

The 8th International Congress on Applied Mineralogy, ICAM 2004, was held in Águas de Lindóia, São Paulo State, Brazil, from 19 to 22 September, 2004. As the major international meeting on this subject, the Congress brought together researchers and scientists from academia, government organizations and industrial sectors to discuss topics related to basic and applied research and to have the most recent overviews with contributions from international specialists on applied mineralogy.

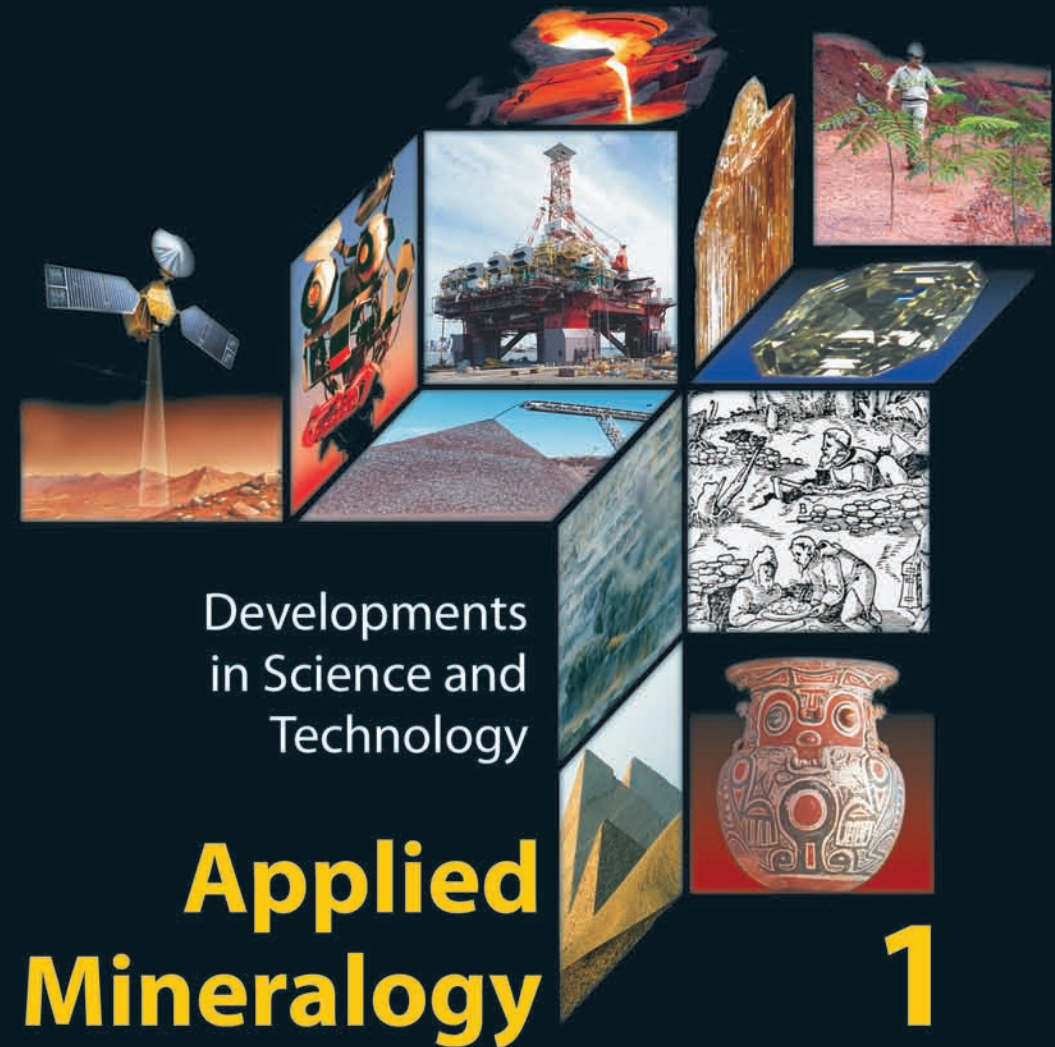
This book compiles 249 papers grouped in 13 technical sessions and 7 plenary lectures according to the Congress themes. They covered applied mineralogy, in the broadest sense, and application on mineral, metallurgical, chemical, oil, and materials industries, as well as in waste recycling, cultural heritage, and environmental assessment and monitoring, offering an overview on its role in all aspects of life.



Applied Mineralogy

Developments in Science and Technology

Volume 1



Editors | M. Pecchio | F. R. D. Andrade |
L. Z. D'Agostino | H. Kahn |
L. M. Sant'Agostino | M. M. M. L. Tassinari |

Applied Mineralogy
Developments in Science and Technology

Applied Mineralogy

Developments in Science and Technology

Edited by

Marcelo Pecchio

Brazilian Portland Cement Association (ABCP)

Fábio Ramos Dias de Andrade

University of São Paulo, Geosciences Institute, Department of Mineralogy and Geotectonics

Liz Zanchetta D'Agostino

University of São Paulo, Polytechnic School, Department of Mining and Petroleum Engineering

Henrique Kahn

University of São Paulo, Polytechnic School, Department of Mining and Petroleum Engineering

Lilia Mascarenhas Sant'Agostino

University of São Paulo, Geosciences Institute, Department of Sedimentary and Applied Geology

Maria Manuela Maia Lé Tassinari

University of São Paulo, Polytechnic School, Department of Mining and Petroleum Engineering

Volume 1



International Council for Applied Mineralogy do Brasil, ICAM-BR

Published by ICAM-BR - International Council for Applied Mineralogy do Brasil
www.appliedmin.org
2004, ICAM-BR, São Paulo
Printed in Brazil

Fundação Biblioteca Nacional

ISBN 85-98656-01-1



**Applied Mineralogy: Developments in Science and Technology / ed. by
M. Pecchio, F.R.D. Andrade, L.Z. D'Agostino, H. Kahn, L.M.
Sant'Agostino, M.M.M.L. Tassinari – São Paulo : ICAM, 2004.
2 v.**

ISBN

v.1 : 85-98656-01-1

v.2 : 85-98656-02-X

**1. Applied mineralogy 2. Advanced materials 3. Analytical instrumentation
4. Biominerals and biomaterials 5. Ceramic, glasses and cement 6. Cultural
heritage 7. Environmental mineralogy and health 8. Gem materials
9. Industrial minerals 10. Mineral exploration 11. Oil reservoirs 12. Ore
mineralogy 13. Process mineralogy I. International Council for Applied
Mineralogy do Brasil II.t.**

Applied Mineralogy: Developments in Science and Technology / ed. by

Table of contents

Volume 1

Preface	XIII
Editorial	XV
Organization	XVII

Plenary Lectures

Applied Mineralogy – an Important Driving Force Towards a Sustained Development of Future Technologies <i>R.B.Heimann</i>	3
Mars Mineralogy: Preliminary Results from Mars Exploration Rovers Spirit and Opportunity <i>P.A. de Souza Jr., S.Squyres, R.Arvidson, G.Klingelhöfer, R.V.Morris, C.Schröder, D.Rodionov, R.Rieder, P.Christensen, K.Herkenhoff, S.Gorevan, H.McSween, N.Cabrol, B.Bernhard, R.Gellert, W.Calvin, F.Renz and the Athena Science Team</i>	13
Platinum-group Element Mineralizations in the Bushveld Complex, South Africa - Focusing on Small-scale Variations <i>R.K.W.Merkle</i>	19
Modern Times and Trends in Industrial Minerals <i>P.W.Harben</i>	25
Recycling of Industrial Wastes – an Overview about Successful Case Studies <i>J.M.F.Ferreira, P.J.S.Guedes, P.Torres, R.S.Manjate, H.R.Fernandes</i>	33
Automation, Integration, and Interpretation – the Future for Process Mineralogy and Practising Mineralogists <i>A.R.Butcher</i>	37
Overview of the Brazilian Gemstone Industry <i>E.P.Salomão, E.Reis, W.K.Daoud</i>	39

Advanced Materials

Aluminosilicate Nanocomposite Material <i>J.L.Capitaneo, F.T. da Silva, V.R.Caffarena</i>	45
Synthesis of (Co-Zn)-Z- Type Barium Hexaferrite for Use as Microwave Absorber <i>V.R.Caffarena, T.Ogasawara, J.L.Capitaneo, M.S.Pinho</i>	49
Preparation of Layered Polyvinyl Chloride (PVC)-Kaolinite Nanocomposites <i>J.L.Capitaneo, F.T. da Silva, V.R.Caffarena</i>	53
Colloidal Processing of Advanced Ceramic Materials <i>J.M.F.Ferreira, S.M.H.Olhero, Xu Xin, M.L.Oliveira</i>	57

Crystal Chemistry and Crystal Structures of Complex Hexa-aluminates and Hexa-ferrites <i>M.Göbbels</i>	61
Synthesis and Characterization of Pillared Smectites with Al <i>D.L.Guerra; V.P.Lemos; R.S.Angélica, M.L.Costa, E.F.Fernandes</i>	65
Transmission Electron Microcopy Studies of Grain Boundary Structures Formed at Elevated Temperatures <i>H.J.Kleebe</i>	69
Nanomineralogy and Nanotechnology <i>I.L.Komov</i>	73
Synthesis and Properties of Organic Acid – Intercalated Manganese Nanocomposites Based on LDHs <i>U.König, H.Pöllmann</i>	77
Manganese Nanocomposites Based on LDHs – Synthesis, Properties, and Characterization <i>U.König, H.Pöllmann</i>	81
Cracking in Graded, Layered Structures <i>I.E.Reimans, J.Chapa-Cabrera</i>	85
Synthesis of a Mesoporous Material from Diatomite <i>V.Sanhueza, U.Kelm, L.López-Escobar, R.Cid</i>	89
Graphite-hexagonal Diamond Transition and Surviving Compressed Graphite <i>A.Yoshiasa, A.Nakatsuka, M.Okube, H.Okudera</i>	93
Sintering of Alumina Nano-sized Powders Produced by Combustion Synthesis Process <i>A.Zimmer, J.C.Toniolo, C.P.Bergmann</i>	97
 Analytical Instrumentation	
Automated, Adaptive Thresholding Procedure for Mineral Sample Images Generated by BSE Detector <i>C.L.Schneider, R.Neumann, A.Alcover-Neto</i>	103
Rietveld Analysis of Ferrimagnetic Minerals from Different Parent Materials in Tropical Soils <i>M.P.F.Fontes, H.Stanjek, U.Schwertmann</i>	107
In Situ EPMA Dating of Monazites from the Morro da Pedra Preta Formation, Serra do Itaberaba Group (São Paulo, Brazil) <i>G.M.Garda, P.Beljavskis, M.S.Mansueto</i>	111
The Application of Synchrotron Radiation Techniques to the Study of Mineralogy <i>A.R.Gerson</i>	115
Rapid Mineral Liberation Analysis with X-Ray and BSE Image Processing <i>Y.Gu</i>	119
Quantitative X-Ray Analysis of Light Elements Boron and Oxygen in Tourmaline Samples <i>A.C.Joaquim, E.S.Mano, H.Kahn, G.C.Fronzaglia, C.A.I.Oba</i>	123
State-of-the-art Quantitative Phase Analysis by X-ray Powder Diffraction <i>A.Kern</i>	125

Problems of the Quantitative Rietveld Phase Analysis of Complex Samples <i>R.Kleeberg</i>	129
Martian Surface ⁵⁷ Fe Mössbauer Analysis <i>G.Klingelhöfer, B.Bernhard, Ch.Schröder, D.Rodionov, J.Foh, F.Renz, R.Gellert, P.A. de Souza Jr., E.Kankeleit, U.Bonnes, R.V.Morris, S.W.Squyres</i>	133
The LIBD Technology - A Powerful Tool For The Highly Sensitive Detection of Particulate Content of Process Water <i>R.Köster, T.Wagner, T.Bundschuh</i>	137
The First Precambrian Detrital Monazites from the Polish Eastern Carpathian <i>M.A.Kusiak, M.Paszkowski, B.Dziubińska</i>	141
EBSD Microstructure Measurements of Marble <i>K.Moen, T.Malvik, J.Hjelen, J.R.Leinum, L.Alnæs</i>	145
Comparison of Different Extraction Methods in the Determination of Gold in Geological Samples for Exploration Studies Using the Atomic Absorption Spectrometric Technique <i>P.V.Sunder Raju</i>	149
Image Analysis of Iron Oxides Under the Optical Microscope <i>E.Pirard, S.Lebichot</i>	153
The Mineralogy of Sediments as Determine by XRD and Rietveld; Comparison with Jade and SEM Image Analysis <i>J.A.R.Stirling, M.Bonardi</i>	157
Brazilian Organoclays: Morphological Characterization Combining AFM and SEM Studies <i>A.T.De León, G.Englert, J.Rubio</i>	161
Mineralogical Approach to Solving Customer Complaints on Various Types of Contamination in Industrial Glass by Using SEM and EDS <i>D.M.van Tonder, M.Cloete, M.Atanaso</i>	165
Application of Combined Cathodoluminescence and Energy-dispersive X-ray Spectroscopy for Analysis of Mineral Raw Materials <i>W.Vortisch</i>	169
Focused Ion Beam (FIB) Specimen Preparation in Applied Mineralogy and Geosciences <i>R.Wirth</i>	173
 Biominerals and Biomaterials	
Degradable Bone Substitution Material Based on Cellular Ca-phosphates <i>F.Goetz-Neunhoffer, R.Enderle, M.Göbbels, J.Neubauer, J.Zeschky</i>	179
Calcium Carbonate Polymorphism in Shells of the Mollusc <i>Physa</i> sp. <i>S.M. de Paula, M.Silveira</i>	183
Assets of Biogenic Carbonate Sands that Justify their Applications in Geomedicine: the Case of the Beach Sands of Porto Santo Island, Madeira Archipelago <i>C.Gomes, J.Silva</i>	187

Corundum Blasted Titanium Implants in Total Hip Arthroplasty - A Surface Characterization <i>J.Göske, W.Kachler, U.Holzwarth, G.Zeiler, A.Schuh</i>	191
Titanium Deposits on Ceramic Heads of Dislocated THR <i>J.Göske, W.Kachler, U.Holzwarth, G.Zeiler, A.Schuh</i>	195
Surface Characterisation of Shot Peened Implants with Glass Beads in Total Hip Arthroplasty <i>J.Göske, T.Müller, W.Kachler, U.Holzwarth, G.Zeiler, A.Schuh</i>	199
Technical Silicification of Wood Materials <i>N.Langhof, J.Götze, M.Hengst, R.B.Heimann</i>	203
Hydroxyapatite Formation in Human Blood <i>A.T.Titov, P.M.Larionov, A.S.Ivanova, V.I.Zaikovskii</i>	207
 Ceramic, Glasses and Cement	
Manganese in Cement <i>H.Pöllmann</i>	213
Evaluation of Powder Densification as Function of Size Distribution and Pressing Additives and Its Influence on Alumina Properties <i>A.K.Alves, C.P.Bergmann</i>	217
Inorganic Sol-gel Processing of Sodium Aluminium Silicate Materials <i>D.Böschel, H.Roggendorf, H.Pöllmann, P.Pollandt</i>	221
Structural Evaluation of an Adobe from Minas Gerais <i>J.Calábria, W.L.Vasconcelos</i>	225
Disintegration in High Grade Titania Slags: Fracture Behaviour of Pseudobrookite <i>J.P.R. de Villiers, A.Tuling., J.Göske</i>	229
Mineralogical and Microstructural Characterization of a Silicon Carbide Refractory <i>E.E.Ferreira, P.R.G.Brandão</i>	233
Inorganic Waste as Ceramic I st Part <i>M.G.Lefter, N.Moreno</i>	237
Sinterability, Microstructure and Glass-Ceramic Properties I st Part <i>M.G.Lefter, N.Moreno</i>	241
Polymerization Reactions by Thermal Treatment of Gyrolite-group Minerals – an IR Spectroscopic and X-ray Diffraction Study Based on Synchrotron Radiation <i>K.Garbev, L.Black, A.Stumm, P.Stemmermann, B.Gasharova</i>	245
Fuel and SO ₃ Influence in Some Portland Cement Clinker <i>L.A.Gobbo, L.M.Sant'Agostino</i>	249
Quantitative Analysis of White Cement Clinker with Rietveld Method <i>L.A.Gobbo; L.M.Sant'Agostino, L.L.Garcez</i>	253
The Influence of Cooling Rate in White Cement Clinker – an Industrial Example <i>L.A.Gobbo; L.M.Sant'Agostino, C.C.F.Guedes</i>	257

Basalt: an Alternative to Shales in Cement Industry <i>M.M.Hassaan, A.El-Sheshtawy, M.Y.Hassaan, A.A.Alashkar</i>	261
Mineralogical Evaluation of Commercial Ceramic Tiles <i>A.A.P.Mansur, H.S.Mansur, W.L.Vasconcelos</i>	265
Mineralogical Analysis of the Micro-Textural Characteristics of the Refractory Coating in the Pierce-Smith Converter <i>C.Marcos, M.Martinez, I.Rodríguez, L.F.Verdeja</i>	269
Synthesis of Mullite After Wastes Derived from Kaolin Processing Industries from the Amazon Region <i>M.C.Martelli, R.F.Neves, R.S.Angélica</i>	273
Fast Industrial X-ray Analysis for Process Control and Automation <i>R.Meier, T.Degen, M.Fransen</i>	277
Hydroceramic Sealants for Geothermal Wells <i>N.Meller, C.Hall</i>	281
Sintering and Crystallization Studies of Industrial Waste Glasses <i>C.H.Oliveira, R.Neumann, A.Alcover Neto, M.V.A.Fonseca</i>	285
Glass-Ceramic Foam Synthesis Using Industrial Wastes <i>C.H.Oliveira, R.Neumann, A.Alcover Neto, M.V.A.Fonseca</i>	289
Properties of Clays Sintered with GLP for Application in Structural Ceramic <i>E.A.Pereira, J.Y.P.Leite, C.Sales, W.Acchar</i>	293
From Raw Materials to Mineral Wastes <i>H.Pöllmann, R.S.Angelica, M.da Costa</i>	297
Pozzolanes as Raw Materials for Cementitious Systems – Testing Methods for Characterization and Properties <i>H.Pöllmann</i>	301
Investigation of Phase Composition and Microstructure of Fused Corundum-Mullite Refractories <i>S.Seifert, S.Saaro, J.Götze, R.B.Heimann, M.Magnus</i>	305
Characterization of Clays Used in the Ceramic Manufacturing Industry by Reflectance Spectroscopy: An Experiment in the São Simão Ball-Clay Deposit, Brazil <i>J.A.Senna, C.R. de Souza Filho</i>	309
Experimental Design to Formulation of Ceramic Coating Masses <i>J.Silveira, J.Pereira Leite, J.Herbert Echude, L.Renato Pontes</i>	313
The Course of Hydration of OPC Pastes Related to the Crystal Chemistry of the Hydration Phases Under the Influence of Sulfonic Admixtures <i>S. Stöber, H.Pöllmann</i>	317
Phase Assemblages in the System $\text{Ca}_2\text{Al}_2\text{SiO}_7$ – “ $\text{Ca}_2\text{MnSi}_2\text{O}_7$ ” Related to a Modified CAC Clinker <i>S.Stöber, H.Pöllmann</i>	321
Influence of Particle Size of Nephelyne Syenite Mineral on Formation of Liquid Phase in Ceramic Masses <i>J.C.Toniolo, H.C.M.Lengler, C.P.Bergmann</i>	325

The Use of Fe-Mn Submerged-arc Furnace Slag in Composite Portland Cement – a Pilot Study <i>S.M.C.Verryn, H. Pöllmann, E.Kearsley</i>	329
The Comparisation of Optical Microscopy and Cathodoluminescence Technique on Ordinary Portland Cement Clinkers <i>N.Winkler, H.Pöllmann, J.Göske</i>	333
Firing Transformations of Clays from Santa Gertrudes Ceramic District <i>R.T.Zauberas, M.D.Cabrelon, R.C.Gennari, F.A.Guastala, A.O.Boschi</i>	337

Cultural Heritage

Mineralogy and Chemistry of Ceramics from Anthropogenic Black Earth of Amazon Region <i>M.L.da Costa, M.S.do Carmo, D.C.Kern</i>	343
Characterisation of Binder Related Particles (lime lumps) in Historic Lime Mortars <i>J.Elsen</i>	347
Brazilian Cultural Heritage under a New Light <i>D.L.A.de Faria, M.C.Afonso, S.C.Lima, H.G.M.Edwards</i>	351
The Vitriified Forts of Europe: Saga, Archaeology, and Geology <i>P.Kresten</i>	355
The Simulation of Copper Chlorides Formation on the Surface of Bronze Monuments in Urban Environment <i>E.V.Meshchanova, O.V.Frank-Kamenetskaya, E.B.Treivus</i>	359
Geoarchaeology: Geological Analysis of Scottish Medieval Carved Monuments <i>S.Miller, F.M.McGibbon, D.H.Caldwel, N.A.Ruckley</i>	363
Characterization by XRD and SEM of Natural and Artificial Patinas on Copper and Copper Alloys <i>A.C.Neiva, H.G.de Melo, R.del P.Bendezú H., R.P.Gonçalves, S.C.Lima</i>	367
Mineralogical Characterization and Raw Materials Provenance of Some Archaeological Masks from Mexico <i>J.Robles-Camacho, R.Sánchez-Hernández</i>	371
The Tropical Weathering Alteration of Palacete Pinho's Façade Tiles in Belém, Brazil <i>T.A.B.C.Sanjad, M.L.da Costa, R.S.Paiva</i>	373

Environmental Mineralogy and Health

Mineralogical and Geochemical Characterization of Sediments and Suspended Particulate Matter in Water from the Potaro River Area, Guyana: Implications for Mercury Sources <i>D.Paktunc, D.Smith, R.Couture</i>	379
Asbestos Release through Degradation of Fibercement <i>F.R.D.Andrade, R.B.Santini, Y. Kihara</i>	383
Mineralogy and Remobilization Processes in the Weltz-clinker Dump Site, Plovdiv Region, Bulgaria <i>R.Atanassova, T.Kerestedjian, I.Donchev</i>	387

In Vitro Accessibility Results of Lead in Soil Dust, Solid Wastes, Sediments and Pb Minerals from Adrianópolis-PR, Ribeira River Basin <i>S.T.Bosso, D.B.Cardoso, J.Enzweiler</i>	391
Radioactive Scales from a Natural Gas Production Facility in the Altmark Region, Germany <i>S.Ceccarello, S.Black, D.Read, H.Weiss, M.Schubert, Ch.Kunze, J.Grossmann</i>	395
Hydrotalcite-like Minerals $\text{CuZn}_3\text{Al}_5(\text{OH})_{17}[\text{CO}_3,\text{SO}_4]_3 \cdot n\text{H}_2\text{O}$: Synthesis and Characterization <i>J.A.M.Corrêa, H.Pöllmann</i>	399
A Preliminary Study of the Environmental Management of Sludges from AODL Reactors <i>A.R.Correa, E.A.Villegas</i>	403
Mineralogical Status of Metals in MSWI Fly Ashes Solidified/Stabilized in Cement and Long Term Stored in Landfills <i>D.Antenucci, G.Lorenzi, D.Leclerq, M.Veschkens, J.Yvon, E.Jdid, P.Nelsen, V.Dutre</i>	407
Mg-Mica Formation in Alkaline Environment of the Nhecolândia, South Mato Grosso, Brazil <i>S.A.C.Furquim, J.P.Queiroz Neto, S.Furian, L.Barbiéro, R.C.Graham</i>	411
Thermodynamic and Structural Properties of Clay Minerals <i>H.Gailhanou, J.Olives, M.Amouric, R.Perbost, J.Rogez, F.Brunet, C.Alba-Simionesco, P.Blanc, E.Gaucher</i>	415
Environmental Aspects of Waste Dumps at the Peña de Hierro Mine (Iberian Pyrite Belt SW Spain) <i>I.González, A.Romero, E.Galán</i>	419
Franca's Smectites as Organophilic Clays <i>R.A.Hanna, A.L.Vieira, A.C.Vieira Coelho, F.R. Valenzuela Diaz, P.Souza Santos</i>	423
Soil Phases and Heavy Metal Distribution in a Gold-silver Mining Area in South-eastern China <i>C.He, E.Makovicky, J.Li</i>	427
Salt Horizons – as Heavy Metal Barriers Within the Monofill for MSWI Residues <i>S.Heuss-Aßbichler</i>	431
Porous Material with Zeolite and Carbide from Paper Sludge and the Application <i>H.Ishimoto, O.Sasaki, M.Yasuda, T.Wajima, O.Tamada</i>	435
Transformation of Technogenic Soot on the Earth Surface <i>T.Moroz, E.Shcherbakova, G.Korablev</i>	439
Asbestos Characterization from Brazil and their Effects in Mine Workers Health <i>M.C.B.Oliveira, J.M.V.Coutinho, E.Bagatin, S.Kitamura</i>	443
Molecular-scale Characterization of Arsenic in Metallurgical Wastes <i>D.Paktunc</i>	447
Potential Contaminant Elements Retention Using Structural 2:1 Layer Clay Minerals <i>W.C.Pereira, D.M.Silva, J.O.Carvalho, N.M.B.Amaral Sobrinho, R.C.Villas Boas</i>	451
Role of Mineralogy in Areas Affected by Acid Saline Seeps, Southwestern Australia <i>M.Raghimi, M.F.Aspondiar</i>	455
Fast Hardpan Formation on Slag Material from Selebi Phikwe, Botswana <i>D.Rammlmair</i>	459

Potential Use of the Chemical Kaolin-Leaching Residue as Soil Fertilizer <i>F.R.Ribeiro, J.D. Fabris, W.N.Mussel, R.F.Novais</i>	463
Effects of Redox Reactions on the Structure of Garfield Nontronite: A Mössbauer Spectroscopic Study <i>F.R.Ribeiro, K.Lee, J.W.Stucki, J.D.Fabris</i>	467
Degradation of Oxamyl by Redox-modified Smectites: Effects of pH, Layer Charge, and Extent of Fe Reduction <i>F.R.Ribeiro, J.W.Stucki, R.A.Larson, K.A.Marley, P.Komadel, J.D.Fabris</i>	471
Mineralogical Characterization and Environmental Evaluation of TSP, PM10 and PM2,5 Atmospheric Inorganic Aerosol of Oviedo (Asturias, Spain) <i>I.Rodríguez, C.Marcos</i>	475
Heavy Metals Concentrations in Mangroves Swamps <i>A.L.F.Santos, G.R.Boaventura, A.C. de Oliveira, V.K.Garg, T.Cassia de Brito Galvão</i>	479
Concentration and Speciation of Heavy Metals in Lagoa da Pampulha Sediments (Belo Horizonte / Minas Gerais; Brazil) <i>G.T.Schmidt, K.Friese, H.A.Nalini, J.C. de Lena, D.W.Zachmann</i>	483
Natural Decontamination of Metalliferous Mining Leachates by Reservoir Mineral Formation <i>M.Schubert, R.Wennrich, H.Weiss, P.Schreck, H.H.Otto</i>	487
Environmental Concerns Regarding the Castromil Gold Mine – A Mineralogical Approach <i>L.Serrano Pinto, E.Ferreira da Silva, C.Patinha, F.Rocha</i>	491
Healing Clays: Need of Certification for Suitable Uses <i>M.Setti, F.Veniale, A.López-Galindo, P.Fenoll Hach-Alí, C.Viseras</i>	495
Autoconservation of Mining Industry Waste as a Result of Prolonged Storage <i>E.Shcherbakova, G.Korablev</i>	499
Attenuation of Metals by Iron-phases from Surface and Ground Water of Ni-Cu Mine Waste <i>N.V.Sidenko, B.L.Sherriff</i>	503
Characterization of Muds and Waters of the Copahue Geothermal Field, Neuquén Province, Patagonia, Argentina <i>J.M.Vallés, M.T.Baschini, G.R.Pettinari, N.García</i>	507
Author Index Vol. I & II	

Preface

We are glad to present the Proceedings of the 8th International Congress on Applied Mineralogy (ICAM2004), an effort to gather researchers from all continents to discuss the latest results and future trends of applied mineralogy.

In the Proceedings there are articles by the invited lecturers, who presented up-to-date overviews of different fields of applied mineralogy.

These two volumes contain 249 papers that cover the broad range of subjects discussed at the ICAM2004. The volumes are organized in chapters according to the technical sessions of the Congress, namely: advanced materials, analytical instrumentation, biominerals and biomaterials, ceramic, glasses and cement, cultural heritage, environmental mineralogy and health, gem materials, industrial minerals, mineral exploration, oil reservoirs, ore mineralogy, process mineralogy, and general session.

The papers published here reveal a wide variety of topics, ranging from talc to diamond, from archeology to nanotechnology, from waste management to the mineralogy of Mars, and in several cases going far beyond the traditional frontiers of Mineralogy and Earth Sciences.

The editorial handling was only possible due to the invaluable assistance provided by the referees. The Organizing Committee is particularly grateful to the chairmen of the sessions and to those who supported the organization of the Congress and the editing of the Proceedings.

We would like to express our appreciation to the participants from all countries who attended the ICAM2004 and made it happen.

Thank you!

Fábio R.D. Andrade & Marcelo Pecchio
Scientific Committee
September, 2004

Editorial

Applied mineralogy embraces numerous applications of mineralogy in the mineral, metallurgical, chemical, and materials industries, as well as in waste recycling and environmental assessment and monitoring. As an interdisciplinary field, it involves characterization of a wide variety of ores, mineral concentrates, engineered materials, industrial residues, and also data interpretation regarding the industrial processes, products, and environmental regulations. The content of these two volumes covering the 13 session headings of the conference reflects the highly interdisciplinary meaning of the applied mineralogy moving towards a materials science approach.

Since the first “International Congress on Applied Mineralogy” (ICAM 1981), in South Africa, it has been an internationally recognized forum that works to bring together researchers from industry, research organizations and academia working in the field of applied mineralogy.

This Congress is considered the main scientific event of the “International Council for Applied Mineralogy”, a loose organization founded to serve the needs of applied mineralogists by providing a board for international activities. Until 1993 the Congresses were held at irregular intervals; after that with co-sponsoring of the International Mineralogical Association (IMA) and its Commission on Applied Mineralogy, it was established a regular 4-year interval and the Congress became more highly interdisciplinary. Previous meetings were held in Johannesburg (1981), Los Angeles (1984), Montreal (1989), Pretoria (1991), Perth (1993), Warsaw (1996), and Göttingen (2000).

ICAM 2004 was organized by University of São Paulo through Polytechnic School and Geosciences Institute, and the International Council for Applied Mineralogy do Brasil (ICAM-BR) in addition to ICAM and IMA-CAM and with a partnership of Brazilian Geological Society (SBG), Brazilian Ceramics Association (ABC), Brazilian Metallurgy and Materials Association (ABM), Brazilian Mining Institute (IBRAM), and Revista Minérios e Minerales. Some particular sessions were also co-sponsored by other international associations; Mineral Exploration and Ore Mineralogy sessions by the International Association on the Genesis of Ore Deposits (IAGOD), Environmental Mineralogy and Health by the Canadian Institute of Mining, Metallurgy and Petroleum (CIM), and Ore Mineralogy and Process Mineralogy sessions by the International Mineralogical Association - Commission on Ore Mineralogy (IMA-COM). Sponsorship from many Brazilian funding agencies, analytical instruments, and mineral and oil industry related companies was crucial to achieve the success of the conference.

Brazil was chosen by the International Council for Applied Mineralogy to held a conference due to its significance in the world mineral industry, nest of ICAM conferences, and to promote a higher integration with other Latin American countries. The Congress brought a unique integration opportunity for applied mineralogists to present their latest research results and an open discussion of the current state-of-the-art stimulating their own enhancement and also the development of new technologies and products and winning productivity into the several application fields.

Despite other parallel international conferences that reduced the attendance in some sessions such as Mineral Exploration, Ore Mineralogy, and Environmental Mineralogy, the submission of 378 Abstracts which resulted in 249 papers accepted for oral and poster presentations, with delegates coming from no less than 35 countries of the five continents, is a result of the firm importance of applied mineralogy in our lives and the strength of ICAM conferences in the international community.

Nevertheless, ICAM 2004 would not have been possible without the firm dedication and enthusiasm of many people, in particular ICAM 2004's organizing and scientific committees consisting of Lilia Mascarenhas Sant'Agostino, vice chair; Marcelo Pecchio, scientific committee chair; Fabio Ramos Dias de Andrade, scientific committee vice-chair, Maria Manuela Maia Lé Tassinari, 1st secretary; Liz Zanchetta D'Agostino, 2nd secretary, as well as all the members of the Scientific Committee and Vanilda Queiroz Sganzerla and her team from Joy Eventos e Promoções.

The high standard of this two-volume publication could not have been achieved without the efforts of the authors to prepare their manuscripts, the reviewed by members of the Scientific Committee and the Advisory Board, and the final editing of Liz Zanchetta D'Agostino and Miguel de Oliveira and his team from Diagrama Estúdio de Artes Gráficas.

Henrique Kahn, São Paulo
ICAM 2004 Chairperson

Organization

ICAM 2004 is organized by:

International Council for Applied Mineralogy, ICAM
International Mineralogical Association - Commission on Applied Mineralogy, IMA-CAM
University of São Paulo, Polytechnic School
University of São Paulo, Geosciences Institute
International Council for Applied Mineralogy do Brasil, ICAM-BR

Sponsorship



Partnership

Brazilian Ceramics Association (ABC)
Brazilian Metallurgy and Materials Metallurgical Association (ABM)
Brazilian Geological Society (SBG)
Brazilian Mining Institute (IBRAM)
Revista Minérios e Minerales
International Association on the Genesis of Ore Deposits co-sponsored Mineral Exploration and Ore Mineralogy sessions
CIM - Canadian Institute of Mining, Metallurgy and Petroleum co-sponsored Environmental Mineralogy and Health session
International Mineralogical Association - Commission on Ore Mineralogy co-sponsored Ore Mineralogy and Process Mineralogy sessions

Organizing Committee

Henrique Kahn
Lilia Mascarenhas Sant'Agostino
Marcelo Pecchio
Fábio Ramos Dias de Andrade
Maria Manuela Maia Lé Tassinari
Liz Zanchetta D'Agostino
Reiner Neumann

Chairperson
Vice-Chairperson
Scientific Committee Chairperson
Vice-Scientific Committee Chairperson
1st Secretary
2nd Secretary
Field Trips

Scientific Committee Board

Advanced materials
Peter Greil
Jose Carlos Bressiani

Gem materials
Pedro Luiz Juchem

Analytical instrumentation
Jan D. Miller
Claudio L. Schneider

Industrial minerals
Richard D. Hagni
Valdir Zampieri

Biominerals and biomaterials
Robert B. Heimann
Anselmo Ortega Boschi

Mineral exploration
Hans Albert Gilg
João Carlos Biondi

Ceramic, glasses and cement
Herbert Pöellmann
Sergio Centurione

Oil reservoirs
Sylvia Couto dos Anjos

Cultural heritage
Tamas Weiszbarg
Marcondes Lima da Costa

Ore mineralogy
Roland K. W. Merkle
Nelson Angeli

Environmental mineralogy and health
Dogan Paktunc
Mirian Cruxen B. de Oliveira

Process mineralogy
Alan Butcher
Rogerio Kwitko Ribeiro

Advisory Board

Allen Pratt
Andre Tabanez
Bernhard Dold
Bertrand Devouard
Brendan Laurs
Caetano Juliani
Carlo Aurisicchio
Carlos Alberto Rosière
Cheryl Seeger
Chris Hamilton
Cristiano Honório de Oliveira
Daniel Atencio
Danieli Ferreira
Danielle Fortin
Dieter Rammlmair
Eduardo Brandau Quitete
Erich Petersen
Erick Raymond Ramanaidou
Excelso Ruberti
Fernando Joaquim F. Tavares Rocha
Fernando Roberto Mendes Pires
Gabriela Campos Fronzaglia
Gergely Andres Julio Szabó
Gianna Maria Garda
Gianni Schena
Giulio Morteani
Gláucia Cuchierato
Hyomin Lee
Inez Valeria Pagotto Yoshida
Jacques Yvon
Jean-Marie Dereppe
Jeanne Percival
Jens Götze
José Barbosa Madureira Filho
José Manoel dos Reis Neto
José Padilha Chrispim Neto
Juergen Neubauer
Karl Schmetzer
Klaus Krambrock
Lauro Nardi
Leonardo Lagoeiro
Linda H. Fujikawa
Luciano de Andrade Gobbo
Lucy Gomes Sant'Anna

Marco Antonio Schiavon
Maurício Veloso Brant Pinheiro
Musa Karakus
Nelson Luiz Chodur
Oscar Jesus Choque Fernandez
Otávio da Fonseca Martins Gomes
Paul Weber
Paula Regina Alves
Paulo Antônio de Souza Junior
Paulo Roberto Gomes Brandão
Peter Scott
Reiner Dohrmann
Reiner Neumann
Reinhard Kleeberg
Robert Marschik
Roberto Perez Xavier
Samuel Toffoli
Silvio Roberto Farias Vlach
Stephan Kaufhold
Tania Mara Dussin
Thomas Karl Fehr
T-T Chen
Vagner Maringolo
Vitor Paulo Pereira
William MacDonald
Willian Petruk
Won Park
Ying Gu
Yushiro Kihara

National Representatives

Argentina	Julio Oyarzabal
Australia	Erick R. Ramanaidou
Belgium	Eric Pirard
Bulgaria	Thomas Kerestedjian
Canada	Dogan Paktunc
Chile	Eugenia Fonseca Pedraza
Colombia	Hildebrando Leal Mejia and Analia del Valle Pantorrilla
Croatia	Goran Kniewald
Egypt	Mohamed Ali Mandour
Finland	Kari Kojonen
France	Jacques Yvon
German	Dieter Rammlmair
Greece	Konstantinos Kitsopoulos
Italy	Marcello Mellini
Japan	Tadato Mizota
Mexico	Mikhail Ostroumov
Netherlands	Eric Pirard
Poland	Adam Piestrzynski
Portugal	Álvaro M. M. Pinto
Spain	Emilio Galan Huertos
South Africa	Sabine Verryn
USA	Richard Hagni

Plenary Lectures

Applied Mineralogy – an Important Driving Force Towards a Sustained Development of Future Technologies

R.B.Heimann

Department of Mineralogy, Technische Universität Bergakademie Freiberg, Germany

ABSTRACT: Today applied mineralogy provides an important bridging function between classical mineralogy *sensu strictu*, and materials science and engineering. While in the past applied mineralogy was busy to assist research and development into the discovery, exploitation, processing, beneficiation and application of resources of energy, ores and minerals, increasingly its focus is shifting to novel, advanced materials and technologies. During this process applied mineralogy has become an important driving force towards a paradigm shift to environmentally benign or even neutral energy technologies and sustainable technology developments. Based on the logistic Volterra-Lotka equation examples will be discussed that include the development of high temperature-resistant materials and coatings for gas turbine blades, the various stages of the application of advanced materials in energy-related engineering systems as well as aspects of past and future energy supply. A novel quaternary trends space (QTS) model will be proposed to forecast the market penetration of the materials foundation of non-fossil fuel-based energy technologies such as nuclear ceramics, photovoltaic materials, and ceramic solid state electrolytes and electrodes for high temperature batteries and solid oxide fuel cells (SOFCs).

1 INTRODUCTION

The vast majority of processes in the universe irreversibly degrade organized energy, *i.e.* work to disorganized energy, *i.e.* heat. As a byproduct entropy is generated so that the global entropy content constantly increases by converting structural order to disorder. However, there is one noticeable exception to this rule: life. Since life goes against the “arrow of entropy” large amounts of energy have to be expended to sustain it. In particular, human life depends crucially on societal structures based on *materials technologies* and, increasingly *information technologies*. Indeed, one of the rather worrying consequences of modern development is the fact that more and more material products are being replaced by the virtual product “information”. This information generation proceeds at ever increasing speed hence producing entropy defined as a dramatic multiplication of probabilistic options in the phase space of “strange attractors” that appear to govern our societal and technological presence. As a consequence increasing amounts of energy must be expended to offset the vast entropy generation of our developed societies. There is little doubt today that generation of energy by burning fossil fuels such as

coal, oil or natural gas not only has a profoundly negative impact on our global climate but also creates megamasses of waste products through mining activities (Fig.1). Hence replacement of conventional energy technologies by regenerative energy sources is at the forefront of worldwide technological development. Applied mineralogy will have an increasing share in these activities and in this contribution some more pertinent aspects of this will be discussed.

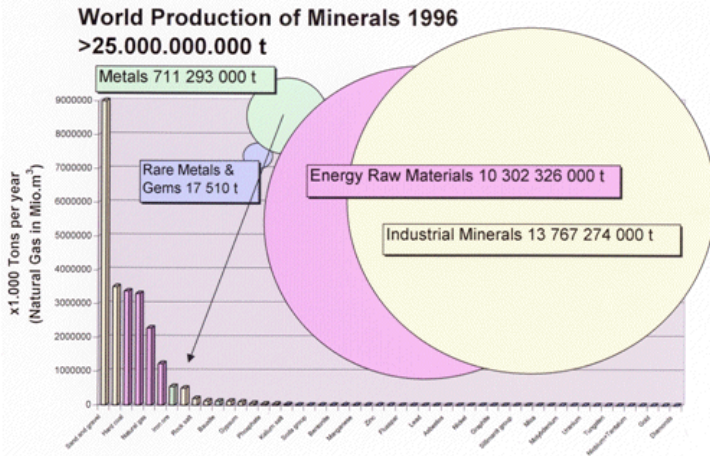


Figure 1: World production of minerals exceeded 25 billion tons in 1996. Industrial mineral and energy raw materials constituted 97 % of all minerals mined.

2 MATERIALS TECHNOLOGIES

The history of the development of useable materials (Fig. 2) started with the utilisation by man of natural ceramic and polymeric composites: stone, bone, wood, plant fibers, leather. Native metals were only sparingly used, mostly for decorative purposes.

All these early materials had a low technological information content, *i.e.* anyone could collect, work and use them without materials-based special skills. Hence holistic technologies marked the begin of the technological development of humankind. This changed with the inception of the first artificial

material, ceramics, since the knowledge required to produce it greatly exceeded that necessary to fashion simple tools from stone, wood or bone (Hench 1988). On the other side, mastering high temperature technologies such as firing of ceramics was the precondition of transformation of ore into metals such as copper or iron, and its purification and remelting to alloys such as bronze or steel. Each of these new technologies required new, more specialised knowledge and consequently the information content increased initially in a gently sloping curve (Fig. 3).

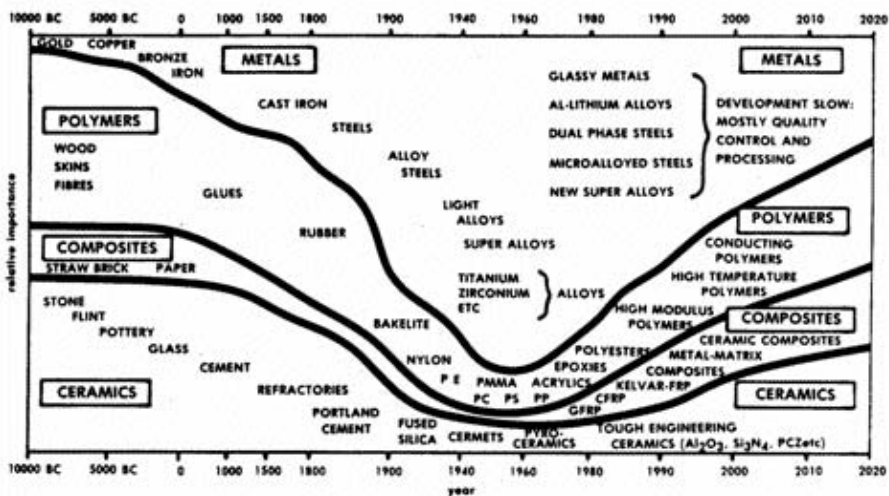


Figure 2: Relative importance of traditional and advanced materials (Froes 1990)

This development stagnated in the Western world during the ‘dark ages’. Only the Renaissance broke this stagnation equilibrium and consequently the innovation curve rose steeply through the development of prescriptive technologies and the input by modern quantitative sciences.

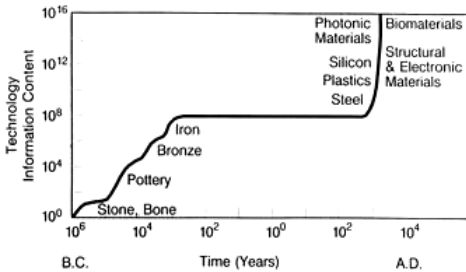


Figure 3. Increase of technological information content with time (Hench 1988).

This is technology at its best: application of scientific knowledge to real-life needs and problems. However, the steep increase of the technology information content shown in Fig. 3 clearly cannot go on forever. In the future it will slow down or even stagnate again. Which route the development will take depends essentially on the wisdom of mankind. Either we will choose a path of voluntary technological restriction through sustained development or will succumb to the cataclysm of global war and an irreversible collapse of the environment and hence our present societal framework.

3 STRANGE ATTRACTORS

To install a voluntary global sufficiency strategy a paradigm shift is required towards environmentally friendly technologies and a sustained development philosophy. Since the interaction between technology and society obeys the rules of complex systems theory this paradigm shift can be recast in terms of strange attractors such as the Lorenz attractor (Ruelle 1980) that describes the inner structure of a chaotic process. A paradigm shift corresponds to a jump from one attractor to the next probable one, *i.e.* the ‘neighbouring’ attractor can be reached by the stochastic process of oscillations within the phase space of possibilities (Kafka 1994a). Figure 4 shows a computed rendering of the Lorenz attractor (Gleick 1987).

As one of the most pressing problems at the beginning of the third millenium is the ever increasing ‘global acceleration crisis’ (Kafka 1994b) it must express itself also in the structure, efficiency and longevity of the strange attractors. In the past

the technological society selected only those attractors that had proved to be useful, *i.e.* had moved in a cyclic fashion through identical orbits hence providing an impression of everlasting continuity in the ways societies worked. The lives of grandfathers, fathers and sons differed little since in the past comparable technologies, materials, and thought and action pattern were preferred and sustained over long time. However, today in our Western industrial society attractors will be left already before a single cycle has been completed, *i.e.* before its stability has been established and unambiguously confirmed. As a result the system tumbles into mathematical chaos until it regains the force field of old, less complex but well established attractors. Current examples of such mechanism are the worldwide rebirth of nationalism and religious fundamentalism as well as the “back to nature” mentality and the enmity towards modern technology of some sectors of society and political parties in developed countries.

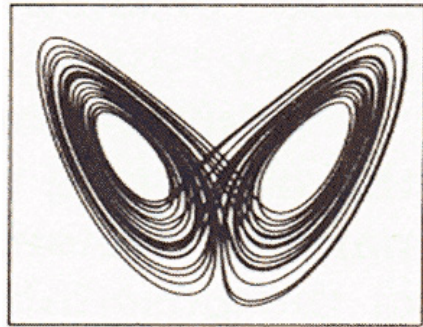


Figure 4. Lorenz attractor (Gleick 1987)

In the search for new attractors it becomes less and less probable that individuals or groups will be able to access them by stochastic ‘oscillation’ in the phase space of possibilities. The critical innovation rate will be exceeded and the technological information content and hence the ‘social’ entropy will increase hyperbolically according to the EVOLON model (Albrecht 1997). Such hyperbolic growth is characterised by the creation of new interaction mechanisms and structures with unknown final state through cooperatively stimulated coupling of synergetically acting individual processes. Consequently entropy increases dramatically by an inflation of information. As a result materials technologies that by definition *decrease* entropy by creation of new ordered structures will be replaced by the virtual product ‘information’ that *produces* entropy since the number of choices, *i.e.* the probability of ‘hits’ in the phase space of possibilities hyperbolically

increases. Inflationary entropy production can only be reversed by providing high amounts of energy that allow a systems to go against the arrow of entropy and to locally create ordered structures. In the future our society runs the risk of not being able to provide enough energy to counteract the global hyperbolical entropy increase. Metaphorically speaking this means that society will energetically starve but entropically drown.

4 LOGISTIC EQUATIONS

Coupled with the increase of the technological information content is an ever decreasing 'half-life' of a new material or a new technology (Fig. 5, Hench 1988).

In the past it used to take hundreds or even thousands of years until systems changes, *i.e.* paradigm shifts materialised. Today this half-life has shortened dramatically.

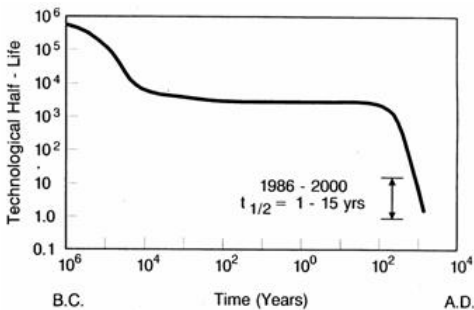


Figure 5: Decrease of technological half-life with time (Hench 1988)

The rate of change of information content is coupled to the likewise increasing rate of information and technology transfer within our modern society. Both processes are linked by a positive feedback (Arthur 1990) and hence an autocatalytic relation exists between materials and technologies that develops preferably in technological niches struggling with each other for survival and growth.

According to Prigogine (Prigogine & Stengers 1984) associated with this is also a struggle of competing philosophical thoughts. If social systems decline, necessarily far from equilibrium, new ways to look at the world emerge. With the demise of feudalism in Western Europe Newtonianism developed at the beginning of the Machine Age. As the Information Age ('The third wave' according to Alvin Toffler) takes now shape its declining predecessor produced quantum mechanics and the

relativity theory. At decision points determinism will be replaced by a chance development at a 'bifurcation point' where the existing social system breaks down and move on a trajectory to a new dissipative structure, *i.e.* a new strange attractor (see above) on a world scale (see also Marchetti 1994). Because of its stochastic nature a prediction of the direction of the change is impossible.

Emergence and disappearance of a technology depends on the interaction of complex and not yet in all details clarified mechanisms. The competition for techno-logical niches can be described by the so-called logistic equation (Verhulst equation, Volterra-Lotka equation). Its quantitative expression is $dN(t)/dt = rN(K-N) - mN$ and closely related to the EVOLON model mentioned above. It shows that for most growth processes independent of the size of N its temporal evolution approaches a stationary value $N(t) = K - m/r$ (Fig. 6).

The equation was developed in the realm of biology and ecology to describe quantitatively the development of a population of N members with a birth rate r , a death rate m , and a given number of resources K accessible to the population.

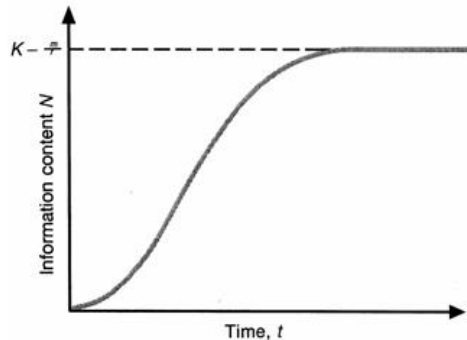


Figure 6: Logistic equation (Volterra-Lotka equation). K = number of resources (carrying capacity of the environment), r = birth rate, m = death rate (Prigogine and Stengers 1984).

To apply this equation to the technological progress the parameters can be assigned to N = sum of information content, r = number of innovations per unit time, m = rate of replacement of old materials or technologies, and K = societal demand as economic driving force. Each technological equilibrium reached is only temporary and the move to a new technology or a new material involves breaking of the established equilibrium and hence the jump to a new attractor. Each materials technology follows its own time line, arrives at a saturation point and will be replaced by a new one with a higher information content $N(t)$ characterised by better materials performance and hence higher market penetration. Consequently a family of

logistic curves emerges with increasing $(K-m/r)$ value. A logistically defined market niche will be filled by a succession of materials or processes in that the preceding one will be replaced by a new one if its capacity to exploit a given or created niche exceeds that of the precursor akin to Darwinian 'survival of the fittest'.

Figure 7 shows a typical example of the development of advanced materials for high temperature-resistant materials and coatings for gas turbine blades of stationary and aerospace applications. Superalloys based on nickel were developed in the fifties of the last century and reached their maximum market share around 1960. With time they were replaced by a succession of diffusive nickel aluminide coatings, plasma-sprayed $(Ni,Co)CrAlY$ coatings, partially stabilised zirconia coatings and finally laser-glassed $MCrAlY$ coatings.

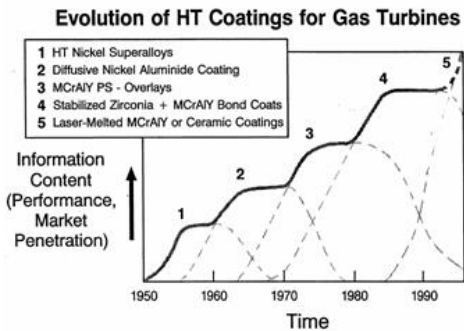


Figure 7: Development and market penetration of high temperature materials for gas turbine blades expressed by a succession of logistic curves (after Sivakumar and Mordike 1989)

Obviously the target of each technological development is to maximise the $K-m/r$ value. This can be achieved in two ways: either by maximising the innovation rate r ("r-strategy" or technology push) or by maximising the demand K ("K-strategy" or market pull).

Since technological systems can not be judged in isolation from society criteria for their efficiency are not being determined by technical factors alone but also by the acceptance of the technology by society (Ishigai 1989). Technologies not easily accepted are those that are intrinsically dangerous to society or perceived as such like weapons, nuclear or gen technologies and those practises that may harm the environment.

On the other hand a new material or technology will not always find an existing market niche. In this case the innovation may transform the sociocultural environment towards creation of such a niche. This is a hallmark of a "K-strategy", *i.e.* creation of a

demand, typical for the capitalist free market economy.

5 ENERGY SUPPLY

As for all materials and technologies the utilisation of primary energy sources follows the principle of logistic evolution.

At present humanity is consuming about 1010 tons of coal equivalent annually corresponding to 10 TW. This ought to be compared to forest shed such as dead trees, branches and leaves that amount to about 100 TW of biomass.

Figure 8 shows the replacement within time of wood by coal, oil, natural gas and nuclear energy. The maxima (saturation) of the market penetration of the primary energy sources are spaced approximately 54-60 years apart (Kondrat'ev cycles). Due to political decisions of several countries to phase out nuclear energy for safety reasons there is an urgent need of replacement since the depletion midpoint of natural gas appears to be 2015, *i.e.* half of the known deposits of conventional natural gas will be exhausted by then (German Federal Institute for Geosciences and Natural Resources, BGR, 1995). As shown in Fig. 8 the energy sources waiting in the wings may be either nuclear fusion or solar energy. This energy source whatever it will be will reach 10% market penetration only around 2050. Hence the world is facing an energy shortage of yet unknown magnitude within the next 20 years or so. As a consequence the call for development and implementation of new regenerative energy technologies takes on a more urgent nature. Applied mineralogy will be one important field of research and technology to reach this goal since it is ideally positioned to combine knowledge and expertise in the geosciences with those in materials science and technology.

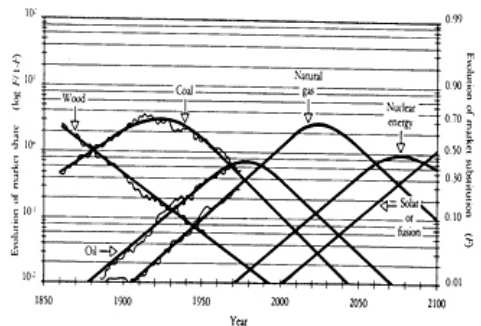


Figure 8: Worldwide use of primary energy sources since 1850. F is the fraction of market penetration. The wavy lines represent real data. The slopes for nuclear, solar and fusion energies are hypothetical (Marchetti 1981)

6 QUATERNARY TREND SPACES

Technology is not only the sum of innovations, inventions and products but a very complex system that besides its material components involves sociocultural factors such as organisations, structures, processes and a mindset (Franklin 1999). This also means that technological development can only be weighted and vaguely predicted in a multidimensional parameter space called a 'quaternary trend space' (Heimann 1991). For energy technologies this QTS comprises three quantifiable extrinsic parameters (net energy production, NEP; availability and accessibility of resources (RMA); and environmental impact, ENV) as well as one rather ambiguous intrinsic sociocultural factor, SCF (Fig. 9).

The latter attempts to measure how a new product or a new technology will be accepted and supported by industry and society as a whole. The main ambiguity arises from the profound differences in risk perception of people of different walks of life (Slovic 1987; Kepplinger 1990). According to Millendorfer & Gaspari (1971) the SCF defined above contains several subfactors such as the *technological efficiency* of a society correlating, surprisingly, strongly with religion, the so-called *productivity function* expressed by the gross national product (GNP) of a country, and a *stress function* that considers the interchangeability of material (use of electric energy per capita) and immaterial input (number of engineers per 10,000 population).

Depending on the effect of individual parameters *i.e.* its relative importance the corners of the tetrahedron shift along the connecting lines between the center point and the corners (positive = opportunity, outward moving corner; negative = threat, inward moving corner). Hence the relative volume of the tetrahedron is a (subjective) measure of the market chance of a product or a technology.

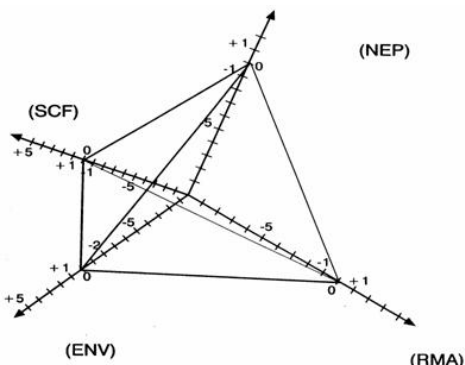


Figure 9: Quaternary trend space tetrahedron to assess the viability of the materials base of regenerative energy technologies (Heimann 1991). For explanation see text.

Comparable models were used by Altenpohl (1979) to describe the position of metal-working industry in Western Europe and by Razim (1990) to optimise the materials selection for automotive industry including advanced materials.

Such QTS have been applied to nuclear ceramics, photovoltaic materials, and ceramic solid state electrolytes and electrodes for high temperature batteries and solid oxide fuel cells (SOFCs) (Heimann 1991). As examples will be shown the situation of nuclear ceramics (uranium dioxide) as the materials base of nuclear energy production by fission as well as the position of high temperature superconducting ceramics as possible material for superconducting magnetic energy storage (SMES) rings in tandem operation with a nuclear power reactor.

6.1 Nuclear ceramics

As in all QTS shown the net energy production (NEP) parameter is defined as

$$NEP = E(v) - E(p) - E(r),$$

where $E(v)$ = energy produced or saved through use of endproducts, $E(p)$ = energy required to produce the material (uranium oxide or carbide, solar silicon, superconducting yttrium barium copper oxide, β -aluminium oxide, perovskites etc.), and $E(r)$ = energy demand during recycling or waste disposal.

The QTS of nuclear ceramics shown in Fig. 10 is determined by the strong negative environmental factor ENV and the associated strongly negative sociocultural factor SCF. The ENV is much affected by the need of safe final disposal of used fuel elements and if politically acceptable, the recycling of fissionable ^{235}U . While the technology of energy production by nuclear fission is environmentally friendly in that it does not emit greenhouse gases, the need for safe final disposal of waste products for at least 100,000 years and the risks associated with it led to strong discord within many societies worldwide. The risk perception is usually quite emotional and strongly dependent on the ethical convictions of the beholder, coupled with an extraordinary divergence of the real risk and its demonstration in the media (Kepplinger 1990). Fig. 10 shows a QTS with $ENV = -4$ that reflects the risk perception of the American League of Women Voters (group 1) and a QTS with $ENV = -0.5$ that reflects the opinion of experts, *i.e.* nuclear physicists and engineers (group 2).

Both groups were asked to rate 30 technologies and activities according to their perceived risk (Slovic 1987; Wilson & Crouch 1987). Group 1 put nuclear energy in first place of their risk list whereas group 2 put it in place 20, far behind medical X-rays

and non-nuclear energy production by burning fossil fuel!

6.2 High temperature superconductors

High temperature superconducting ceramics based on yttrium barium copper oxide (YBCO) were discovered in 1987 and at this time hailed as an environmentally friendly and extremely energy efficient, loss-free answer to existing transmission cable technology.

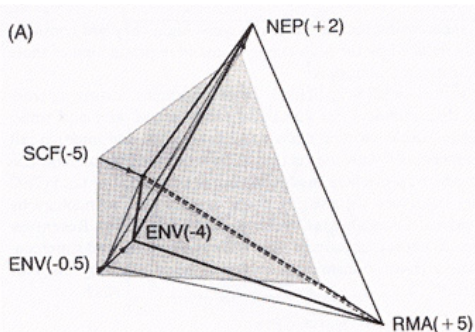


Figure 10: Standard QTS with NEP:0, RMA:0, ENV:0 and SCF:0 (left, gray) and two QTS of nuclear ceramics as perceived by the American League of Women Voters (NEP:+2, RMA:+5, ENV:-4, SCF:-5) and a group of experts (ENV:-0.5, RMA:+5) (right, light).

Similar predictions can be made for photovoltaic and perovskite materials for solar and solid oxide fuel cell (SOFC), respectively. However, this treatment is not confined to energy related materials and/or technologies but can be usefully applied to functional and structural ceramics for cutting tools, electronic substrates, capacitors, sensors and coatings of all kind. In these cases the extrinsic parameter NEP could be replaced by others that specify different economic or technological advantages such as cutting speed, lifetime, switching speed, Q factor, or wear and corrosion resistance.

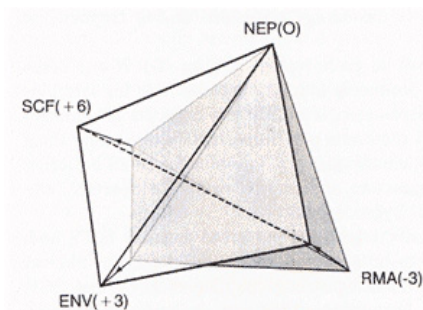


Figure 11: Standard QTS with NEP:0, RMA:0, ENV:0 and SCF:0 (right, gray) and QTS of high temperature superconducting ceramic (NEP:0, RMA:-3, ENV:+3, SCF:+6) (left, light).

In contrast to nuclear ceramics the QTS of high temperature superconducting ceramics (Fig. 11) shows that (i) the material itself is not net energy producing (NEP:0), (ii) both ENV and SCF are strongly positive at +3 and +6, respectively, and (iii) the raw materials required to produce this ceramic are in scarce supply hence rendering RMA as low as -3. HTSC materials are based on yttrium and rare earth elements that are considered strategic materials whose availability in case of a global conflict would essentially annihilate its use as superconducting magnetic energy storage (SMES) rings in tandem with nuclear power reactors.

Moreover, HTSC ceramics constitute a competency destroying product discontinuity for high tension overland transmission cables, electric motors and generators as well as microcircuit switch components. In terms of the logistic equation the high information content of HTSCs jeopardises the existing high voltage technology through breaking of a technological equilibrium.

According to earlier (1990) Japanese estimates this should happen around 2010. However, today reaching of the break-even point between conventional and superconducting technologies appears to be postponed indefinitely.

7 ARENA OF APPLIED MINERALOGY

It would surely overstress this contribution to provide a complete list of activities and research in which applied mineralogists are involved worldwide. In the field of energy technologies there are many aspects surrounding, for example nuclear energy issues, and the development of photovoltaics and solid oxide fuel cells that are providing important research and development stimuli to applied mineralogists. In particular, the safe disposal of radioactive waste constitutes a vast arena of activities. These include but are not limited to

- Prospection and geological analysis of potential host rocks
- Petrographical investigation of host rocks
- Geochemical analysis of groundwater in contact with host rocks
- Distribution of fissures and circulation of water
- Analysis of accessory minerals in rock fissures and their sorption behaviour
- Stress analysis within repositories in hard rock

- Sorption properties of compressed clay deposits
- Immobilisation mechanisms of radioactive ions in glass, ceramics, concrete and synthetic rocks
- Chemical and radiolytic interactions between waste materials, canisters, clay buffer, groundwater and rock in multicomponent systems tests
- Long-term mineral transformations
- Chemical and radiolytic corrosion of glass, ceramics and metals
- Radiation damage of crystalline and amorphous materials

For the development of energy efficient solid oxide fuel cells the following R&D tasks are of interest:

- Synthesis of chemically and mechanically stable perovskites as catalytically active electrodes of SOFCs
- Research into pore-free, highly ionic conductive stabilised zirconia electrolytes
- Development of monolithic SOFCs as well as coatings
- Optimisation of interconnect materials
- Development and optimisation of protective layers to prevent high temperature diffusion of chromium
- Improvement of electrical efficiency of SOFCs
- Decrease of systems degradation over time

In all of these R&D aspects applied mineralogists are involved and will play an ever increasing role. They are particularly qualified to do this since their education and professional expertise are located at the interfaces with scientific disciplines such as chemistry, physics, and geosciences as well as engineering disciplines of various kind. Hence a hallmark of applied mineralogy is the application of typical mineralogical methods including x-ray diffraction, polarisation microscopy and materials analysis to technical processes and products. Frequently applied mineralogist in industry are involved in

- Analytical process control and quality assurance
- Materials and product development, production and application management
- Recycling of secondary products, environmental engineering, and safe disposal

of toxic and otherwise undesirable waste products

These activity field involve, among many others,

- Improvement of traditional and development of novel materials by management of natural resources in an energetically and ecologically desirable manner
- Immobilisation and stabilisation of toxic heavy metals and radioactive waste materials in glass, ceramics or concrete to isolate them near permanently from the biological environment
- Investigation of the influence of environmentally deleterious agents such as acid rain, corrosive effluents and noxious gasses on the stability of building stones and development of methods to conserve and restore ancient buildings.

These are truly important issues that are being explored by universities, research organisations and industrial R&D departments worldwide. Hence it is particularly aggravating that mineralogy is under attack when policy makers and research support agencies look for convenient targets of cutting expenses (Heimann 2000). In several European countries politicians consider mineralogy a scientific discipline that has nearly completed its mandate and thus should be phased out and removed from the curricula of universities. But on the contrary the breadth of scientific exploration in general and applied mineralogy is constantly increasing as is the attendance of international conferences such as ICAM. Owing to the position of applied mineralogy at the cross roads of the classical geosciences and materials science and technology university training in this field is ever expanding to non-traditional areas today. Hence applied mineralogist enter increasingly professional sectors unknown to them only a few decades ago. It is clearly the unique blend of training in chemistry, physics, geology, materials science and also ecology that qualify young applied mineralogists to find their field of endeavour in a bewildering range of diverse interests and research needs.

8 REFERENCES

- Albrecht, K.F. 1997. Present. Interdiscipl. Ecol. Center (IOeZ), Technische Universität Bergakademie Freiberg, July 3.
- Altenpohl, D.G. 1979. The metal industry in a changing world. Mater. and Soc. 3:315.
- Arthur, W.B. 1990. Positive feedback in the economy. Sci. Am. 262(2): 92.

- Franklin, U.M. 1999. *The Real World of Technology* (revised ed.). Toronto: Anansi Press
- Froes, H. 1990. Aerospace materials for the twenty-first century. *Swiss Mater.* 2(2): 23.
- Gleick, J. 1988. *Chaos. Making a New Science*. Penguin Books.
- Heimann, R.B. 1991. Technological progress and market penetration of advanced ceramics. *Bull.Am.Ceram.Soc.* 70(7): 1120.
- Heimann, R.B. 2000. Editorial of 'Applied Mineralogy in Research, Economy, Technology, Ecology and Culture'. Proc. 6th ICAM, Gottingen, Germany, July 17-19. Vol.1, xv. Rotterdam: Balkema
- Hench, L.L. 1988. Ceramics and the challenge of change. *Adv.Ceram.Mater.* 3(3): 203.
- Ishigai, S. 1989. Intrinsic laws of development of technics. Part1. *Technovation* 9:9.
- Kafka, P. 1994a. *Gegen den Untergang – Schöpfungsprinzip und globale Beschleunigungskrise*. München: Carl Hanser
- Kafka, P. 1994b. *Attraktive Gestalten. Schöpfungsprinzip und globale Beschleunigungskrise*. *Süddeutsche Zeitung*, Dec 8.
- Kepplinger, H.M. 1990. Wertewandel: Technikdarstellung in den Medien und Technikverständnis der Bevölkerung. *Chem.-Ing.Tech.* 62(6):465.
- Marchetti, C. 1981. Society as a learning system: discovery, invention, and innovation cycles revisited. Present. Donald S. MacNaughton Symp., Syracuse Univ., N.Y., January 14-15.
- Marchetti, C. 1994. Millenarian cycles in the dynamics of the catholic church. A systems analysis. *Technol. Forecast. Social Change* 46:189.
- Millendorfer, H. & Gaspari, C. 1971. Immaterielle und materielle Faktoren der Entwicklung. *Z. Nationalökon.* 31:81.
- Prigogine, I. & Stengers, I. 1984. *Order out of Chaos. Man's New Dialogue with Nature*. Toronto: Bantam Books
- Razim, C. 1990. in: *Adv.Mater.Proc.* 1/90:75.
- Ruelle, D. 1980. Strange attractors. *Math. Intell.* 2:126.
- Sivakumar, R. & Mordike, B.L. 1989. High-temperature coatings for gas turbine blades: A review. *Surf. Coat. Technol.* 37:139.
- Slovic, P. 1987. Perception of risk. *Science* 236:280.
- Wilson, R. & Crouch, E.A.C. 1987. Risk assessment and comparison: an introduction. *Science* 236:267.

Mars Mineralogy: Preliminary Results from Mars Exploration Rovers *Spirit* and *Opportunity*

P.A. de Souza Jr.¹, S.Squyres, R.Arvidson, G.Klingelhöfer, R.V.Morris, C.Schröder, D.Rodionov, R.Rieder, P.Christensen, K.Herkenhoff, S.Gorevan, H.McSween, N.Cabrol, B.Bernhard, R.Gellert, W.Calvin, F.Renz and the Athena Science Team

¹ *Companhia Vale do Rio Doce, CVRD, 29090-900 Vitória, ES, Brazil*

ABSTRACT: Mars mineralogy was studied by a suite of instruments onboard of Mars Exploration Rovers *Spirit* and *Opportunity* at their landing site and surroundings. At Gusev Crater, ferrous mineral groups (olivine and pyroxene) were found in rocks and, surprisingly, in soil as well. Non-stoichiometric magnetite was also found in rock and soils. Also, systematically, an unspecific ferric phase was observed in the Mössbauer results. At the *Opportunity* landing site, in addition to olivine, hematite and jarosite were identified. Millimeter-sized spheres, named blueberries, were associated with hematite concretions.

1 SPIRIT AT GUSEV CRATER

The Mars Exploration Rover *Spirit* landed at Gusev Crater, hypothesized to have been a site of possibly past lacustrine (Milam et al. 2003) and fluvial (Cabrol et al. 1998) environments. Therefore, sedimentation may have occurred in such conditions. Mineralogical analysis can reveal evidences of these sedimentary deposits.

Columbia Memorial Station (CMS), the *Spirit* landing site, is situated within the low albedo region, consistent with sand-sized particles. MOC images of this unit show numerous dark, possibly dust devil tracks.

Rocks: The site is littered with angular, fine grained dark rocks, some of which have pits resembling vesicles and vugs, consistent with mafic volcanic rocks patterns. The angular rocks may be ejecta from impacts into flows inside or outside the crater, or fragments of larger, somewhat rounded boulders that also occur at this site. Visible/near-infrared Panorama Camera (Pancam) spectra of the dark rocks exhibit reflectance maxima at 673 nm (shorter than the maxima for Mars Pathfinder gray rocks at 750 nm), consistent with the presence of olivine, which has a broad (composite) absorption band. A shorter band center at 930 nm also suggests

the presence of pyroxene or contamination from ferric oxides. The Gusev rock spectra resemble those of uncommon black rocks at the Pathfinder site, which have been interpreted as olivine-bearing basalts (Rieder et al. 1997).

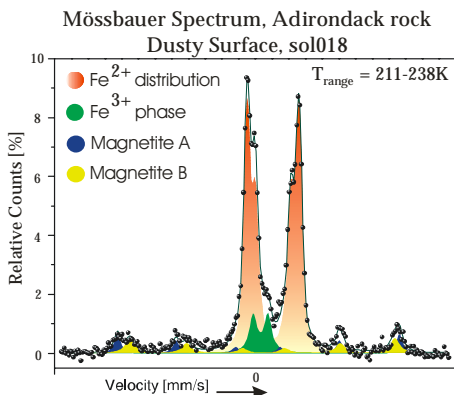
Deconvolving the mineralogy of rocks from their thermal emission spectroscopy data (mini-TES) is confounded by surface observation effects, and corrections are presently being formulated (Calvin et al. 2003).

Despite of some “white” rock registered by Pancam images, all of the rocks that have been imaged by Mini-TES at the Gusev landing site appear to be spectrally similar. However, detailed Pancam and in-situ observations suggest that the white rocks are actually dark rocks mantled with high albedo dust and/or a cemented coating or weathering rind. An example of dark rock studied in detail is Adirondack (Figure 1). It is a rock possibly coated in part by high albedo material.



Figure 1. True color image taken by the panoramic camera onboard *Spirit* shows "Adirondack" the first analyzed by the rover. Images from the panoramic camera's blue, green and red filters (480, 530 and 600 nm filters, respectively) were combined to make this picture (<http://marsrovers.nasa.gov>).

The chemical analysis performed with the alpha-particle X-ray spectrometer (APXS) of the coated surface of Adirondack was taken in the early evening when the temperature was high but still gave acceptable results (Rieder et al. 2004). Preliminary assessment of the measurement indicate sulfur and chlorine contents about half those of the nearby soil. Mars soil is enriched in these elements by more than a factor of ten compared to martian meteorites and the deduced composition of Mars Pathfinder rocks. The elevated sulfur and chlorine abundances support the presence of a coating of dust or, if it is an alteration rind, the process must introduce sulfur and chlorine (e.g., reactions with volcanic exhalations). The bulk composition of this rock surface is basaltic. Mössbauer spectra sample a greater depth of material than do APXS spectra.



Quadrupole Splitting Distribution Profile

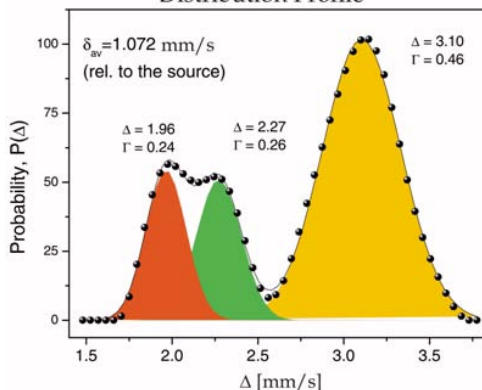


Figure 2. (a) Least-squares fitted Mössbauer spectrum measured at the dusty surface of Adirondack rock. The spectrum was fitted with magnetite sextets, a Fe^{3+} doublet and the distribution of quadrupole splitting values for Fe^{2+} . The quadrupole distribution is presented in Figure 2(b). (b) Least-squares fitted quadrupole splitting distribution profile obtained for dusty surface of the Adirondack rock. Three Gaussians were used to fit the profile. This indicates that three distinct doublets can be used for the final fitting. Γ is the LWHM of the gaussian and Δ (i.e., quadrupole splitting) is its central value of a given gaussian in mm/s.

The Mössbauer spectra of many martian rocks and soils are characterized by a two sextet pattern whose peaks progressively overlap from low to high velocity. This pattern is characteristic of magnetite, where the sextets are derived from the octahedral (mixed valence Fe^{2+} , Fe^{3+}) and tetrahedral (Fe^{3+}) sites. To our knowledge, magnetite has not been reported in the Mössbauer spectrum of any bulk martian meteorite, although Vieira et al. (1986) describes a magnetite spectrum for a magnetic separate from Nakhla (Morris et al. 2004), and small amounts in ALH84001. The intensity ratio of octahedral to tetrahedral sites in stoichiometric magnetite is ~ 1.9 . For Gusev magnetite the ratio is about 1, so it is non-stoichiometric, resulting from oxidation and/or isomorphous impurities (e.g., Ti). Nevertheless, there is a real lack of determining proof of isomorphous substitution on magnetite. The Mössbauer experiment for such purpose has to be performed longer to increase spectral statistics.

The genesis of the soil at Gusev plains is strongly associated to physical weathering. As Mars is known to have intense wind activity and there might exist different basaltic composition. The ferric doublet ($\delta = 0.38 \text{ mm/s}$, $\Delta \sim 0.85 \text{ mm/s}$), visible in Mössbauer spectra, results from Fe^{3+} and is not mineralogically specific (Klingelhöfer et al. 2004).

Ferric oxides, possibly nanophase, are characterized by a doublet and may include the superparamagnetic forms of hematite and goethite, lepidocrocite, akaganéite, schwertmannite, hydronium jarosite, ferrihydrite, and the ferric pigment in palagonitic tephra (e.g., Morris et al. 1989), or a combination of them. Within Martian temperature range (+10°C to -90°C) no significant variation in the Mössbauer pattern and their parameters or relative spectral area was detected for these Fe³⁺ and Fe²⁺ doublets. Sulfur in Gusev Crater soils (Rieder et al. 2004) possibly is present in part as sulfate sorbed on fine-grained ferric oxides under acidic conditions, a process reviewed by (e.g., Myneni 2000 and Morris et al. 2004).

Some geologically reasonable pathways that result in this Fe³⁺ doublet include incorporation into silicate phases during crystallization (e.g., pyroxene and glass) and oxidative alteration (weathering) of ferrous bearing-phases to form ferric-bearing alteration products. The measured ferrous iron/total iron ratio for the surface of Adirondack is 0.8, similar to that for fresh terrestrial basalts (0.85-0.9).

The brushing action with the Rock Abrasion Tool (RAT) was intended to remove any loose dust on the rock surface or to grind into the rock. The APXS analysis of the brushed surface is not significantly different from the pre-brushed surface. The drilled surface showed apparently no outer coating.

Soil: The regolith at the Gusev landing site is a mixture of fine-grained to sandy reddish materials and small rocks. In places, termed "hollows," finer-grained sediments appear to have accumulated, so that any small rocks are not visible. Aprons around some larger rocks also exhibit distinct soil textures and might be haloes of weathered detritus shed from the rocks. Pancam spectra show that a combination of poorly crystalline and nanophase ferric components occur in the soils. A >1300 cm⁻¹ feature in the global TES soil spectra has been interpreted to reflect the presence of small amounts (2-5%) of carbonate (Bell et al. 2002), and that same spectral feature is present in Mini-TES soil spectra.

A microscopic image of the analyzed soil appears uniformly fine-grained, although small rocks may lie below the visible surface. The soil is porous, and micro-scale topography on the soil was maintained even after being depressed by the Mössbauer contact plate. Tiny white grains, some tubular, may be chemically cemented material. The preliminary APXS soil analysis indicates oxide concentrations that are similar to those determined by Mars Pathfinder APXS analyses (Rieder et al. 2004), except for higher MgO, and lower total iron, TiO₂, and K₂O. The higher MgO content could reflect a rich magnesium sulfate concentration, maybe the presence of basalt particles and/or Mg substitution in magnetite in the analyzed sample. Measured concentrations of Cr and Ni in the soil are modest

and do not support the hypothesis that the soil contains fragments of chondritic meteorites.

Based on Mössbauer parameters isomer shift and quadrupole splitting the ferrous iron/total iron ratio is ~ 0.6. The spectrum shows two ferrous doublets, which can be interpreted as three doublets, and one ferric doublet. The most intense ferrous doublet is assigned to olivine, and the other one or two ferrous doublets can be related to pyroxene. This assignment is still uncertain. The finding of olivine in the soil is surprising, given that no rock fragments are visible in the microscope image. The ratio of the two ferrous doublets in the soil and Adirondack are different (McSween et al. in press).

Mössbauer spectrum of El Capitan: Meridiani Planum
Jarosite: (K, Na, X⁺¹)Fe₃(SO₄)₂(OH)₆

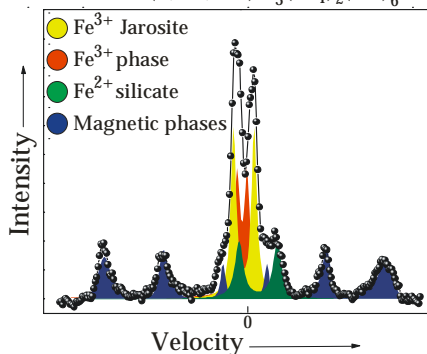


Figure 3. Least-squares fitted Mössbauer spectrum recorded at El Capitan. Jarosite and olivine doublets are identified. The Fe³⁺ is unspecific and the magnetic phases include hematite.

2 OPPORTUNITY AT MERIDIANI PLANUM

The landing site of the Mars Exploration Rover Opportunity was selected largely on the basis of the discovery of gray crystalline hematite by the Mars Global Surveyor (MGS) Thermal Emission Spectrometer (TES) currently in orbit around Mars (Hynek et al. 2002). A Mössbauer spectrum has been obtained for one soil (Figure 4) near the lander in a region having low hematite content according to Mini-TES (Hofen et al. 2003). Preliminary analysis indicates the Mössbauer spectrum is described by two ferrous doublets, a ferric doublet, and a magnetic sextet with very broad lines, possibly from a distribution of sites and/or more than one magnetic phase. The most intense doublet is assigned to forsteritic olivine, based on its Mössbauer parameters (P. de Souza, unpublished database). Preliminary results indicate that the olivine found here in Meridiani Planum and the olivine identified on the other side of the planet at Gusev Crater are not distinguishable on the basis of their Mössbauer

parameters. Olivine has also been identified from orbit by Mars Global Surveyor-TES in the *Nilli Fosse* region (Hoefen et al. 2003). The Mössbauer spectrum recorded at *Meridiani Planum* outcrops is characterized by hematite, jarosite, olivine and a Fe^{3+} doublet (e.g., Figure 3).

The X-ray fluorescence spectrum obtained in soil at *Meridiani Planum* shows many similarities to the Gusev spectrum. Peak areas for P, Ni and Zn could be well detected (Rieder et al. 2004). Phosphorous could be evaluated with great difficulty in the Pathfinder soil spectra. A mean value of 0.4 %wt was calculated (e.g., Brückner et al. 2003). The soils at Gusev and *Meridiani* have comparably high P contents. Compared to Earth the Martian crust is enriched in phosphorous.

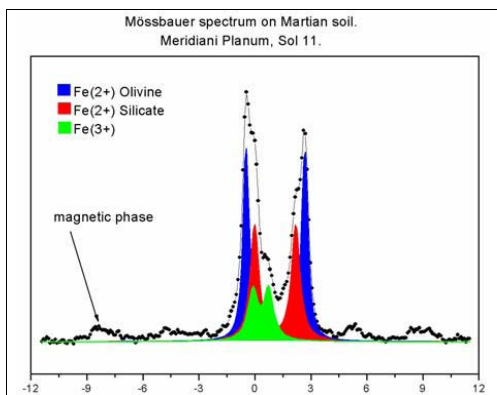


Figure 4. Mössbauer spectrum of the soil measured on Sol 11 as reported by G. Klingelhöfer et al. 2004.

The Gusev and *Meridiani* soil spectra reveal weak Ni peaks. Ni could be added to the Martian surface over time by impacts of meteorites.

The lower content of Ti, Cr, Mn, and Fe in the Gusev soil could be explained by a fractionation of heavy minerals (e.g., ilmenite, chromite, titanomagnetite, magnetite) in the soil during the fluvial and aeolian transport on the Martian surface).

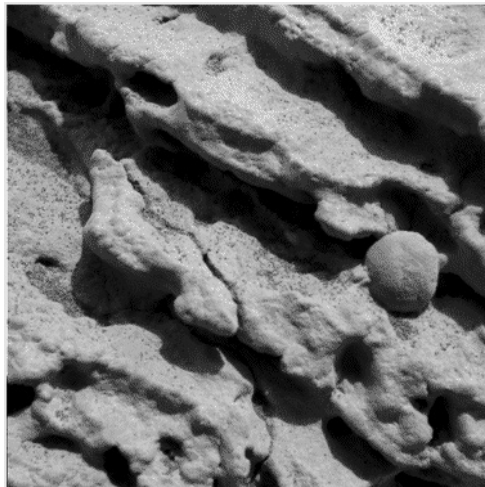


Figure 5. Microscope image of a “blueberry”.

Spherical units we found littered at the Opportunity landing site. Those units were resistant to contact-plate-pressure and were named Blueberries (Figure 5). Some evidences suggest the blueberries are hematite concretions. It can be found in erode from the sulfur-rich outcrop visited by Opportunity at *Meridiani Planum* (e.g., Eagle, Fram and Endurance craters). These units are interpreted as impure sedimentary evaporate sequences with depositional and diagenetic history (Cavin et al. 2004).

Reported as analogous to the blueberries were terrestrial concretions and oolitic iron in the United States (Chan et al. 2004; Guilbert & Park 1986). Both examples have strong contrasts with what is observed on Mars, such as differing composition of the host rock (quartz sandstone or limestone vs sulfate), size, shape and significant interior lamination that cannot be seen in the martian blueberries (Figure 6).



Figure 6. Pancam enhanced false color of McKittrick drilled hole in Eagle Crater. Two sliced “blueberries” are highlighted by the circles.

3 CONCLUSION

Gusev Crater surface mineralogy is characterized by olivine (high Fo%), and in soil it is probably a composite of powdered rocks. In addition non-stoichiometric magnetite, probably pyroxene and octahedrally coordinated Fe^{3+} oxide, oxide-hydroxide or sulfate were found. Traces of Ni, Cr and P were also detected.

Meridiani Planum is characterized by olivine, jarosite and hematite. The octahedrally coordinated Fe^{3+} material could also be detected. Hematite concretions were identified. Mineral diversity of the landing site will be characterized as the mission develops.

4 REFERENCES

- Bell J.F. et al. 2002. *Icarus* 158:56.
Brückner J. et al. 2003. *JGR* 108, E12:8094.
Cabrol N. A. et al. 1998. *Icarus* 133:98-108.
Calvin, W.M. et al. 2003. *Sixth International Conference on Mars*, abstract 3075.
Cavin W. et al. 2004. "Blueberries": A summary of the Hematite Concretions found at the Opportunity Landing Site, Early Mars Conference.
Chan et al. 2004. *Nature*, 429,731.
Guilbert & Park, *The Geology of Ore Deposits*, Ch. 15, 1986.
Hoefen et al. 2003. *Science* 302,627.
Hynek B. et al. 2002. *JGR* 107, E10,5088.
Klingelhöfer, G. et al. 2004. LPSC XXXV. Abstract #2148.
McSween H. et al. *Science*, in press.
Milam K. et al. 2003. *JGRPlanets* 108, E12.
Morris R.V. et al. 1989. *JGR* 94:2760.
Morris R.V. et al. 2004. *Science*, in press.
Myneni S.C.B. 2000. In *Sulfate Minerals*, ed. C.N.Alpers, J.L.Jambor, D.K.Nordstrom, *Rev. Min. Geochem*, vol. 40, MSA, Washington.
Rieder R. et al. 1997. *Science* 278: 1771-1774.
Rieder R. et al. 2004. Lunar and Planetary Science Conference XXXV. Abstract # 2172.
Vieira V.W.A. et al. 1986. *Physica Scripta.*, 33:180.
<http://marsrovers.nasa.gov/gallery/press/spirit/20040119a.html>.

Platinum-group Element Mineralizations in the Bushveld Complex, South Africa - Focusing on Small-scale Variations

R.K.W.Merkle

Applied Mineralogy Group, Department of Geology, University of Pretoria, Pretoria 0002, South Africa

ABSTRACT: Although characteristics of the Merensky Reef and the UG-2 chromitite layers stay constant over large distances along strike, small scale variation in lithologies, grade, and mineral chemistry reflect a much more complicated picture of the nature of these platinum ores in the Bushveld Complex. Individual profiles through the Merensky Reef and the UG-2 show deviations from commonly accepted distribution patterns of the platinum-group elements (PGE) and consequently imply as yet ill understood variations to genetic models. Within both ores, cryptic variations and signs for distinct magmatic events or the effects of magmatic fractionation are common and allow statistically reliable distinction between rock units. It is, to some degree, possible to correlate the mineralising event to magmatic processes. However, the trigger mechanisms for ore formation and the reasons for many of the observed distribution pattern of the PGE remain enigmatic.

1 INTRODUCTION

It appears to be human nature to try to make sense of complex observations, to look for similarities, to extrapolate, and to come up with a simple summary. The Bushveld Complex in general, and its platinum ores in particular, are no exception. Despite a huge body of scientific publications on the Bushveld Complex (of which ca. 21 % focus on the Merensky Reef and a further ca. 13 % on the UG-2 chromitite layer), the small-scale variability in these ores escapes the general attention. "Typical" distributions of grade are shown in reviews and textbooks, and complex and highly sophisticated models are based on such simplified observations.

This contribution will not attempt to remedy the situation, because this would not only require the evaluation of huge data bases which either do not exist or are not publicly available, but it also would require an integrating model which would defeat the purpose of this communication. Instead the presentation focuses on anecdotal evidence for small-scale variability with the hope to create a critical awareness of the complexity these ores harbour and for the need to generate large data sets.

Only if many systematic studies in different localities become available will it be possible to

evaluate the reliability of anecdotal observations, to detect potentially present systematic variations, and ultimately derive at more robust genetic models.

2 MERENSKY REEF

Although the use of the term Merensky Reef should be restricted to the part of the Merensky Unit that can be economically mined, and should bear no implications on the rock types present, it is often associated with the presence of a pegmatoidal pyroxenite bound by chromite stringers and overlying an anorthositic footwall. However, the lithological character of the Merensky Unit changes considerably along strike, with up to 3 chromite stringers present, with pegmatoidal pyroxenite absent in many areas, and ranging in thickness from a few 10's of cm to more than 10 m.

The distribution of the platinum-group elements (PGE) is not restricted to the pyroxene-rich rocks of the Merensky Unit, but may occur up to several m (10 observed, but what is the limit?) below the footwall contact. As a rule of thumb, the highest grades of PGE are located close to the chromite stringers, but increasing thickness of the Merensky pyroxenite typically leads to a patchy distribution of

grade, which makes mining uneconomical.

During mining operations, the best mining cut has to be determined to assure economic mining. In some parts of the Bushveld this parameter stays constant for long distances along strike, while in other areas high fluctuations in the grade distribution requires constant monitoring. An evaluation from Karee Mine in the western Bushveld over a distance of ca 150 m (at a sampling interval of 5 m and sample spacing vertically across the Merensky Reef of typically 10 cm over a distance of up to 2.5 m) allows to demonstrate that the averaged observation (Fig. 1) confirms the expectation of higher grades being associated with the chromite stringers (the grades being lower at the stratigraphically higher chromite stringer), while individual profiles can vary distinctly from this pattern (Fig. 2).

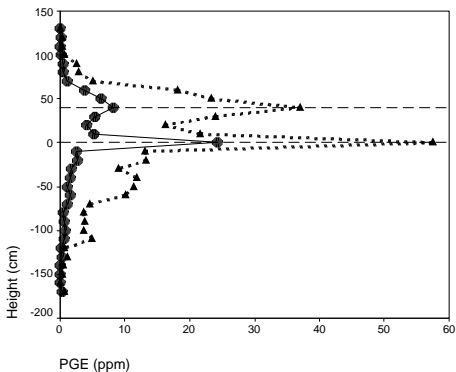


Figure 1. Average PGE concentration (solid line, round symbol) and upper limit of the 90% confidence interval (stippled line, triangles) of a mining panel of the Merensky Reef. Horizontal dashed lines represent chromite stringers.

If interpretations are based on smaller volumes of samples (e.g. different deflections of bore holes), variations in concentrations and distribution pattern can be even more dramatic.

If the lithologies that make up the Merensky Reef are subdivided into the anorthositic footwall (leuconorite), the Merensky pegmatoid (based on distinctly larger grain sizes), the Merensky pyroxenite, and the melanorite in the hangingwall, it can be demonstrated that systematic differences between the rock-types exist. A distinction between Merensky pyroxenite and Merensky pegmatoid is possible with a high degree of statistical certainty (Fig. 3), which implies that systematic petrological differences exist. But even within the pyroxenite and the pegmatoid, the presence of negative and positive europium anomalies testify to distinct variations (Fig. 4). Consequently, relationships between economically important elements like Ni, Cu and the

PGE differ between sub-units of the Merensky lithologies and published relationships, which do not differentiate between these rock-types, represent over-simplifications.

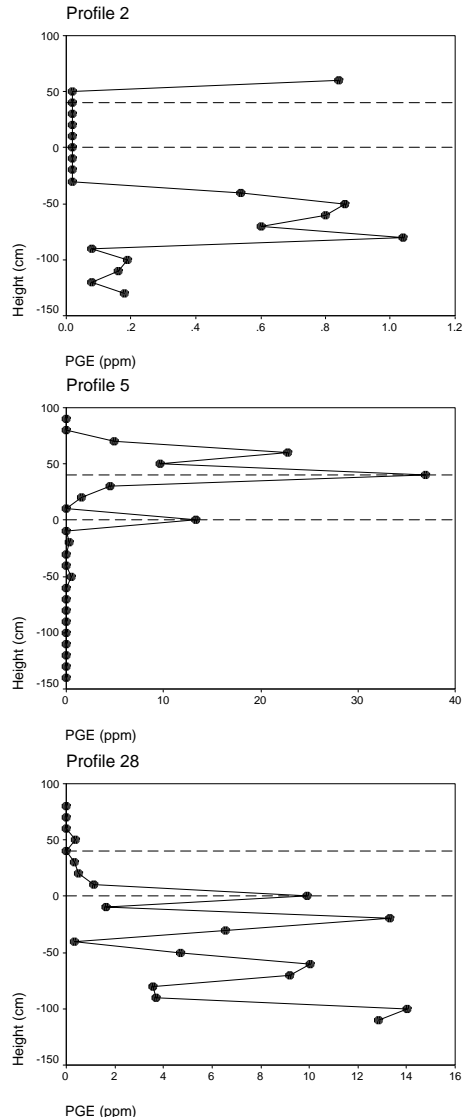


Figure 2. Selected profiles (channel sampling with 10 cm sample height) of a mining panel of the Merensky Reef to demonstrate the variability of PGE distribution. Horizontal dashed lines represent chromite stringers.

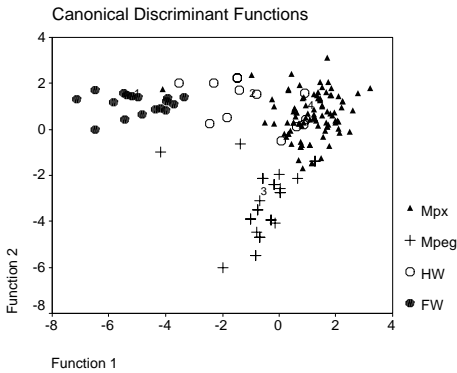


Figure 3. Discrimination between anorthositic footwall (FW), the melanorite hangingwall (HW), Merensky pyroxenite (Mpx) and Merensky pegmatoid (Mpeg). Numbers indicate the group centroids.

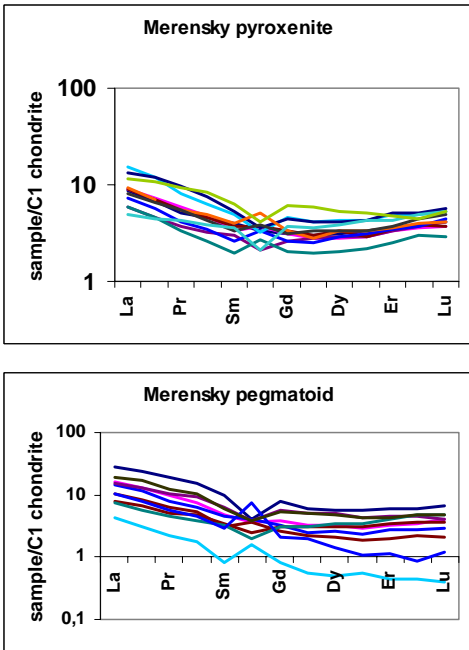


Figure 4. REE pattern of Merensky pyroxenite and Merensky pegmatoid with positive and negative europium anomalies.

Obtaining statistically reliable data on proportions of platinum-group minerals (PGM) requires huge data sets, which are typically much larger than obtained in routine mineralogical investigations. It is therefore at present not possible to substantiate the empirical observation that different rock-types in the Merensky Reef have different proportions of PGM. It is also presently not possible to ascertain whether

the compositions of individual PGM like braggite, (Pt,Pd,Ni)S and cooperite, PtS reflects lithological differences. However, overall the typical compositional variation of braggite in the Merensky Reef seems to be rather limited (Fig. 5).

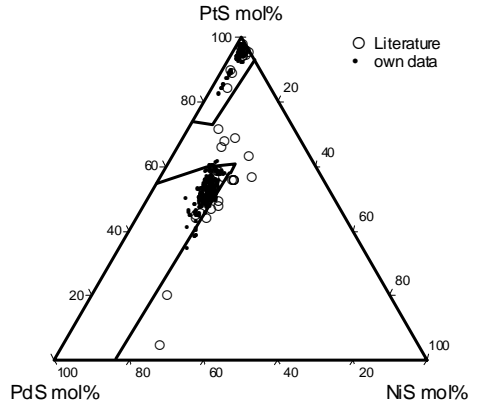


Figure 5. Compositional variation of braggite and cooperite from the Merensky Reef relative to the experimental solubility limits at 700°C (Verryn & Merkle 2002).

3 UG-2 CHROMITITE

The distribution of PGE in the UG-2 is known for a long time not to be homogeneous, but rather to follow a pattern with elevated values at the base, which decline upwards and to form a second peak further up in the layer (Hiemstra 1985).

In some localities it is easily possible to demonstrate that the UG-2 layer consists of 2 or 3 sub-layers, which can be related to variations in the mg# of orthopyroxene (Fig. 6), and the concentrations of PGE. However, like in the Merensky Reef, variations on small scale can exist (Fig. 7) which appear to be related to petrological processes, but are not necessarily laterally consistent. A more general relationship can be observed between the position of the upper PGE peak and a change in the Cr/V ratio of the chromite. Although the variation in the Cr/V ratio of chromite in the UG-2 is not consistent laterally, it is possible to demonstrate that positions of distinct changes and enrichment of PGE in the second peak coincide.

Like in the Merensky Reef, regional differences in the proportions of PGM have been observed in the UG-2, but it is an unresolved issue, to what degree the proportions of PGM in the Merensky Reef and the UG-2 in the same locality are related.

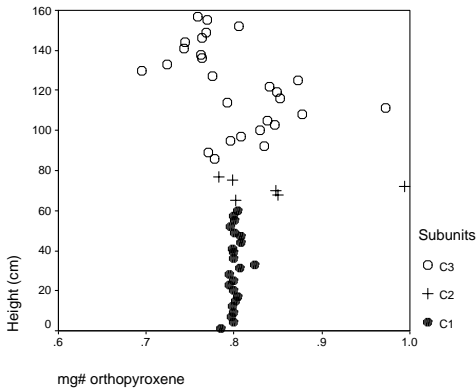


Figure 6. Variation of mg# of orthopyroxene with height in sub-units of the UG-2.

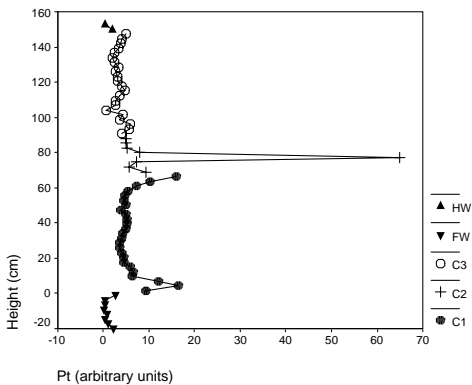


Figure 7. Distribution of Pt in a UG-2 profile consisting of 3 sub-units. Please note that an unusually high value is observed at the same stratigraphic level as an extreme mg# of orthopyroxene in Figure 6.

In the UG-2, PGM proportions appear to vary with height, but to date no statistically reliable study of this aspect has been published. However, the implication is that non-representative sampling may lead to distinct misinterpretations.

Not only do PGM proportions vary with height in the UG-2, the composition of individual PGM may vary as well. So far, this aspect has only been evaluated for braggite because for other minerals the available data base is insufficient. Figure 9 summarizes available data on braggite from the UG-2 and comparison with Figure 5 demonstrates that a much larger variation in composition is observed than in the Merensky Reef.

Electron microprobe analyses of braggite as a function of height are summarized in Figure 10. Although there is a large compositional scatter at

each stratigraphic level examined, a statistical evaluation shows that the fractionation of the Pt/Pd ratio (Hiemstra 1985) is also reflected in the average compositions of braggite. Compositions from different stratigraphic positions can be discriminated, if enough analyses are available (Fig.11). It appears that it is possible to distinguish populations of braggite grains from the Merensky Reef and the UG-2, but it will be rather difficult to identify a “typical” UG-2 composition.

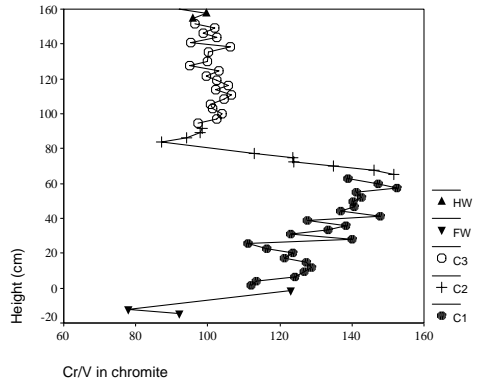


Figure 8. Variation of Cr/V ratio of chromite (based on electron microprobe analyses) in a profile through the UG-2.

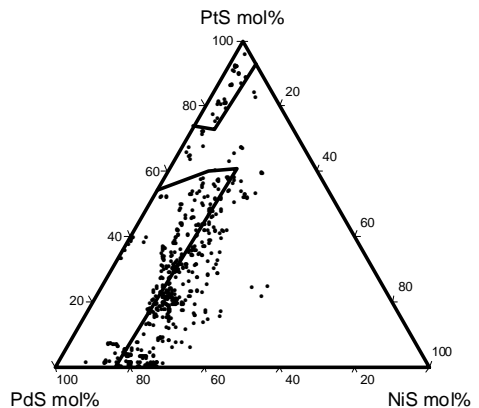


Figure 9. Compositional variation of braggite and cooperite from the UG-2 relative to the experimental solubility limits at 700°C (Verryn & Merkle 2002).

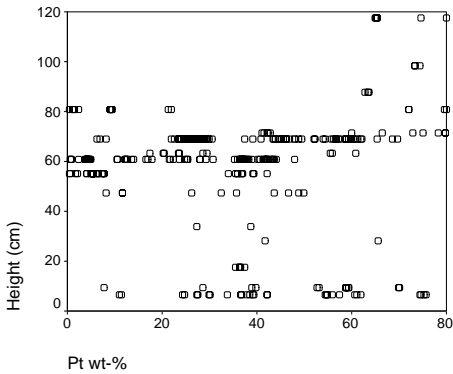


Figure 10. Variation of Pt content in braggite and cooperite in a UG-2 profile.

5 REFERENCES

- Hiemstra, S. A. 1985. The distribution of some platinum-group elements in the UG-2 chromitite layer of the Bushveld Complex. *Economic Geology*. 80:944-957.
- Verryn, S. M. C. & Merkle, R. K. W. 2002. The system PtS-PdS-NiS between 1200°C and 700°C. *Canadian Mineralogist*. 40:571-584.

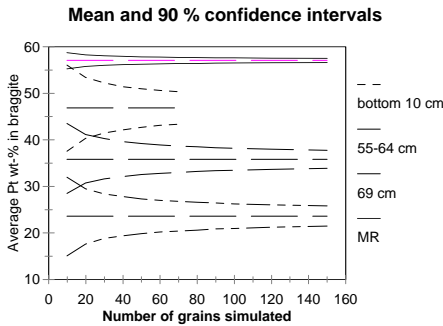


Figure 11. Systematic differences in the Pt content of braggite/cooperite at different height in the UG-2 chromitite layer. MR refers to Merensky Reef.

4 CONCLUSIONS

Although a huge volume of literature on the platinum ores of the Bushveld Complex already exists, there is a distinct need for very detailed investigations to determine the small-scale variability in these ores. Criteria are needed to distinguish them from medium and large-scale variations. It is unlikely that the observations presented in this communication are the only ones that do not conform (or add additional aspects) to presently popular genetic models. However, we need to develop towards integrated models, which can account for all these observations. Only concepts which can explain not only the common systematic relationships, but also the deviations, will stand the test of time.

Modern Times and Trends in Industrial Minerals

P.W.Harben

Peter W. Harben, Inc., Industrial Minerals Consultants, Las Cruces, New Mexico, USA

ABSTRACT: The field of industrial minerals covers the more than 50 diverse nonmetallic and non-fuel materials ranging from low unit value, high place value commodities like aggregates to high unit value, low place value materials like industrial diamond. The majority fall between these two extremes of unit value and place value. Similarly, typical prices range from a few dollars per tonne to more than \$10,000 per tonne for the same extremes with most in the \$100 - \$1,000/tonne category and much of the rest between \$10 and \$100/tonne. At the same time, the number industrial minerals and the price range increases dramatically when individual minerals are broken out by grade based on physical and chemical criteria and then synthetic minerals and downstream products are added. These industrial minerals are market driven and the nature of this market is constantly changing as the population grows, economies become more sophisticated, technical needs and even fashions for raw materials change, and producers and consumers attempt to stay competitive. The nature of the market and these changes – which will influence the ability of the industrial minerals to be exploited commercially – require careful market evaluation before investing.

1 INTRODUCTION

The field of industrial minerals covers the more than 50 diverse nonmetallic and non-fuel materials listed in the table. At one extreme are sand and gravel and crushed stone used in large tonnages and sold for a few dollars per ton and so must be produced close to the point of use (low unit value but a high place value). At the other extreme is industrial diamond whose occurrence in minute quantities thousands of kilometers from markets is no deterrent to commercial exploitation (a high unit value but a low place value). The majority of industrial minerals fall between these two extremes of unit and place value – some will be able to service local markets in Brazil or regional markets in Latin America whilst others are competitive in more distant markets such as North America, Europe, and Asia.

At the same time, the fifty or so industrial minerals reviewed for this paper increase dramatically when individual minerals are broken out by grade based on physical and chemical criteria and then synthetic minerals and downstream products are added.

Industrial minerals are market driven – to quote a well-known saying “without a market, a deposit is merely a geological curiosity”. The nature of this

market is constantly changing as the population grows, economies become more sophisticated, technical needs and even fashions for raw materials change, and producers and consumers attempt to stay competitive. The nature of the market and these changes – which will influence the ability of the industrial minerals to be exploited commercially – include some of the factors outlined below.

2 WORLD MARKETS AND TRADE

2.1 Overall Market Growth

As the world’s population grows and societies shift from a rural farming to an urban manufacturing base, economies become more advanced. As a result, the market for industrial minerals increases, typically with less volatility than metallic or even energy products, and the demands of the consumers become more sophisticated.

2.2 Regional growth rates

North America, Western Europe, and parts of Asia including Japan, Korea, and Taiwan continue to be the largest consumers of industrial minerals. These regions completely dominate the consumption of

1. Construction materials: sand & gravel, crushed rock/aggregates	25. Limestone: calcium carbonate, cement, lime
2. Antimony oxide	26. Lithium minerals: lepidolite, spodumene, petalite, lithium carbonate
3. Asbestos	27. Magnesite & magnesia
4. Barite	28. Manganese
5. Bauxite & alumina	29. Mica
6. Beryllium minerals	30. Nepheline syenite
7. Borates	31. Nitrates
8. Bromine	32. Olivine
9. Celestite	33. Perlite
10. Chromite	34. Phosphates/apatite
11. Clays: attapulgite, bentonite, flint clay, hectorite, kaolin, sepiolite	35. Potash
12. Corundum/emery	36. Pumice
13. Diamonds	37. Pyrophyllite
14. Diatomite	38. Rare earths: xenotime, bastnasite, monazite
15. Dimension stone: marble, granite, slate, limestone/travertine, sandstone	39. Salt
16. Dolomite	40. Silica/quartz
17. Feldspar/aplite	41. Soda ash/trona
18. Fluorspar	42. Sodium sulfate
19. Garnet	43. Sulfur/pyrite
20. Graphite	44. Talc
21. Gypsum	45. Titanium minerals: anatase, ilmenite, rutile
22. Iodine	46. Vermiculite
23. Iron oxide	47. Wollastonite
24. Kyanite/andalusite/sillimanite	48. Zeolites
	49. Zircon/baddeleyite

high-tech products such as beryllium and rare earths, often importing the raw materials for conversion into the specialized products that are then consumed in a local manufacturing process. On the other hand, as manufacturing activity transfers to developing countries, so too does the demand for commodity industrial minerals. Consequently, these traditional industrial minerals markets have become saturated with growth prospects flat compared with the rapid rate of growth in developing regions like parts of Asia and Latin America. In the case of product from Brazil, modest local and regional demand may increase rapidly from a low base whereas Europe has an existing market that represents an immediate target.

2.3 National dominance

Outside of the traditional leaders, China and India with a combined population of more than 2 billion have a tremendous influence on world industrial minerals markets as both consumers and suppliers. In particular, China tends to disrupt mineral markets through dumping (for example, magnesia products in the EU), drastic price undercutting (barite exports

to the United States), rapid conversion from a net importer to exporter (soda ash in the 1990s), and the like. At the same time, India protects its domestic market through severe import duties while at the same time actively exporting material such as garnet and titanium minerals. Therefore, any market evaluation of the potential of most industrial minerals needs to account for the influence of China and India as both a potential customer and competitor.

2.4 Changing trading partners

Old regimes like COMECON have fallen, and new partnerships are emerging to encourage international trade. This includes taking advantage of NAFTA, MERCOSUR, and other trade organizations within the region.

2.5 Deep-sea trade

Since mineral resources are distributed unevenly throughout the world, deep-sea trade in industrial minerals continues to grow. More highly developed techniques of materials handling and transportation

have been a contributing factor, as has the demand by consumers for materials with special or unique properties irrespective of where these materials are found. Wyoming bentonite is delivered to oilrigs all around the world, soda ash from the western United States is transported via dedicated unit trains, port facilities, and ships to glass plants in Latin America, and caustic soda from the US Gulf is exported to alumina plants in Australia. Kaolin from Brazil is exported to the paper markets of North America, Europe, and Asia, and lithium carbonate from Chile now dominates world markets. Low production costs and/or exceptional quality can overcome distance from market and compete successfully with more local products.

3 CORPORATE INFLUENCE

3.1 *Dominant corporations*

A decade or more of rationalization through mergers and acquisition as well as mine closures have resulted in fewer but larger companies that can dominate industries – Unimin is the sole producer of nepheline syenite and a dominant force in silica and other minerals utilized in glass and ceramics, whereas Imerys of France has emerged as the world's major supplier of white filler minerals such as kaolin and calcium carbonate used in paper, plastics, paints, and the like.

Other examples of producers dominating an industry include the following:

- Talc de Luzenac (part of Rio Tinto) – talc
- Plüss Stauffer of Switzerland – GCC
- Specialty Minerals Inc. of the USA – PCC
- Western Garnet of the USA – garnet
- World Minerals of the USA – diatomite
- DeBeers of South Africa – diamonds
- SQM of Chile – lithium
- Tolsa SA of Spain – sepiolite
- Etibor of Turkey and US Borax of the USA - borates.

These major forces are potential competitors – or partners – in any new venture that includes these minerals.

3.2 *Supplier-customer relations*

Rather than the traditional adversarial approach, the supplier and consumer of minerals now liaise over specifications and supply through a close relationship that requires sophisticated electronic transmission of analysis data, allows quality control to reside with the supplier, and encourages joint R&D projects. There are some examples of backward integration whereby large-scale mineral consumers control some or all of the raw material

supply through outright ownership, partial ownership, or long-term technical agreements.

One of the consequences of this domination is the move toward national contracts whereby large consumers can purchase all the silica sand or GCC required for its plants from one company in exchange for an attractive price based on volume.

4 PRODUCT DEVELOPMENT

4.1 *Minerals processing*

There is a trend toward the use of increasingly elaborate processing techniques and the production of value-added grades. Kaolin, for example, may be ground and airfloated to produce a low-cost filler used locally for rubber, waterwashed for use nationally as a fine, white filler in paper, or floated, delaminated, calcined, and magnetically separated to produce bright “engineered material” for use in lightweight-coated grades of paper all over the world. The production of value-added grades in Brazil has expanded the market worldwide.

4.2 *Stringent specifications and service requirements*

Fast, automated methods of manufacture demand raw materials with a high degree of uniformity that in turn places heavy responsibilities on the suppliers of raw materials. Minerals are no longer purchased on price alone – today it is price plus quality, consistency, and service. Certain specifications can only be met by blending minerals from various sources, for example graphite houses may blend graphite from China, Brazil, and Canada to satisfy the needs of a consumer using just 10 tonnes a year.

In contrast, a large paper plant may work with a kaolin producer to develop a specification required to produce a special paper type. In both cases, any producer may need to cooperate with an existing producer so that the mineral product can be added to a range available from the supplier.

4.3 *Development of new applications*

The use of industrial minerals is expanding into many new areas. Over the past decade the market for pet litter, for example, has experienced phenomenal growth giving an enormous boost to the demand for attapulgite, sepiolite, bentonite, diatomite, zeolites, and even gypsum. A potential new producer should be aware of new developments and remain vigilant in seeking new concepts and markets. This is an ongoing process as the markets change.

4.4 Prospects for substitution

Substitution has always been an important aspect of the industrial minerals scene and continues to be critical for success. For example, in the paper industry calcium carbonate is a major challenger to kaolin as a filler and coater, and precipitated calcium carbonate competes with ground calcium carbonate in many applications. In certain parts of the world, most notably in Scandinavia, talc is a potential substitute for both carbonate and kaolin. Regional bans on the use of phosphates in detergents encouraged the use of synthetic zeolites that in turn aided sodium silicate producers and therefore silica sand and chloralkali suppliers.

Substitution offers opportunities and dangers for potential new suppliers, and therefore when evaluating the merits of a kaolin deposit, the markets for carbonate, talc, and even mica should be assessed. In addition, regional differences in use patterns need to be considered. For example, kaolin still dominates paper coating in North America, whereas carbonates are popular in Europe; in the United States the use of precipitated calcium carbonate has skyrocketed due to the scarcity of good-quality ground calcium carbonate.

5 GREEN MOVEMENT

5.1 Coproduct and byproduct competition

Involuntary mineral production influences the supply position and so can disrupt the supply/demand balance. Increasingly, environmental considerations influence the supply of minerals – prime examples include sulfur and sulfuric acid recovered during the refining of crude oil and sour natural gas and gypsum precipitated from a flue gas desulfurization (FGD) plant attached to a coal-burning power plant or the neutralization of acid in a titanium dioxide pigment plant.

Byproduct minerals are produced as the result of a manufacturing process itself such as sodium sulfate derived from rayon spinning or calcium chloride from the Solvay soda ash manufacturing process. The need to dispose of these minerals in a responsible and cost-effective manner encourages sale on the merchant market even at low prices that in turn depress the price of any commercial equivalent or rival. Byproduct generating processes more driven by economics than the green movement include the electrolysis of salt which produces equal parts of chlorine and caustic soda irrespective of the market conditions; similarly, when feldspar is separated from a granite or alaskite by flotation, silica and mica are produced and sold as is or even upgraded to value-added products; another example

would be the extraction of titanium minerals like ilmenite and rutile from mineral sands which invariably yields monazite, garnet, zircon and other heavy minerals.

Revenues from these coproducts may be critical for the economic viability of the operation even though the rate of production is not influenced by demand. It is difficult to compete with a byproduct or coproduct mineral based on price alone.

5.2 Environment and health and safety

Mineral-related environmental and health issues range from simple mineral dusting problems at ports through the need to label mineral content and use specialized containers to the alleged health hazards associated with certain minerals and mineral-related products. At the very least they can represent additional handling or transportation costs, create barriers to sales and impinge on the prospects for future growth, and may even pose a long-term threat to the financial stability of the producing company due to the potential for litigation.

Several minerals have been singled out for scrutiny – in particular silica, asbestos, fluorspar, and bromine. Crystalline silica is classified as a Class 1, Known Carcinogen by the International Agency for Research on Cancer (IARC), a unit of the World Health Organization, and any mineral containing more than 0.1% crystalline silica must be so labeled. Asbestosis, claimed to be the cause of chronic lung disease, triggered the severe restrictions on the use of chrysotile asbestos in many countries and outright bans in others like France and Belgium which have crippled the asbestos market and encouraged substitution (see above).

At the same time, the use of beryllium products is said to cause berylliosis, a serious chronic lung disease. In a similar fashion the demand for fluorspar and bromine has been adversely affected by the Montreal and Kyoto protocols which aim to limit the use of products blamed for the apparent depletion of the ozone layer such as chlorofluorocarbons (CFCs), hydrofluorocarbons (HFC's), perfluorocarbons, sulfur hexafluoride, and methyl bromide. Several other minerals have health and safety concerns: the acicular nature of wollastonite and attapulgite crystals, the asbestiform mineral content in talc, the heavy metal content of barite used in drilling, the eutrophication of lakes through phosphates, the toxicity and carcinogenicity of hexavalent chromium, and the radioactivity associated with monazite and certain byproduct gypsum products.

Industrial Minerals by Price				
\$1-\$10/t				
Aggregates	Anhydrite	Gypsum	Salt	Sand & gravel
\$10-\$100/t				
Aplite	Cement	Ilmenite	Olivine	Salt
Aragonite	Celestite	Kaolin	Phosphates	Salt cake
Barite	Chromite	Lime	Potash	Soda ash
Bentonite	Dolomite	Magnesite	Pumice	Zeolites
Calcium carbonate	Feldspar	Nepheline syenite	Pyrophyllite	
\$100-\$1,000/t				
Alumina	Calcium carbonate	Kaolin	Petalite	Vermiculite
Anatase	Chromite	Kyanite	Rare earth oxides	Wollastonite
Andalusite	Diatomite	Magnesite	Rutile	Xenotime
Asbestos	Emery	Manganese	Sepiolite	Natural zeolites
Attapulgite	Flint clay	Mica	Silica	Zircon
Barite	Fluorspar	Monazite	Sillimanite	
Bauxite	Garnet	Nepheline syenite	Spodumene	
Bentonite	Graphite	Nitrates	Sulfur	
Borax	Iron oxide	Perlite	Talc	
\$1,000-\$10,000/t				
Antimony oxide	Bastnaesite	Graphite	Rutile	
Asbestos	Bromine	Rare earth oxides	Synthetic zeolites	
Over \$10,000/tonne				
Diamonds	Iodine	Rare earth oxides		

5.3 Increased recycling and conservation

Both recycling and material conservation have reduced the demand for virgin raw materials used to make everything from aluminum and glass containers, paper, and plastics to refractories, steel, and even roadbeds.

6 PRICES

Industrial minerals range in price from less than a few dollars per tonne for aggregates to more than \$10,000 per tonne for industrial diamonds. However, most are in the \$100 - \$1,000/tonne category and much of the rest between \$10 and \$100/tonne. The accompanying table classifies minerals by price, although various grades based on inherent quality and processing generate numerous exceptions. Nevertheless, the FOB plant price dictates if it can be mined commercially and CIF port or delivered price how far it can be shipped. This is used as a rough indication of where the mineral can be sold profitably.

7 CONCLUSIONS

Market studies are an almost instinctive part of everyday life. The purchase of everything from a can of soup to a new car requires some sort of market assessment. To set the sales price of a house, the realtor performs a comparative market analysis or CMA by researching the price levels of recent sales of similar properties in the area and adjusting for condition, size, location, etc. Finding and developing an industrial minerals prospect should be no different. After all, if market research is required to buy a 75¢ can of soup, surely the effort to determine the potential profitability of an industrial minerals resource should be commensurately larger. Curiously enough the answer is often "yes, but . . ."

7.1 Without a market . . . still build it

Most would agree with the adage, "Without a market, a mineral deposit is merely a geological curiosity". Yet most modern mining companies employ a crew of managers, accountants, lawyers, investor relation gurus, engineers of all stripes, plus the odd geologist and even botanist, yet very few

feel the need to engage in-house market research help. Like the international engineering firms, they tend to go out a subcontract the market research work.

At the same time, companies continue to build mines and plants on the fly and exploration geologists still scour the far corners of the world for industrial mineral deposits without the slightest notion of whether anything found could be sold at a profit or even sold at all. The concept that industrial minerals demand strong market analysis in order to become viable and valuable is lost in the rush to drill, raise capital, engineer, construct, debug, and produce a product on schedule.

Our experience in this field has ranged from the rare client intent on understanding every nuance of a new market to those that rush where angels with an understanding of the market fear to tread. Most clients fall somewhere between these two extremes.

7.2 The need for independent thought

Recent corporate scandals and indictments have brought home the realization that merchant banking and investment advice need to be separated in order to generate independent research and a level playing field for investors. This would seem as obvious as not asking a used car salesperson whether to buy a car or take the bus. Advice needs to be independent of a stake so that the outcome of the study has little or no effect on the well being of the researcher. It is often an unpopular sentiment, but a market study that advises against getting to a given market might save more money than a positive result will make. Positive bias in a market study may come from on or more sources including the desire to:

- ❖ retain employment by management and staff
- ❖ build the plant and infrastructure by the engineering company
- ❖ develop the local economy through the creation of jobs and a tax base by a government body
- ❖ raise capital and boost share prices by investors

Because of these desires, some marketing studies may be half hearted, under funded afterthoughts that actually follows rather than precedes the considerable time, effort, and capital sunk into drilling holes, developing processing flow sheets, and even building the facility. By that stage of the project, reputations and egos may be on the line.

Most projects have to be sold to management or financial partners, and the initial enthusiasm of the project's champion may be such that it is difficult to back down when bad news is "discovered" about the market. In many cases, the idea of a market study is to simply to confirm the gut feeling that this is a

profitable venture, or as ammunition just in case management or investors ask tough questions.

Alas, industrial mineral deposits are not like that fabled baseball field full of paying fans and legendary players; "build it and they will come" is a romantic concept for the silver screen, but not a prudent business strategy in this line of work.

8 REFERENCES

- Allen, J.B., and Charsley, T.J., 1968, *Nepheline Syenite and Phonolite*, Monograph, Her Majesty's Stationery Office, London, 169 pp.
- Andrews, R. W. 1970, *Wollastonite*, Inst. Geol. Sc., Her Majesty's Stationery Office, London, 114 pp. Anon., 1981, *Manganese Reserves and Resources of the World and their Industrial Implications*, Nat. Materials Advisory Board/US Bur. Mines, Rpt. no. NMAB-374, Nat. Academy Press, Washington DC, 360 pp.
- Anstett, T. F., and Porter, K.E., 1985, *Asbestos Availability — Market Economy Countries*, US Bur. Mines Inf. Circ 9036, 21 pp.
- Barker, J.M., Chamberlin, R.M., Austin, G.S., and Jenkins, D.A., 1996, "Economic geology of perlite in New Mexico, USA" in *Proceedings, 31st Forum on the Geology of Industrial Minerals*, G.S. Austin, G.K. Hoffman, J.M. Barker, J. Zidek, and N. Gilson, eds., New Mexico Bur. Mines and Mineral Resources Bull. 154, pp. 165–170.
- Bleiwas, D.I., and Coffman, J.S., 1986, "Lithium availability — market economy countries", US Bur. Mines Inf. Circ. 9102, 23 pp.
- Boynton, R.S., 1980, *Chemistry and Technology of Lime and Limestone*, 2nd ed., Wiley (Interscience), New York 578 pp.
- Bristow, C.M., 1987, "World kaolins Genesis, exploitation, and application", *Industrial Minerals*, no. 238, July., pp. 45–59.
- Brobst, D.A., and Pratt, W.P., eds., 1973, *United States Mineral Resources*, U.S. Geological Survey Professional Paper 820, 722 pp. (various chapters).
- Brown, C.E., 1973, "Talc" in *United States Mineral Resources*, US Geol. Surv. Prof. Paper 820, D.A. Brobst and W.P. Pratt, eds., pp. 619–626.
- Burnett, W.C. and Riggs, S.R., eds., *Phosphate Deposits of the World*, v 3, Genesis of Neogene to Recent Phosphorites, Cambridge University Press. Bearden, S.D., 1990, "Celestite resources of Mexico" in *Proceeding, 26th Forum on the Geology of Industrial Minerals*, P.C. Sweet, ed., Virginia Div. Min. Res. Publication 119, pp. 13–15.
- Coffman, J.S., and Palencia, C.M., 1984, *Manganese Availability Market Economy Countries A Minerals Availability Program Appraisal*, US Bureau Mines Inf. Circ. 8978, 26 pp.
- Durham, D.L., 1973, "Diatomite" in *United States Mineral Resources*, US Geol. Survey Prof. Paper 820, D.A. Brobst and W.P. Pratt, eds., pp. 191–195.
- Dyni, J.R., and Jones, R.W., eds., 1998, *Proceedings of the First International Soda Ash Conference*, Rock Springs, WY, vol. I, Wyoming State Geol. Surv. Pub. Inf. Circ. no. 39, 95 pp.
- Edward, H.B., Shields, D.J., and Wagner, L.A., 1993, "Chromium availability in market economy countries and network of world chromium supply", US Bur. Mines Inf. Circ. 9337.

- Ericksen, G.E., 1981, "Geology and origin of the Chilean nitrate deposits," US Geol. Surv. Prof. Paper 1188, 37 pp.
- Fantel, R.J., Buckingham, D.A., and Sullivan, D.E., 1986, "Titanium minerals availability — market economy countries", US Bur. Mines Inf. Circ. 9061, 28 pp.
- Fogg, C.T., and Boyle, Jr., E.H., 1987, *Flake and High-Crystalline Graphite Availability — Market Economy Countries: A Minerals Availability Appraisal*, US Bur. Mines Inf. Circ. 9122, 40 pp.
- Force, E.R., 1991, "Geology of titanium — mineral deposits", Geol. Soc. America Sp. Paper 259, 112 pp.
- Flawn, P.T., 1966, *Mineral Resources*, Rand McNally, Chicago, IL, 406 pp.
- Garrett, D.E., 1992, *Natural Soda Ash - Occurrences, Processing, and Use*, Van Nostrand Reinhold, New York, 636 pp.
- Govett, G.J.S., and Govett, M.H., eds., 1976, *World Mineral Supplies: Assessment and Perspective*, Elsevier Scientific Publishing Company, Amsterdam, 472 pp.
- Grim, R.E., 1968, *Clay Mineralogy*, 2nd edition, McGraw-Hill, New York, 596 pp.
- Harben, P.W., 2002, *Industrial Minerals HandyBook — A Guide to Markets, Specifications, & Prices*, 4th edition, IMIL, London, UK, 412 pp.
- Harben, P.W., and Kuzvart, M., 1997, *Industrial Minerals A Global Geology*, Industrial Minerals Information Ltd., London, 462 pp.
- Haynes, W., 1959, *Brimstone, the Stone that Burns*, Van Nostrand, Princeton, NJ, 308 pp.
- Jackson, W.D., and Grey, C., 1993, *International Strategic Minerals Inventory Summary Report — Rare-Earth Oxides*, US Geol. Surv. Circ. 930-N, 67 pp.
- Jaster, M.C., 1956, "Perlite resources of the United States", US Geol. Surv. Bull. 1027-I, 28 pp.
- Kilgore, C.C., Kraemer, S.R., and Bekkala, J.A., 1985, "Fluorspar availability market economy countries and China", US Bur. Mines Inf. Circ. 9060, 57 pp.
- Kilgore, C.C., and Thomas, P.R., 1982, *Manganese Availability — Domestic: A Minerals Availability Program Appraisal*, US Bureau Mines Inf. Circ. 8889, 14 pp.
- Klemic, H., et al., 1973, "Zirconium and hafnium" in *United States Mineral Resources*, D.A. Brobst and W.P. Pratt, eds., US Geol. Surv. Prof. Paper 820, pp. 713–722.
- Lefond, S.J., 1969, *Handbook of World Salt Resources*, Plenum Press, New York, 384 pp.
- Oates, J.A.H., 1998, *Lime and Limestone: Chemistry and Technology, Production and Uses*, Wiley, London, UK, 445 pp.
- Palencia, C.M., and Mishra, C.P., 1986, "Antimony Availability Market Economy Countries A Minerals Availability Appraisal," US Bur. Mines Inf. Circ. 9098, 20 pp.
- Prud'homme, M., 1994, "Potash", Energy Mines and Resources Canada, 100 pp.
- Sand, L.B., and Mumpton, F.A., eds., 1978, *Natural Zeolites — Occurrence, Properties, Use*, Pergamon Press, 546 pp.
- Schlitt, W.J., ed., 1985, *Salt and Brines '85, Proceedings, Symposium Solution Mining of Salts and Brines*, New York, SME, 209 pp.
- Singer, A., and Galan, E., eds., *Palygorskite-Sepiolite: Occurrences, Genesis and Uses*, Developments in Sedimentology 37, Elsevier Pub. Co., 352 pp.
- Stanton, R.L., 1972, *Ore Petrology*, McGraw-Hill, New York, 713 pp.
- Towner, R.R., 1992, *International Strategic Minerals Inventory Summary Report — Zirconium*, USGS Circ. 930-L, 47 pp.
- Varley, E.R., 1952, *Vermiculite*, Inst. Geol. Sc., Her Majesty's Stationery Office, London, 70 pp.
- Varley, E.R., 1965, *Sillimanite*, Inst. Geol. Sc., Her Majesty's Stationery Office, London, 165 pp.
- Weiss, S.A., 1977, *Manganese: The Other Uses*, Metal Bulletin Books Ltd., London, 360 pp.
- White, D., 1988, "Ball clays in the United States" in *Proceedings, 24th Forum on the Geology of Industrial Minerals*, A-J.W. Zupan and A.H. Maybin, III, eds, S. Carolina Geol. Surv., pp. 145–147.
- Wilburn, D.R., 1986, *Magnesium availability — market economy countries: a minerals availability appraisal*, US Bur. Mines Inf. Circ. 9112, 24 pp.

Recycling of Industrial Wastes – an Overview about Successful Case Studies

J.M.F.Ferreira, P.J.S.Guedes, P.Torres, R.S.Manjate, H.R.Fernandes

Department of Ceramics and Glass Engineering, CICECO, University of Aveiro, 3810-193 Aveiro, Portugal

ABSTRACT: Waste management is a very important issue both from the public health perspective, and the environmental and industrial view points, because an ever-increasing amount of inert or hazardous materials need to be disposed in a safe and economical way or, preferably, reused whenever possible. In fact, the residues produced by a given industry can often be regarded as useful raw materials for the related industry and others, thus reducing the negative environmental impact associated with landfill and preserving non-renewable natural resources. The recycling needs should be also regarded as new opportunities for innovation and creativity. Making use of suitable combinations of waste materials, better physical or aesthetical properties can sometimes be obtained for the recycled products. Several successful case studies about recycling different industrial wastes mostly in traditional ceramic formulations will be presented along this contribution. They include sludge from cutting natural stones (e.g., granite sludge); glaze sludge derived from the residual water treatment plants of ceramic industries; refractory materials from the kiln furniture; and fired rejected pieces of porcelain in porcelain compositions.

1 INTRODUCTION

For industry to be sustainable, it will have to mimic nature, reusing and recycling every chemical or material that it uses in cyclical processes, rather than discarding them as waste. In fact, the residues produced by a given industry can often be regarded as useful raw materials for the related industry and others, thus reducing the negative environmental impact associated with landfill and preserving non-renewable natural resources. Waste minimisation and reuse techniques differ according to the type of industrial process involved and company conditions, but it has been possible to implement relatively simple solutions in a great number of industrial plants.

Industrial activities are responsible for the generation of significant amounts of solid wastes and by-products containing hazardous inorganic compounds that are usually accumulated elsewhere. Some of them are accumulating at an alarming rate and there is increasing public concern regarding the environment and ecology. Owing to the growing environmental concerns in recent years, deriving from the large amount and variety of solid wastes and by-products, several studies aiming at minimising wastes during the industrial processes

and at reusing the produced wastes in the same production process have been undertaken over the last decades (Boesmans et al. 1984; Tay 1994; Churchill 1994; Dondi et al. 1997). Most of these studies, carried out both at a laboratory and/or industrial scale, point out brick formulations as being the more tolerant ones for incorporating several kinds of sewage sludge, urban wastes, and a variety of other industrial inert residues. This industrial sector has in fact a great potential for consuming a large quantity of inorganic wastes since even a medium size company might process more than 500 metric tones of raw materials per day.

Recent studies (Perez et al. 1996; Ferreira et al. 1999) demonstrated the feasibility of incorporating sludge produced by the physico-chemical treatment of waste-waters generated by electroplating plants into clay-based ceramic products. From the reported results it could be concluded that the incorporation of these potentially toxic sludge (due to the appreciable amounts of mobile heavy metals) into a brick-type ceramic matrix was a good inertization method even for incorporation rates much higher than those at which sludge are produced. However, brick-type formulations are not a suitable host for all kinds of residual wastes. In fact, some compatibility between the hosting matrix and the incorporating

residue should exist if the quality of the processes and/or the final products is to be preserved. For example, both the ceramic matrix and the residue should have similar thermal behaviours in terms of shrinkage and maturing degrees in a suitable temperature range. This is not the case when Al-rich sludge derived from aluminium anodizing and surface coating processes are considered for red clay products. Therefore, other approaches (incorporation in refractory alumina- or mullite-based products) have been adopted for recycling Al-rich sludge (Olhero et al. 2002; Ribeiro et al. 2002; Tulyaganov et al. 2003). The aim was to find suitable ways for recycling the huge amounts that are annually produced, $\approx 100,000$ metric tons per year only in EU countries (Olhero et al. 2002), posing serious problems in terms of waste management.

Good recycling practices need to be adopted taking into account the specific characteristics of the wastes and of the products in which they are incorporated. When made in a creative way, the reuse of wastes (sludge, unfired scrap and fired crock) in ceramics industries enables to keep or even improve the overall properties of the final products. The aim of the present work is to report the results of some successful case studies about recycling several kinds of industrial wastes such as sludge from cutting granite stones; refractory materials from the kiln furniture; and fired rejected pieces of porcelain in porcelain compositions.

2 SUCCESSFUL CASE STUDIES

2.1 Sludge from cutting natural stones

Granite cutting industry produces large amounts of solid wastes worldwide, which are expected to increase owing to the fact that the world production of granite industry has been increasing annually at a rate of 6% in the recent years. Deposition of huge amounts of granite sludge wastes creates necrotic conditions for flora and fauna while, after drying, fine particles can be deposited in the lungs of mammals via breath.

Granite sludge (GS) kindly offered by “Incoveca” (Viseu, Portugal) was used as raw material to replace feldspar in porcelain-tile industrial formulations. The raw other materials included two clays, clay-E (E) and clay-A (A) and feldspar (F), all from (ADM, Pombal, Portugal). The chemical and mineralogical compositions are presented in Table 1 and in Figure 1, respectively. Samples of different compositions (Table 2) in the form of pellets and extruded cylindrical bars were prepared and their fired properties were evaluated according to the ISO-13006 standard, Group B-I. Sludge incorporation must not jeopardize materials’ properties at the intermediate stages of production process.

Table 1 - Chemical compositions of raw materials (wt.%).

Oxide	Clay A	Clay E	Feld (F)	(GS)
SiO ₂	64.69	64.87	72.29	71.65
Al ₂ O ₃	27.91	29.79	16.72	14.25
Fe ₂ O ₃	2.39	1.75	0.31	2.86
CaO	0.19	0.10	0.71	1.83
MgO	0.58	0.34	0.20	0.86
Na ₂ O	0.80	0.65	5.79	3.72
K ₂ O	2.43	1.70	3.22	4.43
TiO ₂	0.93	0.72	0.02	0.24
MnO	0.01	0.01	0.02	0.03
P ₂ O ₅	0.07	0.07	0.72	0.13

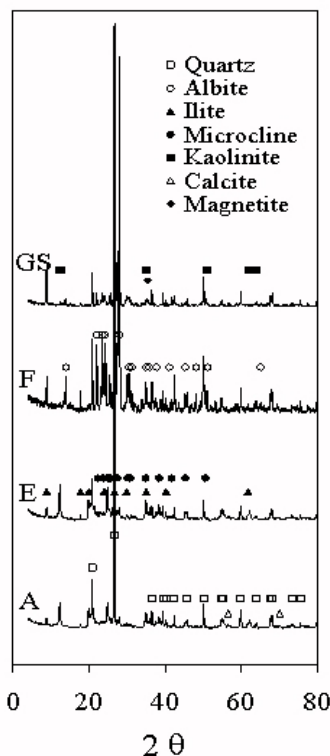


Figure 1. XRD spectra of the A, E, F, and GS (the position of the peaks of the phases are also marked [26]).

Otherwise, extended and costly modifications in the industrial production line would be necessary (e.g. size and speed of caring belts, storing and transportation facilities from one unit to another etc.).

Table 2 – Formulations tested (wt.%).

Formulation	Clay A	Clay E	Feld (F)	(GS)
1	20	30	0	50
2	25	25	0	50
3	20	25	5	50
4	15	30	5	50
5	20	0.34	30	20
6	20	30	25	25
7	20	30	20	30
8	20	30	15	35
9	20	30	10	40
10	20	30	5	45

The fired properties of the as produced samples were compared with those of a commercial porcelain tiles, Keratec® (K), made from the same raw materials, excepting GS (Figures 2 and 3).

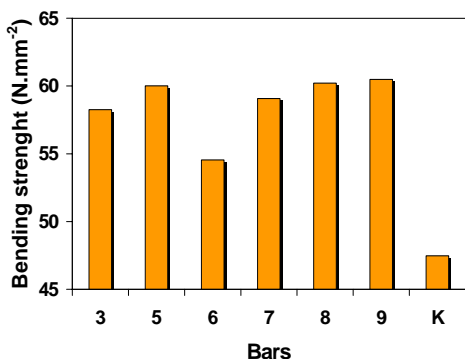


Figure 2 - Three point bending strength of sample formulations listed in Table 1 and Keratec® (K), fired at the optimal temperature of 1180°C for 1 h.

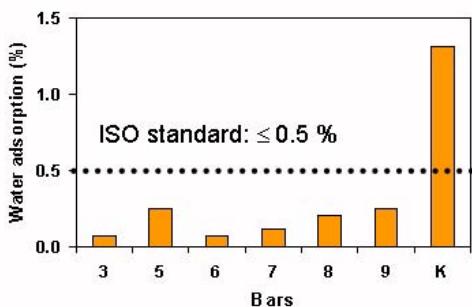


Figure 3 - Water absorption of sample formulations listed in Table 1 and Keratec® (K), fired at the optimal temperature of 1180°C for 1 h.

Figure 2 shows the mechanical strength of the most performing formulations. It can be seen that all formulations containing GS perform better than the commercial one (K). Accordingly, the water absorption values (Figure 3) for the GS containing formulations are also lower than the standard values ($\leq 0.5\%$), contrarily to the reference composition. Based on these results, a correction to the reference composition could be suggested, which enabled to achieve similar results as those exhibited by the GS containing formulations.

2.2 Refractory materials from kiln furniture

Broken kiln furniture cordierite-based refractories were reused to design stoneware products with low coefficient thermal expansion (CTE) able to outstanding thermal shocks in cooking (oven, flame) applications. Very simple formulations containing 50-wt% of cordierite (C) + 50-wt% of a ball clay, BL3 (ADM, Pombal, Portugal) were designed. Cordierite plates were first crashed in a hammer mill up to particles sizes below 1 mm and then ball milled to particle sizes below 63 μm . The milled cordierite powder was wet mixed with the ball clay to get a plastic paste containing about 25-wt.% water. Cylindrical test samples were performed in a vacuum extruder, dried (at room temperature for 24 h, followed by drying at 110°C for another 24 h period) and fired at different temperatures (1100, 1150, 1200 and 1250°C), using a heating rate of 5°C/min and holding for 1 h at the maximum temperature.

The sintered material properties evaluation was made by measuring the water absorption, the firing shrinkage, the flexural strength and the CTE. The results presented in Table 3 show that excellent properties in terms of water absorption and flexural strength were obtained after firing at the highest temperature. The CTE (50-500°C) of the new designed product was compared with that of an industrial stoneware formulation produced by Cerutil, Viseu, Portugal ($\text{CTE} = 9.3 \cdot 10^{-6} \text{ } ^\circ\text{C}^{-1}$). A semi-industrial test was also carried out at this factory using the new designed composition.

Table 3 – Fired properties of the new stoneware products

Temp./Prop.	1100°C	1150°C	1200°C	1250°C
Water abs. (%)	13.9	10.3	2.7	0.05
Shrinkage (%)	4.6	6.5	9.8	12.2
Bend. Strength (MPa)	36	47	52	87
CTE ($10^{-6}\text{ } ^\circ\text{C}^{-1}$) (50-500°C)	-	-	-	8.8

The difference in the CTE means that the new recycled material has a higher thermal shock resistance, while resulted in a very fine *crackle* effect in the glazed pieces. Therefore, an alternative approach was followed to get a CET similar to that of the industrial composition by adding 7.5-wt% of glaze sludge (GZS) to the 50C:50BL3 composition. Figure 4 shows that besides correcting the CET, the addition of GZS also enable the lowering of the sintering temperatures from 1250°C to 1150°C, while keeping similar values for the remaining fired properties.

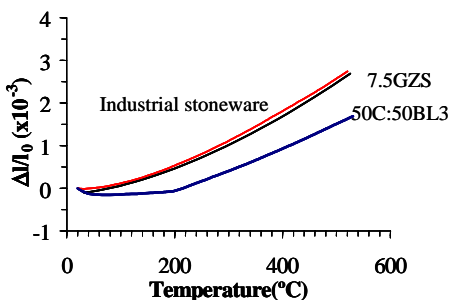


Figure 4 - Effect of composition on the CTE of fired products.

2.3 Recycling fired rejected pieces of porcelain in porcelain compositions

An industrial porcelain (VA, Portugal) was used alone as a reference composition, and mixed with unglazed and glazed fired rejected pieces of porcelain. The solids concentration of the *as-received* slip was about 44-45-vol%. The fired rejects were first crashed and then ball milled for 12 h, at a laboratory scale. Several incorporation levels (from 0-100-wt%) were first attempted by adding unglazed milled rejected pieces (MRP) and suitable amounts of water and dispersant. Adding 50-wt% MRP enabled to increase the solids loading to 60-vol%.

Cylindrical rod-like pieces (8*120 mm) were consolidated by slip casting for pyroplasticity tests. The results revealed that incorporation of wastes in ceramic formulations might enable maturation of the products at lower temperatures even with the unglazed MRP. After correcting the compositions for the pyroplastic index, hollowware pieces incorporating up to 45-wt% glazed MRP could be produced by slip casting and fired under the same conditions as the original virgin composition (1360°C). This enables significant energetic savings (>30%) on spray drying, while the fired properties could not be distinguished from those of the reference composition (Ferreira et al. 2000).

3 CONCLUSIONS

Successful recycling industrial wastes can be made aiming at several goals: lower production costs; Preserve natural resources; save energy; clean the environment and reduce land fill; maximise waste incorporation; no changes in intermediate processing steps; keep, or even improve the final product properties; develop new products, with new functionalities; etc.. This requires creative and innovative approaches in order to achieve simple solutions.

4 REFERENCES

- Boesmans, B., Colon, F. J. and Van der Velden J. H. 1984 Bricks manufactured from clay and municipal refuse, *Interceram*, Nr.3, 27-30.
- Churchill, M. 1994. Aspects of sewage sludge utilization and its impact on brickmaking, *Global Ceram. Rev.*, 1, 18.
- Dondi, M., Marsigli, M. and Fabbri, B. 1997 Recycling of Industrial and Urban Wastes in Brick Production – A Review (Part 2), *Tile & Brick Int.* Volume 13, N°. 4, 302-308.
- Ferreira, J. M. F., H. M. Alves and Mendonça, A. M. 1999. Inertization of Galvanic Sludge by its Incorporation in Ceramic Products, *Bol. Soc. Española de Cerámica y Vidrio*, 38 [2]:127-131.
- Ferreira, J.M.F., & Lemos, I. A. F. 2000 Método de Reciclagem de Caco de Porcelana. Patente Portuguesa N° 102546 de 22/12/2000.
- Olhero, S. M. & Ferreira J. M. F. 2002. Al-rich Sludge Treatments Towards Recycling, *J. Europ. Ceram. Soc.*, 22 (13) 2243-49.
- Perez, J. A., Terradas, R., Manent, M. R., Seijas, M. and Martinez S. 1996. Inertization of industrial wastes in ceramic materials. *Industrial Ceramics*, 16, 7.
- Ribeiro, M. J., Tulyaganov, D. U., Ferreira, J. M. F. and Labrincha, J. A. 2002. Recycling of Al-rich Industrial Sludge in Refractory Ceramics Pressed Bodies. *Ceramics International*, 28 (3) 319-326.
- Tay, J.H. 1987. Bricks manufacture from sludge”, *J. Envir. Eng.*, 113, 278.
- Tulyaganov, D. U., Olhero, S., Ribeiro, M. J., Labrincha, J. A. and Ferreira, J. M. F. 2003. Mullite-Alumina Refractory Ceramics Obtained from Mixtures of Natural Common Materials and Recycled Al-rich Anodizing Sludge. *Journal of Materials Synthesis and Processing*, 10 (6): 313-318.

Automation, Integration, and Interpretation – the Future for Process Mineralogy and Practising Mineralogists

A.R.Butcher

Intellection Pty Ltd. Milton, Brisbane, Queensland, 4064, Australia

Process mineralogy is still a relatively new area of endeavour and continues to be under utilised and under valued in the earth resources industries. This situation is starting to change with the gradual adoption of automated technologies which can now take away operator subjectivity and boredom, and replace it with greater statistical reliability, versatility and higher productivity.

Given this new era of mineralogical data collection, it is important, more than ever before, that the information gained be integrated and interpreted appropriately so that the disciplines of geology, mining, mineral processing, and waste management all benefit.

This paper will illustrate some of the many benefits returned to industry using these new automated technologies. The key to success, now and into the future, lies in technology integration within a culture of cross-discipline collaboration.

Overview of the Brazilian Gemstone Industry

E.P.Salomão
GEOS Ltd.

E.Reis
Minex Ltd.

W.K.Daoud
Geogemas Ltd.

ABSTRACT: This presentation includes a general overview of the Brazilian precious stone industry and its participation in the productive chain of the jewelry sector. Brazilian gems are part of our historical heritage since their discovery by the Portuguese in 1500. In the following century, precisely in 1674, Fernão Dias Paes Leme makes an incursion to the interior searching for emeralds at the request of the king of Portugal. Fernão dies in 1681, clutching green stones he thought were emeralds but were in fact tourmalines. The discovery of diamonds in Minas Gerais in 1732, and the Portuguese Crown's control of its production establish the beginning of the standard production of Brazilian precious stones.

Along the following centuries, several new gemstone provinces were discovered, especially for colored stones, establishing Brazil as one of the leading gemstones producers in the world. Nevertheless, the majority of the production is informal and comes from artisanal mining sites (garimpos), where the small scale production and environmental issues are not satisfactorily addressed. Emerald, aqua marine, amethyst, topaz, alexandrite and tourmaline are the main gems produced in Brazil in addition to diamonds.

Two of them are exclusively produced in Brazil: "The Imperial Topaz", that is found in the proximity of Ouro Preto; and the famous Paraíba Tourmaline, described as "neon" or "electric" due to its magical bright colors. These tourmalines are found only in a specific site in the municipality of São Miguel da Batalha, in the State of Paraíba. The deposit seems to be exhausted, causing the stone's market prices to increase absurdly due to its rarity and beauty.

Although Brazilian geology is favorable for the occurrence of rubies and sapphires, these noble gems have not been found in Brazil yet. The main reason could be the fact that our prospectors ("garimpeiros") are not familiar with these gems and its mineralization. The same happened to emeralds: only after their first discovery in the province of Paraíba, Bahia in 1963, the garimpeiros were able to learn about the occurrence and characteristics of these gems, which led to the discovery of emeralds in various parts of Brazil. There are references to non-gem quality rubies and sapphires in Bahia and Mato Grosso do Sul. Due to the lack of formal exploration in Brazil, our future discoveries of colored stones will rely on the garimpo activity and the determination of the garimpeiros in searching for new occurrences.



Figure 1. Main gemstones production areas.

Diamonds in Brazil have a special chapter all of their own. At present, Brazil produces about 1 million carats/year, almost entirely from secondary sources (alluvium, terraces and conglomerates). The mining giants such as De Beers and Rio Tinto, in addition to others, have invested around US\$1B over the last 40 years, exploring primary sources of diamonds in all latitudes of Brazil. Although thousands of kimberlites have been found, there is no primary diamond mines in the country, all production comes from the garimpos. Accordingly, one can verify that although diamonds are present in almost all of the country, the exploratory methods that has been applied to find the primary sources, all supported by the classic chemistry, geology and mineralogy for kimberlites, did not succeed. Therefore, it is speculated that eventually our fertile kimberlites will not follow the general rule, leaving to the geologists and mineralogists the task of identifying the missing point that will lead us to the discovery of primary mineralization. Recently, a new cluster of kimberlites has been found in the region of Cacoal/Pimenta Bueno, in the State of Rondônia, right in the middle of serious conflicts between garimpeiros and Indians. The present production of this place is estimated in 20.000 carats/month and the diamonds are reported to be of excellent quality. This new province could become of great importance in the near future.

The great informality of mineral production is reflected in the Brazilian commercial balance. Although Brazil is one of the top suppliers in the

world market, the official numbers are extremely modest, as shown in the table below. The exportation of raw and cut stones were of only around US\$ 100 Million in 2003, while the real commercialization value is estimated in at least three times more.

Table.1. Brazilian gemstone export (in US\$1,000,00).

	2000	2001	2002	2003
Rough gemstones	36.440	34.494	44.655	47.629
Cut&polished gemstones	71.373	62.650	74.157	55.697
Total	107.813	97.144	118.812	103.326

Source: IBGM, 2004

The Brazilian Institute of Gems and Precious Metals - IBGM projects a substantial increase in the formal commerce if a number of demands of the sector are implemented by the Government. Historically, the high taxation of gems and jewels in Brazil has prevented its formalization. Given that the market prices are international, there is no chance of competitiveness for Brazilian gems if they are marked by the high taxes practiced in the country.

The depletion of our superficial colored stone reserves is accentuated. In the last decade, the market has been progressively unsupplied due to the decrease of traditional mining work, environmental restrictions, and lack of new significant discoveries. Although there are isolated actions of incentives to

the sector, there is great incoherency among mineral production, which is still artisanal and low-tech, and the down stream segment of the productive chain, the jewelry. In fact, the national jewelry sector achieved a lot of significant improvements in the last years. There were improvements in taxation, international insertion through the intensive participation in international fairs and a spectacular performance in the Brazilian design, which holds today a position of great distinction in the international scenery. A large part of the merit of this performance is credited to IBGM, the Brazilian Institute of Gems and Precious Metals that organized the jewelry industry with realistic goals and carried out a competent political job. On the other hand, production and commerce of raw stones is Informal, disorganized, inefficient and unassisted, being far from reaching the achievements verified in the rest of the productive chain.

Brazilian stones are mostly exported in their raw state to be lapidated in other countries where the labor force cost is more accessible. Lapidating technology is available in the country but social taxes make the cost almost prohibitive and take away the stone's competitive value. This is not the case for the large and valuable special gem, for which there will be special procedures of cutting and polishing, but about the medium quality stones that makes the large consumer market. The industry that produces the prêt-à-porter jewel is interested in calibrated stones, cut in standard format and size, ready to be set in a pre-fabricated piece. Unfortunately, the erroneous concept of the maximum utilization of each piece still prevails in the country, which means that each stone is lapidated in a way to preserve the maximum of its weight. For a better understanding of the meaning of this concept, imagine a footwear industry producing shoes in various sizes and shapes for a better utilization of the leather. Therefore, there is a great challenge to add value to our gems, which will only be achieved by specific public policies for the sector. Adequate taxation, larger integration of the productive chain, training of technical people, incorporation of technology and regular exploration to find new deposits are some of the issues that should be part of a policy aiming to increase and add value to the Brazilian gem production.

Advanced Materials

Aluminosilicate Nanocomposite Material

J.L.Capitaneo & F.T. da Silva

Department of Metallurgical and Engineering Materials, COPPE, Federal University of Rio de Janeiro, Rio de Janeiro, Brazil

V.R.Caffarena

Centro Brasileiro de Pesquisas Físicas (CBPF), CMF, Rio de Janeiro, Brazil

ABSTRACT: Natural clay from Silva Jardim (Silva Jardim clay), Rio de Janeiro - Brazil, was used in the present study. Samples of this clay were studied in different conditions to be used as filler in a nanocomposite material. Manufactures fill polymers with particles in order to improve the stiffness and toughness of the materials, to enhance their barrier properties, to enhance their resistance to fire and ignition or simply to reduce cost. Nanocomposites are a new class of composites with special properties and they can be obtained from layered aluminosilicate, such as kaolinite, $\text{Al}_2\text{Si}_2\text{O}_5(\text{OH})_4$, is a dioctahedral layered hydrated aluminosilicate of the 1:1 type with two distinct interlayer surfaces. The organofunctionalization of this clay mineral can be made after the intercalation of small polar molecules, which widens the interlayer distance. In this work, kaolinite intercalation with dimethyl sulfoxide (DMSO) into the interlamellar spaces of this clay mineral was studied. The new composite was characterized by X-ray fluorescence (XRF), X-ray diffraction (XRD), thermal analysis (TG/DTA) and Fourier transform infrared (FTIR) spectroscopy.

1 INTRODUCTION

Nanocomposites are a new class of composites, that are particle-filled polymers for which at least one dimension of the particles is in the nanometric range. Amongst all the potential nanocomposite precursor, those based on clay and layered silicates have been more widely investigated probably because the starting clay materials are easily available and because their intercalation chemistry has been studied for long time (Alexandre & Dubois 2000).

Regardless of the extensive use of the clay mineral kaolinite in industrial processes, there is little information about its use in nanocomposites.

The ability to modify clay minerals by insertion of an inorganic and/or organic guest species into the interlamellar region opens up a range of potential uses for these materials. The smectite group of minerals possesses exchangeable cations within their interlayers that facilitate the encapsulation of polar organic molecules.

Kaolinite is devoid of this property as there are no exchangeable cations within its layers. However, the kaolinite interlayer region can react with a small group of organic and/or inorganic materials, a process called intercalation (Ray & Okamoto 2003).

Kaolinite $\text{Al}_2\text{Si}_2\text{O}_5(\text{OH})_4$, is a dioctahedral layered hydrated aluminosilicate of the 1:1 type with two distinct interlayer surfaces (gibbsite and silica-like structures). Van der Waals bonds between the aluminol and Si-O groups link adjacent lamella to each other, and frequently make the intercalation processes difficult (Komarneni 1992)

Molecular compounds cannot be intercalate directly in kaolinite, because it needs first opening the clay sheets (displacement reaction). This process, generally, implies the prior intercalation of precursors such as dimethyl sulfoxide (DMSO) (Michalková et al. 2002).

In this work, the process to obtain expanded kaolinite-DMSO is reported. This composite can be used to obtain others by displacing DMSO. Moreover, there was used natural clay from Silva Jardim – RJ, which was previously treated to remove impurities and separate the clay fraction.

2 MATERIALS AND METHODS

2.1 Treatment of natural clay

To obtain the “treated” samples, the natural clay from Silva Jardim was firstly desegregated using a mortar and pestle, weighed (about 20 g), and

dispersed in a dilute ammonium hydroxide solution (5.0 ml NH₄OH and 200 ml of water) during 24 hours. Then, the dispersion were decanted and the suspension, separated. This procedure was repeated until a relative large quantity of aqueous solution containing clay fraction was obtained.

Afterward the water was removed by drying at 70°C during 24 hours. Then, a clay-water solution (60 mg of clay in 1 cm³ of distilled water) was made. A sample with about 3-ml of this solution was dried at 100°C.

The impurities were removed chemically: Fe oxides by using citrate-bicarbonate-dithionite (CBD) method; organic matter by using strong oxidant agent (hydrogen peroxide) and carbonates by using buffer solution of acetic acid/acetate.

After this, the clay fraction (< 2 μm) was separated and characterized. Capitaneo et al. (2004) studied this method to separate nanometric particles using NH₄OH and ethylene glycol and identify the clay minerals presented. The analyzed clay fractions from Rio de Janeiro have kaolinite as the majority clay mineral in its compositions.

2.2 Nanocomposite preparation

The kaolinite clay fraction employed in this work was separate from Silva Jardim natural clay and no crystalline impurities were detected by XRD.

Approximately 1 g of this clay fraction was transferred to a 250-ml round-bottom flask and suspended in 100 ml of DMSO (Aldrich PA) solution (95% v/v DMSO:water). The suspension was stirred at 60°C for 192 hours and then centrifuged at 4000 rpm to recover the solids. The resultant material was dried at 40°C for 120 hours to remove the residual DMSO and characterized.

2.3 Characterization

X-ray fluorescence (XRF) measurements were carried out in a model PW 2400, Philips spectrometer.

For the powder X-ray (XRD) analysis, the solid materials were placed on a glass sample holder and spread out to form a thin layer. A Miniflex diffractometer using Cu-Kα radiation with a dwell time of 1°/min, in the θ-2θ Bragg-Brentano geometry was employed (2-90°).

Both thermogravimetry (TG) and differential thermal (DTA) measurements were carried out using a Shimadzu 50 H equipment. The experiments were performed in static air, using platinum crucibles from 20 to 1000°C with a heating rate of 10°Cmin⁻¹.

Fourier transform infrared (FTIR) spectroscopy was carried out using a NICOLET MAGNA-IR 760 spectrometer. The KBr discs were prepared after mixing each of test samples with dry KBr. Analyses were performed in the transmission mode in the 400-

4000 cm⁻¹ range, with a resolution of 4 cm⁻¹ and accumulation of 32 scans.

3 RESULTS AND DISCUSSION

The chemical composition of natural clay and clay fraction was obtained by XRF. It was observed that % SiO₂ decreased and % Al₂O₃ (and loss of ignition) increased, indicating quartz removal (Table 1). The impurities were also removed.

Table 1- Chemical composition of the natural clays and clay fractions (mass %) obtained by XRF:

Determinations (mass %)	SILVA JARDIM	
	Natural clay	"treated"
SiO ₂	49.45	42.234
Al ₂ O ₃	31.31	37.492
Fe ₂ O ₃	1.44	0.120
TiO ₂	1.68	0.725
K ₂ O	3.26	0.648
Na ₂ O	0.34	-
CaO	0.29	-
MgO	0.39	-
Loss of ignition	11.44	16.94

When kaolinite was reacted with DMSO a expanded kaolinite-DMSO complex was obtained with an intercalation ration of about 88%. The extent of the modification process was determined from X-ray diffractograms given in Figure 1 and 2.

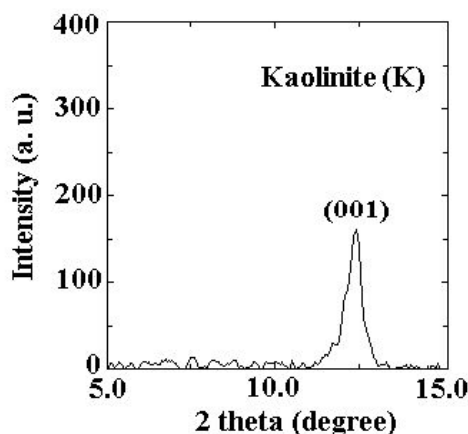


Figure 1: Powder X-ray diffractogram of pure kaolinite.

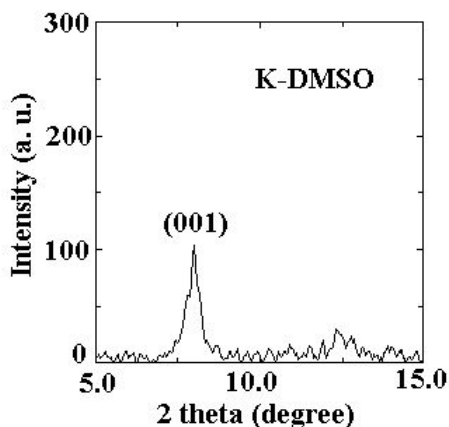


Figure 2: Powder X-ray diffractogram of K(DMSO) complex.

Table 2 summarizes the data obtained by X-ray diffractometry. Basal interplanar spacings were obtained in relation to the basal reflection of the highest order.

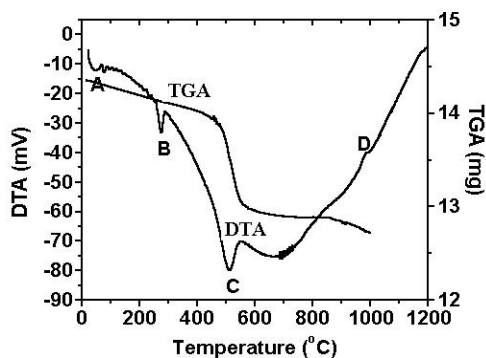
Table 2: Identification of the phases, basal distances and interlayer expansion ($\Delta d = d_{001}$ (of the substituted phase) - d_{001} (of kaolinite) (Å))

Phase	d_{001} (Å)	Δd (Å)
K	7.12	0
K-DMSO	11.03	3.91

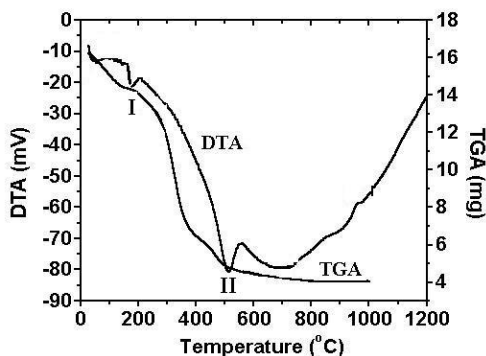
The basal space of this modified material was 11.10 Å, which represents an expansion of 3.91 Å, related to the basal space of the raw kaolinite (7.12 Å).

TG/DTA curves for Silva Jardim clay fraction (K) are shown in Figure 3-a. The initial curves mass loss (endothermic valley), in the DTA curve, is associated with elimination of adsorbed/absorbed water molecules (point A). The second endothermic valley (point B), at about 270°C, is associated with decomposition of gibbsite, $\text{Al}(\text{OH})_3$ and goethite, $\alpha\text{-FeOOH}$. The third endothermic valley (point C), at about 508°C, is related to the dehydroxylation of kaolinite. The last exothermic peak (point D) at about 980°C is related to metakaolinite transformation to mullite.

The K-DMSO phase (Figure 3b) also presents endothermic peaks, once centered at 176°C (peak I), which can be attributed to DMSO elimination, and the other centered at 510°C (peak II) that corresponds to the kaolinite dehydroxylation process.



(a)



(b)

Figure 3: TG/DTA measurements of K (a) and K-DMSO (b) phases, during heating in air with 10°C/min:

Kaolinite is characterized by signature O-H stretching pattern (bands at 3694, 3669, 3653 and 3621 cm^{-1}) in the FTIR study (Table 3).

The band at 3621 cm^{-1} has been unambiguously assigned to the stretching frequency of the internal hydroxyl group of kaolinite and it is not usually influenced very much influenced by interlamellar modifications. This band is also observed for K-DMSO complex.

K-DMSO shows bands at 1428, 1410, 1395, 1320, 3662, 3538 and 3503 cm^{-1} .

The two most intense vibrations of kaolinite at 1033 and 1008 cm^{-1} are often shifted slightly upon intercalation of guest species such as DMSO, where these bands are shifted to 1038 and 1112 cm^{-1} .

Table 3: Peaks observed for the clay fraction and the respective interpretations.

Wavenumbers (cm ⁻¹)	Assignments
3694	O-H
3669	O-H
3653	O-H
3621	O-H
1635	H ₂ O
1107	Si-O-Si
1033	Si-O
1008	Si-O
912	O-H surface
790	Si-O-Si
754	Si-O-Si
697	Si-O-Si
532	Al-Si-O
472	Si-O
431	Si-O

Upon intercalation of DMSO, the band at 912 cm⁻¹ decreases greatly in intensity and another band of 10 cm⁻¹ lower frequency appears at 902 cm⁻¹, presumably due to a repulsive interaction between one of the methyl groups of DMSO, which is proposed to be keyed into the (SiO-) macroring of the silicate surface and the internal hydroxyl of kaolinite (Gardolinski 2001).

4 CONCLUSIONS

The kaolinite sample employed came from Silva Jardim (Rio de Janeiro) and the clay fraction (< 2 μm) was obtained by chemical treatment with impurities removing. After this, it was used to prepare nanomaterials.

To obtain new nanocomposites by using intercalation reaction within the kaolinite matrix, is necessary the preexpansion of the lamellar structure of kaolinite with DMSO. This process was available in this work.

The results reported here confirm that the direct intercalation of DMSO molecules into the interlayer space of kaolinite is possible and that the obtained

kaolinite-DMSO complex (K-DMSO) allows an expansion of 3.91 Å in the interplanar distance.

Due to the low temperature of DMSO elimination (176°C), which was determined by thermal analysis (TG/DTA), it is possible to assume that the process involves integral elimination of the molecule instead of combustion. This fact is corroborated by the absence of exothermic peak attributed to DMSO combustion.

5 ACKNOWLEDGEMENTS

The authors gratefully acknowledge the financial support and other forms of aid provided by CNPq, FAPERJ, PEMM/COPPE/UFRJ, NUCAT/PEQ/UFRJ, CBPF, Instituto de Química/UFRJ and Instituto de Geociências/UFRJ (all Brazilian institutions), which were crucial for the success of this research.

6 REFERENCES

- Alexandre, M.; Dubois, P. 2000. Polymer-layered nanocomposites: preparation, properties and uses of a new class of materials. *Materials Science and Engineering*, v. 28: 1-63.
- Ray, S. S., Okamoto, M. 2003. Polymer/layered silicate nanocomposites: a review from preparation to process. *Progress in Polymer Science*, v. 28, n. 11: 1-103.
- Komarneni, S. 1992. Nanocomposites, *Journal of Materials Chemistry*, v. 2, n. 12: 1219-1230.
- Michalková, A., Tunega, D., Nagy, L. T. 2002. Theoretical study of interactions of dickite and kaolinite with small organic molecules. *Journal of Molecular Structure (Theochem)*, v. 581: 37-49.
- Capitaneo, J. L., Silva, F. T., Vieira, C. M. F., Monteiro, S. N., Caffarena, V. R. 2004. Method to separate nanometric particles of Clays. *Journal of Metastable and Nanocrystalline Materials*, in press.
- Gardolinski, J. E. F. C. 2001. *Compostos de intercalação derivados da caulinita*, Tese de M. Sc. Universidade Federal do Paraná, Curitiba - PR, Brasil.

Synthesis of (Co-Zn)-Z- Type Barium Hexaferrite for Use as Microwave Absorber

V.R.Caffarena

Centro Brasileiro de Pesquisas Físicas (CBPF), CMF, Rio de Janeiro, Brazil

T.Ogasawara & J.L.Capitaneo

Department of Metallurgical and Engineering Materials, COPPE, University of Rio de Janeiro, Rio de Janeiro, Brazil

M.S.Pinho

Brazilian Navy Research Institute (IPqM), Rio de Janeiro, Brazil

ABSTRACT: Z-type hexaferrite may be used in multi-layer chip inductors (MLCI), which are fabricated by interleaving ferrite layers with internal conductors such as silver, and then co-firing the stack to form a monolithic structure. The development of lower sintering temperature Z-type modified hexaferrite will enable the ceramics to be co-fired with less expensive material in production of MLCI. To solve this problem and obtain this Z-type phase at lower temperature, the citrate precursor method was used to obtain nano-sized powders of Co-Zn doped Z-type barium hexaferrite ($\text{Ba}_3\text{Co}_{1,6}\text{Zn}_{0,4}\text{Fe}_{24}\text{O}_{41}$). Moreover, this material can be used both in civil and military applications to suppress microwaves reflected from metal structures and to reduce the radar signatures by using RAM (radar absorbing material). The complex permittivity and complex permeability of hexaferrite-polychloroprene composites were measured by transmission/reflection method in the range from 2.6 GHz - 4 GHz and 8.0 GHz - 16.0 GHz. X-ray diffraction (XRD), X-ray fluorescence (XRF), TGA and DTA and scanning electron microscopy (SEM) were used to characterize the material. Magnetic properties of Z-type hexaferrite and microwave absorption properties of hexaferrite-polychloroprene composites were evaluated by using vibrating sample magnetometer and a waveguide measurement set-up, respectively.

1 INTRODUCTION

Interest in materials that absorb radio frequency energy has existed for many years. In the digital age all the radio frequency spectrum is utilized, from the quasi-microwave band (1-3 GHz) for wireless telecommunication up to the mm waves in the 70-100 GHz range.

The problem of the interference between various sources, prevention of reflections and multiple reflections, and numerous other applications require efficient, inexpensive and lightweight absorbers of electromagnetic radiation.

Ferrites and composites are well suited for this application, as μ (permeability) and ϵ (permittivity) can be modified independently.

Z-type hexagonal ferrites ($\text{Ba}_3\text{Me}_2\text{Fe}_{24}\text{O}_{41}$, where Me is a divalent ion) are promising materials for these applications, possessing high permeability, frequency of resonance in the band of GHz and high thermal stability, being able to be used in inductors and in UHF communication (Hankiewicz et al. 1991, Zhang et al. 2002).

However, formation of Z-type barium hexaferrite only occurs at high temperatures (1300 °C) when using conventional ceramic method, because of complex crystalline structure of the ferrite. Several

other synthesis methods have been developed to overcome the disadvantages of powder mixing method: coprecipitation, sol-gel, citrate method and hydro-thermal synthesis.

In an attempt either to promote the formation of Z-type ferrite at a lower temperature or to improve the magnetic properties, Co-Zn substituted Z-type hexaferrites synthesized by a sol-gel-citrate precursor method were investigated. The influences of the substitution of Co with Zn on magnetic properties and on reflectivity curves have been reported in this paper.

2 MATERIALS AND METHODS

In the citrate precursor method, the cations stoichiometric content present in the aqueous solution reacts with the polyfunctional organic acid, citric acid, under controlled pH conditions to give an organometallic precursor complex. The citrate precursor decomposes at temperatures lower than 500 °C allowing barium hexaferrite to be formed at lower temperature than that of power mixing method, thereby providing an useful way for producing nanophase systems (Caffarena 2004).

Ultrafine $(\text{Zn-Co})_2\text{Z}$ powders were synthesized

by using this method and reagent grade $\text{Fe}(\text{NO}_3)_3 \cdot 9\text{H}_2\text{O}$, $\text{Ba}(\text{NO}_3)_2$, monohydrate citric acid and $\text{Co}(\text{NO}_3)_2 \cdot 6\text{H}_2\text{O}$ and $\text{Zn}(\text{NO}_3)_2 \cdot 6\text{H}_2\text{O}$, in stoichiometric molar ratios to achieve $\text{Ba}_3\text{Co}_{1.6}\text{Zn}_{0.4}\text{Fe}_{24}\text{O}_{41}$ ferrite. The preparation of the solutions was carried out weighing solids and placing then into adequate vessels. Distilled water was added to each one, under agitation until total dissolution of solids.

Then, solutions have been transferred to a balloon and mixed therein. The resulting mixture was heated up to 80°C to have completed the reaction, under reflux in order to make possible future additions of NH_4OH . Ammonia solution was added drop by drop into solution to make it neutral or slightly alkaline (pH 7 – 8) for subsequent precipitation of organo-metallic complex.

Each of several key-metal cations reacted with citric acid, under controlled pH conditions, to give the respective metal citrate, making up a homogeneous joint metallic citrate precursor complex.

Ethanol was then added under vigorous stirring, into reacting mixture to promote the precipitation of a complex citrate gel of barium, iron, zinc and cobalt. After that the remaining aqueous solution was removed by drying at 70°C , thereby leaving the desired solid phase (a highly viscous residue). All the synthesis process was carried out in inert atmosphere (N_2).

Determination of an ideal temperature for the citrate gel decomposition, as well as all the behavior of the complex under heating was carried out by using thermogravimetric analysis (TGA) and differential thermal analysis (DTA). Based on results from this thermal analysis, the gel was submitted to calcination inside muffle furnace with temperature variation from 600 to 1200°C .

The calcination was performed in the following heating schedule: $2^\circ\text{C}/\text{minute}$ up to 400°C , a 400°C plateau during 1 hour, $10^\circ\text{C}/\text{minute}$ up to the final calcination temperature with a residence time at the calcination temperature of 4 hours. Then, it was cooled down at $10^\circ\text{C}/\text{minute}$ to room temperature.

The calcined product was subjected to X-ray diffraction in order to assure the formation of the crystalline and magnetic phase of barium hexaferrite. Evaluation of the microstructure was performed by using TEM, while vibrating sample magnetometry allowed determination of magnetic hysteresis loop.

Figure 1 shows schematically the experimental procedure employed.

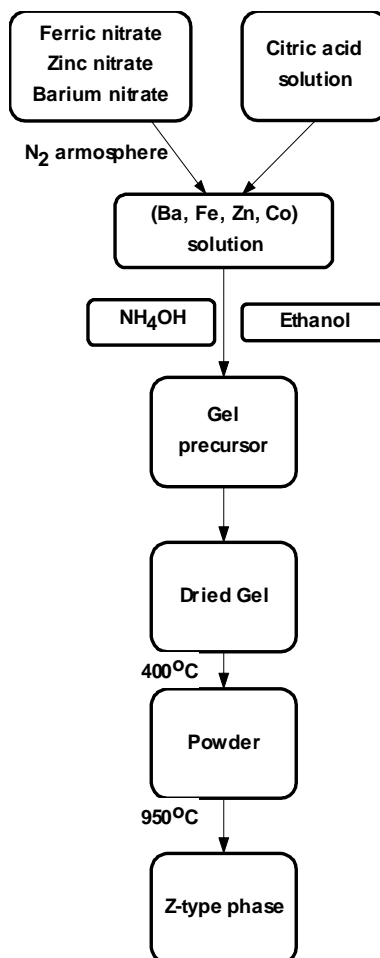


Figure 1: Schematic diagram of the preparation by citrate precursor method.

Thermogravimetry (TG) and differential thermal (DTA) measurements were carried out using TA Instruments SDT-2960. The experiments were carried out in static air, using platinum crucibles between 20 and 1000°C with a heating rate of $10^\circ\text{C}/\text{min}^{-1}$.

X-ray fluorescence (XRF) measurements were carried out on a Philips model PW 2400 sequential spectrometer. This quantitative method was used to determine the stoichiometry of ferrite samples obtained, which were analyzed in form of a fused bead using lithium tetraborate flux.

For the powder X-ray diffraction (XRD) analysis, the solid materials were placed on a glass sample holder and spread out to form a thin layer. A Siemens AXS D5005 diffractometer using $\text{Co-K}\alpha$ radiation with a dwell time of $1^\circ/\text{min}$, in the θ - 2θ

Bragg-Brentano geometry was employed. Silicon powder was used as the internal standard.

The morphological study was performed using JEOL 2000 FX transmission electron microscope and ZEISS scanning electron microscope model DSM 940 A, operated at accelerating voltages of 20 kV, 24 kV and 25 kV. The magnetic hysteresis loop was obtained using VSM PAR model 4500.

In order to obtain the composites for the measurement of the microwave absorber properties, the powder was mixed with polychloroprene rubber (CR), in a 80:20 w/w (ferrite:CR) concentration. The processing was carried out in a Berstorff two roll mill, at room temperature, with velocities of 22 and 25 rpm (back and forward). Vulcanized samples with 4.00 x 4.00 x 0.15 cm were obtained by compression molding in a hydraulic press at 150 °C and 6.7 MPa. The vulcanisation times were determined by the data obtained in the Monsanto Rheometer TM100.

The microwave measurements conducted in this work were based on the transmission/reflection method using a rectangular waveguide as the confining medium for the samples. Using the data obtained from each of the samples measured, an expected prediction of the microwave reflectivity levels for sheet absorbers was made. The materials were analyzed for the frequency range from 2.6 to 4 GHz (S-band) and 8.0 to 16.0 GHz (X/Ku- bands).

3 RESULTS AND DISCUSSION

Results from X-ray fluorescence analysis confirmed that the synthesized powders achieved the planned stoichiometry. In turn, Figure 3 shows TGA and DTA curves of the gel.

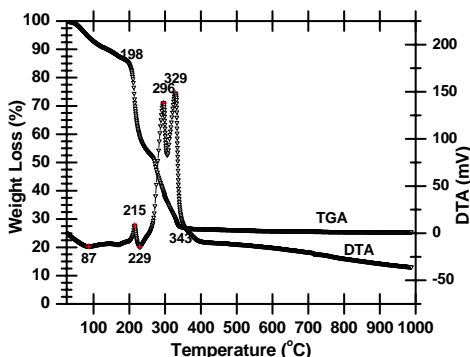


Figure 2: DTA and TGA curves for the metal citrate precursor behavior during heating, in air with heating rate of 10 °C/min.

Above 400 °C, there was no significant weight loss indicating that organic material was completely eliminated likewise the previous finding of Wang et

al. (2002). From this information, decision was taken to carry out gel calcination above 400°C; the crystalline nature of the powders was confirmed by XRD.

Z-type hexaferrite seemed not to be formed directly from simple oxides, but gradually transitioned from simple oxides or spinels to M and Y phases, finally to Z-type hexaferrite.

At 900 °C, Z-type hexaferrite had become the predominant phase; and at 950 °C, this Z-type phase was clearly the majority phase. However, according to Pullar et al. (1998), this material contains small undetectable amounts of Y-type phase ($Ba_2Co_2Fe_{12}O_{22}$) coexisting with the Z-type phase.

TEM was used to characterize powders obtained at 950 °C. It is observed that the particles are more or less uniform in size and this shape is sharply hexagonal plates with nanometric size.

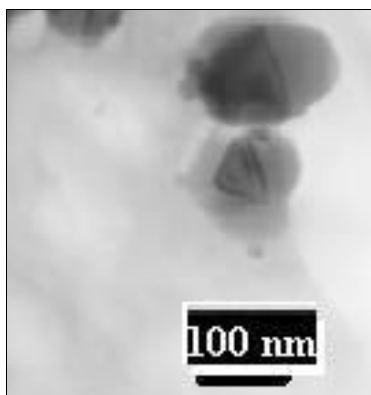


Figure 3: TEM micrograph of $Ba_3Co_{1.6}Zn_{0.4}Fe_{24}O_{41}$ powder.

The magnetization curves (Figure 4) of this material were determined by using the vibrating sample magnetometer and show typical features of magnetically soft ferrites.

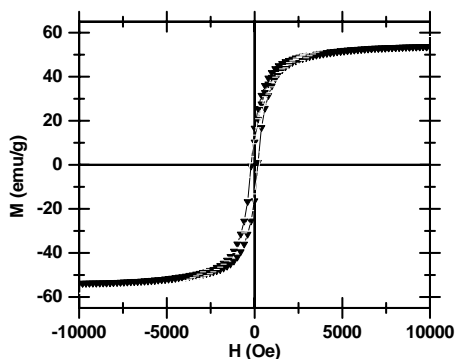


Figure 4: Magnetic hysteresis curve of Zn substituted Z-type hexaferrite calcined at 950°C/4h.

For (Zn-Co)Z-type hexaferrite ($\text{Ba}_3\text{Co}_{1.6}\text{Zn}_{0.4}\text{Fe}_{24}\text{O}_{41}$), saturation magnetization is about 54 emu/g and coercive force is 150 Oe, due to Zn^{2+} doping. This fact can be explained by the following: when Zn^{2+} ions enter the lattice interstitially, Fe-Fe strong interactions that dominate in saturation magnetization are partially replaced by Zn-Fe antiferromagnetic interactions. Fe-Fe interactions are in isotropic arrangement and Zn-Fe interactions counteract some of these and consequently, the anisotropy and magnetization of the ferrites increase.

The results obtained from the reflectivity measurements (Reflection/Transmission Method) are illustrated in Figures 5 and 6, for different thicknesses of composites.

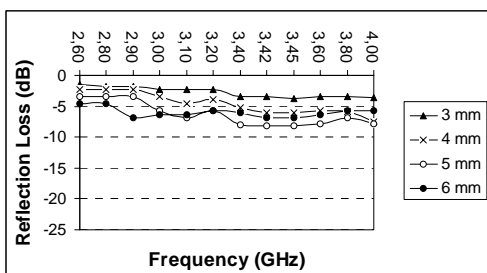


Figure 5: Reflection Loss (dB) as a function of frequency (GHz) in S-band (2.6 – 4.0 GHz).

This material shows good microwave absorption at X/Ku bands (8.0-16.0 GHz) for all thickness, as illustrated in Figure 6 by reduction of the reflection loss value (dB).

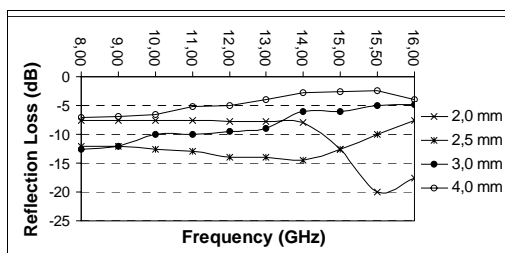


Figure 6: Reflection Loss (dB) as a function of frequency (GHz) in X/Ku-bands (8.0 – 16.0 GHz)

Figure 7 shows the morphology and good dispersion of Z-type hexaferrite in polychloroprene matrix (80:20, wt. %).

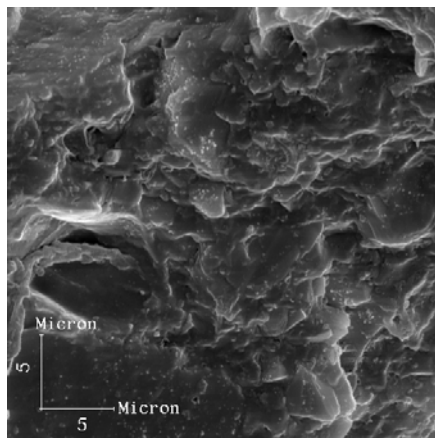


Figure 7: Scanning electron micrograph of (Co-Zn)-Z-type hexaferrite:polychloroprene (80:20, wt. %). Magnification = 3000.

4 CONCLUSIONS

- (1) Ferroplana ferrite $\text{Ba}_3\text{Co}_{1.6}\text{Zn}_{0.4}\text{Fe}_{24}\text{O}_{41}$ has been successfully synthesized by the citrate precursor method at a relatively low temperature of 950 °C under inert atmosphere of N_2 .
- (2) The substitution of Co with Zn ion in Co_2Z could increase the specific saturation magnetization and consequently improve the magnetic permeability of the ceramics.
- (3) This material can be used as microwave absorber for X/Ku bands.

5 ACKNOWLEDGEMENTS

The authors gratefully acknowledge the financial support and other forms of aid provided by CNPq, FAPERJ, PEMP/COPPE, CBPF, IPqM and IGeo/UFRJ (all Brazilian institutions), which were crucial for the success of this research.

6 REFERENCES

- Hankiewicz, J. H., Pajak, Z., Murakhowski, A. A. 1991, *JOURNAL of Magnetism and Magnetic Materials* Vol. 101, pp. 134-137.
- Zhang, H., Zhou, J., Wang, Y., Li, L., Yue, Z., Gui, Z. 2002: *Materials Letters* Vol. 55, pp. 351-355.
- Caffarena, V. R. 2004: Estudo das Propriedades Magnéticas e Absorvedoras de Microondas da Hexaferrita de Bário Tipo Z ($\text{Ba}_3\text{Me}_2\text{Fe}_{24}\text{O}_{41}$) Obtida pelo Método do Citrato (D. Sc. Thesis, UFRJ – Brasil)
- Wang, X., Li, L., Shu, S., Zhou, J. 2002: *Materials Chemistry and Physics* Vol. 77, pp. 248-253.
- Pullar, R. C. et al. 1998: *Journal of Magnetism and Magnetic Materials*, v. 186, pp. 313-325, 1998.

Preparation of Layered Polyvinyl Chloride (PVC)-Kaolinite Nanocomposites

J.L.Capitaneo & F.T. da Silva

Department of Metallurgical and Engineering Materials, COPPE, Federal University of Rio de Janeiro, Rio de Janeiro, Brazil

V.R.Caffarena

Centro Brasileiro de Pesquisas Físicas (CBPF), CMF, Rio de Janeiro, Brazil

ABSTRACT: Kaolinite is an alternative for the intercalation reactions (mechanism to immobilize organic compounds through strong hydrogen bonds into the silicate layer) because it is an abundant clay mineral (nanometric size) available at low prices. However, polar molecules cannot be intercalate directly in kaolinite, because it needs first opening the clay sheets using a displacement reaction which implies the prior intercalation of precursor dimethyl sulfoxide (DMSO). In this work, was reported the intercalation of PVC into the interlamellar spaces of kaolinite from Rio de Janeiro - Brazil. Although PVC is one of the most largely used thermoplastics, only little attention has been paid to PVC layered silicate nanocomposites. Moreover, polymer/layered silicate nanocomposites are a new class of materials with enhanced properties compared to parent conventional (micro)composites and unfilled polymers. Among other improvements, tensile properties are increased, permeability to oxygen and other gases are decreased and thermal stability and flame retardancy are enhanced. The PVC/ kaolinite nanocomposite was obtained and characterized by X-ray diffraction (XRD), thermal analysis (TG/DSC), X-ray fluorescence (XRF), and Fourier transform infrared (FTIR) spectroscopy.

1 INTRODUCTION

Over the last decade, interest in polymeric materials containing dispersed inorganic nano-particles has increased due to the potential for significant advances in mechanical, thermal and flammability properties (Komarneni 1992).

Although it has been long known that polymers can be mixed with appropriately modified clay mineral and synthetic clays, the field of polymer/clay nanocomposites has gained a large momentum recently. There exist many different natural and synthetic clays, dispersible in various polymers, in this paper we shall example from polyvinyl chloride (PVC) (Lebaron et al. 1999).

Kaolinite, $\text{Al}_2\text{Si}_2\text{O}_5(\text{OH})_4$, is a dioctahedral layered hydrated aluminosilicate of the 1:1 type with two distinct interlayer surfaces (gibbsite and silicalike structures). Van der Waals bonds between the aluminol and Si-O groups link adjacent lamella to each other, and frequently make the intercalation processes difficult.

The successful intercalation agents decrease the electrostatic attraction between the lamellae by causing an increase in the dielectric constant when the compounds penetrate between the layers. Intercalating compounds also have a certain

hydrogen bonding capacity. Dimethyl sulfoxide (DMSO) and *N*-methylformamide (NMF) are known to directly intercalate, resulting in an increase of the interlayer spacing within the kaolinite. This increase depends on the size and arrangement of the guest species.

Although not many compounds have the ability to directly intercalate, the number may be extended by the so-called "displacement method". Displacement involves the replacement of a directly intercalated species (e.g., DMSO) by a second organic molecule. The use of a directly intercalating compound as an intermediate for the intercalation of other polar organic compounds opens up new areas for basic, strategic, and applied research. The resultant hybrid materials combine the features of the clay and of the guest species (polymer) (Gardolinski et al. 2000).

Polyvinyl chloride (PVC) has been studied and used widely in industrial fields for many years. However, due to its inherent disadvantages, such as low thermal stability, PVC and its composites are subject to some limitation in certain applications.

In this work, the preparation and characterization of a new PVC/kaolinite nanocomposite (by using Melt Intercalation) was described.

The resultant composite (K-PVC) was characterized by powder X-ray diffractometry (XRD), thermal analysis (thermogravimetry and differential thermal, TG and DTA), and Fourier-transformed infrared spectroscopy.

2 MATERIALS AND METHODS

2.1 K-DMSO complex

To obtain the “treated” samples, the natural clay from Silva Jardim was firstly desegregated using a mortar and pestle, weighed (about 20 g), and dispersed in a dilute ammonium hydroxide solution (5.0 ml NH₄OH and 200 ml of water) during 24 hours. Then, the dispersion were decanted and the suspension, separated. This procedure was repeated until a relative large quantity of aqueous solution containing clay fraction was obtained.

Afterward the, water was removed by drying at 70°C during 24 hours. Then, a clay-water solution (60 mg of clay in 1 cm³ of distilled water) was made. A sample with about 3-ml of this solution was dried at 100°C.

The impurities were removed chemically: Fe oxides by using citrate-bicarbonate-dithionite (CBD) method; organic matter by using strong oxidant agent (hydrogen peroxide) and carbonates by using buffer solution of acetic acid/acetate.

Approximately 1 g of this clay fraction was transferred to a 250-ml round-bottom flask and suspended in 100 ml of DMSO (Aldrich PA) solution (95% v/v DMSO:water). The suspension was stirred at 60°C for 192 hours and then centrifuged at 4000 rpm to recover the solids. The resultant material (K-DMSO complex) was dried at 40°C for 120 hours to remove the residual DMSO and characterized.

2.2 Synthesis of PVC-Kaolinite Nanocomposite

Immediately after drying and characterization, the K-DMSO intercalate was used as precursor to prepare intercalates conducted as follows: polyvinyl chloride was heated to 175°C in a 50-ml round-bottom flask placed in a silicone oil bath. He clay content was fixed at 3% (mass fraction) for the system.

Then, to this viscous melt, 2.0 g of K-DMSO was added at once, and the reaction was allowed to proceed for a total of 120 hours (5 days). The final product (K-PVC) was worked up by washing/centrifuging in methanol three times, followed by air-drying at 25°C and then drying in an oven at 100°C for 3 days.

2.3 Characterization

X-ray fluorescence (XRF) measurements were carried out in a model PW 2400, Philips spectrometer. For the powder X-ray (XRD) analysis, the solid materials were placed on a glass sample holder and spread out to form a thin layer. A Miniflex diffractometer using Cu-K α radiation with a dwell time of 1°/min, in the θ -2 θ Bragg-Brentano geometry was employed (2-90°).

Both thermogravimetry (TG) and differential scanning calorimeter (DSC) measurements were carried out using Shimadzu 50 H equipment. The experiments were performed in static air, using platinum crucibles with a heating rate of 10°Cmin⁻¹.

Fourier transform infrared (FTIR) spectroscopy was carried out using a NICOLET MAGNA-IR 760 spectrometer. The KBr discs were prepared after mixing each of test samples with dry KBr. Analyses were performed in the transmission mode in the 400-4000 cm⁻¹ range, with a resolution of 4 cm⁻¹ and accumulation of 32 scans.

3 RESULTS AND DISCUSSION

In this work, Melt Intercalation was used to obtain the nanocomposites. In this method, the layered silicate is mixed with the polymer matrix in the molten state. Under these conditions and if the layer surfaces are sufficiently compatible with the chosen polymer, in this case PVC, the polymer can crawl into the interlayer space and form an intercalated nanocomposite. In this technique, no solvent is required.

Firstly, the chemical composition of natural clay and clay fraction was obtained by XRF. It was observed that % SiO₂ decreased and % Al₂O₃ (and loss of ignition) increased, indicating quartz removal (Table 1). The impurities were also removed after the chemical treatments.

Table 1: Chemical composition of the natural clays and clay fractions (mass %) obtained by XRF:

Determinations (mass %)	SILVA JARDIM	
	Natural clay	“treated”
SiO ₂	49.45	42.234
Al ₂ O ₃	31.31	37.492
Fe ₂ O ₃	1.44	0.120
TiO ₂	1.68	0.725
K ₂ O	3.26	0.648
Na ₂ O	0.34	-
CaO	0.29	-
MgO	0.39	-
Loss of ignition	11.44	16.94

Table 2 summarizes the data obtained by X-ray diffractometry. Basal interplanar spacings were obtained in relation to the basal reflection of the highest order.

Table 2: Identification of the phases, basal distances and interlayer expansion ($\Delta d = d_{001}$ (of the substituted phase) - d_{001} (of kaolinite) (Å))

Phase	d_{001} (Å)	Δd (Å)
K	7.12	0
K-DMSO	11.03	3.91
K-PVC	35.60	28.48

There was no evidence that any DMSO had remained cointercalated within K-PVC matrix, unless at a relatively low concentration that would not interfere with the measured interplanar spacing.

Variations in the interplanar spacing were determined by subtracting the basal lattice parameter of the intercalated kaolinite from the basal lattice parameter of raw kaolinite (7.12 Å).

The basal space of this modified material was 35.60 Å, which represents an expansion of 28.48 Å, related to the basal space of the raw kaolinite (7.12 Å).

Figure 1 shows a typical TGA thermogram of weight loss as a function of temperature for polymer-kaolinite nanocomposite material along with PVC, as measured under air atmosphere.

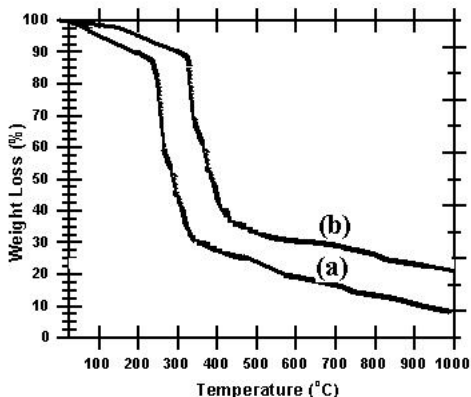


Figure 1: TGA curves of (a) PVC and (b) K-PVC nanocomposite, during heating in air with 10°C/min:

In general, major weight losses are observed in the range of ~200-500°C for PVC and K-PVC fine powders, which may be correspondent to the structural decomposition of the polymers. Evidently, the thermal decomposition of that polymer-kaolinite nanocomposite shift slightly

toward the higher temperature range than that of PVC, which confirms the enhancement of thermal stability of intercalated polymer. After ~800°C, mainly the inorganic residue (Al_2O_3 , SiO_2) remained.

DSC traces of PVC and K-PVC materials are shown in Figure 2.

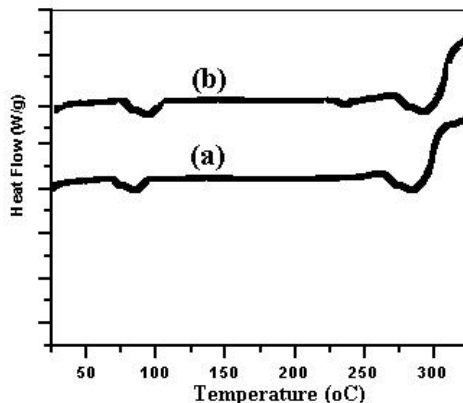


Figure 2: DSC curves of (a) PVC and (b) K-PVC nanocomposite, during heating in air with 10°C/min:

PVC exhibits an endotherm at 81°C corresponding to the glass transition temperature (T_g) of PVC. The K-PVC material is found to have a high T_g compared to the bulk PVC. This is attributed to the confinement of the intercalated polymer chains within the clay galleries that prevents the segmental motions of the polymer chains.

Another endotherm of bulk PVC at higher temperature (275°C), corresponding to the crystalline melting point T_m of PVC, is also found in the DSC thermograms. The nanocomposite has a higher T_m compared to the pure PVC and presents two new phases with melting points below (230°C) and above (300°C) that of the crystalline phase, as shown in Figure 2-b.

In the FTIR spectrum of kaolinite, four bands at 3620, 3651, 3669, and 3693 cm^{-1} appear. The band at 3620 cm^{-1} is assigned to an internal OH group, and the others to outer surface OH groups. By intercalation reactions, the outer OH groups may be perturbed and the OH groups hydrogen-bonded with guest species show new bands at lower wavenumbers, whereas the internal OH group is not influenced. Thus, taking the band at 3620 cm^{-1} as a reference, interactions between OH groups and guest species can be observed (Capitaneo et al. 2004).

The band at 3620 cm^{-1} has been unambiguously assigned to the stretching frequency of the internal

hydroxyl group of kaolinite and it is not usually influenced very much influenced by interlamellar modifications.

K-DMSO shows bands at 1428, 1410, 1395, 1320, 3662, 3538 and 3503 cm^{-1} .

The two most intense vibrations of kaolinite at 1033 and 1008 cm^{-1} are often shifted slightly upon intercalation of guest species such as DMSO, where these bands are shifted to 1038 and 1112 cm^{-1} .

Upon intercalation of DMSO, the band at 912 cm^{-1} decreases greatly in intensity and another band of 10 cm^{-1} lower frequency appears at 902 cm^{-1} , presumably due to a repulsive interaction between one of the methyl groups of DMSO which is proposed to be keyed into the (SiO-) macroring of the silicate surface and the internal hydroxyl of kaolinite.

The intercalation process of K-DMSO with polyvinyl chloride (PVC) also generated three new absorption bands in the FTIR spectra of the resulting K-PVC intercalation compound. These bands were tentatively attributed to the axial deformations of hydroxyl groups that are involved in hydrogen bonding.

4 CONCLUSIONS

The kaolinite sample employed came from Silva Jardim (Rio de Janeiro) and the clay fraction ($< 2 \mu\text{m}$) was obtained by chemical treatment with impurities removing. After this, it was used to prepare nanocomposites.

Intercalation of polyvinyl chloride (PVC) within the matrix cannot be achieved without preexpansion of the lamellar structure of kaolinite with dimethyl sulfoxide (DMSO). PVC intercalation thus proceeds by gradual displacement of DMSO molecules.

The polyvinyl chloride (PVC)/kaolinite nanocomposite was prepared by melt blending of PVC with kaolinite clay fraction. As-synthesized K-PVC materials are characterized by FTIR spectroscopy, TG/DSC measurements and XRD.

Both glass transition (T_g) and crystalline melting point (T_m) was shifted higher temperature compared to the pure PVC, which confirms the enhancement of thermal stability of intercalated polymer.

5 ACKNOWLEDGEMENTS

The authors gratefully acknowledge the financial support and other forms of aid provided by CNPq, FAPERJ, PEGEMM/COPPE/UFRJ, CBPF, NUCAT/PEQ/UFRJ, Instituto de Química/UFRJ and Instituto de Geociências/UFRJ (all Brazilian institutions), which were crucial for the success of this research.

6 REFERENCES

- Komarneni, S. 1992. Nanocomposites. *Journal of Materials Chemistry*, v. 2, n. 12: 1219-1230.
- Lebaron, P. C., Wang, Z., Pinnavaia, T. J. 1999. Polymer-layered silicate nanocomposites: an overview. *Applied Clay Science*, v. 15: 11-29.
- Gardolinski, J. E. F. C., Ramos, L. P., Souza, G. P., Wypych, F. 2000., Intercalation of Benzamide Into Kaolinite. *Journal of Colloid and Interface Science*, v. 221: 282-290.
- Capitaneo, J. L., Silva, F. T., Vieira, C. M. F., Monteiro, S. N., Caffarena, V. R. 2004. Method to separate nanometric particles of clays. *Journal of Metastable and Nanocrystalline Materials*, in press.

Colloidal Processing of Advanced Ceramic Materials

J.M.F.Ferreira, S.M.H.Olhero, Xu Xin

Department of Ceramics and Glass Engineering, CICECO, University of Aveiro, 3810-193 Aveiro, Portugal

M.L.Oliveira

Polytechnic Institute of Bragança, Campus de Santa Apolónia, 5301-854, Bragança, Portugal

ABSTRACT: The present contribution gives an overview about the use of colloidal shaping techniques involving liquid removal or based on different setting mechanisms for direct consolidation green bodies of advanced ceramic materials. Innovative methods for protecting AlN powders against hydrolysis and for preparing stable and high concentrated (≥ 50 -vol.% solids) aqueous suspensions for slip casting, tape casting, and for granulation of powders for dry pressing technologies will be presented. Full dense AlN materials could be obtained by sintering at 1750°C for 2 h. The results achieved will have a tremendous positive impact at both scientific and technological levels. For complex multicomponent systems such as precursor SiAlON compositions (α -Si₃N₄, AlN, Y₂O₃ and Al₂O₃) with different requirements in terms of pH for aqueous dispersion, organic-based suspensions containing as high as 60-vol.% solids have been successfully adopted to consolidate homogeneous green bodies by slip casting, tape casting, and by Temperature Induced Gelation (TIG), a new developed direct consolidation technique. Full dense and α -SiAlON *in situ* reinforced with rod-like α -SiAlON crystals could be obtained from the homogeneous green precursor SiAlON bodies

1 INTRODUCTION

Colloidal shaping techniques have the capability to reduce the strength-limiting defects when comparing with dry pressing technologies (Lewis 2000). Besides traditional processing methods, such as slip casting, tape casting, pressure casting and injection moulding, some new colloidal forming technologies have been developed in the past decade for the near-net-shape forming of complex ceramic parts, including Gel-Casting (GC), Freeze Forming (FF), Starch Consolidation (SC), Hydrolysis Assisted Solidification, (HAS), Direct Coagulation Casting (DCC), Temperature Induced Forming (TIF), etc.

The use of such performing techniques on the processing of advanced ceramics is expected to favour the quality and price of the products. Furthermore, healthier and more environmentally friend production will result if water can replace organic solvents, such as in the processing of AlN. This requires the suppressing of the hydrolysis reactions through protecting the surface of AlN particles, while keeping a good dispersion degree. Such an achievement will have tremendous economic and environmental advantages over the organic-based processing.

Previous attempts on aqueous processing of AlN

(Shimizu et al. 2000; Kosmac et al. 1999; Uenishi et al. 1990) still presented serious shortcomings. Meanwhile, a new method including innovative features has been proposed (Oliveira et al. 2003), which enables the preparation of stable and high concentrated (≥ 76 -wt.%) suspensions suitable for slip casting. Moreover, it has been shown that adding suitable amounts of compatible binders and plasticizers to the previous aqueous suspension enabled the fabrication of AlN-based substrates by tape-casting, or the granulation of powders by freeze granulation for the dry pressing technologies.

Most studies on α -SiAlON ceramics are based on high cost hot-pressing sintering and gas pressure sintering, because α -SiAlON ceramics are difficult to pressurelessly sinter due to the low amount of transient liquid phase during the last stage of sintering. Recently, it was demonstrated that these limitations could be overcome by using suitable colloidal processing routes (slip casting, TIG) that assure high levels of density and homogeneity in the green compacts, which could be full densified by pressureless sintering at 1750°C, 2 h (Xu et al. 2003).

The present work reviews the most important achievements by the authors on the colloidal processing of non-oxide advanced ceramics.

2 EXPERIMENTAL PROCEDURE

2.1 Materials

For aqueous processing of AlN-based ceramics, commercially available AlN-Grade C (H.C. Starck, Germany; $\rho=3.26 \text{ g/cm}^3$) and CaF_2 (Grade-325 mesh, 99.9%, Aldrich, Germany; $\rho= 3.18 \text{ g/cm}^3$) powders with average particle sizes of $0.33 \mu\text{m}$ and $1.06 \mu\text{m}$, respectively, were used in this work. CaF_2 was used as sintering additive (5-wt.%). For the tape casting and granulation processes a latex emulsion (AgoraMat, Portugal) was used as a binder (BI). In order to increase the flexibility of the green tapes and the dry pressing ability of the granules, a plasticizer P200 (AgoraMat, Portugal) was used.

For the preparation of α -SiAlON ceramics the following starting powders were used: 76.92-wt.% Si_3N_4 (H.C. Stark, Germany, $d_{50}=0.38 \mu\text{m}$) + 13.46-wt.% AlN (H.C. Stark, Germany, $d_{50}=2 \mu\text{m}$) + 5.77-wt.% Y_2O_3 (H.C. Stark, Germany, $d_{50}=0.75 \mu\text{m}$) + 3.85-wt.% Al_2O_3 (Alcoa Chemicals, USA, $d_{50}=0.38 \mu\text{m}$).

2.2 Preparation and characterization of suspensions and the green bodies

An aqueous suspension containing 50-vol.% solids (95AlN+5CaF₂ in wt.%) could be prepared as described previously (Oliveira et al. 2003), using 0.5-wt.% of a surface active agent (AS1) and 0.4-wt.% of a protective agent (H_3PO_4). After deagglomeration, several crucibles with different shapes and sizes could be consolidated by slip casting. The so-obtained greens were then sintered in a graphite furnace (Thermal Technology Inc, USA), using a powder bed of 50AlN-50BN (wt.%), in a nitrogen atmosphere at 1750°C for 2 h.

The precursor suspensions for α -SiAlON ceramics were prepared as described elsewhere (Xu et al. 2003) in an azeotropic mixture of 60-vol.% methylethylketon (MEK) (Riedel-de Haën, Germany) and 40-vol.% ethanol (E) (Merck, Germany) and dispersed with a hypermer KD1 (ICI, England). The green bodies obtained by slip casting and TIG were then placed inside a powder bed composed of about 30-wt.% BN + 70-wt.% of precursor α -SiAlON powder and sintered in a graphite furnace under N_2 atmosphere at 1750°C , 2h. Relative sintered densities were determined using the Archimedes immersion technique in mercury.

AlN substrates could be prepared by adding different combinations of binder (10 and 15 -wt.%) and plasticizer (5, 10-wt.%) to the 50-vol.% solids aqueous suspension, using a laboratory tape caster (Elmetherm, Oradom Sur Vayres, France) with a gap of 2 mm under the blade and a fixed casting speed of $\approx 3 \text{ cm.s}^{-1}$. Lower amounts of the same binder (5-wt.%) and plasticizer (2.5-wt.%) were added to the starting AlN suspension to prepare granules by

freeze granulation (PowderPro, Goteborg, HB) for dry pressing technologies.

Rheological characterisation of all suspensions was carried out using a rotational rheometer (Bohlin C-VOR Instruments, UK). The morphology of the granules and the microstructure of the green and sintered samples were observed by scanning electron microscopy (SEM, Hitachi, Tokyo, Japan).

3 RESULTS AND DISCUSSION

3.1 Aqueous processing of AlN ceramics

Figure 1 shows some green bodies consolidated by slip casting from the aqueous AlN suspension containing 50-vol.% solids loading. Cylindrical samples were also obtained and used to evaluate the green and sintered densities, $> 71\%$ and $\approx 98\%$ of theoretical density, respectively.



Figure 1. AlN crucibles obtained by aqueous slip casting.

Figure 2 presents a characteristic microstructure of a fracture surface of the sintered AlN-based ceramics, prepared from the AlN aqueous suspension by slip casting.

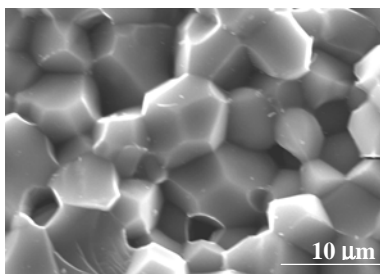


Figure 2. SEM microstructure of a fracture surface of the AlN after sintering at 1750°C for 2 h.

This microstructure shows the well-developed polyhedral AlN crystals and confirms the high densification level achieved at a temperature, which is $100\text{-}150^\circ\text{C}$ lower than the usual temperatures used for AlN ceramics.

Figure 3 presents the viscosity curves of the aqueous AlN suspensions with 50-vol.% total solids loading in the presence of different amounts of

binder and plasticizer. All the suspensions present a shear thinning behaviour desirable for the tape casting process, with a slight increase in viscosity as the content of binder increases from 10 to 15-wt.%.

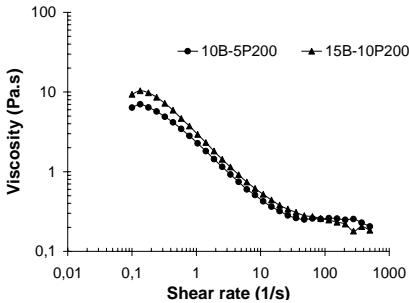


Figure 3. Viscosity curves of the aqueous AlN-based suspensions containing 50-vol% solids, 10- and 15-wt.% binder combined with 5- and 10-wt.% of the plasticizer, P200.

From these suspensions it was possible to obtain un-cracked green tapes, presenting smooth and uniform surfaces, as those presented in Figure 4.

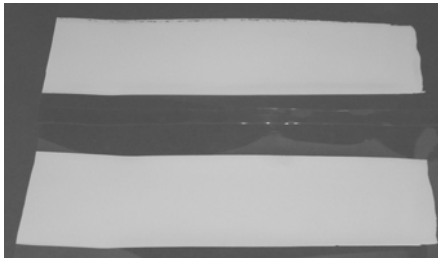


Figure 4. Typical green tapes obtained from aqueous 50-vol.% AlN-based suspensions.

3.2 Freeze Granulation of AlN

Figure 5 presents the rheological behaviour of the 50-vol.% AlN suspensions used to produce granules by freeze granulation, after adding suitable combinations of binder and plasticizer.

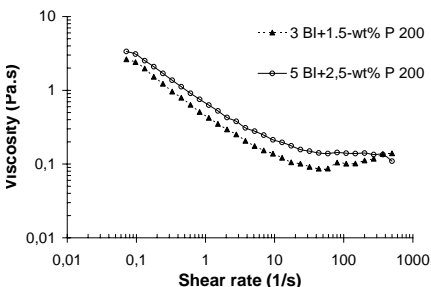


Figure 5. Viscosity curves of the 50-vol.% solids AlN-based suspensions used for freeze granulation, after addition of suitable combinations of binder and plasticizer.

Both suspensions were shear thinning at low shear rate values and suitable for a good spraying and to avoid clogging of the spray nozzle. As shear rate increases a slightly shear thickening trend is apparent for the suspension with lower amounts of binder and plasticizer.

Figure 6 presents the granules obtained after spraying and freezing of the AlN-based suspensions.

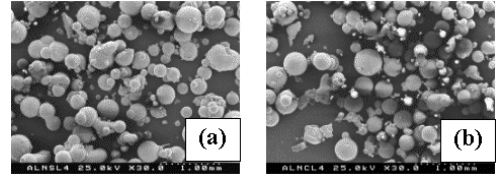


Figure 6. Granules obtained by freeze granulation from the 50-vol.% solids suspensions with different combinations of binder and plasticizer: (a) 3 BI+1.5P200 and (b) 5 BI+2.5P200.

It is important to note that no significant differences were introduced on the characteristics of the granules obtained from the AlN-based aqueous suspensions, by almost doubling the content of binder and plasticizer. This result is in agreement with the similar rheological behaviour of the suspensions (Figure 5). Accordingly, the high homogeneity of the binder and plasticizer in both starting suspensions was determinant for the reproducibility of granules characteristics after spraying and freezing, namely: (i) granules size ($\approx 100\text{-}800\ \mu\text{m}$), (ii) wide granule size distribution, and (iii) predominant round shaped and smooth granule surfaces.

3.3 Preparing dense α -SiAlON ceramics by slip casting and pressureless sintering

Green compacts of precursor α -SiAlON ceramics could be prepared from 60MEK-40E suspensions containing 50-vol.% solids dispersed with 3-wt.% KD1 (Xu et al. 2003). Green densities $> 68\%$ of theoretical density and high degrees of homogeneity have been obtained, as shown in Figure 7 (a). These samples could be full densified by pressureless sintering at a relatively low temperature of 1750°C for 2 h. Furthermore, the sintered microstructure presented in Figure 7 (b) shows that *in situ* α -SiAlON grains could be developed, which act as a reinforcing phase enhancing the typically low fracture toughness of α -SiAlON ceramics. This means the as-obtained dense α -SiAlON could combine the typical high hardness of this crystalline phase with a high fracture toughness imparted by the elongated α -SiAlON grains, while taking advantage of the high potential for cleaning up grain boundaries from the glassy phase, which is incorporated in the crystalline structure.

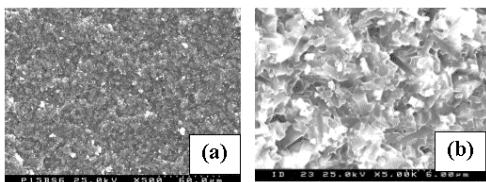


Figure 7. Fracture surface of (a) green sample and (b) sample sintered at 1750°C for 2 hours.

Such microstructural development could be attributed to the relatively high green density and to the homogeneously dispersed small pores. Using a theoretical model, it was concluded (Shaw 1986) that it is desirable to have a fraction of small pores as large as possible in order to maintain a high driving force for sintering, and high powder packing densities must be achieved for optimum sintering.

3.4 Preparing α -SiAlON ceramics by temperature induced gelation (TIG)

While carrying out the studies mentioned in the previous section (2.3), it could be realised that the solubility of KD1 in the azeotropic mixture of 60-vol.% MEK - 40-vol.% E significantly changed with temperature, decreasing as temperature decreases. This effect was then explored and a new direct consolidation method do not involving liquid removal has been developed (Xu et al. 2003). In fact, the solvency of the dispersant in MEK/E decreased dramatically on cooling leading the system to consolidate and form strong rigid bodies.

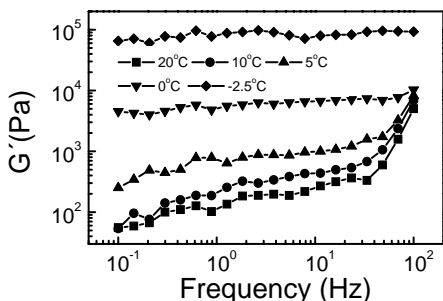


Figure 8. Elastic modulus (G') as a function of frequency for 60-vol.% suspensions with 4-wt.% KD1 measured under different testing temperatures.

Figure 8 shows the evolution of the elastic modulus (G') as a function of frequency for a suspension containing 60-vol.% solids and 4-wt.% KD1. The magnitude of the storage modulus, G' , strongly increases and becomes less dependent on frequency with decreasing temperature, indicating that the precursor SiAlON suspension changes from

being predominantly viscous at the highest temperature to displaying a strong elastic behaviour at the lowest temperature.

4 CONCLUSIONS

The present work shows that significant breakthroughs have been made on colloidal processing of advanced ceramics, both in aqueous media and organic media. Accordingly, the processing of AlN-based ceramics from aqueous suspensions is now possible, which have great advantages in terms of environment, health and security and lower productions costs. Such advantages are expected to bring a tremendous positive impact to industry, as well at the scientific level with a better understanding of the hydrolysis reactions and their control.

For a multi-component and incompatible system in water, such as the precursor powders of α -SiAlON, organic media is the best choice for dispersing the powders. The degrees of dispersion and homogeneity of the green bodies enables to obtain dense and *in situ* reinforced α -SiAlON ceramics by pressureless sintering.

5 REFERENCES

- Kosmac, T., Krnel, K. & Kos, K. 1999. "Process for the protection of AlN powder against hydrolysis", International Patent N. WO 99/12850, 18.03.
- Lewis Jennifer. 2000. "Colloidal Processing of Ceramics", J. Am. Ceram. Soc., 83 [10] 2341-2359.
- Oliveira M., S. Olhero, J. Rocha & J.M.F. Ferreira. 2003. "Controlling hydrolysis and dispersion of AlN powders in aqueous media", J. of Colloid and Interface Science, 261, 456-463
- Shaw T. M. 1986. "Liquid Redistribution during Liquid-Phase sintering," J. Am. Ceram. Soc., 69 [1] 27-34.
- Shimizu, Y., Hatano, J., Hyodo, T. & Egashira, M. 2000. "Ion-exchange loading of yttrium acetate as a sintering aid on aluminium nitride powder via aqueous processing", J. Am. Ceram. Soc., 83 [11] 2793.
- Uenishi, M., Hashizume, Y. & Yokote, T. 1990. "Aluminum nitride powder having improved water resistance", Unites States Patent N. 4.923.689, 08/05.
- Xin Xu, Marta, I.L.L. Oliveira, & José J. M. Ferreira. 2003. " α -SiAlON Ceramics Obtained by Slip Casting and Pressureless Sintering", J. Am. Ceram. Soc., 86 [2] 366-368.
- Xin Xu & José M. F. Ferreira, (submitted) "Temperature Induced Gelation of Concentrated SiAlON Suspensions", Journal of Am. Ceram. Soc.

Crystal Chemistry and Crystal Structures of Complex Hexa-aluminates and Hexa-ferrites

M.Göbbels

Institute of Geology and Mineralogy, University of Erlangen-Nuremberg, Germany

ABSTRACT: In this study hexa-phases in the Al- and Fe-rich parts of the ternary systems CaO/SrO/BaO-Al₂O₃/Fe₂O₃-MgO will be discussed correlating the dependence of crystal structure and crystal chemistry. All crystal structures of these hexa-phases, such as magnetoplumbite, β -alumina or related, can be described as mixed layer structures originating from the spinel structure. The characteristic cations as Ca, Sr or Ba essentially lead to the actual structure present. For industrial application small changes result in large effects. Phosphors such as "BAM:Eu" (BaMgAl₁₀O₁₇:Eu) exhibit the luminescent property just by the replacement of Ba by Eu. This leads to the study of the solid solution series of the β -alumina compound BAM:Eu.

1 INTRODUCTION

Hexa-aluminates and -ferrites exhibiting magnetoplumbite, β -alumina and related structures present a group of materials with a wide variety of properties. Ion-conductivities and optical properties due to doping and magnetic properties are only few examples leading to different applications.

The group of hexa-phases can be generally derived from two basic crystal structures. The crystal structures actually present in the large number of compounds are quite complicated, but basically they can be explained in a very simplified way: The two basic structures are on one hand the magnetoplumbite structure (Adelsköld 1938) and on the other hand the β -alumina structure (Beevers & Ross 1937). The name "hexa-phases" is derived from the chemical formula rather than from the hexagonal or trigonal symmetry. The chemical composition of magnetoplumbite compound hibonite is CaAl₁₂O₁₉. This can be written as CaO • 6 Al₂O₃ or abbreviated CA₆. In case of the β -alumina compound NaAl₁₀O₁₇ or 1/2 Na₂O • 5.5 Al₂O₃ related to one large cation (here Na) the relation is also roughly 1:6.

Both structures magnetoplumbite and β -alumina can be explained as modified spinel-types. In the spinel structure tetrahedral and octahedral coordinations are formed by the suitable stacking order of O-

layers. This stacking is in the [111] direction of the spinel structure. The same kind of stacking is also found in case of the hexa-phases where the stacking direction is parallel to the c-axis of the hexagonal or trigonal structures. This spinel-like stacking sequence is interrupted by inserting modifying units (blocks) which follow a different atomic arrangement. So there are structural units of spinel-type (S-block) and magnetoplumbite defining R-blocks or β -alumina defining B-blocks. The magnetoplumbite compound hibonite CaAl₁₂O₁₉ can be given as a mixed layer structure consisting of S- and R- blocks in the ratio 1:1, the β -alumina compound NaAl₁₀O₁₇ can be given as a mixed layer structure consisting of S- and B- blocks in the ratio 1:1. The only difference between both structures can be focused on the principal difference in the atomic arrangement in the central part of the R- and B-blocks (Fig. 1).

In case of the magnetoplumbite structure (here CaAl₁₂O₁₉) the atomic arrangement with 1 Al 3 O and 1 Ca is quite closely packed whereas in case of β -alumina (here NaAl₁₀O₁₇) the atomic arrangement with 1 Na and 1 O is quite spacious. It can be understood that the size of the large cations such as Ca or Na strongly influence the geometrical and bonding parameters of these structural blocks. The geometrical and bonding parameter mismatch of the S-blocks and the R- or B-blocks sensibly influence the actual

crystal structure present in the compounds. Making it even more interesting as an additional possibility a perovskite-type structural T-Block can also be taken into consideration.

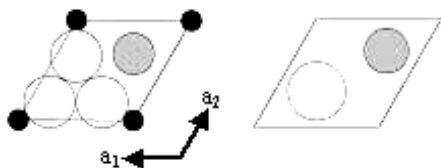


Figure 1: Comparison of the atomic arrangement in the central part of the R-block for magnetoplumbite (left) and B-block for β -alumina (right) based on one unit cell.

Black circles: Al^{3+} , white circles: O^{2-} , grey circles: large cations such as Ca (left) or Na (right).

Among the huge number of possible hexa-phases only a small number has been described so far. We find a group of mixed layer structures representing suitable combinations in kind and number of the different structural units.

2 EXPERIMENTAL PROCEDURE

2.1 Synthesis

For the syntheses of appropriate samples pure components of the following reagent grade chemicals were used: CaCO_3 , SrCO_3 , BaCO_3 , Al_2O_3 , Fe_2O_3 and MgO . Calculated batches were weighed, homogenized in agate mortars under acetone and pre-fired at 1100°C . Finally small samples of the starting mixtures were equilibrated at temperatures in the range from 1100 - 1850°C in a vertical Super Kanthal furnace controlled by a commercial Eurotherm electronic temperature controller. Depending on the temperature and the presence or absence of a melt equilibration periods of 2 hrs up to 2 weeks were selected.

The temperature was measured up to 1600°C by using a Pt/Pt₉₀Rh₁₀ thermocouple and at temperatures up to 1850°C by using a Pt₈₀Rh₂₀/Pt₆₀Rh₄₀ thermocouple. Calibrations were performed against melting points of diopside ($\text{CaMgSi}_2\text{O}_6$) at 1393.5°C , pseudowollastonite (CaSiO_3) at 1546°C and platinum at 1772°C . All temperatures correspond to the IPTS-68 temperature scale.

The experiments were performed in air, except the ones concerning the quaternary system $\text{BaO-Al}_2\text{O}_3\text{-MgO-EuO}$. In order to stabilize Eu^{2+} a strongly reducing H_2 -atmosphere was chosen. Quenching in water was avoided because of possible reactions. Instead the samples were quenched by dropping them on a thick brass block with a high heat capacity.

2.2 Characterization of syntheses products

The quench products were polished and investigated by reflected light microscopy. In many cases the reflectivities of the coexisting phases were quite similar. Thus it was difficult to distinguish them optically.

All samples were studied by electron probe microanalysis (EPMA) on Camebax Cameca or Jeol JXA 8200 equipment using the ZAF evaluation program. On the backscattered electron image of the samples it was possible to distinguish the different phases and to select grains of sufficient size of the coexisting phases in paragenesis. Different series of measurements of coexisting phases in mutual contact were taken. Only analyses of a total within the range $100 \pm 2\%$ were taken into consideration.

3 RESULTS

3.1 Hexa-aluminates in the system $\text{CaO-Al}_2\text{O}_3\text{-MgO}$

The Phase relationships in the Al-rich part of the system $\text{CaO-Al}_2\text{O}_3\text{-MgO}$ have been presented (Göbbels et al. 1995, Iyi et al. 1995). Only magnetoplumbite-type phases (Mp-type) are present:

- $\text{CaAl}_{12}\text{O}_{19}$	Hibonite	(Mp-type)
- $\text{Ca}_2\text{Mg}_2\text{Al}_{28}\text{O}_{46}$	CAM-I	(Mp-type)
- $\text{CaMg}_2\text{Al}_{16}\text{O}_{27}$	CAM-II	(Mp-type)

3.2 Hexa-aluminates in the system $\text{SrO-Al}_2\text{O}_3\text{-MgO}$

In the System $\text{SrO-Al}_2\text{O}_3\text{-MgO}$ both magnetoplumbite-type (Mp-type) and β -alumina-type (β -type) phases and combinations have been reported (Lindop et al. 1975, Stevels & Schrama-de Pauw 1976, Iyi & Göbbels 1996):

- $\text{SrAl}_{12}\text{O}_{19}$	SA_6	(Mp-type)
- $\text{Sr}_2\text{MgAl}_{22}\text{O}_{36}$	SAM-I	(β - & Mp-type)
- $\text{SrMgAl}_{10}\text{O}_{17}$	SAM-II	(β -type)

3.3 Hexa-aluminates in the system $\text{BaO-Al}_2\text{O}_3\text{-MgO}$

In the Al-rich part of the system $\text{BaO-Al}_2\text{O}_3\text{-MgO}$ only β -alumina-type (β -type) phases have been found (Göbbels et al. 1998, Iyi et al. 1998):

- $\text{Ba}_{0.75}\text{Al}_{11}\text{O}_{17.25}$	Ba- β -alumina	(β -type)
- $\text{BaMgAl}_{10}\text{O}_{17}$	BAM-I	(β -type)
- $\text{BaMg}_3\text{Al}_{14}\text{O}_{25}$	BAM-II	(β -type)

Between Ba- β -alumina and BAM-I a continuous solid solution range exists.

3.4 Hexa-ferrites in the system SrO-Fe₂O₃-MgO

The hexa-phases in the system SrO-Fe₂O₃-MgO are crystallizing in structures of magnetoplumbite-type (Mp-type):

- SrFe ₁₂ O ₁₉	SF ₆	(Mp-type)
- Sr ₂ Mg ₂ Fe ₂₈ O ₄₆	SFM-I	(Mp-type)
- SrMg ₂ Fe ₁₆ O ₂₇	SFM-II	(Mp-type)

3.5 Hexa-ferrites in the system BaO-Fe₂O₃-MgO

In the system BaO-Fe₂O₃-MgO the hexa-ferrites exhibit magnetoplumbite-type (Mp-type) phases, not only modified by spinel-units in addition perovskite structural units (P) widen the variation of crystal structures:

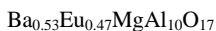
- BaFe ₁₂ O ₁₉	BF ₆	(Mp-type)
- Ba ₂ Mg ₂ Fe ₂₈ O ₄₆	BFM-I	(Mp-type)
- BaMg ₂ Fe ₁₆ O ₂₈	BFM-II	(Mp-type)
- Ba ₃ Mg ₂ Fe ₂₄ O ₄₁	BFM-III	(Mp-type & P)
- Ba ₂ Mg ₂ Fe ₁₂ O ₂₂	BFM-IV	(Mp-type & P)

3.6 Hexa-aluminate phosphors in the system BaO-Al₂O₃-MgO-EuO

For industrial applications the blue phosphor BAM:Eu is widely used (Oshio & Matsuoka 1998). As host material the phase BAM-I (BaMgAl₁₀O₁₇) is doped with suitable amounts of Eu²⁺ following the substitution formula



In this study the solid solution range was determined. The Eu-rich end member could be found corresponding the chemical formula



Subsequently the x parameter for the solid solution range can be given as

$$0 \leq x \leq 0.47$$

4 CONCLUSIONS

In table 1 all hexa-phases and the ratios of the structural blocks forming the actual mixed layer structure are given in comparison.

In the system CaO-Al₂O₃-MgO only magnetoplumbite-type compounds are stable. The size of the Ca nicely fits the arrangement within the defining structural R-block. In case of the system BaO-Al₂O₃-MgO the Ba-ion is far too large for an atomic arrangement in the R-block. Therefore a β-alumina-type B-block is stabilized. In the binary sub-system SrO-Al₂O₃ the Sr-ion takes an intermediate role just

fitting within the atomic arrangement of the magnetoplumbite-type R-Block. On addition of Mg in the ternary system the S-block in the structure subsequently changes the size-relations of the different blocks in the structure, forcing the formation of a B-block due to the need of the combination possibility of S-block and B-block.

Table 1. Comparison of hexa-phases based on magnetoplumbite-type RS and β-alumina-type BS and their combination with additional structural blocks (S-, T-) per unit-cell forming the mixed layer structure present.

Compound	Structural blocks			
	RS	BS	S	T
System CaO-Al₂O₃-MgO				
CaAl ₁₂ O ₁₉	Hibonite	1		
Ca ₂ Mg ₂ Al ₂₈ O ₄₆	CAM-I	2	1	
CaMg ₂ Al ₁₆ O ₂₇	CAM-II	1	1	
System SrO-Al₂O₃-MgO				
SrAl ₁₂ O ₁₉	SA ₆	1		
Sr ₂ MgAl ₂₂ O ₃₆	SAM-I	1	1	
SrMgAl ₁₀ O ₁₇	SAM-II		1	
System BaO-Al₂O₃-MgO				
Ba _{0.75} Al ₁₁ O _{17.25}	Ba-β-alumina		1	
BaMgAl ₁₀ O ₁₇	BAM-I		1	
BaMg ₃ Al ₁₄ O ₂₅	BAM-II		1	1
System SrO-Fe₂O₃-MgO				
SrFe ₁₂ O ₁₉	SF ₆	1		
Sr ₂ Mg ₂ Fe ₂₈ O ₄₆	SFM-I	2	1	
SrMg ₂ Fe ₁₆ O ₂₇	SFM-II	1	1	
System BaO-Fe₂O₃-MgO				
BaFe ₁₂ O ₁₉	BF ₆	1		
Ba ₂ Mg ₂ Fe ₂₈ O ₄₆	BFM-I	1	1	
BaMg ₂ Fe ₁₆ O ₂₇	BFM-II	1	1	
Ba ₃ Mg ₂ Fe ₂₄ O ₄₁	BFM-III	1		1
Ba ₂ Mg ₂ Fe ₁₂ O ₂₂	BFM-IV			1

Going to the ferrite systems the general size relations change due to the different cations Al and Fe³⁺. The system SrO-Fe₂O₃-MgO is structurally completely the same as the corresponding compounds in the system CaO-Al₂O₃-MgO. The larger size of the Sr is compensated by the larger size of the Fe³⁺. In case of Ba in the system BaO-Fe₂O₃-MgO similar size correlations take place. Due to the larger Ba in comparison to the Sr even the possibility to add a perovskite T-block forming additional mixed layer structures is realized.

Looking to the quaternary system BaO-Al₂O₃-MgO-EuO within a rather wide substitution range Ba can be replaced by Eu²⁺. With respect to eightfold coordination in the β-alumina structure the ionic radii of Ba²⁺ = 1.42 and Eu²⁺ = 1.25 are different (Shan-non 1976). Due to the rather spacious atomic arrangement in the B-block the difference in size of Ba and Eu²⁺ can be compensated up to almost 50% of substitution.

5 REFERENCES

- Adelsköld, V. 1938. „X-ray studies on magnetoplumbite, $\text{PbO} \cdot 6 \text{Fe}_2\text{O}_3$, and other substances resembling 'beta-alumina' $\text{Na}_2\text{O} \cdot 11 \text{Al}_2\text{O}_3$. Ark. Kem. Miner. Geol. 12a (29): 1-9
- Beevers, C.A. & Ross, M.A.S. 1937. The crystal structure of 'beta-alumina' $\text{Na}_2\text{O} \cdot 11 \text{Al}_2\text{O}_3$. Z. Krist. 97: 59-66
- Göbbels, M., Woermann, E., Jung J. 1995. The Al-rich part of the system $\text{CaO-Al}_2\text{O}_3\text{-MgO}$, Part I: Phase relationships. J. Solid State Chem. 120.: 358-363.
- Göbbels, M., Kimura, S., Woermann, E. 1998. The Aluminium-rich part of the system $\text{BaO-Al}_2\text{O}_3\text{-MgO}$, Part I: Phase relationships. J. Solid State Chem. 136.: 253-257.
- Iyi, N., Göbbels, M. & Matsui, Y. 1995. The Al-rich part of the system $\text{CaO-Al}_2\text{O}_3\text{-MgO}$, Part II: Structure refinement of two new magnetoplumbite related phases. J. Solid State Chem. 120.: 364-371.
- Iyi, N. & Göbbels, M. 1996. Crystal structure of the new magnetoplumbite related compound in the system $\text{SrO-Al}_2\text{O}_3\text{-MgO}$. J. Solid State Chem. 122.: 46-52.
- Iyi N., Göbbels M., Kimura, S. 1998. The Aluminium-rich part of the system $\text{BaO-Al}_2\text{O}_3\text{-MgO}$, Part II: Crystal structure of the β -alumina-related compound, $\text{Ba}_2\text{Mg}_6\text{Al}_{28}\text{O}_{50}$. J. Solid State Chem. 136.: 258-262.
- Lindop, A. J., Matthews, C., Goodwin, D.W. 1975. The refined structure of $\text{SrO} \cdot 6 \text{Al}_2\text{O}_3$. Acta Cryst. B 31: 2940-2941
- Oshio, S. & Matsuoka, T. 1998. Mechanism of particle growth of a $\text{BaMgAl}_{10}\text{O}_{17}:\text{Eu}^{2+}$ phosphor by firing with AlF_3 . J. Electrochem.Soc. 145 (11): 3898-3903.
- Shannon, R.D. 1976. Revised effective ionic radii and systematic studies of interatomic distances in halides and chalcogenides. Acta Cryst..32 A.: 751-767.
- Stevens, A.L.N. & Schrama-de Pauw, A.D.M. 1976. Eu^{2+} luminescence in hexagonal aluminates containing large divalent or trivalent cations. J. Electrochem. Soc. 123 (5): 691-697.

Synthesis and Characterization of Pillared Smectites with Al

D.L.Guerra; V.P.Lemos; R.S.Angélica & M.L.Costa

Department of Geochemistry, Geosciences Center, Federal University of Pará, Pará, Brazil

E.F.Fernandes

Pos-graduation in Chemistry, Federal University of Pará, Pará, Brazil

ABSTRACT: Hydroxy-polymers of Al were synthesized after hydrolysis of its respective salts and are being used in the intercalation and pillarization of smectites of different chemical composition). The intercalation methodology consists mainly in the substitution of interlamellar cations by bigger cations (Keggin Ion), followed by further drying at 80°C. The resultant material of the intercalation must suffer calcination at 450°C, with the main purpose of removing interlayer water and produce more porous material than the pillared smectite. The materials were characterized by XRD, FTIR, DTA-TG, and textural aspects (surface area and porosity measurements). The XRD data indicated the displacement of $d_{001} = 15,3-15,6 \text{ \AA}$ to $d_{001} = 18,36-18,92 \text{ \AA}$. FTIR results have proved smectites pillarization with the Keggin Ion. DTA-curves are very similar. Endothermic peaks were observed between 100-200°C and 500-600°C, related to loss of water and dehydroxilation, respectively. Textural parameters have also increased thus resulting in the classification of this pillared smectite as a mesoporous material.

1 INTRODUCTION

Pillared interlayer clays (PILC) are potential catalysts and adsorbents. PILC are generally prepared by exchanging Na^+ , Ca^{2+} , and Mg^{2+} ions, that are normally found between these layers, with inorganic metal ions of larger size and charge (Vaughan 1988). Inorganic polymeric metal ions derived from water-soluble salts of Al, Fe, Ti, Cr, and Zr appear to be the most widely explored pillaring agents (Volzone 2001, Budali et al. 2003). The aluminum polyhydroxipolymer (structural formula $[\text{Al}_3\text{O}_4(\text{OH})_{24}(\text{H}_2\text{O})_{12}]^{+7}$) the so-called Al_{13} complex of Keggin structure, is composed of 12 Al octahedra and one Al tetrahedron. It exists in aluminic solution having $1 < \text{OH}/\text{Al molar ratio} < 2.5$ and its concentration increases with increasing OH/Al molar ratio. It contains the four layers of superimposed oxygen atoms (or water or hydroxyls) needed for expanding the clay basal spacing to 18 Å. The first objective in pillaring clays is to achieve as large a basal spacing as possible. These properties contributes to the development of large surface areas and porous volume (Ooka et al. 2001). The aim of the present work was to study the pillarization of smectites at 300- 600°C, with respect to various OH/Al molar ratio and Al/clay ratio.

2 EXPERIMENTAL

Sample clays from Sierra de Maicuru-Pará are composed specially by smectites and goethites traces of Kaolinites. The samples presents: A_1 and A_2 $\text{Al}_2\text{O}_3/\text{FeO}_3 = 0.42$; A_3 $\text{Al}_2\text{O}_3/\text{FeO}_3 = 0.39$ (Lemos & Costa 1997).

2.1 Preparation of the pillaring agent

Aluminum polyhydroxipolymer solutions were prepared by adding 0,2 mol/L NaOH solution dropwise to 0,2 mol/L $\text{AlCl}_3 \cdot 6\text{H}_2\text{O}$ solution, to give various OH/Al molar ratio ratios within the range 1,8-2,4. Vigorous stirring was essential to prevent local accumulations of OH ions which might cause precipitation of $\text{Al}(\text{OH})_3$ in the form of gibbsite (Brindley & Sempels 1977).

2.2 Pillaring process

Dilute aqueous dispersions of the starting smectites were prepared by prolonged mixing (12 hr) with a magnetic stirrer followed by aging of the products for 12 hr. The dispersions were prepared for give meq Al/g of smectites ratios within the range 10, 15 and 25. The precipitated products were separated

from the solution by centrifugation and washed with deionized water. The materials were dried at 100 °C and calcined for 2h at 300, 450, 500, and 600 °C.

2.3 Characterization of the PILC

X-ray powder diffraction (XRD) analyses of the PILC were performed with oriented samples prepared by spreading about 0.5ml of a water suspension of the smectite on a glass slid and drying the slide at room temperature. The XRD patterns were obtained with a Philips diffractometer using $\text{CuK}\alpha$ radiation. BET surface areas and porosity measurements of PILC samples were determined using an Quantachome/Nova Surface Area Pore Volume Analyzer, Model 1200/5.01. The samples were first degassed at 150°C and their surface areas determined at liquid nitrogen temperature, using N_2 as the sorbate. Specific total pore volume and average pore diameter were evaluated from nitrogen uptake at $P/P_0 = 0.99$. The BET equation was used to determine surface area. The mesopore size distribution was obtained by applying the Barret-Joyner-Halenda (BJH) method to the adsorption branch of the isotherm. Thermal analysis was conducted in a Stanton Redcroft 1000/1500 coupled to a DC amplifier and temperature controller. Data from DTA-TG were obtained in all cases at a heating rate of 20°C/min between 36°C and 1000°C and under static air atmosphere. Inorganic groups were identified in FTIR equipment Perkin Elmer, model FT-IR 1760 X in the 450-4000 cm^{-1} spectral range.

3 RESULTS AND DISCUSSION

Table 1 shows $d(001)$ reflections for natural, intercalated (Inter₈₀ °C) and pillared samples and their textural aspects. $d(001)$ reflections=18.63-18.91Å is typical of pillar formation. It was observed for samples A₁ and A₃ d_{001} =14.88 and 14.19 Å, respectively and this generally attributed to presence of a non-pillared fraction (Pergher et al. 1999) of the clays. Meaningful differences in the $d(001)$ reflections were not observed when the calcination temperature was increased from 300 to 450°C (Figure 1).

The FTIR spectra of the sample are similar (Figure 2). The starting samples presents intense absorption near 3700 cm^{-1} due to the OH stretching of SiOH species. Similar to silanol groups, which absorb at 3747 cm^{-1} on silica are either located at corners and fracture of sheets or are formed by the tetrahedral inversion (Plee et al. 1985), i.e., the rearrangement which may take place in two outer Si-O layers by which Si-O-Al bond is hydrolyzed and the Si atom acquires a hydroxyl pointing out words. Such process is thought to be important in the

pillaring mechanism of the clay (Bodoardo et al. 1994). In PILC a new band is found, at 3738 cm^{-1} which is likely to be due to SiOH species perturbed by pillars. In all PILC which Al_{13} is observed a weak shoulder at 3715 cm^{-1} and peaks between 650 and 950 cm^{-1} . The shoulder at 3715 cm^{-1} is characteristic of isolated hydroxyl groups on octahedral aluminum in Al_2O_3 . The peak at 667 cm^{-1} indicates the cation composition in the octahedral sheet. The OH-bending mode of the Al_2OH group absorbs near 920 cm^{-1} and Al-O from the Al_2O_3 absorbs near 667 cm^{-1} (Farmer 1974).

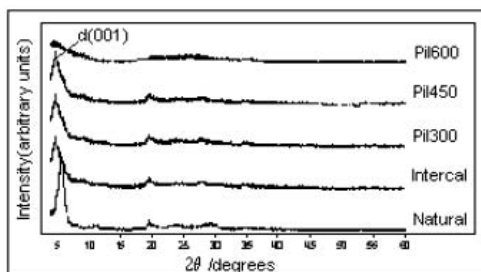


Figure 1: d_{001} of the samples and their evolution with the temperature calcination.

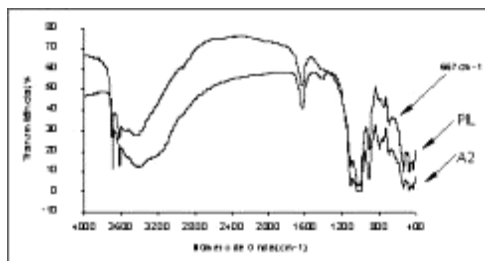


Figure 2: FTIR spectra for starting sample A2 and Al-PILC at 450°C.

Figure 3 depicts the thermal curves DTA-TG in the 36-1000°C range, corresponding to the starting sample and PILC. The general feature of the thermal curve, clearly reveals two steps: one in the 100-150°C and the other in the 500-700°C.

The first step corresponds to the loss of physically adsorbed water (7,5wt%) whereas the second one is attributed to either the dehydroxylation of the clay structure removal of any remaining hydroxide from the pillars (Valverde et al. 2002) or even the transformation of the pillars into Al_2O_3 . The dehydroxylation of hydroxide groups associated with interlayer pillars began to occur at 150°C and caused continuous weight loss to 450°C. Dehydroxylation continues between 500 and 600°C.

This step is related with the stability of the pillars and indicates the collapse of the clays structure.

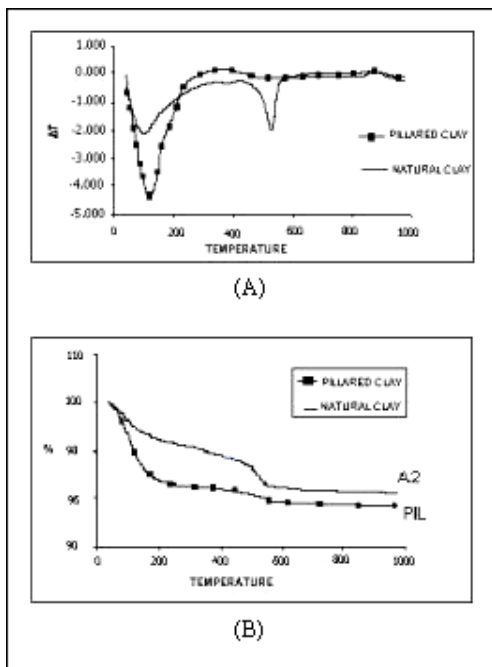


Figure 3: DTA (A) and TG (B) curves for starting sample and Al-PILC.

Surface area and total pore volume were increased from 51 to 122 m²/g and from 0.0652 to 0.1023cm³/g (Figure 5). These values are near to those of Al₂O₃ pillared clays prepared in the past researches (Leite et al. 2000). Average pore diameter calculated from the isotherms were in the range from 45.1 to 177 Å, characteristic to mesoporous solid. Figure 4 A and Figure 4B shows the adsorption-desorption isotherms for starting sample and Al-PILC. The adsorption isotherms are of type IV in the Brunauer, Deming, Deming and Teller (BDDT) classification (Greag et al. 1991) which is typical of microporous and mesoporous solids. Al-PILC at 450°C shows an isotherm similar to the starting sample. On the other hand, the hysteresis loop type H2 in the IUPAC classification is consistent with the expected for mesoporous materials. The BJH mesoporous distribution showed a narrow centered at 36,7 Å for Al-PILC A2. This result indicates a homogeneous pillaring process.

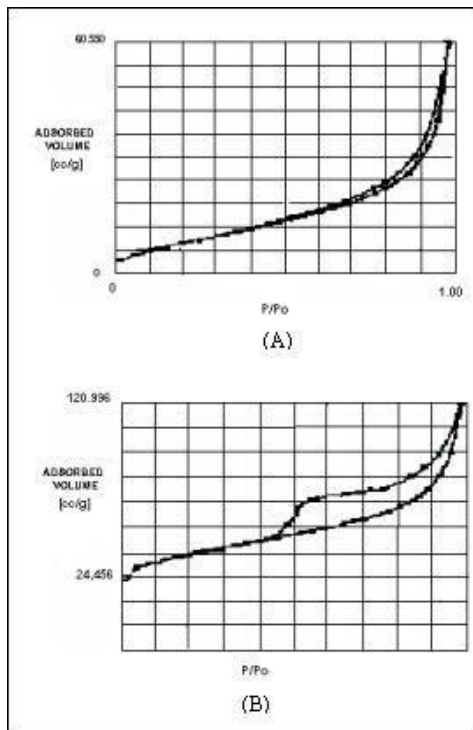


Figure 4: Adsorption-desorption isotherms of N₂ for starting sample(A) and Al-PILC(B) at 450 °C.

Samples	Natural d ₀₀₁ (Å)	Inter ₂₀₀ ^o C d ₀₀₁ (Å)	PILC ₃₀₀ ^o C d ₀₀₁ (Å)	PILC ₄₅₀ ^o C d ₀₀₁ (Å)	Surface area (m ² /g)	Total pore volume (cm ³ /g)	Average pore diameter (Å)
A ₁	15,60	18,63	18,59/14,88	18,49/13,39	44,37(nat) 112 m _{11c}	0,1259 (nat) 0,1454 m _{11c}	45,1
A ₂	15,30	18,89	18,93	18,92	51 122 m _{11c}	0,0652 (nat) 0,1023 m _{11c}	120,12
A ₃	14,50	18,91	18,39/14,19	18,36/14,22	44(nat) 106 m _{11c}	0,0872 (nat) 0,1733 m _{11c}	177
**	15,00	18,50		18,50	88	0,031	24

* Pergher et al (1999); ** Leite et al (2000).

Figure 5: d₀₀₁ of the samples and their textural aspects.

4 CONCLUSIONS

Smectites with Al₂O₃/Fe₂O₃= 0.39-0.42, were pillared with Al₁₃ using OH/Al=2; meq Al/g Clay=15 and pillarization at 450 °C. Homogeneous, pillared samples with high basal spacing (18,36-18,92 Å), average pore diameter (45-176 Å) and surface (121m²/g) were obtained. FTIR spectra clearly indicates a weak shoulder at 667cm⁻¹ in all PILCS where Al₁₃ is observed. This peak indicates the absorption of Al-O from the Al₂O₃. DTA-TG curves indicates the loss adsorbed water (7.5 Wt%) at 100-150 °C and dehydroxilation of groups associated with interlayer pillars. This reaction began to occur at 150 °C and continues between

450-500°C. Al-PILC at 450 °C shows isotherm similar to the starting samples. On the other hand, the hysteresis loop type H2 in the IUPAC classification is consistent with the expected for mesoporous materials.

5 REFERENCES

- Blindley, G.W., Sempels, R.E. 1997. Preparation and properties of some hydroxy-aluminium beidellites Clay Clay miner., v.12, p.229-237.
- Bodoardo, S., Figueiras, F., Garrone, E. 1994. IR study of Brønsted acidity of Al-pillared montmorillonite. Journal of catalysis, v.147, p.223-230.
- Boudali, L.K., Ghorbel, G., Amri, H., Figueiras, F. 2001. Propriétés catalytiques de la montmorillonite intercalée au titane dans l'oxydation de l'alcool allylique (E)-hex-2-én-1-ol. Chimie/Chemistry, v.4, p.67-72.
- Farmer, V.C. 1974. The infra-red spectro of mineral. Mineralogical society, p.539.
- Greeg, S.G., Sing, K.S.W., 1991. Adsorption, surface area and porosity. Academic Press London.
- Leite, S. Q., Dieguez, L.C., San Gil, R.A.S., Menezes, S. M. C. 2000. Pilarização de esmectita brasileira para fins catalíticos. Emprego de argila pilarizada na alquilação de benzeno com 1-dodeceno. Química nova, v.23, p.149-154.
- Lemos, V.P., Costa, M.L. 1997. Transformações mineralógicas e geoquímicas de lateritos do tipo ferruginoso-fosfático-titanífero. Geociências, v.16, n.1, p.87-108.
- Ooka, C., Yoshida, A., Horio, M., Suzuki, K., Hattori, T. 2003. Adsorptive and photocatalytic performance of TiO₂ pillared montmorillonite in degradation of endocrine disruptores having different hydrophobicity. Applied catalysis, v.41, p.313-321.
- Plee, D., Gatineau, L., Fripiat, J.J. 1997. Pillaring processes of smectites with and without tetrahedral substitution. Clay & Clay minerals, V.35, p.81-88.
- Pergher, B.C., Corma, A., Fornes, V. 1999. Materiales laminares pilareados: preparación y propiedades. Química nova, v.22, n.5, p.693-709.
- Valverde, J.L., Sanchez, P., Dorado, F., Molina, C.B., Romero, A. 2002. Influence of the synthesis conditions on the preparation of titanium-pillared clays using hydrolyzed titanium ethoxide as the pillaring agent. Microporous and mesoporous materials, v.54, p.155-165.
- Vanhan, D.E.W. 1988. Pillared clays-A historical perspective. Catalysis today, v.2, p.187-1988.
- Volzone, C. 2001. Pillaring of different smectite members by chromium species (Cr-PILCs). Microporous and mesoporous materials, v.49, p.197-202.

Transmission Electron Microcopy Studies of Grain Boundary Structures Formed at Elevated Temperatures

H.J.Kleebe

Colorado School of Mines, Metallurgical and Materials Engineering Department, 1500 Illinois St., Golden, CO 80401, USA

ABSTRACT: Microstructure evolution of Si_3N_4 ceramics can be effectively altered via the control of processing parameters in the early stage of densification. It is well established that amorphous intergranular films strongly limit potential applications at high temperature of such liquid-phase sintered ceramic polycrystals. A recently processed Sc_2O_3 -doped Si_3N_4 material did not show wetted interfaces up to 1640 °C, which makes it an interesting candidate for high-temperature structural applications. In contrast to the Si_3N_4 ceramic, wetting occurred in a HIPed $z=1$ SiAlON material at temperatures exceeding 1350 °C upon re-annealing. Spontaneous wetting of interfaces at elevated temperatures, leading to the formation of low-viscosity siliceous intergranular films is expected to also be a potentially important mechanism for temperature-activated geological processes such as volcanic eruptions.

1 INTRODUCTION

The structural behavior of silicon-based ceramics at elevated temperature primarily depends on the secondary phases formed during densification and their respective distribution within the microstructure. When such ceramics are heated up to temperatures exceeding 1200 °C, the presence of amorphous intergranular films is of major concern, in particular, due to the low softening temperature, which strongly limits their potential application. Although amorphous phase at triple-grain junctions tend to readily crystallize (Thompson 1990), intergranular grain-boundary films in this system have never been reported to be of crystalline nature. They rather solidify as a thin amorphous film between adjoining matrix grains both at grain as well as phase boundaries. The thickness of these films is normally on the order of 1-2 nm (Kleebe et al. 1992, Ernst et al. 1999), with the exception of homophase low-angle interfaces and twin boundaries that are commonly free of residual glass (Schmid & Rühle 1984). Wetting of internal interfaces by siliceous thin films have been found to exist basically in all Si_3N_4 and SiAlON systems and their thickness was reported to be rather insensitive to the volume fraction of residual glass (Greil &

Weiss 1982). Such a fairly rapid, spontaneous wetting phenomenon at high temperatures was also reported for a Ca-Al-silicate liquid in high purity Al_2O_3 (Shaw & Duncombe 1991), for liquid LiF in direct contact with polycrystalline spinel (Lange & Clarke 1982), and for liquid Ga in certain Al-alloys (Kargol & Albright 1977). However, it should be noted that in the aforementioned systems, the liquid remains at the interface upon cooling, forming a thin glass film, similar to Si_3N_4 and SiAlON ceramics.

Dewetting of the liquid phase from grain boundaries was observed in AlN ceramics, when annealed at high temperature in a highly reducing atmosphere. More-over, dewetting of grain boundaries at high temperatures was reported for Mg-doped partially stabilized zirconia (PSZ), containing SrO and SiO_2 , upon annealing under reducing atmosphere (Drennan et al. 1994). The observation of the migration of an anorthite liquid, $\text{CaAl}_2\text{Si}_2\text{O}_8$, from the interface of a Al_2O_3 bicrystal to its polished surface during annealing was rationalized by the difference in wetting behavior, i.e., the different temperature dependence of the wetting parameters of the free surface and the grain boundary, respectively (Branda & Clarke 1997). However, despite the above experimental findings, dewetted interfaces at room temperature have not

been monitored for Si_3N_4 and SiAlON ceramics as yet, with the only exception of special low-energy grain boundaries.

In this paper, experimental evidence is presented that (i) non-wetted interfaces can be present in Si_3N_4 ceramics at temperatures below 1640 °C, which however showed continuous wetting at higher sintering temperatures, and (ii) that also in the SiAlON system studied non-wetted interfaces formed upon densification at high temperature and pressure (HIPing), while spontaneous wetting occurred when this material was re-annealed at 1380°C (and then quenched to room temperature in order to freeze-in the high-temperature microstructure).

2 EXPERIMENTAL PROCEDURES

Si_3N_4 green bodies were prepared by aqueous slip casting. A commercial Si_3N_4 -powder (Ube SN-E10) was used in this study with 4 vol.% Sc_2O_3 addition as sintering aid. The samples were sintered in a two-step gas-pressure sintering cycle with a maximum temperature of 1850 °C for 1 hour and a N_2 -overpressure of 2 MPa. The sintering cycle was interrupted at different temperatures to study the nucleation/crystallization behavior of this material and to gain detailed information about the corresponding intermediate-temperature microstructures.

The SiAlON material was prepared by hot-isostatic pressing (HIPing) of high purity submicron sized powder (0.2 microns) of corresponding composition (Ube Industries, Ltd., Ube, Japan). Specimens were processed by cold isostatic pressing at 200 MPa, BN coating and preheating at 1200 °C for 2 hrs under a vacuum of $\sim 10^{-5}$ Pa. HIPing was conducted at 2000 °C for 1 hour at an Ar-overpressure of 180 MPa, which led to a relative density of >99.5 %.

Overall microstructure characterization was performed by transmission electron microscopy (TEM) in conjunction with analytical electron microscopy (AEM) employing a thin-window energy-dispersive X-ray spectroscopy system (EDX, PGT-Spirit). A FEI CM20STEM instrument was used, operating at 200 keV, with a point-to-point resolution of 0.24 nm. TEM foils were prepared by standard ceramographic techniques including ultrasonic disc cutting, grinding, polishing and dimpling, followed by Ar-ion thinning to perforation. The samples were subsequently lightly coated with carbon to minimize electrostatic charging under the electron beam.

Quenching from 1380 °C was performed, using a thin dimpled specimen, in order to freeze-in the high-temperature microstructure of the SiAlON sample. A modified apparatus designed for thermal

shock testing was used to heat the center of the sample. Here, a Nd/YAG laser was employed as the radiation source holding the specimen at temperature for 1 minute. Quench rates adequate to maintain the actual high-temperature microstructure within a 120 microns thin TEM-sample (not perforated) was achieved, as rationalized in detail elsewhere (Cinibulk et al. 1993).

3 RESULTS AND DISCUSSION

The main focus of the Si_3N_4 -related research was to verify whether the final microstructure of the materials, starting from the very same green body, can in fact be altered considerably by only changing the processing parameters during sintering. This approach involves the change of sintering parameters at the early stage of densification, in order to affect the nucleation behavior of the β - Si_3N_4 polymorph and, consequently, to change the overall microstructure of the component. In order to verify that nucleation events are affected by the processing parameters, TEM-foils were prepared of samples that were only partially sintered, i.e., densified at a temperature of about 200 °C below the maximum sintering temperature of 1850 °C. Figure 1 shows the overall microstructure of the Sc_2O_3 -doped Si_3N_4 material annealed at 1640 °C for 1 hour.

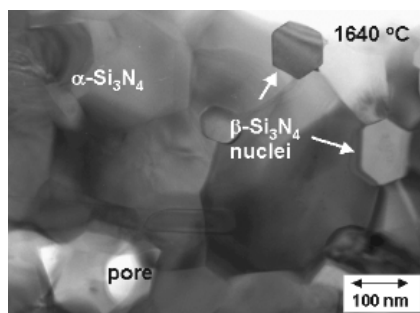


Figure 1: TEM image of the overall microstructure of Sc_2O_3 -doped Si_3N_4 sintered at 1640 °C for one hour.

As shown in Figure 1, the general microstructure of this material is rather complex, containing both silicon nitride polymorphs, α and β , as well as a small volume fraction of a crystalline secondary phase, $\text{Sc}_2\text{Si}_2\text{O}_7$, present at triple grain junctions (typically 5-10 nm in diameter). Note that no amorphous residual glass phase was observed in this sample. The latter observation is also true for the internal interfaces, shown in Figure 2. Here, similar to the overall microstructure, no amorphous grain-

boundary films were observed, which is commonly considered to be a characteristic feature of Si_3N_4 .

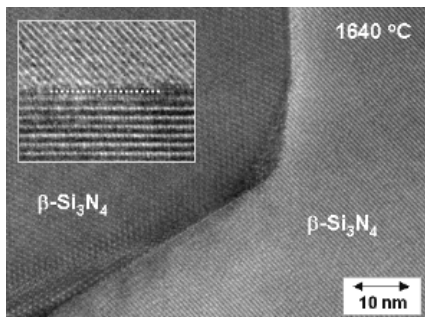


Figure 2: HRTEM image of the grain-boundary structure of Sc_2O_3 -doped Si_3N_4 sintered at 1640 °C (1 hour).

As shown in Figure 2, non-wetted interfaces are present in this material upon sintering at rather low temperature. However, it is important to emphasize that the “common” wetting phenomenon of Si_3N_4 grain boundaries in fact occurs when the material is exposed to a processing temperature exceeding 1680 °C. This is the first time that an Si_3N_4 material was processed that does not contain siliceous intergranular films and can, therefore, be considered a potential high-temperature material for aerospace applications.

The overall microstructure of the $z=1$ SiAlON material was composed of equiaxed β -SiAlON grains with an average grain diameter of 1.5-2.0 microns. Most of the triple junctions observed in this material are formed by direct contact of adjacent SiAlON grains with no residual glass phase present. However, some multi-grain pockets, up to 800 nm in diameter, were observed within the material that revealed an Al-containing siliceous glass, as shown in Figure 3. In some areas of those glass-containing regions, small precipitates of mullite, $\text{Al}_6\text{Si}_2\text{O}_{13}$, were observed, as indicated by the boxed area in Figure 3.

Employing high-resolution TEM imaging (HRTEM) of the area between SiAlON grains that were in the immediate vicinity of such glass pockets did not reveal any evidence for grain boundary wetting. Therefore, it was concluded that at room temperature, these glass pockets are not interconnected by intergranular films, but represent isolated reservoirs of residual glass; a very unusual microstructure evolution. As emphasized before, even interfaces adjacent to such a glass-filled pocket were not wetted by a thin siliceous film. However, when using the Fresnel fringe imaging technique, i.e., imaging the interface region with a slightly over- or underfocused objective lens, the presence of paired dark or bright fringes were seen, similar to

Si_3N_4 interfaces that are wetted by an amorphous grain-boundary film (Kleebe 1997, Ernst et al. 1999, Schmid & Rühle 1984). It was recently reported that such paired Fresnel fringes were also observed in liquid-phase sintered SiC polycrystals, which revealed Y-segregation along SiC interfaces. Hence, it is assumed here that the interface chemistry, although no individual second phase was observed, is slightly different, as compared to the adjacent SiAlON matrix grains.

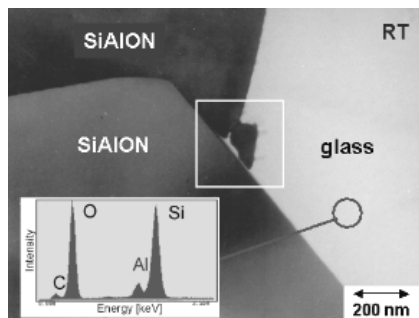


Figure 3: TEM micrograph of the SiAlON material showing a large triple junction filled with residual Al-Si-glass.

In order to compare the RT-microstructure with the actual microstructure at high temperature, the SiAlON sample was again heated to 1380 °C for 1 minute by Nd/YAG laser radiation and then rapidly quenched, in order to freeze-in the actual high-temperature microstructure. TEM observations of the overall microstructure of the quenched sample did not reveal any major differences, with the exception of a rather low fraction of small mullite precipitates (20-50 nm) were observed, epitaxially grown onto SiAlON grain facets (which revealed an orientation relationship between the host lattice and the mullite precipitates). Multi-grain pockets filled with residual Si-Al-O(N)-containing glass were also seen in this sample. However, in contrast to the room-temperature microstructure, HRTEM observations revealed the presence of a thin intergranular glass film along all SiAlON interfaces, as shown in Figure 4. This is the first example of a Si-based ceramic polycrystal that reveals clean interfaces at room temperature, but shows wetted interfaces at elevated temperature.

Since Si_3N_4 and Al_2O_3 and/or AlN can form a solid solution, although limited, it has been commonly anticipated during SiAlON processing that the liquid phase, which forms at high sintering temperature, is finally consumed either by nucleation and growth of new SiAlON matrix grains or as an epitaxial layer on the pre-existing SiAlON grain facets. However, the only SiAlON material

reported thus far that revealed non-wetted interfaces in addition to isolated alumino-silicate glass reservoirs at RT, is the sample studied here, with an overall composition of $z=1$, Si_5AlON_7 . Since mullite precipitates were observed in the RT-sample, but were no longer (or to a much lesser extent) seen upon quenching, dissolution of mullite must have occurred at elevated temperature. This in turn changes the overall composition of the residual glass (increased Al content, decreased Si/Al-ratio). Similarly, as the grain-boundary energy depends on grain-boundary misorientation, it also depends on the overall glass composition, under the assumption of a fixed orientation relationship between the adjoining SiAlON grains.

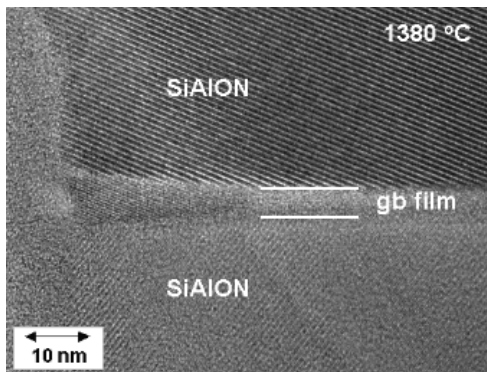


Figure 4: HRTEM image of the SiAlON sample quenched from 1380 °C showing the spontaneous wetting of the interface.

With respect to the as-processed SiAlON sample, it is assumed that during the slow cooling process to RT, heterogeneous nucleation of mullite occurs on SiAlON facets. This nucleation event will have a dual effect on the wetting/dewetting behavior of the material: (i) a change in overall glass composition, i.e., creating a higher Si/Al-ratio and (ii) generating a lower solid-solid interface energy. Similar to the thermodynamic approach to wetting and dewetting of grain boundaries reported by Brada and Clarke (1997), it is thought here that a strong temperature dependence of the wetting parameters, promoted by a continuous change in residual glass chemistry during cooling, which is, in particular, affected by the nucleation of mullite, favors the dewetting of grain boundaries. In contrast, when the material is re-annealed and then quenched to RT, the high-temperature microstructure and the corresponding grain-boundary structure (presence versus absence of intergranular films) can be monitored. In this case, the interfaces revealed spontaneous wetting when the re-annealing temperature exceeded 1350°C.

4 CONCLUSIONS

For first time, a wetting/dewetting process was imaged for Si_3N_4 -based materials. HRTEM imaging showed in two materials non-wetted interfaces at room temperature, while spontaneous wetting occurred at elevated temperatures. This wetting phenomenon is related to the gradual change in interface chemistry with increasing temperature, accompanied by a lowering of the solid-solid interface energy. The presented results are expected to also be important for temperature-activated geological processes such as volcanic eruptions and/or high-temperature, high-pressure deformation in subduction zones.

5 REFERENCES

- Thompson, D. P. 1990. Alternative Grain-Boundary Phases for Heat-Treated Si_3N_4 & α -Sialon Ceramics," Proc. Br. Ceram. Soc., 45 1-13.
- Kleebe, H.-J., Hoffmann, M. J., & Rühle, M. 1992. "Influence of Secondary Phase Chemistry on Grain Boundary Film Thickness in Si_3N_4 ," Z. Metallkd., 83 [8] 610-17.
- Kleebe, H.-J. 1997. "Structure and Chemistry of Interfaces in Si_3N_4 Ceramics Studied by Transmission Electron Microscopy," J. Ceram. Soc. Jpn., 105 [6] 453-75.
- Ernst, F., Kienzle, O., & Rühle, M., 1999. "Structure and Composition of Grain Boundaries in Ceramics," J. Eur. Ceram. Soc., 19: 665-73.
- Schmid, H. & Rühle, M., 1984. "Structure of Special Grain Boundaries in SiAlON Ceramics," J. Mater. Sci., 19: 615-27.
- Greil, P. & Weiss, J., 1982. "Evaluation of the Microstructure of α -SiAlON Solid Solution Materials Containing Different Amounts of Amorphous Grain-Boundary Phase," J. Mater. Sci., 17: 1571-78.
- Shaw, T.M. & Duncombe, P.R. 1991. "Forces Between Aluminum Oxide Grains in a Silicate Melt and Their Effect on Grain Boundary Wetting," J. Am. Ceram. Soc., 74 [10] 2495-505.
- Lange, F.F. & Clarke, D.R. 1982. "Morphological Changes of an Intergranular Thin Film in a Polycrystalline Spinel," J. Am. Ceram. Soc., 65 [10] 502-506.
- Kargol, J.A. & Albright, D.L. 1977. "The Effect of Crystal Orientation on the Liquid Metal Fracture of Al-Bicrystals," Metall. Trans., 8A [1] 27-34.
- Drennan, J., Clarke, D.R., Hannink, R.H.J., & Shaw, T.M. 1994. "Effect of Oxygen Partial Pressure During Sintering on the Microstructure of Mg-PSZ with Strontia & Silica Additions," J. Am. Ceram. Soc., 77 [8] 2001-2008.
- Brada, M.P. & Clarke, D.R. 1997. "A thermodynamic Approach to the Wetting and Dewetting of Grain Boundaries," Acta Mater., 45 [6] 2501-508.
- Cinibulk, M.K., Kleebe, H.-J., Schneider, G.A., & Rühle, M. 1993. "Amorphous Intergranular Films in Silicon Nitride Ceramics Quenched From High Temperatures," J. Am. Ceram. Soc., 76 [11] 2801-808.

Nanomineralogy and Nanotechnology

I.L.Komov

Department of Geochemistry, Institute of Environmental Geochemistry, Kyiv, Ukraine

ABSTRACT: This abstract summarizes the results of our studies on formation of nanostructures. The calculation of the special features of the forms and the presence of noble metals and the physical essence of their behavior under different influences give basis to understand processes, proceeding under the conditions of natural scattering, and the development of the new technologies of its extraction. The resulting increased surface activity improves filler-polymer interactions and reduces rolling resistance and, consequently, fuel consumption (approx. 2%) and exhaust emissions. Another important type of carbon filler is carbon nanotubes and nanofibres. This is a complex and fundamental problem that affects all aspects of inorganic chemistry and materials science such as oxides, metals, alloys, catalysts, corrosion, degradation, and thermal stability. Experimental approach is to study the fundamental aspects of the amorphization process in natural sample, and characterize the structural changes involved during the radiation-induced transformation. Using molecular modeling software, engineers of the future will design molecular building blocks that fit perfectly with each other. Materials with small particle size and large surface areas have properties different from those of conventional bulk phases.

1 INTRODUCTION

Nanomineralogy - it refers to inorganic solid-state materials in the little size range of 1 nm to 100 nm. Nanominerals have the following typical characteristics: small grain size, large reactive surface area, and modifiable and catalytic properties. Nanocrystalline materials are generally defined as single-phase or multi-phase polycrystals of ultra fine grain sizes (1-25 nm), and they may consist of crystalline, quasicrystalline or amorphous phases. Nanocrystalline materials can be classified into several categories according to the nanostructure dimensionality (Wang et al. 2000), i.e. zero-dimensional atomic clusters and cluster assemblies, quantum dots, one-dimensional nano-tubes, two-dimensional modulated multilayers, and three-dimensional equated nanostructures. Importance of nanominerals: reserves of raw materials (crude oil, nonmetallic minerals, hydro- and biosphere); ecological problems (material cycles, contaminant sorption – and transport); problems in earth sciences (weathering, formation and transformation of minerals, sedimentology, petrography).

2 NANOMINERALS

Nanostructured have the following features: single molecules- not compositionally fluxional assemblies of molecules. Clusters are good examples while planar hydrocarbons, dendrimers and particulates are not. Nanoscopic size- approximate range is 0.7 to 50nm. They are larger than small molecules but smaller than macromolecules. Systematic established methodologies exist that enable control over stereochemistry, reactivity, and physical properties. Of all fundamental properties, controlling the stability of atoms, clusters, and particles on a surface or support is the most important one. Recently it has become possible to experimentally measure the metal atom-surface bond strength on a per-atom basis using adsorption micro-calorimetry on ultra thin single crystal metal or metal oxide surfaces. Nanocrystalline materials can be obtained through irradiation of coarse-grained intermetallic or ceramic materials with energetic particles without the incorporation of the implanted species (Wang et al. 2000). By carefully controlling the experimental conditions, nanostructures composed of either nanocrystals in an amorphous matrix or only nanocrystallites have been achieved. The irradiation-induced nanocrystals can be either the original phase

of the target material or phases with different compositions and crystal structures. The process may involve radiation-induced partial amorphization, radiation induced- or enhanced-recrystallization and radiation induced-phase decomposition, through mechanisms such as cascade quenching, defect accumulation and radiation-induced segregation (Wang et al. 2000). These effects can be achieved by either collision or ionizing irradiation or a combination of both. The data of decomposition of the target material has been observed in natural materials that have suffered irradiation from the decay of constituent radioactive elements and in nuclear reactor fuels that have been irradiated by fission neutrons and other fission products. The mechanisms involved in the process of this nanophase formation are discussed in terms of the evolution of displacement cascades, radiation-induced defect accumulation, radiation-induced segregation and phase decomposition, as well as the competition between irradiation-induced amorphization and recrystallization. Minerals such as zircon and titanite are known to undergo amorphization as a consequence of the structural damage caused by alpha decay of radioactive impurities (mostly uranium and thorium) that they contain. Understanding the self-radiation damage observed in these minerals is important, as they can provide fundamental data for the confirmation of extrapolated behavior in nuclear waste forms, over long periods of time. We have been studying the impact of radiation damage on natural materials using a mixture of experimental and computational techniques.

The calculation of the special features of the forms of the presence of noble metals and physical essence of their behavior under different influences gives basis for understanding of the processes, proceeding under the conditions of natural scattering, and the development of the new technologies of its extraction. In recent years, ion beam technologies have increasingly been used as an effective tool for creating. Experiments completed to date have not revealed any significant instability of CaO under further electron irradiation. Both collision and ionizing radiation effects can also be used to promote the precipitation of implanted species at relatively low annealing temperatures in ion-implanted samples through radiation-enhanced diffusion and chemical segregation. The results of a study in the contiguous fields of experimental mineralogy are connected with the nanomineralogy. Radiation pressure based on the law of conservation of momentum is produced on small particles in a converged laser light. Micromanipulation of small particles is possible using laser radiation pressure.

The nanoparticles is ultra small colloids or cluster colloids - all words that means that the particles are at a size where their physical properties begin to

differ from a bulk macroscopic sample of the same material. Nanomineralogy made it possible to conduct: study of Au and Pt in the black shale's; to develop the new methods of the extraction of finely dispersed gold from the scatterings; to propose the methods of cleaning the films of the diamonds before the flotation; to study the smallest mineral in the diamonds; the large part of gold in the natural objects is located in the form of the submicroscopic finely dispersed particles of the virgin metal by size into the tenth- thousandth shares of micrometer. Gold, represented in the form of such nanoparticles, is localized in different minerals, predominantly in the quartz and sulfides. High interest in the forms of gold in sulphides is due to the commercial concentrations of gold in sulphide minerals in some gold-ore deposits. At the same time, the character of its distribution in these minerals is not yet clear in many respects. Some investigators believe that gold in sulphides is an atomic-molecular dispersion isomorphously replacing Fe, Cu, As, and Pb; others (the majority) consider gold as a mechanical admixture in the native crystalline state. New data were obtained on gold distribution in sulphides (pyrite and arsenopyrite) containing more than 200 ppm of gold. It is established that such concentrations are related to the submicrometre inclusions of native gold forming ordered or irregularly distributed groups of gold micro-particles.

Materials with small particle size and large surface areas have properties different from those of conventional bulk phases. In addition zeolites, mesoporous materials, and octahedral molecular sieves are materials with immense internal surface areas. Such nanomaterials are important as catalysts, ion exchangers, adsorbents, detergent additives, and in many other applications. They occur as minerals in soils, hot springs, altered volcanic rocks, and in other environments. They are major transporting agents for heavy metals and other contaminants. Colloids have been suggested as potential carriers of radionuclides in diffusive transport through the compacted bentonite clay to be used as backfill in repositories for radioactive wastes and also in flowing water in fractures in the surrounding rock (Stevens-Kalceff & Phillips 1995). One of the most significant findings has been the observation of the polymerization of the silicon and oxygen atoms in zircon following the original impact made by the recoiling atom. It is hoped that a better understanding of the way that the structures of natural materials such as zircon and titanite will facilitate development of better ceramics for long-term storage of radioactive waste. In recent years, the area of nanocomposites has received considerable attention with the expectation that nanotechnology can lead to lighter, better materials for engineering applications.

Colloids are fine-grained particulates (1 nm - 1 μ m) present in near surface geologic materials. They result from the degradation of organic detritus, and mineral weathering. Colloidal materials enhance the sorption capacity of the solid phase when aggregated or bound to the surfaces of larger, immobile particles because their high surface area, electrostatic properties, and surface functional groups favor inorganic solute complex. Under aqueous conditions that promote their dispersion and stability, colloidal material can facilitate the migration of radio elements that strongly sorbs to them leading to more widespread dispersal.

Groundwater colloids, which adsorb actinide ions, play an important role in actinide migration. Colloid transport can be retarded due to the filtration effect, which is caused by the deposition of colloidal particles onto stationary grain surfaces from flowing suspensions. The deposition behavior depends on the chemical characteristics of the particle surfaces and grain surfaces and on the solution chemistry. The behavior of colloid filtration and investigated the filtration effect on colloid migration by conducting column was indicated the effect of colloidal particle size and solution ionic strength on colloid migration. The particles, which have higher kinetic energy than those in the batch experiments could surmount the interaction potential energy barrier, resulting in higher deposition rate (Chinju H. et al. 2003). The reason for the difference may be the existence of trapped particles at a stagnation point or in cavern sites. In nanotech-land, chemistry meets silicon micromachining techniques through a melding of the appropriate natural laws. The mechanisms that bond atoms together into useful molecules are well understood, as are the principles governing the growth of crystals. Together these chemistries can control how raw materials are transformed — how sand is processed into microchips.

Important deposits of fine-grained industrial minerals are associated with ultramafic rocks. These commodities include magnesium compounds (salts, metal), vermiculite, talc, asbestos, serpentinite, soapstone, and aggregates. In some settings, deposits of platinum-group elements, nickel, cobalt, and (or) gold are associated with ultramafic rocks. Mining processes, novel uses, and building reclamation of these resources will increase the potential for associated environmental hazards (for example, asbestiform minerals dusts). To date, nanoscale materials - ranging in size from 0.1 to 100 nanometers - have found use in a number of applications, including sunscreens, polymer composites. Their characterization is important for understanding phenomena such as weathering, heavy-metal deposition, and soil development. These low-temperature assemblages typically occur in intimate, heterogeneous mixtures of fine-grained minerals.

Natural nuclear fission reactors (hereafter reactors) are unique places in the world where fission reactions took place spontaneously 2 000 millions years ago and have been sustained for quite a long time (100 000 to 500 000 years) in a natural environment. The reactors now contain high-grade uranium ores with high content of fission products and their end members decay. The oxygen isotopic composition of uranium minerals and their nanostructures are sensitive monitors of fluid events and provide key tools for studying the evolution of the Oklo-Okelobondo and Bangombe uranium deposits. The post-criticality evolution of the uraninite is only partially understood because the results from the few studies that have reported oxygen isotopic data present conflicting results (Gauthier-Lafaye & Holliger 1996). The study of uranium deposits is also complicated by the susceptibility of uraninite to alteration and radiation damage and because the effects of these processes are most evident at the nano- scale. Oxygen isotope analysis of uraninite on the micrometer scale has been demonstrated using secondary ion mass spectrometry (SIMS), but such measurements have not yet been related to specific nanostructures. Adsorption of U, together with P, mainly occurs on Fe-oxyhydroxides, but this U retention process seems less efficient than the precipitation one, at least in the close vicinity of the reactor. Uraninite crystals have shown good capacities to retain most of the actinides produced by the fission reactions and most of the fission products that have ionic radii close to that of uranium.

3 ENVIRONMENTAL NANO-GEOSCIENCE

Covers the concepts of size-dependent properties, processes, behavior, and implications of phenomena associated with nanoparticles for materials science and earth and environmental science applications. Fundamental studies on the nature of the aqueous solution/mineral interface and on the structure of near-aqueous solvated ions and colloids are also being performed. The aim of these studies is to provide improved modeling capability for contaminant migration, weathering, and sediment transfer, ion exchange and nutrient cycles. Nanocrystals in the environment have been of great interest and concern because of their high surface activity and instability compared to large particles. In our research we focused on the nano occurrence of heavy toxic elements. Uraninite nanocrystals were found in atmospheric particulates. Some crystals were encapsulated in well-crystallized fulleroid of carbon. This finding leads a new insight into the process of the transport of uranium by aerosol (Chinju H. et al. 2003). Another environmental issue concerns on arsenic poisoning. Nano-scale

occurrences of arsenic-bearing phases were found in association with magnetite nanocrystals, and the phase was identified as the iron arsenide, westerveldite. The high content of released arsenic is attributed to the instability of the reduced arsenic phase in the nano-scale form.

The subject of hybrids based on layered inorganic compounds such as clays has been studied for a considerable time, but the area is enjoying a resurgence of interest and activity as a result of the exceptional properties, which can be realized from such nanocomposites.

4 NANOTECHNOLOGY

Nanotechnology has not been a part of the new direction of synthesis of minerals. Nanotechnology ups the ante by downsizing chemistry from mixing vats containing billions of atoms, to individual atoms bonding together into smart molecular building blocks. In addition zeolites, mesoporous materials, and octahedral molecular sieves are materials with immense internal surface areas. Such nanomaterials are important as catalysts, ion exchangers, adsorbents, detergent additives, and in many other applications. They occur as minerals in soils, hot springs, altered volcanic rocks, and in other environments. They are major transporting agents for heavy metals and other contaminants. Inorganic materials science today is critically lacking in the knowledge of predictive reaction pathway mechanisms that would allow the design and synthesis of materials with specified reactivity and properties. Major efforts in nanoparticle synthesis can be grouped into two broad areas: gas phase synthesis and sol-gel processing. Nanoparticles with diameters ranging from 1 to 10 nm with consistent crystal structure, surface derivation, and a high degree of monodispersity have been processed by both gas-phase and sol-gel techniques. The study of the nature of the dissolution of silica gel and opal forms of amorphous silica is carried out in the wide temperature range. It is established that the solubility of silica gel linearly increases with an increase in the temperature. It is shown that in the means, which were preliminarily subjected to hydrothermal treatment, the equilibrium in the solution is reached more rapidly. The conducted investigations showed that the new types of lasers and optical amplifiers could be developed on the base of opal structures. The matrices of opal were obtained from the monodisperse ashes of the oxide of silicon in the form of globules by the method of sedimentation with the subsequent hydrothermal annealing. Nanoparticles has been observed by in a number of intermetallic compounds and ceramics during high-energy electron or ion irradiations when the ions completely penetrate

through the specimen (Wang et al. 2000). A porous material contains voids or tunnels of different shapes and sizes. These could be utilized as molecular sieves if the tunnels are small enough, or, to put clusters into if they are large enough. By designing the size of the channels the potential applications of such materials are very interesting. Mesoporous materials with varying compositions of inorganic compounds could lead to high-surface-area electrodes, catalysts, optoelectronic devices and sensors. Mesopores are 30–300 Å in diameter.

5 CONCLUSIONS

A study of natural ultra-dispersed systems initiated the creation of new, nanomaterial for the development of new nanotechnology. Importance of nanominerals is for reserves of raw materials (crude oil, nonmetallic minerals, hydro- and biosphere), for ecological problems (material cycles, contaminant sorption – and transport).

6 REFERENCES

- Chinju H. et al. 2003. Deposition behavior of latex particles in filtration process through glass packed column. Dept of Environmental Safety Research, Ibaraki, Japan.
- Gauthier-Lafaye F.& Holliger P. 1996 Nature analogy. *Geochim. et Cosmochim. Acta*, 60, 4831-4852.
- Wang L. et al. 2000. Irradiation-induced nanostructures. *Materials Science & Engineering*. A286, 72-80.

Synthesis and Properties of Organic Acid – Intercalated Manganese Nanocomposites Based on LDHs

U.König, H.Pöllmann

Dept. of Mineralogy and Geochemistry, University of Halle-Wittenberg, Germany

ABSTRACT: Layered double hydroxides (LDHs) are an important class of materials with permanent anion exchange capacity. Because of a high surface charge density they react easily with various types of organic anions. Short- and long-chain anions are rapidly exchanged for inorganic interlayer anions. Negatively charged carboxylic acids and sulfonic acids have been intercalated within the gallery space of LDHs. The chemical composition can be described with the following general formula: $[\text{Mn}_2^{2+}\text{Al}^{3+}(\text{OH})_6]^+[\text{A}^r \cdot n\text{H}_2\text{O}]^x$. Compounds with A^r = carboxylic acid and sulfonic acid molecules were synthesized. The exchange of inorganic interlamellar anions by organic ions was investigated. The $[\text{Mn-Al-NO}_3]$ LDH was selected as precursor for the anion exchange against organic acids. The basal spacing for the formiate derivate is 11,1 Å and increases with the chain length lineary whereas the basal spacing increases more with even C-atoms than uneven.

1 INTRODUCTION

There has been a growing interest in the intercalation of organic molecular anions between the layers of LDHs (Drezdzonek 1988, Kopka et al. 1988, Chibwe et al.1989, Kanezaki 1999, Meyn et al. 1990). Exchange of interlamellar anions by organic ions (dicarboxylic acid anions) was first reported by Miyata et al. 1973. Boehm et al. 1977 described preparation and anion exchange reactions of $[\text{Zn}_2\text{Cr}(\text{OH})_6][\text{NO}_3 \cdot 2\text{H}_2\text{O}]$.

This paper describes the exchange of anorganic anions (nitrate) against different organic acid anions (carboxylic acid, sulfonic acid) in LDHs containing manganese as divalent cation and aluminum as trivalent cation within the brucite-like layers.

2 STRUCTURE

The chemical composition of LDHs can be described with the following general formula: $[\text{Me}^{2+}_{1-x}\text{Me}^{3+}_x(\text{OH})_2]^+[\text{A}^r \cdot n\text{H}_2\text{O}]^x$. The structural principle of the LDHs is the substitution of Me^{2+} ions by other metal ions (Me^{3+}) in brucite like hydroxide layers. Substitution of Me^{2+} by Me^{3+} ions (compounds $[\text{Me}^{2+}_{1-x}\text{Me}^{3+}_x(\text{OH})_2]^+$) produces

positively charged layers. The excess positive charge of the layers is compensated by the negative charges of the interlayer anions. In many cases the interlayer anions can be exchanged by other anorganic and short-chain and long-chain organic anions, such as carboxylates or sulfonates, or anionic surfactants.

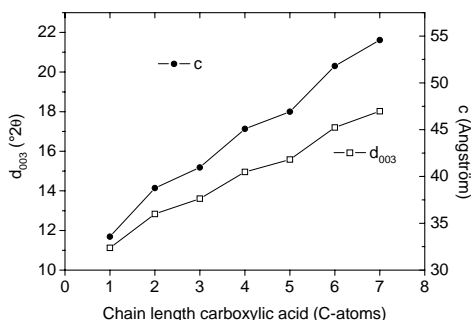


Figure 1. Chain length versus c - lattice parameter and basal spacing d of LDHs containing manganese as divalent cation and carboxylic acids at the interlayer

3 METHODS

3.1 Intercalation of organic anions into LDHs

The direct synthesis of materials with organic anions is limited, requiring the total exclusion of other anorganic anions at each stage (Reichle 1985). For that reason anion exchange reactions of layered double hydroxides are the more successful way to synthesis organic intercalated LDHs. Nitrate was selected as the precursor since carbonate or chloride anions are often difficult to be exchanged.

Manganese aluminum hydroxide $[\text{Mn}_2\text{Al}(\text{OH})_6]^+ [\text{NO}_3 \cdot n\text{H}_2\text{O}]^-$ was prepared with the coprecipitation method according to Miyata 1975, by reacting aqueous solutions containing a stoichiometric mixtures of the metallic nitrates and sodium hydroxide for 1 week at pH 9 and 60°. The solid was filtered and washed three times with deionised and decarbonated water. The double hydroxide was dispersed in an aqueous solution of organic acid salts (C1 to C10) to excess and allowed to react for 1 day at room temperature. The samples were continuously shaken during this period. The precipitate was further washed with deionized and decarbonated water three times. The whole synthesis of the manganese LDHs and the anion exchange reactions were performed under a CO_2 -free atmosphere. A glove box with continued circulation of N_2 was used to avoid carbonatisation and oxidation of Mn^{2+} to Mn^{3+} . The final cream-coloured slurry was investigated immediately by X-ray powder diffraction at 100% rh.

3.2 Investigating methods

X-ray pattern of wet pastes were obtained at 100% relative humidity (rh) with a Philips X'Pert diffractometer (Cu K α radiation) and a X'Celerator detector module with measurement times of 2.5 minutes and maximum intensities > 4 million counts per second. Scanning electron microscopy (SEM) techniques were used to get informations on particle size and habitus of the LDHs (Fig.2). Chemical analysis was carried out using inductiv coupled plasma - atomic emission spectroscopy (ICP-AES) to determine the MnO_2 and Al_2O_3 concentrations. Nitrogen, carbon and hydrogen amounts were analysed quantitatively by direct element analysis.

4 RESULTS

The exchange produce integral series of basal reflections in the XRD pattern (Fig.3). The basal spacings of the manganese aluminum LDHs with the carboxylic acid anions increase with the chain length. Figure 4 shows the d-values and the c-lattice parameter versus the chain length of the carboxylic

acids. The basal spacings are strictly higher than the spacing of the precursor.

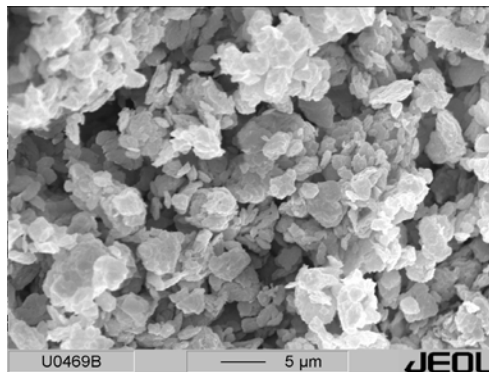


Figure 2 SEM image of $[\text{Mn-Al-C}_9\text{H}_{19}\text{SO}_3]$ LDH

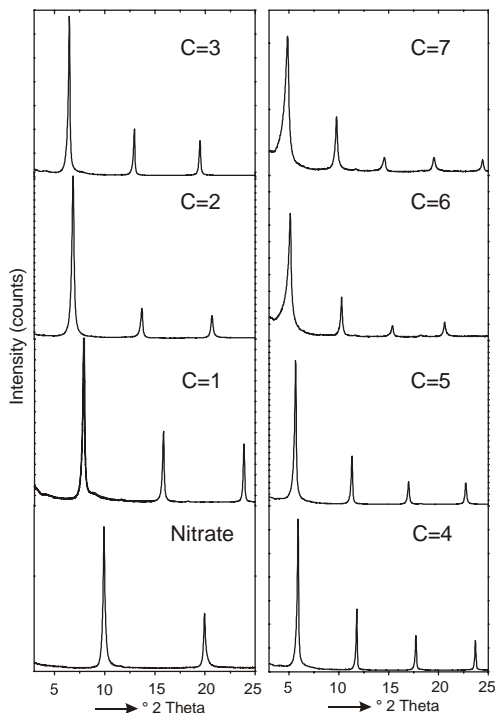


Figure 3 X-ray powder diffraction diagrams of basal reflections (00l) of manganese aluminum LDHs (maximum intensity 65000 counts (C2-C5), 40000 counts (C1), 15000 counts (nitrate, C6, C7)), C=chain length

The basal spacing for the formiate derivate is 11,1 Å and increases with the chain length lineary

whereas the basal spacing increases more with the even C-atoms than the uneven chain length.

The diffraction peaks are indexed using a hexagonal cell with rhombohedral symmetry (R-3m), where the *c* parameter corresponds to 3 times the interlamellar distance (d_{003}), and the *a* parameter, which represents the average intermetallic distance,

is calculated from the position of the d_{110} . If no (001) reflection can be measured the *a*-lattice parameter is taken from manganese aluminum nitrate hydrate before anion exchange. The lattice parameters, refined using least squares methods are shown in Table 1.

Table 1.

	a_0 (Å)	c_0 (Å)	d_{003} (Å)	V (Å ³)	Sp. G group	D_c (g * cm ⁻³)
[Mn ₂ Al(OH) ₆] [NO ₃ · 1,4 H ₂ O]	3.1707	26.6105	8.9	231.69	R-3m	2.337
[Mn ₂ Al(OH) ₆] [CHOO · 1,2 H ₂ O]	3.1728	33.5272	11.1	292.28	R-3m	1.736
[Mn ₂ Al(OH) ₆] [CH ₃ COO · 1,2 H ₂ O]	3.1707 ^{*1}	38.6883	12.9	336.84	R-3m	1.575
[Mn ₂ Al(OH) ₆] [C ₂ H ₅ COO · 1,2 H ₂ O]	3.1707 ^{*1}	40.9496	13.6	356.53	R-3m	1.554
[Mn ₂ Al(OH) ₆] [C ₃ H ₇ COO · 1,2 H ₂ O]	3.1707 ^{*1}	45.0311	15.0	392.06	R-3m	1.472
[Mn ₂ Al(OH) ₆] [C ₄ H ₉ COO · 1,2 H ₂ O]	3.1707 ^{*1}	46.9297	15.6	408.59	R-3m	1.470
[Mn ₂ Al(OH) ₆] [C ₅ H ₁₁ COO · 1,2 H ₂ O]	3.1693	51.8010	17.2	450.61	R-3m	1.384
[Mn ₂ Al(OH) ₆] [C ₆ H ₁₃ COO · 1,2 H ₂ O]	3.1707 ^{*1}	54.6760	18.1	476.03	R-3m	1.359

Metric parameters of carboxylic acid intercalated manganese LDHs at 100% relative humidity, *a*-lattice parameter taken from manganese aluminum nitrate hydrate before anion exchange

Exchange of nitrate against alkan-sulfonates or aromatic-sulfonates occurs in the same way. Results are in progress.

5 REFERENCES

- Boehm, H.P., Steinle, J. & Vieweger, C. (1977): [Zn₂Cr(OH)₆]X·2H₂O, neue Schichtverbindungen mit Anionenaustausch- und Quellvermögen. *Angew. Chem.*, 89, 259-260.
- Chibwe, K. & Jones, W. (1989): Intercalation of Organic and Inorganic Anions into Layered Double Hydroxides. *J. Chem. Soc., Chem. Commun.* 926-927.
- Drezdzon, M.A. (1988): Synthesis of Isopolymetalate-Pillared Hydrotalcite via Organic-Anion-Pillared Precursors. *Inorg. Chem.*, 27, 4628-4632.
- Kanezaki, E. (1999): Intercalation of naphthalene-2,6-disulfonate between layers of Mg and Al double hydroxide: preparation, powder X-ray diffraction, fourier transform infrared spectra and X-ray photoelectron spectra. *Mat. Res. Bull.*, Vol. 34, No. 9, 1435-1440.
- Kopka, H., Beneke, K. & Lagaly, G.J. (1988): Anionic Surfactants between Double Metal Hydroxide Layers. *J. Colloid Interface Sci.*, 123, 427-436.
- Meyn, M., Beneke, K. & Lagaly, G. (1990): Anion-exchange reactions of layered double hydroxides. *Inorganic Chemistry*, 29, 5201-5207.
- Miyata, S. & Kuruma, T. (1973): Synthesis of new hydrotalcite-like compounds and their physico-chemical properties. *Chem. Lett.*, 843-848.
- Miyata, S. (1975): The synthesis of hydrotalcite-like compounds and their structures and physico-chemical properties-I: the system Mg₂+Al₃+ClO₄⁻, Ni₂+Al₃+Cl⁻ and Zn₂+Al₃+Cl⁻. *Clays and clay minerals*, Vol. 23, 369-375.
- Reichle, W.T. (1985): Catalytic Reactions by Thermally Activated, Synthetic, Anionic Clay Minerals. *Journal of Catalysis*, 94, 547-557.

Manganese Nanocomposites Based on LDHs – Synthesis, Properties, and Characterization

U.König, H.Pöllmann

Dept. of Mineralogy and Geochemistry, University of Halle-Wittenberg, Germany

ABSTRACT: Synthetic manganese layered double hydroxides of the hydrotalcite-type, $[\text{Mn}_2\text{Al}(\text{OH})_6][\text{Cl}\cdot 1.5 \text{H}_2\text{O}]$ and $[\text{Mn}_2\text{Al}(\text{OH})_6][\text{NO}_3\cdot 1.4 \text{H}_2\text{O}]$ were prepared by the coprecipitation method. The physico-chemical properties were studied by high temperature and ultra rapid in situ X-ray diffraction measurements, thermal analysis infrared absorption spectra and chemical analysis. The influence of temperature (20°C, 40°C, and 60°C), pH (7, 8, 9, 10, and 11) and reaction time (1d, 4d, 7d, 14d, and 21d) were examined. The crystallinity of the phases increases with the reaction temperature rapidly. Best crystallinities were obtained at pH 8.5-9.5. The crystallinity of the phases increases with the reaction time. Thermal behaviour was investigated with thermal analysis and in-situ X-ray investigations. Dehydration is carried out at two stages. Interlayerwater not necessary for the structure dehydrates up to 160°C. Dehydroxylation of the brucite-like sheets starts at 200°C.

1 INTRODUCTION

The investigation of layered double hydroxide materials (LDHs) becomes an active field in nanocomposite research owing to their many important applications due to their synthetic flexibility in preparing catalyst and ceramic precursors and in tailor-making anion adsorbents, anion exchangers, scavengers, medicine and polymer stabilizers and the hydration of cements (Reichle 1986, Cavani et al. 1991, Rives et al. 1999, Xu et al. 2001).

LDHs are also known as mixed-metal layered hydroxides (MMLHs), or hydrotalcite-like compounds (HTLcs) belonging to a class of natural or synthetic anionic clays with the generic formula $[\text{Me}^{2+}_{1-x}\text{Me}^{3+}_x(\text{OH})_2]^{x+}[\text{A}^{n-}_{x/n}\cdot m\text{H}_2\text{O}]^{x-}$ where Me^{2+} and Me^{3+} are the metal cations, A^r the charge compensating anion and x is ideally between 0.20 and 0.33.

Despite the interesting properties of Mn^{2+} , like its d^5 paramagnetic structure and its potential use in oxidation catalysis, only one successful synthesis of [Mn-Al-Cl] LDH by Malherbe et al. 1999 has been reported as yet. Ribí 1951 described different manganese hydroxides. Taylor 1984 mentioned the preparation of [Mn-Al- CO_3] by induced hydrolysis

but without a single phase material. The crystal structures of the natural minerals shigaite, $[\text{Mn}_6\text{Al}_3(\text{OH})_{18}][(\text{SO}_4)_2\text{Na}\cdot 12\text{H}_2\text{O}]$, and charmarite, $[\text{Mn}_4\text{Al}_2(\text{OH})_{12}][\text{CO}_3\cdot 3\text{H}_2\text{O}]$, has been described by Cooper et al. 1996 and by Chao et al. 1997.

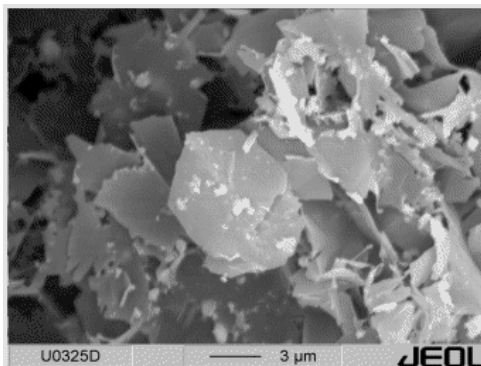


Figure 1 SEM image of [Mn-Al-Cl] LDH

The aim of the work is the synthesis of compounds with $\text{Me}^{2+} = \text{Mn}$, $\text{Me}^{3+} = \text{Al}$, $\text{A}^r = \text{Cl}^-$, NO_3^- and SO_4^{2-} and $x = 0.33$. The main problems encountered in preparing Mn^{2+} LDHs were due to

the difficulty in preventing oxidation of Mn^{2+} in basic solutions. A constant nitrogen atmosphere was used to avoid these effects.

2 STRUCTURE

The crystal structure of hydrotalcite is rhombohedral, R-3m. Synthetic hydrotalcite-like compounds have a structure consisting of brucite-like octahedral layers. Both divalent and trivalent cations are located in the center of oxygen octahedra formed by six hydroxyl groups. To balance the net positive charge, carried by trivalent cations, anions have to be intercalated into the interbrucite-like sheet space during the synthesis, which leads to the formation of a sandwich-like structure. Water molecules occupy residual space in the interlayer region. Additional single charged cations occur in the interlayer if sulfate is used as charge compensating anion. Structure plot q.v. Shigaite at same issue.

3 METHODS

3.1 Synthesis of LDHs containing manganese as divalent and aluminum as trivalent cation

Pure phases of lamellar manganese LDHs (Fig.1) were prepared, according to Miyata 1975, by reacting aqueous solutions containing a stoichiometric mixtures of metallic chlorites, nitrates or sulfates and sodium hydroxide at different temperatures (Fig.2), pH values (Fig.3) and reaction times (Fig.4). For the final synthesis the metallic salts were placed in sealed polyethylene bottles and dissolved under stirring conditions with deionized and CO_2 -free water with a water/solid ratio of 12.5 at 60°C. A 1M NaOH solution was slowly added up to pH 9. The whole synthesis of the manganese LDHs were performed under a CO_2 -free atmosphere. A glove box with continued circulation of N_2 was used to avoid carbonatisation and oxidation of Mn^{2+} to Mn^{3+} . The resulting precipitate was left for 1 week at 60°C into a drying chamber. During aging the pastes were shaken daily. The precipitate was further washed with deionized and CO_2 -free water three times. The final cream-coloured slurry was left to dry in a desiccator under nitrogen atmosphere and 35% relative humidity (rh) using saturated $CaCl_2$ solution.

3.2 Investigating methods

The precipitates of these reactions were filtered in a glove box and immediately investigated by X-ray powder diffraction. X-ray pattern of wet pastes were obtained at 100% relative humidity (rh) on a Philips X'Pert diffractometer (Cu $K\alpha$ radiation) and a

X'Celerator detector module with measurement times of 2.5 minutes and maximum intensities > 4 million counts per second. The samples were investigated again after drying under nitrogen atmosphere at a rh of 35%.

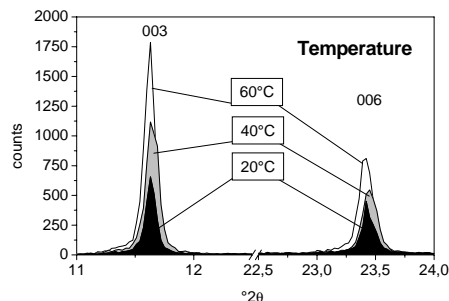


Figure 2 XRD pattern of [Mn-Al-Cl] LDHs synthesized under different temperatures

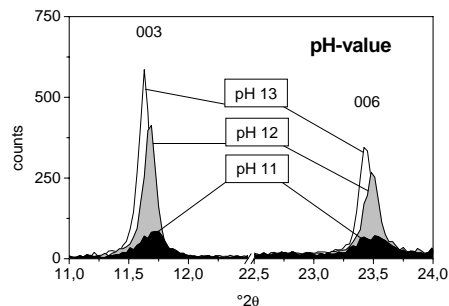


Figure 3 XRD pattern of [Mn-Al-Cl] LDHs synthesized under different pH values

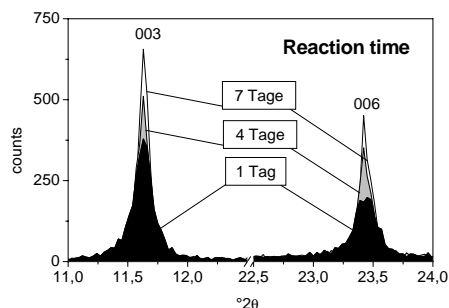


Figure 4 XRD pattern of [Mn-Al-Cl] LDHs synthesized under different reaction times

The dehydration behaviour was investigated with a high-temperature cell HTK 16 (Anton Paar). The measurements were performed on a platinum strip under air conditions up to 250°C. The patterns were

measured after 10 min equilibration at each temperature step of 5 °C in the range 25-250°C, and a heating rate of 60 K/min.

Scanning electron microscopy (SEM) techniques were used to get information on particle size and habits of the LDHs. Chemical analysis was carried out using inductive coupled plasma - atomic emission spectroscopy (ICP-AES) to determine the MnO₂ and Al₂O₃ concentrations. Nitrogen and chlorine amounts were analysed quantitatively by direct element analysis. The amount of water and stability ranges of different hydration stages of the LDHs were carried out by thermal analysis. Infrared (IR) spectroscopy was used to control CO₂ exclusion.

4 RESULTS

Best crystallinities (FWHM₍₀₀₆₎ 0,102 °2θ) were found at a pH value of 9, a temperature of 60°C and a reaction time of 1 week. The XRD pattern shown in Figures 5 and 6 give evidence for well crystallized single phase hydrotalcite-like material.

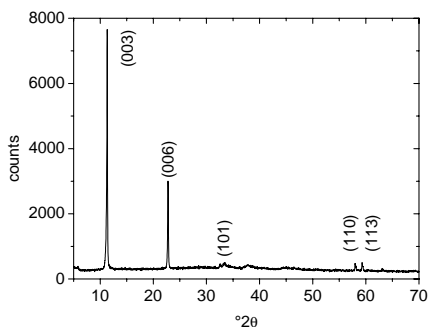


Figure 5 XRD pattern of a coprecipitated [Mn-Al-NO₃] LDH

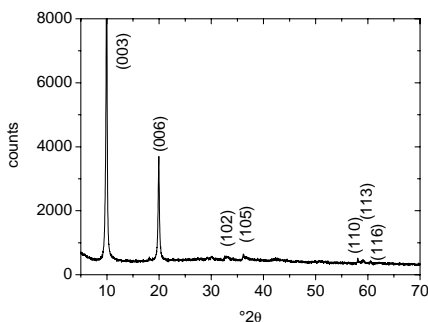


Figure 6 XRD pattern of a coprecipitated [Mn-Al-Cl] LDH

Because of the lamellar aggregates, the XRD pattern shows strong preferred orientation. The diffraction peaks are indexed using a hexagonal cell with rhombohedral symmetry (R-3m), where the *c* parameter corresponds to 3 times the interlamellar distance (*d*₀₀₃), and the *a* parameter, which represents the average intermetallic distance, is calculated from the position of the *d*₁₁₀. The lattice parameters, refined using least squares methods are shown in Table 1.

Table 1. Metric parameters of manganese LDHs at 35% rh.

	[Mn-Al-Cl] LDH	[Mn-Al-NO ₃] LDH
a₀ (Å)	3.18	3.17
c₀ (Å)	23.41	26.61
V (Å³)	204.74	231.69
Sp. Group	R-3m	R-3m
D_c (g*cm⁻³)	2.444	2.337

The elemental composition of the material (Table 2) was determined by inductively coupled plasma-atomic emission spectroscopy (ICP-AES).

Table 2. Chemical analysis of alkali-substituted shigaites.

(weight %)	[Mn-Al-Cl] LDH	[Mn-Al-NO ₃] LDH
Al₂O₃	16.9	15.6
MnO	45.4	41.1
Cl⁻	11.6	n.a.
NO₃⁻	n.a.	19.0
H₂O	26.4	24.3
sum	100.3	100.0

The IR spectrum corresponds to a non-contaminated material, i.e. there is no peak that can be attributed to the presence of carbonate (determination limit 0,1 mass%).

Figure 7 shows a general view of the high-temperature XRD patterns of [Mn-Al-Cl] LDH in the whole temperature range. There are 3 temperature regions that are classified by the XRD pattern: 25 ≤ T ≤ 160°C, 160 ≤ T ≤ 200°C and 200°C ≤ T. In the pattern of the first region, the (003) and (006) reflexes are due to that of the hydrotalcite-like layered structure of [Mn-Al-Cl] LDH. Up to 160°C interlayer water dehydrates from the structure and a dehydrated phase appears at this temperature. This phase is stable at 160-200°C and diminishes completely at 250°C. The dehydration processes of the synthesised phases investigated with X-ray diffractometry are in accordance with the results of the thermal analysis. Total weight loss of sample mass throughout the temperature range for the TG curve agrees well with the summation of all volatile components (H₂O) in the chemical formula.

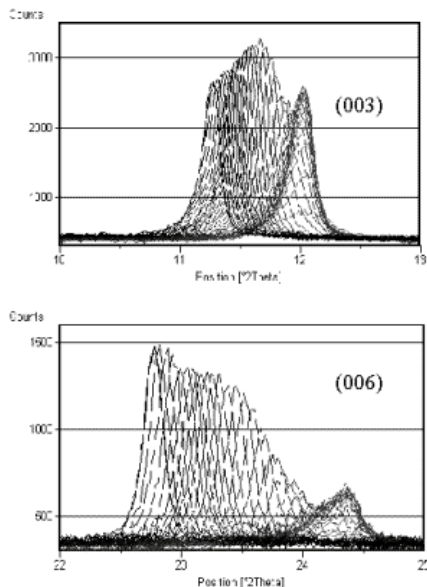
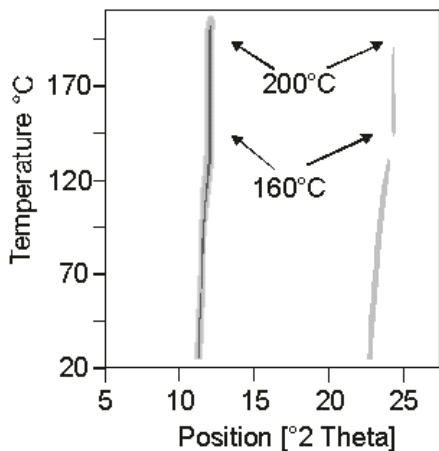


Figure 7 X-ray pattern of [Mn-Al-Cl-] LDH versus temperature (Scan number: 1=25°C, 10=70°C, 20=120°C, 30=170°C, 40=220°C) and (003), (006) reflection at different hydration stages

Two stages of weight loss (endothermic reactions) appear. Interlayerwater not necessary for the structure dehydrates up to 160°C. Dehydroxylation of the brucite-like sheets starts at 200°C.

5 CONCLUSIONS

In summary, we have shown that, when particular care is taken regarding the absence of oxygen (nitrogen atmosphere), it is possible to obtain by coprecipitation hydrotalcite-like compounds with manganese as the divalent cation and chlorite and nitrate as the charge balancing anion. Sulfates of the shigaite-type are described at a separate publication. The XRD pattern showed that the predominant phase is the double hydroxide. Several hydration stages of the synthesis products in the temperature range $25 < T < 160^\circ\text{C}$ followed by decomposition at temperatures above 200°C could be proved.

6 REFERENCES

- Cavani, F., Trifiro, F. & Vaccari, A. 1991. Hydrotalcite-type anionic clays: Preparation, properties and applications. *Catalysis Today*, 11, 173-301.
- Chao, G.Y. & Gault, R.A. 1997. Quintinite-2H, Quintinite-3T, Charmarite-2H, Charmarite-3T and Caresite-3T, a New Group of Carbonate Minerals Related to the Hydrotalcite – Manasseite Group. *Can. Min.*, 35, 1541-1549.
- Cooper, M.A. & Hawthorne, F.C. 1996. The crystal structure of shigaite, $[\text{AlMn}_2^{2+}(\text{OH})_6]_3(\text{SO}_4)_2\text{Na}(\text{H}_2\text{O})_6\{\text{H}_2\text{O}\}$, a hydrotalcite-group mineral. *Canadian Mineralogist*, 34, 91-97.
- Malherbe, F., Forano, C. and Besse, J.P. 1999. First coprecipitation of an LDH containing manganese as the divalent cation. *J. Mat. Sci. Letters*, 18, 1217-1219.
- Miyata, S. 1975. The synthesis of hydrotalcite-like compounds and their structures and physico-chemical properties-I: the system $\text{Mg}^{2+}\text{-Al}^{3+}\text{-ClO}_4^-$, $\text{Ni}^{2+}\text{-Al}^{3+}\text{-Cl}^-$ and $\text{Zn}^{2+}\text{-Al}^{3+}\text{-Cl}^-$. *Clays and clay minerals*, Vol. 23, 369-375.
- Reichle, W.T. 1986. Synthesis of anionic clay minerals (mixed metal hydroxides, hydrotalcite). *Solid state Ionics*, 22, 135-141.
- Ribi, E. 1951. Über die Hydroxiverbindungen des Mangans. PhD Thesis, Short edition, Bern, 16p.
- Rives, V. & Ulibarri, M.A. 1999. Layered Double Hydroxides (LDH) intercalated with metal coordination compounds and oxometalates. *Coordination Chemistry Reviews*, 181, 61-120.
- Taylor, R.M. 1984. The rapid formation of crystalline Double Hydroxy Salts and other compounds by controlled hydrolysis. *Clay Minerals*, 19, 519-603.
- Xu, Z.P., Xu, R. & Zeng, H.C. 2001. Sulfate-Functionalized Carbon/Metal-Oxide Nanocomposites from Hydrotalcite-like Compounds. *Nanoletters*, Vol.1, No.12, 703-706.

Cracking in Graded, Layered Structures

I.E.Reimanis & J.Chapa-Cabrera

Department of Metallurgical and Materials Engineering, Colorado School of Mines, Golden, Colorado, USA

ABSTRACT: Many materials that are optimized for performance are comprised of graded, layered structures. These structures typically contain complex residual stress distributions which may influence the fracture behavior, including both the crack driving force and the crack path. The effects of residual stress on fracture behavior are discussed for elastic and elastic-plastic discretely layered systems using numerical models and experimental results. One of the interesting results is that in the presence of residual stress, the fracture toughness is an independent parameter in determining the crack path. The implications for the design of advanced materials are discussed.

1 INTRODUCTION

1.1 Motivation

Many advanced materials are made using graded and/or layered composition so that properties may be spatially tailored to achieve optimum overall performance. Such materials include coatings for tools and dies, multilayer packages for electronics, fuel cells and airplane structures. Because of the intentional compositional variations, the fracture behavior of graded and layered materials is difficult to predict, and currently no general theories for failure exist. The prediction of crack paths is also of interest in the fracture of heterogeneous rock for mining applications in which costs are reduced when fractures occur with the minimum amount of energy. The goal of this work is to examine how property mismatches may alter crack paths and how that information may be used to better predict fracture.

1.2 Background

Crack propagation in brittle materials occurs in the direction of maximum principal stress (Lawn 1992). This direction is the same as the direction in which the shear stress is equal to zero. If in a monolithic body, a well-known applied load dominates the

stress field, then it is straightforward to determine the crack path; it is in the direction in which the normal principal stress is maximum. For an inhomogeneous material, such as a layered composite, calculations must be made to determine how the applied load, as affected by the material inhomogeneities, affects the crack tip stresses. If residual stresses are present, as is typical for composites, then these may superimpose onto the applied loads to produce a stress field that is difficult to predict.

The particular configuration and material system considered here is a notch or crack lying parallel to the layers in a graded, layered composite as depicted in Figure 1. When the specimen is loaded in four point bending, crack propagation occurs at a critical load that corresponds with the crack tip stress intensity factor exceeding the critical stress intensity factor, generally termed the toughness. If the crack is not located symmetrically within the specimen geometry, it will deviate out of the plane of the notch (Gu & Asaro 1998). Copper and tungsten have been chosen to represent a model brittle-ductile material combination in which no chemical reactions are present. Thus, the elastic, plastic and thermal properties of different layers may be controlled by mixing the appropriate ratio of Cu and W. Measured

properties of the layers used here are shown in Table 1, adapted from Chapa & Reimanis (2002). Cu-rich compositions are more compliant and exhibit lower yield strengths. While the stiffness and yield strength are important properties that determine the crack path (i.e., the crack is drawn towards the more compliant material), the thermal residual stress field may dominate the cracking behavior. The objectives of the work are to benchmark a numerical model with experiments (described next), and then to use the model to understand how residual stress plays a role.

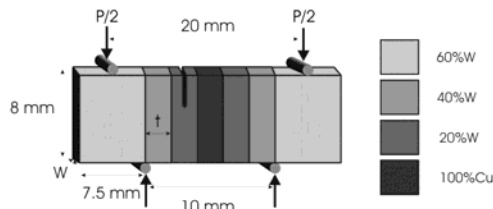


Figure 1. Specimen configuration for the modeling and experiments. The asymmetric geometry means the crack will kink out of the plane of the notch. The problem is to determine the crack kink angle.

Table 1. Properties of different compositions of Cu.W composites, measured by the present authors (Chapa & Reimanis 2002). Percentages are by volume.

	E (GPa)*	σ_y (MPa)	TEC ($^{\circ}\text{C}^{-1}$) ¹	K_{IC} (MPa $\text{m}^{1/2}$) Experimental
Cu	106	35	17.5	NA
20%W	160	146	14.9	18
40%W	203	311	11.2	16
60%W	190	369	8.9	NA

2 EXPERIMENTS: METHODS AND RESULTS

Layered composites similar to that shown in Figure 1 were made by hot pressing powders of Cu and W at 985°C for 15 minutes under 40 MPa applied uniaxial pressure in a graphite element furnace. The resulting dense composites were machined into specimens for testing in the geometry shown in Figure 1. Four specimen types were examined: in two types the interlayer thickness, t , was 2 mm and the notch was placed either in the 40%W layer or the 20%W layer. In the other two types, the layer thickness was 4 mm. Further details are discussed elsewhere (Chapa & Reimanis 2002; Chapa 2001).

A uniaxial mechanical tester was used to load the specimen such that it experienced four point bending. At a critical load, a crack propagated from the notch base. The angle at which the crack deviated out of the initial notch plane was measured for each experiment. A typical experimental result is

shown in Figure 2. Ductile failure modes were observed for all fracture; this indicated that plastic deformation accompanied fracture.

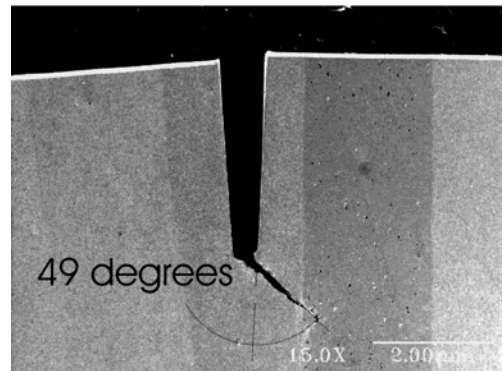


Figure 2. An example crack paths after testing in the configuration shown in Figure 1. The notch was in the 20%W layer and deflects towards the 100% Cu layer to the right, at an angle of 49°.

3 FINITE ELEMENT MODELING: METHODS AND RESULTS

Finite element modeling was conducted using the software ABAQUS. The model treated a 3 mm deep crack instead of a notch. The mesh is described in detail in Chapa & Reimanis (2001). After meshing, the model is subjected to a thermal cool from 300°C, the temperature below which Cu no longer relieves thermal residual stress, to 25°C. In this way, thermal residual stresses are imposed on the specimen. Additionally, the specimen is loaded in four point bending as shown in Figure 1. The stress field around the crack tip is determined and plotted as a function of radial angle around the crack tip. In this way, the direction in which the normal stress is maximum is found. This direction is expressed as the angle from a line parallel to the initial crack, and is the same angle as measured experimentally in Figure 2. For the modeling, it is termed the crack kink angle. The crack kink angle is generally a function of the applied load because the stress field is determined by both the thermal residual stress and the applied load; as the applied load increases, the stress distribution around the crack tip changes accordingly. The model was calibrated by reproducing the experimental results, like the one shown in Figure 2. It was also observed that for all the experiments in which the crack deflection angle was non-zero, plastic deformation in the adjacent layer was responsible for the cracking behavior observed. In other words, the residual stress field did not substantially perturb the overall stress field that governed the crack path. On the other hand, a more

interesting result is observed when no plastic deformation is present, as described next.

The finite element model was used to predict the crack kinking angle when no plasticity was present. The same properties were used above (Tab.1), except that linear elastic elements were employed. A simpler and more general loading configuration is used to depict the results: instead of a four point bending, the load was applied by displacements at the ends of the bar in Figure 1, in a single edged notched type specimen geometry, as depicted in Figure 3.

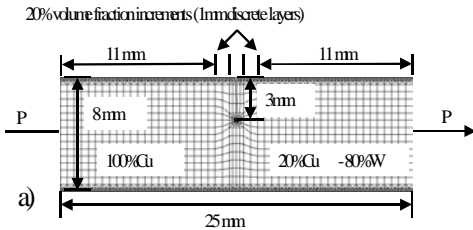


Figure 3: The single edge notch test specimen used for the finite element modeling. The central portion of the specimen is graded in 20 vol % increments.

Because the crack kinks, an equivalent stress intensity factor must be calculated from the main crack stress intensity factor. The equivalent stress intensity factor increases as a function of increasing applied load. When the equivalent stress intensity factor reaches a critical value, the toughness of the material, then the crack will extend. Results for a specific case of the model are shown in Figure 4. The curve is applicable to any linear elastic material combination. Two example materials are indicated with the dashed lines: one material has a toughness of $7 \text{ MPa m}^{1/2}$ and the other $16 \text{ MPa m}^{1/2}$. It is apparent that the angle of crack kinking is highest for the material with the lowest toughness. The thermal residual stress has a strong influence on cracking behavior when the material has a low toughness. Also shown is a line labeled 'No Residual Stress', calculated by running the model such that the thermal expansion coefficients of Cu and W are identical. The crack kink angle in this case is entirely determined by the applied stress field.

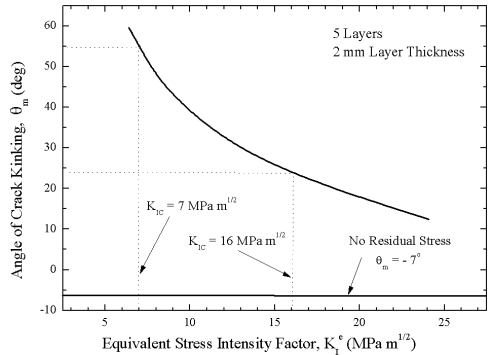


Figure 4: Angle of crack kinking as predicted from numerical model, as a function of the stress intensity factor for a kinked crack. When no thermal residual stress is included in the model, then the crack kink angle is a constant (-7°), simply governed by the elastic mismatch. A rich behavior is observed when residual stresses are present: for tough materials, the crack kink angle is smaller than for brittle materials.

4 CONCLUSIONS

The modeling results above show that the crack path in graded, layered structures may be directly linked with the fracture toughness of the material containing the crack. This dependence only occurs when thermal residual stresses are present. The dependence is more pronounced when the toughness is low; that is, weak materials are more susceptible to the effects of thermal residual stress.

The results have implications in predicting crack paths in layered or inhomogeneous materials in which thermal residual stresses exist. The results also have implications on the relative stability of cracks near interfaces. In particular, if a stable crack is driven and kinks into a material with lower toughness, the conditions for stability may change. Thus, the residual stress must be included in any complete model that describes crack paths in materials. The effect is most important for brittle materials.

5 REFERENCES

- Chapa-Cabrera, J. & Reimanis, I. E. 2001. Effects of Residual Stress and Geometry on Crack Kink Angles in Graded Composites. *Int. J. of Eng. Fract. Mech.* 69: 14-16, 1667-1678.
- Chapa-Cabrera, J. & Reimanis, I. E. 2002. Crack Deflection in Compositionally Graded Cu-W Composites. *Phil Mag. A*, 82: 17/18, 3393-3403.
- Gu, P. & Asaro, R. 1998. Cracks in functionally graded materials. *Int. J. Solids Struct.* 34: 1-17.
- Lawn, B. 1992. *Fracture of Brittle Solids*. Cambridge Solid State Series.

Synthesis of a Mesoporous Material from Diatomite

V.Sanhueza, U.Kelm, L.López-Escobar & R.Cid

Instituto de Geología Económica Aplicada, Universidad de Concepción, Concepción, Chile

ABSTRACT: A mesoporous material was synthesized from diatomite, a natural raw material. The synthesis was carried out under hydrothermal conditions at 135°C for 24 h. The following were the molar proportions of the reaction gel: 222.3 SiO₂: 5.7Al₂O₃: 1.0Na₂O: 101.0 H₂O: 1.1 CTAB (cetyltrimethylammonium bromide). The solid obtained was identified by X-ray diffraction (XRD) and characterized by scanning electron microscopy (SEM), thermal gravimetry and differential thermal analysis (DTA-TGA).

1 INTRODUCTION

The interest for porous materials is not only academic but also industrial. In fact, a significant part of the world economy depends upon nonoporous materials (Zamarev & Kuznetsov 1993). It is interesting to note that zeolitic materials are used in refining processes at the petrochemical industry. The utilization of natural zeolites in catalysis and adsorption is limited by their low adsorption capacity and the presence of contaminants such as Fe and other poisonous materials (Giannetto et al. 2000). For these reasons, the efforts are actually oriented to prepare synthetic zeolites that fit the requirements of the industrial processes. Since it was necessary to process larger molecules than those commonly accepted by zeolites, in the 90 decade scientists began to synthesize the M41S mesoporous family. This family is integrated by the following materials: MCM-41, MCM-48 and MCM-50.

In this work we report the synthesis of a mesoporous material from diatomite (Table 1), a natural raw material. In previous papers (Sanhueza et al. 2003; 2004) we have reported the synthesis of mordenite and ZSM-5 zeolites also using diatomite as starting material. Diatomite is a fine grain sediment consisting of amorphous silica derived from skeletons of diatoms. The SiO₂ content of this

sediment normally fluctuates between 80 and 90%, existing even purer varieties. Minor contents of aluminum, iron, alkaline, and alkaline earth elements allow the presence of co-sedimentary minerals such as clays, quartz, gypsum, and feldspars. Synonymous of diatomite are: diatom earth and kiesselguhr. Obsolete synonymous are: tripolite, "tripoli powder", and "infusorial earth".

2 EXPERIMENTAL PROCEDURE

The synthesis of the mesoporous material from diatomite was carried out under hydrothermal conditions at 135°C, being the following the molar proportions of the reaction gel: 222.3 SiO₂ : 5.7Al₂O₃: 1.0Na₂O: 101.0 H₂O: 1.1 CTAB.

Parr steel autoclave reactor was used in the experiments. In a Teflon vessel was firstly introduced 2.78 g of CTAB, and then 12.82 g of distilled H₂O and 10.18 g of SBR OH anion exchange resin (SUPELCO 13418-U). The mixture was stirred for 24 h and then filtered. Finally, 1.00 g of diatomite and 0.12 g of NaAlO₂ (Riedel of Haën 13404) were added to the CTAB/OH filtrated. The Teflon vessel was then placed into the steel autoclave, under autogenic pressure, and kept at 135°C for 24 hours in a static system oven. Once the run was completed

and the system cooled down, the products were washed with abundant distilled water, filtered using Advantec 5B filter paper and dried at 120°C for 15 hours.

Table 1. Normalized composition (100 wt %) of the starting diatomite material.

Oxide (wt%)	Diatomite
SiO ₂	74.50
TiO ₂	0.18
Al ₂ O ₃	14.31
Fe ₂ O ₃	1.23
MnO	0.08
MgO	0.26
CaO	0.91
Na ₂ O	4.08
K ₂ O	4.42
P ₂ O ₅	0.02
Total	100.00

3 CHARACTERISATION

The micrograph was obtained with an ETEC Corporation microscope, Autoscan model, operated at 30 KV. The crystalline phase synthesized was identified by XRD (Rigaku Diffractometer "Geigerflex" D/max-IIC) using vanadium filter CrK α radiation (CrK α =0.229100). Thermal gravimetry and differential thermal analysis (TGA-DTA) were performed on a RIGAKU TAS 100 equipment under air atmosphere.

4 RESULTS

Figure 1 shows the XRD pattern of the material obtained. This exhibits a more intense peak at degree 2 theta ($d=41.5211\text{\AA}$), indicating that a mesoporous material, with a cell parameter of approximate 47.9 \AA , crystallized. In Figure 2, it is possible to appreciate cumulus of spheres that correspond to a mesoporous material.

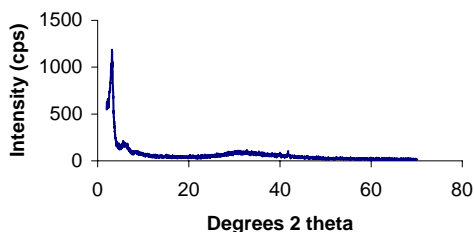


Figure 1. X-ray diffractogram of the mesoporous material synthesized from diatomite.

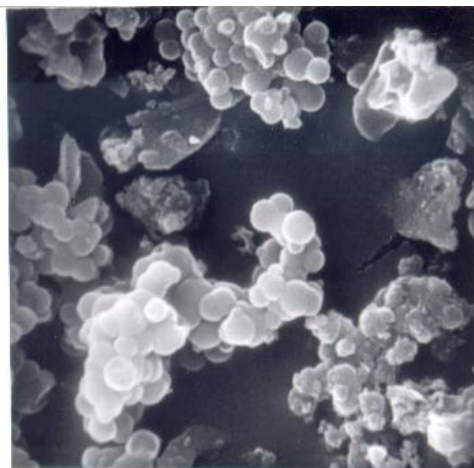


Figure 2. SEM micrograph of mesoporous material formed from diatomite (X40000).

Thermogravimetric analysis (TGA) (Figure 3) of the material shows three distinct weight losses. A first weight loss corresponds to the desorption and removal of water molecules physisorbed on the external surface area of the material or occluded in the macropores present between material aggregates. A second weight loss, accompanied by exotherms, occurs between 200°C and 600°C and is attributed to the removal of the CTAB. Finally, a third weight loss above 600°C is related to the loss from the condensation of adjacent silanol groups to form siloxane bonds. The DTA indicates that this material has a thermal stability at least up to 900°C.

5 CONCLUSIONS

The results presented in this paper demonstrate that it is possible to obtain a mesoporous material under hydrothermal conditions, at 135°C, with a thermal stability at least up to 900°C and a reaction time of 24 hours. This can be achieved with the presence of CTAB as a template agent, using natural diatomite, as a starting material. Actually, we have already synthesized two zeolites (mordenite and ZSM-5) from diatomite, but under different conditions.

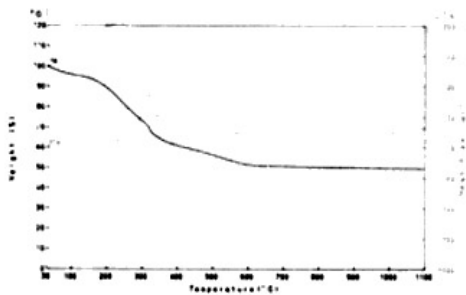


Figure 3. DTA and TG curves of the mesoporous material.

6 ACKNOWLEDGEMENTS:

The authors acknowledge the support of Instituto GEA de la Universidad de Concepción. V. Sanhueza thanks the financial support of the Doctoral FONDECYT Project N°200-0131.

7 REFERENCES

- Giannetto, G. Montes, A & Rodríguez, G (edited by Giannetto, G. Montes, A & Rodríguez, G) 2000. Zeolitas: Características, Propiedades y Aplicaciones Industriales. Venezuela: Innovación Tecnológica Facultad de Ingeniería, Universidad Central de Venezuela.
- Sanhueza, V. Kelm, U. & Cid, R. Synthesis of mordenite from diatomite: a case of zeolite synthesis from natural material. *Journal of Chemical Technology and Biotechnology* 78(2003)485-488.
- Sanhueza, V. Kelm, U. Cid, R. & López-Escobar, L. 2004. Synthesis of ZSM-5 from Diatomite: A case of zeolite synthesis from a natural material. *Journal of Chemical Technology and Biotechnology* (Submitted).
- Zamarev, KI & Kuznetsov (Rao, CRN ed.) 1993. *Chemistry of Advanced Materials*. Oxford.

Graphite-hexagonal Diamond Transition and Surviving Compressed Graphite

A. Yoshiasa

Department of Erath Science, Faculty of Science, Kumamoto University, Kumamoto 860-8555, Japan

A. Nakatsuka

Department of Advanced Material Science and Engineering, Yamaguchi University, Yamaguchi 755-8611, Japan

M. Okube

Department of Erath and Space Science, Osaka University, Toyonaka 560-0043, Osaka, Japan

H. Okudera

Max-Planck-Institute FKF, Heisenbergstr. 1, 70569 Stuttgart, Germany

ABSTRACT: Detail structure of surviving compressed graphite (GR) is reported and formation of the surviving GR is discussed based on the graphite-hexagonal diamond transition mechanism. Surviving compressed GR were always observed when hexagonal diamond (hDIA) was synthesized at 20 GPa from 800 to 2000 C°. Diffraction patterns were analyzed by a Whole Powder Pattern Fitting method and Rietveld method in order to determine the intensity and full width at half maximum for each peak of surviving compressed graphite. Broad and asymmetric 002 Bragg peak of GR corresponds to the summation of the ordinary uncompressed and compressed GR. The mass fraction of the residual uncompressed GR and compressed GR is estimated to be 3:97 at 1200 C°. Our experimental observations indicate that the thermal equilibrium in the system at 20 GPa is not satisfactory attained even at 2000 C°. Considerable amount of residual GR is trapped and surviving within the host diamond crystals, because the simultaneous domain growth of both hDIA and cDIA does not proceed without discontinuity.

1 INTRODUCTION

Carbon exhibits several crystalline forms and has been studied many aspects because of its fascinating physical properties. Lonsdaleite (Fron del & Marvin 1967) is a hexagonal modification of cubic diamond found in meteorite. Hexagonal diamond (hDIA) has been synthesized directly from graphite (GR) under high pressure and high temperature by means of both static and shock compression (Aust & Drickamer 1963, Bundy & Kasper 1967, Clarke & Uher 1984). It always coexists with cubic diamond (cDIA) and graphite (Fron del & Marvin 1967, Hanneman et al. 1967). Detailed structures of hDIA was revealed by Rietveld refinements and transition mechanism from GR to hDIA was discussed by comparing the experimental results and those of previous simulation studies (Yoshiasa et al. 2003).

Considerable amount of residual uncompressed GR and surviving compressed GR co-exists with hDIA but detail structures for these GR were not reported so far. Precise structural characterization of the phases is of fundamental importance for understanding the physical properties. In this study, detail structure of surviving compressed GR is determined by Whole Powder Pattern Fitting method (WPPF) (Toraya 1986) and Rietveld methods.

Formation of the surviving compressed GR is discussed based on the GR-hDIA transition mechanism.

2 EXPERIMENTAL

2.1 Synthesis

Hexagonal diamond and surviving compressed GR were synthesized using a Kawai-type high-pressure apparatus at 20 GPa under various temperatures from 800 to 2000 C°. Starting GR sample used in this study is a pyrolytic graphite for monochromator similar to the sample used by Bundy & Kasper (1967). Detail of the syntheses is shown in the literature (Nakatsuka et al. 1999, Yoshiasa et al. 2003). The sample temperatures were monitored by a W25%Re-W3%Re thermocouple. The sample was first compressed at room temperature up to the prescribed pressure and then temperature was raised under constant applied load. After being kept at the desired condition for 20 min, temperature was quenched by shutting off the electrical current supply to the heater. The pressure was released slowly and the products were recovered at ambient conditions. The obtained specimens were in the form of a hard, gray, and brittle polycrystalline mass.

2.2 Diffraction intensity data collection

X-ray diffraction experiments for recovered specimens are performed using an imaging plate (IP) detector having a wide dynamic range and rotating capillary specimens were used in order to reduce a preferred orientation effect for the WPPF method and Rietveld method. Measurements were carried out on a Rigaku RAXIS-IV system with a rotating anode (50 kV, 250 mA, monochromatized MoK α -radiation, $\lambda=0.71069$ Å and 50 kV and 150 mA, monochromatized CuK α -radiation, $\lambda=1.54184$ Å) (Yoshiasa et al. 2000). The specimen was filled in a 0.30 mm diameter capillary which was rotated with a scan speed of 4°/min in ϕ . For data reduction and processing the programs PROCESS (Rigaku Co. Ltd) and PIP (Fujihisa & Aoki 1998) were used. Two dimensional diffraction image on the IP was integrated and converted into one-dimensional intensity-2 θ diffraction patterns.

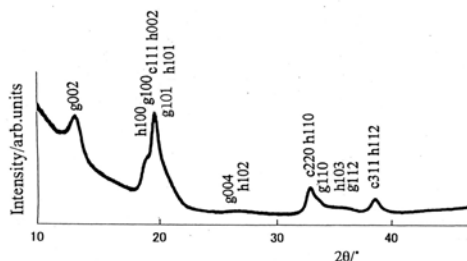


Figure 1. Typical X-ray diffraction profiles (MoK α radiation) of a recovered specimen from 1200 °C and 20 GPa, where g, h and c indicate graphite, hexagonal diamond and cubic diamond, respectively.

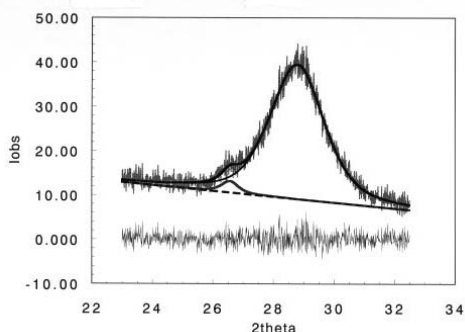


Figure 2. Profile (CuK α radiation) near the 002 peak position of graphite. The reflections at $2\theta=26.5^\circ$ and $2\theta=28.8^\circ$ are the 002 peaks of ordinary uncompressed and compressed graphite, respectively. Observed and calculated profile intensities are represented. Difference between the two intensities are plotted at the bottom of the diagram on the same scale as above.

2.3 Analysis

Observed diffraction patterns for the specimen annealed at 1200 °C were resolved into individual peaks using the computer program WPPF (Toraya 1986) and Rietan-2000 (Izumi 2000). The intensity and full width at half maximum for each peak was determined. Detail of analyses is shown in literature (Yoshiasa et al. 2003). A part of the profile fitting results is shown in Fig. 2. Six independent reflections could be observed and successfully indexed by assuming the hexagonal cell (Tab.1 and 2), though the intense lines for GR is only the GR.002. Here, GR.002 represents the 002 reflection from GR. No further reflection could be observed.

Table 1. Observed and calculated d (Å) values for observed diffraction peaks of surviving compressed graphite ($a=2.486(7)$ c=6.23(4) (Å)).

hkl	I(f)	d _{obs}	d _{calc}
002	100	3.10	3.11
100	5	2.14	2.15
101	8	2.02	2.03
004	5	1.56	1.56
110	5	1.25	1.24
112	5	1.15	1.15

Table 2. Full width at half maximum (°) for compressed graphite (comGR) and uncompressed graphite (uncomGR) in hexagonal diamond sample and for compressed graphite-like BN (comBN) and uncompressed graphite-like BN (uncomBN) in wurtzite-type BN sample.

hkl	comGR	uncomGR
002	2.2	0.8
100	1.3	-
101	1.5	-
004	2.3	-
110	1.2	-
112	1.3	-

hkl	comBN*	uncomBN*
002	2.7	0.3

*Data from Yoshiasa et al. 2003

3 RESULTS

3.1 Graphite phases in the products

Peaks for surviving compressed GR were observed at the 002, 100, 101, 004, 110 and 112 Bragg peak positions. In Fig. 2, broad and asymmetric peak was observed at the strongest 002 Bragg peak positions of GR. The reflection at 3.1 Å ($2\theta=28.8^\circ$) is GR trapped within the host crystals of hDIA and cDIA (Bundy & Kasper 1967, Yoshiasa et al. 2003). The broad and asymmetric peak of GR.002 is made up by the two peaks of an ordinary uncompressed GR ($2\theta=26.5^\circ$) and a surviving compressed and broad 3.10 Å line ($2\theta=28.8^\circ$) due to compressed GR trapped within the crystallites of diamonds. The

broad and asymmetric peak profile for GR.002 in diamond is similar to that for 002 Bragg peak from graphite-like BN in wurtzite-type BN (Yoshiasa et al. 2003).

The FWHM of the 00l reflections for surviving compressed GR is large than that of the h00 and hk0 reflections. Though the GR.002 of surviving compressed GR is extremely broad, the FWHM of GR.002 for residual uncompressed GR is relatively small. The feature was confirmed for the 002 Bragg peak from graphite-like BN in wurtzite-type BN.

The formation of surviving compressed GR was confirmed in all the present products (synthesized under the condition of 20Gpa 800-2000 C°) though residual uncompressed GR extinguished at the temperature higher than 1600 C°. The mass fraction of hDIA, cDIA and total GR was published in the literature (Yoshiasa et al. 2003). The mass fraction of hDIA, cDIA and total GR is 37:38:25 in the specimens annealed at 1200 C°. The mass fraction of the residual uncompressed GR and surviving compressed GR is estimated to be 3:97 based on comparing the both integrated intensities (Fig. 2).

3.2 Lattice constants and bond distances of surviving compressed graphite

The determined crystal data and selected interatomic distances are listed in Tab. 3. The lattice parameters for surviving compressed GR is extremely different from ordinal GR: the c-axis is largely compressed while the a-axis is elongated slightly. The C-C apical distance parallel to the c-axis in surviving compressed GR is shorter than that in ordinal graphite. The C-C basal distance is longer than that in ordinal graphite. Namely, the effect of compression under the condition trapped within the host diamond crystals results in the enhanced covalency of apical bond and the reduced covalency of basal one. The sp² characteristics is different in both compressed and ordinal graphite. The character of bonding for carbon atom in surviving compressed GR lies between hDIA and ordinal graphite.

Table 3. X-ray data of hexagonal diamond, graphite (GR) and compressed graphite (comGR).

	hDIA	comGR	GR
a (Å)	2.508(4)	2.486(7)	2.470(1)
c (Å)	4.183(6)	6.23(4)	6.724(1)
Distance (Å)			
C-C apical	1.59(4)	3.12(2)	3.362(1)
C-C basal	1.53(2)	1.44(2)	1.426(1)

4 DISCUSSION

4.1 Crystallite size of surviving compressed graphite

The FWHM for 00l peak is larger than those for h00 and hk0 peaks. The approximate crystallite sizes of surviving compressed graphite were determined by Sherer's method using X-ray diffraction profile broadening. The obtained crystallite size based on 00l reflections indicates the approximate thickness of graphite layer along <00l> direction and the average thickness is a few tens of Angstroms. The average crystallite width determined by h0l and hk0 reflections is ca. 50 Å. Peak broadening in profile can be explained by the morphology of graphite crystals. The diffraction peaks for 00l reflections are significantly broadened and this feature is similar to the peak profiles observed in hDIA. The crystallite size of surviving compressed GR has smaller size than those of both diamonds.

4.2 GR-hDIA transition mechanism and surviving compressed graphite

The hDIA structure is metastable compared to the cDIA structure and the transformation to hDIA can occur only from GR crystals under nonequilibrium condition (Yoshiasa et al. 2003). The transition probability from GR to hDIA is same as that into cDIA in the samples annealed between 800 and 1400 C°. Real GR crystals have enough macroscopic sizes with long-range order of stacking layers (ABAB stacking). For the growth of cDIA domain, the puckering the GR layers and the collective slide of the layers to ABCABC stacking need simultaneously to achieve the long-range order. The puckering the GR layers and the collective slide of the layers to AB'AB' stacking also need simultaneously for the growth of hDIA domain. The manner of the puckering the graphite layers for cDIA (chair-shaped 6-rings) is different from that for hDIA (boat-shaped 6-rings). GR have a delocalized orbital in the layer and relatively feeble bonding between the atoms of different layers, which easily slide over one another. The metastable hDIA appears, because the cooperative phenomenon of the puckering the GR layer and the collective slide with long-range order for cDIA is not achieved satisfactorily.

Orientation relations of the phase transformation from GR to hDIA and cDIA were revealed by many authors (Bundy & Kasper 1967, Yagi et al. 1992, Yoshiasa et al. 2003): GR<120> is parallel to hDIA<00l>, GR(002) is parallel to hDIA(100) and GR(002) is parallel to cDIA(111). Here, GR(002) and GR<120> represent the 002 plane and 120 crystal zone of graphite. hDIA<00l> and cDIA<111> is equal to the stacking direction of hexagonal and cubic closest packing, respectively.

The stacking direction of GR layer ($//$ c -axis) is equal to that of c DIA while it disagree with that of h DIA. The simultaneous domain growth of both h DIA and c DIA does not proceed without discontinuity (Fig. 3). Considerable amount of residual uncompressed and compressed GR is, therefore, trapped and surviving within the host diamond crystals.

The proportion of h DIA to c DIA decreases with increase in temperature higher than $1600\text{ }^{\circ}\text{C}$. In the present system, the graphite phase as a trapped and surviving phase in DIA still remain even at $2000\text{ }^{\circ}\text{C}$. Our experimental observations indicate that the thermal equilibrium in the system at 20 GPa is not satisfactory attained even at $2000\text{ }^{\circ}\text{C}$. No GR observed in synthesized diamond at temperature higher than $2300\text{ }^{\circ}\text{C}$ (Irifune et al. 2003). It seems that diffusion process with break C-C bonds is probable and the thermal equilibrium in the system is attained at $2300\text{ }^{\circ}\text{C}$.

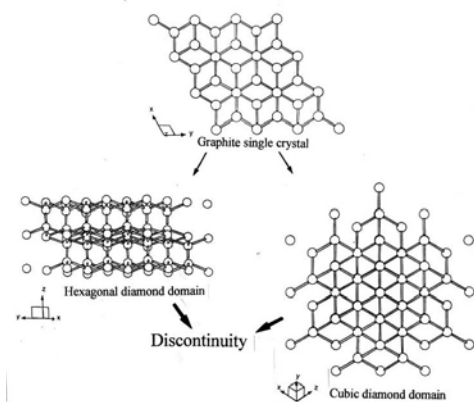


Figure 3. Local changes of atomic configuration for the GR-to- h DIA and GR-to- c DIA transformations. The c axis of GR coincides with $[1-210]$ of h DIA and $[111]$ of c DIA.

5 CONCLUSIONS

Surviving compressed GR were always observed when h DIA was synthesized at 20 GPa from 800 to $2000\text{ }^{\circ}\text{C}$. Residual uncompressed GR extinguished at the temperature higher than $1600\text{ }^{\circ}\text{C}$. The mass fraction of the residual uncompressed GR and compressed GR is estimated to be 3:97 at $1200\text{ }^{\circ}\text{C}$. The sp^2 characteristics is different in both compressed and ordinal graphite. The character of bonding for carbon atom in surviving compressed GR lies between h DIA and ordinal graphite. Peak broadening in profile can be explained by the morphology of graphite crystals. The h DIA structure is metastable compared to the c DIA structure and the

transformation to h DIA can occur only from GR crystals under nonequilibrium condition. The stacking direction of GR layer ($//$ c -axis) is equal to that of c DIA while it disagree with that of h DIA. Considerable amount of residual uncompressed and compressed GR is trapped and surviving within the host diamond crystals because the simultaneous domain growth of both h DIA and c DIA does not proceed without discontinuity. Thermal equilibrium in the system is not satisfactory attained even at $2000\text{ }^{\circ}\text{C}$. In the system, diffusion process with break C-C bonds is probable and the thermal equilibrium is attained at $2300\text{ }^{\circ}\text{C}$.

6 REFERENCES

- Aust, R.B. & Drickamer, H.G. (1963): Carbon: A new crystalline phase. *Science* 140, 817-819.
- Bundy, F.P. & Kasper, J.S. (1967): Hexagonal diamond – A new form of carbon. *J. Chem. Phys.* 46, 3437-3446.
- Clarke, R. & Uher, C. (1984): High pressure properties of graphite and its intercalation compounds. *Adv. Phys.* 33, 469-566.
- Fron del, C. & U.B. Marvin, (1967): Lonsdaleite, a hexagonal polymorph of diamond *Nature*, 214, 587-589
- Fujihisa, H. & Aoki, K. (1998): High pressure x-ray powder diffraction experiments and intensity analyses. *Rev. High Pressure Sci. Technol.* 8, 4-7.
- Hanneman, R.E., Strong, H. & Bundy, F.P. (1967): Hexagonal diamonds in Meteorites. *Science*, 155, 995-997
- Irifune T., Kurio, A., Sakamoto, S., Inoue, T. & Sumiya, H (2003): Ultra polycrystalline diamond from graphite. *Nature* 421, 599-600.
- Nakatsuka, A., Yoshiasa, A., Yamanaka, T., Ohtaka, O., Katsura, T. & Ito, E. (1999): Symmetry change of majorite solid-solution in the system $\text{Mg}_3\text{Al}_2\text{Si}_3\text{O}_{12}$ - MgSiO_3 . *Am. Mineral.* 84, 1135-1143.
- Toraya, H. (1986): Whole-powder-pattern fitting without reference to a structural model. *J. Appl. Cryst.* 19, 440-447
- Yagi, T, Utsumi, W., Yamakata, M., Kikegawa, T. & Shomomura, O. (1992): High-pressure in situ x-ray-diffraction study of the phase transformation from graphite to hexagonal diamond at room temperature. *Phys.Rev.* B46, 6031-6039
- Yoshiasa, A., Yagyuu, G., Ito, T., Yamanaka, T. & Nagai, T. (2000): Crystal structure of the high pressure phase (II) in CuGeO_3 . *Z. Anorg. Allg. Chem.* 626, 36-41.
- Yoshiasa, A., Murai, Y., Ohtaka, O. and Katsura, T. (2003): Detailed structure of hexagonal diamond and wurtzite-type BN. *Jpn. J. Appl. Phys.* 42, 1694-1704.

Sintering of Alumina Nano-sized Powders Produced by Combustion Synthesis Process

A.Zimmer, J.C.Toniolo & C.P.Bergmann

LACER, Department of Materials, Federal University of Rio Grande do Sul, Porto Alegre, Brazil

ABSTRACT: This work investigates the sintering behavior of amorphous nanometric powders obtained by combustion synthesis via glycine-aluminum nitrate. Firstly, it was evaluated the agglomeration effect on sintered density when they were consolidated by uniaxial pressing. The material was disagglomerated through Planetary Balls Mill under different rates of dry milling, which were analyzed by granulometer laser. Calcining was carried out to evaluate the transformation of phases. The sintered samples characterization revealed a difficult densification of bodies using the pressing technique.

1 INTRODUCTION

Growth in consumption of ultra-fine particles for sintering, as alumina nano-sized powder, has received much attention over the last years (Gleiter 2000).

The use of nanopowders has been increasing interest due to outstanding improve on their mechanical properties and sinterability.

Combustion synthesis is particularly an easy, safe and rapid production process wherein the main advantages are energy and time savings. This quick, straightforward process can be used to produce homogeneous, high-purity, crystalline oxide ceramic powders (Kiminami et al. 2000). This method is versatile to synthesize a broad range of particle sizes, including alumina nano-sized powders as related by Patil et al. (2001).

However, GNP (glycine-nitrate combustion process) powders are not well-suited for the fabrication of those ceramics that must retain nanometer scale grain size during sintering to full density. This is because GNP synthesized powders tend to be agglomerated; the nanometer size primary crystallites are necked together, forming an open, high-surface area network. Although these agglomerates are easily broken down to sub-micron

size by milling or ultrasonication, they cannot be broken down to fully independent, nanometer size particles such as those necessary for ultra-high packing efficiency with small primary pores that can be eliminated during sintering without substantial grain growth (Chick et al. 1994).

GNP powders are appropriate for applications in which the powders in which micron- or submicron-size grains are acceptable in the sintered products. In these latter applications, processing steps are often used to break down the agglomerates and increase the consolidated or "green" density prior to sintering. For example, it was found that heating at 1000°C to "pre-sinter" the agglomerates before consolidation resulted in increased green densities and optimum sintering of GNP-produced chromite powders (Chick et al. 1993; Bates et al. 1994).

In the work reported in this paper, a sintering evaluation for alumina produced by GNP and characterization has been developed and applied on a specific sintered piece. Several tests were carried out in order to establish the main properties of this product: mechanical resistance, apparent density and porosity.

2 EXPERIMENTAL PROCEDURE

Aluminum nitrate $\text{Al}(\text{NO}_3)_3 \cdot 9\text{H}_2\text{O}$ was obtained from Vetec Química, Brazil, and glycine from Bio-Rad, USA. Both were capable of being mixed with minimum amount of deionized water. Water evaporation occurred naturally on this solution during the process. Under continuous intense heating, the precursor mixture auto-ignited at approximately 140-150°C and underwent combustion spontaneously forming a powder which did not contain crystallite phases. In fact, it resulted in a brownish voluminous product identified by XRD as an amorphous structure, which indicates the incomplete combustion probably due to characteristics of fuel employed. Subsequently, these powders were calcined at 800, 900, 1000, 1050 and 1100°C, at a heating rate of approximately 9 K/min, during one hour of soaking time.

Simple equipment was necessary to use as Bunsen-type burner and aluminum milk container.

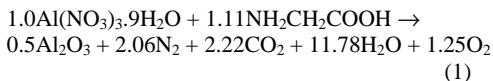
Particle size analyzes have been carried out by laser scattering (Cilas 1180). The powders as-synthesized were dry milled under 5, 10, 20 and 40 minutes.

X-ray diffraction was executed on combustion-synthesized powders for phase characterization, at a rate of 1°/min, using Cu-K radiation on a Philips X-ray diffractometer, (model X'Pert MPD). In order to extract the crystallite size of the coherent diffracting domains from diffraction peak was used the Scherrer method.

Samples with 20mm x 60mm were previously compacted using a hydraulic pressing under 40MPa. They were dried during 24 hours in order to eliminate the humidity. Some of them were previously calcinated at 900 and 1000°C before the sintering process. Finally, the samples were sintered on electric furnace under temperature of 1700°C at a heating rate of 300°C/h.

3 RESULTS AND DISCUSSIONS

The as-synthesized powder was prepared by glycine fuel with lean-stoichiometric composition. The chemical reaction is exothermic in nature and can be expressed as:



It is seen in equation 2, that the average crystallite grain size (t) was in the range of 70 nm which was determined by the X-ray line broadening method using Scherrer equation (Scherrer 1918). Scherrer

gave a definition of the “apparent” domain size, which is a volume-weighted quantity:

$$t = \frac{K \times \lambda}{FWHM} \times \cos \theta \quad (2)$$

Where K is a constant close to unity, λ is the wavelength width of the $K_{\alpha 1}$, $FWHM$ corresponds to the full width at half maximum of the peak and θ the Bragg angle of the $[h\ k\ l]$ reflection.

Before the sintering step was executed a milling process in order to eliminate the agglomerates or at least avoid the clamorous agglomeration. The particle size decreased with increasing time but more effectively until 10 min for dry milling. Comparative value of particle size obtained after this time was highest instead of improvement of their particle sizes as shown on Figure 1.

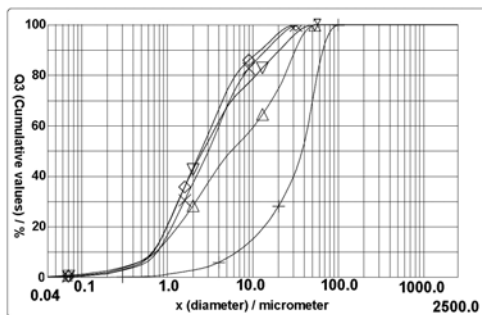


Figure 1. Cumulative values for different milling times.

The XRD of the as-synthesized powder confirmed the amorphous structure, which denotes the absence of crystalline phase from precursor solution for all compositions.

After the calcination procedure the XRD identification was performed, revealing presence of well-crystallized α -alumina at 1100°C as shown in Figure 2. The γ -phase has been detected since 800°C.

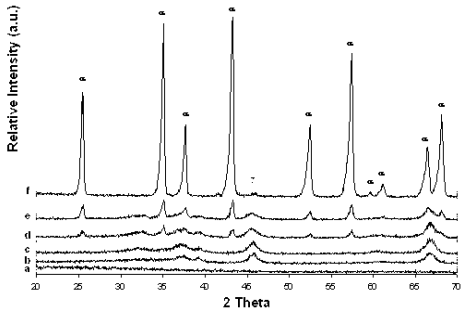


Figure 2. X-ray diffractions of α -alumina ceramic powder: (a) as-synthesized, (b) 800°C, (c) 900°C, (d) 1000°C, (e) 1050°C and (f) 1100°C.

The TG and DTA analysis were also performed to investigate the existence of an unreacted residue in the as-synthesized powder and the phase transformations.

Accordingly, in Figure 3 the TG analysis demonstrates two weight loss steps. First, it was verified on a drastic fall by about 20%. The particle size has leveled off at 500°C. The second drop was slight by about 2.5%. Afterwards the curve has become vertical once more at lower rate up to 1040°C.

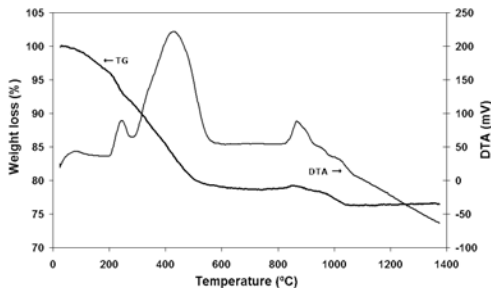


Figure 3. DTA/TG analysis curves of alumina as-synthesized powder by the combustion reaction.

With DTA analysis it was possible to confirm phase transformation into the thermodynamically stable crystallographic alpha alumina just above 1000 °C. It plays an important role as showed on both XRD and TG analysis. Actually, the temperature of phase transformation is clearly identified on the same manner.

The main parameters obtained by these dense bodies are not typical values obtained by nano-sized sintered ceramics. In fact, we observed that are not justified the employ of these nano-sized powders in sintered bodies.

Although not good values of densities have been achieved with this study (Tab.1), the others parameters since as absorption, porosity apparent, water absorption were investigated and they confirmed the low densification for sintered nanomaterials bodies using pressing technique in particular for powders obtained by combustion method.

As we can see in the Table 1, both samples evaluated (samples which underwent calcinations previously at 900, 1000°C and non-calcined) have presented high shrinkage, i.e. due to in part of loss on ignition (mainly for non-calcined sample) and due to worst packing conformation from the last samples mentioned. The degree of agglomeration have a major influence on the packing achievable in green bodies.

Table 1. Sintering properties of alumina without calcination and with two different temperature of calcinations.

Properties	Calcination Temperature		
	Without	900 °C	1000 °C
Shrinkage (%)	30,00	22,50	21,83
Water Absorption (g/cm ³)	0,82	4,15	4,80
Apparent Porosity (%)	2,69	10,02	11,02
Apparent Density (g/cm ³)	3,38	2,70	2,58
Loss on Ignition (%)	20,77	7,41	6,50

4 CONCLUSIONS

Nanoparticles were prepared by the glycine-nitrate combustion method. Typical particles sized 70 nm were obtained. Agglomeration plays an important role in the sintering of nanoscale alumina nanoparticles. Subsequent studies should be necessary on the way to detect the viability of dense pieces application by the GNP process.

5 REFERENCES

- Gleiter, H. 2000. Nanostructured materials: basic concepts AND microstructure. *Acta Mater.* 48:1-29.
- Kiminami, R. M. G. A. et al. 2000. Microwave synthesis of alumina powders. *Am. Ceram. Soc. Bull.* 79:63-67.
- Patil, K. C. et al. 2001. Solution combustion synthesis of nanoscale oxides and their composites. *Mater. Phys. Mech.* 4:134-137.
- Chick, L. A. et al. 1994. Glycine-nitrate synthesis of a ceramic-metal composite. *Nanostr. Mater.* 4:603-614.
- Chick, L. A. et al. 1993. Proceedings 3 International Symposium on Solid Oxide Fuel Cells, Electrochem. Soc., Pennington, NJ. 374.
- Bates, J. L. et al. 1994. Report-94/0042, Gas Res. Inst., Chicago, IL.
- Scherrer, P. 1918. *Nachr. Ges. Wiss. Göttingen.* 26,98.

Analytical Instrumentation

Automated, Adaptive Thresholding Procedure for Mineral Sample Images Generated by BSE Detector

C.L.Schneider, R.Neumann & A.Alcover-Neto

SCT - Setor de Caracterização Tecnológica, CETEM - Centre for Mineral Technology, Rio de Janeiro, Brazil

ABSTRACT: The relationship between average atomic number, BSE detector response, brightness and contrast is fairly well understood. However, it is difficult to positively threshold BSE images due to extraneous factors, such as the presence of edge pixels that usually present an intermediate gray level between the neighboring phases, and due to complex variations in chemical composition that can be observed in a single mineral. The presence of phases with similar average atomic number is another factor that complicates effective thresholding, and sometimes these phases cannot be resolved in the image histogram. It is reasonable to assume that a single phase/mineral will generate a Gaussian distribution of detector responses. A more realistic mineral will generate a distribution of gray levels that is better modeled by a combination of Gaussians, as its chemical composition vary spatially with a range of defects, substitutions, alterations and solid solutions. Another difficulty is to maintain constant contrast and brightness throughout a set of images of mounted particle specimens. Usually, contrast and brightness will only remain constant under very strict conditions. In this work, an automated adaptive thresholding procedure, that allows for the most commonly found phase variations and that self adjusts for changes in brightness and contrast, is implemented. The procedure is based on individual phase models represented by sums of Gaussians. The procedure is tested in a complex copper ore containing magnetite, chalcopyrite and silicates.

1 INTRODUCTION

Automated image processing is not only convenient, but necessary. In order to obtain statistically smooth distributions from particle cross-section measurement, it is necessary to process thousands of cross-sections, in sets of images that contain anywhere from 20 to 100 images. Depending on the complexity of the mineralogy, the processing and thresholding procedures may involve several steps such as filtering, fingerprinting, watershed feature separation, area, linear and perimeter measurements. Reproducing all these steps manually for say 50 images is error prone, and boring. Furthermore, a particle sample is usually split into several narrow sized samples, and each of the sizes imaged, processed and measured. This generates anywhere from five to ten specimens for the average mineral processing plant stream. This may very well be the case for field and laboratory samples. The result is that the microscope operator is commonly presented with jobs that involve processing 500 images. When back-scattered electron images can be used for positive mineral identification and thresholding, acquisition time is significantly reduced. Another advantage is the relative low cost of and simplicity of a BSE detector relative to EDS and WDS.

Therefore, BSE imaging is the preferred source of mineralogy data. A typical BSE image is shown in Figure 1.

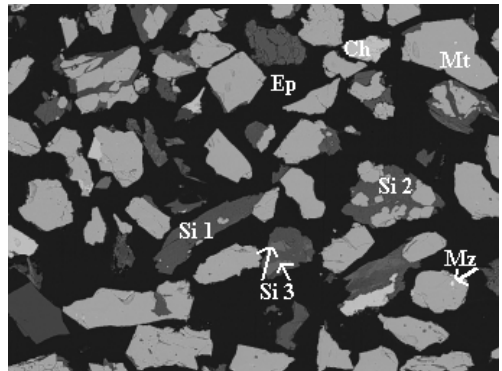


Figure 1: A BSE image showing epoxy (Ep), three different silicates (Si1, Si2 and Si3), magnetite (Mt), chalcopyrite (Ch) and a spec of a monazite (Mz). Particles are in the 104x75 μm size range.

The dependence of detector response on the average atomic number of the phases is readily

noticeable. BSE response increases from epoxy to the various silicates, then magnetite, chalcopyrite and finally the monazite, with the brightest phases corresponding to those of more intense BSE response. The gray level histogram for this image is shown in Figure 2.

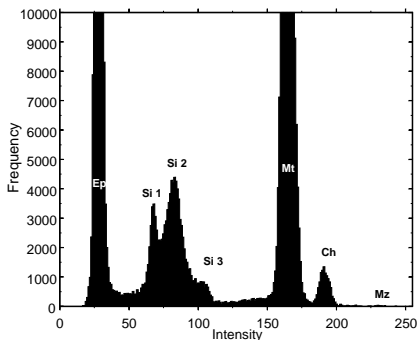


Figure 2: Intensity histogram corresponding to the BSE image in Figure 1.

This intensity histogram has been clipped at 10,000 counts to enhance the smaller peaks. The smallest count between chalcopyrite and magnetite is registered at intensity 183, and for chalcopyrite and monazite at 220. These are good thresholding values to separate the chalcopyrite from the other phases in the image. The problem is that, during acquisition, contrast and brightness may change, so for the next image in the set these values will be different, and an automated procedure is required to find the best thresholding values for all images in the set, without operator interference.

Global automated thresholding procedures such as Otsu (1979) and maximum entropy (Pun 1981) are just not appropriate for such complex gray level histograms. Complex procedures such as split-and-merge and region growing, used in robotics, may very well work, but the alternative presented in this work is more attractive: a method to model the histogram that is constrained by the average atomic number of the phases. The main advantage is that a global analysis of the histogram also provides information such as the probability that a pixel belong to a specific phase or another, or none, the variance of the composition of a phase, preliminary volume fraction assessment, complex processing sequences for multiphase systems, etc. However, all these aspects are not explored in this paper, and the primary objective here is to present a working model and test it for a real set of images from a mineral sample.

2 A MODEL FOR THE INTENSITY HISTOGRAM

Each phase in a BSE image produces a peak at a mean position, and with an area under the peak that is equal to the proportion of the phase in the image. Here we will refer to the total count as the volume fraction of the phase times the number of pixels in the image, since the images are from particle cross-sections, and the first law of stereology is assumed to apply. The third variable is the peak's variance, and this is a function of composition changes within a phase, detector resolution, beam stability, etc. The first concern is to predict where the mean value of a phase peak will be located in the histogram. Harding (2002) has made an important contribution in describing how this problem can be equated using the average atomic number of the phase, and the contrast and brightness at acquisition time. Harding's work is partially based on data gathered here, aimed at describing how atomic number and mean gray level behave in BSE images, as shown in Figure 3.

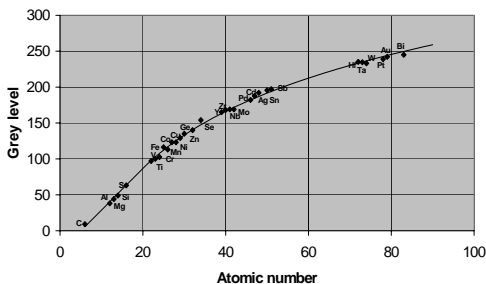


Figure 3: Mean gray level versus atomic number at constant brightness and contrast.

Samples of 31 different elements, from carbon to bismuth, were mounted in epoxy and BSE imaged with an aluminum standard. For all 31 images, the epoxy and aluminum peaks were set at a constant position, ensuring constant brightness and contrast, and the average gray level of the element noted. The resulting plot shows linear behavior at low atomic numbers and logarithmic behavior at higher values of Z . With this data, Harding developed a model based on an auxiliary variable S , defined as:

$$S = \begin{cases} \frac{Z}{Z'} + \ln(Z') - 1 & Z \leq Z' \\ \ln(Z) & Z > Z' \end{cases} \quad (1)$$

where Z is the atomic number of the element. Here, we've found the value of Z' to be 19.75. The value of S varies linearly with contrast and brightness, i.e.

$$I = C S + B \quad (2)$$

where I is the gray level intensity, C is the contrast and B is the brightness level. When a mineral instead of an element is imaged, Z can be substituted by the phase's mass weighed average atomic number in equation (1). The implication is that for known C and B , the mean of a peak in the global histogram is defined if the phase's composition is known.

The histogram model requires a distribution of intensities around the mean values. At this time, it is not known what probability function would be the most appropriate to describe this distribution. The Gaussian distribution function was used here because it has all the desired properties. It is not necessary, for the purpose of determining the best thresholding point, that the histogram model be completely accurate, and the exact shape of the peaks in the model may differ from the actual histogram, as long as the mean values are in the right position. The complete cumulative histogram H_x is therefore modeled by a sum of Gaussians, each Gaussian with an arbitrary variance, and weighed by the volume fraction of phase in the image, i.e.

$$H_x = N \sum_j v_j G_x(\mu_j, \sigma_j) \quad (3)$$

where v_j is defined as the volume fraction of phase j , μ_j its mean intensity and σ_j its variance. N is the total number of pixels in the image. Cumulative distributions are required because the measured histogram is discrete, and the model histogram is continuous. Substituting Equation (2) into Equation (3), we get

$$H_x = N \sum_j v_j G_x(C S_j + B, \sigma_j) \quad (4)$$

and the histogram model is complete.

3 PROCEDURE IMPLEMENTATION

The thresholding procedure was implemented in MMIA™, Minerals and Metallurgical Image Analyzer (King & Schneider 1993). The values of contrast and brightness, and the volume fractions and variances of all phases are obtained by minimizing the sum of squares of residuals between the model and the measured histograms for any given BSE image. The optimization procedure used is based on Sequential Quadratic Programming, and allows for equality constraints as well as bounds for each optimization variable (Schittkowski 1985). The number of parameters to be optimized is $2n+2$, with n equal to the number of phases in the model. A variance and a volume fraction are calculated for

each phase, as well as C and B . The SQP procedure allows for upper and lower bounds for each optimization variable, and in this implementation, each volume fraction is bounded within the [0,1] grade interval. Bounds for the variances are difficult to assess without experiencing with the model, so at implementation, the bounds were set at very wide intervals, equal to the domain of an entire histogram, [0,256]. In practice these bounds are not restrictive at all, and the volume fractions and variances may assume any possible/practical value. One equality constraint was implemented,

$$\sum_j v_j = 1 \quad (4)$$

and this is straight forward. Bounds for contrast and brightness were also implemented, and the actual values are discussed in the experimental session.

4 EXPERIMENTAL

In order to test the thresholding procedure, a copper ore sample from northern Brazil was prepared by hand crushing followed by wet grinding in a rod mill at 50% solids for 15 minutes. The ground product was wet sieved immediately after grinding to avoid sulfide oxidation. The various size fractions were dried under vacuum, embedded in epoxy, polished and carbon coated. Fifty-eight images were acquired from the 104x75 μm mound, using a solid-state back-scattered electron detector on a LEO S440 SEM. Contrast and brightness were set to ensure good phase resolution between the gray levels of chalcopyrite, and the other phases, magnetite and silicates (mainly chlorite, amphiboles and pyroxene). One of the images in the set is shown in Figure 1 and its histogram in Figure 2. For this image, the mean of the chalcopyrite peak is located at gray level 193 and the magnetite is located at 165. These values were obtained simply by locating the cursor at the tip of each peak in MMIA's graphics canvas, and reading the corresponding values. The average atomic number of chalcopyrite (CuFeS₂) is 23.544 and of magnetite (Fe₃O₄) is 21.025. These values are easy to calculate, and MMIA™ has an average atomic number calculator, for convenience. Quoting Harding (2002) "*Howell et al. (1998) found that Castings method of mass weighting the atomic numbers gave the best results*".

$$\bar{Z} = \sum \frac{N_i A_i Z_i}{N_i A_i} \quad (5)$$

This is the procedure adopted in MMIA's average atomic number calculator. The corresponding S values are calculated using Equation (1), and for the

chalcopyrite $S = 3.1589$ and for the magnetite $S = 3.0457$. The two values of S combined with the mean intensities from the histogram are sufficient to calculate the contrast and brightness, using Equation (2). For the image in Figure 1, $C = 208.82$ and $B = -466.63$. These values of C and B define the average atomic number of every phase in the image, by using the procedure described above in reverse order. The values obtained are shown in Table 1.

Table 1: Calculated average atomic numbers of the phases with unknown composition in the image in Figure 1.

	Ep	Si1	Si2	Si3	Mz
I	31	70	85	105	233
S	2.38	2.57	2.64	2.74	3.35
Z	7.9	11.59	13.01	14.9	28.51

The values of average atomic number in Table 1, together with those for chalcopyrite and magnetite were used to define the seven phases in the histogram model. For all 58 images, the initial values of C and B were set equal to the calculated values for the image in Figure 1. The upper and lower bounds for C and B were set at $\pm 10\%$ of the initial values. The initial values of variance were set at 5 for all phases. The initial values of the volume fractions for each phase were obtained from the image in Figure 1, without much care for precision, but satisfying the equality constraint in Equation (4). The values entered were $v_{Ep} = 0.5$, $v_{Si1} = 0.06$, $v_{Si2} = 0.06$, $v_{Si3} = 0.03$, $v_{Ma} = 0.32$, $v_{Ch} = 0.02$ and $v_{Mz} = 0.01$.

A macro was written for MMIA™ to read an image, run a 3x3-delineation filter, calculate the histogram of the delineated image and then fit the histogram with the phases defined above. The routine returned two segmentation levels, one between the epoxy and the first silicate and one between the chalcopyrite and the magnetite. The criterion for the thresholding point was to find the smallest frequency in the measured histogram between the positions of the two adjacent phases.

The macro was run for all 58 images in the set and the results noted.

5 RESULTS, DISCUSSION AND CONCLUSIONS

The most important result to report is that the thresholding points returned by the routine were correct for all images in the set. This is a good indication that the approach is correct. In order to verify how the model fits the data it is necessary to plot an interpolated histogram against the measured histogram. This is shown in Figure 4.

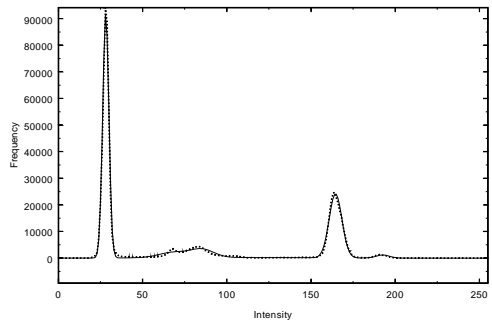


Figure 4: The measured histogram (dotted line) and the fitted histogram using sums of Gaussians (solid line) for the BSE image in Figure 1.

The comparison shows a very good fit, and this is a good indication that the shape of the Gaussian is sufficient to describe a real histogram.

Another interesting result is shown in Figure 5. How does contrast and brightness change during acquisition?

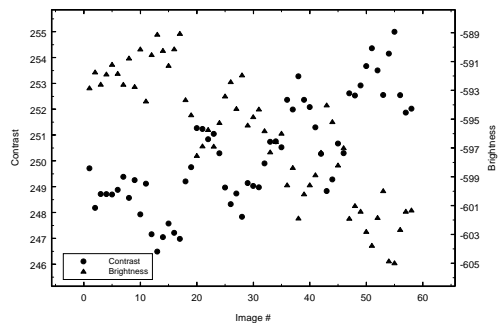


Figure 5: Variation of C and B with acquisition time.

6 REFERENCES

- Harding,D.P. 2002. Mineral identification using a scanning electron microscope. *Minerals and Metallurgical Processing*, 19(4): 215-219.
- Howell,P.G.T., Davy, K.M.W and Boyde, A., 1988. Mean atomic number and backscattered electron techniques. *Mineralogy Mag.*, 51: 3-19.
- King,R.P. and Schneider,C.L. 1993. An Effective SEM-Based Image Analysis System for Quantitative Mineralogy, *KONA*, 11: 165.
- Otsu,N. 1979. A Threshold Selection Method from Gray-Level Histogram. *IEEE Trans. Image Processing*, 2(2): 62-66.
- Pun,T. 1981. Entropy thresholding: a new approach *Comput. Vision Graphics Image Process*, 16: 210-239.
- Schittkowski,K. 1985. NLPQL: A Fortran subroutine for solving constrained nonlinear programming problems, *Annals of Operations Research*, 5, 4850-5000 (1985/86).

Rietveld Analysis of Ferrimagnetic Minerals from Different Parent Materials in Tropical Soils

M.P.F.Fontes

Departamento de Solos, Universidade Federal de Viçosa, 36571-000, Viçosa, MG, Brasil

H.Stanjek

Institut fuer Mineralogie und Lagerstaettenlehre, RWTH Aachen, Wuellnerstr. 2, 52056 Aachen, Germany

U.Schwertmann

Lehrstuhl für Bodenkunde, Technische Universität München, 85350 Freising-Weihenstephan, Germany

ABSTRACT: The two most important magnetic minerals in soils are magnetite and maghemite because they display a magnetic behavior called ferrimagnetism. Another type of behavior called antiferromagnetism is displayed in minerals such as hematite and goethite, with hematite displaying an additional very weak ferrimagnetism due to the imperfect antiparallelism in the alignment of oppositely directed magnetic moments. Magnetite and maghemite are both ferrimagnetic and, therefore, dominate the magnetic behavior of soils, even when present in much lower concentrations than the antiferromagnetic minerals. In Brazil the soils influenced by magnetism cover extensive areas subjected to intense agricultural utilization and, generally, the minerals magnetic properties of these soils have been interpreted in terms of parent material lithology, which provides for the initial magnetic minerals. There are solid evidences that maghemite is present in many highly weathered Brazilian soils as result of aerial oxidation of magnetite originally present in the parent material. The Rietveld method has been applied for the derivation of crystal structure information from powder diffraction data and it is been increasingly used for the refinement of diffraction patterns of soil samples. The objective of this work was to gain more insight in the behavior of the ferrimagnetic minerals from different parent materials from tropical soils, by using the Rietveld analysis. Results showed that the parent materials for the soils influenced the ferromagnetic minerals formed as observed by the unit cell parameters calculated. It was also shown that maghemite was, apparently, the only ferromagnetic mineral that appeared in the samples studied.

1 INTRODUCTION

The two most important magnetic minerals in soils are magnetite (Fe_3O_4) and maghemite ($\gamma - \text{Fe}_2\text{O}_3$) (Mullins 1977) because they display a magnetic behavior called ferrimagnetism. Another type of behavior called antiferromagnetism is displayed in minerals such as hematite ($\alpha - \text{Fe}_2\text{O}_3$) and goethite, with hematite displaying an additional very weak ferrimagnetism due to the imperfect antiparallelism in the alignment of oppositely directed magnetic moments. Magnetite and maghemite are both ferrimagnetic and, therefore, dominate the magnetic behavior of soils, even when present in much lower concentrations than the antiferromagnetic minerals (Stanjek 2000).

In Brazil the soils influenced by magnetism cover extensive areas subjected to intense agricultural utilization and, generally, the minerals magnetic properties of these soils have been interpreted in terms of parent material lithology, which provides for the initial magnetic minerals. Although Schwertmann & Fechter (1984) have demonstrated that maghemite in soils, specially of topsoils from tropics and subtropics, can be originated by the transformation of secondary iron oxides by the

influence of fire, Fontes & Weed (1991) provided very solid evidences that this ferrimagnetic mineral is present in the majority of the highly weathered Brazilian soils as the result of aerial oxidation of magnetite originally present in the parent material. With the development of these soils, the ferrimagnetic minerals usually remain in the formed soil, sometimes altered, but, normally, they still remain ferrimagnetic.

Magnetite and/or titanomaghemite have been reported in the coarser soil fractions (Fontes et al., 2000), while maghemite has been identified in the soil clay fractions (Fontes & Weed 1991; Da Costa et al. 1999; Fontes et al. 2000) of Brazilian soils containing iron-rich spinel phases, which characteristically imparts magnetization higher than 1 JT-1 kg-1 to soil materials.

The Rietveld method (Rietveld 1967, 1969) has been extensively applied for the derivation of crystal structure information from powder diffraction data employing the entire powder diffraction pattern, thereby overcoming the problem of peak overlap and allowing the maximum amount of information to be extracted from the pattern (Post & Bish 1989). This method is been increasingly used for the refinement of diffraction patterns of soil samples (Jackman et al.

1997; Weidler et al. 1998; Jones et al. 2000; Kahle et al. 2002).

The main objective of this work was to gain more insight in the behavior of the ferrimagnetic minerals from different parent materials from tropical soils, by using the Rietveld analysis.

2 MATERIALS AND METHODS

2.1 Sample selection

Samples from B and C horizons of a soil derived from diabase and from B horizons of soils derived from basalt and itabirite were collected and passed through a 2 mm sieve.

2.2 Particle size fractionation and magnetic segregation

For the magnetic separation, subsamples were dispersed ultrasonically and sand, silt, and clay fractions were separated by sieving the coarser components and using centrifuge for the finer ones. The NaOH was used as the chemical dispersant according to Jackson (1979).

For the magnetic segregation, dry separation for the sand fraction and the wet separation for the silt fraction, a hand magnetic separator was used. For the magnetic wet segregation of the clay fraction, it was submitted to a pre-treatment for the dispersion of the material, consisting of 15 or 30 minutes ultrasonic probe treatment and dilution ($< 5 \text{ g L}^{-1}$) in 2 L plastic flasks using a solution of $0.0045 \text{ mol L}^{-1}$ of Na_2CO_3 ($\sim \text{pH } 10.5$). The magnetic filter was prepared and assembled to make up an apparatus similar to the described in Schulze & Dixon (1979) and Fontes (1992). The filter consisted of a recipient coupled to a magnet where the suspension had to go through. The flasks containing dispersed clay were linked to a peristaltic pump enabling continuous flow with the material being collected after passing the magnet. After passing the suspension through the filter for a variable number of times the Na_2CO_3 solution of pH 10.5 was passed through to displace material retained mechanically in the filter. The material that passed through was considered the nonmagnetic fraction. Then, the magnet was turned off and the magnetically trapped material, to be called the magnetic fraction, was flushed out.

2.3 Mineralogical analysis

2.3.1 X-ray powder diffraction data

X-ray diffractometry (XRD) was performed in the separated fractions using a Philips PW 1710 goniometer using $\text{Co K}\alpha_{1+2}$ with a graphite monochromator in the diffracted beam. Both soller slits were installed and the divergence slit was 1°

and the receiving slit 0.1° . The samples were back filled in sample holders and the scans were run from 4 to $120^\circ 2\theta$ with 0.02° increment and 10 seconds counting time. The XRD spectra were analyzed using the software XRD Pattern Processing Jade Plus Release 6.1 (Materials Data, Inc.).

2.3.2 Rietveld method

The X-ray powder diffraction patterns were fit with Rietica (LHPM, a Computer Program for Rietveld Analysis of X-Ray Powder Diffraction Patterns) (Hunter & Howard 2000). The Rietveld analysis was performed using the peak profile function Pseudo-Voigt (How. Assym.). The parameters refined included cell parameters, except for the internal standard Si with a constant $a = 0.543094 \text{ nm}$, 2θ zero, shift, phase scale factors, line width and line shape factors. The variation of the full widths at half maximum (FWHM) was modeled by a quadratic function of $\tan\theta$ with U, V, and W as refinable parameters (Caglioti et al. 1958).

The background was modeled by a refinable polynomial function with four or five free parameters. Whenever necessary, preferred orientation was taken into account using the March-Dollase function. Positional parameters and site occupancy were refined for cations in the structure of most minerals.

The sample mineralogical composition was expressed by the weight fraction of each phase (p) calculated by the following formula: $W_p = (\text{SVVM})_p / \sum (\text{SZVM})_i$ where S is the scale factor, Z is the number of formula units per unit cell, M is the molecular weight of the formula unit, V is the unit cell volume and i is an index running over all phases (Hunter & Howard 2000).

The quantities used to estimate the agreement between the observations and the model during the course of the refinement were: the profile, R_p , the weighted profile, R_{wp} , the Bragg R_b , the expected R_{exp} , the goodness of fit, χ^2 , and the Durbin-Watson d-statistics.

3 RESULTS AND DISCUSSION

The parent materials compared were diabase, a medium-grained and shallow intrusive rock, basalt, a fine-grained frozen lava, and itabirite, a iron-rich metamorphic rock.

3.1 Mineralogy

The mineralogical composition of the samples showed large differences among the soil samples from the three different parent materials. The C horizon of the soil derived from diabase showed ilmenite, maghemite, quartz, smectite, and goethite in the sand fraction. In the silt fraction the same

minerals appeared also with kaolinite and in the clay fraction ilmenite and quartz did not appear, but a little amount of maghemite was still present in this clay fraction. In the B horizon of this soil the pattern repeated for most minerals with the difference that the 2:1 silicate mineral and maghemite completely disappeared from the sample. Another important feature of this sample was the presence of hematite which was not present in the C horizon and has been postulated (Fontes et al., 2000) that it is formed by the transformation of the maghemite present in the saprolite of this soil.

The B horizon of the soil derived from basalt had its mineralogy composed of quartz, ilmenite, maghemite, hematite, and rutile in the coarse fraction, ilmenite, hematite, maghemite, quartz, anatase, rutile, gibbsite, and kaolinite in the medium fraction and gibbsite, hematite, maghemite, anatase, kaolinite, and goethite.

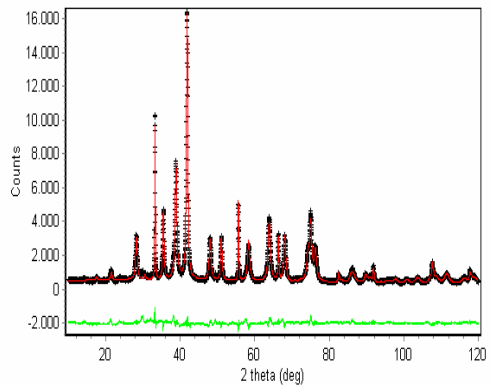
The B horizon of the soil derived from the itabirite presented the simplest mineralogy of all, showing hematite, quartz, and maghemite in all fractions and goethite appearing additionally in the silt and clay fractions. This mineralogy is in consonance with its formation environment.

3.2 Rietveld analysis

Results of Rietveld showed that, in general, the correspondence between the measured and the calculated profile was very good, as demonstrated by the difference curves. According to (McCusker et al. 1999), the most important criteria for judging the quality of a Rietveld refinement are: (i) the fit of the calculated pattern to the observed data and (ii) the chemical sense of the structural model. The former can be evaluated on the basis of the final profile plot (using the complete range of data collected) and the latter on a careful examination of the atomic parameters. Although a difference profile plot is probably the best way of following and guiding a Rietveld refinement, the fit of the calculated pattern to the observed data can also be given numerically. This is usually done in terms of agreement indices or R values such as the *weighted profile R* value, *R_{wp}*. Ideally, the final *R_{wp}* should approach the *statistically expected R* value, *R_{exp}*.

The values for the different *R_s* and goodness of fit showed figures below the ones given in the literature as acceptable for x-ray data refinement and in the range of those obtained in the literature for multiminerall geological samples.

The figure below shows, as an example, the observed intensities, the calculated profile and the difference curves for one of the samples of the soil derived from basalt.



Based on unit cell parameters maghemite was the only ferrimagnetic present in most samples whereas magnetite seemed to be absent in all the fractions analyzed. The a dimension of the maghemite showed values in the range of 0.83138 to 0.83471 which are well below 0.839, characteristic of the magnetites.

The maghemites from diabase were found only in the sand fraction and showed the highest values for the a dimension (0.83471). The maghemites from basalt and itabirite appeared in the sand, silt and clay fraction and showed a dimensions smaller than the ones from diabase but similar between them. The values were 0.83208; 0.83138 for the basalt sand and clay, respectively, and 0.83328; 0.83176, respectively.

4 CONCLUSION

The Rietveld method for structure refinement showed to be an excellent tool to study the ferrimagnetic minerals present in samples from tropical soils derived from different parent materials.

5 REFERENCES

- Caglioti, G.; Paoletti, A. and Ricci, F.P. 1958. Choice of collimators for a crystal spectrometer for neutron diffraction. *Nuclear Instruments and Methods*, 3: 223- 226.
- Fontes, M. P. F. 1992. Iron oxide-clay minerals association in Brazilian Oxisols: a magnetic separation study. *Clays and Clay Minerals*, 40:175-179.
- Fontes M.P.F. and Weed, S.B. 1991. Iron oxides in Brazilian Oxisols: I. Mineralogy. *Soil Science Society of America Journal*, 55: 1143-1149.
- Fontes, M.P.F.; Oliveira, T.S. de; Costa, L.M. da and Campos, A.A.G. 2000. Magnetic separation and evaluation of magnetization of Brazilian soils from different parent materials. *Geoderma*, 96(1-2): 81-99.
- Hunter, B.A. and Howard, C.J. 2000. LHPM. A computer Program for Rietveld Analysis of X-Ray and Neutron Powder Diffraction Patterns. Lucas Heights Research

- Laboratories, Australian Nuclear Science and Technology Organization.
- Jackman, J.M.; Jones, R.C.; Yost, R.S. and Babcock, C.J. 1997. Rietveld estimates of mineral percentages to predict phosphate sorption by selected Hawaiian soils. *Soil Science Society of America Journal*, 61: 618-625.
- Jackson, M. L. 1979. *Soil Chemical Analysis, Advanced Course*. 2nd ed., Published by the author. Department of Soil Science, University of Wisconsin, Madison, WI, USA.
- Jones, R.C.; Babcock, C.J. and Knowlton, W.B. 2000. Estimation of the total amorphous content of Hawai'i soils by the Rietveld method. *Soil Science of America Journal*, 64: 1100-1108.
- Kahle, M.; Kleber, M. and Jahn, R. 2002. Review of XRD-based quantitative analyses of clay minerals in soils: the suitability of mineral intensity factors. *Geoderma*, 109: 191-205.
- McCusker, L.B.; Von Dreele, R.B.; Cox, D.E.; Louer, D. And Scardi, P. 1999. Rietveld refinement guidelines. *Journal of Applied Crystallography*, 32: 36-50.
- Mullins, C.E. 1977. Magnetic susceptibility of the soil and its significance in Soil Science: A review. *Journal of Soil Science*, 28: 223-246.
- Post, J.E. and Bish, D.L. 1989. Rietveld refinement of crystal structures using powder X-ray diffraction data. In: Bish, D.L. and Post, J.E. (Eds). *Modern Powder Diffraction. Reviews in Mineralogy, Volume 20*. Mineralogical Society of America, Washington, DC. pp 277-308.
- Rietveld, H.M. 1967. Line profiles of neutron powder diffraction peaks for structure refinement. *Acta Crystallographica*, 22: 151-152.
- Rietveld, H.M. 1969. A profile refinement method for nuclear and magnetic structures. *Journal of Applied Crystallography*, 2: 65-71.
- Shim, S.H.; Kim, S.J. and Ahn, J.H. 1996. Quantitative analysis of alkali feldspar minerals using Rietveld refinement of X-ray diffraction data. *American Mineralogist*, 81: 1133-1140.
- Stanjek, H. 2000. Formation processes of ferri-magnetic minerals in soils. *Habilitationsschrift. Lehrstuhl für Bodenkunde, Technische Universität München, Freising-Weihenstephan*. 166 p
- Weidler, P.G.; Luster, J.; Schneider, J.; Sticher, H. and Gehring, A.U. 1998. The Rietveld method applied to the quantitative mineralogical and chemical analysis of a ferralitic soil. *European Journal of Soil Science*, 49: 95-105.

In Situ EPMA Dating of Monazites from the Morro da Pedra Preta Formation, Serra do Itaberaba Group (São Paulo, Brazil)

G.M.Garda, P.Beljavskis & M.S.Mansueto

Institute of Geosciences, University of São Paulo, São Paulo, Brazil

ABSTRACT: In situ dating techniques using the electron microprobe (EPMA) have been successfully applied in the determination of the ages of granites and metamorphic rocks from southeastern Brazil. Monazites from two metasedimentary rocks (a metapelite and a graphite schist) and an exhalite (tourmalinite) of the Morro da Pedra Preta Formation (MPPF), Serra do Itaberaba Group (São Paulo, Brazil) were analyzed for Si, Ca, P, LREE, U, Th, Pb and Y. In comparison with the monazites of the metasedimentary rocks, the tourmalinite monazites have high LREE and low Y, Th, U, Pb, Si and Ca contents. These monazites also stand out for their chondrite-normalized LREE patterns, a set being characterized by Sm and Nd enrichments and La (and Ce) depletions, and another by a steep curve ($La/Gd = 10$) that coincides with the pattern obtained for the monazites of the metasedimentary rocks. Two main age intervals, 700-800 Ma and 400-600 Ma, were defined by EPMA. All the values older than 600 Ma correspond to tourmalinite monazites, including well-shaped, zoned crystals. The older ages mark seafloor hydrothermal activity events that took place during the MPPF backarc regime, whereas the younger ages are close to those obtained for Brasiliano granites of the Ribeira Belt (São Paulo), represented in the study area by the Pau Pedra Stock. The spreading of data (*e.g.* some metapelite monazites yield ages younger than 400 Ma) is attributed to isotopic re-equilibrations and elemental redistributions, imposed by fluid circulation during both time intervals.

1 INTRODUCTION

In situ dating techniques using the electron microprobe (EPMA - electron probe microanalysis) have been successfully applied in the determination of the ages of granites and metamorphic rocks from southeastern Brazil, being monazite [(LREE)PO₄] the preferred mineral for such analyses (*e.g.* Vlach et al. 1999, Vlach & Gualda 2000).

EPMA was applied to monazites from three rock types of the Morro da Pedra Preta Formation (Serra do Itaberaba Group - São Paulo, Brazil), aiming at the study of LREE behavior in relation to hydrothermal alteration and its possible interference when dating minerals and rocks by conventional methods.

2 THE MORRO DA PEDRA PRETA FORMATION

The Morro da Pedra Preta Formation (MPPF) is the basal metavolcanic-sedimentary sequence of the Serra do Itaberaba Group, located in the central portion of the Ribeira Belt in São Paulo State (Beljavskis 2003). The MPPF is mainly constituted by metamafic and metapelitic rocks. Calc-silicate

and metavolcaniclastic rocks, banded iron formations, tourmalinites, metachert, metandesites, and metarhyolites occur subordinately.

The MPPF is overlain by andaluzite-rich metapelites and Fe-Mn schists of the Nhanguçu Formation, and quartz schists of the Pirucaia Formation (Juliani 1993, Juliani & Beljavskis 1995).

Deep marine environment admitted for MPPF is attested by the presence of meta-spilites and pillow lavas (Juliani 1993). Intermediate rocks (metandesites and metadacites) originated from partial melting of a subducting oceanic crust under backarc regime were heat sources for hydrothermal fields, in the vicinity of which tourmalinites and metachert are found (Beljavskis et al., submitted). Above and laterally to the metandesite and metadacite bodies, volcanic metagglomerates and metatuffs occur, overlain by sulfide-bearing graphite schists and calc-silicate rocks.

Two metamorphic events affected the Serra do Itaberaba Group, the first reaching the amphibolite facies and the second, the greenschist facies. In the Neoproterozoic, the emplacement of granitic bodies was widespread in the Ribeira Belt, furnishing heat that helped remobilize metals (gold, silver), especially along fractures and faults associated with shear zones.

3 MICROANALYSIS OF MONAZITES

Monazites from three MPPF rock types were analyzed for Si, Ca, P, LREE, U, Th, Pb and Y, totaling 60 analyses. Mapping of the carbon-coated, polished thin rock sections was carried out at the Scanning Electron Microscope Laboratory of the Geosciences Institute of the State University of Campinas (IGe-UNICAMP), equipped with a LEO Scanning Electron Microscope 430 I.

The monazite-bearing rocks chosen for EPMA were a sulfide-bearing graphite schist (SRT11-145, Fig. 1A), a chloritized, tourmaline-bearing mica-quartz schist (SRT8-77, Fig. 1B), and a tourmalinite (T12, Fig. 1C). These rocks were deposited during the MPPF backarc phase, the tourmalinite corresponding to exhalites related to iron formations and metachert. Gold appears disseminated in the three rock types.

Monazite textures, shapes, and sizes vary in a single thin section, indicating more than one

monazite generation event. Sample SRT11-145 presents a poikilitic variety, associated with sulfides (Fig. 1D). Unzoned, potato-shaped monazites are found mingled with micas in sample SRT8-77, having caused pleochroic haloes in biotite (Fig. 1B). This type, showing serrated rims, also appears imbricated with quartz and tourmaline in sample T12 (Fig. 1C). In turn, zoned monazites may be fractured (Fig. 1E) or well-shaped (Fig. 1F).

The analyzed monazites vary from 20 to 100 micra in size. The microanalyses were carried out at the Electronic Microprobe Laboratory of the Geosciences Institute of the University of São Paulo (IGc-USP), equipped with a JEOL Superprobe JXA-8600. Operating conditions were: accelerating voltage: 20 kV; beam current: 100.1 ± 0.1 nA, and beam diameter: 5 micra.

Th and U oxides and galena were the standards used for Th, U and Pb respectively. Maximum counting time for Pb and U was 300s.

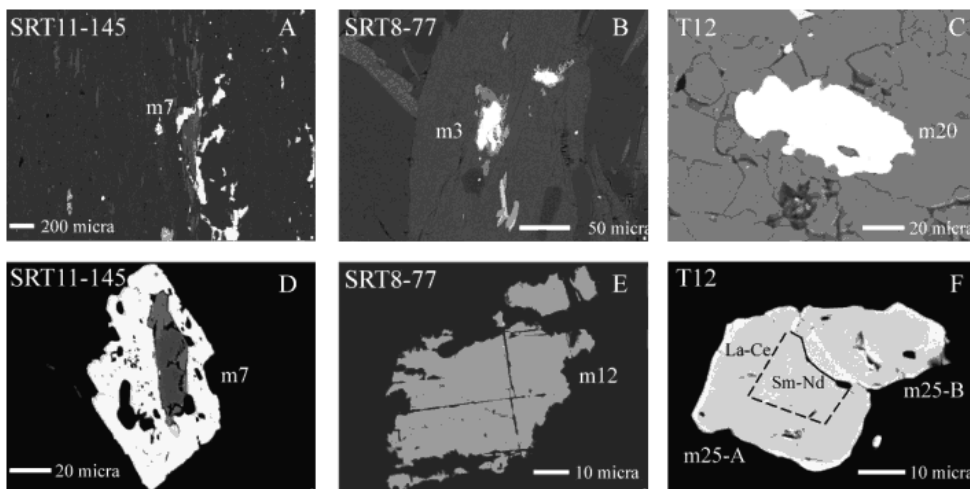


Figure 1. Back-scattered scanning electron microscope images of monazites and their host rocks.

4 RESULTS

Figure 2 shows the histograms of the ages calculated using EXCEL worksheets developed by Vlach & Gualda (2000), based on the statistical method of Montel et al. (1996). Peaks at 500-600 Ma are present in the histograms for the three rock types. Because a second peak at 700-800 Ma appears for T12 (Fig. 2C), the T12 data set is further divided in two groups, named "T12 < 600 Ma" and "T12 > 600 Ma". Figure 3 shows that the LREE contents of T12 monazites are usually high, when compared to SRT11-145 and SRT8-77 monazites. Most "T12 > 600 Ma" monazites present low La + Ce contents (< 37 wt%, Fig. 3A), that correspond to high Sm + Nd

contents (> 13%, Fig. 3B). In particular, zoned monazite T12-m25-A (> 600 Ma) has a nucleus richer in Sm + Nd (Fig. 1F). The majority of the T12 monazites have low Y (Fig. 3C), Th + U (Fig. 3D), Pb (Fig. 3E), and Si + Ca contents (Fig. 3F).

T12 monazites also present distinct chondrite-normalized curves (Fig. 4). Whereas SRT11-145, SRT8-77, and T12 monazites with high La + Ce yield steep curves, with La/Gd = 10, the shapes of the curves for "T12 > 600 Ma" monazites (Figs. 4A, 4B) evidence Sm and Nd enrichments and La (and Ce) depletions. Despite the similar shape of "T12 < 600 Ma" monazites with the steep curves with La/Gd = 10, La contents are variable (9 to 15 wt%).

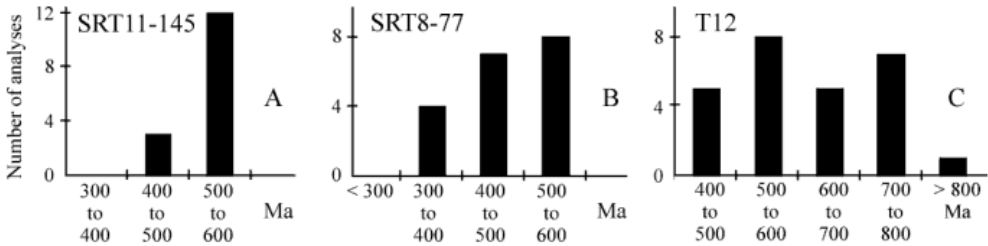


Figure 2. Histograms of the ages calculated using an Excel worksheet developed by Vlach & Gualda (2000).

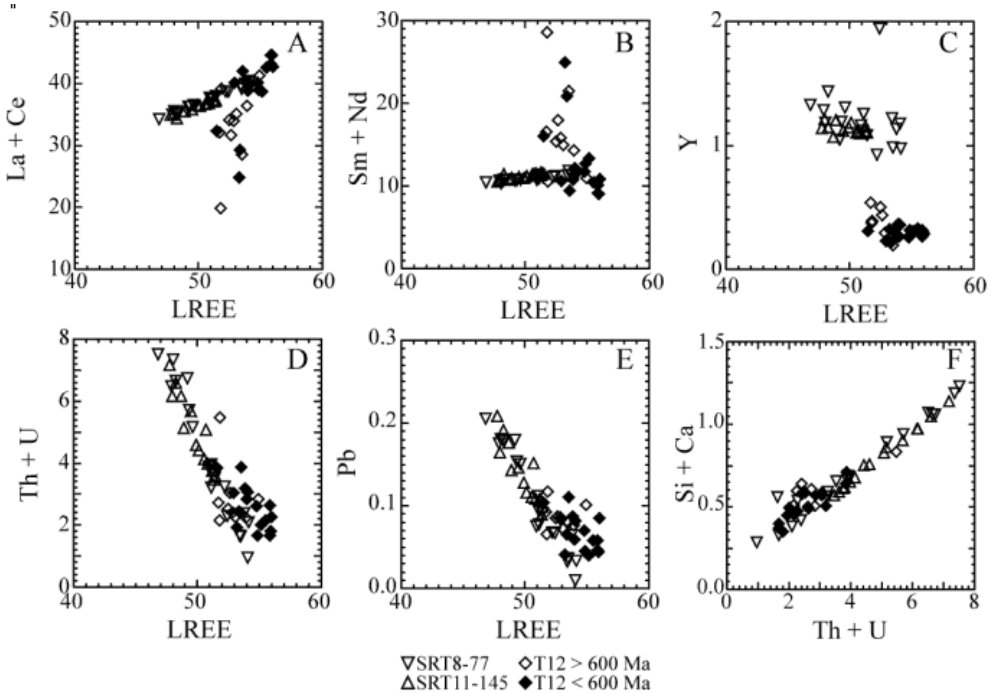


Figure 3. Variation diagrams of elemental compositions (wt%) of the MPPF monazites.

5 DISCUSSION

Beljavskis (2003) used the conventional Sm-Nd method to date the graphite schist SRT11. Whole rock and titanite, garnet, and pyrrhotite concentrates were analyzed, yielding an age of the order of 500 Ma. The estimated error was 100 Ma, attributed to partial mobilization of REE by hydrothermal fluids.

The errors obtained by EPMA of monazites were of the order of 50 Ma for SRT11-145 and 70 Ma for SRT8-77. Additionally, SRT8-77 monazites yielded ages younger than 400 Ma (Fig. 2B). Once the metapelite is more permeable than the graphite schist, the remobilization of elements must have been more intense in the former, changing the

original elemental (Th, U and Pb) concentrations and leading to the spans in age and error values.

For T12 monazites, the errors were much higher, varying from 70 to 150 Ma, indistinctive of ages. The LREE patterns indicate remobilizations, especially for “T12 > 600 Ma” monazites with high Sm and Nd contents. Substitutions of La (and Ce) for Sm and Nd were detected in larger (zoned) crystals. Considering that the older monazites were formed during the hydrothermal activity installed at the MPPF backarc phase, they would certainly be affected by the following hydrothermal events powered by the Neoproterozoic granite genesis.

It is not clear whether Th, U and Pb contents vary according to specific LREE concentrations.

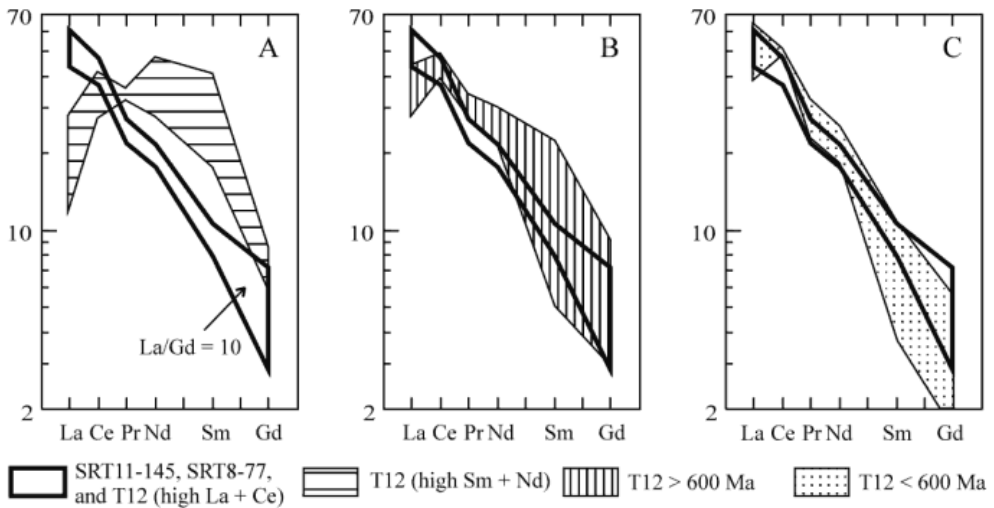


Figure 4: Chondrite-normalized (vertical scale $\times 10^4$) plots. Each area represents a distinct group of monazites.

6 CONCLUSIONS

EPMA helped define two main age intervals, 700-800 Ma and 400-600 Ma, the former registered in “T12 > 600 Ma” monazites and the latter in the monazites of the three MPPF rock types analyzes.

The 700-800 Ma interval corresponds to the seafloor hydrothermal activity installed when MPPF underwent backarc conditions, powered by the intrusion of metandesites and metadacites.

The 400-600 Ma interval is close to the ages obtained for monazites from Brasileiro granites (Janasi 1999, Vlach & Gualda 2000).

The errors, age spans and LREE behavior indicate conspicuous elemental remobilizations, promoted by hydrothermal fluid circulation. In the case of the younger monazites, fluid circulation was favored by shearing.

Thanks to the EPMA method, a 700-800 Ma interval, not detected by conventional dating methods, was defined in the Morro da Pedra Preta Formation and may contribute to explaining such timing in the Ribeira Belt (e.g. Vlach 2001, Cordani et al. 2002, Janasi et al. 2003).

7 REFERENCES

Beljavskis, P. 2003. Caracterização das mineralizações e os ambientes deposicionais dos sulfetos, turmalinas e ouro no contexto da Formação Morro da Pedra Preta, Grupo Serra do Itaberaba - SP. São Paulo, University of São Paulo, 158p. (Unpublished Ph.D. Thesis).

Beljavskis, P.; Garda, G.M.; Mansueto, M.S.; Silva, D. Turmalinitos da Formação Morro da Pedra Preta, Mesoproterozóico do Grupo Serra do Itaberaba (SP): Implicações genéticas e econômicas. Submitted to

Geologia USP.

Cordani, U.G.; Coutinho, J.M.V.; Nutman, A.P. 2002. Geochronological constraints on the evolution of the Embu Complex, São Paulo, Brazil. *Journal of South American Earth sciences* 14:903-910.

Janasi, V.A. 1999. *Petrogênese de granitos crustais na Nappe de Empurrão Socorro-Guaxupé (SP-MG): Uma contribuição da geoquímica elemental e isotópica*. São Paulo, University of São Paulo, 304p. (Unpublished “Livro Docência” Thesis).

Janasi, V.A.; Alves, A.; Vlach, S.R.F.; Leite, R.J. 2003. Granitos peraluminosos da porção central da Faixa Ribeira, Estado de São Paulo: Sucessivos eventos de reciclagem da crosta continental no Neoproterozóico. *Geologia USP - Série Científica* 3:13-24.

Juliani, C. 1993. *Geologia, petrogênese e aspectos metalogenéticos dos grupos Serra do Itaberaba e São Roque na região das Serras do Itaberaba e da Pedra Branca, NE da cidade de São Paulo, SP*. São Paulo, University of São Paulo, 2 vol. (Unpublished Ph.D. Thesis).

Juliani, C. & Beljavskis, P. 1995. Revisão da litoestratigrafia da faixa São Roque/Serra do Itaberaba (SP). *Revista do IG* 16(1/2):33-58.

Montel, J.-M.; Foret, S.; Veschambre, M.; Nicollet, C.; Provost, A. 1996. Electron microprobe dating of monazite. *Chemical Geology* 131:37-53.

Vlach, S.R.F. 2001. Microprobe monazite constraints for an early (ca. 790 Ma) Brasileiro Orogeny: The Embu Terrane, Southeastern Brazil. In: *South American Symposium on Isotope Geology, 3. Extended Abstracts...* Pucón, Chile, p. 265-268.

Vlach, S.R.F. & Gualda, G.A.R. 2000. Microprobe monazite dating and the ages of some granitic and metamorphic rocks from Southeastern Brazil. *Revista Brasileira de Geociências* 30(1):214-218.

Vlach, S.R.F.; Gualda, G.A.R.; Chiessi, C.M. 1999. Electron microprobe monazite dating: first results for two granites from Southeastern Brazil. In: *South American Symposium on Isotope Geology, 2. Actas...* Cordoba, Argentina, p. 518-521.

The Application of Synchrotron Radiation Techniques to the Study of Mineralogy

A.R.Gerson

Ian Wark Research Institute, University of South Australia, Mawson Lakes, Adelaide, South Australia

ABSTRACT: The Australian synchrotron is scheduled to be commissioned in 2007. A major focus of the planning of the end-station facilities is the provision of techniques which are readily applicable to mineralogy, minerals processing and exploration. Two such end-stations will be described both of which incorporate mapping capabilities with a 1-2 μm resolution. The ambient mapping X-ray photoelectron spectrometer end-station will provide the means to probe surface speciation (selectively one to two monolayers and up to tens of monolayers) both under vacuum and in an atmosphere of up to 20 Torr. This will enable reactions to be monitored in situ, for instance oxidation in the presence of O_2 and/or H_2O . Many minerals are either wide band-gap semiconductors or insulators. The provision of an ambient atmosphere alleviates the problem of sample charging as occurs for conventional XPS measurements of insulating materials. The microdiffraction fluorescence microprobe end-station will enable simultaneous X-ray fluorescence and X-ray diffraction to be undertaken via application of a broad bandpass incident X-ray beam. A monochromatic incident X-ray beam will also be available which will enable selective XRF measurements and also X-ray absorption spectroscopy measurements. XAS enables the definition of elemental oxidation states and local geometry. There exists many applications for these end-stations in the areas of geological/mineralogical sciences including mineral exploration; elemental-mineral phase relationships; process control; environmental / whole-earth geochemistry / mineralogy R&D, and also in the environmental sciences including mineral weathering – acid rock drainage and acid mine drainage, release of toxic elements (bioavailability).

1 THE AUSTRALIAN SYNCHROTRON

Plans for the Australian synchrotron, to be based at a site at Monash University (Melbourne), are now well advanced with construction of the facilities having commenced in 2003. It is envisaged that commissioning of the facility will be complete by mid 2007. The central infrastructure required to generate the synchrotron radiation consists, basically, of a linear accelerator to generate an electron stream, a booster ring to accelerate the electrons up to the desired speed, close to the speed of light, and a storage ring.

X-rays are emitted tangentially from the storage ring and are guided down beamlines. The actual experimental facilities are housed at end-stations along these beamlines. The synchrotron is likely to be the single most widely used piece of scientific infrastructure in Australia with an estimated user base of 1200-1300 scientists within 5 years of operation.

Two facilities, of the initial suite of beamlines, have particular application to minerals-based research. These facilities are a Microdiffraction and

Fluorescence Probe (MDF Probe) and an Ambient Mapping X-ray Photoelectron Spectrometer (AM-XPS). Both facilities will provide experimental capabilities not possible via laboratory-based apparatus.

Both techniques provide composition, structure and speciation information although the exact nature of the information varies between the two facilities. The main contrast exists in the depth of analysis. The MDF Probe will provide bulk information (i.e. depth penetration $> 10 \mu\text{m}$) while the X-ray photoelectron spectrometer will enable surface specific (from 1 atomic monolayer to 50 nm) measurements to be carried out.

2 XPS

2.1 *The technique*

X-ray photoelectron spectroscopy (XPS) involves the selective excitation of an electron from a particular atomic shell. XPS measures the intensity of the emitted electrons as a function of their kinetic energy. The X-ray photoelectron spectra are

displayed as a function of the electron binding energy, BE (the energy required to excite the electron from the atomic orbital to the Fermi level) which is determined from

$$BE = h\nu - KE - \phi_p \quad (1)$$

where KE is the kinetic energy of the electron and is the quantity that is measured, $h\nu$ is the energy of incident monochromatic X-rays and ϕ_p is the work function. The BE is not only a function of the atomic shell from which the electron has been excited but also the local environment and hence is a measure of the local speciation. A schematic of the excitation process is shown in Figure 1.

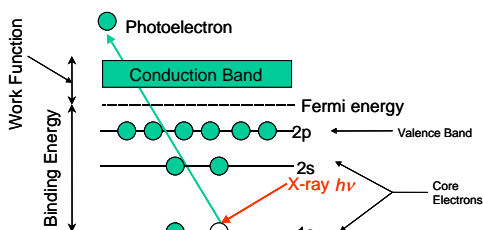


Figure 1: A schematic of the excitation process undergone by an electron on irradiation by X-rays with sufficient energy to excite the electron to the vacuum level (= binding energy + work function).

The depth of measurement is determined by the energy of the incident radiation. Whereas this is fixed for a laboratory based XPS, and is dependent on the X-ray tube used, this can be selected when using a synchrotron radiation source. In this way the surface composition and speciation as a function of depth can be accurately determined with a surface layer sensitivity of as little as 1 monolayer being obtainable. The depth sensitivity of a typical laboratory based XPS is 3-5 nm (approx. 10 monolayers).

The AM-XPS facility will enable both XPS and XAS (X-ray absorption spectroscopy) measurements to be carried out at pressures up to 20 Torr. Traditionally XPS measurements have always been carried out in ultra-high vacuum. Moreover mapping of the surface inhomogeneities will be possible with a resolution of approximately 1 μm . This will enable a more accurate picture to be built up of a surface than via 'spot' analysis. The design of this end-station enables real time surface analysis under a variety of atmospheres including water, oxygen, helium, nitrogen etc... For instance, where it is desired to study the oxidation reaction of a mineral surface it will be possible to carry out the measurement 'in situ' and in real time.

2.2 Examples of AM-XPS applications

Figure 2 shows the non-destructive depth profiling power of synchrotron XPS where the S 2p spectra for chalcopyrite (CuFeS_2 , cleaved in vacuum) as a function of incident X-ray energy is given. The ratios of the bulk states remain the same regardless of incident X-ray energy however, the surface state accounts for 15% of the S 2p signal for the spectra recorded with the lower incident X-ray energy, 252 eV. The surface S state occurs as a result of cleavage of S bonds.

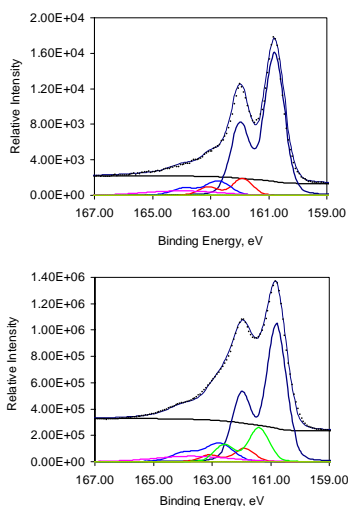


Figure 2: Chalcopyrite S 2p spectra taken with an incident X-ray energy of 568 eV (top) and 252 eV (bottom). The dark blue line doublet indicates S2-, the red doublet S22-, the light blue line Sn2-. The green line, indicative of a S surface state, is only observed at low incident X-ray energies. The data was taken using the SuperESCA XPS at the Elettra synchrotron, Italy.

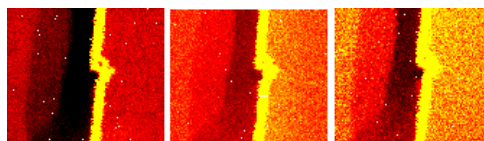


Figure 3: Shows a high resolution XPS image of an oxidised galena surface: (a) Pb 4f, (b) O 1s and (c) S 2p. Each image is approximately 6 μm in width. The brighter areas indicate regions of greater atomic concentration (ESCAMicroscopy facility at Elettra synchrotron). (Prince et al. 2002)

Figure 3 shows XPS images of an oxidised stepped surface of galena. By background subtraction and relative normalisation it is possible to remove topographical affects. It then becomes apparent, for instance, that there is a high concentration of O not only at the step but also a

concentration gradient of O away from the step in the both the left and right-hand directions.

3 MDF PROBE

3.1 The technique

The MDF Probe will provide extremely rapid sample mapping, simultaneously of diffraction and fluorescence data. The incident X-ray beam size will be easily adjustable from mm to 1-2 μm . On application of the small beam size the diffraction patterns measured will, in most scenarios, be indicative of single crystal diffraction rather than powder diffraction (i.e. spots not rings).

The innovative use of a broad bandpass incident X-ray beam will ensure that sufficient diffraction data will be obtained per incident beam position, regardless of crystalline grain size, to enable crystalline phase identification. The depth penetration of the high energy, high flux broad bandpass incident X-ray beam will enable 3D mapping of phase. In addition the provision of monochromatic radiation will enable X-ray absorption spectroscopy (XAS), and fluorescence measurements at wavelengths defined to highlight a specific element.

Only the application of synchrotron radiation offers the possibility of simultaneous XRF and XRD mapping at a micron scale. In a laboratory setting a powder diffraction pattern is carried out using a monochromatic source as a function of diffraction angle (θ) but with synchrotron radiation diffraction data may be collected as a function of X-ray energy:

$$E(\text{keV}) = hc/\lambda = hc/2d \sin\theta \approx 6.2/d \sin\theta \quad (2)$$

where d is the distance between Miller planes in \AA for the crystalline solid, h is Planck's constant, c is the speed of light and λ is the wavelength of the incident X-ray radiation. In this instance broadband Laue diffraction, will be used in order to maximize the diffraction data collectable by application of an area detector without the necessity for sample or detector rotation. This is not possible using a conventional X-ray source.

It has long been recognised that X-rays provide a number of advantages for highly sensitive determination of elemental composition as compared to electron or proton based analytical techniques in that X-rays are efficient at causing excitation of inner-shell electrons, they produce low backgrounds and the samples require a minimum of preparation.

As synchrotron radiation provides white radiation the incident X-ray energy can be selected to create maximum excitation for the element of interest. This, in addition to the high flux provided by a synchrotron X-ray source, can give rise to sensitivities in the order of ppb. As very short

wavelength X-rays are available that have a high sample depth penetration, analysis can be undertaken of melt and fluid inclusions without the necessity for destroying them.

3.2 Examples of MDF probe applications

Figure 4 shows diffraction patterns collected of the $\text{Al}(\text{OH})_3$ phases, gibbsite (G) and bayerite (B) crystallizing in situ from concentrated caustic liquors. The highly penetrating nature of synchrotron radiation enables a wide range of in situ cells and environments to be employed. These diffraction patterns were collected at the Australian Synchrotron Radiation Facility at the Photon Factory synchrotron in Tsukuba.

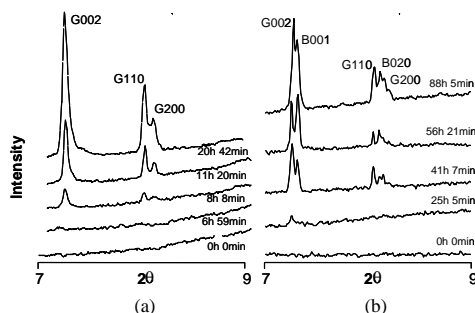


Figure 4: In situ X-ray diffraction patterns of gibbsite and bayerite crystallizing from synthetic Bayer liquors: (a) gibbsite precipitation from liquors made by the dissolution of gibbsite at 160 °C and (b) gibbsite and bayerite precipitation made by the dissolution of gibbsite at atmospheric pressure. (Gerson et al. 1996).

In addition to diffraction and fluorescence capabilities it will also be possible to carry out X-ray absorption spectroscopy measurements on the MDF Probe. These measurements enable the oxidation states of specific elements to be determined as well as their local geometry. This is particularly useful for elements that are not present as an intrinsic part of a crystalline phase or are not in a crystalline form.

Separation of valuable minerals from valueless gangue is often achieved by selective mineral flotation processing. Hydrophobic collector molecules are added to the mineral slurry. These molecules are designed to selectively interact with the valuable components of the ore thus rendering them hydrophobic. In some cases however, the collector molecules do not interact sufficiently with the mineral surface to induce hydrophobicity and the surface must first be 'activated'.

The activation mechanism in which sphalerite (ZnS) is conditioned with $\text{Cu}(\text{II})$ (normally as nitrate or sulfate), prior to adsorption of xanthate and

flotation, has been extensively studied over more than three decades. Until recently, the nature of the copper species formed on the surface of sphalerite was the subject of some controversy. EXAFS (extended X-ray absorption fine structure, a form of XAS) analysis (carried out at the Australian National Beamline Facility, Photon Factory, Tsukuba) has been used to clarify the form of the Cu on the sphalerite mineral surface (Gerson et al. 1998). Figure 5 shows a Cu atom that has replaced a Zn atom on the (110) surface of sphalerite to form a slightly distorted trigonal planar structure bonded to three S atoms.

However, the main strength of the MDF Probe will be the capability to correlate XAS, XRF and XRD and to be able to carry out XRF and XRD simultaneously. Figure 6 shows the analysis of a soil nodule where these three techniques have been applied. This has enabled the identification of Zn in all the phases identified by XRD whereas Ni only occurs in the lithioporite. The application of XAFS has enabled the location of these elements within these phases to be established.

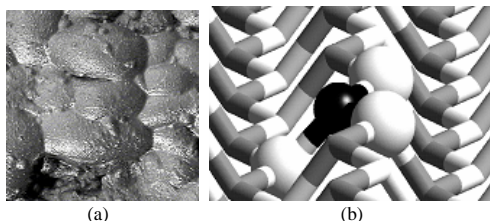


Figure 5: (a) A typical industrial froth flotation slurry and (b) an example of the structure of Cu activated sphalerite, one of the fundamental processes that occurs during mineral processing. The Cu atom is represented as a black sphere, the S atoms are white and the Zn atoms are grey. The three S atoms bonded to the Cu atom are also shown as spheres.

4 CONCLUSIONS

The unique and very powerful characteristics of synchrotron radiation provide wonderful new opportunities for the increased understanding of earth science processes, in the natural environment and in the laboratory and industrial context.

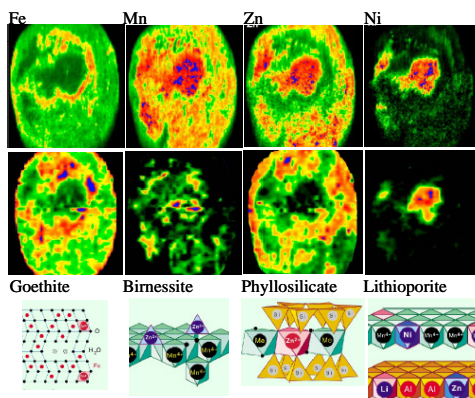


Figure 6: Microanalysis of a soil nodule. Elemental maps are shown at the top of the Figure, phase maps in the central portion and the structures identified through application of EXAFS, for each particular phase, at the bottom. This data was recorded using station 10.3.2 at the Advanced Light Source, Berkeley Laboratories. (Manceau et al. 2002).

The AM-XPS and the MDF Probe will be able to provide an enormous range of measurement capabilities within the Earth Science arena, for both pure and applied research including analyses of: very fine particles, multiphase mixtures, complex textures (e.g. micro-porous), variable compositions (e.g. zoning), phase stability (e.g. exsolution), inclusions (e.g. fluid, crystals), biological interactions rimming, armouring, passivation, secondary mineralisation, trace element-phase associations, core samples, mineral weathering, acid mine drainage and corrosion and elemental partitioning.

5 REFERENCES

- Gerson, A.R., Counter, J.A. & Cookson, D.J. 1996. Influence of solution constituents, solution conditioning and seeding on the crystalline phase of aluminium hydroxide using in situ X-ray diffraction, *Journal of Crystal Growth*, 160, 346-354.
- Gerson, A.R., Lange, A.G., Prince, K.E. & Smart, R.St.C. 1998. The mechanism of Cu activation of sphalerite, *Applied Surface Science* 137, 207-223.
- Manceau, A., Tamura, N., Marcus, M.A., MacDowell, A.A., Celestre, R.S., Sublett, R.E., Sposito, G. & Padmore, H.A. 2002. Deciphering Ni sequestration in soil ferromanganese nodules by combining x-ray fluorescence, absorption and diffraction at micrometer scales of resolution, *American Mineralogist* 87, 1494-1499.
- Prince, K.C., Heun, S., Gregoratti, L., Barinova, A. & Kiskinova, M. 2002. Long-term oxidation behaviour of lead sulfide surfaces, in *Nanoscale spectroscopy and its applications to semiconductor research*, Watanabe, Y., Huen, S., Salvati, G. And Yamamoto, N. (ed.) Heidelberg, Germany: Springer Verlag, pp 111-120.

Rapid Mineral Liberation Analysis with X-Ray and BSE Image Processing

Y. Gu

JKMRC, The University of Queensland, Brisbane, Australia

ABSTRACT: Scanning electron microscope (SEM) based quantitative mineral analysis systems have become increasingly important in minerals processing. Two types of signals from the SEM, X-ray and BSE, are commonly used separately or in combination for this purpose. The X-ray signal has proven to be very reliable for mineral identification, while the BSE signal is very fast. Judicious use of a combination of X-ray and BSE signals can optimize the speed and accuracy of an automated mineral analysis system. This paper presents some of the novel strategies of flexible use of X-ray and BSE capabilities at the particle level that are employed in the recently developed JKMRC/FEI Mineral Liberation Analyser (MLA).

1 INTRODUCTION

1.1 Mineral Liberation Analysis

In modern applied mineralogy studies, mineral liberation analysis is usually carried out with an optical microscope based system or a scanning electron microscope (SEM) system. An optical microscope has only limited capabilities of spatial resolution, automation, and mineral identification. Hence, it is usually used for semi-quantitative work. In contrast, an SEM based system can produce high quality mineral liberation measurements automatically. The increased use of SEM systems in the mining industry in recent years demonstrates its success in mineral liberation analysis.

Several SEM based systems have been developed in the past for mineral liberation analysis (Hall 1977; Pignolet-Brandom & Reid 1988; Jones 1987; King 1993; Lastra et al. 1998; Petruk 2000; Gu 2003). All these systems use X-ray analysis and BSE image processing to varying degrees. The prudent application of both X-ray analysis and BSE image processing in a system can significantly improve its speed and reliability.

1.2 Characteristics of BSE and X-Ray

The BSE (back scattered electron) signal in an SEM is generated from the surface of the sample. Its intensity is proportional to the average atomic number (AAN) of the sample. The two distinctive advantages of BSE signal are high spatial resolution (<0.1 micron) and high speed of acquisition (10,000 points per second). The disadvantage of a BSE signal is so called "grey level overlapping", where two minerals can have a very similar AAN, thus making it impossible to differentiate them based on BSE signal only.

The characteristics of an X-ray signal complement that of BSE. An X-ray spectrum can be used to uniquely identify a mineral. However, X-ray acquisition is very slow (100 points per second) and its resolution low (1 – 5 micron).

The challenge is then to make best use of both BSE and X-ray signals in a system to achieve the required speed, resolution and reliability. This paper introduces two new concepts that are used in the recently developed MLA system: particle level BSE image analysis and mineral level X-ray mapping.

2 PARTICLE LEVEL BSE IMAGE ANALYSIS

2.1 Field of View

To obtain suitable statistical confidence, many fields of view of each sample are usually measured. Depending on the image resolution selected, each field of view can contain a few hundred particles or more (Figure 1). It is possible to perform image analysis at field level, so that particle and mineral identification are obtained in a single step. However, this limits the resolution and sensitivity of the analysis. For example, the histogram of the image is relatively complex (Figure 2). Advanced image analysis techniques are required and they are usually computationally intensive and therefore slow.

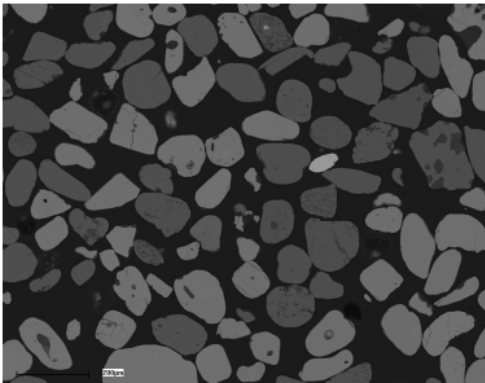


Figure 1. BSE image – a field of view for image analysis

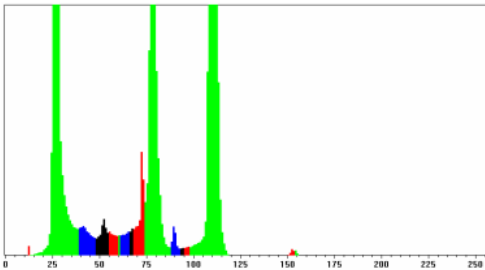


Figure 2. Histogram of the image in Figure 1

2.2 Particle Level

Alternative to the above single step approach, the image analysis can be carried out in two steps. The first step is to separate particles and the second step is to perform mineral recognition on each particle. This approach breaks down the complexity to more manageable parts. Figure 3 shows one of the more complex particles from Figure 1. This particle has five mineral phases and they are clearly indicated in

its histogram (Figure 4). The histogram resolution of Figure 4 is much higher than that of Figure 2, as can be seen from comparing the peak width.



Figure 3. BSE image of a particle from lower left corner of the image in Figure 1.

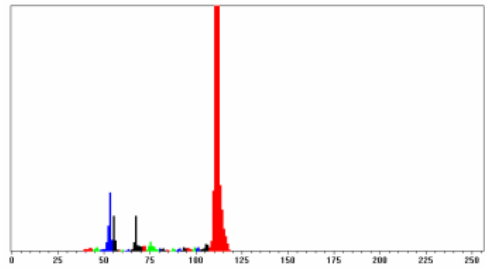


Figure 4. Histogram of particle in Figure 3.

A single particle is much simpler to process than the whole field of view. The mineral composition of the particle is shown in Figure 5.

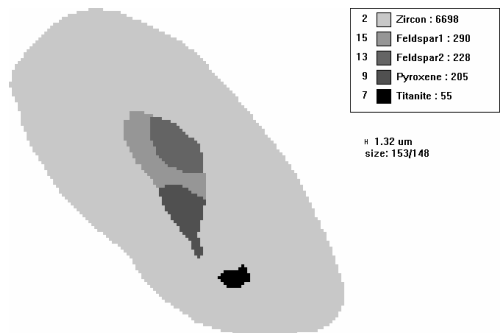


Figure 5. Particle after segmentation and mineral identification.

3 MINERAL LEVEL X-RAY MAPPING

3.1 Particle X-Ray Mapping

Particle X-ray mapping produces an X-ray dot map of the particle in question. Each dot in the map is one X-ray analysis (Figure 6).

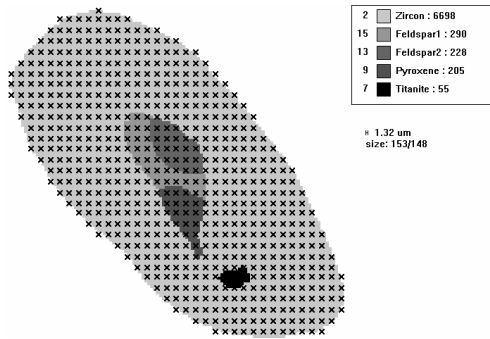


Figure 6. Particle X-ray map, each X-ray is represented by a cross.

Particle X-ray mapping is quite simple and can produce reliable mineral identification if mixed spectra are not prevalent. However, it is slow and in most cases it is not necessary, such as for the zircon mineral in Figure 6 particle.

Over the years, area scan X-ray analysis has been used as a fast alternative.

3.2 Area Scan X-Ray Analysis

Area scan X-ray analysis rasters the electron beam over an area of interest, such as the area occupied by a mineral grain in a particle or in the field of view, for a very short period of time to obtain one X-ray spectrum. This technique is used in some systems (Petruk 2000; Gu 2003) to improve the efficiency of liberation measurements. For example, the particle in Figure 5 would need only 5 X-ray analysis points to identify the mineral phases with the area scan technique.

The disadvantage of this technique is that it can not be applied to particles that contain two or more minerals of very similar grey level (grey level overlapping). For those cases X-ray mapping is the only method to resolve the boundary between those minerals. However, the mapping can be restricted to areas that potentially have grey level overlapping.

3.3 Mineral Level X-Ray Mapping

Mineral level X-ray mapping combines the area scan and X-ray mapping in the analysis of a single particle, thereby providing flexible application of these two levels of X-ray analysis options. Figure 7

shows that the second feldspar is measured with X-ray dot map, while the other minerals in the particle are measured with a single area scan X-ray analysis.

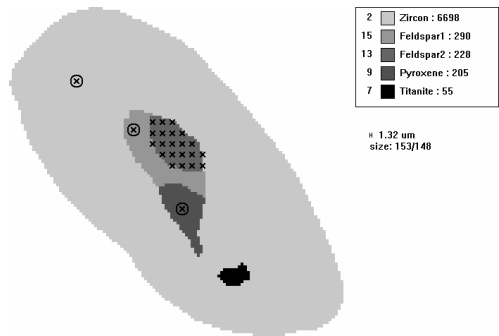


Figure 7. The "Feldspar2" is measured with X-ray dot mapping, with each X-ray dot represented by a cross; the other minerals in the particle are measured with an area scan, with each analysis shown by a circled cross.

4 DISCUSSION AND CONCLUSION

The ideal SEM-based mineral liberation analysis system should make the best use of both BSE and X-ray, handling different ore types and minerals with a suitable combination of those two signals to meet the required reliability and speed. The novel particle level image analysis and mineral level X-ray mapping techniques presented in this paper represent a step forward in this direction.

5 ACKNOWLEDGEMENT

The author wishes to thank Professor Tim Napier-Munn, Dr Rob Morrison, Dr Robert Schouwstra, Kurt Moeller, Eugene Louwrens and other MLA users for useful comments and discussions, and more importantly for their support of the MLA development project over the past seven years.

6 REFERENCES

- Gu, Y. 2003. Automated scanning electron microscope based mineral liberation analysis. *J. Minerals & Materials Characterization & Engineering*, 2: 33-41.
- Hall, J.S. 1977. Composite mineral particles – analysis by automated scanning electron microscopy. *PhD thesis*. JKMR. The University of Queensland, Brisbane.
- Jones, M.P. 1987. *Applied mineralogy – a quantitative approach*. London: Graham & Trotman.
- King, R.P. 1993. Basic image analysis for mineralogy, in *ICAM'93 Demonstration Workshop Manual*, 119-139.
- Lastra, R., Petruk, W. & Wilson, J. 1998. Image analysis techniques and applications to mineral processing, in

- Modern Approaches to Ore and Environmental Mineralogy*, eds. Cabri, L.J. & Vaughan, D.J., Mineral. Assoc. Can., Short Course Vol 27: 327-366.
- Petruk, W. 2000. *Applied mineralogy in the mining industry*. Amsterdam: Elsevier.
- Pignolet-Brendom, S. & Reid, K.J. 1988. Mineralogical characterization by QEM*SEM, in *Process Mineralogy VIII*, eds. Carson, D.J.T. & Vassoilou A.H., TMS, Warrendale, PA, 337-346

Quantitative X-Ray Analysis of Light Elements Boron and Oxygen in Tourmaline Samples

A.C.Joaquim, E.S.Mano, H.Kahn

Minining and Petroleum Engineering Department, Polytechnic School, University of Sao Paulo, Sao Paulo, Brazil

G.C.Fronzaglia

Technological Centre of Research of Vale do Rio Doce Company – Santa Luzia, Minas Gerais, Brazil

C.A.I.Oba

Multigeo Company- Sao Paulo, Sao Paulo, Brazil

ABSTRACT: Boron quantification is a hard task, because boron is a very light chemical element. Few techniques can be applied in order to quantify it. At the same time, boron is an important constituent of the mineral tourmaline and its quantification can define the potential uses of the tourmaline in the manufacturing industry. The microanalysis by SEM/WDX can be an alternative method to perform this task. In this study SEM/EDX and SEM/WDX applied for tourmaline microanalysis. The WDX results are very close to the ones acquired by ICP-AES and atomic absorption performed other laboratories. The results obtained by WDX analysis are 2.88 of boron, 50.4 of oxygen, 0.91 sodium, 0.38 of magnesium, 18.2 of aluminium, 16.4 of silicon and 10.7 of iron in weight percent. Comparing the analysis performed by EDX and WDX, the results originated by WDX present a little variation between distinct analyses while EDX shows a greater variation especially for the light elements such as boron and oxygen. The observed dispersion in B analysis is related to small chemical composition variations from particle to particle as previously indicated by BSE images. WDX technique showed to be a reliable tool for B analysis in tourmaline samples.

1 INTRODUCTION

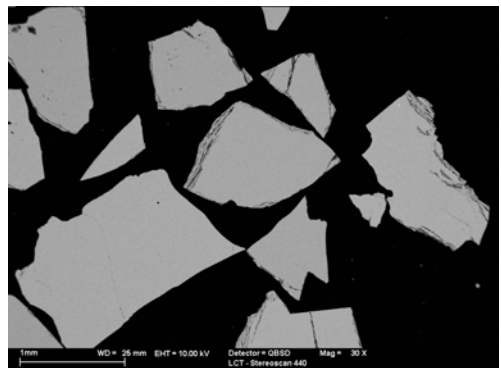
Boron represents only 0.001% of elements in the Earth, however it has many utilities, as example, it is used to in the manufacturing of cloths, woods, ceramics and glasses.

Some techniques have been used to quantify the boron in the tourmaline. The most indicated method is the ICP for bulk analysis, although SEM/WDX analysis can be applied for analysis in micro-scale.

2 METHODS

Small particles of tourmaline, with grain size bellow 100 μm , were used in the analysis. Thin-polished sections were made and then the samples were covered with a carbon film. The images were acquired by LEO SEM, model S440, coupled with two X-ray spectrometers: Oxford EDX, Isis 300 and WDX, Microspec 600i.

Backscattered electrons image, BSE, from tourmaline showed very weak heterogeneity, almost imperceptible, as illustrated in Photomicrography 1.



Photomicrography 1 - BSE image of tourmaline particles.

Even with a ultrathin window with Ge EDX detector the B peak was not observed on the spectrum as illustrated in figure 1.

Standards of boron nitride (BN), quartz (SiO_2), sodium chlorate (NaCl), olivine ($(\text{Mg,Fe})_2 \text{SiO}_4$), jadeite ($\text{NaAl}(\text{Si}_2\text{O}_6)$) and magnetite (FeFe_2O_4) were used to calibrate the WDX spectrometer for analysis. WDX's analysis measurements were processed with 10 keV and 100 nA current measured in a Faraday's cup; the boron spectrum is shown in spectrum 2.

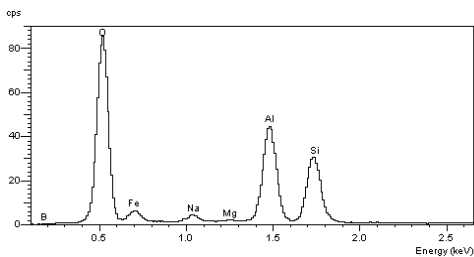


Figure 1. EDX spectrum showing the major elements of tourmaline; boron resolution is not good.

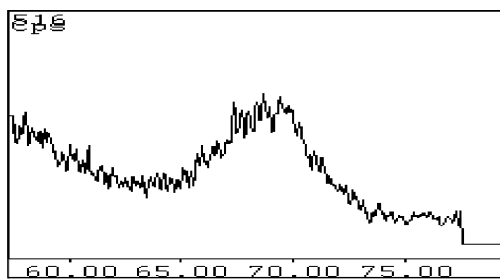


Figure 2. EDX spectrum showing the major elements of tourmaline; boron resolution is not good.

Before the quantitative analysis measurements, it was verified the existence (or absence) of secondary peaks of the major constituents potentially interfering with the boron peak using the pulse discrimination (SCA window voltage mode). In order to minimize or even to avoid chemical bonding shifts of the boron peak, it was selected the option of "peak search" for the standard and sample measurements. LSM 200 crystal was used for boron analysis.

After calculating the relative intensities sample/standard for each analyzed element it was applied Phi-Rho-Z corrections.

3 RESULTS

The attained results, expressed in weight percent, are presented on table 1.

The analysis results carried out by EDX (Fig 1) and WDX (Fig 2) are presented on Figures 3 and 4. The WDX results show a little variation between distinct analysis while EDX shows a greater variation, especially for light elements such as oxygen and boron.

The observed dispersion in B analysis is mainly related to small chemical composition variations from particle to particle, as previously indicated by BSE images, than properly to the analysis itself.

Table 1. Weight percent of elements acquired by WDX..

B	O	Na	Mg	Al	Si	Fe
2.62	50.3	1.04	0.15	18.5	15.9	11.5
2.62	49.6	0.73	0.11	18.6	16.1	11.4
2.63	51.0	1.23	0.17	18.0	16.1	10.9
3.23	50.1	0.63	0.13	18.4	16.5	11.0
3.26	50.3	0.88	1.60	18.0	17.0	8.91
3.14	50.3	0.75	0.38	18.3	16.7	10.5
2.77	50.8	0.93	0.13	18.1	16.5	10.7
2.71	50.6	1.17	0.59	17.6	16.5	10.8
3.30	50.6	0.85	0.17	18.0	16.1	11.0

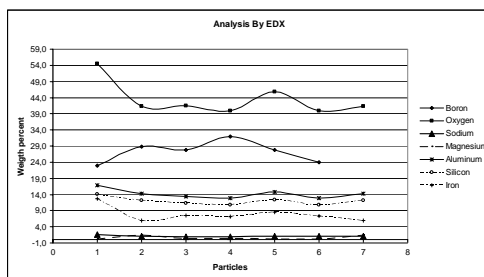


Figure 3. Analysis variation by EDX analysis.

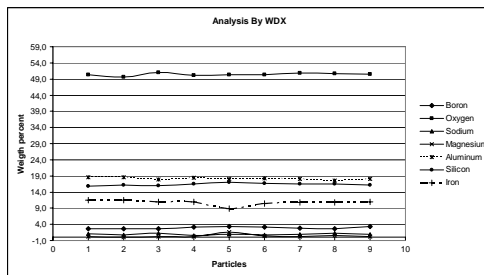


Figure 4. Analysis variation by WDX analysis.

4 CONCLUSIONS

WDX technique confirmed to be a reliable tool for B microanalysis in tourmaline samples. The results coming from a outside laboratory in Japan, by ICP and AAS techniques, gave an average value of 2.95% for B which are basically the same average figure achieved by SEM-WDX, 2.92%±0.3% w/w.

5 REFERENCES

Goldstein, J.I., Newbury, D.E., Echlin, P., Joy, D.C., Romig, A.D., Jr., Lyman, C. E., Fiori, C., Lifshin, E. 1992. Scanning Electron Microscopy and X-Ray Microanalysis. A Text for Biologist, Materials Scientists, and Geologists. Plenum Press.

State-of-the-art Quantitative Phase Analysis by X-ray Powder Diffraction

A.Kern

Bruker AXS GmbH, Karlsruhe, Germany

ABSTRACT: X-ray Diffraction is one of the most powerful methods that exist for qualitative and quantitative phase analysis. Recent developments in analysis and data management software now allow fully automatic operation and will extend the role of X-Ray Diffraction in industrial applications, such as phase quantification or determination of structural and microstructural properties. Nowadays XRD is a well established tool for quality and process control in several industries, examples of which include the aluminium, cement and mining industry.

1 INTRODUCTION

In the cement industry, XRD techniques were introduced in the late 1970's to allow process control operators to analyse the Free Lime content. This is still done by a straightforward calibration based method which just requires the measurement of a single peak. Unfortunately full clinker and cement analysis could never be realised with these methods. Therefore quantitative analysis of the clinker has mostly been carried out by the use of the Bogue method or by optical microscopy, although it's deficiencies, especially when using the Bogue calculation, are well known.

Now the automated quantification of the full clinker composition using the so called Rietveld method is possible by stable and fast software packages like the TOPAS software.

2 CLINKER ANALYSIS

In contrast to classical calibration based quantification, the Rietveld method is standardless and requires a complete X-ray scan and therefore a full blown diffractometer. Of course the data acquisition of a complete diffractogram takes more

time than just measuring one or two peaks. To make this technique workable for quality or process control, in an industrial environment, advanced detector technology like the new 1-dimensional Detector VANTEC-1 developed by BRUKER AXS. Using this detector technology cement clinker quantification can be realised in a few minutes with high accuracy and reproducibility.

The reliability of the Rietveld method has been shown several times by different studies (Angles et al. 2002, Füllmann et al. 2002, Madsen & Scarlett 2000, Möller 1998, Neubauer et al. 1997). In the last three years the automated version of the TOPAS software, TOPAS BBQ, has proven its reliability in several installations in cements plants worldwide and opened the path for quality and process control of kiln operation, based on real numbers.

Apart from clinker analysis the Rietveld method can, of course, be used for all other relevant applications in cement manufacturing where the knowledge of the phase composition is necessary for the production process. This starts with the control of raw materials, intermediate products and ends with the finished cement. It will be shown that quantitative X-ray diffraction is an excellent tool especially for controlling the sulphate composition.

3 BREAKTHROUGH IN CEMENT ANALYSIS

In the final step of Portland Cement production raw materials like Gypsum or Gypsum/Anhydrite mixtures are ground up with clinker in cement mills. This grinding procedure elevates the temperature of the mill feed leading to partial dehydration of the Gypsum phase ($\text{CaSO}_4 \cdot 2\text{H}_2\text{O}$) to Hemi-Hydrate ($\text{CaSO}_4 \cdot 1/2\text{H}_2\text{O}$) (also named Bassanite) or even Anhydrite (CaSO_4). As all sulphate phases do considerably differ in both solubility and reactivity the degree of dehydration has a direct effect on the setting behaviour. Gypsum for example shows a moderate solubility and Hemi-Hydrate is a highly soluble phase.

Knowledge about the absolute phase abundance of the sulphate phases in cements therefore allows monitoring and control of the cement mill operation.

Up to now, most cement plants use chemical analysis to control only the total sulphate content of the cement. Quality control generally is done by time consuming physical test methods to determine parameters, such as setting time and strength. There was no access to the actual mineralogical information, because there was not any satisfactorily working analytical tool.

Now quantitative X-ray Diffraction phase analysis offers the possibility to analyse the sulphate phases, as well as Calcite, in cement directly, with high accuracy and reproducibility.

4 ACCURACY AND REPRODUCIBILITY IN ANALYSIS OF CALCITE AND SULPHATES

To test analytical performance, pseudo-reference samples were prepared as there are no certified cement standards with known phase composition available. This set of standards was made by mixing and homogenizing an industrial clinker with Gypsum, Anhydrite, Hemi-hydrate and Calcite as used in the technical process. For all phases the concentration range from 0 to 6 weight % was covered. In order to determine the reproducibility of the measurement each sample was analysed ten times.

Quantitative results are shown in Figures 1 to 4. In each figure the black line indicates the actual phase composition and the red data points represent the calculated values. The results demonstrate the perfect ability of XRD for quantitative phase analysis of cements. Tables 1 to 4 give the measurement reproducibility from a selection of samples. The Tables give the actual value, the average and the standard deviation in one σ , as well as the observed minimum and maximum value. Accuracy is always better than 0.3 weight %. Reproducibility varies from phase to phase. For Anhydrite it is for example always better than 0.09 weight % (Std. Dev). The results indicate that

quantitative X-ray diffraction is a powerful tool for analysing the Sulphates and Calcite in Cements of the type CEM I.

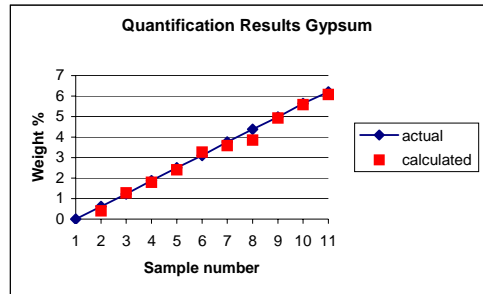


Figure 1. Accuracy in quantitative phase analysis of Gypsum.

Table 1: Gypsum Quantification: Accuracy and Reproducibility. Standard deviation calculated of ten measurements per sample (all values in weight %).

Gypsum			
	Sample3	Sample6	Sample9
Actual composition	1.22	3.10	4.98
Average calculated	1.27	3.26	4.92
Average Stdev	0.10	0.12	0.17
Min _{observed}	1.14	3.06	4.63
Max _{observed}	1.49	3.45	5.25

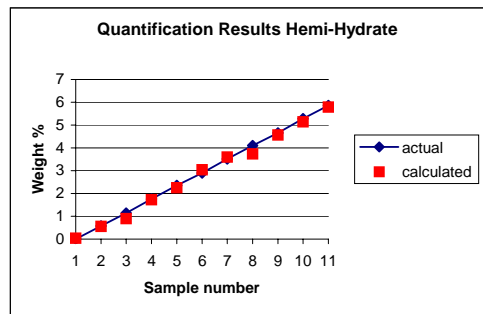


Figure 2. Accuracy in quantitative phase analysis of Hemi-Hydrate.

Table 2: Hemi-Hydrate Quantification: Accuracy and Reproducibility. Standard deviation calculated of ten measurements per sample (all values in weight %)

Hemi-Hydrate			
	Sample 3	Sample 6	Sample 9
Actual composition	1.14	2.90	4.66
Average calculated	0.84	3.04	4.57
Average Stdev	0.10	0.12	0.15
Min _{observed}	0.67	2.78	4.40
Max _{observed}	0.99	3.20	4.92

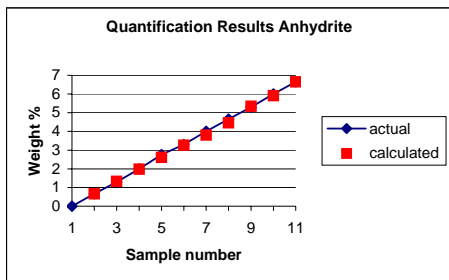


Figure 3. Accuracy in quantitative phase analysis of Anhydrite.

Table 3: Anhydrite Quantification: Accuracy and Reproducibility. Standard deviation calculated of ten measurements per sample (all values in weight %)

Anhydrite			
	Sample 3	Sample 6	Sample 9
Actual composition	1.30	3.30	5.30
Average calculated	1.34	3.26	5.35
Average Stdev	0.06	0.07	0.09
Min _{observed}	1.26	3.12	5.21
Max _{observed}	1.43	3.36	5.45

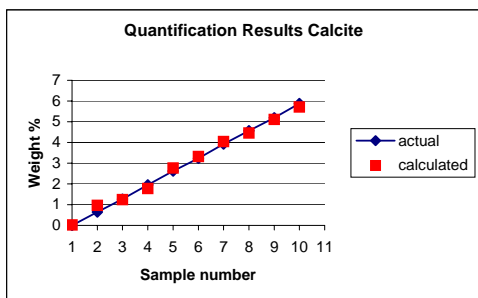


Figure 4. Accuracy in quantitative phase analysis of Calcite.

Table 4: Calcite Quantification: Accuracy and Reproducibility. Standard deviation calculated of ten measurements per sample (all values in weight %)

Calcite			
	Sample3	Sample 6	Sample 9
Actual composition	1.27	3.23	5.19
Average calculated	1.24	3.32	5.11
Average Stdev	0.24	0.24	0.21
Min _{observed}	0.95	3.00	4.71
Max _{observed}	1.52	3.78	5.31

5 REALIZATION IN A CEMENT PLANT

In order to implement Rietveld clinker and cement analysis in a production control system a joint project of Deuna Zement and the Wilhelm-Dyckerhoff-Institute in Wiesbaden (Germany) together with BRUKER AXS and POLYSIUS AG, a producer of automated laboratory systems was initiated.

Installation and Set-up was done in May 2003 and since June 2003 the Deuna cement plant is world-wide the first continuously monitored cement plant in terms of clinker and cement quality.

Under production conditions the Rietveld data turned out to be superior to any classical Bogue calculation. The Rietveld analysis can continuously monitor changes, which can not be seen by classical analysis methods. Detailed information is published in (Paul et al. 2004).

6 CONCLUSION

Until today mineralogical information about the clinker and sulphate phases in cements was impossible, simply because an analytical tool that allows fully automatic analysis was not available. As a result quality control was limited to testing physical parameters such as setting time and strength development. Process control itself has not been possible. Today, XRD analysis now allows the accurate and fast phase quantification. Cement samples are directly measured and require a minimum amount of sample preparation which can be integrated into a lab automation system. This technique opens the path for real time control of clinker and cement production using parameters such as the dehydration of Gypsum in the cement mill. Quality and process control in Portland cement manufacturing can now be dramatically improved.

7 REFERENCES

- Angles G. De La Torre, Sebastian Bruque, Javier Campo, Miguel A.G. Arranda. 2002. The superstructure of C_3S from synchrotron and neutron powder diffraction and its role in quantitative phase analyses, *Cement and Concrete Research*, 32, 1347-1356
- Füllmann, T., Walenta, G., Pöllmann, H., Gimenez, M., Lauzon, C., Hagopian-Babikian, S., Dalrymple, T., and Noon, P. 2001. Quantitative Rietveld Analysis of Portland Cement Clinkers and Portland Cements using the TOPAS Software - Application as a Method for Automated Quality and Process Control in Industrial Production - Part I, *International Cement Review*, January, 41-43.
- Madsen, I.C., and Scarlett, N.V.Y. 2000. Cement: Quantitative Phase Analysis of Portland Cement Clinker, in *Industrial Applications of X-Ray Diffraction* (ISBN: 0-8247-1992-1), Marcel Dekker, New York.
- Möller, H. 1998. Automatic profile investigation by the Rietveld method for standardless quantitative phase analysis, *ZKG International*, 1, 40-50.
- Neubauer, J., Pöllmann, H., and Meyer, H.W. 1997. Quantitative X-ray analysis of OPC clinker by Rietveld Refinement, *Proc. 10th Int. Congr. Cem. Chem.*, Göteborg, Vol. 1, Ii056, 8 p.
- Paul, M., Hornung, D., Enders, M., and Schmidt, R. 2004. Process monitoring in a cement plant: the combination of optimized preparation procedures for clinker and cement and Rietveld analysis, *Cement International* 2, No. 1

Problems of the Quantitative Rietveld Phase Analysis of Complex Samples

R.Kleeberg

Institute of Mineralogy, Freiberg University of Mining and Technology, Freiberg, Germany

ABSTRACT: The Rietveld method is widely accepted as a modern tool for quantitative phase analysis by X-ray diffraction. A lot of successful applications have been published. Nevertheless, the method requires a deep understanding of crystallographic and analytical details. To get accurate and precise results, it is necessary to develop new user-independent software programs and to formulate “rules” for the creation of starting models. The aim of the talk is to demonstrate problems and pitfalls in practical Rietveld analysis as well as some methods to improve the results. Special attention is paid to the preparation and measurement of the samples, to the correction of preferred orientation, the application of models for line broadening, and methods for handling a large number of parameters during the refinement process.

1 INTRODUCTION

Quantitative phase analysis (QPA) by X-ray powder diffraction is a traditional method in material sciences as well as in geosciences. The physical background is well known and taught in excellent textbooks, e.g. Klug & Alexander (1954) and Bish & Post (1989). Presently, traditional single line methods are still in use as well as full profile summation algorithms or profile fitting procedures like the Rietveld method (see Cranswick & Kruger 2002). The application of the latter is rapidly growing because of its obvious advantages like standard-free calculation, insensitivity to grain statistics and the capability for the correction of preferred orientation. Other reasons for the growing interest in the Rietveld technique are the intense advertising for commercial programs and the publication of excellent results of phase quantification for complex mixtures like rocks (e.g. Hill et al. 1993; Hillier 2000; Monecke et al. 2001; Ward & Gomez-Fernandez 2003) or cement materials (e.g. Taylor & Aldrige 1993; De la Torre & Aranda 2003). Additionally, the Rietveld method provides the basis for fast, automated phase analysis in process control (e.g. Füllmann et al. 2001; Scarlett et al. 2001). On the other hand, the Rietveld

method is known to require a deep understanding of crystallography and considerable skills in using the programs. Significant errors in quantitative phase analysis caused by the users are common in practice, but they are documented only as outcomes of international round robins (Madsen et al. 2001; Scarlett et al. 2002).

In general, accurate results of Rietveld phase analysis can be achieved by two methods: (i) by programming of an appropriate refinement strategy inclusive extensive fixing of known parameters for a given, well known system like cement materials (e.g. Füllmann et al. 2001) or (ii) a careful choice of physically meaningful models and a user guided step-by-step procedure for parameter fixing/refining like recommended for structure refinement (McCusker et al. 1999). The first method can be applied only to a set of similar samples and requires an intensive “trial-and-error” work to optimize the control file. Details are not published in order to protect the know how of the authors. The second method is the only one to be useful in a laboratory that has to analyze different types of samples, but only very experienced users are able to interact with their Rietveld program in a way ensuring accurate results even for complex samples. The aim of this talk is to give some hints to improve the quality of

Rietveld quantitative phase analysis of complex samples in every day laboratory work. The talk is focussed on the application of the modern Rietveld code BGMN (Bergmann et al. 1998), but the principles should also be valid for other programs.

2 BASICS OF RIETVELD QPA

The Rietveld method is, first of all, a method of profile fitting for refining of crystal structures. Every point of the diffraction pattern is described as

$$y_i = \sum_p \left[S_p \sum_k \left[L_k P_k H_k |F_k|^2 G(\Delta\Theta_{ik}) P_{ok} \right] \right] + y_{bi} \quad (1)$$

with

- y_i intensity on measuring point i
- S_p scale factor (proportional to the scattering volume of the phase)
- L_k, P_k, H_k Lorentz-, polarisation- and multiplicity factors (line k)
- $|F_k|^2$ structure factor
- $G(\Delta\Theta_{ik})$ profile function
- P_{ok} preferred orientation correction (hkl dependent)
- y_{bi} intensity of the background.

In all Rietveld QPA methods, the relative mass fraction of a phase must be derived from the volume-weighted scale factors:

$$X_p = \frac{S_p \rho_p V_p^2}{\sum_j S_j \rho_j V_j^2} \quad (2)$$

with

- X mass fraction
- S Rietveld scale factor
- ρ density
- V cell volume
- p phase p
- j number of phases.

Therefore, the QPA result will be biased by incorrectly determined scale factors or cell contents of the analyzed phases. This is also true if an internal standard is used and all phases have been related to the standard. During the optimization procedure, structural parameters of the phases have to be refined as well as nonstructural ones. The problems of parameter correlation and instability of some parameters are well known from structure refinement work (McCusker et al. 1999). They become much more complicate in a multicomponent system because of the enlarged number of parameters and the restricted information (intensity) per phase. It is obvious that generalized refinement strategies cannot be formulated easily because of sample-to-sample variations of the phase contents.

Additionally, the restricted information coming from a routinely aquired powder pattern of a multiphase sample will clearly prohibit the refinement of the complete set of structural and non-structural parameters. Consequently, the task of the user is to decide (i) what parameters can or must be refined for the actual measurement, and (ii) how to reach convergence e.g. by the application of an appropriate parameter-turn-on-sequence and by introduction of meaningful parameter constraints or restraints. Another question is what mathematical methods can be used by the program to make some of these decisions automatically. If the program can take over the control of some of these issues, the method will become more user-independent and the potential of errors will be reduced.

3 PRACTICAL PROBLEMS

3.1 Sample preparation and measurement

Although the Rietveld method is known to be relatively insensitive to grain statistics and has the principle capability to correct for preferred orientation effects, the material should be ground carefully to reach the optimal particle size of about 1-2 micron, but at least of about 5 micron. This is necessary in order to correct the effect of microabsorption as well as to minimize preferred orientation (Monecke et al. 2001). The grinding can be done effectively by wet grinding in a McCrone micronizing mill (O'Connor & Chang 1986). The most effective way to avoid preferred orientation during filling the sample holder is spray drying (e.g. Hillier 1999). Moderate preferred orientation of simply ground mineral powders in front- or sideloaded holders can be successfully corrected by the application of symmetrized spherical harmonic functions (e.g. Bergmann et al. 2001). The measurement strategy should be designed to get maximal intensity from a maximal sample volume.

From this point of view, wider divergence geometry should be preferred and the use of Θ -compensating divergence slits is recommended. On the other hand, an excessively wide divergence will prohibit the peak separation necessary for qualitative phase identification. Therefore, a compromise of "medium resolution" should be applied, e.g. an instrumental line width of about $0.1-0.15^\circ 2\Theta$ in the $20-30^\circ$ range. Consequently, the step width has to be about $0.02-0.03^\circ 2\Theta$ to fulfill the common rules of profile analysis. The choice of counting time should ensure at least 2000-3000 counts for the 3-4 maximum lines, but more is, of course, better.

3.2 Profile modeling

One of the most important problems in Rietveld analysis is the choice of an adequate profile shape

model. The peak shape in a laboratory X-ray powder pattern represents a folding of contributions from wavelength distribution, geometrical effects and sample introduced broadening. Only the latter contribution must be refined if the others are pre-determined by learning from standards or by the application of a so-called fundamental parameter approach (Cheary & Coelho 1998, Bergmann et al. 2000). An incorrect choice of the broadening model of any phase in a mixture can bias the QPA results.

This is especially true for strongly broadened lines and heavily overlapping profiles of structurally similar phases (Kleeberg & Bergmann 2002). The profiles of disordered phases can be approximated by hkl-dependent broadening and shifting parameters (Bergmann & Kleeberg 1998).

3.3 Preferred orientation correction

Preferred orientation (PO) in conventional powder mounts is caused by “brick-by-brick” stacking of anisotropic grains during the filling of the sample holder. The simple March-Dollase model cannot correct PO resulting from multiple cleavages of minerals. Therefore, symmetrized spherical harmonic functions must be applied (e.g. Järvinen 1993; Bergmann et al. 2001). Unfortunately, these models introduce a lot of additional parameters in the refinement model, especially for lower symmetric Laue classes. Convergence problems may occur especially for minor phases, and meaningless correction factors as well as wrong QPA results can be caused. Traditionally, the user has to choose a certain PO correction model for any phase. This is a laborious job and often a source of errors. In the BGMN program, an algorithm is used that decides automatically whether a previously chosen model is applicable. Such a feature helps to avoid time consuming computer sessions.

3.4 Use of restraints

The danger of complementary parameter changes during refinement grows with the number of phases, the similarity of structures, the line widths and the number of lines in the pattern. Especially complicated is the correct determination of structural and microstructural parameters for the minor phases: The low intensity of the phase and the weighting scheme used by the minimization algorithm often cause physically meaningless values for lattice parameters, occupation factors and line broadening.

Mostly, the minor phases tend to “absorb” the intensity around the peak base of the main phases and sometimes of the background by calculation of extreme line breadths. The inspection of the correlation matrix by the user as recommended for traditional structure refinement work is impracticable in every day QPA work. A simple and

general approach can be applied to minimize these problems: All these parameters should be restrained to physically meaningful intervals in the start model. Such a limitation of the parameter space can prohibit an “adiabatic” distribution of intensity between structurally similar phases. For example, the restraints of the lattice parameters of adjoining members of solid solution series can be chosen according to the Vegard’s law. In this way, phases showing strongly overlapping lines can be quantified without the well known problems of complementary parameter changes. In the same way the definition of upper limits of line broadening (e.g. upper limits for microstrain, lower limits for domain size) helps to avoid the overestimation of minor phases caused by the calculation of overmuch broadened line profiles as mentioned above. The introduction of restraints is also recommended for site occupation factors.

Because of the correlation of occupation factors and PO in their impact on peak intensities, the direct refinement of occupation factors is sometimes impossible. A practical way can be the use of constraints of the occupation factors to lattice parameters: The lattice parameters can be refined more easily and empirical relations between lattice parameters and chemical composition can be used.

3.5 Parameter-turn-on sequence

For complex mixtures and daily changing samples it seems to be impossible to define rules for a user-guided parameter-turn-on sequence. The only practicable way is the use of modern minimization algorithms ensuring the stability of the refinement process by statistical methods. For example, the program BGMN (Bergmann et al. 1998) uses variable regularization and generalization in a restricted gradient – conjugated direction algorithm.

The program uses a very global, automatically decided parameter-turn-on sequence: First all isotropic parameters/models, than PO correction models, than anisotropic line broadening models. Together with statistical methods to decide about the applicability of the anisotropic models, this approach ensures convergence without any user interaction.

4 EXAMPLES

In the talk the problems will be shown for samples containing up to 15 phases like rocks, tailings and artificial mixtures as used in the Reynolds Cup contest in QPA (McCarty 2002). More than 200 parameters could be refined automatically, and the difference plot is used for the identification of minor phases.

5 SUMMARY

The quantification of complex mixtures by the Rietveld method is possible by the use of modern mathematical methods, physically meaningful models and constraints for the parameters to be refined. The task of the user is to provide an appropriate sample and measurement and to decide about the models to be used. Some frequent pitfalls are discussed in detail.

6 REFERENCES

- Bergmann, J., Friedel, P. & Kleeberg, R. 1998. BGMN - a new fundamental parameters based Rietveld program for laboratory X-ray sources, it's use in quantitative analysis and structure investigations. Commission of Powder Diffraction, International Union of Crystallography CPD Newslett. 20: 5-8.
- Bergmann, J. & Kleeberg, R. 1998. Rietveld analysis of disordered layer silicates. *Mat. Sci. Forum* 278-281 (1): 300-305.
- Bergmann, J., Kleeberg, R., Haase, A. & Breidenstein, B. 2000. Advanced fundamental parameter model for improved profile analysis. *Mat. Sci. Forum* Vols. 347-349 (2): 303-308.
- Bergmann, J., Monecke, T. & Kleeberg, R. 2001. Alternative algorithm for the correction of preferred orientation in Rietveld analysis. *J. Appl. Cryst.* 34: 16-19.
- Bish, D.L. & Post, J.E. (eds.) 1989. *Modern Powder Diffraction. Reviews in Mineralogy* 20, Washington, Mineralogical Society of America.
- Brindley, G.W. 1945. The effect of grain or particle size on X-ray reflections from mixed powders and alloys considered in relation to the quantitative determination of crystalline substances by X-ray methods, *Phil. Mag.*, Ser. 7, 36: 347-369.
- Cheary R.W. & Coelho A.A. 1998. Axial divergence in a conventional X-ray powder diffractometer. II. Realization and evaluation in a fundamental-parameter profile fitting procedure, *J. Appl. Cryst.* 31: 851-861.
- Cranswick, L. & Kruger, G. (eds.) 2002. *Powder diffraction in mining and minerals. Commission on Powder Diffraction Newsletter* 27: International Union of Crystallography.
- De la Torre A.G. & Aranda M.A.G. 2003. Accuracy in Rietveld quantitative phase analysis of Portland cements. *J. Appl. Cryst.* 36: 1169-1176.
- Füllmann, T., Pöhlmann, H., Walenta, G., Gimenez, M., Lauzon, C., Hagopian-Babikian, S., Dalrymple, T. & oon, P. 2001. Quantitative Rietveld analysis of Portland cement clinkers and Portland cements using the TOPAS software - Application as a method for automated quality and process control in industrial production - Part I. *International Cement Review, Analytical methods*: 41-43.
- Hill, R.J., Tsambourakis, G. & Madsen, I.C. 1993. Improved petrological modal analyses from X-ray powder diffraction data by use of the Rietveld method; I, Selected igneous, volcanic, and metamorphic rocks. *J. Petrol.*, 34, 867-900.
- Hillier, S. 1999. Use of an air-brush to spray dry samples for X-ray powder diffraction, *Clay Miner.* 34: 127-135.
- Hillier, S. 2000. Accurate quantitative analysis of clay and other minerals in sandstones by XRD: comparison of a Rietveld and a reference intensity ratio (RIR) method and the importance of sample preparation. *Clay Miner.* 35: 291-302.
- Järvinen, M.J. 1993. Application of symmetrized harmonics expansion to correction of the preferred orientation effect. *J. Appl. Cryst* 26: 525-531.
- Kleeberg, R. & Bergmann, J. 2002. Quantitative phase analysis using the Rietveld method and a fundamental parameter approach. In: S.P. SenGupta & P. Chatterjee (Eds.) *Powder Diffraction. Proc. II Int. School on Powder Diffraction*, IACS, Kolkata, Allied Publishers Ltd, ISBN 81-7764-262-6: 63-76.
- Klug, H.P. & Alexander, L.E. 1954. *X-Ray Diffraction Procedures*. New York, London: John Wiley & Sons.
- Madsen, C., Scarlett, N.V.Y., Cranswick, L.M.D. & Lwin, T. 2001. Outcomes of the International Union of Crystallography Commission on Powder Diffraction round robin on quantitative phase analysis: samples 1a to 1h. *J. Appl. Cryst.* 34: 409-426.
- McCarty, D.K. 2002. Mineral analysis of clay-bearing mixtures: The Reynolds Cup contest. *Commission on Powder Diffraction Newsletter* 27: 12-15.
- McCusker, L.B., Von Dreele, R.B., Cox, D.E., Louer, D. & Scardi, P. 1999. Rietveld refinement guidelines. *J. Appl. Cryst* 32: 36-50.
- Monecke, T., Köhler, S., Kleeberg, R., Herzig, P. & Gemell, J.B. 2001. Quantitative phase-analysis by the Rietveld method using X-Ray powder-diffraction data: application to the study of alteration halos associated with volcanic-rock-hosted massive sulfide deposits. *Can. Mineral.* 39: 1617-1633.
- O'Connor, B.W. & Chang, W-J. 1986. The amorphous character and particle size distributions of powders produced with the micronizing mill for quantitative X-ray powder diffractometry. *X-Ray Spectrometry* 15: 267-270.
- Scarlett, N.V.Y., Madsen, I.C., Cranswick, L. M. D., Lwin, T., Groleau, E., Stephenson, G., Aylmore M. & Agron-Olshina N. 2002. Outcomes of the International Union of Crystallography Commission on Powder Diffraction round robin on quantitative phase analysis: samples 2, 3, 4, synthetic bauxite, natural grandiorite and pharmaceuticals. *J. Appl. Cryst.* 35: 383-400.
- Scarlett, N.V.Y., Madsen, I.C., Manias, C. and Retallack, D., 2001. On-line X-ray diffraction for quantitative phase analysis: application in the Portland cement industry. *Powder Diffraction* 16: 71-80.
- Taylor, J.C and Aldridge, L.P. 1993. Phase analysis of Portland cement by full profile standardless quantitative XRD-accuracy and precision. *Advances in X-Ray Analysis* 36: 309-314.
- Ward, C.R. & Gomez-Fernandez, F. 2003. Quantitative mineralogical analysis of Spanish roofing slates using the Rietveld method and X-ray powder diffraction data. *Eur. J. Mineral.* 15: 1051-1062.

Martian Surface ^{57}Fe Mössbauer Analysis

G.Klingelhöfer, B.Bernhard, Ch.Schröder, D.Rodionov, J.Foh, F.Renz, R.Gellert
Institute for Inorganic and Analytical Chemistry, Johannes Gutenberg University, Mainz, Germany

P.A. de Souza Jr.

Pelletizing Department, Research & Development, Companhia Vale do Rio Doce, Vitória, ES, Brazil & Institute for Inorganic and Analytical Chemistry, Johannes Gutenberg University, Mainz, Germany

E.Kankeleit & U.Bonnes

Nuclear Physics Institute, Darmstadt University of Technology, Darmstadt, Germany

R.V.Morris

NASA Johnson Space Center, Houston, Texas, USA

S.W.Squyres

Department of Astronomy, Cornell University, Ithaca, New York, USA

ABSTRACT: Mössbauer spectroscopy is a powerful tool for quantitative analysis of Fe-bearing materials. The miniaturized Mössbauer spectrometer MIMOS II is part of the Athena science payload landed in Mars in January 2004 on both Mars Exploration Rover missions. The instrument has two major components: (1) a rover-based electronics board which contains power supplies, a dedicated central processing unit, memory, and associated support electronics, and (2) a sensor head that is mounted at the end of the instrument deployment device (IDD) for placement of the instrument in physical contact with soil and rock. The scientific measurement objectives of the Mössbauer investigation are to obtain for rock, soil and dust (1) the mineralogical identification of iron-bearing phases (e.g. oxides, silicates, sulfides, sulfates, and carbonates), (2) the quantitative measurement of the distribution of iron among these iron-bearing phases (e.g. the relative proportions of iron in olivine, pyroxenes, and magnetite in basalt), and (3) the quantitative measurement of the distribution of iron among its oxidation states (e.g. Fe^{2+} , Fe^{3+} , and Fe^{6+}). Special geologic targets of the Mössbauer investigation are dust collected by the Athena magnets and exterior and interior rock and soil surfaces exposed by the Rock Abrasion Tool and by trenching with rover wheels, respectively.

1 INTRODUCTION

1.1 The Mars Exploration Rover mission

For the first time in history a Mössbauer spectrometer was placed on the surface of another planet. The miniaturized Mössbauer spectrometer MIMOS II (Klingelhöfer et al. 2003) is part of the Athena payload of NASA's twin Mars Exploration Rovers (MER) "Spirit" and "Opportunity". It determines the Fe-bearing mineralogy of Martian soils and rocks at the Rovers' respective landing sites, Gusev crater and Meridiani Planum. First results of soil and rock measurements at both landing sites confirm a generally basaltic composition of Martian surface materials.

1.2 Instrument Design

MIMOS operates in backscatter geometry. Because of the complexity of sample preparation, this is the choice for an in situ planetary Mössbauer instrument. No sample preparation is required, the instrument is simply presented to the sample for analysis. Because of mission constraints for minimum mass, volume, and power consumption, the MIMOS II is extremely miniaturized compared to standard laboratory Mössbauer spectrometers and

is optimized for low power consumption and high detection efficiency. All components were selected to withstand high acceleration forces and shocks, temperature variations over the Martian diurnal cycle, and cosmic ray irradiation. Because of restrictions in data transfer rates, most instrument functions and data processing capabilities, including acquisition and separate storage of spectra as a function of temperature, are performed by an internal dedicated microprocessor and memory. The dedicated CPU is also required because most Mössbauer measurements will be done at night when the rover CPU is turned off to conserve power. High detection efficiency is extremely important in order to minimize experiment time. Experiment time is also minimized by using as strong a main $^{57}\text{Co}/\text{Rh}$ source as possible.

Physically, the MIMOS II Mössbauer spectrometer has two components that are joined by an interconnect cable: the sensor head and electronics printed-circuit board. On MER, the sensor head is located at the end of the IDD and the electronics board is located in an electronics box inside the rover body. The sensor head contains the electromechanical transducer (mounted in the center), the main and reference $^{57}\text{Co}/\text{Rh}$ sources, multilayered radiation shields, detectors and their

preamplifiers and main (linear) amplifiers, and a contact plate and sensor. The contact plate and sensor are used in conjunction with the IDD to apply a small preload when it places the sensor head, holding it firmly against the target. The electronics board contains power supplies/conditioners, the dedicated CPU, different kinds of memory, firmware, and associated circuitry for instrument control and data processing.

2 FIRST RESULTS AND DISCUSSION

The first three Mössbauer spectra from the planet Mars were acquired from a soil spot in Gusev crater, just after Spirit had driven off the lander platform, from the rock Adirondack in Gusev crater, and from a soil spot at the bottom of the ~20 m crater which Opportunity landed in at Meridiani Planum. All three spectra show a basaltic mineral composition.

Comparing the soil spectrum from Gusev crater (Fig. 1) with the spectrum from the rock Adirondack (Figs. 2, 3) reveals a similar mineralogical composition, comprising of the dominant forsteritic olivine Fe^{2+} doublet (de Souza Jr., unpublished & de Souza Jr. et al. 2003), a second silicate Fe^{2+} -doublet, and less intense Fe^{3+} -doublet. We tentatively assign the second Fe^{2+} -doublet to pyroxene, but further investigation is necessary to confirm this identification. The rock spectrum shows two small additional sextets, indicative of the mineral magnetite or low-Ti magnetite. This mineral seems to be absent in the soil. However, the rock spectrum came from 12 hours integration and shows good counting statistics whereas the soil spectrum, typical 3 hours integration, has poor counting statistics. Thus, we simply might not be able to see the magnetite in this noisy background. The ratio of ferric to ferrous iron also differs in the rock and the soil spectrum. $\text{Fe}^{2+}/\text{Fe}_{\text{Total}}$ is ~0.6 in the soil sample and ~0.8 in the rock. Thus, as expected, the amount of ferric Fe is higher in the soil than in the rock. Pancam images of Adirondack revealed a dust coating of the rock. Planned activities on Adirondack include using the rock abrasion tool (RAT) to first brush off the dust, and then abrade a possible rock coating. Mössbauer spectra taken after each of these operations will offer further clarification of the differences between rock and soil components at Gusev crater.

The first spectrum of soil at Meridiani Planum, taken at the bottom of the crater Opportunity landed in, again shows a similar pattern of three central doublets. (Fig. 4). The dominant phase is again an olivine Fe^{2+} doublet accompanied by a second Fe^{2+} -silicate phase and a Fe^{3+} -phase. In addition, we see a weak sextet, which agrees well with the Mössbauer parameters of hematite. However, since the sextet is very weak and the linewidths are broad, we do not

want to make a mineralogical assignment yet. We note, however that this spectrum is consistent with the Mini-TES result that the soil in this area has a very low hematite index.

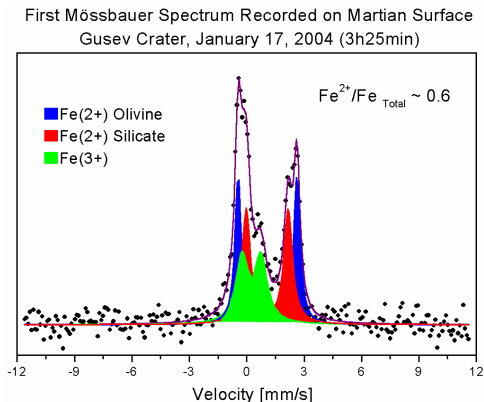


Figure 1. Mössbauer spectrum of soil in Gusev crater.

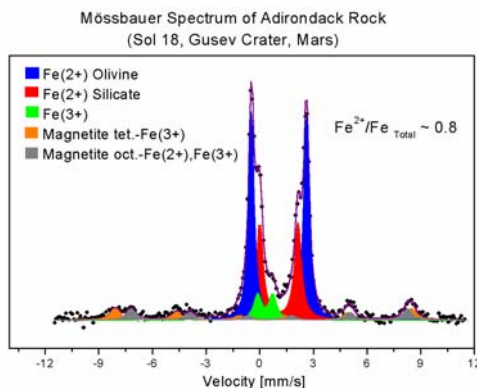


Figure 2. Mössbauer spectrum of Adirondack rock in Gusev crater.

3 CONCLUSIONS

The first Mössbauer measurements on Mars confirm the general basaltic nature of Martian surface materials. All Mössbauer spectra are dominated by the mineral olivine. Olivine has also been detected in the Nilli Fosse region from orbit by the Mars Global Surveyor Thermal Emission Spectrometer (Hoefen et al. 2003).



Figure 3. True color image taken by the panoramic camera onboard Spirit shows “Adirondack” the first rover’s target rock. Rock picture taken by the Panorama Camera. <http://marsrovers.nasa.gov/gallery/press/spirit/20040119a.html>

Mössbauer spectrum on Martian soil.
Meridiani Planum, Sol 11.

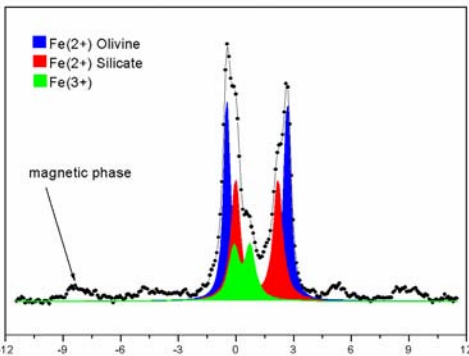


Figure 4. Mössbauer spectrum of soil near the lander in Meridiani Planum.

Detection of olivine at three widely spaced locations on Mars implies its widespread occurrence on the planet and the inefficiency of alteration processes (at least in recent times) that would act to reduce this highly-alterable mineral to weathering products. Only minor amounts of magnetically split ferric components were detected in the first spectra. Because of the presence of magnetite (possibly containing Ti), the Mössbauer spectrum of Adirondack is unlike that for any bulk sample of known SNC meteorite (Morris, unpublished). From our observations, soils seem to be derived from basaltic rocks. We do not see a mineral assemblage (e.g., higher proportion of ferric minerals) indicative

of a recent lacustrine deposit or water percolation. On the other hand, the outcrop rocks from Meridiani Planum landing site are partially formed by jarosite, and hematite (Fig 5). This observation, and other instrument evidences (e.g. high S content seen by the APXS) indicates that this place was once wet.

Mössbauer spectrum of El Capitan: Meridiani Planum

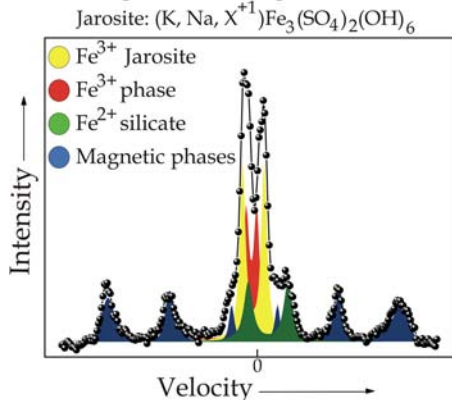


Figure 5. Mössbauer spectrum of a rock (named El Capitan) in the Meridiani Planum.

4 REFERENCES

- Klingelhöfer G., Morris, R. V., Bernhardt, B., Radionov, D., de Souza Jr., P. A., Foh, J., Kankaleit, E., Bonnes, U., Gellert, R., Schröder, Ch., Linkin, S., Evlanov, E., Zubkov, B., Priloutski, O. 2003. Athena MIMOS II Mössbauer Spectrometer Investigation, *Journal of Geophysical Research* 108(E12), 8067.
- de Souza Jr., P. A., unpublished database;
- de Souza Jr., P. A., Morris, R. V., Klingelhöfer, G. and the Athena Science Team. 2003. Analysis of Mössbauer Data from Mars: a Database and Artificial Neural Network for Identification of iron-bearing phases, Sixth International Conference on Mars, Houston, TX 3143.
- Hoefen, T. M., Clark, R. N., Bandfield, J. L., Smith, M. D., Pearl, J. C., Christensen, P. R. 2003. Discovery of Olivine in the Nili Fossae Region of Mars, *Science*, vol. 302, n.5645, 627.
- Morris, R. V., unpublished database.

The LIBD Technology - A Powerful Tool for The Highly Sensitive Detection of Particulate Content of Process Water

R.Köster, T.Wagner, T.Bundschuh

Institute for Technical Chemistry, Division Water Technology and Geotechnology, Forschungszentrum Karlsruhe GmbH, Karlsruhe, Germany

ABSTRACT: Aquatic particulate material plays an important role e.g. in waste water treatment as well as in drinking water technology (Shaw 1980). For the production of drinking water according to current microbial and hygienic quality standards the effective retention of particles (colloids resp. nano-particles) down to the 10 nm size range is necessary. Due to their high surface to volume ratio they can adsorb e.g. heavy metals or toxic organic compounds. Therefore the treatment technology for waste water and drinking water is connected to an effective particle removal. Microbial impurities like bacteria or viruses with particles sizes down to the lower nanometer range are also colloids and/or may adsorb to them. In order to assess the separation efficiency esp. for small particles in the nanometer range a highly sensitive analytical tool is necessary. The quantification of aquatic colloids is quite a difficult task because they are frequently found in small concentrations and often show a colloid size distribution where small particles ($d < 100$ nm) dominate. Commercial laser light scattering and laser light obscuration techniques allow for a direct, non-invasive quantification. However, the detection limits are often not sufficient for small particles with diameters below 100 nm. The rather novel Laser-induced Breakdown Detection (LIBD) method, however, is suitable for the direct, non-invasive determination of both size and concentration of nano-particles down to the lower nm size and concentration (ppt) range. It has been successfully used for particle characterization in drinking water treatment and for investigations in transport mechanisms of colloidal particles in the groundwater flow.

1 LIBD METHOD AND INSTRUMENTATION

The principle of the new developed technique, LIBD, is based on the generation and counting of breakdown events on colloidal particles in liquids. Light of very high intensity can lead to a breakdown of the dielectric property of matter. The necessary power densities can be generated by focusing a pulsed laser beam with pulse energies typically under 1 mJ and pulse lengths of several ns. As a result of the very high electrical field strength (up to 10^{11} V/m (Bettis 1992)) the electrons of atoms and molecules are released by multi-photon absorption. The initially released electrons absorb further light quanta and are accelerated within the electrical field of the laser pulse (inverse bremsstrahlung).

These electrons in turn knock further electrons out of atoms which in the end leads to an electron avalanche. The ionization increases strongly, and a plasma is generated (Radziemski & Cremers 1989, Fujimori et al. 1992). During the process described the plasma heats up to several thousand Kelvin and expands quickly, resulting in a shock wave. After the end of the laser pulse the plasma cools down, recombination processes and emission of light occur. The minimally required critical power density for

plasma generation (breakdown threshold) depends on the state of aggregation of matter. It is highest for gases, lower for liquids and lowest for solids (Bettis 1992). The LIBD principle is based on this difference of breakdown thresholds between liquid and solid matter. The laser pulse energy is adjusted so that in the pure liquid no breakdown event occurs but in presence of solids (colloids) the breakdown threshold within the focal area of the focused laser beam is exceeded. The breakdown events can be detected piezo-electrically and/or optically (plasma light emissions) by means of a camera.

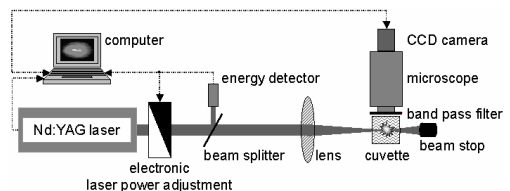


Figure 1: Experimental setup of the LIBD instrumentation.

The number of breakdown events per number of laser pulses is defined as the breakdown probability and dependent both on particle concentration and size. We followed the approach to determine the

spatial distribution of the breakdown events within the focal area by use of an image processing system. From the statistical distribution of the determined local plasma coordinates in the plane of projection of the breakdown events information about the expansion of the effective focal volume and the effective focal length is available. By recording a sufficient number of plasmas, a spatial distribution of breakdown events is obtained that reflects the ignition range of the colloids in the focus.

For the calculation of the particle concentration, the effective focal volume is computed according to (Knopp 1996, Scherbaum et al. 1996) using the mean particle diameter derived from the ignition length. Based on this procedure it is possible to determine the number-weighted mean particle diameter of colloids in unknown samples (Bundschuh 1999, Hauser & Bundschuh 2000, Bundschuh et al. 2003).

The experimental setup of our LIBD instrumentation which up to now is not commercially available is illustrated schematically in Figure 1. A frequency doubled, pulsed Nd:YAG laser (Continuum Surelite I) is used at a wavelength $\lambda_{em.} = 532$ nm and a repetition rate of 20 Hz. After passing a servo-motor controlled variable attenuator controlling the laser pulse energy, the laser beam is focused by a plano-convex lens of 60 mm focal length into the sample dispersion in a rectangular cuvette with a volume of 3.5 mL. The incident laser pulse energy is monitored by a calibrated pyroelectric detector (Newport 818J-09B) and adjusted just below the breakdown threshold of ultra pure water (MilliQ synthesis A10, UF-module with 5 kD cut-off, UV-module). The plasma light emissions generated during the breakdown process are magnified by a microscope (Leica) and recorded by means of a triggered CCD camera. The images are transmitted to a personal computer for data storage and evaluation. The average laser pulse energy and the x, z -coordinates of each plasma event are determined using a newly designed, fully automatic image processing software and are subjected to further data processing.

2 APPLICATIONS AND RESULTS

For calibration of the LIBD instrumentation various diluted polystyrene standard colloid dispersions (delivered by Polymer Standards Service GmbH) with particle diameters of about $0.02 \mu\text{m}$ to about $1 \mu\text{m}$ are used. The polystyrene particles are dispersed in ultra pure water at the concentration desired and measured in quartz sample cells. After calibration and parametrization of the LIBD system by the procedure described in (Bundschuh 1999, Hauser & Bundschuh 2000, Bundschuh et al. 2001a, c) the LIBD is used for the characterization of

particles in a special process water treatment, the drinking water processing (Bundschuh et al. 2001b; Wagner et al. 2002) with subsequent distribution via a water pipeline network of app. 1,700 km total length.

The main obligations of water purification plants are the water purification, supply and the continuous quality inspection. During the purification process of raw water the particulate content must be effectively reduced in order to minimize the risk of contamination by toxic substances as well as the risk of germination of microorganisms. For an efficient removal of bacteria, viruses, and parasites, it is important that colloidal particles are held back equally well as the larger suspended particles (typically $> 1 \mu\text{m}$). Also, during the distribution over a pipeline network there must be no colloid generation, e.g. by bacterial growth. Therefore, it is of major importance that both the size and the number of particles in the colloidal size range are monitored. The new technique offers the possibility of the sensitive detection of particulate contents in the range $\ll 1 \mu\text{m}$. Classical techniques like laser light obscuration (LLO) or photon correlation spectroscopy (PCS; based on laser light scattering) are very much too insensitive in the nanometer range.

The water taken from Lake Constance in Germany in a depth of 60 m already meets the legal requirements regarding chemical and physical quality parameters. Therefore, water treatment at the processing plant *Sipplinger Berg* mainly aims at a reliable deactivation and removal of pathogenic germs and any particulate water content. In the first step of water purification (Fig. 2) the water from Lake Constance is pumped from a depth of 60 m below sea level and micro-sieved ($15 \mu\text{m}$ cut-off). The following oxidation step using ozone ($1.0 - 1.2 \text{ mg/L}$) is designed for disinfection and oxidation of solid matter in the water. Next a small amount of FeCl_3 (0.1 mg/L) is added before filtration through rapid sand filters. This iron assisted filtration was shown to be very efficient (Winzenbacher 2000). Finally, chlorine is added for disinfection. The purified water is then stored in tanks and distributed via two main lines.

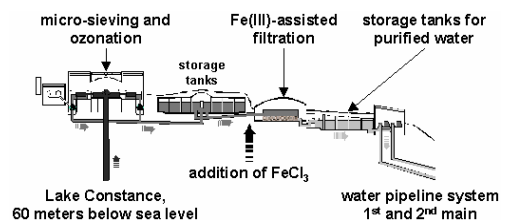


Figure 2: Water purification steps.

The *Zweckverband Bodensee-Wasserversorgung* supplies many communities in Southern Germany with drinking water from Lake Constance. A pipeline network of app. 1,700 km total length with mainly large-caliber pipes is used for this purpose. The pipe diameters range from 0.1 m (small supply pipe) up to 1.6 m directly after the water processing plant *Sipplinger Berg*. Two water mains form the skeleton structure of the water pipeline system. They are made of reinforced or prestressed concrete. Additional water tanks, pumping stations and turbines are part of the distribution system.

For examination of the purification process the suspended matter (particles $> 1 \mu\text{m}$ in diameter) has been quantified with laser light obscuration. Particles in the colloidal size range and in lower concentrations like in natural waters or drinking water cannot be detected with this method since it is not sensitive enough as already mentioned. The same applies to the photon correlation spectroscopy. Therefore, the water samples taken after different steps of water purification and at various points of the pipeline network have also been analyzed by LIBD.

A comparison of the methods for particle analysis is given in Figure 3, showing the limits of detection (LOD) as a function of the mean particle size of the particles investigated. To determine the LOD for LIBD, a 3σ value (triple standard deviation) of the background was evaluated by multiple measurements on pure water. The laser light obscuration data was taken from literature (Hofmann et al. 2003) for the machine CIS-1 (Galai Inc.). This technique is very sensitive for suspended particles with diameters $> 1 \mu\text{m}$, but not in the condition to detect colloidal particles (typically $< 1 \mu\text{m}$). The laser light scattering data were determined using a commercial PCS (photon correlation spectroscopy) machine (model: ZetaSizer 5000, Malvern Instruments Inc.). The intensity of the scattered light strongly depends on the particle diameter (d). In the range of Rayleigh-scattering ($d \leq \lambda/10$), the intensity of scattered light is proportional to d^6 . Consequently, light scattering techniques such as PCS are very insensitive for particles smaller than app. 50 nm in diameter. Figure 3 shows significantly higher sensitivity for detection of colloids with LIBD compared with laser light scattering, especially for colloids smaller than 100 nm.

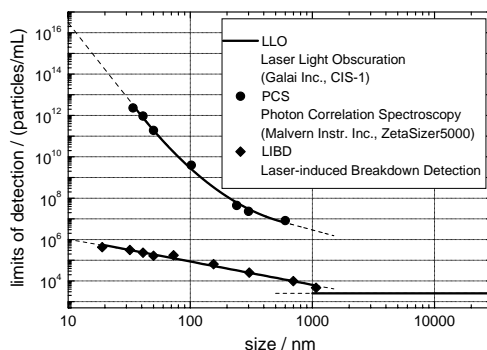


Figure 3: Comparison of detection limits of the non-invasive particle detection methods LLO, PCS, and LIBD.

The concentration of suspended particulate matter (particles with a diameter typically above $1 \mu\text{m}$) in the drinking water was reduced from 5,000 - 30,000 (typically around 15,000) to merely 50 - 150 particles per mL (Schick et al. 2002), widely independent of seasonal fluctuations of the particulate content of the lake water. By using LIBD analysis it could be shown that the Fe(III)-assisted filtration step is highly effective for the removal of the much smaller colloidal water content, too. After micro-sieving, but before the filtration step, $5 \cdot 10^5 - 8 \cdot 10^8$ colloids per mL were found depending on the time of year, and the number-weighted mean diameter ranged from $0.02 \mu\text{m}$ to $0.7 \mu\text{m}$ with a volume concentration of 10^{-7} to $10^{-9} \text{m}^3/\text{m}^3$. After the filtration step the values had decreased to only 1 to 10 % of the original values (Wagner et al. 2002).

In order to find out about possible changes in the particle population of the purified water from Lake Constance during transport and storage, investigations on the particulate content have been carried out at several points of the pipeline network since late 2001. It was found that both the number and the size of colloids and particles $> 1 \mu\text{m}$ remains quite constant, even if the water is transported and stored for up to 15 days in total. There was no sign of an increase (e.g. by smashing of aggregates/agglomerates, precipitation and flocculation phenomena, germination) or a decrease (e.g. by precipitation, biological decomposition, adsorption) in particulate water content. This may be due to the fact that the whole distribution system is inspected and maintained on a regular basis.

Figure 4 shows the total particle concentration (particles $> 1 \mu\text{m}$ and colloids together) at the different sampling points throughout the pipeline system. They have been examined both by laser light obscuration and Laser-induced Breakdown Detection. The colloid number densities varied from $4.7 \cdot 10^6$ to $6.6 \cdot 10^6 \text{mL}^{-1}$.

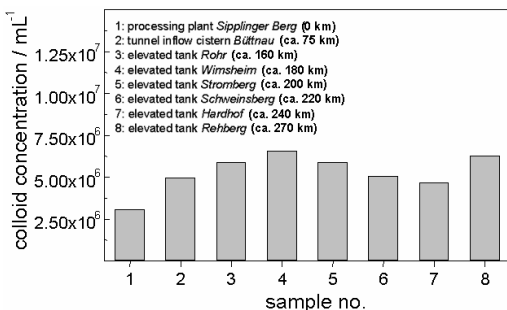


Figure 4: By means of LIBD it could be shown that the colloidal content of purified drinking water does not change during transport and storage.

In the scope of a demonstration field project near the city of Karlsruhe/Germany, the application of natural attenuation technology is tested. The transport of particulate matter in the main water flow direction in the aquifer was investigated by LIBD. The result obtained could exclude the aqueous transport of PAHs (Wege et al. 2002).

3 CONCLUSIONS

Both the laser light obscuration and the rather novel Laser-induced Breakdown Detection as a highly sensitive tool for the direct, non-invasive characterization of aquatic colloids have been used successfully to prove the efficiency of the water purification procedure used by the *Bodensee-Wasserversorgung* for treatment of water from Lake Constance. While the laser light obscuration was useful for the determination of the particle number density of larger particles ($d > 1 \mu\text{m}$), it was not capable of detecting colloids with diameters typically $< 1 \mu\text{m}$. This was, however, no problem for the LIBD method that gives a number-weighted mean particle diameter of all the particles in the sample. The main advantage of the LIBD in comparison to light scattering techniques such as photon correlation spectroscopy (PCS) is a higher sensitivity of several orders of magnitude, especially in the particle size range $< 100 \text{ nm}$.

Within those restrictions, both methods have proved useful for the examination of the particle population during transport and storage of drinking water.

4 REFERENCES

Bettis J. R. (1992). Correlation among the Laser-Induced Breakdown Thresholds in Solids, Liquids, and Gases. *Appl. Opt.*, 31(18), 3448-3452.

Bundschuh T. (1999). Entwicklung und Anwendung der Laser-induzierten Breakdown-Detektion zur Quantifizierung aquatischer Kolloide und Actinidenkolloide. PhD thesis, Institute of Radiochemistry, Technical University Munich, Germany.

Bundschuh T., Hauser W., Kim J. I., Knopp R. and Scherbaum F. J. (2001a). Determination of Colloid Size by 2-D Optical Detection of Laser Induced Plasma. *Colloids Surf. A*, 180(3), 285-293.

Bundschuh T., Knopp R., Winzenbacher R., Kim J. I. and Köster R. (2001b). Quantification of Aquatic Nano Particles after Different Steps of Bodensee Water Purification with Laser-induced Breakdown Detection (LIBD). *Acta Hydrochim. Hydrobiol.*, 29(1), 7-15.

Bundschuh T., Knopp R. and Kim J. I. (2001c). Laser-Induced Breakdown Detection (LIBD) of Aquatic Colloids with Different Laser Systems. *Colloids Surf. A*, 177(1), 47-55.

Bundschuh T., Wagner T. and Köster R. (2003). Hochsensitive Partikelbestimmung mittels der Laser-induzierten Breakdown Detektion. *Chem. Ing. Tech.*, 75(4), 386-390.

Fujimori H., Matsui T., Ajiro T., Yokose K., Hsueh Y. and Izumi S. (1992). Detection of Fine Particles in Liquids by Laser Breakdown Method. *Jpn. J. Appl. Phys.*, 31(Pt. 1, No. 5A), 1514-1518.

Hauser W. and Bundschuh T. (2000). Verfahren zur Bestimmung der Größe von Partikeln in einer Lösung. Patent DE 198 33 339 C1 (Internat. Public. No.: WO 00/06993), Munich, Germany.

Hofmann T., Baumann T., Bundschuh T., von der Kammer F., Leis A., Schmitt D., Schäfer T., Thieme J., Totsche K. U. and Zänker H. (2003). Aquatische Kolloide II: Eine Übersichtsarbeit zur Probenahme, Probenaufbereitung und Charakterisierung. *Grundwasser*, 8(4), 213-223.

Knopp R. (1996). Laserinduzierte Breakdowndetektion zur Charakterisierung und Quantifizierung aquatischer Kolloide. PhD thesis, Institute of Radiochemistry, Technical University Munich, Germany.

Radziemski L. J. and Cremers D. A. (1989). Laser-Induced Plasmas and Applications. Marcel Dekker Inc., New York.

Scherbaum F. J., Knopp R. and Kim J. I. (1996). Counting of Particles in Aqueous Solutions by Laser Induced Breakdown Photoacoustic Detection. *Appl. Phys. B*, 63(3), 299-306.

Schick R., Faißt M. and Stabel H.-H. (2002). Erfahrungen mit der weitergehenden Partikelentfernung durch Zugabe geringer Mengen an Eisen-(III)-Salzen bei der Aufbereitung von Bodenseewasser. In: *Stuttgarter Berichte zur Siedlungswirtschaft*, vol 167, 1st edn, Industrieverlag GmbH, München, pp. 87-103.

Shaw D.J. (1980). Introduction to Colloid and Surface Chemistry, 3rd ed. Butterworth, London.

Wagner T., Bundschuh T., Schick R., Schwartz T. and Köster R. (2002). Investigation of Colloidal Water Content with Laser-induced Breakdown Detection during Drinking Water Purification. *Acta Hydrochim. Hydrobiol.*, 30(5-6), 266-274.

Wege R. and Klaas N. (2002). Stürmlinger Sandgrube: Erkundung und Monitoring. *VEGAS Statuskolloquium 10. Oktober 2002 – Kurzfassungen der Beiträge*, p. 29-35.

Winzenbacher, R. (2000). Untersuchungen zum Filtrationsprozess mit geringen Mengen an Fe(III)-Salzen bei der Aufbereitung von Oberflächenwasser. PhD thesis, Institute of Technical Environment Protection, Technical University Berlin, Germany.

The First Precambrian Detrital Monazites from the Polish Eastern Carpathian

M.A.Kusiak & M.Paszkowski

Polish Academy of Sciences, Institute of Geological Sciences, Kraków, Poland

B.Dziubińska

Jagiellonian University, Institute of Geological Sciences, Kraków, Poland

ABSTRACT: Detrital monazites from sandstones of the Dukla Unit and from rocks in close neighborhood of the Silesia Unit, in the eastern part of the outer flysch belt of the Carpathians, were selected for chemical analysis. The maximum thorium (ThO₂) content in the analyzed monazite grains is 9 wt.%. However there are grains with < 2 wt.% of ThO₂. All grains contain also a significant amount of calcium, suggesting that brabantite formed as part of the monazite-brabantite isomorphous series. The average La/Nd value of analyzed monazites is 1.2, indicating a sialic rock source for the grains. Published data on the ages of detrital monazite from the Carpathian flysch have circum-Variscan age clusters. Attained age data from this study show, besides young ages, surprisingly old, Precambrian dates. This suggests a possible link to so-called Chivchin gneisses from the Rahiv massif in the Ukraine.

1 INTRODUCTION

Monazite is a phosphate of rare earth elements, mostly cerium [Ce,La,Th]PO₄. It selectively concentrates light rare earth elements (LREE). This mineral usually contains Th, U, and radiogenic lead, making it a very useful geochronological tool. For dating monazite grains we used chemical Th-U-total Pb (CHIME; Suzuki & Adachi 1991) method, based on data obtained by electron microprobe microanalysis. The age calculated by this method has a geological meaning if non-radiogenic lead is negligible and the system remained closed, i.e. no modification of U/Th/Pb ratios has occurred except by radioactive decay (Montel et al. 1996, Harrison et al. 2002). The calculation of the CHIME ages, was carried out using the CHIME age calculation program (Kato et al. 1999; <http://ganko.esp.nagoya-u.ac.jp/gsd/CHIME/>). While CHIME has been used widely for the dating of igneous (Mougeot et al. 1997) and metamorphic rocks (Bingen & van Breemen 1998, Braun et al. 1998, Parrish 1990), it is also well suited for provenance analysis in sedimentary and metasedimentary lithologies (Kusiak et al. 2001, Lekki et al. 2003), where mineral grains are compositionally and genetically heterogeneous. CHIME provides no information on

discordance in the Th-U-Pb system, and consequently Pb loss occurred, as expected for isotopic dating methods. However, this method has all advantages of a microprobe analysis: it is non-destructive, has an excellent spatial resolution and provides the possibility to work on normal polished thin-sections (Montel et al. 1996). The time-efficiency and cost-effectiveness of CHIME makes it ideal for provenance studies, where a large number of analyses are required to characterize age populations.

Detrital monazites from sandstones of the Dukla Unit and from rocks in close neighborhood of the Silesia Unit, the Polish eastern part of the outer flysch belt of the Carpathians were selected for chemical analysis.

2 GEOLOGICAL SETTING

The Outer Carpathians, also known as the "Flysch Carpathians", comprise a series of imbricated nappes consist mainly of variable flysch deposits, upper Jurassic to lower Miocene in age (Książkiewicz 1960). The research was carried out on rocks from different lithostratigraphic layers outcropping in Jaśliska, Wisłok, Maniów, Roztoki, Wetlina,

Majdan, which are located in the eastern and western parts of the Dukla Unit and in nearby Bystre, which belongs to the Silesia Unit (Fig. 1). Analyzed

samples are Eocene, Paleocene and late Cretaceous in age.

(A)



(B)

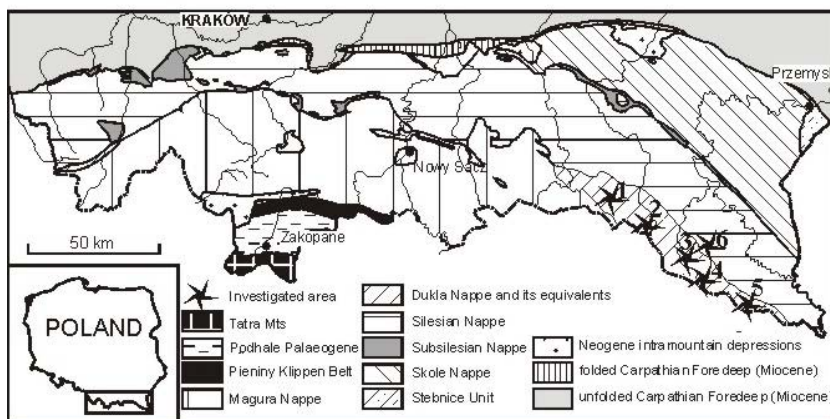


Figure 1. (A) The Carpathian Arc in Europe, (B) Location and simplified geologic map of the Polish Carpathians, samples from: Dukla Unit – 1: JA-Jasliska; 2: WI-Wisłok; 3: MN-Maniów; 4: RO-Roztoki; 5: WE-Welina; and Silesian Unit – 6: BY-Bystre.

3 METHOD

Although the details of the CHIME age calculation had been reported elsewhere (e.g. Suzuki & Adachi 1991, 1994), for convenience reasons, an outline of isochron calculations of Th-rich monazite is given below.

In the first step of the CHIME method we calculate an apparent age (t) from each set of ThO_2 , UO_2 and PbO analyses (wt.%) by solving the equation:

$$\frac{PbO}{W_{Pb}} = \frac{ThO_2}{W_{Th}} (\exp(\lambda_{232}t) - 1) + \frac{UO_2}{W_U} \left[\frac{\exp(\lambda_{235}t) + 137.88\exp(\lambda_{238}t)}{138.88} - 1 \right] \quad (1)$$

where W symbolizes the gram-molecular weight of each oxide ($W_{Pb}=224$ for monazite, $W_{Pb}=222$ for zircon and xenotime, $W_{Th}=264$ and $W_U=270$, $^{238}U/^{235}U=138$).

To eliminate the effect of variations in the Th/U ratio on total Pb produced over a given time span, we turn the sum of ThO_2 and UO_2 into ThO_2^* by:

$$ThO_2^* = ThO_2 + \frac{UO_2 W_{Th}}{W_U (\exp(\lambda_{232}t) - 1)} \left[\frac{\exp(\lambda_{235}t) + 137.88\exp(\lambda_{238}t)}{138.88} - 1 \right] \quad (2)$$

If individual parts of a single monazite grain and/or co-genetic monazite grains contain the same amounts of initial Pb but different amounts of Th and U, all analytical data will plot on a straight line with the slope (m) and intercept (b); i.e.:

$$PbO = m ThO_2^* + b \quad (3)$$

A best-fit regression line is determined through the procedure of York (1966), taking into account of uncertainties in the microprobe analyses, and the first approximation of age (T) is calculated from the slope (m) of equations:

$$T = \frac{1}{\lambda_{232}} \ln \left\{ 1 + m \frac{W_{Th}}{W_{Pb}} \right\} \quad (4)$$

Then, we can obtain the second approximation by replacing the apparent ages (t) with the first approximation age (T), and so on. The intercept (b) of the line is assumed to represent the concentration (wt.%) of the initial PbO. A significant amount of initial Pb or Pb-loss, if present, would shift the intercept of the regression line from the origin, or would not form an isochronal. Normally, the regression for monazite passes through the origin. Evidently, the CHIME age calculation is not applicable for monazite that shows little variation in the Th and U concentrations. If this is the case, an arithmetic average of apparent ages approximates the date of monazite formation.

Analytical conditions of EMPA measurements were: the accelerating voltage: 20 kV, the probe current: 100 nA, and the probe diameter: 5-7 μ m.

4 RESULTS

120 analyses of monazite grains were completed, seven from sandstone samples from Dukla Unit and one from sandstone sample from Silesia Unit. In each of eight samples, there were more than ten monazites analyzed. For inhomogeneous grains, there were selected more than one analytical points. Analyzed monazites from all samples are quite homogeneous in chemical composition, whereas ages they yield are not. The maximum thorium (ThO_2) content in these grains is 9 wt.%. However there are grains with < 2 wt.% of ThO_2 . Surprisingly there are monazites lacking Th. U (UO_2) in analyzed grains reaches up to 1,15 wt.%. All grains contain also about 1 wt.% of CaO, suggesting that in some cases brabantite formed as part of the monazite-brabantite isomorphic series. The average La/Nd ratio is 1.2, indicating a sialic rocks source for the grains.

Despite of the wide range of age dates (Tab.1) we can distinguish at least three age clusters.

Table 1. Table showing the range of calculated CHIME ages detrital monazites [Ma].

Unit	Age of strata	Eocene	Paleocene	Late Cretaceous
Dukla	JAŚLISKA			151-315 1803
	WETLINA			115-205 411, 571
	WIŚŁOK			109-311
	MANIÓW	156-219		
	MANIÓW2		259-379 450	
	MANIÓW5		452-478	
	ROZTOKI			624-797 1122-1885
Silesian	BYSTRE			140-250 340

Firstly, late Mesozoic ages, $109 \pm 9 - 219$ Ma, these are in Wiślók, Wetlina, Maniów and Jaśliska. Secondly, a Paleozoic cluster of ages, $259 - 478$ Ma, generated from nearly all samples except from Maniów, where only Paleogene data were produced and from Roztoki with only older data. And finally the oldest, Precambrian data. Finally, Precambrian dates 1122-1885 Ma resulted from the analysis. A monazite grain example of Precambrian age is shown in Figure 2.

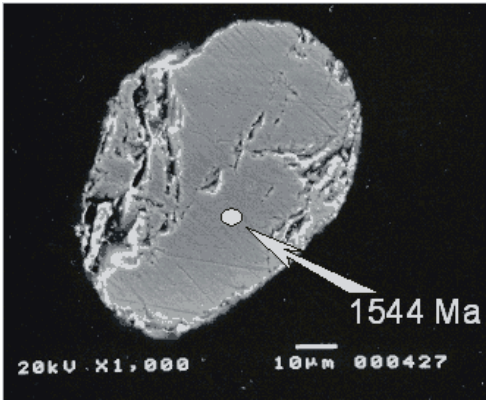


Figure 2. Back-scattered electrons image (BSE) of monazite grain from Roztoki, with marked point of analysis.

5 CONCLUSIONS

In this study we document, for the first time, Monazites of the Carpathian domain that yielded pre-Cadomian Proterozoic ages (1122-1885 Ma).

The nearest occurrence of such old ages is the 1.8 Ga-old zircons from the Austroalpine basement (Schulz & Bombach 2003). These Svekofenian age cluster are typical for the Baltica and Peribaltic terrenees, e.g. the Małopolska Block. It is possible, that this oldest group of monazite grains has been recycled and was derived from the pre-rift Mesozoic sedimentary cover (Jurassic siliciclastic ?) of source terrain Cordillera.

The Cadomian ages (571-797 Ma) from Roztoki and from one Wetlina sample, correspond to widely distributed ages from the Inner and Median Dacides (Kräutner 1991), the Austroalpine Basement and the Brno-Upper Silesia Massif. The younger data from our analyses are Caledonian (411-478 Ma) Variscan (311-379 Ma), Permo-Triassic (205-259 Ma) and Alpine cluster (109-156 Ma).

Published data on the ages of detrital monazite from the Carpathian flysch yielded much younger, circum Variscan age clusters. Our data suggest a crystalline basement of some intra-basinal ridges (cordilleras) as a possible source terrain. The most probable source of detrital material is the eastern prolongation of the so-called Silesian Cordillera which crops out as the Rahiv and Maramureş Massif around Ukrainian/Romanian border. This crystalline massif is known as the Median Dacides (East Carpathian Crystalline Zone) by Kräutner (1991), and the western prolongation of this unit is the West Carpathian Crystalline Zone or Inner Dacides. The source rocks for the detritus could be the Chivchin gneisses and their equivalents from the Rahiv massif and from its Mesozoic sedimentary cover.

6 REFERENCES

- Bingen, B. & van Breemen, O. 1998. U-Pb monazite ages in amphibolites- to granulite-facies orthogneiss reflect hydrous mineral breakdown reactions; Sveconorwegian province of SW Norway. *Contrib. Mineral. Petrol.*, 132: 336-353.
- Braun, I., Montel, J. M. & Nicollet, C. 1998. Electron microprobe dating of monazites from high-grade gneisses and pegmatites of the Kerala Khondalite Belt, southern India. *Chem. Geol.*, 146: 65-85.
- Harrison, T. M., Catlos, E. J. & Montel, J. M. 2002. U-Th_Pb dating of phosphate minerals. In: Phosphates: Geochemical, Geobiological and Materials Importance, Ed: M. J. Kohn, J. Rakovan & J. M. Hughes. *Reviews in Mineralogy & Geochemistry*, 48: 523-558.
- Kato, T., Suzuki, K. & Adachi, M. 1999. Computer program for the CHIME age calculation. *Jour. Earth Sci.*, Nagoya Univ., 46: 49-56.
- Kräutner, H. G. 1991. Pre-Alpine geological evolution of the East Carpathian Metamorphics. Some common trends with the West Carpathians. *Geol. Carpathica*, 42: 209-217.
- Książkiewicz, M. 1960. Outline of the paleogeography in the Polish Carpathians. (in Polish) *Prace IG*, 30: 209-231.
- Kusiak, M., Suzuki, K. & Paszkowski, M. 2001. Preliminary report of CHIME dating on detrital monazite grains from the Namurian Poruba Beds and the Stephanian Kwaczala Arkose in the Upper Silesia Coal Basin, Poland. *J of Earth and Planet. Sci.*, 48: 15-41.
- Lekki, J., Lebed, S., Paszkowski, M. L., Kusiak, M., Vogt, J., Hajduk, R., Polak, W., Potempa, A., Stachura, Z. & Styczeń, J. 2003. Age Determination of Monazites Using the New Experimental Chamber of the Cracow Proton Microprobe. *Nuclear Instruments and Methods in Physics Research B*, 210: 472-477.
- Montel, J. M., Foret, S., Veschambre, M., Nicollet, Ch. & Provost, A. 1996. Electron microprobe dating of monazite. *Chemical Geol.*, 131: 37-53.
- Mougeot, R., Respaut, J. P., Ledru, P. & Marignac, Ch. 1997. U-Pb chronology on accessory minerals of the Velay anatectic dome (French Massif Central). *Eur. J. Mineral.*, 9: 141-156.
- Parrish, R. R. 1990. U-Pb dating of monazite and its application to geological problems. *Can. J. Earth. Sci.*, 27: 1431-1450.
- Schulz, B. & Bombach, K. 2003. Single zircon Pb-Pb geochronology of the Early-Palaeozoic magmatic evolution in the Austroalpine Basement to the South of the Tauern Window. *Jb. Geol. B.-A.*, 143:303-321.
- Suzuki, K. & Adachi, M. 1991. The chemical Th-U-total Pb isochron ages of zircon and monazite from the Gray Granite of the Hida terrane, Japan. *Jour. Earth Sci.*, Nagoya Univ., 38: 11-37.
- Suzuki, K. & Adachi, M. 1994. Middle Precambrian detrital monazite and zircon from the Hide gneiss on Oki-Dogo Island, Japan: their origin and implications for the correlation of basement gneiss of Southwest Japan and Korea. *Tectonophysics*, 235: 277-292.
- York, D. 1966. Least-square fitting of straight line. *Can. J. Phys.*, 44: 1079-1088.

EBSDB Microstructure Measurements of Marble

K.Moen & T.Malvik

Department of Geology and Mineral Resources Engineering, Norwegian University of Science and Technology, Norway

J.Hjelen, J.R.Leinum

Department of Material Science, Norwegian University of Science and Technology, Norway

L.Alnæs

SINTEF Civil and Environmental Engineering, Rock and Soil Mechanics, Norway

ABSTRACT: Bowing of crystalline marble when used as exterior thin claddings is experienced occasionally on buildings around the world. A European Research Project (TEAM) is investigating this deterioration phenomenon and influencing intrinsic and extrinsic parameters. One of several approaches for investigation of intrinsic parameters is microstructure measurements by Electron Backscatter Diffraction (EBSDB). The rock fabrics of two marbles have been investigated and the EBSDB analyses show that the microstructure is intuitively different when comparing them. While the no bowing marble shows xenoblastic microstructure with sutured grain boundaries, subgrains and a lot of twinning, the bowing marble shows granoblastic and polygonal microstructure. The EBSDB results indicate that the stable marble shows a stronger texture than the bowing marble, which shows more random orientation. This trend confirms the statement of Barsottelli et al. (1998) and is also in accordance with knowledge from materials science for metals.

1 INTRODUCTION

Several modern buildings around Europe are covered by marble claddings panels. At certain buildings the panels start to bow and loose strength after some years on the wall (see Figure 1) This phenomenon is experienced occasionally for crystalline marble when used as exterior cladding, see e.g. Cohen & Monteiro (1991), Hook (1994), and Schouenborg et al. (2001) and is assumed to be controlled by temperature variations and moisture, see Yates et al (in prep).

An extensive European research project (TEAM – Testing and Assessment of Marble and Limestone) is investigating this deterioration phenomenon and influencing intrinsic and extrinsic parameters. The project is partly funded by the European Commission under the contract no. G5RD-CT-2000-00233 (see also www.sp.se/Building/TEAM). The TEAM partners have managed to simulate bowing in the lab (Grelk et al. in prep). But why does it happen only to certain crystalline marbles? A lot of rock fabric investigations have been done (Alnæs et al. in prep), but it is difficult to quantify the important rock fabric elements by means of ordinary imaging (optical, SEM) and image analysis.

Electron Backscatter Diffraction (EBSDB) detects microstructure by means of crystallography. That means preferred lattice and grain orientations, grain morphology, grain size etc. EBSDB can be a potentially method for detecting and quantify such marble microstructure. The challenge is to quantify differences by EBSDB and correlate the results with bowing tendencies.

This paper presents some EBSDB results for two marbles, one with strong bowing and one with very weak to absent bowing experienced in both buildings and accelerated laboratory bow test.

2 ELECTRON BACKSCATTER DIFFRACTION

The EBSDB technique is based on the weak diffraction pattern that forms when a focused, stationary, primary electron beam strikes a polished sample, backscatters and diffracts. The diffraction pattern is formed on a fluorescent screen and transferred by a camera to the computer (Hjelen 1990).

Rapid developments in both hardware and software in the past 10 years have made EBSDB easy



Figure 1. Bowing of marble claddings (from TEAM brochure, see also www.sp.se/Building/TEAM)

to use and ideal for the rapid analysis of microstructures of crystalline materials. The collection of an electron backscatter diffraction pattern (EBSP) in the SEM is obtained as follows: A polished sample must be tilted to a high angle (typically 70°) inside the SEM. The electron beam is then directed at the point of interest on the sample surface. Initial elastic scattering of the incident beam causes the electrons to diverge from a point just below the sample surface and to impinge upon crystal planes in all directions. Wherever the Bragg condition for diffraction is satisfied by atomic lattice planes in the crystal, 2 cones of diffracted electrons are produced. These cones are produced for each family of lattice planes (Schwartz et al. 2000). These cones of electrons can be imaged using a transparent phosphor screen viewed by a sensitive camera. The camera is usually positioned horizontally, so that the phosphor screen is close to the sample in order to capture a wide angle of the diffraction patterns. Where the cones of electrons intersect with the phosphor screen, they appear as thin, bright bands (see Figure 2 and Figure 3). These are called backscatter "Kikuchi" bands (Kikuchi 1928). The resulting EBSP is made up of many Kikuchi bands. Every band in the diffraction pattern represents a set of lattice planes in the crystal that is analysed, and the points of intersection between the bands represent crystallographic directions of the crystal (see Figure 3). The diffraction pattern is therefore characteristic for the crystal structure and space orientation of the crystal.

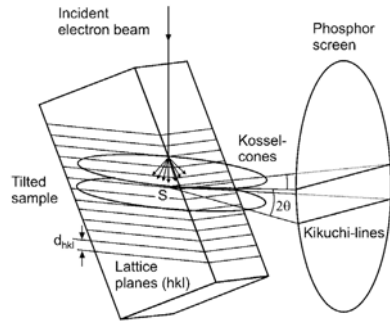


Figure 2. Origin of Kikuchi lines from EBSD (Schwartz et al. 2000)

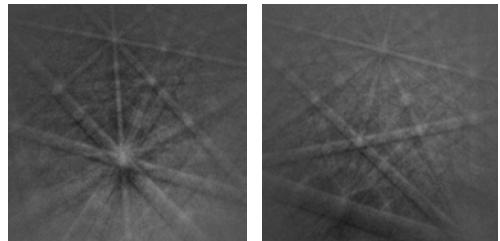


Figure 3. EBSD patterns from 2 orientations of calcite.

The EBSD software automatically locates the positions of individual Kikuchi bands, compares these to theoretical data about the relevant phase and rapidly calculates the 3-D crystallographic orientation. The whole process from start to finish can take from 0.025 sec. to more than one second dependent on the phases analysed.

For each pixel the phase and orientation are stored and can be visualised by phase or orientation maps where phase or orientation are given colour codes. Different kinds of plots can show misorientation, grain size, poles etc. The spatial resolution of this technique is superior to x-rays, since elastic backscattered and diffracted electrons have a smaller interaction volume than x-rays. The interaction volume is dependent on acceleration voltage and atomic number of the analysed minerals, but is usually in the sub micron range. (Moen et al. 2003)

3 EXPERIMENTAL

3.1 Sampling and preparation

The marble specimens are sampled from two neighbouring quarries. Both are calcitic marbles (calcite content > 99 %weight), but one has a problem with bowing while the other has not. For the EBSD analyses the specimens were prepared by cutting, grinding and polishing, to give a polished rock section of diameter 25 mm. A chemical-

mechanical polishing was performed in the end, to make a deformation free surface that makes lattice diffraction possible.

3.2 Microscopy

Before put into the Scanning Electron Microscope (SEM), the sample is covered by aluminium foil along the flanks and carbon paint along the edges to make it as conductive as possible without carbon coating it. To get an optimal EBSD pattern, the analysis is performed in a low vacuum SEM without a conductive carbon layer.

The equipment applied for the experiments is listed in Table 1 and the running and processing conditions in Table 2.

Table 1. Equipment applied for EBSD mapping

Equipment	Type
Low-vacuum SEM	Hitachi S-3500N
EBSD camera	Nordif EBSD dig. camera
EBSD software	TSL, OIM version 3,08/3,5

Table 2 Running and processing conditions for EBSD mapping

Parameter	Setting
WD	20 mm
V _{acc}	20 kV
Pressure	40 Pa
Tilt	70°
Magnification	90x
Binning	2x2
Step size	5 μm
Processing	Gaussian convolution Half with 15° Expansion L=22 Harmonic calculus

4 RESULTS

The results are presented in Figure 4 as orientations maps colour coded by the inverse pole figure (top) and grain boundary map including grains with preferred lattice orientation (bottom), in Figure 5 as pole figures and in Figure 6 as grain size distributions (top) and misorientation angle plots (bottom).

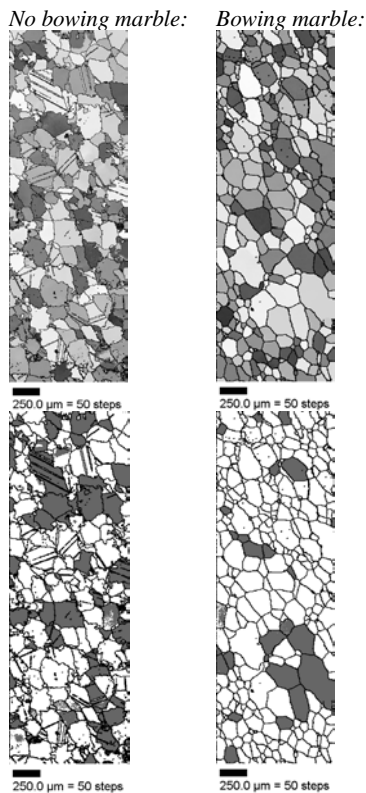


Figure 4. Inverse pole maps (top), grain boundary maps including grains with a preferred orientation (plotting in the dark maxima of the <0001> pole figures (bottom).

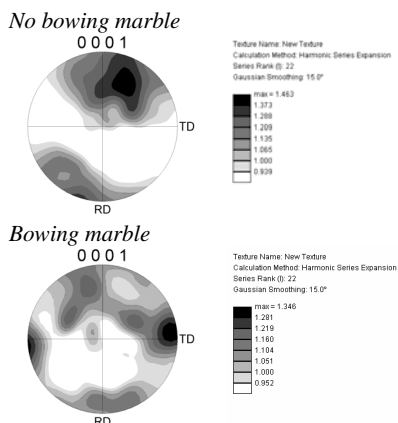


Figure 5. Pole figures of orientation densities in logarithmic scale, upper hemisphere, equal area projection: no bowing marble (top), bowling marble (bottom) based on stage scan of more than 6000 grains.

No bowing marble:

Bowing marble:

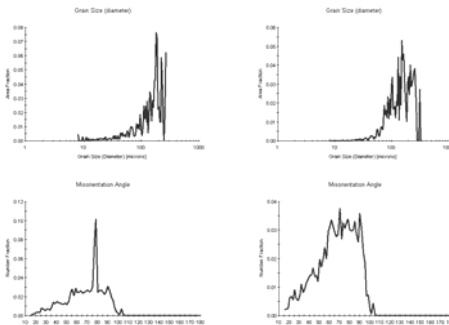


Figure 6. Grain size distribution (top) and misorientation angles (bottom). The peak around 77° characterising the no bowing marble represents the twin boundaries.

5 CONCLUSIONS

EBSDB seems to be well suited to describe microstructure elements in marble (e.g. grain size distribution, grain boundary geometry, grain shape preferred orientation, and lattice preferred orientation (texture)). The first experiments are regarded as successful and are presented here.

The feature characteristics of the two marbles are intuitively different. While the no bowing marble shows a lot of subgrains, twinning and sutured grain boundaries (xenoblastic microstructure), the bowing marble shows clean grain boundaries, equally distributed grain size and almost no twinning. This means granoblastic and polygonal microstructure with triple point grain boundary intersections of approximately 120°, which is typical for a statically recrystallised microstructure (Pieri et al. 2001).

From Figure 5, one can see that the stable marble has got one distinct pole (dark maximum) in the (0001) pole figure, while the bowing marble has the orientations more smeared out. Figure 4 (bottom) shows grains with a preferred lattice orientation, which means grains plotting in the maximum of the pole figures. In the bowing marble it is seen fewer grains with a preferred lattice orientation. The figures 4-5 indicate that the stable marble shows more preferred orientation (stronger texture) than the bowing marble, which on the other side shows a more random orientation. This trend is in accordance with the findings of Koch and Siegesmund (in press) and also confirms the statement of Barsotelli et al. (Barsotelli, Fratini & Giorgetti 1998) who cite Rosenholts and Smith, 1950: "Decohesion of marble due to thermal expansion anisotropy of the calcite crystal only occurs in marble with weak or absent crystallographic orientation".

The findings are also in accordance with knowledge from material science for metals where it

is known that recrystallised metal, free of tension and weak crystallographic orientation, is ductile and easy to form. Contrary, deformed metal contains preferred crystal orientation and a great number of dislocations, which reinforce the structure and makes it more resistant against external forces.

The EBSD technique is at present in use for investigation of additional marble types and also to study the potential relationship between bowing, in *situ* rock stresses and rock fabric.

6 REFERENCES

- Alnæs, L., Koch, A., Schouenborg, B., Åkesson, U. & Moen, K. 2004. Influence of Rock and Mineral properties on the durability of marble panels. *In prep. Proc. Dimension Stone 2004*.
- Barsotelli, M., Fratini, F. & Giorgetti. 1998. Microfabric and alteration in Carrara marble: a preliminary study. *Science and technology for Cultural Heritage* 7 (2), 115-126.
- Cohen & Monteiro 1991: Durability and Integrity of Marble Cladding " A state of the art review". *Journal of the Performance of Constructed Facilities*. 5(2), pp 113-124.
- Grelk, B., Golterman, P., Schouenborg, Koch, A. & Alnæs, L. 2004. The laboratory testing of potential bowing and expansion of marble. *In. prep. Proc. Dimension Stone 2004*.
- Hjelen J. 1990. Teksturutvikling i Aluminium, studert ved Elektronmikrodiffraksjon (EBSD) i Scanning Elektronmikrosko. Ph.D. Thesis. Trondheim, Norway: University of Trondheim.
- Hook, K. 1994: Look out below – The Amoco Building Cladding Failure. *Progressive Architecture*, Feb., 75, pp 58-62.
- Kikuchi S, 1928. Diffraction of cathode rays by mica. *Jap. J. Phys.*, 1928. 5:83.
- Koch, A. & Siegesmund, S. 2004. The combined effect of moisture and temperature on the anomalous expansion behavior of marble. *In: S. Siegesmund, H. Viles & T. Weiss (eds), Stone Decay hazards; Environmental Geology*, in press.
- Moen K, Malvik T, Hjelen J, Leinum JR, 2003 Automatic Material Characterization by means of SEM-techniques, Proceeding, 9th Euroseminar on Microscopy Applied to Building Materials, Ed: M.A.T:M: Broekmans et.al
- Nordtest 2000, Field method for measurement of bowing of cladding panels, <http://www.sp.se/building/team/results.htm>
- Pieri M, Burlini L, Kunze K, Stretton I, Olgaard DL, 2001. Rheological and microstructural evolution of Carrara marble with high shear strain: results from high temperature torsion experiments. *Journal of Structural Geology*. 23:9, p 1393-1413.
- Schouenborg, B., Grelk, B., Alnæs, L., Brundin, J.A., Blasi, P., Yates, T., Marini, P., Tschegg, E., Unterweiger, U., Tokartz, B., Kock, A., Bengtsson, T., Mladenovic, A & Goralezzyg, S. 2003: TEAM – Testing and Assessment of Marble and Limestone.
- Schwartz AJ, Kumar M, Adams BL, 2000. Electron Backscatter Diffraction in Materials Science. NY, Kluwer Academic/ Plenum Publishers, ISBN 0-306-46487-X.
- Yates, T.; Brundin, J-A; Goltermann, P. & Grelk, B., 2004. Observations from the inspection of marble cladding in Europe. *In prep. Proc. Dimension Stone 2004*.

Comparison of Different Extraction Methods in the Determination of Gold in Geological Samples for Exploration Studies Using the Atomic Absorption Spectrometric Technique

P.V.Sunder Raju

National Geophysical Research Institute, Hyderabad, India

ABSTRACT: Different petrochemically-varied lithological samples were collected from the Chitradurga schist belt, Karnataka, to identify auriferous zones. The efficiencies of gold estimation at very low levels by different extraction methods were compared. The extraction methods used were: fire-assay (FA), cyanide leach, and MIBK solvent extraction. The rock samples included banded iron formations (silicate, oxides, carbonate, and sulphide facies), ferruginous cherts, massive milky white quartz veins, and highly sheared fractured translucent dark grey to bluish grey quartz veins. After separation and pre-concentration gold {Methyl isobutyl ketone (MIBK)} solvent extraction procedures have been studied using flame atomic absorption spectrophotometer (F-AAS).

1 INTRODUCTION

In nature gold occurs as native and refractory type. Refractory gold ores are found to be in association with sulphides (pyrite, arsenopyrite and chalcopyrite), while as native, gold is associated with tellurides, bismuthides, silver, antimony, and copper. In general fire-assay (FA), bromine-hydrobromic acid, cyanide leach, open aqua regia – microwave (closed) are some of the important extraction methods. The present study was undertaken in an attempt to answer the following questions:

1. Is there any difference in the Au content of the splits of large sample after crushing? 2. What is the efficiency of these analytical methods based on NaCN leach, MIBK extraction methods, when compared to the classical and widely accepted lead fire assay method?

We approach the problem by studying samples from Gadag and Chitradurga Schist belts (CSB) of Archaean geological age. Gadag and Ajjanahalli in CSB contain both native and refractory gold.

2 EXPERIMENTAL

2.1 Sampling and powdering

Samples were collected from geologically favourable lithounits containing gold. Each sample is unique with varying mineralogical characteristics. 10-15 kg of bulk samples were collected and powdered to (-250) mesh. Samples were weighed out up to 20g. Prior to chemical dissolution the samples were mixed with ammonium nitrate and subjected to open air roasting at 600-650 °C in a porcelain crucible. The sample preparation flow chart described by (V.Balaram 1997) was followed.

2.2 Instrumentation

For this study the model SpectrAA 220 (Varian, Australia) flame atomic absorption spectrophotometer with deuterium background correction was utilized. Details of the instrumental parameters are given later in this paper, (V.Balaram 1999). A model Z 300 bench top centrifuge (Hermle Labor Technik, Germany) was employed for centrifuging the sample solutions in MIBK extraction. The gold speck obtained by cyanidation process was weighed using a model UMT-2 microbalance (Metler,

Switzerland). The instrumental parameters (Table 1) were optimized for maximum absorbency.

Table 1 Instrumental parameters

Wave length	nm	242.8
Slit width	nm	1.0
Lamp Type	-	Hollow C lamp
Lamp current	mA	4
Background correction	-	Deuterium
Flame Type	-	Air acetylene
Measurement time	Sec	1.5
Air flow	L/min	3.5
Acetylene flow	L/min	1.50

3 ANALYTICAL METHODS

3.1 Lead Fire Assay

The traditional fire assay method can measure gold concentration in the range ppb-ppm. The samples analysed by this method, in which litharge and glass forming fluxes, were mixed with finely powdered sample (80-90% <75 µm). The sample, in a crucible, was charged at 850°C in a muffle furnace and the temperature raised and maintained well above 1000 °C for 30-40 minutes until complete fusion. The lead circulates through the molten mass and collects the precious metal forming an alloy (Au-Ag-Pb) that is recovered as a button after cooling and separation from the glassy slag containing base metal and other impurities. The bone ash and marborite cupel heated to 1000 °C was charged with lead button. This process results in a precious metal bead that is parted by dissolution in nitric acid. Alternatively the lead may be dissolved in aqua-regia and analysed for gold and silver by F-AAS. Fire assay is considered to be the most accurate, economical, and consistent method for gold with maximum recovery. The lead fire assay (FA) analysis was carried out on 50 g samples at the chemistry laboratory of Chitradurga gold unit Karnataka. The gold specks were weighed.

3.2 Sodium Cyanide Leach

The sample (200g) was weighed into a bottle and 200ml of distilled water were added. The pH was adjusted to 11 by the addition of 3g of CaCO₃ and solution was made to 2% with respect to NaCN. The open bottle was laid on its side on a bottle roller and allowed to roll for 24 hrs. The bottles and its contents were weighed before and after the cyanide leach to estimate the amount of evaporation. The solution was filtered and heated to not more than 30 °C. Then 2g of lead acetate was added and the solution was stirred. After 15-20 minutes the contents were heated up to 60-65°C. Simultaneously 2g of zinc dust was added and the contents were stirred. Then 10 to 12 ml conc. HCl was added with

a pipette drop wise, while keeping the beaker on a hot plate for 5 minutes. Sponge was formed and allowed to cool to room temperature and then, the sponge containing solution was filtered. The sponge was washed 2-3 times with distilled water. Excess water was squeezed out and spongy mass was rolled in to lead foil after adding 0.1-0.5 g of metallic silver granules. The rolled lead foils were cupelled at 1000°C for about 1 hour. The complex bead containing gold and silver was dissolved in 1:4 HNO₃ for ~10 min and then in 1:1 HNO₃ to separate gold from silver. The gold speck was weighed on a microbalance (K. Fletcher 1988).

3.3 MIBK Procedure

Each 10g sample was transferred into a porcelain crucible with 1g ammonium nitrate, mixed thoroughly, and roasted for one hour in a muffle furnace at 650°C. After roasting, the samples were transferred to 250 ml glass beakers and 30 ml of freshly prepared aqua-regia was added to stabilize the gold chloride complex, during evaporation on a hot plate (I.Rubeska 1980). Each beaker was covered with a watch glass and heated on a hot plate. Heating was continued for at least four hours and enough aqua-regia was added at regular intervals to maintain the free acid level at about one centimeter above the sample surface (S.L. Ramesh 2001). The watch glasses were removed and the contents evaporated slowly until the residue became nearly dry. 40ml of 3M HCl was added to each beaker and warmed until it was clear. These sample solutions were cooled and filtered using Whatman 40 filter paper. The residue was discarded and the filtrate used for the determination of gold. The filtrate of each sample was transferred to a 250ml-separating funnel. The beaker was washed with a minimum amount of 3M HCl and the washings were transferred to a separating funnel and shaken for 5 minutes. After the phases were clearly separated, the aqueous phase was drained off. A 10ml washing solution (10 ml of Conc.HCl+10 ml Conc.HBr to 500ml with DD water) was added and the separating funnel is shaken for two minutes. After the phases were completely separated the aqueous phase was discarded and the organic phase was collected for FAAS gold estimate.

Table 2 Comparison of different extraction methods

Rock Type	(µg/mL)		
	MIBK	Cyanidation	Fire assay
BIF	0.42	0.40	0.32
BIF	0.52	0.40	0.60
BIF	0.78	0.40	0.60
BIF	0.49	0.20	0.40
Metavolcanics	0.44	0.60	0.10
Metavolcanics	0.40	0.42	0.32
Metavolcanics	0.52	0.40	0.60

Table 3 Mean recoveries for Au using NaCN leach, MIBK for different sample sizes of the samples: the fire-assay recovery for 50-g sample is assumed to be 100%.

Area	Mode of Occurrence Au	Recovery %			
		NaCN leach		MIBK leach	
		20g	200g	10g	20g
Gadag	Au associated With pyrite and as Si inclusions	75	nd	94.0	85.3
Ajjanahalli	Metallic Au In silicate and pyrites	95	103	105	99

4 RESULTS AND DISCUSSIONS

The samples were analysed for Au using the three analytical methods described above. Each determination was carried out for five times. The lead fire assay method was taken as standard method. Standard reference materials were used intermittently to cross-check the quality of data obtained.

4.1 Evaluation of homogeneity of the samples after crushing and splitting

Samples collected from two different areas were made as split A and split B for each of the seven samples, two sub samples of different grain size were prepared. Considering that each sub sample was studied five times, there were ten Au results for samples of both splits. A through statistical evaluation of results was carried out and discussed elsewhere. None of the Au values for the seven samples is above the critical value, indicating that there are no significant differences in the Au contents of split A and B.

4.2 Efficiency of different extraction procedures

The slightly lower recovery of Au with the cyanidation technique can be explained due to a variable mineralogical composition of the samples: Au has been found as inclusions in the silicate minerals which are not attacked by cyanide. There is ambiguity between Fire Assay and MIBK results because of lower Au concentration, variable and detectable amounts of Au remain in the slag after fire assaying causing variation in the results. The lower recovery of Au by MIBK technique is due to gold found as inclusions in pyrite and silicates as shown in Table 3.

5 CONCLUSIONS

Mathematical methods for determining the sample size developed by (Clifton et al 1969) were taken into consideration; however, it is difficult to apply these methods because Au may vary in size and shape. Sodium cyanide leach results were lower in comparison to fire assay and aqua-regia leach due to the non-effective leaching of sulphide and silica bearing samples containing gold. The advantage of MIBK method is primarily associated with its cheaper cost, when compared to the fire assay fluxes. It dissolves and extracts the entire platinum metal group in addition to gold and silver. The combination of a fire assay fusion with AAS technique offers the advantage of using large quantity of subsample together with a very sensitive technique to yield better detection limits. The results obtained in this study show that both NaCN leach and MIBK solvent extraction techniques, act as potential alternatives for the fire assay method. However the explorers looking for the best resolution of low-level gold anomalies will find out that the alternative chemical procedures play a vital role when deciding about the economics of the deposit, as proved in the case of gold exploration studies in Gadag and Ajjanahalli in Chitradurga Schist Belts in Karnataka, India.

6 REFERENCES

- Balaram.V., Rao, T.G, Anjaiah, K.V., Ramesh, S.L, Manikyamba, C., Naqvi, S.M 1996. in proceeding volume of National seminar on exploration and exploitation of gold resources in India. NGRI Hyderabad.
- Balaram, V., S.M. Hussain S.M., Uday Raj , Charan S.N., D.V. Subba Rao D.V, K.V. Anjaiaha K.V and Illangovan, 1997 Atomic Spectroscopy,18 (1),17.
- Balaram,V., SunderRaju P.V., Ramesh, S.L., Anjaiah, K.V., Dasaram B, Manikyamba. C., Ram Mohan .M. and Sarma.D.S. 1999 Atomic Spectroscopy, 20 .4.
- Clifton H.E., Hunter RE., Sawson,F.T and Phillips R.L, 1969 US Geolo.Surv .Pap 625C ,17 .
- Chao T.T and R.F.Sauzalone, 1992. Journal of Geochemical Exploration, 44 , 65.
- Fletcher, K., Horsky. S. 1988. Journal of Geochemical exploration, 30, 29.
- Jackwert E. and Gomisceck., 1984 Pure Appl.Chem ,56 ,478
- Langmyr F.J. and Sween .S. 1965. Anal Chim. Acta, 32 1.
- Mathhes S.A., Farell R.F, Mackie, A.J , 1983. Tech .Prog. Rep –U.S.Burea of Mines, 120, 9.
- Rubeska I., Thomas, V.A., Baby, T.V., Thomas, O., Interim report CH-5, UN assisted project, Trivandrum, 1980, India 1-12.
- Ramesh S.L, Sunder Raju P.V., K.V. Anjaiah K.V , Rao T.G, Ramavathi Mathur, Dasaram .B, Nirmal Charan, S., Subbarao.D.V., and V. Balaram., 2001 Atomic Spectroscopy, 22, 263.

Image Analysis of Iron Oxides Under the Optical Microscope

E.Pirard & S.Lebichot

Mineral Georesources and Geo-Imaging Group, GeomaC Department, Université de Liège, Liège, Belgium

ABSTRACT: Many mineralogists have disregarded reflected light microscopy for automated mineral identification since the advent of electron microscopy and particularly EDX microanalysis systems. Although obviously such systems are capable of resolving delicate mineral identification questions they suffer from high operating costs and low image acquisition rates. An additional reason for having disregarded optical microscopy in quantitative ore mineralogy during the last decades is that poor results have been obtained so far because of a very careless attention to the image acquisition protocol. In this paper, we demonstrate how taking advantage of all available information under the optical microscope may improve the identification of some important minerals. By using several interference filters and by rotating the polarizer / analyzer filter set, we obtain a stack of multispectral and multiradial images that can be segmented using multivariate discrimination techniques. In such a way, absolute reflectance, pleochroism, bireflectance and optical anisotropy contribute to the optimal classification of individual pixels into the user-defined mineral species that form the paragenesis under study. Preliminary results are shown on some parageneses where backscattered electron imaging typically proves to be poorly discriminating or useless: Hematite-Magnetite-Goethite in Banded Iron Formations; Ilmenite-Magnetite-Hematite in Magmatic-Ti ores; etc.

1 APPLIED MINERALOGY OF IRON ORES.

The mineralogy of iron ores, particularly those of sedimentary origin, is extremely simple and only involves three major iron-bearing mineral species: Hematite (Fe₂O₃), Magnetite (Fe₃O₄) and Goethite (FeO.OH), not to mention the more or less hydrated mineral mixtures designated under the generic but confusing term of Limonite. The traditional trading of iron ores is based on chemical specifications and size distribution requirements. However, in recent years, detailed studies of iron ores and their behavior in steelmaking processes have drawn attention on the need for a more detailed description of the microtexture of iron ores (Vieira et al. 2003; Clout 2003). Of particular interest are the size distribution of hematite crystals (microplaty, recrystallised, granular,...), the mineral intergrowth (martite, hematite/goethite,...) and the microscopic arrangement of crystals (microporosity, ...). In order to perform such a detailed analysis, mining and steelmaking companies have no alternative to the tedious visual inspection of thousands of grains either under the scanning electron microscope or the reflected light microscope. Despite spectacular progress in instrumentation (Sutherland & Gottlieb 1991) the automatic identification of minerals under

the microscope and the consequent description of microtextural arrangements still stumble over difficulties. This is particularly true for iron ores where all major minerals display poor contrast in their physical / chemical properties (Table 1).

Table 1: Reflectances, composition and average atomic number of major iron oxides and iron sulphides (from Jones 1987; Criddle & Stanley 1993).

Mineral	R ₄₇₀	R ₅₄₆	R ₆₅₀	Fe % wt	\bar{Z} mean atom.nb.
Magnetite	20.9	20.7	20.7	72	21
Hematite	32.5/28.3	31.0/26.8	26.6/23.3	70	20.1
Goethite	17.2/19.9	15.5/17.5	14.4/16.1	63	19.2
Limonite				~60	~18.7
Ilmenite	19.7/16.9	19.2/16.4	20.2/18.0	37	19
Pyrrhothite	32.1/37.0	36.3/41.4	41.5/45.4	64	22.4
Marcasite	44.8/51.6	49.1/56.2	48.3/53.4	47	20.7
Pyrite	45.6	51.7	54.4	47	20.7
Pentlandite	41.9	48.9	53.4	39	~23.4

2 PRINCIPLES OF QUANTITATIVE ORE IMAGING

Digital imaging of mineral assemblages under the microscope can be achieved in several ways: either by using scientific grade CCD cameras or by scanning a scene with an electron beam and digitizing the output of a Robinson Backscattered Electrons detector (BSE imaging) or an X-Ray detector (EDX imaging). When high spatial resolution is a strong requirement, optical imaging cannot compete with scanning electron microscopy. However, in many cases, as with iron ores, optical imaging is a cheap and flexible alternative solution. The widespread availability of scanning electron microscopes has attracted a lot of attention and impeded the development of research work on a rigorous visible light spectrometric imaging in optical microscopy. This lack of interest has been reinforced by the poor results obtained when trying to perform image analysis using color video or still video cameras. Considering the comprehensive measurement and compilation of visible specular reflectance curves published by Criddle and Stanley (1993) on behalf of the Commission for Ore Microscopy (IMA-COM), it appears worth attempting to reconcile both spectroscopy and imaging modes. This is only possible by using multispectral imaging and a proper calibration procedure as proposed in Pirard (2004). Fig. 1 shows how the use of narrow bandwidth (10nm) interference filters improves discrimination between Pyrite and Pentlandite as compared to the tristimulus color filters.

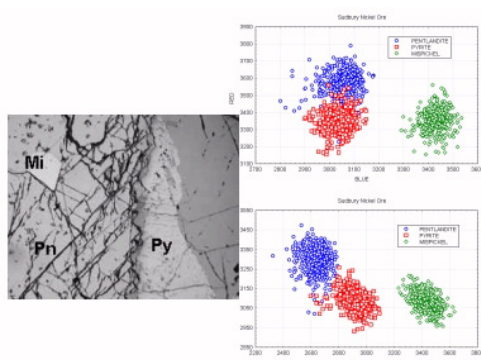


Figure 1. Optical microscopy of a nickel ore showing Pyrite (Py), Pentlandite (Pn) and Arsenopyrite (Mi). Scatterplots represent selections of 400 representative pixels from each phase when using red vs. blue imaging (upper diagram) or 438 nm vs. 692 nm imaging (lower diagram).

Backscattered electrons imaging under the electron microscope is a very convenient method for quickly discriminating between some major sulphides or sulphides and gangue (Lastra 1998). It is sensitive to the mean atomic number of a mineral. If an 8 bit depth digitization is used and considering the range of intensities between gangue (typically $\bar{Z}=10$) and galena ($\bar{Z}=73,2$) or gold ($\bar{Z}=79$) the spectral resolution is about $\Delta\bar{Z}=0,27$, meaning in practice that magnetite and hematite and to a lesser extent goethite can hardly be discriminated. Not to say that pyrite also falls within the same interval.

Energy Dispersive X-Ray analysis is by far the most accurate and sensitive method. It delivers semi-quantitative chemical analysis of a pear-shaped region hit by the electron beam within a few milliseconds. As a complementary tool to BSE it immediately reveals the difference between pyrite and hematite. However, to differentiate minerals made of the same elements in different proportions, longer integration times are needed (e.g. Pyrite vs. Pyrrhotite). The trilogy of iron oxides is a very subtle case necessitating a light-elements detector for oxygen and exceptional accuracy to distinguish hematite (70 % O) from magnetite (72% O).

Both BSE and EDX imaging modes in scanning electron microscopy cannot reveal a difference between polymorphs or between grains of identical composition but different crystallographic orientations. This requires orientation imaging based on electron diffraction patterns (Adams et al. 1993), which is increasingly used in materials sciences for single phase materials, but still not widespread in geological materials (Prior et al. 1996).

On the contrary, it is common practice to exploit polarization modes in optical microscopy and deduce anisotropy and crystal orientation from light behavior. But, surprisingly again, few efforts have been made to cope with this information quantitatively in optical image analysis (Fueten 1997). Because specular reflectances are quite close and may vary in practice with composition, polishing compound and even grain size it is worth adding anisotropic information to help contrasting magnetite from hematite and goethite.

Finally, imaging of the microporosimetry is also an important topic in iron ore characterization. Here again, due to the limited depth of focus of optical microscopy, excellent contrast is achieved between the polished surface and any default (scratch, cleavage, pore,...) whether imaging under the scanning electron microscope is less favourable except if resin impregnation is used in BSE mode.

3 MULTIRADIAL IMAGING OF OPAQUE MINERALS.

In order to take maximum advantage of optical information, an imaging system combining both multispectral and multiradial (polarised light) capabilities was set up. This system uses a Peltier cooled scientific grade 12 bit CCD camera and a series of interference filters mounted on a filter wheel. Additionally, the microscope has a rotating polar (incident light path) and a rotating analyser (reflected light path). Each image is acquired using a precise background correction protocol and time-averaging of a sequence of images to reduce noise (Pirard 2004).

Multispectral imaging consists in stacking a series of subsequent images taken at different wavelength in plane polarised light. In order to add information about the anisotropy, another series of images must be taken at different orientations of the polarisation plane with respect to the mineral surface. To gather complete information this should be done at different wavelength under plane polarised light and repeated at these wavelength for analysed light (crossed polars) (Criddle 1998). Practical considerations make it cumbersome, particularly because image warping (rotation) is necessary to co-register images, so a simplified and approximate procedure has been used in this work.

In transmitted light microscopy, multiradial imaging has been developed by Fueten (1997) by synchronously rotating the polarizer / analyzer instead of the specimen stage. This cannot be achieved in reflected light microscopy because of the semi-reflecting mirror architecture (Criddle 1998, p21). In other words, polarisation of rays is rotated at oblique angles of incidence and hence the polarisation state varies within the cone of light. If the plane of polarisation of incident light is no longer parallel to the semi-reflecting mirror, this will also induce elliptical polarisation. The result of this being that isotropic minerals will display a false anisotropy and ghost images (secondary glare) might appear (Galopin & Henry 1972).

For sake of mineral identification in a section relative to one another, it is not mandatory to have the exact measurement of bireflectance / pleochroism intensities. The same holds for anisotropic reflectance curves (anisotropic tints) which are still poorly understood. Hence, in this work, a series of images have been acquired from the same scene when rotating the incident light polar and these were simply stacked together with multispectral information to see whether this could improve discrimination among mineral species.

4 RESULTS

Several characteristic textures of itabirite iron ores were pictured and processed by using supervised classification algorithms available within the MultiSpec software. The richness of multispectral / multiradial information is best shown using false color, alternatively figure 2 presents reflectance and bireflectance images derived from a set of images taken at five different wavelengths and using polarization steps of 15°.

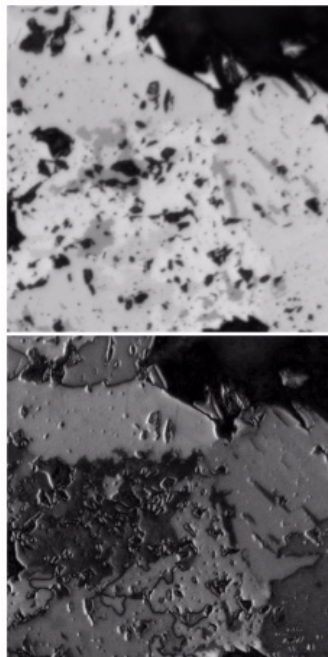


Figure 2a. Reflectance image at 589 nm displaying porosity (black); magnetite (dark grey) and hematite (light grey) and Fig. 2b. Bireflectance image of the same scene computed from the difference between maximum and minimum reflectance at different orientations of the polarizer.

Clearly, a reflectance image at any wavelength allows for discriminating reasonably well between magnetite and hematite. Average grey levels are in the range of 152 for magnetite and between 186 and 218 for hematite (due to bireflectance). However, by stacking several images while rotating the polarizer, the average grey level difference between the maximum intensity for magnetite and the minimum intensity for hematite increases by about 36 %, thereby improving the robustness of the classification algorithm. If instead of pooling all brightest pixels together, one adds a bireflectance intensity criterion to the segmentation process, it is

straightforward to obtain a mapping of individual hematite crystals (Fig. 3) from which grain size distribution or preferred orientation planes can be derived by image analysis (Launeau et al. 1990).

In practice, despite the non-adequate polarization conditions, isotropic sections of hematite remain relatively constant (0 to 5 grey levels variation). All magnetite crystals show variations of the order of 10 to 15 grey levels, while anisotropic sections of hematite reach bireflectance intensities up to 40 grey levels.

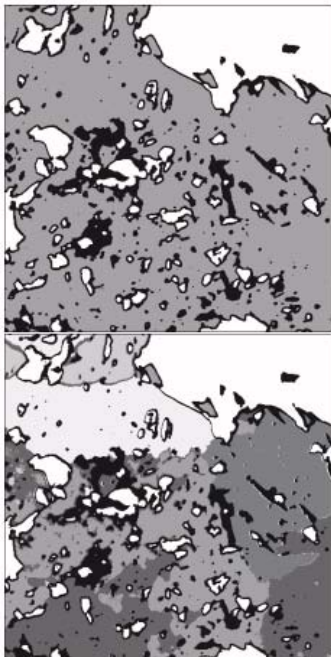


Figure 3a. Fisher Linear Likelihood classification of hematite (grey); magnetite (black) and pore (white) pixels based on a stack of five spectral and four polarized images. Fig. 3b. Classification of the same set of images by taking into account a segmentation criterion based on the bireflectance intensity. Magnetite (black), various hematite crystals (from dark to light grey).

5 CONCLUSION

Correct mineral identification is an absolute prerequisite for proper image analysis of ores. This can be achieved by using several imaging methods having their own advantages and disadvantages. Clearly, optical microscopy image analysis still has a promising future if optimal imaging conditions are used and a maximum of information is pooled together in a multivariate classification system.

The exact measurement of optical properties is

hard to achieve without major modifications in the microscopical setup, but nevertheless indicative anisotropy is often sufficient to enhance differences and reveal textural informations of interest to the applied mineralogist.

When comparing the relative performance of electron microscopy vs. optical microscopy based instruments, one should not forget the higher productivity of optical instruments. These can possibly inspect much larger sample sets at very high speed, thus putting into practice the famous slogan of stereology and sampling theory claiming "do more less well".

To reach this goal however, additional work has to be performed to improve the automated acquisition of optical image analysis systems using spectral and polar filter sets.

6 REFERENCES

- Adams, B.L., Wright, S.I. & Kunze, K. (1993) Orientation imaging: the emergence of a new microscopy. *Metall. Trans.* 24A, 819-831.
- Clout, J. (2003): Upgrading processes in BIF-derived iron ore deposits: implications for ore genesis and downstream mineral processing, IMM Transactions section B, 112, 1, pp. 89-95
- Criddle, A.J. (1998) Ore microscopy and photometry (1890-1998). pp. 1-74 in: *Modern Approaches to Ore and Environmental Mineralogy* (Cabri, L.J. & Vaughan, D.J., editors). Short Course Series, 27. Mineral. Assoc. of Canada, Ottawa.
- Criddle, A.J. & Stanley, C.J. (editors) (1993): *Quantitative Data File for Ore Minerals*, 3rd ed., Chapman & Hall, London, UK, 635 pp.
- Fueten, F., (1997): A computer controlled rotating polarizer stage for the petrographic microscope, *Comp. & Geosci.*, 23, 203-208.
- Galopin, R. and Henry, N.F.M. (1972) *Microscopic Study of Opaque Ore Minerals*. Heffers, Cambridge, UK, 322 pp.
- Lastra, R., Petruk, W. & Wilson, J., (1998): Image analysis techniques and applications to mineral processing, pp. 327-366 in: *Modern Approaches to Ore and Environmental Mineralogy* (Cabri, L.J. & Vaughan, D.J., editors). Short Course Series, 27. Mineral. Assoc. of Canada, Ottawa.
- Launeau, P., Bouchez, J-L., & Benn, K., (1990): Shape preferred orientation of object populations : automatic analysis of digitized images, *Tectonophysics*, 180, 201-211.
- MultiSpec: <http://dynamo.ecn.purdue.edu/~biehl/MultiSpec/>
- Pirard E., 2004, Multispectral imaging of ore minerals in optical microscopy, *Mineral. Mag.*, 68, 2, 323-333.
- Prior, D.J., Trimby, P.W., Weber, U.D., Dingley, D.J., 1996. Orientation contrast images of microstructures in rocks using forescatter detectors in the scanning electron microscope. *Mineral. Mag.*, 60, 859-869.
- Sutherland, D. & Gottlieb, P. (1991): Application of automated quantitative mineralogy in mineral processing. *Minerals Engineering*, 4, 735-762.
- Vieira, C., Rosiere, A., Pena E., Seshadri V. & Assis P. (2003), Avaliação técnica de minerios de ferro para sinterização nas siderúrgicas e minerações brasileiras : uma análise crítica, *Rev. Esc. Minas Ouro Preto*, 56, 2, 97-102.

The Mineralogy of Sediments as Determined by XRD and Rietveld; Comparison with Jade and SEM Image Analysis

J.A.R. Stirling

Geological Survey of Canada, Ottawa, Canada

M. Bonardi

ISMAR-CNR (Istituto di Scienze Marine-Consiglio Nazionale delle Ricerche), Italy

ABSTRACT: The Geological Survey of Canada recently acquired a new X-ray diffractometer (Bruker D8) that included a software package "TOPAS" which is based on the Rietveld method. The first major group of samples to be analyzed with this system were sediment samples from the Lagoon of Venice, Italy. From previous studies, it was determined that the samples were predominately mica, carbonates, quartz, and feldspar with traces of oxides, pyrite and gypsum. A standard was prepared which contained muscovite, calcite, quartz and albite. This standard was processed with the TOPAS program and the results considered acceptable. However, the mineralogy of the new batch of samples was far more complex. The major minerals could be quartz, albite, orthoclase, muscovite, biotite, chlorite, calcite, aragonite, dolomite, ankerite, hastingsite and enstatite with traces of gypsum, Fe-oxides, pyrite, apatite, ilmenite, monazite and bassinite. Obviously, a more complex approach was necessary. On selected samples a detailed mineralogical study was carried out using SEM methods (X-ray mapping, and EDS analysis), X-ray diffraction and powder diffraction on mineral concentrates. This was necessary to completely characterize the minerals so as to find a structure as close as possible to a given mineral. A few samples were processed using SEM image analysis, Rietveld and JADE. Image analysis allows for the identification of trace minerals, which are not always identified by XRD, however the sample analyzed is smaller and the method takes longer. Rietveld is preferable over JADE in complex systems because of overlapping peaks and the lack of standards.

1 INTRODUCTION

The Geological Survey of Canada was contracted by Consiglio Nazionale delle Ricerche to determine the mineralogy of samples of sediments collected from the Lagoon of Venice, Italy. The primary method of study was by X-ray diffraction analysis using a Rietveld method of data reduction. In order to assess the merits of the Rietveld method (which is new to this laboratory), a standard was prepared which contained muscovite, calcite, quartz and albite and it was analyzed using the JADE and Rietveld methods. Also, three samples of the sediments were processed using Rietveld, JADE, and image analysis of EDS X-ray maps.

2 ANALYTICAL METHODS

2.1 Sample Preparation

The samples that were received dry were pulverized to a fine powder in a micro ball mill. The samples were packed into front-loading sample holders and a micro pattern (Peters 1970) was stamped on the surface to help disrupt the orientation of the minerals.

Polished grain mounts were prepared from the unpulverized samples for the SEM/EDS X-ray mapping. A method was used to produce a monolayer of grains so as much as possible not to have overlapping or touching grains.

2.2 X-ray Diffraction and X-ray Mapping

The samples were analyzed with a Bruker Advanced D8 using the following settings: Co Tube (40 kV and 40 mA), range 3 to 86 degrees, divergence and anti-scatter slit 0.5 degrees, receiving slit 6 degrees, step size 0.04 degrees, time/step 4 seconds and sample rotation.

A Cambridge S200 SEM (Cambridge Instruments Ltd.) with a 4PI operating system (4pi Analysis, Inc.) was used to produce X-maps. The operating conditions were 20 kV and 1 nA. Maps were collected at 1024 x 1024 with a dwell time of 20 ms. Approximately 500 grains for each sample were mapped for Na, Mg, Al, Si, P, S, Cl, K, Ca, Ti, and Fe. An example of Si X-map is given in Figure 1.

2.3 Data Reduction: XRD and Image Analysis

The XRD data were analyzed with Eval (a program supplied by Bruker AXS) to determine the mineralogy and the best fit from the ICDD data file.

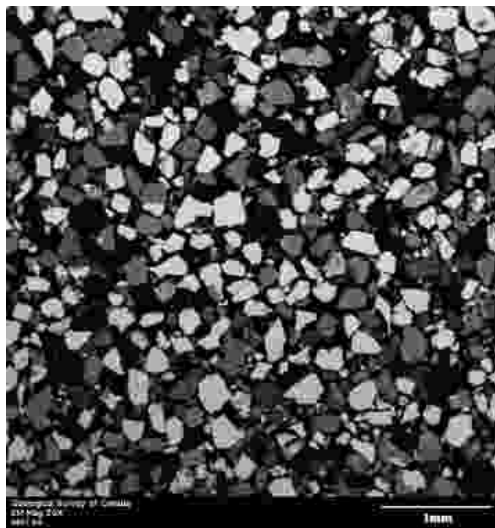


Figure 1. EDS X-ray map of Si for sample 134.

The semi-quantitative mineralogy was determined using TOPAS 2.1 (Bruker AXS 2003) (a

Rietveld based program supplied by Bruker AXS) and JADE 3.1 (supplied by Materials Data Inc.). Scion Image for Windows Beta 4.0.2 (freeware Scion Corporation) was used to process X-ray maps.

3 RESULTS

3.1 Standard

A standard was prepared in order to have a measure of accuracy and precision. Pure minerals from the National Reference Collection of Canada were used to prepare the samples. X-ray maps were not collected for the standard because it had been prepared approximately ten years ago and had been pulverized and was much too fine for x-ray mapping. XRD scans were collected for three preparations of the standard. The results are given in Table 1.

In all cases the results from JADE deviate more from the known mineral composition than TOPAS, however the reproducibility is similar for both methods.

3.2 Samples

Three samples of the sediments were chosen for detailed studies. The XRD mineralogy was determined using EVAL and qualitative SEM/EDS

Table 1: Comparison of the results from TOPAS and JADE on the prepared Standard

Mineral Composition	R-Factors	Calcite		Quartz		Albite		Muscovite	
		TOPAS	JADE	TOPAS	JADE	TOPAS	JADE	TOPAS	JADE
1	Rexp : 12.08 Rwp : 16.58 Rp : 12.90 GOF : 1.37	23	15	43	53	27	27	7	4
2	Rexp : 12.05 Rwp : 17.66 Rp : 13.82 GOF : 1.47	23	15	40	50	29	33	8	3
3	Rexp : 12.08 Rwp : 17.10 Rp : 13.51 GOF : 1.42	22	15	42	54	28	30	7	2
Mean		22.6	14.9	41.9	52.3	28.2	29.9	7.2	3.0
STD		0.29	0.05	1.27	1.85	0.70	2.13	0.37	1.11
Deviation from given value		-11%	-41%	10%	37%	-8%	18%	17%	-52%

Analyses were made on grain mounts. In some cases mineral concentrates were hand picked and X-rayed. This was done in order to select the best crystal structure of that mineral, as was the case for the amphibole, where a Fe-hastingsite was the best fit. The results for the samples are given in Table 2.

Overall the results are comparable, with a few glaring exceptions (quartz in sample 107 and absence of clinocllore in sample 103 as determined by image analysis) and only TOPAS reported

ankerite. At approximately 5% concentrations, JADE is slightly less reliable than TOPAS. In the study no effort was made to optimize the JADE technique. One of the purposes was to evaluate the standard operating procedure in the laboratory with TOPAS (a new procedure for this laboratory). Only image analysis identified trace (<1%) minerals.

4 CONCLUSIONS

As with most techniques, not any one method will do everything. The TOPAS and JADE methods for XRD analysis are comparable for majors, however TOPAS is slightly better for lower concentrations and for sorting out minerals of similar crystallography (dolomite and ankerite). Also, JADE should have reference intensity ratio RIR for the minerals analyzed, thus requiring standards. On the other hand, TOPAS requires that the crystal structure for the mineral be available. Neither method will reliably identify trace phases. With image analysis there is always the question of sampling. The surface of a polished section is a very small sample as compared to the fine-grained powder of a XRD sample. From a practical point of

view, image analysis requires the preparation of a polished sample with care given to sample representation, and considerable time for high-resolution X-ray maps and data reduction.

5 ACKNOWLEDGEMENTS

This work was partially carried out within the framework and with the financial supports of the CO.R.I.L.A. (Consorzio per la Gestione del Centro di Coordinamento delle Attività di Ricerca inerenti il Sistema Lagunare di Venezia) (Subproject 3.2-Hydrodynamics and Morphology) and of the Regione del Veneto and APAT (CARG Project: Fogli "Venezia" and "Chioggia-Malamocco", coordinator Dr Federico Toffoletto).

Table 2: Comparison of the results from TOPAS, JADE and image analysis for the three sediment samples.

	Dolomite	Ankerite	Calcite	Quartz	Albite	Orthoclase	Clinochlore	Amphibole	Pyrite	Ilmenite	Rutile	Fe-Oxide	Pyroxene	Muscovite	Total
Density	2.866	2.71	2.648	2.62	2.57	2.65	3.3	5.011	4.788	4.245			3.2092	831	
Sample	103														
R Factors for TOPAS	Rexp : 12.09	Rwp : 15.50	Rp : 11.89	GOF : 1.28											
TOPAS	50	2	15	19	6		1							6	100
JADE	49		19	24	8		2							0	101
Image Analysis	46		22	23	4				trace		trace			6	100
Sample	107														
R Factors for TOPAS	Rexp : 12.71	Rwp : 14.95	Rp : 11.01	GOF : 1.18											
TOPAS	50	7	21	15	4		2							2	101
JADE	52		22	19	6										100
Image Analysis	61		19	7	3		2			2	1			5	100
Sample	134														
R Factors for TOPAS	Rexp : 11.01	Rwp : 18.54	Rp : 14.33	GOF : 1.68											
TOPAS	2			57	19	10	6	trace					2	4	100
JADE	3			66	21	7	2							2	101
Image Analysis	4		1	51	20	5	2	5	2	2	trace	trace	2	6	100

6 REFERENCES

- Bruker, A.X.S. 2003. TOPAS V2.1: General profile and structure analysis software for powder diffraction data. – User's Manual, Bruker AXS, Karlsruhe, Germany.
- Peters, Tj. 1970. A simple device to avoid orientation effects in X-ray diffractometer samples. Norelco Reporter, v17, No 2, p. 23-24.

Brazilian Organoclays: Morphological Characterization Combining AFM and SEM Studies

A.T.De León

Departamento de Materiales y Metalurgia - Facultad de Ingeniería Mecánica - Universidad Tecnológica de Panamá

G.Englert

Laboratório de Pesquisa em Corrosão - Escola de Engenharia - Universidade Federal do Rio Grande do Sul - Brasil

J.Rubio

Laboratório de Tecnologia Mineral e Ambiental - Escola de Engenharia - Universidade Federal do Rio Grande do Sul - Brasil

ABSTRACT: A combination of SEM (Scanning Electron Microscopy) and AFM (Atomic Force Microscopy) techniques was used to characterize the morphology of Brazilian montmorillonites before and after the intercalation of some organic compounds. AFM revealed that the layers are stacked one upon the others. The surface of the particles consisted of layers bounded with smooth flat basal planes and larger edges ending in some cascade-like steps, 184 μm wide. Some micro and macro valleys (0.6 μm deep) are distributed throughout the whole area and irregularities on basal planes may be attributed to the crystallographic conditions of the genesis of these Brazilian montmorillonites. The mapping performed over 20 x 40 areas showed adhesion forces of 11 nN magnitude on bare clay mineral in the Na^+ form and 40 nN for the calcium form. Forces between 10 and 6 nN were found after organic intercalation. In general, the intercalation caused significant changes in the surface properties of clay mineral. The combination of AFM and SEM studies provided evidence of the poor crystallinity of the Brazilian montmorillonites.

1 INTRODUCTION

Even though the production of modified montmorillonites by the intercalation of organic compounds has been studied in many areas (De León et al. 2003; Krishna et al. 2001; Mortland & Berkheiser 1976; Appleton et al. 1999; Cox et al. 2001), little is known about the influence on the morphological structure when these compounds are grafted onto the solid surfaces.

The morphology of clay mineral has been studied by electron microscopy (Zbik & Smart 1998; Thompson et al. 1981); and these studies revealed a multiplicity of microsteps on the clay mineral surfaces.

Atomic Force Microscopy (Binnig et al. 1986) has rapidly spread throughout many fields of science due to its high versatility (Senna et al. 2001; Oréfice & Brennan 1998; Ikai et al. 2002; Zbik & Smart 1998; Johnson & Lenhoff 1996). While height images provided quantitative topographic information, deflection images often revealed finer surface details. The AFM can also record the force felt by the cantilever as the probe tip is brought close to - and even into - a surface and then pulled away (Ikai et al 2002). This technique can be used to measure long range attractive or repulsive forces between the

probe tip and the surface, elucidating local chemical and mechanical properties and even the thickness of adsorbed molecular layers or bond rupture lengths (Binning et al. 1986).

The aim of this work was to characterize the surface morphology of a Brazilian montmorillonite firstly in the calcium and sodium form and secondly after the intercalation of two organic compounds using a combination of SEM and AFM techniques.

The intercalation of the organic compound was made with the goal to improve the adsorptive capacities of the raw clay, so that it could be used as an alternative adsorbent to remove heavy metals from wastewater.

2 MATERIALS AND METHODS

2.1 Materials

BRASGEL: an industrial Brazilian montmorillonite in Na^+ form from Campina Grande - Paraíba, Brazil. BENTOCAL: a montmorillonite saturated with calcium cations. The organoclays used in this study (named FENAN and ETIL) were obtained by the intercalation of two organic compounds, 1,1 Orthophenanthroline and Ethylenediamine

respectively onto BENTOCAL montmorillonite (De León et al. 2003).

2.2 Atomic force microscopy studies

The morphological structure of different montmorillonites samples and its contact force curve were determined by AFM by the contact mode (Digital Nanoscope IIIa, 3000 system, Si₃N₄ micro cantilever). The force curve obtained for each montmorillonite sample was utilized to calculate the nominal contact force of the tip on the surface samples, defined by the equations:

$$F = k\Delta z \quad (1)$$

$$\Delta z = ADP \quad (2)$$

where: F = Contact force in nN; k = spring constant of the micro cantilever, 0.6 Nm⁻¹; Δz = distance from de control point, nm; A = number of divisions of the cantilever deflection; D = potential applied, V/divisions; P = piezo sensitivity constant, 2 nmV⁻¹.

The time elapsed in one cycle of approach and retraction of the tip was in the range of ~ 2 s and, because the tip was in contact with the clay mineral surface for at least 10% of this time, the contact time was approximately 200 ms. AFM imaging and force-distance measurements were made at room temperature (20°C) and the contact mode topographic images were recorded in height and deflection mode.

2.3 Scanning electron microscopy studies

SEM studies were performed with a Phillips XL-30 ESEM scanning microscope operating normally with up to 30 kV acceleration voltage field emission gun. The samples were attached to a metal mount by carbon tape. Due to the insulating nature of the materials, the samples were coated with a 20 nm thick layer of gold (Balzer Union SCD 040 Sputter Coater system under argon vacuum.)

3 RESULTS AND DISCUSSION

3.1 Topographical analysis

The nanotopography of BRASGEL sample is shown in Figure 1.

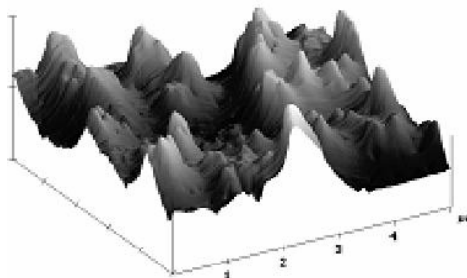


Figure 1. Contac Mode Atomic Force Microscopy (CM-AFM – 3D) images of sodium Brazilian montmorillonite (BRASGEL).

The image of the sample show different topography at various levels. The surface of BRASGEL – a raw clay - shows complex morphological features with irregular and elongated edges, well-defined “hills” and several depressions, suggesting a surface with great roughness; the edges of the flakes, not clearly defined, are ragged and irregular. It also shows a successive “mountain range” with intermittent micro and macrovalleys (~ 0.6 μm deep). In general, this irregular surface is characteristic of bad-developed crystals with no right angles between edge and basal planes. This observation may be linked to a poorly crystallization conditions (Zbik & Smart 1998) whereby the Brazilian montmorillonites were formed (Gopinath et al. 1981).

Figure 2, for the Ca-montmorillonite (BENTOCAL) shows the presence of a large jagged and an irregular edge and an isolated nanovolcano (~184 nm height) in the surface. Nevertheless microvalleys and grooves can be seen (arrow marks)

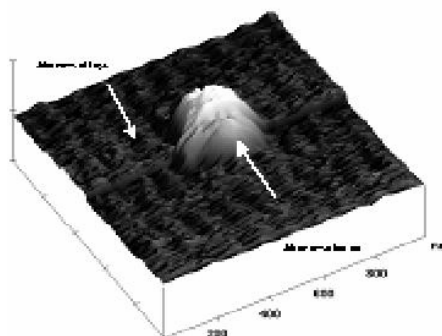


Figure 2. AFM micrographs from the surface of BENTOCAL.

The surface is continuous and appears smooth. Cascade-like step structures may also be appreciated, 280-345 nm wide, as described by Zbik

& Smart (1998), who studied the nanomorphology of well and poorly crystallized kaolinites.

The results clearly show that the surface of non intercalated samples (BRASGEL and BENTOCAL) is not smooth but rough in nature.

Figure 3, obtained after Orthophenanthroline intercalation, shows a seemingly smooth surface, despite the raw clay was not well developed.

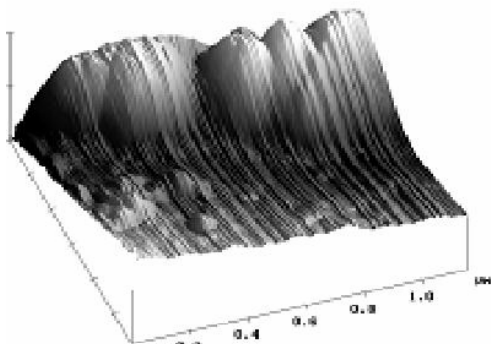


Figure 3. AFM micrographs on well-ordered montmorillonite after Orthophenanthroline intercalation (FENAN).

The overall topography is relatively regular and the basal planes are stacked one over the other. The image shows that the surface topography of the organoclay became smoother and presented a massive cascade-like structure at the layer edges. This may due to the formation of a homogeneous phase after organic intercalation and a subsequent uniform structure.

Figure 4 shows a typical F-E (force vs. extension) curve obtained on the BRASGEL surface. The slope of the curve suggests that the tip moved on a hard surface, and a typical large adhesion interaction curve was represented (Ikai et al. 2002).

The force curve represents the deflection signal for each complete trace-retrace cycle of the piezo. At point *a*, the cantilever is not deflected but due to attractive forces between the tip and the montmorillonite surface, the tip sticks to the sample, and the cantilever is pulled down as the piezo continues to retract. Eventually, the spring force of the bent cantilever overcomes the attractive forces, and the cantilever quickly returns to its non-deflected, non-contact position. This is represented by point *c*. At point *b*, the spring force of the cantilever equals the attractive forces between the tip and the surface. The indentation in the surface was extremely “rough” (677.32 nm) and the extension of the sample was in the range of 5 x 5 µm. The contact forces for the other samples were calculated by employing equations 1 and 2 (Tab. 1).

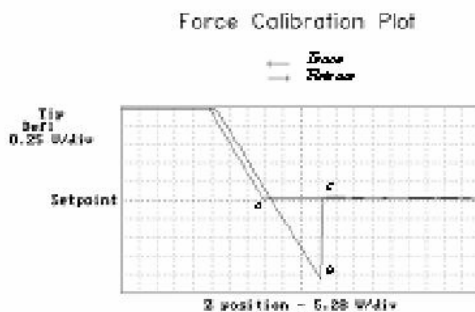


Figure 4. Computing contact force obtained by AFM to the BRASGEL montmorillonite.

Table 1. Contact forces onto Brazilian motmorillonites.

Samples	Resulting contact force, nN
BRASGEL	11
BENTOCAL	40
FENAN	10
ETIL	6

The BRASGEL sample presents an attractive contact force of 11 nN, between the sodium montmorillonite surface and the silicon nitride tip. In the case of calcium montmorillonite (BENTOCAL) the force increased to 40 nN. After the intercalation of Orthophenanthroline and Ethylenediamine onto BENTOCAL montmorillonite the superficial force was significantly reduced. These results indicated that the intercalation of the organic compound and possibly, its orientation inside the basal spacing of montmorillonite, could be responsible for the reduction of the observed superficial contact force.

3.2. Micro structural analysis

The morphology of the montmorillonite, treated and un-treated with organic compounds were determined with SEM. One of these images is shown in Figure 5. The SEM image of BRASGEL montmorillonite shows a continuous surface, even though it contains small particles and the edges of the lamellar are jagged and irregular. The presence of a greater number of smaller size particles between the lamellar make the sample less compact and less rigid (Frost et al. 2002). The appearance presented by the Brazilian montmorillonite, is a typical “terraces landform” and remains the Brazilian crystallization regions (Gopinath et al. 1981).

In addition to particle size and particle distribution in 2:1 clay minerals such as Brazilian montmorillonite, aspect ratio and association structure have a dominant influence on the

intercalation of organic compounds. For instance, the presence of tiny and small clay particles – as shown in the Figure 5 – on the outside of larger particles may block the interlayer space to the penetration of the organic molecules.

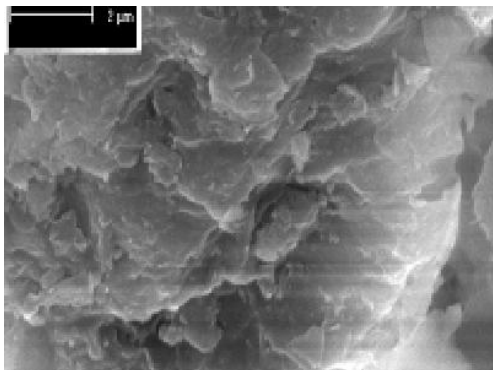


Figure 5. SEM micrographs of the BRASGEL montmorillonite (sodium form).

4 CONCLUSIONS

One of the main conclusions was that the results of these studies reveal that AFM and SEM are important complementary tools for investigating clay mineral surfaces before and after organic compounds are grafted. SEM studies showed that the surface of the FENAN was found to be continuously smooth and non porous, and these results compare well with those obtained from AFM analyses and the intercalation of EP and OP molecules caused a significant change on the surface properties of the Brazilian montmorillonite. The correlation between the AFM and SEM studies provided information about the poor crystalline genesis of the Brazilian montmorillonite particles which, despite the poor crystallinity, were very easy to graft with organic compound.

5 ACKNOWLEDGEMENTS

The authors are grateful to UTP (Panama), UFRGS (Brazil) and to the University of Nevada, Reno, Nevada, (USA) for technical support. Bentonit União Nordeste S.A. is also thanked for the supply of the montmorillonite clay samples.

6 REFERENCES

Binnig, G.; Quate, C. F.; Gerber, Ch. 1986. Atomic force microscope. *Physical Review Letters*. 56: 930-933.

- Cox, M.; Rus-Romero, J. R.; Sheriff, T. S. 2001. The application of montmorillonite clays impregnated with organic extractants for the removal of metals from aqueous solution Part I. The preparation of clays impregnated with di-(2-ethylhexyl) phosphoric acid and their use for the removal of copper (II). *Chemical Engineering Journal*. 84: 107-113.
- De León, A. T.; Nunes, D. G.; Rubio, J. 2003. Adsorption of Cu ions onto a 1.10 phenanthroline-grafted Brazilian bentonite. *Clays and Clay Minerals*, 1: 58-64.
- Frost, R. L.; Gaast, S. J.; Zbik, M.; Klopogge, J. T.; Paroz, G. N. 2002. Birdwood kaolinite: a highly ordered kaolinite that is difficult to intercalate – an XRD, SEM and Raman spectroscopic study. *Applied Clay Science*. 20: 177-187.
- Gopinath, T. R.; Schuster, H-D.; Schuckmann, W. K. 1981. Modelo de ocorrência e gênese da argila bentonítica de Boa Vista, Campina Grande, Paraíba. *Revista Brasileira de Geociências*. 11: 185-192. (In Portuguese)
- Ikai, A.; Afrin R.; Itoh, A.; Thogersen, H. C.; Hayashi, Y.; Osada, T. 2002. Force measurements for membrane protein manipulation. *Colloids and Surfaces B: Biointerfaces*. 23: 165-171.
- Krishna, B. S.; Murty, D. S. R.; Jai Prakash, B. S. 2001. Surfactant-modified clay as adsorbent for chromate. *Applied Clay Science*. 20: 65-71.
- Mortland, M. M.; Berkheiser, V. 1976. Triethylene diamine-clay complexes as matrices for adsorption and catalytic reactions. *Clays and Clay Minerals*. 24: 60-63.
- Oréface, R. L.; Brennan, A. 1998. Evaluation of the interactions between polymeric chains and surfaces with different structures performed by an atomic force microscope. *Materials Research*. 1: 19-28.
- Senna, L. F.; Achete, C. A.; Simão, R. A.; Hirsch, T. 2001. Comparative study between the electrochemical behavior of TiN, TiCxNy and CrN hard coatings by using microscopy and electrochemical techniques. *Materials Research*. 4: 137-141.
- Thompson, D. W.; Macmillan, J. J.; Wyatt, D. A. 1981. Electron microscope studies of the surface microstructures of layer-lattice silicates. *Journal of Colloid and Interface Science*. 82: 362-372.
- Zbik, M.; Smart, R. St. C. 1998. Nanomorphology of kaolinites: comparative SEM and AFM studies. *Clays and Clay Minerals*. 46: 153-160.

Mineralogical Approach to Solving Customer Complaints on Various Types of Contamination in Industrial Glass by Using SEM and EDS

D.M.van Tonder, M.Cloete, M.Atanasova
Council for Geoscience, Pretoria, South Africa

ABSTRACT: Customer complaints on defects occurring in various industrial glass products were investigated by means of SEM imagery and EDS analysis. Defects in industrial glass are caused by contaminated raw material, inadequate mixing, imprecise proportions of raw material in mixture and temperature variations. Defects in the end products include the formation of gaseous bubbles, inclusions, scratch marks, cords and striae as well as discolourations. In order to understand the formation of such artefacts mineralogical investigations were carried out on several glass specimens using a Leica 440 Stereoscan Scanning Electron Microscope (SEM) attached to a LINK (OXFORD) EDS (energy dispersive system). The aim was to identify the various inclusions as well as to investigate their textures and comment on the possible origin of these features in order to assist the client in identifying conditions in the plant contributing to the formation of these defects. Three glass samples were selected for discussion in this paper. Image analysis showed the inclusions to consist of both undissolved raw material as well as recrystallised material. Recrystallised material is reminiscent of dendrites which suggests a devitrification origin. Microanalysis showed the inclusions, occurring in the aluminous viscous sacks, to be corundum and nepheline in two instances and wollastonite in the other. The ability of the SEM with attached EDS to view and obtain elemental information allows rapid problem solving for commercial clients often helping to avoid costly plant shutdowns.

1 INTRODUCTION

A local South African glass producer required assistance in investigating various forms of contamination in several glass products. Defects caused by contamination often result in plant shut down and inevitably production losses.

Defects observed in container glass products include gaseous bubbles, inclusions, cords, striae and discolourations (Domarus 1973). These defects are formed by: contaminated raw material, inadequate mixing, imprecise proportions of material in the raw material mix and temperature variations

Material used in the production of the glasses under discussion here includes alkali feldspar and soda ash. Defects observed were needle-like to granular stony inclusions set in glassy solution (viscous) sacks which are in some instances stretched to a cord.

The aim of the investigation was to ascertain the textural relationships and compositions as well as possible origin of the defects. The suspected source for the formation of defects in the glasses investigated here was the feldspar raw material potentially contaminated by wollastonite. The results

were applied in rectifying the problem and continuation of production.

2 METHODOLOGY

The glass samples were studied macroscopically as well as by means of light and polarising microscopy. Cross cuts, exposing the inclusions, were mounted in epoxy, polished and carbon coated for use in a Leica 440 Stereoscan Scanning Electron Microscope (SEM) attached to a LINK (OXFORD) EDS (energy dispersive system). Image analysis were done using the SEM with operating conditions set at 20kV. Identification and quantification of the chemical composition of the glass as well as the contaminated areas were done using the EDS detector. Analytical traverses, from the clear glass across the contaminated areas and into clear glass again, were investigated and the results presented in Tables 1 and 2 as well as Figure 3 below.

3 RESULTS

Inclusions viewed with the aid of a light microscope showed all inclusions are imbedded in viscous sacks. Polarising microscopy revealed textural differences in the inclusions investigated. Inclusions range from ~8mm long, translucent laths cut by parallel microfractures containing dendritic growths to translucent, four or six sided rhomb-shaped platelets as well as granular stone relicts. Three samples selected for discussion are:

- Glass 1: Glass containing lath-shaped inclusions
- Glass 2: Glass containing four or six sided rhomb-shaped platelets.
- Glass 3: Glass containing granular stones.

3.1 Glass 1

SEM imagery of the contaminated area revealed a deformed viscous sack enclosing an irregular area of dendritic crystals in which several euhedral, tabular crystals are set (Fig.1). EDS analysis showed the viscous sack has a higher Al₂O₃ content when compared to the ordinary glass. The dendritic crystals lining the sack have the composition of nepheline whereas the tabular crystals have the composition of corundum. The dendritic texture suggests that *in situ* crystallisation occurred after solidification of the glass (i.e. devitrification). The euhedral shape of the corundum suggests super saturation and subsolidus crystallisation occurred.

Results of the analytical traverse, shown in Figure 1, are presented in Table 1. Variations in composition of the viscous sack are related to mixing between the ordinary glass and the Al₂O₃-rich viscous sack.

The bulk chemistry of the viscous sack, including its contents, were calculated on the weighting of the spot analysis according to the proportions of the bulk it represents. The bulk composition of the sack together with data from Table 1 and composition of some minerals are presented in Figure 3. The analysis of the sack (small circles) and devitrified nephelinitic crystallites (DN) (crosses) plot in a line towards the composition of ordinary glass.

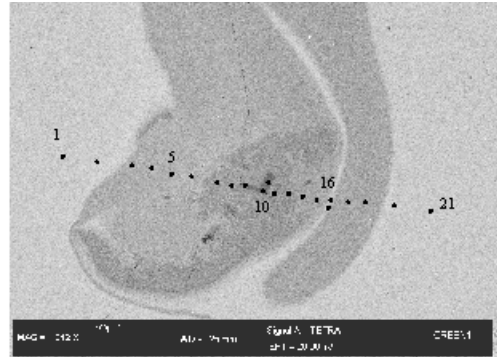


Figure 1. SEM backscatter image of Glass 1 showing the viscous sack lined by dendritic crystals of nephelinitic composition which encloses Al₂O₃ crystals (center of view). EDS analysis along the traverse shown here are presented in Table 1.

3.2 Glass 2

In this glass a viscous sack containing four and six-sided rhomb-shaped platelets were sectioned. SEM imagery showed skeletal growths, generally indicative of rapid crystal growth driven by super saturation, embedded in a flow deformed viscous sack (Fig. 2). The EDS analysis of the analytical traverse are presented in Table 2 and Figure 3. EDS analysis demonstrate the tabular crystals have a wollastonite composition whereas the viscous sack is generally Al₂O₃-rich (Sack 2, represented by squares in Figure 3). Variations exist in the composition of the viscous sack as evidenced by a nutrient deficient area bordering the wollastonite laths suggesting nutrients were consumed during crystal growth. The analysis of the sack plot in a line towards the composition of ordinary glass.

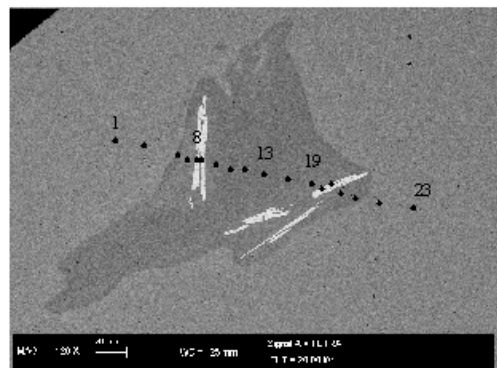


Figure 2. SEM backscatter image of Glass 2 showing the analytical traverse across the flow deformed viscous sack (dark grey) and enclosed elongate wollastonite crystals.

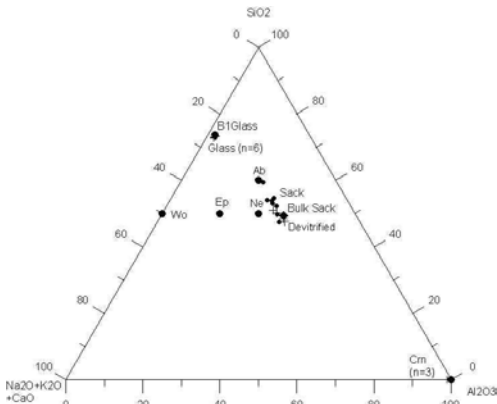


Figure 3. Ternary diagram of SiO₂-(Na₂O+CaO+K₂O)-Al₂O₃ of the analytical traverse in Glass 1 and 2. Indicated on the diagram is Crn=corundum, Ab=albite, Ne=nepheline, Wo=wolastonite, Mul=mullite, Musc=muscovite and Ep=epidote, DN=devitrified nepheline. B1Glass is the reference glass. Also shown : Sack 1 () , Sack 2 () and Bulk sack ()

3.3 Glass 3

SEM imagery showed the presence of nepheline hosting acicular crystals and granular relicts of corundum. The tabular shapes of nepheline crystals suggest *in situ* crystallisation, conforming to a devitrification origin. This is also consonant with the fact that they host the acicular corundum, also inferred to have a devitrification origin. The granular textured corundum, however, clearly show grain boundaries with 120° triple junctions indicative of textural equilibrium.

Table 1: Quantitative major element analysis of Glass 1

Spot	Phase	Na ₂ O	Al ₂ O ₃	SiO ₂	K ₂ O	CaO
1	G	12.89	2.00	72.45	0.87	11.24
2	G	12.27	2.08	72.80	0.80	11.57
3	S	14.30	25.09	53.87	1.29	4.95
4	S	13.87	31.64	47.28	0.97	5.95
5	S	12.46	21.39	59.18	1.27	5.19
6	S	13.10	26.96	52.78	1.02	5.66
7	D	13.97	28.11	50.76	0.93	5.69
8	D	15.66	32.88	47.64	0.81	2.85
9	C	bd	100.00	bd	bd	bd
10	C	bd	100.00	bd	bd	bd
11	C	bd	100.00	bd	bd	bd
12	D	16.39	32.27	48.64	0.97	2.02
13	D	16.30	29.60	50.09	1.08	2.74
14	S	15.21	28.47	52.02	1.50	2.37
15	S	15.64	29.85	49.63	1.12	3.37
16	S	12.63	5.21	71.08	1.02	9.51
17	S	12.67	3.85	71.14	0.74	10.91
18	S	14.87	26.50	53.75	1.35	3.20
19	S	14.58	26.74	54.52	1.52	2.51
20	G	13.08	1.84	73.72	0.85	10.80
21	G	12.78	2.43	72.98	0.77	10.71
22	G	13.20	2.03	72.64	0.96	11.05
23	G	12.94	2.19	72.95	0.85	10.63
B1	G	13.25	1.76	75.57	1.04	10.76

G=glass, S=sack, D=devitrified crystals, C=Corundum
bd= below detection limit

4 DISCUSSION

Analytical data show the presence of a mixing line between glass and the viscous sacks. The relative bulk composition of the sack plot between the compositions of devitrified nepheline (DN) and the varied compositions of the viscous sack in Glass 1. SEM imagery of Glass 2 showed skeletal crystal growths of wollastonite indicative of rapid crystal growth rather than contamination relicts. It could therefore be concluded that the source of contamination could not be tied to wollastonite contaminated feldspar raw material as the bulk composition of the sacks points to a more aluminous source, possibly refractory material used in the glass melting furnace.

Table 2: Quantitative major element analysis of Glass 2

Spot	Phase	Na2O	Al2O3	SiO2	K2O	CaO
1	G	12.66	1.91	74.16	0.74	10.25
2	G	12.27	1.42	73.97	0.64	11.51
3	S	12.28	19.87	61.81	1.05	4.50
4	S	12.49	19.19	62.74	1.22	4.34
5	S	9.57	8.55	72.42	0.81	7.71
6	S	9.00	9.48	72.89	0.78	7.31
7	W	<i>bd</i>	<i>bd</i>	52.38	0.03	47.51
8	W	<i>bd</i>	<i>bd</i>	52.23	0.09	48.05
9	S	10.51	14.82	67.97	0.98	5.60
10	S	10.20	13.75	68.38	0.86	5.88
11	S	12.02	19.90	62.64	0.91	4.19
12	S	11.90	20.88	60.93	1.22	4.46
13	S	11.73	18.52	62.79	1.08	5.07
14	S	11.79	20.40	61.70	1.23	4.27
15	S	11.50	20.11	62.26	1.19	4.47
16	S	11.35	19.23	62.46	1.07	5.51
17	S	11.13	18.04	64.06	1.10	5.18
18	S	10.68	14.73	67.15	1.07	5.98
19	W	<i>bd</i>	<i>bd</i>	51.60	<i>bd</i>	47.89
20	W	<i>bd</i>	<i>bd</i>	50.16	<i>bd</i>	49.63
21	S	10.99	14.21	67.74	1.03	5.84
22	S	11.66	14.78	67.62	1.20	4.62
23	G	12.76	1.46	74.49	0.75	10.46
24	G	12.85	1.83	73.98	0.80	10.45
25	G	12.78	1.68	74.42	0.86	10.19
26	G	13.05	1.68	74.19	<i>bd</i>	10.49

G=glass, S=sack, D=devitrified crystals, W=wollastonite
bd= below detection limit

5 REFERENCES

R.H. Domerus, *Glass SCIENCE*, John Wiley & Sons, Inc., New York, 1973

Application of Combined Cathodoluminescence and Energy-dispersive X-ray Spectroscopy for Analysis of Mineral Raw Materials

W.Vortisch

Institut für Geowissenschaften, Prospektion und Angewandte Sedimentologie, Montanuniversität Leoben, Leoben, Austria

ABSTRACT: Energy-dispersive X-ray spectroscopy (EDS) attached to the cathodoluminescence (CL) equipment enables the analyst to identify minerals and other components readily and simultaneously with CL and polarising microscopy. It is especially helpful when rapid analysis has to be carried out of samples of rocks or mineral raw materials with complex composition. Moreover, the instrumentation described here, can be used as a microprobe for easily mounted pellets of finely ground powders. The results rapidly obtained by this method represent reproducible data and are comparable to those obtained by EDS systems of scanning electron microscopes. The analytical procedure was successfully tested on thin sections, rock specimen and powders of various sedimentary raw materials and hydrocarbon reservoir rocks, containing transparent and opaque, as well as luminescent and non-luminescent minerals and rock fragments.

1 INTRODUCTION

The importance of thin section analysis carried out by means of polarising microscopy combined with cathodoluminescence (CL) microscopy has been proven for many years. For example, in applied industrial research related to mineral raw materials and hydrocarbon exploration (e.g. Houseknecht 1991, Götze 2000, He et al. 1997). A significant progress in this area can be seen in the possibility to combine this technology with simultaneous energy dispersive spectroscopy (EDS). Results obtained by combined CL-EDS analysis from a series of sandstone samples were recently published (Vortisch et al. 2003). The present publication is focusing on the application of this technology to the study of raw materials, including hydrocarbon reservoir rocks.

2 ANALYTICAL PROCEDURES

For simultaneous CL-EDS analysis of uncoated thin sections, rock slabs and powder pellets a cold cathode equipment combined with an energy dispersive X-ray detector was applied for the present study (manufacturer: CITL – Cambridge Image Technology Ltd.; for technical details see Vortisch

et al. 2003). Powder pellets were produced by pressing finely ground rock powder mixed with a small amount of distilled water on a glass slide. The CL-EDS equipment is used together with a standard polarising microscope. Thus polarising microscopy, CL and EDS can be carried out simultaneously. The EDS results are comparable to those obtained by an EDS system (with Be window) attached to a scanning electron microscope (SEM), except for the larger spot size ($< 100 \mu\text{m}$). Advantages, compared to the SEM (non-environmental), are the much easier handling (no coating, no high vacuum system) and the possibility of simultaneous light optical and CL observation, and also the lower price of the equipment.

3 SAMPLES ANALYSED

3.1 *Clinoptilolite (thin section, Figs. 1, 2)*

This sample was taken from a Slovakian economic sedimentary clinoptilolite deposit of Cenozoic age. The sodium content of this clinoptilolite deposit is very low (XRF whole rock analysis: 0.29% Na₂O). Considerable sodium concentrations were only found in feldspar grains (essentially plagioclase, potassium feldspar very rare) which represent almost

all luminescing grains in Figure 1. Quartz occurs only in trace amounts. The CL colour of the plagioclase grains is very uniform (between “moderate yellow green” and “moderate yellowish green” according to the “Rock-Color Chart” of Goddard et al. 1984). No CL could be observed on the very fine-grained clinoptilolitic matrix of this sample. EDS spectra of the clinoptilolitic matrix and a plagioclase grain are shown in Figure 2 (spectra 1 and 2). For comparison the EDS powder spectrum of another clinoptilolite sample (used as standard) with

3.60% Na₂O (XRF) is shown as well (Fig. 2, spectrum 5). With exception of sodium and calcium the chemistry of the Slovakian clinoptilolite is very similar to the one of the standard as is shown by the EDS spectra. Proportions of main elements by XRF: Slovakian clinoptilolite – 66.4% SiO₂, 12.2% Al₂O₃, 3.33% K₂O; standard – 66.8% SiO₂, 11.3% Al₂O₃, 3.74% K₂O.

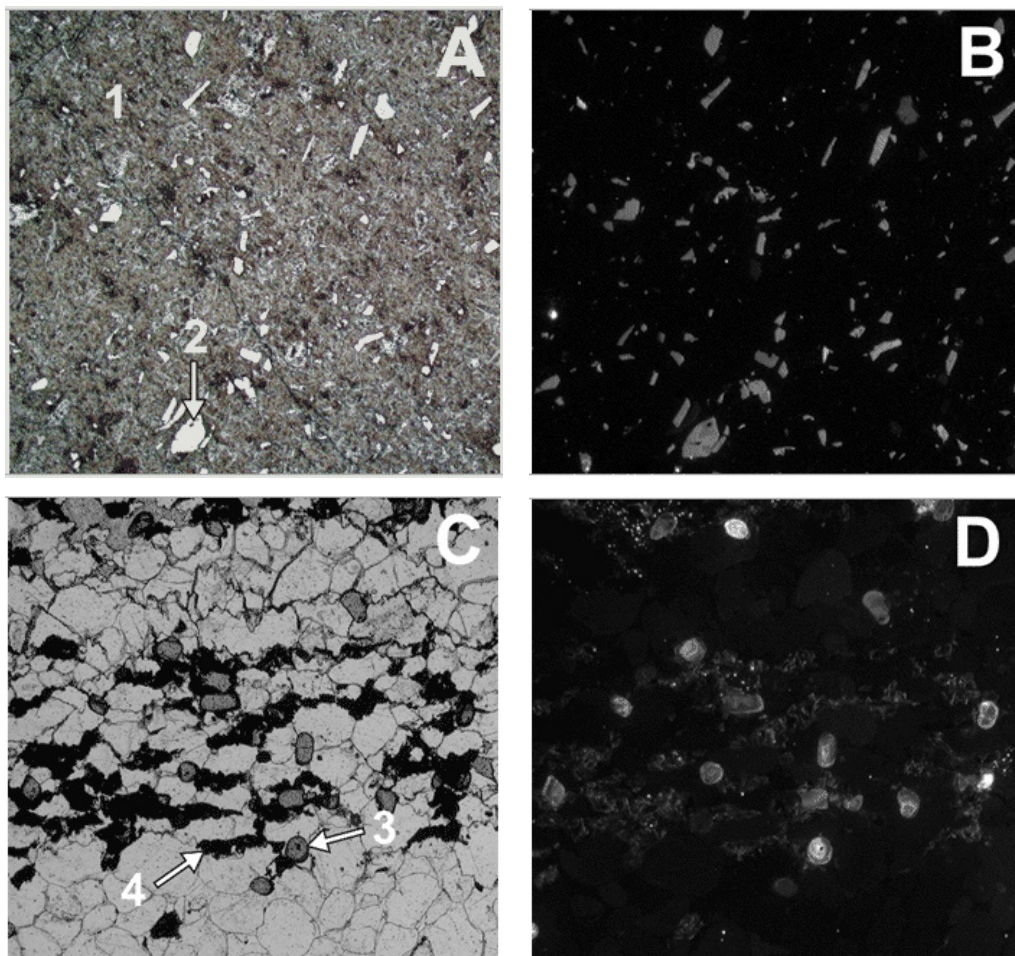


Figure 1. Optical (A, C; plane polarized light) and CL images (B, D) of thin sections (width of all images c. 3 mm). A: Clinoptilolite with feldspar grains (essentially plagioclase) which correspond to nearly all brightly translucent grains. B: CL image of A, showing essentially plagioclase (see text). C: Lower Cambrian heavy mineral placer, consisting mainly of quartz (detrital and cement, low relief, medium grey), detrital zircon (high relief, dark grey, example: arrow 3) and authigenic anatase (opaque in black and white copy, example: arrow 4). D: CL image showing mainly zircon grains. Anatase (originally greenish CL) in black and white copy only faintly visible. Very short exposure time in order to prevent overexposure of zircon, CL of quartz therefore not visible (detrital quartz and quartz cement can easily be differentiated in these sandstones by CL, see e.g. Vortisch et al. 2003, Fig.2).

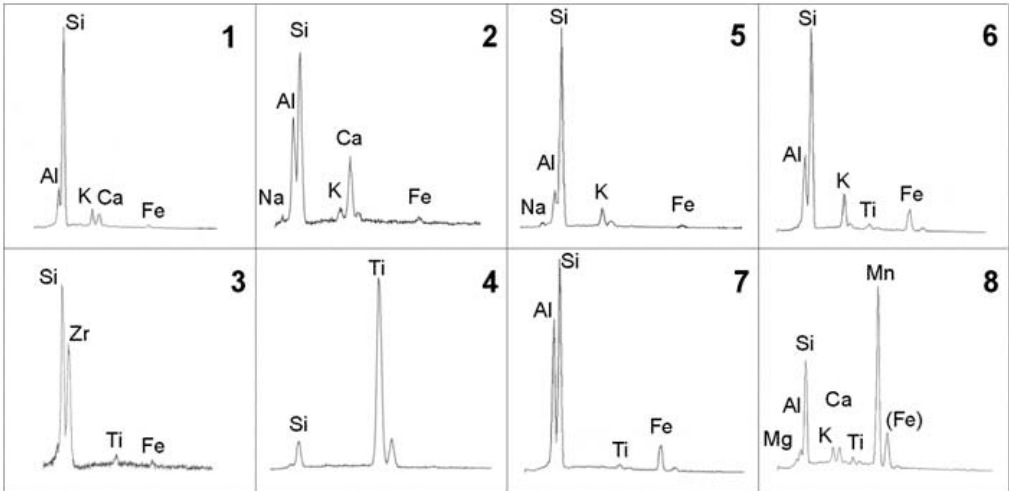


Figure 2: EDS spectra of thin sections and powders described in the text; with exception of zirconium (L peak) only K peaks (where K_{α} and K_{β} can be differentiated only K_{α} peaks) are indicated. 1: Slovakian clinoptilolite (paragraph 3.1); 2: plagioclase in 1; 3, 4: Lower Cambrian heavy mineral placer (3.2); 3: zircon (Si, Zr), with minor influence of neighbouring anatase (Ti) and ?iron staining (Fe, probably due to weathering influence); 4: aggregate of fine-grained anatase (Ti) with small amount of quartz cement; 5: standard clinoptilolite, powder, for comparison with 1; 6: red brick clay (3.3), powder; 7: red ceramic clay (3.4); 8: black ceramic stain (3.5); see text.

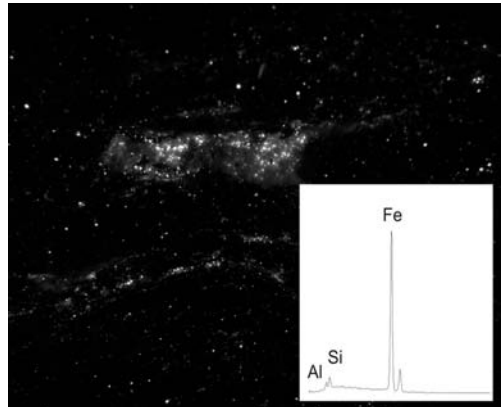


Figure 3: High grade iron ore from Minas Gerais, Brasil (paragraph 3.6). Left: hand specimen and analysed slab (right side), length of scale 4 cm. Right: CL in part of the slab, width of image 4.6 mm; between dots with bright luminescence: area of faintly blue luminescence (very faintly visible in black and white copy), inserted EDS spectrum from this area.

3.2 Heavy mineral placer (thin section, Figs. 1, 2)

The heavy mineral suite of this Lower Cambrian heavy mineral placer from South Sweden consists essentially of detrital zircon and diagenetically formed anatase, a wide-spread TiO_2 polymorph (Vortisch 1975). Zircon shows mainly light bluish CL colours with zoning in some grains, as noted by other authors (see e.g. Marshall 1988), whereas the anatase luminescence is greenish. Typical EDS spectra of these minerals are shown in Figure 2

(spectra 3 and 4). minerals optically similar to those identified here (e.g. monazite that might be similar to zircon) can easily be excluded by means of EDS.

3.3 Red brick clay (powder, Fig. 2)

Main elements of this clay from a German economic clay deposit are Si, Al, Fe and K (see spectrum 6). Proportions of oxides according to X-ray fluorescence analysis (XRF): 64.25% SiO_2 , 17.60% Al_2O_3 , 5.93% Fe_2O_3 , 4.29% K_2O , 4.35% LOI. The

chemical composition of this carbonate-free clay reflects the mineralogy determined by X-ray diffraction (XRD): dominant components are quartz and illite (in clays, the latter is the essential bearer of the flux potassium), occurring together with some kaolinite and hematite. Thus, technically important features of this clay can readily be recognised by EDS analysis of a powder pellet.

3.4 Red ceramic clay (powder, Fig. 2)

This clay is used for the production of traditional indigenous ceramics in a Costa Rican village. Main chemical components are only SiO₂, Al₂O₃ and Fe₂O₃. The relatively high content of aluminium besides dominant silicon as well as the absence of alcalies and alcali earths clearly indicate the main mineralogical components: kaolinite (dominant), quartz, and some hematite. This mineralogy was confirmed by XRD.

3.5 Black ceramic stain (powder, Fig. 2)

This material is applied for the staining of the indigenous ceramics mentioned above. It consists predominantly of manganese (Fig. 2, spectrum 8). As further elements with considerable proportions occur silicon, potassium, calcium, and with minor proportions titanium, iron (indicated FeK_α peak superimposed on MnK_β peak), aluminium and magnesium. Corresponding to the EDS spectrum the manganese minerals cryptomelane and bixbyite were identified by XRD as dominant mineral components. Moreover, quartz and traces of zeolite are visible in the diffractograms.

3.6 High grade iron ore (hand specimen, Fig. 3)

This hand specimen from an itabirite mine in Minas Gerais is almost purely composed of hematite. The analysed slab was cut off by means of a diamond saw. For analysis no further treatment was necessary. The combined CL-EDS analysis proved the existence of a variety of non-hematitic components. Minute lenses of whitish material revealed bluish CL (e.g. Houseknecht, 1991, Plate 5) and EDS spectra typical for clay minerals of the kaolinite subgroup: Si:Al ratios of 1:1, no measurable amounts of alcalies and alcali earths.

The CL-EDS features presented in Figure 3 indicate the admixture of finely dispersed quartz + clay minerals within the predominantly hematitic matrix. Besides these components, others containing sulfur or phosphorus were observed. More research will be carried out on this type of iron ore samples.

3.7 Hydrocarbon reservoir sandstones

CL-EDS analysis was applied for various reservoir sandstones. It proved to be extremely helpful for rapid petrographic analysis of sandstone thin sections. Both, clastic grains as well as cements are readily determined and quantifiable. In the case of carbonate cements the analytical conditions for establishing a cement stratigraphy are considerably improved.

4 CONCLUSIONS

The potential of combined CL-EDS analysis was tested for various raw materials and sedimentary rocks. Thin sections, unpolished rock slabs as well as easily mounted powder pellets, were studied without further treatment. Based on this test it can be stated that mineral raw materials as well as rocks in general can be analysed faster and with more accuracy by means of this technology. Moreover, it helps the analyst to understand more rapidly the samples he has to study, thus shortening the time of individual training.

5 REFERENCES

- Goddard, E.N., Trask, P.D., De Ford, R.K., Rove, O.N., Singewald, J.T. & Overbeck, R.M. (1984): Rock-color chart. Geol. Soc. America, Boulder, Colorado.
- Götze, J. (2000): Cathodoluminescence microscopy and spectroscopy in applied mineralogy. Freiburger Forschungshefte, C 485, Geowissenschaften, 128 pp.
- He, Z., Gregg, J.M., Shelton, K.L. & Palmer, J.R. (1997): Sedimentary facies control of fluid flow and mineralization in Cambro-Ordovician strata, southern Missouri. In: Montañez, I.P., Gregg, J.M. & Shelton, K.L. *Basin-wide diagenetic patterns: integrated petrologic, geochemical, and hydrologic considerations*. SEPM, Spec.Publ. 57, 81-99.
- Houseknecht, D.W. (1991): Use of cathodoluminescence petrography for understanding compaction, quartz cementation and porosity in sandstones. In: Barker, C.E. & Kopp, O.C. *Luminescence microscopy and spectroscopy: qualitative and quantitative applications*. SEPM, Short Course 25, 59-66.
- Marshall, D.J. (1988): Cathodoluminescence of geological materials. 146 pp, Boston (Unwin).
- Vortisch, W. (1975): Schwermineralkonzentrationen im Unterkambrium SO-Schonens (Schweden). Beobachtungen zur Sedimentation und Diagenese. N.Jb. Geol. Paläont. Abh. 150, 44-72.
- Vortisch, W., Harding, D. & Morgan, J. (2003): Petrographic analysis using cathodoluminescence microscopy with simultaneous energy-dispersive X-ray spectroscopy. *Mineralogy and Petrology* 79, 193-202.

Focused Ion Beam (FIB) Specimen Preparation in Applied Mineralogy and Geosciences

R. Wirth

GeoForschungsZentrum Potsdam, Department 4, Telegrafenberg, 14473 Potsdam, Germany

ABSTRACT: The focused ion beam (FIB) tool has been successfully used as both a means to prepare site-specific specimens for subsequent analysis by TEM, SEM and SIMS and a stand-alone instrument for micromachining of materials. The present paper focuses on the unique capability of the FIB instrument to prepare TEM foils from the specific location of interest in the specimen and the achieved results in applied mineralogy and in geosciences. The advantages and capabilities of FIB are demonstrated by several TEM studies on mineral and melt inclusions in crystals, on synthetic forsterite grain boundaries, coatings of a turbine blade from the hot section of a jet engine and finally by an example of micromachining diamond with FIB. Site-specific TEM foils with typical dimensions 20 x 10 x 0.150 micrometer can be cut from nearly any sample by means of a focused Ga-ion beam. The preparation of a TEM-ready foil with such dimensions takes about 4 hours, which is significantly faster than using conventional argon ion milling technique. A FEI FIB200 instrument has been operated at the GFZ Potsdam for two years, and TEM foils from many rock-forming minerals such as olivine, garnet, pyroxene, amphibole, quartz, apatite or glass, metals and alloys, ceramic materials and even microfossils have been successfully prepared and investigated by TEM. In conclusion, FIB substantially expands the application of TEM, AEM and EELS in applied mineralogy, geosciences and materials science.

1 INTRODUCTION

The original use of Focused Ion Beam (FIB) technique was that of a nano-technique in semiconductor industry. Already in 1993 FIB technique was successfully applied to the preparation of thin foils for TEM investigation Overwijk et al. (1993). The basic principle of FIB is the removal of atomic layer by atomic layer of material from a selected area in the specimen using Ga-ions accelerated to 30 kV. There are several good reasons to use a FIB for transmission electron microscope (TEM) foil preparation in applied mineralogy, geosciences and materials science. In the past it was often a demanding task for electron microscopists to prepare an electron transparent foil from just that volume they were interested in. Investigating thin sections of rocks or synthetic material by optical microscopy, mineralogists occasionally observe very small inclusions, which cannot be identified by optical or microprobe analysis. TEM is the appropriate technique to identify a particular inclusion; however, conventional specimen preparation techniques such as argon ion milling or electrochemical polishing will fail because of different hardness of the components. Very small specimens are used in

experiments with diamond anvil cells (DAC) and multi anvil devices and the chemical composition of the constituting phases needs to be analysed after the experiment. In such cases only with FIB a TEM foil can be prepared. Imagine a small single crystal (< 30 micron Ø) has been investigated by IR- or Raman spectroscopy. If it is too small to get oriented for X-ray diffraction and proper data evaluation needs the precise orientation of the sample with respect to the beam, then a TEM foil cut from that sample with FIB and subsequent diffraction analysis using TEM will rapidly solve that problem leaving material enough for further investigations.

Successful application of FIB in applied mineralogy, geosciences and materials science in combination with TEM methods is presented. After a short introduction into the technique (details cf. Overwijk et al. 1993; Young et al. 1998; Roberts et al. 2001; Heaney et al. 2001) the paper focuses on results, which could only be achieved using FIB.

2 DESCRIPTION OF FIB METHOD

Electron transparent foils for TEM investigations are prepared by FIB starting from uncovered thin sections, single crystals, polished pieces of rocks and

even from powder material embedded in epoxy resin. Semiconductors or insulators need carbon coating prior to FIB cutting. A FIB-prepared TEM foil is typically 10 - 20 micron wide, 5 - 15 micron high and 100 -200 nm thick. The final thickness can be less than 50 nm. Inelastic interaction of the ion beam with the sample creates secondary electrons, which are used to image the specimen or to monitor the cutting progress. The surface of the thin foil must be protected from erosion by the Ga-ion beam by a thin layer of platinum (1- 2 μm), which is deposited by decomposing an organic Pt-gas by the ion beam. Beam shift and sample drift are automatically controlled by the computer system using markers that have been cut into the surface of the sample near the final location of the foil as a reference. The first step of foil preparation excavates 10-15 micron deep trenches in front and in the back of the foil. Approaching a foil thickness of about 500 nm the specimen is tilted about 45° and the foil is cut on both sides and at the base, leaving only a small amount of material on both sides to stabilise the foil for final polishing to electron transparency. When the final thickness of about 100 - 150 nm is achieved, the foil is cut free completely by the ion beam and ready for lift-out (Fig.1).

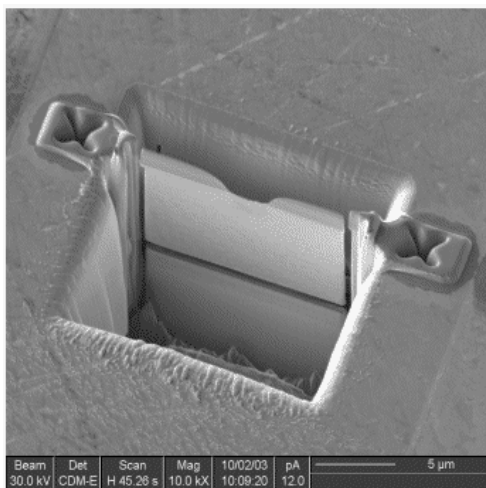


Figure 1 SE image of a FIB-cut foil ready for lift out.

The removal of the foil from the specimen is performed *ex situ* with the aid of an optical microscope equipped with a micromanipulator. The membranes are removed from the excavation site by a glass fibre using electrostatic forces and placed onto a TEM grid. The foil is now ready for TEM investigation and needs no further carbon coating.

3 RESULTS

3.1 Melt inclusions

FIB prepared specimens of melt inclusions in clino- and ortho-pyroxene from a mantle-derived garnet pyroxenite xenolith from Salt Lake Crater (Hawaii, Oahu) have been investigated by TEM. The melt inclusions represent trapped low-degree melt, which has metasomatised the Hawaiian mantle before eruption of the host magma. The inclusions consist of a C-Cl-S-rich glass of basaltic composition with polycrystalline aggregates of nanometer-sized diamonds coexisting with calcite and other nanocrystalline phases such as native Fe and Cu, FeS, FeS₂, ZnS, AgS and several Ti, Nb, Zr, Ir, In, Pd-rich phases of unknown composition (Wirth & Rocholl, 2003).

3.2 Mineral inclusions in diamond

Micro-inclusions in diamonds from the Diavik mine in Canada have been studied by TEM, analytical electron microscopy (AEM) and electron energy-loss spectroscopy (EELS). Detailed analysis of individual inclusions revealed the internal structure of single inclusions. Carbonate (Cc) and silicate phases (phlogopite) were determined by diffraction analysis and chemical analysis. The major advantage in using FIB-prepared TEM foils is the possibility to study the mineral assemblages in inclusions as nature has created them in contrast to the usual method of burning diamonds and investigating the residuum. In Figure 2 a typical idiomorphic phlogopite micro-inclusion is presented.

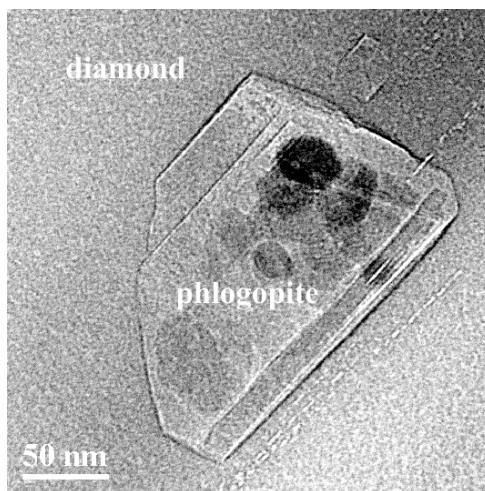


Figure 2. TEM bright field image of a phlogopite crystal included in diamond from Diavik mine, Northern Canada.

3.3 Synthetic grain boundaries in forsterite

Recently synthetic K-feldspar grain boundaries were produced for the first time by diffusion bonding (Heinemann et al. 2003). The same bonding technique was applied to forsterite and tilt grain boundaries with different angles (9°, 12°, 15° and 21°) were synthesised. TEM foils were FIB-cut normal to the grain boundary and polished to a homogeneous thickness of about 150 nm. Additionally, an area of approximately 2-3 micron left and right of the boundary plane was polished to a final thickness of about 70 nm, which is suitable for high-resolution electron microscopy (HRTEM). In contrast to conventional argon ion milling, the FIB technique avoids preferential thinning of the interface region and therefore the HRTEM image can be interpreted much easier. The TEM investigations of forsterite bicrystals reveal that in contrast to observations with metals, dislocations are visible up to a misorientation of 21° of the two grains, and their cores do not yet overlap. In metals the transition from low-angle to high-angle grain boundaries is in the range of 10° to 15°. Burgers vector of the edge dislocations in the forsterite grain boundary is *c*. Increasing the tilt angle of the two grains, the spacing of the dislocations decreases. This result gives a new insight in the structure of silicate grain boundaries.

Another application of FIB in grain boundary studies is demonstrated by diffusion studies on isotopically doped thin films on olivine. Grain boundary diffusion in enstatite-rich pyroxene was studied in pulsed-laser deposited thin films (Milke et al. 2003). The knowledge of the film thickness and the microstructure of the grains in the film are crucial for that kind of experiments. TEM foils cut normal to the film surface by FIB, easily answered these questions.

3.4 FIB application with fossils

Etched cross sections through fibres of a deep sea sponge (*monorhaphis chuni*) exhibit concentric bright and dark rings in the SE images. TEM investigation reveals the nature of the rings. Therefore, TEM foils were cut normal to the rings in such a way that one foil contains one dark ring and two bright rings and vice-versa. The investigations showed that the bright rings are composed of water-containing amorphous silica, whereas the dark rings are mainly organic material that could be mapped with EELS using the Carbon K-edge. The microstructure of the fibre suggests the fibre to be a natural composite material inhibiting crack growth and failure of the fibre.

3.5 Coatings on jet engine turbine blades

Fractography of electron beam plasma vapor deposited EB-PVD TBC coatings from jet engine turbine blades has shown that failure is closely related to the flaw size distribution and the particular phase assemblages of the thermally grown oxide (TGO) layer. The TGO layer comprises a coarse-grained corundum bottom layer close to the bond-coat followed by a fine-dispersed mixed zone consisting of alumina and zirconia adjacent to the thermal barrier coating (TBC). The dynamic pattern of coexisting phases during nucleation and thickening of the TGO layer obtained via FIB cut foils by TEM investigation is supplemented by thermodynamic and constitutional considerations. The microstructural model so derived emphasises that the microstructural approach as pursued in this study is mandatory for TBC lifetime assessment (Fritscher et al. 2004).

3.6 Micromachining of diamonds

We recently used the FIB instrument at the GeoForschungsZentrum, Potsdam to micromachine diamond anvils in a hydrothermal diamond anvil cell. The hydrothermal diamond anvil cell (HDAC) was designed and constructed specifically for the purpose of making observations on fluid and fluid plus solid samples at high temperatures and pressures. Bassett et al. (2000) and Anderson et al. (2002) modified the HDAC by laser drilling a sample chamber and grooves into the diamond anvil to enhance the transmission of X-rays entering and exiting the fluid sample chamber. Precise milling of diamond with a FIB is useful for removing the exact amount of diamond to optimise x-ray transmission without compromising the strength of the anvil.

It is also important in X-ray spectroscopic experiments with the HDAC to observe phase behaviour within the sample chamber as temperature and pressure is changed. However, the optical quality of a laser ablated sample chamber is generally poor due to the irregular surface of the floor. This problem is overcome by milling a sample chamber with a focused ion beam. Figure 3 shows a pit (114 X 108 X 65 micrometers) that was cut within 114 hours (FEL FIB200, Ga-source, 30kV, 11500pA). The smooth floor produced by FIB milling provides excellent observation of the contained sample using a transmitted light microscope. The precise machining of diamond as shown here opens new opportunities for designing diamond anvils to be used with various in situ microanalytical probes.

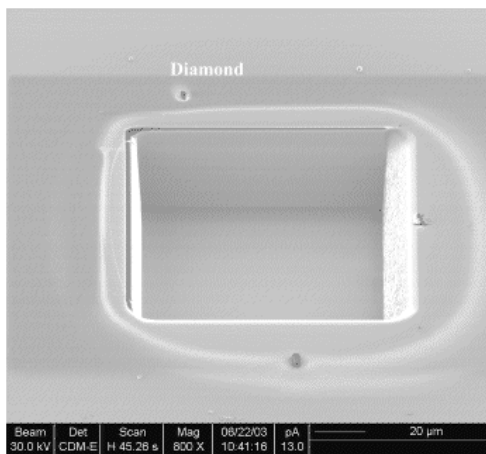


Figure 3. SE image of a diamond. The pit has been milled by FIB (image tilted about 45°).

Young, R.J., Carleson, P.D., Da, X. and Hunt, T. (1998) High-Yield and high-throughput TEM sample preparation using focused ion beam automation. Proceedings 24th Int. Conference for Testing and Failure Analysis, 15-19 November 1998, Dallas, Texas.

4 REFERENCES

- Anderson, A.J., Jayanetti, S., Mayanovic, R.A., Bassett, W.A. & Chou, I-M. (2002) X-ray spectroscopic investigations of fluids in the hydrothermal diamond anvil cell: The hydration structure of La³⁺ from ambient to 300 °C and 1600 bars. *American Mineralogist*, 87, 262-268.
- Bassett, W.A., Anderson, A.J., Mayanovic, R.A. & Chou, I.M. (2000) Hydrothermal diamond anvil cell for XAFS studies of first-row transition elements in aqueous solution up to supercritical conditions. *Chemical Geology*, 167, 3-10.
- Fritscher, K., Braue, W., Schulz, U., Leyens, C. and Wirth, R. (2004) Nucleation and growth of oxide constituents on NiCoCrAlY Bondcoats during different stages of EB-PVD TBC deposition and upon thermal loading. Abstract, 6th Int. Symposium High Temp. Corrosion and Protection of Materials, Les Embieux, France
- Heaney, P.J., Vicenzi, E.P., Giannuzzi, L. and Livi, K.J.T. (2001) Focused ion beam milling: a method of site-specific sample extraction for microanalysis of Earth and Planetary materials. *Amer. Min.* 86, 1094-1099.
- Heinemann, S., Wirth, R. and Dresen, G. (2003) TEM study of a special grain boundary in a synthetic K-feldspar bicrystal: Manebach twin. *Phys. Chem. Minerals*, 30, 125-130.
- Milke R., Dohmen, R., Wiedenbeck, M., Wirth, R., Abart, R. & Becker, H-W. (2003) Rim growth experiments in isotopically doped thin films: grain boundary diffusion on a nano scale. *Europ. Journal of Mineralogy, Beiheft*, 15, 130.
- Overwijk, M.H.F. & van den Heuvel, F.C. (1993) Novel scheme for the preparation of transmission electron microscopy specimens with a focused ion beam. *Journal of Vacuum Sci. & Technology*, B11, 2021-2024.
- Roberts, S., McCaffrey, J., Giannuzzi, L., Stevie, F. and Zaluzec, N. (2001) Advanced techniques in TEM specimen preparation. In: Xiao-Feng Zhang and Ze Zhang (Eds.) *Progress in Transmission electron microscopy*, Springer Series in Surface Sciences 38, Springer.
- Wirth, R. and Rocholl, A. (2003) Nanocrystalline diamond from the Earth's mantle underneath Hawaii. *Earth and Planetary Science Letters*, 211, 357-369.

Biominerals and Biomaterials

Degradable Bone Substitution Material Based on Cellular Ca-phosphates

F.Goetz-Neunhoeffler, R.Enderle, M.Göbbels, J.Neubauer

Institute of Geology and Mineralogy, University of Erlangen-Nuremberg, Germany

J.Zeschky

Department of Material Science, University of Erlangen-Nuremberg, Germany

ABSTRACT: The objective of the study was to synthesize cellular composites of Hydroxy Apatite (HAP) and β -Tricalcium-Phosphate (TCP) for application as bone constitution material. In a first step of the presented investigation different starting compositions for synthesis by solid-state process of HAP-TCP-composites were selected. Phase compositions of the synthesized ceramic composites were investigated by X-ray powder diffraction analysis. The different phases were additionally quantified and characterized for their crystallite sizes by Rietveld refinement using TOPAS 2.1 with fundamental parameter approach. Additionally stereological data from computerized micro-tomography of selected composites were collected and interpreted.

1 INTRODUCTION

Bone constitution material is used very widely for implantation surgery. Further improvement of the available materials is required with respect to degradation behavior and the possibility of depositing organic substances, which favor the healing process after implantation. For that reason we have synthesized an intelligent, cellular structured bone constitution material with two different functions.

Firstly the calcium phosphate containing material must have a cellular structure for fluid transportation purposes and should offer the possibility of infiltration by bone growth and differentiation factors and other organic components, which can be released time controlled.

Secondly the Calcium phosphate must be degradable to be displaced by newly generated bone. By this double functionality a very effective depot material for bone regeneration processes can be provided.

The evolutionary bone building processes are adapted by a synthetically produced and organically modified composite of Hydroxy Apatite (HAP) and β -Tricalcium-Phosphate (TCP). The cellular structure of the HAP-TCP-composite is corresponding with the structure in a naturally grown human bone and is offering very favorable conditions for its inte-

gration and a directed growth of blood vessels from outside to inside the composite.

By modification of porosity an ideal cellular structure can be produced, which is optimized for permeability purposes and at the same time it still disposes of enough compressive strength to fill the cavity after implantation for a certain time. With organic modification of the inorganic HAP-TCP-composite degradation of the Ca-phosphates and also bone regeneration process can be strongly influenced.

In the first step the chemical composition of the ceramic HAP-TCP-composites was optimized to get defined phase compositions. The foaming process was controlled by water to solid ratio in the slurry, which is leading to different porosities in the precursor material for the ceramic sintering process. Reconstructed data from computerized tomography were derived in order to optimize fractional and connectivity densities.

2 EXPERIMENTAL PROCEDURE

2.1 Synthesis of calcium phosphates

Pure phases of HAP and TCP were synthesized from reagent grade chemicals in a laboratory furnace in air. The quenched samples were ground several times in a disk mill (agate) during synthesis procedure.

The ceramic cellular HAP-TCP composites were sintered at 1250 °C for 2h.

2.2 XRD-characterization of syntheses products

All samples were characterized by XRD powder methods with $\text{CuK}\alpha$ radiation. For examinations a SIEMENS D5000 diffractometer equipped with a diffracted beam graphite monochromator using the following adjustments was applied in continuous step mode with fixed slits (Tab. 1).

Table 1: Instrument parameter for quantitative X-ray powder diffraction analysis

Generator: 30mA/40kV	Detector slit: 0.2mm
Tube: fine focus	Detector: scintillation
X-ray: $\text{CuK}\alpha$	Step/Time: 0.02°/4s
Slits: fixed = 0.5°	Range: 5-75° 2 θ

Preparation of the investigated samples was standardized. All samples were ground in a disc mill (agate) and sieved <25 μm to get the required grain sizes for X-ray powder diffraction. Front-loading sample holders were utilized for preparation.

The following Table 2 summarizes the ICSD-codes of the structural data (ICSD 1995), which were used for the Rietveld refinement of synthesized phases.

Table 2: ICSD-Data used for Rietveld refinement and quantification

Phase	Starting data	
	ICSD-Code	Authors
β -C ₃ P (Calcium phosphate)	73712	Boudin et al. (1993)
HAP (Hydroxyapatite)	87668	Wilson et al. (1999)
β -TCP (Whitlockite)	6191	Dickens et al. (1974)
C ₄ P (Hilgenstockite)	2631	Dickens et al. (1973)
α -TCP (Tricalcium phosphate)	923	Mathew et al. (1977)

2.3 Rietveld quantification of HAP and β -TCP

Accuracy (absolute error E_a) and precision (standard deviation s) of Rietveld quantification for HAP-TCP phase compositions was verified on five different synthetic mixtures, which were prepared from the pure synthetic phases HAP and β -TCP.

Measurement of eight independent preparations led to the determination of accuracy and precision. All other quantification results are average values from at least five independent preparations followed by Rietveld refinement of XRD-patterns. From the statistical evaluation of different synthesized samples purity of calibration samples and determination limits of all possible minor phases could be obtained, which was always lower than 0.24 ma.%.

Table 3: Purity of calibration samples for calibration of quantification

Phase	Purity [ma.%]
β -C ₃ P	99.9 \pm 0.1
HAP	99.8 \pm 0.2

The software TOPAS 2.1 with fundamental parameters approach was employed for Rietveld refinements.

Refined parameters were: scale factor, zero displacement, background as Chebyshev polynomial of the 5th grade together with $1/X$, crystallite size, micro strain, and lattice parameters; occupancy factors were included in case of refinement of solid solutions of β -TCP with minor MgO. All parameters were refined simultaneously.

2.4 Controlling and characterization of porosity

For our investigation metallic Al-powder was used as foaming agent. The concentration and size of Al-powder was constant and only the ratio of water to solid was changed in the foaming process to get different porosities in the cellular bodies. The sintered cellular ceramic composites were investigated with respect to their porosities. Additionally cell morphology of four samples was investigated by computerized tomography (μCT 40, Scanco Medical AG, Bassersdorf, CH) with an X-ray tube operating at 40 kV and 80 μA at a wavelength of 0.024 nm. The specimens were scanned in a near isotropic resolution of $37 * 37 * 38 \mu\text{m}^3$. A CCD line array was used to detect the transmitted intensity through the sample. X-ray source and detector were covered with slit collimators. The object was rotated over 360° with one step per degree and the raw data was recorded as sinograms.

Two-dimensional reconstructions of the slices were calculated from the sinograms by Radon back transformation using a Compaq DC10 Alpha workstation. From the 2D images the fractional density ρ_f was calculated as the ratio of transmitted material in the measured slice to the complete slice. A three dimensional reconstruction of the examined volume of interest (VOI) was obtained by stacking the 2D images.

The morphometric structure model index (SMI) was calculated from the three dimensional tomographic data. The SMI was introduced for quantification of bone micro architecture and can be used for foam structure analysis to characterize the shape and anisotropy of cellular materials as well (Hildebrand & Rüegsegger 1997). The SMI is calculated according to:

$$SMI = 6 \cdot \frac{V \cdot \frac{dS}{dr}}{S^2} \quad (1).$$

S is the strut surface in a volume V and dS/dr is the surface area derivative. The foam surface area is rendered by triangulating the surface of a specific VOI with the Marching Cubes method and the volume is defined by setting up polyhedrons inside the VOI that match the bounding surface triangles. A SMI value of 4 describes spherical pores, any deviation of the spherical cell geometry results in lower values. A rod cell structure is described by a SMI value of 3 and plate pores have a SMI of 0. Negative SMI values result from cells with concave surface areas, which is common if coalescence of pores takes place.

The surface/volume ratio and strut thickness were calculated using the distance transformation (DT) method as described in Guilak (1994).

Degree of anisotropy (DA) is calculated by the maximum value of the three axes (H1, H2, H3) divided by the lowest value of the three axes (Hildebrand & Rüeggsegger 1997).

3 RESULTS

3.1 Structural refinement of β -TCP and HAP

A method for quantitative phase analysis for β -TCP and HAP is required to control the phase composition of the sintered ceramic composites of HAP and β -TCP. Different quantitative phase contents are strongly influencing mechanical properties and degradation behavior of the ceramic composites. The developed quantification method on the one hand can be applied to optimize the mechanical properties. On the other hand structural data from the same refinement procedure can be interpreted with respect to crystal sizes.

Results of Rietveld refinement of TCP were derived from coupling of ten XRD-diagrams by using starting data of Dickens et al. (1974) for β -TCP (Tab.4).

Table 4: Results of coupled refinement of β -TCP-synthesis with starting data of Whitlockite (ICSD-No. 6191)

Space group R 3 cH	Refined parameter
a [10^{-10} m]	10.4324 \pm 0.0007
c [10^{-10} m]	37.383 \pm 0.004
Crystal size L [nm]	1305
Micro strain	0.047
R _{Bragg}	7.48

Rietveld refinement of synthesized pure HAP, which was obtained from coupling of ten XRD-diagrams by using starting data of Hydroxy Apatite of Wilson et al. (1973), is shown in Table 5.

Table 5: Results of coupled refinement of HAP-synthesis with starting data of Hydroxy Apatite (ICSD-No. 87668)

Space group P 6 ₃ / m	Refined parameter
a [10^{-10} m]	9.4150 \pm 0.0003
c [10^{-10} m]	6.8839 \pm 0.0007
Crystal size L [nm]	709
Micro strain	0.025
R _{Bragg}	6.25

3.2 Calibration of quantitative phase analysis

Accuracy (absolute error E_a) and precision (standard deviation s) of Rietveld quantification was verified on three different synthetic mixtures, which were prepared from pure HAP and β -TCP. Eight independent measurements led to determination of the plotted values in Figure 1. The values for accuracy of β -TCP in the mixes was always better than 1.2 ma.%. The determined maximum value for precision s is not exceeding 1.6 ma.% (Tab.6). This shows the very good quality of quantitative phase analysis by Rietveld method.

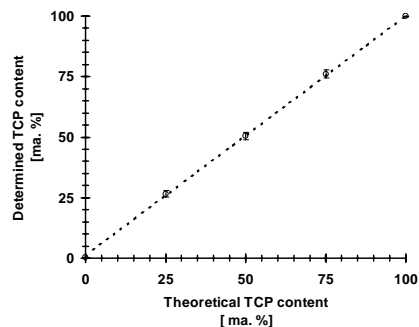


Figure 1: Calibration curve for β -TCP in β -TCP-HAP mixes

Table 6: Calibration data of mixes of β -TCP and HAP

β -TCP/HAP ratio in mix	Calculated β -TCP [ma.%]	Calculated HAP [ma.%]
100:0	99.9 \pm 0.1	0.1 \pm 0.1
75:25	76.1 \pm 1.6	23.9 \pm 1.6
50:50	50.5 \pm 1.5	49.5 \pm 1.5
25:75	26.6 \pm 1.4	73.5 \pm 1.4
0:100	0.2 \pm 0.2	99.8 \pm 0.2

3.3 Synthesis and mineralogical characterization of cellular β -TCP-HAP-composites

By modification of porosity an ideal cellular structure can be produced. Both is favorable for permeability and degradation of calcium phosphates.

The influence of phase composition together with porosity controlled by water to solid ratio (w/s-value) was another aspect of this investigation.

Characterization of cell morphology was performed by μ CT-investigations. The derived stereological data for four different porous materials were evaluated (Tab. 6).

Fractional density is increasing with w/s-value from 0.7 to 1.0. Surface per volume is fairly constant. SMI values below and around 0 are indicating very concave elongated pores. The pores are elongated along the XY-plane (Fig. 2 and 3).

H1, H2, and H3 in Figures 2 and 3 are showing the orientation of the three axes of the ellipsoidal shaped pores.

Table 7: Stereological data of β -TCP cellular ceramic (w/s= 0.7 to 1.0) after sintering at 1250°C

w/s-value of foaming process	0.7	0.8	0.9	1.0
Fractional Density [%]	63	67	66	79
Surface/Volume [1/mm]	11.1	12.6	11.1	11.1
Structure Model Index (SMI)	-1.4	-0.9	-1.1	0.3
Degree of Anisotropy (DA)	1.37	1.18	1.27	1.39

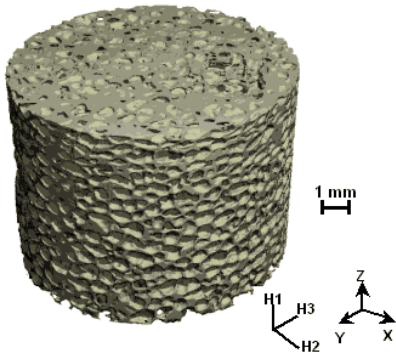


Figure 2: Three-dimensional micro computer tomographic (μ CT) reconstruction of β -TCP cellular ceramic (w/s= 0.7) after sintering at 1250 °C

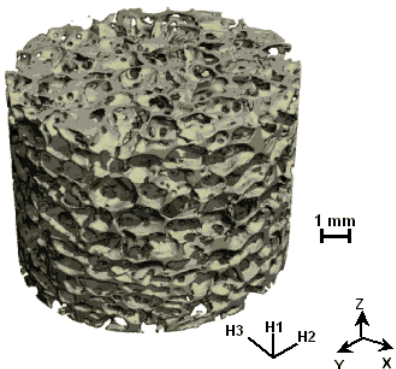


Figure 3: Three-dimensional micro computer tomographic (μ CT) reconstruction of β -TCP cellular ceramic (w/s= 1.0) after sintering at 1250 °C

4 CONCLUSIONS

Quantification of phase composition in cellular ceramic β -TCP/HAP-composites is a very powerful tool for optimizing synthesis conditions of the foaming and sintering processes. Quantitative data are required for determination of the changes in phase contents of degraded cellular TCP-HAP-composites from in-vitro experiments at pH 4.4, simulating osteoclastic processes. Phase specific resorption effects can be correlated with the rate of dissolution of β -TCP and HAP in the ceramic composites. The results are very interesting with respect for changes in the high temperature process of synthesis

The cellular structure with respect to porosity and permeability can be tailored by changing w/s-values during the foaming process. The interesting stereological values from human bone samples (Merz & Schenk 1970, Shors & Holmes 1993) show porosities of 75 - 80% compared to the investigated TCP-samples that show slightly smaller values ranging from 63 - 79 %. Very similar data for surface per volume compared with TCP samples could be calculated from micro-CT-analysis: TCP 11-13 mm^{-1} and human bone 17 mm^{-1} (Soldner & Herr 2001).

5 REFERENCES

- Boudin, S. et al. 1993. Redetermination of the beta- $\text{Ca}_2\text{P}_2\text{O}_7$ structure. *Acta cryst. (C)* 49: 2062-2064
- Dickens et al. 1973. $\text{Ca}_4(\text{PO}_4)_2\text{O}$, tetracalcium diphosphate monoxide. Crystal structure and relationships to $\text{Ca}_5(\text{PO}_4)_3\text{OH}$ and $\text{K}_3\text{Na}(\text{SO}_4)_2$. *Acta cryst. (B)*. 29: 2046-2056
- Dickens et al. 1974. Crystallographic studies of the role of Mg as stabilizing impurity in beta- $\text{Ca}_3(\text{PO}_4)_2$ I. The crystal structure of pure beta $\text{Ca}_3(\text{PO}_4)_2$. *J. of solid state chemistry*. 10:232-248
- FIZ Karlsruhe, ICSD, Inorganic Crystal Structure Database, 1995
- Guilak, F. 1994. Volume and Surface Area of viable Chondrocytes in situ using Geometric Modelling of Serial Confocal Sections. *Journal of Microscopy*, 173: 245-256.
- Hildebrand, T. & Rüegsegger, R. 1997. Quantification of Bone Microstructure with Structure Model Index. *Computer Methods in Biomechanical Engineering*, (1): 15-23
- Hildebrand, T. & Rüegsegger, R. 1997. A new Method for the Model-independent Assessment of Thickness in three-dimensional Images. *Journal of Microscopy*, 185 (1): 67-75
- Mathew et al. 1977. The crystal structure of alpha- $\text{Ca}_3(\text{PO}_4)_2$. *Acta cryst. (B)*. 33 : 1325-1333
- Merz, W. & Schenk, R. 1970. Quantitative structural analysis of human cancellous bone. *Acta anatomica* 75: 54-66
- Shors, E. & Holmes, R. 1993. Porous Hydroxyapatite. In: Hench, L. Wilson, J. (eds.) *An Introduction to Bioceramics*, Vol.1. World Scientific Publishing, Singapore: 181-198.
- Soldner, E. & Herr, G. 2001. Knochen, Knochentransplantate und Knochenersatzmaterialien. *Trauma und Berufskrankheit* 3: 256-269.
- Wilson et al. 1999. Rietveld refinement of the crystallographic structure of human dental enamel apatites. *Am. Mineralogist*. 84: 1406-1414

Calcium Carbonate Polymorphism in Shells of the Mollusc *Physa* sp.

S.M. de Paula & M.Silveira

Electron Microscopy Laboratory, Physics Institute, University of São Paulo, São Paulo, Brazil

ABSTRACT: The complex process of biomineralization is being studied with increasing interest recently, regarding the possibility of devising new materials for technological applications. Nature provides many mineralizing organisms, that produce inorganic deposits with hard and complex structures (Addadi & Weiner 1997). Mollusk shells have a complex microstructure as a result of an organized arrangement of crystals, grown upon an organic matrix. Different crystals of CaCO_3 are deposited along different sites on the inner surface during growth of the shell. They occur mostly as calcite and/or aragonite (Watabe 1984), and to a lesser extent as vaterite polymorphs (Kato 2000; Lowenstam 1981). In this work we have investigated by scanning electron microscopy the calcium carbonate polymorphism in shells of the freshwater mollusk *Physa* sp. (Gasteropoda) ranging in size from 0,5 mm to 10 mm. Crystals with different habits occur in the several sites examined: rhombohedra, hexagonal plates and prisms, in addition to spherulitic and disk-shaped crystals. All these different crystal habits were found in regions near the apex; spherulites occur in the inner surface of the apex itself, whereas in the juvenile *Physa* sp. (0,5 mm) only the circular units were observed so far on their outer surface. The mineral phases were analysed by X-Ray diffraction and the data refined with the Rietveld method, and by Fourier transform infrared spectroscopy (FTIR), demonstrating the presence of only aragonite.

1 INTRODUCTION

Biomineralization is a common process in nature, through which the organisms convert ions in solution into solid minerals (Simkiss & Wilbur 1989). Mineralizing organisms are able to synthesize a variety of biominerals with different habits, the calcium carbonate being the most abundant one (Sikes & Wheeler 1988): it occurs as calcite, aragonite and vaterite (Falini et al. 1996).

In this work we have investigated some aspects of the biomineralization process in shells of the mollusc *Physa* sp. This organism provides an interesting system for such studies for it is able to build arrangements of calcium carbonate crystals that grow quite rapidly.

The crystal regularity, orientation and mechanical properties of mollusc shells bear an intimate relation to organic matrix (Addadi & Weiner 1997), known to contain aminoacids, proteins and polysaccharides (Weiner 1979).

2 MATERIALS AND METHODS

The pulmonate freshwater *Physa* sp. is a mollusc of the Class Gasteropoda. The shell has the shape of a cone (Rhoads & Lutz 1980) about 10-15 mm wide.

Animals raised in small aquaria at about 26 °C were used throughout the present work.

To investigate the mineral phase, shell fragments were ground in a mortar, the resulting powder was passed through a 200 mesh sieve and analyzed by X-Ray (powder method) using an X-pert MPD Philips diffractometer. The data were collected in steps of 0.02° at scattering angles (2θ) ranging from 20 to 90°. The FTIR analyses were performed with a Nicolet 560 FTIR spectrometer and were recorded at 4 cm⁻¹ resolution. Aliquots of the powder were included in KBr pellets for these essays.

For scanning electron microscopy (SEM), shells between 0,5-10 mm in height were carefully removed from the mollusc and washed in distilled water for 12 hours; shells larger than 2 mm in length were cleaned with 40% NaClO (sodium hypochloride) solution for 24 h to removed the organic matter.

Partly decalcified samples were prepared by use of either 2% EDTA (ethylenediamine tetraacetic acid) or 1 mol.L⁻¹ HCl.

All samples were dried at room temperature for 12 h, mounted on the stub with silver paste and gold-sputtered for morphological studies with the Jeol JSM 840-A electron microscope, operated at 12, 15 or 25 kV.

3 RESULTS

Our X-ray diffraction results indicate high crystallinity for the calcium carbonate, further identified as aragonite used the Rietveld refinement (Figure 1) and FTIR spectroscopy (Figure 2).

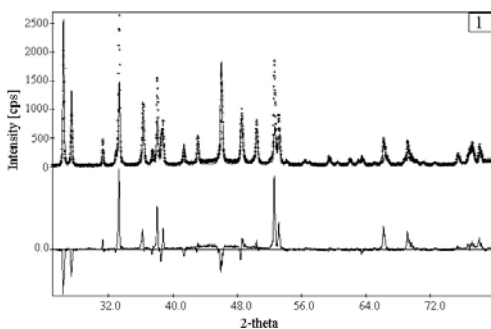


Figure 1: Rietveld refinement of diffraction pattern of the shells, demonstrating the typical spectrum of aragonite.

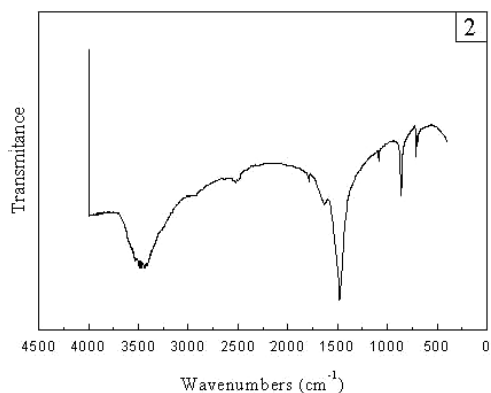


Figure 2: Infrared spectrum showing peaks characteristic of aragonite.

Scanning electron microscope studies presented interesting structures in the shells.

Shells in the initial stages of development showed an arrangement of circular units, about 1.6 μm in diameter (Figure 3) all along their external surface.

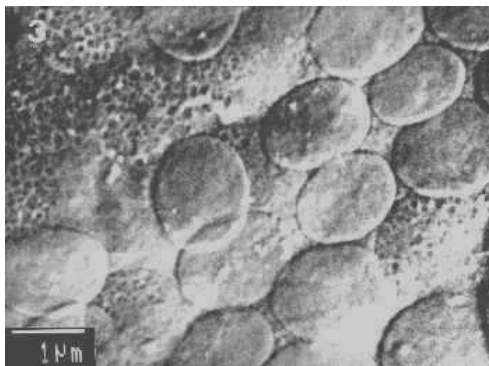


Figure 3: Arrangement of the circular units covering the external surface of a shell (distilled water). x 15,000

Shells ranging between 5-9 mm in height showed many spheres about 1 μm or less in the apex (Figure 4).

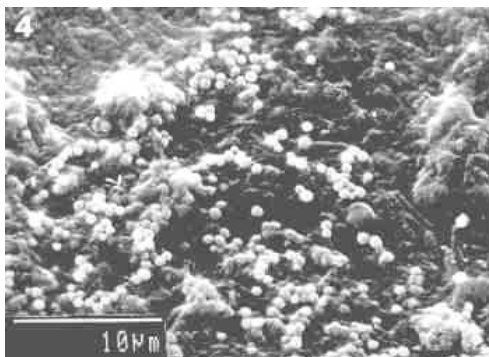


Figure 4: Spheres of calcium carbonate (2% EDTA for 1.5 min). x 2800

Crystals exhibiting a greater variety of forms and habits occur along the columella (Figure 5) and near the apex of the shells (Figures 6 and 7).

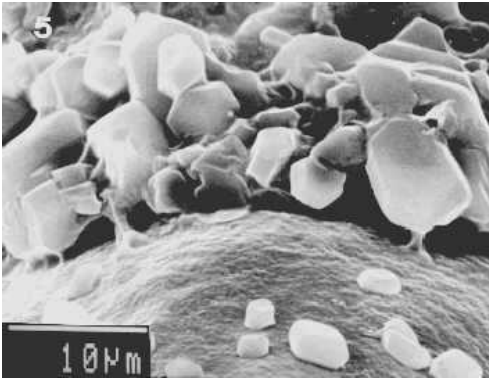


Figure 5: Aragonite crystals found in the columella. x 1800

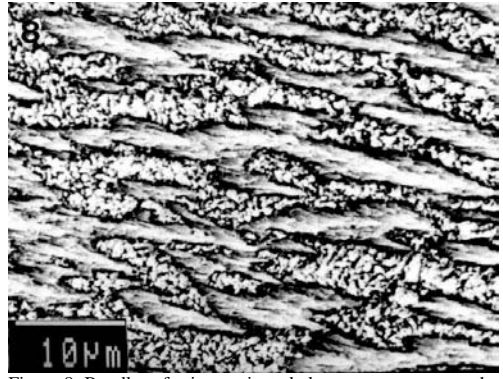
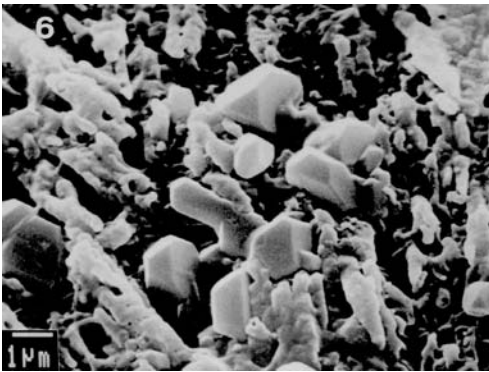


Figure 8: Bundles of prisms oriented along two axes cover the inner surface of the shell, near its opening (1mol.L⁻¹ HCl for 5 min.). x 1600



Figures 6 and 7: Crystals with the most different habits (NaOCl for 24 h). x 7500

Other regular, characteristic arrays crystals occur in the inner surface near the aperture of the shell (Figure 8).

We have found prismatic aggregates with a relatively uniform orientation in the inner surface of the *Physa* sp. The orientation of the prisms is relatively constant for every shell of a same species, and characteristic for the species (Boggild in Watabe 1984).

In our material, both X-ray diffraction and the infrared spectra demonstrate that aragonite is the main inorganic phase. So far, we have no information about the organic composition of this shell.

We could demonstrate here, several polymorphs in different sites of the shells. The mechanisms by which crystal polymorphism occurs are not well understood, but the crystal growth is known to keep an intimate linkage with the organic matrix. Factors as temperature and salinity also influence crystalline habits.

4 DISCUSSION

Mollusc shells are an excellent system to study the biomineralization process once these organisms provide crystals of calcium carbonate with interesting organization and great variations in their crystalline habits.

Different types of crystals are deposited at the same time in diverse parts of the shell. Crystals near the shell edge may be elongate, whereas in central regions of the shell tabular forms are found (Simkiss & Wilbur 1989).

The mineral phase of the shell of *Physa* sp. was followed from its initial stages, when the shells were about 0,5 mm. Only plates of aragonite were present, but no other crystalline polymorphs.

Spheres of calcium carbonate, probably vaterite, were found only in the apex; our X-ray diffraction and the infrared spectra data could not yet confirm

this identification, because they occur in very small amount. This crystalline form was found in the apex of mollusc shells for several other authors in which small amounts of vaterite were detectable with synchrotron X-ray diffraction (Hasse et al. 2000).

In some other molluscs prisms originate from spherulites that develop on the inner surface of the newly formed sheet of periostracum (Taylor & Kennedy 1969).

Many studies on biomineralization process are still needed, including *in vitro* and *in vivo* investigations for clarifying the formation mechanism of mineralized materials.

5 ACKNOWLEDGEMENTS

CNPq fellowship (process 140929/2001-0). We would like to express our thank to Valquíria de Fátima Justo Kozievitch (Escola Politécnica – USP) for the XRD and Astrogildo de Carvalho Junqueira (Instituto de Pesquisas Energéticas e Nucleares-IPEN) for discussion about Rietveld Method.

6 REFERENCES

- Addadi, L & Weiner, S 1997. A pavement of pearl. *Nature* 389: 912-915.
- Falini, G., Albeck, S., Weiner, S., Addadi, L. 1996. Control of aragonite or calcite polymorphism by mollusk shell macromolecules. *Science* 271: 67-69.
- Hasse B., Ehrenberg, H., Marxen, J.C., Becker, W., Epple, M. 2000. Calcium carbonate modifications in the mineralized shell of the freshwater snail *Biomphalaria glabrata*. *Chem. Eur. J.* 6: 3679-3685.
- Kato, T. 2000. Polymer/calcium carbonate layered thin-film composites. *Advanced Materials* 12: 1543-1546.
- Lowenstam, H A. 1981. Minerals formed by organisms. *Science* 211: 1126-1131.
- Rhoads, D.C. & Lutz, R. A. 1980. *Skeletal Growth of Aquatic Organisms*. New York Plenum Press
- Sikes, C.S. & Wheeler, P. 1988. Regulators of biomineralization. *Chem Tech.* 18 (ISS 10): 620-626.
- Simkiss, K & Wilbur, K.M. 1989. *Biomineralization – Cell Biology and Mineral Deposition*. City:Publisher San Diego, Academic Press, Inc.
- Taylor, J. & Kennedy, W.J. 1969. The influence of the periostracum in shell structure of bivalve molluscs. *Calc. Tissue Res.* 3 : 274-283.
- Watabe, N. Shell. Chap. 25, in Bereiter-Hahn J.; Matoltsy A. G. Richards, K. S. (eds) 1984 *Biology of the integument–Invertebrates*. Springer-Verlag , Berlin.
- Weiner, S. 1979. Aspartic Acid-Rich Proteins: Major Components of the soluble Organic Matrix of Mollusk Shells. *Calc. Tissue Int.* 29: 163-167.

Assets of Biogenic Carbonate Sands that Justify their Applications in Geomedicine: the Case of the Beach Sands of Porto Santo Island, Madeira Archipelago

C.Gomes & J.Silva

Centro de Investigação "Minerais Industriais e Argilas" da FCT (Fundação para a Ciência e a Tecnologia) e Universidade de Aveiro, 3810-193 Aveiro, Portugal.

ABSTRACT: The major goal of the present paper is to demonstrate, as much as possible on a scientific basis, that the Porto Santo island of the Madeira archipelago has natural resources that could make the island an ideal place to introduce and develop processes of naturotherapy. These processes presently deserve more and more attention and interest of people who suffer particularly from osteo-articular and muscular affections. It is the case, for instance, of the fine grained biogenic carbonate beach and dune sands existent in Porto Santo island, which have been used with success for many years, according to medical reports, under the form of sand baths. The studied sands display particular thermal (high specific heat and low heat diffusiveness) and chemical properties (rich in Ca, Mg, Sr, P and S that get easily freed during sand-baths by chemical dissolution when in contact with the sweat exsuded by the human body). These properties could justify the traditional application of biogenic carbonate sand, under the form of sand-baths, in geomedicine. This type of sand was formed and deposited during the Late Quaternary (31-15 ma BP) in relation with the pronounced sea level changes verified as consequence of the Last Great Glaciation. Such changes promoted the dismantling of the reefs mainly constituted of calcareous rhodophyta algae that have been developed on the island shallow continental shelf.

1 INTRODUCTION

Unfortunately, research in recent years has been mainly addressed to the negative effects of minerals in the human health.

However, it is well established that some particular minerals are of paramount importance for good human health, either being part of the composition of drinkable spring waters and eatable vegetables and fruits, or being incorporated in many pharms after being submitted to some degree of industrial processing.

The positive effects of minerals in human health have been reported by several authors, such as: Carretero 2001; Galán et al.1985; Ferrand & Yvon 1991; Gomes & Silva 1996, 1999, 2001; Reinbacher 1999; Veniale & Setti 1996.

Presently, there is a growing interest on treatments using natural means, alternative to those of the conventional medicine. It is the so-called naturotherapy, that involves distinct processes and methods, such as: phytotherapy, hydrotherapy, mudtherapy, thermotherapy, etc.

Whenever naturotherapy involves minerals or other mineral resources we can name it geomedicine, a scientific area that comprises the

fundamentals and practises of the application of geomaterials as conditioners of human health.

In fact, particular types of clay/mud, sand, rock salt and spring water, intervene both as chemical and physical conditioners in human health.

The relevant properties of biogenic carbonate sand for applications in geomedicine are described in the present paper.

2 MATERIALS, METHODS, RESULTS AND DISCUSSION

Beach sand of Porto Santo Island, belonging to the Madeira Archipelago, has been used for many years under the form of sand-baths, on an empirical basis, for the treatment of osteo-articular and muscular diseases. This sand did derive from the dismantling, during the Last Great Glaciation that in the northern hemisphere had its maximum around 21ma BP, of a reef that was developed around the island, particularly in its shallow northern continental shelf.

¹⁴C dating carried out on several samples of biogenic carbonate sands from Porto Santo, collected either on beaches or on dunes, provided values within the range 31ma-15ma BP, the highest values corresponding to consolidated dune sand

from deposits located in the northern coast of the island, and the lowest values corresponding to sand from both beaches and non consolidated frontal dunes existent in the southern coast.

Similar sands, more or less contemporary, occur in other Atlantic volcanic islands of the biogeographic region named Macaronesia, such as: Gran Canaria, Fuerteventura and Lanzarote from the Canarias archipelago, Boavista, Sal, Maio, Santiago and S. Vicente from the Cape Verde archipelago, and Santa Maria and Terceira from the Azores archipelago. Other occurrences are known in islands from the Caribbean Sea and from the Great Barrier Reef.

Sand grains consist mainly of bioclasts essentially of calcareous rodophyta algae (Coralline). Mineralogically the biogenic carbonate component of the sand is composed of magnesian calcite (95%) and aragonite (~5%).

Chemically, the biogenic carbonate sand from Porto Santo are particularly rich in Ca, Mg and Sr (Tables 1 and 2).

The analysed sample exhibiting a yellowish colour was collected at the beach, where the volcanoclastic component, consisting mainly of black (basalt) and brown (trachytic tuff) clasts is much higher than in the frontal dune due to aeolian classification. In some sectors of the beach the volcanoclastic component can reach contents around 30%. Traditionally sand-baths are taken at the transition zone of the beach to the frontal dune.

Texturally beach's biogenic carbonate sands are fine grained (most of grain size falls within the range 0,250mm-0,125mm).

Dating using the radiocarbon method provided ages in the range 31,000-15,000 years BP.

Research being carried out found that the assets that could justify, on a scientific basis, sands therapeutic interest, are particularly the thermal properties (specific heat, heat diffusiveness, cooling rate) and chemical properties (chemical composition, chemical dissolution rate in an acidic environment).

Biogenic carbonate beach sand compared with the quartz rich sand current in most beaches which occur worldwide, requires more time to warm up and to cool down to reach the same temperature.

Porto Santo biogenic carbonate sand occurring at the transition zone from the beach to the frontal dune, can reach temperatures, in summer sunny days, around 65 °C.

The distinct behaviour of quartz rich sand and of Mg-calcite rich sand is based on the distinct crystallochemical properties, in what concerns, for instance, particle shape and packing, atomic packing and chemical bonds exhibited by these two minerals.

During the application of sand-baths human body receives and stores heat, and the acid (pH 4.1-6.5) sweat produced reacts with the carbonate sand liberating, in the ionic form, cations such as Ca^{2+} , Mg^{2+} , Sr^{2+} and P^{5+} , which being freed at the skin surface, can be absorbed through it.

Due to the tabular shape of most sand grains, they become stuck to the skin after sand-bathing, and they should remain as so during some minutes till the skin gets dry.

The relevant properties of other natural resources of Porto Santo island, such as seawater, spring water, climate as well as eatable vegetables and fruits grown up in soils developed on biogenic carbonate sand were investigated too, in order to enable their integration, together with sand-bathing, in a comprehensive programme of naturotherapy to be carried out in Geomedicine Centers, which are being installed in Porto Santo island.

The reaction that takes place between carbonate sand and human body appears to be similar to the one already described (Gomes & Silva 2001) for the reaction clay/human body during the application of peloid cataplasms made of bentonite, clay that occurs in Porto Santo too. Such reaction corresponds to a cation exchange reaction between cations, such as Na^{+1} and K^{+1} , highly concentrated in the sweat coming out from the body, and cations, such as Ca^{+2} , Mg^{+2} and Sr^{+2} , which are freed through the dissolution of the carbonate sand grains and become more concentrated in the sweat. Ca^{+2} and Mg^{+2} also exist in the sweat exsuded from the body but in very low concentration. Therefore, between the inner and outer sides of the skin there is a concentration gradient in terms of Ca^{+2} and Mg^{+2} .

Table 1. Chemical analysis data (in %) corresponding to major elements of the biogenic carbonate sand from Porto Santo

SiO ₂	Al ₂ O ₃	TiO ₂	Fe ₂ O ₃	MnO	MgO	CaO	Na ₂ O	K ₂ O	P ₂ O ₅	I.L.
6.10	1.90	0.09	0.52	0.03	2.69	47.12	0.43	0.06	0.25	40.14

* I.L.(the ignition loss determined at 1.000°C for 3 hours, corresponds essentially to CO₂ evolution)

Table 2. Chemical analysis data (in ppm) corresponding to minor and trace elements of the biogenic carbonate sand from Porto Santo

Sr	Ba	Zr	Y	As	Zn	Ni	Cu	Cr	S	V
1259	105	21	-	-	16	3	2	-	44	3

In order to potentiate the cation exchange referred to it was found to be advisable to leave the sand stuck to the skin for some time (around 15 minutes) after leaving the sand bath and until the skin becomes almost dry. Only after that should the sand be removed with a shower.

Treatments with carbonate sand, however, could be more effective for certain affections than treatments with bentonite, due to either the continuous renewal of exchangeable Sr, Ca and Mg during sand treatment, or to the low heat diffusiveness and heat attenuation, which are specific characteristics of the Porto Santo biogenic carbonate beach/dune sand.

As a final note, it should be mentioned that Porto Santo has other natural resources able to be used complementarily to sand-baths. Besides bentonite interesting for applications in mudtherapy (Gomes & Silva 2001), sea-water as well as vegetables and fruits cultivated on soils developed on the biogenic carbonate sands can be used too. As a matter of fact, Porto Santo sea-water compared with other sea-waters exhibits specific properties (pH=8.4; electric conductivity, $48.7\text{mS}\cdot\text{cm}^{-1}$; higher contents of Ca^{+2} , Mg^{+2} , HCO_3^{-1} , SO_4^{-2} and lower contents of Na^{+1} and Cl^{-1} , comparatively to the reference sea-water. Vegetables and fruits are particularly enriched, for instance, in Ca, Mg and Sr. Either under the form of sea-bathing or part of appropriate patients's diet, each one of these resources could be introduced in treatment programmes to be carried out locally in Geomedicine Centres (Gomes & Silva 2001).

3 CONCLUSIONS

The research being carried out did show that Porto Santo biogenic carbonate sand, occurring both on beaches and on dunes, has thermal and chemical properties considered important for human health. In contact with the skin during sand-bathing the carbonate particles that make up the sand, particularly the algae clasts which are relatively more unstable under acidic conditions, are partially dissolved by the exsudation liquid (pH 4.1-6.5) coming from the body if the temperature of the sand is higher than the temperature of the body.

Sand-bathing can take place, either outdoors in the transition zone of beach/frontal dune during sunny days, or indoors in the geomedicine clinics where the ambient temperature is artificially maintained around 40-42 °C, that is, little above the body temperature. Exchange reactions would take place through the epidermis, between the chemical elements (Ca, Mg, Sr, P, etc) that become free due to dissolution of the sand and the elements existent the sweat (Na, K, Cl, etc).

4 REFERENCES

- Gomes, C. & Silva, J. 1996. Estudo das propriedades físicas e químicas da areia de praia da ilha do Porto Santo, tendo em consideração o seu uso para fins terapêuticos. Departamento de Geociências, Universidade de Aveiro, Internal Report, 31p.
- Gomes, C. & Silva, J. 1999. Therapeutic assets of the beach sand of Porto Santo island. Saber Soft, Madeira News Magazine. O Liberal-Empresa de Artes Gráficas, Lda, Câmara de Lobos, RAM, Ano I, n.º 0, Maio.
- Gomes, C. & Silva, J. 2001. Beach sand and bentonite of Porto Santo island: Potentialities for Applications in Geomedicine. C. Gomes and J. Silva (eds), O Liberal, Empresa de Artes Gráficas, Câmara de Lobos, Madeira, 60p
- Carretero, M. I. 2002. Clay minerals and their beneficial effects upon human health: a review. Applied Clay Science, 21, 155-163.
- Ferrand, T. & Yvon, J. 1991. Thermal properties of clay pastes for pelotherapy. Applied Clay Science, 6, 21-38.
- Galán, E., Liso, M. J., Forteza, M. 1985. Minerales utilizados en la industria farmacéutica. Bol. Soc. Esp. Min., 369-378.
- Reinbacher, W. R. 1999. A brief history of clay in medicine. Clay Minerals Society News, 11,1,22-23.
- Veniale, F. and Setti, M. 1996. L'argilla di Pontestura (AL): Potenzialità d'impiego nella formulazione di fanghi peloid. Atti Conv. "Argille Curative" (Veniale, F. ed.), Salice Terme (PV), 139-145.

Corundum Blasted Titanium Implants in Total Hip Arthroplasty - A Surface Characterization

J.Göske & W.Kachler

Zentrum für Werkstoffanalytik Lauf GmbH, Hardtstrasse 39b, 91207 Lauf a.d. Pegnitz, Germany

U.Holzwarth

Peter Brehm, Chirurgie Mechanik, Am Mühlberg 30, 91085 Weisendorf, Germany

G.Zeiler & A.Schuh

Orthopedic Clinic Rummelsberg, Schwarzenbruck, Rummelsberg 71, Germany

ABSTRACT: Alumina blasting techniques, using highly pure Al_2O_3 -particles to create a rough surface of titanium implants in cementless total hip arthroplasty achieve a better osteo integration. An increasing number of publications shows that there is a significant contamination on alumina blasted surfaces. Latest research studies published reveals an effect of contaminant particles on early failure of endoprostheses. Our work aimed at evaluating the amount and particle size of Al_2O_3 on the implant surface. The surface of four different geometries (ARR-Titan acetabular reinforcement ring, anisotropic Vektor cup, Vektor-Titan stem, and modular MRP-Titan stem) were analysed with respect to Al_2O_3 -particles. Field emission scanning electron microscopy combined with a backscatter electron detector was utilized for the detection of the Al_2O_3 -particles on the implant surface. The average area of the covered surface was calculated by means of an image analyzing software. The surface of the Vektor cup was contaminated at an average of $41.7 \pm 4.9\%$, the Vektor-stem at an average of $33.3 \pm 4.7\%$, the MRP-stem at an average of $30.6 \pm 4.2\%$ and the ARR-ring at an average of 23.2 ± 1.6 with Al_2O_3 -particles. Discussion: the results of this study clearly show, that high percentage contamination of rough titanium surfaces with Al_2O_3 -particles does exist. With respect to third body wear in total hip arthroplasty further studies are necessary to minimize contamination of roughened surfaces.

1 INTRODUCTION

Pure titanium and titanium alloys are frequently used for producing implants, because of the high resistance to corrosion and excellent biocompatibility. To enhance the osseous integration of cementless (hip) titanium implants, numerous techniques have been developed to regulate or increase the roughness of surface by plasma spray coating (Ti-VPS) or rough-blasting, using a highly pure corundum (Negre 1995). Goldberg (1995) was able to prove that roughened titanium implants are capable of increasing the rate and amount of fresh bone formation on the implant surface. Publications from maxillofacial-surgery and orthopaedic surgery reveal that, if blasting techniques using highly pure Corundum are employed, residual particles will be left on and in the surface of the implant (Böhler 2002, Darvell 1995, Moberg 1989, Ricci 1992, Witt 1991). Very recently, several studies considered residues of blasting material on the surfaces of highly pure Corundum blasted hip total endoprostheses, possibly responsible for third-body wear (Böhler 2002). Abraded ceramic particles are non-toxic themselves, but numerous papers prove that ceramic particles are capable of inducing the production of osteolytic cytokines and leading to

abrasion-induced periprosthetic osteolysis (Hatton 2003, Petit 2002). Aim of our work was to evaluate the amount and particle size of Al_2O_3 on the implant surface.

2 MATERIALS AND METHOD

The surfaces of four different geometries (5 parts each, ARR-Titan acetabular reinforcement ring, anisotropic Vektor cup, Vektor-Titan stem and modular MRP-Titan stem) were analysed with respect to Al_2O_3 -particles. Grit blasting was performed with Al_2O_3 -particles, Alodur@SWSK, Fa. Treibacher, Germany. Fig. 1 shows the highly pure corundum Alodur@SWSK at a 30-fold magnification.

The Al_2O_3 -particles were detected on the implant surfaces by means of a field emission scanning electron microscope (LEO 1525) with a backscatter electron detector (BSE detector). The respective particle size distribution as well as the surface it covers were determined with digital image analysis (analySIS, Soft Imaging System GmbH). Representative BSE analyses were verified by random sampling using EDX element distribution.

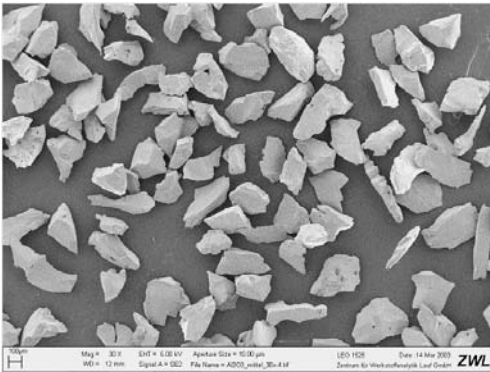


Figure 1. Alodur@SWSK at a 30- fold magnification.

This method graphically illustrates the respective elements and their frequencies in different colours in a selected, defined image portion and thus allows to localize and identify them.

2.1 Sample characterization

A detection of the Al_2O_3 percentage was made by scanning electron microscopy on the surface of:

ARR-Titan acetabular reinforcement ring (Figure 2a), Anisotropic Vektor cup (Figure 2b), Vektor-Titan stem (Figure 2c) and MRP-Titan stem (Figure 2d). Measurements were performed in areas at 10 measuring points which are depicted in the respective figures shown below.



Figure 2. Measuring points on the surface of the ARR -Titan acetabular reinforcement ring (a), Anisotropic Vektor cup (b), Vektor - Titan stem (c), and the MRP - Titan stem (d).

To guarantee a consistent analysis, the following instrument settings on the FE SEM (field emission scanning electron microscope) and BSE detector (backscattered electron detector) were meticulously abided:

- Exactly the same image width: Image portion: 1,800 x 1,230 μm
- Setting of the aperture on the FE REM (diaphragm): 30 μm
- Accelerating voltage: 20 kV
- Magnification: 200 times
- Contrast set on the backscatter electron detector: 100%
- Brightness set on the backscatter electron detector: 80%
- Working distance of the sample from the objective lens: 11 mm

The scanning electron microscope (SEM), amongst other things, serves for imaging the topography of rough surfaces (topography contrast) and differences of material (material contrast).

If the SEM setting is as above the BSE detector permits to localize the corundum particles on the surface against the rest of the sample by showing a difference in contrast, and to analyze them with respect to the grain size and distribution pattern via a brightness modulation. The software parameters for a digital image evaluation were normalized and standardized by hand to obtain the per cent error for each individual measurement. This was accomplished with the aid of 20 individual manual measurements on an object measuring point. The data obtained from these measurements were averaged and the standard deviation calculated. All the measuring points mentioned were analyzed using this standardized software settings.

Each measuring point and each sample was accurately described with regard to the following characteristics: work piece, sample number, measuring spot, magnification, detectors 1 = SE, 2 = QBSD (1 = Secondary Electron detector, 2 = Quadrant Back Scattered Electron detector).

For instance, the description "Vektor-stem-1-p1-200x-2" means: No. 1 Vektor-stem, measuring point 1 at a magnification of 200 times, QBSD.

3 RESULTS

The surface of the anisotropic Vektor cup was contaminated at an average of $41.7 \pm 4.9 \%$, the Vektor-Titan stem at an average of $33.3 \pm 4.7 \%$, the MRP-Titan stem at an average of $30.6 \pm 4.2 \%$ and the ARR-Titan acetabular reinforcement ring at an average of 23.2 ± 1.6 with Al_2O_3 particles over the whole surface orientated to the bone from the top of the type area.

Figures 3a and 3b illustrate an Al_2O_3 contamination of 26.7 % on the surface of the ARR-Titan acetabular reinforcement ring at the measuring point ARR-1-p4-200x obtained with the secondary electron detector (a) and the backscatter electron detector (b).

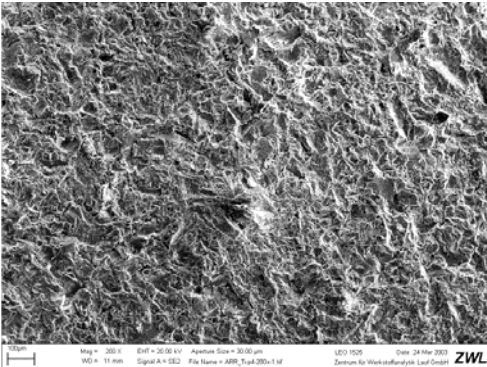


Figure 3a. Al_2O_3 contamination of 26.7% shown by the example of the ARR-Titan supporting ring at the measuring point ARR-1-p4-200x-1 (secondary electron detector).

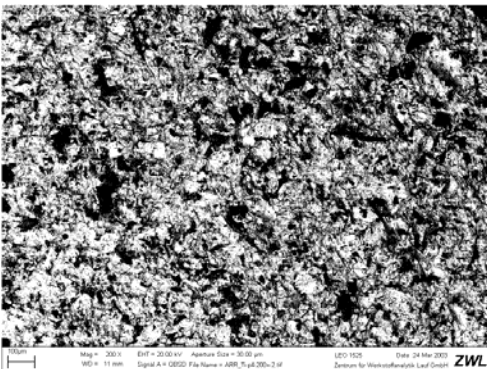


Figure 3b. Precisely the same sample and measuring point as shown in Figure 3a (ARR-1-p4-200x-2), this time observed with the backscatter electron detector.

4 DISCUSSION

Experimental examinations made by Goldberg (1995) on titanium pins were successful in proving that roughened titanium surfaces increase the rate of osteogenesis on the implant surface. The rough surface, similar to the surface of sand abrasive paper, results in an apposition of bone. (Goldberg 1995, Negre 1995, Wennerberg 1996).

Negre (1995) describes a favourable osseous ingrowth behaviour of rough-blasted titanium surfaces having a surface roughness $R_z = 50 \mu\text{m}$. The diameter of the blasting material grains is of immense importance for the favourable osseous ingrowth of rough-blasted titanium surfaces.

The present study shows that titanium surfaces of hip endoprosthesis implants rough-blasted with high-grade Corundum exhibit a large degree of residues of Al_2O_3 particles. Such superficial residues of rough-blasted titanium surfaces

containing Al_2O_3 particles are increasingly regarded as a problem in the reference literature (Böhler 2002, Darvell 1995, Ricci 1992, Witt 1991).

In 1992, Ricci described a pronounced contamination with silicon and aluminium containing particles in explanted, rough-blasted hip implants. The same contaminations were proved to exist in the granulation tissue which adhered to the implants. As experiments have shown there is no adverse effect on the osseous ingrowth behaviour of the implants (Böhler 2002). In 1989 Moberg for the first time described the delivery of major amounts of aluminium-containing particles in conjunction with commercially available titanium plates which were used for osteosynthesis of jaw fractures. Darvell (1995) showed that the Al_2O_3 particle residues were caused by rough-blasting with highly pure Corundum. Böhler (2002) succeeded in finding Al_2O_3 particles, which were associated with rough-blasting using highly pure corundum, in the granuloma of a loosened Zweymüller stem. In addition, he located Al_2O_3 -particles in deep scratches of the metal-on-metal articulation. He reasoned that the aluminium particles obviously penetrate into the periprosthetic tissue, provoke metallic abrasion on the implant surface and, finally, can result in implant loosening. The so-called expanded joint space does not only seem to be open to the transport of abrasive particles from the articulation to the bone implant interface, but vice versa also to the transport of the Al_2O_3 particles into the articulation. Böhler concluded that third-body wear by Al_2O_3 particles needs further study.

Apart from causing third-body wear, the Al_2O_3 particles also pose a problem in respect to the macrophages reaction and, hence, the formation of granulation tissue.

Petit and Catelas (2002) showed that macrophages can be activated by Al_2O_3 -particles. Cell mortality rises significantly in response to the size and concentration of the Al_2O_3 -particles. As does the release of TNF- α .

Hatton (2003) described that Al_2O_3 abrasion particles can induce the production of osteolytic cytokines.

In 1995 Darvell suggested that blasted-particle residues, their effect on the implant surface and the reactions on the implant-to-tissue interface are considered a potential factor for the failure of implants. Darvell required that rough-blasted titanium surfaces should be checked for Al_2O_3 -particles before implantation.

5 CONCLUSION

This study revealed an unexpectedly high percentage of contamination with highly pure Corundum particles on rough-blasted titanium surfaces. Third-

body wear and possible induction of osteolysis by such ceramic particles are potential problems. More studies aiming at minimizing the percentage of residual particles on implant surfaces while maintaining adequate, constant surface roughness, are urgently and utterly needed.

6 REFERENCES

- Böhler M, Kanz F, Schwarz B, Steffan I, Walter A, Plenk H Jr, Knahr K. 2002. Adverse tissue reactions to wear particles from Co-alloy articulations, increased by alumina-blasting particle contamination from cementless Ti-based total hip implants. A report of seven revisions with early failure. *J Bone Joint Surg (Br)*; 84 - B: 128- 36.
- Darvell BW, Sammant N, Luk WK, Clark RKF, Tideman H. 1995. Contamination of titanium castings by aluminium oxide blasting. *J Dent*. 23: 319- 322.
- Goldberg VM, Stevenson S, Feighan J, Davy D. 1995. Biology of gritblasted titanium alloy implants. *Clin. Orthop*. 319: 122- 9.
- Hatton A, Nevelos JE, Matthews JB, Fisher J, Ingham E. 2003. Effects of clinically relevant alumina ceramic wear particles on TNF-alpha production by human peripheral blood mononuclear phagocytes. *Biomaterials*. 24: 1193- 204.
- Moberg LE, Nordenram A, Kjellman O. 1989. Metal release from plates used in jaw fracture treatment. A pilot study. *Int J Oral Maxillofac Surg*. 18: 311- 4.
- Negre J, Henry F. 1995. Bone reaction to contact with a granulated titanium surface. Apropos of 101 total hip prostheses with six years follow-up. *Rev Chir Orthop Reparatrice Appar Mot*. 81: 106- 13.
- Petit A, Catelas I, Antoniou J, Zukor DJ, Huk OL. 2002. Differential apoptotic response of J774 macrophages to alumina and ultra-high-molecular-weight polyethylene particles. *J Orthop Res*. 20: 9- 15.
- Piatelli A, Manzon L, Scarano A, Paolantonio M, Piattelli M. 1998. Histologic and histomorphometric analysis of the bone response to machined and sandblasted titanium implants. An experimental study in rabbits. *Int J Oral Maxillofac Implants*. 13: 805- 810.
- Ricci JL, Kummer FJ, Alexander H, Casar RS. 1992. Technical note: embedded particulate contaminants in textured metal implant surfaces. *J Appl Biomater*. 3: 225- 230.
- Wennerberg A, Albrektsson T, Andersson B. 1996. Bone tissue response to commercially pure titanium implants blasted with fine and coarse particles of aluminum oxide. *Int J Oral Maxillofac Implants*. 11: 38- 45.
- Witt JD, Swann M. 1991. Metal wear and tissue response in failed titanium alloy total hip replacements. *J Bone Joint Surg (Br)*. 73- B: 559- 63.

Titanium Deposits on Ceramic Heads of Dislocated THR

J.Göske & W.Kachler

Zentrum für Werkstoffanalytik Lauf GmbH, Hardtstrasse 39b, 91207 Lauf a.d. Pegnitz, Germany

U.Holzwarth

Peter Brehm, Chirurgie Mechanik, Am Mühlberg 30, 91085 Weisendorf, Germany

G.Zeiler, A.Schuh

Orthopedic Clinic Rummelsberg, Schwarzenbruck, Rummelsberg 71, Germany

ABSTRACT: Introduction: The incidence of dislocation after THR ranges between 1.36% and 3.2%. In cases of revision with acetabular titanium components with dislocations in the past, metallic deposits are frequently found on ceramic heads. Material and method: Ten ceramic heads of revised THR were investigated, which showed metallic deposits. The patients suffered from 1 to 6 dislocations. 4 left and 6 right hip implants of 6 women and 4 men were examined. The prosthesis lifetime ranged between 2 weeks up to 12 years. The surface structure was investigated in a scanning electron microscope (LEO 1525), the metallic deposits were characterised by means of energy dispersive X-ray analysis (EDX). Results: In the area of the metallic deposits titanium was detected by EDX. Edges with significant increase of surface roughness were observed, partially accompanied by spalling of the surface structure and loosening of alumina. Discussion: Titanium deposits increase surface roughness in definite areas, which probably cause wear of ceramic-ceramic or ceramic-polyethylene articulations due to different roughness values and surface properties. Further investigations are necessary, to analyse the importance of these findings with respect to wear and loosening of total hip arthroplasty.

1 INTRODUCTION

Total hip replacement (THR) is one of the most successful principles in orthopedic surgery. Postoperative dislocation remains one of the most frequent complications following total hip replacement. The overall dislocation rate is 1.36 to 3.2% (Morrey 1992, Van Stralen 2003, Woo 1982). Wear debris is the main reason for aseptic loosening in total hip. Most troublesome is the wear of polyethylene cups (Bankston 1993, Bizot 2001, Clarke 2000, Elke 2001, Linder 1983, Lombardi 1989). Ceramic femoral heads were introduced about 20 years ago. The combination ceramic-on-polyethylene reduces the wear and the loosening rate.

To improve the longevity of hip endoprosthesis, the main goal is to reduce wear. Polyethylene together with metal or ceramic is currently the most frequently used combination. Their clinical success is well documented in the literature. The most recent competitors of ultra-high molecular weight polyethylene (UHMWPE) are the highly cross-linked polyethylenes (HCLPE) and the hard-on-hard couplings such as metal-on-metal or ceramic-on-ceramic. In the 1970s it was first realized that the properties of alumina ceramics could be exploited to

provide better implants for orthopaedic applications. Applications depend on the fact that ceramics provide wear characteristics suitable for bearing surfaces in total hip replacement. To date more than 2.5 million alumina femoral heads have been implanted (Hamadouche 2002, Fruh 1997, Willmann 1998, Willmann 2000).

Using inlays and ceramic heads of the latest generation offers the possibility of reducing the wear rate to as low as 0.005 mm per year. In comparison wear rate of metal/ polyethylen articulations is 0.2 mm, ceramic / polyethylen articulations is 0.1 mm and 0.01 mm for metal/ metal articulations (Elke 2001).

In cases of revision of total hip arthroplasties with acetabular titanium components with dislocations in the past, metallic deposits are frequently found on ceramic heads. There is only one case report about similar findings in a revised THR after dislocation. As the question about the significance of these findings with respect to e.c. third body wear still remains we investigated the surface of ten revised ceramic heads.

2 MATERIALS AND METHOD

Ten ceramic heads of revised THR which showed metallic deposits were investigated. The patients

suffered from 1 to 6 dislocations. 4 left and 6 right hip implants of 6 women and 4 men were examined. The prosthesis lifetime ranged between 2 weeks up to 12 years (Tab. 1).

Table 1. Data of the patients.

Nr	Patient	Gender	Age (in years)	Side	Lifetime of the prosthesis (in months)	Revision because ...	Number of Dislocations	Approach	Implantat
1	R.E.	f	61	left	35	Dislocation	3	dorsal	CLS- stem, cementless standard- cup
2	B.M.	f	63	right	12	Loosening of cup	1	dorsal	Wagner- Revisionstem, cementless standard- cup
3	R.E.	f	60	left	96	Loosening of cup	1	dorsal	cementless stem, ARR
4	L.C.	f	66	right	134	Loosening of cup	6	dorsal	CLS- stem, ARR
5	S.D.	m	62	right	12	Dislocation	2	lateral	Vektor- Titan stem, Anisotropic Vektor- cup
6	H.G.	m	62	right	96	Loosening of cup and stem	1	lateral	cementless stem, ARR
7	L.J.	m	62	right	98	Loosening of cup and stem	1	lateral	CLS- stem, cementless standard- cup
8	D.G.	f	59	left	18	Dislocation, Instability	1	lateral	Vektor- Titan stem, ARR
9	D.E.	f	56	left	50	Loosening of cup and stem	1	dorsal	Müller straight stem, ARR
10	K.U.	m	62	right	17	Loosening of cup and stem	1	dorsal	Müller straight stem, ARR

3 RESULTS

In the area of the metallic deposits titanium was detected by EDX.

Edges with a significant increase of surface roughness were observed, partially accompanied by spalling of the surface structure and loosening of alumina.

Case- report (Number 5, see Tab. 1):

Revision and open reduction after dislocation after THR of the right hip was performed in a 62 year old patient. In the past the patient suffered from one dislocation with closed reduction. A cementless Vektor - Titan stem (Alloy: Ti6Al7Nb), a cementless anisotropic Vektor- cup (Alloy: Ti5Al2,5Fe) and an alumina ceramic head was used. Intraoperatively metallic deposits on the ceramic head were detected (Fig.1).

The surface structure was investigated in a FE-SEM (field emission scanning electron microscope) (LEO 1525) with a secondary electron detector (SE). The metallic deposits were characterised by means of energy dispersive X-ray analysis (EDX).

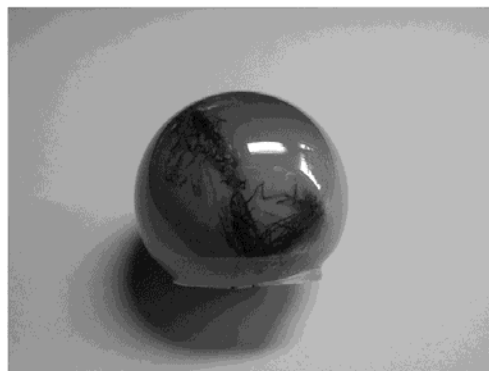


Figure 1. Metallic deposits on a revised ceramic head.

Figure 2 shows titanium deposits with edges and a significant increase of the surface roughness with a 27 fold and 2000 fold magnifying. EDX analysis proved the metallic deposits as titanium.

4 DISCUSSION

Femoral ball heads of aluminium oxide or zirconium oxide ceramics are used for total hip replacement. This application is based on their attractive tribological properties. Ceramic materials have been used as a coupling in total hip arthroplasty since the 1970s to solve the problem of polyethylene particle disease. Using inlays and ceramic heads of the latest generation offers the possibility of reducing the wear rate to as low as 0.001 mm per year (Willmann 1998, Willmann 2000). We could show that titanium can be transferred on ceramic heads after dislocation of total hip arthroplasties. To our knowledge there is only one case report about titanium deposits on ceramic heads (Luchetti 1998). Luchetti found transfer of titanium debris to a ceramic femoral head from contact with an acetabular shell during reduction of a dislocated total hip arthroplasty. Using SEM and EDX he found two markings on a revised ceramic head. EDX proved that these markings consisted from titanium. He discussed that one of the markings was produced during dislocation while the other was produced by closed reduction. It is of concern that this metal transfer occurred in a region of the head located within the acetabular cup during normal gait. The presence of metal might contribute to increased ultrahigh molecular weight polyethylen through either abrasive, plowing wear of the polymer counterface, or as a contributor of third-body particles (Luchetti 1998). It is well documented that both polyethylen and titanium particulate debris are associated with macrophage activation and cytokine release, resulting in osteolysis and aseptic loosening (Elke 2001, Lombardi 1989).

According to our experience and the actual study metallic deposits after dislocation of THR are a frequent finding. These deposits can also occur in primary total hip replacement if intraoperatively there are any difficulties in reduction or if multiple dislocation/ relocation manoeuvres during the surgery are necessary. Titanium deposits at single surface areas surface wear characteristics changed. Limits for roughness values of Alumina heads are $R_a < 0.02$ according to the manufacturer (CeramTec). This roughness value determined by visual inspection is definitively higher at surface areas contaminated with Titanium scratches. Exact measurements could not be performed in this study.

Elke showed linear annual wear rates of 0.2 mm/a for Metal-Polyethylene wear couples due to a higher friction coefficient in comparison to Ceramic – Polyethylene wear couples with 0.1 mm/a abrasive wear (Elke 2001).

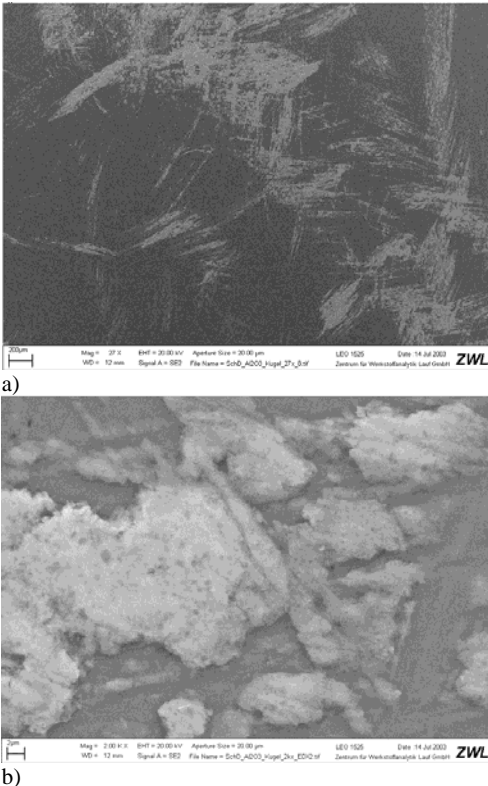


Figure 2. Metallic deposits detected with a SE detector with 27 fold (a) and 2000 fold magnification (b).

In two cases we found spalling of the surface structure and loosening of alumina particles after recurrent dislocations (Fig. 3).

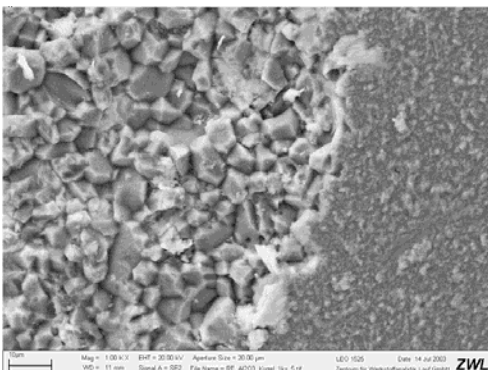


Figure 3. Spalling of the surface structure and loosening of alumina particles after 3 dislocations by means of a secondary electron detector.

5 CONCLUSION

Further investigations have to be made to analyze roughness surfaces locally especially detecting corresponding effects to early Polyethylene wear debris causing osteolysis et cetera. Another problem is caused by interrupting smooth ceramic surfaces as a result of luxation or reposition especially after several times of luxation. This problem occurs also at situations performing difficult reposition at primary hip operations with metal backed acetabular cup designs. Therefore special tools are required to realize protected reposition procedures.

6 REFERENCES

- Bankston AB, Faris PM, Keating EM, Ritter MA 1993. Polyethylene wear in total hip arthroplasty in patient-matched groups. A comparison of stainless steel, cobalt chrome, and titanium-bearing surfaces. *J Arthroplasty* 8: 315-22
- Bizot P, Nizard R, Hamadouche M, Hannouche D, Sedel L 2001. Prevention of wear and osteolysis: alumina-on-alumina bearing. *Clin Orthop*. 393: 85-93
- Clarke IC, Good V, Williams P, Schroeder D, Anissian L, Stark A, Oonishi H, Schuldies J, Gustafson G 2000. Ultra-low wear rates for rigid-on-rigid bearings in total hip replacements. *Proc Inst Mech Eng* 214: 331-47
- Elke R 2001. Particle disease. Is tribology a topic in revision surgery? *Orthopade* 30: 258-65
- Fruh HJ, Willmann G, Pfaff HG 1997. Wear characteristics of ceramic-on-ceramic for hip endoprostheses. *Biomaterials* 18: 873-6.
- Hamadouche M, Boutin P, Daussange J, Bolander ME, Sedel L 2002. Alumina-on-alumina total hip arthroplasty: a minimum 18.5-year follow-up study. *J Bone Joint Surg Am* 84: 69-77.
- Linder L, Lindberg L, Carlsson A 1983. Aseptic loosening of hip prostheses. A histologic and enzyme histochemical study. *Clin Orthop*. 175: 93-104.
- Lombardi AV Jr, Mallory TH, Vaughn BK, Drouillard P 1989. Aseptic loosening in total hip arthroplasty secondary to osteolysis induced by wear debris from titanium-alloy modular femoral heads. *J Bone Joint Surg Am* 71: 1337-42.
- Luchetti WT, Copley LA, Vresilovic EJ, Black J, Steinberg ME 1998. Drain entrapment and titanium to ceramic head deposition: two unique complications following closed reduction of a dislocated total hip arthroplasty. *J Arthroplasty* 13: 713-7.
- Morrey BF 1992. Instability after total hip arthroplasty. *Orthop Clin North Am*. 23: 237-48.
- Van Stralen GM, Struben PJ, Van Loon CJ 2003. The incidence of dislocation after primary total hip arthroplasty using posterior approach with posterior soft-tissue repair. *Arch Orthop Trauma Surg*. 123: 219-22.
- Willmann G 1998. Ceramics for total hip replacement-what a surgeon should know. *Orthopedics* 21: 173-7.
- Willmann G 2000. Ceramic femoral head retrieval data. *Clin Orthop*. 379: 22-8.
- Woo RY, Morrey BF 1982. Dislocations after total hip arthroplasty. *J Bone Joint Surg Am* 64: 1295-306.

Surface Characterisation of Shot Peened Implants with Glass Beads in Total Hip Arthroplasty

J.Göske, T.Müller & W.Kachler

Zentrum für Werkstoffanalytik Lauf GmbH, Hardtstrasse 39b, 91207 Lauf a.d. Pegnitz, Germany

U.Holzwarth

Peter Brehm, Chirurgie Mechanik, Am Mühlberg 30, 91085 Weisendorf, Germany

G.Zeiler, A.Schuh

Orthopedic Clinic Rummelsberg, Schwarzenbruck, Rummelsberg 71, Germany

ABSTRACT: Alumina-blasting is used to create a rougher surface of titanium implants to achieve a better bony ingrowth. An increasing number of publications in maxillofacial and orthopaedic surgery show that there is a significant contamination on alumina blasted surfaces. The same technique is used for inducing internal stresses or cleaning of implant surfaces with glass beads. Due to our knowledge no previous study analysed surface contamination of hip endoprostheses with glass beads. Our work aimed at evaluating the percentage of contamination on these surfaces. The surface of 5 Ti-VPS sprayed Phoenix cups and 5 Morse-taper-junctions of the MRP-Titan revision stem (Peter Brehm, Chirurgie Mechanik, Weisendorf) were analysed with respect to glass particles. Shot peening was performed with glass beads "BALLOTINI" MGL, Fa. Würth Strahlmittel. A field emission scanning electron microscopy (LEO 1525) was used for the detection of the glass-particles on the implant surface with a backscattered electron detector. The area covered by particles was calculated by means of an imaging analyze software. The surface of the Ti-VPS sprayed Phoenix cups showed an average contamination with glass particles of 9.2 ± 1.3 %, Morse taper junctions of the MRP-Titan stem were at $6.7\% \pm 0.8\%$. The results of this study clearly show that a significant contamination of shot peened titanium surfaces with glass particles exists. With respect to third body wear in total hip arthroplasty, further studies are necessary to minimize contamination.

1 INTRODUCTION

Shot peening is used in several procedures in manufacturing orthopaedic implants. To enhance the osseous integration of cementless (hip) titanium implants, numerous techniques have been developed to regulate or increase the roughness of surface by vacuum plasma spray coating (Ti-VPS) or rough-blasting using a highly pure corundum (Eberhardt 1995, Emerson 1999, Hozack 1996, Negre 1995, Vercaigne 1998). Shot peening with glass beads is used for both, cleaning surface hardened titanium implants or cleaning Ti-VPS-coated implants. (SAE J 1173 1988, SAE J 2441 2000, SAE J 445 1996). Publications from maxillofacial surgery and orthopaedic surgery reveal that, if blasting techniques using highly pure alumina were used, residual particles will be left on and in the surface of the implant (Böhler 2002, Darvell 1995, Ricci 1992, Witt 1991). Very recently, several studies considered residues of blasting material on the surfaces of highly pure alumina blasted hip total endoprostheses, possibly responsible for third-body wear (Böhler 2002). Due to our knowledge no previous study analysed surface contamination of hip endoprostheses with glass beads. Aim of our

work was to evaluate the percentage of contaminated surface of hip endoprostheses with glass particles.

2 MATERIALS AND METHOD

The surface of 5 Ti-VPS sprayed Phoenix Titan cups and 5 Morse taper junctions of the MRP-Titan revision stem (Peter Brehm, Chirurgie Mechanik, Weisendorf) were analysed with respect to glass particles. Shot peening was performed with glass beads "BALLOTINI" MGL, Fa. Würth Strahlmittel, Germany.

Figure 1 shows the glass beads at a 250-fold magnification.

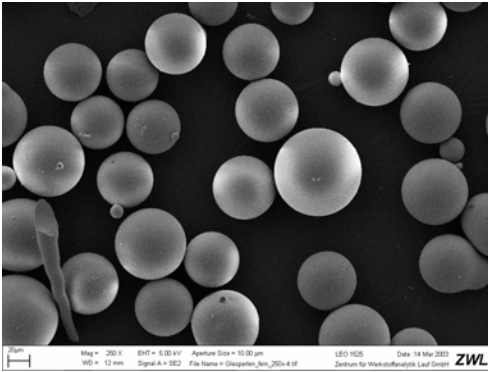


Figure 1. Glass beads "BALLOTINI" MGL at a 250-fold magnification.

The glass particles were detected on the implant surfaces by utilising of a field emission scanning electron microscope (LEO 1525) with a Back Scattered Electron Detector (BSE detector). The surface coverage with glass particles was determined by means of digital image analysis (analySIS, Soft Imaging System GmbH). Representative BSE analyses were verified by random sampling using EDX element distribution. This method graphically illustrates the respective elements and their frequencies in different colours in a selected, defined image portion and thus allows to localize and identify them.

2.1 Sample characterization

A measurement of the percentage of glass was made by scanning electron microscopy on the surface of:

Morse taper junction of the MRP-Titan stem: Measurements were performed in areas at 10 measuring points which are depicted in Figure 2a.

Phoenix Titan cup: Measurements were performed in areas at 10 measuring points which are depicted in Figure 2b.

For an analysis, the constant instrument settings below were always used on the FE SEM (field emission scanning electron microscope) and BSE detector (backscattered electron detector):

- Exactly the same image width: Image portion: 1,800 x 1,230 μm
- Setting of the aperture on the FE REM (diaphragm): 30 μm
- Accelerating voltage: 20 kV
- Magnification: 200 times
- Contrast set on the backscatter electron detector: 100%
- Brightness set on the backscatter electron detector: 80%
- Working distance of the sample from the objective lens: 11 mm

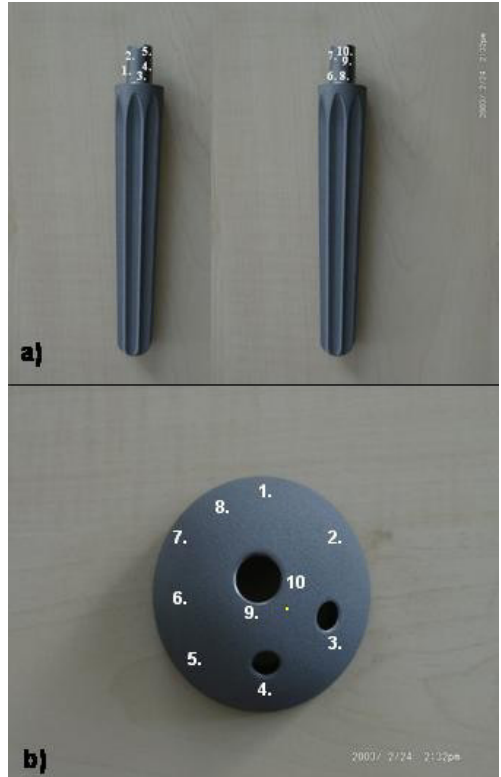


Figure 2. Measuring points on the surface of the Morse taper junction of the MRP-Titan stem (a) and the Phoenix cup (b).

In the present case, the material examined is composed of a metallic component (the implant) which has a high atomic number (e.g. the mean atomic number = 22 for the alloy Ti6Al7Nb of the MRP-stem), and glass particles (70% SiO_2 , 10% CaO , 5% MgO , 14% Na_2O , balance: Al_2O_3 , K_2O , Fe_2O_3) with a mean atomic number of 10.5. Each sample was examined by means of a BSE detector for glass particles at sites precisely localized before and the result was confirmed by using an EDX analysis. If the SEM settings are as specified above, the BSE detector permits to localize the glass particles on the surface against the rest of the sample by showing a difference in contrast. The analysis is performed with respect to the grain size and distribution pattern via a brightness modulation. The software parameters for the digital image evaluation were normalized and standardized by hand to obtain the per cent error for each individual measurement.

This was accomplished with the aid of 20 individual manual measurements on an object measuring point. The data obtained from these measurements were averaged and the standard deviation calculated. All the measuring points

mentioned were analyzed by applying of this standardized software setting.

Each measuring point and each sample was accurately described with regard to the following characteristics:

Workpiece, sample number, measuring spot, magnification, detectors 1 = SE, 2 = QBSD (1 = Secondary Electron detector, 2 = Quadrant Back Scattered Electron detector).

3 RESULTS

The surface of the Phoenix cup was contaminated at an average of $9.2 \pm 1.3\%$, the MRP-Titan stem at an average of $6.7 \pm 0.8\%$ with glass particles over the whole surface.

Figure 3 illustrates a glass contamination of 10% on the surface of the Phoenix cup at the measuring point Phoenix-1-p2-200x-2.

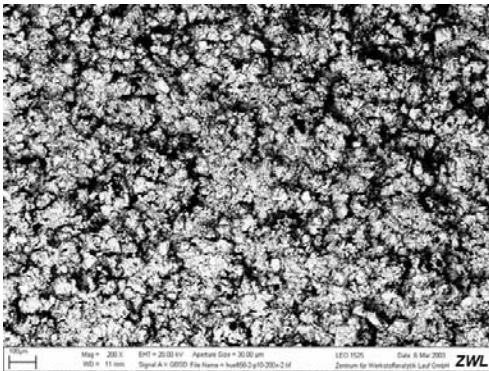


Figure 3. Glass contamination of 10% shown by the example of the Phoenix cup at the measuring point Phoenix-1-p2-200x-2. Image was taken with the Back Scattered Electron Detector.

Figure 4 Illustrates glass particles found on the surface of a Phoenix cup.

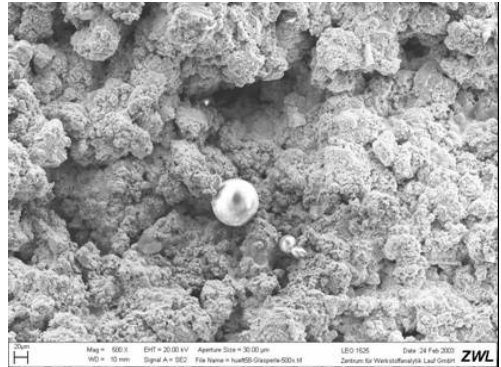


Figure 4. Surface contamination with glass on the surface of the Phoenix Titan cup with a 500 fold magnification, using a secondary electron detector.

4 DISCUSSION

Shot peening is used in several procedures in manufacturing orthopaedic implants. Shot peening with glass beads is used for cleaning Ti-VPS-coated implants to enhance bony ingrowth of cementless titanium implants. A second type of technical application uses shot peening with glass beads to clean surfaces which are shot peened with steel balls first (Eberhardt 1995, Emerson 1999, Gil 2002, Hozack 1996, Vercaigne 1998, SAE J 1173 1988, SAE J 2441 2000, SAE J 445 1996, Vercaigne 1998).

The present study shows that titanium surfaces of hip endoprosthesis implants shot peened with glass beads exhibit a large degree of residues of glass particles. Al_2O_3 particles on rough-blasted titanium surfaces are increasingly regarded as a problem in the reference literature (Böhler 2002, Darvell 1995, Ricci 1992, Witt 1991). In 1992, Ricci described a significant contamination with silicon and aluminum containing particles in explanted, rough-blasted hip implants. The same type of contamination was proved to exist in the granulation tissue which adhered to the implants. As experiments have shown there is no adverse effect on the osseous ingrowth behaviour of the implants (Böhler 2002). Darvell (1995) showed that the Al_2O_3 particle residues were caused by rough-blasting with highly pure alumina. Böhler (2002) succeeded in finding Al_2O_3 particles, which were associated with rough-blasting, using highly pure alumina, in the granuloma of a loosened Zweymüller stem. Additionally, he found Al_2O_3 particles in deep scratches of the metal on metal articulation. He reasoned that the alumina particles obviously penetrate into the periprosthetic tissue, provoke metallic abrasion on the implant surface and, finally, can result in implant loosening. The so-called expanded joint space not only seems to be

open to the transport of abrasive particles from the articulation to the bone implant interface, but vice versa also to the transport of the Al_2O_3 particles into the articulation. Böhler concluded that third-body wear by Al_2O_3 particles needs further study. Till today there is no data available about the effects of glass particles with respect to the induction of osteolysis. It seems that all particles can induce periprosthetic osteolysis (Elke 2001). In 1995 Darvell arrived at the conclusion that blasted-particle residues, their effect on the implant surface and the reactions on the implant-to-tissue interface are considered as potential factor for the failure of implants. Darvell required that rough-blasted titanium surfaces should be checked for Al_2O_3 particles before they are implanted. The same conclusion has to be drawn with respect to glass particles.

5 CONCLUSION

This study revealed an unexpectedly high percentage of contamination with glass particles on shot peened titanium surfaces. Third-body wear and possible induction of osteolysis by such glass particles are potential problems. More studies aiming at minimizing the percentage of residual particles on implant surfaces while maintaining adequate surface characteristics are urgently needed.

6 REFERENCES

- Böhler M, Kanz F, Schwarz B, Steffan I, Walter A, Plenk H Jr, Knahr K. 2002. Adverse tissue reactions to wear particles from Co-alloy articulations, increased by alumina-blasting particle contamination from cementless Ti-based total hip implants. A report of seven revisions with early failure. *J Bone Joint Surg Br.* 84: 128-36.
- SAE J 1173 Issue 1988: Size classification and characteristics of glass beds for peening.
- SAE J 2441 Issue 2000: Process- shot- peening.
- SAE J 445 Issue 1996: Metallic- shot and Grit- mechanical- testing
- Vercaigne, S., Wolke, J.G., Naert, I., Jansen, J.A. 1998. The effect of titanium plasma-sprayed implants on trabecular bone healing in the goat. *Biomaterials* 1998 Jun; 19: 1093-9.
- Witt, J.D., Swann, M. 1991. Metal wear and tissue response in failed titanium alloy total hip replacements. *J Bone Joint Surg (Br).* 73- B: 559- 63.
- Darvell, B.W., Sammant, N., Luk, W.K., Clark, R.K.F., Tideman, H. 1995. Contamination of titanium castings by aluminium oxide blasting. *J Dent*; 23: 319- 322.
- Eberhardt, A.W., Kim, B.S., Rigney, E.D., Kutner, G.L., Harte, C.R. 1995. Effects of precoating surface treatments on fatigue of Ti-6Al-4V. *J Appl Biomater.* 6: 171-4.
- Elke, R. 2001. Particle disease. Is tribology a topic in revision surgery? *Orthopäde.* 30: 258-65.
- Emerson, R.H. Jr, Sanders, S.B., Head, W.C., Higgins, L. 1999. Effect of circumferential plasma-spray porous coating on the rate of femoral osteolysis after total hip arthroplasty. *J Bone Joint Surg Am.* 81: 1291-8.
- Gil, F.J., Planell, J.A., Padros, A. 2002. Fracture and fatigue behavior of shot-blasted titanium dental implants. *Implant Dent.* 11: 28-32.
- Hozack, W.J., Rothman, R.H., Eng, K., Mesa, J. 1996. Primary cementless hip arthroplasty with a titanium plasma sprayed prosthesis. *Clin Orthop.* 333: 217-25.
- Negre, J., Henry, F. 1995. Bone reaction to contact with a granulated titanium surface. Apropos of 101 total hip prostheses with six years follow-up. *Rev Chir Orthop Reparatrice Appar Mot.* 81: 106- 13.
- Ricci, J.L., Kummer, F.J., Alexander, H., Casar, R.S. 1992. Technical note: embedded particulate contaminants in textured metal implant surfaces. *J Appl Biomater.* 3: 225-230.

Technical Silicification of Wood Materials

N.Langhof, J.Götze, M.Hengst, R.B.Heimann

Department of Mineralogy, TU Bergakademie Freiberg, Germany

ABSTRACT: Technical silicification of wood was performed to improve the properties (e.g. wear resistance, water absorption, hardness) of the material. Experimental studies were carried out using two types of wood (oak and spruce) and three different sources of silica including sodium metasilicate (Na_2SiO_3), a colloidal suspension of silica, and tetraethoxysilane (TEOS). Experiments were done in the temperature range between 40°C and 80°C under normal pressure in glass beakers and at higher temperatures (up to 138°C) and pressures (up to 12 bar) in autoclaves. Besides microscopic investigations (binocular, polarizing microscopy, SEM, cathodoluminescence microscopy), measurements of water absorption and hardness were performed. CL microscopy proved to be the most effective method to reveal the distribution of SiO_2 within and on the surface of the wood samples. Material silicified with colloidal silica and TEOS, respectively absorbed about 40% less water than untreated specimens. Likewise, the Brinell hardness of treated samples could be increased by nearly 100% compared to fresh wood samples, which is mainly caused by vitreous silica coatings (generated by sol-gel transformation) at the sample surface.

1 INTRODUCTION

Recently, different chemical und physical methods are being used to improve the structure of industrially used wood and to avoid damages caused by weathering. Most of these procedures use rather toxic chemicals such as chromated copper arsenate leading to certain environmental problems (Tanno et al. 1998). An appropriate silicification procedure would provide a new and harmless way to prevent the mechanical and chemical decay of wood materials.

In nature many examples are known where silica-bearing solutions cause the permineralization of wood. Vitreous and crystalline silica minerals (opal, chalcedony, quartz) increase the hardness (up to Mohs 7) and improve the resistance against chemical, biological and weathering processes. The density of silicified wood is approaching 2.6 Mg/m^3 . This fact leads to the conclusion that surface coating of wood may be suitable to obtain a new composite with moderate density.

Previous studies concerning the artificial silicification of wood were reported by Drum (1968 a, b), Leo & Barghoorn (1976), McCafferty (1992), Oehler & Schopf (1971), Saka & Tanno (1996) and Tanno et al. (1998). Their results show the general

possibility of technical silicification. Drum (1968 a, b) generated siliceous replicas of birch twigs and small pieces of plants by placing them in sodium metasilicate solutions. Oehler & Schopf (1971) examined the artificial permineralization of blue-green algae in silica gel at 165°C and 3000 bar. This appears to be a relevant experiment since the chemical surface structure of algae and wood are comparable in term of terminating OH groups. Hydrogen bondings between silica and the OH-groups cause the preservation of these algae filaments (Schultze-Lam et al. 1995). McCafferty (1992) impregnated wood by soaking in a solution containing silicon and aluminium compounds. However, besides the increase of hardness (up to 120%) no other conclusions about the properties of the wood-ceramic were drawn.

Leo & Barghoorn (1976), Saka & Tanno (1996) and Tanno et al. (1998) tried to "petrify" wood in a different way by using silicon-alkoxides (e.g. tetraethoxysilane TEOS). During sol-gel transformation these compounds hydrolyze to silicic acid $\text{Si}(\text{OH})_4$, one form of silica found in nature. Saka & Tanno (1996) and Tanno et al. (1992) examined only a few properties of silicified specimens. They found that the resistance against fungal attacks increases, and that treated samples

absorbed significantly less water than untreated ones.

In this study more than 100 experiments with different silica sources (sodium metasilicate, colloidal silica suspension, tetraethoxysilane) were performed to silicify samples of oak and spruce wood by hydrothermal treatment, vacuum impregnation and by soaking with silica-containing solutions. Different analytical methods were used to estimate the degree of property enhancement.

2 MATERIALS AND METHODS

2.1 Samples

Cube-shaped samples (1 cm^3) were prepared from oak and spruce woods containing about 4% moisture (25°C) and volatile substances. After a 24 h treatment with acetone the specimens were oven-dried (50°C, 24h). Some experiments were run with untreated samples to compare the results.

Oak wood samples possess significantly higher density and hardness than spruce (Table 1). Therefore one would expect that silicification occurs much faster in spruce wood, since its lower density, i.e. higher porosity.

Table 1: Selected properties of spruce and oak wood (hardness after Nennwitz et al. 1999).

Kind of wood	density [Mg/m^3]	Brinell hardness [N/mm^2]
Spruce	0.45	< 35
Oak	0.65	60-65

2.2 Experimental engineering and methods

Three distinct silicification methods were applied. Hydrothermal experiments at higher temperatures (100 – 138°C) and pressures (1 – 12 bar) were realized in a PTFE-lined steel autoclave. In all experiments the degree of filling was 25% and the reaction time about 3 hours. The second method used was vacuum impregnation of the specimens. The wood samples were penetrated by solutions under reduced pressure ($\approx 100 \text{ mbar}$) at room temperature for about 10 minutes.

In the third method the wood samples were placed in glass beakers containing silica-bearing solutions. These experiments were run in the temperature range between 40°C and 80°C at normal pressure. The solutions were stirred (3h) and subsequently kept overnight to allow sol-gel transformation and diffusion processes.

All treated specimens were dried in an oven at 50°C for at least 48h. To evaluate the water absorption of the material, the samples were placed

in distilled water for 6 days (at 25°C and normal pressure). The Brinell hardness of selected samples was determined and the changes of mass through silicification measured.

Microscopic methods (binocular and polarizing microscopy, SEM, CL) were applied to characterize the sample material.

2.3 Silica sources

Three different sources of silica were used. Sodium metasilicate solutions containing up to 2.5 wt% SiO_2 were prepared for hydrothermal experiments and soaking experiments in glass beakers. Colloidal suspensions of silica (40 wt% SiO_2) were applied during vacuum impregnation and in glass beaker experiments.

In most experiments TEOS was used, which was initially treated with isopropanol to hydrolyse. TEOS and a colloidal colloidal suspension of silica (CSS) contain about 30 wt% and 40 wt% silica, respectively. Their solutions were applied in glass beakers (only TEOS) and under vacuum conditions (both silica sources).

3 RESULTS AND DISCUSSION

3.1 Sodium metasilicate solutions

Aqueous solutions of Na_2SiO_3 have a high pH value (>10) that causes damage and dissolution of the wood material, especially under high pressure and temperatures. Particularly, oak samples showed large loss of mass (up to 30%), whereas spruce decreased in mass by only about 7%. Additionally, water absorption and Brinell hardness of treated specimens were lower than those of fresh samples. These facts considerably limit the further use of sodium metasilicate as silicification agent.

3.2 Colloidal suspension of silica (CSS) and tetraethoxysilane (TEOS) solutions

Although the CSS behaves similar to Na_2SiO_3 solutions (pH value of about 10), the former contains much more silica ($\approx 40 \text{ wt}\%$). Nevertheless, wood samples placed for longer time ($> 20 \text{ min}$) in CSS began to disintegrate. Therefore, only short time vacuum experiments were made with colloidal silica. On the other hand, organic TEOS solutions with alcohol and less diluted acetic acid caused no damage in wood.

Figure 1 illustrates comparable results of experiments in glass beakers (TEOS solution, 80°C, normal pressure) and with the vacuum impregnation technique. In particular, the mass of spruce wood increases during silicification up to 45%. Less porous oak wood shows substantially lower mass gain (10-20%).

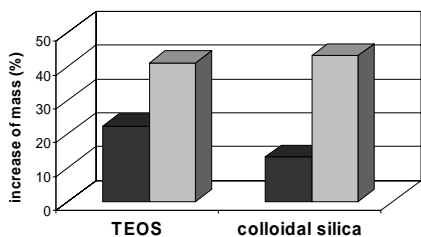


Figure 1: Increase of weight during silicification by TEOS in glass beakers and colloidal silica under vacuum (black = oak wood, grey = spruce wood).

Significant differences could be detected for the formation of vitreous silica. The experiments in glass beakers (40 – 80°C) lead to the deposition of silica coatings at the surface of the wood samples (Fig. 2).

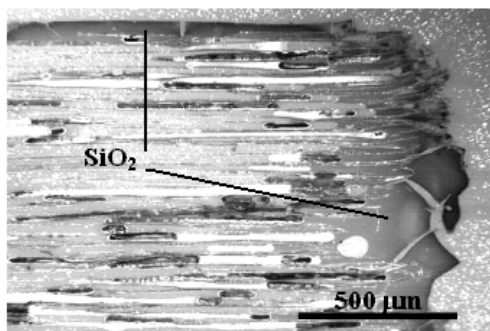


Figure 2: CL micrograph of silicified spruce wood (TEOS, 80°C, glass beaker) showing silica surface coatings.

In contrast to this, vacuum impregnation caused a deeper penetration of the silica-bearing solutions into the wood resulting in silicification of inner parts of the wood material (Fig. 3). Visible cracks and mechanical damage of the solid silica coatings resulted presumably from drying and preparation of the samples for microscopic examinations. Tetraethoxysilane (TEOS) hydrolyses during sol-gel transformation, followed by the formation of monosilicic acid which subsequently polymerizes. Hydrogen bonds can be formed between silicic acid and hydroxyl groups of cellulose (Tanno et al. 1998, Schultze-Lam et al. 1995).

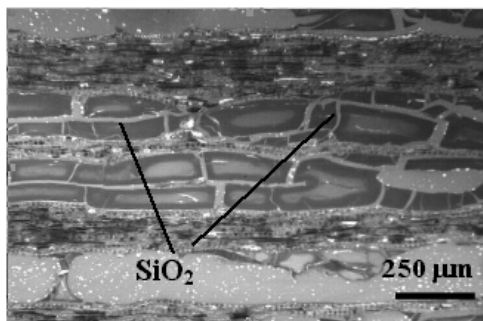


Figure 3: CL micrograph of silicified oak wood (vacuum impregnation with CSS).

Several experiments with TEOS (80°C, glass beaker) resulted in silica deposition not only in cell cavities but also in cell walls (Figure 4).

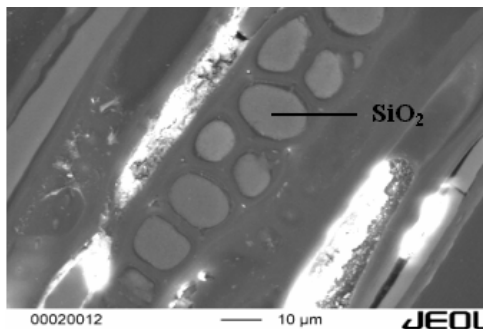


Figure 4: SEM micrograph of silicified vessels in the cell walls of oak wood (TEOS, 80°C, glass beaker).

Both wood samples of vacuum and glass beaker experiments with TEOS and CSS showed significantly decreased water absorption (up to 40 mass%) than untreated specimens (Figure 5). The precipitated solid silica in the interior of the wood samples partially prevents the penetration of water. The silica coatings of samples produced in glass beakers show similar effects. Only cracks in the silica coatings enable the water to penetrate.

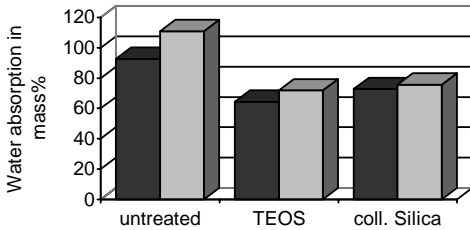


Figure 5: Water absorption of untreated and silicified wood samples (black = oak wood, grey = spruce wood).

The evaluation of the Brinell hardness shows significant differences between samples from vacuum experiments and those treated in glass beakers (Figure 6). An increased hardness is likely caused by silica surface coatings. The experiments in glass beakers result in an increase of hardness of spruce wood of 100%, in oak samples of about 60%.

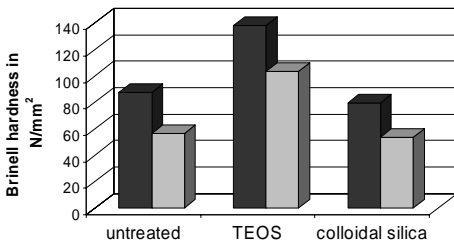


Figure 6: Brinell hardness of untreated and silicified wood samples (black = oak wood, grey = spruce wood).

In contrast, in samples impregnated under vacuum conditions nearly all silica was precipitated in the inner part. Therefore, no protecting coating with increased hardness develops at the wood surface.

4 CONCLUSIONS

In the present study, different methods were tested to produce non-toxic silica coatings on wood samples, which should improve several properties such as mechanical and chemical resistance, water uptake, etc. Successfully applied, these techniques could also help to reduce the demand for products of rain forests and hence protect the environment.

Suitable sources for technical silicification are colloidal silica and TEOS, which contain at least 30 wt% SiO₂. Wood samples of oak and spruce were impregnated under vacuum conditions with both

silica sources. Additionally, samples were soaked in glass beakers containing TEOS solution.

The results show that treatment at moderate temperature (40 to 80°C and ambient pressure) in glass beakers and vacuum impregnation improve the weathering resistance by lowering water absorption. Furthermore, an increase of surface hardness of both oak and spruce wood (nearly 100%) was observed for samples treated in glass beakers. On the surface of these specimens vitreous silica coatings (thickness up to 100µm) could be detected resulting from sol-gel transformation processes.

Methods that combine high alkaline solutions (pH >10, e.g. sodium metasilicate solutions) with low silica content and temperatures above 100°C are unable to silicify wood materials in short-time experiments (several days).

Further studies are required to optimize chemical composition, drying procedures and other variables in order to generate a silica coating without cracks or other defects. Moreover, further studies should combine experiments in glass beakers with the vacuum impregnation technique.

5 REFERENCES

- Drum, R.W. 1968a. Silicification of *Betula* woody tissue in vitro. *Science* 161: 175 – 176.
- Drum, R. W. 1968b. Petrification of plant tissue in the laboratory. *Nature* 218: 784 – 785.
- Leo, R.F. & Barghoorn, E.S. 1976. Silicification of wood. *Harvard Bot. Mus. Leafl., Harvard Univ.* 25: 1 – 47.
- McCafferty, P. 1992. Instant petrified wood. *Popular Science* 241 (4): 56 – 57.
- Nennewitz, I., Nutsch, W. & Peschel, P. 1999. *Holztechnik, Tabellenbuch*. Haan-Gruiten: Nourney, Vollmer GmbH & Co., Verlag Europa-Lehrmittel. 327p.
- Oehler, J. H. & Schopf, J. W. 1971. Artificial microfossils: experimental studies of permineralisation of blue-green algae in silica. *Science* 174: 1229 – 1231.
- Saka, S. & Tanno S. 1996. Wood-inorganic composites prepared by the sol-gel process. Part VI. Effects of a property-enhancer on fire-resistance in SiO₂-P₂O₅ and SiO₂-B₂O₃ wood inorganic composites. *Mokuzai-Gakkai-shi* 42 (1): 81 – 86.
- Schultze-Lam, S., Ferris, F.G., Konhauser, K.O. & Wiese, R.G. 1995. In situ silicification of an Icelandic hot spring microbial mat: implications for microfossil formation. *Can. J. Earth Sci.* 32: 2021 – 2026.
- Tanno, F., Saka, S., Yamamoto, A. & Takabe, K. 1998. Antimicrobial TMSAH-Added Wood-Inorganic Composites Prepared by the Sol-Gel Process. *Holzforschung* 52: 365 – 370.

Hydroxyapatite Formation in Human Blood

A.T.Titov

Department of Mineralogy, United Institute of Geology, Geophysics and Mineralogy SB RAS, Novosibirsk, Russia

P.M.Larionov

Department of Medicine, Institute of Circulation Pathology, Novosibirsk, Russia

A.S.Ivanova & V.I.Zaikovskii

Department of Chemistry, Borekov Institute of Catalysis SB RAS, Novosibirsk, Russia

ABSTRACT: In existing models of the soft tissue mineralization the role of blood is limited to transport of calcium and phosphorus ions. In present study we prove a tissue mineralization mechanism stating that hydroxyapatite (HAP) is produced in the blood plasma. This mechanism is based on the observation of HAP microcrystals, which are similar to hydroxyapatite calcificates on heart valves and the bone apatite, in the dry blood rests of healthy donors. Modeling experiments were carried out under adjustable conditions ($T=37^{\circ}\text{C}$, $\text{pH}=7.4$) with respect to the ionic composition of the main elements (Ca, P, Mg and NaCl) in aqueous solutions close to their contents in the blood plasma. The basic blood protein albumin was used as a biological component. Serum bovine albumin was used as the modeling protein. On the basis of experimental data it was concluded that the blood proteins promote the formation of hydroxyapatite microcrystals. Albumin plays a special role in this process.

1 INTRODUCTION

Mineralization in blood-vascular organs is known to exist solely as a pathological genesis phenomenon. Mineral deposits on natural and bioprosthetic cardiac valves and blood vessels are represented by calcium phosphate. From the physicochemical point of view, a necessary condition for calcium phosphate crystallization is oversaturation of calcium and phosphorus ions in a tissue fluid. Till now the nature and parameters of the tissue fluid responsible for the physiological and pathological mineralization remain unexplained.

The most commonly accepted hypothesis is the formation of primary calcific deposits on the aorta and cardiac valves by the membrane mechanism similar to bone mineralization (Anderson 1983). Here the role of blood is limited to transport of Ca and P ions. In intercellular matrix vesicles with membrane properties their concentrations reach values required to form hydroxyapatite (HAP) $\text{Ca}_{10}(\text{PO}_4)_6(\text{OH})_2$ or other calcium phosphates. Acid phosphates formation: octacalcium phosphate (OCP)- $\text{Ca}_8\text{H}_2(\text{PO}_4)_6 \cdot 5\text{H}_2\text{O}$ or dicalcium phosphate digidrate (DCPD-brushit)- $\text{CaHPO}_4 \cdot 2\text{H}_2\text{O}$ is assumed to be more preferable as precursor phases that undergo transformation into the most stable one

- hydroxyapatite (Tomasic 2001; LeGeros 2001; Mavrilas 1999).

In the present paper we prove an alternative mechanism assuming that hydroxyapatite forms in the blood plasma without participation of any intermediate phases. It is assumed that it participates in the tissue mineralization, whereas the formation of more acid calcium phosphates results from secondary transformations.

This concept is based on: a) investigation of the atomic structure and morphology of calcific deposits of heart valves; b) our observation of hydroxyapatite microcrystals in the human blood and lymph (Titov 2000); c) experimental results on modeling of the ionic blood composition in aqueous solutions.

2 MATERIALS AND METHODS

2.1 *Objects of in vivo mineralization*

In the present study we used intraoperative material – mineralized aortic and mitral cardiac valves obtained from patients with acquired valvular diseases of rheumatic and septic genesis. Their macroscopic and histological analysis was performed. In addition, blood has been taken from patients with mineralization of the cardiac valves

proved by the ultrasonic method. The dry rests of the blood plasma was studied. For comparison a similar analysis was performed with the blood and lymph from a patient with disseminated sclerosis.

2.2 Calcium phosphate synthesis conditions

The modeling of the calcium phosphate formation in the human blood was performed under controlled conditions with constant $\text{pH}=7.4\pm 0.05$ and temperature $T=37\pm 0.2^\circ\text{C}$. The concentrations of the main elements (Ca and P) in the aqueous solution corresponded to their ionic contents in the blood of a healthy adult.

The influence of the Mg and NaCl presence in the initial solution on the phase composition and microstructure of calcium phosphate was also studied. In this case, the concentrations of calcium and phosphorous ions in the final aqueous solution remained at the same level.

The ionic concentrations in the blood of a healthy adult and in the final aqueous solution are presented below in the order of performed experiments.

In blood: Ca – (1.05-1.3) mM; P – (1-1.5) mM; Mg – (0.75-1.25) mM; NaCl – 0.15 M; albumin – (35-55) g/L; pH – 7.36-7.46

In the experiments:

- (1). Ca – 1.33 mM; P – 1.5 mM
- (2). Ca – 1.33 mM; P – 1.5 mM; Mg – 0.4 mM
- (3). Ca – 1.33 mM; P – 1.5 mM; Mg – 0.8 mM
- (4). Ca – 1.33 mM; P – 1.5 mM; NaCl – 0.05 M
- (5). Ca – 1.33 mM; P – 1.5 mM; NaCl – 0.15 M
- (6). Ca – 1.33 mM; P – 1.5 mM; NaCl – 0.15 M; Mg – 0.8 mM
- (7). Ca – 1.33 mM; P – 1.5 mM; NaCl – 0.15 M; Mg – 0.8 mM; albumin – 38.6 g/L

We used the main blood protein albumin as a biological component. Bovine serum albumin, which is available in a high-purity form and easily soluble in water, was chosen as the model protein. Mixing of the initial aqueous solutions of K_2HPO_4 (+NaCl) and CaCl_2 (+ MgCl_2) was carried out at 6.4-6.6 mL/min rate to reach 800 mL of total volume. Such a slow reagent mixing was applied because it matches the human organism conditions best. In each experiment the solution was continuously stirred at the predetermined temperature for 7 hours.

2.3 Methods of investigation

In the present work we used local structural and chemical analysis methods: transmission electron microscopy (TEM), high resolution electron microscopy (HREM), electron diffraction, scanning electron microscopy (SEM), and X-ray microprobe analysis with the energy (EDX) and wave (WDX) dispersion. The instruments used in the study were JEM100-CX, JEM2000 equipped with EDX EDAX, LEO1430VP equipped with EDX OHFORD and

WDX CAMEBAX-micro. Also a Bruker X-ray diffractometer D8 GADDS was used.

3 RESULTS

The investigation of the mineralized parts of cardiac valves by optical and scanning electron microscopy demonstrated that the calcificates exist as an aggregates of fine particles, which form larger particles of varying density up to several centimeters in size.

The hydroxyapatite stoichiometry in cardiac valves was determined by X-ray microanalysis (WDX). Synthetic apatite was used as a standard. The Ca/P molar ratios in the deposits were in the range of 1.72-1.80. The total contents of Na, Mg, Cl, S, Si, Fe, and Mn in each sample did not exceed 1%.

According to the IR spectroscopy data, the valve HAP contained about 4 – 5 wt.% of CO_3^{2-} ions. The presence of carbonate is typical for human apatites where CO_3^{2-} ions substitute PO_4^{3-} groups in the structure (Posner 1984).

According to the TEM data, the calcificate aggregates of the cardiac valves consist of primary particles different in size, morphology and structural ordering. The largest crystals comprising a small part of the volume in the samples of different mineralization degrees have a plate-like shape and are about 5 nm thick and 1 μm to 5 μm in cross size. They are well structurally ordered and sometimes show hexagonal habitus typical for apatite crystals. The most developed planes in these crystals are basal planes (0001). The major part of the valve HAP consists of 10-100 nm microcrystals similar to the bone apatite (c-axis in the crystal plane). Large grains normally consist of disoriented blocks with the sizes from 5 nm to 20 nm. It is remarkable that the samples that are poorly crystallized according to the XRD data are observed as block microcrystals in the high resolution electron microscope.

Mineralization of different type was observed in some valves with HAP. Plate-like crystals and aggregates of sharp-cornered crystals growing from a common center were found. They are 2 to 10 μm in size and are distributed throughout the whole valve tissue. These deposits are also calcium phosphate, and only P and Ca signals are registered by EDX. The Ca/P ratios obtained from comparison with the apatite standard are between 0.95 and 1 for different measurements, which corresponds better to brushite. The brushite crystals do not make oriented adhesion with the surrounding fibers but rather tear the interfiber connections. We have discovered the hydroxyapatite crystals (10-70nm), which are structurally and morphologically similar to the bone apatite and the fine fraction of the cardiac valve calcification, both in the solid residue of the blood plasma of patients with calcinosis, and in the blood

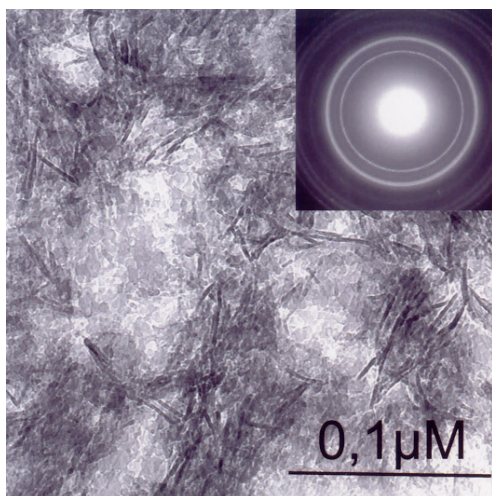


Figure 1. TEM – image and electron diffraction of HAP synthesized in the aqueous solution (exp.1.).

of healthy donors (Titov 2001). Furthermore, in the lymph of a patient with disseminated sclerosis we found plate-like crystals up to 2.5 μm in size similar to the microcrystals with (0001) planes in cardiac valves. It also contains needle-like microcrystals, but they differ from the microcrystals of the fine fraction of valve HAP. Hydroxyapatite of the solid residue of blood and lymph was identified by electron diffraction and X-ray spectra (EDX).

The method of HAP isolation from the solid residue of blood and lymph developed by us was reported earlier (Titov 2001).

To gain further proof of the hypothesis on the blood HAP participation in the tissue calcification and use it in the diagnostics of mineral metabolism disorder in the human organism, we performed model experiments under controlled conditions.

The synthetic product obtained under controlled conditions (exp.1) is HAP as proven by electron diffraction and X-ray microanalysis (EDX). Hydroxyapatite is an aggregate of microcrystals of different morphology and structure. There are needle-like crystals up to 200 nm in length and 5 nm in width with a typical contrast ratio on TEM photos – a light central line and darker edges. The needle-like crystals with a similar contrast ratio of the TEM photos were observed in the patient's lymph. According to the high-resolution electron microscopy and electron diffraction data, the c-axis direction of the needle-like crystals is parallel to their axial line. The remaining part consists of thin plates with different structural ordering varying from an aggregate of nanocrystals consisting of several elementary cells to large crystals with long range structural order.

Adding 0.4 mM magnesium solution into the batch (exp.2) resulted in a considerable decrease of the total weight of synthetic HAP. The needle-like HAP microcrystals became 1.5-2 times smaller compared to the sample in the experiment (1). Under the conditions of experiment (3) when the Mg concentration in the solution was increased to 0.8 mM, both the size and morphology of the HAP crystals changed. The resulting hydroxyapatite consisted of uniform microcrystals 40-70 nm in size with the shape close to that of the bone apatite.

The amount of the HAP synthesized under these conditions is close to the detection limit.

In experiment (4) with 0.05 M NaCl concentration in the aqueous solution, a decrease of the total mass of synthetic HAP and size of the microcrystals was observed. No calcium phosphate was produced when the NaCl concentration in the aqueous solution was 0.15 M with the concentration of Ca and P equal to 1.33 mM and 1.5 mM, respectively (exp.5). Under the conditions of experiment (6) with the NaCl concentration of 0.15 M, and Mg concentration of 1 mM in the final aqueous solution containing 1.33 mM calcium ions, and 1.5 mM concentration of phosphorous ions, calcium phosphate was not produced even after the solution was aged for one year at room temperature.

However, albumin addition to a similar solution resulted in the calcium phosphate formation. It should be noted that the time of the experiment equal to 7 hours turned out to be insufficient for production of the calcium phosphate amount required for preparation of samples and reliable diagnostics of the phase composition of the obtained product.

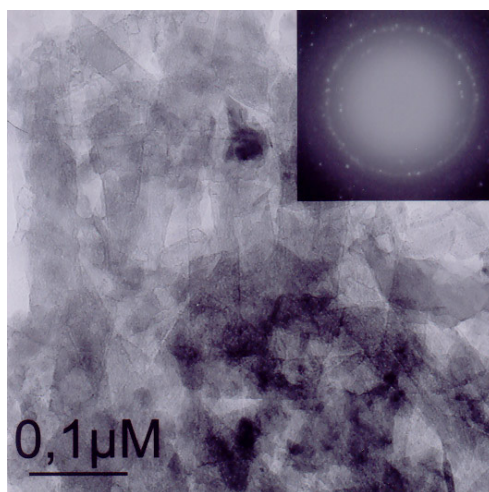


Figure 2. TEM - image and electron diffraction of HAP synthesized in the aqueous solution at presence albumin

However, the precipitate in the solution was correctly identified in 10 days as hydroxyapatite by electron diffraction and X-ray analysis (EDX). The TEM images show hydroxyapatite as thin plates of prolate shape with the length of 50-150 nm.

4 DISCUSSION

Calcification of the forming bone tissue means deposition of calcium phosphates into a neogenic matrix. Pathological calcification causes the calcium phosphate deposition in the tissues of different organs. It is known that the bone apatite consists of thin-plate microcrystals elongated along the c-axis with the average size of $\sim 45 \times 20 \times 3$ nm (Mann 1988). Based on the similarity of the microstructure and chemical composition between the inorganic bone tissue and calcinosis masses on cardiac valves, it was assumed that their mineral elements are formed in the human blood. The HAP microcrystals found in the solid blood residues of healthy donors are structurally and morphologically similar to the bone apatite (Titov 2000). Needle-like HAP crystals found in the lymph of sick patients are similar to those obtained in experiments (1) and (4) where there was no Mg, or its concentration was much lower (exp. 2) than the normal concentration in the human blood. Magnesium is not only an inhibitor of the HAP formation (Montel 1981), but it also makes the microcrystals more isometric and similar in shape to the bone apatite (exp. 3). Identical needle-like microcrystals were also observed during *in vitro* mineralization of tendon (Yamaguchi 2003) and were formed in an aqueous solution in the presence of polyacrylic acid (Sz-Chain 2003). It is significant that these experiments were performed without Mg.

The effect of NaCl as an inhibitor of the HAP formation is evidently due to an increase of the ionic stress in the solution. However, the sodium salt can completely inhibit the HAP formation in an aqueous solution (exp. 4, 5).

The joint action of Mg and NaCl in an aqueous solution in concentrations close to those of the blood plasma (exp.6) completely inhibits the HAP formation. The blood proteins promote the hydroxyapatite formation. The presence of HAP nanocrystals in the blood of healthy donors is an indicative of their physiological origin. The experimental findings indicate that the formation of hydroxyapatite microcrystals in the blood is possible only in the presence of albumin and, presumably, other proteins and ferments, which may accelerate or inhibit the formation of hydroxyapatite.

HAP microcrystals formed in the blood may also participate in mineralization of cardiac valves and cardiovascular calcification. An endothelium injury may promote penetration of HAP microcrystals formed in the blood into collagen fibers followed by

their deposition. At the late mineralization stage the transformation of HAP to brushite in the valve tissue may be accompanied by the pH decrease. The latter may be result from deep degradation changes in the valve tissue related to functional abnormalities due to calcification or because of septic processes.

5 CONCLUSION

Hydroxyapatite microcrystals found in the human blood and lymph as well as HAP synthesis under conditions modeling the ionic composition of the blood elements prove direct formation of HAP in the blood without participation of any intermediate phases. A special role of albumin in the soft tissue calcification may be assumed taking into account that the matrix of a growing bone absorbs albumin from the blood (Owen 1976).

This work was supported in part by ISTC-1858 and RFBR - 02-05-64756.

6 REFERENCE

- Anderson H.C. 1983. Calcific diseases. A concept. Arch. Pathol.Lab. Med.107: 7, 341-348.
- LeGeros R.Z. 2001. Formation and transformation of calcium phosphates: relevance to vascular calcification. Z. Cardiol. 90:3, III/116-III/124 .
- Tomasic B.B. 2001. Physicochemical principles of cardiovascular calcification. Z. Cardiol. 90:3, III/68-III/80.
- Mann S. 1988. Molecular recognition in biomineralization. Nature..332: 119-124.
- Mavrilas D., Apostolaki A., Kaposos J.et.al. 1999. Development of bioprosthetic heart valve calcification in vitro and in animal models: morphology and composition. J. Crystals Growth. 205: 554-562.
- Montel G., Bonel G., Heughebaert J.S. et.al. 1981. New concept in the composition, crystallisation and growth of the mineral component of calcified tissue. J. Crystals Growth. 53: 74-99.
- Owen M., Triffitt J.T. 1976. Extravascular albumin in bone tissue. J. Physiol..257: 293-307.
- Posner A.S., Blumental N.C., Betts F. 1984. Chemistry and structure of precipitated hydroxyapatites. Phosphate minerals. New York. Springer- Verlag.:330-350.
- Titov A.T., Larionov P.M., Shchukin V.S.et al. 2000. Possible formation of hydroxyapatite in blood. Doklady Biochemistry. 373: July-August.132.
- Titov A.T., Larionov P.M., Zaikovskii V.I. 2001. Hydroxyapatite in man blood. Surface investigation: x-ray, synchrotron and neutron techniques.7: 72-76.
- Sz-Chain L., San-Yuan C., Dean-Mo L. 2003. Synthesis and characterization of needlelike apatitic nanocomposite with controlled aspect ratios. Biomaterials. 24: 3981-3988.
- Yamaguchi I., Kogure T., Sakane M. 2003. Microstructure analysis of calcium phosphate formed tendon. J. Mater. Science:Mat. in Med. 14: 883-889.

Ceramic, Glasses and Cement

Manganese in Cement

H.Pöllmann

Department of Mineralogy and Geochemistry, Martin-Luther University, Halle, Germany

ABSTRACT: Cement is still used world-wide in increasing amounts and is a prosperous branch of industry. New demands for cements are increasing quality, the use of secondary raw materials and alternative fuels. The production of new cement types also can be an interesting topic. In this study it is shown how manganese influences the properties of cement. The synthesis of a new cement is shown. Different sources of manganese are used.

1 INTRODUCTION

Manganese additions to cements were not studied in detail in the past. Beside other uses no use as a component in HAC-applications was described (Harben et al. 1998). The manganese containing CaMn_2O_4 (Marokite) is the related structure to monocalciumaluminate $\text{CaO}\cdot\text{Al}_2\text{O}_3$ which is the dominant phase in HAC (Füllmann 1997, Harben et al. 1998, Motzet, Pöllmann 2001, Scrivener & Capmas 1998, Sourie & Glasser 1991, Walenta 1997). Marokite crystallizes in a distorted spinel structure and is therefore not a hydraulic mineral.

The addition of manganese oxides to the raw meal leads to the formation of a new type of highly reactive HAC (Wicks 1985, Pöllmann 2001, Pöllmann & Oberste-Padtberg 2001).

Depending on the raw materials and the temperature applied, the new formed phases are solid solutions of manganese with the primary minerals of a HAC, like CA and C_4AF but also calciummanganates and different Ca-Al-Si-Fe-Mn-oxides with varying stoichiometry are formed.

The hydration of these primary minerals leads to different new hydrates partially also incorporating manganese in their crystal lattices. Solid solution series of manganese brownmillerites were described

in (Füllmann 1997, Motzet & Pöllmann 1998, Pöllmann & Oberste-Padtberg 2001, Puertas et al. 1990, Zötzl & Pöllmann 2001, Zötzl & Pöllmann 2002).

2 PREPARATION & EXPERIMENTAL

The sample preparation was made by mixing calciumcarbonate, manganese oxide and aluminium oxide \pm iron oxide in different proportions – these mixtures were carefully homogenized and sintered at temperatures between 1150 and 1350°C with varying times (2h-30h). The range of compositions of these mixtures is shown in Figure1. Pt- and Al_2O_3 -crucibles were used for the sinter procedure.

The sintered products were afterwards crushed and investigated by X-ray powder diffractometry to determine the phase compositions. New compounds were described and their properties determined. X-ray powder data of new phases were measured and their crystallographic data established. The powdered samples were tested by calorimetry to determine the hydraulicity (Bayoux et al., Pöllmann et al. 1991, Pöllmann & Oberste-Padtberg 2001). Special samples were also investigated by scanning

electron microscopy to demonstrate differences in microstructure and phase formation.

iron phases with brownmillerite structure. The solid solution of monocalciumaluminate can be given by:

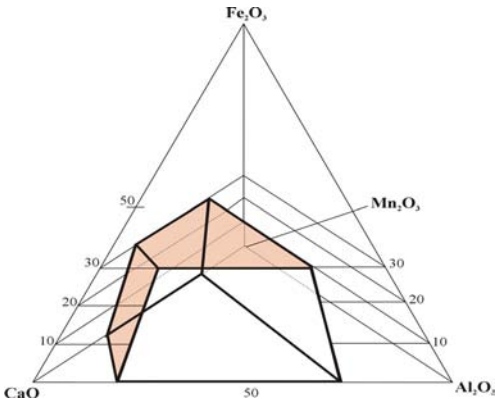
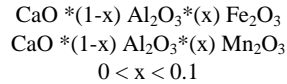


Figure 1. Tetrahedron CaO – Al₂O₃ – Mn₂O₃ – Fe₂O₃ with the region of hydraulic manganese- containing mixtures including classic HAC.

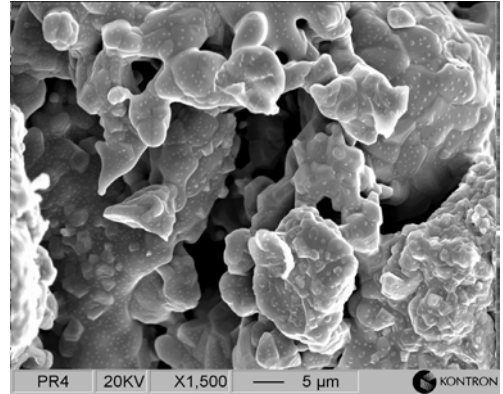


Figure 2. SEM micrograph of sintered manganese cement.

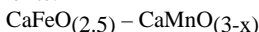
3 RESULTS

Depending on the mineralogical compositions different hydraulic compositions are formed. It is highly important to avoid compositions with high amounts of Calcium manganates with perovskite or spinel structure type, because these phases are only poorly hydraulic. It was necessary to determine X-ray powder data of pure phases to establish identification possibilities in cementitious systems. The following phases were obtained and characterized (Table 1).

Table 1. Phases containing manganese.

1. C(A,Mn)
 2. C₄(A,F,Mn)₂
 3. Spinels
 4. CaMnO(3-x)
- a) Marokite CaMn₂O₄
 b) True spinels with (Fe,Mn)

The relationship between Brownmillerite and Perovskite structure type can be explained by the following equation showing the oxygen deficiency in Brownmillerite.



Brownmillerite – Perovskite

The typical microstructure of a sintered sample is shown in Figure 2, whereas figure 3 shows well crystallized perovskite crystals. The hydraulicity of perovskite containing sintered samples is drastically decreased. Manganese is also incorporated in different calcium aluminates and calcium aluminium

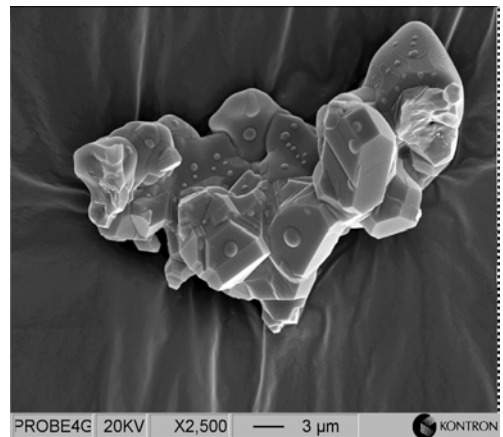


Figure 3. SEM-micrograph of sintered sample showing especially non-hydraulic perovskite.

Special investigations to the phase formation in pure C₂F-C₂Mn-C₂A (Brownmillerite)-system including manganese were performed to establish stability areas of phases (Figure 4).

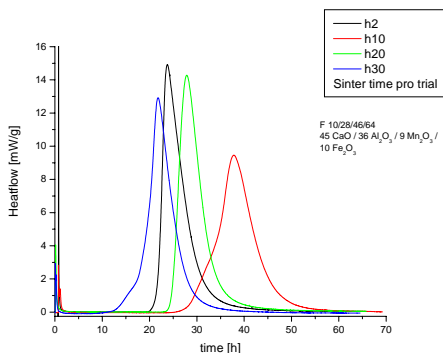


Figure 8. Calorimetric curves of sintered products with chemical composition $45\text{CaO}/36\text{Al}_2\text{O}_3/9\text{Mn}_2\text{O}_3/10\text{Fe}_2\text{O}_3$.

4 SUMMARY AND CONCLUSION

The advantages of manganese for production of HAC's can be summarized as follows:

1. Enlowered sintering temperatures (100 °C – 300 °C) (due to high amounts(20-30%) of manganese present)own phases are formed –(no additional fluxes were used)
2. Use of widely available and cheap raw materials
3. High strength development
4. High early strength development
5. Weathering stability
6. High water bonding capacity due to phase formation with high water bonding capacities
7. Complex use of this cement in construction industry possible due to good strength development
8. Use of this cement in environmental applications for immobilization of soluble manganese salts to form insoluble hydrates
9. High chemical resistance, low leaching rates
10. Workability at low temperatures possible due to high heat evolution
11. Admixtures control of hydraulic properties in applications possible similar to HAC.

5 OUTLOOK

New raw materials (low manganese ores) and secondary resources (manganese slags and fines) will be used for clinker production to further decrease production costs. Also the production of manganese cement in small scale technical furnaces will be investigated.

6 ACKNOWLEDGEMENT

Special thanks are due to ICDD for providing financial help to establish X-ray powder data of new manganese phases.

7 REFERENCES

- Bayoux, J.B., Bonin, A. & Verschaeve, M. Study of the Hydration Properties of Aluminous Cement and Calcium Sulphate Mixes, Calcium Aluminate Cements, R.J. Mangabhai, ed., E. & FN Spon, London, p. 320-334.
- Fillmann, Th. 1997. Quantitative Rietveld-Phasenanalyse von Tonerdezementen, Dissertation Erlangen.
- Harben, P., Raleigh, C. & Harris, J. 1998. Manganese Uses and Markets, Industrial Minerals Information Ltd., London.
- Mangabhai, R.J. 1990. ed.: Calcium Aluminate Cements, E & FN Spon, London.
- Motzet, H. Entwicklung eines Sinterverfahrens zur Herstellung von eisenreichen Tonerdezementen, Dissertation, Halle/Saale.
- Motzet, H. & Pöllmann, H. 1998. Quantitative Phase Analysis of High Alumina Cements, Proceedings of International Conference Cement Micr. p. 187-206.
- Peacor, D.R., Dunn, P.J., Kato, A. Wicks, F.J. 1985. Shigaite, a new manganese aluminum sulfate mineral fom the Ioi mine, Shiga, Japan, N. Jb. Min., Mh. 453-457.
- Pöllmann, H., KUZEL, H. J. & MEYER, H. W. 1991. Heat-Flow Calorimeter in Cement Chemistry-Construction and Application of a Low Cost High Sensitive Calorimeter, Proc. 13th International Conference on Chemical of Cement, Tampa. p. 254-272.
- Pöllmann, H. 2001. Shigait-Synthese, Eigenschaften und Anwendung – Z. Krist.
- Pöllmann, H. & Oberste-Padtberg, R. 2001. Manganese in High Alumina Cement, Calcium Aluminate Cements, IOM Communications, 139-148.
- Pöllmann, H. 2001. Mineralogy and Crystal chemistry of calcium aluminate cement – Int.Conf.on Calc. Aluminate Cements, Edinburgh, Scotland, S. 79-98.
- Puertas, F., Blanco-Varela, M.T. & Dominguez, R. 1990. Characterization of $\text{Ca}_2\text{AlMnO}_5$. A comparative study between $\text{Ca}_2\text{AlMnO}_5$ and $\text{Ca}_2\text{AlFeO}_5$ – Cem.Concr.Res. 20, 429-438.
- Scrivener, K.L. & CAPMAS, A. 1998. Calcium Aluminate Cements in Lea's Chemistry of Cements and Conrete, PC Hewlett, ed., Arnold, London. p. 709-778.
- Sourie, A. & GLASSER, F.P. 1991. Studies on the Mineralogy of High Alumina Cements, British Ceramics, Trans. Journal, 90. p. 1772-1776.
- Walenta, G. 1997. Synthesen und Rietveld Verfeinerung der Einzelphasen von Tonerdezementen – Dissertation Erlangen.
- Zötzl, M. & Pöllmann, H. 2001. Diadochiebeziehungen im System $\text{Ca}_2\text{Fe}_2\text{O}_5$ – $\text{Ca}_2\text{Mn}_2\text{O}_5$ – $\text{Ca}_2\text{Al}_2\text{O}_5$ – Ber. Dt. Min. Ges., 206.
- Zötzl, M. & Pöllmann, H. 2002. Phasenstabilitätsbereiche im System $\text{CaMnO}_2.8$ – „ $\text{CaAlO}_2.5$ “ bei 1300 oC – Ber. Dt. Min. Ges.

Evaluation of Powder Densification as Function of Size Distribution and Pressing Additives and Its Influence on Alumina Properties

A.K.Alves & C.P.Bergmann

Department of Materials, Federal University of Rio Grande do Sul, Porto Alegre, Brazil

ABSTRACT: The densification of a solid body by pressing in ceramic processing depends directly on the granulometry of the raw material and the pressing additives. This work evaluates the mechanical properties of alumina as function of both size distribution of the raw material powder and pressing additives. Alumina Alcoa 3000 was used as raw material. The different size fractions were carried out by sieve classification. The additives were PVA (polyvinyl alcohol), CMC (carboxymethyl cellulose) or PEG (polyethylene glycol). Green density, linear shrinkage after sintering, mechanical strength, apparent porosity and water absorption were evaluated. The results indicate that fine bimodal size distribution associated with PVA binder led to more intense densification, by the same sintering conditions for all samples.

1 INTRODUCTION

Ceramic sintering has been extensively researched due to its technological importance. The first requirement for an efficient ceramic processing is the attainment of a good powder. This powder must have not only high purity, but also other characteristics such as high packaging density and good sintering capability. Many methods has been developed towards improve the quality of the available powders, such as fine milling. Reed (1998).

The properties of the sintered product reflect the nature of the compacted particles. Powder with great activity (great power of sintering) simultaneously with the study of the phenomena that occurs during the sintering can help in the achievement of a product with better characteristics. Özkan & Briscoe (1997).

Although it is common sense that grain size distribution with single size can produce samples with uniform density and fine grains, the most commercial powders possess a certain distribution of size to help the sintering and to minimize the average retraction. On the other hand, a very wide distribution can difficult the sintering of the body, since the small sintering ability of coarser particles,

and lead to a structural nonhomogeneity as result of particle segregation. Say et al (2002).

The densification rate is inversely proportional to the particle size at any temperature. The volume diffusion increases by reduction of the particle size in a ratio 1.5:1. This means that the smaller particle size the more active will be this powder in the sintering process. A reduction of ten times in the particle size reduces about 200°C the sintering temperature.

Petterson & Benson (1999) observed that materials with a wide particle size distribution sintered easily. Also noticed that pressed samples with narrow particle size distribution had few and large pores while those samples with a wide particle size distribution had many and small pores.

Another factor of basic importance in the pressing of ceramic bodies is the type of additive used to assist the pressing stage. These additives have many functions such as lubricant, plasticizer and bounding agent. Baklouti et al (2001). However the characteristics of these elements can damage of the ceramic element. In accordance with the particle size distribution of the powder and its superficial area, will be necessary adding one specific type of pressing additives.

This work verifies which of the particle sized distribution confers the best characteristics to ceramic alumina samples, as well as which is the best pressing additive to this material.

2 EXPERIMENTAL PROCEDURES

2.1 Compositions

Four compositions with different particle size distribution of commercial alumina (Alcoa3000) have been formulated. The powder passed through an increasing sequence of sieves under mechanic vibration, originating four compositions.

2.2 Preparation of the samples

To each one of the compositions a different kind of additive was added. An aqueous solution of PVA (polyvinyl alcohol) 10%wt and an aqueous solution of CMC (carboxymethyl cellulose) 10%wt were added as bounding agents. The plasticizer used was Zuzoplast, a type of polyethylene glycol (PEG). PVA, CMC and, PEG had been added in the ratio of 10% wt.

After the manual homogenization of the mixture, each one of the compositions passed for an 18 meshes sieve in order to complete the homogenization, and to form spherical alumina granules. This stage aimed a best fulfilling of the mold in the pressing stage. The pressure used was 60MPa.

After pressing, the bodies had been measured and weighed. The conformed samples had been left air drying for 24 hours and a period of drying in stove (110°C for 24 hours). The sintering occurred in an oven with normal atmosphere (air and 1atm) 1540°C for 3 hours. The rate of heating was 150°C/h.

After the sintering, the samples were characterized by flexure resistance, water absorption and apparent porosity. Also it was followed the compacting of the powder, the linear and volumetric retraction and the weight loss in the sintering process.

3 RESULTS

The D_{50} of the four compositions were represented in Table 2.

Table 2: Sieve mesh and D_{50} of the compositions.

Composition	Mesh	D_{50} (μm)
G1	Less than 65	3,95
G2	65>115	9,03
G3	115>200	70,14
G4	200>270	97,14

The first fact to be observed is that the particle size distribution has a great influence in the compacting of the samples. In fact the particle size distribution is important in usual systems when the retraction must be minimized. A greater content of large particles and a sufficient amount of small particles, to fill the interstices left for the wrapping up of thick particles, will result in a high density body. The narrowest particle size distribution (G4) was the one with the greatest compacting mainly in comparison to the one which possess only coarse particles (G1), applying the same pressure and pressing agent. PVA shows the smallest compacting for any particle sized distribution. (Figure 1).

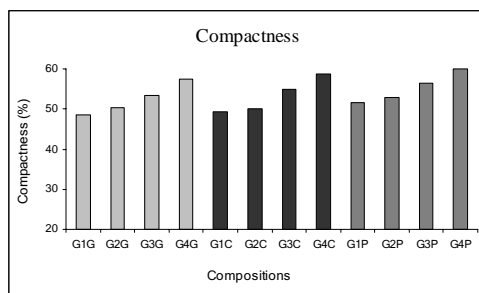


Figure 1: Compactness of samples.

The linear retraction in sintering can indicate the degree of sintering of a ceramic material. Constancy is observed indicating that the sintering happened in similar degree for the different particle sizes.

Another measure of the sintering degree is the densification, defined as the reason between the density after the sintering and the theoretical density of the material. It is observed that for bounding agent PEG and CMC the densification was independent of the particle size distribution, being around 95%. However for PVA, the particle size acts on the densification in a significant way. The samples with narrow particle size distribution possess densification 94% in comparison with 92% of the material of coarse particles. It is important to observe that the densification using PVA was poorer than one using PEG or CMC.

The flexure resistance before sintering was relatively constant. The coarser particles present resistance lower than fine particles, as depicted in Figure 2. The bounding agent that provided the best resistance before sintering was PEG for any particle size distribution and the worst additive was PVA.

The flexure resistance after sintering presented a fall with the increase of particles size. This is expected since finer particles have greater ability of sintering and the material attains greater densification and resistance. The bounding or

plasticizer that provided the best resistance after firing was CMC, but it presented the worst behavior considering the coarse particle size. The best plasticizer when the samples were prepared with

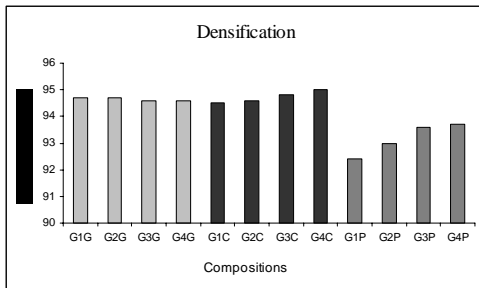


Figure 2: Sample densification.

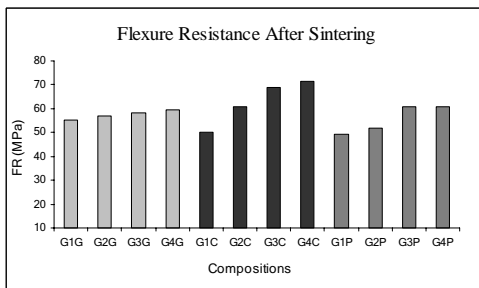


Figure 3: Flexure resistance after sintering.

coarse particles was PEG. As observed in Figure 3, PVA show intermediate results for any particle size composition, justifying its ample applicability.

In Figure 4, an increase in the apparent porosity was observed along with the increase of particle size. This result can be explained, since between bigger particles there were more empty spaces, which during the sintering will be scarcely filled leading to the formation of pores. The apparent porosity is bigger in the samples whose additive was PVA. The lower porosity was observed in samples using PEG, considering the same particle size of the material.

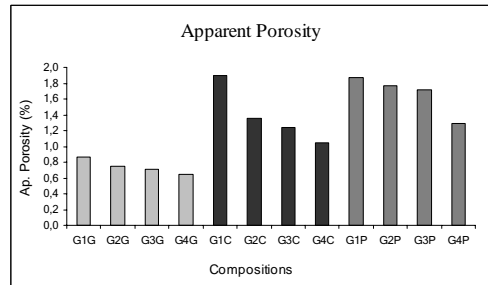


Figure 4: Apparent porosity of samples.

The water absorption acts on a similar way to apparent porosity. There was an increase in the water absorption along with the increase in the particle size. This fact can be explained since more porous samples leave more water infiltrate in its interior.

4 CONCLUSIONS

The results obtained in this study allowed approaching to the following conclusions:

The narrowest particle size distribution provides the best sintering.

The bounding agent which provides the best proprieties (flexure resistance before and after sintering, densification and apparent porosity) for narrow particle size was PEG (polyethylene glycol). PVA shows intermediary values, justifying its wide applicability.

5 REFERENCES

- Reed, J.S. 1998. Introduction to the Principles of Ceramics processing. New York: John Wiley & Sons, 486p.
- Özkan, N. & Briscoe, B.J. 1997. Overall Shape of Sintered Alumina Compacts; Ceramics International, 23, 521-536.
- Say, C.A., Earl, D.A. & Thompson, M.J. 2002. Optimization of the Sintered Density of Aluminum Oxide Compacts; Materials Letter, 53, 262-267.
- Baklouti, S., Bouaziz J., Chartier T. & Baumard, J.F. 2001. Binder Burnout and Evolution of the Mechanical Strength of dry-pressed Ceramics Containing PVA; Journal of the European Ceramic Society, 21, 1087-1092.
- Özkan, N. & Briscoe, B.J. 1997. Compaction behavior of agglomerated alumina powders; Powder Technology, 90, 195-203.

Inorganic Sol-gel Processing of Sodium Aluminium Silicate Materials

D.Böschel & H.Roggendorf

Department of Engineering Sciences, Institut für Werkstoffwissenschaft, Martin-Luther-Universität Halle-Wittenberg, D-06099 Halle, Germany

H.Pöllmann

Department of Geosciences, Institut für Geologische Wissenschaften, Martin-Luther-Universität Halle-Wittenberg, D-06099 Halle, Germany

P.Pollandt

Department of Chemistry, Institut für technische u. Makromolekulare Chemie, Martin-Luther-Universität Halle-Wittenberg, D-06099 Halle, Germany

ABSTRACT: Sol-gel processing with inorganic precursors was applied to synthesize sodium aluminium silicate gels. Sodium silicate solutions were used as silicatic gel former, whereas sodium aluminate solutions were used as aluminium source. Additionally, heat treated suspensions containing pyrogenic silica and alumina colloids were investigated. The $\text{Al}_2\text{O}_3:\text{SiO}_2$ mole ratio was varied from 0.3 to 2.1. Further treatment of the gels included drying at temperatures up to 500 °C, thermal densification (up to 1200 °C) and ion exchange. The heat treated gels were characterized by X-ray diffraction, thermal analysis and in some cases by chemical analysis. Depending on composition and treatment of the gels sodium aluminium silicates like carnegite or aluminium silicates like mullite were obtained.

1 INTRODUCTION

Sol-gel processing is an established method to produce ceramic materials (Brinker & Scherer 1990). Usually, metalorganic compounds dissolved in organic solvents or colloids are applied as precursors. In recent years water based gels have been developed to reduce costs of raw materials and handling (Kawasaki et al. 2000). A further alternative is the use of inorganic gel formers like sodium silicate solutions (Roggendorf & Böschel 2000). Sodium silicate solutions are well known inorganic gel formers. Their gel forming capabilities are known for a long time (Henisch 1970), but their alkali content prohibits many applications in the ceramic context. In combination with sodium aluminate solutions inorganic sodium aluminium silicate gels can be realized. Gels of that type are well known in zeolite synthesis (e. g. Arnold et al. 2004).

Gels for zeolite synthesis contain only small amounts of alumina (molar $\text{Al}_2\text{O}_3:\text{SiO}_2$ ratios between 0.005 and 0.2). Other materials of the $\text{Na}_2\text{O} - \text{Al}_2\text{O}_3 - \text{SiO}_2$ system with higher alumina contents are of special interest for ceramists:

- sodium aluminosilicate glasses (e. g. with albite composition),

- crystalline aluminosilicates like mullite (usually $3\text{Al}_2\text{O}_3:2\text{SiO}_2$) or Al_2SiO_5 polymorphs (e. g. sillimanite),
- crystalline sodium aluminosilicates, and
- alkali activated kaolin cements called “geopolymers” (Davidovits 1991).

Therefore, sodium aluminium silicate gels with higher alumina contents were made in order to investigate their potential for ceramic powder synthesis. Results concerning mainly the preparation of amorphous materials were already presented elsewhere (Böschel & Roggendorf 2003). This study was focused on gels treated by ion exchange in order to reduce the sodium content, a technique already described in literature (Henisch 1970).

As alternative starting materials pyrogenic alumina and silica colloids were applied. The materials prepared by this route do not contain alkalis. The results on their structural development during heat treatment should give further hints on the role of the alkalis.

2 EXPERIMENTAL

2.1 Raw materials

The following raw materials were applied:

- Sodium silicate solution; molar ratio $\text{SiO}_2:\text{Na}_2\text{O} = 3.3$; 27.3 wt % SiO_2 ; 8.6 wt % Na_2O (Roth, Karlsruhe, Germany).

- Solid sodium aluminate; stoichiometry: Na_xAlO_2 ($x = 1.32$); by chemical analysis: 41.7 wt % Na_2O and 51.3 wt % Al_2O_3 , (Giulini-Chemie, Ludwigshafen, Germany).

- NaOH (solution with 40 wt % NaOH, Merck, Darmstadt; Germany).

- Pyrogenic silica (Aerosil 200, Degussa, Hereaus; Germany).

- Pyrogenic alumina (Aluminimoxid C, Degussa, Hereaus; Germany).

The compositions of the solid sodium aluminate and of the sodium silicate solutions were determined by chemical analysis.

2.2 Gel Preparation

The gels were prepared by mixing sodium aluminate and silicate solutions. Gel composition, water content of the gels, conditions of drying ion exchange and heat treatment were varied. Details are given in (Böschel & Roggendorf 2003). The sodium aluminium silicate gels were dried at temperatures between 90 and 500 °C. Then ion exchange was applied to reduce the alkali content. The ion exchanged materials were then heat treated at temperatures up to 1200 °C. A scheme of the process is shown in Fig. 1.

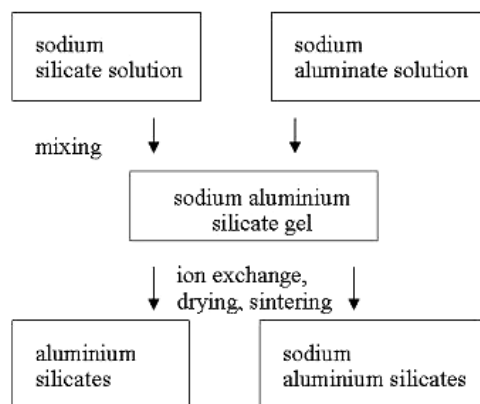


Figure 1: Scheme of the preparation of sodium aluminium silicate materials by inorganic sol-gel processing.

The exact preparation of the gels described in Table 1 included the following steps (type I):

- Preparation of a diluted sodium silicate solution by mixing 3 g of original sodium silicate solution, 0.44 g of NaOH solution and 20 ml deionised H_2O . The diluted solution was kept 24 h at room temperature before further processing.

- Dissolving a given amount of sodium aluminate in a given amount of deionised water (e. g. 2.73 g sodium aluminate in 11.9 g H_2O in the case of gel Ia). $\text{Al}_2\text{O}_3:\text{SiO}_2$ ratio was varied between 1.02 and 2.09.

- Mixing both solutions at room temperature.

- Gelation (primary gel) occurred within 10 s.

- Drying the gels at 100 °C for 3 d.

- Ion exchange in 100 ml deionised H_2O (three times).

- Drying of the ion exchanged gels at 120 °C.

- Heat treatment up to 1000 °C.

The molar $\text{Al}_2\text{O}_3:\text{SiO}_2$ ratios shown in Table 1 are close to the compositions of known aluminium silicates. One of the gels (Ib) was prepared a second time in an upscaled process (factor 10).

Deionised water was applied as medium for ion exchange, since the solubility of both “ceramic” components - silica and alumina - was expected to have minima in the neutral pH range. The efficiency of the ion exchange was checked by chemical analysis of the filtrate.

Additionally, two further synthesis routes were investigated:

- Type II: Preparation of sodium aluminium silicate gels with molar $\text{Al}_2\text{O}_3:\text{SiO}_2$ ratios of 0.28, 0.42, and 0.57. Drying of primary gels and of ion exchanged gels was accomplished at 90 °C. The samples were then heat treated for 1 h at 1200 °C.

- Type III: Preparation of aluminium silicate sols by mixing aqueous dispersions of pyrogenic SiO_2 and Al_2O_3 , (molar $\text{Al}_2\text{O}_3:\text{SiO}_2$ ratios: 0.45 to 1.78), drying at 90 °C, thermal analysis up to 1400 °C, tempering for 1 h at 1350 °C.

Table 1: Starting Composition of three of the gels prepared according type I; Na_2O , Al_2O_3 , and SiO_2 are given as mass fraction of the solid content in %; H_2O content of the gels: 90 wt %; the compositions of the gels were calculated from the educts.

Gel	Ia	Ib	Ic
Na_2O	40.8	41.7	42.3
Al_2O_3	37.5	42.0	44.7
SiO_2	21.8	16.3	13.0
$\text{Al}_2\text{O}_3:\text{SiO}_2$ (mole)	1.01	1.52	2.02

2.3 Analytical methods

The resulting materials were analyzed by:

- Optical microscopy (Jenapol u, Carl Zeiss Jena).

- X-ray diffraction (Seifert XRD 3000 PTS) for phase identification ($\text{CuK}\alpha$, 0.05 ° steps).

- Simultaneous thermal analysis (Netzsch STA 409). Heating rate 10 K/min. Alumina as crucible and reference.

- Chemical analysis: SiO₂ by precipitation and ICP-OES (inductively coupled plasma – optical emission spectroscopy). Al₂O₃ and Na₂O by ICP-OES.

3 RESULTS

Type I: The materials obtained by drying after ion exchange were already crystallised (gibbsite and akdalaite (Al₂O₃·4H₂O)). By DTA crystallisation peaks at about 920 °C were detected. X-ray characterisation yielded carnegieite (NaAlSiO₄) as main crystallisation product (Fig. 2). The filtrate analysis showed that ion exchange extracted more than 90 % of the Na⁺ of the original composition. On the other hand, certain amounts of SiO₂ and Al₂O₃ were dissolved, too. Therefore, the composition of the heat treated gel was analysed chemically. The SiO₂ concentrations of the first analyses were rather low. The upscaled charge of gel Ib (additionally Na₂O was analysed) yielded more reliable results (sum of the oxides = 84.6). The results of the chemical analysis are presented in Table 2. Important is the verification of the Na₂O content of the heat treated gel showing that the ion exchange is incomplete.

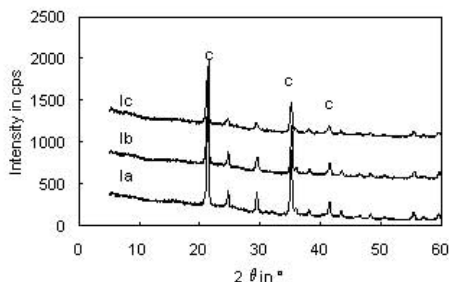


Figure 2: X-ray diffraction graphs of the gels described in table 1. Base lines of samples Ib (+ 500 cps) and Ic (+ 1000 cps) are shifted. c indicates peaks of carnegieite (PDF 33-1203).

Table 2: Composition according to chemical analysis of three of the gels of Table 1; Na₂O, Al₂O₃, and SiO₂ are given as mass fraction of the ion exchanged gel heat treated for 1 h at 1200 °C.

Gel	Ia	Ib (1)	Ib (2)	Ic
Na ₂ O	-	-	15.4	-
Al ₂ O ₃	33.0	34.4	33.0	40.1
SiO ₂	-	-	36.2	-
Al ₂ O ₃ :SiO ₂ (mole)			1.86	

Type II: Most of the materials dried after ion exchange at 90 °C were amorphous. Only in Al₂O₃ rich compositions nordstrandite (Al(OH)₃) was detected.

The further water release was investigated by TG: the residual water content of samples dried at 90 °C was about 20 wt % and mass constancy was reached at about 600 °C. With DTA an exothermic peak at about 950 °C was detected, which was supposed to be caused by a crystallisation reaction. X-ray analysis showed that the materials were still amorphous after heat treatment at 900 °C. At higher temperatures crystalline diffraction patterns were obtained which can be attributed to mullite (Fig. 3). A rough analysis of peak widths of the diffraction pattern yields a particle size of about 15 nm.

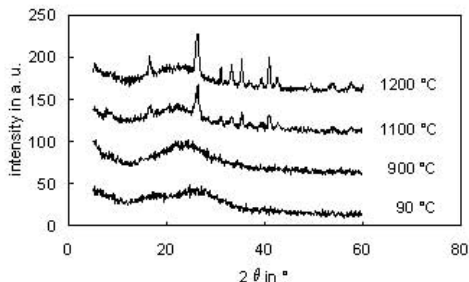


Figure 3: X-ray diffraction graphs of heat treated sodium aluminosilicate gels after ion exchange; type II, temperature of heat treatment (1 h) indicated at the graph; molar Al₂O₃:SiO₂ ratio = 0.57.

Type III: The mixed dispersions of colloids did not form gels. Nevertheless, they could be dried to solid materials. Since one of the precursors (Aluminiumoxid C) has already a crystalline structure, the dried materials were already partly crystalline. DTA showed in nearly all cases (one exception: Al₂O₃:SiO₂ ratio = 1.78) an endothermic peak at about 1300 °C succeeded by an exothermic peak at about 1350 °C. Fig. 3 compares DTA graphs of an ion exchanged (Type I) sodium aluminium silicate gels and a dried dispersion (Type III). A similar sample of a dried dispersion with a molar Al₂O₃:SiO₂ ratio = 1 was heat treated for 1 h at 1350 °C for X-ray diffraction analysis. The diffraction pattern could be explained by a mixture of mullite with minor amounts of cristobalite (SiO₂).

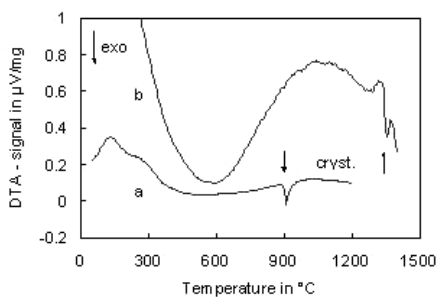


Figure 4: DTA graphs of sodium aluminumsilicate gels after ion exchange; a: type I, molar $\text{Al}_2\text{O}_3:\text{SiO}_2$ ratio = 1.05; b: type III, molar $\text{Al}_2\text{O}_3:\text{SiO}_2$ ratio = 0.90.

4 DISCUSSION

Inorganic sodium aluminium silicate gels are easily formed by mixing sodium silicate and sodium aluminate solutions. The gels can be processed by drying, ion exchange and heat treatment. Crystallisation is enhanced by high Al_2O_3 and Na_2O contents. These components can be regarded as mineralisers. Drying alone of Al_2O_3 rich gels leads to the formation of crystalline aluminium hydrates.

The efficiency of ion exchange $\text{Na}^+ \leftrightarrow \text{H}^+$ in gels with high Al_2O_3 contents was not sufficient to obtain nearly alkali free materials. The reason is probably the high affinity of Al^{3+} and Na^+ , which prohibited the synthesis of pure aluminium silicates. Heat treatment of these gels led to the crystallisation of carnegieite, even if they have $\text{Al}_2\text{O}_3:\text{SiO}_2$ ratios of nearly 1.5 or 2.0, which are the respective molar ratios of mullite.

Ion exchanged gels with low alumina contents stay amorphous up to 900 °C. At higher temperatures the formation of mullite is observed. The onset temperature of mullite formation is in the lower range compared to literature values (Schneider, H. & al.). If both components are introduced as colloids the crystallisation temperature is shifted to significantly higher values. Sodium aluminate solutions are reported to have a molecular structure (Chen 1993) and least part of the silica in sodium silicate solutions is dissolved molecularly (Iler 1979). It is concluded that a molecular dispersion of Al^{3+} and Si^{4+} favours the formation of mullite at lower temperatures.

5 SUMMARY

Inorganic sodium silicate gels were heat treated after ion exchange. Depending on composition and processing conditions sodium aluminium silicates like carnegieite or aluminium silicates like mullite were obtained. The synthesis of pure materials was not

achieved, which is attributed to the incomplete ion exchange.

6 ACKNOWLEDGEMENTS

The help of Dr. J. Trempler (microscopy), S. Brinke (laboratory), and H. Schwalbe (laboratory) is gratefully acknowledged.

7 REFERENCES

- Arnold, A., Hunger, M. & Weitkamp, J., 2004, *Micropor. Mesopor. Mater.* 67: 205-213.
- Böschel, D. & Roggendorf, H., In: B. Samuneva, B., Gutzov, I. & Dimitriev Y. (eds.), 2003: Proc. 2nd Balkan Conference on Glass Science and Technology and 14th Conf. on Glass and Ceramics, Varna, Bulgaria 25-28.09.2002, Publishing House "Science Invest", Sofia (in press).
- Brinker, C.J. & Scherer, G.W., 1990: *Sol-Gel Science*. San Diego, Academic Press.
- Chen, N.Y., Y.L. Liu, B. Tang & M. Hong 1993: Studies on the anionic species of sodium aluminate solutions. *Science in China (Ser. B)*. 36: 32-38.
- Davidovits, J., 1991: *J. Therm. Anal.* 37: 1633-1656.
- Henisch, H. K., 1970: *Crystal growth in gels*, London, University Press.
- Iler, R.K., 1979: *The chemistry of silica*, Chichester, John Wiley & Sons.
- Kawasaki, S. & al., 2000, *J. Mater. Sci. Letters* 19: 11-14
- Schneider, H., Okada, K. & Pask, J.A. 1994: *Mullite and mullite ceramics*. Chichester, John Wiley & Sons.

Structural Evaluation of an Adobe from Minas Gerais

J. Calábria & W.L. Vasconcelos

Department of Metallurgical and Materials Eng., Federal University of Minas Gerais, Belo Horizonte, Brazil

ABSTRACT: In this work we characterized the structure of an adobe (raw earth ceramic brick) from Minas Gerais and its clay. We used techniques of X-ray diffraction, X-ray fluorescence, nitrogen adsorption-desorption (BET method), scanning electron microscopy (SEM), electron microprobe (EDS), and Fourier transform infrared spectroscopy (FTIR). The clay and the adobe are composed mainly by kaolinite and quartz. Concerning the clay, the average pore size obtained from the BET method was 19.2 nm and the specific surface area observed was 61 m²/g. The BET specific surface area of the adobe is 44 m²/g and its average pore size is 22.0 nm. The microstructure of the adobe is formed by irregular particles and pores, matching closely the morphology of the clay particles. Leaching experiments showed the compositional variation of the brick. We found in the surface of the adobe the presence of OH groups linked to both silicon and aluminum atoms.

1 INTRODUCTION

Clay bricks are very resistant to weather and don't require much maintenance. They have moderate thermal insulation and good fire resistance. Another important characteristic is that they don't burn. Because they are porous, the clay bricks are poor thermal conductors. That makes the buildings made with clay bricks fresh in the summer and warmer during winter (Somayaji 1995, Bentz et al. 2000).

The adsorption of water by the adobe is proportional to its porosity. The average pore size and the pore size distribution define the extent of water adsorption by the material. On its turn, the apparent density decreases as porosity increases (Vasconcelos 1997, Altin et al. 1999, Andreola et al. 2000, Juang et al. 2002).

The permeability and porosity play a key role on water incorporation and retention inside the pores and on the water mobility through the block. The destructive action of the humidity can enhance water absorption, resulting on surface energy changes, dissolution and loss of particles, destruction and loss of bondings and also on pressure rising in the pores, leading to the appearance of destructive internal stresses (Kerali 2000, Xian-Qing et al. 2003).

Clays are substances with high capacity of adsorption of metals and of low permeability. The permeability of clays avoids or reduces the flow of liquid effluents through the material and its high capacity of adsorption immobilizes the metals present in the effluents (Tavani et al. 1999).

The infrared spectra, of clays belonging to the group of smectites, show the following bands: 3620; 3425; 1034; 914; 835; 794; 523; and 464 cm⁻¹. In most cases of an attacks acidic media on a material, the intensities of the bands can be changed. This behavior usually means that the crystalline structure has been damaged. In many cases, these alterations on the crystalline structure are not meaningful (Tavani et al. 1999, Wan et al. 2002).

The goal of this work is to describe the microstructure of adobes. Another aim is the evaluation and correlation of microstructural characteristics with a process of environmental degradation.

2 METHODOLOGY

The X-ray diffraction data was obtained using an equipment Phillips, model PW-3710, with Cu- α (radiation, 30 mA, 40 kV, scanning with 0.060 steps

and acquisition time of 1 second per step. The samples used were powders.

In order to carry out a microstructural evaluation, the samples were prepared by ceramography. The surfaces of the samples were coated with gold using sputtering. The equipment used was a JEOL model JSM-5410. In other experiment, powdered samples were dispersed with sodium hexamethaphosphate during 24 hours and dried in an open to air oven. After sputtering with gold, the particles were observed using an equipment JEOL, model JSM 840A with EDS capability.

The nitrogen adsorption-desorption experiments (BET method) were carried out using an equipment Autosorb-1, Quantachrome. The samples were degassed at 120°C. The typical experimental errors are less than 5%.

The equipment used for the Fourier transform infrared spectroscopy measurements was a Perkin-Elmer, model Paragon-1000. The technique employed was diffuse reflectance (DR).

The samples for the leaching tests were prepared with dimensions of approximately 2x1x1 cm. The leaching tests were carried out using 7 mL of a Na₂S₂O₅ 0,001M solution or 7 mL of deionized water.

After leaching, the liquid was removed and the samples were weighted. After drying at 60°C for two days the sample were weighted again.

3 RESULTS AND DISCUSSION

From Figure 1 it is possible to state that the major phases, in both the clay and the adobe, are quartz (Q), kaolinite (K), gibbsite (Gib) and goethite (Go).

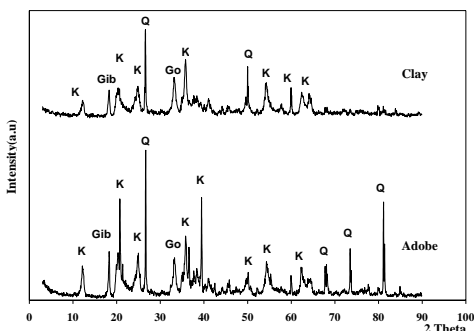


Figure 1. X-ray diffraction spectra.

From X-ray fluorescence analyses it was possible to verify the presence of iron in the clay used to make the adobes. It was also possible to observe, in the clay and in the adobe, the occurrence of silicon and

aluminum, and lower contents of titanium, copper, nickel, chromium, manganese, potassium, sulfur phosphorus and calcium.

The SEM analyses (Fig.2) revealed that the lamellar features of the clays were kept in the adobe microstructure. This kind of geometry can be associated to the low mechanical resistance of the adobe, since the bondings between the lamellae are mostly weak. Figure 3 shows the EDS spectrum obtained for the same region of Figure 2.

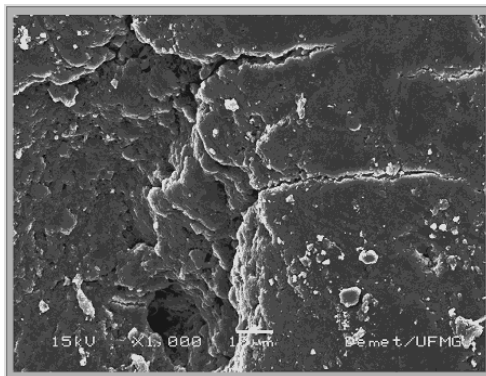


Figure 2. SEM photomicrograph of the adobe.

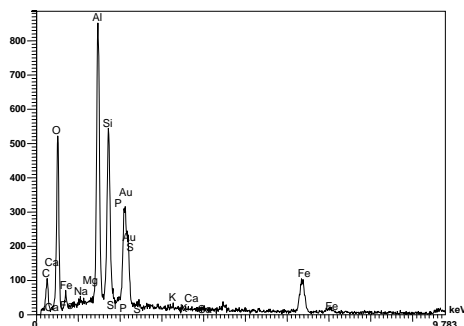


Figure 3. EDS chemical composition of the adobe. Taken in the area shown on Fig. 2.

Figure 4 presents the adsorption isotherms for the clay and the adobe. It can be observed that the volume of nitrogen incorporated in the pores of the adobe is four orders of magnitude larger than the volume incorporated into the clay. This reveals the larger porosity present in the adobe when compared to the clay (Altin et al. 1999, Juang et al. 2002).

The pore size distribution by volume is shown in Figure 5. This Figure represents the larger porosity observed for the adobe. Figure 5 also shows a similar shape for both curves of pore size distribution.

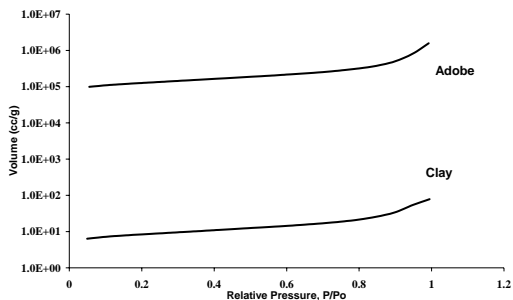


Figure 4. Adsorption isotherms for the clay and the adobe.

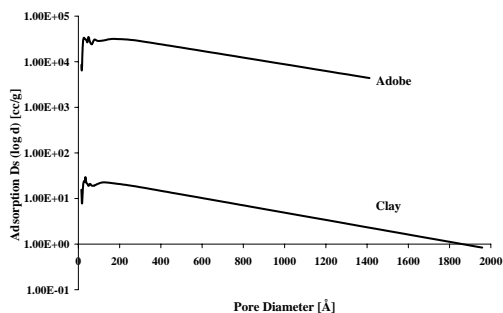


Figure 5. Pore size distribution by volume for the clay and the adobe.

The results obtained from the nitrogen adsorption tests, for the clay and the adobe, of specific surface area (S_p), specific volume of pores (V_p) and average pore diameter (D_p) are shown in Table 1 (Vasconcelos 1997, Altin et al. 1999).

Table 1. Specific surface area, specific volume of pores and average pore size for the clay and the adobe.

Surface Areas and Pore Size Of Clay and Adobe			
Sample	S_p (m ² /g)	V_p (cm ³ /g)	D_p (nm)
clay	61	0.294	19.2
Adobe	44	0.243	22.0

Using the data obtained from the nitrogen adsorption tests (specific volume of pores and specific surface area), it is possible to create a geometric model of the porosity and connectivity of the adobe, as presented in Figure 6 (Reis 2000).

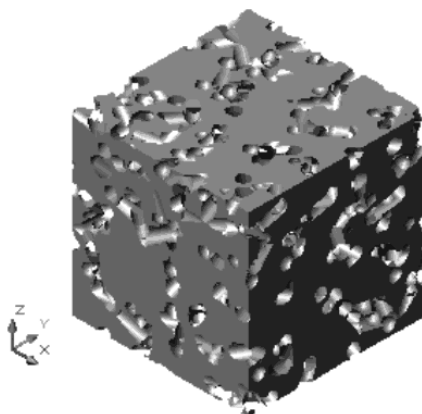


Figure 6. Geometric model of porosity and connectivity applied to the adobe.

Figure 7 shows a typical nanostructure of kaolinite particles present in the clay, as revealed by SEM. This observation is in agreement with the X-ray diffraction results. The typical lamellar aspect of kaolinite clay is kept for the adobe, as shown by Figure 7. The darker regions of Figure 7 suggest the presence of pores in the nanometric range.

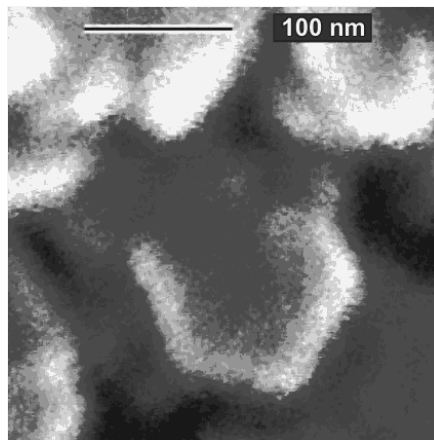


Figure 7. SEM photomicrograph of the adobe

The nanostructural evolution (Table 2) observed in the structural clay products can be associated to their chemical behavior, when in contact with an aggressive environment.

Table 2. Specific surface area, specific pore volume and average diameter of pores of the adobe.

	Before Process	1day - water	1day - acid rain	30 days - water	30 days - acid rain
SP (m ² /g)	44	36	36	18	17
VP (cm ³ /g)	0.243	0.29	0.29	0.28	0.28
DP (nm)	22.0	32.0	32	64	69

Figure 8 exhibits the structural evolution of the adobe during the leaching process in an aqueous media and in simulated acid rain media. Figure 8a shows the model for the adobe before leaching. Figures 8b, 8c, 8d and 8e show, respectively, the model for the adobe after 1 day in water, 1 day in acid rain, 30 days in water and 30 days in acid rain. It can be observed that the structure becomes more damaged in the acid rain media. During the last step of the leaching process in the acid rain media, the adobe loses its dimensional characteristics. It is observed a tendency of increasing the pore diameter as the leaching proceeds.

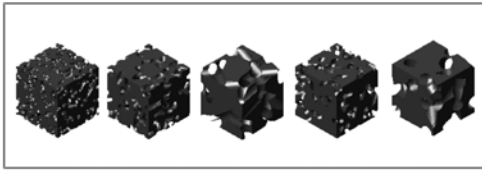


Figure 8. Evolution of the pore nanostructure of the adobe during leaching in an aqueous media and in a simulated acid rain media.

The leaching process took place in a simulated acid rain media ($\text{Na}_2\text{S}_2\text{O}_5$) and in a deionized water media during different time intervals. As a result of this process, the adobe lost its physical integrity. Using Fourier transform infrared spectroscopy it was possible to follow the evolution of water and also to evaluate the reactivity tendency of the surface of the adobe (Fig.9). From Figure 9 one can observe the occurrence of peaks related to Si-O-Si bondings (1079 cm^{-1}) and Al-OH bondings (914 cm^{-1}) in both spectra. The widening of 3620 cm^{-1} band in acid media is due to OH groups and the widening of 3425 cm^{-1} band has been associated to the OH groups bonded to adsorbed water. The 1034 cm^{-1} peak referent to the Si-O-Si bondings shifts to 1079 cm^{-1} . Both bands can undergo some broadening under the effects of an acidic media. In this media, the Al-OH peak at 914 cm^{-1} and the Mg-Al-OH peak at 835 cm^{-1} show a small decrease in intensity. By its turn, the Si-O-Si peak at 1079 cm^{-1} exhibits an increase in intensity when exposed to an acidic media. The peaks at 523 cm^{-1} (Si-O-Al) and 464 cm^{-1} (Si-O) appear with reduced intensities, specially the Si-O-Al peak (Tavani et al. 1999).

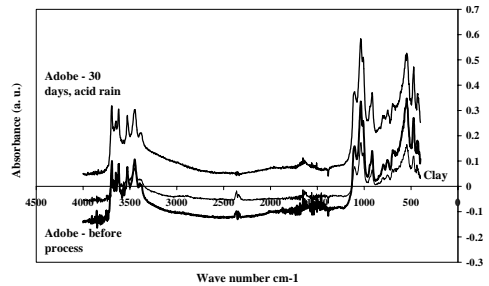


Figure 9. Fourier transform infrared spectroscopy spectra for adobe exposed to 30 days in a simulated acid rain media and with no leaching.

4 CONCLUSIONS

The primary particles observed in the adobe kept the morphological characteristics of the raw material (clay). The lamellar aspect is preserved, as seen by the hexagonal shape of kaolinite particles. The adobe does not go through a firing step and therefore presents only weak bondings, which favors degradation processes. The damage is enhanced due to the presence of large amounts of OH groups on the surface of the adobe. Using a geometric model, it is possible to observe the evolution of the nanostructure of pores. As a result of the leaching process, the average pore diameter increases and the specific surface area reduces in more than 50%.

5 REFERENCES

- Altin, O., Ozelge, O. H., Dogu, T. 1999. *Journal of Colloid and Interface Science* v. 217: p.19-27.
- Andreola F., Leonelli C., Romagnoli M., Miselli P. 2000. *The American Ceramic Society Bulletin*, v.79 n. 7.
- Bentz, D. P., Quenard, D. A., Kunzel, H. M., Baruchel, J., Martys, N. S., Garboczi, E. J. 2000. *Materials and Structures*, v. 33: p.147-153.
- Juang, R-S., Lin, S-H., Tsao, K-H. 2002. *Journal of Colloid and Interface Science* v. 254: p.234-241.
- Kerali, A. G. 2000. Destructive Effects of Moisture on the Long-term Durability of Stabilized Soil Blocks. Working Paper n.52. Development Technology Unit School of Engineering, University of Warwick, UK.
- Reis, S. C. 2000. Aplicação de Modelagem Geométrica Computacional na Obtenção, Visualização e Análise de Estrutura de Poros de Materiais. Master Thesis, Belo Horizonte: Federal University of Minas Gerais.
- Somayaji, S. 1995. Civil Engineering Materials Indian Institute of Technology. New Jersey. Prentice Hall, Inc.
- Tavani, E. L., Volzone, C. 1999. *Cerâmica*. v. 45. São Paulo.
- Vasconcelos, W. L. 1997. *Cerâmica*. v. 43 n. 281-282. p. 120-123.
- Wan, J., Tokunaga, T, K. 2002. *Journal of Colloid and Interface Science* v. 247: p.54-61.
- Xien, X-Q., Fan, T-X., Sun, B-H., Zhang, D., Sakata, T., Mori, H., Okabe, T. 2003. *Materials Science and Engineering*, v. 342: p. 287-293.

Disintegration in High Grade Titania Slags: Fracture Behaviour of Pseudobrookite

J.P.R. de Villiers & A.Tuling

Departments of Geology and Metallurgical Engineering, University of Pretoria, South Africa

J.Göske

Zentrum für Werkstoffanalytik Lauf, Germany

ABSTRACT: Cooling of solidified titania slag in air results in the oxidation of a pseudobrookite phase (M_3O_5 where $M = Fe, Ti$) to form phases that are associated with the disintegration of the solid slag. Extensive disintegration of the slag at temperatures below 500°C is accompanied by the formation of a disordered MO_x phase, which is a unit cell intergrowth of anatase and M_3O_5 structural elements. In-situ X-ray diffraction measurement and Rietveld refinement of the pseudobrookite unit cell parameters yielded values for spontaneous strain associated with the oxidation of the slag. The components of the spontaneous strain tensor for the most reactive sample at 200°C are $e_{11} = -0.0060$, $e_{22} = 0.0033$, $e_{33} = 0.0098$ and $e_{23} = e_{13} = e_{12} = 0$. Lattice energy calculations with the GULP code was used to calculate values for the elastic constants and Young's moduli for M_3O_5 . These values, together with experimental values for the spontaneous strain tensor and the fracture toughness of M_3O_5 were used to calculate the critical crack size for crack propagation. Crack sizes of 0.4 - 1 microns are sufficiently small to explain the cracking that preceded the extensive formation of MO_x and the subsequent segmentation of the solid slag into very small particle sizes.

1 INTRODUCTION

The production of titania slag involves the smelting of an ilmenite concentrate using a carbonaceous reductant (de Villiers et al. in press). After iron reduction and tapping of the liquid metal, the liquid slag is tapped into ladles and cooled with water spraying until solid. The ladles are then emptied and the slag is allowed to cool to ambient temperatures. All producers of high-grade ($>85\%$ TiO_2) slag encounter the problem of disintegration of the solidified tapped slag at relatively low temperatures when the slag blocks cool down.

The disintegrated slag consists of a large proportion of oxidized fine material ($<100\ \mu\text{m}$) that is unsuitable for subsequent use in fluidized-bed chlorination reactors. The fine-grained fraction is normally sold to sulfate pigment producers, usually at a discount.

Remedial action consists of rapid water-cooling of the solid slag blocks down to room temperature, but this is not always effective, and in some instances excessive amounts of fine material are still generated. This study aims to determine the cause of the disintegration and the mechanism.

2 EXPERIMENTAL

A pilot plant slag containing 7.6% FeO and 88.1% TiO_2 was used for the study. Dynamic X-ray diffraction measurements were done while the sample was heated and oxidized in situ, as well as measurements during isothermal oxidation, in order to determine the dimensional changes taking place during oxidation. The slag sample was finely ground in acetone and then transferred onto a platinum heating strip in an Anton Paar HTTK 1600 XRD furnace. The measurements were done using a PANalytical X'Pert Pro MPD with an X'Celerator RTMS Detector-System system at the Martin Luther University at Halle (Saale). Rietveld refinement was used to refine both the M_3O_5 and Pt cell dimensions. Selected partially oxidized single crystals of M_3O_5 were oriented in a precession camera along the $[100]$ and $[010]$ zone axes, and polished for optical microscopy.

Fracture toughness measurements using the Vickers indentation technique were also done on sample J5. The method described by Anstis et al. (1981) was used for this purpose. A constant load of 0.98N (100g) was used in the experiments. The indentation sizes were measured optically and the

radial crack lengths were measured from scanning electron microscope images. See Fig. 1.

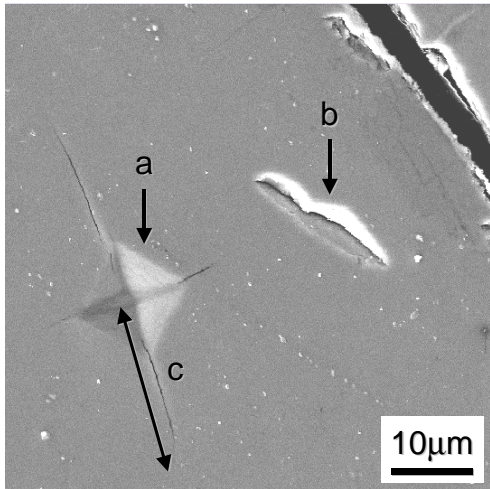


Figure 1. SEM Backscatter image of Vickers micro-indentation with associated crack formation (a and c), together with naturally occurring crack (b).

3 RESULTS

3.1 Dimensional changes on heating of M_3O_5

Changes in unit cell dimensions of M_3O_5 at temperatures from 50°C to 350°C in 10°C steps were determined using simultaneous Rietveld refinement of both the M_3O_5 and platinum metal peaks (from the heating strip). To check the reliability of the refinements, the experimental platinum cell dimensions are compared with those calculated from thermal linear expansion data given by Touloukian et al. (1975). The average deviations from the calculated a-cell values of Pt is 0.0005 Å. (Fig. 2).

To determine the dimensional changes due only to oxidation and to eliminate the effect of thermal expansion, isothermal high temperature refinements were done on the sample over a period of 12 hours at 200°C. The deviations in the M_3O_5 cell dimensions are similar to those in the heating experiments and are due solely to the oxidation reaction.

The changes in cell dimensions of pseudobrookite are shown in Fig. 3. The a-cell dimensions contract, the b-cell dimensions expand slightly, and the c-cell dimensions expand significantly with increase in temperature (and degree of oxidation).

3.2 Strain due to oxidation

Spontaneous strain is defined by Carpenter et al. (1998) as the strain that accompanies a phase transition. In the case of the oxidation reaction

involving the precursor M_3O_5 phase, it is possible to calculate the lattice strain in the orthorhombic M_3O_5 structure before actual formation of the product MO_x . The components of the spontaneous strain tensor as derived from the isothermal data are $e_{11} = -0.0060$, $e_{22} = 0.0033$, $e_{33} = 0.0098$, and $e_{23} = e_{13} = e_{12} = 0$

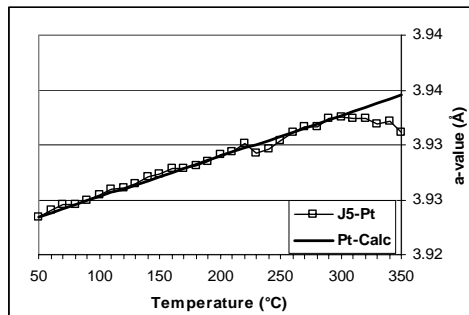


Figure 2. Unit cell data of the platinum heating strip as compared with the values calculated from thermal linear expansion data.

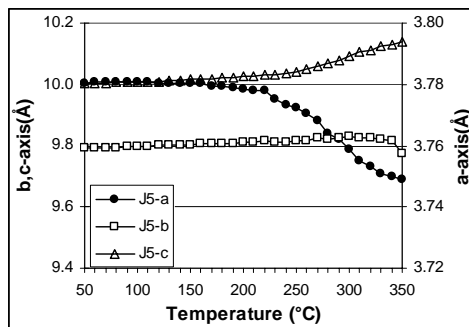


Figure 3. Change of the cell dimensions of M_3O_5 with temperature

3.3 Calculated Elastic constants for sample J5

The elastic constants and Young's moduli were calculated using the GULP code (Gale1994) for M_3O_5 at 200°C. Potential values (Fe-O and Ti-O) of Woodley et al. (1999) as well as the elastic constants of rutile (Grimsditch et al.1976) were used. The composition used in the calculation is $(Fe_{0.4}Ti_{0.6})(Ti_{0.4}Ti_{0.6}^{3+})_2O_5$. The calculated elastic constants of rutile were used to check the validity of fitting. The calculated elastic constants of M_3O_5 : $C_{11}=2.958$ Gpa, $C_{12} = 1.889$ Gpa, $C_{13} = 0.814$ Gpa, $C_{22}=3.312$ Gpa, $C_{23}=0.674$ Gpa, $C_{33}=1.419$ Gpa, $C_{44}=0.405$ Gpa, $C_{55}=1.103$ Gpa, $C_{66}=1.058$ Gpa; were used in the calculation of stresses associated

with the oxidation that could lead to cracking of the crystal before the formation of the MO_x phase. The values are approximate because of the demonstrated problems in modelling elastic constants using crystal structure data only (Collins & Smith 1996).

The Young's Moduli were calculated as: $E_x = 174$ GPa, $E_y = 208$ GPa, $E_z = 118$ GPa in the a, b, and c-crystallographic directions respectively.

3.4 Fracture Toughness

The fracture toughness of M_3O_5 was calculated from crack lengths and micro-indentation lengths measured by scanning electron and optical microscopy respectively. Using the formulas quoted in Anstis et al.:

$$H = P/\alpha_0 a^2$$

with $\alpha_0 = 2$ if a is taken as the impression half-diagonal ($6.4 \mu\text{m}$) and ϕ

$$K_{IC} = \xi_v^R \left(\frac{E}{H}\right)^{1/2} \left(\frac{P}{a^{3/2}}\right)$$

where $\xi_v^R = 0.016$ is a dimensionless constant, E is an averaged Young's modulus, (taken as 166 GPa), H the hardness, P the load (0.98N), and c_0 the crack half-length. A median $c_0 = 12.5 \mu\text{m}$ was used in the calculation, (see Fig. 2). The fracture toughness is calculated as $K_{IC} = 1.32 \text{ MPa}\cdot\text{m}^{1/2}$. This is compared to values of 2.1-4.6 $\text{MPa}\cdot\text{m}^{1/2}$ for Al_2O_3 and 0.75 $\text{MPa}\cdot\text{m}^{1/2}$ for soda-lime glass as given by Anstis et al.

3.5 Crack propagation

The resultant stresses associated with the oxidation of the M_3O_5 were estimated using the calculated elastic constants given above. These are: $\sigma_{xx} = -354$ Mpa, $\sigma_{yy} = 620$ Mpa, $\sigma_{zz} = 1124$ Mpa (σ_{xx} , σ_{yy} , and σ_{zz} are along the a,b, and c crystallographic directions respectively).

It is apparent that during oxidation, the M_3O_5 is under compression along the a-axis and under tension along the other two axes, with the tensile stress being a factor of 2 larger along the c-axis than along the b-axis.

Using the relation, $K_{IC} = Y\sigma_c(a)^{1/2}$, (Tromans & Meech 2002) the critical crack sizes for brittle crack propagation can be estimated, using the calculated tensile stresses above. This was done for edge cracks, with a Y value of $1.12\pi^{1/2}$. This was done along the b and c-axes where tensile stresses prevail. This is shown graphically in Fig. 4.

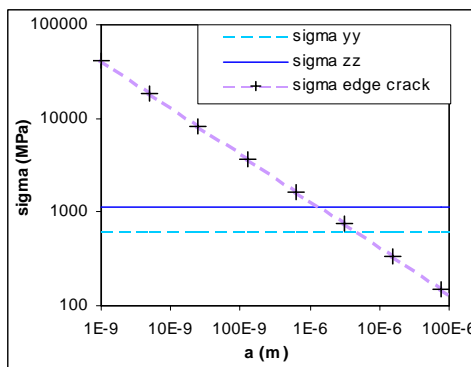


Figure 4. Plot of crack length vs calculated stress

It is apparent that crack sizes as small as 0.4 to 1 μm are sufficient to initiate and propagate cracking (perpendicular to the c-axis) in M_3O_5 during initial oxidation. Visible cracks far in excess of these dimensions are already present in the slags as shown in Fig. 1. These would easily propagate further to provide additional surfaces for exposure to air and further oxidation to MO_x .

3.6 Optical microscopy

Crystals of partially oxidized M_3O_5 were oriented along the [010] zone axis, polished and examined by optical microscopy. Oil immersion optics was used under partially polarized light. From the micrograph it can be seen that transformation occurs along pre-existing cracks in the form of triangular domains, (Fig. 5).

The mechanism of disintegration seems to proceed in two steps. Initially large cracks, oriented approximately along the a-axis and perpendicular to the c-axis, form as a precursor to MO_x formation. This is a result of the development of spontaneous strain in the M_3O_5 during oxidation. The subsequent formation of triangular domains of MO_x causes secondary cracking in the center of the domains along the c-axis, and perpendicular to the large cracks. These secondary cracks eventually join up to segment the crystal into small rectangular fragments as small as 10 μm in size. Fresh surfaces will be exposed, further oxidation will be facilitated and disintegration of the slags will be propagated into the bulk of the sample.

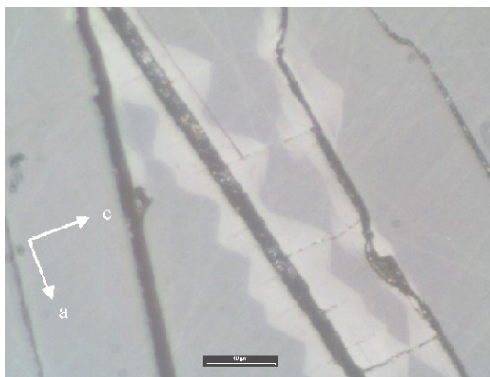
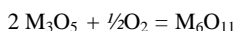


Figure 5. Reflection micrograph showing transformation domains along major cracks in a single crystal of M_3O_5 . Secondary cracks form perpendicular to the triangular domains. The secondary cracks are parallel to the c-crystallographic axis. The bar represents 10 μm .

3.7 Relation with MO_x formation

In all cases, the disintegration of the solid slags is associated with the formation of the MO_x phase. This phase is related to the M_6O_{11} phase described by Grey et al 2000. Rietveld refinement was attempted using cell dimensions and atomic parameters given by Grey et al. The resultant cell was refined as $a = 9.888(7)\text{\AA}$, $b = 3.751(2)\text{\AA}$, $c = 20.78(1)\text{\AA}$, $\beta = 93.00(4)^\circ$ (Rwp = 12.3%), as compared with the values of $a = 9.946(2)\text{\AA}$, $b = 3.744(2)\text{\AA}$, $c = 20.994(3)\text{\AA}$, $\beta = 93.3(1)^\circ$ of Grey et al. If the oxidation reaction can be written as:



The volume changes using the different unit cells may be found in Table 1.

Table 1. Volume changes due to formation of M_6O_{11} .

Phase	Volume (\AA^3)	Δ Volume (%)
2x M_3O_5 (J5)	740.4	
M_6O_{11} Grey et al.	780.5	5.4
M_6O_{11} This study	769.9	4.0

The volume changes are probably the cause for the formation of secondary cracks as observed microscopically, segmenting the slag grains and finally causing the solid slag to disintegrate into a mixture of fine-grained powder and coarser-grained unoxidized M_3O_5 .

4 CONCLUSIONS

The mechanism of disintegration is a dual one. Initially, the M_3O_5 is oxidized on the surface of the

cast slag blocks, resulting in lattice strain. This causes crack propagation in the sample, and fresh surfaces are exposed to air. The oxidation product, MO_x , forms on the crack surfaces and enlarges to form triangular-shaped domains that eventually join up with domains from adjacent cracks. Secondary cracks form, dissecting the domains and these cracks segment the crystals into very small fragments. The disintegration also seems to be related to a volume expansion due to the formation of the MO_x phase. The disintegration then proceeds from the surface of the slag blocks inwards until the whole block disintegrates.

5 ACKNOWLEDGMENTS

The help and support of Deon Bessinger and Hanlie du Plooy from Kumba Resources are gratefully acknowledged. Helpful discussions with Prof D Tromans provided understanding into the use of fracture dynamics.

Financial assistance from the Foundation for Research Development for travel is acknowledged.

Lastly, thanks to Dr Julian Gale for the use of the GULP programme and for helpful discussions on its use.

6 REFERENCES

- Anstis, G.R., Chantikul, P., Lawn, B.R. and Marshall, D.B. 1981. A critical evaluation of indentation techniques for measuring fracture toughness: I, Direct crack measurements *J. Am. Ceram. Soc.* 64 (9): 533-538.
- Carpenter, M.A., Salje, E.K.H. and Graeme-Barber, A. 1998. Spontaneous strain as a determinant of thermodynamic properties for phase transitions in minerals. *Eur. J. Mineral.* 10: 621-691.
- Collins, D R and Smith, W. 1996. Evaluation of TiO_2 force fields. *Daresbury Lab Report, Jan 8, ISSN 1362-0207.*
- de Villiers, J.P.R., Verryn, S. and Fernandes, M. *In press.* Disintegration in high grade titania slags: Low temperature oxidation reactions of pseudobrookite.
- Gale, J.D. 1992-1994. *General Utility Lattice Program (GULP)*. London: Royal Institution and Imperial College.
- Grey, I.E., Cranswick L.M.D., Li C., White T.J., and Bursill L.A. 2000. New M_3O_5 - Anatase intergrowth structures formed during low-temperature oxidation of anosovite. *J. Solid State Chemistry* 150: 128-138.
- Grimsditch, M.H., Ramdas, A.K. 1976. Elastic and elasto-optic constants of rutile from a Brillouin scattering study, *Phys. Rev. B14*: 670.
- Touloukian, Y.S., Kirby, R.K., Taylor, R.E. and Desai, P.D. 1975. Thermal Expansion: Metallic elements and alloys. in *Thermophysical Properties of Matter* 12: 254. New York-Washington: Plenum.
- Tromans, D. and Meech, J.A. 2002. Fracture toughness and surface energies of minerals: theoretical estimates for oxides, sulphides, silicates and halides. *Minerals Engineering* 15: 1027-1041.

Mineralogical and Microstructural Characterization of a Silicon Carbide Refractory

E.E.Ferreira

FOSFERTIL – Fertilizantes Fosfatados S/A – Rod. MG 341, km 25 - Tapira, MG, Brazil

P.R.G.Brandão

Department of Mining Engineering. Federal University of Minas Gerais – UFMG. Belo Horizonte, MG, Brazil

ABSTRACT: Three types of silicon carbide refractory muffles were characterized in order to clarify the cause of their excessive expansion in a firing tunnel kiln. The characterization was carried out by X-ray diffraction, quantitative chemical analysis by X-ray fluorescence, reflected light microscope and scanning electron microscope with microprobe analyses. Also, apparent porosity values were determined for each type of refractory muffle. The results of X-ray diffraction showed the presence of silicon carbide and cristobalite phases for all muffles. The tridymite phase occurred only in muffle C. The observation of the polished sections by reflected light microscopy showed the phases detected in the X-ray diffraction and a vitreous phase, probably silica (SiO₂). For the muffle A, its matrix displayed a high degree of oxidation with few fine particles of silicon carbide and different pore sizes. As for muffle B, its microstructure showed a low degree of particles sintering with a lack of fine particles (<50nm) and its pore diameters were relatively high and mainly interconnected. Contrarily to muffle B, muffle C had a wide silicon carbide particle size distribution in its matrix, with excellent particles sintering. Therefore, its porosity value was lower than the other refractory muffles. Then, this work demonstrated that the cause of the excessive expansion of muffle A was the lack of silicon carbide fine particles fraction in its matrix and low sintering degree, which contributed for the silicon carbide oxidation and, consequently, to the pronounced expansion.

1 INTRODUCTION

Silicon carbide is considered the most important structural ceramic material because of its excellent properties, like high temperature strength, thermal shock resistance, due to its high thermal conductivity and oxidation resistance. Also, its density is relatively low when compared to steel and other refractory materials (Izhevskiy et al. 2000; Strecher et al. 1999; Marchi et al. 2001).

According to Izhevskiy et al. (2000), these excellent properties are due to the covalent bonds, which represent more than 88% of the chemical bond between silicon and carbon atoms.

In this work, three samples of silicon carbide refractory muffles were characterized in order to clarify the excessive expansion of one muffle after its installation in a firing tunnel kiln. These muffles were installed inside this tunnel kiln to avoid the exposure of the burning pieces to direct flame (at the temperature of 1250°C).

2 EXPERIMENTAL

Three samples of the silicon carbide refractory muffles were collected and were called A, B and C.

Sample A was collected from the muffle that had an excessive expansion 90 days after its installation; sample B corresponded to a new muffle that had never been installed and came from the same production group of muffle A. Sample C was a portion of an old muffle, which was used during a long period (four years) in the same tunnel kiln.

To characterize these refractories, the following procedure was carried out: X-ray diffraction; quantitative chemical analysis by X-ray fluorescence and scanning electron microscope (SEM) with attached EDS microanalyser and reflected light microscope. Also, apparent porosity was measured according to the ABNT standard (number 6220).

3 RESULTS AND DISCUSSIONS

The quantitative chemical analyses showed the differences between the muffles and confirmed the oxidation occurred in muffle A. For muffle A, the SiO₂ grade was higher than in muffle B, what was due to the oxidation of the silicon carbide into SiO₂. It means that part of the silicon carbide was transformed into cristobalite and a vitreous phase, high in SiO₂ (Tab. 1). In the case of muffle C, the SiO₂ grade was relatively lower than in the other

muffles. This lower value could be due to its original chemical content and/or some silicon carbide oxidation.

For all muffles, TiO₂, Al₂O₃, Fe₂O₃, CaO and MgO were minor components with grades less than 0,75%. Table 1 presents these results.

Table 1. Quantitative chemical analyses.

Muffles			
Oxide	A (%)	B (%)	C (%)
TiO ₂	(0.05±0.01)	(0.04±0.01)	(0.05±0.01)
Al ₂ O ₃	(0.88±0.02)	(0.41±0.01)	(1.12±0.02)
Fe ₂ O ₃	(0.46±0.01)	(0.79±0.01)	(0.66±0.01)
CaO	(0.01±0.01)	(0.04±0.01)	(0.07±0.01)
MgO	(0.07±0.02)	(0.06±0.01)	(1.12±0.02)
SiC	(68.52±1.00)	(74.89±1.00)	(87.38±1.00)
SiO ₂	(30.01±1.00)	(23.77±0.80)	(10.71±0.90)
Total	100.00	100.00	100.00

Table 2 shows the X-ray diffraction results for the three muffles. Silicon carbide was the abundant phase for all muffles as α-SiC; cristobalite was abundant for muffles A and C and middle for muffle B; tridymite occurred only for muffle C, as a minor phase.

Table 2. X-ray diffraction results.

Phase	Muffle A	Muffle B	Muffle C
Silicon carbide	abundant	abundant	abundant
Cristobalite	abundant	middle	abundant
Tridymite	absence	absence	minor

When the diffractogram of muffle A is compared to that of muffle B, cristobalite, oxidized phase, was more abundant in A than in B (new and original muffle), Table 2 and Figure 1. In Figure 1, the characteristic peak of cristobalite (C) was higher for muffle A compared to the others. It was due to the excessive oxidation of α-silicon carbide, which produced the cristobalite and some vitreous phase.

For the muffle C, there were two oxidized phase, tridymite and cristobalite; this occurrence was due to the relative oxidation that had happened during the long period that this muffle was used.00

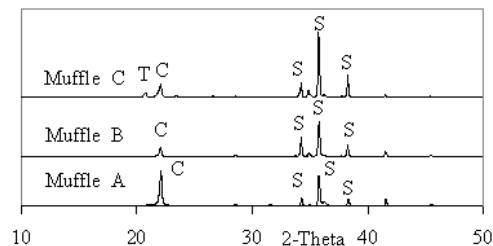


Figure 1. X-ray diffraction pattern for muffles A, B and C. Symbols: T – tridymite; C – cristobalite and S – silicon carbide.

The reflected light microscope study demonstrated that the microstructures of all muffles were relatively different. For muffle B, its microstructure had low sintering degree of the silicon carbide particles and had an interconnected pores network in the refractory matrix, as shown in Figure 2. Also, there is a lack of fine silicon carbide particles, less than 50µm and the majority of particles seems to be in the size between 50 and 200µm. The absence of fine particles associated with the low particles compaction could be responsible for the deficiency in the particles sintering.

For muffle A, which had an excessive expansion, most part of the silicon carbide particles was oxidized to the silica phase (cristobalite and vitreous phase), as demonstrated in Figure 3. As a consequence, the silicon carbide particles smaller than 50µm have disappeared and the others had their outline smoothed by silicon carbide oxidation. Contrarily, muffle B (Fig. 2) showed mainly sharp-edged particles. The silicon carbide oxidation was facilitated by the low particles sintering in muffle A, what made easy the gas entrance into the refractory matrix, as demonstrated in Figure 3.

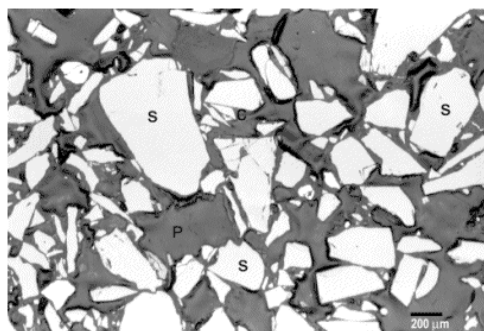


Figure 2. Reflected light micrograph – muffle B, 100X. (S) silicon carbide; (P) pore; (C) cristobalite + vitreous phase.

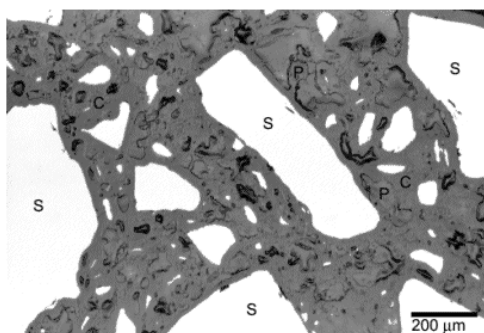


Figure 3. Reflected light micrograph – muffle A, 200X. (S) silicon carbide; (P) pore; (C) cristobalite + vitreous phase.

As for muffle C, the reflected light microscope study showed a wide particle size distribution of silicon carbide in its matrix (Fig. 4). The sintering degree of the particles was excellent, with low porosity and the pore sizes were small or in the middle range.

Due to the long period that this muffle was exposed to the oxidizing atmosphere, it was common to find some oxidized phases (cristobalite or vitreous phase), originated from the silicon carbide particles. However, the velocity of this oxidation seems to have been very slow. The number of small and sharp-edged silicon carbide particles confirmed this fact (Fig. 4).

The scanning electron microscope (SEM) with the EDS microanalyses study has confirmed the previous observation by the reflected light microscope. For muffle A, the excessive oxidation of silicon carbide particles was confirmed and the EDS microanalyses showed the silica phase as result of the particles oxidation, figure 5. In this figure, according to the EDS microanalyses, the area C refers to cristobalite and some vitreous phase (Table 3); the area S refers to the silicon carbide phase.

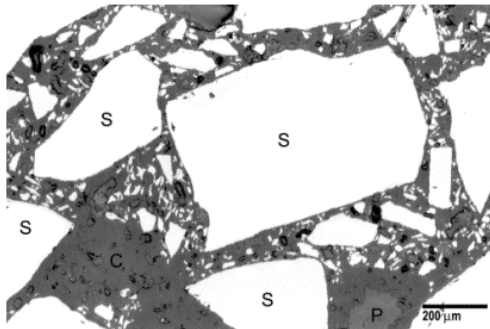


Figure 4. Reflected light micrograph – muffle C, 200X. (S) silicon carbide; (P) pore; (C) cristobalite + vitreous phase.

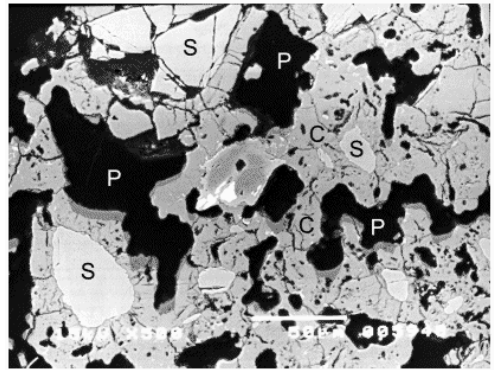


Figure 5. Scanning electron micrograph – muffle A; backscattered electrons image. (S) silicon carbide; (P) pore ; (C) cristobalite + vitreous phase.

Table 3. EDS microanalyses for muffle A.

Area	SiO ₂	Si	Interpretation
S	0.0	100	silicon carbide
C	99.6	-	cristobalite + vitreous phase

For muffle B, the SEM study confirmed the lack of fine silicon carbide particles and high porosity (Figure 6).

In the case of muffle C, this study demonstrated clearly that its microstructure is very different of the others; in Figure 7, the EDS microanalyses (Table 4) confirmed the presence of oxidized phases cristobalite and vitreous phase (area C) and the silicon carbide phase (S). In addition to these phases, tridymite, detected by X-ray diffraction, was associated to the cristobalite phase. The occurrence of tridymite is an indication that the oxidation rate was very slow, since there was time for the crystallization of the vitreous phase as tridymite.

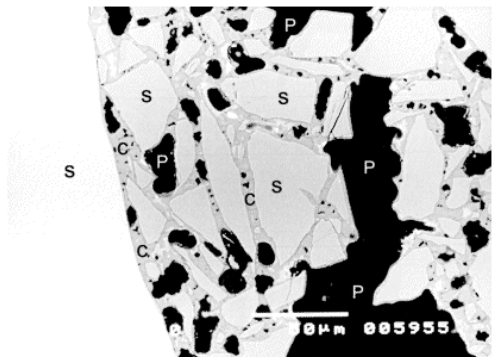


Figure 6. Scanning electron micrograph – muffle B; backscattered electrons image. (S) silicon carbide; (C) cristobalite; (P) pore.

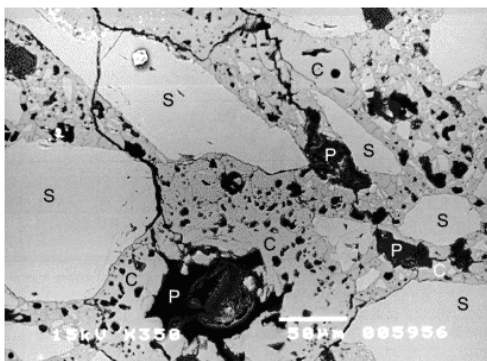


Figure 7. Scanning electron micrograph for muffle C; backscattered electrons image. (S) silicon carbide; (C) cristobalite; (P) pore.

Table 4. EDS microanalyses for muffle C.

Area	SiO ₂	Si	Interpretation
S	-	100	silicon carbide
C	98.0	-	cristobalite, tridymite and vitreous phase

The apparent porosities for muffles A and B were much higher when compared to muffle C, approximately three times (Table 5). It means that the sintering process for muffles A and B was not perfect, what could be due to the lack of fine particles and low particles compaction.

These high apparent porosity values confirmed the previous observations, what demonstrated that the insufficient particles sintering was responsible for the low oxidation resistance of muffle A and, consequently, for its pronounced expansion of muffle A.

Table 5. Apparent porosity of the three muffles.

Muffles	Apparent porosity (%)	
	Average	Standard Deviation
A	23,5	±0,04
B	21,3	±0,28
C	8,6	±0,9

4 CONCLUSIONS

Muffle B had a low sintering degree between the silicon carbide particles and the binder phase, silica. Its porosity was relatively high with relatively wide particle size distribution. This low particles sintering was caused by the absence of fine particles and the low particles compaction.

Due to the similar characteristics of muffle A, after its installation, the rate of silicon carbide oxidation was relatively high, due mainly to the high

apparent porosity value. As a result, the muffle became so fragile and displayed an excessive expansion.

As a comparison, the muffle C was used for a much longer period, has kept its good characteristics with only a little degree of degradation; as an example, the silicon carbide oxidation degree was smaller and, also, its apparent porosity was much lower than the others.

5 REFERENCES

- Izhevskiy, V. A., Genova, L. A., Bressiani, J. C., Bressiani, H. A. 2000. Review articles: silicon carbide. Structure, properties and processing. *Cerâmica*, 46 (297): 4-13.
- Marchi, J., Bressiani, J. C., Bressiani, H. A. 2001. Densification studies of silicon carbide-based ceramics with yttria, silica and alumina as sintering additives. *Materials Research*. 4(4): 231-236.
- Strecker, K., Ribeiro, S., Camargo, D., Silva, R., Vieira, J., Oliveira, F. 1999. Liquid phase sintering of silicon carbide with AlN/Y₂O₃, Al₂O₃/Y₂O₃ and SiO₂/Y₂O₃ additions. *Material Research*, 2(4): 249-254.

Inorganic Waste as Ceramic Ist Part

M.G.Lefter & N.Moreno

Facultad de Ingenieria-Consejo de Investigacion, Universidad Nacional de Salta, Salta, Argentina

ABSTRACT: The purpose of this work was to characterize and evaluate some properties of inorganic waste containing ceramic material. An overview is given of a mechanochemical process for the preparation of a value-added material. Ceramics were obtained using caolinite clay, borax industry residue with calcite and quartz at a sintering temperature of 950°C. Boron free specimens have a sintering temperature of 1050°C. Different types of glass-ceramics were made: caolin, caolin-50% residue caolin-60% residue at temperature up to 1050°C. The aggregates were characterized in term of mineral phases, modulus of rupture. Attempts were made to correlate these properties with corresponding structure and phases. Infrared Spectroscopic and RX investigations has been carried out to study the structural changes as a function of composition; the spectral patern show bands corresponding to Al-O-Al and B-O-Si vibrations. The shifting of the asymmetric stretching frequencies of the Si-O-Si and Al-O-Si to higher wave numbers indicate the formation of mullite. Amorphous phase indicate glass sintered process involved. The amorphous phase transformation was carried out at 950°C. We attempt to give an example of material design using a contaminating residue.

1 INTRODUCTION

Contamination of ground water resources and soil has been one of the major environmental concerns during the past few decades due to its effects on public health. Management of contaminated ground water resources has been a difficult challenge because of the limited resources that can be committed to remediate a large number of contaminated sites. The boron concentration of surface and groundwaters in Lerma Valley, Salta Argentina where several factories produce boric acid and sodium tetraborate has abnormally high values (Lomniczi et al. 1997). The climate is high altitude sub-tropical with dry season, so that agriculture is dependent on irrigation with water from rivers as well as with groundwater.

Industry development caused that the amounts of waste materials is on the increase. The sludge they produce still contains variable amounts of boron. It seems obvious that proper management of these material is necessary. Renewed interests in recyclability and environment sustainability has arisen in the last few years. Environmental legislation increasing the pressure on manufacturers of materials and end-products to consider the environmental impact of their products at all stages

of their life cycle, including recycling and ultimate disposal. This environmental issue has recently generated considerable interest in the development of composite materials (Baillie 2003).

Studies were made on the mechanochemical reaction of the system from the viewpoint of elucidating how solid state reactions occur and propagate from the contact boundary of dissimilar solids. Were shown a number of similar reactions leading to heterobridging bonds (HBBs) or hetromatalloxane bonds (HMBs) when two dissimilar atoms are connected by an oxygen atom serving as a hinge (Senna 2001).

B₂O₃ has been found to be a useful fluxing agent to densify the MgO-CaO-SiO₂-Al₂O₃ (MCAS) composite glass powders. The temperature needed to fully densify MCAS decrease with increase of B₂O₃ addition. MCAS glass powders were used as precursor to prepare dense ceramics and develop its sintering characteristics at less than 1000 °C. (Yang & Cheng 1999). Because of the low melting point of B₂O₃, the procedure of sintering would be a reactive liquid phase sintering process, much easier densification and crystallization of quartz and mullite is evidenced.

2 MATERIAL AND METHODS

As a fundamental raw material, sludge, containing B_2O_3 , as sodium tetraborate, calcium and magnesium metaborate, from borate industry was used. Ceramic pieces were obtained using sludge from a local borate industry and commercially available caolin type clay. The chemical composition of the crude material is shown in Table 1.

Table 1: Samples composition in % oxides

Sample	B_2O_3	SiO_2	Al_2O_3	Fe_2O_3	Na_2O	K_2O	Cao	MgO
1 0% res		48.4	17.56	4.71	1.8	2.20	11.62	2.73
2 50%res	3.6	42.8	14.20	5.30	6.70	3.10	18.50	2.50
3 60%res	5.10	40.10	12.70	5.05	7.12	3.20	19.60	2.40

The flow sheet for obtaining and characterization of the glass ceramic material is shown in Figure 1:

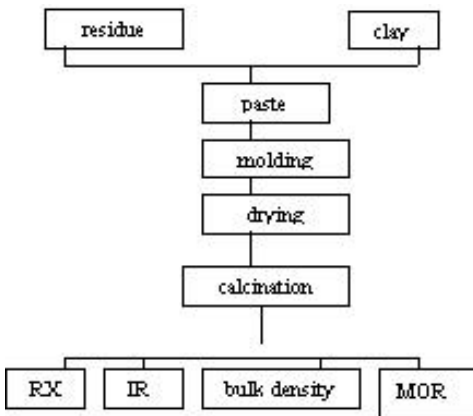


Figure 1: flow sheet for obtaining and characterization of the glass ceramic material.

Chemical analysis used were: gravimetric method for Si; atomic absorption spectrophotometry in a Shimadzu-AA-6500F for Al, Fe, Ca, Mg, Na, K; UV-Visible spectrophotometry in a Spectronic 401, for boron with azomethine H method (Harris, 1992).

Structural characteristics were determined by X-Ray diffraction in a RIGAKU DENKI D/Max II-C using $Cu K\alpha$ radiation, Ni filter, 1° receiving and divergence slits and 0,15 mm dispersion slit. The scanning rate was $2q/min$ and the sample path $0,02^\circ$.

IR spectra were obtained in a FTIR Bruker IFS 88 spectrophotometer.

The density of the green and sintered compacts was determined by Archimedes' method.

3 RESULTS AND DISCUSSION

The crystalline phases were determined by X-ray diffraction. The X-ray diffraction patterns of ceramic pieces with different amounts of B_2O_3 addition, isothermally treated at $950^\circ C$ are shown in Figure 2. Boron free samples had partially densified, the liquid-phase sintering process effect of B_2O_3 was pronounced because the crystallization rates of quartz increased with the amount of B_2O_3 in the sample. No borate mineral was detected.

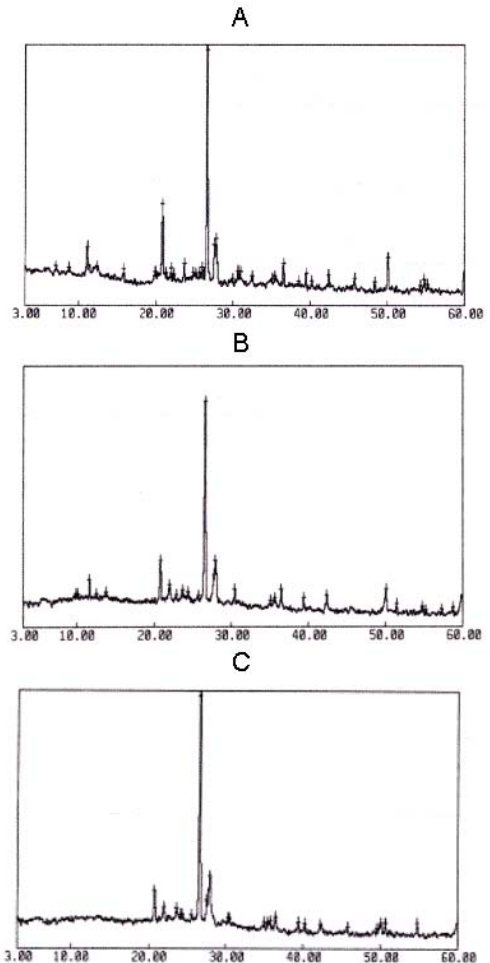


Figure 2: X-ray diffraction patterns: A-boron free; B-50% residue; C-60% residue.

The IR spectra (Figure 3) of the samples calcined at temperatures $950^\circ C$ indicate the structural evolution during mullitization showing a very broad

band without fine structure in the 400-900 region. During heat treatment removal of the hydroxyl groups and of the organics is expected. The removal of OH-groups in the sample results in a increase in Al-O-Al and Si-O-Si linkages. In addition to these, the two hydroxides can condense together resulting in a Al-O-Si linkage and B-O-Si linkages are also present fig. 3 (b) and (c). The existence of nanostructured Al_2O_3 , SiO_2 and $\text{Al}_2\text{O}_3\text{-SiO}_2$ agglomeration in the amorphous state was predicted by the absence of fine structure in the 400-900 cm^{-1} .

4 CONCLUSIONS

The sintering density increases with the addition of B_2O_3 . Analysis showed that the influence of the phases on mechanical strength is related with boron amount, being superior as boron amount increases.

These parameters are good values for a ceramic material. The developed compositions of the ceramics on the basis of a residue are fully qualified for immobilization of boron. This work has demonstrated the suitable conditions for using borate industry residue as a clay additive to produce an engineering quality of brick.

5 REFERENCES

- Bailie, C. Eco-Composites, Composites Science and Technology, Vol. 63, Issue 9, 1223-1224, 2003.
- Harris, C. D. Quantitative Chemical Analysis, Editorial Group Iberoamerica, Mexico, 1992
- Lomniczi, I. and Musso, H, Assesment of Boron Concentration in Surface and Grounwaters in the Lerma and Calchaqui Valleys (Province of Salta, Argentina), Anales de la Asocacion Quimica Argentina, Vol 85, N° 5/6, 283-293, 1997.
- Senna, M. Recent development of materials design through a mechanochemical route, International Journal of Inorganic Materials, Vol. 3, Issue 6, 509-514, 2001.
- Yang, C. F. and Cheng, C. M. The Influence of B_2O_3 on the sintering of $\text{MgO-CaO-Al}_2\text{O}_3\text{-SiO}_2$ composite glass powder.

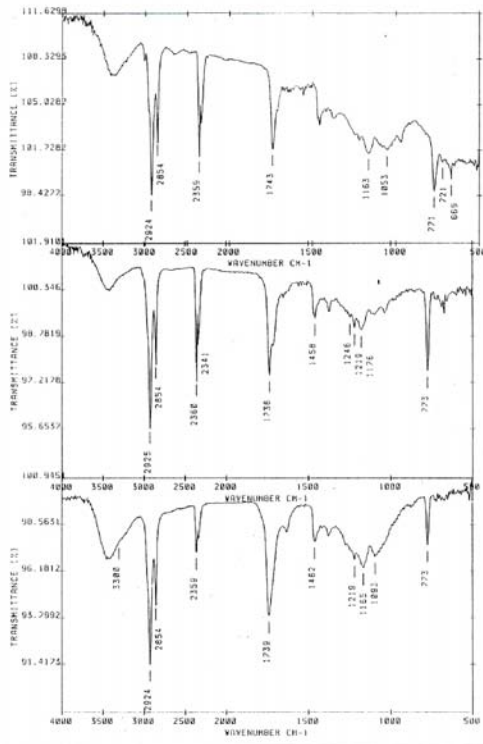


Figure 3: IR spectra: (a) boron free, (b) 50% residue, (c) 60% residue.

Table 2 shows a MOR increase with boron amount, a strong glass phase was formed in the structure and crystalline particles were united and porosity reduced.

Table 2: Physical properties.

sample	bulk density	mineral phases	MOR
1 0% res	1.84 g/cm^3	quartz, illite	123 Kg/cm^2
2 50% res	2.43 g/cm^3	quartz, feldspars	176 Kg/cm^2
3 60% res	2.85 g/cm^3	quartz, mullite	185 Kg/cm^2

Sinterability, Microstructure and Glass-Ceramic Properties 1st Part

M.G.Lefter & N.Moreno

Facultad de Ingenieria-Consejo de Investigacion, Universidad Nacional de Salta, Salta, Argentina

ABSTRACT: The aim of this work is to study some aspects of the physical properties of ceramics fabricated using borax industry residue. Two series of glass-ceramic composites were prepared from borax industry residue and kaolin clay at a sintering temperature of 950°C. A glass-ceramic composites is an effective material sintering at low temperatures. In this paper, the effect of boron on sinterability at different temperatures was investigated. Mullite is a promising material for both conventional and advanced ceramic applications due to low density, high refractoriness, low creep rate, low thermal expansion, low thermal conductivity, good thermal and chemical stability, all properties increased when boron oxide was added. Mullite is the only stable crystalline phase in the aluminosilicate system; its chemical composition ranges from $3 \text{ Al}_2\text{O}_3 - 2 \text{ SiO}_2$ to $2\text{Al}_2\text{O}_3 - \text{SiO}_2$. During a sudden temperature change there occur transient temperature distributions which induce thermal stresses. Boron addition leads to formation of a vitreous phase at lower temperature. Microscopic, RX, spectra, porosimetry studies were carried out in order to characterize the ceramic material obtained. A small amount of glassy phase and a number of small pores were observed in the samples which also have higher density values when the temperature and the amount of boron increase. It is possible to avoid preferred orientation of the porosity and to achieve a uniform density distribution. The results of this work show the effect of boron on sinterability, as expected for a material with good physico-mechanical properties.

1 INTRODUCTION

Several approaches to obtaining glass-ceramics exist. A typical glass component in the composites system is borosilicate glass. B_2O_3 was chosen for its low melting point. In the present study boron oxide was used to obtain dense ceramic at low sintering temperatures (Merge & Aslanoglu 2003). Glass/mullite and glass/spinel composites which consist of borosilicate glass and mullite or spinel respectively are expected to suppress cristobalite precipitation as they contain aluminium ions which are responsible for the cristobalite formation (Bertrand et al. 2003).

There are various experimental methods to investigate phase separations in the glass-forming oxide systems. Techniques such as microscopy, small-angle X-ray scattering are based on physical properties. There exist many controversies between the results from the different techniques. The metastable immiscibility in boric oxide-silica and alkali borate systems has been repeatedly investigated by various methods (Kim & Sanders Jr. 2000). Regular, quasi-regular and subregular solution models were applied to describe the SiO_2 - and B_2O_3 -rich regions of binary liquid solutions.

In this context this work has the objective to study the effect of the firing temperature and the amount of boron containing residue on the microstructure (Vieira & Montero 2003), mineralogical changes and physical properties of ceramics obtained from kaolin type clay and borate industry residue. The reasons are its low softening temperature, which is assumed to decide the sintering temperature of the glass/mullite and glass/spinel composites, its superior chemical resistance property, its lower thermal expansion, and its ease for mass production (Coimbra et al. 2002).

2 MATERIAL AND METHODS

In the brick molding process, two different sludge proportions, 50% and 60% were mixed with ground clay and water using a crushing machine. The mixtures were then introduced into a series of brick molds (10×6×1 cm). After 48 hours maturation followed by 24 hours 100°C oven-dried period, the dried bodies were calcinated at the temperature ranging from 700°C up to 1000°C at low rate heating, steps of 100°C each. The produced bricks then underwent test including: firing shrinkage,

porosity, water absorption, to determine the quality of bricks (Carretero et al. 2002). Following criteria evaluation, the test of toxic characteristics leaching process were presented in previous papers Gamarra et al. 2000).

The microstructure observation on the sintered specimens were done using a ORTHOMAT-POL-LEITZ microscope by transmission with CB 12 filter, 100% light and parallel nicols on 30 μ width prepreates (Braganca & Bergmann 2003) (Almeida et al. 2001).

The crystalline structures of sintered glass-ceramics were investigated using X-Ray diffraction patterns in a RIGAKU DENKI D/Max II-C using Cu K α radiation, Ni filter, 1 $^\circ$ receiving and divergence slits and 0,15 mm dispersion slit. The scanning rate was 2 θ /min and the sample path 0,02 $^\circ$ (Park et al. 2003).

3 RESULT AND DISCUSSION

Physical properties are shown in Table 1. The quality of brick can be assured according to the degree of firing shrinkage. As shown, the firing shrinkage has no increase with increasing boron amount or increasing temperature after 800 $^\circ$ C.

Porosity and water absorption decrease with an increased boron amount and temperature increase. The glass phase dissolve most of the particles and also eliminate porosity.

Table 1: Physical properties of glass ceramic bricks.

sample	porosity % volum	shrinkage cm m $^{-1}$	water absorbion %	aparent density g· cm $^{-1}$
50%res 700 $^\circ$ C	3.6	5	0.43	2.40
50%res 800 $^\circ$ C	3.2	6	0.30	2.55
50%res 900 $^\circ$ C	3.2	6	0.05	2.75
50%res 1000 $^\circ$ C	2.8	6	0.02	2.80
60%res 700 $^\circ$ C	3.4	5	0.35	2.43
60%res 800 $^\circ$ C	3.4	4	0.30	2.57
60%res 900 $^\circ$ C	3.0	4	0.02	2.95
60%res 1000 $^\circ$ C	2.8	4	0.015	3.07

Microscopic observation on boron added specimens sintered at temperature from 600 up to 950 $^\circ$ c are shown in Figure 1- The coalescence of glass particles, pore elimination and the enhancement of densification were promoted by the viscous flow of B $_2$ O $_3$ as shown in Fig. 1(a-700 $^\circ$ C, b-800 $^\circ$ C, c-900 $^\circ$ C, d-1000 $^\circ$ C) for 50% residue samples. Minerals as quartz, plagioclase, small pores and no borate mineral were present. The morphology of samples calcinated at 900 $^\circ$ C is modified slightly.

Viscous flow of the flux coalesced the glass particles and densification becomes more complete as the amount of B $_2$ O $_3$ rises as shown in Figure 1 (e-700 $^\circ$ C, f-800 $^\circ$ C, g-900 $^\circ$ C, h-1000 $^\circ$ C) for 60% residue samples. Densification is more apparent and fewer pores are recognized. Boron is part of glass phase, with small quartz cristals around.

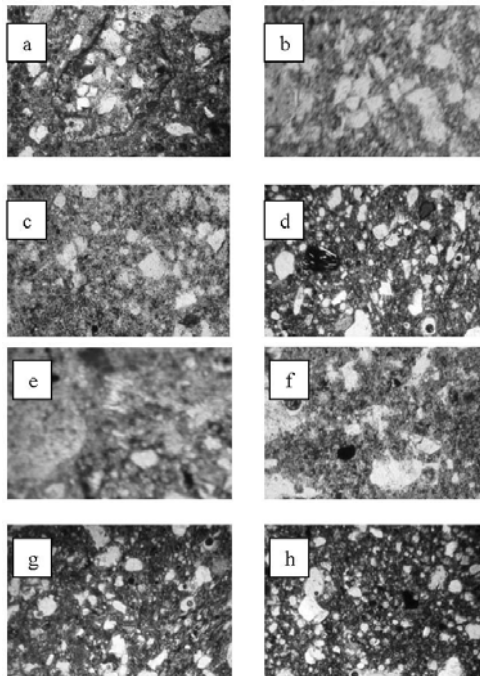


Figure 1: Micrography at different temperatures and composition.

The RX diffractograms of brick samples after heat treatment at various temperatures are presented (Figs. 2, 3). The amorphous to γ -Al $_2$ O $_3$ mullite phase transformation was carried out at temperatures higher than 800 $^\circ$ C. At temperature higher than 900 $^\circ$ C only crystalline mullite peaks were observed and small crystalls of quartz were present too. The possible phase transformation sequence in this system is:

amorphous - γ Al $_2$ O $_3$ - spinel - crystalline mullite

No borate mineral was present in samples fired at temperature higher than 900 $^\circ$ C as was expected, B $_2$ O $_3$ is part of glass-phase.

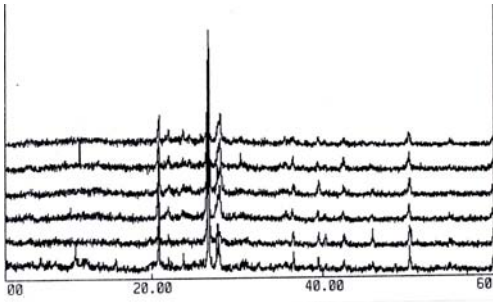


Figure 2: RX patterns of 50% residue bricks fired at temperature ascending from 700°C up to 1000°C.

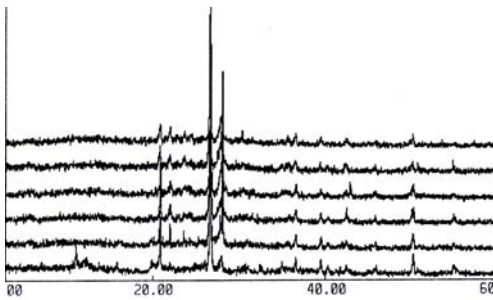


Figure 3: RX patterns of 60% residue bricks fired at temperatures ascending from 700°C up to 1000°C.

4 CONCLUSIONS

The temperature and the amount of B_2O_3 have been found to influence the sintering behaviour of the mixture residue – kaolin. Reaction sintered products showed always a higher sintered density as the amount of boron and temperature increase.

It might be a good way to control boron contamination by immobilizing and recycling a contaminated residue.

5 REFERENCES

- Almeida A.F.L, Thomazini D., Vasconcelos I.F., valente M.A.,Sombra A.S.B. 2001 Structural studies of lithium triborate ($LBO-LB_3O_5$) in borophosphate glass-ceramics, *International Journal of Inorganic Material*, Volume. 3 Issue 7, 829-838.
- Bertrand S. Michalet T., Giraud A., Parlier M., Bataille A. Duclos R., Crampon J. 2003. Processing microstructure and mechanical strength of reaction bonded Al_2O_3 ceramics. *Ceramics International*, Volume 29, Issue 7, 735-744.
- Braganca S.R., Bergmann C.P. 2003. A view of white wares mechanical strength. *Ceramics International*, Volume 29 Issue 7, 801-806.
- Carretero M.I., Dondi M., Fabbri B., Raimondo M., 2002. The influence of shaping and firing technology on ceramic

- properties of calcareous and non calcareous illitic-chloritic clays, *Applied Clay Science*, Volume 20, Issue 6 301-306.
- Coimbra M.A., dos Santos W.N., Morelli M.R. 2002. Recuperação de resíduos inorgânicos para a construção civil. *Ceramica*, Volume 48, Issue 306.
- Gamarra M., Moreno N., Alcorta J. Re L., 2000. estructura y propiedades físico-mecánicas de vidrio cerámico producto de residuo reciclado. VI Jornadas Argentinas de Tratamiento de Minerales, Volume II, 315-319.
- Kim S.S., Sanders Jr. T.H. 2000. Calculation of subliquidus miscibility gaps in the $Li_2O-B_2O_3-SiO_2$ system. *Ceramics International*, Volume 26, Issue 7, 769-778.
- Mergen A., Aslanoglu Z., 2003. Low –temperature fabrication of anorthite ceramics from kaolinite and calcium carbonate with boron oxide addition. *Ceramics International*, Volume 29, Issue 6, 667-670
- Park Y.J., Moon S.O., Heo J. 2003. Crystalline phase control of glass ceramics obtained from sewage sludge fly ash. *Ceramics International*, Volume 29, Issue 2, 223-227.
- Vieira C.M.F., Monteiro S.N. 2003. Influencia da temperatura de queima na microestrutura de argilas de Campos dos goytacazes-RJ. *Ceramica*, volume 49 Issue 309

Polymerization Reactions by Thermal Treatment of Gyrolite-group Minerals – an IR Spectroscopic and X-ray Diffraction Study Based on Synchrotron Radiation

K. Garbev, L. Black, A. Stumm, P. Stemmermann

Forschungszentrum Karlsruhe GmbH (ITC-WGT), Eggenstein-Leopoldshafen, Germany

B. Gasharova

Forschungszentrum Karlsruhe GmbH (ANKA-ISS), Eggenstein-Leopoldshafen, Germany

ABSTRACT: We have investigated the thermal behavior of the calcium-silicate-hydrate gyrolite: $\text{Ca}_{16}[\text{Si}_8\text{O}_{20}]_3(\text{OH})_8 \cdot 14\text{H}_2\text{O}$. Upon heating in air ($t^\circ > 400^\circ\text{C}$) gyrolite is transformed to a truscottite-like phase, which appears to be stable at least up to 600°C . It then loses its crystallinity to great extent between 600 and 700°C . IR-spectroscopic evidence clearly demonstrates polymerization of the silicate anionic structure (Q3-Q4) upon heating in the range 400 - 600°C . Some considerations about the possible positioning of interstitial Ca are given.

1 INTRODUCTION

1.1 Importance (Motivation)

Gyrolite is a member of the large family of the calcium-silicate-hydrate (C-S-H) phases, which are of great importance in cement chemistry. It occurs in hydrothermally-treated cement systems with low CaO/SiO₂-ratios (known as C/S-ratio). Recently, some studies have showed formation of C-S-H phases at elevated temperatures around nuclear waste as a result of reactions of ground water with high-level radioactive waste glass (Gong et al. 1998). Gyrolite itself possesses the interesting property to change its *c*-unit cell reversibly up to 3Å upon heating up to 350°C , which may find many industrial applications. Some minerals structurally related to gyrolite possessing double silicate sheets (reyerite, truscottite, fedorite) show 8-ring channels in their structure and thus are similar to zeolites. Unfortunately, these minerals are extremely rare in nature. Conversely, gyrolite (with single silicate sheets) is one of the most stable phases existing over the temperature range 150 - 230°C under hydrothermal conditions, and can be readily synthesized. Truscottite, reyerite and fedorite may also be synthesized under hydrothermal conditions, but at much higher temperatures.

1.2 Structural aspects

The gyrolite group consists of minerals such as gyrolite $\text{Ca}_2[\text{Si}_8\text{O}_{20}]_3[\text{Ca}_7(\text{OH})_4]_2 \cdot 14\text{H}_2\text{O}$, tungusite $\text{Ca}_{14}[\text{Si}_8\text{O}_{20}]_3\text{Fe}^{2+}_9(\text{OH})_{22}$ and orlyamanite $\text{Ca}_4\text{Mn}_3[\text{Si}_4\text{O}_{10}]_2(\text{OH})_6 \cdot 2\text{H}_2\text{O}$. Characteristic features of their structures are single silicate sheets of 6-membered $[\text{SiO}_4]$ rings. The reyerite group on the other hand includes truscottite $\text{Ca}_{14}[\text{Si}_8\text{O}_{20}][\text{Si}_8\text{O}_{19}]_2(\text{OH})_8 \cdot 2\text{H}_2\text{O}$, fedorite $(\text{K},\text{Na})_2(\text{Ca},\text{Na},\text{Al})_7(\text{Si},\text{Al})_{16}\text{O}_{38}(\text{OH},\text{F})_2(\text{H}_2\text{O})$ and reyerite $(\text{Na},\text{K})_2\text{Ca}_{14}[\text{Si}_8\text{O}_{20}][\text{AlSi}_7\text{O}_{19}]_2(\text{OH})_8 \cdot 6\text{H}_2\text{O}$, which have double silicate sheets of 6-membered rings of $[\text{SiO}_4]$ tetrahedra. Thus, in terms of polymerization, the minerals of the reyerite group possess higher condensate silicate anionic structures than those of the gyrolite group.

2 EXPERIMENTAL

2.1 Synthesis of gyrolite and thermal treatment

Gyrolite was synthesized by hydrothermal treatment of CaO (obtained after burning of CaCO₃ at 1000°C) and SiO₂ (Aerosil) at 220°C for 33 days in a Teflon-lined steel autoclave. Gyrolite samples were subsequently heated at 400 , 500 , 600 and 700°C in air for 10 hours.

2.2 XRD study

XRD measurements were performed with conventional radiation (D5000 with rotating MoK_α anode). A gyrolite powder sample heated at 400°C was measured on the diffraction beamline of the ANKA synchrotron facility in Karlsruhe with a wavelength of 1.1003\AA in reflection geometry with analyser crystal (Si cut along 111).

2.3 IR-study

FT-IR bulk spectra in the $25\text{--}10000\text{ cm}^{-1}$ range were recorded at the infrared (IR) beamline of the ANKA synchrotron facility in Karlsruhe on a Bruker IFS 66vs FT-IR spectrometer with 4 cm^{-1} spectral resolution. An undoped silicon single crystal was used as a holder for the powder samples. The reference was taken with the empty sample holder. All measurements were performed in vacuum.

3 RESULTS AND DISCUSSION

Gyrolite treated at 400 , 500 and 600°C in air shows similar powder pattern to truscottite (ICDD 29-0382) or reyerite (ICDD 29-1039) (Figure 1). Thus, shrinkage of the structure along the c -axis occurs, leading to a decrease in the value of the basal reflection (001) from 22.4 to 19\AA . Another interesting feature is the increased intensity of reflection (002) at about 9.7\AA for the heated samples. The heated samples show good crystallinity (Figure 2).

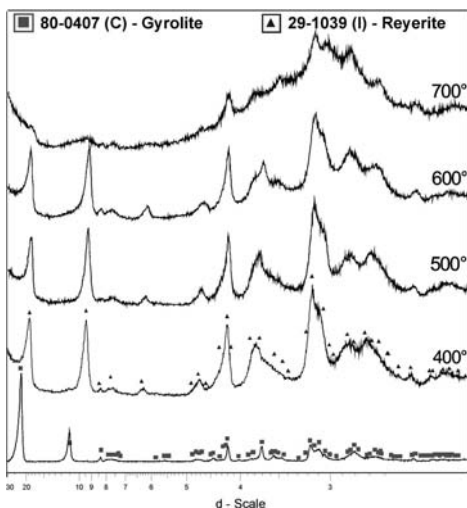


Figure 1: XRD patterns of synthetic gyrolite at room temperature (bottom) and heated at 400 , 500 , 600 and 700°C .

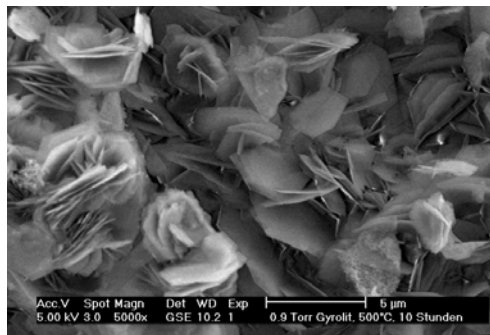


Figure 2: Secondary electron image (ESEM-mode) of gyrolite heated at 500°C for 10 hours.

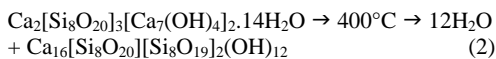
The sample heated at 700°C shows breakdown of the structure and a high percentage of amorphous material, in agreement with the data of Okada et al. (1994) Some reflections of truscottite (reyerite) are still resolvable (211, 213).

Along with the important question of whether 2 (of 3) single silicate sheets condense to double sheets as seen in reyerite and truscottite, we are also interested in the fate of the molecular water upon heating at 400°C . The proposed structural formula of truscottite is $\text{Ca}_{14}[\text{Si}_8\text{O}_{20}][\text{Si}_8\text{O}_{19}]_2(\text{OH})_8 \cdot 2\text{H}_2\text{O}$ (Lachowski, 1979). Supposing that, upon heating at 400°C , gyrolite transforms into truscottite, there are two additional Ca atoms per formula unit (p.f.u.), which must further occupy definite crystallographic positions in the structure. We suppose that this additional Ca does not influence the polymerization of the structure, thus most probably occupying “zeolite like” interstitial positions, as reported for reyerite and fedorite. The additional calcium leads to a surplus $4+$ charge p.f.u., which can be balanced by two possible mechanisms. The first one is partial deprotonisation of the octahedral sheet $(\text{OH})_4 \rightarrow (\text{O})_4$ leading to the formula $\text{Ca}_{16}[\text{Si}_8\text{O}_{20}][\text{Si}_8\text{O}_{19}]_2(\text{OOH})_4 \cdot 2\text{H}_2\text{O}$. This is unfeasible because of the need for charge transfer along the whole structure, and there is no possibility of representing the dehydration in a simple way. Another possible mechanism is reaction of molecular H_2O with two “redundant” oxygen atoms promoted by the condensation:



Thermogravimetric studies of natural and synthetic gyrolite show that until 400°C the phase loses about 12 of 14 H_2O molecules (Shaw, 1999).

The dehydration of gyrolite at 400°C and the building of a truscottite-like phase thus can be represented according to the equation:



The loss of the water molecules is the trigger for the gyrolite – truscottite phase transition at 400°C. Our theory is supported by infra-red spectroscopy studies. There exists a correlation between the decrease in the intensity of the main H₂O bending band at 1633cm⁻¹, the disappearance of the shoulders at 1595 and 1666cm⁻¹, and the appearance of two additional OH stretching bands at about 3697 and 3740cm⁻¹ after heating at 400°C (Figure 3) The higher frequencies show that these OH-groups are less disturbed than those in the untreated gyrolite. The latter have uniform neighborhoods comprising 3 Ca atoms, as in portlandite. We suppose that the new OH groups are coordinated only by one Ca atom in the interstices of the truscottite-like structure. The lattice modes arising in the far IR (FIR) spectra reflect the changes in the Ca structure (Figure 4).

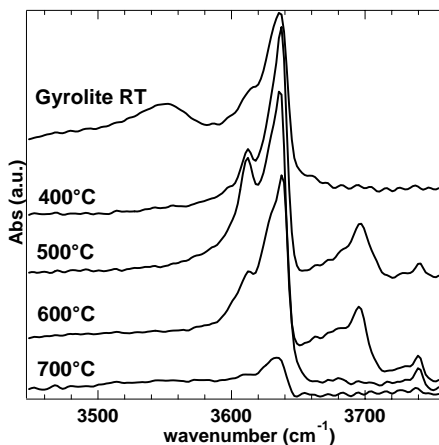


Figure 3: FT-IR spectra in the OH stretching region.

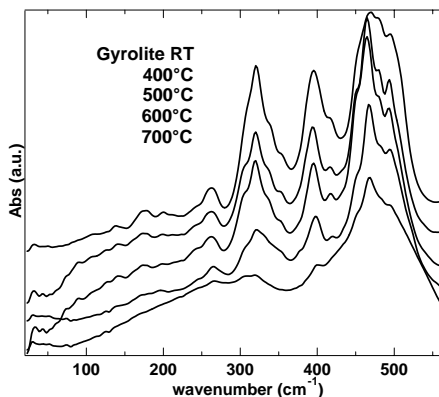


Figure 4: FT-IR spectra in the far IR region.

The FIR spectra of gyrolite heated at 400 and 500°C are very similar, implying that the main changes in the Ca structure occur during the gyrolite – truscottite phase transition at 400°C. As mentioned above, these are related to the transformation of two of the water molecules coordinating the Ca_x cations into OH groups (1) thus provoking the breakdown of the Ca X-sheet. At the same time, two S₂ silicate sheets condense (Fig. 6), forming new 180° Si-O-Si bonds and giving rise to new symmetrical and asymmetrical Si-O-Si (Q⁴) stretching bands at about 806 and 1253cm⁻¹, respectively (Fig. 5) in accordance with Chalmers et al. (1964) and Henning (1974). The band at 1134 cm⁻¹ in untreated gyrolite disappears at 400°C. We assume that this vibration involves terminating oxygen bound to the Ca X-sheet (O-Si₂, Q³) that disappears upon condensation of the S₂ silicate sheets. The next remarkable structural change occurs at 600°C. The newly formed OH groups (3697cm⁻¹) disappear, provoking the next change in the Ca structure, as also seen in the FIR spectra.

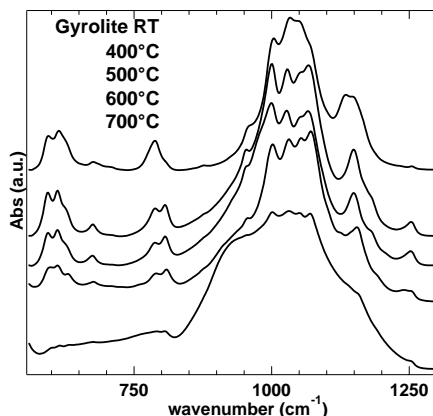


Figure 5: FT-IR spectra in the mid IR region.

In order to develop a model of the structure we investigated the already known reyerite and fedorite structures, which readily incorporate additional cations in their channel-like interstices. Generally, the double silicate layer in these structures may be imagined as mirrored single silicate layers, which in turn consist of alternating regular 6-membered rings of Si-tetrahedra all pointing in the same direction (*uuuuuu* or *dddddd*) and irregular 6-membered rings (*uuduud* and *duuddu*, respectively). In reyerite and fedorite the interstices of the regular double rings are occupied out of plane (closer to one of the single rings). The interstices of the irregular double rings are occupied on the imagined mirror plane. In the first case the coordination of an interstitial cation (in our case Ca) through the oxygen atoms of the silicate framework is 6-fold, but almost all in one

plane. This explains why additional oxygens (OH or H₂O) are needed for proper coordination of the interstitial cation. In the second case, the coordination of a cation situated in the middle of the irregular double ring by oxygen atoms from the framework is also 6-fold but the polyhedron formed has a larger "volume". Nevertheless, it is far too deformed and the interatomic distances are between 2.6 and 2.9Å, i.e. they are too large for 6-fold coordination. Also in this case, additional anions are required for proper coordination, which may be 8-fold. Following this we suggest that OH groups in the plane of the "zeolitic" calcium occupy the irregular interstices. In the case of K-phase, the synthetic analogue of fedorite, (Gard et al. 1981) putting the zeolitic Ca in the irregular interstices produced more acceptable bond lengths and the same 6-fold coordination by the framework oxygen atoms. We suppose that the positions in the interstices of the regular rings are not occupied by Ca because the analogue Na-position in the X-layer is not occupied in the case of synthetic gyrolite with Ca/Si=2/3. On the contrary, we regard the other cation position of the X layer (Ca₈, Merlino, 1988^b) as fully occupied. This position is situated above or beneath the irregular 6-fold rings. After heating and the consequent shrinkage, this Ca is most probably trapped in these interstices. In both cases, introducing an additional two OH groups to give meaningful bond lengths resulted in 8-fold coordination of the "zeolitic" Ca. The OH groups point to the regular rings and most probably the positive charges (H atoms) are concentrated in the regular 6-fold rings, thus balancing the structure.

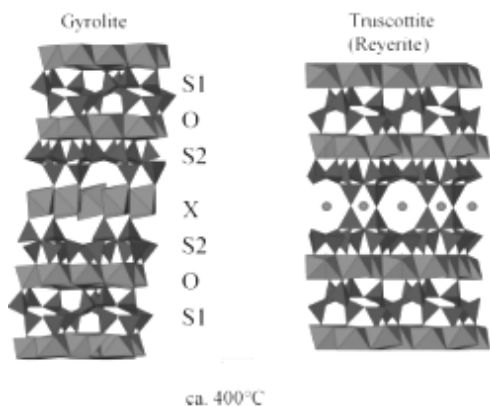


Figure 6: Transformation of gyrolite into truscottite upon heating 400-600°C. Two symmetrically equivalent silicate S2 single sheets polymerize to double sheets. Redundant Ca from X-sheet occupies interstitial positions within the double sheet. Notation after Merlino (1988^{a,b}).

To prove this we simulated the powder pattern of reyerite with Ca in positions in the middle of the

irregular 6-fold rings. The calculated structure factors for reflexions (001) and (002) showed $|F_{(001)}| < |F_{(002)}|$, which is unusual compared with the known patterns for gyrolite, reyerite and truscottite. On the other hand, it is in accordance with the powder patterns of gyrolite heated at 400, 500 and 600°C.

In order to obtain information about the space group and unit cell parameters we studied the powder pattern of the sample heated at 400°C using synchrotron radiation. Preliminary results of the Le-Bail powder pattern decomposition show that the space group P-3 (reyerite) does not fit very well. Better residuals were obtained with space group P-1 and $a=b=9.61\text{Å}$, $c=18.9\text{Å}$, $\alpha=92.8^\circ$ $\beta=90.6^\circ$ $\gamma=120^\circ$. Surprisingly good results have been obtained using space group R-3m and $a=16.6\text{Å}$ and $c=57\text{Å}$.

4 CONCLUSIONS

Synthetic gyrolite transforms into a truscottite-like phase upon heating at 400-600°C in air as evidenced by XRD and IR-spectroscopy.

The presence of additional OH groups, as proved by IR-spectroscopy and XRD pattern simulations, point to occupation of interstitial positions within double silicate sheets by Ca coordinated with OH.

Synthesis of highly polymerized calcium silicate hydrates of the reyerite group could be simplified.

5 REFERENCES

- Chalmers, R.A.; Farmer, V.C.; Harker, R.I.; Kelly, S.; Taylor, H. F. W. 1964. Reyerite. *Mineral. Mag.*, 33, 821-840.
- Gard, J.A.; Luke, K.; Taylor, H.F.W. 1981. The crystal structure of K-phase Ca₇Si₁₆O₄₀H₂. *Kristallografiya*, 26, 1218-1223.
- Gong, W.L.; Wang, L.M.; Ewing, R.C.; Vernaz, E.; Bates, J.K.; Ebert, W.L. 1998. Analytical electron microscopy study of surface layers formed on the French SON68 nuclear waste glass during vapor hydration at 200°C. *Journal of Nuclear Materials*, 254 (2-3) 249-265.
- Henning, O. 1974. Cements; the hydrated silicates and aluminates. In: Farmer, V.C. Ed., *Infrared Spectra of Minerals*. Mineral Society, London, 445-463.
- Lachowski, E.E.; Murray L.W.; Taylor H.F.W. 1979. Truscottite: composition and ionic substitutions. *Mineral. Mag.*, 43, 333-336.
- Merlino, S. 1988^a. The structure of reyerite, (Na,K)₂Ca₁₄Si₂₂Al₂O₅₈(OH)₈·6H₂O. *Mineral.Mag.*, 52, 247-256.
- Merlino, S. 1988^b. Gyrolite: its crystal structure and crystal chemistry. *Mineral. Mag.*, 52, 377-387.
- Okada, Y; Fang, Yh; Ishida, H; Nishido, H. 1994. Dehydration processes of gyrolite. *Journal of the Ceramic Society of Japan*, 102 (5) 449-455.
- Shaw, S. 1999. Hydrothermal formation and high temperature dehydration of calcium silicate hydrate (C-S-H) phases: an *in situ* synchrotron study. *PhD thesis*, University of Manchester.

Fuel and SO₃ Influence in Some Portland Cement Clinker

L.A.Gobbo & L.M.Sant'Agostino

Department of Sedimentary and Environmental Geology, Geosciences Institute, University of Sao Paulo, São Paulo, Brazil

ABSTRACT: The increasing use of alternative fuels as the petroleum coke in the cement industry is due to the significant economy of energy in the manufacturing process. This work was performed using 12 samples of Portland clinker, collected in 4 kilns operated with different raw materials and fuels. Different fuels were used in the Portland clinker production: coal, oil, petroleum coke (pet coke) and also some admixtures of both. Two different pet coques were used, one more enriched in SO₃. Techniques as chemical analysis, optical microscopy, XRD with Rietveld refinement and SEM-EDS were applied in this research. The most important difference in the samples was observed in the belite crystals composition. In clinkers produced using the oil, no SO₃ content was detected in the belite crystals. In contrast, those produced with pet coke showed more than 1,5% of SO₃. Also good correlation was found between the SO₃ and SiO₂ content in crystals, which suggests the substitution of SO₃ in the SiO₂ site. In other hand, high grades of SO₃ in alkalis enriched clinkers led to the formation of cubic C₃A in spite of the orthorhombic polymorph, which makes the cement setting time better. In clinkers produced with pet coke SO₃ enriched, arcanite and Ca-langbeinite were identified, normally present in those with also high K₂O grades in raw mix. Those phases are known to reduce the setting time of cement and also improve the initial resistance performance.

1 INTRODUCTION

The aim of this study is to show the characteristics of some clinkers produced in clinkering process with different kind of fuels as oil, coal, petroleum coke and also mineralizers, with different sulfur content. Fuels and calcium sulfate as mineralizer (anhydrite, gypsum) are normally the main source of SO₃ in the clinker, and especially in this research.

The increasing use of alternative fuels as the petroleum coke in the cement industry is due to the significant economy of energy in the manufacturing process. According to Centurione et al (1999), the mineralization process can bring beneficial effects to the cement industry; economical (fuel consumption), strategic (longer raw materials mine life), ecological (NO_x emission reduction, valorization of industrial waste) and also technical (higher performance of the product). In other hand, the excess of sulfur from mineralization process and also from fuels enriched in SO₃ in the clinkering process can lead to the elevation of SO₂ gas emission and also can lead to the formation of coating rings inside the kiln (Duda 1977). Moir (1992), Blanco-Varela et al (1996, 1997) and Centurione (1999) presented characteristics of clinkers produced with the mineralized pair CaSO₄ and CaF₂.

The SO₂ formed inside the kiln can also react with the alkalis from the raw mix to form the alkaline sulphates, as Ca-langbeinite and arcanite. The alkaline sulphates can lead to the increasing of initial strength (Jons, 1981) and decrease the final strengths (Jons 1981; Sarkar 1989). According to Moir (1982) and Campbel (1999) the Ca-langbeinite is known as a setting time controller in mineralized cements; it can decrease the setting time.

Some chemical and crystallographic modification can occur in the presence of sulfur in the clinkering process. Strunge and Knofel (1985, 1986) confirm that the sulfur is preferentially incorporated to the belite crystals. According to Bonafous et al (1995) in SO₃ enriched clinkers, the SO₃ in the belite probably occur from the substitution $3\text{Si}^{4+} \leftrightarrow 2\text{Al}^{3+} + \text{S}^{6+}$. Gobbo (2003) worked on samples with different content of SO₃ in clinker and presented the correlation of SO₃ and SiO₂ in belite crystals by SEM-EDS microanalysis, suggesting the partial substitution of SiO₂ by SO₃ in the cationic site of SiO₂.

Some XRD studies from Borgholm and Jons (1997) and Gobbo (2003) show that the clinkering with the mineralization pair CaSO₄ and fluorite lead

to the formation of an alite crystal with a narrower peak in the 51.7°2 θ , and also with higher intensity.

2 METHODS

This work was performed using 12 samples of Portland clinker, including two of white cement clinkers, collected in 4 kilns (A, B, C and D) operated with different raw materials and fuels. This samples collection makes possible to compare the sulfur and fuel effect on different clinking processes considering that the applied raw materials have almost no sulfur content.

Different fuels were used in the Portland clinker production: coal, oil, petroleum coke (pet coke) and also some admixtures of both. Two different pet coques were used, one more enriched in SO₃. Some samples were from kilns that produce mineralized clinker, where some gypsum is added in the process, increasing the SO₃ content in clinker. The Table 1 shows the kind of fuel or sulfur origin used in the clinker production of each studied sample.

Table 1: Kind of fuel and sulfur origin in the clinker production of each studied sample.

Sample	Fuel in clinking process	SO ₃ in fuel (%)	Other SO ₃ origin
A1 / A2 / A3	Petroleum coke	4.0	Anhydrite (mineralization)
B1 / B2	Coal	0.1	-
B3 / B4	Coal + Petroleum coke	5.3	-
C1 / C2	Oil	0.8	Gypsum in preheater
C3 / C4	Oil	0.8	-
D1	Petroleum coke	13.0	Anhydrite (mineralization)

2.1 X-Ray Diffraction

The samples were reduced to powder in agate ball mill and mounted in 10g holder by hydraulic pressing. The measurements were carried out in the range of 10 to 70 °2 θ with a step size of 0.02 °2 θ and a counting time of 2s/step. The powder diffraction analysis (XRD) were done with a broad focus CuK α tube anode, applying 40kV/40mA under configuration of 1/2° divergent slit, graphite monochromator, 0.2mm receiving slit and proportional detectors. Data sets were refined by the Rietveld method using GSAS software (Larson & Von Dreele 1999).

2.2 Sem-EDS

The SEM (Scanning Electron Microscopy) analysis of circa 0,3 cm diameter samples was performed on a Leo electronic microscope model Stereoscan 440, the coating was done using Carbon. X-ray spectrometry was used to obtain the clinker phases chemical microanalysis, in a EDS system coupled to SEM. For each analysed phase at least five measurements were done considering the presence of the most common oxides (CaO, Al₂O₃, SiO₂, Fe₂O₃, MgO, Na₂O, K₂O, SO₃ and Mn₂O₃). The literature shows that the alkalis and SO₃ are preferentially incorporated by the belite crystals (Strunge and Knöfel,1985), and the C₃A phase incorporates K₂O and Na₂O leading to the stabilization of the prismatic phase when in higher contents (Strunge and Knöfel,1986). To verify the sulfur incorporation in the belite, some crystals were selected to the microanalysis.

3 RESULTS

3.1 Chemical Composition

The Table 2 presents the chemical composition of the different studied samples.

Table 2: Chemical composition of 12 different clinkers.

Oxide	Sample (weight %)					
	A1	A2	A3	B1	B2	B3
SiO ₂	20.3	20.9	20.5	21.6	21.5	20.9
Al ₂ O ₃	5.0	5.2	5.2	5.6	5.4	5.0
Fe ₂ O ₃	3.5	3.5	3.2	3.4	3.3	3.2
CaO	64.9	66.0	64.9	65.8	64.3	63.5
MgO	1.8	1.3	1.4	0.8	1.2	1.5
SO ₃	2.8	2.1	2.1	0.2	0.8	2.0
Na ₂ O	0.1	0.1	0.1	0.4	0.5	0.5
K ₂ O	0.9	0.8	0.9	0.9	1.0	1.1
Total	99.3	99.9	98.3	98.7	98.0	97.7
FSC	99.7	98.6	98.7	95.0	93.5	95.7
MS	2.4	2.4	2.4	2.4	2.5	2.5
MA	1.4	1.5	1.6	1.7	1.6	1.6

Oxide	Sample (weight %)					
	B4	C1	C2	C3	C4	D1
SiO ₂	21.2	23.3	23.4	23.4	24.3	19.6
Al ₂ O ₃	5.2	5.5	5.0	5.5	4.7	4.8
Fe ₂ O ₃	3.3	0.2	0.2	0.2	0.2	2.8
CaO	64.3	67.5	67.6	69.5	70.3	62.6
MgO	1.5	0.4	0.3	0.3	0.3	2.0
SO ₃	1.4	1.1	1.0	0.3	0.2	3.4
Na ₂ O	0.5	1.4	1.1	0.1	0.1	0.2
K ₂ O	1.1	0.2	0.3	0.1	-	1.1
Total	98.5	99.6	98.9	99.2	95.4	96.5
FSC	95.4	94.0	94.7	96.2	95.5	100.3
MS	2.5	4.1	4.6	4.1	5.0	2.6
MA	1.6	36.7	29.1	34.4	26.2	1.7

3.2 X-Ray Diffraction

The qualitative analysis by XRD showed that the sample D1 (produced with the mineralized pair CaSO_4 and CaF_2 and also with a pet coke more enriched in SO_3) have a narrower peak and with more intensity in the $51,7^\circ 2\theta$, as shown in the Figure 1. The same peak with less intensity and wider was found in the sample B4, produced without the mineralization pair.

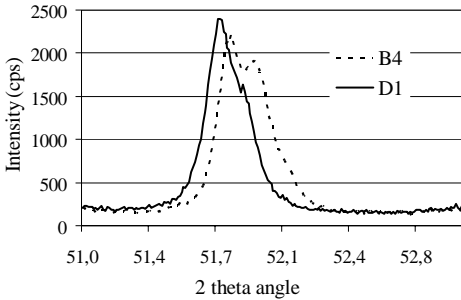


Figure 1: Narrower and with higher intensity peak produced in clinker with higher SO_3 content in sample D1.

The mineralogical composition of clinkers obtained by the Rietveld method is presented in the Table 3.

Table 3: Phases compositions of clinkers obtained by Rietveld method.

Phase	Sample (weight %)					
	A1	A2	A3	B1	B2	B3
Alite	59.7	60.6	58.9	66.1	66.6	68.8
Belite	19.6	19.5	21.5	17.9	16.1	13.7
$\text{C}_3\text{A-cub.}$	3.4	3.4	4.5	-	1.4	2.3
$\text{C}_3\text{A-ort.}$	-	-	-	8.0	6.1	3.1
C_4AF	12.7	13.8	13.3	7.8	9.6	11.6
C_{12}A_7	-	-	-	-	-	-
Free lime	0.9	0.4	0.6	0.2	0.2	0.5
Periclase	0.9	-	-	-	-	-
Sulfates	2.8	2.3	1.3	-	-	-
Total	100	100	100	100	100	100

Phase	Sample (weight %)					
	B4	C1	C2	C3	C4	D1
Alite	61.0	77.7	65.8	72.1	64.2	62.5
Belite	21.0	12.4	24.4	15.4	25.6	18.0
$\text{C}_3\text{A-cub.}$	5.3	-	-	6.1	6.0	9.9
$\text{C}_3\text{A-ort.}$	2.3	8.5	8.1	1.7	1.4	-
C_4AF	10.1	-	-	-	-	5.3
C_{12}A_7	-	0.8	1.8	2.7	1.0	-
Free lime	0.3	0.5	-	0.3	0.4	0.9
Periclase	-	-	-	-	-	0.2
Sulfates	-	-	-	1.8	1.4	3.2
Total	100	100	100	100	100	100

3.3 Sem-EDS

In the belite crystals microanalysis was verified the presence of higher sulfur grades in samples from mineralization clinkering process, as observed in samples A1, A3 and D1. Also elevated levels of SO_3 were verified in those produced with pet coke as fuel, as occurred in the sample A2. The pet coke used was enriched in 5% SO_3 . In samples in which the oil was the fuel used in the process, SO_3 was higher only in samples from clinkering with few gypsum contents. The chemical microanalysis in belite crystals can be observed in the Table 4.

Table 4: Chemical microanalysis composition of belite crystal (SEM-EDS).

Oxide	Sample (weight %)					
	A1	A2	A3	B1	B2	B3
Na_2O	-	0.2	0.1	-	0.4	0.6
Al_2O_3	2.1	1.4	3.6	1.8	1.3	1.4
SiO_2	29.0	31.2	27.7	31.4	31.5	31.1
SO_3	1.7	1.0	2.0	-	-	0.5
K_2O	0.2	0.7	0.9	1.5	0.9	0.5
CaO	65.3	65.4	63.3	64.0	64.6	64.4

Oxide	Sample (weight %)					
	B4	C1	C2	C3	C4	D1
Na_2O	0.3	1.6	1.3	0.3	-	0.1
Al_2O_3	1.4	1.9	2.1	0.9	0.8	1.9
SiO_2	31.2	31.8	31.4	33.3	32.1	28.5
SO_3	0.5	1.0	0.9	0.3	-	1.7
K_2O	0.3	0.2	-	0.2	0.2	0.3
CaO	65.5	63.6	64.3	65.1	66.7	66.0

The Figure 2 shows the fuel and/or clinkering process characteristic that promotes different SO_3 content in belite crystals.

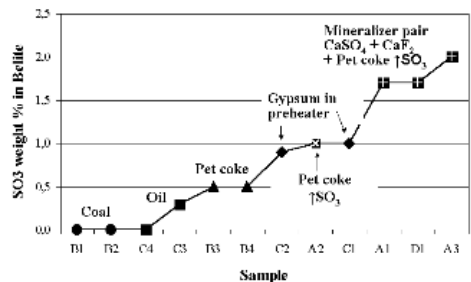


Figure 2: Different SO_3 content in belite crystals and its origin.

The Figure 3 presents the correlation between SO_3 and SiO_2 content in belite crystals suggesting the substitution of SO_3 in the SiO_2 site, as showed by Bonafous et al (1995) and Gobbo (2003).

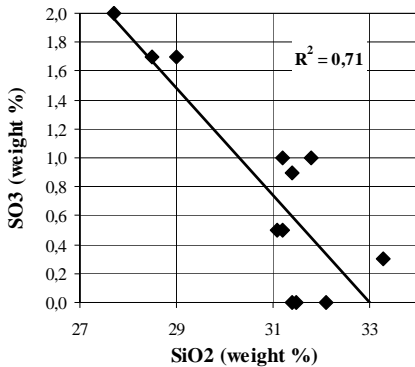


Figure 3: Correlation between SO₃ and SiO₂ content in belite crystals.

4 CONCLUSIONS

Analyzing clinkers produced with different fuels and also different SO₃ contents possibility to have some conclusions about their performance on clinker.

In clinkers produced using the oil, no SO₃ content was detected in the belite crystals. In contrast, those produced with pet coke showed more than 1,5% of SO₃. Clinkering process with high SO₃ pet coke and mineralization pair CaSO₄ + CaF₂ produced clinkers with 2,0% of SO₃ in belite crystals. Also good correlation was found between the SO₃ and SiO₂ content in crystals, which suggests the substitution of SO₃ in the SiO₂ site, as showed by Bonafous et al (1995) and Gobbo (2003). In other hand, high grades of SO₃ in alkalis enriched clinkers led to the formation of cubic C₃A in spite of the orthorhombic polymorph, which can make the cement setting time better. In clinkers produced with pet coke enriched in SO₃, arcanite and Ca-langbeinite were identified, normally present in those with also high K₂O grades in raw mix. Those phases are known to reduce the setting time of cement and also improve the initial resistance performance.

The differences in clinkers with high SO₃ content were also possible by XRD. Those clinkers enriched in SO₃ presented the narrow and with high intensity peak in the 51,72° θ , as suggested by Borgholm and Jons (1997).

5 ACKNOWLEDGEMENT

The authors thank the support gave with X-ray diffraction analysis by LCT-EPUSP (Laboratory of Technological Characterization of the Polytechnic School of the University of São Paulo).

6 REFERENCES

- Blanco-Varela, M.T.; Puertas, F.; Vázquez, T. & Palomo, A. 1996. Modelling of the burnability of white cement raw mixes made with CaF₂ and CaSO₄. *Cement and Concrete Research*. v.26, n.3, pp.457-464.
- Blanco-Varela, M.T.; Palomo, A.; Puertas, F. & Vázquez, T. 1997. CaF₂ and CaSO₄ in white cement clinker production. *Advances in Cement Research*. v. 9, pp.105-113.
- Bonafous, L.; Bessada, C.; Massiot, D.; Coutures, J. P.; LeRolland, B. & Colombet, P. 1995. *Journal of American Ceramic Society*, 78, 2603.
- Borgholm, H. E. & Jons, E. S. 1997. Assessing the benefit of mineralisation from laboratory tests. In: *International Symposium on Cement Industry, 1, Proceedings...* 1997, Assiut, p.1-10.
- Campbell, D. H. 1999. *Microscopical examination and interpretation of portland cement and clinker*. 2.ed. Stokie: Portland Cement Association, 202pp.
- Centurione, S. L. 1999. *Mineralização do clínquer Portland e seus benefícios tecnológicos*. In *Portuguese*. São Paulo, 168pp. (PhD – Institute of Geosciences – University of São Paulo).
- Duda, W. H 1985. *Cement-data-book*. 3rd ed. Wiesbaden, Berlin: Bauverlag, V.1.
- Gobbo, L.A. 2003. *Os compostos do clínquer Portland: sua caracterização por difração de raios-X e quantificação por refinamento de Rietveld*. São Paulo, 157pp. In *Portuguese*. (MSc Dissertation – Institute of Geosciences – University of São Paulo).
- Jons, E. S. 1981. Continuous Measurement of Mortar Strength at Early Ages. *II Cemento*, N, 2, pp. 3-11.
- Larson & VonDreele, R. 1999. *GSAS - General Structure Analysis System*. <http://public.lanl.gov/gsas>.
- Moir, G. K. 1982. *Mineralized High Alite Cements*. *World Cement*, December 1982, pp. 374-382.
- Moir, G. K. & Glasser, F. P. 1992. Mineralizer, modifiers and activators in the clinkering process. In: *International Congress on the chemistry of cement*, 9, Delhi, September 1992. *Proceedings...*Delhi, V.1.
- Sarkar, S. 1989. *Microstructural Investigation of Strength Loss in a Type 10 Cement*. *Proceedings of the 11th International Conference on Cement Microscopy*, International Cement Microscopy Association, New Orleans, Louisiana, pp. 101-114.
- Strunge, J. & Knöfel, D. 1985. Influence of alkalis and sulphur on the properties of cement, Part II, *Zem.- Kalk-Gips*, 38, pp. 441-450.
- Strunge, J. & Knöfel, D. 1986. Influence of alkalis and sulphur on the properties of cement, Part III, *Zem.- Kalk-Gips*, 39, pp.380-386.

Quantitative Analysis of White Cement Clinker with Rietveld Method

L.A.Gobbo; L.M.Sant'Agostino & L.L.Garcez

Department of Sedimentary and Environmental Geology, Geosciences Institute, University of São Paulo, São Paulo, Brazil

ABSTRACT: White Portland clinker is composed of three basic oxides (CaO, Al₂O₃ and SiO₂) and minor components such as Na₂O, K₂O, SO₃, etc. Alite (Ca₃SiO₅), belite (Ca₂SiO₄) and C₃A (Ca₃Al₂O₆) are the most common crystalline phases in white cement clinker. The interstitial phase is composed almost only by C₃A. Different analyses were used in some samples of industrial white cement clinker to check the phase's proportions obtained by the XRD-Rietveld method. Chemical analyses by XRF were performed to provide the Bogue results for alite, belite and C₃A. The optical microscopy was used on point-counting quantification. The absence of C₄AF in the white cement clinker make possible to analyze different C₃A polymorphs formed in the clinker. Selective chemical dissolution was applied to the quantification of interstitial phase residue, and was done on samples with only cubic C₃A and on that with orthorhombic C₃A. The XRD-Rietveld method was applied on the quantifications of five prepared residues; a strong correlation was found between the expected dissolution/prepared mixtures results and Rietveld method results. The analysis also allowed to the detection of C₁₂A₇, a phase commonly formed in high AM cements. The orthorhombic C₃A was found in samples produced with high Na₂O grades in raw mixes. This research shows the Rietveld Method as an accurate tool for qualification and quantification of special cement, when the clinker qualification is greatly dependent on the characteristics of the different forms of aluminates.

1 INTRODUCTION

Composed of three basic oxides (CaO, Al₂O₃ and SiO₂) and minor components such as Na₂O, K₂O and SO₃, the obvious difference from white Portland clinker to grey cement is colour, which represents an important and decisive criterion for evaluating the quality. To reach the required whiteness level, the colouring elements content (Fe, Mn, Cr, Ti, etc.) in raw mixes must be highly accurate. The absence of Fe₂O₃ represents not only a higher temperature for liquid formation but also a higher viscosity and a lower liquid content (12-14%) than in grey cement.

White cement Portland clinker is mainly composed by alite, belite and C₃A. In air of ordinary humidities, a phase of approximate composition C₁₂A₇ is formed. It reacts rapidly with water and occurs in some of the calcium aluminate cements (Taylor 1997). The high AM in white cement raw mixes and also the rapid cooling rate in H₂O vapour can lead to the formation of C₁₂A₇. C₃A can occur as orthorhombic form when the Na₂O reach 3.7% in the phase (Regourd et al. 1975). Gobbo et al. (2004) present an industrial example of the Na₂O influence in white cement clinker, where the increase of Na₂O led to the formation of orthorhombic C₃A. The C₄AF is not present due to the absence of Fe₂O₃ and

possible minor compounds are free lime and periclase.

The clinker phases quantification represents an important tool on quality control of Potland cement production. Until nowadays the most frequently applied method to estimate clinker phases composition is the Bogue procedure. Microscopical techniques are well recognized not only on phases quantification, but also on clinker microstructure informations.

In the Rietveld method (Rietveld 1969) applied to XRD, a theoretical pattern is calculated and fitted to an observed powder diffractogram until the calculation describes the observed pattern as closely as possible. The calculation of a theoretical powder pattern requires crystal structure information about the phases to be quantified. The accuracy of the quantification is directly dependent upon the quality of the structural and instrumental parameters. Overviews concerning the application of the Rietveld method to clinker phase analysis have been more recently given (Taylor et al. 1993; Neubauer et al. 1997; Meyer et al. 1998; Möller 1995; Taylor et al. 2000).

2 METHODS

Eight samples from a medium-scale factory with dry manufacturing technology were used in this study. The clinkerization process occur in a 68.0m longness kiln with a diameter of 3.4m, producing 370 tonnes of white cement clinker per day. The clinker is cooled in a water vapour cooler process. Limestone, silicatic rocks and few gypsum percentages composed the raw mix. Marble was added in a range proportion of 10-11% due to the whiteness and the gypsum was used in an approximate proportion of 4%.

Different analyses were used in some samples of industrial white cement clinker to check the phase's proportions obtained by the XRD-Rietveld method. Chemical analyses by XRF were performed to provide the Bogue results for alite, belite and C_3A . The optical microscopy was used on point-counting quantification of main phases and also on interstitial phase qualitative analysis.

The absence of C_4AF in the white cement clinker make possible to analyze different C_3A polymorphs formed in the clinker. Selective chemical dissolution was applied to the quantification of interstitial phase residue, and was done on samples with only cubic C_3A and on that with non-cubic C_3A .

2.1 Chemical Analysis and Bogue Calculation

Chemical analysis were performed in a Philips PW1660 XRF equipment. The XRF specimens discs were prepared in a flux by fusing a mixture of finely crushed clinker and lithium-tetra-borate. Determination of free lime content was held separately by conventional methods. The potential phase composition of the clinker was calculated based on the results of chemical analysis, according to the Bogue method. The Bogue calculation results were standardized to a total of 100% to enable the comparison with Rietveld analysis and microscopical determination.

2.2 Optical Microscopy

The reflected optical microscopy (Nikon Microscope) was used to qualify and quantify the different clinker samples. The surface of the polished section was etched by potassium hidroxide to the interstitial phase observation and with NH_4Cl solution to distinguish alite and belite crystals. It also permitted to differ the kinds of C_3A formed based on their crystal features. Quantitative analysis was performed by 4000 points counting using two operators.

2.3 Selective Dissolution

The selective dissolution was applied in order to obtain the interstitial phase. The systematic dissolution of calcium silicate was held by organic acid solution with salicylic acid (Takashima 1958) was used on this stage. The dissolution was done on the samples with only cubic C_3A (R1) and in that with non-cubic C_3A (R1), that was observed in the phases quantification by microscopical quantification. With the two residual material, three other samples were prepared. The first with 50% cubic C_3A and 50% non-cubic C_3A (R4), the second with 75% cubic C_3A and 25% non cubic C_3A (R3) and the last one with 25% cubic plus 75% non-cubic (R2). The five prepared samples were used in XRD analysis.

2.4 X-Ray Diffraction

The powder diffraction analysis (XRD) were held in a Bragg-Brentano diffractometer (Philips PW1820) with a broad focus $CuK\alpha$ tube anode applying 40KV/40mA. The samples were reduced to powder in agate ball mill and mounted in 10g holder by hydraulic pressing. The measurements were carried out in the range of 10 to 80 $^{\circ}2\theta$ with a step size of 0.02 $^{\circ}2\theta$ and a counting time of 2s/step, under configuration of $\frac{1}{2}^{\circ}$ divergent slit, graphite monochromator and 0.2mm receiving slit.

The Rietveld refinement, based on comparison of an observed X-ray pattern and a pattern calculated from structure data of each phase, is successfully finished when the residual error is minimized by the refinement of global and structural parameters. Structural data of alite (Nishi et al. 1985), belite (Jost et al. 1977), cubic C_3A (Mondal & Jeffery 1975), orthorhombic C_3A (Nishi & Takeuchi 1975), free lime and $C_{12}A_7$ were used for refinement and quantification.

Data sets were refined by the Rietveld method using GSAS (Larson & von Dreele 1999). The background was fitted with a Chebyshev function with 4 terms. The peak profiles were modelled using a pseudo-Voigt function with one Gaussian and Lorentzian coefficient. The lattice constants, the phase fraction, and zero shift were also refined.

3 RESULTS

3.1 Bogue Composition

The Bogue results based on clinker chemical composition is shown on Table 1.

Table 1. Composition of different studied clinkers by Bogue (wt.%).

Phase	Sample (wt.%)			
	W1	W2	W3	W4
Alite	54.0	55.5	62.7	59.9
Belite	26.5	25.5	20.2	24.7
C ₃ A	14.5	13.0	14.0	12.2
C ₄ AF	0.5	0.5	0.5	0.6
Free lime	0.9	1.4	0.9	2.3
Total	96.4	95.9	98.3	99.6

Phase	Sample (wt.%)			
	W5	W6	W7	W8
Alite	68.0	62.2	64.6	64.9
Belite	18.1	23.3	18.1	18.5
C ₃ A	11.4	11.4	14.0	12.9
C ₄ AF	0.7	0.7	0.4	0.4
Free lime	0.7	2.3	0.7	1.0
Total	98.9	99.8	97.8	97.6

3.2 Optical Microscopy

The qualitative analysis by optical microscopy permitted to identify an essentially prismatic well crystallized C₃A in the samples W1 and W2 and the cubic C₃A in all other samples. The Figure 1 shows the cubic C₃A from the sample W8 and the Figure 2 presents the prismatic C₃A from sample W1, known as the orthorhombic phase.

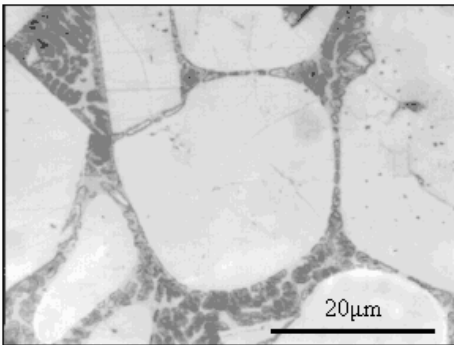


Figure 1. Cubic C₃A from sample W8.

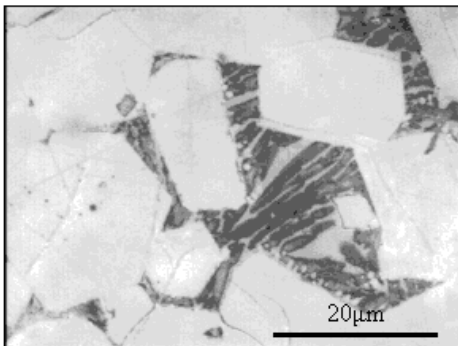


Figure 2. Orthorhombic C₃A from sample W1.

The point counting results are shown in Table 2.

Table 2: Crystallographic composition of clinkers by point-counting.

Phase	Sample (wt.%)			
	W1	W2	W3	W4
Alite	78.8	67.2	74.8	64.9
Belite	4.0	20.1	12.1	23.7
C ₃ A	16.3	11.7	12.5	10.8
Free lime	0.9	1.0	0.6	0.6
Total	100	100	100	100

Phase	Sample (wt.%)			
	W5	W6	W7	W8
Alite	74.0	67.3	67.4	77.1
Belite	15.9	22.0	20.6	9.0
C ₃ A	10.0	10.5	11.1	13.3
Free lime	0.2	0.2	0.9	-
Total	100	100	100	100

3.3 X-Ray Diffraction

The X-Ray diffraction possibiled the identification of the orthorhombic C₃A in the samples W1 and W2 and also the identification of the phase C₁₂A₇, difficult to identify by other techniques.

3.3.1 Clinker Composition

The Rietveld Method applied to white cement possibility the different C₃A quantification in the same sample, and also the quantification of the C₁₂A₇. The phase composition of clinkers based on Rietveld Method is shown on Table 3. The residue R² represents the minimized difference between the calculated and the observed diffractograms.

Table 3. Clinker composition of white cement clinker samples by XRD-Rietveld Method.

Phase	Sample (wt.%)			
	W1	W2	W3	W4
Alite	77.7	65.8	72.1	64.2
Belite	12.4	24.4	15.4	25.6
C ₃ A-cub.	-	-	6.1	6.0
C ₃ A-ort.	8.5	8.1	1.7	1.4
C ₁₂ A ₇	0.8	1.8	2.7	1.0
Free lime	0.5	-	0.3	0.4
Total	100	100	100	100
R ²	4.3	4.4	3.6	2.6

Phase	Sample (wt.%)			
	W5	W6	W7	W8
Alite	69.5	63.9	64.5	73.0
Belite	22.1	26.1	24.9	15.8
C ₃ A-cub.	6.5	7.5	6.2	8.0
C ₃ A-ort.	1.0	1.4	0.9	1.3
C ₁₂ A ₇	0.3	1.1	1.7	1.4
Free lime	-	-	-	0.5
Total	100	100	100	100
R ²	2.9	3.2	2.5	2.9

R²: Rietveld Refinement Residue

3.3.2 Interstitial Phase Composition

Quantitative results of interstitial phases by Rietveld method are shown in Table 4.

Table 4: Quantitative results of interstitial phases by XRD-Rietveld Method.

Phase	Samples (wt.%)				
	R1	R2	R3	R4	R5
C ₃ A-cub.	6.0	32.4	39.3	58.4	79.3
C ₃ A-ort.	92.9	58.6	46.6	23.7	0.0
C ₁₂ A ₇	1.12	9.0	13.8	18.0	20.7
Total	100	100	100	100	100
R ²	1.9	3.7	3.2	3.2	1.7

R²: Rietveld Refinement Residue

4 CONCLUSIONS

The XRD-Rietveld method was applied on the quantifications of five prepared residues; a strong correlation was found between the expected dissolution/prepared mixtures results and Rietveld method results. The analysis also allowed to the detection of C₁₂A₇, a phase commonly formed in high AM cements. The orthorhombic C₃A was found in samples produced with high Na₂O grades in raw mixes.

This research shows the Rietveld Method as an accurate tool for qualification and quantification of special cement, when the clinker qualification is greatly dependent on the characteristics of the different forms of aluminates.

5 REFERENCES

Campbell, D. H. 1999. Microscopical examination and interpretation of portland cement and clinker. 2.ed. Stokie: Portland Cement Association, 202p.

Gobbo, L. A.; Sant'Agostino, L. M. & Garcez, L. L. 2004. C₃A polymorphs related to industrial clinker alkalis content. *Cement and Concrete Research*, vol.34/4, p.657-664.

Goetz-Neunhoeffer, F. & Neubauer, J. 1997. Crystal structure refinement of Na-substituted C₃A by Rietveld analysis and quantification in OPC, 10th International Congress on the Chemistry of Cement, 389.

Jost, K. H.; Ziemer, B. & Seydel, R. 1977. Redetermination of the structure of β-dicalcium silicate, *Acta Cryst., Sect. B* 33 (6) 1696-1701.

Larson & VonDreele, R. 1999. GSAS - General Structure Analysis System, <http://public.lanl.gov/gsas>.

Meyer, H. W.; Neubauer, J. & Malovrh, S. 1998. Neue Qualitätssicherung mit standard-freier Klinkerphasenbestimmung nach der Rietveld-Verfeinerung im Einsatz, ZKG International 3, pp. 152-162.

Möller, H. 1995. Standardless quantitative phase analysis of Portland cement clinkers, *World Cement* September issue, 75-84.

Mondal, P. & Jeffery, J. W. 1975. The Crystal Structure of Tricalcium Aluminate, Ca₃Al₂O₆, *Acta Crystallogr., Sect. B* 31 (3), p. 689-697.

Neubauer, J.; Pöllmann, H. & Meyer, H. W. 1997. Quantitative X-ray Analysis of OPC Clinker By Rietveld Refinement, International Congress on the Chemistry of Cement, 10, p. 569-580.

Nishi, F. & Takeuchi, Y. 1975. The Al₂O₃ Rings of Tetrahedra in the Structure of Ca_{8.5}NaAl₆O₁₈, *Acta Crystallogr., B* (31), 1169.

Nishi, F.; Takeuchi, Y. & Maki, I. 1985. Tricalcium silicate, Ca₃O(SiO₄): The monoclinic superstructure, *Z. Kristallogr.*, 297.

Regourd, M. & Guinier, A. 1975. Cristalochimie des constituants du clinker de ciment portland, *Revue des Matériaux de Construction*, 695, pp. 201-215.

Rietveld, H. M. 1969. A profile refinement method for nuclear and magnetic structures, *J. Appl. Crystallogr.* 65-71.

Takashima, S. 1958. Systematic Dissolution of Calcium Silicate in Commercial Portland Cement by Organic Acid Solution, Japan Cement Engineering Association, Review of the Twelfth General Meeting - held in Tokyo, pp. 12-13.

Takeuchi, Y. & Nishi, F. M. 1980. Crystal-chemical characterization of the 3 CaO.Al₂O₃ solid-solution series, *Z. Kristallogr.* 152, pp. 259-307.

Taylor, J. C. & Aldridge, L. P. 1993. Full-profile Rietveld quantitative XRD analysis of Portland cement: Standard XRD profiles for the major phase tricalcium silicate (C₃S: 3CaO . SiO₂), *Powder Diffraction* 8 (3): 138.

Taylor, H. F. W. 1997. *The Chemistry of Cements*, Academic Press, London.

Taylor, J. C.; Hinczac, I. & Matulis, C. E. 2000. Rietveld full-profile quantification of Portland cement clinker: The importance of including a full crystallography of the major phase polymorphs, *Powder Diffraction* 15 (1).

The Influence of Cooling Rate in White Cement Clinker – an Industrial Example

L.A.Gobbo; L.M.Sant'Agostino & C.C.F.Guedes

Department of Sedimentary and Environmental Geology, Geosciences Institute, University of São Paulo, São Paulo, Brazil

ABSTRACT: With three basic oxides (CaO, Al₂O₃ and SiO₂) and minor components such as Na₂O, K₂O, SO₃, the main and obvious difference of white cement with respect to grey cement is color, which is a decisive criterion on quality evaluation. It is mainly composed by alite (Ca₃SiO₅), belite (Ca₂SiO₄) and C₃A (Ca₃Al₂O₆). The grey color of normal Portland cements is caused primarily by the iron oxide content and secondarily by chromium and manganese oxides. The effects of these components are therefore usually minimized by producing the clinker under slightly reducing conditions and by rapid quenching. Water-vapor cooler is commonly used in white cement cases to achieve the required whiteness. Higher burning temperature than usual is needed (ca. 1550°C) to achieve clinkering in the CaO-Al₂O₃-SiO₂ system. Oil or gas is normally used as fuel, since with coal the ash acts as a contaminant. This work is based in two samples collected in the sampler located after the water vapor cooler. One specimen was collected in processing cooling conditions of abundant water and sample temperature of 27°C. The other one was collected under environment of no water in the cooler and the temperature arriving to 300°C. Chemical analyses, optical microscopy, SEM-EDS and XRD/Rietveld method made possible the investigation. Results allowed confirming that almost no chemical changes occurred from different cooling rates samples, but remarkable crystallographic and whiteness differences were detected in the clinker specimens.

1 INTRODUCTION

Composed of three basic oxides (CaO, Al₂O₃ and SiO₂) and minor components such as Na₂O, K₂O, SO₃, the main and obvious difference of white cement with respect to grey cement is color, which is a decisive criterion on quality evaluation. It is mainly composed by alite (Ca₃SiO₅), belite (Ca₂SiO₄), C₃A (Ca₃Al₂O₆) and also mayenite (C₁₂A₇), formed with rapid cooling rate under H₂O vapor conditions, in high AM (Alumina Modulus) cements. It reacts rapidly with water and occurs in some of the calcium aluminates cements (Taylor, 1997). The C₄AF is not present due to the absence of Fe₂O₃ and possible minor compounds are free lime and periclase. The high AM in white cement raw mixes and also the rapid cooling rate in H₂O vapour can lead to the formation of C₁₂A₇. C₃A can occur as orthorhombic form when the Na₂O reach 3.7% in the phase (Regourd & Guinier 1975). Gobbo et al. (2004a) present an industrial example of the Na₂O influence in white cement clinker, where the increase of Na₂O led to the formation of orthorhombic C₃A.

The grey color of normal Portland cements is caused primarily by the iron oxide content and secondarily by chromium and manganese oxides. To

reach the required whiteness level, the colouring elements content (Fe, Mn, Cr, Ti, etc.) in raw mixes must be highly accurate. The absence of Fe₂O₃ represents not only a higher temperature for liquid formation but also a higher viscosity and a lower liquid content (12-14%) than in grey cement. The effects of these components are therefore usually minimized by producing the clinker under slightly reducing conditions and by rapid quenching. In grey cement production, satellite and grate coolers are used; water-vapor cooler is commonly used in white cement cases to achieve the required whiteness. Higher burning temperature than usual is needed (ca. 1550°C) to achieve clinkering in the CaO-Al₂O₃-SiO₂ system.

A cement kiln is normally operated with what is commonly described as an oxidizing atmosphere. Fe²⁺ is almost all converted to Fe³⁺ during cooling in reducing atmosphere. For white cements, which contain very little Fe, reducing conditions may be preferred because they yield a whiter product (Taylor 1999).

Oil or gas is normally used as fuel, since with coal the ash acts as a contaminant. Blanco-Varela et al. (1997) presents the fluxing and mineralizing effects of CaF₂ and CaSO₄ during the clinkering process.

The phase diagram of Figure 1 shows the system CaO-Al₂O₃ in air of ordinary humidity (Smirnov et al. (1973), where interstitial phases commonly formed in white cements are presented. This system contains the stable phases C₃A, CA, C₁₂A₇ and CA₂. All binary phases in the CaO-Al₂O₃ system except CA₆ are hydraulically active at room temperature, however C₃A is the most important of these phases in Portland cements, heavily influencing the initial set characteristics due to its rapid hydration, which requires retardation, normally by gypsum addition.

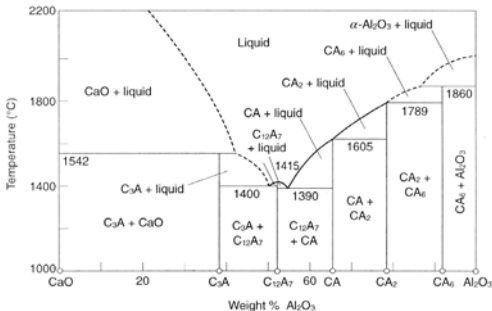


Figure 1: The system CaO-Al₂O₃ in air of ordinary humidity (Smirnov et al. (1973).

2 METHODS

This work is based in two samples from a medium-scale factory with dry manufacturing technology were used in this study. The clinkerization process occur in a 68.0m longness kiln with a diameter of 3.4m, producing 370 tonnes of white cement clinker per day. The clinker is cooled in a water vapour cooler process. Limestone, silicatic rocks and few gypsum percentages composed the raw mix. Marble was added in a range proportion of 10-11% due to the whiteness and the gypsum was used in an approximate proportion of 4%.

Samples were collected in the sampler located after the water vapor cooler. One specimen, named "Sample A" was collected in processing cooling conditions of abundant water and sample temperature of 27°C. The other one was collected under environment of no water in the cooler and the temperature arriving to 300°C, and was named as "Sample B". Ten minutes were taken from one sample collection to the other one, assuring that the pre-homogenized available raw mix was the same in both produced clinkers.

Chemical analyses by were performed to phase's quantification by Bogue equations and point-counting under optical microscopy led to the quantification of main phases. SEM-EDS analyses were performed to obtain the phase's chemical

microanalysis and also minor phases identification and XRD/Rietveld method made possible the phases quantification.

2.1 Chemical Analysis and Bogue Calculation

Chemical analysis were performed in a Philips PW1660 XRF equipment. The XRF specimens discs were prepared in a flux by fusing a mixture of finely crushed clinker and lithium-tetra-borate. Determination of free lime content was held separately by conventional methods. The potential phase composition of the clinker was calculated based on the results of chemical analysis, according to the Bogue method.

2.2 Optical Microscopy

The reflected optical microscopy (Nikon Microscope) was used to qualify and quantify the different clinker samples. Samples were prepared according to Campbell (1999) procedure. The surface of the polished section was etched by potassium hydroxide to the interstitial phase observation and with NH₄Cl solution to distinguish alite and belite crystals. It also permitted to identify the cubic C₃A formed based on the crystal features. Quantitative analysis was performed by 4000 points counting using two operators.

2.3 Sem-EDS

The SEM (Scanning Electron Microscopy) analysis of circa 0,3 cm diameter samples was performed on a Leo electronic microscope model Stereoscan 440, the coating was done using Carbon. X-ray spectrometry was used to obtain the clinker phases chemical microanalysis, in a EDS system coupled to SEM. For each analysed phase at least five measurements were done considering the presence of the most common oxides (CaO, Al₂O₃, SiO₂, Fe₂O₃, MgO, Na₂O, K₂O, TiO₂ SO₃ and Mn₂O₃).

2.4 X-Ray Diffraction

The powder diffraction analysis (XRD) were held in a Bragg-Brentano diffractometer (Philips PW1820) with a broad focus CuK α tube anode applying 40KV/40mA. The samples were reduced to powder in agate ball mill and mounted in 10g holder by hydraulic pressing. The measurements were carried out in the range of 10 to 70 °2 θ with a step size of 0.02 °2 θ and a counting time of 2s/step, under configuration of 1/2° divergent slit, graphite monochromator and 0.2mm receiving slit.

Data sets were refined by the Rietveld method using GSAS (Larson & von Dreele 1999), with the refinement conditions suggested by Gobbo et al. (2004b).

3 RESULTS

3.1 Whiteness

The whiteness was determined in a Minolta Spectrum Colorimeter. The sample "A", produced in rapid cooling with water, presented 84% of whiteness and that produced almost without water conditions presented 71% of whiteness. The whiteness range of 13% from the samples indicates that the cooling rate is directly related with the whiteness degree.

3.2 Chemical Composition

Clinkers chemical analysis possibiled to demonstrate that almosty no chemical changes occur from one sample to the other.

The clinker chemical composition of samples A and B are shown on Table 1. Bogue results based on chemical analysis is presented in Table 2.

Table 1: Composition of different studied clinkers (wt.%).

Phase	Sample (wt.%)	
	A	B
SiO ₂	23.49	23.83
Al ₂ O ₃	5.13	4.85
Fe ₂ O ₃	0.14	0.12
CaO	69.51	69.81
MgO	0.4	0.33
SO ₃	0.34	0.29
Na ₂ O	0.00	0.00
K ₂ O	0.14	0.19
Mn ₂ O ₃	0.035	0.034
LSF	96.66	96.26
SR	4.45	4.79
AR	37.22	39.11
Whiteness	83.76	70.68

Table 2: Phases composition by Bogue method (weight %).

Phase	Sample (wt.%)	
	A	B
Alite	61.15	64.43
Belite	21.54	20.06
Interstitial phase	13.37	12.66
Free lime	1.86	1.22
Total	98.34	98.75

3.3 Optical Microscopy

The qualitative analysis by optical microscopy permitted to identify a well crystalized interstitial phase with different non identified phases. The alite crystals are subhedral with few belite inclusions and with alite sizes of 30µm and 32µm to samples A and B respectively. Belite crystals are dirperse and round, with sizes of 38µm and 40µm respectively to samples A and B. The point counting results are shown in Table 3; interstitial represents essentially C₃A crystals.

Table 3: Crystallographic composition of clinkers by point-counting.

Phase	Sample (wt.%)	
	A	B
Alite	75.3	78.1
Belite	12.4	12.2
Interstitial Phase	10.0	8.7
Free lime	2.3	0.9
Total	100	100

3.4 SEM-EDS

The SEM-EDS microanalysis allowed the identification of phases with chemical composition "close to" the C₃A and C₁₂A₇ in the sample A and "close to" the C₁₂A₇ and CA phases in the sample B. The microanalysis results of calcium aluminate phases are shown in the Table 4.

Table 4: SEM-EDS chemical composition of some phases groups identified in the samples A and B.

Phase	Sample A (wt.%)		Sample B (wt.%)	
	C ₃ A	C ₁₂ A ₇	C ₁₂ A ₇	CA
SiO ₂	4.83	5.04	7.34	1.63
Al ₂ O ₃	35.90	43.50	44.59	65.14
Fe ₂ O ₃	0.62	1.07	0.23	-
CaO	57.84	48.88	46.95	31.80
MgO	0.47	0.74	-	-
SO ₃	-	-	-	-
Na ₂ O	0.22	-	0.62	1.01
K ₂ O	0.12	0.52	0.27	0.42
Mn ₂ O ₃	-	-	-	-
TiO ₂	-	0.24	-	-
Total	100	100	100	100

(-) Under detection limit

The Figure 2 shows the SEM electronic images from samples A and B respectively. C₁₂A₇ and C₃A are shown in sample A and C₁₂A₇ and CA are presented in the sample B.

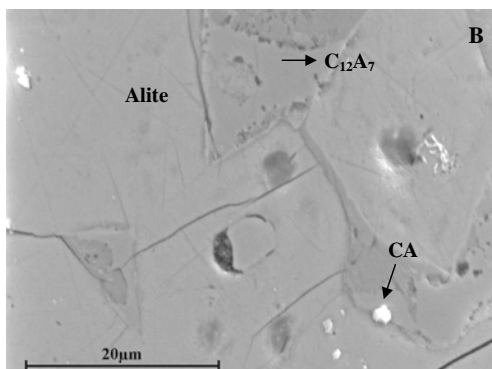
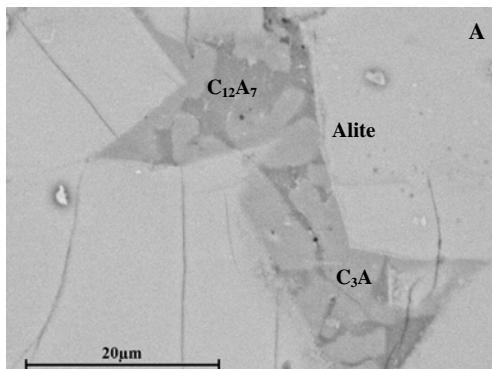


Figure 2: SEM electronic images from samples A and B.

3.5 X-Ray Diffraction

The Rietveld Method applied to white cement possibility the interstitial phase quantification. The phase composition of clinkers based on Rietveld Method is shown on Table 5.

Table 5: Clinker composition of white cement clinker samples by XRD-Rietveld Method.

Phase	Sample (wt.%)	
	A	B
Alite	75.0	77.0
Belite	14.5	14.2
Calcium aluminate	10.5	8.3
Free lime	0.0	0.2
Total	100	100

4 CONCLUSIONS

Results allowed confirming that almost no chemical changes occurred from different cooling rates samples, but crystallographic and whiteness differences were detected in the clinker specimens A and B. Phase with composition close to C_3A and $C_{12}A_7$ were identified in the sample “A” and close to $C_{12}A_7$ and CA in the sample “B”. The cooling rate with humidities lead to the rapid formation of the $C_{12}A_7$ and also the reducing atmosphere, probably leading to the transition from Fe^{2+} to Fe^{3+} and consequent increase on clinker whiteness. The work was an industrial experiment to improve the clinker whiteness.

5 ACKNOWLEDGEMENT

The authors thank the support gave with X-ray diffraction analysis by LCT-EPUSP (Laboratory of Technological Characterization of the Polytechnic School of the University of São Paulo).

6 REFERENCES

- Campbell, D. H. 1999. Microscopical examination and interpretation of portland cement and clinker. 2.ed. Stokie: Portland Cement Association, 202pp.
- Gobbo, L. A.; Sant’Agostino, L. M. & Garcez, L. L. 2004a. C_3A polymorphs related to industrial clinker alkalis content. Cement and Concrete Research, Vol 34/4, pp. 657-664.
- Gobbo, L. A.; Sant’Agostino, L. M. & Garcez, L. L. 2004b. Quantitative Analysis of White Cement Clinker with Rietveld Method, ICAM 2004, *in press*.
- Larson & VonDreele, R. 1999. GSAS - General Structure Analysis System, <http://public.lanl.gov/gsas>.
- Regourd, M. & Guinier, A. 1975. Cristalochimie des constituants du clinker de ciment portland, Revue des Matériaux de Construction, 695, pp. 201-215.
- Rietveld, H. M. 1969. A profile refinement method for nuclear and magnetic structures, J. Appl. Crystallogr., pp. 65-71.
- Smirnov, G. S.; Chatterjee, A. K. & Zhmoidan, G. I. 1973. The phase equilibrium diagram of the ternary sub-system $CaO-CaO.Al_2O_3-11CaO.7Al_2O_3.CaF_2$. Journal of Materials Science, 8; pp. 1278-82.
- Taylor, H.F.W. 1997. The Chemistry of Cements, Academic Press, London.

Basalt: an Alternative to Shales in Cement Industry

M.M.Hassaan & A.El-Sheshtawy

Department of Geology, Faculty of Science. University of Al-Azhar, Cairo, Egypt

M.Y.Hassaan

Department of Physics, Faculty of Science. University of Al-Azhar, Cairo, Egypt

A.A.Alashkar

Egyptian Cement Company, Ain Sukhna, Suez, Egypt

ABSTRACT: The Cairo-Suez district is characterized by extensive Middle Eocene limestones, suitable for cement industry and shortage of the suitable shales. Meanwhile extensive Olig-Miocene subalkaline tholiitic basalts in the form of 3 successive sheets occur in the vicinity of the limestones. The use of basalt in cement industry is recommended before by M.Y.Hassaan. The experimental works on raw mixtures prepared from the 3 basalt sheets produced typical 2 clinkers of ordinary portland cement and sulfate resistant cement. The testing of prepared 2 cement samples from the 2 clinkers indicated that the produced cement match well in its chemical, physical and mechanical properties with the standard specifications. Therefore the use of these basalts in stead of shales in the Cairo-Suez district, Egypt is recommended based on several advantages.

1 INTRODUCTION

The Cairo – Suez district in Egypt lies between longitudes 31°15'00" and 32°20'00" E and latitudes 29°45'00" and 30°15'00" N. The widespread rock units are as follows:

Marine Miocene sediments

Unconformity

Basalt (3 Sheets)

Unconformity

Oligocene sands and gravels

Unconformity

Upper Eocene calcareous shaley sandstones

Middle Eocene limestones

The limestones are chemically suitable for cement industry (Hassaan et al. 1993; Hassaan 2004). The ranges of the major chemical components for 147 samples are SiO₂ 13.3 - 04 Al₂ O₃ 5.6 -0.33, Fe₂ O₃ 7.1-0.2, CaO 53.6-35.5, MgO 5.4-0.13, N₂O + K₂O < 1.5. The district is poor in the suitable shale beds particularly in the eastern part. There, 2 cement companies use shales transported for more than 40 km.

The use of basalt in cement industry was investigated and recommended by Hassaan (2001) as a typical raw material to substitute shales.

The Oligo - Miocene subalkaline tholiitic basalts in the form of 3 successive sheets are extensive. Sheet (A) at the base is altered, the middle (B) is fresh and the upper (C) is weathered.

The basalt is composed essentially of plagioclase, commonly anorthite, pyroxene and basaltic glass with quartz, apatite and opaque minerals as minor constituents. The plagioclase occurs as phenocrysts in either major groundmass forming porphyritic texture and/or in glomerophytic aggregate with pyroxene crystals forming ophitic and subophitic textures. In the altered and weathered basalt plagioclase is completely or partially altered to clay minerals and quartz filling amygdaloids and vesicles. The XRD analysis detected presence of anorthite, augite, montmorillonite, chlorite, ilmenite and goethite. The ranges of the major elements oxides of the 3 sheets are given (Tab. 1).

The present work investigates the suitability of these basalts to substitute shales in cement industry in Cairo - Suez district.

Table 1. Ranges of chemical elements oxides for basalt sheets.

Basalt	Sheet A	Sheet B	Sheet C
SiO ₂	49.3-48.2	50.9-48.6	50.4-49.9
Al ₂ O ₃	18.7-16.1	18.8-16	19.0-18.0
Fe ₂ O ₃	4.6-3.1	7.9-3.3	8.0-4.5
FeO	4.9-3.0	5.5-3.0	4.6-3.4
MgO	8.5-7.9	8.0-6.1	8.2-6.2
CaO	10.1-8.02	10.9-7.0	8.0-5.8
N ₂ aO	3.2-3.0	2.5-2.0	3.1-2.2
K ₂ O	0.8-0.5	0.8-0.4	0.7-0.2

Table 2. Composition of the raw mixtures.

Sample No	1	2	3	4
Basalt %	20.5	18	22	19
Limstone%	76.5	76	76	77.5
Iron ore %	3	5	2	3.5
Sand %	0	1	0	0

Table 3. The chemical analyses of the clinker raw mixtuers and their modules.

Sample	No.1	No.2	No.3	No.4
SiO ₂	13.54	13.41	13.18	13.62
Al ₂ O ₃	3.69	3.79	3.36	3.56
Fe ₂ O ₃	2.84	2.76	2.91	3.23
CaO	42.96	43.05	42.00	42.84
LSF	97.39	98.27	98.25	96.42
SM	2.07	2.07	2.17	2.01
AM	1.30	1.37	1.15	1.10

Table 4. The chemical analysis of clinkers (1,2,3,4), modules and phases.

Item	1	2	3	4
SiO ₂	23.38	21.74	19.51	21.33
Al ₂ O ₃	5.79	5.68	4.50	5.04
Fe ₂ O ₃	4.49	4.33	5.03	4.61
CaO	61.48	62.42	65.82	63.79
MgO	1.73	1.20	1.78	1.86
SO ₃	0.35	0.33	0.28	0.18
K ₂ O	0.23	0.23	0.20	0.12
a	0.70	0.86	2.21	0.60
b	0.79	1.01	2.43	0.62
LSF	81.74	88.68	104.10	92.90
SM	2.27	2.17	2.05	2.21
AM	1.29	1.31	0.89	1.09
C ₃ S	48.43	41.04	73.26	54.69
C ₂ S	24.60	31.37	0.67	19.90
C ₃ A	7.75	7.73	3.41	5.56
C ₄ AF	13.66	13.18	15.31	14.03
c.	29.78	28.53	27.08	27.74

a-Freelime determined by X-Ray method

b-Freelime determined by wet method

c = Liquid phase = 6.1 Fe₂O₃ + MgO + K₂O + SO₃,
for AM < 1.38 at 1450 °C

2 EXPERIMENTAL WORK

Four representative basalt samples were powdered to minus 200 microns. Samples 1, 2, & 3 represent the sheets A, B and C at a locality and sample 4 is a representative to sheet B at another locality.

Each mixture sample was ground for 2 minutes without grinding aid till the powder passed through 200-micron sieve.

Each one represents a basalt sample. Four raw clinker mixtures were prepared. Each clinker mixture was prepared using the raw materials (limestone, basalt and sand) according to three modules called Lime Saturation Factor (LSF), Silica Module (SM), and Alumina Modules (AM) calculated according to the equations 1,2 & 3.

$$MAS = 100 \text{ CaO} / 2.8 \text{ SiO}_2 + 1.18 \text{ Al}_2\text{O}_3 + 0.65 \text{ Fe}_2\text{O}_3 \quad (1)$$

$$SM = \text{SiO}_2 / \text{Al}_2\text{O}_3 + \text{Fe}_2\text{O}_3 \quad (2)$$

$$AM = \text{Al}_2\text{O}_3 / \text{Fe}_2\text{O}_3 \quad (3)$$

The four raw mixtures were fired at 1100°C for 20 minutes inside the furnace, then, for 30 minutes at 1450°C in air to form cement clinker.

The samples, raw mixtures and clinkers were analyzed and measured using XRF, XRD and Mössbauer techniques. The XRF analysis was carried out using an apparatus of ARL type. The Mössbauer spectra were measured at room temperature using ⁵⁷Co radioactive source of 109 Bq used in (Rh) matrix. The analysis is given relative to α-iron oxide.

The composition of the raw mixtures and the chemical analyses of the mixtures and clinkers are given (Tabs. 2, 3 & 4).

3 RESULTS AND DISCUSSION

3.1 Clinkers

A clinker produced from basalt samples 1, 2, 4 is typical portland cement clinker (OPC), while that from basalt sample n.3 is sulphate resisting cement clinker (SRC).

3.2 Cement

Two cement mixtures were prepared from the 2 clinkers as follows OPC 92 wt% clinker mixture and 8 wt % natural gypsum, SCR 94.3 wt% clinker

mixture and 5.7 wt% natural gypsum. The two mixtures were ground without grinding aid in disk mill for 2 minutes. The chemical analyses of the OPC and SRC samples point to that the values of insoluble residue (0.51 and 0.43 wt %), MgO (1.92 and 2.12 wt %), SO₃ (2.02 and 1.75 wt %) and LOI (3.41 and 2.14 wt %) are less than the specification maximum of each item.

Two cement pastes were prepared using water to the cement powder at room temperature. The mechanical and physical properties of the produced 2 cements, were tested for one inch cube mould of the paste. After one day it was remolded and inserted in water for 3 and 7 days for measuring the compressive strength.

The physical properties of the OPC sample are as follows: Fineness (m²/kg) 3133; Initial setting time (minutes) 180, Final setting time (hours) 4.40 and Standard consistency 27.75%. Those of the SRC sample are: 3077, 175, 4.40 and 27.25. respectively. The compressive strength of the two cement samples are as follows: 3 days (N/mm) 30.80, 42.60 and 7 days (N/mm) 36.45 and 42.60 respectively. These values match well with the standard specifications. The four Mossbaur spectra of basalt samples are nearly similar. They show 4 iron phases representing Fe²⁺ and Fe³⁺ ions in both tetrahedral (T) and Octahedral (O) coordination. Such data is the same as that given before (Hassaaan 2001). The spectra of the clinkers are the same as the previous data (Hassaaan 2001; Eissa et al. 1984). Each spectrum contains one doublet for Fe²⁺ and 2 doublets for Fe³⁺ (T & O).

The advantages of using basalt instead of shales in cement clinker are as follows:- 1- New cement factories could be established in Cairo-Suez district where the limesones are located near basalts. 2- Basalt saves the costs of adding either pyrite ash or sand, to compensate the lack of the iron oxide and silica content in the raw mixture of the clinkerization. 3- Basalt has a density equals to about twice that of shales which could save half of the costs of the transportation of shale and the expected diminishing of by-pass dust problem due to the neglected sulphate content in basalt. 4 - The relative high percentage of iron oxide in basalt decreases the heat of formation of the clinker from 1450 °C to 1300 °C. So the use of basalt instead of shale saves about 150 °C which minimizes fuel cost (Hassaaan, 2003). 5- Quarrying and crushing a ton of basalt (to 1 cm) costs 0.75\$. This introduces a saving of 1.25\$ per ton compared to the cost of quarrying and transporting a ton of shale (2\$). 6- The shales have a high average humidity (~18%). Two steps are needed to prepare the shales: (a) storage of 200-300 thousand tons in open air for long period to get rid of 5%, H₂O⁺ in average, (b) using specially designed mills to introduce heated air current through shales to remove completely H₂O⁺. These two aeration

steps include the following cost elements; mills cost/maintenance, fuel for heating the air current, electrical power for aeration and storage: area. The total cost for the above elements is 2-3 times the cost of grinding the crushed basalt to -200 microns.

4 CONCLUSION

The subalkaline tholiitic basalt sheets in the Cairo-Suez district can be used as typical raw material to replace shales, in producing portland cement clinker. This will lead to add new cement factories needed for economic development of Egypt.

5 REFERENCES

- Eissa, N. A.; Hassaaan, M. Y.; Sallam, H. A.; Abo ElEnein, S. H. 1984. Mossbaur spectroscopy in cement manufacture. *J. Mater. Sci. Lett.* 3:88-90.
- Hassaaan, M. M. 2004. The economic potential of the mezozoic – cenozoic carbonate rocks in Egypt. *Sedimental Egypt*, 12:1-22.
- Hassaaan, M. M.; Mohamed, M. H.; Hathout, M. H. & Abd El-Moniem, S. M. 1993. Eocene chemo-litho-facies maps and significance to depositional pattern. *Sedimental Egypt*, 4:207-238.
- Hassaaan, M. Y. 2001. Basalt rock as an alternative raw material in portland cement manufacture. *Materials letter*, 50:175-178.
- Hassaaan, M. Y. 2003. Reducing the formation temperature of Clinker as basalt rock replaces Clay in Cement manufacture. Abstracts ICAME 2003, Muscat, Sultanate Of Oman.

Mineralogical Evaluation of Commercial Ceramic Tiles

A.A.P.Mansur, H.S.Mansur & W.L.Vasconcelos

Department of Metallurgical and Materials Engineering, Engineering School, Federal University of Minas Gerais, Minas Gerais, Brazil

ABSTRACT: In the study of ceramic tiles pathologies and properties, the evaluation of microstructure is very important. However, when dealing with commercial products this investigation is not so straightforward because their previous processing is usually unknown. In order to research the mineralogical composition of six commercial ceramic tiles, we developed a procedure which consists of the determination of tile water absorption, chemical analyses, XRD, and SEM/EDX evaluations, based on a literature summary of changes that may occur during firing. We have used two different groups of ceramic tiles, with very similar chemical composition of Si and Al contents. The quantities of fluxing elements and neomineralization agent are different but they are in the same range within each water absorption group under investigation. Previous information about the expected crystalline phases was obtained through ternary diagrams and XRD diffractograms have confirmed the great majority of them in our samples. The literature about the subject was crucial for connecting chemical analyses results with XRD patterns. SEM/EDX techniques were effective for identification of quartz and the composition of glassy phase. Although we were able to observe other phases immerse in glassy matrix through SEM images, we couldn't specify them. The adopted procedure allowed us to accomplish complete identification of the mineralogical composition of the ceramic tiles under evaluation.

1 INTRODUCTION

In the study of ceramic tiles pathologies and properties, the evaluation of the microstructure is very important. Some properties, like porosity and surface area, could directly be assessed through Mercury Intrusion Porosimetry (MIP) and adsorption isotherms, respectively. However, the study of crystalline phases and amorphous structure, despite of being obtained using X-Ray Diffraction (XRD) and Scanning Electron Microscopy (SEM) coupled to Energy Dispersive Spectroscopy (EDX), is not so easy to be done when dealing with commercial ceramic tiles with unknown previous processing (raw materials and firing thermal profile).

This work describes a path to evaluate these former aspects of ceramic tiles through their physical properties and chemical analyses and assisted by a summary of changes that may occur during firing at kiln.

2 EXPERIMENTAL PROCEDURE

First you should know the group of water absorption (WA) that the ceramic tile belongs to. This physical property was indicated at the ceramic tile box. In the absence of it, WA could be determined by water boiling as described in ISO 10545.

The next step was the material chemical analysis. This could be made by aqueous titration route using a powder sample (passing # 200 mesh) obtained from a ceramic tile after the removal of its glaze. The usual elements to be investigated are Si, Al, Mg, Fe, K, Na, Ca, and Ti.

The XRD analyses must be conducted in a powder sample, similar to the one used in the chemical analysis. It is important to know that the range of 20° to 70° (2θ) contains the strongest diffraction lines intensities of ceramic tiles crystalline phases. In this study the X-ray patterns were recorded using a PHILIPS PW 1710 diffractometer.

Images of SEM can be obtained from freshly fractured surfaces or from samples whose surfaces were polished (silicon carbide abrasive and diamond polishing paste). Both kinds of samples must be

coated with a thin layer of gold to make the specimen conductive. Photomicrographs were obtained from polished samples using a JEOL JSM 5410 microscope.

All this information must be coupled to literature-concerned transformations that may occur on ceramic tiles raw materials at different temperatures.

We have used the methodology previously described to evaluate crystalline phases of six commercial ceramic tiles.

3 RESULTS AND DISCUSSIONS

Four ceramic tiles belonged to water absorption group BIIa (3 % < WA < 6 %) and the last two to BIII (WA > 10%). Considering these results, one could expect that the BIIa tiles would have more glassy phase than BIII. This amorphous phase is responsible for the porosity reduction observed in this group of tiles, because their sintering occur in the presence of a liquid which penetrates in the porosity among particles due to capillarity forces (Reed 1995). Also, the BIII tiles may have a higher content of carbonates (calcite and dolomite) as raw materials. The CO₂ release due to decomposition of these materials creates the open porosity (Yekta & Alizadeh 1996).

The chemical analysis (Table 1) has indicated SiO₂ (≈64%) and Al₂O₃ (≈24%) as major constituents with very similar contents in all samples. Samples BIIa have exhibited a high percentage of fluxing constituents (K₂O + Na₂O + Fe₂O₃) while the others have had lower amounts. Ceramics from BIII have presented an average of 4,5% of neomineralization agent (CaO) in opposition to a less than 1% in BIIa. Based on these data one could expect a higher quantity of non-crystalline phases in samples of BIIa group and more calcium silicates in BIII tiles (Borba et al. & Yekta et al. 1996, Lira et al. 1997). These results were in agreement with the WA information.

Table 1: Chemical composition of BIIa and BIII tiles (wt.% in oxide equivalent.

Oxide Equiv.	Samples			
	BIIa		BIII	
	Range %	Average %	Range %	Average %
Al ₂ O ₃	22.0-25.6	23.7	23.6-23.9	23.8
SiO ₂	62.3-65.9	64.5	64.2-64.4	64.3
MgO	1.3-2.2	1.7	1.0-4.1	2.6
Fe ₂ O ₃	2.4-5.6	4.1	1.2	1.2
K ₂ O	2.9-3.5	3.3	1.0-1.5	1.3
Na ₂ O	0.4-1.2	0.9	0.4-0.9	0.7
CaO	0.2-1.0	0.6	3.4-5.6	4.5
TiO ₂	0.6-0.8	0.7	0.6	0.6
PPC	0.3-0.5	0.4	0.3	0.3

The results of chemical analysis were placed in ternary phases diagrams to identify the crystalline phases which could be expected. As could be seen in CaO-Al₂O₃-SiO₂ diagram (Fig. 1), the samples were all within the quartz-mullite-anorthite stability triangle. Other diagrams were evaluated (MgO-Al₂O₃-SiO₂, Na₂O-Al₂O₃-SiO₂, and K₂O-Al₂O₃-SiO₂) and in all the cases, the samples were in the same area and they indicated that quartz, mullite, anorthite, albite, leucite, and cordierite were the expected phases. It is important to note that this is only a reference, because an equilibrium state is not reached during the ceramic tile firing. Besides that, ternary systems consider only three components neglecting the influence of the others (Segnit & Anderson 1972, Jordán et al. 2001).

The XRD diffractograms (Fig. 2) were analyzed based on these previous results and literature using ICDD (International Centre for Diffraction Data) patterns. From literature, some information were crucial for diagrams interpretation and they are summarized as follows:

- Dehydroxylation of clays generally occurs between 450°C and 550°C (SACMI 1995);
- The study of mineral transformations shows the persistence of clays (chlorite, illite, muscovite, and kaolinite) crystalline structure up to 900°C during firing (Segnit & Anderson 1972, SACMI 1995, Lira et al. 1997, Jordán et al. 1999, Jordán et al. 2001);
- Decomposition of calcite (CaCO₃), dolomite (CaMg(CO₃)₂), and magnesite (MgCO₃) occurs at temperatures between 800°C and 950°C (Ferrari et al. 2000);
- Samples with poor content of CaCO₃ give very simple mineralogical composition (quartz and hematite) (Jordán et al. 1999);
- Calcium carbonates have high reactivity, therefore they would easily react with quartz and other minerals from destroyed clays, producing crystalline phases such as gehlenite, anorthite and wollastonite (Yekta & Alizadeh 1996, Lira et al. 1997, Jordán et al. 2001);

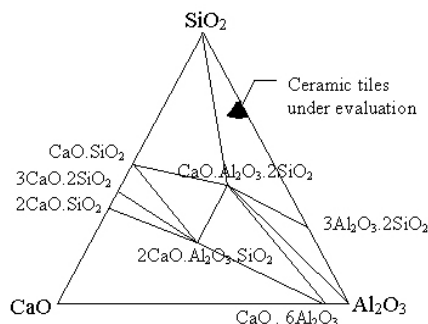


Figure 1: System CaO-Al₂O₃-SiO₂ and the position of assessed ceramic tiles.

- The presence of periclase is usually observed (MgO) after firing ceramic tile bodies with magnesium carbonates. MgO has lower reactivity than CaO (Yekta & Alizadeh 1996, Lira et al. 1997);

- The neomineralization of mullite is observed from temperatures of 1000°C upwards. A large amount of kaolinite is necessary in mullite formation. The kaolinite layer-lattice structure undergoes a progressive reorganization through an intermediate cubic spinel-type phase and it finally reaches the chain structure of mullite-like (Brindley & Nakahira 1958, Jordán et al. 1999, Ferrari et al. 2000, Abadir et al. 2002);

- Gehlenite is formed when a CaO nuclei reacts with clay's Si and Al. This reaction is observed above 800°C. This phase is metastable because it can react with quartz to give wollastonite and plagioclase (anorthite and albite) (Jordán et al. 2001);

- Feldspars play key role to obtain the glassy phase. The large majority of feldspars used at ceramic tile industry are orthoclase, albite, and anorthite. Vitrification of ceramic bodies could be detected from temperatures of 950°C upwards. Sometimes one can observe the presence of residual feldspars which were not completely melted (Borba et al. 1996, Ferrari et al. 2000, Abadir et al. 2002).

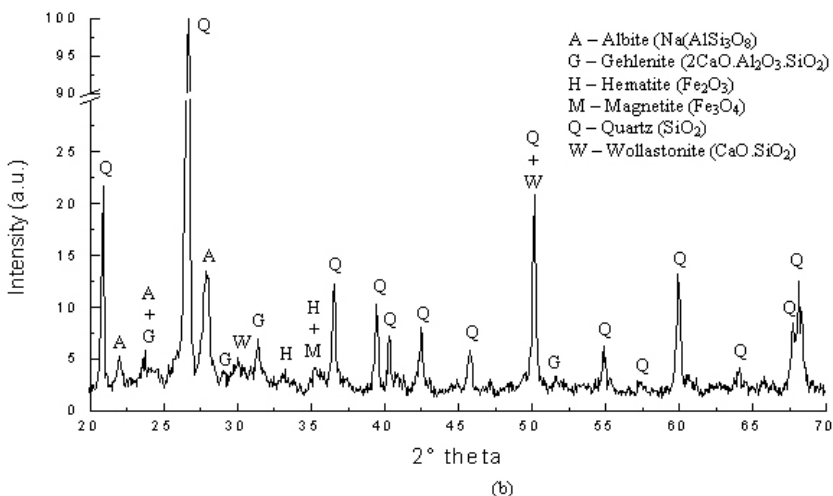
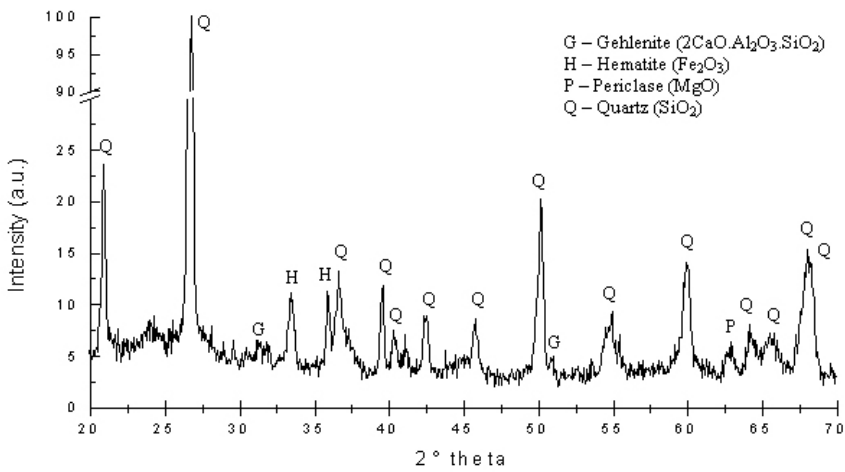


Figure 2: XRD spectra of (a) a ceramic tile, which belongs to BIIa group, and (b) a ceramic tile which belongs to BIII water absorption group.

Based on this information, a typical sample from BIIa group (Fig. 2a) has presented a very simple mineralogical composition with quartz, hematite, gehlenite, and periclase as crystalline phases and BIII tiles (Fig. 2b) have shown a great number of crystalline constituents (albite, gehlenite, hematite, magnetite, quartz, and wollastonite). XRD results also allowed us to verify the presence of a higher amount of glassy phase in BIIa tiles than BIII. This could be observed by the diffractogram background area, which was larger for BIIa.

It was possible to observe crystalline phases immersed on glassy matrix by SEM images. This amorphous phase is characterized through its smooth texture. EDX evaluation of this area has indicated K, Al, and Si as major constituents. Energy dispersive spectroscopy analyses also allowed the identification of other phases helping us to study the mineralogical composition of tiles.

Quartz grains are easily identified, as it can be seen in Figure 3, because of their dimensions and amounts (usually not lesser than 10%).

In Figure 4 we can see a particle whose EDX spectrum has shown a calcium content about four times higher than the average concentration obtained from the sample matrix. We could describe it as calcium-alumino-silicate, probably anorthite ($\text{CaO} \cdot \text{Al}_2\text{O}_3 \cdot 2\text{SiO}_2$) or gehlenite ($2\text{CaO} \cdot \text{Al}_2\text{O}_3 \cdot \text{SiO}_2$), which are often observed in this kind of tile.

4 CONCLUSIONS

Data from water absorption group has given an initial direction about the ceramic tile mineralogical complexity and the amount of glassy phase.

Chemical analyses were important to reveal chemical elements that constitute the sample and provided their quantity in the system. Based on these results, through ternary diagrams, a first evaluation of the expected crystalline phases was possible. Although the actual phases in such complex systems were not known, an estimate can be derived from a consideration of simpler systems. In the six tiles in study, the majority of XRD results have confirmed ternary diagrams information.

Literature concerned with transformations during firing has proved to be a fundamental source of data that are verified in actual systems.

SEM coupled with EDX were effective only for identification of quartz and the composition of the glassy phase.

The results have indicated that a good evaluation of crystalline and amorphous phases from commercial ceramic tiles is possible even when information from processing is unknown.

5 REFERENCES

- Abadir, M. F. et al. 2002. Preparation of porcelain tiles from Egyptian raw materials. *Ceram. Int.*, 28, 303-310.
- Borba, C. D. G. et al. 1996. Estudo de matérias primas fundentes. *Cerâmica Industrial*, 01 (01), 34-39.
- Brindley, G. W. & Nakahira, M. 1958. A new concept of the transformation sequence of kaolinite to mullite. *Nature*, 181, 1333-1334.
- Ferrari, K. R. et al. 2000. Transformações das matérias-primas do suporte cerâmico durante a queima de revestimento cerâmico. *Cerâmica Industrial*, 5 (2), 53-58.
- Jordán, M. M. et al. 1999. Firing transformations of cretaceous clays used in the manufacturing of ceramic tiles. *Appl. Clay Sci.*, 14, 225-234.
- Jordán, M. F. et al. 2001. Firing transformations of Tertiary clays used in the manufacturing of ceramic tile bodies. *Appl. Clay Sci.*, 20, 87-95.
- Lira, C. et al. 1997. Efeitos da composição e da temperatura de queima na expansão por umidade de corpos cerâmicos. *Cerâmica Industrial*, 02 (01/02), 27-30.
- Reed, J. S. (2nd) 1995. *Principles of Ceramics Processing*. New York: John Wiley & Sons.
- SACMI 1995: *Tecnologia de la fabrication de azulejos*. Valencia: Asociacion Tecnicos Ceramicos.
- Segnit, E. R. & Anderson C.A. 1972. Scanning electron microscopy of fired illite. *Trans. Brit. Ceram. Soc.*, 71 (3), 85-88.
- Yekta, B. E. & Alizadeh, P. 1996. Effect of carbonates on wall tile bodies. *Am. Ceram. Soc. Bull.*, 75 (5), 84-86.

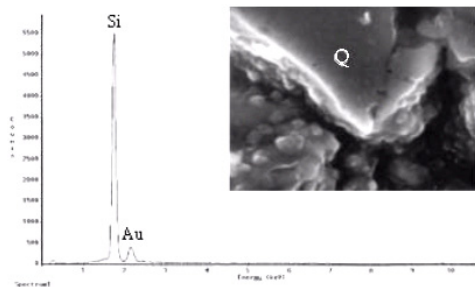


Figure 3: A quartz grain indicated by Q and the EDX spectrum obtained over the grain ($\times 5000$).

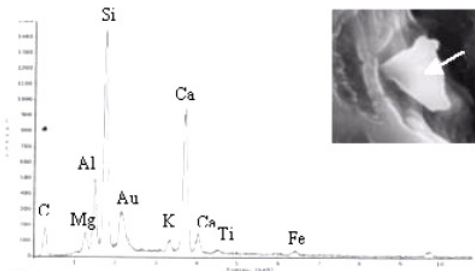


Figure 4: Scanning electron micrograph and EDX spectrum of a particle (arrow) ($\times 5000$).

Mineralogical Analysis of the Micro-Textural Characteristics of the Refractory Coating in the Pierce-Smith Converter

C.Marcos, M.Martínez, I.Rodríguez

Dpto. Geología, Universidad de Oviedo.C/. Jesús Arias de Velasco, s/n, 33005, Oviedo (Asturias), Spain

L.F.Verdeja

Dpto. Ciencia de Materiales, Universidad de Oviedo.C/. Gil de Jaz, s/n, 33003, Oviedo (Asturias), Spain

ABSTRACT: A mineralogical analysis of samples from an used magnesite-chrome brick and another one, not yet used by the metallurgical recovery process of copper was carried out. The used refractory brick was chosen from the region of a Pierce-Smith converter tuyère line because these areas deteriorate more quickly than the rest of the refractory wear. Comparing the results of both sample types it was possible to identify the most vulnerable zones. The identified phases by X-Ray diffraction in the unused sample were: periclase, forsterite, aluminum, and magnesiochromite. In the used sample, cupric phases were identified in addition to mentioned ones. These phases are located in the matrix of the sample, as confirmed by scanning electron microscope. Porosity of used and unused samples was obtained with analysis of images. The decrease of porosity of the used sample (~5%) against the unused sample (~15%) is explained as a result of the chemical attack of the slag filling the porous.

1 INTRODUCTION

The magnesite-chromium refractory is the most widely used brick as coating in the Pierce-Smith converter in the metallurgical recovery process of copper (Chesters 1983). This is due to its stability against high temperatures and its chemical and mechanical resistances. These refractories have a relatively brief life-time, 90 to 100 days, because of their wear and, therefore, they have to be periodically changed (Biswas & Davenport 1993). It implies loss of time and money because the extraction plant must be shut-down to change the coating material. It is difficult to establish the mechanisms involved in the wearing process and what is the phenomenon which causes it.

In addition to technical factors, environmental ones are taken into account more and more, and actually, there is a trend to avoid materials with chromium content due to its toxicity for environment and health. Therefore, it is necessary to know the chemical, physical, and mechanical characteristics of the Pierce-Smith converter coating due to the possibility to change the coating nature. In this work a mineralogical and textural characterization of samples of an used magnesite-chrome brick and another one, not yet used by the conversion process

was carried out. Comparing the results of both sample types it was possible to identify the most vulnerable zones.

2 EXPERIMENTAL

For the mineralogical and textural characterization (Marcos et al. 2002) of samples the following instruments were used:

- A Philips PW 1729-1710 instrument from Servicios Científico-Técnico de la Universidad de Oviedo (Spain) to identify the mineralogical phases of both used and unused refractory brick.

- A CAMEBAX SX-50 electron microprobe analyser with four dispersive spectrometers from Servicios Científico-Técnico de la Universidad de Oviedo (Spain) was used to analyse the phases of the used and unused refractory brick.

- A MEB JEOL-6100 scanning electron microscope (SEM) with a secondary electrons detector and a retrodispersive electrons detector from Servicios Científico-Técnico de la Universidad de Oviedo (Spain) was used to obtain the semiquantitative analysis of the present elements in the refractory samples. This instrument was also

used to obtain the images to be analyzed by the image analyser.

The analysis of images taken with the scanning electron microscope was carried out with a Quantimet image analyser (typical instrument of a number of television-based, optical image analysers) from Servicios Científico-Técnicos de la Universidad de Oviedo (Spain) to determine porosity in the used and unused refractory brick.

Electron microprobe analysis and scanning electron microscope require a very flat and well polished surface, so the refractory samples were mounted in plastic moulds (blocks of 2x1x1 cm). After the pouring resin became hard, the samples were polished. The samples for X-Ray diffraction were grounded as finely as possible.

3 RESULTS AND DISCUSSION

The X-Ray patterns obtained for the used and unused refractories are shown in Figures 1 and 2, respectively.

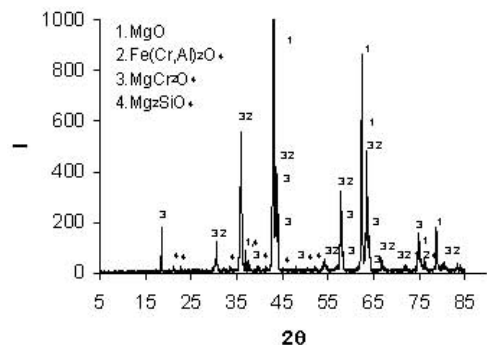


Figure 1: X-Ray diffraction pattern of used refractory.

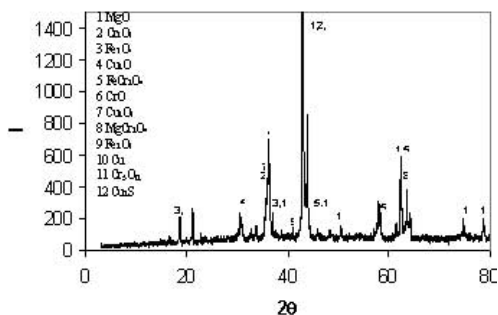


Figure 2: X-Ray diffraction pattern of unused refractory.

The mineralogical phases identified by X-Ray diffraction for the used and unused refractory sample were the following: periclase (MgO), forsterite (Mg_2SiO_4), chromite-aluminum ($\text{Fe}(\text{Cr},\text{Al})_2\text{O}_4$), and magnesio-chromite (MgCr_2O_4). In the used sample there are also phases with copper (Cu_2O , Cu , CuO , Cu_2S). These phases were formed due to the chemical attack of the slag to the refractory brick. Moreover, there are some chromium and iron oxides that the unused sample does not have due to the high temperature condition into the converter.

The electron microprobe analysis allowed us to verify that in the magnesio-chromite grains of the unused brick, the chrome and magnesium oxides contents are high, and the aluminum and iron oxides contents are low. CaO and SiO_2 , which give rise to a lower melting point of the refractory and the decreasing in brick strength, are present as impurities.

The percentages of MgO and Cr_2O_3 are similar in both used and unused bricks, but Al_2O_3 and MnO are found in a lower amount in the unused sample.

A qualitative and then a quantitative analysis allowed us to distinguish between periclase and magnesio-chromite grains as shown in Figures 3 and 4 for the unused and used samples, respectively, which was essential to carry out the image analysis.

The elements scanned were: O, Mg, Cr, Al, Fe, Si in all the unused samples.

In the used sample the elements scanned were: O, Mg, Cr, Al, Fe, Si, Cu, and S.

A mapping of Cu and S elements (Figure 5) revealed that they are located at the matrix and surrounding magnesio-chromite and periclase grains as it is shown in Figure 4.

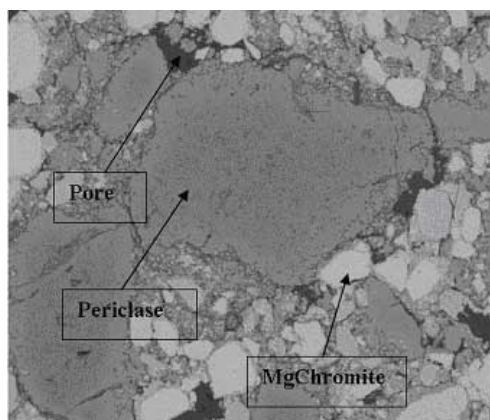


Figure 3: SEM view of the unused refractory sample.

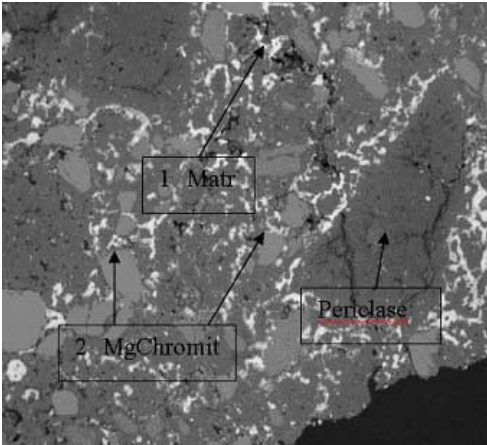


Figure 4: SEM view of the used refractory sample.



Figure 5: SEM view of a copper mapping.

The Fe content in the used sample is higher than in the unused one because this element is present in the chalcocite (Sancho et al. 2000).

For the unused sample, 27 images were analysed in order to obtain the percentages of periclase, magnesio-chromite, and pores into the refractory bricks. The results were: 24.98 % of periclase, 59.83 % of magnesio-chromite, and 15.19 % of pores. These results agree with the manufacturer's values.

The images (~240) of the used samples analysed named 1, 2, 3, and 4 in accordance with its position in the tuyère (Liow et al. 1998): 1 is the sample nearest to the converter (inside) and 4 is the furthest one. Table 1 shows the average percentages of periclase, magnesio-chromite, and porous.

Table 1: Percentage of porous, matrix, and grains for used refractory brick samples.

Sample	% porous	% matrix	% Grains
1	4,28	25,06	70,67
2	2,63	11,66	85,72
3	2,24	10,76	87,00
4	8,26	6,81	84,92

The decreasing in porosity in the used sample (~5%) is explained as a result of the chemical attack of the slag filling the porous.

However, porosity over 25% was obtained in some of the number 4 samples since high temperatures cause breaks and these areas of the refractory brick do not suffer the slag attack.

4 CONCLUSIONS

The refractory brick suffered important modifications during the copper manufacturing process, both in chemical composition and textural conformation.

Matrix is the most altered side because due to the slag attack towards the refractory brick; the unused sample has a high volume of oxides of Mg and Cr, and the used refractory matrix contains important amounts of copper and Cu_2S .

Porosity is also affected due to the attack of the slag filling the porous.

Grains are the less affected because nor periclase neither magnesiochromite show variations from unused sample to the used one.

The refractory brick also suffered mineralogical transformations, specially in the matrix, as revealed by X-Ray diffraction and scanning electron microscope.

5 REFERENCES

- Biswas, A.K. & Davenport W.G. 1993. El Cobre: Metalurgia Extractiva. Santiago de Chile: Ed. Limusa.
- Chesters, J.H. 1983. Refractories Production and Properties. Ed. The Metals Society.
- Liow J.L., Tsirikis P., Gray N.B. 1998. Study of Refractory Wear in the Tuyere Region of a Peirce-Smith Nickel Converter Canadian Metallurgical Quarterly, Vol. 37, No2, 99-117.
- Marcos, C., Llorca, M.A., Camblor, P., Verdeja, L.F. 2002. Caracterización de refractarios monolíticos. Cerámica y Vidrio, Vol 41 Núm. 2, 241-251.
- Sancho, J., Verdeja, L.F., Ballester, A. 2000. Metalurgia Extractiva. Volumen II. Procesos de obtención. Oviedo: Ed. Síntesis.

Synthesis of Mullite After Wastes Derived from Kaolin Processing Industries from the Amazon Region

M.C.Martelli & R.F.Neves

Department of Chemistry and Food Engineering, Universidade Federal do Pará, Pará, Brazil

R.S.Angélica

Department of Geosciences, Universidade Federal of Pará, Pará, Brazil

ABSTRACT: Mullite, $Al_6Si_2O_{13}$, is a relatively rare mineral in nature, formed under exceptional conditions of high temperature and pressure, which can be used to synthesize this mineral. Mullite presents excellent mechanical resistance at high temperature, low thermal expansion coefficient; good chemical and thermal stability. Such characteristics explain the importance of mullite in traditional and advanced ceramics. This research proposes the development of a process to synthesize mullite using the wastes from kaolin processing industries located in the Rio Jari (Monte Dourado-PA) and Rio Capim (Ipixuna-PA) districts. The synthesized materials will be studied for application as base-material for grog and silicon-aluminum refractory bricks. The steps are mineralogical and chemical characterization, verifying the differences between the materials processing through firing of the wastes at increasing levels of temperature with 100 °C increments, ranging from 600 to 1000 °C and 1200 to 1500 °C, during 3 hours at each level, in order to follow mineralogical changes. Methods include the study of temperature and impurities effects through X-ray-powder diffraction and scanning electron microscopy.

1 INTRODUCTION

The use of kaolin in any industrial segment requires previous physical and chemical treatment to minimize the amounts of impurities to or below standard levels established according to the desired application.

In the Amazon region, northern Brazil, more specifically in the States of Pará (PA) and Amapá (AP), huge kaolin deposits can be found in two important districts: 1) Rio Jari (Morro do Felipe – AP), exploited by CADAM Company (Caulim da Amazônia S.A.) and 2) Rio Capim District (Ipixuna – PA), exploited by two main companies: PPSA (Pará Pigmentos S.A.) and IRCC (Imerys Rio Capim Caulim), who are processors of paper coating. These kaolin deposits represent about 70% of the Brazilian reserves, which have been the object of many economic and scientific studies: Coura et al. (1986), Murray & Keller (1993), Silva (1997), Costa & Moraes (1998), Kotschoubey et al. (1999), Sousa (2000), Carneiro (2003), among others.

Kaolin processing units normally produce two types of wastes: quartz in the form of sand which is returned to the mining site, and an aqueous suspension mainly composed of kaolinite, that

corresponds to approximately 25% of the processed ore. Both are disposed of in large ponds and do not have a proper use.

Barata (1998) and Flores (2000) have already studied such kaolin wastes, concerning their physical, chemical, and mineralogical characteristics, and point out good results for their application in ceramics.

The method for mullite sintering uses oxides, hydroxides, salts, and aluminum silicates as starting materials and the mullitization temperature is controlled by the following parameters: grain size of the starting material's powder, the kaolinite degree of crystallinity (well crystallized at around 1000 °C and badly crystallized at around 1200 °C), and also by the presence of impurities, which influence the formation of mullite, promoting the crystallization of different mineral phases and increasing resistance (Schneider et al. 1994).

This work presents a preliminary study of the process of mullite synthesis using kaolin wastes as starting materials and showing the effect of the mullitization temperatures as well as the mineralogical, physical, chemical and technological aspects for their use in refractory materials.

2 MATERIALS AND METHODS

The materials used in the present work are wastes from centrifuges used in kaolin processing by the PPSA and CADAM companies described before. The wastes are named as PR to identify PPSA wastes and CR for the wastes from CADAM. The indexes 600, 700, 800, 900, 1000, 1200, 1300, 1400, and 1500 refer to the firing temperatures applied to the materials. During heating, all samples were kept at the temperatures indicated above for 3 h.

2.1 Firing and Loss by Heating.

The firing process was carried out at 1000°C during three hours at a heating rate of 10°C/min, in the presence of air to guarantee the elimination of all organic material that may have been present. The loss of mass (LOI) by heating was measured.

2.2 Chemical Analysis

Chemical analysis was done by X-ray fluorescence, atomic absorption and flame photometry to measure the amounts of the oxides: SiO₂, Al₂O₃, Fe₂O₃, TiO₂, CaO, MgO, K₂O, and Na₂O.

2.3 X-Ray Diffraction

X-ray diffraction analyses were carried out with a Philips PW 3020 goniometer, using the following conditions: CuK α -radiation, operating at 45kV and 40 mA; continuous scan from 5° to 65° 2 θ , step-size 0.02 and time per step of 0.5s. Powders were disaggregated and packed into aluminum powder mount holders with back loading filling to produce random mounts.

2.4 Scanning Electron Microscopy – SEM

A LEO 1450VP scanning electron microscope was used to study the microstructure and particle size.

3 RESULTS AND DISCUSSION

Data from the chemical analysis and loss of mass by heating are compiled in Table 1. One can observe that mass loss for both samples of wastes, and alumina and silicate content are quite close to the theoretical ones for kaolinite. The theoretical composition is Al₂O₃·2SiO₂·2H₂O (39,50 % Al₂O₃, 46,54 % SiO₂, 13,96 % H₂O or mass loss). The composition is approximate and may vary depending on the kaolinite formation process.

Table 1. Chemical Composition of the wastes.

Oxides (%)	CR	CR-1000	PR	PR-1000	Caulinita
SiO ₂	44,1	50,8	46,50	53,3	46,54
Al ₂ O ₃	37,4	43,2	38,40	44,6	39,50
Fe ₂ O ₃	1,96	2,40	0,69	0,76	
TiO ₂	2,14	2,94	0,96	1,03	
CaO	0,011	0,015	-	0,005	
MgO	-	-	-	-	
Na ₂ O	-	-	-	-	
K ₂ O	0,05	0,10	0,10	0,10	
LOI	13,7	0,41	13,60	0,27	13,96

Figures 1 and 2 display XRD patterns for the CR and PR samples, for each firing temperature - 600°C, 700°C, 800°C, 900°C, 1000°C, and 1200°C in order to observe the series of transformations that take part with kaolinite during heating. The kaolinite characteristic peaks (7.14 9 Å, 4.468 Å, and 3.578 Å) and anatase was observed at 600 °C for the CR sample, for the PR-600, kaolinite (7.161 Å, 4.425 Å, and 3.579 Å), anatase, and quartz. The two figures also show the formation of two bands (d= 2.39 Å / 37.67 2 θ and d=1.97 Å / 45.81 2 θ) in the CR-900 and CR-1000 samples, the second one (45.81 2 θ) was reported by Sen & Thiagarajan, (1988) to be a metastable phase (Al-Si spinel/ γ Al₂O₃). However, a better technique would be electron diffraction on a selected area to confirm this assumption.

For the PR-1000 sample besides the anatase and quartz peaks, two mullite peaks also appear.

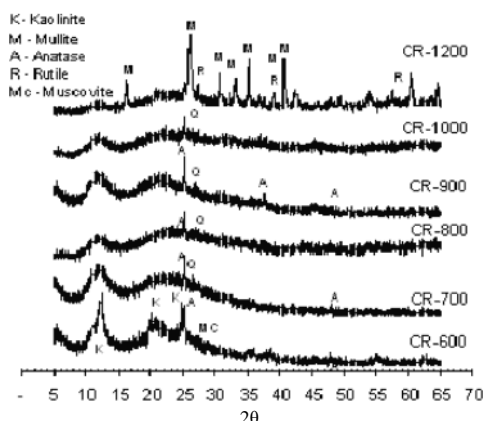


Figure 1. XRD patterns for CR samples after firing at various temperatures.

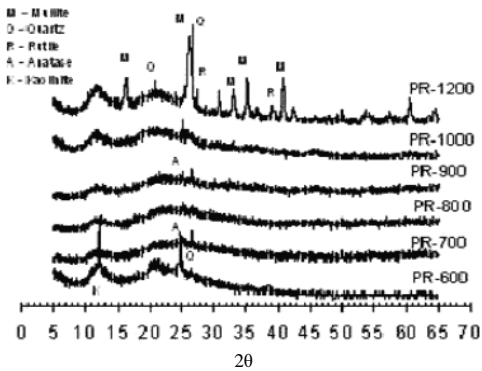


Figure 2. XRD patterns for PR samples after firing at various temperatures.

Figures 3 and 4 show the XRD patterns for the CR and PR samples fired at 1300°C, 1400°C, and 1500°C. The three samples have similar patterns, exhibiting the characteristic peaks of mullite, cristobalite, and rutile.

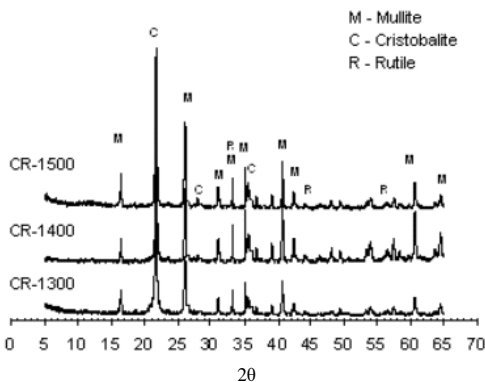


Figure 3. XRD patterns for CR samples after firing at 1300, 1400 and 1500°C.

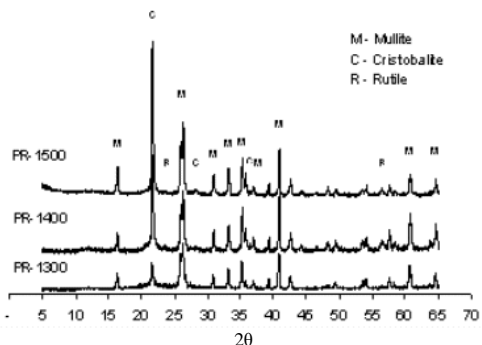


Figure 4. XRD patterns for PR samples after firing at 1300, 1400 and 1500°C.

The SEM pictures for the polished-section specimens of CR and PR samples fired at 1500 °C without HF etching, can be seen in Figures 5 and 6. The CR picture shows clearly acicular prismatic interlaced mullite crystals inside a wide pore. No particle morphology can be observed outside this void, although the composition determined by X-ray diffraction reveals the presence of mullite and cristobalite, besides a non-crystalline silicate phase, as a result of phase transformation reactions. The PR picture also shows a cavity where both inside and outside the void, prior pseudo-hexagonal particles are well sintered. The sample is mainly composed of mullite, cristobalite and vitreous silicate. A supposed glass-phase covers the mullite particles.

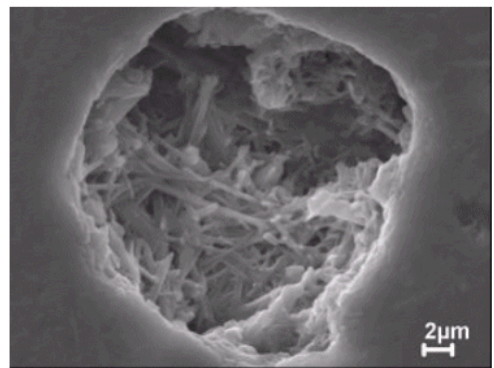


Figure 5. Scanning Electron Microscopy, in polished section, from fired waste CR at 1500°C, without HF etching.

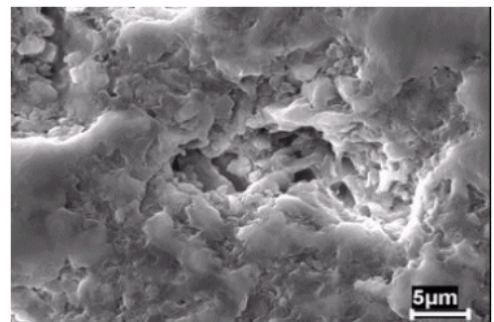


Figure 6. Scanning Electron Microscopy, in polished section, from fired waste PR at 1500°C, without HF etching.

In order to enhance crystal morphologies, hydrofluoric acid was used as etching solution. Figures 7 and 8 display the SEM image of polished surfaces from fired CR and PR wastes, fired at 1500°C and after 4 min of 5% HF solution etching.

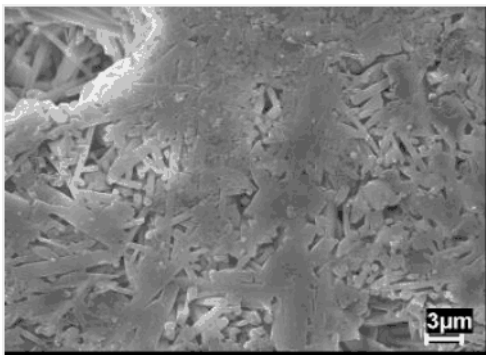


Figure 7. Scanning Electron Microscopy, in polished section, from CR waste fired at 1500°C, etched with HF.

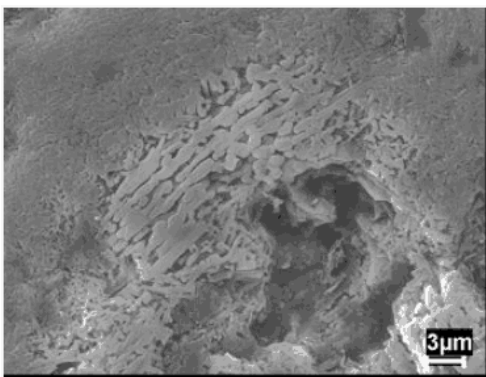


Figure 8. Scanning Electron Microscopy, in polished section, from PR waste fired at 1500°C, etched with HF.

After HF treatment, the CR sample showed well-defined prismatic interlaced mullite particles, even around the cavity, with a uniform size distribution around 5 μ m.

The PR picture shows that the HF etching on the vitreous silicate enhanced the view of the prismatic interlaced mullite particles with a non-uniform size distribution in the cavity contour region.

4 CONCLUSIONS

Chemical analysis of the wastes from kaolin processing allows us to conclude that these materials are mainly composed of kaolinite and due to the very high alumina contents, both wastes are very promising to be used in white grog for white and refractory ceramics application. The high contents of Fe and Ti in the CR sample, in comparison to the PR one, may prevent its use in refractory materials.

The X-ray diffraction results on the 1500°C samples show that metakaolinite quartz (>1200°C)

and non-crystalline silicate, in higher proportion when compared to quartz, are transformed into cristobalite.

Although published results set the transformation of anatase into rutile at around 750°C or close to 900°C, its presence was detected in the samples at 1200°C and above.

The HF etching on the specimens revealed better-defined acicular mullite particles in the CR sample – which has higher Fe and Ti contents – than in the PR sample.

5 REFERENCES

- Barata, M.S. 1998. Estudo da viabilidade técnica e econômica de produção de concreto de alto desempenho com os materiais disponíveis em Belém, através do emprego de adições de sílica ativa e metacaulim. Porto Alegre- (RS), Dissertação de mestrado. UFRS
- Carneiro, B. S. 2003. O Caulim Duro da Região do Rio Capim, Pará –Mineralogia, Geoquímica e Avaliação das Propriedades Cerâmicas. Belém, Universidade Federal do Pará. Centro de Geociências. (Dissertação de mestrado).
- Costa, M. L. & Moraes, E.L. 1998. Mineralogy, geochemistry and genesis of kaolins from the Amazon region. Springer-Verlag. Mineralium Deposita, 33., p. 283-297.
- Coura, F.; Moeri, E.N.; Kern, R.S. 1986. Geologia do caulim do Jarí. In: Cong. Bras. Geologia, 5., Goiânia. Anais....p.2248-2258.
- Flores, S. M. P. 2000. Aproveitamento do rejeito de caulim na produção de alumina para cerâmica e sílica de baixa granulometria. Belém, Universidade Federal do Pará. Centro de Geociências. (Tese de doutorado).
- Kotschoubey, B.,; Truckenbrodt, W.; Duarte, A.L.S. 1999. Cobertura bauxítica e origem do caulim do morro do Felipe, baixo Rio Jarí, estado do Amapá. Revista Brasileira de Geociências 29 (3): 331-338.
- Murray, H. H. & Keller, W. D. 1993. Kaolins, kaolins and kaolins. Kaolin genesis and utilization. Murray, H., Bundy, W., Harvey, C. (Eds.). The Clay Minerals Society. (Special Publication, 1), 341p.
- Schneider, H.; Okada, K.; Pask, J. A. 1994. Mullite and Mullite Ceramics. Chichester, England: John Wiley and Sons.
- Sen, S. & Thiagarajan, S. 1988. Phase transformations in amorphous 3Al₂O₃-2 SiO₂ system prepared by sol-gel method. Ceramics International. 14: 77-86.
- Silva, S.P. 1997. Depósitos de Caulim do Morro do Felipe, Amapá In: BRASIL. Departamento Nacional de Produção Mineral. Rochas e Minerais Industriais. Brasília. caps.12 e 13, p.131-145.(Principais depósitos minerais do Brasil, v.4).
- Sousa, D.J.L.de. 2000. Caracterização geológica, mineralógica química e física do caulim da mina de RCC – Rio Capim Caulim (PA). Belém, Universidade Federal do Pará. Centro de de Geociências. (Dissertação mestrado).

Fast Industrial X-ray Analysis for Process Control and Automation

R.Meier & T.Degen & M.Fransen
PANalytical, Almelo, the Netherlands

ABSTRACT: X-ray analysis of polycrystalline powder samples has grown way beyond its roots in the world of laboratory research and is becoming one of the most powerful industrial process-control tools in the fields of building materials and mining. It is the key to characterizing both the element concentrations and the crystalline phase composition of the materials involved. The development of industrial X-ray analytical systems such as PANalytical's twin solution, has transformed these advanced analytical techniques into a robust, workmanlike and easy-to-use tool for today's heavy industries. The combination of X-ray fluorescence (element analysis) and X-ray diffraction (phase analysis) opened enormous possibilities for process and quality control. Moreover, the recent development of high-speed X-ray detectors allows 'on the fly' quantitative X-ray diffraction analysis and process control in real time.

1 INTRODUCTION

Industrial environments like those used to process building materials and minerals are notoriously harsh on sensitive test and analysis equipment. The need to work often in dusty conditions, high humidity and extreme temperatures places heavy demands on such equipment, which must combine ruggedness and reliability with the precision and sensitivity of a laboratory instrument. This transition from a laboratory instrument to industrial system is difficult, but essential if the industry is to benefit from the latest analytical tools.

One of the most recent techniques to make this transition is X-ray diffraction (XRD). Although the power of XRD as the only analytical technique capable of distinguishing crystalline phases is well recognized, it has long been considered a tool best suited to the laboratory because of its low measurement speed and need for specialist knowledge. However, all this has changed with the introduction of the latest generation of industrial XRD equipment. These instruments are not only able to withstand the rigors imposed by an industrial regime; but they are also designed to be exceptionally easy to use even by non-specialist operators.

Moreover, even measurement speed is no longer an issue with the introduction of PANalytical's fast X'Celerator XRD detector based on proprietary solid-state Real Time Multiple Strip (RTMS) technology. Nowadays XRD is a truly practical and indispensable industrial tool in areas such as quality and production control, enabling manufacturers to maximize the efficiency of their processes and improve the quality of their product.

2 PHASE IDENTIFICATION WITH XRD

In minerals and building materials production, accurate information about the phase composition is essential for determining the quality of the semi-finished products and allowing manufacturers to optimize the efficiency of their process. Although there are many non-destructive analytical techniques that can analyze the elemental composition, for most products the properties are not only determined by the relative amounts of chemical elements, but also by the amount of crystalline phases present.

3 INDUSTRIAL XRD PHASE ANALYSIS

The introduction of Philips' CubiX XRD systems several years ago was something of a milestone in X-ray diffractometry for industry. Successor to the company's PW1800 series, which was the first ever fully automated diffractometer, the CubiX XRD family has continued the trend towards automation but now combined it with an exceptionally small footprint of 0.8 x 0.8 m to meet the space requirements of modern laboratories. Moreover, it has been specifically developed to satisfy stringent quality control requirements in production environments. To help achieve high-throughput, the CubiX systems also incorporate a fast, robust sample-loading mechanism that is suitable for robotic sample handling and integration into an automated conveyor system.

This system is mostly used for reliable and reproducible quantitative phase analysis based on intensity calibrations and peak measurements. Other applications are qualitative phase identification and troubleshooting.

The latest offspring is CubiX Fast, equipped with PANalytical's X'Celerator X-ray detector. Here an integrated array of parallel solid-state detectors replaces the single detector of traditional systems providing up to 100 times faster data acquisition. A scan formerly requiring three hours of data collection time is now recorded in less than two minutes. Moreover, in contrast to other high-speed detector technologies such as the Position Sensitive Detector, this dramatic increase in recording speed comes without compromising resolution. The smallest peak widths measured with this detector are well below 0.04° (Full Width Half Maximum). Additionally the X'Celerator detector is a semiconductor device and maintenance-free, requiring no gas, cooling water, liquid nitrogen or regular re-calibration and re-alignment.

The dramatic increase in speed offered by the new CubiX Fast system has had profound consequences on XRD as a process-control tool. It allows traditional phase analysis in real time for monitoring and production control. The most dramatic change, however, is the ability to measure a complete scan in minutes and to use full pattern profile analysis in place of an intensity calibration. This allows control over many complex industrial processes, where massive peak overlaps and intensity changes either made calibrations impractical or demanded excessive measurement time.

4 THE CUBIX TWIN CONCEPT – COMBINING XRD AND XRF

The ultimate in process control is the combination of elemental analysis by XRF and phase analysis by XRD. PANalytical has developed a new integrated instrument coupling together a diffractometer and a spectrometer without compromising on either XRD or XRF performance. This is called the CubiX TWIN and it includes a range of sample-handling and advanced automation features. It enables manufacturers in heavy industries to streamline their sample preparation and analysis and provide the high speed and high throughput essential for modern interactive process-control.

5 NEW SOFTWARE DEVELOPMENTS ENHANCE EASE-OF-USE

Simplifying diffractometer operation and automating complicated tasks such as phase identification is achieved by new software developments. They helped to transform XRD from a specialist technique requiring considerable knowledge and experience into a routine tool suitable for use in an industrial environment even by relatively inexperienced users. Special subroutines are now available that can be set up to run continuously in a process-control environment with the flexibility to detect and analyze unsuspected constituents.

X'Pert Industry is the software platform developed for PANalytical's industrial XRD equipment. Intended for process and quality control, X'Pert Industry is easy to use and is capable of running an entire analytical routine unattended. Featuring a full Multiple Document Interface (MDI) running under Windows®, it is easy to learn and provides a familiar feel that even inexperienced operators find comfortable to work with. It also contains a customizable report generator and transmits results as text, graphics, or evaluated expressions, all under full user control. On demand the functionality can be extended with modules for specialist applications such as semi-quantitative phase identification or full pattern Rietveld analysis.

The X'Pert HighScore software module uses a powerful search-match algorithm, which optimally combines peak and profile data from the diffraction pattern to assemble a list of candidate phases – ranked in order of probability. When a phase is identified, the software recalculates the list of candidates based on the remaining unexplained features in the pattern. In this way, a complex mixture of phases in a sample can be determined automatically, including generation or transmission of a results report. This module is used for fast automatic screening of compositional changes and for semi-quantitative analysis.

The exact relative proportions of the phases are determined by calibration methods and X'Pert Industry, or in the laboratory by the Rietveld method using the HighScore Plus software, or by using the X'Pert RoboRiet module in a production plant. RoboRiet offers a fully automated Rietveld analysis with encrypted control files, auto-start, a minimal user interface and complete protection against any changes.

8 REFERENCES

- Allman R., Roentgenpulverdiffraktometrie, Berlin, Springer
Young R. A., The Rietveld Method, IUCR
Jenkins R. & Snyder R., Introduction to X-ray powder diffraction, Wiley

6 RIETVELD ANALYSIS

Sometimes a mixture of phases produces an X-ray diffractogram with a lot of overlapping peaks. This means that a simple measurement of the intensities of selected peaks is no longer possible. In this case another technique known as Rietveld analysis, which uses the full diffraction pattern instead of only a few intensities can be used. A calculated pattern derived from known crystal structures of each phase is fitted to the measured pattern using a least-squares algorithm, thus enabling the relative quantities and properties of the crystalline phases in the sample to be deduced without the need for a calibration. The acquisition of a complete pattern with sufficient quality took at least one hour on a traditional powder diffractometer, but is ready within minutes on a CubiX FAST system.

7 REFERENCED RIETVELD ANALYSIS

In the traditional Rietveld method a high quality full diffraction profile is fitted according to a model with known crystal structures and a refinement strategy. Often this is the only method to analyze complex mixtures of several crystalline phases that show strong peak overlaps. The method yields precise, relatively correct results, but lacks absolute accuracy in complex cases.

PANalytical has linked the precise Rietveld quantitative data to other results obtained by established techniques like optical microscopy. This unique "referenced" Rietveld method allows an absolutely correct XRD quantification, accurate enough to push the limits of process control.

Examples of the analysis of Portland clinker and Portland cement will be shown. These more accurate determinations of all phases in cement allow the use of the maximum amount of possible additions and saves valuable clinker. One can also achieve a tighter control of the different sulfate phases in OPC, resulting in more constant hydraulic properties, which facilitates the use of the final product in building projects.

Hydroceramic Sealants for Geothermal Wells

N.Meller & C.Hall

Centre for Science at Extreme Conditions, The University of Edinburgh, Erskine Williamson Building, The Kings Buildings, Mayfield Road, Edinburgh, EH9 3JZ, United Kingdom

ABSTRACT: Portland cement based sealants are currently used to seal geothermal and high temperature oil and gas wells by filling the annulus between a steel casing and the rock through which the well is drilled. This prevents loss of the fluid of interest from the well (e.g. hot water, oil) and contamination by ground water. No systematic research approach has been taken to cement containing inorganic additives other than silica over the temperature range typically encountered in deep hot oil and gas wells or geothermal wells (200 to 400oC). Here we present the initial findings of our work on the CASH (CaO-A₁₂O₃-SiO₂-H₂O) system. The CASH system is based on cement plus silica and alumina additives and has the ability to mimic naturally occurring mineral assemblages in hydrothermal areas. A phase diagram for the system at 200oC is already under construction at the time of writing. We also discuss some of the technical issues associated with well engineering such as rates of reaction of cement formulations, intermediate phase formation and long term durability.

1 INTRODUCTION

Hydrothermal synthesis of inorganic materials is a hot topic. We approach hydrothermal synthesis from a new and different direction based on paste reaction at high solids/liquid ratios. This is more akin to cement technology and we believe it may provide a single-step energy-efficient route to strong structural hydroceramics. In paste synthesis, mineral reactions occur by dissolution/nucleation/crystal growth pathways via solution species while most of the material remains in the solid form. The end product is a cohesive solid material and potentially the composition space is huge.

The choice of the system is driven by an urgent need in energy engineering for new bulk sealants for the construction of hot, deep wells. Traditionally portland cement based materials are used to seal deep hot wells (Nelson 1990). These wells can either be very deep oil and gas wells (depth in excess of approximately 6000m) or shallow to deep hydrothermal wells. In both situations the temperature attained in the well is higher than those encountered in normal well engineering and consequently the cement based sealants used now do not prove durable over the lifetime of a well.

Attempts to modify the composition of portland cement to enhance its suitability at more extreme

conditions commonly entails adding silica to the system (Taylor 1964) to form more durable minerals. However the higher temperatures in geothermal or deep hot oil and gas wells means that the normally robust cement plus silica systems used for such wells are no longer durable. Added to this is the further complication of durability in the presence of formation waters which may take the form of hot aggressive brines. The cement plus silica system has already been shown to be unstable in carbonate rich environments (Nelson 1990) and hence it is likely that it is not durable in the long term in many hot well environments, be they deep oil and gas wells or geothermal wells.

Additions other than silica have been proposed as suitable for such environments (e.g. Sugama & Carciello 1992, Barlet-Gouedard & Vidick 2001) but have not yet been proven as sufficiently durable. However one system does show potential and builds on the original cement plus silica concept. Preliminary investigations by Barlet-Gouedard & Vidick (2001) have shown that the cement plus silica system can be modified with the addition of alumina. At temperatures of approximately 300oC this system produces a suite of minerals similar to those found in hydrothermally altered basalt. If these phases are found in such natural environments then

it is possible that a cement composed of such phases would also be stable.

Barlet-Gouedard & Vidick (2001) appear to have tested only a few compositions in the system over a very restricted temperature range. Hence we decided to take this work a step further. Using their original concept of the CaO-Al₂O₃-SiO₂-H₂O (CASH) system based on portland cement we are undertaking a systematic study of the phase equilibria and kinetics over a range of temperatures (150 to 350oC). The work we report here is in progress but we can however present some of the initial findings of the work, including a partial phase diagram of the CASH system at 200oC. We also discuss some of the problems particular to determining phase equilibria of cement systems in temperatures normally considered to be 'low', geologically speaking.

2 CURRENT METHODOLOGY

Class G oilwell cement was used as the basis for the hydroceramics. Oilwell cement is chosen over construction cement as it has a more consistent composition hence results should be more reproducible. Silica was added in the form of silica flour and is composed of 98 % silica in the form of quartz (SiO₂) with trace impurities. Reagent grade alpha-alumina (corundum) was used as the source of Al₂O₃.

Different samples were made up of a combined total of 10 g of the three starting materials in varying proportions and 4 g of de-ionised water. Only hydroceramics with ≥50% cement were formulated as low cost cementing formulations were of primary interest. Each sample was placed in a sealed vessel and heated to 200oC and allowed to stabilise over 5 days. The temperature was chosen to reflect mid-range temperatures that might be encountered in geothermal or deep oilwells.

After 5 days the sample was removed from the oven and allowed to cool. When at room temperature the samples were removed from their containers and air dried. A few grams were ground up for X-ray diffraction (XRD) phase identification. Duplicate samples showed that the results are reproducible.

3 A NEW CASH PHASE DIAGRAM

From the phases found in each sample a new phase diagram has been determined for the CASH system at 200°C (Figure 1). At 200°C the following secondary phases are observed: gyrolite (Ca₅Si₁₂O₃₀(OH)₄·7H₂O), hillebrandite (Ca₂SiO₃(OH)₂), jaffeite (Ca₆Si₂O₇(OH)₆), portlandite (Ca(OH)₂), quartz (SiO₂), 11Å

tobermorite (Ca₅Si₆O₁₆(OH)₂·4H₂O), xonotlite (Ca₆Si₆O₁₇(OH)₂) and hibschite (Ca₃Al₂Si₂O₈(OH)₄) and katoite (Ca₃Al₂(SiO₄)(OH)₈) of the hydrogrossular series (Ca₃Al₂Si₃O₁₂-Ca₃Al₂(OH)₂). When plotted on a CaO-Al₂O₃-SiO₂ diagram the mineral assemblages produced the following 3-phase triangles:

- Gyrolite + Quartz + Xonotlite
- Corundum + Tobermorite + Xonotlite
- Corundum + Hibschite + Xonotlite
- Corundum + Hibschite + Jaffeite
- Corundum + Jaffeite + Katoite
- Hibschite + Jaffeite + Portlandite
- Hibschite + Jaffeite + Xonotlite.

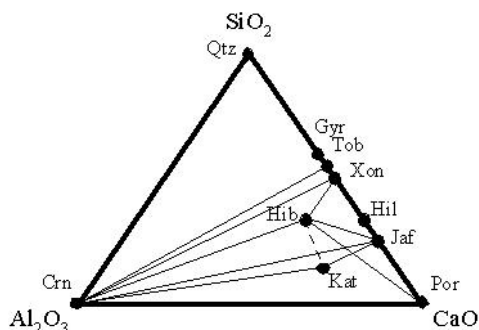
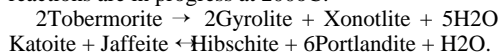


Figure 1. Phase diagram illustrating co-existing phases in the CASH system after 5 days at 200oC.

Abbreviations: Crn=corundum; Gyr=gyrolite; Hib=hibschite; Hil=hillebrandite; Jaf=jaffeite; Kat=katoite; Por=portlandite; Qtz=quartz; Tob=tobermorite; Xon=xonotlite. Solid lines illustrate coexisting phases. The dashed line represents the hydrogrossular solid solution between hibschite and katoite.

Crossing tie-lines indicate that the following reactions are in progress at 200oC:



The direction of the former reaction can be determined from the reactions of Taylor (1964) whereby xonotlite and gyrolite replace tobermorite. The direction of the latter reaction with regard to temperature is currently unknown.

In addition to creating the above phase assemblages the addition of aluminium has a two-fold effect. First it stabilises tobermorite, a phase not normally stable over 150oC, to higher temperatures by Al incorporation into the crystal structure. This has also been observed by previous authors (Liu et al. 2000, Shaw et al. 2000). This may be useful in hot well construction as permeability and compressive strength are key issues. According to Taylor (1964) tobermorite transforms to xonotlite+gyrolite at temperatures over 150°C. The latter have a lower compressive strength in

comparison to tobermorite and are also less permeable. Hence stabilising tobermorite to higher temperatures is beneficial for well construction providing the same strength and permeability are maintained when Al is incorporated into the crystal structure.

Crystallinity improves if alumina is added to the system. Whether the Al-bearing phases of this system intrinsically have better crystallinity than Al-deficient phases is unknown. This latter effect is also observed when xonotlite is present.

4 EQUILIBRIUM ISSUES

Not all samples contained the ideal phase assemblage according to their composition. Additionally many of the samples contain assemblages including quartz or corundum. Corundum normally forms at much higher temperatures suggesting the corundum present in this system is a relict hence its presence on the phase diagram is not thermodynamically correct. Similarly the presence of quartz is more likely to be as a relict phase from the original reactants. This is confirmed by the sharpness of quartz peaks observed by XRD whereby the peaks are much sharper than those of phases produced during hydrothermal synthesis. However it is possible that some quartz forms at this temperature. Hence its presence on the phase diagram may be true.

In some samples the presence of phases outside the ideal composition suggests that equilibrium has not been fully attained. The samples were allowed to equilibrate at 200°C for five days but no samples were synthesised in shorter or longer amounts of time to examine the effects of time on rates of equilibrium. Furthermore the presence of intermediates is currently unknown as all analysis so far has been post mortem. Hence it is proposed to resolve these issues using synchrotron energy dispersive diffraction techniques as detailed by Barnes et al. (1992, 2000, 2002). In situ observations can yield a detailed insight into the very earliest reactions and the presence of intermediates (Meller et al. 2004, Colston, in prep). While the final hydroceramic may be stable in certain geological environments the initial or intermediate phases formed may not be and the final composition may never be reached. Hence it is important to understand the in-situ dynamics of this system over a range of temperatures to ensure a high quality of well engineering.

5 CONCLUSIONS

Hydroceramics based on the CASH system show potential as sealants for deep hot wells. Little is

known about the CASH system at geologically low temperatures (<400°C) and interest from both the oil industry and renewable energy industries have boosted our efforts in elucidating this system under such conditions. Preliminary work shows that phase diagrams can be obtained at such low temperatures although equilibrium issues need to be considered together with the 'ideal' phase assemblage to be certain that the material will produce the correct phase assemblage under well conditions.

The final aim of this work will be to determine the stability of such phase assemblages under different well conditions. This information will be invaluable to well engineers in determining the correct sealant formulation for wells once the down hole conditions are known.

6 REFERENCES

- Barlet-Gouedard, V. & Vidick, B. 2001. A non-conventional way of developing cement slurry for geothermal wells. *Geothermal Resources Council Transactions* 25: 85-91.
- Barnes, P., Clark, S. M., Häusermann, D., Henderson, E., Fentiman, C. H., Muhamad, M. N. & Rashid, S. 1992. Time-resolved studies of the early hydration of cements using synchrotron energy-dispersive diffraction. *Phase Transitions* 39: 117-128.
- Barnes, P., Colston, S. L., Craster, B., Hall, C., Jupe, A. C., Jacques, S., Cockcroft, J. K., Morgan, S., O'Connor, D. & Belloto, M. 2000. Time- and space- resolved dynamic studies on ceramic and cementitious materials. *Journal of Synchrotron Radiation* 7: 117-177.
- Bensted, J. & Barnes, P. (eds.) 2002. The use of synchrotron sources in the study of cement materials. London & New York: Spon Press.
- Colston, S. L., Barnes, P., Jupe, A. C., Jacques, S., Hall, C., Livesey, P., Dransfield, J. & Meller, N. in prep. An in situ synchrotron energy-dispersive diffraction study of the hydration of oilwell cement systems under high temperature/autoclave conditions up to 130°C.
- Liu, F., Chen, D., Ni, W. & Cao, Z. 2000. Effect of Al₃₊ on tobermorite crystallinity. *Journal of University of Science and Technology Beijing* 7: 79-81.
- Meller, N., Hall, C., Jupe, A. C., Colston, S. L., Jacques, S., Barnes, P. & Phipps, J. 2004. Time resolved studies of the hydration of brownmillerite with and without gypsum: a synchrotron diffraction study at ambient and elevated temperature. *Journal of Materials Chemistry* 14: 428-435.
- Nelson, E. (ed.) 1990. *Thermal Cements*. Sugar Land, Texas: Schlumberger Educational Services.
- Shaw, S., Clark, S. M. & Henderson, C. M. B. 2000. Hydrothermal formation of the calcium silicate hydrates, tobermorite (Ca₅Si₆O₁₆(OH)₂·4H₂O) and xonotlite (Ca₆Si₆O₇(OH)₂): an in-situ synchrotron study. *Chemical Geology* 167: 12-140.
- Sugama, T. & Carciello, N. R. 1992. Alkali carbonation of calcium aluminate cements: influence of set-retarding admixtures under hydrothermal conditions. *Journal of Material Science* 27: 4909-4916.
- Taylor, H. F. W. (ed.) 1964. *The Calcium Silicate Hydrates*. London: Academic Press. 168-232.

Sintering and Crystallization Studies of Industrial Waste Glasses

C.H.Oliveira, R.Neumann, & A.Alcover Neto

Centro de Tecnologia Mineral – CETEM/MCT – Rio de Janeiro, Brazil

M.V.A.Fonseca

Instituto de Química – IQ/UFRJ – Rio de Janeiro, Brazil

ABSTRACT: This work evaluated the feasibility of obtaining glass-ceramics (controlledly crystallized glasses) from Brazilian industrial waste glasses. The wastes used were blast-furnace slag, exhaust cracking catalyst and chromite jigging tailings. The glasses were batched only using the wastes, in ratios that generated different contents of iron and chromium (nucleation agents). The careful selection and batching of the wastes allowed not using commercial raw materials, decreasing production costs. The glass crystallization studies (XRD and DTA) showed that higher content of transition metals improved bulk nucleation and lowered crystal growth temperatures. The sintering studies, performed using heating microscopy, showed that the sintering of glasses with lower content of transition metals ranged from 840 to 920°C, while the higher contents one, from 1160 to 1280°C. In the first case, the sintering temperatures were lower because it worked through glassy phase sintering, differently from the other one, where it worked through crystalline particles sintering. The different sintering/crystallization behaviors of the glasses allows glass-ceramic production by bulk crystallization of glass monoliths (higher and intermediate content of iron and chromium) or by simultaneous sintering/crystallization of glass powders (lower and intermediate content). This work shows an alternative usage for industrial wastes, generating a relatively high aggregate value product (glass-ceramics).

1 INTRODUCTION

The huge quantities of solid wastes generated by industries might be very harmful to the environment. Their disposal is costly and frequently inappropriate, so their usage as raw materials for different applications is an important scientific and technological challenge. Inorganic solid wastes are already used in glass, ceramic and cement industries.

These wastes can also be used in glass-ceramics (Rabinovich 1982, Pelino et al. 1997), polycrystalline solids prepared by the controlled crystallization of glasses. These materials usually show much better properties than their related glasses or ceramics, but they are more expensive as they demand more energy (Hlavac 1983). Glass-ceramics production can be briefly described as raw materials melting, glass casting and heat treatment (crystallization). So, incorporation of industrial wastes in batch formulations would decrease raw materials cost.

Industrial waste glass-ceramics have been produced since the 1970's in Europe, being used as electric insulators, facing panels, roof coverings, abrading agents, paving tiles and pipes (Rabinovich 1982, Strnad 1986). In a previous work (Oliveira 2000), Brazilian industrial wastes such as blast-

furnace slag from iron industry (BFS – rich in CaO, SiO₂, Al₂O₃ and MgO – generated during industrial iron oxide reduction), exhaust cracking catalyst from a refinery (ECC – rich in SiO₂ and Al₂O₃ – cracking catalyst is used for transforming long chain hydrocarbons into smaller ones, but after some time its activity decreases and part of it is removed from the reactor and replaced with fresh catalyst) and chromite jigging tailings from Medrado Mine, Bahia (CJW – rich in SiO₂, MgO, Fe₂O₃, Al₂O₃ and Cr₂O₃ – waste of chromite concentration plant) were used in different proportions for production of glasses with different contents of Fe₂O₃ and Cr₂O₃, possible nucleating agents (Strnad 1986, McMillan 1979).

Glass crystallization comprises nucleation and crystal growth (Navarro 1968). Nucleation provides the sites where the crystals will start to grow (Rincon 1992). When nucleation happens all over the bulk of the glass, fine-grained glass-ceramics can be obtained by heat treatment of a glass monolith (Strnad 1986, Hlavac 1983, McMillan 1979). When nucleation is not effective, the crystal growth starts at the few nuclei formed and external surfaces. An alternative is to ground the glass, cast it just like a ceramic powder, and heat treat it for sintering and crystallization (Strnad 1986, Pannhorst 1997, Rabinovich 1982, Gonzalez-Oliver 1997).

2 EXPERIMENTAL

The maximum nucleation temperature (T_{nuc}) determined with DTA (Buri 1982) demands fast heating the glass until a selected temperature, keeping it stable for two hours, and then heating at a $10^{\circ}\text{C}/\text{min}$ rate. After several analyses with different soaking temperatures, a graph $(1/T_c - 1/T_{c0}) \times T_n$ can be plot (T_n is soaking temperature, T_c is the maximum of the crystallization peak with soaking temperature, and T_{c0} is the maximum of the crystallization peak in a simple DTA – constant heating rate). The maximum of the curve is the maximum nucleation temperature, important issue for heat treatment optimization and for evaluation of the nucleation agents effect.

The apparent activation energy of crystal growth was determined with the Kissinger (1956) and modified Kissinger (Kemeny & Sestak 1987, Weinberg 1991, 1992) methods. In the Kissinger method, DTAs at different constant heating rates are acquired and plot as $\ln(\beta/T_c^2) \times 1/T_c$ (β is the heating rate and T_c is the maximum of the crystallization peak). The angular coefficient of the obtained straight line is $-E_a/R$ (E_a is apparent activation energy and R is the perfect gas constant). In the modified Kissinger method, the glasses are rapidly heated, soaked at the nucleation temperature and then heated at different constant heating rates. This procedure eliminates the influence of nucleation that may occur during heating. The Avrami parameter (n), present in the kinetic law of most crystallization processes, the KJMA equation (Zanotto 1992)

$$x = 1 - \exp(-K \times t^n) \quad (1)$$

was determined by means of

$$n = \frac{2.5 \times R \times T_c^2}{\Delta T_{hh} \times \Delta E_a} \quad (2)$$

derived by Augis & Bennett (1978), where ΔT_{hh} is half-height width of the crystallization peak. The Avrami parameter ranges from 1 to 2 for needle-like crystals, from 2 to 3 for lath-like crystals, and from 3 to 4 for three-dimensional ones. The application of a glass-ceramic may depend on crystal dimensionality.

The glasses used in this study came from the following batches (Oliveira 2000): glass 1 (70% BFS and 30% ECC), glass 2 (40% BFS, 30% CJW and 30% ECC), and glass 3 (70% CJW and 30% ECC). They were ground in 100% below $105 \mu\text{m}$ in a ceramic ball mill, and characterized by chemical analysis and X-ray diffraction, XRD, (Bruker AXS D5005, Cu $K\alpha$ radiation, 5 to $70^{\circ} 2\theta$).

Their crystallization properties were studied with a Perkin Elmer thermodifferential analyzer DTA7 (Pt crucibles, 20 mg and alumina as reference).

Heat treatment of the glasses (according to DTA) were performed in a Thermolyne 46128 furnace, and crystalline phases characterized by XRD.

Shape changes (sintering, softening, flowing) of 3 mm side cubic compacts of the glass powders during heating were studied with a Leica Leitz 1A heating microscope at $10^{\circ}\text{C}/\text{min}$ rate.

After being mixed with polyvinyl alcohol, the glass powders were dry pressed and heat-treated in the Thermolyne furnace (according to the heating microscopy results). Specific weight and porosity were determined by measuring the dry, wet, and immersed weights of the sintered bodies obtained.

3 RESULTS AND DISCUSSION

The chemical composition (acid dissolution, volumetric and gravimetric analyses) of the glasses (Table 1) shows Glass 1 with high CaO, Al_2O_3 , SiO_2 , and MgO contents while glass 3 contents high MgO, Al_2O_3 , SiO_2 , Fe_2O_3 and Cr_2O_3 . Glass 2 has an intermediate chemical composition.

Glasses 1 and 2 displayed fully amorphous XRD patterns (hump), while glass 3 showed the hump and some small peaks with the diffraction pattern of magnesiochromite, $(\text{Mg,Fe})(\text{Cr,Al})_2\text{O}_4$, probably arising from the not fast enough cooling of the melt.

Table 1: Chemical composition of the glasses.

Content (%)	Glass 1	Glass 2	Glass 3
SiO_2	44.1 ± 0.1	50.6 ± 0.1	53.2 ± 0.1
Al_2O_3	22.6 ± 0.1	18.8 ± 0.1	16.3 ± 0.1
CaO	27.5 ± 0.1	15.7 ± 0.1	1.4 ± 0.1
MgO	4.9 ± 0.1	9.8 ± 0.1	18.8 ± 0.1
Na_2O	< 0.1	< 0.1	0.5 ± 0.1
K_2O	< 0.1	0.1 ± 0.1	0.7 ± 0.1
Fe_2O_3^*	0.8 ± 0.1	3.2 ± 0.1	4.8 ± 0.1
MnO	< 0.1	0.3 ± 0.1	0.2 ± 0.1
Cr_2O_3	< 0.1	1.4 ± 0.1	4.0 ± 0.1

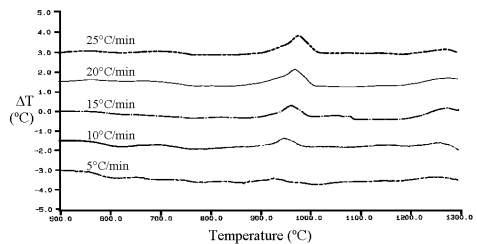


Figure 1: DTA curves of non-nucleated glass 3.

Examples of DTA and nucleation curves are in Figures 1 and 2, respectively. The exothermal peaks

due to crystallization show up on the DTA at Figure 1, and the maximum nucleation temperature might be derived from Figure 2.

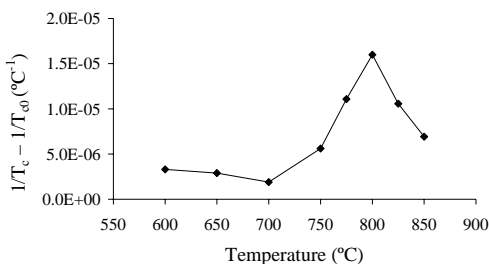


Figure 2: Nucleation curve of non-nucleated glass 2.

Table 2 summarizes the results obtained with DTA for the performed crystallization studies.

Table 2: Crystallization Properties.

Glass	E _a (kJ/mole)	n	T _c (°C)	T _{nuc} (°C)	E _a * (kJ/mole)	n*
Glass 1	396	1.3	1093	925	-	-
Glass 2	338	2.8	1002	800	489	1.9
Glass 3	369	2.2	948	800	418	1.7

* Glasses nucleated before the crystal growth exotherm.

The DTAs of glass 1 showed wide and not intense crystallization peaks, that disappeared after nucleation. The higher T_{nuc} (error ± 5 °C) of this glass, occurring very close to the crystallization peak onset (not shown), could indicate simultaneous crystal growth and nucleation. The Avrami parameter (error ± 0.2) of this glass near 1 and the wide exotherms are indicative of surface crystallization mechanism (Fonseca et al. 1993, 1994, Oliveira et al. 1995, 1997).

Glasses 2 and 3 show the same T_{nuc}, and when pre-nucleated E_a (error ± 20 kJ/mole) increases n decreases. Differently from glass 1, their T_{nuc} values are just a little higher than glassy transition, T_g, (≈ 770°C for glass 2 and ≈ 750°C for glass 3). Glasses 2 and 3 Avrami parameters indicate bulk nucleation and lath-like crystals (for just one crystalline phase).

The crystalline phases generated in the heat-treated glasses were identified by XRD (Table 3). The chemical formulas of these phases are in agreement with the main components of the glasses. The crystalline phases start to appear in XRD at the temperatures assigned in Table 4, agreeing with the DTA crystallization onset temperatures (not shown). Glasses 2 and 3 when heat-treated generate two crystalline phases, one of them presenting unidimensional growth (the pyroxenes diopside and enstatite) and the other one, three-dimensional structure (the feldspar anorthite and the spinel magnesiochromite). Therefore the Avrami parameter

values for these glasses near 2 reflect the effect of both phases in the crystallization kinetics.

Table 3: Crystalline phases generated in the glasses.

Crystalline Phases	1	2	3
T _{cryst,XRD} (°C)	950	925	925
Anorthite CaAl ₂ Si ₂ O ₈	•	•	
Gehlenite Ca ₂ Al ₂ SiO ₇	•		
Diopside Ca(Mg,Al)(Si,Al) ₂ O ₆	•	•	
Enstatite MgSiO ₃			•
Magnesiochromite (Mg,Fe)(Cr,Al) ₂ O ₄			•

Heating microscopy (Table 4, Figures 3, 4) indicated higher characteristic temperatures (error ± 5 °C) for glass 3, also showing sintering temperature range very close to softening temperature, indicating that crystallization precedes sintering.

Table 4: Characteristic Temperatures (DIN 51730).

	Sintering (°C)	Softening (°C)	Melting (°C)
Glass 1	840-920	1230	1260
Glass 2	840-920	1222	1237
Glass 3	1180-1270	1298	1350

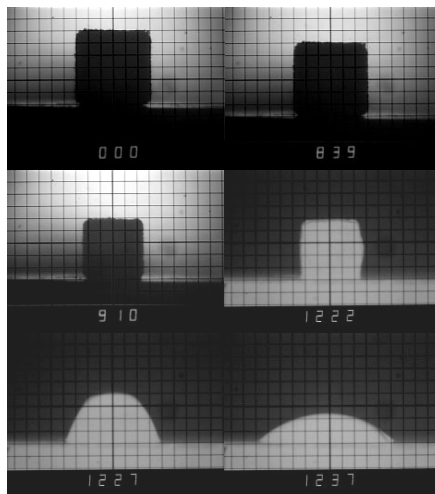


Figure 3: Heating microscopy images of glass 2.

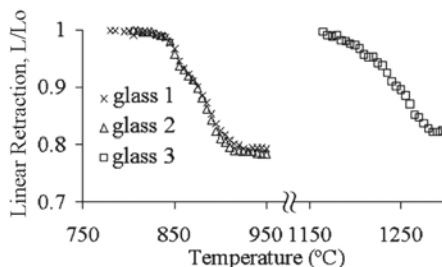


Figure 4: Sintering curves of the glass powders.

Glasses 1 and 2 sinter while still glassy, and their sintering curves end before the beginning of crystallization (XRD and DTA).

Table 5 shows the sintering temperatures applied to the glass compacts (determined by sintering curves in Figure 4) and some properties of the solid bodies obtained. The high specific weight (closed pores + solid) and low open porosity values indicate effective sintering and possibility of obtaining good quality glass-ceramics.

Table 5: Properties after heating the compacts.

Glass	Sintering Temperature (°C)	Specific Weight (g/cm ³)	Open Porosity (%)
1	900	2.80 ± 0.02	1.2 ± 0.1
2	900	2.84 ± 0.02	0.8 ± 0.1
3	1200	2.83 ± 0.02	0.5 ± 0.1

4 CONCLUSIONS

The sintering and crystallization studies indicated the best suited glass-ceramic production procedures for each glass. Glass 1 (sintering at lower temperatures than surface crystallization) is adequate for glass-ceramic sintering route. Glass 3 (sintering at temperatures much higher than bulk crystallization and near melting point) is adequate for glass-ceramic production by heat treating glass monoliths. Glass 2 (sintering at lower temperatures than bulk crystallization) is adequate for both routes.

Iron and chromium oxides confirmed their nucleating properties in the glasses studied.

Glass-ceramic production from only industrial wastes as raw materials is technically feasible.

5 ACKNOWLEDGEMENTS

CNPq - Conselho Nacional de Desenvolvimento Científico e Tecnológico, for D.Sc. scholarship, and Carbox Resende Química e Industrial, for chemical analyses.

6 REFERENCES

Augis, J.A., Bennett, J.E. 1978. Calculation of the Avrami parameters for heterogeneous solid state reactions using a modification of the Kissinger method. *J. Thermal Anal.* 13: 283-292.

Buri, A., et al. 1982. Thermal Evolution of Inorganic Glasses: Glass Transition, Phase Separation, Nucleation and Crystal Growth. *Gazz. Chim. Ital.* 112: 65-70.

Fonseca, M.V.A. et al. 1993. Escória de alto-forno e catalisador exausto: matérias-primas para vitro-cerâmicas. In: *Anais do 37º Congresso Brasileiro De Cerâmica, Curitiba.* p.1071-1078.

Fonseca, M.V.A., et al. 1994. Estudos por ATD da Concentração Ótima de Agente Nucleante para a Cristalização de um Vidro de Escória de Alto-Forno. In: *Anais do 38º Congresso Brasileiro De Cerâmica, Blumenau.* p.1275-1280.

Gonzalez-Oliver, C.J.R. 1997. Sintering of Glass-Ceramics. In: Manfredini, T. et al. (ed.) *Glass-Ceramic Materials: Fundamentals and Applications.* Madrid: Mucchi Editore. p. 93-100.

Hlavac, J. 1983. *The Technology of Glass and Ceramics.* New York: Elsevier.

Kemeny, T. & Sestak, J. 1987. Comparison of Crystallization Kinetics Determined by Isothermal and Non-Isothermal Methods. *Thermochim. Acta* 110: 113-129.

Kissinger, H.E. 1956. *J. Res. Nat. Bur. Stand.* 57: 217-221.

McMillan, P.W. 1979. *Glass Ceramics.* London: Academic Press.

Navarro, J.M.F. 1968. Nucleación y Cristalización en Vidrios. *Bol. Soc. Esp. Cerám.* 7(4): 431-458.

Oliveira, C.H. et al. 1995. Desenvolvimento de materiais vitro-cerâmicos a partir da sinterização de fritas de escória de alto-forno e catalisador exausto de craqueamento de petróleo. In: *Anais do 1º Simpósio Nacional De Vidros, Águas de Lindóia.* p. 123-132.

Oliveira, C.H. et al. 1997. Thermal evolution of a crystalline surface layer on blast furnace slag glasses. In: *Anais do 41º Congresso Brasileiro de Cerâmica, São Paulo.* p. 967-970

Oliveira, C. H. 2000. Reaproveitamento de Rejeitos Industriais Inorgânicos Sólidos: avaliação do potencial de desenvolvimento de materiais vítreos e vitro-cerâmicos. Tese (Doutorado) – UFRJ, IQ.

Pannhorst, W. 1997. Glass Ceramics: state-of-the-art. *J. Non-Cryst. Solids* 219: 198-204.

Pelino, M. et al. 1997. Glass-ceramic materials obtained by recycling industrial wastes. In: Manfredini, T. et al. (ed.) *Glass-Ceramic Materials: Fundamentals and Applications.* Madrid: Mucchi Editore. p. 223-242.

Rabinovich, E. M. 1982. Glass-Ceramics from Israeli Slag and Coal Ash. In: Simmons, J.H. et al. (ed.) *Nucleation and Crystallization in Glasses.* *Advances in Ceramics* vol. 4. Columbus: American Ceramic Society, p. 334-340.

Rincon, J.M. 1992. Principles of Nucleation and Controlled Crystallization of Glasses. *Polym.-Plast. Technol. Eng.* 31(3-4): 309-357.

Strnad, Z. 1986. *Glass-Ceramic Materials.* Amsterdam: Elsevier.

Weinberg, M.C. 1991. On the Analysis of Non-Isothermal Thermoanalytic Crystallization Experiments. *J. Non-Cryst. Solids.* 127:151-158.

Weinberg, M.C. 1992. The Use of Site Saturation and Arrhenius Assumptions in the Interpretation of Non-Isothermal DTA/DSC Crystallization Experiments. *Thermochim. Acta.* 194: 93-107.

Zanotto, E. D. 1992. Crystallization of Liquids and Glasses. *Braz. J. Phys.* 22(2): 77-84.

Glass-Ceramic Foam Synthesis Using Industrial Wastes

C.H.Oliveira, R.Neumann, & A.Alcover Neto

Centro de Tecnologia Mineral – CETEM/MCT – Rio de Janeiro, Brazil

M.V.A.Fonseca

Instituto de Química – IQ/UFRJ – Rio de Janeiro, Brazil

ABSTRACT: This work evaluated the feasibility of obtaining glass-ceramic foams (porous controlledly crystallized glasses) from industrial wastes. These foams might be useful materials for thermal and acoustic insulation as they present high porosity, low density, mechanical resistance and no inflammability. Dimensional changes, surface aspects and crystallization of an industrial waste glass with thermal expansion properties were studied. The glass was batched with blast furnace slag and exhaust cracking catalyst. DTAs showed the shift of the exotherms with different particle sizes (surface processes). Kinetic evaluation showed two crystallization processes with different activation energies. XRD indicated the formation of wollastonite and diopside. Optical micrographies of the heat-treated glasses showed large quantities of bubbles inside the glass matrix, explaining the bloating process. Heating microscopy images show expressive expansion without deformation between 850 and 950°C (~25%). Softening only occurs at 1200°C. Heat treatments of glass powder compacts resulted in solid expanded bodies (glass-ceramic foam), indicating simultaneous sintering and thermal expansion processes. This work shows an alternative usage for industrial wastes, glass-ceramic foam, a potentially valuable and useful building material.

1 INTRODUCTION

As already stated in the previous work, industrial wastes disposal is an important concern nowadays, so the search for alternative usage of these materials is always an welcome theme.

Some wastes have been used in cement and other building materials industries. Glass-ceramics are polycrystalline materials obtained from the controlled crystallization of glasses, show very improved properties but their high energy consumption process increases production costs. So, the use of industrial wastes as raw materials could decrease production and waste disposal costs. (Rabinovich 1982, Pelino et al. 1997, Hlavac 1983),

Industrial waste-based glass-ceramic products such as electric insulators, facing panels, roof coverings, abrading agents, paving tiles and pipes have already been produced in Europe since the seventies (Rabinovich 1982, Strnad 1986).

In previous works (Oliveira 2000, Fonseca et al. 1993, 1994, Oliveira et al. 1995, 1996, 1997), blast-furnace slag from iron production (BFS – rich in CaO, SiO₂, Al₂O₃ and MgO – generated during industrial iron oxide reduction), and exhaust cracking catalyst from an oil refinery (ECC – rich in SiO₂ and Al₂O₃ – cracking catalyst is used for

transforming long chain hydrocarbons into smaller ones, but after some time its activity decreases and part of it is removed from the reactor and replaced with fresh catalyst) have already been used as raw materials for production of industrial waste based glass. Oliveira (1996) reported that a mixture of these wastes, when melted in an induction furnace using graphite crucibles, generated a gray colored glass, differently from the amber ones obtained in electric furnaces with ceramic crucibles. It was also reported that powder compacts of this gray glass presented thermal expansion properties (Oliveira 1996).

This work studies the different properties shown by this gray glass obtained from the same batch of one of the glasses of the previous work, but melted in different condition.

2 EXPERIMENTAL

The glasses used in this study came from the melting of 25 kg of a mixture of 70% of BFS and 30% of ECC at 1450°C in an induction furnace, AJAX model 140. The gray glass obtained was ground in a ceramic ball mill, and classified with 500, 300, 105 and 53 µm sieves. Chemical analysis and X-ray

diffraction (Bruker AXS D5005, Cu K α radiation, 5 to 70° 2 θ) characterized the glass.

Crystallization properties were studied with a Perkin Elmer thermodifferential analyzer DTA7 (Pt crucibles, 20 mg and calcined alumina as reference).

The apparent activation energy of crystal growth was determined with the Kissinger method (Kissinger 1956), by acquisition of DTAs at different constant heating rates and plotting $\ln(\beta/T_c^2) \times 1/T_c$ graph (β is the heating rate and T_c is the maximum of the crystallization peak). The angular coefficient of the straight line obtained is $-E_a/R$ (E_a is apparent activation energy and R is the perfect gas constant).

The glasses were heat-treated (constant heating rate until the selected temperature and cooling) in a Thermolyne 46128 furnace, and crystalline phases characterized by X-ray diffraction. The heat treatments were chosen according to DTA results.

Shape changes (sintering, softening, melting) of 3 mm side cubic compacts of the glass powders during heating were determined with a Leitz 1A heating microscope at 10°C/min rate.

After being mixed with polyvinyl alcohol, the glass powders were dry pressed and heat-treated in the Thermolyne furnace (according to the heating microscopy results). Specific weight and porosity were determined by measuring the dry, wet, and immersed weights of the sintered bodies, following Brazilian standard ABNT MB-67.

Some larger fragments of the glass (centimeter sized) were heat-treated, cut with a diamond saw and polished with SiC paper sheets until grit 600. Images were acquired with a Zeiss Axioplan optical microscope.

3 RESULTS AND DISCUSSION

The chemical analysis (acid dissolution, volumetric and gravimetric analyses) show SiO₂, CaO, Al₂O₃ and MgO as the main components (Table 1). The differences from the analogue amber one (Oliveira 2004) might arise from some material projection from the induction furnace during melting. It is amorphous, as confirmed by its XRD (Fig. 3).

Table 1: Chemical composition of the glass

	Content (%)
SiO ₂	43.5 ± 0.1
Al ₂ O ₃	16.8 ± 0.1
CaO	32.5 ± 0.1
MgO	5.6 ± 0.1
Na ₂ O	0.4 ± 0.1
K ₂ O	0.3 ± 0.1
Fe ₂ O ₃ (total iron)	0.4 ± 0.1
MnO	0.5 ± 0.1

Figure 1 shows DTAs of coarse fraction of the glass, with the assignment of the glassy transition temperature (T_g). The wide exotherm was associated to crystallization, and, at higher temperatures, two endotherms could be result of melting processes (indicating the formation of at least two different crystalline phases). Differently from T_g and the melting valleys, crystallization takes place at shifting temperatures with heating rate changes, allowing the apparent activation energy for crystal growth to be determined using the Kissinger (1956) method (Table 2).

In Figure 2, the DTAs of the finer glass grains show the same thermal profile of the coarser ones, except for a shift of the crystallization exotherm to lower temperatures, and its resolution to three condensed peaks (assigned in Fig. 2). This kind of dislocation is indicative of a surface process (Strnad 1986), whereas the higher the surface area, the lower the temperature where the phenomena occur. The higher surface energy may have also been the driving force for the resolution of the peaks.

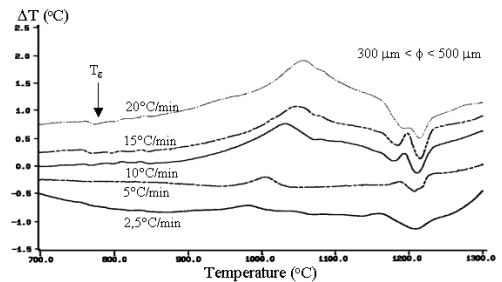


Figure 1. DTA curves of the 300 $\mu\text{m} < \phi < 500 \mu\text{m}$ fraction.

Table 2: Apparent Activation Energy for Crystal Growth.

Gray Glass	300 $\mu\text{m} < \phi < 500 \mu\text{m}$	$\phi < 53 \mu\text{m}$ 2 nd peak	$\phi < 53 \mu\text{m}$ 3 rd peak
E_a (kJ/mol)	351 ± 20	427 ± 20	343 ± 20

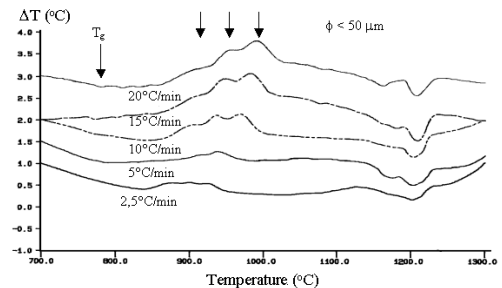


Figure 2: DTA curves of the $\phi < 53 \mu\text{m}$ fraction.

The application of the Kissinger (1956) method to the exotherms of the DTAs (Figs. 1, 2) allowed the apparent activation energies for crystal growth to be calculated (Table 2), except the lowest temperature exotherm for the finer fraction. In this case, the method showed problems, indicating that this exotherm may not be the thermal response of a crystallization process (more discussed ahead). Table 2 shows similar values for the peak of the coarser fraction and the third one of the finer fraction, indicating that the coarser fraction crystallization peak follows the same behavior of the third exotherm in the finer one.

XRD (Fig. 3) of larger fragments of the glass indicated that the first part of the exotherm in DTA plot (until 1000°C) did not generate crystalline phases. That explains why the Kissinger plot of the first exotherm of the finer fraction did not result in a straight line (being probably another kind of exothermic process). The generated crystalline phases, aluminous diopside and wollastonite, are coherent with the chemical composition of the glass.

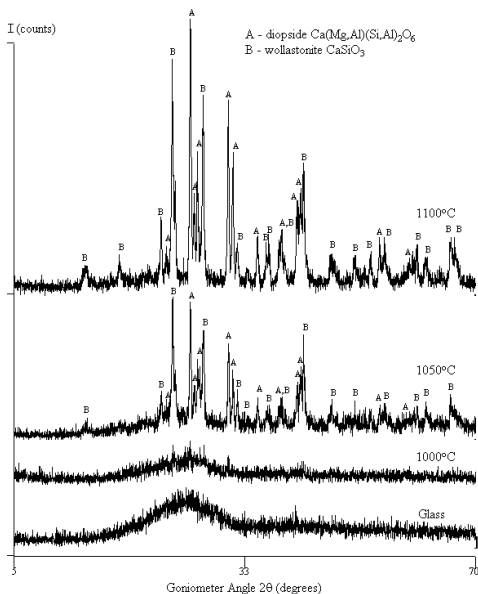


Figure 3: XRD of heat-treated glass samples (Cu K α).

The heating microscopy analysis (Fig. 4) confirmed the thermal expansion properties of this glass, defining its temperature range (Fig. 5). It also determined the softening, half-sphere and melting temperatures (error ± 5 °C), indicating that the maximum temperature such material could be used should stay below 1200°C.

Figure 5 defines the thermal expansion range, from 850 to 950°C, the first part of the DTA exotherm, confirming the different nature of such exothermic process. Table 3 shows some properties of bodies obtained from glass compacts heat-treated according to the expansion curve (Figure 5). As these compacts resulted in porous solid bodies, the expansion process should have happened simultaneously to sintering of the grains. The specific weight (closed pores + solid material) showed values much lower than would be expected for a glass with that composition (2.80 g/cm³, Oliveira 2004), indicating great content of closed pores. Table 3 points out that, in the range analyzed, higher temperatures generated more porosity (closed and open), and longer times decreased the closed porosity and increased the open one (more actuation of sintering).

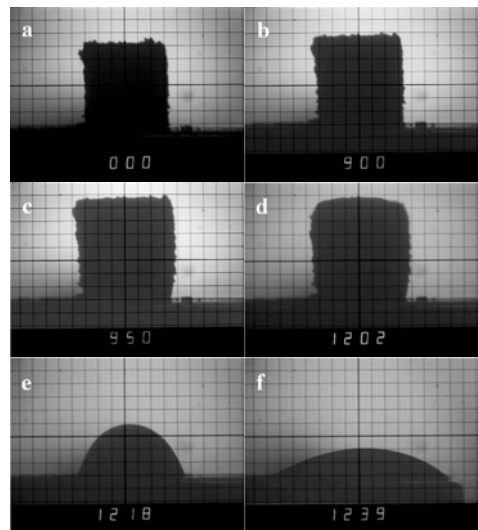


Figure 4: Heating microscopy images: a) room temperature, b) beginning of expansion, c) end of expansion, d) softening, e) half-sphere, f) melting.

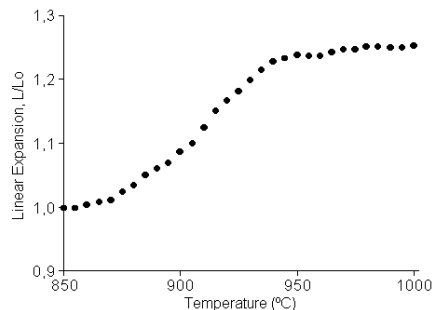


Figure 5: Expansion curve of the glass powder.

Table 3: Properties of heat-treated glass compacts.

Soaking Temperature (°C)	Soaking Time (min)	Specific Weight (g/cm ³)	Open Porosity (%)
900	0	1.90 ± 0.02	0.6 ± 0.1
900	20	1.94 ± 0.02	0.9 ± 0.1
950	0	1.79 ± 0.02	1.4 ± 0.1
950	20	1.88 ± 0.02	2.3 ± 0.1

The image in Figure 6 was acquired from a glass heat-treated at a temperature slightly after the beginning of the DTA exotherm, and points to gas release from the glass matrix as the cause of the expansion process. These gas bubbles were released at temperatures where the glass structure became sufficiently looser. They may be result of the fast melting process performed in the induction furnace, not allowing the complete release of the gases dissolved in the melt. Figure 7 shows that after the glass crystallization, the porous structure was maintained.

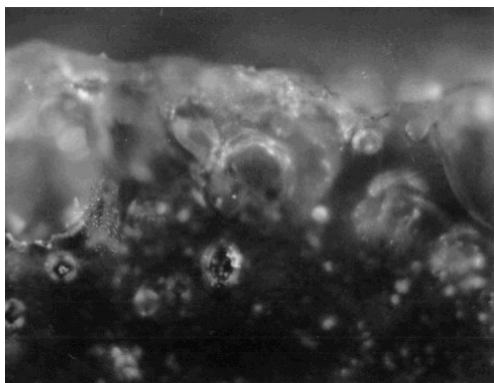


Figure 6: Optical micrography of the surface of the heat-treated glass (900°C).

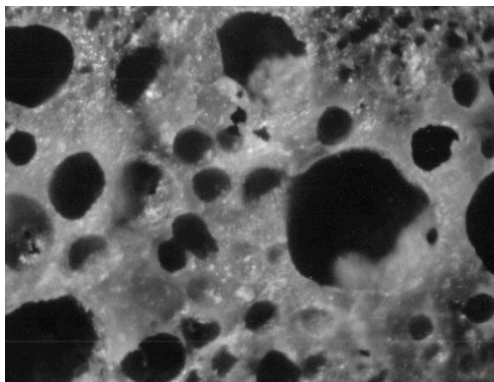


Figure 7: Optical micrography of the surface of the heat-treated glass (1050°C) after crystallization (polished surface).

4 CONCLUSIONS

A glass-ceramic foam with low density, thermal stability up to 1200°C, retaining high closed porosity although fully sintered and well-crystallized, was synthesized from industrial wastes as raw materials. Its properties prove the technical feasibility of recycling industrial wastes for potential high-performance end product, an environmentally friendly and probably self-sustained recycling route.

5 ACKNOWLEDGEMENTS

Companhia Siderúrgica Nacional (CSN), for the use of the induction furnace, CNPq (Conselho Nacional de Desenvolvimento Científico e Tecnológico), for the D.Sc. scholarship, and Carbox Resende Química e Industrial, for the chemical analyses.

6 REFERENCES

- Fonseca, M.V.A. et al. 1993. Escória de alto-forno e catalisador exausto: matérias-primas para vitro-cerâmicas. In: Anais do 37º Congresso Brasileiro De Cerâmica, Curitiba. p.1071-1078.
- Fonseca, M.V.A. et al. 1994. Estudos por ATD da Concentração Ótima de Agente Nucleante para a Cristalização de um Vidro de Escória de Alto-Forno. In: Anais do 38º Congresso Brasileiro De Cerâmica, Blumenau. p.1275-1280.
- Hlavac, J. 1983. The Technology of Glass and Ceramics. New York: Elsevier.
- Kissinger, H.E. 1956. J. Res. Nat. Bur. Stand. 57:217-221.
- Oliveira, C.H. et al. 1995. Desenvolvimento de materiais vitro-cerâmicos a partir da sinterização de fritas de escória de alto-forno e catalisador exausto de craqueamento de petróleo. In: Anais do 1º Simpósio Nacional De Vidros, Águas de Lindóia. p. 123-132.
- Oliveira, C.H. et al. 1996. Meios porosos a partir de vidro de uma mistura de escória e catalisador exausto. Cerâmica 42: 677-680.
- Oliveira, C.H. et al. 1997. Thermal evolution of a crystalline surface layer on blast-furnace slag glasses. In: Anais do 41º Congresso Brasileiro de Cerâmica. São Paulo. p. 967-970.
- Oliveira, C. H. 2000. Reaproveitamento de Rejeitos Industriais Inorgânicos Sólidos: avaliação do potencial de desenvolvimento de materiais vítreos e vitro-cerâmicos. Tese (Doutorado) – UFRJ, IQ.
- Oliveira, C.H. et al. 2004. Sintering and Crystallization Studies of Industrial Waste Glasses. In: Proceedings of the 8th International Congress on Applied Mineralogy. Águas de Lindóia. (in press).
- Pelino, M. et al. 1997. Glass-ceramic materials obtained by recycling industrial wastes. In: : MANFREDINI, T. et al. (ed.) Glass-Ceramic Materials: Fundamentals and Applications. Madrid: Mucchi Editore, p. 223-242.
- Rabinovich, E. M. 1982. Glass-Ceramics from Israeli Slag and Coal Ash. In: Simmons, J.H. et al. Nucleation and Crystallization in Glasses. Advances in Ceramics vol.4. Columbus : American Ceramic Society, p. 334-340.
- Strnad, Z. 1986. Glass-Ceramic Materials. Amsterdam : Elsevier.

Properties of Clays Sintered with GLP for Application in Structural Ceramic

E.A.Pereira, J.Y.P.Leite, C.Sales

Laboratory of Mineral and Waste Processing – CEFET/RN, Natal – RN – Brazil

W.Acchar

Department of Physics - Federal University of Rio Grande do Norte, Natal -RN – Brazil

ABSTRACT: Special clays are used for the development of structural clay products with special application in building industry for fabrication of bricks, tiles, sewer pipes and others artifacts. The Rio Grande do Norte has three major regions of red ceramic: Assú, Seridó, and Potengi. Clay raw materials were obtained directly in the mineral deposit. This work presents a study of two types of clay material sintered with GLP. The samples were characterized by the plasticity and plastic indexes of Atterberg; size distribution according to the sedimentation method. The results indicated that this material can be used to fabricate structural bricks and tiles.

1 INTRODUCTION

The properties of fired clay products largely depend from the structures and chemical compositions of starting raw materials. The industries of structural red ceramics in Rio Grande do Norte still use clay materials without knowing their properties. The purpose of this paper is to study the potential use of two types of clays from Assú-Brazil (Barro Vermelho e São João) under GLP atmosphere. Brugerá¹ and Santos² observe that it is necessary to control temperature, acidity, alkalinity, chemical, and mineralogical composition, associated to the physical characteristics, as plasticity and liquidity limit (Atterberg indices), to get the mixture.

2 MATERIAL AND METHODS

The clays were obtained in natural deposits in Assu ceramic industries, RN State, Brazil. Samples with dimensions of 60x10x05 mm³ were compacted in a steel matrix under 200 kgf/cm² pressures, and sintered between 900°C and 1050°C in liquefied petroleum gas (LPG) for two hours. The identification of crystalline phases was carried out by means of X-ray diffraction. The samples were

characterized using thermal analysis, apparent porosity, water absorption, linear retraction, and flexion rupture. Figure 1 shows the experimental procedure used in this work.

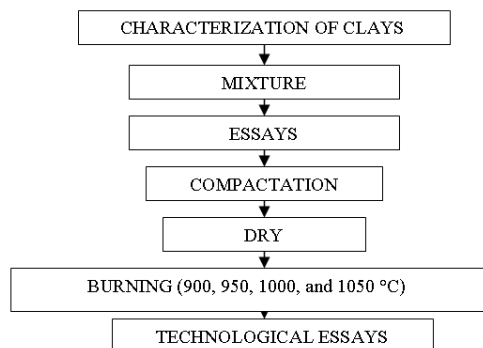


Figure 1: Experimental procedure used in this work.

Plasticity index (IP) was determined by the difference between the value of liquidity limit (LL) and plasticity limit (LP). The results are presented in Table I and show that the two types of clay can be

classified as medium plastic clays. The São João clay has lower plasticity and it is called no plastic clay; the Barro Vermelho clay is the plastic one. Table 1 presents the results of these characteristics.

Table 1: Liquidity limits, Plasticity limits and Plasticity indexes of investigated clays.

Samples	LL (%)	LP (%)	IP (%)
Barro Vermelho	38,5	24,1	14,4
São João	36	26,4	9,6

The particle size distribution of clays is presented in Figure 2. The results indicated that these clays are adequate to be used in the manufacture of tiles and bricks.

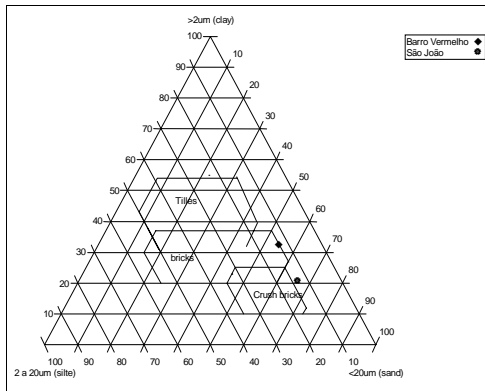


Figure 2: Winkler Diagram of particles size distribution of clays.

Figure 3 presents the conditions of sample 1. Figure 3 shows the linear shrinkage values as a function of sintering temperature and no plastic clay content. The results have showed no significant dependence of the linear shrinkage on the concentration of no plastic clay. The shrinkage values remain practically constant. The linear shrinkage showed low shrinkage values at all temperatures investigated (<3 %). Apparent porosity of sintered bodies are presented in Figure 4. The specimens show a decrease of the porosity values with increasing temperature. Figures 5 and 6 show the flexural strength and water absorption values of the sintered samples, respectively. The results have indicated that the no plastic clay content has no influence on both the properties. The best values were obtained at 1050 °C. Figures 4, 5, and 6 present these results.

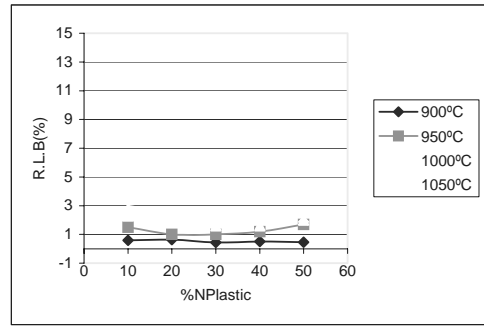


Figure 3: Linear shrinkage values as a function of sintered temperature and no plastic clays content in the mixture.

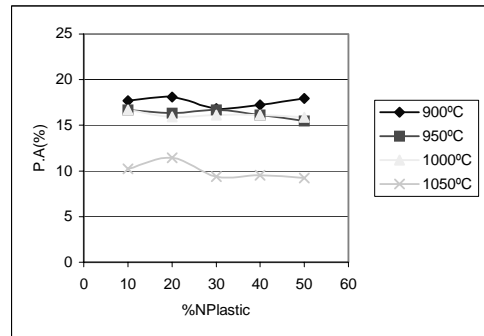


Figure 4: Apparent porosity values

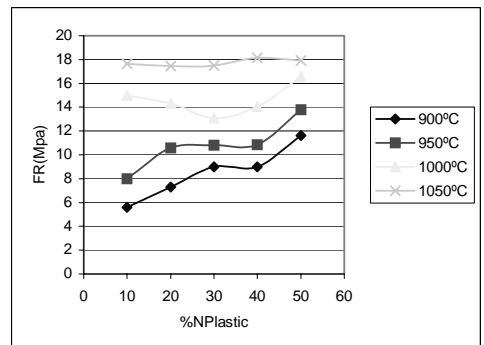


Figure 5: Flexural strength values

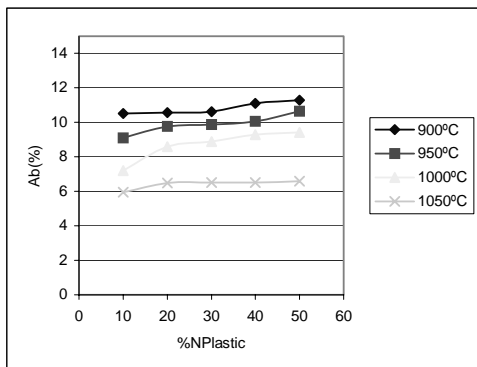


Figure 6: Water absorption values.

3 CONCLUSIONS

The results obtained in this work have shown that these clays are suitable for conformation of red ceramics products. The best properties of the sintered material were obtained at a temperature of 1050°C.

The study has also shown that it is possible to sinter clay products with good properties using liquefied petroleum gas (LPG).

4 REFERENCES

- Bruguera, Jordi. Manual Práctico de Cerámica; 1a Edição, Editora Omega, Barcelona, 1986.
- Santos, P.S. Ciência e Tecnologia de Argilas; 2a Edição, Vol. 1, Editora Edgar Blucher Ltda, São Paulo, 1989.
- Pereira, E. A. and at all., Caracterização Tecnológica de argilas para aplicação em cerâmica vermelha. 46 Congresso Brasileiro de Cerâmica, São Paulo, 2002.
- Pereira, E. A. and at all., Technological characterization of clays for application in structural ceramics. In: I Encontro da Sociedade Brasileira de Pesquisa em Materiais. Rio de Janeiro, 2002.

From Raw Materials to Mineral Wastes

H.Pöllmann

Department of Mineralogy and Geochemistry, Martin-Luther University, Halle, Germany

R.S.Angelica & M.da Costa

Universidade Federal do Para, Belem, Brazil

ABSTRACT: Different mineral occurrences in the Amazon region produce high quality products. Despite some mineral residues are occurring. These residues can be reused for other applications after treatment as secondary raw material. In this study, caolinities, laterites and red muds were characterized and their probable reuse investigated. This is part of a cooperation project throughout the MLU Halle-Wittenberg and UFPA, granted by BMBF and CNPQ.

1 INTRODUCTION

The project deals with the investigation of different brazilian mineral deposits in the Amazon region and with a probable reuse of the non usable amounts of mineral products for primary use (Angelica 1996, Costa 1997, Costa et al. 1996, Costa & Moraes, de Sousa 2000, Kotschoubey & Truckenbrodt 1992). Due to the tremendous amounts of materials available a reuse is mainly useful in the field of building materials. This fulfills the requirements that large amounts of materials can be treated and an economic reuse seems to be possible. Also easy applicable techniques are known, can be developed or adapted. In this study especially deposits for china clay, laterites and processing residues from aluminium production (red mud) were investigated. The basic applications deal with the fabrication of bricks which is widely known. In this study it is the main goal to form hydraulic binders by thermal treatment or to produce at least some latent hydraulic materials (Ferrari 1939, Ringsholt, Korndörfer et al. 2000, Korndörfer 2000, Korndörfer & Pöllmann 1998a, Korndörfer & Pöllmann 1998b, Korndörfer & Pöllmann 1998c, Martelli 2003, Osokin et al. 1992, Osula 1991, Pera et al. 1992, Sahu & Majling 1993). Therefore some other

sources for limestone must be included. Also in special cases additional calciumsulfate is necessary. Deposits included in this study are lateritic residues from gold mining (Igarape Bahia, Carajas), different caolin products from Rio Capim mining area, limestones and gypsum products from Amazon area and red mud from aluminium production (Parastate). In some cases a dehydration process to form metaphases and use of these materials were studied. Especially metakaolinite was produced by a thermal process. This metakaolinite is an excellent pozzolanic material and can be used as an additive to ordinary Portland cements. In the fabrication of concretes parts of OPC are replaced by Metakaolinite and therefore less CO₂ is produced due to reduced amounts of limestone decarbonated in the process of OPC fabrication.

2 PREPARATION & EXPERIMENTAL

All mineral residues were tested for their chemical and mineralogical composition and variation with time to obtain reliable data for probable longer application times. New hydraulic binders were formulated and tested for their mineralogical compositions and some technical properties. The

hydration behaviour was followed by heat flow calorimetry. Mineralogical phases were determined by X-ray diffractometry using SIEMENS D5000 X-ray machine equipped with special cells to follow the hydration behaviour. Depending on materials available different reaction ways were tested and the results documented. The economic aspect of producing new hydraulic binders was considered.

3 DESCRIPTION OF OCCURENCES AND RESIDUES

Different deposits and their residues were included in this study. In Figure 1-3 kaolinite-(Rio Capim) and laterite-(Igarape Bahia) deposits were chosen and these minerals used to produce a cementitious material.



Figure 1. Rio Capim deposit of caolin, showing different qualities of kaolin.



Figure 2: Laterites from Igarape Bahia gold mining area



Figure 3. Sampling of lateritic muds in an old leaching residue deposit from pilot plant.

The different residues can be characterized by their chemical and mineralogical composition:

1. Kaolinites (soft):

SiO_2 : 44.7 % Al_2O_3 38.2 Fe_2O_3 1.0 TiO_2 1.33 Na_2O 0.05 K_2O 0.06 MgO 0.02 CaO <0.04 (de Sousa 2000).

The variation of laterites coming from different sources at Igarape Bahia are shown in Figure 4.

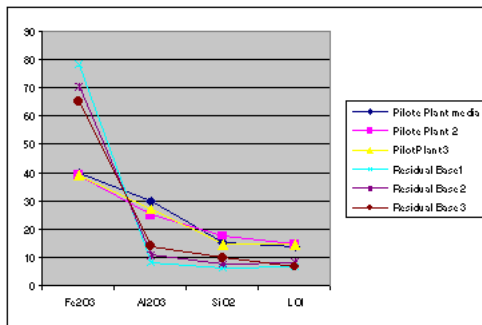


Figure 4. Variation of chemical composition of laterites from Igarape Bahia (Costa et al. 1996).

The different compositions of mineral residues from Igarape Bahia mine area based on mainly hematite (40-73%), kaolinite (12.8-41%), gibbsite (4-25%), goethite (0-13.3%), anatase (0.7-1.8%) and Al-fosphate (0.6-1.6%) (Costa et al. 1996).

4 DEVELOPMENT OF NEW CEMENTITIOUS MATERIALS

The aim of the work was to use the residues to produce some cementitious material for immediate application. Besides the use as an additive to OPC to form soil cement mainly new cementitious materials should be formed by thermal treatment of optimized raw meals (Figure 5). Also the use of metakaolinite formed by thermal treatment of “waste kaolinites” was included. The treatment of metakaolinite was investigated in the course of application of pozzolanic materials.

The following types of cementitious materials were investigated:

1. OPC + laterite ---→ soil cement
2. Iron-rich cements -→Ferrari-cements
3. Laterite + CaO ± kaolinite ± gypsum ± $\text{Al}(\text{OH})_3$
4. Hydrothermally treated mixtures
5. Metakaolinite addition to OPC
6. Sulphoaluminate cement

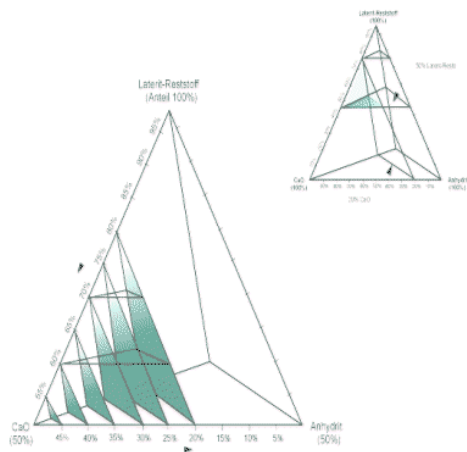


Figure 5. Areas of interest of hydraulic mixtures (Korndörfer 2000).

The residues were treated with different ratios composed of laterite, kaolinite, lime and gypsum (Figure 5). It could be proved that besides C_2S also gehlenite is formed above $900^{\circ}C$. With increasing temperature the amount of gehlenite increases.

Hydrothermal treatment of these mixtures leads to the formation of Strätlingite (gehlenitehydrate).

The results of selected different mixtures from laterite + addition of lime \pm kaolinite \pm gypsum is shown in figures 6-9 (selected graphs from PHD-work J. Korndörfer (Korndörfer 2000)). The use of calcined kaolinite + additions of gypsum can lead to the formation of sulphoaluminate clinkers. The addition of metakaolinite to OPC also can lead to some pozzolanic reactions. Some results on the formation of new phases is shown in Figure 9 (Korndörfer 2000). It can be seen clearly that it is strongly dependant from the type of raw meal mixture given and also from the absolute temperature. Due to the inhomogeneous raw meal compositions mainly coming from the laterite source it is often difficult to establish constant conditions.

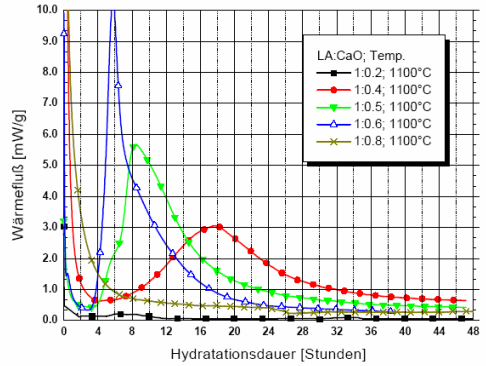


Figure 6. Heat flow calorimetric curves of mixtures containing laterite with addition of CaO sintered at $1100^{\circ}C$ (Korndörfer 2000).

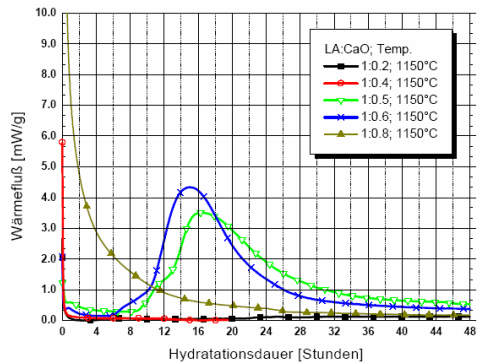


Figure 7 : Heat flow calorimetric curves of mixtures containing of laterite with addition of CaO sintered at $1150^{\circ}C$ (Korndörfer 2000).

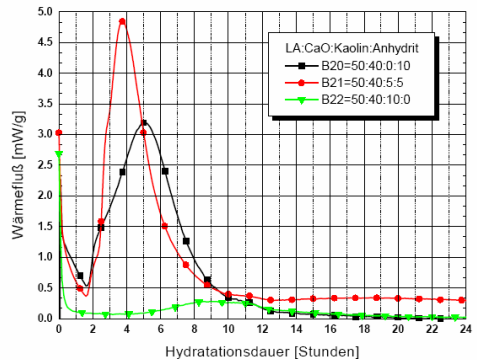


Figure 8. Heat flow calorimetry of mixtures sintered at $1100^{\circ}C$ (Korndörfer 2000).

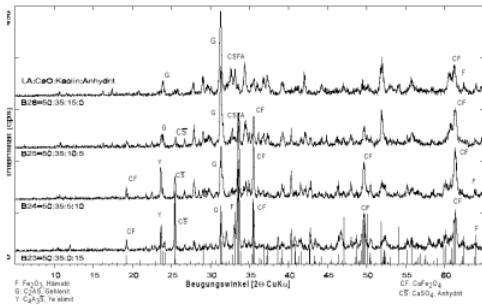


Figure 9. X-ray powder diffractograms showing phase formation of heat treatment of LA:CaO 50:35 at 1100°C (Korndörfer 2000).

5 CONCLUSIONS

Laterites, kaolinites, metakaolinites, bauxites, red muds and other residues can be used for special applications in the building industry but more basic work is necessary to build up an optimized building material. In some cases it is even more easy to produce bricks from argillaceous materials at low. The high amounts of iron in laterites lead often to the existence or formation of nonreactive hematite. In the case of lower iron-containing precursor materials it is often easier to obtain cementitious materials.

6 REFERENCES

Angelica, R.S. 1996. Mineralogie e geochimica de gossans e lateritos auriferos na regio de Carajas: depositos de Igarape Bahia e Aguas Claras – Tese de Doutorado UFPA, 115p

Brosch, H. & Ney, P.: Reaktionen der Hauptgemengteile von Lateriten mit Calciumhydroxid unter niedrigthermalen Bedingungen im Hinblick auf die Herstellung von Baustoffen in Entwicklungsländern – ZKG, 33,6, 283-291, 1980

Costa, M. L. 1997. Laterization as a major process of ore deposit formation in the Amazon region. - Explor. Mining Geol., 6, 179-194.

Costa, M.L. 1991. Aspectos geologicos dos lateritos da Amazonia – Rev. Bras. De Geociencias 21(2), 146-160

Costa, M. L.; Moraes, E. L.; Angélica, R. S. & Pöllmann, H. 1996. Contrates geoquímicos nas bacias de rejeitos da mina de ouro supergênico do Igarapé (Carajás- Pa). - Symp. de Geologia da Amazonia. Belém. - Anais. Belém. SGB/NO, 356-360.

Costa, M.L. & Moraes, E.L.: As grandes reservas de caulim e da lateritzacao na Amazonia – in Cong.Bras.Geol. 37, Sao Paulo, Boletim de resumos expnadidos, SBG V.1, 588-589

De Sousa, D.L. 2000. Caracterizacao Geologica, Mineralogica, Quimica e Fisica do Caulim da Mina da RCC – Rio Capim Caulim (PA – Tese de Mestrado , Belem.

Ferrari, F. 1939 Zur Kenntnis des Ferrari-Zements. - Tonindustrie-Zeitung, 63(81), 873- 876.

Ringsholt, T.: Development of a steam-cured building material on the basis of lateritic soils and lime – United Nations Development Program – Technical Report No. 11,116S., United Nations Indonesia

Korndörfer, J., Pöllmann, H., Da Costa, M.L. & Angelica, R. 2000. Mine Tailings from the lateritic gold mine Igarape Bahia (Carajas Region), a basis for active hydraulic binders – Zeitschrift für Angew. Geologie, Sonderheft, 187- 192, Korndörfer, J.: Dissertation University of Halle.

Korndörfer, J. & Pöllmann, H. 1998a. Zemente auf Basis eines lateritischen Materials mit besonderer Berücksichtigung von Boden-Zementen – Schriften der Alfred-Wegener Stiftung 3/98 ISSN 0946-8978

Korndörfer, J. & Pöllmann, H. 1998b. Zemente auf Basis eines lateritischen Materials mit besonderer Berücksichtigung von Boden-Zementen – Ber.dt.min.Ges., Abstract, 163

Korndörfer, J. & Pöllmann, H. 1998c. Ein eisenreicher Reststoff zur Bildung von hydraulischen Phasen – 3.Symp. Techn. und Angew. Mineralogie Halle/Saale

Kotschoubey, B. & Truckenbrodt, W. 1992. Occorencias de argila semi-flint no nordeste do Para – in Congr.Bras.Geol. 37, Sao Paulo – Boletim de resumos expandidos SBG,v.2, 17p.

Martelli, M.C. 2003. Sintese de mulita a partir dos rejeitos de beneficiamento de caulim para a producao de tijolos refratarios – exame de qualificao.

Osokin, A. P.; Krivoborodov, Y. R. & Dukova, N. F. 1992. Sulfoferrite cements. - Proc. of the 9th Inter. Congress on Chemistry of Cements, New Delhi, India, 236.

Osula, D. O. 1991. Lime modification of problem laterite. – Engineering Geology, 30(2), 141-154.

Pera, J.; Ambroise, J. & Momtazi, A. S. 1992. Investigation of pozzolanic binders containing calcined laterites. - Mat. Res. Soc. Symp. Proc., 245, 25-35.

Sahu, S. & Majling, K. 1993 Phase compatibility in the system CaO-SiO₂-Al₂O₃-Fe₂O₃- SO₃ referred to sulphoaluminate belite cement clinker. - Cement and Concrete Research, 23, 1331-1339.

Pozzolanes as Raw Materials for Cementitious Systems – Testing Methods for Characterization and Properties

H. Pöllmann

Department of Mineralogy and Geochemistry, Martin-Luther University, Halle, Germany

ABSTRACT: Different artificial and natural pozzolanes are well studied because of their hydration properties similar to cements. Pozzolanes offer advantages and disadvantages in comparison to cements. Methods for characterization of hydraulicity like calorimetry, selective dissolution, phase composition, free lime and portlandite content will be mentioned and some preliminary results presented.

1 INTRODUCTION

Different natural and artificial pozzolanic materials are used increasingly as an additive to cements because of reusing waste materials but also because of their increased resistance against aggressive agents in comparison with OPC's.

Due to their origin, pozzolanic materials can contain amorphous glassy phases but also crystalline components. Often the glassy parts form spherical particles or are sometimes irregularly formed. Pumice with volcanic origin can be described by an open microstructure coming from degassing effects. The chemical compositions can vary strongly depending on the origin of the materials (Buchwald et al. 2001, Kruspan 2000, Heide 2001, Malhotra & Mehta, Massazza, Schwiete & Ludwig 1961, Schwiete & Ludwig 1961, Schwiete et al. 1961).

Natural pozzolanes include tuffs, altered volcanic rocks, trass, vitreous rocks and Santorin earth but also pumice products. Natural altered clays and diatomaceous earth are among the products from sedimentary origin. Artificial products include fly ashes, rice husk ash, silica fumes and thermally activated and sintered clay products.

Pozzolanic activity can be described by the reactions occurring in the hydrating system and can

be represented by a decreasing amount of free lime in the system. Also the amount of soluble silica and alumina is increasing with increasing reaction times. Thus the amount of reactable Lime and the time needed for the reaction are important factors. (Huppertz et al., Massazza, Pöllmann et al. 1991). Several methods for determination of the pozzolanic activity can be used. Besides the determination of chemical and mineralogical compositions, the microstructure and specific surface are important properties (Heide 2001, Huppertz et al., Massazza). The overall reaction behaviour of these mixtures can be measured by heat flow calorimetry. The compositions of several of pozzolanic materials are given in Figure 1. No measurements of strength development were included up to the present stage.

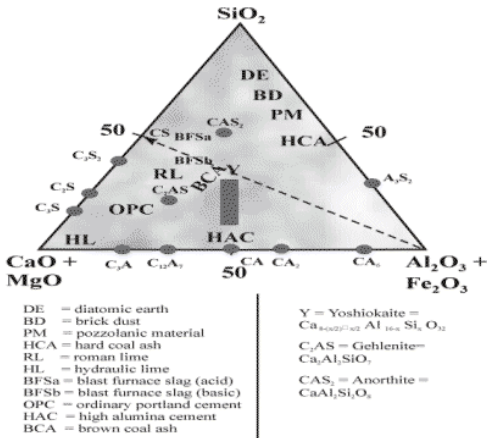


Figure 1. Compositions of cementitious and pozzolanic materials in the ternary diagram $\text{CaO}+\text{MgO} - \text{Al}_2\text{O}_3+\text{Fe}_2\text{O}_3 - \text{SiO}_2$.

2 PREPARATION & EXPERIMENTAL

The methods for the characterization of pozzolanic materials used in this study are mainly based on the determination of the heat of reaction, because other factors like chemistry and mineralogy were already known and some examples are shown in Figures 2-6. The development of future testing methods of hydration will include calorimetry, determination of free lime contents by titration techniques, in-situ X-ray methods, and thermal methods for determination of portlandite contents. Also some measurements of electric conductivity will be included. The preliminary results using calorimetry are summarized in this preliminary report. The heat of reaction was determined from pozzolanic materials added to different Portland Cements and a comparison was made on the varying type of course of hydration. The increased rate of hydration on applying elevated hydration temperatures was included partly and will be reported separately. A new calorimeter was constructed for that reason and will be described elsewhere. In Figure 7 the calorimeter and surrounding is shown.

The overall judgement of pozzolanicity will be performed by DIN EN 196 part 5 using a comparison of $\text{Ca}(\text{OH})_2$ -content against a suspension of a saturated $\text{Ca}(\text{OH})_2$ - solution or by the

1. Application of calorimetry
2. Determination of alcalinity
3. Determination of reactive parts
4. Determination of reaction products
5. Thermoanalytical measurement

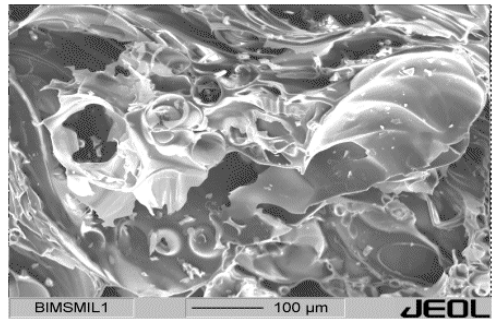


Figure 2. Santorin earth material.

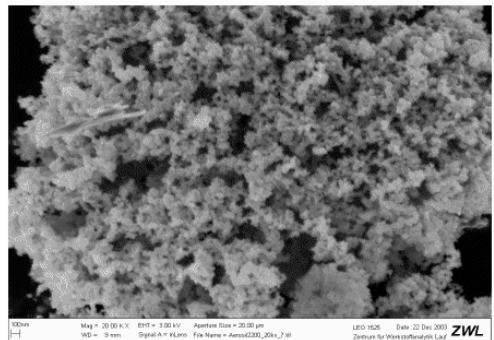


Figure 3. Brick dust from low burnt Brazilian bricks.

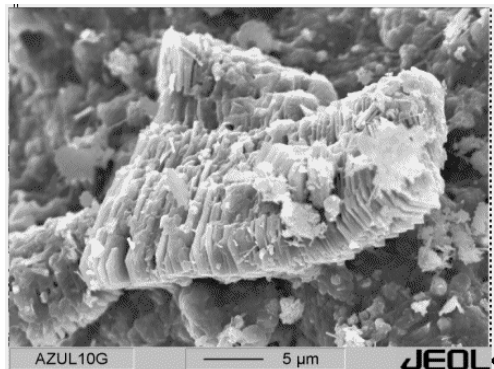


Figure 4. Metakaolinite aggregate showing delamination of layers.

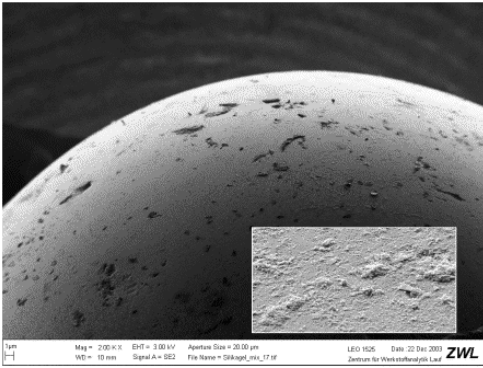


Figure 5. Surface of Silica gel grain.

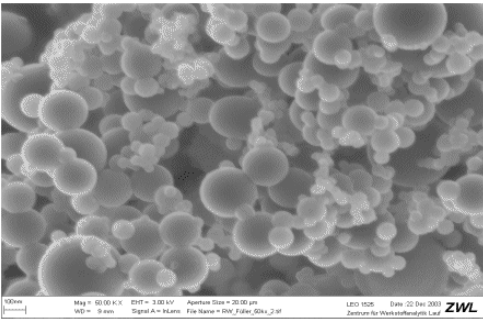


Figure 6. SEM –micrograph of microsilia grains.



Figure 7. Calorimeter with data acquisition, temperature control and quadruplet arrangement.

To be able to make a comparison the following examples show the reaction behaviour of typical OPC's with different additions of brick dust. The reaction of brick dust which is composed mainly by glass and metakaolinite is initiated by the portlandite which is set free during the hydration reaction of Alite. For the application and use of calorimetry in determination of pozzolanity a new calorimeter was constructed which includes a temperature range from 5 to 80°C (Figures 8-11). (Pöllmann, Pöllmann et al. 1991, Pöllmann & Kuzel 1992).

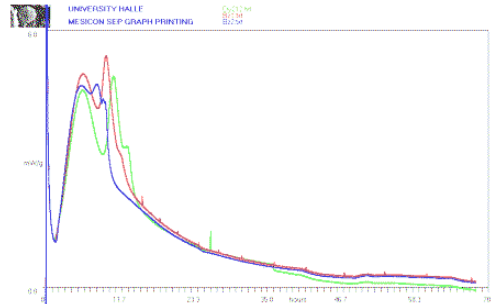


Figure 8. Calorimetric measurements of OPC-1 with brick dust addition(0%,10%,20%).

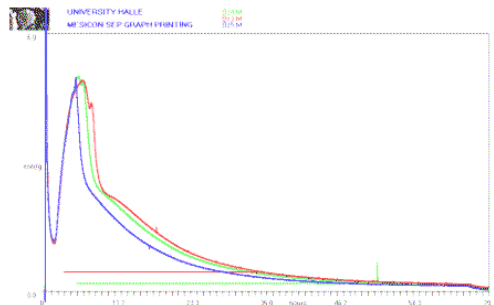


Figure 9. Calorimetric measurements of OPC-1 with brick dust addition(30%,40%,50%).

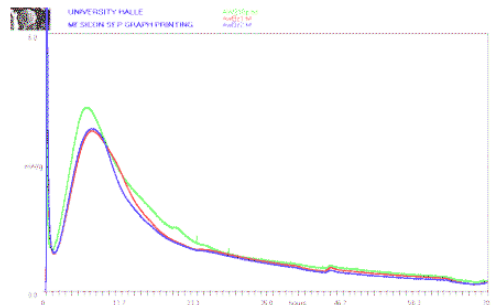


Figure 10. Calorimetric measurements of OPC-2 with brick dust addition(0%,10%20%).

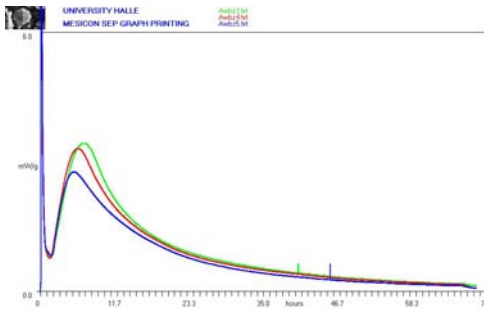


Figure 11. Calorimetric measurements of OPC-2 with brick dust addition(30%40%,50%).

As it is visible in Figures 8-11 the reaction behaviour is also influenced by the type of OPC added. The amount of brick dust and the shift in the maxima of heat hydration is also clearly visible. The comparison to other techniques will be performed in the next future.

3 CONCLUSIONS

It could be proved from literature and by own results that the reaction behaviour of pozzolanic materials depends from :

1. Type of reactive phases
2. amorphous content of mixtures
3. crystalline content of mixtures
4. Amount of reactive phases
5. Specific surface of reactive phases
6. Content of SiO₂ of reactive phases
7. The lime/Pozzolan ratio of the mixes
8. Duration of reaction
9. Temperature of reaction
10. Water/solid ratio of mixes

The main advantages of use of pozzolanes can be summarized in the usage of a cheap and easily available material which can be used instead of materials producing CO₂ in the course or production. The new necessary control measurements and techniques will be developed in the next future.

4 OUTLOOK

These preliminary results will be opened up for investigation of testing methods for absolute determination of relevant parameters, starting with pure phases or pure mixtures to be able to control relevant parameters.

5 REFERENCES

- Buchwald, A., Kaps, Ch., Hohmann, M. 2001. Alkali-activated Metakaolin Cement – 7th CANMET/ACI Conference on Fly Ash, Silica Fume, Slag and Natural Pozzolans in Concrete, Chennai (Madras).
- Franke, B. 1941. Bestimmung von Calciumoxyd und Calciumhydroxyd neben wasserfreiem und wasserhaltigem Calciumsilikat – Z.anorg.allg.Chemie 247, 180-184.
- Kruspan, P.R. 2000. Natürliche und technische Petrogenese von Pozzolanen – Ein Beitrag zur Herstellung mineralischer Sekundärrohstoffe – Dissertation ETH Zürich.
- Heide, M. 2001. Brennprodukte von Tonen als Pozzolane für hydraulisch erhärtende Mörtel : früher und heute – Dissertation Univ. Siegen, (-)
- Huppertz, F., Rankers, R., Wiens, U.: Methoden zur Bestimmung der Reaktivität von Zementen und Pozzolanen – GIT Labor-Fachzeitschrift 6/99, 655-659
- Malhotra, V.M., Mehta, P.K.: Pozzolan and cementitious materials, in Advances in Concrete Technology, I , Gordon and Breach Publishers
- Massazza, F.: Pozzolana and pozzolanic cements, in Lea's chemistry of cement and concrete (Hewlett, P.C., Ed.) Arnold, London, 471-631.
- Pöllmann, H.: The development of a new low temperature and high temperature calorimeter – in prep.
- Pöllmann, H., Kuzel, H.-J. & Meyer, H.. 1991. The usage of heat flow calorimetry in cement chemistry – Construction and application of a low cost high sensitive calorimeter – Proc. XIIIth Int.Con.on Cement Micr., Tampa, 254-272.
- Pöllmann, H. & Kuzel, H.-J. 1992. Konstruktion und Anwendung eines empfindlichen Wärmeflusskalorimeters – Ber.Dt.Min.Ges. Bh.z.Eur.J.Min., Vol.4, 220.
- Schläpfer, P. & Bukowski, R.: Untersuchungen über die Bestimmung des freien Kalkes und des Kalziumhydroxydes in Zementklinkern, Zementen, Schlacken und abgebundenen hydraulischen Mörteln – Eidgenöss. Materialprüfanstalt – Bericht No.63
- Schwiete, H.E. & Ludwig, U. 1961. Das Verhalten von rheinischem und bayerischem Trass in hydraulischen Bindemitteln, Forschungsberichte des Landes Nordrhein-Westfalen, Nr. 978, Westdeutscher Verlag, Köln.
- Schwiete, H.E. & Ludwig, U. 1961. Der Tuff, seine Entstehung und Konstitution und seine Verwendung im Baugewerbe im Spiegel der Literatur, Forschungsberichte des Landes Nordrhein-Westfalen, Nr. 948, Westdeutscher Verlag, Köln.
- Schwiete, H.E., Ludwig, U., Wigger, K.H. 1961. Die Konstitution einiger rheinischer und bayerischer Trasse, Forschungsberichte des Landes Nordrhein-Westfalen, Nr. 956, Westdeutscher Verlag, Köln.
- Schwiete, H.E. & Ludwig, U. 1961. Die Bindung des freien Kalkes und die bei den Trass-Kalk-Reaktionen entstehenden Neubildungen, Forschungsberichte des Landes Nordrhein-Westfalen, Nr. 979, Westdeutscher Verlag, Köln.

Investigation of Phase Composition and Microstructure of Fused Corundum-Mullite Refractories

S.Seifert, S.Saaro, J.Götze & R.B.Heimann
Department of Mineralogy, TU Bergakademie Freiberg, Germany

M.Magnus
Department of Geology, TU Bergakademie Freiberg, Germany

ABSTRACT: Fused corundum-mullite refractories of type SGM were investigated in an attempt to optimize their microstructure. Samples were taken from different SGM bricks produced under specific conditions and from different parts of the bricks to reveal internal variations presumably depending on the production parameters (e.g. cooling conditions). The material was analysed by a combination of various analytical methods including XRD (Rietveld refinement), polarizing microscopy (transmitted and reflected light), cathodoluminescence (CL) microscopy as well as chemical analysis. For the first time a combination of CL microscopy and image analysis was used to quantify the amounts of different crystalline constituents (mullite, corundum, baddeleyite) and glass, and to visualize the microstructure of the refractories with high contrast. All investigated SGM bricks contain different amounts of mullite and show partly different microstructures probably depending on melting temperature, speed of cooling and/or tempering conditions. Furthermore, heterogeneities within the SGM bricks were detected. Using the chemical composition of the glassy phase of the refractories, an estimation of the contents of the crystalline constituents was possible.

1 INTRODUCTION

Refractory materials are commonly used due to their high-temperature properties in several fields of industrial processes. The lifetime and efficiency of any technical furnace plant depend largely on the suitable choice, the quality and the correct installation of the refractory furnace material. To enhance the service time of refractory materials their microstructure should be well understood.

Technological parameters during production processes and varying properties of the raw materials can considerably influence the properties of the manufactured refractory material (Schulle 1990).

In the present study, fused corundum-mullite refractories of type SGM were investigated in an attempt to optimize their microstructure. The study focuses on the crystallization of mullite depending on the Na₂O content of the melt. Furthermore, all phases occurring in the corundum-mullite refractories should be characterized and quantified by a combination of selected analytical methods.

2 MATERIALS AND METHODS

2.1 Sample material

Different SGM bricks (600x300x250 mm) produced under specific conditions were selected for the investigations. The material includes three conventional squared stone bricks and one channel-stone, which represents fast cooled material.

Samples were taken from different parts of the bricks to reveal internal variations possibly depending on the production parameters (e.g. cooling conditions). Three sample pieces of each brick were drilled from the marginal part (0-15 mm), the working zone (45-60 mm) and the lunker zone (75-90 mm), respectively.

The sample material was powdered for chemical analysis and X-ray diffraction. Furthermore, polished thin sections were prepared from each sample piece for microscopic investigations and microprobe analysis.

2.2 Analytical methods

The chemical composition of the samples was analyzed using atomic absorption spectroscopy, photometric and gravimetric methods. The phase composition was quantified by X-ray diffraction

(Rietveld refinement with AUTOQUAN software) using a XRD-3000 TT (Rich. Seifert & Co).

Microscopic investigations included thin section analysis in transmitted and reflected polarized light using a JenaLab microscope (Zeiss). The microscopic images were documented using a Fujix HC-300 digital camera. Detailed investigations concerning grain size, morphology and intergrowth of the components were obtained by scanning electron microscopy using a JEOL JSM-6400 SEM.

The chemical composition of the glassy phase was analyzed by EDX analyses (10x10 μm analytical spots, 20 kV acceleration voltage, 1.3 pA beam current, 60s accumulation time).

CL studies were performed on carbon-coated, polished thin sections using a >hot cathode= CL microscope HC1-LM (Neuser et al. 1995). The system was operated at 14 kV acceleration voltage and with a current density of about 10 $\mu\text{A}/\text{mm}^2$.

Luminescence images were captured "on-line" during CL operations by an adapted digital video-camera (KAPPA 961-1138 CF 20 DXC with cooling stage) coupled with computer-aided image processing equipment. Quantification of the phase composition was performed by an image analysis configuration based on the image-processing software KS-300 (ZeissVision).

3 RESULTS AND DISCUSSION

The variation of the chemical composition of the SGM bricks is summarized in Table 1. Among the investigated chemical components, the contents of Na_2O , Al_2O_3 , SiO_2 and ZrO_2 are of special significance. The results demonstrate that the samples have a relative homogeneous chemical composition and that there are only slight differences among the different samples.

Table 1: Variation ranges of the main chemical components of the investigated SGM bricks (in mass-%)

Sample	Na_2O	Al_2O_3	SiO_2	ZrO_2
I	0.88-0.90	77.1-77.3	17.2-17.3	4.08-4.13
II	1.06	74.2	19.0	5.21
III	0.96-0.98	74.9-75.0	18.6	4.89-4.92
IV	0.76-0.78	75.1-75.4	17.2-17.5	6.0-6.1

In contrast, the phase composition shows significant variations both between the different samples and also within the bricks themselves (Table 2). Especially the contents of corundum and mullite are heterogeneously distributed within the bricks.

Table 2: Variation ranges of the phase composition in the investigated SGM bricks (in mass-%)

Sample	corundum	mullite	baddeleyite	glass
I	38.6-44.5	39.0-45.8	4.3-4.7	10.7-15.6
II	51.7	30.5	4.4	13.4
III	37.4-44.2	39.2-42.4	4.6-5.0	11.9-15.3
IV	11.1-14.8	30.1-43.9	5.4-5.7	11.1-11.3

The variations of the mineralogical composition of the bricks can also be detected in the phase composition and texture of the samples observed by transmitted and reflected light polarizing microscopy. In general, the samples show a distinct zoning with characteristic features in the marginal zone, the working zone and the lunger zone.

The marginal zone is characterized by a fine crystalline matrix of radial fibrous crystals of corundum and/or mullite (Fig. 1). Radiating crystals of mullite oriented along direction of cooling are intergrown with corundum crystals. The interspaces are filled by fine crystals of baddeleyite and randomly distributed glass.

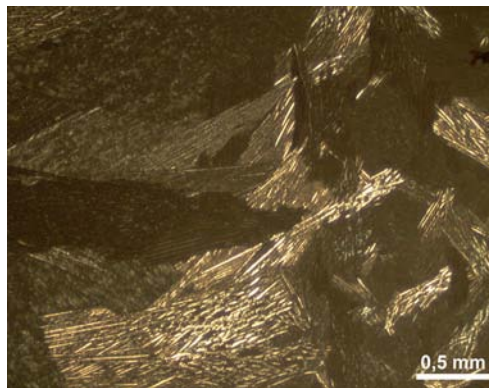


Figure 1: Fine-crystalline corundum within a matrix of glass in the marginal zone of a SGM brick (crossed polars).

The working zone shows an irregular texture of different crystals. Corundum occurs as skeletal or lath-shaped crystals, whereas mullite crystals of different shape can be detected between the corundum. Baddeleyite develops skeletal crystals, mostly intergrown with the glassy phase (Fig. 2).

A typical peritectic texture with oriented crystals of different size is the common feature of the lunger zone. Lath-shaped crystals of corundum are fringed by mullite and have areas of glass in the interspace.

Baddeleyite is mostly intergrown with this glassy phase (Fig. 3).

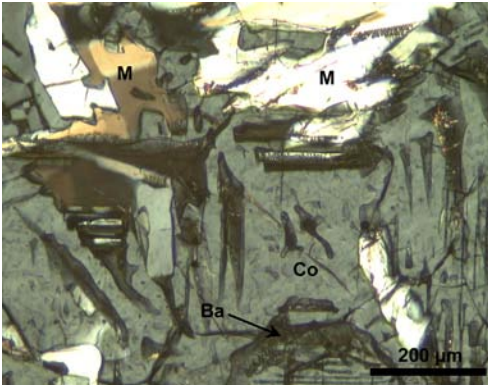


Figure 2: Skeletal crystals of corundum (Co) with irregular crystals of mullite (M) and baddeleyite (Ba) in the interspace of the working zone (crossed polars).

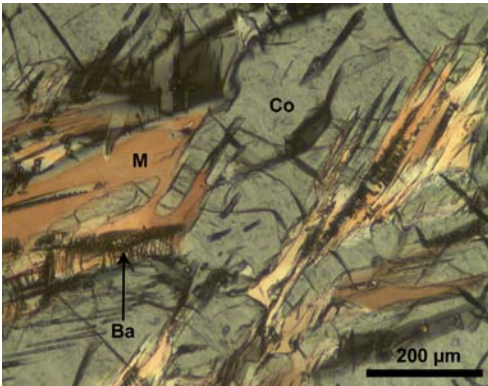


Figure 3 Crystals of corundum (Co) fringed by mullite (M) and partially baddeleyite (Ba) in the lunker zone (crossed polars).

The glassy phase was further investigated by microchemical analysis to get information about its chemical composition. The results (Table 3) illustrate that the average glass composition is comparable in all samples with high contents of SiO_2 and Al_2O_3 , and Na_2O contents of ca. 6 mass-%.

The content of ZrO_2 is below 2 mass-% in all samples.

Table 3: Average chemical composition (in mass-%) of the glassy phase within the investigated SGM bricks

Sample	Na_2O	Al_2O_3	SiO_2	ZrO_2
I	6.38±0.22	21.7±0.9	65.3±0.9	1.23±0.29
II	5.19±0.27	19.8±0.8	68.7±0.8	1.83±0.44
III	6.35±0.34	22.3±1.3	65.1±1.6	1.55±0.44
IV	5.41±0.51	22.4±2.0	63.2±1.8	0.87±0.32

Furthermore, no dependence of the amount of glassy phase on the content of Na_2O in the samples could be detected. The correlation of the amounts of crystalline phases vs. the concentration of chemical compounds within the glassy phase shows an almost linear trend (Fig. 4). Using these results, it is possible to estimate the mineral composition based on the chemical composition of the interstitial glass within the bricks (Seifert 2003).

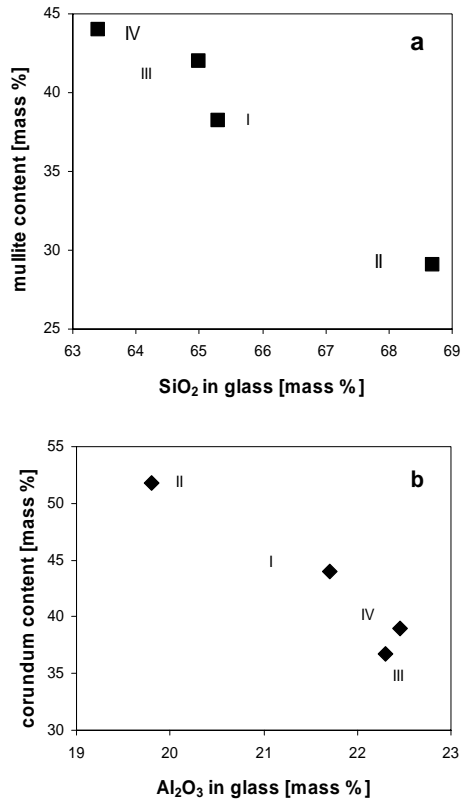


Figure 4: Correlation diagrams showing the mullite content in the SGM brick vs. the SiO_2 content of the glassy phase (a) and corundum content in the brick vs. Al_2O_3 content of the glass (b), respectively.

Cathodoluminescence (CL) studies of the samples provided further information concerning the occurrence and distribution of the different phases within the SGM bricks. In general, the different phases exhibit different luminescence colours during electron irradiation, which enables to detect and quantify them.

Corundum shows a typical red luminescence caused by the activation of Cr^{3+} (Galoyssi & Calas

1993), which is incorporated as traces in the Al position of the crystal lattice (Fig. 5). Baddeleyite can easily be recognized by its bright greenish-blue CL. In contrast, mullite shows a dull blue-violet CL, may be related to electron defects within the SiO₄ tetrahedra (Fig. 6). The glassy phase shows almost no luminescence.

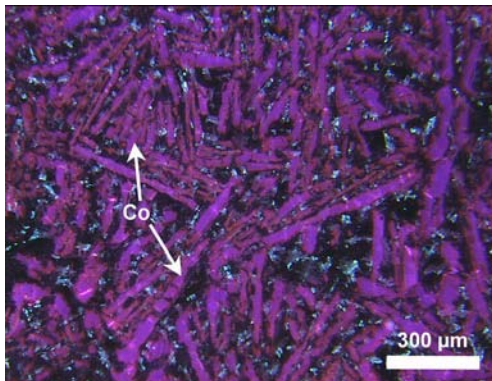


Figure 5: CL micrograph of sample II with lath-shaped crystals of corundum showing a typical reddish luminescence.

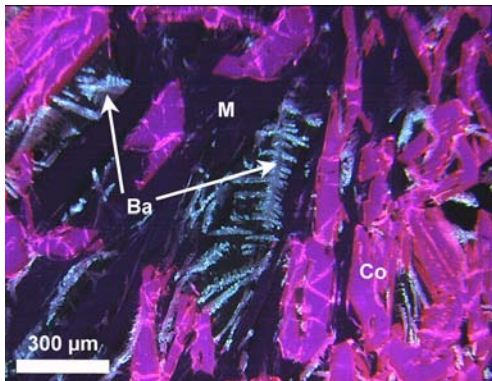


Figure 6: CL micrograph of sample III showing the different luminescence behaviour of corundum (Co: red CL), baddeleyite (Ba: bright greenish-blue CL) and mullite (M: dull blue-violet CL).

We attempted to quantify the phase composition of the SGM bricks by combined CL microscopy and image analysis, since the mineral phases were clearly distinguishable due to their luminescence.

Threshold parameters for phase differentiation based on their luminescence colours were evaluated and an image processing algorithm developed (Götze & Magnus 1997). The first results confirmed that a successful quantification of the phase

composition is possible by combined CL and image analysis (Saaro 2004).

4 CONCLUSIONS

In the present study, the phase composition and microstructure of fused corundum-mullite refractories could be successfully investigated with a combination of various analytical methods. XRD (Rietveld refinement), polarizing microscopy (transmitted and reflected light), CL microscopy as well as chemical analysis were applied to determine and quantify mineral phases in SGM bricks. For the first time a quantification of the different phases was realized using CL microscopy and image analysis.

The advantage of this method is, that it is possible to get simultaneously information about mineral composition and texture of the investigated samples.

The study revealed that the different cooling conditions within single SGM bricks lead to variations in mineral composition and texture. Based on these results it should be possible to optimize the quality of the refractories (textural homogeneity, high content of mullite).

5 ACKNOWLEDGEMENT

We thank R. Buchholz, W. Otto and S. Sachse for providing samples and fruitful discussions during the present study.

6 REFERENCES

- Galoisy, L. & Calas, G. 1993. Inhomogeneous distribution of Cr impurities in α -Al₂O₃ during refractory aging. *J. Mater. Res.* 8: 1153-1157.
- Götze, J. & Magnus, M. 1997. Quantitative determination of mineral abundance in geological samples using combined cathodoluminescence microscopy and image analysis. *Europ. J. Mineral.* 9: 1207-1215.
- Neuser, R.D., Bruhn, F., Götze, J., Habermann, D., Richter, D.K. 1995. Cathodoluminescence: Method and application. *Zentralbl. Geol. Paläont. Teil I, H. 1/2:* 287-306.
- Saaro, S. 2004. Kathodolumineszenz von Korund/Mullit-Steinen. Unpubl. Fourth years thesis. TU Bergakademie Freiberg, Germany.
- Schulle, W. 1990. Feuerfeste Werkstoffe: Feuerfestkeramik – Eigenschaften, prüftechnische Beurteilung, Werkstofftypen. Dt. Verl. Grundstoffind., Leipzig, 494 p.
- Seifert, S. 2003. Gefügeoptimierung von schmelzgegossenen Feuerfest - Korund/Mullit – Steinen (Typ SGM). Unpubl. fourth years thesis. TU Bergakademie Freiberg, Germany.

Characterization of Clays Used in the Ceramic Manufacturing Industry by Reflectance Spectroscopy: An Experiment in the São Simão Ball-Clay Deposit, Brazil

J.A.Senna & C.R. de Souza Filho

Department of Geology and Natural Resources, Geosciences Institute, University of Campinas, São Paulo, Brazil

ABSTRACT: The characterization of clays from the physical, chemical, and ceramic standpoint in pre- and -within mining stages is a necessary step. However, succinct mining planning, lack of industry-oriented standards and the usual bond to empirical discrimination of clays as regards their use, put chemically and technologically different materials as similar standards, with serious consequences to the mining and manufacturing process. Taking the alluvium-derived, ball-clay deposit of São Simão (SS) as a study case, this work aims to evaluate the potential of reflectance spectroscopy (RS) as a method to define types and purity of clays and to seek for possible relations between spectral characteristics of clays and their use in the ceramic industry. The SS deposit hosts three types of clays that were spectrally set apart based on RS. The technique indicated that the white clays comprise kaolinite with varying but high crystallinity, expansive clays, micas and lepidocrosite (first finding in Brazilian alluviums). The gray clays, also kaolinite-rich, display an intrinsic relation between organic matter, expansive clays and goethite. The brown clays contain expansive clays and siderite (first finding in this alluvium). Each of the clay classes typified in the SS deposit has a specific application in the fine ceramic industry, indicating the striking potential of RS to characterize industry-aimed materials.

1 INTRODUCTION

The São Simão (SS) ball-clay deposit comprises a very important type of clay used in the Brazilian ceramic industry, particularly in manufacturing porcelains and pottery. These clays are fine-grained (< 20µm), rich in hexagonal kaolinite but also contain expansive clay-minerals, mica adsorbed to kaolinite crystal faces (Pressinotti 1991) and organic matter. The SS clays are characterized by their high plasticity, resistance under dry conditions, low suitability for vitrification and light colour on burning (Souza Santos 1975, Wilson 1983). The deposit is located in the northeastern region of the São Paulo State, about 8km to the west of the São Simão town.

Despite the unique characteristics of the SS clays, their characterization from the physical, chemical, and ceramic standpoint in pre- and -within mining stages is a difficult task. Considering the intrinsic complexities involved in describing clays by conventional methods (e.g., X-ray diffraction), this work aims (i) to evaluate the potential of reflectance spectroscopy as a relevant, expedite method to characterize clays, including definition of their type, composition and purity, and (ii) to study the possibility to relate clays' spectral variables and parameters to their

specific uses in the ceramic industry, using the SS deposit as a case study.

2 REFLECTANCE SPECTROSCOPY

Spectroscopy is a tool that has been used for decades to identify, understand, and quantify solid, liquid or gaseous materials, especially in the laboratory. In several disciplines, spectroscopic measurements are used to detect absorption features due to specific chemical bonds, and detailed analyses are used to determine the abundance and physical state of the detected absorbing species (Clark 1999). Reflectance spectroscopy (RS), in particular, is a key tool used in remote sensing sciences and it is an extremely sensitive method in detecting clay minerals in the shortwave infrared range (1,3-2,5µm) of the electromagnetic spectrum. This is a fast, non-destructive and operational method that can be applied in mineral determination and mapping (Hunt 1979, 1980). RS of natural surfaces are sensitive to specific chemical bonds in materials, having the advantage of being sensitive to both crystalline and amorphous materials, unlike some other methods, like X-ray diffraction. It aims to

measure, along different and continuous wavelengths, the amount of radiation reflected by the surface of materials, which is displayed as reflectance spectra (e.g., Fig.2). Absorption features in the spectra of minerals are due to the presence of specific molecular groups and, depending on wavelength position, shape and intensity, can be often used to diagnose minerals present in a sample, providing clues on their relative proportion and abundance (Clark 1999).

3 GEOLOGICAL SETTING OF THE SÃO SIMÃO DEPOSIT

The geology around the SS deposit (Fig. 1) comprises lithostratigraphic units of the São Bento Group (sedimentary rocks of the Pirambóia and Botucatu Formations and basalts of the Serra Geral Formation) and Cenozoic sediments. The Tamandua channel (Fig. 1) occupies a N/S-trending open valley, formed in Mesozoic sediments. This valley hosts a fluvial system filled by alluvial sediments.

Sediment deposition started some 30.000 years ago (Turcq et al. 1997). Basaltic dykes and sills

restrain the channel morphology, whereas the floodplain shows two distinct terraces: alluvium I - the actual level of the river, corresponding to a lower terrace; alluvium II - an earlier, higher terrace (Tanno et al. 1994, Pressinotti 1991). The alluvium II is made up of conglomerates, at the base, followed by a thick bed of sandstones at the top, which are intercalated with turfaceous and clay-rich layers. In the latter, clays are concentrated in lenticular bodies up to 2m thick (Tanno et al. 1994), which can be mapped inside a terrace with an average thickness of 8m (Ruiz 1990). These layers are vertically discontinuous, but can be laterally correlated (Pressinotti 1991). The SS ball-clay deposit corresponds to these lenses and comprises mainly fine kaolinites displaying a bi-modal granulometric distribution (Tanno et al. 1994). The clays formed during the Pleistocene - information based on age determinations in organic material associated to them (Turcq et al. 1997, Pressinotti 1991). Paleohydrological studies indicate clay deposition in two stages (wet and dry periods), framed by erosive periods.

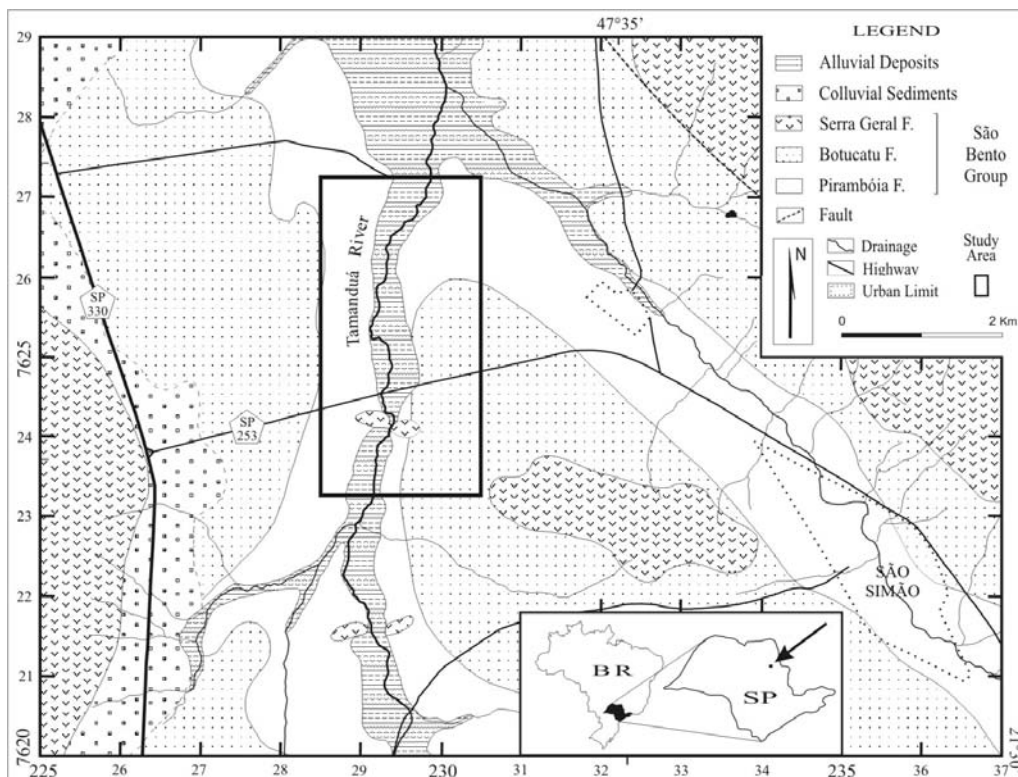


Figure 1. Locality map and geological setting of the study area.

4 MATERIALS AND METHODS

Field work was aimed at collecting a large number of samples in the study area, in which distinct color, texture and any other aspect were verified. In this process, three classes comprising white, gray and brown clays were identified. The spectral characterization of these clays was carried out with the aid of X-ray diffraction (XRD) analysis. The notion here was to establish the necessary parameters for qualitative and quantitative discrimination between the samples. Using XRD results, it was possible to approximate the modal composition of samples considered as representatives of each class. A FieldSpec Full Resolution (0.35 μm - 2.5 μm) spectrometer was employed for RS measurements, which were performed in two stages. Firstly, raw samples collected in the field were submitted to several types of readings, depending on the diversity of materials involved; this was followed by readings of finely crushed samples (i.e., prepared for XRD). Crushed samples stemmed from an integral part of a raw sample or from a specific portion of it, where a particular material was identified. In order to obtain a standard spectra for each class of clay, the arithmetic mean of their respective spectral readings was computed.

5 RESULTS

XRD analyses showed that all clay classes are rich in kaolinite (>70%), but the brown clay is the wealthier one. Quartz is present in every class and varies between 5-20%. Micas reach up to 10% in white clays, 5% in brown clays and are almost absent in gray clays. Gray clays host plenty of expansive clays (5-10%), which are negligible in the white specimens. Lepidocrosite (10%) occurs in white clay layers and siderite (5-10%) within sandy portions of the brown clays.

RS analysis revealed a number of different spectral characteristics between these three clays. The inspection of absolute reflectance spectra (Fig. 2) for each endmember showed that white clays have stronger absorption features around 2.2 μm , followed by brown and gray clays. The shape (sharp) and gradient of the 1.4 e 2.2 μm absorption features are also indicative that the white clays are more crystalline specimens, particular due to the intensity and inflection of the doublet centered around these wavebands. Moreover, the combined appearance of the 1.4 μm and 1.8 μm features, as observed for the white clays, are reliable indicators of higher crystallinity (Pontual et al. 1997). Although the brown clays contain more organic matter than the other samples, which usually imply

in attenuation of spectral features, the ubiquitous presence of kaolinite enhanced the doublet at 2.2 μm (Fig. 2).

The use of the full spectrum, including VIS and VIR wavelengths (0.35-1.30 μm) (Fig. 3), allows the distinction of these three classes in terms of not only their relative crystallinity but also regarding their composition, including the presence of critical impurities.

A set of continuum-removed and stacked spectra of two representative samples of each class is displayed in Fig.3. Sample WC2 (white clay) shows a feature at 0.95 μm that is due the presence of Fe³⁺ host by lepidocrosite (Townsend 1987, Clark et al. 1993). Samples BC1 (brown clay) shows absorptions at 1.05-1.25 μm , typical of siderite (Whitney 1983, Gaffey 1987). Samples WC2, BC1 and BC2 show a feature at 0.5 μm that is related to Fe-bearing minerals. Samples GC1 e GC2 (gray clays), show an absorption feature at 0.6 μm that is linked to the presence of goethite, which in turn is associated to larger concentrations of organic matter, specially found in gray clays.

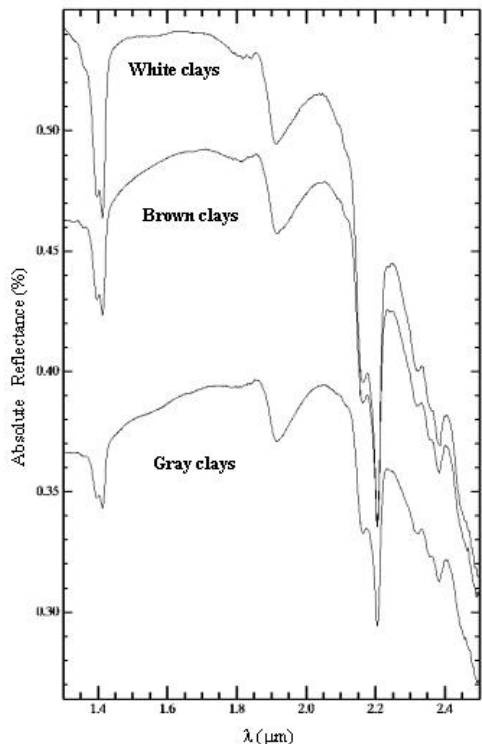


Figure 2. Absolute reflectance spectra of SS clays (white, brown and gray), in the SWIR region.

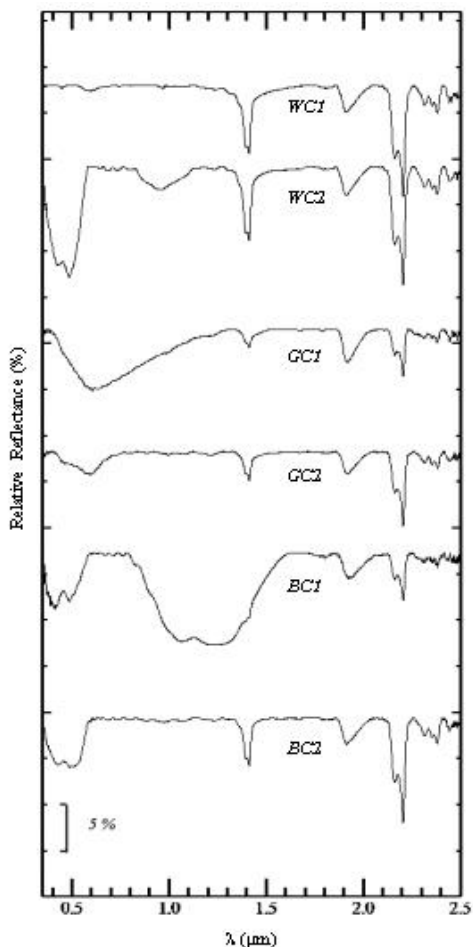


Figure 3. Relative (continuum removed and stacked) reflectance spectra of SS clays – white (WC1, WC2), gray (GC1, GC2) and brown (BC1, BC2), throughout the VNIR and SWIR region.

6 DISCUSSIONS AND CONCLUSIONS

RS successfully characterized the three classes of clays observed in the SS ball-clay deposit in terms of their detailed composition, purity and crystallinity. The occurrence of lepidocrosite (first finding in Brazilian alluviums) and siderite (first time described in the Tamanduá River) in samples of white and brown clays, respectively, is a signature of these two clay classes. Of great interest is the fact that the presence (or absence), type and amount of impurities determined by RS in such clays showed a remarkable correlation with their application in the ceramic manufacturing industry for which they are presently delivered. So, in view of the exploratory nature of this research, the results using RS to

characterize particular industry-aimed clays proved very promising.

7 REFERENCES

- Clark, R. N. 1999. Spectroscopy of Rocks and Minerals, and Principles of Spectroscopy, chapter 1. In: A.N. Rencz (eds.) Remote Sensing for the Earth Sciences: Manual of Remote Sensing, 3ed., vol. 3, John Wiley & Sons, Inc., New York, pp.: 03-58
- Clark, R.N., Swayze, G.A., King, T.V.V., Calvin, W.M. 1993. Digital Spectral Library, version 1, 0.2 to 3.0 μm , U.S. Geological Survey, Open File Report 93-592, 1326p.
- Gaffey, S.J. 1987. Spectral Reflectance of Carbonate in the Visible and Near Infrared (0.35-2.55 μm): Anhydrous Carbonate Minerals. *Journal of Geophysical Research*, 92(B2): 1429-1440
- Hunt, G. R. 1980. Electromagnetic Radiation, The communication link in Remote Sensing, Chapter 2. In: Siegal B.S. and Gillespie A.R. (eds). Remote Sensing in Geology, John Wiley & Sons, New York, pp.: 5-45
- Hunt, G.R. 1977. Spectral Signatures of Particulate Minerals in the Visible and Near Infrared. *Geophysics*, 42(3):501-513
- Pontual, S., Merry, N., Gamson, P. 1997. Spectral Interpretation Field Manual, G-Max. Spectral Analysis Guides for Mineral Exploration, vol. 1. AusSpec Int. Pty.Ltd. 169 p.
- Pressinotti, M.M.N. 1991. Caracterização Geológica e Aspectos Genéticos dos Depósitos de Argilas Tipo "Ball Clay" de São Simão, SP. Dissertação de Mestrado, Instituto de Geociências, Universidade de São Paulo, 141p.
- Ruiz, M.S. 1990. Argilas - Perfil 4, capítulo IV. In: IPT - Instituto de Pesquisas Tecnológicas, Mercado Produtor Mineral do Estado de São Paulo - Levantamento e Análise. Pró-Minério - programa de Desenvolvimento de Recursos Minerais. São Paulo, pp.: 61-86.
- Senna, J.A. 2003. Caracterização de Argilas de Utilização na Indústria Cerâmica por Espectroscopia de Reflectância. Dissertação de Mestrado, Instituto de Geociências, Unicamp, Campinas. 221p.
- Souza Santos, P. 1975. Caulins e Argilas para Cerâmica Branca, cap.21. In: Tecnologia de Argilas aplicada às argilas brasileiras vol.2. Ed. Blücher Ltda. SP, p.468-505
- Tanno, L.C., Motta, J.F.M., Cabral, Junior M., Kaseker, E.P., Pressinotti, M.M.N. 1994. Depósitos de Argilas para uso Cerâmico no Estado de São Paulo, cap.9. In: Schobbenhaus C., Queiroz E.T., Coelho C.E.S (eds.), Principais Depósitos Minerais do Brasil-DNPM, Brasília, vol. IV-B - Rochas e Minerais Industriais, pp.: 99-110
- Townsend, T.E., 1987. Discrimination of Iron Alteration Minerals in Visible and Near-Infrared Reflectance Data. *Journal of Geophysical Research*, 92 (B2): 1.441-1.454
- Turcq, B., Pressinotti, M.M.N., Martin, L. 1997. Paleohydrology and paleoclimate of the Past 33,000 years at the Tamanduá River, Central Brazil. *Quaternary Research*, 47(3): 284-294
- Whitney, G., Abrams, M.J., Goetz, A.F.H. 1983. Mineral Discrimination Using a Portable Ratio-Determining Radiometer. *Economic Geology*, 78(4): 688-698
- Wilson, I.R. 1983. Ball Clays inglesas - origens, propriedades e usos em cerâmica. *Cerâmica*, 29(165): 217-2

Experimental Design to Formulation of Ceramic Coating Masses

J.Silveira, J.Pereira Leite, J.Herbert Echude, L.Renato Pontes

Department of Mechanical Technology, Technology Center, Federal University of Paraíba, João Pessoa, Brazil

ABSTRACT: The present work aims at proposing an experimental methodology based on experimental modeling for the formulation of ceramic masses to be used as ceramic coatings. The project of simplex mixtures in pseudo-components allowed to reduce the total number of experiments to the optimal minimum number. Six raw materials were considered as control factors: talc, quartz, limestone, dolomite, phyllite, and clays. The analyzed output responses was the linear retraction, bending resistance and absorption of water which were selected in account of customer needs since they strongly affect the quality of the ceramic products during the production process.

1 INTRODUCTION

This article presents the optimization of ceramic masses for coating based on mathematical expression denominated as loss function, which allow selecting the best mass among a treatment group elaborated based on a planning matrix. This criterion takes into account the characteristic types of the required qualities, respecting the interests of the types “major is better” and “minor is better.”

The experimental design for simplex mixtures is one of the available options for a systematic study of ceramic masses formulation and lead to a good understanding of the interactions that can exist among the components of the mixture.

2 EXPERIMENTAL DESIGN

The planning matrix was elaborated using as reference a ceramic mass pattern produced in a local industry, denominated as MP.

The transformation of pseudo-components was obtained according to the equation bellow mentioned (Montgomery 1991, Cornell 1991, Bittencourt et al 2001). The Table 1 shows the

values so obtained under the “codified levels” column.

$$X'_i = \frac{X_i - L_i}{1 - \sum_1^6 L_i}$$

Equation: X'_i represents the value in pseudo-components i , $\sum L_i$ is the addition of the inferior limits of the components, and X_i is the real percentage of the component i .

Table 1 shows the planning matrix with the 21 elaborated masses and the MP mass, in terms of both real formulations and pseudo-components.

3 DISCUSSION OF RESULTS

Table 2 shows the individual modeling of the responses for the quadratic model.

It can be observed that quartz addition when combined with limestone provokes a reduction in the linear retraction given by the term $-1,92 X_2X_3$ and also a reduction in the bending resistance as shown by the term $-169X_2X_3$. However, in the production line the target is to obtain a minimum linear retraction combined with a maximum bending resistance. These conflicting results, force to find a

conciliatory solution in order to optimize the ceramic masses. This subject will be studied as follows.

Table 1: Planning matrix of the masses elaborated.

	Formulation of the Masses in%						B: Codified Levels					
	X 1	X 2	X 3	X4	X 5	X 6	X1	X2	X3	X 4	X 5	X 6
M1	18	3	3	12	4	60	1	0	0	0	0	0
M2	8	13	3	12	4	60	0	1	0	0	0	0
M3	8	3	13	12	4	60	0	0	1	0	0	0
M4	8	3	3	22	4	60	0	0	0	1	0	0
M5	8	3	3	12	14	60	0	0	0	0	1	0
M6	8	3	3	12	4	70	0	0	0	0	0	1
M7	13	8	3	12	4	60	,5	,5	0	0	0	0
M8	13	3	8	12	4	60	,5	0	,5	0	0	0
M9	13	3	3	17	4	60	,5	0	0	,5	0	0
M1	13	3	3	12	9	60	,5	0	0	0	,5	0
M1	13	3	3	12	4	65	,5	0	0	0	0	,5
M1	8	8	8	12	4	60	0	,5	,5	0	0	0
M1	8	8	3	17	4	60	0	,5	0	,5	0	0
M1	8	8	3	12	9	60	0	,5	0	0	,5	0
M1	8	8	3	12	4	65	0	,5	0	0	0	,5
M1	8	3	8	17	4	60	0	0	,5	,5	0	0
M1	8	3	8	12	9	60	0	0	,5	0	,5	0
M1	8	3	8	12	4	65	0	0	,5	0	0	,5
M1	8	3	3	17	9	60	0	0	0	,5	,5	0
M2	8	3	3	17	4	65	0	0	0	,5	0	,5
M2	8	3	3	12	9	65	0	0	0	0	,5	,5
M P	10	4	3	14	5	64	,2	,1	0	,2	,1	,4

X1: Talc; X2:Quartz; X3:Limestone
X4: Phyllite; X5:Dolomite X6:Clays

Table 2: Regression Model.

Response (Yi)	R2	Quadratic model
Linear Retraction (Y1)	97%	Y1 = 3,26X1+ 2,42X2+ 1,1X3+ 3,23X4 +1,48X5 + 3,07X6-1,79 X1X3 - 1,03 X1X5 - 1,92 X2X3 -1,88 X2X4 - 1,42 X2X4 -2,32 X3X4+ 2,01 X3X5 -1,87 X3X6 - 2,48 X4X5 + 1,16 X4X6.
Bending Resistance. (Y2)	76%	Y2=147X1+136X2+135X3 +167X4+116X5+165X6+ 142X1X4+101X1X5 +116X1X6-169X2X3 +114X3X5+96X4X5 +96X4X6+ 119X5X6.
Absorption of water (Y3)	94,3%	Y3=13,12X1 + 17,35X2 +20,65X3 + 15,85X4 +22,3X5 +15,5X6 - 5,15X1X2 + 0,65X1X3 - 1,7X1X4 -4,0X1X5--- 3,2X1X6 + 6,6X2X3 -3,9X2X4 -13,65X2X5 -7,2X2X6-10,75X4X5- 5,20X4X6- 2,7X5X6.

3.1 Optimization of the ceramic mass

The experimental methodology was accomplished according to the function quality loss. (Caten 1998, Alarcon, 1998). The loss function developed by Taguchi (Moorish et al. 1991) was adapted to deduce an expression that represents the summation of the total losses for each mass.

The responses are those that display a larger approaching to the target values, in accordance with these conditions: the target value is the inferior limit for the responses of the type “as minor as better”, and the target value is the superior limit for the response of the type “as major as better.”

The Equations (1) and (2) represent the calculation evolution of the quality losses for ceramic mixtures.

$$\check{Z}(I) = \sum [1/(LS-LI)^2 X (IR) x [(Y_i-LI)^2]] \quad (1)$$

$$\check{Z}(I) = \sum [1/(LS-LI)^2 X (IR) x [(LS-Y_i)^2]] \quad (2)$$

For equation (1), minor is better:

LI= Inferior Limit = Target: it is the value that would be ideal;

LS= Superior Limit, is the worst response found, (when minor is better).

For equation (2), major is better:

LI= Inferior Limit: is the worst response found (when major is better).

LS= Superior Limit = Target: is the better response found.

IR: it is the relative importance (weigh) of the responses to each other. Those values can undergo alterations in agreement with the required priorities. Y_i is the response found for the mass M_i.

Table 3 shows the results of the quality loss of the masses, using the Equations 1 and 2.

The larger losses in crescent order were: M19<M13<M10... → M19 was the best mass.

The Figure 3 shows the behavior of the masses in relation to the quality losses.

The optimization of the loss model can be found in function of the independent variables Xi, because, Y=F(x) and Z=F(y) → Z= F(x). The expression represents the loss model Z(i) in the raw materials function: it is observed in absolute terms, that the dolomite is the raw material for it contributes more with the quality loss of the masses (10,16 X5), and clays tends to minimize the quality losses (2,82X6). In relative terms, phyllite and dolomite minimize the quality loss (-22,26X4X5):

$$Z(I) = 2,92X1 + 3,66X2 + 7,53X3 + 3,41X4 + 10,16X5 + 2,82X6 + 1,08X1X2 - 3,9X1X3 - 3,54X1X4 - 17,44X1X5 - 2,72X1X6 + 18,02X2X3 - 6,82X2X4 - 15,56X2X5 - 2,48X2X6 - 6,16X3X4 - 8,58X3X5 - 9,54X3X6 - 22,26X4X5 - 0,66X4X6.$$

Table 3: Summary of the Quality Loss of the masses.

Mass	LR	AW	BR	LOSS SUM
M1	2,24	0,00	0,68	2,92
M2	0,82	0,89	1,10	2,81
M3	0,00	2,83	2,29	5,12
M4	2,19	0,37	0,47	3,03
M5	0,08	4,19	3,08	7,35
M6	1,80	0,28	0,45	2,53
M7	1,59	0,03	1,90	3,53
M8	0,25	0,77	0,83	1,85
M9	2,19	0,04	0,01	2,24
M10	0,56	0,64	0,43	1,63
M11	2,09	0,01	0,09	2,19
M12	0,04	2,83	5,05	7,92
M13	0,86	0,31	0,47	1,02
M14	0,18	0,54	1,40	2,12
M15	1,53	0,11	0,88	2,53
M16	0,22	1,67	0,41	2,30
M17	0,20	2,85	0,94	3,99
M18	0,20	1,23	0,20	1,63
M19	0,29	0,00	0,29	0,58
M20	2,77	0,08	0,00	2,85
M21	0,86	1,29	0,01	2,26

LR: Linear Retraction
 BR: Bending Resistance
 AW: Absorption of Water

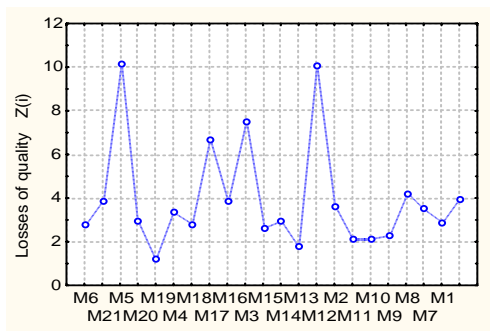


Figure 3: Behavior of the quality losses.

Table 4 shows comparative data between the best mass selected among those elaborated at the planning matrix using the function loss (mass 19) and the mass pattern (MP).

4 CONCLUSION

The equations of quality losses that were developed in this work, allowed the selection the best mass among the several ones of the planning matrix. The use of this technique for analysis of the experiments was shown to be effective to optimize the formulation of ceramic masses. It also brought a

better understanding of the influences of the raw materials in the response behavior of the masses used in the industry. This can lead to the improvement of the quality of the final product, with less refuse and, consequently, with smaller production costs.

Table 4: Comparison of the best masses, in relation to the mass pattern MP.

Mass A: Formulation (%)							LR	BR	A.W
Mass	X1	X2	X3	X4	X5	X6			
MP	10	4	3	14	5	64	2,7	172	14,7
M19	8	3	3	17	9	60	1,8	166	16,4

LR: Linear Retraction;
 BR: Bending Resistance
 A.W. Absorption of Water

5 REFERENCES

Alarcon, O.; L; Dachamir, H 1998. "Formulação de Massas Cerâmicas de Revestimentos através de Delineamento de Misturas" UFSC/CPCEM – Revista Cerâmica
 Bittencourt, L.E.; Júnior, J.C. 2001. "Metodologia Experimental para Desenvolvimento de Formulação de Revestimentos em Processo de Monoporosa, através de Programação Linear". Revista Cerâmica Industrial, Vol.6.
 Caten, C.T.; Pedrassani J.; Ribeiro. 1998 Otimização Experimental de Um Processo de Moagem : Descrição de um Método e Estudo de Caso". Universidade Federal do Rio Grande do Sul. / PPGEP.
 Cornell, J. 1981. THE "Experiments with mix" John Wiley & Sons, Inc.
 Montgomery, A.D. 1991. "Design and Analysis of Experiments." John Wiley and Sons, New York.
 Moorish, E. C.; Taguchi, S. (1999) "Practic application of the Robust Engineering" Control of Quality. São Paulo, no. 81 p. 82-86, feb.

The Course of Hydration of OPC Pastes Related to the Crystal Chemistry of the Hydration Phases Under the Influence of Sulfonic Admixtures

S. Stöber & H. Pöllmann

Institute for Geological Science Mineralogy/Geochemistry MLU Halle, Germany

ABSTRACT: Different admixtures (Benzene sulfonic acids and alkenesulfonic acid sodium salts) change systematically the setting of Ordinary Portland Cement (OPC) pastes. Variable concentrations, systematic changes of the chain lengths of alkenesulfonic acids sodium salts and systematic variations in number and orientation of the CH₃ - substituents on the Benzene ring caused specific acceleration or retardation effects on the cement pastes. Lamellar Calcium Aluminate Benzenesulfonate Hydrates and Lamellar Calcium Aluminate Alkenesulfonate Hydrates were purely synthesized. The metric parameters were refined by Least-Squares Methods.

1 INTRODUCTION

It is estimated, that more than 80% of the concrete production in Northern America contains one special recipes of admixtures. These substances of inorganic or organic origin are added with the water or added after a certain hydration time.

Admixtures are added to concrete in order to optimise the performance of concrete workability and hardening for special applications and to save energy for economic purposes.

The different properties of admixtures like acceleration or retardation of the setting time; decreased water requirements without a change in workability, durability enhancements, and increased rate of strength development are provided by RILEM, ACl, ASTM or CSA standards and specifications. Admixtures do not only modify the properties of concrete, the crystal chemistry of hydration phases, will be modified, too. Especially the Aft - and Afm - phases in OPC and in CAC have the ability to fix inorganic and organic ions in their crystal structures. Ettringite (Aft-phase) is built up of a channel like structure and Lamellar Calcium Aluminate Hydrates are built up of layer sequences perpendicular $c_0, 0, 0, 0$.

Different Benzene- and alkenesulfonic acids and sodium salts were used to demonstrate the effect of acceleration and retardation as a function of admixture concentration and the direct effect of the systematic variation of the molecular structure:

1) Variation of number and orientation of CH₃ - substituents on the Benzene ring of different Benzenesulfonic acids.

2) Variation of the chain length of Alkenesulfonic acids sodium salts $C_nH_{2n-1}SO_3Na$ $n = 1, 3, 5, 7, 8, 9$.

2 INSTRUMENTATION

XRD (X-Ray Diffraction) kinetic measurements of OPC pastes were performed using a D 5000 Diffractometer. The cement pastes were kept for 4 weeks at 35% r. h. under N₂ - atmosphere in a desiccator. 10g cement were prepared on a single crystal Silicon sample holder and measured according to the instrumentation parameters in Table 1.

The precipitates of different Afm-phase synthesis were performed on a SIEMENS 5000 Diffractometer with Cu K α radiation. For the temperature and humidity controlled measurements a TDK camera from PAAR was used. During the

measurements the interior of the camera was purged with N_2 . In order to install different relative humidities, N_2 was pumped slowly through different saturated salt solutions. The following parameters in Table 2 were used for the measurements.

Table 1. D 5000 parameters for OPC scans.

Parameters	Value
2Theta range [°]	3...20
Voltage [kV]	40
X-ray current intensity [mA]	40
Step 2 Theta [°]	0.03
Count time [s]	10
Slits	variable

Table 2. Parameters for XRD measurements of pure Afm phases.

Parameters	Values
2Theta [°]	3...80
Voltage [kV]	40
Current strength [mA]	30
Step 2Theta [°]	0.01
Count time [s]	1
Scatter- and Antiscatter slit	Variable

For the investigations on the effects of sulfonic acids and sodium salt additions, a commercial OPC CEM I 32,5 R with a measured specific surface of $3870 \text{ cm}^2/\text{g}$ was used.

Heat - flow calorimetry was used to investigate the course of hydration of the OPC 0, 0. The instrument is built up of an alumina block with 4 measuring cells. On site is used as a reference in a copper vessel with cover filled with hydrated OPC CEM I. On 3 cells the heat evolution of the exothermic cement reactions were detected. Due to the exothermal heat evolution of the cement hydration, the evolved heat is measured in difference ($\text{Heat}_{\text{Sample}} - \text{Heat}_{\text{Reference}}$). This construction allows the determination of corrected heats per time as voltage (mV) without underground heat effects. The heat is detected by BiTe semiconductors and registered by a digital multimeter from PREMA. The measured mV-values are stored on the HD of the PC and were analysed and interpreted by commercial scientific software.

For the determination of the Afm - phase water concentrations, a TG/DTG 320CU in combination with a Karl-Fischer Instrument was used. Chemical analysis of CaO and Al_2O_3 were performed by AAS and ICP/OES. The organic compounds of the sulfonic acids were directly determined by the total organic carbon method.

3 RESULTS

3.1 Addition of different $\text{C}_6\text{H}_5\text{SO}_3\text{H}$ concentrations to OPC pastes

To 1g OPC, 0.5 ml of Benzenesulfonic acid in the concentration range of 10^{-5} mole was added. The different heat - flow calorimeter plots (Fig. 1) show that the heat - flow of the paste CEM I + 1 mole $\text{C}_6\text{H}_5\text{SO}_3\text{H}$ is extremely low (beneath 0.3 mW/g) during the hydration time 72 hours. After the decrease of evolved heat due the adsorption of water on the surface of cement particles the hydration reactions of the cement phases is strongly retarded.

With the decrease of the $\text{C}_6\text{H}_5\text{SO}_3\text{H}$ concentration in the cement paste, the retarding effect on the cement hydration is systematically lowered. Firstly the minima of the induction period (\bullet) were shifted to lower hydration times. The same tendency is demonstrated for the maxima of the main hydration (+). They were shifted to lower hydration times, too. The heat of hydration, which has been set free between the interval of the minimum of the induction period and approximately 36 h, also called the area of the main cement hydration increase strongly. The determined heat - flow in pastes OPC + $0.05 \dots 0.00001 \text{ m C}_6\text{H}_5\text{SO}_3\text{H}$ is however higher compared to the heat flow of the reference OPC + H_2O .

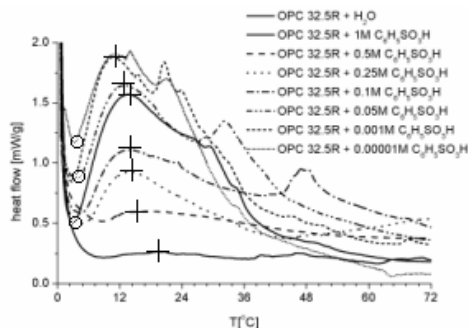


Figure 1. Heat-Flow plots of OPC 32,5 R + different Benzenesulfonic acid concentrations.

3.2 The Influence of the molecular structures of sulfonic acids on the OPC hydration.

3.2.1 Addition of 1 molar Benzenesulfonic acids to an OPC CEM I 32,5 R

As a result of the addition of 1 molar Benzene-, p-Toluene-, Xylene- and Mesitylenesulfonic acid to OPC pastes 32%, 33%, 57% and 75% of the total heat flow between 72h was released. The influence of the admixtures increase the heat-flow from the beginning of the hydration until the minimum of the induction period was reached and reduced the heat

flow until 72 h. The influence of 1 molar Benzene - and p - Toluenesulfonic acids on the course of hydration is higher than the influence of 1 molar Xylene - and Mesitylenesulfonic acids. In general, the minima of the induction period and the maxima of the main hydration were shifted to higher hydration times (Fig.2).

The same acids act at very low concentrations (10-6 mol/l) as accelerators. Xylene- and Mesitylene-sulfonic acids increase the heat-flow and therefore accelerate the course of hydration of OPC pastes stronger than Benzene- and p-Toluenesulfonic acids (Fig. 3).

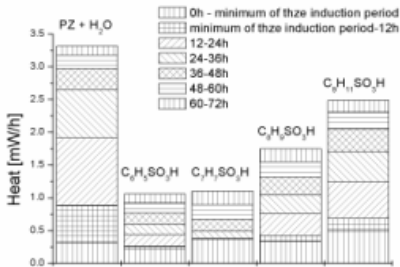


Figure 2. Heat evolution: OPC 32,5R + 1 mol/l Arenesulfonic acids.

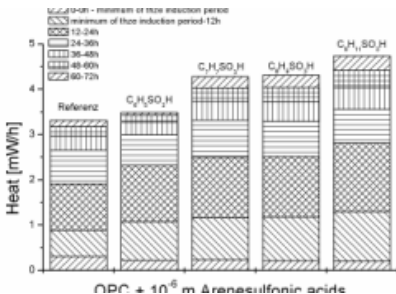


Figure 3. Heat evolution: OPC 32,5R + 10⁻⁶ mol/l Arenesulfonic acids.

3.3 Addition of 0.25 molar Alkenesulfonic Acid Sodium Salts to an OPC CEM I 32,5 R

The addition of the 0.25 mol/l $C_nH_{2n+1}SO_3Na$ with $n = 1,3,5,7,8$ and 9 retard the OPC hydration reactions. The increase of the chain length of the different alkenesulfonic acids shifts the main hydration to higher hydration times, the induction period of the pastes takes longer and the heat flow detected for the investigated cement admixture pastes 72 h is decreased.

The evolved heat in the range of 72 h divided in certain time intervals demonstrates that the influence of the additive is particularly strong at the addition of the sulfonic sodium salts until the minimum of the

induction period and in the range „minimum of the induction period until 36h (Fig. 4).

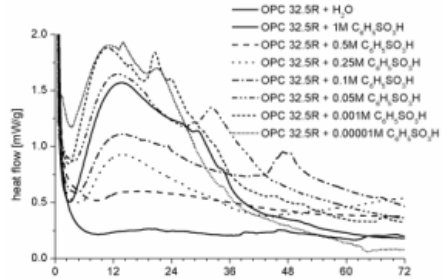


Figure 4. Calorimetry: OPC 32,5R + $C_nH_{2n+1}SO_3Na$ $n=1,3,5,6,7,8,9$.

3.4 Phase formation of Aluminates and Ferrates in OPC

In OPC, C_3A and C_4AF reacts with $CaSO_4 \cdot nH_2O$ and water to Ettringite, which was detected by XRD after 0.17 d. As the result of the conversion reaction of Ettringite + C_3A to lamellar Calcium Aluminate hydrates (Aft-phases) $C_3A \cdot CaSO_4 \cdot nH_2O$ or because of the presence of CO_2 Mono- and Hemicarbonate crystallize in the cement paste (Fig. 5).

However, the new Afm-phase was detected with a different layer distance c' and c_0 . In 0, the base reflections (00l) of the newly crystallized phase were detected after 4 d. Not only the addition of Benzenesulfonic acids (OPC + 1 m Xylenesulfonic acid), also the addition of $C_3H_7SO_3^-$ ions results in the formation of newly in-situ formed Afm phases. In comparison with the different Benzenesulfonic acids Calcium Aluminate Alkenesulfonate Hydrates crystallize at lower degree of crystallinity. The refinement of the layer distances c' are listed in Table 3.

3.5 Metric parameters of lamellar Calcium Aluminate Sulfonate Hydrates

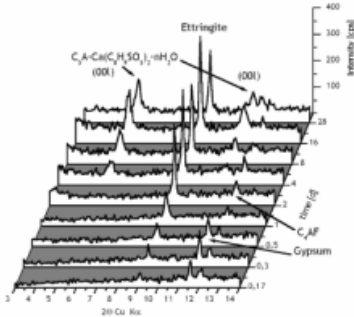
3.5.1 Metric parameters of lamellar Calcium Aluminate Alkenesulfonate Hydrates

All investigated lamellar Calcium Aluminate Alkenesulfonate hydrates crystallize in the trigonal system. R3-R-3, R3m and R-3m were determined as possible space groups.

The unit cell of these AFm-phases is built up of 6 sequences $[Ca_2Al(OH)_6]_n[X \cdot nH_2O]$ ($X =$ Alkenesulfonic ion) at different relative humidities 100% and 35% perpendicular [00l]. The lattice parameter dimension a_0 is about $0,577 \pm 0.002$ nm. The dimension c_0 is strongly influenced by origin of the organic ion fixed in the interlayer area of the crystal structure (Tab. 4).

3.6 Metric parameters of lamellar Calcium Aluminate Benzenesulfonate hydrates

Calcium Aluminate Benzenesulfonate Hydrate and Calcium Aluminate p-Toluenesulfonate Hydrate crystallize on the basis of a hexagonal primitive unit cell with a sequence $[\text{Ca}_2\text{Al}(\text{OH})_6]^+[\text{X}\cdot\text{nH}_2\text{O}]^-$ per unit cell perpendicular [001]. The unit cell of Calcium Aluminate Sulfonate Hydrates crystallize similar to Lamellar Calcium Aluminate Alkanesulfonate Hydrates with 6 sequences $[\text{Ca}_2\text{Al}(\text{OH})_6]^+[\text{X}\cdot\text{nH}_2\text{O}]^-$ (X = Alkanesulfonic ion) perpendicular [001]. Calcium Aluminate Mesitylenesulfonate Hydrate crystallized monoclinic (Tab. 5).



Phase Assemblages in the System $\text{Ca}_2\text{Al}_2\text{SiO}_7 - \text{Ca}_2\text{MnSi}_2\text{O}_7$ Related to a Modified CAC Clinker

S.Stöber & H.Pöllmann

Institute for Geological Sciences Mineralogy/Geochemistry MLU Halle (Saale), Germany

ABSTRACT: Phase assemblages in the binary system $\text{Ca}_2\text{Al}_2\text{SiO}_7 - \text{CaMnSi}_2\text{O}_7$ are presented. As a result of the MnO concentration provided in the starting material, 3 types of phase assemblages were detected. 1). Mn^{2+} occupies together with Al^{3+} ions the T1 tetrahedral position in the Gehlenite solid solution structure. 2). Gehlenite solid solutions $\text{Ca}_{1.95}\text{Al}_{2.03}\text{Mn}_{0.04}\text{Si}_{0.99}\text{O}_7$ crystallize with calcium deficient Akermanite solid solutions $\text{Ca}_{1.36}\text{Al}_{0.83}\text{Mn}_{0.46}\text{Si}_{1.93}\text{O}_7$ 3). Gehlenite solid solutions with the chemical composition $\text{Ca}_{2.31}\text{Al}_{1.49}\text{Mn}_{0.02}\text{Si}_{1.21}\text{O}_7$ crystallize with Wollastonite and Mn_3O_4 .

1 INTRODUCTION

Iron rich CAC is produced by a fusion process of the raw materials bauxite and limestone or chalk. The standard low alumina CAC usually contains about 3-5 % SiO_2 (Pöllmann 2001) and $\text{Mn}_2\text{O}_3 \ll 0.1$ % (Touzo et al. 2001). Pöllmann & Oberste-Padtberg (2001) showed that the addition of manganese oxides to the raw meal of a typical CAC leads to the formation of highly reactive CACs. A lower production temperature and decreased costs of raw material, besides a highly reactive new CAC, are the main advantages. Depending on the raw material and the clinkering temperature used the newly formed phases are solid solutions of manganese with the primary minerals of CAC. This paper is concerned with the substitution $\text{Mn}^{2+} + \text{Si}^{4+} \Leftrightarrow 2\text{Al}^{3+}$ in Melilites in the system $\text{Ca}_2\text{Al}_2\text{SiO}_7 - \text{Ca}_2\text{MnSi}_2\text{O}_7$.

Gehlenite ($\text{Ca}_2\text{Al}_2\text{SiO}_7$) is a common phase of Calcium Aluminate Cements (CAC). Approximately 11...15 % and 3...6 % Gehlenite contain commercial CACs with intermediate and high Iron concentrations (Walenta 1997).

Gehlenite is an end member in the binary system Gehlenite – Akermanite ($\text{Ca}_2\text{MgSi}_2\text{O}_7$). The solid solutions are called Melilites.

Warren (1930) firstly described the crystal structure of Melilites ($(\text{Ca}, \text{Na})_2(\text{Mg}, \text{Al})(\text{Si}, \text{Al})_2\text{O}_7$). Raaz (1930) determined the crystal structure of Gehlenite.

The Melilite crystal structure is built up of twisted T_2O_7 -layers 8 (T = tetrahedral site) with two different tetrahedral sites T1 and T2 perpendicular (001). Cations X links the T_2O_7 - layers.

In the Akermanite structure, Mg^{2+} ions are exclusively placed in the larger tetrahedral sites T1 and the Silicon ions occupy the position T2. The T_2O_7 -layers are linked by Ca^{2+} ions. The Gehlenite structure is deduced from the Akermanite structure due to the substitution $\text{Mg}^{2+} + \text{Si}^{4+} \Leftrightarrow 2\text{Al}^{3+}$. Al^{3+} ions occupy T1 and share the position T2 with Si^{4+} .

Recent studies on the crystal chemistry of Melilites with the unique formula $\text{X}_2\text{ZT}_2\text{A}_7$ demonstrated, that the substitution of cations on the specific positions is controlled by the ion radii and the charge balance in the Gehlenite structure (Röthlisberger 1989):

X = Na, Ca, Ba, Sr, Yb...
Z = Li, Be, Al, Zn, Co...
T = B, Be, Al, Fe, Si, Ge...
 $\text{A}_7 = \text{F}_7, \text{S}_7, \text{O}_7, \text{S}_6\text{O}$

Röthlisberger (1990) studied the substitution of $Mg^{2+} \Leftrightarrow Mn^{2+}$. He reported, that 40...50% of Mg^{2+} can be substituted by Mn^{2+} in Akermanite compared to the substitution $Mg^{2+} \Leftrightarrow Fe^{2+} = 80\%$ (Seifert 1974).

Related to the investigation of Melilite phases in cement clinkers, Sorrentino & Glasser (1975) studied the substitution $Al^{3+} \Leftrightarrow Fe^{3+}$ in Gehlenite. They demonstrated that 50 mole-% of C_2AS were substituted by " C_2FS ". Fe^{3+} occupied just the T1 positions. Sourie & Glasser (1993) demonstrated, that the (Al, Fe) totals in synthetic Melilites of the system $CaO - Al_2O_3 - Fe_2O_3 - SiO_2$ exceed the theoretical values and are accompanied by a deficiency of Si. The Si deficiency increased with a faster cooling rate.

2 EXPERIMENTAL TECHNIQUES

The materials used in starting mixtures were reagent grade chemicals $CaCO_3$, $Al(OH)_3$, MnO , and SiO_2 . CaO was prepared by decarbonation of $CaCO_3$ at 1100C for 2 h.

10 - 12g mixtures were prepared by weighing out the desired concentrations according to the composition $Ca_2Mn_xAl_{2-2x}Si_{1+x}O_7$ $0 \leq x \leq 1$ with $x = 0.05$. The weight concentrations were homogenized in a disk mill for 15 min and pressed to pellets. The pellets were placed in Alumina crucibles sintered in a muffle furnace with a temperature program as shown in Table 1. The maximum sinter temperature changed according to the MnO concentration in the sinter material.

Table 1. Temperature program.

T ₁ [°C]	t ₁ [h]	T ₂ [°C]	t ₂ [h]
800	0	1350 - 1100	24
T ₃ [°C]	t ₃ [h]	T ₄ [°C]	
1350 - 1100	1	800°C	

The sinter products were homogenized in between several times by disc milling in order to optimize the performance of the synthesis.

The sinter products were investigated by XRD using a PANalytical X'Pert system. The samples were prepared by the backloading technique. XRD measurements were performed with Ni filtered $CuK\alpha$ radiation at 45 kV and 40 mA. The range for Rietveld analysis was $7...130^\circ 2\theta$. A step time of 10 s and a step of $0.01^\circ 2\theta$ were chosen due to the average FWHM of the peaks. Lattice parameters were refined by Least Squares Methods using the software packages POWD and Cellref or by the Le Bail method.

For the refinement of the crystal structure the software package TOPAS 2.0 was used. In a first step, scale factor, zero displacement, background (Chebyshev 5th polynomial), crystallite size and lattice

parameters. The site occupancies of Mn^{2+} , Al^{3+} (T1), Al^{3+} (T1) and Si^{4+} (T2) were refined in second step and in a third step the general positions. For peak fitting the pseudo Voigt profile shape function was used.

3 RESULTS

3.1 X-Ray Diffraction

Three different types of phase assemblages were determined in the binary system $Ca_2Al_2SiO_7 - Ca_2MnSi_2O_7$ by XRD.

Batches with the target compositions $Ca_2Mn_xAl_{2-2x}Si_{1+x}O_7$ $0 < x \leq 0.15$ mole are single phased. Gehlenite solid solutions crystallize without side products. The lattice dimension a_0 increases slightly until 0.15 moles MnO . The c - dimension is quite stable, because the ion substitution influences mainly the tetrahedral layer T_2O_7 that is oriented along a_0 and b_0 . Huckenholtz & Ott (1978) postulated that the expansion of the cell volume at a maximum $Al^{3+} \Leftrightarrow Fe^{3+}$ substitution is 2%, whereas the increase of a_0 is definitively higher than c_0 . Structure refinements of Gehlenite solid solutions with yielded the following results (Tabs. 2-5).

Table 2. Refined Residue Values R and Goodness of Fit (GoF).

Target Composition	R _{bragg}	R _w	GoF
$Ca_2Al_{1.9}Mn_{0.05}Si_{1.05}O_7$	6.129	11.85	0.98
$Ca_2Al_{1.8}Mn_{0.1}Si_{1.1}O_7$	7.508	9.70	1.27
$Ca_2Al_{1.7}Mn_{0.15}Si_{1.15}O_7$	9.021	10.71	1.85

Table 3. Site occupancies and calculated composition for the target chemistry $Ca_2Al_{1.9}Mn_{0.05}Si_{1.05}O_7$.

Target Composition	Calculated Composition	
$Ca_2Al_{1.9}Mn_{0.05}Si_{1.05}O_7$	$Ca_2Al_{1.84}Mn_{0.05}Si_{1.11}O_7$	
	OCC	OCC error
Ca ²⁺	1	--
Al ³⁺ (T1)	0.9467	0.003
Mn ²⁺	0.0533	0.003
Si ⁴⁺ (T2)	0.5533	0.003
Al ³⁺ (T2)	0.4467	0.003
O	1	--
O	1	--
O	1	--

Table 4. Site occupancies and calculated composition for the target chemistry $Ca_2Al_{1.8}Mn_{0.1}Si_{1.1}O_7$.

Target Composition	Calculated Composition	
$Ca_2Al_{1.8}Mn_{0.1}Si_{1.1}O_7$	$Ca_2Al_{1.84}Mn_{0.05}Si_{1.10}O_7$	
	OCC	OCC error
Ca ²⁺	1	--
Al ³⁺ (T1)	0.9502	0.003
Mn ²⁺	0.0498	0.003
Si ⁴⁺ (T2)	0.5498	0.003
Al ³⁺ (T2)	0.4502	0.003
O	1	--
O	1	--
O	1	--

Table 5. Site occupancies and calculated composition for the target chemistry $\text{Ca}_2\text{Al}_{1.7}\text{Mn}_{0.15}\text{Si}_{1.15}\text{O}_7$.

Target Composition	Calculated Composition	
$\text{Ca}_2\text{Al}_{1.7}\text{Mn}_{0.15}\text{Si}_{1.15}\text{O}_7$	$\text{Ca}_2\text{Al}_{1.67}\text{Mn}_{0.10}\text{Si}_{1.20}\text{O}_7$	
	OCC	OCC error
Ca^{2+}	1	-.-
$\text{Al}^{3+}(\text{T1})$	0.8913	0.004
Mn^{2+}	0.1087	0.004
$\text{Si}^{4+}(\text{T2})$	0.6087	0.004
$\text{Al}^{3+}(\text{T2})$	0.3913	0.004
O	1	-.-
O	1	-.-
O	1	-.-

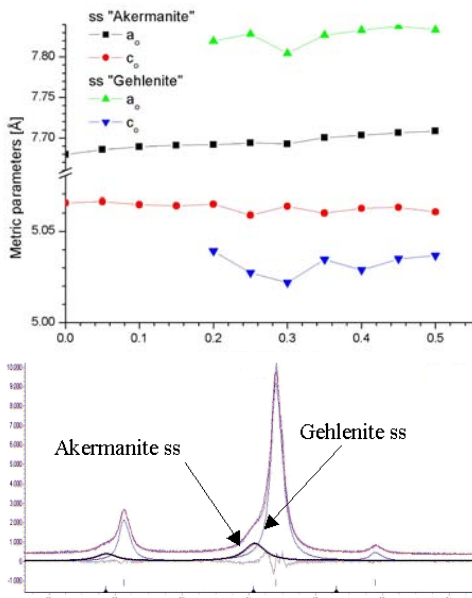


Figure 2 show a strong overlapping of two XRD patterns in the range $28 \dots 35^\circ 2\theta$. With the increase of the MnO in the starting material the concentration of the “Akermanite ss” increase and the patterns of both phases are easier to decompose (Figs. 1, 2).

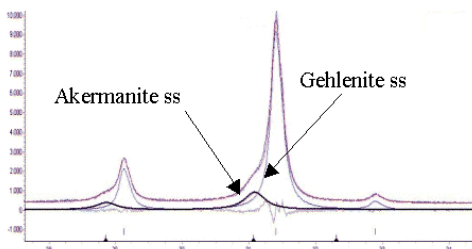


Figure 2. Le Bail Fit of the XRD pattern $\text{Ca}_2\text{Al}_{1.6}\text{Mn}_{0.20}\text{Si}_{1.20}\text{O}_7$.

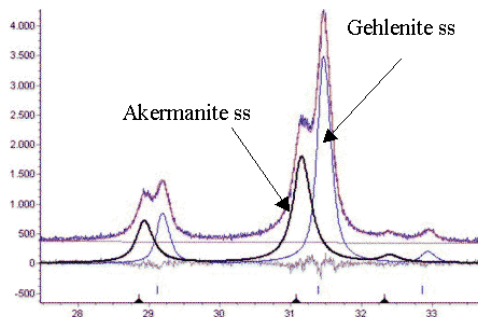


Figure 3. Le Bail Fit of the XRD pattern $\text{Ca}_2\text{Al}_{1.6}\text{Mn}_{0.20}\text{Si}_{1.20}\text{O}_7$.

The refined metric parameter a_0 and c_0 of the Akermanite solid solution in

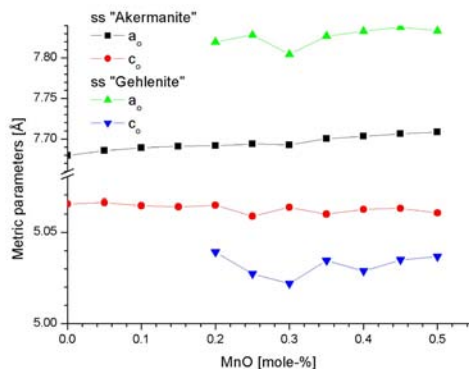


Figure 1 are extremely unstable and differ, whereas a_0 and c_0 show a slight increase in good agreement with the refined lattice parameters in the single phased samples $\text{Ca}_2\text{Mn}_x\text{Al}_{2-2x}\text{Si}_{1+x}\text{O}_7$ $0 < x \leq 0.15$ mole.

XRD measurements of sinter products with $\text{Ca}_2\text{Mn}_x\text{Al}_{2-2x}\text{Si}_{1+x}\text{O}_7$ $0.5 < x \leq 0.95$ mole indicate, that the “Akermanite” solid solution is not longer stable. $\text{Mn}_3\text{O}_4 + \text{CaSiO}_3 + \text{Gehlenite}$ solid solutions were determined as phase assemblages by XRD.

3.2 Microprobe analysis & SEM investigations

Polished sections of the samples “ $\text{Ca}_2\text{Al}_{1.9}\text{Mn}_{0.05}\text{Si}_{1.05}\text{O}_7$ ”, “ $\text{Ca}_2\text{Al}_{1.8}\text{Mn}_{0.10}\text{Si}_{1.10}\text{O}_7$ ”, “ $\text{Ca}_2\text{Al}_{1.6}\text{Mn}_{0.20}\text{Si}_{1.12}\text{O}_7$ ” and “ $\text{Ca}_2\text{Al}_{1.1}\text{Mn}_{0.45}\text{Si}_{1.45}\text{O}_7$ ” were investigated. The chemical compositions were exclusively determined for big enough crystals, which appeared to be free of inhomogeneities and inclusions. On the homogenous surface of the polished section “ $\text{Ca}_2\text{Al}_{1.9}\text{Mn}_{0.05}\text{Si}_{1.05}\text{O}_7$ ” and “ $\text{Ca}_2\text{Al}_{1.8}\text{Mn}_{0.10}\text{Si}_{1.10}\text{O}_7$ ” chemical analysis of 7 points were chosen. The calculation to the unit cell

contents of Gehlenite yielded a Gehlenite endmember composition of $\text{Ca}_{1.95}\text{Al}_{2.03}\text{Mn}_{0.04}\text{Si}_{0.99}\text{O}_7$.

The SEM images of polished section of sample “ $\text{Ca}_2\text{Al}_{1.6}\text{Mn}_{0.20}\text{Si}_{1.20}\text{O}_7$ ” showed idiomorphic dark crystals and a xenomorphic interstitial phase. The microprobe analysis performed on 6 crystals lead to the Gehlenite composition $\text{Ca}_{1.98}\text{Al}_{1.92}\text{Mn}_{0.05}\text{Si}_{1.04}\text{O}_7$ - $\text{Ca}_{2.08}\text{Al}_{2.02}\text{Mn}_{0.02}\text{Si}_{0.93}\text{O}_7$ comparable to the sample with 0.05 moles MnO. The xenomorphic phase was determined based on the chemical analysis of 5 points: The chemistry of P1 - P3 resemble Akermanite like solid solutions with P1: $\text{Ca}_{1.33}\text{Al}_{0.94}\text{Mn}_{0.53}\text{Si}_{1.86}\text{O}_7$, P2: $\text{Ca}_{1.36}\text{Al}_{0.83}\text{Mn}_{0.54}\text{Si}_{1.93}\text{O}_7$, P3: $\text{Ca}_{1.34}\text{Al}_{0.83}\text{Mn}_{0.54}\text{Si}_{1.93}\text{O}_7$. P4 and P5 indicate the presence of manganese containing Gehlenite solid solutions (P4: $\text{Ca}_{1.75}\text{Al}_{1.38}\text{Mn}_{0.16}\text{Si}_{1.51}\text{O}_7$ P5: $\text{Ca}_{1.79}\text{Al}_{1.09}\text{Mn}_{0.32}\text{Si}_{1.62}\text{O}_7$).

Long tabular crystals were identified as CaSiO_3 associated with Mn_3O_4 . In the sample “ $\text{Ca}_2\text{Al}_{1.1}\text{Mn}_{0.45}\text{Si}_{1.45}\text{O}_7$ ”, idiomorphic Gehlenite solid solutions $\text{Ca}_{2.31}\text{Al}_{1.49}\text{Mn}_{0.02}\text{Si}_{1.21}\text{O}_7$ with Ca in excess and $\text{Ca}_{2.32}\text{Al}_{1.17}\text{Mn}_{0.06}\text{Si}_{1.44}\text{O}_7$ with variable Al/Si ratios were determined.

4 DISCUSSION & CONCLUSIONS

In the Melilite system with the endmembers Gehlenite and the hypothetical $\text{Ca}_2\text{MnSi}_2\text{O}_7$, different phase assemblages were determined. The substitution $\text{Mn}^{2+} + \text{Si}^{4+} \Leftrightarrow 2\text{Al}^{3+}$ cause a complex Melilite solid solution chemistry, just the combination of XRD and microprobe analysis make it possible to get basic informations.

Only the samples with the target composition “ $\text{Ca}_2\text{Al}_{1.9}\text{Mn}_{0.05}\text{Si}_{1.05}\text{O}_7$ ” and “ $\text{Ca}_2\text{Al}_{1.8}\text{Mn}_{0.10}\text{Si}_{1.10}\text{O}_7$ ” are single phased. Provided 0.05 and 0.10 moles MnO occupy the T1 positions in the Gehlenite crystal structure. The fixation limit for divalent Manganese must be approximately 0.1 – 0.15 moles in Gehlenite. Structure refinements of the further Gehlenite solid solution yield too low site occupancies for Mn^{2+} on the T1 position. The results of the microprobe analysis gave the proof that the sample was not single phased; Gehlenite solid solutions with the substitution $0.05\text{Mn}^{2+} + 0.05\text{Si}^{4+} \Leftrightarrow \text{Al}^{3+}$ coexist with Akermanites $\text{Ca}_{1.33}\text{Al}_{0.94}\text{Mn}_{0.53}\text{Si}_{1.86}\text{O}_7$.

In the sample with a concentration higher than 0.15 moles MnO, Akermanite solid solutions were detected by XRD and the calculation of the different microprobe analysis showed that Gehlenite solid solutions with 0.05 moles MnO crystallized in contact with Akermanite solid solutions of variable compositions. All of them are CaO deficient and showed increased SiO_2 concentrations.

Akermanite solid solutions are not longer stable in samples provided with MnO concentrations higher than 0.5 moles. They decompose to Mn_3O_4 and Calcium Aluminum Silicate phase comparable to Wollastonite.

The substitution mechanism in Melilites is not as clear as proposed. Beside the exchange $0.05\text{Mn}^{2+} + 0.05\text{Si}^{4+} \Leftrightarrow 1\text{Al}^{3+}$ in the Gehlenite solid solutions, the mechanism in CaO deficient Akermanite phases must be investigated in detail, especially the occupancy of the octahedral site and the role of divalent Mn ions. Usually they occupy the T1 site, however Mn^{2+} ions might have the ability to occupy the octahedral coordinated site of Ca^{2+} because of the small differences of the effective ion radii ($\text{Mn}^{2+} = 0.83$ & $\text{Ca}^{2+} = 1.00$) (Shannon 1976).

5 ACKNOWLEDGEMENTS

The author wishes to express his thanks to Dr. Th. Döring, Institut für Mineralogie & Kristallographie University Leipzig for microprobe analysis.

6 REFERENCES

- Huckenholz, H.G. & Ott, W.D. 1978. Synthesis, stability, and aluminum substitution in Gehlenite-ferrighelenite solid solutions N. Jb Min. Mh. 12 521-536
- Pöllmann, H. (2001): The mineralogy and Crystal Chemistry of Calcium Aluminate Cement Proc. Int. Conf. on Calcium Aluminate Cements (CAC) Edinburgh pp. 80-119
- Pöllmann, H. & Oberste-Padtberg, R. (2001) Manganese in High Alumina Cement (HAC) Proc. Int. Conf. on Calcium Aluminate Cements (CAC) Edinburgh pp. 139-148
- Raaz, F. (1930): Die Struktur des synthetischen Gehlenits $2\text{CaO}\cdot\text{Al}_2\text{O}_3\cdot\text{SiO}_2$ Anz. Akad. Wiss. Wien, Math Naturwiss. Kl. 18, 203
- Röthlisberger, F. (1989): Zusammenhang Zwischen Chemismus, Stabilität und struktureller Variation der Melilite Dissertation Bayreuth p 178
- Shannon, (1976) Revised effective ionic radii and systematic studies of interatomic distances in halides and chalcogenides Acta Cryst.. A32, 751-767
- Sorrentino, F.P. & Glasser F.P. (1975): The system $\text{CaO}\text{-Al}_2\text{O}_3\text{-Fe}_2\text{O}_3\text{-SiO}_2$. The Pseudoternary Section $\text{Ca}_2\text{Fe}_2\text{O}_5\text{-Ca}_2\text{Al}_2\text{O}_5\text{-SiO}_2$ Trans. Br. Ceram. Soc. 74 pp.253-256
- Sourie, A. & Glasser, F.P. (1993): Composition of Melilites Crystallized from $\text{CaO}\text{-Al}_2\text{O}_3\text{-Fe}_2\text{O}_3\text{-SiO}_2$ Melts Trans. Brit. Ceram. 92 4 pp.152-154
- Touzo, B., Gloter, A. & Scrivener, K.L. (2001): Mineralogical Composition of Fondu Revisited Proc. Int. Conf. on Calcium Aluminate Cements (CAC) Edinburgh pp. 129-138
- Walenta, G. (1997): Synthesen und Rietveld- Verfeinerungen der Einzelphasen von Tonerdezementen Dissertation Erlangen p 109
- Warren, B.E. (1930): The structure of Melilite $\text{Ca}_2\text{Na}_2(\text{Mg},\text{Al})(\text{Si},\text{Al})_2\text{O}_7$ Z. Krist. 74,pp.131-138

Influence of Particle Size of Nephelyne Syenite Mineral on Formation of Liquid Phase in Ceramic Masses

J.C.Toniolo, H.C.M.Lengler, C.P.Bergmann

LACER, Department of Materials, Federal University of Rio Grande do Sul, Porto Alegre, Brazil

ABSTRACT: This work investigates the effect on particle size of nephelyne mineral from the southern part of Brazil (Lages) in liquid phase formation. In order to optimize the mass, it was performed differentiated particle size distribution for each defined formulation. Samples obtained by pressing were submitted to some tests, establishing the main properties of ceramic products: mechanical resistance, apparent density, and porosity.

1 INTRODUCTION

Nephelyne syenite is a rock composed of nephelyne, potassic feldspar and sodium-rich plagioclase (Klein 2001). It is used as a flux, like feldspar, lowering the firing temperature of a ceramic body during firing and forming a glassy phase (USGS 1994).

Additionally to the reduction in energetic costs, the Nephelyne syenite diminishes water absorption increasing linear retraction and mechanical resistance of floor tiles. It also increases the compressive strength in glasses, reducing the chance to nucleate cracks (Singh 2003).

The occurrence of alkaline rocks is abundant in Brazil, mainly near the northeast and southeast regions. Most of them were originated by an intrusive process on Precambrian period and some of them appear intruded on sedimentary rocks from Paleozoic era (Barbieri et al. 1987).

In the work reported in this paper, a milling evaluation for nephelyne syenite and characterization has been developed and applied on a typical porcelain formulation. Several tests were carried out in order to verify the influence of particle size on the main properties of ceramic bodies: mechanical strength and porosity.

2 EXPERIMENTAL PROCEDURE

The nephelyne syenite was milled under wet and dry conditions and mixed with the others selected materials of the porcelain formulation. The Figure 1 gives the overall steps involved until the complete porcelain characterization.

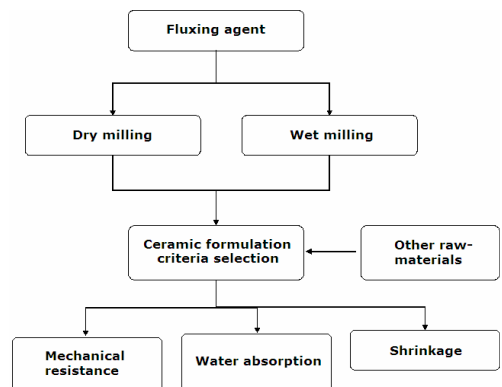


Figure 1: Flowchart of porcelain characterization.

Mechanical resistance, shrinkage, and water absorption properties are often overlooked when formulating ceramic bodies and, for this reason, they were also measured. These attributes are important in developing durable, sellable pottery.

2.1 Materials

The nephelyne syenite used in this mass was obtained from CCU (Urussanga Coalmine Company) Lages, RS, Brazil. It contains low yield of silica and high content in alkalis which were fundamental for its selection. Table 1 shows the typical chemical composition of nephelyne syenite:

Table 1: Chemical composition of nephelyne syenite.

Oxide	(%)
SiO ₂	58.81
Al ₂ O ₃	23.3
Fe ₂ O ₃	0.3
MgO	0.0
CaO	0.4
Na ₂ O	11.4
K ₂ O	5.8
TiO ₂	0.1
P ₂ O ₅	0.1
Ignition loss	1.2
Total	100

Other raw materials are necessary to produce the mass for porcelain formulation and they were selected in accordance with their properties and purity, such as clay, quartz, and talc.

Clay was obtained from São Simão city (São Paulo, Brazil) because it has high plasticity; quartz from Sibelco Corp., and talc from Socavão district (Castro, PR, Brazil), which offers high thermal shock resistance. Table 2 illustrates the two porcelain formulations used on this work:

Table 2: Composition of porcelain formulation.

Materials	C1 (%)	C2 (%)
Clay	40	40
Quartz	15	15
Talc	10	10
Nephelyne sy. (Dry milled)	35	-
Nephelyne sy. (Wet milled)	-	35
Total	100	100

Two batches, C1 and C2, were prepared with nephelyne syenite which had been ground ball milled into two distinct conditions (wet and dry milling) with the aim to investigate the particle size behavior effect on two different porcelain formulations.

Particle size analyzes have been carried out by laser scattering (Cilas 1180). The milling time considered was set in 2, 4, 14, 24, 60, and 90 minutes.

Samples with 20 mm x 60 mm were previously compacted using a hydraulic press under 20 MPa. They were dried during 24 hours in order to eliminate the humidity.

Finally, the samples were sintered in an electric furnace under soaking temperature of 1200 °C established as typical temperature to consolidate the porcelain bodies.

3 RESULTS AND DISCUSSIONS

Milling is an inefficient and energy-intensive process. Typically, only 7 to 13% of the input energy is utilized for size reduction during ball milling, while the remaining energy dissipates mostly as heat (Straimond 1976). The energy provided to the milling process is distributed among different sub processes within a mill.

The size reduction that occurs in a mill is based on a combination of the following mechanisms (Crabtree et al. 1964): impact with media, abrasion with media, and attrition with particles and media.

The sum of media and mass occupied in the ball milling was partially filled with 50% in volume.

Cumulative values revealed slight variation among all the conditions investigated. Figures 2 and 3 show for each milling their respective grinding time. The lowest value found of particle size was 3 μm (dry milling).

The particle size decreased with time increase but it was more effectively for dry milling than wet milling. Figure 4 shows the comparative values of particle size obtained under wet and dry milling.

Within 60 min, approximately, the particle size has leveled off at the 3 μm (dry milling) and 4 μm (wet milling), which reveals no milling efficiency in 90 min.

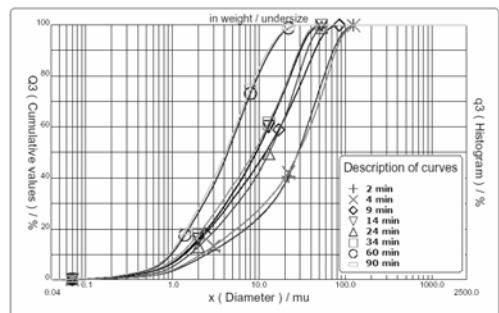


Figure 2: Cumulative values for different wet milling times.

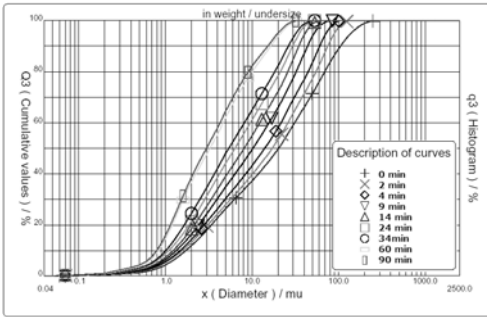


Figure 3: Cumulative values for different dry milling times.

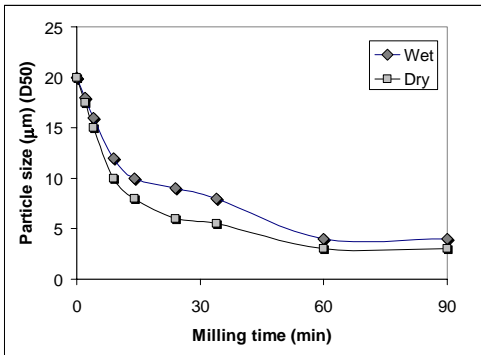


Figure 4: Particle size in function of milling time.

Table 3 explains that water absorption values showed significant difference between both formulations while mechanical resistance did not show high divergence of data. The highest shrinkage, C2, promotes reduction and facilitates the formation of closed porosities.

Table 3: Properties of Porcelain bodies.

Formulation	Mechanical resistance (MPa)	Shrinkage (%)	Water absorption (%)
C1	31.86	7.85	-
C2	30.42	10.09	0.59

4 CONCLUSIONS

In porcelain, nephelyne syenite acts as fluxing agent and it is also dependent on particle size influence.

Porcelain formulation based on dry-milled Nephelyne syenite is the most effective way to promote lower particle size and provides better properties than wet-milled porcelains.

A successful grinding mill combined with an advanced criterion of materials selection is

providing new opportunities for producing extremely fine, high-quality ceramic mass for porcelains.

5 REFERENCES

Klein, G. 2001. Application of Feldspar Raw materials in the Silicate Ceramics Industry. *Interceram* vol. 50 n1., p. 8-11.

U.S. Geological Survey. 1994. Nephelyne Syenite. Ch. in *Industrial Mineral and Rocks*.

Singh, V.K. 2003. Key Ceramic Materials. Department of Ceramic Engineering. Banaras Hindu University.

Barbieri, M. et. al. 1987. Petrological and Geochemical Studies of Alkaline Rocks from Continental Brazil I. The Phonolite Suite From Piratini, RS. *Geochimica Brasiliensis*, 1 (1): 109-138.

Straimond, C.J. 1976. The energy efficiency of the milling process, *Dechema-monographien*, NR 1549-1579, Verlag Chemie, GMBH, Weinheim/Bergstrasse. p. 1-18.

Crabtree, D.D. et al. 1964. Mechanisms of size reduction in comminution systems, 1, impact, abrasion and chipping grinding, *Trans. AIME*, Vol 229. p. 201-206.

The Use of Fe-Mn Submerged-arc Furnace Slag in Composite Portland Cement – a Pilot Study

S.M.C.Verryn

Department of Geology, XRD & XRD Laboratory, University of Pretoria, Pretoria, 0002 South Africa

H.Pöllmann

Martin-Luther-University Halle-Wittenberg, Geological Institute, Halle/Saale, Germany

E.Kearsley

Department of Civil Engineering, University of Pretoria, Pretoria, 0002 South Africa

ABSTRACT: Ferromanganese alloy production in a submerged arc-furnace results in the creation of large amounts of slag. Storage of the slag is becoming an increasing problem, which initiated this study, i.e. to utilize ferromanganese slag (Fe-Mn slag) in blended Portland cement. The main components of the slag used in this investigation are glaucocroite, some bustamite, gehlenite, quartz and minor glassy phases. The approximate chemical composition, in weight per cent, is as follows: 33 % SiO₂, 29 % CaO, 19 % MnO, 8 % MgO, 6 % Al₂O₃, 2 % FeO and 1% SO₃. The Fe-Mn slag was mixed with raw Portland cement clinker in 50:50, 65:35 and 80:20 cement : slag ratios. Two mixing procedures were used, i.e. blending and inter-grinding. Commercially available blast-furnace slag was blended with the Portland cement in the same way for comparison. ISO compressive strength tests were performed and hydration characteristics were measured using a heat-flow calorimeter. The results indicate that the amount of heat developed increases with increasing cement content within each sample group. Comparison of each ratio shows that the Fe-Mn slag containing composite cements show less heat involvement than the respective composite blast-furnace slag cement of the same ratio. Compressive strength of the cement – Fe-Mn slag mixtures is lower than that of the respective cement-blast furnace slag mixtures. The blended Cement – Fe-Mn slag mixtures show greater strength than the inter-ground mixtures comparing each ratio used.

1 INTRODUCTION

Slag originating from the production of iron in a blast furnace, has been used in blended cements since before 1900. In South Africa manganese ore is converted into alloys at a plant in Meyerton in the Gauteng Province. In the production of ferromanganese alloy in a submerged arc-furnace large amounts (approximately 140 000t) of slag are produced yearly. Although a portion of the slag is used in the civil and road building industry, storage of the slag is becoming an increasing problem. This resulted in the initialization of this study, i.e. to utilize ferromanganese slag in blended Portland cement.

2 EXPERIMENTAL

2.1 Raw Materials

Ferro Manganese Slag (FeMn): The Slag consists mainly of glaucocroite and some bustamite, gehlenite and quartz as well as minor unidentified glass phases (determined by X-ray powder diffraction). The typical chemical composition

determined by X-ray fluorescence spectroscopy is: 33 % SiO₂, 30.0 % CaO, 19 % MnO, 8 % MgO, 6 % Al₂O₃, 1.7 % Fe₂O₃, and 1.7 % SO₃

Ordinary Portland Cement (Cem): This cement is milled in our own laboratory from cement clinker adding of 3.5% gypsum.

Granulate blast furnace slag (corex): This slag is widely used in South African cements and performs extremely well. It is used here for comparison.

Commercially available Lafarge 42.5 cement was used for additional comparison in the compressive strength tests.

2.2 Mixtures

The raw materials were mixed in various proportions as indicated in Table 1 below. Two mixing procedures were used:

Inter-grinding: The cement clinker and slag fragments are ground together in the proposed proportions (IG)

Inter-blending: the fine material is blended in rotary ball mill in the proposed proportions (IB).
SABS-ENV196

Table 1: Proportions of raw materials and mixing procedures (IG – intergrinding, IB – blending)

Slag Type	Proportions		Method	Abbreviation
	Cement	Slag		
FeMn	50	50	IG	50/50 Cem/FeMn IG
FeMn	65	35	IG	65/35 Cem/FeMn IG
FeMn	80	20	IG	80/20 Cem/FeMn IG
FeMn	50	50	IB	50/50 Cem/FeMn
FeMn	65	35	IB	65/35 Cem/FeMn
FeMn	80	20	IB	80/20 Cem/FeMn
Corex	50	50	IB	50/50 Cem/Corex
Corex	65	35	IB	65/35 Cem/Corex
Corex	80	20	IB	80/20 Cem/Corex
	100			Cement 100%

2.3 Testing

The strength development was measured at 2, 7 and 28 days using the SABS-ENV196 compressive strength test method on 40x40x160 mm blocks. 450g cementitious material, 225g water and 1350g standard sand were used in each test, which were carried out in duplicate an average values are used here.

The course of hydration was determined by isoperibolic heat-flow calorimetry (Pöllmann et al. 1991). 1ml of water was mixed with 2g cement/slag mixture.

3 RESULTS

3.1 Compressive Strength Tests

Results of the compressive strength after 28 days are shown in Fig 1. The compressive strength of the cement – Fe-Mn slag mixtures is lower than that of the respective cement-corex slag mixtures. It is interesting to note that the blended Cement – Fe-Mn slag mixtures have greater strength than the inter-ground mixtures comparing each ratio used. Strength development from 2 to 28 days is shown in Fig. 2. Comparing the results with the compressive strength requirements of BS12:1996 (Bye 1999), the 50/50 Cem/FeMn interground and blended mixtures fall outside the requirements for all cement classes, the 65/35 Cem/FeMn mixtures fall within the limits for class 32.5N and the 80/20 Cem/FeMn mixtures fall into the 42.5N class.

3.2 Heat-flow Calorimetry

Figures 3 to 5 show the heat evolution of the mixtures displaying the curve for pure cement (Cement 100%) for comparison. Maximum hydration of the corex blends occurs slightly earlier than that of the pure cement and the Fe-Mn-slag blends. Comparing each ratio, heat evolution within the blended cement – Fe-Mn slag mixtures is increased relative to the inter-ground mixtures. This

compares well with the results obtained in the compressive strength tests.

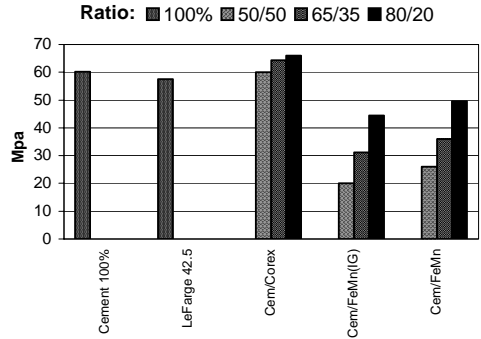


Figure 1: SABS-ENV196 Compressive Strength after 28 days.

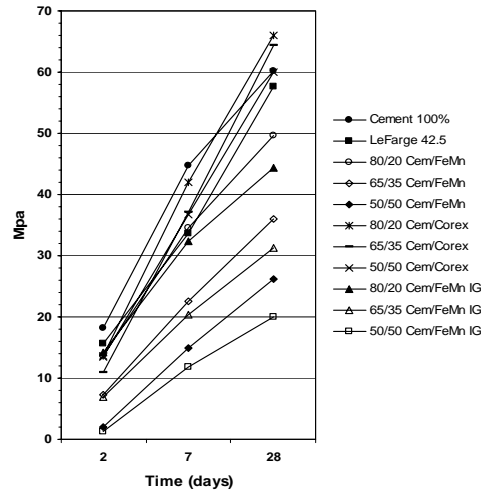


Figure 2: Compressive strength at 2, 7 and 28 days.

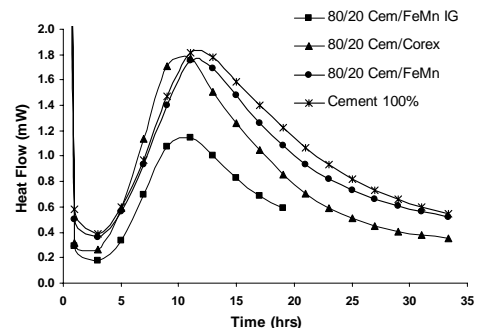


Figure 3: Heat flow curves for 80/20 cement-slag mixtures.

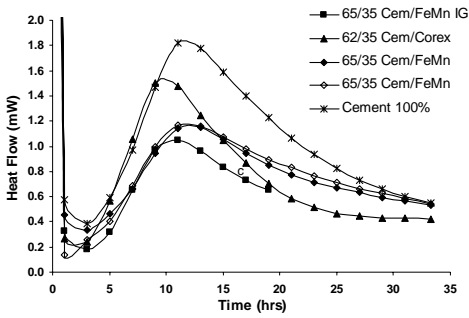


Figure 4: Heat flow curves for 65/35 cement-slag mixtures.

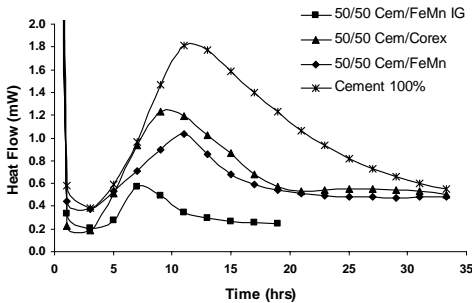


Figure 5: Heat flow curves for 50/50 cement-slag mixtures.

The Heat flow curves for the blended 80/20 ratios and the pure cement are similar, whereas the compressive strength tests show larger differences. In the 65/35 and 50/50 blends, the corex slag blends show greater heat flow, which compares well with the results of the compressive strength tests.

There is a weak positive correlation between the integrated area of the heat development curve and the compressive strength (Fig. 6) supporting the results discussed above.

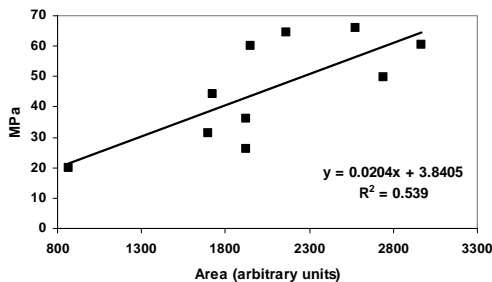


Figure 6: Compressive strength (Mpa) versus integrated area under heat development curve measured from 4 minutes to 20 hours (in arbitrary units). The solid line indicates the best linear fit with the equation and the correlation factor shown at the right hand.

Preliminary results of further tests using different cement types are promising, but show variable behaviour of the Fe-Mn slag, indicating that the use of Fe-Mn slag in different cements should be investigated further.

The authors would like to thank Prof. JPR de Villiers for fruitful discussions and Mr. HF Mostert for the compressive strength tests. The financial assistance provided by the National Research Foundation of South Africa and the Forschungsgemeinschaft Jülich in Germany is greatly appreciated.

4 REFERENCES

Bye, G.C. 1999. *Portland Cement 2nd ed.* Thomas Telford Publishing, London, 225pp.
 Pöllman, H., H.-J. Kuzel & H. Meyer 1991. Heat flow calorimetry in cement chemistry – *Pro. 13th Int. Conf. Cem. Micr., Tampa, 254-272.*

The Comparisation of Optical Microscopy and Cathodoluminescence Technique on Ordinary Portland Cement Clinkers

N.Winkler & H.Pöllmann

Department of Mineralogy and Geochemistry, Martin-Luther University, Halle, Germany

J.Göske

Center for material analysis, Lauf a. d. Pegnitz, Germany

ABSTRACT: The cement industry is interested in new methods for phase analysis and quantification. Time and precision are the decisive factors. This abstract will demonstrate the possibilities of the cathodoluminescence technique for cement investigations. Making explanations to preparation, experimental, advantages and disadvantages.

1 INTRODUCTION

For the determination of clinker structure and phase composition the examination with optical microscopy and point counting analysis is the classic way (Campbell; VDZ). In the last years the importance of the Rietveld method (Pritula & Smrcok 2003, Stutzmann 1996, Füllmann et al. 2001) for the calculation the phase composition increased. A third method will be demonstrated: Cathodoluminescence (CL) technique with Digital Image Analysis (Motzet et al. 1997). The further development of the Cathodoluminescence technique offers the possibility to perform phase structure examinations, phase identification and cement phases quantifications. For this purpose the MonoCL of the company GATAN was coupled with a FE REM of the company Leo. The basic processes involves the excitation of an electron to a state of higher energy followed by the emission of a photon in the UV, visible or IR parts of electromagnetic spectrum when the electron returns to a state of lower energy (Ozawa 1990).

2 PREPARATION & EXPERIMENTAL

The sample preparation for cathodoluminescence technique is similar to optical microscopy. A polished clinker microsection is used. It is possible to differentiate between the Alite, Belite, the interstitial materials and pores (Winkler et al. 2003). The CL image shows several gray colors. Belite is the brightest cement phase followed by

Alite (light gray). The interstitial materials are black. Unfortunately, it isn't possible to differentiate between the Aluminate and Ferrate (Fig. 1).

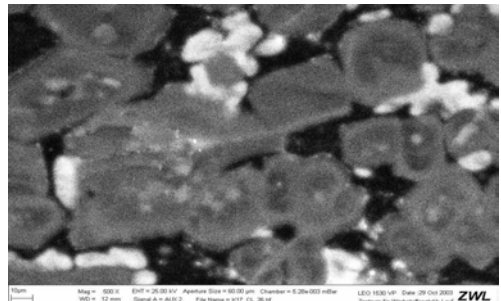


Figure 1. REM-CL image of clinker microsection.

For the better orientation the clinker surface is etched by salicylic acid. The REM image shows the idiomorphic Alites and rounded Belites accurately. Additional a primary (pores) and secondary (rifts) roughness is recognizable. Pores are filled with polished powder (Fig. 2). The same characteristics can be seen in the CL image and in the optical microscopy image.

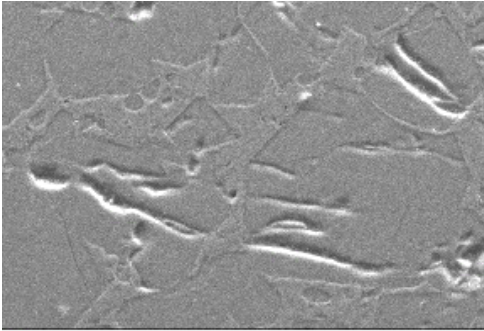


Figure 2a. REM image of clinker microsection.

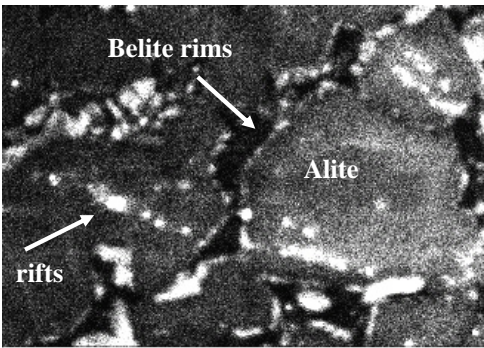


Figure 2b. REM-CL image of clinker microsection from fig. 2a.

It is important to differentiate between the several Belite habits, because information on the clinkering conditions can be obtained. Furthermore microscopical examinations can often give evidence of the cause of disturbances which occur in manufacturing of clinker.

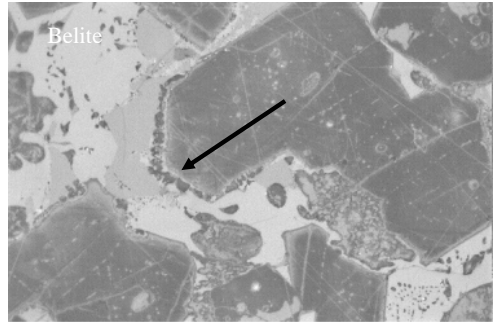


Figure 2c. optical microscopy image of clinker – Belite rims.

In the optical microscopy rounded Belite crystals with or without lamellae, secondary Belites as Belite rims or ternary Belites and ragged Belites can be seen. With cathodoluminescence technique it is possible to differentiate between rounded Belites, rims and ragged Belites. For more precise habit informations the resolution is not sufficient. The following images (Fig. 3) show example for ragged Belites.

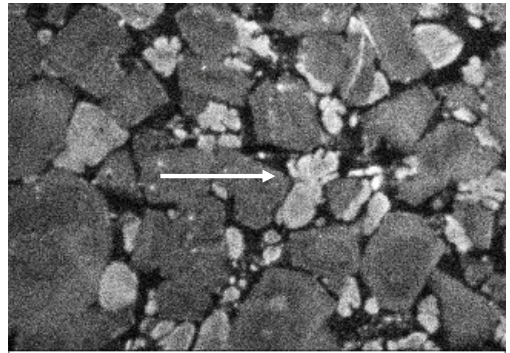


Figure 3a. REM-CL image of clinker – ragged Belites microsection.

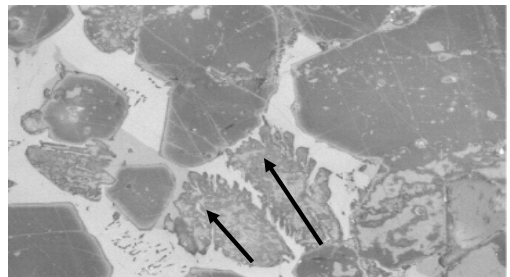


Figure 3b. optical microscopy image of clinker – ragged Belites.

Another disadvantage is the cross dissolve of embedding media and pores filled with polished powder. In fig. 4 the negative influence of filled pores with impregnation is visible. In this case it is only a differentiation between pores and clinker phases. Nevertheless the luminescing embedding media is important for the calculation, because volume percents are part of a precise description. For that purpose the pores must have an other color than the clinker minerals. In this image the embedding media is an epoxy resin.

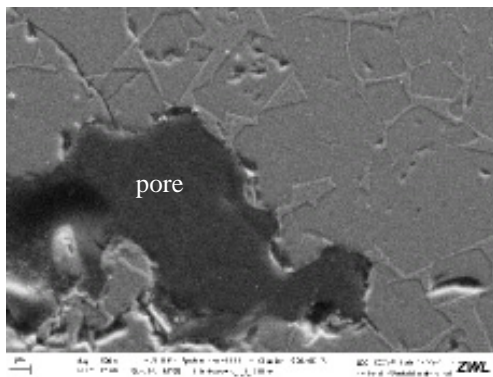


Figure 4a. REM image of clinker microsection.

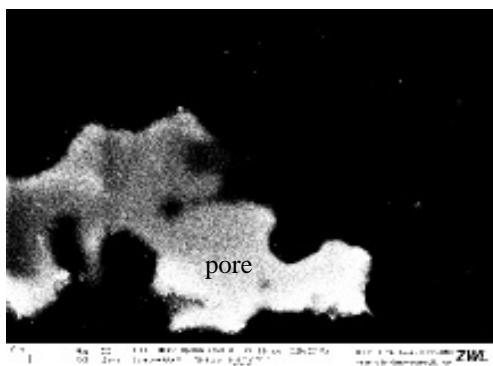


Figure 4b. REM-CL image of clinker microsection.

To minimise interferences of luminescence effects a smooth and clean surface is important, because the polish powder have high luminescence. Therefore it is possible to quantify the clinker with CL technique in combination with Digital Image Analysis, get weight percents of the main phases Alite and Belite, as well as the interstitial minerals and the pore rate. This application isn't possible with the optical microscopy because of the very probable irregular coloring by etching.

3 CONCLUSIONS

For the quantitative calculation the images are transformed in a digital image analysis program. At first the grey colors for each phases are defined as color code. The program calculate from the regular grey colors the volume percents. Table 1 shows first results. The next table (Table 2) shows a comparison to other quantitative methods.

Table 1. Quantification results for CL with Digital Image Analysis.

image number	Alite [vol%]	Belite [vol%]	Aluminate & Ferrate [vol%]
CL01	67	19,7	13,3
CL02	66,1	24,2	9,7
CL07	67,4	5,9	26,7
CL08	69,2	8,5	22,3
CL11	72,2	24,8	3,9
CL12	60,1	1,9	37,9
CL15	74,8	5,5	19,7
mean value	68,1	12,9	19,1

Table 1 shows first results. The Alite contents vary from 60,1 vol% to 74,8vol%. The variation for Belite, Aluminate and Ferrate are greater. A possible reason is the even distribution of Alite, because it's the main phase. The variation of the other phases dependently on the selected images. The contents are converted in wt%. The pores are don't calculated, because the luminescence of the epoxy resin is too high.

Table 2. Quantification results for CL with Digital Image Analysis.

	Alite [wt%]	Belite [wt%]	Aluminate [wt%]	Ferrate [wt%]
point counting	72,5	11,0	16,5	
Rietveld	70,6	12,6	3,8	13,0
CL	66,1	12,8	21,1	

The results of the point counting analysis, Rietveld analysis and Cathodoluminescence technique are comparable. Alite concentrations differ from 66,1wt% to 72,5wt%. With Digital Image Analysis the Alite content are too low, because the Aluminate and Ferrate contents are calculated to high. Possible explanations are: not enough measurements for sufficient statistic or not correct defined color code.

3.1 Advantages

1. CL and optical microscopy can be directly compared;
2. Examination is more objective – even coloring of the CL images;
3. Differentiation between: Alite, Belite, Clinker slag, embedding media and polished powder is possible;
4. Automation is possible;
5. Use of computer-aided image analysis is possible.

3.2 Disadvantages

1. No differentiation between Aluminate and Ferrate can be obtained;
2. Cross dissolve of embedding media and pores occurs;
3. Calculation for Aluminate and Ferrate is too high;
4. Needing a grain size up to circa 0,01mm.

4 OUTLOOK

It is planned to use other embedding media for reducing luminescence. The media should have the property, there is no cross dissolve to the other clinker phases. There is the possibility to determine the pore weight percents. Additional measurements to calculate the standard deviations are in progress.

5 REFERENCES

- Campbell, D.H. Portland Cement Association, Illinois, 1986 Verein Deutscher Zementwerke, Mikroskopie des Zementklinkers, Beton Verlag Düsseldorf, 75 p. 1965.
- Pritula, O. Smrcok, L., On reproducibility of Rietveld analysis of reference Portland cement clinkers, Powder Diffraction, 18, p. 16-22, 2003.
- Stutzmann, P.E. Guide for X-ray powder diffraction analysis of Portland cement and clinker, NIST, Gaithersburg, 38p., 1996.
- Füllmann, T. Walenta, G. Pöllmann, H. Gimenezs, M. Lazon, C. Quantitative Rietveld analysis of Portland cement clinker and Portland cement – application as a method of automated quality and process control in industrial production, Intern. Cement Research, 1, 41-43, 2001
- Motzet, H.; Göske, J.; Pankau, H.G. & Pöllmann, H. Spezielle Analysemethoden von Zementen, GDCh München, Bd. 11, p. 70, 1997.
- Ozawa, L. Cathodoluminescence- Theory and Application, VHC Tokio, 308 p., 1990.
- Winkler, N. Pöllmann, H. Göske, J. Ries, R. Vergleich von Kathodolumineszenz und Auflichtmikroskopie an OPC Klinkern, Eur. J. Mineral., Vol 15, p. 217, 2003.

Firing Transformations of Clays from Santa Gertrudes Ceramic District

R.T.Zauberas & M.D.Cabrelon

Post-Graduate Program in Materials Science and Engineering, Laboratory of Ceramic Tiles, Department of Materials Engineering, Federal University of São Carlos, São Carlos, Brazil

R.C.Gennari, F.A.Guastala & A.O.Boschi

Laboratory of Ceramic Tiles, Department of Materials Engineering, Federal University of São Carlos, São Carlos, Brazil

ABSTRACT: Santa Gertrudes ceramic district products more than 50% of Brazilian ceramic tiles, and most of the 50 tiles industries located there use clay materials extracted from Corumbataí Formation. Composed of 280 million years marine sediments, clays from this Formation are almost ready to use in tile production, with no need for adding extra raw materials. Mineralogical composition of Corumbataí Formation, however, shows lateral and vertical variations, with occurrence of non-clay minerals associated with clay minerals, like feldspars, chalk, quartz and hematite, beside others, being these variations associated with firing behavior of tiles produced. This work evaluates microstructural changes during firing of four clays from Corumbataí Formation, with distinct mineralogical characteristics, industrially used for ceramic tiles production. Clays were characterized to chemical-mineralogical composition, particle size distribution, morphology and thermal behavior. Test bodies were processed and fired at six different temperatures, and microstructure of fired bodies was investigated through X-ray diffraction and electron and optical microscopy. Finally, microstructural transformations of bodies studied in lab scale were related to thermal behavior of clays in plant-scale. The comprehension of microstructure evolution during firing showed that non-clay minerals (impurities) highly affect ceramic tile properties.

1 INTRODUCTION

Santa Gertrudes ceramic district, located in São Paulo State, products more than 50% of Brazilian ceramic tile production (floor tiles), and most of these ceramic industries uses clays extracted from Corumbataí Formation as raw material.

Composed of 280 million years marine sediments, clays from this Formation are almost ready to use in tile production with no need for adding extra raw materials. Due to its high percentage of soft clay constituents, dry milling is preferred rather than wet milling, cheapening manufacturing costs. On the other hand, dealing with only one raw material makes industrial process less predictable because of clays physical, chemical and mineralogical heterogeneity on the same mining pit. Lateral and vertical variations are observed on clay deposits, with associated occurrence of non-clay minerals like feldspars, chalk, quartz and hematite (Christofaletti et al. 2003), beside others, altering tiles final properties if no adjust are made on processing parameters.

Defects related to these variations directly affect product aesthetic, causing different gages and pyroplastic deformation of tiles, and pin holes, bubbles or cracks on glazed surface (Biffi 2000);

extreme situations cause product inadequacy and mild ones raises stock management costs.

Purpose of present work is to evaluate how different physical, chemical and mineralogical characteristics of clays extracted from the same Formation affect floor tile properties, aiming to make industrial process more predictable.

2 EXPERIMENTAL PROCEDURE

Four hammer-milled and moisturized clays from Corumbataí Formation used as raw materials for floor tiles production (BIIB class, 6-10% water absorption) at Santa Gertrudes ceramic district were analyzed. Samples were characterized according to its chemical and mineralogical composition, particle size distribution (sieve and sedimentation procedures) and ceramic properties.

30 test bodies of each clay (7% humidity, dry basis) were pressed in a 6cm X 2cm die to an apparent density after drying of $1.85 \pm 0.02 \text{ g/cm}^3$ and sintered on a laboratory fast-firing kiln at 650°C, 750°C, 850°C, 950°C, 1050°C and 1100°C (5 minutes soaking time).

Characterization of fired samples involved the determination of linear shrinkage and loss on fire; water absorption of samples fired at 1050°C and

1100°C were also evaluated. Mineralogical analysis (Siemens D5005 X-ray diffractometer, CuK α radiation at 40kV and 40mA) were conducted in as-fired test bodies, and samples for microstructural analysis (Zeiss 940A SEM for back-scattered electron images – BSI - coupled with an Oxford EDS) were transversally cut, mounted on polyester resin and polished to 6 μ m superficial finish.

3 RESULTS AND DISCUSSION

Chemical analysis and particle size distribution (PSD) of four clays, named A, B, C and D, are presented at Table 1 and Figure 1.

Table 1. Chemical composition of clays.

Oxides (wt %)	Clays			
	A	B	C	D
SiO ₂	69.8	68.5	63.1	63.1
Al ₂ O ₃	14.1	15.2	12.3	11.2
Na ₂ O	1.5	0.6	2.9	1.1
K ₂ O	3.3	3.3	2.8	3.4
MgO	1.6	1.7	2.9	2.4
CaO	0.5	0.4	5.4	6.8
Fe ₂ O ₃	5.4	5.5	4.0	3.8
TiO ₂	0.6	0.6	0.6	0.5
others	0.3	0.2	0.3	0.2
LOI	2.9	4.0	5.7	7.5

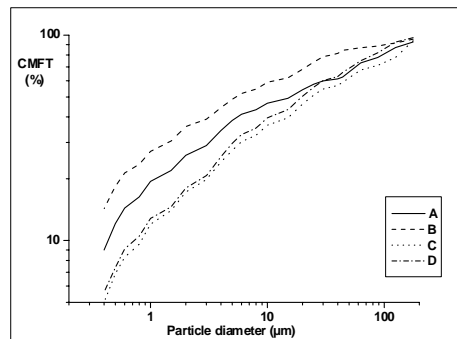


Figure 1: PSD of clays A, B, C and D.

All clays possess a high iron content, responsible for the red-brownish color of fired bodies. K₂O percentage is similar in all clays, Na₂O percentage is higher in clay C and alkaline-earth oxides content is significantly smaller in clays A and B.

Clay B possesses the highest percentage of particles finer than 10 μ m, clay A has an intermediate PSD and clays C and D are the coarser ones. Mineral identified on four clays by XRD are:

- clay A, quartz, illite, montmorillonite, hydrobiotite, plagioclase (anorthite and albite), orthoclase, goethite, hematite, calcium phosphate, iwakiite and manganese oxide;

- clay B, quartz, illite, montmorillonite, plagioclase (anorthite and albite), orthoclase, hematite, rutile, carbonatehydroxylapatite and iwakiite;

- clay C, quartz, illite, montmorillonite, calcite, plagioclase (anorthite and albite), orthoclase, hematite, rutile, calcium hydrogen phosphate and jacobite; and

- clay D, quartz, illite, montmorillonite, hydrobiotite, calcite, plagioclase (anorthite and albite), orthoclase, goethite, rutile, calcium phosphate, pyrolusite, iwakiite and esseneite.

The linear shrinkage (LS), loss on fire (LOF) and water absorption (WA) characterization of fired samples are presented in Tables 2-4.

Table 2: Linear shrinkage of fired samples.

Temperature (°C)	Linear shrinkage (%)			
	A	B	C	D
650	-0.3	-0.3	-0.2	-0.3
750	-0.4	-0.2	-0.2	-0.3
850	0.0	0.2	0.0	0.3
950	1.3	2.5	-0.1	0.8
1050	4.8	5.7	1.1	3.3
1100	7.5	8.0	6.6	6.9

Fired bodies of clays A, B and D had little dimensional change when fired at $\leq 850^\circ\text{C}$, and experienced a greater change above this temperature. Bodies from clay C showed a different behavior, with almost no shrinkage till 950°C and a sudden dimensional change above 1050°C ; in floor tile production, excessive shrinkage in a narrow temperature range may cause problems related to dimensional variation of fired tiles.

Table 3: Loss on fire of fired samples.

Temperature (°C)	Loss on fire (%)			
	A	B	C	D
650	2.0	2.7	1.9	2.5
750	2.3	2.7	3.1	3.8
850	2.5	3.5	4.9	6.4
950	2.7	3.6	5.5	7.1
1050	3.0	3.9	5.8	7.6
1100	3.1	3.9	6.0	7.6

Fired bodies from clays A and B had a somewhat linear LOF, smaller than from clays C and D, that showed a greater LOF for temperatures under 850°C . Relating measurements made on lab scale to plant scale (clays A, B, C and D are industrially processed under 25-30 minutes firing schedules at $1050\text{-}1150^\circ\text{C}$ maximum temperatures, and lab firing schedules were 15 to 20 minutes longer), it was observed that degassing was still occurring on clays A and C even in temperatures higher than 1050°C . This situation can originate bubbles and pinholes on glassy layer, affecting products aesthetic.

Table 4: Water absorption of samples fired at 1050°C and 1100°C.

Temperature (°C)	Water absorption (%)			
	A	B	C	D
1050	6.6	6.0	16.1	11.6
1100	1.8	2.0	4.4	3.0

Clays C and D showed an abrupt water absorption reduction at 1050-1100°C range, that is, they have a lower workability and its processing parameters must be strictly under control to ensure product uniformity and standard adequacy.

XRD of fired samples (Figs. 2-5) indicated that quartz was present in all samples and that illite and montmorillonite patterns persisted at temperatures as high as 950°C, although dehydroxylated. Calcite decomposition (clays C and D) occurred at different temperatures, and plagioclase (Na- and Ca-feldspars) seems to experience some alterations at >850°C, with Na-feldspar pattern losing its intensities and Ca-feldspar augmenting. K-feldspars do not seem to experience any alteration at evaluated temperatures. Legends of mineral phases are: montmorillonite (M), illite (I), goethite (G), quartz (Q), K-feldspars (Fk), plagioclases (P), calcite (C) and hematite (H).

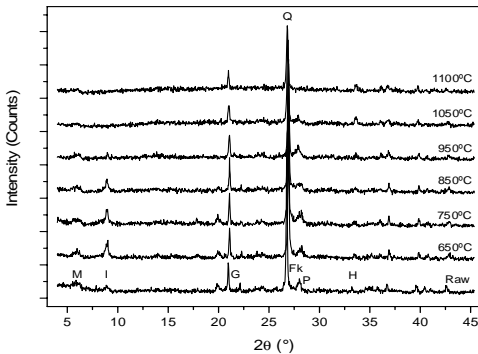


Figure 2: X-ray diffraction patterns of clay A.

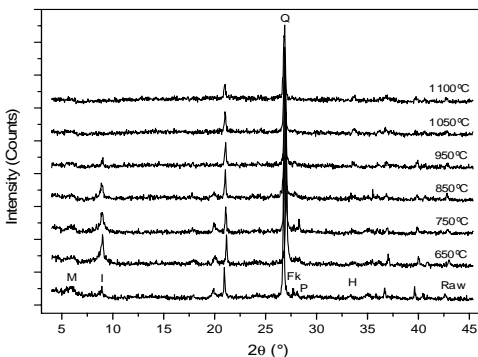


Figure 3: X-ray diffraction patterns of clay B.

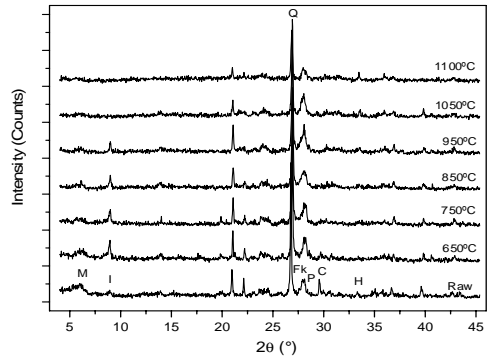


Figure 4: X-ray diffraction patterns of clay C.

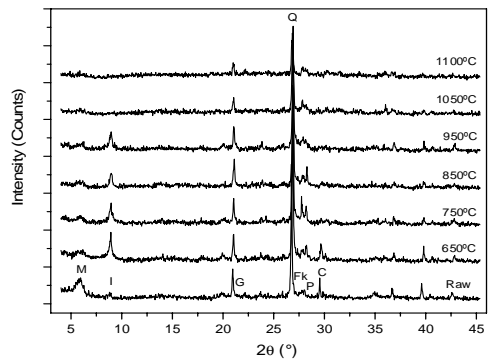


Figure 5: X-ray diffraction patterns of clay D.

BSI of test bodies fired at 1050°C revealed some features of clays. Clay A (Fig. 6) shows a dense structure, with quartz particles (Q) embedded in a matrix composed of clay relicts (porous structures). EDS analysis of brighter particle indicated the presence of Fe and Ti.

Clay B also presents a dense and homogeneous structure (Fig. 7), similar to clay A. A large quartz grain can be observed, presenting peripheral and internal cracks (due to quartz inversion between low and high temperature polymorphs). BSI of clay C (Fig. 8) shows a less dense structure and Ca-rich regions (relicts of calcite, labeled C) around pores; calcite decomposes originating CO₂, responsible for the low firing shrinkage of this clay at < 1050°C.

As shown in Figure 9, it can be noted an intermediate densification of clay D related to others clays and also a bright porous particle, with a high Fe- content (probably a goethite relict, since XRD pattern was noted at < 950°C).

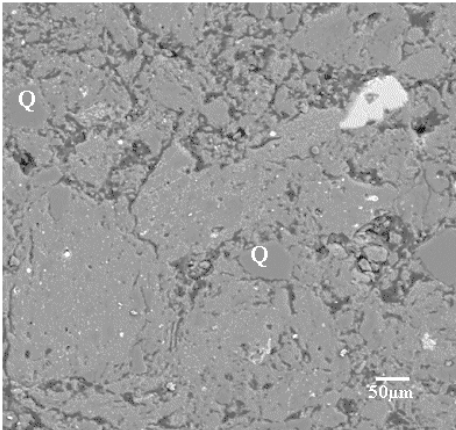


Figure 6: BSE of clay A.

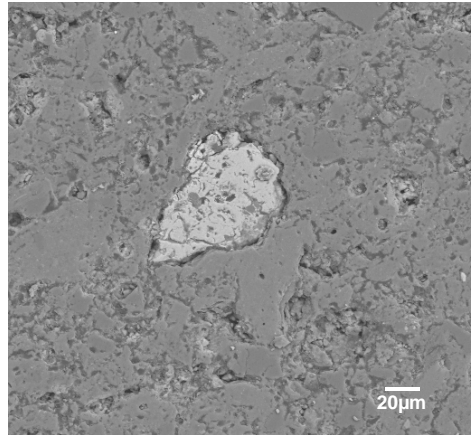


Figure 9: BSE of clay D.

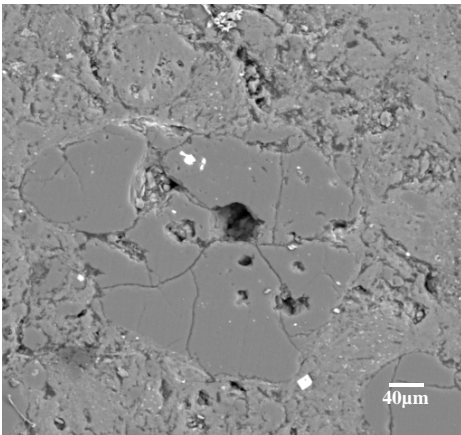


Figure 7: BSE of clay B.

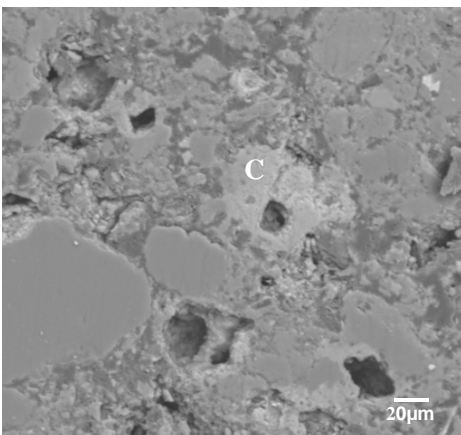


Figure 8: BSE of clay C.

4 CONCLUSIONS

Analyzed clays from Corumbataí formation, extracted from pits not more than 50km far, showed different firing behaviors. Clays A and B presented more predictable transformations on firing than clays C and D, which presented a very narrow firing range (less than 50°C), being more prone to product inadequacy according to floor tile standards (regarding to water absorption and dimensional tolerances), and these differences can be attributed to impurities present, mainly calcium and iron bearing minerals. That is, some of the industrially used clays from this formation do not seem to be proper raw materials for floor tiles production and, since dry milling is not an effective technique for mixing raw materials (and adjusting chemical and mineralogical composition to a desired target), more attention must be spent on adequate prospecting and characterization techniques of new clay pits, instead of trusting only on clay-extractor personal knowledge (nowadays common practice).

5 REFERENCES

- Biffi, G. 2000. Defeitos de fabricação de placas cerâmicas. Rio Claro: Faenza Editrice do Brasil Ltda.
- Christofoletti, S. R. et al. 2003. Os principais contaminantes minerais das rochas sedimentares da formação Corumbataí e sua influência na matéria-prima cerâmica. *Cerâmica Industrial* 8(1): 35-41.

Cultural Heritage

Mineralogy and Chemistry of Ceramics from Anthropogenic Black Earth of Amazon Region

M.L.da Costa & M.S.do Carmo

Department of Geosciences, Federal University of Para, Para, Brazil

D.C.Kern

Department of Ecology, Museu Paraense Emílio Goeldi (MPEG), Belém, Pará, Brazil

ABSTRACT: Fragments of archaeological ceramic are very frequent in archaeological sites with Black Earth all over the Amazon area. The ceramic fragments concentrate mainly on the A-horizons of the soil profile. An important Amazon area with great density of sites with Black Earth is Caxiuana, where the present work was accomplished. Mineralogical and geochemical studies and material potter's of Amazon were also shown effective for identification of the making raw material, production techniques, use identification and characterization of cultural lines. The Manduquinha site located in the Caxiuana bay, is 0,5 ha large, and A-horizon reaches 23 to 31 cm in thickness inside of Black Earth. The tempers found in the ceramic fragments are cauxi, cariapé, sands and crushed ceramics. Cauxi and cariapé are the main tempers and they are formed of organic silica-rich substances amorphous to the x-ray diffraction. The fragments are constituted of quartz, clay-minerals partially crystalline (modified during the burning) (illite and kaolinite), albite, anatase, variscite and iron oxides like maghemite. The chemical composition shows little variation between the distinct fragments and the tempers, and it is independent of the horizon of the soil. The P₂O₅ contents are relatively high and they meet in the form of amorphous phosphates of Al-Fe. Those values indicate contamination with phosphorus, coming from animal diet, and they show that the fragments can represent potteries of daily use.

1 INTRODUCTION

The study of archaeological ceramic vessels can aid in the determination of the origin and of the composition of the material used in its making as well as the making techniques, and, consequently the culture of the people that produced them. The geology, mineralogy and the geochemical have been applied with success in the study of ceramic of archaeological sites (Costa et al. 1991; 1993; 2001; *in press*).

The first mineralogical and chemical investigations of fragments of ceramic of Amazon carried out Costa et al. (1991), Kern (1996), Oliveira et al. (1997), Kern et al. (1997a), Nicoli et al. (2001); Latini et al. (2001), Filho et al. (2001), Appoloni et al. (2001), and Kennett et al. (2002). In the area of Caxiuana, placed in Lower Amazons region, 400 km far from Belém. Several anthropogenic (archaeological) black earth (ABE) sites with ceramic fragments were along the margins of bay and one, called Manduquinha, was selected to realize the present study.

1.1 The Manduquinha site

The Manduquinha site has an area of 0,5 ha, ellipsoidal contour is with larger axis parallel to the

margin of the bay of Caxiuana, and is located 6 m above the water bay level. The soil profile presents the horizons A_p, A₁, A₂, AB, BA, B₁, B₂ and B₃. The color of the horizons A is black (7,5YR 2/0), 23 to 31 cm thick and displays great density of ceramic fragments. It corresponds the occupation layer or a layer with human influence. Multi-element geochemical investigations conducted by Kern (1996) and Costa & Kern (1999) led to identify the possible form human settlement in the site occurred 600 year BP after radiocarbon dates, and consequently the maximum age of the ceramic fragments studied here.

2 MATERIALS AND METHODS

In the site Manduquinha were collected 45 samples of ceramic fragments in trenches, located inside of the ABE site: 26 samples from the A₁ horizon, where meets most of the ceramic fragments; 3 samples from AE; 2 samples from AB; and 14 from A₂. Mineralogical determinations were accomplished by XRD using Philips diffractometry model PW 3710. The mineralogical study were also supported using an optic microscope ZEISS, model AXIOLAB POL, in natural and polarized light, with

ocular (ACHROMATIC 50X) 10X, and lens objectives of 2.5X, 10X and 50X coupled with a photographic camera FUJITSU. The chemical analyses were involved: SiO₂ and loss on ignition-LOI (gravimetric analysis); Fe₂O₃ (dichromatometry); P₂O₅ and TiO₂ (colorimetry) and Al₂O₃ (complexometry-EDTA). CaO, MgO, MnO, Na₂O and K₂O (atomic absorption). All these analyses were realized at the facilities of the Centro de Geociências/Universidade Federal do Pará. With the scanning electronic microscope-SEM with energy dispersive system-EDS (LEO 1450VP.) Museu Paraense Emílio Goeldi we try to identify microcrystalline phases, as the phosphates.

3 RESULTS AND DISCUSSIONS

3.1 Classification of the ceramic fragments tempers

The fragments were classified after the tempers in: ceramic with cauxi (Cx), ceramic with sand (S), ceramic with older crushed (Cm) and ceramic with cariapé (Cp).

The ceramic fragments with cauxi are most abundant and those with sands are less frequent. Cauxi is sponge-like microorganisms (*Parmula batesii* Crankcase and *Tubella reticulata* Crankcase) very common in trees close to the margin of Caxiuanã bay and as suspend load in its water and as part of its bottom sediments (Costa et al. 2002).

3.2 Textural aspects

Ceramic with cauxi presents a micro the cryptocrystalline matrix, interpreted to derived from a clayish material impregnated with cryptocrystalline iron oxy-hydroxide, also cryptocrystalline, denounced by the brown color. Inside of this matrix, floating, occur aggregates cauxi spicules oriented or random distributed. Besides cauxi aggregates also occur many anhedral to subhedral quartz grains.

Ceramic with cariapé displays the same clayish cryptocrystalline matrix, inside of it float small platty and elongated pallets of brown color made of cariapé (*Bignoniacea moquilea* and *Licania utilis*), a outer tree skin, besides anhedral to subhedral quartz grains.

Ceramic with sand shows matrix characteristics similar to the other tempers. It differs from the other ones through the great amount of mineral grains in the sand fraction, mainly represented by quartz and feldspar or rock fragments.

Ceramic with older crushed distinguished from the others ones because it presents fine grained crushed ceramic remains inside of its cryptocrystalline matrix. Older ceramics were, intentionally triturated and reused in the making of new pieces. This still contains quartz, cauxi and

cariapé, in textural arrangement similar observed in the other tempers.

3.3 Mineralogical composition

The ceramic fragments are mainly constituted of quartz, thermal-modified clay mineral (partly burned kaolinite probably), illite, feldspar (albite), anatase, besides iron oxides as maghemite (γ -Fe₂O₃) or hematite (α -Fe₂O₃) and amphibole some times. Albite is found in the samples of ceramic fragments practically independent of the each temper. The amphibole was just observed in the sample CX-42.

Phosphates are present, after the chemical analyses but were not identified by either by x-ray diffraction nor by optical microscope. The SEM/EDS semiquantitative analyses indicate an aluminum phosphate as variscite well distributed in the clayish matrix but especially close to cariapé and cauxi.

3.4 Chemical composition

The ceramic fragments are dominantly constituted by SiO₂ (71.35%), besides of Al₂O₃ (8.6%), Fe₂O₃ (4.54%), P₂O₅ (1.31%), Na₂O (0.98%), K₂O (0.59%), TiO₂ (0.4%), MgO (0.26%), CaO (0.19%). The LOI is relatively high (11.63%). The high values of SiO₂ detach the high contents of quartz, besides cauxi and cariapé, and when associated to Al₂O₃ the clay minerals (burned kaolinite dominantly) and the feldspars. The still relatively elevated values of Na₂O and K₂O confirm the presence of albite and illite, respectively. The diagram Al₂O₃-Fe₂O₃-P₂O₅ (Fig. 1) shows small chemical variation specially for phosphorus. The ceramic fragments with cauxi display enrichment toward Al₂O₃. In the diagram MgO-P₂O₅-TiO₂ (Fig. 2) the ceramic fragments with cariapé can be discriminate by enrichment toward TiO₂. On the other hand the diagram with the earthy alkaline and alkaline metals (Na₂O, K₂O, CaO and MgO) show two field composition, one with higher values of Na₂O (Fig. 3) including the majority of the samples of fragments and another one with higher values of K₂O. The Na₂O field correspond to ceramics with cariapé temper.

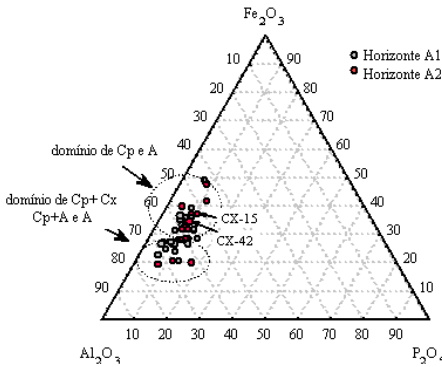


Figure 1. Ternary diagram Al_2O_3 - Fe_2O_3 - P_2O_5 (S=sand, Cp= cariapé, Cx= cauxi, Cm= crushed ceramic) showing quite homogeneous composition for all tempers.

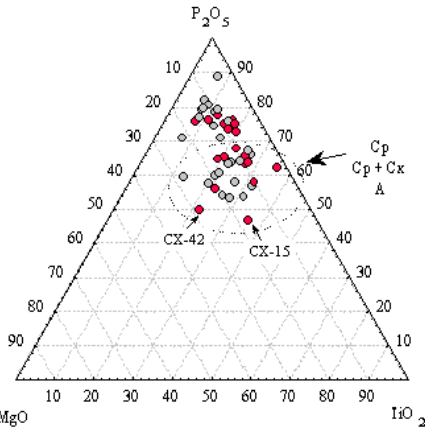


Figure 2. Ternary diagram MgO - P_2O_5 - TiO_2 showing enrichment of TiO_2 in ceramic with cariapé.

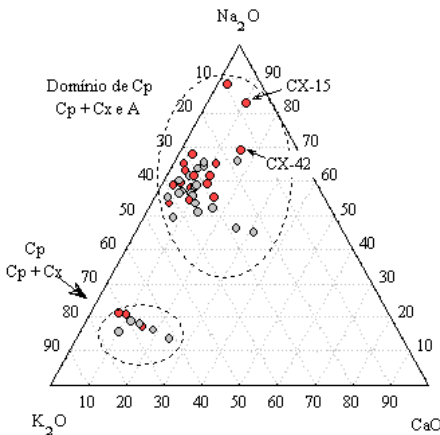


Figure 3. Ternary diagram Na_2O - K_2O - CaO showing clearly two field composition.

These K_2O - Na_2O antagonism with the discrimination of the two fields is also shown by the K_2O - Na_2O correlation ($r=0.52$). The field of the Na_2O , with most of the samples, represents the fragments with albite presence that it is found in those with cariapé, cauxi and sand tempers, mainly. The field of K_2O indicates the illite presence, confirmed by the positive correlation K - Mg ($r=0.86$). The illite can also contain Ti indicated by the slight positive correlation TiO_2 - MgO ($r=0.49$) or it bears anatase micro-inclusions, as observed by Costa et al. (*in press*) in Cachoeira Porteira.

3.4.1 The phosphorous

An aspect a lot of striking in the chemical composition of the ceramic is the relatively high values of P_2O_5 , already verified in ceramic fragments associated to the black earth in the Amazon Region (Costa et al. 1993, 2001; Costa & Kern 1999; Latini et al. 2001; Lima et al. 2002; Costa et al. *in press*).

The P_2O_5 values (0.71 to 2.1%) found at Manduquinha are slightly lower than those described by Costa et al. (1993) in other sites of Amazon Region. Costa et al (1993) found phosphates type variscite and rhabdophanite locally. In Cachoeira Porteira they were found elevated of P_2O_5 similar or same values and even so it was not found apatite. The analyses of SEM allowed to observe the presence common of phosphates of aluminum together cryptocrystallines or inside of the fabric of the cariapé fragments and cauxi, or same distributed in the matrix. The analysis semiquantitative for SEM/EDS in a point of the clayish matrix with cariapé temper suggests the presence of very small and well distributed crystals contends P, Al and Fe, besides Ca and K, interpreted as amorphous phosphates of Al-Fe.

4 CONCLUSIONS

The archaeological ceramic fragments of Caxiuana show the present tempers: 1) cariapé; 2) cauxi; 3) sand (feldspars and/or quartz); 4) tritulated ceramic. The most common are those ones with cariapé and cauxi. All fragments are made of quartz, burned clay mineral (interpreted to be kaolinite-derived), albite, illite and hematite. The mineral composition does not show any relation to the different types of temper and this way can not use for ceramic classification. Exception can be made only for the sand temper, where illite is not frequent. It is outstanding the relatively elevated values of P_2O_5 , interpreted to occur as amorphous (Al, Fe)-phosphates, and come from food cooking, which can promote the contamination the ceramic vessel walls with phosphorus. The cooking liberates phosphorous

from the food to the liquid during the concoction, which reacts with the amorphous to cryptocrystalline clay mineral of the wall body leaving form amorphous aluminum phosphates (Costa et al. 1991). A contamination through soils is discarded, because the variations of P_2O_5 in the ceramic fragments do not display any dependence nor to the soils horizons, neither to the tempers. The raw material for elaboration of ceramic vessel of Caxiuana was constituted of clayish material with kaolinite and quartz, and some illite. To them was added albite, rocks fragments (granites: quartz and feldspars), or cariapé and/or cauxi, separately, or even two or more of these tempers, which come from the surrounding area.

5 REFERENCES

- Appoloni, C. R.; Quiñones, F.R.E.; Aragão, P.H.A.; Santos, A. O.; Silva, L. M.; Barbieri, P.F.; Nascimento Filho, V.F.; Coimbra, M.M. 2001. EDXRF Study of Tupy-Guarani Archaeological Ceramics. *Radiation Physics and Chemistry*. 711-712.
- Costa, M. L.; Kern, D.C.; Souza, J.R.T.; Pinto, A.H.E. 1991. A Mineralogia e a Geoquímica na Cerâmica Arqueológica de Oriximiná-PA. 3º Congr. Bras. de Geoquímica, São Paulo, p.1-3.
- Costa, M.L.; Kern, D.C.; Pinto, A.H.E.; Souza, J.R.T. 1993. Geochemical contribution to archaeological ceramics of Cachoeira-Porteira (Oriximiná-PA). *International Symposium on the Quaternary of Amazonia*, Anais. Manaus. Pág.: 09.
- Costa, M. L. & Kern, D.C. 1994. Geoquímica Aplicada à arqueologia (Arqueogeoquímica da Amazônia). IV Simpósio de Geologia da Amazônia, SBG, Belém, 261-263.
- Costa, M.L. & Kern, D.C. 1999. Geochemical signatures of tropical with archaeological black earth in the Amazon, Brazil. *Journal of Geochemical Exploration*. 66: 369-385.
- Costa, M.L.; Kern, D.C.; Pinto, A.H.E.; Souza, J.R. T. 2001. Mineralogia de Artefatos cerâmicos de Sítio arqueológico com terra preta no baixo Amazonas. XI Congr. Arqueologia, Rio de Janeiro, SAB pág 65.
- Costa, M.L., Kern, D.C., Behling, H., Borges, M.S., 2002, Geologia. In: Pedro Lisboa (org.). Caxiuana: populações tradicionais, meio físico & diversidade biológica. Museu Paraense Emílio Goeldi, Belém-PA, p.179-205.
- Costa et al., (in press) – Archaeological ceramic of dark earth sites from Lower Amazon region: Mineralogy. *Acta Amazônica*.
- Costa, M. L.; Kern, D. C.; Pinto, A. H. E.; Souza, J. R. T. (submetido). Mineralogy and origin of the phosphates in the ceramic artifacts from archaeological black earth in the lower Amazon region. *Acta Amazonica*.
- Filho, U.M.V.; Latini, R.M; Bellido, A.V.B.; Buarque, A.; Rossi, A.M. 2001. Cerâmicas Arqueológicas da Região de Araruama no Estado do Rio de Janeiro. VI Congresso de Geoquímica dos Países de Língua Portuguesa XII Semana de Geoquímica. pág.: 679-682.
- Kennett, D.J.; Sakai, S.; Neff, H.; Gossett, R.; Larson, D.O. 2002. Compositional Characterization of Prehistoric Ceramics: A New Approach. *Journal of Archaeological Science*, 443-455.
- Kern, D.C. 1996. Geoquímica e Pedogeoquímica em Sítios Arqueológicos com Terra Preta na Floresta Nacional de Caxiuana (Portel-PA). Centro de Geociências-UFFPA. Tese de Doutorado, 124p.
- Kern, D.C. & Costa, M.L. 1997a. Cerâmica arqueológica (sítio PA-GU-5; Manduquinha) e cabocla na região de Caxiuana-Pará. *Revista de Arqueologia*. 10: 107-125.
- Latini, R.M.; Bellido Jr., A.V.; Vasconcelos, M.B.A.; Dias Jr., O. F. 2001. Classificação de cerâmicas arqueológicas da bacia amazônica. *Química Nova*, 24 (6): 724-729.
- Lima, H.N.; Schaefer, C.E.R.; Mello, J.W.V.; Gilkes, R.J.; Ker, J.C. 2002. Pedogenesis and pre-colombian land use of "Terra Preta Anthrosols"(Indian black earth") of western Amazonia. *Geoderma*. 110:1-17.3

Characterisation of Binder Related Particles (lime lumps) in Historic Lime Mortars

J.Elsen

Department of Geology, Katholieke Universiteit Leuven, Leuven, Belgium

ABSTRACT: The results of chemical-mineralogical analyses of binder related particles presented here are part of a broad investigation of historic lime mortars from different periods (Byzantine, Roman, Carolingian and Romanesque) and from different monuments and excavations in Belgium and Turkey. The results of the study of a great number of historic mortars by optical microscopy indicate that most samples contain smaller or greater 'lime lumps'. These binder related particles are generally rounded often porous structures, appearing distinctly in the mortar matrix. A great number of these lime lumps were investigated in more detail by SEM/EDX and microprobe methods to investigate the nature of these particles. Three distinct groups of lime lumps *sensu stricto* could be identified and even a non-hydrated calcium silicate phase could be observed in the central part of one particle. Apart from these three groups several other binder related particles consist of mixtures of different phases with unclear mineralogical composition or unclear origin. The results of the characterisation of these binder related particles have clearly proved to be useful for a better knowledge about the various technologies used in lime production and mortar preparation and to determine the hydraulicity of ancient lime mortars.

1 INTRODUCTION

The results of chemical-mineralogical analyses of binder related particles presented here are part of a broad investigation of historic lime mortars from different periods (Byzantine, Roman, Carolingian and Romanesque) and from different monuments and excavations in Belgium and Turkey. The characterisation of historic lime mortars enables us to refine our knowledge of the mortar composition, the original materials and their provenance, to specify the various technologies used in lime production and mortar preparation and to distinguish improvement or deterioration in the composition and qualities of mortars throughout time.

The results of the study of a great number of historic mortars by optical microscopy indicate that most samples contain smaller or greater 'lime lumps' as mentioned by several authors to be often present in historical lime mortars (Knöfel 1991, Schouenborg et al. 1993, Hughes et al. 1999, Hughes et al. 2001). These lime lumps are generally rounded often porous structures, appearing distinctly in the mortar matrix. The origin of these is not agreed upon, but there are a couple of explanations

stated by different authors. Some binder related particles are considered to be partly-sintered particles formed in traditional kilns where there are hot zones sufficient to initiate fusing or sintering of the lime. When sintered the lime is weakly reactive, or dead burned and when in a mortar, over time it will hydrate and carbonate. According to Knöfel (1991), Hughes et al. (2001), Callebaut et al. (2001) and others, the presence of well-rounded porous lime lumps indicate that the lime used was dry-slaked, that is slaked with a minimum amount of water to convert all CaO in Ca(OH)₂. A method mentioned in literature for the production of dry-slaked lime is thoroughly mixing of wet sand with burnt lime fragments (Kraus et al. 1989). From experimental work, these lime lumps *sensu stricto* are indeed formed by such dry-slaking method (Callebaut et al. 2001).

Probably different types of binder related particles, inclusions occur in ancient mortars with a different origin but the nature of a certain lime lump or particle is not easily determined by optical microscopy alone. Therefore, a great number of these binder related particles were investigated in more detail by SEM/EDX and microprobe methods.

2 MATERIALS AND METHODS

Historical mortar samples from different periods (Byzantine, Roman, Carolingian and Romanesque) have been taken from several monuments and excavations in Belgium and Turkey. Since 1990 regular archeological excavations have been carried out in the Hellenistic and Roman city of Sagalassos (Burdur province, Southwestern Turkey) by the Catholic University of Leuven (Degryse et al. 2002). Another series of samples were taken during excavations around the Cathedral at Tournai in Belgium and are investigated as part of a broader study considering the transition of ancient cities and their rural territories from Roman to late Roman society and the transformation to the early middle ages.

The samples were taken using hammer and chisel and their location is described and illustrated with photographs. All samples have been characterised using a combination of chemical and microscopical (PFM and SEM) techniques. Polished thin sections have been analysed by SEM/EDX (PHILIPS-SEM-XL30i/EDAX) using a solid state Back-Scattered Electron detector with a gold coating and have been analysed by a JEOL microprobe after carbon coating.

3 RESULTS

A number of point analyses of ca 5-10 μm^3 in binder related particles, selected using optical microscopy, were carried out with the following results; one group of particles consists of 56 wt% CaO (100 wt% on a volatile-free basis = pure CaCO_3); a second group consists of one phase containing mainly CaO ($\text{Ca}(\text{OH})_2$ and CaCO_3) with a certain amount of SiO_2 (2-10 wt%); a third group consists of two zones, an outermost carbonated zone and an internal zone with the chemical composition of 33-39 wt% SiO_2 and 34-37 wt% CaO, which can be interpreted as composed of calcium silicate hydrate (CSH). In the central part of one particle of this third group, the remains of a non-hydrated phase could be observed (Fig. 1) with a composition of 42-45 wt% SiO_2 and 55-58 wt% CaO, which can be interpreted as a calcium silicate phase. Apart from these three groups several other binder related particles consist of mixtures of different phases with unclear mineralogical composition or unclear origin.

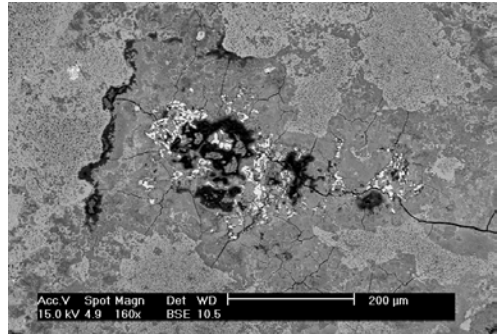


Figure 1 : BSE-image of the central part of a binder related particle. Two main zones can be distinguished, an outermost carbonated zone (pure CaCO_3) and a central, dark-grey zone with a chemical composition corresponding to a calcium silicate hydrate phase. In the central part of the figure, porous zones (black) and white particles with a chemical composition corresponding to a calcium silicate phase can be distinguished.

4 CONCLUSIONS

The results of the study of a great number of historic mortars by optical microscopy indicate that most samples contain smaller or greater binder related particles also named 'lime lumps' in literature. These binder related particles are generally rounded often porous structures, appearing distinctly in the mortar matrix. A great number of these particles were investigated in more detail by SEM/EDX and microprobe methods to investigate the nature of these particles. Three types of binder related particles can be distinguished; underburned fragments, overburned fragments and lime lumps sensu stricto. Underburned fragments can provide information about the type of limestone that has been used to burn the lime and thus also about the hydraulicity of the lime. Results of mineralogical analyses on overburned fragments can provide information about maximum burning temperatures used. The results of SEM/EDX and microprobe analyses on lime lumps sensu stricto inform us about the hydraulicity of the lime binder.

We can conclude that binder related particles can provide information for the assessment of the nature and the provenance of the raw materials and of the historic technologies which have been used in lime production and mortar preparation.

5 REFERENCES

- Callebaut K. & Elsen J. 2001. Nineteenth century hydraulic restoration mortars in the Saint Michael's church (Leuven, Belgium): natural hydraulic lime or cement? *Cement and Concrete Research* (31) 397-403.
- Degryse P., Elsen, J. & Waelkens M. 2002. Study of ancient mortars from Sagalassos (Turkey) in view of their

- conservation, *Cement and Concrete Research*, (21), 1457-1463
- Hughes J.J., Cuthbert S. & Bartos P. 1999. Alteration textures in historic Scottish lime mortars and the implications for practical mortar analysis. In: *Proceedings of the 7th Euroseminar on Microscopy Applied to Building Materials*, Delft, 417-426.
- Hughes J.J., Leslie A. & Callebaut K. 2001. The petrography of lime inclusions in historic lime based mortars. In: *Proceedings of the 8th Euroseminar on Microscopy Applied to Building Materials*, Athens, Greece, 359-364.
- Knöfel D. 1991. Alte und neue Mörtel. Materialkundliche Untersuchungen und Empfehlungen für Instandsetzungsmörtel. *Arbeitshefte des Sonderforschungsbereiches 315 "Erhalten historisch bedeutsamer Bauwerke"* (10) 32-38.
- Kraus K., Wisser S. & Knöfel D. 1989. Über das Löschen von Kalk vor der Mitte des 18. Jahrhunderts – Literaturauswertung und Laborversuche. *Arbeitsblätter für Restauratoren* (1), 206-221.
- Schouenborg B., Lindqvist J.-E., Sandström H., Sandström M., Sandin K. & Sidmar E. 1993. Analysis of old lime plaster and mortar from southern Sweden. Swedish National Testing and Research Institute, SP Report 34.

Brazilian Cultural Heritage under a New Light

D.L.A.de Faria

Institute of Chemistry, University of São Paulo, C.P. 26077, 05513-970, São Paulo, Brazil

M.C.Afonso & S.C.Lima

Museum of Archaeology and Ethnology, University of São Paulo, Av. Prof. Almeida Prado 1466, 05508-900 São Paulo, Brazil

H.G.M.Edwards

Department of Chemical and Forensic Sciences, University of Bradford, BD7 1DP, Bradford, UK

ABSTRACT: The growing interest in the development of new and more powerful methods of investigation of cultural heritage problems has been motivated by the needs of conservators. Very rare and/or valuable objects can't be damaged during the analysis and in these cases the use of non-destructive techniques is mandatory. Raman microscopy is being recognised as one of the most powerful tools in the investigation of art and archaeology problems, allowing the object to be studied as it is, directly on the microscope stage or using fibre-optics. Many collaborative works on Brazilian cultural heritage objects are currently in course and some examples are given in the present work, where the use of Raman spectroscopy in the investigation of biomaterials (bones and teeth) from sambaquis, archaeological and ethnographic resins is reported. Inorganic compounds used in ceramics are also here focused. Important informations were obtained for (i) red-pigmented bones (very pure unprocessed haematite) collected in a sambaqui (Santa Catarina); (ii) ethnographic resins (mostly diterpenic ones); (iii) resin tembetá (unprocessed triterpenoid resin) found in São Paulo and (iv) pigments in ceramics (metal oxide based pigments, charcoal and kaolin).

1 INTRODUCTION

The scientific study of cultural heritage objects and the materials used in their creation has provided an impetus for the application and development of non-destructive, micro-sampling analytical techniques. The complexity in composition of the source materials used in their construction, the lack of precise knowledge about their preparation and ancient technologies used in their production provide some of the most challenging problems for analysis.

Environmental damage is another key feature to be addressed when exposition to the elements occur; in particular, the aggressive colonisation by microbes and lichens of exposed stone, rock and plaster surfaces found in rock art, wall-paintings and frescoes, as well as the obvious substratal damage caused by acid rain or hydrocarbons from vehicles and habitation combustion processes, are urgent problems which require some rapid solutions. Objects that were buried for centuries put another interesting question since the nature of the degradation also depends on the burial conditions (soil composition and acidity, humidity, temperature etc) apart from the burial time.

In these cases, therefore, analytical techniques are required not only simply to furnish information about the original construction of an object, but also to identify the sources and extent of chemical or biological deterioration therein, and, if possible, to provide some "early warning" signals to alert conservators to major potential problems. In this area infrared and Raman microscopy have been particularly relevant in their applications as well as providing information about pigment composition, resins used in varnished and the original sourcing of materials (Faria et al. 2002).

In this work some recent results using Raman microscopy in the investigation of Brazilian cultural heritage objects is reported. The study encompasses archaeological (Faria et al. 2004 in press) and ethnographic resins (Faria et al. 2003), pigments on ceramics and pigmented bones collected from sambaquis (Edwards et al. 2001). Regarding degradation, the archaeological resin and the pigmented bones are of particular interest because they were collected in excavations thus allowing a better understanding of the effect of the burial site conditions on the degradation. In the case of pigments on ceramics, the main purpose is the identification of materials and techniques used.

2 EXPERIMENTAL

FT-Raman spectra were obtained using a Bruker IFS/66 FRA 106 and a Bruker RFS 100/S instrument, both with Nd³⁺/YAG laser excitation at 1064 nm. Spectra were recorded with 4 cm⁻¹ spectral resolution and, in most cases, with 2000 scans accumulated to provide better signal-to-noise ratio; the laser spot was approximately 100 µm in diameter at the sample. Raman spectra excited in the visible were also obtained (Renishaw Raman microscope, using the 632.8 and 785 nm lines); in some cases the vibrational bands were swamped by the strong fluorescent background.

Samples

The bones were excavated from a sambaqui (Jaboticabeira II, burial No. 32 at Locus 2.16, trench 15) in the south of Santa Catarina State, which are being investigated by the Camacho Archaeological Project. Almost all of the bones and bone fragments (ca. 3000 years old) exhibited pronounced ochre coloration landmarks, which were particularly thickly layered on the humerus. All specimens were in a fragile and friable condition. For our Raman spectroscopic work, particular attention was paid to this heavily coloured humerus specimen, where in places the pigment could be seen lying on the surface of an indefinite mass which was attached to the bone.

The resin *tembetá* (lip-plug) was recovered from an excavation of a guarani tribe habitation in the archaeological site named Pernilongo at Iepê, south of São Paulo State, Brazil. It is about 1600 years old and in appearance it is a tapered cylinder with a cross-bar at the top. It was found split in pieces together with other smaller fragments, which probably were used as ear adornments; they were found buried inside a 50 cm sediment layer, close to a water reservoir and it is thus believed that the fragments were covered by water (ca. 20 cm) and, in drier periods, only by the sediments.

Ethnographic resins were nine different resin samples from the Amazon and Central areas in Brazil and belonging to the MAE collection. Their age ranged from about 40 to 100 years; externally they generally present a black or dark brown surface but an inspection in the internal regions reveals bright and mostly red resins.

Indian pottery fragments belong to MAE and are representative of Tupi-guarani tradition. The specimens present areas with black, white and red pigments.

3 RESULTS AND DISCUSSION

Although it is easy to find information about the presence of ochre in burials located in *sambaquis* in the archaeological literature, this material has

actually never been analysed to date. The archaeologists have identified the ochre form, if it appears in pebbles or powder deposits, where on the body it was found and its colour (bright red, red–yellowish). However, archaeological ochre analysis hitherto has been restricted to the pigments used in rock art.

Thus, Raman spectroscopic techniques were used to the analysis of red ochre-stained archaic human bones aiming to address the following questions: (i) is there evidence for an ancient technology of red ochre preparation for body painting? (ii) was any binding agent, organic or inorganic, used to apply the pigment to the body? (iii) can the presence of biodeteriorative chemicals caused by the reaction of tissue degradation materials and the pigment be observed?

The heavily pigmented area of the bone shows bands at 244, 292, 409 and 610 cm⁻¹, which are characteristic of haematite, providing for the first time a clear indication of the generic term ‘red ochre’ used by archaeologists to describe this pigmentation. It has long been realized that red ochre formulations varied in ancient times and that this usually included fine sand or clays, however, the bands are sharp and the absence of goethite peaks or a sharp Raman band at 465 cm⁻¹ from α -quartz (sand particles) clearly indicates that the haematite was not derived from goethite heating and was in a very pure form.

Analysis of the FT-Raman spectrum of the unpigmented area of the bone also shows that almost complete leaching out of the organic component (mainly collagen) has occurred. A comparison of the bone spectrum from the 3000-year-old skeleton and from a Roman bone specimen shows the extensive mineralization of the *sambaqui* specimen; the proteinaceous $\nu(\text{CONH})$, $\delta(\text{NH})$ and $\delta(\text{CH}_2)$ modes of collagen at 1650, 1450 and 1230 cm⁻¹ in younger bone have been considerably reduced in intensity for the ancient specimen. Also, in the 3000-year-old sample the presence of carbonate (weak intensity peaks at 1086, 712 and 283 cm⁻¹) can be seen, which indicates mineralization of this specimen through absorption of carbonaceous material into the inorganic matrix on vacation of the sites occupied by the collagenic component.

A deeply pigmented area on the humerus seems to be overlying what appeared to be an amorphous mass microscopically. This could be detritus from the grave site or organic residues from the body deterioration, but it could be an important area for more detailed examination since the ochre is firmly adhered to the paler amorphous mass, which itself is adherent to the bone. No Raman signals indicative of an organic origin were obtained of the amorphous material, only a weak $\nu(\text{PO})$ band from phosphatic bone and absence of $\nu(\text{SiO})$ indicates that it is not a

proteinaceous, phosphatic or sandy deposit. However, a new broader feature appeared at 790, 710 cm^{-1} , which is here ascribed to a 'limewash-like' phase (calcium oxide-hydroxide). It is not clear yet, however, whether this later archaic culture intentionally prepared the body with 'limewash,' or it was the result of years of slow exchange of calcium (from the bone) by iron (from haematite). If it was intentionally prepared the purpose could be to facilitate the adhesion of the pigment to the bone or to accelerate the body decomposition. It would be important archaeologically to study the artefacts and habitation of this culture to see if there is evidence of an ancient technology associated with lime production from sea-shells which contain a form of calcium carbonate known as aragonite and on heating to temperatures of about 750 °C breaks down into lime (calcium oxide); such investigation is currently being undertaken.

Concerning archaeological resins, a ca. 1600 years-old *tembetá* was investigated. *Tembetá* is a lip-plug used in some cultures to signify the attainment of adulthood by a male member of the tribe. The specimen is rare and only a few other resin *tembetás* are known as these adornments were mostly constructed from wood or stone. In none of them the resin composition was accessed. There is a coating of brick-red material over the dark red resin; the coating is badly degraded and has flaked off in several parts, thereby exposing the resin beneath. There is a suggestion that the coating is possibly red ochre from its appearance and colour. The purpose of non-destructive Raman spectroscopic analysis here is to learn something about the chemical composition of the resin, which may assist conservators in urgent restoration of the artefact, and to confirm the presence of red ochre as the coating on the resin.

Several regions of resin and the coating were examined, followed by a comparison of the spectral results with a database of archaeological resins. The outer surface "coating" of the *tembetá* is not iron(III) oxide or any other mineral pigment since its spectrum is similar to the clear, dark red resin interior of the specimen. A decrease in band sharpness, however, is attributed to a degradation of the resin at its outer surface in contact with the burial environment.

Most resins used in antiquity are composed of mixtures of terpenes with diterpenoids (C_{20} compounds) and triterpenoids (C_{30} compounds) being most common. Resins such as those belonging to the *Pinus* (*Pinaceae*), *Agathis* and *Hymenaea* (*Caesalpiniodeae*) species are predominantly diterpenoid, those of the *Pistacia* (*Anacardiaceae*), *Commiphora* and *Boswellia* species, however, are predominantly triterpenoid. It is extremely rare to find a natural resin which contains both diterpenoid and triterpenoid

components, hence the distinction between these through their Raman spectra will provide a sound means of indicating some possibilities of identification of an unknown resin and will exclude other likely sources.

An earlier research on the discrimination protocol for diterpenoids and triterpenoids has shown that the wavenumber region 1520-1750 cm^{-1} is crucial for the discrimination in the terpenoid classification. When the Raman spectra of *tembetá* is compared with *Pinus halepensis*, *Cedrus libani* and *Pistacia lentiscus* resins the presence of two major Raman bands in this region, namely 1702 and 1656 cm^{-1} is indicative of a triterpenoid resin as diterpenoid ones, containing predominantly abietane compounds, have strong bands at approximately 1650 or lower and 1611 cm^{-1} , sometimes with a band near 1635 cm^{-1} whose intensity increases with specimen degradation. On the other hand, *Pistacia* resins always have a slightly higher wavenumber feature at about 1655 cm^{-1} and a weaker band near 1705 cm^{-1} . Degradation produces a weaker shoulder around 1620 cm^{-1} . Hence, the obtained spectra indicate that the *tembetá* resin is a triterpenoid, whose composition is near that of *Pistacia* resins. A confirmation of the triterpenoid classification of the *tembetá* resin is the presence of a doublet at about 1460/1440 cm^{-1} , in which the two bands are of similar intensity. The $\nu(\text{CH})$ stretching region (not shown) is not definitive enough for unambiguous identification or classification of the unknown resin as diterpenoid or triterpenoid.

There is a tradition that Indian tribes from the south-east of Brazil and Paraguay used a resin from *Hymenaea stigonocarpa* Mart. (*Jatobá*) to construct artefacts; the Raman spectrum of such resin was obtained and on the basis of the protocol used here, the *Jatobá do Cerrado* resin is unambiguously not the source for the *tembetá* artefact, since it is a diterpenoid in composition as indicated by a strong feature at 1634 cm^{-1} , with weaker shoulders at about 1650 and 1640 cm^{-1} . We are as yet unable to obtain specimens of likely contemporary alternatives, which could have been used in the construction of the resin *tembetá* and, indeed, it appears that geocologists are of the opinion that changes in climate and population movement make it unlikely that the precise botanical sourcing of the *tembetá* resin will emerge.

The successful investigation of the *tembetá* inspired the investigation of ethnographic resins, aiming the construction of a database with Raman spectra of Brazilian resins, which can be applied to museum objects. The results obtained so far have revealed some interesting features: although the resins look similar by visual inspection, their Raman spectra are significantly different allowing the samples to be classified into 4 groups: (i) diterpenoid resins in association with carotenoids

(intense bands at 1517 and 1153 cm^{-1}); (ii) diterpenoid resins, probably with its structure based on the labdane skeleton (most significant bands at 3080, 2930, 2870, 1520, 1155 and 1012 cm^{-1}); (iii) gum, probably, with bands of similar intensities between 1650 and 800 cm^{-1} and (iv) poor light scatterer resins. Such classification is based on previous studies reported in the literature involving a large number of resins and gums from different sources; unfortunately none of them included resins from the Amazon area. Mass spectrometry is currently in use to confirm the information obtained from Raman spectroscopy.

The non-destructive character of Raman microscopy is not of importance in the case of ceramic fragments due to their abundance. However, such samples are very heterogeneous and the possibility of discriminating the components is undoubtedly attractive as some informations can be lost when the sample is pulverized. The major drawback for the use of Raman spectroscopy in this case, even with excitation at 1064 nm, is the fluorescence inherent to clays materials. Another problem arises from the fact that the pigments are usually minerals (typically metal oxides or oxihydroxides), which are poor light scatterers.

The question to be addressed here is the occupation area by tupi-guarani groups in the Paranapanema basin as São Paulo seems to be a frontier between occupation in the north of the State by tupinambá groups and the guaranis in the south. The most important vestige of such occupations are the ceramics and a more detailed study can contribute to a better understanding of these groups and their spatial distribution. The initial step in such investigation involves the characterization of the pigments used by the different indian cultures above mentioned. The preliminary results obtained are affected by a strong fluorescent background even with excitation in the NIR. Pigments (red, white and black in most cases, outer layer of the fragment and the ceramic paste itself, which could be useful in the identification of antiplastics used in the preparation of the object.

Contrarily to what happen in the IR, Raman spectroscopy allows the investigation of the low frequency region of the spectrum, permitting the identification of substances such as kaolinite (strongest peak at 186 cm^{-1}). Thus, the white pigment used in the guarani ceramics was identified as being a mixture of sand and kaolinite. In the black pigment, a large amount of charcoal was found and it is possible that the pigment was applied using grease, due to the high fluorescent background associated. The possibility that the charcoal particles have been incorporated during the firing step in the ceramics preparation can be ruled out because the pigment was found in the bulk not at the external surface.

4 CONCLUSIONS

In the present work Raman spectroscopy with excitation in the visible and in the NIR were used in the investigation of cultural heritage objects. The specimens studied were archaeological and ethnographic resins, human bones excavated from sambaquis and ceramic fragments from tupi-guarani groups.

Concerning the archaeological resin, its triterpenoid composition was inferred from the spectra whereas the ethnographic ones are mostly diterpenic ones.

The pigmented bones investigated revealed that a highly pure form of hematite was used, which was not produced by goethite heating. It is not clear so far when the pigment was applied: just after death or directly over the bare bones. This point is still under investigation.

With the ceramic fragments, the identification of the pigments used are more difficult due to the fluorescence presented by the samples, but even so it was possible to identify iron oxydes (hematite and magnetite), quartz, calcite and charcoal.

The results reveal the potential of the technique in the investigation of valuable and/or rare objects as it is a non-destructive tool, capable to provide very specific structural information, with spatial resolution when necessary.

5 REFERENCES.

- Edwards, H.G.M.; Faria, D.L.A.; Monteiro, A.M.F.; Afonso, M.C.; Farwell, D.W.; De Blasis, P.; Eggers, S. 2001. Raman Spectroscopic Study of 3000 Year-old Human Remains from a Sambaqui, Santa Catarina, Brazil, *J. Raman Spectrosc.*, 32 (1), 17-22.
- Faria, D.L.A.; Afonso M.C.; Edwards, H.G.M. 2002. Espectroscopia Raman: uma nova luz no estudo de bens culturais, *Revista do Museu de Arqueologia e Etnologia*, 12:249-267.
- Faria, D.L.A.; Edwards, H.G.M.; Afonso, M.C.; Brody, R.H.; Morais, J.L.; 2004. Raman Spectroscopic Analysis of a Tembétá: a Resin Archaeological Artefact in Need of Conservation, *Spectrochim. Acta A*, in press.
- Faria, D.L.A.; Lima, S.C.; Edwards, H.G.M. 2003. Raman Investigation of Brazilian Ethnographic Resins, *International Conference on the Applications of Raman Spectroscopy in Art and Archaeology*, Ghent, Bélgica.

The Vitrified Forts of Europe: Saga, Archaeology, and Geology

P.Kresten

National Heritage Board, Portalgatan 2A, SE-754 23 Uppsala, Sweden, and GeoData, Tövädersgatan 18, 754 31 Uppsala, Sweden.

ABSTRACT: In all, more than 200 ancient fortifications in Europe have ramparts that show evidence of extensive firing. In cases where silicate rocks were used as building materials, vitreous melts formed. In limestone areas, the rocks were transformed into burnt lime. For over two centuries, it has been debated whether the ramparts are the results of constructive efforts, or of the destructive firing by enemies. While most archaeologists favour the destructive hypothesis, most geologists believe in the construction of vitrified ramparts. The Nordic sagas, as well as those from Ireland, France, or Bohemia, tell us both of constructive and destructive efforts. The results of analyses of some fifty sites from all over Europe suggest that while some sites show clear evidence of construction, other sites are probably related to burning down the defences, while still other sites could be classified as incidental vitrification. At every individual site, the possible purpose of the vitrified rampart has to be questioned. Of utmost importance are reliable data on peak temperatures achieved, estimates of the water pressure during the process, availability and possible transport of fusible material and, last but not least, availability of required fuel material.

1 INTRODUCTION

Vitrified forts have been defined as prehistoric fortifications where the building stones of the rampart are bound together by vitreous material in situ by the action of heat (Christison 1898). For carbonate instead of silicate rocks, the result is calcination rather than vitrification. In all, more than 230 hill-forts with vitrification (and calcinations) are known, several of which only poorly documented.

For more than two centuries, scholars and scientists have debated whether vitrified forts should be seen as the results of constructive efforts, or of the destructive firing by enemies. In addition, incidental firing (by lightning, signal-fires, hearths, metallurgic activities, etc.) may be an explanation for some sites. At present, most scholars seem to advocate the destructive model, while most scientists are in favour of a constructive hypothesis.

2 SAGA

Whatever caused vitrification of a rampart, the scene itself must have made a lasting impression. The story of the “hill-fort alight” would have been told for generations to come. Indeed, even today, in most

cases more than fifteen centuries later, local folklore is still vivid on that issue.

Existing stories tell about constructive or destructive firing, or more mythical backgrounds. One of the most famous examples is depicted in the final scene of “Die Walküre” by Richard Wagner, with Wotan calling upon Loge to light a ring of fire around the hill-top where Brünnhilde sleeps, awaiting the bravest of men (i.e., Siegfried) to free her. One does not need too much imagination to link that scene to the burning rampart of a hill-fort.

A more specific example is provided by Sainte-Suzanne (France), where the story tells us that it took seven years to construct the “glass wall” in order “to keep out the wild beasts”. In Scotland, the lords of Fettercairn and Dunsinane were a bit sour at each other, resulting in the mutual destruction of their hill-forts by fire (both sites are extensively vitrified). Much later, Shakespeare seems to have made use of that story in “Macbeth” – the apparition tells him “Macbeth shall never vanquish’d be until great Birnam wood to high Dunsinane hill shall come against him” (Act 4, Scene 1). Dragging lots of wood to a hill-fort could of course have had the purpose to burn the place down, alternatively, to smoke out the inhabitants. According to Shakespeare, Macbeth was unfortunately at

Dunsinane, when Birnam wood started to move. Fortunately for him, the date of firing Dunsinane was determined to AD 455±120 by TL-methods (Kresten & Goedicke 1996), i.e., several centuries before the reign of Macbeth.

Other examples of destructive efforts are found in the Irish sagas, specifically mentioning 150 blacksmiths with their bellows providing forced draught to the charcoal (Thurneysen 1921, p. 473). By contrast, diverse tales from Bohemia are more mythical, referring to the ramparts as dwellings for the “little people” (dwarfs, elves). Else, gold and other precious items are supposedly hidden in the ramparts. These latter stories stem from the frequent occurrence of hollow spaces in the ramparts due to the combustion of fuel (charcoal, wood).

3 ARCHAEOLOGY

During the 18th and 19th centuries, more and more vitrified forts were recognised as such, mainly in Scotland, but also in France, Germany, and other countries. Most archaeologists believed that vitrification was a constructive method, either Scottish or Celtic. It was also popular to involve the druids, the Celtic sages, which were accredited with everything grand or mysterious on the British Isles (often wrongly, as we know now). However, after the experimental production of vitrification by Childe & Thorneycroft (1937), the pendulum swung to the other side – most, if not all vitrification was due to enemy action. Excavations, as well as ¹⁴C- and TL-dates were most often interpreted in favour of this model. Today, the number of archaeologists believing in the constructive origin of vitrified forts is not very great.

The problem is really that most findings can be interpreted both ways. For instance, many vitrified hill-forts date back to times of turmoil, like the Migration Period. Thus, one may conclude that during that time many hill-forts were burnt down. Alternatively, one may state that these uncertain times called for more stable (such as: vitrified) defences.

In most cases, archaeology is unable to determine who struck the match, to put it simply. Close-Brooks (1986) correctly pointed out that whoever fired the rampart had to be in control of the fort itself. This makes distinguishing between defenders and attackers even more difficult, as it would hardly be possible to find out the difference between them any more.

The archaeologist would have to investigate the possible purpose of the vitrification. If it occurs only at the inner entrance of a bivallate fort, and nowhere else (like at Caer Euni, Wales), one could take this as indication for an enemy attack. In times of turmoil, the entrance would have been barred using

timber and similar combustible material which, when set on fire, could result in local vitrification at that spot. Broborg (Sweden), on the other hand, is vitrified all over except for at the entrance (Kresten et al 1993) – which is much more difficult to explain by enemy action.

An example of incidental vitrification could be Kollerborg, Sweden (Damell & Kresten 1996), with scattered pieces of vitrified material within the rampart, seemingly without any function. Locals informed about frequent lightning strikes on that particular hill-top, particularly during summer. One may safely assume that when lightning strikes now, it even struck 1300 years ago, when the vitrified material was formed.

4 GEOLOGY

By contrast, most geologists studying vitrified forts (Brothwell et al. 1974, Youngblood et al. 1978, Kresten & Ambrosiani 1992, Kresten et al. 1993) seem to have favoured the constructive hypothesis. At many sites, temperatures in excess of what can be reached by natural draught have been recorded. Also, selection of readily fusible rock material, in some cases transported for many kilometres, indicates careful planning for constructive purposes. The section-wise firing found at some sites (Kresten et al. 1993), as well as the use of charcoal (instead of timber) again both are constructive details.

Besides temperature, water partial pressure is a critical (and often overlooked) factor. Experiments conducted by the author on material (amphibolite, gneiss) from the vitrified fort Broborg (Sweden) has shown that even applying forced draught does not lead to the formation of melts. The rocks merely crack and oxidise. Therefore, vitrification must have taken place in a confined space, keeping the water partial pressure at level to facilitate melting. This, again, would be a clear indication of constructive efforts.

One may add that calcined walls, with the solid limestone blocks reduced to rubble and powder, could only be the result of destructive firing. However, Camp d’Affrique (France) was shown to be constructive – excavation and analyses revealed that the rampart did not consist of burnt lime but rather of a type of reinforced Portland cement dated to Hallstatt B-C (Ploquin et al. 1993).

5 CONCLUSIONS

From the above, it is evident that interdisciplinary studies are required in order to solve the problems posed by the vitrified hill-forts. However careful excavations that are performed, archaeology only can not provide the complete picture. Geology, on

the other hand, provides data on the process itself, but little, if anything, on the people that had carried out the process.

In the sagas, vitrified forms can be the results of either construction or destruction. If we combine all archaeological and geological evidence that has been presented, we arrive at a similar conclusion. It is quite obvious that every single occurrence has to be evaluated from available facts, and broad generalisations to cover all vitrified (calcined) forts are uncalled for.

6 ACKNOWLEDGEMENTS

The author acknowledges constant support by *Berit Wallenbergs Stiftelse* (the Berit Wallenberg Foundation) for the study of the vitrified forts of Europe.

7 REFERENCES

- Brothwell, D.R., Bishop, A.C. & Woolley, A.R. 1974. Vitrified forts in Scotland: a problem in interpretation and primitive technology. *Journal of Archaeological Science* 1: 101-107.
- Childe, V.G. & Thorneycroft, W. 1937. The experimental production of the phenomena distinctive of vitrified forts. *Proceedings of the Society of Antiquaries of Scotland* 72: 44-55.
- Christison, D. 1898. *Early Fortifications in Scotland. Motes, Camps, and Forts*. Edinburgh and London, Blackwood & Sons.
- Close-Brooks, J. 1986. Excavations at Clatchard Craig, Fife. *Proceedings of the Society of Antiquaries of Scotland* 116: 117-184.
- Damell, D. & Kresten, P. 1996. Swedish vitrified hill-forts, with special reference to Kollerborg (Närke). - *Proceedings from the 6th Nordic Conference on the Application of Scientific Methods in Archaeology, Esbjerg 1993*, 67-76. Arkæologiske Rapporter nr. 1, 1996. Esbjerg Museum
- Kresten, P. & Ambrosiani, B. 1992. Swedish vitrified forts – a reconnaissance study. *Forvännan* 87: 1-17.
- Kresten, P. & Goedicke, Chr. 1996. TL-Dating of vitrified ramparts: Did Birnam Wood go to Dunsinane Hill in A.D. 455? *Iskos* 11: 99-106.
- Kresten, P., Kero, L. & Chyessler, J. 1993. Geology of the vitrified hill-fort Broborg in Uppland, Sweden. *Geologiska Föreningens i Stockholm Förhandlingar* 115: 13-24.
- Ploquin, A., Duval, P., Eveillard, J., Lagadec, J.-P. & Leroy, M. 1993. Les noyaux calcinés du rampart Hallstättien de la Cité d'Affrique (Messein, 54): Données archéométriques et interprétation. *Archaeologia Mosellana* 2: 175-199.
- Thurneysen, R. 1921. *Die irische Helden- und Königssage bis zum siebzehnten Jahrhundert*. Halle (Saale), Max Niemeyer.
- Youngblood, E., Fredriksson, B.J., Kraut, F. & Fredriksson, K. 1978. Celtic vitrified forts: Implications of a chemical-petrological study of glasses and source rocks. *Journal of Archaeological Sciences* 5: 99-121.

The Simulation of Copper Chlorides Formation on the Surface of Bronze Monuments in Urban Environment

E.V.Meshchanova, O.V.Frank-Kamenetskaya, E.B.Treivus

Department of Crystallography, Saint Petersburg State University, Saint Petersburg, Russia

ABSTRACT: The simulation of corrosion films formation on the surface of artistic bronzes (brasses) of different composition in HCl (2 or 4 moles/l) vapor was carried out. Synthetic analogues of Cu-minerals formed on a surface of bronze monuments (tenorite CuO, cuprite Cu₂O, nantokite CuCl, and atacamite Cu₂Cl(OH)₃), have been received. The sequence of their crystallization: oxides (mainly cuprite) → nantokite → atacamite, has been established. Phase transition of the orthorhombic atacamite in monoclinic clinooatamite is connected, probably, with ordering distribution of copper; zinc cations in crystal structure is revealed. Time variations of mass of formed phases have been investigated. Kinetic laws of their development at the initial stage of phases formation, indicating simple (non chain) heterogeneous reactions, have been revealed. It has been shown, that atacamite formation may occur at the expense of nantokite. The composition of the brass, representing homogeneous solid solutions with copper crystal structure, essentially impacts not only the mineral composition of corrosion film, but also the rate of crystallisation process. The ancient art bronzes, containing microimpurities of Sn, S or Fe (Zn excepted), are characterized by the most stable component.

1 INTRODUCTION

Because of the humid climate and strong industrial pollution the problem of the unique bronze memorial art conservation is of real importance for Saint Petersburg.

Among the products of the atmospheric corrosion film (patina) on the surfaces of bronze monuments high soluble copper chlorides (nantokite, atacamite) appear often (Kalish 1971, Frank-Kamenetskaya et al. 2000, Bulakh et al. 2001 among other). The last frequently leads to penetrating of corrosion deep into copper alloy material (Figure 1).

The study of the multifactor corrosion process *in situ* presents many difficulties. For this reason it is not clearly understood. In the present work we have made an attempt to study copper chlorides formation on the artistic bronze surfaces by means of simulated experiment.

2 SIMULATED EXPERIMENT

Copper alloys discs (18 mm in diameter) with different content of Zn, Sn, and other chemical elements typical for artistic bronze (Table 1) were placed into the exsiccator together with the glass containing HCl solution 2 (tests 1-6) and 4 (test 7) mole/l for a period of three month approximately.

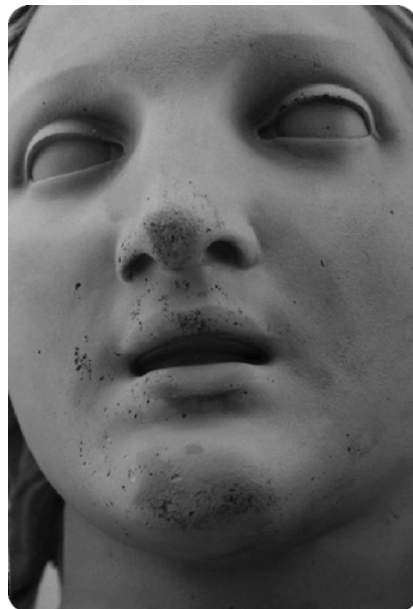


Figure 1. Display of "stomach ulcer" on bronze monuments. A figure of an angel on the Alexander column. Dvorzovaya square, Saint Petersburg.

Optical control of corrosion products was exercised every day. X-ray phase analyses (diffractometer DRON, CuK α) were carried out every 3-4 days. Time variations of mass of newly formed phases were estimated by measuring relative intensities of the control diffraction reflections. By choice of peaks their intensities and absence of other phases overlapping were taken into account.

The selection of kinetic model of phase crystallization at the initial stage of their formation was done with use the equation:

$$M=at^n, \quad (1)$$

Table 1. Provenance and average chemical composition of copper alloys used in the simulation experiment. All surfaces are grounded and, on the alloy surface (Test 4), numerous cavities are seen.

Test	Monument (place of sampling) Chemical composition, atomic fractions
1	"Angel", Alexander column Saint Petersburg (pedestal, internal party) Cu _{0.79} Zn _{0.18} Sn _{0.02} (S+Fe) _{0.01}
2	"Angel", Alexander column Saint Petersburg (pedestal, external party). Cu _{0.79} Zn _{0.19} Sn _{0.01} (S+Fe) _{0.01}
3	"Millennium of Russia" Great Novgorod (modern alloy) Cu _{0.88} Zn _{0.09} Sn _{0.02} (Fe+Ni) _{0.01} + Pb
4	"Millennium of Russia" Great Novgorod (support of power) Cu _{0.88} Zn _{0.07} Sn _{0.04} S _{0.01}
5	"Tamers of horses", Anichkov bridge Saint Petersburg (group 2, plinth). Cu _{0.89} Zn _{0.09} S _{0.01} (Sn+Fe) _{0.01}
6	Modern monument Saint Petersburg Cu _{0.89} Zn _{0.11}
7	Identical as Test 6

3 RESULTS AND DISCUSSION

3.1 Sequence and factors of phase formation

During simulation the synthetic analogues of the Cu-minerals, formed on a surface of bronze monuments, were received: tenorite CuO (in tests 6, 7), cuprite Cu₂O, nantokite CuCl, and atacamite Cu₂Cl(OH)₃. The individual phase of zinc (zinkite ZnO) has been received only in tests 6 and 7, allowing to assume that zinc, as the isomorphic impurity, is included into crystal structures of the formed copper compounds. Phase transition of the orthorhombic atacamite in monoclinic clinoatacamite (tests 6 and 7) is connected, probably, with ordering distribution of copper and zinc cations in crystal structure.

On initial stage of formation the crystallizing phases are well identified by color. Grains of tenorite – brown, brown-yellow, cuprite – black and black-red, nantokite – grayish and light green,

atacamite – dark green, clinoatacamite – bright green.

The formation sequence of corrosion film minerals was established: oxides (mainly cuprite) → nantokite → atacamite → clinoatacamite. At the first stage on a surface of bronze a separate cuprite grains (Figure 2a) and other oxides, and then gatherings of them, gradually enlarging, are formed. Simultaneously on black cuprite grains the first individual green grains of copper chlorides start to be formed (Figure 2b). The most intensively process goes on edges of the discs and in microcracks. Time decrease of the mass of nantokite, which then disappears, indicates that the formation of atacamite may occur on its account. At the final stage of the experiment on the surface of copper alloys, a dense two-layer corrosion film is formed (Figure 2c).

Results of experiment have shown that the composition of the brass, representing homogeneous solid solutions with copper crystal structure, essentially impacts not only mineral composition of corrosion film, but also the rate of corrosion process (Fig.3). The ancient art bronzes, containing, except for Zn, microimpurities of Sn, S or Fe (tests 1,2,5) are considerably more resistant in comparison with modern bicomponent systems (Tests 6 and 7). During the experiment the increase in the rate of corrosion also has been demonstrated at the increase of pressure HCl vapors (Tests 6 and 7), distortions of the homogeneity of an alloy (Test 3) and manifestation of the macro deficiency of surface structure (Test 4).

3.2 Kinetic laws

Time increase of the mass of crystallized phases at the initial stage of their formation is well described by the exponential equation (1) (Figure 4). Values degree index n vary from 0.34 to 3.98. According to Jacobs & Tompkins theory, it indicates on simple (non chain) heterogeneous reactions.

The chemical composition of a brass is clearly reflected in kinetic laws of the patina minerals development (Table 2).

According to the theory adopted (Jacobs & Tompkins 1955, Barret 1973) the following assumptions were made based on the interpretation of the results received:

1. The greatest possible supersaturation in the gas medium with regard to neogenic phases is created in the closed exsiccator volume practically instantly after the beginning of experience.

2. As the mass of forming phases is irrelevant and the quantity of a hydrochloric acid is great, supersaturation remains permanent during all experiment.

3. Already formed crystals do not prevent formation and growth of new grains. It is obviously

possible, if their number per area unit of a surface is small.

4. The rate of crystal grains nucleation and the linear rate of their growth in tangential and normal directions are constant in time at the initial stage of corrosion process.

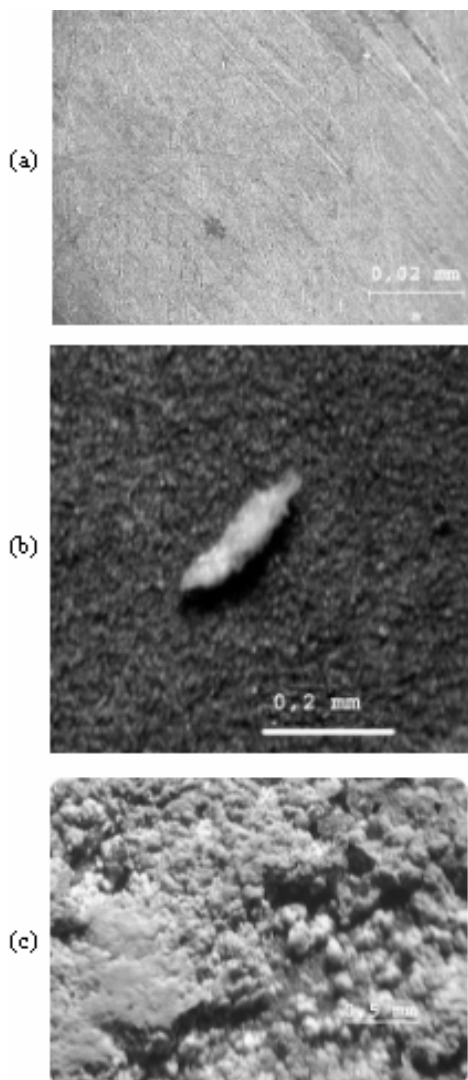


Figure 2. The various moments of synthetic patina minerals' formation: a) cuprite grains, b) nantokite grain, c) corrosion film.

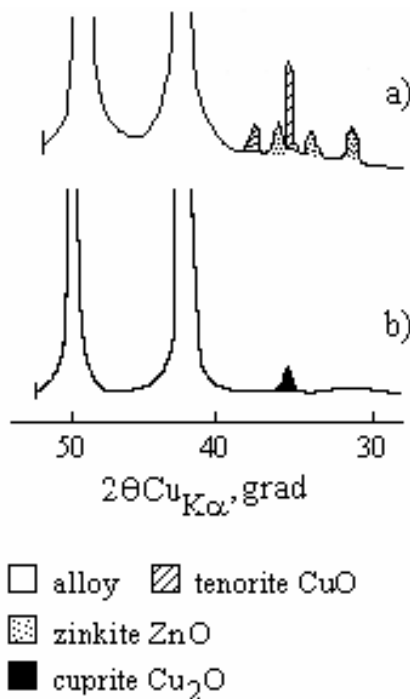


Figure 3. Fragments of X-ray diagrams of corrosion products for alloys of different composition after ~50 hours since the experiment beginning: a) modern bronze (test 6); b) old bronze (test 2).

Under these conditions n in the equation (1) has to be equal to 4. In the process of crystals' growing and increasing their thickness, the normal rate should be become too small in comparison with tangential, and then $n=3$. When grains begin to prevent the grow of each other, but do not form a continuous film, growth rate decreases, and $n=2$. In the final stage of the process of a continuous film formation, the increase in thickness of a film is determined by solid phase diffusion, and $n=0.5$.

As cuprite and nantokite formation is accompanied by their decomposition and transformation into other copper compounds, the above described theory failed when applied to them. In atacamite case in one of the tests at an early stage of patina formation, value n is close to 4, which indicates the equality of tangential and normal crystal grows rates. Values of parameters n in other tests (Table 2) specify later stages of crystallization of this compound at which, according to the theory described above, birth and growth of isolated grains occurs. At a final stage of the process in the most tests n is near to 0.5 and kinetics of the developments of atacamite is characterized by the formation of a continuous film.

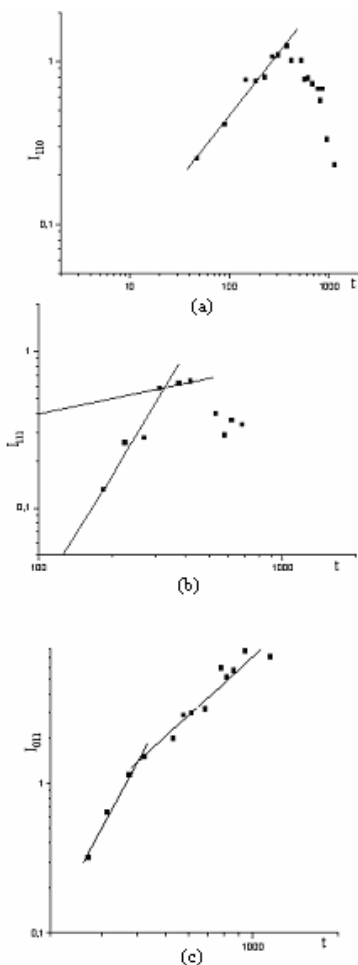


Figure 4. Relative intensity time changes example of diffraction reflections of formed phases (test 6): a) cuprite R=0.98, b) nantokite R=0.96, R=0.99, c) atacamite R=0.99, R=0.94. R- correlation coefficients

Table 2. Example of influences of copper alloy composition on crystallization of patina minerals analogues.

Modern alloy (test 6)		Old bronze (test 5)	
Value n in equation (1)	Time, hours	Value n in equation (1)	Time, hours
cuprite			
0.78	48-360	0.53	24-415
nantokite			
2.56	180-310	0.45	415-968
0.34	310-420		
atakamite			
3.50	270-400	1.52	303-930
1.76	400-1200	0.56	930-1450
clinoatakamite			
1.80	600-1200	not fixed	not fixed

4 CONCLUSION

During the simulation the synthetic analogues of the Cu-minerals formed on a surface of bronze monuments (tenorite CuO, cuprite Cu₂O, nantokite CuCl, and atacamite Cu₂Cl(OH)₃) have been received. The sequence of their crystallization has been established. The impact of the chemical composition on the brass and other factors (pressure HCl vapors, distortions of the homogeneity of alloy, and manifestation of the macro deficiency of surface structure) on the corrosion rate have been analyzed. Kinetic laws of the patina minerals' development at the initial stage of phases formation, indicating simple (non chain) heterogeneous reactions, have been established.

As a whole, it was shown that the simulation approach used in the present research is very effective to study the corrosion film formation on the surface of bronze monuments in urban environment. Experiments, in which the corrosion processes on the bronze monuments are investigated under conditions very near to nature, are now in progress.

5 ACKNOWLEDGEMENTS

The authors would like to acknowledge A.G. Bulakh, T.N. Kaminskaya, S.M. Sukharzhevskii, and A.A. Knizel for their contribution to this work.

This research work is supported by Russian Foundation of Fundamental Investigation (project N° 02-06-80123).

6 REFERENCES

- Barret P. 1973. *Cinétique hétérogène*. Paris: Jauthier-Villars.
- Bulakh A.G., Frank-Kamenetskaya O.V., Vlasov D.Yu., Zolotarev A.A., Turchinskii S.G. 2001. Razrushenie kamnya i metalla v pamyatnikakh kul'tury Sankt-Peterburga. Metody i rezul'taty issledovaniya (Destruction of a stone and metal in monuments of culture of Saint Petersburg. Methods and results of research). *Dizain i stroitel'stvo* 3: 62, 63, 78.
- Frank-Kamenetskaya O.V., Bulakh A.G., Mironova A.A., Nesterova A.N., Efremova N.N., Rytikova V.V., Turchinskii S.G. 2000. Experience of monument mineralogical mapping in Saint Petersburg. *Applied Mineralogy* 2: 981-984.
- Jacobs P., Tompkins F. 1955 Classification and theory of reaction in solid. *Chemistry of the solid state*. Garner W.B. (ed.) London: Butterworths Sc. Publ.: 245-282.
- Kalish .M.K. 1971. *Estestvennye zaschitnye plenki na mednyh splavah (Natural protective films on copper alloys)*. Moscow: Metallurgiya

Geoarchaeology: Geological Analysis of Scottish Medieval Carved Monuments

S.Miller, F.M.McGibbon & D.H.Caldwell

National Museums of Scotland, Chambers Street, Edinburgh, UK, EH1 1JF

N.A.Ruckley

The Old School House Kirkbuddo, by Forfar, Angus, Scotland, UK, DD8 2NQ

ABSTRACT: Geological surveys of early medieval sculptured stones from a number of related sites in central Scotland and of late medieval sculptured stones from a number of related sites in the west of Scotland has been undertaken to assess the geological make-up of the sculptured stones and identify possible source areas for the raw materials. Non-destructive petrological studies (including grain size, mineralogy and textural and structural characteristics) and examination of previously and newly collected magnetic susceptibility measurements are used to characterize the sculptured stones and potential source material. The results of the project indicate that for the early medieval sculpture: (1) all the sculptured stones are sandstone with the exception of one siltstone and one granite, (2) the sedimentary rocks are consistent with sources in the Lower Old Red Sandstone (LORS) of the area and (3) from within the LORS, a number of different geological units have been utilized for the procurement of the stones. For the late medieval sculpture, the results indicate: (1) various rock types have been used including amphibolite, schist, slate and sandstone and (2) non-locally derived material is used extensively in some areas suggesting a more developed network for procurement of raw materials. The techniques used also aid the art historical interpretation of a number of carved stones in providing identification of carved fragments from the same monument.

1 INTRODUCTION

Medieval sculpture in central eastern Scotland (Angus, Perthshire and Tayside) is exemplified by some 120 8th – 10th century sculptures and sculptural fragments, published and catalogued by Cruden (1964). The Royal Commission for Ancient and Historical Monuments Scotland (RCAHMS) are in the process of drawing and photographing the collections.

Medieval West Highland sculpture was defined and surveyed in an important monograph published by Steer and Bannerman (1977). There are some 600 examples ranging in date from the 14th to the 16th century, spread over 86 sites. These sculptures are located at various sites throughout the Western Highlands of Scotland.

Many of the sculptures are in the care of Historic Scotland (e.g. the St Vigean collection) whilst others are part of the collections of the National Museums of Scotland, are in local authority care or are held privately.

The present project was initiated with the aim of improving previous interpretation of the sculpture by bringing geological knowledge and skills to bear on the subject, leading to a reassessment of where the sculpture was carved and result in a new

understanding of power and patronage in medieval Scotland. The project has involved close collaboration with RCAHMS and Historic Scotland.

A petrological survey, backed up by magnetic susceptibility readings, of the most representative sculptures has been undertaken. Early medieval sculpture collections surveyed include: St Vigean, Aberlemno, Meigle, Pictavia and Meffan together with individual sculptures at other sites (Fig. 1). Late medieval sculpture collections surveyed include: two of the largest and most representative collections of sculpture at Iona and Oronsay (Fig.1).

2 METHODOLOGY

2.1 Petrology

All available sculptured stones have been examined using non-destructive petrological techniques in order to provide a 'field identification' of the rock type. This type of petrological analysis has provided a basic identification of rock type and has been used to distinguish between general rock types. All examination includes the following measurements:

a) colour (with reference to Munsell standard colour charts). Colour measurements from all weathered surfaces were obtained. In a small

b) number of cases, it was possible to make observation of the unweathered colour of the sculptures.

c) grainsize (with reference to standard grainsize measurements on the ϕ scale)

d) macroscopic mineralogy (i.e. mineralogical content that can be ascertained by hand-specimen examination with hand lens)

e) textural & structural characteristics such as bedding, cross-bedding, jointing, other planar fabric, grainsize variation, sediment maturity

f) clast distribution and composition

g) weathering characteristics

Division of the specimens into "rock types" has been primarily based on the textural characteristics. Colour has been used only as a general guide to overall appearance since, in many cases, the sculptures have undergone varying degrees of weathering and/or cleaning, both activities that could significantly alter the colour of the surface of the specimen.

All outcrop specimens (i.e. potential source rocks) have been examined using petrological techniques in order to classify rock type. In addition to the measurements taken for the sculptures, all examinations of outcrop specimens also include microscopic mineralogy i.e. mineralogical content from thin section examination.

Classification of the specimens into rock types is based on mineralogical and textural characteristics. Colour has been used only as a general guide to overall appearance.

All sandstones are classified according to their mineralogy and using the sandstone classification scheme of Folk where all rocks containing less than 15% fine grained matrix are classified in terms of the three principal components; quartz, feldspar (plus granite and gneiss clasts) and other rock fragments.

Sediment maturity is based on a combination of mineralogical maturity (content of chemically stable and physically resistant minerals) and textural maturity (content of fine grained matrix and the sorting and roundness of the grains). The assessment of textural maturity is based upon the schemes of Folk (1951, 1974) and Pettijohn et al (1973).

In addition to the above observations, all outcrop specimens were also identified according to detailed thin section petrology.

2.2 Magnetic susceptibility

The magnetic susceptibility was measured with an Exploranium KT-9 Kappameter giving a measurement of the true susceptibility.

The KT-9 has several operating modes but to achieve a consistency of readings the "pin mode" of working was used throughout. The accuracy on a flat rock is estimated to be +/- 3% in the "pin mode".

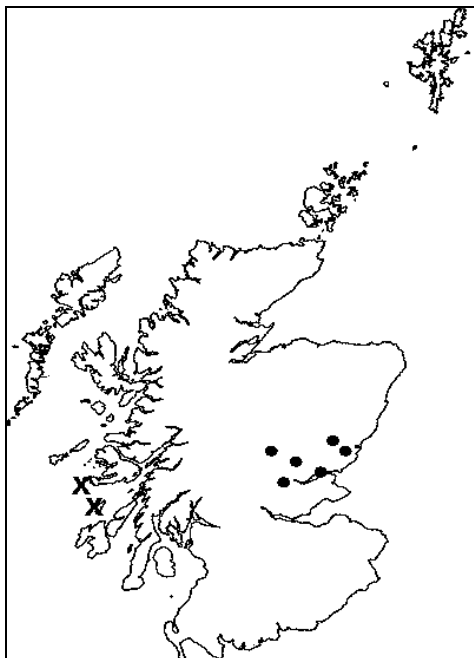


Figure 1. Map of Scotland showing the localities of early medieval sculpture in Central Scotland (.) and late medieval sculpture on Iona and Oronsay in the West Highlands (x).

Whenever feasible a series of a dozen readings were taken from the front and rear faces of the carved stones away from all possible sources of magnetic contamination. Twelve readings represent one data set. Over 230 data sets of sculpture were taken and the average and standard deviation of each set of readings determined. Almost 180 data sets taken from quarry or outcrop locations have been utilized to provide a magnetic susceptibility data set.

3 RESULTS

3.1 Early medieval sculpture

The geological analyses of the early medieval sculptures indicate that all the sculptured stones are sandstone with the exception of one siltstone and one granite. Each of the units used in the carvings can be characterised using a combination of petrological features and magnetic susceptibility values (Fig. 2). For the sandstones, the features are consistent with sources in the Lower Old Red Sandstone (LORS) of the area and would indicate that, from within the LORS, a number of different geological units have been utilized for the procurement of the stones.

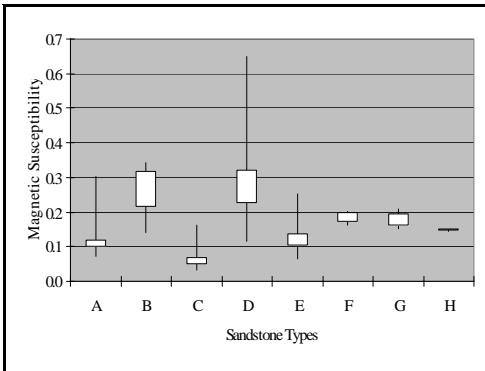


Figure 2. Range of magnetic susceptibility values of the sandstone groups characteristic of the early medieval carved sculpture form Central Scotland.

From the geological survey, sampling and thin section analysis of rocks cropping out in the area, it is clear that there are distinctive lithological differences between stratigraphical groups and even between formations. This is encouraging for potential identification of sources of carved stone. However, there is also considerable variation within groups, even on an outcrop scale. In addition, there has been considerable change in landscape and many potential quarry sites are in-filled and are no longer accessible for sampling. Nevertheless, the samples collected provide a comprehensive set of comparative material from potential sources in the LORS of the area.

Comparing sculpture from different early medieval sites, it is apparent that a number of the sculptures from individual sites could be from the same source. Also, some rock types at each locality appear to be specific to individual sites.

The feasibility of local production of the sculptures at each site is supported by local quarrying evidence. There are a number of sandstone quarries in the immediate area of each of the sites visited and a detailed study of the history of quarrying throughout the area suggests more numerous early working quarries across the region. In addition, the nature of the LORS units would allow very local, non-quarry sources such as outcrop in river-cuttings to be utilized for the production of stone.

3.2 Late medieval sculpture

Based on the examinations carried out there are a significant number of macroscopic differences in the stone types use for the sculptures at all of the sites examined.

All petrological analysis was undertaken independently of the magnetic susceptibility

measurements to ensure that no bias was recorded in the grouping of the rock types.

Based on petrological examination, the rocks used for the Iona sculptures include slate, a number of varieties of schist (mica schist, chlorite schist, garnet chlorite schist, garnet biotite schist and talc schist), metabasite, trachyte/dacite, gabbro, metadolerite, metagranodiorite, amphibolite, sandstone and quartzite.

The rock types used for the Oronsay sculptures is more restricted and includes mica and chlorite schist, pelitic mica schist, metabasite, amphibolite and sandstone.

On both Iona and Oronsay the most commonly used rock type is schist. The notable difference between Iona and Oronsay is that Iona has a greater variety of schist types with the exception of a distinctive pelitic mica schist that appears only on Oronsay.

Combined magnetic susceptibility data and petrological classifications for Iona and Oronsay sculptures indicate there is a good correlation between different rock types and average magnetic susceptibility measurements. In particular, slate (Iona) and pelitic mica schist (Oronsay) have consistently low magnetic susceptibility measurements whilst the other rock types, including all the other varieties of schist) exhibit higher average magnetic susceptibility measurements (Fig. 3).

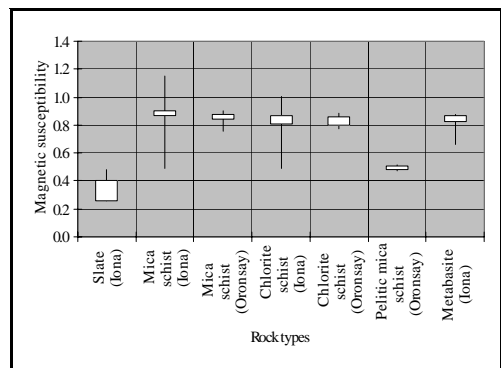


Figure 3. Range of magnetic susceptibility values of five rock types from medieval carved stones on Iona and Oronsay.

The rock types used for sculptures on both Iona and Oronsay cannot be locally derived. In addition, they cannot have a single source location since the range of rock types used indicates that a number of quarry localities must have been utilized. This is clear from the petrology (when compared to the local geology). However, all of the rock types identified could have been sourced within the West

Highlands. Steer and Bannerman (1977) suggested a possible source for many of the Iona sculptures as Doide “quarry” on the Kintyre peninsula.

It is clear from this work that both the petrological and magnetic susceptibility data indicate that this could not have been the only source if, indeed, it was a rock source at all. Of the late medieval sculpture examined in other west coast localities (such as the Outer Hebrides) results indicate that local stone procurement may have been more routine in these more remote areas since there is a direct correlation between the stone used for carved sculpture and that used for building construction at the time.

4 CONCLUSIONS

Initial conclusions for early medieval sculpture in Central Scotland, are that the majority of the sculpture is located very close to the stone source. It appears that little, if any, large scale movement of raw materials or carved sculpture took place at this time.

From our work here, it is evident that there are many more sources of stone used by medieval sculptors in the West Highlands than hitherto postulated, and that immediately local sources were no longer the norm.

However, is it credible, as has been previously postulated, that, in late medieval times, the carvers imported blocks of stone over long distances for their work? There would presumably have been a significant amount of wastage in the process of shaping and carving the slabs and crosses, best left at the quarry itself. Stone is heavy and expensive to transport. Most craftsmen would surely have wished to have been closely involved with selecting the actual slabs they were going to carve. It therefore seems much more likely to the writers that the carvers would be based at the quarries and that long sea or land voyages would have been the exception rather than the rule. Work by scholars in England on other medieval grave slabs and covers suggests that such a picture would be the norm (Butler 1958, 1964). Further research may reveal a more complex picture of individual craftsmen or workshops based at several quarries, or indeed opening up quarries from time to time to deal with local commissions.

This study has shown the potential benefits of combining hand specimen petrological identification and magnetic susceptibility measurements of sculptures with thin section analysis and magnetic susceptibility measurements of outcrop specimens. Only by using this combination of techniques can a potential source be identified with any reasonable degree of certainty.

Clearly, consideration of the origin of the stones is central to the thinking about economic implications for the procurement and movement of raw materials and about the place of carving. Also, in order to assess the importance of links between sites, future geological examination would need to concentrate on more detailed identification of geological features of the sculptures. Following directly from the work reported here, more detailed petrological examination of the sculptures e.g. from thin sections would yield more detailed comparisons and potentially more robust matches between sculptures and source rocks. In addition, consideration of the carving properties of the different stone types relative to the type of sculpture produced may indicate a preference for particular materials depending on the desired outcome. There is clearly much more research to be done on medieval sculpture in Scotland – more petrological and chemical analyses, the identification of additional quarry sources, and a complete reassessment of the stylistic characteristics of the carvings. Results to date demonstrate the scope there is for redefining the nature of the culture and society of Medieval Scotland.

5 REFERENCES

- Butler, L. A. S. 1958. Some Early Northern Grave Covers – A Reassessment. *Archaeologia Aelania*, 36, 4th series: 207-220.
- Butler, L. A. S. 1964. Minor Medieval Monumental Sculpture in the East Midlands. *Archaeological Journal*, 121: 111-153.
- Cruden 1964. *The Early Christian and Pictish Monuments of Scotland. Official Guide.*
- Folk, R L, 1951 ‘Stages of textural maturity in sedimentary rocks’, *J of Sedimentary Petrology* 21, 127-130
- Folk, R. L. 1974. *Petrology of Sedimentary Rocks*, Austin: Hemphills.
- Pettijohn, F. J., Potter, P. E. & Siever, R. 1973. *Sand and Sandstone*. Berlin: Springer.
- Steer, K. A. & Bannerman, J. W. M. 1977. *Late Medieval Monumental Sculpture in the West Highlands*. Edinburgh: The Royal Commission on the Ancient and Historical Monuments of Scotland

Characterization by XRD and SEM of Natural and Artificial Patinas on Copper and Copper Alloys

A.C.Neiva, H.G.de Melo, R.del P.Bendezú H., R.P.Gonçalves

Department of Chemical Engineering, Polytechnic School, University of Sao Paulo, Sao Paulo, Brazil

S.C.Lima

Laboratory of Restoration and Conservation, Museum of Archeology and Ethnology, University of Sao Paulo, Sao Paulo, Brazil

ABSTRACT: X-Ray diffraction (XRD) and scanning electron microscopy (SEM) with energy-dispersive X-Ray analysis (EDXA) were used to identify compounds in both natural and artificial corrosion layers of copper and copper alloys. The natural patinas were present in metallic pieces of the Museum of Archeology and Ethnology of the University of São Paulo (MAE-USP). The artificial patinas were obtained by dabbing nitrate and chloride-containing solutions on the surfaces of copper and bronze samples. For the natural patinas, we describe the corrosion products of two Ogboni edan figures. Very small samples of the corrosion products were taken off from the pieces and analysed by XRD and SEM-EDXA. X-Ray Fluorescence spectra revealed high Cu and Zn for piece A, and high Cu, Pb and Zn for piece B. Most corrosion products presented no Cu, but high contents of Zn or Pb. In both alloys, this should be ascribed to selective corrosion. For piece A, $Zn(CO_3)$ was the main corrosion compound. For piece B, PbO_2 and $Pb(CO_3)_3$ were clearly identified. For the artificial patinas, SEM results have shown the formation of compact and porous layers, whose morphologies were dependent on the substrate and also on the solutions employed. EDXA analysis have shown the presence of Cu, O and Cl, and minor amounts of Zn. XRD has shown the presence of gerhardite ($Cu(NO_3)(OH)_3$), nantokite ($CuCl$), atacamite ($Cu_2Cl(OH)_3$) and cuprite (Cu_2O).

1 INTRODUCTION

Restoration and conservation of the architectural, artistic and ethnological metallic heritage includes for one side the prevention of corrosion and the restoration of corroded pieces, and for the other side the preparation of artificial patina layers to mimetize natural patina layers on replacement pieces or cleaned surfaces. Both activities require the characterization of corrosion layers. The present work deals with metallic pieces of the African collection of the Museum of Archeology and Ethnology of the University of Sao Paulo (MAE-USP), and with artificial patina layers obtained on copper and bronze samples. MAE-USP has many metallic pieces in the African, Pre-Colombian and Mediterranean collections. Some of them are suffering a strong process of corrosion. With the acquisition of a chamber with controlled umidity and temperature conditions for the technical reserve, new strategies for the restoration and conservation are being defined. In order to accomplish this, sistematic characterization of the pieces and of their conservation condition is necessary. In this field, the present work describes the characterization of the alloy and of the corrosion products of two Nigerian edan figures of the Ogboni Society. In the field of

artificial patina layers, the work describes the characterization of patinas obtained with the application of two different solutions, both by dabbing at room temperature on copper and bronze surfaces. These recipes for the obtention of patina layers were chosen because they can be easily applied to offshore and huge structures, in opposition to traditional recipes which use high temperature or immersion, for instance.

2 METHODS

2.1 Preparation and characterization of artificial patina layers

The patina layers were prepared by dabbing the copper and bronze samples with solution S1 or S2 twice a day for five days. The compositions of the solutions, taken from Costa (2003), are given in Table 1.

Table 1 – Compositions of Solutions S1 and S2.

Solution	Composition	
S1	$Cu(NO_3)_2$ – 85g/L $FeCl_3$ – 3g/L	$ZnNO_3$ – 85g/L H_2O_2 – 3%
S2	$Cu(NO_3)_2$ – 200g/L	$ZnCl_2$ – 200g/L

The samples were characterized by Scanning Electron Microscopy (SEM) with Energy-Dispersive X-Ray Analysis (EDXA) and by X-Ray Diffraction (XRD). SEM observation was performed at the Department of Metallurgy and Materials of the Polytechnic School of the University of Sao Paulo (EPUSP). XRD was performed on Philips diffractometers at the Laboratory of Technological Characterization and at the Laboratory of Particulate Raw Materials and Non-Metallic Solids, both at the EPUSP. X-Ray was generated at 40kV/40A, and the scanning was made with 30 or 50s steps of 0.05° . The behavior of the patina layers on NaCl 0.5M solutions, which would simulate very aggressive marine environments, was studied by electrochemical impedance spectroscopy and polarization curves.

2.2 Sampling and characterization of the corrosion products of the edans

The edans, denominated Piece A and Piece B, were first observed with a binocular microscope, and analysed by X-Ray Fluorescence Spectroscopy. After corrosion products with different colors and morphologies were identified, very small samples were taken from each one. These samples were analysed by SEM-EDXA and XRD, as described in the previous section.

3 RESULTS

3.1 Artificial patina layers

The patina layers obtained with both S1 or S2 solution have homogeneous color and good adherence after prepared. For S1 patinas, these properties remained after exposition to air or after immersion in a NaCl 0,5 M solution for three days. For S2 patinas, the exposition to air resulted in a heterogeneous appearance, and the immersion in the NaCl solution resulted in poor adherence.

The MEV-EDXA observation revealed that S1 patinas are formed by two layers, both on copper and on bronze (Figs. 1, 2). The internal one, apparently more compact, presented high Cu and Cl contents. The external one, very porous, presented faceted crystals with high Cu, O and N contents. XRD patterns (Fig. 3) revealed the presence of gerhardite ($\text{Cu}(\text{NO}_3)(\text{OH})_3$, 14.687 JCPDS file), nantokite (CuCl , 6.344 JCPDS file) and cuprite (Cu_2O , 5.667 JCPDS file), on copper. On bronze, atacamite ($\text{Cu}_2\text{Cl}(\text{OH})_3$, 25.269 JCPDS file) was also observed, but cuprite was not (Figure 4). On copper, the layers are less thick (2.7 and $3.8\mu\text{m}$, respectively) than on bronze (2.4 and $7.9\mu\text{m}$, respectively), and lines from the substrate (cfc-Cu), with some texture, can be seen. Combining EDXA and XRD results, one can conclude that the internal

layer is composed of CuCl , and the external layer is mainly composed of nitrates, both on copper and on bronze.

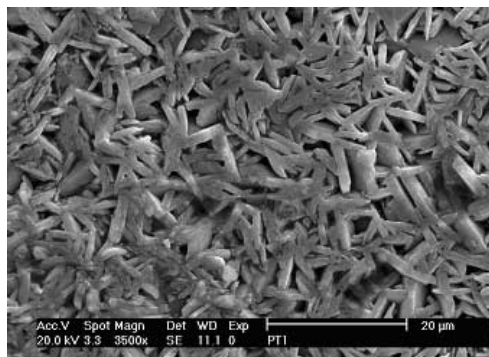


Figure 1: MEV (secondary electrons) of copper with S1 (superficial image).

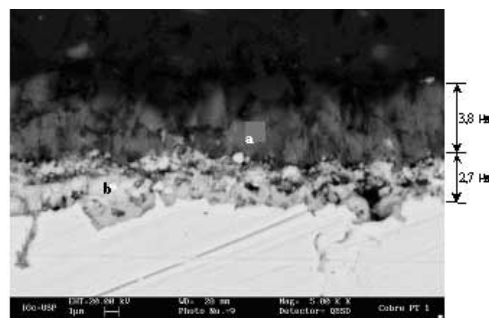


Figure 2: MEV (secondary electrons) of copper with S1 (transversal image).

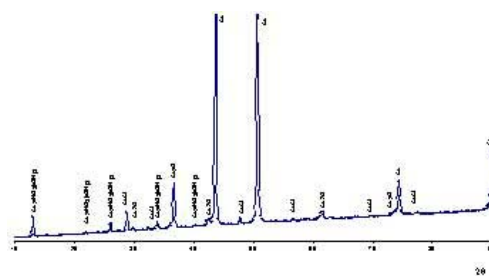


Figure 3: XRD of copper with S1.

A MEV surface image of S2 patina on copper is shown in Figure 5. One can see that there are two kinds of structures. They do not form two superimposed layers as with S1. Instead, both structures grow from the substrate. The triangular crystals have high Cu and Cl contents. The smaller

crystals have high O, Cu and Zn contents. Their shape and amount is different on copper and on bronze, what can be ascribed to the presence of Zn as a alloy element in the bronze, thus inducing an easier growth of Zn-containing compounds. No Zn compound, however, was identified in the XRD spectra, shown in Figures 6 and 7. The only identified phases were gerhardite ($\text{Cu}(\text{NO}_3)(\text{OH})_3$, 14.687 JCPDS file), nantokite (CuCl , 6.344 JCPDS file) and atacamite ($\text{Cu}_2\text{Cl}(\text{OH})_3$, 25.269 JCPDS file), both on copper and on bronze. One can suppose that Zn is dissolved in the nitrate, with just a small effect on lattice parameters.

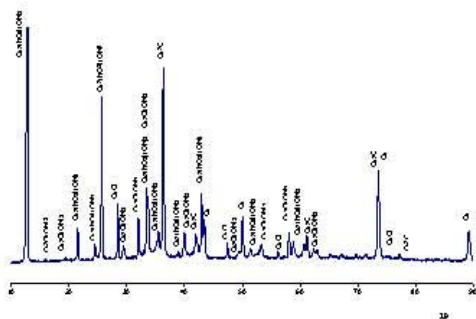


Figure 4: XRD of bronze with S1.

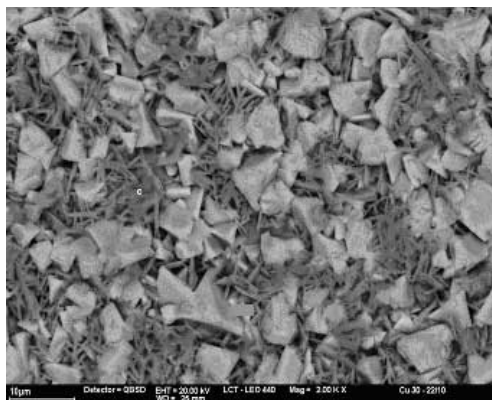


Figure 5: MEV (secondary electrons) of copper with S2 (surface image).

The electrochemical results on NaCl solutions are coherent with the microstructural observation. The dissolution process has a mixed electrochemical-transport control. The diffusion-controlling species probably is $[\text{CuCl}_2]^-$. This process should be occurring in the pores observed in both structures. After three days in the solution, there is a change in the behavior, which can be ascribed to the blocking of the pores by the new corrosion products, leading

to better protection against corrosion. For S2 patinas, however, there is a degradation of this electrochemical behavior, which can be ascribed to the lower adherence observed in the samples after exposed to NaCl solutions. These results are described with detail elsewhere (Bendezú et al. 2003).

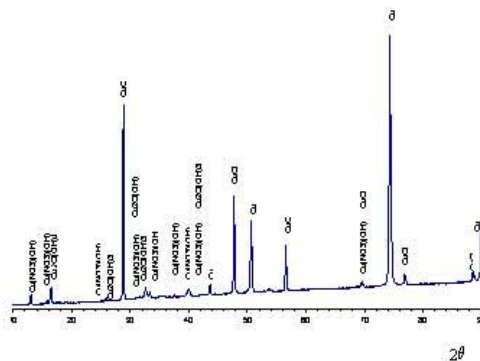


Figure 6: XRD of copper with S2.

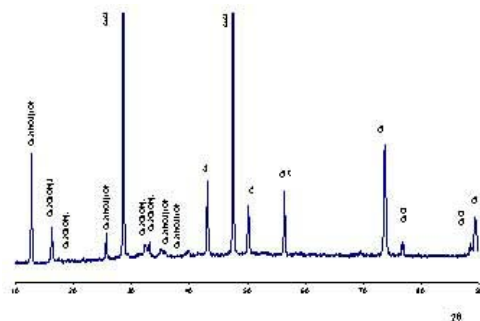


Figure 7: XRD of bronze with S2.

3.2 The Ogboni edans

X-Ray Fluorescence spectra obtained on regions not covered by corrosion products revealed high Cu and Zn (55,7 and 41,9%, respectively) for Piece A. Smaller amounts of Fe (0,3%), Co (0,3%) and Ni (1,8%) were also observed. The main corrosion products were white and black. Their XRD patterns are shown in Figures 8 and 9, respectively. In the white one, ZnO and possibly $\text{Zn}(\text{CO})_3$ were identified. This is coherent with the MEV-EDXA results, which show high Zn (51%) and O (22%). In the black one, XRD shows mainly $\text{Zn}(\text{CO})_3$ and probably some small amounts of ZnO and Al_2O_3 .

No Cu-containing compounds were observed in these white and black corrosion products. So, selective corrosion has occurred. Just one of the corrosion products presented some Cu. It was a

Mineralogical Characterization and Raw Materials Provenance of Some Archaeological Masks from Mexico

J.Robles-Camacho & R.Sánchez-Hernández

National Institute of Anthropology and History, Laboratories and Academic Support. Mexico.

ABSTRACT: Geoarchaeological studies have a great variety of applications and lapidary analysis is one of them. The problem related to the mineral composition of archaeological masks from Mesoamerican cultures was studied, and in this paper we present three case studies; two masks from the Maya culture and the last from the Teotihuacan culture. The main interest in this investigation was the mineralogical characterization of the green tessellae mask to determine its raw material provenance, in order to learn of these socio-cultural implications. The Pacal Mask is the first case, and it is composed of more than 300 tiles of albite, albite-kosmochlor, jadeite-albite, and veined quartz. The Oxkintok Mask has 339 tessellae and their homogeneous green color is also reflected in the mineralogical composition; omphacite and kosmochloric omphacite pyroxen minerals are the main constituents. These characteristics were assayed with X-ray diffraction (XRD), petrography, scanning electron microscope analysis (SEM-EDS) and infrared spectroscopy (IR). The third case (The Malinaltepec Mask) was performed using the blue-greenish optical properties of minerals and their visible exfoliation. This mask is a tessellae mosaic composed of amazonite and turquoise. In reference to the probable raw material provenance of the masks' constituents, there is previous analytical information that indicates a jadeite and minerals associated with the source from Motagua Valley (Guatemala) and a not well-defined source of amazonite.

1 INTRODUCTION

1.1 Historical preceding

The use of masks in the pre-Columbian societies has been recognized from the years 1000 B. C., however, it is possibly an older tradition. The masks were used mainly to represent divinities for funeral furniture and rituals. They were also an important part of the warriors' attire. In the Aztec Culture, the Jaguar Mask represented the highest rank: The Warrior. The Spanish chronicles from the Conquest times mentioned a variety of animals represented in masks: 1) monkeys were associated with dancing and singing; 2) the horned owl was recognized as an unlucky omen; 3) another animal was the snake, which still in different regions of Mexico symbolizes the Rain.

Outstanding in the cultural area known as Mesoamerica is the use of mask in funerals. The masks which were important objects as a part of the funeral furniture of emperors and high ranking people. Because of this tradition, the most beautiful mosaic masks were made with tessellae of different kinds of blue-green minerals and rocks, such as jadeite, turquoise, amazonite, malachite, travertine, diorite, serpentinite, etc. The mosaics

were mounted on wood, stone or even flint chips and ceramic, with or without plaster supports.

1.2 Case studies

Recently, three archaeological pieces were studied: "the Pacal Mask" (Chiapas state), the "Oxkintok Mask" (Yucatan state), both belonging to the Maya Culture, and the "Malinaltepec Mask" (Guerrero state), a Teotihuacan-style piece.

The Pacal Mask was a surpassing piece of the Pacal, the Great mortuary furniture. Pacal was the most famous emperor from Palenque, which is an important ancient Mayan city located in Chiapas state in southeast Mexico. This mask was elaborated with more than 300 tiles mounted on a wood and paster base, and has diverse green shades moving to white, and is between 2 millimeters to 7 centimeters long. The Oxkintok Mask was found associated with the remains of an adult male of unknown identity in Tomb 5, Building CA-3 in the archaeological site at Oxkintok, located in Yucatan State in southeast Mexico. In this case the Mask is composed of 339 tessellae, part of them mounted on a base made with flint chips and plaster and the other part on ceramic. The Malinaltepec Mask is a piece which was found in the town of Malinaltepec, in Guerrero State in

southern Mexico. In this case, the support is serpentinite.

2 METHODOLOGY AND RESULTS

2.1 Analyses

The mineralogical and chemical characterization of mosaic elements was carried out with X-ray diffraction (XRD) and chemical analysis by Scanning Electron Microscopy/Energy Dispersive System (SEM/EDS). More recently, reflection infrared spectroscopy (IR) was used to examine archaeological objects because of its non-destructive character and efficiency in mineral studies. The "Malinaltepec Mask" was studied based on its optical properties.

2.2 Mineral composition of the tessellae

The composition of the Pacal Mask tiles corresponds to minerals such as kosmochlor and jadeite, albite and quartz, usually as a vein filling. Likewise, the minerals found in the dark-green Oxkintok Mask tessellae were omphacite and kosmochloric omphacite. Finally, more than 90 per cent of the Malinaltepec Mask tiles were classified as amazonite (amazonstone) and a few bluish turquoise pieces.

2.3 Raw material provenance

It was established that the raw material of the Mayan masks possibly comes from the Motagua River Valley in Guatemala where jadeite, albite and associated rock deposits are found (Foshag 1955, 1957; Harlow 1993, 1994). In the case of the amazonite, its provenance is not yet well-established, but it is now known that a deposit is located in Chihuahua State, in northern Mexico (Sanchez-Hernandez et al., 2002). Turquoise deposits are widely distributed, mainly in the southwest and south of the USA, and there are also some minor deposits in northern Mexico.

3 CONCLUSIONS

The study of three Mesoamerican masks made it possible to distinguish mineralogical differences between greenish and blue-greenish tessellae. The pyroxene minerals, like kosmochlor, omphacite and jadeite give green color to the Pacal and Oxkintok Mayan Masks. The blue color of the Malinaltepec Mask mosaic is due to amazonite and turquoise. This information helps also to deduce that, for each object, there is a different raw material provenance: 1) Motagua River Valley (Guatemala): pyroxene (jade stone and associates); 2) North of Mexico,

probably: amazonite and turquoise. Finally, it is important to say that mineralogical study of archaeological objects needs non-destructive techniques; the SEM analysis is well established, however, it requires a mineralogical precision complement such as XRD which and requires less than 50 milligrams of powder. Actually, the non-destructive IRS is being developed and applied to archaeometry with good results.

4 REFERENCES

- Foshag, W.F., 1955. Chalchihuitl - A Study in Jade. *American Mineralogist*, 40. p. 1062-1069.
- Foshag, W.F., 1957. Mineralogical Studies on Guatemalan Jade. *Smithsonian Miscellaneous Collections*, Vol. 135, N. 5. USGPO, Washington, D.C. p. 1-60.
- Harlow, G.E., 1993. Middle American Jade. Geological and Petrologic Perspectives on Variability and Source. In: Frederick W. Lange (ed.). *Pre-Columbian Jade. New geological and cultural interpretations. University of UTAH press*. P. 9-29.
- Harlow, G.E., 1994. Jadeites, Albitites and Related Rocks from the Motagua Fault Zone, Guatemala. *J. Metamorphic Geol.* 12, p. 59-68.
- Sanchez-Hernandez, R., Robles-Camacho, J. and Reyes-Salas, M.A., 2002. Uso Alternativo de Amazonita y Turquesa en Objetos Arqueológicos Mesoamericanos. Resúmenes-GEOS. *III Reunión Nacional de Ciencias de la Tierra. Puerto Vallarta, Jal. México.* p. 287-288.

The Tropical Weathering Alteration of Palacete Pinho's Façade Tiles in Belém, Brazil

T.A.B.C.Sanjad & M.L.da Costa

Department of Geochemistry and Petrology, Geosciences Center, Federal University of Pará, Pará, Brazil

R.S.Paiva

Department of Biology, Biologic Sciences Center, Federal University of Pará, Pará, Brazil

ABSTRACT: The use of tiles on external walls in historical constructions of Brazil could have been the solution found by Portuguese constructors of the 18th century to protect, decorate and render impermeable the larges externals walls of buildings. In Belém city, located in the tropics at Amazon region, the tiles were used on façades since the middle of the 19th century. The Palacete Pinho was constructed at the end of the 19th century. It presents three types of pattern tiles: two German (PPA and PPAC) used on the most part of façade and other Portuguese applied only on the lower part of façade (PPP). These tiles displayed different manufacture techniques, chemical and mineralogical composition and, as counterpart, behave differently against tropical weathering. The degradation process started since the tiles were fixed on the building façades, an answer of the material to the external tropical environment. The rate of degradation action depends on physical, chemical and mineralogical characteristics of tiles. The main alterations observed in ancient tiles of Palacete Pinho are: detachment, stains from the traffic pollution and microorganisms colonization, loss of glazing with subsequent darkening. The weathering action occurs more rapidly on the Portuguese tiles than on the German ones.

1 INTRODUCTION

The façade tiles from the 19th century are suffering several composition alterations caused mainly by the tropical environment. The Palacete Pinho (Fig. 1) is a building that has three kinds of tiles with different alterations. Understand the microorganisms action, its possible alterations and how the weathering can benefit from the degradation are important information to save this Brazilian cultural heritage. Chiari (2000), Oliveira (2001), Malhoa (2001) have demonstrated the importance of the sciences to preserve the cultural heritage.



Figure 1: Main façade of Palacete Pinho.

1.1 The Palacete Pinho Building

It was built at the end of the 19th century by Camilo de Amorim to be the Antônio Pinho's residence. Derenji (1987) explains that it is one of the most important constructions of eclectic architecture of Belém that shows the application of tiles in this period.

Alcântara (unpubl.) identified in this building three types of pattern tiles: one German, used on the most part of façade (PPA), the second one (PPAC) is German too and it is a kind of frame for the main tile composition of façade. The third one is Portuguese; it was applied only on the lower part of façade (PPP). The samples PPA and PPAC have a colorful paint with low relief covered by colorless glazed. The Portuguese sample looks like an opaque marble paint.

1.2 Information about the environmental characteristics of façade tiles

The climate of the city Belém is characterized by high precipitation, high humidity combined with high temperature and sun light irradiation (a typical tropical weather). Together with traffic pollution these are the main factors to promote weathering alterations on buildings materials of the Palacete

Pinho. Other decay factors have been introduced through past interventions with inadequate building materials.

2 MAPPING OF THE FAÇADES

The number of tiles that exist in the façade of Palacete Pinho was registered in a cadastral map drawing using AutoCAD 2000. For each tile, the alterations were freehand sketched. The weathering forms may be identified, according to the legend with different kinds of hachure.

3 MATERIALS AND METHODS

Three samples of different kinds of tiles were collected (PPA, PPAC, PPP). Additionally to those, some punctually samples of alterations products were taken from other tiles for lab investigation. Other samples were collected from other building materials such mortars, joints materials, bricks from the masonry, grating, and roof gutter.

To identify mineral phases we used X-Ray diffraction with micro preparation techniques and optical microscope. For chemical analyses and to support mineral identification we employed X-Ray fluorescence spectroscopy, infrared spectrometry, and scanning electronic microscopy.

4 RESULTS AND DISCUSSION

4.1 Mapping of the types of weathering alterations

The alterations identified in German tiles are: detachment with the mortar from the masonry, dark patina on the glazed from the traffic pollution, dark stains under the glazed, gray powder near the mortar joints, rust stains on the glazed, and some mortar joints without adherence. At the Portuguese ones the alterations are: loss of glazed in the most tiles with subsequently darkening, dark patina from the urban pollution and rust stains on the glazed. All these alterations are located in the detail of the map (Fig.2).

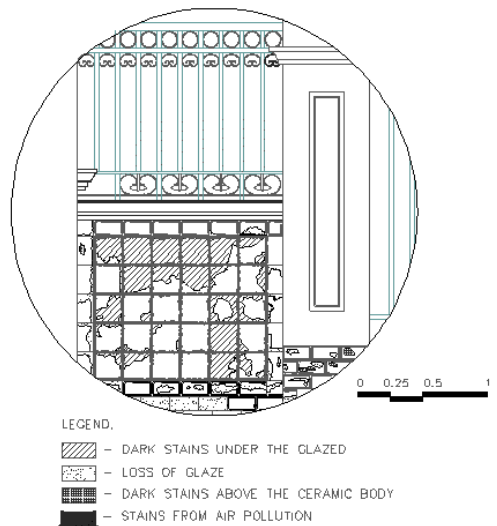


Figure 2: Detail of the weathering alterations map.

4.2 Mineralogical aspects

The German tiles (PPA and PPAC) have a similar mineralogical composition on the ceramic body, mainly constituted by quartz, mullite, tridymite, and calcite. Quartz, calcite, diopside and gehlenite were found in the ceramic of Portuguese tile (sample PPP). The crystalline material observed at the glazed in all the samples is quartz. Only the blue and gray glazes from PPA and PPAC samples, present cassiterite. All glazes present high backgrounds that suggest presence of amorphous material due be a vitreous material.

Quartz, calcite and kaolinite were found in all samples of mortars. Kaolinite can be a weathering mineral. Some joints present the same minerals. In the bricks from the masonry quartz, hematite and muscovite were mainly identified. Goethite was localized at the grading and is a typical weathering mineral.

The dark patina located on the glazed is mainly constituted by quartz, kaolinite and calcite identified by X-Ray diffraction and infrared spectrometry. They possibly come from the traffic pollution. The gray powder near the joints is constituted by calcite and the rust stains above the Portuguese tiles are formed by goethite, a weathering mineral. The dark stain under the glazed shows the same minerals found in its ceramic body

4.3 The color painting elements

The glaze's colors of Germans and Portuguese samples were analyzed by X-Ray fluorescence spectrometry and the results show that lead is the

main chemical element used as pigments for all tiles. Ramos et al. (2002) also have observed lead in some ancient tiles. The transparent yellowish glazed of the sample PPA presents: lead, iron, zinc, copper, nickel and manganese. Since these elements are present in the other colors one conclude that tin and cobalt detected in the gray color should be the responsible for that color; iron for ocher; tin, antimony and cobalt for blue; tin and antimony for light orange; manganese for brown; and copper and cobalt for green. The light yellow glazed based of Portuguese tile contains lead, copper, zinc, nickel, iron, manganese and chromium. The antimony probably is responsible for the orange color and the element cobalt for the blue color. When tin is present in PPA and PPAC samples, their glazing become more opaque than transparent.

4.4 Physical properties

The German tiles presents 11.50% water absorption and the Portuguese 24.42%. The glazed thickness of PPA and PPAC is about 0.04 to 0.2 mm and the ceramic body is 1.10 to 1.12 cm. The sample PPP is approximately 0.08 to 0.1 mm of glazed thickness and 0.8 to 1.30 cm of ceramic body due the furrow behind the tile. Optical microscopic analyses show some fissures in the PPP ceramic body parallel to the glazed. Some defects were observed in the glazing of both tiles, such as fissures and many bubbles probably caused by the firing process.

4.5 Microorganisms activity

The most important biodegradation observed at Palacete Pinho is caused by the algae belonging to *Cyanophyta* and *Bacillariophyta* divisions: *Chroococcus*, *Cyanosarcina*, *Scytonema* and *Navicula* (Fig. 3). Torraca (1988) explains that the algae on masonry are frequently present in the tropical climate. Caneva et al. (1991) told that some *Bacillariophytes* had been recognized in some building surfaces in the tropics and the algae subsequently retard drying of the surface and increase the water content, what favors the adherence of other substances to the patina, and the growing of other microorganisms, as well as lower and higher plants.

The presence of fissure in the glazed of the German tiles and its transparency together luminosity, humidity, and some nutrients like silicates favor the surviving of algae. On the other hand, the algae do not attack Portuguese tiles with opaque glazing; only after the loss of glazing and, therefore, above the ceramic body. The first results or impressions from this kind of microorganism alterations is the development of dark stains, pores rupture with grain desegregation and some physical changes in the tiles, becoming a pulverulent

material. This kind of alteration was observed only in the Portuguese tiles.

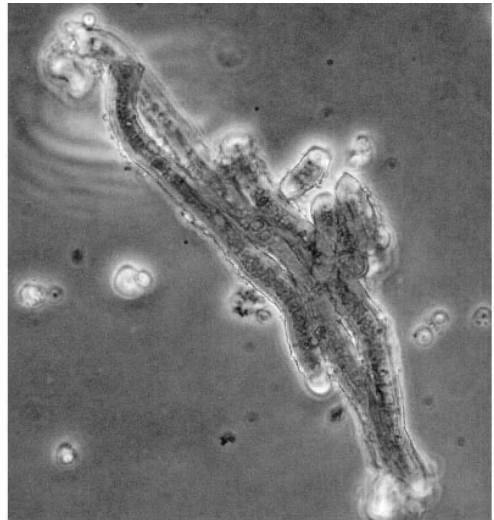


Figure 3: Microorganism (*Scytonema sp.*) observed at PPP sample .

5 CONCLUSIONS

The three types of tiles studied show all kinds of weathering alterations, but the Portuguese one show the most severe alterations such as, quick loss of glazing becoming an earthy material. This kind of alteration was not observed in the German glazed tiles that present weathering resistant minerals, such as cassiterite, and also a lower porosity that turns percolation of soluble salts in the porous ceramic body very difficult.

Jeannette (1997) explains that the porous structure is important to the alteration process by soluble salts. The fissures existing in the ceramic body of Portuguese tiles increase the porosity, contributing to the capillary rise.

The fissures in the colorless glazing permit the colonization by algae, on the other hand, it avoids the attack of other kind of microorganisms. Other characteristics, such as the small glazing thickness, fissures in the ceramic body and the position at the lower part on the façade, favors the degradation of the Portuguese tiles.

The most tiles located at the east façade do not present the dark stains coming from air pollution. They receive rain precipitation, wind blowing and sunlight in the morning.

The action of the plant roots contributes to the release of tiles from masonry.

The goethite formed over some Portuguese tiles

is a typical product of the actual weathering, coming from the oxidation of nearby iron grating.

The results showed that some properties of the tiles inherited from the manufacture processes are contributing for its alteration by the tropical weathering. To avoid or retard the weathering alteration we need know more details about the nature of the tiles. This can also be useful for new ceramic architectural products as a way to prevent the occurrence of the same alteration process in the near future. The study of historic façade tiles, as for example, Palacete Pinho, shows the necessity to use suitable materials, more resistant to the tropical weathering (glazed and ceramic body), and to control some defects that occur during the manufacture.

6 REFERENCES

- Alcântara, D (unpubl.). Azulejos em Belém do Pará. Subprojeto. Belém: IPHAN, 1982, 52p.
- Caneva, G.; Nugari, M. P. & Salvadori, O. 1991. Biology in the Conservation of Works of Art. Roma: ICCROM, 182p.
- Chiari, G. 2000. Mineralogy and cultural heritage. In: Vaughan, D.J. & R.A. Wogelius, (Ed.) Environmental Mineralogy. Budapest: Eötvös University Press, vol.2, p. 351-381.
- Derenji, J. 1987. Arquitetura eclética no Pará – no período correspondente ao ciclo da borracha: 1870 – 1912.. In: Fabris, A. (Ed) Ecletismo na arquitetura brasileira. São Paulo: Nobel, Edusp, p. 147 a 175.
- Jeannette, D. 1997. Importance of the pore structures during the weathering process of stones in monuments. In: Soils and sediments mineralogy and geochemistry. Germany: Springer, p. 177-190.
- Malhoa, M. 2001. A importância do diagnóstico. In: Dias, M. C. V. L. (Ed) Patrimônio azulejar brasileiro – aspectos históricos e de conservação. Brasília: Ministério da Cultura, p.111 –125.
- Oliveira, M. M. 2001. Materiais de revestimento aplicados na conservação de azulejos. In: Dias, M. C. V. L. (Ed) Patrimônio azulejar brasileiro – aspectos históricos e de conservação. Brasília: Ministério da Cultura, p. 141 – 163.
- Ramos, S.S.; Reig, F. B.; Adelantado, J. V. G.; Marco, D.J.Y.; Carbó, A.D. 2002. Study and dating of medieval ceramic tiles by analysis of enamels with atomic absorption spectroscopy, X-Ray fluorescence and electron probe microanalysis. *Spectrochimica Acta Part B* 57: 689-700.
- Torraca, G. 1988. Porous Building Materials. Roma: ICCROM, 149p.

Environmental Mineralogy and Health

Mineralogical and Geochemical Characterization of Sediments and Suspended Particulate Matter in Water from the Potaro River Area, Guyana: Implications for Mercury Sources

D.Paktunc, D.Smith, R.Couture

Mining and Mineral Sciences Laboratories, CANMET, 555 Booth Street, Ottawa, Ontario, K1A 0G1, Canada

ABSTRACT: Sediments and suspended particulate matter in water along a 60 km stretch of the Potaro River area in Guyana were characterized to better understand the sources of increased Hg in the carnivorous fish species. Quartz and gibbsite are the most abundant minerals in the river bottom sediments. The tributaries affected by land mining operations contain larger fractions of the fine particles and are characterized by the presence of aluminosilicate minerals. It appears that the Hg concentrations increase exponentially as a function of the proportion of fine particles (<62 µm). In addition, the high Hg concentrations correspond to samples containing kaolinite and muscovite. There is an overall increase in Hg concentrations in the sediments downstream. Selective extraction tests indicate that organocomplexed Hg is the predominant Hg species in most of the sediment and tailings samples; however, this does not rule out the significance of non-humic bound Hg species. The increased levels of Hg in the sediments appear to be resulting from the placer gold mining activities by which large amounts of soil and sediments are excavated and processed. The source of Hg in soil may include atmospheric deposition.

1 INTRODUCTION

There are health concerns over the mercury exposure of Amerindians in the Amazon basin. Due to increased levels of Hg in carnivorous fish species, Amerindians, who regularly consume fish, have significantly high levels of Hg in their hair. In order to investigate the sources of Hg in the food chain, a mineralogical and geochemical study was conducted along a 60 km stretch of the Potaro River basin, heavily influenced by placer gold mining operations. The objectives of this study were (1) to determine the mineralogical characteristics of the sediments and tailings in relation to Hg concentrations, (2) to assess the impact of Hg contamination from small and medium-scale placer gold mining operations, and (3) to contribute to the conception of anthropogenic vs. natural sources of Hg in the Potaro River basin.

2 METHODOLOGY

2.1 Sampling

Water samples taken at 1m depths and at a depth of 90% of the water column were diluted with distilled water in the laboratory and filtered onto 0.2 µm

polycarbonate filters. A vacuum apparatus was used to achieve a uniform distribution and light loading of the particulate matter on the filters.

Sediments from the bottom of the Potaro River and its tributaries along the 60 km stretch, and tailings from the abandoned dredge near Tumatumari were sampled (Fig. 1). In addition, sediments from an undisturbed open cut at an active land mine at White Hole were sampled to provide a basis for the natural background data. The samples were dried at room temperature, classified and sieved to remove the large pieces of organic debris. The samples were then homogenized and split for chemical, mineralogical and particle size analyses.

2.2 Analytical techniques

A variable pressure scanning electron microscope (VP-SEM) interfaced to an image analyser was used to analyze the particulate matter on polycarbonate filters. Following automated detection of about 1000 particles in each sample, a semi-quantitative X-ray microanalysis was performed. Mineralogical compositions of the sediment and soil samples were determined by a Rigaku rotating-anode X-ray powder diffractometer.

Particle size measurements were performed using a Microtrac particle analyzer. The silt and clay size fractions (i.e. <63 μm) were combined and reported as the fine fraction.

Total Hg analyses were performed at Flett Research Ltd. Mercury analyses were based on the SnCl_2 reduction method, gold amalgam trapping with fluorescence detection. The precision of the analytical technique, based on duplicate analysis of a selected number of samples, was very good.

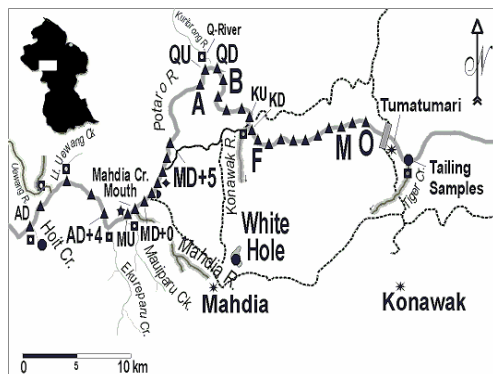


Figure 1. The Potaro River transect and sampling locations. River bottom sediments are marked by triangles. The study area is marked by the white rectangle in a sketch of Guyana at upper left corner. AD: Amatuk Falls downstream; MD: Downstream of the confluence of the Mahdia Creek. Water flow is from left to right.

Selective extraction tests were performed by Frontier Geosciences Inc. The samples were sequentially leached to obtain the following fractions: (F0) leachable elemental Hg (Hg^0), (F1) water soluble Hg, (F2) pH 2 soluble Hg, (F3) 1N KOH extractable Hg, (F4) 12N HNO_3 soluble Hg, and (F5) aqua regia soluble Hg. The analytical variability was determined through the analysis of duplicate, spiked and blank samples. The overall recovery of certified reference materials was 85.1 %, indicating high accuracy of the procedure. Kim et al. (2003) provide an independent evaluation of the selective extraction methodology by X-ray absorption fine structure spectroscopy. Although the species represented by the F4 fraction are well determined by the selective extraction technique, more than 10 % variability is possible for the F1, F2 and F3 species. In addition, there is the likelihood of overlap in the extraction of the species.

3 RESULTS

3.1 Suspended particulate matter in water

The principal particles observed in the water column consist of Al-Si, Si, Al and Fe particles with minor amounts of Ti, Fe-Al-Si and Fe-Al particles. In general, the particulate matter showed minor variations in mineralogy with respect to water column depth. The Al-Si particles are in greater abundance in the water column downstream of Mahdia Creek (i.e. 60-67 %) than they are in an upstream location (i.e. 29-36 %). In contrast, there is a decrease in the abundance of Al-Fe and Al particles. These suggest a major influx of Al-Si particles from Mahdia Creek, which is heavily influenced by land mining activity.

3.2 Soil

The undisturbed soil as sampled in advance of a land dredge operation at White Hole contain two distinct units: (1) the lower unit of white silt loam and (2) the upper unit of pale brown sandy loam. The fine fraction (i.e. <63 μm) forms 64 % of the lower unit and 29 % of the upper sandy soil unit. Kaolinite is more abundant in the lower silty soil unit. Mercury concentrations are much higher in the sandy soil unit than in the underlying finer grained soil (Fig. 2). The selective extraction test results indicate that the Hg associated with humic organic matter (F3) forms the most dominant Hg fraction in the upper sandy soil unit. Changes in the other Hg species across the vertical soil profile are less pronounced. The F0 and F2 fractions are below the detection limits throughout the soil profile. The absence of F2 fraction and the abundance of F3 in the sandy soil unit suggest the presence of Hg as adsorbed species on humic organic matter. The F4 fraction representing the non-humic bound Hg^{2+} adsorbed to particle surfaces is relatively uniform throughout the profile forming the secondmost abundant fraction in the sandy unit and the most abundant fraction in the silty unit. Abundance of the organocomplexed Hg species in the upper horizon is essentially the reason for the strong enrichment in the total Hg concentrations. The preferential enrichment in the upper sandy soil regardless of the particle size and mineralogical composition seems to suggest an extraneous source of Hg such as atmospheric deposition.

3.3 Sediments

Quartz and gibbsite are the most abundant minerals in the river bottom sediments. Kaolinite and muscovite are present in all the tributary samples affected by land mining activity while the samples from the unaffected tributaries do not contain kaolinite or muscovite. The sample from the

Uewang River, which is thought to be weakly affected by land mining, contains muscovite only. The sediments sampled along the Potaro River, downstream of the Amatuk Falls show an increase in the fine fraction beginning with the large influx at Mahdia Creek (Fig. 3). The tributaries affected by land mining operations contain larger fractions of the fine particles (e.g. 93 %) than those of the unaffected tributaries.

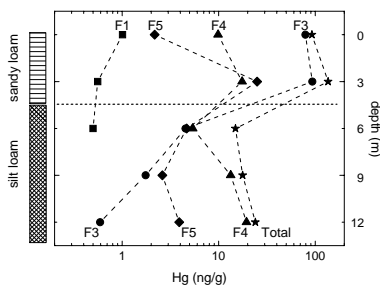


Figure 2. Mercury speciation in a vertical soil profile from White Hole. Total Hg is the sum of species.

Mercury concentrations in the Potaro River sediments range from 6 ppb below the Amatuk Falls to 214 ppb at the end of the transect near Tumatumari. Downstream of the Mahdia Creek confluence, Hg concentrations appear to display an increase (Fig. 4). Mercury concentrations range from 68 to 321 ppb within the tributaries affected by mining activities. On the contrary, Hg concentrations are lower (i.e. 5-32 ppb) in the sediment samples from the tributaries unaffected by mining.

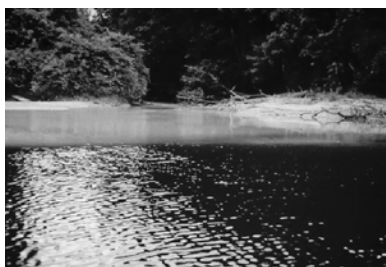


Figure 3. Confluence of Mahdia Creek (background) with Potaro River (foreground). Note the color contrast between the Mahdia Creek (grey) affected by mining and the Potaro River (black).

There is a correlation between the particle size and Hg concentrations (Fig. 4). Increases in the Hg concentrations correspond to the samples having greater proportion of finer size fractions. It appears

that the Hg concentrations increase exponentially as a function of the proportion of fine particles. The increases in the fine size fractions of the sediment samples with downstream (Fig. 4) are related to the placer gold mining activities by which large amounts of sediments are dredged from the river bottom.

The sediments containing more than 44 ppb Hg have kaolinite and muscovite in addition to gibbsite. Although it has been well documented that Hg has a strong affinity for the fine fraction of soils, a mineralogical control may have been overlooked as suggested by the results presented in this study.

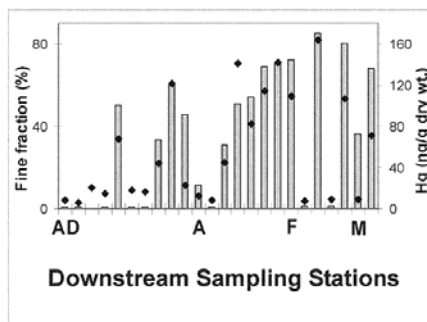


Figure 4. Variation of particle size as a percentage of the fine fraction (i.e. <63 μm) shown in vertical bars and total Hg concentrations (diamond symbols) in sediments along the Potaro River transect from east (left) to west (right). Horizontal axis not to scale.

The selective extraction tests produced similar results for the Potaro River samples. On average, approximately 70 % of the total Hg in the sediments are organocomplexed Hg species (Fig. 5). The remainder is made of strong complexed Hg (11-14 %) and relatively insoluble Hg (14-30 %) species. No elemental, water soluble or pH 2 soluble Hg fractions is present. Abundances of the aqua regia Hg fraction remain relatively low in all the samples with the exception of Station O where it is 4 times greater than the other stations.

Selective extraction test results from the tributary samples are similar. Samples from the Mahdia Creek mouth and Tiger Creek contain on average 52 % organocomplexed Hg, 24 % strong complexed Hg and 24 % Hg sulfide or selenide species.

3.4 Tailings

The tailing samples contain 16 to 27 % fine fractions. Quartz and gibbsite are the dominant minerals in the tailings samples. The tailing samples contain total Hg concentrations ranging from 9 to 42 ppb. The high end of this range is attributed to the presence of an organic-rich layer (Fig. 6). This

sample is also characterized by the presence of kaolinite and muscovite in addition to quartz and gibbsite. Selective extraction tests indicate that the majority of the Hg can be characterized as the organocomplexed Hg.

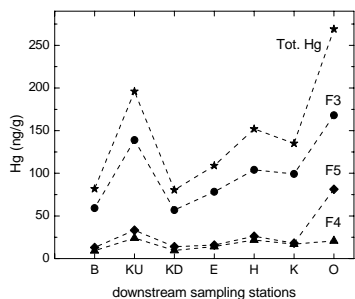


Figure 5. Mercury speciation results in sediment samples along the Potaro River transect. Tot. Hg is the sum of species. Horizontal axis not to scale. See Fig.1 for station locations.

4 CONCLUSIONS

Quartz and gibbsite are ubiquitous in the sediments. Kaolinite and muscovite are confined to the sediments containing more than 44 ppb Hg. In addition, the Hg concentrations appear to increase exponentially as a function of the proportion of fine particles. The correlation between the fine fraction and Hg concentration of the Potaro River and its tributary samples and the mineralogical observations suggest that aluminosilicate minerals such as kaolinite and muscovite play a role in controlling the observed Hg distributions in the sediment samples.

Increases in the fine fractions of the sediments downstream appear to be related to the placer gold mining activities by which large amounts of soil and sediments are excavated or dredged.

It is possible that the high Hg concentrations present in the undisturbed sandy soil horizon at White Hole are due to atmospheric deposition as well as being natural.

Anthropogenic Hg input to the river systems probably involves not only the amalgamation process used to extract gold but also the disturbance of the natural soil and sediments by dredging and excavation operations. This is similar to the findings of Howard et al. (2002) and Telmer et al. (2000) in the Amazon basin.

The Hg speciation results indicate that the majority of the Hg within the sediments can be characterized as organocomplexed thus having a potential for methylatability. The Hg speciation results, suggesting a control by the soil organic matter, are not necessarily compatible with the

correlations that exist between the mineralogy or particle size data and the total Hg concentrations where sorption to aluminosilicate particles is postulated. The similarities in the downstream profiles of the Hg fractions as shown in Figure 5 seem to suggest nonspecific or overlap in extraction of Hg species by various solvents.

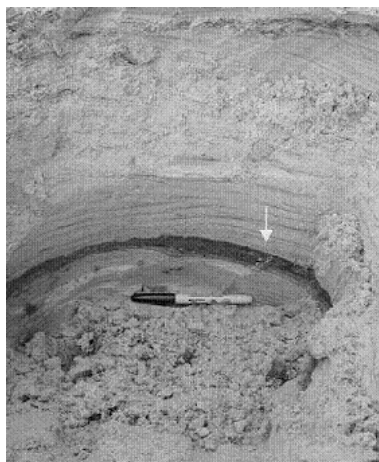


Figure 6. Photo showing a 1 cm thick organic-rich layer (marked by the arrow tip) in the tailings near the abandoned river dredge near Tumatumari.

5 ACKNOWLEDGEMENTS

The study was funded by the Canadian International Development Agency (CIDA). Sampling of the sediments and soil was carried out by the personnel of Guyana Geology and Mines Commission under the guidance of the third author (RC). The senior author thanks Ayalew Legesse for logistic help in Guyana, and Bryan Tisch and Bill Howell for reviewing the paper.

6 REFERENCES

- Kim, C.S., Bloom, N.S., Rytuba, J.J. and Brown, G.E. (2003) Mercury speciation by X-ray absorption fine structure spectroscopy and sequential chemical extractions: A comparison of speciation methods. *Environmental Science and Technology* 37, 5102-5108.
- Howard, B.M., Malm, O., Payne, I. and Thornton, I. (2002) Mercury in Amazonia: Assessing the role of artisanal gold. *Mining Environmental Magazine*, 20-21.
- Telmer, K., Costa, M., Araujo, E.S., Angelica, R.S. and Maurice, Y (2000) The source and distribution of mercury in the Tapajos River basin – The importance of suspended sediments from alluvial gold mining, Para Brazilian Amazon. *31st International Geological Congress, Rio de Janeiro, Brazil, Extended Abstracts*, pp. 221-226.

Asbestos Release through Degradation of Fibercement

F.R.D.Andrade, R.B.Santini, Y.Kihara*

Department of Mineralogy and Geotectonics, Geosciences Institute, University of Sao Paulo, Sao Paulo, Brazil

**Brazilian Portland Cement Association, Sao Paulo, Brazil*

ABSTRACT: Degradation of fibercement tiles due to weathering enhances porosity and may cause detachment of mineral fibers. A 25 years old fibercement roof was analysed by microscopy and X-ray diffractometry, and compared to a non-weathered sample. Mineralogical composition of the old tiles comprises chrysotile, calcium hydrosilicates, calcite and calcium sulfates, the two latter occurring in the weathered tiles only. Weathered fibercement surfaces are rough, and loosen asbestos fibers can be seen with the naked eye and easily removed by touching. The lower, unexposed surface of the weathered tiles has much lower porosity and its fibers are better fixed in the cement compared to the upper surface of the tile. Microscopic analysis revealed that the weathered portion of the tiles is about 2mm thick, in which enhanced porosity and detachment of asbestos contrasts with the well preserved inner parts of the tile. Particulate matter in the atmosphere was sampled right above the tiles. Analysis of particulate solids carried away by water impact and flow over the tile surface was also done. Among the solids identified in the atmosphere and water samples, there is a large predominance of soot, while fibers are much lesser in volume, comprising mostly cellulose and rare asbestos. Solid fraction carried by water also contains quartz and clay minerals, besides soot and fibers. Chemical weathering of fibercement caused by acid rain is stronger in industrial urban areas.

1 INTRODUCTION

Asbestos-reinforced fibercement is a low-cost building material widely used in Brazil and other developing countries. Its low price and several technical properties contributed to make this material a commercial success. Around 50 to 70% of the buildings in Brazil are covered with fibercement, and almost 90% of the Brazilian asbestos production is consumed in fibercement production. Asbestos-reinforced fibercement is composed by portland cement, asbestos (mostly chrysotile) and smaller amounts of cellulose. The asbestos content in the tiles is around 12.5 wt. %. Although asbestos is widely recognized as hazardous to human health, fibercement is traditionally neglected as a potential source of asbestos contamination. It is usually handled as an inert material and asbestos release is considered only under such conditions as cutting, drilling or crushing fibercement pieces. Construction debris containing fibercement are considered in several countries as inert and no special care is taken concerning their disposal. Degradation of fibercement due to weathering is still relatively underestimated. As any concrete body, fibercement tiles are prone to undergo degradation when exposed to chemical, physical and biological weathering.

Degradation of the cement matrix enhances porosity and may lead to detachment of the mineral fibers.

We studied a 25 years old fibercement roof in São Paulo City, Brazil. Tiles were analyzed under optical and scanning electron microscope, and their mineralogical composition was determined by X-ray diffraction. Samples of new, non-weathered tiles were analyzed for comparison. The mineralogical composition of the old tiles comprises chrysotile (asbestos), calcium hydrosilicates (cement), calcite and calcium sulfates. The latter two minerals are not present in new tiles and are formed by carbonic and sulfuric acid attack during chemical weathering.

2 PREVIOUS STUDIES

There are relatively few studies assessing open air asbestos concentration. Spurny (1989) studied asbestos release from weathered tiles. Measured emissions of asbestos fibers longer than 5 µm were in the range of 106 to 108 fibers/m².h, while the mean release of asbestos from weathered and corroded fibercement into the environment was estimated at about 3 g/m³.year. Maximum values of ambient air concentrations of asbestos fibers longer than 5 µm at distances of 0.5 to 1.0m from corroded

fibercement plates was 0.001 fibers/cm³. The author observed that, although chrysotile fibers were chemically changed due to weathering, animal experiments did show that their carcinogenic potential did no differ from the unaltered chrysotile. Spurny (1989) considered that mineral fibers dispersed into the air contribute to the total carcinogenic potential of the polluted atmosphere and increase the health risk for the general population.

Felbermayer & Ussar (unpubl.) compared asbestos concentration in the atmosphere of several locations, including an asbestos mine and an asbestos cement plant, urban areas with heavy and low traffic densities, sites with and without asbestos cement roofing, and compared them with the natural background in areas unaffected by asbestos contamination or human activity. Highest fiber concentrations were observed in the asbestos mine (avg 0.0024f/cm³; min 0.0006; max 0.0088) and in the urban area with heavy traffic density (avg 0.0046 f/cm³; min 0.0008; max 0.0079), corresponding respectively to ten- to twenty-fold enrichment compared to the natural background (avg 0.0002 f/cm³; min 0.000; max 0.0005). The site with asbestos cement roofing presented lower fiber concentration (avg <0.001 f/cm³; min 0.000; max 0.0004) than the natural background, although it must be emphasized that these values are close to the detection limit of the applied measuring technique (0.0001 f/cm³).

Several efforts have been made to access the relative risk to human health of the main mineral fiber types. It is widely recognized that amphibole fibers are considerably more hazardous than chrysotile, mainly because of the much higher biopersistence of the former compared to the latter. The risk of pure chrysotile inhalation is still under debate, as it is particularly difficult to access because of the common association of amphibole and chrysotile in nature. Contamination of chrysotile deposits by amphibole fibers may contribute to the carcinogenic effects of occupational exposure, as tremolite is usually the predominating fiber present at death (e.g. McDonald & McDonald 1997). While some authors consider as very small the risk of exposure to commercial chrysotile (McDonald & McDonald 1997; Rees et al. 2001), other consider that the exposure to chrysotile alone induces asbestosis, lung cancer and mesothelioma, together with an increased prevalence of non-malignant respiratory symptoms (Stayner et al. 1996; Niklinski et al. 2004).

3 SURFACE ANALYSIS

Exposed surfaces of old fibercement tiles have rough surfaces, and loosen asbestos fibers can be easily

seen with hand lenses or even with the naked eye. The fibers are easily removable by touching. Weathering features are more pronounced along the hinges of wave-like corrugated tiles, as these regions are more fractured, probably due to residual tensions from the manufacture process. There is a clear contrast between the upper and the lower surfaces of the weathered tiles; the unexposed surface has much lower porosity and its fibers are quite fixed in the cement. The same contrast is observed where tiles overlap, whereas the underlying portions of the tiles remain unaltered, resembling new ones.

Under the scanning electron microscope, the upper surface of the tiles display an enhanced porosity, revealing huge amounts of asbestos fibers detached from the degraded cement (Figure 1). A weathered upper portion, about 2mm thick, is clearly seen, contrasting with the inner parts of the tile which are still well preserved. Biogenic structures resembling bacteria colonies were observed inside some of the pores.

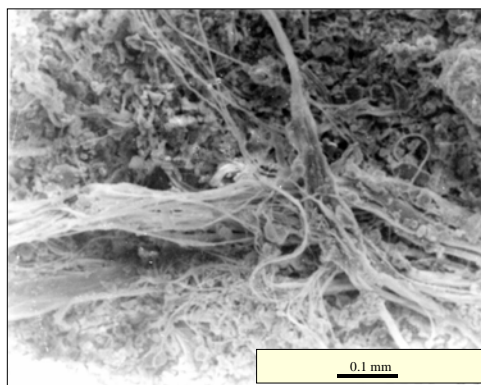


Figure 1. Scanning electron microscope image of loosen asbestos fibers in the upper, weathered surface of an old fibercement tile.

4 ASBESTOS RELEASE

Looking for detached asbestos particles in the environment around the tiles, two procedures were performed: (a) sampling of particulate solids in the atmosphere right above the tiles; and (b) analysis of particulate solids carried away by water impact and flow over the tile surface. The air sample corresponds to 330m³, continuously sampled along 17 days in a pump apparatus placed 1 meter above the tile. While, for the other test, 20 liters of water were poured over the tiles and collected in its lower end. Solid fractions in air and water samples were collected in filters and analyzed under the electron scanning microscope.

Among the solids identified in the atmosphere and water samples, there is a large predominance of soot, as the sampling site is not far from major urban roads. Fibers are much lesser in volume, comprising mostly cellulose and rare asbestos. Solid fraction carried by water also contains quartz and clay minerals.

5 WEATHERING SIMULATION

An experiment of accelerated weathering was performed with fibercement samples immersed in distilled water at 60°C in a glass beaker. The whole experiment took 56 days, corresponding to approximately 15 years of natural weathering. Four samples of new fibercement were cut under current water to avoid inhalation of asbestos, and carefully clean before being immersed in water. The samples were taken from the water, each at a time, after 14, 28, 42 and 56 days to measure their porosity. Using a non-weathered sample as a reference, a steady, non-linear increase in porosity was observed. Our preliminary data indicate that the longer the weathering, the higher the rate of cement degradation. Solid residues were collected from the bottom of the beaker and analyzed under the electron scanning microscope, which confirmed the presence of asbestos fibers detached from the tile samples.

6 CONCLUSIONS

Fibercement tiles are potential sources for asbestos contamination. Progressive degradation of the cement matrix enhances porosity and loosens mineral fibers from the tiles. Preliminary results from fibercement roofs in São Paulo, Brazil, confirmed previous observations that asbestos is released from corroded fibercement plates, which, therefore, cannot be considered as entirely inert building materials.

Additionally, chemical weathering caused by acid attack of fibercement is stronger in industrial urban areas, where rain water has a higher acidity than elsewhere. Taking into account the vast areas covered by fibercement in Brazil and other countries, as well as the cumulative effects of progressive weathering of old fibercement roofs, the positive effects of a possible prohibition of asbestos-reinforced fibercement in civil construction would be only fully achieved if old fibercement roofs were replaced by safer materials. After removal, fibercement should be disposed in controlled sites to avoid asbestos contamination of the surroundings.

Our ongoing research aims to quantify asbestos emissions and asbestos concentration in the atmosphere in the vicinity of asbestos tiles, together

with the natural asbestos background in São Paulo, in order to complete the preliminary results presented in this paper.

7 REFERENCES

- Felbermayer, W. & Ussar, M.B., unpublished. Environmental pollution by weathering of asbestos cement sheets. 5 p.
- McDonald, J. C. & McDonald, A. D., 1997. Chrysotile, tremolite and carcinogenicity. *Ann. occup. Hyg.*, 41:699-705.
- Niklinski, J., Niklinska, W., Chyczewska, E., Laudanski, J., Naumnik, W., Chyczewski, L., Pluygers, E., 2004. The epidemiology of asbestos-related diseases. *Lung Cancer*, in press.
- Rees, D., Phillips, J.I., Garton, E., Pooley, F.D., 2001. Asbestos lung fibre concentrations in South African Chrysotile mine workers. *Ann. Occup. Hyg.*, 45(6):473-477.
- Spurny, K.R., 1989. On the release of asbestos fibers from weathered and corroded asbestos cement products. *Environm. Res.*, 48:100-116.
- Stayner, L.T., Dankovic, D.A., Lemen, R.A., 1996. Occupational exposure to chrysotile asbestos and cancer risk: a review of the amphibole hypothesis. *Am. J. Public Health*, 86:179-186.

Mineralogy and Remobilization Processes in the Weltz-clinker Dump Site, Plovdiv Region, Bulgaria

R. Atanassova & T. Kerestedjian

Geological Institute, Bulgarian Academy of Sciences, 1113 Sofia, Bulgaria

I. Donchev

Central Laboratory of Mineralogy and Crystallography, Bulgarian Academy of Sciences, 1113 Sofia, Bulgaria

ABSTRACT: The Pb-Zn smelter (KCM) is the biggest Pb and Zn producer in the country. Clinker dumps have been deposited in the vicinity of the smelter during the last 35-40 years. The present study aimed at identification and characterization of the initial mineral composition of the clinker material and the recent mineral phases formed on the dump surfaces as well as the component remobilization processes. Over 30 minerals were identified in the initial material: elements (metals and alloys), oxides, silicates, sulphides, carbonates, and noble metals (Au and Ag). Clinker heaps were found to be affected by active self-initiated chemical processes – high temperature chemical burning and component transport phenomena, facilitated by gas and fluid movement. The main result of the chemical activity of the dumps is the deposition of recent sulphates minerals. More than 10 mineral phases as well as their deposition mechanisms were described. Other phenomena and measurable physical and chemical parameters in the dump bodies were registered too. Based on the study results, the clinker bodies were found to be sources of both usable metal contents and hazardous environmental threat. The results of the remobilization of the heavy metals are a secondary metallic contamination and acidification of the surface and ground waters, soils and river sediments. On the other hand, it became obvious, that the reuse of this material as a source of metal is technologically possible and it would lead to both economic and environmental benefits.

1 INTRODUCTION

The remainders of the KCM Pb-Zn smelter, near the town of Plovdiv, produced during its 40-year long activity, have been stored in large heaps in a neighbouring area. Main industrial products of the smelter are lead, zinc, and cadmium ingots as well as various alloys. Sulphuric acid is also component of its production. Classical pyro-metallurgical flow sheet, comprising sintering, shaft furnace reduction smelting and pyro-refining is applied for the lead production. The flow sheet for the zinc production is a classical hydro-metallurgical one, comprising roasting of zinc concentrates, treatment of gases to sulphuric acid, conventional two stage calcine leaching, weltz process to treat residues, solution purification, and electrolysis, melting, and casting of zinc ingots.

The clinker heaps were found to be affected by active self-initiated chemical processes – high temperature chemical burning and component transport phenomena, indicated by gas and fluid exhalations. The main result of the chemical activity of the dumps is the deposition of significant amounts of recent minerals (mainly sulphates).

This study is aimed at identification and characterization of the initial mineral composition of

the clinker material and the recent mineral phases formed on the dump surfaces as well as the component remobilization processes.

2 METHODS

The initial minerals in the clinker were studied by optical microscopy. The mineral composition was analyzed by electron microprobe (Philips 515). Recent mineral species were identified both by microprobe JEOL JSM 35 and X-ray diagram patterns (Debye-Scherrer method) compared with PDF card. The morphology of crystals was studied by Scanning electron microscopy (SEM). DTA was also used.

3 MATERIALS

Three visibly different types of materials are observed.

- Currently produced remainder. Weltz-clinker, rusty-brown, non-agglomerated. No chemical activity is observed, except gypsum formation on the surface, a few days after deposition.

- Chemically active material. 5-20 years old, slightly agglomerated, with some highly agglomerated spots. Chemical activity is noticed by the intensive exhalation of acid (pH 2) gases and high temperature – mostly about 40°C on the surface, but over 200°C measured in some active spots.

- Materials with moderate chemical activity. 20-40 years old, with no external signs of chemical activity, but with temperature (up to 110 °C) at a depth of 1 m or more.

4 INITIAL CLINKER MATERIAL

Over 30 minerals were identified in the initial clinker material: elements (native metals, including Fe, Cu, Au & Ag, and their alloys), sulphides (chalcopyrite, cubanite, bornite, pyrrhotite, chalcocite, coveline, troilite), silicates (fayalite, quartz, silica glass). Oxides (magnetite, hematite, goethite, etc.) and carbonates (malachite) are less abundant, while Pb, Zn sulphides (sphalerite, wurtzite, galena), and precious metal minerals are rare. Detailed characteristic is given by Donchev & Mitov (1997). Collomorph, porphyric, breccious, and porous structures are most typical for this material. Degraded sulphides are the most characteristic content of the investigated material. These are former sulphides that have partly lost their structure during incomplete melting. Under microscope they look much like the original phases, but their structure is closer to this of natural glasses, and hence their composition is remarkably non-stoichiometric. Especially pyrrhotite-cubanite intermediate phases are registered. The analyzed phases were attributed to intermediate members, in some cases with composition close to the natural analogue “chalcopyrrhotite”.

5 RECENT MINERALS DEPOSITION

5.1 Iron sulphates

HALLOTTRICHITE $FeAl_2[SO_4]_4 \cdot 22H_2O$. Represented by dusty or earthy yellowish masses, sometimes with visible tiny fibrous or acicular crystals.

MELANTERITE $FeSO_4 \cdot 7H_2O$. Found exclusively around smoke exhalation outlets. Represented by light-blue masses, changing to yellowish upon exposure to dry air.

COPIAPITE ($FeFe_3[SO_4]_6(OH)_2 \cdot 20H_2O$) Found as shapeless yellowish masses, always in close association with melanterite. DTA curve registered shows endotherm at 315°C with weight loss about 45%, corresponding to simple dehydration. The second 745°C endotherm corresponds to major loss of sulphur probably as SO_2 gas.

5.2 Copper sulphates

CHALCANTHITE $CuSO_4 \cdot 5H_2O$. Represented by platy crystals or kidney-like aggregates with typical blue color.

ANTLERITE $Cu_3[SO_4](OH)_4$. Represented by fine grainy or acicular rims with greenish color. Often mixed with chalcantinite.

BONATTITE $CuSO_4 \cdot 3H_2O$. Observed as vermiform masses, bright blue in color. Hard to distinguish from chalcantinite.

CHALCOCYANITE $CuSO_4$. Represented by stalactite like rims.

5.3 Al and Ca containing sulphates and native sulphur

APIJOHNITE $MnAl_2[SO_4]_4 \cdot 22H_2O$. Represented by white rims or shapeless masses. Often together with HALOTRICHITE $FeAl_2[SO_4]_4 \cdot 22H_2O$.

GYPSUM $CaSO_4 \cdot 2H_2O$. Represented by dusty masses on fresh clinker material, as well as growing around smoke exhalation outlets. The second type represents both chemical and structural evidences of a transition to anhydrite.

NATIVE SULPHUR α -S. Found as perfect acicular crystals up to 1 cm long but less than 1 mm wide. Greenish yellow in color. The acicular shape is an expression of a skeletal growth. The skeletons consist of parallel orthorhombic bipyramids $p\{111\}$. Slight rounding of the crystal edges, probably due to dissolution by acid gases, is observed under SEM (Fig. 1).

Sometimes fine droplets of sulphuric acid (14%) are found on their crystal faces. These droplets are hygrostatic and do not evaporate.

6 PROCESS

The represented data form the following overall picture of the observed process:

1. The sulphides are decomposed with the formation of H_2SO_4 ;
2. The coke is oxidized, using atmospheric oxygen and probably agitated by the sulphuric acid.
3. Initially insoluble phases, are metamorphosed into highly soluble material.
4. Observed chemical transformations are characterized by elevating stages of oxidation of the negative divalent sulphidic sulphur (S^{2-}), through zerovalent elementary S and tetravalent (SO_2) to hexavalent (SO_3).



Figure 1. SEM image of skeletal sulphur crystal.

5. This is supposed to happen in non-equilibrium conditions and thus depends a lot on minor local differences.

6. Bacteria take part in this process too and probably initiate most of redox processes.

7. Some or all of the observed processes are exothermic.

8. The composition of the gas exhalations is: CO₂ 16.7; Ar 1.04; O₂ 1.06; N₂ 81.2, and SO₂ - 0.36 vol.%. Formed gases SO₂ and CO₂ elevate the metallic components mobilized during sulphide decomposition. On the surface, both gases and liquid solutions deposit sulphate minerals.

9. The environmental consequences of the above described process are significant pollution levels in the close vicinity of the dumps. Leaching test results of the clinker material show concentrations of hundreds times above MPL (Maximum permissible limit): f. ex. Cu 800 mg/l = 3200 times MPL; Zn 270 mg/l = 20 times MPL.

7 CONCLUSIONS

Based on the study results, the clinker bodies were found to be sources of both usable metal contents and hazardous environmental threat. Concentrations times over the regulation limits for the main pollutants (Pb, Cu, Zn, Cd) in soils are observed around the residue dumps. Same localization were found for the over regulatory concentrations of main pollutants in ground and surface waters (Watmetapol 2003).

The remobilization of the heavy metals results in a secondary metallic contamination and acidification of the surface and ground waters, soils and river sediments. On the other hand, it became obvious, that the reuse of this material as a secondary source of metal is technologically possible.

Recently it has been treated in the "Elshitsa" plant by ore dressing technology for production of copper and coke concentrates. This use leads to both economic and environmental benefits.

8 ACKNOWLEDGEMENT

This study was funded in the frame of the NATO SfP 973739 WATMETAPOL project.

9 REFERENCE:

- Donchev, I. & K. Mitov. 1997. Mineralogy of clinker waste and opportunities for its useful components extraction. – *Geol. and mineral. resour.*, 2-3, 26-29.
 Watmetapol - NATO SfP 973739, 2003, Progress report

In Vitro Accessibility Results of Lead in Soil Dust, Solid Wastes, Sediments and Pb Minerals from Adrianópolis-PR, Ribeira River Basin

S.T.Bosso, D.B.Cardoso, J.Enzweiler

Department of Geology and Natural Resources, Geosciences Institute, State University of Campinas, São Paulo, Brazil

ABSTRACT: During decades, lead mining and smelting activities in the eastern part of Parana state, Brazil, generated wastes and tailings, which mostly are up to now disposed near to the old plant and neighbor villages. Previous studies of other authors revealed that part of villagers have concentrations of lead, in blood, higher than normal and the results can clearly attributed to the exposure to the high levels of lead in the environment. Some suggestions were made regarding the contamination routes, but they could not clearly stated yet. To help in clarifying this point, bioaccessibility experiments with surface soils, minerals and mine tailings were conducted under conditions that simulate human gastric juice. All lead from solid wastes and great part of Pb from nearby soils lead were be dissolved, while little Pb was dissolved from some typical lead minerals. The soil samples contain 70-680 mg kg⁻¹ Pb, which is not enough to detect Pb phases by EDS-SEM analysis. But in one sample, a grain of pyromorphite [Pb₅(PO₄)₃Cl] was identified. In the solid waste and sediments samples, lead is incrustated in the matrix as PbO. From X-ray diffraction results of a soil dust sample, feldspar and a clay mineral (saponite) were identified, among other minor phases. In the solid wastes from the smelter process, just one lead phase (PbO) was identified. In the residues from the flotation process, none Pb phase could be identified, just some clay minerals (biotite and phlogopite), calcite, dolomite and barite.

1 INTRODUCTION

1.1 Area description

Adrianópolis city is located on the Ribeira de Iguape river basin, which is situated in an area comprised both at the northeast of Paraná and at southeast of São Paulo states. This area was responsible, in the past, for great lead production and also zinc and silver. Beside the mining activities, in the decade of 1950, a smelting and refining company was installed.

1.2 Pollution history

During decades, solid wastes of the mining and smelter process were piled up and disposed near to the village and at the margin of Ribeira River. Contamination of the river sediments was detected the 80's decade (e.g. CETESB 1988).

Cunha (2003) reported up to 900 mg kg⁻¹ lead in soils. The contamination of the environment, particularly the soils probably is due to several factors like the presence lead mineralized phases, atmospheric emissions from the former metallurgic plant and aeolic transport of fine particles from the solid wastes piles. Paoliello et al. (2002) and Cunha (2003), showed that a significant number of children

at school age, which live in the village near the abandoned refining plant have high levels of lead in blood (> 10 µg dL⁻¹). In adults, up to 48 µg dL⁻¹ of lead in blood was measured (Paoliello et al. 2003).

Despite the evidences of Pb in the environment, no clear contamination route could be established for observed high levels of Pb in human blood in the area. Brown et al. (1999) comparing similar situations in other areas of the world, showed that it is not always possible to establish a correlation between lead in the environment and lead levels in blood of people who live in such places. Their conclusion was that bioavailability is mainly concerned with the speciation of the element (i.e. its chemical form, valence and physical state), rather than the total concentration. The molecular speciation of lead species in soils, has been done, in some cases, by EXAFS (extended X-ray absorption fine structure) and XANES (X-ray absorption near-edge structure) techniques (Manceau et al. 1996, Brown et al. 1999, Ostregreen et al. 1999).

Different phases can present different reactivity and consequently behavior, regarding bioavailability. *In vitro* bioaccessibility tests were proposed to infer about bioavailability (Hamel et al. 1998, Oomen et al. 2002) by simulating the metabolic conditions of the human gastric tract. Since people who live the

area of the study have great chance of having contact with the soils and solid wastes, samples from those materials and also of some lead minerals and compounds were tested to evaluate Pb solubility in solutions which simulate gastric juice acidity and complexing capacity.

2 MATERIALS AND METHODS

2.1 Sample collection

A composed sample of topsoil (just the upper loose part of the soil) was collected at a distance of about 1 km from the former ore plant. Other soil samples (from the first upper 30 cm of the soil horizon), collected at different distances from the plant were also used. Composed samples from different points of the same pile of the mine tailings and solid wastes piles (slag), were collected. A sample of sediment from a flooding area (wetland) near to the mine tailing pile was also collected.

2.2 Grain size

The samples were sieved (62 μm) to evaluate the amount of fine particles. The fine fraction of all samples was separated for the bioaccessibility tests. The coarsest fraction was grinded for chemical analysis.

2.3 Characterization

Samples were analyzed by XRF (X-ray fluorescence) to determine whole Pb concentration. XRD was used for determination of the mineral phases. Not grinded samples were also analyzed by energy dispersive spectrometry on a scanning electronic microscope (SEM-EDS).

2.4 Bioaccessibility experiments

The bioaccessibility test presented by Hamel et al. (1998) consists in determining the amount of lead that is soluble when the sample is in contact with organic acid solutions. 1 g of each sample was transferred to Teflon bottles and 100 ml of 0.4 M of glycine solution, previously acidified to pH 1.5 with HCl was added. The bottles were closed with their lids, placed in a thermostatic bath at 37 °C and left under constant orbital agitation, during 1 h. Phases were separated by centrifugation, at 3500 rpm for 10 min, and the liquid phase was analyzed by atomic absorption spectrometry (AAS). A second method, used by Oomen et al. (2002), consists in using a solution with 3.2 g of pepsin, 7.0 mL of HCl and 2.0 g of NaCl in 1 L of ultrapure water. The final pH of this solution is 1.5. In a third experiment, water acidified to pH 1.5 with HCl was used. The remaining conditions (time of contact, separation

method and the quantification of the lead) were identical to the procedure with glycine solution.

3 RESULTS

3.1 Grain size

In the soil samples, coarser particles (> 62 μm) are predominant, i.e., represent 60% of the whole sample, in average. In the slag, the fine fraction corresponds just to 1.2% sample taken (3.5 kg), and in the mine tailing samples, about 20% of the material are fine particles (< 62 μm).

3.2 XRF Analysis

The total lead concentrations in the fine fractions of the collected samples are shown in Table 1. The mine waste samples contain significant amount of lead, while in soils concentrations are much lower. The relative difference of concentration between the fine and the coarse fractions is about 50% in soils and 15% in average in solid wastes. The mine tailings sample from Vila Mota also presents 624 mg kg^{-1} of Cd and 1070 mg kg^{-1} of As, and in the solid waste sample from Rocha mine 1880 mg kg^{-1} of As were determined.

Table 1: XRF results for Pb quantification in finest fraction of the samples

Sample (location)	Pb (mg kg^{-1})
Topsoil (1.0 km*)	682
Soil 1 (5.0 km*)	450
Soil 2 (1.0 km*)	263
Soil 3 (0.5 km*)	93
Soil 4 (1.4 km*)	68
Mine tailings (Vila Mota)	3770
Wetland (Vila Mota)	4680
Slag (Plumbum)	3.4%
Mine tailing (Rocha mine)	1.7%

* Distance from the plant

3.3 SEM Analysis

From the soils, just the topsoil was analyzed by EDS-SEM. and the only phase of lead which was clearly identified was a particle with composition which was associated to the secondary Pb mineral pyromorphite ($[\text{Pb}_5(\text{PO}_4)_3\text{Cl}]$). In the mine tailings, slag and sediment, litharge (PbO) was found incrustated with silicatic phases.

3.4 XRD Analysis

XRD analysis of the topsoil sample showed, in order of predominance, quartz, feldspar and clay minerals (saponite-montmorillonite). In the mine tailings quartz, micas and one lead phase, identified as lanarkite ($\text{Pb}_2(\text{SO}_4)\text{O}$), and baryte (BaSO_4) were

identified. In the slag, several oxides were identified: PbO, Fe₂O₃ and TiO₂.

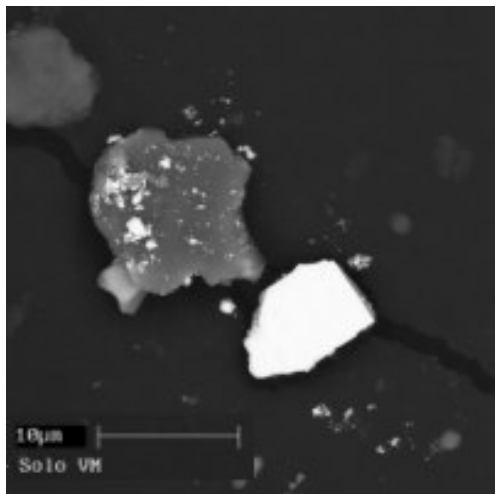


Figure 1: EDS-SEM image showing a grain, in white, of a Pb phosphate (probably pyromorphite) in the topsoil sample.

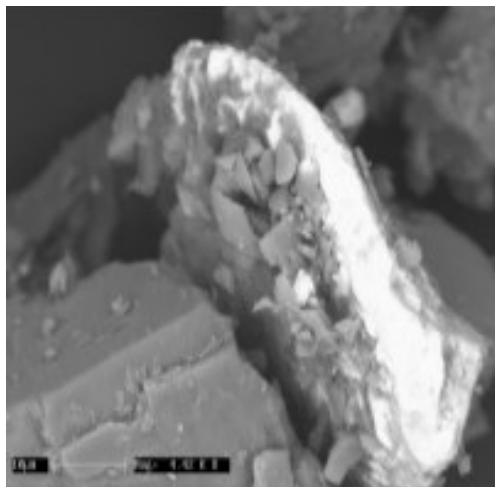


Figure 2: SEM image of a portion of a mine tailing sample, showing PbO (in white) in a silicate matrix, according to EDS analysis

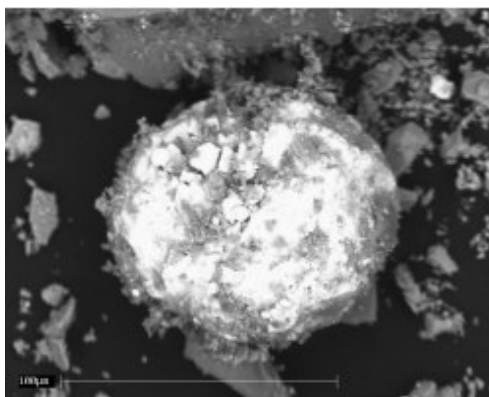


Figure 3: SEM image of a portion of smelter solid waste sample, showing PbO (white) on a silicate matrix, according to EDS analysis

3.5 Pb Bioaccessibility

Data in Figure 4 are the averages of lead solubility results and the respective standard deviation (1s - when available) in the topsoil and soils samples, in glycine, pepsin and acid solutions.

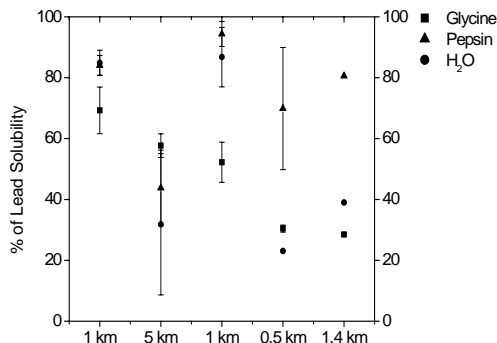


Figure 4: Pb solubility in organic solutions (pH 1.5) for soil samples. When included, error bar represents one standard deviation (n=4). For sample at 1.4 km, n=2.

All lead present in solid waste and wetland samples, was soluble in the three solutions. Complete lead solubility from the slag sample, just occurred in glycine solution, while in pepsin solution and water at pH 1.5, the measured solubilities were just 17% and 16%, respectively. Lead minerals (PbS and Pb₂SO₄O) presented low solubilities, with an average of about 15%. Synthetic compounds as Pb(NO₃)₂, Pb₃O₄ and PbCO₃ presented high solubility in all tested solutions.

4 DISCUSSION

The solubility tests using glycine, pepsin and acid solutions showed that the soil samples contain lead phases, which are soluble in those media at great extent. Comparing the results obtained in soil samples with the solubility of the solid wastes, including that of the slag in glycine solution, it is highly probable that most lead in soils is due to the contamination from the solid wastes. The tested lead minerals presented low solubility and we attribute the insoluble lead in soils to the presence of lead mineral phases, despite we were able to identify just a lead phosphate. Among lead minerals, the phosphates are the least soluble (Langmuir 1997) and Pb from chloropyromorphite $[Pb_5(PO_4)_3Cl]$ is considered nonbioavailable (Zhang et al. 1998).

The contamination of soils probably occurred by dry and wet depositions (at the time when the plant was active), and from particles of the tailings pile carried by the wind. In a pilot study, it was shown that dusts in some of the villager's houses, contain more than 1000 mg kg⁻¹ lead (Figueiredo et al. 2003). The formation of new species, formed by weathering (physical, chemical and biological) cannot be precluded.

According to the results of the solubility tests, the acid pH has a fundamental role in lead bioaccessibility (bioavailability) and in some cases more significant than glycine and pepsin solutions. The pH of the tests is similar to the gastric pH, so similar reactivity is supposed to occur in the human digestive tract. The presence of glycine and pepsin can change the speciation in solution and increase solubility, by complexing the metallic ion. Glycine, a small amino acid, forms chelate complexes with metals and has an important role in metal bioabsorption, being used in alimentary supplements and medicine, to assist the metabolism of certain metals (as zinc, magnesium, iron and calcium - Ashmed et al. 1985). Similar metal-chelates can be expected with pepsin, the enzyme that in gastric juice digests proteins, but its absorption is expected to be lower, compared to glycine, because the distinct sizes of the two compounds. Further metabolic transformations need also to be accounted for.

5 CONCLUSIONS

Lead in soils and especially in mine tailings from the area of the study is significantly soluble in conditions that simulate human digestive fluid, indicating that in case of ingestion, there is risk of contamination. Additional data with more samples and mineral phases (e.g. pyromorphite) will be obtained to confirm this preliminary conclusion. Reactions between lead and other metals at the conditions of the experiments will also be

considered. nd Fe) for binding sites could change the reactivity. For example, the role of competing metals (e.g. Ca and stability of the Pb-chelates). Further investigations will focus on these aspects, and on speciation in solution after solubility products and stability constants of the Pb chelates and other metals.

6 REFERENCES

- Ashmead, H. D., Graff, D. J., Ashmead, H. H. 1985. In: *Intestinal Absorption of Metal Ions and Chelates*; Charles C. Thomas: Springfield, IL; pp 76-77.
- Brown, G.E., Foster, A.L., Ostergren, J.D. 1999. Mineral surfaces and bioavailability of heavy metals: A molecular-scale perspective. *Proc. National Academic Science* 96: 3388-3395.
- CETESB - Companhia de Tecnologia de Saneamento Ambiental 1988. *Iguape-Cananéia/ Vale do Ribeira: caracterização ecológica e avaliação toxicológica da população da bacia*. São Paulo, CETESB. 108p.
- Cunha, F.G. 2003. *Contaminação humana e ambiental por chumbo no Vale do Ribeira, nos estados de São Paulo e Paraná*. Doctorate Thesis. Geosciences Institute, State University of Campinas, Brazil. 120p.
- Figueiredo, B. R., Cunha, F.G., Paoliello, M.M.B., Capitani, E. M.de, Sakuma, A., Enzweiler, J. 2003. Environment and human exposure to lead, cadmium and arsenic in the Ribeira Valley, In: *6th International Symposium on Environmental Geochemistry - Edinburgh, Scotland, Vol. 1*, pp.49.
- Hamel, S.C., Buckley, B., Liou, P.J. 1998. Bioaccessibility of metals in soil for different liquid to solid ratios in synthetic fluid. *Environmental Science & Technology* 32: 358-362.
- Langmuir, D. 1997. *Aqueous Environmental Geochemistry*. Prentice-Hall, New Jersey. 600p.
- Manceau, A., Boisset, M.C., Sarret G., Hazemann, R.L., Mench, M., Caambier, P., Prost, R. 1996. Direct determination of lead speciation in contaminated soils by EXAFS spectroscopy. *Environmental Science & Technology* 30: 1540-1552.
- Oomen, G.A., Hack, A., Minekus, M., Zeijdner, E., Cornelis, S. C., Schoeters, G., Verstraete, W., Van de Wiele, T., Wragg, J., Rempelberg, C.J.M., Sips, A., Van Wijnen, J.H. 2002. Comparison of five in vitro digestion models to study the bioaccessibility of soil contaminants. *Environmental Science & Technology* 36: 3326-3334.
- Ostergren, J.D., Brown, G.E., Parks, G.A., Tingle, T.N. 1999. Quantitative speciation of lead in selected mine tailings from Leadville, CO. *Environmental Science & Technology* 33: 1627-1636.
- Paoliello, M.M.B., De Capitani, E.M., Da Cunha, F.G.A., Matsuo, T., Carvalho, M.D., Sakuma, A., Figueiredo, B.R. 2002. Exposure of children to lead and cadmium from a mining area of Brazil. *Environmental Research* 88 (2): 120-128.
- Paoliello, M.M.B., De Capitani, E.M., Da Cunha, F.G.A., Matsuo, T., Carvalho, M.D., Sakuma, A., Figueiredo, B.R. 2003. Determinants of blood levels in an adult population from a mining area in Brazil. *Journal de Physique IV, Proceedings - XIIth International Conference on Heavy Metals in the Environment, Volume I*: 127-130.
- Zhang, P.C., Ryan, J.A., Yang, J. 1998. In vitro soil Pb solubility in the presence of hydroxyapatite. *Environmental Science & Technology* 36: 2763-2768.

Radioactive Scales from a Natural Gas Production Facility in the Altmark Region, Germany

S.Ceccarello & S.Black

University of Reading, UK

D.Read

Enterpris, University of Reading and University of Aberdeen, UK

H.Weiss & M.Schubert

UFZ Centre for Environmental Research, Leipzig, Germany

Ch.Kunze

WISUTEC Wismut Umwelttechnik GmbH, Chemnitz, Germany

J.Grossmann

GICON GmbH, Dresden, Germany

ABSTRACT: Radioactive scale is widespread in oil and gas production facilities. The most common scale mineral is barite (BaSO_4), which incorporates radium isotopes by ionic substitution in the barite lattice, though other phases also occur. In the Altmark region of East Germany, crusts of metallic lead and mercury-lead compounds (mm to cm in size) have been found in both the well tubing and surface installations of a gas field. Early analyses of the deposits obtained an approximate composition HgPb_2 , tentatively denoted 'altmarkite', but did not address the issue of natural radioactivity. Consequently, a more detailed programme of chemical and mineralogical analysis was undertaken in an attempt to better understand the nature of the deposits and their mode of formation. Several handling and disposal options for the scales and radioactively contaminated plant exist. However, any solution chosen for remediation of the sites must conform to German and EU regulatory criteria and requires careful assessment of local environmental factors. The method chosen is discussed. The incidence of radioactive Hg-Pb deposits could be much more widespread than is thought at present owing to the recent discovery of the 'new mercury ore belt' in Western Europe, extending through Poland, Germany and the Netherlands to the south of England.

1 INTRODUCTION

The Altmark region in the State of Sachsen-Anhalt, Germany hosts major gas production fields. The reservoir rocks are Lower Permian (Sachsen) sandstones and production wells can reach a depth of 3500 m. Formation waters are of NaCaMg-Cl and CaNaMg-Cl types with mineralisation leading to dissolved solids around 360 g/dm^3 (Müller 1990). The gas itself contains mercury at concentrations up to 4 mg/m^3 .

Kaemmel et al. (1977) described lead and mercury-rich scales from installations at these gas fields. They identified a lead amalgam (HgPb_2) and tentatively gave it the mineral name 'altmarkite', subsequently rejected by the International Mineralogical Association (1980) on the grounds that the material may not be of natural origin but an industrial artifact. However, a naturally occurring lead amalgam of similar composition was discovered in a platinum-bearing Cu-Ni sulphide deposit from China and hence altmarkite was re-defined and accepted as a mineral in 1985 (Dunn et al. 1985). These early studies classified the scales and the encrusted tubes on which it forms as hazardous substances (or waste) owing to its chemical composition. They did not establish that

the material is also highly enriched in radionuclides of the natural U-Th decay series. The present paper describes recent radiochemical and supplementary analyses, which suggest that altmarkite is more appropriately classified as Naturally Occurring Radioactive Material (NORM).

2 SAMPLING

Samples were obtained from production well tubes at the Salzwedel-Peckensen field, Altmark, and date from 1988. Macroscopically, they comprise massive, apparently amorphous deposits with a pronounced metallic lustre. The material is a soft, friable amalgam and easily cut with a scalpel (reported hardness values are 1.5-2 for altmarkite (Fleischer et al. 1979) and Pb-Hg (62.38%-32.62%wt) (<http://webmineral.com/data/leadamalgam.shtml>). The colour on a freshly polished surface is white-silver to grey. Darker areas (dark grey to black) are visible on some surfaces suggesting partial oxidation or possibly, local accumulation of different phases (Fig.1).

3 EXPERIMENTAL

The mineralogy, bulk composition and γ -ray activity of the material have been determined. X-ray diffraction analysis (XRD) was used to determine the mineralogy and microcrystallinity of the samples (X-ray Diffractometer SIEMENS D5000). The bulk composition was determined by ICP-OES (Perkin Elmer Optima 3000 with AS90 Auto Sampler) after complete dissolution in HNO_3 solution. Five samples from both the surface and interior of the deposit were analysed to assess homogeneity. Gamma (γ) activity was measured on a B5030 Canberra Broad Energy Germanium Detector (3800mm^2 active area) on the dissolved samples. Finally, a Scanning Electron Microscope (Jeol LV5900) equipped with an Oxford Instruments INCA Energy 400 microanalysis system attachment for Energy Dispersive X-ray analysis (EDX) was used to provide information on the morphology and to obtain further compositional information. The latter includes an EDX trace for elemental analysis, elemental mapping and quantitative element determination on polished surfaces. Polishing was achieved through Focused Ion Beam-Secondary Ion Mass Spectroscopy (FEI-FIB200SIMS).

4 RESULTS AND DISCUSSION

The material resembles a synthetic tetragonal lead-mercury amalgam (serial number 39-0395 of the International Centre for Diffraction Data- 1601 Park Lane, Swarthmore, Pennsylvania, 19081-2389 U.S.A.). However, the strongest XRD lines at 2.77, 2.48 and 1.67Å are shifted slightly in terms of both their position and relative intensity when compared to the main X-ray peaks from the reference sample, indicating some differences in composition and crystallography. The spectrum also shows other diffraction peaks ($d=3.337$, $d=3.087$), which correspond to quartz and lead oxide (PbO). The latter is represented by a rather broad peak, which is probably due to chemical interaction with mercury. Black areas are noticeable on the surface of the mineral indicating partial oxidation of metallic Pb to PbO. Overall, the Pb-Hg deposit analysed in this study appears to give a very close match to the signature of tetragonal altmarkite (strongest XRD lines 2.78, 2.49 and 1.67Å), as reported by Fleischer et al. (1979). The bulk composition of the material is shown in Table 1. The deposit consists mainly of Pb and Hg with accessory Ba, Fe, S, Ca and Sr.

Table 1. Bulk composition determined by ICP-OES analysis (composition expressed as elemental wt%). * By difference on bulk, confirmed by spot analysis.

As	Ba	Ca	Cu	Fe	Hg*	Pb	S	Sr	Zn
0.06	0.28	0.09	0.04	0.13	37.7	61.48	0.14	0.06	0.01

The mercury content determined initially by Atomic Absorption, after complete dissolution in HNO_3 , ranged between 20-40% (wt/wt). Likely sources of error were the volatility of Hg, which can be released during HNO_3 digestion and the high dilution factor needed. The composition was confirmed, therefore, by quantitative EDX analysis of a polished surface (Fig.2).

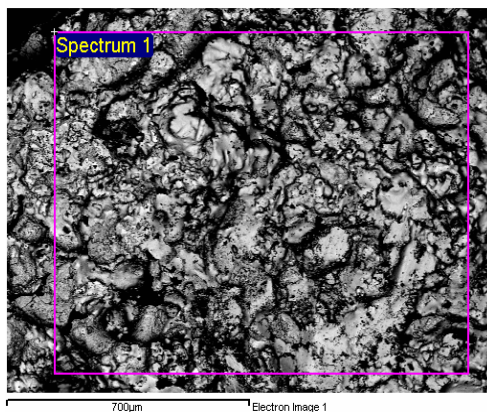


Figure 1: SEM image of the Hg-Pb deposit.

The sample displays a high degree of heterogeneity on unpolished surfaces. Amalgams with compositions ranging from 5.1 – 94.3 to 90.6 – 8.9 (Hg-Pb wt%) were found over a wide area of the sample through EDX microanalysis (Fig.3). Dark inclusions were identified on the external surface, containing primarily Ba, Sr, Ca, S, O and Pb. These components were absent in analyses of polished surfaces and, hence, it is reasonable to suspect the presence of a surface film in which altmarkite loses its microcrystalline structure and within which other mineral phases, such as $(\text{Ba},\text{Sr})\text{SO}_4$, CaCO_3 and PbO are deposited. This aspect merits further investigation.

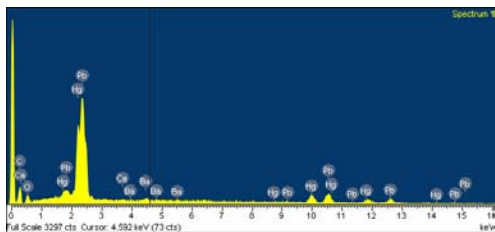


Figure 2: EDX trace of the area highlighted in Figure 1 (1.19mm²).

The sample contains natural series isotopes from the ²³⁸U (²²⁶Ra, ²¹⁴Bi, ²¹⁰Pb) and ²³²Th (²²⁸Ra, ²¹²Pb) decay series. The Pb-Hg deposit shows significant activity with regards to all of the radionuclides cited above with the exception of ²²⁸Ra. ²¹⁰Pb is the main radionuclide present in the mineral with an activity of 4285 Bq/g. Five different areas of the Hg-Pb deposit were monitored. The value quoted represents the mean though ²¹⁰Pb appears to be distributed homogeneously within the regions sampled.

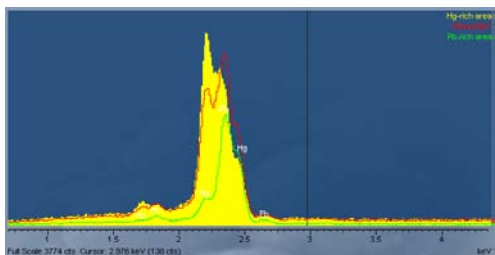


Figure 3: Overlaid EDX traces of three Pb-Hg surface amalgams showing compositional variation.

Owing to the volume of contaminated plant accumulated over the past few years, handling, clean-up and disposal of the scales poses a number of technical and economic problems. Any solution chosen for remediation must conform to German and EU regulatory criteria and requires careful assessment of local environmental factors.

Different handling and disposal options for scales and radioactively contaminated plant exist (Read et al. 2004). The first issue to resolve is whether the plant has significant residual value (e.g. specialised stainless steel equipment) or can be disposed of directly. Cleaning options are invariably costly and can lead to relatively high radiation exposure for workers. In the case of altmarkite, problematic residues would require solidification and, almost certainly, prior processing to remove mercury. Removal of mercury from the HgPb₂ is technically feasible though the materials remaining are still hazardous and fall within the ambit of NORM waste.

In those cases where cleaning is the only accepted option, owing to environmental, regulatory or economic constraints, a geopolymer containing an alkali-activated aluminosilicate matrix, has been developed to encapsulate scale material recovered by high-pressure water jetting. The matrix has proven long-term stability and has been accepted by the German regulators for the disposal of NORM wastes in municipal landfills.

Should a decision be made not to clean the plant, available options essentially reduce to smelting and direct disposal. Smelting has the advantage of recovering steel value, but the potential for cross-contamination during steel production is critical. Limits to throughput capacity may be set too low for this solution to be viable. Direct disposal is simpler with fewer problems regarding capacity. National legislation defines clearance and exemption levels below which NORM wastes can be disposed of in ordinary or industrial landfills. For example under the German Radiation Protection Act, provided the specific activity of the combined steel and attached scales does not exceed 50 Bq/g, it can be consigned to this route. In this case, the challenge is finding a separation method that allows the amount of waste requiring treatment to be minimised. Semi-automatic activity measurement equipment with high throughput has been developed for this purpose. It incorporates automated recording and database management for large quantities of wastes ensuring traceability of individual items, if required by the regulatory authorities. Results for material from the Altmark region indicate that only 1 – 2% of the total amount of steel scrap requires special treatment (smelting or cleaning); the remainder can be disposed of to industrial landfills.

Similar deposits rich in ²¹⁰Pb have been found on gas production equipment from the UK and the Netherlands suggesting that the incidence of radioactive Hg-Pb deposits may coincide with the recent discovery of the 'new mercury ore belt' in Western Europe. The latter extends through Poland, Germany and the Netherlands to the south of England. If so, the results of the current study and the technology applied to remediation would be applicable to other industrial sites contaminated by NORM materials.

5 ACKNOWLEDGEMENTS

The authors would like to thank Richard Chater and Dr David McPhail (Department of Materials, Imperial College London) for sample preparation by FIB-SIMS and Dr Terry Williams and Anthony Kearsley (Mineralogy Department, National History Museum London) for help with the SEM-EDX analyses.

6 REFERENCES

- Dunn, P.J., Chao, G.Y., Fleischer, M., Ferraiolo, J.A., Langley, R.H., Pabst, A. and Zilczer, J.A. 1985. New mineral names. *American Mineralogist* 70: 214-221.
- Fleischer, M., Chao, G.Y. and Mandarino, J.A. 1979. New mineral names. *American Mineralogist* 64: 652-659.
- International Mineralogical Association; Commission on New Minerals and Mineral Names 1980. *Mineralogical Magazine* 43: 1053-1055.
- Kaemmel, T., Mueller, E.P., Krossner, L., Nebel, J. Unger, H. and Ungethuem, H. 1977. Altmarkit, ein neues Mineral. *Z. ang. Geologie* 23(10): 535.
- Müller, E.P. 1990. Genetische Modelle der Bildung von Erdgaslagerstätten im Rotliegenden. *Nds. Akad. Geowiss. Veroefftl.* 4: 77-90.
- Read, D., Rabey, B., Black, S., Glasser, F.P., Grigg, C. and Street, A. 2004. Implementation of a strategy for managing radioactive scale in the China Clay industry. *Min. Eng.* (in press).

Hydrotalcite-like Minerals $\text{CuZn}_3\text{Al}_5(\text{OH})_{17}[\text{CO}_3,\text{SO}_4]_3 \cdot n\text{H}_2\text{O}$: Synthesis and Characterization

J.A.M.Corrêa

Department of Geochemistry and Petrology, Federal University of Pará, Pará, Brazil

H.Pöllmann

University of Halle/Mineralogy, Saxen Anhalt, Germany

ABSTRACT: Hydrotalcite-like layered double hydroxides (LDHs), using the system [(Cu,Zn)-Al- CO_3 - SO_4], have been prepared and the products characterised with XRD, DTA-TG, IR and SEM-EDX analysis. The syntheses were carried out by co-precipitation method and hydrothermal treatment in PP bottles at 80°C for 1-7 days. Two structures were determined, one with basal spacing $d = 7.52 \text{ \AA}$ ($a = 3.0621 \text{ \AA}$ and $c = 22.0665 \text{ \AA}$) compared with Copper Zinc Aluminium LDHs and other with basal spacing $d = 11.11 \text{ \AA}$ ($a = 3.0480 \text{ \AA}$ and $c = 33.3415 \text{ \AA}$) compared with copper glaucocerinite. The main advantages of LDHs over the traditional anionic exchange resins are their higher anionic exchange capacity and the fact that LDH are resistant to high temperature treatments. This characteristic permits therefore that LDHs may be used as ion exchanger in some high temperature applications such as in the treatment of water sulfide mine and cooling water of nuclear reactors.

1 INTRODUCTION

Hydrotalcite is an anion clay that is found in nature and can be easily synthesized in the laboratory by co-precipitation of dilute solutions of magnesium and aluminum chlorides with sodium carbonate. It is composed of mixed layers of Mg and Al, $[\text{Mg}_{1-x}\text{Al}_x(\text{OH})_2]_{x+}$, with interlayer anions, most commonly carbonate, to provide overall charge neutrality.

Layered double hydroxides form spontaneously in a wide range of environments, however the thermodynamic data on their solubility and stability need more intensive investigations. These data are vary important because LDHs can be used as reservoir mineral in the control of contaminant mobility in soils and wastes. Their flexible structure are capable of accommodating a wide range of bivalent and trivalent cations like Zn, Ni, Co, Fe and Cr in natural minerals and Cd, Cs, Li and Cu in synthetics. Ion size appears to play an important role in stabilizing the LDHs structures, e.g. large cations like Pb cannot be incorporated (Pöllmann & Keck 2003). Other wise it is expected that the adsorption of metal ions will be non-selective and dependent only on the charge of the cations (Li et al. 1996).

2 METHODS

2.1 Synthesis

An aqueous solution of the appropriate Cu^{2+} and Zn^{2+} sulphate salts was prepared at different Cu:Zn ratios. This mixture was added drop by drop to a basic solution containing NaOH (approximately 1M) and early dissolved Al^{3+} with vigorous stirring under normal atmosphere. Different pH values were tested (Table 1). The precipitate was aged at 80°C for different periods of time, between 24 and 168 hours, filtrated and washed with deionised water.

2.2 Characterization

Mineral d spacings were determined from XRD ($\text{CuK}\alpha 1$, 1.540598 Å, 45kV, 40 mA) in a Phillips xPert diffractometer. IR spectra were recorded on samples pressed into KBr discs using a Bruker-EQUINOX 55 spectrophotometer. Electron microscopy was performed on ground samples using a JEOL- JSM 6300 raster electron microscope with attached EDAX. Thermal analyses of powdered samples up to temperatures of 1.000 °C were carried out at a ramp rate of 10°C min⁻¹ using a SEIKO-TG/DTA 320U instrument.

3 RESULTS

3.1 Characterization of the LDHs

Figure 1 shows the XRD patterns for the materials prepared under different conditions of pH during precipitation and hydrothermal treatment. The XRD spectra of the LDH minerals correspond to spectra found in the literature (e.g. Cavani et al. 1991; Rives 2001). A general analysis of these patterns shows that the materials prepared with (Cu,Zn)-Al cation combination presented higher crystallinity. Under different pH values and MII/MIII ratio were observed phase impurities (ZnO and CuO), that disappear under special conditions (Table 1).

Table 1. Different parameters (R, x e pH) and new formed minerals. $R = M^{2+}/M^{3+}$, $x = M^{3+}/(M^{2+} + M^{3+})$, $M^{2+} = (Cu+Zn)$, $M^{3+} = Al$.

Samples	R	x	pH	Paragenesis
LDH-10-01	1,43	0,41	12,38	LDH+CuO+ZnO
LDH-13-01	1,54	0,39	12,38	LDH+CuO+ZnO
LDH-13-02	1,68	0,37	12,3	LDH+CuO+ZnO
LDH-13-03	1,83	0,35	12,22	LDH+CuO+ZnO
LDH-14-01	1,84	0,35	12,14	LDH+CuO+ZnO
LDH-14-02	1,86	0,35	12,15	LDH+CuO+ZnO+Zn(OH) ₂ +Cu(OH) ₂
LDH-14-03	1,87	0,35	12,16	LDH+CuO+ZnO+Zn(OH) ₂ +Cu(OH) ₂
LDH-15-01	1,88	0,35	12,2	LDH+CuO+ZnO
LDH-15-02	1,90	0,34	12,13	LDH+CuO+ZnO
LDH-15-03	1,91	0,34	12,18	LDH+CuO+ZnO
LDH-10-03	1,92	0,34	12,03	LDH+ZnO traços
LDH-16-03	2,18	0,31	11,93	LDH+ZnO
LDH-16-01	2,2	0,31	11,92	LDH+ZnO
LDH-16-02	3,04	0,25	11,83	LDH+Glauco+ZnO
LDH-09-01	3,97	0,2	12,12	LDH+CuO+ZnO
LDH-09-02	3,99	0,2	12,05	LDH+CuO+ZnO
LDH-09-03	4	0,2	12,09	LDH+CuO+ZnO

The *d* spacings show the characteristic values for trigonal structures with symmetrical peaks assigned to the (003), (006), (104) and (105) planes.

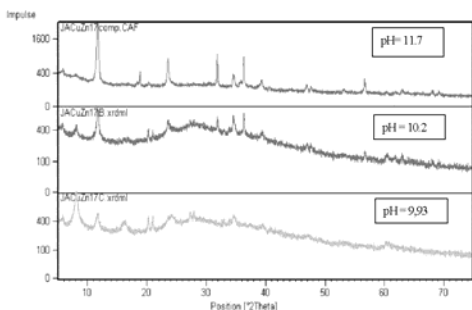


Figure 1. XRD patterns of synthetic [(Cu, Zn)-Al-SO₄,CO₃] LDH under different pH values.

The indexing of the diffraction peaks was obtained by the POWD program. The c-axis and a-axis parameters of the hydroxalite like mineral were

calculated to be 22.6005 Å and 3.0631 Å respectively and the basal spacing is 7.52 Å. The Cu-glaucocerinite-like structure has basal spacing *d* = 11.11 Å and the c-axis and a-axis parameters are 33.3415 Å and 3.0480 Å, respectively.

The SEM micrographs show the different crystal forms. Sheet crystals may be observed with hexagonal form in the sample with LDH-like structure (Fig. 2A). The structure similar to glaucocerinite shows rosette-like crystals (Fig. 2B).

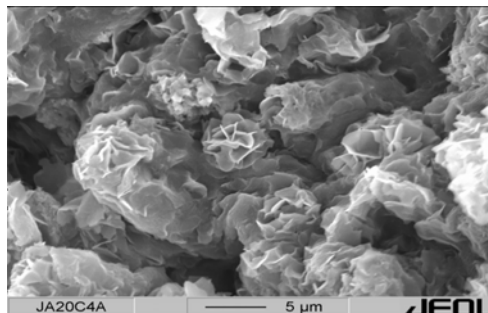
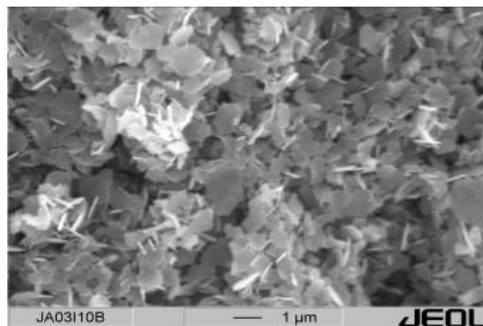


Figure 2A – SEM-images of well crystallized sheet crystals of [(Cu, Zn)-Al-SO₄,CO₃] LDH. Note the hexagonal sheet crystals in the center of the micrograph. 2B Crystals of glaucocerinite-like minerals with rosette forms

The IR spectra of the minerals are similar (Fig. 3). The absorption at 3500-3600 cm⁻¹ can be attributed to the H-bonding stretching vibrations of the OH group in the brucite-like layer. The shoulder present at around 3000 cm⁻¹ has been attributed to hydrogen bonding between H₂O and the anion in the interlayer (Cavani et al. 1991). The small absorption between 1100 and 1150 cm⁻¹ can be ascribed to sulfate. The absorption at ~1400, 800 and 620-650 cm⁻¹ are attributed to CO₃.

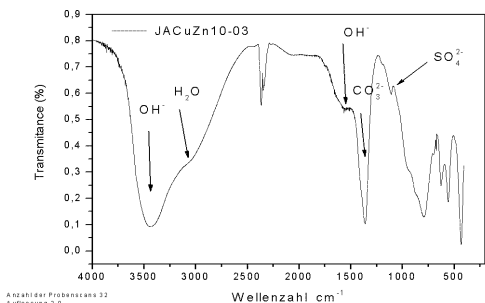


Figure 3. IR spectra of [(Cu, Zn)-Al-SO₄,CO₃] LDH with basal spacing 7.52 Å

Thermo-gravimetric measurements show two transitions (Fig. 4): 1) the first one, endothermic, at low temperatures (147 – 360 °C) corresponds to the loss of interlayer water, approximately 29.3% of weight loss; 2) the second one, endothermic, at higher temperature (400 – 800 °C) is due to the loss of hydroxyl groups from brucite-like layer, as well as of the anions, approximately 8,32% of weight loss. The total weight losses vary in the range of 27.7 and 37.6%. These behaviors are in agreement with those reported for LDHs (Bellotto et al. 1996)

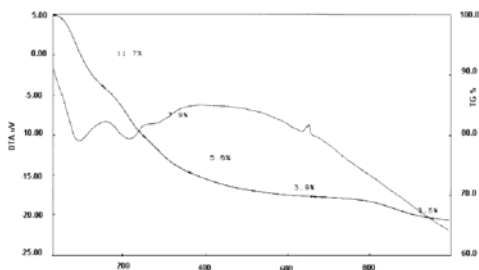


Figure 4. TG-DTA of [(Cu, Zn)-Al-SO₄,CO₃] LDH with basal spacing 7.52 Å

4 DISCUSSION

The synthesis of [(Cu,Zn)-Al-SO₄,CO₃] LDH shows that it can be used as a reservoir mineral to fixate or immobilize heavy metals in industrial wastes and likewise can be used as water decontamination product in sulfide mines. LDH minerals have, as the clay minerals, adsorbing properties due to their large interlayer space which may be accessible to molecular polar species and anions. Gade et al. (2001) investigated drill cores from Bavarian hazardous waste landfill and showed that several hydrotalcites-like minerals containing heavy metals (III, II) were present.

The main advantages of LDH over the traditional anionic exchange resins are their higher anionic exchange capacity and the fact that LDH are resistant to high temperatures treatments. This characteristic permit therefore that LDH may be used as ion exchanger in some high temperature applications such as in the treatment of cooling water of nuclear reactors

5 ACKNOWLEDGMENTS

This research was supported by CAPES (Fundação Coordenação de Aperfeiçoamento de Pessoal de Nível Superior, Brazil) through a pos-doctoral program. The Institute of Geological Science/Mineralogy of Halle University, Germany provided laboratory facilities.

6 REFERENCES

- Allmann, R. (1968a): The Crystal Structure of Pyroaurite. *Acta Crystallographica*, 24, 972-977.
- Allmann, R. (1968b): Die Doppelschichtstruktur der plättchenförmigen Calcium-Aluminium-Hydroxide am Beispiel des 3CaO*Al₂O₃*CaSO₄*12H₂O. *Neues Jahrbuch für Mineralogie, Monatshefte*, 140-144.
- Allmann, R. (1968c): Magnesium Aluminium Carbonate Hydroxide Tetrahydrate: A Discussion. *American Mineralogist*, 53, 1057-1059.
- Allmann, R. (1977): Refinement of the hybrid layer structure [Ca₂Al(OH)₆]⁺[1/2SO₄*3H₂O]. *Neues Jahrbuch für Mineralogie, Monatshefte*, 136-144.
- Allmann, R. & Jepsen H.P. (1969): Die Struktur des Hydrotalkits. *Neues Jahrbuch für Mineralogie, Monatshefte*, 544-551.
- Allmann, R.; Maghsudnia, H. (1991): Synthese von Sulfat-Hydrotalkiten. *Berichte Europäischen Journals für Mineralogie*, 3(1), 177.
- E.R.Andrew (1971): The Narrowing of NMR Spectra of Solids by High-speed Specimen Rotation and the Resolution of Chemical Shift and Spin Multiplet Structures for Solids. *Progress in NMR Spectroscopy*, 8, 1-39.
- Bellotto, M.; Rebours, B.; Clause, O.; Lynch, J.; Bazin, D.; Elkaïm, E. (1996): A re-examination of hydrotalcite crystal chemistry. *Journal of Physical Chemistry*, 100(20), 8527-8534.
- Brindley, G.W.; Kikkawa, S. (1980): Thermal Behavior of Hydrotalcite and of Anion-exchanged Forms of Hydrotalcite. *Clays and Clay Minerals*, 28(2), 87-91.
- Cavani, F.; Trifiro, F.; Vaccari, A. (1991): Hydrotalcite-type anionic clays: preparation, properties and applications. *Catalysis Today*, 11(2), 173-301.
- Delmas, C.; Borthomieu, Y. (1993): Chemie Deuce Reactions: A New Route to Obtain Well Crystallized Layer Double Hydroxides. *Journal of Solid State Chemistry*, 104, 345-352.
- Feitknecht, W.; Gerber, M. (1942): Zur Kenntnis der Doppelhydroxide und basischen Doppelsalze III: über Magnesium-Aluminiumdoppelhydroxyd. *Helvetica Chimica Acta*, 25, 131-137.

- Feitknecht, W. (1942): Über die Bildung von Doppelhydroxiden zwischen zwei- und dreiwertigen Metallen. *Helvetica Chimica Acta*, 25, 555.
- Frondel, C. (1941): Constitution and polymorphism of the pyroaurite and sjögrenite groups. *American Mineralogist*, 26(5), 295-315.
- Gade, B.; Pöllmann, H.; Heindl, A.; Westermann, H. (2001): Long-term behavior and mineralogical reactions in hazardous waste landfills: a comparison of observation and geochemical modeling. *Environmental Geology*, 40 (3):248-256.
- Hernandez-Moreno, M.; Ulibarri, M.; Rendon, J.L.; Serna, C.J. (1985): IR Characteristics of Hydrotalcite-like Compounds. *Physics and Chemistry of Minerals*, 12, 34-38.
- Kooli, F.; Kosuge, K.; Hibino, T.; Tsunashima, A. (1993): Synthesis and Properties of Mg-Zn-Al-So₄ Hydrotalcite-like Compounds. *Journal of Materials Science*, 28, 2769-2773.
- Kooli, F.; Kosuge, K.; Tsunashima, A. (1995b): Mg-Zn-Al-CO₃ and Zn-Cu-Al-CO₃ Hydrotalcite-like Compounds: Preparation and Characterization. *Journal of Materials Science*, 30, 4591-4597.
- Miyata, S. (1975): The Syntheses of Hydrotalcite-like Compounds and their Structures and Physico-Chemical Properties - I: The System Mg²⁺-Al³⁺-NO³⁻, Mg²⁺-Al³⁺-Cl⁻, Mg²⁺-Al³⁺-ClO⁴⁻ and Zn²⁺-Al³⁺-Cl⁻. *Clays and Clay Minerals*, 23, 369-375.
- Pöllmann, H. and Keck, E. (2003): Hydrotalkit vom Gr. Teichelberg bei Pechbrunn/Oberpfalz. *Aufschluss*, 54, 249-255.
- Reichle, W.T. (1986): Synthesis of anionic clay minerals (mixed metal hydroxides, Hydrotalcite). *Solid State Ionics*, 22, 135-141.
- Reichle, W.T.; Kang, S.Y.; Everhardt, D.S. (1986): The Nature of the Thermal Decomposition of a Catalytically Active Anionic Clay Mineral. *Journal of Catalysis*, 101, 352-359.
- Rives, V. ed. (2001): *Layered Double Hydroxides: Present and Future*, Nova Science Publishers Inc., EUA, 439 p.
- Thevenot, F.; Szymanski, R.; Chaumette, P. (1989): Preparation and characterization of Al-rich Zn-Al hydrotalcite-like compounds. *Clays and Clay Minerals*, 37(5), 396-402.

A Preliminary Study of the Environmental Management of Sludges from AODL Reactors

A.R.Correa & E.A.Villegas

Department of Metallurgical Engineering and Materials Science, Federal University of Minas Gerais, Belo Horizonte, Brazil

ABSTRACT: AODL sludges are solid wastes generated during the production of stainless steels. They are composed mainly of inorganic oxides of constituent metals of these materials. In most cases they constitute wastes that can release toxic elements, mainly hexavalent chromium, to the environment. During the present work these sludges were classified in fine and coarse fractions and toxic components distribution was studied in order to apply separation methods like wet magnetic distribution and selective solubilization in deionized water. The main results show that selective separation is not very efficient for the fine fraction and that toxic chromium is released on both fractions. A brief discussion of the main routes used to achieve decontamination of AODL sludges is also given in this paper.

1 INTRODUCTION

1.1 Sludge generation in AODL reactors

During the production of stainless steels in AODL (“Argon Oxygen Decarburization with Lance”) reactors, the blowing of argon and oxygen inside the molten bath generates an exhaustion gas full of solidified droplets.

Since this gas stream contains several pollutants hazardous to the atmosphere, cleaning and decontamination is necessary before its releasing to the environment. When this is accomplished using wet scrubbers a solid wet-phase called *sludge*, is generated. Usually sludges contain most of the pollutants originally present in the gas stream.

1.2 Environmental management of sludges

Sludges containing amounts of toxic substances like hexavalent chromium are classified as hazardous wastes and must not be released to the environment. Up to now several routes to treat the sludges for decontamination have been investigated. The most important ones are reviewed in the next section.

However successful the process may be, no one is of general application due to the different nature of the sludges. Hence, in every case proper good sense

and technical experience may be necessary to choose an adequate decontamination procedure. The present work investigated fractional classification of the sludges followed by wet magnetic separation and solubilization in deionized water.

2 REVIEW OF STAINLESS STEELMAKING SLUDGES ENVIRONMENTAL MANAGEMENT

2.1 Pyrometallurgical recycling methods

According to Fosnacht (1981), methods for treatment of steelmaking wastes involving reduction at high temperatures (above 1000°C) have been widely accepted. One basic feature of these processes is the removal of volatile compounds, accompanied by the reduction of iron oxides. But these processes have high installation and operational costs that can make them economically unfeasible, especially in small mills.

According to Sobrinho & Tenório (2000), new processes were developed for recovering chromium and nickel contained in flue dust gases generated during the production of stainless steels. These processes are efficient but have high installation and operation costs. Such is the case of processes like

STAR, INMETCO and ENVIROPLAS (Correa 2003).

According to the last author pyrometallurgical methods for recycling stainless steelmaking wastes were invented in developed countries and are not economically feasible in Brazilian conditions, due to the fact that Brazilian wastes have much less zinc and nickel, the most valuable metals to recover.

2.2 Agglomeration techniques

According to Nascimento et al. (2000), the sintering of steelmaking wastes should be avoided, because of their particle size distribution (great percentage below 0,105 mm). The pelletizing of these wastes is feasible.

According to Sobrinho & Tenório (2000), the briquetting of stainless steelmaking wastes is more efficient and cheaper, if compared to other agglomeration techniques. The addition of iron borings improves the briquettes properties.

2.3 Magnetic separation

According to Geldenhuis (2001), the concentration of stainless steelmaking flue dusts through magnetic separation is feasible. In relation to nickel, this author relates the achievement of recoveries of about 50% and concentrations of six-fold in relation to the feed.

2.4 Ultra-sonic assisted gravimetric separation

According to Souza et al. (2002), it is possible to concentrate the coarse fraction of carbon steelmaking sludges using ultra-sonic devices. The sludge is dispersed by ultra-sonic vibrations, and then the particles are separated by density and size. This method achieves iron recovery of about 60-70%, and iron concentrations of 95%, with low energetic consumption and without the use of chemicals. The concentrate may then be briquetted and recycled.

Research is needed to evaluate the possibility of using this technique for concentrating stainless steelmaking sludges, especially the fine fraction, which would permit the making of briquettes for recycling.

2.5 Immobilization in cement-based materials

According to Lee et al. (1995), chromium-bearing wastes are commonly immobilized in cement-based materials. XANES analysis revealed that most of the immobilized chromium remains in the hexavalent form, if only Portland cement is added, but can be reduced to the trivalent form if slag is also added to the moisture.

2.6 Reduction of hexavalent chromium

According to Heller & Roy, there are several agents that can reduce the hexavalent chromium to its trivalent form, which is much less toxic and less soluble. The most commonly used are, in decreasing order:

- Sodium bisulfite - NaHSO_3 ;
- Sulfur dioxide - SO_2 ;
- Sodium hydrosulfite - $\text{Na}_2\text{S}_2\text{O}_4$;
- Ferrous sulfate - FeSO_4 .

2.7 Disposal in landfills

According to Sobrinho&Tenório (2000), great world steel producers like USA and Japan have very restrictive environmental laws, which demand the removal or stabilization of heavy metals before landfilling.

In Brazil the legislation demands stainless steelmaking sludges to be disposed in landfills for hazardous wastes (Associação Brasileira de Normas Técnicas, Standards Series 10.000).

3 EXPERIMENTAL

3.1 Materials and equipment

During this work sludge samples were obtained from an AODL reactor in a steel mill located in Minas Gerais-Brazil. In this particular reactor, the cleansing of the exhaust gases was carried out by a wet scrubber generating a liquid effluent from which the suspended solids were collected in two different points generating, this way, the coarse and the fine fractions of the sludge. According to the company engineers, the coarse fraction of these sludges can be recycled after a briquetting operation.

Six samples of each fraction were collected monthly, during 6 consecutive months. With these, 1 composed sample was prepared for each fraction of the sludge.

3.2 Sludge characterization

X-Ray Diffraction studies showed that the sludges were composed almost entirely of crystalline matter with very small quantities of amorphous material. These studies also revealed the presence of synthetic ferrites, especially chromium-bearing magnetite, maghemite, calcium ferrites, manganese oxides, calcium carbonate, and other oxides of iron, chromium, calcium and nickel.

Table 1 shows a typical distribution of some physical properties between the coarse and fine fractions.

Table 1. Particle size, density, and wet content.

	Coarse fraction	Fine fraction
Particle size	0.1 mm	1.2 μ m
Density (g/cm ³)	5,5	3,5
Water content (%)	14-15	35-45

SATMAGAN (Saturation Magnetization Analysis) revealed the presence of approximately 33% of (artificial) magnetite in both fractions. It should be pointed out that since the magnetite present in these sludges is a chromium-bearing material, an equal distribution of it in both fractions is not a desirable condition.

It is also remarkable the absence of significant concentrations of zinc, and the almost complete absence of lead and cadmium. This comes from the fact that the mill does not use galvanized or contaminated scrap as a feed-mixture.

Table 2. Magnetic separation results.

	Sample 1		Sample 2		Sample 3		Sample 4	
	Conc	Tail	Conc	Tail	Conc	Tail	Conc	Tail
Mass (%)	0,42	0,58	0,45	0,55	0,27	0,73	0,21	0,79
Fe _t	43,74	39,61	47,75	42,97	46,82	32,64	46,83	30,67
Cr _t	10,10	6,01	9,80	8,11	7,52	6,95	7,13	6,59
Ni	1,31	1,15	1,88	1,11	1,66	1,18	1,60	0,90
Zn	0,116	0,060	0,044	0,038	0,051	0,053	0,046	0,056
P	0,019	0,020	0,020	0,020	0,017	0,019	0,026	0,028
Heat losses	8,34	8,73	5,45	6,48	5,52	9,08	3,99	8,63

The magnetic separation tests aimed at concentrating the valuable metals nickel, chromium and iron in the magnetic fraction without significant losses, while concentrating the undesirable elements, especially phosphorus, in the non-magnetic fraction.

The results show that selective distribution of the above elements was not efficient. It was observed that this was mainly due to the occurrence of "magnetic flocculation", phenomenon in which magnetic particles assembly, entrapping non-magnetic particles in the floc. This may have occurred due to one or more of the following reasons:

- Poor fine particle dispersion (Wills 1997; Gonçalves et al. 2000; Souza et al. 2002);
- Utilization of a magnetic separator with a continuous magnetic field (Wills 1997);
- Low dissolution of solids in pulp and/or too high flow rates (Correa 2003).

The solubilization results show that, in most cases, the sludges can release chromium, in the trivalent and hexavalent forms, to the environment. Therefore, the sludges will have very high potentials for environmental impacts if they are not correctly

3.3 Magnetic separation

Magnetic separation was conducted with four 50g samples of the fine fraction, diluted in 8 liters of water, at flow rate of 0,2 l/min. After this the tailings and the concentrate, were dried and analyzed to determine their chemical composition.

Solubilization was conducted with 50g samples, 3 samples for each fraction, diluted in 0,8 l of water, agitated continuously for 24 hours. After filtration under pressure the liquor was analyzed for chemical composition.

The magnetic separator was of the "CARPO WHIMS" Model "WHIMS 3X4L" type, with continuous current high field for wet operation. The mixers used in the solubilization steps were "FANEM" 258.

4 RESULTS AND DISCUSSION

Table 2 shows the results for magnetic separation of the fine fraction.

handled, transported and properly stored. It is also noteworthy the high pH of the liquors due mainly to the dissolution of calcium oxides. This is unfortunate as reduction of hexavalent chromium is not quite feasible in alkaline liquors.

Table 3 shows the results for solubilization in deionized water.

Table 3. Solubility in deionized water.

	Coarse fraction liquors			Fine fraction liquors		
	1	2	3	1	2	3
Cr _t (mg/l)	0,456	0,440	0,413	0,186	0,223	0,154
Cr (VI) (mg/l)	0,039	0,035	0	0,033	0,033	0,036
Ni (mg/l)	0,058	0,041	0,039	0,069	0,087	0
pH	12,34	12,27	12,27	12,15	12,22	11,99

5 CONCLUSIONS

- Pyrometallurgical methods for recycling AODL sludges, invented in developed countries, are not feasible in most of Brazilian conditions, due to lower levels of zinc and nickel in the sludges.

- The coarse fraction of the sludges considered in this work is richer in iron, chromium and nickel than the fine fraction and can be recycled to the process after a briquetting operation;

- Magnetic separation of the fine fraction was not efficient with the equipment used during this work;

- Fine fraction efficient distribution of the chromium-bearing magnetite between magnetic and non-magnetic fractions cannot be accomplished with a continuous high field magnetic separator in the conditions of this work;

- Effective reduction of hexavalent chromium will not be feasible due to the high pH of the resulting liquors;

- Research is needed to evaluate the feasibility of using techniques like magnetic separation and ultrasonic assisted gravimetric separation, for the development of new routes for recycling these wastes at lower costs;

- The sludges have very high environmental impact potentials, especially because they can release chromium, in the trivalent and hexavalent forms, to the environment, if they are not correctly handled, transported and stored;

- Regarding domestic steel mills sludges, disposal in landfills for hazardous wastes may be a good option for the fine fraction.

6 REFERENCES

- Associação Brasileira de Normas Técnicas. Norms serie 10.000.
- Correa, A.R. 2003. Caracterização e Estudo Preliminar do Gerenciamento Ambiental das Lamas do Reator AODL da ACESITA.. 93p. Dissertation (Master Course in Metallurgical and Mining Engineering) – Engineering School, Federal University of Minas Gerais, Belo Horizonte.
- Fosnacht, D.R. 1981. Recycling of ferrous steel plant fines, State-of-the-art. Iron and SteelMaker, 22-26.
- Geldenhuis, J.M.A. 2001. Recovery of valuables from flue dust fines. Minerals Engineering, Sept. 4 p.
- Gonçalves, I.N., Araújo, S., Machado, O. 2000. Gerenciamento de Resíduos Sólidos da ACESITA: Caracterização e Potencial de Aplicação. In: 55° Congresso da Associação Brasileira de Metalurgia e Materiais. Rio de Janeiro. Anais: CD-ROM ABM 55° Congresso da Associação Brasileira de Metalurgia e Materiais, 2000, Rio de Janeiro.
- Heller, R.J., Roy, C.H. Hexavalent Chromium Reduction. ENVIROSCOPE.
- Lee, J.F., Bajt, S., Clark, S.B., Lamble, G.M., Langton, C.A., Oji, L. 1995. Chromium speciation in hazardous, cement-based waste forms. Physica B, 208&209. 577-578.
- Nascimento, R.C., Lenz, G., Santos, D.M., Capocchi, J.D.T., Takano, C., Mourão, M.B. 2000. Caracterização e Viabilização Para Reciclagem De Resíduos Siderúrgicos Sólidos. In: 55° Congresso da Associação Brasileira de Metalurgia e Materiais. Rio de Janeiro. Anais: CD-ROM ABM 55° Congresso da Associação Brasileira de Metalurgia e Materiais, 2000, Rio de Janeiro.
- Sobrinho, P.J.N., Tenório, J.A.S. 2000. Geração de Resíduos Durante o Processo de Fabricação De Ferro e Aço. In: 55° Congresso da Associação Brasileira de Metalurgia e Materiais. Rio de Janeiro. Anais: CD-ROM ABM 55° Congresso da Associação Brasileira de Metalurgia e Materiais, 2000, Rio de Janeiro.
- Sobrinho, P.J.N., Tenório, J.A.S. 2000. Processos para o aproveitamento de poeiras geradas durante a fabricação de aço. In: 55° Congresso da Associação Brasileira de Metalurgia e Materiais. Rio de Janeiro. Anais: CD-ROM ABM 55° Congresso da Associação Brasileira de Metalurgia e Materiais, 2000, Rio de Janeiro.
- Souza, E.L., Araújo, F.G.S., Tenório, J.A.S., Gomes, J.E.L., Oliveira, C.P. 2002. Tratamento de lamas siderúrgicas com de recuperar seu conteúdo metálico. In: 57° Congresso Anual da Associação Brasileira de Metalurgia e Materiais. São Paulo. Anais: CR-ROM ABM 57° Congresso Anual da Associação Brasileira de Metalurgia e Materiais, 2002, São Paulo.
- Wills, B.A. 1997. Mineral Processing Technology. 6th ed. Oxford: Butterworth & Heinemann. 486p.

Mineralogical Status of Metals in MSWI Fly Ashes Solidified/Stabilized in Cement and Long Term Stored in Landfills

D. Antenucci, G. Lorenzi, D. Leclercq, M. Veschkens
Institut Scientifique de Service Public (ISSEP), Liège, Belgium

J. Yvon & E. Jdid
Laboratoire Environnement et Minéralurgie (LEM), École Nationale Supérieure de Géologie, Centre de Recherche François Fiessinger, Vandoeuvre-Les Nancy, France

P. Nelsen & V. Dutre
Vlaamse Instelling voor Technologisch Onderzoek (VITO), Mol, Belgium

ABSTRACT: In order to improve the knowledge about the behavior laws affecting the MSWI fly ashes solidified/stabilized in cement and long term stored in landfills, a multidisciplinary study of two different monoliths has been performed. Materials were examined through leaching tests, petrographical observations, X-ray diffraction and EDS based TEM and SEM. Rather high leached amounts of chlorides, sulfates and lead have been detected. The texture of the various samples has revealed a network of connected micro-cracks. Pb, Zn, Cr, are distributed between inherited stable phases and inherited or neo-formed unstable phases. In contrast with the data available from room temperature experiments, the neo-formed sulfates, complex Ca-hydroxides and ordered Ca-silicate-hydrates, crystallized during a prolonged storage where temperature ranges higher than 70°C, are mostly free of heavy metals. The knowledge of the mineralogical status of various heavy metals gives valuable informations on their possible mobility. Since the status of Pb in ordered Ca-minerals is almost null, the Pb mobility is conditioned by the segregation in leachable submicronic phases (hydroxides, chlorides and hydroxy-chlorides) precipitated from the solution after a local decrease of pH due to the metallic aluminum hydrolysis. In some conditions, these submicronic phases are trapped in complex hydroxides.

1 INTRODUCTIONS

Hydraulic binders are often used for the solidification/stabilization (S/S) of hazardous Municipal Solid Waste Incineration (MSWI) fly ashes (Robert 1995). In this procedure, the solids are usually mixed with cement and water, with or without other additives (lime, pozzolanic reagent). At the moment, the S/S MSWI residues are disposed of in appropriate landfills, where they produce huge monoliths, but the question of potential utilization of these solid products is explored as well. Thus, the knowledge of the long-term behavior of such materials is a prerequisite. The long-term durability of S/S MSWI fly ashes disposed of in landfills still remains an unanswered question because most of the knowledge available at present time about the element mobility depends on models the validity of which have been established only on the short term, using small sized proofs, (Lin et al.1993; Brault 2001). In these conditions, the energy developed by exothermal reactions is quickly dissipated and contrarily to the huge landfill conditions, the proofs stay close to the room temperature. The present study aims at clarifying the mineralogy of S/S MSWI residues stored in huge landfills, in order to predict the long-term behavior of several heavy

metals, in particular Pb, Zn, Cr, and anions, mainly $\text{SO}_4^{=}$ and Cl^- .

2 MATERIALS AND METHODS

2.1 Sampling

The study is based on the sampling of two landfill sites. One is 10 years of age, where the MSWI fly ashes were stabilized with Portland cement without any previous treatment (samples series labeled I), and the other is 5 years of age, where the MSWI fly ashes were stabilized with cement after a partial leaching of soluble species, mainly chlorides, and sulfidation of heavy metals using Na_2S (samples series labeled II).

2.2 Compliance leaching test

Compliance tests, carried out under water leaching conditions, are established to verify whether a material complies with the regulation. For granular materials, the compliance tests are set up by CEN/TC292/WG2 and identified as EN 12457. In this study, the part 4 of the draft has been used. The samples are crushed to less than 10 mm and leached with demineralized water at a liquid to solid ratio of

10 (L/S = 10). The eluates were analysed for Pb, Zn, Cr, chlorides and sulfates.

2.3 Petrographical analysis

Petrographical analysis is carried out on thin sections of 30 microns thick. The intrinsic characteristics of the materials force to a specific preparation due to the low cohesion of materials, the potential toxicity of their sawn products and the very high solubility and/or the limited thermal stability of some components.

2.4 X-ray diffraction analysis

Major mineral phases identification is obtained by X-ray diffraction using a Philips PW 1390 diffractometer equipped with monochromatized $Fek\alpha$ radiation.

2.5 Scanning electron microscopy (SEM) and transmission electron microscopy (TEM)

A preliminary identification of heavy metals bearing phases in the solidified MSWI is performed using a "K.E. Development" Back Scattered Electron Imaging device, then refined using a Hitachi S-2500 SEM, equipped with a "superquantum DELTA" EDS micro-analyzer. The SEM analysis of solidified MSWI have been performed on carbon vaporized, polished thin sections. TEM characterization was performed with a Philips SM20 apparatus, fitted with EDS micro-analyzer. The observations and microanalyses were made on powders spread from alcohol suspension on a carbon film supported by a copper grid.

3 RESULTS AND DISCUSSION

3.1 Compliance leaching tests

Compared with the European directive (2002), the leached concentrations measured with Pb and Cl⁻ (Table 1) oblige to range the series I of S/S MSWI residues in the hazardous category "C", whereas the series II could be accepted, *a priori*, in the category "B" i.e. "stable and not reactive hazardous wastes". Nevertheless, for these kind of wastes the European directive points out the fact that their leaching behavior must not evolve noxiously at long-term. Because of the method itself, the compliance leaching tests cannot predict, alone, the long-term evolution of pollutants. Supplementary techniques are needed to reach this goal.

Table 1: Leached amounts (in mg/Kg of dry matter) of Pb, Zn, Cr, Cl⁻ and SO₄²⁻; S/S MSWI Residues (I and II); A= inert wastes, B= stable and non reactive hazardous wastes, C= hazardous wastes following the European directive based on compliance test values admitted at L/S = 10 l/Kg. The pH of leacheates is greater than 12.5.

Residues	Leached amount, mg/kg				
	Pb	Zn	Cr	Cl ⁻	SO ₄ ²⁻
I	1.28 to	0.13 to	<0.05 to	8 000 to	100 to
	9.24	0.45	0.15	60 000	130
II	<0.1	<0.1 to	<0.05 to	800 to	140 to
		0.55	1.3	14 500	1 290
A	0.5	4	0.5	800	1 000
B	10	50	10	15 000	20 000
C	50	50	70	25 000	50 000

3.2 Petrographical analysis

Networks of micro-cracks, related to hydration-dehydration cycles and/or to shrinkage cracks are easily visible. Such a texture promotes fluids circulation and facilitates leaching processes as well as precipitation reactions affecting the S/S MSWI fly ashes.

3.3 X-ray diffraction analysis

The various samples of S/S MSWI fly ashes display the following essential minerals: portlandite, Ca(OH)₂; calcite, CaCO₃; hydrocalumite, Ca₂Al(OH)₆(Cl,OH)·3H₂O; ettringite, Ca₆Al₂(SO₄)₃(OH)₁₂·26H₂O; katoite, Ca₃Al₂(SiO₄)₃·Ca₃Al₂(OH)₁₂; tobermorite, Ca₅Si₆O₁₆(OH)₂·4H₂O; gonnardite, Na₂CaAl₄Si₆O₂₀·7H₂O.

Considering the well known high solubility of hydrocalumite at any pH, and the increasing solubility of ettringite with decreasing pH (Van der Sloot 1999), one can infer that Cl⁻ and SO₄²⁻ cannot be ideally immobilized through these minerals.

The *in situ* temperature, measured between 1 and 1.5 meter depth during the sampling of S/S MSWI residues of the series II, was close to 70°C. Taking into account the identified zeolites, hydrogarnets and tobermorite, it is plausible to consider that in monofills the temperature reaches 80-100°C and generates a convection of fluids, a situation which promotes the crystallization of ordered silicate-hydrates since they grow slowly and reach thermochemical conditions closer to equilibrium. These considerations are also supported by available data on the hydrothermal synthesis of various silicate-hydrates under high alkali conditions (Mimura et al. 2001; Shaw et al. 2000).

3.4 SEM and TEM analyses

The main heavy metal-bearing minerals are reported in Table 2. It can be seen that Pb, Zn and Cr are distributed between inherited stable phases (metallic

alloys, spinels, glasses, refractory oxides, titanates, phosphates) and inherited or neo-formed unstable phases (amphoteric metals, hydroxides, carbonates, metal chlorides, chromates).

Table 2: Heavy metal speciation: * inherited phases; (*) inherited or neo-formed phases; ** neo-formed phases

Metal	Mineralogical compounds
Pb	Pb*; PbCl ₂ * (cotunnite); PbO ^(*) ; (Pb,Hg,Cu)S; PbS; Pb ₄ Cu(SO ₄) ₂ (OH) ₆ ** ^(*) ; Pb(OH) ₂ ** ^(*) ; Pb ₂ Cl ₃ (OH)** (Penfieldite); PbClOH** (laurionite); Pb ₂ CuCl ₂ (OH) ₄ ** ^(*) Pb ₂ Cl ₂ ·x(O,OH) _{2x} ** (blixite); Pb ₃ (OH) ₂ (CO ₃) ₂ ** ^(*) ; CSH** ^(*) ; Glass*
Zn	Zn*; ZnO*; Spinel <i>s.l.</i> *; Zn(OH) ₂ *; FeO*, MnO*; Zn(PO ₄) ₂ ** ^(*) ; (Ca,Mg)-phosphates ^(*) ; Cu-Zn Alloys*; Zn-Al Alloys *; Zn-Al-Ni Alloys *; CSH** ^(*) ; ZnTiO ₃ ** ^(*) ; Glass*
Cr	Ca ₃ Al ₂ (SiO ₄) ₃ -Ca ₃ Al ₂ (OH) ₁₂ ** (hydrogarnet)
Cr	Cr ₂ O ₃ *; FeCr ₂ O ₄ * (chromite); ZnCr ₂ O ₄ * (zincchromite) Fe ₃ O ₄ * (magnetite); CaCrO ₄ ** ^(*) ; (Ba,Zn)(Cr,S)O ₄ ** (Hashemite); Fe-Cr-V-Nb* Alloys Fe-Cr-Ni-Mo * Alloys; Fe-Cr-Ni* Alloys

As already shown by Antenucci et al. (2003), the aluminum hydrolysis promotes the precipitation of the neo-formed Pb-oxy-hydroxychlorides. Typically, this phenomenon leads to concentric distributions with an aluminum nucleus, a first crown out of aluminum hydroxide and an external shell out of hydrocalumite, free of Pb in its lattice, trapping submicronic Pb-phases. Hydrocalumite precipitated in micro-cracks is also free of lead. The cationic substitutions are limited to some Zn²⁺ for Ca²⁺ in ordered silicate-hydrates (katoite), and concern Zn²⁺ and Cr²⁺ for various divalent cations in the minor heavy metal-bearing minerals. Small quantities of Pb are accepted only in the host disordered Ca-silicate-hydrates (CSH). The reason why Pb does not substitute for Ca²⁺ in the rather regular Ca-sites of ordered neo-formed silicate-hydrates, for instance katoite (Sacerdoti & Passaglia 1985), is suggested to arise from the stereochemically active 6s² lone pair, a chemical property of Pb²⁺ which leads to one-sided arrangement of bonds to anion thus to asymmetrical Pb-polyhedra (Welch et al. 2000); this phenomenon is revealed only when the Ca-minerals can reach the equilibrium. In cementitious conditions such a situation can be responsible for the precipitation of unstable Pb-minerals, thus leading to appreciable Pb leached amounts. On the contrary, the rather low leached concentrations of Zn and Cr can be explained by the fact that a significant part of the status of these cations is irreversibly fixed in the raw

MSWI fly ashes through stable compounds, actually spinels *s.l.*, glasses, etc., formed during the incineration process at very high temperature. Small quantities of zinc and lead also occur in disordered calcium silicate hydrate (CSH).

4 CONCLUSION

Monofills of S/S MSWI fly ashes using hydraulic binders are affected by a prolonged increasing of temperature (up to 80-100°C for several years) which governs the evolution of major mineral phases and the differentiation of the heavy metal-bearing species. The neo-formed-ordered Ca-silicate-hydrates contain practically no heavy metals in their lattice. The cementitious conditions combined with the stereochemically active 6s² lone pair of Pb²⁺ are suggested to be responsible for the lack of extended cationic substitution mechanisms involving Pb.

Regarding the long-term behavior of toxic inorganic elements, their mineralogical status indicates that the majority of zinc and chromium bearing phases are stable, whereas most of mineral species containing lead and anions (Cl⁻, SO₄²⁻) are characterized by an instability which will not be enhanced by maturation.

In other words, the low temperature crystallization of disordered calcium-silicate hydrates leads to a structural immobilization of lead and zinc, whereas the recrystallization process at high temperatures generates ordered Ca-minerals free of Pb and promotes a segregation of Pb in soluble submicronic Pb-phases. In addition, the recrystallization produces a change in textural properties, then micro-cracks increase the permeability.

5 REFERENCES

- Antenucci, D., Barres, O., Dreesen, R., Dutré, V., Jdid, E. A., Kenis, C., Leclerq, D., Lhote, F., Lorenzi, G., Nielsen, P., Veschkens, M., Yvon, J., 2003. Evaluation du comportement à long terme des résidus fins d'incinération des ordures ménagères (REFIOM) stabilisés aux liants hydrauliques. LIFE99 ENV/B/000638, Technical Final report.
- Brault, S., 2001. Modélisation du comportement à la lixiviation à long terme de déchets stabilisés à l'aide de liants hydrauliques. PhD thesis, Université Pierre et Marie Curie, Paris VI. 266 pp.
- Directive 1999/31/CE, annexe II, concernant la mise en décharge des déchets. 2002, 31p.
- Lin, T.T., Lin, C.F., Wel, W.C., Lo, S.L., 1993. Mechanism of Metal Stabilization in Cementitious Matrix : Interaction of Tricalcium Aluminate and Copper Oxide/Hydroxide. Environ. Sci. Technol. 27, 1312 – 1318.
- Mimura, H., Yokota, K., Akiba, Y., Onda, Y., 2001. Alkali Hydrothermal Synthesis of Zeolites from Coal fly ash and

- Their Uptake Properties of Cesium Ion. *J. Nucl. Sci. Technol.* 38, 9, 766 – 772.
- Robert, H., 1995. Stabilisation au bitume de cendres volantes d'usines d'incinération d'ordures ménagères avant dépôt en décharges contrôlées. *Congrès International sur les procédés de solidification et de stabilisation des déchets.* Société Alpine de Publications, p 223 – 227.
- Shaw, S., Clark, S.M., Henderson, C.M.B., 2000. Hydrothermal formation of the calcium silicate hydrates, tobermorite ($\text{Ca}_5\text{Si}_6\text{O}_{16}(\text{OH})_2 \cdot 4\text{H}_2\text{O}$) and xonotlite ($\text{Ca}_6\text{Si}_6\text{O}_{17}(\text{OH})_2$): an in situ synchrotron study. *Chem. Geol.* 167, 129 – 140.
- Sacerdoti, M., Passaglia, E., 1985. The crystal structure of katoite and implications within the hydrogrossular group of minerals. *Bull. Minéral.* 108, 1 – 8.
- Van der Sloot, H.A., 1999. Characterization of the leaching behaviour of concrete mortars and of cement – stabilized wastes with different waste loading for long term environmental assessment. *Congrès International sur la Stabilisation des Déchets et Environnement.* Société Alpine de Publication, Grenoble, p 131-139 .
- Welch, M.D., Cooper M.A., Hawthorne, F.C., Criddle, A.J., 2000. Symesite, $\text{Pb}_{10}(\text{SO}_4)_7\text{Cl}_4(\text{H}_2\text{O})$, a new PbO-related sheet mineral: Description and crystal structure. *Amer. Min.* 85, 1526 – 1533.

6 ACKNOWLEDGEMENTS

Authors are grateful to LIFE for financial support (Programme Research LIFE99 ENV/B/000638).

Mg-Mica Formation in Alkaline Environment of the Nhecolândia, South Mato Grosso, Brazil

S.A.C.Furquim, J.P.Queiroz Neto, S.Furian

Department of Geography, University of São Paulo, São Paulo, Brazil

L.Barbiéro

Department of Metallurgy, Indian Institute of Science, Bangalore, India

R.C.Graham

Department of Environmental Sciences, University of California, Riverside, USA

ABSTRACT: The geochemical control of Mg in alkaline environment is still subject to debate. Precipitations of stevensite, sepiolite or Mg-montmorillonite are usual in alkaline water but the formation of Mg-silicate has been deduced from geochemical equilibrium between solid and liquid phases rather than actually observed from mineralogical investigations. The knowledge of exact stoichiometry involved in Mg precipitation is necessary to elaborate a chemical tracer in order to realize hydro-chemical balances. In the Nhecolândia, a sub-region of the Pantanal wetland in Brazil, recent studies have shown that saline water arises from present day concentration of fresh water under the influence of evaporation. The geochemical processes involving the major elements as the solutions become more saline are the precipitation of calcite or Mg-calcite, magnesium-silicates and eventually sodium-carbonates. In the Pantanal framework, the precipitations occur in sandy horizons, making possible the accurate identification of the Mg-involving silicate formation. The clay (<2mm) and medium silt fractions were analyzed using x-ray diffraction, electron microprobe, and observed under SEM and TEM. The results indicate that magnesium is incorporated in small quantities (2 to 3 %) in amorphous material and in the neof ormation of a low-charge mica. The consequences in terms of hydro-chemical budget are presented.

1 INTRODUCTION

The geochemical control of Mg²⁺ in natural alkaline waters subjected to evaporation has been reported in the literature through two main processes: 1) precipitation of Mg-carbonates (Cheverry 1974, Eugster & Hardie 1978, Barbiéro 1995) and 2) formation of Mg-silicates (Garrels & Mackenzie 1967; Gac et al. 1977, Jones et al. 1977, Jones & Galan 1988, Valles et al 1989; Marlet et al. 1996).

The first process seems to occur when the Mg/Ca ratio of diluted waters increases after calcite precipitation, being responsible for the origin of endogenic minerals as Mg-calcite and magnesite (Eugster & Hardie, 1978). The second process apparently takes place in the early stages of water concentration (Gac et al. 1977) and possibly occurs both in waters depleted and enriched in Al, producing stevensite and sepiolite in the former (Darragi & Tardy, 1987) and smectite in the latter (Jones 1986; Valles et al. 1989). Stevensite (Velde 1985, Jones 1986, Torres Ruiz et al. 1994) and sepiolite (Garrels & Mackenzie 1967, Gac et al. 1977, Torres Ruiz et al. 1994, Singer et al. 1998) are usually considered as endogenic minerals when formed in highly evaporative environments. Smectite, however, seems to be formed either by

direct precipitation (endogenic origin) or by transformation from pre-existing clays (authigenic origin) (Gac et al. 1977). However, the formation of these minerals has been more frequently predicted through geochemical equilibrium between solid and liquid phase than actually observed from mineralogical investigations (Gac et al. 1977, Valles et al. 1989, Marlet et al. 1996). In most of the studies, the exact stoichiometry involved in the Mg control processes has not been accurately identified.

The identification of the processes involved in the water evolution of alkaline environments, including those related to the Mg control, can provide important information in order to elaborate a quantitative tracer for the hydro-bio-geochemical balance (Ribolzi et al. 1996; Barbiéro et al. 2001).

The Nhecolândia, a sub-region located in the Pantanal wetland in central-western Brazil (16°-20°S and 50°-58°W), presents as a distinctive feature both freshwater and saline lakes with a huge chemical variability and co-existing in close proximity, the latter currently evolving in an alkaline way under the influence of concentration by evaporation (Valles et al. 1991). The processes responsible for most water chemical variability are the precipitation of calcite or Mg calcite, the formation of Mg silicates and eventually Na-carbonates as water becomes more

saline (Barbiéro et al. 2002). In this sub-region of Pantanal wetland, most of the sediments and soil materials are sandy (Del'Arco et al. 1982; Silva 1986; Queiroz Neto et al. 1996), which favors the discrimination of the neoformed minerals from pre-existing clays and allows the accurate identification of the Mg-silicate stoichiometry.

The objective of this study is to identify the mineralogical composition of Mg-clay suspected to be responsible for the control of Mg in the soil solution.

2 MATERIALS AND METHODS

The present study was achieved at Nhumirim Farm (18°59'S and 56°49'W) and sampling was around a representative saline lake of Nhecolândia. The soil materials around this lake are formed by a light, sandy and structureless surficial horizon, which overlies a light and sandy horizon with abundant blackish volumes of organic matter, polyedric substructure and with common presence of carbonate nodules. Beneath, there is a gray horizon (2YR 5/2) with polyedric substructure and higher amounts of clay than the above horizons. The gray horizon overlies a green horizon (5Y 5/2), that contains the highest amount of clay of the profile (12 to 20%) and is sodic and alkaline ($\text{Na/T} > 50\%$ and pH ranging from 9 to 11) (Barbiéro et al. 2000).

X-ray diffraction (XRD) and scanning electron microscopy (SEM) analyses were performed on the gray and green horizons whereas transmission electron microscopy (TEM) analysis was performed only in the latter.

X-ray diffraction analyses were accomplished on silt and clay fractions, both of them separated by centrifugation and sedimentation after destruction of the organic matter with NaOCl (pH 9.5) (Anderson 1963). Oriented specimens were analyzed through five different treatments: ethylene glycol solvation, Mg saturation, K saturation and heating of the K saturated clay at 350°C and 550°C (Jackson 1979) using a Siemens D-500 diffractometer (CuK radiation with graphite crystal monochromator). Analyses were run with a step size of a 0.02° 2θ and a count time of 1.0 s per step.

Samples of the whole soil material and the medium silt fraction were examined using a FEI XL30-FEG SEM fitted with a semi-quantitative elemental analyzer (EDAX).

The <2μm clay fraction of the green layer was selected for analysis using a FEI-CM300 TEM linked with a x-ray detector EDS, model Phoenix, and with a elemental analyzer EDAX. A drop of a diluted suspension with the clay was placed on a standard Cu grid with carbon film.

Quantitative analyses were performed on compacted clay patches using electron microprobe

(SX50) fitted with wavelength dispersive spectrometers (WDS).

3 RESULTS AND DISCUSSION

The microprobe analysis indicates that the clay fraction of both grey and green horizons is composed of Si (60 to 70%), and secondarily of Al (15 to 25%), K (6 to 9%), Fe (4 to 7%), Mg (2 to 3%), and Ca (1 to 6 %). The mineralogical composition of the clay fraction consists mainly of mica, kaolinite and quartz (Figure 1). The medium silt is dominated by quartz in the gray horizon whereas it presents a mineral composition similar to that of the clay fraction in the green layer. The SEM observations revealed that this medium silt fraction in the green horizon is composed of clay aggregates rather than silt-sized mineral grains.

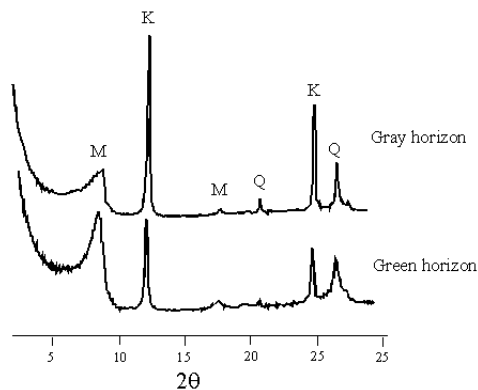


Figure 1: X-ray patterns of clay in both gray and green horizons. M: mica; K: kaolinite; Q: quartz.

The TEM analysis was consistent with both x-ray diffraction and SEM results, as mainly amorphous materials enriched in Si and a well-crystallized low charge mica were identified (Figure 2). According to this preliminary observation, it seems that the clay mineralogy of the <2μm fraction and medium silt fraction may be arising from precipitation of mica in a matrix of amorphous silica-rich phase. Grey and green horizon, that were clearly distinguished in the field, differ mainly in the composition of the silt fraction, which is predominantly composed of quartz in the first one and of quartz grains and clay aggregates in the second one. Neoformation of mica from smectite has already been described in African alkaline lakes (Singer & Stoffers 1980; Jones & Weir 1983). To our knowledge, direct neoformation of mica or crystallization of mica from amorphous material has never been described in alkaline environments.

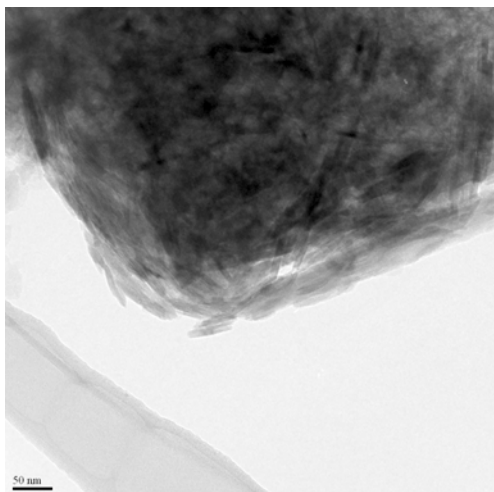


Figure 2. Amorphous silica-rich phase with mineral crystallization, identified in the TEM.

The results also indicate that Mg is not a major component of the neoformed clay fraction, which presents higher K contents. The results are in agreement with the geochemical studies carried out at the regional scale (Barbiéro et al. 2002) that emphasized that Mg was controlled by both carbonate and silicate precipitation.

The formation of Mg-involving silicates may have a significant influence in the control of Mg, because Mg is present in low quantities in the water. Even though the proportion of K is higher in the precipitating clay, the clay formation may have much less effect on K contents in the solution because they are about 100 times higher than Mg contents in the equilibrating solution (Barbiéro et al. 2002).

4 CONCLUSIONS

The preliminary investigations carried out on the clay and silt fraction seem to indicate that the green horizon developed around and beneath the saline lakes of the Nhecolândia is composed of amorphous silica in which the neoformation of mica is occurring. These formations involve transfer of protons that should be taken into account in the hydro-geochemical balance carried out on these alkaline lakes.

Although the proportion of Mg involved is low, clay precipitation may contribute significantly in the control of magnesium in the soil solution, and may have a strong qualitative impact on the water chemistry. The next research efforts should focus first on the proportion of Mg included in the Mg-calcite, and then on the simulation of evaporation

taking into account Mg-calcite precipitation and the clay neoformation identified in this study.

5 REFERENCES

- Anderson, J.U., 1963. An improved pretreatment for mineralogical analysis of samples containing organic matter. *Clays Clay Miner.*, 10:380-388.
- Barbiéro, L., 1995. Les sols alcalinisés sur socle dans la vallée du fleuve Niger. Origine de l'alcalinisation et évolution des sols sous irrigation. *Travaux et Documents Microfichés Orstom* 138, 209 p.
- Barbiéro, L. Queiroz Neto, J.P. Ciornei, G. Sakamoto, A.Y. Capellari, B. Fernandes, E. Valles, V., 2002. Geochemistry of water and ground water in the Nhecolândia, Pantanal of Mato Grosso, Brazil: variability and associated processes. *Wetlands*, 22: 528-540.
- Barbiéro, L., Valles, V., Regeard, A., Cheverry, C., 2001. Residual alkalinity as tracer to estimate the changes induced by a forage cultivation in a non-saline irrigated sodic soil. *Agricultural Water Management*, 50: 229-241.
- Barbiéro, L. Queiroz Neto, J.P., Sakamoto, A. 2000. Características geoquímicas dos solos relacionadas à organização pedológica e à circulação de água (Faz. Nhumirim da EMBRAPA, Nhecolândia, MS). III Simpósio sobre Recursos Naturais e Sócio-Econômicos do Pantanal. Corumbá, 27 a 30 de novembro de 2000, p.90-100.
- Cheverry, C., 1974. Contribution à l'étude pédologique des polders du lac Tchad. Dynamique des sels en milieu continental subaride dans les sédiments argileux et organiques. Thesis. Sci., U.L.P. Strasbourg, 257 pp.
- Darragi, F., Tardy, Y. 1987. Authigenic trioctahedral smectites controlling pH, alkalinity, silica and magnesium concentrations in alkaline lakes. *Chemical Geology*, 63: 59-72
- Del'Arco, J.O., Silva, R.H. Tarapanoff, I. Freire, F.A. Pereira, L.G. Souza, S.L. Luz, D.S. Palmeira, R.C.B. Tassinari, C.C.G., 1982. Geologia da Folha SE.21 Corumbá e Parte da Folha SE.20. In *Radam Brasil-Levantamento dos Recursos Naturais*. Rio de Janeiro, p.25-160.
- Eugster, H.P., Hardie, L.A., 1978. Saline Lakes. In Lerman, A. (ed.) *Lakes: chemistry, geology and physics*. Springer-Verlag, p. 237-294.
- Gac, J.Y., Droubi, A., Fritz, B., Tardy, Y., 1977. Geochemical behavior of silica and magnesium during the evaporation of waters in Chad. *Chemical Geology*, 19: 215-228.
- Garrels, R.M., Mackenzie, F.T., 1967. Origin of the chemical compositions of some springs and lakes. In *Equilibrium Concepts in Natural Water Systems*. Am. Chem. Soc., Adv. Chem., 67:222-242.
- Jackson, M.L., 1979. *Soil Chemical Analysis-Advanced Course*. 2nd ed. M.L. Jackson, Madison, WI.
- Jones, B.F., Galan, E., 1988. Palygorskite-sepiolite. *Reviews in Mineralogy*, 19:631-674.
- Jones, B.F., 1986. Clay mineral diagenesis in lacustrine sediments. In: Mumpton, F.A. (Ed.), *Studies in Diagenesis*. US Geol. Surv. Bull., 1578: 291-300.
- Jones, B.F., Eugster, H.P., Rettig, S.L., 1977. Hydrochemistry of Lake Magadi Basin, Kenya. *Geochim. Cosmochim. Acta* 41:53-72.
- Jones, B.F., Weir, A.H., 1983. Clay minerals of Lake Abert, an alkaline, saline lake. *Clays and Clay Minerals* 3:161-172.
- Marlet, S., Valles, V., Barbiéro, L., 1996. Field Study and Simulation of Geochemical Mechanisms of Soil

- Alkalinization in the Sahelian Zone of Niger. *Arid Soil Research and Rehabilitation*, 10:243-256.
- Queiroz Neto, J.P.; Sakamoto, A.; Lucati, H.M.; Fernandes, E., 1996. Dinâmica Hídrica de uma Lagoa Salina e seu entorno na Área do Leque, Nhecolândia, Pantanal- MS. In II Simpósio sobre Recursos Naturais e Sócio-Econômicos do Pantanal. Corumbá, MS, p.51.
- Ribolzi, O., Valles, V., Bariac, T., 1996. Comparison of hydrograph deconvolutions using residual alkalinity, chloride and oxygen 18 as hydrochemical tracers. *Water Resources Research*, 32:1051-1059
- Silva, T.C., 1986. Contribuição da Geomorfologia para o Conhecimento e Valorização do Pantanal. In *Anais do I Simpósio sobre Recursos Naturais e Sócio-Econômicos do Pantanal*, 27 de novembro a 4 de dezembro de 1984, Corumbá (MS), 77-90.
- Singer, A., Stoffers, P., 1980. Clay mineral diagenesis in two East African lakes. *Clay Minerals*, 15: 291-307.
- Singer, A., Stahr, K., Zarei, M., 1998. Characteristics and origin of sepiolite (Meerschaum) from Central Somalia. *Clay Minerals*, 33: 349-362.
- Torres Ruiz, J., López-Galindo, A., González-López, J.M., Delgado, A., 1994. Geochemistry of Spanish sepiolite-palygorskite deposits: genetic considerations based on trace elements and isotopes. *Chemical Geology*, 112: 221-245.
- Valles, V., N'Diaye, M.K., Bernadac, A., Tardy, Y., 1989. Geochemistry of waters in the Kouroumari Region, Mali; Al, Si, and Mg in Waters Concentrated by Evaporation: Development of a Model. *Arid Soil Research*, 3: 21-39.
- Valles, V., Pachepsky, I., Ponizovsky, A.A., 1991. Invariant criteria for irrigation water quality assessment in arid and semi-arid regions. In : *Genesis and Control of Fertility of Salt Affected Soils*. ISSS Subcommittee on Salt Affected Soils Science, pp. 330-333 USSR, V.V. Dokuchaev Soil Institute, Moscow.
- Velde, B., 1985. Clay Minerals: a physico-chemical explanation of their occurrence. *Developments in Sedimentology*, 40. Elsevier, 427 p.

Thermodynamic and Structural Properties of Clay Minerals

H.Gailhanou^{*}, J.Olives, M.Amouric, R.Perbost
CRM-CNRS, Campus de Luminy, Marseille, France

^{*} Andra (N.Michau), Châtenay-Malabry, France. PhD Thesis, Andra-ANRT-BRGM-CNRS-Univ Agreement

J.Rogez
TECSEN, Faculté des Sciences de St Jérôme, Marseille, France

F.Brunet
ENS, Paris, France

C.Alba-Simionesco
LCP, Faculté des Sciences d'Orsay, France

P.Blanc & E.Gaucher
BRGM, Orléans-la-Source, France

ABSTRACT: The knowledge of the thermodynamic behaviour of clay minerals is very important in the management of industrial or radioactive waste. Clay minerals (smectite, illite-smectite mixed-layer minerals) are here studied, both experimentally (HRTEM, calorimetry) and theoretically (energy modelling). Dissolution calorimetric measurements and energy calculations are consistent and show that illite-smectite interstratified minerals are slightly more stable than the two-phase assemblage, illite + smectite. Using adiabatic calorimetry, specific heat values of dehydrated smectite, from 0 K to 265 K, are also presented. These first calorimetric measurements are needed to determine all the thermodynamic functions of these clay minerals.

1 INTRODUCTION

The study of clay minerals is of high interest in various scientific fields, concerning both applied and fundamental research. For example, clays containing smectite and illite-smectite have ideal properties (impermeability, plasticity) for their use as confinement barriers for industrial or radioactive waste. Nevertheless, their thermodynamic properties, which are essential to understand their long-term behaviour, are still almost unknown. The final aim of this work is to obtain all the thermodynamic functions concerning clay minerals, such as smectite, illite and mixed-layer illite-smectite. Owing to their very small size and the presence of various impurities, these clay minerals need to be very well characterized, structurally and chemically, up to the nanometre scale (including impurities). The structure and the thermodynamic properties of these clay minerals are then studied, both experimentally (HRTEM, calorimetry) and theoretically (energy modelling, interatomic potentials). First results, concerning characterization calorimetry and modelling, are here presented.

2 MATERIALS

The studied samples are (1) a smectite and (2) illite-smectite mixed-layer minerals.

Smectite — referenced as a montmorillonite — was obtained from the Wyoming bentonite MX-80, after purification, exchange with Na cation and extraction of the < 2 µm clay fraction.

Illite-smectite interstratified minerals belong to the hydrothermal series from the Shinzan area (Japan) (Inoue et al. 1987, Olives et al. 2000). They represent a complete series from the smectite to the illite end-members.

3 CHARACTERIZATION, HRTEM-AEM

HRTEM observations, on various samples from the hydrothermal smectite-to-illite conversion series, reveal different ordering types in the illite-smectite layer sequences: from randomly disordered (R0), in the less transformed samples, to R1 and R2 ordered, with, locally, regular ...*isis*... and ...*iisiis*... sequences (*i* = illite, *s* = smectite) (Fig. 1).

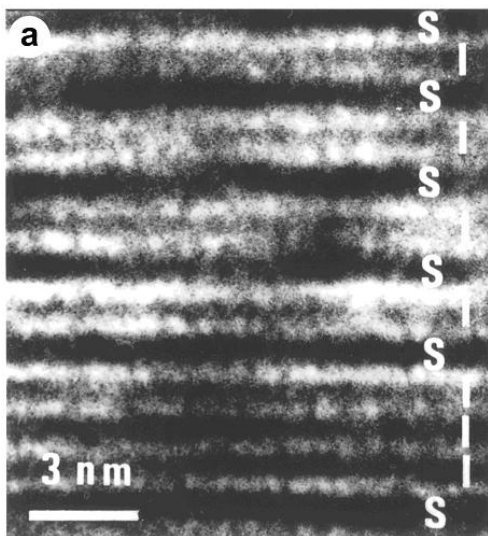


Figure 1. Locally ordered ...*isis*... sequence, observed by HRTEM.

AEM microanalyses (coupled with HRTEM) indicate a general chemical trend from montmorillonite to illite.

In the smectite sample, IRTF analyses reveal the presence of 7.5 wt.% of quartz and 7.5 wt.% of cristobalite. Moreover, AEM microanalyses indicate an amount of 20 wt.% of SiO₂ impurities, which suggests that 5 wt.% of amorphous SiO₂ is also present. As a consequence of such an important amount of SiO₂ impurities, the resulting composition of the smectite is less rich in SiO₂: it shows a beidellite-montmorillonite composition, instead of the referenced montmorillonite one.

4 CALORIMETRY

The purpose of this work is to determine the complete set of thermodynamic properties of these clay minerals, *i.e.* enthalpies of formation, entropies and Gibbs free energies of formation, at any temperature.

Standard enthalpies of formation may be obtained by dissolution calorimetry. This method is based on the measurements of the heats of dissolution, in a reference solution, of the clay mineral, of its oxide — or hydroxide — constituents, and of the impurities.

Specific heats, Cp, are determined using adiabatic calorimetry, from 5 K to 300 K, and DSC (Differential Scanning Calorimetry), from 300 K to 500 K. The entropy is then obtained by integrating Cp/T from 0 K to T.

From the previous values of the standard enthalpies of formation, the entropies and the specific heats, Gibbs free energies of formation can be deduced, at any temperature.

4.1 Dissolution calorimetry

An original application of the dissolution calorimetry method was used to determine the enthalpies of mixing of the illite-smectite clays. The measured enthalpies of dissolution (in a reference solution) of these samples may be well represented in a 3D-space, using two relevant chemical parameters (obtained from statistical analysis). They were then modelled by a second-degree polynomial surface (Fig. 2).

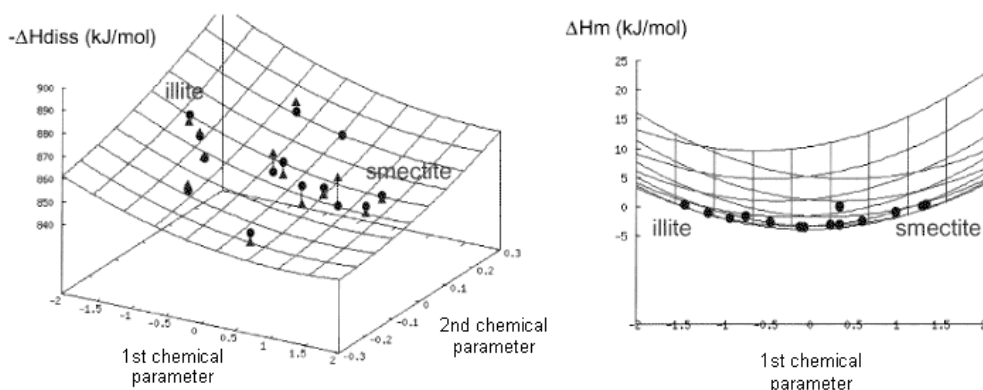


Figure 2. Left diagram: enthalpy of dissolution (with opposite sign) as a function of the two relevant chemical parameters. Right diagram: enthalpy of mixing of the layers (the 2nd chemical parameter axis is normal to the figure). Triangles = experimental points; circles = modelled points.

determination of the entropy function between 0 K and 265 K.

Further calorimetric measurements (dissolution calorimetry, adiabatic calorimetry, DSC) are in progress in order to obtain all the thermodynamic functions related to these clay minerals, namely, enthalpies of formation, entropies and Gibbs free energies of formation.

7 REFERENCES

- Inoue, A. , Kohyama, N., Kitagawa, R. & Watanabe, T. 1987. Chemical and morphological evidence for the conversion of smectite to illite. *Clays and Clay Minerals* 35: 111-120.
- Olives, J. , Amouric, M. & Perbost, R. 2000. Mixed layering of illite-smectite: results from high-resolution transmission electron microscopy and lattice-energy calculations. *Clays and Clay Minerals* 48: 282-289.

Environmental Aspects of Waste Dumps at the Peña de Hierro Mine (Iberian Pyrite Belt SW Spain)

I.González, A.Romero, E.Galán

Dpto. Cristalografía, Mineralogía y Química Agrícola. Universidad de Sevilla 41071-Sevilla. Spain.

ABSTRACT: Waste dumps, stream water and sulphate efflorescences sampled in the pyritic Peña del Hierro mine have been studied in order to identify the processes and factors implicated in the genesis of the acid mine drainage (AMD) and the release of pollutants to the stream water. Waste dumps include: volcanic tuffs, gossan, shales, roasted pyrite ashes and floated pyrite. Volcanic tuffs, which are rich in pyrite, are the main source of AMD. Gossan and ashes are mainly composed of iron oxides and they are rich in trace elements (As up to 1710 ppm, Pb up to 3455 ppm, and heterogeneous concentration in Hg, Zn, Cu and Mo). The streams springing from the waste dumps present a typical and very advanced case of AMD, with pH 1.8 on average. This extreme pH caused the alteration of minerals and the mobilization of major and traces elements (for instance Zn, Cu and Mn sometimes over 100,000 µg/l and As up to 72,200 µg/l). The sequence of mobility is: Mn > Co, Zn, Cd > Cu, Ni >> As, Mo, Cr >> Pb, Hg. The efflorescent compounds are dominated by Fe-Mg- and Al hydrated sulphates and hydroxy-sulphates. The main phases are coquimbite, halotrichite and copiapite, and sporadically melanterite, hexahydrate, epsomite and starkeyite. Geochemical analysis show that As have affinity to precipitate with coquimbite, Co and Ni can be removed partially by copiapite and halotrichite and Zn, Cd, Cu and Mn are bounded to melanterite and epsomite when they appear.

1 INTRODUCTION

The high activity of the polymetallic sulfide mines in the Iberian Pyritic Belt (SW of Spain) has originated a strong acid drainage and the release of many trace elements. Stream water enter the Tinto River, which is one of the most polluted rivers in the world. In this work, the old mine site Peña del Hierro, located in the catchment area of this river, has been studied.

In order to identify the processes and the factors involved in the genesis of the acid mine drainage and the remediation possibilities, the aims of this work were a) to characterize the mineralogy and geochemistry of the waste dumps, b) to study the geochemistry and physical properties of the stream water, and c) to identify the different sulphate efflorescences that precipitate during summer.

2 MATERIAL AND METHODS

Waste dumps were studied from 58 samples coming from drill holes. Fifty water samples were collected from 9 main streams around the waste dumps in four campaigns: two in summer (dry station), and two in

winter, after a continuous period of rainfall. Headwaters and downstream waters were taken from every channel (Fig.1). Efflorescences (57 samples) were taken from the same water sampling points. Selection was according to their physical aspects (colour, fragility of the crust, morphology).

The mineralogy of the efflorescences and the waste dumps (rock fragments and the <2mm fraction, the most weathering fraction) was determined by X-ray powder diffraction, using a Philips PW1130/90 instrument with automatic slit and Ni filtered Cu K α radiation under 20 mA and 40 kV conditions. Morphology was observed by optical and scanning electron microscopy (SEM), with the last instrument spot analyses were realized with and X-ray energy dispersive spectrometer (EDS).

Some spoil, and efflorescence, selected samples were used for determining major and trace elements by Instrumental Neutron Activation Analysis (INAA) and Inductively Coupled Plasma-Optical Emission Spectrometry (ICP-OES). The selected waters were analyzed by Inductively Coupled Plasma-Mass Spectrometry (ICP-MS).

3 RESULTS AND DISCUSSION

3.1 Waste dumps

Waste rock dumps in Peña del Hierro are very heterogeneous and they are mainly composed of barren rock: acid volcanic tuff, gossan and shales (Fig.1). The ore transformation has also produced roasted pyrite ashes along the XIX century and remains of floated pyrite coming from the concentration process of the ore in the last stage of the mining. The cartography of these materials and the depths of the drill holes carried out allow us to calculate an approximate volume of every unit (Tab. 1).

Table 1. Surface and approximate volume of the waste dumps.

	Surface (Ha)	Volumen (m ³)
Tuffs	9	1,000,000
Tuff-Gossan	6	625,000
Gossan	4.5	325,000
Pyrite Ashes	2	100,000
Washed Pyrite	0.2	4200
Others	1.5	25,000

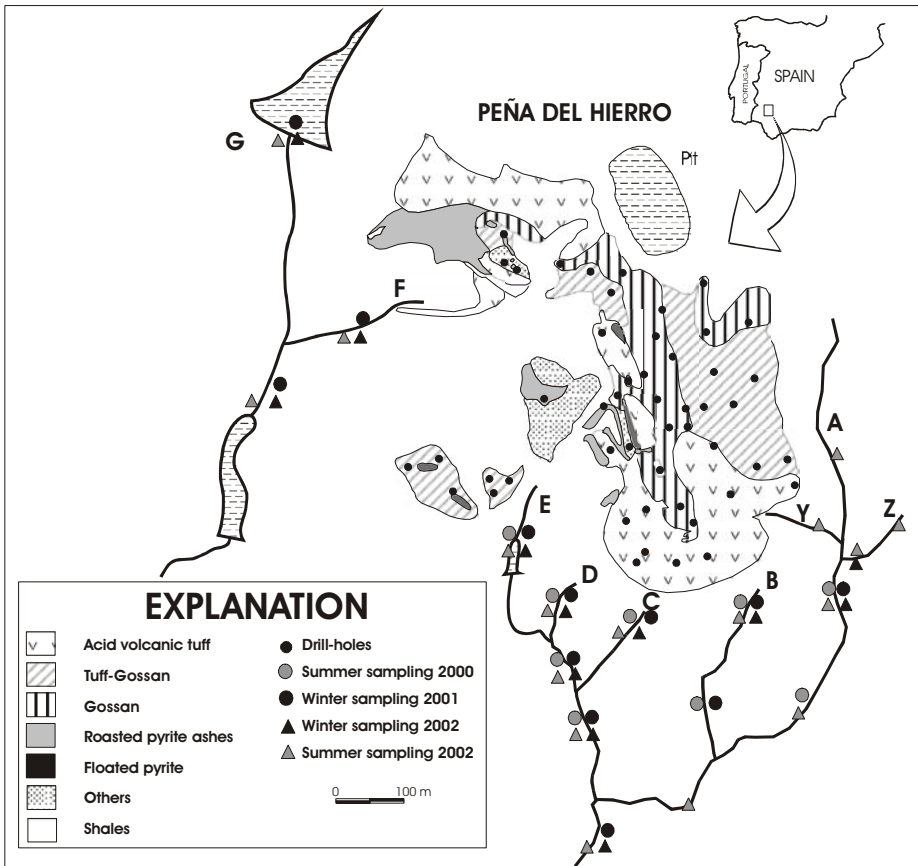


Figure 1. Cartography of the waste dumps and sampling location.

Volcanic tuffs and shales are dominated by quartz and muscovite, but the most important mineralogical characteristic is the occurrence of pyrite veins crossing the tuffs. The pyrite oxidation causes the precipitation of jarosite, that commonly occurs in the <2mm fraction of these materials. Barite, chlorite and kaolinite have been also identified, as accessory phases.

Dumps mainly composed of gossan and the roasted pyrite ashes dumps are characterized by a high content of poorly crystalline Fe-oxy/hydroxides and hematite. Goethite is also abundant in gossan, but it does not appear in the ashes. Quartz and barite appear usually as accessory minerals, and pyrite can occur in the ashes as a rest of the original sulphides. The high content in low crystallinity Fe-oxides can hide accessory minerals.

The geochemistry of the dumps (analyzed in the <2mm fraction, Tab. 2) is related with the type of accumulated material. For instance, gossan and roasted pyrite ashes dumps are rich in iron (23 and 46% respectively on average) and trace elements. Arsenic presents the highest concentration in gossan (538-1710 ppm), and lead in the ashes (1995-3455 ppm). Other important metals in these units are Hg (1-53 ppm), Cu (90-895 ppm) and Mo (45-331 ppm). On the other hand, tuffs presents the highest contents of S (1.2-7.2%) and the trace element concentration are lower than in the other materials.

The high correlations between some elements as As or Mo and Fe content ($r^2=0.81$ and 0.74 respectively) suggests that these trace elements are adsorbed on the Fe-oxides, as the results obtained by other authors (Müller & Seiler 1999, Galán et al. 2003).

Table 2. Geochemistry of the waste dumps (<2mm fraction).

	Tuffs			Gossan			Ashes		
	Max.	Min.	Av.	Max.	Min.	Av.	Max.	Min.	Av.
S (%)	7.2	1.2	4.1	1.3	0.1	0.6	1.5	0.6	0.7
Fe (%)	10.9	4.0	7.4	30.8	16.1	23	52.1	36.3	52.2
Al (%)	5.5	2.1	4.0	4.6	0.8	2.7	1.2	0.3	0.7
K (%)	3.9	1.2	2.2	1.6	0.6	1	0.6	0.1	0.3
Mg (%)	0.7	0.1	0.3	0.2	0.1	0.1	<0.1	<0.1	
Na (%)	0.7	0.1	0.3	0.2	0.1	0.1	<0.1	0.1	
Ca (%)	<0.03	0.01		<0.06	0.02		<0.07	0.05	
As (ppm)	263	46	160	1710	538	979	971	21	504
Pb (ppm)	628	113	302	989	318	591	3455	584	2173
Cu (ppm)	1487	16	342	895	90	322	527	213	409
Zn (ppm)	392	19	107	434	56	200	536	102	306
Mo (ppm)	95	21	55	331	143	221	351	45	158
Cd (ppm)	<1	0.2		<4		1	3	1	2
Hg (ppm)	<2	0.8		53	1	15	<16		8
Co (ppm)	64	7	27.8	8	3	5	58	18	36
Ni (ppm)	15	5	10.4	18	2	9	<18		11
Cr (ppm)	39	15	27.8	<42		27	<32		20
Mn (ppm)	113	7	33	79	33	55.5	44	27	37

3.2 Stream water

The streams surrounding the waste dumps present a typical and very advanced case of acid mine drainage, with pH ranging from 0.7 to 3.2 and an average value of 1.8 (Tab. 3). Acid volcanic tuffs seem to be important in the genesis of acid mine drainage as streams springing from the bottom of them are lower in pH. For instance, streams Y, B, C and D are usually between 0.7 and 1.6. Streams E and F range from 1.7 to 2.7 (Fig. 1). The pH \approx 7 determined in stream G, which was taken in clean waters, shows the influence that these spoils have on the waters.

This extreme acid mine drainage causes the alteration of the minerals and the mobilization of major and trace elements in high concentrations (Tab. 2), although many of them are in a low content in the dumps (Tab. 1). For instance, Fe is up to 30,200 mg/l, but Mg and Ca (up to 1680 and 470 mg/l respectively) have a higher mobility according to the concentration that they presented in the waste dumps. Other elements like K shows very low values (average 4.5 mg/l), in this case, probably because it is precipitating in the dumps forming jarosite (Bigam et al. 1996).

Table 3. Geochemistry of stream water.

	Maximum	Minimum	Average
pH	3.2	0.7	1.8
Conductivity (μ S)	47,080	1002	14,612
Al (mg/l)	4180	1	1341
Ca (mg/l)	470	21	173
Fe (mg/l)	30,200	41	7705
K (mg/l)	35	0.2	4
Mg (mg/l)	1680	93	531
Na (mg/l)	60	4	25
Si (mg/l)	134	8	55
Ba (μ g/l)	28	5	14
Co (μ g/l)	26,100	599	8317
Mn (μ g/l)	152,000	9730	47,617
Mo (μ g/l)	11,300	0.0	1779
Ni (μ g/l)	1470	177	841
As (μ g/l)	72,200	2	11,204
Cd (μ g/l)	849	0.4	304
Cr (μ g/l)	1110	0.0	278
Cu (μ g/l)	161,000	139	47,823
Hg (μ g/l)	0.3	0.0	0.0
Pb (μ g/l)	1390	9	163
Zn (μ g/l)	142,000	5280	72,025

Regarding trace elements, Zn, Cu and Mn (sometimes over 100,000 μ g/l) present the highest concentrations, followed by As, Co and Mo (11,204, 8317 and 1779 μ g/l on average respectively). Cadmium (up to 849 μ g/l) shows a high mobility

according to the concentrations presented in the waste dumps (<4 ppm). The sequence of mobility obtained from the relationship between the average concentrations in the waters and those observed in the dumps is the following:

Mn> Co, Zn, Cd> Cu, Ni>> As, Mo, Cr >> Pb, Hg

The extreme acidity is involved in the mobility of the elements. Indeed, some of them as Fe, Al, As, Cu, Mo or Co present a high negative correlation with the pH. Others as K, Cd, Pb or Zn are not correlated with the pH, probably because they are influenced by other factors like chemical and mineralogical speciation.

3.3 Sulphate efflorescences

Sulphate efflorescences are mainly composed of coquimbite, copiapite and halotrichite. Other phases appearing sporadically are melanterite, epsomite, hexahidrite, rhomboclase and starkeyite. Iron, Mg, Al and trace elements like Zn (51-8016 ppm), Cu (10-2413), As (2-592 ppm) and other like Cd, Co, Ni, Mo, Pb or Mn are the major elements (Tab. 4). Arsenic is bonded exclusively to coquimbite, as only appear when this mineral is present, and the highest concentrations occur in coquimbite monomineralic samples. Epsomite and melanterite, when they appear, can storage Zn, Cu and Mn, as they have been seen by SEM. High correlation among these elements, these phases and Ni suggest that it can be also sorbed by them. When epsomite and melanterite don't occur, Co and Ni can be bounded to copiapite+halotrichite, and Zn, Cu and Cd can be immobilized by accessories phases.

Table 4. Geochemistry of sulphate efflorescences.

	Maximum	Minimum	Average
S (%)	22.1	12.2	17.7
Fe (%)	18.1	0.8	11.8
Mg (%)	10.1	0.3	2.4
Al (%)	4.9	0	2.1
Na (%)	3.3	0	0.3
K (%)	0.4	0	0.1
Ca (%)	0.4	0	0.1
Ba (ppm)	19,000	0	1046
Co (ppm)	580	71	206
Mn (ppm)	26,224	112	4045
Mo (ppm)	183	0	29
Ni (ppm)	142	3	42
As (ppm)	592	2	170
Cd (ppm)	28	1	6
Cr (ppm)	24	0	6
Cu (ppm)	2413	10	776
Hg (ppm)	2	0	0
Pb (ppm)	262	0	26
Zn (ppm)	8016	140	1810

The pH is probably one of the main factors controlling the precipitation of these minerals (Jambor et al. 2000), but the geochemistry of the water can play an important role in the characteristics of the mineralogy.

4 CONSIDERATIONS

The relationship Fe/SO_4^{2-} in stream water is more than three times the theoretical one obtained from the oxidation of pyrite. This suggests that gossan and the roasted pyrite ashes are dissolving, as the precipitation of jarosite ($SO_4^{2-}/Fe = 1.2$) doesn't seem to be enough to compensate Fe exceeding, and many trace elements are releasing to the water.

Physical-chemical conditions of the waters ($pH \leq 2$ and $Eh \approx 500$ mV) prevent the precipitation of Fe-ochres minerals (Bigham et al. 1996; Monterroso & Macías 1998), keeping major and trace elements in solution.

Although sulphate efflorescences trap trace elements, the immobilization is only temporal, as the high solubility of these sulfates causes polluting plumes after the first rainfall (Jambor et al. 2000).

5 REFERENCES

- Bigham, J. M., Schwetmann, U., Traina, S. J., Winland, R. L. & Wolf, M. 1996. Schwetmannite and the chemical modeling of iron in acid sulfate waters. *Geochimica et Cosmochimica Acta*. 60, 12: 2111-2121.
- Galán, E., Gómez Ariza, J. L., González, I., Fernández-Caliani, J. C., Morales, E., Giráldez, I. 2003. Heavy metal partitioning in river sediments severely polluted by acid mine drainage in the Iberian Pyrite Belt. *Applied Geochemistry*. 18: 409-421.
- Jambor, J. L., Nordstrom, D. K., Alpers, Ch. N. 2000. Metal-sulfate Salts from sulfide mineral oxidation. In: Alpers, C. N, Jambor, J. L & Nordstrom, D. K. (eds). Sulfate minerals: Crystallography, Geochemistry and Environmental Significance. 405-452 Washington. *The Mineralogical Society of America*.
- Monterroso, C. & Macias, F. 1998. Drainage waters affected by pyrite oxidation in a coal mine in Galicia (NW Spain): Composition and mineral stability. *The Science of the Total Environment*. 216: 121-132.
- Müller, J. & Seiler, P. 1999. Relevance of self-sealing processes in pyrite sinters for heavy metal mobility. In Åmansson (ed). *Geochemistry of the Earth's Surface*. 211-214, Rotterdam: Balkema.

Franca's Smectites as Organophilic Clays

R.A.Hanna & A.L.Vieira
CNPq - Brazil

A.C.Vieira Coelho, F.R. Valenzuela Diaz, P.Souza Santos
LMPSol - Metallurgical and Materials Engineering Department, Polytechnic School, University of São Paulo, São Paulo, Brazil.

ABSTRACT: Several studies of organic pollutants adsorbed by smectites modified with alkylammonium ions have been reported. The adsorption capacity of the modified clay is usually determined according to the preparation method used, the nature of the surfactant cation and the value of the interlamellar space. Preliminary results of Na-smectites from Franca – São Paulo State, Brazil showed a consistent increase of the original 1.4 – 1.5 nm basal spacings when the samples were treated with cetrinmonium chloride. Franca's smectites are modified by other two quaternary ammonium salts; gasoline, kerosene and diesel fuel are tested for adsorption experiments with the modified smectites. XRD, Foster's swelling and hydrocarbon adsorption tests are used for characterization and evaluation of the adsorption capacity of the organoclays.

1 INTRODUCTION

Organophilic clays, among several others uses, have been used to adsorb and remove undesirable compounds from solutions or from the environment. Its adsorption capacity can be applied in many fields and the smectites (or bentonites) are the favourite clays for this purpose. Brazil, despite of the fact that is one of the major world producers of clays, is still considered poor in the smectites production. The smectites from the region of Franca, north-east of São Paulo State, have been poorly cited in the literature in terms of their technological properties (IPT 1975; Zandonadi 1976, 1978; Valenzuela 2001; Santos 1996; Abreu 1997).

The smectite structure is essentially a crystalline and layered aluminium hydrosilicate. Smectites in the sodium form present a high water adsorption capacity but this property can be modified through the cationic changes between sodium smectites and quaternary ammonium salts containing long alkyl chains. The hydrophilic character of the sodium smectite is changed to hydrophobic and organophilic. An expansion of the basal spacing (d_{001}) occurs caused by the presence of the long chain alkylammonium ions. Organophilic clays adsorb organic compounds by several mechanisms

such as ionic reactions and complexation (Grim 1968).

It is possible to optimize the adsorption of a specific compound by selecting the smectite, the quaternary ammonium salt and the exchange cations methods. Many toxic compounds as phenol, vinasse, benzene, trichlorobenzene and toluene have been successfully adsorbed by organophilic clays. (McBride 1985; Valenzuela 1995; Büchler 1986; Stul 1978; Lagaly 1993).

2 MATERIALS AND METHODS

In this work, three types of smectites were compared:

- a national organoclay (BF Clays);
- a sodium commercial bentonite imported from Wyoming, USA (Aldrich Ltd);
- polycationic smectites from Franca.

Franca's polycationic samples were changed to the sodium form using Na_2CO_3 (Merck) as dispersant based on Padua's process (Santos 1989). Franca's smectites in the sodium form and the Wyoming bentonite samples were changed to the organophilic form by the following procedure:

- preparation of a water-clay dispersion (4%);

- mechanical stirring for 20 minutes;
- resting of the dispersion for 24 hours at the room temperature;
- addition of the quaternary ammonium salt (cetrimmonium chloride /Clariant Brazil) in a 50% aqueous solution;
- mechanical stirring for 20 minutes;
- resting of the dispersion for more 24 hours at the room temperature;
- filtration using a Büchner funnel;
- drying of the filter cake for 72 hours at 60° C;
- grounding of the filter cake to minus # 200 for DRX analysis to compare the basal expansions (d_{001});

Besides the procedures described above, an exploratory experiment based on Foster's swelling (Foster 1953) were carried out by slowly adding 1g of organophilic clay to 100ml of the organic compound tested (gasoline, alcohol, kerosene and diesel fuel) in a sealed graduate tube. The system was left to stand for 24 hours, stirring with a glass rod during 02 minutes and allowed to rest for more 24 hours, when the swelling was recorded. Foster's swelling can be adopted as a method to indicate the organophilic character of the clay. However there is controversy about the adaptations of the method, originally used for water, for organic compounds.

3 RESULTS AND DISCUSSION

The expansions in the basal spacing can be seen in the Table 1 and Figure 1. It is clear that the basal spacing expansions obtained for the samples of Franca'smectites are similar to the imported smectite (Wyoming) when they are changed to the organophilic form. The adopted changing methods caused a good interlayer intercalation of the cetrimmonium chloride cations.

The initial swelling values are shown in the Table 2. Wyoming bentonite samples showed the best performances. The samples of Franca'smectites presented good values for gasoline. BF clay was "more organophilic" for diesel fuel and gasoline.

Table 1. Basal spacings (d_{001}) obtained for the smectites.

CLAY	d_{001}	OBSERVATION
Wyoming (sodium)	12.35	250 meq Na+ /100g of dried clay
Wyoming (organophilic)	19.69	-
BF Clay	15.43	-
Franca 1 (sodium)	12.67	250 meq Na+ /100g of dried clay
Franca 2 (sodium)	12.21	100 meq Na+ / 100g of dried clay
Franca 1 (organophilic)	19.22	-
Franca 2 (organophilic)	19.35	-

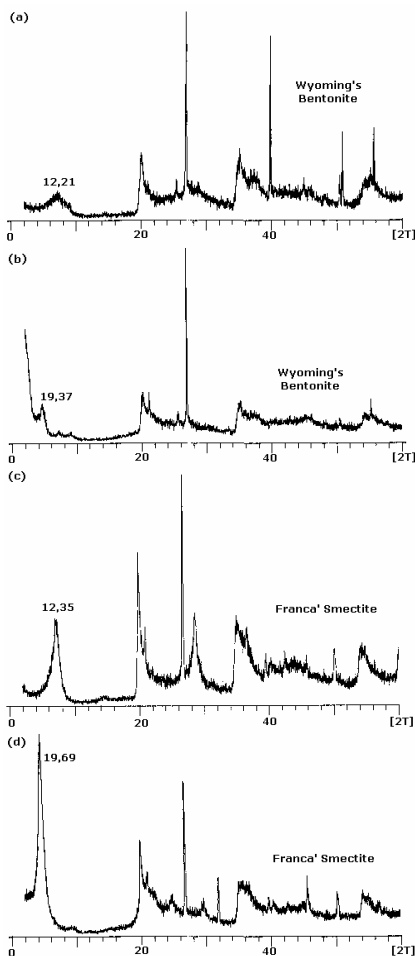


Figure 1. X-Ray curves showing d_{001} expansions after the treatment with cetrimmonium chloride: 12,21Å to 19,37Å for Wyoming' Bentonite (a, b) and 12,35Å to 19,69Å for Franca' Smectite (c, d).

Table 2. Swelling values for the organophilic clays

Organic Compound	Organophilic Clays		
	Franca	Wyoming	BF clay
Gasoline (Standard/ Shell)	09	18	-
Gasoline (V-Power/ Shell)	10	17	-
Gasoline (Standard/Petrobra)	06	19	2.5
Fuel Alcohol (Petrobras)	2.5	08	2.5
Kerosene (Vimak P.Q.Ltd)	2.5	3.0	2.5
Fuel oil (Petrobras)	2.5	09	-

4 CONCLUSIONS

Based on the d_{001} expansions obtained, it can be concluded that the smectites from Franca can be successfully changed to the organophilic form. The initial swelling values suggest the study of new variations in the adaptation of Foster's swelling method and the use of others quaternary ammonium salts and changing methods to get increased adsorptions for the petrochemical studied. The synthesis of organophilic clays from these Brazilian smectites can give an adsorber material in cases of fuel spills or others types of soil and water pollution.

5 REFERENCES

Abreu, L. D. V. 1997. Estudo da Pilarização, com Alumina, de Argilas Esmectíticas Brasileiras. 135p. Dissertação (Mestrado em Engenharia Química). Escola Politécnica, USP, São Paulo.

Büchler, P. M.; Warren, D.; Clark, A. I. & Perry, R. 1986. The use of clay liners in the attenuation of the organic load of vinasse in developing countries. In: International Conference on Chemicals in the Environment, Lisboa. Anais. p.715-724.

Foster, M. D. 1953. Geochemical studies of clay minerals (II)-Relation between ionic substitution and swelling in montmorillonite. *American Mineralogy*, USA., v.38, p.994-1000.

Grim, R. E. 1968. *Clay Mineralogy*. 2.ed. New York: McGraw-Hill.

Instituto de Pesquisas Tecnológicas 1975. Publicação 1045: Argilas Montmoriloníticas Brasileiras como Agentes Descorantes de Óleos Vegetais e Minerais. São Paulo.

Galaly, G. 1993. Surface and interlayer reactions: bentonite as adsorbents. In: 10th International Clays Conference, Adelaide, Australia. Anais. p.137-144.

McBride, M. B.; Pinnavaia, T. J. & Mortland, M. M. 1985. Adsorption of aromatic molecules by clays in aqueous suspension. *Advanced Environmental Science Technology*, USA. n.8, p.145-154.

Santos, P. S. 1989. *Ciência e Tecnologia de Argilas*. São Paulo: Edgard Blücher Ltd., 2 ed, v. 1,2,3.

Santos, P. S.; Vieira, A. C. C. & Abreu, L. D. V. 1996. Estudo da pilarização, com alumina, de argilas esmectitas brasileiras. *Cerâmica*. São Paulo, v.42, p. 150-153.

Stul, M. S.; Maes, A. & Uytterhoeven, J. B. 1978. The adsorption of n-aliphatic alcohols from dilute aqueous solutions on RNH₃ - Montmorillonites, Part I - Distribution at infinite dilution. *Clay and Clay Minerals*, USA. v.5. p.309-315.

Valenzuela, F. R. D. & Santos, P. S. 1995. Obtenção de argilas esmectitas organofílicas partindo-se de três bentonitas sódicas comerciais. In: 39 Congresso Brasileiro de Cerâmica, Águas de Lindóia. Anais, p. 237-242.

Valenzuela, F. R. D. & Santos, P. S. 2001. Studies on the acid activation of Brazilian smectitic clays. *Química Nova*. São Paulo, v.24, p.345-353.

Zandonadi, A. R. & Santos, P. S. 1978. Propriedades reológicas de montmorilonitas ou esmectitas brasileiras. *Cerâmica*. São Paulo, n.25, p.355-371.

Zandonadi, A. R. & Santos, P. S. 1976. Propriedades reológicas em fluidos tixotrópicos para perfuração de poços de petróleo de algumas argilas montmoriloníticas brasileiras - Boletim Técnico da PETROBRAS, Rio de Janeiro, n. 19, jan./mar. p.21-26.

Soil Phases and Heavy Metal Distribution in a Gold-silver Mining Area in South-eastern China

C.He

Geographic Institute, University of Copenhagen, Oster Voldgade 10, DK1350, Copenhagen, Denmark

E.Makovicky

Geological Institute, University of Copenhagen, Oster Voldgade 10, DK1350, Copenhagen, Denmark

J.Li

Institute of Mineral Deposits, Chinese Academy of Geological Sciences, Beijing, China

ABSTRACT: Two series of soil samples were collected. One situated downslope of an old mining pit and the other downstream of a main tailing pond of an ore refinement factory. Chemical analyses and chemical speciation of five heavy metals: Cu, Pb, Zn, Ag and as well as clay mineralogy, grain size distributions and total organic carbon of the soils, were investigated. Quartz, feldspars, illite, kaolinite and smectite are the common mineral phases. No principal heavy metal-bearing minerals were detected. Accumulation of heavy metals in the soils was obvious. The results of the speciation indicated that a significant quantity of the metals was accommodated in the structure of the minerals. Illite was the most abundant clay mineral in the area. However, it did not show any influence on the heavy metal distribution, nor did kaolinite. Instead, a positive correlation was observed between smectite and total contents of nearly all the heavy metals investigated. Contents of organic carbon showed also some relation to the distribution of the heavy metals while the grain size of the soils did not seem to have impact upon the heavy metal retention.

1 INTRODUCTION

Heavy metals are some of the main contaminants in the ecological system. Ore which contains heavy metals is the important pollution source (Alloway 1990; Bowell et al. 1999). The purpose of the present work was to investigate distribution of heavy metals in soils and their relationship with the soil phases, and to evaluate the potential pollution around one of the principal Chinese gold-silver mines.

The mine is located in a well cultivated and densely populated area of the prosperous Zhejiang Province, South-Eastern China. The mining history can be traced back for at least 400 years.

Its geological background consists of amphibolites facies metamorphic rocks forming the Proterozoic basement and of Late Jurassic intermediate to acid volcanic. The deposit is a low-sulphidation epithermal deposit with Au/Ag mineralization hosted by fine grained sulfides/tellurides in crustiform quartz/carbonate stockworks.

It is recognized that the virtual environmental impact of heavy metals depends not only on their total concentration but also on the physical and chemical forms they assume (Yong et al. 1992;

McBride 1994). Selective chemical extractions have hence been widely used in environmental sciences although it is understood that the interpretation of the extraction results is more "operationally defined" than a real speciation of the heavy metals (Tessier et al. 1979; Ure & Davidsen 2002). Single extraction with its advantages and limitations was employed by some scientists (Tack et al. 1996; Tack & Verloo 1999; Sutherland 2002; Dassenakis et al. 2003; Luo et al. 2003) it also was adopted in the present investigation.

2 MATERIALS AND METHODS

Two profiles of soil samples were taken, supplemented by a few randomly placed ones. One profile was situated about 20 meters downslope from an old ore-pit, the other was taken about 200 meters downstream of a main tailing pond and about 30 meters from the nearest village houses. The sample profiles started from the top soil and downward, comprising 4-5 samples. Each sample weighed about one kilogram, covering 10 cm of the profile thickness. Three samples were taken from the bottom of a dried tailing pond. A sample was collected from the stream bottom below the first

profile. Two reference samples were taken from a hill slope about 8 meters above the tailing pond. All samples were sealed in double layer plastic bags before further treatments.

The samples were oven-dried at 80°C overnight and plant roots and coarse pieces were sifted away. The sifted fraction was ground in agate mills for further analyses. Trace elements were analysed by ASS (flame and MH5-20). Mineralogy of the samples was analysed by XRD (Philips PW3710, automatic divergence slit, graphite monochromator and CuK α radiation in 40 kV and 40 mA). For clay mineralogy (<2 μ m), oriented specimens were made with a pipette to sediment the suspensions on glass slides. Semiquantitative estimation of clay mineralogy was done by integrating the area of the selected peaks of the respective clay minerals from the powder patterns using APD program and mineral intensity factors (Moore & Reynolds 1997).

Considering their many advantages, we adopted the single independent extractions corresponding to the well know 5 step sequential extractions (Tessier et al. 1979). The extraction method and the reagents used were same as that for sequential extraction detailed by Tessier et al. (1979) with small modifications. The assessing calculation was according to Tack et al (1996). The extraction types and the corresponding speciations are: (1) cation exchangeable (absorbed on surfaces and interlayer), (2) acid extractable (bound to carbonates), (3) reducible (bound to Fe- or Mn- oxides), (4) oxidizable (bound to organic matters) and (5) residual (the metals accommodated in the mineral structures). The extractions were duplicated and the average of the results was used. The extracts were analysed by ASS (flame and MH5-20) with external standards GFX to control the analytical quality.

3 RESULTS AND DISCUSSIONS

The mineralogy was rather uniform for all the samples which were dominated by quartz and feldspars. Importantly, no mineral phases of heavy metals were detected by XRD in all the samples. The absence of heavy metal phases was confirmed by electron microprobe analyses which failed to find any hot-spots with significant heavy metal concentration in back-scattered electron photographs of the investigated samples. The clay fraction (<2 μ m) (Fig. 1) comprised primarily illite, kaolinite and smectite with various concentrations.

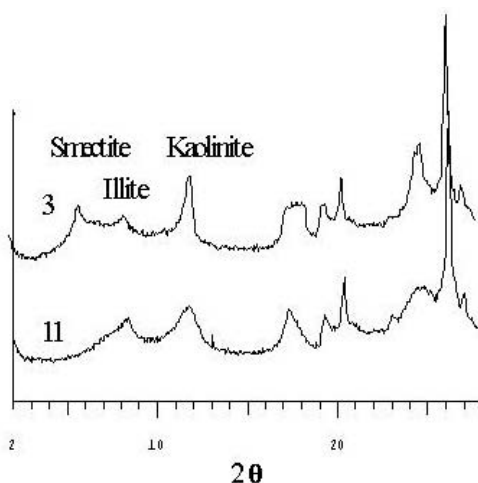


Figure 1. XRD of clay minerals.

The total concentration of the heavy metals and the fraction of residuals were shown in table 1 together with the other properties of the soil samples. For Pb, some negative numbers resulted from the calculation of the residual fraction; this is due to selectivity overlaps among of the extractants. Compared with the reference samples, accumulation of Ag, Cu, Pb, Zn and As in the first profile (downslope of the old mining pit) was obvious. The average contents of Cu, Ag Zn and As in the samples from profile 1 are about 2-4 folds of the reference sample, whereas Pb is over 7 fold. However, the contents of heavy metals in the profile 2 are close to the background values (except As). The As content is generally as high as 10 times that of the reference. However since the content of As in the tailing samples themselves is low in comparison to the reference, and the chemical speciation of the As suggested geogenic origin of the As in all samples from profile 2, the tailing pond could be excluded as the pollution source of As. A local As source has to be assumed instead.

Illite is the most abundant clay mineral in all the investigated samples but it did not exert any influence on the heavy metal distribution, nor did kaolinite. Instead, a positive relation was observed between concentration of smectite and the total contents of nearly all the investigated heavy metals (Fig.2). It is widely accepted that large surface area and high cation exchange capacity re responsible for high absorption of heavy metals on smectite (Spooner & Giusti 1999).

Relation of smectite and the heavy metals

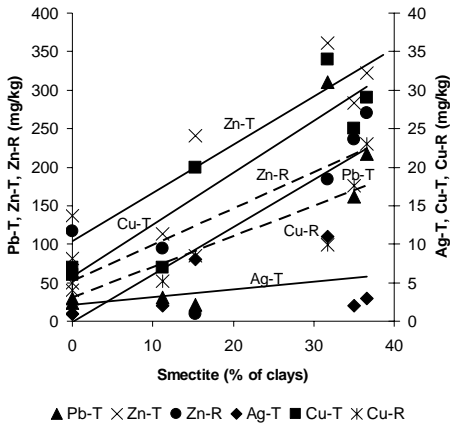


Figure 2. Relation of smectite and the heavy metals T- is total metal and R- is residual.

Table 1

Samples		1	3	5	7	9	11	14
TOC (%)		27.61	13.01		0.18	0.88	10.65	
<1 u (%)		6.25	8.20	9.09	1.56	8.32	8.70	7.07
<5u (%)		24.04	29.78	31.04	5.20	30.86	33.99	30.64
kao (%)		18	16	16	19	11	14	17
ill (%)		50	47	49	66	78	86	83
sme (%)		32	37	35	15	11	0	0
Total	Ag	11.00	3.00	2.00	8.00	2.00	1.00	1.00
(ppm)	Cu	34.00	29.00	25.00	20.00	7.00	7.00	6.00
Pb		310.00	217.00	162.00	21.00	31.00	29.00	24.00
Zn		361.00	322.00	283.00	241.00	113.00	82.00	137.00
As		13.00	12.00	12.00	1.00	3.30	36.00	39.00
Residual	Ag	6.90	1.95	1.50	7.30	1.65	0.50	0.45
(ppm)	Cu	9.90	23.00	17.55	8.55	5.15	4.95	4.00
Pb		-112.30	23.95	-40.35	-7.05	2.10	-16.50	-13.00
Zn		183.85	270.35	236.40	9.50	94.55	61.80	116.60
As		10.20	10.95	10.75	0.15	2.85	33.35	36.60

4 CONCLUSIONS

Quartz, feldspars, illite, kaolinite and smectite are the common mineral phases in the soils of the mining area. No mineral phases of heavy metals were present in detectable concentration. Accumulation of Ag, As, Zn, Cu and Pb was observed in the samples taken from downslope of the old mining pit; however chemical speciation revealed that generally only a minor portion of the heavy metals was easily extractable, i.e. with high mobility and bioavailability in the nature. The majority of the heavy metals were accommodated in mineral structures that are rather stable in the natural environment. Smectite had generally a high retention capacity for heavy metals. A significant quantity of the retained Zn and Cu in smectite was probably accommodated in the smectite structures or

associated secondary mineral. Fine particle sizes did not favour the retention of heavy metals while the organic matter in the investigated soils was active in retaining some types of the heavy metals.

However, this explanation seems not always satisfactory. For Zn and Cu, their residual fractions showed similar relationships with smectite as that of total content (Fig. 2, dashed lines) suggesting that the increase in heavy metals with the increase in smectite was not due to weakly "absorbed" metals on the surfaces or in the interlayer of smectite but was accommodated in the smectite structure (Zn) or as associated secondary mineral (Cu) so that it survived several severe chemical extractions. These concentrations were too low to be detected by XRD or microprobe. The contents of the heavy metals did not show any relation with the size distribution of the sample (Tab.1) what in a way supports this interpretation. The contents of total organic carbon (TOC) exert strong influence on the concentration of different cations as well. A positive correlation was found with Pb and As in fraction (4), Ag and Cu in fraction (3) and Cu and Zn in fraction (1).

associated secondary mineral. Fine particle sizes did not favour the retention of heavy metals while the organic matter in the investigated soils was active in retaining some types of the heavy metals.

5 REFERENCES

- Alloway, B.J. 1990. *Heavy metals in soils*. London: Blackie.
- Bowell, R.J., Williams, K.P., Connelly, R.J., Sadler, P.J.K., Dodds, J.E. 1999. Chemical containments of mine waste. In: Metcalfe, R. & Rochelle, C.A. (eds). *Chemical containments of waste in the geosphere*. Geological Society Special Publication n^o.157. London.
- Dassenakis, M., Andrianos, H., Depiazi, G., Konstantas, A., Karabela, M., Sakellari, A., Scoullas, M., 2003. The use of various methods for the study of metal pollution in marine sediments, the case of Euvoikos Gulf, Greece. *Applied Geochemistry*. 18: 781-794.

- Luo, Y., Jiang, X., Wu, L., Song, J., Wu, S., Lu, R., Christie, P. 2003. Accumulation and chemical fractionation of Cu in a paddy soil irrigated with Cu-rich wastewater. *Geoderma*. 115: 113-120.
- McBride, M. B. 1994. *Environmental Chemistry of Soils*. Oxford University Press. New York, Oxford. p. 308-341.
- Moore, D. M. & Reynolds, R. C. Jr. 1997. *X-ray diffraction and the identification of clay minerals*. Oxford University Press, Oxford, New York.
- Spooner, A. J. & Giusti, L. 1999. Geochemical interactions between landfill leachate and sodium bentonite. In Metcalfe, R. & Rochelle, C. A. (eds): *Chemical Containment of waste in the geosphere*. Geological Society Special Publication no.157. London.
- Sutherland, R.A. 2002. Comparison between non-residual Al, Co, Cu, Fe, Mn, Ni, Pb and Zn released by a three-step sequential extraction procedure and a dilute hydrochloric acid leach for soil and road deposited sediment. *Applied Geochemistry*. 17: 353-365.
- Tack, F. M. G., Vossius, H. A. H., Verloo, M. G. 1996. A comparison Between Sediment Metal Fractions, Obtained from Sequential Extraction and Estimated from Single Extraction. *Intern. J. Environ. Anal. Chem.* 63: 61-66.
- Tack, F. M. G., Verloo, M. G. 1999. Single extractions versus sequential extraction for the estimation of heavy metal fractions in reduced and oxidised dredged sediments. *Chemical Speciation and Bioavailability*. 11, 2, 43-50.
- Tessie, A., Campbell, P. G. C., Bisson, M. 1979. Sequential Extraction Procedure for the Speciation of Particulate Trace Metals. *Analytical Chemistry*. 51, 7, 844-851.
- Ure, A. M., Davidsen, C. M. 2002. *Chemical Speciation in the Environment*. Blackwell, Oxford.
- Yong, R. N., Mohamed, A. M. O., Warkentin, B. P. 1992. *Principles of Contaminant Transport in Soils*. Elsevier. 327p.

Salt Horizons – as Heavy Metal Barriers Within the Monofill for MSWI Residues

S.Heuss-Abbichler

Department of Earth and Environmental Sciences, Ludwig-Maximilians University, Munich, Germany

ABSTRACT: The residues of municipal solid waste incinerators (MSWI), e.g. bottom ashes and air pollution control (APC) residues, are a potential problem for the environment, due to their elevated contents of heavy metals and salts. APC residues, containing high amounts of soluble salts and heavy metals, are indeed classified as hazardous materials. Various solutions were developed to fix the soluble ecotoxic elements in primary or secondary reservoir minerals with low solubility. These solutions require the input of energy or additives, leading to extra costs. In a monofill for MSWI residues, however, the leachates show low concentrations of these components. A detailed study of borehole samples from this landfill revealed that a salt layer has developed at seven metres depth. The precipitation of various salts within this zone is caused by changed permeability conditions within the monofill. The concentration of the heavy metals exceeded the mean value in fresh MSWI residues. These observations indicate that soluble heavy metals may be trapped at a deliberately generated salt horizon and, this way, may reduce the total ecotoxic components output.

1 INTRODUCTION

The thermal treatment of municipal solid waste aims to reduce the waste volume and to produce inert materials. The organic contents of bottom ashes are less than 5 wt.-%. Nevertheless, several studies have shown that MSWI residues do indeed contain reactive materials. Elevated temperatures up to 80°C, observed only in monofills for bottom ashes, reflect the effect of exothermal reactions (Speiser 2001). The accumulation of hydrogen gas within a monofill for MSWI residues may result from hydration reactions of non-noble metals, especially aluminium, under alkaline conditions (Magel et al. 2002). In general it is assumed that most of the leachable heavy metals and salts are washed out within the first weeks. It has been recently suggested, however, that the period of desalting, and thus of elevated charge of the leachate, may be prolonged over months or several years (Hirschmann & Förstner 2000).

Leaching tests of fresh APC residues show high contents of soluble salts and heavy metals, such as lead. None the less, in the leachate of the monofill of Waldering in Bavaria, Germany, a landfill for MSWI residues only, the concentrations of these elements are much less than expected.

Analysis of a sample taken from a borehole in the monofill in 1995 revealed a high percentage of ettringite $\text{Ca}_6\text{Al}_2(\text{SO}_4)_3(\text{OH})_{12}\cdot 25\text{H}_2\text{O}$ (Picolab 1996). Because reservoir minerals like ettringite may incorporate heavy metals like copper, lead and zinc in their structure, it was suggested that their growth may maintain the leachate pollution at low levels.

2 OVERVIEW OF SIMULTANEOUS STUDIES

Lab experiments were carried out with APC residues of semi-dry injection processes (MSWI of Rosenheim). No reservoir minerals like ettringite were observed, even after 300 days of storage. Leaching tests (German Test DIN 38414-S4) showed unequivocally that this material has a low capacity to retain soluble components in newly formed reaction phases (Speiser et al. 2002).

Better results were obtained in lab experiments by mixing APC residues with aluminium-rich additives (Heuss-Abbichler et al. 2002), and the release of ecotoxic elements, like lead, were reduced.

Field tests were prepared with mixtures of APC residues and aluminium-rich additives like MSWI bottom-ashes and aluminium hydroxide sludge (a residue of anodization of aluminium). The reaction

progress of these materials was studied over a period of 28 months. The leachate from each of these fields was collected separately. The results show that the chloride content in the leachate was initially very low, but after two months exceeded 5 g/L. Wash-out of heavy metals was not observed during the first period, even though the pH value was above 10. However, lead was abruptly mobilized after five months disposal and concentrations up to 22 mg/L were obtained. Even after 2 years disposal, the discharge of Pb in the leachate was still around 10 mg/L.

These results are in contradiction with the low concentration of ecotoxic elements in the leachate, observed in the monofill. Other effects must therefore control the composition of the leachate.

3 ANALYTICAL METHODS

The chemical composition of the material was analyzed by means of X-ray fluorescence spectrometer (XRF Philips PW2400). Leaching tests of solid materials were carried out according to the German Test DIN 38414-S4. Heavy metal, chloride and sulfate concentrations of the leachate samples were measured by ICP-OES (Perkin Elmar Optima 3000). Phase analysis was conducted by X-Ray Diffraction (XRD, Siemens D5000).

4 RESULTS

4.1 Fresh APC residues and bottom ashes

The main elements of the APC residues and bottom ashes are shown in Table 1. The values obtained for other heavy metals in MSWI residues, are very low: Cr < 1050 ppm, Ni < 500 ppm, and Co, As, Cd < 60 ppm.

The values obtained in the leachates of the concomitant materials are also listed in Table 1. Fresh APC residues are alkaline (pH > 12). The high conductivity of the leachate (35 mS/cm) corresponds to high chloride contents (11.3 g/L). The concentration of soluble heavy metals varies: while high concentrations were obtained for Zn, Cu and Pb, the values for Cd (< 0.2 µg/L), As (< 2 µg/L), Ni (< 0.05 mg/L) and Cr (< 0.05 mg/L) were below the detection limit. In general, the concentrations in the leachate of bottom ashes are low. The chloride content is generally less than 500 mg/L.

Table 1. Main elements in fresh MSWI residues (APC residues and bottom ashes) and the elements determined in the leachate of the samples (*n.a.* not analyzed).

		APC residue		Bottom ash	
wt.-%	mg/L	wt.-%	mg/L	wt.-%	mg/L
Na ₂ O	Na	0.3	n.a.	3.4	n.a.
K ₂ O	K	0.2	n.a.	0.8	n.a.
CaO	Ca	58.7	n.a.	19.2	n.a.
MgO	Mg	2.0	n.a.	3.2	n.a.
Al ₂ O ₃	Al	1.7	n.a.	10.8	n.a.
Fe ₂ O ₃	Fe	2.3	n.a.	15.2	n.a.
SiO ₂	Si	6.0	0.2	34.6	0.5
Cl	Cl	13.4	11290	0.6	208
SO ₃	SO ₄	7.2	1365	2.0	120
Pb	Pb	0.6	78.7	0.3	18.3
Zn	Zn	2.1	5.1	0.7	1.7
Cu	Cu	0.1	0.4	1.0	0.9

4.2 Monofill

In the monofill, APC residues and bottom ashes (1:1 ratios) are deposited in layers. The ages range from 7 year at the top to 12 years at the bottom. A borehole with 300 mm diameter and 16.5 m length was constructed just beside the borehole of 1995 and samples were collected in 1 metre intervals.

4.2.1 Sample composition

The composition of the aged MSWI residues deviates from that of the fresh materials. In particular, the chlorine content shifts: APC residues at the top of the monofill exhibit low chlorine concentrations (< 0.8 wt.-%). The amount increases with increasing depth: at 7 m depth a maximum value of 16 wt.-% chlorine was measured. The concentration decreases again beneath this layer. At the bottom of the monofill 1 - 5 wt.-% chlorine was analyzed. The chlorine content of the altered bottom ashes varies between 2 and 5 wt.-%. The concentration of sulfur (SO₃) ranges between 1 and 4 wt.-%. The results are in good accordance with those of the borehole of 1995.

For heavy metals, in bottom ashes, high values were determined for samples at 4 m depth: Cu 14,200 ppm and Zn 59,800 ppm. Pb concentrations vary between 800 and 3000 ppm. In APC residues the values range for Cu between 600 and 1900 ppm, for Zn between 2900 and 7700 ppm and for Pb between 1500 and 2800 ppm.

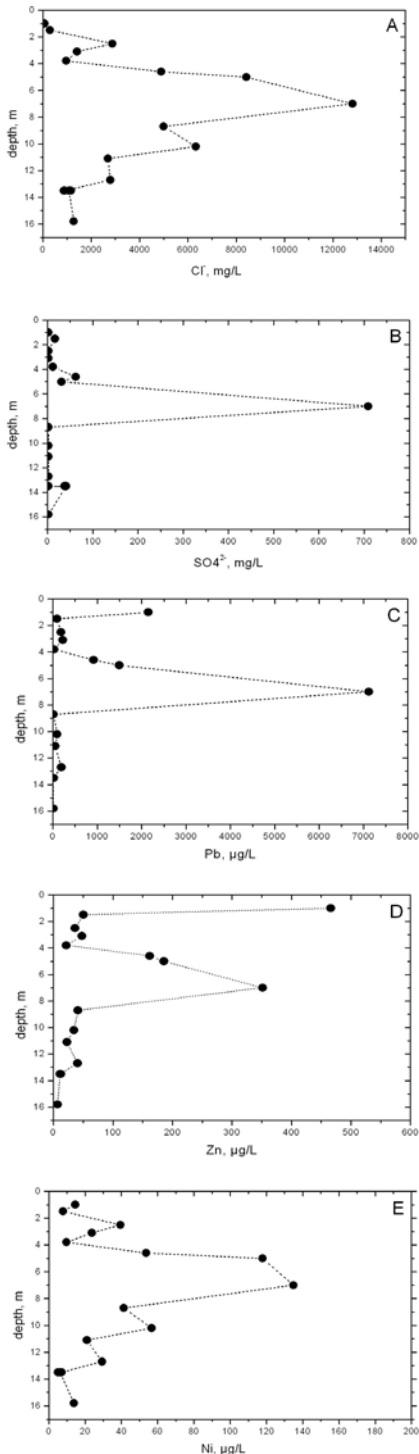


Figure 1: Concentration of chloride, sulfate and the heavy metals Pb, Zn, Ni, Cu and As in the leachate of borehole samples from the monofill Waldering, Bavaria

4.2.2 Chemical analysis of the leachate

The pH-value in the leachate of the samples varies between pH 12.3 and pH 11.5. The concentration of chloride in the bottom ashes ranges between 297 and 4990 mg/L. For the APC residues, only 70 mg/L chloride was determined in the upper zone (Figure 1a). With increasing depth, at 7 m, a maximum value of 12,800 mg/L was analyzed. The concentration decreases to 2790 mg/L in the lower zone of the monofill

The sulfate contents in the leachates of the solid phases are low, been less than 40 mg/L for bottom ashes and less than 60 mg/L for APC residue, with one exception: 700 mg/L was measured at 7 m depth (Figure 1b).

The concentrations of the heavy metals correlate with the chloride content (Figure 1 c – h). Elevated concentrations in the leachate of the uppermost sample were determined only for Pb (2 mg/L) and Zn (0.5 mg/L). The concentration of the heavy metals also increases with increasing depth. Maximum values were observed at 7 m depth: the measured concentrations were for Pb 7.1 mg/L, Zn 350 µg/L, Ni 140 µg/L, As 45 µg/L and Cr 85 µg/L. Note the low value for Cu (55 µg/L) observed at 7 m depth. Above this layer the concentration was 320 µg/L and below this zone 240 µg/L (Figure 1 f).

4.2.3 Mineralogical investigations

Phase analyses have shown high contents of salts, like halite NaCl, sylvine KCl and calcium chloride hydroxide CaClOH especially in samples taken from 5 up to 7 m depth. Furthermore, the concentration of gypsum $\text{CaSO}_4 \cdot 2\text{H}_2\text{O}$ and hydrocalumite $\text{Ca}_2\text{Al}(\text{OH})_6\text{Cl} \cdot 2\text{H}_2\text{O}$ is elevated. Remarkable bright blue aggregates, up to 5 mm diameter, have grown in aged APC residues stored in plastic buckets for 3 years.

5 DISCUSSION AND CONCLUSIONS

MSWI residues, especially APC residues, have a low storage capacity for heavy metals such as lead. Only part of the heavy metals is fixed in solid phases. Depending on water content and saturation conditions in the landfill, it may be mobilized, even after a longer ageing period.

Chemical and mineralogical investigations of the monofill samples show that a salt-rich layer has been developed within the landfill. In the leachate, the concentration of lead correlates with that of chloride. This indicates that lead is precipitated as a soluble solid phase on the pore surfaces. Even heavy metals like Zn, Cu, Ni and Cr, which were not analyzed in the leachate of fresh MSWI residues, are enriched within the salt rich zone. Note that even the concentration of As in the leachate exceeds the average contents of fresh APC residues by several orders of magnitude.

The porosity of five APC residues was determined. At 2.5 m, the sample has a porosity of 67 %, and at 5 m a porosity of 48 % was determined. Beneath this area the porosity is higher, varying at 53 %. At 13.5 m the porosity decreases again, being 43 %. Obviously the reduction of the porosity at 5 m is caused by the operation of heavy vehicles at civil works in the landfill.

The change in porosity is reflected in the water content of the samples: the APC residues show above 4 m and below 12 m high values up to 45

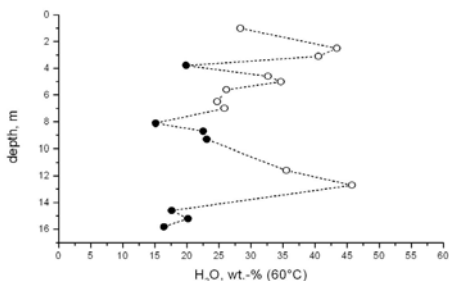


Figure 2: Water content (60°) of the APC residues (open circle) and bottom ashes (solid circle) of the monofill Waldering, Bavaria

wt.-% H₂O (Figure 2). Below 4 meters, however, the water content decreases. Between 5 and 9 m low values at about 25 wt.-% was determined. The lowest water content was measured for bottom ash at 8 m depth.

Obviously, the inhomogenities in the porosity of the materials induced the formation of a barrier within the monofill. The leachate cannot infiltrate homogenously and the elements mobilized by washing-out processes are accumulated. The salts may precipitate from the oversaturated solutions.

These results indicate that the salt layer may act as a filter system. To date, several solutions have been proposed to fix soluble ecotoxic elements within a deposit. The need for a high energy input and for additives turn these solutions unfeasible. According to this study, a deliberately generated salt horizon within the landfill may offer an effective and low cost method to inhibit the discharge of ecotoxic elements into the environment.

6 ACKNOWLEDGEMENTS

The results presented in this paper are part of a wider study supported by the Bavarian State Ministry for Regional Development and Environmental Affairs (projects E53 and F188). The author wishes to acknowledge Dr. G. Magel and Dr. C. Speiser for their helpful collaboration.

7 REFERENCES

- Heuss-Aßbichler, S., Speiser, C. & Spiegel, W. 2002. Lab- and field experiments of mixtures of APC residues of municipal solid waste incinerators and Al-rich additives. In: R02 - 6th World Congress on Integrated Resources Management, 6 pp., Geneva
- Hirschmann, G. & Förstner, U. 2000. Langzeitverhalten von Schlackedeponien, Hamburger Berichte 16, Deponietechnik 2000
- Magel, G., Unzeitig, H., Heuss-Aßbichler, S., Fehr, K. T. & Gerthner, F. 2002. Wasserstoffproduktion auf einer Deponie für MV-Rückstände. Müll und Abfall, 6, pp. 338 – 343
- Picolab 1995. Mineralogisch-chemische Untersuchung einer Bohrkernprobe der Monodeponie Waldering: Bindungszustand der Salze und Schwermetalle, LfU-Bericht, 44 pp.
- Speiser, C. 2001. Exothermer Stoffumsatz in MVA-Schlackedeponien: Mineralogische und geochemische Charakterisierung von Müllverbrennungsschlacken, Stoff- und Wärmebilanz. Dissertation, Technische Universität München, 261 pp.
- Speiser, C., Heuss-Aßbichler, S. & Spiegel, W. 2002. The significance of ettringite for the long-term stability of boiler ashes and gas cleaning residues of municipal solid waste incinerator. In: R02 - 6th World Congress on Integrated Resources Management, 6 pp., Geneva.

Porous Material with Zeolite and Carbide from Paper Sludge and the Application

H.Ishimoto, O.Sasaki, M.Yasuda

Access Network Service Systems Laboratories, Nippon Telegraph and Telephone Corporation, Ibaraki, Japan

T.Wajima, O.Tamada

Graduate School of Human and Environmental Studies, Kyoto University, Kyoto, Japan

ABSTRACT: The authors are promoting research and development to recycle the papermaking sludge discharged during the old paper recycling process, with the ultimate aim of achieving zero waste products (zero emissions). Thus far technology has been developed for converting the ash produced by incinerating papermaking sludge into Micro Porous Material (MPM), and some types of MPM have been applied as water purification materials. However, the amount of papermaking sludge discharged each year in Japan is said to be three million tons, and achieving zero emissions will be difficult if application is limited to water purification materials. Therefore, development to further expand the range of application for papermaking sludge is required. This study attempted the development of new MPM made from the base materials of papermaking sludge and papermaking sludge ash that can effectively purify water and adsorb gas. As a result, MPM containing hydroxy sodalite, zeolite A and zeolite P as zeolite types were successfully fabricated. In addition, materials containing the above zeolites and which also have a superior specific surface area were fabricated from papermaking sludge. These MPM exhibit characteristic properties in terms of specific surface area and cation exchange capacity, and application can be expected in the fields of water purification and gas adsorption.

1 INTRODUCTION

Japan's domestic reuse rate and recovery rate for old paper are 57.0% and 58.0% (both as of 2000), respectively, so Japan could be considered one of the most advanced countries in using old paper. However, the old paper recycling process also produces an industrial waste known as papermaking sludge (PS) which cannot be reused as paper. PS consists of paper fiber components which have become too short due to repeated recycling and clay components used to ensure a smooth paper surface. While some of PS is reused in cement materials or for other applications, most is still incinerated and disposed of in sanitary landfills. Therefore, the development of technology for effectively reusing PS is required.

The authors have developed a new material called "Micro Porous Material (MPM)" that makes use of the fiber and clay components of PS as one technology for reusing PS, and some of these MPM have been practically applied as water purification materials (Ishimoto & Yasuda, 1997; Ishimoto et al. 2000; Ishimoto et al. 2003). Figure 1 shows the concept for a total paper recycling system using MPM.

This paper introduces the results of attempts to generate MPM with varied characteristics from PS and papermaking sludge ash (PSA) with the aim of application to even more diverse fields.

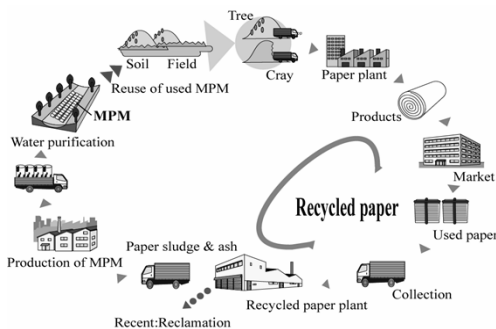


Figure 1 Total recycling design for paper by MPM

2 MPM BASE MATERIALS PS AND PSA

Currently, most PS is incinerated to PSA at incineration facilities.

The composition, cation exchange capacity of Na (hereafter CEC) and specific surface area of the PS

and PSA used in this study are shown in Table 1, the SEM photograph and the XRD waveforms of PS in Fig. 2(a), those of PSA in Fig. 2(b).

Table 1. Composition, CEC and Surface area

	Composition(%)					CEC (cmol/kg)	Surface Area(m ² /g)
	C	Na	Al	Si	Ca		
PS	24	0.1	5.9	7.1	8.6	15	8.2
PSA	1.8	0.2	11	14	17	7.3	10.8

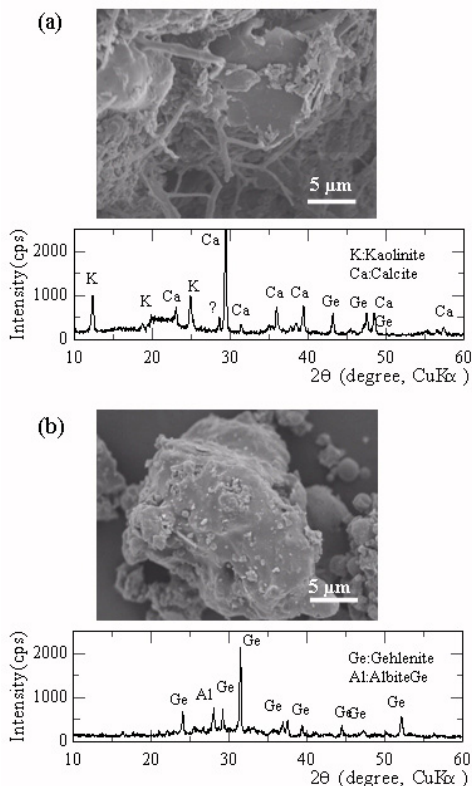


Figure 2. SEM and XRD : (a) PS , (b) PSA.

During the process of incinerating PS to PSA, the kaolinite ($\text{Al}_2\text{Si}_2\text{O}_5(\text{OH})_4$) used to smooth the paper surface and the calcite (CaCO_3) added to increase the whiteness melt at the high temperature and then crystallize into globular gehlenite ($\text{Ca}_2\text{Al}_2\text{SiO}_7$). Gehlenite once crystallized it is extremely difficult to melt again.

3 MPM MADE FROM PSA

3.1 Hydrothermal Synthesis Reaction

The Japanese papermaking process is systematized up to the point where PS is incinerated into PSA. Therefore, the effective use of PSA was first investigated.

As shown in Table 1, the main components of PSA are Si, Al and Ca, and of these, zeolite can be synthesized by using the Si and Al. Therefore, hydrothermal synthesis was performed under the following conditions.

- Temperature: 80°C
- Time: 15 hours
- Solution: 3 mol/l NaOH
- Solid to liquid ratio: 1:4

Figure 3(a) shows the SEM photograph and the XRD waveform of the material generated. Some hydroxy sodalite ($\text{Na}_4\text{Al}_3\text{Si}_3\text{-OH}$) peaks can be confirmed from the XRD waveform, and the SEM photograph shows that minute crystals on the order of several hundred nanometers have formed on the surface (hereafter "PSA-ZHS"). Measurements of CEC of PSA-ZHS showed the relatively high value of 110 cmol/kg. Also, the specific surface area was not so high at 28.8 m²/g, so PSA-ZHS can be used mainly as a water purification material.

However, the XRD waveform clearly shows a gehlenite peak and the crystals visible in the SEM photograph are minute, indicating that only a part of the Si and Al contained in the PSA have been converted into zeolite. This is thought to be due to the two factors that the gehlenite is an extremely difficult to dissolve format, and that there was insufficient Si supply relative to Al. Therefore, countermeasures were attempted for these factors. For the former, the Ca in the gehlenite was removed through a neutral reaction with a strong acid to transform the gehlenite into an easily dissolved format. For the latter, the Si was eluted from diatomite which contains large amounts of Si, and this solution was then used as the reaction fluid.

3.2 Hydrothermal Synthesis Reaction after Acid Treatment

The acid treatment conditions are as follows (Wajima et al. 2003).

- Temperature: 20°C
- Time: 1 hour
- Solution: 1 mol/l HCL
- Solid to liquid ratio: 1:10

Following acid treatment, the solid and liquid were separated by suction filtering, and the solid was washed thoroughly using distilled water and then dried. Hydrothermal synthesis was then performed on that solid under the following conditions.

- Temperature: 80°C
- Time: 15 hours
- Solution: 3 mol/l NaOH
- Solid to liquid ratio: 1:4

Figure 3(b) shows the SEM photograph and the XRD waveform of the material generated. Zeolite A ($\text{Na}_{12}\text{Al}_{12}\text{Si}_{12}\text{O}_{48}\cdot\text{H}_2\text{O}$) peaks can be confirmed from the XRD waveform, and the SEM photograph clearly shows the formation of cubical crystals approximately 1 to 2 μm in size (hereafter "PSA-ZA"). PSA-ZA has a CEC of 310 cmol/kg and a specific surface area of 30.7 m²/g. Although the specific surface area does not differ greatly from PSA-ZHS, the CEC has increased to approximately three times that of PSA-ZHS, indicating that PSA-

ZA can be used as an even higher performance water purification material.

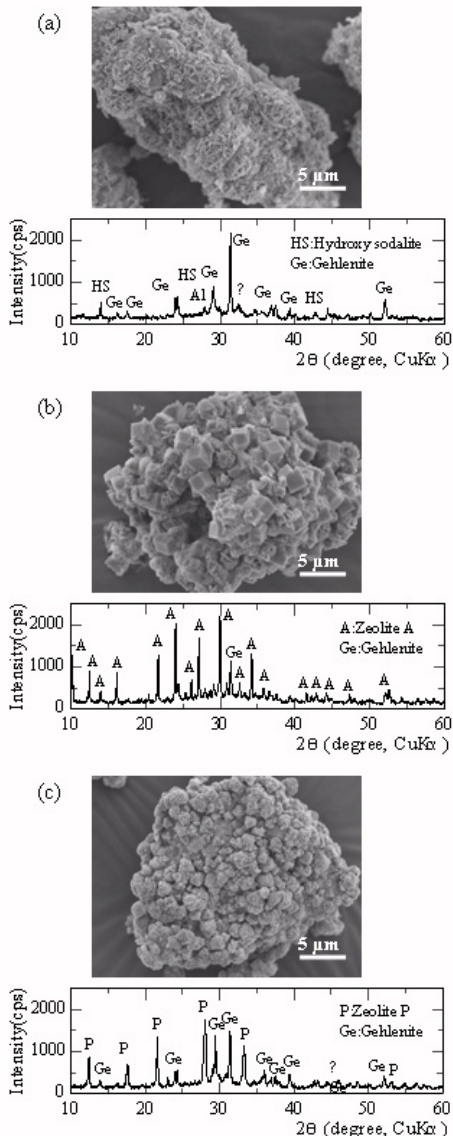


Figure 3. SEM and XRD : (a) PSA-ZHS , (b) PSA-ZA , (c) PSA-ZP.

3.3 Hydrothermal Synthesis Reaction Using a Diatomite Effluent

A diatomite-based effluent was prepared under the following conditions.

- Temperature: 80°C
- Time: 1 hour
- Solid: Diatomite

- Solution: 3 mol/l NaOH
- Solid to liquid ratio: 1:4

The solid and liquid were separated by filtering, and the solution was collected and used as the reaction fluid for hydrothermal synthesis under the following conditions.

- Temperature: 80°C
- Time: 15 hours
- Solution: Diatomite effluent
- Solid to liquid ratio: 1:4

Figure 3(c) shows the SEM photograph and the XRD waveform of the material generated. Zeolite P ($\text{Na}_6\text{Al}_6\text{Si}_{10}\text{O}_{32}\cdot\text{H}_2\text{O}$) peaks can be confirmed from the XRD waveform, and the SEM photograph shows the formation of countless crystals approximately 1 μm in size (hereafter "PSA-ZP"). PSA-ZP has a CEC of 200 cmol/kg and a specific surface area of 70.1 m^2/g . Both the CEC and the specific surface area have increased to approximately twice that of PSA-ZHS. In addition to use as a water purification material, PSA-ZP also has a surface area that can be expected to allow use as a gas adsorbent, which allows use over a relatively wide range of fields.

4 MPM MADE FROM PS

The results described above clearly show that MPM with a CEC that is mainly effective for water purification can be produced using PSA as the base materials. However, when PSA is used as the starting material, the fiber component of the PS cannot be used.

Therefore, the PS was carbonized to increase the surface area of the fiber component, and then hydrothermal synthesis was performed. The carbonizing conditions are as follows.

- Temperature: 650°C
- Time: 3 hours
- Atmosphere: N_2

The carbide is referred to hereafter as PSC. Three patterns of processing were carried out using this PSC in the same manner as PSA.

4.1 Hydrothermal Synthesis Reaction

Hydrothermal synthesis was performed on PSC under the same condition of section 3.1.

Figure 4(a) shows the SEM photograph and the XRD waveform of the material generated. Some hydroxy sodalite peaks can be confirmed from the XRD waveform, and the SEM photograph shows the formation of crystals on the surface (hereafter "PSC-ZHS"). PSC-ZHS has a CEC of 85 cmol/kg or slightly less than PSA-ZHS which also contains hydroxy sodalite, but the specific surface area has increased by more than three times to 98.1 m^2/g . The specific surface area is relatively large, so use of PSC-ZHS can be expected mainly for gas purification rather than water purification.

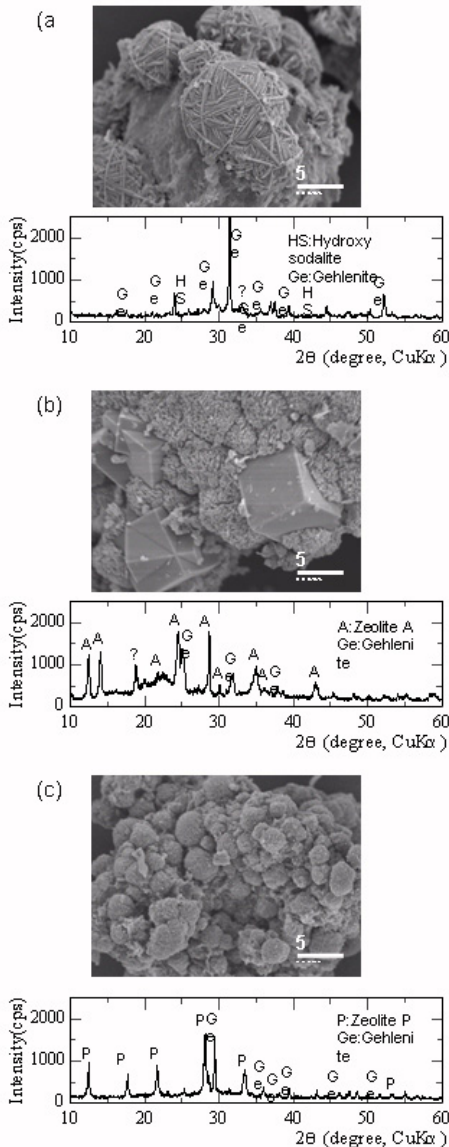


Figure 4. SEM and XRD: (a) PSC-ZHS, (b) PSC-ZA, (c) PSC-ZP

4.2 Hydrothermal Synthesis Reaction after Acid Treatment

The acid treatment conditions and hydrothermal synthesis are as same as section 3.2.

Figure 4(b) shows the SEM photograph and the XRD waveform of the material generated. Zeolite A peaks can be confirmed from the XRD waveform, and the SEM photograph shows the formation of cubical crystals 5 μm or more in size (hereafter

"PSC-ZA"). PSC-ZA has a CEC of 190 cmol/kg and a specific surface area of 87.5m²/g. As expected the CEC is lower but the specific surface area has increased compared to PSA-ZA. Both the CEC and the specific surface area are relatively high, so PSC-ZA can be used over a wide range of fields.

4.3 Hydrothermal Synthesis Reaction Using a Diatomite Effluent

Making condition of a diatomite-based effluent and hydrothermal synthesis are as same as section 3.3.

Figure 4(c) shows the SEM photograph and the XRD waveform of the material generated. Zeolite P peaks can be confirmed from the XRD waveform, and the SEM photograph shows the formation of countless rough, minute crystals (hereafter "PSC-ZP"). PSC-ZP has a CEC of 230 cmol/kg and a specific surface area of 71.6 m²/g. Both the CEC and the specific surface area are relatively high values, so use is expected both as a water purification material and a gas adsorbent.

5 SUMMARY

- Three patterns of processing were carried out using PSA as the base materials. These patterns were: 1.Hydrothermal synthesis, 2.Hydrothermal synthesis after acid treatment, 3.Hydrothermal synthesis using a diatomite effluent. As the result, three types of MPM : concluding hydroxy sodalite, zeolite A, zeolite P. These MPM have CEC of 85, 310, 200 cmol/kg and surface area of 28.8, 30.7, 70.1 m²/g each. These MPM mainly can be expected as water purification materials.

- Three patterns of processing were carried out using PS as the base materials. As the result, different types of MPM containing hydroxy sodalite, zeolite A and zeolite P could also be generated. And these MPM have CEC of 85, 190, 230 cmol/kg and surface area of 98.1, 87.5, 71.6 m²/g each. These MPM mainly can be expected as water purification and gas adsorption materials.

6 REFERENCES

- Ishimoto H. & Yauda M. 1997. Technology for Converting Papermaking Sludge into Micro-porous Crystal Materials. NTT REVIEW Vol.9 No.4 , 51-56.
- Ishimoto H. et al. 2000. Use of Papermaking Sludge as New Material. Journal of materials in civil engineering ASCE Novenver 2000 , 310-313.
- Ishimoto H. et al. 2003. Application of New Materials from Paper Recycling for Purifying Domestic Wastewater. NTT REVIEW Vol.15 No.1 , 43-47.
- Wajima T. et al. 2003. Zeolite Synthesis from Paper Sludge Ash at Low Temperature. The Japan / Korea International Symposium on Resources Recycling , 173-178.

Transformation of Technogenic Soot on the Earth Surface

T.Moroz

United Institute of Geology, Geophysics & Mineralogy, Novosibirsk, Russia

E.Shcherbakova & G.Korablev

Institute of Mineralogy, Miass, Russia

ABSTRACT: In regions where the atmosphere has been polluted as a result of human industrial activity the rock surface weathering leads to specific formations non-typical of pre-industrial time. Near Karabash (the South Ural, Russia) the exposures of magmatic and metamorphic rocks have been covered by dense black crust with thickness to 0.7 mm. The sulphate-carbonaceous composition of the crust as well as its localization make it possible to connect its formation to acidic sulphate-soot emissions of the Karabash metallurgical plant. The thickest crust is developed on lizardite serpentinites exposed quite near the source of emissions. Raman spectroscopy was used to provide structural characterization of carbonaceous component from the crust so as from primary aerosol soot. It has been shown that the carbon-rich phases have various degrees of graphitization and different carbon forms. In comparison with primary aerosol soot, content of graphite is increased in the black crust. It seems that metals of iron group (Fe, Co, Ni) may be catalysts of graphitization process.

1 INTRODUCTION

In the old European cities, phenomenon of formation of specific black crust (black patina) of the sulphate-carbonaceous composition on the walls of the stone buildings and monuments are well known (Marszalek 2000; Matovic & Vashkovic 2000; Posfai & Molnar 2000). The similar crusts very often cover the exposures of various rocks in regions where the atmosphere has been polluted as a result of human industrial activity. In both cases, these crusts are formed as a result of deposition from the atmosphere of the sulphate-soot aerosol and its following interaction with an open surface of solid substance.

Composition and structure of primary soot particles produced to the atmosphere as a result of incomplete combustion of fossil fuel or vegetation have been studied in detail (Posfai & Molnar 2000). On the other hand, numerous papers have been devoted to study of carbonaceous materials from the natural geological formations (Beyssak et al. 2002; Buseck & Huang 1985; Pasteris & Wopenka 1991; Wopenka & Pasteris 1993). Nevertheless, the products of transformation of emissional soot have not been studied practically until now. We made an attempt to fill this gap using the Raman

spectroscopy to research the products of soot transformation from the black crust that covers the exposures of various magmatic and metamorphic rocks near Karabash, one of the oldest centres of the copper metallurgy of the South Ural, Russia.

2 ENVIRONMENTAL INFLUENCE OF THE KARABASH METALLURGICAL PLANT

History of the Karabash Metallurgical Plant (KMP) goes back to 1907 when the copper deposits began to be processed there. Thus its influence to environment is in progress almost a hundred years. At present, the KMP includes numerous mines, concentrating mill, and copper-melting works.

In the emissions of the KMP, the soot content is variable from 6 to 42 %. SO₂ content is changed to 47 – 93 %. Owing to high air humidity, SO₂ is transformed to H₂SO₄ and the aerosol deposited from the atmosphere to solid rocks will consist mainly of sulphuric acid and soot. The acid aerosol component slowly interacts with the rock surface and the soot component takes a role of a compress keeping an acid on the open surface of the rock exposure. Thus, as a result of this process, the dense black crust of sulphate-carbonaceous composition

with thickness to 0.7 mm is formed on the exposures of magmatic and metamorphic rocks. It is known that the greater the SiO₂ content of a rock the greater the resistance to sulphuric acid (Jambor et al. 2000). Therefore, among the Karabash rocks, ultramafites (lizardite and antigorite serpentinites) are the most unstable, followed by mafites (gabbro-amphibolites) with quartz-containing rocks (granite-gneiss) affected least. The serpentinite surface is completely covered by black crust but in amphibolite and granite-gneiss exposures it is clearly seen that black crust is developed on feldspars and melanic minerals (amphiboles, black micas) but quartz grains are not changed. The thickest crust is developed on lizardite serpentinites exposed quite near the source of emissions.

Sulphates in the black crust form very thin light-coloured veinlets or rimes making a boundary between the rock and the black crust. On serpentinites, sulphate veinlets consist of epsomite and its dehydration products MgSO₄ × nH₂O where n = 1 – 7.

3 RAMAN SPECTROSCOPY OF TECHNOGENIC CARBON

Raman spectroscopy is a standard nondestructive technique for the characterization of crystalline, nanocrystalline, and amorphous carbons (Tuinstra & Koenig 1970, Ferrary & Robertson 2000, Kawashima & Katagari 1995). The Raman spectra of carbonaceous component from the black crust so as from primary aerosol soot were measured in right-angle scattering geometry using Jobin Ivon spectrometer RAMANOR U1000. Exciting was performed with 514.5 nm line of Ar ion laser using cylindrical focalized lens for the heat decrease. Photon detection was by single-channel analysis, with an photomultiplier tube that was thermoelectrically cooled. KBr pellet technique also applied. The spectrum of carbon-rich material from the lizardite serpentinites (sample 830/4) is presented in the Figure 1.

The first-order Raman line of graphite was observed at 42 and 1581 cm⁻¹ (G peak) (Kawashima & Katagari 1995). The first-order spectrum of microcrystalline graphite showed additional bands at about 1350 and 1600 cm⁻¹ not observed in single graphite crystal. These additional bands become observable not only in microcrystalline graphite but also in the defect-rich graphite due to the breakdown of translational and local lattice symmetries. The theoretical visible Raman spectra of amorphous carbon present a broad feature between 1200 and 1700 cm⁻¹ associated with sp² stretching as found in experiments (Profeta & Mauri 2001). Raman spectroscopy with the 514.5 nm wavelength of the incident laser beam is much more sensitive to sp²

than sp³ carbon hybridisation. In disordered graphite, nanocarbon and sp² carbon materials the disordered-induced Raman D peak has been observed around 1350 cm⁻¹. The empirical correlation between the intensity ratios R = I_D/I_G has been used as a measure of the concentration of lattice defects present in the graphite structure (Lespade et al. 1982). Characteristic feature of the D-band is that relative intensity of the G-band increases with increasing disorder and decreasing crystallite size (Ferrary & Robertson. 2000). The general shape of the first-order spectrum can be used as a good metamorphic-grade indicator (Pasteris & Wopenka 1991; Wopenka & Pasteris 1993, Beyssak et al. 2002).

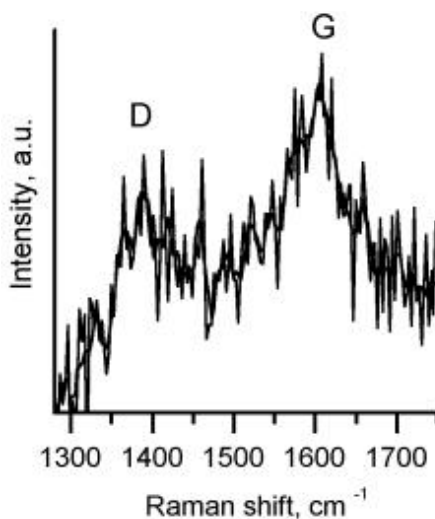


Figure 1: The first-order Raman spectrum of developed on lizardite serpentinites carbon-rich thickest crust with 514.5 nm incident radiation.

In the carbonaceous particles from the Karabash serpentinites rocks G peak is broader and is shifted to about 1600 cm⁻¹. In this poorly organized sample, it was impossible to separate the contributions of the D' (about 1620 cm⁻¹) component from that of the G band. The broadening of the graphite characteristic band (G peak) can be interpreted as the influence of the disorder in the graphite plane. The D peak of the sample is also broad and shifted to higher wavenumber. It has the shoulder at about 1330 cm⁻¹. The results observed can be explained by the formation of new carbon phases of a mixture of tetrahedral (sp³) (peak at 1330 cm⁻¹) and trigonal (sp²) (peaks at about 1380 and 1600 cm⁻¹) bonding structures. The 1380 cm⁻¹ band can be interpreted as A_{1g} mode, which becomes Raman active due to the

finite crystal size (Tuinstra & Koenig 1970). This peak arises when the crystallite size of the graphite decreases below some minimum value; its development is therefore a reliable indicator of the degree of disorder in the carbonaceous material (Lespade et al. 1982).

For the comparison of Raman data with the correlation curve between specific area of D peak (approximated by $[D/(D+G)]*100$) from original data by Wopenka & Pasteris (1993), we performed decompositions of spectrum using conventional fitting methods. The profile used for each band is a Lorentz (average approximation by two Lorentzian curves), and Voigt functions (with 1382, 1457, 1519, 1574, 1603 band positions).

The value G band position, G band width (full width at half maximum FWHM ≈ 50 , for Voigt functions), D/G intensity ratio (about 0.99) and $[D/(D + G)]*100$ integrated area ratio (60 for Lorentz and 53 for Voigt curves) both in the first, and second cases have similar values and correspond to a low degree of a metamorphism.

4 CONCLUSIONS

As stated above, the carbon-rich phases have various degrees of graphitization and different carbon forms. In comparison with primary aerosol soot, content of graphite is increased in the black crust. Raman parameter $R = 1.2$ is characteristic of the black crust from lizardite serpentinites exposed quite near the KMP. The similar values of R have been established for natural carbonaceous material from the rocks transformed under conditions of the lowest metamorphic stages (Wopenka & Pasteris 1993; Kribek et al. 1994). For lack of high temperature or pressure necessary for graphitization of natural carbonaceous materials (Beyssak et al. 2002; Pasteris & Wopenka 1991; Wopenka & Pasteris 1993;), metals of iron group (Fe, Ni, Co) may be catalysts of graphitization of technogenic soot on the Earth surface. The structure of underlying rock may play a role of catalyst too. It is known that the ions of various metals may be introduced between the graphitic layers of soot. Therefore the heavy metals from the emissions of the KMP may be partially kept off in the black crust and negative environmental influence of the KMP may be decreased in that way.

This work is supported in part by the Siberian Branch of Russian Academy of Sciences project No. 6.4.1.

5 REFERENCES

- Buseck, P. & Huang, Bo-Jun. 1985. Conversion of carbonaceous material to graphite during metamorphism. *Geochim. Cosmochim. Acta.* 49: 2003 - 2016.
- Beyssak, O., Rouzaud, J.-N., Goffe, B., Brunet, F. & Chopin, C. 2002. Graphitization in a high-pressure, low-temperature metamorphic gradient: a Raman microspectroscopy and HRTEM study. *Contrib. Mineral. Petrol.* 143: 19 - 31.
- Jambor, J.I., Blowes, D.W. & Ptacek, C.J. 2000. Mineralogy of mine waste and strategies of remediation. In: *Environmental Mineralogy /EMU Notes in Mineralogy.* 2: 255 - 290.
- Ferrary, A. & Robertson, J. 2000. Interpretation of Raman spectra of disordered and amorphous carbon. *Phys. Rev. B.* 61: 14095 - 14107.
- Kawashima, Y. & Katagari, G. 1995. Fundamentals, overtones, and combinations in the Raman spectrum of graphite. *Phys. Rev. B.* 52: 10053 - 10059.
- Kribek, B., Hrabal, J., Landais, P. & Hladikova, J. 1994. The association of poorly ordered graphite, coke and bitumens in greenschist facies rocks of the Ponikla group, Lúgicum, Czech Republic: the result of graphitisation of various types of carbonaceous matter. *J. metamorphic Geol.* 12: 493 - 503.
- Lespade, P., Al-Jishi, R. & Dresselhaus, M.S. 1982. Model for Raman scattering from incompletely graphitized carbons. *Carbon.* 20: 427 - 431.
- Marszałek, M. 2000. Soiling of stone monuments: mineralogical and chemical analyses of dark surficial layers (castles around Krakow in Poland). *Acta Mineral. Petrograph.* XLL: 49.
- Matovic, V & Vashkovic, N. 2000. Environmental influence on stone monument «OSLOBODIČINA BEOGRADA 1944». *Acta Mineral. Petrograph.* XLL: 52.
- Pasteris, J.D. & Wopenka, B. 1991. Raman Spectra of Graphite as indicators of degree of metamorphism. *Can. Mineral.* 29: 1 - 10.
- Posfai, M. & Molnar, A. 2000. Aerosol particles in the troposphere: a mineralogical introduction. In: *Environmental Mineralogy /EMU Notes in Mineralogy,* 2: 197 - 252.
- Profeta, M. & Mauri, F. 2001. Theory of resonant Raman scattering of tetrahedral amorphous carbon. *Phys.Rev. B.* 63: 245415.
- Tuinstra, F. & Koenig, J.L. 1970. Raman spectra of graphite. *J. Chem. Phys.* 53: 1126 - 1130.
- Wopenka, B. & Pasteris, J.D. 1993. Structural characterization of kerogens to granulite-facies graphite: Applicability of Raman microprobe spectroscopy. *Amer. Mineral.* 78: 533 - 557.

Asbestos Characterization from Brazil and their Effects in Mine Workers Health

M.C.B.Oliveira

Instituto de Pesquisas Tecnológicas, Divisão de Geologia, Cidade Universitária, São Paulo, Brazil

J.M.V.Coutinho

Departamento de Mineralogia e Petrologia, Instituto de Geociências, Universidade de São Paulo, São Paulo, Brazil

E.Bagatin & S.Kitamura

Departamento de Medicina Preventiva e Sócial, Faculdade de Ciências Médicas, Universidade Estadual de Campinas, São Paulo, Brazil

ABSTRACT: The asbestos ore from Minaçu is made up of serpentine minerals, mainly chrysotile, present both in matrix and in veinlets, which cut the serpentinite body. Chrysotile occurs in sub-millimetric to millimetric silky, flexible and lustrous fibers. In the asbestos ore of the São Felix do Amianto, serpentine minerals, mainly chrysotile, predominate in serpentine matrix and in veinlets. Minerals of the amphibole group, such as tremolite and tremolite-actinolite were detected in the mine area. Tremolite-actinolite appears as needle-shaped crystals as well as asbestos. Asbestiform tremolite occurs in straight and sharp-pointed fibers. The health effects observed among 4,220 asbestos mine workers submitted to clinical examination, conventional chest radiography, spirometric measurements and assessment of occupational exposure were related with the pleural and pulmonary diseases. The objective of the study was to estimate the morbidity of asbestos related diseases among mine workers. The progressive improvement in the workplace conditions is likely to be related to a significant decrease in the morbidity of those workers.

1 GEOLOGY

1.1 Asbestos from Minaçu

The Cana Brava mine situated in the county of Minaçu, Goiás, accounts for nearly all the Brazilian asbestos production. It was opened in serpentinites from the so-called Cana Brava Complex, which is an anorogenic stratiform mafic-ultramafic body formed by fractional crystallization of a olivine-tholeiite magma (Correia 1994). Field relationships indicate that the parental magma intruded a volcano-sedimentary sequence previously deformed and metamorphosed. The magma crystallized at pressures below 7 Kbar and was emplaced at about 2.0 Ga in extensional environment related to a crustal rifting. Metamorphism and deformation occurred at about 1.3 Ga and converted the igneous sequence amphibolite, metawebsterite and metagabbro from bottom to top.

Serpentinites are now found as lenses intermingled with unchanged parent rocks. They developed between 400-600 Ma in two phases of hydrothermal processes acting on the metabasic and metaultrabasic rocks.

The first, oxidizing phase promoted the production of antigorite and/or lizardite plus hematite in "type 1", brown serpentinite. During the

second, reducing phase, chrysotile was formed inside distensive fractures of "type 2", green serpentinite.

Petrographical, mineralogical and technological studies were carried out on more than a hundred samples of rock and fibers (Oliveira 1996).

The brown serpentinite (type 1) contains frequent reliquiar olivine and pyroxene together with antigorite and/or lizardite, some chrysotile and opaque minerals (hematite and magnetite). Such composition causes the host rock to become more resistant to mechanical stresses.

The green serpentinite (type 2) does not contain minerals from the mother rock. Chrysotile is the main serpentine and the chief opaque mineral is magnetite.

Chrysotile is present also in veinlets, which cut the serpentinite body, it occurs in sub-millimetric to millimetric silky, flexible and lustrous fibers (Fig. 1)

Chrysotile was the only asbestos mineral found in the two types of serpentinite from Cana Brava mine.

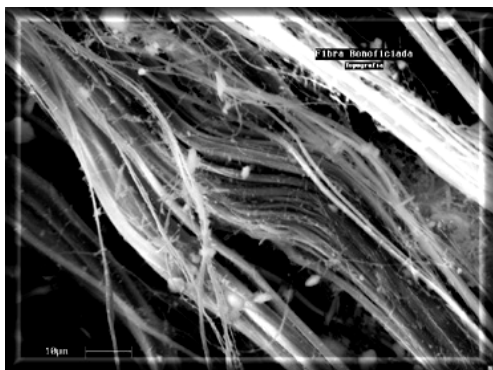


Figure 1: Backscattered electron microscopy image. Chrysotile gently curved fibres bundle showing a flexible appearance.

1.2 Asbestos from São Félix do Amianto- BA

The deposits from São Felix do Amianto (Bom Jesus da Serra county), in Bahia, was mined from the 1930's until 1967 for the extraction of the chrysotile asbestos.

The serpentinite levels are found in the lower unities of an Archean granulitic complex. The host rocks: garnet enderbite and charnoenderbite are associated with gabbronorites and pyroxenites of possible komatiite affiliation.

The asbestos mineralization is shaped as 1-5 cm. Thick irregular "cross" on "slip-fiber" chrysotile veins and lenses dispersed or concentrated along shear zones that cut green, fine-grained, frequently silicified serpentinites. Oliveira & Coutinho (1999) made the x-ray diffractometric and microscopic studies of 23 samples from São Felix do Amianto. They had in mind the possible detection of amphibolic asbestos. In two samples the mineral was present (Fig. 2).

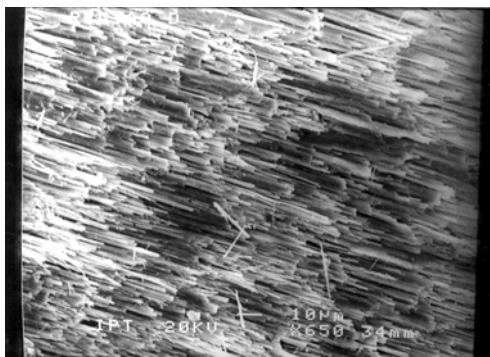


Figure 2: Backscattered electron microscopy image. Tremolite bundles showing an unflexible and a needle-like appearance.

One sample presented a sheaf of centrimetric tremolite fibers formed, possibly in a shearing zone. The tremolite displays elongated habit, with aspect-ratio from 40:1 to 50:1, that, as stated by EPA (1993) configure asbestiform mineral.

The second sample was collected in a calc-silicate band interbedded with serpentinites. It consist of bundles of prismatic or sometimes micrometric needles and fibers of tremolite-actinolite, with aspect-ratios of 20:1 to 30:1, characterists of asbestiform minerals (EPA 1993).

They were found associated with chlorite and were probably formed by hydrothermal alteration of diopside.

2 ASBESTOS AND MINE WORKERS HEALTH

A high number of asbesto studies concerning incidence and prevalence of all kinds of asbestosis is available in the literature (NIOSH 1992).

This peculiar situation of asbestos exploration in Brazil deemed to us as particularly suitable for the evaluation of the effects of such improved working conditions upon the respiratory health. No previous study has specifically looked at the longitudinal consequences of beneficial changes on environmental work conditions in a large cohort of miners and millers from developing countries (EPA, 2001). This was the first epidemiological study in Brazil aimed to evaluate and follow the relationship between radiographic evidence of parenchymatous and/or pleural disease and pulmonary functional abnormalities among asbestos miners and millers, taking into account the progressive changes in occupational exposure to asbesto fibers. (Bagatin 2000).

2.1 Methods

2.1.1 Subjects

The study group comprised all workers and ex-workers of a single asbestos mining and milling company (S.A.M.A. SA) who have been exposed from 1940 to 1996.

2.1.2 Measurements

- Occupational and Smoking History:

A standardized occupational history was obtained for each subject, detailing the start and end of exposure, the specific workplace(s) and the estimated level of exposure (Finish Inst. Occup. Health 1997).

- Radiographic Evaluation

Standard high-kilovoltage, posteroanterior chest radiographs were performed on a single center

before the physiological evaluation. Radiographs were classified according to the ILO Classification of Radiographs of Pneumoconiosis (ILO 2000).

-Spirometry

Spirometric tests were performed with a calibrated pneumotacograph (Fleisch No. 3). The subjects completed at least three acceptable maximal forced expiratory maneuvers: technical procedures, acceptability and reproducibility criteria were those recommended by the American Thoracic Society.

3 RESULTS

3.1 Population Characteristics

From the 10157 eligible subjects, 4220 were evaluated (41.5 %). Rate of recruitment success was particularly high in the older cohorts. Therefore, while 72.6 % of the subjects with less than 5 years of exposure were not examined, more than 92 % of the workers with longer time of exposure were successfully recruited.

There was a significant effect of group of exposure on the demographic and occupational variables. Higher cumulative exposure was also found in group of the older cohort subjects as compared to the other groups. In similarity with the aforementioned results, the median values for cumulative exposure (fibre/year/cc) were remarkably different for those groups : 51.2, 20.2 and 2.4, respectively.

3.2 Clinical Findings

A positive smoking history was found in 63.4% of the subjects. A heavy smoking history was especially found in the older cohort, 13.4 % of these patients smoked more than 50 cigarette pack per year. In contrast, only 9.7 % of those workers were considered as heavy smokers. There was a significant association of smoking with obstructive impairment and dyspnea.

Thirty seven percent of the workers related breathlessness on daily activities. The prevalence of dyspnea was particularly high in older groups. The symptom was independently associated with age, a positive smoking history, functional impairment (both restrictive and obstructive) and cumulative exposure (≥ 10 fiber/year/cc).

3.3 Radiographic Abnormalities

Parenchymatous abnormalities on the chest X-ray were found in 77 (1.8 %) and pleural findings 136 (3.8 %) of the workers, respectively. Combined parenchymatous and pleural findings were found in 4.7 % of the population. Prevalence of these alterations was significantly higher in older group:

these workers also had more extensive lesions. Overall, there were only mild to moderate roentgenographic abnormalities and the ILO profusion scores typically ranged from 1/0 to 2/1. We found 18 subjects with asbestosis and pleural plaques, 17 only asbestosis, 71 only pleural plaques and 3 with lung cancer. In conclusion, the progressive improvement in the workplace conditions is likely to be related to a significant decrease in the morbidity of those workers.

4 FINAL CONSIDERATIONS

Physical and chemical characteristics of amphibole - hard fibres, needle-like, splintery and with ferric iron ions - makes it more toxic, especially because of a longer biopersistence time and smaller intralung solubility. Chrysotile has a smaller oxidative stress and forms less free radicals because of the absence of iron in the chemical formula. For being unfibrilable and having a higher solubility, chrysotile has a smaller biopersistence and consequently produce less inflammation mediators.

5 REFERENCES

- Bagatin, E. (coord.). 2000. Morbidade e mortalidade entre trabalhadores expostos ao asbesto na atividade de mineração - 1940-1996. Relatório Final do Projeto Temático Asbesto-Mineração - FAPESP.
- Correia, C.T. 1994. Petrologia do Complexo Máfico-Ultamáfico de Cana Brava, Goiás. Tese de doutoramento, IG-USP. 151 p.
- Environmental Protection Agency. - EPA. 1993. Method for determination of asbestos in bulk building materials. EPA/600/R-93/116.
- Environmental Protection Agency. - EPA. 2001. Asbestos health effect conference - www.epa.gov.
- Finish Institute of Occupational Health. 1997. Asbestos, asbestosis and cancer. Proceedings of an international experts meeting. Helsinki.
- International Labour Office. Revised 2000. International Classification of Radiographs of Pneumoconiosis. n° 22.
- National Institute of Occupational Health - NIOSH. 1992. Asbestos, publications Depto. of Health and Human services-Center of Diseases Control-CDC.
- Oliveira, M.C.B. 1996. Caracterização tecnológica do minério de crisotila da Mina de Cana Brava, Goiás. Tese de doutoramento, IG-USP. 250 p.
- Oliveira, M.C.B. & Coutinho, J.M.V. 1999. Estudo petrográfico-mineralógico de amostras de rochas e fibras procedentes da região de Vila Nova Amianto, Bom Jesus da Serra, BA. Rel. IPT n° 42 409.47p.

Molecular-scale Characterization of Arsenic in Metallurgical Wastes

D.Paktunc

Mining and Mineral Sciences Laboratories, CANMET, 555 Booth Street, Ottawa, Ontario, K1A 0G1, Canada

ABSTRACT: Common forms of As precipitates used by the metallurgical industries to control As in the effluents include ferric arsenates and Fe(III) oxyhydroxides with variable levels of arsenic. In addition, jarosite is a potentially attractive phase for arsenic control. Synchrotron X-ray absorption fine structure spectroscopy (XAFS) was utilized to characterize the common forms of arsenical precipitates with the objective to assess their stabilities. The results indicate that the As-O interatomic distances are uniform at 1.68 to 1.69 Å and the coordination numbers range from 4 to 5 which suggest tetrahedral coordination of the first shell of atoms. The As-Fe distances of individual goethite grains with varying As concentrations range from 3.24 to 3.32 Å and the coordination numbers are in the 1-3 range, indicating inner-sphere bidentate-binuclear arsenate complexes. The main As-Fe distance is 3.30 Å for the ferric arsenates whereas the As-Fe distances vary from 3.30 to 3.34 Å for arsenical ferrihydrites. Coordination numbers range from 2 to 4 for the ferric arsenates and from 4 to 9 for the arsenical ferrihydrites. It appears that the coprecipitation of arsenate with Fe (III) oxyhydroxides is responsible for the wide range of As concentrations observed in goethite and ferrihydrite. The results from the jarosite samples indicate that arsenate substitutes for sulfate in the jarosite crystal structure. Such a substitution leads to distorted tetrahedra and vacancies in the octahedral sites.

1 INTRODUCTION

Arsenic is a common contaminant in effluents and tailings resulting from gold and base-metal processing and extractive metallurgy operations. It occurs in various forms such as sulfides, oxides, arsenates, and arsenical ferrihydrites and goethites in the solid wastes. Our understanding of the nature and characteristics of such As compounds is limited. This limitation has important bearings on the assessment of their stability and the prediction of long-term behavior of As in the wastes.

Accordingly, detailed mineralogical studies including synchrotron X-ray absorption fine structure spectroscopy (XAFS) were carried out to determine the molecular-scale characteristics of the common forms of As.

2 METHODOLOGY

The samples used in this study are laboratory precipitates and mineral specimens. They were selected to represent a broad range of compositions that are common and/or potentially useful in the metallurgical industries. The list includes ferric arsenates, arsenical ferrihydrite, arsenical goethite

and jarosite.

Arsenical goethite specimens are from the Ketza River gold mine in Yukon as described by Paktunc et al. (2003; 2004). Ferric arsenates and arsenical ferrihydrites are laboratory precipitates prepared at INCO Ltd. as described by Krause & Ettl (1989) and at the Imperial College of London by Dr. Peter Swash. Jarosites are synthetic material as described by Paktunc & Dutrizac (2003).

X-ray powder diffraction analyses were performed using a Rigaku rotating anode with CuK α radiation at 55kV, 180 mA, step-scan 0.04°, scan rate at 4° per minute in 2 θ .

The bulk XAFS experiments were carried out at the Stanford Synchrotron Radiation Laboratory on wiggler beamlines. Finely ground samples were mixed with boron nitride to dilute the concentrated samples to about 1 wt % As or less. The XAFS spectra were collected at room temperature in the fluorescence mode. Micro-XAFS experiments involving grains of goethite mounted on polished sections were carried out at the PNC-CAT's undulator beamline of the Advanced Photon Source. Micro-XAFS spectra were collected from the center of mineral grains by a beam size of ~5 μ m in the fluorescence mode. A minimum of four XAFS scans

were made on each sample. Data reduction was accomplished by EXAFSPAK (George & Pickering 1995). XAFS data analysis was performed with theoretical phase and amplitude functions generated in FEFF7 (Zabinsky et al. 1995). Estimated uncertainties in the coordination numbers are ± 1.7 for As-O and ± 0.4 for As-Fe. Interatomic distances have the following uncertainty values: ± 0.01 Å for As-O and ± 0.02 Å for As-Fe.

3 RESULTS

Shown in Figure 1 are k^3 -weighted XAFS spectra from a series of goethite grains with a range of As concentrations from 2 to 26 wt % As_2O_5 . These oscillations are electronic signals produced as a result of singly scattering of core level electrons ejected from central As atoms causing constructive and destructive interference between the propagated and reflected waves. The signals coming from different shells are separated by Fourier filtering. The major peak on the Fourier transformed spectra at approximately 1.3 Å corresponds to the oxygen shell (Fig. 2). XAFS analysis indicates that the oxygen atoms around the central arsenic occur in tetrahedral coordination in all the samples. The peak at approximately 2.7 Å corresponds to scattering from Fe atoms. The third peak that occurs approximately 3.3 Å in goethite corresponds to scattering from Ca atoms. The As-Fe distances ranging from 3.24 to 3.32 Å and the coordination numbers from 0.7 to 2.6 suggest that arsenate ions occur as adsorbed species forming bidentate-binuclear complexes on goethite (Fig. 3). It appears that the availability and coprecipitation of arsenate during the formation of goethite is responsible for the wide range of As concentrations observed in goethite. The presence of Ca scatterers around As in goethite at approximately 4.15 Å distance suggests coprecipitation of Ca-Fe arsenates with goethite in the form of nanoclusters or small crystallites.

The Fourier-transformed XAFS spectra of the ferric arsenate and arsenical ferrihydrite precipitates are shown in Figure 4. XAFS analysis indicates that the precipitates with Fe/As molar ratios ranging from 1 to 6 have a similar local coordination environment. The As-Fe interatomic distances are around 3.3 Å. The coordination numbers vary from 2.4 to 4.1 . The precipitate with Fe/As ratio of 10, subjected to accelerated aging, has a different local structure. It is characterized by a longer As-Fe interatomic distance (3.34 Å) and high coordination number of 9.4 . The As-Fe interatomic distance of this precipitate is closer to that of scorodite. XRD analysis indicates that this precipitate has a long-range structure that is similar to 6-line ferrihydrite (Fig. 5). The precipitates with lower Fe/As ratios

(i.e. 1 to 6), on the other hand, possess different long-range structures.

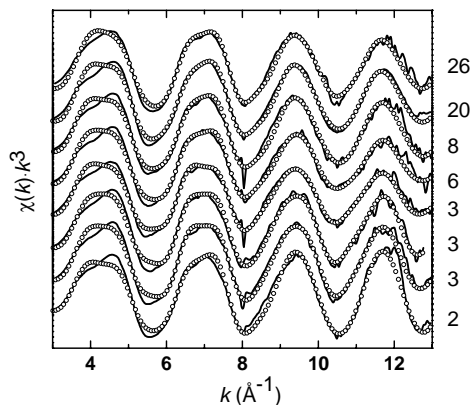


Figure 1. Micro-XAFS spectra of goethite grains with variable As concentrations ranging from 2 to 26 wt % As_2O_5 , as marked along the vertical axis on the right. Experimental spectra are shown by solid lines and fitted spectra by circles.

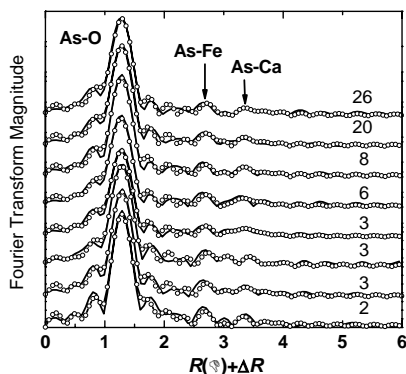


Figure 2. Fourier-transformed XAFS spectra of goethite grains as in Fig.1.

XRD patterns of the precipitates with low molar Fe/As ratios of 1 and 2 are similar that are characterized by two broad peaks: one at 2.98 Å and the other at 1.57 Å. These are similar to the “amorphous” ferric arsenate of Carlson et al (2002) and the natural arsenical hydrous ferric oxide of Rancourt et al. (2001). The profiles are also similar to the barren 2-line ferrihydrite (Fig. 5) but with greater d-spacings displaced to longer distances. It appears that the profiles begin to resemble the 6-line ferrihydrite structure more closely as the molar Fe/As ratio is increased.

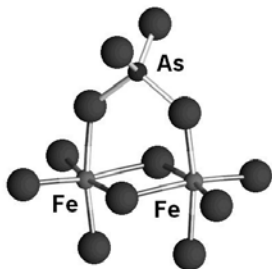


Figure 3. Polyhedral representation of bidentate-binuclear attachment of an arsenate ion on a edge-sharing Fe-O dioctahedra.

Ferric arsenate precipitates having molar Fe/As ratios of 1 to 4 can be conceptualized by bidentate-binuclear attachment of arsenate onto 2 Fe-O dioctahedra that are linked along O-O edges. The Fe-O dioctahedra themselves are composed of face-sharing octahedra. Although this arrangement is possible based on geometric considerations, it is not realistic because the apical oxygens to which arsenate is attached are doubly-coordinated and are considered as unreactive sites. Furthermore, a molar Fe/As ratio that is between 1 and 4 would be difficult to maintain with this kind of configuration. The other possibility is based on the scorodite structure where arsenate tetrahedra is corner-linked to isolated Fe-O octahedra. A difference between scorodite and ferric arsenate in this case would be in the As-O-Fe angles. A smaller angle is required for ferric arsenate to achieve shorter As-Fe distances. In addition, such an arrangement makes lower coordination numbers possible. Occasional octahedral site vacancies could be the reason for long-range disorder for ferric arsenates. A possible local structure for the ferric arsenate precipitate having molar Fe/As ratio of 10 and displaying 6-line ferrihydrite structure involves the ferrihydrite structure of Drits et al. (1993). There are octahedral vacancies in the 6-line ferrihydrite structure. If arsenate tetrahedra are located in cavities resulting from octahedral vacancies in the ferrihydrite structure, the observed high coordination numbers (e.g. 9.4) can be achieved while maintaining the As-Fe interatomic distances.

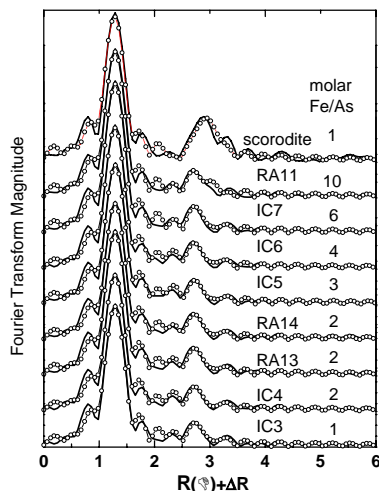


Figure 4. Fourier-transformed XAFS spectra of synthetic ferric arsenate and arsenical ferrihydrites with variable As concentrations. Numbers next to labels are molar Fe/As ratios. Scorodite spectra shown for comparative purposes.

The XAFS spectra from K-jarosite precipitates with AsO_4 concentrations ranging from 1.3 to 9.9 wt % indicate As-Fe interatomic distances of $\sim 3.26 \text{ \AA}$ and Fe coordination numbers of ~ 2 (Paktunc & Dutrizac 2003). Substitution of sulfate by arsenate is limited to 17 mole % AsO_4 and requires octahedral vacancies in the structure in addition to expansion of the unit-cell to accommodate the larger arsenate tetrahedra. Since jarosite is a common precipitate in metallurgical waste streams, demonstration of its ability to fix up to $\sim 10 \text{ wt \%}$ AsO_4 is important for As control practices in the metallurgical industry.

4 CONCLUSIONS

Arsenate ions occur as adsorbed species forming bidentate-binuclear complexes on goethite. The wide range of As concentrations observed in goethite (up to $\sim 26 \text{ wt \%}$ As_2O_5) appears to result from the availability and coprecipitation of arsenate during the formation of goethite. High As sorption results from the bidentate-binuclear attachment on small Fe-O polyhedral chains. Ca-Fe arsenates can coprecipitate with goethite by forming nanoclusters or small crystallites.

Ferric arsenate and arsenical ferrihydrite precipitates with molar Fe/As ratios ranging from 1 to 6 possess similar local coordination environments around As. Long-range structures resemble the "amorphous" ferric arsenate compounds and the 2-line ferrihydrite having greater d-spacings displaced

to longer distances. The precipitate with Fe/As ratio of 10 has a different local structure which is characterized by a longer As-Fe interatomic distance and a higher coordination number. This precipitate has a long-range structure that is similar to 6-line ferrihydrite.

Jarosite can incorporate up to ~10 wt % AsO₄ in its crystal structure. This and other properties of jarosite such as its relative stability and disposal properties make it potentially attractive for long-term disposal of arsenical wastes.

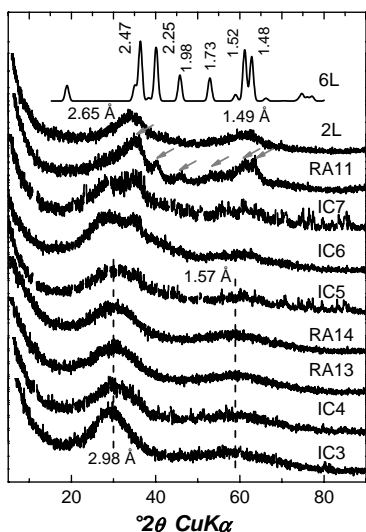


Figure 5. XRD patterns of synthetic ferric arsenate and arsenical ferrihydrites. Two-line ferrihydrite (2L) is represented by a barren synthetic precipitate prepared by Dr. Patricio Riveros (CANMET) and six-line ferrihydrite (6L) is a simulated profile based on the structure proposed by Drits et al. (1993). Refer to Fig.4 for description of labels. Arrows on RA11 point to corresponding peaks of 6L.

5 ACKNOWLEDGEMENTS

XAFS experimental work on synthetic samples was carried out at the Stanford Synchrotron Radiation Laboratory, a national user facility operated by Stanford University on behalf of the U.S. Department of Energy, Office of Basic Energy Sciences. Micro-XAFS experiments on goethite grains were carried out at the Pacific Northwest Consortium - Collaborative Access Team's (PNC-AT) beamline at the Advanced Photon Source (APS) in Argonne. The latter was supported by the Natural Sciences and Engineering Research Council of Canada through a major facilities access grant. Research at both facilities is also supported by the

US Department of Energy under contracts W-31-109-Eng-38 (APS) and DE-FG03-97ER45628 (PNC-CAT). Drs. Eberhard Krause and Peter Swash kindly provided the synthetic materials. Dr. Andrea Foster's help with data acquisition and analysis is greatly appreciated. Review of the paper by Dr. Patricio Riveros is acknowledged.

6 REFERENCES

- Carlson, L., Bigham, J.M., Schwertmann, U., Kyek, A. and Wagner, F. (2002) Scavenging of As from acid mine drainage by schwertmannite and ferrihydrite: A comparison with synthetic analogues. *Environmental Science and Technology*, 36, 1712-1719.
- Drits, V.A., Sakharov, B.A., Salyn, A.L. and Manceau, A. (1993) Structural model for ferrihydrite. *Clay Minerals*, 28, 185-207.
- George G. N. and Pickering I. J. (1995) EXAFSPAK: a suite of computer programs for analysis of X-ray absorption spectra. Stanford Synchrotron Radiation Laboratory.
- Krause E. and Ettl V. A. (1989) Solubilities and stabilities of ferric arsenates. *Hydromet.* 22, 311-337.
- Paktunc, D. and Dutrizac, J. (2003) Characterization of arsenate-for-sulfate substitution in synthetic jarosite using X-ray diffraction and X-ray absorption spectroscopy. *Canadian Mineralogist*, 41, 905-919.
- Paktunc, D., Foster, A., Heald, S. and Laflamme, G. (2004) Speciation and characterization of arsenic in gold ores and cyanidation tailings using X-ray absorption spectroscopy. *Geochimica et Cosmochimica Acta*, 68 (in press).
- Paktunc A D., Foster A., and Laflamme J. (2003) Speciation and Characterization of Arsenic in Ketzar River Mine Tailings Using X-Ray Absorption Spectroscopy. *Environmental Science and Technology*, 37, 2067-2074.
- Rancourt, D.G., Fortin, D., Pichler, T., Thibault, P.-J., Lamarche, G., Morris, R.V. and Mercier, P.H.J. (2001) Mineralogy of a natural As-rich hydrous ferric oxide coprecipitate formed by mixing of hydrothermal fluid and seawater: Implications regarding surface complexation and color banding in ferrihydrite deposits. *American Mineralogist*, 86, 834-851.
- Zabinsky S. I., Rehr J. J., Ankudinov A., Albers R. C., and Eller M. J. (1995) Multiple scattering calculation of x-ray absorption spectra. *Phys. Rev. B* 52, 2995-3009.

Potential Contaminant Elements Retention Using Structural 2:1 Layer Clay Minerals

W.C.Pereira & D.M.Silva & J.O.Carvalho

Department of Ambient Health, ENSP, Instituto Oswaldo Cruz – FIOCRUZ, Rio de Janeiro, Brazil

N.M.B.Amaral Sobrinho

Agronomy Institut, UFRRJ, Rio de Janeiro, Brazil

R.C.Villas Boas

Centro de Tecnologia Mineral – CETEM, MCT, Rio de Janeiro, Brazil

ABSTRACT: The purpose of this work is a study of the potentially contaminant trace elements, present in industrial residues that are transferred to the environment through the percolated liquid. This study examines the performance of clays as sorbents, applied to elements retention. This work deals with the development of an industrial residues disposal process. Two types of residues were studied, the Cia. Ingá residues, passive environmental of the Galvanoplasty Industry, classified as dangerous, Class I (ABNT, 1987), and another one, refuse slag from Cia Siderúrgica Nacional – CSN, used as alkalizer in the experiment. The chosen residue, the slag from steel works, currently represents a huge environmental liability from the steel industry. Even though this residue has been considered relatively stable within the established standards by the rules in force at the moment, due to its characteristics ($Cd < 0,5$, $Pb < 10$, $Co < 5$, $Cu = 61$, $Cr = 280$, $Mo < 10$, $Ni < 1,5$, $Se < 3,0$, $Zn = 75$), so far it does not have an alternative for an adequate reutilization. The use of this residue as an alkalizer associated to the use of clay minerals with a layer structure of 2:1 in industrial and sanitary landfill can contribute to a more efficient solution of a final disposal problem.

1 INTRODUCTION

1.1 Goal

This work is based on the study of the characteristics, properties, and availability of the mentioned materials, in order to elucidate the necessary parameters for its use for the control of liquid effluents, originating from the percolation of potentially contaminated residues.

This work deals with the development of an industrial residues disposal process. Two types of residues were studied, the Cia. Ingá (Electroplating) residues, ($Zn = 22294,4 \text{ mg Kg}^{-1}$, $Cd = 175,2 \text{ mg Kg}^{-1}$, $Pb = 2486,8 \text{ mg Kg}^{-1}$, $Cu = 123,2 \text{ mg Kg}^{-1}$, $Ni = 32,0 \text{ mg Kg}^{-1}$) and another one to alkalize (refuse slag from Cia Siderúrgica Nacional – CSN) Pinheiro (2003). The clay minerals were studied with the objective of adsorption and the consequent retention of the potentially contaminant elements that could be bio-available in the environment. The concern about the mobility of the potentially toxic elements are greater when the edaphic (a large part of acid soil) and the tropical zone climatic factors are taken into account and the interactions amongst those kinds of residues and the several physicochemical parameters. The chosen alkalizer residue, the slag from steel works, currently represents a huge

environmental liability from the steel industry. Even though this residue has been considered relatively stable within the established standards by the rules in force at the moment, due to its characteristics ($Cd < 0,5 \text{ mg Kg}^{-1}$, $Pb < 10 \text{ mg Kg}^{-1}$, $Co < 5 \text{ mg Kg}^{-1}$, $Cu = 61 \text{ mg Kg}^{-1}$, $Cr = 280 \text{ mg Kg}^{-1}$, $Mo < 10 \text{ mg Kg}^{-1}$, $Ni < 1,5 \text{ mg Kg}^{-1}$, $Se < 3,0 \text{ mg Kg}^{-1}$, $Zn = 75 \text{ mg Kg}^{-1}$), there is no alternative for an adequate reutilization, so far. In this way, the use of this residue as an alkalizer associated to the use of clay minerals with a layer structure of 2:1, in industrial and sanitary landfill, can contribute to a more efficient solution of a final disposal problem.

1.2 General

The chemical attenuation consists of minimizing the migration of contaminants to the subsurface of the soil. Those techniques are based on the incorporation of the agents with heavy metals immobilization potential. Some forms of attenuation in situ have been having prominence in the literature, among them we can find: oxide, hydroxides, and oxi-hydroxides of Fe and Mn that are important adsorbents of metals in the soils. The silicates and aluminosilicates represent the unions of Si, Al and of the anionic radicals with cation which

present constituent of elements such as Al, Fe, Mg, Mn, Ca, Na, K as well as Li, B, Be, Ti, Zr, TR, Cs, Sr, Y, Zn, Cu, etc. The constituent anionic radicals, besides Si and Al, are also Ti, Zr, Be, B, Fe³⁺. The role of the complementary anions is carried out by the groups (OH)⁻, F⁻, O₂⁻, S₂⁻, Cl⁻, and [BO₃]₃⁻, as well as [O₃]₂⁻, [SO₄]₂⁻, etc.. The smectite clay group is being thoroughly studied due to its diverse properties, such as: a) the versatility of cationic change, making possible the introduction of a variety of ions among their layers, b) swelling capacity, accommodating a great number of molecules of several sizes between the layers 2:1 and c) capacity to be exfoliated and later rearranged without changes in the crystalline structure of the layers.

2 EXPERIMENTAL SECTION

2.1 Sampling and Analytical Methods

With reference to the materials, the choice was for the residues of Ingá, environmental liabilities from the Galvanoplasty Industry, that can be observed in Figure 1. These residues have been studied, in search of a solution for the pollution caused by the leached material from the residues in Sepetiba Bay. The residues of Cia. Siderúrgica Nacional (Steel Industry) were also studied, and they will be used as neutralizer in the process, due to its high alkalinity. These residues are produced in the steel manufacture. The materials studied were, in the first place, the ones that would be used as sorbents; smectite was chosen to start the process, and its physical and chemical properties, superficial area and mineralogical composition was studied.



Figure 1. Environmental liabilities from Galvanoplasty Industry Ingá.

The samples were submitted to several steps of preparation which involved comminution, homogenization, and quartering. The determination of the superficial area and the study of the porosity

of the material were accomplished using ASAP (Accelerated Surface Area and Porosimetry System), Micromeritics, 2010, using the technique of adsorption/desorption of nitrogen. The mineralogical analyses were made in the Center of Mineral Technology (CETEM) an X-Ray diffractometer (XRD), Siemens AXS, D505, and the technique of X-Ray fluorescence (Phillips, I model TW2400). Hydraulics conductivity tests were made with the use of a permeameter, according to Darcy law ($q = -K (\Delta\Psi_B - \Delta\Psi_A) / \Delta Z$).

2.2 Experimental setup

The tests were done in an experimental apparatus in bench scale, consisting of transparent acrylic cells filled with the residues to be studied and the clay mineral to be used as adsorbent and material composed of grains of quartz, inert to the process, filter, recipient for the liquid effluent, and containers for the storage of acidified water with pH 4 to 4.5. The affluent acidified liquid, that simulates the precipitation of acidified rain water, is pumped through hoses for the cells, going through the material in study, in a lixiviation process, and is collected in containers for subsequent analysis. The pH was defined as a function of the average presented in pluviometric precipitations in areas of heavy industrialization (metallurgy, thermoelctrical etc.) in the State of Rio de Janeiro. The experimental set-up scheme is shown in Figure 2.

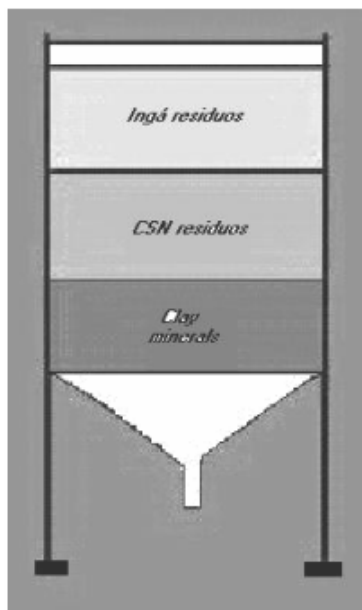


Figure 2. Experimental setup scheme.

2.3 Results and discussion

Six days after the starting point of the experiment it was observed the beginning of a drip, and approximately 56 days afterwards the drainage was interrupted. Figure 3 displays the experimental assembly, simulating, in laboratory scale, the possibilities of industrial landfill. It was then observed a cementation in the CSN residue, and the consequent blockage of the introduced liquid circulation.

The chemical composition of the materials was obtained using the technique of X-Rays fluorescence, for determination of the CaO, MgO, K₂O, etc. Table 1 presents the results obtained. The studied smectite is policationic, presenting a small swelling. The results of X-Rays diffraction in the sample presented basal interference lines in the montmorillonite group, and kaulinite group. The diffraction results also presented bands that indicate the presence of mixed layers of illite-montmorillonite, irregularly inter-stratified, as we can observe in the diffractograms shown in Figure 4. Quartz is present in small proportions.

Table 1. XR Fluorescence chemical analysis results.

	Smectite (%)
CaO	0,79
MgO	2,2
Na ₂ O	0,4
SiO ₂	60,9
Fe ₂ O ₃	7,4
K ₂ O	3,4
Al ₂ O ₃	12,1

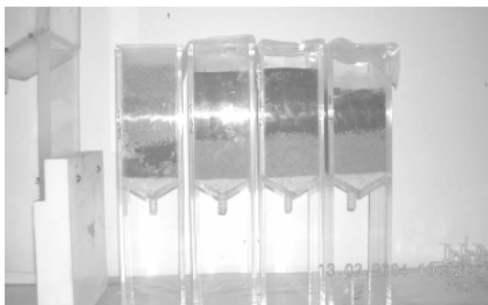


Figure 3. Transparent acrylic cell with 70cm height, 20cm X, 20 cm width.

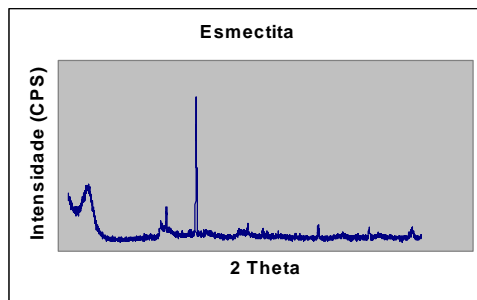


Figure 4. The XRD results show records corresponding to montmorillonite, kaulinite, and illite (primary and secondary peaks).

The value of the hydraulic conductivity was measured by means of a permeameter of the type "constant height water column". The results were the following: Ingá residues, $2,19 \times 10^{-4}$ cm/s, CSN residue, 0,01 cm/s, and for the smectite $0,9 \times 10^{-5}$ cm/s.

The ionic substitution of Al⁺³ for Si⁺⁴ in the tetrahedral layer, or Mg⁺² or Fe⁺³ for Al⁺³ in the octahedral is the origin of the permanent negative load in smectite. That could explain the retention process of potentially contaminant elements. However, as it was seen above, the contact among the studied residues promotes a cementation, a white layer is formed among the Ingá and CSN residues. The clay mineral, probably due to the swelling capacity and retention of liquids, contributes in that process. At the end of the process cell 2 presents a layer with crystalline aspect, as shown in Figure 5. Up to now we have not had the opportunity to analyse this layer using an appropriate method. The next step will be to analyse all the residues, obtained at the end of the process.

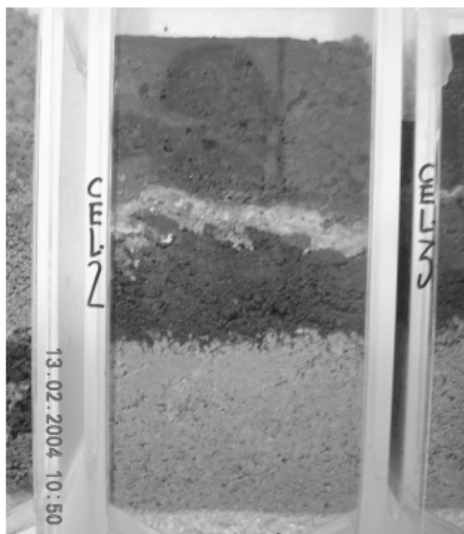


Figure 5. Acrylic cell showing a cementation process of Ingá and CSN residues.

3 CONCLUSIONS

The expected results are that the contaminated residue will be partially neutralized by the alkaline residue, immobilizing harmful elements, associated to the clay minerals. However, it was observed that the CSN residue, when placed in layers immediately below Ingá residues, form a cement in a relatively short time. The continuity of the study should bring more detailed results for the process. The mixture in differentiated percentages of both kinds of residues can improve the process performance.

4 ACKNOWLEDGMENTS

This research was supported by the FIOCRUZ PED Program (Pesquisa Estratégica, Desenvolvimento e Inovação). We would like to express our gratitude to CSN for allowing access to sampling and to Maíra Matos, Fioacruz trainee.

5 REFERENCES

- ASSOCIAÇÃO BRASILEIRA DE NORMAS TÉCNICAS (ABNT). NBR 10004. Resíduos Sólidos – Classificação. São Paulo, Projeto 1.63.02-001, 1987. 48p.
- Bergaya F. & Lagaly G. 2001. Surface modification of clay minerals. *Applied Clay Science*. 19, 1-3.
- Fitch A., Song J., Stein J. 1996. Molecular structure effects on diffusion of cations in clays. *Clays and Clays Minerals*. 44, 3: 370-380.
- Griffin R. A., Frost R. R., Robinson G.D., Shimp, N.F.. 1997 Attenuation of pollutants in municipal landfill leachate

by clay minerals: Heavy metal adsorption. *Environmental Geology Notes*, 79, 1 – 47.

Khalil C.M., Teixeira L.C.F.L. 1992. Método analítico de determinação da capacidade de troca catiônica de argilominerais. II seminário de Química Analítica. CENPES, Rio de Janeiro, Brasil.

Pinheiro R.S. 2003. Inertização de resíduo perigoso através do uso de resíduos industriais alcalinos. Tese de Mestrado. Instituto de Agronomia, Universidade Federal Rural do Rio de Janeiro, Brasil. 74 pp.

Role of Mineralogy in Areas Affected by Acid Saline Seeps, Southwestern Australia

M.Raghimi

Department of Applied Geology, Curtin University of Technology, Perth, Australia and Gorgan University of Agricultural Sciences & Natural Resources, Gorgan, Iran

M.F.Aspandiar

Cooperative Research Centre for Landscape Environments and Mineral Exploration, Department of Applied Geology, Curtin University of Technology, Perth, Australia

ABSTRACT: The study of morphological and mineralogical changes within an acid saline seep affected landscape revealed seasonal differences in surface mineralogy, reflecting the operation of sulfidization and oxidative sulfide weathering processes. During the wet season, the surface and near surface of the waterlogged seep and marsh areas is dominated by black sulfidic materials (pyrite) and minor salt crusts, with negligible iron oxides and oxyhydroxides. The Fe and S emerging from seeps contribute to the sulfidization processes operative in reducing conditions within the waterlogged zones. During the dry season, the surface mineralogy of the seepage zone is dominated by salt (halite), sulfates (gypsum and barite) and importantly, iron oxyhydroxides gel precipitates and crusts (ferrihydrite, goethite, schwertmannite). The gradual drying of previously waterlogged zones during summer facilitates oxidative weathering of the sulfides, which together with rapid oxidation of Fe^{2+} emerging from the still persisting minor seeps, results in the formation of iron oxyhydroxides and acid generation. The visible near infra-red (VNIR) reflectance spectra of the surface minerals from unaffected, salt crusted and acid seep areas, showed spectral differences expressed in the VNIR region due to absorption bands of iron oxides and hydroxides. The spectral difference can be utilized for regional scale mapping of acid seeps and acid sulfate soils via hyperspectral and multispectral remote sensing.

1 GENERAL INSTRUCTIONS

1.1 Type area

The study area is located in the West Dale catchment, which is approximately 100 km SW of Perth, Western Australia (Fig 1). The climate is Mediterranean and land use is dominated by pasture and grazing activity. The study area setting is typical of the region, dominated by saline groundwater seeps in the valleys, which is an increasing problem facing much of agricultural land in SW Australia (George et al. 1997). In addition to saline seeps, acid sulfate soils associated with acid conditions are being increasingly recognized in inland agricultural areas of Australia (Fitzpatrick 2002) and are an emerging problem in the wheatbelt region of SW Australia (George 2002).

1.2 Physiography and Geological Setting

The geology of the area is dominated by Archaean granitoids cut by NW – SE trending multiple dolerite dykes. Locally only one dolerite dyke outcrop is present that marks a ridge, but magnetic intensity images suggest two NW-SE trending dolerites dykes and a fault approximately 500 m to the north of the sampling locality.

Geomorphologically the area is of undulating hills with near flat hilltops and subdued but narrow valleys. Much of the area is covered by thick regolith, which can reach a depth in excess of 40 m in some valleys.

1.3 Methods

Soil samples were collected by hand augering down to around 1.5 m and in the marsh area. The pH and Eh of waters was measured in field after calibrating the electrodes. Bulk mineralogy was determined using X-ray diffraction (XRD) with random powder mounts, scanned using $CuK\alpha$ radiation. Samples were step scanned from $4 - 80^\circ 2\theta$ using a 0.2° step size and with a 1 s counting time, but for some iron samples, 3 s counting times were employed. Diffuse reflectance spectra of surface and subsurface materials were collected with an ASD Fieldspec within the wavelength range of 350 – 2500 nm with increments of 1 nm with a 34 ms integration time. The samples for spectroscopy were dried and crushed mildly to form coarse powders. The spectra were run in a dry laboratory environment. Continuum removal procedures were not employed on the spectra. Some minerals were identified via a combination of scanning electron microscopy

(SEM), both in backscatter and secondary electron mode, and energy dispersive X-ray analysis (EDAX). Some sulfidic samples were studied in a moist, uncoated state in the SEM, which reduced resolution of the images.

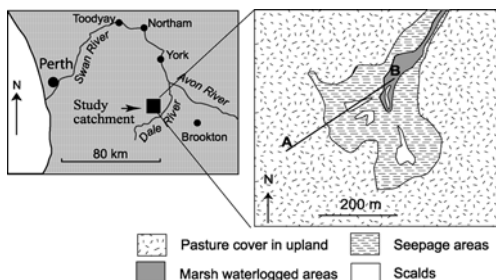


Figure 1. Location map of the study area showing distribution of surface features. A-B is the transect for soil study shown in figure 2.

2 RESULTS

2.1 Toposequence characteristics of regolith

Based on the nature of the surface and groundwater conditions, the landscape was divided into three areas along the toposequence: unaffected zone in the upper catchment, seepage zones in the mid slope, and permanently waterlogged zone (marsh) in the valley floor (Fig 2). This classification is similar to landform settings of many inland acid seeps and potential acid sulfate soils in Australia (Fitzpatrick et al. 1996).

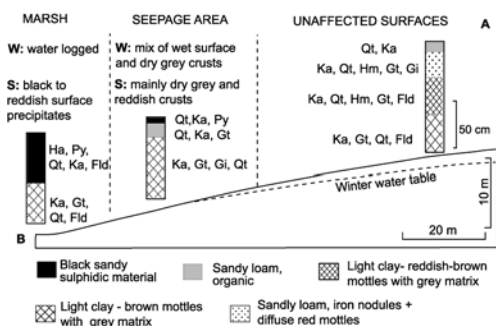


Figure 2: A soil toposequence across the acid saline seep affected landscape showing the main surface and subsurface soil morphological features. W – winter (wet) season, S – summer (dry). Mineralogy of individual soil horizon morphologies only: Qt-quartz, Ka- kaolinite, Hm – hematite, Gt – goethite, Gi – Gibbsite, Ha – halite, Py – pyrite, Fld-feldspar.

The affected land area represented by the waterlogged and seepage zones migrate upwards in the toposequence thereby gradually increasing the degraded land area and reducing pastures. Six soil

profiles were sampled and studied along a toposequence, but the locations and morphological properties of only three profiles, representative of the three main landscape positions, are shown in Figure 2.

2.2 Dry unaffected zones (upper catchment)

Grassland or pastures dominate the surface of topographically higher unaffected land. The soils in the unaffected part are duplex, sandy loams, with red to dark red nodules in the B horizon grading into reddish mottles and eventually into brown to dark brown mottles with grey matrix colours in the C horizons (> 80 cm). The dominance of gley colours coincides with winter perched groundwater levels. Some sub-vertical mottles along voids are present. The nodules and various mottles (pore linings and Fe masses) are redoximorphic features indicative of oxidation-reduction conditions in a saturated environment (Bigham et al. 2001). The mineralogy of individual horizons is documented in Figure 2, with the secondary iron minerals showing a gradual change from dominant hematite in the reddish nodules near the top to dominant goethite lower down in the brown mottles.

2.3 Seepage zones (mid slope)

During winter, the seep zones are saturated and have either micro-relief soggy areas with blackish material mixed with bare grey crust scalds. In summer, the same seepage areas are considerably drier, have reddish-brown and grey crusts with only minor seeps emerging at the surface. Many parts of seepage zone have hard, bare localized patches or scalds interspersed with rills and gullies. The rills are a few centimetres in depth and occur along the slopes where seeps emerge, and gullies around 2 m wide and up to 1 m deep dominate the valley floor. During winter, the pH of seeps is > 4.5 while in summer it drops to < 3.5. The morphology and mineralogy of soil profiles underlying the seepage zone are similar to the unaffected zone, except that a dark A horizon is present in the seepage zone (Fig. 2). The main difference is the presence of minor quantities of pyrite in the dark surface material. The differences in morphology of surface material during winter and summer are expressed in the differences in mineralogy, with reddish crusts being dominated by ferrihydrite (6-line), halite, gypsum and minor schwertmannite and goethite (Table 1).

2.4 Marsh zones (valley floors)

During winter, the marsh area is waterlogged and mostly submerged. During summer, parts of the marsh zone dry up and have reddish to black surface crusts, while parts remain waterlogged. The pH of

water in the marsh areas is > 5.5 in both winter and summer, but with reducing conditions ($Eh \sim -20$ mV). The marsh area profiles have 30-60 cm thick black “ooze” type material which when disturbed emanates a strong rotten egg smell, indicative of black sulfidic material as observed by Fitzpatrick et al. (1996). Below this sulfidic material, brown to dark brown mottles in a grey matrix dominate. The nodules and mottles are redoximorphic features that relate to saturation and redox conditions. Moist, uncoated sulfidic materials observed with the SEM revealed sub-rounded particles composed of S and Fe and interpreted as pyrite (Fig. 3), and presence of pyrite was confirmed by XRD. These particles could be an agglomeration of smaller particles. In winter, much of the seep and marsh area is saturated and only blackish material and minor halite are present on the surface.

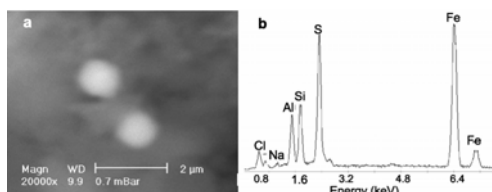


Figure 3. a) SEM backscatter image of black sulfidic material from the marsh area showing sub-rounded bright, high atomic number particles. b) EDX spectrum of the brighter particles indicating S and Fe (pyrite). The other minor spectrum peaks are from kaolinite (Al and Si) and halite (Na and Cl) from the surrounding material.

Table 1: Mineralogy as determined by XRD, of the different surface precipitates within the seep and marsh area during dry summer month.

Surface morphology	Mineralogy
Dry grey crusts	Halite, gypsum, barite, kaolinite, quartz
Reddish crusts	Ferrihydrite, schwertmannite, halite, gypsum, quartz
Reddish gelatinous precipitates	Ferrihydrite, schwertmannite, goethite, halite, gypsum

2.5 Reflectance Spectroscopy (VNIR)

The reflectance spectra of surface materials collected in summer from the unaffected land, the seepage area (grey and reddish crusts), and the marsh area (black sulfidic materials), showed marked differences according to their mineralogy. Figure 4 shows the diffuse reflectance spectra of the three different surface materials: the reddish crust (seepage zone), grey scalds (seepage zone) and black surface (seepage and marsh zone). The grey scald area shows absorption features representative of presence of minor amounts of kaolinite (Al-OH vibrational modes at 2200 nm) and none indicative of halite, because of the lack of absorption features from chloride minerals within the observed

wavelength range. The reddish crusts present in some minor active seeps and ubiquitous in the dried seep areas show broad absorption features around 900 nm. These wavelength features are assigned to the crystal field transitions of ferric iron (${}^6A_{1g} \rightarrow {}^4T_{2g}$ transition), and a subtle shoulder at 640 nm due to the ${}^6A_{1g} \rightarrow {}^4A_{1g}$ transition (Crowley et al. 2003). The broad and intense absorption peaks at 1400 & 1900 nm are indicative of molecular vibration transitions of bound water. The iron crust spectra correspond to those of ferrihydrite reference spectra (Crowley et al. 2003), and possibly a shoulder at 640 nm indicative of schwertmannite. The high amount of bound water suggests that the material is dominated by ferrihydrite with lesser amounts of schwertmannite, and XRD of the same material confirmed this interpretation (Table 1).

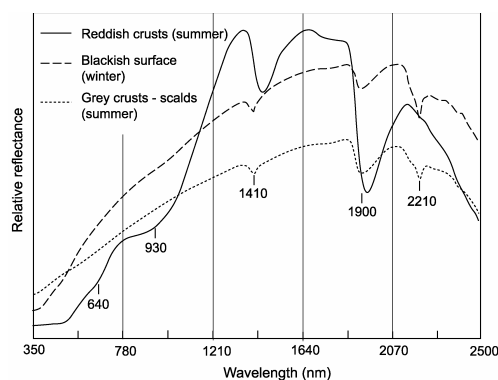


Figure 4: Reflectance spectra in the UV-visible-near infrared range of different surface materials in summer and winter months. The positions of visible wavelength region reflectance minima (before continuum removal) are indicated.

3 DISCUSSION

The differences in morphology and mineralogy of the surface and near surface materials during the wet winter and dry summer months indicate the operation of seasonal dynamic groundwater and geochemical processes, that are expressed in the surface and near surface soil mineralogy. During the wet winter months, water tables are higher with redoximorphic features (mottles, nodules, pore linings) forming in response to saturation and reducing-oxidation conditions within the subsolum. The presence of hematite and goethite in the subsolum of the entire toposequence indicates operation of redox conditions due to water table effects. The presence of pyrite bearing black sulfidic materials in the waterlogged marsh areas (valley floors) indicate the formation of pyrite within the upper horizons of the submerged soils, dominantly during winter. Iron and S, released from the topographically higher regolith profiles in response

to rising water tables due to deforestation, combine to form sub-micrometer pyrites grains, a reaction catalyzed by microbial processes and organic matter at or near the surface. The oxidation of Fe^{2+} emerging from the seeps is restricted due to waterlogged and reducing conditions prevailing on and near surface. The significant changes in surface material during summer in the seepage zone indicate the operation of two processes linked to the drying of the surface (lowering of perched water table) and onset of oxidizing conditions, both being responsible for increasing acidity. Firstly, in contrast to wet water logged surfaces, the emergence of Fe^{2+} in the seeps results in rapid oxidation and hydrolysis of iron leading to formation of ferrihydrite and goethite as precipitates, and subsequent increase in H^+ , a reaction similar to the first part of ferrollysis. Secondly, drying of much of the seep area and marsh area leads to oxidation of near surface sulfidic material followed by Fe^{3+} hydrolysis, resulting in the formation of ferruginous precipitates and creation of acid conditions in the regolith, stream and shallow groundwater (Fitzpatrick et al. 1996). Complete drying results in the formation of crusts with ferrihydrite, goethite, halite, gypsum and barite that precipitate in relation to evaporation.

The understanding of the seasonal processes and its effect on surface and near surface mineralogy are critical to the recognition and management of an increasing number of *acid* saline seeps across the vast land area of the West Australian wheatbelt, as opposed to the much publicized salinity issues. Firstly, the recognition of surface ferruginous minerals via spectral reflectance in summer months will enable the use of hyperspectral and multispectral remote sensing to cost effectively identify and monitor acid generation areas and acid sulfate soils (discriminated via presence of surface iron oxyhydroxides in summer months), as opposed to purely saline seeps that are dominated by halite. Such mapping of acid areas via surface mineralogy has been applied to acid mine drainage environments (Swayze et al. 2000). Secondly, the hematite-goethite ratio with respective hues and chromas (Bigham et al. 2001) in soil profiles can be used as indicators of saturation state during any month, and used to estimate waterlogging conditions in particular parts of the landform. Thirdly, the iron oxide and hydroxide minerals found in soils and surface precipitates act as metal adsorbants (Manceau et al. 2002), and their solubility during different seasons will affect metal concentrations of surface and groundwater. However, to fruitfully apply the rapid but robust methods of spectral reflectance of minerals to land management issues, it is imperative to understand the processes by which the minerals form, and then accordingly formulate and implement land and water management strategies.

4 CONCLUSIONS

This study demonstrates dynamic, seasonally influenced changes to surface and near surface mineralogy of an acid saline seep affected landform. During the wet months, due to waterlogging, the sulfidization process dominates, while during the drier months, oxidative weathering of pyrite and iron hydrolysis results in precipitation of iron oxyhydroxides at and near the surface with the generation of acidity. The study found the iron oxyhydroxide minerals present in the surface crusts and precipitates reflect acid conditions, as opposed to halite and gypsum that reflect only saline conditions. This difference in the surface mineralogy during summer months can be readily identified via multispectral and hyperspectral remote sensing methods mainly during summer, and therefore regionally mapped to identify spatial and temporal distribution of acid seeps.

5 REFERENCES

- Bigham J.M., Fitzpatrick R.W., Schulze D. 2001. Iron Oxides. In J.B.Dixon and D.G. Schulze (eds). Soil Mineralogy with Environmental Applications. Soil Science Society of America Special Publications. Madison, Wisconsin, USA. 323-366.
- Crowley, J.K., Williams, D.E., Hammarstrom, J.M., I-Ming, C., and Mars, J.C. 2003. Spectral reflectance properties (0.4-2.5 μm) of secondary Fe-oxide, Fe-hydroxide, and Fe-sulphate hydrate minerals associated with sulphide-bearing mine wastes. *Geochemistry: Exploration, Environments and Analysis*. 3, 219-228.
- Cudahy, T and Ramanidou E. 1997. Measurement of the hematite:goethite ratio using field visible and near-infrared reflectance spectrometry in channel iron deposits, WA. *Australian Journal of Earth Sciences*, 411-420.
- Fitzpatrick R.W. 2002. Inland acid sulfate soils: A big growth area. In 5th International Acid Sulfate Soils Conference, Tweed Heads, NSW (Book of Extended Abstracts).
- Fitzpatrick R.W., Fritsch, E., & Self P.G. 1996. Interpretation of soil features produced by ancient and modern processes in degraded landscapes: V Development of saline sulfidic features in non-tidal seepage areas. *Geoderma* 69: 1-29.
- George, R.J., McFarlane, D.J., & Nulsen, R.A. 1997. Salinity threatens the viability of agriculture and ecosystems in Western Australia. *Hydrogeology Journal*, 5 6-21.
- George, R.J (2002) Secondary acidification an emerging problem in wheatbelt. *Focus on Salt* 23, 10.
- Manceau, A., Marcus, M.A., & Tamura, N. 2002. Quantitative speciation of heavy metals in soils and sediments by Synchrotron X-ray Techniques. In Applications of synchrotron radiation in low-temperature geochemistry and environmental science (Fenter, P.A, Rivers, M.L., Sturchio, N.C. & Sutton, S.R eds). 341-428.
- Swayze, G.A., Smith, K. M., Clark, R.N., Sutley, S.J., Pearson, R.M., Vance, J.S., Hageman, P.L., Briggs, P.H., Meier, A.L., Singleton, M.J., Roth, S. Using imaging spectroscopy to map acidic mine waste. *Environmental Science and Technology*. 34, 47-54.

Fast Hardpan Formation on Slag Material from Selebi Phikwe, Botswana

D.Rammlmair

Section Geochemistry, Rocks and ores, BGR, Hannover, Germany

ABSTRACT: After deposition the Fe-rich slag from the Ni-Cu-smelter at Selebi Phikwe, NE-Botswana shows despite the fact of a very short rainy season, strong agglutination of slag fragments taken place within 10 years generating a well developed, 40 cm thick, hardpan on loosely deposited coarse grained slag spheres (95% between 0.2 mm and 20 mm in diameter). This fast agglutination contributes to the stabilization of the dump to an enhancement of surface run-off of rainwater, to a reduction of water input, air exchange and therefore a reduction of reactions taking place in the heap. A process which is responsible for a significant reduction of rock drainage.

1 INTRODUCTION

Hardpan formation is a widespread natural process, well known from e.g. silcrete, ferricrete, calcrete. Hardpan formation takes place also at slag heaps, tailings and waste rock piles in various climatic environments and in relatively short time compared to natural systems.

Hardpans can be observed micro- and macroscopically measured, simulated and partially modeled and are dependent on material, climate and age. They consist of a mixture of un- and dissolvable primary and secondary phases - especially of gels, which are sinks of certain elements, protection against erosion by wind and water. They control the rain water introduction and the oxygen diffusion, and therefore the alteration and rock drainage in quantity and quality (Blowes et al. 1991; Chermak & Runnells 1996; Agnew & Taylor 2000, Niederleithinger et al. 2000; Rammlmair & Meyer 2000; Jung et al. 2001; Rammlmair et al. 2001; Rammlmair 2002).

2 SELEBI PHIKWE

2.1 General

The Selebi Phikwe Ni-Cu-mine is situated in the medium to high-grade metamorphic Limpopo Belt. Country rock are garnet, anorthite, biotite gneisses. The ore contains pyrite, pentlandite and chalcopyrite. The ore concentrate is self-burning due to the high pyrite content. A Ni-Cu-Co-matte is produced with considerable PGE contents.

The slag spheres are deposited by lorry on a heap and exposed surfaces are younger than 10 years (Fig.1).



Figure 1. Slagheap and smelter at Selebi Phikwe.

2.2 Material characterization

The Selebi Phikwe slag appears to be highly reactive. The Fe-rich slag spheres are composed according to the cooling history of a homogeneous quenched glass I or a mixture of glass II and plagioclase, fayalite, magnetite crystals (Fig. 2).

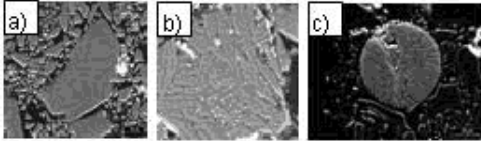


Figure 2. Slag fragments of a) homogeneous glass I, b) fayalite+magnetite+glass II, c) sulfide sphere with leaching channels.

Despite the unfavorable grain size distribution (Fig. 3) the capillary transport in the slagheap seems to be extraordinarily fast. This fast transport is probably due to the development of micro-channels on the sphere surfaces (Fig. 4) and transport of supersaturated solutions within this capillary system and instantaneous precipitation at the air/solution boundary, resulting in the formation of a 40 cm thick hard pan within 10 years on a heap flank in loosely deposited material (Fig. 5).

The semiarid climate favors this fast accumulation of agglutinating matter, but does not really explain the enormous amount of precipitated material since water contents in the slagheap even after rainfalls should be extremely low all over the year.

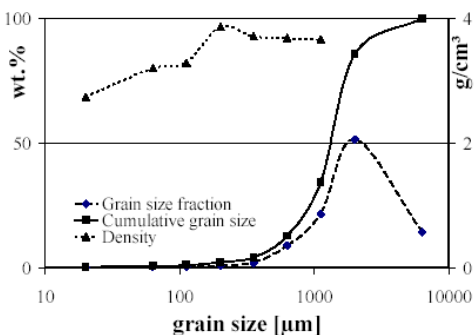


Figure 3. Grain size and density distribution of slag fragments.

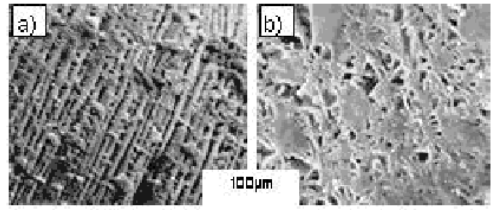


Figure 4. Scanning electron microscope secondary electrons (SEM SE) images showing micro-channels due to selective leaching of slag material from Botswana a) of the rim of a slag sphere with fayalite strings with deep channels, and b) from the core of the sphere showing plagioclase laths with relic glass. Leaching conditions 1 minute in 30% H₂O₂ steam, 25°C.

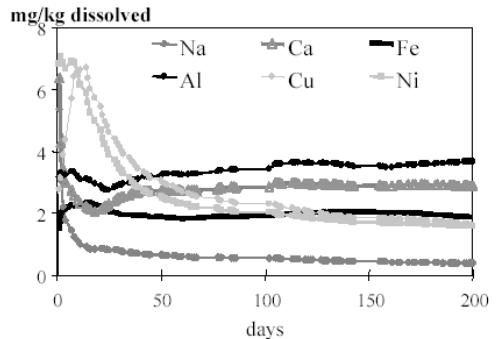


Figure 5. Immediate, retained and reduced availability related to grain size, mineralogy and coating effects.

2.3 Experimental work

In the SOXHLET experiment instantaneous and retained bleeding (first flash), due to dissolution of fine grained material, secondary soluble matter and selective leaching of components (Figs. 2c, 4a, b), preferentially glass II, is responsible for the elevated contents during the first days of the experiment. Due to reduced accessibility, diffusion becomes later the controlling factor.

The concentrate shows high Fe, Cu, Co, Ni contents (Tab. 1). The slag is enriched in Si, Al, K, Na, P, Ba and Cr. The efflorescent material is enriched in Mn, Mg, and Ni. The hardpan shows elevated Mg, Ca, Co, Cu, and Ni.

The experiments caused a relative enrichment / depletion of a number of elements in the pH3/7 treated slags relative to the starting conditions.

Ni and Cu, concentrated in the embedded sulphide spheres appear to be relatively slowly dissolved. Si, Fe, Ca, K, Na, P, Rb and Sr enrichment in the glass fraction preferentially go into solution, but Fe appears to be rapidly fixed under pH7 conditions.

Table 1. Chemistry of ore concentrate, slag, experiments and hardpan

Sample	SiO ₂	TiO ₂	Al ₂ O ₃	Fe ₂ O ₃	MnO	MgO	CaO	Na ₂ O	K ₂ O	P ₂ O ₅	(SO ₃)	LOI	Total	Co	Cr	Cu	Ni
ore concentrate	7.24	0.117	2.35	64.74	0.041	1.34	1.3	0.34	0.2	0.038	0.21	14.5	92.42	1726	140	29626	29028
original slag	31.21	0.177	5.54	60.79	0.044	1.22	1.65	1.1	1.13	0.053	3.19	-6.93	99.28	1073	271	3015	1511
pH7-treated slag	31.02	0.163	5.71	59.94	0.040	1.05	1.23	0.7	0.92	0.034	2.49	-4.24	99.11	979	282	2744	1440
pH3-treated slag	31.77	0.171	5.70	61.28	0.041	1.09	1.37	0.78	1.03	0.038	2.77	-7.08	99.09	1003	279	3027	1466
pH3-eluate *	0.64	0.001	0.06	1.25	0.002	0.08	0.19	0.24	0.20	0.009			2.69	32	1	75	74
hardpan	31.13	0.201	5.93	54.64	0.045	1.47	1.89	0.92	1.08	0.058	2.91	-1.77	98.51	1176	387	6160	4275

XRF-analyses (Major elements in wt.%, trace elements in ppm; LOI Loss On Ignition); * ICP-OES-analyses

2.4 Hardpan

At the slagheap at Selebi Phikwe hardpans occur in various positions. At the loosely deposited flanks, thick hardpans evolve within a 10 years period. At the flat top of the heap due to the compaction by the trucks a one to two cm thin hardpan evolves right in one season (Fig.6). Due to the continuous deposition of material in layers on top of the heap the time of exposure of a flank and heap top is limited to a few years. Most probably numerous, more ore less well developed top and flank hardpans have been generated within the depositional history of the slagheap. Within the hardpan itself a continuous replacement of pores by agglutinating Fe-hydroxides/oxides and Ni/Cu/Fe-sulfates, partially highly soluble, but with increasing degree of agglutination more and more inaccessible, reduces the pore size and volume from almost 35% down to 6% and less (Fig. 7).

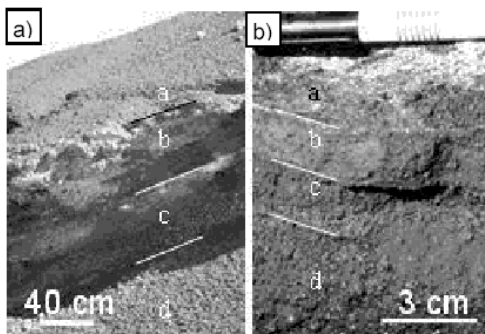


Figure 6. Hardpan development at the flank and the top of the slagheap. a) loose material with some efflorescence, b) hardpan, c) oxidized zone, and d) fresh material.

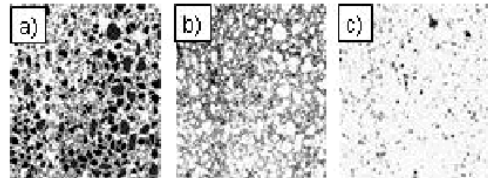


Figure 7. Hardpan from the road sections with a) fragments (65.6%), agglutinated by b) Fe-oxide / hydroxide (28.5%) and pores (5.9%) being isolated and reduced in size. In black item of interest.

3 CONCLUSION

In Selebi Phikwe rapid dissolution of slag material caused by chemical or biological weathering takes place. An effective hard pan formation can be observed after ten years in loosely dropped material in this semi-arid climate. In compacted finer grained matter a hard pan evolves right after one year. SOXHLET tests have shown that hardpan quality and effectivity is controlled by the pH and can be used for characterization of the crust forming potential and the retention capacity of a material. Hardpans are sinks for elements (Fe, Ni, Cu), inhibit wind and water erosion, reduce water input and air exchange and therefore further oxidation and AMD. Hardpan formation - a natural attenuation phenomenon - is highly effective unless interrupted mechanically and might be a better alternative than remediation. Problems arise in quantifying the time required by the process and its effectiveness.

4 ACKNOWLEDGEMENTS

Many thanks for logistical support to the Geological Survey of Botswana, Lobatse and to Selebi Phikwe Mine, Botswana RST Ltd.

5 REFERENCES

Agnew, M. & Taylor, G. 2000. Laterally extensive surface hardpans in tailings storage facilities as possible inhibitors of acid rock drainage. In: Proceedings of the 5th Intern. Conf. Acid Rock Drainage (ICARD 2000), vol.II. p.1337-1346.

- Blowes, D. W., Reardon, E. J., Jambor, J. L. & Cherry, J. A. 1991. The formation and potential importance of cemented layers in inactive sulfide mine tailings. *Geochim. Cosmochim. Acta.* 55: 965-978.
- Chermak, J. A. & Runnells, D. D. 1996. Self-sealing hardpan barriers to minimize infiltration of water into sulfide-bearing overburden, ore, and tailings piles. In: Tailings and mine waste '96. Proc. Intern. Conf. Tailings and Mine Waste. 3: 265-273.
- Jung, H. G., Rammlmair, D., Tacke, K. D. & Tufar, W. 2001. Crust formation processes on Tailings Impoundments simulated by Column Experiments. In: Securing the Future, Proc. Int. Conf. Mining and Envir., Skellefteå. June 25-July 1 2001. vol. 1: 327-335.
- Niederleithinger, E., Grisseemann, C. & Rammlmair, D. 2000. SIP geophysical measurements on slag heaps: A new way to get information about subsurface structures and petrophysical parameters. In: Proceedings of the 6th International Congress on Applied Mineralogy, ICAM 2000, vol. 2: 607-610. Rotterdam, A.A.Balkema.
- Rammlmair, D. & Meyer, L. 2000. Crust formation: Via column experiments to mathematical modelling. In: Proceedings of the 6th International Congress on Applied Mineralogy, ICAM 2000, vol. 2: 641-644. Rotterdam, A.A.Balkema.
- Rammlmair, D., Tacke, K-D. & Jung, H. G. 2001. Application of new XRF-scanning techniques to monitor crust formation in column experiments. In: Securing the Future, Proc. Int. Conf. Mining and Envir., vol. 1: 683-692, Skellefteå.
- Rammlmair, D. 2002. Hard pan formation on mining residuals. In: B. Merkel et al., Proceedings UMH III, Freiberg, 2002.

Potential Use of the Chemical Kaolin-Leaching Residue as Soil Fertilizer

F.R.Ribeiro, J.D.Fabris, W.N.Mussel

Department of Chemistry, ICEX, UFMG, Belo Horizonte, MG, Brazil

R.F.Novais

Department of Soil Science, UFV, Viçosa, MG, Brazil

ABSTRACT: The industrial beneficiation of kaolin involves removal of iron (hydr)oxides and other impurities that impart unwanted colors to the final product, which depreciate its commercial value, particularly if destined for the paper industry. The chemical leaching process in the industrial line may then require treatments with metallic zinc and sulfuric and phosphoric acids in order to reduce, dissolve, and remove iron. To mitigate the environmental impact of these treatments, the acid residue is usually neutralized with calcium oxide. The resulting solid residue is commonly disposed in the industrial area without further treatment to prevent environmental damage. Consequently, percolation through the soil alters the chemical composition of the soil solution and may promote pH variations as well as the release of heavy elements. Alternative disposal methods are needed. In the present study, the potential use of this solid industrial waste as a soil fertilizer was evaluated, owing to the fact that it is high in calcium and other essential plant nutrients. The partially aged residue was tested with soil samples under greenhouse conditions using a clayey and a medium textured soil. A small (~ 0.5) downward shift in pH was observed by applying the residue to the soil, but this effect is not considered a limiting factor to the agricultural productivity of the soil. The amounts of phosphorous, calcium, and zinc in the soil increased linearly with the amount of residue added, which greatly favors plant growth and confirms the potential for the residue to be used as a fertilizer.

1 INTRODUCTION

Iron (hydr)oxides are removed from kaolin by submitting the ore in the industrial line to chemical leaching with metallic zinc and sulfuric and phosphoric acids (Trawinski 1980). The resulting acid residue is neutralized with calcium oxide, resulting in a solid residue that was the focus of study in the present work. The residue is commonly disposed around the industrial area, with no treatment for environment protection. The percolation of this material into the soil affects the chemical composition of the soil solution and may promote pH variations and release hazardous chemical components to the environment. On the other hand, the high calcium sulfate content, as well as the existence of other essential plant nutrients, suggests some potential agronomic use of this material, which depends also on its solubility. The main purposes of this study were: (i) to characterize the mineralogical phases of the solid residue; (ii) to carry out soil tests to evaluate its potential as a source of nutrients for agricultural purposes, and (iii) to evaluate indirectly the environmental impact of residue use as soil fertilizer in agricultural areas.

2 MATERIAL AND METHODS

The partially aged material was collected from a solid residue deposit of the industrial plant of Caolim Azzi Ltda., located in the city of Mar de Espanha (geographical coordinates, 21° 52' 02" S and 43° 00' 35" W), State of Minas Gerais, Brazil. The sample was studied using X-ray powder diffraction (XRD), thermogravimetric analysis, differential thermal analysis, Mössbauer spectroscopy, and conventional chemical analysis. Kaolinite, lepidocrocite, gypsum, goethite, and hematite were the major minerals identified (Ribeiro 2002). The behavior of the residue as a fertilizer was tested under greenhouse conditions without plants. Two soil samples were used for the incubation tests: a clayey (Sete Lagoas sample) and a medium textured soil (João Pinheiro sample), as described in more detail by Oliveira et al. (1999). After mixing the industrial residue in doses of 0, 200, 600, 1,800, 5,400 and 16,200 kg ha⁻¹, the soils were watered until field capacity and left in the greenhouse for 20 days. Soil samples were collected after 5, 10, and 20 days of incubation. The pH of the soil:water mixtures at a mass ratio of 1:2.5 was measured, and chemical elements collected with the Mehlich1 extractor (Mehlich 1953) were quantified by

inductively coupled plasma emission spectroscopy (ICP) and atomic absorption spectrometry (AAS). Statistical correlations between pH, P, Zn, or Ca and the industrial residue dose after different incubation times were also calculated.

3 RESULTS AND DISCUSSION

pH in aqueous soil systems is used as a qualitative evaluation of the overall fertility status of the soil (Tomé 1997). Under controlled conditions plants can tolerate a pH range of 3.0 to 9.0 with no vital damage if nutrients are supplied in suitable quantities. In the natural soil environment, however, if the pH is below 4.5 or above 7.5 plant growth may be inhibited by deficiencies in Ca, Mg, P, and microelements or by toxicity from free Al^{3+} .

The partially aged solid residue used in this work was relatively rich in Fe ($Fe_2O_3 = 5.50$ mass%), S ($SO_3 = 9.63$ mass%), Ca ($CaO = 4.48$ mass%), P ($P_2O_5 = 3.99$ mass%), Si ($SiO_2 = 21.10$ mass%), and

Al ($Al_2O_3 = 24.50$ mass%). The relative amounts of Si and Al and XRD analysis indicate that the solid residue contains kaolinite (ideal formula, $Al_4(Si_4O_{10})(OH)_8$) and gypsum ($CaSO_4 \cdot H_2O$) (Ribeiro 2003).

As a general trend, calcium sulfate has little or no effect on the soil pH, but other chemical components of the solid residue evidently do affect the pH, decreasing the initial soil acidity to pH 4.6. This pH value would be low enough to promote the release of heavy elements to the environment. In the present case, the pH of both soils decreased by 0.6 as the dose of the solid residue reached $16 \times 10^3 \text{ kg ha}^{-1}$ (Fig. 1). The incubation time also affects acidity, but pH became stable after 10 days. The fitted functions are shown in Table 1. Both soils behave as good buffer systems, and no heavy metals or other toxic elements were detected with the residue dose range studied. The observed variation in acidity should, therefore, have little or no adverse effect on plant growth.

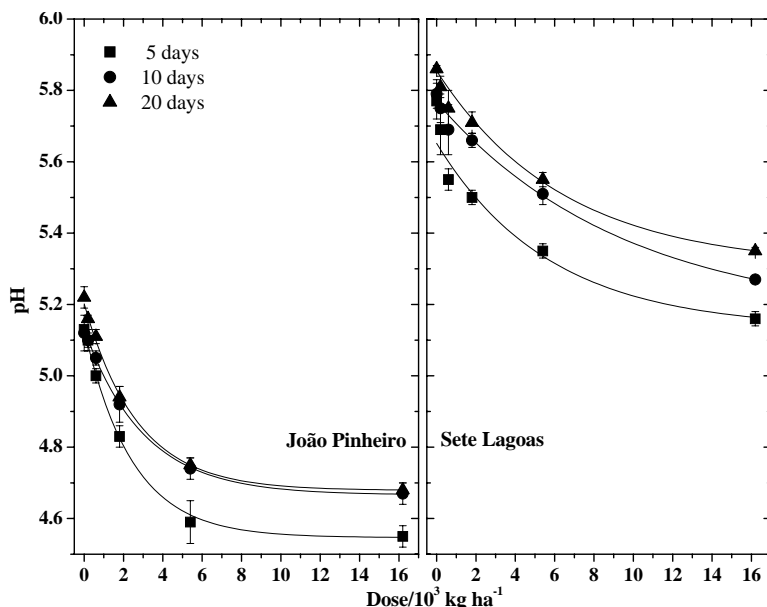


Figure 1 – Increasing acidity with applied doses of the kaolin-residue for the two soil samples, Sete Lagoas and João Pinheiro.

Soil pH is assumed to have a great effect on the release of phosphorus to the soil solution. The optimum availability of phosphorus to plants commonly occurs in soils with pH ranging from 6.0 to 7.0. Increasing soil acidity increases the solubility of iron and aluminum, which tend to fix or remove phosphorus from the soil solution and limit its availability to plants. On the other hand, in soils with high pH, phosphorus reacts with calcium and

magnesium to form insoluble compounds. The amount of available phosphorus, as measured by the Mehlich1 extractor, increased after applying the solid residue (Figure 2). The high linear regression coefficients (Table 1) reveal that dose and time are important factors in the release of phosphorus to the soil solution. For the clayey Sete Lagoas soil, the phosphorus availability after applying the solid residue is higher than for the João Pinheiro soil. In

fact, for the Sete Lagoas soil, the residue application increased soil acidity toward the optimum pH range, thus releasing phosphorus into the soil solution. Because the initial pH of the João Pinheiro soil is less than the Sete Lagoas soil, the increased acidity

due to residue application extends the pH of the João Pinheiro soil outside the optimum range for P availability, thus potentially causing an adverse impact on its fertility with respect to P.

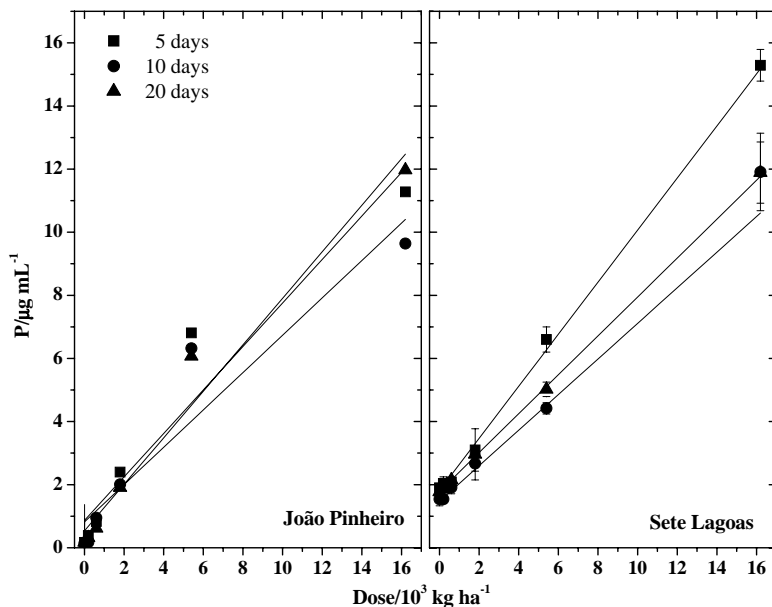


Figure 2 – Availability of phosphorous with applied doses of the kaolin-residue for the two soil samples, Sete Lagoas and João Pinheiro.

Zinc is one of the essential micronutrients to plants, and its availability is highly dependent upon the soil pH (Pierzynski & Logan 1993). In the present case, the Mehlich1 extractable Zn contents also increase linearly with the applied residue dose

(Fig. 3). In both soils, Zn availability is approximately the same. In the Sete Lagoas soil, however, the availability clearly decreases as the time of incubation increases, as seen by comparing the linear regression coefficients (Table 1).

Table 1 – Regression models to the soil pH and Mehlich1 extractable P and Zn as function of incubation time and doses (D).

	5 days		10 days		20 days		
	Equation	R ²	Equation	R ²	Equation	R ²	
João Pinheiro	pH	4.55 + 0.58 e(-D/2.4 x 10 ⁴)	0.999	4.67 + 0.47 e(-D/3.0 x 10 ⁴)	0.999	4.68 + 0.52 e(-D/2.7 x 10 ⁴)	0.999
	P	0.9 + 6.9 x 10 ⁻⁴ D	0.938	0.8 + 5.9 x 10 ⁻⁴ D	0.908	0.5 + 7.4 x 10 ⁻⁴ D	0.972
	Zn	0.9 + 1.32 x 10 ⁻² D	0.999	0.6 + 1.26 x 10 ⁻² D	0.999	0.8 + 1.30 x 10 ⁻² D	0.999
Sete Lagoas	pH	5.13 + 0.52 e(-D/6 x 10 ⁴)	0.963	5.16 + 0.61 e(-D/9 x 10 ⁴)	0.999	5.31 + 0.55 e(-D/6 x 10 ⁴)	0.998
	P	1.82 + 8.2 x 10 ⁻⁴ D	0.994	1.47 + 5.6 x 10 ⁻⁴ D	0.992	1.78 + 6.2 x 10 ⁻⁴ D	0.998
	Zn	0.87 + 0.012 D	0.974	0.3 + 0.0103 D	0.982	0.5 + 0.0105 D	0.994

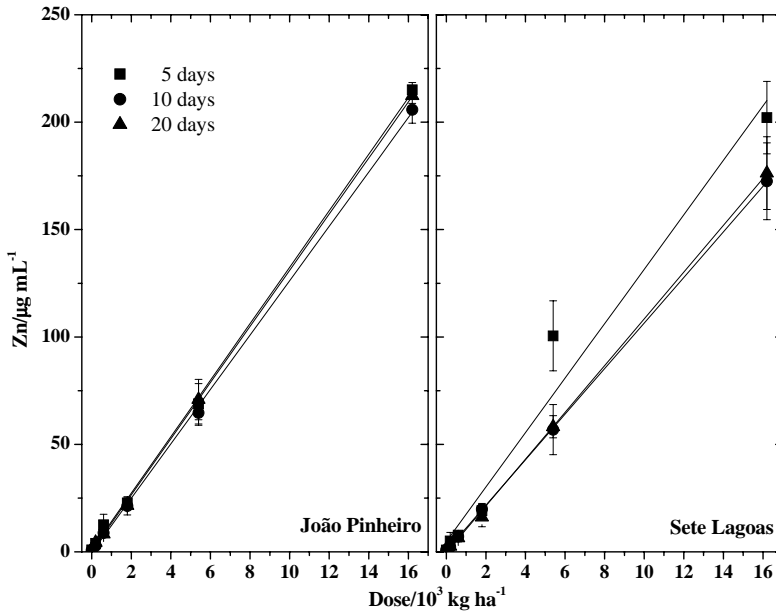


Figure 3 – Availability of zinc with applied doses of the kaolin-residue for the two soil samples, Sete Lagoas and João Pinheiro.

4 CONCLUSIONS

Even though the soil application of solid residue from the industrial leaching of kaolin increased the acidity in both soil samples studied, this increase was not a limiting factor to the use of the residue in agriculture. The small decrease in pH itself presents no problem for plant growth, and it had no apparent effect on releasing heavy or other toxic elements to the soil solution. Residue application also enriches the soil with respect to P, Ca, Mg, and Zn, which favors plant growth and confirms the potential for using this residue as a soil fertilizer.

5 ACKNOWLEDGMENTS:

To Professor Joseph W. Stucki (University of Illinois, USA) for reading the manuscript and for his valuable suggestions. The authors also thank the Caolim Azzi industry (Brazil) for providing all studied samples, and CNPq (Brazil) for fellowship funding for FRR.

6 REFERENCES

Mehlich, A. 1953. Determination of P, Ca, Mg, K, Na, NH₄. Raleigh, NC. *Soil Testing Division Publication*. n. 1-53.
 Oliveira, M. F. G., Novais, R. F., Neves, J. C. L., Vasconcellos, C. A., Alves, V. M. C. 1999. Relação entre o zinco

“disponível”, por diferentes extratores, e as frações de zinco em amostras de solos. *R. Brás. Ci. Solo*, 23:827-836.
 Piersynski, G. M., Logan, T. L. 1993. Crop, soil, and management effects on phosphorus soils test levels. *J. Prod. Agric.* 6:513-520.
 Ribeiro, F. R., Mussel, W. N., Fabris, J. D., Novais, R. F. 2002. Caracterização química-mineralógica e avaliação do potencial de aproveitamento do resíduo sólido proveniente da extração e do tratamento do minério de caulim da região de Mar de Espanha (MG). Belo Horizonte: UFMG/ICEx/DQ.
 Ribeiro, F. R., Mussel, W. N., Fabris, J. D., Novais, R. F., Garg, V. K. 2003. Identification of iron-bearing minerals in solid residues from industrial kaolin processing. *Hyperfine Interactions*, 148/149:47-52.
 Tomé Jr., J. B. 1997. Manual para interpretação de análise de solo. Livraria e editora agropecuária.
 Trawinski, H. 1980. *Cerâmica*, 26:(122)25.

Effects of Redox Reactions on the Structure of Garfield Nontronite: A Mössbauer Spectroscopic Study

F.R.Ribeiro, K.Lee, J.W.Stucki

Department of Natural Resources and Environmental Sciences, University of Illinois, Urbana, IL, USA

J.D.Fabris

Department of Chemistry, Federal University of Minas Gerais, Belo Horizonte, MG, Brazil

ABSTRACT: The oxidation state of structural Fe in smectite clay minerals asserts a great influence on the physical, chemical, and surface properties of the clay; but, little is known about the mechanisms by which this influence occurs. Knowledge of the mechanism would enable better management and exploitation of this phenomenon for the benefit of the environment, industry, and agriculture. The purpose of this study was to determine changes in the clay structure, especially regarding the environment of Fe, that accompany changes in Fe oxidation state. Nontronite in its unaltered, reduced, and reduced-re-oxidized states were characterized by Mössbauer spectroscopy at 87 K and by chemical analyses for structural Fe(II). Octahedral Fe environments in the smectite clays were distinctively changed as reduction progressed. Particularly, Fe(III) quadrupole splitting distributions (QSD) of the highly reduced samples showed a bimodal distribution pattern, which was interpreted to indicate the co-existence of the Fe(III) trioctahedral and dioctahedral domains, even though they were quantitatively very small in the highly reduced state. Re-oxidation restored virtually all of the Fe to the Fe(III) state, but the Fe environment (QSD) of the re-oxidized samples differed from that of the unaltered sample to increasing degrees depending on the initial level of Fe reduction. Iron(III) QSD showed that the structural changes due to redox reactions were irreversible. The greater the extent of reduction, the more the distortion in the structure and the more the irreversibility upon re-oxidation. These differences indicated that the reversibility of the redox process depends on the initial extent of reduction.

1 INTRODUCTION

Reduced nontronite and other Fe-bearing smectites have been studied by Mössbauer spectroscopy in the past (Rozenon & Heller-Kallai 1976a, b, Russell et al. 1979, Komadel et al. 1995), but those studies were limited either by failures to apply important precautions to preserve the reduced state during handling by only a modest level of reduction, or by the lack of advanced methods for analyzing the Mössbauer spectrum. Other previous studies revealed that the redox states of structural Fe in smectites extensively change structural OH groups and the coordination environment of Fe (Lear & Stucki 1985, Manceau et al. 2000, Drits & Manceau 2000, Fialips et al. 2001). While the exact relationships between changes in Fe oxidation state and changes in clay surface chemistry have yet to be fully identified, links to changes in crystal structure are believed to be important. As reduction progresses, the structural disorder becomes more extensive and reversibility upon re-oxidation is degraded. The purpose of the present study was to further probe the changes in the state and environment of Fe at various stages of Fe reduction and re-oxidation in order to fill gaps in our

knowledge of this subject. This Mössbauer study of Fe-rich smectites is the first to utilize systematic reduction-re-oxidation treatments with a technique capable of achieving advanced (virtually 100%) levels of reduction.

2 MATERIALS AND METHODS

2.1 Clay sample

The <0.5- μm size fraction of the Garfield, Washington, nontronite (API #33a) was prepared for this Mössbauer study. The clay was dispersed and saturated in 1 mol/L NaCl solution, fractionated by successive centrifugations in 5 mmol/L NaCl solution and deionized water, dialyzed, and freeze-dried.

2.2 Redox treatment of structural Fe

Reduced smectite clays were prepared using sodium dithionite as the reductant. A portion of Garfield (~30 mg) was dispersed in 20 mL of deionized water in a septum-sealed centrifuge tube followed by addition of 10 mL CB-buffer solution (2 parts of 1.2 mol/L sodium citrate and 1 part of 1.0 mol/L

sodium bicarbonate). The sample was then placed into a water bath at 73°C, and 150 mg of sodium dithionite was added. Reduction periods of 10, 30, 60, and 240 min were selected to obtain different reduction levels (Fe(II)/total Fe). Following reduction samples were washed 4 times with deoxygenated 5 mmol/L NaCl solution. The re-oxidized sample was prepared by purging O₂ gas into washed, reduced suspension held at 73°C for 12 hr. The Fe-reduction levels of the reduced samples were measured by both the 1,10-phenanthroline method of Komadel & Stucki (1988) and by Mössbauer spectroscopy at 87 K.

2.3 Mössbauer spectroscopy

⁵⁷Fe Mössbauer spectra were obtained using a constant acceleration type spectrometer with a 512 channel analyzer and a 25-mCi ⁵⁷Co/Rh source. All spectra were collected at 87 K in a bath-type cryostat and recorded at a velocity range of ±4 mm/s and ±12 mm/s. A metallic Fe foil was used to calibrate the velocity scale and zero velocity was set to the centroid of the room-temperature spectrum of the Fe foil. Most of the absorber clay samples were prepared with thicknesses of 4 to 5 mg Fe/cm².

Spectra were folded into 256 channels and fitted with quadrupole-split doublets assuming Lorentzian line shapes. The areas and widths of both peaks in each doublet were constrained to be equal. Distributions of quadrupole splittings for the octahedral ferric and ferrous doublets were calculated with line width (FWHM) fixed at 0.20 mm/s and all doublets constrained to have the same isomer shift.

3 RESULTS AND DISCUSSION

Mössbauer spectra of the unaltered Garfield nontronite at 87 K displayed no peaks characteristic of Fe oxide phases nor of Fe(II) in the velocity ranges of ±12 mm/s (Fig. 1). In the velocity range of ±4 mm/s (no figure displayed), the spectrum of unaltered Garfield was fitted with two doublets for octahedral Fe(III) and with no tetrahedral Fe(III). The fitted parameters (Tab. 2) showed identical isomer shift and quadrupole splitting values to those in other studies (Goodman et al. 1976, Murad 1987).

The Mössbauer spectra obtained from the reduced Garfield showed that octahedral Fe(II) sites (the high-energy doublet lines around 2.5 mm/s) increased with increasing extent of iron reduction (Fig. 2). Each spectrum of the reduced clays was fitted in the same way with two octahedral Fe(III) and two octahedral Fe(II) doublets. After 10 min of reduction, structural Fe(II) was clearly evident as the main broad envelope was partitioned into multiple parts, including one with a large isomer shift and

quadrupole splitting distinctive of high spin Fe(II).

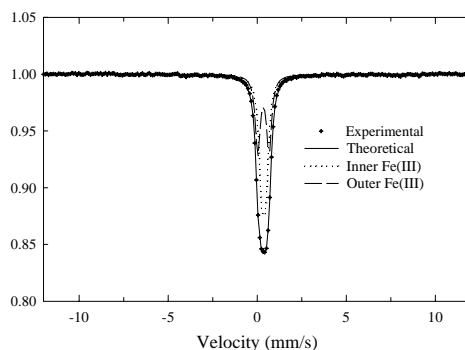


Figure 1. Mössbauer spectra of unaltered Garfield at 87 K in a velocity range ±12 mm/s.

With increasing reduction time, Fe(II) peaks became greater and Fe(III) peaks decreased accordingly. Areas of the Fe(III) doublets were significantly decreased after 60 min of reduction. None of the fitting parameters of the 10- to 60-min reduced clays was significantly changed except for peak area. Highly reduced Garfield (240-min reduction treatment) yielded two major Fe(II) peaks with only small doublets for Fe(III). The Fe(III) peak areas amounted to only 4% of the total. The spectra of this sample required more than two Fe(III) doublets to achieve an acceptable fit and the isomer shift for Fe(III) was smaller than in the other samples. Chemical analysis of the 10-, 30-, 60-, and 240-min reduction treatment revealed Fe(II)/Total to be, respectively, 23%, 45%, 69%, and 95%. The relative Fe(II) peak areas from fits to the spectra agreed well with the Fe(II)/total ratios obtained by chemical analysis.

A series of Mössbauer spectra were collected from the re-oxidized Garfield samples after the various reduction treatments (Fig. 3). Samples re-oxidized after the larger reduction periods yielded spectra with broader line widths and larger quadrupole splittings (Tab. 1). The sample re-oxidized after 10 min of reduction had almost identical hyperfine parameters to those of the unaltered Garfield. The two octahedral Fe(III) doublets in the spectrum of the sample re-oxidized after the 240-min reduction treatment were, however, much broader than in the unaltered Garfield. The quadrupole splitting of the outer Fe(III) doublet from the re-oxidized forms of the 60- and 240-min reduced clays were more than 1.0. This observation indicates that highly reduced samples may not recover their original, unaltered structure upon re-oxidation due to the large degree of distortion created by the intensive reduction treatment.

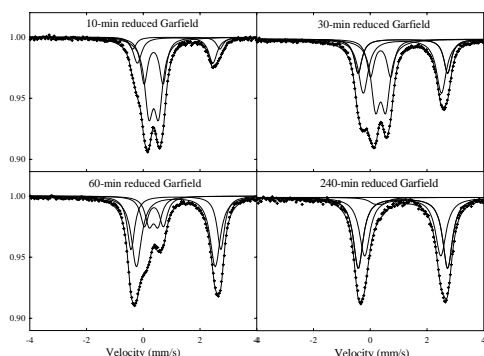


Figure 2. Mössbauer spectra of the reduced Garfield. The spectra were collected at 87 K after reduction for various periods as indicated.

Table 1. Mössbauer parameters for Na-Garfield at 87 K.

Treat [†] / χ^2	Comp [‡]	δ (mm/s)	Δ (mm/s)	Γ (mm/s)	Area* (%)
U/ 2.38	1 Fe(III)	0.468(1)	0.23(1)	0.37(2)	52(5)
	2 Fe(III)	0.463(1)	0.64(1)	0.38(1)	48(5)
10-min R/ 1.70	1 Fe(III)	0.476(1)	0.34(2)	0.35(2)	48(5)
	2 Fe(III)	0.473(1)	0.67(2)	0.30(2)	27(5)
	1 Fe(II)	1.232(3)	2.66(1)	0.36(1)	7(1)
	2 Fe(II)	1.273(6)	3.07(2)	0.28(2)	18(1)
30-min R/ 2.27	1 Fe(III)	0.475(1)	0.36(2)	0.36(2)	34(4)
	2 Fe(III)	0.474(2)	0.71(2)	0.31(2)	17(3)
	1 Fe(II)	1.242(1)	2.75(1)	0.32(1)	16(2)
	2 Fe(II)	1.259(1)	3.15(1)	0.36(2)	33(2)
60-min R/ 2.15	1 Fe(III)	0.478(2)	0.33(3)	0.34(3)	15(3)
	2 Fe(III)	0.487(3)	0.69(2)	0.32(2)	13(3)
	1 Fe(II)	1.260(1)	2.79(1)	0.43(1)	22(2)
	2 Fe(II)	1.259(1)	3.19(1)	0.30(1)	50(2)
240-min R/ 2.67	1 Fe(III)	0.394(1)	0.29(2)	0.47(2)	4(1)
	2 Fe(III)	-	-	-	-
	1 Fe(II)	1.252(2)	2.68(2)	0.45(1)	44(4)
	2 Fe(II)	1.258(1)	3.15(1)	0.41(1)	51(4)
10-min RO/2.68	1 Fe(III)	0.471(5)	0.23(1)	0.36(2)	50(4)
	2 Fe(III)	0.463(6)	0.64(1)	0.37(8)	50(4)
30-min RO/2.47	1 Fe(III)	0.471(1)	0.28(1)	0.43(2)	45(5)
	2 Fe(III)	0.466(1)	0.72(1)	0.49(1)	55(5)
60-min RO/2.05	1 Fe(III)	0.461(1)	0.48(2)	0.59(3)	62(7)
	2 Fe(III)	0.467(2)	1.02(3)	0.57(3)	38(7)
240-min RO/2.04	1 Fe(III)	0.463(1)	0.69(1)	0.61(1)	73(3)
	2 Fe(III)	0.478(2)	1.28(2)	0.52(2)	27(3)

[†]Treatment (U=unaltered; R=reduced; RO=reduced, reoxidized). [‡]Component (1=Inner; 2=Outer). δ =isomer shift. Δ =quadrupole splitting. Γ =line width. The figures in parentheses are one standard deviation except for those in Area column. *the figures in parentheses are error (%).

Curve fitting of the spectra from the Garfield samples, using only Lorentzian line shapes, generally produced acceptable statistical parameters; however QSD for Fe(III) and Fe(II) in these spectra were performed for comparison.

Unlike the fits with two Lorentzian doublets, the Fe(III) QSD of the unaltered Garfield (Fig. 4) showed only a broad and continuous, but asymmetrical, distribution. In other words, no assignment of Fe to multiple sites could be made.

After partial reduction of the sample (10-, 30-, and 60-min reduction treatments), the Fe(III) QSD remained a single, continuous distribution that was somewhat narrower than in the unaltered sample, but shifted to slightly greater value although still located within the same range. After the 240-min reduction, however, the QSD changed dramatically to a bimodal distribution having two sharp peaks.

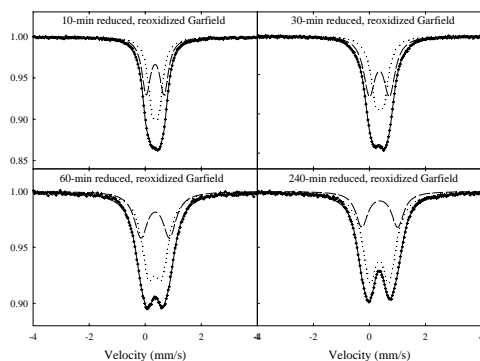


Figure 3. Mössbauer spectra of reoxidized Garfield at 87 K. The spectra were collected after reoxidizing each reduced Garfield for 12 hr in water bath at 73° C.

The first peak was centered at a value similar to the unaltered smectite (0.3 mm/s), indicating that some of the Fe(III) is still located in a dioctahedral environment even after significant reduction. The second peak, however, was shifted to about 0.9 mm/s, which is consistent with Fe(III) in a trioctahedral structure (compare with a value of 1.0 mm/s for Fe(III) in biotite). This conclusion is also supported by the observations by Manceau et al. (2000) and Fialips et al. (2001) that structural Fe reduction causes the migration of some structural Fe to form trioctahedral domains.

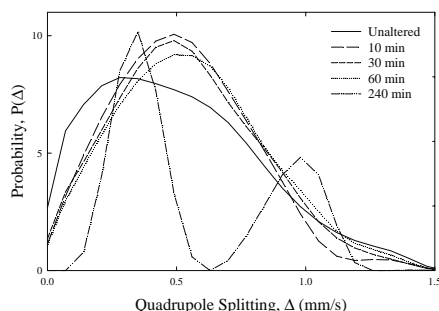


Figure 4. Fe(III) quadrupole-splitting distributions from fits to the spectra of the reduced Garfield with various reduction periods.

The Fe(II) QSD was also calculated and revealed no great differences among the reduced samples

(Fig. 5), except the average value for the 10-min treatment was less than the other treatments. These differences were identical to the differences reported for the fitting parameters in Table 2. After 30 min of reduction, both the peak maximum and the average QSD position increased slightly and may indicate a displacement in the coordinating anions (OH^- , O^{2-}), around Fe(II).

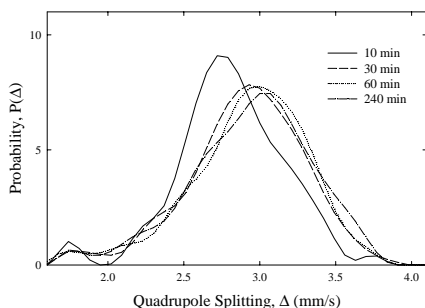


Figure 5. Comparison of Fe(II) quadrupole-splitting distribution from fit to the spectra of reduced Garfield with different reduction periods.

After re-oxidation of the samples, further interesting features were found in the Fe(III) QSD (Fig. 6). First, the distributions were distinctly different from the unaltered samples, indicating a lack of reversibility. Second, the bimodal distribution observed for Fe(III) in the partially reduced states was retained after re-oxidation, with one component positioned at about 0.25 mm/s, and the other component steadily shifted from about 0.5 mm/s to about 0.9 mm/s as the reduction treatment progressed toward completion, and, third, the components became broader as the initial reduction level increased. The fitted parameters for the unaltered and the 10-min reduced, re-oxidized clay were almost the same, but the Fe(III) QSD were different. The QSD could, therefore, be a good indicator of the irreversibility of reduction-re-oxidation reactions on Fe-bearing clays.

4 CONCLUSION

Quadrupole splitting distribution analysis applied to Garfield nontronite provides clear criteria for observing the structural changes that occur upon reduction and re-oxidation of structural Fe in the clay. The Fe(III) QSD in the highly reduced sample is consistent with the formation of trioctahedral domains and the co-existence of Fe(III) in both tri- and dioctahedral environments, even though quantitatively the trioctahedral domain size is very small. The QSD for Fe(III) in the re-oxidized Garfield sample showed that the structural changes due to redox reactions are not completely reversible.

The greater the extent of reduction, the more the distortion in the structure and the more the irreversibility upon re-oxidation.

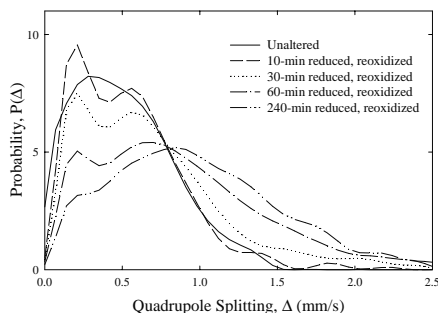


Figure 6. Fe(III) quadrupole-splitting distributions from fits to the spectra of the re-oxidized Garfield via different reduction periods.

5 ACKNOWLEDGMENTS

The authors acknowledge financial support from the National Science Foundation, Grant N° EAR 01-26308; and DOE-NABIR Grant N° FSU F48792.

6 REFERENCES

- Drits, V. A., Manceau, A. 2000. A model for the mechanism of Fe^{3+} to Fe^{2+} reduction in dioctahedral smectites. *Clays and Clay Mineral.*, 48:185-195.
- Fialips, C. I., Huo, D., Yan, L., Wu, J., Stucki, J. W. 2001. Effect of iron oxidation state on the IR spectra of Garfield nontronite. *Am. Mineral.*, 87:630-641.
- Komadel, P., Madejova, J., Stucki, J. W. 1995. Reduction and reoxidation on nontronite: questions of reversibility. *Clays and Clay Mineral.*, 45:105-10.
- Lear, P. R. and Stucki, J. W. 1985. Role of structural hydrogen in the reduction and reoxidation of Fe in nontronite. *Clays and Clay Mineral.*, 33:539-545.
- Manceau, A., Lanson, B., Drits, V. A., Chateigner, D., Wu, J., Huo, D., Gates, W. P., Stucki, J. W. 2000. Oxidation-reduction mechanism of iron in dioctahedral smectites. 2. Structural chemistry of reduced Garfield nontronites. *Am. Mineral.*, 85: 153-172.
- Murad, E. 1987. Mössbauer spectra of nontronites: structural implications and characterization of associated iron oxides. *Z. Pflanzenernähr. Bodenk.*, 150:279-285.
- Rozenon, I. & Heller-Kallai, L. 1976a. Reduction and oxidation of Fe(III) in dioctahedral smectites. 1: reduction with hydrazine and dithionite. *Clays and Clay Mineral.*, 24:271-282.
- Rozenon, I. & Heller-Kallai, L. 1976b. Reduction and oxidation of Fe(III) in dioctahedral smectites. 2: reduction with sodium sulphide solutions. *Clays and Clay Mineral.*, 24:283-288.
- Russell, J. D., Goodman, B. A., & Fraser, A. R. 1979. Infrared and Mössbauer studies of reduced nontronites. *Clays and Clay Mineral.*, 27:63-71.

Degradation of Oxamyl by Redox-modified Smectites: Effects of pH, Layer Charge, and Extent of Fe Reduction

F.R.Ribeiro, J.W.Stucki, R.A.Larson, K.A.Marley

Department of Natural Resources and Environmental Sciences, University of Illinois, Urbana, IL, USA

P.Komadell

Institute for Inorganic Chemistry, Slovak Academy of Sciences, Bratislava, Slovakia

J.D.Fabris

Department of Chemistry, Federal University of Minas Gerais, Belo Horizonte, MG, Brazil

ABSTRACT: The redox states of structural iron in clay minerals may profoundly affect the chemical fate of agrochemicals. The pesticide oxamyl can be degraded either through a redox pathway, to produce N, N-dimethyl-1-cyanoformamide (DCMF), or through a base-catalyzed hydrolysis, to produce oxamyl oxime. In a preliminary study, we found that in the presence of reduced reference clay, oxamyl degraded rapidly, completely, and exclusively to oxamyl oxime (base hydrolysis pathway). This result was surprising because the reduced smectite is presumably a strong reducing agent and a priori predicts the alternative redox pathway, yielding preferentially DCMF. The main objectives of this study were therefore to: (i) better understand the basis of the observed degradation mechanism of oxamyl in the presence of reduced smectite, and (ii) evaluate if these degradation reactions would occur in nature. The hypotheses tested were: (i) the neutralization of the Brønsted basicity of the reduced smectite precludes the hydrolysis degradation pathway and invokes the redox pathway, (ii) this degradation depends on the smectite Fe(II) content and redox cycle, and (iii) oxamyl degradation occurs in soil clays reduced under natural conditions. Results revealed that for both reference clays, which were reduced to varying degrees at circum-neutral pH, oxamyl actually degrades to oxamyl oxime. As the pH of the oxamyl solution decreases, however, the Brønsted basicity of the clay surface becomes increasingly neutral, yielding preferentially DCMF. At pH 2.5, DCMF was the only observable product. Reoxidation of the smectites restores some but not all of the original clay properties.

1 INTRODUCTION

The swelling nature of smectite clays permits H₂O and other molecules to be accommodated in the interlayer space, where numerous chemical processes may occur, including the induced transformation of organic compounds. These molecules experience short- and long-range interactions at the clay-water interface that may determine their chemical fate. The oxidation state of structural Fe in smectite is known to profoundly influence its surface interfacial properties (Stucki 1997), which, in turn, affects the clay's interactions with organic compounds. Specifically, the effective surface acidity is dramatically altered when structural Fe(III) is reduced to Fe(II). Cervini-Silva et al. (2000) showed that pentachloroethane is transformed to tetrachloroethene through the reduced clay surfaces that act as a Brønsted base.

Oxamyl is a pesticide that degrades via a hydrolytic mechanism, or via an electron transfer process. Since reduction of structural Fe in smectite alters both the surface acidity and reduction potential, which of these two pathways is favored under low- vs. high-pH conditions is unclear.

The objectives of this work were (i) to correlate

pH changes and redox state of smectite with oxamyl degradation; (ii) to determine the effect of different initial pH of oxamyl on degradation products; (iii) to evaluate the relative importance of different oxamyl:smectite ratios, and (iv) to identify any different behavior between low- and high-Fe smectites on these oxamyl degradation reactions.

Since the reduced smectite surfaces possess an elevated Brønsted basicity as well as an increased reduction potential, the question is which of these, i.e., base-catalyzed hydrolysis or reductive transformation, dominates the main chemical pathway governing the oxamyl degradation.

2 MATERIALS AND METHODS

Two smectite samples were used in this study: (i) Wyoming montmorillonite ([sample labeled Upton, similar to API #25, Na_{0.72}(Si_{7.82}Al_{0.18})(Al_{3.06}Fe³⁺_{0.30}Fe²⁺_{0.02}Mg_{0.65})O₂₀(OH)₄; Low 1980) obtained from American Colloid Company, Arlington Heights, Illinois, USA (same sample used by Yan et al. 1996), and (ii) ferruginous smectite from Grant County, Washington, USA, (sample labeled SWa-1, Na_{0.87}(Si_{7.38}Al_{0.62})(Al_{1.08}Fe³⁺_{2.67}Fe²⁺_{0.01}Mg_{0.23})O₂₀(OH)₄; Manceau et al. 2000), purchased from the

Source Clays Repository of The Clay Minerals Society.

Oxidized smectites were prepared by suspending portions of the Na-saturated, freeze-dried stock material in 5 mmol L^{-1} NaCl solution. Reduced forms of the clays were prepared by a procedure described by Stucki et al. (1984). Reoxidized forms were obtained by flowing oxygen gas for 24 hours at room temperature through the reduced clay suspension, after removing the reducing agent by centrifuge-washing three times with 5 mmol L^{-1} NaCl solution. The amounts of Fe(II) and total structural Fe were determined by the analytical method of Komadel & Stuchi 1988.

The oxamyl solution was prepared by dissolving oxamyl powder either in acid solution, so as to obtain a final solution concentration of 25 mg L^{-1} , at pH 3.5, or in deionized water to the same final concentration, except at pH ≈ 7.0 .

Thirty mL of oxamyl:smectite suspension in a ratio of $37.5 \mu\text{g} : 1 \text{ g}$ was reacted overnight in a capped teflon vessel, placed horizontally in a reciprocal shaker. A 1-mL aliquot of a 25 ppm CaCl_2 solution was then added to each sample, and centrifuged at 6000 rpm for 10 minutes in an IEC Clinical Centrifuge model Sorvall RC 5C Plus. The supernatant was collected and submitted to HPLC analysis and pH determination. The chemical composition of the oxamyl samples and their degradation products were determined by reverse-phase HPLC (Perkin Elmer 250 Binary LC Pump) with UV detection at 233 nm, an Alltech C18 ($5 \mu\text{m}$, $250 \text{ mm} \times 4.6 \text{ mm}$) column, and an isocratic mobile phase of 5 mmol L^{-1} acetic acid:acetonitrile (85:15 v/v), at a flow rate of 1 mL min^{-1} . The retention times of oxamyl, oxamyl oxime, and DCMF were identified by comparing HPLC profiles with authentic standards and by photodiode array spectroscopy (Groton PF1 Diode Array Detector System). Concentration values in samples were determined from a standard curve.

3 RESULTS AND DISCUSSION

Levels of structural Fe(II) obtained by dithionite reduction, as determined by the Komadel & Stucki (1988) procedure for SWa-1 and Upton clays, were over 90 mass% (relative to the total Fe) and 80 mass%, respectively. Reoxidation decreased the Fe(II) content to 10 mass% and 42 mass%, respectively.

Reduction of structural Fe greatly affects the physical and chemical properties of clays, increasing their tendency to aggregate. Previous studies also found changes in the surface area, layer charge, cation exchange capacity, swelling pressure, and color, following chemical reduction of structural Fe (Stucki et al. 1988). For SWa-1 clay, color changed

from yellow, in the oxidized form, to blue-gray in the dithionite-reduced form, and back to yellow in the reoxidized form. For Upton, color was unchanged by variations in oxidation state of the structural iron.

The rate and extent to which the oxamyl disappears in the presence of dithionite-reduced smectites were greater than in the presence of the oxidized clays. The higher the structural Fe(II) content, the lower the final concentration of oxamyl in solution (Fig. 1).

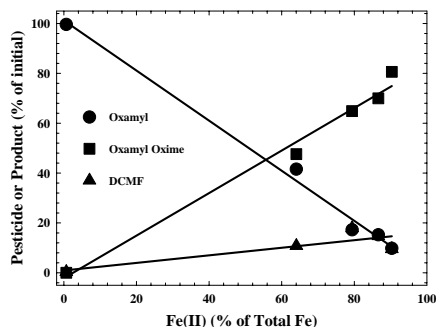


Figure 1. Degradation products of oxamyl as a function of structural Fe(II) in SWa-1.

The major degradation product in all cases, however, was the hydrolysis product, oxamyl oxime, rather than the reduction product, DCMF. These results are consistent with the hypothesis that the smectite basal surface enhances Brønsted base catalysis. The surface catalyzed reaction might, however, be mediated through the bulk water. Strong interaction with water molecules occurs at the smectite basal surface through Si-O and H-O-H coupling, which is further strengthened by reduction of structural Fe (Yan & Stucki 2000). This interaction polarizes the interlayer water toward the Si-O basal group, and makes Fe(II)-bearing smectite a strong nucleophilic reactant that accelerates the hydrolysis. Organic compounds may then interact with the basal surface through the polarized water (Cervini-Silva et al. 2000, 2001).

Despite the main interaction between smectite and oxamyl following the base-catalyzed hydrolysis pathway for both the oxidized and reduced iron states, a small amount of reductive degradation product, DCMF, was observed in dithionite-reduced smectite. The rate of DCMF production, however, was lesser than that following the hydrolysis pathway.

The pH of the oxamyl solution and the equilibrium pH of the $37.5 \mu\text{g} : 1 \text{ mg}$ oxamyl:smectite oxidized, reduced, or reoxidized SWa-1 suspension were measured. Results revealed several interesting effects (Tab.1): i) the reaction with oxamyl reoxidizes some of the structural Fe(II); ii)

reoxidation with oxygen gas was incomplete; iii) pH increases with increasing Fe(II) content; iv) reduced clay buffers the solution pH to 7-9, depending on the initial pH.

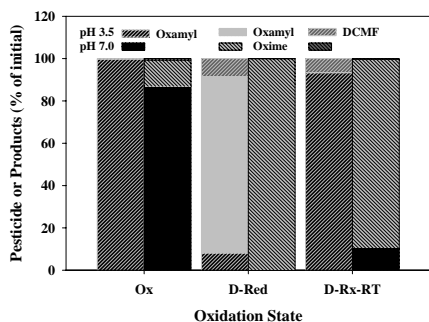


Figure 2. Degradation products of oxamyl as a function of structural Fe(II) in SWa-1.

Table 1. Changes in the oxamyl:smectite SWa-1 suspension pH and structural Fe(II) before and after oxamyl application.

	Solution pH			Fe(II)/%		
	Ox	D-Red	D-Rx-RT	Ox	D-Red	D-Rx-RT
No oxamyl	6.9	8.4	8.4/9.2	0.67	90.34	10.15
Oxamyl pH = 3.5	3.4	7.1	3.9	0.00	39.57	2.35
Oxamyl pH = 7.0	6.6	9.0	6.9	0.47	65.57	6.45

3.1 Oxidized smectite SWa-1

Adding oxamyl solution at pH \approx 3.5 to oxidized SWa-1 in suspension decreased the pH to 3.4. At this point, no oxamyl was decomposed by the hydrolysis pathway and the clay had no Fe(II) to promote degradation by the reduction pathway (Fig.2). Addition of oxamyl solution at pH \approx 7 to the suspension decreased the pH only slightly (to 6.6) and degraded oxamyl by the hydrolysis pathway. In this case, the Fe(II) content in the clay decreased slightly after reaction with oxamyl.

3.2 Reduced smectite SWa-1

For the reduced SWa-1, adding oxamyl solution at pH \approx 7 decreased the resulting pH to 7.1 from the initial pH of 8.4 in the reduced smectite, but increased relative to the pH \approx 3.5 of the oxamyl solution. Figure 2 indicates the high amount of oxamyl oxime rather than DCMF formed by oxamyl reaction with the reduced clay. Iron(II) in reduced clay favored initially the reduction pathway, decreasing the oxamyl content from 90 to \sim 40 mass%. However, if the initial pH of the suspension was increased, the hydrolysis product

was favored. When oxamyl solution at pH \approx 7 was added to the reduced clay, the pH of the final suspension increased to 9.0, and oxamyl was decomposed exclusively by the hydrolysis pathway.

Contrary to observations from the oxidized and reoxidized clays, the pH in the oxamyl:smectite suspension increased relative to the added oxamyl solution when it was in contact with reduced clay.

In all conditions studied, the structural Fe(II) content decreased after reaction with oxamyl solution. However, the greatest decrease in Fe(II) was observed after the application of oxamyl solution at pH \approx 3.5. At this pH, but not at pH \approx 7, DCMF was preferentially produced.

3.3 Reoxidized smectite SWa-1

With the reoxidized clay, the degradation of oxamyl produced a small amount of DCMF, which was attributed to the remaining Fe(II) in the reoxidized clay. Although the initial pH of the clay was high, 9.2, adding oxamyl solution at pH \approx 3.5 led to a decrease of the final pH \approx 3.9, disfavoring degradation by the hydrolysis pathway. Fe(II) content in the clay decreased from 10 to about 2 mass% by reacting with oxamyl, which confirms the Fe(II) consumption in this reaction. By adding oxamyl solution at pH \approx 7, the final pH of the suspension decreased from \approx 9.9 to \approx 6.9 and higher amounts of oxamyl oxime were produced. In this case, no DCMF was detected and the iron consumption was lesser (about 3.5mass %) than when oxamyl solution at pH \approx 3.5 was applied (about 7.5 mass%)

3.4 Upton versus SWa-1

Upton clay showed the same general behavior as observed for SWa-1. However, taking into account its lower total iron content, some specific characteristics were observed for this clay. Upton oxidized and reoxidized clays have a similar behavior to the oxidized and reoxidized SWa-1, respectively (Tab. 2). Figure 3 indicates the formation of a small quantity of DCMF in oxidized clay at both pHs studied. Compared to oxidized SWa-1, oxidized Upton has more structural Fe(II), which explains degradation through the reduction pathway, producing DCMF.

Results obtained with the reduced Upton must be understood also on the basis of its relatively lower total iron content, i.e. only 3 mass% (in SWa-1 total iron content is about 16 mass%). After adding oxamyl solution at pH \approx 3.5 to the reduced Upton, the pH of the resulting suspension decreased four units, compared to the initial pH of the clay; and the final pH is closer to that of the original oxamyl solution. In the same conditions, the pH for the final suspension decreased by only one unit for the

reduced SWa-1. Regarding oxamyl degradation, contrary to observations from reduced SWa-1, only DCMF was produced at pH \approx 3.5. Only the hydrolytic degradation product was observed by adding the oxamyl solution at pH \approx 7 to the reduced Upton. Regarding the Fe(II) consumption in the reduced Upton during the oxamyl degradation process at pH \approx 3.5, the behavior was opposite to that observed for SWa-1 clay. The correlation between these two clays indicated that hydrolysis and reduction pathways did not occur separately; but, instead, they were closely interrelated during oxamyl degradation.

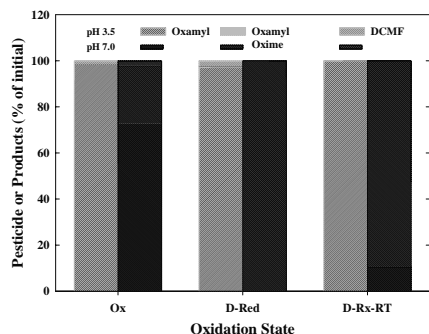


Figure 3. Degradation products of oxamyl as a function of structural Fe(II) in Upton.

Table 2. Changes in the oxamyl:smectite Upton suspension pH and structural Fe(II) before and after oxamyl application.

	Solution pH			Fe(II)/%		
	Ox	D-Red	D-Rx-RT	Ox	D-Red	D-Rx-RT
No oxamyl	7.2	8.7	8.7/9.9	12.94	80.37	42.22
Oxamyl pH = 3.5	3.8	4.5	3.8	3.64	51.19	20.17
Oxamyl pH = 7.0	6.9	8.2	7.1	9.16	27.67	21.63

4 CONCLUSIONS

Iron redox reactions on clay mineral surfaces play an important role on the degradation of agrochemicals. Oxamyl can be degraded through two different mechanisms. In the hydrolysis pathway, oxamyl oxime was the most important product and in the reduction one, N, N-dimethyl-1-cyanoformamide (DCMF) was mainly produced. In the presence of reduced SWa-1 clay, hydrolysis and reduction products were found. Oxamyl oxime was always produced in higher quantity. In the presence of oxidized or reoxidized clays, only oxamyl oxime was detected. The rate at which oxamyl disappears was higher for reduced than for oxidized smectites. The surface basicity of the interlayer interface was

the major cause for the hydrolysis and the presence of structural Fe(II) was primarily responsible for the reduction reaction of the oxamyl.

The extent to which the redox reactions take place depends upon the structural iron content, in tetrahedral sites of the clay structure and also upon the acidity of the oxamyl solution. At room temperature and circum-neutral pH, even the oxidized clay decomposed the studied agrochemical. However, a more important effect was observed with the reduced clay, which shows more effective degradation either at circum-neutral or at lower pH, where the oxamyl solution tends to be more stable.

Reduced smectites can promote the degradation of the oxamyl in simultaneously both pathways. At lower pH, the predominant product is DCMF whereas at higher pH, the oxamyl oxime is the main product.

5 ACKNOWLEDGMENTS

FRR, JWS, and JDF acknowledge financial support from the National Science Foundation, Grant N° EAR 01-26308; PK acknowledges the J.W.Fulbright Commission for fellowship support.

6 REFERENCES

- Cervini-Silva, J., Larson, R. A., Wu, J., Stucki, J. W. 2001. Transformation of chlorinated aliphatic compounds by ferruginous smectite. *Environ. Sci. Tech.*, 35: 805-809.
- Cervini-Silva, J., Wu, J., Stucki, J. W., Larson, R. A. 2000. Adsorption kinetics of pentachloroethane in iron-bearing smectites. *Clays and Clay Min.*, 48: 132-138.
- Komadel, P. & Stucki, J. W. 1988. Quantitative assay of minerals for Fe(II) and Fe(III) using 1, 10-phenanthroline: *Clays and Clay Min.*, 36: 379-381.
- Low, P. F. 1980. The swelling of clay. II. Montmorillonites. *Soil Sci. Soc. Am. J.*, 44: 667-676.
- Manceau A, Lanson, B., Drits, V. A., Chateigner, D., Gates, W. P., Wu, J., Huo, D., Stucki, J. W. 2000. Oxidation-reduction mechanism of iron in dioctahedral smectites. *Am. Miner.*, 85: 133-152.
- Stucki, J. W. 1997. Redox processes in smectites: Soil environmental significance. Auerswald, K. and Stanjek, H. eds., *Advances in GeoEcology*, 30. Catena-Verlag: Amsterdam. 395-406.
- Stucki, J. W., Golden, D. C., Roth, C. B. 1984. The preparation and handling of dithionite-reduced smectite suspensions. *Clays and Clay Min.*, 32: 191-197.
- Stucki, J. W., Goodman, B. A., Schwertmann, U. 1988. eds., *Iron in soils and clay minerals*, D. Reidel: Dordrecht, The Netherlands.
- Yan, L., Low, P. F., Roth, C. B. 1996. Swelling pressure of montmorillonite layers versus H-O-H bending frequency of the interlayer water. *Clays and Clay Min.*, 44:749-765.
- Yan, L. & Stucki, J. W. 2000. Structural perturbations in the solid-water interface of redox transformed nontronite. *Journal of Colloid and Interface Science*, 225:429-439.

Mineralogical Characterization and Environmental Evaluation of TSP, PM10 and PM2,5 Atmospheric Inorganic Aerosol of Oviedo (Asturias, Spain)

I.Rodríguez & C.Marcos

Dpto. Geología, Universidad de Oviedo.C/. Jesús Arias de Velasco, s/n, 33005, Oviedo (Asturias), Spain

ABSTRACT: Investigations from September of 2000 to August of 2001 and February of 2003 to April of 2003 in the atmospheric inorganic aerosol of Oviedo (Spain) were carried out in order to characterize and to compare the TSP (total suspended particulate matter), PM10 and PM2.5 (particulate matter with an aerodynamic diameter lesser than 10 and 2.5 μm , respectively) and evaluate the air quality, are the first in this scientific field in this city. TSP, PM10 and PM2.5 collected with a high and medium-volume sampling was characterized by X-ray diffraction and electron microscope scanning with EDX. Compositional distribution of particulate matter in the studied zones of the Oviedo city was obtained by factorial analysis and cluster.

1 INTRODUCTION

The atmospheric pollution can be defined as “the presence of substances in the outdoor air in concentrations sufficient to interfere with health, comfort, safety, or with full use and enjoyment of property”. Seen over longer periods, pollution in mayor cities tends to increase during the built up phase and the global number of cars has increased. Air pollution poses risks to and adverse effects on human health (Guthrie & Mossman 1993) as well as natural and man-made environments (Connor 1990). Health-related air pollution is represented by particulate matter (PM), NO_x, tropospheric ozone and SO₂. Actually, in most of the industrialised world urban air pollution is monitored routinely.

Particulate matter is the general term used for a mixture of solid particles and liquid droplets found in the air. Particulate matter can be either primary or secondary in nature. Primary particles are emitted directly into the atmosphere either by natural or anthropogenic processes, whereas secondary particles have a predominantly man made origin and are formed in the atmosphere from the oxidation and reactions of the other components in the air.

The parameters that determine the danger of the particles as air pollutants in the environment, are:

shape, size, nature, composition, concentration and duration of exposure.

Suspended particulate matter (SPM) is all particles surrounded by air in a given, undisturbed volume of air. Fine particulate matter is defined as specific fractions of suspended particulate matter as particles which pass through a size selective inlet with a 50% efficiency cut-off at 10 μm (PM10) and 2.5 μm (PM2.5) (UNEP/WHO 1994) aerodynamic diameter, respectively. Fine particles penetrate and are retained more deeply in the human respiratory tract.

In this work the TSP, PM10 and PM2.5 measured in Oviedo (Asturias, Spain) from September of 2000 to August of 2001 and from February of 2003 to April of 2003 was used to characterize the aerosol and evaluate the air quality of the city.

2 EXPERIMENTAL

TSP, PM10 and PM2.5 were collected with a high and medium volume sampling in the monitoring stations of Oviedo, Plaza de Toros and Palacio de los Deportes which are near a traffic road, and Purificación Tomás situated in a park with the same name.

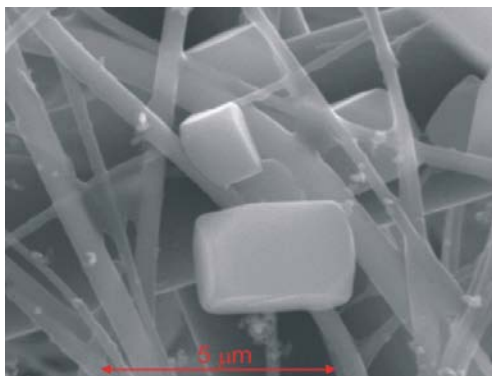


Figure 5. Halite particles.

The classification and compositional distribution of particulate matter (PM10 and PM2.5) in the studied zones of Oviedo city were obtained by factorial and cluster analyses starting from the data obtained by EDX. To determine the distribution of the particles collected in the samplers they were classified according to their composition by cluster analysis. Firstly, hierarchical and non-hierarchical methods were used and the number of particles of each cluster (method of K partitions: “quick cluster of SPSS”) and the relative average percentage of the studied elements of each cluster was estimated. Secondly, this methodology was successively repeated in the cases where groups of particles were not well defined until the most of particles were correctly classified. The number of classes of PM10 was 10, 7 and 8 in Palacio de los Deportes, Plaza de Toros and Purificación Tomás, respectively. The number of classes of PM2.5 was 9, 9 and 11 in Palacio de los Deportes, Plaza de Toros and Purificación Tomás, respectively. The most abundant phases in the PM10 and PM2.5 particulate in all the investigated zones of the city are silicates and aluminosilicates, carbonates, sulphates and halite, but sulphates are the most abundant in PM2.5 in all the zones and halite is more abundant in PM10 than in PM2.5.

In relationship with the concentration, the TSP annual average value along the year 2000-2001 was of $55\mu\text{g}/\text{m}^3$ in Plaza de Toros, $58\mu\text{g}/\text{m}^3$ in Purificación Tomás and $77\mu\text{g}/\text{m}^3$ in Palacio de los Deportes. These values have not exceeded the limit value stabilised by the European Community, $150\mu\text{g}/\text{m}^3$ (38/1972 law, on December 22). The TSP concentration media value has reduced about 20% compared to the registered between 1993-1997 (Ferrón de la Fuente 1999). During 13 days of sampling for site in Plaza de Toros, Purificación Tomás and Palacio de los Deportes, the daily averages values of PM10 exceeded the limit value ($50\mu\text{g}/\text{m}^3$) established by the European Community

(Directive 1999/30/EC) 8, 4 and 6 days respectively. The maximum PM2.5 concentration occurred in Plaza de Toros.

In Oviedo, as urban area, the main anthropogenic source of airborne particulates are the Soto de Ribera coal-fired power plant, motor vehicle exhaust and residencial combustion sources (coal and diesel oil). The main natural source of airborne particulates is resuspended soil dust, as in the Europe. These particulates concentrate mainly in TSP and PM10 fraction. So, the natural particles are: Calcite, quartz, gypsum, dolomite, muscovite, hematite, halite and vegetal particles. The anthropogenic particles are: Gypsum, iron oxides, wollastonite, mascagnite, cerussite, lead, selenides, carbonaceous particles and spherical particles.

3 CONCLUSIONS

The phases identified in the particulate matter collected with high volume sampler in Oviedo city are spherical, irregular or with crystalline habit. Inorganic particulate matter of TSP, PM10, PM2.5 is made up of: Silicates and aluminosilicates of Ca, Na, K, Mg, S, Cl, carbonates of Ca and Na, sulfates of Ca and/or Na, iron oxides, calcium oxide, chlorides, carbonaceous particles. The more abundant mineral phases were quartz, calcite and gypsum, although the concentration of the last is higher in PM2.5 and PM10 than in TSP, as revealed by X-ray diffraction and as it was to be expected.

The decreasing of the TSP in Oviedo city is due to the increase of pedestrian streets and to the street cleaning and the decrease of the domestic coal burning. The exceeded value of the PM10 concentration is common because is Mediterranean country where the contribution of natural particulate matter is higher than other countries of North of Europe.

4 REFERENCES

- Connor, M. 1990. *Les aerosoles antropogenes et l'alteration de la pierre*. Project de Diplome. Ecole Polytechnique de Lausanne.
- Ferrón de la Fuente, E. 1999. *Calidad del aire en Asturias 1986-1997*. Oviedo: Servicio de Publicaciones del Principado de Asturias. Gobierno del Principado de Asturias.
- Guthrie, G.D. jr. & Mossman, B.T. 1993. Merging the geological and biological sciences: An integred approach to the study of mineral-induced pulmonary diseases. In: *Health effects of mineral dusts*. Guthrie, G.D. jr. & Mossman, B.T. (ed.). Reviews in Mineralogy, Vol. 28, Mineralogical Society of America (P.H. Ribbe, ed.).
- UNEP/WHO 1994. *GEMS/AIR Methodology Reviews* Vol. 3: Measurement of suspended particulate matter in ambient air. Nairobi: WHO/EOS/94.3, UNEP/GEMS/94.A.4. UNEP.

Heavy Metals Concentrations in Mangroves Swamps

A.L.F.Santos & G.R.Boaventura

Institute of Geosciences, University of Brasília, 70910-900 Brasília, DF, Brazil.

A.C. de Oliveira & V.K.Garg

Institute of Physics, University of Brasília, 70910-900 Brasília, DF, Brazil

T.Cassia de Brito Galvão

School of Engineering, Federal University of Minas Gerais, Belo Horizonte, MG, Brazil

ABSTRACT: Mangrove sediments in contact with metal rich water, nutrients, and complex organic matter suffer mineralogical transformation – dissolution of some and transformation of others minerals. In addition to that, some compounds of Fe^{3+} are reduced to Fe^{2+} forming carbonates, phosphates, and sulfide minerals like amorphous sulfides (FeS), greigite (Fe_3S_4), pyrite (FeS_2), mackinawite ($Fe_{1+x}S$) and pyrrhotite ($Fe_{x-1}S_x$). Under such conditions heavy metals precipitate as refractory sulfides and accumulate in mangrove sediments. Deposited metals strongly affect sediment characteristics. One of the most important parameters is grain size, Lucas (1986). Fine sediments with surface area scavenge much higher amounts of metals than sand. Induced coupled Plasma spectroscopy (ICP-AES), Mössbauer spectroscopy, and X-rays diffraction have been used to identify and to analyze the sediment composition of associated minerals like quartz, pyroxenes, amphiboles, muscovite, as well as minerals e.g. illite, kaolinite, etc. The observed increase of Zn, Cd, and Cr and Ni elements concentrations in some areas is probably due to the transport of the elements by tidal dynamic and upstream river from industrial effluents. The studied sediments have pyroxenes, amphiboles, muscovite, quartz, kaolinite and illite, suggesting a derivation starting from the gneissic and constituent maghemites, and of the covering sedimentary Cenozoic corresponding to the Formation Barriers.

1 INTRODUCTION

The river Paraíba do Sul (RPS) emerges in Serra da Bocaina in the state of São Paulo at an altitude of 1800 meters. It flows more than 1150 km to reach São João da Barra in Rio de Janeiro. The whole region from Serra da Bocaina to São João da Barra is densely populated, with sufficient industrial and agricultural activity. Decades of intense use of hydro potential of the river in industry, energy, urban and agriculture have caused quality degradation of environment of the region. In the Fluminense region only about 2% of the population has sewage facilities. Nearly 2.6 million tones of urban waste, and around 30 million tons of industrial waste are deposited in the river every day. In its journey RPS and its tributaries (Paraibuna, Pomba and Muriaé rivers) show heavy metal contamination (Zn, Pb, Cu and Cr) caused by industrial and urban waste deposit, Malm (1986), Torres (1992) and Azcue (1987). The primary aim of the present study is to find out heavy metal concentrations of Zn, Cd, Cr and Ni in mangrove sediments at Convivência Island in the estuary of river Paraíba do Sul - Aragon et al. (1996). The map of the site from where the samples were collected is depicted in Figure 1.

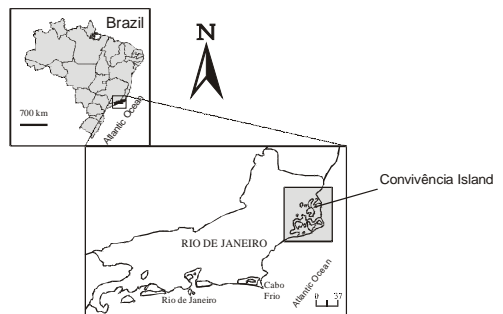


Figure 1. - Map of the area studied (Convivência Island).

Chemical analyses results of sediments from Convivência Island (from the estuary of river Paraíba do Sul) along with the chemical analysis of sediments from the different places of the journey of the river have been compared with the standards values from shale rocks. The present results give a geochemical correlation between heavy metals (Zn, Ni, Cu e Cr) and organic matter (OM), carbon/sulfur (C/S) relation and small granulometric fractions (clay/silt) in the sediments.

Mangrove vegetation occurs, preferentially; in areas where water is still, occupying areas with sandy saline silts, that happen due to sea tide. Aragon et al. (1996) observed that water flow from the river, and that the rainy season reduce the salt content in such areas. Mangrove sediments present certain characteristics, which may favor metal accumulation. Sheltered, slack water conditions allow deposition of fine particles normally enriched with trace metals. High organic matter and sulfide content helps in fixing heavy metals as insoluble sulfides and precipitated organic-metal complexes. Therefore, three major aspects are involved in the accumulation and distribution of heavy metals in mangrove sediments: (a)- preferential accumulation of sediments of fine grains (b)- accumulation of high organic matter content, and (c)- precipitation of metal sulfides present as by-product of the sulfate reduction based metabolism. Mangroves are an important receptor of pollutants from atmospheric deposition, continental runoff and tidal currents.

2 MATERIALS AND METHODS

The samples studied were obtained from three different places (stations E1, E2, and E3 - Figure 1) in the region of river Paraíba do Sul (RPS), situated in the Convivência Island (21° 35' 00'' S and 41° 02' 00'' W). These locations were selected on the basis of vegetation density and the characteristic of Mangrove. Acrylic tubes of 8.5 cm diameter and 1.0 m of length were inserted vertically in the sediments. The sediments samples obtained were cut to 2 cm width from the base of the acrylic tube. Plasma spectroscopy (ICP- AES) was used for the elemental analysis of Fe, Ni, Cu, Cr and Zn. Mineralogical analysis by the X-ray diffraction were recorded with a Siemens model D5000 operated at 40kV at 20mA, and a tube of Cu-K α in a 2 θ range from 4° a 70° with a velocity of 2° per minute. Mössbauer spectroscopy measurements, both at room temperature and liquid nitrogen temperature were carried out using a Co⁵⁷ source in Rh matrix, with an initial activity of 50 mCi, and all the spectra were least square fitted. A typical room temperature Mössbauer spectrum of one of the samples is depicted in Figure 2. The present study allowed an estimate of a stable environment in relation to the other areas. The results were statistically treated and are discussed in comparison with regional geochemical views aiming to reference to any future program for local, regional environment monitoring.

The present results give a geochemical correlation between heavy metals (Zn, Ni, Cu e Cr) and organic matter (OM), carbon/ sulfur (C/S) relation and small granulometric fractions (clay/silt) in the sediments.

Table 1. – Heavy metals concentrations in surface sediments from mangroves Convivência Island- estuarine of river Paraíba do Sul (RPS) –Station E1.

	1	2	3	4	5	6	7
	1.01	0-2	0.79	86.13	6.12	85.14	22.11
	1.02	2-4	0.68	<DL	<DL	2.00	2.42
	1.03	4-6	3.79	32.44	<DL	25.69	11.27
	1.07	12-14	1.65	31.56	<DL	22.13	10.58
	1.10	18-20	2.66	38.42	<DL	23.93	11.33
	1.16	30-32	1.88	19.02	<DL	13.08	8.01
	1.16r	30-32	1.78	18.65	<DL	12.92	6.78
	1.20	38-40	0.67	13.83	<DL	11.13	4.55
	1.26	50-52	0.51	<DL	<DL	<DL	1.86
	1.35	68-70	0.71	<DL	<DL	4.55	2.87
	1.37	72-74	0.73	6.13	<DL	4.32	3.45
	1.39	76-78	1.32	7.50	<DL	9.58	4.02
	1.43	94-96	1.88	14.12	<DL	14.87	6.18
\bar{x}			1.41	26.78	<DL	25.87	7.34
(n=16)			2.66	86.13	6.12	85.14	22.11
Maxima			0.51	<DL	<DL	<DL	1.86
Minima							

1 Samples, 2 Depth (cm), 3 Fe₂O₃ (%), 4 Zn (mg/Kg), 5 Ni (mg/Kg), 6 Cr (mg/Kg), 7 Cu (mg/Kg), DL Detection limit

The analytical results are in Tables 1 (similar results not shown here are from stations 2 and 3). Average concentrations of Fe, Zn, Ni, Cr and Cu (from stations 1, 2 and 3) are reported in Table 2 and 3. These values have also been compared with the standards values from shale rocks particles normally enriched with trace metals. High organic matter and sulfide content helps in fixing heavy metals as insoluble sulfides and precipitated organic-metal complexes.

Table 2. – Average contents of heavy metals: Zn, Ni, Cr, Cu (mg/Kg) and Fe (%) in surface sediments from studied Mangroves compared with those from the Standard Shale.

Elements	Station 1	Station 2	Station 3	Standard shale*
Fe	1.41	4.35	13.34	4.7
Zn	26.78	62.78	54.09	95
Ni	<DL	<DL	<DL	0.3
Cr	25.87	40.96	40.29	90
Cu	7.34	16.60	18.30	45

DL Detection limit

Table 3 – Average contents of heavy metals: Zn, Ni, Cr, Cu (mg/Kg) and Fe (%) in the studied sediments compared with those from the medium and inferior portion of south Paraíba river.

	1	2	3	4	5	6
Fe		6.36	6.00	11.00	6.00	.94
Zn		47.88	327.0	222.0	102.0	7.0
Ni		<DL	<DL	<DL	<DL	---
Cr		35.71	265.0	91.0	73.0	7.0
Cu		14.08	105.0	74.0	11.0	7.0

1 Elements,

2 Mangrove Convivencia Island,

3 RPS Medium Portion Malm (1998),

4 RPS fluvial inferior portion Molisani (1997),

DL Detection limit

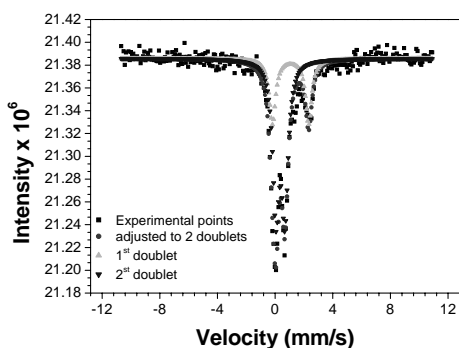


Figure 2. Typical room temperature Mössbauer Spectrum of one of the samples.

It can be observed that the mean values of mangrove sediment elements from 3 stations are less than the values from standard shale. Also, the mean value of element concentrations of Zn, Ni, Cr and Cu of the studied sediments can be compared with the reported values of Malm (1998). These concentrations values of elements from the sediments studied are of the order 7 times less (table 2) compared to the values reported by Malm (1998) (obtained while studying the medium flow of the river Paraíba do Sul (RPS), while studying the estuary of river Paraíba do Sul, also observed reduction in concentration values of elements Zn, Ni, Cr, and Cu from the values obtained from mean flow of RPS. Santos et al. (2002) confirmed that indeed there is reduction in values of element concentrations in the mangrove sediments of river Paraíba do Sul. They also suggested the main processes that cause the reduction in concentrations-enrichment and deposit of these elements at preferred locations, dilution of concentrations because of lack of local pollution points. The Mössbauer spectra (Figure 2) of the sediments

studied showed the presence of iron oxides and hydroxides.

In mangroves swamps the mud predominantly consists of fine sediments generally of clays and slit. This fine fraction of sediments helps geochemical formations by complex formation of organic metallic formations and adsorption. Earlier Santos et al. (2002), and Queiroz (1992) studied the mangrove swamps of river Joanes, Bahia showed the important association between heavy metals, Fe and Mn. The fact that Fe and Mn form oxides and hydroxides in estuary zones indicate the co precipitation processes also taking place. The most significant results of mangroves swamps of Convivência Island are shown in Table 4.

Tabela 4: Pearson coefficient matrix (r), calculated as different concentration fractions (metal fractions, granulometric fractions, organic matter, pyrite, carbon sulfur and susceptibility).

	Fe	Zn	Cr	Cu	FeS ₂	C/S	OM	MS	Clay/ slit
Fe	1.00								
Zn	0.64	1.00							
Cr	0.60	0.58	1.00						
Cu	0.37	0.57	0.84	1.00					
FeS ₂	0.26	0.27	0.16	0.24	1.00				
C/S	0.61	0.08	0.39	0.36	-0.80	1.00			
M.O.	0.25	0.56	0.11	-0.02	0.54	0.11	1.00		
S.M.	0.20	0.55	0.02	-0.10	0.36	-0.22	0.93	1.00	
ARG	0.43	0.46	0.31	0.30	0.51	0.26	0.67	0.59	1.00
SILT	-0.03	0.03	-0.35	0.33	-0.12	0.08	0.51	0.44	0.51

OM=Organic matter, C/S= Carbon-Sulfur relation, MS= Magnetic Susceptibility

The presence of Cr and Zn and the relation C/S showed high and positive correlation similar to Fe. Studies have shown that the concentration of some trace elements could have the effect of diagenetic process. In this context the iron sulfides could have some role for the presence of trace elements (diffusions and redistribution within the sediments). The trace elements in mangroves swamps of Convivência Island show a low coefficient relation.

3 CONCLUSIONS

The present report is a study of concentration of elements of Fe, Zn, Ni, Cr and Cu in the sediments from the mangrove sediments from Convivência Island of river Paraíba do Sul (RPS).

In spite of the low mean concentrations of toxic metallic oxides compared to other elements used for comparison (standard shale and other regions), and

non availability of geochemical conditions of the mangroves studied we can not conclude that mangroves of Convivência island are not undergoing important ambiental changes. The low concentration of these elements in the studied area is caused by the enrichment of these elements at the preferred deposit sites and dilution process associated to lack of local pollution.

The presence of iron is associated to the superficial flow of the river. The presence of iron is caused by the local soil that is naturally rich in iron oxides; it is non-toxic to the regional population. The presence of iron oxides and iron hydroxides is an important factor in recycling of heavy metals specifically in the aqueous system.

Torres J. P. M. (1992). Ocorrência e distribuição de metais pesados no Rio Paraibuna. *M.Sc. Desertation*, Juiz de Fora-MG, Brazil.

4 REFERENCES

- Aragon, G. T., Ovale, A. R. C., Miguens, F. C., Rezende, C. E., & Carmouze, J. P. (1996). Pyrite formation in mangrove sediments, Brazil. *Proceedings of the Fourth International Symposium on the Geochemistry of the Earth's Surface, Leeds – England, 22-28 July, 29-33*, Editor S. H. Bottrell, International Association of Geochemistry and Cosmochemistry, the Geochemistry Group of the Mineralogical Society, England.
- Azcue, J. M. P. (1987). Possíveis vias de acesso de metais pesados provenientes do sistema hídrico *Rio Paraíba do Sul Gandú, RJ, até o homem*. *M.Sc. Desertation*, Universidade Federal do Rio de Janeiro, Brazil, pp.1-85.
- Lucas, M. F. (1986). Distribution of mercury in the sediments and fishes of the Lagoon of Aveiro. *Water Science & Technology*, 18, 141-148.
- Malm, O. (1998). Estudo da poluição ambiental por metais pesados no sistema Rio Paraíba do Sul - Rio Gandú (RPS-RG) através da metodologia da abordagem pelos parâmetros críticos. *M.Sc. Desertation*, Universidade Federal do Rio de Janeiro, Brazil.
- Molisani, M. M. (1997). Distribuição de metais pesados associados ao *sedimento* de fundo na porção inferior e estuário interno do rio Paraíba do Sul-RJ, *Undergraduate Monograph*, Universidade Estadual Norte Fluminense, Brazil, pp.1-34.
- Queiroz, A. F. S., (1992). Mangroves de la baía de Todos Santos-Salvador-Bahia-Brésil: Sés caractéristiques et l'influence anthropique sur as géochimie. *Doctorate thesis, University Louis Pasteur, Strasbourg, France*, 148.
- Santos, A. L. F., Queiroz, A. F. S., Argolo, J. L., Carvalho, I.G., Barbosa, R. M., Oliveira, O. M. C., Mascarenhas, L. S., & Rocha, S. A. (1998). Caracterização Geoambiental do Estuário do Rio Joanes-Lauro de Freitas-Região Metropolitana de Salvador-Subsídio Para Um Estudo Ambiental Sistemático. *Revista Escola de Minas, Ouro Preto, Brazil*, 51, 3, 67-71.
- Santos, A. L. F., Boaventura, G. R., Aragon, G. T., Oliveira, A. C. de & Garg, V. K. (2002). Evolution and identification of iron bearing minerals; magnetic and mineralogical study of trace metals (Zn, Cd, Cr, Ni) in mangrove sediments of Convivência Island of South Paraíba River (RJ). *Proceedings 6th International Symposium on Environmental Geotechnology and Global Sustainable Development*, Chung-Ang University, Korea, 2- 5 July (2002). Editor Hong Won-Pyo, Chung-Ang University, Korea, 701-712.

Concentration and Speciation of Heavy Metals in Lagoa da Pampulha Sediments (Belo Horizonte / Minas Gerais; Brazil)

G.T.Schmidt

Department of Environmental Geochemistry, Geosciences Institute, Gutenberg University, Mainz

K.Friese

Department of Inland Water Research, Centre for Environmental Research, Magdeburg, Germany

H.A.Nalini

Department of Geology, UFOP, Ouro Preto, Brazil

J.C. de Lena

Department of Chemistry, UFOP, Ouro Preto, Brazil

D.W.Zachmann

Department of Geochemistry, Environmental Geology Institute, TU Braunschweig, Germany

ABSTRACT: The artificial reservoir Lagoa da Pampulha has been increasingly affected by sediment deposition and pollution from urban and industrial sources. This study investigates heavy metal concentrations and their speciation in the lake sediment using ICP-OES, ICP-MS, and XRD analysis. Speciation analysis was done by sequential elution under inert gas as well as after oxidation. Carbon, sulfur, and most of the analyzed heavy metals are enriched in the top sediment layer with a pronounced downward decrease, indicating the presence of an anthropogenic influence. Statistical analysis, including correlations and a PCA of depth-related total concentration data, helps distinguish presumably anthropogenic heavy metals from geogenic components. Some samples with high element concentrations in the sediment also show elevated concentrations in their pore water. Analyses of element distribution between sediment and pore water suggest a strong bonding of heavy metals to the anoxic sediment. The trend toward elevated solubility in the pore water of oxidized samples is clear for most of the analyzed elements. Speciation analysis yields characteristic fractionations for each element. In addition, it indicates that the behavior of heavy metals in the sediment is strongly influenced by organic substances. These substances provide buffering against oxidation, acidification, and metal release. In the future, care must be taken to reduce the supply of contaminants and to prevent the release of heavy metals from dredged sediments.

1 INTRODUCTION

1.1 Study Area

Lagoa da Pampulha is a reservoir which was built in 1958 in the northern part of Belo Horizonte. It is approximately 4.4 km long and 450 m wide, covering a total of 2.7 km² with a mean depth between 4 and 6 m. Its water volume of about 12 to 14 million m³ is exchanged, on average, every 4 months (CPRM 2001, Pinto Coelho et al. 1994).

The catchment covers an area of 97.9 km² which includes the urban areas of Belo Horizonte and Contagem (42.7%) plus mostly grass land (CPRM 2001). A total of eight tributaries flow into the reservoir. There is a spillway in the dam with an average outflow of about 1.6 m³/s.

The reservoir was built primarily to prevent flooding during the rainy season, but also to serve as a drinking water reservoir and recreational area. These functions have been severely affected due to increasing settlement and industrialization after 1958.

The extraction of drinking water was stopped in 1980 because influx of urban wastewater has caused

eutrophication and proliferation of cyanobacteria. Algal blooms have become more and more frequent. In recent studies, the water was found to be almost free of dissolved oxygen below the surface (Pinto Coelho et al. 1994). This was confirmed in the present study. Effluents from industrial sites, gas stations, landfills, and uncontrolled waste dumps have added to chemical pollution. The most significant sources of contamination are situated alongside the largest tributaries, the Sarandi and the Ressaca.

Increasing soil erosion in the catchment area, triggered by deforestation and uncontrolled urban sprawl, have caused a massive influx of sediments, estimated at 200,000 to 400,000 m³ per year (Cena 2001, CPRM 2001). Between 1979 and 1998, some 7 million m³ of sediment were dredged and deposited on islands in the reservoir.

The local administration has initiated several remediation programs; the most recent one, PROPAM, was started in 2002 and is still running. It includes repair works on the dam and several tributaries, enhanced sewage treatment and water aeration, dredging of lake sediments, and measures against deforestation and urban sprawl.

1.2 Scope of Investigation

This study focuses on heavy metals found in the reservoir sediments. Their total concentration was studied as well as environmental availability, which was done by pore water analysis and a six-step sequential elution procedure. In order to study the effect of oxidation following air exposure of dredged material, both analyses were done with samples that were kept well-preserved under inert gas, and with samples that had been exposed to air.

2 MATERIALS AND METHODS

2.1 Sample Collection

Samples were collected from three spots, marked as A, B, C in Figure 1, during two campaigns; one in May and one in August 2001.

Sedimentary material was extracted from the bottom with a "Mondseecorer". The undisturbed cores were split up into separate samples in layers of a few cm in depth and filled into airtight plastic containers. One set of samples from each point was immediately put under argon to avoid any exposure to oxygen.

2.2 Sample Processing and Analysis

Pore water was extracted with a centrifuge (diameter 26 cm, 4000 rpm) and filtered (pore size 0.2 μm). The solid material was dried at 60°C. Grain size fractions were separated by sieving and flotation (Bachmann et al. 2001). X-ray diffraction of clay minerals was done in a three step procedure (untreated, glycolated, 550°C). Carbon concentrations were measured using a Leco CS 144 spectrometer.

The total concentration of the main components and trace elements were analyzed after digestion with a $\text{HNO}_3\text{-HClO}_4\text{-HF}$ mixture (7:2:7) in open PFA vessels. For speciation analysis, a six-step sequential elution method was applied (Jakob et al. 1990). This method is a variant of the 5-step scheme developed by Tessier et al. (1979). The following fractions were obtained: 1. exchangeable (ammonium acetate), 2. carbonatic (sodium acetate), 3. easily reducible (hydroxyl ammonium chloride), 4. less easily reducible (ammonium oxalate + oxalic acid), 5. organic/sulfidic (hot hydrogen peroxide, ammonium acetate), and 6. residual (HF digestion, see above).

Element analysis was done using ICP-OES (Bausch & Lomb ARL 3520 ICP Sequential Spectrometer and Fissons Instruments Maxim) and ICP-MS (Micromass Platform ICP). The analysis included the following elements: Al, As, Ba, Ca, Cd, Co, Cr, Cu, Fe, K, Mg, Mn, Na, Ni, P, Pb, S, Sb, Sn, Sr, Ti, V, Zn, and Zr.

3 RESULTS AND DISCUSSION

3.1 Sediment Properties

The material was found to be very fine-grained, consisting mainly of fine silt and clay. The clay fraction rises from roughly 10% at point A to over 20% at point C, while the silt fraction shows the opposite trend. Point B shows an intermediate composition. The obvious reason is the increasing distance of the points A to C from the main tributaries (Fig. 1).

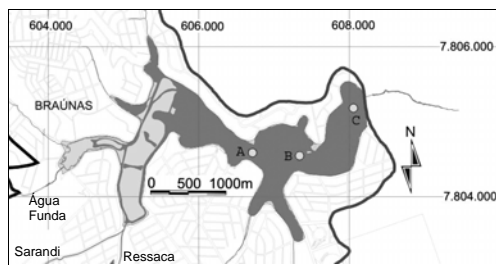


Figure 1: Sampling points in the reservoir. Light gray areas = islands; black line = border of catchment area

X-ray diffraction shows that the mineral composition of the sediment appears to be uniform throughout the whole reservoir. The main identified components are kaolinite (dominant), illite, and gibbsite. Goethite and hematite were also detected.

3.2 Total Element Concentrations

The depth profiles of element concentrations provide insights into the geochemistry of sedimentation. Some examples are shown in Figure 2. The dominant component, Al, shows an even distribution with a slight decrease in the top layer, where organic material is more abundant than below. The distribution of S, Zn, and Cr concentrations consist of a strong enrichment in the top layer and a pronounced decrease towards constant values in lower depths. The same distribution is found for C, P, Mn, Cu, and Sb. A similar but less clear pattern is found for Fe, Pb, Ni, Sn, and Cd. The mean concentration in the top 5 cm and the corresponding enrichment factors (divided by the minimum concentrations averaged from all sampling points) are listed in Table 1.

The distinct enrichment in the upper layers of the depth profiles clearly indicates the presence of anthropogenic sources, whereas the deeper layers represent something close to the geogenic background.

The concentrations of C, S, and P are a clear indication of organic pollution as a consequence of urban wastewater discharge. Previous studies have shown that the reservoir is a sink for large amounts of nutrients introduced from the tributaries (Barbosa 1998). The high sulfur contents are manifest especially in the top sediment layer through a strong H_2S smell and black color.

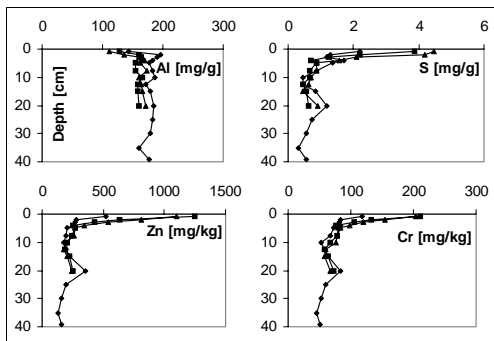


Figure 2: Depth profiles of selected element concentrations in three different sediment cores from sampling point A.

Table 1: Mean concentration c [mg/kg] in top layer (5 cm) and enrichment factors EF of selected elements in the sediment.

Element	S	P	C	Zn	Sb	Cd	Cu	Cr	Sn	Pb	Ni
c	4780	2170	37640	383	1.07	1.09	36.8	102	8.0	43.5	42.6
EF	11	4.1	3.5	3.1	2.5	2.4	2.1	2.0	1.9	1.8	1.4

Two-element correlations (Fig. 3) reveal some more striking differences between specific elements. C and P show a clear unique correlation with no differences between the sampling points. C and S, in contrast, are correlated differently for each sampling point. Obviously, organic substances in the sediment have higher S contents at point C than at point A, with point B possessing intermediate amounts. The same is true for the correlation of C and Ni, indicating that Ni is uniquely correlated with S (Fig. 3). Cr shows a different behavior. Plotted against C, the steepest correlation line is at point A and the flattest one at point C. This trend is even more pronounced in the correlation against S. Zn and Cu display the same pattern as Cr (not shown here). The different correlation patterns indicate that S is deposited not only in organic material with C and P, but also occurs as sulfide, more notably in the deeper water regions at point C. The correlations also reflect the supply of heavy metals to the lake sediments by the main tributaries, the Sarandi and the Ressaca.

Ni is obviously closely linked to S, whereas Zn, Cr and Cu seem more related to C, with a tendency to precipitate closer to the main tributaries than S and Ni. None of these elements shows any clear correlation to Fe or Mn concentrations.

A principal component analysis (PCA) was done as a statistical summary of all the analyzed total concentrations. Three principal components were found, with communalities of 40.9%, 27.4%, and 8.2%, respectively. Taking a factor loading of 0.6 as a limit, the elements were assigned as follows: component 1: C, P, S, Fe, As, Cd, Cr, Cu, Ni, Pb, Sb, Sn, and Zn; component 2: Al, Ca, K, Mg, Na, Ba, Sr, and V; component 3: Pb. This is a rather clear confirmation of the assumption that many elements, particularly heavy metals, are from anthropogenic

sources (PCA component 1), while others are of geogenic origin (PCA component 2).

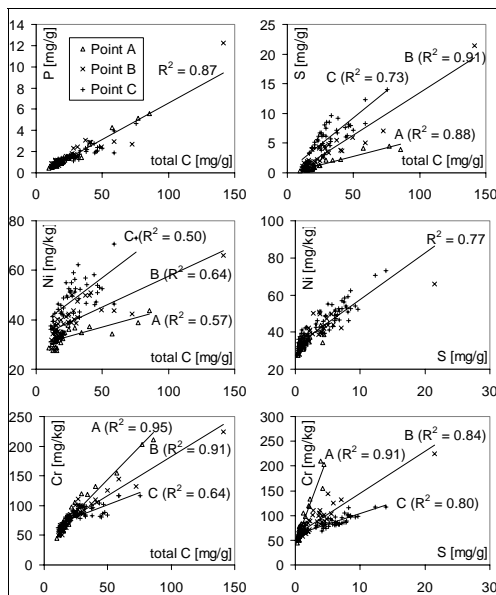


Figure 3: Correlations of selected pairs of total element concentrations in sediment samples from the three sampling points.

3.3 Pore Water and Speciation Analysis

Some samples with exceptionally high elemental concentrations in the sediment also show high elemental concentrations in the pore water. Zn is the most easily soluble of the trace elements, reaching up to $>100 \mu\text{g/l}$, followed by Ni with up to $20 \mu\text{g/l}$.

Differences of elemental concentrations in pore water between anoxic and oxidized samples are summarized in Figure 4. The distribution coefficient K_d is calculated by dividing the mean concentration in the sediment by the mean concentration in the corresponding pore water samples. Most elements become more soluble (lower K_d) after oxidation; exceptions are Zn, Cu, and Cr. S shows the most significant difference, as can be expected from the conversion of sulfide to sulfate. Due to sulfide oxidation the pH of the pore water drops below 3.

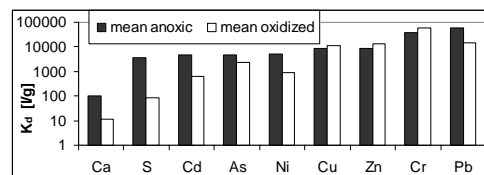


Figure 4: Distribution of selected element concentrations between sediment and pore water.

The pH of the sediment is in the range of 7. In contrast to the pore water, the sediment samples show no change in pH even after several weeks of oxidation. The logical conclusion is that the sediment provides strong Eh and pH buffering.

The elemental concentrations in the sequential elution fractions are shown in relation to the total concentrations. Figure 5 displays the averaged results from six well-preserved (anoxic) and four oxidized samples for the elements Fe, Zn, Cr, and Ni.

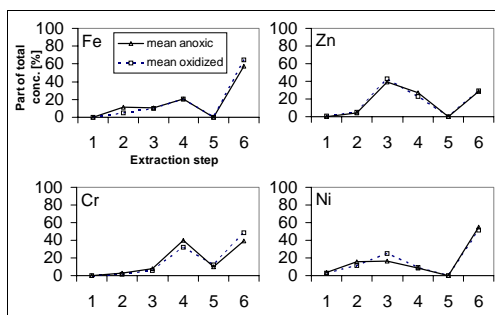


Figure 5: Mean parts of concentrations found in the fractions of the sequential elution.

1 = exchangeable, 2 = carbonatic, 3 = easily reducible, 4 = less easily reducible, 5 = organic/sulfidic, 6 = residual fraction.

With Fe we observe a remarkably high share of the residual fraction, which increases in the oxidized samples. The increase of this share is attributed to an increased presence of highly crystalline Fe oxides.

Zn is mainly found in the 3rd, 4th, and 6th elution steps. Zn found in steps 3 and 4 is bound to Fe oxides. It is not detectable in step 5, which was unexpected because the close correlations between the total concentrations of C, S, and Zn suggest a dominating organic/sulfidic speciation. Thus the residual fraction might contain some sulfidic residue not extracted in the 5th step. Zn fractionation shows no differences between anoxic and oxidized samples.

Cr dominates in the 4th and 6th elution steps, with a slight increase of the residual fraction for the oxidized samples. This is in good agreement with the well-known association of Cr and Fe oxides.

Ni is partly soluble in the first four elution steps, but the major part remains insoluble (residual phase). Part of the carbonatic fraction is apparently dissolved during oxidation and incorporated into newly-formed oxides. From the very clear Ni/S correlations mentioned above, one would expect to find a substantial amount in step 5, which is not the case. Again, we assume that the extraction was ineffective and Ni compounds remained insoluble up to step 6.

The small differences between the anoxic and the oxidized samples and the missing evidence of a sulfidic fraction by sequential elution indicate strong Eh and pH buffering of the sediment.

4 CONCLUSIONS

The upper sediment layers and the pore water of Lagoa da Pampulha are contaminated by P, S, and heavy elements (especially Cr, Cu, Ni, and Zn). The distribution of elemental concentrations in the sediment points to the main tributaries as the most significant supply of contaminants.

High nutrient loading causes reducing conditions in the lake sediment. These conditions trigger the accumulation of sediments rich in S²⁻, which stabilizes the fixation of heavy elements. The results of the sequential elution indicate the presence of a redox buffer in the sediment (most likely organic C), which prevents (i) fast oxidation of sulfides, (ii) buildup of acid conditions, (iii) fast release of heavy metals, and causes (iv) increasing accumulation of heavy elements in the sediment.

The higher concentrations of heavy metals found in pore water give evidence for the availability of contaminants under oxidizing conditions.

The situation requires a fast implementation of the initiated remediation programs. They should not only focus on reducing eutrophication, which, although necessary, might lead to increased metal mobility, but also on identifying and eliminating the sources of metal pollution. Care should be taken with dredged material, from which increasing amounts of metals may be released after oxidation.

5 REFERENCES

- Bachmann, T.M., D.W. Zachmann, K. Friese 2001. Redox and pH conditions in the water column and in the sediments of an acid mining lake. *Journal of Geochemical Exploration* 73: 75-86.
- Barbosa, F., F. Garcia, M. Marques, F. Nascimento 1998. Nitrogen and Phosphorus balance in a eutrophic reservoir in Minas Gerais: A first approach. *Rev. Brasil. Biol.* 58(2): 233-239.
- Cena, T. 2001. R\$ 215 milhões são jogados pelo ralo. *Estado de Minas* 02.08.2001: 25.
- CPRM 2001. Estudo hidrogeológico da Bacia da Pampulha. Belo Horizonte: CPRM/SUREG-BH.
- Jakob, G., L. Dunemann, D. Zachmann, T. Brasser 1990. Untersuchungen zur Bindungsform von Schwermetallen in ausgewählten Abfällen. *Abfallwirtschaftsjournal* 2(7-8): 451-457.
- Pinto Coelho, R., A. Giani, E. von Sperling (eds.) Ecology and human impact on lakes and reservoirs in Minas Gerais with special reference to future development and management strategies. Belo Horizonte: SEGRAC.
- Tessier, A., P. Campbell, M. Bisson 1979. Sequential Extraction Procedure for the Speciation of Particulate Trace Metals. *Analytical Chemistry* 51(7): 844-850.

Natural Decontamination of Metalliferous Mining Leachates by Reservoir Mineral Formation

M.Schubert, R.Wennrich & H.Weiss
UFZ Centre for Environmental Research, Leipzig, Germany

P.Schreck
Institute of Geophysics and Geology, Leipzig University, Leipzig, Germany

H.H.Otto
Department of Applied Crystallography, Tech. Univ. Clausthal-Zellerfeld, Clausthal-Zellerfeld, Germany

ABSTRACT: The Mansfeld region in Saxony-Anhalt, Germany, has been known for the mining and processing of copper ore for more than 800 years. One of the processing residues is a fine-grained scrubber dust consisting of agglomerates of submicroscopic metal sulfide particles in a matrix of highly viscous hydrocarbons. In the late 20th century, substantial quantities of this scrubber dust eventually totaling 100,000 tons were deposited in a dump. Heavy metal contaminated seepage water emerging from this dump is now the main threat to the local surface water and groundwater. The point of discharge into the local surface water system is a spring situated at the foot of the dump. The extremely high heavy metal and sulfate concentrations in the spring water trigger the precipitation of a variety of minerals containing considerable amounts of heavy metals. This precipitation process was studied in detail. The research is the first step in a study designed to optimize and utilize this natural precipitation process to clean up the site. By identifying and enhancing the precipitation procedures, such self-cleaning processes could be used as part of a remediation scheme to clean up the local surface waters. Moreover, the metal-rich precipitate is considered to have economic potential as a secondary source of metals or as a catalyst precursor material.

1 INTRODUCTION

For several centuries the Mansfeld region in Saxony-Anhalt, Germany, has been known for the mining of a low-grade black shale copper ore known as *Kupferschiefer*. Although copper mining and ore-processing were abandoned in 1990, residues from these activities are still abundant in the region and are nowadays the main source of contamination impairing the local surface water. The processing residue with the most serious impact on the local environment is a fine-grained scrubber dust which consists of agglomerates of inorganic particles in a matrix of various highly viscous hydrocarbons (Weiss et al. 1997, Schubert et al. 2003). The concentrations of the predominant elements in the scrubber dust are listed in Table 1 (Weiss et al. 1997). Apart from the major elements such as Zn, Pb, Cu, Fe, Al, Sn, Si, and S, substantial concentrations of Mn (930 mg/kg) and Mo were determined (590 mg/kg).

Table 1: Predominant elements in the scrubber dust [w/w %].

Zn	Pb	Cu	Fe	Al	Sn	Si	S _{tot}
19.3	14.3	1.3	1.3	1.3	1.1	8.0	11.3

While the agglomerates in the scrubber dust may reach several hundred microns in diameter, the median diameter of the individual particles is only about 1.25 μm . The high carbon content of the material stems from the organic matter of the copper ore. The inorganic particles are crystalline, nanocrystalline or amorphous solid solutions of mainly metal sulfides. The predominant crystalline phases are listed in Table 2 (Weiss et al. 1997).

Table 2: Main crystalline phases in the scrubber dust [%].

ZnS*	ZnS**	PbS	PbSO ₄	SiO ₂	amorph.
19.5	17.5	6.9	6.3	2.6	38.0

*: wurzite, **: sphalerite

During the years of ore-processing, the viscous scrubber dust was piped to several local storage facilities. Most of the material was dumped in an impoundment situated on the top plateau of a huge slag heap. Eventually the pond contained about 100,000 m³ of a more or less consolidated sludge. Since the bottom of the pond was not sealed, substantial amounts of the slurry randomly infiltrated the fractured slag heap. The sludge which impregnated the slag heap and which is subject to

recent leaching processes is considered to be the main local source of heavy metal emissions into the environment.

Today's main seepage water outflow from the slag heap is a highly contaminated spring situated at the foot of the heap. The process of water contamination is thought to occur as follows: Uncontaminated groundwater emerging from a sandstone aquifer layer covered by the slag heap migrates at the base of the heap through a zone heavily interspersed with scrubber dust. In this zone, the slow but constant oxidation of heavy metal sulfides and the subsequent leaching of the easily soluble oxidation products (mainly metal sulfates) lead to the contamination of the water emerging at the foot of the heap.

Recent study has addressed the precipitation of a variety of hydroxide and sulfate minerals found immediately at the spring. Since these naturally formed reservoir minerals contain considerable amounts of heavy metals, it seems appropriate to investigate whether this natural precipitation process can be exploited for leachate decontamination. By enhancing the natural processes, it might be possible to use mineral precipitation to remediate the local surface water system. This paper discusses the natural precipitation processes observed and the chemical and mineralogical characteristics of the precipitates.

2 EXPERIMENTAL

2.1 On-site activities

Spring water was sampled automatically over a six-month period on a diurnal schedule. To compile information on local background concentrations, additional samples were taken at two uncontaminated springs as well as four monitoring wells situated nearby.

To characterize the precipitate, five samples were collected. Three of them were taken immediately at the spring. The mud-like, pale green material found here is only a few months old. Two other samples stem from another sampling point a few meters away. Since the second location is situated in a part of the brook that dried up several decades ago, the samples can be considered typical of aged precipitate.

2.2 Laboratory analysis

All spring water samples were analyzed for Pb, Zn, Cu, Mn, Mo, Al, and SO₄. Because of the high element concentrations, ICP AES (CIROS, Spectro A.I.) with pneumatic nebulization (cross flow) was used. Depending on the concentration levels, the elements were analyzed in undiluted or diluted water samples (sample + deionised water: 1 + 9 or 1 + 99,

respectively). The standard addition method (SAM) was used for calibration (Danzer & Currie 1998).

The precipitate samples were analyzed for their bulk chemical compositions using energy dispersive X-ray fluorescence EDXRF (XLAB 2000, Spectro A.I.). Given the high metal concentrations, the material was diluted with SiO₂ powder to reduce the concentrations to a level which matched the working range of the XRF spectrometer. The aluminum content was determined semi-quantitatively in the original material using a wavelength dispersive XRF spectrometer (SRS 3000, SIEMENS).

The mineralogical composition of the precipitates was studied using XRD. Two different diffractometers were employed. The 'young' samples were analyzed with a high-performance Guinier double-radius diffractometer (Otto & Hofmann 1996), which is equipped with an imaging plate detector and a Ge(111) monochromator, separating CuK α ₁ radiation ($\lambda = 1.5406 \text{ \AA}$). The patterns of the matured samples were recorded using a commercially available Bragg-Brentano diffractometer (CuK α radiation, $\lambda = 1.54179 \text{ \AA}$).

3 RESULTS

3.1 Spring water

The analyses of the spring water revealed very high concentrations of sulfate and heavy metals. The concentrations of the analyzed elements in the spring water and the respective background concentrations as determined in uncontaminated samples are listed in Table 3.

Table 3: Mean elemental concentrations in the spring water (SW; n=122) compared to typical background values (BG; n=8) in mg/l.

	Cu	Mn	Pb	Zn	Al	Mo	SO ₄
SW	21.8	18.2	2.1	1953	16.8	0.011	46650
BG	<0.06	0.07	<0.07	0.29	0.39	0.0012	458

During the sampling period, the pH and temperature of the spring water remained constant at about T = 7°C and pH = 5.7. The pH value, which is comparably low for regional spring waters, can be explained by the sulphide oxidation processes occurring in the scrubber dust scattered in the slag heap.

3.2 Precipitate

The average chemical composition of the precipitate samples is shown in Table 4. The mineral composition is dominated by Zn, Cu, Al, Mo, Pb, Si,

and SO_4 . Other anionic components are CO_3 and $(\text{OH})_2$.

Table 4: Mean metal and sulfur concentrations of the precipitates (n=5).

Zn	Cu	Al	Pb	Mo	Mn	S _{tot}
[%]	[%]	[%]	[mg/kg]	[mg/kg]	[mg/kg]	[%]
14.4	10.1	8.4	9100	2600	120	4.5

A Guinier pattern typical of the young precipitate is displayed in Figure 1. It shows some very distinctive and some broader peaks. All the sharp peaks belong to the tetragonal mineral wulfenite, PbMoO_4 , which can be detected easily, even in very low concentrations. Its lattice parameters were determined to be $a = 5.381(1) \text{ \AA}$ and $c = 12.154(5) \text{ \AA}$, tallying closely with the reference data. The broader peaks, which represent most of the sample material, suggest a high proportion of the nanocrystalline phases. Comparing the 2θ values of the broad peaks with JCPDS file data reveals that the fresh phase is mainly composed of brucite-like $(\text{Cu,Zn,Al})_3(\text{O,OH})_6$ sheets intercalated with layers of H_2O molecules and SO_4^{2-} anions. The highest d-value of about $9.1\text{--}9.2 \text{ \AA}$ may represent the layer repeat-unit in the c direction. The results indicate that mineral formation is only at an early stage. Considering the proposed $(\text{Cu,Zn,Al})_3(\text{O,OH})_6$ sheets and the high concentrations of SO_4 , Al, Cu, and Zn, the formation of zincowoodwardite, $(\text{Cu,Zn})_{4-5.5}\text{Al}_{2.5-4}(\text{SO}_4)_{1.5-2}(\text{OH})_{16} \cdot 5-8\text{H}_2\text{O}$, the zinc-containing analogue of woodwardite, seems to be likely. Its crystal structure is rhombohedral, with lattice parameters $a = 5.31 \text{ \AA}$ and $c = 26.77 \text{ \AA} (= 3 \times 8.92 \text{ \AA})$.

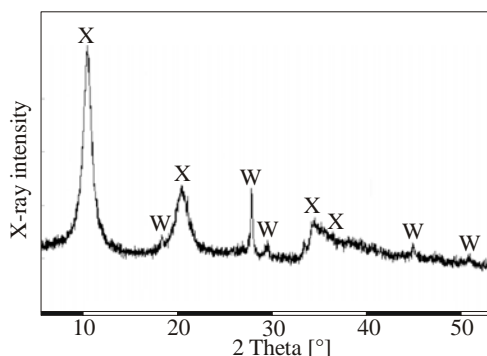


Figure 1: Guinier pattern by way of example for the young precipitate taken with $\text{CuK}\alpha$ radiation ($\lambda = 1.5406 \text{ \AA}$); X = nanocrystalline phase (zincowoodwardite), W = wulfenite.

A typical XRD pattern for the matured samples is shown in Figure 2. It shows mainly distinctive peaks, which apart from a small amount of α -quartz indicate a (Zn,Cu) hydroxide carbonate. It was, however, difficult to find a correct indexing of the monoclinic unit cell due to some peak overlaps and peak broadening. The lattice parameters obtained are $a = 13.74(2) \text{ \AA}$, $b = 6.342(5) \text{ \AA}$, $c = 5.376(4) \text{ \AA}$ and $\beta = 95.3(1) \text{ degrees}$. These parameters were compared to those given for the minerals hydrozincite, $\text{Zn}_5[(\text{OH})_6(\text{CO}_3)_2]$, and aurichalcite, $\text{Zn}_3\text{Cu}_2[(\text{OH})_6(\text{CO}_3)_2]$. It was shown that the lattice parameters of the matured precipitate are situated between the parameters of these two zinc minerals. The observed trend of the lattice parameters is indicative of the partial substitution of Zn by Cu on the octahedrally coordinated sites of the hydrozincite structure.

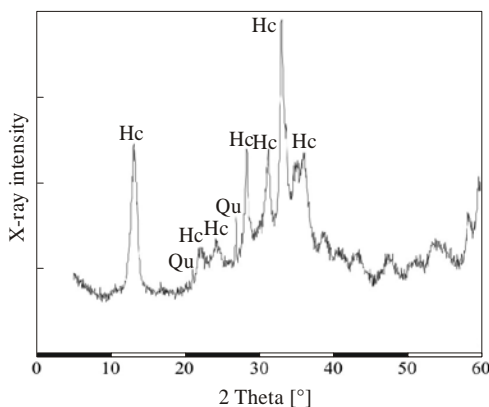


Figure 2: XRD diagram by way of example for the matured precipitate taken with $\text{CuK}\alpha$ radiation ($\lambda = 1.54179 \text{ \AA}$); Qu = quartz, Hc = (Zn,Cu) hydroxide carbonate.

4 DISCUSSION AND CONCLUSIONS

4.1 Spring water

Sulfate originating in the weathered scrubber dust can be distinguished from naturally occurring sulfate from the Triassic aquifer by sulfur isotope analysis. Strauch et al. (2001) determined the sulfur isotope signature of the leachates from the weathered scrubber dust as $\delta^{34}\text{S} = -14.3 \text{ ‰ CDT}$. This value differs strongly from the respective value of the uncontaminated aquifer water, which is $\delta^{34}\text{S} = 0$ to $+4 \text{ ‰ CDT}$. The contaminated spring water has a mean sulfur isotope signature of $\delta^{34}\text{S} = -13 \text{ ‰ CDT}$. These values indicate that uncontaminated groundwater from the aquifer enters the slag heap and interacts with the secondary metal sulfates formed by the oxidation of the scrubber dust. This enrichment in sulfate gives rise to a substantial

change in the isotopic signature of the water. It implies that the high heavy metal content in the spring water also stems from the weathering of the scrubber dust.

The extent and intensity of the mobilization process occurring inside the slag heap depends mainly on the solubility of the metal sulfates. The solubilities of the sulfates discussed here decrease in the order $\text{ZnSO}_4 > \text{MnSO}_4 > \text{Al}_2(\text{SO}_4)_2 > \text{CuSO}_4 > \text{PbSO}_4$ (Lide 1993). Since the respective sulfide solubilities are very poor under standard conditions, it can be assumed that sulfide leaching plays only a minor role in the water contamination.

Judging by comparison of the metal concentrations in the scrubber dust and in the spring water, it is evident that Zn and Mn are mainly enriched in the leachates. This corresponds to the high solubility of the respective sulfates. Al plays a major role for the precipitation of the observed zinc-copper-aluminum hydroxides. Cu, which forms easily soluble sulfates as well, is mobilized to a lesser extent. Pb is leached from the sludge only in minor amounts compared to its abundance in the scrubber dust due to its low sulfate solubility.

4.2 Precipitate

Summarizing the results of the chemical and XRD analyses of the young precipitate, the following formation process can be concluded. The oxidation of metal sulfides, which occurs in the slag heap, mobilizes metals and sulfate from the scrubber dust and gives rise to very high metal and SO_4 concentrations in the spring water. At first a gel is formed from the metal and SO_4 containing solution, absorbing substantial amounts of heavy metals. Zinc-copper-aluminum hydroxides start to crystallize from the newly formed gel, forming particularly octahedrally coordinated $(\text{Zn,Cu,Al})_3(\text{O,OH})_6$ layers. These precursor layers take up H_2O and SO_4^{2-} as intercalated sheets, and may finally form hydroxide-sulfates, such as zincwoodwardite. In contrast to the slow formation of zinc minerals, the less soluble PbMoO_4 already forms well-developed micro-crystals of wulfenite at low metal concentrations at early stages.

The maturing of the precipitate is characterized by the interaction of the precipitate with atmospheric CO_2 , which triggers the transformation of the zinc-copper-aluminum hydroxide-sulfates into zinc-copper hydroxide-carbonates. The resulting crystalline phase is situated between a copper-rich hydrozincite and aurichalcite.

Further research is to be conducted into whether forced precipitation can be applied for further heavy metal immobilization and thus be used as part of a remediation scheme for the site. The initial results suggest that adding trivalent cations, e.g. Al^{3+} , would increase the precipitation rate (Schreck et al.

2000). The question of whether the metal-rich precipitates can be used as secondary resource materials for these metals is of economic significance and thus will remain at the center of interest. Finally, we notice that the nanocrystalline precipitate may be of use as a precursor material for copper/zinc oxide catalysts for industrial hydrogenation processes (Waller et al. 1989, Joyner et al. 1991, Pollard et al. 1992).

5 REFERENCES

- Danzer, K., Currie, L. A. 1998. Guidelines for Calibration in Analytical Chemistry, Part 1. Fundamentals and Single Component Calibration (IUPAC Recommendations 1998). Pure & Appl. Chem. 70: 993-1014.
- Harding, M.M., Kariuki, B.M., Cernik, R., Gressey, G. 1994. The Structure of Aurichalcite, $(\text{Cu,Zn})_3(\text{OH})_6(\text{CO}_3)_2$, Determined from a Microcrystal. Acta Crystallogr. B 50: 673-676.
- Joyner, R. W., King, F., Thomas, M. A., Roberts, G. 1991. The influence of precursor structure and composition on the activity of copper/zinc oxide catalysts for methanol synthesis. Catal. Today 10: 417-419.
- Lide, D. R. (ed.) 1993. CRC Handbook of Chemistry and Physics (73 ed.). Boca Raton: CRC Press.
- Otto, H. H., Hofmann, W. 1996. Construction of a double-radius Guinier diffractometer using $\text{MoK}\alpha_1$ radiation and an one- or two-dimensional detection system. J. Appl. Crystallogr. 29: 495-497.
- Pollard, A. M., Spencer, M. S., Thomas, R. G., Williams, P. A., Holt, J., Jennings, J. R. 1992. Georgeite and azurite as precursor in the preparation of co-precipitated zinc/copper oxide catalysts. Appl. Catal. A 86: 1-11.
- Schreck, P., Witzke, T., Pöllmann, H. 2000. Heavy metal fixation in leachates from copper mining by optimising natural reservoir mineral precipitation. In Rammilmair D. et al. (eds.) Applied Mineralogy. Rotterdam: Balkema.
- Schubert, M., Morgenstern, P., Wennrich, R., Freyer, K., Weiss, H. 2003. The weathering behavior of a complexly contaminated scrubber dust from the Mansfeld Region, Germany. Mine Water and the Environment 22: 2-6.
- Strauch, G., Schreck, P., Nardin, G., Gehre, M. 2001. Origin and Distribution of Sulfate in Surface Waters of the Mansfeld Mining District (Central Germany) - A Sulfur Isotope Study. Isotopes Environ. Health Stud. 37: 101-112.
- Waller, D., Stirling, D., Stone, F. S., Spencer, M. S. 1989. copper-zinc oxide catalysts - activity in the relation to precursor structure and morphology. Faraday Discuss. Cem. Soc. 87: 107-129.
- Weiss, H., Morency, M., Freyer, K., Bourne, J., Fontaine, D., Ghaleb, B., Mineau, R., Möder, M., Morgenstern, P., Popp, P., Preda, M., Treutler, H.-C., Wennrich, R. 1997. Physical and chemical characterization of a complexly contaminated scrubber dust - a by-product of copper smelting in Sachsen-Anhalt, Germany. Sci. Total Environ. 203: 65- 78.

Environmental Concerns Regarding the Castromil Gold Mine – A Mineralogical Approach

L.Serrano Pinto, E.Ferreira da Silva, C.Patinha & F.Rocha
Department of Geosciences, University of Aveiro, Aveiro, Portugal

ABSTRACT: The Castromil mine was one of the several gold mines in Portugal. This mining area is abandoned since the mid 40's and nowadays one can see the consequences of a careless exploitation. The study area is located on the contact between a Variscian granitic batholith and the Silurian metasediments. The gold occurs within the pyrite and arsenopyrite, galena, native bismuth, chalcopyrite and pyrrhotite are associated with the auriferous mineralization. The mineralogical studies were based on X-ray diffraction (XRD) determinations, carried out in the <80 "mesh" (about <180 µm) grain size fraction, using a Phillips PW 3040/60 diffractometer. The clay fraction (<2 µm fraction) was separated by sedimentation, according to the Stokes law. Oriented specimens for subsequent X-ray diffraction analysis were then analysed after drying, glycolation and heating to 375°C and 550°C. All samples were analysed from 2° to 40° 2θ, at 1° 2θ/min, with Cu-Kα radiation. The selective chemical sequential extraction used 6 steps where each reagent or mixture is able to dissolve, in a selective way, a particular mineralogical constituent corresponding to an assumed potential carrier of trace elements in the sample. Results show that As and Pb could go into solution by dissolution of the less resistant mineralogical phases surpassing the target values.

1 INTRODUCTION

Castromil is an old gold mining area located in the NW of Portugal, some 23km East of Oporto, belonging to the district of Paredes and parish of Sobreira.

According to statistics of 1991, that same parish is suffering a strong demographic growth (413%) due to the presence of major cities surrounding it and good communication routes.

The Castromil gold mine is abandoned since the mid 40's and because at that time no environmental laws and/or education were employed, nowadays one can see the consequences of a careless exploitation. There are tailings at open air, wells and adits without fencing and some of these last are in danger of collapsing.

The geology of the area is characterised by the presence of black schists, coarse grained porphyritic granites (regional rocks) and an aplitic/pegmatitic vein responsible for the auriferous mineralization (Fig. 1). The ore deposit is of Hercinian age and has a hydrothermal origin.

Three stages of mineralization are present; the first is the iron - arsenic stage characterised by the formation of quartz, arsenopyrite, pyrite, pyrrhotite

and bismuth. The pyrite is dominant, followed by arsenopyrite. The gold could be associated to these sulphides and the presence of bismuth is vestigial. The second stage is the zinc stage where sphalerite is rare and chalcopyrite occurs in inclusions in pyrite and sometimes is associated to pyrrhotite. The final stage is called the remobilization stage where gold is associated to galena which fills the micro-fractures of pyrite and arsenopyrite. Covelite, goethite, scorodite and other carbonates and sulphates are present as well (Couto 1991).

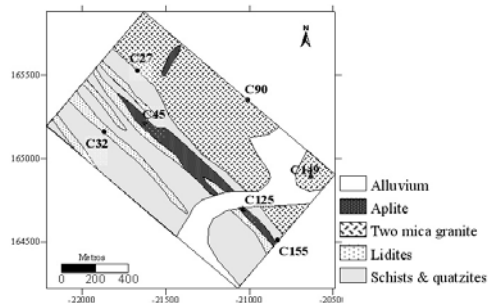


Figure 1: Simplified geology of the study area.

The topography is favourable to surface run-off from the mining site to an agricultural valley where there are large diameter wells used to water the agricultural fields.

A previous work was done at the site showing that in some areas the soils present high concentrations of arsenic and lead and with this present study one pretends to understand the mineralogical behaviour of these toxic elements.

2 MATERIALS AND METHODS

On the previous study mentioned above 106 soil samples covering an area of 1.4km² using a square grid of 100 × 100m were collected. This grid covered not only the area affected by the old mining activities but the surrounding agricultural and urban areas as well. The soils were collected to a depth of 15cm, then oven dried (temperature always below 40°C) and sieved. The fraction used to this study was that below 0.177mm. From each sample an amount of 0.5g was leached in hot (95°C) aqua regia (HCl-HNO₃-H₂O) for 1 hour and analysed by Inductively Coupled Plasma-Emission Spectrometry (ICP-ES) for 35 elements. A rigorous quality control program was used including reagent blanks, duplicate samples and certified international reference materials. Precision and accuracy of the chemical analysis were better than 10% for all the analysed elements. The analysis was performed in an accredited Canadian laboratory (ACME Anal. ISO 2002 Accredited Lab. – Canada).

From those 106 soil samples 13 were chosen for this study, representing the three lithologies present at the site having a high range of arsenic content.

In order to study the mineralogical and chemical speciation of the two most important trace elements related to the contamination – As and Pb (Pinto et al. (2002), X-Ray diffraction (XRD) and selective sequential chemical extraction techniques (SSCE) were used.

For mineralogical analysis by XRD, the samples were dried, washed with distilled water and wet sieved to separate the clay/silt size fraction. The samples were then dried in an oven at 60°C and gently disaggregated with a porcelain mortar. XRD was used following the methodology proposed by Rocha (1993).

Regarding the SSCE, the soils were submitted to a series of 6 extractions where each reagent or mixture is able to dissolve, in a selective way, a particular mineralogical constituent corresponding to an assumed potential carrier of trace elements in the sample. The sequential extraction was carried out on 1g of the selected samples according to the procedure described by Cardoso Fonseca & Ferreira da Silva (1998). The extractants were as follows (Cardoso Fonseca 1982, Cardoso Fonseca & Martin

1986). Step 1 – Ammonium acetate (1M NH₄Ac, pH 4.5); Step 2 – Hydroxylamine hydrochloride (0.1M NH₄OHHCl, pH 2); Step 3 – Ammonium oxalate in darkness (0.175M (NH₄)₂C₂O₄ – 0.1M H₂C₂O₄, pH 3.2); Step 4 – H₂O₂, 35%; Step 5 – Ammonium oxalate under U. V. radiation (0.175M (NH₄)₂C₂O₄ – 0.1M H₂C₂O₄, pH 3.3); Step 6 – Three-acid mixture (HCl_{conc.} + HNO_{3conc.} + HF_{conc.}) decomposition gently heated until dryness.

3 RESULTS

3.1 Pollution index

Heavy metal contamination in the surface environment is frequently associated with a mixture of contaminants rather than a single element. The Pollution Index (PI) was used in this study to evaluate the degree of trace element contamination and it is the sum of the average ratios of the total concentration of trace metals to the hazard criteria divided by the total number of analysed elements (assumed tolerable level of Ag-10 mg.kg⁻¹, As-20 mg.kg⁻¹, Cu-100 mg.kg⁻¹, Mo-50 mg.kg⁻¹, Pb-100 mg.kg⁻¹, Sb-150 mg.kg⁻¹, V- 10 mg.kg⁻¹, and Zn-300 mg.kg⁻¹). These tolerable values derive from the threshold that indicates the phytotoxically excessive level (Kabata-Pendias & Pendias, 1984). A pollution index higher than 1 indicates that the metal concentrations are above the phytotoxically permissible levels.

Figures 2-4 show the pollution index and the As and Pb mapping in soils.

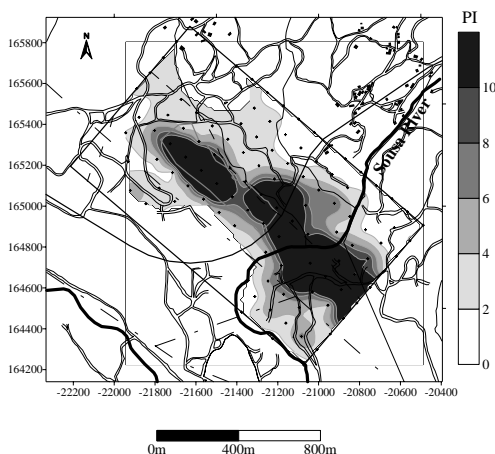


Figure 2: Pollution Index.

Looking at the pattern given by Figure 1, one can see the area where this index is greater than 1 is quite large and one shall emphasize that the areas

affected by the old mining works present a PI greater than 5.

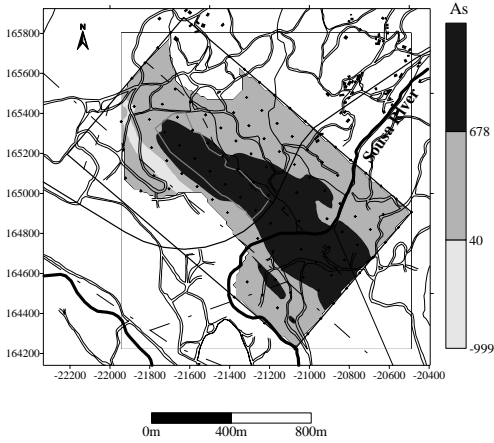


Figure 3: As grades in soils (values in ppm).

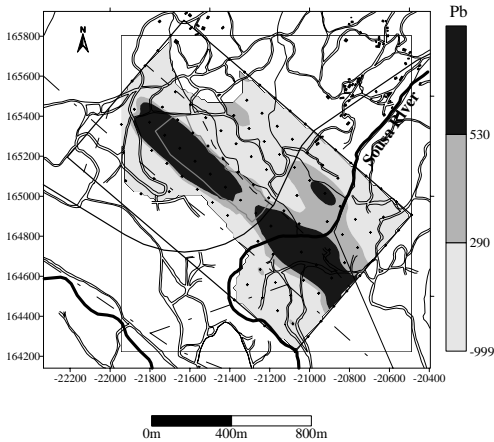


Figure 4: Pb grades in soils (values in ppm).

3.2 Results from SSCE and XRD

The results given by the SSCE allowed distinguishing the different bearing phases for the studied samples. Figures 5-7 show the different percentages of extraction of As, Fe and Pb regarding the six extractants used when SSCE was performed.

The soil samples belonging to the metasediments strip (C27 and C32 with total concentrations of As-280 and 202 ppm, Fe-2.79 and 2.14%, Pb-88 and 107 ppm) present, in general, a similar behaviour regarding the extraction of the elements As, Fe and Pb. For As, the highest percentage is extracted by ammonium oxalate either in darkness (50%) and under UV radiation (40%), although the soil sample

located near the granites present a different ratio as there is more As linked to the matrix and less to the crystalline and/or amorphous Fe oxides. Despite this, in both cases the majority of As is linked to the Fe oxy-hydroxides. The diffraction patterns show the possible presence of Fe minerals such as hematite, goethite, pyrrhotite and cryptocrystalline phases. According to Bose & Sharma (in press) these compounds are able to adsorb As onto their surface. Regarding Pb, the soil samples collected over the metasediments are characterised by presenting a low concentration of this element.

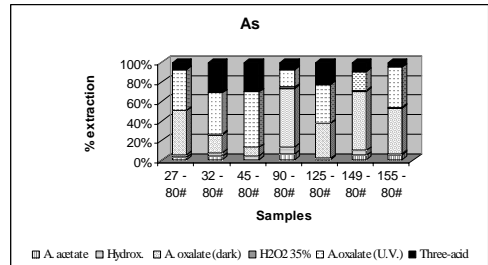


Figure 5: Percentages of extraction for As.

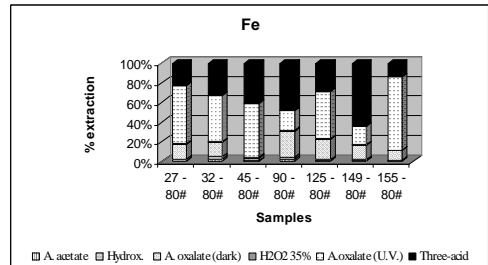


Figure 6: Percentages of extraction for Fe.

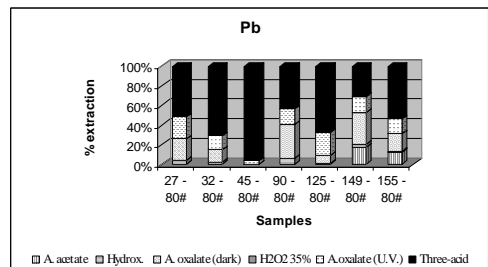


Figure 7: Percentages of extraction for Pb.

According to the SSCE results, Pb was extracted with the three acid mixture (Pb linked to very resistant phases - silicates) and in less extent with ammonium oxalate in darkness and under UV radiation (Pb linked to amorphous and/or crystalline

Fe oxides). Once again, the sample located farther of the granites is the one with higher percentage of extraction of Pb linked to the residue.

The behaviour of the soil samples collected in the area where granites are present (C90 and C149) is similar as well. With total concentrations between 80 and 135ppm for As, 1.9 and 3.05% for Fe and 69 and 175 ppm for Pb. The highest concentrations of As are extracted with ammonium oxalate in darkness, showing this element is linked to the amorphous Fe oxides. The contribution of the extraction with ammonium oxalate under UV radiation is lesser but even so around 20%. The results from the XRD show no evidence of As bearing minerals. This is understandable considering the soil has 100-200 ppm As and the detection limit for XRD is at best 1 wt%. For Pb the results are slightly different once the highest percentage of extraction is associated to the three acid digestion (between 35 and 45%). This means the mineralogical phase for this element is the residue. Despite this fact, amorphous and crystalline Fe oxides could be the bearing phase of this element. The hypothesis given for As regarding the diffractograms can be applied for Pb.

Three soil samples (C45, C125 and C155) were chosen, representing the mineralised area, to perform the sequential chemical extraction and the XRD (total concentrations vary between 2560 and 6900 ppm for As, 2.71 and 5.42% for Fe and 556 and 3196 ppm for Pb). Comparing the SSCE results one conclude that As and Fe have a similar behaviour because percentages of extraction for both elements are identical for each extractant. As expected, the highest percentage of extraction was obtained with the ammonium oxalate (both in darkness and under UV radiation) although some As and Fe was extracted with the three acid mixture. These suggest that As could be adsorbed onto Fe oxy-hydroxides. One must mention that despite the low percentage of extraction (5%) obtained by the ammonium acetate (assumed as corresponding to water soluble and dissolved exchange ions), the high As total concentrations measured in the soil samples can originate concentrations in this element in ground and surface waters above the tolerable limit (10 ppb) (World Health Organisation). The diffraction patterns indicate the presence of As and Fe bearing minerals, such as scorodite and goethite. Regarding the other elements, the behaviour of Pb depends on the sample location. In one sample (C-45) all the extracted Pb is linked to the matrix while in the others it is associated to different mineral phases (amorphous and crystalline Fe oxides and residue). It is important to emphasize that the low percentage of extraction linked to ammonium acetate could be responsible for the presence of high concentrations of Pb in the environment. As an example, in sample C-125, 25% of the existing Pb

was extracted by the ammonium oxalate, representing 750 ppm which could be turn soluble – the target level is 15 ppb (Swartjes 1998). Plumbogummite is probably the Pb bearing mineral responsible for the presence of this element in soils.

4 CONCLUSIONS

This study was elaborated with the aim to know in which mineralogical phases support As and Pb. The results showed that the bearing phases of As are the amorphous and crystalline Fe oxides and regarding Pb the bearing phases are the silicates and the amorphous Fe oxides.

In terms of the present minerals, scorodite, plumbogummite, goethite and hematite as well as some amorphous Fe minerals are the most likely to exist.

5 REFERENCES

- Bose, P. & Shma, A. (in press). Role of iron in controlling speciation and mobilization of arsenic in subsurface environment. Water Research.
- Cardoso Fonseca, E. 1982. Emploi de l'extraction chimique sélective séquentielle et détermination des phases-support du Pb et du Zn en milieux silico-alumineux lors de l'altération supérgene du prospect de Sanguinheiro (SE Aveiro – Portugal). Comunicações Serviços Geológicos Portugal, 68 (2): 267-283.
- Cardoso Fonseca, E. & Ferreira da Silva, E. 1998. Application of selective extraction techniques in metal bearing phases identification. A South European case study. J. Geochemical Explor. 61: 203-212.
- Cardoso Fonseca, E. & Martin, H. 1986. The selective extraction of Pb and Zn in selected mineral and soil samples. Application in geochemical exploration (Portugal). J. Geochem Explor., 26 (3): 231-248.
- Couto, M. H. M. 1993. As mineralizações de Sb-Au da região Dúrio-Beirã, unpublished PhD Thesis, Faculdade de Ciências do Porto.
- Kabata-Pendias, A & Pendias, H. 1984. Trace elements in soils and plants. Boca Raton, FL: CRC Press.
- Pinto, L. S. 2001. Caracterização ambiental da zona envolvente à mineralização de Castromil – Paredes, unpublished MSC. Thesis, Universidade de Aveiro.
- Rocha, F. 1993. Argilas aplicadas a estudos litoestratigráficos e paleoambientais na Bacia Sedimentar de Aveiro, unpublished PhD. Thesis, Universidade de Aveiro.
- Swartjes, F. A. 1998. Risk assessment of soil and groundwater quality in the Netherlands. Risk Analysis, 19 (6): 1235-1249.

Healing Clays: Need of Certification for Suitable Uses

M.Setti & F.Veniale

Dipartimento di Scienze della Terra, University of Pavia, Pavia, Italy

A.López-Galindo & P.Fenoll Hach-Alí

Instituto Andaluz de Ciencias de la Tierra, CSIC – University of Granada, Granada, Spain

C.Viseras

Departamento de Farmacia y Tecnología Farmacéutica, University of Granada, Granada, Spain

ABSTRACT: Clay minerals are used in the preparation of pharmaceutical products as excipients and coadjuvants in tablets and suspensions improving the drug bio-availability, for hygienic applications and as “peloid” muds in spa-centres. Healing clays vary in mineral composition, but normally they should have high content of smectite, whereas mixtures of kaolinite, illite and mixed layers seem more suitable for internal uses. Peloid-therapy is the application of thermal muds (“peloids”) for recovering rheumatism, osteoarthritis and traumatic muscle-bone damages. The calorific capacity and cooling rate of the aqueous pastes are determined by mineral composition, granulometry, exchange capacity, hydric degree and adhesivity. Artificial pastes made up of clay geomaterials (natural or modified) mixed with salty mineral waters are currently used in spa centers. They should possess suitable properties which are in relation with time and procedures of ageing (“maturation”), and with the chemo-physical and biological reactions which are occurring in the admixtures. Regulations (standard criteria) are needed for certifying the suitable quality of clay geomaterials to be used in peloid-therapy and in pharmaceutical-cosmetic formulations.

1 INTRODUCTION

Clay minerals (as laminar, smectite, kaolinite, talc and fibrous sepiolite-palygorskite) are used in the preparation of pharmaceutical and cosmetic products; mixed with animal feeds as active chemisorbents for protective coatings of stomach and intestine against toxins, bacteria, and even viruses; for hygienic applications as deodorants, cat litters, cigarette filters, household pollutants removal, etc. Furthermore, for the preparation of thermal muds (a poultice called *peloid* obtained after suitable maturation by mixing with mineral water) used in spa-centres for the therapy (local or generalized cataplasms) of rheumatism, arthritis and bone-muscle traumatic damages (also due to sport performances), for the treatment of skin diseases as acne, seborrhoea and psoriasis, and for cosmetic cleaning masks, and aesthetic clay-water baths to recover lipo-dystrophies and cellulite. Special healing materials are the para-muds, admixtures of clay minerals with paraffin.

2 CLAYS AS DRUGS

Products intended for use in the preparation of medicines must fulfil certain requirements regarding safety, stability, and chemical inertia; other important attributes are colour and taste, affecting the acceptance by the patient. On the other hand, it is known that the bioavailability of scarcely soluble compounds can be increased by adsorption on solid templates; another mechanism is provided by solubilisation due to colloidal-dispersed solids. Water content and texture influence the technical processes. In fact, it is important to maintain the phases separate before use, or to obtain a system easy to disperse before administering to the patient. Besides their own (re)active properties, clay minerals serve as excipients and coadjuvants (stabilisers, dispersants, lubricants, surfactants, binders and fillers) in the preparation of medicinal products. In some cases, the interaction between drugs and clay minerals is used to influence drug release, modifying the biopharmaceutical profile of the drug, that is controlling the release of the drug from the medicinal. Recent developments of chemotherapy have requested clay minerals with high cation exchange capacity, aiming to realise new functional and durable medicaments. Preformulation

studies have shown the possibility of effective control of the release of several actives (including tetracyclines, beta-blockers, and anti-inflammatory drugs) by means of interaction with selected clay minerals.

X-ray diffraction and chemical analyses carried out by our team on various pharmaceutical drugs and herbalist's clays allowed to recognise significant differences in composition, mainly concerning the content of smectite, kaolinite, carbonate, quartz and cristobalite; the latter phase could be dangerous when the bearing medicament is used for oral administration.

We have investigated the mineralogical and chemical purity of fibrous sepiolite-palygorskite and laminar bentonites, determining several parameters concerning their suitability for use in tablet manufacture: (i) yellowish-white colour does not need correction; (ii) water content varies according to the structure of clay minerals and storage conditions; (iii) adsorption capacity of methylene blue (indicating suitability as anti-diarrhoeic product) is affected by the amount of hydration water, dehydration temperature and kind of exchangeable cation(s) present in the clay.

Our studies on the effect of mixing conditions and on the influence of textural characteristics on the flow and rheological behaviour of some clay-water dispersions have evidenced that the pharmaceutical grade is different for fibrous and laminar clay minerals: sepiolites showed the highest viscosity, whereas palygorskites resulted in low to medium viscosity gels; bentonites provided medium viscosity systems. Viscosity greatly increased in bentonites dispersions after low shear treatment (as a result of swelling), whereas viscosity stayed for fibrous clay dispersions. Drastic pH changes highly influenced the rheological behaviour of fibrous clay dispersions, whereas the laminar clay/water systems were found less sensitive.

3 CLAY FOR PELOOTHERAPY

The preparation of peloid muds consists in mixing a clay geomaterial with saline water. The main factors contributing to the peloid mud features are: composition and granulometry of the virgin clay, geochemistry of the mineral water and maturation procedure. The maturation treatments are varying with respect to the mixing procedure and lasting time. Clay/water ratio and workability of the mud paste are usually matter of empirical valuation depending on the spa-center tradition. Stockage and re-cycling of peloid muds is a further problem.

To be suitable for thermal therapy, certain qualities of the peloid muds are much appreciated: low cooling rate, high-exchange capacity, good adhesivity, ease of handling and pleasant sensation

when applied to the skin. Worse applications of peloid-therapy could produce non-beneficial effects, or cause relapse.

The aim of our investigation was to evaluate the effect of different mineral waters and maturation procedures on the minerals constituting the virgin clay geomaterial. Mineralogical changes were mainly concerning the degradation of smectite and illite; dissolution of calcite is subordinate. Furthermore to determine the physico-chemical properties and rheological behaviour of the maturated muds. For this purpose, peculiar parameters have been tested. The $< 2\mu\text{m}$ fraction was generally decreased due to clay particle agglomeration. Cation exchange capacity, soluble salts, water retention, swelling index, activity, consistency parameters (WL, WP and PI), thermal behaviour and cooling kinetics are influenced by the geochemistry of mineral water used for the maturation treatment, but there are some opposite trends for Br-I-salty, and for sulphureous and Ca-sulphate waters, respectively.

The temperature reached by the peloid muds after 20 min of application (calculated after an innovative mathematical model) is influenced by water retention; such measurement is also important for the spa-center management, especially when high-energy costs have to be met for the peloid mud heating. An increase in plasticity index and a slower cooling are considered to improve the quality of the peloid mud. The different cation exchange behaviour and soluble salt content could be discriminant for either dermatological masks or thermal body cataplasms.

Leaching tests have shown that the release-exchange between skin sweat and peloid mobile chemical elements is depending on the amount of swelling clay minerals.

Furthermore, a protocol has been developed for testing the bio-adhesivity of the peloid mud, an important parameter for evaluating the effectiveness of peloid application on the body skin; it is based on innovative rheological and tensiometric approaches.

Attention has also been paid to the bio-activity occurring during the maturation processes; some interesting results are concerning the lipidic fraction of virgin, maturated and regenerated muds; it was verified that the mature mud contains higher concentration of phospholipids than the regenerated one.

Investigations addressed to radio-activity are in progress concerning dangerous ionising radiations as radon (a volatile element) and non-volatile daughter products that could remain into the lung tissue for long time. This can be especially dangerous when the peloid mud is recycled, a common praxis in many spa-centres.

Finally, we have put in evidence the need of regulations (standard criteria) for certifying the

suitability of clay geomaterials for the formulation of peloid muds, also with respect to differentiated therapies. As a matter of fact, the characterisation of clays to be used for dermatological-cosmetic products is not under rigorous regulation. Moreover, the clay geomaterials used for the preparation of peloid muds are only empirically evaluated.

As preliminary suggestion, we recommend the following parameters for qualifying clay geomaterials to be used in the preparation of peloid muds:

- granulometry: fraction $< 2\mu\text{m}$ at least 70-80%;
- specific surface area: it can be roughly calculated on the base of grain-size distribution;
- mineralogy of bulk sample and clay fraction, content of swelling clay minerals (at least 60-70%), abrasive minerals (quartz, feldspars), hazardous constituents (free silica, asbestiform minerals, Fe-oxy-hydroxides), carbonates (can play a role on the rheological and physico-chemical behaviour);
- chemistry: essential and trace elements, especially the toxic ones;
- pH;
- cation exchange capacity (total and Na^+ , K^+ , Ca^{2+} , Mg^{2+});
- soluble salts;
- water retention;
- consistency parameters (liquid and plastic limits, plastic index);
- rheology: activity, adhesivity, viscosity;
- thermal behaviour: DTA, TG and DTG analyses, heat capacity and conductivity, cooling kinetics.

The increasing success of natural health remedies is somewhat jeopardising: not all that does glitter is gold!

4 REFERENCES

- Veniale F. (Ed.) 1996. *Argille curative (Healing clays)*. Proc. Meeting Gruppo Ital. AIPEA, Salice Terme/PV (Italy), 142 pp.
- Veniale F. 1997. Applicazioni e utilizzazioni medico-sanitarie di materiali argillosi naturali e modificati. (Medical and sanitary applications and uses of natural and modified clays). *Proc. Worrkshop Gruppo Ital. AIPEA*, Rimini (Italy), 205-239.
- Veniale F. (Ed.) 1999. Argille per fanghi peloidi termali e per trattamenti dermatologici e cosmetici (Clays for thermal peloid muds and for dermatological and cosmetic treatments). Proc. Symposium Gruppo Ital. AIPEA, Montecatini Terme/PT (Italy). *Miner. Petr. Acta*, XLII, 261-335.
- Veniale F. 2004. Formulation of muds for pelo-therapy: effects of maturation by different mineral waters. *Appl. Clay Sci.*, 19 (in press).
- Viseras C. and López-Galindo A. 1999. Pharmaceutical applications of some spanish clays (sepiolite, palygorskite, bentonite): some preformulation studies. *Appl. Clay Sci.* 14, 69-82.

Autoconservation of Mining Industry Waste as a Result of Prolonged Storage

E.Shcherbakova & G.Korablev
Institute of Mineralogy, Miass, Russia

ABSTRACT: In the South Ural, the oldest mining/metallurgical region of Russia, about 3500 millions m³ of solid and liquid waste of the industries have been accumulated already. To develop ways of better waste utilization, their structure, chemical and mineral composition, and influence to environment were studied. Flotation wastes of Cu-Zn sulphide ores, or the so-called tailings, are disposed as a pulp to the open tailing ponds where their composition is considerably changed. The originally friable tailings become transformed into compact rocks (technogenic sandstones) in which separate mineral grains are cemented by the newly formed sulphates, and a quartz-sulphate crust is formed on the settling pond surface. Over time, water-soluble sulphates in the crust are changed into practically insoluble sulphate minerals. In 15-25 years, the settling pond becomes completely covered by a crust, which remediates the negative impact of the waste to environment. Any attempt to develop the settling pond as a potential technogene deposit will likely result in disturbance of the surface crust and the established equilibrium, and posed renewed environmental risk.

1 INTRODUCTION

At many mining sites, the extraction and processing of sulphide ores produce pyrite-containing waste oxidation of those results in generation of low-pH conditions and the consequent release of heavy metals into ground and surface waters. Various programs of utilization, remediation or revegetation of mining waste are elaborated to decrease their negative influence to environment (Jambor et al. 2000a, b).

In the South Ural (Russia), mining/metallurgical industries have been developed since 1780s. Presently, more than 3500 millions m³ of solid and liquid waste are stored in waste dumps or special reservoirs. The semi-liquid flotation waste of Cu-Zn sulphide ores are disposed as a pulp to the open tailings impoundments. In the late nineties of last century, there were six closed and four active tailings impoundments. The surface area of tailings impoundments varied from 15 to 285 hectares, with tailing quantities in each impoundment ranging from 3 – 40 million tons. The total resources of tailings exceeded 90 million tons. During storage of the tailings, some valuable components such as Au and Ag are accumulated. To develop ways of better utilization of the tailings, their structure, chemical

and mineral composition, and influence to environment were studied (Shcherbakova & Korablev 1998).

2 METHODS

The surface of each tailing impoundment was sampled. When possible, the surface was drilled to a depth of 2 – 3 to 10 – 20 meters, and samples were removed throughout the profile of drilled holes.

In the samples of tailings, the contents of SiO₂, TiO₂, Al₂O₃, Fe₂O₃, FeO, MnO, MgO, CaO, K₂O, Na₂O, P₂O₅, SO₃, CO₂, H₂O, and S²⁻ were determined by wet silicate analysis; Cu, Pb, Zn, Cd, Ni, Co, Ag, As, Sb, and Bi by atomic absorption spectroscopy and X-ray fluorescence analysis. The mineral composition of tailings was determined by X-ray diffractometry, IR, and Raman spectroscopy. Mössbauer spectroscopy was used for more precise determination of minerals containing Fe²⁺ and Fe³⁺.

3 RESULTS

3.1 Structures

Fresh tailings are a friable fine-grained material. In the impoundments, the tailings are differentiated according to their density, as governed by sedimentation in the natural water basins, resulting in alteration of coarse-grained (0.05 – 0.06 mm), middle-grained and fine-grained (0.01-0.02 mm) bands in the tailings impoundments after closure. Due to the irregular flow of pulp, the complex beach zones with prevalence of coarse-grained sediments are formed on the periphery of the tailings impoundments and zones with fine-grained fractions of tailings are situated in the central parts.

3.2 Mineral composition

The fresh tailings contain on average (wt.%): pyrite 45, quartz 35, aluminosilicates of K, Na, and Ca (feldspar, mica) 10, carbonates (dolomite, calcite) 5, primary Cu-Zn sulphides (chalcopyrite, sphalerite) 2 - 4.

In the old tailings, aluminosilicates and carbonates practically disappear, and Cu and Zn sulphides occur as single grains only in the deeper levels of the impoundments. The major minerals of the old tailings are pyrite, quartz, and gypsum. Pyrite content varies from 20 - 80 %, with the general trend of decreasing from deeper levels to the surface of the impoundments along with the relative concentration of fine-grained bands. On the surface of the old closed impoundments, the pyrite content is significantly lower up to the absolute disappearance of this mineral. Quartz content varies from 10-35 %, increasing towards the top levels of the old tailings impoundments, where, as a rule, a sharp increase of the average size of quartz grains is also observed. Gypsum content varies from 5-40%, generally increasing towards the surface of the impoundments.

In the near-surface parts of tailing impoundments, sulphate minerals are abundant. The simple soluble sulphates of the type $M^{2+}(SO_4) \times nH_2O$ ($M^{2+} = Fe^{2+}$, Zn, Mg, Mn, Cu, Ni, Co, $n = 1 - 7$) predominate. These salts are unstable, and their hydration states are dependent on the local humidity or moisture conditions. The simple hydrated sulphates are commonly accompanied by those of more complex composition such as copiapite $AFe^{3+}_4(SO_4)_6(OH)_2 \times 20H_2O$ ($A = Fe^{2+}$, Mg, Zn, Cu, Al, Fe^{3+}) and halotrichite $A(Al,Fe^{3+})_2(SO_4)_4 \times 22H_2O$ ($A = Fe^{2+}$, Mg, Zn).

On the surface of the old closed tailings impoundments, jarosite $KFe_3(SO_4)_2(OH)_6$ (to 15 %) is most usual. Rozenite $M^{2+}SO_4 \times 4H_2O$ (to 10%) occurs on the surface and in the upper levels of the old tailings impoundments. Szomolnokite $M^{2+}SO_4 \times H_2O$ prevails in the young impoundments. Melanterite $M^{2+}SO_4 \times 7H_2O$ is conserved as relics

inside the aggregates of rozenite; sometimes it forms the abundant accumulations in the deeper levels of the tailings impoundments. Although the sulphate minerals in the tailings impoundments are typically Fe-dominant, the Mg-containing sulphates such as magnesiocopiapite have been noted to form abundantly where the primary carbonate minerals contain Mg. As well, the identification of Zn or Cu-containing minerals such as zinc-melanterite, zincocopiapite, and ferroan boothite serves to emphasize that the composition of the sulphate salts will reflect those of the oxidizing source materials.

3.3 Chemical composition

In fresh tailings, the mean contents of Cu and Zn are lower than in the primary ores by at least 1.5 – 4 times (0.25 and 0.90 %, respectively). In the old tailings, the concentration of Cu and Zn decline to 0.06 and 0.50 % respectively, and in the near-surface zones of the impoundments, to 0.03 and 0.10%. These elements are concentrated in the foot of the sand horizons and in the fine-grained bands, which are characterized by high pyrite content. A similar trend of decreasing concentrations from ores → fresh tailings → old tailings is also typical for Pb, Cd, and Bi.

The inverse trend is observed for Ag. In the old tailings, the average concentrations of Ag are higher than in the primary ores by at least four times, increasing toward the deeper levels of the impoundments with relative higher concentrations of fine-grained bands. Similar behaviour is characteristic for Au and As, which increase in the series ores → fresh tailings → old tailings; higher concentrations of Au are associated with the beach zones of the impoundments.

4 DISCUSSION

The features of the structure and composition of the tailings indicated consisted stages of tailing transformations as a result of prolonged storage, in relation to the age of the impoundments.

In the transformation processes of tailings, pyrite is oxidized under the action of oxygen-enriched atmospheric waters to form of sulphuric acid and hydrous ferroan sulphates, firstly in the surface zone with coarse-grained bands of tailings (aeration zone). In the active impoundments where new tailings are constantly being loaded on the surface, due to the limited residence time of oxidizing conditions, transformation fails to proceed significantly.

Hydrous ferroan sulphates, the primary products of oxidation of pyrite, are found only in the impoundments that have been closed for at least five years. In the aeration zones of the impoundments

aged less than five years since closure, only residual sphalerite and chalcopyrite are decomposed, which are less stable to oxidation than is pyrite.

Sulphuric acid has a major role in the chemical transformation of tailings in the impoundments aged more than five years since closure, resulting in direct crystallization of minor-hydrous ferroan sulphates (formation of szomolnokite instead of melanterite and rozenite), oxidation of ferroan sulphates to ferroan ones (formation of copiapite), and decomposition of aluminosilicates (mainly mica) and carbonates with formation of secondary quartz along with Ca, K, and Al sulphates.

As a result of these processes, the originally friable tailings are transformed into compact rocks (technogenic sandstones) in which separate mineral grains (mainly quartz and pyrite) are cemented by the newly formed sulphates. The sandstone's quartz nearly disappears with depth. In the deeper levels of the impoundments, pyrite concentrations reach 70 – 80 %. In contrast, a quartz-sulphate crust is formed on the surface of the impoundments. In the composition of this crust, insoluble sulphate minerals (jarosite) replace the water-soluble sulphates (melanterite, rozenite) for a time. Such crust, varying in thickness, covers the surface of the impoundments completely within 15-25 years, isolating the impoundment and causing difficult access to the inner parts by atmospheric waters and preventing the further oxidation of pyrite. This autoconservation phenomenon has been observed in practically all old impoundments.

Pyrite and the noble metals, Ag and Au, accumulate in the tailing impoundments as a result of prolonged storage of tailings, and they may be extracted from the impoundments by the appropriate technologies. At the same time, the tailings impoundments are great generators of pollutants; the environmental influence of an impoundment is most intensive when it is actively working and gradually decreases after closure as a result of the autoconservation phenomena. For this reason, any attempt to develop the impoundment as a potential technogene deposit will likely result in disturbance of the surface crust and the established equilibrium, and pose renewed environmental risk.

5 REFERENCES

- Jambor, J.I., Nordstrom, D.K. & Alpers, C.N. 2000a. Metal Sulfate Salts from Sulfide Mineral Oxidation. In: *Sulfate minerals: Crystallography, Geochemistry, and Environment significance / Reviews Mineral. Geochem.*, 40: 304 – 350.
- Jambor, J.I., Blowes, D.W. & Ptacek, C.J. 2000b. Mineralogy of mine waste and strategies of remediation. In: *Environmental Mineralogy / EMU Notes in Mineralogy*, 2: 255-290.

- Shcherbakova, Elena & Korablev, George. 1998. Autocconservation of mining industry waste in the South Ural, Russia. *Proc. Latvian Acad. Sci.* 52: 286-288.

Attenuation of Metals by Iron-phases from Surface and Ground Water of Ni-Cu Mine Waste

N.V.Sidenko & B.L.Sheriff

Department of Geological Sciences, University of Manitoba, Winnipeg, Manitoba, R3T 2N2 Canada

ABSTRACT: This study was designed to understand processes of Cu, Zn, and Ni attenuation from water within sulfide mine tailings, at INCO Ltd, Thompson, Manitoba, Canada. Surface water from small pools, and ground water from pits in the tailings was tested for pH, filtered immediately and analyzed for metals, SO_4^{2-} , Fe^{2+} , and Fe^{3+} . Unacidified water samples were stored for two months, while precipitates formed by the oxidation of dissolved Fe^{2+} . These sediments were separated from the solution by filtration, the solutions reanalyzed and precipitated minerals identified by a combination of scanning electron microscopy and X-ray diffraction. A selective dissolution technique measured element partitioning between phases of different crystallinity. Initially, ground water was characterized by a pH of 5.7-6.2, and concentrations of SO_4^{2-} 6-13 g/l, Fe^{2+} 1 g/l, Fe^{3+} 100 mg/l, Cu 0.05 mg/l, Zn 0.3 mg/l, and Ni 3 mg/l. Precipitation of goethite and schwertmannite resulted in the pH decreasing to 2.8-3.3 and the Cu, Zn, and Ni to 23, 82, 25% of their initial values, respectively. Surface water was initially more acidic (pH = 2.7-3.2), with similar concentrations of SO_4^{2-} , Cu, Zn, but less Fe^{2+} at 120-180 mg/l, and more Fe^{3+} (12-210 mg/l) and Ni (10-107 mg/l). Formation of schwertmannite and jarosite decreased the initial concentrations of Cu, Zn, and Ni in surface waters by 14, 23, and 7.7 %, respectively. The affinity of metals to goethite and jarosite decreases in the sequence $\text{Cu} > \text{Zn} > \text{Ni}$, while poorly crystalline schwertmannite accumulated the metals in the reverse order, $\text{Cu} < \text{Zn} < \text{Ni}$.

1 INTRODUCTION

Oxidation of sulfides in mine wastes result in the acidification of water and the release of Fe^{2+} , SO_4^{2-} and metals into solution. Further oxidation of Fe^{2+} to Fe^{3+} and hydrolysis can lead to the precipitation of Fe hydroxides or hydroxysulfates depending on the geochemical conditions (Nordstrom & Alpers 1999; Bigham & Nordstrom 2000). These Fe-phases play important roles in reducing the environmental impact of acidic drainage by the sorption of the metals (Plumlee et al. 1999; Webster et al. 1998; Lee et al. 2002). Despite numerous studies in this field, there remain questions about the occurrence, stability and absorption capacity of Fe phases with regard to the oxidation of mine tailings.

The aim of this study was to understand the processes controlling the attenuation of Ni, Zn, and Cu, from surface and ground waters within mine tailings. The specific objectives of the study were (1) to characterize water chemistry, (2) to identify the mineralogical composition of precipitates, and (3) to determine the metal concentration in precipitates and partitioning between phases of differing crystallinity.

This study is based on mine tailings, produced by INCO Ltd's Ni-Cu mine at Thompson, 645 km north of Winnipeg, Manitoba. Since 1960, about 40 Mt of

tailings have been produced. Tailings discharged during last 10 years contain from 4.0 to 15.7 wt. % sulphur. Sulfide minerals are predominantly pyrrhotite, with minor pentlandite, chalcopyrite, and pyrite. Gangue minerals consist of biotite, quartz, potassic and albitic feldspars with minor amphibole and calcite.

2 METHODOLOGY

Water samples, T9W and T10W, were collected from the bottom of pits dug in the tailings and T5W, T6W, T7W, and T16W from small pools on the surface. The water was filtered through a 0.45 μm filter and unstable parameters such as Eh, pH, and dissolved oxygen (DO) measured immediately. Samples were divided into four aliquots; one was acidified with HNO_3 to preserve metals in the solution, another with HCl for iron speciation and two aliquots preserved unacidified, with one being sent for anion analysis. All samples were stored at temperatures below 4°C until analyzed by Evirotest Laboratories Ltd., Winnipeg. Total concentrations of metals were determined by ICP-MS, SO_4^{2-} by turbidimetry, and Cl⁻ by a colorimetric technique. Concentration of Fe^{2+} and Fe^{3+} was separated by ion chromatography and detected by UV spectrometry.

Samples of unacidified water were stored at 10°C for two months during which time precipitates formed. The T9F, T10F, T5F, T6F, T7F, and T16F precipitates were separated from the solutions with a 0.45 µm filter and dried at room temperature. The T9WF, T10WF, T5WF, T6WF, T7WF, and T16WF samples of filtrate, were analyzed as described above. Minerals in the precipitates were identified with powder X-ray diffraction (XRD), scanning electron microscope (SEM) equipped with an X-ray energy-dispersive spectrometer (EDS) and electron microprobe (EMP).

Sequential leaching was used to separate elements bound with Fe-phases of differing crystallinity (Dold 2003). Poorly crystalline phases were extracted by shaking 25 mg aliquots of the precipitates in 10 ml of 0.2 M ammonium oxalate solution adjusted to pH 3 by oxalic acid, for 45 minutes in the dark, at room temperature. Then, the solid residue was separated by centrifugation and the liquid collected for analysis. 10 ml of the same reagent were added to the residue, and the samples heated at 80°C for 2 hours, sufficient to dissolve all Fe-hydroxides and hydroxysulfates (Dold 2003). The separated aliquots were analyzed for Fe, Ni, Cu, and Zn using induced coupled plasma optical emission spectroscopy ICP-OES. Extraction of 98% total Fe from sample T7F, consisting of only schwertmannite, demonstrated the effectiveness of the selectivity of this technique.

3 RESULTS AND DISCUSSION

3.1 Geochemistry of surface and ground water

Both surface and ground water can be classified as Mg-Ca-Fe-SO₄ water with the content of total dissolved solids ranging from 1.3 to 13 g/l (Table 1).

Initially, ground water was characterized by pH 5.7-6.2. The dominant form of iron in the ground water is Fe²⁺. The metal concentrations in the solutions are in the order Cu<Zn< Ni. After two months of storage, Fe²⁺ decreased and Fe³⁺ increased as precipitates were formed by Fe²⁺ oxidation. Further hydrolysis of Fe³⁺ and precipitation of hydroxides resulted in the pH decreasing to 2.8-3.3. Metal were reduced by co-precipitation to 23, 82, and 25% of initial concentrations for Cu, Zn, and Ni, respectively.

Surface water was initially more acidic (pH=2.7-3.2) than the ground water, containing more Fe³⁺ and metals, but less Fe²⁺ (Table 1). The relative order of concentrations of Cu, Zn, and Ni in surface waters is the same as in ground water. During storage, the concentrations of Fe²⁺ decreased to <0.1-6.7 g/l, while the level of Fe³⁺ and acidity were close to the initial values. Initial concentrations of Cu, Zn, and Ni decreased to 14, 23, and 7.7%, respectively. Initial concentrations differed from the final ones by a few percent, within the reproducibility of the analyses.

Higher percentages of metals were precipitated from the ground water than from the surface solutions. This could be due to either oxidation of the higher initial content of Fe²⁺ producing more precipitate, or to the higher pH of the ground water affecting the adsorption of metals. At pH>3.5, iron hydroxides and hydroxysulfates adsorb divalent metals more effectively than under acidic conditions (Dzombak & Morel 1990, Webster et al. 1998). At pH<3.5, the attenuation of metals by co-precipitation and formation of solid-solutions dominate over adsorption on the surface of iron hydroxides and hydroxysulfates.

Table 1. Analyses of water samples: initially (W) and after precipitation (WF), mg/l.

Sample	pH	Eh	TDS	Ca	Mg	Na	K	SO ₄ ²⁻	Fe	Fe ²⁺	Fe ³⁺	Cu	Zn	Ni
Ground water														
T9W	6.22	0.01	1320	411	1150	95.8	128	6130	949	1010	38	0.036	0.42	2.29
T9WF	3.64	0.51	-	304	1080	87.1	103	6660	816	510	150	0.083	0.08	1.73
T10W	5.80	0.07	2270	428	2490	630	188	13000	1620	1380	148	0.051	0.24	3.71
T10WF	3.24	0.71	-	321	2360	607	182	13100	1290	864	290	0.039	0.15	3.03
Surface water														
T7W	3.20	0.59	1540	457	335	15.4	3.1	2200	139	117	12	0.26	0.16	9.74
T7WF	3.09	0.67	-	402	300	20.7	4.4	2530	64.1	<0.1	47	0.27	0.26	8.99
T16W	2.74	0.55	-	480	1960	274	43.4	9420	433	178	210	0.16	1.25	107
T16WF	2.89	0.63	-	389	1800	288	32.4	10000	288	3.7	253	0.13	0.96	111
T5W	2.58	0.69	15000	513	1740	233	15.1	9940	346	41.5	293	0.30	0.47	46.9
T5WF	2.54	0.75	-	458	1690	254	2.51	9620	265	<0.1	171	0.31	0.48	43.8
T6W	2.49	0.63	6900	463	433	166	29.2	4350	551	419	137	0.039	0.30	23.8
T6WF	2.49	0.79	-	453	467	184	32.2	4320	340	6.7	148	0.053	0.27	23.1

3.2 Mineralogy of precipitates

Goethite, FeOOH , was identified by XRD as the principal crystalline phase precipitated from the ground water (Fig. 1). The precipitate consisted of 0.5-2 μm spherules, sometimes covered by a thin layer of fibrous crystals, difficult to resolve by SEM. The raised background at 2θ of 35° between the two goethite peaks matches the major broad reflection of schwertmannite $\text{Fe}_8\text{O}_8(\text{OH})_{8-2x}(\text{SO}_4)_x \cdot n\text{H}_2\text{O}$ (Fig. 1). The fibrous morphology, XRD data, and presence of S found by SEM-EDS indicate that the poorly crystalline phase associated with goethite is schwertmannite.

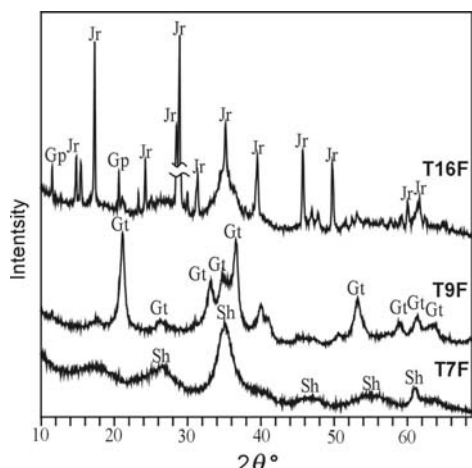


Figure 1. XRD patterns of sediments precipitated from ground (T9F) and from surface water (T5F, T7F, T16F) showing the positions of reflections of goethite (Gt), jarosite (Jr), schwertmannite (Sh) and gypsum (Gp).

Only schwertmannite precipitated from the surface water sample T7W. The XRD pattern of this schwertmannite is similar to synthetic and natural analogs (Bigham et al. 1990). Schwertmannite can form web-like aggregates made of interwoven crystals (Fig. 2a). Schwertmannite formulae calculated from EMP analyses are $\text{Fe}_8\text{O}_8(\text{OH})_{(8-2x)}(\text{SO}_4)_x \cdot n\text{H}_2\text{O}$, where x varies from 1.04 to 1.60, which is in agreement with previous studies of schwertmannite (Bigham et al., 1994, Yu 1999 et al.). In T6F and T16F, jarosite, $\text{KFe}_3(\text{SO}_4)_2(\text{OH})_6$, identified by XRD, was associated with fibrous crystalline schwertmannite overgrowing jarosite (Fig. 2b).

Mineralogical differences between the precipitates from ground and surface water can be explained by different values of pH, SO_4^{2-} content and red/ox conditions (Bigham & Nordstrom 2000). Jarosite is usually stable at $\text{pH} < 3$ and high SO_4^{2-} but

goethite precipitates between pH 3 and 8. Schwertmannite is a metastable phase found between pH 2.5 and 6 in more oxidized waters than goethite.

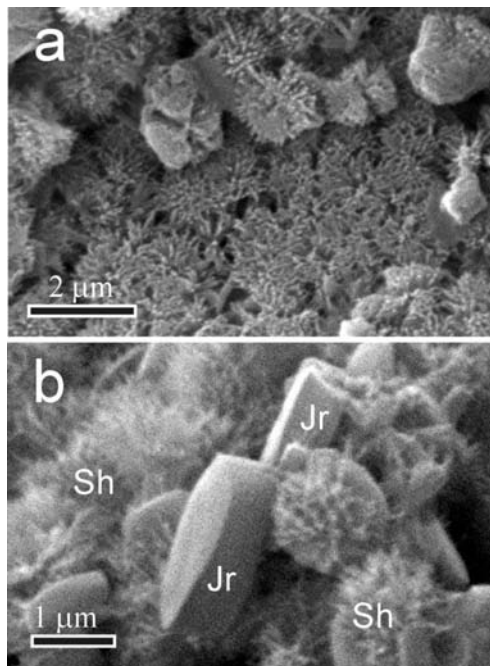


Figure 2. SEM pictures showing (a) web-like aggregates of schwertmannite from T7F; (b) schwertmannite (Sh) overgrowing jarosite (Jr) in T16F.

3.3 Metal partitioning between Fe-phases

About half of the iron in the ground water was precipitated as poorly crystalline schwertmannite and the remainder as goethite (Table 2). Most Ni and Zn was bound to schwertmannite.

Ni and Zn were also co-precipitated with schwertmannite from surface waters. In the schwertmannite from T7F, concentrations of metals are in the order $\text{Cu} < \text{Zn} < \text{Ni}$, which is the order of their concentrations in the solution.

Concentrations of the metals in jarosite from T5F decreased in the order $\text{Cu} > \text{Zn} > \text{Ni}$, the reverse of schwertmannite. This sequence agrees with the order of incorporation of metals by jarosite $\text{Cu} > \text{Zn} > \text{Co} \sim \text{Ni} > \text{Cd}$ found by Dutrizac & Jambor (2000).

The average portion of metals in crystalline phases decreased in the sequence $\text{Cu} > \text{Zn} > \text{Ni}$ (Table 2), which is similar to their ease of hydrolysis. In contrast, schwertmannite accumulates the metals in reverse order $\text{Cu} < \text{Zn} < \text{Ni}$, which corresponds to observed concentrations of the metal concentration in solutions.

Table 2. Mineralogy, concentrations, and partitioning of metals between poorly- (1) and well-crystalline phases (2) of the precipitates.

Sample	Minerals	Fe		Cu		Ni		Zn					
		Total	1	2	Total	1	2	Total	1	2			
T10F	Sh+Gt	47.2	64	36	20.9	76	24	22.3	99	1	8.6	53	47
T9F	Sh+Gt	49.9	48	52	7.4	33	67	23.8	99	1	13.1	94	14
T7F	Sh	42.5	98	2	6.0	78	22	53.3	91	9	8.7	85	15
T6F	Sh+Jr	44.5	86	14	43.4	50	50	13.7	85	15	69.9	100	0
T16F	Jr+Sh	35.1	61	39	9.9	3	97	196	92	8	24.9	47	53
T5F	Jr	31.0	4	96	80.9	24	76	3.5	32	68	18.5	20	80
Average			60	40		44	56		83	17		66	35

On average, most Ni (83%) and Zn (66%) were accumulated in schwertmannite regardless of the fact that only 40% of the total Fe is in this phase. The recrystallization of unstable schwertmannite into the stable phases, observed by Bigham et al. (1990), may cause the release of metals into solution in acidic conditions.

4 CONCLUSIONS

- More Cu, Zn, and Ni, was precipitated from the ground water than from surface waters due to the higher initial content of iron and pH of ground waters. These parameters result in a larger quantity of precipitates and an increase in the effectiveness of metals sorption onto Fe hydroxides.
- The metals co-precipitated from ground water with goethite and schwertmannite, while the formation of schwertmannite and jarosite controlled the metal attenuation from surface waters. Difference in the mineralogy of the precipitates is attributed to initial pH and SO_4^{2-} concentrations.
- The affinity of metals to goethite and jarosite decrease in the sequence $\text{Cu} > \text{Zn} > \text{Ni}$, while schwertmannite accumulates them in reverse order $\text{Ni} > \text{Zn} > \text{Cu}$. Most Ni and Zn are bound with poorly crystalline schwertmannite, and could be released back into solution. This should be taken into account during remediation of mine sites.

5 ACKNOWLEDGEMENTS

This work was financially supported by a Collaborative Research and Development grant from NSERC, Canada matched by INCO Ltd. Thompson operations. NVS is supported by a NATO-NSERC Research Fellowship.

6 REFERENCES

Bigham J.M. 1994 Mineralogy of ochre deposits formed by sulphide oxidation. In: J.L. Jambor & D.W. Blowes (eds.),

Short course handbook on Environmental geochemistry of sulphide mine waste. Mineral. Assoc. Can., Waterloo: 103-132

Bigham J.M. & D.K. Nordstrom 2000. Iron and aluminium hydroxysulfates from acid sulfate waters. In N.C. Alpers., J.L. Jambor, & Nordstrom D.K. (eds.) Sulfate minerals: Crystallography, Mineralogy and Environmental Significance. *Rev. Miner. Geochem.* 40: 351-404

Bigham J.M. Schwertmann, U., Carlson L. & E. Murad 1990 A poorly crystallized oxyhydroxysulfate of iron formed by bacterial oxidation of Fe(II) in acid mine waters. *Geochim. Cosmochim. Acta.* 54:2743-27-58

Dold B. 2003 Dissolution kinetics of schwertmannite and ferrihydrite in oxidized mine samples and their detection by differential X-ray diffraction (DXRD) *Appl. Geochem.* 18: 1531-1540.

Dutrizac J.E. & J.L. Jambor 2000 Jarosites and their application in hydrometallurgy. In N.C. Alpers., J.L. Jambor, & Nordstrom D.K. (eds.) Sulfate minerals: Crystallography, Mineralogy and Environmental Significance. *Rev. Miner. Geochem.* 40: 405-453

Lee, G., Bigham J.M. & G. Faure 2002. Removal of trace metals by coprecipitation with Fe, Al and Mn from natural waters contaminated with acid mine drainage in the Ducktown Mining District, Tennessee. *Appl. Geochem.* 17: 569-581.

Nordstrom D.K. & C.N. Alpers 1999. Geochemistry of acid mine water. In G.S. Plumlee & M.J. Logston (eds.), *Environmental Geochemistry of Mineral Deposits Part A. Processes, methods and health issues.* *Rev. Econ. Geol.* 6A: 133-160.

Plumlee G.S., Smith K.S., Montour M.R., Ficklin W.S. & E. Mosier 1999. Geologic controls on the composition of natural waters and mine waters diverse mineral deposit types. In G.S. Plumlee & M.J. Logston (eds.), *Environmental Geochemistry of Mineral Deposits Part B. Case studies and research topics.* *Rev. Econ. Geol.* 6B: 373-432.

Webster J.G., Swedlund P.J. & K.S. Webster 1998. Trace metal adsorption onto and acid mine drainage iron (III) oxyhydroxysulfate. *Env. Sci. & Tech.* 32: 1361-1368.

Yu J.-Y., Heo B., Choi I.-K., Cho J.-P. & H.-W. Chang 1999. Apparent solubilities of schwertmannite and ferrihydrite in natural stream waters polluted by mine drainage. *Geochim. Cosmochim. Acta.* B63: 3407-3416

Characterization of Muds and Waters of the Copahue Geothermal Field, Neuquén Province, Patagonia, Argentina

J.M.Vallés*, M.T.Baschini, G.R.Pettinari & N.García

CIMAR (Centro de Investigaciones en Minerales Arcillosos), Facultad de Ingeniería, Universidad Nacional del Comahue, Buenos Aires 1400, Neuquén, 8300, Argentina, email: miria@uncoma.edu.ar

* *CONICET, Consejo Nacional de Investigaciones Científicas y Técnicas, Argentina*

ABSTRACT: The Copahue-Caviahue geothermal field is located in the Andes Cordillera of western Neuquén Province, Patagonia, Argentina. Several geothermal features such as hot springs, ponds, and fumaroles occur in the surroundings of Villa Copahue, near an active volcano. In this place a thermal complex was developed for therapeutic treatments. In the first stage of this study, the inorganic composition of waters and natural muds are evaluated. These results, together with additional research, might allow a better control of the quality of the system, and will be useful in the matured artificial peloids preparation. The physical and chemical conditions vary within ponds. Water temperature ranges from 35°C to practically boiling. Some waters are neutral and others are very acidic. Monovalent cations predominate, sodium being the most abundant, with an important contribution of potassium. Divalent cations like calcium and magnesium are present in low proportions. Among anions, sulphate is the most abundant. High conductivities were measured, particularly in acidic waters. X-Ray diffraction and infrared spectroscopy show that muds are composed mainly by clay minerals accompanied by elementary orthorhombic sulfur, natroalunite, cristobalite, and pyrite together with quartz and K and Na-Ca feldspars. Clay minerals are kaolinite and a mixed-layered illite/smectite (I/S) with a high smectite component (95% or more). Two regional clay materials were evaluated in order to be used in the production of artificial peloids. They are kaolinite and bentonite in the vicinity of the thermal center.

1 INTRODUCTION

The Copahue-Caviahue geothermal field is located in the Andes Cordillera of western Neuquén Province, Patagonia, Argentina, close to the Chilean boarder.

Several geothermal features like hot springs, ponds, and fumaroles occur in the surroundings of Villa Copahue, near an active volcano. In this place an international-level thermal complex was developed for therapeutic treatments under medical supervision. Natural peloids with separate waters are used for pelotherapy in treatments of rheumatism, arthritis, and traumatologic effects as well as cutaneous illnesses and treatment of respiratory illnesses.

A first stage of study of natural muds in inorganic phases is presented and also, a physicochemical characterization of the waters. The program include also the biological characterization of the microbiology, flora and fauna.

These basic studies will allow us to develop a program of periodic measurement of quality indicators that facilitate the detection of possible alterations caused by anthropogenic action or by natural changes.

In addition, these activities will serve as a starting point to study the raw materials and processes essential for obtaining artificial peloids. These processes will enable us to mature clays from other locations through contact with the waters of Copahue and thereby avoid exhaustion of this natural resource.

2 MATERIAL

We worked on 7 samples of muds took from artificial pools or from natural ponds as well as their supernate liquid. Other waters from ponds, small springs and independent upwelling waters where also analyzed. The samples correspond to those indicated in Table 1. Likewise, it was made a first evaluation of two regional materials, kaolinite and bentonite, available in proximities of the thermal baths, to begin studies about the possibility of producing artificial therapeutic peloids.

Table 1: Sample location.

Source	Water sample	Mud sample
Laguna del Chanco	01LCH	02LCH
Laguna Sulfurosa Madre	05LSM	06LSM
Laguna Verde Oeste	07LVO	08LVO
Laguna Verde Este	09LVE	10LVE
Baño 2	13B2	12B2
Las Maquinitas	17LM1	18 M1
Las Máquinas	23LM2	28LM2
Agua de "Vichy"	14AV	
Agua Sulfurosa	25AS	
Agua Ferruginosa	26AF	
Agua del Limón	38AL	
Agua de Mate	39AM	

They are kaolinite from Chita Mine and bentonite from Barda Negra, both belonging to Zapala Department, Neuquén province, Argentina.

3 METHODS

Mineralogical composition of bulk powder of the muds and raw materials was analyzed by X-Ray diffraction with a Rigaku D-MAX-II-C X-Ray diffractometer. In addition, oriented preparations of the less than 4 micrometer size fraction were analyzed glycol solvated and heated. Moreover, Infrared Spectroscopy (with a Buck Scientific model 500) on pressed-disc KBr technique, in the regions of 4000-600 cm^{-1} was performed.

Previously organic matter was removed with sodium hypochlorite. Mechanical sieve analyzes were carried out as well.

Chemical analysis of waters were carry out following the techniques stated in Díaz de Santos, Ed. (1992).

Table 2. Mineralogical composition of muds..

	Silt-clay grain-size % < 62 μm	Bulk mineralogy	Clay minerals	
			Smectite (1) %	Kaolinite %
02LCH	99	Clay minerals - orthorhombic sulfur - quartz - pyrite	75	25
06LSM	92	Clay minerals - orthorhombic sulfur - natroalunite - pyrite - quartz - K feldspar	85	15
08LVO	92	Clay minerals - plagioclase - natroalunite - pyrite - quartz	45	55
10LVE	96	Clay minerals - orthorhombic sulfur - plagioclase - natroalunite - pyrite - quartz	25	75
12B2	80	Clay minerals - cristobalite - natroalunite - pyrite - quartz -	50	50
18LM1	92	Clay minerals - orthorhombic sulfur - natroalunite - pyrite - quartz - K feldspar	75	25
28LM2	94	Clay minerals - natroalunite - pyrite - quartz -	35	65

(1) Mixed-layered illite/smectite, smectite 95 % or more.

4 EXPERIMENTAL RESULTS

4.1 Mineralogical composition of muds

Muds are composed mainly by clay minerals accompanied by minor amounts of accessory minerals. Smectite and kaolinite are the two most common clay minerals ranges from 85% to 25% smectite and 75% to 15 % kaolinite (Table 2). So-called smectite is actually a mixed-layered illite/smectite (I/S) with random ordering and 95% or more smectite. Figure 1 is a XRD pattern of less than 4 μm size fraction of some of the samples. Abundance of kaolinite and smectite is confirmed by IR spectrum (Figure 2) in all samples analyzed (Farmer 1979).

Elementary orthorhombic sulfur is a frequent mineral, mainly present in some ponds. Colloidal sulfur is also found in the less 4 micrometer size fraction. Natroalunite, cristobalite and pyrite are present, together with quartz and K and Na-Ca feldspars.

4.2 Raw clay materials

In this first step, only the mineralogical composition of both materials was determined. Clay from Chita Mine is almost pure white kaolinite with less than 3% quartz. XRD analysis in Zapala bentonite shows that dioctahedral smectite - montmorillonite - predominates the mixture, although accessory minerals, such as quartz, feldspars, and opal-CT, are also present, as are smaller amounts of zeolites and gypsum.

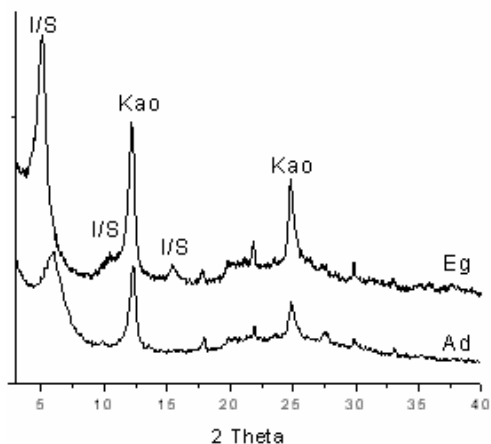


Figure 1: XRD traces of $< 4 \mu\text{m}</math> size fraction. Eg: ethylene - glycol, Ad: air dried$

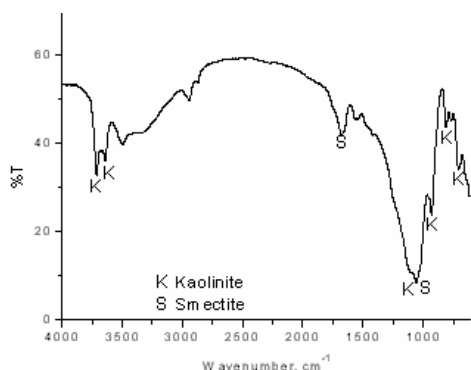


Figure 2: IR spectrum

4.3 Physicochemical characteristic of waters

Physicochemical characteristics of the Copahue thermal waters are shown in Table 3. Waters belongs to two great groups: acid and near the neutrality. In acid waters (pH between 1,60 to 2,82) the main cationic component is H^+ ion, with important amounts of mono, di, and trivalent ions (Na^+ , K^+ , Ca^{2+} , Mg^{2+} , Fe^{2+} , Fe^{3+}), whereas the predominant anion, between the evaluated ones, is the sulphate. In waters where pH is between 5,58 to 7,10 predominate monovalent cations sodium and potassium, whereas among anions acquire importance the presence of carbonates, bicarbonates and silicates. The chlorides are in low proportions in both systems.

5 DISCUSSION

Host rocks of geothermic reservoir and those outcropping in the place studied are volcanic rocks of andesitic and basandesitic composition, tuffaceous breccias, volcanic conglomerates, and pyroclastics (Pesce, 1989). Such rocks show evidences of strong hydrothermal alteration produced by steam rising from geothermal reservoirs, gases of magmatic origin and surficial waters heated by steam. Underground thermal water reservoirs are located at a depth of 800-1000 m, the shallower, and more than 1400 m the deeper. (Pannarello, 2002).

Muds are composed by alteration minerals from host rocks, precipitates from dissolved salts and reaction products from gases of magmatic origin.

The volcanic origin of the system generates gaseous hydrogen sulfide within the pools. The presence of this gas, easily identifiable by its scent, is the main source of contribution of H^+ in the waters analyzed. Additionally, the hydrogen sulfide oxidation generates sulfur as deposits founded in the surface, crystals incorporated to muds and the colloidal sulfur present in muds and waters. The high amount of sulphates would be the end product of a series of reactions redox favored by the presence of oxygen and/or microorganisms. The general conditions of pH do not favor the dissolved sulfide, but these are found as precipitates, mainly under the iron sulfide form (pyrite). The acid waters have dissolved an important amount of di and trivalent cations, favored by the pH effect over the solubility of salts. This fact is concordant with a high conductivity in such systems.

Since natural muds are largely composed of clay minerals belonging to the kaolinite and smectite groups in variable proportions, raw materials were selected to fulfill that mineralogical requirement.

6 CONCLUSIONS

As it is of practice in European spas, artificial muds could be made in Copahue, using clays of the smectite and kaolinite groups obtained in the outskirts as basic ingredient. Future studies will require the analysis of the rheological characteristics, parameters of consistency, ionic exchange capacity, water retention, and thermal behavior, among others, of the artificially obtained peloids.

We propose to use two types of clays available in the region of the spas to be tested in maturation processes: kaolinite of the Chita mine and bentonite of the Barda Negra region, previously analyzed by Pettinari and Vallés (1999) and by Impiccini and Vallés (2002).

The acid waters are proposed as the most convenient for the maturation processes, because they are those that could cause the biggest effects in the basic materials in the shortest time.

Table 3: Physicochemical characteristics of waters.

	01LCH	05LSM	07LVO	09LVE	13B2	17LM1	23LM1	27LM2	14AV	25AS	26AF	38AL	39AM
Temp. Field °C	28	58	24	27	42	30/40	92	35	40	72	55	53/58	59
pH (field)	2.35	5.58	2.70	2.82	2.30	2.10	6.78	1.75	6.06	7.10	6.27	1.60	6.10
pH (lab)	2.82	6.00	2.73	2.87	2.82	2.35	7.24	2.04	8.08	8.45	8.55	1.97	6.41
Cond. μ S/cm	2700	820	1560	1410	1200	7600	1140	5600	680	920	1030	6720	600
Sulfate *	700.0	236.4	392.3	176.9	300.0	1305.6	144.4	733.3	8.0	14.1	9.6	1357.7	43.2
Bicarbonate*	n/d	20.5	n/d	n/d	n/d	n/d	40.9	n/d	158.6	422.4	868.2	n/d	245.5
Carbonate *	n/d	n/d	n/d	n/d	n/d	n/d	n/d	n/d	5.0	14.3	17.2	n/d	n/d
Silicate *	220	150	150	150	70	220	110	80	110	110	80	400	220
Chloride *	12.5	10.8	5.6	6.6	5.6	3.4	6.3	16.0	4.5	6.9	6.6	2.8	2.8
H+ *	19.9	-	6.5	4.8	5.5	31.0	-	27.5	-	-	-	45.4	-
Na+ *	30.4	26.8	29.8	30.3	10.1	27.8	21.2	12.6	17.7	49.9	70.6	119.6	32.0
K+ *	15.3	13.4	14.1	14.6	3.4	12.5	8.3	6.3	5.7	29.9	46.4	12.0	18.9
Ca ²⁺ *	56.6	22.2	28.8	27.7	26.6	16.6	6.9	17.8	31.6	26.6	33.3	7.2	35.1
Mg ²⁺ *	17.2	6.7	9.4	6.8	4.0	6.1	2.9	8.7	10.4	24.2	27.6	14.0	10.4
Fe ²⁺ *	n/d	n/d	n/d	0.3	0.1	n/d	n/d	n/d	n/d	n/d	n/d	0	n/d
Fe ³⁺ *	25.0	n/d	2.5	2.2	4.9	50.0	n/d	12.5	n/d	n/d	n/d	35	n/d
Fe tot. *	25.0	n/d	2.5	2.5	5.0	67.2	n/d	18.5	n/d	n/d	n/d	35	n/d
Solid res *	2123	739	681	784	493	3360	555	1478	253	444	692	2600	-

Given the relationship between the composition of waters and muds used for medical treatments, we recommend periodic controls of the main physicochemical parameters of the waters in order to evaluate the variability over time.

acqua sulfurea e salso-bromo-iodica per la preparazione di fanghi peloidi termali e per trattamenti dermatologici. In Veniali, F. (Ed.) *Mineral. Petrogr. Acta*, vol. XLVII: 267-275.

7 REFERENCES

- Díaz de Santos, Ed., 1992. Métodos normalizados para análisis de aguas potables y residuales, American Public Health Association, American Water Works Association, Water Pollution Control Federation.
- Farmer, V.C., 1979. Infrared Spectroscopy in Mineral and Inorganic Chemistry, *Special Publication n.98*, The British Ceramic Research Association.
- Impiccini, A. y J.Vallés. 2002. Los depósitos de bentonita de Barda Negra y Cerro Bandera, departamento Zapala, provincia del Neuquén, Argentina. *Revista de la Asociación Geológica Argentina*, 57 (3): 305-314.
- Pannarello, H., 2002. Características isotópicas y termodinámicas de reservorio del campo geotérmico Copahue-Caviahue, provincia del Neuquén. *Revista de la Asociación Geológica Argentina*, 57 (3): 328-340.
- Pesce, A., 1989. Evolución Volcano-Tectónica del complejo Efusivo Copahue-Caviahue y su modelo geotérmico preliminar. *Revista de la Asociación Geológica Argentina*, 44 (1-4): 307-327.
- Pettinari, G. y J. Vallés., 1999. Análisis Cuantitativo de materias primas arcillosas para cerámica por Difracción de Rayos X. *Revista Información Tecnológica*, Vol. 10 N° 5: 47-55.
- Veniale, F., M. Setti, M. Soggetti, F., Lofrano, F. Trailo., 1999. Esperimenti di maturazione di geomateriali argillosi con

Author Index (Volumes I & II)

Acchar, W.	293	Black, L.	245	Cid, R.	89
Addad, J.E.	579	Black, S.	395	Ciftci, E.	537, 643, 873
Afonso, M.C.	351	Blanc, P.	415	Cloete, M.	165
Alashkar, A.A.	261	Boaventura, G.R.	479	Clout, J.M.F.	993, 1047
Alba-Simionesco, C.	415	Boiocchi, M.	529	Conceição, S.I.	619, 669
Alcover-Neto, A.	103, 285, 289	Bonardi, M.	157	Correa, A.R.	403
Allard, T.	745	Bonás, T.B.	607, 861, 977	Correia, J.A.M.	399
Almendras, E.	1039	Boni, M.	781	Correia-Silva, R.H.	877
Alnaes, L.	145	Bonnes, U.	133	Correia, E.	587
Alves, A.K.	217	Boschel, D.	221	Costa, M.L.	65, 741
Alves, D.B.	819	Boschi, A.O.	337, 713	Coutinho, J.M.V.	443
Alves, P.R.	653	Bosso, S.T.	391	Couture, R.	379
Amaral Sobrinho, N.M.B.	451	Braga, G.C.B.	543	Crósta, A.P.	773
Amaral, A.M.	571	Brandão, A.G.	977	Cuchierato, G.	607
Amorim, L.V.	657, 961	Brandão, P.R.G.	233, 869, 893, 989	Cucarella, J.	881
Amosov, R.A.	965	Braz, A.B.	981	Cui, X.	697
Amouric, M.	415	Brizola, R.M.	639	Cupertino, J.A.	831
Andrade, F.R.D.	383, 759	Broekmans, M.A.T.M.	661	Cutmore, N.G.	969
Angeli, N.	849	Brum, T.M.M.	513, 559		
Angélica, R.S.	65, 273, 297	Brunet, F.	415	da Costa, M.	297
	665, 685, 741, 773	Brunnacci-Ferreira-Santos, N.	935	da Costa, M.L.	343, 373, 989
Angulo, S.C.	763	Bundschuh, T.	137	da Silva, F.T.	45, 53
Anjos, S.M.C.	811, 815	Butcher A.R.	37	D'Agostino, L.F.	673
Antenucci, D.	407	Bychkov, G.L.	575	D'Agostino, L.Z.	673
Aquino, J.A.	869			Dalakashvili, Z.B.	965
Arango, Y.C.	627	Cabral, A.R.	865	Daoud, W.K.	39
Arduini, M.	835	Cabrelon, M.D.	337	de Araújo, J.G.	1025
Arvidson, R.	13	Cabrol, N.	13	de Faria, D.L.A.	351
Aspandiar, M.F.	455	Caddah, L.F.G.	819	de Farias, J.B.	1025
Atanasova, M.	165	Cadile, S.	793	de Lena, J.C.	483
Atanassova, R.	387	Caffarena, V.R.	45, 49, 53	De León, A.T.	161
Atencio, D.	919	Calábria, J.	225	de Melo, H.G.	367
Auriscchio, C.	611	Caldwell, D.H.	363	de Oliveira, A.C.	479, 543
Ávila, C.A.	919	Calvin, W.	13	de Oliveira, M.P.	1025, 1029
Ávila, J.C.	521	Capitaneo, J.L.	45, 49, 53	de Pablo-Galán, L.	823
		Cardoso, D.B.	391	de Paula, S.M.	183
Bagatin, E.	443	Cardoso, M.	533	De Ros, L.F.	815, 831, 843
Banaszak, A.	923	Carneiro, B.S.	665	de Souza Filho, C.R.	309
Barbiéro, L.	411	Carvalho, C.I.P.	725	de Souza Jr., P.A.	13, 133
Barbosa, M.I.R.	657	Carvalho, F.M.S.	759	de Souza, R.S.	831
Barbosa, M.S.C.	785	Carvalho, J.O.	451	de Villiers, J.P.R.	229
Barilo, S.N.	575	Carvalho, P.R.S.	769, 777, 857	De Vito, C.	611
Barros, L.A.F.	997	Cassia de Brito Galvno, T.	479	Death, D.L.	969
Barrueto, H.R.	919	Castañeda, C.	591	Debacher, N.A.	1025, 1029
Baschini, M.T.	507	Castro, P.T.A.	745	Degen, T.	277
Basei, M.A.S.	733	Caucia, F.	529	Dí Giulio, A.	835
Beljavskis, P.	111	Ceccarello, S.	395	Dias Filho, D.C.	843
Belogub, E.V.	853, 897, 915	Chambel, L.	533	Dias, G.O.	539
Benevides, T.	877	Channer, D.M. DeR.	563	Diogo Pinto, A.	533
Bennett, D.W.	969	Chapa-Cabrera, J.	85	Dixon, R.D.	901
Bendezú H., R.del P.	367	Chaves, M.	533	do Carmo, M.S.	343
Bergmann, C.P.	97, 217, 325	Chávez-García, M.L.	823	Domoney, R.M.	649
Bermanec, V.	525	Chernet, T.	985	Donchev, I.	387
Bernhard, B.	13, 133	Chodur, N.L.	513	Donskoi, E.	993
Bettencourt, J.S.	877	Choque Fernandez, O.J.	989	Drozдова, I.A.	749
Biesinger, M.	973	Christensen, P.	13	Ducart, D.F.	773
Biondi, J.C.	769, 777, 857	Chula, A.M.D.	869	Dutre, V.	407

Dziggel, A.	789	Gaspar, J.C.	1017	Holzwarth, U.	191, 195, 199
Dziubińska, B.	141, 677	Gaucher, E.	415		
		Gellert, R.	13, 133		
		Gennari, R.C.	337	Ihlen, P.M.	693
Eberhardt, J.E.	969	Gerson, A.R.	115	lishi, K.	631
Ebina, T.	717	Gilg, H.A.	781	Ikuta, Y.	631
Edwards, H.G.M.	351	Givan, A.	583	Isaia, G.C.	639
Elsen, J.	347	Gobbels, M.	61, 179	Ishimoto, H.	435
El-Sheshtawy, A.	261	Gobbo, L.A.	249, 253, 257	Ivanova, A.S.	207
Emelchenko, G.A.	575	Goetz-Neunhoeffer, F.	179		
Enderle, R.	179	Gomes, O.F.M.	1043		
Endo, I.	889	Gomes, C.	187, 681	Jacamon, F.	693
Englert, G.	161	Gomes, C.M.	961	Jaksch, H.	525
Enzweiler, J.	391	Gomes, C.S.F.	725	Jansen, E.	947
Escudero, R.	615	Gomes, D.L.	737	Jarmolowicz-Szulc, K.	827
		Gomes, V.	681	Jdid, E.	407
		Gomes-Jr, A.A.S.	885	Joaquim, A.C.	123
Fabris, J.D.	463, 467, 471	Gonçalves, R.P.	367	John, V.M.	763
Falck, H.	547	González, I.	419	Juchem, P.L.	513, 559
Farias, K.V.	657	Gorevan, S.	13	Juliani, C.	879
Fenoll Hach-Ali, P.	495	Göske, J.	191, 195, 199, 229, 333		
Fernandes, E.F.	65	Götze, J.	203, 305, 685		
Fernandes, H.R.	33	Goulart, E.P.	713	Kachler, W.	191, 195, 199
Ferreira da Silva, E.	491	Graça, L.M.	517	Kahn, H.	123, 763, 981, 997, 1009
Ferreira, E.E.	233	Graham, R.C.	411	Kalmykov, A.E.	753
Ferreira, H.C.	657, 961	Graphchikov, A.A.	749	Kaminsky, F.V.	563
Ferreira, J.M.F.	33, 57, 619, 669	Grebenshchikova, E.A.	749	Kankeleit, E.	133
Ferreira, M.Q.	619	Griffin, W.L.	563	Karfunkel, J.	525
Firth, B.A.	993	Groat, L.A.	547	Kasic, V.	931
Fischer, A.C.	513	Gross, J.M.	725	Kastner, G.F.	571
Fiss, G.F.	1029	Grossmann, J.	395	Kearsley, E.	329
Fogliata, A.S.	521	Gu, Y.	119	Kelm, U.	89, 1001
Foh, J.	133	Guastala, F.A.	337	Kerstedjian, T.	387
Fonseca, M.V.A.	285, 289	Guedes, C.C.F.	257	Kern, A.	125
Fontes, M.P.F.	107	Guedes, K.J.	539, 567	Kern, D.C.	343
França, K.B.	961	Guedes, P.J.S.	33	Khachatryan, G.K.	563
Francis, J.	973	Guerra, D.L.	65	Kihara, Y.	383
Franke, N.D.	769, 777, 857	Guimarnes, G.B.	759	Kijko, A.	901
Frank-Kamenetskaya, O.V.	359	Gurhan Yalcin, M.	643	Kisters, A.F.M.	789
Fransen, M.	277	Guttler, R.S.	551	Kitamura, S.	443
Friese, K.	483			Kleebe, H.J.	69
Fritsch, E.	595			Kleeberg, R.	129, 685
Fronzaglia, G.C.	123	Hagni, R.D.	649, 653, 873	Klingelhöfer, G.	13, 133
Frost, B.R.	927	Hall, C.	281	Klingenberg, B.	947
Furian, S.	411	Hamilton, C.	957	Kniewald, G.	525
Furlan, L.	1029	Hanna, R.A.	423	Kolayli, H.	537
Furquim, S.A.C.	411	Haralyi, N.E.	551	Komadel, P.	471
		Harben, P.W.	25	Komov, I.L.	73
		Hart, B.	973	König, U.	77, 81, 623
Gablina, I.F.	951	Hassaan, M.M.	261	Korablev, G.	439, 499
Gailhanou, H.	415	Hassaan, M.Y.	261	Köster, R.	137
Galán, E.	419	Hayashi, H.	717	Krambrock, K.	517, 539, 567
Gallego, A.N.	1055	He, C.	427	Kresten, P.	355
Gandini, A.L.	785	Heimann, R.B.	3, 203, 305	Kühn, T.	689
Garbev, K.	245	Helle, S.	1001	Kunze, Ch.	395
Garcez, L.L.	253	Henderson, I.	693	Kunze, K.	947
García, A.	627	Hengst, M.	203	Kurnevich, L.A.	575
García, N.	507	Herbert Echude, J.	313	Kusiak, M.A.	141, 677
Garda, G.M.	111	Herkenhoff, K.	13	Kuzmann, E.	543
Garg, R.	543	Heuss-Aßbichler, S.	431	Kwitko-Ribeiro, R.	865
Garg, V.K.	479, 543	Hjelen, J.	145	Lacerda, M.A.S.	571, 591
Gasharova, B.	245	Hofmeister, W.	555	Lagoeiro, L.	517, 885, 889

Lamberg, P.	1005	Menabdishvili, B.Z.	965	Ostrooumov, M.	595
Langhof, N.	203	Mendes, J.C.	709	Otto, A.	789
Larionov, P.M.	207	Merkle, R.K.W.	19, 805, 901	Otto, H.H.	487
Larsen, R.B.	693	Merzweiler, K.	635	Oyarzábal, J.	729, 793
Larson, R.A.	471	Meshchanova, E.V.	359	Oyarzún, J.	881
Lasnier, B.	595	Miano, S.C.	905		
Lastra, R.	1021	Miljak, D.G.	969		
Lebichot, S.	153	Miller, D.	973	Paciornik, S.	1043
Leclerq, D.	407	Miller, S.	363	Paiva, R.S.	373
Lee, K.	467	Mizusaki, A.M.	815	Paktunc, D.	379, 447, 1021
Lefrant, S.	595	Moen, K.	145	Pariy, A.S.	965
Lefter, M.G.	237, 241	Monte, M.B.M.	741	Paszkowski, M.	141, 677
Leinum, J.R.	145	Monteiro, L.V.S.	877	Patinha, C.	491
Leite, J.Y.P.	293	Morad, S.	843	Penha, F.G.	1025, 1029
Lemos, V.P.	65	Morales-Carrera, A.M.	709	Perbost, R.	415
Lengler, H.C.M.	325	Moreno, N.	237, 241	Pereira Leite, J.	313
Leonyuk, N.I.	575, 721	Moroz, I.	583	Pereira, E.	657
Li, J.	427	Moroz, T.	439	Pereira, E.A.	293
Liccardo, A.	513, 579	Morris, R.V.	13, 133	Pereira, L.	619
Liipo, J.	1005	Mortensen, J.K.	547	Pereira, M.	861
Lima, S.C.	351, 367	Motta, J.F.M.	713	Pereira, M.C.	885
Lira, H.L.	657, 961	Moura, A.	587	Pereira, R.M.	919
Lodziak, Je.	805	Moya, F.A.	737, 759	Pereira, W.C.	451, 797
López-Escobar, L.	89	Müller, I.L.	639	Persiano, A.I.C.	517
López-Galindo, A.	495, 835	Müller, T.	199	Pettinari, G.R.	507
Lorenzi, G.	407	Mussel, W.N.	463	Pieczonka, J.	923
Lu, X.	697			Piestrzyński, A.	923
Lubachesky, R.	559			Pinheiro, M.V.B.	517, 539, 567
		Nagase, T.	717	Pinho, M.S.	49
		Nakatsuka, A.	93, 631	Pino, G.A.H.	1043
Madood Hussain, T.S.	801	Nalini, H.A.	483	Pirard, E.	153
Magalhães, M.S.	893	Naumann, M.	947	Pires, F.R.M.	905, 927
Magela, G.	517	Nefyodova, I.V.	721	Pitkajarvi, J.	1005
Magnus, M.	305	Neiva, A.C.	367	Plötze, M.	685
Makovicky, E.	427	Neiva, A.M.R.	911	Pollandt, P.	221
Maltsev, V.V.	575	Nelsen, P.	407	Pöllmann, H.	77, 81, 213, 221, 297, 301, 317, 321, 329, 333, 399, 623, 635, 689, 989
Malvik, T.	145	Netto, A.M.	919	Pratt, A.	1021
Manjate, R.S.	33	Neubauer, J.	179		
Mano, E.S.	123, 997, 1009	Neufeld, H.	547		
Mansueto, M.S.	111	Neumann, R.	103, 285, 289, 919, 1031, 1035		
Mansur, A.A.P.	265, 1013	Neves, R.F.	273, 665, 741	Qiu, J.	697
Mansur, H.S.	265, 1013	Newman, J.A.	785	Queiroz Neto, J.P.	411
Maraschin, A.J.	815	Norman, M.	831		
Marcos, C.	269, 475, 627	Novaes, L.E.S.M.	725		
Marley, K.A.	471	Novais, R.F.	463	Radosavljevic, S.	705, 931
Marmo, J.	985	Novoselov, C.A.	853, 915	Radosavljevic-Mihajlovic, A.	705
Márquez, M.A.	1017, 1055			Raghimi, M.	455
Marshall, D.D.	547	Oba, C.A.I.	123	Rammilmair, D.	459, 805
Martelli, M.C.	273	Ogasawara, T.	49	Ratti, G.	939, 981, 997
Martin, C.	957	Okube, M.	93	Read, D.	395
Martínez, M.	269	Okudera, H.	93	Rebelo, A.M.A.	733
Mas, G.	521	Olhero, S.M.H.	57	Reimanis, I.E.	85
Masalov, V.M.	575	Oliveira, C.H.	285, 289	Reis, E.	39
Matos, M.J.	701	Oliveira, E.F.	571, 579, 591	Reis Neto, J.M.	733, 737
McGibbon, F.M.	363	Oliveira, M.C.B.	443	Remacre, A.Z.	797
McKay, N.	957	Oliveira, M.L.	57	Remus, M.V.D.	831
McSween, H.	13	Olives, J.	415	Renato Pontes, L.	313
Medeiros, S.M.	567	Olivito, J.P.R.	607	Renz, F.	13, 133
Meier, R.	277	Orlandi, P.	611	Rezende, N.G.A.M.	741
Melcher, F.	805	Ortenzi, A.	835	Ribeiro, F.R.	463, 467, 471
Melcher, F.	897			Rieder, R.	13
Melekestseva, I. Yu.	897				
Meller, N.	281				

Rieseberg, C.E.	737	Silveira, M.	183	Viana, R.R.	601
Robles-Camacho, J.	371	Simakov, S.K.	749, 753	Vieira Coelho, A.C.	423
Rocha Filho, O.G.	865	Smart, R. StC.	973	Vieira, A.L.	423
Rocha, F.	491	Smith, D.	379, 1021	Vigdergauz, V.E.	1051
Rocha, F.J.F.T.	725	Soares, L.	673	Viladkar, S.G.	649
Rodionov, D.	13, 133	Song, R.	599	Villanova, S.N.	769, 777, 857
Rodrigues, C.R.O.	843	Sorokin, L.M.	753	Villas Boas, R.C.	451
Rodriguez, I.	269, 475, 627	Soto, O.A.J.	1043	Villegas, E.A.	403
Rogers, C.A.	969	Sousa, D.J.L.	755	Viseras, C.	495
Rogez, J.	415	Sousa, J.J.	701	Vlach, S.R.F.	849
Roggendorf, H.	221	Souza Filho, C.R.	773	Vortisch, W	169
Roldan, A.A.	713	Souza Santos, P.	423		
Romano, R.C.	885, 889	Souza, R.S.	839, 843		
Romero, A.	419	Spaeth, J-M.	567	Wagner, Ch.	635
Roquet, M.B.	729	Squyres, S.W.	13, 133	Wagner, T.	137
Rosière, C.A.	935	Stanjek, H.	107	Waichel, B.L.	559
Roth, M.	583	Stasiulevicius, R.	571, 591	Wajima, T.	435
Rubio, J.	161	Stemmermann, P.	245	Weiss, H.	395, 487
Ruckley, N.A.	363	Stirling, J.A.R.	157	Wennrich, R.	487
Rybacki, E.	947	Stöber, S.	317, 321, 635	Wiedemann, P.	685
		Stojanovic, J.	705, 931	Williams, S.	957
		Stucki, J.W.	467, 471	Winkler, N.	333
		Stumm, A.	245	Wirth, R.	173
Saaro, S.	305	Suh, C.E.	865		
Sabot, B.	583	Sunder Raju, P.V.	149, 801		
Sales, C.	293	Szabó, G.A.J.	759	Xu Xin,	57
Salomão, E.P.	39				
Sánchez-Hernández, R.	371				
Sanhuesa, V.	89				
Sanjad, T.A.B.C.	373	Tamada, O.	435	Yagovkina, M.A.	749
Sant'Agostino, L.M.	249, 253, 257, 607, 861, 939, 977	Tassinari, M.M.M.L.	939, 981, 997	Yakovleva, V.A.	853
		Tavares, R.P.	893	Yalcin, G.	873
Santini, R.B.	383	Tavera, F.J.	615	Yalcin, M.G.	537
Santos, A.L.F.	479	Tesalina, S.G.	897	Yalcinalp, B.	537
Santos, M.D.C.	745	Tewelde, M.	635	Yang, Z.	599
Sasaki, O.	435	Titov, A.T.	207	Yasuda, M.	435
Savelieva, G.N.	943	Tomašić, N.	525	Yoshiasa, A.	93, 631
Schäfer, W.	947	Toniolo, J.C.	97, 325	Young, J.M.	993, 1047
Schmidt, G.T.	483	Torres, P.	33	Yvon, J.	407, 745, 755
Schneider, C.L.	103, 1031, 1035	Treivus, E.B.	359		
Scholz, R.	525	Trudu, A.G.	993, 1047		
Schreck, P.	487	Tuling, A.	229	Zachmann, D.W.	483
Schröder, C.	13	Turunen, J.	1005	Zaikovskii, V.I.	207
Schröder, Ch.	133			Zakharchenko, O.D.	563
Schubert, M.	395, 487			Zambonato, E.	843
Schuh, A.	191, 195, 199	Ulsen, C.	763	Zanardo, A.	713
Schwertmann, U.	107			Zanetti, A.	529
Seifert, S.	305	Vagheti, M.A.O.	639	Zapata, D.M.	1055
Senna, J.A.	309	Valenzuela Diaz, F.R.	423	Zauberas, R.T.	337
Sequeira, C.	681	Vallés, J.M.	507	Zaykov, V.V.	897, 915
Serrano Pinto, L.	491	van Tonder, D.M.	165	Zeiler, G.	191, 195, 199
Setti, M.	495, 835	Vapnik, Ye.	583	Zeschky, J.	179
Shcherbakova, E.	439, 499	Varajão, A.F.D.C.	709, 745, 755	Zhokhov, A.A.	575
Sherriff, B.L.	503	Vasconcelos, P.	815	Zimmer, A.	97
Shivdasan, P.A.	649	Vasconcelos, W.L.	225, 265		
Sidenko, N.V.	503	Velho, J.	619, 669		
Siegel, P.	1039	Veniale, F.	495		
Siemes, H.	947	Venturini, P.N.	885, 889		
Silva, C.M.A.	811	Verdeja, L.F.	269		
Silva, D.M.	451	Verryn, S.M.C.	329		
Silva, F.L.H.	961	Veschkens, M.	407		
Silva, J.	187	Viana, J.D.	657		
Silveira, J.	313				

The 8th International Congress on Applied Mineralogy, ICAM 2004, was held in Águas de Lindóia, São Paulo State, Brazil, from 19 to 22 September, 2004. As the major international meeting on this subject, the Congress brought together researchers and scientists from academia, government organizations and industrial sectors to discuss topics related to basic and applied research and to have the most recent overviews with contributions from international specialists on applied mineralogy.

This book compiles 249 papers grouped in 13 technical sessions and 7 plenary lectures according to the Congress themes. They covered applied mineralogy, in the broadest sense, and application on mineral, metallurgical, chemical, oil, and materials industries, as well as in waste recycling, cultural heritage, and environmental assessment and monitoring, offering an overview on its role in all aspects of life.



ISBN 85-98656-02-X



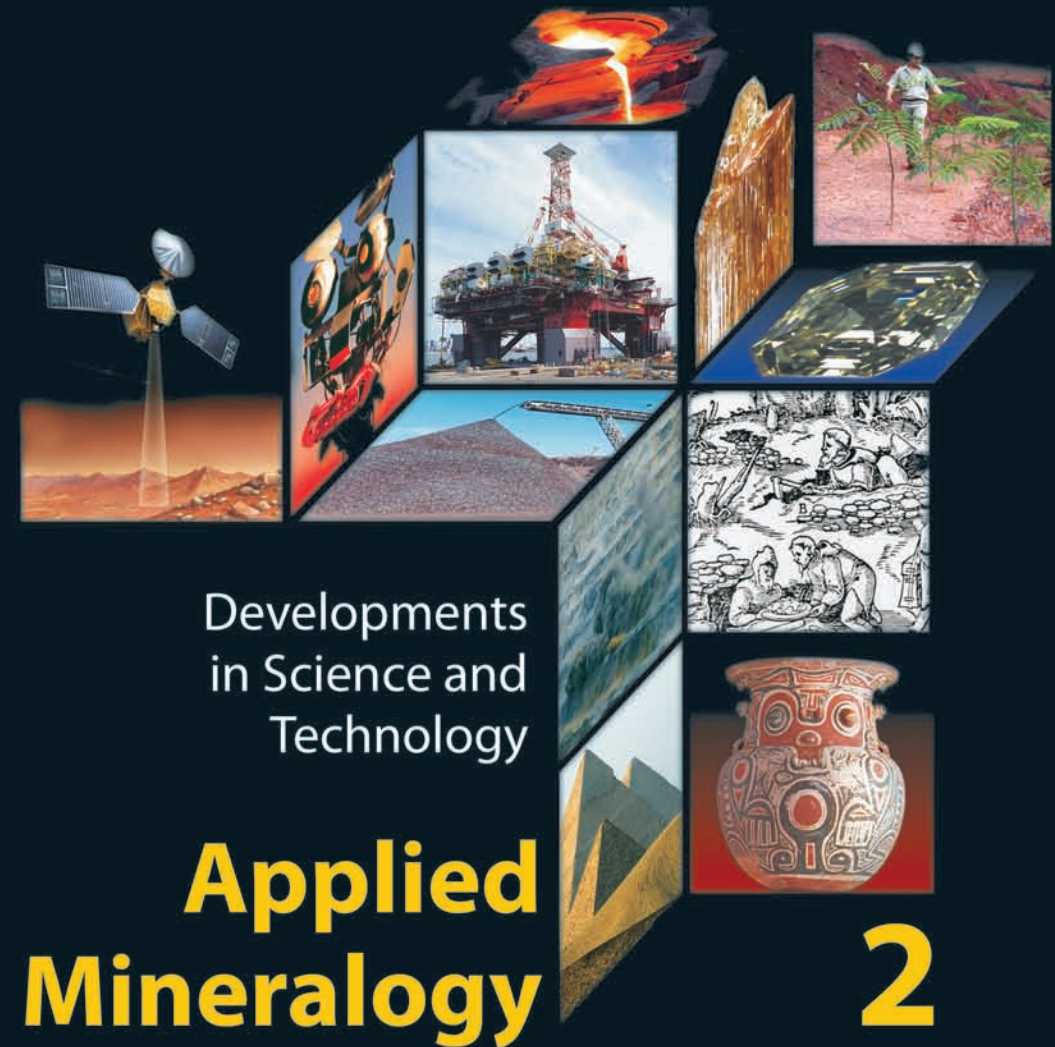
9 788598 656014



Applied Mineralogy

Developments in Science and Technology

Volume 2



Editors | **M. Pecchio | F. R. D. Andrade |**
L. Z. D'Agostino | H. Kahn |
L. M. Sant'Agostino | M. M. M. L. Tassinari |

Applied Mineralogy
Developments in Science and Technology

Applied Mineralogy

Developments in Science and Technology

Edited by

Marcelo Pecchio

Brazilian Portland Cement Association (ABCP)

Fábio Ramos Dias de Andrade

University of São Paulo, Geosciences Institute, Department of Mineralogy and Geotectonics

Liz Zanchetta D'Agostino

University of São Paulo, Polytechnic School, Department of Mining and Petroleum Engineering

Henrique Kahn

University of São Paulo, Polytechnic School, Department of Mining and Petroleum Engineering

Lilia Mascarenhas Sant'Agostino

University of São Paulo, Geosciences Institute, Department of Sedimentary and Applied Geology

Maria Manuela Maia Lé Tassinari

University of São Paulo, Polytechnic School, Department of Mining and Petroleum Engineering

Volume 2



International Council for Applied Mineralogy do Brasil, ICAM-BR

*Published by ICAM-BR - International Council for Applied Mineralogy do Brasil
www.appliedmin.org
2004, ICAM-BR, São Paulo
Printed in Brazil*

Fundação Biblioteca Nacional

ISBN 85-98656-02-X



**Applied Mineralogy: Developments in Science and Technology / ed. by
M. Pecchio, F.R.D. Andrade, L.Z. D'Agostino, H. Kahn, L.M.
Sant'Agostino, M.M.M.L. Tassinari – São Paulo : ICAM, 2004.
2 v.**

ISBN

v.1 : 85-98656-01-1

v.2 : 85-98656-02-X

**1. Applied mineralogy 2. Advanced materials 3. Analytical instrumentation
4. Biominerals and biomaterials 5. Ceramic, glasses and cement 6. Cultural
heritage 7. Environmental mineralogy and health 8. Gem materials
9. Industrial minerals 10. Mineral exploration 11. Oil reservoirs 12. Ore
mineralogy 13. Process mineralogy I. International Council for Applied
Mineralogy do Brasil II.t.**

Applied Mineralogy: Developments in Science and Technology / ed. by

Table of contents

Volume 2

Gem Materials

Gem Materials Map of South Brazil Region <i>P.L.Juchem, T.M.M.Brum, A.C.Fischer, N.L.Chodur, A.Liccardo</i>	513
Crystal Chemistry of Aquamarines: A Case Study in Pegmatites Hosted in Migmatites from the NE of Minas Gerais State, Brazil <i>L.Lagoeiro, L.M.Graça, G.Magela, A.I.C.Persiano, M.V.B. Pinheiro, K.Krambrock</i>	517
Topaz of Papachacra, Catamarca, Argentina: Mineralogical Description <i>J.C.Ávila, A.S.Fogliata, G.Mas</i>	521
Nanocrystals of Tridymite in Opal Cavities <i>V.Bermanec, N.Tomašić, J.Karfunkel, R.Scholz, G.Kniewald, H.Jaksch</i>	525
Gemological and In-Situ Chemical Analyses of Emeralds from Vigizzo Valley (Italy) and other World-wide Occurrences <i>M.Boiocchi, F.Caucia, A.Zanetti</i>	529
A Geological Model of Angolan Diamond Populations <i>L.Chambel, A.Diogo Pinto, M.Chaves, M.Cardoso</i>	533
Mineralogical and Physical Characterization of the Oltustone, a Gemstone Occurring around Oltu (Erzurum-Eastern Turkey) <i>E.Ciftci, M.G.Yalcin, B.Yalcinalp, H.Kolayli</i>	537
About the Color in Natural, Gamma and Neutron Irradiated Spodumene <i>G.O.Dias, M.V.B.Pinheiro, K.J.Guedes, K.Krambrock</i>	539
Effect of Energetic Heavy Ion Radiation and Site Distribution Studies in Brazilian Emeralds by Mössbauer and Optical Methods <i>V.K.Garg, G.C.B.Braga, A.C. de Oliveira, R.Garg, E.Kuzmann</i>	543
Gem Beryl Mineralization in the Northern Cordillera of Canada <i>L.A.Groat, J.K.Mortensen, H.Neufeld, D.D.Marshall, H.Falck</i>	547
Spectroscopy of Colored Diamonds <i>R.S.Guttler, N.E.Haralyi</i>	551
The Relevance of Small Scale Paragenetic Relations Derived from the Structural Topology of Gem-minerals for Technological Processes and Products <i>W.Hofmeister</i>	555
A New Opal Occurrence In Volcanic Rocks Of Paraná Basin, Brazil <i>P.L.Juchem, R.Lubachesky, T.M.M. de Brum, B.L.Waichel</i>	559
Diamond from the Los Coquitos Area, Bolivar State, Venezuela <i>F.V. Kaminsky, O.D. Zakharchenko, G.K. Khachatryan, D.M.DeR. Channer, W.L. Griffin</i>	563
Pink Tourmaline Studied by Optical Detection of Magnetic Resonance <i>K.Krambrock, S.M.Medeiros, K.J.Guedes, M.V.B.Pinheiro, J.-M.Spaeth</i>	567
Trace Elements and Colors in Gemological Varieties of Spodumene Mineral <i>M.A.S.Lacerda, E.F.Oliveira, R.Stasiulevicius, G.F.Kastner, A.M.Amaral</i>	571

Synthetic Ruby with Different Levels of Chromium Concentration and Crystal Morphology Depending on the Growth Conditions <i>N.I.Leonyuk, V.V.Maltsev, S.N.Barilo, G.L.Bychkov, L.A.Kurnevich, G.A.Emelchenko, V.M.Masalov, A.A.Zhokhov</i>	575
Chemical Fingerprints of Sapphires in Alluvial Diamond Deposits from Coxim, MS, Brazil <i>A.Liccardo, J.E.Addad, E.F.Oliveira</i>	579
Crystal Chemistry and Inclusions of Chinese Emerald <i>I.Moroz, M.Roth, B.Sabot, Ye.Vapnik, A.Givan</i>	583
Multiple Fluids in a Single Emerald Crystal: What May it Means? <i>A.Moura, E.Correia</i>	587
Application of Neutron Activation Analysis in the Determination of Trace Elements in Tourmalines <i>E.F.Oliveira, M.A.S.Lacerda, R.Stasiulevicius, C.Castañeda</i>	591
Infrared Reflection Spectrometry of Minerals and Gemstones <i>M.Ostrooumov, E.Fritsch, B.Lasnier, S.Lefrant</i>	595
The Hetian Jade of China <i>R.Song, Z.Yang</i>	599
The Beryl to Bromellite Transformation: In Situ High Temperature X-ray Observations <i>R.R.Viana</i>	601
 General Session	
Mineralogical and Petrographical Studies of Manufactured Fine Aggregates <i>G.Cuchierato, L.M.Sant'Agostino, T.B.Bonás, J.P.R.Olivito</i>	607
Nb-Ta Oxides from Vigezzo Valley Pegmatites – Northern Italy <i>C.De Vito, C.Auriscchio, P.Orlandi</i>	611
True Viscosity and Drift Flux Analysis <i>R.Escudero, F.J.Tavera</i>	615
Mineralogical Characterization of a Pelite from Triassic (Coimbra, Portugal) <i>M.Q.Ferreira, L.Pereira, S.I.Conceição, J.M.F.Ferreira, J.Velho</i>	619
Synthesis of Alkali-Substituted Shigaite <i>U.König, H.Pöllmann</i>	623
Behaviour of Vermiculites with Different Composition at Different Temperatures <i>C.Marcos, A.García, I.Rodríguez Marcos, Y.C.Arango</i>	627
The Crystal Structure of Synthetic Palenzonaite $\text{Ca}_2\text{NaMn}_2\text{V}_3\text{O}_{12}$ <i>A.Nakatsuka, Y.Ikuta, A.Yoshiasa, K.Iishi</i>	631
Metalsulfonate Hydrates – Synthesis and Investigation <i>H.Pöllmann, S.Stöber, M.Tewelde, Ch.Wagner, K.Merzweiler</i>	635
Behavior of Steel Corrosion Potential of Concrete with Mineral Additions <i>M.A.O.Vagheti, I.L.Müller, G.C.Isaia, R.M.Brizola</i>	639
Geochemical Characteristics of the Kolsuz Area Clays (Nigde-Central Anatolia) <i>M.Gurhan Yalcin, E.Ciftci</i>	643

Industrial Minerals

Fluorite Replacement of Carbonatite and Marble at Okorusu, North-central Namibia <i>R.D.Hagni, P.A.Shivdasan, S.G.Viladkar, R.M.Domoney</i>	649
Bunge's Cajati Apatite Mine, SE Brazil: Mineralogy and Petrography of the Carbonatite Intrusions and the Relationship to Mineral Processing <i>P.R.Alves, R.D.Hagni</i>	653
Polymeric Additives Effects in the Rheological Properties of Bentonite Clay Dispersions from Paraíba, Brazil <i>M.I.R.Barbosa, J.D.Viana, L.V.Amorim, H.L.Lira, H.C.Ferreira, K.V.Farias, E.Pereira</i>	657
Qualities of Quartz and the Alkali-Silica Reaction in Concrete <i>M.A.T.M.Broekmans</i>	661
Mineralogical and Geochemical Characterization and Ceramic Properties Evaluation of the Hard Kaolin from the Capim Region, Northern Brazil <i>B.S.Carneiro, R.S.Angélica, R.F.Neves</i>	665
Rheology of Precipitated Calcium Carbonate Slurries: A Comparative Analysis with CMC, HEC And MHPC <i>S.I.Conceição, J.M.F.Ferreira, J.Velho</i>	669
Image Analysis for the Determination of Roundness and Sphericity Grades of Sandy Grains <i>L.Z.D'Agostino, L.Soares, L.F.D'Agostino</i>	673
Heavy Minerals from the Polish Part of the Eastern Carpathian Sandstones <i>B.Dziubińska, M.A.Kusiak, M.Paszkowski</i>	677
Appraisal of the Delamination Efficiency Produced by Low Energetic Sonication Carried out on a Kaolin Unusually Rich in Kaolinite Stacks <i>C.Gomes, V.Gomes, C.Sequeira</i>	681
Mineralogical Characterization of Kaolin from the Capim Region, Pará State (Brazil) <i>J.Götze, R.Kleeberg, P.Wiedemann, M.Plötze, R.S.Angélica</i>	685
Synthesis of Zn-Al-layered Double Hydroxides Precursor Phases Containing Carboxylic Acids in the Interlayer <i>T.Kühn, H.Pöllmann</i>	689
Natural Refinement of Quartz Raw Materials for the Production of Polycrystalline Silicon <i>R.B.Larsen, F.Jacamon, P.M.Ihlen, I.Henderson</i>	693
Study on the Synthesis of 4Å Zeolite from Bentonite <i>X.Lu, J.Qiu, X.Cui</i>	697
Stereological Reconstruction of Planar Composition Using the Method of Schneider <i>M.J.Matos, J.J.Sousa</i>	701
Zeolitic Tuffs from Serbian Deposits and their Acid Modification <i>A.Radosavljevic-Mihajlovic, J.Stojanovic, S.Radosavljevic</i>	705
Bentonite from Guayaquil, Ecuador: Characterization and Possible Industrial Applications <i>A.M.Morales-Carrera, A.F.D.Varajão, J.C.Mendes</i>	709
Alternative Feldspathic Rocks for Porcelainized Ceramics in SE Brazil <i>J.F.M.Motta, A.Zanardo, E.P.Goulart, A.A.Roldan, A.O.Boschi</i>	713
Hydrothermal Synthesis and Characterization of Fe(III) and Fe(II)-Bearing Smectite <i>T.Nagase, T.Ebina, H.Hayashi</i>	717

Industrial Growth and Properties of Calcite Single Crystals <i>I.V.Nefyodova, N.I.Leonyuk</i>	721
Assessment of Technological Properties of Granitoids from South Brazil <i>L.E.S.M.Novaes, C.S.F.Gomes, F.J.F.T.Rocha, C.I.P.Carvalho, J. M.Gross</i>	725
Geochemical and Structural Characterization of K-feldspar from the Valle Fértil Field Pegmatites, Pampean Ranges, Argentina <i>J.Oyarzábal, M.B.Roquet</i>	729
Jura-Cretaceous Hydrothermalism as Genesis of Mineralization in Dolomitic Marbles of Itaiacoca Belt, Brazil <i>J.M.Reis Neto, A.M.A.Rebelo, M.A.S.Basei</i>	733
Petrographic Characteristics of Calcareous Rocks and their Implications in the Cement Manufacturing Process: A Case Study <i>J.M.Reis Neto, C.E.Riesemberg, F.A.Moya, D.L.Gomes</i>	737
Potential Uses of Natural Zeolites (Stilbite and Laumontite) from Brazil <i>N.G.A.M.Rezende, R.S.Angélica, M.L.Costa, R.F.Neves, M.B.M.Monte</i>	741
Crystallochemical Parameters as Support for Interpretation of Facies Variation in a Kaolin Deposit from Brazil <i>M.D.C.Santos, A.F.D.C.Varajão, P.T.A.Castro, J.Yvon, T.Allard</i>	745
Carbon Nanotubes and Fullerene-Like Phase Formation at Low Temperature and Pressure Parameters <i>S.K.Simakov, A.A.Graphchikov, I.A.Drozdova, M.A.Yagovkina, E.A.Grebenshchikova</i>	749
Chaoite Synthesis from Fluid at Low Temperatures and Pressures <i>S.K.Simakov, A.E.Kalmykov, L.M.Sorokin</i>	753
Kubelka-Munk Procedure for Brightness Evaluation of Blended Kaolins from Rio Capim, North Brazil <i>D.J.L.Sousa, A.F.D.C.Varajão, J.Yvon</i>	755
Genesis of Talc Deposits and the Metamorphic History of the Itaiacoca Group Metadolomites, Southern Brazil <i>G.A.J.Szabó, F.R.D.Andrade, G.B.Guimarães, F.A.Moya, F.M.S.Carvalho</i>	759
Applied Mineralogy Characterization of Construction and Demolition Waste from Brazilian Recycling Plants <i>C.Ulsen, H.Kahn, S.C.Angulo, V.M.John</i>	763
 Mineral Exploration	
Shear Zone Gold Deposits from Santa Catarina and Paraná States, Southern Brazil <i>J.C.Biondi, N.D.Franke, P.R.S.Carvalho, S.N.Villanova</i>	769
Characterizing Hydrothermal Alteration Minerals at Los Menucos, Patagonia Argentina, Using Reflectance Spectroscopy <i>D.F.Ducart, A.P.Crósta, C.R.Souza Filho, R.S.Angélica</i>	773
Contrasting Mineral Deposit Styles from Peixoto de Azevedo Region, Mato Grosso, Brazil <i>N.D.Franke, P.R.S.Carvalho, S.N.Villanova, J.C.Biondi</i>	777
Stable Isotope Studies on Zn and Pb Carbonates: Could they Play a Role in Mineral Exploration? <i>H.A.Gilg, M.Boni</i>	781

Geophysical and Geological Data Integration Using a New Statistical Approach for Mineral Target Selection Applied to Emerald Prospection in the Itabira Map Quadrangle, Minas Gerais, Brazil	785
<i>J.A.Newman, M.S.C.Barbosa, A.L.Gandini</i>	
The New Consort Gold Mine in the Barberton Greenstone Belt, South Africa: Orogenic Gold Mineralization in a Condensed Metamorphic Profile	789
<i>A.Otto, A.Dziggel, A.F.M.Kisters</i>	
Geology, Geochemistry and Petrogenesis of the Yatasto-San Bernardo Li-Bearing Pegmatite, Argentina	793
<i>J.Oyarzábal, S.Cadile</i>	
The Use of Mineralogical Data for Estimating Iron Ore Reserves	797
<i>W.C.Pereira, A.Z.Remacre</i>	
Petrology and Geochemistry of Mafic-Ultramafic Pods Around Bababudan – Nallur Lineament in Western Dharwar Craton, India: Implication for PGE Mineralisation	801
<i>P.V.Sunder Raju, T.S.Madoom Hussain</i>	
Detailed EDXRF-based Chemostratigraphy of Pt-ore of the Bushveld-Complex, SA	805
<i>D.Rammilmair, F.Melcher, Je.Lodziak, R.Merkle</i>	
Oil Reservoirs	
Clay Minerals in Oil Reservoirs of Brazil	811
<i>S.M.C.Anjos, C.M.A.Silva</i>	
Determination of the Depositional Age of Hydrocarbon Reservoir Sandstones through the Argon/Argon Radiometric Dating of Diagenetic Potassic Feldspar	815
<i>A.M.Mizusaki, L.F.De Ros, A.J.Maraschin, S.M.C. dos Anjos, P.Vasconcelos</i>	
Opals in Oil Reservoirs	819
<i>D.B.Alves, L.F.G.Caddah</i>	
Monte Carlo Simulation of Na- and Ca-montmorillonite at 353 K and 625 bar	823
<i>L.de Pablo-Galán, M.L.Chávez-García</i>	
Studies on Quartz as the Tracer of Fluid Migration	827
<i>K.Jarmolowicz-Szulc</i>	
A New Method to Trace the Provenance of Single Zircon Grains: Implications for Petroleum Exploration	831
<i>M.V.D.Remus, L.F.De Ros, M.Norman, R.S. de Souza, J.A.Cupertino</i>	
Implication of Authigenic Illite Growth on the Quality of Oil Reservoirs	835
<i>M.Setti, A.Di Giulio, A.López-Galindo, A.Ortenzi, M.Ardolini</i>	
Diagenetic Chemical Reactions and Products as a Result of Rock-water Interactions in a Petroleum Reservoir from Deposition to Deep Burial	839
<i>R.S.Souza</i>	
Albitization of Detrital Feldspars in Petroleum Reservoir Rocks, Brazil	843
<i>R.S.Souza, C.R.O.Rodrigues, D.C.Dias Filho, L.F.De Ros, E.Zambonato, S.Morad</i>	

Ore Mineralogy

Chromite Composition, Metamorphism, and PGM Distribution in Chromitites from the Espinhaço Ridge - Brazil <i>N.Angeli, S.R.F.Vlach</i>	849
Supergene Sulphides and their Analogues in the Supergene Profile of the Urals VMS Deposits <i>E. V.Belogub, C.A.Novoselov, V.A.Yakovleva</i>	853
Ore Mineralogy of Shear Zone Gold Deposits from Santa Catarina State (Brazil) <i>J.C.Biondi, N.D.Franke, P.R.S.Carvalho, S.N.Villanova</i>	857
A Mineralogical Guide Supporting Reserve Evaluation and Mining of Cajati Phosphate Ore <i>T.B.Bonás, L.M.Sant'Agostino, M.Pereira</i>	861
Brittle Microstructures in Gold Nuggets: Evidence for Seismogenic Failure of Gold <i>A.R.Cabral, C.E.Suh, R.Kwitko-Ribeiro, O.G.Rocha Filho</i>	865
Characterization of an Argillaceous Phosphate Ore Type from the Tapira Mine, MG, Brazil <i>A.M.D.Chula, P.R.G.Brandão, J.A.Aquino</i>	869
Significant Characteristics of Volcanogenic Massive Sulfide Deposits of the Eastern Pontides (NE Turkey): A through Comparison to Japanese Kuroko Deposits <i>E.Ciftci, G.Yalcin, R.D.Hagni</i>	873
Textural Patterns of Sulfides Related to a Paleoproterozoic Low-Sulfidation Epithermal System in Tapajós Gold Province, Pará State, Brazil <i>R.H.Corrêa-Silva, C.Juliani, T.Benevides, J.S.Bettencourt, L.V.S.Monteiro</i>	877
Condoriaco Silver District: a Mineral Heritage in La Serena, Chile <i>J.Cucurella, J.Oyarzún</i>	881
Mineralogy of the Iron Formation in the Itabira Mines, Iron Quadrangle, Brazil <i>L.Lagoeiro, R.C.Romano, P.N.Venturini, M.C.Pereira, A.A.S.Gomes-Jr</i>	885
Iron Ore Mineralogy of Paleoproterozoic Iron Formations from Iron Quadrangle, Brazil <i>L.Lagoeiro, P.N.Venturini, R.Roman, I.Endo</i>	889
Types of Goethite from Quadrilatero Ferrifero's Iron Ores and their Implications in the Sintering Process <i>M.S.Magalhães, P.R.G.Brandão, R.P.Tavares</i>	893
Sulpharsenides and Arsenides in Massive Sulphide Deposits Connected with Ultramafites, South Urals <i>I.Yu.Melekestseva, V.V.Zaykov, E.V.Belogub, S.G.Tesalina</i>	897
Trace Element Characterization of Gold and Platinum-group Element Deposits and Products in South Africa <i>R.K.W.Merkle, R.D.Dixon, A.Kijko</i>	901
Geochemical and Mineralogical Zoning Derived from the Weathering of the Alkaline Rocks in the Itatiaia Massif, Rio de Janeiro, Brazil <i>S.C.Miano, F.R.M.Pires</i>	905
Geochemistry of Cassiterite and Wolframite from Tin and Tungsten Deposits in Portugal <i>A.M.R.Neiva</i>	911
Cervelleite-like Sulphotellurides from the Urals HVMS Deposits <i>C.A.Novoselov, E.V.Belogub, V.V.Zaykov</i>	915

Zirconiferous Hafnon and Hafniferous Zircon from São João Del Rei, Minas Gerais, Brazil <i>R.M.Pereira, A.M.Netto, C.A.Ávila, H.R.Barrueto, R.Neumann, D.Atencio</i>	919
Unconventional Precious Metal Deposits <i>A.Piestrzyński, J.Pieczonka, A.Banaszak</i>	923
Parageneses Generated by the Oxidation During the Metamorphism of the Itabira Iron Formation in the Quadrilátero Ferrífero, Minas Gerais, Brazil <i>F.R.M.Pires, B.R.Frost</i>	927
Mineralogical Balance of Gold of the Bor Metallogenic Zone, Serbia <i>S.Radosavljevic, J.Stojanovic, V.Kasic</i>	931
Dolomitic Itabirites and Generations of Carbonates in the Cauê Formation, Quadrilátero Ferrífero <i>C.A.Rosière, N.Brunnacci-Ferreira-Santos</i>	935
Nugget Effect in Gold Grade Determination – An Historical Case <i>L.M.Sant'Agostino, M.M.M.L.Tassinari, G.Ratti</i>	939
Chromites of the Polar Urals, Russia <i>G.N.Savelieva</i>	943
Glide Systems of Hematite Single Crystals in Deformation Experiments <i>H.Siemes, B.Klingenberg, E.Rybacki, M.Naumann, W.Schäfer, E.Jansen, K.Kunze</i>	947
Sulfides of the Cu-S-system in the Endogenic and Exogenetic Ores <i>I.F.Gablina</i>	951

Process Mineralogy

Correlating QemSCAN Mineralogy with Metallurgy in Feasibility Studies <i>C.Hamilton, C.Martin, N.McKay, S.Williams</i>	957
Study of Electrodialysis Applied to Verde-Lodo Bentonite Clay Dispersions From Paraíba, Brazil <i>L.V.Amorim, H.L.Lira, H.C.Ferreira, F.L.H.Silva, K.B.França, C.M.Gomes</i>	961
“Gravitational” and “Flotational” Gold in Ores of Madneuli Copper Deposit (Georgia) <i>R.A.Amosov, A.S.Pariy, B.Z.Menabdishvili, Z.B.Dalakishvili</i>	965
On-Line Measurement of Mineralogy for Ore Sorting and Characterisation <i>D.W.Bennett, N.G.Cutmore, D.L.Death, J.E.Eberhardt, D.G.Miljak, C.A.Rogers</i>	969
Principal Component Analysis Applied to Surface Chemistry in Process Mineralogy <i>M.Biesinger, D.Miller, J.Francis, B.Hart, R.StC.Smart</i>	973
Technological Characterization of Carbonatic Raw Material Manufacture from Cajati (SP) <i>A.G.Brandão, L.M.Sant'Agostino, T.B.Bonás</i>	977
Technological Characterization of Low Grade Phosphate from Salitre, MG-Brazil <i>A.B.Braz, H.Kahn, G.Ratti, M.M.M.L.Tassinari</i>	981
Direct Comparison on Mechanical and Digital Size Analyses of Kemi Chromite, Finland <i>T.Chernet, J.Marmo</i>	985
Ore Microscopy, Origin, and Beneficiation Problems of Copper Ore from Salobo, Brazil <i>O.J.Choque Fernandez, M.L. da Costa, H.Pöllmann, P.R.G.Brandão</i>	989
Transforming Process Mineralogy Data into Improved Hydrocyclone Performance <i>J.M.F.Clout, A.G.Trudu, E.Donskoi, J.M.Young, B.A.Firth</i>	993

Process Mineralogy Studies of a “Foscorite” Ore from Salitre Alkaline Carbonatitic Complex <i>H.Kahn, G.Ratti, M.M.L.Tassinari, E.S.Mano, L.A.F.Barros</i>	997
Effects of Smectite and Kaolinite- rich Gangue on Sulphuric Acid Leaching of Exotic Copper Ore <i>U.Kelm, S.Helle</i>	1001
Grain Size and Liberation of Chromite in Ground Chrome Ore from Kemi Mine, Finland <i>J.Liipo, P.Lamberg, J.Turunen, J.Pitkääjärvi</i>	1005
Technological Characterization of Ni-Cu-Co Ore from Fortaleza de Minas, MG, Brazil <i>E.S.Mano, H.Kahn</i>	1009
Characterization and Production of Novel Ceramic Roof Tiles Obtained Using Slate Powder Waste <i>H.S.Mansur, A.A.P.Mansur</i>	1013
Gold Reprecipitation in the São Bento Mine Process <i>M.A.Márquez, J.C.Gaspar</i>	1017
Assessment of Uncertainties in Modal Analysis and Liberation Measurements by Synchrotron-based X-Ray Microtomography <i>D.Paktunc, D.Smith, R.Lastra, A.Pratt</i>	1021
Coal and Clay Flotation Using Dodecyltrimethylammonium Bromide (C ₁₂ TAB) and Sodium Dodecylsulfate (SDS) <i>F.G.Penha, M.P. de Oliveira, J.G. de Araújo, J.B. de Farias, N.A.Debacher</i>	1025
Mixture Coal-Pyrite Flotation Using Potassium Ethylxanthate (C ₂ XK) and Sodium Dodecylsulfate (SDS) <i>F.G.Penha, M.P. de Oliveira, G.F.Fiss, L.Furlan, N.A.Debacher</i>	1029
Experimental Verification of the Three-phase Linear Grade Distribution Prediction Method by Direct Measurement <i>C.L.Schneider, R.Neumann</i>	1031
Quantitative Measurement of Exposed Area by Image Analysis of Particle Cross-section <i>C.L.Schneider, R.Neumann</i>	1035
Automatic Gold Process Mineralogy with the “Precious-X” Image Analysis System <i>P.Siegel, E.Almendras</i>	1039
Native Copper Analysis through Digital Microscopy <i>O.A.J.Soto, O.F.M.Gomes, G.A.H.Pino, S.Paciornik</i>	1043
Nanometer Size Iron Oxides in Australian Iron Ores: Implications for Mineral Processing <i>A.G.Trudu, J.M.F.Clout, J.M.Young</i>	1047
Methods of the Evaluation of Mineral Surface Wettability <i>V.E.Vigdergauz</i>	1051
Definition of the Type of Refractoriness in El Zancudo Gold Mine, Antioquia, Colombia <i>D.M.Zapata, A.N.Gallego, M.A.Márquez</i>	1055
Author Index Vol. I & II	1059

Gem Materials

Gem Materials Map Of South Brazil Region

P.L.Juchem, T.M.M.Brum, A.C.Fischer

Gemological Laboratory, Department of Mineralogy and Petrology, Geosciences Institute, Federal University of Rio Grande do Sul, Porto Alegre, Brazil

N.L.Chodur

Department of Geology, Federal University of Paraná, Curitiba, Brazil

A.Liccardo

Sea and Earth Sciences Institut, Vitória, Brazil

ABSTRACT: This map shows the most important gem material localities and their geological features in South Brazil Region - Rio Grande do Sul (RS), Santa Catarina (SC) and Paraná (PR) States. RS is worldwide known by huge gem quality agate and amethyst geode deposits in tholeiitic basalts of Paraná Basin. Rose quartz, rock crystal, opal, calcite, gypsum, zeolites, apophyllite, onyx and jasper also occur in these deposits. Salto do Jacuí is the main agate production region, where mining activities are done by open-pit in an altered andesite-basaltic rock. The main amethyst deposits are in Alto Uruguai region, north of RS, where large amethyst-bearing geodes are extracted from a fresh basalt in underground adits. Similar deposits occur sparsely in west of SC and southwest of PR. Diamond alluvial deposits in Tibagi river valley (PR) are known by the special quality of the stones and are sporadically exploited. In Barra Velha region (SC) there are large colluvial deposits of ruby and sapphire associated to granulitic rocks. The crystals are opaque to translucent and can exhibit special features like color zoning, silk, chatoyance and asterism, which produce nice cutted and collection stones. A large deposit of petrified wood is known in central region of RS, in Gondwanic sedimentary rocks, but are not properly studied and its commercial use is prohibited. Serpentinities in Precambrian crystalline rocks are exploited in southwest RS and are used as carving objects.

1 INTRODUCTION

Many important gem materials deposits occur in south Brazil, related to different geological settings (Figure 1). These materials are used as cutted gems, ornamental gems or collectors gems.

South Brazil Region comprises the States of Rio Grande do Sul (RS), Santa Catarina (SC) and Paraná (PR), where five main important geological units occur. Crystalline rocks constitute the Precambrian shield and are represented by two main groups: the metamorphic rocks (granulitic gneisses, migmatites, amphibolites, deformed granitoids and mafic and ultramafic rocks) with 2.0 to 2.5 Ga; and younger granitic and metamorphic rocks (tonalites, granodiorites, alcali granites, sienites and schists, phyllites, quartzites and marbles) with 550 to 650 Ma (Almeida et al. 1984). In RS, these rocks are in the Sul Riograndense Shield, in SC they are mainly in the Granulitic Complex of Santa Catarina, and in PR they correspond to Açungui Group.

The Gondwanic sedimentary rocks are composed by glacial beds, shallow marine to continental transitional facies and desert sandstones deposited in Parana Basin, a huge sedimentary basin located in southeastern South America. These rocks are covered

by lava flows of Jurassic-Cretaceous age, which represent one of the most extensive flood basalt province in the world. This volcanic event originated from deep fractures related to Gondwana rupture and South Atlantic Ocean opening (Piccirillo & Melfi 1988). This unit is known as Serra Geral Formation and is mainly composed of tholeiitic basalts, locally covered by dacitic and rhyolitic flows in the southern States of Brazil (Chies & Roisenberg 1993).

Cretaceous sediments are represented by continental sandstones with reddish violet colour, covered by recent sediments in several regions. The Coastal sediments are mainly Quaternary to recent continental, marine and transitional units, originated during sea level oscillations.

2 VOLCANIC ROCK DEPOSITS

The largest and more important gem materials deposits are found in RS. This State is worldwide known by huge gem quality agate and amethyst geode deposits in Serra Geral Formation, which are included in the most important deposits of the world.

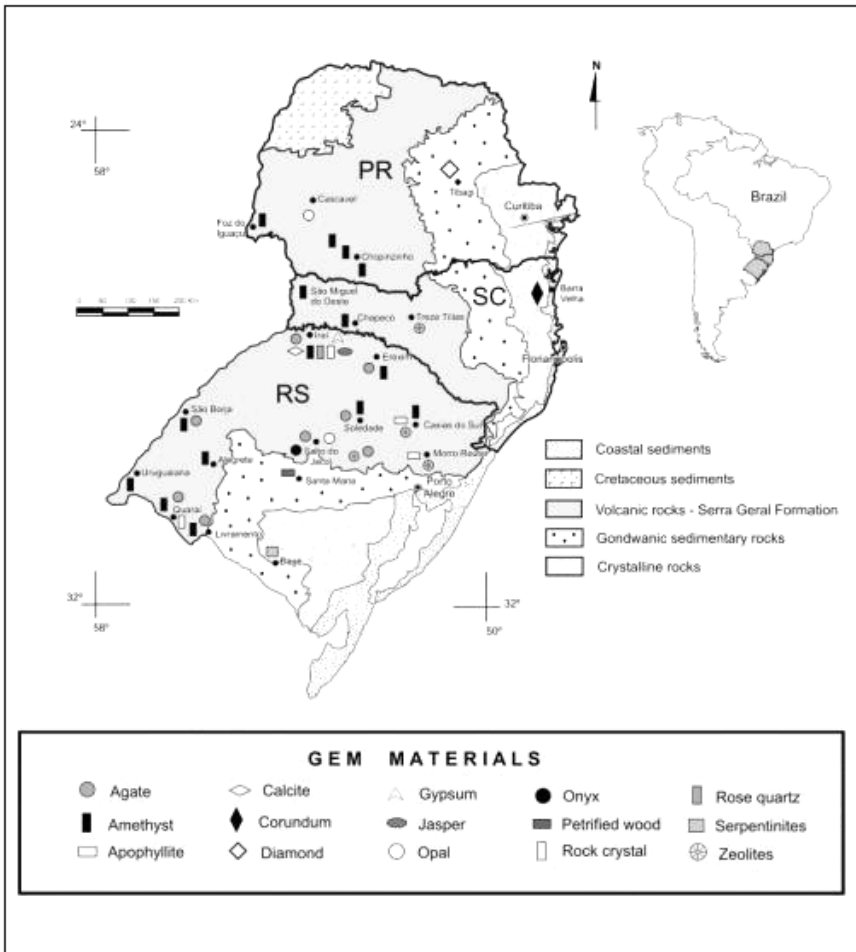


Figure 1. Gem Materials Map of south Brazil region, showing the most important gem deposits localities and their geological settings.

Agate occurs in almost all known geode deposits. Salto do Jacuí is the main agate production region, where mining activities are done by open-pit in an altered andesite-basaltic rock, in more than 150 mine fronts (Juchem & Brum 1998). Agate usually occurs completely filling roundish to egg-shaped decimetric geodes, but in several cavities it can be followed by a fractured colourless to milky quartz layer and sometimes by late calcite.

Agate is mainly used as ornamental material in polished plates or in carvings as bowls, vases and watches. It is also used in jewelery as cutted gems or as rings and bracelets. This mineral is usually dyed in order to improve or modify the natural colours. The "Umbú agate" (a massive bluish gray chacedony with weak or absent bands at naked eye) is the most appreciated in the international trade, since it shows

the best results after dyed, producing strong colored bands. Onyx deposits may occur near Salto do Jacuí, but most of this mineral in the trade is, in fact, dyed agate.

Gem quality opal with white, yellow, blue, pink and orange-red colours can also occur associated with these deposits. Black colour opal filling small cavities and thin fractures was recently discovered in SW of PR, in the same volcanic formation.

There are many amethyst occurrences in RS, but the most important mining area is in Alto Uruguai region, north of the State. In this region, large amethyst-bearing geodes over one meter long are extracted from a fresh basalt in horizontal underground adits from more than 300 mine fronts (Juchem 1999). Similar deposits occur in west of SC and southwest of PR which seems to form a

continuous mineral province with the RS deposits. Recent mining in Chopinzinho region (PR) has produced high gem-quality crystals (Chodur et al. 2002). Amethyst is used as cutted gem, and the geodes as ornamental material. Significant amounts of this mineral are heat-treated in order to produce citrine, the yellow variety of quartz.

The geodes are filled by a thin wall-layered of massive or banded microcrystalline quartz, followed by a centimetric layer of colourless to milky quartz with progressive colour change to amethyst. The colour of amethyst varies from a light violet to deep rich hues. There are some amethyst crystals with bluish, pinkish, grayish and purplish violet colours. Color zoning and irregular color distribution are common, visible under the microscope and even to the naked eye. Colourless quartz can occur as clear prismatic specimens (rock crystal variety), and in this case is used as cutted gem. Centimetric euhedral rose quartz crystals may rarely be associated with amethyst.

Late minerals are represented by calcite, gypsum (selenite variety) and barite, which occur as euhedral crystals covering the silica minerals (Juchem et al. 1990). These mineral species are used as ornamental stones or as collection specimens. Many superb mineral samples are disputed by collectors and museums around the world. Calcite, the more common late mineral, occurs in a variety of crystal forms and colours. Pseudomorphs of calcite replaced by microcrystalline quartz, and rock crystal and/or amethyst encrusting calcite are observed.

Selenite is found only in two mines in Alto Uruguai. The crystals are always euhedral with prismatic to tabular habit in parallel aggregates, ranging from few centimeters to one meter of length. The crystallization of selenite in geodes, as well as its mineralogical and crystallographic features indicates that this is a unique and exceptional deposit in the world (Juchem et al. 2000).

Mineralogical and chemical results, including solid and fluid inclusion studies and oxygen isotope data, show that these geode minerals have been deposited in epithermal conditions (Juchem 1999; Juchem et al. 2002).

The material commercially classified as jasper, correspond to breccias composed by irregular fragments of chalcedony, basalt and sandstone, cemented by agate. This material occurs at the base of some geodes or as discontinuous layers at the top of a mineralized basalt flow. Jasper is mainly used as ornamental carvings and sometimes as cutted gems. Glass and glassy rocks that occur at the limit between lava flows, have been used as carvings and improperly named in the market as jasper.

Zeolites associated with apophyllite and sometimes calcite and colourless quartz occur in several regions filling geodes in basalt and acid flows of Serra Geral Formation. Some deposits in

RS and SC are in economic concentrations, where special samples of beautiful mineral aggregates can be extracted for use as ornamental or collection gems. Apophyllite occurs as centimetric colourless to greenish well-formed samples. Zeolites are usually small crystals, being identified until now stilbite, mordenite, heulandite, scolecite, laumontite, epistilbite, chabazite, analcime, stellerite and levyne.

3 CRYSTALLINE ROCK DEPOSITS

Serpentinites in Precambrian rocks are exploited in southwest RS, and are used as carving objects for ornamental purposes. These rocks were originated from gabbros and peridotites from Cerro Mantiqueiras Formation (Cesar 1980). Antigorite, chrysotile, magnetite, amphiboles, pyroxenes, talc and olivine in mesh, ribbon and deformed textures are its main petrographic characteristics. The colour varies from light yellowish green to dark green, with patches, veins and bands with black, white, yellowish white, brown and purple colours, in irregular distribution. Polychromated serpentinites, a rare and appreciated ornamental gemstone in the international trade (Cipriani & Boreli 1986) also occur in this region.

4 GONDWANIC DEPOSITS

A large deposit of petrified wood is known in central region of RS, in Gondwanic sedimentary rocks, that is one of the most important earth silicified fossil wood records (Sommer & Scherer 1999). The fossils are included in Mata Sandstone and in Santa Maria and Caturrita Formations, of Triassic age. According to the authors cited above, the fossil woods comprises conifer-related gymnosperm forms and possibly represents a mesophytic flora originated due to climate changes that took place during the Meso-Neotriassic transition. Fragments of trunks that can reach up to 20 meters of length are widespread in an area of about 305 Km², but the main important occurrences are in São Pedro do Sul and Mata region, near Santa Maria (Bolzon & Guerra-Sommer 1994). The samples can exhibit gray, white, pinkish, reddish, yellowish and brown pigmented colours, with different degrees of silica replacement and preserved vegetable structures. Many samples may be cutted and polished in order to produce ornamental objects, showing good gem quality.

This abundant paleobotanic record constitutes an important scientific inheritance on which protection and conservation activities have recently been performed, and its commercial use is now prohibited.

5 SEDIMENTARY DEPOSITS

In Barra Velha region (SC) there are large recent colluvial deposits with ruby and sapphire, associated to granulitic rocks. The sediments are poorly sorted, composed by rough blocks, gravels and pebbles of milky quartz and fragments of quartzites and quartz-feldspar rocks, with a sandy to clay-size matrix. These features characterize debris flows sedimentation with little transport (Chodur 1977). Centimetric opaque to translucent corundum crystals with short prismatic to tabular habit are common in these sediments. Reddish colours characterizing ruby variety are the most common but sapphire variety with rose, white, brown, gray and black colours can also occur. Corundum can exhibit special features like color zoning, silk, chatoyance and asterism, which produce nice cutted and collection stones. Special stones are obtained from the black variety, that shows a velvet-like appearance after polished.

Diamond occurrences in alluvial deposits, usually associated with gold, are known in Tibagi region (PR). This gemstone are found in several rivers of this region, but the highest concentrations are in Tibagi river and affluents that drain Gondwanic sedimentary rocks (Chierigati 1989). Usually the stones are of small size and may exhibit several fractures. These features suggest a long sedimentary transport and prevent the determination of the diamond source areas. In the beginning of the last century, there were many mine areas exploited by local people (garimpos) which produced good gems. Despite the small size of most of the stones, the Tibagi diamond is famous for its special gem quality. Nowadays this gemstone is occasionally exploited, but there are some reports of special clear rough stones with up to 5 carats.

6 REFERENCES

- Almeida, F.F.M.; Hasuy, Y.; Litwinsky, N. 1984. O Pré-Cambriano no Brasil. São Paulo-Editora Edgard Blücher, 318 p.
- Bolzon, R.T.; Guerra-Sommer, M. 1994. Considerações sobre a Tafonomia da Lignitoflora Mesozóica do Rio Grande do Sul. *Acta Geológica Leopoldensia*, 39/1 (27): 109-115.
- Cesar, A.R.S.F. 1980. O craton do Rio da Prata e o cinturão Dom Feliciano no Escudo Uruguaio-Sul Riograndense. *Cong. Bras. Geol.*, XXXI. Anais. Camboriú.V.5, p.2879-92.
- Chies, J. O. & Roisenberg, A. 1993. Modelos para geração do vulcanismo ácido da Bacia do Paraná, na região ocidental RS/SC. *Cong. Bras. Geol. Anais. V. IV*, p. 23-24.
- Chierigati, L. A. 1989. Aspectos mineralógicos, genéticos e econômicos das ocorrências diamantíferas da região nordeste do Paraná e sul de São Paulo. Dissertação de Mestrado. Instituto de Geociências/USP. 180 p.
- Chodur, N. L. 1997. Mineralogia e geologia dos depósitos de rubi e safira da região de Barra Velha, SC. São Paulo. Tese de Doutorado-Instituto de Geociências/USP. 110p.
- Chodur, N.L.; Juchem, P.L.; Liccardo, A.; Splendor, F. 2002. Ametista de Chopinzinho, PR. *XLI Cong. Bras. Geol.*. Anais. João Pessoa - SBG. p.593.
- Cipriani, C.; Boreli, A. 1986. Guia de Piedras Preciosas. Barcelona - Ediciones Grijalbo, S.A.. p. 384.
- Juchem, P.L. & Brum, T.M.M. 1998. Geologia e Mineralogia. In: *Ágata do Rio Grande do Sul. DNPM. Brasília. Série Difusão Tecnológica nº 5. Cap. 2, p. 25 - 35.*
- Juchem, P. L. 1999. Mineralogia, geologia e gênese dos depósitos de ametista da região do Alto Uruguai, Rio Grande do Sul. São Paulo, 225 p. (Tese - Doutorado) Curso de Pós Graduação em Geociências - programa de mineralogia aplicada. Universidade de São Paulo.
- Juchem, P.L.; Brum, T.M.M.; Svisero, D.P. 2000. A unique occurrence of selenite in geodes of basalts from RS, Brazil. 31st Intern. Congress Rio de Janeiro. Anais. General Symposium 8-1(CD-ROOM).
- Juchem, P.L.; Brum, T.M.M.; Fischer, A.C.; Svisero, D.P. 2002 The amethyst from Alto Uruguai Mining District, Parana Basin, Brazil: mineralogical and chemical signature. 18th IMA General Meeting. Abstracts. Edinburgh. p. 146.
- Piccirillo, E.M.; Melfi, A.J. eds. 1984. The Mesozoic Flood Volcanism of the Paraná Basin - petrogenetic and geophysical aspects. São Paulo, USP-Instituto Astronômico e Geofísico. p. 179-205.
- Sommer, M.G.; Scherer, C.M.S. 1999. Sítios Paleobotânicos do Arenito Mata nos Municípios de Mata e São Pedro do Sul, RS. In: Schobbenhaus, C.; Campos, D.A.; Queiroz, E.T.; Winge, M.; Berbert-Born, M. (Edit.) Sítios Geológicos e Paleontológicos do Brasil. Publicado na Internet: <http://www.unb.br/ig/sigep/sitio009/sitio009.htm>.

Crystal Chemistry of Aquamarines: A Case Study in Pegmatites Hosted in Migmatites from the NE of Minas Gerais State, Brazil

L.Lagoeiro, L.M.Graça

Department of Geology, Federal University of Ouro Preto, Ouro Preto, Brazil

G.Magela

Department of Chemistry, Federal University of Ouro Preto, Ouro Preto, Brazil

A.I.C.Persiano, M.V.B. Pinheiro, K.Krambrock

Institute of Physics, Federal University of Minas Gerais, Belo Horizonte, Brazil

ABSTRACT: A total of 15 samples of varieties of blue beryl (aquamarine) was selected for crystal chemistry characterization. Three sets representing main range of colors were selected for analyses. The first set corresponds to samples of light blue colors. A second set represents sample of intermediate blue tones. Samples included in third set are dark blue. Microprobe analyses showed that the content of alkalis ($\text{Na}_2\text{O} + \text{K}_2\text{O}$) increases linearly with the increase of intensities of blue. The intensity of blue is also directly related to the (Fe + Mg) content. There is a negative correlation between (Fe + Mg) and (Al + Si) contents. The results of the Mössbauer spectroscopy analyses indicated that Fe^{2+} (approximately 70%) and Fe^{3+} (30%) are the main ions and they are allocated preferentially in the octahedral sites, replacing Al^{3+} ions. In addition to the Mössbauer spectroscopy, we also used optical absorption spectroscopy to correlated the spectral bands generated by the optical absorption with the presence of $\text{Fe}^{2+}_{\text{Al}}$ (replacing Al^{3+} ions in octahedral sites), Fe^{2+}_1 , $\text{Fe}^{3+}_{\text{Al}}$, $(\text{CO}_3)^{2-}$ ionic group, and structural H_2O of type I and II. The absorption of the visible light responsible for the shades of blue is influenced essentially by the absorption bands corresponding to $\text{Fe}^{2+}_{\text{Al}}$, Fe^{2+}_1 and CO_3^{2-} groups. With respect to the Fe ions in the crystallographic sites, the optical absorption helped to identify $\text{Fe}^{2+}_{\text{Al}}$, $\text{Fe}^{3+}_{\text{Al}}$ and Fe^{2+}_1 and the Mössbauer spectroscopy correlated the doublets to the ions $\text{Fe}^{2+}_{\text{Al}}$, $\text{Fe}^{3+}_{\text{Al}}$ and Fe^{2+}_1 in tetrahedral sites.

1 INTRODUCTION

A total of 15 samples of gem-quality Beryl with different shades of blue (acquarines) was selected to investigate the cause of color and the relationship between the concentration of the color-caused elements and the variation of blue shades. The samples were collected in pegmatites hosted in granitic-gnaissic-migmatitic rocks. All samples came from a location called "Tatu Mine", in the District of Santa Maria de Itabira, Minas Gerais State, Brazil. A few geochronological data available for these rocks indicates that they have a minimum age of 2.7 Ga years (Grossi Sad et Al. 1990). REE studies (Müller et al. 1986) suggested that these rocks originated by partial melting and crystallization of former granitic rocks. The pegmatite bodies associated to the migmatization and crystallization processes are mostly of tabular shape and parallel to the gneissic-migmatitic foliation. Some pegmatite bodies also occur as apophysis mainly oblique to the main regional foliation. Most of the analyzed samples were taken from tabular pegmatite bodies parallel to the regional foliation (gneissic layering). These bodies are in average 2 to 3 meters long and 30 cm thick. Na-plagioclase, K-feldspar, quartz and muscovite

are the main minerals of the pegmatites. Fluorite, titanite pyrite, garnet and beryl are present in minor amounts. The beryl minerals have well-developed faces. Locally the beryl fills voids or indents into the plagioclase twin boundaries which give mineral boundaries corroded figures, suggesting that an interaction between Be-bearing fluids and crystallized feldspar minerals.

2 SAMPLE PREPARATION AND APPLIED ANALYTICAL TECHNIQUES

Three major groups of colored beryl with different shades of blue were taken from the set of 15 samples and chosen for analyses. They are: 1) light blue; blue; and dark blue. The samples were oriented and cut parallel and perpendicular to their crystallographic *c*-axis. Microprobes were taken in points randomly chosen with respect to the crystallographic axes since samples are homogeneous coloured. The optical absorption was measured with incident light parallel to the crystallographic *c*-axis. The spectrum band corresponds to a range from the ultraviolet (180nm) to the near infrared (3600 nm), passing through the visible region (380nm to 760 nm). Mössbauer

absorption technique was applied in order to determine the relative proportion of Fe^{2+} to Fe^{3+} and the their crystallographic sites as well.

3 RESULTS

3.1 Electron Microprobe Analysis

The Table 1 shows the results of the microprobe analysis in the light blue, blue and dark blue beryl samples. As a general tendency, the content of alkalis ($\text{Na}_2\text{O} + \text{K}_2\text{O}$) increases as the blue shade changes to dark blue, although, in average the bulk concentration of alkalis in all samples is smaller than those found in alkalis-bearing beryl around the world. In the dark blue samples the Fe contents are higher than those of the light blue ones. There is a positive linear correlation between the iron and the alkalis concentrations for all analysed samples. The MgO concentrations appear to have the same behavior of the Fe ions, that is, their contents increases as the alkali contents get higher, although the MgO concentrations are much smaller than those of FeO. The contents of FeO and MgO show positive linear correlations. Contrasting the concentrations of the pair Al_2O_3 and SiO_2 with those of FeO, it appears that the Al and Si concentrations drop as the blue shades get darken, suggesting a negative linear correlation between the contents ($\text{Al}_2\text{O}_3 + \text{SiO}_2$) and FeO. A similar relationship appears when the concentrations of Al_2O_3 and ($\text{FeO} + \text{MgO}$) are compared.

Table 1. Electron microprobe analyses of the studied samples

Sample/wt %	SiO_2	Al_2O_3	FeO	MgO	Na_2O	K_2O
Light Blue	66,3	17,94	0,73	0,004	0,25	0,016
Blue	66,3	17,61	1,04	0,014	0,27	0,022
Dark blue	65,9	17,08	1,68	0,038	0,49	0,043

3.2 Optical Absorption Spectroscopy

In the whole spectrum of the analysed samples (Fig.1) five distinct bands of absorption appears. One of them appears just partially which means that its absorption peak is missing. This may be caused by the interference with one superposed band. The first absorption band is common to all samples. It has a maximum around 1,5 eV, in the infrared region. The second one is centred at 1,8 eV, and, again, is common to all analysed samples. At this time, it appears in the visible region. It is responsible for the absorption of the red and part of the orange color. The third band is broader than first two and has its peak of maximum in the ultraviolet region, out of the area covered by the graph. It corresponds to the blue to purple color. The forth band is superposed to the first (centered around 1,5 eV),

with a small shift, which results in a maximum around 1,7 eV. It is less intense when compared to the three first bands and it is wider too. The fifth and last band is narrower than the others and appear in all samples. It occurs in a region of the infrared, between 0.6 e 0.7 eV. These two peaks are related to the presence of water molecules of type I and II (Wood & Nassau, 1968). The transmission valleys for the beryl specimens analysed appear in the spectral ranges correspondent to the colors, blueish green, greenish blue and blue.

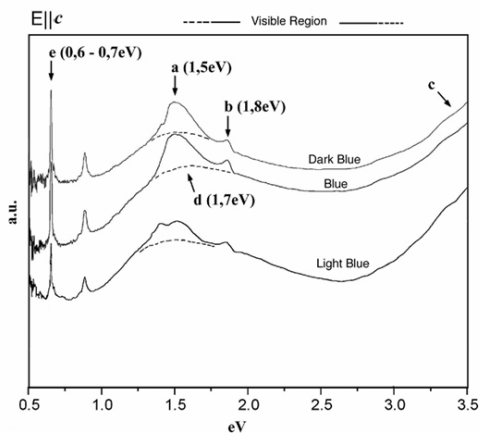


Figure 1. Optical absorption spectrum for the studied samples.

3.3 Mössbauer absorption spectra

Figure 2 shows the Mössbauer absorption spectra for the blue varieties of beryl. The doublet with δ of 1,3 mm/s and quadrupole splitting of 2.7 mm/s suggest that the Fe^{2+} ions occupy the same octahedral sites of Al^{3+} . The Fe^{2+} ions in tetrahedral coordination are related to the doublet with δ of 1.0 mm/s and quadrupole splitting of 1.5 mm/s (Prince et al. 1976; Parkin et al. 1977).

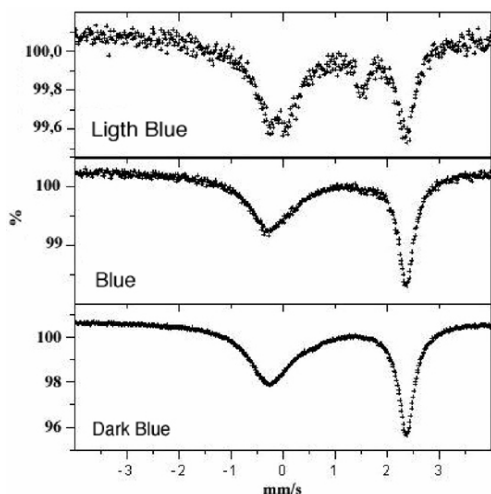


Figure 2. Mössbauer spectrum for the light blue, blue and dark blue samples.

4 INTERPRETATION AND CONCLUSIONS

The microprobe analyses of the beryl specimens showed that although the beryl minerals in the sampled pegmatites are poor in alkalis ($\text{Na}_2\text{O} + \text{K}_2\text{O} < 0.5\%$) there is a positive correlation between the alkalis and the FeO content. The dark blue beryl specimens are enriched in FeO and depleted in alkalis when compared with the light blue samples. The same relationship occurs for FeO and Al_2O_3 . The content of FeO rises proportionally with intensity of blue shades of the samples, whereas the concentration of Al_2O_3 drops gradually. The content of SiO_2 also drops as the samples get darker (dark blue) and the FeO concentration becomes higher. The increase of FeO and MgO contents and the correspondent rise in the ($\text{Na}_2\text{O} + \text{K}_2\text{O}$) concentration suggest that Fe might be considered the main exchange ion in the variation of colors registered in the beryl specimens. The alkalis might be located in the beryl channel to adjust the charge unbalance caused by the replacement, mainly by Al^{3+} , in the octahedral sites, and, at less extent, Be^{2+} and Si^{4+} , in the tetrahedral sites, by Fe ions.

The optical absorption spectra also provide valuable information about nature of the ions, radicals and molecules and their structural positions. The first absorption spectrum (1,5 eV) is interpreted as a result of the replacement of octahedral Al^{3+} by the Fe^{2+} ions ($\text{Fe}^{2+}_{\text{Al}}$). The second absorption spectrum might be associated to the presence of the CO_3^{2-} group. The substitution $\text{Fe}^{3+}_{\text{Al}}$ are thought to be responsible for the appearance of the third absorption spectrum. The fourth spectrum might be caused by the interstitial Fe^{2+} ($\text{Fe}^{2+}_{\text{i}}$) in the channels.

The last absorption spectrum individualized might be related to the structural H_2O of the types I and II.

Mössbauer spectroscopy indicated that the Fe^{2+} ions predominate over the Fe^{3+} in an average proportion of 70% to 30%, respectively, in dark blue samples. In light blue specimens the $\text{Fe}^{2+}/\text{Fe}^{3+}$ proportions are about 50% to 50%, with a slight predominance of the Fe^{2+} ions. According to the doublets and quadrupole splittings obtained, it was possible to determine for Fe ions the following structural position: $\text{Fe}^{2+}_{\text{Al}}$; $\text{Fe}^{3+}_{\text{Al}}$ and Fe^{2+} in tetrahedral sites. This is in a good accordance with the result obtained from the optical absorption spectroscopy which allow for Fe ions the following structural sites: $\text{Fe}^{2+}_{\text{Al}}$; $\text{Fe}^{3+}_{\text{Al}}$; and Fe^{2+} interstitial (inside the channels).

5 REFERENCES

- Grossi Sad, J. H., Chiodi Filho, C., Santos, J. F., Magalhães, J. M. M., Carelos, P. 1990. Duas suítes graníticas do bordo sudeste do cráton Sanfranciscano, em Minas Gerais: petroquímica e potencial metalogenético. In: *Proceedings of the 36th Brazilian Geological Congress*, 4, 1836-1848, Natal, RN.
- Muller, G., Hohndorf, A., Lauenstein, H. J., Lenz, H. 1986. Petrological and Geochemical Data on a High Metamorphic Archean BIF – bearing rock sequence near Guanhões, Minas Gerais, Brasil. *Geol. J.*, D79: 3-20.
- Parkin, K. M.; Loeffler, B. M.; Burns, R. G. 1977. Mossbauer spectra of kyanite, aquamarine, and cordierite showing intervalence charge transfer. *Physics and Chemistry of Minerals*, 1:301-311.
- Prince, D. C.; Vance, E. R.; Smith, G.; Edgard, A.; Dickson, B. L. 1976. Mössbauer effect studies of beryl. *Journal de Physique*, C6: 811-817.
- Wood, D. L. & Nassau, K. 1968. The characterization of beryl and emerald by visible and infrared absorption spectroscopy. *American Mineralogist*, 53:777-800

Topaz of Papachacra, Catamarca, Argentina: Mineralogical Description

J.C.Ávila

CONICET, Facultad de Ciencias Naturales, Universidad de Tucumán, Argentina

A.S.Fogliata

Facultad de Ciencias Naturales, Universidad de Tucumán, Argentina

G.Mas

CONICET; Departamento de Geología, Universidad del Sur, Argentina

ABSTRACT: Topaz mineralization in Piedra Calzada minesite is hosted near the contact between metamorphic rocks of Precambrian Eocambrian age and Paleozoic granitoids. Topaz occurs in crystals and veinlets associated to quartz, muscovite, fluorite, columbite and limonite. They are yellow to colorless prismatic crystals with ending bipyramidal. Topaz contains fluid inclusions with variable size. They are mainly two (L+V) and three (L+S+V) phase inclusions, and as a whole they homogenized in liquid phase, although frequently near the critical point at temperatures between 370° and 420°C.

1 INTRODUCTION

The studied area Piedra Calzada minesite is located in the east slope of Sierra de Papachacra, approximately 3 km south from the Papachacra locality in the regional setting of Sierras Pampeanas Occidental, province of Catamarca, Argentina. The geographical coordinates are 27°01'27''S and 66°53'51''W (Fig.1).

2 GEOLOGICAL SETTING

The geology of the area is characterized by metamorphic and granitic rocks. Metamorphic rocks are metasedimentites of Loma Corral Formation. They are dark grey schists, quartzites, gneises and phyllites striking NE and plunging 30°O to 80°E. They have granoblastic texture and are composed by quartz, biotite, muscovite and plagioclase. Loma Colorada Formation is inferred to be Precambrian- Early Paleozoic (Aceñolaza & Toselli 1981).

Granitic rocks, mainly medium grained and light yellow monzogranites, belongs to Papachacra Formation. They have grainy hypidiomorphic texture and are composed by quartz, perthitic potash

feldspar, sodium plagioclase, biotite, muscovite, apatite, zircon and opaque. Geochemical and petrographical data show that they are peraluminous, evolved and postorogenic. Papachacra Formation is inferred to have carboniferous age (Lazarte 1991).

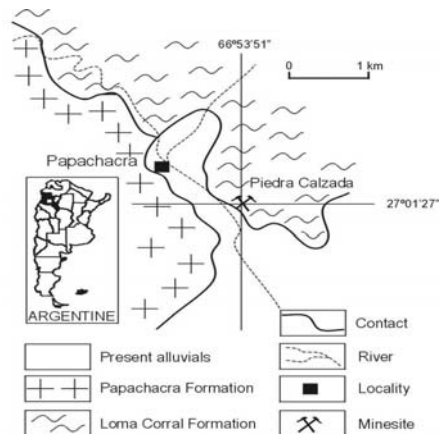


Figure 1. Simplified geologic map showing the location of Piedra Calzada Topaz mine (modified from Avila y Porto 1982).

3 TOPAZ MINERALIZATION

Topaz mineralization occurs near the contact of metamorphites with granites. Wall-rock alteration of the granite adjacent to the metamorphites is greisenization, characterized by an assemblage which consists mainly of quartz and muscovite with minor amount of fluorite and topaz and scarce columbite. Brecciated sectors are often by clast of the metamorphites and granite.

Outcrops are mined by surficial methods. Topaz is recovered by artisanal process and selected specimens have been cutted in foreign countries. The size range of the faceted stone varies from 0.4 cm to 1 cm.

3.1 Mineralogy

Topaz crystals have been examined by optic microscopy, XRD and fluid inclusions study. Topaz appears in crystals and veinlets associated to quartz, muscovite, fluorite, columbite and limonite. Crystals are mainly transparent of yellow color to colorless, with vitreous to translucent shine. Their size varies from 0,2 cm and 2,5 cm. The density is about 3,4. Often found in short to long prismatic crystals, sometimes with characteristics terminal faces. They are prismatic crystals with ending bipyramide. They have perfect cleavage {001} and have columnar habitus and crystalline striated face. Microscopic characteristic are: colorless, refractive indices near to each other n_x 1.610, low birrefringence, first order gray.

XRD patterns show that the samples corresponds to ICDD topaz card. It is almost pure of F⁻ with minimal substitution of OH⁻ (Fig.2).

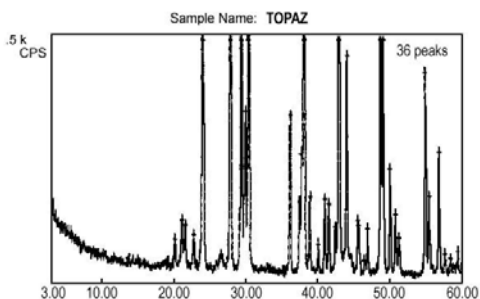


Figure 2. X-ray diffraction pattern of topaz, Piedra Calzada.

3.2 Fluid Inclusions

Topaz contains numerous fluid inclusions with variable size from 5 to 150 μ . Two types of fluid inclusions have been recognized based on their appearance at room temperature: two phases

inclusions (L+V) and three phases inclusion (L+V+S).

-Two phases inclusions: they are the most abundant and can be divided in three different groups (II₁, II₂ y II₃) characterized by their form, relation liquid-vapour and size.

II₁: liquid rich, with liquid vapour ratio range from 8:2 to 9:1. Are small, about 20-30 μ in size, with regular shapes. They have negative crystal shapes and have isolated occurrence. II₂: with liquid vapour ratio about 6:4. They are big, lengthened and occur in clusters aligned in trains parallels to the c crystallographic axis of the crystal. They homogenized in liquid phase, although frequently near the critical point.

Both groups show almost the same salinity, about 16 to 18 wt% NaCl eq. Homogenization temperatures vary between 370°C and 420°C (Fig.3).

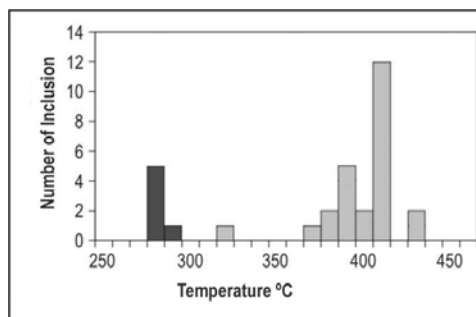


Figure 3. Homogenisation temperature of fluid inclusions of topaz, Piedra Calzada. Black: II₃ ; Gray: II₁ , II₂.

II₃: very small inclusions with liquid vapour ratio 9:1. Homogenization temperatures vary between 270°C and 300°C which means that this group would correspond to a late fluid.

-Three phases inclusions: they are scarce. The solid phase is halite. Show salinity about 40wt% NaCl eq. Homogenization temperatures about 400°C, after crystal solution which means that the solution is saturated after trapping temperature of the fluid.

4 CONCLUSIONS

The mineral assemblage (quartz, muscovite, topaz, fluorite, and columbite) and fluid inclusions thermometry suggests that Piedra Calzada is an hydrothermal high temperature deposit.

Mineralogical characteristic and occurrence suggest that crystal topaz from Piedra Calzada deposit could be used as gems of medium value.

5 ACKNOWLEDGEMENTS

The authors would like to express their gratitude to Tucumán University, South University and The National Investigation Council for the support in the realization of the present work.

6 REFERENCES

- Aceñolaza, F.G. & Toselli, A.J. 1981. Geología del noroeste argentino. Publicacion Especial, Facultad de Ciencias Naturales, U.N.T. n°1287 pp 1-212.
- Avila, J.C. & Porto, J.C. 1982. Presencia de topacio en el contacto granito-basamento del área de Papachacra, provincia de Catamarca. Acta Geológica Lilloana XVI 1:215-220.
- Lazarte, J.E. 1991. Estudio petrológico y geoquímico de los granitoides de las sierras de Papachacra y Culampajá. Relaciones metalogenéticas. Facultad Ciencias Naturales e Instituto Miguel Lillo, U.N.T. Tesis Doctoral (inédito) 275 pp.

Nanocrystals of Tridymite in Opal Cavities

V.Bermanec & N.Tomašić

Institute of Mineralogy and Petrography, Faculty of Science, University of Zagreb, Horvatovac bb, 10000 Zagreb, Croatia

J.Karfunkel & R.Scholz

Instituto de Geociências, Universidade Federal de Minas Gerais, Brazil

G.Kniewald

Center for Marine and Environmental Research, Rudjer Boskovic Institute, POB 180, 10002 Zagreb, Croatia

H.Jaksch

LEO Elektronenmikroskopie GmbH, Carl-Zeiss-Straße 56, 73447 Oberkochen, Germany

ABSTRACT: Two opal samples were investigated by X-Ray diffraction and FESEM. Green opal from Goleš ultramafic rocks was designated as opal-CT. Reddish opal from the Spančevski rid sedimentary sequence was also determined as opal-CT, although it could be considered as a boundary case with opal-C. Both opals contain other mineral phases like sepiolite or kaolinite and hematite. FESEM images showed on both opal samples the presence of cavities filled with spheres. The spheres are covered with hexagonally shaped crystals presumably being tridymite. Common morphological properties of the low and high temperature forms of tridymite cannot unambiguously confirm the high temperature hydrothermal stage in the formation of the investigated opal-tridymite association.

1 INTRODUCTION

Opal is a mineral substance frequently showing a range of properties and specimen-specific variations. Therefore, its thorough characterization is essential not only for the material recognition, the interpretation of origin, but also for its evaluation.

Two opal samples, one originating from Goleš, Kosovo (Serbia and Montenegro) and another from Spančevski rid, Macedonia, were investigated. Opal from Goleš is pale green with vitreous luster and associated with ultramafic rocks. White opal with dull lustre was found in a sedimentary sequence in Spančevski rid, probably of lacustrine provenance, and is somewhere red tinted due to hematite inclusions. Both opal samples show characteristic conchoidal fracture. The geological setting of both localities in terms of opal formation has not been described in detail yet.

2 EXPERIMENTAL

The X-Ray diffraction data for both opals were collected by Philips X'Pert PRO powder diffractometer using CuK α radiation excited by 45 kV and 40 mA. The opal samples were mounted

with silicon disk into the sample spinner to improve signal to noise ratio as well as counting statistics.

SEM images were obtained on a Gemini Supra 55 VP LEO FESEM system. Field emission SEM (FESEM) enables high resolution images obtained by low accelerating voltages, in this case 1.34 kV. Therefore, the charging of an investigated material is minimized and there is no need for sample coating what eliminates charging artifacts. The high resolution imaging is additionally improved by the application of InLens detection. InLens secondary electron detection is characterized by an ultra high resolution and precise imaging with low energy electron beam, thus being suitable for the investigation of nano-scale crystals.

3 RESULTS AND DISCUSSION

The investigated opal samples show signatures of both opal-C and opal-CT. However, the diffraction line at approximately 4 Å appears in the case of Goleš opal at 4.11 Å, what designates it as opal-CT (Elzea et al. 1994). The opal from Spančevski rid with the same line at 4.07 Å could be also treated as opal-CT following the same criterion, although it is very close to the boundary with opal-C.

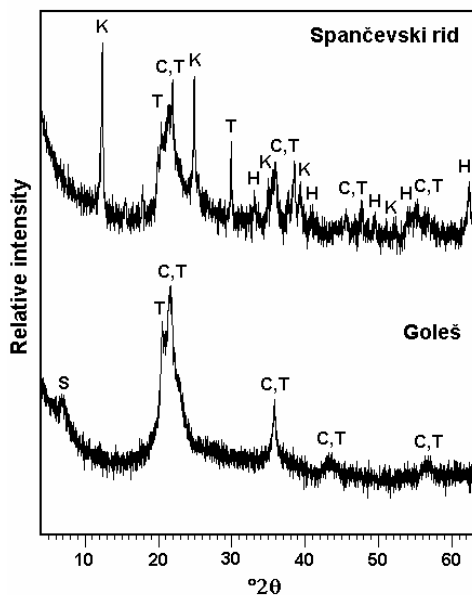


Figure 1. Diffraction patterns of opal from Goleš and Spančevski rid with peak identification (C – cristobalite, T – tridymite, S – sepiolite, H – hematite, K – kaolinite).

Along with opal, the diffraction patterns also indicate the presence of other mineral phases (Fig. 1). Sepiolite is present in the case of Goleš opal. The association of Goleš opal with ultramafic rocks suggests sepiolite to be the product of their hydrothermal alteration (Bonatti et al. 1983, Muthuraman 1986) rather than to be directly precipitated from the solutions enriched in Mg (Ispording 1973). On the other hand, kaolinite and hematite are found in the opal from Spančevski rid, the latter being responsible for its local reddish appearance. These inclusions seem to be very finely intergrown with opal and are not very likely to be separated from the opal matrix. Such an association has been already reported as a product of hydrothermal alteration of rhyolitic ignimbrite (Henneberger & Browne 1988).

SEM analysis was performed in order to explore micro-features of the investigated opals since it was found to be very important in the general opal description. Both opals show properties of so called lepidospheric textures (Esenli et al. 2003). Namely, spheres of less than 10 μm are found in the cavities on the opal surface (Fig. 2). The spheres are connected in clusters and there are tens of them in each cavity. At higher magnification the tiny plates covering the surface of the spheres become visible (Fig. 3). The plates are rather equal in size, approximately 0.5-1 μm in diameter and are tens of

nanometers thick. Some plates clearly exhibit hexagonal morphology and according to their habit they could be recognized as tridymite (Fron del 1962). In the case of green opal from Goleš a few surface fractures contain only a few spheres but then, these are significantly larger than those arranged in clusters. However, they are again covered with the plates seemingly belonging to tridymite. Such an occurrence of opal spheres covered with tridymite crystals indicates two-stage formation. This is probably caused by an oscillation or change of crystallization conditions. The hexagonal habit of the tridymite crystals suggests them to be high-tridymite although low temperature forms are known to be pseudomorphs after the high temperature form (Fron del 1962). Low-high tridymite transformation starts at 110°C and high temperature hexagonal phase is stable above 380°C (Nukui et al. 1978), however common morphological properties of different tridymite phases cannot directly imply a role of high temperature hydrothermal solutions in the formation of this opal-tridymite association. Unfortunately, X-ray diffraction pattern do not show sufficient diagnostic features that would differentiate low and high tridymite modifications, what is additionally emphasized by the presence of other phases in the opal samples.

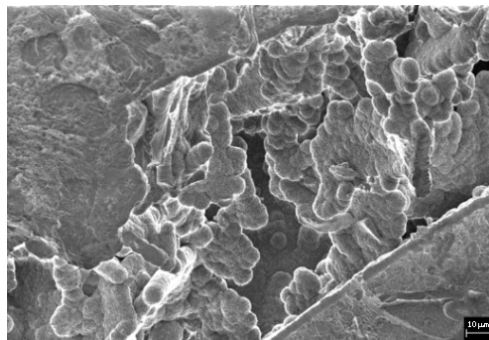


Figure 2. SEM image of the Spančevski rid opal showing a cavity filled with spheres.

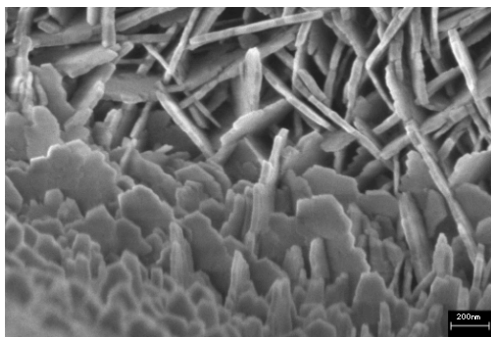


Figure 3. SEM image of the Goleš opal with tridymite crystals covering a sphere in a cavity.

4 CONCLUSIONS

Using FESEM at low accelerating voltages it is possible to observe tridymite crystals in nano-scale range and thus confirm their presence inferred by X-Ray diffraction patterns. The crystals are well-shaped with hexagonal habit and cover the spheres situated in cavities of the investigated opals. These findings indicate that both opals have suffered at least two stages of formation. However, hexagonal habit of the tridymite crystals observed is characteristic for both hexagonal high temperature form and other lower temperature tridymite modifications, and thus is not strongly indicative for a participation of high temperature hydrothermal solutions in the formation of this opal-tridymite association.

The work shows the opal nano-features being potentially important in the material evaluation and handling. Also, employing FESEM in characterization of opals proves to be advantageous.

5 REFERENCES

- Bonatti, E., Simmons, E. C., Breger, D., Hamlyn, P. R., Lawrence, J. (1983). Ultramafic rock seawater interaction in the oceanic crust: Mg-silicate (sepiolite) deposit from the Indian Ocean floor. *Earth and Planetary Science Letters*, 67(2), 229-238
- Elzea, J. M., Odom, I. E., Miles, W. J. 1994. Distinguishing well ordered opal-CT and opal-C from high temperature cristobalite by x-ray diffraction. *Analytica Chimica Acta* 286(1): 107-116
- Esenli, F, Kumbasar, I., Esenli, V., Kirikoglu, S. 2003. A study on the characteristics of some opals from Turkey. *Neues Jahrbuch für Mineralogie – Monatshefte* 2003(4): 177-192
- Fron del, C. 1962. The System of Mineralogy. Vol. III, 7th edition, John Wiley & Sons, New York
- Henneberger, R. C. & Browne, P. R. L. 1988. Hydrothermal alteration and evolution of the Ohakuri hydrothermal system, Taupo volcanic zone, New Zealand. *Journal of Volcanology and Geothermal Research* 34(3-4): 211-231
- Ispording, W. C. 1973. Discussion of the occurrence and origin of sedimentary palygorskite-sepiolite deposits. *Clays and Clay minerals* 21(5): 391-401
- Muthuraman, K. (1986). Sea water-basalt interactions and genesis of the coastal thermal waters of Maharashtra, India. *Geothermics* 15(5-6): 689-703
- Nukui, A., Nakazawa, H., Akao, M. 1978. Thermal changes in monoclinic tridymite. *American Mineralogist* 63:1252-1259

Gemological and *In-Situ* Chemical Analyses of Emeralds from Vigezzo Valley (Italy) and other World-wide Occurrences

M.Boiocchi

Centro Grandi Strumenti and Department of Earth Science, University of Pavia, Pavia, Italy

F.Caucia

Department of Earth Science, University of Pavia, Pavia, Italy

A.Zanetti

IGG-CNR, Section of Pavia, Pavia, Italy

ABSTRACT: Complete gemological analyses have been carried out on cut gems from Vigezzo Valley (Italy), El Chivor and Muzo (Colombia), Carnaiba and S. Terezinha (Brazil), Irondro and Malakialina (Madagascar), Takovaya (Russia), Miku (Zambia), Habachtal (Austria). The results of this study are reported in gemological cards. Unit-cell edges determination has been obtained by single crystal X-ray diffraction analysis, whereas LA-ICP-MS analyses have been performed to determine the Al_2O_3 content, along with that of other relevant minor and trace elements. Among the samples object of this study, the best "emerald green" tonality is shown by the gems from El Chivor and Carnaiba likely due to their Cr- and V-rich composition (ppm level). The amount of Al_2O_3 is variable and inversely related to the abundance of minor elements, such as MgO and FeO. Nevertheless, the Al_2O_3 chemical variability does not seem to influence the colour of gems. For example, El Chivor emeralds show a high chemical purity while Carnaiba samples show a greater amount of minor and trace content. Vigezzo Valley materials, as beryl crystals from other European occurrences, show a fairly good gem quality. In particular, they are characterised by a pale green-bluish colour that is likely due to the extremely low content in V and Cr, associated to appreciable Fe amount.

1 INTRODUCTION

Green beryl samples were found near Pizzo Marcio and Alpe Rosso, Vigezzo Valley, Northwestern Italian Alps. In the seventies, these localities were important mining areas for green beryl (emerald variety), which occurred in albitic veins and mica-schist rocks (Appiani et al. 1995). Nowadays, gem quality samples are rare and this area is not economically important. Only collectors or mineralogists are interested in samples from this locality, because of the good morphology of emerald crystals, a peculiarity of this area among the Italian deposits.

During the summer of the 2003, a new sampling was carried out in the Vigezzo Valley that allowed us to collect various morphologically-perfect beryl crystals. However, only a very little number of crystals showed optical quality suitable to give reason to cut facets to obtain emerald gems.

Cut gems were subjected to complete gemological investigations and their optical and physical properties are reported in gemological cards. Small fragments of the residual rough material were used to select beryl single crystals for unit-cell edge determination (by means of single crystal X-ray diffraction). Moreover, with the aim to

characterise the relation between the minor and trace element concentration and the gemological quality of beryl crystals, other fragments were picked up for chemical analysis by Laser Ablation - Inductively Coupled Plasma - Mass Spectrometer (LA-ICP-MS). In particular, this analysis has allowed the determination of the Al_2O_3 content, along with that of relevant minor and trace elements (e.g., Na_2O , MgO, FeO, Cr_2O_3 , V_2O_5 and TiO_2).

Gemological, X-ray diffraction and *in-situ* chemical analyses have been also carried out on emerald samples from other world-wide mining areas (El Chivor and Muzo, Colombia; Carnaiba and S. Terezinha, Brazil; Irondro and Malakialina, Madagascar; Miku, Zambia; Takovaya, Russia; Habachtal, Austria) and their characteristics have been discussed in comparison with those of Italian samples.

2 EXPERIMENTAL

2.1 Gemological investigation

Morphology, inclusions and optical properties were evaluated by means of a gemological optical microscope (A. Kruss Optronic) equipped with devices to measure size of gems and birefringence,

Table 1: Unit-cell edges (Å), volume (Å³), c/a ratio, measured density (g cm⁻³) and refractive indexes of beryl samples.

Locality	<i>a</i>	<i>c</i>	<i>c/a</i>	<i>V</i>	ρ	ω	ϵ
Vigezzo Valley - Italy	9.257(1)	9.201(1)	0.994	682.82	2.74	1.591	1.583
Muzo-Colombia	9.220(1)	9.189(1)	0.997	676.49	2.71	1.580	1.570
El Chivor-Colombia	9.219(1)	9.192(1)	0.997	676.56	2.69	1.579	1.570
Carnaiba-Brazil	9.263(1)	9.196(1)	0.993	683.33	2.72	1.588	1.583
S. Terezinha-Brazil	9.226(1)	9.192(1)	0.996	677.59	2.69	1.588	1.580
Irondro-Madagascar	9.241(1)	9.203(1)	0.996	680.61	2.73	1.584	1.582
Malakialina-Madagascar	9.237(1)	9.190(1)	0.995	679.06	2.72	1.587	1.582
Miku-Zambia	9.274(1)	9.199(1)	0.992	685.18	2.77	1.602	1.592
Takovaya-Russia	9.243(1)	9.235(1)	0.999	683.27	2.74	1.588	1.580
Habachtal -Austria	9.249(1)	9.200(1)	0.995	681.57	2.73	1.591	1.584

reflection indexes, dichroism, fluorescence and visible absorption. Weight was measured using a hydrostatic balance.

2.2 X-ray diffraction

Selected beryl single crystals were analysed on a Philips PW-1100 four-circle diffractometer (graphite-monochromatized Mo-K α X-radiation). Hexagonal unit-cell edges were obtained from least-square refinement of the *d* values obtained for 60 rows of the reciprocal lattice by measuring the barycentre of each reflection and of the corresponding antireflection in the 2 θ -range -60 < 2 θ < 60°.

2.3 LA-ICP-MS microprobe

Beryl fragments were mounted on epoxy resin, polished and analysed by LA-ICP-MS. Operating conditions were as follows: 213 nm laser wavelength, 10 Hz laser repetition rate, 40-50 μ m spot diameter. The ablated material was analysed with a double-focusing sector-field ICP-SFMS model Element 1, ThermoFinnigan Mat (Bremen, Germany). Quantification was done by using SiO₂ (stoichiometric value) as internal standard and NIST SRM 610 synthetic glass as external standard. Precision and accuracy were estimated by analysis of BCR-2 standard and resulted better than 5 and 10%, respectively.

3 DISCUSSION

Gemological investigation has shown the presence of a high amount of lamellar inclusions (micas), fluid inclusions and fractures in the Italian beryl crystals. Refractive index and density are reported in Table 1 (where the unit-cell parameters are also shown) and compared with the values of other gems. The colour of Italian materials is a pale green variable from bluish to yellowish green and it is very similar to Russian and Austrian gems (as well as refractive index and density).

Brazilian emeralds are deep brilliant green in colour and characterised by different types of

inclusions, e.g. biphasic fluid-gas inclusions (Leone 1993) and crystalline inclusions. Colombian gems show typical triphase inclusions (solid-fluid-gas), crystalline inclusions and colour zoning. The transparency is very good and the colour is a deep velvet green. Miku emeralds are characterised by mineral inclusions (schorl black tourmaline) that produce a deep bluish green colour. Habachtal gems show a pale bluish green colour due to glaucophanic inclusions. Gems from Madagascar have a good green colour and transparency even if crystalline inclusions are present.

Optical spectroscopy shows that absorption at 690 nm (red) characterises Brazilian and Colombian gems, while absorption at 400-510 nm and 590-620 nm occur in all gems with the exception of Italian emeralds.

Unit-cell edge of analysed samples are reported in Table 1. The *c/a* ratio ranges from 0.992 to 0.999 and it is inversely related to the *a* unit-cell edge (Fig.1).

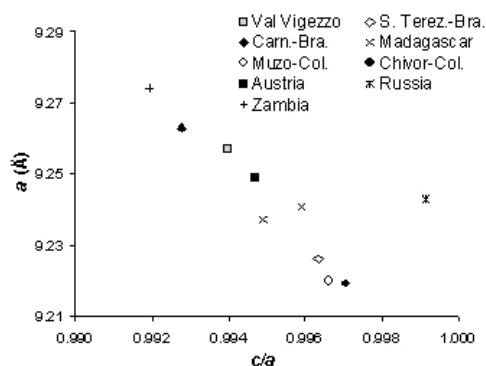


Figure 1: Unit-cell edge *a* versus *c/a* ratio for beryl crystals.

Both these behaviours correspond to octahedral substituted beryl (Auriscchio et al. 1988), i.e., beryl crystals in which the Al octahedron hosts a little and variable amount of divalent cations.

In-situ chemical analyses (Fig. 2) show the inverse relation between the Al₂O₃ content and the

amount of other less abundant oxides (i.e., excluding alkali ions: MgO + FeO). This suggests that these cations are vicarious of aluminium in the octahedral Al-site of beryl. The deficiency of positive charge resulting from the replacement of Al by cation of lower valence (Mg and Fe²⁺) is generally balanced by alkali cations in the void channels of the beryl structure. Actually, in the analysed samples, the amount of Na₂O is linearly related to the sum of the other less abundant oxides (Fig. 3). On the whole, El Chivor emeralds show the largest chemical purity, with Na₂O and MgO content less than 1 wt%. A slightly higher amount of these elements results in the sample from S. Terezinha, while the other specimens are characterised by a greater amount of alkali, MgO and other minor elements (~ 4 wt%).

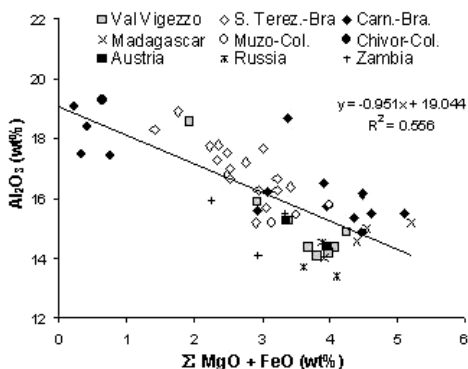


Figure 2: Al₂O₃ content versus the sum MgO + FeO obtained from LA-ICP-MS analysis.

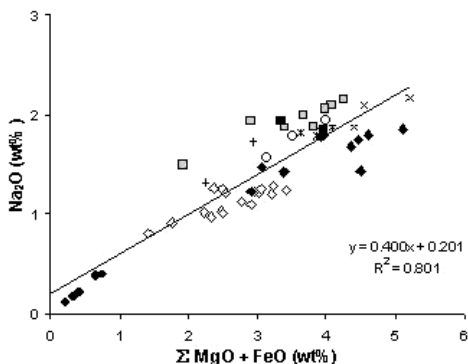


Figure 3: Na₂O content versus the sum MgO + FeO obtained from LA-ICP-MS analysis. Symbols are the same as in Fig. 2.

Chromium and vanadium are assumed as chromophore of emerald. In our samples, the amount

of these trace elements are variable (Fig. 4), but it is actually higher in emeralds with most intense green colour. In particular, gems of the same deep green colour are rich in V at El Chivor, rich in Cr at Carnaiba, rich both in V and Cr in the Madagascan mines. Italian emeralds are poor in these elements and, as other European gems (Austrian and Russian), do not show a deep green emerald tonality.

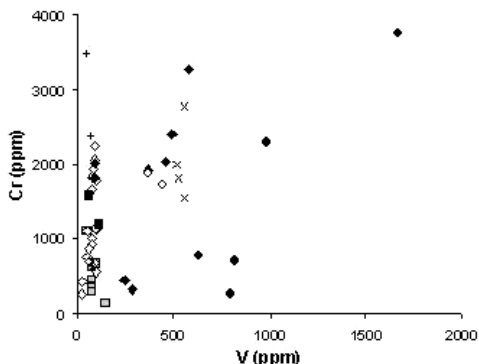


Figure 4: Content of Cr versus V (ppm level) in beryl samples. Symbols are the same as in Fig. 2.

Ti content is low and rather similar in all the analysed samples, whereas a low Fe content characterises the gems from El Chivor (Fig. 5). The other samples are more rich in Fe and the presence of this element is probably the reason for the bluish tonality of the gems poor in Cr or V (as European beryl).

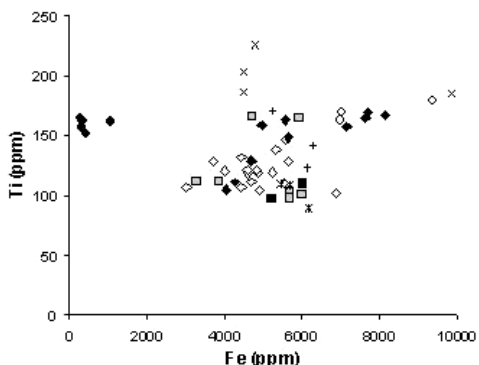


Figure 5: Content of Ti versus Fe (ppm level) in beryl samples. Symbols are the same as in Fig. 2.

4 CONCLUSIONS

The results of gemological, single-crystal X-ray diffraction and *in-situ* chemical analysis of emeralds from Italy and from several world-wide occurrences are shown. Gem quality emeralds occur in all the investigated mining areas. The quality of gems does not result strictly related to the presence of octahedral substitution. Actually, the substitution of Al for divalent cations (Mg and Fe²⁺) is detected with variable amount in the investigated gems without relations with the gem colour.

As far as the trace content is concerned, Italian emeralds are poor in Cr and V and for this reason they do not show a deep green colour. However, Italian materials result slightly rich in Fe and this, very likely, produces the light green-bluish tonality characteristic of these gems.

The best emeralds are that coming from Colombian and Brazilian mines, in which occur gems of intense and homogeneous green colour, with a low number of inclusions. However, also among Italian materials occur fairly good gem quality samples, that result in intermediate terms between the emerald and the aquamarine variety.

5 REFERENCES

- Appiani, R., Cini, V., Gentile, P., Mattioli, V., Preite, D., Vignola, P. 1995. *Val Vigizzo – I Minerali delle Albititi*. 300 pp., Edizioni Linea Due, Milano.
- Aurischio, C., Fioravanti, G., Grubessi, O., Zanazzi, P.F. 1988. Reappraisal of the crystal chemistry of beryl. *Am. Mineral.*, 73, 826-837.
- Leone, A. 1993. Giacimenti di smeraldo e relative inclusioni. *Scienze delle Gemme*, 2, 15-24.

A Geological Model of Angolan Diamond Populations

L.Chambel

CVRM – Centro de Geo-sistemas, Instituto Superior Técnico, Universidade Técnica de Lisboa, Lisboa, Portugal

A.Diogo Pinto

Laboratório de Geologia Aplicada, Instituto Superior Técnico, Universidade Técnica de Lisboa, Lisboa, Portugal

M.Chaves

Instituto de Geociências, Universidade Federal de Minas Gerais, Belo Horizonte, Brazil

M.Cardoso

ISCTE – Instituto Superior de Ciências do Trabalho e da Empresa, Lisboa, Portugal

ABSTRACT: This paper's objective is to describe the properties of Angolan diamond deposits namely in what concerns their geological setting and diamond populations and to study the relationship between diamond populations' characteristics and their deposits' location. The exploration for new deposits is a practical consequence of this project's results. The data used in this project consists of information concerning the classification of over five hundred separate diamond parcels. The analysis performed on the available data (22,054 diamonds from 66 Angolan diamond deposits, based on the joint color-clarity categories relative frequencies) suggests the existence of five diamond population types in the studied deposits. Two unequal size types account for more than 80% of the cases, the other three being very subordinate in importance. The color factor seems to be more important than clarity in the clusters' definition, an observation that agrees with results obtained in exploratory work done with K-means (not presented here). The results obtained suggest the directing further investigation into the joint use of all diamond classification factors in connection with geographical and geological variables.

1 INTRODUCTION AND OBJECTIVES

Angolan diamond deposits are among the world's richest due to their mining characteristics and to their diamonds' unit value. At present, diamonds are the second most important mineral resource in Angola (after oil). Numerous foreign and Angolan companies are now exploring for, developing and operating diamond mines.

Angola's main diamond-producing region is located in the Lundas provinces - NE Angola.

Different diamond deposits are characterized by specific properties of the populations of their diamonds – Figure 1 and Figure 2 for examples of different grain size distributions. This fact can be used in diamond exploration, trade control and marketing. Although recognized a long time ago, those relationships have always had an empirical and subjective character.

5.1 Objective

This paper's objective is to describe the properties of Angolan diamond deposits namely in what concerns their geological setting and diamond populations and to study the relationship between diamond populations' characteristics and their deposits'

location. The exploration for new deposits is a practical consequence of this project's results.

2 ANGOLAN DIAMOND GEOLOGY

With a surface of a little over 1 M km², Angola has a complex geology, subject of (Carvalho 1983), (Nunes 1991) and (Sínese 1998).

Angolan mineral deposits are varied and include iron, gold, copper, phosphates, underground water and natural stone, just to name a few (Gouveia et al. 1992). However, it's carbon-based substances (oil and diamonds) that constitute the backbone of a reviving mineral industry.

Angolan diamond deposits have either a primary or a secondary nature – Table 1. Diamonds have been found in most of the Angolan river basins although the largest and richest deposits are concentrated in the Lundas region (NE Angola). They are described in (Monforte 1988a,b,c), (Chambel 2000) and elsewhere.

2.1 Primary deposits

Of the 700+ Angolan kimberlites some are world class deposits, namely the Catoca (in production,

>1Mct/y) and Camafuca-Camazambo (Real 1958), (Real 1959) and (Reis & Aires-Barros 1981). The Camútúè kimberlite, although with lower reserves, has high-quality diamonds. Other kimberlites, like Camatchia, Camagico and others where diamonds are known to occur, are in different stages of the deposit evaluation to mine implementation process.

Table 1. Angolan diamond formations stratigraphic position.

Surface formations		Holocene to Upper Pliocenic	
Coverage terrains	Kalahari System	Lower Pliocenic to Eocenic	
	Calonda Formation	Middle to Upper Cretacic	
		Kimberlite eruption	Middle Cretacic
	Intercalar Continental System	Upper Jurassic to Lower Cretacic	
	Karoo System	Cassange Series Lutõe Series	Recian to Upper Carbonic
Bedrock terrains	Luana Group	Cartuchi-Camaungo Formation Luana Formation	Upper Precambrian
	Metamorphic Series of NE Angola (formerly Kibaras System)	Upper Series Lower Series	
	Metasedimentar Complex (?)	Middle	
	Base Complex	Upper System	Lower
		Lower System	

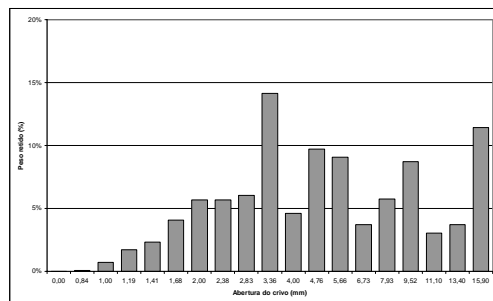


Figure 1. Diamond size distribution of the Camútúè kimberlite (Angola).

Angolan kimberlitic structures can be classified into six (Gouveia et al. 1992) or seven (Reis & Aires-Barros 1980) groups (*provinces*, according to both authors), the most important of which is, in economical terms, the Northern Lunda group, which occupies (approximately) the basins of the Luachimo and Chicapa rivers. It can be subdivided on geostructural criteria into four subgroups: Camútúè - (Monforte 1960), (Menezes 1973a), (Menezes 1973b), (Menezes 1974a), (Reis & Monforte 1981) - Calonda, Camatchia - (Menezes

1974a) and (Menezes 1974b) - e Lôva. Over sixty kimberlitic occurrences were mapped in this group.

2.2 Secondary deposits

Angolan alluvial deposits' diamonds constitute the bulk of the production in Angola and represent a large fraction of the existing reserves. The Chumbe, Luembe, Luachimo and Chicapa rivers' deposits are the most important, only surpassed by Cuango River's. It is also important to note that the Calonda Formation conglomerates have an increasingly important role in secondary deposits mining.

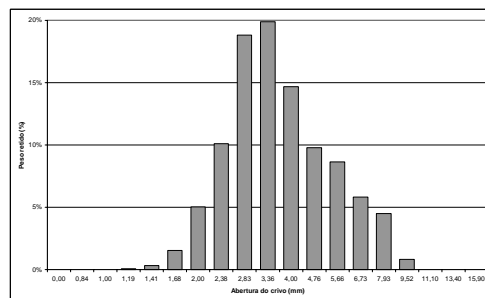


Figure 2 - Diamond size distribution of an alluvial deposit in Angola.

According to (Monforte 1988b), the Angolan secondary deposits can be classified into two major groups:

A- Deposits independent of the present hydrographic network:

- Calonda Formation deposits.
- Planalts gravel beds.
- Elluvial (slope) deposits.

B- Deposits related with the present hydrographic regime, in its old or recent activity:

1. In relation with rivers' old activity:
 - Terrace deposits.
 - Alluvial plain deposits.
2. In direct and immediate relation with the present activity of rivers:
 - River bank/island deposits.
 - River bottom deposits.

3 METHODOLOGICAL APPROACH

The data used in this project consists of information concerning the classification of over five hundred separate diamond parcels (one hundred and thirty five different Angolan diamond deposits and occurrences).

Each deposit is characterized by a sample of diamonds with octahedral morphology. The

samples' diamonds are classified into three (decreasing quality and unit value) color (A, B, C) and clarity levels (1, 2, 3) – Table 2.

Each diamond deposit or occurrence has thus an associated table with the joint color-clarity relative frequencies.

Table 2 - Used variables.

Used variables		Colour level		
		A	B	C
Clarity level	1	A1	A2	A3
	2	B1	B2	B3
	3	C1	C2	C3

3.1 Analysis techniques

A mixture model is adopted to perform the diamond deposits clustering. LATENT GOLD (Magidson & Vermunt 2000) is used for estimation. The flexibility of this type of approach makes it able to deal with the complexity of real problems considering multivariate and mixed bases for clustering modeled by appropriate (in our case normal) distributions. It also provides criteria to deal with the selection of the number of segments.

The number of clusters to use in the model is one of the crucial choices: too many groups turn the results difficult to interpret; too few make the model less useful. In the particular case of this application, unlike other type of clustering applications, there is a special interest in finding exotic groups (even if with a small size) of deposits given its possible link to unknown primary sources. LATENT GOLD identifies an appropriate number of clusters via the traditional Information Theory measures, e.g. AIC and BIC based on log-likelihood (Magidson & Vermunt 2000) – Figure 3 for the application of these criteria in this problem.

4 RESULTS OBTAINED

Table 3 presents the profile (average proportion of diamonds in each color-clarity class) of the five groups defined in the analysis. Table 4 is designed to assist the results' interpretation by comparing each group's profile with the global sample profile (proportions ratio).

The defined deposit clusters are:

- Cluster 1: the largest cluster, corresponding to 41 (62% of total) deposits – Table 3. It's

- characterized by concentration in the A and depletion in the C color categories, in comparison with the global sample – Table 4.
- Cluster 2: the second largest cluster, corresponding to 14 (21%) of total deposits. Depletion in A and B and concentration in C categories characterize it.
- Cluster 3: 5 (8%) of the deposits. It's characterized by concentration in the B3 and C3 and depletion in the A, C1 and C2 categories
- Cluster 4: 4 (6%) of the deposits. It's characterized by concentration in the B2, C1 and C3 and depletion in the A color-clarity categories.
- Cluster 5: 2 (3%) of the deposits. It's characterized by (strong) concentration in the C and (very strong) depletion in the A and B color-clarity categories.

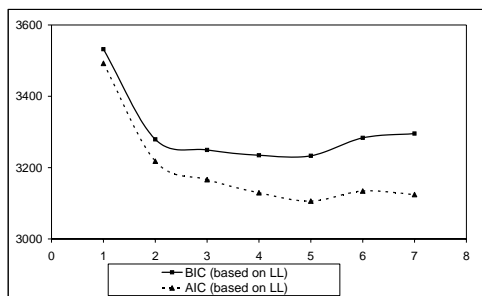


Figure 3 – Determination of the number of groups – BIC and AIC criteria.

Table 3 - Clusters' means profiles.

	Cluster 1	Cluster 2	Cluster 3	Cluster 4	Cluster 5
Size	61,4%	21,0%	7,9%	6,5%	3,3%
	41	14	5	4	2
A1	5,58%	1,67%	3,44%	2,53%	0,44%
A2	13,96%	4,98%	6,24%	5,04%	1,67%
A3	12,19%	5,46%	3,71%	7,68%	2,00%
B1	9,21%	7,87%	9,11%	9,32%	5,94%
B2	23,37%	17,85%	21,14%	28,78%	10,15%
B3	25,01%	22,55%	39,41%	24,06%	15,34%
C1	1,53%	6,73%	1,30%	3,90%	9,32%
C2	4,16%	17,39%	5,42%	8,62%	25,71%
C3	4,82%	15,49%	10,23%	10,07%	29,44%
A	31,73%	12,12%	13,38%	15,26%	4,11%
B	57,60%	48,27%	69,66%	62,16%	31,42%
C	10,51%	39,62%	16,96%	22,59%	64,47%
1	16,33%	16,27%	13,85%	15,75%	15,70%
2	41,50%	40,23%	32,80%	42,43%	37,53%
3	42,02%	43,50%	53,35%	41,82%	46,78%

Table 4 - Clusters' concentration analysis.

	Global average	Cluster1	Cluster2	Cluster3	Cluster4	Cluster5
		Concentration				
A1	4,23%	1,32	0,40	0,81	0,60	0,11
A2	10,49%	1,33	0,47	0,59	0,48	0,16
A3	9,48%	1,29	0,58	0,39	0,81	0,21
B1	8,82%	1,04	0,89	1,03	1,06	0,67
B2	21,95%	1,06	0,81	0,96	1,31	0,46
B3	25,25%	0,99	0,89	1,56	0,95	0,61
C1	3,01%	0,51	2,23	0,43	1,29	3,09
C2	8,03%	0,52	2,17	0,68	1,07	3,20
C3	8,63%	0,56	1,80	1,19	1,17	3,41
A	24,20%	1,31	0,50	0,55	0,63	0,17
B	56,02%	1,03	0,86	1,24	1,11	0,56
C	19,67%	0,53	2,01	0,86	1,15	3,28
1	16,06%	1,02	1,01	0,86	0,98	0,98
2	40,47%	1,03	0,99	0,81	1,05	0,93
3	43,36%	0,97	1,00	1,23	0,96	1,08

5 CONCLUSIONS

The analysis performed on the available data (22,054 *Stone* type diamonds from 66 Angolan diamond deposits, based on the joint color-clarity categories relative frequencies) suggests:

- The existence of five diamond population types in the studied deposits. Two unequal size types account for more than 80% of the cases, the other three being very subordinate in importance. All groups including the later, more exotic, groups should be considered as candidates for further analysis aiming to relate their characteristics, location and genetical processes.
- The color factor seems to be more important in the clusters' definition than clarity, an observation that agrees with results obtained in exploratory work done with K-means (not presented here).

The results obtained suggest the directing further investigation into the joint use of all diamond classification factors in connection with geographical and geological variables.

6 ACKNOWLEDGEMENTS

This work had the financial support of *FCT - Fundação para a Ciência e Tecnologia*, a Portuguese Government scientific development institution. *SPE - Sociedade Portuguesa de Empreendimentos SA*, the source of most information used, also supports this project through its participation in the *DiaGenesis* project.

7 REFERENCES

- Carvalho, H. d. (1983). "Notice explicative préliminaire sur la géologie de l'Angola." *Garcia de Orta, Sér. Geol* 6(1-2): 15-30.
- Chambel, L. (2000). "Evolução do peso dos diamantes ao longo do rio Chicapa (Lunda, Angola)." *REM, Revista da Escola de Minas* 53(3).
- Gouveia, J. A. d. C., Moncada, P. C. d., Monteiro, J. F. A. & Neto, M. G. N. M. (1992). *Riquezas minerais de Angola*, Instituto para a Cooperação Económica (ICE).
- Magidson, J. & Vermunt, J. (2000). Latent class cluster analysis. *Applied latent class analysis*. J. A. A. a. A. L. McCutcheon. Cambridge, Cambridge University Press.
- Menezes, R. (1973a). *Ensaios em diamantes da mina Camutuê*, DIAMANG, Divisão dos Serviços de Prospecção, Secção de Geologia.
- Menezes, R. (1973b). *Mina do Camutuê: ensaios efectuados sobre diamantes recolhidos entre 21 e 31 de Maio de 1973*. Relatório inédito.
- Menezes, R. (1974a). *Estudo de diamantes dos quimberlitos do Camatchia e do Camutuê*, DIAMANG, Secção de Geologia.
- Menezes, R. (1974b). *Estudo dos diamantes do quimberlito do Camagico*, DIAMANG, Divisão de Prospecção e Geologia, Secção de Geologia.
- Monforte, A. (1960). *Estudo dos diamantes do Goege*, Relatório da DIAMANG, Companhia de Diamantes de Angola.
- Monforte, A. (1988a). *O diamante em Angola nas rochas quimberlíticas e nos jazigos secundários. Vol. 1 - Geologia Geral*. Lisboa, Sociedade Portuguesa de Empreendimentos.
- Monforte, A. (1988b). *O diamante em Angola nas rochas quimberlíticas e nos jazigos secundários. Vol. 2 - Jazigos de diamantes*. Lisboa, Sociedade Portuguesa de Empreendimentos (SPE).
- Monforte, A. (1988c). *O diamante em Angola nas rochas quimberlíticas e nos jazigos secundários. Vol. 3 - Metodologia Geral de prospecção*. Lisboa, Sociedade Portuguesa de Empreendimentos (SPE).
- Nunes, A. d. F. (1991). *A investigação geológico-mineira em Angola*. Lisboa, Instituto para a Cooperação Económica (ICE).
- Real, F. (1958). "Sur les roches kimberlites de la Lunda (Angola)." *Boletim do Museu e Laboratório Mineralógico e Geológico da Faculdade de Ciências da Universidade de Lisboa* 26(7ª série): 3-33.
- Real, F. (1959). *Intrusões quimberlíticas da Lunda - Contribuição para o conhecimento do Karroo de Angola*. Lisboa, Serviços Geológicos de Portugal, Direcção Geral de Minas e Serviços Geológicos.
- Reis, B. & Aires-Barros, L. (1980). *Sur quelques quimberlites de l'Angola*. 26.º Congr. Géol. Int., Paris.
- Reis, B. & Aires-Barros, L. (1981). "Sur quelques quimberlites de l'Angola." *Comunicações dos Serviços Geológicos de Portugal* 67(1): 3-18.
- Reis, B. & Monforte, A. (1981). "Nota preliminar sobre o maciço quimberlítico ocidental de Camutuê (Lunda - Angola)." *Boletim da Sociedade Geológica de Portugal XXII*, Volume de homenagem ao Professor Doutor Carlos Teixeira: 327-338.
- Sinise (1998). *geoAngola®*, base de dados geológica de Angola.

Mineralogical and Physical Characterization of the Oltustone, a Gemstone Occurring around Oltu (Erzurum-Eastern Turkey)

E.Ciftci & M.G.Yalcin

Nigde University, Department of Geological Engineering, 51200 Nigde, Turkey

B.Yalcınalp & H.Kolaylı

Karadeniz Technical University, Department of Geological Engineering, 61200 Trabzon, Turkey

ABSTRACT: The oltustone, occurring in the nearby area of the town of Oltu (Erzurum-eastern Turkey) has been a source of income for the local people for centuries. It is used mainly for counting beads, ornaments, and a variety of other souvenirs. It is a highly diagenetic coal with resin impregnation, which is extremely brittle and a light rock (specific weight is about 1.2 g/cm^3). It is dull black to brownish black in color when it is fresh and unprocessed. Its carbon content is between bituminous coal and anthracite. It is also soft when fresh and hardens very quickly when exposed to atmosphere (HVC: 35.44 ± 2.61 ; using 300 g). The oltustone has highly diverse trace element contents. In particular, iron, aluminum, barium, calcium, magnesium, titanium, silicon, and sodium are the most abundant elements. The Oltustone is also rich in organic compounds. Main components are barbital, phenanthrene (anthracene), and metyl-naphtalene. Investigations carried out on polished-sections revealed abundant presence of micron-sized pyrite framboids and quartz.

1 INTRODUCTION

Subject area is located in the easternmost corner of Turkey, called town of Oltu (Erzurum) (Fig. 1). Although Oltustone occurrences are not restricted to the town of Oltu, it is named after this town due perhaps to its more abundance around it: Güzelsu, Dutlu, Güllüce, and Gökçedere (Parlak 1994). It is also mined out in Bayburt and Haymana (Ankara) to a lesser extent. The Oltustone is treated as gemstone and used for a dozen of souvenirs, jewelry and gifts. Major use of the Oltustone (about >90%) is in counting beads (Fig. 2).

2 FIELD OCCURRENCES

Oltustone occurs as very thin layers (3-5 cm-thick beds with inconsistent lateral extension) in flysches of Cretaceous age, intercalated with marl and clay layers (Bozkus 1990). It may occur as vertically positioned, irregular, short, and thin lenses (lenticular bodies) (a few cm in thickness and up to 15 cm in length) in about 1 m thick marl horizons of Neogene age.

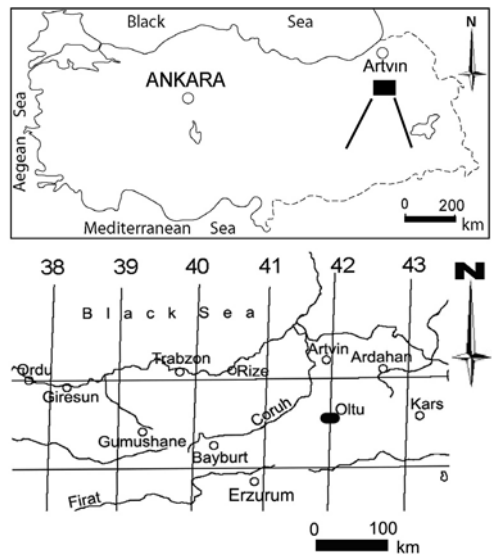


Figure 1: Location map of the subject area.

Although lignite occurrences are present in the same basin, Oltustone does not occur with lignite.

Oltustone has long been mined by local people through rather primitive underground mining methods. Thus, no reliable data on past productions and reserves are available.



Figure 2: Raw and processed Oltustone.

3 CHEMICAL COMPOSITION OF OLTUSTONE

XRD, Gas Chromatography, Reflected Light Microscopy (RLM), and Inductively Coupled Plasma (ICP) techniques have been employed to analyzed oltustone: Only inorganic phases detected by XRD were pyrite and quartz, which are approved by RLM observations. Based on Gas Chromatography analyses, phenanthrene (anthracene), barbital, and methyl naphthalene were the most abundant organic components. Most abundant elements determined by ICP were C (~85 wt %), Al, Ba, Fe, Mg, Na, Ca, Si, and Ti (Çiftçi et al., 2002). Carbon content of the Oltustone is between bituminous coal and anthracite. Its calorific value is 8064 kcal/kg.

4 PHYSICAL CHARACTERISTICS

The Oltustone is relatively soft when it is mined out and brownish black in color. It is shaped and cut into desired size while soft or fresh. It gets harder once it is mined out upon losing its moisture which occurs relatively fast.

It is also a light material with a specific gravity of 1.2 g/cm^3 . Conchoidal fracturing is another property of it (Fig. 2). Hardness tests conducted on the ground mass yielded 35.44 ± 2.61 in Vicker's scale. cal Bulletin of Turkey, V. 33, 47-56, 1990, Ankara, Turkey.

5 FORMATION OF OLTUSTONE

Oltustone can be considered as a sedimentary formation.

Most convincing information on how it is formed comes from fossilized woods (juniper tree) enveloped by oltustone layers, found in some of the galleries. This strongly suggests that it is composed of lignite soaked by resin. Micron-sized pyrite spheres are always present. Its compact structure could be due to diagenesis.

6 CONCLUSIONS

The Oltustone is a diagenetic lignite impregnated by resin. Resin is the major component distinguishing it from the regular lignite. It is polished better, harder (upon losing moisture content once mined out), and brighter than lignite. Its carbon content is very close to anthracite.

6 REFERENCES

- Çiftçi, E., Coşkun, S. and Yalçınalp, B., "Oltustone – Mineralogical and physical properties", 55. TJK; Bildiri Özetleri, s. 51, 11-15 Mart, 2002, Ankara, Turkey.
- Parlak, T., Oltustone Turkish folk jewellery, Faculty of Fine Arts, Ataturk University, 1994, Erzurum.
- Bozkus, C., Stratigraphy of northeast part of the Oltu-Narman (Kömürlü) Tertiary basin, Geologi

About the Color in Natural, Gamma and Neutron Irradiated Spodumene

G.O.Dias, M.V.B.Pinheiro, K.J.Guedes & K.Krambrock

Departamento de Física, ICEx, Universidade Federal de Minas Gerais, CP. 702, 30.123-970 Belo Horizonte, MG, Brazil

ABSTRACT: Natural spodumene from Minas Gerais, Brazil, is investigated by electron paramagnetic resonance (EPR), electron microprobe, optical absorption and photoluminescence. Spodumene has chemical formula $\text{LiAlSi}_2\text{O}_6$ with monoclinic symmetry. Natural colors include yellow, green and pink. In yellow spodumene EPR spectra of Fe^{3+} , substituting for Al^{3+} are found and analyzed. The yellow color is generally attributed to charge transfer transitions of Fe^{3+} with absorption bands in the near UV and a tail extending to the violet/blue spectral range. The color and the EPR lines are not influenced by gamma irradiation. Pink spodumene (called kunzite) shows intense EPR signals of Mn^{2+} in different configurations, small amounts of Fe^{3+} and some extra not yet identified EPR lines. In green spodumene (hiddenite), Cr^{3+} was identified from its typical R_1 and R_2 photoluminescence lines. Comparison of the EPR spectra of kunzite and hiddenite let us conclude, that the additional EPR lines are due to Cr^{3+} substituting for Al^{3+} . However, analysis of the spectra is complicated because of superposition of many lines. Gamma irradiation does not change the color of hiddenite, however, most kunzite turns green with two new absorption bands (470 and 620 nm). The green color induced in kunzite is very unstable. By neutron irradiation all specimen of spodumene acquire a yellow-brown color that is stable until 500°C and therefore can be considered as a color enhancing process.

1 INTRODUCTION

Spodumene belongs to the pyroxene minerals. It is a lithium aluminum silicate with chemical formula $\text{LiAlSi}_2\text{O}_6$. The symmetry of α -spodumene, the low temperature form, is monoclinic with space group $C2/c$ (C_{2h}^6) and unit cell parameters $a = 9.52 \text{ \AA}$, $b = 8.32 \text{ \AA}$, $c = 5.25 \text{ \AA}$ and $\beta = 69.4^\circ$ with four molecules per unit cell. Brazilian spodumene appears in huge transparent crystals in the state of Minas Gerais with pale yellow, green and pink colors (Karfunkel et al. 2002). Green, chromium bearing spodumene is called hiddenite and the pink variety kunzite. Bad quality spodumene is used for extraction of lithium.

The search for color-enhancing processes of colorless and pale colored gemstones is still a great motivation for scientist, apart from the identification of color centers. It is known that most pink kunzite turns dark green by gamma irradiation, however, the color fades in a few days in sunlight or in a few minutes at about 100°C (Nassau 1983). The reason for the color change is not well understood. The same holds for the natural colors.

The main objective of our work is the investigation of the natural colors and the color causing centers of Brazilian spodumene using

electron microprobe analysis, electron paramagnetic resonance (EPR), optical absorption and photoluminescence. In addition, different color enhancing irradiation techniques like gamma and neutron irradiation together with thermal treatments are employed.

2 EXPERIMENTAL

Electron paramagnetic resonance (EPR) measurements were done in a custom-build spectrometer working at X-band frequencies (8.8 – 10 GHz). For signal improvement a common 100 kHz field modulation was employed using a Lock-In detection system. The samples were inserted in a He flux cryosystem (OXFORD) allowing temperatures between 10 and 350 K. Optical absorption measurements were done at room temperature in a commercial equipment (HITACHI) working in UV-visible spectral range. Photoluminescence measurements were done using an Ar^+ ion laser (488 nm, 300 mW max.) in the visible spectral range using a photomultiplier detection system.

Samples have been oriented from the natural faces using the cleavage plane of spodumene. The small rectangular parallelepipeds with dimensions of

about $3 \times 2 \times 5 \text{ mm}^3$ were polished to optical quality. One specimen of all samples was hold as a reference sample, two other were subjected to gamma irradiation from a ^{60}Co source with dose up to 5 MGy and neutron irradiation (dose $5 \times 10^{17} \text{ n/cm}^2$).

3 EXPERIMENTAL RESULTS

Table 1 shows the results of electron microprobe analysis of three representative samples. Li content was not analyzed. From the table we note that the ratio of FeO/MnO concentration is about 0.3 for kunzite, 3 for hiddenite, and 7 for yellow spodumene. Kunzite has more or less the double in concentration of Mn compared to the other two. In addition, Cr could not be detected in all samples.

Table 1: Electron microprobe analysis of three representative samples (Kun: kunzite, Ysp: yellow spodumene and Hid: hiddenite) in wt.%.

	SiO ₂	Al ₂ O ₃	Na ₂ O	MnO	FeO	Cr ₂ O ₃
Kun	65.26	27.41	0.11	0.16	0.05	≤0.01
Ysp	65.17	27.44	0.11	0.08	0.58	≤0.01
Hid	64.91	27.46	0.12	0.06	0.17	≤0.01

Figure 1 shows the optical absorption spectra of the three specimen of natural spodumene. Kunzite shows absorption bands at 545 and 685 nm, hiddenite at 420, 500 and 600 nm and yellow spodumene at 430 and 545 nm.

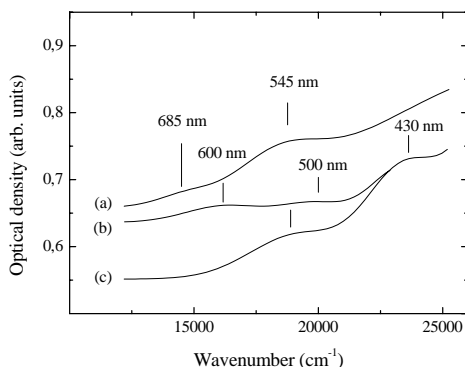


Figure 1: Optical absorption spectra measured at room temperature for (a) kunzite, (b) hiddenite and (c) yellow spodumene. The numbers indicate line positions of optical bands (see text).

After gamma-irradiation the absorption spectrum of kunzite is dominated by a band centered at 600 nm (not shown), leaving the crystal dark green. This band is similar a band in natural hiddenite, however,

much less stable. The band fades out by thermal treatment at about 100°C in a few minutes.

Electron microprobe analysis of hiddenite did not show any Cr content in the samples. However, photoluminescence measurements show that Cr is really present in small concentrations in hiddenite. Figure 2 shows a spectrum measured at room temperature with excitation of Ar⁺ ion laser (488 nm). The typical R lines (R₁ and R₂) of Cr³⁺ are observed together with a broad band centered at 730 nm and a less intense at 585 nm. The latter band is also observed in kunzite and yellow spodumene.

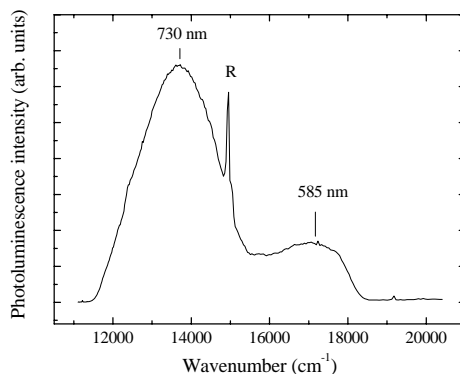


Figure 2: Photoluminescence spectrum of hiddenite measured at room temperature. Excitation with Ar ion laser. R denotes the R lines of Cr³⁺.

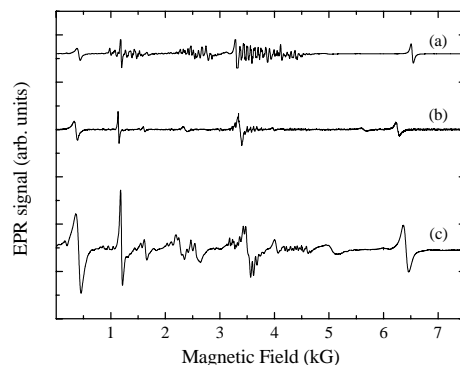


Figure 3: EPR spectra for (a) kunzite, (b) hiddenite and (c) yellow spodumene measured at room temperature in X band with microwave frequency of 9.38 GHz for B || c-axis. Slight line shifts are related to small misalignments of the samples.

Figures 3 shows the EPR spectra of the three samples of spodumene measured at room temperature for B || c-axis. The EPR lines belong to Fe³⁺ (Manoogian et al. 1965, Gaite & Michoulier

1973) and Mn^{2+} (Holuj 1968, Holuj & Manoogian 1968). Fe^{3+} lines are more intense for yellow spodumene, while that of Mn^{2+} for kunzite. The EPR lines of both are intermediate in intensity for hiddenite. These results are consistent compared with electron microprobe analysis. It is assumed that both impurities occupy Al^{3+} sites in the spodumene structure. The question arise, what is the compensation mechanism for Mn^{2+} and where are the EPR lines of Cr^{3+} . The latter may be answered by low concentration and the superposition of the many lines of Fe^{3+} and Mn^{2+} . No work has been published which identify Cr^{3+} EPR spectra in spodumene.

After gamma-irradiation the EPR spectra in the different samples are not modified including kunzite which turned green.

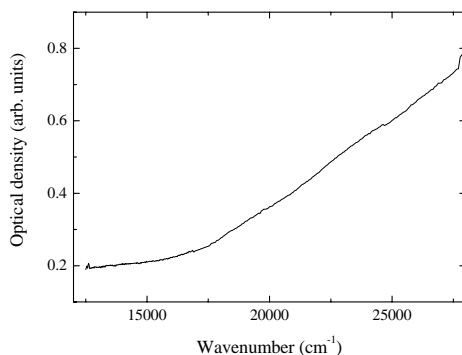


Figure 4: Optical absorption spectrum of neutron-irradiated kunzite measured at room temperature. The samples turned yellow-brown. The color as well as the absorption spectra for neutron-irradiated hiddenite and yellow spodumene are identical and stable up to 500°C.

Neutron irradiation of all types of spodumene results in a yellow-brown color. Figure 4 shows the absorption spectrum of kunzite after neutron irradiation with a dose of $5 \times 10^{17} \text{ cm}^{-2}$. The absorption spectrum is dominated from a band centered in the UV. All absorption bands of the natural sample are masked by this strong absorption. The spectra for hiddenite and yellow spodumene are identical to the spectrum shown in figure 4. The color and the absorption band are stable up to 500°C.

4 DISCUSSION

The pink color of different gem minerals has been attributed to Mn impurities as for example in pink tourmaline and red beryl (bixbite). There are different indications for that, however, a definitive proof is still missing. The valence state of the Mn

ions and the position in the crystal structures is discussed controversy. From optical absorption measurements in natural and irradiated kunzite, the pink color has been attributed to Mn^{4+} substituting for Al^{3+} with the need of compensation (Fujii & Isotani 1988, Isotani et al. 1991). The same authors explain the green color after irradiation with Mn^{3+} . Mn^{2+} was also discussed, however, from our results this model can be clearly excluded because the EPR spectra of Mn^{2+} are not influenced by irradiation or heat. Other model includes a metal ligand field transition in order to explain the color change (Nassau 1983). In this case the valence states of Fe and Mn impurities can be changed by irradiation: Mn^{3+} (pink) + Fe^{3+} (colorless) \Rightarrow Mn^{4+} (green) + Fe^{2+} (colorless). Heat restores the initial configuration. Such a model may explain many observations, however, it is not proven by EPR. EPR spectra are explained only by Mn^{2+} which are not changed by irradiation. An intrinsic color center produced by irradiation is another possibility. However, such a center should be diamagnetic, because it is not seen by EPR. In such a model the question arise why this center is not produced in yellow spodumene. Further, from our measurements it seems that the same center is stable in hiddenite.

The green color of hiddenite has been attributed to Cr^{3+} impurities. Cr^{3+} is known to be a strong coloring ion in many minerals like ruby, emerald and alexandrite. In our samples Cr^{3+} was only identified from the R photoluminescence lines (Walker et al. 1997). They belong to transitions from the 2E excited state to the 4A_2 ground state and do not change much in position in different crystal fields (Marfunin 1979). The broad luminescence band centered at 730 nm should correspond to a transition from the state 4T_2 to 4A_2 . The broad absorption bands centered at 500 and 600 nm are due to the transitions from the ground state of Cr^{3+} to the 4T_2 and 4T_1 excited states. Minimum absorption falls in the green spectral region. All of our measurements can be explained within this model. Therefore, we conclude that Cr^{3+} substituting for Al^{3+} is the color center in green hiddenite. Unfortunately, the Cr^{3+} in our samples was very low, therefore, a clear identification by EPR is still missing.

The yellow color of many minerals is often attributed to Fe impurities. The yellow color is produced from an optical absorption band centered in the near UV which is attributed to charge transfer transitions between Fe^{3+} and Fe^{2+} (Nassau 1983). Such model is consistent with the observation that irradiation does not modify the color. Fe is the dominant impurity in yellow spodumene. In addition, the EPR spectra are dominated by Fe^{3+} EPR lines. We agree with such explanation. Because also hiddenite and kunzite contain reasonable concentrations of Fe the color should somewhat be

influenced by this absorption. The questions about the Fe^{2+} site and the compensation mechanism are still open.

Gamma-irradiation is not very successful for color enhancing of spodumene. Some kunzite specimen can be enhanced slightly in color. Neutron-irradiation is by far a better way for changing the color of pale colorless spodumene. The produced color is a yellow-brown which is stable up to 500°C . Whether such color is commercial or not we do not know. The color center responsible for the absorption band in the near UV spectral range is not known. The absorption band is similar to the charge transfer transition involving Fe impurities. However, our EPR measurements did not show an increasing Fe^{3+} concentration after neutron irradiation.

5 CONCLUSIONS

Different specimen of Brazilian spodumene have been investigated in relation to its color and color enhancing processes. It is concluded that only neutron irradiation results in drastic change in color for all types of spodumene, leaving a dark yellowish brown color which is stable up to 500°C . The color of yellow spodumene is basically produced from charge transfer transitions involving Fe. The green color of hiddenite is most probably related to Cr^{3+} . Most doubts are still left for the association of the pink color of kunzite with manganese. The same holds for the unstable green color produced in kunzite by gamma irradiation.

6 ACKNOWLEDGEMENTS

The authors are grateful to J. Menezes and J. Karfunkel for providing the samples; R. Ferracini and A. Leal (CDTN) for the gamma irradiations and neutron irradiations, respectively, and A.I.C. Persiano for the electron microprobe analysis. We acknowledge financial support from the Brazilian agencies FINEP (CORGEMA 4856), CNPq and CAPES (Probral 125/01) and the DAAD.

7 REFERENCES

Fujii, A.T. & Isotani, S. (1988): Optical absorption study of five varieties of spodumene, *An. Acad. Bras. Ci.*, 60, 127.
Isotani, S., Fujii, A.T., Antonini, R., Pontuschka, W.M., Rabbani, S.R. & Furtado, W.W. (1991): Optical absorption study of radiation and thermal effects in Brazilian samples of spodumene, *An. Acad. Bras. Ci.*, 63, 127.

Gaite, J.M. & Michoulier, J. (1973): Electron paramagnetic resonance of Fe^{3+} in diopside and spodumene, *J. Chem. Phys.*, 59, 488.
Holuj, F. (1968): EPR of Mn^{++} in spodumene. I. Natural crystals, *Can. J. Phys.*, 46, 287.
Holuj, F. & Manoogian, A. (1968): EPR of Mn^{++} in spodumene. II. Heated crystals, *Can. J. Phys.*, 46, 303.
Karfunkel, J., Quéméneur, J., Krambrock, K., Pinheiro, M.V.B., Dias, G.O. & Wegner, R. (2002): Edelsteine aus dem Gebiet nördlich von Araçuaí (Minas Gerais, Brasilien): Vorkommen, Eigenschaften und Behandlungsmethoden, *Z. Dt. Gemmol. Ges.*, 51/4, 171.
Manoogian, A., Holuj, F. & Carswell, J.W. (1965): Electron spin resonance of Fe^{3+} in single crystals of spodumene, *Can. J. Phys.*, 43, 2262.
Marfunin, A.S. (1979): Spectroscopy, luminescence and radiation centers in minerals, Springer Verlag.
Nassau, K. (1983): The physics and chemistry of color, John Wiley & Sons.
Walker, G., Jaer, A.E., Sherlock, R., Glynn, T.J., Czaja, M. & Mazurak, Z. (1997): Luminescence spectroscopy of Cr^{3+} and Mn^{2+} in spodumene ($\text{LiAlSi}_2\text{O}_6$), *J. of Luminescence*, 72-74, 278.

Effect of Energetic Heavy Ion Radiation and Site Distribution Studies in Brazilian Emeralds by Mössbauer and Optical Methods

V.K.Garg, G.C.B.Braga, A.C. de Oliveira, R.Garg
University of Brasília, Institute of Physics, 70919-900 Brasília, DF, Brazil

E.Kuzmann
Department of Nuclear Chemistry, Eötvös University, Budapest, Hungary

ABSTRACT: In Brazil gem-quality emeralds are found at Campos Verdes, Goiás (GO) and Salinhas, Bahia (BA); samples from these two locations have been analyzed using transmission ^{57}Fe Mössbauer spectroscopy, X-ray diffraction, electron microprobe analysis and optical methods. Mössbauer spectra were decomposed into four subspectra associated with Fe ions at different sites. We found that Fe^{2+} substitutes both Al and Be sites in different proportions (varied with the origin of emerald samples); and about 1/3 of iron ions in Fe^{3+} valence state are located primarily in two different sites. Emerald samples originating from Goiás, Brazil, containing a significant portion of Fe^{3+} beside Fe^{2+} were irradiated with 209 MeV ^{89}Kr ions to study the effect of irradiation on the valence state of iron. Using ^{57}Fe transmission Mössbauer spectroscopy a valence state transition from Fe^{3+} to Fe^{2+} was clearly observed as a result of irradiation. The results indicate that the $3+$ state of iron is metastable in this system.

1 INTRODUCTION

Emerald belongs to the beryl family. In natural beryl the occurrence of main constituent oxides are BeO (14%), Al_2O_3 (19%) and SiO_2 (67%). The iron content of emerald is usually between¹ 0.3 - 3.14%. The basic structure and general physical and chemical properties of beryls have already been studied, however, much less is known about the parameters exclusive to emerald, such as its cation distribution. Our aim was to study the sites and distribution of Fe ions in Brazilian emeralds. For this we performed ^{57}Fe Mössbauer spectroscopy, XRD, and optical measurements on gem-quality natural emeralds.

2 EXPERIMENTAL

We collected gem-quality emeralds of varied sizes from Campos Verdes, Goiás (GO) and Salinhas, Bahia (BA). The samples were identified as emerald by optical methods, X-ray diffractometry, and electron microprobe analysis, based upon their characteristic color, photoluminescence of Cr, crystal structure and composition. ^{57}Fe Mössbauer spectra of emerald samples (both powdered and

single crystal) were recorded by a conventional Mössbauer spectrometer (WISSEL) using a proportional detector in transmission geometry, both at room temperature and at liquid nitrogen temperature (78K) using a 108 Bq activity $^{57}\text{Co}(\text{Rh})$ source. The samples were prepared by applying a small force to press the powdered emeralds in the sample holder. To decrease the disturbing effect of texture, powdered samples with a surface density of 50 mg/cm^2 were used for the measurements. In order to collect more than 10^7 counts in each channel and in view of the low iron content and to reduce the scattering in the resonant absorption each spectrum was recorded over the course of 20 days (still there is ample scattering in the Mössbauer spectra). Isomer shifts in this paper are reported relative to the $\alpha\text{-Fe}$. A least square fitting program evaluated the Mössbauer spectra, and the quadrupole splitting distributions were obtained by modified Hesse-Rübartsch methods. The samples were irradiated with 209 MeV Kr ions, available at the U-400 cyclotron of JINR, in Dubna. Irradiations were carried out at room temperature in a vacuum better than 10^{-6} Pa. As the irradiation flux was maintained at a relatively low level ($109 \text{ ions/cm}^2\cdot\text{s}$), the temperature did not increase more than 15°C during the irradiation. The fluence of irradiation was 1012

ions/cm². The thickness of the sample was in the range of the penetration depth of the applied Kr ions.

3 RESULTS AND DISCUSSION

The intensity of the pale green color characteristic of the emerald depends on the concentration of Cr³⁺ in the crystal lattice. The addition of other impurities leads to the presence of additional bands of light absorption, which alter the emerald's typical color. Thus, identifying extra impurities allows one not only to confirm the emerald's origin but also the feasibility of neutralizing the effect of the impurities through suitable treatment.

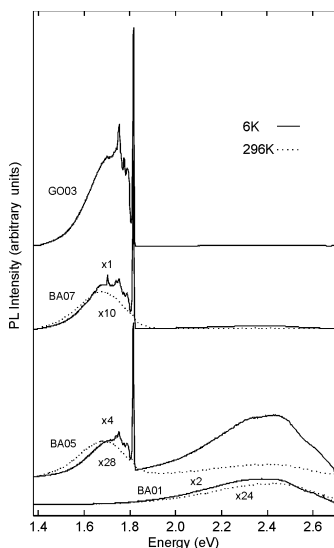


Figure 1. depicts the PL spectra of four samples (BA01, BA05, BA07 and GO03) measured at 6K and 296K, represented by a continuous and a dotted line respectively.

In the spectra of all except BA01 we can see the emission bands associated with chromium and iron. However, there is also a new large band of emission with a maximum at ~2.4 eV, extending from 1.6 eV to beyond the end of the figure at ~2.7 eV. This new band is the only emission detected in BA01. Detailed analysis of the PL spectra of this specimen shows the presence of a pack of fine lines of low intensity, between 2.60 eV and 2.68 eV, which are probably related to the electronic transitions of V³⁺ impurities. In the samples studied we observed that Goiás samples have large Cr³⁺ incorporation, large Fe contamination but very little vanadium contamination; whereas in samples from Bahia – less Cr incorporation, less Fe contamination but much larger vanadium contamination. This variability in the relative abundance of these

impurities is responsible for the different color tones.

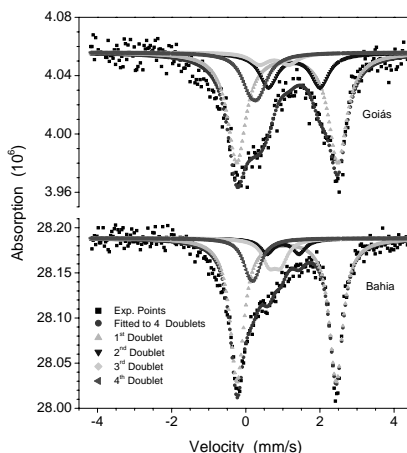


Figure 2. Depicts typical room temperature Mössbauer spectra of powdered samples of Brazilian emerald.

Since each Mössbauer spectrum is complex, with many subspectra, and the absorption percentage is small, hence, as in most iron-bearing minerals, the Mössbauer spectra were decomposed by fitting a few quadrupole split subspectra of Lorentzian lines in the frame of an appropriately chosen model containing the constraints between the Mössbauer parameters of subspectra and the different iron sites. In the model, the site assignment of the Mössbauer subspectra corresponds well to the distinct cation positions at different crystallographic sites. The result of this procedure depends first and foremost on correct knowledge of the number of iron positions distinguishable by Mössbauer spectroscopy. This number can be different from the exact number of crystallographic iron sites because different microenvironments of the same site (e.g., having different cation neighborhoods) can also be distinguished by the Mössbauer method. The presence of numerous microenvironments can make conventional evaluation unreliable. For such cases we can calculate the quadrupole splitting distribution derived from the Mössbauer spectrum. Correspondence can be obtained between the peaks of the distribution curve and the different microenvironments. With this method we can distinguish different microenvironments better than by conventional spectrum evaluation.

We used the quadrupole splitting distribution method to estimate the Mössbauer spectra of the emeralds. By decomposition of the quadrupole splitting distribution, we found four peaks associated to the four iron microenvironments. Based on the results of the quadrupole splitting distribution method, four Lorentzian doublets were used for

conventional decomposition of the Mössbauer spectra. This way all Mössbauer spectra could be decomposed into four doublets (D1, D2, D3 and D4) with corresponding parameters. The Mössbauer spectra of the samples, polished and ground down to 0.3 mm thickness, indicated similar texture effect as observed earlier with iron-bearing beryls. Powdered samples also exhibited some texture effect. Nonetheless, much less temperature-dependent relaxation was observed compared to the effect reported with aquamarine. The site assignment of the doublets observed in the Mössbauer spectra of emerald is based on (Braga et al. 2002):

1) Knowledge of Mössbauer parameters in minerals

2) Expectation of crystallographic sites for iron in the emerald structure

3) Earlier Mössbauer and other studies of iron-containing beryl

Iron can be expected to be situated at the following positions in this structure:

- at substitutional cation sites
- octahedral Al site as Fe^{2+} or Fe^{3+}
- tetrahedral Be site as Fe^{2+} or Fe^{3+}
- tetrahedral Si site as Fe^{3+}

Doublet D1 is attributed to Fe^{2+} located at octahedral Al site in the emerald lattice. The isomer shift and the quadrupole splitting of doublet D1 are typical for octahedrally coordinated Fe^{2+} ion in minerals. Doublet D2 is associated with Fe^{2+} ions occupying the tetrahedral Be site. The isomer shift is characteristic for a Fe^{2+} ion and the quadrupole splitting indicates a four-coordinated micro-environment. Be and Si are both in tetrahedral coordination, however, the substitution of Si by Fe^{2+} ion is unlikely; in that case the quadrupole splitting would be expected to be much less than is measured. Price et al (Price et al. 1976) have studied Mössbauer spectra of another beryl, and found a doublet with parameters similar to D2. Doublets D3 and D4 certainly represent two different Fe^{3+} microenvironments. The occurrence of Fe^{3+} at both Al and Be sites has already been predicted but not shown directly. The observed Mössbauer parameters of doublets D3 and D4 are not characteristic for any known mineral or compounds, which are usually part of an emerald ore. EPR measurements confirmed the presence of Fe^{3+} inside the lattice. Previous Mössbauer studies of iron-bearing beryls indicated a smaller contribution (Platonov of Fe^{3+}). The larger percentage of Fe^{3+} in Brazilian emeralds can be explained by the higher relative abundance of Fe in Brazilian minerals than those from elsewhere. This agrees with the Mössbauer analysis of bazzite – the natural scandium analog of beryl found in an iron-rich area of Kazakhstan – which displayed about 50% Fe^{3+} micro-environments. We found no evidence of Fe ions in structural channels, where iron sites have been postulated earlier, probably

because of their small recoilless fraction that might not be observable in Mössbauer spectra at room temperature. Considering the above arguments we can describe doublets D3 and D4 as following:

Doublet D3 is associated with Fe^{3+} ion substituted into the octahedral Al site. The Mössbauer parameters of this doublet correspond to the octahedrally coordinated Fe^{3+} site. Similar parameters were derived from the magnetically split spectrum obtained with a beryl in an external magnetic field (6T). Doublet D4 can be associated with Fe^{3+} ion substituted into the tetrahedral Be site. The isomer shift and the quadrupole splitting confirm a tetrahedral coordination for Fe^{3+} ion. This site assignment agrees with the expectation that Fe^{3+} substituted Be (as mentioned above), even in beryls with lower iron content. We found no evidence of Fe ions in structural channels probably because their small recoilless fraction might not be observable in the Mössbauer spectra.

The Brazilian emeralds contain a large amount of Fe^{3+} , not found in any other iron-containing beryls in earlier works. Interestingly enough, the relative population of iron in Al sites compared to iron at Be sites was the same in every sample. The most striking difference between the two types of emeralds was that in GO samples Fe^{3+} preferred the Al site, while in the BA samples Fe^{3+} preferred the Be site. Fe^{2+} prefers the Al site in both cases, but this choice is more than three times stronger in BA than in GO emeralds. One can interpret these differences as consequence of how these emeralds were formed. Our measurements show that the emeralds from Bahia (BA samples) contained vanadium and chromium as principal color centers, but those from Goiás (GO samples) had only chromium.

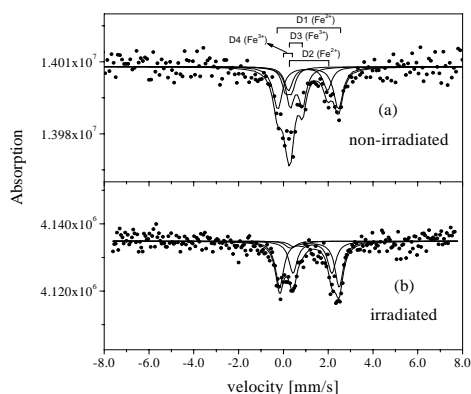


Figure 3. (a) non irradiated and (b) irradiated emerald room temperature ^{57}Fe Mössbauer spectrum.

Figure 3 shows the room temperature ^{57}Fe Mössbauer spectrum of the emerald sample before

and after the irradiation. The spectra can be decomposed into four doublets (D1, D2, D3 and D4) representing four distinct iron sites (Kuzmann et al. 1998).

Comparing the relative intensities of subspectra belonging to the emerald before irradiation (Tab. 1), we can make two main observations:

- Before the irradiation Fe²⁺ and Fe³⁺ distribute about equally among the Al and Be sites .

- The relative occurrence of Fe³⁺ is very large in the non-irradiated Brazilian emerald (43 %).

The ⁵⁷Fe Mössbauer spectrum of the irradiated emerald (Fig. 3b) differs significantly from that of non-irradiated one (Fig. 3a). The most striking change is the decrease of the relative area of the subspectra belonging to Fe³⁺. The corresponding area fractions are depicted in Table. It is clear that as a result of irradiation the relative area of the doublets D3 and D4, belonging to Fe³⁺, diminished strongly at the expense of the relative area of doublets D1 and D2 representing Fe²⁺. This finding indicates the reduction of Fe³⁺ to Fe²⁺ as the main result of the energetic heavy ion irradiation. It is consistent with the earlier results obtained in connection with light ion irradiations.

Table 1. Mössbauer parameters of non-irradiated and irradiated samples.

Mössbauer parameters	Emerald	
	non-irradiated	irradiated
IS (D1) (mm/s)	1.10±0.01	1.11±0.01
IS (D2) (mm/s)	0.95±0.01	0.96±0.01
IS (D3) (mm/s)	0.58±0.01	0.55±0.02
IS (D4) (mm/s)	0.23±0.01	0.22±0.02
QS (D1) (mm/s)	2.71±0.02	2.65±0.02
QS (D2) (mm/s)	1.74±0.02	1.73±0.03
QS (D3) (mm/s)	0.55±0.02	0.41±0.02
QS (D4) (mm/s)	0.28±0.02	0.20±0.02
A (%) (D1)	36±3	54 ±4
A (%) (D2)	21±2	37 ±3
A (%) (D3)	29±2	5 ±2
A (%) (D4)	14±1	4 ±2

Considering that irradiation promotes the transformation of metastable states to the equilibrium one, the observed reduction of Fe³⁺ indicates that iron in the 3+ valence state can be considered to be metastable in emerald. The metastability of Fe³⁺ in emerald is in accordance with the heat treatment induced reduction of Fe³⁺ to Fe²⁺ as observed in some beryls. However, given that the Fe³⁺ to Fe²⁺ transformation was not possible via heat treatment at 600° C for 3 hours, in emerald the Fe³⁺ state seems to be more stable than in other kinds of beryl. This increased stability of Fe³⁺ may be connected to the higher iron content found in the Brazilian emerald.

In the case of heavy ion irradiation the energy of the Kr ion is transferred to the target material in two different ways, by energy deposition in electronic excitations and by elastic collisions with the atoms

of the target material. In the case of emerald being an insulator, the energy deposition by electronic excitations is expected to dominate. Accordingly, the reduction of Fe³⁺ to Fe²⁺ via energetic heavy ion irradiation in emerald can be explained as follows.

The energetic Kr ions transfer their kinetic energy to the emerald mainly by creating so called thermal spikes, where the local temperature can extend well over 600° C. Although Kr ions will undoubtedly create new defects in the system, the ensuing high local temperature can change the original defect structure around Fe³⁺ cations at both Al and Be sites. Thus it can promote the transformation of Fe³⁺ to the more stable Fe²⁺.

As the site occupancy of Fe (2+ and 3+) at the Al and Be sites did not change considerably through irradiation, the reduction process is likely to occur without considerable diffusion process. Thus, the irradiation affects mainly the electronic state of Fe³⁺ without altering its site occupancy considerably.

4 CONCLUSIONS

Mössbauer spectroscopy of natural Brazilian emeralds revealed two Fe²⁺ and two Fe³⁺ sites in the crystal. The Fe²⁺ and Fe³⁺ substitute both the octahedral Al and the tetrahedral Be sites. The distribution of Fe²⁺ and Fe³⁺ ions among the crystallographic sites is characteristic of the emerald location. The photoluminescence studies of samples from Bahia show less of Cr and Fe³⁺ but much contamination of vanadium and absence of characteristic doublet of emerald peaks where as in samples from Goiás large Cr and Fe³⁺, but very less contamination of vanadium is indicated.

With the help of energetic heavy ion irradiation we have shown that the Fe³⁺ → Fe²⁺ transformation, observed earlier in some beryls due to thermal treatment, takes place in emerald at Al as well as at Be sites. Our results indicate that the Fe³⁺ state can be metastable in emerald. The reduction process due to energetic heavy ion irradiation occurs locally, without considerable diffusion process.

5 REFERENCES

- Braga, G.C.B., Garg, V.K., Oliveira, A.C., Freitas, J.A., Kuzmann, E., and Garg, R.: *Optical And Mössbauer Study Of Brazilian Emeralds*, Physica Status Solidi (a) 194 (1) 36-46 (2002).
- Kuzmann, E., Nagy, S., Vértes, A., Weiszburg, T.G., Garg, V.K.: *Geological and Mineralogical Applications of Mössbauer Spectroscopy*, in *Nuclear Methods in Mineralogy and Geology* (eds. A. Vértes, S. Nagy, K. Sívegh) Plenum Press, NY (1998)
- Price, D.C., Vance, E.R., Smith, G., Edgar, A., Dickson, B.L.: *Mössbauer effect studies of beryl*, J. Phys. (Paris) 37 (1976) C6-811.

Gem Beryl Mineralization in the Northern Cordillera of Canada

L.A.Groat, J.K.Mortensen, H.Neufeld

Department of Earth and Ocean Sciences, University of British Columbia, Vancouver, Canada

D.D.Marshall

Department of Earth Sciences, Simon Fraser University, Burnaby, Canada

H.Falck

C.S. Lord Northern Geoscience Centre, Yellowknife, Canada

ABSTRACT: Three gem beryl occurrences have recently been discovered in northwestern Canada. The first is the Lened emerald property in the southwestern Northwest Territories, where pale-green V-dominant crystals occur in quartz-carbonate veins in a garnet-diopside skarn. The source of the Be is thought to be the Lened granite, with ~7 ppm Be. The source of the V is a black shale, with up to >3000 ppm V. In 1998 Cr-dominant emerald was discovered at the Regal Ridge property in southeastern Yukon. The mineralization is associated with quartz veins and aplite dikes which intrude metavolcanic rocks of the Yukon-Tanana Terrane. Green beryl crystals up to 4 cm in length are found in 12 mineralized zones within a 900 × 450 m area. Some of the smaller crystals, and sections of larger crystals, are gem-quality. The source of the Be is thought to be a nearby granite, with ~12 ppm Be, and the source of the Cr is the schist (~960 ppm Cr). In 2003 blue gem beryl was discovered at the True Blue property in southern Yukon. The crystals occur in a swarm of closely-spaced quartz ± siderite ± fluorite ± tourmaline veinlets that cut a syenite stock. The veins, which occupy a dense network of tension gashes, are 0.5 to 20 cm thick. Over 100 individual beryl showings have been discovered in a zone measuring 700 × 200 m. Much of the aquamarine is an unusual cobalt-blue colour, and electron microprobe analyses show up to 5.81 wt.% FeO.

1 INTRODUCTION

Emerald is green gem beryl ($\text{Be}_3\text{Al}_2\text{Si}_6\text{O}_{18}$), in which the colour is related to minor amounts of contained Cr or V. Emerald is the third most valuable gemstone (after diamond and ruby) and can be worth more than US\$100,000 per carat. Canada is not presently a producer of coloured gemstones, but this could change as a result of several exciting new discoveries in the northern Cordillera.

2 LENED

In 1997 an occurrence of V-dominant emerald was discovered near the mid-Cretaceous Lened pluton in the southwestern Northwest Territories (Fig. 1). Pale to medium green emerald crystals up to 3 cm in length occur where quartz veins cut a garnet-diopside skarn. The skarn formed from a limestone of the Rabbitkettle Formation, and overlies V-rich (2070-3170 ppm) black shales of the Earn Group. The close proximity of the granite suggests that it is the source of the Be, although the Be content is low (6-7.3 ppm), and the source of the V is undoubtedly the shale. A fluid inclusion study (Marshall et al. 2004) suggests that the emerald crystals formed at

temperatures of 250-550 °C and pressures <3,700 bars. Questions remain about the relative timing of the different events (skarn formation, vein emplacement, thrust faulting, etc.).

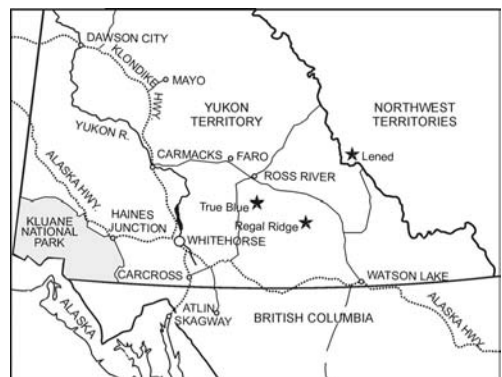


Figure 1: Location map.

3 REGAL RIDGE

3.1 Introduction

In 1998 a major occurrence of emerald was discovered at Regal Ridge in the southeastern Yukon Territory in northwestern Canada. The mineralogy, geology, and origin of the occurrence are described in Groat et al. (2002). The mineralization is associated with quartz veins and aplite dikes which intrude metavolcanic rocks of the Yukon-Tanana Terrane. Green beryl crystals up to 4 cm in length are found in 12 mineralized zones within a 900 × 450 m area. Chromium (average 3208 ppm) is the predominant chromophore. Some of the smaller crystals, and sections of larger crystals, are gem-quality, and a number of small gems (up to ~2.4 ct) have been fashioned from the Regal Ridge samples.

3.2 Regional geology

The Yukon-Tanana Terrane in the Regal Ridge area is composed of mainly Devonian quartz-rich metaclastic rocks and carbonates and Devonian and Mississippian metavolcanic and metaplutonic rocks which are inferred to have formed in continental magmatic arc (Mortensen & Jilson 1985, Mortensen 1992, Murphy & Piercey 2000) and back-arc settings (Piercey et al. 2000). The oldest rocks are in the Devonian to Mississippian Grass Lakes succession. The Fire Lake unit, a mafic metavolcanic unit composed mainly of chloritic phyllite (Murphy et al. 2002), is the second-oldest unit within the succession. The rocks were thrust onto the North American miogeocline between late Triassic and earliest Cretaceous time. The Yukon-Tanana rocks are intruded by several ca. 112 Ma intrusions of the Cassiar-Anvil plutonic suite. The Tintina fault lies 14 km southwest of the property.

3.3 Host rocks

The main host rock for the mineralization is a chlorite-plagioclase schist which forms part of the Fire Lake unit (DF unit of Murphy et al. 2002). Geochemical analyses show that the schist is a high-Ca boninite. The Cr in the emerald is most likely from the schist (average 960 ppm Cr). A leucogabbro unit (Dmi unit) is closely interfingering with the mafic schist. Variably-serpentinized ultramafic rocks occur in the western and northern parts of the map area. Murphy et al. (2002) suggest that these represent intrusive sills that fed the overlying DF rocks via gabbroic dikes (Dmi).

3.4 Granite and aplite

The occurrence is underlain (at a depth of approximately 800 m) by a 112 Ma two-mica (biotite > muscovite) quartz monzonite, which

outcrops to the east, south, and north. It is weakly foliated to unfoliated, with shallowly dipping contacts. The pluton belongs to the Anvil plutonic suite (Mortensen et al. 2000) of 112-100 Ma felsic intrusions, which are typically rich in W, Mo, Au, and Bi. The close proximity of the granite suggests that it is the source of the Be, although the Be content is low (12-13.2 ppm). Numerous aplite dikes from 40 cm to 10 m in width occur on the property.

3.5 Quartz veins

Quartz veins are abundant throughout the property. The majority of the veins appear to be related to Cretaceous deformation. Early veins are typically thin, foliation-parallel, sulfide-rich, and contain no tourmaline. All of the other quartz veins, including those that contain beryl and emerald, are associated with at least some tourmaline, either within the veins or in the vein selvage. The degree of alteration surrounding the veins varies from none to m-wide horizons of rusty-weathering schist. This rustiness is likely due to weathering of finely disseminated sulfides (especially pyrrhotite) that are commonly present in the alteration zones adjacent to the veins.

3.6 Emerald

Emerald is found associated with veins at several different orientations. Mineralization appears to be particularly well developed in the area of intersection between the youngest generation of veins and older, more deformed veins. Emeralds occur along the margins of quartz veins in highly-altered schist, as well as within the quartz veins themselves. The mineralizing event is interpreted to have occurred over a considerable period of time, but was mainly syn- to late- tectonic, coinciding with the waning stages of quartz monzonite intrusion. Late ductile deformation has also affected some of the emerald-bearing veins, as evidenced by the presence of healed fractures in emerald and micro-boudinage of tourmaline grains within vein quartz. At least two of the aplite dikes contain beryl or emerald, which confirms our hypothesis that there is a continuum from the quartz monzonite intrusion through aplite dikes to beryl-bearing quartz veins (Neufeld et al. 2003).

4 TRUE BLUE

The True Blue property is located in the Ketz-Seagull District of the southern Yukon Territory, within the Cassiar Platform and southwest of the Tintina Fault. Beryl was discovered on the property in 1976, and gem beryl in 2003 (Rohtert et al. 2004). The crystals occur in a swarm of closely spaced quartz ± siderite ± fluorite ± tourmaline veins that

fill tension gashes in a Mississippian-age (~360 My) syenite stock. The veins range in thickness from 0.5 to 20 cm, and locally comprise up to 30% of the rock. The vein zone measures 700 × 200 m in outcrop at the surface, and is exposed over an elevation range of 100 m. Within this area, more than 100 individual occurrences have been discovered. The vein zone is developed near the upper contact of the syenite body with Lower Paleozoic pelitic and carbonate country rocks. The syenite is sodic in composition (~8 wt.% Na₂O) and contains moderately high concentrations of Be (to ~10 ppm) and F (to ~4000 ppm).

The beryl crystals range in size from a few mm to 5 × 2.5 cm, and in colour from pale to medium green and from pale to dark blue. Some of the crystals, especially those occurring with tourmaline, show a blue core and green rim. The dark blue material is noteworthy for the hue (which is maintained at very small sizes for aquamarine) and for the exceptionally strong dichroism. Electron microprobe analyses show high concentrations of Fe (to 5.81 wt.% FeO), Mg (to 3.27 wt.% MgO), and Na (to 2.51 wt.% Na₂O). Preliminary crystal-structure analysis suggests that all of the Fe is at the octahedral site, and also shows Be substitution at the Si site (to 0.33 Be apfu). Iron is most likely the chromophore responsible for the dark blue colour.

5 OTHER BE AND BERYL OCCURRENCES IN NW CANADA

A literature review (of assessment reports and other published and unpublished reports) shows that numerous other Be and beryl occurrences exist in southern Yukon and northern British Columbia. Analyses of a scheelite-bearing skarn at the Myda claim, approximately 20 km south of the Regal Ridge showing, show 0.05 to 0.09 wt.% BeO. Beryl has also been reported from the Logtung W-Mo deposit, the JC Sn-bearing skarn claims, and the Ice Lakes area, all in southern Yukon close to the British Columbia-Yukon border. Beryl has also been reported from the Jennings River, Ash Mountain, Blue Light, Gazoo, Low Grade, Haskins Mountain, and Cassiar Beryl showings and prospects in northern British Columbia. Most of these are associated with Cretaceous plutons, in particular the Cassiar batholith.

The discovery of emeralds at Regal Ridge and Lened and of gem beryl at True Blue, along with numerous reports of anomalous levels of Be and/or the presence of beryl in the northern Cordillera, suggest the potential for more emerald and gem beryl occurrences in the Yukon, western Northwest Territories, and northern British Columbia. This area could represent one (or possibly more) distinct

beryl/emerald camp(s), as has been recognized at other places in the world.

6 REFERENCES

- Groat, L.A., Marshall, D.D., Giuliani, G., Murphy, D.C., Piercey, S.J., Jambor, J.L., Mortensen, J.K., Ercit, T.S., Gault, R.A., Mathey, D.P., Schwartz, D.P., Maluski, H., Wise, M.A., Wengzynowski, W. & Eaton, W.D. (2002) Mineralogical and geochemical study of the Regal Ridge showing emeralds, southeastern Yukon. *Canadian Mineralogist*, 40, 1313-1338.
- Marshall, D.D., Groat, L.A., Falck, H. & Giuliani, G. (2004) The Lened emerald prospect, Northwest Territories, Canada: Insights from fluid inclusions and stable isotopes, with implications for northern Cordilleran emerald. *Canadian Mineralogist*, 42 (in press).
- Mortensen, J.K. (1992) Pre-Mid-Mesozoic tectonic evolution of the Yukon-Tanana Terrane, Yukon and Alaska. *Tectonics*, 11, 836-853.
- Mortensen, J.K. & Jilson, G.A. (1985) Evolution of the Yukon-Tanana Terrane: Evidence from southeastern Yukon Territory. *Geology*, 13, 806-810.
- Mortensen, J.K., Hart, C.J.R., Murphy, D.C. & Heffernan, S. (2000) Evolution of early and mid-Cretaceous magmatism in the Tintina Gold Belt. In: *The Tintina Gold Belt: Concepts, Exploration, and Discoveries*, J.L. Jambor, ed. British Columbia and Yukon Chamber of Mines, 2, 49-57.
- Murphy, D.C. & Piercey, S.J. (2000) Syn-mineralization faults and their re-activation, Finlayson Lake massive sulphide district, Yukon-Tanana Terrane, southeastern Yukon. In: *Yukon Exploration and Geology 1999*, D.S. Emond and L.H. Weston, (eds.), Exploration and Geological Services Division, Yukon Region, Indian and Northern Affairs Canada, 55-66.
- Murphy, D.C., Colpron, M., Roots, C.F., Gordey, S.P., & Abbott, J.G. (2002) Finlayson Lake targeted geoscience initiative (southeastern Yukon), Part 1: Bedrock geology. In: *Yukon Exploration and Geology 2001*, D.S. Emond, L.H. Weston and L.L. Lewis, (eds.), Exploration and Geological Services Division, Yukon Region, Indian and Northern Affairs Canada, 189-207.
- Neufeld, H.L.D., Groat, L.A., & Mortensen, J.K. (2003) Preliminary investigations of emerald mineralization in the Regal Ridge area, Finlayson Lake district, southeastern Yukon. In: *Yukon Exploration and Geology 2002* D.S. Emond & L.L. Lewis (eds.), Exploration and Geological Services Division, Yukon Region, Indian and Northern Affairs Canada, 281-284.
- Piercey, S.J., Murphy, D.C., Mortensen, J.K. & Paradis, S.A. (2000) Arc-rifting and ensialic back-arc basin magmatism in the northern Canadian Cordillera: evidence from the Yukon-Tanana Terrane, Finlayson Lake region, Yukon. *Lithoprobe Report*, 72, 129-138.
- Rohtert, W.R., Quinn, E.P., Groat, L.A. & Rossman, G.R. 2003 Blue beryl discovery in Canada. *Gems & Gemology*, 39,

Spectroscopy of Colored Diamonds

R.S.Guttler

Department of Mineralogy, Geosciences Institute, University of São Paulo, São Paulo, Brazil

N.E.Haralyi

Department of Mineralogy, Geoscience Institute, University of São Paulo State, Rio Claro, Brazil

ABSTRACT: A data bank of UV/VIS/NIR and IR spectra of colored diamonds has been compiled. This will aid in the analysis of the defect centers responsible for the colors of fancy diamonds. Besides, it is of utmost importance to have a reference of spectra of natural material to define the range of intensities and concentrations of the color producing defects for any investigation of possible treatments of fancy diamonds. Some absorption spectra of natural, synthetic, and treated diamonds are shown and the main defects indicated.

1 INTRODUCTION

Brazil was the main producer of diamonds during the eighteenth century, before the discovery of the huge deposits in South Africa in the middle of the nineteenth century. From the main alluvial mining areas, millions of carats of high quality stones flooded the market in Europe leading to a heavy drop in value (Lenzen 1966).

Considering the most valued types of diamond, the so called fancy diamonds, or diamonds in shades of pink, lilac, blue, green, yellow, orange, and red, beside black and champagne, Brazil has enriched to a considerable extent the list of known colored stones. Copeland (1974) lists one hundred and one colored stones of historic importance and large sizes and of these, twenty seven colored diamonds as coming from Brazil, mainly from Minas Gerais. During the last 30 years, few descriptions can be found, but the last find in 1997 refers to a rough red diamond of 13.90 carats, cut to a shield shaped gem of 5.11 carats (Genis 1998, Sauer 2001) and recently exposed at the Smithsonian, shows the importance of Brazil as a producer of outstanding gems. On the other hand, in Brazil, very little has been investigated or documented of all those colored diamonds and hardly nothing had been undertaken to

mount a databank of spectra of natural colored diamonds. Considering the problem of color enhancement of natural and synthetic diamonds, it is of utmost importance to have a reliable reference library of spectra at disposition. Only then, one can make comparisons.

2 DEFECTS IN DIAMOND AND COLOR

Pure diamond does not absorb visible light selectively and is therefore colorless. The energy of the visible light cannot excite electrons to overcome the energy of the large band gap. Therefore, diamonds that are colored by absorbing light in the visible region do so because there exist defects with electronic levels in the band gap permitting electrons to move. These may be "point defects" with dimensions of interatomic distances or these may be "extended defects" involving few or large groupings of atoms in the structure of diamond. A search in the specific literature, cited by Collins (1982) and Harlow (1998) dealing about natural, synthetic, and Chemical Vapor Deposited Diamonds (CVD), revealed more than 500 different defects possible in the diamond structure and their interactions at higher temperature, where these become mobile. These

defects show up very often as fine absorption lines, called Zero Phonon Lines (ZPL) accompanied by secondary minor absorptions in absorption spectra. The shape of these and the number and form of the secondary maxima are characteristic of the type of defect (Walker 1979, Zaitsev 2000). It may be stressed that those fine ZPL as such do not impart a color, but only the additional more or less broad bands of absorption of the secondary peaks. It appears an impossible task to monitor all of these and their interactions as can be seen by the wealth of recent work published in the journal "Diamond and Related Material". Fortunately, in natural diamonds, it is mainly Nitrogen up to about 3000 ppm, Boron up to tens of ppm, interstitial Carbon and Vacancies (not occupied structural sites) which dominate the defect chemistry and physics as a function of growth history, concentration and temperature. A good review about the fundamental work on these defects can be found in Berman (1965), Walker (1979), and Collins (1982). Not all of these defects interact with light, in that case they do not impart any coloration on the diamond. Sometimes, they even quench optical responses of nearby active defect centers. Four major forms of Nitrogen related defects exist – isolated substitutional Nitrogen (C-center), occupying tetrahedral sites in the structure, the A- and B-aggregate composed of two and four nitrogen, respectively, and the N3 complex with three nitrogen. The first three absorb also in the infrared part of the electromagnetic spectrum, and these are even used to classify diamonds by Infrared Spectroscopy in type Ib, IaA, and IaB or even IaA/B using the specific absorptions in the one-phonon region at about 1000 to 1500 cm⁻¹ wave number range. Diamonds with very little nitrogen are called type II and Type IIb contains some ppm Boron. The C-center with maximum absorption in the UV at 270 nm absorbs still in the visible blue region, producing intense yellow colors at low concentrations (the so-called Canary Diamonds) or green colors at higher concentrations. The A- and B-centers are optically inactive. If isolated substitutional nitrogen, the normal stage at diamond growth, aggregate during the further history of the diamond in the mantle, it forms the A-, B-aggregates. The original yellow diamond will turn colorless. Combinations of three nitrogen with carbon give rise to the N3-centers at a wavelength of 415 nm. These and the related N2-centers (478 nm) absorb light and impart light yellow colors, producing the Cape color diamonds.

Combinations of nitrogen with vacancies produced by radiation treatment and further annealing form the ND1, H3, H4, and N-V centers with their different charge states. They are all optically active. The N-V center in its negative charge state is responsible for treated red and pink to purple colored diamonds. Natural pink diamonds, however, are colored by a broad absorption band

with peak at about 550 nm, whose identity is still in debate. Boron related defect centers produce absorption in the red end of the spectra producing a blue color in diamonds, like the famous "Hope Diamond". Brown or champagne colored diamonds, natural or synthetic, show an increasing absorption to the violet end or high energy range. Microscopic evidences link the color forming defect center to episodes of plastic deformation of the crystal structure during the history of the diamond

3 COLOR ENHANCEMENT OF DIAMOND

3.1 Irradiation

By artificial irradiation of diamonds with electrons, gamma-rays or neutrons, one produce defects in the crystal structure of diamond. These defects may be of Schottky or Frenkel type by creating interstitial atoms or vacancies. They are known as the GR1 defect system at about 741 nm, accompanied by a large absorption band to higher energy produced mainly by the presence of carbon-interstitials, and impart a green or blue color on the diamond as function of radiation dose and type of diamond used. The GR1 system produces a typical absorption spectrum independent of type of irradiation.

3.2 Heat treatment

By subsequent heat treatment, these radiation-produced defects become mobile and will recombine or combine with chemical impurities in the structure to form defects similar to those found in the natural counterparts. Depending on the original composition of the diamond and on its history, the colors so produced may be orange, yellow, red, lilac and pink, imitating very well the natural fancy colored diamonds. The implications of this treatment are quite obvious. A diamond colored by this method will never be so rare as his natural counterpart.

4 EXPERIMENTAL

Using natural and treated material from the collection of the senior author, UV/VIS/NIR and IR spectra have been taken with the Guided Wave System and the FTIR facilities at the Chemical Institute of University of São Paulo. About 150 spectra of various types of colored diamonds have been collected. This Guided Wave system works very well on cut stones. By use of an optical fiber, light is being directed into the stone and the same light conductor collects the light which passed through the stone. This setting does not allow to quantify the absorption coefficient because of lack of knowledge of the path length of the light. The cooling system has still to be optimized to get good

low temperature spectra and the following discussion of the results concentrates on room temperature spectra. During the presentation of the figures, the main features of spectra of colored diamonds, natural, synthetic, and treated, as already outlined above, will be discussed and some differences between natural colored and artificially produced will be highlighted.

5 RESULTS

At first, spectra of the very common yellow diamonds will be shown. In that case, one has to differentiate between the natural Canary and the Cape Diamonds. The color of the former is due to isolated substitutional nitrogen, the color of the latter produced by defects called N3 and N2. Fig.1 shows a typical Cape Diamond with quite a strong yellow color due to the N3 and N2 defect. It should be kept in mind, that the strength of color is related to the concentration of these defects.

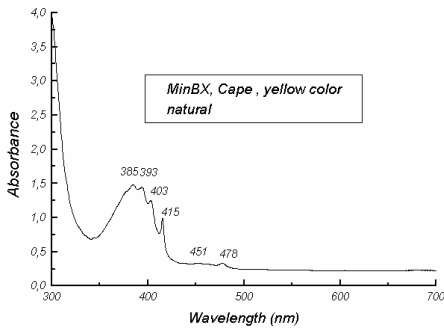


Figure 1. Cape yellow diamond, natural, with N3 and N2 defects at 415 and 478 nm wavelength. The large absorption band from 415 to 350 nm is clearly seen.

An other type of yellow natural diamond is shown in Figure 2, showing the N3 but not the N2 defect.

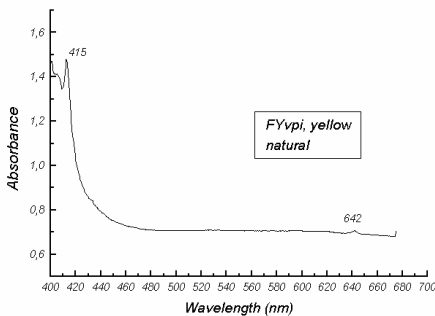


Figure 2. Natural yellow diamond with strong N3 absorption at 415 nm wavelength.

Some representative spectra of brown and yellow-brown natural and synthetic diamonds are shown in Figure 3 and 4. The absorption in both increases to higher energy continuously in the synthetic stone, the natural diamond shows additionally shoulders on the absorption slope, indicating coexisting defects.

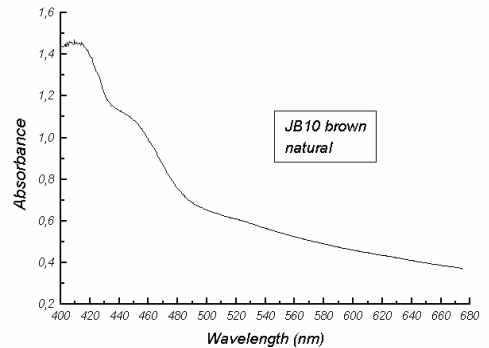


Figure 3. Absorption spectrum of natural brown diamond from Juína, Brazil.

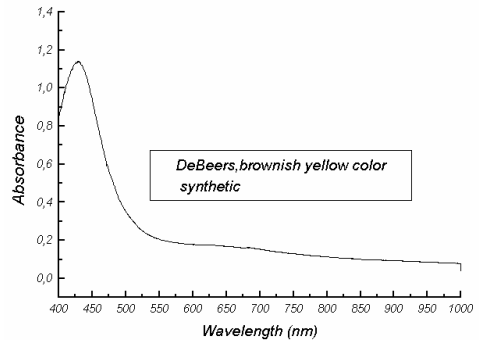


Figure 4. Absorption spectra of synthetic brown diamond, produced by De Beers.

The problem of the pink color in diamonds is still under investigation. The following Figure 5 shows an absorption spectra of a strongly pink colored natural diamond. At about 550 nm the spectrum shows a strong broad peak of absorption imparting the fine pink color on the stone.

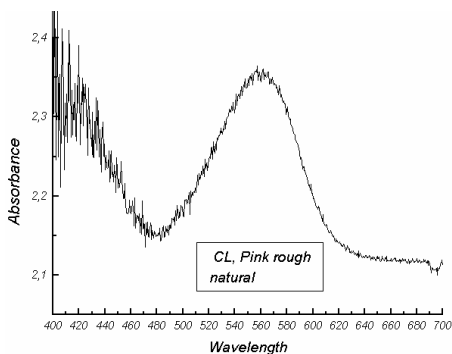


Figure 5. Pink colored diamond from Juína, the strong absorption at about 550 nm is responsible for the color.

The pink color can also be produced by using irradiated diamonds containing nitrogen and vacancies. By heat treatment up to 800 degree they form the N-V-defect imparting a pink, red or mauve color.

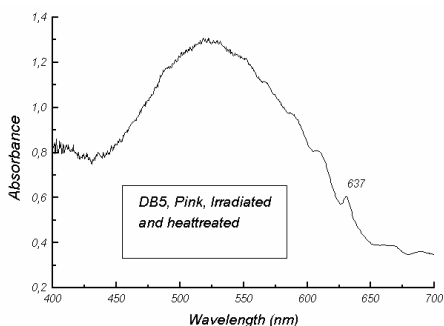


Figure 6. Pink diamond. Color is due to irradiation and heat treatment. The N-V defect at 637 nm is indicated.

The blue color in diamond may be a result of treatment or due to substitutional boron. Figure 7 and 8 show typical absorption spectra for both types of coloration.

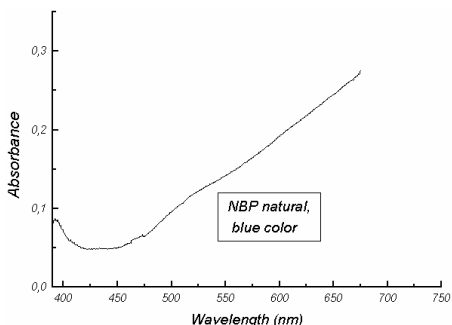


Figure 7. Absorption spectrum of boron-containing natural blue diamond with absorption increasing to higher wavelength.

To differentiate the two types, one has to test the electrical conductivity. Boron colored diamonds show electrical conductivity, the irradiated ones on a much smaller scale, below the detection limits of most conductivity meters. Infrared spectra, not shown here, give evidence of the presence of boron related defects.

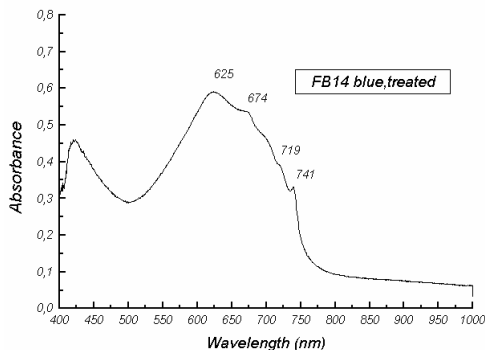


Figure 8. Blue color produced by irradiation. The GR1 defect system with ZPL at 741 nm is clearly seen.

In case of the diamond shown in Fig.8, the dose of radiation used produced a blue color. This can be clearly seen by the low absorption between 400 and 500 nm and the higher absorption at 550 nm and larger wavelength. A smaller dose of radiation will produce a green stone. Natural green colored diamonds will show the same features of the 741 nm defect, but to a much smaller extent and intensity. It is therefore quite difficult to assign without doubt a natural green color to a diamond.

6 REFERENCES

- Berman, R.1965. Physical Properties of Diamond. Clarendon Press – Oxford.
- Collins, A.T. 1982. Colour Centers in Diamonds. Journal of Gemmology 18: 37-75.
- Copeland, W. 1974. Famous and Unique Diamonds. Gemol. Institute of America, GIA.
- Genis, R. 1998. The Gemstone Forecaster. Vol.16 No.2, Collector Corner.
- Harlow, G. E. 1998. The Nature of Diamonds. Cambridge University Press.
- Lenzen, G. 1966. Produktions-und Handels- Geschichte des Diamanten. Berlin.
- Sauer, R.J. 2001. Eras do Diamante. Amsterdam-Sauer, Rio de Janeiro.
- Walker, J. 1979. Optical Absorption and Luminescence in Diamond. Rep. Prog. Phys. 42: 1605-1659.
- Zaitsev, A.M. 2000. Vibronic Spectra of impurity- Related optical centers in diamond. Physic. Rev. B. 61: 12909-12922.

The Relevance of Small Scale Paragenetic Relations Derived from the Structural Topology of Gem-minerals for Technological Processes and Products

W.Hofmeister

Department of Geosciences, Applied Mineralogy and Gemstone Research, Johannes-Gutenberg-University, Mainz, Germany

ABSTRACT: Known from gem mineralogy, the oxidic system MASB has several features ruled by actual chemical composition with appropriate structural topology, which makes it an exiting base for small scale phase mineralogy applicable to the development of new substrate materials and glass ceramic systems. Special emphasis must be put on grain boundaries and on crystalline gradient properties in this system, and the challenge may be summarized as “potential of small scale paragenesis”: There is a clear benefit developed by structural changes in the region of coexisting crystal surfaces at intergranular boundaries if local adjustments of coordination polyhedra are taken into consideration.

1 INTRODUCTION

The vast majority of gemstones are homogeneous, crystalline, naturally grown, inorganic materials, just minerals with some special properties. Many of them are members of the MAS-system (MgO, Al₂O₃ and SiO₂ given as m:a:s) with some, minor additives and/or replacing elements, as, for example, chromium, boron, beryllium, fluorine, and hydrogen. Some members of system are prominent minerals and gemstones for its own: Quartz (0:0:1) with its open framework structure as the most common polymorph of a vastly spread family, and corundum (0:1:0), with its famous relatives sapphire and ruby. Periclase (1:0:0) provides the system with all the features of a typically cubic close packed oxidic structure. Compounds in between the corners of the MAS-triangle are known as minerals too, but usually are more famous as crystalline products with essential properties for solid state technologies. The fact, that the MAS-system is responsible for about 89 % of the crystalline products of the Earth's mantle (Gasparik 2003) proves the stability of the crystal structures for the given chemistry under the prevailing pT-relations.

2 CRYSTAL CHEMISTRY AND STRUCTURAL TOPOLOGY

The increasing demand in having materials for enduring tools, as for substrates or glass ceramics, asks for basic solids with high strength, hardness and/or high Young's Modulus (e-module). Some of the MAS-members are highly qualified in this sense, like corundum (0:1:0), or spinel (1:1:0), or sapphirine (7:9:3), or cordierite (2:2:5). Their physical properties as homogeneous crystals clearly depend on the individual crystal structures, the bonding between the building units and the purity of the chemical compounds involved in the actual phase, since impurities, as long as they are not soluble in the host, will result in inclusions which interact with the host. The host-guest relationship is very essential for the whole object and its properties, depending on grain size, energy at the grain boundaries and intergranular texture of the “whole rock”. The relation between a large single crystal and its minor inclusion-phases (voids, gas, fluid, crystals) is comparable to a glass-ceramic system, where crystallites and glass are combined with the result of special physical properties.

The MAS-system is not only relevant due to its crystalline compounds, it is a glass system too. Therefore, the combination of glassy and crystalline phases may be of great advantage for technical applications. One of the main features of the physical properties of MAS-minerals is the architecture of their crystal structures, which are widely dominated by backbones of aluminium-oxygen-polyhedra, connected via two common edges thus building infinite octahedral chains (Peacor et al. 1999). These chains now may be interconnected in different ways with different coordination polyhedra around other or the same cations, which to characterize is a task of extended topological analysis of crystal structures.

Usually, in the pure MAS-system there is a limited diversity in the principal kind of coordination polyhedra due to the restricted chemistry of the cations. Extension of the MAS-system with B_2O_3 (Grew & Anovitz, 1996) results in more complex gemstone minerals (m:a:s:b; sinhalite 2:1:0:1, grandierite 2:3:2:1, etc.) with typical features like high density, transparency, high index of refraction, high hardness etc.. Here, polyhedral diversity within a chemical system climaxes, as there are at least three principally different polyhedra around Mg^{2+} , three around Al^{3+} , two around B^{3+} , and one around Si^{4+} . And obviously, there is interdependence between these possible arrangements of cations and anions in the individual crystal structures, also depending on nucleation and crystal growth conditions. These effects have their influence on the dimensions of polyhedra and in this way on the physical properties of the crystalline phases and their interaction.

Werdingite (2:7:4:4) / m:a:s:b) (Niven et al. 1991), for example, is built up of magnesium-oxygen trigonal-diprisms, aluminium-oxygen octahedra and tetrahedra, silicon-oxygen tetrahedra, boron-oxygen tetrahedra and triangles. This is a bad example for Pauling's rule of parsimony; it shows the principal possibility of ruling the crystallization behaviour of a chemically complex composition by temperature, pressure and crystallization kinetics with the aim to get one complex or some more but less complex crystalline phases. And in kornerupine (Moore & Araki 1979) (ca. 8:12:8:1 / m:a:s:b), there is one tetrahedral site which may be occupied by more or less boron, being the central tetrahedron in a T_3O_{10} group, which affects the bridging angle of the trimer during changes in site occupancy. This may influence the physical properties of a composite material having kornerupine as an essential crystalline compound.

3 OBSERVING CRITICAL PARAMETERS

The observation and characterization of inclusions in

gem mineralogy is very essential for at least three purposes: 1. The origin of gem material may be defined by certain inclusions which can be a witness for the geological context or the crucible of laboratory synthesis. 2. During a necessary heat treatment, frequently applied to optimize some properties of gemstones, the gem itself and its relation to the host must be known to prohibit unintentional destruction of the host by the guest. 3. The inclusion may be resolved by the gem material itself by applying the appropriate technique and leave the gem in a better context.

Some years ago, a very powerful method has been adapted to analyze small particles in situ without any interference: The Raman-Microprobe basing on Raman-Micro-Laser-Spectroscopy (e.g. Nasdala 2002). It has the advantage of analyzing what is to be seen, independent of being solid, crystalline, fluid or gaseous, and it is also able to deliver clear signals of the actual stress and strain state of objects embedded in other materials (Nasdala et al. 2003). Due to the resolution of only some μ^3 the next neighborhood and even the grain-boundaries between different phases may be analyzed in situ, showing the direct relationship of them in paragenesis. If there are, for example, crystalline or fluid inclusions within a transparent corundum crystal which has to be heat treated for colour enhancement, there will be changes in the next area around the inclusions during the heating and cooling processes. Depending on the nature of the inclusion there may be a cotectic reaction, a partial melting followed by crystallization or absorption of material. The small scale reaction usually is not the center of further investigations, but it is really worth to be so in the future. For some substances the crystallization out of a glass is an appropriate way to get single crystals. The result may be some kind of a glass ceramic. The behavior of spinel or sinhalite or sapphirine crystals within a ruby or sapphire crystal during primary bulk crystallization or during secondary solid state reactions has a pronounced influence on the physical properties of the host mono-crystal.

4 CONCLUSIONS

So, if there is any strong stress and strain regime between the different phases, this will influence the "whole rock" stability, or the glass ceramic compound. It is the aim of further investigations to reduce the intergranular differences within a given basic system by crystal chemical engineering according to the structural variability of the compounds. There is not only the way of producing chemical compounds of principally different crystal structure and topology; there is the possibility of taking advantage of polytypism, of increasing or

decreasing the amount of solid solution and of chemically concurring end members of a restricted solid solution series or closely related crystal structures.

Therefore, the well known oxidic systems used so long and fruitful in technology are not at their evolutionary end, we know too much about the phases involved. It is only necessary to combine the sub-nano crystal structure data with the chemical potential of the compounds involved across the intergranular borderlines of the solid phases and extrapolate them to a scale of physically practicable properties.

5 REFERENCES

- Gasparik, T. (2003): Phase Diagrams for Geoscientists. Springer, Berlin.
- Grew, E. S. & Anowitz, L. M. (eds.) (1996): Boron. Mineralogy, Petrology and Geochemistry. Rev. Mineralogy 33, Min. Soc. Amer.
- Moore, P. B. & Araki, T. Komerupine (1979): a detailed crystal-chemical study. N. Jb. Miner. Abh., 134, 317-336.
- Peacor, D. R., Rouse, R. C. & Grew, E. S. (1999): Crystal structure of boralsilite and its relation to a family of boroaluminosilicates, sillimanite, and andalusite. Amer. Mineral., 84, 1152-1161.
- Nasdala, L. (2002): Mineralogical applications of Raman microprobe mapping. – Federation of Analytical Chemistry and Spectroscopy Societies, 29th Annual Meeting, Providence, RI, USA, 2002.
- Nasdala, L., Brenker, F. E., Glöckner, J., Hofmeister, W., Gasparik, T., Harris, J. W., Stachel, T., Reese, I. (2003): Spectroscopic 2D-tomography: Residual pressure and strain around mineral inclusions in diamonds. – Eur. J. Mineral. 15, 6, 931-936.
- Niven, M. L., Waters, D. J. & Moore, J. M. (1991): The crystal structure of werdingite, $(\text{Mg,Fe})_2\text{Al}_2(\text{Al,Fe})_2\text{Si}_4(\text{B,Al})_4\text{O}_{37}$, and its relationship to sillimanite, mullite, and grandidierite. Amer. Mineral., 76, 246-256.

A New Opal Occurrence in Volcanic Rocks of Paraná Basin, Brazil

P.L.Juchem, R.Lubachesky, T.M.M. de Brum

Gemological Laboratory, Department of Mineralogy and Petrology, Geosciences Institute, Federal University of Rio Grande do Sul, Porto Alegre, Brazil.

B.L.Waichel

State University of West Parana, Brazil.

ABSTRACT: A new opal occurrence was recently discovered in SW of Paraná State, Brazil, in Serra Geral Formation, a late Jurassic-early Cretaceous volcanic sequence of Paraná basin. This material is deposited mainly inside small roundish to ovoid cavities but also filling thin fractures in a basaltic rock. This opal occurs as an opaque massive material, sometimes in botryoidal aggregates, exhibit black colour and is brittle, resembling volcanic glass. It is optically isotropic with a refractive indice of 1,49. X-ray measurements show diffraction pattern of a mixture of non-crystalline opal and opal-CT. When viewed under petrographic microscope in thin section, it is usually translucent with reddish brown colours and do not show remarkable growth structures or inclusions. On petrographic and SEM/EDS microscopy, some native copper inclusions were identified. Chemical data obtained by X-ray fluorecence showed that this opal contains 40% of SiO₂, 31% of Fe₂O₃, approximately 20% of water, followed by MgO (4%), CaO (1,9%) and Al₂O₃ (1,4%), and small amounts ($\leq 0,2\%$) of MnO, Na₂O, K₂O, TiO₂ and P₂O₅. Although it does not occur in large quantities, reports of other opal occurrences in neighbouring areas will encourage exploratory works in order to determine its gemmological quality and commercial potential.

1 INTRODUCTION

Gem quality opal deposits are known in Rio Grande do Sul State, in rocks from Serra Geral Formation, a late Jurassic-early Cretaceous volcanic sequence of Paraná basin (Augustin et al. 2003). A new black colour opal occurrence was recently discovered in SW of Paraná State filling cavities in the same volcanic formation. This paper is the first report about these occurrences and presents the preliminary results about geological and mineralogical characteristics. In spite the small occurrences, the study of this material is an important approach on the mineralogical properties of this material in order to determine its gemmological potential. Geological and mineralogical characteristics will also contribute to understand the genesis of geode minerals.

According to Ball (1985) and Schumann (1991) the term "black-opal" will be used for any precious opal of dark grey or black body colour in hue. Despite the black colour of the Paraná opal, samples obtained until now do not show the play of colour that characterizes the precious opal. For this reason, opal studied here will be named as "black colour opal".

2 ANALYTICAL TECHNIQUES

Mineralogical and petrographic analyses were performed in laboratories of Geosciences Institute of Federal University of Rio Grande do Sul.

Mineral data were obtained with a Schneider polariscope and gemmological microscope, a Topcon refractometer and a Leitz petrographic microscope; the later was used also for host rock petrographic analysis. Specific gravity was determined with a Marte hydrostatic balance. Krüss ultraviolet lamps of short and long wavelenght were used in order to observe fluorescence in opal samples. X-ray diffraction (XRD) spectra of powdered opal samples were produced in a Siemens diffractometer. Operation conditions were: Cu K α radiation, 30 kV, 30 mA and 2 θ varing from 2 to 80 $^{\circ}$. A Jeol JSM 5800 scanning electron microscope (SEM) was used to analyse the internal structure and solid inclusions; this inclusions were also identified by semiquantitative chemical analyses using an energy dispersive system (EDS) equipment. A Rigaku RIX 2000 X-ray spectrometer was used to determine opal major chemical elements.

3 GEOLOGY AND OCCURRENCES

As it can be observed in Figure 1, Paraná State have five main important geological settings. Crystalline rocks constitute the Precambrian shield and are represented by metamorphic and granitic rocks included in Açungui Group (Almeida et al. 1984). The Gondwanic sedimentary rocks are composed by glacial, marine and continental units, deposited in Paraná Basin, a huge sedimentary basin located in southeastern South America. These rocks are covered by lava flows of Jurassic-Cretaceous age, originated from deep fractures related to Gondwana rupture and

South Atlantic Ocean opening (Piccirillo & Melfi 1988). This unit is known as Serra Geral Formation and is mainly composed by tholeiitic basalts, locally covered by dacitic and rhyolitic flows in the southern States of Brazil (Chies & Roisenberg 1993). Cretaceous sediments are represented by continental sandstones, covered by recent sediments in several regions. The Coastal sediments are mainly Quaternary to recent units, originated during sea level oscillations.

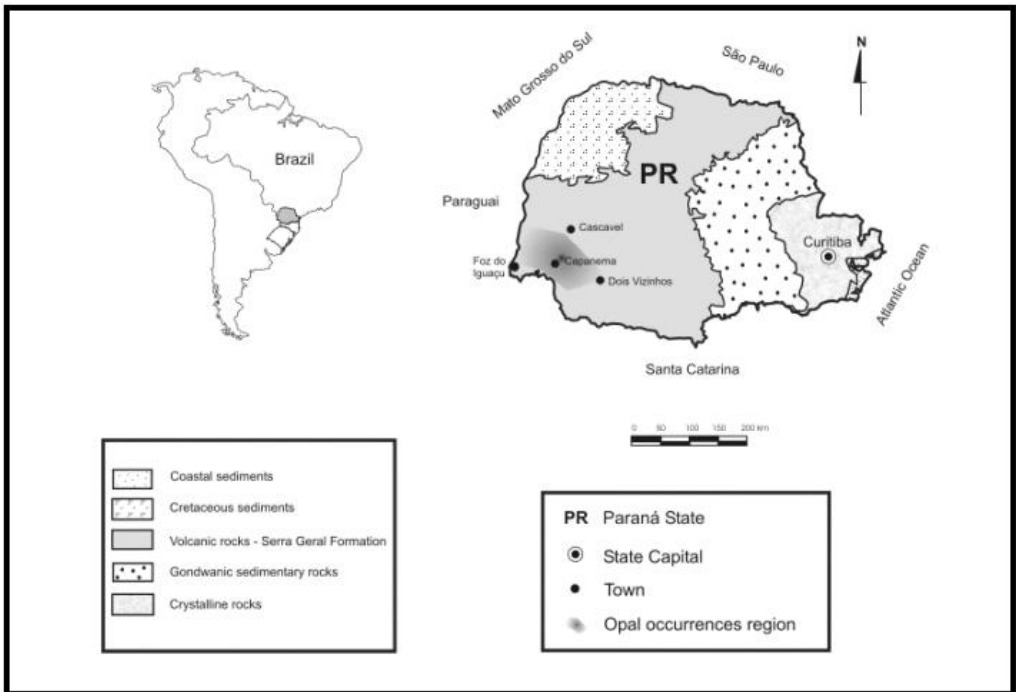


Figure 1. Localization map of Paraná State (Brazil), showing the main geological settings and the black colour opal occurrences region.

Black colour opal was found firstly in a paving stone quarry during a geological field trip near Capanema town, and further in other dispersed occurrences in two localities, Cascavel and Dois vizinhos region. Some occurrences near Foz do Iguaçu town have also been reported. The host rock of these occurrences is a sparsely to highly opal-bearing amygdaloidal basalt with dark gray colour and aphanitic to micro-porphyrific texture. Fine to medium grains of labradorite, augite, Ti-magnetite and native copper comprise the mineralogical composition.

The deposits occur mainly inside small roundish to ovoid lava cavities that can reach from few

millimeters up to 10 centimeters in length. Usually, the smaller cavities are entirely filled with black coloured opal, while centimetric cavities may be incompletely filled with thick opal layers; in this larger cavities, opal can be followed by gray chalcedony and colourless to milky quartz, and sometimes amethystine crystals (Figure 2). In some occurrences, thin veins of black colour opal fill fractures in the basaltic rock.

4 MINERALOGICAL CHARACTERISTICS

Opal occurs as a black opaque massive material,

sometimes in botryoidal aggregates (Figures 2 and 3). This opal exhibit black colour, vitreous to resinous luster and is brittle, resembling volcanic glass. It shows irregular to conchoidal fracture, 5 to 6 Mohs hardness and 1,88 specific gravity. It is optically isotropic with a refractive indice of 1,49. When viewed under petrographic microscope in thin section, it is usually translucent with reddish brown colours and does not show remarkable growth structures or inclusions. In rare samples it is possible to observe minute inclusions of a yellow metallic material, visible under the loupe and even to the naked eye. With SEM/EDS microscopy, they were identified as native copper inclusions. Euhedral crystals of this mineral may also occur deposited inside small cavities of the basaltic rock.

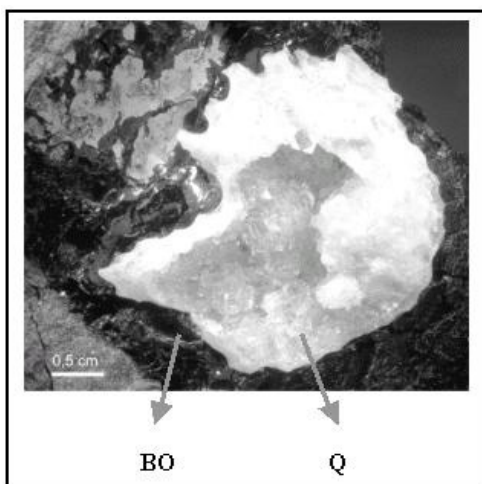


Figure 2. A cavity in basaltic rock filled with black colour opal (BO), followed by colourless to milky quartz (Q).

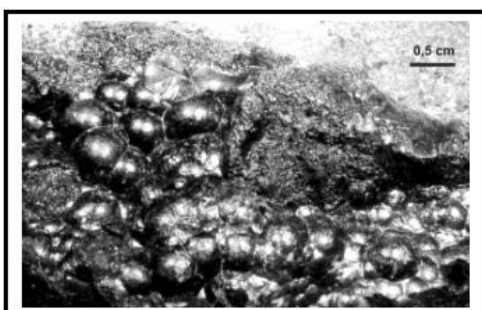


Figure 3. Black colour opal in botryoidal aggregates filling a cavity in a basaltic rock.

Chemical data obtained by X-ray fluorescence (Figure 4) show that this opal contains approximately 40% of SiO₂, 32% of Fe₂O₃ and 20% of water, followed by MgO (4%), CaO (1,9%),

Al₂O₃ (1,4%), and small amounts ($\leq 0,2\%$) of MnO, Na₂O, K₂O, TiO₂ and P₂O₅. These results are very different of those obtained in opal from other regions. The black colour opal from Paraná shows a smaller content of SiO₂ and higher content of Fe₂O₃ and H₂O than opal from other occurrences (e.g Frondel 1962; Gomes & Costa 1994; Augustin et al. 2003).

SiO ₂ = 40,20	CaO = 1,93	K ₂ O = 0,07
Fe ₂ O ₃ = 31,79	Al ₂ O ₃ = 1,43	TiO ₂ = 0,06
H ₂ O = 20,10	Na ₂ O = 0,26	P ₂ O ₅ = 0,02
MgO = 3,95	MnO = 0,20	

Figure 4: Chemical composition of black colour opal from Paraná State, Brazil.

X-ray measurements show diffraction patterns that resemble a mixing of non-crystalline opal (opal-A) and opal-CT, according to the classification of Graetsch (1994). As it can be observed in Figure 5, the diffraction of the analysed opal shows a small peak characteristic of opal-CT (at $\sim 35.70^{0}2\theta$) due to tridymite and a broad irregular peak between 20 and 30⁰2 θ , resembling Opal-A. On SEM observations in opal fragments, it was not possible to identify cristobalite and/or tridymite crystals neither the amorphous silica spheres, characteristic of internal structure of opal-A.

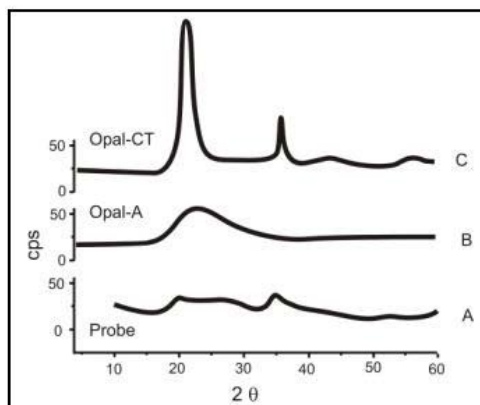


Figure 5: X-ray diffractograms of black colour opal from Paraná (A), opal-A and opal-CT. The probe opal diffractogram shows a small peak characteristic of opal-CT and a broad irregular peak resembling Opal-A.

5 CONCLUSIONS

Although black colour opal from Paraná was not found in large quantities until now, preliminary geological and mineralogical results presented in this paper show it is a unique and interesting

occurrence in volcanic rocks of Paraná basin. Mineralogical and chemical data of this opal are very different of those obtained in opal of other regions (e.g Frondel 1962; Smith 1988; Gomes & Costa 1994; Banerjee & Wenzel 1999; Augustin et al 2003). Reports of other opal occurrences in neighbouring regions will encourage other exploratory and research works in order to determine its gemmological quality and commercial potential.

6 REFERENCES

- Almeida, F.F.M; Hasuy,Y.; Litwinsky, N. 1984. O Pré-Cambriano no Brasil. São Paulo-Editora Edgard Blücher, 318 p.
- Augustin, A. H.; Brum, T.M.M.; Juchem, P.L 2003. Características mineralógicas da opala da região do Salto do Jacuí, RS. XV Salão de Iniciação Científica, UFRGS. CD-ROOM. Sessão de Mineralogia e Petrologia I, Trabalho 01.
- Ball, R.A. 1985. Black opal: a brief review. Australian Gemmologist, 15, p. 310-314.
- Banerjee, A.; Wenzel, T. 1999. Black opal from Honduras. European Journal of Mineralogy. 11, p. 401-408.
- FrondeL, C. 1962. The system of mineralogy of J. D. Dana & E. S. Dana. New York. Yale University, 1837-1892 ed. 7 ed. John Wiley & Sons, Inc., 334 p.
- Gomes, E.R.; Costa, M.L. 1994. Contribuição à gênese das opalas de Pedro II (Piauí). Geochimica Brasiliensis, v 8, n 1, p. 79-98.
- Chies, J. O. & Roisenberg, A. 1993. Modelos para geração do vulcanismo ácido da Bacia do Paraná, na região ocidental RS/SC. Cong. Bras. Geol. Anais. V. IV. p. 23-24.
- Juchem, P.L.; Hofmeister, T.; Brum, T.M.M. 1990. Substâncias Gemológicas no Rio Grande do Sul - Modos de Ocorrência e Caracterização Gemológica. XXXVI Cong. Bras. Geol. Anais. Natal, RN. V.3. p.1436-1449.
- Piccirillo, E.M.; Melfi, A.J. eds. 1984. The Mesozoic Flood Volcanism of the Paraná Basin - petrogenetic and geophysical aspects. São Paulo, USP-Instituto Astronômico e Geofísico. p. 179-205.
- Schumann, W. 1991. Gemas do Mundo. Rio de Janeiro. 3a. ed. Ed. Ao Livro Técnico S.A. 254 p.
- Smith, K.L 1988. Opal from Opal Butte, Oregon. Gems & Gemology. V. 2, n. 4. p. 229-236.

Diamond from the Los Coquitos Area, Bolivar State, Venezuela

F.V. Kaminsky, O.D. Zakharchenko, G.K. Khachatryan

KM Diamond Exploration Ltd., 2446 Shadbolt Lane, West Vancouver, British Columbia, V7S 3J1, Canada

D.M.DeR. Channer

Guaniamo Mining Company, Centro Gerencial Mohedano, Office 9D, La Castellana, Caracas, Venezuela

W.L. Griffin

GEMOC, Department of Earth and Planetary Sciences, Macquarie University, NSW, Australia

ABSTRACT: The Los Coquitos placer is located approximately 50 km north of the Guaniamo area in Bolivar State, Venezuela, and no obvious primary diamond sources are associated with it. Diamond in the Los Coquitos placer is generally similar to the Quebrada Grande diamond; however Los Coquitos diamond has a higher relative abundance of A-type nitrogen impurities with respect to complex nitrogen centers, and has a higher proportion of isotopically heavy diamond crystals. Diamond from the Los Coquitos area has a unimodal (rather than bimodal) distribution of crystals based on the concentration of A nitrogen impurity centers, and a higher relative abundance of A-type nitrogen centers with respect to B and P centers. Generally, the $\delta^{13}\text{C}$ value of the Los Coquitos diamond varies from +0.4 to -20.5 ‰. Minerals of the eclogitic suite predominate among the diamond inclusions from the Los Coquitos placer, as is the case with the Quebrada Grande placer and kimberlite sills. Los Coquitos mineral inclusions in diamond show a lower calcium index of garnets, wider compositional variations in pyroxene, and lower forsterite component in olivine, as compared with Quebrada Grande diamond. This suggests that the Los Coquitos diamond has the same, kimberlitic type of primary source, but it may be a different, new source from the known kimberlite sills in Guaniamo.

1 INTRODUCTION

Earlier we studied diamond from placer deposits of the Quebrada Grande River in the Guaniamo area, Venezuela and demonstrated that, in contrast to previous conclusions, they were not recycled from Proterozoic Roraima sediments but are of local origin, and have been derived from 700-800 Ma kimberlite sills (Kaminsky et al. 2000, Channer et al. 2003). This is why prospecting works for diamond in the Guaniamo area were extended by the Guaniamo Mining Company, and led to the discovery of new diamondiferous placer deposits.

For this research we comprehensively studied 77 diamond crystals from the new, Guaniamo placer (Fig.1). The main objective of this study was to evaluate the conditions of formation of Guaniamo diamond, and to identify the primary sources for the placer diamond crystals in the Guaniamo valley and nearby alluvial areas.

2 DIAMOND MORPHOLOGY

Diamond crystals from the Guaniamo placer include dodecahedroids (36.3%), octahedra (24.7%), O-D combination crystals (28.6%), and their twins

and aggregates. 84.4% of the Guaniamo diamond crystals bear green pigmentation spots.

Epigenetic (post-growth) alterations of diamond crystals include surface features due to post-growth processes such as natural oxidation dissolution and plastic deformation and mechanical erosion marks caused by transportation of crystals in alluvium. None of the studied diamond crystals from the Guaniamo placer exhibits any marks of intense mechanogenic erosion.

3 NITROGEN IMPURITIES

All Guaniamo diamond crystals can be subdivided into three groups based on their IR spectral features: Group I includes diamond crystals with a sharp predominance of B nitrogen impurity centers over A centers; Group II includes diamond crystals with approximately equal proportions of A and B centers; and Group III diamond crystals have low (compared to that of Groups I and II) concentrations of all nitrogen impurity centers, with unequal proportions of A and B centers. They all belong to Group 2 moderate-nitrogen diamond (which includes most of the known diamond populations) with an average nitrogen aggregation %B=60-70% (Fig.2).



Figure 1. Location map.

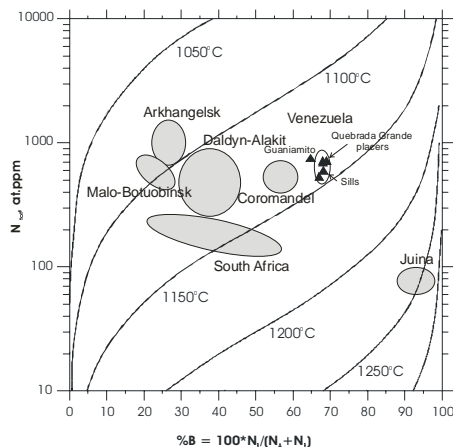


Figure 2. Taylor-Milledge (1995) diagram for diamond crystals from different area worldwide. Isotherm curves are for 3 Ga.

In general, IR spectra of diamond crystals from the Guaniamo placer are similar to those from

diamond crystals from the Guaniamo sills and the Quebrada Grande placer that were recorded in our previous study (Kaminsky et al. 2000). The similarity between diamonds from Guaniamo and Quebrada Grande placers is confirmed by comparison of average values of nitrogen B centers, hydrogen impurity and platelets. Average hydrogen and platelets values in Guaniamo diamond crystals are comparable with the ones in Quebrada Grande crystals.

At the same time, diamond crystals from Guaniamo placer have a higher total nitrogen content (N_{tot}) and lower level of its aggregation ($\%N_B$) comparing to Quebrada Grande crystals. As a result, the figurative point of Guaniamo diamond is located out of the field of diamond crystals from the Guaniamo area (Fig.3). This difference may point to dissimilar thermal and/or kinetic parameters of diamond crystals formation processes.

Based on these data, despite the fact that diamond crystals from the Guaniamo placer have much in common with diamond crystals from the Quebrada Grande deposits, it can not be excluded that some as-yet unknown primary source was involved in the formation of the Guaniamo placer.

4 CARBON ISOTOPIC COMPOSITION

Isotope analyses were performed with the VARIAN-MAT-230 mass-spectrometer, with an accuracy of $< 0.1\%$ PDB ($^{13}C/^{12}C$ PDB = 0.0112372). After initial preparation, crystals of diamond were oxidized to CO_2 using an O_2 flux (circular system, 900 °C).

The $\delta^{13}C$ value of the Guaniamo diamond crystals varies from +0.4 to -20.5‰. Like in the Quebrada Grande sills and placer, isotopically light diamond crystals with $\delta^{13}C < -10\%$ predominate (58%). One of the diamond crystals studied has a positive $\delta^{13}C$ value (+0.4‰). The majority of diamond crystals with inclusions of eclogite-suite minerals are isotopically light.

The variation in $\delta^{13}C$ in the Guaniamo placer diamond (Fig.3) suggests the Quebrada Grande sills and placer were not the suppliers of diamond crystals to the Guaniamo placer. This variation would suggest that an unknown deposit, in which the proportion of isotopically heavy diamond crystals is higher than in the Quebrada Grande deposits, was involved in the formation of the Guaniamo placer.

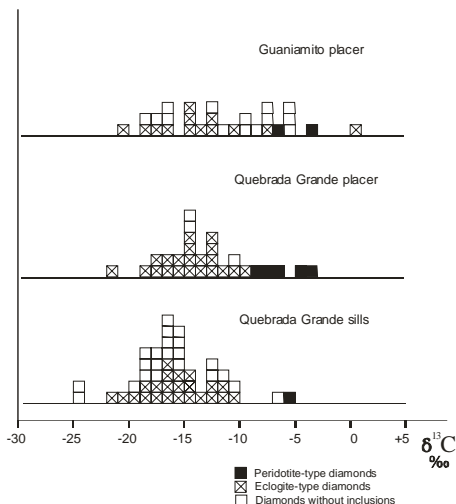


Figure 3. $\delta^{13}\text{C}$ distribution in diamond crystals from the Guaniamito and the Quebrada Grande placers and sills.

For the diamond crystals with crystalline mineral inclusions, a correlation was observed between the isotopic composition and the paragenetic affinity of the mineral inclusion. The rare diamond crystals with mineral inclusions of ultramafic paragenesis are isotopically heavy. The majority of diamond crystals with inclusions of eclogite-suite minerals are isotopically light.

5 MINERAL INCLUSIONS IN DIAMOND

High-pressure minerals (other than sulphides) account in the Guaniamito placer in approximately 23% of diamonds. They contain mineral inclusions of eclogitic and ultramafic suites. A characteristic feature of the Guaniamito diamond crystals is the sharp predominance of crystals with mineral inclusions of eclogitic suite: seventeen diamond crystals (89.5%) are of the eclogitic association, and only two crystals (10.5%) appeared to be minerals of the ultramafic suite.

Eclogitic-type inclusions in the Guaniamito diamond crystals are represented by garnet (pyrope-almandine), clinopyroxene (omphacite), ilmenite, coesite and ferroan periclase.

Garnet of the pyrope-almandine series (10 grains) has mg value in the limit of 0.487 to 0.586, what is similar to garnet included in Guaniamo diamonds (Fig.4). The calcium index in these grains varies from 15 to 26 with an average of 19.5.

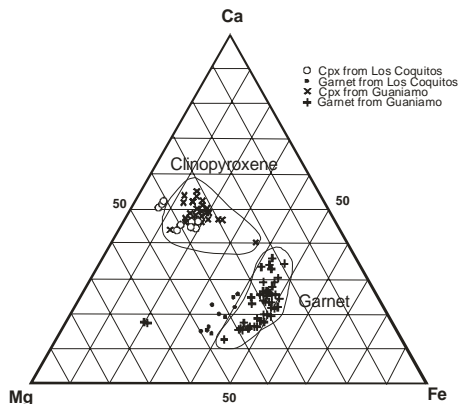


Figure 4. Mg-Ca-Fe composition of pyrope-almandine garnet and clinopyroxene included in Guaniamito diamond.

Pyroxene (omphacite) is also abundant among the E-type mineral inclusions in Guaniamito diamond crystals. The Na_2O content varies from 3.2 to 6.6%, with an average of 5%. Al_2O_3 content varies from 8.6 to 12.6% and shows a positive correlation with Na_2O . A characteristic feature of the pyroxene inclusions in the Guaniamito diamond crystals is the high proportion of K_2O (0.5 to 1.0%, average of 0.76%). Guaniamito pyroxene includes three groups of omphacite: a high-magnesium group with $mg = 0.843\text{--}0.849$, a relatively low-magnesian group with $mg = 0.683\text{--}0.699$, and a transition group of a wider composition with $mg = 0.738\text{--}0.771$ (Fig.4).

Coesite occurs in the Guaniamito diamond crystals as small colorless inclusions, and in some cases, is associated with orange garnet and omphacite. Three coesite inclusions were analyzed; they are virtually pure SiO_2 .

A single ilmenite inclusion was found in association with omphacite. It is characterized by a low MgO content (0.10%) and a higher than usual MnO content (2.35%). We observed such specific, low-Mg manganiferous ilmenite grains in superdeep diamonds from Juina, Brazil (Kaminsky et al. 2001); some of them were in association with ferroan periclase, majorite and CaTi-perovskite. However, in this case low-Mg manganiferous ilmenite associates with omphacite and belongs to the eclogitic association.

A single ferroan periclase inclusion was recorded. The carbon isotopic composition of hosting diamond is $\delta^{13}\text{C} = 12.4\text{‰}$ PDB and is likely to be of E-type. The ferroan periclase has 97% FeO with only 0.09% MgO and $mg = 0.002$. This is unusual for lower-mantle ferroan periclase which has a wide mg variation range from 0.38 to 0.85 (Harte et al. 1999, Kaminsky et al. 2001). Probably, the iron index of ferroan periclase can be used in future as a criterion for distinguishing of lower-mantle ferroan periclase.

Ultramafic-type inclusions are represented only by olivine. Three olivine inclusions were found; they have similar forsterite components ($mg = 0.926-0.932$) and contain small amounts of NiO (0.25-0.33%) and Cr₂O₃ (0.05- 0.11%). They are similar to olivine inclusions occurring in diamond crystals from other regions.

6 DISCUSSION

The equilibrium temperature and pressure estimates for the eight pyroxene inclusions in Los Coquitos diamond are in a wide range of 1060-1767 °C and 41-83 kbar. These figures, in general, correspond to the P-T estimates for Guaniamo diamond crystals (1025-1450 °C and 55-61.5 kbar; Kaminsky et al. 2000). However, they demonstrate presence of higher P-T conditions for Los Coquitos diamond comparing to Guaniamo diamond.

Like in Guaniamo diamond crystals, in Los Coquitos, crystals of the eclogite suite are sharply predominant. Earlier we suggested that this fact may have been caused by involving in diamond origin carbon incorporated in volcano-sedimentary lithospheric rocks which later underwent subduction into the mantle. This idea was supported recently by studying of oxygen isotope composition in coesite included in Guaniamo diamond crystals. Schulze et al. (2003) have established that the oxygen isotope ratio $\delta^{18}\text{O}$ VSMOW in coesite preserved in diamond is in range of +10.2 to +16.9‰, what is abnormal of subcratonic mantle. These values are typical of subduction-zone meta-basalts.

On the other hand, Los Coquitos diamond crystals differ of Guaniamo crystals by their morphology, physical properties, nitrogen impurities, carbon isotope composition and mineral inclusions. This suggests that the Los Coquitos diamond crystals may have a similar, kimberlitic primary source like the Guaniamo diamond crystals, but the location of the sources are different. Each locality has its own sources. Judging by almost a full lack of mechanical erosion marks on Los Coquitos diamond crystals, their sources are local.

7 REFERENCES

Channer, D.M.DeR., Egorov, A. & Kaminsky, F. 2001. Geology and structure of the Guaniamo diamondiferous kimberlite sheets, South-West Venezuela. *Revista Brasil. Geocienc.* 31(4), 615-630.

Harte, B., Harris, J.W., Hutchison, M.T., Watt, G.R. & Wilding, M.C. 1999. Lower mantle mineral associations in diamonds from Sao Luiz, Brazil. In: Yingwei Fei, C.M. Bertka and B.O. Mysen (eds.), *Mantle Petrology: Field Observations and High Pressure Experimentation. A Tribute to Francis R. (Joe) Boyd*. The Geochemical Society Special Publication No. 6, 125-153.

Kaminsky, F. V. & Khachatryan, G. K. 2001. Characteristics of nitrogen and other impurity in diamond, as revealed by infrared absorption data. *Canadian Mineralogist* 39(6), 1735-1745.

Kaminsky, F.V., Zakharchenko, O.D., Griffin, W.L., Channer D.M.DeR & Khachatryan-Blinova, G.K. 2000. Diamond from the Guaniamo area, Venezuela. *Canadian Mineralogist* 38(6), 1347-1370.

Kaminsky, F.V., Zakharchenko, O.D., Davies, R., Griffin, W.L. & Shiryaev, A.A. 2001. Superdeep diamonds from the Juina area, Mato Grosso State, Brazil. *Contr. Mineral. Petrol.* v. 140(5), 734-753.

Schulze, D.J., Harte, B., Valley, J.W., Brenan, J.M. & Channer D.M.DeR. 2003. Extreme crustal oxygen isotope signatures preserved in coesite in diamond. *Nature* 423(6975), 68-70.

Simakov, S.K. 2003. Physico-chemical aspects of diamond-bearing eclogites formation in the upper mantle and earth crust rocks. Magadan: Far East Branch RAN, 187 pp.

Taylor, W.R. & Milledge H.J. 1995. Nitrogen aggregation character, thermal history and stable isotope composition of some xenolith-derived diamond crystals from Roberts Victor and Finch. In: *Sixth Internat. Kimberlite Conf. Extended Abstr.*, Novosibirsk, August 1995, 620-622.

Pink Tourmaline Studied by Optical Detection of Magnetic Resonance

K.Krambrock, S.M.Medeiros & K.J.Guedes

Departamento de Física, ICEx, Universidade Federal de Minas Gerais, CP. 702, 30.123-970 Belo Horizonte, MG, Brazil

M.V.B.Pinheiro & J.-M.Spaeth

Fachbereich Physik, Universität Paderborn, 30098 Paderborn, Germany

ABSTRACT: The pink color of tourmaline from the elbaite family is generally attributed to manganese impurities or intrinsic radiation-induced defects. Pink tourmaline samples from different regions in Minas Gerais, Brazil, are investigated by electron microprobe, electron paramagnetic resonance (EPR) and optical absorption. The color is caused from three absorption bands centered at 390 nm (strong), 515 nm (strong) and 680 nm (weak). EPR spectra reveal the presence of manganese and iron impurities consistent with electron microprobe analysis. However, the EPR lines are very broad and their angular dependencies complicated, inhibiting a conclusive structure analysis. More information is obtained from the optical detection of magnetic resonance (ODMR) using the magnetic circular dichroism of the absorption (MCDA). The temperature and magnetic field dependence of the MCDA is analyzed for the spin state by the Brillouin function. From that analysis we conclude that the dominant absorption band at 515 nm is due to Mn^{3+} and the band at 680 nm is due to Mn^{2+} . Most samples can be decolorized by thermal treatments at about 600°C, while gamma irradiation restores the pink color. The color of some brownish-pink samples can be enhanced when first decolorized by thermal treatment and afterwards irradiated leaving them pure pink.

1 INTRODUCTION

Tourmaline is known for its great variety in colors with gem-quality. The most common tourmaline from Brazil are pink, green and blue. The knowledge about the cause of color is very poor. Most colors were explained by transition metal impurities like Fe and Mn in different valence states incorporated basically in Y-sites in the tourmaline structure. The models for the color centers are generally based only on optical absorption data in combination with crystal-field theory. The color of pink tourmaline, related with an absorption band centered at 515 nm, is discussed. It has earlier been attributed to an intrinsic O' hole center produced by irradiation (Berhov et al. 1969) or it has been related to manganese impurities (Petrov 1990).

Tourmaline exhibits a very complex chemical composition with trigonal structure (space group $R3m - C_{3v}^5$). The chemical formula can be written as $XY_3Z_6(BO_3)_3Si_6O_{18}(OH,F)_3(OH,F)$ (King et al. 1994), where the X-sites are normally Na, Ca or vacancies, sometimes Mg, Fe or Mn. The Z and Y-sites are generally occupied by Al, however, substitution of nearly all transition metals can be found in the Y-sites.

Krambrock et al. (2004) have shown by optical detection of magnetic resonance (ODMR) that the O' hole center interacting with two Al ions is produced by gamma irradiation in O₁ sites of tourmaline. It is correlated with an absorption band centered at 365 nm with a band tail extending in the visible spectral range inducing a yellow color (Krambrock et al. 2004). In this work we show by ODMR that the dominant absorption band in pink tourmaline centered at 515 nm is related to trivalent manganese impurities.

2 EXPERIMENTAL

All pink tourmaline samples investigated originate from Minas Gerais, Brazil, and belong to Li-bearing elbaites. The Mn and Fe content varied in between 0.25 – 0.15 wt.% and 0.02 – 0.08 wt.% as determined by electron microprobe analysis. Samples were oriented using the natural faces perpendicular to the c-axis, afterwards cut to dimensions of 3 x 2 x 5 mm³ and polished to optical quality.

Optical detection of magnetic resonance was carried out via the magnetic circular dichroism of absorption (MCDA). The equipment consists of a

superconducting split-coil magnet with the monochromatic, circularly polarized light propagating along the magnetic field direction. Optically detected electron paramagnetic resonance (ODEPR) were done in a split K-band resonance cavity working at 24 GHz. More details can be found elsewhere (Spaeth & Overhof 2003).

3 EXPERIMENTAL RESULTS AND ANALYSIS

Figure 1 (a) shows the optical absorption spectrum of natural pink tourmaline measured at room temperature. Three absorption bands can be observed in the natural sample: 680 nm (weak), 515 nm (strong), a strong increase in absorption towards the UV spectral range with a shoulder at 390 nm (strong). All absorption bands disappear in thermal annealing experiments at about 600°C leaving the sample colorless (Fig. 1b). Gamma-irradiation restores the color. Figure 1 (c) shows the spectrum obtained after gamma irradiation with a dose of 400 kGy. The bands appear in different intensities depending on the dose. The bands centered at 680 nm, 515 nm and the shoulder at 390 nm are restored, however, the strong UV transition is still less intense than in the natural sample.

The color of natural brownish-pink samples can be enhanced with the combination of thermal annealing and gamma-irradiation. The brown hue in such samples does not appear again and the sample acquires a pure pink color.

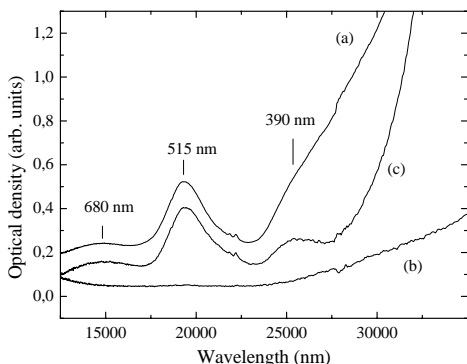


Figure 1: Unpolarized optical absorption spectra measured at room temperature of pink tourmaline (a) natural pink (b) after thermal treatment at 600°C and (c) after thermal treatment and gamma irradiation with a dose of 400 kGy.

Figure 2 shows the MCDA spectra of the same pink tourmaline sample measured at two different temperatures (1.63 K and 4.2 K) and two magnetic fields (1.0 T and 2.0 T). From the dependence with

temperature we can conclude that the absorption bands belong to paramagnetic color centers.

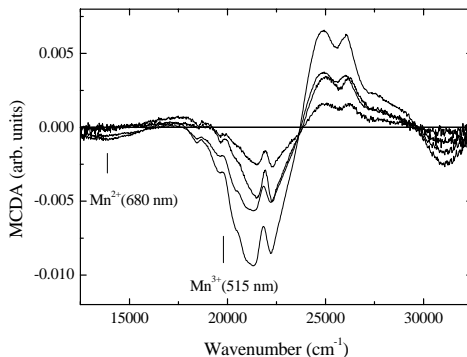


Figure 2: MCDA spectra of pink tourmaline measured for two temperatures (1.63 K and 4.2 K) and two magnetic fields (1.0 T and 2.0 T) for $B \parallel c$ -axis.

Figure 3 shows the ODEPR spectrum measured at 1.5 K with microwave frequency of 24.02 GHz in the MCDA band at 515 nm for $B \parallel c$ -axis. Different EPR transitions can be observed which have large line widths (about 100 mT). The results are similar to conventionally detected EPR spectra. For some orientations the typical 6 line hyperfine spectrum of manganese was observed. However, a complete analysis of the spectra is difficult. By measuring the excitation spectra of the ODEPR lines it is found that all belong to the same paramagnetic center. The different ODEPR lines are attributed to fine structure transitions of manganese. The analysis of the spin Hamiltonian leaves to the g -factor for $B \parallel c$ -axis equal to 1.98 ± 0.02 .

However, more information about the manganese impurities can be obtained analyzing the temperature and field dependence of the MCDA. The MCDA of a paramagnetic defect is proportional to the spin polarization which is given by the Brillouin function

$$B_s(x) = \frac{1}{S} \left[\left(S + \frac{1}{2} \right) \coth \left(S + \frac{1}{2} \right) x - \frac{1}{2} \coth \frac{x}{2} \right] \quad (1)$$

where x is $x = g\mu_B B/kT$ and S is the spin state of the paramagnetic defect. The other constants have their usual meaning. Measuring the MCDA for two different temperatures and two magnetic fields allows one to calculate the ratio R_{exp}

$$R_{exp} = \frac{MCDA(B1, T1) - MCDA(B1, T2)}{MCDA(B2, T1) - MCDA(B2, T2)} \quad (2)$$

which can be compared to the theoretical ratio R_{the} using the Brillouin function for the same temperatures and magnetic fields (Spaeth & Overhof 2003). For the ratios diamagnetic contributions to the MCDA are eliminated. The results of such an analysis are shown in Table 1.

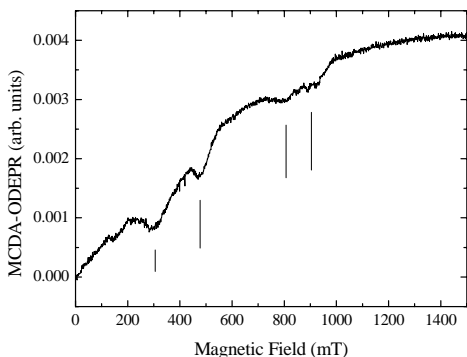


Figure 3: ODEPR spectrum of pink tourmaline measured at 1.5 K with microwave frequency of 24.02 GHz in the MCDA band at 515 nm for $B \parallel c$ -axis. Straight lines indicate different fine structure transitions.

Table 1: Analysis of spin state using the Brillouin function (equ. 1) for the magnetization. Ratio $R = R_{exp}/R_{the} \approx 1$ determines the spin state.

MCDA (cm^{-1})	MCDA (nm)	S=1.5	S=2.0	S=2.5
14265	700	0.74	0.87	0.99
19420	515	0.93	0.99	1.04
21275	470	0.90	0.98	1.07
22245	450	0.86	0.95	1.03
24915	401	0.92	1.00	1.10
26075	384	0.96	1.04	1.14

From the above results it is proposed that the dominant optical absorption band of pink tourmaline centered at 515 nm is associated with Mn^{3+} in the high spin state with spin $S = 2$, which best reproduce the Brillouin function. The other absorption band at 680 nm with weak intensity is probably related to the Mn^{2+} ion. We can only speculate about the site in which the manganese ion enters. The Y-site has a bigger volume for accommodation of impurities and also it has the same trivalent charge state leaving the crystal neutral.

4 DISCUSSION

The discussion about the color in tourmaline is very complicated and controversy because of the different chemical compositions and possible substitutions,

together with high concentrations of impurities. Electron paramagnetic resonance studies, very successful for the analysis of color centers and impurities in ionic crystals and many minerals, are nearly absent in tourmaline.

The pink color of tourmaline is discussed to originate from manganese impurities (Petrov 1990) or intrinsic O⁻ hole centers (Bershov et al. 1969). From our study it is clear that the absorption bands in pink tourmaline are related to manganese impurities. The irradiation-induced O⁻ hole center is responsible for a yellow color (Krambrock et al. 2004). The dominant absorption band in pink tourmaline at 515 nm is due to a paramagnetic defect with spin $S = 2$ and a g-factor for $B \parallel c$ -axis of 1.98. These data are consistent with Mn^{3+} ions in the high spin state $S = 2$ in weakly distorted octahedral sites. This model is consistent with earlier results (Manning 1973). The best site in the tourmaline lattice for Mn^{3+} is that of the Y-site substituting Al^{3+} ions because of the higher volume compared to the Z-site.

The color of other minerals like red beryl (bixbite) or pink spodumene (kunzite) was also attributed to manganese impurities (Nassau 1983). What type of optical transition is responsible for the absorption band in the visible spectral range is not clear at the moment. Intrinsic d-d transitions are in general not allowed and therefore should be less intense. However, in low symmetrical environments the electric dipole transition probabilities can be enhanced. Charge transfer transitions involving Mn ions or Mn and Fe ions in different valence states can also explain some of the optical transitions.

An open question is still the thermal annealing process at about 600°C, in which the pink tourmaline loose its color. From this investigation it is concluded that the absorption bands at 390 nm and 515 nm have different origins. However, what kind of physical process is involved by the treatments is not easily answered. In EPR measurements the signals which were attributed to Mn^{2+} ions did not enhance after thermal treatment at about 600°C, where the crystal turns colorless, neither new paramagnetic defects were observed. More experiments are necessary to find an answer to this question.

5 CONCLUSIONS

The dominant absorption band of pink tourmaline at 515 nm is due to manganese impurities in the trivalent charge state in high spin configuration with $S = 2$. It is suggested that the Mn^{3+} ions occupy preferably the Y-sites. The color of brownish-pink tourmalines (elbaïtes) from Brazil can be enhanced when first receive a thermal treatment at about 600°C and afterwards gamma-irradiation.

6 ACKNOWLEDGEMENTS

The authors are grateful to V. J. Ferreira, C. Castañeda and J. Karfunkel for providing the samples; R. Ferracini (CDTN) for the gamma irradiations and A.I.C. Persiano for the electron microprobe analysis. We acknowledge financial support from the Brazilian agencies FINEP (CORGEMA 4856), CNPq and CAPES (Probral 125/01) and the DAAD.

7 REFERENCES

- Bershov, L.V., Martirosyan, V.O., Marfunin, A.S., Platonov, A.N. & Tarashchan A.N. (1969): Color centers in lithium tourmaline (elbaite), *Sov. Phys. Crystallog.*, 13, 629.
- King, V.T., Foord, E.E. & Gaines, R.V. (1994): Die Turmalingruppe, Christian Weise Verlag extraLapis, 6, 8.
- Krambrock, K., Pinheiro, M.V.B., Guedes, K.J., Medeiros, S.M., Schweizer, S. & Spaeth, J.-M. (2004): Correlation of irradiation-induced yellow color with the O[•] hole center in tourmaline, *Phys. Chem. Min.*, 31, 167.
- Manning, P.G. (1973): Effect of second-nearest-neighbor interaction on Mn³⁺ absorption in pink and black tourmalines. *Can. Mineral.*, 11, 971.
- Nassau, K. (1983): The physics and chemistry of color, John Wiley & Sons.
- Petrov, I (1990): Role of natural radiation in tourmaline coloration – discussion, *Am. Mineral.*, 75, 237.
- Spaeth, J.-M. & Overhof, H. (2003): Point Defects in Semiconductors and Insulators, Springer Series in Material Science, CHAP. 4.

Trace Elements and Colors in Gemological Varieties of Spodumene Mineral

M.A.S.Lacerda, E.F.Oliveira, R.Stasiulevicius, G.F.Kastner, A.M.Amaral

Centro de Desenvolvimento da Tecnologia Nuclear, Comissão Nacional de Energia Nuclear, Belo Horizonte, Brazil.

ABSTRACT: This work presents the results of characterization and irradiation treatment of two spodumene mineral varieties (greenish and lilac). To determine the concentration of trace elements in the samples the k_0 Instrumental Neutron Activation Analysis (k_0 -INAA) was used. A ^{60}Co irradiator was used for the treatment of the specimens. The change of color, when they were submitted to high intensity gamma rays, was analyzed. The results obtained in characterization and irradiation treatment showed relatively good agreement with the literature. The k_0 -INAA method, showed its potential as an analytical multi-elemental determination tool. Some elements in trace quantities were detected in the samples, suggesting a possible influence of these elements on spodumene colors.

1 INTRODUCTION

The spodumene mineral, from pyroxene group, represented by the general formula $\text{LiAlSi}_2\text{O}_6$, is a source for the production of Li salts. The transparent varieties of beautiful coloration are gemstones.

Gemological varieties of spodumene are rare in nature, being known as kunzite (lilac) and hiddenite (green). Colorless, yellow-straw and pale-green varieties do not have specific denominations.

Mineral varieties show well-known coloration changes whenever they are submitted to gamma rays, X-rays, electrons, and ultraviolet rays. Most authors associate the coloration change, as well as the luminescence phenomenon presented by some spodumene varieties, to the main impurities concentration: Mn, Fe and Cr (Claffy 1953; Holuj 1968; Webster 1970; Ito 1980; Fujii & Isotani 1988; Isotani et. al. 1991).

This work presents the results of characterization and irradiation treatment of some spodumene mineral varieties. The k_0 Instrumental Neutron Activation Analysis (k_0 -INAA) was used to determine the concentration of trace elements in 4 samples of 2 varieties (greenish and lilac) of spodumene mineral. The k_0 -INAA is a non-destructive technique that provides an accurate

multielemental analysis (De Corte 1986; Menezes et al. 2003). It has long been one of the most sensitive used to measure the concentration of trace amounts of many elements in gemstones.

2 EXPERIMENTAL

Lilac and greenish varieties of spodumene obtained in Minas Gerais, Brazil, were analyzed. The samples, weighing about 300 mg, were irradiated in the reactor Triga Mark I IPR-R1 (100 kW – neutron flux of $6.6 \cdot 10^{11} \text{ n} \cdot \text{cm}^{-2} \cdot \text{s}^{-1}$) in the Centro de Desenvolvimento da Tecnologia Nuclear (CDTN/CNEN), Belo Horizonte, Brazil. Reference certified material of International Atomic Energy Agency (IAEA/Soil-7) was simultaneously irradiated for quality control purposes.

The k_0 -INAA in lower layer rotatory rack was applied using Na as comparator. Trace elements concentrations were determined through three schemes of irradiation performed in rotary rack: (i) 4 minutes of irradiation time, 2-15 minutes of decay time and about 10 minutes of measuring time to determine short half-life isotopes; (ii) 4 hours of irradiation time, 36-48 hours of decay time and about 3 hours of measuring time to determine

isotopes with medium half-life values and; (iii) 16 hours of irradiation time, 20-25 days of decay time and about 6 hours of measuring time to determine long half-life isotopes.

Gamma-spectroscopy analysis was performed in two coaxial CANBERRA HPGe detectors, models GC1518 and GC5019, coupled to a multichannel analyzer. The first detector was used to determine long half-life isotopes and the second one to determine short and medium half-life isotopes. Technical problems did not allow the use of the same detector model for all measurements.

Color changes on spodumene samples, when they were submitted to high intensity gamma rays, were analyzed too. A ^{60}Co irradiator, with activity of about 40.000 Ci was used for this approach.

3 RESULTS AND DISCUSSION

Major and trace elements concentrations of reference certified material and samples are listed in Tables 1 and 2, respectively.

Table 1. Experimental and certified elemental concentrations (in $\mu\text{g} \cdot \text{g}^{-1}$) for IAEA/SOIL-7 reference.

Element	E.V	C.V	C.I
Al	49442 ± 9400	47000	44000 – 51000
As	15.8 ± 0.6	13.4	12.5 – 14.2
Ce	49.6 ± 0.5	61	50 – 63
Co	8.5 ± 0.2	8.9	8.4 – 10.1
Cr	42.3 ± 0.5	60	49 – 74
Cs	5.0 ± 0.2	5.4	4.9 – 6.4
Cu	ND	11	9 – 13
Dy	4.9 ± 0.4	3.9	3.2 – 5.3
Fe	24455 ± 82	25700	25200 – 26300
Ga	8.7 ± 1.4	10	9 – 13
K	11533 ± 127	12100	11300 – 12700
La	25.2 ± 0.2	28	27 – 29
Mn	679 ± 2	631	604 – 650
Na	2402 ± 34	2400	2300 – 2500
Rb	ND	51	47 – 56
Sb	ND	1.7	1.4 – 1.8
Sc	7.3 ± 0.2	8.3	6.9 – 9.0
Ti	ND	3000	2600 – 3700
V	59.5 ± 15	66	59 – 73

E.V: Experimental values; ND: Not detected
C.V: Certified values; C.I.: Confidence Interval

Table 1 shows that experimental results present good agreement with certified values. Some elements were not determined due to inherent interference. These results also agree with previous analyses performed in Radiochemical Laboratory in CDTN (Menezes et. al. 2003) and permit to check the reproducibility and accuracy of experimental results for spodumene mineral samples.

Table 2. Major and trace elements concentrations (in $\mu\text{g} \cdot \text{g}^{-1}$) in 4 samples of 2 varieties (greenish and lilac) of spodumene mineral.

Element	Greenish varieties		Lilac Varieties	
	A	B	A	B
Au	< 0.5	< 0.5	< 0.5	< 0.5
Ce	16.0 ± 3	18.0 ± 3	15.9 ± 2	10.2 ± 1
Cr	ND	ND	ND	ND
Fe	440 ± 50	925 ± 30	280 ± 30	195 ± 30
Ga	42.8 ± 3	43.0 ± 2	145 ± 4	53 ± 3
Hf	ND	ND	< 0.5	< 0.5
K	670 ± 70	620 ± 50	530 ± 100	420 ± 90
La	8.6 ± 0.5	7.5 ± 0.5	5.5 ± 0.5	4.7 ± 0.5
Mn	470 ± 10	490 ± 10	840 ± 10	390 ± 10
Na	990 ± 50	830 ± 50	1170 ± 50	1180 ± 50
Os	3.1 ± 1.1	3.0 ± 0.5	ND	ND
Rb	ND	ND	3.6 ± 0.7	ND
Sc	15.5 ± 0.5	17.1 ± 0.5	< 0.5	< 0.5
Sm	< 0.5	< 0.5	< 0.5	< 0.5
V	14.5 ± 2	17.6 ± 2	ND	ND
[Fe]/[Mn]	0.93	1.89	0.33	0.50

Table 2 shows an approximate Mn content in two samples of greenish spodumene. The sample B shows much higher Fe concentration. Probably, the high concentration of Fe is associated to the green color of the samples, once the greenish varieties of spodumene sampled are not true hiddenite: they are not coloured by chromium (Webster 1970). On the other hand, as the [Fe]/[Mn] ratio is low (< 2) the samples are not intense green. Contrary to green varieties sampled by Fujii & Isotani (1988).

The Mn appears in higher concentration in lilac samples. This fact is probably associated to the lilac color of these spodumene samples.

Considerably high concentration of Ga and low concentration of La and Ce in all the samples were detected. Os was detected only in greenish samples and Sc present a much higher concentration in greenish compared to the lilac samples. These elements may be substituting Al in $\text{LiAlSi}_2\text{O}_6$ crystal.

V was detected only in greenish samples and Cr was not detected in the studied samples (probably, its concentration is below the detection limit). Vanadium in the samples is too low in concentration to cause the green color.

High concentration of Na and K was found in all the studied samples. These elements may be substituting Li in $\text{LiAlSi}_2\text{O}_6$ crystal.

Irradiation of the greenish samples to high intensity gamma-rays from ^{60}Co irradiator (radiation dose of about 20 kGy) did not influence the color of these samples. But, lilac spodumene turned deeply green under gamma irradiation. When heated to temperatures above 120 °C the green color disappears in a few hours. This fact, already observed in the literature (Claffy 1953; Holuj 1968; Webster 1970; Ito 1980; Fujii & Isotani 1988;

Isotani et. al. 1991), may be associated to higher Mn concentration and the great mobility of Li ion in the crystal force field.

4 CONCLUSION

The results obtained in characterization and irradiation treatment of two varieties of spodumene mineral (greenish and lilac) showed relatively good agreement with the literature.

The k_0 -INAA method, applied for trace elements determination in samples, showed its potential as an analytical multi-elemental determination tool. Applying this technique was possible to identify some elements in trace quantities. Some of these elements, as V, Fe and Mn, found in samples, may suggest a possible influence on color which the spodumene possess. Since the color of spodumene is a complex function of Mn/Fe/Cr/V concentrations and valence states, to determine only trace elements concentrations is not sufficient to solve the problem.

5 ACKNOWLEDGMENT

This work was supported by the Fundação de Amparo à Pesquisa do Estado de Minas Gerais – FAPEMIG (Research Support Foundation of Minas Gerais State, Brazil).

6 REFERENCES

- Claffy, E.W. 1953. Composition, tenebrescence and luminescence of spodumene minerals. *American Mineralogist*, v. 38, p. 919-931.
- De Corte, F. 1986. The k_0 - standardisation method: a move to the optimisation of neutron activation analysis. Ryksuniversiteit Gent, Faculteit Van de Wetenschappen, p. 464.
- Fujii, A. T. & Isotani, S. 1988. Optical absorption study of five varieties of spodumene. *Anais da Academia Brasileira de Ciências*, v. 60, p. 127-135.
- Holuj, F. 1968. EPR of Mn^{++} in spodumene natural crystals. *Canadian Journal of Physics*, v. 46, p. 287-306.
- Isotani, S., Fujii, A. T., Antonini, R., et. al. 1991. Optical absorption study of radiation and thermal effects in brazilian samples of spodumene. *Anais da Academia Brasileira de Ciências*, v. 63, p. 127-139.
- Ito, A.S. 1980. Study of radiation damage and heat treatments in spodumene. Ph. D. Thesis, Institute of Physics of the University of São Paulo, São Paulo.
- Menezes, M.A.B.C., Sabino, C.V.S., et. al. 2003. K₀-Instrumental Neutron Activation Analysis establishment at CDTN, Brazil: A successful story. *Journal of Radioanalytical and Nuclear Chemistry*, v. 257, N^o 3, p. 627-632.
- Webster, R. 1970. *Gems. Their sources, descriptions and identification*. Butterworth & Co., London, 836 p.

Synthetic Ruby with Different Levels of Chromium Concentration and Crystal Morphology Depending on the Growth Conditions

N.I.Leonyuk & V.V.Maltsev

Geological Faculty, Lomonosov Moscow State University, Moscow 119999/GSP-2, Russia

S.N.Barilo, G.L.Bychkov, L.A.Kurnevich

Institute of Physics of Solids and Semiconductors, BAS, Minsk 220072, Belarus

G.A.Emelchenko, V.M.Masalov, A.A.Zhokhov

Institute of Solid State Physics, Chernogolovka 142432, Moscow District, Russia

ABSTRACT: Single crystals of ruby with size up to 2.5 cm have been obtained from fluxed melts based on the systems $\text{Li}_2\text{O} - \text{MoO}_3$, $\text{Li}_2\text{O} - \text{WO}_3$, $\text{Na}_2\text{O} - \text{WO}_3$, $2\text{PbO} - 3\text{V}_2\text{O}_5$, $\text{PbO} - \text{V}_2\text{O}_5 - \text{WO}_3$, $\text{PbF}_2 - \text{Bi}_2\text{O}_3$ and Na_3AlF_6 by both the top-seeded solution growth method and spontaneous crystallization at temperatures 1330 - 900°C. Al_2O_3 solubility has been measured for the flux composition of $2\text{Bi}_2\text{O}_3 - 5\text{PbF}_2$ in the temperature range 1200-1000°C and dissolution enthalpy has been found as 29.4 KJ/Mol. The composition of grown crystals was studied by electron microprobe analysis. The synthetic ruby contains 0.51 to 6.38 at % of chromium admixture depending on the crystal growth conditions. Mo, W, Pb and Bi concentration in grown crystals does not exceed 0.01 wt %. The amount of vanadium impurities varies from 0.02 to 0.06 at %. The crystallographic forms {0001}, {01-12}, {11-23}, {10-14}, {10-10} and {10-10} are distinguishing features of the crystals grown. Synthetic crystals obtained within 1150 - 900°C have a plate-like habit with a strongly developed pinacoid, except the crystallization of ruby from Li-enriched fluxed melts at elevated temperatures. Ruby crystals tend to grow with more equidimensional shape in the interval of 1330 - 1100°C. In this case, the {0001} faces are rarely developed. Increasing WO_3 concentration in $\text{PbO} - \text{V}_2\text{O}_5 - \text{WO}_3$ system also promotes more isometric ruby crystals.

1 INTRODUCTION

Corundum, $\alpha\text{-Al}_2\text{O}_3$, belongs to the most popular materials with device potential, and colored crystals, for example, ruby and sapphire are found as a highly prized gemstones. Particularly, the red of natural ruby corundum is due to contents of Cr^{3+} up to 1%, and additional V^{3+} (as a rule, 0.03-0.05%) intensifies the color (Deer et al. 1962).

The interest in ruby crystals for gemology applications has led to a demand for crystals of color, real structure and habit like natural red corundum. For this reason, attempts have been made to grow these crystals by flux method or under hydrothermal conditions, but most of them are impracticable for the commercial production of isometric crystals. The synthetic ruby contains maximum 2 - 3% of Cr_2O_3 admixture (Balitski & Lisitsyna 1981), and it tends to grow with a plate-like habit having strongly developed {0001} faces (Elwell & Scheel 1975).

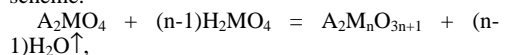
Only a few authors could obtain the isometric crystals, especially with {22-43} faces from high-temperature tungstate solutions for example, see (Yanovskii et al. 1970). Additionally, a complex flux of the $\text{PbF}_2 - \text{Bi}_2\text{O}_3$ system has been used for the growth of isometric ruby crystals by Chase & Osmer

(1967). However, the lack of the Al_2O_3 solubility data for this flux composition holds back of the progress towards developing growth technology of large ruby single crystals.

On the whole, the influence of the type of solvent, impurities and temperature on the corundum habit is yet to be understood precisely. This paper deals with experimental results on the growth conditions, solubility, composition, and morphology of ruby crystals obtained from high-temperature solutions using $\text{Li}_2\text{O} - \text{MoO}_3$ (I), $\text{Li}_2\text{O} - \text{WO}_3$ (II), $\text{Na}_2\text{O} - \text{WO}_3$ (III), $\text{SrO} - \text{WO}_3$ (IV), $\text{PbO} - \text{V}_2\text{O}_5$ (V), $2\text{PbO} - 3\text{V}_2\text{O}_5 - \text{WO}_3$ (VI), $\text{PbF}_2 - \text{Bi}_2\text{O}_3$ (VII) and Na_3AlF_6 (VIII) as fluxes.

2 EXPERIMENTAL

Before the flux growth experiments, all complex flux compounds were synthesized at 600-900°C. For example, alkaline molybdates and tungstates were obtained in accordance with the following reaction scheme:



where A = Li or Na and M = Mo or W. The $\text{MO}_3/\text{Li}_2\text{O}$ molar ratio was varied from 2 to 3 (fluxes

I and II), but these values were 2.5 and 3.5 for the III and IV systems, respectively. WO_3 concentration in the system VI does not exceed 34.2 mol %. Al_2O_3 solubility in the flux VII (71.8 mol % PbF_2 /28.2 mol % Bi_2O_3) was measured in the temperature range of 1200 – 900°C with a special labyrinth-type arrangement of the liquid lock, because of high volatility of this system.

Synthetic ruby crystals with different chromium concentration were obtained from high-temperature solutions by both the top-seeded solution growth (TSSG) method and spontaneous crystallization in the temperature interval 1330 - 900°C. The Al_2O_3 concentration was varied from 5.62 to 9.11 mol % in the most of high-temperature solutions, and it was kept at 17 and 34.3 mol % in the case of VII and VIII systems. The Cr_2O_3 admixture was up to 1.7 mol % of $(\text{Al,Cr})_2\text{O}_3$ in initial load.

In the runs of spontaneous crystallization, platinum crucibles (volume ~ 100 - 150 ml) with the starting charge were usually cooled down to 1100 or 900°C at a rate of 0.2 - 0.5°C/h. Then, the temperature was lowered to 350°C at 10 - 15°C/h.

Before the TSSG, saturation temperatures of the fluxed melts were precisely determined by a probe technique based on the observation of changes in the micro-relief of faces of small crystals measuring 3-5 mm and weighing up to 0.03 - 0.04 g. The relative saturation temperature could be measured with a precision of $\pm 0.3^\circ\text{C}$. In the crystal growth process, supersaturation was kept within certain limits by the cooling of fluxed melts in the range of 2 - 5°C/day following the experimental data on the solubility as well as by a temperature gradient between zones of crystal growth and solubility of initial $(\text{Al,Cr})_2\text{O}_3$ ($\Delta T = 1 - 5^\circ\text{C}$).

The Al, Cr, V, Mo, W, Pb, and Si concentrations in grown crystals were measured by electron microprobe analysis (EMPA) using a CAMEBAX-SX50 analyzer with accuracy better than 2 %. For each crystal, five to seven points were analyzed on the mirror-like surfaces.

3 RESULTS AND DISCUSSION

3.1 Solubility and crystal growth

Figure 1 shows the measurement results of the Al_2O_3 solubility in $5\text{PbF}_2 - 2\text{Bi}_2\text{O}_3$ melt both in the linear coordinates solubility – temperature (Fig.1a) and in the semilogarithmic coordinates $\ln C - 1/T$ (Fig.1b). Al_2O_3 solubility ranges from 5.4 to 8.5 wt % at 990°C and 1200°C, respectively. Calculated dissolution enthalpy value of Al_2O_3 is 29.4 KJ/Mol for this flux composition.

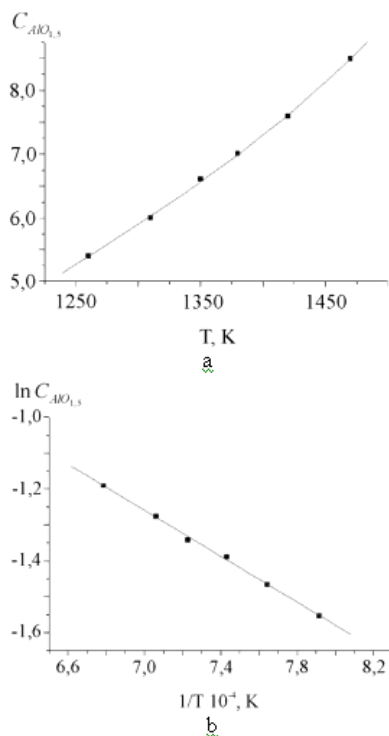


Figure 1: Al_2O_3 solubility in the $5\text{PbF}_2 - 2\text{Bi}_2\text{O}_3$ melt: (a) solubility- temperature linear coordinates; (b) $\ln C - 1/T$ semilogarithmic coordinates.

The quality of ruby crystals grown under different conditions, as it might be expected, was enhanced with a lower cooling rate of fluxed melt. Clear and transparent bulk crystals up to 2.5 cm were grown by TSSG method at the growth rate of 0.1 mm/day (Fig.2). No cracks and inclusions could be observed with the naked eye in these crystals.

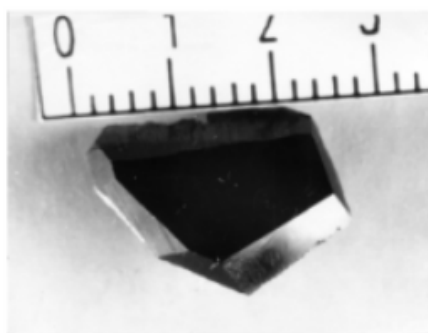


Figure 2: Ruby crystal grown from $5\text{PbF}_2 - 2\text{Bi}_2\text{O}_3$ based fluxed melt.

3.2 Composition of synthetic ruby

There is a correlation between growth conditions and composition of synthetic ruby. As a matter of fact, the admixtures of Mo and W (I, II, III, IV and VI solvents), Pb (V, VI and VII systems) and Bi (flux VII) in grown crystals does not exceed 0.01 wt %. The amount of vanadium impurities varies from 0.02 to 0.06 at % for V and VI flux based systems. However, the chromium concentration in ruby crystals results from the crystallization temperature, the type of flux, the composition high-temperature solutions, the $\text{Cr}_2\text{O}_3/\text{Al}_2\text{O}_3$ ratio in initial mixture (Table 1). It increases up to 6.38 at % in the case of solvent VI, but these values are equal to 0.55 and 0.67 for systems VII and VIII, respectively.

Table 1. Chromium concentration (C_{Cr}) in ruby crystals grown from V and VI flux based systems.

Composition of solutions, mol %					$T_{\text{cryst}}, ^\circ\text{C}$	$C_{\text{Cr}}, \text{at.}\%$
Al_2O_3	Cr_2O_3	PbO	V_2O_5	WO_3		
5.67	0.08	37.67	56.58	0	1330-1310	1.28
5.62	0.05	37.72	56.61	0	1170-1100	0.52
					1250-1190	1.34
5.78	0.08	32.96	49.70	11.56	1270-1165	6.38
7.62	0.05	30.35	45.53	16.45	1290-1155	1.13
6.74	0.05	30.64	45.96	16.61	1080-1070	0.53
5.65	0.05	26.40	39.50	28.40	1110-1060	0.63
9.11	0.06	23.12	34.72	32.99	1135-1115	0.51
5.75	0.05	24.00	36.00	34.20	1140-1120	0.53

Since the concentration of chromium atoms in grown crystals usually increases with increasing crystallization temperature, it can be concluded that the distribution of aluminum and chromium components also depends on the solubility of Al_2O_3 and Cr_2O_3 in these complex fluxes. Following to the Ruff's rule (Chernov et al. 1980), for example, the chromium component should be higher in the ruby crystals grown at elevated temperatures.

At the same time, the C_{Cr} value slightly decreases with an increase in the cooling rate of fluxed melts, i.e. with increasing supersaturation of high-temperature solutions. Taking into consideration that growth of ruby crystals is very slow and, most likely, this process characterizes as a kinetic growth regime. On this basis, the chromium incorporation can be understood using the equation for the effective trapping coefficient of a strongly adsorbed impurity at step sites (K_{eff}) in the layer-by-layer crystallization mechanisms (Chernov et al. 1980):

$$K_{\text{eff}} = K_0 / (1 + \Delta\mu/\Delta\mu^*) \quad (1)$$

Here, K_0 is the equilibrium trapping coefficient by a step which is equal to the equilibrium concentration in a surface layer, $\Delta\mu$ is the supersaturation, and $\Delta\mu^*$ is a function which

depends on the attachment and detachment frequencies of both impurity and host atoms. The $\Delta\mu^*$ value is positive if the impurity adsorption parameter at kink sites is higher than the same parameter for the host atoms. As for negative $\Delta\mu^*$, the opposite situation takes place as well. Therefore, this equation would hold true for chromium, if it is postulated Cr^{3+} ions to be strongly adsorbed impurities. In the case of positive $\Delta\mu^*$, the effective trapping coefficient of chromium will decrease with an increase in the relative supersaturation.

In the meantime, there are variations in chromium distributions over the entire volume of grown crystals during the crystal growth process even if the cooling rate was reduced to $2^\circ\text{C}/\text{day}$. Some of these "irregularities" may also result from analysis errors of crystal regions near micro-cracks due to induced stress during cutting and polishing of the grown crystals. Therefore, in order to eliminate the possibility of this mechanical factor, special care was necessary in processing samples for microprobe analysis.

3.3 Crystal morphology

The crystallographic forms $\{0001\}$, $\{01\text{-}12\}$, $\{11\text{-}23\}$, $\{10\text{-}14\}$, $\{10\text{-}10\}$ and $\{10\text{-}10\}$ are distinguishing features of the crystals grown (Fig. 3).

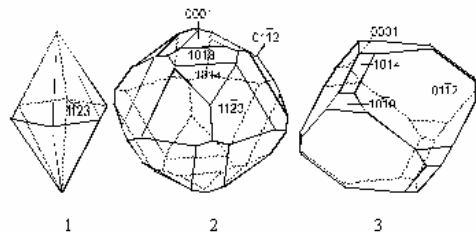


Figure 3. Drawings of ruby crystals grown under different conditions: (1) fluxes I and II, $T = 1160 - 1130^\circ\text{C}$; (2) flux VI, $T = 1135 - 1115^\circ\text{C}$; (3) flux VII, $T = 1270 - 900^\circ\text{C}$.

Ruby crystals obtained within $1150 - 900^\circ\text{C}$ (I and II fluxes) have a plate-like habit with a strongly developed pinacoid, except the crystallization from Li-enriched fluxed melts at elevated temperatures (Table 2). The crystals obtained in the interval of $1330 - 1100^\circ\text{C}$ (III, IV, VI, VII and VIII fluxes) have more equidimensional crystal shape. In this case, the $\{0001\}$ faces were rarely developed.

Table 2. Habits of ruby crystals depending on growth conditions

* Plate-like habit

** Isometric habit

Flux	T _{cryst.} , °C	Faceting and habit
Li ₂ O-2MoO ₃	1140-1120	{0001}, {11-23}, {01-14}* {11-23}, {01-14}**
Li ₂ O-3MoO ₃	1140-1100	{0001}, {11-23}, {01-14}* {11-23}, {01-14}**
Li ₂ O-2WO ₃	1160-1130	{0001}, {11-23}, {01-14}* {11-23}, {01-14}**
Li ₂ O-3WO ₃	1150-900	{0001}, {11-23}, {01-14}* {11-23}, {01-14}**
2Na ₂ O-5WO ₃	1220-1195	{11-23}, {01-12}, {01-14}**
2SrO-7WO ₃	1200-1100	{11-23}, {01-12}, {01-14}**
5PbF ₂ -2Bi ₂ O ₃	1270-900	{01-12}, {0001}, {10-14}, {10-10}**

In contrast to II fluxes, increase in the concentration of WO₃ in the solvent, VI also promotes more isometric ruby crystals (Table 3).

Table 3. Effect of WO₃ concentration (C_{WO3}) in the flux VI on the shape of ruby crystals.

C _{WO3} , mol.%	Faceting
0	{0001}, {01-12}
16.45	{0001}, {01-12}, {11-23}, {10-14}
28.40	{11-23}, {10-14}, {0001}, {01-12}, {10-18}
32.99	{11-23}, {0001}

4 CONCLUSIONS

As a result, single crystals of ruby have been obtained from fluxed melts based on the systems Li₂O - MoO₃, Li₂O - WO₃, Na₂O - WO₃, PbO - V₂O₅ - WO₃, PbF₂ - Bi₂O₃, and Na₃AlF₆ by both the TSSG method and spontaneous crystallization in the temperature range of 1330 - 900°C. The composition of grown crystals was studied by electron microprobe analysis. The synthetic ruby contains from 0.51 to 6.38 at % of chromium admixture, depending on the crystal growth conditions. Experimental data on growth conditions, composition and morphology of grown crystals are presented for each flux and temperature interval.

A major problem which is not yet clarified concerns the detailed nature of the crystallization process. A choice of appropriate flux may be a way to grow the isometric ruby crystals in a wide temperature range.

5 ACKNOWLEDGEMENTS

The authors thank Mr. Yu.V. Titov and Dr. I.A. Bryzgalov for the microprobe analysis of ruby crystals. V.V. Maltsev acknowledge the Program of the Russian President for Young Scientists (Grant MK-1430.2003.05), for partial support of this work, at the final stage.

6 REFERENCES

- Balitski V.S., Lisitsyna E.E. 1981. *Sinteticheskiye analogi i imitatsii prirodnykh dragotsennykh kamney*. Moscow: Nedra (in Russian).
- Chase A.B., Osmer J.A., 1967. Flux growth of ruby crystals. *J. Amer. Ceram. Soc.* 50: 325-328.
- Chernov A.A., Givargizov E.I., Bagdasarov Kh.S., Kuznetsov V.A., Demyanets L.N., Lobachyov A.N. 1980. *Sovremennaya kristallografiya 3: Obrazovaniye kristallov*. Moscow: Nauka (in Russian).
- Deer W.A., Howie R.A., Zussman J. 1962. *Rock-forming minerals 5: Non-silicates*. Longmans.
- Elwell D., Scheel H.J. 1975. *Crystal growth from high-temperature solutions*. London: Academic Press.
- Yanovskii V.K., Voronkova V.I., Koptsik V.A. 1970. Absorption effect of tungstate melt on forms and growth mechanisms of corundum crystals. *Kristallografiya* 15: 362-366 (in Russian).

Chemical Fingerprints of Sapphires in Alluvial Diamond Deposits from Coxim, MS, Brazil

A.Liccardo & J.E.Addad
Instituto CTM – Vitória – Brazil

E.F.Oliveira
Centro de Desenvolvimento de Tecnologia Nuclear – Belo Horizonte - Brazil

ABSTRACT: Alluvial deposits of Coxim, Mato Grosso do Sul contain corundum, BGY sapphire type, in association with diamonds. No evidence of rock source are found to both minerals, diamond and corundum. These sapphires were analyzed by NAA and ICP to main trace-elements (Fe, Cr, Ti, Ga, Mn, V and Na). The ratio Cr/Ga<1 indicates alkaline basaltic source to the corundum in other places in the world. High iron contents can suggest Fe²⁺ - Fe³⁺ type of cause of color, typical to basaltic-sapphires. Coxim sapphires presented values around 1- 48ppm of Cr, 150-156ppm of Ga, 4572-6340ppm of Fe, 374-405ppm of Ti, 13-22ppm of Mn, 9-13ppm of V and 64-71ppm of Na. The ratio Cr/Ga to the Coxim samples is lower than 1 and indicates basaltic origin to corundum. The contents of Fe and low Ti indicates Fe²⁺ - Fe³⁺ mechanism to cause of colors in these sapphires. The presence of this kind of corundum suggest the possibility of alkaline-basalts among the rocks in Paraná Basin border or at the source lithologies to clastic stones, as Aquidauana Formation. High levels of chemical attack resistance, hardness and density of both, corundum and diamond, indicate a sedimentary reworking survival and a depositional convergence at fluvial traps. High roundness of the sapphires from Coxim indicates a long distance transport vector. Great difficulties to obtain chemical informations in diamonds and few data existent about its origin, mainly in sedimentary deposits, can turn useful the corundum fingerprintings as a tool in prospection.

1 INTRODUCTION

In alluvial diamond deposits at Coxim River, and also in some affluents as Jauru, Taquari and Piquiri rivers, in Mato Grosso do Sul (Brazil) sapphire grains are recovered. This association is founded in fluvial segments along 100km N-S and 40km E-W in the Coxim region (54° 20' to 54° 40'S and 17° 50' to 18° 55'W). These sapphires (BGY type) were analyzed chemically and the results are presented and correlated to cause of color and genetic possibilities.

2 CONTEXT AND MATERIAL DESCRIPTION

The diamond/sapphire occurrences in the Coxim region are recent non-consolidated gravel and sand deposits and there are no evidence of source-rocks for both diamond and corundum. Only sedimentary rocks are presents in the region, the sandstones of Aquidauana Formation related to Parana Basin (paleozoic basin).

Sapphire grains recovered by diamond “*garimpeiros*” show sizes from ~1 to 12mm. They present low euedrism, low sphericity, medium to high roundness and the shape of the grains is

conditioned by fracturing (Figure 1). These sapphires present typical blue-green-yellow colors (BGY), with intense parallel color zoning. This kind of corundum in other places in the world is usually related to alkali-basalts.

Basic composition to corundum is Al₂O₃ (~99%) and some others constituents can be present as trace elements. Chemical analyses have been made to search for trace elements in order to understand their role in the cause of color of the Coxim sapphires and to obtain data about genesis.

The ratio Cr/Ga<1 indicates alkaline basaltic source to the corundum in others occurrences (Sutherland et al. 1998; Schwarz & Stern 2001; Sutherland & Schwarz 2000). High iron contents can suggest a participation of Fe²⁺ - Fe³⁺ type of cause of color, typical to basaltic-sapphires (Smith et al. 1995). Considering these relations, the investigation about corundum genetic conditions depends directly of trace elements quantification.

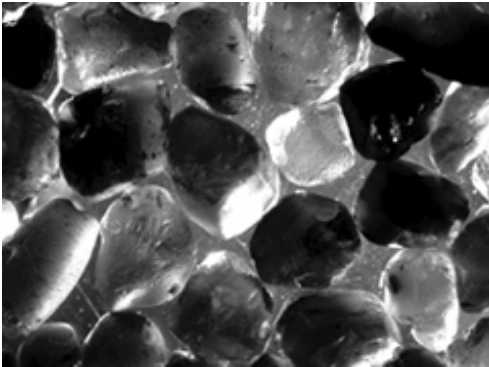


Figure 1: Corundum grains recovered from the Coxim deposits.

3 SAMPLES AND ANALYSIS

Samples of corundum were collected, selected and prepared in slices or powder to submit to analytic methods. Neutron Activation Analysis (NAA), Ultra Violet-Visible spectroscopy (UV-Vis) and Ion Coupled Plasma (ICP), were used to obtain data about chemical composition, mainly concerning trace elements. The UV-Vis analysis required transparent slices. For NAA the material was reduced to powder and cleaned with HF, HCl and HNO₃. A part of same powder was fused and dissolved to ICP analysis. Three samples of the predominant blue-color sapphire from Coxim deposits were used to proceed in NAA, two to ICP and one to UV-Vis.

4 RESULTS

Results from Neutron Activation analysis related to the main trace elements are showed in Table 1. ICP have been realized to complement the data, mainly because Ti, V and Mn have no possibilities of detection in NAA in function of interference of excess Al. The results of ICP are showed in Table 2. Coxim sapphires presented values around 1- 48ppm of Cr, 150-156ppm of Ga, 4572-6340ppm of Fe, 374-405ppm of Ti, 13-22ppm of Mn, 9-13ppm of V and 64-71ppm of Na. Cr contents analyzed by ICP showed higher values than results from NAA.

The UV-Vis spectra obtained to blue sapphire indicates only the presence of Fe³⁺, as showed in Figure 2.

Table 1: Results of Neutron Activation Analysis (ppm).

Elements	COX-1	COX-2	COX-3
Cr	8	1	9
Fe	6340	4572	4887
Ga	156	148	152
Na	64	68	71
Tb	-	-	-
Th	-	1	-
Ce	-	-	-
La	-	-	-
W	-	-	-
As	-	-	-
Ta	2	-	-
Sb	-	-	-
Sc	-	-	-
Co	-	-	-

Table 2: Results of ICP-OES (ppm).

Elements	COX-Blue	COX-Green
Cr	48	9
Ti	405	374
Mn	13	22
V	13	9

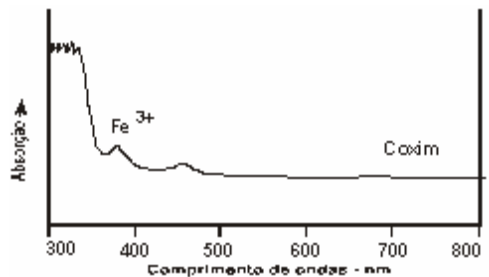


Figure 2: Characteristic spectrum in UV-Visible to blue sapphires from Coxim River.

5 DISCUSSION

Chemical data indicates high contents in Fe to the Coxim corundum. Otherwise low contents in Cr, Mn, V and Na was found. Contents of Ti, revealed by ICP (374-405ppm), indicate the possibility of participation of this element as cause-of-color together Fe²⁺, as classic mechanism IVCT (Intervalence Charge Transfer) – Fe²⁺ - Ti⁴⁺ ⇒ Fe³⁺ - Ti³⁺. However the high contents in Fe suggest also the possibility of the same mechanism between Fe²⁺ and Fe³⁺. UV-Vis spectra show peaks attributed to Fe³⁺ in 380 and 450nm and no answer between 500 and 600nm (usually the zone that shows IVCT mechanism). Earth Rare Elements are not detected in these sapphires, differently than corundum from granulites in other parts of Brazil (Liccardo 2003).

The ratio Cr/Ga to these samples is lower than 1 and indicates basaltic origin to corundum, in conformity with Sutherland et al. (1998) proposition.

Corundum found in alkaline basalts has its origin in lower portions of crust, and these extrusive rocks are only an agent of transport to xenocrystals (Guo et al. 1992; Levinson & Cook 1994), like diamonds at kimberlites.

The presence of this kind of corundum indicates the possibility of alkaline-basalts among the rocks in Paraná Basin border or at the source lithologies to sediments, as Aquidauana Formation. High levels of chemical attack resistance, hardness and density of both, corundum and diamond, suggest a sedimentary reworking survival and a depositional convergence at fluvial traps. However, differently of diamond, corundum presents features of transport in its morphology and surface texture. High roundness of sapphires from Coxim indicates a long distance transport vector.

Great difficulty to obtain chemical information in diamonds and few data existent about its origin, mainly in sedimentary deposits, can become useful the corundum fingerprinting as a tool in prospection in these kinds of occurrences.

6 REFERENCES

- Guo J.F., O'Reilly, S.Y., Griffin W.L. 1992. Origin of sapphire in eastern Australian basalts, inferred from inclusion studies. *Journal of Geological Society of Australia*, 32: 219-220.
- Levinson, A. A. & Cook, F. A. 1994. Gem Corundum in Alkali Basalt: Origin and Occurrence. *Gems & Gemmology*, 30: 253-262.
- Liccardo 2003 – Coríndon no Brasil – ocorrências, mineralogia, química e gênese. Doctorate Thesis – Universidade Federal de Ouro Preto – Ouro Preto, Minas Gerais. 186p.
- Schwartz, D. & Stern, W.B. 2000. Chemical Fingerprinting as a tool for the Characterisation of Gem Corundums from different genetic environments. In: *International Geological Congress*, 31. Rio de Janeiro, Brasil (CD-ROM).
- Sutherland, F.L.; Schwartz, D.; Jobbins, E.A.; Coenraads, R.R.; Webb, G. 1998. Distinctive gem corundum suites from discrete basalt fields: a comparative study of Barrington, Australia and West Pailin, Cambodia gemfields. *Journal of Gemmology*, 26: 65-85.
- Sutherland, F.L. & Schwartz, D. 2001. Origin of gem corundums from basaltic fields. *The Australian Gemmologist*, 21(1):30-33
- Smith, C.P.; Kammerling R.C.; Keller A.; Peretti A.; Scarratt K.V.; Khoa N.G.; Repetto, S. 1995. Sapphires from southern Vietnam. *Gems & Gemology*, v.31, p. 168-186.

Crystal Chemistry and Inclusions of Chinese Emerald

I.Moroz & M.Roth

Department of Applied Physics, The Hebrew University of Jerusalem, 91904 Jerusalem, Israel

B.Sabot

BP 34, 42450 Sury le Comtal, France

Ye.Vapnik

Department of Geological and Environmental Sciences, Ben-Gurion University of the Negev, 84105 Beer-Sheva, Israel

A.Givan

Department of Inorganic and Analytical Chemistry, The Hebrew University of Jerusalem, 91904 Jerusalem

ABSTRACT: Chinese emerald, sampled in a deposit near Malipo in the Wenshan area of Yunan province, occurs in the Nanwenhe Cambrian metamorphic core complex. Mineralization is hosted by pegmatite intruded predevonian gneisses and biotite-muscovite schists and induced by metasomatic fluids that are attributed to late cretaceous circulations. Electron microprobe, optical absorption spectroscopy and microthermometry analysis methods were applied in the study. The investigated emerald is characterized by a very high content of V_2O_5 and very low content of Cr_2O_3 . Unusually high concentration of V and very low of Cr is confirmed by visible absorption spectra of the emerald. The mineral is also characterized by relatively high concentrations of Cs_2O , Na_2O , MgO , FeO , NiO , and CuO . Mineral inclusions of black tourmaline, muscovite (and V-bearing muscovite), calcite, arsenopyrite, ilmenite, Fe oxides and oxides of other elements are common in the emerald. Fluid inclusions are rare, related to healed fractures and are likely to be of pseudosecondary origin. Inclusions are composed of two phases (gas and liquid), and the homogenization temperature (T_h) is between 200-300°C into the liquid phase; fluid inclusions are of low salinity (up to 8 wt%) and most likely are composed of KCl-rich solutions.

1 INTRODUCTION

Very little is known about the real gem potential of China and very few natural as well as synthetic emeralds from China have been marketed in western countries. However, the production of emeralds has been increased lately.

Chinese emerald, sampled in a deposit near Malipo in the Wenshan area of Yunan province, occurs in the Nanwenhe Cambrian metamorphic core complex. Biotite from an intrusive leucogranite has been dated using the K-Ar method by the age of 186.2 My (Zhang Shitao et al. 1999). Numerous pegmatites' bodies have been seen at 4 km around the granite. Mineralization is hosted by pegmatite intruded predevonian gneisses and biotite-muscovite schists. The mineralization is related to metasomatic fluids that are attributed to late cretaceous circulations (Zhang Shitao et al. 1999). A regional shear zone is reported on a geological map, but any geotectonic control on the mineralization has not been reported previously. According to Zhang Shitao (1999), two kinds of deposit exist: a first one is related to hydrothermal activity that has occurred at the final stage of pegmatitic emplacements. This type of mineralization is associated with 90% of the produced gems and some other emeralds that are

found within shear zone among gneisses. The mineralogy of the gangue is as follows: potassium feldspath, quartz, albite, tourmaline, fluorite, muscovite, biotite, chlorite, calcite, cassiterite and wolframite. In second occurrences (Zhang et al. 1999) emerald is embedded within quartz-biotite matrix together with tourmaline and arsenopyrite. The succession of metasomatic lithologies is: gneiss -> Al_2SiO_5 small band within gneiss -> quartz-feldspar rock -> biotite with emerald -> amphibolites.

In 1999 the productive zone was 20 m wide and up to 25 m deep. Six veins were producing emerald exhibiting the (0001) and (1010) crystallographic habits. Crystals were generally 10 to 200 mm long and their diameter could reach 50 mm.

2 CRYSTAL CHEMISTRY

Electron microprobe, optical absorption spectroscopy and microthermometry were employed as analytical tools in this study.

The mineral inclusions' composition in emerald was analyzed by a JEOL JXA-8600 electron microprobe (the Institute of Earth Sciences of the Hebrew University of Jerusalem). This instrument

was equipped with an energy-dispersive spectrometer, which displayed the entire spectrum of those elements (with atomic numbers of six and above) that had been exposed to the focused spot of the electron beam. The microprobe was operated using a 15 kV acceleration voltage, and a beam current of 10 nA. The Pioneer Norvar EDS (133 eV) computerized automation system was used to collect, store and subsequently analyze the accumulated data. Standards used consisted of suitable natural minerals and synthetic materials. The detection limits for elements were generally in the range of hundreds to thousands of parts per million. As the electron microprobe spectrometer cannot resolve the energies for variable oxidation states of individual elements the total iron content is expressed as FeO in spite of the fact that part of the iron in emerald exists as Fe₂O₃ (Wood & Nassau 1968; Platonov et al. 1984; Schwarz et al. 1996; Moroz et al. 1999). Vanadium can occur also in

multiple valence states. Mineral formulae for emerald were calculated on the basis of the ideal beryl formula having 18 oxygens per formula unit. A theoretical value for BeO was computed by assuming that 3 beryllium cations would be present in the beryl crystal structure.

The investigated emerald is characterised by a very high content of V₂O₃ (on the average - 0.53 wt%) and very low content of Cr₂O₃ (on the average - 0.037 wt%). There is a strong color zoning in the emerald: it is colorless in the center of the mineral and green outwards. The V content is practically constant, whereas the Cr content increases from below the detection limit in the center to the border of the mineral. As the emerald is usually not homogeneous in terms of chemical composition, it displays distinctive color zoning which correlates directly with the variations of both chromium and iron contents (see Table 1 for detail) according to the color bands.

Table 1. Malipo (China) emerald composition.

Oxides											Average
BeO	14.00	14.00	14.00	14.00	14.00	14.00	14.00	14.00	14.00	14.00	14.00
SiO ₂	63.93	63.41	63.93	59.28	63.53	63.42	62.15	64.74	62.45	61.40	62.82
Al ₂ O ₃	15.74	16.15	16.08	14.70	16.12	15.78	15.32	15.92	16.35	15.71	15.82
Cr ₂ O ₃	0.00	0.11	0.06	0.12	0.00	0.00	0.00	0.03	0.00	0.00	0.04
V ₂ O ₃	0.74	0.83	0.57	0.55	0.51	0.78	0.57	0.61	0.51	0.74	0.64
FeO	0.55	0.67	0.28	0.76	0.45	0.37	0.19	0.13	0.25	0.47	0.41
MgO	0.79	0.84	0.81	1.30	0.56	0.94	0.88	0.65	0.53	0.49	0.78
TiO ₂	0.00	0.08	0.00	0.00	0.08	0.10	0.10	0.04	0.39	0.08	0.09
MnO	0.00	0.01	0.00	0.00	0.17	0.00	0.00	0.05	0.05	0.09	0.025
CuO	0.00	0.49	0.00	0.31	0.00	0.30	0.00	0.00	0.00	0.00	0.11
NiO	0.51	0.00	0.00	0.01	0.00	0.25	0.00	0.00	0.29	0.27	0.14
Na ₂ O	0.82	0.75	0.76	0.75	0.59	0.89	0.84	0.76	0.61	0.67	0.74
K ₂ O	0.00	0.01	0.05	0.02	0.07	0.03	0.07	0.03	0.03	0.00	0.03
Cs ₂ O	0.00	0.32	0.00	0.00	0.24	0.00	0.22	0.00	0.81	0.45	0.21
CaO	0.09	0.13	0.06	1.77	0.09	0.07	0.00	0.08	0.00	0.13	0.07
BaO	0.00	0.11	0.00	0.40	0.00	0.00	0.06	0.00	0.16	0.00	0.04
SO ₃	0.04	0.09	0.00	0.15	0.07	0.25	0.19	0.00	0.11	0.00	0.09
La ₂ O ₃	0.00	0.07	0.00	0.34	0.23	0.16	0.00	0.00	0.11	0.00	0.06
F	0.30	0.00	0.02	0.24	0.30	0.00	0.00	0.00	0.00	0.13	0.10
Cl	0.00	0.03	0.00	0.00	0.04	0.00	0.00	0.00	0.00	0.02	0.01
Total wt%	97.50	98.11	96.62	94.70	97.04	97.34	94.59	97.04	96.65	94.65	

Chromium is the usual element claimed to be responsible for the attractive green color of emerald. However, the Malipo emerald contains up to 0.83 wt.% V₂O₃, which contributes to its emerald-green color (Brown 1984; Platonov et al. 1984; Wood & Nassau 1968). The emerald shows the highest V content comparing with emeralds from other studied deposits (Moroz & Eliezri 1998). Some variation of iron (Table 1) is due to the possibility of incorporating iron, either as Fe²⁺ or Fe³⁺, at different sites of the beryl lattice. Examination of the visible absorption spectra of emeralds from various deposits

(Moroz et al. 1999) has helped to explain the effect of iron content variation on the color of the resulting emerald. The mineral is also characterized by relatively high concentrations of Cs₂O (average - 0.21 wt%), Na₂O (0.74 wt%), MgO (0.78 wt%), FeO (0.41 wt%), NiO (0.135 wt%), CuO (0.114 wt %) and F (0.10 wt%). The MgO:FeO ratio in the emerald is 1.90. Oxides of other elements such as CaO, BaO, TiO₂, MnO, CoO, K₂O, La₂O₃, Ce₂O₃, SO₃ and Cl have been found either in small amounts close to the detection limit of the instrument or have not been detected at all in some volume parts. As

Mg, Fe, Cr, V, Ti, Mn, Ni, Co, La, and Ce enter the beryl structure, generally by substituting for aluminum, the correlation between these elements and Al is negative. Such substitution of Al^{3+} by bivalent ions, such as Mg, Fe, Mn, Ni, Cu and Co, requires coupled substitution normally with Na and/or K and Cs. As a consequence, emerald from this deposit is enriched in MgO , FeO and Na_2O and Cs_2O , while having a lower Al_2O_3 content.

3 THE VISIBLE ABSORPTION AND IR SPECTROSCOPY

The samples were studied by visible absorption spectroscopy at the Division of Applied Physics of the Hebrew University. The absorption spectra in the visible region were recorded using a Perkin Elmer Lambda 15 spectrophotometer. The (190-900) nm range versatile, high performance double-beam ultraviolet/visible (UV/VIS) instrument version was used. The spectral slit width was 2 nm in all experiments, which provided a reasonably good spectral resolution in view of the broad bands measured.

It should be emphasized, that an unusually high concentration of V and a very low content of Cr are confirmed by the visible absorption spectra of emerald, namely by the absence of narrow R-lines of chromium in the 685-687 nm range, in contrast to the quoted studies of optical absorption spectra of emerald crystals from Brazil (Santa Teresinha), Colombia and synthetic emerald (Moroz et al. 1999). A broad band at 820-830 nm due to Fe^{2+} in the octahedral Al^{3+} sites, or channel sites, is almost absent in these emeralds likewise the Chinese emerald. However, in contrast to these emeralds, intensive broad absorption bands near 430 nm and 612 nm in the Malipo emerald are due to V or a combination of V + Cr + Fe (at 612 nm). It is noteworthy that the V_2O_3 concentration (0.53 wt%) in the Malipo emerald is clearly higher than that of iron (0.41 wt%). Therefore, it may be concluded that iron in this emerald is found in other forms, for example as Fe^{3+} .

IR spectroscopic studies were carried out on powdered samples dispersed in KBr excess. The apparatus of type Bruker 113 v (FTIR) was used at the Department of Inorganic and Analytical Chemistry of the Hebrew University of Jerusalem. Rather intense fundamental vibrations of H_2O molecules appeared in these spectra. In the water stretching modes range ($3700-3500\text{ cm}^{-1}$) three distinct bands were normally observed. The sodium content (0.74 wt%, medium alkali-bearing emerald) is the main control of the intensity ratio of the bands observed which, as a consequence, are attributed to the presence of the free water molecule (3697.5 cm^{-1} -A) and water-sodium complexes (3649.7 cm^{-1} -C and 3594.9 cm^{-1} -B). The intensity ratios of the

bands are: $B > C > A$, that is in accordance with data of K. Schmetzer (1989). There are also H_2O bending modes at the 1635.1 and 1576.0 cm^{-1} sites.

4 INCLUSIONS

Mineral inclusions of black tourmaline, muscovite (and V-bearing type), arsenopyrite (Zhang Liangju et al. 1999) and, according to electron microprobe analysis, calcite, ilmenite (Fe:Ti ratio ~ 3.3:1), Fe oxides (sometimes Ni-Cr-bearing Fe oxide), Cu oxide (tenorite?), Zn oxide and Pb oxide are common in the emerald.

For fluid inclusion investigation, 0.1-0.2 mm thick emerald wafers polished on both sides were prepared. Fluid inclusions were studied at temperatures between -190 and $+500^\circ\text{C}$ using a Fluid INC. heating-freezing stage. The accuracy of temperature measurements was about $\pm 0.5^\circ\text{C}$ in the low-temperature range (-190 - $+50^\circ\text{C}$) and $\pm 2^\circ\text{C}$ in the high temperature range (100 - 500°C).

According to fluid inclusions studies of Zhang Shiato et al. (1999), the temperature of formation of the deposit is 325 - 372°C , NaCl salinity is 13-18 wt%, $P = 66.7$ - 77.9 Mpa. According to our present observations, fluid inclusions are rare; they are related to healed fractures not crosscutting the host emerald and are most likely of pseudosecondary origin. The inclusions are composed of two phases (gas and liquid). Small inclusions (about 10-20 μ) are isometric whereas bigger ones are elongated and exhibit irregular forms. The homogenization temperature (T_h) in the liquid phase is between 200 and 300°C . In a single inclusion the first melting temperature of ice has been observed at -8.0°C , whereas the final melting temperature is recorded in several inclusions between -5.5 and 3.5°C . Thus, fluid inclusions are of low salinity (up to 8 wt%) and most likely are composed of KCl-rich solutions. Several solitary inclusions, probably of primary genesis, have been observed in calcite. T_h is recorded in two inclusions at 250 and 305°C , other inclusions were decrepitated at $T > 230^\circ\text{C}$. The final melting of ice has been observed at -4.0 and -1.5°C . Thus, the salinity is about 6 wt%. It is likely, that inclusions related to the same stage are hosted by emerald and calcite.

Inclusions of low-salinity chloride solutions are typical for the investigated emerald and they are associated with calcite. Elsewhere, a low salinity of fluid inclusions in emerald seems typical for other schist-type deposits (Moroz & Vapnik 1999) and it distinguishes them from inclusions in emeralds formed in deposits of different origin.

5 CONCLUSIONS

Malipo is a rare type of vanadium-bearing emerald

deposit. Vanadium, due to its higher concentration, is the main coloring agent rather than chromium; there is a possibility of the effect of varying contents of iron on the color of the resulting emerald. Since the pegmatite has intruded gneisses and biotite-muscovite schists, it appears that vanadium, chromium, and iron have been leached from these rocks by fluids associated with pegmatite formation. Unusually high concentration of vanadium and a very low one of chromium is confirmed by the visible absorption spectra of the emerald. The mineral is also characterized by relatively high concentrations of Cs₂O, Na₂O, MgO, FeO, NiO, and CuO. Mineral inclusions of black tourmaline, muscovite (and V-bearing type), calcite, arsenopyrite, ilmenite, Fe oxides, Cu oxide, Zn oxide, and Pb oxide are common in the emerald. Low-salinity aqueous inclusions have been found in emerald and calcite. This type of inclusions is common for emeralds from schist-type deposits.

6 REFERENCES

- Brown, G. & Snow, J. 1984. Inclusions in Biron synthetic emeralds. *Australian Gemmologist*, 15: 167-171.
- Moroz, I. I. & Eliezi, I. Z. 1998. Emerald chemistry from different deposits: an electron microprobe study. *The Australian Gemmologist*, 20, 2: 64-69.
- Moroz, I. I. & Eliezi, I. Z. 1999. Mineral inclusions in emeralds from different sources. *Journal of Gemmology*, 26: 357-363.
- Moroz, I. & Vapnik, Ye. 1999. Fluid inclusions in emeralds from schist-type deposits. *Canadian Gemmologist*, XX, 1: 8-14.
- Moroz, I., Roth, M., Deich, V. 1999. The visible absorption spectroscopy of emeralds from different deposits. *The Australian Gemmologist*, 20, 8: 315-320.
- Platonov, A. N., Taran, M. N., & Balitsky, V. S. 1984. Nature of gems coloring. Moscow: Nedra.
- Schmetzer, K. 1989. Types of water in natural and synthetic emerald. *N. Jb. Miner. Mh.*, H. 1: 15-26.
- Schwarz, D., Kanis, J. & Kinnaird, J. 1996. Emerald and green beryl from Central Nigeria. *Journal of Gemmology*, 25, 2: 117-141.
- Wood, D. L. & Nassau, K. 1968. The characterization of beryl and emerald by visible and infrared absorption spectroscopy. *The American Mineralogist*. 53: 777-800.
- Zhang, Liangju et al., 1999. Gemmological characteristics and deposit geology of Yunan emerald. *Acta Mineralogica Sinica*, vol. 19: 2 (in Chinese).
- Zhang Shito et al., 1999. Geological features and genesis of emerald deposit in Malipo county, Yunan province, China. *Geological Science and Technology Information*, vol. 18, 1, March issue: 50-54 (in Chinese).

Multiple Fluids in a Single Emerald Crystal: What May it Means?

A.Moura & E.Correia

Departamento de Geologia, Faculdade de Ciências, Universidade do Porto, Portugal. Centro de Geologia da Universidade do Porto.

ABSTRACT: Fluid inclusions in emeralds have been studied in deposits in many parts of the World. In most of these studies researchers found more than one fluid inclusion type that are interpreted as coeval to the emerald formation. In the Capoeirana and Socotó productive areas in Brazil, we could observe at least six fluid inclusion types in one isolated emerald crystal. Here we discuss how this multiple fluids could be interpreted in relation to the emerald genesis.

1 INTRODUCTION

Studies of fluid inclusions (FI) on emeralds from many places in the World frequently reveal a great variety of FI populations. De Souza et al. (1992) in a study of the FI of the *garimpo* at Capoeirana found monophasic to polyphasic fillings with triphasic as the most abundant FI type. FI identical with this last one were found by Grundmann & Morteani (1989) in emeralds from Habachtal (Austria) and Leydsdorp (South Africa). Some of this FI have solid daughter phases but others only present H₂O and CO₂ phases.

Moroz et al. (2001) in a study of emeralds from Lake Manyara and Sumbawanga deposits (Tanzania) also found H₂O-CO₂ FI with numerous daughter phases. Another type of inclusions (an H₂O-CO₂-CaCl₂ rich fluid) is also found in these emeralds. A nahcolite-bearing fluids as the main fluid type in emeralds was found by Vapnik & Moroz (2002) in samples from the Maria deposit (Mozambique). As in precedent examples here the fillings (namely the water/gas ratio) and the number of solid phases are heterogeneous. Many workers have studied the Colombian emeralds. Ottaway et al. (1994) found

hypersaline aqueous carbonic inclusions (with liquid and vapour CO₂) but Deneele et al. (1999) stated that CO₂ have been detected by Raman spectrometry only as a minor component. Here once more the fluids could be very heterogeneous. Vapnik & Moroz (2000) found two fluid types in emeralds from the Jos complex (Nigeria). One of the fluids is a hypersaline multiphase Na-Ca-Cl aqueous carbonic fluid while the other is a low-density volatile -rich water -free fluid. In this case the authors found strong evidences of a primary genesis for these fluids as they are along growth zones. Hypersaline multisolid phase inclusions (with salinities up to 80-90 wt.%) and unusual compositions (FeCl₂, BaCl₂, KCl) were studied by Vapnik & Moroz (2001) inside emeralds from Panjshir (Afghanistan).

Giuliani et al. (1997) in a state-of-the-art study about the genesis and types of the Brazilian emeralds presents abundant evidences that the fluids in emeralds are often of multiple composition.

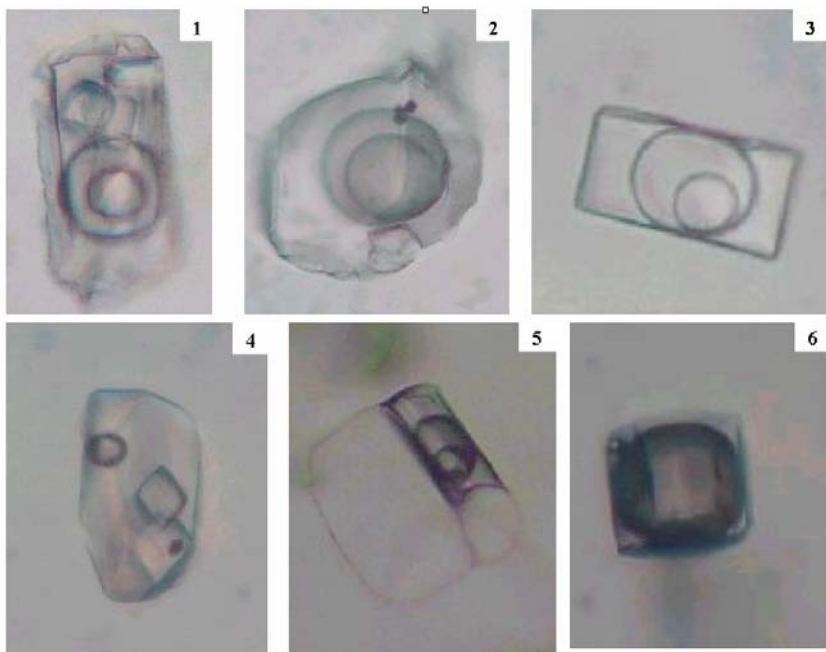


Figure 1- Typical fluid inclusions found on a single emeralds crystal from Capoeirana and Socotó areas (Brazil). 1. Lc-w-p, 2. Lc-w, 3. Lw-p, 4. Lw-s, 5. Lc-w-e and 6. Vc-w (abbreviations: L for dominant liquid phase, V for dominant vapour phase, c- carbonic phase (CO₂- rich), w- liquid water, p- polyphasic solid inclusions (daughter minerals), s- single solid phase, e- emerald entrapped in the inclusion). Maximum fluid inclusions dimension between 20 and 60 μ m.

2 THE ABUNDANCE OF FLUID INCLUSION TYPES ON EMERALDS

The petrographic observation of centimetric single emerald crystals from Capoeirana and Socotó areas in Brazil have shown at least six FI types (fig.1).

Most of the observed fluids could be interpreted as primary in origin because they occur isolated or in small groups without any visible alignment.

In the same crystal it is possible to observe groups of only one fluid type (in the case of this emeralds this is a H₂O-CO₂-(CH₄)-multi salt fluid, with a volumetric gas content of 0.5 ± 0.2 . However, in other places in the crystal it is possible to observe distinct FI (in composition and density). Few inclusions could be considered as secondary as they are along trails that crosscut the entire crystal.

The firsts fluid type (fig. 1-1) is an hypersaline H₂O-CO₂-(\pm CH₄ \pm N₂)- multi salt fluid. The filling ratio (Flw = water volume/total FI volume) is variable but normally between 0.2 and 0.7. A second type of FI (fig. 1-2) is identical of the precedent except in that it only has one daughter phase (occasionally with additional vary small black phases possibly metallic ores). The main difference between these two fluids is salt composition (simpler in the second FI type). A third FI type (fig. 1-3) is

even simpler in composition as it has no visible daughter phases. The main difference for the precedent fluids is again the lower salinity and eventually the salt components. A fourth FI type (fig. 1-4) is a multi salt H₂O fluid, with no detected gas component. A more rare fluid type (fig. 1-5) is an aqueous carbonic fluid (with liquid and vapour CO₂) with one or more giant solid phases. Although petrographically different this FI are analogous to the type three FI with the difference of having an entrapped emerald portion(s). The sixth FI type (fig. 1-6) is a vapour-rich fluid (gas phase volume > 50 %), which in same cases presents one or more very small (and difficult to see) solid phases.

3 INTERPRETING THE FLUID VARIATION

Barros & Kinnaird (1985) and Cassedanne & Barros, (1986) concluded that in the case of the pegmatitque associated Porangatu occurrence (Brazil) there was the contemporaneous circulation of three types of fluids.

Giuliani et al. (1997) propose that the aqueous carbonic fluid present in emeralds from the shear zone deposits (also related with an alkaline metassomatic hydrothermalism) have been resulted

from a mechanical mixture of an H₂O-NaCl fluid with an CO₂-N₂+CH₄ fluid.

Vapnik & Moroz (2000) consider possible that the gas and hyper saline fluids have been entrapped coeval and that the fluid was heterogeneous at least considering the entire formation of the studied emeralds. These authors sustain that an influx of low-density CO₂ bearing fluid must have existed during the middle and outer stages of emerald growth. If this was the case we must consider that emeralds can crystallize at least from two very different fluid types. Another fluid (an alkaline, nahcolite-bearing type) is proposed by the same authors for the case of the Maria deposit (Mozambique).

Precluding post entrapment modifications the fluid variety often observed at the scale of a single crystal could have originated from two situations: (1)- heterogeneous trapping, and (2)- homogeneous trapping of different fluids in different moments of the crystal growth. Immiscibility, an important mechanism on precipitation, does not seem relevant in the case of emerald formation.

It is well known that the concept of heterogeneity - homogeneity could depend on the scale of observation (Diamond, 2001). The fact that the great majority of the observed FI, in our samples, are of one type suggests that the majority of the fluid could have been trapped in the homogeneous field. The existence of multiple fluids and particularly the variation on density in the H₂O-CO₂-NaCl fluids (fig. 2) could be envisaged as fluctuations in the fluid composition during the period (thousands of years?) of the emerald growth. The evidences that emeralds can grow from fluids of different composition support the hypothesis that P-T conditions could have been important on emerald formation, particularly those with an orogenic metamorphic origin. In this environmental attention must be focus on pressure drops as this is a very well known mechanism favouring deposition in hydrothermal systems (Sibson, 1973; Sibson et al. 1975; Mullis, 1988; Roedder & Bodnar, 1980; Moura, 2001).

Apart a proper geochemistry and geodynamic settings of emerald findings and the importance of physical-chemical changes during emerald growth it is very likely that an hypersaline fluid was a extremely favourable condition for the transfer of mass needed for emerald formation.

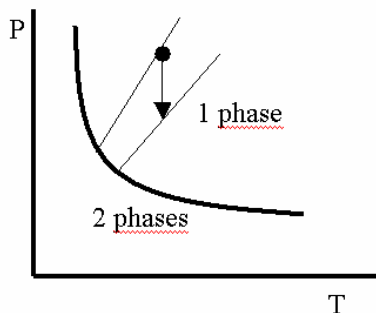


Figure 2- P-T field for an H₂O-CO₂-NaCl fluid with isochors (thin lines) and immiscibility curve (thick curve line). Arrow represents the pressure drop. From Moura (2001).

4 REFERENCES

- Barros, J.G.C. & Kinnaird J.A. (1985)-Fluid inclusion studies of emeralds and green beryls from the Porangatu deposit, Goiás state, Brazil. In: VIII ECROFI Symposium, Gottingen Abstracts, p.2
- Cassedane, J.P. & Barros, J.G.C. (1986)- Quelques gîtes d'émeraudes de Goiás. Rev. Gemmol., AFG, 88, 9-12.
- De Souza, J.L.; Mendes, J.C.; Silveira Bello, R.M.; Svisero, D. P. & Valarelli, J.V. (1992)- Petrographic and microthermometrical studies of emeralds in the "Garimpo" of Capoeirana, Nova Era, Minas Gerais State, Brazil. Mineral. Deposita, 27, 161-168.
- Deneele, D., Dubois, M., Cheilletz, A., Branquet, Y. & Giuliani, G., (1999)- Pressure-temperature conditions and fluid evolution in the emerald deposits of Colombia. Terra Nostra, 99/6, 75-76.
- Diamond, L. (2001)- Review of the systematics of CO₂-H₂O fluid inclusions. Lithos, 55, 69-99.
- Giuliani, G.; Cheilletz, A.; Zimmermann, J-L., Ribeiro-Althoff, A.M.; France-Lanord, C.; Feraud, G. (1997)- Les gisements d'émeraude du Brésil: genèse et typologie. Chr. Rech. Minière, 526, 17-61.
- Grundmann, G. & Mortelli, G., (1989)- Emerald mineralization during regional metamorphism: Habachtal (Austria) and Leydsdorp (Transvaal, South Africa) deposits. Economic Geology, 84, 1835-1849.
- Moroz, I., Vapnik, Y., Eliezri, I. & Roth, M., (2001)- Mineral and fluid inclusion study of emeralds from the Lake Manyara and Sumbawanga deposits, Tanzania. Journal of African Earth Sciences, 33 (2), 377-390.
- Moura, A. (2001)- Quartz geobarometry: insight using favourable fluid inclusions entrapped in the homogeneous P-T field. Bol. Soc.Española de Mineralogia, 24-A, 33-34.
- Mullis, J. (1988). Rapid subsidence and upthrusting in the Northern Apennines, deduced by fluid inclusions studies in quartz crystals from Porretta Terme. Schweiz. Mineral. Petrogr. Mitt, 68, 157-170.
- Ottaway, T.L.; Wicks, F.J.; Bryndzia, L.T.; Kyser, T.K. & Spooner, E.T.C. (1994)- Formation of the Muzo hydrothermal emerald deposit in Colombia. Nature, 369, 552-554.
- Roedder, E. & Bodnar, R., (1980)- Geological pressure determinations from fluid inclusions studies. Ann. Rev. Earth and Planetary Sci., 8: 263-301.

- Sibson, R., (1973)- Interactions between temperature and pore-fluid pressure during earthquake faulting and a mechanism for partial or total stress relief. *Nature*, 243, 66-68.
- Sibson, R., Moore, M. & Rankin, A. (1975)- Seismic pumping- a hydrothermal fluid transport mechanism. *J. Geol. Soc. Lond.*, 131, 653-659.
- Vapnik, Y. & Moroz, I., (2000)- Fluid inclusions in emerald from the Jos Complex (Central Nigeria). *Schweiz. Mineral. Petrogr. Mitt* , 80, 117-129.
- Vapnik, Y. & Moroz, I., (2001)- Fluid inclusions in Panjshir emerald (Afghanistan). In: Noronha, F., Dória, A. & Guedes, A. (Eds.), Abstracts, XVI ECROFI. Universidade do Porto, Portugal, 451-454.
- Vapnik, Y. & Moroz, I., (2002)- Compositions and formation of conditions of fluid inclusions in emerald from the Maria deposit (Mozambique). *Mineralogical Magazine*, 66 (1), 201-213.
- Vrolijk, P. & Myers, G., (1990)- Fluid pressure history in subduction zones: evidence from fluid inclusions in the Kodiak Accretionary Complex, Alaska. In: *Studies in Geophysics: The role of fluids in crustal processes*, pp.148-157. National Academy Press, Washington, D.C.

Application of Neutron Activation Analysis in the Determination of Trace Elements in Tourmalines

E.F.Oliveira, M.A.S.Lacerda, R.Stasiulevicius

Centro de Desenvolvimento da Tecnologia Nuclear, Comissão Nacional de Energia Nuclear, Brazil.

C.Castañeda

Centro de Pesquisa Manoel Teixeira da Costa, IGC/UFMG, Brazil.

ABSTRACT: The present work reports a methodology to determine trace elements in tourmaline by neutron activation analysis. The interference effect of ^{10}B was demonstrated by irradiating samples of different weight from the same tourmaline and plotting a graph of specific activity against the sample weight. The ideal weight with minimal interference effect was obtained in the straight line deviation. Instrumental neutron activation analysis can be applied to the ideal weight with minimal interference effect. Radionuclides ^{65}Zn , ^{59}Fe , ^{60}Co , ^{51}Cr , ^{46}Sc , ^{82}Br , ^{140}La , $^{24\text{m}}\text{Na}$, ^{42}K , ^{85}Sr , ^{182}Ta , ^{134}Cs , ^{124}Sb were detected.

1 INTRODUCTION

Trace elements studies are very important in modern petrology because they are more capable of discriminating between petrological processes than are major elements. Trace elements allow and are capable to understand the processes controlled by crystal-melt or crystal-fluid equilibria. Tourmalines are important as petrogenetic indicators because they can incorporate by total or partial substitution of a great variety of chemical elements depending on the mineralogical and metalogenetic history of the rock (Oliveira et al. 2002; Hawthorne et al. 1993; Hawthorne 1996; Hawthorne & Henry 1999; Slack 1996; Cleland et al. 1996; Henry & Dutrow 1996; Henry & Guidotti 1985; Koval et al. 1991).

Tourmalines are structurally and chemically complex borosilicate minerals that can be represented by the general formula $\text{XY}_3\text{Z}_6\text{T}_6\text{O}_{18}(\text{BO}_3)_3\text{V}_3\text{W}$, where $\text{X} = \text{Na}^+$, Ca^{2+} , K^+ , and vacancy (); $\text{Y} = \text{Mg}^{2+}$, Fe^{2+} , Mn^{2+} , Al^{3+} , Fe^{3+} , Mn^{3+} , Cr^{3+} and Li^+ ; $\text{Z} = \text{Al}^{3+}$, Mg^{2+} , Fe^{3+} , Cr^{3+} , V^{3+} . The T site is occupied by Si or Al in fourfold coordination with oxygen and in threefold coordination with boron. These structurally distinct positions have been assigned to the W site, which is dominated by O^{2-} , OH^- , F, Cl, and the V site, which

is dominated by OH^- , or, more rarely, O^{2-} . In addition, several other trace elements can also be present in sites X, Y and Z (Hawthorne & Henry 1999).

This paper reports a methodology of determination of trace elements in boron rich minerals by instrumental neutron activation analysis (INAA) where tourmaline was the mineral investigated. INAA in samples containing boron is problematic due to the large neutron-capture cross section of ^{10}B (3838 barns in thermal energy 0.0253 eV). This results in different nuclear production rates in different parts of the samples and this is undesirable. As a consequence of the neutron-capture effect, the concentration of the elements determined by neutron activation is lower than it really. One of them is to use a graph of the specific activity against the sample weight and determine the smallest sample where interference effect is eliminated or minimum.

The determination of trace element in tourmalines by neutron activation analysis has been investigated by some authors (Koval et al. 1991; Laul & Lepel 1987; King et al. 1988; Jolliff et al. 1987). King et al. (1988) studied the REE distribution in tourmalines by INAA technique involving pretreatment by boron volatilization. Jolliff et al.

(1987) and Laul & Lepel (1987), studied the REE distribution in tourmalines by radiochemical neutron activation analysis (RNAA). The analytical methods described by these authors are very hard and/or contamination can occur.

2 METODOLOGY DESCRIPTION

The methodology used in this work is based on studies for determination of trace-element by INAA when during irradiation there is a suppression of the incident neutron flux in the target sample (Bowen & Gibbons 1963; Ehmann & Vance 1991). This interference effect can be demonstrated by irradiating the same sample of different weights and then, after determining the activity of each sample, plotting a graph of specific activity against sample weight. From the graph it is possible to determine the maximum weight where interference effect was eliminated or minimized and thus limit irradiation to the samples of that determined weight. This occur in the straight line deviation.

3 SAMPLING AND ANALYTICAL TECHNIQUES

Brazilian tourmalines from granitic pegmatites were carefully selected. Five tourmaline samples were selected from several hundreds of fragments based on quality and color homogeneity. Special care was taken to separate the different color zones from zone samples. The tourmalines from granitic pegmatites occur in northeastern Minas Gerais States, multi-colored tourmalines of the pegmatites belong to the Eastern Gemological Province and were formed by partial melting of metasedimentary rocks during the granitogenic episode of the Neoproterozoic Araçuaí Belt (Pedrosa & Wiedemann-Leonardo 2000; Pinto & Pedrosa 2001). Firstly, electron microprobe and Mössbauer spectra have been acquired for tourmaline in study, Mössbauer spectra of the samples selected estimated the lower Fe^{3+}/Fe^{2+} ratio (Oliveira et al. 2002).

For INAA the irradiation was performed in the reactor TRIGA Mark I IPR-R1 at 100 kW_t with thermal neutron flux of 6.6×10^{11} n.cm⁻².s⁻¹. The acquisition parameters the gamma spectroscopy and the irradiation used were carefully defined in order to better sensitivity. The elements were determined through irradiation for 16 hours. Following a cooling time of about a week, samples were counted for one hour. After a further delay to permit shorter half-life activity to decay, about fifteen days, the samples were recounted for about one day (86000 s) to obtain the gamma activity for longer lived radioisotope. The gamma spectroscopy was performed using a hyperpure germanium detector (HPGe) with a

resolution (FWHM) 1.75 keV at 1332 keV peak of ⁶⁰Co, a relative efficiency of about 50%. All counting was performed at constant geometry in a position where the analyser dead-time registered about 0,1%. Thirty-three powdered samples of the same tourmaline of weight between 0,003-0,45 g were irradiated in order to approximate to the "no interference weight" condition. For radionuclides that showed an inadequate sensitivity it was necessary to tolerate higher degrees of interference. Reference certified material (Soil-7) was irradiated simultaneously with the tourmaline to provide reproducibility of results of the analysis and for the quality control. The results of three investigations for five tourmalines was realized and plotted for all radionuclides in order to provide reproducibility of method and check if the interference effect is lost.

4 RESULTS AND DISCUSSION

Table 1 presents the weight of samples, induced activity and specific activity for ⁶⁵Zn and ⁵¹Cr detected in the a tourmaline sample.

Table 1 - INAA experimental and acquisition parameters Weight activated (g); Induced activity (counts/s); Specific activity (counts/s/g)

Isotope	⁶⁵ Zn, E _γ = 1115 keV		⁵¹ Cr, E _γ = 320 keV	
	Weight activated	Induced activity	Specific activity	Specific activity
0,003	0,44	130,40	0,03	8,68
0,005	0,63	131,94	0,04	8,62
0,007	0,83	123,16	0,06	8,73
0,007	1,16	172,58	0,05	8,12
0,009	1,14	132,19	0,08	8,77
0,009	1,18	129,68	0,08	8,95
0,011	1,42	133,89	0,09	8,31
0,011	1,39	126,23	0,08	7,59
0,015	1,93	128,68	0,11	7,43
0,017	2,09	125,84	0,14	8,25
0,018	2,15	121,26	0,14	7,75
0,019	2,32	125,26	0,15	8,20
0,021	2,63	127,69	0,17	8,08
0,027	3,30	120,94	0,20	7,26
0,032	3,78	118,78	0,24	7,45
0,054	5,73	105,46	0,39	7,15
0,058	6,10	105,18	0,41	7,00
0,079	7,81	98,44	0,55	6,91
0,086	8,41	97,42	0,59	6,88
0,100	9,45	94,54	0,69	6,88
0,132	12,01	90,77	0,91	6,86
0,170	15,38	90,35	1,12	6,59
0,184	16,32	88,84	1,26	6,84
0,217	19,51	89,79	1,41	6,51
0,219	19,82	90,37	1,48	6,76
0,261	23,14	88,72	1,73	6,64
0,281	24,82	88,38	1,80	6,40
0,300	26,79	89,29	2,00	6,67
0,333	29,54	88,81	2,19	6,59
0,356	31,39	88,18	2,33	6,56
0,360	32,24	89,57	2,29	6,35
0,400	35,05	87,63	2,63	6,57
0,450	39,55	87,88	2,90	6,44

The graphs of specific activity against sample weight for some radionuclides are shown in Figure 1 and 2, where it is possible to observe the deviation from the straight line around 0,1g. In tourmaline samples weighing around 0,1g the interference effect does not occur, or occurs to a lesser extent.

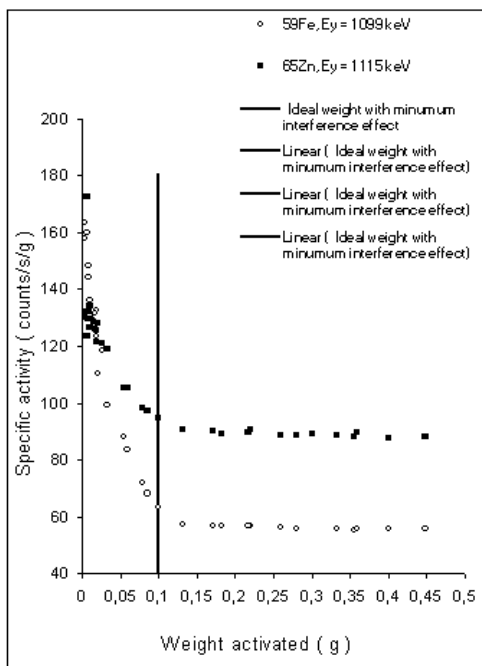


Figure 1 - Variation of induced specific activity with weight of tourmaline

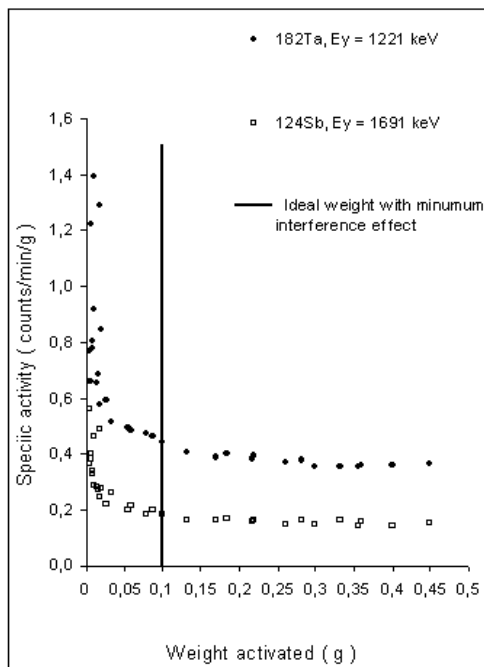


Figure 2. Variation of induced specific activity with weight of tourmaline

All radionuclides showed good agreement in the deviation from the straight line. Small systematic discrepancy was noted for ^{134}Cs , ^{182}Ta , ^{124}Sb , ^{46}Sc , due to their low concentration.

The isotopes investigated were: ^{187}W , ^{140}La , ^{199}Au , ^{72}Ga , ^{76}As , ^{42}K , ^{131}Ba , ^{75}Se , ^{203}Hg , ^{82}Br , ^{85}Sr , ^{51}Cr , ^{124}Sb , ^{134}Cs , ^{46}Sc , ^{86}Rb , ^{59}Fe , ^{60}Co , ^{182}Ta , ^{233}Pa , ^{65}Zn , $^{110\text{m}}\text{Ag}$, ^{152}Eu , ^{160}Tb , ^{175}Hf , $^{177\text{m}}\text{Lu}$, $^{24\text{m}}\text{Na}$. In the tourmaline samples, the radionuclides ^{65}Zn , ^{59}Fe , ^{60}Co , ^{51}Cr , ^{46}Sc , ^{82}Br , ^{140}La , $^{24\text{m}}\text{Na}$, ^{42}K , ^{85}Sr , ^{182}Ta , ^{134}Cs , ^{124}Sb were detected.

5 CONCLUSION

INAA has been used traditionally to determine trace element in mineral samples. Among the trace element analysis techniques, there are many advantages associated with the use of INAA when compared with other analytical methods. When interference effect of ^{10}B is eliminated, INAA can be used to determined trace element in tourmaline. However, special carefully in irradiation, experimental and acquisition parameters, since sensitivity can be affected by interference effect.

6 ACKNOWLEDGMENT

The authors are indebted to the FAPEMIG – Fundação de Amparo à Pesquisa do Estado de Minas Gerais, Brasil by financial support, in special mineral gems project development in CDTN/CNEN - Centro de Desenvolvimento da Tecnologia Nuclear/Comissão Nacional de Energia Nuclear.

7 REFERENCES

- Bowen, H.J.M. Gibbons, D. (1963): *Radioactivation Analysis*. 1st Ed., Oxford: Clarendon Press, 295p.
- Cleland, J.M., Morey, G.B., and McSwiggen, P.L. (1996): Significance of tourmaline-rich rocks in the north range group of the Cuyuna iron range, East Central Minnesota. *Economic Geology*, v. 91, p.1282–1291.
- Ehmann, W.D. Vance, D.E. (1991): *Radiochemistry and Nuclear Methods of Analysis*. 1st Ed., New York: John Wiley & Sons, 531p.
- Hawthorne, F.C. (1996): Structural mechanisms for light-element variations in tourmaline. *Canadian Mineralogist*, v.34, p.123–132.
- Hawthorne, F.C. and Henry, D.J. (1999): Classification of the minerals of the tourmaline group. *European Journal of Mineralogy*, v.11, p.201–215.
- Hawthorne, F.C., McDonald, D.J., and Burns, P.C. (1993): Reassignment of cation site occupancies in tourmaline: Al-Mg disorder in the crystal structure of dravite. *American Mineralogist*, v.78, p.265–270.
- Jolliff, B.L. Papike, J.J. Laul, J.C. (1987): Mineral records of pegmatite internal evolution: REE contents of tourmaline from the Bob Ingersoll pegmatite, South Dakota. *Geochimica et Cosmochimica Acta*, v.51, p.2225–2232.
- Laul, J.C. Lepel, E. A. (1987): Rare earth element patterns in biotite muscovite and tourmaline minerals. *Journal of Radioanalytical and Nuclear Chemistry*, v.112(2), p.461–471.
- Henry, D.J. and Dutrow, B.L. (1996): Metamorphic, Tourmaline and its petrologic applications. *Reviews of Mineralogy*, v.32 p.503–558.
- Henry, D.J. and Guidotti, C.V. (1985): Tourmaline as petrogenetic indicator mineral: an example from the staurolite-grade metapelites of NW Maine. *American Mineralogist*, v.70, p.1–15.
- Koval, P.V., Zorina, L.D., Kitajev, N.A., Spiridonov, A.M., and Ariunbileg, S. (1991): The use of tourmaline in geochemical prospecting for gold and copper mineralization. *Journal of Geochemical Exploration*, v.40, p.349–360.
- King, R.W. Kerrich, R.W. Daddar, R. (1988): REE distributions in tourmaline: An INAA technique involving pre-treatment by B volatilization, *American Mineralogist*, v. 73, p.424–431.
- Oliveira, E.F. Castañeda, C. Eeckhout, S.G. Gilmar, M.M. Kwitko, R.R. grave, E. Botelho, N.F. (2002): Infrared and Mössbauer study of Brazilian tourmaline from different geological environments. *American Mineralogist*, v. 87, p. 1154–1163.
- Slack, J.F. (1996): Tourmaline associations with Hydrothermal ore deposits. *Reviews of Mineralogy*, 33, 559–643.
- Pedrosa-Soares, A.C., and Wiedemann-Leonardos, C.M., (2000): Evolution of the Araçuaí belt and its connection to the Ribeira belt, eastern Brazil, 265–285. In *Tectonic Evolution of South America*, Cordani, U.G., Milani, E.J., Thomaz, A. and Campo, D.A., Eds., Rio de Janeiro: *31st International Congress of Geology*, August 6–17, 2000, 856 p.
- Pinto, C.P. and Pedrosa-Soares, A.C. (2001): Brazilian gem provinces. *Australian Gemmologist*, v.21, p.12–16.

Infrared Reflection Spectrometry of Minerals and Gemstones

M.Ostrooumov

Department of Geology and Mineralogy, Metallurgical Institute, University of Michoacan, Morelia, Mexico

E.Fritsch, B.Lasnier & S.Lefrant

Jean Rouxel Institute of Materials, University of Nantes, Nantes, France

ABSTRACT: The purpose of this work is to inform the mineralogical community about the availability of a catalogue and a new database with automatic search software for mid and far infrared reflection spectrometry (IRS) of rock-forming minerals and natural and synthetic gemstones (<http://www.geocities.com/ostrooumov>). The highly advantageous peculiarities of the IRS make it extremely suitable for different investigations in Advanced Mineralogy and Gemology. IRS is the method of choice for the examination of minerals and gemstones, as they are non-destructive in nature. Using IRS, practically all mineralogical and gemological objects can be identified. In particular, quick and precise identification of gemstones, loose or mounted, as well as the non-destructive analysis of different mineral phases in objects of archaeological interest, museum collections and ancient artifacts are possible. Existing infrared spectral databases for minerals are comprised of data collected from powder dispersions. Therefore the necessity of a new database of reference infrared reflection spectra is extremely important. In support of IRS techniques, a catalogue and new spectral database, with over 500 infrared reflection spectra in mid and far domains from more than 250 different minerals, natural and synthetic gemstones, has been created. The reflectance spectrum serves as a “fingerprint” of the minerals and gemstones and IRS is capable of solving many current problems in Advanced Mineralogy as well as in cosmic geology, volcanology, planetology, astronomy, and ecology.

1 INTRODUCTION

The purpose of this work is to inform the mineralogical community about the availability of a catalogue and a new database with automatic search software for mid and far infrared reflection spectrometry (IRS) of rock-forming minerals and natural and synthetic gemstones. The infrared reflection spectrum of a single mineral is a characteristic of its kind. That is why the spectra can give the structural formula without chemical analysis data (Farmer & Lazarev 1974; Hawthorne 1988; Marfunin 1995). All the characteristics of the infrared spectra of minerals are related to the chemical composition and the crystalline structure of the natural compounds (Niquist & Kagel 1971; Farmer 1974; Nakamoto 1978; Povarennykh 1978).

This study was undertaken to compensate for the absence of published research works referent to the IRS of minerals, particularly gemstones. Indeed, the literature is notably lacking in infrared reflection studies of minerals and gemstones (Ostrooumov et al. 1995). However, IRS is non-destructive method, which is why it is a very important tool for mineralogists and gemologists. Existing infrared spectral databases for minerals are comprised of data collected from powder dispersions (Hofmeister

1995). Infrared reflection spectrometry presents many comparative advantages in comparison to infrared absorption spectrometry of minerals (Ostrooumov et al. 1995). Therefore, the necessity for a new database of reference infrared reflection spectra of minerals and gemstones is extremely important.

2 EXPERIMENTAL DATA

2.1 Methods

The mineral frequency vibrations are generally measured by infrared absorption spectrometry. However, absorption spectrometry has a series of limitations. Firstly, it is a destructive method. Additionally, the infrared measurements of the reflection spectra of minerals are likely to be extended because of the appearance of stable and practical spectrometers with the complementary reflection equipment. The advantages of the infrared reflection spectrometry are numerous: 1) IRS is a non-destructive investigative method that can be used in the study of minerals with natural surface, i.e., crystallographic faces, planes of cleavage, non-uniform surfaces, and of cut and mounted gems for which it can be used to test for identification for

these stones; 2) the usable surface of the samples can vary from a few cm² to a few mm²; and finally, the IRS method is much easier to carry out than absorption spectrometry.

However, the IRS method also has its limitations. For exact determination it is necessary to take into account the effect of the orientation of mineral crystals and rough stones. Anisotropic minerals produce infrared reflection spectra which can be very different depending on the relative orientation of the laser and the crystal lattice. That is why the IRS studies presented here were performed using the mineral crystals in different orientations (all the samples, in the x,y and x,y,z – directions). All experimental data are characterized by the spectra which were obtained for the mineral samples with specific orientation. According to recent results, many minerals may show significantly stronger directional differences in their infrared reflection spectra. In the new database of infrared reflection spectra of minerals and gemstones the software allow to search out the spectrum with similar spectrometric characteristics (positions of the peaks, their relative intensity and configuration). It is concluded that our reliable database will be capable of solving many current problems in mineralogical and gemstone identification as well as in the determination of the crystal orientation.

2.2 Sampling

The creation of an infrared reflection spectra catalog implies obtaining spectra on samples with the greatest possible purity. For this reason, we selected some 250 mineral species of sufficient dimension to be guided, carved and refined. These samples were of the greatest purity and were identified by the traditional gemological and mineralogical methods.

Each "standard" sample was analyzed quantitatively with the electron probe microanalyser CAMECA SX 51 at the Saint Petersburg Geological Institute (Russia). The results of these analysis have been recorded at the Department of Mineralogy at the University of Michoacan, Mexico, and at the Mineralogical and Gemological Laboratory at the University of Nantes, France.

2.3 Obtaining the spectra

The infrared reflection spectra were obtained with the equipment to which we have access to for the spectrometric groups installed at: 1. Mineralogical Laboratory (Saint Petersburg Mining Institute, Russia), 2. Mineralogical and Gemological Laboratory (Mainz University, Germany), 3. Crystal Physics Laboratory (Institute of Materials, Nantes University, France).

2.4 Instruments used

We have used various spectrometric apparatus:

-Spectrometer IRS-29 (Russia)

-Spectrometer UR-20 (Germany)

-Spectrometer Perkin-Elmer FTIR (Germany)

-Spectrometer Bruker IFS-28 (France)

-Spectrometer Nicolet 20SXC-FTIR (France)

We had the possibility of using these various apparatus to compare our results and to benefit from the complementarities of the professionals at the universities involved.

The mineralogical and gemological samples were guided and mounted on the universal accessory of reflection with retro-mirror (Harrick Scientific Corporation). As verification purposes, the same spectra were obtained in various laboratories and with different spectrometric equipment.

The spectra were recorded on diskettes and are available at the Mineralogical Laboratory (University of Michoacan, Mexico) and at the Mineralogical and Gemological Laboratory (University of Nantes, France).

With the results of this investigation, we have elaborated an automatic spectrometric software for the determination of minerals.

3 ANALYTICAL RESULTS

The near-infrared range (13333-4000 cm⁻¹ or 0.8-2.5 μm) is favorable for the identification of the typical bands of some chemical groups or ions such as Fe²⁺ (0.8-1 μm), H₂O (1.4; 1.9 μm), OH (2.2; 2.7 μm), and CO₃²⁻ (1.9; 2.0; 2.17; 2.3 μm). Thus, these absorption bands are used for the qualitative or semi-quantitative analysis of these groups and also to determine various elements.

Table 1. Typical bands of mineral compounds in mid- infrared range.

Class or radicals	v 3	v 4
Carbonates	1570-1500	765-675
Nitrates	1475-1390	750-695
Borates	1430-1350	680-605
Sulphates	1315-1190	680-580
Phosphates	1200-1080	650-525
Orthoborates	1040-940	570-500
Silicates	1000-830	540-435
Chromates	930-800	400-360
Arsenates	900-760	420-310
Vanadates	880-740	390-310
Selenates	870-800	415-375
Molibdates	850-790	375-330
Wolframates	815-785	340-295
Iodates	825-720	400-320
Selenites	770-720	390-350

In the mid-infrared range (MIR: 4000-400 cm^{-1} or 2.5-25 μm) the reflection (Tab.1) or absorption bands are normally visible due to the various minerals atomic groups. The mid-infrared spectra of the mineral offers significant information about the functional groups of which it is constituted. The majority of the mineral's characteristic bands meet in the mid-region of the infrared spectrum. Therefore, research with reference to this region of minerals and gems is bountiful, and a catalog of infrared reflection spectrum of minerals and some gemstones is now on the Internet (Ostrooumov et al. 2003).

The far-infrared range (FIR: 400-10 cm^{-1} or 25-1000 μm) is a range where the fundamental bands of basic frequencies of various atomic groups are observed. To this date, this range has not been studied in depth for mineral compounds.

In the far-infrared range (Tab.2) the reflection spectra are particularly typical for compounds with a relatively weak strength of the inter-atomic bond (sulfides, oxides of the low valence elements, halides, carbonates, sulfates, nitrates). Chemical compounds with relatively high bonding (silicates) also present characteristic profiles. The IRS technique in the far region supplements a well spectrometry in the mid-infrared zone for the various crystallochemical classes of minerals.

To determine the natural or synthetic origin of gemstones, it is necessary to investigate them in the near-, mid- and far-infrared ranges. Each mineral, natural or synthetic gemstone presents a quite particular infrared reflection spectrum, which allows for rapid identification of the mineral species.

4 CONCLUSIONS

In support of IRS techniques, a first systematic catalog and new spectral database (www.geocities.com/ostroum), with over 500 infrared reflection spectra in mid and far ranges from more than 250 different minerals, natural and synthetic gemstones, and automatic search software has been created.

The IRS non-destructive method in the different ranges will contribute to the resolution of current problems of Advanced Mineralogy, such as structural parameters, crystal zonation, optical orientation, inclusions and pleochroism, etc. (Ostrooumov 1991; Ostrooumov et al. 2003).

Using IRS, almost all mineralogical and gemological objects can be identified. In particular, quick and precise identification of gemstones, loose or mounted, as well as the non-destructive analysis of different mineral phases in objects of archaeological interest, museum collections and ancient artifacts is possible.

The IRS has proved very useful in solving some of the most complicated cases of mineralogical and gemstone identification. It primarily aids in the determination of whether minerals and gems are natural or synthetic (man-made) or if they have undergone treatment in a laboratory. IRS, together with Raman spectrometry, has become an efficient and valuable tool for mineralogical and gemological laboratories.

Table 2. Characteristic bands of mineral compounds in far-infrared range.

Mineral	Reflection maximum (cm^{-1})			
	>300	300-200	200-100	<100
Pyrite	405			
	347	294		
Spinnelle	307	258	164	
	365	259	198	
Chrysoberyl	322	258	197	
	396	260	163	85
Quartz II c	367		144	
	331	271	186	94
Apatite	318	238		
	310	260	198	83
Turquoise	320	228	111	
		209	199	95
Wulfenite			182	
	306		123	62
Olivine	360	292	165	
	380	235	192	
Almandine	318		135	
	397		144	64
Zircon	313			
	361	257	145	
Beryl	362	260	198	66
	403	292	144	
Tourmaline	332			
	360	249	137	
Diopside	318	230	131	
	345	259	140	91
Jadeite			106	
			146	
Actinolite			109	
			163	85
Moscovite			114	
			185	95
Microcline	328	272	146	
			109	
Sanidine	380	297	163	85
			114	
Oligoclase	401		185	95
	368			
Labradorite	405	238	125	
	318			

The highly advantageous peculiarities of IRS make it extremely suitable for different investigations in Mineralogy and Gemology. The reflectance spectrum serves as a "fingerprint" of the minerals and gemstones and IRS is capable of solving many current problems in Advanced Mineralogy as well as in cosmic geology, volcanology, planetology, astronomy, and ecology.

5 ACKNOWLEDGMENTS.

The authors wish to thank M.C. Kimberly Anne Brooks-Lewis for the English revision of this work.

6 REFERENCES

- Hofmeister, A. 1995. Infrared Microspectroscopy in Earth Science. In Practical guide to infrared microspectroscopy. Second Edition, Marcel Dekker, Inc. New York-Basel-Hong Kong, 377-415.
- Farmer, V.C. 1974. The Infraed Spectra of Minerals. Mineralogical Society. London.
- Farmer, V.C. & Lazarev, A. 1974. Symmetry and crystal vibrations. In The Infrared Spectra of Minerals (V.C. Farmer ed.), Mineralogical Society, London.
- Hawthorne, F.C. (ed.) 1988. Spectroscopic Methods in Mineralogy and Geology. Mineralogical Society of America, Washington, D.C.
- Marfunin, A. 1995. Advanced Mineralogy. Springer Verlag. Berlin-New York-Heidelberg.
- Nakamoto, K. 1978. Infrared and Raman spectra of Inorganic and Coordination Compounds. John Willey & Sons, New York.
- Niquist, R.P. & Kagel, R.O. 1971. Infrared spectra of inorganic compounds (3800-45 cm⁻¹). Academic Press, New York.
- Ostrooumov, M. 1991. Method of determination of the lattice ordering degree in the alcalin feldspars by infrared reflection spectrometry. Proceedings of the URSS Mineralogical Society, vol. 120, No.5, 94-99.
- Ostrooumov, M., Lasnier, B. & Lefrant S. 1995. Infrared reflection spectrometry of gem materials. Analisis, 23, 39-45.
- Ostrooumov, M., Lasnier, B., Lefrant S. & Fritsch, E. 2003. Infrared reflection spectrometry of minerals and gemological materials. WEB page: <http://www.geocities.com/ostroum>.
- Povarennykh, A.S. 1978. The use of infrared spectra for the determination of minerals. American Mineralogist, vol. 63, 956-959.

The Hetian Jade of China

R.Song & Z.Yang

Key Laboratory of Mineral Resources, Institute of Geology and Geophysics, Chinese Academy of Sciences, Beijing, China

ABSTRACT: The Hetian jade, also called tremolite jade, is one kind of nephrites. It is the aggregation of tremolite minerals. The Hetian jade plays an important role in the Chinese traditional culture. It has been considered as emperor jade in the Chinese history. The Hetian jade was the main material for making jade ware in the history. It has provided plentiful jade culture in China. The Hetian jade comes from the contact metasomatism of mid-acid intrusive rock and dolomite marble in the Kunlun Mountain, Southwest China. The main chemical components of the Hetian jades are SiO₂, MgO and CaO, with minor components of Al₂O₃, FeO, Fe₂O₃, Na₂O, K₂O and H₂O. The weight percentages of SiO₂ are about 53.34% - 57.60%, the MgO 21.30% - 24.99%, and the CaO 11.33% - 17.41%. Usually, the weight percentages of FeO are less than 2%, the Fe₂O₃ less than 1%, the Al₂O₃ less than 2%, both Na₂O and K₂O less than 0.3%, and the H₂O less than 2%. There are about 95 - 99% tremolites in the Hetian jades, whereas, the impurity minerals are very sparse. The impurity minerals of the Hetian jades are usually diopside, epidote, clinozoisite, forsterite, dolomite, quartz, magnetite, pyrite, pleonaste and apatite.

1 THE HETIAN JADE AND CHINESE CIVILIZATION

The Hetian jade comes from the Kunlun Mountain, Southwest China, which is the best jade in China. The word of Hetian is the locality name of the jade. The Hetian jade plays an important role in the Chinese traditional culture, it has been considered as emperor jade in the Chinese history. About 3500 years ago, the Hetian jade became the raw material of jade ware in the Chinese Palace. When the Hetian jades were found by the ancient people of Kunlun, they were transported to the Central Plains of China. As we know, the famous Silk Road was rose in the Han Dynasty (206 B.C. - A.D. 220) in China, so, the Hetian Jade Road was considered as the predecessor of the Silk Road. Since the Spring and Autumn Period (770 - 476 B.C.), the Chinese people have connected the moral character with jade, they thought the moral excellence can be likened to the pretty of jade. The Chinese Jade ware was an important component of the Chinese civilization. In the Chinese history, the Hetian jades were often made into national treasure, jewellery of imperial family, imperial seal and authenticating object of folk.

2 THE COMPOSITION AND CHARACTER OF THE HETIAN JADE

The weight percentages of SiO₂ of the Hetian Jades are about 53.34 - 57.60%, the MgO 21.30 - 24.99%, and the CaO 11.33 - 17.41%. There are few minor components in the Hetian jades. Usually, the weight percentages of FeO of the Hetian jades are less than 2%, the Fe₂O₃ less than 1%, both the Na₂O and the K₂O less than 0.3%, the Al₂O₃ less than 2% and the H₂O less than 2% (Tang et al. 2002). The mineral grain of the Hetian jade is very fine, therefore, the character of the Hetian jade is fine and smooth, and possesses greasy lustre and semitransparent. The Hetian jade possesses high tenacity, so, it is wear-resistant and not easy broken. According to their colours, the Hetian jades can be divided into white, grey and yellow jades etc. The best Hetian jade is one kind of white jades, named mutton-fat jade. The Hetian jades are mainly composed of tremolites. Usually, the tremolite minerals are more than 98%, their grains are very fine. The Hetian jades show microcrystallines with interlocking micro-texture (Chen & Chen 2002). The impurity minerals are very sparse, they are usually diopside, epidote, clinozoisite, forsterite, dolomite, quartz, magnetite, pyrite, pleonaste and apatite etc. The

refraction index of the Hetian jade is 1.60-1.62, the density is 2.93 - 2.97 g/cm³, and the hardness is 6.5 - 6.9 (Yang & Wang 2002). The amphibole group minerals are named according to their crystal chemistries. In the diagram of TSi vs. Mg/(Mg + Fe²⁺) of nomenclature of amphiboles, the Hetian jades are distributed in the tremolite range. The chemical compositions have proved that the Hetian jades are mainly composed of tremolites. The x-ray diffraction data of Hetian jades are very similar to the standard x-ray diffraction data of tremolites (Cui & Yang 2002).

3 THE GENESIS OF THE HETIAN JADE DEPOSIT

The original deposit of the Hetian jade is the metasomatic ore deposit of carbonate rock with intrusive rock. The deposit is a typical contact metasomatic deposit. The intrusive rocks are granite and granodiorite etc. They are usually small dike rocks. The carbonate rocks are mainly dolomite marble rocks, which contain about 20% MgO. They are usually lenticular rocks. The metasomatic ore deposit possesses banded structure. From the intrusive rocks to the carbonate rocks, they are epidotization and potassium feldspar intrusive rocks diopside band tremolite band forsterite band serpentine band dolomite marble band. The Hetian jades usually occur in the tremolite band (Tang et al. 2002). The chemical reaction of the formation of the Hetian jade may be as follows (Cui & Yang 2002):



4 REFERENCES

- Chen, K. & Chen, Z. 2002. Study on compositions and physical features of Hetian jade. *Acta Petrologica et Mineralogica*, 21(Supp.), 34-40. (in Chinese).
- Cui, W. & Yang, F. 2002. Study on Hetian jade (tremolite jade). *Acta Petrologica et Mineralogica*, 21(Supp.), 26-33. (in Chinese).
- Tang, Y., Liu, D. & Zhou, R. 2002. Study on name, culture, quality and mineral deposit of Hetian jade. *Acta Petrologica et Mineralogica*, 21(Supp.), 13-21. (in Chinese).
- Yang, Z. & Wang, S. 2002. Micro-textures and spectrometry characteristics of Hetian jade. *Acta Petrologica et Mineralogica*, 21(Supp.), 57-61. (in Chinese).

The Beryl to Bromellite Transformation: *In Situ* High Temperature X-ray Observations

R.R.Viana

Department of Mineral Resources, Institute of Exact Sciences and Earth, University of Mato Grosso, Cuiabá, Brazil

ABSTRACT: Phase transitions in beryl (aquamarine variety) have been observed at temperatures up to 1200°C, using X-ray diffractometry at high temperature. The samples analyzed already had been chemically well-characterized by Viana et al. (2002). Sodium chloride was added to control any shift due to instrumental errors. At about 780°C, a new phase identified as bromellite (BeO) commences to form. For sample with large content of water type I, it is observed that this new phase is stable together with beryl up to 1200°C and for those with larger content in water type II, they are stable up to 900°C, after this, only bromellite and vitreous phase are formed in this samples. This study suggests that the thermal changes of beryl are directly related to content and the spatial configuration of water inside channel sites. The formation of bromellite seems to occur by the reaction of NaCl and beryl at high temperature.

1 INTRODUCTION

This work was performed on four beryl samples of blue and blue-greenish color of the pegmatites from the Eastern Brazilian Pegmatite Province in the region of Minas Gerais State. The research emphasizes the changing of phase of beryl to bromellite, produced by effect of heating at high temperature investigated from room temperature (RT) up to 1200°C at steps of 20°C, using X-ray diffraction patterns. The variation of both cell parameters with temperature had already been reported before for a synthetic beryl (Morosin 1972, Schlenker et al. 1977), but for that particular sample the *a* axis showed an expansion whereas the *c* axis showed a contraction from RT to 300°C and an expansion at higher temperatures.

2 EXPERIMENT

Powder X-ray diffraction patterns (XRD) were performed on four samples in a D-5000 Siemens apparatus (Cu-K α radiation). The experiments were sequentially from room temperature up to 1200°C, with each run took about 30 minutes, meaning that the four investigated samples remained at

temperatures above 800°C for about 10 hours. Sodium chloride was used as an internal standard and peak positions were determined by fitting the numerical profiles with a Pearson VII function. Cell parameters were determined using the strongest reflections. All the samples used in this work were chemically characterized by Viana et al. (2002).

3 RESULTS AND DISCUSSION

Blue-greenish samples show small amounts of water type II, and consequently greater amounts water type I, whereas those blue samples show smaller amount of water type I (Viana et al. 2002). In Figure 1 is shown diffractograms for blue-greenish samples. In this figure it is observed the stability of beryl up to 1200°C, coexisting with bromellite.

Figure 2 clearly demonstrates that there is no reflection of beryl at 1200°C and keeps a standard pattern at 900°C. Above this temperature only bromellite is present along with vitrea phase.

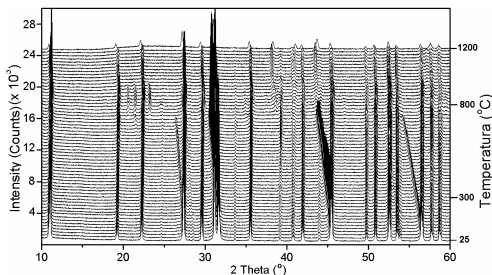


Figure 1: X-ray diffraction patterns (Cu-Kα) of blue-greenish beryl, where is observed that bromellite and beryl coexist at temperature up to 1200°C

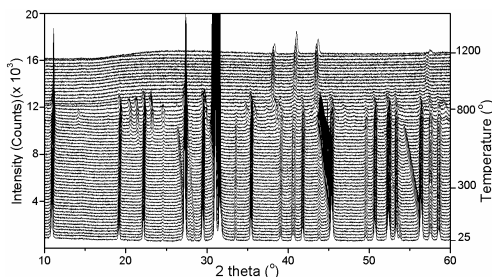


Figure 2: X-ray diffraction patterns (Cu-Kα) of blue beryl. For these samples is present only bromellite and vitreous phase at temperature up to 1200°C. At about 900°C no trace of beryl is observed.

For best view of the beryl in transformation to bromellite phase, it is showed in Figure 3 diffractograms in selected temperatures for sample blue-greenish. It can be learned from this figure that the increase the temperature shift the NaCl lines towards lower angles, indicating an expansion of the lattice; and some beryl-lines are moved toward higher angles, signifying a contraction of the lattice. Close to 300°C the (211) of beryl and (200) NaCl reflection coincide because they were shifted in opposite directions. At 800°C there are no traces of NaCl, and a new phase identified as bromellite (BeO) starts to be formed. This transformation seems to be associated only with the introduction of NaCl, because other experiments without add NaCl, only a vitreous phase and/or beryl is present.

The coefficient of thermal expansion for the sodium chloride and beryl were obtained. For NaCl the coefficients were measured at RT, 300°C, 600°C and 700°C, and the value found was $4.5 \times 10^{-5} \text{C}^{-1}$ (Viana et al. 2002). The thermal expansion coefficients for blue-greenish sample were calculated from the temperature dependence of the cell parameters in the range 25-1200°C (Fig.4). For whose value measured at RT to about 700°C the α_a obtained was $-2.9 \times 10^{-6} \text{C}^{-1}$ and α_c $-8.5 \times 10^{-6} \text{C}^{-1}$. At 850°C they become zero and from that

temperature upwards they are positive and temperature dependent.

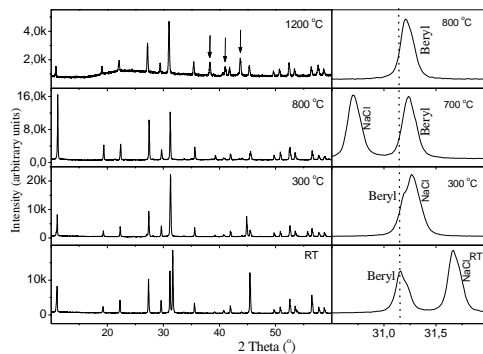


Figure 3: X-ray diffraction patterns (Cu-Kα) of blue-greenish beryl at RT, 300°C, 700°C, 800°C and 1200°C. The right side shows the shift of the (211) beryl and (200) NaCl lines. Arrows point to lines belonging to bromellite (after Viana et al. 2002).

For blue samples, the cell parameters decrease continually at about 800°C, after this temperature occur an increase in both parameters. The coefficient of thermal expansion calculated for these samples were $-5.2 \times 10^{-6} \text{C}^{-1}$ for aa and $-9.1 \times 10^{-6} \text{C}^{-1}$ for ac. The study concerning the effect of heating in the lattice parameters of bromellite is under investigation.

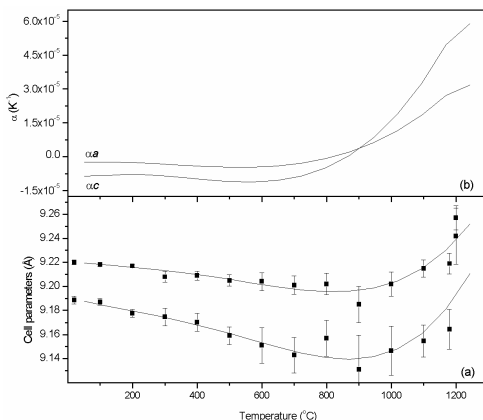


Figure 4. Temperature dependence of the cell parameters (a) and thermal expansion coefficients (b) of blue-greenish sample.

4 ACKNOWLEDGMENTS

This work was partially supported by Capes, CNPq

and Fapemig (Brasil). The author thanks Prof. Dr. Willen B. Stern (Basel University-Switzerland) by X-ray analyzes and Prof. Dr. Dahrani Sundaram (UFMT-Brazil) for the text revision.

5 REFERENCES

- Morosin, B. 1972. Structure and thermal expansion of beryl. *Acta Cryst* B28:1899-1903.
- Schlenker, J. L., Gibbs, G. V., Hill, E. G., Crews, S. S., Myers, R. H. 1977. Thermal expansion coefficients for Indialite, Emerald and Beryl. *Phys Chem Minerals* 1:243-255.
- Viana, R. R., Jordt-Evangelista, H., da Costa, G. M., Stern, W. B. 2002. Characterization of beryl (aquamarine variety) from pegmatites of Minas Gerais, Brazil. *Physics and Chemistry of Minerals*. 29: 668-679.

General Session

Mineralogical and Petrographical Studies of Manufactured Fine Aggregates

G.Cuchierato & L.M.Sant'Agostino

Department of Sedimentary and Environmental Geology, Geosciences Institute of the University of São Paulo

T.B.Bonás

Bunge Fertilizantes S/A.

J.P.R.Olivito

Department of Sedimentary and Environmental Geology, Geosciences Institute of the University of São Paulo

ABSTRACT: As part of a more extensive research, the present paper discuss the behavior of manufactured fine aggregates (MFA) mineralogy and related with the aggregates source rock features. The MFA generated by the crushing process in quarries, are being produced in the Great São Paulo Metropolitan Area (GSPMA) over 3 million m³/year in 39 active mining operations (period 1998 to 2000). The crushed stone total production in the GSPMA is over 18 million m³/y, what means around 4.2 t/hab/year of aggregate per capita. The study covered half of the quarries in activity, their rock sources were collected for petrography and their MFA products were sampled for technological characterization. The characterization comprised sample preparation, textural and mineralogical analyses, grain size classification (sieving and laser diffraction) and microscopic and instrumental analysis (X-ray diffraction and fluorescence). In the GSPMA the aggregates are predominantly obtained from granitic and gneissic rocks of basement (over 90 % of the total) and the majority of the mined granites are porphyritic with feldspar phenocrysts in a mafic medium to fine grained mass, while mined gneisses are generally granolepidoblastics with fine-grained mass. Due to these characteristics, the products originated by crushing in quarries have distinct behavior in the rock comminution, being strongly controlled by the grain size crystallization characteristics of the minerals; as consequence the MFA showed a clear mineral segregation in grain size distribution and the accessory minerals tend to be concentrated in the finest fraction (mainly -0.075 mm), and quartz and feldspar on the coarse fraction.

1 INTRODUCTION

The quarries production in the Great São Paulo Metropolitan Area (GSPMA) is based on the exploitation of basement rocks mainly of granitic composition, coming from 39 active mines in the period covered by this study. Cuchierato (2000) developed technological research of some products and residues from these quarries, specially the manufactured fine aggregates (MFA), aiming enhance their application.

The technical and economical quarries aspects were verified by field work what gave a general picture about the plutons mined in the GMPSA. At the same occasion, sources rocks were collected for petrography and also their fine products (MFA) were sampled for technological characterization.

This paper deals with the MFA investigation focusing their grain size distribution, chemical and mineralogical characteristics as well as technological performance.

2 ECONOMICAL ASPECTS

The aggregates for civil building are the principal Brazilian mineral commodity. Unless their low prices they have an important role in the mineral industry financial movement, even considering that the country has one of the lowest aggregates consumption *per capita* of the world (around 2.1 t/hab/year – DNPM 2000).

São Paulo State is responsible for the industrial minerals the major part of the production of the country, essentially to supply raw material for civil building demanded by urban and industrial development, always exploiting local geological sources. This position is due to a great demographic and industrial concentration that requires raw material for construction and basic infrastructure.

In this context the GSPMA appears as the principal region of aggregates production and consumption of Brazil with around 4.2 t/hab/year, what signifies the double of the national consumption but is far below from that of the developed countries.

3 GSPMA GEOLOGICAL SETTINGS

The GSPMA is situated in the geological domain of pre-Cambrian crystalline rocks that have partial recovering by recent alluvial sediments related to the basin of the main rivers in the region (Coutinho 1980, Riccomini 1989, Juliani 1993, Sabesp/Cepas 1994, Rodriguez 1998 and Sant'Anna 1999).

In the GSPMA basement, which belongs to the Ribeira Folded Belt (Hasui et al. 1975), several rock types are recognized such as gneisses, xistes, filites, amphibolites, quartzites, milonite-gneisses, blastmilonites, milonites and migmatites with variable structures. These rocks were intruded by several generations of granitic bodies related to the *Ciclo Tectônico Brasileiro* or coming from the reworking of older rocks.

The rocks with granitic composition cover large areas of the pre-Cambrian terranes. Several lithotypes are identified such as granites, granodiorites, monzogranites and not differentiated granites, partly gneissified, of the Proterozoic period, normally porphyritic with sin/tardi/pos tectonical features. They form bodies of all dimensions, since large batholites till small stocks (Rodriguez 1998), which are located at the basin boards in high lands.

4 GSPMA QUARRIES SOURCE ROCKS

The crystalline rocks from the basement are exploited for aggregates raw material and it was verified that the majority of the quarries is established at geological unities of similar mineral assembly.

The lithologies observed in the quarries are almost all quartz-feldspar rocks of granitic composition that can be classified as granites (massive or texturally oriented) and gneisses.

Among the source rock studied five main lithotypes were identified: granites 3a and 3b, granodiorites and tonalities, plus biotite-amphibole gneisses. The diagram Quartz-Feldspar-Mafic minerals was applied to a simple categorization of the rocks (Figure 1). The mafic minerals index is a common parameter for igneous rocks mineralogical composition classification being defined as the volumetric proportions of dark minerals in the rock.

Unless the mentioned index is specifically used for igneous rock evaluation, here it was applied also for the metamorphic for comparative purposes, essentially with the conotation of a color indicator. This assumption was supported by the probable igneous rock origem of the GSPMA quarries gneissic rocks (ortogneisses), as suggested by field work.

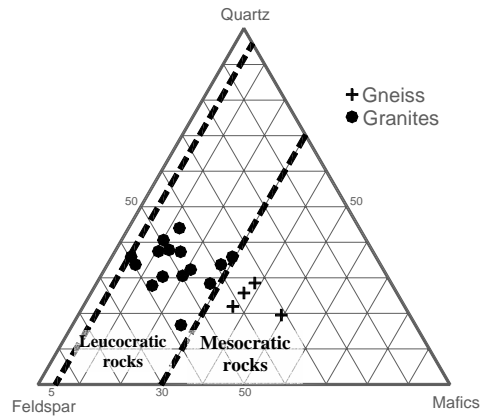


Figura 1 - Diagram of rocks mineral composition

The granites were classified as leucocratic rocks, with mafic index between 5 and 30%. The gneisses showed index corresponding to mesocratic rocks due to their higher quantity of iron-magnesium minerals (pyroxenes and amphiboles).

A common peculiarity was observed in the textural aspects of the exploited rocks: the bulk of the granites are porphyritic with feldspar phenocrysts (centimeters sized) in a mafic medium to fine grained mass, while gneisses are generally granolepidoblastics with centimetric crystals immerse in a fine-grained mass.

5 MANUFACTURED FINE AGGREGATES

The manufactured fine aggregates (MFA) are defined (Ohashi 2001) as the sand resulted from fresh rock crushing, with limited quantity (actual standardized in 5 to 7%) of micro fines accumulated under the 200# sieve (0.075 mm).

It is estimated that this material production is higher than 3 million m³/year in the GSPMA (Cuchierato & Sant'Agostino 2000). The MFA meant from 10 to 42 % of the quarries production and have the general aspects showed in the Figure 2.

For the sampled material, the grain size distribution showed quite similar behavior for the more fine fractions, with the -0.075 mm varying in weight proportions from 7 to 16% of the total sample (Fig.3). The distinct behavior observed are related with rock lithological and textural aspects: higher fines proportions are associated with the gneisses and the fine matrix porphyritic granites.

For the coarser fractions there are significant trend differences of the grain size distribution, also controlled by textural and lithological rock characteristics. The major proportions of coarse

material should be related to faneritic granites and to medium sized matrix porphiritic granites.

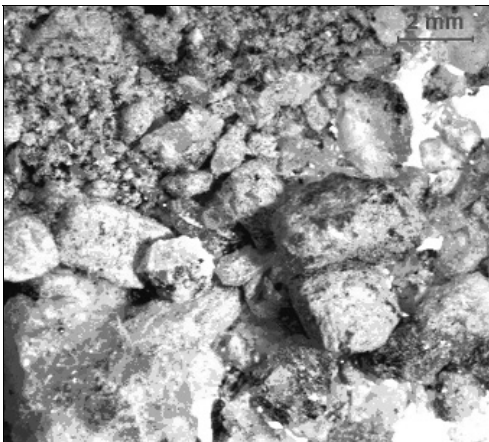
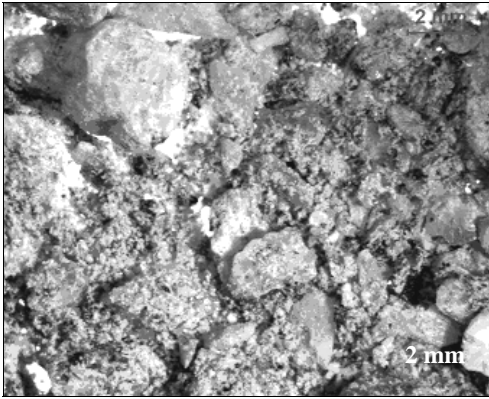


Figure 2: General aspects of the MFA produced at Mairiporã (upper photo) and at Perus (photo below).

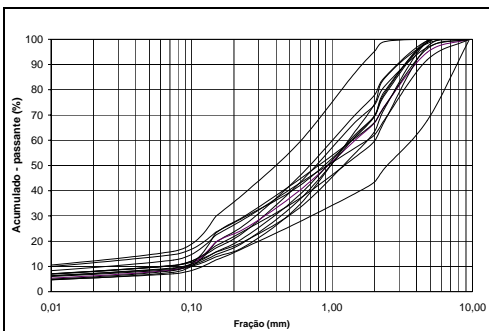


Figure 3: MFA's grain size distributions

There is some relationship between mafic indexes of the aggregate source rocks and the proportions of fine fraction (-0.075 mm) generated in the industrial crushing process, as indicated in the Figure 4. This correlation corroborated the close-fitting interference of source rocks characteristics in their behavior in comminution processing, as well as in the attributes of the MFA produced in this processing.

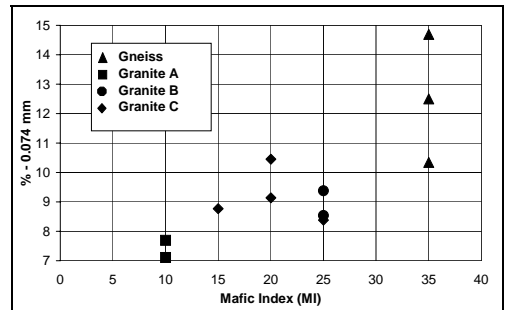


Figure 4: Correlation between the source rock mafic index and the proportion of the fraction -0.075 mm (Granites A = medium faneritic texture; Granites B = porphiritic with medium matrix, Granites C = porphiritic with fine matrix)

It was verified that the MFA obtained from gneissic rocks that have fine fraction (-0.075 mm) weight proportions around 10-15% are those with the higher mafic index (35%).

In the cases of granitic source rocks a scattering trend can be observed, with their mafic index in the range of 10 to 25% and the MFA's fine fraction weight proportions varying below 11%. The source rock with faneritic medium sized texture showed mafic index around 10% and low MFA's fine fraction weight proportions. Those porphiritic source rocks with medium sized faneritic matrix have mafic index about 25% and MFA's fine fraction weight proportions between 8.5 and 9.5%. Finally, for that porphiritic source rocks with fine sized faneritic matrix the mafic index ranged from 15 to 25% and the MFA's fine fraction weight proportions between 8.3 and 10.5%.

6 CONCLUSIONS

The aggregates source rocks features, mainly related with their texture, defined distinct performances in the quarries industrial crushing process. Rocks with fine-grained texture tend to generate higher fine fraction (-0.075 mm) weight proportions.

Also the source rocks texture plus mineral assembly are of great consequence in the characteristics of the MFA's produced in the

industrial comminution. Higher rock mafic index also indicate probable superior fine fraction (-0.075 mm) weight proportions.

The quarries in the GSPMA, region of the cases studied, normally exploited coarse-grained granitic composition rocks of the pre-Cambrian basement, being very common those with porphyritic texture. For those rock types the mafic plus accessory minerals tend to be concentrate in the finest grain size portion of the rock, both in the matrix of porphyritic texture and even in the more homogeneous texture.

The studied cases showed a clear tendency of the mafic plus accessory minerals to be concentrate in the finest grain size fraction produced in the industrial crushing process applied to the granitic composition rock exploited in the GSPMA. Consequently, the coarse aggregates have higher proportions of quartz-feldspar components and the MFA's by-products obtained are enriched in mafic minerals, relatively to the source rocks composition.

7 ACKNOWLEDGEMENTS

For the funding agency FAPESP (Fundação de Amparo à Pesquisa dos Estado de São Paulo) that supported the development of this work also as Research Project, Master Sciences and Scientific Initiation Fellowships.

8 REFERENCES

- Coutinho, J.M.V. (1980) Carta geológica da região metropolitana de São Paulo 1:100.000. São Paulo, EEMPLASA. (2 maps).
- Cuchierato, G. (2000) Caracterização Tecnológica dos resíduos da mineração de agregados da Região Metropolitana de São Paulo, visando seu aproveitamento econômico. São Paulo, 201p. Geosciences Institute Master Sciences Dissertation, University of São Paulo.
- Cuchierato, G.; Sant'Agostino, L.M. (2000) Pó de Pedra: produção na região metropolitana de São Paulo (RMSP) e principais características. In: Seminário Desenvolvimento Sustentável e a Reciclagem na Construção Civil, Práticas Recomendadas, 3, São Paulo, 2000. Meio Ambiente. São Paulo, IBRACON, Comitê Técnico 206. p. 125.
- DNPM – Departamento Nacional de Produção Mineral (2000) Sumário Mineral, v. 20, p. 23-24.
- Hasui, Y; Carneiro, C.D.R.; Coimbra, A.M. (1975) The Ribeira folded belt. Revista Brasileira Geociências, v.5, p. 257-266.
- Juliani, C. (1993) Geologia, petrogênese e aspectos metalogenéticos dos grupos Serra do Itaberaba e São Roque na região das serras do Itaberaba e da Pedra Branca, NE da cidade de São Paulo, SP. São Paulo, 803p. Geosciences Institute PHd Thesis, University of São Paulo.
- Ohashi, T. (2001) Areia de brita com alto conteúdo de microfios na produção de concretos de cimento Portland. Revista Areia & Brita. Associação Nacional de Entidades..., n.14, p.19 + Slides
- Riccomini, C. (1989) O rift continental do sudeste do Brasil. São Paulo, 256p. Geosciences Institute PHd Thesis, University of São Paulo.
- Rodriguez, S.K. (1998) Geologia urbana da região metropolitana de São Paulo. São Paulo, 171p. Geosciences Institute PHd Thesis, University of São Paulo.
- Sabesp/Cepas (1994) Diagnóstico hidrogeológico da região metropolitana de São Paulo (RMSP). São Paulo. (Internal report).
- Sant'Anna, L.G. (1999) Geologia, mineralogia e gênese das esmectitas dos depósitos paleogênicos do rift continental do Sudeste do Brasil. Geosciences Institute PHd Thesis, University of São Paulo.

Nb-Ta Oxides from Vigizzo Valley Pegmatites – Northern Italy

C. De Vito

Dipartimento di Scienze della Terra, Università di Roma “La Sapienza”, p.le A-Moro 5 - 00185 Roma Italy

C. Aurisicchio

IGG, C.N.R., sezione di Roma, p.le A. Moro 5 – 00185 Roma, Italy

P. Orlandi

Dipartimento di Scienze della Terra, Università di Pisa, via S. Maria 53 - 56126 Pisa, Italy

ABSTRACT: A large number of Nb and Ta oxides from Vigizzo Valley pegmatites were analyzed using electron microprobe and X-ray diffraction. Most of the samples come from “beryl-rich type pegmatites”, hosted by gneissic rocks, and some others from albitized pegmatite cutting amphibolite and biotite gneiss. X-ray powder patterns collected with Gandolfi camera and single crystal patterns collected with Weissenberg camera were repeated on single fragments previously heated at 900°C for ten hours. Microprobe analytical data, as revealed also by X-ray-diffraction studies, show that the samples are polycrase-(Y), ferrocolumbite, manganocolumbite and microlite.

1 INTRODUCTION

Study of Nb and Ta oxides and Ti-Nb-Ta complex oxides has recently developed considerably, because of their petrogenetic significance in reconstructing the evolution of rare-enriched-granitic pegmatites (Černý & Ercit 1985, 1989; Černý et al. 1986, Mulja et al. 1996, Aurisicchio et al 2001, 2002, De Vito, 1998, 2002).

In the Vigizzo Valley Nb-Ta oxides and Ti-Nb-Ta complex oxides occur in small miarolitic cavities (e.g. pockets) as accessory minerals of beryl-rich and albitized pegmatites.

The euxenite-polycrase group has the general formula AB_2X_6 where the A-site is occupied mainly by Na, Ca, Y, REE, Th, U; the B-site by Nb, Ta, Ti and the X site by O and OH.

Minerals of the columbite-tantalite group have the general formula AB_2O_6 , with the A-site occupied by Fe, Mn, and a smaller quantity of Mg, Na, and trivalent ions, and the B-site occupied by $Nb > Ta >> Ti > W$.

The pyrochlore group has the general formula $A_{2-m}B_2X_{6-w}Y_{1-n}^*pH_2O$, where the A-site is occupied mainly by Na, Ca, Mn, Fe^{2+} , Fe^{3+} , Sr, Sb, Cs, Ba, REE, Pb, Bi, Th, U; the B-site by Nb, Ta, Ti,

Al, Fe^{3+} , Zr, Sn and W; the X-site by O and OH and finally Y-site by OH, O and also F. Commonly this group of minerals is divided into three major subgroups on the basis of the main occupant of the B-site (betafite $2Ti > Nb + Ta$; pyrochlore $Nb + Ta > 2Ti$, $Nb > Ti$; and microlite $Nb + Ta > 2Ti$, $Ta > Nb$) and in many species on the basis of the cationic populations occupying the A-site (Hogarth 1977, Černý & Ercit 1989).

In this contribution, we report the results of composition and structural state of euxenite-, -columbite and -pyrochlore mineral groups from Vigizzo Valley pegmatitic dikes.

2 OCCURRENCES

The pegmatites of Vigizzo Valley are well known to mineral collectors (Mattioli 1979, Albertini & Andersen 1989) for the numerous rare minerals such as Nb and Ta oxides. They are intruded into metamorphic rocks of the Penninic Unity, which is cut by Sempione-Centovalli Line, the northern branch of the Insubric Line.

Many types of pegmatite were recognized by different researchers and all are divided in two main groups: the first one, made by discordant dikes, is

hosted by gneissic rocks (e.g. Pian dei Lavonchi, Val Trontano, Rio Graia, Val di Crana), whereas the second type, represented by albitized pegmatite occur in amphibolite and biotite gneiss (Alpe Rosso, Pizzo Marcio). The former, showing medium to coarse grain size, contain the following major silicate phases: quartz, alkali-feldspar and micas. The rare mineral species such as gadolinite-(Y), xemotime-(Y), uraninite, and Nb-Ta oxides are found in small pockets, often concentrated at the contact with wall-rock. In the central part of the bodies frequently occurs beryl (blue-beryl). The latter, with medium grain size and smaller dimensions have the paragenetic assemblage dominantly composed by albite, actinolite, epidote, chlorite. In addition to major phases the pegmatites contain a complex variety of minerals including garnet, zircon, bavenite, roggianite, allanite, titanite, rarely beryl (emerald), and Nb-Ta oxides.

3 ANALYTICAL METHODS

The EMP analyses of the Nb and Ta oxides were done with a Cameca Cx 827 instrument equipped with three wavelength-dispersion spectrometers (WDS) and one energy-dispersion spectrometer (EDS), at the IGC-CNR, Sezione di Roma. All the samples were analyzed with an accelerating voltage of 15 kV, a sample current of 30 nA measured on a synthetic andradite, and a beam diameter of 3 μm .

During electron microprobe analysis of minerals containing the REE $L\alpha$ was used for Ce, Pr, Nd, Gd, Er and Yb; $L\beta$ for Sm, Ho and Dy. The others REE were not included in processing, since they were below detection limits. Peaks and backgrounds for each REE were measured according to the approach of Roeder (1985). Synthetic silicate glasses (Drake & Weill 1972, Åmli & Griffin 1975) were used for quantitative determination of REE. Corrections for the matrix effect were calculated by ZAF software (Microbeam Service). Analytical error was ~ 1% rel. for major and ~ 5% rel. for minor elements. Detection limits in the specified working conditions ranged between 0.05 and 0.1 wt. %.

X-ray diffraction analyses were carried out at the Department of Earth Sciences of the University of Pisa, using a Gandolfi camera (114.6 mm diameter, Fe-K α radiation) and single crystal patterns with Weissenberg camera. Unit cell parameters were calculated, after correction for shrinkage, by least-squares refinement of powder diffraction patterns using the program of Appleman & Evans (1973), modified by Garvey (1986).

4 CHEMICAL COMPOSITION

The crystals are tiny, prismatic or tabular from yellow-orange to brownish in colour.

Polycrase of the beryl-rich type pegmatite shows B-site occupied by Ti, Nb, Ta and minor amount of W and Al, whereas A-site by Y, U, Th and REE (Tab. 1).

They generally show low totals because of the altered and disordered structural state of these samples, but this is a common characteristic of metamict minerals.

Table 1. Representative compositions of members of the euxenite group minerals, Vigizzo Valley

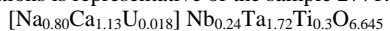
Sample	2766		2767		G		H	
	A.Pol.	A.Pol.	B.R.P.	B.R.P.	B.R.P.	B.R.P.	B.R.P.	B.R.P.
Na ₂ O w%	0.00	0.00	0.17	0.00	0.00	0.00	0.00	0.00
MgO	0.00	0.00	0.45	0.41	0.41	0.42	0.42	0.42
CaO	0.16	0.12	1.14	0.27	0.27	0.83	0.83	0.83
FeO	1.33	0.56	0.43	1.14	1.14	0.67	0.67	0.67
UO ₂	18.85	7.41	1.41	3.17	3.17	4.28	4.28	4.28
ThO ₂	1.41	2.40	3.27	3.78	3.78	3.84	3.84	3.84
Y ₂ O ₃	17.08	21.15	19.98	21.29	21.29	17.29	17.29	17.29
Ce ₂ O ₃	0.00	0.00	0.00	0.29	0.29	0.00	0.00	0.00
Nd ₂ O ₃	0.00	0.00	0.00	0.14	0.14	0.00	0.00	0.00
Gd ₂ O ₃	0.00	0.00	0.38	1.17	1.17	0.00	0.00	0.00
Dy ₂ O ₃	0.89	1.44	2.02	2.35	2.35	1.67	1.67	1.67
Er ₂ O ₃	2.07	1.57	0.00	1.42	1.42	0.00	0.00	0.00
Yb ₂ O ₃	1.08	2.23	0.00	0.00	0.00	1.42	1.42	1.42
Nb ₂ O ₅	25.12	29.40	22.22	21.67	21.67	17.47	17.47	17.47
Ta ₂ O ₅	5.09	5.52	26.24	18.93	18.93	29.12	29.12	29.12
TiO ₂	23.24	24.26	20.24	21.76	21.76	18.96	18.96	18.96
WO ₃	1.02	0.96	0.00	0.97	0.97	1.95	1.95	1.95
Al ₂ O ₃	0.00	0.00	0.00	0.00	0.00	0.33	0.33	0.33
Total	97.33	97.02	97.97	98.76	98.76	98.58	98.58	98.58
Structural formulae based on six atoms of oxygen								
Na <i>apfu</i>	0.000	0.000	0.021	0.000	0.000	0.000	0.000	0.000
Mg	0.000	0.000	0.042	0.038	0.038	0.041	0.041	0.041
Ca	0.011	0.008	0.077	0.018	0.018	0.059	0.059	0.059
Fe	0.071	0.028	0.023	0.060	0.060	0.037	0.037	0.037
U	0.269	0.100	0.020	0.044	0.044	0.063	0.063	0.063
Th	0.021	0.033	0.047	0.054	0.054	0.057	0.057	0.057
Y	0.583	0.685	0.671	0.712	0.712	0.605	0.605	0.605
Ce	0.000	0.000	0.000	0.007	0.007	0.000	0.000	0.000
Nd	0.000	0.000	0.000	0.003	0.003	0.000	0.000	0.000
Gd	0.000	0.000	0.008	0.024	0.024	0.000	0.000	0.000
Dy	0.018	0.028	0.041	0.048	0.048	0.035	0.035	0.035
Er	0.045	0.033	0.000	0.030	0.030	0.000	0.000	0.000
Yb	0.021	0.041	0.000	0.000	0.000	0.028	0.028	0.028
<i>A-site</i>	1.040	0.957	0.951	1.039	1.039	0.932	0.932	0.932
Nb	0.728	0.809	0.634	0.616	0.616	0.519	0.519	0.519
Ta	0.089	0.091	0.450	0.323	0.323	0.521	0.521	0.521
Ti	1.121	1.110	0.961	1.028	1.028	0.938	0.938	0.938
W	0.017	0.015	0.000	0.016	0.016	0.033	0.033	0.033
Al	0.000	0.000	0.000	0.000	0.000	0.026	0.026	0.026
<i>B-site</i>	1.956	2.025	2.045	1.983	1.983	2.037	2.037	2.037
cations	2.995	2.983	2.996	3.022	3.022	2.968	2.968	2.968

Note: A.P. polycrase from miarolitic cavities of albitized pegmatites; B.R.P.= polycrase from beryl-rich type pegmatite;

The ferrocolumbite compositions, with Nb dominant in the *B*-site and Fe in the *A*-site are rare, whereas the member Mn-dominant, manganotantalite, are more diffused in the majority of dikes.

Columbite minerals vary between ferrocolumbite to manganocolumbite (Tab. 2).

Microlite, occurring in the beryl-rich type pegmatites shows *B*-site occupied by Ta with minor amount of Nb and Ti, whereas *A*-site is Ca dominant with minor amount of U and Th. The following structural formulae of microlite based on 2.00 *B*-site cations is representative of the sample 2771:



Polycrase found in miarolitic cavities of the albitized pegmatites are Y-dominant in the *A*-site (Tab. 1), partially substituted by HREE.

Table 2. Representative compositions of members of the columbite group minerals, Vigezzo Valley

Sample	2994	2770	F	.F
	Mn-col.	Mn-col.	Fe-col.	Fe-col.
FeO wt%	5.36	6.83	15.68	14.50
MnO	13.60	12.08	2.91	5.01
Nb ₂ O ₅	46.56	50.51	41.64	43.50
Ta ₂ O ₅	31.72	26.99	37.54	35.45
TiO ₂	2.27	2.24	1.77	1.68
Total	99.91	98.93	99.55	100.14
Structural formulae based on six atoms of oxygen				
Na <i>apfu</i>	0.05	0.04	0.00	0.00
Fe	0.29	0.36	0.87	0.79
Mn	0.735	0.646	0.163	0.276
<i>A</i> -site	1.072	1.043	1.029	1.066
Nb	1.344	1.442	1.244	1.280
Ta	0.551	0.463	0.674	0.628
Ti	0.109	0.106	0.088	0.082
<i>B</i> -site	2.003	2.011	2.006	1.990
Σ cations	3.075	3.055	3.035	3.056

Note: Mn-col=manganocolumbite;

Fe-col.=ferrocolumbite

5 X-RAY DIFFRACTION DATA

X-ray powder and single crystal patterns show that our samples belong to euxenite-, pyrochlore- and columbite- mineral groups. Because U- and Th-rich minerals are often metamict, X-ray powder patterns were repeated on single fragments previously heated at 900°C for ten hours.

Table 3 lists the results of euxenite-minerals calculated on the basis of the space group Pbcn.

In Table 4 are reported the unit-cell parameters of heated crystals of columbite minerals calculated on the basis of the space group Pcan. In the same table we report cell parameter of the sample 2771 (microlite).

Table 3. Unit – cell parameters of selected samples of the euxenite group minerals, Vigezzo Valley

Sample	before heating	<i>a</i> ₀	<i>B</i> ₀	<i>C</i> ₀
2767	metamict	14.58(4)	5.533(3)	5.186(4)
2768	metamict	14.53(4)	5.541(6)	5.196(5)
2769	metamict	14.60(4)	5.56(4)	5.197(2)
H	metamict	14.65(7)	5.578(5)	5.203(7)
G	metamict	14.69(7)	5.629(8)	5.205(4)

Table 4. Unit-cell parameters of selected samples of the columbite group minerals and microlite subgroup (2771), Vigezzo Valley, P. disord = partially disorder columbite

Sample	before heating	<i>a</i> ₀	<i>b</i> ₀	<i>c</i> ₀
2770	P. disordered	14.38(3)	5.742(3)	5.071(3)
2994	p. disordered	14.36(2)	5.750(2)	5.049(1)
F	p. disordered	14.33(2)	5.755(2)	5.084(2)
E	p. disordered	14.33(1)	5.765(2)	5.109(2)
2771	p. disordered	10.365(5)	10.365(5)	10.365(5)

6 DISCUSSION AND CONCLUSIONS

The chemical compositions of the samples, here studied are plotted in the classified diagrams to summarize synthetically the variations on the basis of cation occupancies. Figure 1a shows the *B*-site occupancy of euxenite-polycrase minerals of the all dikes. In Figure 1b are plotted the main occupant of *A*-site (Y+REE, Ca and U+Th). A comparison of the Nb-Ta oxides, found in the pockets of two type dikes, reveal an high level of fractionation (on the basis of Nb/Ta ratio) in former type of pegmatites. Even if the composition of polycrase from these dikes is higher in Ta, this never reaches the tautauxenite. With decreasing Ti and increasing Ta content, polycrase gradually changes its composition.

In Figure 2 is reported the trend Nb/Ta vs Ta showing chemical variations of the all analysed columbite-minerals.

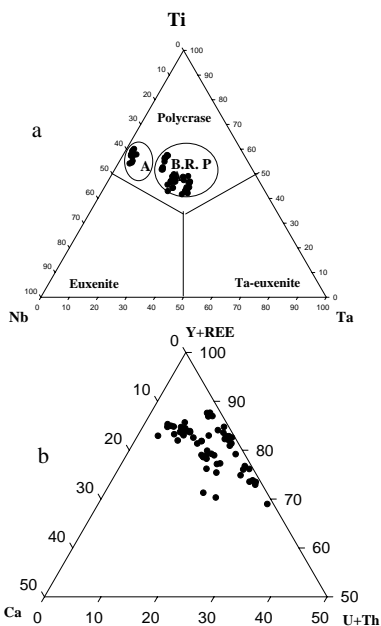
Microlite occurs as primary phase in the pockets of beryl-rich pegmatite in association with polycrase. The occurrence of the Ta-dominant phase suggest high degree of fractionation trend on the basis Nb/Ta ratio (Fig.3).

The data on the Nb and Ta minerals of Vigezzo Valley suggest the following conclusions:

- Nb-Ta oxides found in miarolitic cavities of the beryl-rich type pegmatites show high level of fractionation (on the basis of Nb/Ta ratios);
- the samples from albitized pegmatite dikes have a low degree of Nb/Ta fractionation and do not contain Ta-rich phases;
- euxenite-group minerals of both suites, show structural disorder caused by damage radiation due to radionuclide contents;
- columbite-minerals are partially disordered and after heating become fully ordered.

7 REFERENCES

- Albertini, C. & Aandersen, T. (1989): Non-metamict orthorhombic AB₂O₆ Y-Nb-Ta-Ti oxides from a pegmatite in Arvognio, Crana Valley (Toceno, Vigezzo Valley, N. Italy). *Rendic. Soc. It. Min. Petr.* 43-3, pp. 773-779.
- Amli, R. & Griffin, W.L. (1975): Microprobe analysis of REE minerals using empirical correction factors. *Am. Mineral.* 60, 599-606
- Appleman, D.E. & Evans, H.T., Jr. (1973): Job 9214: Indexing and least-squares refinement of other diffraction data. U.S. Geological Survey, Computer Contributions 29 (NTIS document PB2-16188).
- Aurisicchio, C., De Vito, C., Ferrini, V. & Orlandi, P. (2001): Nb-Ta oxide minerals from miarolitic pegmatite of the Baveno pink granite, NW Italy. *Mineral. Mag.*, 65 (4), 509-522
- Aurisicchio, C., De Vito, C., Ferrini, V. & Orlandi, P. (2002): Nb and Ta oxide phases in the Fonte del Prete granitic pegmatite, Island of Elba, Italy. *Can. Mineral.*, 3, 799-814
- Černý, P. & Ercit, T.S. (1985): Some recent advances in the mineralogy and geochemistry of Nb and Ta in rare-element granitic pegmatites. *Bull. Minéral.*, 108, 499-532.
- Černý, P., Goad, B.E., Hawthorne, F.C. & Chapman, R. (1986): Fractionation trends of the Nb- and Ta- bearing oxide minerals in the Greer Lake pegmatitic granite and its pegmatite aureolae, southeastern Manitoba. *Am. Mineral.*, 71, 501-517.
- Černý, P. & Ercit, T.S. (1989): Mineralogy of Niobium and Tantalum: crystal chemical relationships, paragenetic aspects and their economic implications. In *Lanthanides Tantalum and Niobium*. (Möller P., Černý P., & Saupé R., eds.). 27-79. Springer-Verlag Berlin Heidelberg.
- De Vito, C (1998): Minerali di Nb e Ta nelle pegmatiti dell'Isola d'Elba, di Baveno e della Val d'Ossola: caratterizzazione geochimica e cristallografica. Degree thesis, Univ. Rome "La Sapienza", Italy. pp 190
- De Vito, C (2002): Il giacimento gemmifero e ad elementi rari dell'Anjanabonoina, Madagascar Centrale. Ph.D. thesis, Department of Earth Sciences, University of Rome, Italy, pp230.
- Drake, M.J. & Weill, D.F. (1972): New rare earth element standards for electron microprobe analysis. *Chem. Geol.*, 10, 1179-81.
- Garvey, R. (1986): LSUCRIPC: least squares unit-cell refinement with indexing on the personal computer. *Powder Diffraction*, 1, 144.
- Hogarth, D.D (1977): Classification and nomenclature of the pyrochlore group. *Am. Mineral.*, 62, 403-410.
- Mattioli, V. (1979): Euxenite e tanteuxenite in Valle Vigezzo. *Mineral. Mag.*, 15, 78-89.
- Mulja, T., Williams-Jones, A.E., Martin, R. F. & Wood, S.A. (1996): Compositional variation and structural state of columbite-tantalite in rare-element granitic pegmatites of the Preissac-Lacorne batholith, Quebec, Canada. *Am. Mineral.*, 81,146-157.
- Roeder, P. L. (1985): Electron-microprobe analysis of minerals for Rare-Earth elements: use of calculated peak-overlap corrections. *Can. Mineral.*, 23, 263-71



Figures 1(a, b). Triangular plots of the B-site occupancy (a) and A-site occupancy (b) in euxenite group minerals. A=albitized pegmatites and B.R.P.=beryl rich pegmatite.

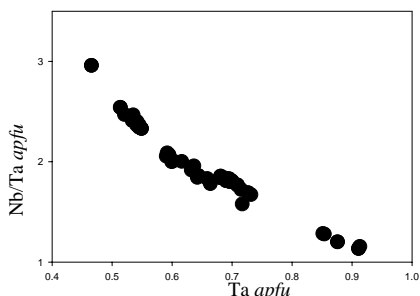


Figure 2. Distribution of Vigezzo Valley columbite minerals with the variation of the Nb/Ta and Ta values.

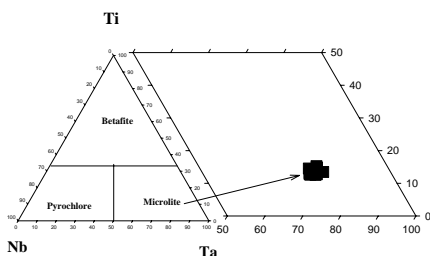


Figure 3. Occupancy of the B site of the pyrochlore-group minerals according to the major elements (Hogarth 1977), showing the composition of the microlite encountered.

True Viscosity and Drift Flux Analysis

R.Escudero & F.J.Tavera

Instituto de Investigaciones Metalúrgicas, Universidad Michoacana de San Nicolás de Hidalgo, México

ABSTRACT: Drift Flux Analysis assumes a constant dynamic viscosity of the continuous phase (one cP or one grame/centimetre-second) not matter the changes as result of the pulp consistency or solids content. This paper shows the relevance of considering the real value of the dynamic viscosity in terms of the characteristics of a gas dispersion. Viscosity of water was varied by using a polymer and the bubble size, bubble surface area, and gas holdup were calculated through the Drift Flux Model. Results show a good agreement between the calculated and measured bubble diameter once the true value of viscosity of the continuous phase is considered during the solution of the drift flux model.

1 INTRODUCTION

Drift flux theory, which was first introduced by Wallis (1964), has been used to relate the fraction of gas with the gas and liquid rates in bubble columns. The concept has been applied to multi-phase systems, and additional parameters have been introduced to try to define the effect of the environment on bubble formation (Dobby et al. 1988; Yianatos et al. 1988). The result is a model to estimate mean bubble size in a system involving a dispersed phase (i.e, flotation columns).

The use of flotation column in applications such as de-inking of recycled paper (Watson et al. 1996), de-oiling of water (Van Ham et al. 1983), and for metal ion recovery from hydrometallurgical solutions (Tavera et al. 2000) is observing renewed interest. In these applications the formation of small bubbles is crucial to collect the fine ink particles or oil droplets. A literature review showed that there is almost no published information regarding the best dispersion characteristics for a given flotation application. On the other hand, the dependence of bubble surface area flux with parameters as flotation rate, recovery, and the metallurgical performance is well documented in the literature (Gorain 1996), where a linear relationship between all the former

parameters is reported. As mentioned by Jameson et al., (1977), the bubble size and the bubble surface area flux should be well predicted (or calculated) in order to consider a proper value of the flotation rate constant for a given column duty.

Dobby and Finch (1988) pointed out that small bubbles are desirable for fine particle flotation because they increase particle-bubble collision probability. They create more stable froth phases and a greater column carrying capacity. Nevertheless, small bubbles (or particle-bubble aggregate) are prone to be trapped by the tailings stream due to their weak buoyancy force, they remain in the pulp and can not lift themselves (Escudero 1998).

During the development of the drift flux model the following two assumptions are made:

- The liquid observes Newtonian behaviour, and
- Small spherical bubbles ascend uniformly, homogeneously distributed over the cross-section of the column.

Another assumption made when the drift flux model is solved is the value of the viscosity of the continuous phase. The viscosity of tap water is considered despite the fact that either mineral pulp

or any liquid different from water observes a viscosity larger or smaller than one centipoise.

A direct method to measured bubble size is by cinephotography (Geary & Rice 1991). Images of bubbles are obtained and the size is measured. Today, this usually involves an image analyser to help process the large number of bubbles (at least 500) that must be examined for statistical reliability. The volume of the bubble is calculated assuming symmetry about the vertical axis. There are other direct methods for measuring bubble volume, such as X-ray cinephotography, γ -ray absorption, and laser techniques, although their application is restricted by the sophistication of the devices (Drew et al. 1970).

Drift flux analysis is a method to estimate average bubble diameter based on the knowledge of the gas holdup and phase velocities. Good agreement between the bubble size determined through drift flux analysis and that from photographic evidence has been reported (Yianatos et al. 1988; Escudero et al. 2000) for gas-water systems. Comparisons between experimental and calculated bubble size for liquids with viscosity larger than that of water has not been tested to date.

This paper compares the mean bubble size measured using photography with that estimated from drift flux analysis for a gas-liquid systems varying the viscosity from 1 to 4.7 centipoises.

2 EXPERIMENTAL SET-UP

The apparatus is shown in Figure 1. A rectangular section of column made with transparent plexiglas was placed at the top of a 5.7 cm (0.057 m) diameter column. This provided a flat section with a cross sectional area equal to that of the circular column. The section was wide enough (0.02 m) to allow the free movement of the rising bubbles, but spread them out to facilitate photographic analysis.

Air was fed through a vertical sparger at the bottom of the column into tap water containing 20 ppm of dowfroth 250C and a certain amount of poly (acrylamide-CO- acrylic acid) to vary the viscosity of the liquid. After conditioning the water in a tank, the column was filled and photographs were taken for every J_g value.

The surface area (A_s) of the sparger used during the test was 79.8 cm^2 ($79.8 \times 10^{-4} \text{ m}^2$) with a nominal pore size $2 \mu\text{m}$ and permeability 1.6 darcy ($1.6 \times 10^{-5} \text{ m}^2$). The variables monitored were: air flowrate (q , L/min), pressure drop between the taps (1.81 m) at which the gas holdup was measured (Δp , cm H_2O), temperature (T , $^\circ\text{C}$), and head pressure at the bottom of the column (p_t , cm H_2O). All tests were run under batch conditions.

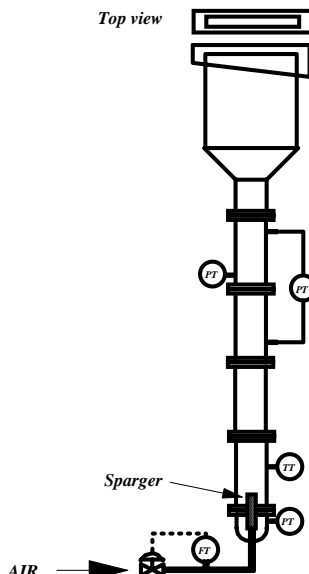


Figure 1. Experimental set-up to obtain photographic measurement of db. The eg (necessary to estimate db from drift flux analysis) was measured over the mid portion of the column.

Pressure drop was measured using differential pressure transducers (Bailey, model PTSDDD1221B2100). The air rate was measured and controlled using a mass flowmeter/controller (MKS Instruments, model 1562A-40L-SV). Corrections to the air flowrate for temperature were made. The temperature was measured by using a ICTD temperature detector (Transduction Ltd., model ICTDP/N1662).

Kinematic viscosities of liquids were determined by using a Cannon-Fenske Routine viscometer type for transparent liquids (Cannon Instrument Company, mod. 50Z185).

Pictures of the bubbles at the flat section were taken for each value of J_g using a stationary digital camera (Sony, mod. Mavica MVC-FD95). Bubble diameters were measured manually employing an image analyzer (Media Cybernetics LP, Image Pro 4.0). The image analyzer was calibrated according to a milimetric tape secured to the inside-front of the flat section. For each condition, about 800 bubbles were measured.

3 RESULTS AND DISCUSSION

3.1 Measured bubble size distribution and mean size.

A typical distribution of bubble sizes as obtained from the image analyzer is shown in Figure 2.

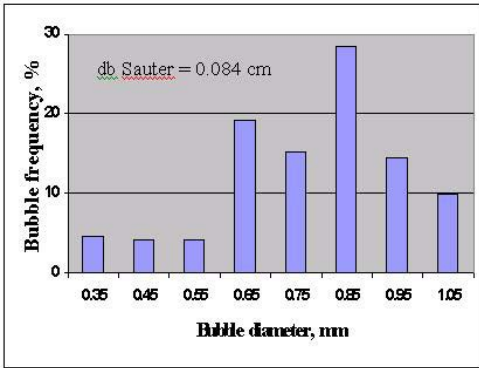


Figure 2. Typical bubble size distribution as obtained from the image analyzer. viscosity 1.6 cP.

From the distribution, a Sauter mean and a number mean bubble diameter were calculated. The number mean diameter was calculated from:

The Sauter diameter, often considered the appropriate one for flotation (Yianatos et al. 1988; Gorain et al. 1995; Gomez et al. 2000) was calculated as follows:

$$d_b = \frac{\sum \text{diameters}}{\text{number of bubbles measured}}$$

$$d_b = 6 \frac{\sum \text{bubble volume}}{\sum \text{bubble area}}$$

The observed trend of bubble diameter increasing with the viscosity is as expected if we consider that the viscous drag force retards the bubble formation since it is opposite to the buoyancy force of the bubble. Differences between the two mean sizes, number and Sauter, is not significant when the bubble size distribution is relatively narrow, however, the Sauter diameter will be designated as that measured and compared with the calculated diameter.

3.2 Comparison between measured and calculated bubble size.

Drift flux analysis was used to estimate a mean bubble size knowing the air and liquid flowrates, the gas holdup, and the true value of viscosity of the liquid, measured as mentioned in a previous chapter of the paper. The bubble diameters are also compared in Figure 3. A complete agreement is observed for the case of viscosity of 1 cP, and for all the air flowrates tested here. In accord with previous experimental evidence, d_b from drift flux analysis compares well with the Sauter mean d_b (Yianatos et al. 1988; Dobby et al. 1988).

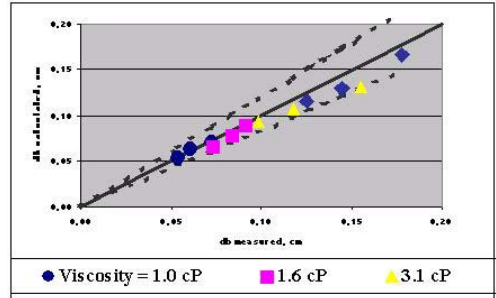


Figure 3. Bubble size measured, and estimated. Surface tension of the liquid 65 dyn/cm². The dotted lines means $\pm 20\%$ error.

The rest of the compared data converges well enough within a $\pm 20\%$ error, after considering the measured value of viscosity of the liquid. In other words, the Drift Flux model calculates with acceptable accuracy a mean bubble diameter once the right values of the physicochemical characteristics of the liquid are considered.

As mentioned above, in most of the processes involving gas dispersions the true value of the viscosity of the liquid is quite different from that of water. The implication in considering the viscosity of the liquid always being as one centipoise, leads to miscalculate or wrongly predict an average bubble size and then the characteristics of the dispersion (gas holdup, bubble size, and bubble surface area flux). An example of the former statement can be demonstrated through the Figure 4. As can be observed all the calculated bubble sizes (for true viscosities different from 1.0 cP) disagree from those measured using the photographic technique, drawing diameters with an error larger than 20%. The consequences of mistakes in predicting a bubble size were pointed out in the introduction.

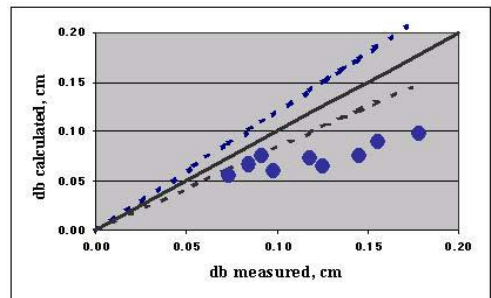


Figure 4. Comparison between diameters, for a constant viscosity 1.0 cP.

4 CONCLUSIONS

Comparisons between measured (using photographic technique), and calculated bubble diameters (through the solution of the Drift Flux model) drawn the following conclusions:

The relevance of considering the true value of the dynamic viscosity in terms of the characteristics of a gas dispersion was determined. The Drift Flux model calculates with acceptable accuracy a mean bubble diameter once the right values of the physicochemical characteristics of the liquid are considered.

If changes in viscosity are not considered and it is taken as one centipoise, an average bubble size and then the characteristics of the dispersion (gas holdup, bubble size, and bubble surface area flux) will be miscalculated. This error in predicting bubble size leads to wrongly predict both the gas holdup the bubble surface area flux.

As is mentioned in the literature, the knowledge of the properties of a gas dispersion are needed in order to design a column flotation for a given duty.

5 REFERENCES

- Dobby, G. S., Yianatos, J. B. & Finch, J. A. 1988. Estimation of Bubble Diameter in Flotation Columns from Drift Flux Analysis. *Canadian Metallurgical Quarterly*. Vol.27, No.2, pp 85-90.
- Escudero, G. R. 1998. Characterization of Rigid Spargers and their Selection for Flotation Columns. PhD Thesis. Department of Mining and Metallurgical Engineering. McGill University. Montreal, Canada.
- Finch, J. A. & Dobby, G. S. 1990 Column Flotation. Pergamon Press. P. 9-58.
- Gómez, C. O., Escudero, R. & Finch, J. A. 2000. Determining Equivalent Pore Diameter for Rigid Porous Spargers. *The Canadian Journal of Chemical Engineering*. Vol.78, p. 785-792.
- Gorain, B. K., Manlapig, E. V. & Franzidis, J. P. 1996. The Effect of Gas Dispersion Properties on the Kinetics of Flotation. Proceedings of the Symposium Column '96. Gomez & Finch Eds. August 26-28. Society of CIM, Montreal, QC, Canada.
- Tavera, F. J., Escudero, R., Finch, J. A. & Uribe, A. 2000. Flotación de Ni-Deta en Medios Acuáticos: Aplicación de Columnas de Flotación. Paper accepted for its publication in the magazine AFINIDAD. Barcelona, España. 2000.
- Wallis, G. B. 1969. One-Dimensional Two-Phase Flow. McGraw Hill Inc. p. 89-122.
- Watson, J. A., Gómez, C. O. & Finch, J. A. 1996. De-inking of Recycled Paper Using Column Flotation. Column'96. Proceedings of the International Symposium on Flotation Columns. Montreal, Canada. p. 195-207.
- Yianatos, J. B., Finch, J. A., Dobby, G. S. & Xu, M. 1988. Bubble Size Estimation in a Bubble Swarm. *Journal of Colloid and Interface Science*, Vol.126, No.1, pp 37-44.

Mineralogical Characterization of a Pelite from Triassic (Coimbra, Portugal)

M.Q.Ferreira & L.Pereira

Department of Earth Sciences, University of Coimbra, 3000-272 Coimbra, Portugal

S.I.Conceição & J.M.F.Ferreira

Department of Ceramics and Glass Engineering, CICECO, University of Aveiro, 3810-193 Aveiro, Portugal

J.Velho

Department of Geosciences, University of Aveiro, 3810-193 Aveiro, Portugal

ABSTRACT: In Portugal, the Triassic lithology is characterized by a sedimentary sequence representing the erosion that the Iberian craton was subjected. The sediments were transported by rivers and brooks to a basin that was evolving to the so-called Lusitanian Basin. In the chronological limit between Triassic and Mesozoic, there is a very interesting geological material, a pelite, environmentally representing a lagoon where slime and mud sediments were deposited. Due to the diapiric tectonic, there are outcrops of this dark gray pelite between Coimbra and Torres Vedras, in a distance about 120 km long. This pelite is a very interesting material because during the raining season shows a very plastic behaviour, causing slope stability problems in urban areas and in highways. Stratigraphically above this pelite, thicker limestone sequences occur and it's normal to observe the collapse of the limestone. In summer season, the pelite loses water and turns to be a high stiffness material, difficult to work with. These so different seasonal behaviours and their consequence on environmental geology motivated the research work on the characterization of the pelite. The pelite was characterized in terms of mineralogical, physical and technological properties, especially density and rheology. The other direction aims at establishing a correlation between the rheological characteristics of this geological material with mineralogy and engineering geology was also analysed.

1 INTRODUCTION

In the chronological limit between Triassic and Mesozoic, in Portugal, there is a very interesting geological material, a pelite, environmentally representing a lagoon where slime and mud sediments were deposited (Soares et al. 1985). The pelite, *in situ*, behaves as a soft rock, but, in the presence of water, it shows a very sharp transformation into a soil or even a mud. Due to its extremely evolutive behaviour, this geological material shows geotechnical problems, like slope instabilities.

The main goal of this research is the characterization of this pelite material in terms of mineralogical, physical, geotechnical and rheological properties trying to understand the reasons of such great modifications in the presence of water.

2 RESULTS

2.1 Particle size distribution

Particle size distributions of two representative samples (A and B) were determined using the laser scattering technique (Coulter LS230) and the results

are presented in Figure 1. The two pelite samples are mainly formed by 60% silt, 30% sand and 10% clay and they show average particle sizes of 5.2 μm (pelite A) and 5.7 μm (pelite B) and similar particle size distributions.

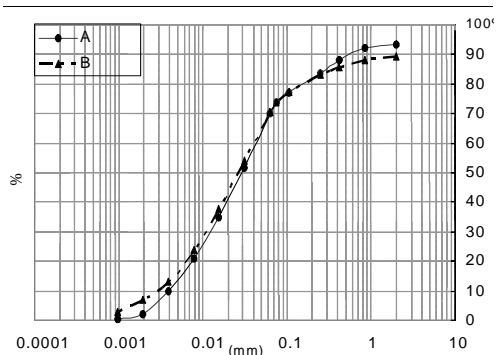


Figure 1: Particle size distribution.

2.2 Mineralogical characterization

Using the Stokes law, sandy, silty and clayey fractions obtained from the original material were

analysed by X-ray diffraction for mineralogical analysis. The characteristic minerals from each granulometric fraction are as follows: Sandy fraction - illite (or muscovite), kaolinite, chlorite, quartz and calcite; silty fraction - illite (or muscovite), kaolinite, chlorite and quartz; clayey fraction - illite (or muscovite), kaolinite and chlorite.

The usual tests using X-ray diffraction with the aim to identify expansive clay minerals, like smectites, showed that these minerals are not present in the pelites.

2.3 Porosity

For pore structure determinations, mercury intrusion porosimetry method was chosen using a Poresizer 9320 apparatus from Micromeritics. The advance of contact angle was 137.0°, while the average sample weight was 0.321 g. Equilibration time was 20 sec. and the maximum intrusion volume was 0.050 mL/g. The results are presented in Table 1.

Table 1: Porosimetric results.

Porosimetric properties	A	B
Total intrusion volume (mL/g)	0.082	0.071
Total pore area (m ² /g)	14.45	10.17
Average pore diameter (µm)	0.023	0.028
Porosity (%)	18.1	15.9

These two pelite samples show a very low mercury intrusion volume and despite these low values, total pore area data are very high. These results show that these pelites have a relatively compact structure characterized by very fine pores.

Both samples show pores with one mode, with values ranging between 0.023 µm and 0.028 µm, reflecting a very uniform material in terms of fabric, with very fine pores, showing a quite narrow dimension distribution. The very low values of mercury intrusion volume are also reflected in terms of a low average porosity of about 17%, considering the two pelite samples.

2.4 Plasticity

For the determination of consistency limits, Portuguese Norm NP-143 (1969) was adopted. The results presented in Table 2 show very similar consistency properties between samples A and B.

Table 2: Consistency limits and methylene blue (VBS).

Properties	Pelite A	Pelite B
LL (%)	35	33
PL (%)	26	22
PI (%)	9	11
VBS (g/100g)	0.5	1.2

2.5 Methylene blue technique

Methylene blue is a very interesting method for characterizing the clay fraction of a geological material in a global way; it means that the final result is a function of the content of clay fraction and of the mineralogical nature. The results obtained by the methylene blue test (VBS) followed the NF P 94-068 (1993) norm for soils. The results obtained for samples A and B are presented in Table 2.

The results range changes between 0.5 g and 1.2 g of methylene blue per 100 g of pelite. In accordance with LCPC/SETRA classification, soils with VBS in the range of 0.2-1.5g/100 g are sandy-silty soils with a sensitive behaviour when in contact with water.

2.6 Point load test and expansibility

The technique for the evaluation of point load strength was made according to the specifications of the ISRM norm (1985). Samples A and B were tested with increased water content levels as a function of submersion time interval. In this way, it is possible to quantify the decreasing of the resistance with the increasing amounts of water.

Table 3: Point load test results.

Samples	W (%)	Is(50) (Mpa)	Uniaxial strength (MPa)
A-"in situ"	12.53	0.07	1.54
A-24 horas	4.13	0.48	10.56
A-oven	0.00	0.80	17.6
A-sat-5 min	13.03	0.19	4.18
A-sat-10 min	13.04	0.03	0.66
A-sat-20min	14.46	0.06	1.32
A-sat-30 min	6.63	0.17	3.74
B-in situ	6.2	0.06	1.32
B-24 horas	3.16	0.68	14.96
B-oven	0.00	1.26	27.72
B-sat-5 min	5.40	0.52	11.44
B-sat-10 min	4.62	0.08	1.76
B-sat-20min	14.05	0.24	5.28
B-sat-30 min	8.22	0.09	1.98

W – Water content; Is(50) – Point load strength;
 σ_c – Uniaxial compressive strength (=Is(50) x 22)

Both samples (A and B) were analysed without water in the following conditions: - "in situ", immediately after collection; - 24 hours after sampling and air dried; - after drying at 105°C for 24 hours. Besides these conditions, other four tests were used for each sample with different water contents achieved after submersion time during 5, 10, 20 and 30 minutes. The results are presented in Table 3.

Figure 2 shows the point load resistance as a function of water content. There is a very clear trend

for a drastic reduction in terms of mechanical strength of the pelites with increasing amounts of water. Even for water contents as low as about 5%, the point load resistance is very low, about 0.5 MPa or even inferior.

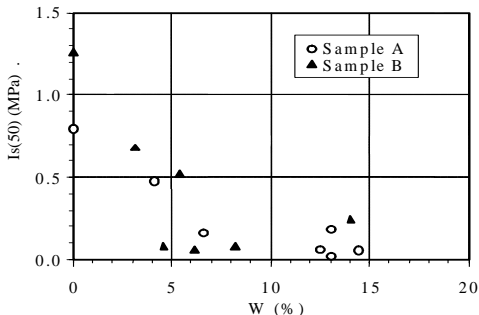


Figure 2: Point load resistance in function of water content.

The highest values in terms of water content after submersing both samples remained under 15%, which are in accordance with data obtained from mercury intrusion porosimetry technique. When pelites are saturated with water such as in the rainy season or due to other reasons, the mechanical resistance shows a dramatic decrease, between 1/5 and 1/20 of the mechanical resistance, when they are dried.

The non-confined linear expansibility results obtained by following the LNEC E 200-1967 norm [5] are displayed in Figure 3.

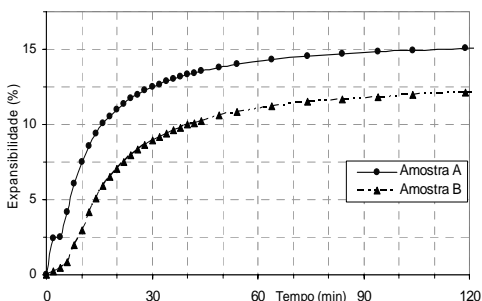


Figure 3: Non-confined linear expansibility results.

It can be observed that the highest expansion rates occurred between the first 5 and 20 minutes, followed by a less accentuated increasing rate and, finally by a trend to plateaux after 60 min submersing time. Sample A had an increase of 15% at the end of 5 days trial while pelite B showed an increase of 13%.

2.7 Rheology

The suspensions were prepared by first adding gradually, into distilled water, pelite powder in different proportions in order to set the final solid loads at 30-, 35- and 40-vol%, in the case of pelite - A, and 35-, 40- and 45-vol% for pelite B.

After adding the whole-required amounts of powder, the mixtures were kept under stirring for further 20 minutes. The suspensions were then transferred to a cylindrical polyethylene and were subjected to a deairing step by rolling them into the milling container for 6 h.

Rheological measurements were performed in a rotational controlled stress rheometer (Bohlin C-VOR, USA) after the 6 h slip-deairing step at a strictly controlled temperature of 20°C. The measuring configuration adopted was a cone and plate ($\varnothing=40$ cm, 4° , gap=150 μ m).

For flow behaviour and viscosity tests, stress sweep and multi-step shear measurements (20 points, max. equilibrium time of 1 min) were performed in the shear rates range from 0.1 s^{-1} up to about 1100 s^{-1} . Shear rate step functions were used to assess the structural decomposition/regeneration features of the suspensions. The results are, however, not shown due to the lack of space. Finally, in order to access the internal structure of the suspensions, oscillatory tests were carried out at a constant frequency of 1 Hz in the shear stress range from 0.01 to 100 Pa.

2.7.1 Viscosity behaviour

The steady shear viscosity curves of Pelite-A and Pelite-B suspensions containing different volume fractions in the range of 30-40-vol.% (in the case of Pelite-A) and 35-45-vol% (in the case of Pelite-B) are displayed in Figures 4 and 5, respectively. It can be seen that all the curves of pelite A reveal a shear thinning behaviour along the lower shear rate range, followed by a trend to a near Newtonian plateau, while the curves of pelite B present a more complex behaviour.

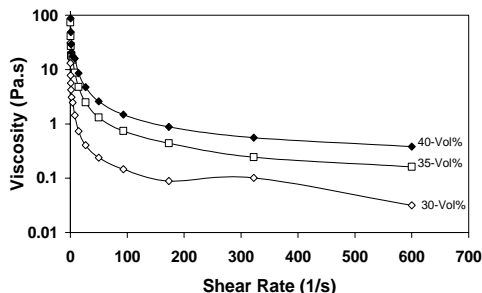


Figure 4: Effects of solids load and the suspension preparation procedure on the steady shear viscosity curves of pelite A suspensions.

There seems to be a sudden viscosity drop/recover between 5-15 s⁻¹ followed by a shear thinning behaviour and then by a possible thickening trend within the higher shear rate range.

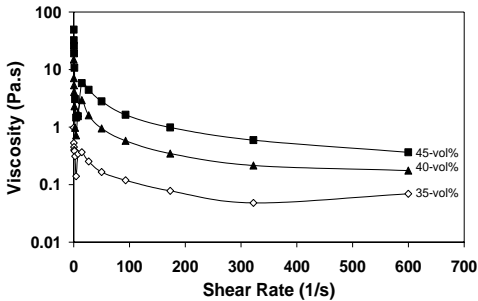


Figure 5: Effects of solids load and the suspension preparation procedure on the steady shear viscosity curves of pelite B suspensions.

2.7.2 Oscillatory shear behaviour

The amplitude stress sweeps of pelite A and pelite B suspensions are displayed in Figures 6 and 7, respectively. It can be seen that increasing the solids volume fraction of both samples (30-40-vol% - pelite A; 35-45-vol% - pelite B) makes G' to increase about two order of magnitude.

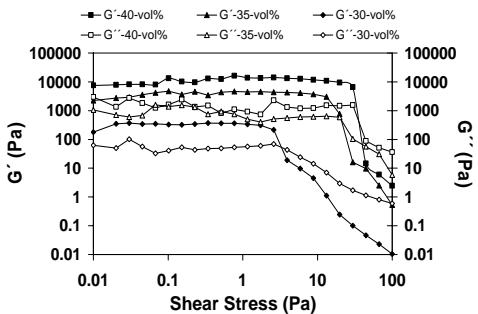


Figure 6: Amplitude sweep: Elastic (G') and Viscous (G'') modulus for pelite A suspensions.

Such changes also increase the crossover point (COP) for about one order of magnitude in the case of pelite A (≈4-40 Pa), while in the case of pelite B each increment of 5-vol% is accompanied by one order of magnitude increase of the COP (≈0.2-20 Pa). Therefore, the COP occurs at much lower stress values in suspensions of pelite B for a given solids loading, e.g., at 40-vol%: 2 Pa for pelite B; and 40 Pa for pelite A. Since the viscous character predominates over the elastic one for shear stresses

above the COP, the slope instability is more serious for pelite B.

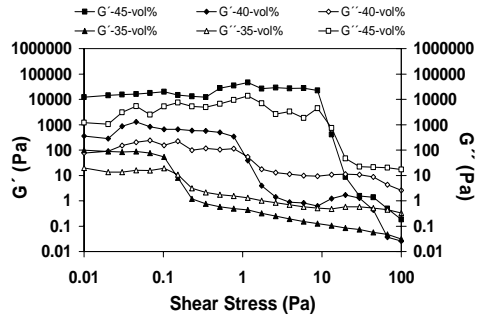


Figure 7: Amplitude sweep: Elastic (G') and Viscous (G'') modulus for pelite B suspensions.

3 CONCLUSIONS

The results presented in this work show that rheology is a very sensitive method to evaluate the slope instability problems posed by pelite-type soils, which are of great concern in urban areas and in highways. These results are according to the lower LL, the higher values of PI and VBS, which might derive from different mineralogical characteristics.

4 ACKNOWLEDGMENTS

Tanks are due to Fundação para a Ciência e Tecnologia through the research project number POCTI/ECM/38444/2001, co participated by FEDER and to "Centro de Geociências da Universidade de Coimbra".

5 REFERENCES

- ISRM 1981. Rock characterization testing & monitoring - ISRM Suggested methods. Ed. por E.T. Brown, Pergamon Press.
- ISRM. Commission on Testing Methods. Working Group on Revision of the Point Load Test Method (1985). Suggested method for determining point load strength.
- AENOR-UNE 103 600:1996. Determinação da expansibilidade de um solo com o aparelho de Lambe.
- LNEC E 200, 1967. Solos. Ensaio de expansibilidade.
- NP-143, 1969. Solos. Determinação dos limites de consistência.
- NF P 94-068, 1993. Determinação do valor de azul de metileno de um solo pelo ensaio da mancha.
- Soares, A. F., Marques, J. F. and Rocha, R. B. 1985. Contribuição para o conhecimento geológico de Coimbra. Memórias e Notícias (100): 131-143.

Synthesis of Alkali-substituted Shigaite

U.König, H.Pöllmann

Dept. of Mineralogy and Geochemistry, University of Halle-Wittenberg, Germany

ABSTRACT: Synthetic manganese Layered Double Hydroxides of the shigaite-type were prepared by the coprecipitation method. The thermal behaviour of the compounds, $[\text{Mn}_6\text{Al}_3(\text{OH})_{18}][(\text{SO}_4)_2\text{X} \cdot 12\text{H}_2\text{O}]$ with $\text{X} = (\text{Li}), \text{Na}, \text{K}, \text{Rb}, (\text{Cs}), \text{NH}_4^+$ was investigated by several experimental techniques. Different conditions were used for the synthesis. The influence of temperature (20°C, 40°C, 60°C), pH (7, 8, 9, 10, 11), reaction time (1d, 4d, 7d, 14d, 21d) and varying manganese/aluminum ratios were examined. Thermal analysis and in-situ X-ray diffractometry show several dehydration stages of the synthesis products in the temperature range of $25 < T < 170^\circ\text{C}$ followed by decomposition at temperatures above 200°C. The main results are as follows. (1) Alkali-substituted shigaite-like compounds were synthesised under CO_2 exclusion (glove box under nitrogen) under defined conditions. (2) Thermal behaviour was investigated with thermal analysis and in-situ X-ray investigations. Dehydration is carried out at three stages (60°C, 90-120°C, 200°C).

1 INTRODUCTION

Shigaite, $[\text{Mn}_6\text{Al}_3(\text{OH})_{18}][(\text{SO}_4)_2\text{Na} \cdot 12\text{H}_2\text{O}]$, is a layered double hydroxide first described from Shiga Prefecture, Japan, by Peacor et al. (1985). Other natural occurrences are known from Iron Monarch, South Australia (Pring et al. 1922) and Wessels Mine, Kalahari manganese field, Cape Province, South Africa (Fig.1). Shigaite is the Mn^{2+} analogue of motukoreaite with the following formula $[\text{Mg}_6\text{Al}_3(\text{OH})_{18}][(\text{SO}_4, \text{CO}_3)_2\text{Na} \cdot 12\text{H}_2\text{O}]$.

Layered double hydroxides, LDHs, also known as hydrotalcite-like compounds (HTs) are an important class of materials with permanent anion exchange capacity (Cavani et al. 1991). The natural and synthetic compounds are important for a wide field of applications, such as storage minerals for environmental remediation, precursor materials for catalyst, heavy metal adsorbant agents and hydration products of cements.

2 STRUCTURE

The crystal structure of shigaite (Fig.1,2) is rhombohedral (Cooper et al. 1996), R-3, consisting of brucite-like octahedral layers. The net positive

charge of the brucite-like octahedral layers is balanced by an equal negative charge from the interlayer anions. Water molecules occupy residual space and additional space with the compensating anions in the interlayer region. Additional +1 charged cations like Li, Na, K, Rb, Cs or NH_4^+ occur in the interlayers (Fig.3).

3 METHODS

3.1 Synthesis of $[\text{Mn}_6\text{Al}_3(\text{OH})_{18}][(\text{SO}_4)_2\text{Na} \cdot 12\text{H}_2\text{O}]$

The preparation of shigaite with different single charged cations was done using different raw materials of reagent grade quality. Pure phases of lamellar shigaite were synthesised in two different ways. For the coprecipitation method according to Miyata (1975) stoichiometric mixtures of $\text{Mn}(\text{SO}_4) \cdot \text{H}_2\text{O}$ and $\text{Al}_2(\text{SO}_4)_3 \cdot 18\text{H}_2\text{O}$ were placed in sealed polyethylene bottles and dissolved with a water/solid ratio of 12.5 under stirring conditions. A 1M NaOH solution was slowly added up to pH9. For preparing shigaite with other single charged cations hydroxides of (Li), K, Rb, (Cs) and NH_4^+ were used. Another way for synthesis was the reaction of $\text{NaAl}(\text{OH})_4$ with $\text{Mn}(\text{SO}_4) \cdot \text{H}_2\text{O}$ and 1M NaOH. The

compounds produced with the coprecipitation method showed the better crystallinities.

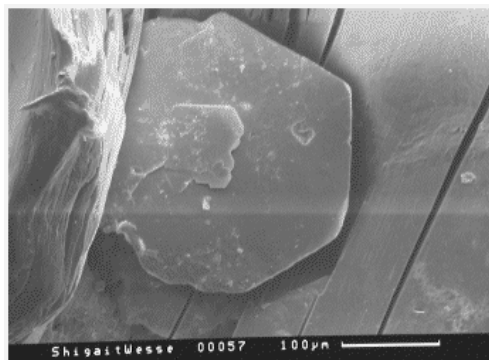


Figure 2 Naturel shigaite from Wessels mine, South africa

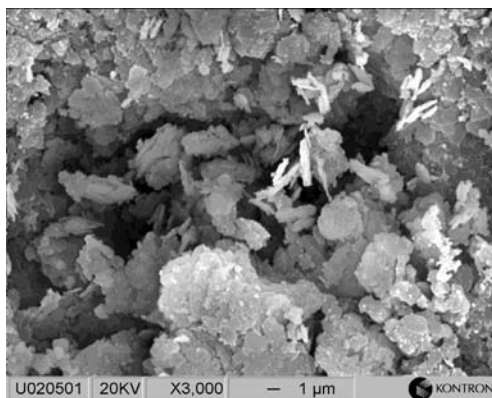


Figure 3 Synthetic shigaite-Na

The whole synthesis of the lamellar shigaite was performed under a CO₂-free atmosphere. A glove box with continued circulation of N₂ was used to avoid carbonatisation that would cause [Mn₂Al(OH)₆]₃ [(SO₄)_{2-x}(CO₃)_xNa(H₂O)₆(H₂O)₆] or oxidation of Mn²⁺ to Mn³⁺. The reaction temperature was kept constant 60°C. During aging for 1 week the pastes were shaken daily.

3.2 Investigating methods

The precipitates of these reactions were filtered in a glove box and immediately investigated by X-ray powder diffraction. X-ray pattern of wet pastes were obtained at 100% relative humidity (rh) on a Philips X'Pert diffractometer (Cu K α radiation) and a X'Celerator detector module with measurement times of 2.5 minutes and maximum intensities > 4 million counts per second. The samples were dried for further investigations in a box under nitrogen atmosphere at a rh of 35% using saturated CaCl₂

solution. A high-temperature cell HTK 16 (Anton Paar) was installed for investigating the dehydration behaviour. The measurements were performed on a platinum strip under air conditions up to 250°C. The patterns were measured after 10 min equilibration at each temperature step of 5 °C in the range 25-250°C, and a heating rate of 60 K/min.

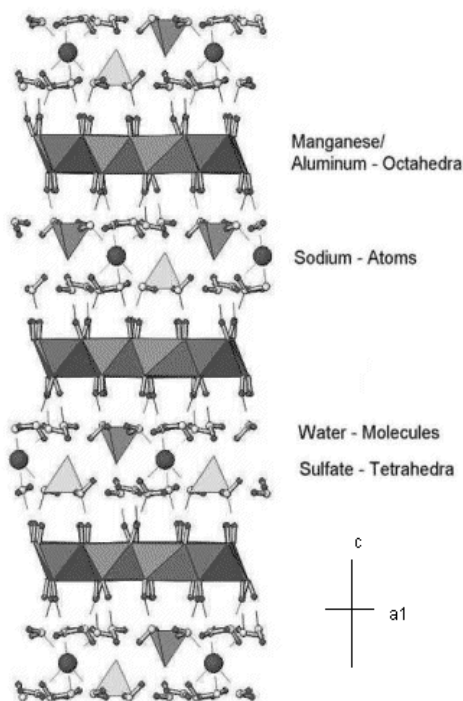


Figure 1 Crystal structure of Shigaite (after Cooper et al. 1996)

Scanning electron microscopy (SEM) techniques were used to get informations on particle size and habitus of the shigaite. Chemical analysis was carried out using inductiv coupled plasma - atomic emission spectroscopy (ICP-AES) to determine the MnO₂, Al₂O₃ and Na₂O concentrations. Sulfur amounts were analysed quantitatively by direct element analysis. The amount of water and stability ranges of different hydration stages of the shigaite were carried out by thermal analysis. Infrared (IR) spectroscopy was used to control CO₂ exclusion because minor contamination can be detected.

4 RESULTS

Best crystallinities were found at a pH value of 9, 60°C and a reaction time of 1 week. The precipitates were investigated immediately by X-ray powder diffraction at 100% rh (Fig. 4). Due to the typical

hexagonal habit (Figs 1,2), a preferred orientation of the crystals in the sampleholder occurs. Therefore the reflections were indexed and refined on the basis of a rhombohedral cell after drying to 35% rh over a saturated CaCl_2 solution and measuring with a

backloading sampleholder (Table 1). The c lattice parameter increases with the ion radius of the single charged cation at the interlayer. The composition was calculated on the basis of the chemical analysis (Table 2).

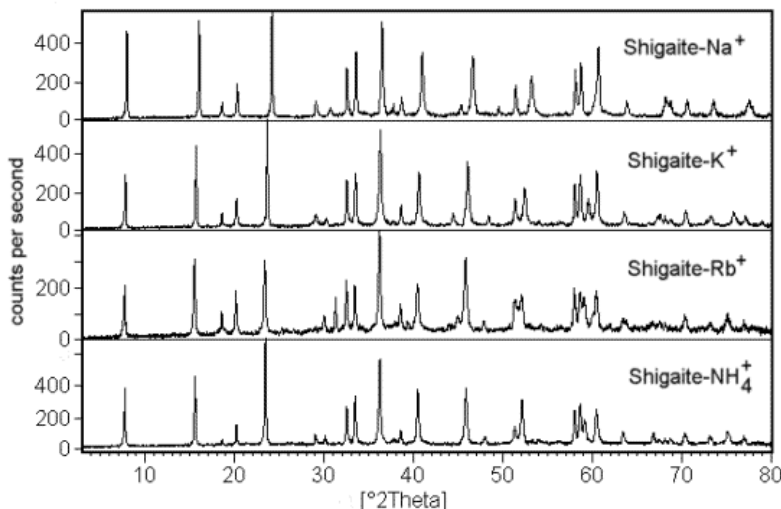


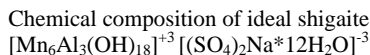
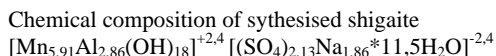
Figure 4. X-ray diagrams of alkali-substituted shigaite, measured at 35% rh.

Table 1. Metric parameters of alkali-substituted shigaite at 35% rh

	Shigaite			
	Na	K	Rb	NH_4^+
a_0 (Å)	9.5143	9.5228	9.5311	9.5278
c_0 (Å)	33.0396	33.7983	34.1858	34.0911
V (Å ³)	2590.12	2654.32	2689.44	2680.11
Sp. Group	R-3	R-3	R-3	R-3
D_c (g*cm ⁻³)	2.208	2.185	2.242	2.125

Using in-situ X-ray diffraction and thermal analysis different dehydration stages were determined at higher temperatures. Figure 5 shows a general view of the high-temperature XRD patterns of a Shigaite-Na in the whole temperature range. There are five temperature regions that can be classified by the XRD pattern: $25 \leq T \leq 60^\circ\text{C}$, $60 \leq T \leq 90^\circ\text{C}$, $90 \leq T \leq 120^\circ\text{C}$, $120 \leq T \leq 170^\circ\text{C}$ and $170^\circ\text{C} \leq T$. In the pattern of the first region, the (003), (006) and (009) reflections are due to that of the shigaite-like layered structure. At 60°C half of the interlayer water (not necessary for the structure) dehydrates and a new phase appears at that temperature. This phase is stable at $60\text{--}90^\circ\text{C}$. The next region $90\text{--}120^\circ\text{C}$ is a transition zone where the rest of the interlayer water dehydrates. This zone is followed by the beginning of the dehydroxylation of the main layer. This phase is stable at $120\text{--}170^\circ\text{C}$ and diminishes completely at 250°C .

The dehydration processes of the synthesised phases investigated with X-ray diffractometry are in accordance with the results of the thermal analysis. Fig. 6 illustrates a TG curve of Shigaite-Na. Three stages of weight loss (endothermic reactions) appear at 60°C , 90°C to 120°C and 170°C . Total weight loss of sample mass throughout the temperature range for the TG curve agrees well with the summation of all volatile components (H_2O) in the chemical formula:



It should be noted that the temperatures of the TG analysis agree with those of the formation and dehydration of the phases in the XRD pattern of this solid sample, respectively. Because the XRD pattern indicates that the layered structure is still maintained, it is reasonable to assume that the weight loss at 60°C and 90°C in the TG curve is due to elimination of interlayer water not necessary for the structure.

Table 2. Chemical analysis of alkali-substituted shigaite

(weight %)	Shigaite			
	Na	K	Rb	NH ₄ ⁺
Al ₂ O ₃	13.2	13.6	13.1	13.2
MnO	38.0	37.7	37.7	39.5
SO ₃	14.8	14.8	15.3	15.9
H ₂ O	32.2	32.5	33.2	33.3
Na ₂ O	2.8	n.a.	n.a.	n.a.
K ₂ O	n.a.	4.0	n.a.	n.a.
Rb ₂ O	n.a.	n.a.	5.2	n.a.
NH ₃	n.a.	n.a.	n.a.	1.3
sum	101.0	102.6	104.5	103.8

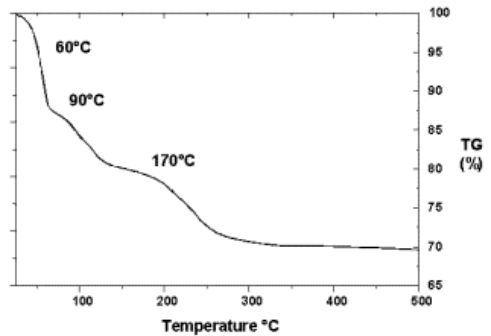


Figure 6 TG curve of shigaite-Na

5 CONCLUSION

It could be proved that alkali-substituted shigaite can be synthesised with the coprecipitation method. The emplacement of K, Rb and NH₄⁺ instead of Na showed pure phases of lamellar shigaite with good crystallinities. No minor phases crystallised. Because of the small ion radius of Li and the large ion radius of Cs synthesis of lamellar shigaite failed.

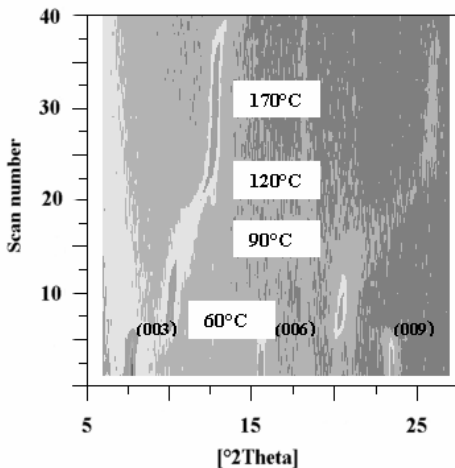


Figure 5 X-ray pattern of shigaite-Na versus temperature (Scan number: 1=25°C, 10=70°C, 20=120°C, 30=170°C, 40=220°C)

No well crystallized single phases were formed. Exact determinations about the influence of the ion radius are in progress. Several hydration stages of the synthesis products in the temperature range 25<T<170°C followed by decomposition at temperatures above 200°C could be proved.

6 APPLICATION

Shigaite is produced if manganese sulfate is used for controlling the hydration behaviour of high alumina cement instead of calcium sulfate. With increasing amounts of manganese sulfate the hydration reaction is retarded. Not only the hydration process could be affected, the fixation of water molecules is good and the harden product is very stable against chemical attacks. Shigaite appears together or instead of ettringite. Thus it is possible to control the thermal resistance of the harden binder with the thermal stability of the shigaite.

7 REFERENCES

- Cavani, F., Trifiro, F. & Vaccari, A. (1991): Hydrotalcite-type anionic clays: Preparation, properties and applications. *Catalysis Today*, 11, 173-301.
- Cooper, M.A. & Hawthorne, F.C. (1996): The crystal structure of shigaite, [AlMn₂²⁺(OH)₆]₃(SO₄)₂Na(H₂O)₆{H₂O}, a hydrotalcite-group mineral. *Canadian Mineralogist*, 34, 91-97.
- Miyata, S. (1975): The synthesis of hydrotalcite-like compounds and their structures and physico-chemical properties-I: the system Mg²⁺-Al³⁺-ClO₄⁻, Ni²⁺-Al³⁺-Cl⁻ and Zn²⁺-Al³⁺-Cl⁻. *Clays and clay minerals*, Vol. 23, 369-375.
- Peacor, D.R., Dunn, P.J., Kato, A. & Wicks, F.J. (1985): Shigaite, a new manganese aluminum sulfate mineral from the Ioi Mine, Shiga, Japan. *N. Jb. Min. Mh.*, 10, 453-457.
- Pöllmann, H. (2001): Shigaite – Synthese, Eigenschaften und Anwendung. *Zeitschrift für Kristallographie, Supplement Issue No. 18*, 138.
- Pring, A., Slade, P.G. & Birch, W.D. (1992): Shigaite from Iron Monarch, South Australia. *Min. Mag.*, 56, 417-419.

Behaviour of Vermiculites with Different Composition at Different Temperatures

C.Marcos, A.García, I.Rodríguez Marcos

Dpto. Geología, Universidad de Oviedo.C/. Jesús Arias de Velasco, s/n, 33005, Oviedo (Asturias), Spain

Y.C.Arango

Universidad Nacional de Colombia, Sede Manizales, A.A 127, Manizales (Caldas), Colombia.

ABSTRACT: Vermiculites have been investigated extensively because of their various industrial applications and scientific interest. These layered silicates present large diversity of behaviours as a result of its lamellar structure, layer charge associated with the numerous isomorphous substitutions, disorder effects and ability for dehydration-rehydration and swelling process. The present study is centered on the results of X-ray diffraction at elevated temperature, *in situ* and *ex situ* processes, of vermiculites from different origin and composition in order to understand their different behaviour as opposed to the composition.

1 INTRODUCTION

Vermiculites present large diversity of behaviours as a result of its lamellar structure, layer charge associated with the numerous isomorphous substitutions, disorder effects and ability for dehydration-rehydration and swelling process. The hydration state of vermiculite is defined by the number of water layers in the interlamellar space, with a development corresponding to different phases, such as zero-, one- and two-water layer hydration states (0-, 1- and 2-WLHS, respectively). Their basal spacings depends on the water vapour pressure, temperature and cation species.

The present study is centered on the results of X-ray diffraction at elevated temperature, *in situ* and *ex situ* processes, of vermiculites from different origin and composition in order to understand their different behaviour as opposed to the composition.

2 EXPERIMENTAL

The vermiculite samples investigated were collected from Sta. Olalla (Huelva, Spain), Paulistana (Piauí, Brasil), Catalão (Goiás, Brasil) and West China, respectively. These vermiculites come from

thioctahedral micas of phlogopite (Sta. Olalla, Paulistana and West China) and biotite type (Catalão), according to the representation of the octahedral sheet cations in a Mg - R³⁺ - R²⁺ ternary diagram (R³⁺ and R²⁺ represent the sum of trivalent and divalent cations, respectively). These cations were obtained from the (CAMEBAX-MBX50 of the Servicios Científico-Técnicos de la Universidad de Oviedo) electron microprobe analyses and using the MINPET software, as reflected in the structural formula (Tab.1). The alteration of mica to vermiculite implies the replacement of the interlayer K⁺ by a hydrated cation as Mg²⁺.

Therefore, the content of potassium reveals that vermiculite from Sta. Olalla is pure because % KO < 0.35 and the other samples are not pure vermiculites because % KO > 2.5, value related to the biotite composition.

Table 1 Structural formula of vermiculites (1, Sta. Olalla; 2, Paulistana; 3, Catalão, 4: China).

$(Mg_{0.75}Ca_{0.05}Na_{0.04})(Mg_{4.92}Al_{0.59}Fe_{0.43}Ti_{0.04})(Si_{5.66}Al_{2.34})O_{20}(OH)_4$
$(Mg_{0.55}K_{0.69}Ca_{0.03}Na_{0.01})(Ti_{0.13}Fe_{0.61}Cr_{0.01}Mn_{0.01}Mg_{5.24})(Si_{6.10}Al_{1.67}Fe_{0.24})O_{20}OH_4$
$(Mg_{0.25}K_{0.20}Ca_{0.01}Na_{0.04})(Al_{0.61}Fe_{1.27}Ti_{0.09}Mn_{0.01}Mg_{4.01})(Si_{6.46}Al_{1.54})O_{20}OH_4$
$(K_{1.17}Ca_{0.05}Na_{0.17})(Ti_{0.09}Mg_{4.43})(Si_{4.88}Al_{1.71})O_{20}OH_4$

X-ray patterns for powder and flakes samples, at atmospheric pressure, have been performed using a Seifert XRD 3000 diffractometer (Servicios Científico-Técnicos de la Universidad de Oviedo), at room temperature; and a Bruker AXS (Laboratorio de Física del Plasma, Universidad Nacional, Sede Manizales) at different temperatures, in the range between 20°C and 1000°C, collected each 10°C. The results at room temperature (Fig. 1) for the samples studied show that Sta Olalla and Paulistana samples are basically vermiculite, China sample is practically phlogopite and the Catalão sample is composed by hydrobiotite and vermiculite.

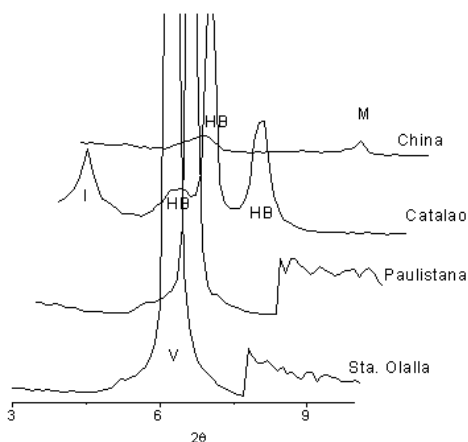


Figure 1. X-ray patterns at room temperature.

Vermiculite obeys to a temperature increase changing its structure. Vermiculites with Mg-cation interlayer show the three dehydration states previously reported (Walker 1956; Collins et al.1992; Reichenbach et al. 1994; Ruiz-Conde et al.1996; Marcos et al. 2003). The silicate structure vanishes after dehydration and the reappearing of a new structure depends on Mg-interlayer content, particle size and time of treatment. It is a dynamic process which depends on chemical composition, size, relative humidity and experimental conditions of process, as shown in Figures 2, 3, 4 and 5.

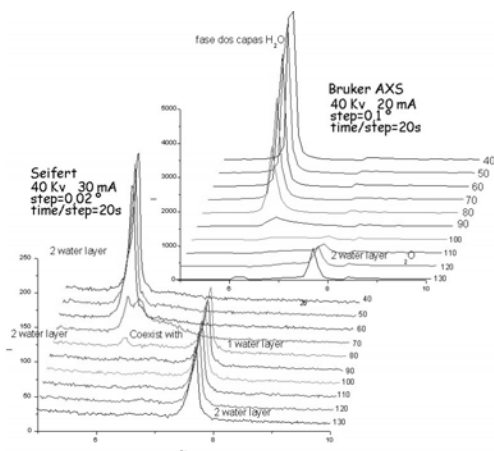


Figure 2. X-ray diffraction patterns at different temperatures *in situ* for Sta. Olalla vermiculite, as example.

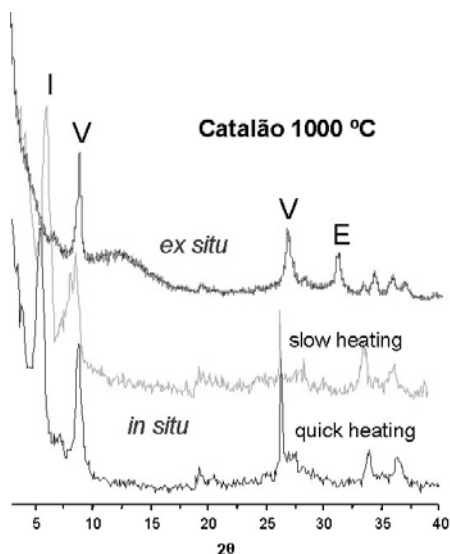


Figure 3. X-ray diffraction patterns at 1000 °C *ex situ* and *in situ* (slow and quick) for Catalão vermiculite, as example. V=vermiculite, E=enstatite, I=interstratified of hydrated vermiculite.

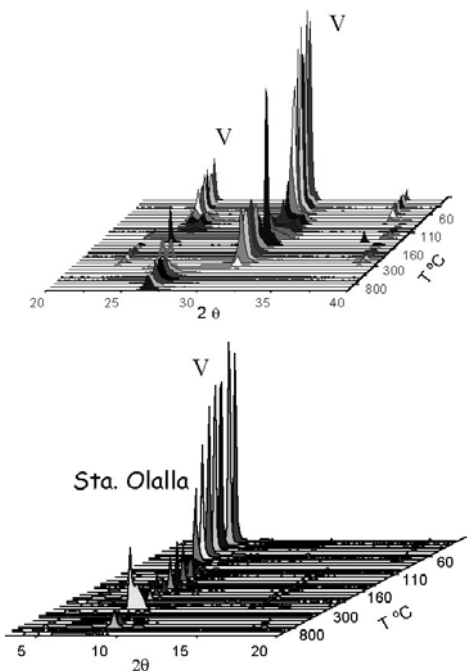


Figure 4. X-ray diffraction patterns at different temperatures *in situ* for Sta. Olalla, as purest vermiculite.

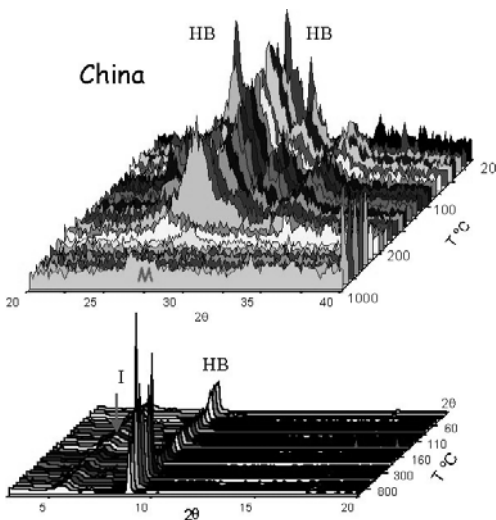


Figure 5. X-ray diffraction patterns at different temperatures *in situ* for China sample, as not pure vermiculite. HB=hydrobiotite, I=interstratified.

The silicate structure vanishes after dehydration and the reappearing of a new structure depends on Mg-interlayer content, particle size and experimental conditions.

The changes occurs faster in powdered samples with the most Mg-interlayer content than in flakes and with less time of treatment.

The behaviour of vermiculites with Mg and/or K in the interlayer differs from the vermiculites which have only K in the interlayer. It is due to K has hydration energy lesser than Mg-cation and it has a high affinity to water molecules.

Vermiculites with Mg-cation interlayer show the three dehydration states previously reported. In the purest vermiculites (Sta. Olalla) these states occur at higher temperatures than in micaceous vermiculites, such a China sample. Vermiculites having a higher K interlayer content and a lack of Mg, and a higher proportion of biotite-vermiculite mixed-layer mineral than in the purest Sta. Olalla vermiculite suffer a slight dehydration but it is not visible by X-ray diffraction.

Changes in the hydration states with temperature increase are displayed by the intensity decrease of the reflections and higher 2θ values.

Changes *in situ* experiments are slower than *ex situ* ones.

Ex situ heating (quick) originates vermiculite with 0 water layer in the interlamellar and enstatite.

In situ heating (slow) originates vermiculite with 0 water layer in the interlamellar, an interstratified of vermiculite with different hydration phases and mica.

The behaviour from 700 up to 1000°C is similar, which is important in order to save energy in the pyroexpansion process for industrial applications of vermiculite, normally made at 1000°C.

3 REFERENCES

- Collins, D. R.; Fitch, A. N. & Catlow, R. A. 1992. Dehydration of vermiculites and montmorillonites: a time-resolved powder neutron diffraction study. *Journal of Material Chemistry*, 8:865-873.
- Marcos, C.; Argüelles, A.; Ruiz-Conde, A.; Sánchez-Soto, P. J. & Blanco, J. A. 2003. Study of the dehydration process of vermiculites by applying a vacuum pressure: formation of interstratified phases. *Mineralogical Magazine*, vol. 67(6): 1253-1268.
- Reichenbach, H. G. & Beyer, J. 1994. Dehydration and rehydration of vermiculites: IV. Arrangements of interlayer components in the 1.43nm and 1.38nm hydrates of Mg-vermiculite *Clay Minerals*, 29: 327-340.
- Ruiz-Conde, A.; Ruiz-Amil, A.; Pérez-Rodríguez, J. L. & Sánchez-Soto, P. J. 1996. Dehydration-rehydration in magnesium vermiculite: conversion from two-one and one-two water hydration states through the formation of interstratified phases, *Journal of Material Chemistry*, 6:1557-1566.
- Walker, G. F. 1956. Mechanism of dehydration of Mg-vermiculite. *Clays and Clay Minerals*, 4:101.

The Crystal Structure of Synthetic Palenzonaite $\text{Ca}_2\text{NaMn}_2\text{V}_3\text{O}_{12}$

A. Nakatsuka

Department of Advanced Materials Science and Engineering, Yamaguchi University, Ube 755-8611, Japan

Y. Ikuta

Department of Chemistry and Earth Sciences, Yamaguchi University, Yamaguchi 753-8512, Japan

A. Yoshiasa

Department of Earth Sciences, Kumamoto University, Kumamoto 860-8555, Japan

K. Iishi

Department of Chemistry and Earth Sciences, Yamaguchi University, Yamaguchi 753-8512, Japan

ABSTRACT: Single crystals of palenzonaite (idealized formula $\text{Ca}_2\text{NaMn}_2\text{V}_3\text{O}_{12}$) were synthesized using the floating zone method and its crystal structure was examined by a single crystal X-ray diffraction technique. The unusually short Mn–O length is observed in the present synthetic palenzonaite. The V–O bonds have 55.1% covalency, and this value is comparable to covalencies of Si–O bonds in silicate garnets. Moreover, comparison of the V–O lengths in the reported vanadate garnets, including the present crystal, shows that the lengths are almost constant at about 1.72 Å regardless of ionic species occupying the octahedral site, as in Si–O lengths in silicate garnets. Such similarities in bonding nature between the V–O and the Si–O bonds yield a mutually similar rotating mode of tetrahedra. A further notable feature of the present crystal is that the dodecahedra and octahedra have the unusually long shared edges.

1 INTRODUCTION

Considerable efforts have been devoted to the crystal chemical studies of garnets because of their importance as constituents of the Earth's crust and mantle. The general formula of garnets can be expressed as $\text{X}^{\text{III}}[\text{X}_3]^{\text{VI}}\{\text{Y}_2\}^{\text{IV}}(\text{Z}_3)\text{O}_{12}$, and the X-, Y- and Z-cations are coordinated dodecahedrally, octahedrally and tetrahedrally by oxygen ions (Fig. 1), respectively. Garnets can accommodate various chemical species as seen in silicate garnets and rare-earth garnets; they commonly have di- or trivalent cations on the dodecahedral site, trivalent cations on the octahedral site and tetra- or trivalent cations on the tetrahedral site. On the other hand, some garnet compounds including pentavalent cations on the tetrahedral site such as vanadate garnets were reported (Bayer 1965, Dukhovskaya & Mill 1974, Basso 1987, Nakatsuka et al. 2003). The general formula of vanadate garnets can be expressed by $\text{X}^{\text{III}}[\text{Ca}^{2+}_2\text{A}^+]^{\text{VI}}\{\text{M}^{2+}_2\}^{\text{IV}}(\text{V}^{5+}_3)\text{O}_{12}$ (A = Na, Li; M = Mg, Mn, Co, Ni, Cu, Zn), and they are characterized by the mean formal valences of 1.67+ on the dodecahedral site, 2+ on the octahedral site and 5+ on the tetrahedral site.

A representative example of natural vanadate garnets is palenzonaite, occurring in manganese ores

at the Molinello mine, Val Graveglia, Northern Apennines, Eastern Liguria, Italy. The natural palenzonaite occurring there has a composition close to the idealized formula $\text{Ca}_2\text{NaMn}_2\text{V}_3\text{O}_{12}$, but significant amounts of As^{5+} and Si^{4+} replace V^{5+} on the tetrahedral site and its composition can be expressed as $\text{Ca}_{2+x}\text{Na}_{1-x}\text{Mn}_2(\text{V,As})_{3-x}\text{Si}_x\text{O}_{12}$ with $x \approx 0.3$ (Basso 1987). Basso (1987) refined the crystal structure of this natural palenzonaite and discussed its crystal chemistry. However, the refined structure of impurity-free palenzonaite has been not reported to date. Describing the crystal structure of impurity-free palenzonaite is important for the progress in the systematic understanding for the crystal chemistry of vanadate garnets. Here, we report the refined structure of synthetic palenzonaite and describe its structural features.

2 EXPERIMENTAL AND ANALYSIS

2.1 Synthesis

Single crystals of palenzonaite $\text{Ca}_2\text{NaMn}_2\text{V}_3\text{O}_{12}$ were grown by the floating zone method. The starting materials were powders of reagents-grade Na_2CO_3 , CaCO_3 , MnCO_3 and V_2O_5 . To eliminate weighing errors due to the presence of VO_2 in V_2O_5 ,

the reagent V_2O_5 had been previously preheated at 773 K for 15 h under oxygen flow and then was stored and weighed in a dry-box. Stoichiometric amounts of the starting materials were well mixed and then calcined at 1123 K for 15 h. After the calcined powder was mixed once again, it was placed into a sealed rubber tube to form a rod of 8 mm in diameter and 60 mm in length and hydrostatically pressed at about 600 kg cm^{-2} , after which the rod was sintered at 1293 K for 2 h in air. For the crystal growth, the sintered rod was put into a single ellipsoidal type of infrared heating furnace with a 3.5 kW halogen lamp as a heat source (Nichiden Machinery Ltd., Model 50X). The crystal growth was carried out under dry-air flow at the flow rate of 200 ml min^{-1} . Upper and lower shafts were counter-rotated at the rate of 30 rpm and the growth rate was 0.5 mm h^{-1} . Chemical composition of the synthesized crystals was examined by an electron microprobe analyzer (Shimadzu EPMA-V6) operated at a 15 kV accelerating voltage and a 15 nA beam current.

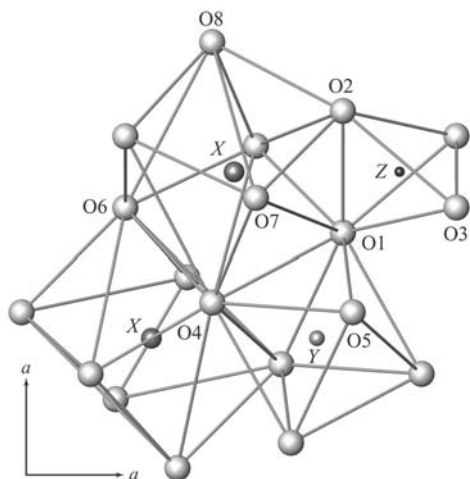


Figure 1: Crystal structure of garnet.

2.2 Single crystal X-ray diffraction

A single crystal ground into a sphere of 0.20 mm in diameter was used for measurements of X-ray diffraction intensities. The measurements were carried out at room temperature using a four circle diffractometer (Rigaku AFC-5S) with the graphite-monochromatized $\text{MoK}\alpha$ ($\lambda = 0.71069 \text{ \AA}$) radiation, and the operating conditions were 40 kV and 30 mA. The unit-cell parameters were determined by the least-squares method from a set of 25 reflections within the range $45^\circ \leq 2\theta \leq 50^\circ$. Intensity data of reflections within $2^\circ \leq 2\theta \leq 100^\circ$, corresponding to

$0.02 \leq \sin\theta/\lambda \leq 1.08$, with $0 \leq h, k, l \leq 27$ were collected by continuous ω - 2θ scan mode, and were corrected for Lorentz-polarization factors and spherical absorption effects ($\mu_r = 0.657$ for $\text{MoK}\alpha$). A total of 4949 reflections was measured and averaged in Laue symmetry $m\bar{3}m$ to give 881 independent reflections, of which 301 observed independent reflections with $|F_o| \geq 3\sigma(|F_o|)$ were used in the structure refinements.

The structure refinements were carried out by minimizing the function $\sum w(|F_o| - |F_c|)^2$ using a full matrix least-squares program RADY (Sasaki 1987). Atomic scattering factors for neutral atoms and anomalous dispersion coefficients were taken from International Tables for X-ray Crystallography (Ibers & Hamilton 1974). During the refinements, the correction for isotropic extinction effect (Becker & Coppens 1974a,b) was made. After several cycles of refinements, displacement parameters were converted to the anisotropic model. The crystallographic data, data collection parameters and refinement parameters are summarized in Table 1. The refined structural parameters are listed in Table 2. The selected interatomic distances are given in Table 3.

Table 1: Crystallographic data, data collection parameters and refinement parameters.

a (\AA)	12.568(1)
V (\AA^3)	1985.1(4)
Space group	$Ia\bar{3}d$
Crystal size (mm, diameter)	0.20
Radiation used	$\text{Mo K}\alpha$
μ (cm^{-1})	65.65
Scan type	ω - 2θ
2θ range ($^\circ$)	2-100
Absorption correction	sphere
No. of measured reflections	4949
No. of observed independent reflections with $ F_o \geq 3\sigma(F_o)$	301
R_{int}	0.0224
R	0.0164
R_w	0.0164

Table 2: Refined structural parameters.

	X-site	Y-site	Z-site	O-site
occupancy	0.66 Ca 0.33 Na	1.0 Mn	1.0 V	1.0 O
x	0.125	0	0.375	-0.0393(1)
y	0	0	0	0.0540(1)
z	0.25	0	0.25	0.1580(1)
U_{11}	0.0084(4)	0.0090(1)	0.0064(3)	0.0118(7)
U_{22}	0.0120(3)	0.0090	0.0073(2)	0.0113(7)
U_{33}	0.0120	0.0090	0.0073	0.0090(7)
U_{12}	0	-0.0005(2)	0	-0.0006(6)
U_{13}	0	-0.0005	0	0.0015(6)
U_{23}	0.0011(4)	-0.0005	0	0.0004(5)
B_{eq} (\AA^2)	0.853(2)	0.711(1)	0.552(1)	0.845(7)

Table 3: Selected interatomic distances (Å).

(Ca,Na)-O1	2.462(2)	O4...O7	2.907(3)
(Ca,Na)-O4	2.547(2)	O1...O4	3.037(3)
Mn-O	2.155(2)	O1...O5	3.058(3)
V-O	1.720(2)	O1...O2	2.682(3)
O4...O6	2.938(3)	O1...O3	2.871(3)

3 RESULTS AND DISCUSSION

3.1 Unusual Mn-O length

As shown in Table 3, the Mn-O length [2.155(2) Å] in the present crystal is considerably short compared with the calculated value (2.210 Å) from Shannon's radii (Shannon 1976) of Mn^{2+} and O^{2-} . The same situation is also observed in the natural palenzonaite occurring in the Molinello mine [2.146(2) Å; Basso 1987] although its chemical composition can be reasonably explained by divalent Mn ions. Moreover, such an unusually short Mn²⁺-O length is observed in MnSiO₃ tetragonal garnet (space group *I*₄*1*/*a*), with three nonequivalent Mn-O lengths [2.170(4) Å, 2.130(4) Å, 2.142(5) Å] on the octahedral site, and its mean Mn-O length is 2.147 Å (Fujino 1986).

3.2 Bonding nature of V-O bond and rotation of VO₄ tetrahedron

Covalency of bonds can be related to bond valence (Brown & Shannon 1973). From the empirical equation proposed by Brown & Shannon (1973), the covalency of V-O bond in the present crystal is calculated to be 55.1%. Thus, the V-O bond has a large covalency comparable to those of Si-O bonds in silicate garnets (about 53%). Moreover, the V-O length in the present crystal [1.720(2) Å; Table 3] is almost the same as those of the previously reported vanadate garnets Ca₂NaMg₂V₃O₁₂ [1.7208(6) Å; Nakatsuka *et al.* 2003] and Ca_{2.05}Na_{0.9}Co₂V₃O₁₂ [1.722(11) Å; Dukhovskaya & Mill 1974]. Thus, the V-O lengths in vanadate garnets are hardly influenced by ionic species on the octahedral site, as well as Si-O lengths in silicate garnets (Novak & Gibbs 1971).

The variations of the mean cationic sizes on the dodecahedral site ($V^{III}R$) and on the octahedral site ($V^I R$) cause the structural variations due to the rotation of tetrahedra (Born & Zeman 1964), and its rotating mode should be influenced by the rigidity of bonds between tetrahedral cations and oxygen ions. In Figure 2, the variation of the "position angles" (Born & Zeman 1964), signifying the rotation of tetrahedra about the c axis, of vanadate garnets as a function of $V^I R/V^{III} R$ agrees excellently with that of silicate garnets. This result will reflect the similarities in bonding nature between V-O bonds in vanadate garnets and Si-O bonds in silicate garnets described above. Thus, the

crystal structure of vanadate garnets will obey the geometric constraints similar to those of silicate garnets. In contrast, rare-earth garnets, in which cations such as Al³⁺, Fe³⁺ and Ga³⁺ that will bond more softly to oxygen occupy the tetrahedral sites, show a different trend from vanadate and silicate garnets (Fig. 2).

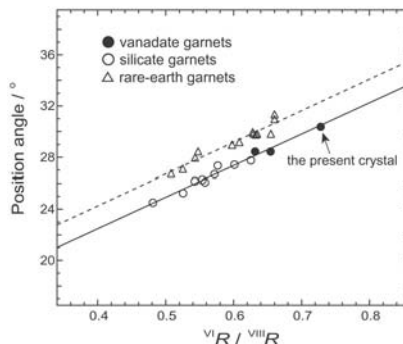


Figure 2: Variation of position angle as a function of the ratio of the mean size ($V^I R$) of octahedral cation to that ($V^{III} R$) of dodecahedral cation. The data of vanadate garnets are based on Dukhovskaya & Mill (1974), Nakatsuka *et al.* (2003) and the present study. The data of silicate and rare-earth garnets are based on Novak & Gibbs (1971) and Euler & Bruce (1965), respectively.

3.3 Edge lengths of polyhedra

3.3.1 VO₄ tetrahedron

In Figure 3, thermal vibrations of the dodecahedral cation (Ca^{2+}, Na^+) and the tetrahedral cation (V^{5+}) are significantly restricted between both cations, indicating the existence of strong $V^{III}(Ca^{2+}, Na^+) - IVV^{5+}$ repulsion. This is also observed in other garnets (Nakatsuka *et al.* 1995, Nakatsuka *et al.* 1999, Nakatsuka *et al.* 2003). As seen in Table 3, the geometric constraints of garnet structure force the tetrahedral-dodecahedral shared edge (O1...O2) to become considerably short compared with the unshared tetrahedral edge (O1...O3) (Meagher 1975), and thereby the fundamentally strong $V^{III}(Ca^{2+}, Na^+) - IVV^{5+}$ repulsion is sufficiently shielded.

3.3.2 (Ca,Na)O₈ dodecahedron and MnO₆ octahedron

The following features common to the reported vanadate garnets (Dukhovskaya & Mill 1974, Basso 1987, Nakatsuka *et al.* 2003) are observed in the edge lengths of dodecahedron and octahedron: (1) the dodecahedral-dodecahedral shared edge length (O4...O6) is considerably longer than the unshared dodecahedral edge length (O4...O7) in contradiction to Pauling's third rule (Pauling 1929); (2) the

octahedral-dodecahedral shared edge length (O1...O4) is very close to the unshared octahedral edge length (O1...O5). According to Nakatsuka *et al.* (2003), the long cation-cation distances and the valence distribution in vanadate garnets yield weak X–X and X–Y repulsions and consequently allow these unusually long shared edges. Such unusually long shared edges of dodecahedron and octahedron are also observed in the present crystal (Table 3).

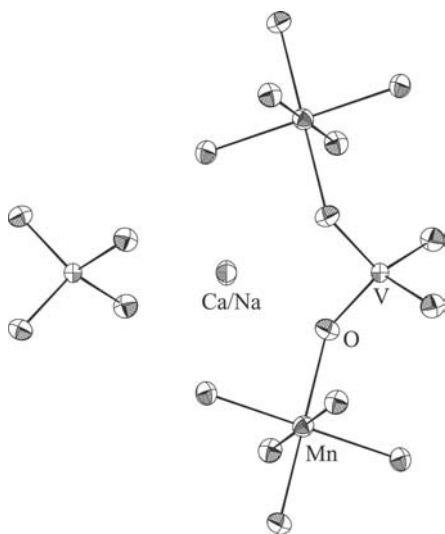


Figure 3: Displacement ellipsoids in the synthetic palenzonaite $\text{Ca}_2\text{NaMn}_2\text{V}_3\text{O}_{12}$, drawn at the 70% probability level.

4 CONCLUSIONS

On the basis of the results of the structure refinements of palenzonaite $\text{Ca}_2\text{NaMn}_2\text{V}_3\text{O}_{12}$, synthesized using the floating zone method, we conclude as follows. (1) The present crystal has unusually short Mn–O bond, as well as the natural palenzonaite. This is also observed in MnSiO_3 tetragonal garnet. (2) The bonding nature of V–O bonds in vanadate garnets is similar to that of Si–O bonds in silicate garnets. Because of this, the VO_4 tetrahedra in vanadate garnets are subjected to the rotating mode similar to that of the SiO_4 tetrahedra in silicate garnets. (3) The dodecahedral-dodecahedral and the octahedral-dodecahedral shared edges are allowed to become unusually long because of weak repulsions between dodecahedral cations and between dodecahedral and octahedral cations. The same situation is also observed in other vanadate garnets.

5 ACKNOWLEDGMENTS

This work was partly supported by grants from the Ministry of Education, Culture, Sports, Science and Technology of the Japanese Government.

6 REFERENCES

- Basso, R. 1987. The crystal structure of palenzonaite, a new vanadate garnet from Val Graveglia (Northern Apennines, Italy). *Neues Jahrb. Mineral. Monatsh.*, 136–144.
- Bayer, G. (1965): Vanadates $\text{A}_3\text{B}_2\text{V}_3\text{O}_{12}$ with garnet structure. *J. Am. Ceram. Soc.*, 48, 600.
- Becker, P.J. & Coppens, P. (1974a): Extinction within the limit of validity of the Darwin transfer equations. I. General formalisms for primary and secondary extinction and their application to spherical crystals. *Acta Cryst.*, A30, 129–147.
- Becker, P.J. & Coppens, P. (1974b): Extinction within the limit of validity of the Darwin transfer equations. II. Refinement of extinction in spherical crystals of SrF_2 and LiF . *Acta Cryst.*, A30, 148–153.
- Born, L. & Zemman, J. (1964): Abstandsberechnungen und gitterenergetische berechnungen an granaten. *Beitr. Mineral. Petro.*, 10, 2–23.
- Brown, I.D. & Shannon, R.D. (1973): Empirical bond-strength–bond-length curves for oxides. *Acta Cryst.*, A29, 266–282.
- Dukhovskaya, E.L. & Mill, B.V. (1974): Refinement of the crystal structure of vanadium garnet $\text{Na}_{0.5}\text{Ca}_{2.05}\text{Co}_2\text{V}_3\text{O}_{12}$. *Kristallografiya*, 19, 84–88.
- Euler, F. & Bruce, J.A. 1965. Oxygen coordinates of compounds with garnet structure. *Acta Cryst.* 19:971–978.
- Fujino, K., Momoi, H., Sawamoto, H. & Kumazawa, M. (1986): Crystal structure and chemistry of MnSiO_3 tetragonal garnet. *Am. Mineral.*, 71, 781–785.
- Ibers, J.A. & Hamilton, W.C. (eds.) (1974): *International Tables for X-ray Crystallography*, vol. IV, Birmingham, Kynoch Press.
- Meagher, E.P. (1975): The crystal structures of pyrope and grossularite at elevated temperatures. *Am. Mineral.*, 60, 218–228.
- Nakatsuka, A., Ikuta, Y., Yoshiasa, A. & Iishi, K. (2003): Vanadate garnet, $\text{Ca}_2\text{NaMg}_2\text{V}_3\text{O}_{12}$. *Acta Cryst.*, C59, i133–i135.
- Nakatsuka, A., Yoshiasa, A. & Takeno, S. (1995): Site preference of cations and structural variation in $\text{Y}_3\text{Fe}_{5-x}\text{Ga}_x\text{O}_{12}$ ($0 \leq x \leq 5$) solid solutions with garnet structure. *Acta Cryst.*, B51, 737–745.
- Nakatsuka, A., Yoshiasa, A., Yamanaka, T., Ohtaka, O., Katsura, T. & Ito, E. (1999): Symmetry change of majorite solid-solution in the system $\text{Mg}_3\text{Al}_2\text{Si}_3\text{O}_{12}$ – MgSiO_3 . *Am. Mineral.*, 84, 1135–1143.
- Novak, G.A. & Gibbs, G.V. (1971): The crystal chemistry of silicate garnets. *Am. Mineral.*, 56, 791–825.
- Pauling, L. (1929): The principles determining the structure of complex ionic crystals. *J. Amer. Chem. Soc.*, 51, 1010–1026.
- Sasaki, S. (1987): RADY, A fortran program for the least-squares refinement of crystal structures, National laboratory for high energy physics, Japan.
- Shannon, R.D. (1976): Revised effective ionic radii and systematic studies of interatomic distances in halides and chalcogenides. *Acta Cryst.*, A32, 751–767.

Metalsulfonate Hydrates – Synthesis and Investigation

H.Pöllmann, S.Stöber & M.Tewelde

Department of Mineralogy / Geochemistry, Martin-Luther-University, Halle, Germany.

Ch.Wagner & K.Merzweiler

Institute of inorganic chemistry, Martin-Luther-University, Halle, Germany.

ABSTRACT: The synthesis of methanesulfonatehydrates occurs through the reaction of metalcarbonates and methanesulfonic acids in an aqueous solution in a stoichiometric-ratio. The methanesulfonate compounds of some alkaline-, alkalineearth- and transitionmetals, which are listed in table 1, were synthesised and their water of hydration determined using TG and DTA. Lithium-, sodium-, calcium-, barium- and silvermethanesulfonate form only unhydrated compounds, while manganese- and cadiummethanesulfonates form hydrated compounds with two molecules of water. Cobalt-, copper- and zincmethanesulfonates contain 4 and strontium 5,5 molecules of water of hydration.

1 INTRODUCTION

Methanesulfonic acids ($\text{CH}_3\text{SO}_3\text{H}$), the general formula being RSO_3H ($\text{R} = \text{C}_n\text{H}_{2n+1}$), are strong organic acids which form compounds when reacting with inorganic and organic bases. Especially their sodium salts play an important role as detergents. The application of sulfonates, as additives, in the field of building chemistry is also known. The compounds crystallize in monoclinic, orthorhombic and triclinic systems and their respective unit cell data are listed below (Table 1).

Research on metalsulfonates has been carried out also by Garaud et al. 1980, Charbonnier 1979, Charbonnier et al. (1975, 1981), Chin Hsuan & Hingerty (1981) and Pöllmann et al. (2002).

2 EXPERIMENTAL METHODS

Grade agents of methane sulfonic acid ($\text{CH}_3\text{SO}_3\text{H}$), metal carbonates and metal hydroxides are used.

All compounds were prepared by mixing methane sulfonic acid with their respective metal-carbonates or metalhydroxides. In all cases, crystals were grown through a slow evaporation of the aqueous solution at room temperature.

The detailed procedure of the experiment is as follows:

0,04 mole methane sulfonate acid ($\text{CH}_3\text{SO}_3\text{H}$) is diluted with approximately 40 ml. of distilled water. An equivalent quantity of carbonates or hydroxides, respectively, were added while constantly stirring up.

The fresh precipitated hydroxides were prepared by adding NaOH to chlorides or sulfates. All precipitates were washed three times with distilled water. A subsequent separation was done using a zentrifugal apparatus.

3 CHARACTERISATION

The crystalline compounds were examined using various methods such as: X-ray diffraction, thermo-analysis and other chemical methods. X-ray diffraction has been carried out using a Siemens powder diffractometer D5000. Operating conditions were 40kV accelerating voltage and 30 mA beam current on a copper anode. Diffractograms were taken in increments of $0,04^\circ$ with a counting time of 2s.

Thermogravimetric measurements for water content controll have been accomplished using TG SEIKO of (TG/DTA 320) typ.

SEM micrographs have been carried out by means of Scanning Electron Microscopy (SEM from JEOL of JSM 6300 typ).

Unknown unit cell datas of some compounds were obtained using a four circle diffractometer. The measured unit cell datas were then further refined with the help of the program POWD.

4 RESULTS

Refinements of the lattice parameters delivers the values listed below (Table 1).

Table 1: Unit-cell parameters of hydrated and unhydrated Methanesulfonates.

	a [Å]	b [Å]	c [Å]	α	β	γ	SG
Li(CH ₃ SO ₃)	7.8647	7.4909	6.5594	90	90.30	90	C2/m
Na(CH ₃ SO ₃)	17.0713	22.0217	5.6058	90	90	90	Pbma
Ca(CH ₃ SO ₃) ₂	17.235	10.08	9.17	90	90	90	Pbca
Sr(CH ₃ SO ₃) ₂ ·5.5H ₂ O	8.6404	6.0795	9.10	90	113.01	90	P21/m
Ba(CH ₃ SO ₃) ₂	6.313	16.60	7.555	90	90	90	Cmcm
Mn(CH ₃ SO ₃) ₂ ·2H ₂ O	5.146	5.675	9.20	114.83	103.21	90.9	P1/P-1
Co(CH ₃ SO ₃) ₂ ·4H ₂ O	9.5229	9.9808	7.2410	90	124.99	90	P21/c
Cu(CH ₃ SO ₃) ₂ ·4H ₂ O	9.3664	9.632	7.3076	90	122.18	90	P21/c
Zn(CH ₃ SO ₃) ₂ ·4H ₂ O	9.47	9.907	7.21	90	124.6	90	P21/c
Ag(CH ₃ SO ₃)	8.70	5.772	8.26	90	100.2	90	P21/c
Cd(CH ₃ SO ₃) ₂ ·2H ₂ O	4.777	6.098	9.993	124.71	91.90	94.4	P-1

Table 1 shows the unit-cell datas of some alkali-, alkaline earth- and transition metal methanesulfonates (hydrated and unhydrated).

Strontiummethanesulfonate forms a hydrated compound with 5,5 Molecules of water of crystallization and crystallizes in monoclinic crystal system. Further cobalt-, copper- and zinkmethanesulfonate form hydrated compounds with 4 molecules of water and crystallize all in monoclinic crystal system.

Manganese- and cadmiummethanesulfonates form also hydrated compounds but with only 2 molecules of water of crystallization and crystallize both in triclinic system.

On the other side, lithium-, sodium-, calcium-, barium- and silvermethanesulfonate form only unhydrated compounds. While lithium-, and silvermethanesulfonates crystallize in monoclinic crystal system, sodium-, calcium- and barium all crystallize in orthorhombic type. Almost all crystals of methanesulfonates listed in table 1, with the exception of cobalt- and coppermethanesulfonate crystals which have a red and green colours respectively, form colourless crystals.

Hydrated methane-sulfonatahydrates which are formed by temperatures < 100°C dehydrate in 2 steps (Figs 6,7).

SEM-micrographs of some methanesulfonates are shown in Figures 1, 2 and 3. SEM image of crystalline aggregates of coppermethansulfonate are

shown in Figure 1. Figure 2 shows a detailed SEM image of Figure 1 with idiomorphic crystals of coppermethanesulfonate.

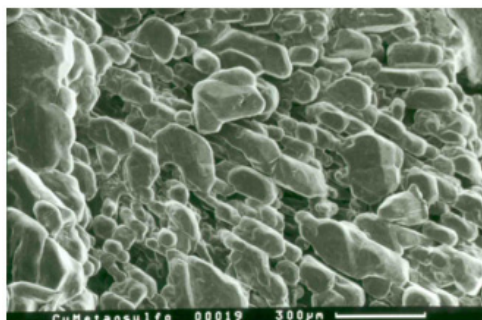


Figure 1: SEM micrograph of crystalline aggregates of hydrated coppermethanesulfonate (Cu(CH₃SO₃)₂·4H₂O).

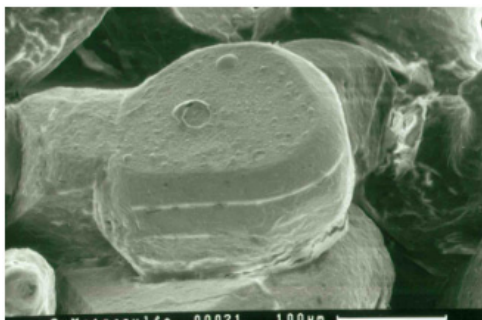


Figure 2: SEM micrograph of idiomorphic Coppermethanesulfonate (Cu(CH₃SO₃)₂·4H₂O) crystals (a detailed image of Fig. 1).

Figure 3 shows aggregates of hydrated manganese-methanesulfonates crystals.

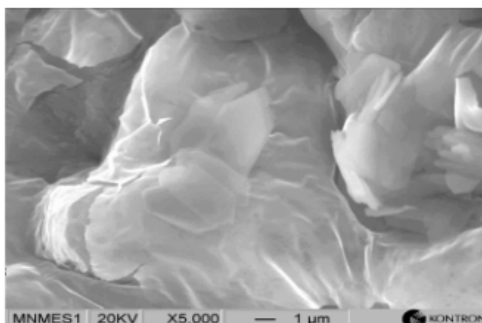


Figure 3: SEM micrograph of hydrated manganese-methanesulfonate (Mn(CH₃SO₃)₂·2H₂O).

Figures 4 and 5 show x-ray diffraction pattern of hydrated manganese- and coppermethanesulfonate.

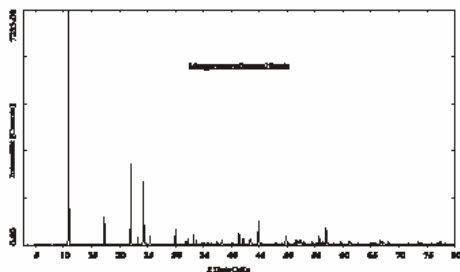


Figure 4: X-ray powder diffraction pattern of hydrated manganese-methanesulfonate ($\text{Mn}(\text{CH}_3\text{SO}_3)_2 \cdot 2\text{H}_2\text{O}$).

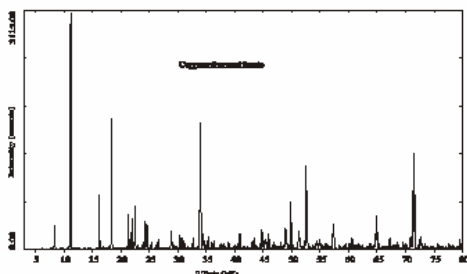


Figure 5: X-ray powder diffraction pattern of hydrated coppermethanesulfonate ($\text{Cu}(\text{CH}_3\text{SO}_3)_2 \cdot 4\text{H}_2\text{O}$).

Thermogravimetry and DTA measurements have been taken in temperature ranges of 25°C to 350°C at a heating rate of $10^\circ\text{C min}^{-1}$. In Figure 6 and 7, the thermogravimetric and DTA results of copper- and cobaltmethanesulfonate are illustrated.

As it is shown on Figure 6, the decomposition of water of crystallization from tetrahydrated coppermethanesulfonate occurs in 2 stages.

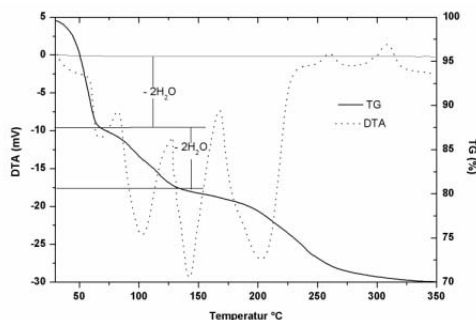
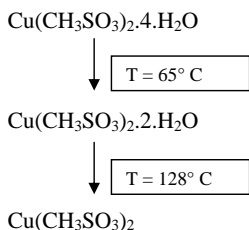


Figure 6: TG- and DTA diagram of hydrated coppermethanesulfonate ($\text{Cu}(\text{CH}_3\text{SO}_3)_2 \cdot 4\text{H}_2\text{O}$ (heating rate: $10^\circ\text{C min}^{-1}$).

Figure 7 shows the TG- and DTA diagram of hydrated cobaltmethanesulfonate. The loss of water of crystallization takes place here also in two stages.

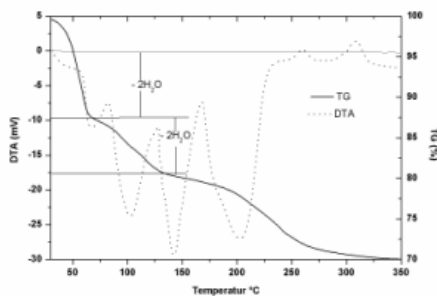
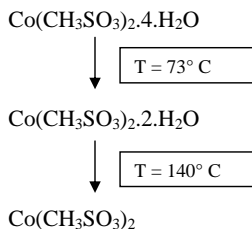


Figure 7: TG- and DTA diagram of hydrated cobaltmethanesulfonate ($\text{Co}(\text{CH}_3\text{SO}_3)_2 \cdot 4\text{H}_2\text{O}$ (heating rate: $10^\circ\text{C min}^{-1}$).

Figure 8 and 9 show crystal structures of hydrated coppermethanesulfonate and unhydrated lithiummethanesulfonate respectively. In both Figures (Figs 8, 9), it can be seen that both compounds consist of layered structures, in which the layers are made up of CH_3SO_3^- . Their respective cations lay between the layers. In case of hydrated coppermethanesulfonate, for example, the copper atoms are octahedrally surrounded by six water molecules.

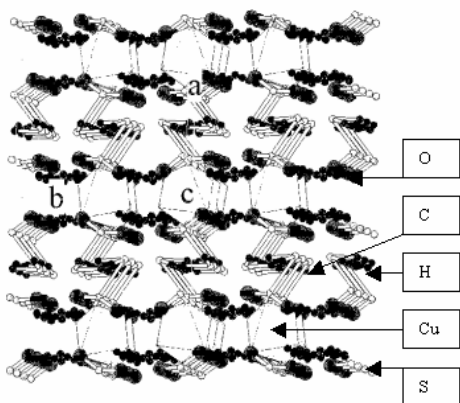


Figure 8: Crystal structure of hydrated copper-methanesulfonate

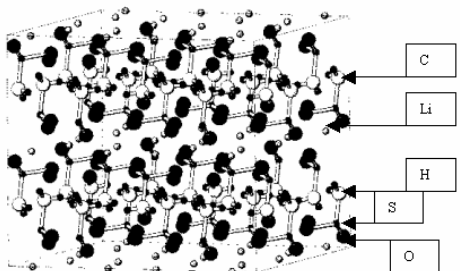


Figure 9: Crystal structure of unhydrated lithium-methanesulfonate

5 CONCLUSIONS

It could be shown that the synthesis of some alkaline-, earthalkaline- and transitionmetal-methanesulfonates occur as a result of the reaction between metalcarbonate and methanesulfonic acids. While lithium-, sodium-, calcium-, barium- and silbermethanesulfonates form unhydrated compounds; manganese- and cadmiummethanesulfonate form hydrated compounds with two molecules of water respectively.

Cobalt-, copper- and zincmethanesulfonates form hydrated compounds with four molecules of water each while strontiummethanesulfonate has 5,5 molecules of water. Their crystal structures are layered and the layers are formed by CH_3SO_3 in which the metal cations lay between the layers.

6 REFERENCES

- Garaud, Y., Charbonnier, F. and Faure, R. 1980. *J. Appl. Cryst.* 13, 190. Charbonnier, F. (1979). *Thermochimica Acta*, 33, 31-39.
- Charbonnier, F., Faure, R. & Loiseleur, H. 1975. *J. Appl. Cryst.* 8, pp 400, 493, 694.
- Chin Hsuan, W & Hingerty, B.E. 1981. *Acta Cryst.* B37, 1992-1997.
- Pöllmann, H., Stöber, S., Tewelde, M., Wagner, Ch. & Merzweiler, K. 2002. *Synthese und Charakterisierung von Methansulfonathydraten mit Mn, Co, Cu, Zn und Cd*. *Ber. Dt. Min. Ges.* 14, 131.

Behavior of Steel Corrosion Potential of Concrete with Mineral Additions

M.A.O.Vagheti & I.L.Müller

Program of Masters degree in Engineering of Mines, Metallurgy and of Materials, School of Engineering, Federal University of Rio Grande do Sul, Rio Grande do Sul, Brazil

G.C.Isaia & R.M.Brizola

Program of Masters degree in Civil Engineering, Center of Technology, Federal University of Santa Maria, Santa Maria, Rio Grande do Sul, Brazil

ABSTRACT: This work aims to show the steel status inside concrete with mineral additions, through corrosion potential electrochemical technique. This technique is useful to identify situations of corrosion risk or steel passivation status with low probability to present corrosion. In the experimental investigation 80 concrete prismatic specimens (7,5 x 7,5 x 5 cm) containing CA-60 steel rebar with 5 mm diameter were molded. Five concrete mixtures, four of them with mineral additions (fly ash, rice husk ash and ground granulated blast furnace slag) and one of reference (CPV-ARI cement) were investigated. The studied water/binder ratios were 0,50, 0,60 and 0,70. To induce corrosion the accelerated carbonation was utilized. The specimens were cured by 49 days at humid chamber, followed by a process for internal humidity equilibrium until to complete 91 days. Afterwards, the specimens were placed in the carbonation chamber by 20 weeks and immediately wetting/drying cycles by 6 months were performed. The primary results indicate too much variation of the potentials (but always in high figures), confirming the steel passive status and the concrete high ohmic resistivity. Later on 12 weeks inside the chamber, with carbonation front advance, tendencies for more negative values were noticed, mainly for the more porous concrete (w/b 0,60 and 0,70) as well as for the rice husk ash and slag mixtures. After the 20 weeks period, just at the beginnings of the wetting/drying cycles, the potentials reached sufficiently negative values (-500 mV) to characterize the period of corrosion propagation of the Tuutti (1982) model.

1 INTRODUCTION

The electrochemistry technique of the corrosion potential for the reinforced or prestressed concrete, it has been showed its efficiency in the qualitative determination of the possible places of degradation by steel corrosion.

Its performance in the potential lines mapping in the structures is satisfactory, and it has been often used in constructions in the evaluation of situations where probability of steel corrosion exists.

Originally, the employment of the technique emerged in the United States, mainly for the need of that country in obtaining effective means for study, evaluation and control of the corrosion, due to the serious problems in bridges decks, especially for the use of deicing salts in the winter for liberation of the highways (Casculo 1997).

After extensive works in 473 bridge decks contaminated with chloride, Van Daveer (1975) it established empiric zones of potentials associated to the corrosion risk. In 1977, ASTM (American Society for Testing and Materials) normalized the corrosion potentials technique for use in concrete.

The work aims to show the steel potentials inside

The necessary equipment for measurement electrochemical potentials is a voltmeter of high

the concretes with mineral additions indicating, along the time, the changes happened since the rebar depassivation to the corrosion properly said. For depassivate the steel inside of the samples, the induction by accelerated carbonation was used and, later, the acceleration of the corrosive process through wetting/drying cycles with baths in potable water.

2 PRINCIPLES AND TECHNIQUE APPLICATION

The operation principle of the electrode potential technique or of corrosion, consists of the potential readings in concrete samples or in the concrete structures properly said.

These readings are taken in relation to a reference electrode and the greatness of the potentials indicate the corrosion risk.

The potential difference registration among two semi cells (steel/concrete semi cell and stable semi cell that is the reference electrode) qualitatively indicates the corrosion probability in certain places of the structure.

entrance impedance (> 10 MOhms) and a reference electrode (for readings in concrete the most

appropriate is it of saturated calomel - SCE). Beyond following: sponge of high conductivity (destined to improve the electric conductivity between the

of those, the used accessories are the electrode and the concrete surface) and the electric connections (spinning).

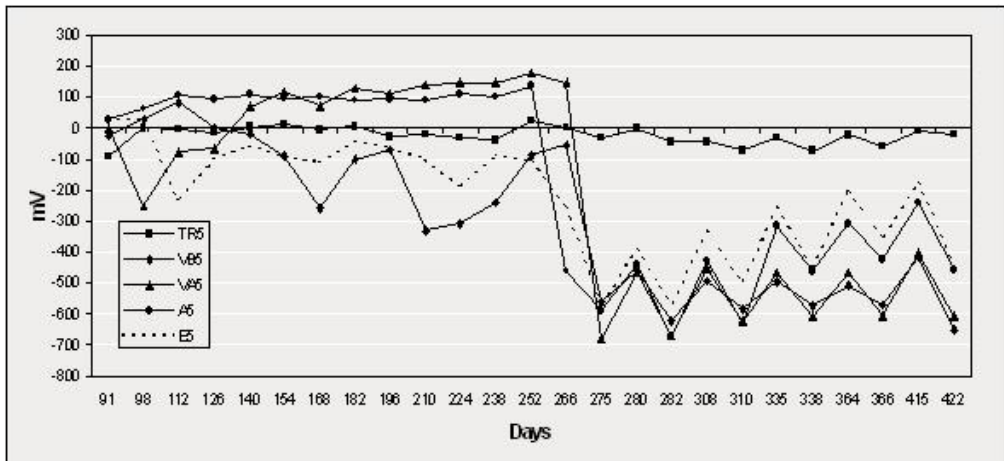


Figure 1 – Potentials for the 5 mixtures with ratios w/b = 0,50.

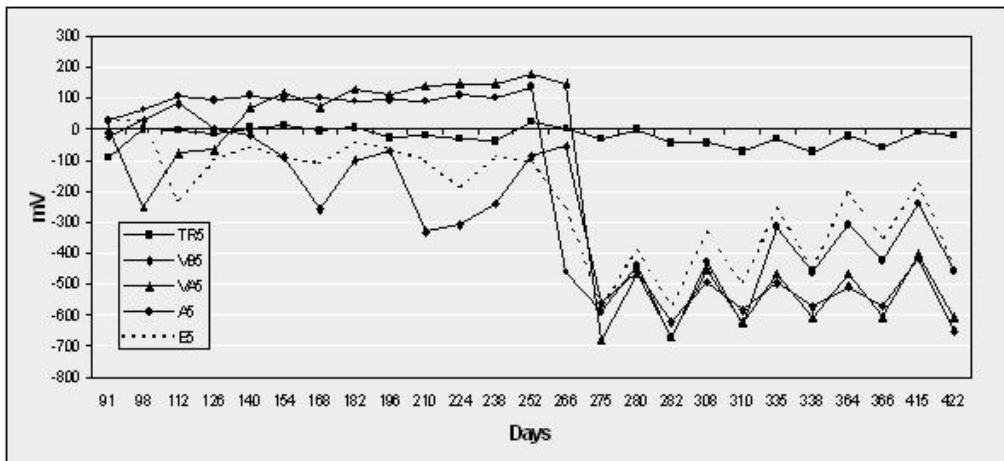


Figure 2 – Potentials for the 5 mixtures with ratios w/b = 0,60.

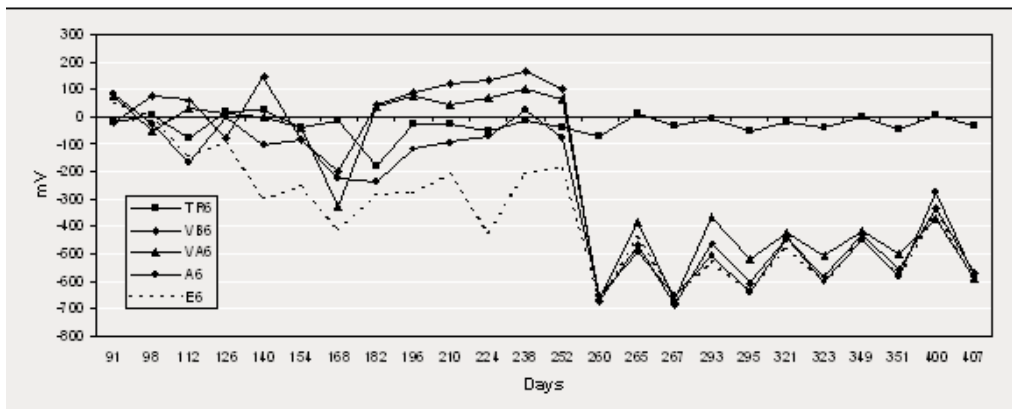


Figure 3 – Potentials for the 5 mixtures with ratios w/b = 0,70.

3 EXPERIMENTAL

3.1 Materials

The materials for the concrete specimens production, were the following: cement CPV-ARI; fly ash of petrochemical industry of the south area of Brazil; rice husk ash of the mill of the municipal district of Santa Maria/RS/Brazil; granulated blast furnace slag was supplied by the National Siderurgical Company (NSC); fine aggregate and coarse aggregate were obtained from Santa Maria/RS/Brazil's area. The employed steel in the tests was of the CA-60 category, with 5 mm diameter, coming from NSC.

3.2 Materials mix proportions

The cement and mineral additions mix proportions are below in the Table 1:

Table 1 - Type and convention to each mixture

Mixture	Composition (% in mass)	
1	100% cement (CPV-ARI)	TR
2	25% fly ash + 75% cement	VB
3	50% fly ash + 50% cement	VA
4	25% rice husk ash + 75% cement	A
5	70% blast furnace slag + 30% cement	E

For each one of the mixtures, three levels of resistances represented by the water-binder ratios (w/b) 0,50; 0,60 and 0,70, were verified. Therefore, the plan of the research foresaw the molding of 15 different concretes groups, three for each one of the mixtures.

3.3 Cure procedures

After the 80 specimens prismatics (7,5 x 7,5 x 5,0cm) casting, they were conditioned in humid

chamber by 49 days. At end of this period, they passed by a preconditioning process (RILEM TC 116-PCD Recommendation) of 42 days for internal humidity equilibrium, completing 91 days for the start of tests properly said.

3.4 Induction and acceleration of the corrosion

For the corrosion induction, the accelerated carbonation test was preceded in a FANEM 345 climatic chamber. This chamber controls the specimen's temperature and the humidity, as well as it regulates the defined CO₂ content emission for the test. The specimens, completing 91 days, were deposited in this chamber with 10% of CO₂ in volume, staying in the same for approximately 160 days.

After, began the wetting/drying cycles for corrosion acceleration for, approximately 6 months period.

4 RESULTS

In the following figures 1, 2 and 3, there are the graphs with the potentials readings along the time, comprising the induction period for accelerated carbonation and the corrosion acceleration period through the wetting/drying cycles.

5 RESULT ANALYSIS

All the analyzed steels, for the 5 concrete mixtures in the first 5 weeks of the induction period, presented great variation in the results, remaining between + 200 mV and -350 mV.

In this 5 weeks period, the steel still remains in the passive state and with the concrete (high pH) protecting the rebar. With the carbonation front

advance, in the 17 following weeks, there was already a tendency for more negative values of the potentials for the concretes with higher porosity ($w/b = 0,70$ ratio), mainly in the slag mixture (E7).

Nevertheless, with the more resistive concretes ($w/b = 0,50$ ratio) it is noted that practically the potentials did not change, except for the VB5 mixture.

In the concretes with $w/b = 0,60$ ratio in the comprehended period between 168 and 252 days, it can be verified until an elevation in the potentials values. This potentials raising, according some authors, among them Andrade et al (1988), it can be due to the humidity reduction in function of the evaporation of water through the carbonation reactions, being that process facilitated in more porous concretes, with higher w/b ratios.

The time for the steel depassivation inside of the different concretes, in this induction period for accelerated carbonation, was not very evident by the graphs analysis. It can be observed just some tendency in the Figure 2 at the 168 days, in which there was an abrupt fall in the potentials for almost all the mixtures, followed again by an elevation. In the Figure 3, possibly, at the 126 days this process also happened. In the Figure 1, does not appear clearly a similar situation along the induction process by carbonation.

In Vieira's research (2003), the author also tells that in the induction process by carbonation, the time for the rebar depassivation was not clearly evident, while in the induction by ions chloride the steel depassivation period appears more clearly, contributing to that the concrete electric conductivity containing chlorides.

In the Figures 1, 2 and 3 analysis for the corrosion acceleration period through the wetting/drying cycles, it is already immediately verified in the cycles start a significant potentials drop, passing from $+150$ mV values up to -700 mV ones.

It is evident that only the concrete carbonation is not enough to cause the steel corrosion, requiring too much that the humidity fill the material pores and contribute to increase the ionic mobility and, more precisely, the ions transport from the anodic areas to cathodic ones through the electrolyte.

During that 6 months period, approximately, the potentials stayed between -300 mV and -700 mV range, accelerating the steel corrosive process, also verified through the polarization resistance technique, with corrosion densities currents of up to $3 \mu\text{A}/\text{cm}^2$.

6 CONCLUSION

Through the readings accomplished along the time of the steel potential of corrosion inside the

concrete specimens with mineral additions, the following could be verified:

- the potentials presented a lot of variation in the results at the first 4 or 5 weeks of accelerated carbonation;
- after that period, the potentials were stabilized, confirming the steel passive status;
- while the carbonation front progressed, it happened a sudden potentials drop, probably indicating the rebar depassivation. That change was not clearly defined for the figure 1, while in the figures 2 (168 days) and 3 (126 days) it became more evident;
- to accelerate the steel corrosion in the concretes it was necessary the humidity supply, once only the action of CO_2 did not proceed sufficiently effective for the corrosion propagation;
- with the wetting/drying cycles it was possible to verify the potentials drop to sufficiently negative values (-500 mV), characterizing the corrosion propagation period foreseen in the Tuutti's model (1982).

7 REFERENCES

- Andrade, C. & Gonzáles, J.A. 1988. Tendencias actuales en la investigación sobre corrosión de armaduras. *Informes de la Construcción*, v.40, n.398, p. 7-14.
- ASTM C 876. 1991. Standard test method for half-cell potentials of uncoated reinforcing steel in concrete. American Society for Testing and Materials. Philadelphia.
- Cascudo, O. 1997. O controle da corrosão de armaduras em concreto - Inspeção e técnicas eletroquímicas. São Paulo: PINI, Goiânia: UFG.
- RILEM. Recommendations of TC 116-PCD. 1999. tests for gas permeability of concrete. *Materials and Structures*. v.32, n.217, p.163-179.
- Tuutti, K. 1982. *Corrosion of steel in concrete*. Stockholm: Swedish Cement and Concrete. Research Institute.
- Vieira, F.M.P. 2003. Contribuição ao estudo da corrosão de armaduras em concretos com adição de sílica ativa. Porto Alegre. 246p. Tese (Doutorado). Escola de Engenharia, Programa de pós-graduação em Engenharia de Minas, Metalúrgica e dos Materiais. Universidade Federal do Rio Grande do Sul.

Geochemical Characteristics of the Kolsuz Area Clays (Niğde-Central Anatolia)

M.Gurhan Yalcin & E.Ciftci

Nigde University, Department of Geological Engineering, 51200 Niğde, Turkey

ABSTRACT: The study area is occupied by marine sediments of late Paleocene-lower Eocene age, lacustrine deposits of late Miocene age, and volcanic rocks of Pliocene age. The Kolsuz clay deposit is hosted by the Kizilbayir Formation of late Miocene age. This formation is consisted, from bottom to top, of conglomerates, red-green clay stuffed with gravel-shale-mudstone sequence and gravel lenses. The Kolsuz clay deposit is 20-150 cm in thickness and occurs as intercalated with mudstone-shale succession. This sequence overlies gravel horizon forming base of the Kizilbayir Formation. Major minerals determined include montmorillonite, albite, quartz, calcite, hematite, and halloysite. Dominating clay mineral in the deposit is montmorillonite. According to the chemical analyses, low Al_2O_3 content could be an indication of high sand content for the clay deposit. Fe_2O_3 content is also high that is deleterious in the cement industry due to its undesired effect on coloring, refractoriness, and cookability. Thus, the material is not suitable for ceramic industry, however suitable for brick and cement production for light constructions. This study suggests that the Kolsuz clay deposit is formed mainly by montmorillonite transported from the neighboring areas where hydrothermal alteration was intense.

1 INTRODUCTION

The study area is located in Niğde, 40 km in the south (M_{33-d_1}). Kolsuz clay district extends in east-west direction through the Katrandetepe-Sansartepe slopes. It is largely exposed in the northern portion facing the Bor plain of the Eocene flysch surrounding the Tauros mountains chain. This study intends to investigate geological, mineralogic, and geochemical characteristics of the clay deposit. Earliest investigations on the general geology include Blumenthal (1956); Ketin & Akarsu (1965); and Demirtaşlı et al. (1973). Oktay (1982) studied the stratigraphy of the lithologies occurring in the area in detail and characterized the magmatic rocks of the area as subduction-related. Baş et al. (1986) investigated general characteristics of the magmatic rocks of Ulukışla-Çamardı (Niğde) area. Atabey (1988) prepared 1:100,000 scale geological map for the region. Çevikbaş and Öztunalı (1991 and 1992) examined the ore mineralizations of Ulukışla-Çamardı (Niğde) with respect to their general geology.

This study attempts to explain the mineralogic and geochemical characteristics of the clay deposit. Samples collected from the area were investigated by employing the reflected light microscopy (RLM),

X-ray diffractometry (XRD), and scanning electron microscopy with energy dispersive spectrometry (SEM-EDS).

2 GEOLOGY

Some of earlier works, particularly Oktay (1982) has been referred to in the stratigraphic terminology. The others include Blumenthal (1956), Ketin and Akarsu (1965), Demirtaşlı et al. (1973), Yoldaş (1973), and Atabey (1988). Lithologic units occurring in the region include, progressing upward, Serenkaya, Güney, Kızılbayır, Katrandetepe, and Beştepeler Formations.

Serenkaya Formation crops out largely in the south of area and it is the oldest lithology of the study area, which is of lower Lutecian-late Paleocene age. It is overlain conformably by the Güney Formation. Base of the formation is not observed in the area. It is consisted mainly of volcanic and subvolcanic rocks.

Güney Formation is of late Paleocene-lower Eocene age. It generally crops out in lower stratigraphic horizons. The Güney Formation is overlain discordantly by the Kızılbayır Formation of late Miocene age. It is comprised of sandstone-limestone-shale-mudstone-siltstone sequence having

flysch character.

Kızılbaş Formation comprises base of the late Miocene deposits. It is overlain concordantly by the Katrandetepe Formation. It is observed side by side with the Güney Formation in the study area due to faulting. It is consisted generally of terrestrial facies including conglomerate, sandstone, red-green clay with gravel, shale, mudstone sequence, and lens-shaped gravels. Sandstones are green and red in color and are very fine-grained, and they also lack any layering. This portion forms the Kolsuz clay deposit and also known as Burç or Altay (Yoldaş 1973) Formations.

Katrandetepe Formation is composed generally of green-white marl, gray lacustrine limestones and it is observed in the mid-upper Miocene sequence. Well-laminated dark color bituminous shale interbeds within the sequence are also observed (Oktay 1982). It is overlain by the Beştepeler formation. This formation is also known as Ulukışla Formation in the region (Yoldaş 1973).

Beştepeler Formation is loosely cemented, and cross-bedded. It is consisted of sand, lenses of conglomerate, shale muddy limestone, mudstone, which are considered to be stream bed deposits. It is of late Miocene age.

3 GENERAL CHARACTERISTICS OF THE KOLSUZ CLAY DEPOSIT

An area of about 35 km² was studied in detail and mapped at 1:25 000 scale. It is observed that subject clay site is hosted by the Kızılbaş Formation which discordantly overlies the Güney Formation. In general, it occurs concordant with topography as river deposits. The formation is consisted mainly of land facies including conglomerates, red-green gravel-bearing clay, shale, and mudstone succession containing gravel lenses. Sandstones are green, locally red in color, loosely cemented and well-sorted but poorly layered. Shale occurs in green and red colors, it is very fine-grained, and lacks any layering. The formation also has loosely cemented conglomerates at the base, and red-green mudstone-shale-clay sequence towards the top. Poorly sorted Kızılbaş Formation is discordantly overlain by lacustrine limestones of the Katrandetepe Formation.

A layer of round conglomerates with 20-100 cm thickness is composed of a variety of clasts including andesite, sandstone, limestone, and basalt at the base of Kızılbaş Formation. A sandstone layer sits on the conglomerates, which is gray and yellow in color and contains sand grains up to 1mm in across. Clay-bearing layers with 20-150 cm thickness sit on the sandstones and these are of Eocene age and they also contain andesite and basalt fragments in the west of the study area. Clay-rich

horizons show layered nature striking NE-SW with a 10°SE dip. A dip-slip normal fault striking NE-SW cuts through the study area.

4 XRD INVESTIGATION OF CLAY AND MARL SAMPLES

About 25 samples collected from the study area, from outcrops and trenches, were analyzed using X-Ray diffractometry at Niğde University. Shimadzu XD1 at 40 mA and 40 KV, with a scanning speed of 2°/min. using Cu-filter has been employed. Major minerals recognized through the XRD examination include the following: montmorillonite, albite, quartz, calcite, hematite, dolomite, and halloysite.

Absence of illite is significant. Abundances of clay species vary from sample to sample. Hematite is also present in some of the samples.

5 SEM OBSERVATIONS

Microstructures, mineralogical compositions, porosity, and diagenetic characteristics were examined in SEM-EDS. Clay minerals occur as flakes with significant porosity. Most importantly, no indications of hydrothermal formation were noticed suggesting that the clay minerals would have been transported to the deposition site from elsewhere.

6 CHEMICAL CHARACTERISTICS

The clay samples collected from the study area were analyzed for their SiO₂, Al₂O₃, Fe₂O₃, CaO, MgO, NaO, K₂O and SO₄ contents at the Cimsa Laboratory (Niğde) using a Spectronic Series 20 spectrophotometer. Na₂O and K₂O measurements were carried out using a Flame Photometer. CaO ability of the clay samples is also tested to measure the free CaO contents. XRD results showed well agreement with the chemical analysis. Arithmetic means of each element-oxide were calculated as follows 48.71% SiO₂, 12.87% Al₂O₃, 6.05% Fe₂O₃, 8.71% CaO, 3.41% MgO, 0.51% SO₃, 2.14% K₂O, 2.89% NaO, and 12.62% LOI.

Samples collected from the trenches showed high SiO₂ contents given rise by the abundance of quartz; high CaO contents were resulted from abundant calcite and high K₂O by presence of alkaline feldspars and subordinate mica. Positive correlation of CaO and MgO indicates presence of dolomite as well. LOI (loss on ignition) amounts show linear relationship with SO₃-bearing samples also containing high CaO, which should account for the presence of gypsum (CaSO₄·2H₂O). Samples with high LOI contents contain low SiO₂ that shows

negative correlation between quartz and clay abundances.

7 CONCLUSIONS

Field studies indicate that the Kolsuz clay deposit occur within the Kızılbayır Formation overlying the conglomeratic layer at the base of formation. It is consisted of a 20-120 cm-thick sequence of mudstone and shale having red-green colors in the field. Gravel lenses were seen near contact with the conglomerates. It is covered by the limestones of Holocene age. According to mineralogical investigation, major clay species is montmorillonite accompanied by albite, quartz, halloysite, chlorite, dolomite, and calcite. Illite is not detected.

The Kolsuz clay deposit is being exploited by Niğde Cimento (OYSA). This study determined that the clay can be used for white cement production. However, high Fe_2O_3 and CaO contents are not desired and will reduce quality of the product. Fe_2O_3 contents range between 2% and 8.10%, thus the clay can not be used for high quality ceramic production. After removal of overburden, Al_2O_3 content of the clay varies between 11.53% and 17.85%. Arithmetic means determined for major element-oxides include 48.71% SiO_2 , 12.87% Al_2O_3 , 6.05% Fe_2O_3 , 8.71% CaO, 3.41% MgO, 0.51% SO_3 , 2.14% K_2O , 2.89% NaO, and 12.62% LOI. Based on these results, LOI positively correlates with SO_3 contents and shows inverse relationship with quartz abundance. Presence of SO_3 and CaO suggest the presence of gypsum as well. Based upon the field observations, the formation containing the clay deposit could extend towards west of the study area suggesting possible of presence of significant clay reserves in the area.

This study suggests that the Kolsuz clay deposit is formed by transported clay species. This is supported by scarcity of hydrothermal alteration in the study area that is also indicated by low Al_2O_3/SiO_2 ratios (< 0.3). SEM observations also support this suggestion. According to the current mining regulations, this deposit is not considered to be economical due to low Al_2O_3 content ($< 30\%$).

This investigation suggests that similar formations should be investigated for their clay potentials. Although the deposit meets local demands at the moment, however, new resources will be required in the near future.

8 REFERENCES

- Atabey, E., 1988, 1/100.000 ölçekli açınısma nitelikte Türkiye Jeoloji Haritaları serisi, Kozan J19 paftası: MTA Genel Mdl., yayını, 125.
- Baş, H., Ayhan, A., ve Atabey, E., 1986, Ulukışla-Çamardı (Niğde) volkanitlerinin bazı petrolojik ve jeokimyasal özellikleri: Jeoloji Müh. Derg., 26,27-34.

- Blumenthal, M. M., 1956, Yüksek Bolkaradağın kuzey kenar bölgelerinin ve bazı uzantılarının jeolojisi: MTA yayını, Seri D, No:7, Ankara 153s.
- Çevikbaş, A., ve Öztunalı, Ö., 1991, Ulukışla-Çamardı (Niğde) havzasının maden yatakları: Jeoloji Müh. Derg., 39, 22-40.
- Çevikbaş, A., ve Öztunalı, Ö., 1992, Ulukışla-Çamardı (Niğde) havzasının jeolojisi: 45. Türkiye Jeoloji Kurultayı Bildiri Özet., 58-59.
- Demirtaşlı, E., Bilgin A. Z., Erenler, F., Işıklar, S., Sanlı, D. Y., Selim, M., Turhan, N., 1973, Bolkaradağının Jeolojisi: Cumhuriyetin 50. yılı Yerbilimleri Kongresi, Tebliğler, MTA yayını, Ankara 608 s.
- Ketin, İ., Akarsu, İ., 1965, Ulukışla Tersiyer havzasının Jeolojik etüdü hakkında rapor: TPAO, No:339.
- Oktay, F. Y., 1982, Ulukışla ve çevresinin stratigrafisi ve jeolojik evrimi: Tür. Jeol. Kur. Bült., 25, 15-23.
- Yoldaş, R., 1973, Niğde- Ulukışla bitümlü şist alanının jeolojisi ve ekonomik olanakları: Yayınlanmamış MTA Raporu, No:5050.

Industrial Minerals

Fluorite Replacement of Carbonatite and Marble at Okorusu, North-central Namibia

R.D.Hagni & P.A.Shivdasan

Department of Geology and Geophysics, 125 McNutt Hall, University of Missouri Rolla, Rolla, Missouri, United States

S.G.Viladkar

Department of Geology, St. Xavier's College, Mahapalika Marg, Mumbai, India

R.M.Domoney

Department of Earth and Environmental Science, University of the Western Cape, Bellville, South Africa

ABSTRACT: The fluorite deposits at Okorusu, in north-central Namibia are closely associated with an alkaline igneous ring complex of late Cretaceous age. The alkaline complex intruded Precambrian Damara regionally metamorphosed rocks and strongly metasomatized to those rocks to green, dense, fine-grained aegirine-augite fenites. Fluorite has been mined at two open pit mines (A and B) where high-grade (~60% CaF₂) fluorite ores have formed largely by massive replacements of carbonatite rocks. Greenish gray, magnetite, pyroxene, pyrrhotite, calcite carbonatite was locally intruded into brecciated fenite and then subsequently was replaced by fluorite ores. Ores that formed by the replacement of carbonatite are characterized by: 1) replacement remnants of the carbonatite, 2) goethite pseudomorphs of the carbonatite minerals, pyroxene, pyrrhotite, and magnetite, and 3) high phosphorus contents. In contrast, fluorite ores formed by marble replacement are much finer-grained, devoid of deleterious apatite, lack goethite pseudomorphs after pyroxene, magnetite, and pyrrhotite, and lack magnetite anomalies. The character of the rocks replaced by the fluorite ores is the determining factor in the development of beneficiation problems associated with the ores. Fluorite ores that have replaced carbonatite retain apatite as a replacement remnant and may present problems with regard to the level of phosphorus present. Fluorite ores that have replaced marble lack phosphorus and may have silica beneficiation problems.

1 INTRODUCTION

1.1 General geology

The fluorite deposits at Okorusu, in north-central Namibia are closely associated with an alkaline igneous ring complex of late Cretaceous age (125±7 Ma) (Milner et al. 1995). The alkaline complex has intruded Precambrian Damara regionally metamorphosed quartzites, marbles, and schists (Van Zijl 1962). The Damara rocks have been strongly metasomatized to green, dense, fine-grained aegirine-augite fenites due to alkali-rich fluids derived from carbonatite magma.

1.2 Character of the fluorite ores

The fluorite ores at Okorusu has been mined principally at two open cast mines, the A and the B pits. The ore deposits are massive high-grade (~60% CaF₂) fluorite ores that have replaced the host rocks. During that replacement small vugs have developed due to volume differences between the host rock and the replacement fluorite ore. Those vugs are partly lined with large, well-developed fluorite crystals that were deposited in open space.

1.3 Purpose of present research

Previous research at Okorusu has shown that the fluorite ore deposits have formed largely by the replacement of carbonatite bodies intruded into brecciated fenite host rocks (Shivdasan & Hagni 2001, Shivdasan 2003). Recent field research has shown that portions or all of some orebodies at Okorusu, in contrast, have formed by the replacement of host rock marbles. This communication treats the diversity of rock types replaced by the fluorite orebodies at Okorusu with some emphasis on the fluorite replacement of marble.

2 FLUORSPAR REPLACEMENT DEPOSITS AT OKORUSU

2.1 Fluorite replacements of carbonatites

The fluorite ores at Okorusu have formed largely by massive replacements of carbonatite rocks. Although as many as five types of carbonatite rocks have been distinguished at Okorusu (Hagni & Shivdasan 2000, Shivdasan & Hagni 2001, Shivdasan 2003), two types of carbonatites are most common and have been most prominently involved in fluorite replacement. The most abundant carbonatite is a

pyroxene carbonatite that is greenish gray, medium-grained, and pyroxene (iron-rich diopside)-rich (pyroxene abundance ranges about 20-45%). The pyroxene carbonatite grades locally into or is traversed by a coarser-grained pegmatitic calcite-rich carbonatite. The pegmatitic carbonatite also contains large crystals of titaniferous magnetite, pyroxene (iron-rich diopside), and hexagonal pyrrhotite. The term pegmatitic is used to indicate very coarse crystal size, and does not have genetic implications. Both types of carbonatite have been intruded into brecciated fenite prior to the introduction of the fluorite-depositing ore fluids.

2.2 Evidence for fluorite replacement of carbonatite

It is not easy to recognize that the fluorite ores have replaced carbonatites, because most or all of the original carbonatite has disappeared in the process of replacement. What remains around the fluorite orebodies is predominantly the fenite into which the carbonatite bodies had been intruded. The fenites are much less susceptible to fluorite replacement and only locally do they experience very limited areas of fluorite replacement that are marked by halos of light green to tan potassic alteration (Hagni 2001).

Several lines of evidence indicate that most of the massive fluorite ores at Okorusu have formed by the replacement of carbonatite. Fluorite ores that have replaced carbonatites are commonly characterized by the prominent presence of brown goethite-rich patches that have the shapes of the pyroxene, pyrrhotite, and magnetite crystals that were formerly present in the carbonatites prior to their replacement by fluorite. Such goethite pseudomorphs may be disseminated throughout the massive replacement fluorite ores. Thick prisms of goethite formed after pyroxene, goethite plates after pyrrhotite, and equant goethite grains after magnetite. Magnetite was the most resistant to the oxidizing fluorite ore fluids, and it commonly was oxidized first to hematite and then oxidized to goethite. Original platy hexagonal pyrrhotite crystals, up to one meter long, in the carbonatites were initially oxidized to marcasite, pyrite, secondary magnetite and hematite by early pre-fluorite hydrothermal fluids, and then subsequently to goethite with the introduction of the fluorite-depositing fluids (Hagni & Shivdasan 2001a).

Fluorite ores that have replaced carbonatites also may contain local remnants of the carbonatite that escaped complete replacement. Remnants several feet across are present locally in the B pit. Some of the replacement remnants of pegmatitic carbonatite contain pyroxene crystals as long as one-third of a meter. Where the remnants are predominantly calcite with only minor amounts of other minerals (pyroxene, magnetite, apatite, and pyrrhotite), the resulting fluorite replacements tend to develop abundant vugs.

The presence of magnetite rims at the margins of essentially all of the fluorite ore pods in the A pit is further evidence for the fluorite replacement of carbonatite pods intruded into fenite. The earliest discovered carbonatite pod in the open pit mines was along the footwall at the west end of the A pit (Kogut 1995, Kogut et al. 2001, Fig. 2F, Hagni 2001). That pod is hourglass shaped, three meters high, and one meter wide. It consists mostly of coarsely crystallized calcite and has coarsely crystallized massive magnetite rims, 15 to 30 centimeters thick, around its entire perimeter. The magnetite evidently crystallized early from very volatile-rich carbonatite magma on the walls of the intruded fenite. Elsewhere in the A pit the calcite portions of the carbonatite intrusions were entirely replaced leaving only their magnetite rims as evidence for the original replaced carbonatite pods.

One of the clearest examples of partial replacement of a carbonatite body is present on the footwall of the A pit. A nearly vertical carbonatite dike, two to three meters wide, has been intruded into fine grained greenish fenite. The dike consists of medium grained, greenish brown pyroxene carbonatite with five to ten centimeter thick rims of coarsely crystallized massive magnetite on both walls. The carbonatite has been replaced by fluorite ores at three levels in the pit: 1) at the lowest level, 2) at an intermediate height, and 3) at the highest level. The carbonatite between those three fluorite ore pods remains unreplaced. Within the three pods of fluorite replacement the magnetite rims persist as insoluble remnants and serve as evidence that the magnetite-rimmed fluorite areas have formed by the replacement of magnetite-rimmed carbonatite.

An even clearer example of carbonatite replacement by fluorite ore has been exposed only recently along the west end of the hanging wall in the A pit where a mining pushback was undertaken to obtain access to lower portions of the north-dipping A orebody (Dawe & Saayman 2000). A sill-like body of pyroxene carbonatite and pegmatitic carbonatite was intruded eastward into partially fenitized rocks. The carbonatite body is 20 meters thick, 900 meters long, and it pinches out to the east (Fig. 3 in Hagni & Viladkar, in press). About one-half of the carbonatite sill has been replaced by fluorite ores and it is clear that the central calcite-rich portions of the sill were favored for fluorite replacement.

Further evidence indicating that the A and B orebodies largely formed by the replacement of carbonatite is provided from core holes that were drilled along the strike to the east of the A orebody and to the southeast of the B orebody. Rather than intersecting the extensions of the two orebodies, those drill holes intersected carbonatite that clearly represents the original rocks that were replaced by the two fluorite orebodies.

Finally, fluorite ores that replaced carbonatite typically are characterized by relatively high phosphorus contents. Because phosphorus is a deleterious substance in fluorite concentrates used in the steel-making industry, fluorite ores and concentrates are routinely analyzed for their phosphorus contents. The apatite crystals, which account for the presence of phosphorus, can be observed with the naked eye in the fluorite ores that replaced carbonatites. Most of these apatite crystals were not deposited at the time of fluorite deposition, but rather represent relict apatite crystals that were originally present in the fluorite-replaced carbonatite.

2.3 Fluorite replacements of marble

Early speculation, before the Okorusu mines had been well developed, proposed that the fluorite orebodies were formed by the replacement of marble (Van Zijl 1962, Prins 1981). With the opening and gradual deepening of the A pit, it became abundantly clear that the ores in that pit had formed almost entirely by the replacement of carbonatite (Hagni & Shivdasan 2000, Shivdasan & Hagni 2001, Shivdasan 2003). A small pod satellite of ore along the hanging wall at the far west end of the A pit, however, was first recognized to have replaced marble.

Similarly, in the B pit most of the fluorite ores appear to have formed by the replacement of carbonatite. In the upper levels, some of the ores exhibited a distinct banded texture and were interpreted earlier to have replaced marble or other regionally metamorphosed Damara rocks (Kogut 1995, Hagni 2001). Recent deepening of the B pit has developed new exposures on the 1650 and 1640 levels that show clear replacement of marble by some of the fluorite ores. The main ore run, the A run, in the B pit has formed at the contact between pyroxene carbonatite and marble. The ores in that run have replaced carbonatite on the northeast side and marble on the southwest side. However, fluorite ores recently mined from the A band on the 1640 level have formed entirely by replacement of marble.

Finally, a third orebody (the C pit) is scheduled for mining in 2005. Examination of drill core from the C pit orebody appears to indicate that it has formed primarily by the replacement of marble.

2.4 Evidence for fluorite replacement of marble

Several features of the fluorite ores formed by replacement of marble help to distinguish those ores from fluorite ores that formed by the replacement of carbonatite. First, the fluorite crystals in the marble replacements are much finer-grained. In contrast to fluorite crystals in the carbonatite replacements that

may be as large as five centimeters across or more, the typical fluorite crystal in the marble replacements is less than a millimeter across.

The character of banding and the degree of its development also differ for the two types of replacements. The fluorite ores that have replaced carbonatite typically lack any banding. Indistinct local banding that is locally present in the carbonatite-replacement fluorite ores is discontinuous and is oriented in indistinct patterns with divergent directions.

Distinctive for the fluorite ores that have replaced marble is their complete lack of goethite pseudomorphs after pyroxene, magnetite, and pyrrhotite, and magnetite. As noted earlier, such pseudomorphs are an especially characteristic feature of the carbonatites replacement fluorite ores.

In contrast to the carbonatite-replacement fluorite ores that contain magnetite as a remnant phase from the original carbonatite, the marble-replacement fluorite ore lack magnetite. For this reason, the fluorite orebody at the C pit lacks a positive magnetite anomaly. The orebody at the B pit, in contrast, has a prominent positive magnet anomaly associated with the carbonatite.

Similarly, in contrast to the carbonatite-replacement fluorite ores that contain apatite that is largely relict from the replaced carbonatite, the fluorite ores that have replaced marble are essentially devoid of deleterious apatite.

2.5 Applications to beneficiation concerns

The character of the rocks replaced by the fluorite ores is the determining factor in the important development of beneficiation problems associated with the ores. Fluorite ores that have replaced carbonatite retain apatite as a replacement remnant and may cause problem levels of phosphorus to be present in the concentrates produced from those fluorite ores (Kogut & Hagni 1995, Hagni & Kogut 1997, Hagni & Shivdasan 2001b). Fluorite ores that have replaced marble lack phosphorus and may have silica beneficiation problems.

3 CONCLUSIONS

The ore fluids that formed the ore deposits at Okorusu replaced a variety of host rock types. The most prominent rock type replaced by fluorite was carbonatite. Fluorite ores formed by the replacement of carbonatite are characterized by coarse grain size, goethite pseudomorphs after crystals of magnetite, pyroxene, and pyrrhotite, and relatively high phosphorus contents. Where the original carbonatite bodies had dense magnetite rims, such as in the A pit, those magnetite rims resist replacement by the fluorite-depositing fluids and they persist as

magnetite rims around the fluorite orebodies. Due to the presence of magnetite in the carbonatites and subsequent replacement fluorite ores, they are characterized by positive magnetic anomalies.

Some orebodies or portions of orebodies have formed by the replacement of Damara host rock marbles. The fluorite ores that formed by marble replacement are much finer grained than the carbonatite replacements. Their phosphorus content is negligible because of the very low apatite content of the replaced marble, in contrast to the high apatite content of the carbonatites. Similarly, these orebodies lack positive magnetic anomalies because the marbles, unlike the carbonatite, lack magnetite.

The importance of recognizing the original rock types replaced by the fluorite ores lies in the fact that deleterious phosphorus contents may be present in fluorite ores that have formed by the replacement of carbonatites. In contrast, fluorite ores that have formed by the replacement of marbles contain insignificant amounts of phosphorus. Although the original carbonatite and marble rocks may be almost entirely replaced, the distinguishing characteristics of the fluorite ores may be used to interpret the nature of the host rock replaced and thereby predict potential beneficiation problems.

4 REFERENCES

- Dawe, M. & Saayman, A. F. 2000. The execution of a pushback under extremely unstable geological conditions at the Okorusu mine in Namibia. The Institute of Quarrying, Southern Africa, Symposium, Cape Town: 23 p.
- Hagni, R. D. 2001. Variations in ores, host rocks, and ore controls for the carbonatite-related fluorite deposits at Okorusu, North-Central Namibia: in Hagni, Richard D. (ed.) Studies on Ore Deposits, Mineral Economics, and Applied Mineralogy: With Emphasis on Mississippi Valley-type Base Metal and Carbonatite-related Ore Deposits. Rolla: University of Missouri-Rolla Press, 143-158.
- Hagni, R. D. & Kogut, A. I. 1997. The character of phosphorus in fluorite ores and concentrates from the Okorusu fluorite deposit, North-Central Namibia: Applied mineralogy. Proceedings of the 5th International Congress on Applied Mineralogy in the Minerals Industry, Warsaw: 216-220
- Hagni, R. D. & Shivdasan, P. A. 2000. Recognition of pegmatitic carbonatite intrusions in sodic fenite, and their importance in the localization of the fluorite ores at Okorusu, Namibia (abs.). Carbonatites 2000, St Etienne: 16.
- Hagni, R. D. & Shivdasan, P. A. 2001a. Origin of large plates of goethite in fluorite ores at Okorusu, Namibia. in Hagni, Richard D. (ed.) Studies on Ore Deposits, Mineral Economics, and Applied Mineralogy: With Emphasis on Mississippi Valley-type Base Metal and Carbonatite-related Ore Deposits. Rolla: University of Missouri-Rolla Press: 159-173
- Hagni, R. D. & Shivdasan, P. A. 2001b. The application of cathodoluminescence microscopy to the study of carbonatite-related fluorite ores, host rock carbonatites, and beneficiation products at Okorusu, Namibia. AIME-SME, Annual Meeting, Denver, CD ROM, SME Paper No. 01-133, 7 p.
- Hagni, R. D. & Viladkar, S. G., in press. A Comparison of the Carbonatite-related Fluorite Deposits at Amba Dongar, India and Okorusu, Namibia. Proceedings of the 38th forum on the Geology of Industrial Minerals, St. Louis, Missouri, Missouri Geological Survey and Resource Assessment Division Report of Investigations.
- Kogut, A. I. 1995. Mineralogy, paragenetic sequence, geochemistry and genesis of the Okorusu fluorite deposit, North-Central Namibia. Unpublished M.S. thesis, University of Missouri-Rolla, Rolla, 365 p.
- Kogut, A. I. & Hagni, R. D. 1995. Mineralogical characterization of phosphorus in fluorite ores and concentrates from Southern Africa. in Hagni, Richard D. (ed.) Process Mineralogy XIII: Applications to Beneficiation Problems, Pyrometallurgical Products, Advanced Mineralogical Techniques, Precious Metals, Environmental Concerns, Ceramic Materials, Hydrometallurgy, and Minerals Exploration. The Minerals, Metals & Materials Society, Warrendale, 15-27.
- Kogut, A., Hagni, R. D. & Schneider, G. I. C. 2001. Geology, mineralogy, and geochemistry of the carbonatite-related fluorite ores at Okorusu, north-central Namibia. in Hagni, Richard D. (ed.) Studies on Ore Deposits, Mineral Economics, and Applied Mineralogy: With Emphasis on Mississippi Valley-type Base Metal and Carbonatite-related Ore Deposits. Rolla: University of Missouri-Rolla Press: 113-142.
- Milner, S. C., Le Roex, A. P. & O'Connor, J. M. 1995. Age of Mesozoic igneous rocks in northwestern Namibia, and their relationship to continental breakup. Journal of Geological Society of London 152: 97-104.
- Prins, P. 1981. The geochemical evolution of the alkaline and carbonatite complexes of the Damaraland Igneous Province, South West Africa. *Annale van die Universiteit van Stellenbosch, Serie al (Geologiese)* 3, 145-278
- Shivdasan, P. A. & Hagni, R. D. 2001. Okorusu fluorite deposits, Okorusu, Namibia: Preliminary results of 1999 field mapping. in Hagni, Richard D. (ed.) Studies on Ore Deposits, Mineral Economics, and Applied Mineralogy: With Emphasis on Mississippi Valley-type Base Metal and Carbonatite-related Ore Deposits. Rolla: University of Missouri-Rolla Press, 159-173.
- Shivdasan, P. A. 2003. Petrology, geochemistry, and mineralogy of pyroxene and pegmatitic carbonatite and the associated fluorite deposit at Okorusu alkaline igneous carbonatite complex, Namibia. Unpublished Ph.D. dissertation, University of Missouri-Rolla, Rolla, 213 p.
- Van Zijl, P. J. 1962. The geology, structure and petrology of the alkaline intrusions of Kalkfeld and Okorusu and the invaded Damara rocks. *Annale van die Universiteit van Stellenbosch* 37, Series A, No. 4, 241-338.

Bunge's Cajati Apatite Mine, SE Brazil: Mineralogy and Petrography of the Carbonatite Intrusions and the Relationship to Mineral Processing

P.R.Alves & R.D.Hagni

Department of Geology and Geophysics, University of Missouri-Rolla, Missouri, USA

ABSTRACT: The apatite deposit at the Cajati mine is contained within carbonatites of the Jacupiranga Alkaline-Carbonatite Complex, located in Sao Paulo state, southeastern Brazil. The complex is Cretaceous (131 Ma), and it has intruded into rocks of the basement. Phosphate ore has been continuously mined since 1943, when mining started out from lateritic residuum. Currently, this deposit is one of few in the world where apatite is economically extracted from bedrock carbonatite, with an average grade of 5 % P₂O₅. Five distinct carbonatite intrusions were previously recognized at the Cajati mine (Gaspar 1989). In this study, more recent field and petrographic works have examined mineralogical, textural, and geochemical variations among the carbonatites to ultimately characterize the styles of apatite mineralization and investigate possible correlation with mineral processing. Microscopic examination, especially by cathodoluminescence (CL) method, has shown that despite variations of physicochemical conditions in the five carbonatites, the crystallization of apatite followed a general trend, with only few exceptions. Cores of apatite crystals commonly contain abundant primary fluid inclusions. The CL method has revealed features of the apatite growth mechanisms, and demonstrated that the ore mineral always shows CL color zoning. A borehole sample of a recently detected, distinct northern carbonatite intrusion was included in this work.

1 INTRODUCTION

The apatite deposit at the Cajati mine is contained within carbonatites of the Jacupiranga Alkaline-Carbonatite Complex, which was emplaced in the Cretaceous (Ruberti et al. 2000). The complex is located 240 km southwest of São Paulo city, in southeastern Brazil.

Bunge, a global leader in agribusiness and agricultural products, has managed to economically mine low grade apatite ore from bedrock carbonatite in Cajati. This deposit has been continuously exploited since 1943. Apatite is concentrated through an specifically designed flotation process, which has been expanded and redesigned in the past few years. The ultrafine fraction, which had been previously discarded, now represents additional 10 % volume of concentrated apatite product. Ores ranging from 3 % to as much as 15 % P₂O₅ are blended to yield a 5 % P₂O₅ plant feed. The final concentrate will typically contain more than 36 % P₂O₅.

The minerals from which apatite is separated are calcite, dolomite and magnetite, but minor phlogopite, olivine and pyrrhotite are also present. Several trace minerals have been described for the Cajati (or Jacupiranga) mine, but they make up far

less than 1 % of the whole rock composition. Although not relevant for processing, some trace minerals, namely ilmenite, pyrite, chalcopyrite, valleriite, baddelleyite, perovskite and pyrochlore, were included in this study due to their geochemical significance and/or textural relationship to the main mineral phases.

Five distinct carbonatite intrusions have been recognized at the Cajati mine (Gaspar 1989).

More recent lithological and structural detailed mapping works (scale 1:500), regularly updated by the company staff, have better delineated the carbonatite intrusions, including several marginal dikes and zones of xenoliths. For the current study, the deposit was thoroughly sampled according to the lithological units determined in the detailed geological map as updated at the time of collection, in 2002. Then, from a large number of samples, 38 specimens were selected for studies, including borehole samples.

A northern extension of the carbonatite deposit, detected by exploration drilling and gravimetry, has shown characteristics distinctive of those from the five older intrusions. The accurate surface and depth extent of this later body remains to be determined, but a borehole sample was included in this study.

2 METHODS

In order to study the selected set of minerals from the Cajati mine, a combination of microscopy methods and techniques was used. The standard petrographic method, microscopy of transmitted light, was complemented by reflected light so that magnetite, ilmenite and sulphides could be investigated. Cathodoluminescence (CL) of hot cathode has targeted apatite, calcite, and dolomite. It was especially useful for promptly distinguishing the carbonate minerals and textures, and for examining apatite zoning and other internal structures. The method of cold cathode, i.e. a CL detector attached to an electron microscope, was tested in apatite from one sample. This method provides higher magnification with better resolution, but the CL colors cannot be seen on the image. A selected number of samples was investigated in detail by Scanning Electron Microscopy and Electron Microprobe Analysis.

3 RESULTS

3.1 *The apatite mineralization*

Three major styles of apatite mineralization may be seen in any of the carbonatite intrusions: 1) veins or veinlets, which may be strongly oriented according to magmatic foliation, 2) small pods or patches, sometimes associated with veins or forming acicular aggregates, and 3) less common disseminated, discrete grains. Massive aggregates of medium to coarse apatite grains occur in phoscorite (apatite-magnetite-olivine) rock in the oldest carbonatite intrusion (Fig. 1).

Apatite crystals show compositional zoning, as numbered on Figure 1, characterized by changes in CL color. The core (1) is pinkish blue/violet and often has euhedral, hexagonal shape, indicating that nucleation and initial growth possibly occurred while most of the carbonates were in the liquidus phase. In coarse apatite grains, sometimes two or more cores are seen, which is evidence that growing crystals have clustered to form one grain. A second zone (2) shows blue CL color and sometimes is not present. The third zone (3) seems to have been more persistent along crystallization, and exhibits light blue to greenish blue CL color. The outermost zone (4) has blue CL color very similar to that of zone 2. Some crystals of the northern, later intrusions also show a fifth zone characterized by bright white CL. These crystals were affected by local hydrothermal fluids, as evidenced by fracturing caused by dolomite and sulphide veins, and later calcitic microveins. However, the alteration effect on apatite crystals from carbonatites in the fault shear zone (southern and central orebody intrusions) have caused distinct fracturing, and locally resulted in

non-cathodoluminescent, dull apatite (Fig. 2). Observation of the internal structure of apatite along its c-axis reveals complex, discontinuous chemical interactions during growth history.

Primary fluid inclusions, parallelly oriented to the apatite c-axis, may be abundant but mostly restricted to the core. These inclusions are generally small (<10 μm), but they can measure as much as 110 μm in apatite from hydrothermally affected carbonatites. Fluid inclusions are usually oblong, but very irregular shapes can also be seen. Most inclusions carry a liquid (L) and a vapor (V) phases, and quite often $L < V$. Rarely, solid phases (including an opaque mineral) are present. The white spots in the cores of apatite crystals seen on Figure 1 are fluid inclusions. Calcite eventually displays tiny fluid inclusions, which have to be distinguished from dolomite exsolution blebs.

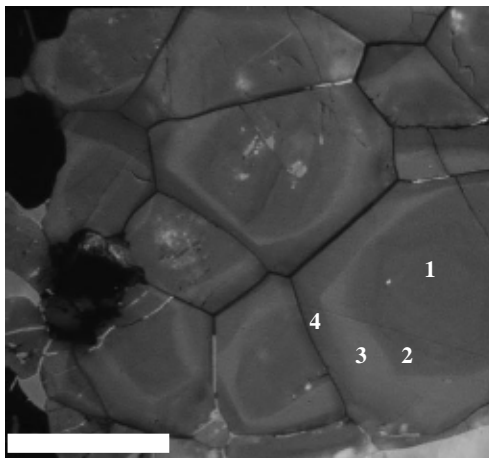


Figure 1: CL image showing apatite zoning (1 to 4). Crystals are from phoscorite developed in the oldest, southern carbonatite intrusion. Note how each crystal affected the growth of another. White spots on the cores are fluid inclusions. Length of horizontal bar is 0.5 mm.

The characteristics described above, except those for samples from areas affected by shear faulting and hydrothermal fluids, can be seen in all carbonatites, with some variation. However, systematic microprobe analyses on apatite grains from the carbonatite intrusions, including the latest one that was recently intercepted by borehole drilling (SP24), show a marked variation in SrO levels, exhibiting a tendency of increasing concentration in the latest intrusions. For instance, SrO measurements in apatite were 0.47 % in the oldest carbonatite, 0.59 % in the northern dolomitic intrusion, and 0.92 % in the sample from drillhole SP24. Other relevant characteristics detected were

the enrichment of LREE (especially Ce), and presence of 0.12 % to 0.21 % of Na₂O. Fe and Mg were significantly increased in some apatites that occur as inclusions in magnetite and olivine, respectively.

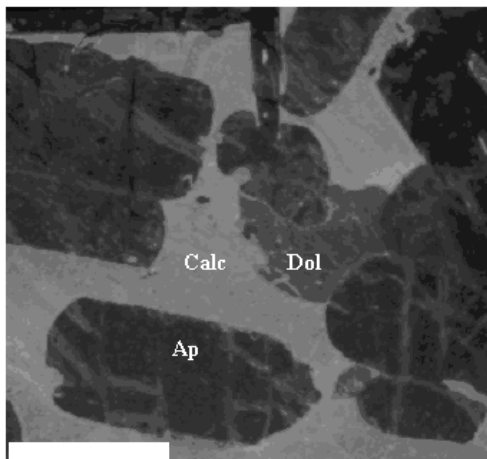


Figure 2: CL image of fractured, dull apatite with calcite and dolomite. Sample collected at level -60m south, in the area of influence of major fault. Length of horizontal bar is 0.5 mm.

3.2 Gangue minerals

Studies on the so called gangue minerals, from a mining and processing standpoint, such as olivine (Gaspar 1989), magnetite (Gaspar 1983a), and phlogopite (Brod et al. 2001, Gaspar 1982), were fundamental for better understanding of the petrogenesis of the carbonatites at Cajati.

Magnetite is approximately as abundant as apatite. Large crystals may appear to have perfect euhedral shape at a glance, but under microscope the grains are commonly resorbed. Magnetite crystals are much denser than the carbonatite melt, and flow banding showing crystal size segregation and settling can be seen in some locations, such as in the northern calcitic intrusion. As magnetite crystals grown, poikilitic texture was frequently developed by inclusion of apatite, dolomite and calcite crystals. Magnetite from the recently discovered, youngest carbonatite intrusion is fine to medium grained, and scarce if compared with its overall average content in the deposit.

Ilmenite with high Mn, Mg and Nb can be found in some of the carbonatites at Cajati as exsolution laths or small inclusions in magnetite. These ilmenites were extensively investigated and used as geothermometer in previous works (Gaspar 1983b, Mitchell 1978). Small, discrete grains also formed outside magnetite, and apparently contain higher Nb than the exsolved laths. Some ilmenite crystals do

not show its typical strong anisotropism character under reflected light, and these usually are associated with higher Nb content.

Phlogopite exhibits ubiquitous complex zoning. The most remarkable chemical variation is that determined by Ba, which replaces K. Phlogopite crystals display variable aspects of alteration, and may themselves be formed as a result of alteration of olivine. Phlogopite is affected preferentially along its rim and cleavage plans. Some grains show undulose extinction and/or evident deformation. Fine grained phlogopite is present in samples from the youngest dolomitic carbonatite intrusion, collected from borehole SP24.

Olivine has high forsterite (Fo) component. Measurements were Fo97 in the northern calcitic intrusion, and Fo93 from the largest southern intrusion, collected from bench toe at level -60m. Olivine is easily altered (Deer et al. 1992), and this feature is evident in the carbonatites. Larger crystals may contain dolomite inclusions.

Pyrrhotite is the main sulphide mineral present. Typically, it does not exceed 2 % of the carbonatite composition. Pyrrhotite twinning was observed in one sample, indicating there was a transition from hexagonal to the lower temperature, monoclinic structure. Few euhedral, hexagonal/pseudohexagonal crystals were observed. Pyrite is the second sulphide in abundance, and it has formed by replacement of pyrrhotite, as well as chalcopyrite and secondary magnetite. Valleriite is also present and corresponds to a later replacement phase, possibly developed by some affinity with carbonates microveins that percolated magnetite. Goethite is not common, but was identified in altered pyrrhotite.

Calcite and dolomite show a variety of textures that can be related to those predicted in experimental phase diagrams of the CaCO₃-MgCO₃ relation at high pressure and temperature (Goldsmith 1983). Dolomite commonly occurs as small exsolution blebs in calcite, or interstitial among earlier calcite grains. Calcite is also often interstitial, forming rounded, anhedral shapes. In the carbonatites with the highest Mg content, dolomite may exhibit CL color zoning (red core and brown rim). Zoning in calcite is usually formed by successive intercalation of yellow and brown CL colors, and is an evidence of recrystallization. Calcite twinning is very common. Grain boundaries may be interlocking, sutured, serrated, rounded or subhedral, angular.

Baddeleyite occurs in very small amounts but it is fairly common in the carbonatites, especially where large magnetite crystals are concentrated. It is easily identified by its twinning, and exhibits zoning. Few, small grains of perovskite and pyrochlore were described. Pyrochlore was found only in the sample SP24, from the recently drilled dolomitic carbonatite. Its complex zoning is marked by variations of Nb (decreasing towards the rim), and Th (increasing

towards rim). Pyrochlore, perovskite and baddeleyite typically form small, subhedral grains.

4 CONCLUSION

Based on the microscopy study of the minerals forming the carbonatites in the Cajati mine, it was possible to better understand some of the processing issues routinely noticed. For instance, the location of the ore denominated by the company staff as “hard apatite” partially coincides with the area most affected by hydrothermal calcitic and dolomitic fluids. This event was local but significant enough to cause recrystallization of grains of the carbonate minerals. The veins in fact have cracked and broken the apatite crystals, but have also affected the rims of the grains, as indicated by development of a bright, white CL zone. Changes in surface properties will affect the flotation recovery, but ore blending minimizes the relevance of this effect.

The ore adjacent to the shearing fault zone is known (and expected) to be very fine. The increase in the “ultrafine” fraction needs to be controlled in order to optimize flotation recovery. Ultrafines are floated in columns. Microscopy demonstrated that very fine, ground calcite was remobilized and recrystallized. Angular, very fine grains of apatite, and in some cases of ground magnetite, occur associated with the fine-grained calcite.

Overall, the apatite crystals are related to textures that draw a parallel with good to moderate capacity of grain liberation. Enveloped apatite grains, especially those engulfed by magnetite, are very difficult to separate, but this case does not comprise a relevant amount of the ore. In other cases, such as that illustrated by Figure 2, apatite is fractured, which would positively affect its grinding behavior. Interstitial apatite was crystallized at angular junctions of dolomite grains in sample from borehole SP24, which would lead to a fairly easy liberation.

5 REFERENCES

Brod, J.A., Gaspar, J.C., de Araujo, D.P., Gibson, S.A., Thompson, R.N. & Junqueira-Brod, T.C. 2001. Phlogopite and tetra-ferriphlogopite from Brazilian carbonatite complexes: petrogenetic constraints and implications for mineral-chemistry systematics. *Journal of Asian Earth Sciences*, 19: 265-296.

Deer, W.A., Howie, R.A. & Zussman, J. (1992). *An introduction to the rock forming minerals*. Harlow, England: Prentice Hall.

Gaspar, J.C. & Wyllie, P.J. (1982). Barium phlogopite from the Jacupiranga carbonatite, Brazil. *American Mineralogist*, 67: 997-1000.

Gaspar, J.C. & Wyllie, P.J. (1983a). Magnetite in the carbonatites from the Jacupiranga Complex, Brazil. *American Mineralogist*, 68: 195-213.

Gaspar, J.C. & Wyllie, P.J. (1983b). Ilmenite (high Mg, Mn, Nb) in the carbonatites from the Jacupiranga Complex, Brazil. *American Mineralogist*, 68: 960-971.

Gaspar, J.C. (1989). *Geologie et mineralogie du Complexe Carbonatitique de Jacupiranga, Bresil*. PhD thesis presented to U.E.R. de Sciences Fondamentales et Appliquées de la Université D’Orleans, France.

Goldsmith, J.R. (1983). Phase relations of rhombohedral carbonates. In: *Carbonates: mineralogy and chemistry*, Reeder, R.J. (ed.). Mineralogical Society of America, Reviews in Mineralogy, 11: 49-60.

Mitchell, R.H. (1978). Manganian and magnesian ilmenite and titanian clinohumite from the Jacupiranga carbonatite, Sao Paulo, Brazil. *American Mineralogist*, 63: 544-547.

Ruberti E., Gomes, C.B. & Melcher, G.C. (2000). The Jacupiranga Carbonatite Complex: geological and petrological aspects of the Jacupiranga alkaline-carbonatite association, southern Brazil. Post-Congress Field Trip Aft 08 Guidebook, International Geological Congress, Rio de Janeiro, Brazil. Part I: 1-21.

Polymeric Additives Effects in the Rheological Properties of Bentonite Clay Dispersions from Paraíba, Brazil

M.I.R.Barbosa, J.D.Viana, L.V.Amorim, H.L.Lira, H.C.Ferreira

Department of Materials Engineering, Federal University of Campina Grande, Paraíba, Brazil

K.V.Farias

Graduate Program of Chemistry Engineering, Federal University of Campina Grande, Paraíba, Brazil

E.Pereira

System Mud Indústria e Comércio Ltda., Itajaí, Santa Catarina, Brazil

ABSTRACT: The aim of this work is to evaluate the effects of polymeric additives and their role as colloidal protector in the rheological control of bentonite clay dispersions from Paraíba, Brazil. These dispersions are used as drilling fluids for oil well. It was studied two samples of sodium bentonite clay: one prepared in laboratory (namely Bofe) and other commercial sample (namely Brasgel PA). It was used two additives: carboxymethyl cellulose of low viscosity (CMC BV) and polyanionic cellulose (PAC). The dispersions were prepared with 4.86% w/w of clay and submitted to two different treatments. First, the dispersions were treated by using different proportions of polymeric additives and after 24 hours it were measured apparent (AV) and plastic viscosities (PV) and water loss (WL). On the other treatment, the dispersions were first treated with additives and submitted to a different proportions of $\text{CaCl}_2 + \text{MgCl}_2$, after 24 hours it was measured AV, PV and WL. The results shown that: (i) the polymeric additives work to increase viscosity and act as a protector agent in the dispersion prepared with Bofe clay. The values of AV, PV and WL are in accordance with the specification to be used as drilling fluids for oil well and, (ii) the rheological properties depend on the interaction of bentonite/polymer and the length of the polymer chain.

1 INTRODUCTION

The bentonite clays are composing predominantly by montmorillonite clay mineral and have several industrial application, such as, in oil well drilling muds, as a bonding agent for foundry molding sands, pelletizing iron ores, pharmaceuticals, emulsions stabilizers, catalysts and paint (Souza Santos 1989).

The biggest deposits of bentonite clays in Brazil are located in Paraíba State and the volume corresponds to 67% of the national deposit (Trindade 2001). These clays are polycationic and were discovered in 60's. They became well known due to the colors and the capacity of to change to sodium form after treatment with sodium carbonate (Na_2CO_3) (Souza Santos 1968). Today, after 40 years of exploitation, it can be found at least three types of clays, namely Bofe, Chocolate and Verde-ldo. These clays have the same mineralogical composition (montmorilonite and quartz impurities) but show different rheological behavior (Amorim 2003).

Several studies has been done in Federal University of Campina Grande, Paraíba, Brazil, to evaluate the rheological properties of these clays, as well as, the effect of addition of polymers to the

bentonite clay-water system to protect from the action of calcium and magnesium chlorides (Amorim 2003).

This way, the aim of this work is to evaluate the effects of polymeric additives and their role as colloidal protector in the rheological control of bentonite clay dispersions from Boa Vista City, Paraíba, Brazil to be used as drilling fluids for oil well.

2 MATERIALS

2.1 Bentonite clays

It was studied two samples of sodium bentonite clays. One prepared in laboratory and namely Bofe, from Juá deposit, Boa Vista City, Paraíba, and another commercial sample, namely Brasgel PA, supplied by Bentonit União Nordeste.

2.2 Polymeric additives

It was studied two polymeric additives of cellulose with long chain, carboxymethyl cellulose with low viscosity, namely CMC BV and polyanionic cellulose with high viscosity, namely PAC. The CMC BV was studied in concentration of 0.3, 0.4

and 0.5g/24.3 g of dry clay, and the PAC was studied in concentration of 0.2, 0.3 and 0.4g/24.3g of dry clay.

Table 1: Technical data of the polymeric additives.

Technical data	CMC BV	PAC
Function	Increase viscosity and control water loss	Increase viscosity and control water loss
Application	Potable water	Salt water
Composition	CMC	Polyanionic
Chain size	Long	Cellulose
Degree of substitution (DS)	0.75	0.95
Purity (%)	>95.00	>98.00

The polymeric additives were supplied by System Mud Indústria e Comércio Ltda. The table 1 shows the technical data for the additives.

2.3 Degrading additives

It was studied calcium chloride PA (CaCl_2) and magnesium chloride PA (MgCl_2) supplied by VETEC. These additives were studied in concentration of 10meq of $\text{CaCl}_2/100\text{g}$ of dry clay + 10meq of $\text{MgCl}_2/100\text{g}$ of dry clay, 20meq of $\text{CaCl}_2/100\text{g}$ of dry clay + 20meq of $\text{MgCl}_2/100\text{g}$ of dry clay and 30meq of $\text{CaCl}_2/100\text{g}$ of dry clay + 30meq of $\text{MgCl}_2/100\text{g}$ of dry clay.

3 METHODOLOGY

3.1 Transformation of natural bentonite clay to sodium bentonite

The natural Bofe clay was transformed into sodium bentonite by addition of concentrated Na_2CO_3 solution (0.2g/mL). The adopted ratio of Na_2CO_3 to clay is 150meq of $\text{Na}_2\text{CO}_3/100\text{g}$ of dry clay and leave 5 days in a chamber with 100% of humidity.

3.2 Preparation of bentonite clays dispersions

The dispersions were prepared with 4.86% w/w of clay according to Brazilian norms (Petrobras 1998a).

3.3 Polymeric treatment

The dispersions were treated with different amounts of polymeric additive and stirred for 5min. After 24 hours it was measured the rheological properties presented in the 3.5 item.

3.4 Degrading treatment

After polymeric treatment the dispersion were treated with different amounts of $\text{CaCl}_2+\text{MgCl}_2$ and stirred for 5 min and rest for 24 hours. After it was measured the rheological properties presented in the 3.5 item.

3.5 Rheological properties

It were measured the apparent (AV) and plastic (PV) viscosities by using a Fann 35A viscometer and water loss (WL) by using a press filter Fann, according to Brazilian norms (Petrobras 1998a).

4 RESULTS

The results show that the treatment with polymeric additives improve the rheological properties of the Bofe clay dispersions and the treatment with 0.4 and 0.5g of CMC BV (Tab. 2) and 0.4g of PAC (Tab. 3) present the best results with values of AV, PV and WL suitable according to Brazilian specifications (Petrobras 1998b). When the polymeric compounds are adding to the clay dispersions the functional groups are adsorbed on the surface of the particles and the long flexible chain increase the viscosity of the system. Also the negative charge of the polymer neutralizes the positive charge of the clay particles and repulsion between them occurs and avoids flocculation (Amorim 2003).

Similar behavior is presented to the Bofe clay dispersion after addition of different polymeric additives. According to Amorim (2003), this result is justified by the long chain of the polymer, although the polymer presents different viscosity degrees.

To the Brasgel PA clay dispersion, the polymeric treatment produces a flocculated state, with high value of AV, except the treatment with 0.3g of CMC BV. This behave is different from Bofe clay dispersion and contradict to the explanation give before. However, the polymeric long chain can produce a flocculation due to the encapsulation and bridge formed by the polymers (Somasudaran et al. 1966). Also parts of the same polymeric chain adsorbed to the surface of different clay particles (Luckham & Rossi 1999).

Table 2. Rheological properties of Sodium Bofe clay dispersions treated with CMC BV, and submitted to degrading additives (CaCl₂ + MgCl₂).

CMC BV (g/24.3g of dry clay)	CaCl ₂ + MgCl ₂ (meq/100g of dry clay)	AV (cP)	PV (cP)	WL (mL)
-	-	12.5	4.8	17.7
0.3	-	13.3	7.0	17.3
0.4	-	15.5	8.0	17.2
0.5	-	18.5	7.0	16.3
-	10 + 10	10.8	4.5	17.8
-	20 + 20	8.5	4.0	21.0
-	30 + 30	9.7	3.8	20.5
0.3	10 + 10	15.3	7.0	17.5
	20 + 20	25.3	8.0	18.0
	30 + 30	31.5	4.0	17.4
0.4	10 + 10	17.3	7.0	16.0
	20 + 20	19.0	7.0	17.0
	30 + 30	20.5	7.0	18.0
0.5	10 + 10	20.5	7.0	15.3
	20 + 20	20.8	7.5	17.8
	30 + 30	21.3	7.0	17.5
Specifications (Petrobras 1998b)		≥ 15.0	≥ 4.0	≤ 18.0

Table 3. Rheological properties of Sodium Bofe clay dispersions treated with PAC, and submitted to degrading additives (CaCl₂ + MgCl₂).

PAC (g/24.3g of dry clay)	CaCl ₂ + MgCl ₂ (meq/100g of dry clay)	AV (cP)	PV (cP)	WL (mL)
-	-	12.5	4.8	17.7
0.2	-	12.8	5.0	14.0
0.3	-	14.0	5.5	12.3
0.4	-	15.0	6.5	11.5
-	10 + 10	10.8	4.5	17.8
-	20 + 20	8.5	4.0	21.0
-	30 + 30	9.7	3.8	20.5
0.2	10 + 10	17.0	5.0	15.5
	20 + 20	36.0	4.0	14.0
	30 + 30	36.5	9.0	16.6
0.3	10 + 10	16.3	6.0	13.3
	20 + 20	29.5	10.0	14.4
	30 + 30	50.3	9.5	15.2
0.4	10 + 10	17.5	6.0	12.5
	20 + 20	36.0	5.5	12.0
	30 + 30	40.8	9.0	13.5
Specifications (Petrobras 1998b)		≥ 15.0	≥ 4.0	≤ 18.0

The addition of CaCl₂+MgCl₂ in the clay dispersions decreases the values of AV and PV and increases the value of WL (Tab. 2, 3, 4, 5). According to Luckham & Rossi (1999) and Amorim (2003) the presence of Ca²⁺ and Mg²⁺ reduce the hydration of the clay particles and increase the attractive force between them, causing interaction face-to-face type.

The Bofe clay dispersion when treated first with polymeric additive and after submitted to the degrading agent CaCl₂+MgCl₂ shows that CMC BV

(Tab. 2) protect the rheological properties with values in conformity with the specifications (Petrobras 1998b). The best results were obtained with 0.4g and 0.5g of CMC BV and different proportion of CaCl₂+MgCl₂ (Tab. 2). According to Pereira (2002) the presence of mono and divalent cations such as Na⁺, Ca²⁺ and Mg²⁺ reduce the lengthening of the polymer and form agglomerate like a ball of thread and decrease their solubility. These results show that the CMC BV acts as a protective colloid to the presence of Ca²⁺ and Mg²⁺ in different proportions. The treatment with PAC carry out to a flocculated state which is characterized by high values of AV. In addition when using Bofe clay dispersions against Ca²⁺ and Mg²⁺ is higher than the resistance of the PAC when using Bofe clay dispersion. Note that PAC is recommended to be used with salt water and present high degree of substitution and purity.

To Brasgel PA clay dispersions the treatment with polymer and after with degrading agent CaCl₂+MgCl₂ carry out to a flocculated-gel form with high values of AV and WL (Tabs. 4, 5). In this case the polymer additives do not act as a protective colloid.

Comparing the results obtained by using the Bofe clay dispersions with the results obtained by using the Brasgel PA clay dispersions, it can be observed that the polymer type and the length of the polymeric chain are important factors in the rheological study of the water and clay dispersions. Besides, the type of clay has a strong influence in the results.

Table 4: Rheological properties of Brasgel PA clay dispersions treated with CMC BV, and submitted to degrading additives (CaCl₂ + MgCl₂).

CMC BV (g/24.3g of dry clay)	CaCl ₂ + MgCl ₂ (meq/100g of dry clay)	AV (cP)	PV (cP)	WL (mL)
-	-	16.1	4.0	16.3
0.3	-	20.8	7.0	14.8
0.4	-	25.5	6.5	15.0
0.5	-	27.8	6.5	13.5
-	10 + 10	16.8	3.5	19.8
-	20 + 20	11.8	3.0	27.5
-	30 + 30	5.0	2.5	39.0
0.3	10 + 10	36.3	3.5	17.5
	20 + 20	38.8	2.5	19.7
	30 + 30	31.5	5.0	23.3
0.4	10 + 10	43.5	4.5	17.0
	20 + 20	46.8	4.0	20.0
	30 + 30	34.3	6.0	22.7
0.5	10 + 10	46.8	3.0	15.5
	20 + 20	50.5	5.5	18.5
	30 + 30	32.8	5.0	21.5
Specifications (Petrobras 1998b)		≥ 15.0	≥ 4.0	≤ 18.0

Table 5: Rheological properties of Brasgel PA clay dispersions treated with PAC, and submitted to degrading additives (CaCl₂ + MgCl₂).

PAC (g/24.3g of dry clay)	CaCl ₂ + MgCl ₂ (meq/100g of dry clay)	AV (cP)	PV (cP)	WL (mL)
-	-	16.1	4.0	16.3
0.2	-	24.8	3.5	13.2
0.3	-	24.0	5.0	11.5
0.4	-	24.8	5.5	10.8
-	10 + 10	16.8	3.5	19.8
-	20 + 20	11.8	3.0	27.5
-	30 + 30	5.0	2.5	39.0
0.2	10 + 10	85.5	11.5	14.0
	20 + 20	60.8	15.5	17.0
	30 + 30	30.8	10.0	22.3
0.3	10 + 10	104.5	15.0	11.5
	20 + 20	75.5	19.5	14.5
	30 + 30	38.5	12.5	17.0
0.4	10 + 10	95.5	7.5	10.2
	20 + 20	104.8	39.5	12.0
	30 + 30	54.5	14.5	12.5
Specifications (Petrobras 1998b)		≥ 15.0	≥ 4.0	≤ 18.0

5 CONCLUSIONS

Through the obtained results it can be concluded that: i) the treatment with polymeric additive improve the rheological properties of the Bofe clay dispersions and make suitable to be used as drilling oil well fluid based on water; ii) the Brasgel PA clay dispersion after treatment with polymeric additive presented a flocculated state; iii) the rheological properties of the clay dispersions are negatively influenced by the addition of CaCl₂+MgCl₂; iv) the CMC BV act as a protective colloid in the Bofe clay dispersions; v) the CMC BV and PAC do not act as a protective colloid in the Brasgel PA clay dispersions and vi) the rheological properties of the clays dispersions are dependent on the interactions between bentonite particles/polymer and the length of the polymer chain.

6 ACKNOWLEDGEMENTS

This work is supported by Agência Nacional do Petróleo - ANP, FINEP, MCT and CNPq/CTPETRO.

7 REFERENCES

- Amorim, L. V. 2003. Melhoria, Proteção e Recuperação da Reologia de Fluidos Hidroargilosos para Uso na Perfuração de Poços de Petróleo. Ph.D. Thesis, Federal University of Campina Grande.
- Luckham, P. F. & Rossi, S. 1999. The Colloidal and Rheological Properties of Bentonite Suspension, *Advances in Colloid and Interface Science* 82: 43-92.

- Pereira, E. Química dos Polímeros e Aplicações – Parte III. www.systemmud.com.br.
- Petrobras 1998a. Ensaio de Viscosificante para Fluido de Perfuração Base de Água na Exploração e Produção de Petróleo, Método, N – 2605.
- Petrobras 1998b. Ensaio de Viscosificante para Fluido de Perfuração Base de Água na Exploração e Produção de Petróleo, Especificação, N – 2604.
- Somasundaran, P., Healy, T. W. & Fuerstenau, D. W. 1996. The Aggregation of Colloidal Alumina Dispersion by Adsorbed Surfactant Ions, *Journal of Colloid and Interface Science* 22: 599-605.
- Souza Santos, P. 1968. Estudo Tecnológico de Argilas Montmoriloníticas do Distrito de Boa Vista, Município de Campina Grande, Paraíba, Tese para Concurso à Cátedra de Química Industrial, DEQ, EPUSP, São Paulo.
- Souza Santos, P. (2 ed.) 1989. *Ciência e Tecnologia de Argilas*, vol. 1, São Paulo.
- Trindade, M. H. A. 2001. Bentonita. www.dnpm.org.br.

Qualities of Quartz and the Alkali-Silica Reaction in Concrete

M.A.T.M.Broekmans

Department of Mineral Characterization, Geological Survey of Norway, N-7491 TRONDHEIM

ABSTRACT: The deleterious alkali-silica reaction in concrete is globally wide-spread, and occurs in virtually all rock types (including sedimentary, metamorphic and igneous) containing substantial free quartz. Locally, a given rock type may behave alkali-reactive, whereas the same rock type behaves innocuous elsewhere. The potentially alkali-reactive quartz is very likely to differ in its mineralogical and geochemical properties, provided the wide range of rock types in which it occurs. A widely accepted method to test the potential alkali-reactivity of quartz is by determining its crystallinity index by means of XRD, conform the method first described by Murata & Norman (1976). However, it is unclear which issues known to affect quartz dissolution are reflected in the crystallinity index. Moreover, when the quartz's CI is determined by alternative methods (DTA cf. Deutsch et al. (1989), or FT-IR cf. Shoval et al. (1991)), the results typically differ greatly from the results by XRD. To rescale XRD crystallinity indices on a scale of <1-10, a rock crystal described 'clear euhedral quartz' is used as an internal standard. A current research project investigates 18 of such crystals with all three above methods, and uses optical cathodoluminescence to reveal their internal structure. All crystals show twinning, lamellar growth, zoning, intergrowth structures, and some also repaired cracks containing secondary quartz, demonstrating their inhomogeneity. Which if these features do affect alkali-silica reactivity, and which if these is reflected in the CI is yet unknown.

1 INTRODUCTION

1.1 Deleterious alkali-silica reaction (ASR) in concrete

Some 12% of the earth's continental crust is made of α -quartz [SiO₂]. Thus, most aggregate materials used in concrete do contain substantial quartz. In concrete of 'favorable composition' and under 'favourable conditions', some quartz may react with available alkalis forming a hygroscopic silica gel that expands when the gel reacts hydraulically with water (Figure 1). Eventually, this cracks up the surrounding concrete, reducing its strength. This is the essence of a deleterious process called alkali-silica reaction, abbreviated as ASR. In fact, deleterious ASR is caused by the undesired dissolution of quartz in the alkaline, high-pH environment of concrete.

To prevent deleterious ASR, global and local legislation puts strict limits to the maximum allowable alkali content of cement, aggregate material, and the concrete as a whole. In addition, the aggregate material has to fulfil certain requirements traditionally reflecting local lithological variation of the aggregate composition (eg. Wigum 2000). On a global scale, virtually any rock type containing substantial quartz including

igneous (volcanic and magmatic), sedimentary and metamorphic has been described to be potentially alkali-silica reactive, posing a potential risk for long-term concrete damage.

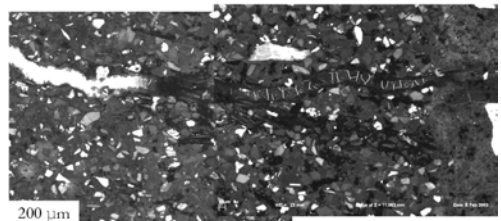


Figure 1: SEM-cathodoluminescence map of alkali-reactive Dutch sandstone (the striped snake is a gel-filled ASR-induced crack). Note the bright angular detrital grains, cemented by dull non-luminescent quartz of diagenetic origin.

However, an aggregate constituent that is considered to be alkali-silica reactive in one region may be considered innocuous in another. In Norway for instance, all sandstone is classified as potentially alkali-reactive (see rock list in Wigum 2000), whereas it is classified as being innocuous in the Netherlands. But, some Norwegian sandstones have

been documented to behave inert in practice, and some Dutch sandstones have been documented to produce gel and expansion cracking (Heijnen et al. 1996, Broekmans 2002), complicating this picture.

1.2 Geological variability of quartz

Determining the content of undesired potentially alkali-reactive constituents in a given aggregate material currently occurs by optical thin section petrography and subsequent classification according to the locally accepted list of acceptance/rejection criteria. In Norway, these criteria include both rock type and quartz grain size, among others. In the Netherlands, aggregate material is classified after its content of porous chert. Ambiguous and/or suspect materials can be assessed additionally by a series of RILEM TC 106 (2000) testing methods.

Given the wide range in geological origin and provenance of alkali-reactive rocks, the quartz in it must have formed in an equally wide range of combinations of P, T, pH and Eh, with a variety of fluids present. Hence, quartz formed under such variable conditions is likely to have different micro-structural and compositional features (as eg. in Figure 1). In what way these and other traits affect the ASR potential of quartz of a certain origin is unknown. However, fundamental mineralogical and geochemical criteria to distinguish between alkali-reactive and inert quartz (in ASR-terms) are lacking.

1.3 Real quartz structure and dissolution

Several issues are known to increase the solubility of quartz under geological conditions, some of which may also apply to the ASR-practice (Dove & Rimstidt 1994, Broekmans 2002). Some of these issues are directly or indirectly related to particular features of the quartz lattice like eg. twinning, domain and/or lamellar structure (Bambauer et al. 1961, Friedlaender 1951), dislocations and foreign species incorporated in the lattice including water, lattice deformation and subgraining, et cetera. Additionally, the presence of moganite with a considerably higher solubility than quartz (Gislason et al. 1997) may also contribute to unwanted quartz dissolution with ASR in certain rock types.

The moganite structure can be modelled as lamellar Brazil twinning of quartz at unit cell scale, reducing its symmetry. Brazil-type twinning can also be synthetically induced by directed stress (Heaney 1994). Moganite is known to be quite common in fine-grained and micro-crystalline varieties, notably chert (Heaney & Post 1992).

2 CURRENT TESTING METHODS

2.1 Determining expansion potential

In cases where thin section petrography remains inconclusive to determine the ASR-potential of a given aggregate (constituent), the expansion of the material is measured in a procedure designed to mimic ASR conditions, to provoke ultra-accelerated expansion (RILEM 2002a, b). Subsequently, the sample needs to be verified by another round of petrography, increasing expenses and duration.

Due to local variability, acceptance criteria need to suit existing local experience with ASR-susceptibility of aggregate materials. However, it would be preferred to have a test method that addresses more fundamental properties that affect quartz solubility directly.

2.2 Assessing quartz

Characterizing quartz can be done in several ways, including crystal-structural and geochemical. With application to ASR and (unwanted) dissolution in concrete, determination of the crystallinity index (CI) by XRD appears to be widely accepted, following the method described by Murata & Norman (1976). To determine the CI, the ratio of the heights over background of the first two peaks in the quintuplet at $67.74^\circ 2\theta$. The ratio is multiplied with instrumental correction factor F, calculated from the CI of a crystal of (supposedly ideal) 'clear euhedral quartz' that is then rescaled to maximum value 10.

The original paper by Murata & Norman (1976) does not provide arguments for the selection of that particular quintuplet, neither from a quartz crystal-structural, nor from an XRD-related point of view. It is currently unknown which features/flaws in the quartz lattice that do affect solubility also do affect this CI, and to what extent. The paper by Kühnel et al. (1975) on goethite in pedogenetic processes discusses factors affecting crystallinity like crystallite size and structural perfection, adding crystallite shape as a third factor.

Alternative methods to determine a CI for quartz include DTA assessing the reversible α - β phase transition at 573°C (Deutsch et al. 1989), and FT-IR to determine absorption at 1145 cm^{-1} (Shoval et al. 1991), who also noted that some samples with a high CI according to FT-IR may have a very low CI when assessed by DTA, or vice versa in a non-systematic way. Crystallinity indices by XRD of Dutch non-metamorphic chert, low-grade American chert, and (relatively) high-grade Norwegian mylonites (ie., silica formed under very different conditions) cover the whole range from <1-10, without any correlation to their ASR-expansion potential as determined by laboratory experiments (Broekmans 2002).

3 CURRENT RESEARCH

3.1 Quartz (in-) homogeneity

The quartz used as an internal standard by Murata & Norman (1976) to calculate instrumental correction factor F is a so-called 'Herkimer diamond' from Herkimer/NY, characterized further only as 'clear euhedral quartz'. The lustrous and close to perfect appearance of a typical Herkimer diamond strongly suggests a near-ideal quartz crystal. However, earlier work by Friedlaender (1951) and Bambauer et al. (1961) on rock crystal quartz from the Alps already showed that inhomogeneity of the interior is the rule rather than the exception, as visualized by eg. optical cathodoluminescence of diverse types of quartz formed under different geological conditions as in Götze et al. (2001). Similarly, recent SEM cathodoluminescence on high-grade rocks from the Bamble Sector, SE Norway, revealed that individual quartz grains may exhibit grain boundary alteration, healed microfractures and/or patches of secondary quartz, as well as euhedral quartz nuclei (Van den Kerkhof et al. 2004).

Technically, crystal structural features including inhomogeneous distribution of luminescent species as well as other properties (Van den Kerkhof et al. 2004) must in principle have an effect on local structural perfection, however, to which extent these are in fact reflected in a CI value is unknown.

3.2 Towards a uniform crystallinity index for quartz

A standard must be well-defined and homogenous, among other crucial properties. Inhomogeneities will for instance lead to peak broadening and increased background noise in XRD analysis, affecting the CI as that is a peak ratio over background.

In all 18 rock crystals of 'clear euhedral quartz' from have been collected from all over the world. Double polished 2mm thick sections have been produced from one half of the crystal, the other half has been cast in epoxy to allow microsampling. All polished samples have been characterized by optical cathodoluminescence at the Bergakademie Freiberg, Germany and by EBSD-mapping to reveal the internal structure with respect to twinning, growth zoning, domain building, and occurrence of secondary quartz in healed cracks. Figure 2 shows complex growth zoning, in the NE direction very finely intergrown, and its oriented termination against a zone of different luminescence along the left edge. Though the surface appears well polished in ordinary light, some 'roughness' is observed along the left edge of the image, probably due to luminescence effects. Decay over time of initially blue luminescence is characteristic of Na+Al replacing Si; the simultaneous activation of a brownish-reddish luminescence can be attributed to

hydroxyl water in the quartz structure (Götze et al. 2001, Götze 2003, pers.comm.).

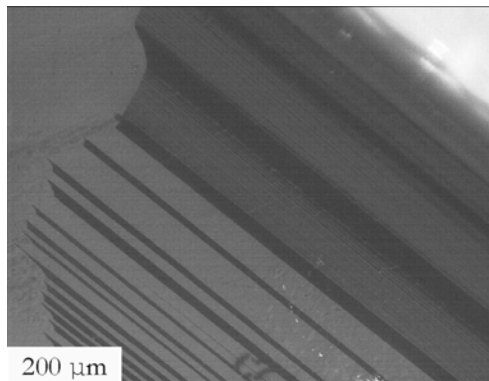


Figure 2: Optical cathodoluminescence of the interior of a single rock crystal of 'clear euhedral quartz' from Norway. Original color image different shades of navy to cobalt blue.

Three to five different locations within one single crystal in the epoxy-cast halves have been sampled by microdrilling to determine crystallinity indices by XRD, DTA, and FT-IR conform the methods mentioned above (Murata & Norman 1976, Deutsch et al. 1989, Shoval et al. 1991), and to determine the variability among crystals of 'clear euhedral quartz' from different localities, the variability within one single rock crystal, as well as the variation between the different methods. Preliminary data by the above methods seem to confirm the inferred variability; full results will be available at the 8th ICAM.

Future research will zoom in on the structural details of the samples with (HR) TEM, Raman and LA-ICP-MS to assess elemental compositions.

4 CONCLUSIONS

Until today, alkali-silica reactive quartz has not been characterized in terms of its mineralogical and geochemical properties. The fact that alkali-reactive quartz seems to originate from diverse geological environments suggests that the dissolution of quartz under ASR-conditions in concrete may be affected by different mineralogical-geochemical features, which future testing methods to determine the alkali-reactivity potential will have to focus on.

Which of the features affecting quartz dissolution are picked up by the crystallinity index of quartz as determined by XRD, DTA or FT-IR is unknown. The standard material used in CI-determinations by XRD of Murata & Norman (1976) described as 'clear euhedral quartz' appears to be quite variable. Optical cathodoluminescence imaging on 18 rock

crystals all show inhomogeneous luminescence due to internal zoning, twinning, intergrowths, etc.

Preliminary determination of crystallinity indices by XRD, DTA, and FT-IR from several world locations demonstrates that the results do vary even within one and the same single rock crystal. Thus, 'clear euhedral quartz' used as such for an internal standard is inappropriate. Therefore, scepticism is justified towards the widely accepted XRD method by Murata & Norman (1976) to determine the CI and interpret the results straight-forwardly as alkali-silica reactivity potential.

5 REFERENCES

- Bambauer, HU, Brunner, GO, Laves, F 1961. Beobachtungen über Lamellenbau an Bergkristallen. *Zeitschrift für Kristallografie* (116): 173-181.
- Broekmans, MATM 2002. The alkali-silica reaction: mineralogical and geochemical aspects of some Dutch concretes and Norwegian mylonites. *PhD-thesis University of Utrecht, Geologica Ultraiectina* (217): pp 144.
- Deutsch, Y, Sandler, A, Nathan, Y 1989. The high-low inversion of quartz. *Thermochimica Acta* (148): 467-472.
- Dove, PM, Rimstidt, JD 1994. Silica-water interactions. *Reviews in Mineralogy* (29): 259-308.
- Friedlaender, C 1951. Untersuchung über die Eignung alpiner Quarze für piezoelektrische Zwecke. *Beiträge zur Geologie der Schweiz, Geotechnische Serie, Lieferung* (29): pp 98.
- Göslason, SR, Heaney, PJ, Oelkers, EH, Schott, J 1997. Kinetic and thermodynamic properties of moganite, a novel silica polymorph. *Geochimica et Cosmochimica Acta* (61): 1193-1204.
- Götze, J, Plötze, M, Habermann, D 2001. Origin, spectral characteristics and practical applications of the cathodoluminescence of quartz - a review. *Mineralogy & Petrology* (71): 225-250.
- Heaney, PJ 1994. Structure and chemistry of the low-pressure silica polymorphs. *Reviews in Mineralogy* (29): 1-40.
- Heaney, PJ, Post, JE 1992. The widespread distribution of a novel silica polymorph in microcrystalline quartz varieties. *Science* (255): 441-443.
- Heijnen, WMM, Larbi, JA, Siemes, AJH 1996. Alkali-silica reaction in the Netherlands. *Proceedings of the 10th International Conference on Alkali-aggregate Reaction in Concrete*: 109-116.
- Kühnel, RA, Roorda, HJ, Steensma, JJ 1975. The crystallinity of minerals - a new variable in pedogenetic processes: a study of goethite and associated silicates in laterites. *Clays & Clay Minerals* (23): 349-354.
- Murata, KJ, Norman II, MB 1976. An index of crystallinity for quartz. *American Journal of Science* (276): 1120-1130.
- RILEM TC 106-AAR 2000a. A-TC 106-2 Detection of potential alkali-reactivity of aggregates - the ultra-accelerated mortar bar test. *Materials and Structures* (33): 283-289.
- RILEM TC 106-AAR 2000b. B-TC 106-3 Detection of potential alkali-reactivity of aggregates - method for aggregate combinations using concrete prisms. *Materials and Structures* (33): 290-293.
- Rykart, R 1995. *Quarz-Monographie. 2nd edition*. Ott Verlag, Thun, Switzerland.
- Shoval, S, Ginott, Y, and Nathan, Y (1991): A new method for measuring the crystallinity index of quartz by infrared spectroscopy. *Mineralogical Magazine* (55): 579-582.
- Van den Kerkhof, AM, Kronz, A, Simon, K, Scherer, T 2004. Fluid-controlled quartz recovery in granulite as revealed by cathodoluminescence and trace element analysis (Bamble sector, Norway). *Contributions to Mineralogy & Petrology* (146): 637-652.
- Wigum, BJ 2000. "Normin2000" - A Norwegian AAR research program. Proceedings of the 11th International Conference on Alkali-Aggregate Reaction in Concrete: 523-531.

Mineralogical and Geochemical Characterization and Ceramic Properties Evaluation of the Hard Kaolin from the Capim Region, Northern Brazil

B.S.Carneiro & R.S.Angélica

Departamento de Geoquímica e Petrologia, Centro Geociências, Universidade Federal do Pará, Brazil

R.F.Neves

Departamento de Engenharia Química, Centro Tecnológico, Universidade Federal do Pará, Brazil

ABSTRACT: The main objective of this work is to carry out mineralogical and geochemical studies of the hard kaolin, a non-processes waste overlaying kaolin ores from the Rio Capim district (Pará state, northern Brazil), and evaluate its possible use as raw material for the ceramic/refractory industry. Different chemical and mineralogical analysis were carried out, including XRD, DTA-DTG, FTIR, and SEM. For the technological assays, prismatic ceramic bodies were made and calcined at the following temperatures: 1200°C, 1300°C, 1400°C and 1500°C. Ceramic properties were measured latter. Results show a mineralogical composition dominated by kaolinite and trace amounts of anatase, besides increasing contents of iron related to hematite and goethite in the upper parts of the hard kaolin horizon. The results of the ceramic properties evaluation show that hard kaolin can be used either for white ceramics purposes (ware, porcelain, etc.) or as refractories.

1 INTRODUCTION

The Capim region (Pará state, northern Brazil) is the most important kaolin district in the Amazon region, with the largest Brazilian reserves of high whiteness kaolin for the paper coating industry (Fig. 1). The main ore (soft kaolin horizon) is located about 20 m depth, being covered by a hard, iron-rich kaolin level, besides a sandy-clay overburden (Tertiary Barreiras Formation). The hard kaolin is also named as Flint or semi-flint kaolin (Kotschoubey et al. 1996) and is a typical example of a non-processed waste. Other kaolin profiles in tropical regions also exhibit the same horizon succession (e.g., Makoro Deposit, Botswana, Africa; Ekosse, 2000).

Although it exhibits very low granulometry and small quartz contents, in comparison with the soft kaolin, iron levels are too high and increase the costs of beneficiation. Two main companies exploit the kaolin of the Capim River: *Pará Pigmentos S/A (PPSA)* and *Imerys - Rio Capim Caulim S.A (IRCC)*. Samples of the hard kaolin collected for this work came from the PPSA's mine.

The main purpose of this paper is to present the results of mineralogical and chemical characterization of the hard kaolin and evaluate the possibility of its use for structural ceramic purposes.

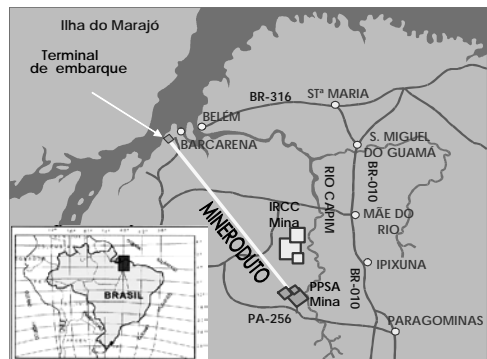


Figure 1: Location Map with the main Kaolin operations at the Capim Region, northeastern part of Pará state (Modified after Bastos & Angélica, 2001).

More details about the geology of the Capim area and the kaolin profiles structuration can be found in Goetze et al. (2004, in this congress), besides additional mineralogical and geochemical data.

2 MATERIALS AND METHODS

About 30 kg of samples of two main types of hard kaolin were collected from the main open pit of the

PPSA mine, and named as follow:

- CDF (Caulim Duro Ferruginoso), for the iron-rich Hard Kaolin; and
- CDB (Caulim Duro Branco), White Hard Kaolin.

Figure 1 shows an interesting outcrop of both facies of the hard kaolin. The lower-ferruginous part exhibits a typical mottled texture.



Figure 1: Geological outcrop of the CDB and CDF hard kaolin samples

All the samples were air-dried during 24 h.

X-ray diffraction analyses were carried out on non-oriented clay specimens using a Philips PW 3020 goniometer, using the following conditions: CuK α -radiation, operating at 45kv and 40 mA; continuous scan from 5° to 65° 2 θ , step- size 0.02 and time per step of 0.5s. Differential thermal analysis (DTA), thermo gravimetric analysis (TGA) and Infrared Spectroscopy (FT-IR) were also carried out.

Chemical analysis of the clayey powders was obtained using different techniques depending on the type of element analyzed. SiO₂ and Loss on Ignition (LOI) - gravimetry, Al₂O₃ - Complexiometry, Fe_{total} and TiO₂ - UV-colorimetry and Ca, Mg, Na and K - Atomic Absorption Spectrometry.

The ceramic properties were studied on a laboratory scale using the same procedures used by the red-ceramic industry. For this purpose, the samples were dried and grinded (hammer mill).

Rectangular ceramic bodies (100x50x13 mm) were obtained by uniaxial pressing at 30 MPa. The bodies were then dried in an oven (105 \pm 5°C) and fired using an electric roller kiln (maximum temperature of 1500°C; 60 min cold to cold). Final products were characterized by measuring the size variations and the bending strength after pressing and after firing. The following properties as-fired have been determined: linear shrinkage, porosity, water absorption and bend strength pressing.

3 RESULTS AND DISCUSSION

3.1 Characterization

The chemical analysis, expressed as oxides are presented in Table 1. The results are compared with a theoretical kaolinite. Concerning SiO₂, Al₂O₃ and loss on ignition (LOI) contents, the CDB sample is very close to the theoretical kaolinite. The main difference can be observed in the iron contents, that reach 10.37% in the ferruginous hard kaolin (CDF).

TiO₂ is also considered a contaminant for the industry and its contents in both samples are very similar and close to 1%.

Table 1: Total Chemical composition of the hard kaolin samples from the Capim region.

Oxides (Wt.%)	CDB	CDF	Theoretical kaolinite
SiO ₂	43.16	38.54	46.54
Al ₂ O ₃	39.03	36.81	39.50
Fe ₂ O ₃	1.29	10.37	-
TiO ₂	1.26	1.12	-
LOI	14.41	13.01	13.96
CaO	<0.01	<0.01	-
MgO	0.01	0.03	-
Na ₂ O	0.013	0.15	-
K ₂ O	0.01	0.07	-
Σ	99.34	100.11	100.00

Figure 2 shows x-ray diffractograms of both hard kaolins.

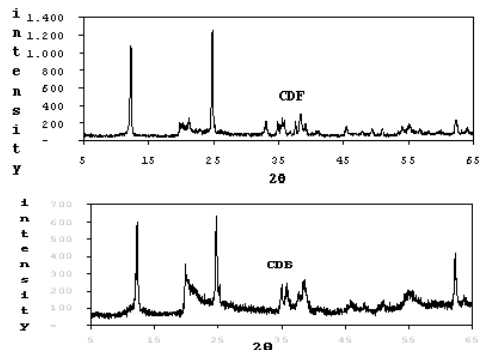


Figure 2: XRD patterns of the CDF and CDB samples

Kaolinite is the dominant phase in all samples and the main difference in the mineralogical composition is related to the presence of hematite in the CDF sample, besides the better crystallinity of the kaolinite, in comparison with the CDB sample. The high values of Fe₂O₃ and TiO₂ are related to the

following accessory minerals, identified by XRD: hematite, goethite, anatase, rutile and ilmenite.

Infrared spectra of the hard kaolin are exhibited in Figure 3. Most bands are characteristic of kaolinite. The bands observed on 3706, 3653 and 3621 cm^{-1} correspond to the OH-stretching, and the band in 916 cm^{-1} refers the OH-deformation. At 695, 754 and 800 cm^{-1} , the bands are associated with the SiO-deformations, while the bands in 1001, 1034 and 1100 cm^{-1} are SiO-stretching.

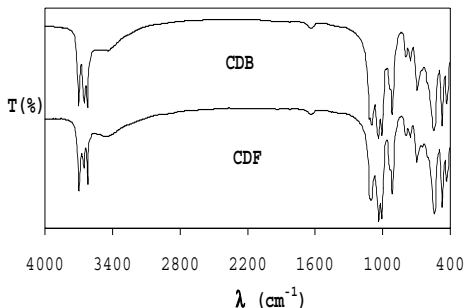


Figure 3: Infrared spectra of the hard kaolin.

DTA and DTG curves exhibited in Figure 4 are also very characteristic of a typical kaolinite spectra.

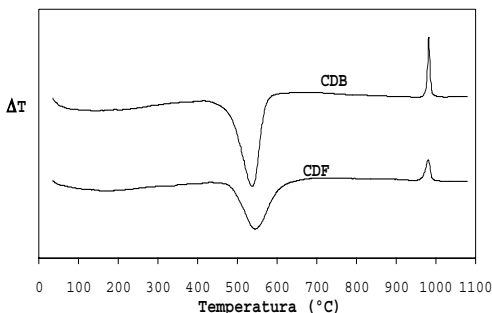


Figure 4: DTA and DTG curves of the CDF and CDB samples

The endothermic peaks at 537°C and 545°C, samples CDB and CDF respectively, correspond to the OH-loss leading to the formation of metakaolinite. The exothermic peaks at 983°C and 979°C (CDB and CDF, respectively) correspond to the decomposition of metakaolinite in amorphous silica and the formation of new crystalline phases, such as Si-containing γ -Al₂O₃ spinel structure (Brindley & Nakahira, 1959) or mullite (Chen et al, 2000). It is still noticed in the sample CDF a small endothermic peak at 350°C related to goethite

decomposition. For the TGA analysis, a mass loss is observed around 13,80% and 12,15% for the samples CDB and CDF, respectively, approaching to the theoretical value of the kaolinite (13,96%).

3.2 Ceramic properties

Table 2 shows the results obtained for the ceramic properties. The results for linear shrinkage (LS) are high in comparison with those found on the literature. This is due to the very low granulometry of the starting materials, giving rise to defects formation, which were observed experimentally.

Results for bending strength (BS) are quite low in comparison with the literature, which are also justified due to the presence of deformations in the ceramic bodies after firing. The results for water absorption (WA) are negatively correlated to the sintering of the material, it means, small WA and apparent porosity imply in higher densities and sintering temperatures. It was easily observed in all the studied samples. The obtained results show that the properties are altered for higher firing temperatures.

Table 2: Ceramic properties of ceramic bodies after firing

Sample	CAF	LS (%)	BS (MPa)	WA (%)
CDF1200°C	red/brown	6,18	2,13	20,30
CDF1300°C	red/brown	11,18	3,98	9,01
CDB1200°C	white	7,51	1,17	23,22
CDB1300°C	white	14,07	2,02	6,80
CDB1400°C	white	15,65	1,49	8,40
CDB1500°C	white	17,79	0,50	8,20

CAF – Color after firing

LS – Linear Shrinkage

BSP – Bending Strength

WA – Water Absorption

4 CONCLUSIONS

The samples studied are basically consisted of a finely grained material, mainly composed by kaolinite. The main difference is related to Fe₂O₃ contents that can reach more than 10% in the hard ferruginous kaolin (CDF) and is mainly related to hematite.

Concerning applications, as a general rule, all studied materials are suitable for structural ceramic products. The White Hard Kaolin exhibited white color after burning at 1200°C, 1300°C, 1400°C and 1500°C, making possible its application for white ceramic (dishes, floors, porcelain, etc.). It has also presented a low sintering level, turning possible its use as refractory.

The iron-rich Hard Kaolin exhibited red/brown color after burning at 1200 °C and 1300°C, suitable for structural ceramic and not proper for refractories due to its high iron contents.

5 ACKNOWLEDGEMENTS

The authors gratefully acknowledge support from the CPGG – Curso de Pós-Graduação em Geologia e Geoquímica from UFPA.

6 REFERENCES

- Bastos, C.H.L. & Angélica, R.S. 2001. Variação Lateral de Alvura no Depósito de Caulim da Pará Pigmentos, Rio Capim, Estado do Pará. In: VII Simpósio de Geologia da Amazônia, Belém. (CD-ROM)
- Brindley, G.W. & Nakahira, M. 1959. The kaolinite-mullite reaction series: I, a survey of outstanding problems. *J. Am. Ceram. Soc.*, 42(7): 311-314.
- Chen, C.Y., Lan, G.S., Tuan, W.H. 2000. Microstructural evolution of mullite during the sintering of kaolin powder compacts. *Ceramics International*, 26: 715-720
- Ekosse, G. 2000. The Makoro kaolin deposit, southeastern Botswana: its genesis and possible industrial applications. *Applied Clay Science*, 16: 301-320.
- Goetze, J., Kleeberg, R., Wiedemann, P., Plötze, M., Angélica, R.S. 2004. Mineralogical characterization of kaolin from the Capim region, Pará State (Brazil). (This Congress)
- Kotschoubey, B., Truckenbrodt, W., Hieronymus, B. 1996. Depósitos de caulim e argila "semi-flint" no nordeste do Estado do Pará. *Revista Brasileira de Geociências*, 26(2): 71-80.

Rheology of Precipitated Calcium Carbonate Slurries: a Comparative Analysis with CMC, HEC and MHPC

S.I.Conceição & J.M.F.Ferreira

Department of Ceramics and Glass Engineering, CICECO, University of Aveiro, 3810-193 Aveiro, Portugal

J.Velho

Department of Geosciences, University of Aveiro, 3810-193 Aveiro, Portugal

ABSTRACT: Precipitated calcium carbonate (PCC) is a very important pigment especially for paper coating applications. PCC is produced in satellite units in different particle size distributions and with different particle shapes. Regarding particle morphology, scalenohedral, rhombohedral and acicular shapes are the most important. PCC can be produced in two crystallized structures, calcite and aragonite. One of the most exigent applications of PCC is in paper coating where rheology is a critical property. Carboxymethyl cellulose (CMC) is a very common co-binder applied in coating colour formulations. New co-binders are positioning as an alternative to CMC. Two of them are hydroxyethyl cellulose (HEC) and methylhydroxypropyl cellulose (MHPC). The main goal of this research is to analyse the potentialities of these two co-binders as possible alternatives to CMC in order to improve rheology of PCC suspensions. Two PCC pigments were selected: one, with scalenohedral habit, calcitic (PCC-C); the other, with acicular particles, aragonitic (PCC-A). The results show a clear difference between rheological characteristics of PCC-C and PCC-A slurries due, essentially, to particle shape effects. Rheological properties of coating colours with added HEC and MHPC co-binders show interesting results which confer these additives a high potential for paper coating applications.

1 INTRODUCTION

The demand for synthetic calcium carbonate powders has been rapidly growing in recent years in various fields of industry including pharmaceuticals, elastomers, foodstuffs, food colorants, toiletries, processing of rubbers and plastics, preparation of inks, paints, sealants and other useful products. Precipitated calcium carbonate is also a widely used mineral pigment for worldwide paper production (You 1998, Virtanen 1999). The principal advantages of using PCC powders are related with their elevated purity, high brightness, gloss, opacity, and smoothness, the uniform dimensional distribution of the particles and the imparted mechanical strengths and abrasion resistance to the above end products when compared to traditional mineral pigments. Furthermore, PCC can be produced with several crystalline habits (acicular, rhombohedral, and scalenohedral) and with different size of particles, depending on the specific reaction process that is used (Virtanen 1999, Conceição et al. 2003). These characteristics influence the rheological properties of the slurries.

Particle size and shape are important for several reasons. A large particle size combined with a wide particle size distribution and a roundish particle

shape will enable to maintain a low viscosity at relatively high solid contents. In the opposite situation, i. e., for small particle sizes, narrow particle size distributions, and when the particles differ significantly from round shape (e. g., needle-like, plate-like), the slurries tend to exhibit high viscosities even at relatively low solid contents.

Cellulosic polymers, CMC (in particular), HEC and MHPC, have been used in paper coating processes to provide rheology control and water retention. These polymers, although generally referred to as “thickeners”, often play a much bigger role than merely thickening coating colours. A cellulosic thickener can affect the state of particles dispersion and hence the structure and rheological behaviour of the coating (Lehtinen 2000, Young & Fu 1991). The present work aims at a better understanding of the influence of the particle shape of pigments and of the type and molecular weight of co-binders on the rheological behaviour of PCC suspensions.

2 EXPERIMENTAL PROCEDURE

2.1 Material and slip preparation

For this research two precipitated calcium carbonate

(PCC) pigments were used: one of calcitic nature, with scalenohedral habit (PCC-C); the other of aragonitic nature, with acicular particles (PCC-A), having average particle sizes of 0.637 μm and 0.643 μm , respectively, measured by using a laser diffraction instrument (Coulter LS230).

The suspensions containing PCC-C were prepared with 50-vol% of solids, while suspensions containing PCC-A were prepared at 48-vol% of solids loading. Two CMC grades with different molecular weights (M_w) were used: CMC35 with a $M_w=35,000$ g/mol and CMC250 with $M_w=250,000$ g/mol. As alternatives to CMCs, two new co-binders were also used, HEC with $M_w=115,000$ g/mol and MHPC with $M_w=200,000$ g/mol. All these co-binders have been added separately in a fixed amount of 0.2-wt.% relative to dry mass of PCC. In the case of CMCs, a 1:1 ratio was also used while keeping the total added amount at 0.2-wt.%. After adding the co-binders, each suspension was transferred to a cylindrical polyethylene container and left rolling in a rotating system for 24 hours for homogenising and deairing.

The coating colours formulations were all based on PCC to which 10 parts (on a weight basis) of carboxylated styrene-butadiene latex and 1 part of acrosol were added.

2.2 Slip characterisation

Rheological measurements were performed in a rotational controlled stress rheometer (Bohlin C-VOR, USA) after the 24 h slip-deairing step at a strictly controlled temperature of 20°C. The measuring configuration adopted was a cone and plate ($\varnothing=40$ cm, 4°, gap=150 μm). For flow behaviour and viscosity tests, stress sweep and multi-step shear measurements (20 points, max. equilibrium time of 1 min) were performed in the shear rates range from 0.1 s^{-1} up to about 1100 s^{-1} , while oscillatory tests were carried out with a constant frequency of 1 Hz and variable shear stress (from 0.01 to 100 Pa).

3 RESULTS AND DISCUSSION

3.1 Influence of particle shape and adding latex/binders on Rheology

3.1.1 Flow and Viscosity behaviour

The flow curves of the coating colours for the two pigments, PCC-C and PCC-A, are shown in Figures 1 and 2, respectively. It can be seen that all the curves exhibit shear thinning behaviours. The flow curves are affected by type and the M_w of the co-binders. These additives seem to play two different roles, namely, as thickeners of the dispersing liquid media, increasing its viscosity; and as surface active

agents. The predominance of one or the other role seems to depend on the interplay among the type and M_w of co-binders, and the particle shape of pigments. In all cases, the shear stress values required for the systems to flow at a given shear rate increase, relatively to the situations in absence of co-binders, which exhibit the more fluid-like behaviour. Furthermore, the hysteresis loop of the flow curves is also sensitive to the type and M_w of the added co-binders.

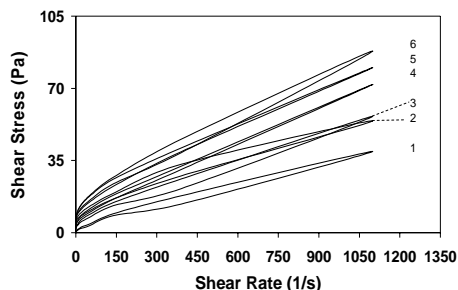


Figure 1: Effects of molecular weight of cellulose binders (for a total added amount of 0.2-wt%) on the flow curves of PCC-C suspensions in the presence of 10-wt% Latex + 1-wt% Acrosol.

- Legend: 1. 50-vol% without binders;
2. 50-vol%, HEC;
3. 50-vol%, CMC35;
4. 50-vol%, MHPC;
5. 50-vol%, CMC250;
6. 50-vol%, Mixture;

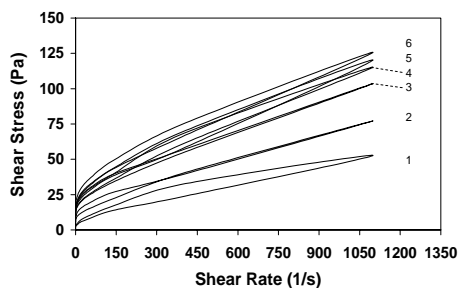


Figure 2: Effects of molecular weight of cellulose binders (for a total added amount of 0.2-wt%) on the flow curves of PCC-A suspensions in the presence of 10-wt% Latex + 1-wt% Acrosol.

- Legend: 1. 48-vol% without binders;
2. 48-vol%, HEC;
3. 48-vol%, CMC35;
4. 48-vol%, MHPC;
5. 48-vol%, Mixture;
6. 48-vol%, CMC250;

The sequence of the curves is almost the same for the two PCC pigments, only the relative position of the curves with added MHPC and (CMC35 + CMC250) mixture appear reversed when changing from PCC-C to PCC-A. It is interesting to note that

the HEC with a $M_w=115,000$ g/mol has a lower thickening effect than CMC35 ($M_w=35,000$ g/mol). This might be attributed to different polymer configurations when adsorbed at the particles surface as well as to different specific interactions between polymers and solid surfaces. The shorter molecules of CMC35 are more prone to form an airy-like conformation, thus increasing more the apparent volume of the dispersed particles when compared to the other longer polymer chains, which might adsorb through small segments, forming loops and tails less extended to the solution. Another interesting feature of the flow curves obtained in the presence of the higher M_w co-binders is the relatively narrow hysteresis loop, i.e. a less accentuated tendency for particles structuration after shear (tixotropy). This can be understood considering that the total added amount of 0.2-wt.% would enable a good surface coverage by the polymeric chains to avoid bridging flocculation effects. However, this might not be the case when the (CMC35+CMC250) mixture was used. In fact, considering the small average size of the particles (high specific surface area) 0.1-wt.% of the fast adsorbing co-binder CMC35 might not be enough to achieve a good surface coverage. Under these circumstances, the longer chains of CMC250 will be able to adsorb simultaneously in more than one particle promoting some bridging flocculation.

Figures 3 and 4 show the steady viscosity curves of the coating colours for the two pigments, PCC-C and PCC-A, respectively. The shear-thinning behaviour is confirmed for all the curves up to shear rates of about 300 s^{-1} followed by near Newtonian plateaus.

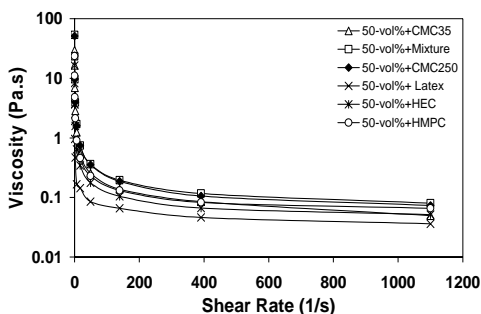


Figure 3: Effects of molecular weight of cellulose binders (for a total added amount of 0.2-wt.%) on the steady shear viscosity curves of PCC-C suspensions in the presence of 10-wt.% Latex + 1-wt.% Acrosol.

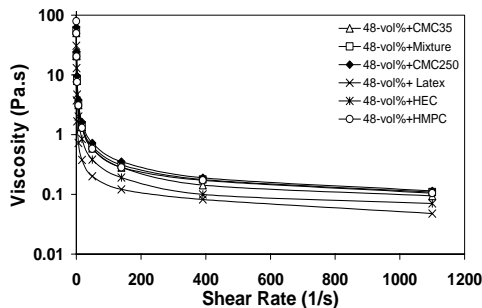


Figure 4: Effects of molecular weight of cellulose binders (for a total added amount of 0.2-wt.%) on the steady shear viscosity curves of PCC-A suspensions in the presence of 10-wt.% Latex + 1-wt.% Acrosol.

The shear-thinning behaviour is confirmed for all the curves up to shear rates of about 300 s^{-1} followed by near Newtonian plateaus. Such behaviours are typical of suspensions containing polymeric binder/thickening agents that help forming a weak network structure, which is gradually disrupted under the applied shear stress field and aligns the particles along the flow direction. The sequences of the curves are essentially the same already observed in Figures 1 and 2, respectively.

3.1.2 Oscillatory behaviour

An amplitude sweep was used to characterise the consistency at rest with regard to dispersion stability during long-term storage. Figure 5 shows the oscillatory curves of PCC-C colours in absence and in the presence of 0.2-wt.% CMC co-binders, while Figure 6 compares the oscillatory curves of the same pigment suspensions but in the presence of 0.2-wt.% CMC35, HEC and MHPC.

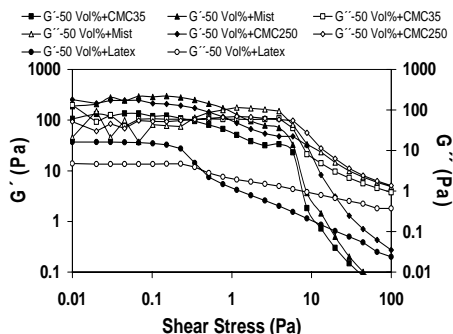


Figure 5: Amplitude sweep: Elastic (G') and Viscous (G'') modulus for PCC-C suspensions, in the presence of 0.2-wt.% of binders (CMC35, CMC250 and the mixture of both) + 10-wt.% Latex + 1-wt.% Acrosol.

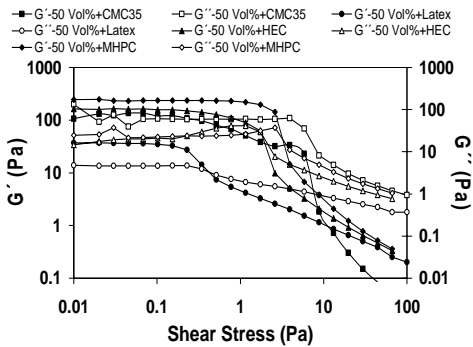


Figure 6: Amplitude sweep: Elastic (G') and Viscous (G'') modulus for PCC-C suspensions, in the presence of 0.2-wt% of binders (CMC35, HEC and MHPC) + 10-wt.% Latex + 1-wt.% Acrosol.

The first obvious observation is that the values of storage modulus (G') and loss modulus (G'') are much larger (≈ 100 -300 Pa) for suspensions containing co-binders in comparison to the one measured in absence of co-binders (≈ 40 Pa). G' represents the elastic (reversible deformation) behaviour of the sample. G'' is a measure of the deformation energy used up in the sample during the shear process and lost to the sample afterwards thus, representing the viscous (irreversible deformation) behaviour of the sample.

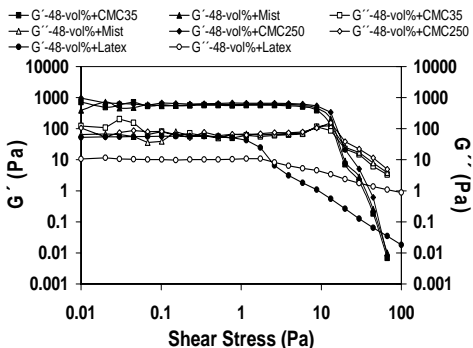


Figure 7: Amplitude sweep: Elastic (G') and Viscous (G'') modulus for PCC-A suspensions, in the presence of 0.2-wt% of binders (CMC35, CMC250 and the mixture of both) + 10-wt.% Latex + 1-wt.% Acrosol.

From the Figures 5 and 6 it can be seen that G' exhibits a more or less extended plateau, revealing that the analysis included the linear viscoelastic (LVE) range. The extent of the plateau increases with increasing co-binders M_w . This means that the crossover point where the viscous character

dominates over the elastic one occurs at increasing shear stress values as M_w of co-binders increases. Furthermore, the comparison of these two Figures suggests that the colours with added HEC or MHPC co-binders would exhibit a better stability at rest since the G' plateaux are more flat. In other words, the same suitable rheological properties might be achieved with smaller added amounts of these additives.

Regarding the influence of different added co-binders, the oscillatory curves of PCC-A exhibited the same trends as observed with PCC-C. However, the acicular form of PCC-A particles resulted in measured G' values (Figure 7), which were almost one order of magnitude greater than those observed for the roundish PCC-C particles. Such differences are significant, especially if one considers the lower solids loading of PCC-A colours. In a consistent way, the crossover point also occurs for higher shear stress values for the acicular PCC particles in the presence of co-binders. However, no apparent differences are observed between the two pigment colours in absence of co-binders.

4 CONCLUSIONS

The results presented in this work show that the co-binders HEC and MHPC are good alternatives to the more commonly used CMC ones since they impart good flow behaviour and a faster structural recovering of the layers after paper coating. On the other hand, the morphology of the pigment particles plays the most relevant role in determining the rheological properties. Elongated particles are more prone to structural regeneration after shear due to the easy bridging of the particles by the adsorbed co-binder molecules.

5 REFERENCES

Conceição, S.I., Santos, N.F., Velho, J.L., Kholkin, A. & Ferreira, J.M.F. 2003. "Relationship between Coating characteristics and Printability", WPP – Chemical Technology of Wood Pulp Paper, Proceedings of WPP'2003, 17-19 September 2003, Bratislava-Slovakia, 161-166.

Lehtinen, E. 2000. "Coating binders – general", in pigment coating and surface sizing of paper, chap. 13, ed. tappi press, 189-195.

Virtanen, P. 1999. "Process for preparing and modifying synthetic calcium carbonate", Patent No: Wo 99/36361, World Patent.

You, K.J. 1998. "Process for producing ultrafine particles of colloidal calcium carbonate", Patent No: Gb 2309691, Uk Patent Application.

Young, T. S. & Fu E. 1991. "Associative behaviour of cellulosic thickeners and its implications on coating structure and rheology", Tappi Journal, April, 197-207.

Image Analysis for the Determination of Roundness and Sphericity Grades of Sandy Grains

L.Z.D'Agostino, L.Soaes & L.F.D'Agostino

Department of Mining and Petroleum Engineering, Polytechnic School, University of São Paulo, Brazil

ABSTRACT: Three distinct sands (alluvial sand, granitic and basaltic quarry fines) were sampled, characterized and utilized as fine aggregate in the preparation of mortars for the civil construction area. Sands sampled were submitted to grain size analysis. After this analysis, some retained fractions in specific sieves of the series adopted were studied using the image analysis. For handling ease the retained size fractions - 4.8 + 2.4 mm, -2.4 + 1.2 mm and -1.2 + 0.6 mm were selected for this analysis. The determination of roundness and sphericity grades is essential in sand characterization because these are important characteristics of the sand used as fine aggregate, and have direct influence in the properties of mortars as workability and mechanical strength. Roundness and sphericity grades of alluvial sands and quarry fines result, among other important factors, from the mineralogy of the alluvial deposits and from the source-rocks used in the production of crushed rock, respectively. The study of roundness and sphericity grades using the image analysis aims to get a deep knowledge of these characteristics of the sands chosen. Based on standardized tests carried out in laboratory, the technological performances of the mortars were checked and the one that were prepared with granitic quarry fines presented the better workability and good results for compressive strengths.

1 INTRODUCTION

In Brazil, the Metropolitan Region of São Paulo is the largest consumer center of aggregates for civil construction. In 2002, this region consumed approximately half of the total volumes of sand and crushed stone produced in the state of São Paulo (Valverde 2002). Of the total volume used, 90% of the sand comes from regions located more than 100 km from the consumer center, a fact that increases its final price, given that transportation accounts for 2/3 of its cost (Valverde 2003). On the other hand, during the production of crushed stone, a fraction of very fine material (< 5mm) called quarry fines is also produced. These fines are stored in great outdoor piles and do not have a steady consumer market. Stockpiles of this material are subject to weathering, causing silting of the nearby drainage systems and air pollution, in addition to occupying large spaces in the quarry areas.

Thus, the study of quarry fines as aggregate for mortar preparation is very important, and knowledge of the form and texture of the grains, compared to those of alluvial sands, is essential for the technological knowledge of these sands. The degree of roundness and sphericity, among other characteristics, of the sand grains used as fine

aggregate for mortar, have a significant effect in their technological performance as already researched by Selmo (1986), Sabbatini (1986), Carneiro (1999) and Zanchetta (2000).

2 METHODOLOGY

2.1 Geology

In order to carry out this survey three types of sandy material were studied. One of them was alluvial sand from Jacareí, SP, representing the Quaternary sands of the flatlands of the Paraíba do Sul river valley, which was sampled at the Oásis Mineração de Areia. The other two types of material are quarry fines: one is the remains of crushed granitic rock from the region of Perus, SP, representing the crystalline foundation rocks of the state of São Paulo (Embu Quarry – Perus Unit) and the other results from the crushing of basaltic rock from the region of Campinas, SP, representing basaltic rocks from the Paraná River Basin (Basalt 5 Quarry).

2.2 Image analysis

First the sands were dried, then they were submitted to homogenization and then separated into fractions, in order to allow the different characterization tests

proposed and carried out in this survey. As part of these tests, a granulometric analysis of the sands was made, adopting a series of sieves recommended by the Brazilian technical standard NBR-7217 – Aggregates – Determination of the granulometric composition (ABNT 1987). The grains forming the fractions - 4.8 + 2.4 mm, - 2.4 + 1.2 mm and - 1.2 + 0.6 mm were studied through the image analysis method (Araújo et al. 2003) for determining the degree of roundness and sphericity of the grains using the QWIN Leica image analysis program. The distribution of these size fractions resulted from granulometric analysis is showed in Table 1.

Table 1. Distribution of the size fractions for the sands.

Size fraction (mm)	Alluvial sand (%)	Granitic quarry fines (%)	Basaltic quarry fines (%)
- 1.2+0.6	28.7	16.8	13.4
- 2.4+1.2	11.7	20.8	22.3
- 4.8+2.4	2.7	18.2	25.1

For capturing the images of grains of basaltic rock fines, it was necessary to use a white base (paper sheet) for contrast with the color of the grains (dark gray). For capturing the images of grains of granitic rock fines and of the alluvial sand (light gray and beige grains), a black opaque cardboard paper was used, which afforded the ideal contrast for obtaining images. Thus, for each fraction of each sample (9 fractions in all), a minimum of one thousand grains were analyzed, to make available high reliability data for the subsequent statistic treatment. The grains were arranged over the bases in such a manner that no grain touched the other, and they were manually separated using thin tip tweezers.

Right after capturing the images of the grains of each fraction of the samples, the program used for analysis of the images (QWIN Leica) calculated, based on a binary image resulting from the image initially captured, various parameters for each grain, as determined at the beginning of this phase. These parameters were: area, perimeter, roundness, aspect ratio and diameter of the equivalent circle.

The roundness of each grain, was calculated according to the following formula (Leica 1996):

$$Roundness = \frac{Perimeter \times Perimeter}{4 \times \pi \times Area \times 1.064} \quad (1)$$

where the adjustment factor of 1.064 corrects the perimeter for the effect of the corners produced by the digitization of the image.

Roundness calculated is a factor of the form of the grains, where a perfect circle has roundness equal to 1 and any other number greater than one 1 represents a grain with a low roundness degree, that

is, with a rough surface. If two grains with the same area present different roundness, the grain that shows the largest perimeter shall have the lowest roundness degree (value > 1) and the one with the smaller perimeter shall have the higher roundness degree (value near 1).

The aspect ratio, another parameter examined, was calculated applying the following formula (Leica 1996):

$$Aspect\ ratio = \frac{L}{B} \quad (2)$$

where *L* is the length of the grain (big axis) and *B* the breadth of the grain (small axis).

The aspect ratio shows the ratio between the axis of a grain. The bigger the ratio, the more elongated will be the grain. A perfect circle would have its aspect ratio equal to 1. Thus, it is possible to rate this parameter with the sphericity. Aspect ratios with values near 1 represent grains with high sphericity (the form of the grain is near that of a sphere); on the other hand, values higher than 1 represent grains with low sphericity (the form of the grain is elongated).

It should be pointed out that the aspect ratio, as well as the roundness degree, were parameters calculated based on bidimensional images and, for this reason, the ratio between length and width is called aspect ratio and not sphericity, given that for evaluation of the later, the grain should be tridimensionally evaluated. Nevertheless, with the aspect ratio it is possible to evaluate the degree of sphericity of the grain analyzed.

The results of the roundness and aspect ratio analyses were statistically treated. From the charts it was possible to view the roundness and aspect ratio behavior of the three fractions of each sand and to compare them.

3 RESULTS

3.1 Size fraction - 1.2+0.6 mm

The distribution chart of grains roundness shows a very similar behavior for the curves of the three types of sand. Even so, the grains of the alluvial sand can be considered to have a greater roundness degree than those of the granitic fines, while the later have a greater roundness degree than the grains of the basaltic fines (Fig.1).

The aspect ratio distribution chart shows that the grains of the alluvial sand have greater sphericity than those of the granitic fines, which, in turn, have greater sphericity than those of basaltic fines (Fig.2). Approximately 8% of these grains of granitic fines and 15% of the basaltic fines, present an aspect ratio greater than 2.

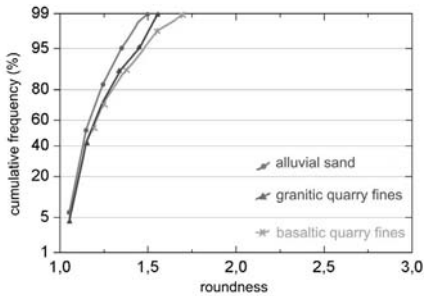


Figure 1. Roundness of size fraction - 1.2 + 0.6 mm.

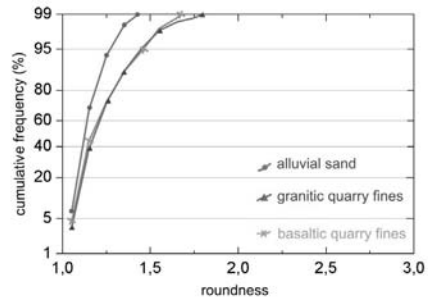


Figure 3. Roundness of size fraction - 2.4 + 1.2 mm.

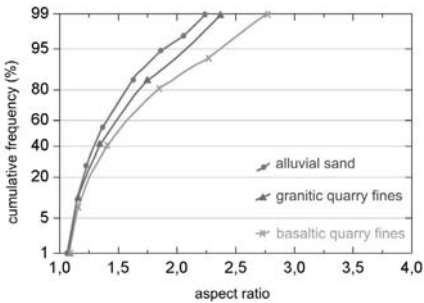


Figure 2. Sphericity of size fraction - 1.2 + 0.6 mm.

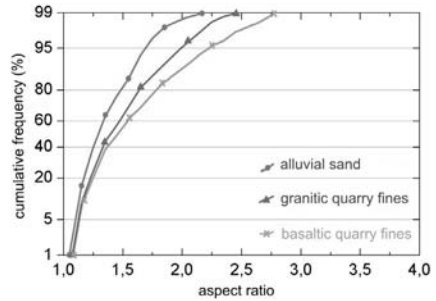


Figure 4. Sphericity of size fraction - 2.4 + 1.2 mm.

3.2 Size fraction - 2.4+1.2 mm

The roundness distribution chart shows a very similar behavior between curves of the granitic and basaltic fines, but different when compared to the curves of the alluvial sand. The three types of sand show 95% of their grains as having a surface not so angular. It also shows that 95% of the grains of alluvial sand have a greater roundness degree than those of granitic and basaltic fines (Fig.3).

In the aspect ratio distribution chart each type of sand has a different distribution, although all three show the same pattern of the distribution curve. Thus, the grains of the alluvial sand have greater sphericity than those of the granitic fines, which, in turn, have greater sphericity than those of basaltic fines (Fig.4).

3.3 Size fraction - 4.8+2.4 mm

The roundness distribution chart shows a very similar behavior between curves of the granitic and the alluvial sand, and very different when compared to the curve for the basaltic fines. Thus, the grains of the basaltic fines may be considered to have a greater roundness degree than the grains of alluvial sand, and these, in turn, have a greater roundness degree than the grains of granitic fines (Fig.5). It should be pointed out that 5% of the grains of granitic fines show a roundness degree higher than 1.7 reaching 20.5, indicating grains with a very angular surface.

In the aspect ratio distribution chart it can be noted that each type of sand presents a different distribution. Approximately 7% of the grains of basaltic fines, 10% of the grains of granitic fines, and 5% of the grains of the alluvial sand have an aspect ratio greater than 2, reaching values of 4.1, 22.9 and 11 respectively. Therefore, the grains of alluvial sand have greater sphericity than the grains of basaltic fines, which, in turn, have greater sphericity than the grains of granitic fines (Fig.6).

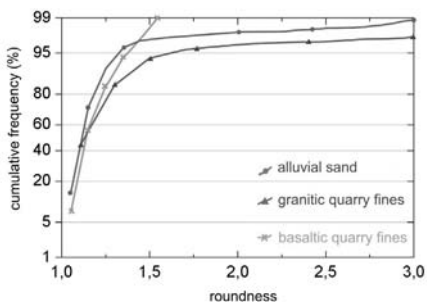


Figure 5. Roundness of size fraction - 4.8 + 2.4 mm.

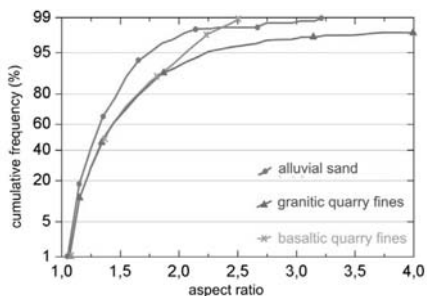


Figure 6. Sphericity of size fraction - 4.8 + 2.4 mm.

4 CONCLUSIONS

The three types of sand that were the object of the study were utilized as fine aggregate for preparation of mortars, and those were submitted to technological tests in order to evaluate properties such as workability and compressive strength.

Workability was one of the aspects deserving attention during preparation of mortars. Mortars prepared with basaltic fines showed to be less easy to work with because they were heavier than those prepared with granitic fines and alluvial sand. Roundness and sphericity of the sand grains also have an effect on this property, since more angular and more elongated grains present much more imbrication than the round and spherical grains. The grains of basaltic fines, considering the three size fractions studied, showed to be more angular and more elongated than those of granitic fines and of alluvial sand.

As to the compressive strength of mortars, three curing periods were set, 7, 28 and 90 days, so that mortars could be tested in accordance with Standard NBR-13279 – Mortar for walls and ceilings – Determination of compressive strength (ABNT 1995). During the three curing periods, mortar prepared with basaltic fines presented greater compressive strength than those prepared with granitic fines and alluvial sand. The form and texture

of the grains also affect this property: more angular grains make for greater imbrication, and this increases the compressive strength of the mortar. After 28 days, mortar with basaltic fines presented 4.5 MPa; that with granitic fines 4.4 MPa and the one with alluvial sand, 4.1 MPa. At 90 days, mortar with basaltic fines, granitic fines, and alluvial sand presented 5.4, 5.1 and 4.9 MPa, respectively.

Based on the results obtained, it is concluded that the study of the form and texture of the grains of the sand that will be used as fine aggregate for mortar is important, since these are characteristics that can have a relevant effect on the performance of mortars. The method adopted in this survey supplied statistical data that are fundamental to complement the complex analysis of the factors that affect the properties and performance of mortars.

5 REFERENCES

- Araújo, G.S.; Bicalho, K.V.; Tristão, F.A. 2003. Determinação da forma das areias através da análise de imagens. In: Simpósio Brasileiro de Tecnologia de Argamassas, 5. São Paulo. Anais. Departamento de Engenharia de Construção Civil, Escola Politécnica da USP / ANTAC: 121-129.
- Associação Brasileira de Normas Técnicas. 1987. Agregados – Determinação da composição granulométrica – NBR 7217. Rio de Janeiro.
- _____. 1995. Argamassa para assentamento de paredes e revestimento de paredes e tetos – Determinação da resistência à compressão – NBR 13279. Rio de Janeiro.
- Carneiro, A.M.P. 1999. Contribuição ao estudo da influência do agregado nas propriedades de argamassas compostas a partir de curvas granulométricas. 169p. Tese (Doutorado). Departamento de Engenharia de Construção Civil, EPUSP.
- Leica QWIN. 1996. User guide & Reference guide. Leica Imaging Systems Ltd. Cambridge.
- Sabbatini, F.H. 1986. Agregados miúdos para argamassas de assentamento. In: *Simpósio Nacional de Agregados, 1*. São Paulo. Anais. Departamento de Engenharia de Construção Civil, EPUSP: 17-25.
- Selmo, S.M.S. 1986. Agregados miúdos para argamassas de revestimento. In: *Simpósio Nacional de Agregados, 1*. São Paulo. Anais. Departamento de Engenharia de Construção Civil, EPUSP: 27-43.
- Valverde, F.M. 2002. Produção e consumo de agregados para a construção civil no Brasil. São Paulo. Associação Nacional das Entidades de Produtores de Agregados para Construção Civil, 02 Out. 2002. /Personal communication.
- Valverde, F.M. 2003. Agregados para construção civil. Sumário Mineral 2003. DNPM. Available in: <www.dnpm.gov.br>. Last access: dez. 2003.
- Zanchetta, L.M. 2000. Características tecnológicas de argamassas elaboradas com diferentes tipos de areias. 79p. Monografia de Trabalho de Formatura (TF-2000/13). Instituto de Geociências, USP.

Heavy Minerals from the Polish Part of the Eastern Carpathian Sandstones

B.Dziubińska

Jagiellonian University, Institute of Geological Sciences, Kraków, Poland

M.A.Kusiak & M.Paszowski

Polish Academy of Sciences, Institute of Geological Sciences, Kraków, Poland

ABSTRACT: The Eastern Carpathians belong to the outer flysch belt of the Carpathian arc and form part of the European Alpides. For the purpose of heavy mineral analysis selected sandstone formations were used from the Dukla and Silesian Units. The heavy, mineral fraction group is dominated by ultra stable minerals such as zircon, tourmaline and rutile (ZTR) in samples coming from the Dukla Unit. Electron-microprobe analysis enabled the possibility to identify monazite, xenotime and chromian spinel, not observed in the Dukla Unit before. From the Silesian Unit, ZTR minerals only account for about 15%, with a lack of tourmaline and rutile, but also with a dominance of opaque minerals. These sandstones show a more polymictic character, with unstable garnets and metamorphic minerals. The detrital material supplied to the Dukla Unit came from crystalline massifs, which was built up of rock types dominated by a felsic character and metamorphic rocks (most probably Precambrian). The distinctive difference between these two spectra of heavy mineral groups may well be a result of the different composition and the structure of source terrains or possibly a different mode of weathering, erosion and sedimentation. Owing to the dominance of euhedral mineral shapes and the low textural maturity of detrital grains, recycling should be excluded as the cause of petrofacial maturity of Dukla Unit sandstones. This is evidence of a high erosion rate and a domination of physical weathering of the source area.

1 INTRODUCTION

A new feature of heavy accessory minerals is their application into the different branches of geological sciences. This is due to the general progress in mineralogy and instrumental analysis techniques. Heavy mineral analysis is a very important tool, especially for the determination of detritus provenance.

2 GEOLOGICAL SETTING

The Outer Carpathians, also referred to as the "Flysch Carpathians", comprise a series of imbricated nappes consisting mainly of variable flysch deposits, upper Jurassic to lower Miocene in age (Książkiewicz 1960). The sampled sandstones, Upper Cretaceous and Paleogene in age, belong to two tectonostratigraphic units (nappes) of the Polish Outer Carpathian flysch arc: the Dukla Unit and the Silesian Unit. Both units represent a thick, lithologically similar and monotonous sequence of deep-water, synorogenic, turbiditic and hemipelagic siliciclastics (additionally calcareous-siliceous).

These range from Cretaceous-Oligocene in the case of the Dukla Unit and Upper Jurassic-Oligocene in the Silesian Unit. Thick sandstone bodies fill narrow sub-basins between elongated, intrabasinal, synsedimentary active rises (traditionally named "cordilleras"). This eroded chain of cordillera, recently completely vanished in Polish segment of Carpathians, accessible only in Ukrainian and Romanian part of orogen, is regarded as a main type of source terrain for dominating part of Carpathian flysch siliciclastics. Section model of particular cordillera, reconstructed from coarse-grained detritus (e.g. Silesian Cordillera) usually show two structural stages: crystalline, pre-Alpine(?) basement and sedimentary Palaeozoic or/and Mesozoic cover.

The research was carried out for rocks outcropping in such lithostratigraphic profiles in Jaśliska, Wisłok, Maniów (3 samples from different lithostratigraphic layers), Roztoki, Wetlina, Majdan, which are located in the eastern and western parts of the Dukla Unit and in Bystre, located in close neighborhood in Silesia Unit (Fig.1). Analyzed samples are Eocene, Palaeocene and late Cretaceous in age.

(A)



(B)

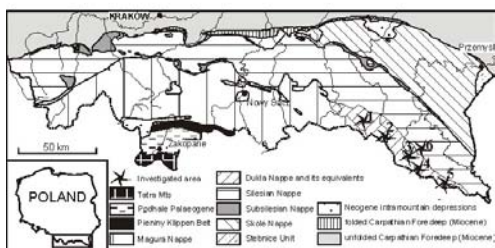


Figure 1. (A) The Carpathian Arc in Europe; (B) Location and simplified geologic map of the Polish Carpathian, samples from: Dukla Unit – 1: JA-Jasliska; 2: WI-Wisłok; 3: MN-Maniów; 4: RO-Roztoki; 5: WE-Welina; and Silesian Unit – 6: BY-Bystre.

3 HEAVY MINERAL SEPARATION

In each of the cases approximately 5kg of sample rocks from outcrops were collected. All samples were crushed and sieved using a 0.32 μm screen. Heavy minerals were preliminary concentrated using the Wilfley's concentrating table (Steward 1986). Each sample was processed once to obtain an initial concentrate, which was then reprocessed to clean up the original separation. This concentrate was then made into a hand-schlich. After drying and sieving the "pre-concentrate" of heavy minerals was used in an isodynamic magnetic separator. This separator can even be used for weak magnetic minerals.

For the removal of the paramagnetic fraction a magnetohydrostatic separator (Kusiak & Paszkowski 1998) was used, where the process of separation of mineral grains mixtures takes place in a water solution of manganous chloride ($\text{MnCl}_2 \cdot 4\text{H}_2\text{O}$), which is based on the density and difference in magnetic susceptibility of particular grains. The fluid contains dissolved paramagnetic ions and in such a medium on the ground of difference in magnetic susceptibility and the specific weight of individual constituents the separation of mixture of mineral grains takes place. The aqueous solution of manganese chloride has the highest magnetic

susceptibility to salts from iron group elements (Brożek 1983). Such procedure provides the opportunity for the separation of a highly selective group of minerals with a very small difference in density, and also the separation of very dense minerals. These methods are more effective and more precise than conventional separations in toxic organic heavy liquids and allow the complete elimination, from laboratory work, of highly toxic and expensive heavy liquids (Paszkowski et al. 1999).

During the first stage all samples were polished with a diamond paste on an 8-inch diamond plate (15 μm) in wet conditions and the final stage involved polishing using a 0.5 μm diamond paste. All samples were polished until the grains were thinned to approximately half-thickness.

4 RESULTS AND CONCLUSIONS

The heavy, mineral fraction group is dominated by ultras stable minerals such as zircon, tourmaline and rutile (ZTR) in samples, which come from the Dukla Unit. From the Silesia Unit, ZTR minerals make up only 15% and are characterized by a lack of tourmaline and rutile, and the dominance of opaque minerals (Fig. 2).

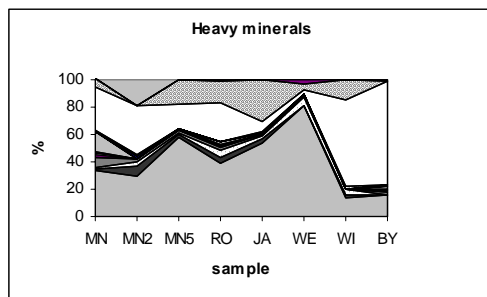


Figure 2. Heavy minerals from samples: from the bottom: zircon (grey), tourmaline (black), rutile, staurolite, dystene, andalusite, apatite, garnet (black), glaukonite, opaque minerals (white), framboidal pyrite (diagonal line pattern) and others (grey).

A characteristic feature is the common occurrence of framboidal pyrite.

The euhedral shape of zircon grains is a distinctive feature, but is also subordinate subhedral and rounded. In some cases there was noticeable presence of apatite, staurolite, andalusite, kyanite and occasionally also garnet. Following EMPA analysis it was possible to first determine the occurrence of xenotime and to confirm the presence of monazite and chromian spinel, not noticed in the

Dukla Unit before. Dukla Unit detrital material was supplied from crystalline massifs, built in rock-type formations dominated by a felsic character and metamorphic rocks (most probably Precambrian). The Presence of detrital chromian spinel, and also the proportion of Y/Ni to Cr/V suggest a presence in ultramafic or mafic source rocks or possibly recycled detritus from these types of rocks. The distinctive difference between these two heavy minerals spectra may be as a result of different composition and the structure of source terrains or a different mode of weathering, erosion and sedimentation. The intensity of chemical weathering is most probably the main reason for such a difference. Owing to the dominance of euhedral mineral shapes and the low textural maturity of detrital grains, recycling should be excluded as the cause of petrofacial maturity of Dukla Unit sandstones.

In contrast to the above-mentioned Dukla Unit sandstones, heavy minerals from Silesian Unit sandstones reveal a more polymictic character with unstable garnets and metamorphic minerals. This is evidence of a high erosion rate and the dominance of physical weathering of the source area. The common presence of framboidal pyrite suggests a reduction condition in the early diagenesis stages.

Such results are preliminary, since a more detailed, chemical analysis of minerals for a reliable reconstruction of particular source areas is necessary.

5 REFERENCES

- Brożek, M. 1983. Magnetic properties and viscosity of fluids containing dissolved paramagnetic ions. *Archiwum górnictwa*, 28,1: 87-95, in Polish.
- Książkiewicz, M. 1960. Outline of the paleogeography in the Polish Carpathians. (in Polish) *Prace IG*, 30: 209-231.
- Kusiak, M. & Paszkowski, M. 1998. Wydzielanie minerałów ciężkich za pomocą separatora magneto hydrostatycznego. *Przegląd Geologiczny*, 46: 674-675, in Polish.
- Paszkowski, M., Kusiak, M. & Banaś, M. 1999. Nowe, niekonwencjonalne metody w preparatyce minerałów akcesorycznych. *Documenta Geonica*, The 4th Czech-Polish Conference about Carboniferous Sedimentology. Peres Publishers. Prague: 147-150, in Polish.
- Stewart, R. A. 1986. Routine heavy minerals analysis using a concentrating table. *Journal of Sedimentary Petrology*, 56: 555-556.
- Ślącza, A. & Kamiński, M. A. 1998. A guidebook of excursions in the Polish flysch Carpathians. *Special Publications of Grzybowski Foundation*, Kraków, 6:171p.

Appraisal of the Delamination Efficiency Produced by Low Energetic Sonication Carried out on a Kaolin Unusually Rich in Kaolinite Stacks

C.Gomes & V.Gomes

MIA (Centro de Investigação "Minerais Industriais e Argilas") da FCT (Fundação para a Ciência e a Tecnologia), Universidade de Aveiro

C.Sequeira

Departamento de Biologia, Universidade de Aveiro

ABSTRACT: The present paper examines the effect of sonication on particle-size and other physical properties (specific surface area, viscosity, and abrasivity) of a kaolin unusually rich in kaolinite stacks. Such kaolin sampled in the Mevaiela deposit, Angola, derives from the alteration of rocks belonging to the Kunene gabbro-anorthosite complex. Delamination of these kaolinite stacks promoted by sonication produced important beneficial changes in the properties referred to, enabling kaolin application for certain functions that could not be accomplished by the raw kaolin, that is, prior to its beneficiation.

1 INTRODUCTION

Kaolinite delamination is a mechanical process used to increase the specific surface area (SSA) of a kaolin, property of paramount importance whenever a kaolin is used as coating or pigment, for instance, in paper and in paint industries.

Significant gains on SSA can be achieved through kaolin milling, however notorious and deleterious changes are recognised both on kaolinite particle shape and on kaolinite structural order.

In most of residual kaolins, kaolinite particles appear, in general, as single crystal plates, exhibiting, pseudo-hexagonal shapes.

However, in some cases, kaolinite particles consist of stacks, piles or books of individual crystal plates. Therefore, in the industry the individualization of the single plates that build up these stacks can be achieved through a method of kaolin processing called delamination. This process essentially promotes the development of basal cleavage, that is the cleavage along the (001) crystal planes.

However, in certain circumstances, such as those performed in the technique called sand-attrition, prismatic cleavage, that is the cleavage along (011) crystal planes, takes place as well.

In the industry kaolin delamination is achieved through the application of mechanical action upon kaolins, either on the plastic (paste) state, or in the liquid (slurry) state.

In the first case, delamination can be produced by repeated extrusion under compression of a semi-dry paste (18-25% of moisture and 60-70% of solids).

In the second case, the kaolin suspension is agitated using a stirrer of blades working at variable speed, the blades having variable orientation.

In both cases kaolinite particle size can be significantly reduced. Delamination can be achieved as well through the shock between kaolinite particles and small plastic balls or quartz sand bearing specific characteristics in sand mills, the so-called sand-attrition technique.

Any of the techniques referred to produce changes on the following kaolin properties: particle size distribution, SSA, viscosity and colour.

Delaminated and calcined kaolins too, within the commercial grades of kaolin, are the most expensive ones.

Velho & Gomes (1991) developed a mechanical-chemical process of kaolin delamination, in the laboratory, that applies the combined effect of sonication and hydrazine hydrate intercalation (to

weaken crystal interlayer energy prior to the ultrasounds action) with good results.

However, this delamination method hardly could be applied at the kaolin processing plants, due to both economic and environmental constraints. A purely mechanical method, but satisfactorily efficient, would be desirable.

On this basis, the present paper discloses the results of the benefits achieved on some relevant kaolin properties (SSA, abrasivity and viscosity) using low energetic sonication to promote the delamination of kaolinite stacks.

Experimental work was carried out on a kaolin unusually rich in kaolinite stacks, and the efficiency of the process could be assessed based upon kaolin relevant properties, such as: grain size distribution, grain morphology, specific surface area, abrasivity and viscosity concentration.

Delamination being promoted both from shock-wave impacts on kaolinite particles and from interparticle collisions.

2 MATERIALS, METHODS, RESULTS AND DISCUSSION

The kaolin deposit of Mevaiela occurs close to Mevaiela, a village located about 50 km to the south of the town of Lubango, Angola. It is the result of the alteration of gabbro-anorthosite rocks belonging to the Kunene complex. Kaolinite particles, except in the superficial layers of the deposit, exhibit as a rule, numerous prismatic stacks consisting, on average, of 15-20 individual pseudo-hexagonal plates.

The mean mineralogical composition of Mevaiela raw kaolin consists of structurally well-ordered kaolinite (> 90%) and halloysite (< 5%). However, in the superficial layers of the deposit halloysite content can reach values around 15%.

The non-clay minerals usually found in raw kaolins, such as, quartz, feldspar and mica, responsible for the relatively high abrasivity values and for the relatively low specific surface area (SSA) values, are not present in the Mevaiela kaolin.

Mineralogical data was determined through the application of X-ray diffraction (XRD) techniques.

High abrasivity, low SSA and low viscosity concentration values are much inconvenient, for instance, whenever kaolin is used in coating formulations for paper manufacturing or as extender in inks and paints.

Mevaiela raw kaolin, exhibits the following properties: pH = 8.4; brightness (84.2) and yellowness (5.5) measured following the DIN method; specific surface area (BET) = $6 \text{ m}^2 \cdot \text{g}^{-1}$; main chemical components determined by X-ray fluorescence (XRF): SiO_2 - 45,27%; Al_2O_3 - 39,40%; Fe_2O_3 - 0,85%; TiO_2 - 0,10%; MgO - 0,10%; Na_2O - 0,15%; abrasivity Einlehner AT 1000 = 12 mg;

viscosity concentration = 56.5 % (Gomes et al. 1994).

The values of the last two parameters referred to were not expected, the first being too high, and the second being too low. To explain these anomalous values, particle size distribution and particle shape have been determined and examined.

Grain size distribution was determined using the grain size analyser Sedigraph 5400, from Micromeritics. The obtained distribution provided a polymodal frequency curve, characterised by the following parameters: median diameter $1.72 \mu\text{m}$; modal diameter $1.68 \mu\text{m}$.

Scanning electron microscopy (SEM) observations, using a Jeol 5100 apparatus, did show that most of the kaolin particles do not consist of single plates. Stacks of kaolinite pseudo-hexagonal plates displaying columnar habits, occasionally vermiform shapes, are very frequent, and the number of platelets forming these stacks, as a rule, varies within the range 10-20.

Velho & Gomes (1991) did delaminate several kaolins from Portugal submitting them to ultrasound treatments and the achieved results, in terms of benefits brought about in relevant properties, such as specific surface area, rheology and colour. Therefore, three aqueous suspensions (using freshly deionised water) of Mevaiela kaolin with 10% concentration (w/v) were submitted to sonication treatments (using an ultrasonic liquid processor with 190 W of output) for periods of 1, 2 and 3 hours. Kaolin suspensions inside cylindrical glass containers were kept at the constant temperature of $21 \text{ }^\circ\text{C}$ during the entire treatment by means of a cooling recirculator.

After sonication, the treated kaolin suspensions were dried in an oven at 50°C .

Particle size parameters, median diameter and modal diameter, saw their values significantly reduced: $1.11 \mu\text{m}$ and $1.00 \mu\text{m}$ for 1 hour; $0.92 \mu\text{m}$ and $0.81 \mu\text{m}$ for 2 hours; $0.83 \mu\text{m}$ and $0.73 \mu\text{m}$ for 3 hours.

Significant gains on SSA values determined by the same method (BET using N_2 as adsorbate) used for raw kaolin were obtained: $9 \text{ m}^2 \cdot \text{g}^{-1}$ for 1 hour; $13 \text{ m}^2 \cdot \text{g}^{-1}$ for 2 hours and $18 \text{ m}^2 \cdot \text{g}^{-1}$ for 3 hours. Changes on particle size and shape due to the delamination of kaolinite stacks could be followed by SEM observations.

Figures 1 and 2 show both size and morphological features of kaolinite particles, prior to sonication treatment and after being submitted to sonication treatment lasting for 3 hours, respectively.



Figure 1- Size and morphological features of Mevaiela kaolin before being submitted to sonication treatment.

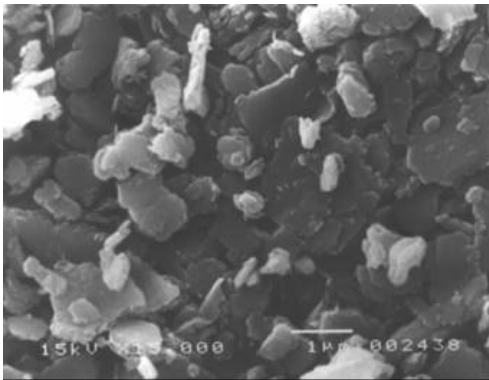


Figure 2- Size and morphological features of Mevaiela kaolin after being submitted to sonication treatment lasting 3 hours.

Only for the treatment that did last 3 hours a very slight change of the kaolinite structural order could be detected by X-ray diffraction (XRD) analysis.

3 CONCLUSIONS

The low energetic sonication treatments being carried out cause changes on kaolinite particle size of the studied Mevaiela (Angola) kaolin did promote mainly the basal cleavage. Based upon the experimental work being carried out it was found that delamination efficiency depends upon several variables: ultrasound energy, kaolin/water (w/v) ratio and time of treatment.

The influence of these parameters, considering progressive increments relatively to those used in the present paper, is being investigated in order to find out the values for which the yield or efficiency of the process is at its maximum, but preserving kaolinite structure and shape.

4 REFERENCES

- Gomes, C.S.F. et al. 1994. Kaolin deposit of Mevaiela (Angola), alteration product of anorthosite: assessment of kaolin potentialities for application in paper. *Appl. Clay Sci.* 9: 97-106.
- Velho, J. A L. & Gomes, C. S. F. 1991. Characterization of Portuguese kaolins for the paper industry: beneficiation through new delamination techniques. *Appl. Clay Sci.* 6: 155-170.

Mineralogical Characterization of Kaolin from the Capim Region, Pará State (Brazil)

J.Götze, R.Kleeberg & P.Wiedemann

Department of Mineralogy, TU Bergakademie Freiberg, Germany

M.Plötze

IGT ClayLab, ETH Zürich, Switzerland

R.S.Angélica

Federal University of Pará, Belém, Brazil

ABSTRACT: The kaolin from the Capim region, northern Brazil, occurs in more than 15m thick layers within the Ipixuna Formation (Cretaceous age) overlaying kaolinitic sandstones and covered by clayey sandstones with “ironstone” lenses. The kaolin itself can be divided in a lower ca. 6.5m thick part of soft kaolin (main ore) and an upper part of ca. 10m hard kaolin. Samples of different stratigraphic or lateritic horizons were investigated concerning grain-size distribution (wet sieving, SEM), phase composition (XRD with Rietveld refinement), chemical composition, thermal behaviour (TG, DTA) and real structure (ESR spectroscopy) to get information about general characteristics of the raw material and to draw conclusions about an industrial use of the kaolin in the industry (paper, ceramics). The main components of the kaolin are low-crystalline kaolinite (Hinkley index 0.33-0.73), quartz and anatase/rutile as accessory minerals. In the upper part of the deposit, the kaolin is mainly iron-rich. Results of ESR analysis revealed that some of the iron is structurally incorporated in the octahedral site of kaolinite. These results are in particular important for refinement processes of the raw material.

1 INTRODUCTION

Kaolinite is one of the most important clay minerals occurring in large amounts in sediments and sedimentary rocks or as alteration product in crystalline rocks. Because of its widespread occurrence and its physical and chemical properties, kaolinite is widely used in certain technical applications (e.g., ceramic industry, filling material, refractory materials). On the other hand, kaolinite is an important mineral in sedimentary petrology as an indicator of specific facies conditions. In the present study, the kaolin from the Capim region, Brazil was investigated by a combination of various mineralogical and chemical methods to provide information concerning an industrial use of the clay material.

2 MATERIALS AND METHODS

2.1 Geological background and sample material

The kaolin from the Capim region (Pará State, northern Brazil) occurs in more than 15m thick layers within the Ipixuna Formation (Cretaceous age). It overlays kaolinitic sandstones and is covered by clayey sandstones with “ironstone” lenses (Fig.

1). The kaolin itself can be divided into a lower ca. 6.5m thick part of soft kaolin (main ore) and an upper part of ca. 10m hard kaolin (De Sousa 2000).

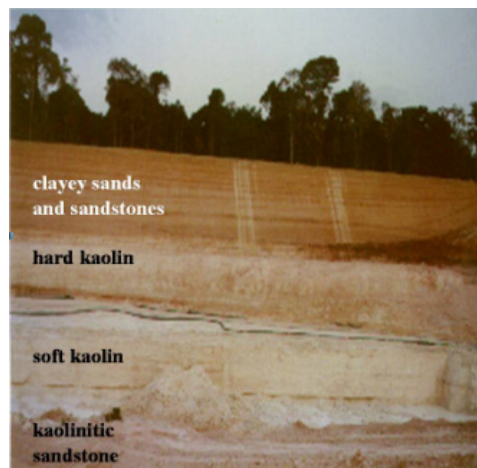


Figure 1: View on a typical kaolin profile from Capim.

A schematic kaolin profile is presented in Figure 2. The numbers are related to the samples, which were collected in different parts and at different levels of the main pit, in order to obtain a composed profile.

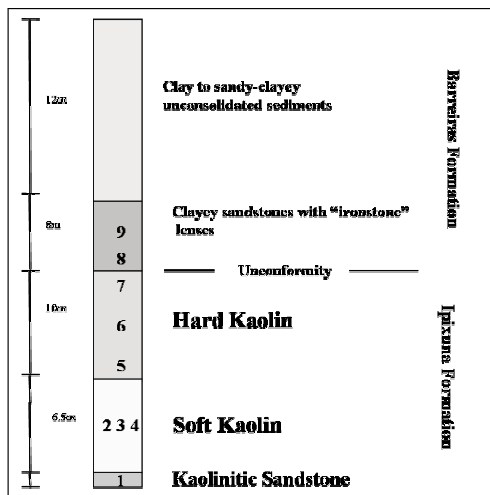


Figure 2: Schematic profile of the kaolin deposit showing the positions of the investigated samples

Sample 1 derives from the kaolinitic sandstone. It is not considered a kaolin-ore because the quartz content is very high. Samples 2 to 4 were collected from the soft kaolin in the same level but representing lateral variations according to different iron contents. Samples from the hard or flint kaolin (5 to 7) were collected from the base (5) to the top (7) of this horizon in order to get vertical Fe variations. Sample 8 represents the ironstone above the hard kaolin, and sample 9 is from very “clean” kaolinite lenses interlayered in the ironstone above, which belongs to the Barreiras Formation.

2.2 Analytical techniques

The grain-size distribution of the samples was determined by wet sieving. The mineralogical composition and the crystal structure of the investigated clay samples were characterized by XRD (BRUKER-AXS D8; $\text{CuK}\alpha$, $4\text{-}70^\circ$ 2θ , 0.02° steps, 3s per step) using Rietveld refinement (AutoQuan/BGMN). The material was additionally studied by SEM (JEOL 6400) to detect variations in grain size and morphology of the different minerals. For the identification of point defects in the crystal structure of kaolinite, paramagnetic centres were investigated in powder samples by electron spin resonance (ESR) spectroscopy (BRUKER ESP

300E) in the X-band at 295 and 70 K (5 G, 40 mW, 100-200 mT and 320-336 mT). The chemical composition of the clay samples was determined by Inductively Coupled Plasma Mass Spectrometry (ICP-MS Agilent 7500).

3 RESULTS AND DISCUSSION

The results of wet sieving (Table 1) show that most of the kaolin material is concentrated in the fraction $<20\ \mu\text{m}$. Only sample 8 from the ironstone has most of the material in the coarser grain fraction.

Table 1: Grain-size distribution of the investigated samples

Sample	$<20\ \mu\text{m}$	[mass-%]	$>20\ \mu\text{m}$
9	51.1		48.9
8	3.2		96.8
7	96.4		3.6
6	98.5		1.5
5	88.3		11.7
4	98.6		1.4
3	75.5		24.5
2	76.3		23.7
1	66.4		33.4

The main mineral components of the kaolin are kaolinite and quartz (Table 2). In samples 1 to 4 more than 98 mass-% kaolinite are present in the fraction $<20\ \mu\text{m}$ and almost no quartz was found in this fraction. In some of the samples, considerable amounts of hematite (sample 5) and goethite (samples 5, 7, 8) were detected (up to >10 mass-%). Anatase/rutile and minerals of the crandallite group were analyzed as the main accessory minerals, which exclusively occur in the fraction $<20\ \mu\text{m}$. Additionally, zircon (sample 5) and muscovite (samples 3, 4) were detected.

Table 2: Mineral composition [mass-%] of the kaolin samples.

Sample	Quartz	Kaolinite	Crandallite	Anatase	Rutile
9	49.6	48.8	0.3	1.1	0.3
8	82.6	-	+	+	+
7	0.4	88.4	0.8	2.0	1.0
6	-	95.6	0.6	1.7	0.6
5	1.0	81.3	0.6	0.1	0.3
4	-	96.0	0.7	0.8	-
3	23.6	75.2	0.5	-	-
2	21.9	77.0	0.6	0.5	-
1	28.1	71.3	0.4	0.2	-

The mineralogy of the kaolin samples is reflected in the main chemical composition (Table 3).

Considerable contents of Fe_2O_3 and TiO_2 were analyzed, whereas the concentrations of CaO , MgO , MnO , Na_2O and K_2O are below 0.1 mass-% in all investigated samples. The differences to 100 mass-% are due to the loss of ignition. These results were confirmed by the TG/DTA analyses.

Table 3: Results (in mass-%) of chemical analyses by ICP-MS

Sample	SiO_2	TiO_2	Al_2O_3	$\text{Fe}_2\text{O}_{3\text{tot}}$	P_2O_5	Σ
9	70.0	1.06	16.9	2.59	<0.01	90.78
8	70.9	0.04	0.94	23.9	0.05	95.93
7	39.7	2.14	33.3	7.64	0.05	83.06
6	42.9	2.39	35.7	1.05	0.06	82.21
5	29.4	1.31	24.3	32.4	0.08	87.76
4	43.2	1.76	36.2	1.21	0.10	82.69
3	55.9	1.16	28.8	0.57	0.07	86.70
2	55.9	1.10	28.2	0.50	0.08	85.90
1	58.8	0.43	26.9	0.29	0.04	86.70

The data illustrate that both mineral and chemical composition of the kaolin can considerably vary, even within a distinct horizon of the deposit. This is also true for the crystallinity of the kaolinite. The Hinkley index varies between 0.33 and 0.73 and shows the highest values within the soft kaolin (sample 3: HI = 0.73) and the lowest within the hard kaolin (sample 6: HI = 0.33). The Hinkley index of the kaolinite from the underlying kaolinitic sandstone was 0.54.

Differences were also found for grain size and morphology of kaolinite from different horizons. Scanning electron microscopy revealed that the kaolinite from the soft kaolin occurs as “books” of pseudohexagonal crystals (Fig. 3), whereas the samples from the hard kaolin show irregular crystals of kaolinite (Fig. 4).

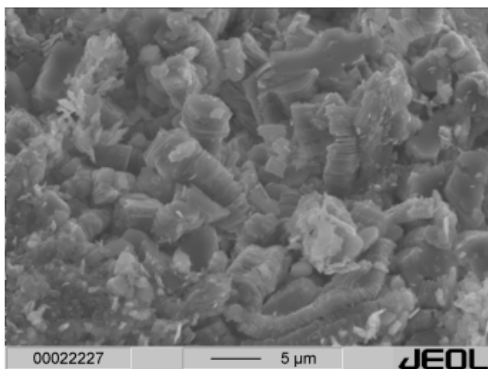


Figure 3: SEM micrograph of sample 3 (soft kaolin) showing well-crystallized “books” of kaolinite.

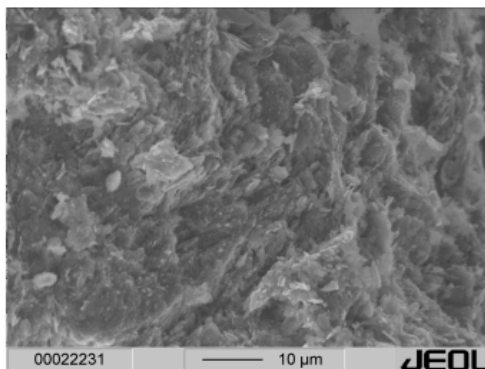


Figure 4: SEM micrograph of sample 7 (hard kaolin) showing irregular fine crystals of kaolinite.

The samples from the overlying sandstones with “ironstone” lenses show clear evidence for processes of mobilization and precipitation. The SEM micrographs revealed collomorph structures with small spheres within the ironstone lenses (Fig. 5).

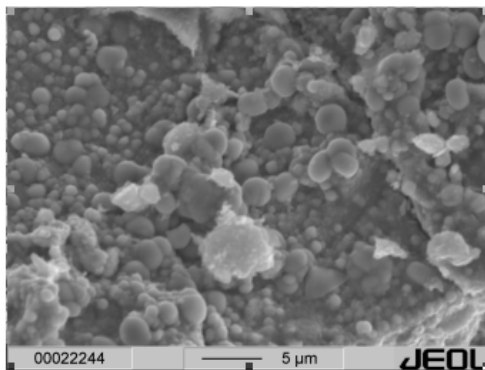


Figure 5: Spheres of silica within “ironstones” of the overlying clayey sandstone (sample 8).

Further results concerning defects in and the incorporation of trace elements into the kaolinite structure were obtained by ESR studies. The ESR spectra of kaolinite usually consist of two regions, low-field resonance with $g = 3.5\text{-}4.9$, which is associated with Fe^{3+} substituting for Al^{3+} , and high-field resonance with $g \sim 2.0$, which can be assigned to radiation induced defects (RID) (Clozel et al. 1994).

Fe^{3+} substitutes for Al^{3+} at two octahedral positions causing the ESR spectra at $g_{\text{eff.}} \sim 4.3$ (Meads & Malden 1975). These spectra were found in the investigated kaolin samples from Capim (Fig. 6). The intensity of the Fe^{3+} signal was high

compared to spectra of standard kaolin samples (e.g., KGa-1/2; Götze et al. 2002). This can be related to high contents of structural iron within the investigated kaolinites.

The other important group of paramagnetic centres represents the radiation induced paramagnetic defect centres (RID - $g_{\text{eff.}} \sim 2.0$). These centres are assigned to electron holes trapped on Si-O or Al-O-Al groups. Compared to kaolinites from other deposits (Götze et al. 2002), the Capim kaolinites show high signal intensities of these defects (Fig. 6).

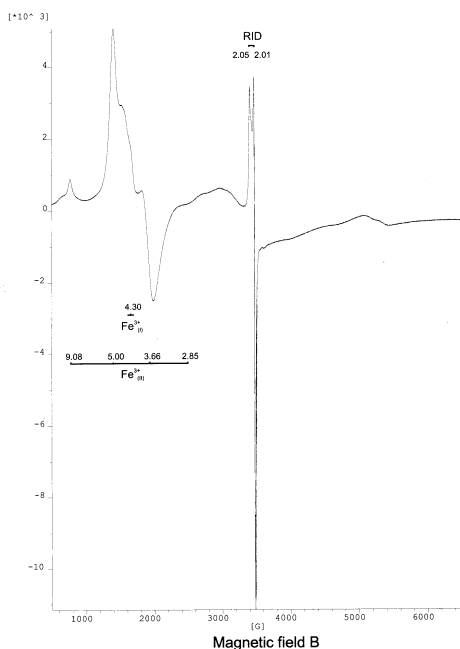


Figure 6: ESR spectrum (X band, 295 K) of a kaolinite sample from Capim showing high concentrations of Fe^{3+} and RID centres.

4 CONCLUSIONS

Samples of different stratigraphic horizons from the kaolin deposit of Capim were investigated concerning grain-size distribution (wet sieving, SEM), phase composition (XRD with Rietveld refinement), chemical composition, thermal behaviour (TG, DTA) and real structure (ESR spectroscopy) to get information about general characteristics of the clay material and to draw conclusions about a potential industrial use of the kaolin in the industry (e.g., paper, ceramics).

In most samples, more than 98 mass-% of kaolinite are concentrated in the fraction $<20 \mu\text{m}$, whereas almost no quartz was found in the fine fraction. Therefore, it is possible to produce a very pure fraction of kaolinite, although it is poorly crystalline (Hinkley index 0.33-0.73). XRD and chemical analysis revealed that Ti oxides and crandallite minerals are also concentrated in the fine fraction, which were probably formed by alteration processes of the parent rock material. Another problem for industrial use may arise from the high amounts of Fe in the kaolin. ESR studies revealed that some of the iron is structurally bound as Fe^{3+} in kaolinite and not removable by conventional dressing methods.

5 REFERENCES

- Clazol, B., Allard, T. & Muller, J.-P. 1994. Nature and stability of radiation induced defects in natural kaolinites: new results and reappraisal of published works. *Clay Clay Miner.* 42: 657-666.
- De Sousa, D.J.L. 2000. Characterization of Geology, Chemistry and Physics of kaolin from the Rio Capim deposit (in Portuguese). M.Sc. thesis, Universidade Federal do Pará, Belém.
- Götze, J., Plötze, M., Götze, Th, Neuser, R.D. & Richter, D.K. 2002. Cathodoluminescence (CL) and electron paramagnetic resonance (EPR) studies of clay minerals. *Mineral. Petrol.* 76: 195-212.
- Meads, R.E. & Malden, P.J. 1975. Electron spin resonance in natural kaolinites containing Fe^{3+} and other transition metal ions. *Clay Miner.* 15: 1-13.

Synthesis of Zn-Al-layered Double Hydroxides Precursor Phases Containing Carboxylic Acids in the Interlayer

T.Kühn & H.Pöllmann²

Martin-Luther-University Halle-Wittenberg, Department of Mineralogy and Geochemistry, Germany

ABSTRACT: Layered double hydroxides (LDH) with the formula $[Zn_{1-x}Al_x(OH)_2]^{x+} [xA * nH_2O]^{x-}$ and $xA = Cl^-, CO_3^{2-}, NO_3^-, SO_4^{2-}$ are a member of the hydrotalcite-group. The crystal structure is based on positive main- and negative charged interlayers. The ability of permanent interlayer-anion-exchange is investigated in this research project. The LDH's were synthesized by coprecipitation method at different pH-values (pH 7-12), reaction temperatures (40°C, 60°C, 80°C, 100°C), reaction time (1d, 3d, 7d and 21d) and different molarities of Me^{2+} (Zn) and Me^{3+} (Al). The synthetic products were analyzed by in situ X-ray diffraction measurements, thermal analysis (TG, DSC), infrared absorption spectra and chemical analysis. The results show an increase of crystallinity depending on the used synthesis condition. The pH- optimum varies between pH 7-7.5 for Zn-Al-LDH with $A = Cl^-, NO_3^-$ and pH 8.5-9 with $A = SO_4^{2-}$. The crystal size increases with increasing temperature and time. Best crystallinities were obtained at molarities of Zn:Al = 2:1 with $A = Cl^-, NO_3^-$ and Zn:Al = 3:1 with $A = SO_4^{2-}$. The results will be used to develop a method for synthesis of Zn-Al-LDH as precursor phase for the fixation of organic anions in the interlayer.

1 INTRODUCTION

Layered double hydroxides (LDH), commonly termed as metal-metal-hydroxysalts and anionic clay minerals, are a group of natural and synthetic materials containing different chemical and structural alternating layers. Negative charged interlayers with reversibly exchangeable anions, additional cations and water molecules occur alternating to the positive charged brucite-like mainlayers (Bish 1980). Furthermore, additional cations and organic molecules can be fixed reversibly within the interlayer.

One of the most important subgroup of the LDH represent the minerals of the hydrotalcite-group. The hydrotalcites are characterized by the ability of permanent interlayer-anion-exchange, which is recently used by industry (building-materials, catalyst) and pharmacy. Through the incorporation of large organic anions in the interlayer, the lamellar structure of hydrotalcite is expanding. Therefore, the hydrotalcites can be used to select ions in accordance to different diameters.

The simplified chemical structure of LDH is $[(Me(II)_{1-x}Me(III)_x(OH)_2]^{x+} [xA*nH_2O]^{x-}$, with Me as metal cation and A as exchangeable anion.

According to the widespread diversity of Me, a large number of LDHs have been synthesized with divalent cations such as Mg, Mn, Fe, Co, Ni, Cu, Zn etc. and trivalent cations such as Al, Cr, Mn, Fe, Co etc. Additionally, a lot of different inorganic anions such as $CO_3^{2-}, Cl^-, NO_3^-, SO_4^{2-}$ etc. can be fixed in the interlayer during direct synthesis and afterwards exchanged with organic anions.

The aim of this study was to develop a method for synthesis Zn-Al-LDH as precursor phases for fixation of carboxylic, sulfonic and amino acids in the interlayer via anion exchange.

2 EXPERIMENTAL

2.1 Synthesis

The following pure chemicals were used for synthesis: $ZnCl_2, AlCl_3*6H_2O, Zn(NO_3)_2*6H_2O, Al(NO_3)_3*9H_2O, ZnSO_4*7H_2O, Al_2(SO_4)_3*18H_2O, NaOH$.

Synthesis of LDHs were performed by coprecipitation method (Miyata 1975, Cavani et al. 1991). Different molar concentrations of Me(III), e.g. $Al(NO_3)_3*9H_2O$ and of Me(II), e.g. $Zn(NO_3)_2*6H_2O$, were dissolved in 50ml decarbonatized H_2O with constant stirring and

heating at 50°C. NaOH was quickly added up to pH 6.5 to prevent the formation of $\text{Al}(\text{OH})_3$ and further slowly added up to a constant pH (7-12). The aqueous solutions were filled in polyethylene bottles and aged at 40°C, 60°C and 80° for 3-21 days. Additionally, Zn-Al-LDH was prepared analogous to the method described above, using $\text{NaAl}(\text{OH})_4$, ZnO and inorganic acid (e.g. HNO_3) for pH fixation.

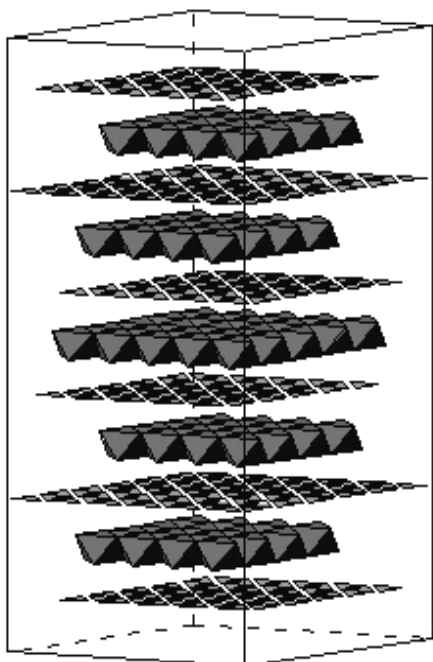


Figure 1. Layered structure of hydrotalcite. Top and bottom layers display the interlayer, separated by Mg/Al-hydroxides. (Pöllmann 1989).

All synthesis and subsequent analysis (e.g. filtering the precipitates) were done under constant nitrogen atmosphere in a glove-box to prevent the contamination with CO_2 , which is emplaced predominantly in the interlayer and complicates an anion exchange. Therefore, Cl^- , NO_3^- and SO_4^{2-} were used as exchangeable anions.

2.2 Characterization of synthesized products

The synthesized products were analyzed by in situ XRD measurements, using $\text{CuK}\alpha$ radiation and a PANalytical diffractometer with X'Celerator detector and silicon ($a_0=5.4308$, 99.999%) as an internal standard. The device was used in step scan mode with fixed slits.

Lattice parameters of LDHs with different anions were refined by Powley method with the software PowdMuld V2.2 and LeBail method with Topas V2.0. The samples were dried at 35% relative humidity and examined with chemical and thermal analysis and infrared absorption spectra.

3 RESULTS

3.1 Synthesis methods

The coprecipitation at constant pH is the most commonly used method for preparation of hydrotalcite-like compounds. The predominant minor phase in the synthesized samples at high pH values was ZnO. Using ZnO and $\text{NaAl}(\text{OH})_4$ implicates a high alkaline initial pH which can be adjusted to pH 7.5 with organic acids during the 'one-pot' or direct synthesis or with inorganic acids to synthesize LDH precursor phases. However, the chemical reduction of ZnO is more difficult than the prevention of the formation of ZnO. Furthermore the Zn-Al-salt reactants provide the anions within the solution that will predominantly be emplaced in the interlayer. According to the observations the coprecipitation method with Zn-Al-salts was the preferred synthesis method.

3.2 Electron microscopy

The samples are well crystallized and contain thin leaf-like crystals (Fig.2) with predominant pseudo-hexagonal shape.

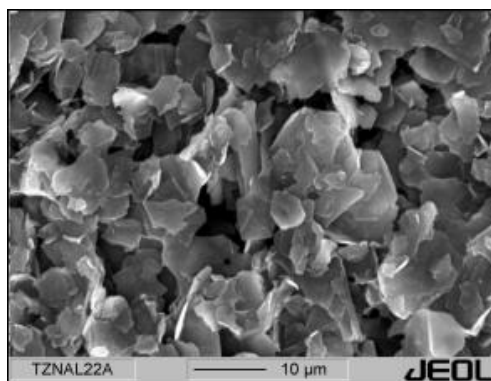


Figure 2. $[\text{Zn}_2\text{Al}(\text{OH})_6]^{+}[\text{NO}_3^* \text{nH}_2\text{O}]^{-}$ -crystals after synthesis at 80°C and pH 7.5. Hexagonal crystal faces are slightly visible.

3.3 Temperature, Time & pH-value

The Zn-Al-LDHs were synthesized at varying temperatures at 40°C, 60°C and 90°C and normal pressure. As shown in Figure 3, an increasing

crystallinity with increasing temperature is observed. At ambient temperature the (003) and (006) peaks of LDH display a wide peak shape and low intensities, additional to a high background. At 90°C the hkl-reflexes are still sharp, even the (116) and (10 14) reflexes at $65^{\circ}2\theta$. A further increasing temperature gives no remarkable enhancement of powder pattern.

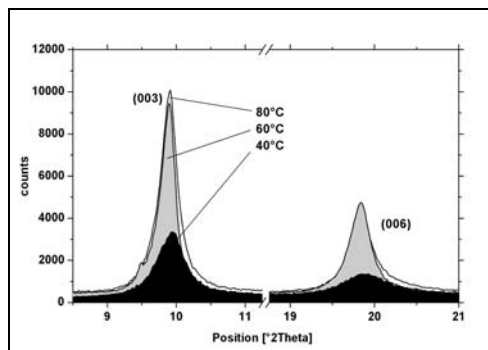


Figure 3. X-ray patterns of $[Zn_2Al(OH)_6]^+[NO_3^nH_2O]^-$ at pH 8 and 7 day altering

Although the formation of hydrotalcite starts even after the synthesis procedure the best intensities were obtained after 7 days at 80°C. The intensities of the (hkl)-reflexes advance with increasing alteration time up to an optimum at one week. X-ray patterns of longer altered samples show only shallow increased intensities of the LDH-peaks.

The pH is the most limiting factor for Zn-Al-LDH formation. As shown in Figure 4 the occurrence of ZnO increases with increasing pH-value, whereas the reflexes of LDH decrease. The best crystallinity of LDH with a Zn/Al-ratio ≈ 2 and monovalent anions (Cl^- , NO_3^-) was obtained at pH 7.5. But synthetic LDH with the divalent anion SO_4^{2-} is well developed at pH 9. Amorphous $Al(OH)_3$ occurs additional to poor crystallized Zn-Al-hydrotalcite at lower pH. At pH=10 (Roy et al. 2001), well crystallized LDH with the M^{2+}/M^{3+} -ratio=3 coexists with ZnO. At higher pH only ZnO reflexes were observed.

Well crystallized hydrotalcite like compounds are described for acidic conditions up to pH 5-6 (Costantino et al. 1999, Goswamee 1999). Using the coprecipitation method are owing small (hkl)-reflexes with low intensities and irregular peak shape. Therefore, only alkaline synthesis methods have been further examined in this research project.

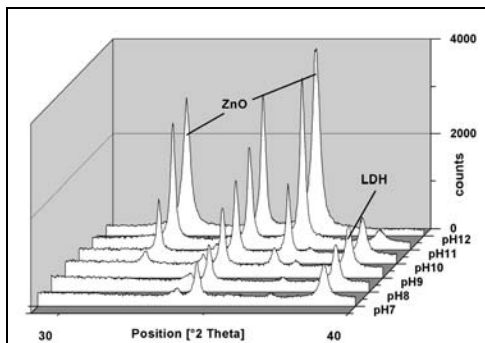


Figure 4. Different pH values used for synthesis Zn-Al-LDH.

3.4 Substitution of anions

In order to evaluate the mobilization potential of Zn-Al hydrotalcite-like compounds with various inorganic anions in the interlayer and the further substitution of organic anions selected synthesis were prepared and analyzed. The following two systems have been performed: Zn-Al-LDH with M^{2+}/M^{3+} ratio=2, pH=7.5, $A=Cl^-$, NO_3^- and M^{2+}/M^{3+} ratio=2, pH=9 and $A=SO_4^{2-}$. After syntheses of the precursor phases analogous to the procedure described above, neutralized carboxylic acids in excess were added. The substitution was carried out at pH 7. Afterwards the samples were altered for one week at 80°C.

As shown in Figure 5 and 6, exchange of inorganic anions by different carboxylic acids leads to an expansion of lamellar structure of the LDH, which depends on the chain size of the substituted organic anions.

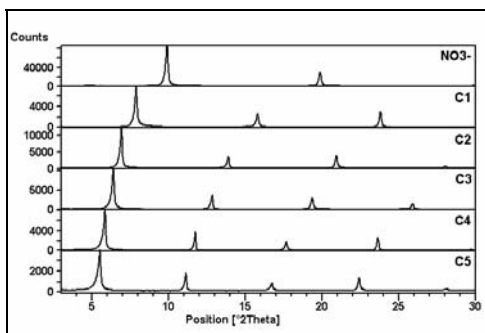


Figure 5. X-ray powder pattern of anion exchange. Upper pattern marks the inorganic-precursor-phase.

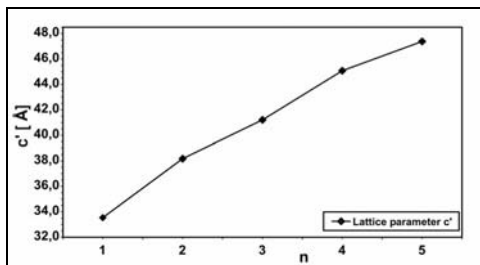


Figure 6. IR-Lattice parameter c' vs. chain length of carboxylic acids.

Replacement of the monovalent anion NO_3^- by carboxylic acids is leading to a complete substitution, while the mobilization potential of Cl^- decreases dependent on the increasing ionic radii of the carboxylic salts. The IR-spectrum (Fig.7) of synthesized Zn-Al-LDH with $\text{C}_5\text{H}_{11}\text{COO}^-$ in the interlayer, which is representative for replacement with C_1 - C_{10} , displays the characteristic absorption bands $\nu_{\text{as}}=1590\text{cm}^{-1}$, $\nu_{\text{s}}=1410\text{cm}^{-1}$ of $-\text{COO}^-$ and of CH_2/CH_3 at 2980cm^{-1} (Günzler & Heise 1996). In contrast to Cl^- and NO_3^- the IR-spectrum of substituted $\text{SO}_4^{2-} \leftrightarrow \text{C}_5\text{H}_{11}\text{COO}^-$ (Fig.8) shows distinctive absorption bands of SO_4^{2-} , additional to the bands of carboxylic acid. That assumes the formation of a LDH with mixed anions.

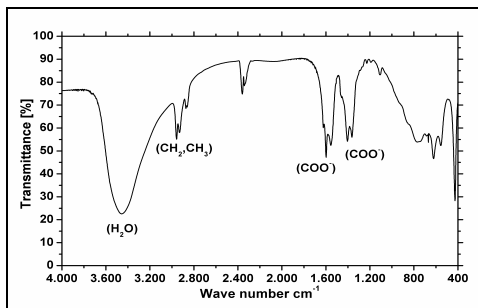


Figure 7. IR-spectrum of Zn-Al-LDH $\text{C}_5\text{H}_{11}\text{COO}^-$. The precursor phase contained Cl^- as anion in the interlayer.

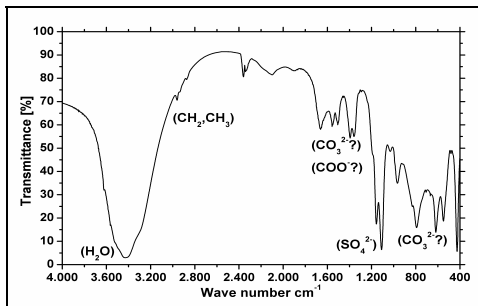


Figure 8. IR-spectrum of Zn-Al-LDH $\text{C}_5\text{H}_{11}\text{COO}^-$. The precursor phase contained SO_4^{2-} as anion in the interlayer.

4 CONCLUSIONS

1. Synthetic Zn-Al-hydroxalcite precursors can be well prepared by the coprecipitation method.
2. Best intensities in X-ray powder patterns were obtained at $\text{M}^{2+}/\text{M}^{3+}$ -ratio=2 for used monovalent inorganic anions and $\text{M}^{2+}/\text{M}^{3+}$ -ratio=3 for SO_4^{2-} . The optimal synthesis conditions are $\text{pH}=7-7.5$ (Cl^- , NO_3^-) and $\text{pH}=9$ (SO_4^{2-}), reaction time of 7d and 90°C aging temperature (Fig.9).
3. Under the same synthesis conditions Zn-Al-LDH with Cl^- and NO_3^- in the interlayer are the most suitable precursor phases for anion exchange with carboxylic acids.

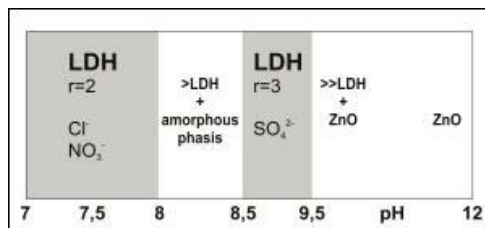


Figure 9. Optimized pH conditions for synthesis of Zn-Al-LDH precursor phase

5 REFERENCES

- Bish, D.L. 1980. Anion-exchange in takovite: applications to other hydroxide minerals. *Bull. Minéral.* 103: 170-175.
- Cavani, F., Trifiro, F. & Vaccari, A. 1991. Hydroxalcite-type anionic clays: Preparation, properties and applications. *Catalysis Today* 11: 173-301.
- Costantino, U., Coletti, N. & Nocchetti, M. 1999. Anion Exchange of Methyl Orange into Zn-Al Synthetic Hydroxalcite and Photophysical Characterization of the Intercalates Obtained. *Langmuir* 15: 4454-4460.
- Goswamee, R.L. 1999. Synthesis and characterization of some mixed metal hydroxides and their applications. *PhD-Thesis, Guwahati: Gauhati University.*
- Günzler, H. & Heise, H.M. 1996. IR-Spektroskopie-Eine Einführung. Weinheim: VCH Verlagsgesellschaft.
- Miyata, S. 1975. The syntheses of hydroxalcite-like compounds and their structure and physico-chemical properties-I: The system $\text{Mg}^{2+}\text{-Al}^{3+}\text{-NO}_3^-$, $\text{Mg}^{2+}\text{-Al}^{3+}\text{-Cl}^-$, $\text{Mg}^{2+}\text{-Al}^{3+}\text{-ClO}_4^-$, $\text{Ni}^{2+}\text{-Al}^{3+}\text{-Cl}^-$ and $\text{Zn}^{2+}\text{-Al}^{3+}\text{-Cl}^-$. *Clays and Clay Minerals* 23: 369-375.
- Pöllmann, H. 1989. Mineralogisch-Kristallographische Untersuchungen an Hydrationsprodukten der Aluminatphase hydraulischer Bindemittel. *Habil. Mineralogisches Institut Universität Erlangen.*
- Roy, A.d., Forano, C. & Besse, J.P. 2001. Layered Double Hydroxides: Synthesis and Post-Synthesis Modification. In Rives, V. (ed.). *Layered Double Hydroxides: Present and Future.* New York: Nova Science Publisher, Inc.

Natural Refinement of Quartz Raw Materials for the Production of Polycrystalline Silicon

R.B.Larsen & F.Jacamon

Department of Geology and Mining Engineering, Norwegian University of Science and Technology, Trondheim, Norway

P.M.Ihlen & I.Henderson

Geological Survey of Norway, Trondheim, Norway

ABSTRACT: An annual growth of the solar cell marked of 15% is expected over the next eight years. Accordingly, by 2010, the world marked demand for solar cell quality polycrystalline silicon is 8000 tons/yr. These requirements exceed the amount of polycrystalline silicon that currently is available from the semi conductor industry. Application of ultra high purity quartz (HPQ) as a raw material may solve this demand shortage and may reduce the final raw material costs. Natural quartz with the desired quality is currently unavailable. However, in this study we outline the geological processes required for the genesis of HPQ in granitic pegmatite. Ti, P, Fe and Al are enriched at high temperatures in quartz forming from primitive mantle derived granitic melts. Al, together with B, is enriched in peraluminous melts, whereas Ti will be relatively low in this setting. The lowest concentrations of Ti, P, Fe and Al, altogether, are found in evolved volatile-rich melts where quartz crystallised at a relatively low temperature. The Li concentration may be greatly reduced by subsolidus recrystallization of igneous quartz by infiltrating aqueous fluids. Solar cell polycrystalline silicon can most likely be refined from low temperature quartz crystallizing from an uncontaminated granitic melt that were exposed to partial subsolidus recrystallization. Several occurrences fulfilling these conditions were discovered in South Norway.

1 INTRODUCTION

In the present study we document the trace element distribution in quartz from the Evje and Froland meta-aluminous granitic pegmatite fields in South Norway. These pegmatite fields are thoroughly documented in terms of their origin, evolution and petrogenetic links from several studies throughout the past eighty years. Given this volume of previous work, we have a solid foundation upon which to interpret the igneous evolution of quartz and to evaluate the genesis of high purity quartz as a future raw material for the solar cell industry.

The scope of the present communication is to document the trace element evolution of granitic pegmatite quartz during the evolution from primitive to evolved granitic compositions and during subsolidus recrystallization of quartz. It will be discussed how the trace element distribution in quartz compare to K-feldspar for which the chemical changes during igneous evolution is well known. We hold that certain CAFCC processes in granitic rocks and subsolidus recrystallization may produce very high purities of quartz.

1.1 Solar cells and quartz

A solar cell comprises two layers of polycrystalline

silicon. Si-ions in one layer is partially substituted by ions having a single charge less than Si^{4+} whereas Si-ions in the other layer are substituted with ions having a single charge more than Si^{4+} . Most commonly, the contaminant ions are B^{3+} and P^{5+} respectively, because they approach the ionic potential of Si^{4+} hence fit very well into the silicon atomic lattice. The excess, respectively deficit of electrons generates an electron current between the two sides given that sunlight (i.e. photon packages) is supplied.

In order for the polycrystalline silicon to work properly, the silicon raw material, i.e. quartz, must comprise a very high purity. Trace amounts of trivalent or pentavalent ions prohibit the required imbalance of electrons between the two sides of the solar cell. Monovalent ions, for example Li, Na and K, may charge balance B and quench the electron flow. Similarly, trivalent ions on the P-enriched side of the solar cell may charge balance P ($2\text{Si}^{4+} = \text{Al}^{3+}\text{P}^{5+}$) and also prevent the flow of electrons. Accordingly, it is required that the quartz raw material for the production of solar cell polycrystalline silicon must contain extremely low concentrations of trivalent, monovalent and pentavalent ions. The P and B content must be less than 1 g/ton and the total concentration of trace

elements in the quartz must be less than 50 g/ton.

Unfortunately, when a trace element is first incorporated in the atomic lattice of quartz, it is normally very energy intensive hence expensive to extract it. Exceptions may be the monovalent ions that can be partially removed by acid leach, but otherwise the quartz raw materials must have experienced natural geological processes that strongly enhance its purity.

2 CHEMISTRY OF QUARTZ

Quartz comprises an exceptionally strong configuration of Si-O bonds that allows only a minimum of other elements into its structure. Accordingly, more than 50 % of the bonds are covalent. However, anywhere from 50 ppm or less to a few thousand ppm of trace elements may be incorporated into the atomic lattice. Trace elements that may fit in to the atomic lattice structure of quartz includes Al, B, Ba, Be, Ca, Cr, Cu, Fe, Ge, H, K, Li, Mg, Mn, Na, P, Pb, Rb, Sr, Ti and U. Not all studies agree with this list of elements.

Normally, the speciation and concentration of trace elements cannot be judged from the macroscopic appearance of quartz. For example, quartz that at first glance appears clear and inclusion-free may contain thousands of ppm of structurally bound trace elements. On the contrary, dark smoky quartz with many solid and liquid inclusions may be nearly free of trace elements in the atomic lattice. The smoky colour is caused by low levels of ionising radiation induced by the decay of radiogenic elements in neighbouring minerals (e.g. ^{40}K in K-feldspar). The quartz itself may contain only a few ppm of structurally bound elements that are confined to colour centres in the atomic lattice. Other colour variations may indeed be signs of abundant trace elements. Amethyst, for example, owes its colour to structurally bound Fe. Rose quartz, owe its colour to high concentrations of structurally bound Fe and Ti, to Al-P substitutions or may be caused by inclusions of sub-microscopic dumortierite $[\text{Al}_7(\text{BO}_3)(\text{SiO}_4)\text{O}_3]$ fibres.

In the current study of quartz from Evje and Froland we are mostly concerned with Al, B, Be, Fe, Ge, K, Li, Na, P and Ti because these elements comprise > 99 % of the trace elements. Ti and Ge, both being tetravalent ions, occur in the quartz lattice as simple substitution for Si^{4+} (Fig. 1b). Phosphorous, which is a pentavalent ion, is integrated as coupled substitutions together with Al^{3+} , or another trivalent ion (Fe^{3+} or B^{3+}), in two neighbouring silicon-tetrahedron (Fig. 1c). Monovalent ions (Li^+ , K^+ and Na^+) are either situated in atomic channels running parallel to the c-axis or at sites of lattice defects (e.g. dislocations). Divalent ions mostly occupy vacancies (Be^{2+}) or

atomic cavities (Fig. 1d). They are charge balanced by trivalent ions, mostly Al^{3+} , which is substituting for Si^{4+} .

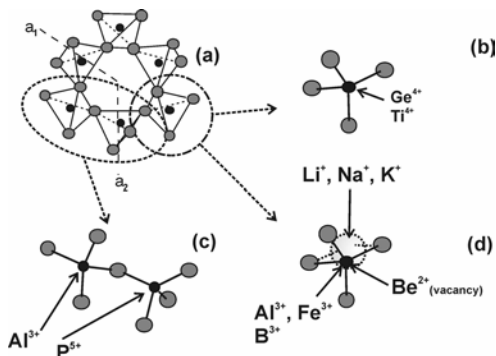


Figure 1: Structurally bound trace elements in quartz. a: atomic model of low-quartz. b: single substitution of Ge and Ti. c: coupled substitution of P and Al pairs. d: stuffed derivatives where a trivalent ion substitute for Si and is charge balanced by a monovalent ion.

3 TRACE ELEMENTS IN QUARTZ

3.1 Structural bound trace elements in quartz

By weight, the dominant trace elements in granitic pegmatite quartz are Al, P, Li, Ti, Ge, Na and B in that order of abundance. In most samples there are >1 ppm of any of these elements and together they comprises > 95 wt.% of the trace elements. The remnant 5% comprises K, Fe, Be, Ba and Sr whereas other elements normally are present at concentrations lower than the detection limit.

3.2 Trace elements in quartz compared to K-feldspar

To fully understand the partitioning of trace elements between quartz and the co-existing granitic melts, the distribution of key trace elements in quartz are compared to the distribution of Rb, Pb and Ga in K-feldspar. In particular Rb, but also Pb and Ga are strongly incompatible elements in granitic melts hence their concentration in K-feldspar will increase as the granitic melt develops from primitive to progressively more evolved compositions (e.g. Larsen R.B. (2002) *The Canadian Mineralogist* 40: 137-151).

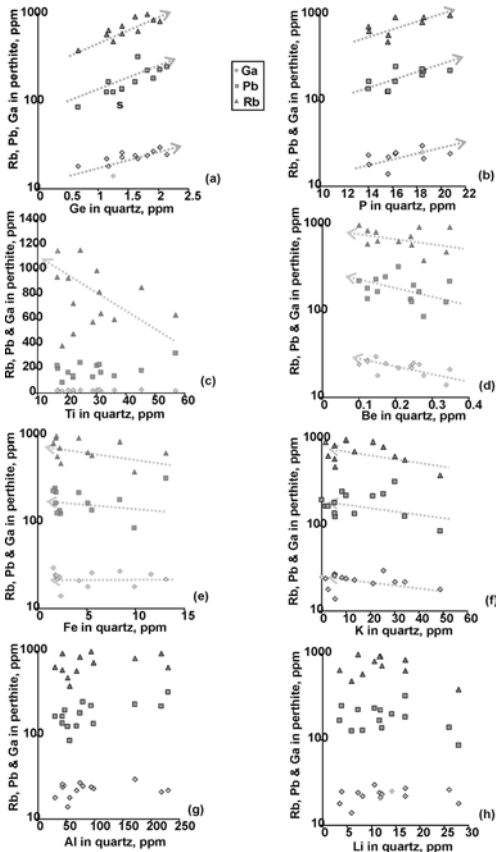


Figure 2: Distribution of trace elements in K-feldspar are compared with the distribution of trace elements in quartz. See text for details.

The concentrations of Ge_{qz} and P_{qz} are increasing proportionally with the concentration of Rb_{kfs} , Pb_{kfs} and Ga_{kfs} in K-feldspar (FIGURE 2a, b). The concentration of Ti_{qz} , Be_{qz} , Fe_{qz} and K_{qz} in quartz is falling as the concentration of Rb_{kfs} , and in most cases also Pb_{kfs} and Ga_{kfs} is increasing in perthite (Figs. 2c-f). The trends for Be_{qz} are well constrained, whereas the trends for Fe_{qz} and K_{qz} are more erratic. Titanium_{qz} shows a strong negative correlation with Rb_{kfs} . The concentration of Al_{qz} and Li_{qz} is inconsistent when compared to Rb_{kfs} , Pb_{kfs} and Ga_{kfs} . Apparently the concentrations of both Al_{qz} and Li_{qz} are increasing up to a certain point after which they follow a path of constant Rb-values (Fig. 2g, h) or, in the case of Li_{qz} , the path becomes negative with the highest concentrations of Li_{qz} coinciding with lowest concentrations of Rb_{kfs} .

3.3 Subsolidus remobilisation

In order to test the sensitivity of Li and other monovalent cations to subsolidus processes, we analyzed Evje and Froland quartz that had recrystallized repetitively during subsolidus conditions. These analyses consistently imply that Ge and Ti maintain constant concentrations even through episodes of pervasive recrystallization (Figs. 3a, b). On the contrary, the concentration of Li is falling with the degree of recrystallization whereas the concentrations of Na and K respectively, are increasing (Na) or nearly constant (K) (Figs. 3c-e). Accordingly, Na partition in favour of quartz whereas Li partition in favour of the aqueous fluids that are associated with subsolidus recrystallization. Potassium is apparently undisturbed by the infiltrating aqueous fluids.

The concentrations of both B and P are nearly constant during both partial and more pervasive recrystallization. Accordingly, the concentration of these elements are not seriously altered.

With these results it is implied that Li and Na has the ability to partially migrate in and out of the quartz lattice during subsolidus hydrothermal alteration.

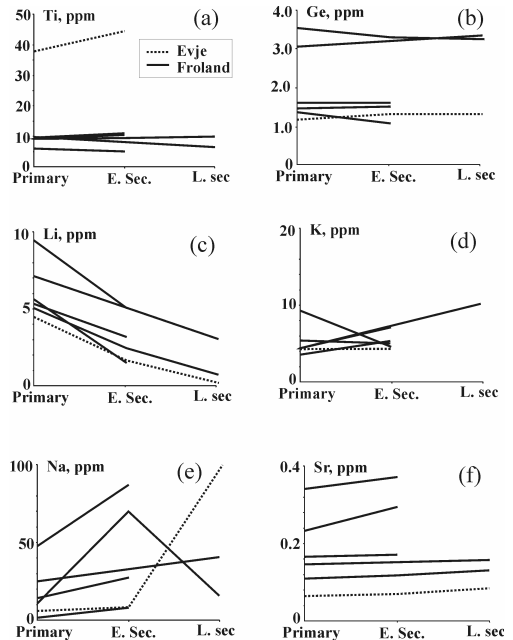


Figure 3: Remobilization of trace elements during progressively more recrystallized igneous quartz. "Primary": unaltered granitic pegmatite quartz. "E. Sec": Early secondary quartz i.e. partially recrystallized quartz. "L. Sec": late secondary quartz i.e. pervasively recrystallised quartz.

4 CONCLUSIONS

- The dominant trace elements that are incorporated in igneous quartz in the Evje and Froland pegmatite fields are Al, P, Li, Ti, Ge, Fe and K in that order of abundance and in concentrations greater than 1 ppm. Be, B, Ba and Sr are common in concentrations from a few ppb to 1 ppm.

- Structural bound trace elements in quartz are highly sensitive to petrogenetic processes. Particularly Ge, P, Ti and Be record both the origin and evolution of the granitic rocks and efficiently discriminate between melts of different origin that otherwise may share many similarities.

- K, Fe, Be and Ti are the most compatible trace element whereas P, Ge, Li, and Al are progressively more incompatible (from P to Li).

- Ge, Ti, P and B are immobile during subsolidus recrystallization of igneous quartz. Li partition in favour of the infiltrating aqueous fluids whereas Na partition in favour of quartz.

- Solar cell polycrystalline silicon can most likely be refined from low temperature quartz crystallizing from an uncontaminated granitic melt that were exposed to partial subsolidus recrystallization.

Study on the Synthesis of 4Å Zeolite from Bentonite

X.Lu, J.Qiu & X.Cui

Department of Chemical and Environmental Engineering, Shandong University of Science and Technology, Qingdao, Shandong 266510, China

ABSTRACT: This paper presents the experimental results of synthesizing 4Å zeolite from Ca-bentonite. A synthesis process consisting of acidification, basification, gelation and crystallization was employed, and the process parameters such as dosages of chemicals, liquid/solid (S/L) ratios, temperatures and retention times at different steps were tested in detail. According to the X-Ray Diffraction (XRD) analysis, the synthesized product under optimal conditions turns to be a typical 4Å zeolite with a cell constant of 12.20 Å and chemical formula of $\text{Na}_2\text{Al}_2\text{Si}_{1.85}\text{O}_{7.7}\cdot 5.1\text{H}_2\text{O}$. And, the Ca^{2+} exchange capacity, whiteness and particle size of the synthesized product were measured as 294.9-311.4mg/g, 90.59-92.90% and 1.02-1.33 μm (d_{50}) respectively.

1 INTRODUCTION

Along with the use of large quantities of detergents containing Sodium Tri-Poly Phosphate (STPP), more and more water areas in China have been growing over-nourished, which has caused serious environmental problems. For this reason, the use of detergents containing STTP has been forbidden in China and many other countries. As a result, the substitutes of STPP are essential in dairy chemical industry, and the 4Å Zeolite has been reported a proper substitute of STPP (Zhu & Song 1993). Previous researches showed that it is technically feasible to synthesize 4Å zeolite from bentonite (Liu 2000 Lu 1991 Wang 2002). The characterizations of the structure and properties of the synthesized 4Å Zeolite were also reported (Han 1997). However, the proper process parameters and the properties of the synthesized products vary from material to material. The aim of this study is to investigate the proper process parameters of synthesizing 4Å zeolite from the Ca-bentonite from Laixi of Shandong Province, China, and to characterize the structure and properties of the synthesized material by means of XRD analysis, whiteness measurement, Ca^{2+} exchange capacity and particle size measurements.

2 EXPERIMENTAL

2.1 Materials and instrumentation

The bentonite sample used in this experiment was obtained from Laixi of Shandong Province, China. The main mineral in the material is montmorillonite with a content of 65-70%, and the minor minerals include quartz, feldspar and calcite. The montmorillonite in the sample was characterized by XRD as typical Ca-montmorillonite with interlayer spacing d_{001} of 15.331 Å.

The reagents used in the experiments include H_2SO_4 (98%, w/w), HCl (37%, w/w), NaOH, NaAlO_2 , and CaCO_3 . All reagents are made in China and of analytical grade.

Atomic Absorption Spectrophotometer (HP3510, Shanghai, China) was used to measure the Ca^{2+} exchange capacity of the 4Å Zeolite by measuring the difference of Ca^{2+} content in solution before and after Ca^{2+} exchange, X-ray diffractometer D/Max-3B, Japan was used to characterize the structures of the raw material and synthesized products, Whiteness-Colorimeter (WS-SD d/o, Zhejiang, China) was used to measure the whiteness of the 4Å Zeolite, and Laser Particle Analyser (JL1166, Sichuan, China) was used to measure the particle distribution of the synthesized 4Å Zeolite.

2.2 Experimental procedure

The raw material was firstly de-gritted to remove quartz and other impurities. Then the refined material was used as the starting material for the synthesis of zeolite. The synthesis process consists of acidification, basification, gelation and crystallization. First, the starting material was reacted with HCl or H₂SO₄ to remove metallic ions such as Ca²⁺, Fe²⁺, Al³⁺ and Mg²⁺ from the material, and then the residue was washed on a vacuum filter and dissolved in NaOH solution to produce Na₂SiO₃. After that, NaAlO₂ was added to react with Na₂SiO₃ to form an aqueous gel product, and finally the gel crystallized to form 4Å zeolite under proper temperature and retention time. The final products were washed and filtered on a vacuum filter and dried at the temperature of 105 . All the experiments were conducted in beakers of 400ml to 600ml under controlled temperatures in a water bath cell, and stirrers were used to disperse the suspensions.

3 RESULTS AND DISCUSSIONS

3.1 Acidification

In this stage, acid types and dosages, L/S ratios, temperatures and duration times were tested in detail. Under the conditions of 30% HCl, L/S ratio of 4/1, temperature of 95 and retention time of 8h, most of the cations in the material were removed and the structure of montmorillonite was destroyed. According to the XRD analysis on the starting material and on the acidified material, the peaks of montmorillonite disappeared after acid treatment (Fig.1, Fig.2) and amorphous silica was formed.

However, the XRD results (Fig.1, Fig.2) also indicate that the quartz in the starting material is unaffected after acid treatment and retains in the residue.

3.2 Basification

The acid treated material, after washing, was subject to the basification process. Using 30%(w/w) NaOH as the basification reagent, the effect of Na₂O/SiO₂ molar ratio on the properties of the final product were tested under L/S ratio of 4/1, temperature of 65 and retention time of 2h. And, gelation conditions were controlled as L/S ratio of 4/1, Si/Al molar ratio of 1/1, gelation temperature of 20-30 and retention time of 1h, and crystallization conditions were controlled as temperature of 90 and retention time of 3h. Results (Table 1) indicate that the best product quality can be obtained when the Na₂O/SiO₂ molar ratio is controlled as 2.25/1. The Ca²⁺exchange capacity of the synthesized product reaches maximum value of 311.4mg/g, and the particle size reaches the finest

value of 1.02µm (d₅₀). But, little variations of whiteness were observed within the tested range of Na₂O/SiO₂ molar ratios.

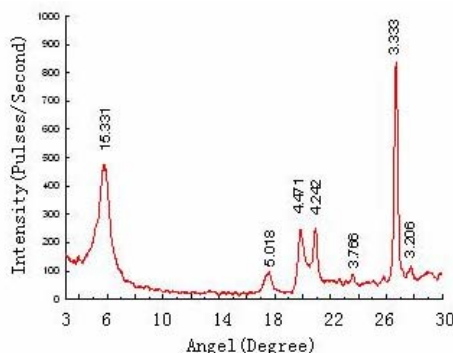


Figure 1: X-ray diffraction pattern of starting material.

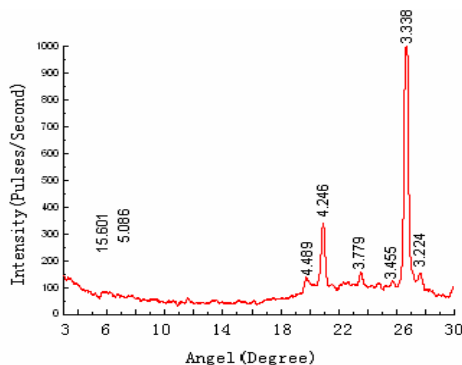


Figure 2: X-ray diffraction pattern of the acidified material.

Table 1: Effect of Na₂O/SiO₂ molar ratio on the properties of synthesized product.

Na ₂ O/SiO ₂ molar ratio	1.5:1	2.25:1	3:1	4:1
Particle size (d ₅₀) (µm)	1.331	1.02	1.176	1.189
Whiteness degree (%)	92.35	91.72	92.20	91.32
Ca ²⁺ exchange capacity (CaCO ₃ mg/g)	295.5	311.4	297.7	293.5

3.3 Gelation

The dosage of NaAlO₂, represented by Si/Al molar ratio is the key parameter for a successful gelation. Under the above mentioned optimal basification conditions the effect of Si/Al in the gelation stage was studied at the temperature of 20-30 and reaction time of 1h. And, crystallization conditions were controlled as temperature of 90 and retention

time of 3h. Results (Table 2) show that the optimal Si/Al ratio is 1/1, and more or less Si/Al ratio will cause negative effects on the Ca²⁺ exchange capacity and the fineness of the product. Again, the whiteness is not obviously affected.

Table 2: Effect of the Si/Al mole ratio on the properties of synthesized product.

Si/Al mole ratio	1.5:1	1:1	1.5:2	1.5:2.5
Particle size d ₅₀ /μm	1.247	1.08	1.177	1.111
Whiteness degree, %	92.80	91.86	92.48	91.93
Ca ²⁺ exchange capacity, CaCO ₃ /mg/g	297.6	311.2	299.7	300.6

3.4 Crystallization

After gelation, the material is subject to the stage of crystallization. Under the foregoing optimal process parameters of basification and gelation, the effects of retention time and temperature at the crystallization stage were studied.

The effect of crystallization time was tested at the temperature of 90 °C. Results (Table 3) show that the retention time should be controlled at about 3h in order to get the maximum Ca²⁺ exchange capacity.

With the retention time controlled at 3h, the effect of the crystallization temperature was further tested. According to Table 4, Ca²⁺ exchange capacity of the synthesized product increases with the temperature when the temperature is less than 90 °C, but higher temperature of more than 90 °C will cause somewhat decrease of the Ca²⁺ exchange capacity. Therefore, the optimum crystallization temperature should be 90 °C.

Based the foregoing experiments, the optimal synthesis conditions for the bentonite sample can be summarized as the following: First, the starting material is treated with 30% HCl solution for 8h at L/S ratio of 4/1 and temperature of 95 °C; and then the washed residue is dissolved in 30% NaOH solution for 2h at Na₂O/SiO₂ molar ratio of 2.25/1, L/S ratio of 4/1 and temperature of 65 °C. After that, the NaOH treated solution was put into reaction with NaAlO₂ to get an aqueous gel under the conditions of Si/Al of 1/1, temperature of 20-30 °C and duration of 1h. Finally the gel is subject to the crystallization stage for 3h at the temperature of 90 °C.

Table 3: Effect of the crystallization time on the Ca²⁺ exchange capacity.

Crystallization time, h	1	2	3	4	5
Ca ²⁺ exchange capacity, CaCO ₃ /mg/g	300.3	298.7	311.4	305.2	294.9

Table 4: Effect of the crystallization temperature on the Ca²⁺ exchange capacity.

temperature/°C	70	80	90	100
Ca ²⁺ exchange capacity, CaCO ₃ /mg/g	297.9	299.6	311.4	308.7

3.5 XRD analysis and characterization of the synthesized material

The synthesized material under optimal process conditions was further detected by XRD. According to Figure 3, the X-ray diffraction patterns of the synthesized product is a typical 4Å Zeolite with the cell constant of 12.20 Å and a chemical formula of Na₂Al₂Si_{1.85}O_{7.7}·5.1H₂O. Also, the peaks of quartz were detected in the synthesized material. This is because that the finely disseminated quartz in the raw material was not efficiently removed in the de-gritting process.

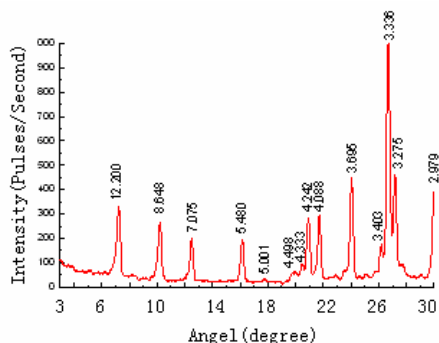


Figure 3: X-ray diffraction pattern of the synthesized material

The properties of the final product synthesized under optimal conditions and the comparison with the quality standard set by the Ministry of Chemical Industry of China (Q/HG02-05091) were listed in Table 5. According to the results, the quality of the synthesized 4Å zeolite fully meets the quality standard. This indicates that the synthesis process of 4Å zeolite from Ca-bentonite is technically feasible.

Table 5: Quality index of the synthesized 4Å Zeolite and comparison with the standard (Q/HG02-05091).

Quality Index	Q/HGJ02-05091 Standard	Synthesized Product
Ca ²⁺ exchange capacity, CaCO ₃ mg/g	≥240	294.9~311.4
Whiteness, %	≥85	90.59~92.90
Particle size<4μm, %	≥80	91.34

4 CONCLUSIONS

Based on the experiments, it is technically feasible to synthesize 4Å Zeolite from bentonite by the process of acidification, basification, gelation and crystallization. The structure of the synthesized product has been confirmed by XRD analysis as a typical 4Å zeolite with a cell constant of 12.20 Å, and the Ca²⁺ exchange capacity, whiteness and particle size of the synthesized zeolite were measured as 294.9-311.4mg/g, 90.59-92.90% and 1.02-1.33μm (d₅₀) respectively. But, it is essential to optimize the process parameters such as the dosages of chemicals, temperatures and retention times because they have notable influence on the properties of the synthesized product. Also, the purification of the raw material and the utilization of the effluent from acid treatment need to be further studied.

5 REFERENCES

- Han, Shuyun, et al. 1997. Studies on the Synthesis, Structure and Properties of 4Å Zeolite Molecular Sieve. *Journal of Qingdao University*, 10(3): 31-36.
- Liu, Zhicheng. 2000. Study on the Synthesis Process of 4Å Zeolite for Detergents from Bentonite. *Non-Metallic Mines*, 23(2): 21-23,16.
- Lu, Peinan. 1991. Preparation of 4Å Zeolite for Detergents by Use of Bentonite. *Daily Chemical Industry*, (4): 1-6.
- Wang, Zhiguo. 2002. Study on Utilizing Bentonite to Synthesize 4Å Zeolite. *Industrial Minerals and Processing*, (6): 11-12,23.
- Zhu, Tiejun and Song, Zongliang. 1993. Study on the Synthesis of New Type 4Å Zeolite and Low-Phosphor Detergent. *Daily Chemical Industry*, (3): 21~22.

Stereological Reconstruction of Planar Composition Using the Method of Schneider

M.J.Matos & J.J.Sousa

Department of Materials & Production Technologies, INETI, 1649-038, Lisboa, Portugal

Abstract: Planar composition distributions were converted into volumic composition distributions, by the stereological method of Schneider. A real ore was used as vehicle of test. Data was acquired on polished sections, mounted from samples of the size fractions obtained by hydroclassification of the ore, ground to 95% -75µm. The higher biases were observed in the classes 0-10% and 90-100%, where the particles, due to the sectioning effect, tend to be 'seen' as free. Stereological correction provided approaching the real (volumic) liberation data..

1 INTRODUCTION

Structures are generally evaluated through measurements on sections which, unless performed according to unbiased procedures (Howard & Reed 1998), contain deviations due to the sectioning effect. Procedures to obtain unbiased data, although currently applied in quantifying biological structures (Gundersen & Jansen 2002), are sometimes difficult, even impossible, to implement for quantifying materials with high natural variability, as is the case of many mineral ores. In these circumstances, the stereological extrapolation, supported by statistically representative planar data, provides useful approaches to the real structure (Underwood 1970).

Methods for volumic reconstruction were developed, under the mathematical support of Statistics and Probabilities. The stereometric relations are deduced taking into account the property of interest, the parameter used to express it, the parameter projections in the sections and the method used for measuring the projections.

The stereologic methodology is unfolded in two main steps, which consist of (1) establishing the mathematical expression of the direct relation (3-D → 2-D) and (2) using it to deduce the expression of the inverse relation (2-D → 3-D). In practice, it

consists of using a known structure (real or simulated) and evaluating how does a given property relate with its projections in random sections. The relation is theoretically expressed as follows:

For a property m , the relation between the volumic data distributions, $p(m_3)$, and the planar data distributions (lineal or areal), $F(m_{1,2})$, is given by the Freedholm integral equation of the 1st species:

$$F(m_{1,2}) = K(m_{1,2}|m_3) \cdot p(m_3) dm_3 \quad (1)$$

In the expression, m assumes values in the interval $[0, x]$; 1,2,3 refer to the spatial dimension of measurements; $p(m_3)$ represents the probability density of the property volumic data distribution; $F(m_{1,2})$ represents the cumulative distribution of the planar measurements and $K(m_{1,2}/m_3)$ represents the function (matrix) of direct transformation, which establishes the relation between the classes of volume and the probability distribution of the random planar projections in each class.

When structures consist of heterogeneous particulate systems and the property is the composition, the volumic reconstruction assumes high complexity. Expression (1) is difficult to apply because generates unstable numeric solutions and requires the knowledge of the kernel of direct

transformation, or matrix **K**. This is determined by subdividing the volumic data range in *n* narrow ranges and measuring, in each range, the *m* planar projections of composition. The discretized form of equation (1) is:

$$f_{(1,2)i} = \sum_{j=1}^n k_{ij} f_{(3)j}, \quad i = 1, \dots, m;$$

or, in matricial notation:

$$f_{1,2} = K f_3 \quad (2)$$

K represents the discretized form of the direct transformation matrix, with dimension (mxn) and generic element k_{ij} ; $f_{1,2}$ represents the vector distribution of the proportions of the classes of planar composition (m components); f_3 represents the vector distribution of the volumic proportions of the classes of volumic composition (n components).

The objective of quantitative stereology is to estimate f_3 , theoretically given by:

$$f_3 = K^{-1} f_{1,2} \quad (3)$$

K^{-1} represents the inverse or stereologic matrix. In practice, however, matrix **K** is almost singular (determinant close to zero), with a high number of condition, which means that the direct inversion leads to obtaining non-admissible solutions. The inversion must be attained by mathematical indirect procedures.

2 THE METHOD OF SCHNEIDER

Matrix **K** was determined by direct experimentation. Matrix inversion was approached by mathematical techniques of iterative indirect reconstruction.

2.1 Obtaining experimental data

Direct experimentation involved:

- classifying real mineral particles (obtained by the primary grind of an ore, considered biphasic) in narrow size fractions; classifying by densities the particles of each fraction;

- defining, from the classes of density, the correspondent classes of volumic composition and measuring, by lineal image analysis, the composition distribution of each class;

- establishing, for each size class, the empirical relation between the classes of volumic composition and the correspondent lineal composition distributions; (the relation is assumed to be independent of the size).

2.2 Functional relation between the volumic composition and the lineal composition distributions

Experimental data provided plotting the curves of variation of the lineal composition distribution with

the volumic composition and the proportion of free particles with the volumic composition. The expressions of functional relation contain parameters, which must satisfy simultaneously the 3 equations (mixed particles, free particles of phase A and free particles of phase B). The parameters were determined by computer, using the method of Romberg to implement the numeric integration, and the method of Rosenbrock, for parameter optimisation.

The shape of the curves is closely related with the ore texture and so do the parameters; the parameters are the coefficients of matrix **K**.

2.3 Matrix K

The function of transformation of the real ore was discretized in 12 classes of linear and volumetric composition. The n-column of matrix **K** represents the cumulative discrete distribution of the linear composition of the particles in the n-class of volumic composition.

2.4 Matrix Inversion

The conversion of planar (1-D or 2-D) into volumic (3-D) distributions, is an ill-posed problem, which was solved by procedures of regularization, to compute reproducible solutions. As the results refer to compositions, the solutions must be constrained to satisfy the conditions of monotonicity and consistency (the sum of the results equals 1).

Matrix inversion followed the Rosenbrock proposal, which consists in minimizing the function objective, NSR (normalized sum of residuals):

$$NSR = \sum_{i=0}^n \frac{|F_i^j - \hat{F}_i^j|}{F_i^j} \quad (j=1, 2, \dots, 12)$$

with $F_V^1 \leq F_V^2 \leq \dots \leq F_V^{12} = 1$, for all j.

In the expression the variates of optimisation are the cumulative fractions F_V^j . F_i^j represents the coefficients of the lineal cumulative distribution (measured) and \hat{F}_i^j represents the coefficients of the lineal cumulative distribution, recalculated using the coefficients calculated for the vector of the volumic composition distributions; monotonicity and consistency are simultaneously satisfied.

The optimal solutions are iteratively estimated, from the initial coefficients of the vector distribution of the volumic composition. The initial values (chosen to be close to the optimal solution, in order to assure the consistent convergence of the biased linear composition data) were estimated by the Tikhonov regularization method, defined in matricial notation:

$$f_v = (K + \lambda I)^{-1} F_e$$

In the expression I represents the matrix identity and λ is the Tikhonov regularization parameter, which filtrates the errors contained in the measurements.

2.5 The algorithm of Schneider

The algorithm developed by Schneider to correct the lineal, or areal, composition distributions, measured in different types of texture, involves the following textural parameters:

- (1) the volumic composition of the mineral of interest, estimated by image analysis;
- (2) the specific gravity of the mineral of interest and the specific gravity, ponderated for the remaining components;
- (3) the texture degree of symmetry;
- (4) the type of distribution to correct;
- (5) the lineal / areal proportions of the particles in each class of composition.

3 EXPERIMENTAL DATA

3.1 The raw ore

An aplite rock, from Guarda, Portugal, provided the experimental data. The rock, mainly composed by feldspars (albite and microcline), quartz and muscovite, was measured for the mineral quantities

and grain size distribution. Mineral quantities were determined by chemical elemental analysis (AQE, average of two reproducible results, expressed as % oxides) and by image analysis (IA, chord analysis of more than 1500 mineral grains). Data are given in Table 1 (Matos et al.1996).

Table 1 - Mineral quantities (wt%) in the unbroken ore

Minerals	AQE	IA
	Albite	35.5
Microcline	16.0	21.4
Quartz	34.5	32.0
Muscovite	14.0	11.0

The grain size distribution provided estimating the practical grind to liberate the feldspar minerals.

3.2 The ground ore

The ore was ground to 95% below $-75\mu\text{m}$, in a rod mill [Matos 1999]; the granulometric distribution is given in Table 2. The size fractions were sampled, mounted in polished sections and measured, by image analysis, for the apparent mean composition (Table 2) and the apparent composition distribution (Matos 1999, pp.115).

Table 2 – Size analysis of the ground ore, as determined by the Cyclosizer. Mean composition of size fractions

Size class (μm)	Size distribution (wt %)	Apparent mean composition of the size fractions (area %)				
		Albite	Microcline	Quartz	Muscovite	Total
+ 75.0*	5.3	n.a.	n.a.	n.a.	n.a.	n.a.
-75.0 + 44.1 – cone 1	20.3	33.47	17.70	41.76	7.06	100.0
-44.1 + 31.1 – cone 2	26.3	28.00	19.69	46.15	6.15	100.0
-31.1 + 21.3 – cone 3	12.3	27.53	15.35	48.48	8.64	100.0
-21.3 + 14.8 – cone 4	11.8	39.89	17.23	42.81	9.07	100.0
-14.8 + 12.1 – cone 5	6.1	32.63	12.85	43.78	10.74	100.0
-12.1**	17.9	n.a.	n.a.	n.a.	n.a.	n.a.
Apparent mean composition of the ore (by ponderation of the size fractions)		30.8	16.7	44.3	8.2	100.0

* by screening; **by difference; n.a – non analysed; ponderation used the data of the contiguous fractions.

3.3 Stereological Correction

The composition was expressed by the proportion of the area occupied by the mineral of interest in the total area occupied by the minerals. Planar cumulative distributions were reconstructed by the method of Schneider, implemented by algorithm 'Invert' (Durão 1998). Cumulative volumic distributions were obtained. (Matos 1999).

Areal and volumic cumulative distributions are compared, for mineral albite (cones 1, 2, 3), in Fig.1. Areal and volumic distributions are compared for all the minerals (cone 1 - Stokes diameter $>44.1\mu\text{m}$), in Fig. 2.

4 DISCUSSION

The curves for albite, given in Fig.1, are representative of the curves obtained for the other minerals, in the different size fractions. As observed in the figure, the different sizes produce similar curves, meaning that in this size range the liberation degree doesn't increase with the size reduction. The most significant differences are observed in the extreme classes of composition ($<10\%$ and $>90\%$) where the measurements are over-evaluated. Such behaviour results from the sectioning effect: in a particle, the most abundant phase has higher probability of being sampled (either during the mounting or on applying the measurement grid -

lineal measurements produce more biased data than areal measurements).

In Fig.2, the areal and volumic composition distributions (coarser fraction) are compared for all the minerals. It is observed the high degree of liberation attained by the actual grind: most particles are in the classes <10% (liberation of the gangue) and >90% (liberation of the mineral of interest).

In the classes 0% and 100%, together with the real free particles, were measured particles in the other classes, mainly in the contiguous classes of composition, as revealed by the volumic distribution; in the middle classes of composition, the particles tend to produce data close to the real. Albite and microcline volumic data reveals the absence of free particles.

The mean composition of the ore, calculated from the planar and volumic composition distributions of the size fractions, is given in Table 3. As expected, the fundamental law of Stereology, $V_v = A_A$, (Underwood 1970), is observed.

Table 3 – Mean composition of the ore, calculated from the areal and the volumic composition distributions.

Minerals		
	% area	% volume
Albite	30.6	29.7
Microcline	15.8	16.0
Quartz	42.2	42.4
Muscovite	11.4	12.9

The similitude of the minerals specific gravity ($\sim 2.6 \text{ g/cm}^3$), allows to assume that %vol \sim %wt, and to compare the actual composition with the obtained by chemical analysis (AQE) and by image analysis (IA). Some discrepancies were observed, in particular in albite and quartz proportions. Although these proportions are identical in the unbroken ore (Table 1), in the ground ore (Table 2) quartz exists in higher proportion than albite, in all the size fractions; this may be the result of different mechanical properties of quartz and albite.

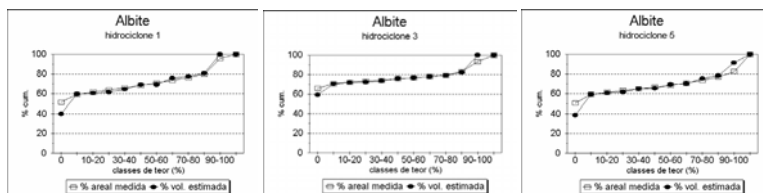


Figure 1 – Cumulative composition distributions, as measured (%area) and as estimated (%volume), by the method of Schneider - Albite, cones 1, 3 and 5.

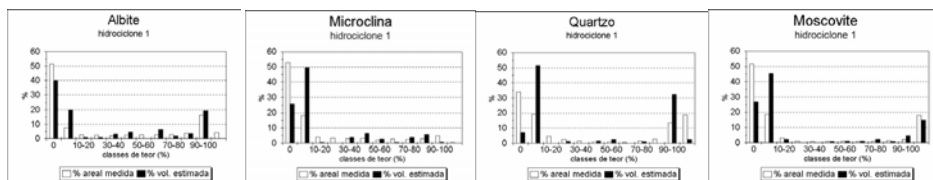


Figure 2 - Composition distributions of the minerals in cone 1, as measured (% area) and as corrected (% volume) by the method of Schneider.

5 CONCLUSIONS AND REFERENCES

Stereological correction of planar composition is important in the quantification of mineral liberation. The technique provides correcting the bias dues to the sectioning effect, enhanced in the (binary) particles mainly composed by one component.

6 REFERENCES

Durão, F.O. (1998), Routines in Annex 8 in 'Contribution to the study of liberation in polimineral ores – Techniques and Models', PhD thesis, IST-Techn. Univ. of Lisbon, Portugal.

Gundersen, H.J.G. and Jansen, E.B., (2002), 'Introduction to quantitative Stereological techniques useful at EM level', Workshop at ICEM15 – 15th Int. Congress on Electron Microscopy, Durban, South Africa.

Howard, C.V. and Reed, M.G., (1998), 'Unbiased Stereology – Three-dimensional measurements in microscopy', BIOS Scientific, Guilford Publ., U.K.

Matos, M. J., Lastra, R. and Petruk, W., (1996), 'Characterization of Feldspar Texture and Liberation by Image Analysis', Trans IMM, Sec.C, 105, C133-C140.

Matos, M.J., (1999), PhD Thesis: 'Contribution to the study of liberation in polimineral ores – Techniques and Models', IST-Technical University of Lisbon, Portugal.

Schneider, C.L., (1995), 'Measurement and Calculation of Liberation in Continuous Milling Circuits', PhD thesis, Univ. Utah, U.S.A.

Zeolitic Tuffs from Serbian Deposits and their Acid Modification

A.Radosavljevic-Mihajlovic, J.Stojanovic, S.Radosavljevic

Institute for Technology of Nuclear and Other Mineral Raw Materials, Applied Mineralogy Unit, P.O. Box 390, 86 Franchet d'Esperey Street, 11000 Belgrade, Serbia, Serbia and Montenegro

ABSTRACT: The mineralogical and crystallochemical characterization and acid stability of two zeolitic tuffs from Zlatokop and Beocin deposits (Serbia) were investigated. Chemical, mineralogical, IR and XRPD analyses characterized the initial and modified samples. Chemical decomposition of the acid treated samples was accompanied by release of tetrahedral coordinated Al^{3+} into the solution. In addition, the substantial losses of inorganic ions: Na^+ , K^+ , Ca^{2+} , and Mg^{2+} in to the solution were observed. These XRPD analyses showed a reduction of unit cell parameters of HEU-type minerals, which were caused by treatment with HCl (1M and above). The results of XRPD and IR analyses indicated that a partial amorphization of acid treated samples occurred. Based on the obtained results of XRPD and crystallochemical analyses, can be seen that the different atomic ratio and different compositions of inorganic ions have great influence of the acid stability of zeolitic tuffs.

1 INTRODUCTION

Clinoptilolite–Heulandite (HEU-type zeolite mineral) with simplified formula $(Na, K, Mg, Ca)(Al_6Si_3O_{72}) nH_2O$ is the most common natural zeolite found mainly in sedimentary rocks of volcanic origin. The crystal structure of clinoptilolite (space group C2/m, $a=17.662$, $b=17.911$, $c=7.407$) contains three types of structural channels confined by tetrahedral ring systems. A and B channels run parallel to the c-axis and are confined by ten- and eight-membered rings, respectively. C channels, confined by another set of eight-membered rings, run parallel to the a-axis and the (102) direction (Koyama & Takéuchi 1977). Cations and H_2O molecules occupy the channels.

Acid treatment of natural and synthetic zeolites improves their adsorption properties by the mechanisms of decationisation and dealumination (Filippidis et al.1996; Radosavljevic-Mihajlovic et al., 2002). The HEU-type zeolites treated with 1M hydrochloric acid loses significant amounts of framework Al and extra-framework cations of the channels whereas only a negligible amount of Si is extracted (Missilidis et al. 1996). Subsequent X-ray single-crystal structure (Wüst et al. 1999) analysis indicated partial rearrangement of framework Al to

hydrated extra-framework Al, where Al preferred octahedral coordination. Thus not only H_3O^+ but also Al^{3+} appeared as extra-framework cations.

In this paper, the results of acid treatment of natural zeolites from two different deposits are presented. The study was carried out with the aim to determine mineralogical and crystallochemical properties of initial and acid treated samples.

2 EXPERIMENTS AND METHODS

The row zeolitic samples used in this study were clinoptilolite-heulandite rich tuffs from two deposits Zlatokop (Vranje, Serbia) and Beocin (Fruska Gora, Serbia). These samples were denoted as SZ and SB. The acid treatment of two zeolitic tuffs was performed by mixing 2g of each sample with 100 ml of 1M HCl, for 2h. After reaction time the samples were left in contact for 24 h at room temperature and then centrifuged, washed and dried. The treated samples were denoted as HZ and HB. The concentrations of inorganic cations released from zeolitic tuffs including dissolved aluminum were determined in supernatants.

The total content of exchangeable inorganic cations (CEC) in initial and acid treated samples was

obtained by Ming and Dixon method (Ming & Dixon 1987).

The concentrations of inorganic cations (Ca^{2+} , Mg^{2+} , Na^+ and K^+) and aluminum were determined on atomic absorption spectrophotometer (Perkins Elmer, Model 703).

XRPD analyses of row zeolitic tuffs and acid treated samples were performed on the Phillips PW-1710 diffractometer with monochromatic $\text{Cu/K}\alpha$ radiation, in the range from 4° - 35° 2θ . Monoclinic crystal system (space group $\text{C2/m} - 12$) was used for determination of unit-cell parameters (a , b , c , V and β) using the crystallographic program "LSUCRIPC" (Garvey 1986). The values of unit cell parameters were calculated for characteristic diffraction reflections of the HEU-type zeolite: [020]; [200]; [-311]; [111]; [131]; [400]; [330]; [151].

IR spectra of initial and acid treated samples were obtained on the Hewlett Packard IR spectrometer, in the range from $4,000 - 400 \text{ cm}^{-1}$, using KBr.

3 RESULTS AND DISCUSSION

3.1 Mineralogical and crystallochemical analyses

The mineralogical analyses of initial materials showed that colour of zeolitic tuff from Zlatokop deposit are pale-yellow with limonite impregnations and pyrite veins. The main mineral in this tuff was clinoptilolite-Ca, while quartz, feldspar, limonite and volcanic glass were present in trace amounts.

The colour of zeolitic tuff from Beocin deposit is whitish. The main mineral in this tuff is heulandite-Ca, while quartz, feldspar, calcite, mica and clay minerals are present in trace amounts.

Table 1. The chemical composition of raw samples

Oxide (%)	Zlatokop - SZ	Beocin - SB
SiO_2	64.60	55.44
Al_2O_3	12.40	15.04
Fe_2O_3	1.84	1.85
CaO	4.02	6.20
MgO	0.80	2.64
Na_2O	0.91	2.32
K_2O	0.82	0.52
IL.	15.47	15.57
Total	100.8	99.58

After acid treatment mineralogical composition of these two samples were changed. Sample from Zlatokop deposit treated by 1M HCl showed partial amorphization of the HEU-type minerals, while quartz and feldspars were practically unaltered. Treated sample from Beocin deposit, also showed partial amorphization of the HEU-type minerals. Carbonates were dissolved and mica minerals were altered.

The chemical composition of initial zeolitic samples (SZ and SB) is given in table 1. Crystallochemical formula (based on the total of 72 O atoms) of HEU-type zeolites calculated from chemical composition is presented in Table 2.

Table 2. Crystallochemical formula of row zeolitic samples (SZ,SB).

SZ	$\text{Ca}_{3,38}\text{Mg}_{0,38}\text{Na}_{1,5}\text{K}_{1,03}(\text{Al}_{6,3}\text{Si}_{29,7}\text{O}_{72}) 21\text{H}_2\text{O}$
SB	$\text{Ca}_{3,7}\text{Mg}_{0,24}\text{Na}_{0,68}\text{K}_{2,54}(\text{Al}_{7,3}\text{Si}_{28,7}\text{O}_{72}) 25\text{H}_2\text{O}$

The Si/Al ratio for HEU-type zeolite from Zlatokop deposit is 4.42 and it is characteristic feature for clinoptilolite. The HEU type zeolite from Beocin deposit has less Si/Al ratio-3.95. These lower Si/Al ratios in this tuff may be caused by different balance of net negative charge of aluminum framework.

During acid treatment, process of dealumination increases content of aluminum in supernatants. Comparing with initial sample SZ, in which the amount of Al was 6.55%, at acid concentration of 1M, the percent of aluminum leached from framework is 3.2%. The amount of Al in SB is 7.95% and after acid treatment, 4.6% of Al is leached out. Inorganic alkali and alkali-earth cations, released from zeolitic tuff showed that these cations were progressively leached out as the concentration of acid increased. The results of content of leached inorganic cations (Ca^{2+} , Mg^{2+} , K^+ , Na^+) and aluminum released during the acid treatment as a function of ratio $\text{H}^+/\text{Al}^{3+}$ are presented in Table 1. The ratio $\text{H}^+/\text{Al}^{3+}$ was calculated by dividing the amount of H^+ ion in exchangeable position by the amount of Al^{3+} released from zeolitic framework, and represents the ratio between ion exchange and dealumination processes.

Table 3. Content of leached cations acid treated sample ($\text{mmolM}^+/100\text{g}$).

Mark	$\text{H}^+/\text{Al}^{3+}$	Al^{3+}	Ca^{2+}	Mg^{2+}	Na^+	K^+
HZ	120	160	85	35	22	8
HB	100	172	156	75	20	30

Inorganic alkali and alkali-earth cations, released from zeolitic tuff showed that these cations were progressively leached out as the concentration of acid increased (Table 3). The different removal rate of the cations can probably be related to the location of cations in the channels and their coordination in the zeolite framework. The content of inorganic cations (Ca^{2+} , Mg^{2+} , Na^+ , K^+) in acid treated samples and the content of leached inorganic cations calculated in $\text{mmolM}^+/100\text{g}$, are presented in Table 4.

Table 4. The content of exchangeable cations initial and acid treated sample (mmolM⁺/100g).

Mark	Ca ²⁺	Mg ²⁺	Na ⁺	K ⁺
SZ	94.0	10.7	21.0	16.4
HZ	35.3	1.3	3.5	7.0
SB	114.0	7.6	9.6	35.4
HB	37.0	0.4	-	15.0

In Table 4, can be seen that the content of calcium in exchangeable position in raw zeolitic tuff (Z) was 138 mmolM⁺/100g. The content of leached calcium at acid concentration 1M, in mmolM⁺/100g was 115 mmolM⁺/100g. Based on these results can be concluded that calcium, mainly from exchangeable position was leached out. The exchangeable cations Na⁺ and K⁺ demonstrated similar behavior during the acid treatment. The higher content of leached Mg²⁺ appears partially from the volcanic glass. The different removal rate of the cations can probably be related to the location of cations in the channels and their coordination in the zeolite framework.

3.2 IR and XRPD analyses

IR spectra of acid treated samples (HZ and HB) were compared with IR spectra of initial samples (SZ and SB) and these results are presented in Figure 1.

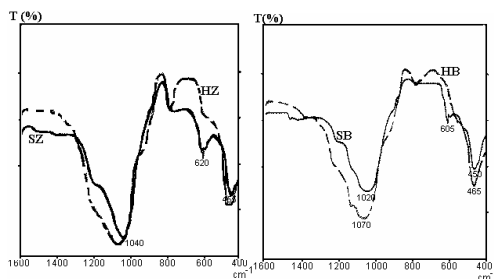


Figure 1. IR spectra of acid treated samples (HZ and HB) and initial samples (SZ and SB)

IR spectra of acid treated samples showed clear changes of all vibration bands. The intensities of asymmetric (~1040cm⁻¹) and symmetric (~830cm⁻¹) stretching vibration of Al-O-Si band, after acid treatment increase and peaks are shift to higher frequency, corresponding to dealumination and decreasing the Si/Al ratio. The vibration band near 600cm⁻¹ disappeared after acid treatment, indicating the dealumination and breaking of Al-O bands inside the zeolitic structure. The new absorption bands at approximately ~870cm⁻¹ may indicate the presence of semi-amorphous phase (Rodriguez-Fuentes et al., 1998).

The powder-XRPD analyses of the row samples (SZ and SB) and for the acid-treated samples (HZ and HB) are presented in Figures 2 and 3.

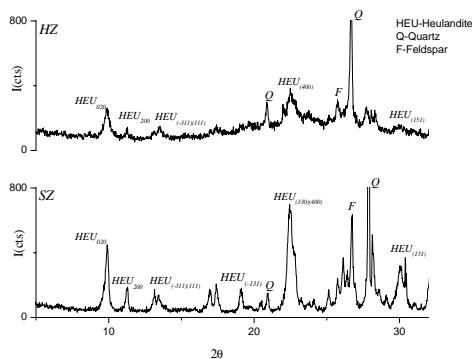


Figure 2. XRPD patterns of row (SZ) and acid-treated sample (HZ) from Zlatokop deposit

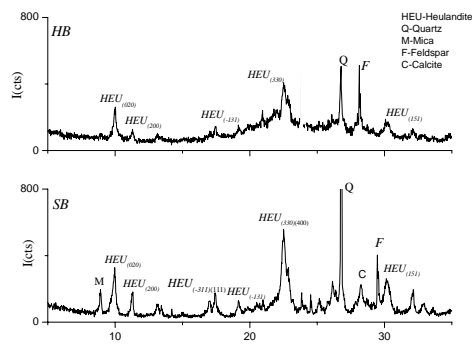


Figure 3. XRPD patterns of row (SB) and acid-treated sample (HB) from Beocin deposit

The XRPD patterns of treated samples showed decrease of intensity and peak broadening, which are indicative for some crystallinity loss. The loss of the crystallinity is related to the extent of dissolution of aluminum from the zeolite framework. Also, the diffraction peaks, characteristic for accessory minerals, after acid treatment, disappeared. Unit-cell parameters of row and acid treated HEU-type zeolite are presented in Table 3.

Table 3. Unit-cell parameters of row and acid treated HEU-type zeolites

	<i>a</i> (nm)	<i>b</i> (nm)	<i>c</i> (nm)	β°	<i>V</i> (nm ³)
SZ	1.766(4)	1.790(4)	0.7426(4)	116.48(6)	2.101
HZ	1.767(4)	1.792(4)	0.7424(5)	116.46(6)	2.105
SB	1.767(3)	1.791(3)	0.7420(3)	116.44(5)	2.103
HB	1.764(4)	1.787(4)	0.7433(4)	116.46(5)	2.095

Calculated unit-cell parameters of the acid treated samples (HZ, HB) showed significant changes in comparison with unit-cell parameters of initial samples (SZ, SB). The changes of the unit-cell parameters of these samples (HZ and HB) point to tension in the HEU-type framework (movement of tetrahedral coordinated aluminum in clinoptilolite framework). Then it may be concluded that extraction of lattice aluminum and eventually its partial replacement by silicon, probably occurred since the unit-cell contraction is related to the smaller length of Si-O-Si bonds with respect to those of O-Al-O.

4 CONCLUSION

Acid treatment of zeolitic tuff leads to exchange of inorganic cations at lower acid concentrations (1M), while at higher concentration this process is accompanied with dealumination of zeolitic tuff.

The different removal rate of the cations can probably be related to the location of cations in the channels and their coordination in the zeolite framework.

Intensity of X-ray diffraction peaks decrease significantly with increasing of acid concentration that corresponds to a loss of crystallinity of zeolitic tuff. A significant reduction in crystallinity of HEU-type zeolite was effected by concentration of hydrochloric acid (1M). The changes of the unit-cell parameters of these samples point to a tension in the HEU-type framework, which can be ascribed as movement of tetrahedral coordinated aluminum. The IR-analysis that was correlated with the results of X-ray analyses indicated an amorphization of acid treated zeolitic tuff from Zlatokop and Beocin deposits.

5 REFERENCES

- Koyama, K. & Takéuchi, Y. 1977. Clinoptilolite: the distribution of potassium atoms and its role in the thermal stability. *Zeitschrift für Kristallographie*, 145, 216- 239.
- Filippidis, A., Godelitsas, A., Charistos, D., Misaelides, P. & Kassoli-Fournaraki, A 1996. The chemical behaviour of natural zeolites in aqueous environments: Interactions between low-silica zeolites and 1MNaCl solutions of different initial pH-values. *Applied Clay Science*, 11, 199-209.
- Radosavljevic-Mihajlovic, A., Dakovic, A. & Tomašević-Canovic, M. 2002. *Journal of Mining and Metallurgy*, 38(1-4) A, 87-96.
- Misaelides, P., Godelitsas, A., Link, F. & Baummann, H. 1996. Application of the ²⁷Al(γ , p)²⁸Si nuclear reaction to the characterization of the near-surface layers of acid-treated HEU-type zeolite crystals. *Microporous Materials*, 6, 37-42.
- Wüst, T., Stolz, J. & Armbruster T. 1999. Partially dealuminated heulandite produced by acidic REECl₃ solution: A chemical and single-crystal X-ray study, 84, 1126-1134.
- Ming, D.W., & Dixon, J.B. 1987. Quantitative determination of clinoptilolite in soils by a cation-exchange capacity method, *Clays and Clay Minerals* Vol.35, No 6, 463-468.
- Garvey R. G. 1986. *Powder Diffraction*, 1, 114.
- Rodriguez-Fuentes G., Ruiz-Salvador A. R., Mir, M., Picazo, O., Quintana G., & M. Delgado 1998. *Microporous and Mesoporous Materials*, vol 20, 269.

Bentonite from Guayaquil, Ecuador: Characterization and Possible Industrial Applications

A.M.Morales-Carrera, A.F.D.Varajão & J.C.Mendes

Department of Geology, School of Mines, University Federal of Ouro Preto, Minas Gerais, Brazil

ABSTRACT: Mineralogical studies by X-ray diffraction (XRD), differential and gravimetric thermal analysis (DTA-GTA), infrared spectroscopy (IR), associated to chemical analysis and cation exchange capacity (CEC), allowed to characterize the clay of Guayaquil (Ecuador). This clay is mainly formed by calcic montmorillonite, and recognized as calcic bentonite, similar to that from Cheto (USA). The calcic bentonite has a large field of applications, that can be increased by acid treatments to improve their physical and chemical properties. The effectiveness of the activation process was determined by surface area and porosity by using BET, and morphological analysis by using scanning electronic microscopy (SEM).

1 INTRODUCTION

The purpose of this work is to characterize the clay found 18 km outside the city of Guayaquil in Ecuador. This city is located west of the Andean Mountains and southeast of the region known as *Costa* (Bristow & Feininger 1977). The referred-to clay is found in mudstone of the Ancón Group formed during the upper Eocene, being originated by the alteration of Andean volcanic ash and by deposition in marine environment. Its origin is similar to know widely sodic bentonite from Wyoming and calcic bentonite from Cheto in the USA (Nemecz 1981).

2 METHODOLOGY

Thirty-two samples were collected from eight profiles. The mineralogical composition was obtained by X-ray diffraction (XRD) and chemical analysis in the all sample. After this step, 13 representative samples were selected for detailed mineralogical study of their clay fraction.

The XRD and cation exchange capacity (CEC) analysis of the clay fraction (EMBRAPA 1997) allowed the identification of the group and specie of

predominant clay mineral. Additionally, 5 select samples were used to get acid activation in order to improve some technological properties.

X-ray diffraction (XRD) analysis, chemical analysis, cation exchange capacity (CEC), surface area, differential and gravimetric thermal analysis (DTA-GTA), infrared spectroscopy (IR) and scanning electronic microscopy (SEM) were used to compare the natural and activated samples.

3 RESULTS AND DISCUSSION

The XRD patterns of the entire thirty two samples show the predominance of the smectite group (14.49Å), mica (9.77Å), kaolinite (7.11Å) and, secondarily quartz (4.24Å and 3.33Å), and feldspar (3.21Å). Some diffractometer patterns also show calcite and others little gypsum.

The Table 1 describes the average chemical composition of the thirty two samples of Guayaquil and of the calcic bentonite of Cheto, USA (Van Olphen & Fripiat 1979). These two clays are mainly composed by magnesium and calcium followed by potassium and sodium. There are greater percents of SiO₂, K₂O, Na₂O and Fe₂O₃ of the Ecuadorian clay than those of Cheto.

Table 1: The average chemical composition of calcic bentonite of Guayaquil, Ecuador and of Cheto, USA (Van Olphen & Fripiat 1979).

% Samples	SiO ₂	Al ₂ O ₃	Fe ₂ O ₃	MgO	CaO	K ₂ O	Na ₂ O
Guayaquil	65.8 ± 2.05	15.3 ± 0.97	5.25 ± 0.42	2.00 ± 0.15	1.68 ± 0.44	1.12 ± 0.11	0.84 ± 0.12
Cheto	60.4	17.6	1.42	6.46	2.82	0.19	0.06

In the clay fraction, the XRD patterns of the saturated samples with MgCl₂ and ethylene glycol show the most intense peak at 17Å (Figure 1) indicating the presence of smectite group. Additionally, non integral sequences of wide and anti-symmetrical peaks point out the occurrence of illite/smectite mixed-layers and traces of illite associated to the smectite. As well as, the peak at 7Å shows the presence of the kaolinite in this clay fraction. Other peaks correspond to quartz and feldspar.

The presence of the smectite group was also confirmed after KCl and ethylene glycol saturation that showed the peak at 14 Å (Brown 1961).

The XRD data of LiCl saturated samples followed by heating to 300°C for 12h (Green-Kelly 1953) and saturated with ethylene glycol allowed to identify the montmorillonite specie by its collapsed state which produced a first order spacing at 9.6 Å.

The main cations exchangeable were quantified for the fraction clay. In natural samples, the values for the Ca²⁺ varied from 32 to 51 meq/100g, for the Na⁺ from 0.3 to 1.1, for the Mg²⁺ from 1.9 to 5.8 and, for the K⁺ from 0.05 to 0.09.

The Ca²⁺ showed the highest values and, then this is main cation exchangeable. Therefore, these results and the origin previously known confirmed that the Ecuadorian clay is a calcic bentonite. The activation treatment (Kooli & Jones 1997, Tkáč et. al. 1994, Frenkel 1974) using H₂SO₄ in the fraction clay was more efficient than that using HCl. The Figure 2 shows that there is no destruction of the crystalline structure of constituent minerals using H₂SO₄ compared to HCl.

Differential and gravimetric thermal analysis (DTA-GTA) confirmed the results obtained using the X-ray diffraction. As a result, the montmorillonite showed two endothermic peaks close to 150°C, one peak at 250°C and another one at 500°C. The illite showed a peak at 150°C, and one peak between 550° and 575°C. The kaolinite showed a peak at 500°C. These results were obtained in either natural or activated samples. Loss of weight in analyzed samples was less than 20% compared to the initial weight.

Transmission Infrared spectroscopy (Wilson 1994, Van de Marel & Beutelspacher 1976), associated with X-ray diffraction and thermal analysis verified the mineralogy of the clay fraction. There is no difference in the mineralogy when IR spectrum of natural and activated were compared.

Generally, the activated samples showed a greater percentage of SiO₂ than natural samples. In fact, these results were also obtained by Grim (1962) and Griffiths (1990). They describe that the basic activation process occurs when there is a selective leaching of cations and relative enrichment of SiO₂.

The effective cation exchange capacity of natural samples ranges from 39.12 to 54.61 meq/100g. These values, low for montmorillonite (Grim 1962), are influenced by the presence of other associated minerals. After activation, these results are lower than those of natural samples ranging from 7.52 to 15.57 meq/100g.

The total volume of pores in the natural samples is 0.03877 cc/g and it is increased to 0.05804 cc/g for the activated samples. The adsorption-desorption isotherms point out the duplication of N₂ adsorbed after activation as consequence of the increasing of micro and meso pores.

The values of surface area for natural samples vary from 16.82 m²/g to 29.51 m²/g that are much lower than those found for pure montmorillonite (50 m²/g) according to Van Olphen & Fripiat (1979). This discrepancy is caused by the interference of other minerals in the natural samples. However, the activated samples showed a significant increase in the surface area from 34.41 to 41.36 m²/g as illustrated in the Figure 3.

4 CONCLUSIONS

The investigation in the Ecuadorian clays identified the clay minerals and other non-clay minerals, where calcic montmorillonite is predominant. These results and its origin due to the alteration of volcanic ash proved that it is a calcic bentonite. This bentonite can be compared to that of Cheto in Arizona, USA.

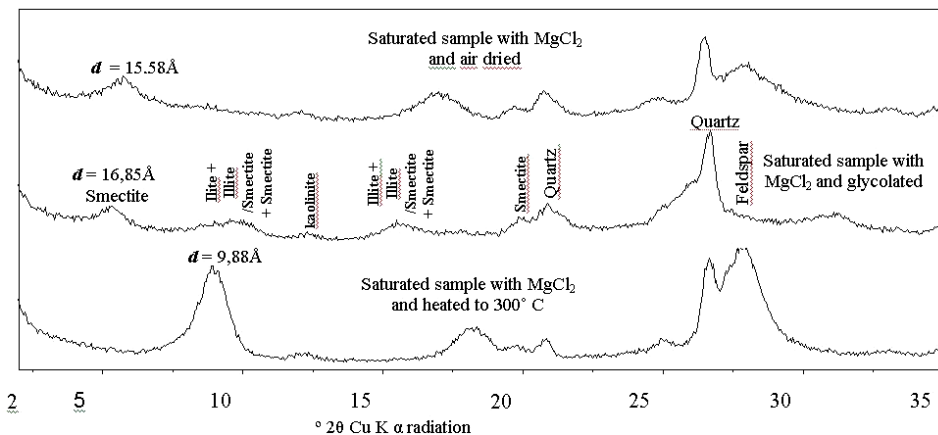


Figure 1. Representative X-ray diffraction patterns of clay fraction saturated with MgCl₂.

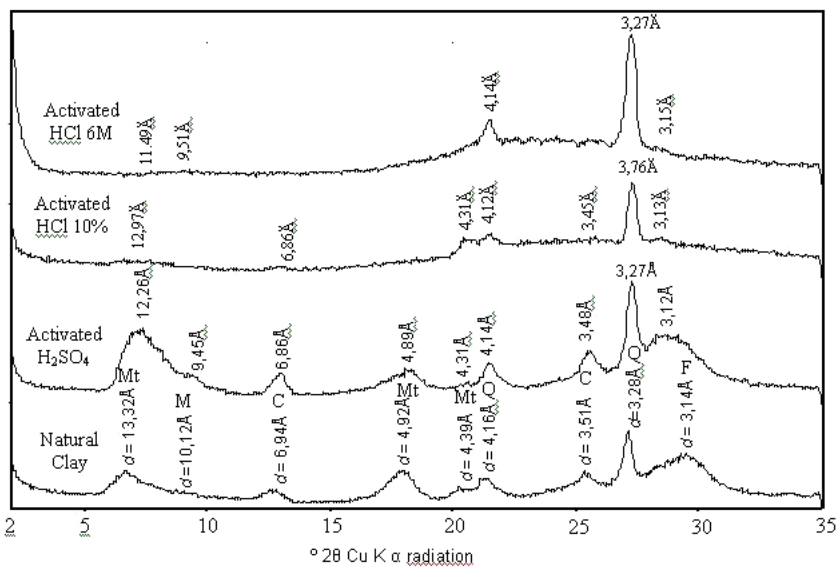


Figure 2 - X-ray diffraction patterns of natural and activated clay with HCl and H₂SO₄.

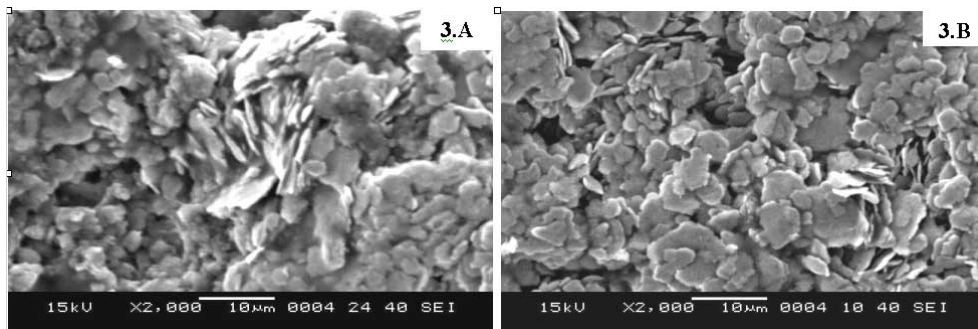


Figure 3 – Scanning electronic microscopy (SEM) micrographs of the natural (A) and activated (B) clay fraction.

Natural calcic bentonite can be used in several industrial applications, as a binder of minerals and food products. The activated calcic bentonite can be used in the purification and bleaching of oils and the catalyses of petroleum derivatives. The activation with 50% of H₂SO₄ showed better result than that with HCl. This performance was due to the primary mineralogy conservation, occurring only the leaching of basic cations. Additionally, a significant increase of the porosity and the surface area allows new possibilities of application of the Ecuadorian calcic bentonite. Actually, the Ecuadorian calcic bentonite is only used in ceramic and cement industries.

5 REFERENCES

- Bristow, C. R. & Feininger, T. (1977). *Léxico Estratigráfico del Ecuador*. 2^a Ed. Centre National de la Recherche Scientifique, 412 p.
- Brown, G. (1961). *The X-ray Identification and Crystal Structures of Clay Minerals*. Mineralogical Society, 453 p.
- EMBRAPA. (1997). *Manual de Métodos de Análises de Solo*. 2 ed., Ministério da Agricultura e do Abastecimento, 212 p.
- Frenkel, M. (1974). Surface acidity of montmorillonites. *Clays and Clay Minerals*, 22: 435-441.
- Green-Kelly, R. (1953). The identification of montmorillonoids in clays. *Journal of Soil Science*, 4: 233-237.
- Griffiths, J. (1990). Acid activated bleaching clays. *Industrial Minerals*, 276: 55-67.
- Grim, R. E. (1962). *Applied Clay Mineralogy*. McGraw Hill, 422 p.
- Kooli, F. & Jones, W. (1997). Characterization and catalytic properties of a saponite clay modified by acid activation. *Clay Minerals*, 32: 663-643.
- Nemecz, E. (1981). *Clay Minerals*. Budapest, Akademiai Kiadó, 547 p.
- Tkáč, I., Komadel, P., Müller, D. (1994). Acid-treated montmorillonites – A study by ²⁹Si and ²⁷Al MAS NMR. *Clay Minerals*, 29: 11-19.
- Van De Marel, H. W. & Beutelspacher, H. (1976). *Atlas of Infrared Spectroscopy of Clay Minerals and their Admixtures*. Elsevier Scientific Publishing Company, Inc., 396 p.
- Van Olphen, H. & Fripiat, J. J. (1979). *Data Handbook for Clays Materials and other Non-Metallic Minerals*. Pergamon Press Inc., 436p.
- Wilson, M. J. (1994). *Clay Mineralogy*. London, Chapman & Hall, 367 p.

Alternative Feldspathic Rocks for Porcelainized Ceramics in SE Brazil

J.F.M.Motta

Mineral Resource Group, Division of Geology, Institute for Technological Researches, Sao Paulo, Brazil

A.Zanardo

Department of Petrology and Metallogeny, IGCE, University of the State of Sao Paulo, Rio Claro, Brazil

E.P.Goulart

Former Ceramic Lab, Division of Chemistry, Institute for Technological Researches, Sao Paulo, Brazil

A.A.Roldan

Former Department of Petrology and Metallogeny, IGCE, University of the State of Sao Paulo, Rio Claro, Brazil

A.O.Boschi

Dept. of Materials Engineering – Federal University of São Carlos – São Carlos – São Paulo State, Brazil

ABSTRACT: Three different rocks were studied as a source of fluxing material for formulation of porcelainized body in whiteware ceramics (Motta 2000). These three mineral prospects are located in São Paulo state and vicinities, in Southeast Brazil, and involve quartz-rich feldspathic rocks related to low metamorphic degree mylonite; high-pressure gneiss; and low degree metamorphic arkose. The study involved geologic mapping and sampling, mineralogical studies, chemical analyses, preliminary ore dressing tests, and ceramic experiments. Ceramic tests were done in laboratory after empirical formulation of the bodies based on current fabrication processes and products. Up to 77% of mylonite, 35% of arkose and 65% of gneiss were included in the composition of the different bodies giving good performance in the physical properties. Further studies were done by scanning electron microscopy (SEM) for evaluation of the microstructure and mineralogical transformations on thermal treatment of the material and their correlation with ceramic properties. This paper presents the results of the studies and points out the geologic potential for fluxing material in the Southeast Brazil as well as the main ceramic characteristics of these raw materials and the possibility for innovative formulations for whiteware and ceramic tiles.

1 INTRODUCTION

This paper shows the studies done to support mineral exploration and final uses for feldspar and related raw materials in the southeastern Brazil (Fig.1) to be used in the silicatic ceramics as fluxing raw materials. Three special prospects were aimed at in this study, both concerning metamorphic ancient environment, but from three different geological-geotectonic settings, as follow: a) mylonites from granitic rocks placed in shear zone; b) arkosean sands and sandstones from low-grade metamorphic rift basin; and c) gneiss from high-grade metamorphic environment. All the three prospects show good economic competitiveness potential due to their feldspar-rich mineralogy, medium to low iron contents and good geological potential for reserves. Final uses for these materials would attend ceramic industries for composition of light color ceramic body, from raw material, up to white ceramic body for processed materials.

1.1 Subject

The main subject of this paper is to present three occurrences of feldspathic rock and to discuss its characteristics and possibilities for silicatic ceramic.

2 MATERIALS AND METHODS

All three prospects were selected in the geological scenario of the State of São Paulo and its vicinity (Southeastern Brazil- Fig. 1), based on previous available data, such as the mineralogy (feldspar-rich rocks and small amount of mafic minerals); chemical composition (high alkali and low iron content); special characteristics for ore dressing (related to work index, magnetic minerals and other physical properties); potential for good reserves and location (nearby the consumers).

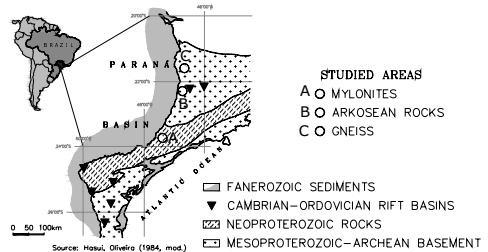


Figure 1 – Area localization in Southeastern Brazil

This study was carried out on the basis of the following work steps: geological mapping and sampling, mineralogical studies, chemical analyses, preliminary ore dressing tests, ceramic tests and post firing microscopy study.

2.1 Geological mapping and sampling

Fieldwork was done to recognize each area through several cross sections and subsequently detail mapping and sampling were done to specific facies of interest for lab analysis and tests.

2.2 Mineralogical studies

Samples were characterised by binocular and optical microscopy, X-ray diffractometry and thermal analyses.

2.3 Chemical analyses

Major oxide contents were determined by X-ray spectrometry.

1.4 Preliminary ore dressing tests

Experimental milling tests for Work Index determination and granulometrical sorting tests were carried out to observe mineralogical and ceramic characteristics in different processed products.

1.5 Ceramic experiments

Fresh and weathered rocks samples were studied to evaluate their ceramic properties, such as water absorption, strength, shrinkage, firing colour and density.

3 RESULTS AND DISCUSSION

The main results from field and lab studies, involving geological aspects, chemical composition and physical and ceramic characteristics are described as follows:

Table 1. Chemical composition of the raw materials (wt %).

Rock kind	Sample	LOI	SiO ₂	Al ₂ O ₃	TiO ₂	Fe ₂ O ₃	Na ₂ O	K ₂ O	CaO	MgO	Total
Fresh mylonite	Average	2.07	71.80	16.70	0.12	0.73	2.79	5.18	0.35	0.25	99.88
	Deviation	0.74	1.62	1.08	0.03	0.24	0.77	0.25	0.18	0.08	0.14
Weathered mylonite	Average	5.77	68.31	19.34	0.15	1.00	0.20	4.16	0.55	0.21	99.60
	Deviation	1.42	2.80	2.58	0.03	0.07	0.06	0.64	0.63	0.08	0.60
Arkose		1.19	78.56	11.49	0.20	1.28	2.47	4.00	0.64	0.36	100.19
Arkosean sand	Average	2.40	80.96	10.40	0.35	1.91	0.27	3.59	0.06	0.47	100.42
	Deviation	0.54	3.64	2.11	0.05	0.36	0.09	0.69	0.02	0.15	0.26
Gneiss	Average	0.83	74.58	13.24	0.10	1.04	3.57	5.39	1.17	0.36	100.32
	Deviation	0.54	2.50	1.16	0.03	0.43	0.76	0.39	0.59	0.32	0.13

3.1 Geology and mineralogy

Mylonites - The mylonitic rocks are inserted in the Taxaquara Shear Zone – TSZ (Figure1), an important structure in the crystalline basement of São Paulo State, formed in the Late Proterozoic to early Phanerozoic periods, described in previous papers such as Hasui et al. (1977). The mylonitic rocks vary from slightly deformed protomylonites to highly deformed ultramylonites. Petrologically, these rocks show reduction in grain size and change in mineralogy, from feldspar-rich to mica-rich facies, a common aspect observed in ductile deformation zones involving quartz-feldspathic rocks. Another characteristic presented is the ductile matrix surrounding fractured feldspar grains. This textural frame was considered important to mineral milling and processing

Arkose – Metamorphic arkose occurs in the sandy facies of the small Neoproterozoic/ Cambrian rift Eleutério Basin in the boundary between São Paulo and Minas Gerais states, studied by Zanardo e Oliveira (1987) and Teixeira (1995). Its facies shows around 40% of quartz, 35% of feldspar, and some opaque mineral, heavy minerals and detritic muscovite, with 12% to 15% of phyllosilicatic matrix. In the weathered areas, it is found arcosean sands poorer in feldspar content.

Gneiss – hololeucocratic orthogneiss, occurring in the southern Minas Gerais State, belonging to Varginha Complex, a unit originated in a high degree of metamorphism (under high pressure and temperature) in the Proterozoic, according to Zanardo (1992). Its mineralogy is composed by quartz (20-35%), feldspar minerals (25 a 35% of plagioclase, 30-50% of alkali feldspar) and 5% or less of accessory mineral such as magnetite, biotite and chlorite.

3.2 Chemical composition

The main oxides are listed in Table 1 and show major values for K₂O and Na₂O for gneiss, followed by mylonite and arkose. The iron content is smaller than 2%, on average.

3.3 Mineral processing characteristics

The following values of WI (work index) were obtained for the three rocks: mylonite (8,9 kWh/ short ton); arkose (13,3 kWh/ short ton); and gneiss (13,5 kWh/ short ton). Additionally, ore dressing tests were done using different processing methods, such as magnetic, densimetric, granulometric and flotation. The iron-bearing phases were simply separated by magnetic means in the gneiss sample; and granulometric sorting works performed well to mylonitic rock to distinguish a feldspar-rich concentrate from a sericite-rich concentrate.

3.4 Ceramic characteristics

Ceramic tests carried out on single sample of rocks indicate good fluxing action for all materials when worked in laboratory experiments (process and firing tests – Figs 2-6). In the Figure 3 is given an example that shows the gresification curve (water absorption *versus* shrinkage at different temperatures), very important diagram according to Melchiades et al. (1997a,b) and Barba et al. (1997) for arkose, gneiss and mylonite. Both rocks show very low water absorption around 1200°C, except when they are weathered.

Additionally, when replacing feldspar in blends to compound ceramic bodies (Fig. 2), all materials show good performance as shown in Figures 4-6.

Ceramic body composition →		Porcelain Stone	Gresified Tile	Sanitary ware
Raw material ↓				
Non plastic	Arkose	20		
	Arkosean sand	15		
	Gneiss	33	15	
	Mylonite	5	20	25
	Weathered Mylonite		20	52
Plastic	Talc		2	3
	Plastic clay	24	43	13
	Kaolin	3		7
Total of fluxing material in ceramic body		73	55	77

Figure 2- Raw materials in ceramic body composition.

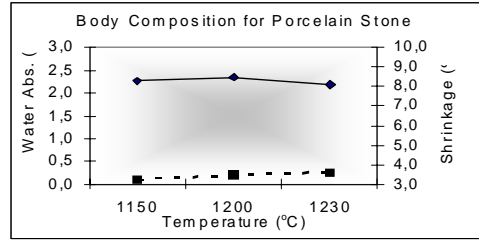


Figure 4- Vitrification curve for porcelain stone.

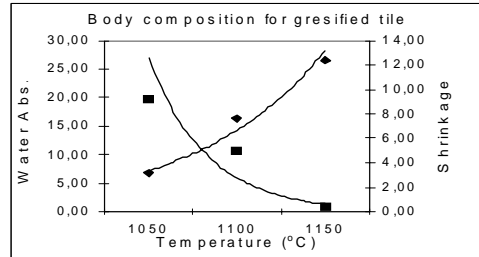


Figure 5- Vitrification curve for porcelain stone.

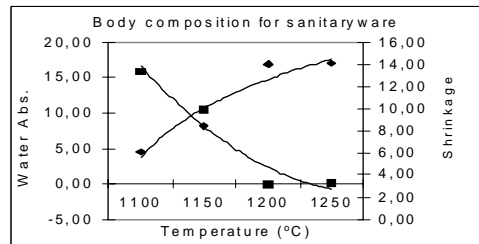


Figure 6- Vitrification curve for porcelain stone

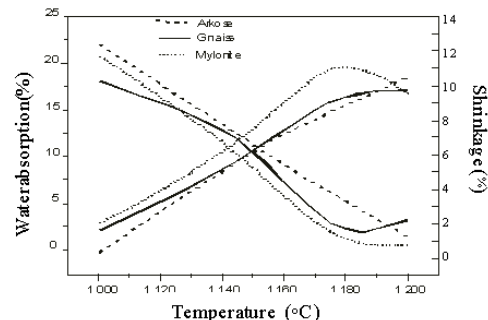


Figure 3- Vitrification curve for the three rocks.

3.5 Micro-structure on SEM

Analyzing some of the ceramic bodies prepared above, it was possible to observe the evolution of vitrification and melting under each steps of temperature.

Around 1250 °C the feldspar transforms in well growth mullite crystals and glass, the clay forms a great deal of very small mullite and less glass and the quartz generates viscous glass and the crystals at the core remain, as shown in Figure 7.

4 CONCLUSIONS

The three prospects studied here present mineralogy rich in feldspar and, two of them also show to be rich in white phyllosilicates, both rich in alkali. Feldspar, from different geological environments shows difference in chemical and mineralogy.

According to the results presented here and additional experiments, it was possible to know that all three studied deposits would be suitable to compound porcelainized ceramic bodies under relatively low temperature. Some of its characteristics are high strength values and the light color of the bodies when fired. The gneiss rock would burn white if adequately dressed.

Under SEM it was possible to see good reactivity and transformation, resulting in a good crystal-liquid fabric, which is responsible for the high strength.

It is still under investigation if the micro-structure is hardly affected or not by the type of feldspar. The feldspar from high-grade metamorphic area appears to react more easily, faster and better than others, but this investigation is still going on.

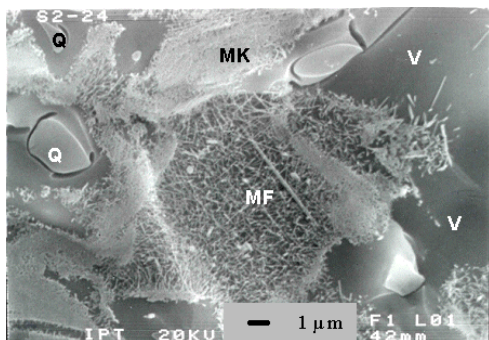


Figure 7 – Photo from Scan Electronic Microscopy showing sanitary ware body sample fired at 1.250 °C, observing the network of mullite from feldspar (MF), from kaolinite (MK), quartz (Q) and glass (V)

5 REFERENCES

- Barba, A. et al. 1997. *Materias primas para la fabricación de soporte de baldosas cerámicas*. Castellón: Instituto de Tecnología Cerámica. 291p.
- Hasui, Y.; Ponçano, W.L.; Bistrichi, C.A.; Stein, D.P.; Galvão, C.A.C. de F.; Gimenez, A.F.; Almeida, M.A. de; Melo, M.S. e Pires Neto, A.G. 1977. The great faults of the east of São Paulo state. In: *Simp. of Reg. Geology (Brazilian Geologic Society-São Paulo section)*, I, 1977, São Paulo, *Proceedings...*, p.369-380. (in portuguese).
- Melchiades, F. G., Quinteiro, E., Boschi, A. 1997a. A curva de gresificação: parte 1. *Cerâmica Industrial*. 1997, 4, p.30
- Melchiades, F. G., Quinteiro, E., Boschi, A. 1997b. A curva de gresificação: parte 2. *Cerâmica Industrial*. 1997, vol.2,nº 1/2, p.23-26
- Motta, J.F.M. 2000 *Ceramic raw material and three case studies of fluxing raw material*. Rio Claro: UNESP-University of São Paulo State (Doctorate Thesis). 208p. (in portuguese).
- Teixeira, A. L. 1995. *Ambientes geradores dos sedimentos da bacia Eleutério*. São Paulo, SP., 122p. *Dissertação (mestrado)* - IGUSP - 23/06/95.
- Zanardo, A; Oliveira, M.A.F. 1990. Aspectos microestruturais e texturais dos metassedimentos da Formação Eleutério. *Geociências*. São Paulo (número especial): 317-330.
- Zanardo, A. -1992- *Análise petrográfica, estratigráfica e microestrutural da região de Guaxupé-Passos-Delfinópolis (MG)*. (Tese de doutoramento). IGCE-UNESP (inédita).

6 AKNOWLEDGMENTS

The authors would like to express their thanks to FAPESP (Proc. 87/13.824-7) for financial support; CNPq for a scholarship contribution; and LaRC-DEMa-UFSCar, IPT and IGCE-UNESP for facilities and technical support.

Hydrothermal Synthesis and Characterization of Fe(III) and Fe(II)-Bearing Smectite

T.Nagase, T.Ebina & H.Hayashi

National Institute of Advanced Industrial Science and Technology, Tohoku

ABSTRACT: Single phase of Fe-dioctahedral smectite were synthesized hydrothermally from Si-Fe(III)-Mg and Si-Fe(III)-Al hydrous oxides within 24 hrs at 100-250 °C. The color of the smectite turned from yellowish brown to green with increase of the reaction rate between the hydrous oxide and tetraethyl ammonium hydroxide (TEAOH) when it was used instead of sodium hydroxide. The Fe(2p)_{3/2} binding energies and ESR spectra of the samples suggested the change of Fe coordination or oxidation state in the smectite with decomposition of TEAOH during the hydrothermal treatments.

1 INTRODUCTION

Nontronite and Fe-montmorillonite belong to the family of Fe-dioctahedral smectite, whose chemical formulae are $\text{Na}_x\text{Fe}^{3+}_2\text{Si}_{4-x}\text{Al}_x\text{O}_{10}(\text{OH})_2 \cdot \text{H}_2\text{O}$ and $\text{Na}_{x+y}\text{Fe}^{3+}_{2-x-y}\text{Fe}^{2+}_x\text{Si}_{4-x}\text{Al}_x\text{O}_{10}(\text{OH})_2 \cdot \text{H}_2\text{O}$ $\text{Mg}_y\text{Si}_{4-x}\text{Al}_x\text{O}_{10}(\text{OH})_2 \cdot \text{H}_2\text{O}$, ($0.2 < x < 0.6$), respectively. In the geological disposal system of high level nuclear waste, smectite, which is main component of bentonite, is expected to adsorb the radio nuclides leaking out from the nuclear waste glass. And Fe-bearing smectites are considered to have high adaptability towards the geological disposal system for their selective adsorption of Ce and some another radio nuclides (Iwasaki et al. 1996; Ames et al. 1983). Fe(III) intercalated Montmorillonite has took attention with its excellent catalytic activity for selective oxidation, such as the dehydroxylation of styrene for epoxide formation. (Wang 1991; Xu et al. 1998; Ewell & Insley 1935). And owing to the oxidation and reduction of Fe(III) and Fe(II) in the octahedral site, the smectites bearing the structural Fe can also act as catalysis for degradation of some organic pollutants. (Wang 1991; Xu et al. 1998) However, it is very hard to obtain the pure phase of natural ferric and ferrous smectite, and it has been very difficult to synthesize a single phase of such

smectites in short time without the precipitation of ferric oxide (Ewell & Insley 1935; Hamilton et al. 1951; Decarreau et al. 1987). The ferric and ferrous smectite have additional Fe site compared to Fe intercalated smectite, the study of its catalytic behavior will take an interest.

Recently, Nagase et al. (1999) achieved to synthesize the Fe-montmorillonite and nontronite, using the phase relationships estimated from solubility of Fe-minerals and controlling the pH, using low concentration of slurry and hydrothermal temperature to avoid the impurity.

In this study, using tetraethyl ammonium hydroxide ($(\text{C}_2\text{H}_5)_4\text{NOH}$) to control the pH, syntheses of Fe-smectite were achieved successfully more short time using more concentrated slurry in comparison with the case using sodium hydroxide (NaOH). And difference in the oxidation state of iron between the samples was discussed.

2 MATERIALS AND METHODS

Fe(III)-Al-Si hydrous oxide was prepared by mixing the metal chloride complex and sodium silicate solution at low pH condition and co-precipitated by titration of ammonium hydroxide. Tetraethyl

ammonium hydroxide (TEAOH) solution was added to the filtrated hydrous oxide to adjust the pH for hydrothermal treatment. Resulted slurry was heated hydrothermally in a teflon container. Then sample were dried at room temperature.

The powdered products were characterized by Rigaku X-ray diffractometer, and observed by JEOL TEM 2000EXII (200kV). ATR visible spectra (370-700nm) were obtained by Shimadzu densitometer CS-9300PC. Fe coordination in the products was examined by analyzing the XP and ESR, using Ulvac PHI 5601ci spectrometer with MgK α radiation and JEOL JES-TE200, ESR spectrometer. FT-IR spectra (4000-400cm⁻¹) were also analysed by KBr technique using Perkin Elmer Spectrum 1000.

3 RESULTS

3.1 Color change of the smectite synthesized in various conditions

The conditions of syntheses were estimated from the solubility diagram of Nagase et al. (1999).

The resulted products listed in table 1 coincide with the estimated phase relationships. When using NaOH, the optimum concentration of slurry at 100 - 200 °C, pH12 was 10-20 wt% and the concentration of slurry and pH became higher than optimal condition, impurities such as analcime, aegirine and hematite were easily precipitated. Upon addition of tetraethyl ammonium hydroxide (TEAOH) instead of NaOH, transformation of smectite to aegirine didn't recognized.

Table 1: Hydrothermal conditions of syntheses and the products characterized by X-ray diffraction patterns.

run No.	starting composition	adjusted pH	conc. of slurry	added alkali	temp. (°C)	time (h)	products by XRD
1	Si-Fe-Al=4-1.7-0.3	12.1	1/10	NaOH	175	24	smectite(Y)*
2	Si-Fe-Mg=4-1.7-0.3	12.4	1/10	NaOH	200	24	smectite(Y)
3	Si-Fe-Mg=4-1.7-0.3	12.0	1/10	NH ₄ OH	200	24	smectite(YG)*
4	Si-Fe-Mg=4-1.7-0.3	13.1	1/10	NaOH	200	24	aegirine, smectite
5	Si-Fe-Mg=4-1.7-0.3	12.3	1/1	NaOH	200	4	aegirine, smectite
6	Si-Fe-Al=4-1.7-0.3	13	1/1	(C ₂ H ₅) ₄ NOH	200	4	smectite(YG)
7	Si-Fe-Mg=4-1.7-0.3	13	1/1	(C ₂ H ₅) ₄ NOH	200	4	smectite(YG)
8	Si-Fe-Mg=4-1.7-0.3	13	1/1	(C ₂ H ₅) ₄ NOH	200	24	smectite(G)*
9	Si-Fe-Mg=4-1.7-0.3	1/1	(C ₂ H ₅) ₄ NOH	225	4	smectite(G)	
10	Si-Fe-Mg=4-1.7-0.3	13	1/1	(C ₂ H ₅) ₄ NOH	250	4	smectite(G)

*Y:yellowish brown color, YG:yellowish green, G: dark green

In comparison with the XRD patterns of the obtained smectite samples, d(001) values of the samples synthesized with TEAOH and NH₄OH were smaller than those of the samples with NaOH.

With ethylene glycole treatment, the interlayer space of Na⁺ smectite is easily expanded, whereas it is difficult for the NH₄⁺ smectite. Usually, quaternary alkyl ammonium intercalated smectite

have larger d-value in comparison with Na⁺ smectite, the sample synthesized with TEAOH should have NH₄⁺ in its interlayer space derived from decomposed TEAOH.

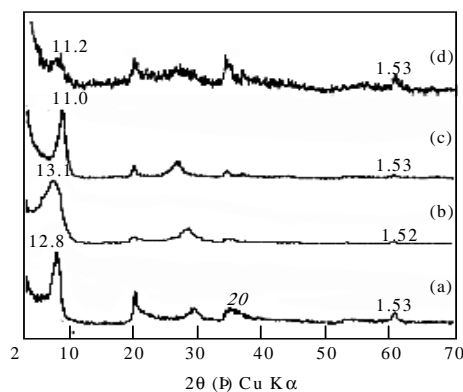


Figure 1: Powder X-ray diffraction patterns of the synthesized nontronite(a) and Fe-montmorillonite at 200°C for 24h upon addition of NaOH(b), NH₄OH(c), and TEAOH(d).

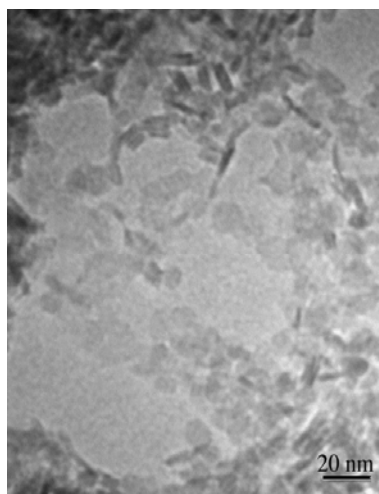


Figure 2: Fe-montmorillonite synthesized at 200 °C for 24h using TEAOH.

3.2 TEM observation

By TEM, the Fe-smectite samples synthesized with NaOH had well crystallized and layered particles more than 50 nm in a diameter with c.a. 20 nm of thickness. From the solid/liquid ratio (S/L) = 1/1 slurry with TEAOH, the smectite sample synthesized at 200°C for 24 h had low crystallinity in comparison with the sample from S/L = 1/10 slurry. The sample synthesized with TEAOH

consisted of almost uniform particles of c.a. 20 nm in a diameter with a thickness of 3- 4 nm, and no particles of aegirine and ferric oxide were observed. Thus, the green color of the samples seemed not to depend on the impurities.

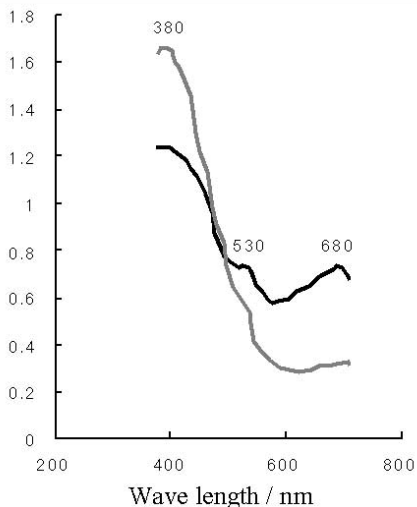


Figure 3: ATR visible spectra of Fe bearing smectite synthesized using NaOH(a) and TEAOH(b).

3.3 Spectroscopic analysis

ATR-visible spectrum of the yellow smectite synthesized with NaOH showed the absorption at around 530 nm and 680 nm, however, in the sample synthesized with TEAOH, these peaks were diminished, and the absorption at 380 nm was increased. The band at 530 nm were usually observed in ferric oxides and can be attributed to presence of ferric state iron with oxygen in octahedral arrangement. The band at 380 nm had been attributed to Fe(III) in tetrahedral framework position in the zeolite structures were increased in the sample with TEAOH (Fejes et al. 2002).

According to the assignment by P. Selvam et al.(2001), both samples synthesized with NaOH and TEAOH had g values of trivalent iron in the structure ($g=2.0$) and no peaks of nano-sized clusters ($g=2.1-2.3$) were observed in ESR spectra (see Figure 4). The intensity of the peak of $g=2$ of TEA-Fe-smectite was decreased in comparison with that of Fe-smectite synthesized with NaOH.

Thus it was suggested that the difference in the color of the samples were derived from the arrangement or oxidation state of iron in the structure.

From X-ray photoelectron spectra (XPS) of the products, the $Fe(2P)_{3/2}$ binding energies of the

products obtained by TEAOH decreased with increase of temperature of syntheses. The value of $Fe(2P)_{3/2}$ binding energy was 711.9, 711.5 and 711.0 eV for the sample synthesized at 200 °C, 225 °C and 250 °C, which was 0.5-1.4 eV lower compared to that of the sample obtained by NaOH (712.4 eV). Since the binding energy of FeO is 1.5 eV lower than Fe_2O_3 (McIntyre & Zelaruk 1977), it can be considered that the reduction of Fe relevance to the decomposition of TEAOH was occurred during the synthesis.

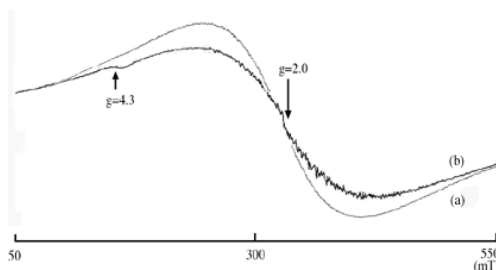


Figure 4: ESR spectra of Fe-montmorillonite samples synthesized using NaOH(a) and TEAOH(b).

The FT-IR spectra of the sample synthesized at 200 °C with TEAOH has a peak at 2987 cm^{-1} assigned to absorption of alkyl chain, which diminished and disappeared in the samples synthesized at 225 °C and 250 °C. No change was observed in the Si-O(b) stretching of 1014 cm^{-1} , which means no perturbation of Si-O tetrahedral sheet. The peak at 1112 cm^{-1} of Si-O(a) shoulder in the sample with TEAOH reflected the lower crystallinity in comparison with the sample with NaOH, which can be also observed in the Na-smectite synthesized at lower pH condition. The Si-O(a) shoulder diminished and shifted to 1107 cm^{-1} in the spectra of the samples at 225 and 250 °C. The peak of FeO-OH deformation was shifted from 815 cm^{-1} to lower frequency in the sample by TEAOH, which means the increase of Fe(III)/Fe(II) ratio according to Stucky and Roth (1976). The sample with TEAOH have a peak at 785 cm^{-1} , which diminished with increase of temperature, which suggests some organic complex of iron.

4 DISCUSSION

Stucky & Roth (1976) were discussed the relationship between FT-IR spectra and Fe(III)/Fe(II) ratio in Fe-smectite by reducing natural nontronite of $Fe(III)/Fe(II) = 13$, and they recommended that the absorption of 3570 , 1030 , and 821 cm^{-1} were lineally shifted to lower frequency

with decrease of Fe(III)/Fe(II) ratio with dithionite-reducing. In this study, those absorptions in the sample with NaOH were found at 3554, 1014, and 815 cm^{-1} . In the case with TEAOH, absorption at 3554 cm^{-1} of structural hydroxyls of Fe^{3+} - Fe^{3+} -vacancy was almost disappeared, and adsorption of FeO-H deformation was shifted to lower side, however, in this case, comparing the samples synthesized at different temperature, which has to be attributed to lower crystallinity of the samples. Since the $\text{Fe}(2\text{P})_{3/2}$ binding energy of the sample at 250 °C was lower in comparison with the lower crystallized sample at 200 °C and 225 °C with higher alkylamine content, the lower $\text{Fe}(2\text{P})_{3/2}$ binding energy of the sample at 250 °C can be attributed to reducing of a part of the ferric ion in the smectite structure.

From the above results, it is considered that TEAOH was decomposed during the synthesis, reducing a part of ferric content, and derived ammonium ion was trapped into the interlayer spaces of smectite.

5 CONCLUSION

Fe-di-octahedral smectite containing Fe(III), Fe(II) ions in the structure could be synthesized from a higher concentration of the slurry of Si-Fe hydrous oxide with TEAOH at higher temperature than 200°C.

The green color of the smectite was considered to be reflected the coordination of iron in the structure.

With TEAOH instead of NaOH, because of low concentration of sodium, co-precipitation of aegirine and analcime were avoided.

Since, the layer charge of Fe-smectite can be controlled reversibly by the oxidation and the reduction of Fe in its octahedral site, synthetic Fe-smectite will be expected to act as a functional catalysis for both industrial and environmental points.

6 REFERENCES

- Ames L. L., McGarrah J. E. and Walker B. A., *Clays and Clay Mines*, 31, 321 (1983).
- Boricha A. B., Mody H. M., Das A., Bajaj H. C., *Appl. Catal. A*, 179, 5 (1999).
- Decarreau A., Bonin D., Badaut-Trauth D., Couty R., and Kaiser P., *Clay Minerals*, 22, 207 (1987).
- Ewell H. and Insley P. R., *J. Res. Nat. Bur. Standards*, 15, 173 (1935).
- Bowers T. S., Jackson K. J., and Helgeson H. C., *Equilibrium Activity Diagrams*, Springer-Verlag, New York Tokyo (1984).
- Fejes P., Kiricsi I., Kovács K., Lázár K., Marsi I., Oszkó A., Rockenbauer A. and Schay Z., *Appl. Catal. A*, 223, 147(2002)
- Hamilton G. and Furtwangler W., *Tschermaks Mineral. Petrogr. Mitt.*, 1951, 3F.

- Helgeson H. C., *Am. J. Sci.*, 267, 724 (1969).
- Iwasaki T., Onodera Y., Torii K., and Hayashi H., *JP Patent* 2500322 (1996).
- McIntyre N. S. and Zelaruk P. G., *Anal. Chem.*, 49, 1521 (1977).
- Nagase T., Iwasaki T., Ebina T., Hayashi H., Onodera Y. and Dutta N.C., *Chemistry Letters*, 1999, 303 (1999).
- Pai S. G., Bajpai A. R., Deshpande A. B., Samant S. D., *Synth. Commun.* 27, 2267 (1997).
- Pai S. G., Bajpai A. R., Deshpande A. B., Samant S. D., *J. Mol. Catal., A*, 156, 233 (2000).
- Stucki J. W. and Roth C. B., *Clays and Clay Mines*, 24, 293 (1976).
- Selvam P., Dapurkar S. E., Badamali S. K., Murugasan M., and Kuwano H., *Catalysis Today*, 68, 69 (2001).
- Wang M. C., *Clays and Clay Mines*, 39, 202 (1991).
- Xu S., Lehmann R. G., Miller J. R. and Chandra G., *Environmental Sci. Technol.*, 32, 1199 (1998).

Industrial Growth and Properties of Calcite Single Crystals

I.V.Nefyodova

All-Russian Research Institute for Synthesis of Minerals, Aleksandrov 601600, Vladimir District, Russia

N.I.Leonyuk

Geological Faculty, Lomonosov Moscow State University, Moscow 119999/GSP-2, Russia

ABSTRACT: In this paper, calcite crystals, CaCO_3 , have been grown under hydrothermal conditions in the CaCO_3 - NH_4Br - LiCl - H_2O system, pure and with an addition of indium. Peculiarities of calcite growth on the seeds oriented parallel to $\{11\text{-}20\}$ and $\{0001\}$ planes are investigated. The number of crystal growth defects is effectively reduced in comparison with conventional hydrothermal synthesis of this materials using rhombohedral seeds. Indium impurity has a certain effect on growth mechanism of calcite crystals: the faces (0001) , $(10\text{-}11)$ and $(02\text{-}21)$ are visibly perfect and no spontaneous crystallization is noted. As a result, this growth conditions allowed to grow the optical grade of this material with variable indium impurity from 0.03 to 0.5 at %. The light transmission is comparable with the best grades of natural Iceland spar. Optical and luminescent characteristics of the crystals grown have also been studied.

1 INTRODUCTION

Optical quality calcite (Iceland spar) is one of the most important materials having high birefringence and transmission over a wide spectral range. There is a large market demand for manufacturing polarizers, beam divergent elements, laser shutters and other optical units.

Hydrothermal synthesis of these crystals is productive because it is possible to use some of the equipment designed for the quartz industrial technology. Since the seventies of the last century, many laboratory studies have reported the growth of these crystals under hydrothermal conditions. For example, an advantage of NH_4Br and NH_4Cl solutions for calcite crystal growth at temperatures over 250 °C is discussed by Gener et al. (1974). Also, CaCO_3 crystals were grown from NH_4Br solutions in steel autoclaves using glass vessel inserts of 3-3.5 mm diameter (Ikornikova 1975). These authors studied the habit function as a function of the growth conditions. Calcite single crystal layers up to 10 mm perpendicular to the $(10\ 11)$ were grown from K_2CO_3 solutions in autoclaves (20 x 275 mm) lined with silver (Kinloch et al. 1974). Later, calcite was also obtained from nitrate solutions (Kikuta & Hirano 1990).

It is known, the natural Iceland spar is characterized by about 70 simple crystallographic forms, and 20 of them are strongly developed (Dana 1953). On the other hand, synthetic calcite grown under hydrothermal conditions has a limited number of crystal faces. The faces of $\{02\text{-}21\}$ and $\{10\text{-}11\}$ rhombohedra as well as $\{11\text{-}20\}$ hexahonal prism are morphologically stable in the crystals obtained from the NH_4Br and NH_4Cl based solutions.

The industrial growth technology of calcite crystals on seed plates parallel to the $\{10\text{-}11\}$ faces (split rhombohedron) has been developed in Russia for the first time in the world (Nefyodova & Lyutin 1995). Serial production of polished rhombohedral cleavages up to 80x80x16 mm became possible by using steel autoclaves of a few cubic meters and vessel inserts made of a special titanium alloy. However, crystals grown on the $\{10\text{-}11\}$ oriented seeds are comparably expensive for making polarizers because of the amount of waste that results and which increases the price of the products. The optical inhomogeneity like V-shaped defects can often occur in growth pyramids of the split rhombohedron (Borodin et al. 2002).

From this point of view, the crystal growth on pinacoidal seeds provides the most economic route for machining optical calcite single crystals. On this

way, using NH_4Br and NH_4Cl mineralizers, it was found that a certain inhomogeneity of calcite crystals is caused by an intense spontaneous nucleation on $\{10\text{-}11\}$ and $\{0001\}$ faces as well as on the walls of liners (Nefyodova et al. 2000). An addition of Li ions to starting $\text{CaCO}_3 - \text{NH}_4\text{Br} - \text{H}_2\text{O}$ system allowed to restrict this spontaneous nucleation, but this admixture lead to the development of $\{0001\}$ simple form.

In this paper, taking into consideration the above results, a further attempt was made to improve the quality of calcite crystals using the $\text{NH}_4\text{Br} - \text{LiCl}$ solvent, pure and with an addition of indium. Homogeneity and optical characteristics of the crystals grown have also been studied. A comparative investigation of the transmission spectra and photoluminescence of natural and synthetic crystals are of great interest for analyzing the mechanisms controlling the optical characteristics of the grown crystals. It is clearly possible to regulate the physicochemical conditions of synthetic calcite crystal growth so as to grow crystals suitably doped and having the requested physical properties.

2 EXPERIMENTAL

24-liter steel autoclaves lined with floating type of 2.5-liter titanium inserts were used for the growth of calcite crystals. Hydrothermal experiments were based on the ammonium bromide solvent doped with lithium chloride and metallic indium or In_2O_3 . The starting crystalline material was prepared of natural CaCO_3 single crystals. This mixture was loaded in a lower part of the lining vessel (dissolution zone). Plate-like seeds of natural calcite oriented parallel to $\{10\text{-}11\}$ and $\{0001\}$ were fixed in an upper section of the liner (crystallization zone). Saturated solutions were transferred from the lower, and most heated, zone into the higher area (more cold) owing to the thermal convection. As a result of supersaturating solution in the upper section of autoclave, an excess of dissolved CaCO_3 deposited on the seeds. Experimental conditions were as follows: temperatures of 250 - 300°C, $\Delta T = 5 - 10^\circ\text{C}$, pressure 50 - 100 Mpa, and duration of 30 - 85 days.

Chemical and spectral analyses of the grown crystals has been made. Optical spectra of indium doped calcite samples were measured by spectrophotometers «Specord-M40» and «SDL-1». The light transmission (T , %) and the light absorption (K , cm^{-1}) parameters in the ultraviolet range of spectrum were determined taking into account reflection losses from the sample surface. The photo-luminescence spectra of the synthetic calcite crystals were measured following the procedure described by Tarashchan (1978).

3 RESULTS AND DISCUSSION

3.1 $\text{CaCO}_3 - \text{NH}_4\text{Br} - \text{LiCl} - \text{H}_2\text{O}$ system

As a result, using the above procedures, calcite crystals having a single crystal layer thickness up to 10 mm were grown (Fig.1).

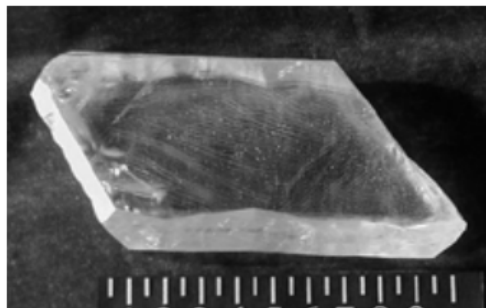


Figure 1: CaCO_3 crystal grown on a seed parallel to $\{0001\}$ face

According to Ikornikova [1], the solubility of calcite in NH_4Br solutions increases exponentially with increasing temperature. It implies a similar temperature dependence for the growth rates of $\{0001\}$ faces from these solutions. However, as it was found experimentally, this dependence practically is linear, and there is intensive spontaneous nucleation at elevated temperatures, and it limits the growth rate of calcite crystals on pinacoidal seeds.

As it might be expected, perfect crystals with stable properties can be grown at a constant growth rate. For this reason, a method of crystal synthesis involving controlled variation of the crystallization temperature mode was suggested for studying the dependence of the calcite homogeneity on the dynamics of the rate changes (Lefauchaux & Rodert 1974).

In experimental long-term runs the autoclave power was periodically switched off for half an hour, and then it was switched on again. Due to this procedure, the temperature in both crystallization and dissolution zones was steeped 6 - 8 °C at each on/off, off/on power change. Results of the autoclave temperature changes are distinctly displayed in the $\langle 0001 \rangle$ crystal growth direction.

There is a tendency to reducing the growth rate during the initial growth (Fig.2). At the end of a run, an increase in the growth rate was observed, and it is connected with the appearance of slit shaped spaces due to hasty growth on roughened surfaces.

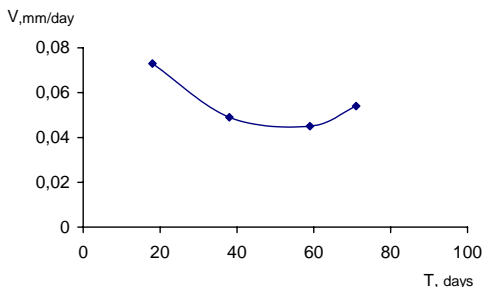


Figure 2: Crystal growth rate (V) vs time (T) during crystallization process

3.2 Indium doped CaCO_3 - NH_4Br - H_2O system

No spontaneous nucleation has been found in experiments with In^{3+} dopant. Normal growth rates of the faces $\{0001\}$, $\{10\text{-}11\}$ and $\{02\text{-}21\}$ were substantially reduced in comparison with the CaCO_3 - NH_4Br - H_2O hydrothermal solutions. Figure 3 shows a calcite crystal grown on pinacoidal seed. No visible defects are in these crystals, but the grown up material has isometric cracks. Also, crystals grown on the seeds parallel to $\{10\text{-}11\}$ have irradiating cracks indicating In^{3+} impurity in crystal structure.

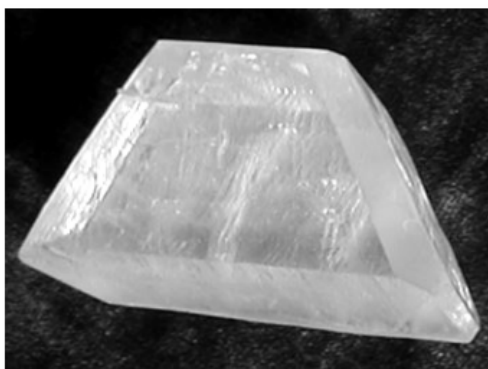


Figure 3: 7 mm thick calcite crystal grown in the CaCO_3 - NH_4Br - H_2O system doped with In

As the results of chemical and spectral analyses, grown crystals have indium concentration from 0.03 to 0.5 % (Table 1). It can be concluded that metallic indium and/or indium oxide differently effect on the growth kinetics. Presence of In_2O_3 reduces normal growth rates of the $\{0001\}$ face to 0.03 mm/day maximum. The faces $\{0001\}$ and $\{10\text{-}11\}$ are not twinned in these crystals and In content in the grown up layer varies from 0.1 to 0.5 %. On the other hand, the metallic indium increase the growth rate along pinacoidal direction to over 0.1 mm/day, and it makes synthetic calcite less homogeneous. In this

case, the indium concentration in crystals grown is found to be in one order lower, 0.03 – 0.08 %.

Table 1. Indium concentration (C_{In}) in calcite crystals resulted from spectral semi-quantitative analysis $^*\text{In}_2\text{O}_3$ used as a dopant, but metallic In was added in other experiments.

In concentration in starting mixture, mol %	(0001)/(1011) growth rate, mm/day	C_{In} , at %
-	0.120/0.125	-
0.002*	0.039/0.005	0.50
0.001	0.092/0.119	0.03
0.001	0.080/0.096	0.03
0.001*	0.026/0.007	0.10
0.0015	0.023/0.009	0.08

3.3 Optical properties

There are three main absorption bands of 280, 310 and 350 nm caused by the $\text{CO}_m^{\text{n-}}$ and Ca^{2+} centers and a wide absorption band of 220 - 500 nm, connected with an organic impurity, the latter being a distinguishing feature in the absorption spectra of natural Iceland spar crystals. Two absorption bands (320 and 240 nm) are a distinguishing feature in the spectra of synthetic optical calcite. The 320 nm absorption band is a characteristic of all growth on $\langle 10\ 11 \rangle$, $\langle 11\ \bar{2}0 \rangle$ and $\langle 0001 \rangle$ pyramids and it is caused by donor centers $[\text{CO}_2]$, but the second one (240 nm) is caused by hole centers $[\text{CO}_3]$ (Platonov 1976). The comparative study of natural and synthetic crystals in the range of wavelength over 500 nm shows that the light transmission is connected with structural features of CaCO_3 , but not with impurities or structural defects.

In contrast to this data, the light transmission curves in the short-wave spectral range, (especially in the ultraviolet), is sensitive to various structural infringements and to impurities depending on the geochemical formation conditions for natural crystals and physics and chemistry of the crystal growth conditions for synthetic crystals. In the range 340 - 500 nm, synthetic calcite has a better light transmission and lower statistical spread in T % values than natural Iceland spar (Fig.4). Transmission spectra of the samples prepared of In^{3+} doped material show a shift of the transmission edge towards the long wave side (from 200 to 240 nm). The light absorption cut off for crystals grown from differently oriented seeds and from regions of different growth pyramids is practically the same; it indicates a very good degree of homogeneity for synthetic calcite crystals. Applications for synthetic calcite, as well as for natural Iceland spar are restricted by photoluminescence in a specific spectral range. In particular, radiation bands at 345, 370, 630 nm maximum were found in grown crystals. Radiation in the range of around 630 nm was studied, and is connected with Mn^{2+} instead of Ca^{2+} ions ($^4\text{T}_1(\text{G}) \rightarrow ^6\text{A}_1(\text{S})$ electronic transition).

Ultraviolet luminescence of Iceland spar is caused by an electronic transition ${}^2D_{3/2} \rightarrow {}^2F_{5/2}, {}^2F_{7/2}$ in Ce^{3+} (Tarashchan 1978). It was found that the intensity of photoluminescence increases from the center to periphery of crystals.

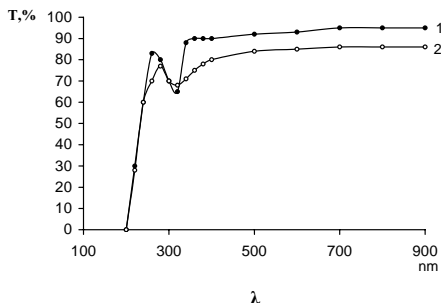


Figure 4. Transmission spectra of synthetic (1) and natural (2) calcite crystal.

Bands of the luminescence due to cerium and manganese impurities, $5 \cdot 10^{-5}$ - $1 \cdot 10^{-4}$ and 0.001 - 0.1 mole % respectively, appear in the spectral ranges of 340 - 370 nm and 610 - 630 nm. Besides, there is also radiation of a different intensity in the range of 400 - 550 nm and, most likely, it is connected with impurities of rare earth elements as well as structural imperfections.

4 CONCLUSIONS

An efficient calcite crystal growth technology under hydrothermal conditions has been developed in order to reduce significantly the amount of waste that can occur in manufacturing optical products. The economic efficiency of the technological process is much improved. The number of crystal growth defects is effectively reduced in comparison with conventional technologies of calcite synthesis using rhombohedral seeds.

Indium impurity has a certain effect on growth mechanism of calcite crystals: the faces (0001), (10-11) and (02-21) are visibly perfect and no spontaneous crystallization is noted.

The light transmission is comparable with the best grades of natural Iceland spar. Though, a certain shift of transmission band to the long wave region can reduce the field use of this material in optics.

5 REFERENCES

Borodin V.L., Nefyodova I.V., Chvanski P.P. 2002 Hydrothermal growth of optical calcite. *X National*

- Conference on Crystal Growth*, November 24-29, 2002, Moscow. Abstracts: 341 (in Russian).
- Dana D. 1953. *Sistema mineralogii*. Moscow: Inostrannaya Literatura.
- Gener F., Bricard M.C., Lemetre R., Aumont R. 1974. Recristallisation hydrothermale de la calcite dans des solution d'halogenures d'ammonium. *High Temperatures-High Pressures* 6: 657-662.
- Ikornikova N. Yu. 1975. Hydrothermal synthesis of crystals in chloride systems. Moscow: Nauka (in Russian).
- Kikuta K., Hirano S. 1990. Hydrothermal growth and dissolution behavior of calcite single crystals in nitrate solutions. *J. Crystal Growth* 99: 895-899.
- Kinloch D.R., Belt R.F., Puttbach R.C. 1974. Hydrothermal growth of calcite in large autoclaves. *J. Crystal Growth* 24/25: 610-615.
- Lefauchaux F., Rodert M.C. 1974. Etude des defauts crees dans des calcites synthetiques soumises a des conditions exterieures de croissance variables. *High Temperatures-High Pressures* 6: 645-656.
- Nefyodova I.V., Lyutin V.I. 1995. Experimental study of optical inhomogeneity in calcite. *Experiment in Geosciences* 4: 77-78.
- Nefyodova I.N., Lyutin V.I., Borodin V.L., Chvanski P.P., Leonyuk N.I. 2000. Hydrothermal growth and morphology of calcite single crystals. *J. Crystal Growth* 211: 458-460.
- Platonov A. N. 1976. *Priroda Okraski Mineralov*, Kyeve: Naukova Dumka.
- Tarashchan A. I. 1978 *Lyuminestsentsiya mineralov*. Moscow: Nauka (in Russian).

Assessment of Technological Properties of Granitoids from South Brazil

L.E.S.M.Novaes

Instituto de Química e Geociências, Universidade Federal de Pelotas, Pelotas, Brazil

C.S.F.Gomes & F.J.F.T.Rocha

Departamento de Geociências, Universidade de Aveiro, Aveiro, Portugal

C.I.P.Carvalho

Instituto Geológico e Mineiro, Portugal

J. M.Gross

Geolinks, Porto Alegre, Brazil

ABSTRACT: Rio Grande do Sul State's territorial area is privileged with a great diversity of lithological types. These litho types vary from the Archean to the Cenozoic and they are distributed in four different geomorphological regions: Plateau, Peripheral Depression, Coastal Plain and Shield. Some of them, especially those present in Plateau and Shield geomorphological regions, represent an enormous potential of rocks that can be industrialized and used, for instance, as a dimension stone. The present work deals with the geology of a region, mostly in the Dom Feliciano Belt's Eastern Domain, Sul-rio-grandense Shield, from which were selected a set of four granitoids, each one with its own chromatic and textural characteristics. These granitoids were investigated in relation to its petrology, chemical and physical-mechanical properties, according to rigorous standard international regulation procedures, in order to be a contribution for its use in civil construction works.

1 INTRODUCTION

Rio Grande do Sul State's territorial area is privileged with a great diversity of lithological types. These litho types vary from the Archean to the Cenozoic and they are distributed in four different geomorphological regions: Plateau, Peripheral Depression, Coastal Plain and Shield. Some of them, especially those present in Plateau and Shield geomorphological regions, represent a potential of rocks that can be industrialized and used, for instance, as a dimension stone.

Despite the notable variety of natural stone potential, mainly granites, the south region of the Rio Grande do Sul State, is still waiting enterprising companies to launch the development in this important mineral sector (Novaes & Azevedo 1995; Gross et al. 1998; Novaes 2003).

As some researchers say, natural stone represents a natural mineral resource, of paramount economic importance that requires both scientific and technological studies (Moura 1991; Chiodi Filho 1993; Costa et al. 1995; Velho et al. 1998).

In regional terms, the dimension stone enterprise, including extractive, manufacturing and commercial activities that uses natural stone as raw material, have not yet revealed its social, cultural and economic potentialities. The study of the main

physical, chemical and technological characteristics of the natural stone pretends to be a contribution for its use in civil construction works.

2 GENERAL FEATURES OF NATURAL STONE'S OCCURRENCES

The granitic rocks that are being researched in this work are grouped into a main geological section named Sul-riograndense Shield, represented by the crystalline basement (Fig. 1).

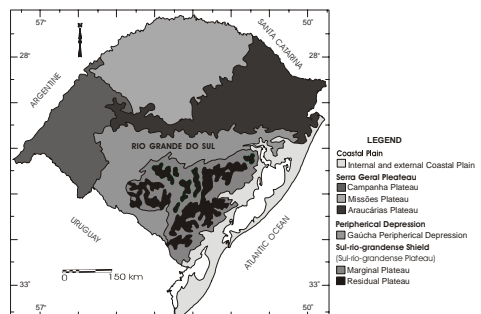


Figure 1. Geomorphological Domain of Rio Grande do Sul State, Brazil (Novaes 2003).

An extremely varied range of igneous rocks of granitoid types and metamorphic rocks of medium and high metamorphic grade forms the crystalline basement. These litho types represent a highly promising field for the discovery of new varieties, due to their textural, compositional, petrographical and color diversifications, as well as due to their broad distribution, along with the small amount of geological research carried out in this area so far (Santos et al. 1989; Novaes & Azevedo 1995; Gross et al. 1998; CPRM 1999).

These four occurrences of granitic rocks that have been studied are located in the very southeastern area of the south region in Rio Grande do Sul State in three distinct districts (Fig. 1): CLJ – Capão do Leão District, PAR and PAZB – Pedras Altas District and PELCS – Pelotas District.

It should be emphasized that besides the geological conditions that are favorable to the occurrence of natural stone resources, this region offers a complete support in infrastructures required for commercial activities, such as road and rail networks, harbor facilities and availability of electric power, besides an exceeding of hard working people (Novaes 2003).

3 CHEMICAL COMPOSITION

Chemical composition of the studied four specimens representative of granitic rocks from south region of Rio Grande do Sul State, Brazil, is shown on Table 1 and was carried out by XRF analysis.

Table 1 – Studied natural stones' chemical composition (Novaes 2003).

Oxides (%)	Natural Stone			
	CLJ	PAR	PAZB	PELCS
SiO ₂	73.86	73.75	76.23	62.22
TiO ₂	0.13	0.22	0.15	1.02
Al ₂ O ₃	12.99	13.21	12.20	16.20
Fe ₂ O ₃	1.43	1.23	0.98	5.40
MnO	0.09	0.05	0.03	0.09
MgO	0.60	0.81	0.80	2.41
CaO	0.60	0.88	0.74	3.78
Na ₂ O	4.08	4.20	3.05	3.24
K ₂ O	4.75	4.12	4.89	4.04
I.L.	0.60	0.59	0.46	0.63

4 PETROGRAPHICAL CHARACTERIZATION

Petrographical characterization based in a QAP Diagram (Streckeisen 1976) of the studied samples of natural stone was carried out on thin sections that were observed with an optical microscope, both in natural and polarized light.

The main petrographical and mineralogical characteristics of the four distinct samples of studied natural stone are as follows (Tab. 2; Fig. 2).

Table 2 – Studied natural stones' mineralogical composition (Novaes 2003).

Rocks Min.	CLJ		PAR		PAZB		PELCS	
	%	SD	%	SD	%	SD	%	SD
Quartz	36	2.3	28	0.5	33	1.3	20	1.0
K-Feldspar	51	2.0	43	1.3	23	0.8	12	0.8
Plagioclase	9	1.5	22	1.5	37	0.3	50	0.3
Biotite	4	0.5	5	1.0	7	0.3	17	0.3
A/S minerals	TR	–	TR	–	TR	–	1*	–

SD=Standard Deviation; A/S=Accessory/Secondary minerals; *Titanite

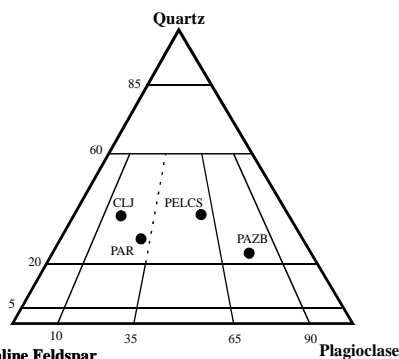


Figure 2 – Studied natural stones' petrographical classification (Streckeisen 1976).

- “CLJ” Siyenogranite – It is a plutonic rock of reddish color; a holocrystalline inequigranular rock that shows medium faneritic texture, hipidiomorphic grains, and as essential minerals has alkaline feldspar, quartz, plagioclase and biotite as a varietal mineral.
- “PAR” Siyenogranite – It is a plutonic rock of reddish color; a holocrystalline inequigranular rock that shows medium faneritic texture, hipidiomorphic grains, and as essential minerals has alkaline feldspar, plagioclase, quartz and biotite as a varietal mineral.
- “PAZB” Monzogranite – It is a plutonic rock of grayish color; a holocrystalline inequigranular rock that shows medium faneritic texture, hipidiomorphic grains, and as essential minerals has plagioclase, quartz, alkaline feldspar; biotite as a varietal mineral and titanite as accessory.
- “PELCS” Granodiorite – It is a plutonic rock of whitish color; a holocrystalline inequigranular rock that shows medium faneritic texture, hipidiomorphic grains, and as essential minerals has quartz, plagioclase, alkaline feldspar and biotite as a varietal mineral.

5 PHYSICAL MECHANICAL CHARACTERIZATION

The physical-mechanical tests (Tab. 3) are of paramount importance for the characterization of the commercial natural stone, since their applications depend upon the physical-mechanical parameters.

Table 3 – Studied natural stones' physical-mechanical characterization (Novaes 2003).

Tests	Units	Natural stones			
		CLJ	PAR	PAZB	PELCS
Compression breaking load	kg/cm ²	3060	2385	2237	3267
Bending strength	kg/cm ²	169	141	182	146
Bending strength after freezing test	kg/cm ²	182	179	140	114
Volum. weight	kg/m ³	2620	2620	2720	2610
Water absorp. (NatP)	% weight	0.1	0.1	0.1	0.2
Apparent porosity	% vol.	0.2	0.3	0.3	0.5
Thermal linear expan. coefficient	x10 ⁻⁶ /°C	9.9	8.9	7.7	6.8
Capon abrasive test	Mm	14.0	13.5	15.5	15.0
Impact test	Cm	55	50	60	65

The technological tests select to be carried out, following recommended standard tests, were considered sufficient for the assessment of the physical-mechanical behavior of the studied natural stones (Moura et al. 2000).

5.1 Compression breaking load

Six (06) cubic specimens with edge measuring 5±0.5 cm were utilized, after being dried till constant weight, and then submitted to progressive compression up to their rupture (CEN/TC 246 – prEN 1926).

5.2 Bending strength and bending strength after freezing test

Twelve (12) test parallelepipedic specimens for each test, with dimensions of 30x10x5 cm were utilized. It has been assessed the maximum tension that could be supported by the test specimens till their rupture being attained (CEN/TC 246 – EN 12372).

5.3 Water absorption at normal atmospheric pressure

This test determines the water mass adsorbed by the test specimen after soaking at normal atmospheric pressure. Six (06) cubic test specimens with edge

measuring 5±0.5 cm was utilized (CEN/TC 246 – prEN 13755).

5.4 Volumetric weight and apparent porosity

This test uses six (06) cubic specimens, for each test, with at least 25 cm³ in volume. After drying to constant mass, the volumetric weight and open porosity are determined by vacuum assisted water absorption and submerged weighing of specimens.

The volumetric weight is expressed by the ratio of the mass of the dry specimen and its apparent volume in kg/m³. The apparent porosity is expressed by the ratio, as a percentage, of the volume of open pores and the apparent volume of the specimen (CEN/TC 246 – EN 1936).

5.5 Thermal linear expansion coefficient

Three (03) rectangular specimens were utilized, having the appropriate dimensions and using a high precision Adamel-Lhomargy dilatometer, in the temperature range 0°C-80°C. The obtained value represents the maximum value of the coefficient of linear thermal expansion (CEN/TC 246 – prEN WI 246-011).

5.6 Capon abrasion test

This test was carried out, knowing as a Capon test, being utilized six (06) parallelepipedic test specimens with dimensions 15x15x3 cm, in order to obtain the result expresses the thickness reduction of the test specimen produced by friction of a disc and an appropriate abrasive (CEN/TC 246 – prEN 14157).

5.7 Impact test

In these test four (04) parallelepipedic plates with dimensions 20x20x3 cm were placed on a sand bed 10 cm thick and then submitted to the impact of sphere of steel weighing 1 kg that falls down from heights progressively 5 cm higher. The result corresponds to the minimum falling height that causes the plate rupture (CEN/TC 246 – prEN 14158).

5.8 Frost resistance

The frost resistance of natural stone units is determined by a test comprising 48 cycles of freezing in air and thawing in water (CEN/TC 246 – prEN 12371). This test uses six (06) parallelepipedic specimens with dimensions 50x50x300 mm and ten (10) parallelepipedic specimens with dimensions 50x100x300 mm.

6 CONCLUSIONS

The results of both petrographical studies and physical-mechanical tests carried out on the studied four types of natural stone of south region of Rio Grande do Sul State, Brazil, allowed to put forward the following comments:

- a) All studied varieties provided higher values of compression breaking load, in accordance with the fact that the normal average for granitic rocks is approximately 800 to 3000 kg/cm².
- b) All studied varieties provided great values of bending strength and bending strength after freezing test, in accordance with the fact that the normal average for granitic rocks is approximately 80 to 360 kg/cm².
- c) All studied varieties provided great values of volumetric weight, in accordance with the fact that the normal average for granitic rocks is approximately 2600 to 2800 kg/cm³.
- d) All studied varieties provided great values of mechanical resistance to water absorption at NATP, in accordance with the fact that the normal value for granitic rocks is approximately 0.20 to 0.50 %.
- e) All studied varieties provided great values of apparent porosity, in accordance with the fact that the normal value for granitic rocks is under 1.50 %.
- f) All studied varieties provided great values of thermal linear expansion coefficient, in accordance with the fact that the maximum value for granitic rocks is approximately 5 to 10x10⁻⁶/°C.
- g) All studied varieties provided great values of Capon abrasion test, in accordance with the fact that the normal value for granitic rocks is approximately 14.3 to 16.6 mm.
- h) All studied varieties provided great values of impact test, in accordance with the fact that the normal value for granitic rocks is approximately 45 to 90 cm.
- i) No color or structural changes on the samples were noticed after 48 cycles of the test frost-defrost being carried out.
- j) The prevailing applications of these rocks are in interior and exterior works.

7 REFERENCES

CEN/TC 246 – Natural stone test methods: prEN 1926 (1998); EN 1936 (1999); prEN 12371 (2001); EN 12372 (1999); prEN 13755 (1999); prEN 14157 (2001); prEN 14158 (2001); prEN WI 246–011 (2001).
Chiodi Filho, C. 1993. A importância da pesquisa geológica para o setor de rochas ornamentais. *Revista Brasil Mineral*, São Paulo, v. 11, n. 110, pp. 46-49.

Costa, L. R.; Leite, M. R. M. & Moura, A. C. 1995. O futuro da indústria das Rochas Ornamentais. *Bol. Minas*, vol. 32, nº 1, pp. 1-13.
CPRM 1999. Programa Levantamentos Geológicos Básicos do Brasil – PLGB: Folha de Pedro Osório. SH.22-Y-C. Estado do Rio Grande do Sul. Escala 1:250.000/Org. Gilberto Emílio Ramgrab [e] Wilson Wildner – Companhia de Pesquisa de Recursos Minerais, MME, Brasília.
Gross, J.M.; Monteiro, A. & Novaes, L.E.S.M. 1998. Mármore e Granitos: Potencialidades da Metade Sul. Porto Alegre, v. 1. 54 p.
Moura, A. C. et al. 1991. Catálogo de Rochas Ornamentais Portuguesas. Edição Instituto Geológico e Mineiro, Lisboa, vols. I,II,III,IV.
Moura, A.C.; Grade, J., Ramos, J.M.F. & Moreira, A.D. 2000. Granitos e rochas similares de Portugal. Instituto Geológico Mineiro, Ministério da Economia, 179 p.
Novaes, L.E.S.M. & Azevedo, M.M. 1995. Tecnologia e difusão de rochas ornamentais na Região Sul do Estado do Rio Grande do Sul – Pólo Graniteiro. Universidade Católica de Pelotas, Instituto Técnico de Pesquisa e Assessoria, Serviço de Apoio às Micro e Pequenas Empresas, Pelotas, RGS, 44 p.
Novaes, L.E.S.M. 2003. Caracterização petrogeoquímica, físico-mecânica e avaliação sócio-econômica da pedra natural para fins ornamentais de depósitos da Zona Sul do Estado do Rio Grande do Sul, Brasil. Tese de Doutorado, Universidade de Aveiro, Portugal, 305 p.
Santos, E.L.; Ramgrab, E.G.; Maciel, A.L. & Mosmann, R. 1989. Mapa Geológico do Estado do Rio Grande do Sul, escala 1:1.000.000 e Parte do Escudo Sul-riograndense escala 1:600.000. Departamento Nacional da Produção Mineral, MME, Porto Alegre.
Streckeisen, A. 1976. To each plutonic rock its proper name. *Earth Sci. Rev.*, v. 12, pp. 1-33.
Velho, J.A.G.L.; Gomes, C.S.F. & Romariz, C. 1998. Minerais industriais: geologia, propriedades, tratamentos, aplicações, especificações, produções e mercados. Coimbra, 591 p.

8 ACKNOWLEDGMENTS

The present work was carried out within the framework of a cooperative project between Universidade Federal de Pelotas, RS, Brazil; Universidade de Aveiro, Portugal; and Instituto Geológico e Mineiro, Portugal.

The executing team would like to thank the geologist Andreia Monteiro, Brazil; Mr. Mário Duarte Monteiro and Mr. António Selores Sousa, from Instituto Geológico e Mineiro, S. Mamede de Infesta, Portugal, for their technical collaboration and efforts to make feasible the research carried out.

Geochemical and Structural Characterization of K-feldspar from the Valle Fértil Field Pegmatites, Pampean Ranges, Argentina

J.Oyarzábal & M.B.Roquet

Departamento de Geología, Proyecto CyT 349001, Universidad Nacional de San Luis, San Luis, Argentina.

ABSTRACT: The Valle Fértil field muscovite-bearing pegmatites are located between 30° 30' and 30° 47' S and 67° 29' and 67° 43' W, in the Pampeana Pegmatitic Province, Argentina. The pegmatites exhibit a heterogeneous complex internal structure, the units of primary crystallization are border, wall, intermediate zones and quartz core, muscovite and albite replacement bodies are always present. The mineral assemblage is characterized by the predominance of K-feldspar, quartz, plagioclase and muscovite. The K-feldspars studied were collected from wall and intermediate zones, all of them show pink or pale brown color and marked perthitic character. Their chemical analyses reflect the pegmatite type, geochemical signature and mineralization of the deposits as well as the evolution of zones within each of them. The K/Rb, K/Cs and Rb/Sr ratios correlate well with the established patterns of geochemical fractionation for muscovite-bearing and barren rare-element pegmatites of LCT signature of Pampeana Pegmatitic Province. (Al,Si) ordering in the tetrahedral sites have been calculated from lattice parameters and selected diffraction-peak positions, the results indicate that the blocky K-feldspars from intermediate zones have a fully ordered structure. The near maximum microcline state suggests conditions of crystallization at low rates of nucleation.

1 INTRODUCTION

Alkali feldspars, quartz and micas are the main granitic pegmatite rock-forming minerals. K-feldspar crystallizes through extensive periods of pegmatite solidification and provides suitable host for Rb, NH₄, Cs, Ca, Sr, Pb, Ba, Eu, La and Li in alkali position, and B, Ga, Ge, Fe, Mg, Ti and P in tetrahedral sites; its subordinate, minor and trace element concentrations reflect aspects related to petrogenetics features, mineralogy and geochemistry, and can be used to correlate them with established patterns of geochemical fractionation in other pegmatitic fields, and for the determination of the pegmatite type, geochemical signature and probable mineralization.

The structural state of K-feldspar, established by the (Al,Si) distribution in tetrahedral sites, is petrologically informative and may reflect the crystallization conditions of the pegmatites. Different authors have studied its determination.

2 METHODOLOGY

K-feldspar samples were collected from the intermediate zone of each pegmatite. The mineral

grains were fragmented in an Abich mortar, selected by picking up under stereomicroscope, and grounded in an agate mortar for this chemical and structural analysis. The chemical analyses were performed by X-ray fluorescence with a Philips PW-1400 spectrometer; Na was analyzed by atomic spectrometry. A Rigaku D-MAX III C diffractometer with CuK α radiation was used. The X-ray powder diffraction data were collected under the following experimental conditions: 30 kV, 20 mA, with a scanning speed of 2° (2 θ)/min and counts recovered every 0.01° (2 θ), between 29° and 31° (2 θ) in order to accurately identify the 131 and 1-31 reflections; full diffractograms were made between 10° and 60° (2 θ) and counts recovered every 0.05° (2 θ). Least-square refinements of cell parameters were performed using the CELREF-V3 program developed by Altermatt & Brown (1987).

3 GEOLOGICAL SETTING

The pegmatitic field is confined to the eastern of the Valle Fértil range, Pampeana Pegmatitic Province, central Argentina, and consists of about 30 barren or muscovite pegmatites assigned to three different groups (from N to S): Balilla, Aurora and Tinacria.

The basement is composed of high-grade amphibolite to granulite facies metamorphic rocks, mainly metabasites and granodioritic gneisses, with intercalated gabbro, tonalite and biotite granite cataclastic bodies. According to Casquet et al. (2003), the pegmatites were emplaced at $\sim 690 \pm 90^\circ\text{C}$ and $\sim 4.1 \pm 0.4$ kb. Some K-Ar date from muscovites have allowed to establish three cycles of pegmatitic activity, the first between 650 and 600 Ma, and the other two among 500 and 430 Ma, respectively (Toubes Spinelli, 1984).

4 THE PEGMATITES

In general, the pegmatite bodies are tabular, with 10-120 m wide and 30-250 m long. They have N25-30°W to N25-45°E predominant strike and 30-45° NE or SW dips. All of them exhibit a heterogeneous, complex internal structure with variable textural characteristics and mineral modes; the units of primary crystallization are border, wall, intermediate zones and quartz core, muscovite and albite replacement bodies are always present. The mineral assemblage is characterized by the predominance of K-feldspar, quartz, plagioclase and muscovite, whereas the accessory minerals are Bt-Vrm-Alm-Tur-Brl-Ep-Mnz-Aln.



Figure 1. Location map of the pegmatites.

The deposits studied are Santa Amalia, San Guillermo, Andacollo and El Chañar. Santa Amalia and San Guillermo mines are in the north of the Valle Fértil field, 18 km at NW of the Usno village, they are members of the Balilla group and constitute the most important reserve of the ceramic minerals of Argentina. Andacollo and El Chañar pegmatites form part of the Aurora group, and they are located at SW of the San Agustín town (Fig. 1).

5 PHYSICAL AND OPTICAL CHARACTERISTICS OF K-FELDSPAR

K-feldspar specimens studied were collected from wall and intermediate zones, all of them show pink or pale brown color and marked perthitic character, in the outer most units contain quartz intergrowths in micrographic texture. In the inner units, K-feldspar shows blocky texture and the crystals exhibit a combination of several pinacoidal forms. In thin sections, the grains occur twinned according to the albite and pericline laws, and show intergrowth texture as micropertthite exsolution of albite, the most frequent patterns are sub-parallel lamellae (3-10 μ in width, in Andacollo samples), veins (35-200 μ in width, El Chañar mine), and oriented rods with diffuse edges in Santa Amalia and San Guillermo deposits. The alteration products are kaolinite and sericite, whereas albite and muscovite, hosted along the cleavage surfaces, are the most frequent replacements.

6 COMPOSITIONAL CHARACTERISTICS OF K-FELDSPAR

The content in subordinate, minor and trace elements constitutes an important guide for the granitic pegmatites exploration, systematic variations in composition of primary feldspars have been applied to the study of several deposits from Pampeana Pegmatitic Province. Table 1 shows the analytical data for the analyzed specimens.

The K₂O contents range from 13.01 to 15.01 wt%, according to K-feldspars from pegmatites of low degree of differentiation (Galliski et al. 1997), whereas Rb varies between 177 and 306 ppm. The K/Rb ratio expresses a low degree of geochemistry evolution in all the considered deposits. The P₂O₅ content reaches 0.031 wt% as a maximum value in the Andacollo pegmatite, none of the obtained values are located over the boundary (0.1 wt% P₂O₅ line) that delimits between muscovite or hybrid pegmatites of LCT signature and deposits more differentiated, with rare-element mineralization.

The deficient occupancy in alkali sites of incompatible elements such as Cs and Rb is very significant in order to distinguish deposits with lower differentiation level. Cs and Rb exhibit a similar behavior, with medium concentrations of 6-22 and 177-306 ppm, respectively. The Sr contents range from 8 to 81 ppm, and the lowest average values correspond to the deposits located in the north of the field (Andacollo and Santa Amalia mines).

Table 1. Compositional data for K-feldspars

		SiO ₂	TiO ₂	Al ₂ O ₃	Fe ₂ O ₃	CaO	MnO	Na ₂ O	K ₂ O	P ₂ O ₅	Ba	Sr	Ga	Rb	Cs
SG	m	66.10	0.01	16.30	0.05	0.09	0.004	1.76	13.66	0.005	518	8	9	249	6
	M	67.10	0.02	17.50	0.08	0.17	0.010	2.66	14.40	0.020	1118	43	13	306	18
	X ₇	66.59	0.02	16.94	0.07	0.12	0.006	2.25	13.92	0.012	923	18	11	272	12
SAM	m	64.21	0.01	16.98	0.03	0.08	0.003	2.47	13.79	0.009	680	8	9	247	15
	M	65.80	0.03	18.01	0.08	0.13	0.010	2.83	14.20	0.021	1121	40	19	305	22
	X ₆	65.04	0.02	17.56	0.05	0.10	0.005	2.62	13.97	0.015	902	24	14	278	18
AND	m	64.77	0.01	16.98	0.03	0.08	0.005	1.98	13.01	0.012	778	43	11	177	6
	M	66.00	0.03	18.01	0.08	0.13	0.012	2.77	14.01	0.031	1530	62	15	230	16
	X ₆	65.17	0.02	17.38	0.05	0.11	0.009	2.23	13.59	0.022	1134	55	12	203	11
ECH	m	64.02	0.01	16.98	0.11	0.13	0.005	2.43	14.43	0.011	1110	41	4	179	6
	M	65.85	0.03	17.51	0.14	0.19	0.013	2.55	15.01	0.019	2530	81	9	236	11
	X ₅	64.98	0.02	17.26	0.12	0.16	0.009	2.49	14.68	0.014	1758	62	7	202	8

References: oxides in wt%, elements in ppm; m: minimum, M: maximum, Xn: average of n analyses.
 SG: San Guillermo, SAM: Santa Amalia, AND: Andacollo, ECH: El Chañar.

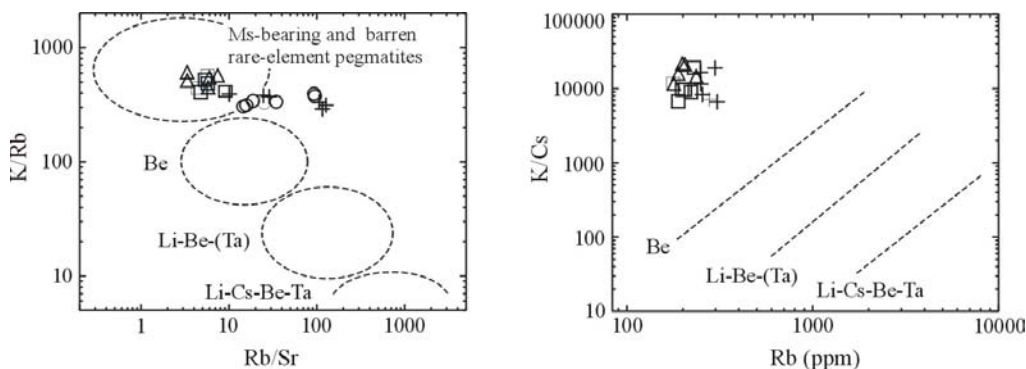


Figure 2. Rb/Sr-K/Rb and Rb-K/Cs diagrams. Symbols: + San Guillermo, o Santa Amalia, □ Andacollo, △ El Chañar.

The Rb/Sr-K/Rb and Rb-K/Cs diagrams (Fig. 2) properly discriminate between different pegmatitic typologies for Pampeana Pegmatitic Province (Galliski et al. 1997) and locate de deposits of the Valle Fértil field in (or near) the sector of muscovite and barren rare-element pegmatites of LCT or NYF signature. The Rb/Sr-K/Rb plot shows that Santa Amalia and San Guillermo samples have a greater Rb/Sr ratio, and consequently these deposits could be considered more differentiated.

The Ba average contents range from 902 to 1758 ppm, the highest values correspond to K-feldspars from Andacollo and El Chañar pegmatites, whereas the concentration decreases in the northern deposits exhibiting the same evolution behavior that Rb and Cs.

7 STRUCTURAL STATE OF K-FELDSPAR

Although not all granitic pegmatites are microcline-bearing, departures from the fully ordered state are petrologically informative and provide valuable information about the physico-chemical conditions during the pegmatite consolidation process. The analyses of the structural state of de K-feldspars were performed using several methods for calculating the Al content (t_n) in individual tetrahedral sites (T_n) by the study of relations among lattice parameters and selected diffraction-peaks positions.

The triclinicity index was calculated using the equations of Goldsmith & Laves (1954) and McGregor & Ferguson (1989). The results range from 0.917 to 1.070, the differences obtained by means of both methods vary between 0.39 and 6.76%.

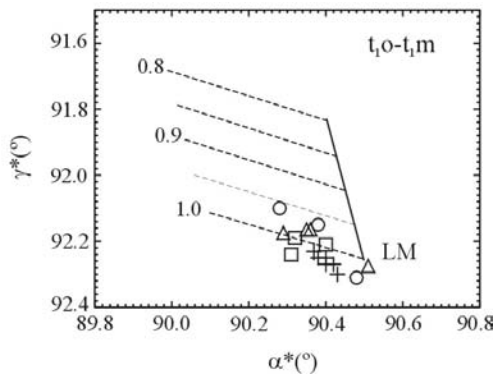
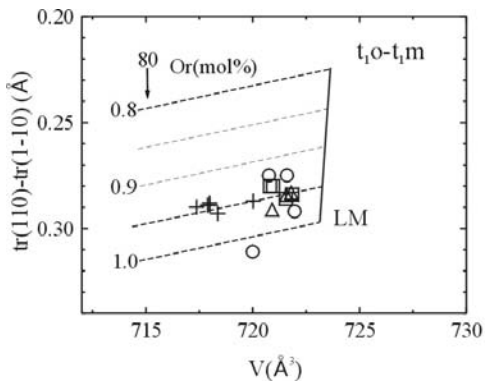


Figure 3. V- Δ tr and α^* - γ^* diagrams. Symbols: + San Guillermo, \circ Santa Amalia, \square Andacollo, \triangle El Chañar.

The (Al,Si) distribution was determined by different methodologies: a) on the basis of b - c^* and γ^* - α^* (Wright & Steward 1968); b) using selected diffraction-peak positions (Kroll & Ribbe 1987); and 3) in terms of the translation distances along [110] and [1-10] (Kroll 1973). The resolution by means of different variables exhibit similar results in each one of the studied samples, the α^* - γ^* and V- Δ tr diagrams (Fig. 3) show that the K-feldspar from different deposits have a full ordering (with $\Sigma t_1 \sim 1.0$) corresponding to low microcline.

8 CONCLUSIONS

The chemistry of the K-feldspar reflects the geochemical characteristics and mineralogy of the deposits studied. On the basis of mineralogical, textural and paragenetical parameters, the pegmatites of the Valle Fértil field can be classified as muscovite class pegmatites (according to Černý 1991), the K-feldspar geochemical data supports this hypothesis.

The correlation diagrams between selected major and trace elements reveal that the northern pegmatites (San Guillermo and Santa Amalia mines) are more geochemically evolved than the southern ones (Andacollo and El Chañar mines).

The near maximum microcline state of blocky K-feldspar from intermediate zones suggests conditions of crystallization at low rates of nucleation; its textures and grain-sizes support the structural data obtained.

The abundance, grain-size, and chemical quality of microcline studied (high K_2O , very low Fe_2O_3) are the main factors that favor the Valle Fértil pegmatites exploitation.

9 REFERENCES

Altermatt U. D. & I. D. Brown 1987. A real-space computer-based symmetry algebra. *Acta Cryst.* (A-43): 125-130.
 Casquet C., Galindo C., Rapela C., Pankhurst R. J., Baldo E., Saavedra J. & J. Dahlquist 2003. Granate con alto

contenido en tierras raras pesadas (HREE) y elevada relación Sm/Nd en pegmatitas de la Sierra de Valle Fértil (Sierras Pampeanas, Argentina). *Bol. Soc. Esp. Min.* (26-A): 133-134.

Toubes Spinelli R. O. 1983. Edades potasio-argón de algunas rocas de la Sierra de Valle Fértil, provincia de San Juan. *Rev. Asoc. Geol. Arg.* (38): 405-411.

Černý P. 1991. Rare-element granitic pegmatites Part I: anatomy and internal evolution of pegmatite deposits. *Geosc. Can.* (18, II): 49-67.

Galliski M., Perino E., Gásquez J., Márquez Zavalía M. & R. Olsina 1997. Geoquímica de feldspatos potásicos y muscovitas como guía de exploración de pegmatitas graníticas de algunos distritos de la provincia pampeana. *Rev. Asoc. Geol. Arg.* (52): 24-32.

Goldsmith J. R. & F. Laves 1954. The microcline-sanidine stability relations. *Geochim. Cosmochim. Acta* (5): 1-19.

Kroll H. 1973. Estimation of Al,Si distribution of feldspars from the lattice translations $tr[110]$ and $tr[1-10]$, I: alkali feldspars. *Contrib. Min. Petrol.* (39): 141-156.

Kroll H. & P. Ribbe 1987. Determining (Al,Si) distribution and strain in alkali feldspars using lattice parameters and diffraction-peaks positions: a review. *Am. Min.* (72): 491-506.

McGregor C. R. & R. B. Ferguson 1989. Characterization of phases and twins in alkali feldspars by the X-ray precession technique. *Can. Min.* (27): 457-482.

Wright T. L. & D. B. Steward 1968. X-ray and optical study of alkali feldspar. I. Determination of composition and structural state from refined unit cell parameters and 2V. *Am. Min.* (53): 38-87.

Jura-Cretaceous Hydrothermalism as Genesis of Mineralization in Dolomitic Marbles of Itaiacoca Belt, Brazil

J.M.Reis Neto

Department of Geology, Federal University of Paraná, Curitiba, Brazil

A.M.A.Rebelo

Brazilian National Nuclear Energy Commission (CNEN) / Federal University of Paraná co-operation agreement, Curitiba, Brazil

M.A.S.Basei

Geosciences Institute, University of São Paulo, São Paulo, Brazil

ABSTRACT: Based on geochemical, mineralogical and petrographic studies this paper characterizes the mineralization typology developed between Proterozoic dolomitic marbles of Itaiacoca Group and a Mesozoic diabase dike of the Serra Geral Formation. The blending of the extracted materials result in the product commercially designed “*Dolomito Talcoso*” (talcose dolomite) that has diversified industrial applications. The studied area is situated in the southeastern portion of the Itaiacoca Belt in the Ponta Grossa Region, Parana State, Brazil. The studies were based on samples from different stratigraphic horizons collected at different distances from the contact between the basic dike and of the dolomitic marbles. The geochemical results are compatible with the paragenesis constituted of dolomite, serpentines (crisotile and antigorite), diopside, talc, brucite and forsterite, resulting from rocks originally constituted by dolomite and ankerite modified by silica addition. In spite of silica concentration raising up to 30% calcium and magnesium silicates dominate and the presence of quartz hasn't been verified. The transformations are more intense near by the dike. The relationship between the mineral paragenesis and the geologic-structural data characterizes a model of hydrothermalism associated with contact metamorphism, caused and controlled by the diabase emplacement, modifying the original dolomitic marbles mineralogy in the contact zone (hornfels). The presence of the alteration minerals associated with the great amount of calcite in relation to dolomite content confers to the extracted material low abrasiveness, raised whiteness and other physical properties that permit diversified industrial applications.

1 INTRODUCTION

The Itaiacoca Region in Paraná State, southern Brazil, is an important producer of talc, which has been exploited for more than 40 years. Besides talc, other materials associated with siliceous dolomitic marbles have also been exploited, with varied uses in the transformation industry.

Several talc deposits found close to diabase dikes have been interpreted as generated due to diabase intrusion in dolomitic marbles (Sobanski et al. 1984). However, a great number of authors now believe that there is no genetic link between the diabase bodies and the talc deposits. The possible relationship would be a consequence of geomorphological processes responsible for modeling the regional landscape (Lima 1993, Gondim 2001, Loyola 2003).

This work presents the geochemical, mineralogical and petrographic studies of a mineral deposit from which the product commercially named “*Dolomito Talcoso*” (talcose dolomite) is obtained. This deposit is enclosed by Proterozoic dolomitic marbles of the Itaiacoca Group, in the contact zone with a Mesozoic diabase dike of the Serra Geral

Formation. The main objective of this research is to characterize the ore typology resulting from hydrothermalism caused by the intrusion of the diabase dike in the dolomitic marbles.

2 GEOLOGIC SETTING

The Itaiacoca Belt belongs to the central part of the Mantiqueira Province (Souza 1990, Reis Neto 1994, Basei et al. 2000). The rocks of the belt, dolomitic marbles, quartzites and metapelitos, constitute the Itaiacoca Group, which is a metasedimentary sequence intercalated with ultrapotassic metavolcanic rocks. This Group underwent greenschist facies metamorphism during the Brazilian Cycle. Two major Neoproterozoic granitic complexes (Cunhaporanga – NW and Três Córregos - SE) limit the Group.

The predominant strike of the metamorphic rocks is N40-50E, given by a fine but marked schistosity (Reis Neto 1994), and is crosscut by N40-60W-striking, Mesozoic diabase dike swarms. A great number of diabase dikes occur in the study area and the dikes are in general associated with the talc

deposits found in the siliceous dolomitic marbles.

2.1 The Study Area

The studied quarries were planned according to the relation of the diabase dike with the host marbles. The quarries fronts are characterized by a sequence of marble levels of different colors. They present plane-parallel (S_0) stratification and two types of metamorphic foliations. One is a fine cleavage (S_1), in general parallel to the stratification (S_0). A second foliation is a fracture cleavage (S_2) that occurs in specific parts of the quarries.

The N50W-striking, thick diabase dike that crops out in the quarries fronts presents irregular contacts with the marbles. The types of marbles are defined according to color, which varies with the proximity to the dike; they are informally named gray marble (GM) and white marble (WM). GM is a very fine-grained rock, with marked primary plane-parallel stratification, and average thickness between 20 and 30 cm. WM, despite in general appearing intercalated with GM, also occurs as large pockets, or as discordant, centimeter-sized, fine veins (Fig.1).

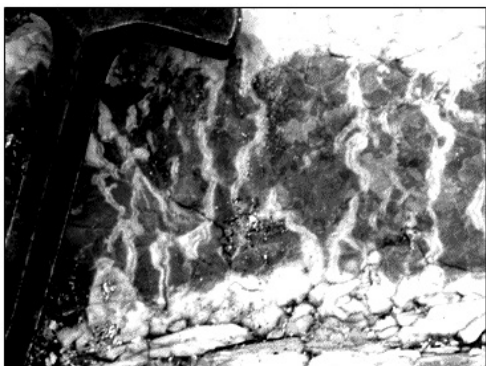


Figure 1. Relations between GM and WM. Example of WM veins inside GM.

3 ANALYTICAL METHODS

Studies were carried out using samples collected in the contact zone of the marbles with the diabase dike. Each sample represents different stratigraphic horizons and was collected at different distances from the basic dike.

Major elements, expressed as oxides, were determined by X-ray fluorescence. The diffractometric analyses were carried out using a powder X-ray diffractometer. For the interpretation of the data the PANalytical's X'Pert HighScore software was used together with the PDF-2 data bank (JCPDS-ICDD).

All rock types were analyzed under the petrographic microscope, aiming at observing the relationship between the minerals determined by X-ray diffractometry. Some samples of siliceous dolomitic marbles were treated with HCl for a better chemical and mineralogical characterization of the silicatic phases.

4 RESULTS

Considering the CaO, MgO and SiO₂ contents, GM shows slight variations, whereas WM presents considerable variations, especially regarding SiO₂ contents. In WM, SiO₂ increases with decreasing MgO, and large variations in CaO occurs (Fig. 2). The sum of CaO and MgO contents decrease with increasing SiO₂.

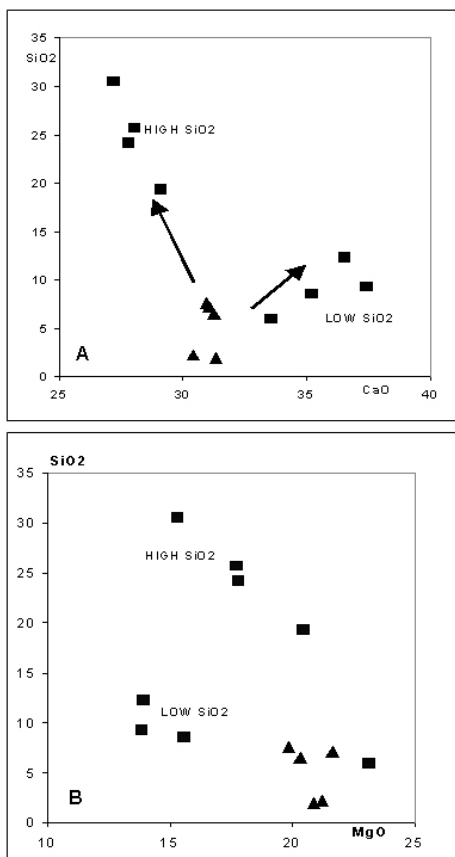


Figure 2. SiO₂ versus CaO (A) and MgO (B) for GM (triangles) and WM (squares).

4.1 Gray Marble (GM)

X-ray diffraction helped distinguish ankerite, dolomite and calcite among the carbonates identified under the microscope. The diffractograms show the existence of two types of GM: the first is characterized by the presence of dolomite and calcite (samples SDAS 2A1 and 2B) and micro- and mesoscopic white veins. In the diffractogram an intense peak corresponding to calcite is identified. The other type (samples SDAS 6B e 7) is mainly constituted by dolomite and ankerite. As basic characteristics, they present massive structure and granoblastic texture, and show neither veining nor the calcite peak.

Thus, by comparing the diffractograms for GM samples, it is possible to distinguish two paragenesis. There is a direct relationship between the appearance of calcite and the decrease of ankerite and dolomite. On the other hand, the petrographic analyses of samples SDAS 2A1 and 2B show the existence of distinct mineral assemblages in the veins and in the matrix.

4.2 White Marble (WM)

Calcite as the main mineral in WM, that is, a pure, or with low magnesium, calcium carbonates. In turn, dolomite appears sporadically. Comparing the diffractograms with the chemical results, it is possible to distinguish two WM types, one of low SiO₂ (<14% SiO₂) and the other with high SiO₂ contents (> 15% SiO₂). Most of the samples show, besides carbonates, antigorite and clinochrysotile and other magnesium silicates. In low- SiO₂ WM, dolomite, brucite and periclase occur together with calcite.

The diffractograms show great similarities between both types of WM. For low-SiO₂ WM, sample SDAS 1A shows a dolomite peak and sample SDAS 1F, the presence of the diopside peak.

Both WM types were also characterized by means of petrographic analyses. Where SiO₂ contents are high, the matrix is fine-grained, greenish white, in general crosscut by white veins. The mineralogical composition and grain size of the veins is distinct from the matrix. In turn, the low-SiO₂ variety presents very fine-grained, equigranular matrix, lacking any preferential orientation. In this case, the mineralogical transformation is pervasive and homogeneous, as a consequence of a broader neoformation.

5 DISCUSSION AND CONCLUSIONS

The exploitation of both types of marbles (WM and GM) takes place parallel to bedding (S₀). The chemical and mineralogical properties of GM

indicate that the marbles underwent hydrothermal alteration in a heterogeneous manner, with the introduction of SiO₂.

Based on field observations and laboratory data, it is verified that the closer to the diabase dike, the more intense was the hydrothermalism and the introduction of SiO₂ with consequent generation of WM, which means formation of calcium and magnesium silicates (forsterite, diopside and clinochrysotile).

To form an assemblage constituted of dolomite, chrysotile, antigorite and forsterite starting from rocks essentially composed of ankerite and dolomite, it is necessary, besides the introduction of SiO₂, an important heat input. It is important to stress out that the generation of calcite is not associated with the increase of CaO.

Chemical data show that WM can contain up to 30% SiO₂. The paragenesis is characterized by the presence of high-temperature magnesium and calcium minerals (forsterite and diopside), coexisting with low-temperature minerals (chrysotile, antigorite and talc) and absence of quartz. The existence of high-temperature magnesium silicates in WM is explained by the action of a hydrothermal alteration process promoted by the diabase intrusion. As temperature conditions changed, SiO₂ entered the system. The introduction was not homogeneous, resulting in high- and low-SiO₂ WM types.

The introduction of SiO₂ was selective, once it generated pockets and alteration of the discontinuity zones along the bedding (S₀). After the saturation of these zones, veins were formed towards the inner parts of the gray limestone (Fig. 1). Therefore, WM can occur either concordant or discordant to GM bedding, but veining always starting from bedding. The structural patterns corroborate with hydrothermalism marked by SiO₂ percolation.

Therefore, WM are the extreme members of the hydrothermal alteration of an ankeritic marble (GM) in a contact metamorphism environment, resulting in a mineral resource rich in either magnesium silicates or calcium and magnesium silicates.

Finally, the characterization of a diabase dike as a conditioning factor for hydrothermal alteration processes, with generation of economic mineral deposits in dolomitic marbles, is the first step to the re-evaluation of the exploration potential in the Itaiacoca Belt. As this belt is constituted by large volumes of dolomitic marbles crosscut by dike swarms, a promising, new model of regional exploration is proposed.

6 ACKNOWLEDGEMENTS

The authors wish to thank the PADCT-CNPq Program and the DIMICAL Project – Limestone

Mining Districts of the State of Paraná (CNPq n. 62.00.32/01-4) for the support to this research. Also to Mineração São Judas for permission to work in the quarry area.

We also thank LAMIR – Laboratory for Analysis of Minerals and Rocks and the Thin Section Laboratory, both from the Geology Department of the Federal University of Paraná.

7 REFERENCES

- Basei, M. A. S., Siga Jr., O., Masquelin, H., Harara, O. M., Reis Neto, J. M., Preciozzi P., F. 2000. The Dom Feliciano belt of Brazil and Uruguay and its foreland domain, the Rio de La Plata craton. In: Cordani, U. G., Milani, E. J., Thomaz Filho, A., Campos, D. A. (Ed.). Tectonic evolution of South América. 31st International Geological Congress, Rio de Janeiro, Brazil, August 2000, pp. 311-334.
- Gondim, A. C. 2001. Exploration of talc deposits in Paraná State, Brazil. *Mineralia Slovaca*, Bratislava, v. 33, n. 6, p. 575-578.
- Lima, R. E. 1993. Evolução geológica e controles dos depósitos de talco na Região de Itaiacoca-Abapã PR. Brasília-DF: UNB. Dissertação de Mestrado. Instituto de Geociências, Universidade de Brasília, 139p.
- Loyola, L. C. 2003. O distrito de talco do Paraná, gênese e características dos minérios. Curitiba-PR: UFPR. Dissertação de Mestrado. Departamento de Geologia, Setor de Ciências da Terra, Universidade Federal do Paraná, 77 p.
- Reis Neto, J. M. 1994. Faixa Itaiacoca: registro de uma colisão entre dois blocos continentais no Neoproterozóico. São Paulo-SP: USP. Tese de Doutorado. Instituto de Geociências, Universidade de São Paulo, 253 p.
- Sobanski, A., Giust, D. A., Chodur, N. L. 1984. As jazidas de talco de Abapã, município de Castro (PR). *Anais do XXXIII Congresso Brasileiro de Geologia*, V. 8, Rio de Janeiro, pp 3799-3808.
- Souza, A. P. 1990. Mapa geológico na escala 1:50.000 e esboço da evolução tectônica e sedimentar do Grupo Itaiacoca, nas folhas Barra do Chapéu e Ouro Verde – SP/PR. São Paulo-SP: USP. Dissertação de Mestrado. Instituto de Geociências, Universidade de São Paulo.

Petrographic Characteristics of Calcareous Rocks and their Implications in the Cement Manufacturing Process: A Case Study

J.M.Reis Neto

Department of Geology, Federal University of Paraná, Curitiba, Brazil

C.E.Riesemberg & F.A.Moya

Laboratory of Microscopy –Technical Center, Votorantim Cimentos, Curitiba, Brazil

D.L.Gomes

Mining Department, Votorantim Cimentos, Curitiba, Brazil

ABSTRACT: The exploitation of different types of metacalcareous rocks from the Votuverava Formation for production of raw meal used in the cement manufacturing process has taken place for decades in the State of Paraná. Based on detailed field cartography, chemical, petrographic, and mineralogical studies of the main lithologic types found in two quarries were carried out. These calcareous rocks show mineralogical characteristics that have important implications in the industrial process. The heterogeneous petrographic characteristics of the studied rocks raise the hypothesis that they resulted from different conditions prevailing during sedimentation, diagenesis and, subordinately, metamorphic processes. These characteristics influence the physical properties of the raw material, with direct implications in ore processing stages. At present, chemical composition, rather than mineral composition and fabric, of the different calcareous rock types (also named “marbles”, according to the regional metamorphic grade) guide the exploitation. A more detailed study, taking into account mineral components such as calcite, dolomite, quartz, and other calcium and magnesium silicate minerals, can better guide the exploitation and supply information for the continuous improvement of the manufacturing process.

1 INTRODUCTION

For decades, the cement production in the State of Paraná has taken place with the exploitation of metacalcareous rocks from the Votuverava Formation of the Açungui Group (Basei et al. 2000). The sedimentation of the Votuverava Formation occurred in the Neoproterozoic and it was later deformed in the Brasiliano Cycle, during the formation of Gondwana. It is located in southern Brazil and integrates the Ribeira Belt of the Mantiqueira Province. In the Mesozoic, the study region was crosscut by diabase dikes related to the Ponta Grossa Arc mafic dike swarm.

This case study aims at the petrographic, chemical and mineralogical characterization of calcareous rock types sampled in two distinct quarries. The petrographic studies, together with the description of the outcrops, allowed characterizing the mineral fabric (structure and texture) and classify the different lithologic types present.

Interacting petrographic description and analysis and interpretation of X-ray diffractograms made the determination of the mineral composition of the studied rocks possible.

The chemical characterization resulted from the application of the X-ray fluorescence method using

calibration curves specific for calcareous and clayey calcareous rocks and marls.

1.1 Objectives

The main objective of this work is to determine the different structural, textural and mineralogical characteristics of the calcareous rocks at the quarry fronts and to relate these characteristics to physical properties of the raw material used in the cement manufacturing process. These characteristics can affect the behavior of these rocks during mining (drilling and blasting), crushing and grinding and of the raw mixes inside the high-temperature kilns.

1.2 Methods

Representative calcareous rock samples were collected in two quarries (here named Quarries 1 and 2), according to the experience of the technicians responsible for prospecting and opening of mining fronts. Depending on the petrographic heterogeneity of the sampled limestone types, the following procedure was adopted:

- Determination of the mineral composition using optical microscopy and X-ray diffractometry analysis;

- Detailed characterization of the structure, texture and mineral composition from macro- and microscopic analyses;

- Identification of distinctive mineral assemblages for different rock groups from both quarries;

- Characterization of the chemical composition of the various lithologic types by X-ray fluorescence.

This procedure led to a better understanding of the relationship between exploited petrographic types and their behavior during the process of clinker production.

The results were analyzed and interpreted by professionals from both the Votorantim Cimentos Technical Center and Mining Department and from the Department of Geology of the Federal University of Paraná.

2 RESULTS

2.1 Quarry 1 Samples

Quarry 1 is composed of at least four different limestone types that show distinct structural, mineralogical and chemical characteristics. These lithotypes also differ chemically, mainly in their CaO, MgO, SiO₂, Al₂O₃ and LOI contents. The results of the chemical analyses are summarized in Table 1.

Table 1 – Chemical analyses of the main types of Quarry 1 calcareous rocks (A: calc-phyllite; B: limestone hornfels; C: massive metalimestone; D: clastic metalimestone).

%	A	B	C	D
CaO	27.11	49.97	49.85	42.78
MgO	2.66	3.33	2.73	8.47
SiO ₂	30.89	6.88	2.81	4.66
Al ₂ O ₃	8.11	0.43	0.18	0.64
Fe ₂ O ₃	1.94	0.67	0.26	0.46
K ₂ O	2.74	0.01	0.05	0.20
Na ₂ O	0.06	0.01	0.01	0.01
MnO	0.02	0.06	0.01	0.01
TiO ₂	0.44	0.02	0.01	0.03
P ₂ O ₅	0.12	0.01	0.01	0.01
LOI	25.56	38.67	43.31	42.69
Total	99.65	100.06	99.23	99.98

X-ray diffractometry data allowed distinguish different mineral assemblages composing the various lithologic types (Figure 1).

The predominant lithologic types can be divided as follows:

- Calc-phyllite: a strongly-foliated rock, due to the iso-orientation of white micas. The typical X-ray diffractogram (Fig.1) shows the conspicuous presence of quartz, besides the marked predominance of calcite over dolomite. High SiO₂ (30.89%), Al₂O₃ (8.11%) and K₂O (2.74%) contents,

represented in Figure 3, are the consequence of the presence of white micas and the derivation from clayey calcareous rocks;

- Limestone hornfels: medium-grained rocks with granoblastic texture that are found in contact with diabase dikes. The predominance of calcite and the lack of quartz and dolomite are characteristic features. The analyses showed that SiO₂ (6.88%) and MgO (3.33%) contents reflect the presence of diopside and amphiboles, both identified by X-ray diffractometry;

- Massive metalimestone: a very fine-grained rock with granoblastic texture and sporadic clasts. Low MgO (2.73%) contents reflect the predominance of calcite over dolomite;

- Clastic metalimestone: a fine- to very fine-grained rock with granoblastic texture. The presence of millimeter- to decimeter-sized, oval-shaped clasts is a characteristic feature. In general this rock has high MgO (8.47%) and somewhat low SiO₂ (4.66%) contents. X-ray diffractometry shows the presence of calcite, dolomite and quartz (Fig. 1).

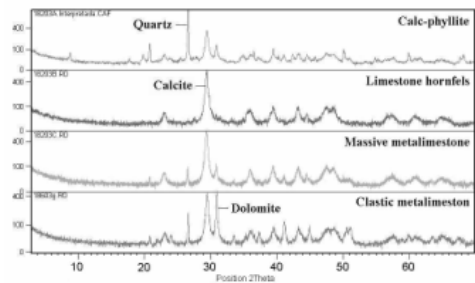


Figure 1- Quarry 1 calcareous rocks.

2.2 Quarry 2 Samples

Applying the procedure adopted for Quarry 1, the main Quarry 2 lithologic types were identified and characterized as follows (Fig. 2):

- Massive metalimestone: a very fine-grained rock with homogeneous granoblastic texture. The textural homogeneity associated with the lack of clasts is its characteristic feature. The analyses show the predominance of calcite and the almost total absence of quartz and dolomite, confirmed by low MgO (1.40%) contents;

- Massive siliceous metalimestone: a rock similar to the massive metalimestone, being very fine-grained and having very homogeneous granoblastic texture and low MgO (1.59%) content. The main distinction between these two rock types is high SiO₂ (6.30%) contents and the marked presence of quartz in the massive siliceous metalimestone;

- Calc-phyllite: a strongly-foliated rock, due to the orientation of white micas. Its main

characteristics are high SiO₂ (30.44%) and MgO (6.34%) contents, corresponding to the predominance of the dolomite peak over that for calcite, and the presence of calciferous and magnesian micas. Al₂O₃ (6.70%) and K₂O (2.19%) contents also attest derivation from clayey limestones.

In a broad sense, Quarry 2 lithotypes have lower MgO contents in comparison with Quarry 1 rocks, except for the calc-phyllite, whose MgO contents are compatible and sometimes even higher than those of certain Quarry 1 lithotypes (see Tabs. 1 and 2).

Table 2 – Chemical analyses of the main types of Quarry 2 calcareous rocks (A: massive metalimestone; B: massive siliceous metalimestone; C: calc-phyllite).

%	A	B	C
CaO	51.27	50.09	23.41
MgO	1.40	1.59	6.34
SiO ₂	2.88	6.30	30.44
Al ₂ O ₃	0.54	0.44	6.70
Fe ₂ O ₃	0.28	0.25	3.37
K ₂ O	0.13	0.12	2.19
Na ₂ O	0.01	0.01	0.10
MnO	0.01	0.01	0.02
TiO ₂	0.03	0.03	0.37
P ₂ O ₅	0.02	0.02	0.08
LOI	42.86	40.98	26.92
Total	99.43	99.84	99.94

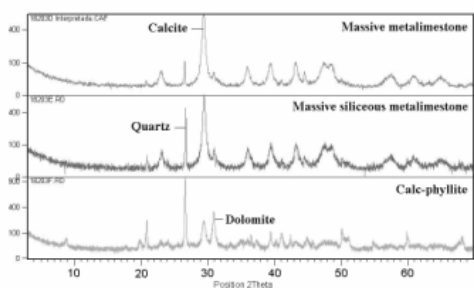


Figure 2 – Quarry 2 calcareous rocks.

3 DISCUSSION AND CONCLUSIONS

Based on comparative analyses involving the main lithotypes found in Quarries 1 and 2, it is possible to conclude that the different petrographic characteristics revealed by this study resulted from prevailing conditions during sedimentation, diagenesis and superimposed metamorphic processes. Metamorphism affected the calcareous rocks differently, producing varied mineralogical (textural and compositional) characteristics that influence, either in a beneficial or harmful way, the quality of the raw material exploited for cement

production. The varied metalimestone mineral compositions, together with chemical, textural and structural characteristics, affect the physical properties (porosity, grinding index, burning temperature, etc) of the raw mixes. The different lithotypes present microscopic characteristics that mirror diagnostic macroscopic features. These features allow the visual identification of the different calcareous rocks in the mining fronts, helping interpret (and eventually optimize costs) the chemical analyses done previously to the opening of the mining fronts, which are necessary to control the material to be exploited. The microscopic (structural, textural and mineralogical) characteristics of the main limestone types of both quarries can be visualized, for example, in micrographic images (Fig. 3).

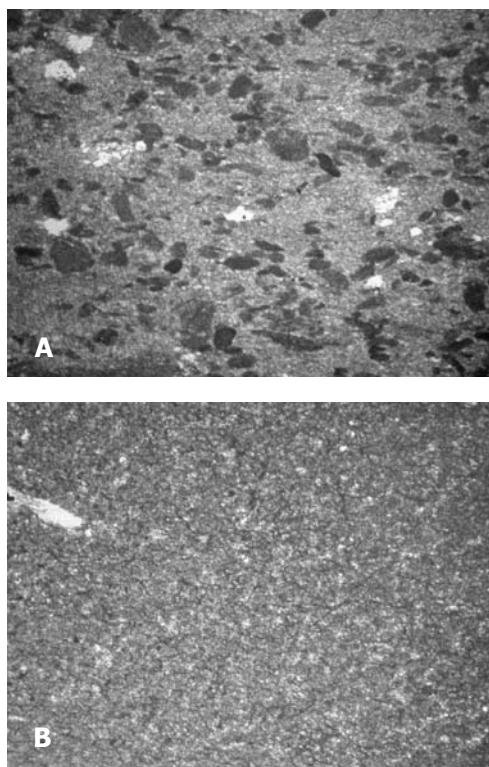


Figure 3 – A: Quarry 1 clastic metalimestone. B: Quarry 2 massive metalimestone with homogeneous equigranular matrix (micrographic images, magnification 15 x).

Higher MgO contents observed in Quarry 1 samples are associated with the presence of clasts. These particular MgO contents, due to the presence of dolomite in the calcareous rocks, is in a way interesting for the manufacturing process, once

MgO, as well as Fe₂O₃, may act as flux inside the kiln, promoting reactions and clinker mineralization. However, the concentration of MgO in calcareous rocks is a limiting factor for cement production, making the use of certain lithotypes as raw material impossible. Another negative factor resulting from high dolomite concentrations is that the desirable raw meal grain size is more difficult to achieve by grinding and consequently energy costs are higher.

Lithologies such as the limestone hornfels, despite its higher SiO₂ contents, have lower quartz contents. The use of such rock as raw material could be viable, once the “free silica” (quartz, cristobalite) problem, which greatly influences grinding and raw meal burning, would not occur. However, these rocks (which appear in 1m to 5m-thick bands in contact with basic dikes) present well-developed granoblastic texture and are medium-grained, again implying in more severe grinding conditions.

The use of calc-phyllites as raw material is also interesting for the cement manufacturing process, in special for the presence of micas that contribute with SiO₂ and mainly Al₂O₃ and alkalis (K₂O, Na₂O) to the raw meal composition. The micas, as well as other silicate minerals, when finely ground, do not interfere in grinding and raw meal homogenization, which is a positive factor when burning is concerned (ABCP, 1987). The presence of alkalis is especially important in the neutralization of sulfur, resulting in alkaline sulfates. Sulfur, when present in excess in the petrol coke (used as fuel) can cause instability inside the kiln and consequently affects the quality of the clinker being produced.

The massive metalimestones present in both quarries, because of their very fine grain size, granoblastic texture and composition, which is basically calcite, offer better grinding conditions and enormously contribute with CaO to the manufacturing process.

The results show that the different petrographic (structural, textural, and chemical) characteristics of the metacalcareous rocks from both quarries greatly influence the industrial process of cement production.

4 ACKNOWLEDGMENTS

The authors are thankful to all Votorantim Cimentos Technical Center and Mining Department professionals for the support given during field work, access to database, discussions and permission to visit the quarry fronts.

They also thank LAMIR – Laboratory of Mineral and Rock Analyses of the Department of Geology of the Federal University of Paraná for the chemical, mineralogical and petrographic analyses.

5 REFERENCES

- ABCP – Associação Brasileira de Cimento Portland - 1987 - Influencia da granulometria do quartzo na fabricação do cimento portland – Boletim Informativo de Microscopia, n. 12, pp. 7-8.
- Basei, M.A.S., Siga Jr., O., Masquelin, H., Harara, O.M., Reis Neto, J.M., Preciozzi P., F. - 2000 - The Dom Feliciano belt of Brazil and Uruguay and its foreland domain, the Rio de La Plata craton. In: Cordani, U. G., Milani, E. J., Thomaz Filho, A., Campos, D. A. (Ed.). Tectonic evolution of South América. 31st International Geological Congress, Rio de Janeiro, Brazil, August 2000, pp. 311-334.
- Deer, W.A.; Howie, R.A.; Zussman, J. -1995 - An Introduction to the Rock-Forming Minerals. Longman Group Limited, 696 p.
- Reis Neto, J.M - 2003 - Avaliação Petrográfica, Química e Mineralógica de amostras de Rochas Calcárias – Relatório Interno da Votorantim Cimentos.

Potential Uses of Natural Zeolites (Stilbite and Laumontite) from Brazil

N.G.A.M.Rezende

CPRM - Geological Survey of Brazil

R.S.Angélica & M.L.Costa

Department of Geosciences, Federal University of Pará, Brazil

R.F.Neves

Department of Chemistry and Food Engineering, Federal University of Pará, Brazil

M.B.M.Monte

Brazilian Centre for Mineral Technology

ABSTRACT: Natural zeolites are focus of growing interest due to their economic potential. Zeolites physico-chemical properties favor their applications in a vast field of important branches of industry such as oil industry, agriculture and waste treatment. Although in Brazil there are no known deposits of these commodities, some prospects point out to the possibility of future availability. That is the case of the large occurrences of stilbite and laumontite in the Parnaíba Basin, Northeastern Brazil. These zeolite form the main cement phase of the sandstones, either on eolian or on fluvial facies. Otherwise, zeolite grade is better in the eolian (with up to 40%) due to its better initial porosity. The first beneficiation studies showed that enrichment is possible through merely mechanical processes. Adsorption assays for copper show that mechanically concentrated phases enriched in laumontite exhibit similar behavior to that of activated alumina. These preliminary investigations of potential uses recommend further research, mainly aiming agricultural and environmental applications. Investigations should emphasize other metals, anions and gases, under varied physico-chemical conditions and different degrees of zeolite activation. Moreover, besides the unusual geological setting of the mentioned stilbite and laumontite-bearing sandstone, these minerals are not among the traditionally explored zeolite deposits in the world. A challenge that is being worth to be faced.

1 INTRODUCTION

The versatility of industrial uses of natural zeolites has increasingly called the attention of prospectors mainly toward deposits hosted by sedimentary and volcano-sedimentary rocks.

Zeolites physico-chemical properties provide them the ability to be applied as molecular sieves, favoring their application in important branches of industry, such as oil industry, agriculture and waste treatment. The better uniformity in size and shape of their channels, when compared to other products such as silica gel and activated alumina and coal, distinguishes zeolites as better adsorbents.

Only by the middle of last decade prospectors woke up to evaluate the potential for natural zeolites in Brazil. The start point was the discovery of important occurrences of stilbite and laumontite in the Corda Formation, NW portion of Parnaíba Basin, in the states of Tocantins and Maranhão (Rezende & Angélica 1997).

The first technological studies carried out on the zeolitic ore of Parnaíba Basin were mainly dedicated to the recovery and concentration of the useful phase (Inglethorpe et al. 1996; Hamelmann et al. 1998).

Such studies showed the liability for concentrating the ore by merely mechanical processes as well speculated about the possibility of using concentrated phases in agriculture and waste treatment. Garcia (1997), based on Cuban tradition, stated that the zeolite-bearing sandstones of Corda Formation could not compete as industrial mineral.

Besides a general overview about geological and mineralogical aspects of zeolite concentrations in Parnaíba Basin, this paper deals with preliminary studies to evaluate potential uses for that ore, experimenting it as adsorbent for Cu^{2+} .

2 GEOLOGICAL SETTING AND ORE GRADE

An important aspect to be considered in case of future exploitation of zeolite occurrences of Parnaíba Basin is the role of geological environment in zeolite content. Stilbite and laumontite comprise the main cement phase of eolian and fluvial sandstones of the Lower Cretaceous Corda Formation that integrate a sedimentary depositional system developed on basaltic flows (Fig.1). Paragenetic evolution of the autigenic phase

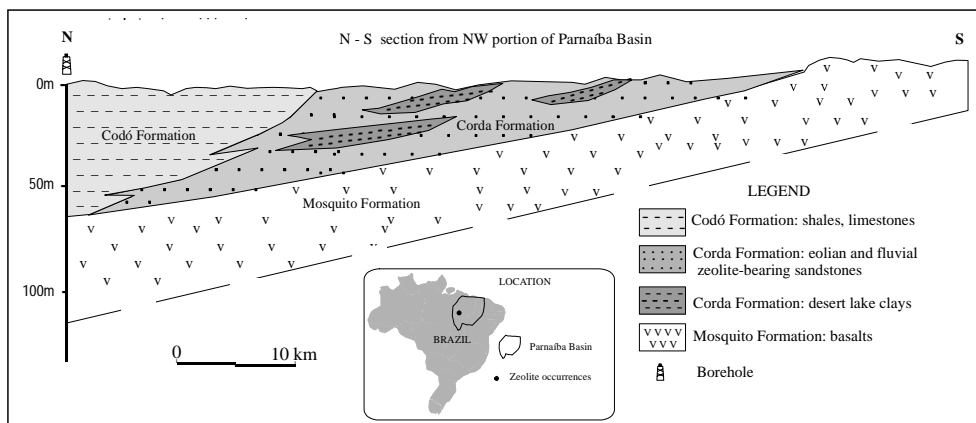


Figure 1: Schematic diagram of stratigraphic relation showing distribution of the zeolite bearing sandstones of Corda Formation.

includes an iron oxide-hydroxide coating on detrital grains, smectite (mainly montmorillonite), and the zeolites and some calcite. It was not possible to define the relative sequence of zeolite/calcite formation since there are some evidences they are all co-genetic. The sandstone texture with loose / punctual packing, the isotopic composition of oxygen and carbon ($\delta^{18}\text{O}$ and $\delta^{12}\text{C}$) in the calcitic cement, and the absence of albitization of detrital plagioclase, besides the well preserved character of smectites, with honeycomb-like texture, are suggestive of a diagenetic environment dominated by temperatures and pressures close to surface conditions. The zeolite formation is related to an open hydrologic system influenced by an arid to semiarid depositional landscape.

Zeolite grade varies from 18 to more than 40% but the better textural maturity of the first (Fig. 2), with better initial porosity, leads to enrichment in the eolian facies.

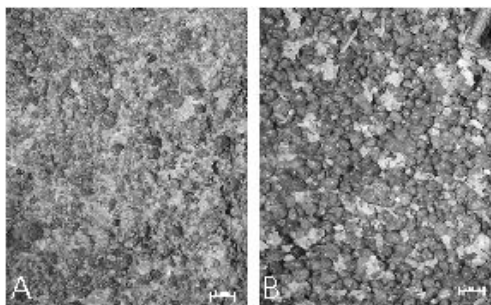


Figure 2: Eolian facies (B) shows better textural maturity than the fluvial facies (A), favoring enrichment in zeolite content.

The zeolitic zone crops out on an area up to 400km^2 , with a thickness of more than 10m.

3 MINERALOGICAL ASPECTS OF THE ZEOLITES

Stilbite and laumontite, as well as some calcite, form a white mass of cement of the reddish sandstone. When the rock is disaggregated, zeolites look like volcanic shards due to the way they grew in the pore space (Fig. 3).

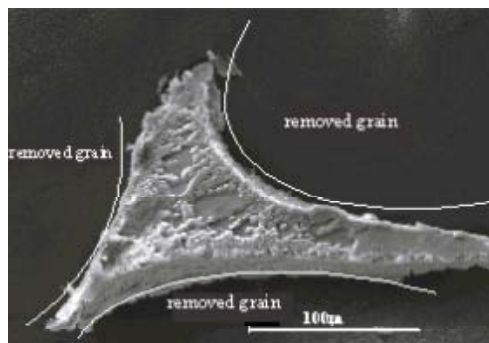


Figure 3: Zeolite crystal after desegregation (SEM image).

Stilbite presents a platy habit while laumontite often tends to form prismatic crystals with radial arrays (Figs. 4, 5). Their chemical composition is also a good tool for diagnosis. WDS and EDS analysis showed that Si:Al ratio is around 3.20 in stilbite, and around 2.14 in laumontite and that Ca is the main cation, with very low K, Na, and Mg contents.

4 TESTS OF ADSORPTION FOR Cu^{2+}

4.1 Materials and methods

The results below are one of the first attempts to search for possible applications to zeolite concentrates from Parnaíba Basin. Procedures were adapted from those described by Neves et al. (2000).

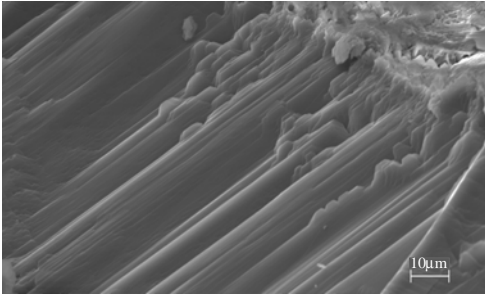


Figure 4: Stilbite crystal with platy habit (SEM image).

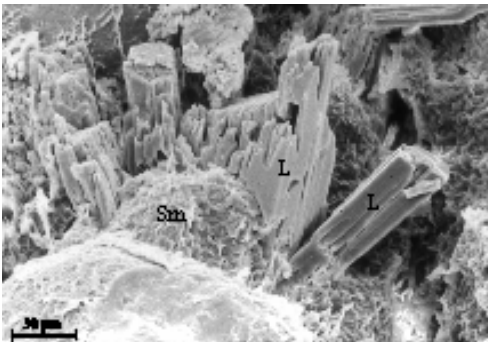


Figure 5: SEM image of Laumontite crystals (L) with prismatic habit and radial arrays, growing on smectite (Sm) rim that cover detrital grains.

Two zeolites concentrates were obtained by desegregation and sieving (150 mesh) of bulk samples and dried at 100°C in an oven for one hour. The following conditions have been used: 1g of adsorbent and 100ml of a copper sulphate solution, diluted in several concentrations (20, 40, 100, 200 and 400ppm of Cu). The system was kept under magnetic agitation at room temperature (26°C) for 20 minutes with subsequent filtration. The filtrate was then diluted to an adequate concentration for further chemical analysis by AAS.

One sample of zeolite concentrate (NR-A-19) was representative of laumontite-rich layer. Sample NR-A-14, of stilbite-rich layer. Due to the mechanism of concentration (simple sieving), some smectite and a very small proportion of detrital

grains must be considered as contaminant. It is very difficult to get pure zeolite concentrates.

4.2 Results and Discussion

Equilibrium data for adsorption of Cu^{2+} , in the presence of SO_4^{2-} (Table 1) were treated by linear regression, using the software Statistica for Windows 5.1B, according to the mathematic model by Freundlich (apud Neves et al. 2000).

Table 1: Equilibrium data of Cu^{2+} adsorption by zeolitic concentrates from Corda Formation.

Initial Concentration (ppm)	Stilbite		Laumontite	
	q (mg/g)	Ce (mg/l)	q (mg/g)	Ce (mg/l)
20	1,9	1	19,4	0,6
40	3,2	8	3,5	5,5
100	5,0	50	6,3	37
200	5,4	146	8,2	118
400	6,8	332	10,4	296

q- retained mass at equilibrium

Ce- Concentration of solution at equilibrium

The kinetics of the reactions, showed as isotherms (Fig. 6), states specific behavior for each material. The laumontite-rich sample presented a better performance toward copper adsorption.

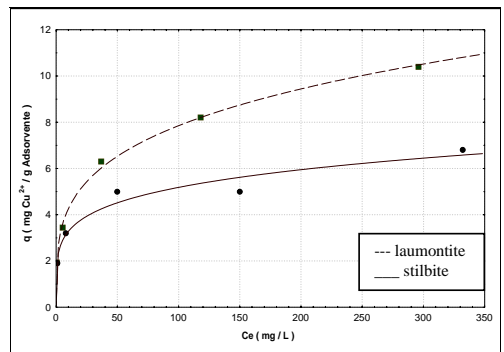


Figure 6: Isotherms of Cu^{2+} adsorption (in presence of anion SO_4^{2-}) by zeolite concentrates from Parnaíba Basin.

The meaning of these values for laumontite can be evaluated by comparison with data registered by Neves et al. (2000) using activated alumina as adsorbent (Fig. 7). Laumontite-rich concentrate exhibited intermediate performance.

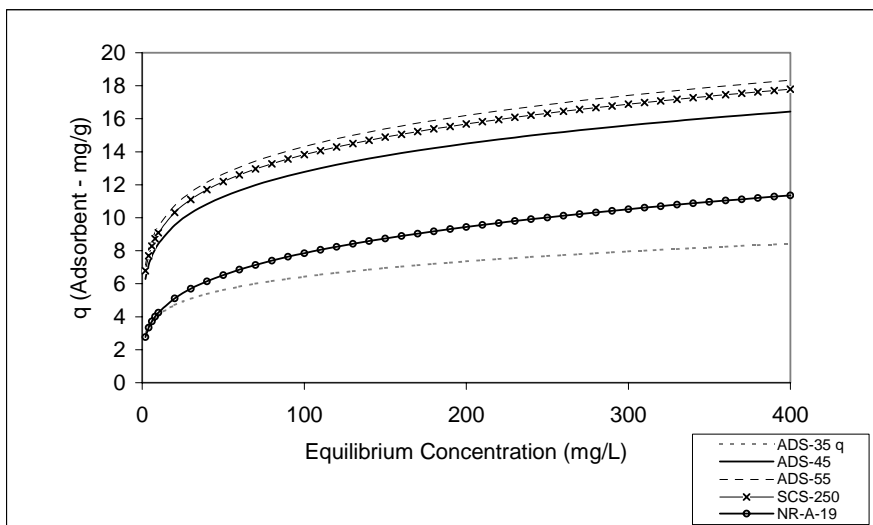


Figure 7: Isotherms of Cu^{2+} adsorption (in presence of anion SO_4^{2-}) by activated adsorbent aluminas compared with laumontite-rich concentrate from Parnaíba Basin.

5 CONCLUSIONS

The stilbite and laumontite occurrences in Parnaíba Basin are the major and most important register of natural zeolites in Brazil, whose potential for these commodities is still unknown.

Considering that the adsorption phenomena is influenced by several conditions, among which pressure, temperature, and quality of the adsorbent raw material and of the material to be adsorbed, the results registered in this paper are relevant.

The reasonable performance of laumontite-rich concentrate as an adsorbent for Cu^{2+} indicates to be wise to increase investigation of possible uses for that material. Cation exchange capacity (CEC) is the only technological market in which natural zeolite can compete with synthetic ones (Colella 1996). Laumontite has a CEC by the order of 4.25 meq/g, highly better than other commercial zeolites (claytonite = 2.22; mordenite = 2.29; heulandite = 2.91 and chabazite = 3.86 meq/g).

Moreover, studies that are being carried out at the Brazilian Center for Mineral Technology (M.B.M Monte, personal communication) have pointed out to the possible use of stilbite concentrates from Parnaíba Basin in agriculture.

This preliminary outlook concerning industrial applications of natural zeolites concentrates from Parnaíba Basin leads to the conclusion that there is much to be done. Investigations must go on with complementary adsorption assays, involving other metal, anions and gases, under variable physico-chemical conditions. Experiments must consider

different level of zeolite grades, grain size and degrees of activation.

The very low tradition in Brazil concerning to exploration of natural zeolite deposits is an additional point recommending persistence in the above-mentioned studies, besides the most unusual character of the large and selective stilbite-laumontite accumulation.

6 REFERENCES

- Colella, C. 1996. Ion exchange equilibria in zeolite minerals. *Mineral. Deposita*, 31:554-562.
- Garcia, OP 1997. Informe de amostra de zeolita. Primeira etapa de el estudio. CIMTEC. Habana/Cuba. (Relatório Inédito).
- Hamelmann, CRA; Luz, AB; Rezende, NGAM 1998. Beneficiamento de zeolitas naturais da Bacia do Parnaíba. Encontro Nacional de Tratamento de Minério e Metalurgia Extrativa 17. Águas de São Pedro: SBQ.
- Inglethorpe, SDJ; Evans, EJ; Mitchel, CJ 1996. Mineral processing of zeolite-bearing sandstone from Parnaíba Basin, Brazil. Internal report. Short Report Series, MPSR/96/51. British Geological Survey, Mineralogy and Petrology Group.
- Neves, AS; Soffiati, IHB; Matelli, MC; Pena, R.S.; Neves, RF 2000. Alumina Ativada I – Efeito da Temperatura de Processamento e de Adsorção na Alumina Ativada. Congresso Brasileiro de Cerâmica, 44. São Pedro (SP). Associação Brasileira de Cerâmica (1 CD-ROM).
- Rezende, NGAM & Angélica, RS 1997. Geologia das zeolitas sedimentares no Brasil. Principais Depósitos Minerais do Brasil. Brasília: DNPM/CPRM, v.4-B. p.193-212.

Crystallochemical Parameters as Support for Interpretation of Facies Variation in a Kaolin Deposit from Brazil

M.D.C.Santos, A.F.D.C.Varajão & P.T.A.Castro

Department of Geology, School of Mines, University of Ouro Preto, Ouro Preto, Brazil

J.Yvon

Laboratory of Environment and Mineralurgy, Geology School, INPL, Nancy, France

T.Allard

Laboratory of Mineralogy and Crystallochemistry, University of Paris IV, Paris, France

ABSTRACT: The present study was developed in the kaolin deposit of Água Limpa located in the Moeda syncline, Quadrilátero Ferrífero, Minas Gerais state. The sedimentological, micromorphological and mineralogical studies, characterized the kaolin deposit as a Tertiary basin filled with colluvial facies originated by gravity mass-flow process associated with sub-arid climate conditions. X-ray diffraction analyses performed on the whole deposit led to the identification of kaolinite as the major clay mineral with a variable crystallinity, from base to top of the deposit. The X-ray coherent scattering thickness and the P1 infrared index, show that the kaolinite crystals at the top have lower amount of packing defects than those at the base. The electron paramagnetic resonance analyses for the kaolinite of the base show spectra typical of high defect kaolinite, with octahedral type(I) Fe³⁺ dominant, usually associated with pedogenic origin. Therefore, the basal facies of the deposit mainly consist of soil kaolinite and the top facies of saprolite kaolinite. These data associated with sedimentological and micromorphological observations suggest that the deposit presents an inversed lateritic profile. The kaolinite was originated in the alteration of white mica of the phengite group. The EDS measurements indicated a chemical composition varying from phengite at the centre to illite followed by kaolinite, at the border. Locally, kaolinite still shows a low potassium content. The kaolinite was formed in the weathering profiles of the local basement before and during the opening of the basin and transported by gravitational process into the basin.

1 INTRODUCTION

Several crystallochemical studies have been realized in kaolin deposits (Cases et al. 1982., Allard 1994, Ballan et al. 1999, Muller et al. 1995, Ballan et al. 1999) in order to evaluate their associated components to the degree of structural defects of kaolinite. Besides, petrological studies performed on lateritic profiles have shown the in situ generation of kaolinite plasma and its differentiation during the process of transfers and accumulation of materials (Tardy & Nahon 1985, Nahon 1986, Muller 1987, Boudeulle & Muller 1988, Tardy et al. 1991, Tardy 1993). Although for the case of allochthonous lateritic profiles (Varajão et al. 2001, Santos 2003, Santos et al. 2004, Santos & Varajão 2004), where pedogenic process have obliterated the transport features, studies evolving the use of crystallochemical parameters to define the relationships between the parent material of kaolinite are little explored in the literature.

The purpose of this paper is a contribution to understanding the process involved in the formation of a colluvial kaolin deposit from Brazil. The investigation, based on the previous sedimentological and pedological studies, were

supported by X-ray diffraction (DRX), scanning (SEM) and transmission electron microscope (TEM), infrared spectroscopy (IR) and electron paramagnetic resonance (EPR).

2 GEOLOGICAL SETTING

The Água Limpa deposit is inserted in the western limb of the Moeda syncline in the Quadrilátero Ferrífero, Southeast of Minas Gerais State, Brazil. Its basement is composed of Precambrian rocks (sericite phyllites, carbonous phyllites, dolomitic phyllites and quartz-bearing dolomites) of the Piracicaba Group, Minas Supergroup. The deposit occurs upon saprolitic material in unconformity contact and shows a NE/SW elongation and a 800m² surface extension.

According to Santos (2003), five principal lithofacies were recognized in the deposit: cohesive sandstone (Cs), white diamictite (Dw), red diamictite (Dr), nodular diamictite (N), and conglomerates. (C). It can be pointed out that the pos-deposition pedogenic process obliterate the pre existent structures and makes difficult the facies differentiation.

4 MINERALOGICAL AND CRYSTALLOCHEMICAL PARAMETERS

3 MATERIAL AND METHODS

Nine samples corresponding to an ideal profile of Água Limpa deposit after DCB extraction (Mehra & Jackson 1960) were analysed by using a Jobin-Yvon Sigma 2080 (CoK α radiation) diffractometer and, the crystallinity indexes R1 and R2 (Liétard 1977) and the size of coherent thickness scattering domains (Scherrer equation, Sherrer 1918) determined. The P1 index (Liétard 1977, Cases et al. 1982) was measured using Fourier transform Infrared Spectroscopy (Bruker IR 55). X-band EPR spectra were obtained using a Bruker ESP300E with cooled (145K) nitrogen flow device and measurements of signals were done at 9,42GHz. Morphological aspects of the clay particles were investigated on 7 samples (5 from the deposit and 2 from the phyllite saprolitic basement) using a scanning electron microscope (SEM - HITACHI S2500) and a transmission electron microscope (TEM - Philips CM20), both fitted with an energy dispersive X-ray detector (EDX).

According to the Table 1, the XRD patterns from the random powder (fraction <30 μ m) of all the facies shows that kaolinite is the major clay mineral with smaller amounts of muscovite, gibbsite, hematite and goethite. Rutile and anatase also are present as heavy minerals. The feldspars were observed only in the phyllite of the basement deposit. The observations on oriented materials do not show the discrete reflections in the [02.,11.] band, used to calculate the Hinckley index (Hinckley 1963). This fact indicates a low crystallinity of the kaolinite crystals (Brindley & Brown 1984) and is compatible with the values of R1 test (Liétard 1977). According to this author values lower than 0.65 are typical for kaolinites with high random defects in the (a, b) plane. In addition, the coherent scattering thickness (Scherrer 1918) shows that kaolinite of top facies (C, N, Dr) of deposit are more ordered than those of base facies (Sc, Dw) and the kaolinite present in the phyllites has coherent thickness typical of ordered kaolinites. Besides, the values P1 index confirm that kaolinites from the top have a better packing order than those from the base.

Table 1 – Mineralogical composition of the different facies and crystallochemical parameters of kaolinite

Facies	Mineralogy of fraction < 30 μ m	Mineralogy After DCB	DC(002) Å	R1 Test	P1 Index	Fe ³⁺ (ppm)
C	K, Gi, H, M, R, An	M, K, Gi, R	168	-	0.0020	4028
N	K, M, Gi, H, Go, R, An	M, K, Gi, R, An	157	-	0.0020	3973
Dr	K, R, A, Gi, Q, H, Go	K, M, An, R	170	0.56	0.0020	-
Dw	K, Gi, R, An, M	K, Gi, Q, M, R	162	0.45	0.0010	-
Dw	K, M, A, R	K, M, R, Q	141	0.55	0.0011	-
Dw	K, M, Q, An, R, H, Go	K, Gi, M, R, An	136	0.40	0.0005	2511
Sc	K, M, Q, R	Q, K, M, R	135	0.65	0.0007	2786
Phyllite 2	M, K, F	M, K, F	283	-	0.0063	-
Phyllite 1	M, H, K, R	M, K, F	192	-	0.0012	5099

Facies: C=Conglomerate; N=nodular, Dr=red diamictite; Dw=White diamictite. Sc= Cohesive sandstone. Mineralogy: K=kaolinite; M=White Mica; Q=quartz; Gi=Gibbsite; H=hematite; Go=goethite; R=Rutile; An=Anatase, F=Feldspar; Phyllite 1=altered graphitic Phyllite; Phyllite 2= altered sericitic phyllite, Fe³⁺(ppm)= structural iron quantification.

The EPR analysis for the kaolinite of the base show spectra typical of high defect kaolinite, with a dominant octahedral type (I) Fe³⁺, usually associated with a pedogenic origin. The top kaolinites present the silhouette of type (II) Fe³⁺ signals (Figure 1). The type (I) Fe³⁺ is related to local symmetry variation created by octahedral clusters and, according Balan et al. (1999), this type occurs in a boundary position of kaolinite crystallites. The Type (II) Fe³⁺ is associated to deformations of octahedral sites of well ordered kaolinites and is considered as randomly spread (Delineau et al. 1994).

Comparing the results of DRX, Infrared Spectroscopy, RPE we can interpret that the defect signals in the kaolinites seem to be connected to iron interlayering or to mica-sheets as suggested by the

relation between the number of packing defects and the amount of total iron. The average coherent scattering thickness of the kaolinites of top deposit is related to less impurities in their growth environment. So, these kaolinites crystallized in the saprolite of the source area and the facies of the base deposit mainly consist of soil kaolinite. This interpretation is supported by observations of Muller (1987) and Fiallips (1999) that described, in weathering profiles, kaolinites with different degrees of crystallinity due to pH variations and the presence of iron in their growth environment. Balan (2000) suggested that in the altered profiles the progressive dissolution of ordered kaolinites, from the base to top, leads to form disordered phases.

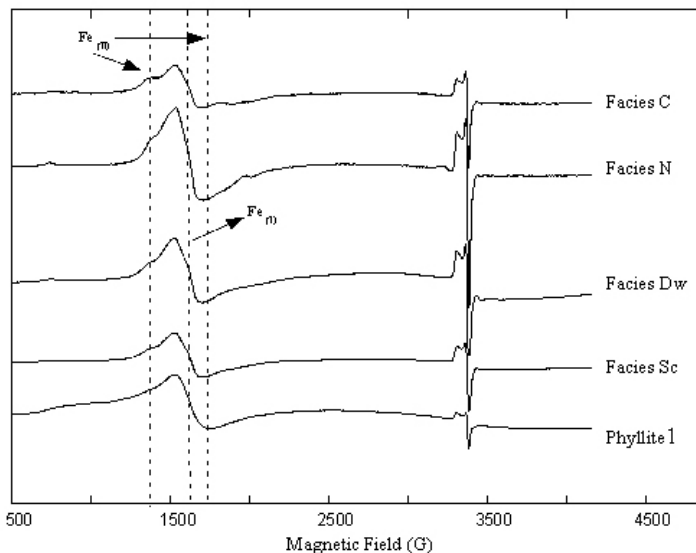


Figure 1- Full range X-band EPR Spectra of kaolinite showing the signals of type (I) Fe^{3+} of the bottom facies and the type (II) Fe^{3+} of top facies. Note the very intense paramagnetic defect center.

SEM and TEM analysis of the kaolinite particles showed sub-hexagonal to hexagonal and irregular shapes predominating in the Dw, Dr, N and C facies of deposit. The kaolinite crystals from the sericitic and graphitic phyllites basement generally have hexagonal forms and occur associated to the white lozenge shaped mica.

EDS analysis of the white micas of the graphitic phyllite reveal compositions belonging to the phengite group (paragonite or celadonite - Bailey 1984): $(\text{Si}_{3.2} \text{Al}_{0.78}) (\text{Al}_{1.1} \text{Mg}_{0.13} \text{Fe}^{3+}_{0.76})_{0.77} (\text{Mg}_{1.1} \text{Fe}^{2+}_{1.9})_{0.23} \text{O}_{10} (\text{OH})_2 \text{K}_{0.79} \text{Na}_{0.12}$; $(\text{Si}_{3.35} \text{Al}_{0.64}) (\text{Al}_{1.62} \text{Mg}_{0.09} \text{Fe}^{3+}_{0.28})_{0.23} \text{O}_{10} (\text{OH})_2 \text{K}_{0.89}$. The white micas of the sericitic phyllites have the following compositions: $(\text{Si}_{3.08} \text{Al}_{0.92}) (\text{Al}_{1.46} \text{Mg}_{0.24} \text{Fe}^{3+}_{0.29})_{0.10} (\text{OH})_2 \text{K}$, passing to $\text{Si}_2 \text{Al}_{1.8} \text{Fe}^{3+}_{0.044} \text{K}_{0.063} \text{O}_5 (\text{OH})_4$, passing to $\text{Si}_2 \text{Al}_{1.79} \text{Fe}^{3+}_{0.20} \text{O}_5 (\text{OH})_4$. So, in this case illite is probably transformed (neomorphosis) to kaolinite with structural Fe and K and finally to kaolinite with structural Fe. An analogous transformation involving the same chemical process (white mica of phengite group and illite to kaolinite) in weathering environment has been described by Varajão et al. (2001). They observed in kaolinites from North of Moeda syncline the d spacing transition from 10\AA to 7\AA and suggested the transformation of white mica into kaolinite.

5 CONCLUSIONS

The studies performed at the Água Limpa deposit showed that the source of sediments was the lateritic profiles developed from the Piracicaba Group where the clay minerals, principally kaolinite was generated by alteration of white mica of phengite group (celadonite and paragonite). This deposit represents an inversed lateritic profile as observed by the space distribution of crystallinity index. It can be suggested as a general chemical process that the white mica of phengite group and illite can convert into kaolinite in supergenical environments conditions.

6 REFERENCES

- Allard T. 1994. La kaolinite: un dosimètre des rayonnements naturels. Application au traçage de migrations anciennes de radioéléments dans la géosphère. Université de Paris VII, Paris, Thèse doctorat 234p.
- Bailey S.W. 1984. Classification and structures of the micas. Reviews in Mineralogy. Mineralogical Society of America, 13. Pg. 584p.
- Ballan E. 2000. Cristalochimie des silicates a la surface de la terre. Evolution de kaolinite e du zircon dans les sediments et les sols du bassin Amazonien. Université de Paris VII, Paris, Thèse doctorat, 222p.
- Ballan E., Allard T. Boizot, B. Morin G. Muller J.P. 1999. Structural Fe^{3+} in natural kaolinites: new insights from electron paramagnetic resonance spectra fitting at X and Q-band frequencies. Clays and Clay Minerals, 47(5):605-616.
- Boudeulle, M. & Muller, J.P. 1988. Structural characteristics of hematite and goethite and relations with kaolinite in laterite from Cameron. ATEM study. Bull. Mineral 11: 149-166

- Brindley G.W. & Brown G. 1984. Crystal structures of minerals and their X-ray identification. London, Mineralogical Society, 495 p.
- Cases J. M., Lietard, O., Yvon J., Delon J. F. 1982. Étude des propriétés cristallochimiques, morphologiques et superficielles de kaolinites désordonnés. Bulletin de Minéralogie 105: 439-457
- Delineau T., Allard T., Muller J. P., Barrès O., Yvon J., Cases J.M., 1994. FRIR reflectance vs.EPR studies of structural iron in kaolinites. Clays and Clay Minerals 10 : 308-320.
- Fiallipsis C. G. 1999. Étude Expérimentale de la cristallinité et des conditions de formation de la Koalinite. l'Université de Poitiers, Poitiers, Thèse Doctorat 249p.
- Hinckley D.N. 1963. Variability in "crystallinity" values among the kaolin deposits of Georgia and South Carolina. Clays and Clay Minerals 2:229-235
- Liétard O. 1977. Contribution 'a l'étude des propriétés physicochimiques, cristallographiques et morphologiques de kaolins. Institute National Politecnique de Lorraine/LEM, Nancy, Thèse de doctorad, 322p.
- Mehra O.P. & Jackson M.L. 1960. Fe oxide removal from soil and clays by a dithionite-citrate system buffered with sodium carbonate. Clays and clay minerals, 7:317-327
- Muller J. P. 1987. Analyse pétrologique d'une formation latéritique meuble du Cameroun. Université de Paris VII, Paris, Thèse de doctorat, 188p.
- Muller J.P., Manceau, A., Callas, G., Allard, T. Ildefonse, P., Hazemann, J.L. 1995. Crystal chemistry of kaolinite and Fe-Mn oxide: relation with formation conditions of low temperature systems. American Journal of Science 295, 1115-1155.
- Nahon D. 1986. Evolution of iron crusts in tropical landscapes. In: Coleman, S.H., Dethier, D.P. (Eds.), Rates of chemical weathering of rocks and minerals. London Academic Press, p.169-191.
- Santos M.C. & Varajão A.F.D.C. 2004. Sedimentation and pedogenic features in a clay deposit in Quadrilátero Ferrífero, Minas Gerais, Brazil. Anais da Academia Brasileira de Geociências 76 (1): 147-159.
- Santos, M.C., Varajão, A.F.D.C. & Yvon, J. 2004. Genesis of clayey bodies in Quadrilátero Ferrífero, Minas Gerais, Brazil. Catena, 55 (3) 277-291
- Santos M.C. 2003. Caracterização dos depósitos argilosos na porção centro-sul do Sinclinal da Moeda, Quadrilátero Ferrífero, MG, Brasil: macromorfologia, micromorfologia, cristalóquímica, gênese e considerações industriais. Doctorat thesis UFOP/INPL. Ouro Preto. 200p.
- Sherrer P. 1918. bestimmung der gröbß und der inneren struktur von kolloidteilchen mittels Röntgenstrahlen. Nachr. Ges. Wiss. Göttingen. 2, 96-100.
- Tardy Y. & Nahon D. 1985. Geochemistry of laterites, stability of Al-goethite, Al-Hemathite and Fe³⁺ -kaolinite in bauxites and ferricretes: an approach to the mechanism of concretion formation. American Journal of Science 285: 865-903
- Tardy Y. 1993. Pétrologie des Laterites et des Sols L'alteration Initiations. Paris, Masson.
- Tardy Y., Kobilsek B., Paquet H., 1991. Mineralogical composition and geographical distribution of African and Brazilian periatlantic laterites. The influence of continental drift and tropical paleoclimates during the past 150 million years and implications for India and Australia. Journal of African Earth Sciences 12:283-295
- Varajão A.F.D.C., Gilkes R.J. & Hart R.D. 2001. The relationships between kaolinite crystal properties and the origin of materials for a brazilian kaolin deposit. Clays and Clay Minerals 49, 44-59.

Carbon Nanotubes and Fullerene-Like Phase Formation at Low Temperature and Pressure Parameters

S.K.Simakov

Geol. Dept., S-Petersburg University, Universitetskaya emb.7/9, S-Petersburg, 199034, Russia.

A.A.Graphchikov

Inst. Exp. Mineral., Chernogolovka, Moscow distr., 142432, Russia

I.A.Drozdova

Institute of Silicate Chemistry, Makarova nab.2, S-Petersburg, 199034, Russia

M.A.Yagovkina & E.A.Grebenshchikova

A.F.Ioffe Physical Institute, Politechnicheskaya 26, S-Petersburg, 194021, Russia

ABSTRACT: Multi-wall fullerite structures and typical carbon nanotubes were synthesised at metamorphic conditions (700-750°C and 5 kbar). Fullerites have overall forms, multilayers structure and reach several hundreds of Å. Nanotubes reach in the length 1 µm and have outer diameter nearly 600 Å and inner diameter nearly 40Å.

1 INTRODUCTION

New carbon forms - fullerenes and fullerene-like phases (fullerites) experimentally were synthesised at temperatures more than 1500° C (Dresselhaus et al. 1996). In nature these forms were discovered in the different geological situations: in the matrix of carbonaceous chondrite meteorite (Buseck & Hua 1993), in thin films within fractures in Karelian shungites (Buseck et al. 1992), in pillow lavas that cut across black shales (Jehlicka et al. 2000), coal (Fang & Wang 1997; Osawa 1999), fossil dinosaur eggs (Wang et al. 1998), a carbonaceous impact breccia from the Canadian Sudbury Structure (Becker et al. 1994; 1996). Most part of fullerenes was found in shungite, a carbon-rich rock in Karelia (Buseck 2002). It's metasediment rocks which also includes rocks of volcanic and metasomatic origin. There are also reports of larger natural fullerenes, sometimes called "giant fullerenes" (Smith & Buseck 1981). These are large and closely resemble the concentric carbon layers in the "carbon onions" that are presumed to be related to fullerenes (Ugarte 1992; Kroto 1992). Some authors suppose that fullerenes can form complexes with metals in the endogenic fluids (Vinokurov et al. 1997). These complexes can transport metals and take part in the kimberlite and carbonatite formations. In spite of

many reports of natural fullerene findings, their origin still remain elusive (Buseck 2002). Becker et al. (2001) state that fullerenes are "highly resistant to metamorphism" and "a robust tracer in the geological environment". The most typical fullerene association in the natural objects is association with graphite. Majority of economic graphite veins have formed at temperatures corresponding to amphibolite or granulite facies. Frost (1979) show that the graphite veins can form from methane-rich fluid during metamorphic processes. That is why we studied the process of carbon pyrolyses at low pressures and temperatures corresponding to metamorphic conditions.

2 EXPERIMENTAL PROCEDURE

The process of carbon formation from hydrocarbon gases were studied at 700-750° C and 5 kbar at the period of run 5-6 days (nearly 20 runs were provided). The source of hydrocarbon gases was polypropylene. The experiments were carried out in cold-seal pressure vessels with vertically mounted furnaces. H₂O was used here as the pressure medium. The structure of the electric furnaces made it possible to create hot spots with gradients of only 2-3° C over 50 mm where the capsules were placed.

Temperatures were measured by chromel-alumel thermocouples and controlled automatically with accuracies of $\pm 5^\circ\text{C}$. The attainment of the run conditions required 1.5-2 hours. Quenching was achieved by cold-air blast. Over 10-12 minutes of quenching, the temperature decreased to 150-200 $^\circ\text{C}$. Pressures were measured by tube manometers with accuracies of ± 10 Mpa. The runs were provided in welded gold capsules with wall thicknesses of 0.2 mm. The inner capsule has a diameter 3 mm and outer - 5 mm. The double capsule technique was used with a Fe-FeO buffer. Gold capsules are sufficiently permeable to hydrogen at these temperatures. In order to perform runs at constant redox conditions, an additional external nickel container was used which was filled with fayalite (as a result oxygen fugacity at the experiments keeps lower CCO buffer).

3 RESULTS AND DISCUSSION

Products of the experiments were studied by the X-ray diffraction and electronic microscopy methods. By the X-ray diffraction's nanographite and ravatite were diagnosed. After that the experimental products were processed in HClO_4 for the graphite destruction. Than 10 mg of dressing specimen powder (under investigation) was suspended in ml of toluene and sonicated for 15 min at 22 kHz (MSE-100W, UK). A small drop of suspended specimen was placed on carbon-coated copper grid for electron microscopy and air-dried. Grids were investigated in TEM (JEM-100S, JEOL, Japan and EM-420, Philips) operating at 100kV. At high magnification it was discovered that specimen contained short multi-wall carbon nanotubes (Fig.1), onion-like and triangle nanostructures with "shoots" (Fig.2) and small amount of thin long (0,5 - 1 micron) nanotubes 10-20 nm in diameter.

4 CONCLUSION

From obtained results we can conclude that rare forms of the carbon - multi-wall fullerenes and nanotubes could be formed from the hydrocarbon gases at P-T parameters corresponding to metamorphic conditions. Some onion-like structures (Fig. 2a) are very closed to natural "giant fullerenes" founded in the Allende meteorite (Smith & Buseck 1981). From previously done experiments it's known that these phases are more characteristic for very high temperatures (Dresselhaus et al. 1996). As a result we can conclude that the origin of the fullerene in metamorphic rocks could be connected with the metamorphic hydrocarbon-rich fluids.

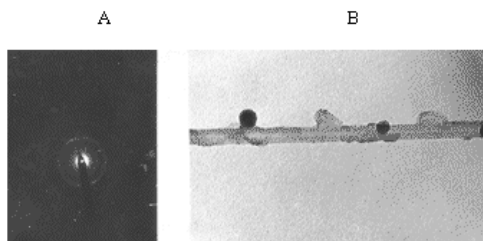


Figure 1. Nanotube under 50,000 magnification (B) and its microdiffraction (A).

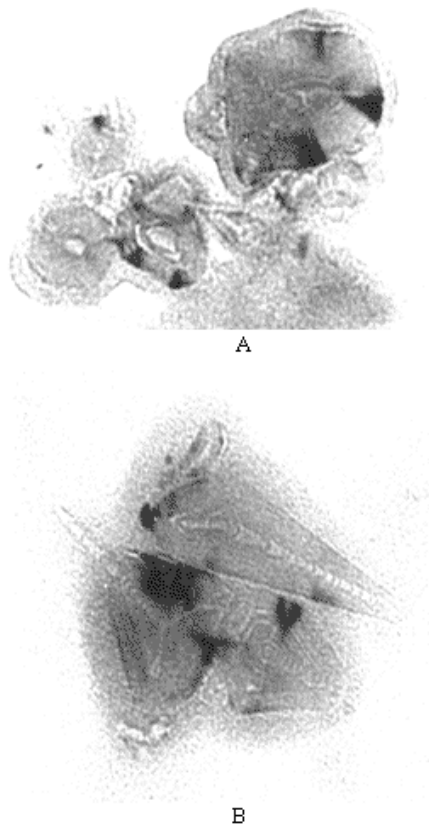


Figure 2. Fullerites 300,000 magnifications (A - onion-like and B - triangle nanostructures with "shoots").

5 REFERENCES

- Becker, L., Bada, J.L., Winans, R.E., Hunt, T.E., Bunch, B.M. & French, B.M. 1994. Fullerenes in the 1.85-billion-year-old Sudbury impact structure. *Science*, 265, 642-644.
- Becker, L., Poreda, R.J. & Bada, J.L. 1996. Extraterrestrial helium trapped fullerenes in the Sudbury impact structure. *Science*, 272, 249-252.
- Becker, L., Poreda, R.J., Hunt, A.G., Bunch, T.E. & Rampino, M. 2001. Impact event at the Permian-Triassic boundary:

- Evidence from extraterrestrial noble gases in fullerenes. *Science*, 291, 1530-1533.
- Buseck, P.R., & Hua, X. 1993. Matrices of carbonaceous chondrite meteorites. *Ann. Rev. Earth Plan. Sci.*, 21, 255-305.
- Buseck, P.R., Tsipursky, S.I. & Hettich, R. 1992. Fullerenes from the geological environment. *Science*, 257, 215-217.
- Buseck, P.R. 2002 Geological fullerenes: review and analysis. *Earth Plan. Sci. Lett.*, 203, 781-792.
- Dresselhaus, M.S., Dresselhaus, G & Eklund, P. 1996. The science of fullerenes and carbon nanotubes. Acad. Press,
- Fang, P.H. & Wong R. 1997 Evidence for fullerene in a coal of Yunnan, Southwestern China. *Mat. Res. Innov.*, 1, 130-132.
- Frost, B.R. 1979. Mineral equilibrium in involving mixed-volatiles in a C-O-H fluid phase: the stabilities of graphite and siderite. *Am. J. Sci.*, 279, 1033-1059.
- Jehlicka, J., Ozawa, M., Slanina, Z. & Ozawa, E. 2000. Fullerenes in solid bitumens from pillow lavas of Precambrian age (Mitov, Bohemian massif). *Full.Sci.Teh.*, 8, 449-452.
- Kroto H.W. 1992 Carbon onions introduce new flavor to fullerene studies. *Nature*, 359, 670-671.
- Osawa, E. 1999 Natural fullerenes - Will they offer a hint to the selective synthesis of fullerenes? *Full.Sci.Teh.*, 7, 637-652.
- Smith, P.P.K. & Buseck, P.R. 1981 Graphitic carbon in the Allende meteorite: A microstructural study. *Science*. 212, 322-324.
- Ugarte, D. 1992. Curling and closure of graphitic networks under electron-beam irradiation. *Nature*, 359, 670-671.
- Vinokurov, S.F., Novikov, U.N. & Usatov, A.V. 1997. Fullerenes in the geochemistry of endigenic processes. *Geohimiya*. No 9, 937-944.
- Wang, Z.X., Li, X.P., Wang, W.M., Xu, X.J., Zi, C.T., Huang, R.B. & Zheng, L.S. 1998. Fullerenes in the fossil of dinosaur egg. *Full.Sci.Teh.*, 6, 715-720.

Chaoite Synthesis from Fluid at Low Temperatures and Pressures

S.K.Simakov

Geol. Dept., S-Petersburg University, Universitetskaya emb.7/9, S-Petersburg, 199034, Russia

A.E.Kalmykov & L.M.Sorokin

A.F.Ioffe Physical Institute, Politechnicheskaya 26, S-Petersburg, 194021, Russia

ABSTRACT: Rare diamond-like carbon-phase chaoite was synthesised at low temperature and pressure metamorphic parameters. We studied the process of carbon formation from organic matter at 500°C and 1 Kbar for a period of 5-6 days. Products of the experiments were studied by the X-ray diffraction and electronic microscopy methods. By the X-ray diffraction's nanographite was diagnosed. By electronic microscopy the hexagonal cut particles were observed regularly in the carrier film. Their microdiffraction patterns have six fold axis of symmetry, which corresponds to hexagonal or cubic lattice. The interplanar spacings are closed to hexagonal structure of chaoite ($a=8,948\text{Å}$, $c=14,078\text{Å}$, ASTM data, card 22-1069).

1 INTRODUCTION

Rare diamond-like carbon phase chaoite was discovered in graphite of meteoritic crater (El Goresy & Donnay 1968). Later it was diagnosed in diamond-bearing meteorite Urei (Vdovykin 1969). Experimentally it was synthesized at temperatures of more than 1500° C (Lloyd et al. 1972). The most typical chaoite association in the natural objects is the one to graphite. The major part of economic graphite veins was formed at temperatures corresponding to that of amphibolite or granulite facies. Frost (1979) shows that the graphite veins can form from methane-rich fluid during metamorphic processes. That is why we studied the process of carbon pyrolyses at low pressures and temperatures corresponding to metamorphic conditions. The hexagonal cut particles were observed regularly in the carrier film.

2 EXPERIMENTAL PROCEDURE

The process of carbon formation from hydrocarbon gases was studied at 500°C and 1 Kbar for a period of 5-6 days. The source of hydrocarbon gases was organic matter. The experiments were carried out in

titanium vessels. The structure of the electric furnaces made it possible to automatically control the temperature with an accuracy of $\pm 5\text{°C}$.

3 ANALYTICAL PROCEDURE

Products of the experiments were studied by the X-ray diffraction and electronic microscopy methods. After that the experimental products were processed in HClO_4 for the graphite destruction. A residual powder after ablation was immersed into an amyl acetate solution of collodion and applied to the water surface. The formed film was transferred on the gauze for the electron-microscopic analysis. The samples were investigated by the electron microscope EM-200 at an accelerating voltage of 100kV.

4 RESULTS

By the X-ray diffraction's nanographite was diagnosed. The hexagonal cut particles were observed regularly in the carrier film (Fig.1). Their microdiffraction patterns have six fold axis of symmetry (Fig. 2), which corresponds to hexagonal

or cubic lattice. The interplanar spacings are close to the hexagonal structure of chaoite ($a=8,948\text{\AA}$, $c=14,078\text{\AA}$, ASTM data, card 22-1069). To confirm that observable particles are chaoite crystal forms the sample was inclined (20°). The

microdiffraction pattern obtained could not be identified as a cubic structure. On the other hand, keeping within regular lattice, registered reflections correspond to the same ones due to the reflection from the planes with the zone axis (1 2 3).

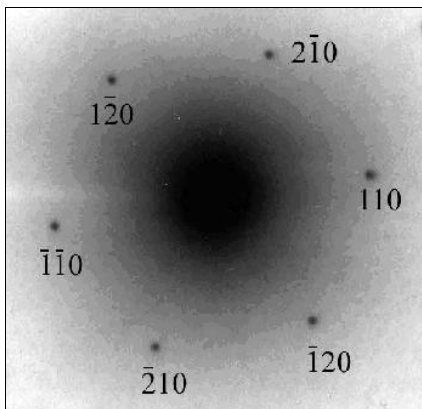


Figure.1 Chaoite particle under magnification

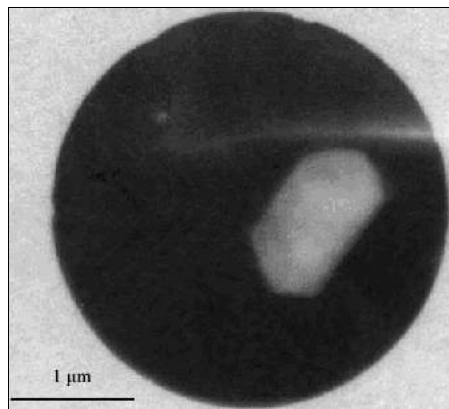


Figure.2. Microelectronogram of the chaoite-like substance particle. Measured interplanar spacing $d=4,48\text{\AA}$, tabulated point ASTM: $d=4,47\text{\AA}$.

5 CONCLUSION

As a result we can conclude that chaoite could be formed from hydrocarbon-rich fluids at metamorphic low temperatures and pressures.

6 REFERENCES

- Frost, B.R. 1979. Mineral equilibrium in evolving mixed-volatiles in a C-O-H fluid phase: the stabilities of graphite and siderite. *Am. J. Scie.*, 279, 1033-1059.
- El Goresy, A. & Donnay, G. 1968. A new allotropic form of carbon from Ries Crater. *Science*, 161, 363 – 365.
- Lloyd, N.S. et al. 1972. The formation of new polymorphs carbon and fluid flow patterns by irradiating solid carbons with CO₂ laser. *High Temp. Sci.*, 4, 445 – 477.
- Vdovykin, G.P. 1969. *Geochimiya*. N 9, 1145-1148 (In Russian)

Kubelka-Munk Procedure for Brightness Evaluation of Blended Kaolins from Rio Capim, North Brazil

D.J.L.Sousa & A.F.D.C.Varajão

Department of Geology, School of Mines, University of Ouro Preto, Minas Gerais, Brazil

J.Yvon

Laboratory of Environment and Mineralurgy, Geology School, INPL, Nancy, France

ABSTRACT: Kaolin is widely used in the paper industry where its brightness is a key parameter. The Rio Capim kaolin district, (Northeast of Pará State, Brazil) is one of the largest high whiteness kaolin reserves in the world. It includes, at the base, the main ore, a soft kaolin that gradually passes to the top into a ferruginous duricrust, followed by a hard (flint) kaolin. The present work not only aims at identifying the chemical composition effect on the final color of the kaolin, but also to characterize the chromophores species, mainly the iron phases associated with kaolinite crystals, by using ultraviolet-visible spectrometry. Physical analysis involved grinding (residue analyses) and laser grain size distribution. According to X-ray diffraction, kaolinite is the major mineral, followed by quartz and minor amounts of hematite, goethite, muscovite, zircon, tourmaline, rutile, staurolite, kyanite, anatase and topaz. Representative samples of the kaolin profile, including the soft and the hard facies, were collected and blended respecting the required quality for the paper industry, such as particle size distribution, viscosity and brightness. The brightness of kaolin mixtures is not a direct consequence of the contained different grades, but a complex function of reflectance of individual samples expressed by means of the Kubelka-Munk equation. In conjunction with geostatistic methods, this equation was used to predict the mass composition to obtain blended samples with controlled optical properties.

1 INTRODUCTION

The Kaolin District of Capim is located in the oriental Brazilian Amazon precisely on NE of the Pará State, on the margin of Capim River. It represents one of the largest reserves of high whiteness kaolin in the country and corresponds to one half of the national production devoted to paper coating for internal consume and exportation to Europe, Asia and United States.

The regional geological context shows two great stratigraphical units: a) inferior unit, related to the ore qualities, including the soft kaolin in the base and the flint above; b) superior unit, composed of sandy-loamy sediments with a lateritic profile at the top.

In the soft kaolin, based on its texture and color, the following facies can be recognized from the base to the top: 1) a sandy kaolin, with an average thickness of 4 m; 2) a stratified white kaolin, with laminations evidenced by concentrations of heavy minerals, its thickness can reach up to 5 meters; in the intermediate portion of this facies, millimetric to decimetric lenses of cream kaolin occur; 3) a rose to reddish kaolin (medium thickness of 1 m) that gradually changes to a red-brown ferruginous duricrust that characterizes the passage to the flint kaolin. A regional unconformity surface marks the

contact between the flint kaolin and the superior unit (Sousa 2000).

The blended material used in the mines process is only composed of the 3 facies from the soft kaolin: the rose to reddish kaolin, that has a low brightness (<80 ISO) and a low residue (<5%); the laminated kaolin that presents a good brightness (range of 80-89) and a medium residue (<10%) and, the sandy kaolin that also has a good brightness (83-90) but a high residue (20-50%). The process is done by blending parts of each kaolin facies to obtain a brightness > 83 and a residue < 20%.

The aim of the present study is to benefit the greatest possible tonnage of ore without depreciating the quality of the final blended product involving the whole set of kaolin facies, including the flint, to obtain a minimum whiteness of 83 (ISO). The brightness values are obtained from the raw samples (ROM), without magnetic separation neither chemical leaching. Besides, other characteristics were acquired such as the % of > 325 mesh size residues and the % of < 2 μ m size particles.

2 METHODOLOGY

Eighteen representative samples of the soft and flint

kaolin were collected covering the largest possible diversity of the types, mainly based on their color and texture. The blended samples were identified as mix-1, mix-2 and mix-3; they are mixtures of the different kaolin types collected. The main goal here is to incorporate the greatest amount of the ore in the commercial products without depreciating its quality, in order to reach a maximal economical benefit of the deposit. The purpose is not only to increase the lifetime of the deposit but also to prevent valuable qualities from becoming waste. The kaolin samples improvement includes disaggregation, quartering, dispersion in water by using dispersing agents (sodium polyacrylate and sodium carbonate), and sieving at 325 mesh. In this stage the percentage of residues that indicates the real ore content is determined. After that, the slurry is centrifuged and conditioned in a standard solid/pulp ratio of 70%. The percent of $< 2\mu\text{m}$ size particles, that is a reference parameter for paper coating, is determined. In addition, the particle size distribution is obtained by using Sedigraph equipment. The brightness determination is carried out using a Technibrite Micro TB-1C device, standardized with magnesium oxide or barium sulfate. The brightness is expressed in reflection percentage of the 457 nm radiation according to the ISO procedure. Brightness was also determined after magnetic treatment (Inbrás-Eriez Magnetics) and after chemical leaching with sodium hydrosulfite (2 kg/ton).

The kaolin brightness determination is a fundamental parameter of quality control to the final product used in the paper industry. For blended products, the brightness determination does not follow simple addition laws (Conceição & Petter

2000; Peroni 1998). This is the reason why the empirical Kubelka-Munk procedure, which has shown its efficiency in other fields, has been chosen here as a composition law. Since the Kubelka-Munk function (equation 1)

$$F(R)=(1-R)^2/2R \quad (1)$$

is a function of the reflectance (R), it can be expressed as the weight mass average of optical densities for each wavelength. Conceição & Petter (2000) and Peroni (1998) applied this method to measure chromatic pollutants contributions and evaluate kaolin reserves. The reflectance is obtained from a Kubelka-Munk value by using the following equation 2:

$$R=1+F_{k-m} (2F_{k-m} + (F_{k-m})^2)^{1/2} \quad (2)$$

3 RESULTS AND DISCUSSION

The XRD analysis of all samples show the dominant presence of kaolinite and quartz; with minor amounts of hematite, goethite, muscovite, zircon, tourmaline, rutile, staurolite, kyanite, anatase and rarely topaz. The UV-visible analysis allowed to distinguish the characteristic bands of the hematite (range of 530 -542 nm) goethite (~550 nm), anatase (310-330 nm) and the band in the range of 240-260 nm related to electrons migration between oxygen and ferric iron.

Among the different facies considered, the sandy kaolin has the highest percentage of residue, as shown in the samples KA and KSC (Table 1).

Table 1: Physical analyses of the Rio Capim kaolin: percentage of residue > 325 mesh, % of size particles $< 2\mu\text{m}$, brightness values (rom, no magnetic and chemical leach) and Kubelka-Munk values

Samples	% Residue >325 mesh	Particle $<2\mu\text{m}$	Brightness (ISO)			% Gain brightness (ISO)			Kubelka-Munk Function		
			ROM	N. Mag.	Chem.L.	N. Mag. - ROM ¹	Chem.L. N. Mag. ²	Chem. L. ROM ³	ROM ⁴	N. Mag. ⁵	Chem L. ⁶
KF	31.90	74.0	75.30	75.30	77.37	2.07	6.82	8.89	0.04051	0.03310	0.01484
KR	11.68	71.3	79.34	79.34	81.15	1.81	5.95	7.76	0.02690	0.02189	0.00955
KSRe	6.74	70.9	84.06	84.06	86.29	2.23	4.02	6.25	0.01511	0.01089	0.00520
KS50	6.72	66.6	86.09	86.09	87.35	1.26	4.37	5.63	0.01124	0.00916	0.00374
K562	7.68	64.7	87.49	87.49	89.15	1.66	3.18	4.84	0.00894	0.00660	0.00319
KS	8.18	54.5	89.01	89.01	89.75	0.74	2.06	2.8	0.00678	0.00585	0.00365
KCSS	2.62	52.3	80.04	80.04	82.59	2.55	3.01	5.56	0.02489	0.01835	0.01211
KSC	35.85	50.7	88.45	88.45	89.71	1.26	1.98	3.24	0.00754	0.00590	0.00377
KA	45.74	54.0	78.29	78.29	82.88	4.59	4.85	9.44	0.03010	0.01768	0.00858
Mix-1	12.70	62.5	84.25	84.25	86.62	2.37	4.03	6.4	0.01472	0.01033	0.00482
Mix-2	5.45	58.5	82.39	82.39	85.06	2.67	3.79	6.46	0.01882	0.01312	0.00700
Mix-3	9.57	66.4	82.22	82.22	84.48	2.26	5.45	7.71	0.01922	0.01426	0.00564

N. Mag. - ROM¹ – gain of brightness after magnetic fraction in relation to the ROM. ROM²– raw sample.

Chem L. - N. Mag.³ – gain of brightness after chem.leach in relation to the no magn. fraction. No Mag.⁵– Sample no magnetic

Chem L. - ROM³ – gain of brightness after chemical leach in relation to the ROM. Chem L.⁶– chemical leach.

The flint sample (KF) shows peculiar characteristics. It does not disaggregate in water and

presents high resistance to the impact. For these reasons its residue is the product of an incomplete

dispersion. For the other samples the % of > 325 meshes residues is < 12. The < 2 μm size fraction content increases towards the top of the profile, reaching the largest accumulated weight of 71.3 and 74% (Table 1) in the rose (KR) and flint (KF) samples, respectively. For the other samples the content of < 2 μm size fraction ranges from 50 to 70%. The figure 1 shows a wide particles sizes range of 50-0.5 μm with a cumulative distribution of 90% for < 10 μm size particles. This fact shows a few heterogeneity in the particle size distribution that is not a problem in the industrial process since delamination reaches up to 35% gain on the rejected fraction (Souza 2000).

The magnetic separation generates a brightness gain ranging from 0.7 to 4.6 points, while the gains due to chemical leaching vary from 2 to 6.8 points, with a 5 points average improvement in the final stage. This effect is directly linked to the elimination of iron and iron-titanium oxi-hydroxides.

According to Petter (1994) a direct application can be carried out on blended kaolin with similar optical indexes and particle size distributions. The Kubelka-Munk function F(R) can be used for a direct ponderable equation (equation 3), that is:

$$F(R)_{1+2+\dots+n} = c_1 F(R)_1 + c_2 F(R)_2 + \dots + c_n F(R)_n \quad (3)$$

Where, $F(R)_{1+2+\dots+n}$ is a KM function of all n blended samples, $F(R)_n$ is the function of each n sample and, c_n is the weight concentration of each n sample.

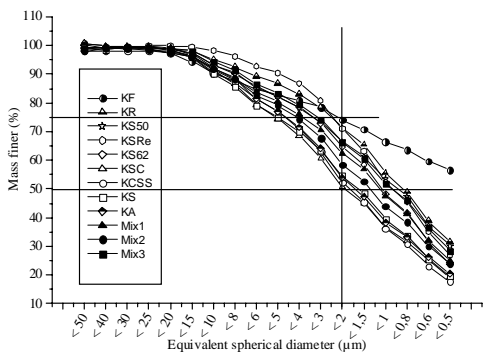


Figure 1: Cumulative frequency of the particle size between 50 and 0.5 μm of the soft, flint and blended samples.

Table 2 presents the data of mix-1, mix-2 and mix-3 samples processed from the Kubelka-Munk function. We can observe a narrow correlation with the results obtained from the individual samples. The figure 2 represents the samples analyzed in the three stages where the whiteness was measured. The

curves were adjusted to fit the Kubelka-Munk equation and express the distribution of the samples; the values of correlation coefficients are reported in the graph.

Tabela 2: Blend of three samples (Mix-1, Mix-2, Mix-3) starting from other six samples (KS62, KR, KA, KCSS, KSRe, KS50) and their respective Kubelka-Munk function as individualized sample and as composed sample.

	Stage	Bright. ^{1a}	F_{K-M}^{1b}	Bright. ^{2a}	F_{K-M}^{2b}	SD ³
Mix-1	ROM	84.25	0.01472	83.29	0.01677	0.00144
	N. Mag.	86.62	0.01033	85.73	0.01188	0.00109
	ChemL.	90.65	0.00482	90.02	0.00554	0.00050
Mix-2	ROM	82.39	0.01882	82.78	0.01791	0.00065
	N. Mag.	85.06	0.01312	85.11	0.01302	0.00007
	ChemL.	88.85	0.00700	88.72	0.00717	0.00012
Mix-3	ROM	82.22	0.01922	83.18	0.01699	0.00158
	N. Mag.	84.48	0.01426	85.28	0.01270	0.00110
	ChemL.	89.93	0.00564	90.03	0.00551	0.00009

^{1a} Brightness and F_{K-M}^{1b} Kubelka-Munk function of individualized sample.

^{2a} Brightness and F_{K-M}^{2b} Kubelka-Munk function of composed sample:

- Mix-1= 0.6 kg (KS62) + 0.6 Kg (KR) + 1.8 Kg (KA)
- Mix-2= 0.857 kg (KCSS) + 2.143 Kg (KSRe)
- Mix-3= 2 kg (KS50) + 0.5 kg (KR) + 0.5 (KA)

³ SD – standard deviation of the function K-M between the individualized samples and the composites.

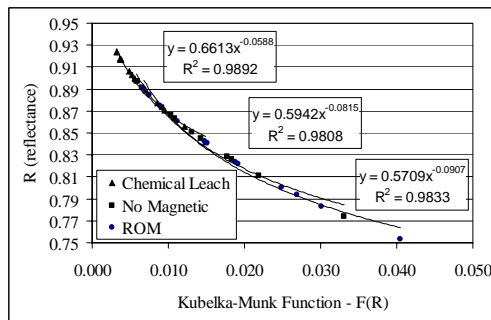


Figure 2: Reflectance versus Kubelka-Munk function.

4 CONCLUSIONS

The particle size distribution and the percentage of >325 meshes residue decreases upwards. The main colored contaminants are iron oxides and hydroxides and, iron-titanium minerals that can be easily removed by magnetic separation and chemical leaching. However, the contribution of kaolinite-included nano chromatophores and the specific coloration due to octahedral iron (Delineau et al. 1994) still remains

For the three samples (mix-1, mix-2 and mix-3) the calculated values by using the Kubelka-Munk procedure are close to the measured values on the

mixtures. This fact shows that the method works very well. However we must point out the fact that the analyzed mixtures were made on crude samples while the ideal particle size to apply the K-M method is $< 2\mu\text{m}$. This fact can explain the minor differences in curves fitting due to the contribution of coarser particles. One part of this problem is, however, minimized since the analyses were standardized to a minimum of 90% of the total mass with particles $< 2\mu\text{m}$.

The main characteristic of this methodology is that, knowing the physical characteristics of the material, the amount of each ore type to be used in the blend can be estimated, based on a minimum value of final whiteness, in order to have the best commercialization.

5 REFERENCES

- Conceição, P. R. N. & Petter, C. O. 2000. Utilização de técnicas espectro-colorimétricas no auxílio à lavra seletiva de caulins: adição de espectros de reflectância. *Revista Escola de Minas*, 53 (2) abril - junho. 125-128.
- Delineau T., Allard T., Malengreau N., Muller J.P., Yvon J., Barrès O., Cases J.M. 1994. Apport des spectrométries RPE, Infrarouge et UV visible pour l'étude des statuts du fer ferrique dans les kaolins : relation avec la couleur et certaines propriétés d'utilisation. *Revue de l'industrie minière. Mines et Carrières, Les techniques* 76, 232-240.
- Peroni, R. L. 1998. Introdução de variável espectro-colorimétrica no modelamento e planejamento de jazidas de caulim e comparação da seletividade produzidas por modelos de diferentes dimensões. UFRGS / PPGEM / LAPROM. Dissertação de mestrado. 125p.
- Petter C. O. 1994. Contribution à l'Étude de la valorisation des kaolins pour l'industrie papetière: mise au point d'une méthodologie colorimétrique, application à la sélectivité minière. *École des Mines de Paris*. 300 p. Thèse de doctorat.
- Sousa, D. J. L. 2000. Caracterização geológica, mineralógica, química e física do caulim da mina da RCC - Rio Capim Caulim (PA). Belém, Universidade Federal do Pará. Centro de Geociências. (dissertação de Mestrado). 116p.

Genesis of Talc Deposits and the Metamorphic History of the Itaiacoca Group Metadolomites, Southern Brazil

G.A.J.Szabó & F.R.D.Andrade

Department of Mineralogy and Geotectonics, Geosciences Institute, University of São Paulo, São Paulo, Brazil

G.B.Guimarães

State University of Ponta Grossa, Paraná, Brazil

F.A.Moya

Cimentos Votoran S.A., Curitiba, Paraná, Brazil

F.M.S.Carvalho

Geosciences Institute, University of São Paulo, São Paulo, Brazil

ABSTRACT: The metadolomites of the Neoproterozoic Itaiacoca Group, Paraná State, southern Brazil, contain an important part of the Brazilian talc reserves. Two main types of talc ore have been recognized: (a) talc schists along transcurrent shear zones; and (b) irregular pockets of fine-grained, massive talc. The Itaiacoca Group underwent four metamorphic episodes: (i) greenschist facies regional metamorphism during the Neoproterozoic Brasiliano orogeny; (ii) thermal metamorphism along the contact with the Neoproterozoic Cunhaporanga granite batholith; (iii) hydrothermalism related to transcurrent shear zones, that formed large volumes of talc schist; (iv) small-scale thermal metamorphism related to Mesozoic diabase dikes. The Itapirapuã transcurrent shear zone defines the contact between the Itaiacoca Group and the Proterozoic Três Córregos granitic batholith, and the main talc deposits are aligned following its branches. Enhanced permeability due to shearing provided channels for percolation of the silica-rich aqueous solutions that reacted with the metadolomite to form the talc deposits. Minor amounts of talc occur as submillimetric films along the sedimentary stratification and fractures. Geothermometry of calcite coeval with talc indicates two intervals of temperature (290-300 °C and 380-400 °C). The massive type of talc (b) replaced the metadolomite without significant volume change and was probably formed at lower temperatures, lacking any direct relation with the shear zones.

1 INTRODUCTION

The Itaiacoca Group is a Neoproterozoic supracrustal low-grade metamorphic belt situated in the eastern part of the Paraná State, southern Brazil. The Group went through a multi-stage metamorphic history, comprising Neoproterozoic regional, dynamic and thermal metamorphism during the Brasiliano Orogeny, and a Cretaceous thermometamorphic event. The metadolomite-related talc deposits of the Itaiacoca Group are responsible for the main Brazilian talc production and constitute the second largest talc reserve. Barbosa (1943) related the genesis of the talc deposits to the thermal effects of the Mesozoic diabase dikes on the metadolomites. Lima and Dardenne (1987) considered that the talc deposits were formed by regional metamorphism and thrust faults, followed by hydrothermalism along transcurrent shear zones. This paper presents a metamorphic framework focused on the Itaiacoca metadolomites, with emphasis on the genesis of its talc deposits.

2 GEOLOGICAL SETTING

The Itaiacoca Group is part of the Proterozoic Ribeira Belt, southern Brazil. The exposure of these basement rocks is particularly large in the Paraná State, as the Phanerozoic Paraná Basin has been eroded due to the up-lift of the Ponta Grossa Arc, during the opening of the South Atlantic. The Itaiacoca Group is composed by volcano-sedimentary low-grade metamorphic rocks, and builds up a narrow NE- to NNE-oriented belt between two granitic batholiths. The NW border of the Itaiacoca Group is defined by the intrusive contact with the Neoproterozoic Cunhaporanga Granitic Complex, while the SE contact of the Itaiacoca Group with the Três Córregos Granitic complex and the medium-grade metamorphic rocks of the Água Clara Formation is defined by the N40E transcurrent Itapirapuã shear zone.

3 METAMORPHIC HISTORY

3.1 Regional metamorphism

During the Neoproterozoic Brasiliano Orogeny, the Itaiacoca Group underwent regional metamorphism

under greenschist conditions (chlorite zone) accompanied by the development of open folds, followed by transcurrent shear zones. Primary structures such as stromatolites, oolites, cross-bedding and parallel layers, and vugs in the metavolcanics, are still partially preserved. Detritic quartz grains in the metadolomite show no evidence of reaction with the surrounding dolomite grains to form talc or tremolite, indicating that the regional metamorphism was of fairly low intensity, and was not responsible for the formation of talc deposits.

3.2 Thermal metamorphism I

The emplacement of the Cunhaporanga Granitic Complex along the NW border of the Itaiacoca Group transformed the grey metadolomites into white granoblastic marbles, bearing forsterite, diopside, tremolite \pm talc \pm calcite, indicating concomitant percolation of silica-rich fluids. The phyllites inside the contact metamorphism aureola contain garnet and andaluzite porphyroblasts, and fibrolite. After the thermometamorphic peak, retrometamorphism partially substituted tremolite by talc, resulting in prismatic and acicular pseudomorphs.

3.3 Dynamic metamorphism

The contact between the Itaiacoca Group and the Três Córregos Granitic Complex is tectonic, lacking evidences of thermal metamorphism. The major talc deposits of the region consist of mylonitic talc-schists, formed along NNE to NE shear zones, parallel to the main shear zone, and subordinately along NNW and NS fault branches. The anastomosed pattern of calcification is self-similar in different scales, consisting of talc in mylonitic foliation surrounding calcite porphyroblasts, lenticular fragments of residual metadolomite and stretched quartz veins, and minor amounts of serpentine or tremolite asbestos.

3.4 Thermal metamorphism II

The Cretaceous diabase dike swarm caused small scale contact metamorphism on the Itaiacoca Group, transforming the originally grey, fine-grained Itaiacoca metadolomite into white granoblastic marble. Metamorphic effects are restricted to few centimetres, with fringes of a fine-grained serpentine-bearing hornfels with a variety of colours (black, violet, brown, green). Fragments of metadolomite surrounded by large volumes of diabase contain brucite, besides chlorite and serpentine pseudomorphs after olivine(?). There is no evidence of calcification related to the diabase dikes, although they protect the talc ore bodies from erosion.

4 PATTERNS OF TALC MINERALIZATION

The following patterns of calcification have been recognized in the Itaiacoca Group:

- talc schists related to transcurrent shear zones, with well developed talc lamellae, with colours varying from white to pink, green, and light- to dark grey. Talc schist bodies have several hundred meters in length, and a few millimeters up to several meters width (Figure 1A). They are mainly concentrated along the eastern border of the Itaiacoca Group, particularly in its southernmost portion. The purest Itaiacoca talc ore belongs to this type;

- films and veins of fine-grained talc along layering planes and fractures in metadolomites not directly affected by shear (Figura 1B). This pattern occurs a few kilometers away from the main shear zones and its dense and irregular fracture nets resembles protocataclastic breccias. Talc was probably formed by fluids from the shear zones;

- irregular pockets of very fine-grained powdery white talc in metadolomites not affected by shear. In this case, transition from metadolomite to talc is gradual, and the original layering is preserved, suggesting a substitution without significant volume change. This type of deposit has no clear relation to shear zones or to igneous intrusions;

- at the contact aureola around the Cunhaporanga granite (Figure 1C), small amounts of talc occur as pseudomorphs after tremolite formed by retrometamorphism.

5 CONCLUSIONS

The complex metamorphic history of the Itaiacoca metadolomites resulted in superimposed mineral assemblages. Among these metamorphic episodes, the most important talc-forming event was the hydrothermal alteration related to the transcurrent shear zones, during which the metadolomites interacted with silica-rich aqueous solutions. Calcite geothermometry indicates peak temperatures around 400-420°C. Smaller amounts of talc occur in fractures resembling protocataclastic breccias further away from the main shear zones, as well as in the thermal aureola along the contact with a granite intrusion; in the latter case, talc is retrometamorphic.

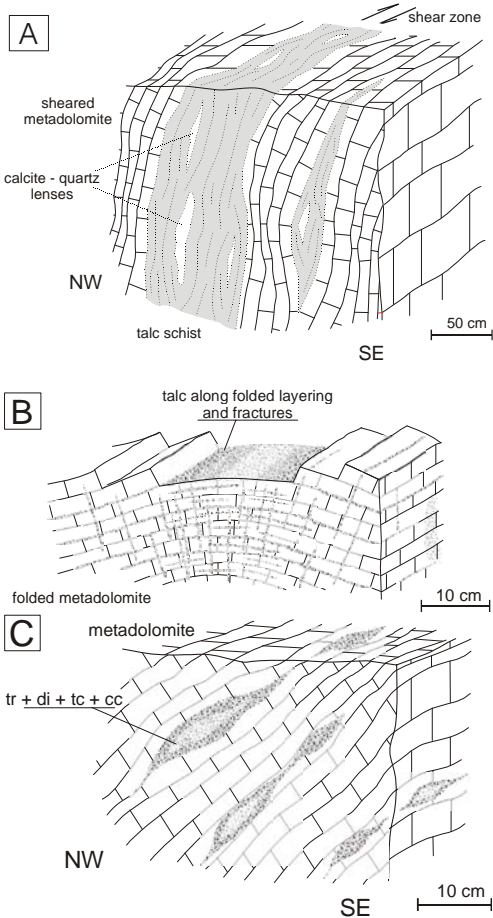


Figure 1. Main talc mineralization styles in the Itaiacoca metadolomites: (a) talc schist in shear zones; (b) weak talcification in open folds and fractures; (c) thermometamorphic aureola in the contact with a granite intrusion (tr=tremolite; di=diopside; tc=talc; cc=calcite).

Besides the talc schists in shear zones, there are deposits of massive fine-grained talc, that replace the metadolomite in a static manner, apparently without significative volume change. This type has a simpler association of metamorphic minerals and seems to have been formed at lower temperatures compared to the talc schist.

Chrysotile and tremolite asbestos represent a restriction to exploitation of talc from the Itaiacoca metadolomites, as asbestos-bearing raw materials have been banned by increasingly severe legislation in various countries, including Brazil. The erratic distribution of these minerals along the mineralized belts is an obstacle to their prediction.

6 REFERENCES

- Barbosa, O., 1943. Pesquisa da jazida de talco de Moura, Distrito de Itaiacoca, Município de Ponta Grossa, Estado do Paraná. (Decreto n^o 13.330, de 13/09/43).
- Lima, R. E., Dardenne, M. A., 1987. Geologia e controle da Mina Grande da Costalco – Itaiacoca (PR). in: Atas III Simp. Sul-Bras. Geol., Curitiba, Soc. Bras. Geol., vol. 2:623-632.
- Lima, R. E., 1993. Evolução geológica e controles dos depósitos de talco da região de Itaiacoca, Abapã, PR. M.Sc. Thesis (unpublished), Univ. Brasília.

Applied Mineralogy Characterization of Construction and Demolition Waste from Brazilian Recycling Plants

C.Ulsen & H.Kahn

Department of Mining and Petroleum Engineering, University of Sao Paulo, Sao Paulo, Brazil

S.C.Angulo & V.M.John

Department of Civil Engineering, School, University of Sao Paulo, Sao Paulo, Brazil

ABSTRACT: Three representative samples of construction and demolition waste recycled as aggregates were taken from two different Brazilian recycling plants. The samples were fractioned by sink-and-float and sieving techniques. The chemical composition, the main mineralogical phases and physical characteristics such as bulk specific gravity of these fractions were determined. The applied mineralogy characterization of CDW from Brazilian recycling plants allows to conclude that the studied recycled aggregates are essentially constituted by silicates and carbonates; hydrated cement-based phases were not detected. They do not differ, in majority, from origin (Itaquera and Vinhedo) or classes (Red and Grey). Phyllosilicates from clays were detected in the size fraction below 0.15 mm. Tectosilicates from natural stones and sand used in construction were found in the heaviest sink product ($d > 2.5 \text{ g/cm}^3$). The binder content is correlated with SiO_2 grades to sink-float products. Mass distributions for sink-float products from individual size fraction indicate distinct behavior due to the liberation of silicates. Physical properties of the attained products indicate that a gravity concentration would allow producing a recycled aggregate for use both in structural concrete as well as in high strength concrete.

1 INTRODUCTION

1.1 Construction and demolition waste management

Several materials such as concrete, mortar, tiles, bricks, soils, plastics, metals, wood, paper, tar compounds, etc. constituted the construction and demolition waste (CDW). In fact, mineral materials represent around 90% (m/m) of the CDW (EC 2000; Ferraz et al. 2001).

CDW represents between 13 and 67% (m/m) of the municipal solid waste (John 2000; Hendriks 2000). In order to reduce environmental and economical impacts of CDW caused by illegal dumping in urban areas, a new management approach has been proposed based on formal CDW collect system and recycling (Pinto 1999; EC 2000).

1.2 CDW recycling

There are several processes to recycle CDW. The mineral materials, the most representative fraction, are recycled using mineral processing applied to mineral raw materials (Angulo et al. 2003). In general, the recycled products are civil construction aggregates mostly used in pavement activities.

However, this use is not sufficient to consume all produced CDW (Hendriks 2000; Angulo et al. 2003).

There is demand to develop other uses such as mortar and concrete aggregates (Angulo et al. 2003). Nevertheless, there is variability in CDW aggregate composition and other physical properties such as bulk specific gravity and water absorption, which interfere in concrete and mortar performances (Angulo 2000).

Only part of CDW recycled aggregate is suitable for use in non-structural concrete. The CDW visual sorting, crushing, and sieving approach is insufficient to produce recycled raw material for use in structural concrete (Angulo et al. 2003). Therefore, fast and reliable characterization techniques must be developed in order to classify CDW according to their possible uses. Furthermore, this variability demands CDW quality control and technological approach to both concrete and mortar applications.

Being so, the purpose of this study is to characterize CDW recycled aggregates from two different Brazilian recycling plants (São Paulo and Vinhedo cities) using the applied mineralogy approach (Sant'Agostino & Kahn 1997).

2 EXPERIMENTAL DESIGN

2.1 Sampling

In the Itaquera recycling plant, recycled CDW mineral waste was visually classified in grey (mostly cement-based construction materials) and red classes (mostly red ceramic construction materials). In the Vinhedo recycling plant, only recycled CDW red class was being produced. These classes of CDW recycled aggregates were sampled after crushing. They were named IR (Itaquera Red), IG (Itaquera Grey), and VR (Vinhedo red).

A 18 dm³ container was collected during each effective hour production for each class during a 20-day period giving almost 2t of each studied recycled CDW. These samples after a homogenization procedure were re-sampled for the applied mineralogical studies (4 containers of 65 kg each).

2.1.1 Crushing and sieving

The CDW recycled aggregate was screening by squared 50 x 50 sieves in the following apertures (mm): 50.8; 38.1; 25.4; 19.1; 12.7; 9.5; 4.8; 2.4; 1.2; 0.6. A dry process was applied to Itaquera samples; Vinhedo recycled CDWs were submitted to a wet process.

The size fractions above 25.4 mm of each recycled CDW sample were submitted to a secondary crushing by a jaw crusher to minus 25.4 mm and then submitted to another size classification by sieve analyses.

Both attained size fractions were submitted to chemical analyses and, since the results were very similar, they were composed for sink-float analyses.

2.2 Heavy media separation

Since the mass balance of the fraction passing in 0.3 mm sieve aperture was not significant, Itaquera and Vinhedo CDW size fractions above 0.3 mm were re-sampled for sequential sink-float separations by heavy liquids with specific gravities of 1.7; 1.9; 2.2; and 2.5 g/cm³. A zinc chloride (ZnCl₂) solution in water was used for the first two specific gravities and bromoform (CHBr₃) with ethylic alcohol for the others. Five products were generated by the sink float separations as follow: 1.7; +1.7-1.9; +1.9-2.2; +2.2-2.5; and +2.5 (g/cm³).

2.3 Chemical analysis

Quantitative chemical analyses were carried out by X-ray fluorescence spectrometry (XRF) in all size fractions and sink-float products for the major oxides - SiO₂, Fe₂O₃, Al₂O₃, CaO, MgO, Na₂O, K₂O, MnO, TiO₂, P₂O₅, SO₃. LOI (loss of ignition at 1050°C) was also determined. Additionally, the

amount of binder (Portland cement, gypsum, and chalk) attached in the aggregate particles from the sink-float products were evaluated by HCl 20% acid leaching assay.

2.4 Mineralogical analysis

Each specific gravity fraction from sink-float separations was submitted to a qualitative mineralogical analysis by X-ray diffraction (XRD) in a Philips MPD 1880 powder diffractometer with of CuK α radiation.

The definition of which size fractions were chosen for mineralogical analyses was based on their macroscopic observations and chemical analyses data.

2.5 Bulk specific gravity and water absorption

The sink-float products from the size fractions above 4.8 mm were submitted to a bulk specific gravity and water absorption analyses according to ASTM C 127-93. These assays are standard tests to evaluate the physical properties of aggregate material used in civil engineering.

3 DISCUSSION

As mentioned before, no substantial distinction was observed in terms of chemical composition between the size fractions from the initial size analyses and the material from secondary crushing (+25.4 mm).

SiO₂ (64-72%), Al₂O₃ (7-12%) and CaO (5-12%) are the major oxides for size fractions above 4.8 mm. The fine fractions (-4.8+0.15 mm) shows a slightly increase on SiO₂ content (63-85%) while the -0.15 mm fractions presents a substantial increase on the amounts of Al₂O₃, CaO and LOI.

In fact, SiO₂ grades show an inverse linear correlation with CaO plus Al₂O₃ as illustrated in Figure 1. These two oxides present also a direct correlation with LOI (Fig. 2).

Silicates and carbonates are the major minerals present in the studied recycled CDWs. Phyllosilicates, such as kaolinite, muscovite-biotite and other soil related minerals, are more significant in -0.15 mm size fractions, suggesting some soil incorporation in the recycled CDW samples.

The SiO₂ and CaO+Al₂O₃ correlation is also observed for the sink-float products. However, the heaviest fractions, which are essentially constituted by tectosilicates (quartz, microcline and albite from natural stone, gravel, and sand), present a distinct correlation from the lighter ones, which present larger amount of phyllosilicates related to clays/ceramics and carbonates from the binders.

The binder content is related to SiO₂ grades for the sink-float products (Fig. 3).

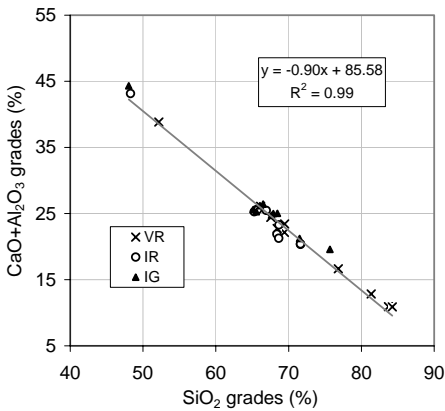


Figure 1. Correlation between SiO₂ and CaO+Al₂O₃ grades.

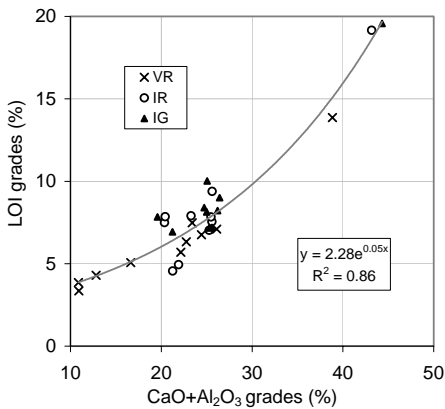


Figure 2. Correlation between CaO+Al₂O₃ and loss of ignition grades.

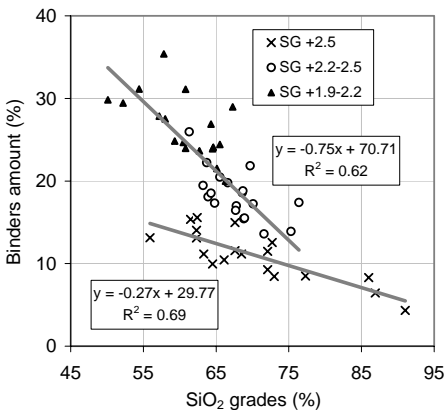


Figure 3. Correlation between SiO₂ grades and binder amount.

The heavier the sink-float products are the higher the SiO₂ grade is (Figure 4) and lower the LOI (Figure 5), which content is also related to the binders presence that, in some cases, can be represented by the sum of CaO+Al₂O₃.

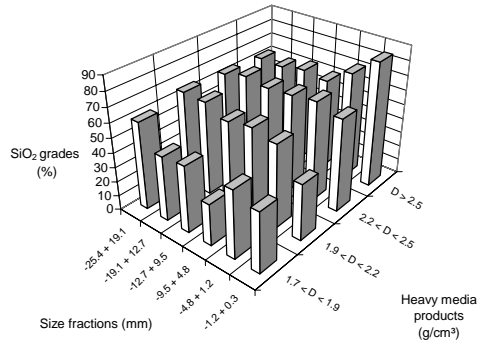


Figure 4. SiO₂ behavior in the sink-float separations for distinct size fractions – Itaquera grey recycled CDW.

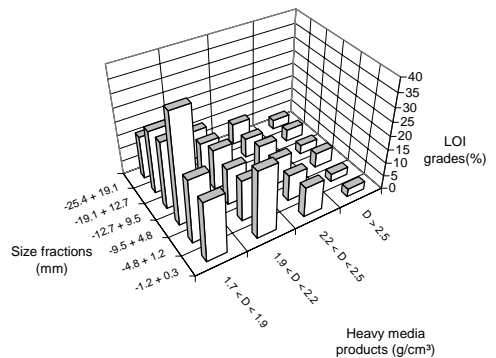


Figure 5. LOI behavior in the sink-float separations for distinct size fractions – Itaquera grey recycled CDW.

Mass distributions for sink-float products from individual size fraction indicate distinct behavior that gradually changes from the coarsest to the fines fractions which are essentially correlated with mineral liberation and indicate that the material above 12.7 mm is not proper liberated (Fig. 7).

Analyzing the specifications of recycled coarse aggregate for concrete (Rilem Recommendation 1994), the sink-float products with specific gravity above 2.3 g/cm³, equivalent to more than 70% (w/w), would present physical qualities to be used in structural concrete which market is essentially dominated by conventional natural aggregates.

The specific gravity product fractions above 1,9 g/cm³ present potential use since no deleterious contaminants (no mineral materials) are present.

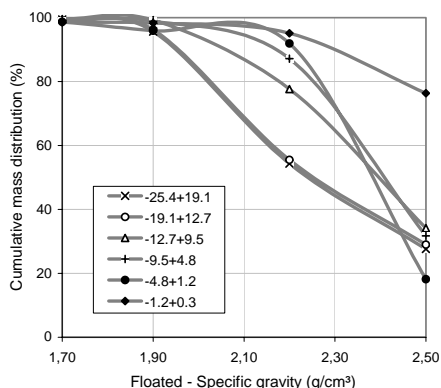


Figure 6. Specific gravity floated separability curves for Itaquera red recycled CDW.

Based on physical properties of the attained products (Fig. 7) a size classification followed by gravity concentration would allow producing an aggregate for use in structural concrete as well as high strength concretes.

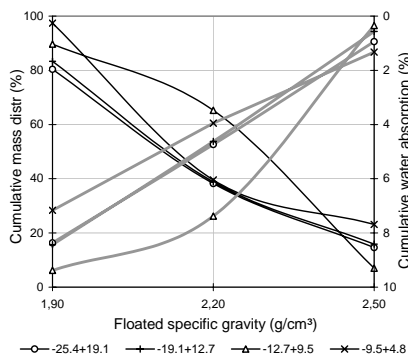


Figure 7. Specific gravity separability curves and water absorption for Vinhedo red recycled CDW.

4 CONCLUSIONS

The studied CDW recycled aggregates are essentially constituted by silicates and carbonates including hydrated cement-based phases non-detected by XRD. They do not differ, in majority, from origin (Itaquera and Vinhedo) or classes (red and grey). Phyllosilicates content is more relevant in the size fraction below 0.15 mm suggesting some soil incorporation. Both the size fractions and sink-float products present a linear correlation between SiO_2 grades and $\text{CaO}+\text{Al}_2\text{O}_3$, which are also correlated with the loss of ignition.

In the sink-float separations the tectosilicates (quartz, microcline and albite) from natural stones,

gravel and sand used in construction were in the heaviest specific gravity product ($d>2.5 \text{ g/cm}^3$); other products are constituted by a mixture of silicates and carbonates.

Mass distributions for sink-float products from individual size fraction indicate distinct behavior that gradually changes from the coarsest to the fines fractions indicate that the material above 12.7 mm is not proper liberated.

The binder content varies according to specific gravity of the sink-float products and is also correlated with SiO_2 and LOI grades.

Physical properties of the attained products indicate that a gravity concentration would allow producing a recycled aggregate for use both in structural concrete as well as high strength concrete, uses that cannot be even considered based on the conventional technological currently applied in Brazil for CDW recycling.

5 ACKNOWLEDGEMENTS

We would like to thank FINEP (Fundo Verde e Amarelo), CNPq, and FAPESP for their support to this research.

6 REFERENCES

- Angulo, S. C. 2000. Variabilidade de agregados graúdos de resíduos de construção e demolição reciclados. M. Eng. Dissertation. University of São Paulo. 155p.
- Angulo, S. C.; John, V.M.; Kahn, H. & Ulsen, C. 2003. Characterisation and recyclability of construction and demolition waste in Brazil. In: Fifth international conference on the environmental and technical implications with alternative materials. Spain. ISBN 84-95520-00-1. p.209-218.
- European Commission. 2000. Management of construction and demolition waste http://europa.eu.int/comm/enterprise/environment/index_home/waste_management/constr_dem_waste_000404.pdf accessed in 09/2002.
- Ferraz, G. R. et al. 2001. Estações de classificação e transbordo na cidade de São Paulo. In: IV Seminário de Desenvolvimento sustentável e a reciclagem na construção civil. Brazil.
- Hendriks, C. F. 2000. The building cycle. Aeneas, Netherlands. 231 p.
- John, V. M. 2000. Reciclagem de resíduos na construção civil – contribuição à metodologia de pesquisa e desenvolvimento. Associate Professor Thesis. University of São Paulo. 102p.
- Pinto, T. P. 1999. Metodologia para a gestão diferenciada de resíduos sólidos da construção urbana. Ph.D.Thesis. University of Sao Paulo. 189 p.
- Sant'Agostinho, L. M & Kahn, H. 1997. Metodologia para Caracterização Tecnológica de Matérias Primas Mineralas. Report – Escola Politécnica, University of São Paulo. 29p.
- Rilem Recommendation. 1994. Specification for concrete with recycled aggregates. *Materials and Structures*. n.27, p.557-9.

Mineral Exploration

Shear Zone Gold Deposits from Santa Catarina and Paraná States, Southern Brazil

J.C.Biondi

Paraná Federal University, Geology Department. C.P. 19.001, 81.531-990 - Curitiba-Brazil

N.D.Franke, P.R.S.Carvalho & S.N.Villanova

Gold Standard Minas S.A., Rua Tibagi 294, s. 1003/1004, 80.060-110 – Curitiba-Brazil

ABSTRACT: Four Shear zone Gold deposits from the states of Paraná (PR) and Santa Catarina (SC) are of the same Brazilian orogeny age (550 – 500 My). They characterize two different deposit types generated in similar geological environments but distinct ore bodies geometry and ores paragenesis. The Tabiporã (PR), Cavalo Branco, and Cristalino (SC) quartz veins fill secondary synthetic shear faults and are hosted by granitic intrusions. At the Tabiporã (PR) mine and Cavalo Branco (SC) deposits the ore bodies are filling thrust-shear faults. Their quartz veins are strongly deformed, what is not observed at the Cristalino (SC) veins. The Schramm mine (SC) is a bonanza-type gold deposit with carbonate pipe-like oreshoots that fill tensional fractures hosted by ultrabasic granulites. Tabiporã, Cavalo Branco and Cristalino have similar ores and hydrothermal paragenesis that contrast with Schramm deposit. The characteristics of these deposits seem to be conditioned by hosting rocks and structures. In southern Brazil, conventional orogenic gold deposits are inside shear zones and hosted by granitic rocks and pelitic schists, while the non conventional deposit is hosted by basic-ultrabasic rocks with ore bodies filling tensional fractures.

1 TABIPORÃ MINE (PR)

The Tabiporã (PR) ore body averages 9g Au/ton. It is hosted by Passa Três granite, in N60°-70°W shear zones related to the N45°-60°E Lancinha mega-shear system (Fig. 1).

The vein has a listric shape (Fig. 1B), with plunge changing gradationally from 60-70° SW on surface, to 15-20° SW 180 m below. The vein aspect, its discontinuities and sigmoidal shape of vein segments suggest that the ore body is hosted by a thrust, low to high angle shear zone.

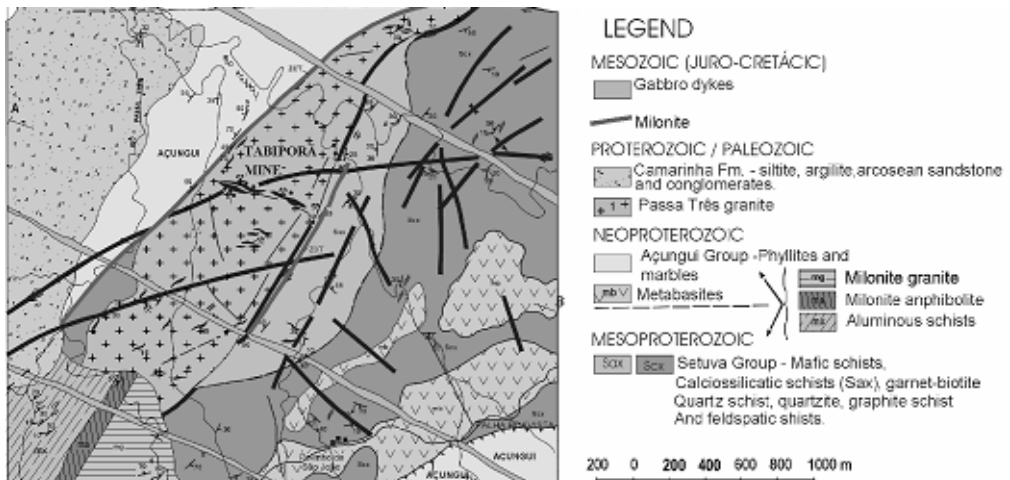


Figure 1 –Regional geology (Piekarz, 1992) of the Tabiporã Mine region.

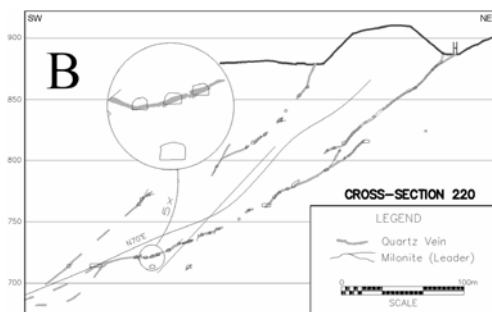


Figure 2 – Tabiporã Mine –Cross-Section - 220 (Gottardi Neto, 2004).

Passa Três is a quartz-amphibole syenitic intrusion that initially had a bulk microcline + biotite (potassic) and fluorite alteration and, latter, was hydrothermally altered to sericite, chlorite, pyrite, biotite and carbonates, with minor magnetite, hematite, pyrite, and chalcopyrite.

Gold, without silver, occurs free or inside pyrite in carbonate-fluorite-adularia quartz veins, with low quantities of chalcopyrite, chalcocite, digenite, bornite, and bismuth sulfosalts. Granite's muscovite were dated 604 Ma (K/Ar), hydrothermal sericite 528 ± 10 Ma (K/Ar), and pyrite lixiviates 510 ± 13 Ma (Rb-Sr).

2 SCHRAMM MINE (SC)

The Schramm Mine ore assays 300 to 2,500 ppm of gold and 150 to 300 ppm of silver. It is hosted by an almost vertical $N75^{\circ}-85^{\circ}E$ tensional fracture (Fig. 3B, Biondi et al. 1992) related to an $N5^{\circ}-15^{\circ}E$ shear zone that belongs to the $N60^{\circ}-70^{\circ}E$ Itajaí shear system (Fig. 3A).

Gold occurs, free or inside sulfides, mainly in siderites and ankerites of hydrothermal, neither sheared nor deformed, quartz-carbonate pipes (Fig. 3C) hosted by 2,8 Ga granulites and magnetic gneisses, which show carbonate, chlorite, sericite, and silica alteration.

The ore contains lamellar hematite, magnetite, sphalerite, pyrite, chalcopyrite, arsenopyrite, gersdorffite, millerite, siegenite, Bi-rich galena, pyrrhotite and cosalite (Biondi et al. 2001). Mineralization postdates the last thermo-tectonic event that affected the area, 594 ± 5 Ma ago (U-Pb in zircon).

3 CAVALO BRANCO DEPOSITS (SC)

The Cavalo Branco deposit ore bodies is a strongly boudinated and sigmoidal-segmented quartz vein (Fig. 4B), with gold averaging 10 to 20 ppm. Gold is found free on quartz or inside pyrite microfractures.

Veins are dipping $40-70^{\circ}S$, filling synthetic shear and thrust faults related to $N70^{\circ}-80^{\circ}E$ shear zones developed along the contact of Brusque Group metapelites with amphibole-rich diorite intrusions dated 610-580 Ma. Shear belong to the Itajaí shear system. The quartz vein is hosted by a small, syntectonic, biotite-hornblende diorite intrusion that was strongly hydrothermally altered (Fig. 4A).

The Cavalo Branco deposit ore body is in the center of a hydrothermal zone. The earliest hydrothermal alteration was sericitization and pervasive Na metassomatism that resulted in crystallization of albite on igneous K-feldspar and plagioclase. Hydrothermal albite forms a rim around sericitized K-feldspar and plagioclase. The hydrothermalism gradually turned from sodic to silico-potassic. Silico-potassic alteration is characterized by crystallization of plagioclase followed by microcline and quartz. Igneous hornblende and biotite are partially replaced by green biotite. Muscovite replaces sericitized feldspars and also crystallizes in the matrix, between quartz and feldspar crystals. Pyritization occurs locally.

Propylitic and sericitic alteration zones are overlapped. Hornblende is totally replaced by biotite, chlorite and epidote and early biotite is replaced by chlorite and muscovite. Quartz, chlorite and sericite crystallize forming polycrystalline zones and veins with diffuse contacts. Bicolor tourmalines occurs locally. Toward the shear zone carbonation increase and pyrite and gold crystallize next to very few chalcopyrite and sphalerite.

4 CRISTALINO DEPOSIT (SC)

The Cristalino deposit ore shoots are made of a swarm of quartz veins with gold also averaging 10 to 20 ppm. Gold is found free on quartz or inside pyrite and chalcopyrite microfractures. Veins are vertical, filling synthetic shear faults related to $N80^{\circ}-85^{\circ}E$ shear zone developed along the contact of a Ti-rich granite dyke and Proterozoic pelitic schist of the Brusque Group. All rocks were strongly sheared and hydrothermally altered, but individually, quartz veins are structurally better preserved than in Cavalo Branco. Hydrothermal alterations on both deposits were similar. Some differences, as the greater presence of chlorite at Cavalo Branco, are consequence of the host rock compositions, more basic at Cavalo Branco than at Cristalino. The ore paragenesis at Cristalino includes, beside pyrite, minor chalcopyrite, sphalerite, and galena. Scheelite and barite occur locally.

After the Cavalo Branco and Cristalino quartz vein emplacement, shear zones and granitic magmatism were reactivated and the deposits were crossed by several granite veins. These intrusions

thermally recrystallized the ore bodies, host rocks and primary hydrothermal paragenesis, as well as restarted the hydrothermal systems (Fig. 4A). More at Cristalino deposit than at Cavalo Branco, the hydrothermal reactivation and thermo-metamorphism caused important changes on hydrothermal paragenesis. The hydrothermal zones received silicic, sodic, and potassic fluids that

crystallized microcline, plagioclase, meso and antiperthitic intergrowths and biotite, followed by a strong silicification. This new hydrothermal phase was developed equally over the granite and the Brusque schists.

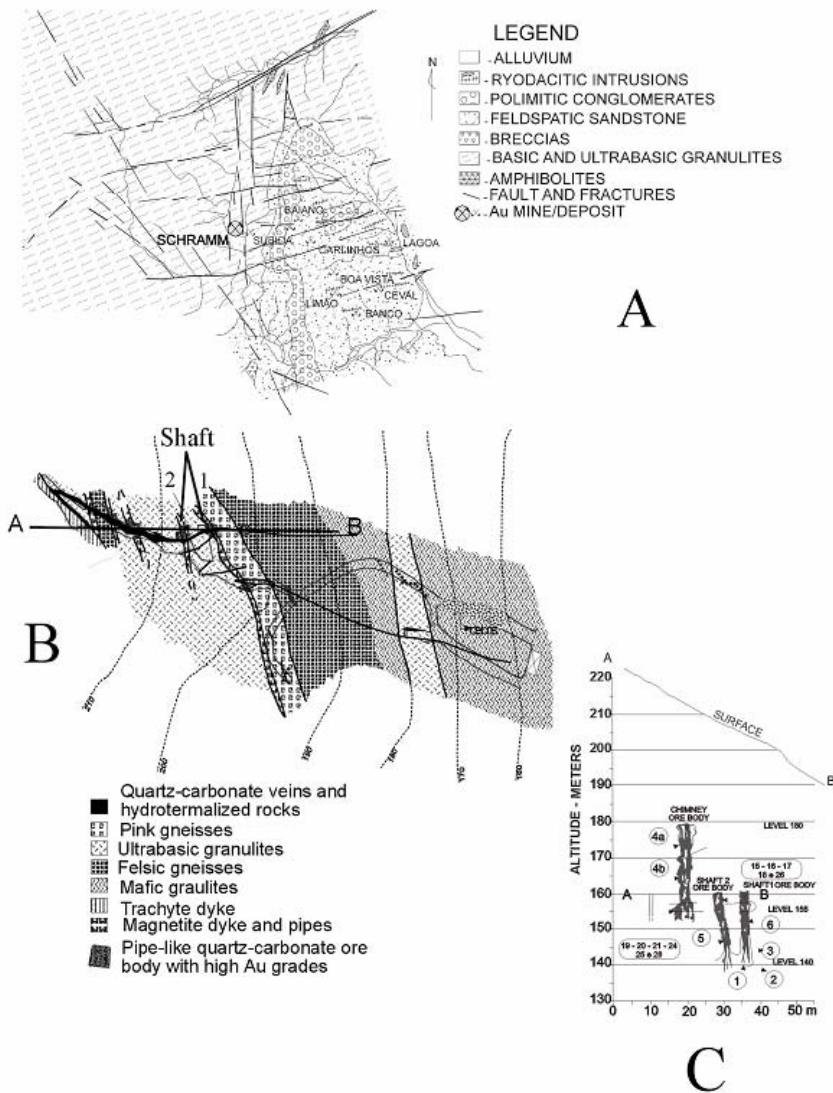


Figure 3: A: Location of the Schramm Mine on shear zone bordering the Itajai Basin (SC-Brazil). B: Level 155 geological map. C: Section across pipe-like ore bodies.

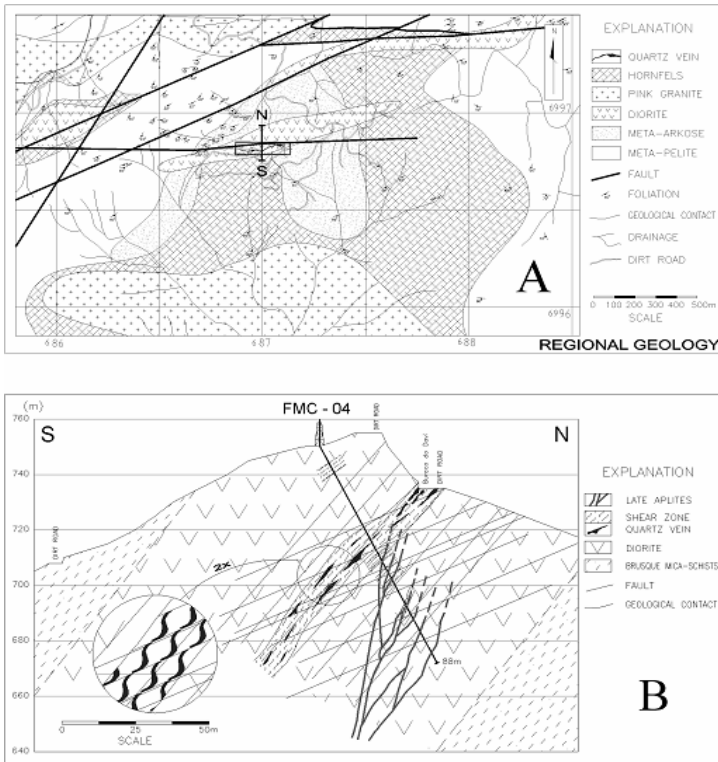


Figure 4: Geology of Cavalo Branco gold deposit. (A) Preliminary regional geological map. (B) Schematic section crossing Cavalo ore body, based on surface geology and the description of drill holes samples.

5 CONCLUSIONS

The four deposits studied are of gold and genetically related to the same thermo-tectonic event comprising two different types. Cavalo Branco, hosted by diorite, has a main quartz vein strongly boudinated and sigmoidal-segmented. Although bigger than Cavalo Branco and hosted by quartz-amphibole syenite, the two quartz veins of Tabiporã Mine are morphologically equal to Cavalo Branco. Both deposits are in low to medium angle plunging thrust faults that were reactivated after the ore emplacements. Cristalino comprises a vertical quartz vein swarm also emplaced in a shear zone. Veins are less deformed than at Cavalo Branco and Tabiporã. The gold grades (10-20 g/ton, without Ag), the ore paragenesis (quartz veins with a great quantity of pyrite and few chalcopyrite, galena and sphalerite), the hydrothermal paragenesis (predominance of quartz, feldspars and mica and low grades of biotite, chlorite and epidote) and the host rocks (always granitic) of Cavalo Branco, Cristalino and Tabiporã are similar. The Schramm's ore bodies are non deformed tensional fracture filling shoots, hosted by ultrabasic-magnetitic rocks. Their ore grades, composition and paragenesis are totally different

from the previous ones. The characteristics of mineralizations seem to be conditioned by host rocks and by hosting structures. In southern Brazil, conventional orogenic gold deposits are in shear zones affecting aluminous granitic rocks and pelitic schists, while the non conventional deposit is hosted by basic-ultrabasic rocks and their ore bodies fill tensional fractures.

6 REFERENCES

- Biondi J.C.; Franke N.D.; Carvalho, P.R.S.; Villanova S.N. 2001. Geologia e petrologia da mina de ouro Schramm (Gaspar - SC). *Revista Brasileira de Geociências*, 31(3):287-298.
- Biondi J.C.; Schicker G.; Bugalho A. 1992. Ore genesis in tardi-orogenic basins - 1. Rigid structures influence on the genesis of MINEPAR (Au) and Ribeirão da Prata (Pb-Zn-Cu) deposits, Itajaí Group (SC, Brazil). *Revista Brasileira de Geociências*, 22(3):275-289.
- Gottardi Neto A. 2004 - Geology of Tabiporã gold Mine (PR). Unpublished Internal Report, Tabiporã Mine, 12p.
- Piekarcz G.F. 1992. O Granito Passa Três - PR e as mineralizações auríferas associadas. *Tese de Mestrado*, UNICAMP, 221 p.

Characterizing Hydrothermal Alteration Minerals at Los Menucos, Patagonia Argentina, Using Reflectance Spectroscopy

D.F.Ducart, A.P.Crósta, C.R.Souza Filho & R.S.Angélica
Geosciences Institute, University of Campinas, Campinas, Brazil

ABSTRACT: Reflectance spectra from hydrothermal altered rocks were measured with a portable Pima radiometer in order to produce a detailed map of the alteration present in the gold-silver prospect of Cerro La Mina, Patagonia Argentina. Alteration minerals such as kaolinite, dickite, alunite, illite and quartz were identified by means rock spectra interpretation, revealing the following alteration haloes: advanced argillic, argillic and silicification. This pattern is characteristic of a high-sulphidation epithermal system. Furthermore, spectra of kaolinite were analyzed aiming to determine the relative crystallinity degree of the samples. A crystallinity index 'Ck' was developed, based on the morphological variations of the spectral curves in the range from 2.162 to 2.182 μm . The results reveal that kaolinites with high crystallinity are located in the northeast sector of the prospect and may be associated with higher paleo-temperatures of alteration fluids that originated them. These results are confirmed by X-ray diffraction and demonstrate the potential of reflectance spectroscopy as an unexpensive and fast technique for hydrothermal alteration mapping in mineral exploration activities.

1 INTRODUCTION

The mineral district of Los Menucos is located in Patagonia, Argentina, and it has been a goal of recent exploration activities for gold-silver deposits associated with quartz veins and hydrothermal alteration breccias. Extensive alteration zones at surface are indicators of this type of mineralization in the district and constitute important targets for mineral exploration using remote sensing data (Crósta et al. 2003). However, the mineralogy, spatial location and distribution of these zones are yet insufficiently understood. Detailed knowledge of alteration assemblages is important in providing information about mineralizing processes.

Portable spectro-radiometers are an effective tool for fast identification of alteration minerals and their variations in terms of their chemical composition and degree of crystallinity (Thompson et al. 1999). These instruments are adequate for analyzing clays, phyllosilicates, sulphates and carbonates, due to active inter-atomic bonds of ions and molecules that form these minerals in the shortwave infrared (SWIR) region of the electromagnetic spectrum (Hunt & Ashley 1979). In general, variations in crystallinity are reflected by variations in the shape and intensity of diagnostic absorption features. The

high degree of crystallinity of these minerals may indicate higher temperatures, which are typical of the regions nearer the paleoconducts of hydrothermal fluids. Hence, the degree of crystallinity can be used to delineating the paleo-isotherms of the forming fluids, thus defining the vectors towards possible ore-bearing zones, an useful information in mineral exploration (Kruse & Hauff 1991, Huston et al. 1999).

In this study, we report on the results of a spectral characterization of the alteration mineralogy of Cerro La Mina prospect, in the Los Menucos district, Patagonia Argentina.

2 GEOLOGICAL BACKGROUND

The Cerro La Mina prospect is part of the mineral district of Los Menucos, located in the Somún Curá Massif. This prospect consists of near horizontal sequences of ignimbrites and rhyolites, which are collectively comprised in the Neo-Triassic Los Menucos Group (Labudía et al. 2001). These rocks host NE-SW-trending hydrothermal breccias containing gold-silver mineralization, with grades ranging from 0.7 to 11 g/t. In association with this

mineralization, there is an intense and widespread hydrothermal alteration, covering near 27 km².

3 DATA AND METHODS

Near 1100 reflectance spectra were measured using the PIMA and FieldSpec-FR instruments. The samples were collected at the surface and the objective was to identify the alteration mineralogy. Sampling was conducted along a regular grid, with sample points spaced of 50m and grid lines spaced of 200m. Mineral identification was based on wavelength, intensity and shape of the main absorption features (Clark et al. 1990), in comparison with reference spectra from the USGS digital spectral library. The analysis was carried out using the SIMIS FeatureSearch 1.6 software. Spectral identification results were spatially interpolated and displayed as an alteration map, thus showing the spatial distribution of these minerals.

Besides mineral identification, quantitative analysis of spectra derived from samples containing mostly kaolinite was carried out, aiming to determine their relative degree of crystallinity. This analysis was based on the application of a crystallinity index. The index, coined 'Ck', is a revised version of the 'Kx' index proposed by Pontual et al. (1997), based on the 2.160-2180µm slope parameters $Kx = [2.180slope - (2.160slope - 2.180slope)]$. The Ck index considers essentially the ratio between the absorption features located at 2.162 µm and 2,182 µm in the kaolinite spectra. The Ck index decreases in value with increasing kaolinite crystallinity (Fig. 1).

The results of spectral analysis were supported by X-ray diffraction (XRD). They were carried out using a Philips PW 3020 goniometer, under the following conditions: CuKα-radiation, operating at 45kv and 40 mA; continuous scan from 5° to 65° 2θ; 0.02 step-size and time per step of 0.5s. Rock powders were packed into aluminum mount holders with back loading filling.

4 RESULTS

Spectral analysis allowed the identification of the following alteration minerals: kaolinite, dickite, alunite, illite and quartz (Fig. 2).

Kaolinite and dickite are widely distributed around the Cerro La Mina prospect (Fig. 3). Kaolinite predominates in the east-northeastern sector, and it is mixed with dickite towards the central sector. In the west-southwestern sector, kaolinite occurs intercalated with dickite.

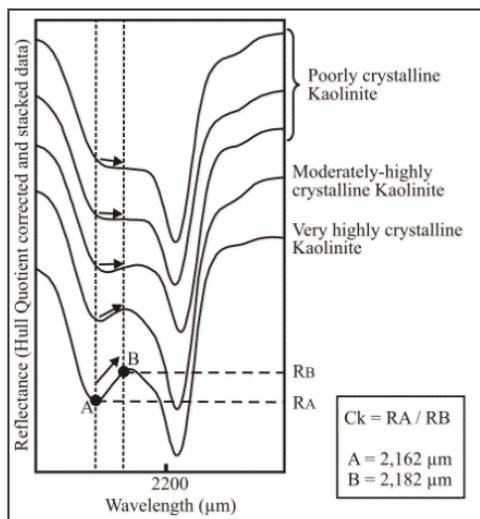


Figure 1. Double absorption features (doublets) at 2.2 µm in kaolinite spectra, showing the variation in morphology of the curves with increasing crystallinity (modified from Pontual et al. 1997). The Ck index used in this work is calculated from the ratio of the reflectance values RA and RB, measured at points A (2.162 µm) and B (2.182 µm), respectively.

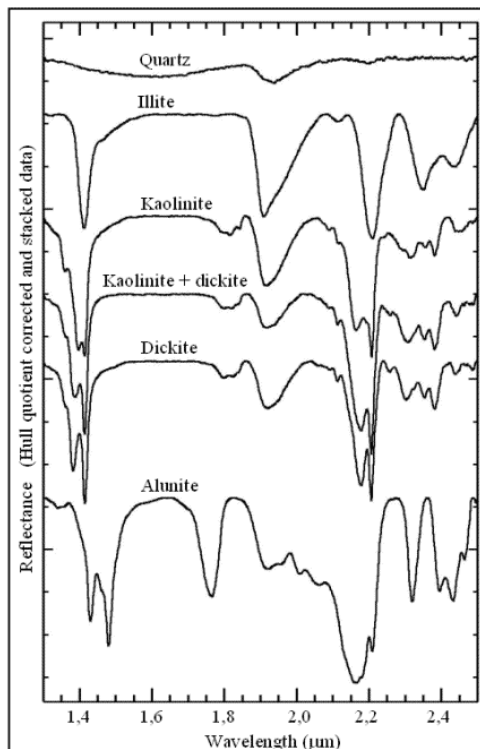


Figure 2. Reflectance spectra of the main minerals identified in Cerro La Mina.

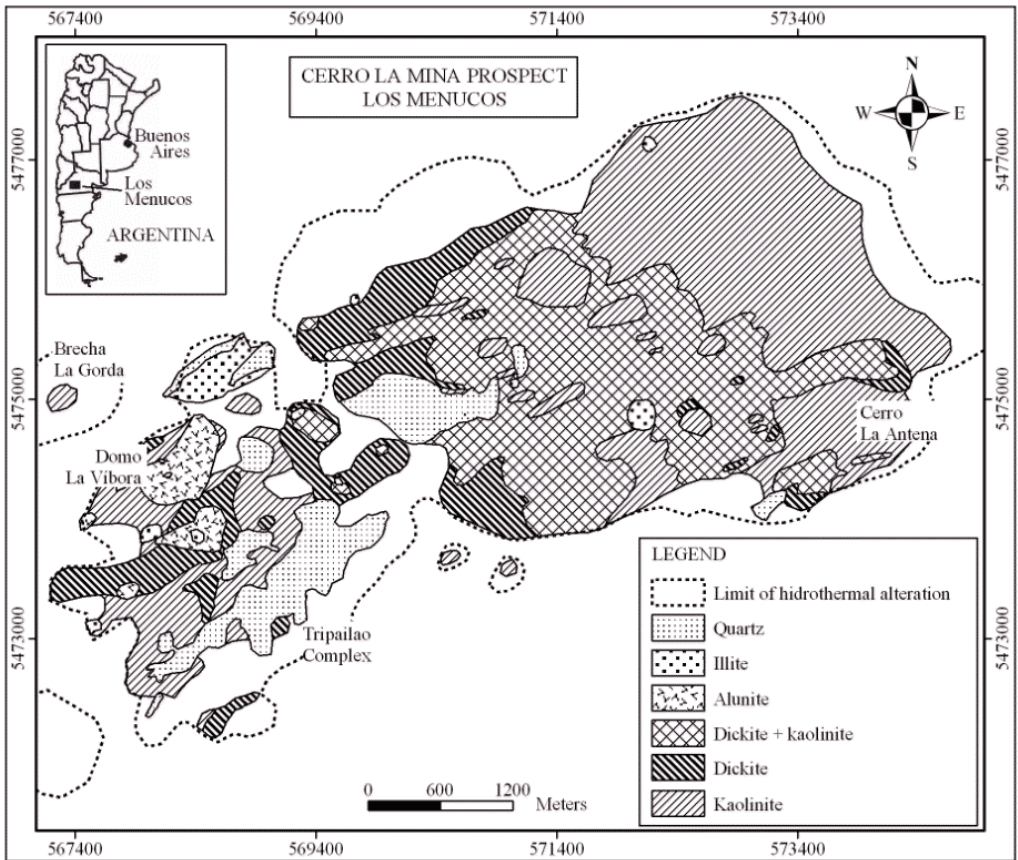


Figure 3: Hydrothermal alteration map of Cerro La Mina prospect based on reflectance spectroscopy.

Distinction between kaolinite and dickite is possible due to differences in their twofold absorption features ('doublet') located at 1.4 μm (OH, H₂O) and 2.2 μm (Al-OH). In contrast, these two minerals are almost undistinguishable in the XRD results.

A zone with intensely silicified rocks was recognized in the area of the Tripailao Complex, in the south-western sector of the prospect. Reflectance spectra of quartz usually lack in diagnostic absorption features. Occasionally, they may show features at 1.4 μm and 1.9 μm due to the presence of water-rich fluid inclusions. The XRD results showed high quartz contents in the samples from Tripailao.

Alunite occurs in the north-western sector of the prospect, at the Domo La Vibora. This mineral is identified on the basis of two absorption features at 1.400 μm (OH-) and 2.178 μm (Al-OH). Diagnostic peaks of alunite in the XRD diffratograms show low intensity, whereas the reflectance spectra of the same samples clearly indicate the presence of such mineral.

Illite occurs in restricted areas of the western and north-western sectors of Cerro La Mina.

The alteration pattern defined by zones of advance argillic alteration (containing quartz + alunite + dickite + kaolinite), intense silicification (quartz) and argillic alteration (dickite, dickite + kaolinite, kaolinite and illite), is characteristic of high-sulphidation epithermal systems (Arribas 1995).

The results of the quantitative analysis of the kaolinite spectra, employing the *Ck* index, showed higher crystallinity degrees in the northeastern sectors, which can be tentatively associated to hydrothermal fluids with higher paleo-temperatures. Further studies will be carried out aiming to gain more information on the physical-chemical characteristics of these fluids and to test the results provided by spectral analysis.

5 CONCLUSIONS

Qualitative analysis of field reflectance spectroscopy data of the Cerro La Mina prospect allowed a detailed description of the main alteration minerals and their corresponding areas of occurrence. Alteration of the advanced argillic type was recognized in the southwestern sector, silicification in the central-southern and argillic in the central and north-eastern sectors. The advanced argillic zone is the main exploration target for gold-silver mineralization in the prospect.

Quantitative analysis applied to reflectance spectra of kaolinite resulted in useful information about the degree of crystallinity of this key clay mineral. Systematic analysis of the crystallinity of kaolinite may be used in exploration to determine relative paleo-temperatures of hydrothermal alteration fluids, thus indicating the likely location of primary conduits. In high-sulphidation epithermal systems, these conduits show a spatial association to higher grade gold-bearing ores.

This paper is a new assessment on the use of reflectance spectroscopy as a tool for mineral exploration. The results reported here further attest its capabilities as a swift, low cost and effective technique to identify minerals associated with hydrothermal alteration processes (usually fine grained), as well as to aid the detection of subtle changes in mineral crystallinity.

6 ACKNOWLEDGEMENTS

The authors would like to thank Francisco Azevedo and Colin Brodie (IAMGOLD Argentina) for field support, discussions and overall assistance. A. P. Crósta and C.R. Souza Filho were supported by research grants from FAPESP and CNPq, Brazil. The Geosciences Institute of the Federal University of Para, Brazil, is acknowledged for allowing access to XRD facilities.

7 REFERENCES

- Arribas A. 1995. Characteristics of high sulfidation epithermal deposits and their relation to magmatic fluid. In: Magmas, fluids and ore deposits of C., MDRU-UBC, 23: 419-455.
- Clark R.N., King T.V.V., Klejwa M., Swayze G.A., Vergo N. 1990. High spectral resolution reflectance spectroscopy of minerals. *J. Geophys. Res.*, 95, No. B-8, 12653-12680.
- Crósta A.P., Souza Filho C.R., Azevedo F., Brodie C. 2003b. Targeting key alteration minerals in epithermal deposits in Patagonia, Argentina, using ASTER imagery and principal component analysis. *International Journal of Remote Sensing*, 24 (21): 4233-4240.
- Hunt G.R. & Ashley R.P. 1979. Spectra of altered rocks in the visible and near infrared. *Economic Geology*, 74: 1613-1629.

- Huston D.L., Kamprad J., Brauhart C. 1999. Definition of high-temperature alteration zones with PIMA: An example from the Panorama VHMS district, central Pilbara Craton. In: Australian Geological Survey Organisation Research Newsletter, 30: 10-12.
- Kruse F.A. & Hauff P.L. 1991. Identification of illite polytype zoning in disseminated gold deposits using reflectance spectroscopy and X-ray diffraction—potential for mapping with imaging spectrometers. *IEEE Transactions on Geoscience and Remote Sensing*, 29: 1101-1104.
- Pontual S., Merry N.J., Gamson P. 1997. Practical Applications Handbook, Vol. 1-8, GMEX spectral analysis guides for mineral exploration. Ausspec International Publications.
- Thompson A.J.B., Hauff P.L., Robitaille A.J. 1999. Alteration mapping in exploration: application of short-wave infrared (SWIR) spectroscopy, *SEG Newsletter*, 39:16-27.

Contrasting Mineral Deposit Styles from Peixoto de Azevedo Region, Mato Grosso, Brazil

N.D.Franke, P.R.S.Carvalho & S.N.Villanova

Gold Standard Minas S.A., Rua Tibagi 294, s. 1003/1004, 80.060-110 – Curitiba-Brazil

J.C.Biondi

Paraná Federal University, Geology Department. C.P. 19.001, 81.531-990 - Curitiba-Brazil

ABSTRACT: Peixoto de Azevedo region exhibits a variety of small deposits and occurrences that are distinguished by their paragenesis. Pombo is a copper-gold sulfide deposit hosted by an hydrothermalized granite, different from Cerro Azul, where ore is a hydrothermalized pyroxenite mineralized with hematite, magnetite, sphalerite, galena, chalcopyrite, argentite, pyrite, and gold, that occurs crystallized on rock mesostase or inside chalcopyrite and/or sphalerite. The Guido area has a pyroxenite float with clinoenstatite, labradorite-bitownite, pyrrhotite, pentlandite, sperrylite-platarsite, magnetite, and goethite.

1 INTRODUCTION

Alta Floresta is the southern domain of the Tapajós-Parima orogenic belt, which crosses the Amazon Craton, extending SE-NW from Peixoto de Azevedo town (MT) up to the Parima domain, in Venezuela (Santos et al. 2001). Many gold and gold-copper epigenetic vein and disseminated/stockwork intrusion related and mesothermal orogenic deposits are known in this belt (Juliani et al. 2002). The Pombo area, that is located around 60 km SE of the Peixoto de Azevedo town (Fig.1), exhibits a variety of small deposits (Pombo, Guido and Cerro Azul) that are distinguished by their contrasting rocks and ore paragenesis.

2 ORE PARAGENESIS

2.1 The Pombo deposit

The Pombo pluton is a 180 km² oval shaped magnetite-hornblende-biotite granodiorite porphyry intrusion. It is intruded by many hornblende-diorite, basalt, and rhyodacite stocks and dykes. Regionally it is hydrothermally albitized and sericitized, with minor potassic, silicic,

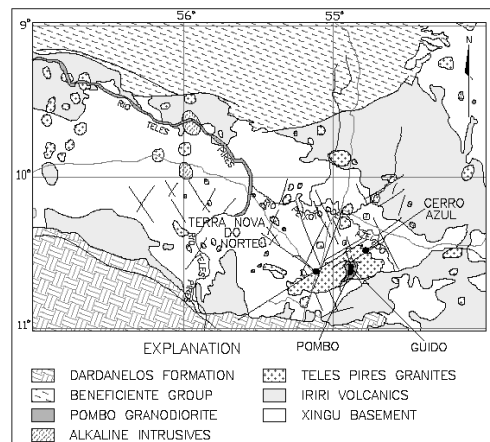


Figure 1 – Geological map of Alta Floresta area (Modified from RADAM-BRASIL 1980).

chloritic alterations, and localized disseminations of pyrite. K-feldspars are perthitic to mesoperthitic and frequently partially inverted to microcline. Oligoclase and K-feldspars cores are sericitized and rimed by exsolved albite.

The Pombo deposit, located inside de Pombo pluton, was developed along a N50⁰-60⁰E shear/fault

structure with known length exceeding 3,0 km. The deposit is a vein and stockworks with gold and copper whose ore zones assay 0,5-37 g Au/ton and 0,1-3,2% Cu. Ore shoots gangue are made of quartz and muscovite and the ore has gold, abundant anhedral and euhedral pyrite, chalcopyrite, and minor sphalerite. Gold, anhedral pyrite and chalcopyrite crystallized on a first hydrothermal phase. Remobilised gold, euhedral pyrite, digenite, chalcocite, bornite, covellite, and sooty chalcocite crystallized on a second phase, on cementation zones of supergenic environments (Fig.2).

The Pombo ore deposit body is in the center of a hydrothermal zone. The earliest hydrothermal alteration was sericitization and pervasive Na metassomatism that resulted in crystallization of albite on igneous K-feldspar and plagioclase. In the perthite crystals, exsolved albite served as nuclei for crystallization of hydrothermal albite. Hydrothermal albite locally also forms a second rim around sericitized K-feldspar and plagioclase. The hydrothermalism gradually turned from sodic to silico-potassic. The main macroscopic feature of this alteration is the change of feldspar colour from grey to red, owing to crystallization of fine-grained hematite. Silico-potassic alteration is characterized initially by crystallization of mesoperthite followed by pervasive replacement of perthite and plagioclase by microcline and quartz. Igneous hornblende and

biotite are partially replaced by green biotite. Muscovite replaces sericitized feldspars and also crystallizes in the matrix, between quartz and feldspar crystals. Intense pyritization occurs locally.

Propylitic and sericitic alteration zones are overlapped. Hornblende is totally replaced by biotite, chlorite, and epidote and early biotite is replaced by chlorite, muscovite, rutile, and pyrite. Quartz, chlorite, and sericitic crystallize forming polycrystalline zones and veins with diffuse contacts. Magnetite is replaced by rutile and, near to shear zone, intense sulphidization occurs, crystallizing chalcopyrite, pyrite, gold, and carbonate. Basalt and andesite dykes around Pombo deposits are also sericitized, chloritized and carbonatized.

2.2 The Guido area

The Guido area is located 2,0 km North of the Pombo deposit, inside the porphyry pluton, too. Geology here is characterized by the occurrence of lamellar hematite-muscovite and magnetite-quartz veins, by small diorite, gabbro, and rhyodacite dykes mineralized with pyrite and chalcopyrite and by a small pyroxenite float. The pyroxenite is not hydrothermally altered. It is made of 55-60% clinoenstatite, 5-10% labradorite-bitownite, 15-20% pyrrhotite, 10-15% pentlandite, <1%

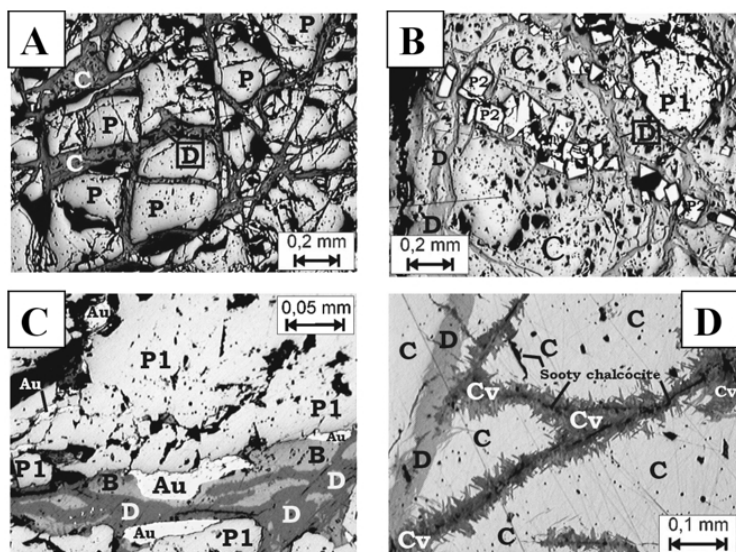


Figure 2: Ore mineral of the Pombo Cu-Au deposit. (A) Brecciated ore, with pyrite cemented by chalcopyrite partially replaced by digenite and chalcocite. (B) Euhedral pyrite, of the second hydrothermal phase, and anhedral pyrite (first phase) cemented by chalcopyrite partially replaced by digenite. (C) Gold, bornite and digenite along fracture inside pyrite. (D) Fracture in chalcopyrite filled with covellite and sooty chalcocite (black), crossing fracture with digenite. Anhedral pyrite = P1; euhedral pyrite = P2; chalcopyrite = C; gold = Au; bornite = B; digenite = D, and covellite = Cv (black, dusty mineral, inside digenite).

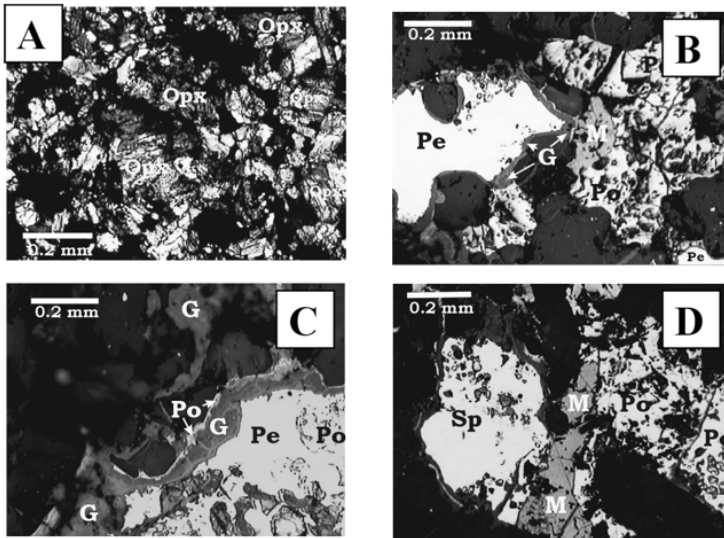


Figure 3: Ore minerals of the Guido area, mineralized with Ni and PGE. (A) Pyroxenite (PB-SV-67), with clinoenstatite, labradorite, and ore minerals. (B) Pentlandite bordered by goethite, magnetite, and pyrrhotite (C) Pentlandite bordered by goethite and hematite. (D) Sperrylite, magnetite, pyrrhotite, and pentlandite crystallized with silicates of the pyroxenite. Orthopyroxene = Opk, sperrylite = Sp, pentlandite = Pe, pyrrhotite = Po, magnetite = M, hematite = H, and goethite = G.

sperrylite - platarsite [Pt(As,S)₂], 1-2% magnetite, and 3-5% goethite (Fig. 3) and assay 1,7% Ni and 2-3 ppm Pt+Pd. Pyroxenite do not outcrops, but a fragment with pentlandite and platarsite was observed within the basalt of a dyke crossed by drill hole near the Pombo deposit. The basalt is chloritized and carbonatized, suggesting that pyroxenite is older than Pombo hydrothermalism.

2.3 The Cerro Azul area

The Cerro Azul is a non active gold deposit that is located 18 Km NE from the Pombo area, outside the Pombo porphyry pluton. Local geology shows small, 20-50 meters diameter, podiform-like intrusions, of highly hydrothermally altered clinopyroxenites emplaced in biotite-hornblende granodiorite stocks.

The clinopyroxenites have been transformed into hydrothermalites with hornblende, tremolite-actinote, chlorite, epidote, talc, anthophyllite, carbonates, and quartz, assaying 60-120 ppm Au, 200-260 ppm Ag, 0,2-0,3% Cu, 0,5-2% Pb and 0,5-1,0% Zn. Ore minerals are hematite (20-25%), magnetite (10-20%), sphalerite (2-8%), galena (3-10%), chalcocopyrite (1-3%), argentite (1 a 2%), pyrite (1-3%), and gold that occurs crystallized on rock mesostase or inside chalcocopyrite and/or sphalerite (Fig. 4). Although the hydrothermal paragenesis of Cerro Azul and Pombo ore, and altered rock are

different, the differences seem to be only a consequence of the rock compositions, being both alteration processes similar.

3 CONCLUSIONS

Alta Floresta, bordering the Amazon Basin, is a frontier of geological knowledge of Brazil, what explains the scarcity of information about regional, local and ore deposit's geologies. Ages, isotopic data, and ore fluids of all these deposits were not definitely settled, so the reasons for the great variation in the ore mineral and alteration paragenesis observed are yet unknown. The rocks of Cerro Azul and Guido deposits are similar, but the Cu-Zn-Pb-Ag sulfide + Au ore and the hydrothermal paragenesis of Cerro Azul can not be compared to Guido, where mineralization is characterized by Ni and Pt-As sulfides related to non altered clinoenstatite. A fragment with pentlandite and parisite, whose composition is similar to Guido ore, was observed in a basalt dyke altered by Pombo hydrothermalism. On the other hand, hydrothermal alteration and gold mineralization of Pombo and Cerro Azul are similar. These facts suggest that Cerro Azul and Pombo gold ores are posterior to Guido Ni-Pt mineralization. Cerro Azul and Pombo are hydrothermal gold+sulfide deposits genetically

from different kind of rocks. Guido is a Ni-Pt an endomagmatic unknown deposit. occurrence in ultrabasic, non altered rock, related to

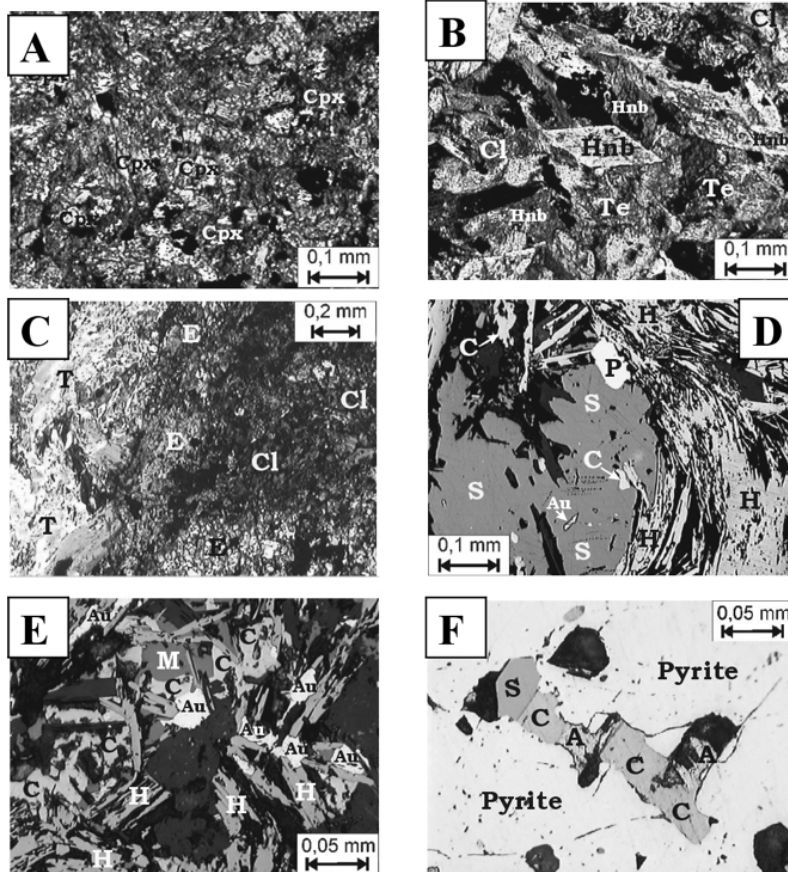


Figure 4: Ore minerals from Cerro Azul Area. (A) Clinopyroxenite with pyrite. (B) Hornblende, chlorite, tremolite-actinolite, and pyrite crystallized due to hydrothermal alteration of clinopyroxenite. (C) Deeply altered clinopyroxenite, with tremolite-actinolite, chlorite, epidote, talc, and carbonate. (D) Sphalerite, with minor pyrite and chalcopyrite, bordered by lamellar hematite. (E) Gold, magnetite, lamellar hematite and chalcopyrite crystal among silicates of altered clinopyroxenite. (F) Chalcopyrite, sphalerite, and argentite included in pyrite. Sphalerite = S; pyrite = Pp; chalcopyrite = C; hematite = H; gold = Au; magnetite = M; argentite = A; chlorite = Cl; epidote = E; talc = T; tremolite-actinolite = Te

The lack of comprehension of the deposits types and styles, all located at the same region, reflect the poor regional geology knowledge of the Alta Floresta – Peixoto de Azevedo region.

Brazil: Hydrothermal alteration and regional implications. *Precambrian Research*, **119**:225-256.

4 REFERENCES

Santos J.O.S.; Groves D.I.; Hartmann L.A.; Moura M.A. and McNaughton N.J. 2001. Gold deposits of the Tapajós and Alta Floresta domains, Tapajós-Parima orogenic belt, Amazon Craton, Brazil. *Mineralium Deposita*, **36**:278-299.

Juliani C; Corrêa-Silva R.H.; Monteiro L.V.S.; Bettencourt J.S. and Nunes C.M.D. 2002. the Batalha Au-granite system – Tapajós Gold Province, Amazonian craton,

Stable Isotope Studies on Zn and Pb Carbonates: Could they Play a Role in Mineral Exploration?

H.A.Gilg

Lehrstuhl für Ingenieurgeologie, Technische Universität München, Munich, Germany

M.Boni

Dipartimento di Geofisica e Vulcanologia, Università di Napoli Federico II, Naples, Italy

ABSTRACT: Stable carbon and oxygen isotope studies on carbonate minerals from nonsulfide Zn-Pb deposits can be useful in characterizing the ore-forming systems, thus providing new strategies for mineral exploration. We have investigated the isotope composition of Pb and Zn carbonates from calamine ores of the Iglesias district, SW Sardinia, and from the giant Angouran Zn deposit, NW Iran, and compare our results to those from other oxidized deposits (La Calamine, Broken Hill, Skorpion). Smithsonites, cerussites and phosgenites from supergene deposits display a common C-O-isotope pattern: $\delta^{18}\text{O}$ values are uniform, thus pointing to a single, meteoric fluid source and constant formation temperatures, while $\delta^{13}\text{C}$ values show a large spread indicating two isotopically distinct sources of carbon. Supergene cerussites have lower $\delta^{13}\text{C}$ values than supergene smithsonites, phosgenites, or calcites from the same deposit. Nonsulfide ores in the Angouran deposit occur in two paragenetic stages: an early, predominant hydrothermal stage I and a late supergene stage II. Oxygen isotope values of hypogene stage I smithsonites are highly variable (18.3 - 23.8 ‰), while $\delta^{13}\text{C}$ values are high and uniform ($+5 \pm 1$ ‰). In contrast, the isotope pattern of stage II smithsonites and cerussites is typical for a supergene origin. Our data imply that the majority of nonsulfide ores at Angouran formed by hydrothermal carbonatization of sulfides in a subsurface hot spring environment.

1 INTRODUCTION

Mineral exploration and scientific research on nonsulfide Zn deposits have experienced a significant revival in the last years as a consequence of new developments in hydrometallurgical acid-leaching, solvent-extraction, and electro-winning techniques. Recently, Large (2001) and Hitzman et al. (2003) suggested new classification schemes for nonsulfide Zn deposits. Both draw a genetic distinction between hydrothermal willemite-dominated deposits, such as Vazante, Brazil, or Beltana, Australia, from various types of supergene deposits consisting mainly of Zn carbonates (smithsonite, hydrozincite) and hydrous Zn silicates (hemimorphite, saucornite). The recent discovery of predominant hydrothermal smithsonite in Angouran, one of the largest and highest-grade non-sulfide Zn deposits (Gilg et al. 2003a), has challenged these genetic classifications.

Stable carbon and oxygen isotope studies on carbonate minerals from nonsulfide deposits are powerful means in elucidating the conditions of ore formation, metal enrichment processes, and sources of mineralizing fluids, thus characterizing the ore-forming system and providing new strategies for mineral exploration. In this study, we evaluate the potentials and present limitations of stable isotope

geochemistry of Zn and Pb carbonates, such as smithsonite (ZnCO_3), cerussite (PbCO_3), or phosgenite ($\text{Pb}_2\text{Cl}_2\text{CO}_3$), for research on ore genesis and use in mineral exploration targeting. We focus on calamine deposits in the Iglesias mining district, SW Sardinia, Italy, and the Angouran deposit, NW Iran, but include in our discussion both published and new results from other deposits, such as Broken Hill (Australia), Skorpion (Namibia), La Calamine (Belgium), and Lavrion (Greece).

2 ISOTOPE FRACTIONATION FACTORS

A prerequisite for the correct interpretation of stable isotope data of carbonate minerals is the accurate determination of isotope compositions and the knowledge of fractionation factors between minerals and water as a function of temperature. The phosphoric acid fractionation factors for smithsonite and cerussite between 25 and 72°C have recently been established by Gilg et al. (2003b). They are used here to (re)calculate the isotope compositions of these carbonates. For phosgenite, we apply the factors of cerussite. Isotope compositions are expressed here as delta values in ‰ relative to V-SMOW (oxygen) and V-PDB (carbon). Oxygen

isotope fractionation in the systems smithsonite-water and cerussite-water are poorly constrained at low temperatures. They have been estimated using thermodynamic calculations by Golyshev et al. (1982) and semi-theoretical bond models by Zheng (1999). Recently, Melchiorre et al. (2001) presented an experimental calibration of the cerussite-water thermometer using a slow precipitation method. We note that the equation of Melchiorre et al. (2001) predicts a small equilibrium oxygen isotope fractionation of only $\sim 2\%$ at 25°C between calcite (O'Neil et al. 1969) and cerussite, whereas much larger fractionations between these minerals of ~ 6 and $\sim 9.5\%$ are suggested by Zheng (1999) and Golyshev et al. (1982), respectively. The equilibrium oxygen isotope fractionation between smithsonite and cerussite at 25°C is $\sim 9.3\%$ (Zheng 1999) or $\sim 12\%$ (Golyshev et al. 1982).

3 STABLE ISOTOPE CHARACTERISTICS OF SUPERGENE NONSULFIDE DEPOSITS

3.1 The Iglesias district, SW Sardinia

The calamine-type deposits of the Iglesias district, SW Sardinia, formed by surface related oxidation of pre-Variscan carbonate-hosted sulfide deposits of MVT and SEDEX style (Boni et al. 2003). The oxidation zones reach to depths of 200 to more than 600 m below the present surface. The mineralogy of nonsulfide mineralization is complex and consists of smithsonite, hydrozincite, hemimorphite, cerussite, anglesite, phosgenite, and many exotic minerals, accompanied by calcite, aragonite, Fe and Mn oxides and oxyhydroxides and residual clays. The smithsonites from the deposits show a very restricted range of $\delta^{18}\text{O}$ values with an average of $27.4 \pm 0.9\%$ (1 σ , $n = 26$) suggesting a single, meteoric fluid source and uniform formation temperatures (Boni et al. 2003). Carbon isotope values of smithsonites scatter between -0.6 and -10.4% indicating at least two isotopically distinct sources of carbon (Fig. 1). The ^{13}C -enriched source can be related to dissolution of diagenetically recrystallized sedimentary and/or hydrothermal carbonates of the immediate wall rocks ($\delta^{13}\text{C} = 0 \pm 2\%$) by sulfuric acids produced during sulfide oxidation. The isotopically light carbon component is generated by oxidation of organic matter, most probably in the overlying soils. The variability of carbon isotope composition reflects crystal morphology and possibly different environments of sulfide oxidation. Botryoidal and stalactitic smithsonites from the vadose zone show high $\delta^{13}\text{C}$ values (-0.6 to -3.9%), while all other smithsonite types (rhombohedral, polycrystalline microaggregates, or "rice grain" shaped, Boni et al. 2003) have $\delta^{13}\text{C}$ values below -3.9% and probably formed in the (epi-)phreatic zone.

New stable isotope data on Pb carbonate minerals mostly from one of the mines (Monteponi) reveal a very similar pattern in a $\delta^{18}\text{O}$ - $\delta^{13}\text{C}$ plot as those indicated by smithsonites (Fig.1). The $\delta^{18}\text{O}$ values of phosgenites are uniform at $20.9 \pm 0.4\%$ ($n = 6$), while $\delta^{13}\text{C}$ values vary from -4.2 to -9.8% . Cerussites are characterized by lower $\delta^{18}\text{O}$ values of $17.4 \pm 0.5\%$ ($n = 10$). The carbon isotope values are more variable ranging from -6.5 to -20.9% . Calcites associated with calamine ore and aragonite speleothems in the mining area have uniform oxygen isotope values ($26.1 \pm 0.5\%$, $n = 5$) and a similar range of carbon isotope values as smithsonites (Fig.1). The oxygen isotope fractionation between calcite and cerussite from the Iglesias district is $\sim 8\%$ and that between smithsonite and cerussite $\sim 10.5\%$. Both values are intermediate between the predictions by Zheng (1999) and Golyshev et al. (1982).

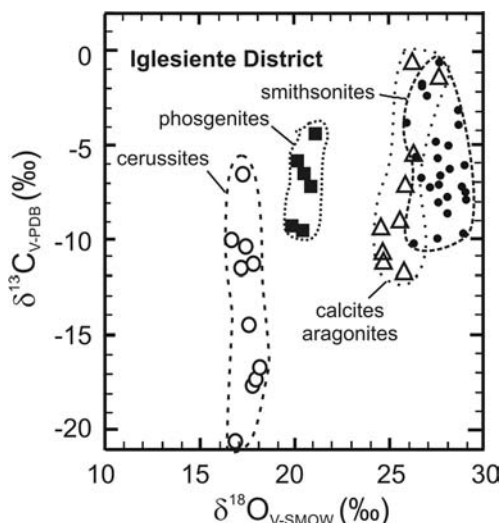


Figure 1: Stable carbon and oxygen isotope composition of smithsonites, phosgenites, cerussites, calcites and aragonites from the calamine ores of the Iglesias district, SW Sardinia.

3.2 Comparison with other supergene deposits

Stable isotope data on Pb and Zn carbonates from supergene oxidation zones of the Broken Hill sulfide deposit, New South Wales, Australia, display a very similar isotope pattern. Cerussites studied by Melchiorre et al. (2001) show a large carbon isotope variation with low $\delta^{13}\text{C}$ values (-13.5 to -19.2%), while oxygen isotope values are rather uniform ($16.1 \pm 0.5\%$, $n = 9$). Smithsonites have oxygen isotope values ($27.5 \pm 0.8\%$, $n = 3$) that are $\sim 11\%$ larger than those of cerussites, and $\delta^{13}\text{C}$ values range from -7.8 to -12.0% (Böttcher et al. 1993, this study). Borg et al. (2003) reported on isotope analyses on

smithsonites from the Skorpion nonsulfide Zn deposit, Namibia. Here, again, $\delta^{18}\text{O}$ isotope values are uniform (27.9 ± 0.3 ‰, $n = 5$) and carbon isotope values vary from -4.0 to -8.0 ‰. Our new data (Boni et al. 2004) on smithsonites from oxidation zones of sulfide deposits in Eastern Belgium (La Calamine, Moresnet, Fossey, Theux, and Welkenraedt deposit) reveal a C-O-isotope pattern that is very similar to other supergene deposits ($\delta^{13}\text{C}$ from -1.5 to -11.6 ‰, $\delta^{18}\text{O} = 28.2 \pm 0.5$ ‰, $n = 15$).

3.3 Implications for isotope fractionation factors

The average $\delta^{18}\text{O}$ values of smithsonites from the investigated supergene deposits of Iglesias, Broken Hill, Skorpion, and Belgium are comparable at 27.8 ± 0.4 ‰ and the oxygen isotope values of cerussites from the Iglesias and Broken Hill deposits are consistently ~ 11 ‰ lower. We note that present-day, local meteoric groundwaters at these localities are also similar at -6.5 ± 1 ‰.

If the smithsonites from all these deposits were formed from waters that are isotopically similar to the present-day local ground waters, equilibrium mineral-water $^{18}\text{O}/^{16}\text{O}$ fractionation at ambient temperatures ($\sim 20 \pm 15^\circ\text{C}$) can be estimated at ~ 34 ‰ for smithsonite, ~ 27 ‰ for phosgenite, and ~ 23 ‰ for cerussite, as compared to a value of ~ 29 ‰ for calcite (O'Neil et al. 1969). Our preliminary oxygen isotope data on cerussites (24.8 ± 0.2 ‰, $n = 6$), phosgenites (27.9 ± 0.8 ‰, $n = 4$) and aragonites (31.5 ± 1.5 ‰, $n = 8$) in ancient Pb-rich slags that were deposited in the Mediterranean Sea ($\delta^{18}\text{O} = +1.5$ ‰), near Lavrion, Greece, corroborate these estimates, but are inconsistent with the predictions of Melchiorre et al. (2001).

The carbon isotope values of supergene cerussites are often more than 5 ‰ lower than those of supergene smithsonites, phosgenites and calcites from the same deposit (see also below). This might indicate carbon isotope fractionation factors between cerussites and CO_2 that are different to those of the other carbonate minerals (cf. Golyshev et al. 1981).

4 STABLE ISOTOPE CHARACTERISTICS OF A HYPOGENE NONSULFIDE DEPOSIT AT ANGOURAN, IRAN

Angouran is located in the Zanjan Province, NW Iran, at an elevation of ~ 2800 m above sea level. It is one of the largest Zn carbonate deposit in the world with resources of 13.5 Mt at 31.2 % Zn in 1999. The deposit hosts also a limited body of primary sulfide and mixed carbonate-sulfide ores (Gilg et al. 2003a). The nonsulfide ores are marked by two paragenetic stages, an early and predominant stage I carbonate ore (where carbonate coexists with

sulfides) and a late stage II carbonate ore (where they coexist with oxides).

Stage I carbonate ore is dominated by smithsonite and displays a variety of textures from massive to brecciated, from botryoidal to euhedral dog-tooth shaped, from vuggy to dense. Stage I smithsonites exhibit locally abundant, tiny euhedral arsenopyrite crystals and less abundant quartz, galena, and pyrite crystals along specific growth zones. The co-precipitation of sulfides, the absence of oxides and the presence of reduced As species exclude the formation of stage I carbonate ores in a supergene oxidation environment. The stability of smithsonite + quartz implies maximum formation temperatures of $\sim 100^\circ\text{C}$ and high CO_2 fugacities. The paragenesis smithsonite plus arsenopyrite is stable under these conditions in reducing environments at a pH of ~ 8 to 9, thus very close to the sphalerite stability field. Oxygen isotope values of stage I smithsonites are highly variable ranging from 18.3 to 23.8 ‰. In contrast, $\delta^{13}\text{C}$ values are unusually high and uniform ($+5 \pm 1$ ‰). The wide range of $\delta^{18}\text{O}$ values indicates either the participation of two isotopically distinct fluids and/or Zn carbonate formation under variable thermal conditions. High carbon isotope values of stage I smithsonites are characteristic for travertines which are abundant in the Angouran area. Active travertine-depositing hot springs with temperatures of 20 to 45°C , as well as cold springs ($<10^\circ\text{C}$) near Angouran, are fed by meteoric waters with $\delta^{18}\text{O}$ values of -10 ‰.

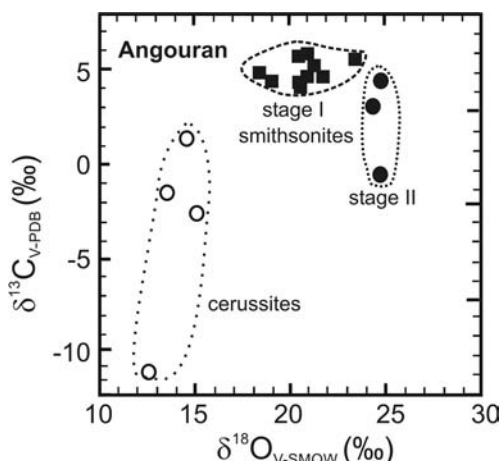


Figure 2: Stable carbon and oxygen isotope composition of smithsonites (stage I and stage II) and cerussites (stage II ores) from the Angouran mine, NW Iran.

The stage II carbonate ores occur as colloform bands in veins crosscutting massive stage I ores, or as euhedral crystals in vugs and open fractures.

However, these ores amount to only a very minor part of the nonsulfide ores. Stage II carbonate ores are characterized by the assemblage smithsonite, hemimorphite, mimetite, goethite, hematite, Mn oxides, calcite and cerussite. Oxygen isotope values of stage II smithsonites are homogeneous at 25 ± 1 ‰ and $\delta^{13}\text{C}$ values variable from +5 to -0.8 ‰, thus clearly distinct from stage I smithsonites. Cerussites from stage II ores have uniform $\delta^{18}\text{O}$ values of 14.0 ± 1.1 ‰ (n = 4), and highly variable carbon isotope values of +1.9 to -11.2 ‰. The stable isotope characteristics of Pb and Zn carbonates from stage II and their mineral paragenesis are indicative for a supergene origin.

Calcite occurs in and around the nonsulfide orebody in a great variety of forms, such as euhedral crystals in vugs, massive sparry fissure fillings, but also as colloform crusts in karst-like cavities in the marble. The stable isotope compositions of these calcites show a negative correlation ranging from $\delta^{18}\text{O}$ values of 16 ‰ and $\delta^{13}\text{C}$ values of +5 ‰ to $\delta^{18}\text{O}$ values of 22 ‰ and $\delta^{13}\text{C}$ values of -2 ‰. The isotope variation of calcites can be interpreted as mixing of ^{13}C -rich hydrothermal fluids with cold, ^{12}C -rich ground waters.

5 CONCLUSIONS

Pb and Zn carbonate minerals from supergene oxidized ore deposits display a very characteristic C-O-isotope pattern of uniform oxygen, but highly variable (> 4‰) carbon isotope values. Supergene smithsonites have $\delta^{18}\text{O}$ values that are ~ 11 ‰ higher than cogenetic cerussites, ~ 6.5 ‰ higher than phosgenites, and ~ 2 ‰ higher than calcites or aragonites. The range of carbon isotope values of supergene smithsonites, phosgenites and calcites reflects variable contributions of carbonate carbon from the wallrocks and reduced organic carbon most probably from the overlying soils and is comparable to the range shown by pedogenic carbonates (Cerling 1984). Cerussites from supergene deposits have much lower $\delta^{13}\text{C}$ values than supergene smithsonites, phosgenites or calcites from the same deposit.

In contrast, the smithsonites from stage I nonsulfide ores at Angouran show a large variation in oxygen isotope values, while carbon isotope values are constant and unusually heavy at +5 ‰. The data suggest that stage I Zn carbonates at Angouran formed by hydrothermal carbonatization of sulfide ores in a subsurface, travertine-related hot spring environment.

These preliminary studies clearly show the potentials of stable isotope geochemistry on Pb and Zn carbonates in characterizing nonsulfide Zn-Pb ore deposits. Further detailed studies are needed to establish consistent oxygen and carbon isotope

fractionation factors for Pb and Zn carbonates for use in geothermometry.

6 REFERENCES

- Boni, M., Gilg, H.A., Aversa, G. & Balassone, G. 2003. The "calamine" of SW Sardinia: Geology, mineralogy and stable isotope geochemistry of supergene Zn mineralization. *Econ. Geol.* 98: 731-748.
- Boni, M., Dejonghe L., Balassone, G., Coppola V. & Gilg, H.A. 2004. The Mesozoic weathering in Belgium and the "Calamine"-type ore deposits. Proceedings of 32nd I.G.C., Florence.
- Borg, G., Kämer, K., Buxton, M., Armstrong, R. & Merwe, S.W. 2003. Geology of the Skorpion supergene Zn deposit, southern Namibia. *Econ. Geol.* 98: 749-771.
- Böttcher, M.E., Gehlken, P.-L., Birch W.D., Usdowski, E. & Hoefs, J. 1993. The rhodochrosite-smithsonite solid-solution series from Broken Hill (NSW), Australia: Geochemical and infrared spectroscopic investigations. *N. Jb. Miner. Mh.* 1993: 352-362.
- Cerling, T.E. 1984. The stable isotopic composition of modern soil carbonate and its relationship to climate. *Earth Planet. Sci. Lett.* 71: 229-240.
- Gilg, H.A., Allen, C., Balassone G., Boni M. & Moore F. 2003a. The 3-stage evolution of the Angouran Zn "oxide"-sulfide deposit, Iran. in: Eliopoulos et al. (eds.): *Mineral Exploration and Sustainable Development*. Rotterdam: Millpress, 77-80.
- Gilg, H.A., Struck U., Vennemann T. & Boni, M. 2003b. Phosphoric acid fractionation factors for smithsonite and cerussite between 25 and 72°C. *Geochim. Cosmochim. Acta* 67: 4049-4055.
- Golyshev, S.I., Padalko, N.L. & Pechenkin, S.A. 1981. Fractionation of stable oxygen and carbon isotopes in carbonate systems. *Geokhimiya* 10: 1427-1441.
- Hitzman, M.W., Reynolds, N.A., Sangster, D.F., Allen C.R. & Carman, C.E. 2003. Classification, genesis, and exploration guides for nonsulfide zinc deposits. *Econ. Geol.* 98: 685-714.
- Large, D. 2001. The geology of non-sulfide zinc deposits - An overview. *Erzmetall* 54: 264-274.
- Melchiorre, E.B., Williams, P.A. & Bevins, R.E. 2001. A low temperature oxygen isotope thermometer for cerussite, with applications at Broken Hill, New South Wales, Australia. *Geochim. Cosmochim. Acta* 65: 2527-2533.
- O'Neil, J.R., Clayton, R.N. & Mayeda, T. 1969. Oxygen isotope fractionation in divalent metal carbonates. *J. Chem. Phys.* 51: 5547-5558.
- Zheng, Y.-F. 1999. Oxygen isotope fractionation in carbonate and sulfate minerals. *Geochim. J.* 33: 109-126.

Geophysical and Geological Data Integration Using a New Statistical Approach for Mineral Target Selection Applied to Emerald Prospection in the Itabira Map Quadrangle, Minas Gerais, Brazil

J.A.Newman, M.S.C.Barbosa, A.L.Gandini

Department Of Geologia, School Of Mines, Federal University Of Ouro Preto. Minas Gerais, Brazil

ABSTRACT: The main approach of this contribution is the application of a mapping technique using probability ratios to estimate the distribution of emerald deposits of the Itabira region, Minas Gerais, and its correlation with potential areas of exploration. The integration of diverse data types has always been an essential activity of any regional exploration program a modeling procedure involving data processing to define new areas with the potential for the discovery of mineral deposits. The results, the analysis and the interpretation of the methodology used to interpret the principal magnetic and gamma spectrometric structures. The ability of the models to predict favorable regions for economic emerald mineralization was verified by a comparison with existing deposits and occurrences. Several models that delineate highly prospective areas were determined. From the regional perspective, the predictive geophysical models convincingly define the majority of host rocks. Most importantly, the predictive models generated for the different mineralized environments delineate prospective areas outside the known mines. The magnetometric images were important to highlight the regional structures. The application of these processing techniques and the interpretation of magnetic structures with the horizontal gradient, first and second vertical derivatives, analytic signal and upward continuation images allowed the characterization of physical discontinuities that represent geological structures. The gamma spectrometric data processing delineated regional geological units. Magnetic data was interpolated into a regular grid by using minimum curvature algorithm. The processing provided first and second vertical derivative, analytic signal, horizontal gradient, vertical integral and upward continuation maps. The interpretation of these images produced maps of the magnetic structures (principal lineaments). Gamma spectrometric maps provide information regarding geology and possible targets for future explorations. By using the interpretative geological map it was possible to outline the major geological units with different radiometric response, which are not represented in the most recent geological maps of the region. The models of probability ratio use the space distribution of host rocks and mineral occurrences to calculate different mineralization signatures, and the results will help focus new exploration activities in the region.

1 INTRODUCTION

The first explorers of the Brazilian territory were known by the name of *bandeirantes*. They used to travel thousands of miles searching for gold, diamond, and emerald. They never found any emerald during those colonial times. Emerald was found in Brazil during the 60's. The first emerald discovery occurred in Salininha (Bahia) in 1963.

From then on, several deposits were discovered such as: Carnaíba (Bahia) in 1964, Itabira (Minas Gerais) in 1978, Santa Terezinha de Goiás known presently as Campos Verdes (Goiás) in 1981, Socotó (Bahia) in 1983, and Capoeirana (Minas Gerais) in 1988.

The last emerald discovery, outside Minas Gerais, occurred in the Tocantins State in February 1997. In this well it was found some green stones. Between

1995 and 1999, new emerald deposits were discovered in Minas Gerais. Among them Toco *garimpo* and Canta Galo mine in Nova Era/São Domingos do Prata. In the Canta Galo mine, both the colluvium and the unweathered rock have been mined to produce emerald of excellent gemological quality. The emerald deposit in Minas Gerais was found in 1999 by the Canadian company Seahawk Minerais while exploring an area between the *Garimpo* da Capoeirana and the Belmont mine. The *Fazenda* (Farm) das Piteiras deposit is currently being explored and in production.

The analyzed region is located between 43°00' and 43°30' West and 19°30' and 20°00' South, with a surface area of 3.000 km². It corresponds to the Itabira sheet (SE.23-Z-D-IV), and the scale is :100.000. The area is westward of Belo

Horizonte. The principal access is made from roads BR-262, BR-120, and MG-436.

The province of Minas Gerais is well-known as the world's largest emeralds producer, with a highlight over the Itabira region deposits, placed inside the Emerald Belt of Minas Gerais (César-Mendes & Svisero 1989). The mines of Belmont and Piteiras, and the Capoeirana's prospection present the geological association of beryllium pegmatites, whose source is related to Borrachudos granites and metaultramafic rocks with colouring elements, such as Cr⁺³, V⁺³ e Fe⁺³ (César-Mendes & Barbosa 2001). Studies fulfilled in that area use an innovator methodology for the emerald research, using radiometric and magnetometric patterns as accessory tools for geological characterization of the area and emerald deposits.

2 GEOLOGICAL CONTEXT

The area is located at the extreme northeast of the Ferric Quadrangle and can be subdivided into several important lithostratigraphical and lithostructural units, identified in minor scale, southern side of the São Francisco Craton.

The basic geology of the terrain underlying Itabira, Santa Maria de Itabira, and Nova Era is characterized by an Archean cratonic basement composed of a gneissic-migmatitic region with a polygenetic and polymetamorphic character, including Borrachudos granite-type rocks; a belt of Archean green rocks (greenstone belt) from the Rio das Velhas supergroup; lower Proterozoic metasediments of the Minas supergroup; and medium Proterozoic metasediments, which are essentially quartzitic, and belong to the Espinhaço supergroup.

It's a classic emerald occurrence region, and belongs to the Emerald Belt of Minas Gerais, as defined by César-Mendes & Souza (1989). The area has lithological units represented by the archean cratonic basement, composed by gneissic-migmatitic polymetamorphic and poligenetic areas, including granitic rocks of the rubber granite kind (possible font of pegmatites); by the arqueans green rock belt (greenstone belt) of the Rio das Velhas Supergroup; by metasediments from the inferior proterozoic of the Minas Supergroup; and, finally, by metasediments of the mean proterozoic, essentially quartzitics, from the Espinhaço Supergroup (Souza 1988) (Table 1).

Table 1 – Lithostratigraphic units of the Geological Skeleton of Emerald Province of Minas Gerais (from Pedrosa-Soares et al. 2001).

2.1.1 Unit	2.1.2 Principal rocks	2.1.3 Age
Espinhaço Supergroup	quartzite, metapelite, metaconglomerate, marble, metavolcanic felsic, and mafic rocks	Paleoproterozoic and Mesoproterozoic
Borrachudos Suite	gneissic granite	Paleoproterozoic
Minas Supergroup	itabirite, quartzite, phyllite, schist, conglomerate, marble	Paleoproterozoic
Juiz de Fora Complex	Granulite, gneiss	Paleoproterozoic
Rio das Velhas Supergroup	metasedimentary and metavolcanic rocks, metaultramafic rocks	Archean
Gneissics Complex	gneiss, migmatite, granite, metamafic rocks, feriferous formation, quartzite	Paleoproterozoic and Archean

As regards the emerald genesis, the deposits and/or occurrences in Minas Gerais are associated to the schist derived from ultramafic rocks, at places with acute percolation of hydrothermals fluids related to the pegmatites, due to specific tectonic conditions. These schists, represented essentially by biotite-flogopite-schist, clorite-schist and tremolite-actinolite-schists, are decimetric to metric intercalations associated to pelitics micaschists and amphibolites, usually altered at its surface.

Pegmatites and schists metaultramafics are the most important lithologies for the mineralizations of precious stone minerals found in the Itabira/Nova Era region. Pegmatitics apophysis have, as characteristic, a great amount of industrial and gemologic beryl (aquamarine). Schist derived from metaultramafic rocks are the lithological kind important to emeralds mineralizations. These rocks occur mostly as centimetric to metric intercalations in the metapelitic schists of the muscovite-quartz-schist and muscovite-biotite-quartz-schist kind. In a petrographical analysis, they are represented by chromite-biotite/phlogopite-schists or, generical-ly, called biotitites, where porphyroblasts of emerald crystals can be found.

The geochemical interaction happened between the pegmatitic beryl (represented by the pegmatitic veins) and the metaultramafic rocks with colouring elements (Cr+3, V+3 e Fe+3). The percolation of fluids from pegmatites, in these rocks, promotes, due to the hydrothermal effect and/or metasomatic of contact, the interaction of elements such as beryllium, among others, with chromium and

subsequent crystallization of emeralds at the alteration halos of the metaultramafic rocks, represented mainly by biotite-phlogopite-schists, chlorite-schists and tremolite-actinolite-schists. These colouring elements are found in higher concentrations at the metaultramafic levels (biotite-phlogopite-schist) of the sedimentary-volcanic sequence.

The geological conditions in the Itabira region are very similar to that of the Belmont mine, the Piteras mine and the Capoeirana garimpo. In stratigraphic terms, the Belmont mine, the Piteras mine and the Capoeirana garimpo are located in an area that is underlain by rocks from the basal paragneisses sequence of the Minas supergroup. Subordinately, there are amphibolitic rocks, intercalations of meta-ultramafic schist, and pegmatitic veins. The two latter lithologies are responsible for the emerald mineralization in the region. As regards the mineralization and genesis, the emerald deposits is dominantly associated to schists, which were originated from meta-ultramafic rocks in sites of intense pegmatitic percolation. The emerald mineralization occurs next to the schist - gneiss contact.

3 OBJECTIVE

The main approach of this contribution is the application of a mapping technique using probability ratios to estimate the distribution of emerald deposits of the Itabira region, Minas Gerais, and its correlation with potential areas of exploration of this mineral. The probability ratio models use the spatial distribution of host rocks and mineral occurrences to calculate different signatures of mineralizations. Therefore, the major purposes of this investigation are: a) to characterize the geological and tectonic context of Itabira region, using radiometric and magnetometric data treatment and interpretation. For this reason, the identification and mapping of regional structures will be made, to understand the regional tectonic and its importance for the mineralization processes; b) the use of radio-metric data to study the variation in the concentration of uranium (U), potassium (K), and thorium (Th) isotopes, to characterize the spatial distribution related to hydrothermal events; c) the mapping, using probability ratios, with the integration of geological and geophysical data in a probability model, using a new technology and methodology, such as diffused logic; d) to study the spatial relation between the geological variables obtained from the probability ratio and make maps with possibility of emerald exploration.

4 METHODOLOGY

The main approach of this contribution is the application of a mapping technique using probability ratios to estimate the distribution of emerald deposits of the Itabira region, Minas Gerais, and its correlation with potential areas of exploration of this mineral. The probability ratio models use the spatial distribution of host rocks and mineral occurrences to calculate different signatures of mineralizations. Integration of this data with available geological data, establishing probability ratio model criteria to predict areas with possible emerald mineralizations.

This research started with the analysis of data from "Stones from Minas Gerais – Magnetometric and Gammaspectrometric Aerial Survey of Itabira–Ferros Region," made in 1996 by an association between DNPM (National Department of Mineral Production) and CPRM (Geological Service of Brazil), which was an aerialgeophysical survey, scale 1:25.000, in a remarkably stone producing area in the State of Minas Gerais, provided by CPRM (Geological Service of Brazil) carrying out a bibliography research about the geology of Itabira, the processing method and interpretation of aerial-geophysical magnetometric and aerial-gammaspectrometric data, with its main filters and the algorithms used for mineral exploration. An intense bibliographic review of the principal emerald deposits models was executed, with application of processing techniques and aerial-geophysical magnetic and gammaspectrometric interpretation in these principal geological models and of the more important magnetometric and radiometric theoretical embasement; using the steps of data interpretation and reprocessing, to generate a geophysical probability model of potential areas for emerald exploration.

The quantitative evaluation of geological data used bibliographic, geochemical (those related similarly to gammaspectrometric data) and geophysical data from the Itabira area. Researches were made about geophysics applied to mineral prospection and its principal relations with mineral exploration. To build the geophysical database, processing data methodology was used to interpret and make the relation with the geology of the studied area. The analysis of regional structures, with magnetometric data. The analysis of magnetic huffiness of deep rocks (magnetometry) allowed the differentiation of metaigneous lithologies from metasedimentar and characterize the tectonic structuralization from relatively high to lower depths, after the application of frequency filters. The gammaspectrometric map is made with the concentrations of U, Th, and K isotopes (counts per second – cps), with information about the sided rock. The analysis of K anomalism, and its relation

with hydrothermal processes. The F parameter and the anomalous potassium method is used to determinate areas with K anomalism due to the antagonism of thorium and potassium, which is typical of alteration processes together with potassium secondary enrichment. Areas with similar characteristics to the mineralized areas were chosen, with the development of a probability ratio model. These models use the host rocks spatial distribution and mineral occurrences to calculate different signatures of mineralizations.

5 CONCLUSIONS

The geophysical approach of this contribution consisted of geophysical data processing, which were interpreted with emphasis at the geological context with GIS (Geographical Information System). The thought was that, talking about exploration, the geophysical anomalisms are not the only aspect to be observed, but the answers related to mineralization, lithology and structures with economic importance.

The interpretation of high resolution magnetic data allowed an outlook of regional architecture, as well as a better comprehension of structural controls of emerald deposits. The radiometric maps (total count, potassium, uranium, and thorium) were highlighted separately, and presented with pseudo-colours (R:G:B = K:U:Th). Single lithological units can be written, since they have different radiometric answers. Mafics, ultramafics, and paleoproterozoic units are darkened; then, the surrounding units, which indicates lower concentrations in all the three radiometric elements. Granite-gneisses have a radiometric response equivalent to high total count, and are shown in white or blue (high uranium). Firstly, it was possible to delimitate the granitic rocks of the Borrachudos granite and those of the metaultramafics from volcano-sedimentary sequence. Due to this lithological differentiation, it was possible to determinate all the subsequent steps of the research.

The ability of models in predicting favourable regions to emeralds mineralization was verified by the comparison of these areas with host rocks and with the occurrence of hosted deposits. Models for geophysical prediction were also studied, to delimitate areas of high possibility for prospection. The spatial analysis of diagnostic criterion of the events related to the genesis of the emerald lead away to targets for prospection. This approach must consider host rocks with high potential, the extension of areas with natural high prospection, and high potentials mapped by this technique. The characterization of favourable host rocks and several known emerald mines gives arguments for this

discussion. The correlation shows the efficaciousness of the applied methodology. If the veracity of these prediction models is tested and proven, then the results will help to bring new exploration activity to the area.

6 BIBLIOGRAPHY

- César-Mendes, J & Gandini, A.L. 2000. History of the Brazilian emerald findings. In: International Geological Congress, 31, Rio de Janeiro, field Tripe Guide. Rio de Janeiro, Field Trip Art 20, 58p.
- César-Mendes, J. & Barbosa, M.S.C. 2001. Esmeralda. In: Castañeda, C.; Addad, J.E.; Liccardo, A. 2001. Gemas de Minas Gerais, Belo Horizonte, Sociedade Brasileira de Geologia – núcleo Minas Gerais, p. 129-151.
- César-Mendes, J. & Ferreira Jr, P. D. - 1997 - Os Garimpos de Monte Santo, TO: uma nova descoberta de esmeralda no Brasil. *Revista Escola de Minas*, 51(2): 30-35.
- César-Mendes, J.; Svisero, D.P. 1989. Aspectos econômicos da esmeralda de Santa Terezinha de Goiás. *REM. Revista da Escola de Minas*, 42: (2): 26-28.
- Pedrosa-Soares, A.C.; Pinto, C.P.; Netto, C.; Araújo, M.C.; Castañeda, C.; Achtschin, A.B.; Basílio, M.S. 2001. A Província Gemológica Oriental do Brasil. In: C. CASTAÑEDA; J.E. ADDAD; A. LICCARDO (orgs.) Gemas de Minas Gerais - esmeralda, turmalina, safira, topázio, quartzo, água-marinha, alexandrita. Belo Horizonte, Sociedade Brasileira de Geologia - Núcleo Minas Gerais, 100 - 127.
- Prospec S/A. Levantamento Aéreo Magnetométrico e Gamaespectrométrico – Projeto Gemas de Minas Gerais, Convênio DNPM/CPRM. DNPM. 1996. V. 1 (Relatório Final).
- Schobbenhaus C.; Campos D. A.; Asmus H. E. 1984. Mapa geológico do Brasil e da área oceânica adjacente. Brasília: MME/DNPM.
- Schorcher, H.D. & Guimarães, P.F. - 1976 - Estratigrafia e tectônica do Supergrupo Minas e geologia do distrito ferrífero de Itabira. In: *Cong. Bras. Geol.*, 29, Ouro Preto-MG. Roteiro das Excursões, p. 75-86.
- Schorcher, H.D.; Santana, F.C.; Polônia, J.C.; Moreira, J.M.P. - 1983 - Quadrilátero Ferrífero - Minas Gerais State: Rio das Velhas greenstone belt and proterozoic rocks. *Excursions anex, ISAP, Brazil*, 44p.
- Souza, J.L.; César-Mendes, J.; Svisero, D.P. 1987. Aspectos mineralógicos e geológicos das esmeraldas brasileiras. *Revista da Escola de Minas*, 40 (3): 18-26.
- Souza J. L. 1988. Mineralogia e geologia da esmeralda da Jazida de Itabira, MG. Instituto de Geociências, Universidade de São Paulo, Tese de Mestrado, 192p.
- Telford, W. M. et al. 1986. *Applied Geophysics – Great Britain*, Cambridge, University Press, 860 p. II, graf.

The New Consort Gold Mine in the Barberton Greenstone Belt, South Africa: Orogenic Gold Mineralization in a Condensed Metamorphic Profile

A.Otto & A.Dziggel

Institute of Mineralogy and Economic Geology, RWTH Aachen University, Aachen, Germany

A.F.M.Kisters

Department of Geology, University of Stellenbosch, Matieland, South Africa

ABSTRACT: The gold mineralization at the New Consort gold mine occurs within discrete, siliceous mylonitic units that are located at or close to the contact between the Onverwacht Group and Fig Tree Groups. We have studied three localities, that are, from West to East, situated in progressively higher-grade metamorphic rocks. Conventional geothermometry reveals a steep temperature gradient of nearly 200 °C over a distance of about 2.5 kilometers, ranging from upper greenschist-facies grades in the west, to amphibolite-facies grades in the east of the mine workings. Combined structural, textural and petrological data suggest a syn-kinematic gold mineralization in all three localities, at or close to the peak of metamorphism. Although the mine is structurally highly complex, the sulfide assemblages in the ore shoots change progressively with metamorphic grade, and include (i) arsenopyrite-pyrrhotite-pyrite in the Western Zone, (ii) arsenopyrite-pyrrhotite-chalcocopyrite in the Central Zone, and (iii) arsenopyrite-loellingite-pyrrhotite-chalcocopyrite in the Eastern Zone.

1 INTRODUCTION

The New Consort gold mine forms one of four active mines that occur closely clustered along the northern margin of the ca. 3.5-3.2 Ga Barberton greenstone belt, South Africa. The gold mineralization is commonly interpreted to be related to the final stages of the tectonometamorphic evolution of the Barberton greenstone belt during the Mesoarchaeon at 3.1 Ga (Harris et al. 1995). As such, the New consort mine represents one of the oldest orogenic gold deposits in the world. The host rocks of the New Consort mine comprise ultramafic and mafic schists of the Onverwacht Group, that are in tectonic contact with overlying sedimentary rocks of the Fig Tree Group (Fig. 1). The complexly folded and imbricated metavolcanosedimentary sequence is floored in the north by the 3.1 Ga granitoids of the Nelspruit batholith and older migmatites and basement gneisses. The gold mineralization is mainly structurally controlled and occurs around the highly sheared and silicified contact between rocks of the Onverwacht and Fig Tree Group. This contact, locally referred to as the Consort Bar, reaches a thickness of up to several meters, and the epigenetic ore shoots may occur in

different stratigraphic levels at or near this structural break.

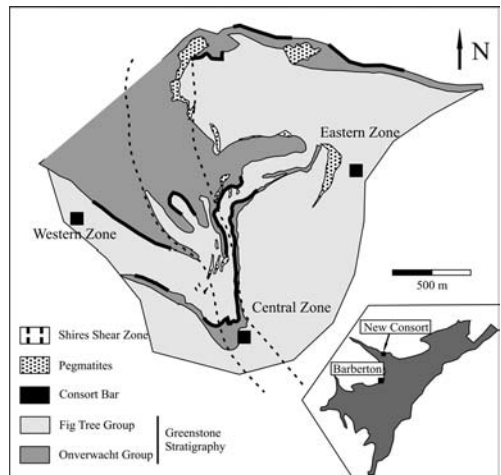


Figure 1. Simplified geological map of the New Consort gold mine, showing the main lithological units. The inset shows the mine location in the Barberton greenstone belt (modified after Voges 1986).

A characteristic feature of the gold mineralization is the development of the relatively continuous and laterally extensive, though structurally highly complicated, mineralized horizons in wall-rocks of significantly different metamorphic grade. This offers the opportunity to study the controls and timing of a hydrothermal plumbing system under different metamorphic and rheologic conditions in one mine.

In order to establish the relative timing of gold mineralization with respect to the metamorphic evolution of the wall-rocks, we have studied three selected localities at the New Consort mine that are located, from west to east, in progressively higher-grade metamorphic wall-rocks. We will first characterize the different P-T conditions of the regional metamorphism experienced by the wall-rocks and then describe the petrologic variations of ore- and alteration parageneses between the different localities. Mineral abbreviations are after Kretz (1983).

2 MINE GEOLOGY

The three localities studied are here referred to as the Western, Central and Eastern Zone (Fig. 1). The mineralization in the Western Zone is situated in shallow southerly dipping and intensely folded metapelites of the Fig Tree Group, and occurs about 1 m above the Consort Bar. The metapelites are interlayered and infolded with thin bands of mafic schists. The rocks are very fine-grained to mylonitic, and appear almost un-metamorphosed in outcrop. Kinematic indicators point to a top-to-the-north reverse sense of movement along the bounding shear zones. Late normal faults (the Bluejacket faults) dip moderately to the south and cut through the lithologies and mineralization.

The mineralization in the Central Zone is situated within the Consort Bar, and is currently mined ca. 1400 m below surface. The wall-rocks are at amphibolite-facies grade and comprise metapelites and ultramafic schists of the Onverwacht and Fig Tree Groups. The E-W trending, strongly foliated wall-rocks and the Consort Bar dip steeply to the south, and contain a mineral stretching lineation that plunges at moderate angles to the west. Shear sense indicators suggest a south block up sense of movement with a sinistral strike-slip component along the Consort Bar.

The mineralization in the Eastern Zone is hosted by Onverwacht Group mafic to ultramafic schists. The variably foliated rocks dip moderately to the southwest and contain a mineral stretching lineation that generally plunges at shallow angles to the southeast. Calc-silicate rocks and highly sheared gneisses occur as intercalated foliation-parallel layers. A weakly foliated, fine-grained amphibolite

occurs as a semi-massive lense within the ultramafic schists. The contact with the overlying metapelitic schist is distinct compared to the development of the Consort Bar in other portions of the mine. It is a sharp, tectonic contact, which dips steeply to the south. Pegmatites show intrusive but commonly strongly mylonitized contacts with the wall-rocks. The latter are parallel to the foliation of the mafic schists and dip at moderate angles to the southwest.

3 WALL-ROCK PETROLOGY

The Fig Tree Group metapelites in the Western Zone consist of quartz-biotite-plagioclase assemblages and occasionally contain syn- to late-tectonic garnet and/or cummingtonite porphyroblasts. Thin bands of garnet-hornblende-biotite-quartz schists are interlayered and infolded with the metapelites, indicating upper greenschist-facies conditions.

The wall-rocks in the higher grade Central and Eastern parts show similar mineral assemblages. The ultramafic schists of the Onverwacht Group consist of syn- to post-tectonically grown tremolite, talc, and serpentine. Accessory minerals include biotite, calcite, and chromite. Intercalated amphibolites are fine- to medium-grained and weakly foliated. The amphibolites contain hornblende-plagioclase-quartz-clinopyroxene assemblages. In places, these assemblages are extensively retrogressed to a fine-grained mixture of titanite, sericitic albite, K-feldspar, and actinolite. Pyrrhotite and arsenopyrite may occur as disseminated anhedral grains. Calc-silicate rocks appear as foliation-parallel layers with a thickness on a dm-scale. The peak assemblage comprises clinopyroxene, grossular, scheelite, and apatite, that have been partly replaced by zoisite, albite, and K-feldspar.

The metapelitic schists of the Fig Tree Group contain garnet, biotite, cummingtonite, plagioclase and quartz. The foliation is defined by biotite and cummingtonite. Rotated garnet porphyroblasts grew syn- to post-tectonically and record a typical bell-shaped prograde zoning pattern. Plagioclase exhibits a prograde zonation, with an anorthite-rich core and anorthite-poor rim. Biotite and cummingtonite are not zoned and in textural equilibrium with garnet (rim), plagioclase (rim) and quartz. Small amounts of chlorite and actinolite replace the peak metamorphic assemblage.

4 GEOTHERMOMETRY

Garnet-biotite, garnet-hornblende and hornblende-plagioclase thermometry was applied to suitable mineral assemblages in the metapelites and amphibolites from all three localities (Fig. 2). The

estimated temperatures clearly confirm the presence of a distinct metamorphic gradient in the mine.

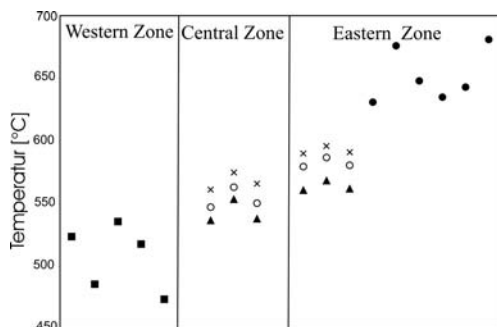


Figure 2. Estimated peak temperatures for representative Grt-Bt, Grt-Hbl and Hbl-Pl pairs; open circle and cross: Bhattacharya et al. (1992), triangle: Pertchuk & Lavrenteva (1993), dots: Holland & Blundy (1994), square: Krogh Ravna (2000).

Grt-Bt thermometry, using the calibrations of Bhattacharya et al. (1992), and Pertchuk & Lavrenteva (1983), produced somewhat low temperatures ranging between 530°C and 570°C in the Central, and 560°C and 600°C in the Eastern Zone. Due to the common resetting of the biotite peak composition during retrogression, these estimates should be regarded as minimum temperatures for the peak of metamorphism. The Hbl-Pl thermometer (Holland & Blundy, 1994) reveals distinctly higher temperatures, ranging between 630°C and 680°C. In general, however, these estimates are in good agreement with upper greenschist- to mid-amphibolite-facies grades at low to medium pressures.

5 GOLD MINERALIZATION

In the Western Zone, the mineralization occurs in foliation-parallel layers infolded with the metapelitic wall-rocks. The ore horizons mainly consist of arsenopyrite, pyrrhotite and pyrite, which are texturally well-equilibrated. Free gold is relatively rare, and occurs at grain boundaries or intergrown with pyrrhotite. Associated silicate phases include biotite and tourmaline. Temperature estimates using the biotite-tourmaline geothermometer reveal temperatures very similar to those estimated for the wall-rocks.

The highly silicified Consort Bar in the Central Zone is strongly laminated and has an approximate width of 2 m. It contains discontinuous and subvertical sulfide-rich lenses and veins that outline the ore shoots. The sulfide assemblage in these

higher grade rocks comprises arsenopyrite, pyrrhotite, and chalcopyrite, that are locally replaced by pyrite. Arsenopyrite occurs in two texturally different varieties. A first variety forms coarse-grained, idiomorphic crystals (~0.5 cm). A second variety occurs as fine-grained needles. Pyrrhotite occurs in fractures and on grain boundaries of the coarse-grained arsenopyrite. Chalcopyrite and pyrite occur as xenomorphic to idiomorphic grains. Gold occurs in different relationship to its host minerals (Table 1): (i) as inclusions in arsenopyrite (Fig. 3) and albite, (ii) along fractures in arsenopyrite, and (iii) intergrown with pyrrhotite and silicate gangue minerals (Fig. 4). The silicate alteration minerals include Cr-muscovite, Cr-tourmaline, albite, rutile, and titanite.

Table 1. Generalized paragenetic diagram illustrating three main mineralization stages observed in the Consort Bar (Central Zone).

minerals	stage I	stage II	stage III
sulfides			
arsenopyrite (blocky)	_____		
arsenopyrite (needles)		_____	
pyrrhotite		_____	
chalcopyrite		_____	
pyrite			_____
silicates/oxides			
Cr-tourmaline		_____	
Cr-muscovite		_____	
albite		_____	
titanite		_____	
rutile		_____	
gold	_____	_____	

Wall-rock alteration is restricted to the lower 50 cm of the metapelitic schists in the hangingwall of the Consort Bar. The pervasive foliation in this zone is parallel to that of the host rocks. Elongated arsenopyrite needles and pyrrhotite define the mineral stretching lineation, indicating a syn-kinematic gold mineralization. The alteration zone further consists of abundant Cr-muscovite, quartz, and small amounts of Cr-tourmaline, rutile and titanite, resulting in the overall intense green coloration. Traces of biotite replaced by Cr-muscovite suggest a metapelitic precursor for this part of the Consort Bar.

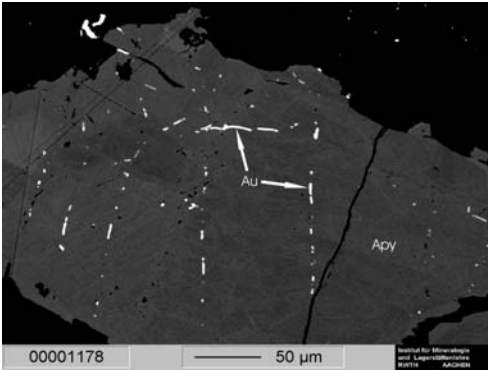


Figure 3. SEM backscattered electron image showing gold inclusions in a zoned arsenopyrite (stage I).

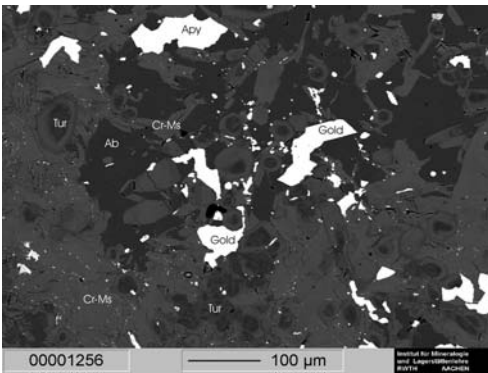


Figure 4. SEM backscattered electron image showing gold grains intergrown with tourmaline, Cr-muscovite and albite (stage II).

The mineralization in the Eastern Zone is associated with massive amphibolites of the so-called Footwall Lense. The mineralization in this part of the mine has not been studied to date, but has been interpreted by previous workers to be similar to that of the Consort Bar. The sulfide assemblage in the ore shoots comprises arsenopyrite, loellingite, pyrrhotite and chalcopyrite (Harris et al., 1995). The presence of loellingite in the Eastern Zone in addition to arsenopyrite suggests higher temperatures at a given sulfur fugacity.

6 DISCUSSION AND CONCLUSIONS

The gold mineralization at the New Consort Gold mine is hosted by variably metamorphosed rocks, ranging from upper greenschist-facies to amphibolite-facies grades. Although more detailed structural and petrological data are needed, the data presented in this study suggest a syn-kinematic gold

mineralization at or close to the peak of metamorphism. Assuming a contemporaneous timing of gold mineralization in low-, medium- and higher-grade host rocks, the distinct change of sulfide assemblages with metamorphic grade indicates that this temperature gradient was present during the gold mineralization. Steep metamorphic gradients are a characteristic feature of the contact between the Barberton greenstone belt and the surrounding granitoid gneisses, pointing to a causal relationship between the juxtaposition of granite-gneiss terrain with the greenstones and fluid flow and gold mineralization.

7 ACKNOWLEDGEMENTS

We thank Barberton Mines Ltd. for support and access to underground workings. J. Kolb is thanked for helpful comments on an earlier version of the manuscript.

8 REFERENCES

- Bhattacharya, A., Mohanty, L., Maji, A., Sen, S. K. & Raith, M., 1992. Non-ideal mixing in the phlogopite-annite binary: constraints from experimental data on Fe-Mg partitioning and a reformulation of the biotite-garnet geothermometer. *Contrib. Mineral. Petrol.*, **110**, 87-93.
- Harris, P.D., Robb, L.J., Tomkinson, M.J., 1995. The nature and structural setting of rare-element pegmatites along the northern flank of the Barberton greenstone belt, South Africa. *S. Afr. J. Geol.*, **98** (1), 82-94.
- Holland, T.J.B., Blundy, J., 1994. Non-ideal interactions in calcic amphiboles and their bearing on amphibole-plagioclase thermometry. *Contrib. Mineral. Petrol.*, **116**, 433-447.
- Kretz, R., 1983. Symbols for rock-forming minerals. *Amer. Mineral.*, **68**, 277-279.
- Pertchuk, L. L. & Lavrenteva, I. V., 1983. Experimental investigations of exchange equilibria in the system cordierite-garnet-biotite. In *Saxena, S. K., (ed.) Kinetics and Equilibrium in Mineral Reactions. Springer, Berlin: 199-239.*
- Krogh Ravna, E.J., 2000. Distribution of Fe²⁺ and Mg between coexisting garnet and hornblende in synthetic and natural systems: an empirical calibration of the garnet-hornblende Fe-Mg geothermometer. *Lithos*, **53**, 265-277.
- Voges, F.D., 1986. The New Consort Gold Mine, Barberton greenstone belt. *Mineral Deposits of Southern Africa. Vols I & II. Geol. Soc. S. Afr.*, 163-168.

Geology, Geochemistry and Petrogenesis of the Yatasto-San Bernardo Li-Bearing Pegmatite, Argentina

J.Oyarzábal & S.Cadile

Departamento de Geología, Proyecto CyT 349001, Universidad Nacional de San Luis, San Luis, Argentina

ABSTRACT: Yatasto-San Bernardo pegmatite consists of a single body classified here as a complex type, spodumene subtype, and rare-element class pegmatite. This deposit is located at 32° 24' 34'' S and 65° 42' 44'' W, in the Conlara field, Pampeana Pegmatitic Province, Argentina. The pegmatite is tabular, 260 m long and up to 14 m wide in the central segment. It strikes N25-35°E and dips 45-60° NW, and is hosted within a fertile LCT pegmatitic granite, intruded in Qtz-Bt-Pl-Ms±Tur-Ap-Zrn schists. K-feldspar and mica geochemistry and structural state were studied. K-feldspar exhibits a high Al:Si order (~1.0), and muscovite shows 2M₁ polytype form; whereas lepidolite has a layer-stacking sequence according to 1M polytype. The K/Rb, K/Cs and Rb/Sr ratios in K-feldspar and muscovite show a marked differentiation process and probable derivation from the hosting granite.

1 GEOLOGICAL SETTING

Yatasto-San Bernardo pegmatite is located in the north of the San Luis ranges at 32° 24' 34'' S and 65° 42' 44'' W, in the Conlara field, Pampeana Pegmatitic Province, Argentina (Fig.1).

The geological setting is typical of Sierras Pampeanas, a pericratonic mobile belt developed during upper Precambrian-lower Paleozoic. The area is characterized by the presence of metamorphic rocks of medium grade, intruded by a suite of granitoids and pegmatites. The metamorphic rocks are represented by Qtz-Bt-Pl-Ms±Tur-Ap-Zrn schist. The pegmatite is hosted in a leucogranite lens characterized by an extreme modal and textural heterogeneity.

2 GEOLOGY OF THE PEGMATITE

Yatasto-San Bernardo pegmatite is emplaced in the eastern part of a leucogranite lens of reduced dimensions (~ 0.3 km²). The deposit is tabular, 260 m long and up to 14 m wide in the central segment. It strikes N25-35°E and dips 45-60° NW (Fig. 1). The contact with host rock are evidenced by abrupt textural and mineralogical changes.

In its complex and asymmetric internal structure (Fig. 1) it is possible to recognize the following units: border (Ab-Qtz-Ms±Tur-Grt-Ap), wall (Qtz-Mc-Ms-Ab-Brl±Tur-Elb-Ap-Grt), outer intermediate (Mc-Qtz-Ms±Ap), inner intermediate (Qtz-Spd-Lpd-Mtb±Elb-Ap) and a quartz core zones. A major tabular replacement, with saccharoidal albite, and several filling and replacement units were recognized.

The pegmatite emplacement suggests a forced character, with displacement of the host rock, within a physical discontinuity generated by tensional strain active during the cooling period of the fertile granite, in semi-fragile rheologic conditions.

The existence of a fine grained border zone is an excellent indicator of thermal differences between the pegmatite and the host rock. The presence of tabular and prismatic minerals (muscovite and schörl) with an oblique orientation over the contact of the border zone, gives evidence that the emplacement developed with mobility, from a generation of ascending pegmatitic fluids.

The presence of granitic xenolites in the wall zone of the deposit suggests a forced pegmatitic emplacement.

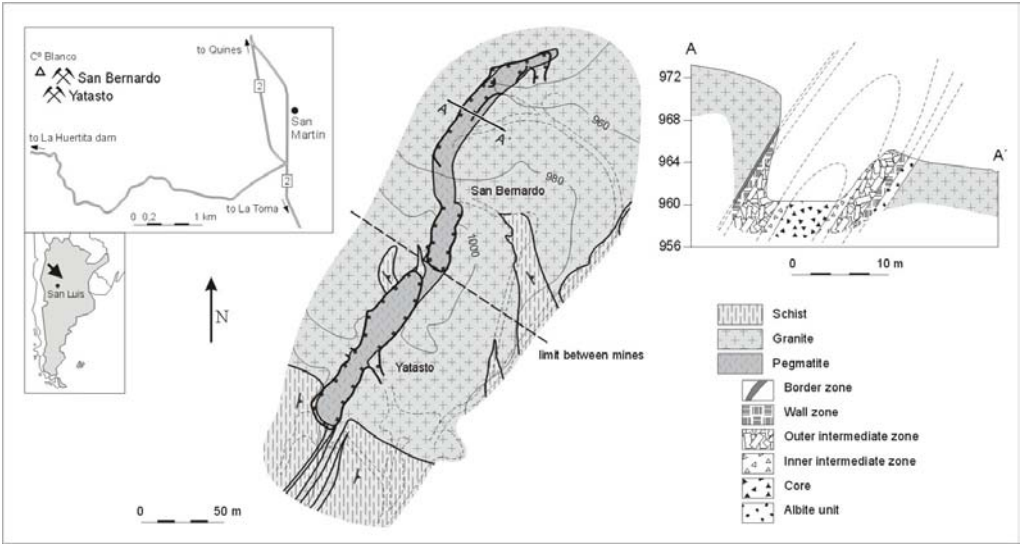


Figure 1. Geological map of the Yatasto-San Bernardo pegmatite (after Cadile 2003).

3 STRUCTURAL STATE OF K-FELDSPAR

The triclinicity index and (Al,Si) distribution in tetrahedral sites were determined by XRD analysis. Values of t_{10} (~ 1.0), obtained by different methods (Kroll 1973, Kroll & Ribbe 1987), indicate a fully ordered structure, corresponding to a low microcline. The $V\text{-}\Delta\text{tr}_{[110]-[1-10]}$ and $2\theta_{(-201)} - \Delta 2\theta_{(130)-(1-30)}$ diagrams (Fig. 2), show the obtained results.

The maximum ordering of the K-feldspars studied, suggests conditions of crystallization at low rates of nucleation and high contents of volatile phases.

4 MUSCOVITE AND LEPIDOLITE POLYTYPES

The obtained X-ray diffraction patterns and cell parameters of muscovite demonstrate remarkable similarities with respect to those obtained by Yoder & Eugster (1955) for synthetic muscovite of $2M_1$ polytypic form. Lepidolite of the replacement units shows stacking sequences according to $1M$ (following the proposal of Bailey 1980).

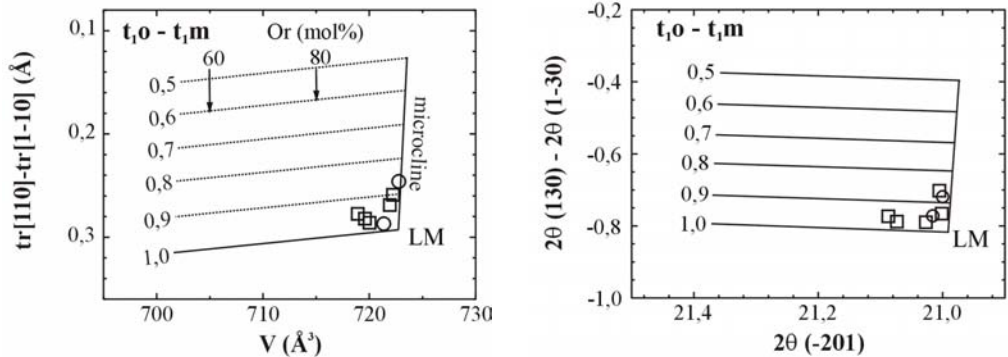


Figure 2. $V\text{-}\Delta\text{tr}_{[110]-[1-10]}$ and $2\theta_{(-201)} - \Delta 2\theta_{(130)-(1-30)}$ diagrams for topochemically triclinic Kfs (after Kroll & Ribbe 1987). References. \square outer intermediate zone (Yatasto-San Bernardo pegmatite); \circ granite.

5 COMPOSITIONAL CHARACTERISTICS OF K-FELDSPAR AND MUSCOVITE

The analyzed K-feldspar samples were collected from the outer intermediate zone of the pegmatite and from the fine coarse grained facies of the host granite lens. The Rb/Sr-K/Rb and Rb-K/Cs diagrams (Fig. 3) show that the samples from the deposit are disposed between the fields corresponding to beryl type and complex type pegmatites with Li mineralization, whereas the samples from the granitic facies evidence in both graphics a lower level of geochemical evolution.

The analyzed muscovite specimens were collected from the wall zone of the pegmatite and from the replacement units of the granitic facies. The Cs-K/Rb diagram (Fig. 4) shows that the samples corresponding to the Yatasto-San Bernardo pegmatite are located between the fields II (beryl type pegmatite) and III (complex type pegmatite, with Li mineralization); whereas the samples from the granite evidence a lower level of geochemical evolution. The K/Cs-K/Rb diagram (Fig.4) confirms the geochemical evolution trend.

6 PETROGENESIS AND CLASSIFICATION

The genesis of the Yatasto-San Bernardo pegmatite is interpreted as a magmatic differentiation process from a related fluid of the granite in which was emplaced. The mineralogical and textural characteristics of the granitic facies are equivalent to those cited by Černý (1991) for fertile pegmatitic granite.

The crystallization process was generated by the emplacement of pegmatitic melt enriched in volatile phases and rare metal elements, that crystallized in a semi closed system with a low rate crystallization,

within a physical discontinuity generated by tensional strain active during the cooling period of the fertile granite, under semi-fragile rheologic conditions.

The presence of a well developed zoned internal structure and this complex characteristics suggest a progressive crystallization from the border to the interior of the deposit; whereas the compositional and textural differences between adjacent zones have been originated by a fractionation mechanism and successive reactions between remnant crystals and fluids under no-equilibrium conditions (Cameron et al. 1949).

The tabular albite replacement unit, located asymmetrically with respect to the general zonation, suggests the generation of a later pulse fully enriched in sodium and volatile components that generates important replacements over the primary units. Similar units were described and studied in the Independencia Argentina (Galliski et al. 1994) and Aqueelarre pegmatites (Oyarzábal 2004).

On the basis of the mineralogical, textural and paragenetic parameters, the Yatasto-San Bernardo deposit can be classified as complex type, spodumene subtype, and rare-element class pegmatite. The K-feldspar and muscovite geochemical data support this hypothesis.

7 ECONOMIC ASPECT

High concentration of ceramic and industrial mineralization (such as microcline, albite, quartz, muscovite, montebrazite, and refractory spodumene), in addition with its coarse grain size, are the main factors favoring the exploitation of this deposit at large scale, with an integral extraction of its ceramics resources.

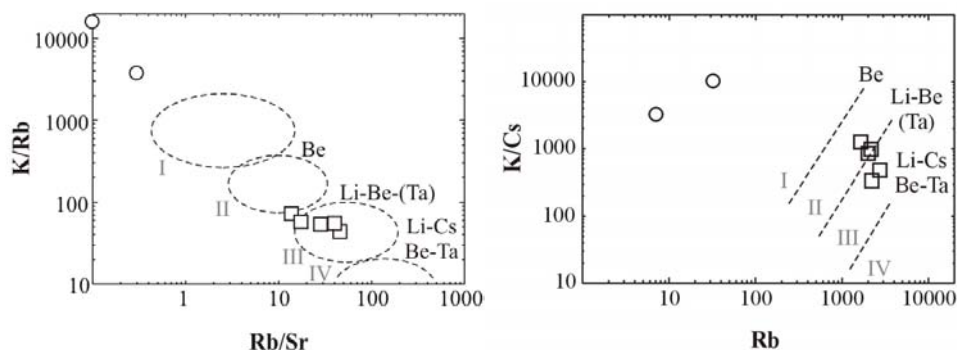


Figure 3. Correlation plots between selected major and trace elements for K-feldspar. Each sector groups: I) barren pegmatites of LCT signature, II) Be-bearing pegmatites, III) complex and albite-spodumene type pegmatites, and IV) albite type pegmatites, for pegmatites of Pampeana Pegmatitic Province (Galliski et al. 1997).

References: □ outer intermediate zone (Yatasto-San Bernardo pegmatite); ○ granite.

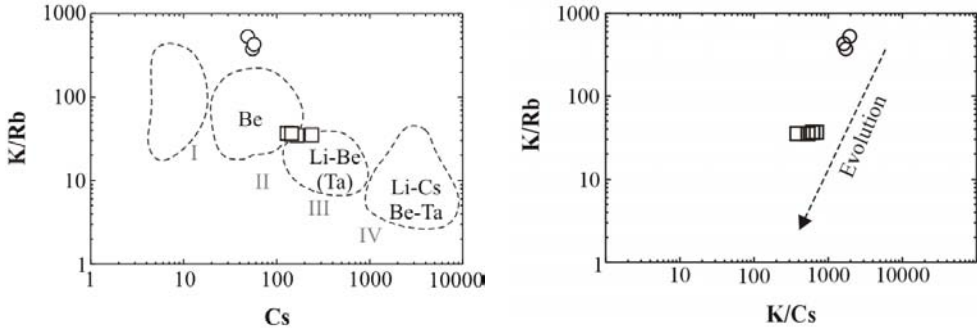


Figure 4. Correlation plots between selected major and trace elements for muscovite. Each sector groups: I) barren pegmatites of LCT signature, II) Be-bearing pegmatites, III) complex and albite-spodumene type pegmatites, and IV) albite type pegmatites, for pegmatites of Pampeana Pegmatitic Province (Galliski et al. 1997).
References: □ wall zone (Yatasto-San Bernardo pegmatite); ○ replacement muscovite over granitic facies.

8 CONCLUSIONS

Yatasto-San Bernardo pegmatite conforms a single pegmatitic body emplaced into a leucogranitic lens. The pegmatite exhibits a complex and asymmetric internal structure, formed by: border, wall, outer intermediate, inner intermediate and a quartz core zones; several filling and replacement units were recognized.

The mineralization is composed by quartz, albite, microcline, muscovite, beryl, spodumene, ambligonite-montebrazite, lepidolite, schorl, elbaite, apatite, garnet, varulite-hagendorfite, dickite, illite, and kaolinite.

The zoning of primary units, the distribution and nature of the mineral assemblages and the geochemical indicators present in this deposit, constitute excellent guides to be applied in the exploration of pegmatites of identical typologies. Concentrations of some major and trace elements in K-feldspar and muscovite provide information related to the mineralization contained in the pegmatite body.

Following the current classification system (Černý 1991) the deposit can be classified as complex type, spodumene subtype, and rare-element class pegmatite. The K-feldspar and muscovite geochemical data support this hypothesis.

9 REFERENCES

Bailey W. 1980. Structures of layer silicates. *Crystal structures of clay minerals and their X-ray identification* (G. W. Brindley and G. Brown Eds.). Min. Soc. London: 1-123.
Brisbin W. 1986. Mechanics of pegmatite intrusion. *Am. Min.* (71): 644-651.

Cadile S. 2003. *Mineralogía, geoquímica, petrogénesis y potencial económico de los yacimientos Yatasto y San*

Bernardo, Departamento San Martín, San Luis, Argentina. Tesis de Licenciatura UNSL. San Luis, Argentina.

Černý P. 1991. Rare-element granitic pegmatites Part. I: anatomy and internal evolution of pegmatite deposits. *Geosc. Can.* (18, II): 49-67.

Chadwick R. 1958. Mechanisms of pegmatite emplacement. *Bull. Geol. Soc. Am.* (69): 803-836.

Galliski M., Márquez Zavalía M., Oyarzábal J. & O. Cortona 1994. Geología de una pegmatita de tipo albíta: la mina Independencia Argentina. *Rev. Asoc. Geol. Arg.* (49): 306-312.

Galliski M., Perino E., Gásquez J., Márquez Zavalía M. & R. Olsina 1997. Geoquímica de feldespatos potásicos y muscovitas como guía de exploración de pegmatitas graníticas de algunos distritos de la provincia pegmatítica pampeana. *Rev. Asoc. Geol. Arg.* (52): 24-32.

Kroll H. 1973. Estimation of Al,Si distribution of feldspars from the lattice translations $tr[110]$ and $tr[1-10]$, I: alkali feldspars. *Contrib. Min. Petrol.* (39): 141-156.

Kroll H. & P. Ribbe 1987. Determining (Al,Si) distribution and strain in alkali feldspars using lattice parameters and diffraction-peaks positions: a review. *Am. Min.* (72): 491-506.

Oyarzábal J. 2004. *Geología, mineralogía, geoquímica y petrogénesis de yacimientos pegmatíticos del Distrito Totoral, Sierra de San Luis, Argentina.* Tesis Doctoral UNC. Córdoba, Argentina.

Yoder H. & H. Eugster 1955. Synthetic and natural muscovites. *Geochim. Cosmochim. Acta* (8): 225-280.

The Use of Mineralogical Data for Estimating Iron Ore Reserves

W.C.Pereira

Mine Operation Superintendent, M.Sc - SAMARCO MINERAÇÃO S.A.

A.Z.Remacre

Ph.D., Professor at the Geoscience Institute – UNICAMP

ABSTRACT: This paper presents a specific mining application to estimate iron ore reserves, which uses mineralogical data, instead of the usual chemical variables. In the suggested procedure, the geostatistical methods of kriging and conditional simulation are used to characterize the mineralogy in block models. Cut-off grades and recoverable reserves are determined by using the recovery functions average grade and ore tonnage, adopting, as an assumption, that the required specification of the reserves is already established, in terms of the mineralogical content mode. Cut-off grades and recoverable reserves calculated by kriggeage model and by conditional simulation model are compared and show significant differences. The methodology was applied in the Alegria Mine, an iron deposit located in the state of Minas Gerais, in the south-east region of Brazil, and it is justified by the influence of the mineralogy in the performance of the industrial processes and in the physical properties of the iron ore products.

1 INTRODUCTION

The mineralogical composition is the principal conditioner of the performance of the iron ores in the stages of mining and industrial steel processes. Among the iron ore minerals, the specular hematite is one of the minerals that contributes to a better physical quality of the iron ore pellets and, as consequence, influences in the productivity of the pelletization and in the subsequent handling of the pellets. The influence in the performance of the industrial processes and in the physical properties of the iron ore products justifies the utilization of the variable grade of specular hematite (SH) for estimating reserves of iron ore and this is the purpose of this work.

2 METHODOLOGY

The methodology used consisted of:

1 – Implementation of estimation and simulation geostatistical models of the variable SH in mine blocks.

2 – Selection of cut-off grades through the use of the recovery function average grade and estimation of reserves through the use of the recovery function ore tonnage.

3 GENERAL INFORMATION OF THE AREA STUDIED

The area studied is localized in a specific region of the Alegria Mine, which is a property of Samarco Mineração S/A, a company that is a producer and exporter of iron ore pellets. Its ore reserves are situated in the east portion of an iron complex named Quadrilátero Ferrífero, localized in the state of Minas Gerais, in Brazil. Although the processes of beneficiation and pelletization in Samarco have flexibility to accept variations in the mineralogical characteristics of iron ore, they are normally adjusted to receive iron ore whose average grade of SH is 47% in mineral volume.

4 LOCALIZATION OF THE MINERALOGY DATA

The data utilized in this study are mineralogical analysis of core samples from exploration diamond core drilling boreholes, composited in 8m, corresponding to research grids of 100x100m and 50x50m in the directions north-south (NS) and east-west (EW), respectively; and also of pneumaticdrilling holes 8m deep, corresponding to a

grade control grid of 25x25m, in the same directions.

The SH data is preferentially located in the south-west portion of the area studied, which corresponds to the region with the highest grades of SH and where the current mining operations are concentrated.

5 STATISTICAL ANALYSIS AND SPATIAL VARIABILITY

To utilize data of exploration and grade control drillholes together, and since the holes are mainly localized in regions with higher grades of SH, a declustering technique was applied, by establishing test grids that permitted an association of one weight for each sample and posterior selection of the grid that produces the lowest average grade {"cell declustering", Isaaks & Srivastava (1989), page 243}. Experimental variograms were made in the main directions NS, EW and vertical. An spherical model was adopted, whose proximity to the origin is approximately linear and with less inclination in the direction north-south, showing this to be the direction of greater continuity.

6 GEOSTATISTICAL SIMULATION AND ESTIMATION MODELS

The method of geostatistical simulation used was the sequential gaussian (SGS), conditioned to the SH data. 50 simulations were made in a fine grid with the dimensions of 3,125 x 3,125 x 8m (dimensions along the directions NS, EW and vertical, respectively), in order to reproduce the variable SH in the level of punctual support, totalling 469.824 simulated knots. After the validation of the results obtained in terms of statistical and spacial characteristics of the simulations of SH in the knots of the grid of 3,125 x 3,125 x 8m, simulations of the SH in mine blocks were implemented. A procedure of change of support was used, in which the value simulated in one mine block was equivalent to the average of the values simulated in the interior knots of this block. The change of support was done for 2 supports of blocks, the first being on 9788 blocks of 12.5 x 12.5 x 24 m and the second on 2447 blocks of 25 x 25 x 24 m (dimensions along the directions NS, EW and vertical, respectively). The choice of these two distinct supports is due to the fact that, in Samarco, a grade control in the grid of 12,5 x 12,5 m is used for chemical variables and another grade control in the grid of 25 x 25 m is used for mineralogy variables. In this way, the purpose is to compare the results of the estimate of reserves in those 2 supports. The results of this procedure are shown in Table 1, where is also shown a comparison

of the results from geostatistical estimates by kriging. In this table are presented, initially, the results of three (3) simulations chosen randomly (simulations 01 (S -01), 27 (S - 27) and 44 (S - 44)), followed by the average result of the 50 simulations. These results reflect a combined action of the effects of support and of information (Matheron 1984) (Rivoirard 1987), besides the characteristic smoothing effect of the real variability in kriging (Journel & Huijbregts 1987) that caused a reduction of the variability of the krigged blocks, when compared with the simulations.

Table 1. Comparative Statistical Summary: Simulation and Kriging

%SH in Mine Blocks	Blocks 12,5 x 12,5 x 24 m	
	Average	Standard Deviation
Simulation		
S_01	27.48	20.36
S_27	27.82	21.17
S_44	27.64	20.85
Average of 50 Simulations	27.80	21.24
Kriging	27.71	19.39

%SH in Mine Blocks	Blocks 25 x 25 x 24 m	
	Average	Standard Deviation
Simulation		
S_01	26.66	19.57
S_27	26.91	20.59
S_44	26.74	20.02
Average of 50 Simulations	26.95	20.58
Kriging	26.66	19.26

7 DETERMINATION OF CUT-OFF GRADES AND ESTIMATION OF RESERVES

According to Rivoirard (1994), the calculation of recoverable reserves depends on the establishment of the relationships between tonnage and grade, which are obtained through specific functions, named recovery functions. With the results of the kriging and the simulations, the curves of the recovery function $m(z)$, average grade versus cut-off grade, were done. The purpose was to establish a group of cut-off grades that guarantees the required specification of SH. These curves are shown in Figure 1, where the values are in percentages of SH.

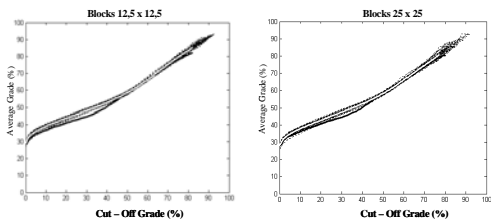


Figure 1. Curves of the function $m(z)$

As mentioned previously, the mining process in Samarco has to produce ores with average grade of 47% of SH. In this way, by analysing the curves of the function $m(z)$, for an average grade of 47%, 50 equiprobable values of cut-off grade are obtained from the simulations and one single value of cut-off grade is obtained from the kriging, for each one of the block supports considered. Table 2 provides the summary of the statistics of the 50 cut-off grades of the simulations, as well as the value of the cut-off grade estimated by kriging. In this table, the code *ct* means cut-off grades and the values are in percentages of SH.

Table 2. Summary Statistics of the cut-off grades to obtain the average grade of 47% SH

Cut-Off Grades	Blocks 12,5 x 12,5 x 24m	Blocks 25 x 25 x 24m
Minimum (Min_ct)	24.16	25.38
Inferior Quarter (Q1_ct)	26.29	28.27
Average (Avg_ct)	27.15	29.07
Superior Quarter (Q3_ct)	27.69	29.86
Maximum (Max_ct)	30.15	32.50
Kriging	34.79	35.30

The curves of the recovery function $T(z)$, ore tonnage versus cut-off grade, are shown in Figure 2. For all curves, the value of $T(z)$ has the meaning of recoverable reserves of iron ore in terms of percentage of the total tonnage of the mineral resource available in the region studied. In this study, the recoverable reserve depends only on the cut-off grade adopted (unique constraint), accepting, for simplification, that the choice of each block is carried out without considering its location and neighbourhood.

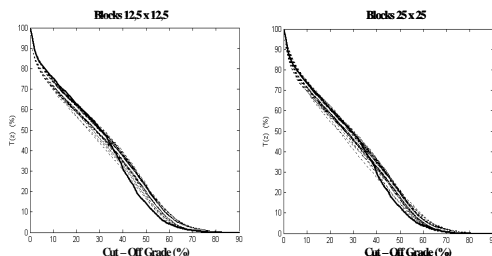


Figure 2. Curves of the function $T(z)$

The analysis of the variation of the 50 resulting reserves per each cut-off grade selected was done considering the minimum, medium and maximum values. The results of this procedure are given on Table 3 (in percentages of total mineral resource). On this table are also shown 2 values of reserves obtained from the kriging, coming from the two krigged cut-off grades, being 1 value for each support. By analysing Table 3, one can affirm that the selection of reserves obtained from the simulations indicates a gain of tonnages in relation to the selection of reserves obtained from the kriging, for all the cut-off grades analyzed.

Table 3. Results of the reserves estimates

Support	Cut-off grades (ct)	Value of ct (%SH)	MINIMUM RESERVE (%)	AVERAGE RESERVE (%)	MAXIMUM RESERVE (%)
Blocks 12,5 x 12,5 x 24 m	Min_ct	24.16	51.25	55.82	58.62
	Q1_ct	26.29	48.36	53.35	56.15
	Avg_ct	27.15	47.19	52.33	55.26
	Q3_ct	27.69	46.53	51.70	54.59
	Max_ct	30.15	43.49	48.78	51.69
	KRIGING			43.17	
Blocks 25 x 25 x 24 m	Min_ct	25.39	49.53	54.40	57.05
	Q1_ct	28.27	45.82	51.02	53.88
	Avg_ct	29.07	44.83	50.08	52.92
	Q3_ct	29.86	43.87	49.12	52.01
	Max_ct	32.50	40.48	45.94	48.95
	KRIGING			39.98	

Selection of reserves by blocks of 25 x 25 x 24m projected losses of tonnage in relation to the selection by blocks of 12,5 x 12,5 x 24m, as much as for the model estimated by kriging, as much as for the simulation model. These results suggest a change of the grid of the grade control of SH, from the current grid of 25 x 25m to the grid of 12,5 x 12,5m. To define the viability of changing the grid of the grade control of SH from 25 x 25m to 12,5 x 12,5m, it was checked if the increase in costs due to the execution of a larger number of grade control boreholes and mineralogical analysis can be compensated economically by removing less tonnages of waste material, when utilizing blocks of

12,5 x 12,5 x 24m. In fact, for each borehole of the grid of 25 x 25m, there will be 4 correspondent boreholes in the grid of 12,5 x 12,5. On the other hand, the selection by blocks of 12,5 x 12,5 x 24m projected higher tonnages of reserves in relation to a selection by blocks of 25 x 25 x 24m and the difference between the reserves of these two supports for each level of cut-off grade is equal to the additional tonnage of waste that would be generated in case of using blocks of 25 x 25 x 24m. Considering the specific costs C_{25} (cost of execution plus mineralogical analysis of boreholes in the grid of 12,5 x 12,5) and CE (cost of waste) in monetary units per percentage of the total mineral resource.

In order for the change of the grade control grid from 25 x 25m to 12,5 x 12,5 to be compensatory, the following condition must be obeyed:

$CE/(C_{12}-C_{25}) > 1$ This condition means that the cost of waste removal must be superior to the increase of cost projected to maintain a finer grade control grid. Since $C_{12} = 4C_{25}$ and $CE = 1923C_{25}$ (in accordance with information provided by Samarco), it results that $CE/(C_{12}-C_{25}) = 641$. So, the proposed change of grid is compensatory enough. The future economy due to the use of the grid of 12,5 x 12,5m in relation to the current 25 x 25m grid can be obtained by : $(R_{12}-R_{25}) * (CE - (C_{12}-C_{25}))$ in monetary units, being R_{12} and R_{25} the recoverable reserves in percentage of total mineral resources obtained from the selection in blocks of 12,5 x 12,5 x 24m and 25 x 25 x 24m, respectively.

8 CONCLUSIONS

1. Compared to kriging, the conditional simulation is a better alternative to reproduce the reality of the grades in terms of their variability, spatial distribution and continuity. In this way, the simulated cut-off grades obtained allowed to calculate reserves that are potential representatives of the unknown real recoverable reserve.
2. Due to the characteristic smoothing effect of the real variability in kriging, the krigged cut-off grade led to a conservative estimate of reserves (underestimation), compared to the estimates obtained by the simulations, for both supports of blocks considered.
3. Through the models of conditional simulation implemented, two groups of cut-off grades and equiprobable reserves were established, one for each support of block considered. In both cases, the intervals of variation of the reserves represent the uncertainty in tonnage. The knowledge of this uncertainty will support the decision in the choice of one specific from the

group of cut-off grades and the consequent determination of the correspondent reserve, as a function of the level of risk tolerance accepted to work with. In the case of kriging, it is not possible to assess this uncertainty, because only one value of reserve is obtained, for each support of block.

4. The results obtained showed that the increase in the mining selectivity, as a result of the change of the dimensions of the mine blocks from 25 x 25 x 24m to 12,5 x 12,5 x 24m, projected gains of tonnage of the ore reserves. These variations are caused by the distinguishable degradation of the curves of the recovery functions $m(z)$ e $T(z)$ for both supports of blocks, which can be explained by the joint combination of the information and support effect. Besides, the cost of the increase of the number of grade control boreholes and mineralogical analysis, due to the change of the grid of the grade control, from 25 x 25m to 12,5 x 12,5m, was very compensated by the economy generated through the reduction of the strip ratio for blocks of 12,5 x 12,5 x 24 m, which validated the increase of the mining selectivity.

9 REFERENCES

- Isaaks, E. & Srivastava, R. 1989. *An Introduction to Applied Geostatistics*. New York: Oxford University Press Inc.
- Journel, A. & Huijbregts, C. J. 1978. *Mining Geostatistics*. New York: Academic Press.
- Matheron, G. 1984. The Selectivity of the Distributions and "The Second Principle of Geostatistics". *Geostatistics for natural resources characterization*. Lake Tahoe USA: D. Reidel Publishing Company: p. 421-433.
- Rivoirard, J. 1987. *Advanced Geostatistics*. Fontainebleau, France: Centre de Géostatistique, École des Mines de Paris, C - 131.
- Rivoirard, J. 1994. *Introduction to Disjunctive Kriging and Non-Linear Geostatistics*. Oxford, England: Oxford University Press: 180p.

Petrology and Geochemistry of Mafic-Ultramafic Pods Around Bababudan – Nallur Lineament in Western Dharwar Craton, India: Implication for PGE Mineralisation

P.V.Sunder Raju & T.S.Madood Hussain
 National Geophysical Research Institute, Hyderabad, India

ABSTRACT: Mafic-Ultramafic (MUMF) suite rocks of Archaean age occur as discontinuous bodies near Bababudan-Nallur (BN) lineament in western Dharwar Craton of South India. Studies were carried out on these MUMF to know the nature, composition, and probable PGE mineralisation in these rocks. These MUMF, which occur as enclaves in gneisses ranging in size from tens of meters up to 4 kms trending NNW with steep dips. These MUMF pods consists of meta-peridotites, tremolite-actinolite schists, serpentinites, amphibolites and metabasalts with minor gabbro dykes and thin chlorite and glimmerite veins. Nodular and ocelli structures occur in the talc-serpentine rocks. EPMA studies carried out on the amphibole grains show presence of subrounded to rounded 20-25µm chromite grains which show presence of platinum. The overall major element composition of MUMF rocks show high MgO (22-40%) and total iron (8.34 -10.01%) contents and few samples show komatiitic affinity. The occurrence of ultramafics as enclaves within the gneisses is similar to the mafic ultramafic association of the nearby Archaean greenstone belts having chromite deposits. But, PGE is not yet reported from these older schist belts. With the encouraging values of PGE in the present MUMF which are comparatively younger and nearer to the BN lineament, these MUMF seems to be a promising target area for PGE mineralisation.

1 INTRODUCTION

Deposits containing Ni,Cu and Pt group elements (PGE) are normally found in association with mafic-ultramafic rocks (Barnes 1999). Keays and Campbell (1981), Barnes and Naldrett (1987) suggest that PGE crystallise directly from silicate magmas, or that they were transported as tiny grains in chromites or olivines or as silicate nucleations evolved by the magma from the mantle. However, the PGE commonly exhibit chalcophile behaviour. Mafic and Ultramafic igneous rocks are the most PGE rich of the common crustal rocks (Crocket 1979). Sequences of differentiated mafic and ultramafics bodies, layered complexes (early to late Archean age) associated with sulphides, chromite and associated titanomagnetite need detailed exploration of PGE in India (Raghunandan 1991). The Western Dharwar Craton host several mafic-ultramafic rocks, and Ti-Vanadiferous magnetite and chromitite deposits existing in and around Bababudan-Nallur lineament (Fig 1). The purpose of this paper is to study the mineralogy of mafic and ultramafic rocks in relation to PGE mineralisation and use major and trace and REE element data to characterize the chemical composition of the mafic

and ultramafic suite of rocks and interpret the geochemical and petrological significance of the mafic-ultramafic hosting PGE mineralisation.

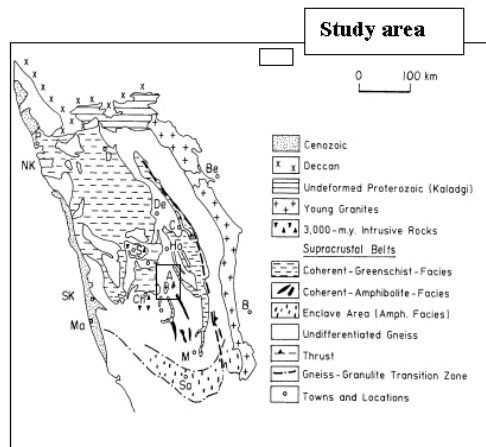


Figure 1. Geological map with Western Dharwaras showing study area as (A) corresponding to Arsikere area which cuts BN lineament. Modified after (Naqvi & Rogers 1997).

2 GEOLOGY OF THE AREA

Mafic-Ultramafic (MUMF) suite rocks of Archaean age occur both as concordant as well as discordant bodies near Bababudan-Nallur (BN) lineament in Western Dharwar Craton of South India.

The area extends up to 400 km² in an north wards trending strike direction. This prominent lineament occur within enclaves (Sargur Schist Complex) in gneisses trending in NW-SE direction (with Arsikere-Banawar granite in South Western part and Kadur granite in the west of the area for more than 50 km in strike length. These MUMF, which occur as enclaves in gneisses range in size from 20x200m to 200x400M with varying lengths up to 5 km trending NNW-NS with steep dips. These MUMF pods consists of metaperidotites, tremolite actinoliteschists, serpentinites amphibolites and metabasalts with minor gabbro dykes and thin chlorite and glimmerite veins. Nodular ocelli structures occur in talc- serpentine rocks.

3 MINERALOGY AND PETRO-CHEMISTRY

Petrological studies reveal that the talc serpentine and tremolite-actinolite schists are peppered with opaque dust mostly at the grain boundaries of the constituent minerals as well as the serpentine rich ground mass. The rocks have mineral assemblage of serpentine, antigorite, talc, tremolite, actinolite, hornblende, chlorite, biotite, sulphide, chromite, magnetite, ilmenite, titanomagnetite and plagioclase. The rocks have undergone greenschist to amphibolite facies metamorphism. EPMA stuides carried out on the amphibole grains show presence of rounded to subrounded chromite grains with chemical compositions varying from (Cr 10-14 in wt%). It is suspected that many minerals occur as euhedral crystals enclosed in chromite grains (Fig.2).

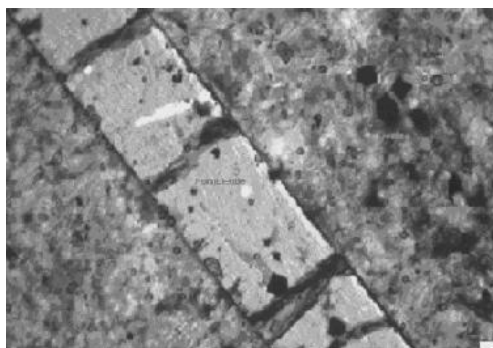


Figure 2. 20-25µm euhedral chromite grains in talc matrix (X 630).

They show varying degree (least-moderate) chemical alterations of serpentinisation, steatitisation and chloritisation. Fresh tremolite actinolite schists and chrome bearing titanomagnetite samples coincidentally are enriched in PGE tenor. The rarity of Pt bearing magmatic PGMs as inclusions in chromite (Merkle 1989, 1992) implies that Pt content of chromite layers was almost exclusively concentrated by the immiscible sulphide melt (Vongruenwaldt & Merkle 1995). Spinel is relatively rich in Pt, constitute a relatively large proportion of this limited partial melt, thus accounting for the high Pt/Pd ratio (Naldrett & Cabri 1976).

Out of 58 samples collected three major rock groups are identified as (metaperidotite/serpentinites, tremolite actinolite schist/Talc actinolite schists or mafic rocks). Twenty samples are Talc/actinolite schists. Sixteen samples are tremolite actinolite schists and twenty samples are mafics with two glimmerite samples. The averages of MgO, TiO₂ and K₂O contents of mafic/ultramafics i.e. 37.00, 0.28 and 0.06% respectively. The CaO/Al₂O₃ ratio is significantly very high with 0.54 to 2.45. The samples containing high CaO/Al₂O₃ ratios are also enriched in PGE concentrations with an average Pt of 400 ppb. The Mg# (Mg/ Mg + Fe⁺⁺) ratio nearer to 0.7 is generally considered to be characteristic feature of cumulates. This ratio for the MUMF rocks is nearer to 0.7. This indicate that these rocks may not be cumulates. High contents of Nickel and Chromium (~5000, 7800 ppm) are reported in these MUMFs. The Table 1 show a partial chemical analysis of varied rocks present.

Table 1. Analyses of mafic-ultramafic rocks.

	1	2	3	4
SiO ₂	46.84	45.99	41.02	48.44
TiO ₂	0.09	0.03	0.04	0.3
Al ₂ O ₃	2.3	0.89	1.34	6.17
Fe ₂ O ₃ T	8.6	10.26	8.56	10.22
CaO	1.58	0.05	0.25	6.31
MgO	37.94	40.06	41.67	26.93
Ni (ppm)	5884	1079	1751	1029
Cr	6000	7200	5200	3200
Cu	42	51	10	33
Zn	157	233	31	66
PGE (ppb)				
Pt	1220	1685	758	650
Pd	800	900	625	800.
Au	78	370	80	75

1.Tremolite actinolite schist 2. Actinolite 3.Serpentinite
4.Glimmerite

The Chondrite normalized REE patterns show pronounced negative europium anomalies (Fig 3).

The REE show slightly fractionated patterns with enriched LREE (LREE/HREE ~ 5.0).

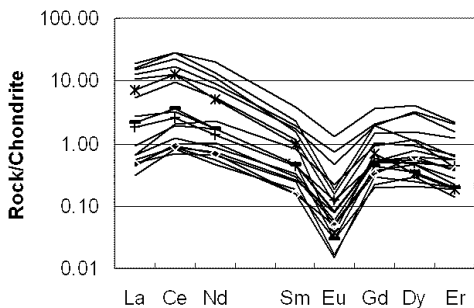


Figure 3. Ree patterns

3.1 Implications for exploration

The present study indicates that the concentration of the PGE in mafic/ultramafic suite of rocks in Western Dharwar are at-least partially controlled by various degrees of partial melting of contrasting geological set-ups. As these MUMF complexes occurring in BN lineament have characteristic features of stratiform intrusions in having calcic clinopyroxene, no orthopyroxene or plagioclase, abundant hornblende, more iron rich chromite, and magnetite and ratios of 0.29 -1.30 (Pt/ Pt+Pd), suggest that they offer prospect for economically important Cr-Pt sulphide deposits in similarity to Alaskan type ultramafites (Naldrett 1976). The summarized data presented here and in (Sunder Raju et al. 2003) suggest that the potential of the MUMF sequences as a potential targets for PGE mineralisation. The PGE and sulphide contents of our samples are, however, relatively variable, in accord with the general lithological heterogeneity of the MUMF along the BN lineament in western Dharwar, India. This raises the possibility that the local structural and lithological controls have played a significant role in elevated sulphide and PGE contents sporadically.

4 CONCLUSIONS

Chromite was probably the principal PGE collector in these mineralized zones. Sulphides are regarded as the primary collectors of PGE and sulphide precipitation is the main controlling factor for the Pt and Pd enrichment.

5 REFERENCES

- Barnes S. J. & Naldrett A. J. 1987. Fractionation of the Platinum Group of Elements and gold in some komatiites of the Abitibi Greenstone belt , Northern Ontario, *Eco.Geol* V82 pg 165-183.
- Barnes ,S.J et , Maier ,W.D. 1999. The fractionation of Ni,Cu and the noble metals in silicate and sulphide liquids. In *Dynamic processes in Magmatic ore deposits and their application in Mineral Exploration*. Edited Par , Keays, R.R,CEG, Geological Association of Canada, Short course volume 13, p 69-106.
- Crocket , J.H. 1979 Platinum group elements in mafic and ultramafic rocks : a survey , *Canadian Mineralogist* V 17 391-398 .
- Keays, R.R. & Campbell, H. 1981. Precious metals in the timber lava intrusion, Western Australia : Implication for the genesis of plantiferous ores in layered intrusion. *Economic Geology* V 76 Pg 1118-1141.
- Merkle, R.K.W. 1989a. Estimation of recovery characteristics of platinum group minerals in some chromiite layers below UG-2 in the Bushveld complex, South Africa. In *Magmatic sulphides- The Zimbabwe volume*. Edited by Prenderghast ,M.D AND Jones, M.J PP 81-86 ,Institution Mining Metallurgy,London
- Merkle, R.K.W. 1992. Platinum group minerals in the middle group chromiite layers at Marikana, Western Bushveld complex: Implication for collection mechanisms and post magmatic modification. *Canadian Journal Earth Sciences* 29, (209-221).
- Naldrett, A.J. & Cabri, L.J. 1976. Ultramafic and related mafic rocks: Their classification with special reference to the concentrations of Ni sulfides and Platinum group elements *Economic Geology* v 71 pp 1131-1158.
- Naqvi, S.M. and Rogers, J.W. 1987 *Precambrian Geology of India*, Oxford Univ.press, pp 1-223.
- Raghunandan 1991. Notes on Geological settings and exploration of PGE in *Journal of Geological Society Of India* , Vol 38 No 6.
- Sunder Raju, P.V & Hussain, S.M. 2003. The use of metal ratios in prospecting for PGE mineralisation in mafic-ultramafic rocks by ICP-MS in and around Bababudan – Nallur Lineament in Western Dharwar in Karnataka, in *ISMAS, Volume II* pages 589- Editor S.K Aggarwal . ISMAS Publication
- VoGruenewaldt, G. & Merkle R.K.E. 1995. Platinum group element proportions in Chromiites of the Bushveld Complex: Implications for fractionation and magma mixing models. *Journal of Africa Earth Sciences*. Vol 21, No 4 pp 615-632..

Detailed EDXRF-based Chemostratigraphy of Pt-ore of the Bushveld-Complex, SA

D.Rammlmair, F.Melcher, Je.Lodziak
BGR, Hannover, Germany

R.Merkle
Univ. Pretoria, South Africa

ABSTRACT: Within the Busveld Complex Ni-Cu-PGE mineralization occurs in individual horizons. Drill cores of the UG-2 chromitite of the “Critical Zone” and the Merensky Reef have been investigated chemically in detail by continuous energy dispersive x-ray fluorescence (EDXRF) scanning in 50 µm steps with the geoscanner. Polished thin sections were obtained from anomalous zones regarding Cr, Ti, Cu, Ni, Pt and Pd contents and mapped in 100 µm steps by the EDXRF-microscope to localize individual mineral grains. Electron microprobe analysis was used to verify PT-anomalous zones and to identify individual PGM grains. The UG-2 drill core was mapped in detail. Ca, Fe, Cr and Ti reflect textural peculiarities showing aggregates of chromite grains being alternating embedded in a plagioclase or pyroxene matrix.

1 INTRODUCTION

In the Bushveld complex, the largest known layered intrusion (66000 km²) a strong mineralogical and geochemical variation in the rock succession and in individual layers can be observed. Factors influencing these changes are density and viscosity of the silicate melt as a function of temperature and composition, cooling rate, assimilation, geometry of the magma chamber, volume ratio of the melts and distance from the magma channel (Penberthy & Merkle 1999).

Both, the Merensky Reef and the UG-2, a chromitite layer of the „Critical Zone“ show significant differences in the thickness of layers, chromite composition, sulfide and platinum-group minerals (PGM) ratios, platinum-group element (PGE) distribution, as well as in intensity and characteristics of late and post-magmatic overprinting. Numerous scientists have investigated the mineralogy of silicates, oxides, sulphides and PGM's, their genesis, alteration pattern, metasomatism, tectonic overprint. The geochemistry of major and trace elements and especially of valuable metals such as Ni, Cu, Co and PGE's has been obtained in the cm- to m-scale. Former investigations have shown a relationship of PGE to

chromitite thickness, variable Pt/Pd and Pt/Rh ratios according to localities.

Magma mixing might explain these distribution patterns. The re-distribution of PGE due to basal erosion, „potholes“, and alteration might create regional differences in the PGM-ratios.

These traditional methods to investigate the vertical and lateral variation are time consuming and cost intensive, and might not always locate the anomalous zones due to in-appropriate sampling.

In this paper new and fast, easy to handle methods are invoked and combined with traditional methods to localize and to approve Ni/Cu/PGE- anomalies, to characterize drill cores chemically and to relate the chemistry to the mineralogy. This might form a valuable base to show the relationship of Ni, Cu, and PGE's to other trace elements within vertical profiles and lateral extension.

2 METHODS

The application of the destruction free energy dispersive x-ray fluorescence analyses (EDXRF) on half cores with a smooth surface shown for examples from UG-2 and Merensky Reef offers a relatively cheap and fast, but not problem free

alternative for acquisition of chemical patterns (standard measurement conditions: Mo-tube, 45 kV, 30 mA, 20 sec, 50 μm x 2000 μm flat beam, 50 μm step size) (Figure 1). The continuous simultaneous measurement of semi-quantitative data of relevant elements (such as K, Ca, Ti, Cr, Mn, Fe, Ni, Cu, Pt, Pd) with high spatial resolution provides information on chemically anomalous zones, cryptic layering and allows a detailed sampling of these zones of the core Rammilmair et al. (2001) described the methods in detail.

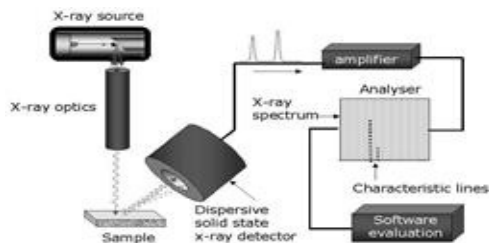


Figure 1: Measurement principle (courtesy of COX Analytical system AB, Sweden)

From these selected samples polished thin sections have been prepared and mapped by EDXRF (Mo-tube, 100 μm \varnothing mono-capillary, 45 kV, 30 mA, 0.5 sec, 100 μm step size). The results manipulated by image analyses and selected groups of elements were combined to false color images to show mineral distribution. Anomalous zones regarding Pt, Pd, Cu, Ni, Ti, and Cr distribution were investigated microscopically and by microprobe. A number of PGM's could be located by these means.

3 MINERALOGY

The mineralogy of the UG-2 chromitite layer is complex and has been described in detail by Penberthy & Merkle (1999) and Cawthorn et al. (2002).

Primary silicates such as plagioclase, orthopyroxene with intercumulus clinopyroxene, some phlogopite and pargasitic hornblende have been reported besides traces of a Zr-Ti-phase, REE-oxide, badellyite, sphene, Cl-apatite, zircon, prehnite, epidote, tremolite, chlorite, quartz, albite, pumpellyite, calcite (partly secondary). Chromite might show a reaction rim of orthopyroxene or plagioclase. Sulides such as pentlandite, chalkopyrite pyrrhotite occur at grain boundaries of chromite and silicates. Pentlandite shows pyrite inclusions, and is partly replaced by millerite. Galena is rarely found.

The PGE concentrations reach 3 to 6 ppm (Pt + Pd + Rh + Au), and are found as discrete grains or as solid solution in pentlandite. A number of PGM's such as Pt-Pd-Ni-sulphide (braggite, vysotzkite), Pt-S (mainly cooperite), Pt-Rh-Ir-Cu-S (cobaltian malanite), Ru-Os-Ir-S (laurite-erlichmanite), PGE-Bi-Te (various tellurides, bismutellurides), PGE-As-S (e.g. hollingworthite, irarsite, ruarsite, sperrylite, majakite) are named by Penberthy & Merkle (1999).

4 RESULTS

Results from the fast scanning method could be approved microscopically and by microprobe investigations. Combined element distribution and ratios of Ca, Fe, Cr, Ni, Cu, PGE along profile show the plagioclase – pyroxene/olivine – chromite – sulfide - PGM distribution, respectively.

4.1 Geoscanner

Element distribution profiles have been combined with optical scans to highlight zones of interest. The Fe and Ca contents reflect basically the plagioclase / pyroxene distribution, Cr stands for chromite and Cr-enriched clinopyroxene. Ni and Cu show zones of sulphide mineralization. Close to chromitite layers Ni might be incorporated in olivine, too. Pt and Pd show local enrichment corresponding to Ni anomalies or being isolated (Figure 2). These anomalies certainly require more detailed investigation by other methods like microprobe.

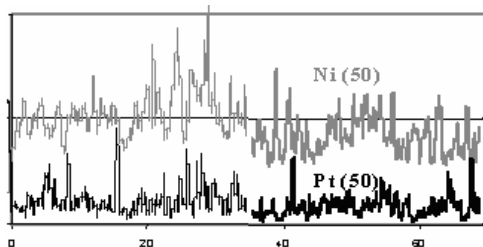


Figure 2: Distance from contact to anorthosite

4.2 EDXRF microscopy

Almost 70 cm of a UG-2 chromitite core of 3 cm \varnothing were scanned in 100 μm steps for major and trace elements. The Element distribution maps were combined by image analytical methods. The combination of three diagnostic elements such as Ca, Fe, Cr separates plagioclase from olivine/pyroxene and chromite and reveals interesting textural pattern (Figure 4) related

probably to magma mixing. Chromite is embedded either in a plagioclase or an orthopyroxene matrix.

K, Al and Si show zones of phlogopite and quartz; Fe, Ni, Cu differentiate between Ni in olivine or sulphide, whilst elevated PGE relate to PGM or to crystallographic signals of pyroxene.

The chemical pattern were controlled by polished thin sections, scanned with 100 μm steps (Figure 5) for chemical pattern and scanned optically by a slide scanner at // and crossed polars providing additional information on grainsize distribution and mineralogy of the material.

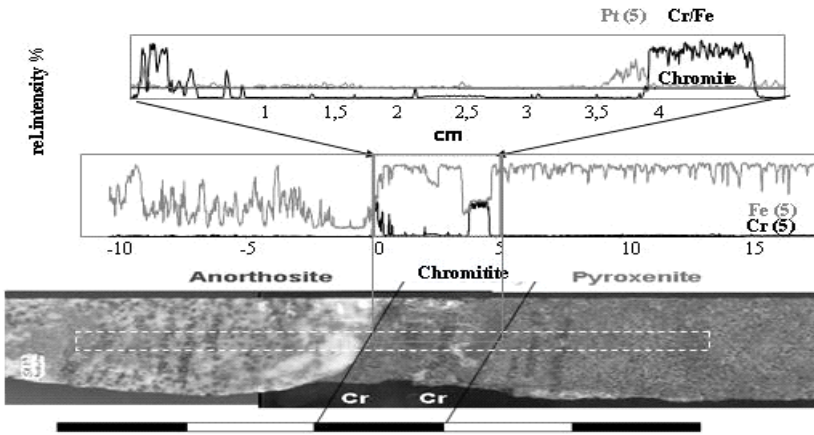


Figure 3: Section through the merensky reef showing the chemical expression of the anorthosite, the chromitite and the pyroxenite. Relative intensities are presented as moving mean of 5 points. Pt shows distinct enrichment close to the chromitite

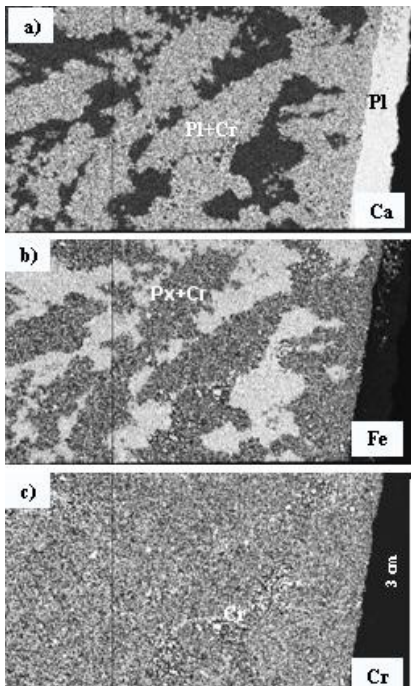


Figure 4: Ca, Fe, and Cr distribution in UG-2 chromitite showing mineral textures. Chromite (c) aggregated by plagioclase (a) or pyroxene (b) (white).

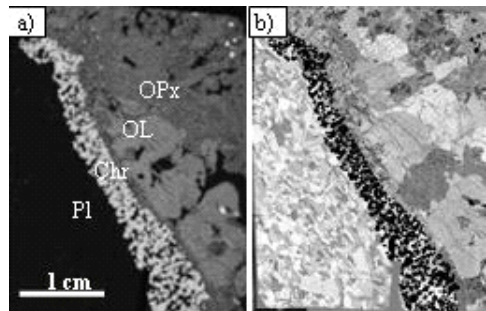


Figure 5: Polished thin section showing plagioclase, chromite, olivine and orthopyroxene identified by a) a mixture of Cr, Fe and Ni obtained by EDXRF, and b) by mixed images obtained from the optical microscope by // and X polars.

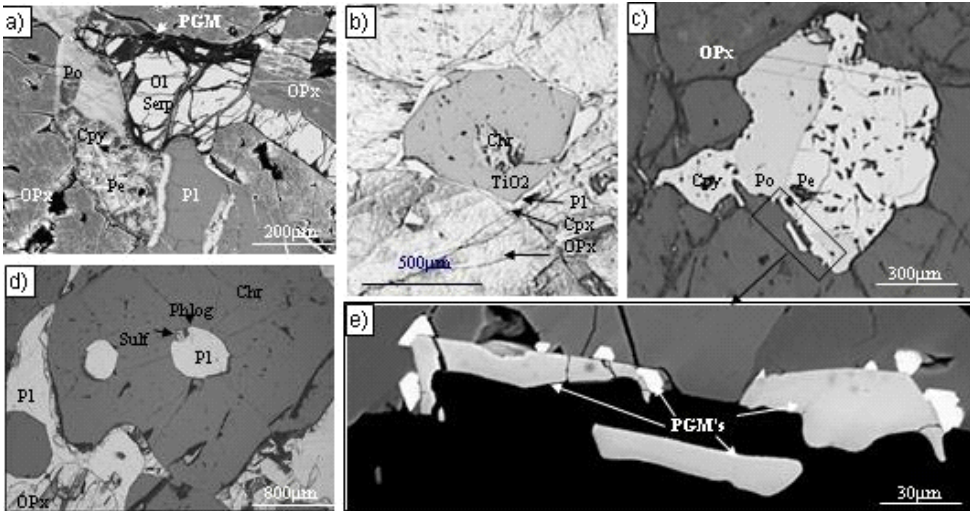


Figure 6: Microprobe back scattered electron (BSE) images showing a plagioclase (Pl), olivine (Ol), serpentine (Serp), ortho- and clinopyroxene (OPx, CPx), phlogopite, (Phlog), chromite (Chr), rutile? (TiO₂) oxides, sulfide? (Sulf), pyrrhotite (Po), pentlandite (Pe), chalcopyrite (Cpy), and various platinum-group minerals.

4.3 Electron microprobe

The zones of interest with anomalous Ni, Cu, and PGE values obtained from the EDXRF-based element distribution maps and microscopy were further investigated in detail by microprobe. A number of platinum-group minerals could be verified by this method (Figure 6).

5 CONCLUSION

EDXRF provides 1D- and 2D-element distribution patterns from drill cores and polished sections and polished hand specimen. A number of trace elements are influenced by matrix changes and diffraction peaks. One dimensional (1D) profiles reflect the mineral ratios of plagioclase, pyroxenes, olivine and chromite and of chalcopyrite and pentlandite. Zones of mineralization, hydrothermal alteration and tectonic overprint can easily be localized and sampled. Two dimensional (2D) distribution patterns provide information on the mineral distribution and rock texture.

Even PGE's can be traced by both the 1D- and 2D-methods, down to sizes around 25µm, verified microscopically and by SEM and microprobe.

The amount of appropriate samples for detailed investigation can be reduced. Problems arise due to the interference of trace element signals, e.g. PGE, with crystallographic peaks of pyroxenes for example. This interference is hardly to be identified along profiles, but can easily be located within the maps due to the size of the particles. This definitely has to be improved for the future via software

optimization. A lateral extension of measurements along strike might provide new aspects regarding genesis of mineralization, metasomatism, magma mixing or tectonic overprint.

6 REFERENCES

- Cawthorn RG, Merkle R.K.W. & Viljoen M.J. (2002) Platinum-group element deposits in the Bushveld Complex, South Africa. In: Cabri L.J., (editor) *The Geology, Geochemistry, Mineralogy and Mineral Beneficiation of Platinum-Group Elements*. Canadian Institute of Mining, Metallurgy and Petroleum, Special Volume, 54, 389-429
- Penberthy C.J. & Merkle R.K.W. (1999) Lateral variations in the platinum-group element content and mineralogy of the UG-2 chromitite layer, Bushveld Complex. *South African Journal of Geology* 102, 240-250.
- Rammelmair D, Tacke KD, Jung H (2001) Application of new XRF-scanning techniques to monitor crust formation in column experiments. In: *Securing the Future, Proceedings of the Internat. Conf. Mining Environment., Skellefteå, Vol 2:683-692*

Oil Reservoirs

Clay Minerals in Oil Reservoirs of Brazil

S.M.C.Anjos & C.M.A.Silva

PETROBRAS/CENPES, Rio de Janeiro, Brazil.

ABSTRACT: Oil reservoirs are porous and permeable sedimentary rocks containing oil in their porous space. Brazilian oil reservoirs are mainly sandstones of quartz feldspathic composition deposited from eolian and fluvial-deltaic to deep marine environments. These reservoirs present a diagenetic evolution during their burial history and minerals are precipitated and dissolved according to pore fluid composition. Clay minerals are phyllosilicates with a variety of forms and habits that precipitate in reservoir pore space causing porosity and permeability reduction, therefore reducing reservoir productivity. This work aims to present examples of typical diagenetic clay minerals in reservoirs from different basins in Brazil.

1 GENERAL GEOLOGY

Oil fields in Brazil occur mainly in passive margin basins formed in response of the breaking up of the Gondwana Continent in the Early Cretaceous (Fig.1). The largest fields are deep marine deposits located in Campos, Santos and Espírito Santo Basins. Oil production also occurs in pre rift phase of some basins, and in the Paleozoic Solimões Basin.

2 CLAY MINERALS

Detrital clay minerals, in general, are incorporated in sandstones by bioturbation or by mechanical infiltration of suspended clay-rich waters as a post-depositional or sindepositional mechanism mainly in continental environments.

Diagenetic clays can be formed by precipitation from pore waters, replacement of framework sand grains and replacement of precursor detrital or diagenetic clay minerals. The prevailing clay mineral groups in sandstones are kaolinite, illite, chlorite, smectite and mixed-layers varieties. They can occur with different habits in sandstones such as pore lining, pore filling or replacing framework

grains (Ali 1981). All these occurrences are related to the origin and the diagenetic processes involved. Clay minerals in sandstones are commonly identified by X-ray diffraction (XRD) and scanning electron microscopy (SEM/EDS).

2.1 Illite

Illite is a dioctahedral clay mineral comprised of one octahedral layer sandwiched between two tetrahedral layers in a 2:1 structure similar to muscovite with a 10 Angstrom d(001) peak by XRD. Illite is a mesogenetic clay mineral, and it commonly occurs in late stages of diagenesis in sandstone reservoirs.

2.2 Kaolinite

Kaolinite is a 1:1 layer structure of aluminum and silica easily recognized in thin section petrography due to its coarse grain size. It occurs as pseudo hexagonal plates stacked in a worm-like vermicular habit. It fills scatter pores in sandstone and is commonly generated by dissolution or replacement of feldspars and mica in both early and late diagenesis. It is identified by its 7 Angstrom peak d(001) by XRD.



Figure 1 – Location map.

2.3 Smectite

Smectite is a 2:1 group of clay minerals both dioctahedral and trioctahedral and presents the important property of expanding and contracting the structure under salinity changes in pore fluids. It is recognized by its 17 Angstrom peak after glycol treatment and a 10 angstrom peak after heating (Moore & Reynolds 1997).

2.4 Chlorite

Chlorite has a 2:1:1 structure of tetrahedral-octahedral-tetrahedral layers. It presents a variety of morphologies such as rosettes, honey-combs, cabbagehead-like growth and plates attached to sand grains. It commonly occurs in late diagenesis but in volcanic –rich sands it may occur in early phases. It is a 14 Angstrom (d001) mineral with a variety of peak intensities as a function of its iron/magnesium content.

2.5 Mixed layers

Mixed layers are clay minerals formed by the interstratification of different mineral layers. The most common mixed layer clays are illite-smectite and chlorite-smectite, and they represent intermediate composition of the end members. The most common mixed layer clays are illite-smectite and chlorite-smectite, and they represent intermediate composition of the end members. They are very common.

3 CLAY IN BRAZILIAN RESERVOIRS

In Brazilian oil reservoirs, illite is only common in Paleozoic eolian sandstones of Solimões basin (Mizusaki et al. 1990). It occurs as thick fibrous filaments growing from surfaces of framework grains (Fig.2) and seems to replace precursor clays. Illite is a potassium rich-clay which favors absolute geochronologic dating. Kaolinite (Fig.3) is very common in early phases of diagenesis. In fan deltaic reservoirs of the Pendência Formation of Potiguar Basin (Anjos et al. 2000), kaolinite is very pervasive, plugging most of the pore space and replacing framework grains. The formation process is related to dilution by meteoric water infiltration close to erosive surfaces. In Sergipe-Alagoas Basin kaolinite is also associated to unconformities in the pre-rift Serraria Formation (Garcia et al. 1990).

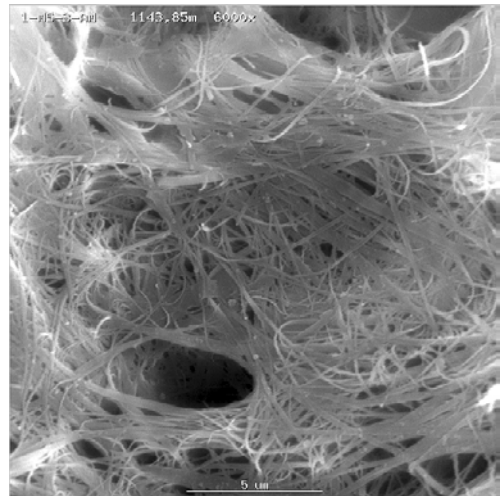


Figure 2. SEM image of fibrous illite in Paleozoic sandstones of Solimões Basin.

Smectite occurs both as post-depositional infiltrated clay (Moraes & De Ros 1988) and as authigenic clay mineral in Brazilian reservoirs. In the fluvial Açú Formation sandstones of Potiguar Basin, smectites are present as clays mechanically infiltrated during flooding periods of a dry climate (Souza 1988) (Fig. 4). In the pre-rift Sergi Formation in the Recôncavo basin, infiltrated clays vary from smectite composition in the shallow Dom João field and changes to mixed-layer illite-smectite gradually enriched in illite layers with increasing depth of the fields (Rodrigues 1990). Smectite is common cement in reservoirs enriched in volcanic rock fragments, as observed in Roncador Field of Campos Basin. On the other hand, a rare occurrence in feldspathic turbidite reservoirs is observed in Fazenda Alegre Field of Espírito Santo Basin, where

diagenetic smectites occur as massive, grain-replacive and pore-filling aggregates, as pore-lining coatings and rims, as complex, multiple coat/rim grain-replacive aggregates, and as pseudomorphic replacement of kaolinite vermicular aggregates and biotite flakes.

Chlorite is frequent but with minor amounts in deeply buried Brazilian reservoirs, except for Upper Cretaceous reservoirs of Santos Basin, where

chlorite (Fig. 5) is an abundant clay mineral which strongly reduces reservoir permeability (Anjos et al. 2003). In Santos Basin deep marine reservoirs are enriched in volcanic rock fragments favoring the basin-wide chlorite formation and distribution. Chlorite occurs replacing framework grains, as pore-filling cement and predominantly as pore-lining cement. It is mainly a ferroan chlorite of the polytype IB, typical of diagenetic chlorites.

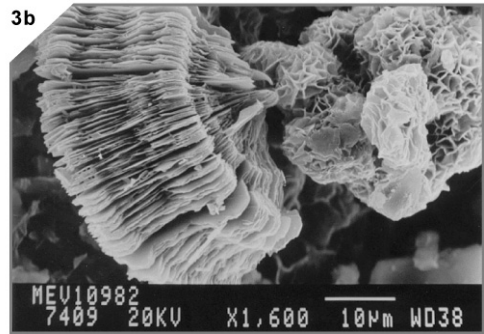
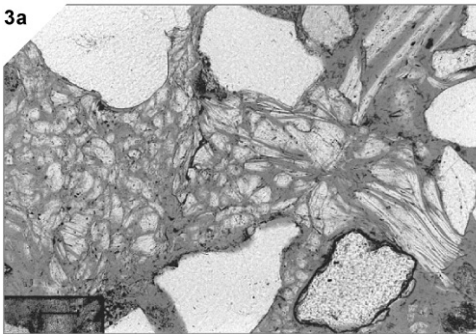


Figure 3. (a) Pore-filling kaolinite in turbidite reservoir of Campos Basin (Thin section petrography). (b) SEM image of pore-filling vermicular kaolinite of Campos Basin.

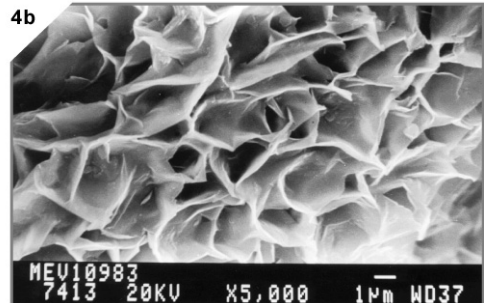
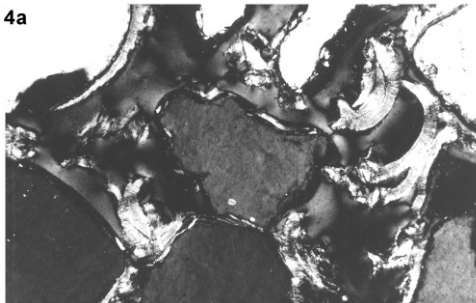


Figure 4. (a) Mechanically infiltrated smectite in sandstones of the Potiguar Basin. (b) SEM image of honey-comb smectite of Espírito Santo Basin.

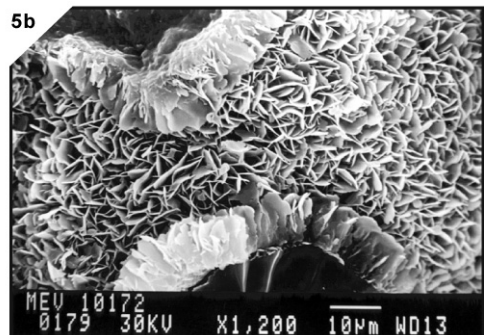
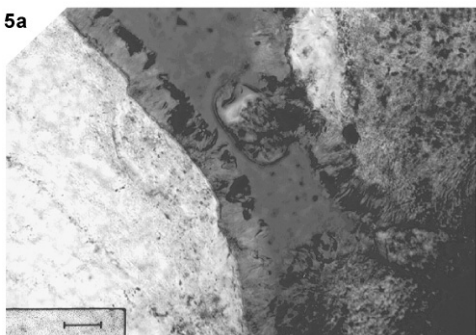


Figure 5. (a) Pore-lining chlorite (thin section) of Santos Basin. (b) SEM image rosette chlorite of Santos Basin.

Mixed layer clays are always present in Brazilian reservoirs associated to the previously described clays or are the predominant clay mineral present. Illite–smectite mixed layer clay with variable amounts of illite layers is a frequent mineral in all reservoirs. A special occurrence is the ordered mixed-layer chlorite-smectite (corrensite) in sandstones of Carmópolis Field of Sergipe/Alagoas Basin which indicates saline conditions.

4 EFFECTS OF CLAY MINERALS ON RESERVOIR QUALITY

Diagenetic clay minerals have a strong control on petrophysical properties of reservoirs, such as porosity, permeability and water saturation. They affect the wire-line logs response such as resistivity, gamma-ray, density, sonic and neutron logs, which are the common tools used to evaluate oil content in reservoirs.

Clay minerals have a large surface area and large cation-exchange capacity which contribute to the interaction with drilling and completion fluids. Caution has to be taken to avoid additional formation damage to reservoirs.

5 CONCLUSION

Clay mineral content in Brazilian oil reservoirs are systematically evaluated in order to avoid misinterpretation of log analysis that could lead to underestimation of oil content, to reduce formation damage, and to increase reservoir productivity.

6 REFERENCES

- Ali, S.A., 1981. Sandstone diagenesis – Applications to hydrocarbon exploration and production. Gulf Science & Technology Company. Pittsburgh, Pennsylvania, 221p.
- Anjos, S.M.C., De Ros, L.F., Souza, R.S., Silva, C.M.A. and Sombra, C.L., 2000. Depositional and diagenetic controls on the reservoir quality of lower cretaceous Pendência sandstones, Potiguar rift basin, Brazil. AAPG Bulletin, v.84, n.2, p.1719-1742.
- Anjos, S.M.C., De Ros, L.F. and Silva, C.M.A., 2003. Chlorite authigenesis and porosity preservation in the Upper Cretaceous marine sandstones of the Santos Basin, offshore eastern Brasil. Int. Assoc. Sedimentol. Spec. Publ., n.34, p.291-316.
- Garcia, A.J.V., De Ros, L.F., Souza, R.S. and Bruhn, C.H.L., 1990. Potencial de reservatórios profundos na Formação Serraria, Bacia de Sergipe/Alagoas. Boletim de Geociências da PETROBRAS, v.4, n.4, p.467-488.
- Mizusaki, A.M.P., Anjos, S.M.C., Wanderley Filho, J.R., Silva, O.B., Costa, M.G.F., Lima, M.P., Kawasita, K., 1990. Datação K/Ar de illitas diagenéticas. Boletim de Geociências da PETROBRAS, v.4, n.3, p.237-251.
- Moore, D.M. and Reynolds Jr, R.C., 1997, X-ray diffraction and the identification and analysis of clay minerals. Oxford University Press, 378p.
- Moraes, M.A.S. and De Ros, L.F., 1988. Caracterização e influência das argilas de infiltração mecânica em reservatórios fluviais da Bacia do Recôncavo, Nordeste do Brasil. Boletim de Geociências da PETROBRAS, v.2, n.1, p.13-26.
- Rodrigues, C.R.O., 1990, Argilominerais na evolução diagenética dos arenitos da Formação Sergi, Jurássico, Bacia do Recôncavo, Brasil. Dissertação de mestrado, Universidade Federal de Ouro Preto, 211p.
- Souza, M.S., 1988, Fatores diagenéticos de controle das qualidades de reservatório da Formação Açú (Ksup) no Campo de Estreito/Rio Panon, Bacia Potiguar – RN. Dissertação de Mestrado, Universidade Federal de Ouro Preto, 89p

Determination of the Depositional Age of Hydrocarbon Reservoir Sandstones through the Argon/Argon Radiometric Dating of Diagenetic Potassic Feldspar

A.M.Mizusaki, L.F.De Ros, A.J.Maraschin

Instituto de Geociências, Universidade Federal do Rio Grande do Sul, Brazil

S.M.C. dos Anjos

PETROBRAS/CENPES, Rio de Janeiro, Brazil

P.Vasconcelos

University of Queensland, Australia

ABSTRACT: Sandstones are the most important hydrocarbon reservoir rocks in many basins of the world. However, several reservoir-sandstones deposited under continental or transitional conditions lack a precise chronostratigraphic determination of their depositional ages, because they do not contain correlatable fossils with defined ages. Such undefinition considerably limits the precision of the generation-migration-accumulation models developed for the exploration and development of these reservoirs. However, many of the continental and transitional sandstones show early diagenetic overgrowths of potassic feldspar, which precipitated on the detrital feldspar grains soon after their deposition. Such occurrence represents the possibility of dating the deposition of these sandstones through the radiometric $^{40}\text{Ar}/^{39}\text{Ar}$ dating of these early diagenetic feldspar overgrowths. An *in situ* $^{40}\text{Ar}/^{39}\text{Ar}$ laser dating technique was developed and applied to early diagenetic feldspars of the Açú sandstones of the Potiguar Basin, main continental oil reservoirs of Brazil. This unit was deposited in fluvial and estuarine environments during the drift stage of the Brazilian continental margin evolution. The minimum $^{40}\text{Ar}/^{39}\text{Ar}$ radiometric ages obtained are compatible to the depositional age of the Açú Formation interpreted from stratigraphic correlations. This method shows excellent potential for determining the depositional age of many sandstones with poorly-constrained chronostratigraphic situation, which biostratigraphic dating is imprecise or inexistent.

1 NEAR - SURFACE K-FELDSPAR AUTHIGENESIS

The fluvial sandstones of the Açú Formation contain abundant, very early, authigenic K-feldspar overgrowths around detrital orthoclase and microcline grains (Maraschin et al., in press). Although early K-feldspar precipitation has been reported in several studies (Sibley 1978; Waugh 1978; Kastner & Siever 1979; Ali & Turner 1982; Girard et al. 1988; Krainer & Spötl 1989; De Ros et al. 1994; Hagen et al. 2001) an extremely early and near-surface authigenesis of overgrowths such as observed in the Açú sandstones is relatively rare. The overgrowths in Açú sandstones are commonly covered by mechanically infiltrated clay coatings (Fig. 1), what indicates their very early, near-surface precipitation. Authigenic smectite (Fig. 2), kaolinite and pre-compactional calcite cement also post-date the overgrowths.

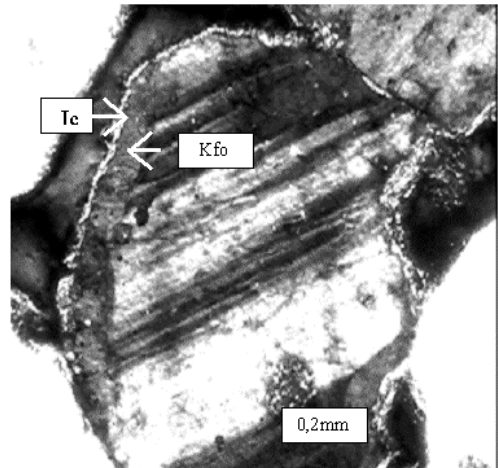


Figure 1. Cross-polarized-light photomicrograph showing authigenic K-feldspar overgrowth (Kfo) around detrital microcline covered by mechanically infiltrated clay coatings (Ic).

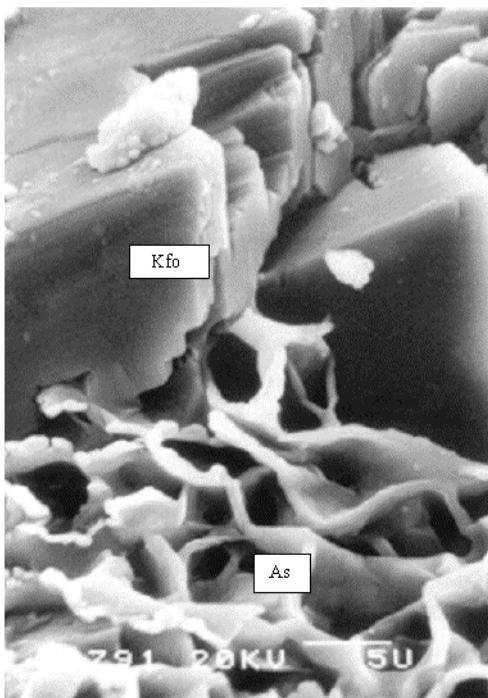


Figure 2. SEM micrograph of authigenic K-feldspar (Kfo) partially engulfing authigenic smectite (As).

The overgrowths are optically discontinuous with the detrital grains, untwined, non-luminescing and were formed directly on grain surfaces, under shallow phreatic conditions, without solid (clays, oxides) or fluid inclusions in between grains and overgrowths. The overgrowths commonly show a rhombohedral (sanidine) shape, and range in thickness from about 0.4 to 1.0 mm. They are composed of chemically pure KAlSi_3O_8 , and constitute up to 6 % of the whole rock. The K, Si and Al ions needed to form the K-feldspar overgrowths were probably derived from the hydrolysis (dissolution and replacement by clay minerals) of detrital feldspars and micas, which occurred in the coarse, alluvial deposits along the basin margins, or also possibly from the leaching of K-feldspar and mica in the granitic-gneissic basement rocks overlain by the Açú Formation. Meteoric fluids with high $\alpha\text{K}^+/\alpha\text{H}^+$ and $\alpha\text{SiO}_{2\text{aq}}$, required to precipitate authigenic K-feldspar at around 30°C and 1 atm, evolved through evaporative concentration along the groundwater circulation pathways throughout the basin.

1.1 Dating overgrowths and detrital k-feldspars

The analytical procedures for dating the deposition of the Açú sandstones through the radiometric $^{40}\text{Ar}/^{39}\text{Ar}$ dating of their early diagenetic K-feldspar overgrowths were performed in $^{40}\text{Ar}/^{39}\text{Ar}$ Laboratory of the University of São Paulo Geosciences Institute, Brazil. Gradual heating with a low-intensity laser beam with a diameter of 10-12 μm was used for extracting the Ar gas from low temperature overgrowths and high temperature detrital K-feldspars.

The 146 individuals grains analyzed yielded a range of age from 139.17 ± 0.99 to 482.43 ± 1.41 Ma for the overgrowths and detrital grains, respectively. The clustering of results for the detrital feldspars around 377.5 ± 5 Ma corresponds to a previously-detected regional uplift that affected the source terrains to the south of the basin. The age obtained from the overgrowths around 120 Ma is compatible with the interpreted time range of the Açú Formation deposition (Albian-Cenomanian; Araripe and Feijó, 1994), with a minimal contamination from the detrital cores.

2 CONCLUSIONS

The Cretaceous fluvial sandstones of the Açú Formation, Potiguar Basin, northeastern Brazil, contain abundant, very early, authigenic K-feldspar overgrowths around detrital orthoclase and microcline grains, precipitated at relatively high pH, $\alpha(\text{K}^+)/\alpha(\text{H}^+)$ ratio, and $\text{SiO}_{2\text{aq}}$ activities.

Despite the lack of precise dating of the unit, due to the lack of correlatable fossils, the extremely early character of K-feldspar authigenesis in the Açú sandstones allowed dating their deposition through radiometric ($^{40}\text{Ar}/^{39}\text{Ar}$) dating of the overgrowths. This technique yielded results that are compatible to the interpreted depositional ages of the Açú reservoir sandstones. This technique shows excellent potential for unraveling the chronostratigraphic setting of this and other continental and transitional units.

3 REFERENCES

- Ali, A.D.; and Turner, P. 1982. Authigenic K-feldspar in the Bromsgrove sandstones Formation (Triassic) of Central England: *Journal of Sedimentary Petrology*, v. 52, p.187-197.
- Araripe, P.T.; and Feijó, F.J. 1994. Bacia Potiguar. *Boletim de Geociências da Petrobrás*, v. 8 (1), p. 114-127.
- De Ros, L.F., Sgarbi, G.N.C. and Morad, S., 1994. Multiple authigenesis of K-feldspar in sandstones: evidence from the Cretaceous Areado Formation, Sao Francisco Basin, central Brazil: *Journal of Sedimentary Research*, v. 64, p. 778-787.
- Girard, J.P., Aronson, J.L.; and Savin, S.M. 1988. Separation, K/Ar dating, and $^{18}\text{O}/^{16}\text{O}$ ration measurements of diagenetic

- K-feldspar overgrowths: an example from the Lower Cretaceous arkoses of the Angola margin: *Geochimica et Cosmochimica Acta*, v. 52, p.2207-2214.
- Hagen, E., Kelley, S.P., Dypvik, H., Nilsen, O.; and Kjøllhamar, B. 2001. Direct dating of authigenic K-feldspar overgrowths from the Kilombero rift of Tanzania: *Journal of Geological Society*, v.158, p.801-807.
- Kastner, M.; & Siever, R. 1979. Low temperature feldspars in sedimentary rocks: *American Journal of Science*, v. 279, p. 435-479.
- Krainer, K.; & Spötl, C. 1989. Detrital and authigenic feldspars Triassic sandstones, Eastern Alps (Austria): *Sedimentary Geology*, v. 62, p. 59-77.
- Maraschin, A.J; Mizusaki, A.M.; and De Ros, L.F. 2004. Near-surface K-feldspar precipitation in cretaceous sandstones from the Potiguar Basin, RN . *Journal of Geology*, v. 112, (3), p. 317-334.
- Sibley, D.F. 1978. K-feldspar cement in the Jacobsville Sandstone: *Journal of Sedimentary Petrology*, v. 48, p. 983-986.
- Waugh, B. 1978. Authigenic K-feldspar in British Permo-Triassic sandstones: *Journal of Geology*, v. 135, p. 51-56.

Opals in Oil Reservoirs

D.B.Alves

Petrobras Research Center, CENPES, Rio de Janeiro, Brazil

L.F.G.Caddah

In memoriam

ABSTRACT: Opal can be found as cement in the Upper Cretaceous sandstones of the Carapeba and the Pargo oil fields of the Campos Basin, Brazil. Unfortunately, the presence of this opal alters the value of rock resistivity and can preclude prompt identification of oil in the reservoirs. For a long time, the source of this diagenetic silica has been an intriguing problem. In this study, the origin of this opal is directly associated with the products of diagenetic changes in the adjacent bentonite (volcanic ash) beds. In the studied area, a great amount of smectite had been formed soon after the deposition of the volcaniclasts originating the bentonite beds. Afterwards, burial diagenesis promoted important mineralogical changes leading to an extensive formation of ordered interstratified illite/smectite ($R = 1$). Following the conversion of smectite to interstratified illite/smectite, a liberation of a great amount of free silica (around 29% of total weight) from the bentonites took place and was directed towards the reservoirs promoting their cementation with opal and microquartz (chalcedony).

1 INTRODUCTION

The biogenic origin of sequences of fine-grained siliceous deposits (bedded or nodular cherts, diatomites, radiolarites, and siliceous shales) has been long established and can be considered well known after several studies including those promoted by the International Geological Correlations Project's from IUGS and sponsored by UNESCO (McBride 1979; Iijima et al. 1983; Hein 1987; Hein & Obradovic 1989). Most siliceous rocks preserved in the geological record were deposited in continental margin basins under zones of coastal upwelling. Less known is the origin of siliceous cements found in sandstones characterized by distinct grain-sizes.

Opal and microquartz (chalcedony) have been found as cements in some sandstones from Upper Cretaceous turbidite deposits of the Carapeba Formation in the Carapeba and the Pargo oil fields of the Campos Basin (Freitas 1987; Moraes 1989; Carvalho et al. 1995). These cements are observed filling the pores and/or recovering the surface of grains of the rock framework and as replacement of clay matrix (squeezed intraclasts). Their mean frequency is 9%, but values from traces to 25-30% have also been reported. The presence of this kind of

cement originated low values of rock resistivity in the induction log, which precluded the immediate identification of oil-bearing intervals for some time. However the microcrystalline quartz did not fill completely the intergranular space of reservoir rock, allowing the existence of relatively big pores where crude oil accumulates.

In an attempt to explain the source of this diagenetic silica, two main hypotheses have been proposed, as follows: the dissolution of the radiolarian siliceous debris which are found in associated pelitic beds; and diagenetic transformation of clay mineral in the adjacent shales and in the pelitic intraclasts found in the sandstones. In this study, the occurrence of microcrystalline silica in the reservoirs of the Carapeba and the Pargo oil fields is directly associated to chemical-mineralogical changes induced by burial diagenesis in the adjacent bentonite beds.

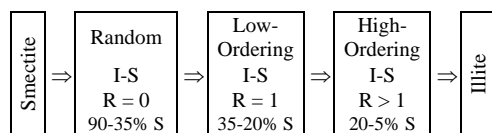
2 BENTONITES OF THE CAMPOS BASIN

Several bentonite beds are observed in the Upper Cretaceous Ubatuba Formation of the Campos Basin where they constitute locally important stratigraphical markers, such as the '3-Dedos'

Marker Bed (Caddah et al. 1994). The bentonites were formed by the subaqueous alteration of volcanic ash fall deposits. The original composition of the volcanoclasts was equivalent to trachytes and soon after their deposition an extensive alteration (halmyrolysis) took place, which originated a great amount of smectite with only residual values of analcime and sanidine. Afterwards, mild burial diagenesis would change the smectite to a highly expandable randomly interstratified illite/smectite (with 85-90% smectite-layers). Bentonites with such a composition can be found all around the basin nowadays, even at depths of around 3000m.

In the Campos Basin, bentonites with same origin but composed of much less expandable ordered interstratified illite/smectite (35-25% smectite-layers) have been found only in the Carapeba and the Pargo oil fields at equivalent depths (Alves et al. 1995).

Illitization of smectites is the most common reaction of bentonites under the action of burial diagenesis (Hoffman & Hower 1979; Nadeau et al. 1985; Inoue et al. 1990; Sucha et al. 1993; Li et al. 1997). It takes place through successive stages, each one characterized by interstratified illite/smectite (I-S) with both distinct composition and structural ordering. In a simple way, the following sequence can be used to represent the pathway of this reaction:



R = for Reichweite, as used by Moore & Reynolds (1997); S = smectite-layer.

The low evolutionary pattern for burial diagenesis of the bentonites of Campos Basin is mostly conformable to the general pattern of this basin since even its shales do not exhibit expressive changes in their clay mineral assemblages with depth/temperature (Anjos 1986). Out of this pattern, the presence of ordered interstratified illite/smectite (R = 1) in the Carapeba and the Pargo oil fields is an effective indicator that these rocks have reached a higher degree of burial diagenesis than those from the rest of the basin. The restricted area where such mineralogical change has been observed favors a local explanation for the mechanism that imprinted such a signature.

3 CHEMICAL CHANGES DURING BURIAL DIAGENESIS

Mineralogical changes induced by burial diagenesis

of the bentonite beds of Carapeba and Pargo are followed closely by corresponding chemical adjustments representative of the new minerals formed. Since the relationships of trace and rare earth elements have shown that all the bentonites of the Campos Basin had the same origin, one approach to evaluate the extension of burial diagenesis over the Carapeba and the Pargo bentonites would be to access the chemical variation, which such a geological process produced. This can be done easily for example by evaluating the magnitude of gains and losses of their major elements.

To compare the variations between the composition of halmyrolytic and diagenetic bentonites, the method used by Krauskopf (1967) was applied. The inconstant behavior of Al under burial diagenesis prevents its use for tracing the chemical reactions (Hower et al. 1976) therefore Ti has been chosen instead (Table 1). A monomineralic sample from '3-Dedos' Marker Bed has been chosen to represent the halmyrolytic bentonites, while a sample from a bentonite from the Carapeba field has been chosen to represent the product of burial diagenesis.

Table 1: Calculation of chemical gains and losses during burial diagenesis of bentonites from Carapeba Field when compared to the halmyrolytic bentonite from the '3-Dedos' Marker Bed.

	A (wt. %)	B (wt. %)	C (wt. %)	Δ_{C-A} (g)	Δ_{C-A}^* (%)
SiO ₂	50.53	51.17	21.26	-29.27	-58
TiO ₂	0.54	1.30	0.54	0.00	0
Al ₂ O ₃	18.18	19.70	8.18	-10.00	-55
FeO _t	5.28	5.14	2.14	-3.14	-59
MnO	0.02	0.03	0.01	-0.01	-50
MgO	3.43	4.22	1.75	-1.68	-49
CaO	0.88	1.02	0.42	-0.46	-52
Na ₂ O	2.44	1.17	0.49	-1.95	-80
K ₂ O	0.29	4.66	11.22	+10.93	+3769
P ₂ O ₅	0.04	0.10	0.04	0.00	0
LOI	18.38	11.50	4.78	-13.60	-74
Total	100.01	100.01	41.55	-58.46	-58

A = halmyrolytic bentonite; B = diagenetic bentonite, C = normalizing with TiO₂ equal A; Δ_{C-A} = gains and losses induced by burial diagenesis; and LOI = loss on ignition.

From Table 1, the losses of practically all the major elements are immediately evident, except for K. Such a relation of losses and gains can be considered effective based on the constancy of Ti/P ratio, which is 13.4 for Carapeba and 13.2 for the '3-Dedos' Marker Bed. In decreasing order, the magnitude of losses (weight) induced by burial diagenesis in the bentonite of Carapeba and the Pargo oil fields corresponds to: SiO₂ >> H₂O > Al₂O₃ >> FeO_t > Na₂O > MgO > CaO >> MnO.

In 100g of original rock, the losses are equivalent to 69g of mass. The increment of around 11g of K₂O

was disproportionately low to reequilibrate all the losses produced by the process as a whole. Therefore, we can say that burial diagenesis gave rise to an effective loss of more than half of the original mass of halmyrolytic bentonite. Of course, such products must have been displaced to the adjacent permeable sandstones, conditioning their secondary cementation. Such a mechanism had already been proposed by Boles & Franks (1979) for the Wilcox sandstone.

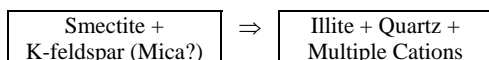
4 DISCUSSION

In the Campos Basin, the presence of ordered interstratified illite/smectite (R = 1) in the bentonites in the area comprising the Carapeba and the Pargo oil fields indicates the existence of an anomaly within this basin, an area with local differentiation of the extension of burial diagenesis.

The most widely used reaction that synthesizes the illitization of smectites was proposed by Hower et al. (1976), and is expressed as:



As can be observed, for the reaction to take place, a supply of Al and K is necessary. In the case of shales, these elements would be supplied by the dissolution of detrital feldspars and micas, which are usually present in this lithology (Hower et al. 1976). It has been proposed also that the liberation of Si would promote the precipitation of secondary quartz in the rock. In other words, new clay minerals would originate by the isochemical redistribution of the elements of the rock. The mineralogical reaction would be synthesized as:



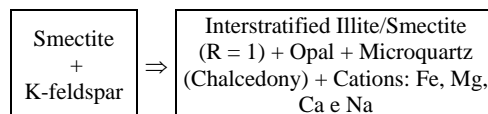
In the case of bentonites of the Carapeba field, this model does not fit completely the facts observed, since the initial composition of bentonite (practically monomineralic) did not allow isochemical displacement that could justify the chemical-mineralogical changes observed. Therefore, an external source of K and Al would be necessary to promote the illitization of the original smectite.

Based on Table 1, it can be seen that except for Ti, P and K, all the cations have been remobilized from the bentonite. However the increase of Al₂O₃ related to SiO₂ necessary to promote the reaction of

illitization is only apparent. Silica has been liberated in higher amount, promoting the relative increase of alumina, which has also been partially removed from the rock. Therefore, the only element extensively added to the diagenetic bentonite would be in reality K₂O.

The presence of small amounts of mica contamination has been observed by Caddah et al. (1998) in the some bentonite associated to the turbidites of the Carapeba Field and it could have been remobilized to form the interstratified illite/smectite with higher content of K. Another potential source of the K necessary to the illitization of smectite would be the adjacent turbidite sandstones, which in the Carapeba and the Pargo fields are essentially arkose in composition. The presence of K-feldspar (mostly orthoclase) highly altered and partially replaced by carbonate can still be seen in thin-section (Moraes 1989; Freitas 1987). Due to the high availability of K in the formation water of reservoir, it might have migrated to the bentonites by means of diffusion or metassomatic process, a mechanism observed by Altaner et al. (1984) and Altaner (1989).

Thus burial diagenesis made available varying amounts of chemical elements, which could migrate to the adjacent rocks. Such a process would alter deeply the composition of the formation water, giving rise to a more intense cementation. For example, the higher content of SiO₂ would certainly promote extensive siliceous cementation in the adjacent lithologies. Such a process would therefore explain the intense opal and microquartz cementation observed in the sandstones of the Carapeba and the Pargo oil fields. In short, the main source of silica to the microcrystalline quartz of the Carapeba and the Pargo oil fields would come from the illitization of smectite from the associated bentonites. Thus the mineralogical reaction that best express such a reaction would be:



5 CONCLUSION

Burial diagenesis promoted important mineralogical changes in the composition of bentonites of the Carapeba and the Pargo oil fields of the Campos Basin, leading to an extensive formation of ordered interstratified illite/smectite. Following the conversion of smectite to interstratified illite/smectite, a great amount of free silica (around 29% of total weight) formed and was directed

towards the reservoirs promoting their cementation with opal and microquartz.

6 REFERENCES

- Altaner, S.P. 1989. Calculation of K diffusional rates in bentonite beds. *Geochimica et Cosmochimica Acta*, 53: 923-931.
- Altaner, S.P.; Hower, J.; Whitney, G. & Aronson, J.L. 1984. Model for K-bentonite formation: evidence from zoned K-bentonites in the disturbed belt, Montana. *Geology*, 12: 412-415.
- Alves, D.B.; Mizusaki, A.M.P. & Caddah, L.F.G. 1995. Diagenetic evolution of the clay minerals of the Upper Cretaceous bentonite beds of the Campos Basin, SE Brazil. In: EUROCLAY'95, Leuven (Bélgica), 19-25.08.1995. Book of abstracts.... Leuven, European Clay Mineral Group Association, p. 363-364.
- Anjos, S.M.C. 1986. Absence of clay diagenesis in Cretaceous-Tertiary marine shales, Campos Basin, Brazil. *Clays and Clay Minerals*, 34 (4): 424-434.
- Boles, J.R. & Franks, S.G. 1979. Clay diagenesis in Wilcox sandstones of Southwest Texas: implications of smectite diagenesis on sandstone cementation. *Journal of Sedimentary Petrology*, 49(1): 55-70.
- Caddah, L.F.G.; Alves, D.B.; Hanashiro, M. & Mizusaki, A.M.P. 1994. Caracterização e origem do marco "3-Dedos" (Santoniano) da Bacia de Campos. *Boletim de Geociências da PETROBRAS*, 8(2/4): 315-334.
- Caddah, L.F.; Alves, D.B. & Mizusaki, A.M.P. 1998. Turbidites associate with bentonites in the Upper Cretaceous of the Campos Basin, offshore Brazil. *Sedimentary Geology*, 115: 175-184.
- Carvalho, M.V.F.; de Ros, L.F. & Gomes, N.S. 1995. Carbonate cementation patterns and diagenetic reservoir facies in the Campos Basin Cretaceous turbidites, offshore eastern Brazil. *Marine and Petroleum Geology*, 12(7): 741-758, 1995.
- Freitas, L.C.S. 1987. Estudo de reservatório do Membro Carapebus (cretáceo) no Campo de Carapeba, Bacia de Campos, Estado do Rio de Janeiro, Brasil. Thesis-Meister. Ouro Preto: Universidade Federal de Ouro Preto, 133 p.
- Hein, J.R. (Ed.). 1987. Siliceous sedimentary rock-hosted ores and petroleum. New York: van Nostrand Reinhold Company.
- Hein, J.R. & Obradovic, J. (Eds.). 1989. Siliceous deposits of the Tethys and Pacific regions. New York: Springer-Verlag.
- Hoffman, J. & Hower, J. 1979. Clay mineral assemblages as low-grade metamorphic geothermometers: application to the thrust faulted disturbed belt of Montana, U.S.A. In: Scholle, P.A. & Schluger, P.R. (Eds.) *Aspects of diagenesis*. Tulsa: Society of Economic Paleontologists and Mineralogist, p. 55-79 (Special Publication n. 26).
- Hower, J.; Eslinger, E.; Hower, M. E. & Perry, E.A. 1976. Mechanism of burial metamorphism of argillaceous sediment: mineralogical and chemical evidence. *Geological Society of America Bulletin*, 87: 725-737.
- Iijima, A.; Hein, J.R. & Siever, R. (Eds.). 1983. Siliceous deposits in the Pacific region. Amsterdam: Elsevier. (Developments in Sedimentology 36).
- Inoue, A.; Watanabe, T.; Kohyama, N. & Brusewitz, A.M. 1990. Characterization of illitization of smectite in bentonite beds at Kinnekulle, Sweden. *Clays and Clay Minerals*, 38(3): 241-249.
- Krauskopf, K.B. 1967. Introduction to geochemistry. New York, McGraw-Hill.
- Li, G.; Peacor, D.R. & Coombs, D.S. 1997. Transformation of smectite to illite in bentonite and associated sediments from Kaka Point, New Zealand: contrast in rate and mechanism. *Clays and Clay Minerals*, 45(1): 54-67.
- McBride, E.F. (Ed.). 1979. Silica in sediments: nodular and bedded chert. Tulsa, Society of Economic Paleontologists and Mineralogists, 184p. (Reprint series number 8)
- Moore, D.M. & Reynolds, R. 1997. X-ray diffraction and the identification and analysis of clay minerals. Oxford: Oxford University Press.
- Moraes, M.A.S. 1989. Diagenetic evolution of Cretaceous-Tertiary turbidite reservoirs, Campos Basin, Brazil. *The American Association of Petroleum Geologists Bulletin*, 73(5): 598-612.
- Nadeau, P.H.; Wilson, M.J.; McHardy, W.J. & Tait, J.M. 1985. The conversion of smectite to illite during diagenesis: evidence from some illitic clays from bentonites and sandstones. *Mineralogical Magazine*, 49: 393-400.
- Sucha, V.; Kraus, I.; Gerthofferova, H.; Petes, J. & Serekova, M. 1993. Smectite to illite conversion in bentonites and shales of the east Slovak basin. *Clay Minerals*, 28: 243-253.

Monte Carlo Simulation of Na- and Ca-montmorillonite at 353 K and 625 bar

L.de Pablo-Galán

Instituto de Geología, Universidad Nacional Autónoma de México, México D. F., México

M.L.Chávez-García

Facultad de Química, Universidad Nacional Autónoma de México, México D. F., México

ABSTRACT: The hydration of Na- and Ca-saturated Wyoming-type montmorillonites is investigated by Monte Carlo simulations at constant stress in the $NP_{zz}T$ ensemble and at constant chemical potential in the μVT ensemble, at the basin temperature of 353 K and pressure 625 bar, equivalent to 4.2 km depth. In this environment, simulations predict a stable 1,2-water layer Na-montmorillonite of water 164.4 mg/g, d_{001} spacing 12.72 Å, density 0.32 g/ml. Sodium ions are coordinated with six molecules of water separated 2.30-2.33 Å. Water molecules are closer to the central interlayer plane and the spacing is larger than that at 300 K and 1 bar. No other hydrates are predicted. Ca-montmorillonite does not form any stable hydrates. The most nearly stable is the monolayer hydrate, of adsorbed water 169.22 mg/g, spacing 12.50 Å, density 0.34 g/ml. Ca ions are in six-fold coordination with water molecules separated 2.70-2.80 Å, energy -21.11 kcal/mol. The interlayer structure is formed by one broad layer of water molecules 0.09 Å off the interlayer midplane, with the protons oriented towards the siloxane surfaces and the midplane. Ca^{2+} takes positions intermediate to protons and the oxygen atoms. Ca-montmorillonite hydrates would be stable at lower depths.

1 INTRODUCTION

The hydration and dehydration of expandable clay minerals in sedimentary basins give rise to swelling and instability, adsorption and release of fluids and chemical species that affect rock strength and pore pressure, contributing to overpressure and subsurface fluid migration. The interaction of these clay minerals and brines are of particular interest in petroleum-rich basins, where they affect the recovery of petroleum and the quality of the reservoir. Na- and Ca-montmorillonite are two of the most common expandable clay minerals. They are well known, largely as a result of their ability to swell in humid environments into one-, two-, and three-layer water complexes, and to develop microscopic swollen colloidal suspensions when immersed in water. The behavior is well known from experimental and simulation studies at the ambient conditions of 300 K and 1 bar, but is less known at the higher pressures and temperatures encountered in sedimentary basins. In the present study, the stability and swelling of Na- and Ca-montmorillonite is investigated by Monte Carlo simulations at constant stress in the $NP_{zz}T$ ensemble and at constant chemical potential in the μVT ensemble, at the reservoir conditions of 353 K and

625 bar, common to petroleum rich sedimentary basins.

2 METHODOLOGY

The hydration of montmorillonite is studied at 353 K and 625 bar by Monte Carlo simulation in the $NP_{zz}T$ and μVT ensembles. These conditions are equivalent to a depth of 4.2 km in terms of the lithostatic gradient. The simulations employ the model and approach described by Chávez-Páez et al. (2001a, b). The clays considered are Na-saturated Wyoming-type montmorillonite of unit cell $(Si_{7.75}Al_{0.25})(Al_{3.50}Mg_{0.50})O_{20}(OH)_4Na_{0.75}.nH_2O$ and Ca-saturated montmorillonite of unit cell $(Si_{7.75}Al_{0.25})(Al_{3.50}Mg_{0.50})O_{20}(OH)_4Ca_{0.37}.nH_2O$. The water-counterion and clay-counterion interactions are simulated using the TIP4P model of water interaction (Jorgensen et al. 1983, Bounds 1985).

3 RESULTS

3.1 $NP_{zz}T$ simulations

The adsorption of 32 water molecules by Na-montmorillonite, at the basin conditions of 353 K and 625 bar, clusters the molecules in two tight

almost one layer in the interlayer mid-plane (Fig. 1a), with their protons on the mid-plane and to both sides closer to the siloxane surfaces. The Na^+ counterions form outer-sphere complexes with the water molecules. Higher adsorption of 64 water molecules separates two layers of oxygen atoms and four layers of protons, with the Na^+ largely on the central plane (Fig. 1b). The separations between layers are indicated in Table 1.

Ca-montmorillonite shows a similar behavior (Fig. 2c, 2d). There are however differences in the location of the Ca^{2+} counterions and on the distances between layers (Table 1). The configurations are illustrated in the snapshots of Figure 2.

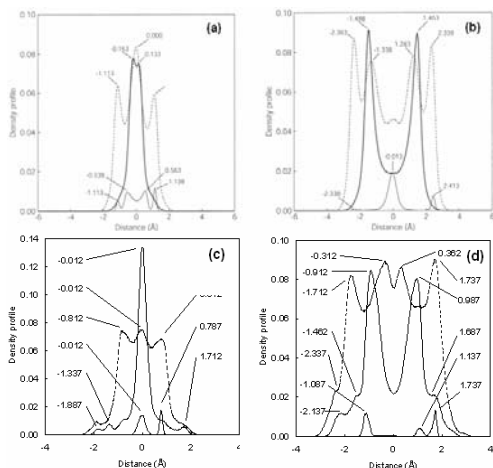


Figure 1: Density profiles of montmorillonite hydrated at 353 K and 625 bar, NP_{zz}T ensemble: (a), Na-montmorillonite, 32 water molecules; (b), Na-montmorillonite, 64 water molecules adsorbed; (c), Ca-montmorillonite, 32 water molecules; (d), Ca-montmorillonite, 64 water molecules. Numbers indicate distances from the interlayer midplane.

Table 1: Monte Carlo simulation of hydrated Na- and Ca-montmorillonite, NP_{zz}T ensemble, 353 K, 625 bar.

Counterion	Na	Na	Ca	Ca
Atom/cell	6	6	3	3
Clay layers	2	2	2	2
Water (molec/cell)	32	64	32	64
Spacing (Å)	12.57	14.92	11.83	13.73
Density (g/ml)	0.20	0.33	0.21	0.36
Energy (kcal/mol)	24.29	6.60	-24.24	-19.66
Lennard-Jones (")	0.61	1.43	-26.37	-13.17
Coulomb (")	23.68	5.17	1.41	-6.68
r (Å)	2.30	2.32	2.78	2.80
O^{\ominus} dist. midplane	0.15	1.47	0.01	0.95
H^{\oplus} dis. midplane	1.11	2.36	0.81	1.71
$\text{Na}^+/\text{Ca}^{2+}$	0.55	2.37	0.01	0.71

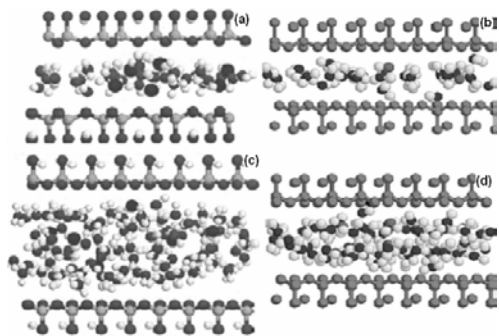


Figure 2: Snapshots of hydrated, NP_{zz}T ensemble: (a), Na-montmorillonite, 32 water molecules adsorbed; (b), Ca-montmorillonite, 32 water molecules; (c), Na-montmorillonite, 64 water molecules; (d), Ca-montmorillonite, 64 water molecules.

The radial distribution function (Fig. 3) shows that the cation-oxygen separations are shorter in Na-montmorillonite than in Ca-montmorillonite. The coordination probability decreases with increasing solvation.

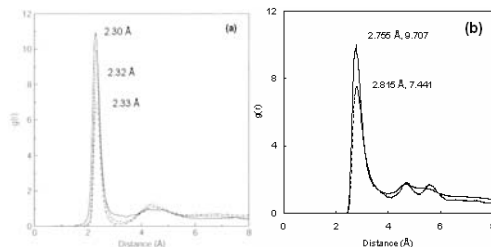


Figure 3: Radial distribution function $g(r)$, NP_{zz}T ensemble: (a), Na-montmorillonite; (b), Ca-montmorillonite.

The adsorptions of 32 and 64 water molecules develop d_{001} spacings of 12.57 and 14.92 Å for Na-montmorillonite and of 11.83 and 13.73 Å for Ca-montmorillonite (Fig. 4a, 4c). Under reservoir conditions, the interlayer structure appears to be in Ca-tighter than in Na-montmorillonite.

The internal energy of Na-montmorillonite decreases from 24.29 to 6.60 kcal/mol as the adsorbed water increases from 32 to 64 molecules, with the Lennard-Jones contribution moving from 0.61 to 1.43 kcal/mol and the Coulomb contribution from 23.68 to 5.17 kcal/mol (Fig. 4b). Ca-montmorillonite shows internal energies of -24.24 and -19.66 kcal/mol, Lennard-Jones contributions of -26.37 and -13.17 kcal/mol, and Coulomb contributions of 1.41 and -6.68 kcal/mol (Fig. 4d). Na- and Ca-montmorillonites have at reservoir

conditions different stabilities, with the latter appearing to form more stable hydrates.

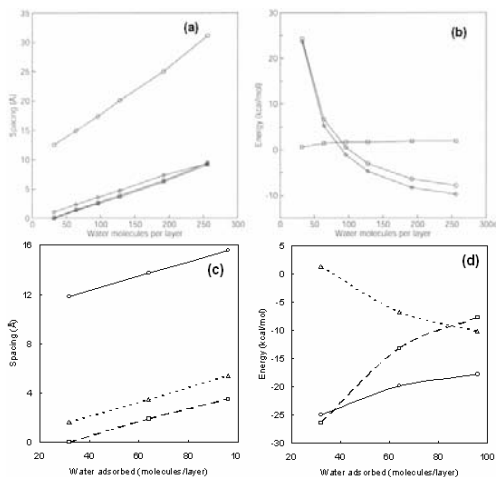


Figure 4: Variation of the d_{001} spacing and the internal energy with the adsorbed water, $NP_{zz}T$ ensemble: (a,b), Na-montmorillonite; (c,d), Ca-montmorillonite.

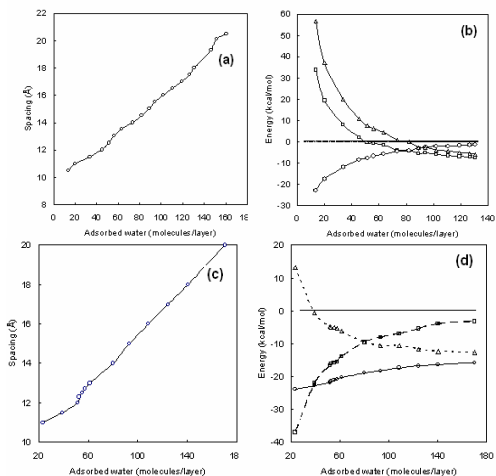


Figure 5: Correlation between the d_{001} spacing and the internal energy with the adsorbed water, μVT ensemble: (a,b), Na-montmorillonite; (c,d), Ca-montmorillonite.

3.2 Grand canonical (μVT) simulations

Simulations in the grand canonical μVT ensemble at reservoir conditions indicated an excess chemical potential for the bulk fluid of -5.58 kcal/mol. The variation of the pressure tensor P_{zz} with the adsorbed water (Figure 6) indicates that in Na-montmorillonite the pressure tensor equals the bulk

pressure when the adsorbed water is 53.37 molecules/cell and the d_{001} spacing is 12.72 Å. It corresponds to a stable monolayer hydrate. No other hydrated complexes are stable under these conditions and depth. Much to the contrary, Ca-montmorillonite does not develop a pressure tensor equal to the bulk pressure, indicating that stable forms of Ca-montmorillonite do not develop at these temperature, pressure, and depth (Fig. 6b). The most nearly hydrated complex would be a monolayer hydrate of 12.50 Å spacing, formed by the adsorption of 55.21 water molecules and having a P_{zz} of 1086.9 bar.

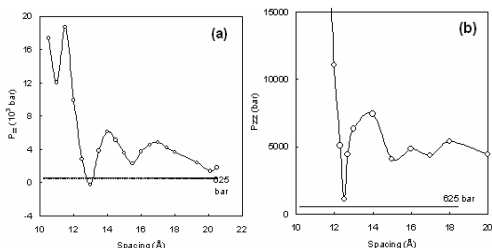


Figure 6: Variation of the pressure tensor P_{zz} with the d_{001} spacing, grand canonical μVT ensemble: (a), Na-montmorillonite; (b), Ca-montmorillonite.

The interlayer configuration of the two hydrates is shown in Figures 7a and 7b. Na-montmorillonite develops two closed water layers, with the Na^+ distributed therein. In Ca-montmorillonite only one single thick layer of water molecules persists, with some molecules closer to the siloxane surfaces. Neither Na^+ nor Ca^{2+} remains in the interlayer midplane.

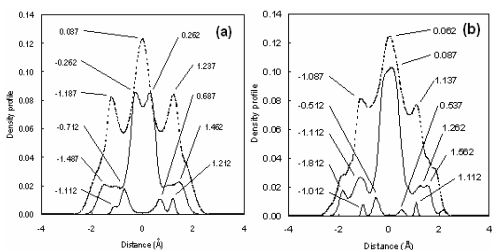


Figure 7: Density profile, μVT ensemble, at 353 K and 625 bar, of: (a) Na-montmorillonite, 1,2-layer hydrate; (b), Ca-montmorillonite, 1-layer hydrate.

4 CONCLUSIONS

Monte Carlo simulations on the hydration of montmorillonite indicate that 1,2-water layer Na-

montmorillonite is the only stable hydrate at 353 K and 625 bar, of a d_{001} spacing of 12.75 Å. This spacing is larger than the 12.2 Å simulated at 300 K and 1 bar, conditions at which the 15.7 Å two-layer and possibly the 18.7 Å three-layer hydrates exist. Ca-montmorillonite is not stable under basin conditions and only the 12.5 Å monolayer hydrate is nearly stable. No other hydrates are stable. They compare with the 12.2, 14.7, and 18.4 Å one-, two-, and three-layer hydrates recognized in the surface environment. Between the surface environment where the various hydrates are stable and the basin environment where only the Na-monolayer is stable, there must be intermediate depths at which the various hydrates cease to exist, leaving the clay layers available to form other minerals.

The coordination of the counter ions in the interlayer decreases with increasing hydration. This, and the instability of the two- and three-layer hydrates with increasing depth, should favor the displacement of water to the bulk.

5 REFERENCES

- Bounds, D.G. 1985. *Mol. Phys.* 54, 1334.
- Chávez-Páez, M., Workum, K. van, dePablo, L. & dePablo, J.J. 2001. Monte Carlo Simulations of Wyoming Sodium Montmorillonite Hydrates. *J. Chem. Phys.* 114, 1405-1413.
- Chávez-Páez, M., dePablo, L. & dePablo, J.J. 2001. Monte Carlo Simulations of Ca-montmorillonite Hydrates. *J. Chem. Phys.* 114, 10948-10953.
- dePablo, L., Chávez, M.L., Sum, A.K. & dePablo, J. J. 2004. Monte Carlo Molecular Simulation of the Hydration of Na-montmorillonite at Reservoir Conditions. *J. Chem. Phys.* 120, 939-946.
- Jorgensen, W.L., Chandrasekhar, J., Madura, J.D., Impey, R.W. & Klein, M.L. 1983. *J. Chem. Phys.* 79, 926.

Studies on Quartz as the Tracer of Fluid Migration

K.Jarmolowicz-Szulc

Centre of Excellence: Research on Abiotic Environment REA, Polish Geological Institute, Warsaw, Poland

ABSTRACT: Quartz in form of the vein fillings in the Carpathian flysch and the cement in the sandstones in the oil reservoir in the Baltic Sea have been studied by means of fluid inclusions, light isotopes and gas chromatography aiming at characteristics and migration of fluids, especially hydrocarbons.

1 INTRODUCTION

Quartz has been one of the best known and studied minerals in the world. It has been occurring in different geological environments, in that as the vein mineral of a certain characteristics called the Marmarosh diamonds, as well as the cement in the sedimentary rocks in the hydrocarbon reservoirs.

The first variety of the quartz mentioned, has been studied for about a century in the Carpathians in Europe, aiming at explanation of the phenomena of its formation and characteristics (Tokarski 1905, Hurai et al. 1989, Dudok et al. 1997, Jarmolowicz-Szulc 2001a). The second type of the quartz filling in the porous space has been the object of numerous analyses for long years, too (e.g. Sikorska & Paczesna 1997). The present case concerns the Cambrian sandstones from the Polish segment of the Baltic Sea, which are the reservoir rocks for oil.

The paper will focus onto the fluid inclusion and isotopic studies of both varieties aiming at the problem of the quartz as the tracer of fluid migration.

2 OBJECTIVES

The aim of the presentation is to show characteristic features of fluid inclusions in the quartz and in the quartz cements as well as to interpret the results of the isotope, microthermometry and fluorescence studies in the context of fluid evolution and formation of the rocks.

3 METHODS AND EQUIPMENT USED

Double-sided-polished thin sections in case of the sandstones, and quartz crystals themselves, were prepared for fluid inclusion studies using two preparation techniques (Jarmolowicz-Szulc 2001a,b). General microscopic observations were conducted applying a polarization microscope both in the transmitted and reflected (UV) lights. These comprised: a microscope analysis of fluid inclusions (Leitz Orthoplan); fluorescence studies together with a microphotography (Nikon microscope and UV device); cold cathodoluminescence studies (CCL 8200 mK3); microthermometric analyses (homogenisation and freezing using Fluid Inc. System). The studies were conducted in the

Petrological Department of the Polish Geological Institute in Warsaw, Poland.

The isotope studies were conducted by means of the method of a point analysis in quartz. Spectrometric (SIMS) isotope analysis of the oxygen was performed at the Arizona State University in Tempe (AZ, USA) according to the procedure of Hervig et al. (1992) and Williams et al. (1997). Determinations were conducted for some dozens of the measured points in the quartz grains, each scanned from 49 to 94 times. They were performed against the Arkansas quartz standard, the characteristic features of which, calibrated against the international standards, have been shown in Hervig (op. cit.). Three grains of quartz (the "Marmarosh diamonds") have been studied, both in automatic and manual modes. Determinations of the oxygen isotopes in the quartz overgrowths on the detrital grains were conducted manually.

Gas composition of the hydrocarbon inclusions in the "Marmarosh diamonds" was determined by use of the chromatograph "Chrom 5" and mass spectrometer MX-1304 in Lviv, Ukraine (Dudok & Jarmolowicz-Szulc 2000; Jarmolowicz-Szulc & Dudok 2000). The analytical studies were performed based on the assumption that the maximum temperatures of the formation of the Marmarosh diamonds have not exceeded 230-240 °C. Three intervals of the short heating in the helium atmosphere were applied (Dudok & Shanina 2000). Gas components have been released gradually, during crystal destruction at room conditions. With this technique, it was possible to measure nitrogen, carbon dioxide and hydrocarbons up to octane. This method was used for the first time on the vein minerals in the Carpathian oil-bearing province (Dudok & Jarmolowicz-Szulc 2000).

The estimation of the pressure and temperature conditions of the formation of the "Marmarosh diamonds" based on the crossing isochore technique using coexisting methane and aqueous inclusions (Kaliuzhnyj 1982). Isochores for pure methane were calculated with Flincor programme (Brown 1982). Calculations for the inclusions in the quartz cement were conducted by means of VT-flinc programme.

4 DESCRIPTION

The Marmarosh diamonds from the Western and Eastern Carpathians contain both hydrocarbon and aqueous inclusions. This type of the bi-pyramidal quartz displays euhedral, transparent crystals of an ideal crystal habit and a perfect reflection (Karwowski & Dorda 1974). The inclusions are either of primary or of secondary origin. Those primary ones may be divided into three phase groups of state. They may be either homogeneous or heterogeneous. The solid inclusions comprise

different bitumens. The liquid inclusions (mostly in the external growth zones) are filled with one or two non-mixing fluids. Gas inclusions contain methane with some admixtures of heavier hydrocarbons. The heterogenic inclusions contain different types of the filling, e.g. gas and liquid hydrocarbon and the aqueous solution; gas and heavy hydrocarbon and the aqueous solution and solid bitumens etc. (Dudok & Jarmolowicz-Szulc 2000).

The Marmarosh diamonds sampled in different regions in the Carpathians (the Bieszczady Mts. and the foreland) show distinct differences in the character of their fluid inclusions. They contain a spectrum of fluids - from methane, through oil to aqueous solutions. Fluid inclusions either display a character of pure substances (e.g. one phase methane) or are complex (e.g. oil-methane, methane-oil, water-methane etc.). The veins where they occur have been paths of fluid migration. The quartz points to the process of migration of the distinct fluids, the complex aqueous-hydrocarbon ones. These palaeofluids were rich in water, light hydrocarbons (methane) and heavy hydrocarbons (oil) and in some localities also in the carbon dioxide. The locality of the quartz points to the directions of the migration of these differentiated types of the fluids, especially suggests possible trends for search of hydrocarbons.

The quartz cement from the reservoir Cambrian sandstones in boreholes in the Polish part of the Baltic Sea contains both the hydrocarbon (HCFI) and aqueous (AQFI) inclusions (Jarmolowicz-Szulc 2001b). The formation of these inclusions has been connected with a fluid migration and trapping in the quartz cements - early and late. The hydrocarbon inclusions, oscillating in their size from one to some micrometers, display the fluorescence features in colours from white-blue to yellow. Basing on the fluorescence features, a type of the petroleum may be determined. It is light and mature. The densities of the oils oscillate from 41 to 45°API. The aqueous inclusions do not fluoresce at all. The AQFI are at the boundary of the detrital and the authigenic quartz, in the early cement and in the late filling of microfractures. The hydrocarbon inclusions are most frequent in the late filling of the fissures, thus pointing out the late hydrocarbon migration to the reservoir.

The fluid inclusions and isotopic studies on both the fluid inclusions and the quartz point to the hydrocarbon migration in the reservoir and the character of the paleofluids responsible for the quartz cement formation and reservoir filling.

5 CONCLUSIONS

The areas of the occurrence of the hydrocarbons in the inclusions in the quartz may be mostly prospective for the search for oil and gas. This

problem was discussed by Jarmolowicz-Szulc & Dudok (2000). Such a suggestion may be supported by the results of the gas chromatography and Rock-Eval studies of the organic matter (Dudok et al. 2002) which prove oil window conditions in NW and gas conditions in SE of the studied area in the Carpathians.

Oil is present in the late cements in the Cambrian sandstones, mostly in the fillings of tectonic microfractures and stylolitic sutures. It migrated together with water and was trapped in the late quartz in the conditions of 107°C and 317 bars. It is light and mature. The abundance of HCFI is restricted to some boreholes and the upper parts of the profiles (Jarmolowicz-Szulc 2001b).

Key words: quartz, quartz cement, Marmarosh diamonds, fluid inclusions, hydrocarbons, isotopes, microthermometry.

6 REFERENCES

- Brown P., 1982: Flincor: a microcomputer program for the reduction and investigation of fluid inclusion data. *Amer. Miner.* 74:1390-1393.
- Dudok I. V. & Jarmolowicz-Szulc K., 2000: Hydrocarbon inclusions in vein quartz (the "Marmarosh diamonds") from the Krosno and Dukla zones of the Ukrainian Carpathians, *Geol. Quart.*, 44 (4), Warsaw, 415-423.
- Dudok I. V., Kaliuznyj V. A. & Vozniak D. K., 1997: The particularities of phase composition and the problems of systematics of the hydrocarbon fluid inclusions in "Marmarosh diamonds" of the Ukrainian Carpathians, XIV ECROFI, Nancy, France, 96-97.
- Dudok I.V., Kotarba M. & Jarmolowicz-Szulc K., 2002: Employment of pyrolytic methods in geochemical studies of organic matter of the vein formations in the flysch of the Carpathians Mts. *Geologia i geochemia goruczych kopalin*. Lviv, 1, 76-87 (in Ukrainian).
- Dudok I. V. & Shanina S. N., 2000: Hydrocarbon composition of the inclusions in the Marmarosh diamonds in the Ukrainian Carpathians (the Krosno & Dukla zones). *Dopovidi NAN Ukrainy*, 176-180 (in Ukrainian).
- Hervig R. L., Williams P., Thomas R. M., Schauer S. N. & Steele I. M., 1992: Microanalysis of oxygen isotopes in insulators by secondary ion mass spectrometry. *Intl. J. Mass. Spec. Ion Proc.*, 120, 45 – 63.
- Hurai V., Francu J., Bajova L. & Gavacova H., 1989: Hydrocarbon inclusions in "Marmarosh diamonds" from flysch sediments of Eastern Slovakia. In : Fluids in geological processes, Czechoslovakian Contributions to the Session devoted to Fluid Inclusions, Bratislava, Abstracts, 5 – 6.
- Jarmolowicz-Szulc K., 2001a: Characteristic features of vein fillings in the southeastern part of the Polish Carpathians (calcite, quartz, bitumens). *Przegl. Geol.* 49, 785-792 (in Polish with English summary).
- Jarmolowicz-Szulc K., 2001b: Fluid inclusion studies in quartz cements in the Middle Cambrian sandstones in the Leba Block in the Baltic Sea – diagenetic, isotope and geochemical implications. *PGI Bull.* 399, 75 pp. (in Polish with English summary).
- Jarmolowicz-Szulc K. & Dudok I. V., 2000: Fluid inclusion studies in vein minerals of the Capathians, Poland – Ukraine. Abstracts of XIth Congress of Regional Committee in Mediterranean Neogene Stratigraphy, Fes, Morocco, 132.
- Kaliuznyj V. A., 1982: The principles of studies of the mineral-forming fluids. Kiev, *Nauk. Dumka*, 240 p. (in Russian).
- Karwowski Ł. & Dorda J., 1986: The mineral forming environment of "Marmarosh diamonds". *Min. Pol.* 17(1), 3 – 12 (in Polish with English abstract).
- Sikorska M. & Paczesna J., 1997: Quartz cementation in Cambrian sandstones on the background of their burial history (Polish part of the East European Craton). *Geol. Quart.* 41, 3: 266-272.
- Tokarski J., 1905: On the Marmarosh diamonds, *Kosmos*, Lvov, 30, 443-460.
- Williams L., Hervig R. L. & Dutton S. P., 1997: Constraints on paleofluid compositions in the Travis Peak Formation, East Texas: evidence from microanalyses of oxygen isotopes in diagenetic quartz. *SEPM Spec. Publ.*, 57, 269-280.

A New Method to Trace the Provenance of Single Zircon Grains: Implications for Petroleum Exploration

M.V.D.Remus & L.F.De Ros

Departamento de Mineralogia e Petrologia, Instituto de Geociências, Universidade Federal do Rio Grande do Sul, Porto Alegre, Brazil

M.Norman

School of Earth Sciences, Australian National University, Canberra, Australia

R.S. de Souza

PETROBRAS Research Center, CENPES/TRO, Rio de Janeiro, Brazil

J.A.Cupertino

PETROBRAS - E & P / CORP, Rio de Janeiro, Brazil

ABSTRACT: A combination of new analytical methods allows for the first time to identify with precision the source areas of individual zircon grains. Zircon is an ultrastable mineral found in sandstones and conglomerates of sedimentary basins of virtually every age. Primary zircons occur in several types of magmatic rocks with a wide range of compositions. In metamorphic rocks zircon is a common accessory mineral in high-grade terrains and also found in high-pressure rocks. The content and distribution of trace elements are related to the environment of zircon formation. Hafnium isotope composition can identify zircons derived from different felsic rocks and rocks from mantle affiliation. Trace element analyses and Hf isotopic compositions of individual zircons are obtained by Laser Ablation ICPMS (Inductively-Coupled Plasma Mass Spectrometry), and by a multi-collector ICPMS for high-precision isotopic analysis. Further, the U-Pb geochronology of individual detrital zircons using SHRIMP (Sensitive High Resolution Ion Microprobe) controlled by cathodoluminescence allows dating the age of their source-terrains. The combination of U-Pb age, cathodoluminescence, trace element and Hf isotopic composition of individual zircon grains, therefore, provides a powerful tool for discriminating the source-lithology of detrital zircons and tracing the provenance of detrital sedimentary sequences of all ages. The impact of this new integrated methodology on provenance studies applied to basin analysis for petroleum exploration will be of great importance. The definition of the source area of specific individual grains will be a powerful tool to interpret the dynamics of source-areas uplift, patterns of sedimentary transport and basin infill.

1 WHY TO USE ZIRCON AS A PROVENANCE-INDICATOR MINERAL?

Sedimentary mineral assemblages commonly contain detrital zircon - an ultrastable heavy-mineral found in sandstones and conglomerates of sedimentary basins of virtually every age. Zircon is chemically resistant and refractory, and can survive both weathering and transport processes. Zircon crystallizes with a high U/Pb ratio in view of their tendency to incorporate large concentrations of U but very little initial (non-radiogenic) Pb and retain the daughter products of U and Th radioactive decay allowing to use it as a very precise geochronometer (Dickin 1995).

Primary zircons occur in several kinds of magmatic rocks, such as leucogranites, calc-alkaline granitoids and felsic volcanics, calc-alkaline basic rocks, alkaline syenites, fenites, carbonatites and kimberlites. In metamorphic rocks zircon is a common accessory mineral in high-grade terrains and also found in high-pressure rocks (blue schists and eclogites). Ages measured on detrital zircon populations yield information about geochronology of crustal segments of the source regions, helping to

trace the provenance of the sediments (Roback & Walker 1995; Morton et al. 1996; Sircombe 1999).

Additionally, the content and distribution of trace elements, such as Y, Th, U, P, Hf and REE elements are related to the environment of zircon formation and can be used for identification of source-rock lithology (Heaman et al. 1990; Belousova et al. 1998; Belousova et al. 2002). Hafnium isotope composition can identify zircons derived from intermediate to mildly felsic rocks, from felsic rocks and evolved aplitic granites, and from rocks from mantle affiliation (Knudstein et al. 2001). Further, the cathodoluminescence (CL) images can decipher the internal structure of zircon crystals, such as inherited cores and younger overgrowths, as well as the colour signatures of individual grains, which are related to trace-element activators (Hanchar & Millar 1993; Belousova et al. 1998). Hence, the population of zircon grains within a sedimentary rock could be used to discriminate both the ages and lithologic types of the source region.

Our aim is to show that these data, obtained by modern integrated microanalytical techniques, will allow the definition of the source areas of specific individual grains. This will constitute a powerful

tool to interpret the dynamics of source-areas uplift, the patterns of sedimentary transport and basin infill. The impact of this new integrated methodology on provenance studies applied to basin analysis in petroleum exploration will be of extreme importance.

2 SHRIMP U-Pb AGES OF INDIVIDUAL ZIRCON GRAINS

U-Pb geochronology of individual detrital zircons using SHRIMP (Sensitive High Resolution Ion Micro Probe) allows in-situ measurements of single zircon grains and even fragments or growth zones within single crystals. The SHRIMP technique is a rapid method to obtain ages of single zircon grains from detrital populations. A data acquisition rate of about 70-100 analyses per 24 hours is now possible, depending on the precision required. The sample populations of zircon are mounted in epoxy and polished, until grains are sectioned in half to expose all zones. A circular section of about 25 μm diameter (~ 2 ng) is sampled by a beam of oxygen ions. The accelerated particles from the crater formed pass into high resolution, high sensitivity mass spectrometer, which counts selected U and Pb ions, from which U-Pb ages are calculated (Morton et al. 1996, Compston 1999).

The radiogenic zircon compositions are plotted on diagrams $^{207}\text{Pb}/^{235}\text{U} \times ^{206}\text{Pb}/^{238}\text{U}$ (for Proterozoic and Archaean zircons), or $^{207}\text{Pb}/^{206}\text{Pb} \times ^{206}\text{Pb}/^{238}\text{U}$ (for samples including Phanerozoic zircons). An example of a studied sample of clastic zircons from a metasedimentary rock from southern Brazil shows four distinct zircon populations (Fig. 1; Remus et al. 2000). These populations were defined by cathodoluminescence and back scattered images of scanning electron microscope combined with SHRIMP U-Pb ages (Fig. 2) and correlated very well with regional source-rocks ages.

3 HAFNIUM ISOTOPES

^{176}Hf is the radiogenic daughter of beta decay from ^{176}Lu . Therefore, variations in Hf isotopic compositions (e.g. $^{176}\text{Hf}/^{177}\text{Hf}$) reflect the time-integrated Lu/Hf ratio of a magmatic source. During igneous processes, Hf behaves like a light rare-earth element, similarly to Sm, so that continental crust has a low Lu/Hf ratio, and the depleted mantle has a high Lu/Hf ratio. This produces significant variations in $^{176}\text{Hf}/^{177}\text{Hf}$ in crustal and mantle source regions over geological time, with the depleted mantle evolving to high $^{176}\text{Hf}/^{177}\text{Hf}$, and continental crust evolving to low $^{176}\text{Hf}/^{177}\text{Hf}$.

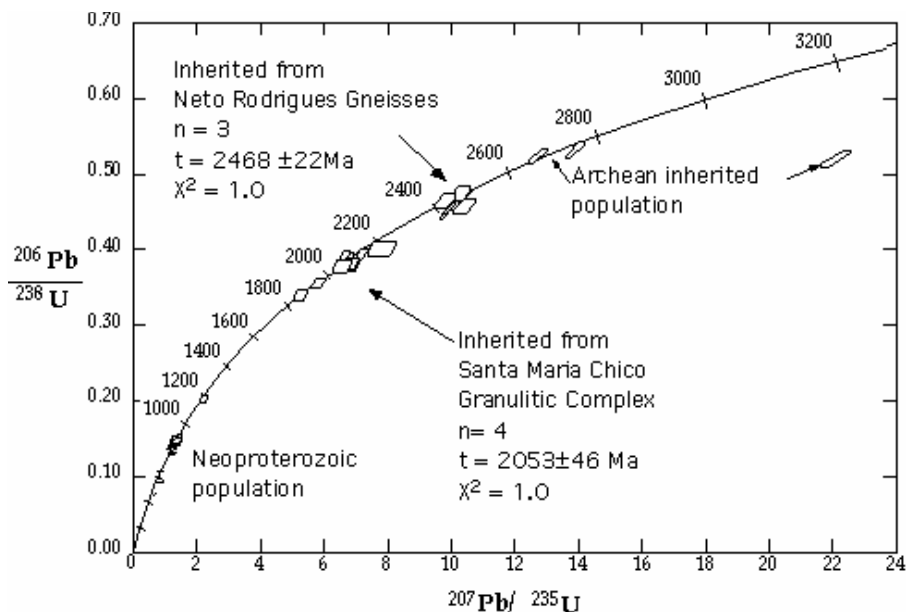


Figure 1: Concordia diagram of zircon populations from Neoproterozoic metasedimentary rocks of southern Brazil (modified from Remus et al. 2000).

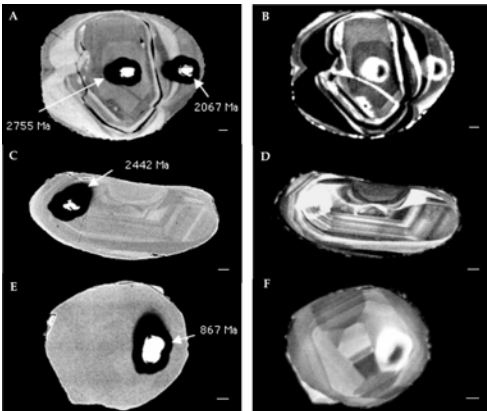


Figure 2: Backscattered electron (left) and cathodoluminescence (right) images of sectioned detrital zircons from Proterozoic metasedimentary rocks from southern Brazil, showing the damage craters formed by the SHRIMP ion beam. A and B show a complex zircon grain with an inherited Archean core surrounded by Paleoproterozoic overgrowths. E and F show a magmatic zircon with complex sector zoning (modified from Remus et al. 2000).

Zircons have very high Hf contents relative to Lu, and so they lock in the initial Hf isotopic composition of the magma from which they crystallized. This allows to trace the relative contributions of crustal and mantle source regions to granitic magmas through the Hf isotopic compositions of individual zircon grains, using laser ablation sampling and a multi-collector ICPMS for high-precision isotopic analysis. The isotopic variations are relatively large, and well within the analytical capabilities of modern instrumentation. Hafnium isotope composition can identify zircons derived from intermediate to mildly felsic rocks, from felsic rocks and evolved aplitic granites, and from rocks from mantle affiliation (Knudstein et al. 2001).

4 ZIRCON TRACE ELEMENTS

Zircon has a tendency to incorporate trace elements and its abundance in magmatic rocks affect the behavior of many trace elements during magma crystallization. Metamorphic zircons from different environments (e.g. high T and high P/T metamorphism) show a large variation in trace element composition (Rubatto 2002). In magmatic systems, zircon controls the distribution of zirconium, hafnium and have a significant influence on the behavior of rare earth elements, Y, Th, U, Nb and Ta (Belousova et al. 2002). These trace elements are incompatible in many rock-forming silicate minerals, and are concentrated in the late-crystallizing zircon. The elemental abundance,

distribution and shape on chondrite-normalized curves of such elements are related to the environments of zircon formation in specific source rocks (Heaman et al. 1990, Belousova et al. 1998, Belousova et al. 2002).

A general trend of increasing trace elements abundance in zircons from ultramafic through mafic to granitic rocks and Th/U ratios typically from 0.1 to 1, reaching 100-1000 in zircons from carbonatites and alkaline pegmatites has been recognized by Belousova et al (2002). A classification and discrimination tree diagram was proposed by Belousova et al. (2002), which determines the fields of zircons from different magmatic source-rocks (Fig. 3).

Metamorphic zircon of granulites formed in equilibrium with partial melting have steep heavy-enriched REE pattern, and are distinguished from magmatic zircons because of their lower Th/U ratio (Rubatto 2002). This author shows that in eclogite facies, zircon also has a low Th/U ratio but reduced heavy rare-earth element enrichment and Eu anomaly, while in low grade metamorphic veins, zircon has low Th/U ratio but is extremely enriched in HREE, Nb and Y.

Trace element analyses of individual zircons are obtained by Laser Ablation ICPMS (Inductively-Coupled Plasma Mass Spectrometry).

5 CONCLUSIONS

The combination of U-Pb age, cathodoluminescence, trace element composition, and Hf isotopic composition of individual zircon grains provides a powerful tool for tracing the specific source terranes of detrital population, allowing to trace the provenance of detrital sedimentary sequences of all ages. This new integrated approach is based on the recent developments of multi-collector ICPMS technology and of SHRIMP dating controlled by cathodoluminescence. The impact of this new integrated methodology on provenance studies applied to basin analysis in petroleum exploration will be of extreme importance.

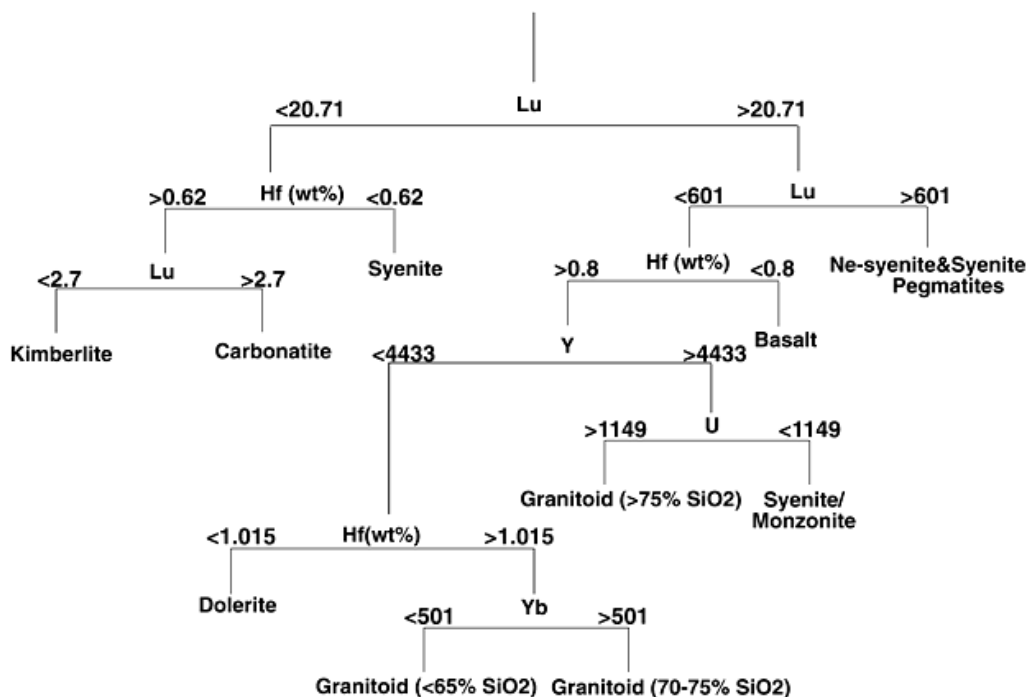


Figure 3: Classification and regression tree diagram for the recognition of zircons from different magmatic rock types based on trace elements (Belousova, 2002).

6 REFERENCES

- Belousova, E. A., Griffin, W.L., Pearson, N.J. 1998. Trace element composition and cathodoluminescence properties of southern African kimberlitic zircons. *Min. Mag.*, 62(3): 355-366.
- Belousova, E. A., Griffin, W.L., O'Reilly, S. Y., Fisher, N. I. 2002. Igneous zircon: trace element composition as an indicator of source rock type. *Contrib. Mineral. Petr.* 143: 602-622.
- Compston, W. 1999. Geological age by instrumental analyses: the 29th Hallimond lecture. *Min. Mag.* 63: 297-311.
- Dickinson, A.P. (1995) Radiogenic isotope geology. Cambridge Univ. Press, 490p.
- Hanchar, J.M. & Millar, C.F. 1993. Zircon zonation patterns as revealed by cathodoluminescence and backscattered electron images: implications for interpretations of complex crustal histories. *Chem., Geol.*, 112:1-13.
- Heaman, L. M., Bowins, R., Crocket, J. 1990. The chemical composition of igneous zircon suites: implications for geochemical tracer studies. *Geoch. Cosm. Acta*, 54, 1597-1607.
- Knudsen et al. 2001. In-situ hafnium and lead isotope analyses of detrital zircons from the Devonian sedimentary basin of NE Greenland: a record of repeated crustal reworking. *Contrib. Min. Petr.*, 141: 83-94
- Morton, A.C., Clauoué-Long, J.C., Berge, C. 1996. SHRIMP constraints on sediment provenance transport history in the Mesozoic Statfjord Formation, North Sea. *J. Geol. Soc., London*, 153: 915-929.
- Remus, M. V. D., L. A. Hartmann, N. J. Mcnaughton, D. I. Groves, and I. R. Fletcher. 2000. The link between hydrothermal epigenetic copper mineralization and the Caçapava Granite of Brasiliano Cycle in Southern Brazil. *J. S. Am. Earth. Sci.*, 13: 191-216.
- Roback, R.C., Walker, N.W. 1995. Provenance, detrital zircon U-Pb geochronometry, and tectonic significance of Permian to Lower Triassic sandstone in southeastern Quesnellia, British Columbia and Washington. *Geol. Soc. Am. Bull.*, 107: 665-675.
- Rubatto, D. 2002. Zircon trace element geochemistry: partitioning with garnet and link between U-Pb ages and metamorphism. *Chem. Geol.*, 184:123-138.
- Sircombe, K.N. 1999. Tracing provenance through the isotope ages of litoral and sedimentary detrital zircon, eastern Australia. *Sedim. Geol.*, 124: 47-67.

Implication of Authigenic Illite Growth on the Quality of Oil Reservoirs

M.Setti & A.Di Giulio

Dipartimento di Scienze della Terra, University of Pavia, Pavia, Italy

A.López-Galindo

Instituto Andaluz de Ciencias de la Tierra, CSIC – University of Granada, Granada, Spain

A.Ortenzi & M.Arduini

ENI S.p.A. – E & P Division – Department of Petrography, Sedimentology and Stratigraphy, Milan, Italy

ABSTRACT: The morphology of illite particles is fundamental to the quality (permeability) of reservoir rocks in oil exploration. We characterize the texture and chemistry of plate and filamentous illite, both of which are found in oil and water sandstones of a hydrocarbon reservoir located in the Southern Viking Graben in the UK North-Sea. The studied samples vary from upper very fine to upper coarse sandstones, with an average porosity of 14.5 %, both primary and secondary in origin. They are mainly made up of quartz (up to 90%) and lesser quantities of illite. The main authigenic minerals are quartz overgrowths and illite, while kaolinite occurs only in subordinate amounts. Filamentous illite and quartz overgrowths may have formed by the reaction $\text{kaolinite} + \text{K-feldspar} = \text{illite} + \text{quartz}$, which explains the intimate relation between illite and quartz overgrowths observed by SEM. In oil samples, the growth of illite seems to occur at the same time as quartz, while in water samples the illite developed after the quartz. The small differences observed in the chemical composition of oil and water illites may suggest that diagenesis was active in the water zone, while it was stopped in the oil zone. The different illite development mechanisms may influence the degree of porosity and the overall efficiency of the rock.

1 INTRODUCTION

The importance of illite in establishing the quality of the reservoir rock has been noticed by many authors (Ehrenberg & Nadeau, 1989; Hassouta et al. 1999; Chuhan et al. 2001; Lima & De Ros 2002; Wilkinson & Haszeldine 2002, among others). Different illite morphologies act differently on reservoir permeability and often a low percentage of a given illite morphology may cause a dramatic drop in permeability (Kantorowicz 1990; Ehrenberg & Boassen 1993), probably due to two different mechanisms: on the one hand, the specific surface of pore walls is greatly increased and, on the other, it has been observed that the migration of fine illite particles could affect the pore network efficiency by plugging the pore-throats (Güven et al. 1980; Weaver 1989).

Illite morphologies have been diversely named by authors (Neasham 1977; Macchi 1987). The main structures are three: platelets, laths and filaments, laths and filaments being considered as filamentous illite, even if filaments are considerably thinner than laths. Observations on reservoir rocks of different ages and basins tend to indicate that, in many cases, the platelets seem to be formed by intergrowing laths as is clearly visible in the examples from the

Ordovician of the Ghadames Basin in Libya and the Lower Cretaceous of the Offshore Congo (Figs A, B). Therefore, apart from the genesis of illite, it is very important to understand its morphological characteristics and their genetic relationships.

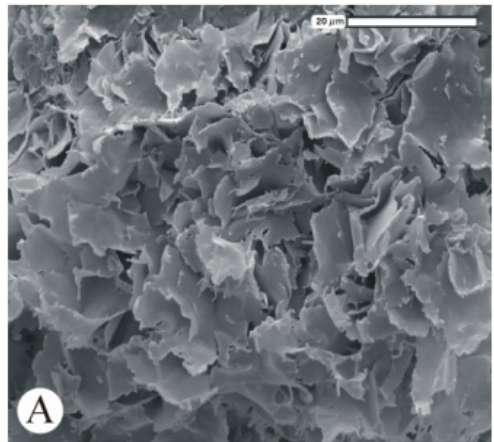


Figure A: Illite platelets from the Lower Cretaceous of the Offshore Congo.

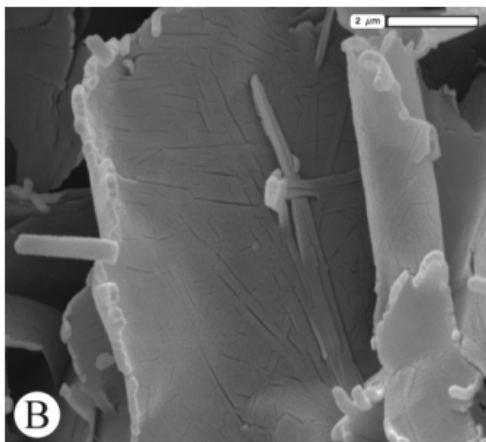


Figure B: Detail of fig. A, showing that platelets seem to be composed of interwoven illite laths.

In the present study, X-ray diffraction, scanning (SEM) and transmission (TEM-AEM) electron microscopy and optical investigation have been used to study the illite in oil and water sandstones of a hydrocarbon reservoir located in the Southern Viking Graben in the UK North Sea. Production is from a thick Jurassic conglomeratic sequence known as the Brae Formation. Illite is found in the pore space of the sandy matrix of the conglomerate and appears with the three basic morphologies mentioned above. This mineral is probably the cause of the net drop in permeability recorded between the oil and water zones.

The aim of this study is to characterize the different illite morphologies and their chemical composition, as well as to explain the possible genesis of illite, in order to determine whether a meaningful difference is recorded between the oil and water zones and if the diagenesis is really more advanced in the latter zone.

2 MATERIALS AND METHODS

Mineralogical analyses were carried out by XRD, following the standard procedures for clay minerals (*cf.* Thorez 1976; Wilson 1987) on the bulk samples (random “powder” preparation). Semi-quantitative percentages of each identified mineral phase were calculated using the “SIROQUANT” software package (Taylor & Clapp 1991). The SEM observations were performed with a ZEISS DSM 950 (equipped with the microanalytical LINK system). The TEM-AEM microanalyses were carried out using a PHILIPS CM 20 (coupled with the EDAX system).

The bulk sample mineralogy is mainly made up of quartz (70-90%) and subordinate illite (3-26%). Also kaolinite and feldspars are sometimes present but in low percentages (< 7%).

A set of 26 sandstone samples was studied by a standard point count by optical polarizing microscope in order to determine the detrital mode, types and amount of cement and porosity, and to evaluate the relative role played by compaction and cementation in the porosity reduction during diagenesis. In addition, textural features were determined microscopically by the use of visual comparators (Beard & Weyl 1973).

3 RESULTS

The studied samples cover a quite wide range of grain-size, from upper very fine to upper coarse sandstones, with good to moderately good sorting. Porosity ranges from 21.6 to 7.3 % (average porosity 14.5 %) and is both primary and secondary in origin; secondary porosity mostly results from the dissolution of detrital feldspars and micas.

The studied samples have a quartz-rich framework with an average original composition, modified during diagenesis to reach their average present day Q96F2L2 composition (figures).

The most abundant authigenic minerals are quartz overgrowths, which represent the 8.8 % of the rock as an average (range 3.4-14.2 % of the rock) and illite (average 6.3 % of the rock, ranging from 2.6-15.4 %) both as pore-lining and pore-filling cement in very variable ratio. Kaolinite occurs only in some samples and in very subordinated amount.

The relative role of compaction and cementation in the porosity reduction during diagenesis has been estimated by the calculation of the Compactional Index as proposed by Lundegard (1992) modified to take into account the texture of the studied samples. The result points out that cementation played a major role with respect to compaction (average CI 0.3).

SEM observations showed that the quartz is characterized by a very well developed habit (Fig. C) due to quartz overgrowths having varies size from few μm to 10-200 μm , developed on the surfaces of detrital quartz grains. The feldspars occur in few amount both in the oil and water samples and show noticeable dissolution features. No diagenetic replacement of feldspar by illite was observed, while, in some cases, the growing of illite at the expense of kaolinite is present.

Illite particles are present as cement inside the pores; they are attached on the quartz grain surfaces and show plate and filamentous morphologies. The filamentous morphologies are often developed on the edges of the plates (Fig. D). Filamentous illite is described to be of authigenic origin and not detrital

because of its delicate morphology, it surely formed after the compaction of the sediment (Bailey 1980; Huggett 1995).

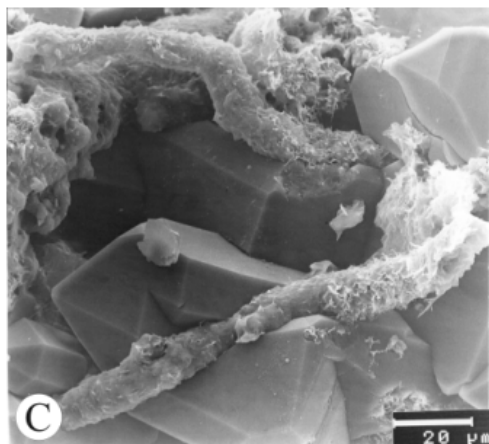


Figure C: Idiomorphic quartz crystals, crossed by an elongated illite aggregate, oil sample 16/17-B4 13304.0.

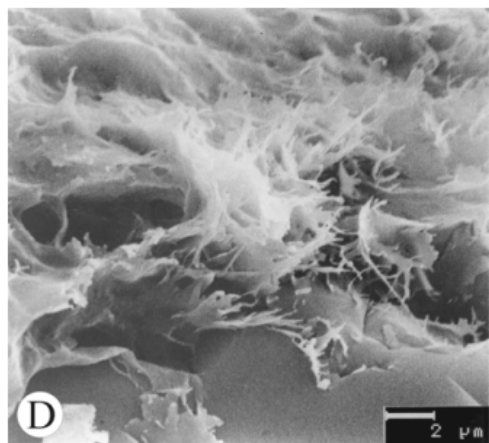


Figure D: Filamentous illite on quartz grain surface, oil sample 16/17-B4 13304.0.

The SEM observations highlighted that the development of illite in the water samples is different from the one in the oil samples. In particular, the authigenesis of illite in the water samples seem to have occurred directly on the quartz surface, as no distinct interruption among the two minerals are observed (Fig. E). In the oil samples illite particles appear generally as leaned on the quartz surfaces (Fig. F).

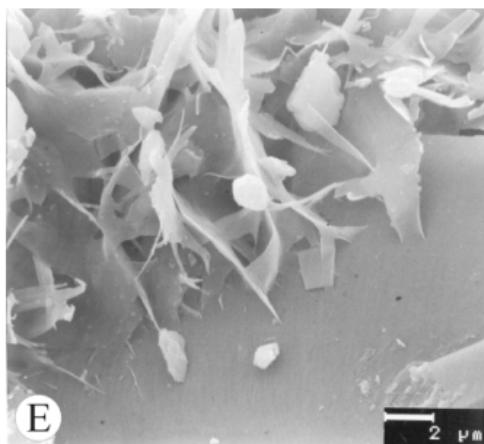


Figure E: authigenic illite on quartz surface water sample 16/17-19 12210.0.

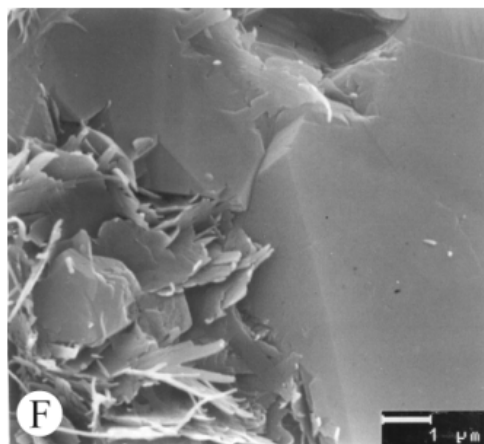
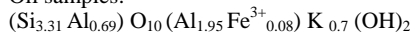


Figure F: Plate illite particles resting on quartz surface, oil sample 16/17-B3 13014.0.

Average crystal-chemical formulae of illite were obtained from the TEM-AEM microanalyses of around one hundred individual particles. They are as follows:

Oil samples:



Water samples:



These formulae represent the typical composition of illite. We observe that these compositions are very similar, although water samples illite is more enriched in K than oil sample illite, and that there is a greater tetrahedral substitution in water samples illites. It is not clear, in any case, if there is a relation

between chemical composition and type of reservoir rocks.

4 CONCLUSIONS

TEM observations invariably suggest that plate illites consist more of interwoven fibrous illite laths, since all crystals have a needle morphology. This confirms the observations made by SEM on various samples, as stated in the introduction.

Several authors attribute the formation of filamentous illite in sandstones to dissolution of aluminous mineral phases, like K-feldspar, kaolinite and smectite (Güven et al. 1980; Morad & AlDahan 1987; Chamley 1989; Bjørlykke 1998).

The scarcity of kaolinite and the abundance of illite in the samples might be related to a less acid pH of migrating K-rich groundwaters of marine origin and to later diagenetic conditions with higher temperatures, over 120°C. In fact, the formation of kaolinite generally occurs during early diagenesis, while illite forms during burial diagenesis (Chamley 1989; Weaver 1989; Bjørlykke et al. 1995).

In conclusion, we think that the filamentous illite and quartz overgrowths present in the samples were formed by the reaction: kaolinite + K-feldspar = illite + quartz, as described by Bjørlykke (1998). This reaction explains the intimate relation between illite and quartz overgrowths observed by SEM. It is possible to hypothesise that, in the oil samples, the growth of illite occurred at the same time, or immediately before the growth of quartz, while in the water samples the illite developed after the quartz. The difference in chemical composition also suggests that the illite diagenesis was active in the water zone, while it was stopped in the oil zone.

We hypothesise that the different mechanisms of development of illite may influence the degree of porosity and the overall efficiency of the rock. In fact the illite which appeared only resting on the quartz surfaces (oil samples) might have better mobility than the illite fixed on the quartz surfaces (water samples).

5 REFERENCES

Bailey S.W. (1980). Structure of layer silicates. In *Crystal structures of clay minerals and their X-ray identification* (Brindley G.W. and Brown G., Eds.). Mineral. Soc., London, 1-123.

Beard D.C. and Weyl P.K. (1973). Influence of texture on porosity and permeability of unconsolidated sand. *A.A.P.G. Bull.*, 57: 349-369.

Bjørlykke K. (1998). Clay mineral diagenesis in sedimentary basins - a key to the prediction of rock properties. Examples from North Sea Basin. *Clay Minerals*, 33: 15-34.

Bjørlykke K., Aagaard P., Egeberg P.K. and Simmons S.P. (1995). Geochemical constraints from formation water

analyses from the North Sea and Gulf Coast Basin on quartz, feldspar and illite precipitation in reservoir rocks. In: *The Geochemistry of Reservoir* (J.M. Cubitt and W.A. England, Eds.). *J. Geol. Soc. London Spec. Publ.*, 86: 33-50.

Chamley H. (1989). *Clay Sedimentology*. Springer-Verlag, Berlin Heidelberg, 623 pp.

Chuhan F.A., Bjørlykke K. and Lowrey C.J. (2001). Closed-system burial diagenesis in reservoir sandstones: Examples from the Garn Formation at Haltenbanken area, offshore mid-Norway. *J. Sedimentary Research*, 71 (1): 15-26.

Ehrenberg S.N. and Boassen T. (1993). Factors controlling permeability variation in sandstones of the Garn Formation in Trestakk Field, Norwegian continental-shelf. *J. Sedimentary Petrology*, 63 (5): 929-944.

Ehrenberg S.N. and Nadeau P.H. (1989). Formation of diagenetic illite in sandstones of the Garn Formation, Haltenbanken area, Mid-Norwegian continental-shelf. *Clay Minerals*, 24 (2): 233-253.

Güven N., Hower W.F. and Davies D.K. (1980). Nature of authigenic illites in sandstone reservoirs. *J. Sed. Petrology*, 50: 761-766

Hassouta L., Buatier M.D., Potdevin J.L. and Liewig N. (1999). Clay diagenesis in the sandstone reservoir of the Ellon Field (Alwyn, North Sea). *Clays and Clay Minerals*, 47 (3): 269-285.

Huggett J. M. (1995). Formation of authigenic illite in palaeocene mudrocks from the central North Sea: a study by high resolution electron microscopy. *Clays and Clay Minerals*, 43: 682-692.

Kantorowicz J.D. (1990). The influence of variations in illite morphology on the permeability of Middle Jurassic Brent Group sandstones, Cormorant Field, UK North-Sea. *Marine And Petroleum Geology*, 7 (1): 66-74.

Lima R.D. and De Ros L.F. (2002). The role of depositional setting and diagenesis on the reservoir quality of Devonian sandstones from the Solimoes Basin, Brazilian Amazonia. *Marine and Petroleum Geology*, 19 (9): 1047-1071.

Lundegard P.D. (1992). Sandstone porosity loss: a big "picture" view of the importance of compaction. *J. Sed. Petrology*, 62: 250-260.

Macchi L. (1987). A review of sandstone illite cements and aspects of their significance to hydrocarbon exploration and development. *Geological Journal*, 22: 333-345

Morad S. and AlDahan A. A. (1987). A SEM study of diagenetic kaolinitization and illitization of detrital feldspars in sandstones. *Clay Minerals*, 22: 237-243.

Neasham J.W. (1977). The morphology of dispersed clay in sandstone reservoirs and its effect on sandstone shaliness, pore space and fluid flow properties. *Society of Petroleum Engineers of AIME*, 6568

Taylor J.C. and Clapp R.A. (1991). New features and advanced applications of SIROQUANT: a personal computer XRD full profile quantitative analysis software package. *Adv. X-Ray Anal.*, 35.

Thorez J. (1976). *Practical identification of clay minerals*. Dison, Belgium, 90 pp.

Weaver C. E. (1989). *Clay, muds and shales*. Elsevier, Amsterdam 819 pp.

Wilkinson M. and Haszeldine R.S. (2002). Fibrous illite in oilfield sandstones - a nucleation kinetic theory of growth. *Terra Nova*, 14 (1): 56-60.

Wilson M. J. (1987). A handbook of determinative methods in clay mineralogy. Chapman-Hall, New York, 308 pp.

Diagenetic Chemical Reactions and Products as a Result of Rock-water Interactions in a Petroleum Reservoir from Deposition to Deep Burial

R.S.Souza

Petrobras, Centro de Pesquisas e Desenvolvimento, Rio de Janeiro, Brazil

ABSTRACT: The original composition of the water deposited along with the Água Grande sands was likely fresh water and its evolution during progressive burial history was a complex non-conservative process including chemical evolution and mixing of waters from different origins. Present-day Ca-rich brines present at greater depth are likely the product of water-rock interaction processes, which might encompass plagioclase dissolution and albitization and calcite dissolution within Água Grande sandstones and associated Candeias mudstones, whereas Na-Ca-Cl saline waters seems to be related to the dissolution of evaporite minerals once present within older rocks (Permian interval) at greater depth. Furthermore between these two compositional end members, more diluted, but still saline waters, with high Na/Ca ratio, likely received an additional supply of Na⁺ from the illitization of smectite ("shale water"). Additional Si, Ca, Na, K, and likely H⁺ was added through sandstone/shale interactions to the basin pore fluid circulating system.

1 INTRODUCTION

Approximately twenty percent of the volume of most sedimentary basins is pore water. Most of this water is hot, salty, under high pressure, and the chemical composition is variable. It is of obvious importance to know how fluids originate in sedimentary basins, what processes determine pathways and mechanisms of migration and solute transport.

The origin and migration of subsurface brines plays an important role in a wide range of geological processes. Particularly significant to diagenesis, as the complex mixture of sedimentary materials and organic matter attempt to achieve chemical equilibrium during burial, transfer of material from one phase to another is performed through pore fluid circulation. Because pore fluids are mobile, they can migrate through a sedimentary rock sequence, carrying with them diagenetically reactive components, heat, hydrocarbons, salts, and metals.

Major objectives of this work include (1) characterization of the Água Grande sandstones formation water; (2) understanding how water composition and origin are related to the diagenetic processes and porosity evolution of these rocks during their burial history; and (3) determination of

geochemical controls that could have significance for either predicting or constraining diagenetic pathways in the sandstones.

2 SAMPLING AND DATABASE

One hundred and seventy samples of formation water were obtained from early Cretaceous Água Grande sandstones, Recôncavo Basin, Northeast Brazil (Fig. 1). Water samples were obtained from 163 wells distributed among 75 oil and gas fields or regions distributed throughout the basin. Because the Água Grande sandstones occur at different depth throughout the basin, they allow a superb opportunity for analyzing water compositional trends with depth. Most samples were obtained from open and cased-hole formation tests and were analyzed for major constituents, but some of them do not present complete analysis for all components. The chemical ionic balance was the chief quality control test on the water analyses. The chemical balance between the sum of major anions and the sum of major cations should be equal. Analyses with more than 5% of difference were discarded from the database.

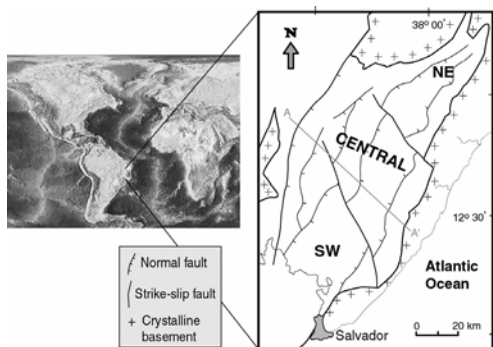


Figure 1: Location map of the Recôncavo Basin, Northeast Brazil.

3 WATER COMPOSITIONAL VARIATION WITH INCREASING DEPTH

Salinity generally increases with increasing depth (Fig. 2A), except for some samples at greater depth (near 3,000 m depth), which show salinities lower than expected. These samples are still more saline than seawater, and their diluted character may be related to mixing with water liberated from shales (“shale-water”).

Temperature increases with increasing depth at a gradient of 35°C/Km, but salinity exerts the dominant control on *in situ* density. Distribution of *in situ* density of water with increasing depth could explain a mechanism for fluid convection within the entire reservoir. Figure 2 also shows that waters with similar density may occur at considerably different depth. Due to that, these waters have potential to move. Based in this effect, deeper waters move upward, while shallower ones sink. This process provides a mechanism for density-driven fluid flow that could control diagenetic modifications (grain dissolution and replacement, and cement precipitation and dissolution) within sandstones (Morton & Land 1987; Land et al. 1988; Ranganathan & Hanor 1989; Land & Macpherson 1992). It is important to remark that this process also yields an efficient mechanism for migration and emplacement of oil within sandstones situated in proper structure.

Although at different rates, a similar tendency with increasing depth is noticed for the major cations (Fig. 2B and C), except for Mg²⁺, which does not show the same distinctive trend (Fig. 2D).

Among the major anions, chloride, by far the most important, mirrors the salinity trend with increasing depth (Fig. 3A).

Regardless of the complexity of bicarbonate determination due to the presence of organic

alkalinity (Carothers & Kharaka 1980), it is obvious from figure 3B that higher bicarbonate concentrations are present at a depth shallower than 1,500 m. It might be related to organic acids, which are thermally destroyed at temperatures higher than 80°C (around 2,000 m depth). The low sulfate content in the studied waters (Fig. 3C) suggests sulfate reduction processes, either bacterially (shallow depth) or thermally induced (greater depth).

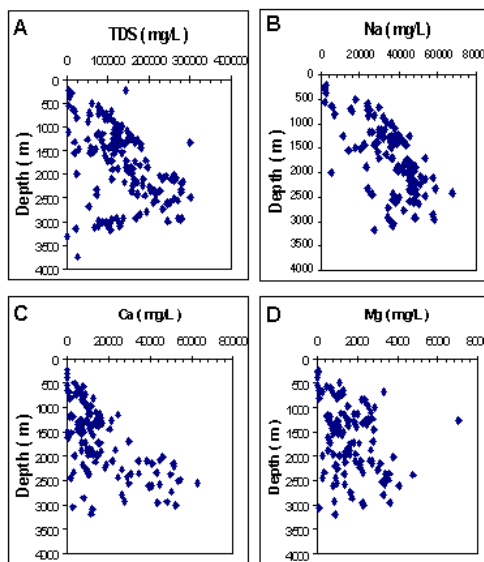


Figure 2. Total dissolved solids and major cations variation through depth.

4 EVOLUTION OF FORMATION WATERS OF ÁGUA GRANDE SANDSTONES

Whatever was the composition of the water deposited along with the Água Grande sands, its evolution during progressive burial was a complex non-conservative process resulting from the chemical evolution and mixing of waters from different origins (Fig. 4). Ca-rich brines, at greater depth, are likely associated with water-rock interaction processes, which might encompass Ca yielded by shales, plagioclase dissolution and albitization, and calcite dissolution, whereas Na-Ca-Cl saline waters seem to be related to dissolution of evaporite minerals once present within older rocks (Permian interval) at greater depth. Furthermore between these two end members, more diluted, but still saline waters, with high Na/Ca ratio, likely received additional supply of Na⁺ from illitization of shales (“shale water”).

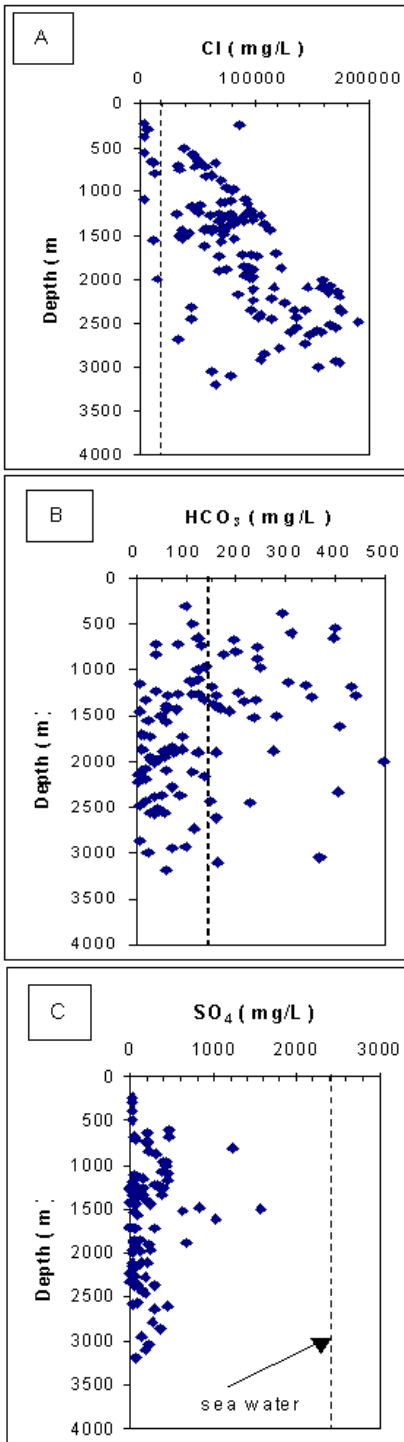


Figure 3: Main anions variation through depth.

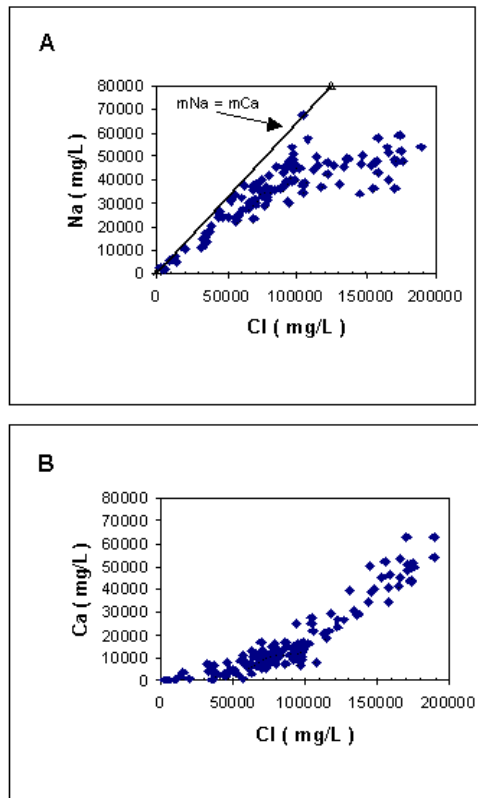


Figure 4: Na versus Cl (A) and Ca versus Cl (B) concentration for all water types of Água Grande sandstones. Saline waters are characterized by $mNa < mCl$ because of progressively greater contribution from calcium with increased salinity. The line is drawn at $mNa = mCl$ (halite line).

5 CONCLUSIONS

Sodium and chloride dominate the ionic composition of most water samples of the Água Grande sandstones, and thus halite is implicated as the primary source of solutes. The more acceptable explanation for the TDS content and high amounts of Cl^- and Na^+ of the Água Grande brine is that a saline fluid originated deep in the Recôncavo Basin by reaction with Permian evaporites (presently almost all dissolved). These waters moved up-dip along faults and/or preferentially through high permeability sandstones, and were diluted at shallow depth (meteoric influence + depositional water). The waters underwent changes in composition due to water-rock interactions such as diagenetic modifications of clay minerals in associated shales (smectite illitization), albitization of feldspars, and chlorite and calcite precipitation within the sandstones.

6 REFERENCES

- Carothers, W.W. & Kharaka, Y.K. 1980. Stable carbon isotopes of HCO₃⁻ in oil-field waters: implications for the origin of CO₂. *Geochem. and Cosmochem. Acta* v. 44: 323-332.
- Land, L.S., Macpherson, G.L., and Mack, L.E. 1988. The geochemistry of saline formation water, Miocene, offshore Louisiana. *Gulf Coast Association of Geological Societies Transactions* v. 38: 503-511.
- Land, L.S. & Macpherson, G.L. 1992. Origin of saline waters, Cenozoic section, Gulf of Mexico sedimentary basin. *AAPG Bull.* v. 76: 1344-1362.
- Morton, R.A. & Land, L.S. 1987. Regional variations in formation water chemistry, Frio Formation (Oligocene), Texas Gulf Coast. *AAPG Bull.* v.71: 191-206.
- Ranganathan, V., & Hanor, J.S. 1989. Perched brine plumes above salt domes and dewatering of geopressured sediments. *Journal of Hydrology.* v. 110: 63-86.

Albitization of Detrital Feldspars in Petroleum Reservoir Rocks, Brazil

R.S.Souza, C.R.O.Rodrigues & D.C.Dias Filho

Petrobras, Research and Development Center, Rio de Janeiro, Brazil

L.F.De Ros

Geosciences Institute, Federal University of Rio Grande do Sul, Porto Alegre, Brazil

E.Zambonato

Petrobras, UN-ES, Vitória, Brazil

S.Morad

Uppsala University, Sweden

ABSTRACT: Albitization was a pervasive diagenetic process in several oil reservoirs in different Brazilian basins, remarkably within the deep Sergi and Água Grande (Upper Jurassic and Early Cretaceous, Recôncavo Basin), Urucutuca (Eocene, Espírito Santo Basin), and Itajaí-Açu (Early Cretaceous, Santos Basin) sandstones. Albitization, as a general term, refers to the formation of authigenic albite, either as a direct precipitate from solution forming overgrowths, ingrowths and healing fractures or by replacement of other minerals, typically potassium feldspar or calcic plagioclase. Detrital feldspars replaced by albite are turbid, contain variable amounts of dissolution voids and are generally untwined or show irregular blocky to tabular extinction. Their turbid appearance is due to the presence of numerous small fluid inclusions and micropores. Optical and electronic microscopy analyses revealed that albitized plagioclase grains are composed of numerous elongated prismatic albite crystals, arranged parallel to each other in one direction related to the lattice of the replaced feldspar. Albite occurs also as small intergranular discrete crystals associated in places with illitic clays. Intrastratal solutions related to the replacement of detrital plagioclases or K-feldspars may be a good source to the albitization reactions. However, sandstones where albite overgrowths predominate may have other sources of elements like brines from the Permian Afligidos Fm. or from the dewatering of nearby shales.

1 INTRODUCTION

The assessment of petroleum reservoir rock quality requires the understanding of burial and diagenetic histories and the characterization of all processes that may affect porosity obstruction or enhancement. The identification of diagenetic mineral paragenesis related to shallow or deep burial help reconstruct a variety of different scenarios that are of extreme importance in the prediction of reservoir quality parameters, among them, permeability

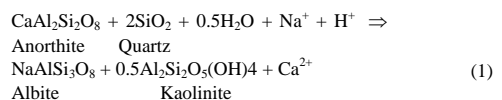
Albitization is a very common process in several Brazilian deep petroleum reservoir rocks. Understanding the albitization patterns in such rocks is extremely important not only for their exploration, but also to relate the distribution of porosity and permeability to diagenetic processes at a reservoir scale, benefiting oilfield development and production.

2 THE ALBITIZATION PROCESS AND MAJOR FEATURES OF ALBITIZED GRAINS

Albitization is a general term that refers to the formation of authigenic albite, either as a direct precipitate from solution or by replacement of other

minerals, typically potassium feldspar or calcic plagioclase (Saigal et al. 1988; Aagard et al. 1990; Ramseyer et al. 1992). A number of studies have highlighted the importance of this diagenetic process, including Land & Milliken (1981), Boles (1982), Walker (1984), McDowell (1986), Milliken (1989) and Morad et al. (1990).

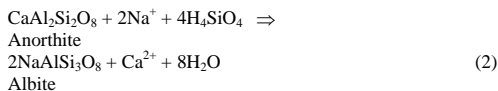
Boles (1982) and Boles & Ramseyer (1987) related albitization of plagioclase to elevated silica activity due to dissolution of quartz at sites of high stress, as follows:



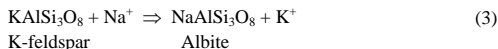
Boles (1982) believed that most of the Na^+ required could be derived from the reactions of smectite illitization within the interbedded shales.

Land (1984) pointed out that the presence of albite overgrowths on albitized plagioclase grains of the Tertiary Frio sandstones, Texas Gulf coast, were suggestive of an external source of Na^+ , i. e. that there was a higher amount of precipitated albite than the one expected if accounting only the remobilization by equal volume of albitized detrital

feldspars. Thus, Land (1984) suggested the following reaction:



Despite the complexity of albitization of potassium feldspar, the reaction requires the exchange of potassium in the detrital feldspar by sodium in order to form albite, as follows:



Although the albitization of plagioclase is recognizably enhanced at temperatures higher than 100°C (Boles 1982), partial replacement has been reported at 75-100°C (Morad et al. 1990). Moreover, Saigal et al. (1988) have shown that K-feldspar albitization can occur at relatively low temperature (~65°C) if a suitable sink for K⁺, such as the illitization of smectite and/or neoformation of illite is provided. Evidence from reservoir sandstones (Morad et al. 1990) and from thermodynamic calculations (Ben Baccar et al. 1993) indicate that the albitization of plagioclase occurs at lower temperatures than those needed for K-feldspar albitization.

Albitized detrital feldspars are turbid, contain variable amounts of dissolution voids and are untwined or show irregular blocky to tabular extinction. Their turbid appearance is due to the presence of numerous small fluid inclusions and of micropores. Optical and electronic microscopy analyses revealed that albitized plagioclase grains are composed of numerous elongated prismatic albite crystals, arranged parallel to each other in one direction related to the lattice of the replaced feldspar. Albite occurs also as small intergranular discrete crystals associated in places with illitic clays. These features, along with their chemical purity (pure NaAlSi₃O₈ in microprobe analyses), indicate an *in situ* diagenetic albitization.

3 ALBITIZATION IN BRAZILIAN SANDSTONES

Albitization was a pervasive diagenetic process in several oil reservoirs in different Brazilian sedimentary basins, remarkably within the deep Sergi and Água Grande (Upper Jurassic and Early Cretaceous, Recôncavo Basin), Urucutuca (Eocene, Espírito Santo Basin), and Itajaí-Açu (Early Cretaceous, Santos Basin) sandstones.

Albitization was pervasive within the deep Água Grande fluviodeltaic and eolian sandstones (Souza

1999). Albite occurs mainly as overgrowths or by replacement of potassium feldspar or calcic plagioclase (Fig. 1).

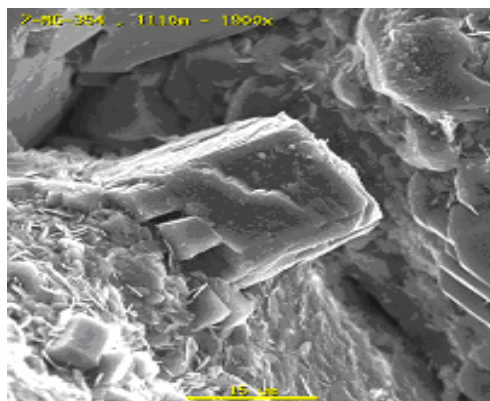


Figure 1: Grains of plagioclase with albite overgrowths. SEM image.

In sandstones buried over 2,500 m feldspars with original composition are extremely rare. Only in the shallower buried Água Grande there is a significant amount of detrital K-feldspars (orthoclase and microcline) and plagioclase (oligoclase-andesine). Albitization likely was contemporaneous with quartz cementation and started at a temperature of about 80°C. Albitization within the Travis Peak Formation (Lower Cretaceous, Texas) was estimated to start at a similar temperature (Dutton 1986), whereas Kaiser (1984) stated that albitization occurred at temperatures ranging from 50° to 85°C in the Frio Formation (Oligocene, Gulf of Mexico).

Fluids responsible for albitization were likely Na-Cl brines that were generated during the rifting stage and that replaced the original meteoric waters of the continental Água Grande red beds. Na-Cl rich brines were likely generated by dissolution of Permian evaporites of the Afligidos Formation during burial. In addition, XRD data of Candeias mudstones show that analcime (Na-rich zeolite) decreases with depth and maturation level, suggesting an additional source of Na⁺ for albitization.

The Al³⁺ was presumably derived from the dissolution and replacement of silicates in the sandstones. The Si⁴⁺ may have been derived in part from these sources and in part from clay mineral transformation within the Candeias mudstones.

Albitization was probably nearly coeval with kaolinite formation, both occurring during a time of relatively abundance of dissolved Al³⁺ after the major phase of grain dissolution. The albitization process resulted in the release of Ca²⁺ into the brine and incorporation of Na⁺ by feldspars, hence modifying the original Na-Cl brine toward a Na-Ca-

Cl brine that presently occurs in the Água Grande Fm. This scenario of formation water evolution is supported by the present day composition of formation water analysis.

The Sergi Fm. sandstones are Upper Jurassic continental red beds deposited by a widespread braided fluvial system under arid to semi-arid climate that allowed the eolian reworking of the top beds. The tectonic evolution of the Recôncavo Basin led to the formation of an asymmetrical graben, deeper in the east. This geometry allows the occurrence of the Sergi Fm. in a variety of present day depths, from outcrops in the west to over 4,000 m deep in the east. Rodrigues (1990), revising the diagenetic evolution of these sandstones in the Recôncavo Basin, emphasizes that the albitization was insipient in shallow samples (less than 1,000 m deep) and widespread in deeper ones.

The albitization process in deep Sergi evolved either over plagioclases or K-feldspars mostly in the form of overgrowths and locally as ingrowths (i. e. inside partially dissolved feldspar grains), as a fracture healing cement and as a total or partial pseudomorphic replacement. Late discrete crystals are also found but are less common.

In deep Sergi sandstones, the albitization reactions are contemporary to chlorite and late quartz precipitation and occur with ordered illite-smectite mixed-layered clays averaging 85% of illite in the clay structure. This paragenesis is indicative of temperatures of about 100 °C or higher, consistent with the stratigraphic position of the Sergi Fm. which is older and deeper than the Água Grande sandstones.

Interstratal solutions related to the replacement of detrital plagioclases or K-feldspars may be a good source to the albitization reactions. However, sandstones where albite overgrowths predominate may have other sources of elements like brines from the Permian Afligidos Fm. or from the dewatering of nearby shales.

In the Urucutuca sandstones (Eocene, Espírito Santo Basin), the observed pervasive albitization is associated with anomalously high porosities. Intense feldspar grain dissolution suggests an internal source of Na⁺ for the precipitation of pure albite.

The combination of diagenetic dissolution and replacement of feldspars by albite and kaolinite changed the original detrital composition of several of the Urucutuca sandstones from arkoses to subarkoses and even to quartzarenites, a significant modification in the original framework composition.

The association of intense albitization with high porosities in some offshore Eocene sandstones suggest that such strong albitization might be associated with processes of porosity enhancement and redistribution of extreme importance for reservoir quality prediction.

Itajaí-Açu (Early Cretaceous, Santos Basin) shelf and turbidite sandstones present a suit of deep diagenetic features including pervasive albite overgrowth (Fig. 2), quartz and chlorite precipitation besides strong compaction. These diagenetic features, coherent with the sandstones present depths of about 5,000 m, are somewhat controlled by provenance, grain size and sedimentary environment but albitization is common in all cases.

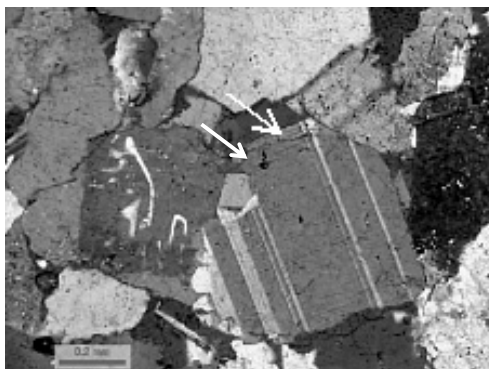


Figure 2: Grains of plagioclase with albite overgrowths. Transmitted light with crossed polarizer.

Albite overgrowths are present whenever there is open pore space and lacks chlorite rims. Albitization by replacement of detrital plagioclases and K-feldspars is common even when there are thick chlorite rims and tight compaction. In some cases, albite overgrowths are followed by the precipitation of calcite, anhydrite or zeolite cements indicating the migration of fluids from underlying evaporitic beds.

4 CONCLUSIONS

Albitization of detrital feldspars is a common diagenetic process identified in a variety of oil reservoir in Brazilian basins. In spite of stratigraphic age, sedimentary depositional environment and geological setting, albitized grains show similar petrographic features. As a general rule, albitized detrital feldspars are turbid, contain variable amounts of dissolution voids and are untwined or show irregular blocky to tabular extinction. Their turbid appearance is due to the presence of numerous small fluid inclusions and micropores. Optical and electronic microscopy analyses revealed that albitized plagioclase grains are composed of numerous elongated prismatic albite crystals, arranged parallel to each other in one direction related to the lattice of the replaced feldspar. Albite

occurs also as small intergranular discrete crystals associated in places with illitic clays.

Possible sources of Na⁺ for albite authigenesis are the illitization of detrital smectitic clays in associated mudrocks and the dissolution of evaporites during burial. Ongoing research will check the relationships of enhanced albitization and porosity with the possible influence of thermohaline circulation of fluids due to the proximity of salt domes, with regional faults, and with intrabasinal magmatic centers.

Major potential external Na⁺ sources for detrital feldspar albitization are Na-Cl brines generated by dissolution of Permian evaporates (Água Grande and Sergi sandstones), dissolution of analcime (Na-rich zeolite) and clay mineral transformations in associated shales. Among the likely internal source of Na⁺ are dissolution of plagioclase and volcanic rock fragments, common framework grains in some of the studied sandstones.

5 REFERENCES

- Aagard, P., Egeberg, P.K., Saigal, G.C., Morad, S., and Bjørlykke, K., 1990, Diagenetic albitization of detrital K-feldspar in Jurassic, Lower Cretaceous, and Tertiary clastic reservoir rocks from offshore Norway, II. Formation water chemistry and kinetics considerations: *J. Sedim. Petrol.*, 60: 575-581.
- Ben Baccar, M., Fritz, B. & Madé, B. 1993, Diagenetic albitization of K-feldspar and plagioclase in sandstone reservoirs: thermodynamic and kinetic modelling. *J. Sedim. Petrol.*, 63: 1100-1109.
- Boles, J.R. 1982. Active albitization of plagioclase. *Gulf Coast Tertiary. Am. J. Sc.*, 282: 165-180.
- Boles, J. R. & Ramseyer, K. 1987. Diagenetic carbonate in Miocene sandstone reservoir, San Joaquin Basin, California. *AAPG Bull.* 71(12): 1475-1487.
- Dutton, S.P., 1986, Diagenesis and burial history of the Lower Cretaceous Travis Peak Formation, east Texas: Ph.D. Dissertation, The University of Texas, Austin, Texas, 165 p.
- Kaiser, W.R., 1984, Predicting reservoir quality and diagenetic history in the Frio Formation (Oligocene) of Texas, in McDonald, D.A., and Surdam, R.C., eds., *Clastic Diagenesis: AAPG Memoir 37*: 195-215.
- Land, L.S., and Milliken, K.L., 1981, Feldspar diagenesis in the Frio Formation, Brazoria County, Texas: *Geology*, 9: 314-318.
- Land, L.S., 1984, Frio Formation diagenesis, Texas Gulf Coast: a regional isotopic study, in McDonald, D.A., and Surdam, R.C., eds., *Clastic Diagenesis: AAPG Memoir 37*: 47-62.
- McDowell, S.D., 1986, Composition and structural state of coexisting feldspars, Salton Sea geothermal field: *Mineralogical Magazine*, 50: 75-84.
- Milliken, K.L., 1989, Petrography and composition of authigenic feldspars, Oligocene Frio Formation, South Texas: *J. Sedim. Petrol.*, 59: 361-374.
- Morad, S., Bergan, M., Knarud, R. & Nystuen, J.P. 1990. Albitization of detrital plagioclase in Triassic reservoir sandstones from the Snorre Field, Norwegian North Sea. *J. Sedim. Petrol.*, 60: 411-425.
- Ramseyer, K., Boles, J.R., and Lichtner, P.C., 1992, Mechanism of plagioclase albitization: *J. Sedim. Petrol.*, 62: 349-357.
- Rodrigues, C. R. O. 1990. Argilominerais na evolução diagenética dos arenitos da Formação Sergi, Jurássico, Bacia do Recôncavo, Brasil. M. Sc. Dissertation. UFOP, Ouro Preto. 211p.
- Saigal, G.C., Morad, S., Bjørlykke, K., Egeberg, P.K., and Aagaard, P. 1988. Diagenetic albitization of detrital K-feldspar in Jurassic, Lower Cretaceous, and Tertiary clastic reservoir rocks from offshore Norway, I. Textures and origin. *J. Sedim. Petrol.* 58: 1003-1013.
- Souza, R. S. 1999. Integrated Diagenetic Modeling and Reservoir Quality Assessment and Prediction of the Água Grande Sandstones, Early Cretaceous, Recôncavo Basin, Northeast Brazil. Ph.D Dissertation, The University of Texas at Austin. 386P.
- Walker, T. R. 1984. Diagenetic albitization of potassium feldspar in arkosic sandstones. *J. Sedim. Petrol.*, 54(1): 3-16.

Ore Mineralogy

Chromite Composition, Metamorphism, and PGM Distribution in Chromitites from the Espinhaço Ridge - Brazil

N. Angeli

Dept. of Petrology and Metallogeny – State University of São Paulo (Rio Claro), Brazil

S.R.F. Vlach

Dept. of Mineralogy and Geotectonics – University of São Paulo (São Paulo), Brazil

ABSTRACT: Textural and mineralogical features, as well as chromite compositions of chromitites from the Espinhaço Ridge resemble those of chromitites associated with stratiform complexes. A metamorphic/hydrothermal overprint led to chromite re-equilibration and to the development of a zoning pattern given by Cr- and Mg-rich cores, Al and Fe³⁺ increase in intermediate zones, and an outer zone with ferritchromite-magnetite. Platinum Group Minerals (sperrylite, laurite, irarsite) occur as inclusions in chromite crystals and as isolated crystals in the chromitite matrix. The greater abundance of PGM in the chromitite matrix in more intensely metamorphosed zones suggests that the PGE were mobile during the metamorphic/hydrothermal event.

1 INTRODUCTION

The Espinhaço ridge comprises an orogenic belt developed on the São Francisco craton, which extends from north of Minas Gerais to Bahia states, E Brazil. A volcanic-sedimentary sequence (Serra Sequence, Knauer 1999), which hosts mafic-ultramafic bodies, crops out in its southeastern limits, along the contact between the Espinhaço Supergroup and the Guanhães granite-gneissic complex (Figure 1). It is composed by serpentinites, actinolite-chlorite-talc schists, chlorite-magnetite schists and talc schists, with intercalations of quartzites, conglomerates and phyllites (Zaparolli 2001).

Chromite compositional variations in relation with metamorphism are important to understand element mobility and Platinum Group Element (PGE) distribution. This paper presents a brief characterization of chromitite lenses enclosed in the metamorphosed mafic-ultramafic bodies from the Alvorada de Minas area, with emphasis on chromite composition and Platinum Group Minerals (PGM) distribution.

2 ANALYTICAL METHODS

After conventional petrographic descriptions of polished thin sections, a detailed study was made under the SEM (LEO-430i), provided with EDS (CatB, OMG), operating under 15 kV and 10 nA, which allow us to characterize chromitite main textural and mineralogical features. Chemical analyses of chromite (WDS) were done with a JEOL JXA-8600 equipment operating under 15 kV and 20 nA. WDS quantitative PGM analysis was not feasible due to the small crystal dimensions (< 12 mm).

3 GEOLOGICAL SETTING AND GENERAL PETROGRAPHY

The Alvorada de Minas mafic-ultramafic rocks comprise mainly NNE trending metahasburgite bodies, enclosed in Archaean to Paleoproterozoic granite-gneissic rocks. They crop out as tectonic slabs limited by thrust faults running from E to W, which caused local stratigraphic inversion. Several chromitite lenses occur within these bodies. They are locally continuous up to 12-14 m, but in most

cases they are disrupted, reaching 2.5 – 4.0 m length (Angeli & De Carvalho 1996).

The chromitite lenses are fine-grained and display cataclastic texture. Most of them presents disseminated ore in the top and a more massive texture in the bottom, in a matrix mainly composed by chlorite and talc. Olivine (F₀₈₇ – F₀₉₂) occurs in a few bottom samples. The chromite crystals (0.1–2.0 mm) have both euhedral and anhedral shapes. Some lense-shaped portions with 75-85 % modal chromite present well-developed layering with fine-grained

(0.1–1.0 mm) chromite layers intercalated with medium-grained (2.0–3.0 mm) ones. The crystals are often poikilitic, with inclusions of Ti-magnetite, ilmenite, some minute PGM crystals, and pseudomorphic chlorite and serpentine. They are often fractured and in-filled by chlorite (kammererite); some of them present also corrosion features in their rims. Pull-apart textures were found in zones of highest strain, where the rocks were strongly affected by brittle deformation.

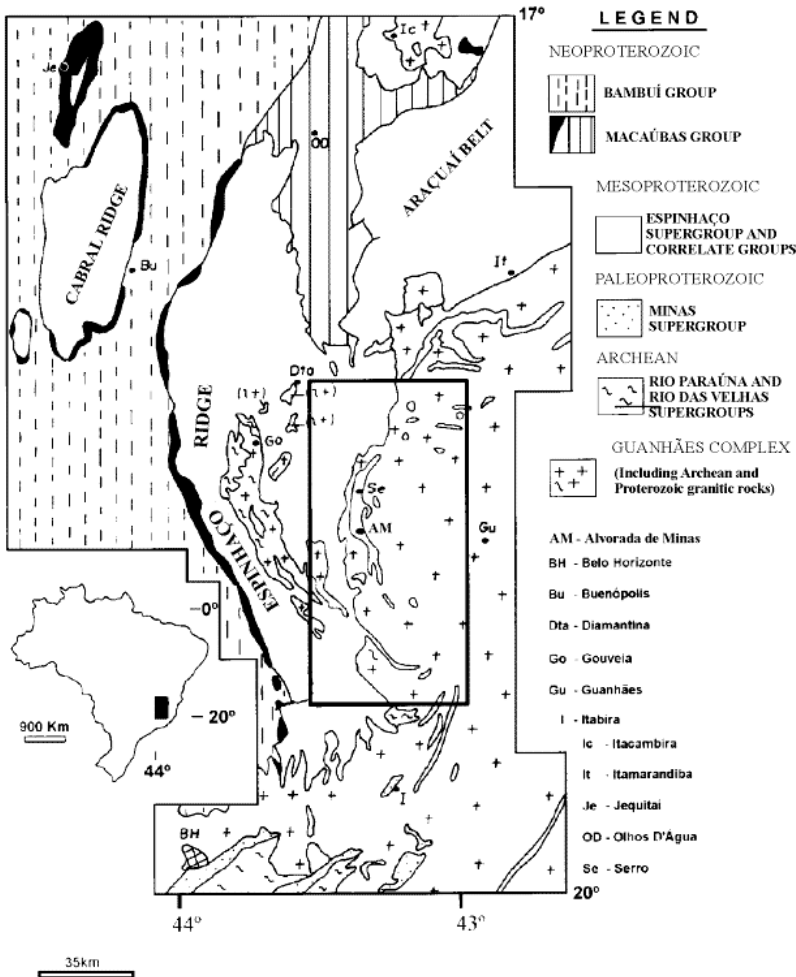


Figure 1. Geological map of Espinhaço Ridge, MG (After Knauer 1999).

Besides kammererite and talc, the chromitite matrix presents serpentine, carbonates (siderite, magnesite, and ankerite), rutile, and opaque minerals, which locally reach up to 5 to 6 vol%. The opaque mineral assemblage comprises magnetite,

pyrite, ilmenite, minor PGM and gold. Rare minute chalcopyrite and pyrrhotite crystals occur associated with the carbonates.

4 CHROMITE CHEMISTRY

Chromite crystals display a zoning pattern which varies from chromite-rich cores to ferritchromite rims (Figure 2). Three main zones have been recognized: a core (dark gray) with higher Cr₂O₃ and MgO contents, ranging from FeCr₂O₄ to (Fe,Mg)Cr₂O₄; an intermediate zone (medium gray) which depicts Al and Fe³⁺ increase, close to Fe(Fe³⁺,Cr,Al)₂O₄; and an outer zone (light gray), with high Fe³⁺, transitional between ferritchromite and magnetite, (FeO) (Fe₂O₃).

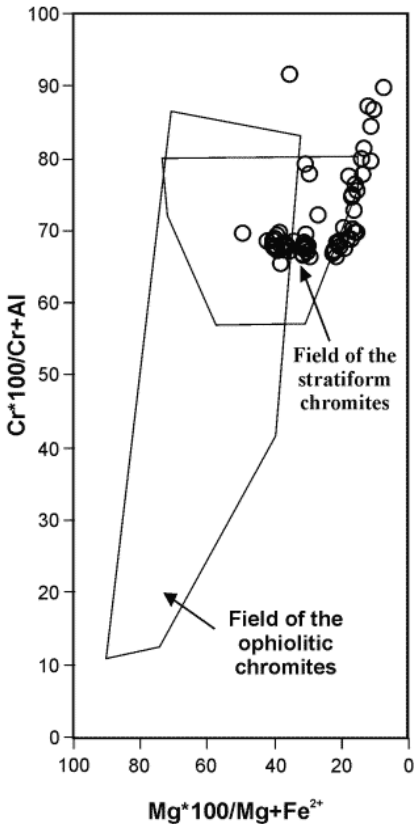


Figure 2. Fields of compositional variation of the analysed crystals (main body of Alvorada de Minas). The composition of the chromites, outside the fields, correspond to rims of the crystals.

The core compositions are similar to chromites from the Bushveld and the Great Dyke Complexes. Average composition is (wt.%): 48.3% (Cr₂O₃), 18.1 (Fe₂O₃), 17.4 (Al₂O₃), 8.9 (MgO), 0.3 (TiO₂), 0.2 (NiO), and 0.2 (MnO); Cr₂O₃ contents are lesser than 62 wt.%. The cores have high Fe and Cr

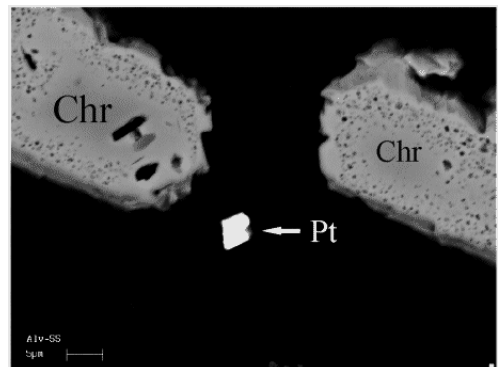
contents, with Cr/Fe ratios up to 2.9. In the Cr*100/Cr+Al vs Mg*100/Mg+Fe²⁺ diagram (Figure 2), our data plot in the field of the stratiform type chromites (Naldrett & Von Gruenewaldt, 1989). It is noteworthy that MgO contents decrease from top to bottom in chromitite layers. The rim compositions have higher Fe/Mg and Cr/Al and plot at the limit or outside the above mentioned field. This zoning pattern is attributed to a metamorphic and/or hydrothermal (?) event, which re-equilibrated chromite composition, while the original magmatic composition was preserved in crystal cores only, as supported by similar studies (Burkhard 1993; Kimball 1990; Fleet et al. 1993).

5 PLATINUM GROUP MINERALS (PGM)

PGM were found in three deposits from the Alvorada de Minas area. They are concentrated in the lenses bottom, like in the Stillwater Complex (Murk 1985), and more common in the ore matrix (Photomicrograph 1), but crystal inclusions are present in the cores, intermediate zones, and rims of chromite crystals. They are euhedral to anhedral and have dimensions between 5 and 12 mm.

A detailed search with SEM and EDS allowed identification of sperrylite (PtAs₂), laurite ((Ru,Os,Ir)S₂), irarsite (Ir,Ru,Rh,Pt)AsS, cooperite (PtS), and a Pt-Ir alloy with about 72 wt.% Ir and 14 wt.% Pt.

Whole rock data for one sample gave anomalous PGE values (ppb): 314 (Pt), 226 (Ru), 120 (Ir), 72 (Pd), and 50 (Rh). This supports the PGM occurrence in these rocks.



Photomicrograph 1. Crystals of Chromite (Chr) and Sperrylite (Pt) enclosed in silicatic matrix composed by chlorite and minor serpentine. The crystals of chromite show a zoning, the core is rich in chromian and the rim is rich in iron. The left crystal presents three inclusions of kammererite.

6 DISCUSSION

Chemical data indicate that the original magmatic composition of chromite in the studied chromitites were preserved in crystal cores only. The compositional variation from top to bottom layers also reflects the earlier igneous evolution. A late metamorphic/hydrothermal event led to element mobilization in chromite crystals turning, causing their rims to be enriched in Fe/Cr and depleted in Al and Mg.

Chromite lost Cr to some extent, which was incorporated into kammererite (Lipin 1984). Al mobility was smaller, which is attributed to the low P-T conditions. According Evans & Frost (1975), when Al starts to move away from chromite, under greenschist to lower amphibolite grade, exsolved Ti-minerals begin to form in chromite, a feature also observed in the present study. Ti have affinity with magnetite, but exhibits a great stability during low-grade reactions. In our samples, Ti-rich lamellae and inclusions of Ti-magnetite in chromites were observed, indicating a preferential partition of Ti to the Fe-rich exsolved portions. Such exsolution probably happened after the unmixing of Fe and Al-Mg-rich phases under subsolidus conditions (Candia & Gaspar 1997).

PGM occur in the kammererite and talc matrix, mainly in the more intensely metamorphosed portions of the chromitites, while in the preserved ones they appear mostly as inclusions in chromite crystals. This feature indicates that the metamorphic/hydrothermal event caused PGE depletion in the structure of chromite.

7 CONCLUSIONS

Our data suggest that chromitites from Alvorada de Minas partially preserved their original magmatic evolution, which appears to be similar to the ones associated with stratiform complexes. Cr₂O₃ content in mafic magmas and suitable fO₂ lead to chromite precipitation in the initial crystallization phases, together with minor olivine as cumulate phases, while orthopyroxene, in small amounts, was intercumulus. PGM crystallized close to chromite and was captured as inclusions.

A later low P-T metamorphic/hydrothermal event led to chromite re-equilibration, as demonstrated by Cr loss in crystal rims and its late incorporation into the matrix kammererite. This event contributed also for PGE mobilization and re-precipitation in the chromite matrix.

8 ACKNOWLEDGEMENTS

We thank D.R.H. Verdugo for the SEM work, G. Angeli for help with figures, and F.R.D. Andrade for text improvement.

9 REFERENCES

- Angeli, N. & De Carvalho, S. G. 1996. Composição química de cromitas em corpos metamórfico/ultramáficos da borda leste do Espinhaço Meridional, Minas Gerais. *Geonomos*, Belo Horizonte, Brazil: 4(1): 11-20.
- Burkhard, D.J.M. 1993. Accessory chromium spinels: their coexistence and alteration in serpentinites. *Geoch. Cosmoch. Acta*, 57: 1297-1306.
- Candia, M.A.F. & Gaspar, J.C. 1997. Chromian spinels in metamorphosed ultramafic rocks from Mangabal I and II complexes, Goiás, Brazil. *Mineral. Petrol.*, 60: 27-40.
- Evans, B.W. & Frost, B.R. 1975. Chrome spinel in progressive metamorphism: a preliminary analysis. *Geoch. Cosmoch. Acta*, 39: 959-972.
- Fleet et al. 1993. Oriented chlorite lamellae in chromite from the Pedra Branca mafic-ultramafic complex, Ceará, Brazil. *Am. Mineral.*, 78: 68-74.
- Kimball, K.L. 1990. Effects of hydrothermal alteration on the compositions of chromian spinels. *Contr. Mineral. Petrol.*, 105: 337-346.
- Knauer, L.G. 1999. Serra do Espinhaço Meridional: considerações sobre a estratigrafia e a análise da deformação das unidades Proterozóicas. PhD Thesis, UNESP, Rio Claro (SP): 324p.
- Lipin, B.R. 1984. Chromite from the Blue Ridge Province of North Carolina. *Am. Jour. Sci.*, 284: 507-529.
- Murk, B.W. 1985. Factors affecting the formation of chromite seams: Part II: Petrology and geochemistry of the G and H chromite seams in the Mountain View area of Stillwater complex - USA. PhD Thesis, Un. of Toronto, Canada: 94p.
- Naldrett, A.J. & Von Gruenewaldt, G. 1989. Association of platinum-group elements with chromitites in layered intrusions and ophiolite complexes. *Econ. Geol.*, 84: 180-187.
- Zapparoli, A.de C. 2001. Os depósitos de cromita da borda leste da Serra do Espinhaço Meridional, Minas Gerais: Petrologia, quimismo e implicações genéticas. MSc Thesis, UNESP, Rio Claro (SP): 133p.

Supergene Sulphides and their Analogues in the Supergene Profile of the Urals VMS Deposits

E.V.Belogub & C.A.Novoselov

Institute of Mineralogy, Urals Branch of Russian Academy of Science, Miass, Russia

V.A.Yakovleva

Geological department, Saint-Petersburg State University, Saint-Petersburg, Russia

ABSTRACT: Supergene zoning of VMS deposits is a result of simultaneous effect from the numerous factors. Superposition of the favourable factors leads to supergene concentrations of the base metals. Supergene sulphides and selenides such as colloform nonstoichiometric pyrite, galena, As-galena, sphalerite, tetrahedrite, pyrrhotite-like, and jordanite-like minerals, metacinnabar, pyrite-dzsharkenite, naumannite, tiemannite, sphalerite, and galena were found above or within the specific subzone which have been distinguished in residual quartz-pyrite sands in the supergene profile of the Southern Urals VMS deposits. Primary massive sulphide ores of these deposits are composed of pyrite, chalcopyrite, sphalerite with minor tennantite, bornite, and galena. Secondary sulphide minerals at VMS deposits of South Urals region are characterized with lightened sulphur isotope composition. Blind position of ore bodies, stagnant regime and bacterial enrichment are favourable conditions for secondary concentration of the base metals as sulphides or their analogues.

1 INTRODUCTION

Formation of the Urals VMS deposits is related to evolution of the Devonian paleo-island arc. The final stage of sulphide-bearing ore system spectacular history was continental supergenesis during Triassic-Quaternary. It resulted in the formation of oxidized ores, which have been the source of gold, silver, copper, and iron during more than 2000 years at the Urals.

The ways of secondary concentration of metals under supergene conditions are different. Gold concentration can be residual, chemogenic, and combined. Copper, silver, and other metals enrichment is of chemogenic character usually. Many kinds of different secondary sulphides and their analogues can be discovered in the supergene zone. Ascertainment of mineral forms of the metals looks very important for exploitation purposes of the upper part of VMS deposits.

The only way to detect and identify the rare secondary sulphides is the integrated use of the precise mineralogical mapping with optical, X-ray and microprobe analysis of samples. An important point is that supergene sulphide minerals are often unstable, so their preservation from air is necessary. Bornite, covellite, chalcocite, and acantite are

common supergene minerals in the cementation zone of VMS deposits (Emmons 1912, Smirnov 1955, and others). The presence of secondary galena, sphalerite, some sulphosalts, and selenides in supergene profile were discovered for VMS deposits at first by the authors' team.

2 GEOLOGICAL SETTING

The Urals VMS deposits are located within Ordovician-Devonian fold belt extending for 2500 km with width of 200 to 400 km. The Urals belt contains about 80 VMS deposits. Copper, zinc, gold, silver, and some trace elements are extracted from them. Only in the South Urals more than 10 VMS deposits are exploited now, and about 30 ones have been prospected. Numerous have an oxidized roof with specific mineral composition, which can be exploited providing advanced economical profit from noble metals and mercury extraction.

Continental supergenesis of the South Urals started at the Triassic under tropical and later semiarid conditions. Weathering resumed after Jurassic-Cretaceous sea transgression. Climate changed from tropical in the Triassic, Jurassic and Cretaceous to arid, semiarid and humid in the

Cainozoic.

The classic model of supergene profile includes (bottom - top): cementation (I), leaching (II) and fully oxidized (III) subzones (Fig. 1).

Cementation subzone is formed below water table as a result of reaction of Cu- and partly Ag-enriched solutions with the primary ore minerals. The galvanic effect plays important role. This interaction leads to formation of high-grade copper (and silver) ores composed of covellite, digenite, chalcocite, acantite, and stromeyerite.

Leaching subzone ordinary consists of residual minerals from primary ores. These are pyrite, quartz, and barite in lower part and quartz and barite in upper part of the subzone.

Specific subzone of the secondary sulphides was determined within low horizon of supergene profile of some VMS deposits in the Urals (Zapadno-Ozernoe, Alexandrinskoye, Dzhusa, possibly – Guy and Blyava). This subzone is presented with sulphide-barite-quartz fine-grained sands, associated with lenses of native sulphur and located above residual pyrite sands but below clear quartz-barite sands. Supergene sulphides and selenides such as colloform stoichiometric pyrite, pyrite, greigite, galena, As-galena, sphalerite, tetrahedrite, pyrrhotite-like and jordanite-like minerals, metacinnabar, pyrite-dzharkenite, naumannite, and tiemannite were found here. All new-formed phases are formed on the relics of primary minerals with evidence of the leaching at their surface. There is supergene differentiation of the base metals as sulphides here.

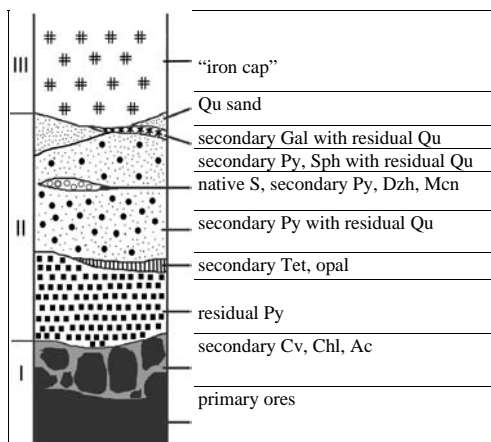


Figure 1: General scheme of the secondary sulphide location in the supergene profile of Urals VMS deposits.

Qu – quartz, Gal – galena, Py – pyrite, Sph – sphalerite, Dzh – dzharkenite, Mcn – metacinnabar, Tet – tetrahedrite, Cv – covellite, Chl – chalcocite, Ac – acantite

The gold enrichment was determined for the

supergene sulphides subzone. For example, average gold content in the quartz-sulphide sands of Zapadno-Ozernoe deposit is 50 ppm, whereas in residual pyrite sands amounts 15 ppm, and in gossans it varies from 8 to 10 ppm. Native gold occurs as spherical grains from 5 to 7 μ across associated with colloform pyrite. Its composition was determined by microprobe analysis as $Au_{0.95}Ag_{0.05}$.

3 SECONDARY SULPHIDES AND THEIR ANALOGUES

3.1 Mineral diversity

Copper sulphides as covellite and chalcocite are most usual secondary sulphide minerals in the cementation subzone. They are the alteration products of chalcopyrite and normally are formed on the boundaries and cracks of chalcopyrite, sphalerite, and galena. Often chalcocite and covellite are characterized with silver admixture up to 0.1 wt.%. Formation of the copper sulphides in leaching subzone as new crystals on the surface of residual sands is not typical.

Secondary tetrahedrite was determined by X-ray, SEM and optical microscopy as a specific horizon between residual pyrite and quartz-barite sands at the Zapadno-Ozernoye deposit only. Tetrahedrite is presented with sparse disseminated grains (about several μ in size (Belogub et al. 2003)) between secondary quartz grains. New-formed sulphosalts of lead were identified in the wall rocks of the partly oxidized sulphide ore body at the same deposit.

Iron disulphides as pyrite and marcasite are widespread in the leaching subzone of many deposits. As a rule, these minerals are fine-grained, colloform or bacteria-like formed. Marcasite forms microconcretions (Fig. 2a). Looking to the results of the exploiting prospecting it can be summarized that secondary iron sulphides bearing layers are enriched with rare elements. For example arsenic content amounts to 1-3 wt.% (German-Rusakova 1962), selenium – 0.44 wt.% for Guy deposit (Zaykov & Sergeev 1993). Microprobe analyses of secondary colloform pyrite from Zapadno-Ozernoye deposit were calculated for stoichiometric formula of pyrite – Se-pyrite – dzharkenite series $Fe(S,Se)_2$. Mineral with maximum selenium content gives the formula $Fe(Se_{0.8}S_{0.2})_{\Sigma 2.0}$ (Fig. 2b) (Yakovleva et al. 2003). Numerous attempts of identification by SEM with EDAX of iron predominated sulphide phases in the secondary sulphide sands from Zapadno-Ozernoye deposit resulted in the identification of pyrite, greigite, pyrrhotite-like sulphides containing silver, arsenic, selenium, occasionally lead, and antimony (particular analysis gives the formula $Fe_{0.98}Ag_{0.02}(S_{0.86}Se_{0.07}Sb_{0.05}As_{0.02})_{\Sigma 1.00}$). These minerals form margins, thin rims around the

colloform pyrite grains. X-ray diffraction patterns show a predominance of pyrite with additional pyrrhotite, greigite or nonidentified minerals.

Silver sulphide acanthite was found in cementation zone of many deposits. Also this mineral forms fine dissemination in bromine-bearing chlorargyrite which corroded pearceite grains in gossans from the Balta-Tau deposit. Acanthite was identified in heavy concentrate of the native sulphur sand from Guy deposit (Zaykov & Sergeev 1993).

X-ray diffraction and optical analysis of the black quartz-bearing sulphide sands from the Zapadno-Ozernoye and Dzhusa deposits detected galena as predominating mineral. It forms cement in quartz microbreccia, skeleton, and case-like crystals (Fig. 2c). The skeleton case-like habit of secondary galena crystals is evident of "starvation" of crystals caused by low diffusion rates of supergene solution, along with stagnant water regime at the time of their precipitation. There is admixture of arsenic in galena from Zapadno-Ozernoye (Belogub et al. 2003). Also there was found a mineral with composition close to jordanite PbS_xAs_y with a varying ratio between sulphur and arsenic. Supergene galena was described before only in the supergene zone of the Broken-Hill, some skarn and SEDEX-type deposits (Yakhontova & Grudev 1987).

Sphalerite was identified by X-ray analysis at the Alexandrinskoe deposit. Also sphalerite was found using optical microscope as zoned spheres.

Metacinnabar was identified using the optical microscope and microprobe. It is characterized with impurities content lower than threshold of detectability of microprobe and occurs as skeleton crystals as rims around relics of sphalerite at the Zapadno-Ozernoye deposit (Fig. 2d). Previously cinnabar was found by SEM with EDAX at the Guy deposit (Zaykov & Sergeev 1993). But there is not any optical or structural information about this mineral. So, taking into account more oxidative stability field for metacinnabar in comparison with cinnabar it can be more real discoveries of metacinnabar in supergene profile.

Tiemannite ($Hg_{0.9}Fe_{0.1}$)Se was identified with pyrite and dzharkenite in the heavy mineral concentrate of the sulphide-quartz sand from Zapadno-Ozernoye deposit. The grain size is less than 0.5μ . Zaykov & Sergeev (1993) described this mineral before from sulphur sands from the Guy deposit.

Naumannite was identified using SEM with EDAX in quartz-pyrite aggregates with dzharkenite and native selenium (Belogub et al. 2003).

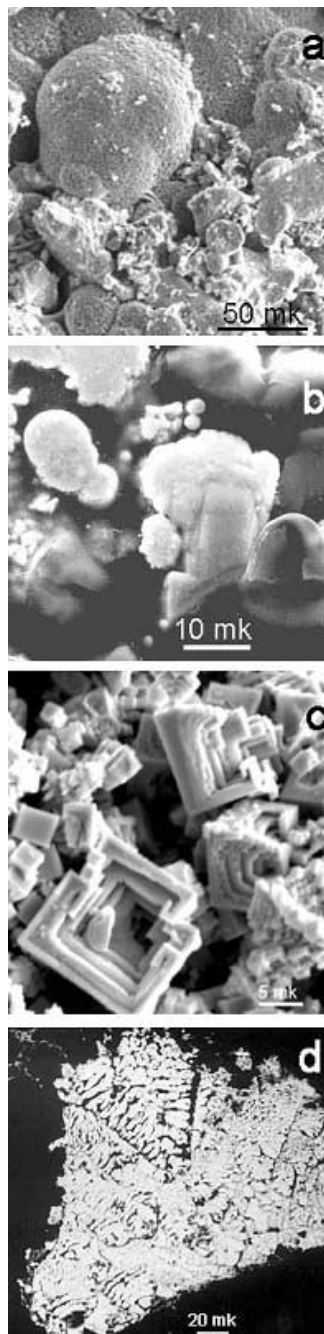


Figure 2. Microconcretions of marcasite from Dzhusa (a), colloform Se-bearing pyrite from Zapadno-Ozernoye (b), case-like galena crystals from Dzhusa (c), and skeleton crystals of metacinnabar from Zapadno-Ozernoye (d). SEM. Photo a, c – V.A. Kotlyarov (Institute of mineralogy, Miass); b, d – A.R. Nesterov (SPb State University, Saint-Petersburg).

3.2 Sulphur isotope composition

Sulphur isotope composition for supergene profile was studied for three VMS deposits of South Urals region. The Alexandrinskoe deposit doesn't demonstrate significant fractionation of sulphur isotopes in supergene profile, so the difference in sulphur isotope composition between that of primary massive sulphide ores and supergene products is minimum.

The lightest sulphur isotope composition at the Guy deposit is characteristic for native sulphur lenses ($-5.5\text{‰ } \delta S^{34}$). There are some lightness for sulphur from quartz-pyrite sands from leaching zone ($-2.9\text{‰ } \delta S^{34}$) in comparison with primary ores ($-1.9\text{‰ } \delta S^{34}$) (Zaykov & Lein 1998). From the author's point of view, the sulphur lightening is connected with microbial separating.

The sulphur isotope composition of secondary sulphides from Zapadno-Ozernoye deposit varies from -8.1 up to $-17.2\text{‰ } \delta S^{34}$, whereas primary sulphides have δS^{34} from $+2.0\text{‰}$ to $+3.2\text{‰}$. The formation of this specific subzone seems to be related with reductive acid conditions during raised ground water level with high bacterial activity (Belogub et al. 2003).

3.3 Genesis

The examples we've discussed so far show wide spectrum of secondary sulphides and their analogues presented at the typical VMS deposits of South Urals region. Their precipitation is controlled by combination of the Eh and pH parameters.

Galena, sphalerite, and tennantite are more soluble under acid conditions than pyrite. Therefore, earlier portions of supergene solutions are enriched with lead, zinc, and mercury. Galvanic processes contribute a lot to advanced corrosion and decomposition of the base metal sulphides. High gradient of Eh and pH, prolonged stagnant regime and bacterial prosperity provide favourable conditions for a differentiation of base metals in the sulphide form. These conditions can realize in the case of blind location of deposit, when supergene processes are in the initial stages. Material of the leached ores can be used as substratum for the new mineral growth. It is important, that all finds of galena-bearing sands have a stratification sign and are separated from residual pyrite sands and covellite-bearing sands.

Special attention should be paid to secondary selenides. These minerals are more stable under oxidative conditions than sulphides and require less activity of selenium for the formation of corresponding selenides. So, when the metals, selenium and sulphur are contained in solution, selenides will precipitate at first.

4 CONCLUSION

Supergene sulphide-bearing subzone is a part of leaching zone of the VMS deposit's supergene profile. It is worth noting the fact of separation of base metals in the supergene profile: the horizon of secondary copper (and sometimes silver) sulphide enrichment doesn't correspond to that of lead and mercury sulphides. This subzone differs from secondary copper enrichment (cementation) subzone by mineral composition, genesis, and geochemical parameters. Supergene zones above blind ore bodies are most favourable for its formation.

So the common opinion on the secondary sulphide enrichment as the matter of copper and silver can be revised, as a number of base metal sulphides and their analogues (galena, metacinnabar, tetrahedrite, sphalerite, dzsharkenite, etc.) were found to precipitate under supergene conditions at VMS deposits of South Urals.

This work was supported by the Fund "Universities of Russia", project No UR.09.01.048: RFBR, project 04-05-64386, and the Ministry of Education of Russia, project A03-2.13-39.

5 REFERENCES

- Belogub E., Novoselov C., Spiro B., Yakovleva B. 2003. Mineralogical and sulphur isotopic features of the supergene profile of Zapadno-Ozernoye massive sulphide and gold-bearing gossan deposit, South Urals. *Mineralogical Magazine*, vol. 67: 339-354.
- Emmons W. 1917. The enrichment of ore deposits. *Bull. U.S. Geol. Survey*, № 625.
- German-Rusakova L. 1962. Elements migration in the supergene zone of the Blyava copper massive sulphide deposit at the Southern Urals. *Transactions of Ore Deposits Institute*. Moscow.
- Smirnov S. 1955. The supergene zone of sulphide deposits. Leningrad: USSR AS. (in Russian).
- Yakhontova L., and Grudev A. 1987. The mineralogy of oxidized ores: reference book. Moscow: «Nedra». (in Russian).
- Yakovleva V., Belogub E., Novoselov K. 2003. Supergene iron sulphoselenides from Zapadno-Ozernoye copper-zinc massive sulphide deposit, South Urals: The new solid solution series between pyrite FeS_2 and dzsharkenite $FeSe_2$. *Mineralogical Magazine*, vol. 67: 355-364.
- Zaykov V. & Leyn A. 1998. Sulphur isotope composition in minerals from Guyskoe copper sulphide deposit supergene zone (S. Urals). *Transactions of Institute of Mineralogy*, № 8: 177-184. (in Russian)
- Zaykov V. & Sergeev N. 1993. Supergene zone of the Guyskoye deposit (Southern Urals). *Geology of ore deposits*, vol 35: 320-332. (in Russian).

Ore Mineralogy of Shear Zone Gold Deposits from Santa Catarina State (Brazil)

J.C.Biondi

Paraná Federal University, Geology Department. C.P. 19.001, 81.531-990 - Curitiba-Brazil

N.D.Franke, P.R.S.Carvalho, S.N.Villanova

Gold Standard Minas S.A., Rua Tibagi 294, s. 1003/1004, 80.060-110 – Curitiba-Brazil

ABSTRACT: The Schramm, Carneiro Branco and Cristalino are the main orogenic shear zone gold deposits from Santa Catarina State, South Brazil. The Schramm is a bonanza-type gold deposit with ore shoots assaying from 300 ppm up to 2,500 ppm of gold. The Carneiro branco and the Cristalino are conventional shear zone deposits with ore shoots made of pyrite bearing quartz veins assaying 10-20 ppm of gold.

1 INTRODUCTION

The Schramm, Carneiro Branco and Cristalino are the main orogenic shear zone gold deposits from Santa Catarina State (South Brazil). Their known gold reserves are small but due to its bonanza-type ore the Schramm is the only enduring mine.

2 GEOLOGY OF THE OROGENIC GOLD DEPOSITS

The Schramm ore bodies are, none sheared nor deformed, quartz-carbonate veins and pipes-like ore shoots developed inside tensional fractures related to a high angle shear system affecting basement Archean basic and ultrabasic granulites and gneisses with intense hypogenic alteration.

Gold occurs associated with nickel, arsenic and cobalt bearing sulfides, in massive and pipe-like lodes in siderite and ankerite (dolomite) formed where the quartz-carbonate veins intersect iron rich gneisses and hydrothermal magnetite zones (Fig. 1 A and B). Although the ore bodies are composed

almost by 70% quartz and 30% carbonates, the gold content in quartz is rarely higher than one ppm.

The Carneiro Branco and Cristalino ore bodies are strongly boudinated, E-W quartz veins dipping 40⁰-80⁰S, filling spaces along secondary synthetic, shear fault splays of N70⁰-80⁰E main shear zones. The Carneiro Branco quartz vein is hosted inside a small, syntectonic, biotite-hornblende diorite intrusion that is strongly hydrothermally altered while the Cristalino ore bodies are composed of a swarm of boudinated quartz veins developed mainly along the sheared contact between a syntectonic, quartz-porphyry dacite dyke and Proterozoic pelitic schists of the Brusque Group. All rocks were also strongly hydrothermally altered just as at the Carneiro deposit. After the Carneiro and Cristalino quartz structures emplacement, the whole region was intruded by several granitic plutons that thermally recrystallized ore bodies, host rocks and primary hydrothermal mineral paragenesis, as well as reactivating the mineralizing hydrothermal systems.

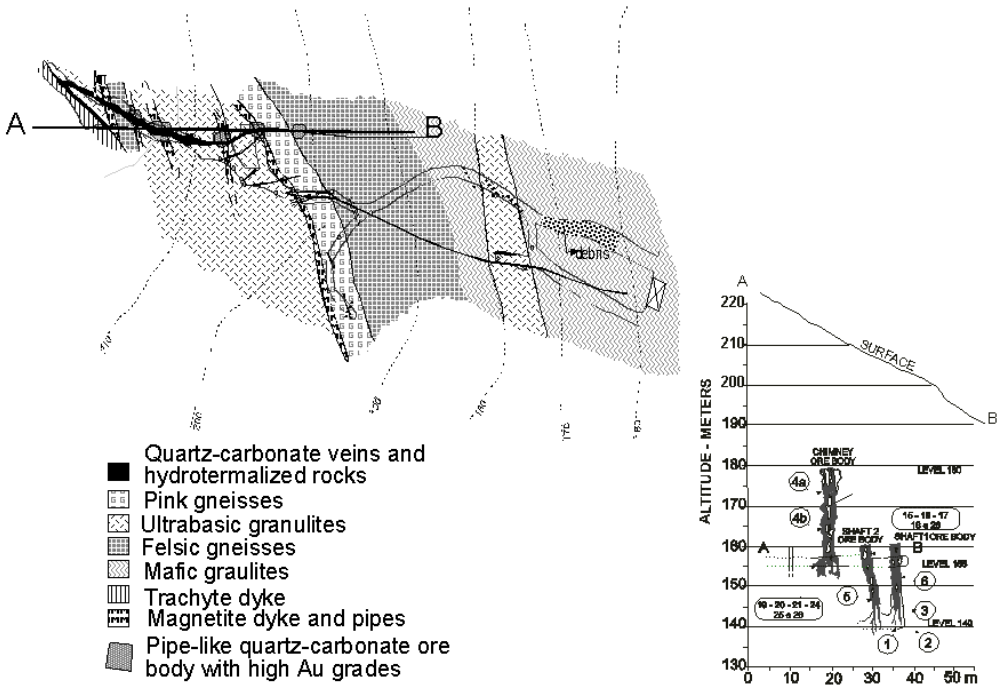


Figure 1. (A) Geological map of the Schramm Mine at level 155, showing the location of shafts 1 and 2 and chimney pipe-like ore bodies (B) Vertical section across the pipe-like ore shoots. Numbers refers to positions from where analyzed samples were taken (Biondi et al. 2001).

3 ORE CHEMISTRY

At the Schramm mine, gold is found free or inside sulfides of the carbonate portions of the pipe-like ore shoots where gold grades vary from 300 and 2,500 ppm. Along with gold there is silver (150 to 300 ppm), arsenic (0.15 to 0.60%) and nickel (0.01 to 1.4 %) and in minor proportions, Zn (250 to 1,600 ppm), Pb (100 to 850 ppm) and Co (40 to 750 ppm). The amount of Sb, Te, Se, W, Mo and Bi are very low or close to 10 ppm. The quartz portions of the lodes show gold grades below 1 ppm with As, Zn, Pb, Ni, Cu, Co, Mo, Te and Bi between 1 and 50 ppm. Outside the mineralized zones the gold grades are below 50 ppb while the other elements vary from 10 and 900 ppm. Rarely the rocks with hypogenic alteration have anomalous gold greater than 50 ppb that do not increase the values of the other elements that range from 1 and 200 ppm.

At the Carneiro Branco and Cristalino deposits the ore shoots gold grades vary between 1 and 350 ppm with gold/silver ratio ≈ 1 . Besides gold, barium (300 to 2,000 ppm) and vanadium (50 to 234 ppm) are elements with abnormal values. The low values of copper (27 to 144 ppm), lead (36 to 377 ppm) and zinc (22 to 244 ppm) reflect the rarity of sulfides

other than pyrite. At the Cristalino deposit there are some small and localized bonanza-type gold oreshoots that run high copper (> 5000 ppm) and high lead (> 5000ppm).

4 ORE AND ROCK PARAGENESIS

4.1 Host rock mineralogy

At Schramm the first hydrothermal manifestation was the crystallization of magnetite pipe-like shoots and veins followed by shear related hydrothermalism whose hosts rock response varied according to its primary mineralogy (Table 1). In all cases, carbonates (siderite and ankerite), chlorite (ripidolite and brunsvigite) and quartz were the most frequent minerals (Biondi et al. 2001). At the Carneiro Branco and Cristalino deposits, the first hydrothermal phase crystallized quartz, dolomite, chlorite (ripidolite) and sericite. The hydrothermal reactivation and thermo-metamorphism caused by granitic intrusions recrystallized the preceding rocks and hydrothermal paragenesis.

Table 1. Schramm host rocks paragenesis (Biondi et al. 2001).

Magnetic gneiss		Basic/ultrabasic granulites		Microcline gneisses	
Transparent minerals	Ore minerals	Transparent minerals	Ore minerals	Transparent minerals	Ore minerals
Quartz (***)	Magnetite (***)	Augite	Ilmenite	Quartz (***)	Magnetite
Siderite (***)	Hematite (*)	Hornblende	Iron oxide (**)	Microcline (*)	Hematite
Ankerite (**)	Euhedric Pyrite (*)	Bitownite		Albite (**)	Euhedric Pyrite (*)
Ripidolite (**)	Matrix pyrite	Biotite		Muscovite (***)	Iron oxide (**)
Brunsvigite (*)	Chalcopyrite	Ripidolite (***)		Chlinoclore (*)	
Penninite (**)		Brunsvigite (**)		Penninite (*)	
Stilpnomelane		Siderite (***)		Siderite (**)	
Biotite		Ankerite (**)		Ankerite (*)	
Esphene		Albite (**)		Beryl	
Muscovite (**)				Pyrophyllite	

(***) Very Common - (**) Common - (*) Few - () Rare

The hydrothermal zones were albitized, potassified (microcline and biotite) and silicified by the reactivation hydrothermal phase while the thermo-metamorphism crystallized muscovite and quartz fenoblasts, together with sillimanite (fibrolite), andalusite, cordierite and chloritoid.

4.2 Schramm's ore body paragenesis

Microscopic description and microprobe analysis of ore minerals revealed that the Schramm's gold occurs associated with an unusual paragenesis composed mainly by sphalerite, pyrite, siegenite-violarite, millerite, and gersdorffite, together with

nickel-cobaltiferous pyrite (rare), magnetite, galena (rare), chalcopyrite (few), arsenopyrite (rare), an unknown Ni-Fe-Co sulfo-arsenate and covelite.

The structural formulas in Table 2 shows that gold has 27.5% of silver and that siegenite is an iron rich variety, transitional to violarite. There is also a nickel-cobaltiferous pyrite and a sulfide with the formula (Co, Fe, Ni)_{7.980}As_{9.000}S_{6.000} that no previous reference was found. The mineral cristalization succession started with gold and was followed by Pb and Cu sulfides, ending with the crystallization of Fe-Ni-Co-As sulfides.

Table 2. Schramm Mine ore mineral chemistry (Biondi et al.2001).

MINERAL	NUMBER OF MOLS	ANALYZED FORMULA	THEORETICAL FORMULA
Arsenopyrite	Fe _{1.053} Co _{0.002} Ni _{0.003} As _{1.065} S _{1.000}	(Fe, Co, Ni) _{1.058} As _{1.065} S _{1.000}	FeAsS
Chalcopyrite	Cu _{0.996} Co _{0.002} Ni _{0.005} Zn _{0.004} As _{0.004} Fe _{0.994} S ₂ Cu _{0.996} (Co, Ni, Zn, Fe) _{1.013} S _{2.000}	(Co, Ni, Zn, Fe) _{1.013} S _{2.000}	CuFeS ₂
Sphalerite	Fe _{0.021} Co _{0.001} Ni _{0.009} As _{0.002} Zn _{0.949} S _{1.000}	(Zn, Fe, Co, Ni, As) _{0.982} S _{1.000}	ZnS
Gersdorffite	Fe _{0.008} Co _{0.011} Zn _{0.006} Ni _{0.953} As _{0.964} S _{1.000}	(Fe, Co, Zn, Ni) _{0.978} As _{0.964} S _{1.000}	NiAsS
Co-Fe-Ni Sulfarsenide	Fe _{0.318} Co _{0.202} Ni _{2.140} As _{3.000} S _{2.000}	(Co, Fe, Ni) _{7.980} As _{9.000} S _{6.000}	Unknown mineral (?)
Millerite	Fe _{0.019} Co _{0.001} Ni _{0.945} S _{1.000}	(Ni, Fe, Co) _{0.965} S _{1.000}	NiS
Siegenite -Violarite	Fe _{0.552} Co _{0.572} Ni _{1.856} As _{0.016} S _{4.000}	(Fe, Co, Ni) _{2.980} As _{0.016} S _{4.000}	(Co, Ni) ₃ S ₄ - Ni ₂ FeS ₄
Euhedric pyrite	Fe _{1.004} Ni _{0.004} Cu _{0.001} S _{2.000}	(Fe, Ni, Cu) _{1.009} S _{2.000}	FeS ₂
Ni-Co pyrite	Fe _{0.988} Co _{0.024} Ni _{0.014} S _{2.000}	(Fe, Co, Ni) _{1.026} S _{2.000}	(Fe, Co, Ni)S ₂
Magnetite	Fe _{0.800} O _{4.000}	Fe _{3.002} O _{4.000}	Fe ₃ O ₄
Gold	Au _{0.448} Ag _{0.123}	Au _{0.725} Ag _{0.275}	Au _{1-x} (Ag, Pt, Pd, Cu, Te) _x

4.3 Vertical changes in ore body paragenesis of the Schramm mine.

The petrography of ore samples collected from level 140 to 180 of the Schramm gold mine show that magnetite-hydrothermalites preceded the crystallization of the quartz-carbonate veins and pipe-like ore shoots. A vertical zonality was characterized by three different ore paragenesis (Fig. 2). Below level 155, carbonate-rich ore, hosted by magnetite-hydrothermalites and composed by lamellar hematite, magnetite, sphalerite and gold, with subordinated pyrite, chalcopyrite, arsenopyrite, gersdorffite and siegenite, typify an environment desulfurized, what determined gold deposition.

Around the 155 level, the carbonate-rich ore is sulfide poor with a paragenesis in which siegenite, gersdorffite and sphalerite are very common minerals along with gold and subordinate pyrite and chalcopyrite.

At this level ore is hosted by ultrabasic granulites and gold was deposited as a consequence of the low pH-intermediate fO_2 environment. Above the 155 level, the main ore minerals are Bi-rich galena, sphalerite and gold, with subordinated gersdorffite, pyrrhotite, pyrite and cosalite. Gold occurs mainly in carbonate but also in quartzveins hosted by granulites. These minerals characterize a reduced fluid and high pH environment.

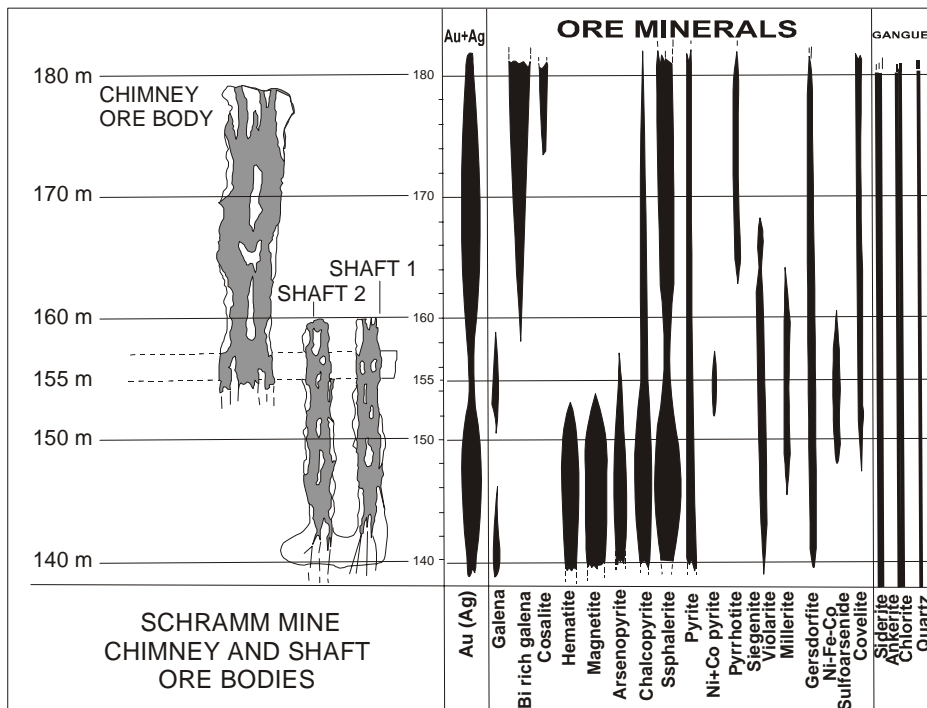


Figure 2: Vertical changes at Schramm's ore body paragenesis.

4.4 Carneiro Branco and Cristalino ore body paragenesis.

Contrasting with the mineralogical complexity of the Schramm mine ore bodies, the Carneiro Branco and the Cristalino ore show very simple and common minerals paragenesis. Gold occurs free in quartz or inside pyrite micro fractures. Beside pyrite, the main sulfide, the ore paragenesis includes minor proportions of chalcopyrite, sphalerite and galena. Very small amounts of wolframite and barite occur locally.

5 CONCLUSION

It seems that there is a relationship between the ore paragenesis and the geological environment. The mineral paragenesis is first conditioned to host rocks and secondary by the related structure.

6 REFERENCES

- Biondi J.C.; Franke N.D.; Carvalho, P.R.S.; Villanova S.N. 2001. Geologia e petrologia da mina de ouro Schramm. (Gaspar - SC). Revista Brasileira de Geociências, 31(3): 287-298.

A Mineralogical Guide Supporting Reserve Evaluation and Mining of Cajati Phosphate Ore

T.B.Bonás

Bunge Fertilizantes S/A.

L.M.Sant'Agostino

Department of Sedimentary and Environmental Geology, Geosciences Institute of the University of São Paulo

M.Pereira

Bunge Fertilizantes S/A

ABSTRACT: The Cajati phosphate mine is located 230 km southeast of Sao Paulo city. The ore body is composed by carbonatites mineralized with apatite, which are disposed in plant as an ellipse N27°W oriented. The carbonatite is subdivided in lithological units defined by variations in the physical aspects (structures) and the mineralogical characteristics of the carbonatic matrix related with the principal accessories and smaller constituents (texture and proportions). Xenolithic zones are remarkable among the lithological units; they comprise portions characterized by mixtures of carbonatite and magnetite-clinopyroxenites, the surrounding waste rock, in proportions that can arrive to almost 100% of clinopyroxenite. Some reaction zones are observed in the described rocks contact, characterizing frequently mineralized bands (silicatic/carbonatic composition) with very peculiar mineralogy. Considering the Xenolithics zones as only partially profitable in function of the clinopyroxenite waste presence and the erratic spatial distribution of this contaminant rock that follow not any known geological settings, efforts were applied in the establishment of mineralogical indicators to define the relative proportions of the constituent rocks. Correlations between chemical and mineralogical compositions associated with mining parameters allowed to set up levels of mineral worthwhile for these lithological units, which were appointed to the data from diamond and percussion drilling. Subsequently, the profitable ore resources contained in these assimilation zones were defined by the mineralogical indicators applied to the mine block model, which are also used in the mining fronts forecasting for the short period plans.

1 INTRODUCTION

A pure carbonatitic low-grade ore has being exploited for phosphate in Cajati mine, southeast Brazil, since 1975.

The mining operation began in 1942 with residual ore, enriched by supergenic processes, and in the 1970's it started the low-grade fresh rock exploitation (5% P₂O₅).

Producing 500.000 t/y of phosphate concentrate as the main product applied for phosphoric acid manufacturing, the industrial park is notable by the optimization of raw material profitability.

Carbonate material is a by product for cement or animal ration or soil acidity correction raw material depending on the MgO grades; magnetite is sold mainly for cement industry as balance raw material

the Complex; it is intruded in pyroxenites (Ruberti et al. 1988) and confines the apatite mineralization defining the mining open-pit configuration. Jacupiranguite is an old-fashioned term for the magnetite clinopyroxenite host rock that is essentially composed by diopside, containing accessory minerals magnetite, biotite, nefeline and olivine (Gaspar 1989).

The carbonatite body represents a low grade ore essentially composed by carbonates, calcite and dolomite, with variable magnetite content and less than 10% of accessory minerals (phlogopite, serpentine, olivine and sulphides).

The ore body has an internal arrangement with peculiar mineralogical and structural features defining several ore lithologies, as a consequence of at least five recurring magmatic events (Fig.1).

1.1 Geological settings

The ore occurs in the south portion of the Jacupiranga Alkaline Complex, a classical geological of alkaline and ultramafic rocks occurrence in Brazil.

A NNW elongated carbonatite body, 1 km long by 0.4 km large, represents the nucleus portion of

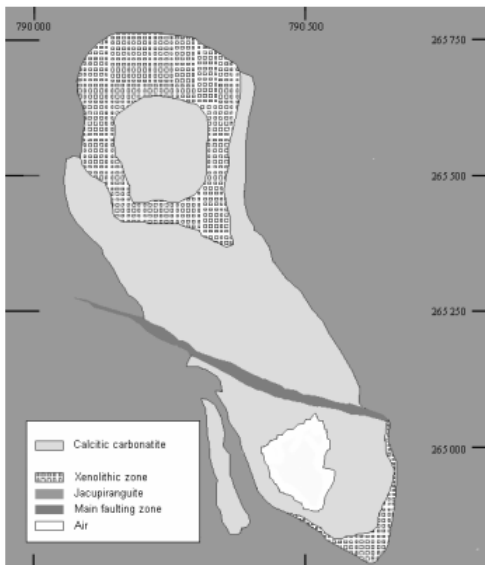


Figure 1: Carbonatite body internal organization, level 60m below sea level, according to the geological 3D-model used at the mine (actualized in October, 2002).

Xenolithic zones of hybrid mineral composition associated with the ore body can be recognized; they contain apatite in high grades sparsely distributed and define a low grade ore type (3% P_2O_5 cut off grade).

1.2 Objectives

The xenolithic zones are only partially exploitable due to the presence of erratic spatial distributed contaminant rocks that are selected at the mine site by color criteria applied in the crumble ore. The portions of the host rock incorporated by the carbonatitic magma are barren and constituted contaminants as well as diluents of the ore.

This work was outcome of the economical interest involved in the establishment of recovery parameters for the ore associated to the xenolithics zones, which is significant in the total mine reserves.

The focus was establishing any indicators, using mineralogical characteristics that could define the relative proportions of the constituent rocks of these zones.

As result of a mixture of pyroxenite host rock in very pure carbonatitic magma, they have a significant mineralogical contrast. Based on the consequent ore chemical composition differences, mineralogical indices were investigated in order to characterize the distinct portions and their relative proportions in the natural blending of the referred zones.

These indices should be applied to the ore chemical composition obtained from drilling samples to support the evaluation of the profitable reserves contained in the xenolithic zones. They also should be used in percussion samples to support mining operation.

2 XENOLITHICS ZONES FEATURES

Three xenolithic zones, corresponding to magmatic breccia, are recognized in the mine scenery: the northeastern (XNE) and the south (XS) transitional zones in the contact with the host rock, besides a prominent one (XN) forming a ring that clearly segregates a north portion in the ore body (Fig.1). They characteristically have rounded xenoliths host rock in a carbonatitic matrix, plus reactions bands (Fig.2).

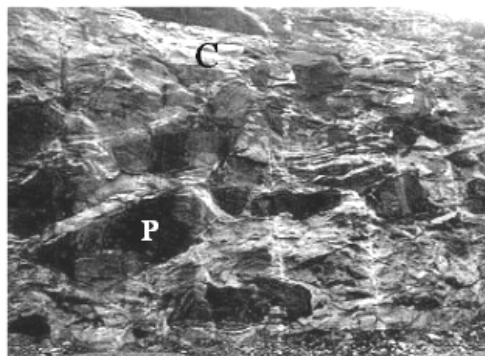


Figure 2: Illustrative aspects of the xenolithics zones (P=pyroxenite; C=carbonatite). High = 10 m.

The xenoliths are considered the pyroxenites that normally have reaction bands associated. Their dimensions vary from centimeters to meters and tend to be concentrated in the mentioned specific zones apart of occur scarcely widespread in others sites of the ore body.

Inside the carbonatite ore body the reactions bands typically form intercalations of silicates and carbonates and occur as thin metasomatic boundaries in the xenoliths. (Bonás 2001). They contain reddish brown milimetric bands constituted mainly by submilimetric phogopite, intercalated with almost pure carbonates bands (Fig.3).

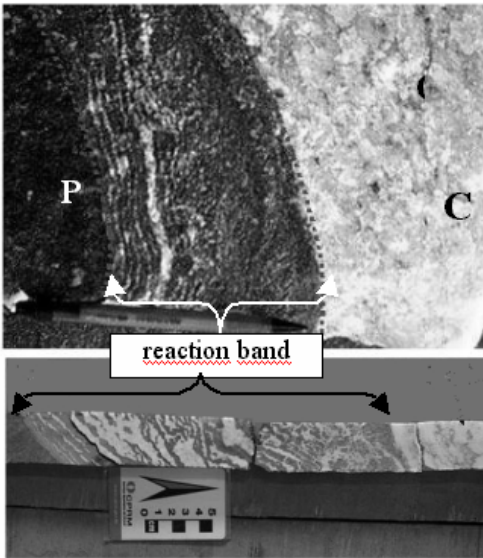


Figure 3. Details of the reaction bands inside the carbonatitic ore body (P=pyroxenite, C=carbonatite). Upper – rock fragment; down - drilling sample.

3 MINERALOGICAL INDICES

The basic criteria to distinguish the lithologies components of the xenolithic zones were their silica grades as reflection of silicates contents.

The typical chemical compositions of the carbonatite, the pyroxenite and the reaction bands contained in these zones were obtained from the database of drilling samples, with the set of samples representative of each lithology selected by geological description.

For indices establishment also the mining block grades resulted from geostatistical interpolation were considered.

The three xenolithics zones were evaluated separately since they probably were formed in distinct geological environments.

3.1 Statistical parameters

The three lithologies can be well characterized by statistical parameters for silica grades (Table 1).

The carbonatites are similar at the XN and XNE zones and a little different at the XS. The pyroxenites show significant differences in the silica grades at the zones, they are similar at XN and XE and higher at XS.

The reaction bands have specific behavior at each xenolithic zone: at the XN significant quantity of carbonatite could be verified while at the XNE they are less representative and at the XS are not present. Table 1 – SiO₂ grades statistical data.

Lithology	parameters	North (XN)	Northeast (XNE)	South (XS)
carbonatites	minimum	0.14	0.23	0.10
	maximum	9.41	9.83	8.19
	mean	1.75	2.91	2.11
	σ^2	2.01	2.46	2.53
	mode	0.62	3.20	0.10
	n^b samples	105	55	22
reaction bands	minimum	10.4	10.8	22.4
	maximum	40.4	38.0	40.1
	mean	23.2	23.7	31.4
	σ^2	7.14	8.21	5.58
	mode	20.0	24.6	---
	n^b samples	138	40	15
pyroxenites	minimum	12.3	21.5	28.8
	maximum	46.1	41.9	44.4
	mean	34.1	34.3	38.9
	σ^2	6.7	5.42	5.68
	mode	32.6	35.7	42.8
	n^b samples	41	29	8

3.2 Criteria

For quantify the xenoliths some equations of silica grades versus xenoliths proportions were built, by weighting these proportions with the SiO₂ of carbonatite and xenoliths (Fig.4).

The xenoliths in the mining sense normally comprise pyroxenite plus reaction bands in proportions assumed, in a first approach, as 70-30% according to geological descriptions; this assumption should be continually checked during mining operation. So, for each zone it was calculated the silica grade relative to the xenoliths to be applied in the correlation equations.

The adopted criteria have tendency to super estimate the xenoliths quantity, but are adequated for a conservative ore reserves evaluation.

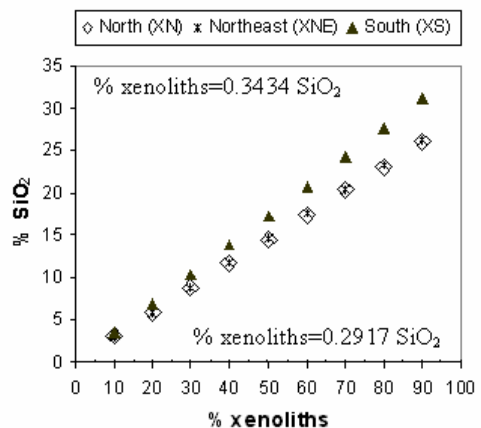


Figure 4 – Established correlations for the three xenolithic zones and respective equations.

4 VALIDATION

The calculated xenolith proportions were compared with that obtained by drilling samples log descriptions in composed intervals compatible with mining bench fronts dimensions. The quantity of xenoliths was obtained using geological criteria and also considering reaction band plus pyroxenite in the same way of the calculations.

The results presented a good correlation considering the bulk of the xenolithics zones, but locally some dispersion of data could be detected. The dispersions are related with two uncommon aspects detected in geological description details.

One aspect is referred to silicates enriched carbonatites inadequately noticed in the geological description. The second appears where reaction bands associations have few or absence of pyroxenites, situation not pondered by the proposed calculations.

5 CONCLUSIONS

Based on the differences between the mineralogical compositions of the lithologies that characterize the xenolithic zones, it was possible to established correlations between the SiO₂ grade of the ore and their relative proportions. Using the characteristics grades of the lithologies, equations were settled up. Intentionally the applied formulas super estimate the xenoliths quantities, but are adequate for conservative reserves evaluation and mining planning purposes.

The validation of the equations by comparing with the drilling geological description was successfully. Some dispersion of results associated with the presence of anomalous associations must be regard.

Procedures to refine the established functions were incorporated in mining operation, meaning systematical geological description of the bench fronts to be compared with the calculations here exposed. The chemical data used for the calculations are both that pointed in block model by geostatistical interpolation and that obtained from percussion drilling of mining control.

6 REFERENCES

- Ruberti, E., Scheibe, L.F. and Gomes, C.B 1988. The Jacupiranga Alkaline Complex. Int. Conf. *Geochemical Evolution of the Continental Crust*, Poços de Caldas, Guidebook, p 11-25.
- Gaspar, J.C. 1989. Geologie el mineralogie du complexe carbonatitique de Jacupiranga, Brésil. *Université d'Orleans PhD Thesis, U.E.R. de Science Fundamentales et Appliquées*, 344 p.
- Bonás, T.B. 2001, Consolidação de critérios de descrição litológica para o minério apatítico do Complexo Alcalino de Jacupiranga. *USP graduation monograph*, TF-2001/36, 48p.
- Sant'Agostino, L.M., Alves, P.R., Shimabukuro, N.T., Bonás,T.B. 2001. Applied mineralogy as a tool for mine planning of phosphate rock. *Minerals and Metallurgical Processing Jour.*, 14(12), 1649-1657.
- Sant'Agostino, L.M, Bonás, T B., Pereira, M.A. 2003. Applied mineralogy supporting phosphate rock cut-off definition. ICAM, International Congress on Applied Mineralogy, Helsinki, Finlândia.

Brittle Microstructures in Gold Nuggets: Evidence for Seismogenic Failure of Gold

A.R.Cabral

Rua Coelho Neto, 32/704, Rio de Janeiro, 22231-110, Brazil

C.E.Suh

Department of Geology and Environmental Science, University of Buea, P.O. Box 63, Buea, South West Province, Cameroon

R.Kwitko-Ribeiro

Companhia Vale do Rio Doce, Rodovia BR 262/km 296, Caixa Postal 09, 33030-970, Santa Luzia, Brazil

O.G.Rocha Filho

Mina do Gongo Soco, Companhia Vale do Rio Doce, Fazenda Gongo Soco, Caixa Postal 22, 35970-000 Barão de Cocais-MG, Brazil

ABSTRACT: Gold nuggets (0.4–2.5 cm across) from specular hematite-rich, sulphide-free, auriferous veins (*jacutinga*) from the Gongo Soco iron ore mine, Minas Gerais, Brazil, have inclusions of palladium arsenide-antimonides (isomertieite and mertieite-II) and hematite. Both isomertieite and mertieite-II are commonly brecciated. More rarely, isomertieite has sub-parallel S-shaped intragranular microfractures terminating in angular edges. Hematite laths show microfracturing and displacement, as well as microgouge formation and slumping. The microstructures are filled by gold without any optically recognisable brittle failure. In some instances, however, gold itself is fractured. It is possible that fluid pressure increase and its sudden (seismogenic?) release could fracture erstwhile ductile gold.

1 INTRODUCTION

Gold is a classic example of ductile and malleable metal. In experiments, however, microscopic cracking of silver–gold alloys occurs in aqueous environments under tensile stress (e.g., Friedersdorf & Sieradzki 1996, Galvele et al. 1996). In nature, fine-grained gold can be seen under the transmitted-light microscope to fill in fissures in minerals (e.g., Ramdohr 1969), but fissures in coarse-grained gold (i.e., nuggets) have rarely been observed, and the conditions under which they form remain enigmatic. Such microstructures include high-fineness gold veinlets with sharp angular bends (Knight et al. 1999) and rift-like faulting (Lange & Gignoux 1999).

Remarkable brittle microstructures in gold nuggets and their inclusions of ore minerals from cross-cutting, specular hematite-rich veins hosted by banded iron formation (itabirite) at the Gongo Soco iron ore mine, Minas Gerais, are here described. The nuggets are characteristically encrusted by Pd–O-bearing ferruginous material, and represent the historically famous *ouro preto* (black gold) of Minas Gerais (Cabral et al. 2003b). It is speculated that the microstructures may be related to sudden (seismogenic) release of fluid pressure.

2 GOLD–PALLADIUM MINERALISATION AT GONGO SOCO

In the past, Gongo Soco was a celebrated underground gold mine (1826–1856). Nowadays, it is one of the numerous iron ore mines of the Quadrilátero Ferrífero of Minas Gerais (see Cabral et al. 2003a for a location map).

The Gongo Soco iron ore mine dominantly encompasses rocks of the Palaeoproterozoic Itabira Group (Dorr 1969). The Itabira Group is the chemical sequence of the metasedimentary Minas Supergroup, and consists of a lower unit of itabirites (Cauê Formation) grading upward into dolomitic rocks (Gandarela Formation). The rocks of the Minas Supergroup were complexly deformed, resulting in the geological map pattern of dome-and-keel structures. Although the tectonic evolution of the Quadrilátero Ferrífero is disputed, the penetrative tectonic fabrics (mylonitic foliation, crenulation cleavage, stretching lineation) in its central and eastern parts are generally attributed to the ~0.6 Ga Brasiliano Orogeny (Hippert & Davis 2000, Rosière et al. 2001, and references therein). In general, regional metamorphic conditions varied from greenschist facies in western and central Quadrilátero Ferrífero to almandine–amphibolite

facies in its eastern part. Gongo Soco is located in central Quadrilátero Ferrífero, in the cummingtonite zone of Pires (1995).

The Gongo Soco gold–palladium mineralisation, known as *jacutinga*, occurs as sulphide-free, specular hematite-rich veins which cross-cut folded itabirite. Based on this cross-cutting relationship, the *jacutinga* veins are considered late- to post-Brasiliano in age. The *jacutinga* veins are soft, commonly thin (<0.5 m) and discontinuous. A single *jacutinga* vein may host auriferous tension gashes and veinlets (<5 cm in width) of specular hematite and quartz. This superposition of structures suggests recurring fracturing and mineralisation. Petrographic evidence for recurring mineralisation at Gongo Soco is given by the overprinting of hematite-bearing tension gashes by masses of randomly oriented crystals of fine-grained hematite (Cabral et al. 2003a).

The Gongo Soco gold is characteristically palladium-bearing and coarse-grained (Hussak 1904). Gold nuggets containing more than 3 wt.% Pd commonly have abundant inclusions of isomertieite, $\text{Pd}_{11}\text{Sb}_2\text{As}_2$, and mertieite-II, $\text{Pd}_8(\text{Sb,As})_3$ (Cabral et al. 2002).

3 GOLD-HOSTED MICROSTRUCTURES

Gold nuggets were obtained from a gravimetric (Knelson) concentrator at the iron ore plant. The microstructures of four nuggets of gold, ranging in length from 0.4 to 2.5 cm, include fracturing and displacement of mineral inclusions without any sign of brittle failure of the host gold (Figs. 1a, b), as well as fracturing of gold proper (Fig. 1c).

Sigmoidal intragranular microfractures are a rarely observed but remarkable deformational feature in gold-hosted isomertieite (Fig. 1a). These microfractures segment the crystal into microdomains relatively displaced to each other, with sharp lobate edges defining a domino-like structure. Such microstructure could indicate the sense of shearing if orientation were known. Fragmentation was experienced by euhedral crystals of hematite included in gold. This is the case of Figure 1b, in which sections of a crystal of hematite were comminuted to microgouge, forming slump-like structures. Note that rigid segments of unharmed hematite bordering the slumped microgouge were not displaced. Segments of hematite laths are only displaced along microfractures without any microgouge. No indication of brittle failure of the host gold is observed in Figures 1a, b. These examples come from the inner parts of gold nuggets.

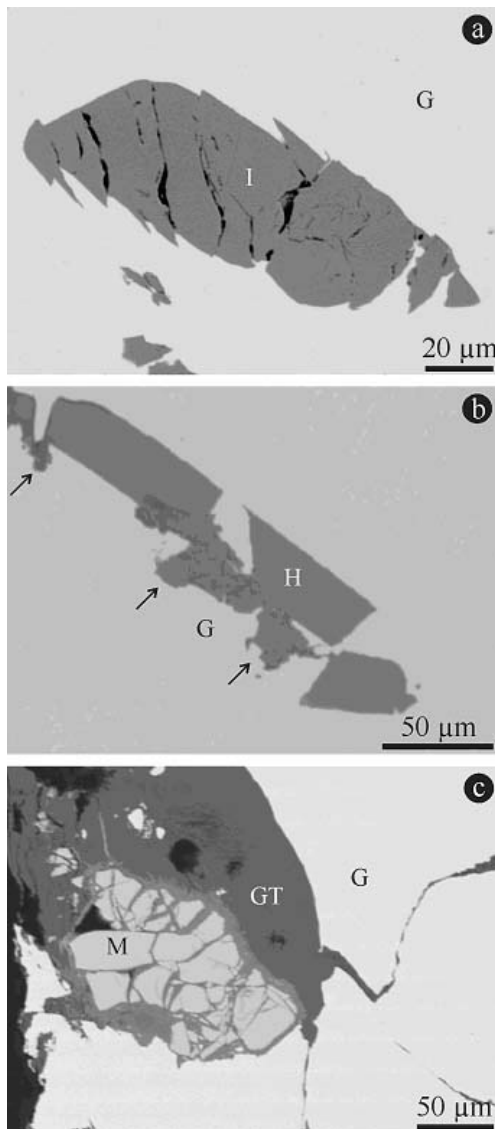


Figure 1: Backscattered electron images of gold (G) and mineral inclusions; black areas are filled by resin. a. Sigmoidal intragranular microfractures in isomertieite (I) terminating in angular edges. b. Microfractures in hematite (H) with microgouge forming slump-like structures (arrows). Note that the hematite lath was only displaced along the microfracture lacking microgouge. c. Brecciated mertieite-II (M) and goethite (GT)-healed fissures at the margin of a gold nugget.

In some cases, the brittle failure of gold seems to have occurred at, or close to, the margins of the nuggets. The mertieite-II crystal of Figure 1c is located at the margin of a nugget and shows extensive fracturing, from which fissures in gold

stem. Deformation twins in hematite (Fig. 2), though rarely observed, appear to be associated with coarse-grained gold (i.e., they are absent in foliation-forming hematite of the itabirite and associated soft hematite ore).

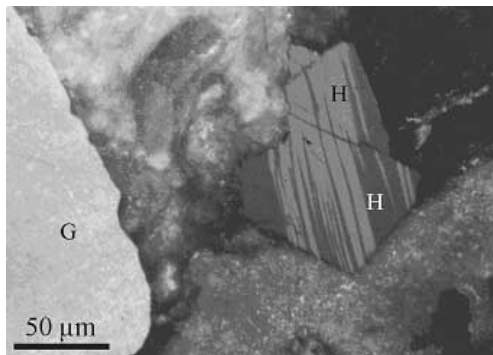


Figure 2: Reflected-light photomicrograph (oil immersion, inclined nicols) of mechanically twinned hematite (H) in limonite-like coating on gold (G).

In other cases, the brittle failure of gold is not obviously close to the margins of the nuggets (Fig. 3). The microfracturing is analogue to dilational fault jogs developed by strike-slip rupturing (cf., Sibson 1987). The fissures are sealed by hematite laths and a goethite-like matrix (Fig. 3, black areas). A late deformational overprint is manifested by fissure-healing by gold containing very fine-grained iron oxide (Fig. 3, black arrows).

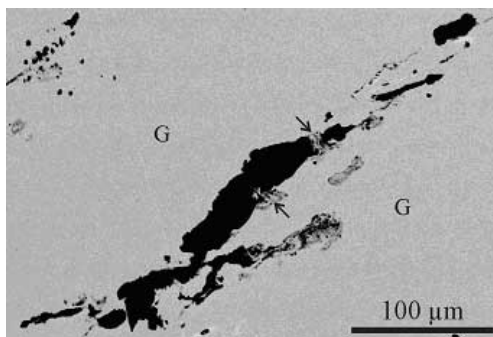


Figure 3: Backscattered electron image of a nugget of Pd-bearing gold. Brittle failure of gold (G) is indicated by the formation of dilational fissures healed by iron oxides (black). Black arrows denote gold that penetrates into iron oxides. This gold (black arrows) has a powdery appearance due to very fine-grained iron oxide.

It is worthy of mention that one nugget of palladian gold (nugget gold) is fragmented and

healed by specular hematite, kaolinite and subhedral to euhedral, fine-grained crystals of palladian gold. This fine-grained gold has a more variable composition in terms of palladium and mercury than the nugget gold (Cabral & Lehmann 2003).

4 DISCUSSION

The presence of brittle microstructures in gold nuggets is somewhat unexpected considering the malleability of gold. Therefore, such microstructures might provide a new approach to the understanding of the evolution of gold-mineralising systems. An immediate question that arises is whether the microstructures are tectonic- or weathering-derived features. The sigmoidal fracturing of isomertieite (Fig. 1a), slumped microgouge of hematite (Fig. 1b) and brecciation of mertieite-II (Fig. 1c), all indicate a tectonic origin. Weathering of residual gold particles commonly results in surface-pitted grains with rounded edges (e.g., Colin et al. 1997, Varajão et al. 2000).

Inevitably, another question emerges: what sort of tectonic regime is capable of fracturing gold? The brittle failure of gold seems to have occurred at, or close to, the margins of the gold nuggets, where fissures are healed by goethite (Fig. 1c). The margins were probably burst by relatively high H₂O-pressure fluids, as indicated by the goethite-healed fissures. However, gold itself hosts brecciated crystals in the inner parts of gold nuggets (Fig. 1b), suggesting recurrent deformation and possible fluid-pressure release. At least, part of the Gongo Soco coarse-grained gold comes from tension gashes and veinlets hosted by veins. In other words, field evidence is also suggestive of episodic hydrofracture veining. Whether this scenario falls within the envisaged fault-valve behaviour, i.e., rapid fluid pressure fluctuations associated with faults that remain active because of fluid overpressure in the seismogenic zone (Sibson 1992, Oliver 2001), is unclear. It is interesting to point out that the microstructure in Figure 1c (fracturing of gold) is similar to that recorded by Galvele et al. (1996) on experimentally deformed silver-gold alloys at strain rate of $\sim 10^{-6} \text{ s}^{-1}$. Microfracturing and twinning in hematite were experimentally produced at strain rates between 10^{-4} and 10^{-5} s^{-1} (Hennig-Michaeli 1977). Although the experiments differ from natural conditions, the strain rates are comparable to those estimated for seismic faulting (Nur 1974, Sibson et al. 1975).

The *jacutinga* mineralisation at Gongo Soco cross-cuts folded itabirite, which is considered to have been deformed in the ductile stage of the Brasiliano deformation. The presence of deformation twins in hematite (Fig. 2) is remarkable because they have only been found in hematite along

post-Brasiliano brittle faults (Rosière et al. 2001). The *jacutinga* veins and associated tension gashes and veinlets are rich in specular hematite and lack any significant amount of sulphide minerals, indicating an oxidising fluid system.

5 CONCLUDING REMARKS

While recognising that much of the discussion presented here is speculative, the petrographic investigation has described rarely, if ever, observed gold-hosted microstructures and also pointed out their intriguing nature. One possible interpretation is that the brittle failure of gold-hosted mineral inclusions and of gold itself may indicate rupturing triggered by sudden release of fluid overpressure in the seismogenic zone. Obviously, more research is needed to elucidate the formation of gold-hosted brittle microstructures in nature.

6 REFERENCES

- Cabral, A.R. & Lehmann, B. 2003. A two-stage process of native palladium formation at low temperatures: evidence from a palladian gold nugget (Gongo Soco iron ore mine, Minas Gerais, Brazil). *Mineralogical Magazine* 67: 453–463.
- Cabral, A.R., Rocha Filho, O.G. & Jones, R.D. 2003a. Hydrothermal origin of soft hematite ore in the Quadrilátero Ferrífero of Minas Gerais, Brazil: petrographic evidence from the Gongo Soco iron ore deposit. *Applied Earth Science (Transactions of the Institution of Mining and Metallurgy B)* 112: B279–B286.
- Cabral, A.R., Lehmann, B., Kwitko, R. & Jones, R.D. 2002. Palladian gold and palladium arsenide–antimonide minerals from Gongo Soco iron ore mine, Quadrilátero Ferrífero, Minas Gerais, Brazil. *Applied Earth Science (Transactions of the Institution of Mining and Metallurgy B)* 111: B74–B80.
- Cabral, A.R., Lehmann, B., Kwitko-Ribeiro, R., Jones, R.D. & Rocha Filho, O.G. 2003b. On the association of palladium-bearing gold, hematite and gypsum in an ouro preto nugget. *Canadian Mineralogist* 41: 473–478.
- Colin, F., Sanfo, Z., Brown, E., Bourlès, D. & Minko, A.E. 1997. Gold: a tracer of the dynamics of tropical laterites. *Geology* 25: 81–84.
- Dorr, J.V.N. 1969. Physiographic, stratigraphic and structural development of the Quadrilátero Ferrífero, Minas Gerais, Brazil. United States Geological Survey Professional Paper 641-A.
- Friedersdorf, F. & Sieradzki, K. 1996. Film-induced brittle intergranular cracking of silver-gold alloys. *Corrosion* 52: 331–336.
- Galvele, J.R., Maier, I.A. & Fernández, S.A. 1996. Stress corrosion cracking of silver-gold alloys in 1 M potassium chloride, potassium bromide, and potassium iodide solutions. *Corrosion* 52: 326–330.
- Hennig-Michaeli, C. 1977. Microscopic structure studies of experimentally and naturally deformed hematite ores. *Tectonophysics* 39: 255–271.
- Hippert, J. & Davis, B. 2000. Dome emplacement and formation of kilometre-scale synclines in a granite-greenstone terrain (Quadrilátero Ferrífero, southeastern Brazil). *Precambrian Research* 102: 99–121.
- Hussak, E. 1904. Über das Vorkommen von Palladium und Platin in Brasilien. *Sitzungsberichte der mathematisch-naturwissenschaftlichen Klasse der Kaiserlichen Akademie der Wissenschaften* 113: 379–468.
- Knight, J.B., Mortensen, J.K. & Morison, S.R. 1999. Lode and placer gold composition in the Klondike District, Yukon Territory, Canada: implications for the nature and genesis of Klondike placer and lode deposits. *Economic Geology* 94: 649–664.
- Lange, I.M. & Gignoux, T. 1999. Distribution, characteristics, and genesis of high fineness gold placers, Ninemile Valley, Central-Western Montana. *Economic Geology* 94: 375–386.
- Nur, A. 1974. Matsushiro, Japan, earthquake swarm: confirmation of the dilatancy-fluid diffusion model. *Geology* 2: 217–221.
- Oliver, N.H.S. 2001. Linking of regional and local hydrothermal systems in the mid-crust by shearing and faulting. *Tectonophysics* 335: 147–161.
- Pires, F.R.M. 1995. Textural and mineralogical variations during metamorphism of the Proterozoic Itabira Iron Formation in the Quadrilátero Ferrífero, Minas Gerais, Brazil. *Anais da Academia Brasileira de Ciências* 67: 77–105.
- Ramdohr, P. 1969. The ore minerals and their intergrowths. Oxford: Pergamon Press.
- Rosière, C.A., Siemes, H., Quade, H., Brokmeier, H.-G. & Jansen, E.M. 2001. Microstructures, textures and deformation mechanisms in hematite. *Journal of Structural Geology* 23: 1429–1440.
- Sibson, R.H. 1987. Earthquake rupturing as a mineralizing agent in hydrothermal systems. *Geology* 15: 701–704.
- Sibson, R.H. 1992. Implications of fault-valve behaviour for rupture nucleation and recurrence. *Tectonophysics* 211: 283–293.
- Sibson, R.H., Moore, J.M.C. & Rankin, A.H. 1975. Seismic pumping – a hydrothermal fluid transport mechanism. *Journal of the Geological Society (London)* 131: 653–659.
- Varajão, C.A.C., Colin, F., Vieillard, P., Melfi, A.J. & Nahon, D. 2000. Early weathering of palladium gold under lateritic conditions, Maquiné mine, Minas Gerais, Brazil. *Applied Geochemistry* 15: 245–263.

Characterization of an Argillaceous Phosphate Ore Type from the Tapira Mine, MG, Brazil

A.M.D.Chula & P.R.G.Brandão

Department of Mining Engineering, Federal University of Minas Gerais – UFMG

J.A.Aquino

Nuclear Technology Development Center – CDTN

ABSTRACT: This work presents the results of the mineralogical characterization carried out on an argillaceous phosphate ore type from the Tapira Mine, Brazil. The studies were developed on two samples (numbers 11 and 12) from less deep parts of the mine (approximately 87-105m in depth) and had the purpose to determine the mineralogy and microstructure compositions of the samples and their alteration degree, with special emphasis on apatite. X-ray diffraction, chemical analyses, optical and electron microscopy/microanalyses (EDS and WDS) and infrared spectrometry were the techniques used to characterize the samples. The ore is classified as an argillaceous clinopyroxenite and although the mineralogy is similar in the two samples, they show variable modal proportions of apatite, mica-like minerals and nontronite. The samples are also composed by magnetite and anatase with minor amounts of ilmenite, goethite, perovskite, pyroxene, carbonates, quartz, titanite, secondary phosphates (monazite/rhabdophane and crandallite group minerals), zirconolite, barite and K-feldspar. Mica-like minerals were identified mainly as mixed-layer phyllosilicates, formed by different proportions of phlogopite/biotite and vermiculite. Pure vermiculite is also observed. The apatite in both samples is classified as carbonate-strontium-fluor-hydroxylapatite, with small amounts of REE, Na, Si and sometimes Mg and Fe; it is essentially primary and well formed. Fluid inclusions are common in sample 12 and in sample 11 apatite displays inclusions of calcite, monazite, barite, K-feldspar, nontronite, ilmenite and zirconolite. The presence of fine clay minerals such as nontronite may cause problems in apatite froth flotation concentration by increasing reagents consumption and contaminating the final concentrate by entrainment.

1 INTRODUCTION

The Tapira mine, which is an important ore deposit of phosphate and titanium, is located at approximately 35Km south-southeast of the town of Araxá, in the northern portion of the Tapira ultramafic-alkaline-carbonatitic complex, western Minas Gerais (SE Brazil). It is one of several alkaline-carbonatitic complexes of the Alto Paranaíba province and was emplaced approximately 70 m.y. ago (Hasui & Cordani 1968) in the Precambrian metasedimentary rocks of the Canastra Group. The deposit is the result of supergenic enrichment of ultramafic rocks (mainly clinopyroxenites and peridotites) rich in phosphorus and titanium and is deeply weathered due to the tropical climate. The total geological reserve of phosphate ore is estimated in 1.2 billion tonnes, with an average grade of 8.2% of P_2O_5 .

The phosphate ore from the Tapira Mine shows a complex mineralogical association and low grade of apatite because of its igneous origin. The clinopyroxenites are the main rock type, showing facies variations defined by the variable modal

proportions of the essential minerals clinopyroxene, mica and similar minerals, perovskite, apatite and magnetite. The concentration of the apatite ore is carried out by froth flotation which is very much influenced by the physical, chemical and crystallinity degree characteristics of the apatite (Rodrigues & Brandão 1993) and by the gangue minerals.

Detailed mineralogical characterization was performed on two samples of argillaceous phosphate ore type collected in the levels 1258 and 1240 (approximately 87-105m in depth) in the mine. The goal of these studies was to determine the mineralogical compositions and the apatite characteristics what is fundamental to the understanding of these ores' behaviour and can contribute to obtaining an apatite concentrate with better grade and recovery.

2 METHODOLOGY

The study of the two samples of argillaceous clinopyroxenites collected in the mine comprised its comminution (crushing) below 2.54cm, followed by

grinding below 0.297mm and desliming at -0.037mm. The +0.037mm material was separated in five size fractions (+0.210mm, -0.210 +0.149mm, -0.149 +0.105mm, -0.105 +0.074mm and -0.074 +0.037mm) by wet screening. The global sample and all the six fractions of each one were submitted to chemical and X-ray diffraction (XRD) analysis and studies by optical microscopy. Representative pieces of rocks in each sampled point, which were used to prepare polished thin sections, were collected for the petrographic description.

Detailed mineralogical analyses were obtained by scanning electron microscopy (SEM) and electron microprobe using energy-dispersive X-ray spectrometry and wavelength-dispersive spectrometry microanalysis (EDS/WDS). The composition of each total sample was determined by the combination of three techniques: particle counting using an optical microscope, chemical analysis and X-ray diffraction. Chemical analyses were accomplished by X-ray fluorescence (Phillips model PW2404), energy-dispersive spectrometry (with americium²⁴¹ excitation source – Kevex system) and selective electrode (only for the fluorine analysis). The following equipments were used: Phillips model PW3710 and a Rigaku model Geislerflex X-ray diffractometers; Leitz Ortoplan optical microscope; SEM JEOL model JSM-5410 with EDS Noran model TN-M3055 and electron microprobe JEOL model JXA8900RL.

A detailed characterization was carried out on the micaceous minerals using the XRD technique. The phyllosilicates were manually separated and pulverized. Three X-ray diffractograms were produced for each mineral: with the sample without any chemical or physical treatment; after heating to 500°C during one hour; and after soaking for two hours in ethylene glycol.

Purified apatite concentrates of these two samples were obtained in the laboratory by means of a combination of techniques: flotation in a Denver cell and heavy liquid separation. The apatite concentrates were submitted to XRD and chemical analysis and optical and scanning electron microscopy studies. Selected apatites from each sample were also analyzed using a JEOL model JXA8900RL electron microprobe. Infrared spectrometry (Bomem Hartmann & Braun, model DA8) was used to identify the ions OH⁻ and CO₃²⁻ in the apatite structure. The samples were prepared using the KBR pellet method.

3 RESULTS

3.1 Petrographical/mineralogical characterization

Petrographically, these two samples were classified as clinopyroxenites and were included in a group called “argillaceous clinopyroxenites” based on the

mineralogical characteristics. These rocks are very altered, show ochre-yellowish to light green color and are fine to medium grained. The mineralogy composition by fraction of the two samples is displayed in Table 1.

Table 1 – Mineral composition of the argillaceous clinopyroxenites

Size (mm)	% weight	Minerals (% weight)						
		ap	mt	pv	at	mc	no	cb
Sample 11								
+0.210	15.7	34	47	3	7	1	4	rare
-0.210 + 0.149	12.3	40	38	3	8	2	6	<1
-0.149 + 0.105	11.0	39	32	1	12	2	11	<1
-0.105 + 0.074	8.3	36	29	1	8	5	18	<1
-0.074 + 0.037	10.9	34	26	1	8	7	20	1
-0.037	41.8	15	3	1	8	15	52	2
Total calc.	100	28	22	2	8	8	28	1
Sample 12								
+0.210	24.8	12	33	3	11	38	2	rare
-0.210 + 0.149	13.9	20	28	2	9	37	2	rare
-0.149 + 0.105	10.8	23	24	3	10	35	3	rare
-0.105 + 0.074	7.9	27	20	3	10	35	3	rare
-0.074 + 0.037	8.7	29	14	2	11	36	5	1
-0.037	33.9	9	8	<1	15	38	26	2
Total calc.	100	16	20	2	12	37	11	1

ap = apatite; mt = magnetite; pv = perovskite; at = anatase; mc = micaceous minerals; no = nontronite and cb = carbonates.

The samples are basically composed by the same minerals, only varying the relative proportions of apatite, micaceous minerals and nontronite. Magnetite and anatase are abundant in both samples and minor amounts of ilmenite, goethite, perovskite, pyroxene, carbonates and quartz are observed. Titanite, zirconolite, barite, secondary phosphates (monazite/rhabdophane and crandallite group minerals) and K-feldspar appear locally. The X-ray diffractograms of the micaceous minerals together with WDS microanalyses showed that these minerals are mainly mixed-layer phyllosilicates, formed by different proportions of phlogopite and vermiculite in sample 11 and by biotite and vermiculite in sample 12. Pure vermiculite was observed less frequently. Magnetite is partially altered to hematite and commonly shows exsolution lamellae of ilmenite. The clay mineral was identified as a little expanded smectite rich in iron (nontronite) by XRD and EDS microanalysis. Figure 1a, b shows that although the composition of the clay mineral is the same in the two samples, its morphology is different.

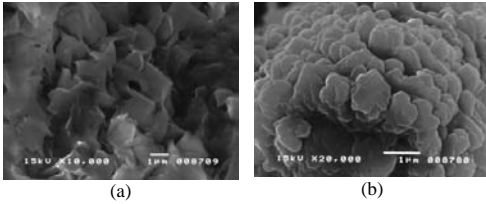


Figure 1 – Nontronite morphology in the samples of argillaceous clinopyroxenites obtained by SEM (secondary electrons image). The EDS microanalyses are in the table below. (a) sample 11. (b) sample 12.

Sample	SiO ₂	TiO ₂	Al ₂ O ₃	FeO	MgO	CaO	P ₂ O ₅
11	52.2	1.2	14.0	27.9	1.1	3.6	0.00
12	48.5	2.7	6.1	35.9	2.6	2.2	1.7

The apatite in these clinopyroxenites is abundant, shows variable granulation (0.05mm to 2.5cm), is disseminated within the rock, filling the intergranular spaces or as inclusions in magnetite, perovskite, micaceous minerals or nontronite and appears as isolated crystals or in aggregates. These characteristics indicate that apatite is one of the first minerals to form. Partial coverings by goethite thin crusts occur in less than 5% of the grains. Apatite shows mainly a clear aspect, although fluid inclusions are common in sample 12 and in sample 11 apatite displays inclusions of calcite, monazite, barite, K-feldspar, nontronite, ilmenite and zirconolite (Figure 2a, b). The apatite content varies from 16-28% (sample 12 and 11) and in sample 12 it increases from the coarse fraction (+0.210mm) to the fine fraction (-0.074 +0.037mm), decreasing in the -0.037mm. The same trend was observed in other samples of clinopyroxenites from the Tapira mine studied by Chula *et al.* (2004). Sample 11 is an exception, as the apatite content increases from the +0.210mm fraction to -0.210 +0.149mm and then decreases toward the finest fraction (-0.037mm). The apatite liberation in the -0.210 +0.149mm fraction varies from 92% to 95%.

Infrared spectrometry and WDS microanalysis results indicate that the apatite is a carbonate-strontium-fluor-hydroxylapatite. Substitutions of Ca²⁺ mainly for Sr²⁺ and rare-earth elements and also for Na⁺, Mg²⁺ and Fe²⁺; of the PO₄²⁻ group for SiO₄⁴⁻ and CO₃²⁻ and of F for OH were detected. The average content of SrO in the apatite varies from 0.88% to 1.30%; F from 1.15% to 1.47% and the REE content is <1%.

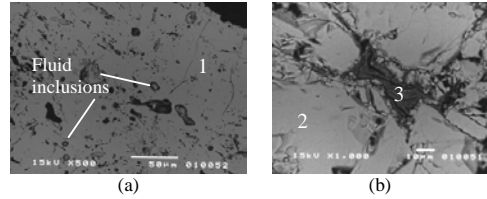


Figure 2 – Apatite aspects in argillaceous clinopyroxenites obtained by SEM (backscattered electrons image). The EDS microanalyses are in the table below. (a) apatite with fluid inclusions – sample 12. (b) apatite with inclusion of nontronite – sample 11.

Area	SiO ₂	Al ₂ O ₃	FeO	MgO	SrO	CaO	P ₂ O ₅	Mineral
1	0.3	0.06	0.09	0.2	1.3	56.4	40.8	apatite
2	0.4	-	0.14	0.03	1.0	56.5	41.9	apatite
3	57.6	13.0	24.3	2.7	-	2.4	-	nontronite

3.1.1 Chemical analysis

The contents of the major oxides and their distribution by size fractions in sample 11 are in Tables 2-3 and in sample 12 in Tables 4-5.

Table 2 – Oxides contents by size fraction in sample 11

Size (mm)	Grades (weight %)							
	P ₂ O ₅	Fe ₂ O ₃	MgO	CaO	Al ₂ O ₃	SiO ₂	TiO ₂	REO [*]
0.210	16.1	35.2	0.89	22.8	0.73	4.5	13.9	0.98
0.149	17.3	29.6	0.93	24.2	1.29	6.9	13.0	0.95
0.105	16.6	28.6	0.98	23.0	1.66	8.8	13.0	0.95
0.074	15.7	27.2	1.13	21.7	2.19	11.0	12.8	0.93
0.037	14.4	26.8	1.18	20.0	2.50	12.8	13.2	0.98
-0.037	6.4	22.0	1.78	9.7	7.65	29.1	7.95	0.81
Total	12.0	26.7	1.33	17.1	4.11	17.0	11.0	0.90

* rare-earth oxides

Table 3 – Weight and oxides distribution by size fraction in sample 11

Size (mm)	Weight (%)	Simple oxide distribution (%)							
		P ₂ O ₅	Fe ₂ O ₃	MgO	CaO	Al ₂ O ₃	SiO ₂	TiO ₂	REO
0.210	15.7	21.0	20.7	10.5	20.9	2.8	4.2	19.8	17.1
0.149	12.3	17.6	13.6	8.6	17.4	3.9	4.9	14.4	12.9
0.105	11.0	15.2	11.8	8.1	14.8	4.5	5.7	13.0	11.7
0.074	8.3	10.8	8.5	7.0	10.5	4.4	5.4	9.6	8.6
0.037	11.0	13.1	11.0	9.8	12.9	6.7	8.3	13.1	12.0
-0.037	41.8	22.2	34.5	56.0	23.5	77.8	71.5	30.1	37.7
Total	100	100	100	100	100	100	100	100	100

Table 4 – Oxides contents by size fraction in sample 12

Size (mm)	Grade (weight %)							
	P ₂ O ₅	Fe ₂ O ₃	MgO	CaO	Al ₂ O ₃	SiO ₂	TiO ₂	REO*
0.210	5.8	33.1	5.7	9.7	5.3	15.2	17.7	0.42
0.149	9.4	27.2	5.3	14.1	4.9	16.4	14.1	0.38
0.105	10.5	25.2	5.2	15.9	4.7	15.9	13.8	0.36
0.074	12.1	23.6	4.6	18.0	4.2	15.4	14.1	0.39
0.037	13.0	23.1	3.7	19.3	3.6	14.7	15.7	0.41
-0.037	4.0	24.7	4.7	5.4	6.2	29.6	11.5	0.31
Total	7.3	27.0	4.98	11.0	5.2	20.3	14.2	0.37

* rare-earth oxides

Table 5 – Weight and oxides distribution by size fraction in sample 12

Size (mm)	Weight (%)	Simple oxide distribution (%)							
		P ₂ O ₅	Fe ₂ O ₃	MgO	CaO	Al ₂ O ₃	SiO ₂	TiO ₂	REO
0.210	24.8	19.7	30.4	28.3	21.8	25.1	18.6	30.8	28.3
0.149	13.9	17.8	14.1	14.9	17.8	13.1	11.3	13.8	14.4
0.105	10.8	15.5	10.1	11.2	15.5	9.6	8.4	10.4	10.5
0.074	7.9	13.1	6.9	7.3	12.9	6.4	6.0	7.8	8.4
0.037	8.7	15.5	7.5	6.5	15.3	5.9	6.3	9.6	9.7
-0.037	33.9	18.4	31.1	31.9	16.7	39.9	49.4	27.4	28.6
Total	100	100	100	100	100	100	100	100	100

The distribution of the major oxides shows the tendency of P₂O₅ to concentrate in the finest size fraction (-0.037mm) and in the coarsest fraction (+0.210mm). The +0.149mm fraction has the highest P₂O₅ content in sample 11, while in sample 12 it corresponds to the +0.037mm fraction. The behavior of CaO is similar to that of P₂O₅ and the Fe₂O₃ content decreases from the coarsest to the finest size fraction. The Al₂O₃ and SiO₂ contents increase in the finest size fraction and TiO₂ has its smallest content in this fraction (-0.037mm).

4 CONCLUSIONS

The two samples are classified as clinopyroxenites and included in a group called “argillaceous clinopyroxenites” based on the mineralogical characteristics. The apatite content is high (varies from 16% to 28%) and the main gangue minerals are magnetite, anatase, micaceous minerals, nontronite and perovskite. The carbonate content is very low (approximately 1%).

The presence of fine clay minerals such as nontronite may cause problems in apatite froth flotation concentration by increasing reagents consumption and contaminating the final concentrate by entrainment.

Micaceous minerals were identified mainly as mixed-layer phyllosilicates, formed by different proportions of phlogopite/biotite and vermiculite

structures; they also can cause problems in the beneficiation of similar ores (Barros et al. 2001; Assis & Brandão 1999).

The apatite has composition of carbonate-strontium-fluor-hydroxylapatite, is essentially primary and well crystallized. The fact that the apatite do not show association with secondary types suggest that these samples would have a good performance in the froth flotation. However, the problems could be the contamination of the concentrate by gangue minerals (mainly nontronite) by entrainment and, in sample 11, due to the presence of gangue minerals inclusions in apatite crystals.

5 ACKNOWLEDGMENTS

The authors would like to thank the following persons and institutions: L.A.F. de Barros, R.S. Aglinskas and L.O. Almeida (Fosfertil, Brazil) for providing the samples and for significant help in this research; W. de Brito (CDTN, Brazil), R.C.B. Malafatte (UFMG) and R.C. Lois (UFMG) for their assistance in X-ray diffraction; S.C.E.M. Teixeira (UFMG) and W.T. Soares (LMA) for their assistance in microanalysis; I. S. B. Carvalho for her assistance in infrared spectrometry studies; the Brazilian research-supporting institutions Capes and CNPq for the grants and scholarships. We also thank the Nuclear Technology Development Centre (CDTN) for the infrastructure and the Electron Microscopy and Microanalysis Laboratory (LMA), pertained to the partnership Physics, Geology, Chemistry – UFGM and CDTN.

6 REFERENCES

- Assis, S. M. & Brandão, P. R. G. 1999. Os minerais micáceos do minério fosfático de Tapira. Parte I. Estudos com os minérios micáceos puros. *Brasil Mineral*, No. 175: p. 32-36.
- Barros, L. A. F. de; Filho, L. S. & Peres, A. E. C. 2001. Plant practice innovations in a phosphate concentrator. *Minerals Engineering*, v.14, No. 1: p. 117-121.
- Chula, A. M. D.; Brandão, P. R. G. & Aquino, J. A. 2004. Caracterização de minérios fosfáticos com elevados teores de carbonatos e silicatos da mina de Tapira-MG. XXENTMME, Florianópolis-SC, disponível em CD, 15-18 de Junho.
- Hasui, Y. & Cordani, U. G. 1968. Idades potássio-argônio de rochas eruptivas mesozóicas do oeste mineiro e sul de Goiás. In: Anais Congr. Bras. Geol., 22, Belo Horizonte: p.139-143.
- Rodrigues, A. J. & Brandão, P. R. G. 1993. The influence of crystal chemistry properties on the floatability of apatites with sodium oleate. *Minerals Engineering*, v.6, No. 6: p. 643-653.

Significant Characteristics of Volcanogenic Massive Sulfide Deposits of the Eastern Pontides (NE Turkey): A through Comparison to Japanese Kuroko Deposits

E.Ciftci & G.Yalcin

Nigde University, Department of Geological Engineering, 51200 Nigde, Turkey

R.D.Hagni

University of Missouri-Rolla, Department of Geology & Geophysics, Rolla 65401, USA

ABSTRACT: The upper Cretaceous volcanogenic massive sulfide deposits (VMS), occurring in northeastern Turkey known as the eastern Pontide tectonic belt are considered as the largest sources for base metals in the country. The Turkish VMS deposits throughout the eastern Pontide tectonic belt share common attributes. They are all hosted by the felsic volcanic pile of Late Cretaceous age and have a strata-bound nature. These deposits belong mainly to the Cu-Zn-type, but Cu-Zn-Pb- (e.g., Lahanos deposit), Cu- (e.g., Murgul deposit), and Zn-Pb-Cu-types (e.g., Köprübaşı deposit) are also present in the region. All the deposits were deposited at temperatures ranging from 320°C to 160°C. The salinities of the fluid inclusions range between 0.5 – 6 wt. % eq. NaCl. Fluid inclusions are generally liquid-rich and have consistent liquid-to-vapor ratios. Almost all of the VMS deposits exhibit a very high Cu/Cu+Zn ratio relative to the Japanese counterparts. The sulfur isotope compositions for all of the deposits fall in a very narrow range suggesting a homogeneous source and temperature formation. The $\delta^{18}\text{O}$ values acquired from quartz gangue are restricted to the magmatic fluid range, but quartz-water fractionation from seawater at about 300°C could account for the $\delta^{18}\text{O}$ values in the Turkish VMS deposits.

1 INTRODUCTION

The study area extends from Ordu in the central Black Sea region, to the Georgian border in the northeast corner of Turkey, comprising an area approximately 300 km by 100 km. The volcanogenic massive sulfide deposits of the region are spatially and temporally associated with late Cretaceous acid volcanism that occurred during the formation of the Pontide island arc system. This region hosts more than 60 massive sulfide economic and subeconomic deposits that vary in reserve and tenor.

2 GENERAL GEOLOGY

The basement of the eastern Pontide is characterized by a tectonic collage of various pre-Liassic units including Carboniferous high-temperature, low-to medium-pressure metamorphic rocks intruded by Permian Gümüşhane granite, Permo-Triassic low-temperature, medium- to high-pressure metamorphic rocks and non-metamorphic Permo-Carboniferous sediments (Topuz et al. 2003).

The metamorphic basement is overlain by arc volcanics erupted in three volcanic cycles, during the Liassic, Upper Cretaceous and Eocene-Pliocene times (Arslan et al. 1997; Aydın et al. 2003): (I) The “Lower Basic Volcanic Complex” (LBVC), a Jurassic-Lower Cretaceous volcanic complex, discordantly overlies the basement metamorphic rocks. The LBVC consists mainly of basalt, basaltic agglomerates, locally spilitized basalts, andesite, andesitic agglomerates, and tuffs; (II) late Cretaceous-early Eocene mafic and felsic rocks are the most widespread in the eastern Pontides. They are predominantly exposed along the Black Sea coast, in an area known as the Eastern Pontides’ northern zone. The felsic volcanic rocks (FVC), known as the mineralized dacites, are of particular interest due to their close association with the VMS

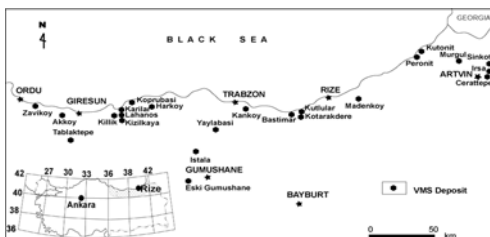


Figure 1. Location map of the eastern Pontide belt and major VMS deposits of the region.

deposits and some of the vein-type mineralizations. They comprise lava flow, tuff and pyroclastics often containing disseminated pyrite. All of these rocks fall in the VAG field as shown in Figure 2a. These volcanic rocks are overlain by marl-limestone (locally mudstone) - barren dacite (regionally known as the “purple dacite”) sequence of Maastrichtian-Paleocene age; (III) middle-post Eocene basaltic-andesitic rocks and intercalated sedimentary rocks are known to be the Upper Basic Volcanic Complex (UBVC).

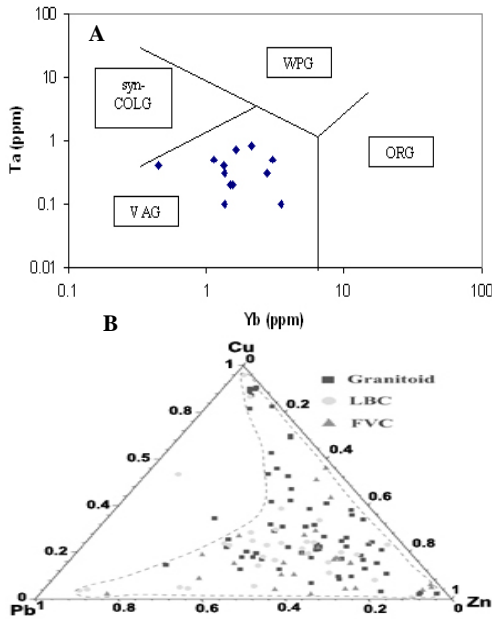


Figure 2. (A) Samples from the FVC on the Yb-Ta diagram; (B) metal contents of the host and underlying rock section (LBC is for lower basic complex of Jurassic-Lower Cretaceous age, FVC is for felsic volcanic complex of late Cretaceous age).

Igneous intrusive rocks (excluding the Gümüşhane granite, which is part of the basement) of two different ages, Lower-Upper Cretaceous (Artvin and Harsit granitoids) and Eocene (Zigana granitoid) crosscut the volcanic and the sedimentary rocks (Moore et al. 1980; Yaşınalp 1992; Köprübaşı 1993). Metal contents of felsic volcanic rocks and underlying rock section indicate that all of these rocks could be the source for the metals.

3 ORE DEPOSITS

The Turkish VMS deposits throughout the Eastern

Pontide tectonic belt show strong similarities with each other, and can be considered as “*sister deposits*”. The common features are similar are the following: (I) They are all hosted by the felsic volcanic pile of Upper Cretaceous age termed “felsic volcanic complex (FVC).” Thus, they are strata-bound in nature; (II) they appear belong mainly to the Cu-Zn-type, but Cu-Zn-Pb- (e.g. Lahanos deposit), Cu- (e.g. Murgul deposit), and Zn-Pb-Cu-types (e.g. Köprübaşı deposit) also are present in the region; (III) these deposits show very similar textural and mineralogical characteristics (Ciftci 2000).

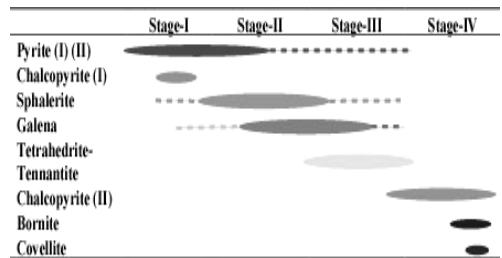


Figure 3. Generalized regional paragenetic sequence for the major ore minerals in the Turkish VMS deposits.

Figure 3 shows generalized paragenetic sequence for the major ore minerals throughout the region. The major differences between Cu-rich and Cu-poor (in the form of chalcopyrite) deposits are that the former do not contain the stage-II mineral association, whereas the latter lacks the stage-IV mineral association. Some of the Cu-poor deposits briefly exhibit indications of this stage, whereas others completely lack it. This could be attributed to the availability of certain metal ions within the ore-forming system. The major difference in mineralogy with Japanese counterparts, is the abundance of yellow ore in the form of chalcopyrite and bornite. Bornite is particularly important due to its widespread presence and its high silver content. Gold occurs associated with the yellow ore, except in the Çayeli deposit, where gold is associated with semiblack ore.

Almost all of the VMS deposits in the Pontids region exhibit a very high Cu/Cu+Zn ratio. The sulfur isotope compositions for all of the deposits investigated fall in a very narrow range that suggests a very homogeneous source and temperature. Figure 4 shows metal ratio vs $\delta^{34}\text{S}$ for the investigated VMS deposits. As Figure 4 indicated the black ore dominated deposits and yellow ore dominated deposits of the region do not differ significantly with respect to their $\delta^{34}\text{S}$ values. The $\delta^{18}\text{O}$ values acquired from quartz are restricted to the magmatic

fluid range, but quartz-water fractionation from seawater at about 300°C could account for the $\delta^{18}\text{O}$ values in the Turkish VMS deposits. Consideration of sulfur isotope data in conjunction with the oxygen isotope values reveals significant similarities between the Japanese Kuroko fluids and the Turkish VMS-forming fluids. Sulfur is believed to have been leached from the basement rocks. The $\delta^{34}\text{S}$ values of the Turkish VMS deposits are restricted to a very narrow range in comparison to the Japanese counterparts, suggesting a very uniform source. This could suggest that the fluids could have originated from seawater or from a mixture of seawater and magmatic waters.

All the deposits investigated were deposited at temperatures ranging from 320°C to 160°C. The salinities of the fluid inclusions were between 0.5 – 6 wt.% equivalent NaCl. Fluid inclusions are generally liquid-rich and have consistent liquid-to-vapor ratios, which indicate lack of boiling, probably due to relatively deep formation for the deposits.

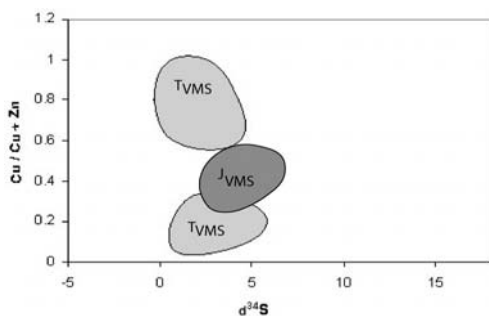


Figure 4. Average $\delta^{34}\text{S}$ values vs Cu/Cu+Zn ratios of the Turkish and Japanese VMS deposits, indicating relatively narrow range for the $\delta^{34}\text{S}$ values (TVMS: Turkish, JVMS: Japanese VMS).

4 CONCLUSIONS

Turkish VMS deposits are essentially similar to Japanese Kuroko-type VMS deposits in many aspects: geological setting, ore mineral paragenesis, lack of metamorphism, formation temperatures, salinity, stable isotope characteristics and host rock lithology. Despite these major similarities, following differences are also present: abundant bornite presence, modes of gold and silver occurrence, relative more abundance of Cu-rich or Cu-bearing sulfide minerals, and age (late Cretaceous).

5 REFERENCES

- Arslan, M., Tüysüz, N., Korkmaz, N., Kurt, H. 1997. Geochemistry and Petrogenesis of the Eastern Pontide Volcanic rocks, Northeastern Turkey. *Chem. Erde* 57, 157-187.
- Aydın, F., Karşı, O., Sadıklar, M.B., Şen, C., Altherr, R. 2003. The youngest K-Ar ages and new petrographical data of the eastern Pontide alkaline volcanics, NE-Turkey. Symposium on the Geology and Mining Potential of Eastern Black Sea Region (Trabzon, NE Turkey), Trabzon, Turkey.
- Ciftci, E. 2000. Mineralogy, Paragenetic Sequence, Geochemistry, and Genesis of the Gold and Silver Bearing Upper Cretaceous Mineral Deposits, Northeastern Turkey. University of Missouri-Rolla, Ph.D. Dissertation (unpublished), 251 p. Missouri, U.S.A.
- Köprübaşı, N., 1993. Petrology and geochemistry of the Jurassic-Cretaceous magmatic rocks between Tirebolu-Harşit (Giresun). *TJK Bull.* v. 36, 139-50, Ankara, Turkey.
- Moore, W. J., McKee, E. H., Akıncı, Ö. T. 1980. Chemistry and Chronology of Plutonic Rocks in the Pontide Mountains, Northern Turkey. *In: European Copper Deposits*, p. 209-216, Belgrade.
- Topuz, G., Çapkınoğlu, Ş. 2003. Preliassic Basement Rocks of the Eastern Pontides. Symposium on the Geology and Mining Potential of Eastern Black Sea Region (Trabzon, NE Turkey), Trabzon, Turkey.
- Van, A. 1990. Pontide Kuşağında Artvin Bölgesinin Jeokimyası, Petrojenezi ve Masif Sülfür Mineralizasyonları. Karadeniz Technical University, Ph.D. Thesis (unpublished). 220 p, Trabzon, Turkey.
- Yalçınalp, B. 1992. Güzelyayla (Maçka-Trabzon) Porfiri Cu-Mo Cevherleşmesinin Jeolojik Yerleşimi ve Jeokimyası. K.T.Ü., Ph.D. Thesis (unpublished). 177 p. Trabzon, Turkey.

Textural Patterns of Sulfides Related to a Paleoproterozoic Low-Sulfidation Epithermal System in Tapajós Gold Province, Pará State, Brazil

R.H.Corrêa-Silva; C.Juliani; T.Benevides; J.S.Bettencourt
Instituto de Geociências, Universidade de São Paulo, São Paulo, Brazil
L.V.S.Monteiro
Instituto de Geociências, Universidade de Campinas, São Paulo, Brazil

ABSTRACT: Well-preserved paleoproterozoic ash-flow caldera complexes were recently discovered in the Tapajós Gold Province. Ring composite volcanoes in these complexes are composed mainly by rhyolite, dacite, ignimbrite, ash tuffs, crystal rich tuffs, welded tuffs and co-ignimbritic breccias flows. Porphyries and shallow granite dikes and stocks that lead to the formation of a Cu–Mo–Au low-sulfidation epithermal mineralization cut the volcanic sequence. The hydrothermal alteration is represented in the rhyolites, granites and porphyries by an early Na-metasomatism, which was followed by K-metasomatism. Sericitic alteration with adularia and propylitic alteration with adularia-affected rhyolites, tuffs, ignimbrites, breccias, tuffaceous sandstones, and granite and porphyry intrusions. Argillic alteration overprints sericitic and propylitic mineralizations in shallow portions of the volcanic rocks. Chalcopyrite, pyrite, molybdenite, and chalcocite mineralization are usually related to propylitic and sericitic alteration zones. Gold mineralization is associated to propylitic and sericitic zones, where gold occurs as inclusions or microveinlets in sulfides. In the shallow portions the sulfides are replaced by hematite and limonite. The base and precious metals mineralization occurs as open space fills and disseminated, which may grade to massive, and are related to large fluid flow and permeability of the host rocks. In the propylitic zones platy calcite occur in veins of quartz + adularia, which could be indicative that boiling activity was responsible, in part, for the deposition of the metals.

1 INTRODUCTION

Textural patterns of sulfide minerals can provide information about ore forming processes and their association with genetic models can lead exploration geologists to target their goals.

Hydrothermal textural patterns in Cenozoic low-sulfidation mineralization were well described by Heald et al. (1987), White & Hedenquist (1990) and Simmons & Browne (2000). However, older well-preserved low-sulfidation mineralization, like the Paleoproterozoic Tapajós occurrence, is very rare and the comprehension of its textural pattern can provide a better knowledge of the genesis and evolution of ancient hydrothermal systems.

1.1 Method

The samples of drill holes and outcrops were described in Zeiss Axioplan and Olympus BX-50 petrographic microscopy linked to OLY-750 digital image equipment with ImagePro software. Mineral analyses were obtained in a JEOL JSM-T330A Scanning Electron Microscopy with IXRF EDS2000 System.

1.2 Geology

The Tapajós Gold province is located in the Amazonian Craton (Almeida 1978), in the boundary between two tectonic–geochronological provinces known as Tapajós–Parima (2.10 – 1.87 Ga) and Central Amazonian (> 2.3 Ga) (Santos et al. 2000). The Tapajós–Parima Province is interpreted as a result of at least two orogenic events (Santos et al. 2000).

In the Tapajós Gold Province, near the Tapajós River, some composite volcanoes occur related to ash-flow caldera complexes (Juliani et al. 2002; Juliiani et al. Submitted; Corrêa-Silva 2002; Corrêa-Silva et al. Submitted; Corrêa-Silva et al. 2003;). These volcanoes are composed of rhyolitic to dacitic flows interbedded with ignimbrites, ash tuffs, crystal tuffs, welded tuffs and breccias from Bom Jardim, Salustiano and Aruri Formations, of the Iriri Group (~1.88 Ga) (Almeida et al. 2000; Bahia & Quadros 2000; Juliiani et al. submitted). Porphyries and shallow granites cut the composite volcanoes and lead to the formation of a Cu–Mo–Au mineralized low-sulfidation epithermal system (Corrêa-Silva et al. 2001; submitted; Corrêa-Silva 2002; Juliiani et al. 2002; Juliiani et al. 2003). The volcanic system was strongly preserved from erosional and metamorphic

processes. In this system, widespread different types and styles of hydrothermal alteration have been recognized.

2 HYDROTHERMAL ALTERATION

2.1 Na-metasomatism

The Na-metasomatism is restrict to granite, rhyolites and porphyries and it is the first alteration stage that occurred in the hydrothermal system. It was responsible by pervasive intergranular crystallization of albite and quartz. Albite also replaces igneous feldspar and fill veins.

2.2 K-metasomatism

The K-metasomatism is characterized by crystallization of microcline, biotite, quartz and pyrite that obliterate the previous textures and mineralogy in rhyolites, granites and porphyries. Two stages of K-metasomatism affected the granites. The first one has a pervasive style and the second is mainly a fissure-controlled hydrothermal alteration, which may grade to a pervasive style. The K-metasomatism is usually accompanied by intense silicification.

2.3 Sericitic alteration with adularia

The sericitic alteration with adularia is the volumetrically most significant alteration type in the Tapajós low-sulfidation epithermal system. It is characterized by sericite, quartz and pyrite crystallization. This alteration type affected all rocks of the system and it was more intense in volcanoclastic and epiclastic rocks. Sericite, quartz, pyrite and adularia replace the original mineralogy, also filling veins and intergranular spaces.

2.4 Propylitic alteration with adularia

The propylitic alteration with adularia also affected a great volume of rocks. Two events can be identified. The first is probably genetically linked to the emplacement of the granitic bodies; it is previous to the early stage of sericitization and affected pervasively the andesitic and rhyolitic flows and portions of tuffs. The andesite original minerals were replaced by hornblende, chlorite, epidote and quartz. In the rhyolite and tuffs the original mineralogy was replaced by chlorite, epidote, calcite, fluorite, albite, adularia, pyrite, and chalcopyrite. The second propylitic stage is posterior to the sericitization event and is predominantly fissure-controlled. This propylitization affected all lithotypes, is probably related to the emplacement of porphyry dikes, and is characterized mainly by chlorite, calcite, epidote, fluorite, albite, adularia, pyrite, chalcopyrite, and minor leucoxene, rutile,

sphalerite, galena and barite crystallization in open space veins and disseminated in the rock matrix.

2.5 Argillic alteration

The argillic alteration was the last hydrothermal alteration event of the low-sulfidation system. It is recognized mainly in rhyolites, tuffs, ignimbrites and tuffites and occurs only near the paleo-surface of the hydrothermal system. It is characterized by widespread rock matrix replacement of feldspars and sericite, or filling vein of minerals of the kaolinite group.

3 ORE MINERALOGY

The main ore minerals are chalcopyrite, pyrite, molybdenite, and chalcocite, which occur mainly in the propylitic and sericitic hydrothermal zones. Minor galena and sphalerite are also found in propylitic zone and small grades of free gold occur in oxidized hematite-rich zones. Two major mineralization styles are observed: open space fills and disseminated, which in some cases, grade to massive sulfide zones.

3.1 Textural hydrothermal patterns

The typical texture of the ore mineral in the propylitic zones is the intergrowths of chalcopyrite and pyrite in paragenesis with chlorite, quartz, epidote, platy calcite and fluorite. This association occurs mainly in veins (Fig 1a) but grade to massive around the veins. The pyrite crystals are well shaped in the rock matrix and in some portions are skeletal.

The second generation of chalcopyrite surrounds the pyrite-chalcopyrite intergrowths and small crystals of galena and sphalerite (Fig. 1c). It occurs mainly along older hydrothermal veins.

Massive zones of chalcopyrite are common in zones of intense rock replacement by chlorite, epidote and quartz.

Molybdenite occurs in typical flake habit (Fig. 1b) in the border or inside quartz-calcite veins mainly in porphyry and rhyolite.

In the deeper level of propylitic zones chalcocite occurs associated with quartz veins. The chalcocite crystals have flaky habit and are < 2 mm.

In the sericitic zones, the sulfide mineralization is mainly in veins but grade to massive in tuffs and epiclastic rocks. In these veins pyrite and chalcopyrite are intergrowth with major amounts of pyrite concentrates in vein borders. Small inclusions of silver-copper-iron sulfide occur in chalcopyrite (Fig.1d), indicating potentiality for silver mineralization in this system. The sulfides from the sericitic alteration are in paragenetic association with sericite, quartz and adularia.

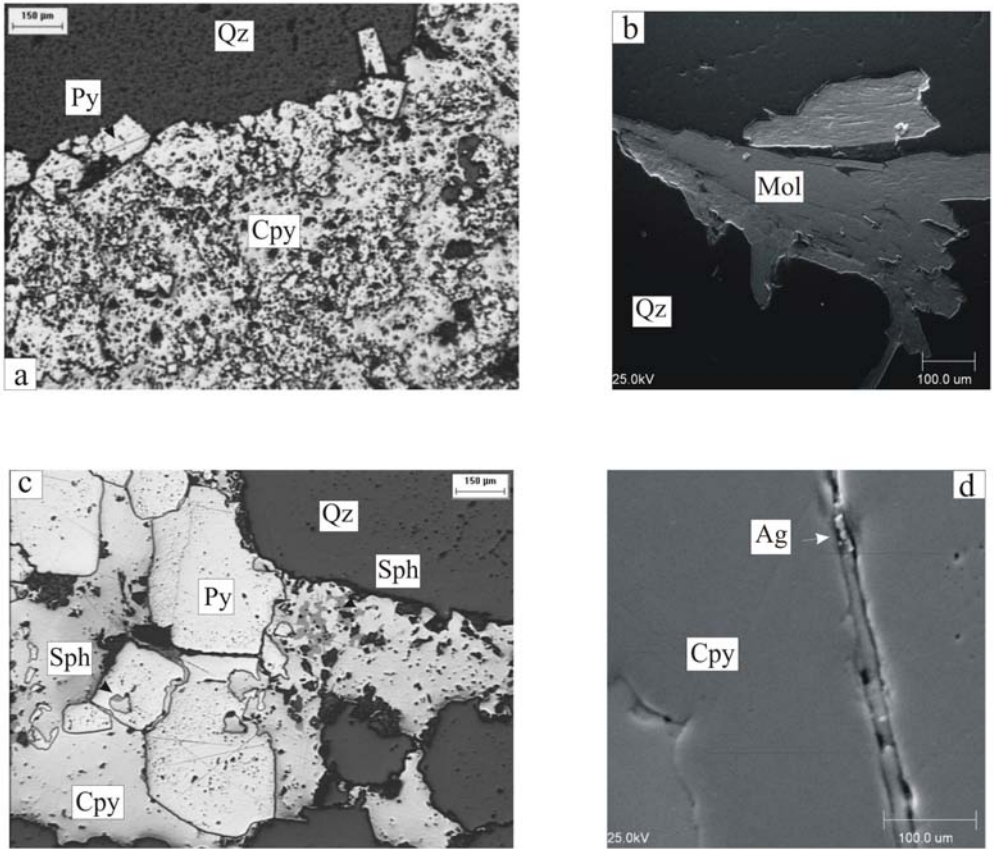


Figure 1. Sulfide minerals in Tapajós low-sulfidation epithermal system. (a) Pyrite–chalcopyrite vein (reflected light), (b) Molybdenite with flake habit in quartz vein (SEM image), (c) Pyrite chalcopyrite intergrowth with sphalerite inclusions (reflected light), (d) Unidentified silver–copper–iron sulfide inclusion in chalcopyrite (SEM image), (Ag) Unidentified silver–copper–iron sulfide, (Cpy) Chalcopyrite, (Mol) Molybdenite, (Py) Pyrite, (Qz) Quartz, and (Sph) Sphalerite.

The molybdenite occurs associated to late quartz veins in sericitic zones. Gold mineralization is related to propylitic and sericitic zones as inclusions or microveinlets in sulfides. In the upper part of the system, the sulfides are replaced by hematite and developed vuggy texture. The sulfitized zones are currently weathered to limonite clusters. In these more oxidized zones gold occurs in the free form.

4 CONCLUSIONS

The margins of ash-flow calderas are an environment with large fluid flow (Heald et al. 1987) that creates a suitable place for the development of epithermal systems. This feature can be observed in Tapajós Paleoproterozoic low-sulfidation system, where the host rocks are strongly affected by hydrothermal alteration in fissure-

controlled and pervasive style. In this site the sulfide mineralization is related to propylitic and sericitic zones where the main ore minerals are chalcopyrite, pyrite, molybdenite and chalcocite that occur in open space fills and disseminated mineralization styles with grade to massive. Minor amounts of galena and sphalerite are also found in propylitic zone as inclusions in chalcopyrite. In propylitic zones occur veins with platy calcite in association with quartz and adularia. This association is indicative of paleo-zones of boiling (Simmons & Browne 2000). Boiling zones are a good environment to deposition of precious metals and thus identification in preserved paleoproterozoic hydrothermal mineralization, may be indicative of the existence of ore-grade deposits.

The successive pulses of hydrothermal alteration types and different stages of sulfides crystallization imply the recurrence of magmatic and hydrothermal

activity that could lead to a widespread sulfide mineralization in a large volume of volcanic rocks. The occurrence of silver–copper–iron sulfide inclusions in chalcopyrite can indicate potentiality for silver mineralization in this system. Both mineralization styles described in Tapajós low-sulfidation epithermal system are related to permeability and large fluid flow in the host rocks and the sulfide concentration is close to paleo-zones of boiling. Juliani et al. (2000, 2002a) recognize high–sulfidation and porphyry–related hydrothermal mineralizations in the Tapajós region where the granites and porphyry have similar hydrothermal alteration styles, types and textural ore patterns, implying a possible genetic, spatial and temporal link among them. The relationships between epithermal and porphyry–related hydrothermal systems could generate world-class base–precious–metals mineralizations and constitute a new model for gold exploration in Precambrian areas.

5 ACKNOWLEDGEMENT

The authors would like to thank FAPESP grant (98/02567–6), CNPq and PRONEX/CNPq/UFPA (662103/1998). We are also thankful to SENAI – Mario Amato for the support at the MEV Lab. and RTDM for the samples and fieldwork support.

6 REFERENCES

- Almeida, F.F.M.de., 1978. A evolução dos Crátoms Amazônico e São Francisco comparada com a de seus homólogos do Hemisfério Norte., Congresso Brasileiro de Geologia. *Anais*, Recife, pp. 2393-2399.
- Almeida, M.E., Brito, M.F.L., Ferreira, A.L. and Monteiro, M.A.S., 2000. Geologia e Recursos Minerais da Folha Mamãe Anã (SB.21-V-D). Estados do Amazonas e Pará. Escala 1:250.000. Nota explicativa. In: M.E. Almeida (Editor), Projeto Especial Província Mineral Do Tapajós. PROMIM Tapajós/ CPRM., Brasília.
- Bahia, R.B.C. and Quadros, M.L.E.S., 2000. Geologia e recursos minerais da Folha Caracol - (SB-21-X-C. Estado do Pará Escala 1:250.000. Nota explicativa. In: R.B.C. Bahia (Editor), Projeto Especial Província Mineral Do Tapajós. PROMIM Tapajós/ CPRM., Brasília.
- Corrêa-Silva, R.H., 2002. Caracterização de um sistema epitermal low-sulfidation (adularia-sericita) mineralizado em Au-Cu-Mo em vulcânicas paleoproterozóicas na Província Aurífera do Tapajós: Implicações metalogênicas e tectônicas. Master Science Thesis, Universidade de São Paulo, São Paulo, 159 p.
- Corrêa-Silva, R.H., Juliani, C., Bettencourt, J.S., Nunes, C.M.D., Almeida, T.I.R., 2001. Caracterização de um sistema epitermal low-sulfidation (ou adularia-sericita) hospedado em vulcânicas e vulcanoclásticas do Grupo Iriri na Província Aurífera do Tapajó, PA, VII Simpósio de Geologia da Amazônia. *Cd-Room*, Belém.
- Corrêa-Silva, R.H., Juliani, C., Bettencourt, J.S., 2003. Paleoproterozoic ash-flow calderas in Tapajós Gold province, Amazonian craton, Brazil: Tectonic significance. EGS-AGU-EUG Joint Assembly, *Geophysical Research Abstracts*, 5(14233).
- Corrêa Silva, R.H., Juliani, C., Monteiro, L.V.S., Benevides, T., Bettencourt, J.S., Submitted. Paleoproterozoic ash-flow caldera-related low sulfidation (adularia-sericite) epithermal Cu-Mo-(Au) mineralization in the Tapajós gold province, Amazonian Craton, Brazil. *Journal of South American Earth Sciences*.
- Heald, P., Foley, N.K., Hayba, D.O., 1987. Comparative anatomy of volcanic-hosted epithermal deposits: acid-sulfate and adularia-sericite types. *Economic Geology*, 82: 1-26.
- Juliani, C., Nunes, C.M.D., Bettencourt, J.S., Corrêa-Silva, R.H., Monteiro, L.V.S.M., Neumann, R., Alcover Neto, A. And Rye, R. O., 2000. Early Proterozoic volcanic-hosted quartz-alunite epithermal deposits in the Tapajós Gold Province, Amazonian Craton, Brazil. , GSA Annual Meeting. Abstracts with programs., Reno.
- Juliani, C., Corrêa Silva, R.H., Monteiro, L.V.S., Freitas, F.C., Bettencourt, J.S., Teixeira, N.P., Chissini, G.B. and Silva, J.M., 2002. Implicações para estratigrafia do vulcanismo ácido no Cráton Amazônico decorrentes da identificação de ash-flow calderas na Província Aurífera do Tapajós, II Simpósio Sobre Vulcanismo e Ambientes Associados, *Boletim de Resumos e Roteiro da Excursão*, pp. 16.
- Juliani, C., Corrêa-Silva, R.H., Monteiro, L.V.S., Bettencourt, J.S. and Nunes C. M. D., 2002a. The Batalha Au-Granite System – Tapajós Province, Amazonian Cráton, Brazil: Hydrothermal alteration and regional implication. *Precambrian Research*, 119(1-4): 225-256.
- Juliani, C., Corrêa-Silva, R.H., Monteiro, L.V.S., Bettencourt, J.S., 2003. Epithermal and plutonic gold mineralizations related to paleoproterozoic acid magmatism in the Tapajós Gold Province, Amazonian craton, Brazil. EGS-AGU-EUG Joint Assembly, *Geophysical Research Abstracts*, 5(14239).
- Juliani, C., Rye, R.O., Nunes, C.M.D., Snee, L., Corrêa-Silva, R.H., Monteiro, L.V.S.M., Bettencourt, J.S., Neumann, R., Alcover Neto, A., Submitted. Paleoproterozoic high-sulfidation mineralization in the Tapajós gold province, Amazonian Craton, Brazil: Geology, mineralogy, alunite argon age and stable isotope constraints. *Chemical Geology*.
- Santos, J.O.S., Hartmann, L.A., Gaudette, H.E., Groves, D.I., McNaughton, N., Fletcher, I.R., 2000. A new understanding of the Provinces of the Amazon Craton based on integration of field mapping and U-Pb and Sm-Nd geochronology. *Gondwana Research*, 3(4): 453-488.
- Simmons, S.F. and Browne, P.R.L., 2000. Hydrothermal minerals and precious metals in Broadlands-Ohaaki Geothermal System: Implications for understanding low-sulfidation epithermal environments. *Economic Geology*, 95: 971-999.
- White, N.C. and Hedenquist, J.W., 1990. Epithermal environments and styles of mineralization: Variations and their causes, and guidelines for exploration. *Journal of Geochemical Explorations*, 36: 445-474.

Condoriaco Silver District: a Mineral Heritage in La Serena, Chile

J.Cucurella

Departamento Ingeniería de Minas. Facultad de Ingeniería. Universidad de La Serena, Chile

J.Oyarzún

Departamento Ingeniería de Minas. Facultad de Ingeniería. Universidad de La Serena & CEAZA, Chile

ABSTRACT: Chilean silver ores were intensively mined during the 19th century. The beauty of red silver sulfosalts (the so-called *rosicleres*), the amount and variety of halides and the huge specimens of native silver, were also valuable aspects of these ores. Although a great number of silver specimens were sent to European museums, a large number of them remain in Chilean institutions, for example the Ignacio Domeyko collection, which is currently displayed at the University of La Serena (ULS) Mineralogical Museum. During the 1990s, the technical and scientific staff of the ULS began a comprehensive mineralogical and metallogenesis study of this collection. The present communication concerns to Condoriaco Ag-Au district, (29° 04'S / 70° 52' W). The district was mined during pre-Colonial time and later in the 1880s. During the first 10 years, one of its mines produced 23.4 t Ag, with grades up to 15 kg/t Ag and Au/Ag ratios of 1:10. The Condoriaco veins are vertical and hosted by a volcanic sequence emplaced within a huge caldera structure. The paragenesis and ore textures, indicate that sulfide, sulfosalts and native silver, were deposited from both hydrothermal and supergene solutions. The oxidation zone is important, and there the enriched secondary sulfides were replaced by silver halides under the semiarid and close to the sea environment. The cultural heritage of this old silver district, along with the Domeyko Collection, is an important asset for the tourism industry. Additionally, the district still has a potential for mineral exploration.

1 INTRODUCTION

The earliest report on Condoriaco dates from 1788 ("Noticias de las Principales Minas Conocidas en el Reino de Chile"; by A. Martínez), and the first chemical-mineralogical analysis of the silver ore, (published by I. Domeyko; Mineralojía, 1897) indicated the presence of silver tellurides. In 1883, began an intensive period of mining, which was sustained for almost 30 years. The "Sociedad Minera Beneficiadora de Plata de Condoriaco" was incorporated in 1921, and remained active until the first half of the 20th century.

During the first years of mining work, only the upper and richest zones of the veins were mined, obtaining grades as high as 15 kg of silver per metric ton (10:1 Ag / Au ratios).

In the first ten years of production, the Mercedes mine yielded 11.000 tons of silver ores, containing about 23.400 kg of fine silver. (Kuntz 1925). When the richest supergene and transitional zones were gradually exhausted and gave way to the primary ores, the mining benefits decreased. Between 1933 and 1935, 3.800 kg Ag and 290 kg Au were recovered. (Lanas 1955)

The waste dumps were reprocessed in the 1980's, when silver prices boomed. Also, small veins and

breccia pipe copper deposits have been mined in the district during the last 40 years.

2 GEOLOGICAL SETTING

Silver deposits in Chile are grouped in two main types: 1) veins and replacement bodies hosted by limestones associated with Jurassic or Lower Cretaceous volcanic rocks (*silver-only* deposits, e.g., Caracoles and Chañarcillo); and 2) epithermal silver-gold deposits in Upper Cretaceous and Tertiary volcanic rocks (e.g. Condoriaco).

The Condoriaco district is located in a volcanic caldera, about 28 km in diameter, which includes andesitic, dacitic and rhyolitic lavas, and ignimbrite flows. These rocks are cut by felsic dikes and stocks and by late granodioritic bodies. (Emparan & Pineda 1999)

The whole sequence is cut by N-S normal faults that host the silver/gold deposits. Mineralization and formation of the large hydrothermal alteration zone occurred during the last phase of caldera development (Muller 1987).

The mineralized structures are grouped in two main N-S trending clusters, which comprise veins that strike for up to 2.4 km long. Both belts are

flanked by parallel structures, which host smaller and lower grade deposits (Fig. 1). Both the oxidation

and the transitional zone in the main deposits were intensively mined and exhausted.

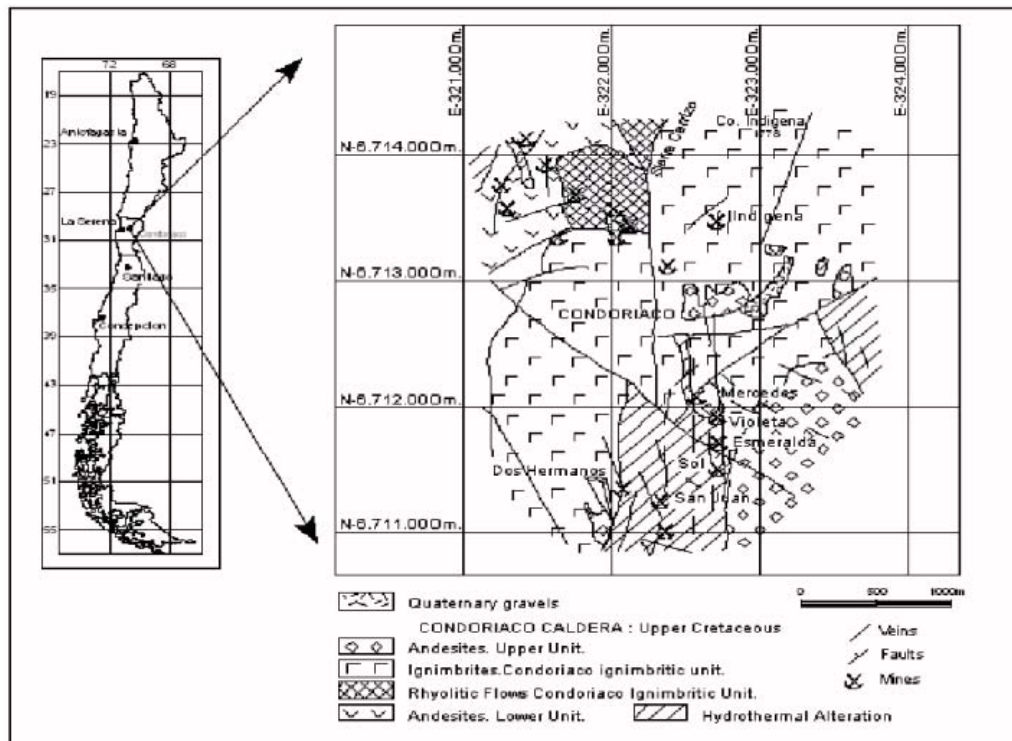


Figure 1.

3 MINERALOGY

The mineralization sequence includes chalcopyrite, pyrrargyrite, pyrite, sphalerite, magnetite, bornite, tetrahedrite, arsenopyrite, native gold, and galena as primary mineralization with native silver, argentite (acanthite), polybasite, stembergite, stromeyerite, embolite (Ag (Br,Cl), and cerargyrite (chlorargyrite) in the supergene enrichment zone.

Among the gangue minerals, quartz is ubiquitous during the whole stage of mineralization, having at least two veins generations. Calcite postdates quartz was present all over the mineralization stage. Barite occurs in two vein generations, one of them, post-mineralization.

The analysis of the fluid phase indicates salinities between 4.9 and 20 % wt NaCl with temperatures between 160°C to 240° C for gangue minerals, whereas temperatures of 220°C to 290°C have been estimated for the sulphides. (Cucurella & Flores 1994).

In silver deposits that have been submitted to intensive processes of supergene enrichment, it is

hard to distinguish between primary and secondary sulphides. In the Condoriaco deposit, argentite probably developed in the upper part of the secondary enrichment zone, as suggested by its relations with silver halides, native silver, cerussite, and by its rhythmical banded texture, common in supergene depositions.

The mineral association and texture data indicate that the native silver precipitated both from ascending (hydrothermal) as well as descending (meteoric) solutions.

The silver halogenides, cerargyrite and embolite, developed in the oxidation zone, are typical of supergene enrichment environment in a semiarid zone close to the sea (Cucurella et al. 1991). These halogenides show small-scale zonation. The less soluble cerargyrite was deposited in the upper part and embolite in the lower sectors of the deposits. It seems likely, that when the ground water level came down, the oxidized zone invaded the secondary enrichment sulphides zone, and some of the oxidized ores become replaced by silver halides.

4 CONCLUSIONS

Condoriaco host epithermal Ag- (Au) veins, contained an extremely rich silver paragenesis including sulfides, sulfosalts, halides, and native silver. The veins occur in clusters within a caldera type volcanic structure.

It is important to point out that, the end of mining activities at Condoriaco was mostly due to the gradual exhaustion of the richest supergene and transitional zones and to the cyclic conditions of ore prices. However, recent geological and structural evidences indicate that new rich zones could be found in blocks displaced by the normal fault system.

The cultural heritage represented by this old silver district, is considered an important asset for the tourism industry and, as such, the site has been selected for a pilot program set up by La Serena Town Council. The Domeyko mineralogical collection at La Serena University offers an important complement to this initiative

5 ACKNOWLEDGEMENTS

The authors gratefully acknowledge the support from the University La Serena and from La Serena Town Council, which made this study possible.

6 REFERENCES

- Cucurella, J, Flores, I, Oyarzún, J. 1991. El valor científico de una colección mineralógica en la reconstitución de tres antiguos distritos argentíferos: Arqueros, Algodones y Rodaito (Norte de Chile). *Estudios Geológicos*. Vol. 47 (3-4). Museo Nacional de Ciencias Naturales. Madrid- España.
- Cucurella, J.; Flores, I. 1994. Condoriaco silver deposit: A geological, mineralogical and genetic reconstitution from I. Domeyko collection of the University La Serena, Chile. *Mineralogia Polonica*, Vol. 25 N° 1. Polonia.
- Domeyko, I. 1897. *Mineralogía*. Imprenta Cervantes. Chile.
- Emparan, C.; Pineda, G. 1999: Área de Condoriaco-Rivadavia. Región de Coquimbo. Servicio Nacional de Geología y Minería. Mapas Geológicos. N° 12. Escala 1:100.000 Santiago, Chile.
- Kuntz, J. 1925. Monografía minera de la provincia de Coquimbo. Folleto N° 13. Publicaciones del Cuerpo de Ingenieros de Minas. Soc. Imp. y Lit. Universo.
- Lanas, E. 1955: Sobre explotación de minas y desmontes de la Sociedad Minera Condoriaco. Inédito. Caja de Crédito y Fomento Minero
- Martínez de Matta y Casamiglia A. 1788. Noticias de las principales minas conocidas en el Reino de Chile. Archivo Museo Nacional de Ciencias Naturales. Madrid España
- Muller, R. 1987. La geología del distrito argentífero de Condoriaco al NW de La Serena, IV Región de Coquimbo, Chile. Inédito. Universidad de La Serena.

Mineralogy of the Iron Formation in the Itabira Mines, Iron Quadrangle, Brazil

L.Lagoeiro, R.C.Romano, P.N.Venturini

Department of Geology, Federal University of Ouro Preto, Minas Gerais, Brazil

M.C.Pereira, A.A.S.Gomes-Jr

Vale do Rio Doce Company (CVRD), Itabira, Brazil

ABSTRACT: Different from the other parts of the Iron Quadrangle, iron formation in the Itabira mines has a complex mineralogy. Interleaved with the iron oxide and silica bands, layers of granitic materials occur. A combination of analytical techniques, including electron microprobe analysis, X-ray diffraction and X-ray fluorescence was applied in order to determine the mineralogy and the chemical composition of the iron formation rocks. The iron rich layers are mainly composed of magnetite and hematite. Goethite is the main mineral phase after iron oxides. The admixture of igneous-related materials, iron formation and a variety content of MnO produced a wide range of mineral composition. These include complex oxides and hydroxides containing Fe, Al, Mn, Mg, Ti, Ca, Na, K, Ba, Li, Be, F as well as some phosphate (monazite) and silicate minerals (such as feldspars and micas).

1 INTRODUCTION

The Iron Quadrangle is considered a classical granite-greenstone terrain (Schorscher et al. 1982) of Archaean and Paleoproterozoic ages (Teixeira & Figueiredo 1991; Babinski et al. 1993). It hosts important mineral resources including one of the largest iron deposits around the world. It is located at the southeastern of Minas Gerais State, Brazil. Mostly, iron formations consist of an alternation of layers of iron and quartz minerals. The thickness of these layers varies from few micrometers to several centimeters. Locally, banded the iron formation gradually passes to massive bodies of almost pure hematite. In some places, besides quartz, layers of carbonates and other silicates phases (mainly amphiboles) can also be found. Some factors may contribute to produce a complex mineralogy in the iron formation, such as, for instance, deposition of terrigenous sediments interleaved with layers of iron and quartz minerals. In addition, horizons of manganese-carrying materials and volcanic rocks contribute to the appearance of minerals with complex composition. When iron formations are surrounded by granitic bodies their mineralogy gets even more complex, reflecting in the appearance of uncommon minerals that are not normally found in

iron formation rocks. A good example of that situation may be found in the Itabira district Mines. The proximity of iron formation with intrusive granites and the fluid activities associated to them promoted the formation of a variety of minerals with complex chemical compositions. We use a combination of techniques, including optical and electron microscopy (combined EDX and WDX microprobe), X-Ray diffraction and fluorescence, to determine the mineralogy and chemical composition of iron formation in the Itabira Mines.

2 SAMPLE SELECTION AND PREPARATION

Iron formation in the Itabira Mines includes banded rocks with alternation of iron and silica minerals and interleaved layers of a varied composition and physical aspects. Most of these materials lays parallel to the compositional banding of the iron formation rocks. In the field, we separated three groups of those layers based exclusively on their physical characteristics. They are in order of abundance: 1) yellowish to brownish layers; 2) white layers and 3) black layers. These materials share some diagnostic characteristics, as for instance, most of them has a massive aspect and very fine-grained

aggregates. We collected around 150 samples of all those materials. The samples were separated for petrographic characterization, X-ray diffraction (XRD) and fluorescence (XRF) and for electron microprobe analyses (EMPA) following the standard procedures for sample preparation for each analytical technique.

3 SAMPLE CHARACTERIZATION

Iron formation rocks themselves consist of alternations of compositional layers of iron and silica minerals. The thickness of the silica layers varies from few millimeters to several centimeters. Iron mineral layers have thickness from few millimeters to several meters. When iron-rich layers (> 90% of iron oxide minerals) get thicker, iron formation receives a local name of hard hematite, a high-grade ore composed mainly by granular or tabular hematite with minor relicts of magnetite grains. Interleaved with the iron formation rocks, three groups of colored materials occur. Mining geologist referred to them in the field as “contaminated iron ores”, because they have a relatively high Fe content and diversified mineralogical and chemical composition. The proportions in which these materials occur are used to classify the iron ores as “contaminated” or not. The “contaminated” materials have a diagnostic massive aspect and fine-grained (clay-sized particles) aggregates. These materials can be recognized in the field mainly by their physical characteristics, such as color and texture. The main physical aspect and composition of the three major groups are given in the following paragraphs.

3.1. Yellowish to brownish layers

Besides their characteristic color, these materials are commonly very fine-grained. At hand-sample scale, they appear as massive aggregates with an average grain size less than 5 μm . Therefore, the mineralogical constituents can only be discernible at the (electron) microscopic scale. Essentially, the yellowish material consists in a complex mixture of minerals, including phyllosilicates (kaolinite, talc and serpentine); uncommon oxo-hydroxides and silicates, containing Fe, Al, Mn, Ca, Na, K and Li; and phosphates (see Tables for a complete list of constituent minerals). These materials occur in bands whose thickness varies from few millimeters to 10's of centimeters.

Table 1. Mineralogy of the yellow to brownish materials.

Material	Mineralogy
	Vermiculite $(\text{Mg}, \text{Fe}^{2+}, \text{Al})_3(\text{Al}, \text{Si})_4\text{O}_{10}(\text{OH})_2 \cdot 4(\text{H}_2\text{O})$
Yellowish to Brownish	Nimite $(\text{Ni}, \text{Mg}, \text{Fe}^{2+})_5\text{Al}(\text{Si}_3\text{Al})\text{O}_{10}(\text{OH})_8$
	Siderite $\text{Fe}^{2+}\text{CO}_3$
	Lizardite $\text{Mg}_3\text{Si}_2\text{O}_5(\text{OH})_4$
	Talc $\text{Mg}_3\text{Si}_4\text{O}_{10}(\text{OH})_2$
	Birnessite $(\text{Na}, \text{Ca}, \text{K})_x(\text{Mn}^{4+}, \text{Mn}^{3+})_2\text{O}_7 \cdot 1.5(\text{H}_2\text{O})$
	Natronambulite $(\text{Na}, \text{Li})\text{Mn}^{2+}_4(\text{Si}_3\text{O}_{14}(\text{OH}))$
	Willemseite $(\text{Ni}, \text{Mg})_3\text{Si}_4\text{O}_{10}(\text{OH})_2$
	Laumontite $\text{CaAl}_2\text{Si}_4\text{O}_{12} \cdot 4(\text{H}_2\text{O})$
	Quartz SiO_2
Yellowish to Brownish	Muscovite $\text{KAl}_2\text{Si}_2\text{O}_6(\text{OH})_{0.9}\text{F}_{0.1}$
	Braunite $\text{Mn}^{2+}\text{Mn}^{3+}_6\text{SiO}_{12}$
	Berlinite $\text{Al}(\text{PO}_4)$
	Sidorenkite $\text{Na}_x\text{Mn}^{2+}(\text{PO}_4)_n(\text{CO}_3)$
	Montmorillonite $(\text{Na}, \text{Ca})_{0.5}(\text{Al}, \text{Mg})_2\text{Si}_4\text{O}_{10}(\text{OH})_2 \cdot n(\text{H}_2\text{O})$
	Goethite $\text{FeO}(\text{OH})$
	Hematite Fe_2O_3
	Bixbyite $(\text{Mn}^{3+}, \text{Fe}^{3+})_2\text{O}_3$
	Kaolinite $\text{Al}_2\text{Si}_2\text{O}_5(\text{OH})_4$

3.2. White layers

In a very similar manner, layers of white material occur parallel to the compositional bands of the iron formation. They are fine-grained too, what makes their minerals resolved only at the (electron) microscopic scale. Their compositions are also complex, although with a lesser extent of minerals than those found in the yellowish materials (see Tables for a comparison). The constituent minerals include: phyllosilicates (talc and kaolinite); a variation of hydroxides and oxides contained Al, Fe, Mg, Mn, Ca, K, Na and Li; and minor amounts of other silicates. They occur mostly as thin layers alternated with iron oxide bands.

Table 2. Mineralogy of the white materials.

Material	Mineralogy
White	Talc $\text{Mg}_3\text{Si}_4\text{O}_{10}(\text{OH})_2$
	Natronambulite $(\text{Na}, \text{Li})\text{Mn}^{2+}_4(\text{Si}_3\text{O}_{14}(\text{OH}))$
	Maghemite $\text{Fe}^{3+}_{23}\text{O}_3$
	Vaterite CaCO_3
	Muscovite $\text{KAl}_2(\text{Si}_3\text{Al})\text{O}_{10}(\text{OH}, \text{F})_2$
	Gibbsite $\text{Al}(\text{OH})_3$
	Goethite $\text{FeO}(\text{OH})$
	Analcime $\text{NaAlSi}_3\text{O}_6 \cdot (\text{H}_2\text{O})$
	Vermiculite $(\text{Mg}, \text{Fe}^{2+}, \text{Al})_3(\text{Al}, \text{Si})_4\text{O}_{10}(\text{OH})_2 \cdot 4(\text{H}_2\text{O})$
	Birnessite $(\text{Na}, \text{Ca}, \text{K})_x(\text{Mn}^{4+}, \text{Mn}^{3+})_2\text{O}_7 \cdot 1.5(\text{H}_2\text{O})$
Kaolinite $\text{Al}_2\text{Si}_2\text{O}_5(\text{OH})_4$	
Hematite Fe_2O_3	

3.2. Black layers

These layers consist of thin to thick horizons (up to few meters) interbedded with the iron formation layers. They consist of very fine-grained particles (clay-sized) that cannot be identified by conventional optical or physical methods. The constituent minerals were identified by X-Ray diffraction and EMPA. The minerals show a wide range of composition comprising oxo-hydroxides (Mn, Fe, Al, Mg, Ca, Na, K, Ba, Li) and silicates (quartz, micas, and clay minerals).

Table 3: Mineralogy of the black materials

Materia	Mineralogy
I	
Hematite	Fe ₂ O ₃
Winchite	(CaNa)Mg ₄ (AlFe ₃)Si ₄ O ₂₂ (OH) ₂
Vermiculitae	(Mg,Fe ²⁺ ,Al) ₃ (Al,Si) ₂ O ₁₀ (OH) ₂ ·4(H ₂ O)
Actinolite	Ca ₂ Mg ₃ Fe ²⁺ ₂ Si ₈ O ₂₂ (OH) ₂
Goethite	FeO(OH)
Romanechite	(Ba,H ₂ O) ₂ (Mn ⁴⁺ ,Mn ³⁺) ₅ O ₁₀
Gibbsite	Al(OH) ₃
Alunite	KAl ₃ (SO ₄) ₂ (OH) ₆
Albite	NaAlSi ₃ O ₈
Saponite	(Ca ^{1/2} ,Na) _{0,3} (Mg,Fe ²⁺) ₃ (Si,Al) ₄ O ₁₀ (OH) ₂ ·(H ₂ O)
Anandite	(Ba,K)(Fe ²⁺ ,Mg) ₃ (Si,Al,Fe) ₄ O ₁₀ (S,OH) ₂
Black	
Cariopilite	(Mn ²⁺ ,Mg,Zn,Fe ³⁺) ₃ (Si,As) ₂ O ₃ 10(OH,Cl) ₄
Talc	Mg ₃ Si ₄ O ₁₀ (OH) ₂
Jarosite	KFe ³⁺ ₃ (SO ₄) ₂ (OH) ₆
Bixbyite	(Mn ³⁺ ,Fe ³⁺) ₂ O ₃
Geikielite	MgTiO ₃
Lepidocrocite	FeO(OH)
Muscovite	KAl ₂ (Si ₃ Al)O ₁₀ (OH, F) ₂
Annite	KFe ³⁺ ₃ AlSi ₃ O ₁₀ (OH, F) ₂
Janggunite	Mn ⁴⁺ _{5,6} (Mn ²⁺ Fe ³⁺) _{1,4} O ₆ (OH) ₆
Birnessite	(Na,Ca,K) _x (Mn ⁴⁺ ,Mn ³⁺) ₂ O ₇ ·1.5(H ₂ O)
Kaolinite	Al ₂ Si ₂ O ₇ (OH) ₄
Quartz	SiO ₂

4 FINAL CONSIDERATIONS AND CONCLUSIONS

The 'contaminated' materials characterized in the Itabira Mines show a wide range of mineral phases with complex chemical composition (see Tables of the identified minerals for each type of 'contaminated' material). Although is not rare to find terrigenous sediments interbedded with the iron formation - which might account for the presence of, for instance, Al- and Mn-carrying minerals - the presence of minerals of more complex composition (Li, REE-carrying minerals, Be, Ba, among others) cannot be attributed only to the terrigenous sediment. A suite of intruded granite (the term granite is used here in its broad sense) bodies are

found in the country rocks of the iron formation in the Itabira Mines. These granites contain accessory minerals such as beryl, Li and REE-bearing minerals whose chemical compositions are compatible to those minerals found in the 'contaminated' material and in the iron formation as well. The source for those elements, not commonly found in the terrigenous components of the iron formation, might be attributed to the fluid activities related to the granite bodies intruded in the country rocks in the adjacent area of the Itabira Mines.

5 REFERENCES

- Babinsk, M., Chemale, F., e Van Schmus, W. R., 1993. A idade das formações ferríferas bandadas do Supergrupo Minas e sua correlação com aquelas da África do Sul e Austrália. Proceedings of the 2nd. Simpósio do Cráton do São Francisco, Belo Horizonte, 152-153.
- Schorscher, H.D., Santana, F.C., Polônia, J.C., e Moreira, J.M.P., 1982. Rio das Velhas Greenstone Belt and Proterozoic rocks, Quadrilátero Ferrífero, Minas Gerais State. Excursion annex of International Symposium on Archean and Early Proterozoic Geological Evolution and Metallogenesis, Salvador, Sociedade Brasileira de Geologia, 1-25.

Iron Ore Mineralogy of Paleoproterozoic Iron Formations from Iron Quadrangle, Brazil

L.Lagoeiro, P.N.Venturini, R.Romano, I.Endo

Department of Geology, Federal University of Ouro Preto, Minas Gerais, Brazil

ABSTRACT: The banded iron formations in Iron Quadrangle, Brazil, consist mostly of alternations of layers mainly composed of silica and iron oxide and hydroxide minerals. Several generations of iron oxide phases are present in those iron formations, and their different fabric imprints resulted from at least two main thermal-mechanic processes (deformation and metamorphism) all over the Iron Quadrangle. We have studied iron oxide minerals to establish the sequences of formation and transformation of iron oxide minerals during deformation, metamorphism and subsequent supergenic alteration. Magnetite minerals represent the oldest recognizable growth of iron oxides in Iron Quadrangle. A fluid-assisted deformation and metamorphic processes promoted the transformation of magnetite and recrystallization of the massive aggregates of hematite. Two distinct types of hematite texture were produced in this stage: aggregates of granular grains resulted of the direct transformation of magnetite crystals and tiny tabular hematite directly precipitated from solution originated by the dissolution of magnetite. Intracrystalline gliding and recrystallization of original hematite aggregates originated grains with high aspect ratios and strong shape and crystallographic textures. It was in this stage that a very well marked tectonic/metamorphic compositional layering was produced. The folding of the compositional layers caused the reorientation, and in some cases, growth of new tabular hematite obliquely to the earlier compositional layering. The later registered iron oxide growth is represented by post-kinematic blastesis of magnetite grains related to an extensive thermal event. The euhedral grains related to this event and the remained magnetite clasts were subsequently altered by supergenic processes.

1 INTRODUCTION

Iron formations from the Iron Quadrangle (QF) in the Southeast of Brazil are part of a major Paleoproterozoic (Alkmim & Marshak, 1998) sequence that consists mainly of metasedimentary (clastic and chemical sediments) and metavolcanic (tuff and pyroclastic) rocks. The iron formation unit itself consists of hundreds of meters of interleaved layers of iron oxide minerals (Mgt, Hem) and Qtz. Compositional layers have thickness from few millimeters to tens of centimeters. Iron oxides layers are commonly thicker than the quartz layers. In many places they may reach hundreds of meters given rise to bodies of hard hematite ores.

Iron formations have a persistent spatial distribution all over the Iron Quadrangle (Dorr 1969). Their present spatial configuration (Fig. 1) and composition resulted from intense tectonic and metamorphic processes started around 2.1 Ga ago (Babinski et al., 1995; Alkmim & Marshak, 1998). In this contribution, we present the results of mineralogical and microstructural studies in iron formation samples from the entire Iron Quadrangle region. Our main goal was to establish a relationship

between the two major thermo-mechanic processes (named D1 e D2) and the generation of iron oxide and hydroxide minerals. To do so we used a combination of techniques including optical and electron microscopy as well as X-ray diffraction and fluorescence for mineral identification.

2 MAJOR GEOLOGICAL PROCESSES AND STRUCTURES

2.1 Underformed structures

The oldest structure recognized in the Iron Quadrangle is a compositional horizon where well-formed magnetite crystals concentrate. The horizons or compositional bands are no thicker than few millimeters. These millimetric bands alternates with thin layers of a mixture of quartz and magnetite grains in a wide range of proportions. The transition between the compositional layers is gradual. These layers are characterized by the absence of deformation features or other evidence for the operation of metamorphic processes that suggest that these structures might result from sedimentary processes.

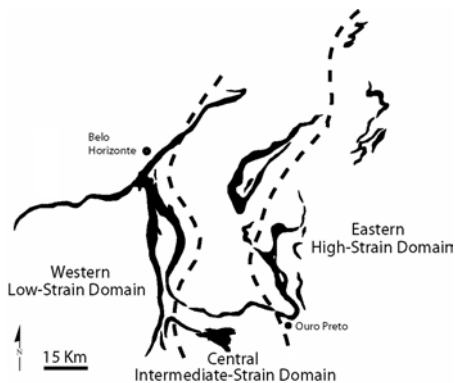


Figure 1. Map of the Paleoproterozoic iron formation in the IQ area showing main domains of strain magnitudes. Limits between domains (heavy dashed lines) approximately follow that found in Rosière et al. 2001. Metamorphic grade increases from west to east (Pires 1995).

2.2 Structures related to the first deformation and metamorphism (D1)

This was the most intense deformation registered in rocks of the Iron Quadrangle, and are related to the Transamazonian contraction (2.1 – 1.8 Ga; Alkmim & Marshak 1998). The metamorphism achieved its peak during the D1 deformation. It was in this stage that most of mineral assemblage developed. An intense folding and transposition of the original layering resulted in a metamorphic foliation (S_1) parallel to the axial plane of isoclinal folds. The transposition produced an alternation of layers of different composition. Contrasting with compositional bands of syn-depositional origin, the metamorphic layering characterizes by abrupt transitions from iron oxides to quartz layers. An extensive recrystallization of the former mineralogy and the development of the new one occurred during the D1 deformation. Fluid activities were an important component operative in the D1 deformation and it had an important role on the mineral transformation and growth of new mineral phases.

2.3 D2 Deformation

This second major deformation process is attributed to the Braziliiano orogeny (0.7 to 0.45 Ga; Alkmim & Marshal 1998) and left only localized imprint over the previously formed (D1) structures and mineralogy. The metamorphic layering S_1 was tightly folded. Transposition related to this deformation is only locally registered. A new foliation (S_2) developed parallel to the axial plane of the tight folds. It is less penetrative at the microscopic level. New mineral growth was very limited when compared with those produced during

the first deformation stage. It consists of tabular Hem grains oriented along the axial plane of tight folds. In some localities, tabular Qtz veins are positioned along the fold axial planes. In several situations these veins are mineralized in gold which occurs associated with goethite. It is worth to note that in most of the Qtz veins associated with the D1 deformation, mainly bedding-parallel veins, gold is generally absent. The common iron oxide mineral found in those Qtz veins is specular Hem. In that situation, Gt, which might be attributed to any sort of hydrothermal process, is not present.

3 DEFORMATION, METAMORPHISM AND MINERAL GROWTH

3.1 Mineral growth during D1 deformation

The main mineral assemblage found in iron formation rocks of the Iron Quadrangle region was syn-kynematically developed during D1 deformation. The original mineral aggregates (Fig. 2), mainly massive to granular Mgt and Hem, were transformed and (re) crystallized into syn-metamorphic iron oxide minerals which are arranged in bands originated by transposition of pre-D1 layers. Metamorphic studies (Hoefs et al 1982; Pires 1995) all over the Iron Quadrangle indicated that the maximum temperature for mineral growth reached 450°C in the east boundary of the IQ, although local thermal gradient is registered in several locations, particularly near gneissic-migmatitic-granitic domes. In places where relicts of original mineralogy are preserved Mgt porphyroclasts show evidences of transformation in aggregates of Hem crystals. The transformation started along crystallographic (111) planes as well as in fractured surfaces (Lagoeiro, 1998) in contact with the oxidizing aqueous fluids (Fig.3). Dissolution of Mgt grains also occurred in situation where crystal faces were oriented normal to the direction of maximum shortening. The dissolved material got into solution and then precipitated in planes that constitute the foliation S_1 . For that reason, two main types of iron oxide aggregates were produced as a result of the operation of combined processes including microfracturing, oxidation of Mgt and dissolution and crystallization of new grains. The oxidation of Mgt produced aggregates of granular Hem (Fig. 4). Grains are typically equant, with irregular boundaries and no preferred crystallographic texture. Conversely, precipitated hematite grains are mainly tabular, with straight boundaries, high aspect ratio and show remarkable textures (Figs. 3 and 5). Crystal plastic processes were also operative during the D1 deformation. Original massive aggregates of iron oxides were recrystallized and new aggregates of hematite grains were produced. The recrystallized Hem grains are tabular and have crystallographic

and shape preferred orientations. They differ from the precipitated tabular hematite grains mainly by their larger sizes and smaller aspect ratios, as shown in Figures 3 and 5.

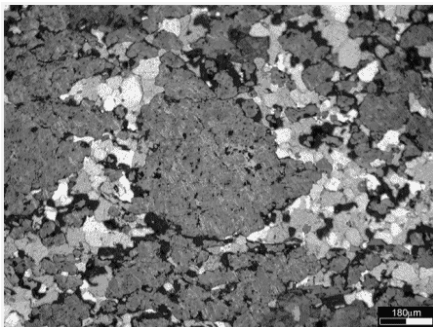


Figure 2. Optical micrograph showing relicts of magnetite porphyroclasts partially transformed into Hem.

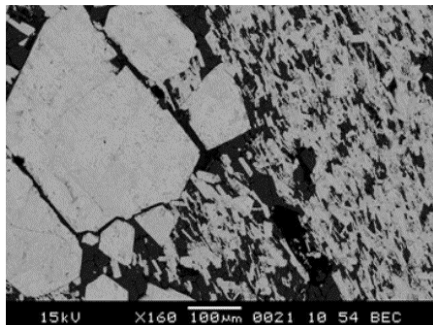


Figure 3. Electron backscattered image of magnetite porphyroclasts and tabular hematite aggregates. Slight grey shades correspond to hematite and dark grey to magnetite.

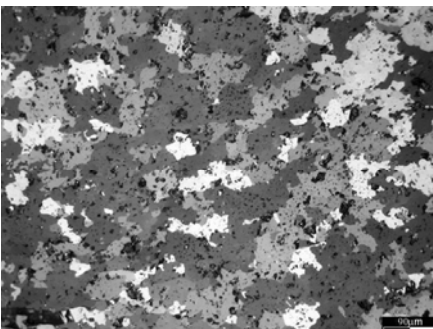


Figure 4. Aggregate of granular Hem originated by oxidation of Mgt clasts, showing characteristic isotropic texture.

3.2 Post-D1 and Pre-D2 mineral growth

The last registered mineral growth, pre- D2 deformation, occurred in some areas of the Iron

Quadrangle. The mineral assemblage produced may be related to thermal activities restricted to some domains in the IQ region. Mgt porphyroblasts are the most representative minerals grown at this stage. Grains are found overprinting the mineral assemblage found in the syn-D1 metamorphic foliation. Mgt grains are larger (up to few cm in diameter) and commonly show well-developed crystallographic faces. This event might be characterized by a static growth (annealing) that produced thicker tabular crystals or somewhat polygonal aggregates (foam textures) with characteristic straight boundaries (Fig.6).

3.3 The D2 deformation and mineral growth

Mineral growth related to the D2 deformation is restricted to some locations, particularly those corresponding to domains of localized strain, such as shear zones. In these localities, such as D2 fold hinges zones (Fig. 7), where transposition features are relatively common, new crystallized aggregates of tabular hematite grew obliquely to the main orientation of the older tabular Hem grains.

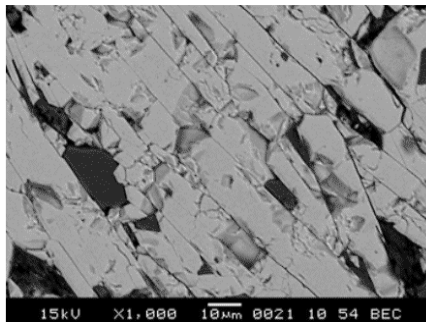


Figure 5. Electron backscattered image of tabular hematite crystals related to the D1 deformation.

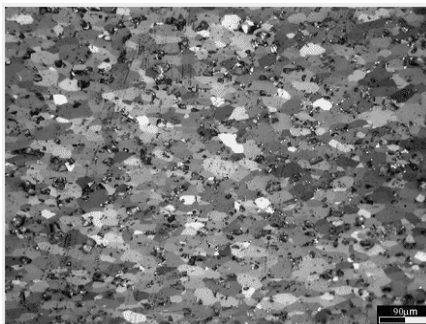


Figure 6. Hematite aggregate with predominance of straight grain boundaries.

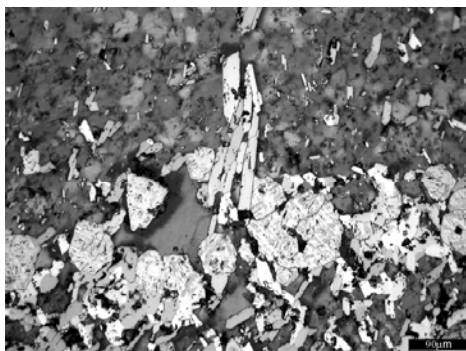


Figure 7. Tabular Hem crystals oriented nearly perpendicular to the foliation S_1 , in region of microfold closure related to D2 deformation. Incident light with polarizers partially crossed.

In some localities axial plane foliation (S_2) is filled by Qtz vein mineralized in gold. Besides Qtz and gold, Gt can also be found in this type of Qtz vein.

3.4 Weathering minerals

The weathering processes were very intense over the entire Iron Quadrangle. Even in the mined areas where hundreds of meters of iron ores have been extracted it is still possible to find horizons in the iron formations showing extensive evidence for weathering process. In the oxidation zones, the original mineralogy, Mgt and Hem, reacted with meteoric oxygenated aqueous fluids and produced massive aggregates of Goethite (Fig. 7). Goethite is also present inside large pores of secondary origin. In this case, goethite may be present as columnar to prismatic crystals spatially arranged perpendicular to the void walls. In rich manganese horizons, Mn-carrying minerals are found associated with goethite filling secondary pores.

4 CONCLUSIONS

The systematic studies of the iron formation rocks, sampled all over the Iron Quadrangle region, allow us to establish a relationship between the geological processes and the mineral growth. The oldest registered mineral growth corresponds to massive and granular Mgt and Hem aggregates that are isotropic with respect to crystallographic and shape. The most pervasive and intense deformation and metamorphic processes, named D1, promoted the transformation the Mgt aggregates and the crystallization of new tabular Hem crystals. A pervasive recrystallization of original Hem aggregates produced aggregates of tabular Hem grains. The subsequent deformation and metamorphic processes (D2) were less severe and

their roles on mineral growth were manifested just locally. Weathering processes were severe in several parts of the Iron Quadrangle. They promoted a profound modification of the mineralogy and texture, generated by the previous processes, which might affect in different ways the mineral processing of the iron ores.

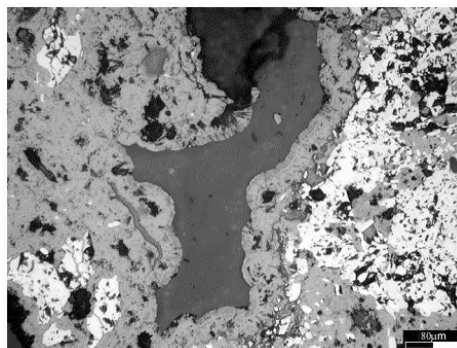


Figure 8. Optical micrograph (incident/plane polarize light) showing magnetite grains (intermediate grey level) and aggregate of hematite (light grey) in a matrix of massive aggregate of goethite (dark grey). In the central part of the micrograph large void are filled with epoxy (dark grey to black).

5 REFERENCES

- Alkmim F. F. & Marshak S. 1998. Transamazonian Orogeny in Southern São Francisco Craton Region, Minas Gerais, Brasil: Evidence for Paleoproterozoic Collision and Collapse in the Quadrilátero Ferrífero. *Precambrian Research*, 90: 29-58.
- Babinski M.; Chemale, F. Jr. & Schumus, W. R. 1995. The Pb/Pb age of the Minas Supergroup carbonate rocks, Quadrilátero Ferrífero, Brazil. *Prec. Res.*, 72:235-245.
- Dorr J.V.N.II. 1969. Physiographic, stratigraphic and structural development of the Quadrilátero Ferrífero, Minas Gerais, Brazil. USGS/DNPM. Professional Paper 641-A. 110p.
- Hoefs, J., Muller, G., Schuster, A.K., 1982. Polymetamorphic Relations in Iron Ores from Iron Quadrangle Brazil: The Correlation of Oxygen Isotope Variations with Deformation History. *Contributions to Mineralogy and Petrology*, 79, 241-251.
- Lagoeiro L. E. 1998. Transformation of magnetite to hematite and its influence on the dissolution of iron oxide minerals. *Journal of Metamorphic Geology* 16:415-423.
- Pires, F.R.M., 1995. Textural and mineralogical variations during metamorphism of the Proterozoic Itabira Iron Formation in the Quadrilátero Ferrífero, Minas Gerais, Brazil. *Anais da Academia Brasileira de Ciência* 67 1, pp. 77-105.
- Rosière, C.A.; Siemes, H.; Quade, H.; Brokmeier H-G, Jansen E. M. 2001. Microstructure, textures and deformation mechanisms in hematite. *Jour. Struct. Geol.* 23(9):1429-1440.

Types of Goethite from Quadrilatero Ferrifero's Iron Ores and their Implications in the Sintering Process

M.S.Magalhaes & P.R.G.Brandao

Mining Engineering Department, Federal University of Minas Gerais (UFMG), Belo Horizonte – MG, Brazil.

R.P.Tavares

Metallurgical and Materials Engineering Department, Federal University of Minas Gerais (UFMG), Belo Horizonte – MG, Brazil.

ABSTRACT: Quadrilatero Ferrifero's iron ores used in the sintering process correspond to mixes of hematitic and goethitic ore typologies. The ores have particle size mainly distributed in the range from 6.35mm to 0.105mm. Goethite (Gt) comprises a low amount in these ore blends; however, it can be relevant in the reactivity during sintering. This research involved techniques such as reflected-light microscopy and scanning electron microscopy – backscattered electron images (SEM-BSE) for microstructure evaluation, and energy dispersive X-Ray spectrometry (SEM-EDS) for microanalytical study. Many morphologies were described considering the three ore blends: colloform type; massive, and thin lamellae (fibrous); Gt with earthy aspect is also present. They have variable degrees of microporosity. Some microanalytical differences among these morphologies were observed: Si-Al-P-bearing Gt, which corresponds to the common type; Al₂O₃-rich Gt and MnO-bearing Gt. These last two types have also Si, Al, and P in their compositions. Although goethite is completely consumed during the sintering processes, its control in the sintering burden is very important due to the impurities mentioned in its composition, which can affect in different ways the composition of the sinter phases. Therefore, the identification of the types of goethite and their amounts in the iron ore mixes, as well as their chemical constitution, can avoid the increase of deleterious elements during the sintering stage.

1 INTRODUCTION

Quadrilatero Ferrifero's iron ores used in the sintering process correspond to mixes of hematitic and goethitic ore typologies. These mixes have particle size mainly distributed in the range from 6.35mm to 0.105mm (sinter feed). Goethite (Gt) is present in relatively low amounts in these ore blends; even then, it is relevant to the reactivity behavior during sintering (Goldring & Fray 1989, Caporali et al. 2002) and also common impurities in its composition are incorporated in some phases of the sinters, which correspond to agglomerates produced by the heating of iron ore mixes with fluxes and coke, which promotes the combustion. Thus, the evaluation of the morphological types and the study of the chemical composition of this mineral distributed in the iron ore blends used in the sintering burden are relevant to control the quality of sinters, although Gt is completely consumed during this agglomeration process.

2 ANALYTICAL PROCEDURES

Polished sections of three different ore mixes (sinter feed) were analyzed by means of microscopy techniques such as optical (reflected light, RLOM)

and scanning electron microscopy (backscattered electron images, SEM-BSE) for evaluation of the goethite morphologies. Also, microanalyses were carried out by an energy dispersive X-ray spectrometer coupled to the SEM (EDS). Approximately 40 polished sections, corresponding to the three mixes of iron ores (SFA, SFB and SFC), were observed by reflected-light microscopy. Each blend is related to three different mines from Quadrilatero Ferrifero. The SEM observations including more than one hundred microanalyses were processed on 13 sections. Both coarser grain size fractions of the samples as finer ones were used to make polished sections, which were carbon coated to SEM evaluations.

3 RESULTS

3.1 Types of Goethite According to the Morphological Aspects

Many morphologies of goethite with variable microporosity were identified considering the three ore blends:

- colloform (fig. 1a);
- massive (fig. 1b);
- thin lamellae (fibrous, fig. 1b);
- Gt with earthy aspect (fig. 1c).

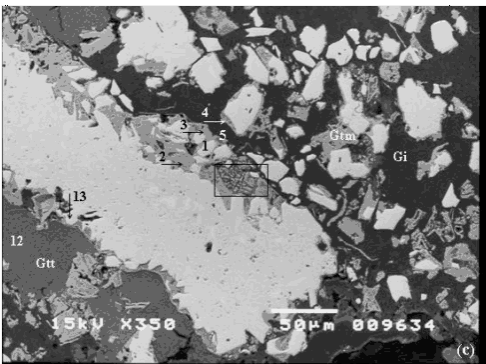
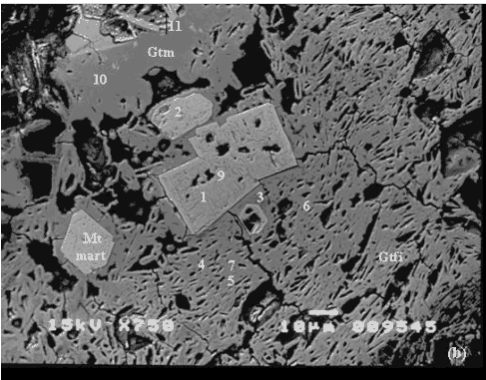
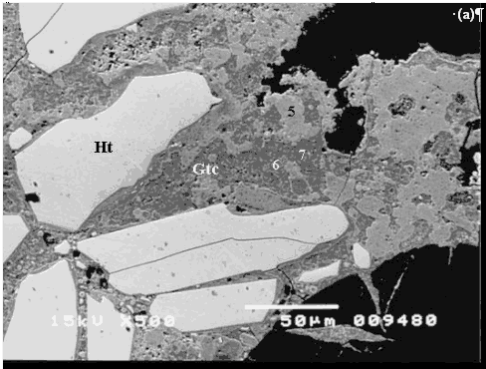


Figure 1: Types of goethite associated to iron ore mixes (sinter feed) from Quadrilatero Ferrifero. (a) A sinter feed (SFA) – microporous colloform goethite (Gtc) showing different compositions, hematite (Ht) crystals are distributed on this goethitic mass. (b) SFC – massive Gt (Gtm) and fibrous Gt (Gtfr) presenting completely martitized magnetite distributed within it and with intragranular Gt (Gtintra). (c) SFB – fragments of Ht and Ht with magnetite relicts (actually remnant microstructure of strongly martitized magnetite, which is not clear in this SEM photo) are distributed in a goethitic mass showing earthy Gt (Gt) and microporous massive Gt (Gtm); gibbsite (Gi) is also associated. SEM-BSE images with EDS microanalyses of areas and points marked (Table 1).

These terms were used by Cornell & Schwertmann (1996) to describe goethitic material textures (fabric), considering that the goethite basic morphology is essentially acicular.

This mineral can occur filling interstitial cavities of hematite (Ht) crystals or constituting individualized portions with Ht fragments and/or aggregates of Ht crystals associated (Figs. 1a, 1c). Portions surrounding large Ht aggregates are also observed. Martitized magnetite can be also distributed in this goethitic material (Fig. 1b).

3.2 Types of Goethite According to the Chemical Composition

From the microanalysis, some compositional differences were observed in the goethitic material (Table 1):

- Si-Al-P-bearing Gt, which corresponds to the common type; Si can also occur in minor values;
- Al₂O₃-rich Gt, which can have Si and P as other impurity elements;
- MnO-bearing Gt (MnO > 1wt%); Si, Al and P are also present as impurities.

The MnO-bearing goethite was described in the studied samples of the SFA and SFC. The general characterization (mineralogy and global chemistry) of these sinter feed samples (SFA and SFC) and the SFB was presented by Magalhães et al. (2004).

4 DISCUSSION AND CONCLUSIONS

Although goethite is completely consumed during the sintering processes, its control in the sintering burden is very important due to the impurities present in its composition, which can affect in different ways the elements distribution of the sinter phases. For example, coalesced Ht of the studied sinters, which were produced with these ore blends, is commonly Al-bearing. Other example of the Gt composition influence in the sinter phases is showed by the P-bearing silicates in these agglomerates (for more details, see Magalhães & Brandão 2003).

The compositional aspects of sinters, which are inherited from the ore minerals, are partially related to the reactivity behavior, which can be completely distinct if the hematite/goethite ratio varies largely, as some researchers have demonstrated (Goldring & Fray 1989, Caporali et al. 2002). Then, the variation of this ratio can indirectly affect the performance of sinters like mechanical strength and reduction capacity (reducibility).

Even though the goethite content is not so high in the sinter feed samples studied, the understanding of its behavior during the sintering is relevant. The proportion of the three blends seems to be very well controlled due to the good metallurgical and physical results of the sinters produced from this ore burden (Magalhães 2003). The proportion of the

goethitic material in the ore mixes seems also to be adequate due to the adjusted values of elements like Al, P and Mn in the sinter feed samples (Magalhães et al. 2004). The knowledge of the goethite types and their amounts in the iron ore mixes, as well as

their chemical constitution with their respective elements distribution, can avoid the increase or decline of some elements in the sintering burden, contributing indirectly to the production of sinters with better metallurgical, physical and chemical performances.

Table 1: Microanalyses of goethites and some associated phases from Quadrilatero Ferrifero's iron ores (sinter feed samples).

1 SEM-EDS	2 Phases	Fe ₂ O ₃	SiO ₂	Al ₂ O ₃	3 MnO	P ₂ O ₅
Figure 1a* (SFA)						
A5	Gt(cl)	95.72	0.32	1.86	0.30	1.81
P6	Gt(esc)	93.64	0.17	3.75	0.00	2.44
P7	Gt(esc)	93.88	0.12	3.67	0.17	2.16
Figure 1b* (SFC)						
A1	Mt mart	98.44	1.04	0.22	0.15	0.15
A2	Mt mart	98.85	1.02	0.09	0.00	0.04
P3	Gt	94.72	2.92	1.70	0.12	0.55
P4	Gt _{fi}	93.59	3.46	1.84	0.46	0.66
P5	Gt _{fi}	94.84	3.28	0.98	0.28	0.62
P6	Gt _{fi}	94.76	2.73	1.46	0.37	0.67
A7	Gt _{fi}	94.35	3.02	1.44	0.46	0.73
P8	Gt _{intra} **	96.37	1.97	1.03	0.18	0.45
P9	Mt mart	98.46	1.44	0.00	0.03	0.07
A10	Gt _m	93.89	3.55	0.92	0.53	1.11
P11	Ht	99.16	0.38	0.17	0.00	0.30
Figure 1c* (SFB)						
A1	Ht	99.37	0.27	0.24	0.04	0.08
A2	Gt _m	94.29	1.46	4.09	0.00	0.16
A3	Gt _m	91.76	1.33	6.01	0.25	0.65
A4	Gt _m	91.20	1.04	7.19	0.00	0.57
A5	Gi	11.71	0.72	87.57	0.00	0.00
P6* ³	Gt	90.36	3.94	4.49	0.00	0.01
P7* ³	Gt	90.40	2.42	4.35	0.62	1.19
P8* ³	Gt	91.47	3.72	3.87	0.14	0.26
P9* ⁴	Gt	83.50	2.68	12.46	0.59	0.77
P10* ⁴	Gt	90.09	1.02	7.96	0.23	0.70
P11* ⁴	Gt	92.98	1.26	4.61	0.00	1.16
A12	Gt _t	91.58	1.52	5.92	0.00	0.97
A13	Ht	99.34	0.38	0.24	0.00	0.04

Results in wt.%. Whole Fe calculated as Fe₂O₃. Abbreviations are explained in the Figure 1; exceptions: cl light and esc dark.

* Microanalysis areas (A) and points (P) are marked on the photomicrographs of the Figure 1.

** This microanalysis is not marked, but it corresponds to goethite distributed intragranularly to martitized magnetite.

³ 1.20; 1.02 e 0.54 wt% CaO, respectively. ³ and ⁴ phases distributed on the area marked in black.

Observe that the results lower than 0.5wt% do not have microanalytical meaning.

5 REFERENCES

Caporali, L.; Oliveira, D.; Ottoni, R. 2002. The concept of iron ore sintering reactivity. *Ironmaking and Steelmaking* v. 29 n. 9: 29-36.

Cornell, R. M.; Schwertmann, U. 1996. *The iron oxides*. VCH: Weinheim.

Goldring, D. C.; Fray, T. A. T. 1989. Characterisation of iron ores for production of high quality sinter. *Ironmaking and Steelmaking* v. 16 n. 2: 83-89.

Magalhães, M. S. 2003. *Minérios de ferro e sínteres industriais: mineralogia, microestruturas, química mineral, comportamento magnético e controle de qualidade*. Belo Horizonte: Escola de Engenharia da UFMG (Ph.D. Thesis in Metallurgical and Mining Engineering).

Magalhães, M. S.; Brandão, P. R. G. 2003. Microstructures of industrial sinters from Quadrilatero Ferrifero's iron ores – Minas Gerais State – Brazil. *Minerals Engineering* v. 16 n. 11 (Applied Mineralogy Issue): 1251-1256.

Magalhães, M. S.; Brandão, P. R. G.; Tavares, R. P. 2004. Characterization of Quadrilatero Ferrifero's iron ores used in sintering processes. In: *International Meeting on Ironmaking, 2, and International Symposium on Iron Ore, 1*. Vitória – ES, Brazil. Proceedings... São Paulo: ABM, 2004 (submitted).

Sulpharsenides and Arsenides in Massive Sulphide Deposits Connected with Ultramafites, South Urals

I.Yu.Melekestseva, V.V.Zaykov, E.V.Belogub, S.G.Tsalina

Laboratory of Applied Mineralogy and Minerageny, Institute of Mineralogy of RAS, Miass, Russia

ABSTRACT: The South portion of the Main Urals Fault zone contain several Co-bearing massive sulphide deposits connected with ultramafites. Ishkinino, Ivanovka, and Dergamysh deposits are the most known and extensively studied. Sulpharsenides and arsenides of cobalt, nickel and iron are widespread all over the ores of these deposits. Studied minerals are the unique feature of these ores such as increased Co, Ni, and Cr contents in ores. Sulpharsenides are represented by cobaltite, arsenopyrite, gersdorffite, alloclastite, and glaucodot; arsenides – by nickeline (monoarsenides), safflorite, löllingite, rammelsbergite, and krutovite (diarsenides). As-bearing mineralization is connected with precious metal (native gold) and bismuth-tellurium (native bismuth and rucklidgeite) mineralization. Ores of deposits are divided on three groups by saturation of sulpharsenides and arsenides and their geochemistry. Forming of sulpharsenides and arsenides was caused by collision processes at the Urals.

1 INTRODUCTION

The Urals is an outstanding place in the world of its concentration of the VMS deposits. Four types of VMS deposits have been determined: copper-zinc massive sulphide (Urals type), gold-bearing massive sulphide polymetallic (Kuroko, or Baymak type), copper massive sulphide (Cyprus type), and Co-bearing copper massive sulphide in ultramafites (Prokin & Buslaev 1999, Zaykov et al. 2001). The last type recently appeared and is one of the most interesting and unstudied in comparison with others. Deposits of this type have some similar peculiarities with massive sulphide ores on ultramafites of the Middle-Atlantic ridge.

Ultramafic-mafic and mafic complexes, which Co-bearing massive sulphide ores are connected with, are partially associated with ophiolite complexes (Fig. 1) of the Early and Middle Paleozoic age. They fix the relics of structures of the Urals paleo-ocean: rift of marginal oceans, back-arc and fore-arc basins, and island arcs. These structures were undergone to collision processes of different intensity and age that brought to the formation of suture zones. Tectonic plates composed of mafic, ultramafic and rhyolite-basalt complexes are combined in these structures.

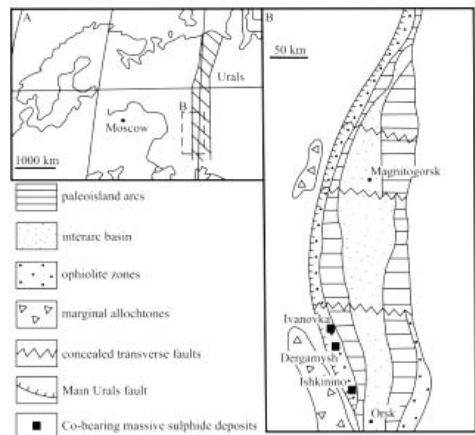


Figure 1. Location of Co-bearing massive sulphide connected with ultramafites on the South Urals geodynamic sketch (composed by V.V.Zaykov).

2 GEOLOGICAL SETTING AND ORE MINERAL COMPOSITION OF CO-BEARING MASSIVE SULPHIDE DEPOSITS

Studied deposits are concentrated in the suture zone – the Main Urals fault. Fragments of island-arc slope

of subduction zone with accretion wedge from the plates of oceanic complexes were preserved here. Boudinaged ore bodies usually lay at the contacts of ultrabasite, basalt and olistostrome tectonic plates.

2.1 *Ishkinino*

Ishkinino deposit is situated 20 km west of the town of Gay (Orenburg district). It is hosted by serpentinites, basalts, and siliceous olistostrome sediments. Geological structure of deposit, which they are formed, is an antiform of three tectonic plates (Zaykov et al. 1999). Ores are localized on the wings of serpentinite plates and accompanied by talc-carbonate aposerpentinite metasomatites.

Ores have been divided into three mineralogical types: pyrite-pyrrhotite, chalcopyrite-pyrite-pyrrhotite, and cobaltite-arsenopyrite-chalcopyrite-pyrite-pyrrhotite (sulpharsenide-sulphide) (Melekestseva & Zaykov 2003). The dominant minerals are pyrrhotite, pyrite, and chalcopyrite. Accessory minerals are arsenopyrite, cobaltite, gersdorffite, nickeline, magnetite, chromite, and pentlandite, four minerals of linnaeite group, safflorite, löllingite, rammelsbergite, and krutovite and rare native gold, sphalerite and rucklidgeite.

Co and Ni contents in ores vary from 0.01 up to 0.31 wt.% for Co and from 0.13 up to 0.49 wt.% for Ni. In sulpharsenide-sulphide ore type Co content was up to 10 wt.% by the geological-prospecting data.

2.2 *Ivanovka*

Ivanovka deposit is situated 20 km west of the town of Buribay, Bashkortostan. It is hosted by variously metasomatized ultramafites, basalts, and gabbro (Zakharov & Zakharova 1975). Geological structure of the deposit is complicated by pre- and post-mineralization fault system.

Ores have been divided into three mineralogical types: pyrite-chalcopyrite-pyrrhotite, chalcopyrite-pyrrhotite, and pyrrhotite-chalcopyrite-pyrite. The main minerals are pyrrhotite, chalcopyrite, and pyrite. Accessory minerals are magnetite, chromite, ilmenite, sphalerite, marcasite, pentlandite, allosclite, and glaucodot, minerals of linnaeite group, and rare nickeline, valleriite, millerite, bornite, native gold, bismuth, and pilsenite (Zakharov & Zakharova 1975, Tesalina et al. 2001).

Co and Ni contents in ores changes from 0.02 up to 0.11 wt.% for Co and from 0.06 up to 0.16 wt.% for Ni.

2.3 *Dergamysh*

Dergamysh deposit is located 25 km South-West of the town of Buribay, Bashkortostan. It is hosted by ultramafites, volcano-sedimentary rocks, and gabbro

(Buchkovsky 1970, Zaykov et al. 2001). Geological structure of deposit is a sinform of tectonic plates. Ore body lies between ultramafite ones.

Ores have been divided into three mineralogical types: pyrite-pyrrhotite, chalcopyrite-pyrite-marcasite, and pyrite-marcasite. The dominant minerals are marcasite, pyrite, and chalcopyrite. Accessory minerals are pyrrhotite, sphalerite, magnetite, chromite, ilmenite, minerals of linnaeite group, and rare native gold, valleriite, cobaltite, arsenopyrite, nickeline (Ismagilov 1962).

Co and Ni grades vary from 0.01 up to 0.14 wt.% for Co and from 0.003 up to 0.08 wt.% for Ni.

3 PECULIARITIES OF SULPHARSENIDE AND ARSENIDE COMPOSITION

Ten sulpharsenides and arsenides have been determined in ores of Co-bearing massive sulphide deposits of the South Urals. Their distribution between the deposits is shown in table 1.

Table 1. Distribution of sulpharsenides and arsenides of Co, Ni, and Fe in studied deposits

Minerals	Ishkinino	Ivanovka	Dergamysh
Sulpharsenides			
Cobaltite	++		+
Arsenopyrite	++		+
Gersdorffite	++		
Alloclasite		++	
Glaukodot		+	
Arsenides			
Nickeline	++	+	+
Löllingite	+		
Safflorite	+		
Rammelsbergite	+		
Krutovite	+		

Notes: ++ – minerals to be often found, + – minerals to be seldom found.

Microprobe analyses of sulpharsenides and arsenides showed peculiarities of their chemical composition (Figs. 2, 3) and microzonality. They are characterized by increased contents of some elements in comparison with analogues from hydrothermal cobalt and cobalt-nickel deposits, cobalt bearing skarns, Co-Ni-Ag-Bi-U deposits, and sulphide copper-nickel deposits.

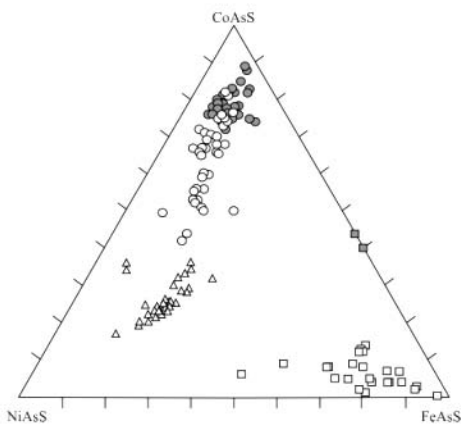


Figure 2. Chemical composition of sulpharsenides of studied deposits: Ishkinino cobaltite (white circles), gersdorffite (triangles) and arsenopyrite (white blocks); Ivanovka alloclasite (grey circles), and glaucodot (grey blocks) in system CoAsS-NiAsS-FeAsS.

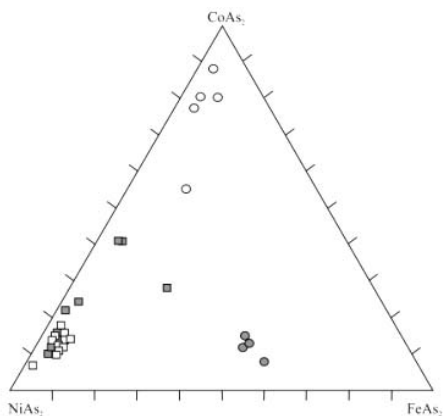


Figure 3. Chemical composition of Ishkinino diarsenides: löllingite (grey circles), safflorite (white circles), rammelsbergite (grey blocks), and krutovite (white blocks) in system CoAs₂-NiAs₂-FeAs₂.

3.1 Ishkinino

Cobaltite, $(\text{Co}_{0.84-0.43}\text{Ni}_{0.12-0.42}\text{Fe}_{0.08-0.17})_{1.04-1.02}\text{As}_{0.98-1.03}\text{S}_{1.02-0.97}$, occurs as euhedral cubic/octahedral and skeletal crystals (from 0.1 up to 2 mm), their intergrowths and accumulations in sulphide matrix and calcite veins (Melekestseva et al. 2003). It is very much enriched in Co – up to 14.69 wt.%. All cobaltite crystals have zonality: increased Co contents peculiar for the centre of crystals, increased Ni contents – for the periphery (“direct” zonality). There are “inverse” and alternate zonalities too.

Arsenopyrite, $(\text{Fe}_{0.89-0.49}\text{Co}_{0.10-0.07}\text{Ni}_{0.05-0.45})_{1.04-1.01}\text{As}_{1.02-1.39}\text{S}_{0.98-0.61}$, occurs as small (~ 0.04 mm) euhedral rhombic, often skeletal, crystals, their intergrowths in sulphide matrix and accumulations of large (up to several mm) brecciated grains. It is also enriched in Ni – up to 14.66 wt.% and has complicate zonality.

Gersdorffite, $(\text{Ni}_{0.30-0.72}\text{Co}_{0.24-0.20}\text{Fe}_{0.22-0.16})_{0.97-1.08}\text{As}_{1.10-1.15}\text{S}_{0.90-0.85}$, occurs as cubic/octahedral crystals (up to 0.5–1 mm) and crystal aggregates in sulphide matrix associating with nickeline. It has the increased Co (up to 12.68 wt. %) and Fe (up to 18.53 wt. %) contents. Gersdorffite has zonality too: increased Co contents are in the centre of crystals, increased Fe contents – in the periphery.

Nickeline, $(\text{Ni}_{0.99-1.01}\text{Co}_{0.01})_{1.00-1.01}\text{As}_{1.00}$, forms tabular grains in cobaltite and xenomorphic aggregates (up to several mm) with gersdorffite. It is free from admixtures and zonality.

Till recently, only nickeline and skutterudite were known in massive sulphide ores of the Urals. Studying Ishkinino ores, safflorite, löllingite, rammelsbergite, and krutovite were firstly found in the Urals massive sulphide deposits. They occur in cobaltite crystals as lamellar and xenomorphic grains (from 2 up to 50 μm) replacing nickeline and gersdorffite. There are seldom found large xenomorphic aggregates (up to 100 μm) of closely accrete diarsenides, nickeline, and gersdorffite grains.

Löllingite, $(\text{Fe}_{0.50-0.56}\text{Ni}_{0.40-0.35}\text{Co}_{0.13-0.06})_{1.03}(\text{As}_{1.96}\text{S}_{0.04})_{2.00}$, is nickeloan (Ni – up to 11 wt.%). Safflorite, $(\text{Co}_{0.83-0.96}\text{Ni}_{0.19-0.08}\text{Fe}_{0.06-0.04})_{1.08}(\text{As}_{2.00-1.98}\text{S}_{0.00-0.73})_{2.00}$, has increased Ni (up to 10 wt.%) and S (up to 13 wt.%) contents. Moreover, nickel always prevails over iron although theoretical formula of safflorite is $(\text{Co,Fe})\text{As}_2$. Rammelsbergite, $(\text{Ni}_{0.49-0.88}\text{Co}_{0.29-0.10}\text{Fe}_{0.23-0.04})_{1.01-1.02}(\text{As}_{1.96-1.92}\text{S}_{0.04-0.08})_{2.00}$, contains slightly increased S (up to 1.3 wt.%), Fe (up to 1.4 wt.%) contents and high Co grades (up to 12 wt. %). Krutovite, $(\text{Ni}_{0.76-0.91}\text{Co}_{0.17-0.08}\text{Fe}_{0.06-0.02})_{0.99-1.01}(\text{As}_{1.54-1.74}\text{S}_{0.46-0.26})_{2.00}$, has slightly increased Fe (up to 2.3 wt. %) and Co (up to 5 wt. %) contents and high S grades (up to 8 wt.%). In addition, Bi contents up to 1 wt.% have been fixed in rammelsbergite and krutovite.

All sulpharsenides and nickeline associate with native gold occurred in them both the small (up to 8 μm) inclusions and crystals (up to 70 μm) in minerals studied. Diarsenides associate with rucklidgeite occurred in them as very small (up to 6 μm in wide) xenomorphic grains.

3.2 Ivanovka

Alloclasite, $(\text{Co}_{0.72-0.91}\text{Ni}_{0.16-0.14}\text{Fe}_{0.13-0.07})_{1.01-1.12}\text{As}_{0.98-0.99}\text{S}_{1.02-1.01}$, occurs as rhombic/prismatic euhedral or skeletal crystals, their intergrowths and accumulations in sulphide matrix. As distinct from

cobaltite it has clear anisotropy and small microhardness in comparison with other Co-sulpharsenides (VHN less than 840 kg/cm²). It contains Ni up to 6.58 wt.% and Fe up to 6.35 wt.%. It's established that alloclaste has zonality: increased Co and decreased Ni and Fe contents are in the center of crystals, in the periphery – vice versa.

Glaucodot, (Fe_{0.68}Co_{0.42-0.53})_{1.10-1.21}As_{1.14-0.97}S_{0.86-0.85}, forms intergrowths of rhombic crystals (up to 100 μm) in pyrrhotite and serpentinite, mostly in disseminated ores. Native gold occurs in it as small (up to 10 μm) xenomorphic inclusions and elongated (up to 50 μm) grains. Native bismuth is observed as small (no more than 10 μm) xenomorphic grains together with gold. Glaucodot contains Co from 14 up to 18 wt.%, free from Ni and is non-stoichiometric very much.

Nickeline is seldom observed in ores as small grains and haven't chemically studied yet.

3.3 Dergamysh

Cobaltite, arsenopyrite and nickeline were only noticed in reports of geological-prospecting organisations as very seldom impregnation in sulphide matrix. We didn't observed them. The basic concentrator of Co is pyrite enriched in it – up to 7.27 wt.%.

4 CONCLUSIONS

Realised researches have showed the distinctive peculiarities of As-bearing mineralization of massive sulphide deposits connected with ultramafites. We can divide studied minerals (and deposits respectively) into three groups: nickeloan, cobaltian, and "normal".

Ishkinino ores have the widest spectrum of As-bearing minerals, nickeloan varieties predominant over cobaltian and cobaltian minerals are very much enriched in Ni. Ivanovka ores have mostly cobaltian arsenic minerals – alloclaste and glaucodot. They don't show high increasing of Ni. As-bearing mineralization in ores of Dergamysh deposit is seldom occurred. Combination of geological and mineralogical features let us say that Dergamysh As-bearing mineralization should be free from admixtures of Ni. By ore and mineral chemistry Dergamysh deposit can be compared with the Lentee massive sulphide deposit (Cyprus type) located at Dombrovsky paleoarc basin. Ores of the Letnee deposit has about 0.11 wt.% of Co (in average) which concentrated mostly in pyrite enriched in it (Massive sulphide 1985).

It's significant that precious metal and bismuth mineralization is always connected with arsenic

minerals. It tells us about their genetic kindred. Enrichment of massive sulphide ores connected with ultramafic by Ni, Co, and Au in industrial grades was caused by collision processes.

5 ACKNOWLEDGEMENTS

Authors thank E.I.Churin (IMin, Miass), N.S.Rudashevsky & Yu.L.Kretser (PC+, Saint-Petersburg), K.Becker (TU-BAF, Freiberg) and J.Spratt (NHM, London) for carrying-out of microprobe analyses. We also acknowledge the financial support of Russian Fund for Basic Researches (project 04-05-96014-p2004ypa1_a).

6 REFERENCES

- Buchkovsky, E.S. 1970. Sulphide mineralization connected with ultramafite intrusions of the western wing of Magnitogorsky megasinklinorium on the South Urals. *Voprosy geologii Vostochnoy okrainy Russkoy platformy i Yuzhnogo Urala*. 10: 114–134 (in Russian).
- Ismaglyov, M.I. 1962. Some features of mineralogy and genesis of the Dergamysh copper-cobalt deposit. *Geologo-mineralogicheskie osobennosti mednorudnykh mestorozhdeniy Yuzhnogo Urala*. 74–97 (in Russian).
- Massive sulphide deposits of the Urals. Geological conditions of location. V.I.Smirnov (ed). 1985. 288 (in Russian).
- Melekestseva, I.Yu. & Zaykov, V.V. Ores of the Ishkininskoe cobalt-copper massive sulphide deposit (the South Urals). 2003. Miass: IMin UB RAS. 122 (in Russian).
- Melekestseva, I.Yu., Zaykov, V.V. & Tesalina, S.G. Sulpharsenides and arsenides of Co, Fe and Ni in ores of the Ishkininskoe cobalt-copper massive sulphide deposit (the South Urals). 2003. *Zapiski VMO (Proceeding of Russian Mineralogical Society)*. 5: 77–77.
- Prokin, V.A. & Buslayev, F.P. 1999. Massive copper-zinc sulphide deposits in the Urals. *Ore Geology Review*. 14: 1–69.
- Tessalina, S.G., Zaykov, V.V., Orgeval, J.-J., Augé, T. & Omenetto, P. 2001. Mafic-ultramafic hosted massive sulphide deposits in Southern Urals (Russia). In: Piastzynski et al. (eds.) *Mineral Deposits at the Beginning of the 21st Century*. Swets & Zeitlinger Publishers Lisse. 353–356.
- Zakharov, A. A. & Zakharova, A.A. 1975. Dependence of ore composition of the Ivanovskoy sulphide deposit on the South Urals from their lithological restriction. *Geologiya i usloviya obrazovaniya mestorozhdeniy medi na Yuzhnom Urale*. 105–110 (in Russian).
- Zaykov, V.V., Maslennikov, V.V., Zaykova, E.V. & Herrington R. 2001. *Ore-formation and ore-facies analysis of massive sulphide deposits of the Urals paleocean*. Miass. 314 (in Russian).
- Zaykov, V.V., Wipfler, E. L., Becker, K. & Buschman, B. Pyrrhotite and gold-arsenopyrite ores of the Ishkininskoe deposit (in the Main Urals fault). 1999. *Metallogenia drevnikh i sovremennykh okeanov-99. Rudonosnost' gidrotermalnykh sistem*. 92–95 (in Russian).

Trace Element Characterization of Gold and Platinum-group Element Deposits and Products in South Africa

R.K.W.Merkle

Applied Mineralogy Group, Department of Geology, University of Pretoria, Pretoria, South Africa

R.D.Dixon

Forensic Science Laboratory, Pretoria, South Africa

A.Kijko

Council for Geosciences, Pretoria, South Africa

ABSTRACT: Trace element fingerprinting of gold and platinum-containing materials is aimed at the unique characterization of materials from ores and precious metal minerals, materials at different stages in the beneficiation and refining process, and commercially available products. Using data obtained from a range of analytical techniques, including PIXE, XRF and mass spectroscopy, the specially designed IPSOLUTE statistical software allocates individual analyses to material groups and performs a probabilistic comparison with other analyses in the database. In geology, understanding the compositional fingerprints should permit the identification of genetic processes, because differences or changes in the ore forming processes should be reflected in the trace element pattern of ore minerals (or associated minerals which are introduced into the beneficiation process). Such fingerprints of gold and platinum-group minerals could therefore be used to understand the sources of mineralization. In South Africa, identification of the source of precious metal materials recovered during police operations is of great importance, with the value of the gold stolen annually estimated between R1.7 to R3.5 billion annually (*ca.* US\$240 to 500 million). Both gold and platinum-group metals have unique problems associated with source identification. In either commodity, anything from ore to final metal products is stolen and the challenge is to use trace element fingerprinting to identify the source despite different beneficiation procedures by companies and illegal syndicates.

1 INTRODUCTION

1.1 *The aim of fingerprinting*

The South African economy is based on mining, especially for precious metals. Theft of precious metals is therefore also a significant factor. In order to find the deposits, and to trace the stolen products, trace element fingerprinting is equally important for Geosciences and Forensic Science. Trace element fingerprinting of gold and platinum-containing materials is a technique aimed at the determination and quantification of minor and trace components, which allows the unique characterization of materials from ores and precious metal minerals to flotation concentrates, smelter products, materials at different steps in the refining process, and finally the commercially available products. The specially designed IPSOLUTE statistical software allows allocation of individual analyses to material groups and performs a comparison and allocation of probabilities for the similarity to other data in the database.

1.2 *Geological applications*

In geology, understanding the compositional fingerprints should permit the identification of

genetic processes, based on the assumption that differences or changes in the ore forming processes (e.g. intrinsic conditions of hydrothermal fluids or magmas) will be reflected in the trace element pattern of ore minerals (or associated minerals which inevitably are also introduced into the beneficiation process). Trace element fingerprints of gold and platinum-group minerals in placer deposits could therefore be used to understand the sources of placer mineralization (Brown et al. 2003, Frimmel & Gartz 1997; Knight et al. 1999). In such a scenario, the trace element pattern of a mineral species will differ between genetic ore types, as will the pattern of different mineral species within a specific ore type. At present, the development of analytical protocols and the creation of databases for comparison are in their infancy. In South Africa, huge deposits of platinum-group elements and of gold are being mined and South Africa is therefore in the forefront of elemental fingerprinting.

1.3 *Forensic applications*

In Forensic Science, identifying the original source of precious metal materials recovered during police operations is very important, due to the extent of the problem (Gastrow 2001). Although crime statistics

are incomplete (it is estimated that only 1.4 to 2.8 % of all stolen gold is recovered), indications are that between 0.8 and 1.6 % of the world gold production gets stolen annually in South Africa. The value of the gold stolen in South Africa is difficult to quantify due to rapid fluctuations in precious metal prices and in the value of the Rand (= South African currency). However, estimates range from 1.7 billion Rand to 3.5 billion Rand annually (at 2 October 2003, this is equivalent to 240 to 500 million US\$).

Theft of platinum-group metals is even more difficult to estimate, but in recent years platinum-group metals to the value of ca 20-25 million Rand (2.9-3.5 million US\$) have been recovered by police and mine security annually. If the recovery rate is similar to that of stolen gold, then the amounts are also very large.

2 PROCESS CONSIDERATIONS

Both gold and platinum-group metals have unique problems associated with source identification. In either commodity, anything from ore to final metal products is stolen and the challenge is to use trace element fingerprinting to identify the source despite different beneficiation procedures by companies and illegal syndicates. The mineralogy of gold ores in South Africa is rather homogeneous and the recovery of the gold is rather easy (panning, amalgamation, cyanidation), compared to platinum, where smelting of the concentrate is required to increase the concentration of the PGE and to transform the large variety of platinum-group minerals into a more easily extractable form.

Due to the large costs involved in the forensic aspects of fingerprinting, the main emphasis has been to obtain tools to identify the source of stolen precious metals, with special emphasis on gold, while the characterization of fingerprints of PGE-containing materials has received a lower priority. It must be pointed out that this is inseparable from the evaluation of the geological questions of ore genesis and the characterization of genetic ore types, but goes beyond the geological needs because metallurgical products have to be considered as well.

2.1 *Depositional factors*

Identifying the mine of origin of materials is complicated by many factors. Different ore-bearing layers (which formed at different times in the Witwatersrand Basin and reflects changes in the source area of the sediments) or ore bodies (such as different vein systems in a mineralised zone in a greenstone belt) may be mined and blended at any stage of the beneficiation process, and differences exist in the beneficiation procedures, depending on the nature of the ore (e.g. native gold versus

refractory gold in arsenopyrite). For the same type of ore, commercial processes will also differ from illegal processes (e.g. amalgamation). It is therefore very challenging to arrive at characteristics that are common to all intermediate products derived from a specific ore body, and also reflect the characteristics introduced by the beneficiation process. It is also important that such fingerprints remain identifiable in the highly refined products. Hierarchical identification of the regional source of gold in South Africa can be achieved by considering elements very indicative of associated ore minerals (e.g. Ni and As being derived from associated sulpharsenides such as arsenopyrite (FeAs₂) or gersdorffite (NiAs₂) in the ores from the Barberton Greenstone Belt, or Te and Sb reflecting the Sb-rich nature of the ores in the Murchison Range).

2.2 *Metallurgical factors*

Concentrations of platinum-group elements in gold-containing products from the Witwatersrand depend on details in the metallurgical process. Small amounts (3-100 ppb estimated *in situ*) of PGE are concentrated in small (typically 100-150 micrometers in diameter) nuggets at the same stratigraphic levels as the gold. Most PGM are not affected by the cyanidation, but were concentrated in the past behind the liners of the mills. This liner concentrate is typically very rich in gold (up to 10s of %) and contains a substantial amount of PGM as well. If this liner concentrate is introduced directly into the smelting process, unusually high amounts of PGE can be found in the gold and may be used as time markers. A change in the liner material from metal to rubber prevents the formation of liner concentrate and therefore changes the usability of PGE contents for source identification in the future.

2.3 *Mineralogical factors*

Mineralogical characteristics of many products allow the identification of the type of material as well. X-ray diffraction and microscopic techniques are useful to identify gold ore and concentrate from the greenstone belts, but are much less diagnostic if the matrix is overwhelmingly dominated by quartz. Similarly, PGE-concentrate derived from the UG-2 chromite layer can easily be identified by the amount of chromite, while a distinction between concentrate from the Merensky Reef and the Platreef requires very careful evaluation.

During the processing of the ore during different stages of the beneficiation, some elements are reduced, while others are enriched (or relatively less reduced) together with the gold or PGE.

3 ANALYTICAL METHODS

3.1 XRF

Bulk chemical analyses (by XRF) or mineral analyses (by EPMA) may be needed to distinguish materials with similar mineralogical matrix or appearance. For example, different PGE-rich mattes (furnace matte or converter matte) from Merensky Reef or UG-2 ore can be easily allocated to the ores from which they were derived, based on their concentrations of Cu, Ni, or Rh. These characteristics remain even during the conversion process, where Fe and S are preferentially removed from the matte. The effects of lateral variations in these ore types (which are mined in many shafts along strike and processed in different concentrators and smelters) on the possibility to allocate products to a specific mine or shaft is still awaiting evaluation.

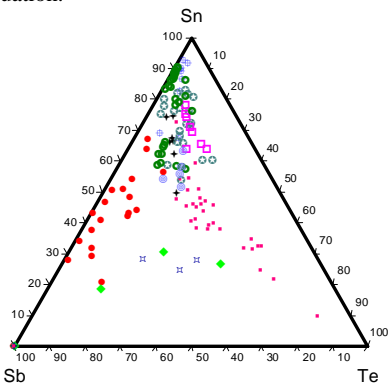


Figure 1. An example of the distinction between gold produced by different Witwatersrand gold mines using 3 elements only.

3.2 ICP-OES

At the Forensic Science Laboratory, all analyses of precious metal containing materials are carried out in triplicate to 1 % relative standard deviation (RSD) and controlled with certified reference materials. The triplicate analyses are to ensure that inhomogeneous materials are detected. Analytical protocols have been developed and are being followed to ensure this level of quality. Analytical procedures for comprehensive chemical analysis vary depending on the type of material identified in preliminary XRF analysis. Typically, the material is dissolved and ICP-OES is used for the determination of major components, and in metallic matrices, ICP-OES is also used to determine components to low ppm levels. If fire assay techniques are employed for pre-concentration, the procedure is carried out in duplicate. For selected trace elements in solution, quadrupole ICP-MS in sequential mode is employed to ppb levels.

3.3 LA-ICP-MS

Recently, laser-ablation ICP-MS has been tested for the determination of trace elements. It was observed that most materials are not homogeneous enough (e.g. small amounts of Ir-rich exsolutions at gold grain boundaries and sub-micron inclusions) to use laser-ablation ICP-MS in sequential mode. The probability that important compositional characteristics may be missed or misinterpreted is considered too high. To overcome the problem of small-scale sample heterogeneity, time-of-flight ICP-MS was introduced to the analytical procedures. Although still under development, it is obvious that with the simultaneous determination of all the isotopes of interest, even transient peaks are determined accurately. Especially for the determination of element or isotope ratios, time-of-flight minimises the adverse effects that fluctuations in the ablation rate have on the sequential determination in ICP-MS.

Obviously, the amount of material to be characterized has to be considered for the selection of techniques. For XRF analysis, typically, several grams of material are required, whereas about 250 milligrams of material (sufficient for accurate weighing) is the minimum for ICP-AES. Because of the small spot size of the laser ablation (with the present 266 nm Cetac LSX 200 Nd:YAG Laser) of 10 - 100 micrometer in diameter and the simultaneous determination of the elements of interest, only very small amounts of material are required. However, one of the fundamental drawbacks of laser ablation is the variable ablation rate as a function of matrix, which makes quantification of the results a difficult task. Presently two approaches are followed to evaluate how this problem could be alleviated: 1) the preparation of suites of matrix matched standards for the more common materials to be investigated, and 2) the use of high-precision analyses by non-destructive techniques (such as EPMA or PIXE) using a minor component as an internal standard.

4 STATISTICAL METHODS

4.1 Database creation

The development of a database for precious metal containing materials from southern Africa has started and is an ongoing process. A huge amount of material has to be characterized in order to increase confidence that the correct source of material can be identified. The identification itself is a hierarchical procedure, in which major elements or ubiquitous minor elements often suffice to identify the genetic type of mineralization. However, the problem becomes exponentially more complex if it is required to identify the source in a specific district.

Adjacent mines in the Witwatersrand or the Bushveld Complex may mine the same stratigraphic horizon, but even adjacent mines in the same deposit can be distinguished as sources, if analyses with very high precision and accuracy are available of a large range of elements and isotopes. This separation is facilitated partly due to lateral variations in the ore bodies and partly by differences in the beneficiation processes.

4.2 Statistical evaluation

To achieve identification of the source of precious metals and other materials, the IPSOLUTE software is continuously fine-tuned and optimised to the material in question. An important aspect is that the software can handle missing values, i.e., even data sets that were produced by different laboratories and incorporating different suites of elements, can be combined and utilized. Two different statistical techniques are applied and compared to ensure consistency. In a first step, the procedure assesses the similarity (or dissimilarity) between the sample to be identified and every object in the database. The procedure calculates the distance between objects (sample to be identified and sample in the database) and allocates a probability for correct allocation. The second procedure is based on principle component analysis and the comparison of unknown and reference data in n-dimensional space.

5 CONCLUSIONS

Obviously, allocation of gold (or other precious metals) to a source is only possible if the source is part of the reference database. With trace element data and multi-variate statistics it is possible to identify source areas of precious metal ores and products. It is essential to collate as much material and their analyses as possible to improve the ability to characterize ores and minerals from many examples of different genetic types, as well as technical products derived from such ores.

6 REFERENCES

- Brown, S.M., Johnson, C.A., Watling, R.J. & Premo, W.R. (2003). Constraints on the composition of ore fluids and implications for mineralizing events at the Cleo gold deposit, Eastern Goldfields Province, Western Australia. *Australian Journal of Earth Sciences* 50: 19-38.
- Frimmel, H.E. & Gartz, V.H. (1997). Witwatersrand gold particle chemistry matches model of metamorphosed, hydrothermally altered placer deposit. *Mineralium Deposita* 32: 523-530.
- Gastrow, P. (2001). Theft from South African mines and refineries. The illicit market for gold and platinum. ISS Monograph Series 54: 72pp.
- Knight, J.B., Mortensen, J.K. & Morison, S.R. (1999). Lode and placer gold composition in the Klondike District, Yukon Territory, Canada: implications for the nature and genesis of Klondike placer and lode gold deposits. *Economic Geology* 94: 649-6

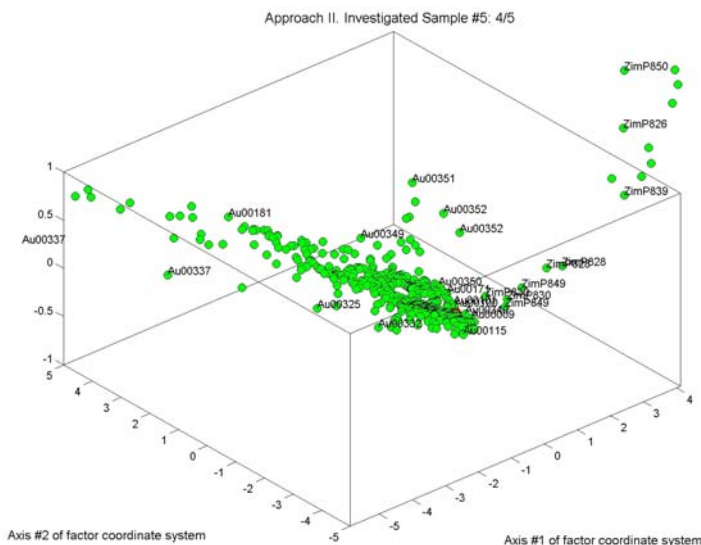


Figure 2. A comparison of gold produced by different Witwatersrand gold mines (Au) and greenstone gold from Zimbabwe (Zim). The combination of all analytical information and the use of multivariate statistics enables the determination the source with a high level of confidence.

Geochemical and Mineralogical Zoning Derived from the Weathering of the Alkaline Rocks in the Itatiaia Massif, Rio de Janeiro, Brazil

S.C.Miano

Brazilian Institute for Environment and Renewable Resources – IBAMA SCEN – Trecho 2, Ed. Sede do IBAMA - 1º Andar - DILIQ - Brasília-DF CEP 70.818-900 Brazil

F.R.M.Pires

UFRJ – Federal University of the Rio de Janeiro –Department of Geology, IGEO, Ilha do Fundão, Rio de Janeiro, RJ, 21949-900

ABSTRACT: The kaolinite and gibbsite deposits at the Itatiaia Alkaline Complex are distributed according to the presently proposed, well established, strongly contrasting four geomorphological domains: Highland, Transitional (Massena plateau), Lateritic (Macieira plateau) and Talus domains. While at the Highland domain the relief is rugged and steep, with altitudes above 2300 m at the Transitional (2300-2100 m) and Lateritic (2100-1800 m) domains the topography is gentler, consisting of mountains formed by weathered material with interspersed blocks and boulders of fresh alkaline rock. Talus (below 1800 m) corresponds to the area of steep slopes composed of a confused mixture of argillaceous material with sparse boulders of alkaline rocks. Field, petrographic, mineralogical, geochemical, textural and XRdiffraction-data supported the characterization of the domains as well as indicated the transitional nature between the domains. The significant differences between the domains are listed below. Highland domain is built by the barren mountains and ranges superficially separated by hanging valleys filled with peat-like material, yellow clays and discontinuous stringers of boulders and cobbles at the bottom of the deposits. The thin saprolite at the Highlands is dominated by whitish kaolinitic clays stained by brownish yellow Fe oxides in Liesegang type structure. Gibbsite is insignificant in general and peat like material contains abundant fragments of feldspar and kaolinite. Metahalloysite, illite, montmorillonite and larger vermiculite flakes. Massena consists of a gentle mountainous relief, with an incipient gully process in development. Concretion formation which is more developed at Massena, consists of a mixture of kaolinite and gibbsite. Goethite “cuirasses” are more ubiquitous at this domain. Macieira plateau can be described as a residual, relatively thick, red bauxite blanket situated at the top of a gentle mountain. Concretioning is abundant, and composed of gibbsite with small amounts of kaolinite, restricted to the saprolite zone. REE and trace elements are relatively enriched at Macieira, in contrast with the other domains. Talus is marked by a steep slope consisting of loose red clay material with boulders of alkaline rock. Vegetation is typically a tropical rain forest. Clays are composed by variable mixtures of kaolinite and gibbsite.

1 INTRODUCTION

The 220 sq km, Itatiaia Alkaline Massif is located at the coordinates 44°45'W and 44°32'W of longitude and 22°15'S and 22°30'S of latitude, nearby Itatiaia township and the Paraíba do Sul river valley (Fig. 1). It consists of an outstanding topographic expression in the southeastern part of Brazil (Barros 1952).

The main purpose of this work is to discuss the existence of four geochemically different domains governed by geomorphological processes. Mineralogical and geochemical studies, XR-diffraction data, and field work are the principal tools to support our conclusion. Variations in climate, morphology and types of vegetations constitute additional criteria to distinguish the four domains. The several lithologic types of alkaline rocks occurring at Itatiaia and the existence of the predominant east-west fracturing and ruptile shear

zones also produced local variations in the weathering and consequently the types of the clay minerals. The main superficial feature exposed in the fresh alkaline rocks corresponds to the east-west disposed, mesoscopic grooves (“caneluras”), apparently controlled by the fracture system.

The fracturing may represent the effects of the neotectonics that has been affected the Itatiaia Massif since its emplacement. We believe that the fracture system affecting the Itatiaia Massif comprehends the fractures and shear zones projected from the Precambrian basement, in a reactivation process during Phanerozoic. The effects of the fracturing and shear zones is best observed at the Highland domain, (altitudes above 2300m), where fresh alkaline rocks are abundant. Spectacular morphological features, such as Pico das Agulhas Negras with 2787m, Prateleiras, Calcanhar do Hermes, Cabeça do Leão are some of the distinct

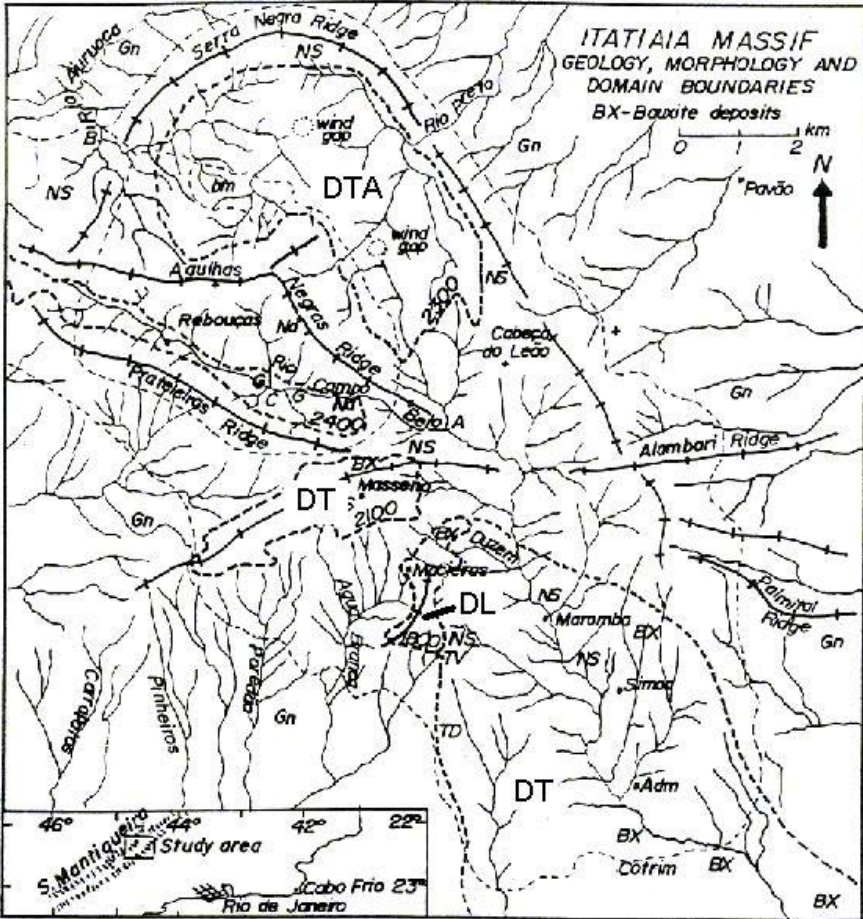


Figure 1. Map of the Itatiaia Massif, showing the geomorphologic domains. DTA = Highland domain; DT = Transitional-Massena domain; DL = Lateritic-Macieira domain; DT = Talus domain.

and sculptured forms of the rugged relief. Remnants of supposedly glacial cirques, separating the highest peaks of the Massif, are covered by fields of boulders and filled by peat like material and areas of discontinuous permafrost. The U-shaped, glaciogenically derived, valleys are limited at their lower parts, by local base levels marked by rocky butresses where rapids and small water falls exist. These features reflect how contrasting is the morphology of the Highlands and its remarkable differences to the remaining domains. The following geomorphological step corresponds to the Massena Plateau or Transitional domain between 2300m and 2100m characterized by gentle relief formed by hills partly covered by a relatively thin weathered mantle with small, sparse and patchy exposures of fresh alkaline rock. A few deposits of peat like material filled the lower portions of the relief, and the

development of yellowish brown, goethitic cuirasses are frequently found. Limited fields of boulders are still existent. The vegetations is formed by extensive grasslands and a few bushes of bamboo trees and speaded "cabeça de negro". Between 2300m and 1800m is the Lateritic or Macieira Plateau domain marked by a few and small elevations in a gentle topography which underwent more degradation than the ones previously described. A relatively dense rain forest marks the physical limit between the Transitional and this domain. Flat hills, typified by the elevation of the Antennas, partly covered by a gibbsite-rich laterite mantle represent this domain. The fourth domain, below the altitude of 1800m, is covered by a very dense rain forest and widespread talus deposits formed by abundant boulders in a clay matrix.

The Itatiaia Massif, dated of Cretaceous age, is inserted in the Serra da Mantiqueira an east-west trending, broad mountain system occupying the boundaries between the States of São Paulo, Minas Gerais and Rio de Janeiro. Serra da Mantiqueira is formed by strongly deformed Precambrian gneisses, migmatites, quartzites, cut by granitic intrusives, locally mylonitized.

2 GEOCHEMICAL CHARACTERIZATION OF THE DOMAINS

The rugged and steep morphology of the Highland domain is built in intrusive, medium-grained nepheline syenite, nordmarkites and alkalic granite, invaded by a magmatic breccia composed of fine-grained fonolite, displaying occasional orbicular texture and disseminated pyrite. Mostly, this domain forms naked peaks and steep hills separated by U-shaped valleys covered by boulder fields and peat-like material. Agulhas Negras, Prateleiras, Cabeça de Leão and Três Picos are some of the higher peaks of the Massif. Glacial boulder clay (Ebert 1960) may be the result of short glacial periods, and could be associated to the hanging valleys.

Thin to very thin weathered crusts form around blocks and exposures of the alkaline rocks. Liesegang rims bordered by fractures and shear zones exhibit a nice and coloured alternance of stained clays varying from yellowish white to brownish yellow color. The fracture system with angles between 50° and 60° facilitated the development of the alteration rims. Black Fe/Mn oxides fill discontinuously the fissures and cracks. In the study section RB-52 (Fig.2) it predominates yellowish white kaolinite as weathering product, forming patches and small blankets on top of the alkaline rocks. Illite, metahalloysite, and montmorillonite detected in the XR-diffractograms, and bronze vermiculite flakes and abundant, 2-3cm long fragments of slightly altered feldspar can be found in the soils and peat-like material surrounding the weathered blocks. Gibbsite exists in meaningless amounts. The general absence of concretions and cuirasses is noteworthy. Mineralogical composition of the clay material, mixed up with feldspar fragments, from this domain revealed after the study of several cross sections showed kaolinite contents varying from 11% to 84%, gibbsite values between none to 18% (a single result about 54%) and goethite in the range 3% and 16% and considerable amounts of feldspar (4% and 73%). The results suggest an immature development of the weathering mantle.

The Transitional/Massena domain is marked by a mountainous relief, incipient gully formation, and a few outcrops. The study soil profile MA-36 (Fig.2) shows a more mature, yellowish brown clay saprolite with the presence of gibbsite (4%-30%) in

most of the sections, the predominance of kaolinite (15% to 80%), and goethite, reaching 72% in the duricrusts, but ranging from 3% to 20%. Feldspar, metahalloysite, illite, sphene and smectite have been identified in the diffractograms and vermiculite, after biotite, in larger flakes directly recognized in the soil samples. Colloform texture exhibited in gibbsite encircled by goethite reveals the differential solubility factors.

In general, the normative calculations for some sections indicate a ratio of 3:1 for kaolinite:gibbsite in the hard concretions mixed within the yellow clay. The yellow clay itself contains 53% kaolinite and 35% fine-grained feldspar. The $\text{SiO}_2/\text{Al}_2\text{O}_3$ ratio in the yellow saprolite is low, tending to a silica impoverishment. However the significant variation in the relative concentrations of kaolinite and gibbsite in the domain defines well its transitional character.

In the Lateritic or Macieira Domain, the section AN 72 (Fig.2) was picked out because it is well exposed, showing the upper portion of the partly weathered nepheline syenite upward to the bauxite at surface. It was sampled at the "Praça da Bauxita", a flat plateau in the Antennas Elevation, covered by dense, tropical rain forest. Decimetric fragments of hard bauxitic concretions can be found almost everywhere in the plateau. It consists, from bottom of whitish yellow, altered fragments of nepheline syenite. Kaolinite is abundant and incipient gibbsite peaks are visible in the diffractogram; goethite is nearly absent. The next shell is composed of less kaolinite with an increase of gibbsite and the appearance of goethite and illite. In the remaining alteration cortexes gibbsite increases significantly, kaolinite decreases, but not steadily, and goethite is more concentrated in the intermediate zone. It should be noticed the relative frequency of K feldspar along the section. Just above the lowest level, the altered material is red, except in the upper portion which contains more yellowish brown concretions. Normative gibbsite over 60%, followed by kaolinite, in the range 8% to 21%, and goethite in the average of 10% express alumina contents among 45% and 51%, silica values between 3.8% and 9.8%, and Fe_2O_3 between 6.5% and 12%. The Ki index was below 0.5, reflecting an alic tendency.

At the Talus domain, the profile HS-46 (Fig.2), from the fresh alkaline protolith to the surface, revealed a thin crust of Mn oxides, gibbsite, kaolinite and relic of K feldspar, sphene, chlorite and ilmenite. Toward the surface the altered material grades from a whitish yellow color, to a brownish red, increasing the amount of clay. This feature is accompanied by an increase of gibbsite and goethite contents, and decrease in kaolinite and K feldspar. Small fragments of alkaline rock are still present close to the cortex.

3 METHODOLOGY

From the 18 alteration profiles, distributed in the 4 Domains, one section in each was selected to this work. For each sample analyses were proceeded using ICP-MS, EAA, DRX, besides morphoscopic and textural observations. In addition, MEV, LOI e pH analyses have been done.

Mineralogical compositions of the analysed soil material were quantified by normative calculations to the indicator minerals: kaolinite, gibbsite, quartz, goethite, K-feldspar, compared with XRD charts.

Geochemical aspects of the whole analytical set, were studied under the Ki (alteration index), WPI e PI (Hassassowitz,1926; Reiche,1943, modificado de Carvalho 1972) viewpoints. Comparisons of the analytical data with the field studies were performed.

4 CONCLUSION

The geomorphological, mineralogical and geochemical subdivision of the weathered alkaline protoliths of the Itatiaia Massif in four domains is well characterized and supported by field and laboratory investigations. The rugged morphology

and whitish, kaolinitic soils, profusely rich with partly altered feldspar fragments and almost absent gibbsite of the Highlands (above 2300m) contrasts with the Transitional domain (between 2300m and 2100m) with yellow kaolinite-rich clays, with a slight increase of gibbsite and abundant goethite concretions, and with the Lateritic domain (between 2100m and 1800m) with gibbsite-rich, kaolinite-poor, hard bauxitic crusts on top of the Macieira Plateau and from the lower Talus domain (Below 1800m) with mixed clays, kaolinite, gibbsite, K feldspar and minor goethite.

5 REFERENCES

- Barros, W.D. 1952. Parques Nacionais do Brasil. R.J. MA/SAI.88p.
- Ebert, H. 1960. Novas observações sobre a glaciação pleistocênica na serra do Itatiaia. Acad. Bras. Ciênc. 32(1):51-73.
- Harrassowitz, H. 1926. Laterit Fortch. Geol. Paleont. Berlin (5):253-565.
- Carvalho, G.S. 1972. Comparação de produtos de meteorização pela sua composição mineralógica virtual e por índices de meteorização e programas em Fortran IV para cálculos. Bol. Serv. Geol. Moçambique. 36:1-46.

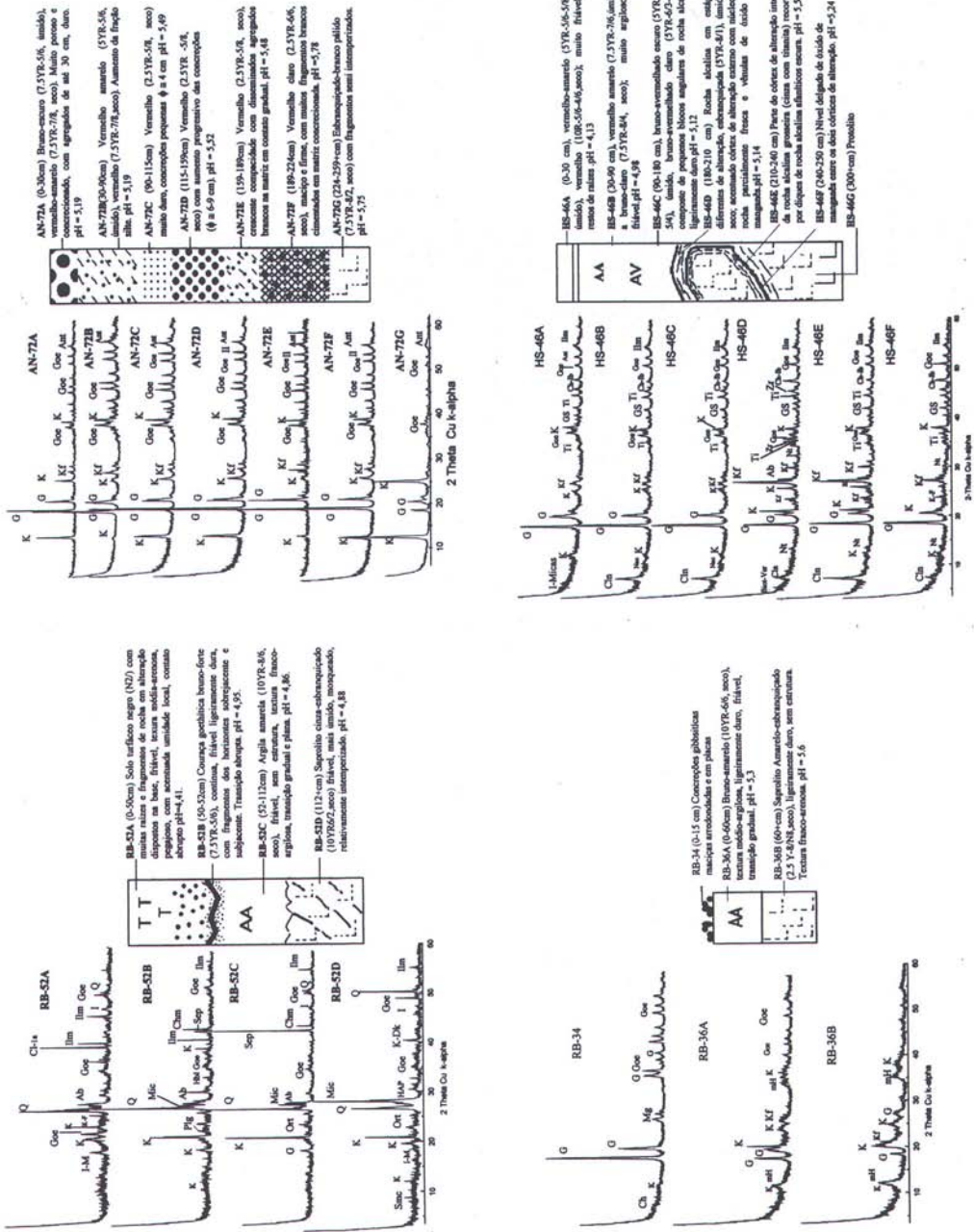


Figure. 2. Diagram showing the section study RB-52 (Highland Domain); RB-34 (Transitional-Massena Domain), AN- 72 (Lateritic-Macieira Domain); HS-46 (Talus Domain).

Geochemistry of Cassiterite and Wolframite from Tin and Tungsten Deposits in Portugal

A.M.R.Neiva

Department of Earth Sciences, Faculty of Sciences and Technology, University of Coimbra, 3000-272 Coimbra, Portugal

ABSTRACT: In Sn>W-bearing quartz veins, euhedral cassiterite shows sequences of alternating parallel lighter and darker zones. The lighter zones consist on nearly pure SnO₂, whereas the darker zones are pleochroic, oscillatory zoned, have higher Nb, Ta and Fe contents and present exsolutions of ferrocolumbite, manganocolumbite and ixiolite. Cassiterite from W>Sn-bearing quartz veins is commonly zoned. The darker zones are homogeneous and slightly pleochroic, but chemically similar to lighter zones. Cassiterite contains inclusions of rutile and ilmenite. Several wolframite crystals are homogeneous, but heterogeneous crystals showing inner patches rich in hubnerite component also occur in two deposits. Normally zoned crystals showing increase in Fe and decrease in Mn from core to rim were found in another deposit. In one deposit, later wolframite contains inclusions of scheelite, partially replaces it and is richer in Fe and poorer in Mn than earlier wolframite. Wolframites from Sn>W-bearing quartz veins and two W>Sn-bearing quartz veins have significant Nb content, which does not depend on the Fe and Mn contents of wolframite. Tungsten is well negatively correlated with Nb. Only very rare single crystals of wolframite show increase in W and decrease in Nb from core to rim. Sn>W-bearing quartz veins contain wolframite poorer in Nb than the darker zones of cassiterite, which exsolved columbite and ixiolite. In W>Sn-bearing quartz veins, wolframite has higher Nb content than cassiterite, which contains rutile inclusions enriched in Nb. The reaction of fluids with country metasediments is responsible for the high Nb content in wolframite of these W>Sn-bearing quartz veins.

1 INTRODUCTION

There are many occurrences of cassiterite and wolframite in northern and central Portugal, and most of them have been exploited. Cassiterite occurs in veins of granitic pegmatite and quartz veins, while wolframite occurs in quartz veins. Pegmatite veins cut granites and surrounding pre-Ordovician, Ordovician and Silurian metapelites, while quartz veins mainly cut these metapelites, but rarely cut the granites themselves. These veins are related to Hercynian S-type granites, but some quartz veins with wolframite are associated with an Hercynian I-type granite.

There are several hypothermal quartz veins containing both cassiterite and wolframite. Euhedral cassiterite occurs among quartz crystals, mainly along vein-schist contact, associated with a muscovite-rich selvage, while wolframite is distributed throughout the veins. Ten quartz veins, from northern and central Portugal, containing both cassiterite and wolframite (Fig. 1) were selected to study the compositions of these ore minerals and their inclusions and products of exsolution by electron microprobe in order to discuss different types of zonation in cassiterite and wolframite and to explain the variations in their compositions.

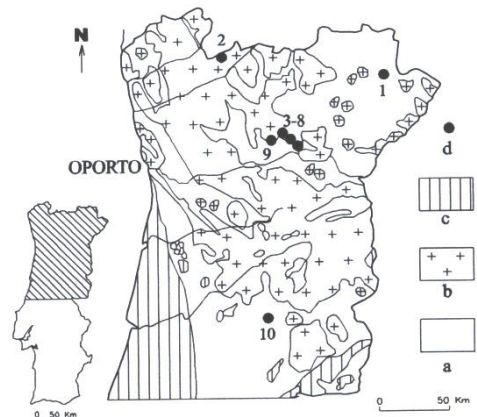


Figure 1. Location of ten Sn and W deposits chosen for study. a. Pre-Ordovician and Paleozoic metamorphic complexes, some ultrabasic and igneous rocks; b. Hercynian granitic rocks; c. Mesozoic and Cenozoic sedimentary rocks; d. quartz veins with cassiterite and wolframite. Sn > W-bearing quartz veins from 1-Argozelo; W > Sn-bearing quartz veins from 2- Carris, 3- Carvalhal, 4- Soutelinho, 5- Filharoso, 6- S. Domingos, 7- Folgar, 8- Bouço, 9- Vale das Gatas, 10- Panasqueira.

2 CASSITERITE COMPOSITIONS AND ZONING

Euhedral cassiterite from Sn>W-bearing quartz veins shows sequences of alternating narrow parallel darker and lighter zones. The darker zones are pleochroic from ε red to ω translucent and colorless, oscillatory zoned, and have higher Nb, Ta and Fe contents than the lighter zones, which consist of nearly pure SnO₂, are colourless to tan and translucent (Tab.1). The darker zones show exsolved ferrocolumbite, manganocolumbite and titanium ixiolite with subordinate W>Sn. These darker zones are heterogeneous and their Ta and Fe contents decrease near the exsolutions and increase with distance from these exsolutions. Consequently, Ta becomes more abundant than Nb with increasing distance from the exsolution products. In the same crystal, significant differences in the Ta/(Ta+Nb) values are found in darker zones that are far apart, although they show the same product of exsolution (either columbite or ixiolite), while closely spaced darker zones do not show significant chemical distinction.

Euhedral cassiterite from W>Sn-bearing quartz veins is generally zoned, with slightly pleochroic darker zones from ε brown to ω light brown, which are chemically similar to the lighter zones (Table 1). However at Carvalhal, the darker zones of some crystals of cassiterite are strongly pleochroic from ε red to ω translucent colorless and have higher Ti content than that of the lighter zones (Table 1). Commonly accidental rutile inclusions are uniformly distributed in the lighter and darker zones, but ilmenite inclusions are only found in the cassiterite from Carris. The cassiterite is fairly homogeneous near the inclusions and lacks any products of exsolution. In each crystal, there is no chemical distinction in successive darker zones.

Table 1. Electron microprobe data on cassiterite from quartz veins from northern and central Portugal.

	Sn > W-bearing quartz veins		W > Sn-bearing quartz veins		
	lighter zone	darker zone	1	lighter zone	darker zone
Nb ₂ O ₅	–	1.06	–	0.01	0.04
Ta ₂ O ₅	0.09	1.71	0.02	0.01	0.30
TiO ₂	0.08	0.13	0.64	0.32	0.97
SnO ₂	99.50	96.64	99.41	99.62	98.39
WO ₃	–	–	–	0.06	0.02
MnO	0.01	–	–	0.02	0.10
FeO	0.08	0.79	0.08	0.02	0.01
Total	99.76	100.33	100.15	100.06	99.83

1 - lighter and darker zones of similar composition;
– not detected.

The darker zones of cassiterite from Sn>W-bearing quartz veins are richer in Nb, Ta and Fe and poorer in Ti than the cassiterite from W > Sn-bearing quartz veins (Table 1, Fig. 2). $2(\text{Nb}+\text{Ta})^{5+} + (\text{Fe}, \text{Mn})^{2+} \rightleftharpoons 3(\text{Sn}, \text{Ti})^{4+}$ is the main mechanism responsible for the incorporation of Fe, Mn, Nb, Ta and Ti in the analyzed crystals of cassiterite (Fig. 2).

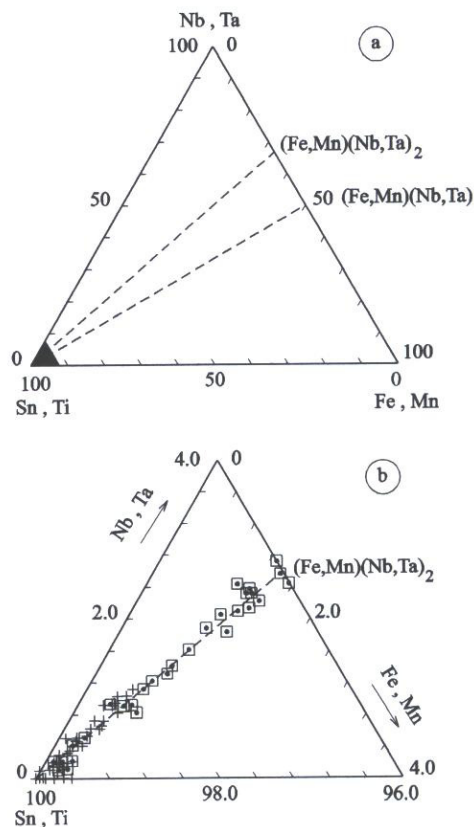


Figure 2. a) (Nb, Ta) - (Fe, Mn) - (Sn, Ti) diagram showing the location of the triangular plot for Portuguese cassiterite from Sn and W-bearing quartz veins expanded in the following Figure b. Symbols: ◻ - Sn > W-bearing quartz veins, ○ - W > Sn-bearing quartz veins.

3 WOLFRAMITE COMPOSITIONS

Several analyzed crystals of wolframite are homogeneous. However, at Panasqueira and Filharoso, some heterogeneous crystals show inner patches, which are richer in Mn than the rest of the crystal (Table 2) and represent an earlier stage of wolframite precipitation.

Table 2. Selected electron microprobe data on wolframite from northern and central Portugal.

	Folgar	Panasqueira			Filharoso		Carris		Vale das Gatas	
		1	2	Core	Rim	3	4	5	6	7
TiO ₂	0.01	0.02	-	0.11	-	0.03	-	0.02	0.02	0.01
MnO	13.83	3.41	5.34	3.59	3.13	15.40	21.07	21.68	6.45	4.28
FeO	11.24	20.63	18.45	21.90	21.72	9.98	4.13	2.24	17.81	20.09
Nb ₂ O ₅	0.20	0.26	0.38	1.88	0.47	0.23	0.22	0.07	0.01	0.63
SnO ₂	0.02	0.02	0.05	0.03	0.07	0.02	-	-	-	-
Ta ₂ O ₅	0.03	-	-	0.05	-	-	-	-	0.02	-
WO ₃	74.87	75.11	75.52	72.19	74.34	74.57	74.65	76.15	75.48	74.61
Total	100.20	99.45	99.74	99.75	99.73	100.23	100.07	100.16	99.79	99.62

Panasqueira: 1 and 2 - from the same crystal, 2 - inner patch; core and rim of a single crystal; Filharoso: 3 and 4 - from the same crystal, 4 - inner patch; Carris: 5 - without inclusions, 6 - with scheelite inclusions; Vale das Gatas: 7 - the richest in Nb₂O₅.

Some crystals of wolframite from Vale das Gatas are zoned and the core has a composition similar to that of homogeneous crystals from the respective vein. The rim of these zoned crystals is poorer in hubnerite content than the core, but has a similar composition to that of crystals in other close veins. The analyzed crystals are not associated with sulfides. Later fluids enriched in Fe, but earlier than those responsible for the precipitation of sulfides, gave origin to the rim of zoned crystals of wolframite and penetrated along fractures of earlier crystals producing heterogeneous crystals.

Wolframite compositions from most of the ore deposits have a dominant hubnerite component, while wolframite from Panasqueira has a dominant ferberite component (Table 2). At Carris, some crystals show a dominant hubnerite component, while others present a dominant ferberite component (Table 2). The latter crystals represent a later generation of wolframite containing inclusions of scheelite and partially replacing scheelite.

Niobium is the only minor element, determined by electron microprobe, which presents significant content in wolframite from three of the deposits studied. Niobium content of wolframite does not depend on the hubnerite content, but it is negatively correlated with W (Fig. 3). Analyzed wolframite crystals do not contain either inclusions or exsolution products of Nb-bearing oxide minerals. Three zoned crystals for W and Nb show increase in W and decrease in Nb from core to rim (Table 2).

4 THE NIOBIUM BEHAVIOUR

At the Sn > W-bearing quartz veins, wolframite contains up to a lower Nb value (0.94 wt.% Nb₂O₅) than the highest (1.12 wt.% Nb₂O₅) found in the darker zones of cassiterite, which exsolved columbite and ixiolite. Wolframite lacks any products of exsolution and is later than cassiterite. The fluids had a lower Nb content during the precipitation of wolframite than during the crystallization of cassiterite.

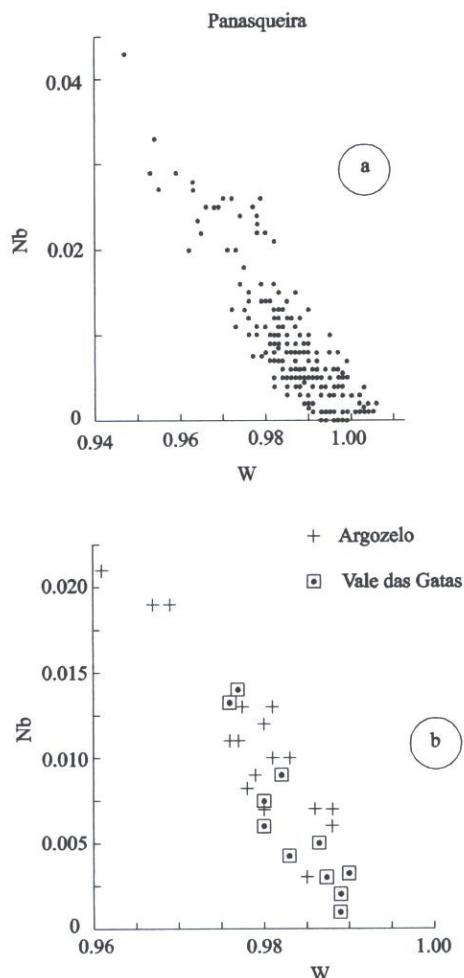


Figure 3. Diagram of Nb versus W of individual analyses of wolframites from northern and central Portugal.

In the W > Sn-bearing quartz veins, cassiterite commonly has a low Nb content. However, wolframites from two of these deposits, Vale das Gatas and Panasqueira, have significant Nb contents up to 0.63 and 1.88 wt.% Nb₂O₅ (Table 2), respectively. Cassiterite from these two deposits has only 0.01 wt.% Nb₂O₅, which is lower than that (0.36 wt.%) in the analyzed cassiterite from the other W > Sn-bearing quartz veins. Cassiterite contains rutile inclusions having 2.54 and 0.30 wt.% Nb₂O₅ at Vale das Gatas and Panasqueira, respectively. Therefore, these was recurrence of Nb.

At Panasqueira, the unaltered S-type granite contains 23 ppm Nb, while the country schist contains less than 15 ppm Nb. During the main sulfide stage, there is evidence for significant interaction of essentially non-magmatic meteoric water-dominated ore forming fluids with organic-rich metasedimentary rocks, including coals given by low D fluids (Polya et al. 2000). In general, wolframite precipitated in the ore veins earlier than sulfides and during the main oxide silicate stage. Anomalously low D waters were found in fluid inclusions in cassiterite and arsenopyrite from this stage (Kelly & Rye 1979), suggesting that there was already some mixing of the magmatic hydrothermal fluids with meteoric water that has interacted with non-magmatic rocks. This mixing must have increased and provided Nb to the hydrothermal fluids within the oxide silicate stage from the precipitation of cassiterite to that of wolframite.

5 CONCLUSIONS

- 1) Euhedral cassiterite from Sn > W-bearing quartz veins is zoned, with alternating parallel pleochroic darker zones richer in Fe, Ta and Nb than the lighter zones. The darker zones are oscillatory zoned and show blebs of columbite and ixolite. Ta/(Ta + Nb) shows a large range of values throughout the red zones, although successive very closed space, red zones have a similar composition.
- 2) Euhedral cassiterite from W > Sn-bearing quartz veins is commonly zoned with slightly pleochroic and chemically indistinct darker zones from alternating parallel lighter zones. Both zones contain rutile ± ilmenite inclusions.
- 3) The cassiterite from Sn > W-bearing quartz veins has darker zones, which are richer in Nb, Ta and Fe and poorer in Ti than cassiterite from W > Sn-bearing quartz veins.
- 4) The main mechanism responsible for the incorporation of Nb, Ta, Fe, Mn and Ti in cassiterite is $2(\text{Nb}, \text{Ta})^{5+} + (\text{Fe}, \text{Mn})^{2+} \rightleftharpoons 3(\text{Sn}, \text{Ti})^{4+}$.
- 5) Some analyzed crystals of wolframite are homogeneous, while others are heterogeneous

and some are zoned. Rare heterogeneous crystals have inner Mn-rich patches representing an early stage of wolframite precipitation. Other heterogeneous crystals have a Fe-rich composition along fractures, while zoned crystals show increase in Fe and decrease in Mn from core to rim. Later fluids enriched in Fe are responsible for the Fe-rich compositions along fractures and rims.

- 6) Later crystals of wolframite containing inclusions of scheelite and replacing scheelite are derived from fluids richer in Fe and poorer in Mn than those responsible for the precipitation of earlier crystals of wolframite.
- 7) In some deposits, wolframite shows significant Nb content and rare crystals present decrease in Nb and increase in W from core to rim. The main mechanism responsible for the incorporation of Nb in wolframite is $\text{W}^{6+}\text{Fe}^{2+} \rightleftharpoons \text{Nb}^{5+}\text{Fe}^{3+}$.
- 8) The fluids of the Sn>W-bearing quartz veins probably had a progressive decrease in Nb content from the cassiterite crystallization to the wolframite precipitation, as suggested by the Nb content of these ore minerals.
- 9) In the W>Sn-bearing quartz veins, the fluids certainly had a decrease in Nb content from the rutile crystallization to the cassiterite crystallization. However, fluids probably reacted with country metasediments and became richer in Nb before the wolframite crystallization.

6 ACKNOWLEDGEMENTS

I am grateful to Prof. M. Machado Leite and Dr. J.M. Farinha Ramos for the use of electron microprobe at the Geologic and Mining Institute, S. Mamede de Infesta, Portugal. Financial support of the Geoscience Centre at Coimbra University is also acknowledged.

7 REFERENCES

- Kelly, W.C. & Rye, R.O. 1979. Geologic, fluid inclusion, and stable isotope studies of the tin-tungsten deposits of Panasqueira, Portugal. *Econ. Geol.*, 74: 1721-1822.
- Polya, D.A., Foxford, K.A., Stuart, F., Boyce, A. & Fallick, A.E. 2000. Evolution and paragenetic context of low D hydrothermal fluids from the Panasqueira W-Sn deposit, Portugal: New evidence from microthermometric, stable isotope, noble gas and halogen analyses of primary fluid inclusions. *Geochim. Cosmochim. Acta*, 19: 3357-3371.

Cervelleite-like Sulphotellurides from the Urals HVMS Deposits

C.A.Novoselov, E.V.Belogub, V.V.Zaykov

Laboratory of Applied Mineralogy, Institute of Mineralogy, Miass, Russia

ABSTRACT: This paper is dedicated to the comparison of the cervelleite-like sulphotellurides from the Urals hydrothermal volcanic massive sulphide (HVMS deposits). These minerals were discovered in the Gayskoe, Yaman-Kasy, Severo-Uvaryazhskoe, Tash-Tau, and Babaryk deposits. They appertain to the chalcopyrite + galena + sphalerite + tennantite ± bornite association. Other silver and/or tellurium minerals are presented with electrum, hessite, stromeyerite, silver-bearing chalcocite, benleonardite-like mineral, sylvanite, and native tellurium. Formation of the sulphotellurides is indicative of the relative low tellurium fugacity which is insufficient for tellurides to be formed. The broad variations of composition and physical properties of cervelleite-like sulphotellurides allow the supposition of a presence of several mineral species, distinguished by structure, copper contents, and tellurium – sulphur ratio.

1 INTRODUCTION

Investigation of the ore minerals, containing tellurium, silver and gold, is an important task for understanding of genesis and transformation processes on the HVMS deposits. Nowadays cervelleite-like minerals are known insufficiently. This mineral group needs accurate definition of physical and structural parameters.

Cervelleite was established as a new mineral in 1989 for the Bambolla Mine (Criddle et al. 1989). Formerly silver sulphotellurides with minor copper contents were described by Aksenov et al. (1969) for the sulphide ores of Zyranovskoe deposit (Altay), by Gadzheva (1985) for Shadiitsa epithermal deposit (Bulgaria), by Karup-Moller (1976) for Ivigtut cryolite deposit. Cervelleite-like mineral from galena-bornite-sphalerite ores of the Um Samiuki volcanogenic Zn-Cu-Pb-Ag deposit (Egypt) was described by Helmy (1999). A series $(\text{Ag,Cu})_6\text{TeS}_2 - (\text{Ag,Cu})_4\text{TeS}$ is found for the gold quartz-vein type Funan deposit (China) (Gu et al. 2003).

2 OCCURRENCES

Urals is the greatest HVMS deposits province (Fig. 1). Tellurides of gold, silver, lead, are the usual accessory minerals for sulphide ores. Some sulphotellurides such as goldfieldite, benleonardite-like mineral, cervelleite have been discovered at the first recently (Maslennikov et al., in press).

Unnamed silver sulphotelluride $(\text{Ag}_{2.92}\text{Cu}_{0.06})\text{Te}_{1.00}\text{S}_{1.00}$ was found accompanied with tennantite, pyrite, luminescenting sphalerite, galena, and bornite in ores from the Gayskoe deposit (Orenburg district). It forms subhedral isometric grains up to 15 μ in size included in galena. Also native gold forms rare veinlets in galena (Moloshag et al. 2002).

Sulphotellurides were detected in the very specific position for the Yaman-Kasy deposit (Orenburg district) (Maslennikov et al., in press). Cervelleite-like $(\text{Ag}_{1.60}\text{Cu}_{0.08})_{1.68}(\text{Te}_{0.48}\text{S}_{0.52})_{1.00}$ and benleonardite-like minerals were determined in the microveinlets cutting hessite and sylvanite grains within chalcopyrite zone of the paleohydrothermal chimneys. Native tellurium associates with sulphotellurides usually.

In the Baymak ore district (Bashkortostan) silver sulphotellurides were established in the Severo-

Uvaryazhskoe and Tash-Tau deposits. In the Severo-Uvaryazhskoe deposit cervelleite forms anhedral, elongated grains up to 0.1 mm size in galena from the chalcopyrite-galena-sphalerite-pyrite stockwork ores. Sometimes cervelleite forms a simple intergrowth with hessite.

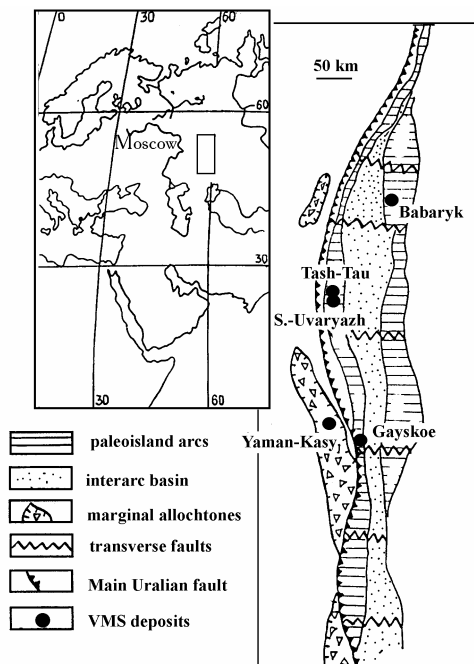


Figure 1: Magnitogorsk-Mugodzhary paleoisland arc and position of HVMS deposits.

Cervelleite-like phase from massive pyrite-bornite-chalcopyrite-sphalerite ores from the Tash-Tau deposit occurs as a small spots on the galena-bornite border. Electrum presents in the ores from both deposits also.

Cuprous cervelleite-like mineral ($\text{Cu}_{0.48}\text{Ag}_{1.49}\text{S}_{1.97}(\text{S}_{0.69}\text{Te}_{0.31})_{1.00}$ from Babaryk deposit (Chelyabinsk district) forms isometric to elongated anhedral grains (up to 0.2 mm). The grains are isolated in galena or restricted to contact bornite and galena in pyrite-chalcopyrite-sphalerite-bornite-galena ores with banded structure. The mineral associates with stromeyerite, silver-bearing chalcosite, and electrum sometimes.

3 CHEMICAL COMPOSITION

Chemical composition of cervelleite-like sulphotellurides from Urals HVMS deposits is

variable and shows a difference in cation – anion ratio and in impurity composition (Fig. 2). Cervelleite from the type locality have the S : Te ratio as 1 : 1 (Criddle et al. 1989). Cervelleite-like mineral from Babaryk deposit have the same ratio as 2 : 1. Copper is a usual admixture in the Urals samples. Copper content varies from 0.1 wt. % (Gayskoe) up to 14.4 wt. % (Babaryk). Some admixture of iron, zinc, arsenic, selenium has been fixed too. A strict negative correlation of Ag and Cu, S and Te contents in the cuprous cervelleite-like mineral from the Babaryk deposit might be an evident of limited isomorphism in these pairs.

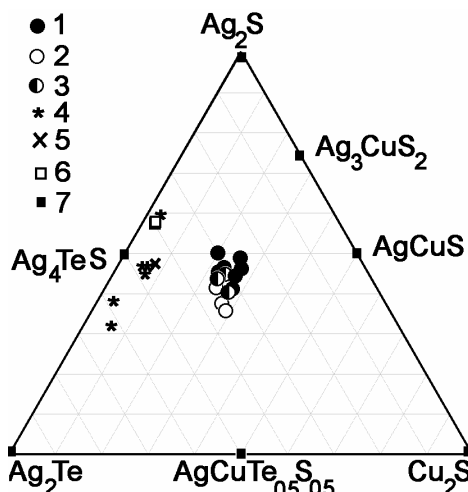


Figure 2: Chemical composition of cervelleite-like minerals in the plot hessite (Ag_2Te) – argentite (Ag_2S) – chalcocite (Cu_2S): 1 - 3 – from the Babaryk deposit: 1 – in galena, 2 – in bornite, 3 – in galena and bornite; 4 – from the Severo-Uvaryazhskoe deposit; 5 – from the Yaman-Kasy deposit; 6 – from the Gayskoe deposit; 7 - end-members: Ag_4TeS – cervelleite, Ag_3CuS – jalpaite, AgCuS – stromeyerite; 7 – synthetical phase $\text{CuAgTe}_{0.5}\text{S}_{0.5}$.

4 PHYSICAL PROPERTIES

Cervelleite-like minerals are the typical “microprobe phases”. Their optical and physical properties have an irregular character. The structure of cervelleite-like minerals is not deciphered. A review of the Urals species and comparison with other ones show the formidable variations of their physical characteristics (Table 1) and chemical composition. So, reflectance spectrum of cervelleite from the Severo-Uvaryazhskoe deposit is different from type locality one (Criddle et al. 1989). Reflectivity of cuprous cervelleite-like mineral from Babaryk deposit is characterized by considerably low values R. It can be explained by copper admixture.

Microhardness values cover a wide range from 44.5 up to 119.4 kg/mm² (Table 1). This phenomenon can be hardly explained with variations in chemical composition of the mineral. It is probably that these variations are resulted of an

influence of grain size and cleavage. Microhardness measuring for cervelleite from Bambolla Mine is unique because of very small size of grains. Obtained values for Urals samples were made on more representative material.

Table 1: Physical properties of cervelleite-like sulphotellurides in comparison with Bambolla and Zyranovskoe minerals

Occurrence	Optical properties	Hardness
Zyranovskoe, phase Z (Aksenov et al. 1969)	R: 40(442) - 40.1(465) - 39.9(493) - 39.5(523) - 39(551) - 38.1(588) - 37.4(621) - 36.2(667) - 35.9(698); isotropic; grey with bluish-green or greenish shade	VHN 84-87; hessite > H < galena
Gayskoe (Moloshag et al. 2002)	Anisotropic	no data
Bambolla (Criddle et al. 1989)	R: 39.75(400) - 39.8(470) - 38.15(546) - 35.6(650) - 34.4(700); isotropic; bluish to greenish white; positive photochemical reaction	VHN ₁₀ 26
Yaman-Kasy (Maslennikov et al. in press)	anisotropic; dark grey with brown shade; strong positive photochemical reaction	no data
Severo-Uvaryzhskoe	R: 36.5(460) - 37.1(520) - 35.8(620) - 35.1(700); isotropic; grey with greenish shade	VHN ₂₀ 119.4; H > galena
Babaryk	R: 32.9(400) - 32.5(460) - 32.1(520) - 30.6(620) - 29.9(700); isotropic; grey with greenish, bluish-greenish shade	VHN ₁₀ 44.5; h < galena

Notes: R – reflectivity, % (in brackets pointed wave length, nm); VHN – microhardness, kg/mm²; h – polishing relief.

It is possibly to assert that cervelleite has more high microhardness then determined for type locality. Described polishing relief of minerals can confirm this thesis.

Cervelleite-like minerals are stable chemically. Very light photochemical reaction was observed for cervelleite isolated from other silver-bearing minerals (acantite and hessite). Intergrowth of silver minerals leads to aggravation of effect (Criddle et al. 1989). The experiments with some of the Urals cervelleite-like minerals (Babaryk, Severo-Uvaryzhskoe) show negative or very weak (with HNO₃) chemical and photochemical reaction.

5 STRUCTURE

Cervelleite from type locality has a primitive cubic cell with *a* 14.03 Å (Criddle et al. 1989). For the cuprous cervelleite-like mineral from Babaryk deposit very poor X-ray data were obtained (*d* (Å), intensity): 5.04, w; 4.16, ew; 3.08, w; 2.54, vw; 2.32, w. Intensities are very weak, estimated as a weak (w), very weak (vw), extremely weak (ew). Obtained set of reflexes is not similar with cervelleite. But low quality of deбаграмms can't be juxtaposed with confidence.

6 CONCLUSIONS

There are hessite Ag₂Te, chalcocite Cu₂S, argentite Ag₂S, stromeyerite AgCuS, jalpaite Ag₃CuS, henryite Ag₃Cu₄Te₄, cervelleite Ag₄TeS in the Ag-Cu-Te-S system. Synthetic phase AgCuTe_{0.5}S_{0.5} was obtained by Yu. Asadov within the broad range of temperature (up to 650 °C and below 440 °C). Cubic

(high-temperature) and monoclinic (low-temperature) polymorph modifications characterize this compound like a hessite, argentite and chalcocite. There are sulphosalts (benleonardite and goldfieldite) with other cation-anion ratio.

Investigated cervelleite-like minerals from Urals HVMS deposits were found in the chalcopyrite ± bornite-galena-sphalerite-tennantite association. Pyrite presents as a minor mineral in relics usually. Other silver and/or tellurium minerals can be presented by electrum, hessite, stromeyerite, silver-bearing chalcocite, benleonardite-like mineral, sylvanite, native tellurium. Ores are disseminated or massive, banded.

The genesis conditions for cervelleite-like minerals were discussed by Gu et al. (2003) for relatively high temperatures 250 °C. From their point of view the stability field of these minerals is determined by superposition of the field of sapphires and tellurides of silver which depend on the activity of the sulphur and tellurium (Gu et al. 2003). In the Babaryk deposit cuprous cervelleite-like mineral associates with bornite, chalcocite, stromeyerite, galena, sphalerite and electrum. There are no argentite and hessite in this mineral assemblage. Only cuprous cervelleite-like mineral is a concentrator of tellurium. So, it is impossible to calculate fugacity of tellurium and sulphur for this association without thermodynamical data for sulphotellurides. This association may be formed under temperatures less 78°C (higher limit of stability for orthorhombic stromeyerite) and high oxidative potential (for the forming of chalcocite, bornite which content some Cu²⁺). These conditions are characterized for the zones of “submarine supergenesis” of massive sulphide ore bodies and resulted the interaction between sea water and

hydrothermal fluids. This was demonstrated by numerous authors in the frame of the recycling model. Formation of the sulphotellurides reflects the low tellurium fugacity which is insufficient for tellurides to be formed. Only sulphotellurides from the Yaman-Kasy deposit were determined in association with native tellurium.

The broad variations of composition and physical properties of cervelleite-like sulphotellurides allow supposing the presence of several mineral species, distinguished by structure, copper contents, and Te–S ratio.

This work was supported by the RFBR (project 04-05-96014-r2004ural_a).

7 REFERENCES

- Aksenov, V. S., Gavrilina, K. S., Litvinovitch, A. N., Bespaev, Kh. A., Pronin, A. P., Kosyak, E. A., Slinsarev, A. P. 1969. Occurrence of new minerals of silver and tellurium in ores of the Zyranovskoe deposit in the Altay. *Izvest. Akad. Nauk. Kazakh. SSR, Ser. Geol.*: 74-78 (in Russian)
- Criddle, A. J., Chisholm, J. E., Stanley, C. J. 1989. Cervelleite, Ag_4TeS , a new mineral from the Bambolla mine, Mexico, and a description of a photochemical reaction involving cervelleite, acanthite and hessite. *Eur. J. Mineral.*, 1: 371-380.
- Gadzheva, T. 1985. A new silver-copper-tellurium sulphide mineral ($(Ag,Cu)_4TeS$) from the Shadiitsa deposit, Central Rhodope Mountains. *Dokl. Acad. Nauk*, 38(2): 211-213 (in Russian).
- Gu, X.-P., Watanabe, M., Hoshino, K., Shibata, Y. 2003. New find of silver tellurosulphides from the Funan gold deposit, East Shandong, China. *Eur. J. Mineral.*, vol. 15, no 1: 147-155.
- Helmy, H. 1999. The Um Samiuki volcanogenic Zn-Cu-Pb-Ag deposit, Eastern Desert, Egypt: A possible new occurrence of cervelleite. *Canadian Mineralogist*, vol. 37, № 1: 143-158.
- Karup-Moller, S. 1976. Arcubisite and mineral B — two new minerals from the cryolite deposit at Ivigtut, south Greenland. *Lithos*, vol. 4: 253-257.
- Maslennikov, V., Herrington, R., Stanley, C., Buslaev, F. Tellurium mineralization in zoned sulfide chimneys from the Silurian Yaman-Kasy copper-zinc massive sulfide deposit, southern Urals. *Canadian Mineralogist* (in press).
- Moloshag, V., Grabezhev, A., Gulyaeva, T. 2002. Forming conditions of tellurides in the Urals sulphide and copper-gold-porphiry deposits. *Proceedings of the Russian Mineralogical Society*, №5: 40-54. (in Russian).

Zirconiferous Hafnon and Hafniferous Zircon from São João Del Rei, Minas Gerais, Brazil

R.M.Pereira & A.M.Netto

Applied Geology Department, Faculty of Geology, University of Rio de Janeiro State, Rio de Janeiro, Brazil

C.A.Ávila & H.R.Barrueto

Geology and Palaeontology Department, National Museum, Federal University of Rio de Janeiro, Rio de Janeiro, Brazil

R.Neumann

Sector for Technological Characterisation, Mineral Analyses Coordination, Center for Mineral Technology, Rio de Janeiro, Brazil

D.Atencio

Department of Mineralogy and Geotectonics, Geosciences Institute, University of São Paulo, São Paulo, Brazil

ABSTRACT: This study describes the identification of hafniferous zircon in Brazil and, at least, the third worldwide occurrence of zirconiferous hafnon. Those minerals were found in pegmatite bodies belonging to the São João del Rei Pegmatitic Province, Minas Gerais State. Hafniferous zircon was identified in the Volta Grande Mine as well as on other neighbor's creeks within such pegmatitic province. SEM/EDS and electron microprobe analyses of several grains of hafniferous zircon of one ore body of the Volta Grande Mine have variable contents of HfO₂ and atomic ratios of HfSiO₄ as well. The obtained results indicate very subordinate zonation patterns of zirconiferous hafnon along the zircon's borders during the continuous growing of the crystal. This restrict chemical zonation demonstrates a little Hf saturation.

1 INTRODUCTION

Hafnium (Hf) is a rare element in nature, usually associated to zirconium (Zr) and replacing it in mineral structures, mainly in zircon (ZrSiO₄) and baddeleyite (ZrO₂). In granitoids and pegmatites, the hafnium content in zircon crystal lattice tends to increase at the later crystallization processes, preferentially in lithium-enriched pegmatites (Knorring & Hornung 1961; Correia Neves et al. 1974). But Hf, which usually occurs together with Zr, even in pegmatites, does not commonly form hafniferous minerals, like hafnon silicate (HfSiO₄).

In Brazil, Cassedanne et al. (1985) reported hafniferous zircons with concentrations of HfO₂ achieving up to 23% wt, more precisely from the Mixeriqueira pegmatite, Minas Gerais.

In this study, we present the chemical results of the second identification of hafniferous zircon in Brazil. This mineral was found in the E ore body of the Volta Grande Mine (Nazareno County) as well as on Cascalho Preto creek (Coronel Xavier Chaves County) and on Pernambuco creek (Ritópolis County), all located within the São João del Rei Pegmatitic Province, Minas Gerais. The

zirconiferous hafnon border of a one zoned hafniferous zircon grain from the E ore body of Volta Grande Mine represents the first brazilian and, at the very least, the third worldwide occurrence of zirconiferous hafnon.

2 GEOLOGY OF THE SÃO JOÃO DEL REI PEGMATITIC PROVINCE

The São João del Rei Pegmatitic Province, located in the southern Minas Gerais State, is close to 70 km long and 20 km wide, spreading out over 1,400 km², from Nazareno up to Resende Costa counties. Two greenstone belt sequences, of unknown age are recognized in the area: the southern Nazareno Greenstone Belt and the northern Rio das Mortes Greenstone Belt. The Rio das Mortes Greenstone Belt is intruded by diverse igneous plutonic rocks, among which the Ritópolis batolith, with a minimum crystallization age (by stepwise Pb zircon evaporation) of $2,121 \pm 7$ Ma (Ávila et al. 2003), constitutes the most expressive intrusion identified. On regional scale, pegmatitic bodies cut not only the amphibolites and schists from the greenstone belt

but also the former granitic batolith and other minor plutonic intrusions (trondhjemite, tonalite, diorite, granodiorite). Both the Rio das Mortes Greenstone Belt and the plutonic bodies are covered by paleo, meso and neoproterozoic lithotypes of the São João del Rei, Carandaí and Andrelândia sequences.

The pegmatites are mineralized in tantalite, microlite and cassiterite, cutting the granitic and amphibolitic rocks with sub-vertical dip planes. They present several variable dimensions, usually lesser than 100 m wide and/or thickness.

Notwithstanding, at the Volta Grande Mine area, the pegmatites were emplaced as sub horizontal tabular bodies, lens-shaped injections, varying from 700 to 1000 m of length (Lagache & Quéméneur 1997). These pegmatites are lithiferous, formerly named A, B, C, D, E and F bodies (Quéméneur 1987) and they have spodumene and sometimes lepidolite as the Li-bearing crystalline phases. This mineral assemblage fits to the albite-spodumene type pegmatite of the classification proposed by Cerný (1992).

3 ANALYTICAL METHODS

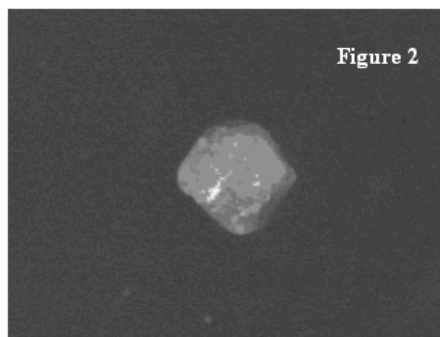
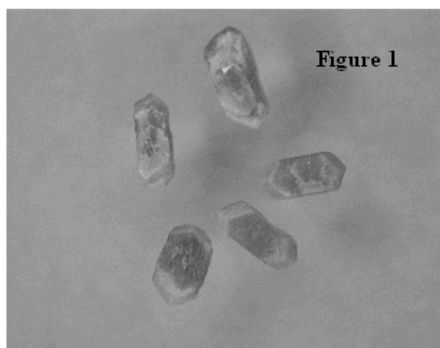
The X-ray diffractometer used was a Bruker D5000, using copper anode ($\text{CuK}\alpha$ $\lambda=1,5418 \text{ \AA}$), secondary graphite monochromator, $0,02^\circ$ 2θ step and 1s count per step. Analyses were performed on finely ground powder samples, and, for samples too small to fill the sample holder, a quartz zero-background sample holder was used.

Scanning electron microscopy (SEM) was performed using a LEO S440 equipment, at 20 kV accelerating voltage, coupled to a Link ISIS L300 energy dispersion X-rays spectrometer (EDS), SiLi Pentafet detector, ultra thin ATW II window, 133 eV resolution @ 5,9 keV. Quantifications, based on ZAF corrections, were calculated by Oxford's ISIS L300 suite SEMQUANT program. Spatial resolution of EDS analyses is around 2 μm diameter and 1.5 to 5 μm deep, depending on the materials density on the analyser spot. SEM images are usually backscattered electrons detector (BSD) images, therefore grey levels are proportional to the mean atomic weight on the pixel, and might be considered compositional images, where lighter grey stands for heavier phase.

Yet electron microprobe analyses were performed on a Camebax SX50 from Cameca, operating at 20 kV electron accelerating voltage and 40 nA sample current, for simultaneous light and heavy element analyses with spatial resolution of 5 μm . Synthetic ZrSiO_4 and HfSiO_4 were used as standards for Zr and Hf, and corrections were calculated by the PAP program.

4 RESULTS

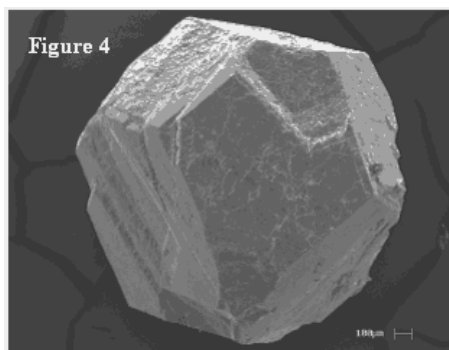
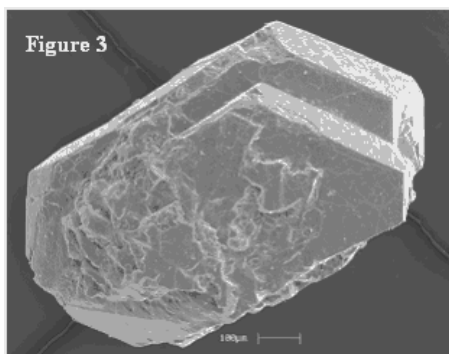
Several samples of heavy minerals concentrates were panned in some creeks between the village of Coqueiros and the city of Coronel Xavier Chaves. Zircon grains collected on a small creek close to the Volta Grande Mine (Nazareno County), as well as on Cascalho Preto (Coronel Xavier Chaves County) and on Pernambuco (Ritápolis County) creeks, were submitted to the SEM's dispersive energy microanalysis. From their results it was possible to observe considerable Hf enrichments. Hafniferous zircon grains usually occur as euhedral crystals with bipyramidal prismatic habits and some of them may be twinned (Figs. 1-4). Grain sizes vary from less than 1 up to 2 mm, with colours ranging from pink to reddish, some of which presenting fluorescing yellowish under short-waved ultraviolet radiation.



Figures 1-2. Hafniferous zircon grains from the Volta Grande Mine, Nazareno County, Minas Gerais, Brazil, magnified using a binocular lens ($\times 20$).

Interplanar crystalline spacings d_{hkl} of hafniferous zircon are slightly higher than the spacings of natural zircon, although they are very close. Synthetic hafnon, on the other hand, presents narrower spacings. In spite of these differences, X-ray diffraction was not precise enough for any

accurate identification of these minerals. Electron microprobe determination of ZrO_2 , HfO_2 , SiO_2 , ThO_2 , FeO , TiO_2 , Al_2O_3 , MgO , CaO and Y_2O_3 contents of three hafniferous zircon grains (Fig. 5) from the E ore body of the Volta Grande Mine are presented in Table 1. The contents of ZrO_2 , HfO_2 , SiO_2 and ThO_2 are very similar to those obtained by SEM/EDS analysis, altogether with other two grains not previously analyzed by microprobe (Table 2). The hafniferous zircon grains display Hf-enriched regions containing from 26.9 to 36.5wt% HfO_2 (SEM/EDS), lighter grey on SEM/BSD images, and predominating darker regions with lower hafnium, from 17.2 to 21.1wt% HfO_2 (Table 2).



Figures 3-4. Back-scattered MEV images of different shapes of two hafniferous zircon grains from the Volta Grande Mine, Nazareno County, Minas Gerais, Brazil. Scale bars = 100 microns.

Hafniferous zircon crystal with very high hafnium content could be identified as inclusion in a cassiterite grain at the same concentrate (Fig. 6). SEM/BSD images also differentiate between lighter, Hf-enriched portions of the crystal, and darker regions with lower contents of such element. The lighter ones are located on the crystal's border and display up to 48.4% HfO_2 (wt%), whereas the darker regions, widespread distributed, averaged from 30.6

to 33.5% (wt% HfO_2). Following the zircon-hafnon series classification proposed by Correia Neves et al. (1974), the dark region corresponds to a hafniferous zircon and the lighter borders to a zirconiferous hafnon (Table 3).

Table 1. Electron microprobe analyses and structural formula (based on 4 oxygen atoms) of three hafniferous zircon grains from the Volta Grande Mine, Nazareno County, Minas Gerais, Brazil. Points A and B are represented in Fig. 5.

	Grain 1			Grain 2		Grain 3	
	A	B		A	B		
SiO_2	30.96	30.42	29.38	28.73	30.34	28.91	30.46
ZrO_2	55.61	51.24	45.28	40.42	54.06	40.47	53.65
HfO_2	15.33	17.46	24.14	29.21	14.51	31.03	15.13
TiO_2	-	0.07	0.03	0.05	0.03	0.02	-
Al_2O_3	0.01	0.11	0.14	0.04	0.10	0.02	0.01
FeO	0.05	-	0.05	-	0.10	-	0.05
MgO	-	-	0.02	0.04	0.01	0.02	-
CaO	0.02	0.01	-	0.02	0.05	-	0.06
ThO_2	0.04	-	-	0.14	0.14	-	0.16
Y_2O_3	0.10	0.02	0.05	0.28	0.56	0.01	0.37
Total	102.1	99.34	99.09	98.92	99.91	100.4	99.92
Si	0.99	1.01	1.00	1.01	0.99	1.01	1.00
Zr	0.87	0.83	0.75	0.69	0.86	0.69	0.86
Hf	0.14	0.17	0.24	0.29	0.14	0.31	0.14
Ti	0.00	0.00	0.00	0.00	0.00	0.00	0.00
Al	0.00	0.00	0.00	0.00	0.00	0.00	0.00
Fe	0.00	0.00	0.00	0.00	0.00	0.00	0.00
Mg	0.00	0.00	0.00	0.00	0.00	0.00	0.00
Ca	0.00	0.00	0.00	0.00	0.00	0.00	0.00
Th	0.00	0.00	0.00	0.00	0.00	0.00	0.00
Y	0.00	0.00	0.00	0.01	0.01	0.00	0.01

Table 2. SEM/EDS analyses and atomic ratio of lighter and darker(*) regions of hafniferous zircon grains from the Volta Grande Mine, Nazareno County, Minas Gerais, Brazil. Points C and D are represented in the Fig. 5.

Grain	SiO_2	ZrO_2	HfO_2	ThO_2	Total	100. Hf/Zr+Hf	
1	29.6	42.3	27.8	-	99.8	27.7	
	29.6	42.7	27.3	-	99.6	27.3	
	29.8	41.4	28.8	0.2	100.2	28.8	
*	30.4	48.6	21.1	-	100.0	20.2	
*	30.6	50.3	19.2	-	100.0	18.1	
2 C	29.6	40.4	29.6	-	99.6	30.1	
	* D	30.4	52.3	17.2	-	99.9	16.0
3	29.4	36.4	34.1	-	100.0	35.4	
	28.7	34.6	36.5	-	99.8	38.1	
	*	30.4	51.4	18.2	-	100.0	17.0
*	29.9	40.4	29.7	-	100.0	30.1	
	29.2	37.2	33.6	-	100.0	34.5	
6*	30.5	51.4	17.7	0.4	100.0	16.6	
	*	30.0	51.6	17.6	0.5	99.8	16.5
	*	30.4	51.5	17.6	0.2	99.8	16.6
7	29.7	43.4	26.9	-	100.0	26.5	

5 CONCLUDING REMARKS

The border of zirconiferous hafnon on hafniferous zircon from the São João del Rei Pegmatitic Province represents the first Brazilian and, probably, the third worldwide occurrence of zirconiferous hafnon hitherto known, after the first description made by Correia Neves et al. (1974) on Zambezi pegmatites, Mozambique.

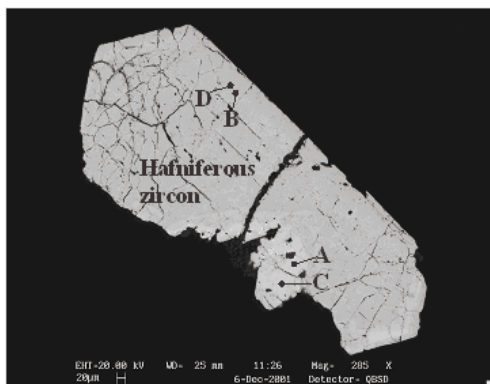


Figure 5. MEV back-scattered image showing hafniferous zircon with different compositional portions. Lighter=more Hf rich; darker=less Hf rich. A and B points - microprobe analysis (Tab.1). C and D points - SEM/EDS analysis (Tab.2). Scale bar = 20 microns.

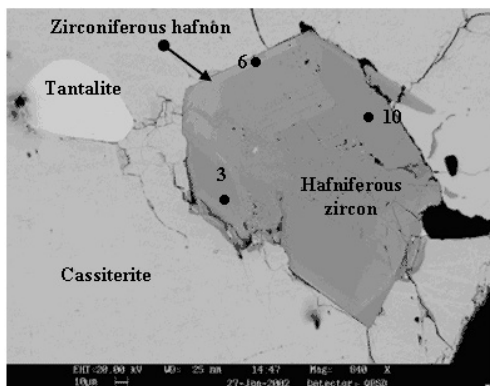


Figure 6. MEV back-scattered image showing inclusions of hafniferous zircon and tantalite in a cassiterite host grain. Zirconiferous hafnbn developed only along of a part of the border the hafniferous zircon. Spots 3, 6 and 10 (SEM/EDS results) are represent in Table 3. Scale bar = 10 microns.

XRD results on the hafniferous zircon grains were quite similar to the published patterns for low-Hf zircon and synthetic hafnbn (Bayliss et al. 1980). A more precise identification of these minerals by X-ray diffraction method won't be possible due to the mineral's structures. Knorring & Hornung (1961) found similar problems in zircons of Karibib Li-bearing pegmatites of Namibia.

SEM/EDS and electron microprobe analyses of several grains of hafniferous zircon of the E ore body indicated HfO_2 contents ranging between 17.2 and 36.5% (wt) and atomic ratios ($100 \cdot \text{Hf}/\text{Zr} + \text{Hf}$) varying from 16.5 to 38.1% (mol) HfSiO_4 . Only in a part of the border of a hafniferous zircon crystal,

hosted in a cassiterite grain, the contents of HfO_2 increased from 47.7 to 48.4% (wt), raising the atomic ratio variation between 54.2 and 54.9% (mol) HfSiO_4 , corresponding to zirconiferous hafnbn. Well-shaped zoned borders of the Hf-bearing portions denote a step and continuous crystal zoning (not progressive) during the zircon formation, under variable saturation levels of such element in the pegmatite.

Table 3. SEM/EDS analyses and atomic ratio of a zircon-hafnbn crystal inclusion in cassiterite. Darker regions correspond to hafniferous zircon and the lighter borders to zirconiferous hafnbn. Zircon from the Volta Grande Mine, Nazareno County, Minas Gerais, Brazil. Points 3, 6 and 10 are represent in Fig. 6.

Spot	SiO_2	ZrO_2	HfO_2	ThO_2	Total	$100 \cdot \text{Hf}/\text{Zr} + \text{Hf}$
<i>Lighter border</i>						
6	28.6	23.1	48.0	0.5	99.9	54.9
7	28.5	23.5	47.7	0.3	100.0	54.2
8	27.6	23.5	48.4	0.5	100.0	54.7
<i>Darker region</i>						
3	29.8	39.8	30.6	-	100.2	31.0
9	29.5	36.4	33.5	0.6	100.0	35.0
10	28.8	37.9	33.4	-	100.1	34.0
11	29.2	39.3	31.1	0.4	100.0	31.5
12	29.5	38.4	32.5	-	100.3	33.2

6 REFERENCES

- Ávila, C.A.; Valença, J.G.; Moura, C.A.V.; Klein, V.C. & Pereira, R.M. 2003. Geoquímica e idade do Trondhjemito Cassiterita, borda meridional do Cráton São Francisco, Minas Gerais. Arquivos do Museu Nacional, 61(4): 267-284.
- Bayliss, B.P.; Berry, L.G.; Mrose, M.E. & Smith, D.K. 1980. Mineral Powder Diffraction File Data Book. Pennsylvania: International Center for Diffraction Data. 1168 p.
- Cerný, P. 1992. Geochemical and petrogenetic features of mineralization in rare element granitic pegmatites in the light of current research. Applied Geochemistry, 7(2): 393-416.
- Cassedanne, J.P.; Baptista, A. & Cerný, P. 1985. Zircon hafnifère, samarskite et columbite d'une pegmatite du Rio Doce, Minas Gerais, Bresil. Canadian Mineralogist, 23(4): 563-567.
- Correia Neves, J.M.; Lopes Nunes, J.E. & Sahama, G. 1974. High hafnium of the zircon-hafnbn series from the granite pegmatites of Zambézia, Mozambique. Contributions to Mineralogy and Petrology, 48(1): 73-80.
- Knorring, O. Von & Hornung, G. 1961. Hafnium zircons. Nature, 190(17): 1098-1099.
- Lagache, M. & Quéminéur, J.J.G. 1997. The Volta Grande pegmatites, Minas Gerais, Brazil: An example of rare-element granitic pegmatites exceptionally enriched in lithium and rubidium. Canadian Mineralogist, 35(1): 153-165.
- Quéminéur, J.J.G. 1987. Petrography of the pegmatites from Rio das Mortes Valley, southeast Minas Gerais, Brazil. Revista Brasileira de Geociências, 17(4): 595-600.

Unconventional Precious Metal Deposits

A. Piestrzyński & J. Pieczonka

AGH-University of Science and Technology, av. Mickiewicza 30, 30-059 Krakow, Poland

A. Banaszak

KGHM Polish Copper Company, Lubin, Poland

ABSTRACT: Platinum-group elements occur not only in the well known mafic layer intrusions, but very often in unconventional environments e.g. anoxic sediments, epithermal deposits related to the porphyry coppers rich in gold, and oxidized redbed-related rocks. Some of them can be of an economic importance. An average Au content in the redbed-type gold deposit related to the Polish Kupferschiefer copper deposit is 2.25 ppm, Pt = 0.138 ppm, and Pd = 0.082 ppm. The precious metal deposit underlies the rich copper deposit, and occurs only in the place with a minor Cu content. Proportions of precious metals in the Santo Tomas II porphyry copper deposit are similar, 1.4, 0.29, and 0.045 ppm, respectively. Although the mechanism of ore mineral crystallization and geological environment are very different, these deposits may have probably the same, deep source, mantle derived mineralized fluids.

1 INTRODUCTION

The occurrence of PGM in ultramafic Ni-Cu-Fe sulphide deposits is documented in many monographs (Cabri & Laflamme 1976; Naldret & Cabri 1976; Vermaak & Hendriks 1976, Cabri 1981; Naldret et al. 1990). Over the last years there is more evidence, that hydrothermal fluids may also be responsible for the transportation and precipitation of PGM minerals in a variety of environments (Stumpfl 1974; Stumpfl & Tarkian 1976; McCallum et al. 1976; 1986; Schiffries & Skinner 1987; Piestrzyński et al. 1994). Geology of several unconventional mineral deposits from around the world is discussed in recent scientific journals. The following deposits are usually mentioned in these papers: Sukhoi Log, Udokan, Natalka and Nezdanskoeye (Russia); Dzhezkazgan and Murantau (Kazakhstan), Zunyi (China); Jabiluka and Coronation Hill (Australia); Lubin - Kupferschiefer (Poland) and Nik (Canada). The presence of platinum-group elements in several porphyry copper deposits is discussed by Tarkian, Stribny (1999), however there is still lack of precise data on the PGM content in this type of deposits. In this work some new information on unconventional precious metals mineral deposits are presented.

2 PORPHYRY COPPER

2.1 Santo Tomas II, Philippines

The Santo Tomas II deposit is an Au-Mo-W-porphyry copper deposit, located in the SW flank of the Cordillera Central in Luzon Is., Philippines. Its geotectonic position and geology are typical of porphyry type of the Pacific Ring of Fire. A suit of diorite and andesite porphyries probably of Miocene age intrudes metavolcanics of the basement complex. Younger dacite-basaltic dikes crosscut older formations. Mineralization is hosted mainly by the hornblende-quartz diorite and metavolcanics composed of andesitic and basaltic flows, volcanic tuffs, pyroclastics, and is structurally controlled. Hydrothermal alteration includes silicification, biotitization, sericitization and propylitization (Tarkian & Koopmann 1995). Ore minerals generally occur as quartz stockwork fillings and disseminations. Primary mineral assemblage consists of chalcopyrite, pyrite, magnetite, bornite, the major ore minerals, and accessory molybdenite, chalcocite, sphalerite and galena. The platinum group minerals are related to one of the latest mineralization stages and are associated with native gold of high purity and minor electrum. Pt-bearing merenskyite, Pt-bearing stibiopalladinite and mertieite, vysotskite,

hessite, sopcheite, kotulskite and Ag_3TeS have been found in this deposit (Piestrzyński et al. 1994). Bulk chemical analyses of raw ore samples reveal the presence of precious metal up to 1400 ppb Au, 290 ppb Pd, 45 ppb Pt and 100 ppb Ag. The precious metal mineral assemblage is related to the highly silicified rock, reach in gold (Piestrzyński et al. 1994).

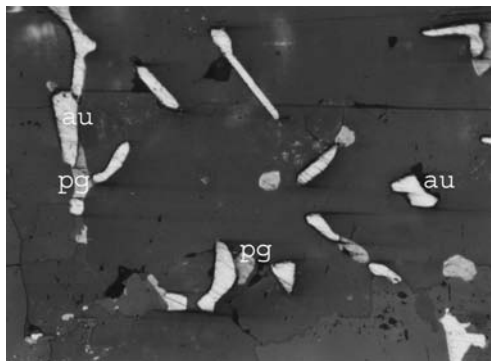


Figure 1. A rich gold (au) and platinum-group mineral (pg-kotulskite) bonanza in quartz-calcite nest. Reflected light, Santo Thomas, Philippines; size of the phot. is 1.0x1.5 mm.

The highest content of gold up to 1-2 wt%, and several tens of PGM have just been observed in the hand specimens collected from the silicified sections (Fig. 1). The Au-PGM assemblage occurs as free space filling and in carbonate nests. In the nearest vicinity of the rich gold – platinum mineral assemblage, red internal reflection of quartz are often observed. Carbonates are the final cement.

2.2 Medet and Elatsite, Bulgaria

Both these deposits are located in the Srednogorie zone that is a part of metallogenic, calc-alkaline belt of the late Cretaceous to Paleocene age (Berza et al. 1998). Bulk chemical analyses of single ore samples and concentrates from Medet and Elatsite deposits (Bulgaria) reveal the presence of 848 ppb Au and 9 ppb Pd, and 8598 ppb Au, 59 ppb Pt and 298 ppb Pd, respectively. A recent study by Tarkian et al. (2003) gives a detailed description of the Elatsite deposit and of its mineral composition containing the mineral assemblage typical of porphyry copper. Within the ore minerals merenskyite and members of the merenskyite-moncheite solid solution have been listed as a minerals responsible for PGM concentration. This information shows that some typical porphyry copper deposits can have a big potential of precious metals and similar geological phenomena are responsible for their formation.

3 REDBED-TYPE GOLD DEPOSIT, THE KUPFERESCHIEFER, POLAND

3.1 Geology

Lubin-Sieroszowice mining district that host a new type of Au, Pt and Pd mineralization is classified as a stratabound polymetallic deposit. The polymetallic mineral assemblage is hosted by sedimentary suit of sandstones followed by the Kupferschiefer black shale and dolomite of Permian age (Wodzicki Piestrzyński 1994). The copper deposit is limited at the south by the deep Odra faults system that controls the structure of the Fore-Sudetic Block. A new discovery of the precious metals assemblage, located in the profile below the economic Cu mineralization could change a general opinion on the genesis of this deposit. Precious metals are located in a continuous, thin horizon (about 40 sq km) with an average thickness of 0.22 m (0.05-1.4 m) and an average ($n = 1,121$ samples) gold content 2.25 ppm, 0.14 ppm Pt and 0.08 ppm Pd (Piestrzyński et al. 2002). This horizon is characterized by red color and low contents of copper and organic matter, and high concentration of gold PGM and oxidized iron. Oxidation environment is peneconcordant in relation to the typical black Kupferschiefer containing copper deposit. The Au- PGM-bearing horizon is situated in the Zechstein sandstone and the lowermost part of the Kupferschiefer (Piestrzyński et al. 2002).

3.2 Mineralogy and geochemistry

Precious metal mineral assemblage consists of high purity native gold, electrum, tetraauricupride, Pt-Pd-arsenides, and some selenides and tellurides. All samples representing the oxide environment contain less than 0.18 wt% of FeO and 0.44 wt% total organic carbon (TOC), and high content Fe_2O_3 ranging between 1.5 wt% and 8.76 wt% and gold ranging from 0.09 to 94.9 ppm (Piestrzyński et al. 2002). Low content of TOC in the red variety of the Kupferschiefer is very significant (Sawlowicz 1994, Pieczonka 2000, Piestrzyński et al. 2002). It suggest strong oxidation of previous existing organic matter of the sapropelitic origin. The typical Kupferschiefer from the copper deposit area contains usually 10 wt% copper and 7-8 wt% TOC and several times lower content of Fe_2O_3 , (Pieczonka 2000). Gold and platinum-group metal contents in the typical Kupferschiefer, rich in copper, are lesser than 5 ppb. Such concentrations are characteristic of normal anoxic sediments (Crocket 1993).

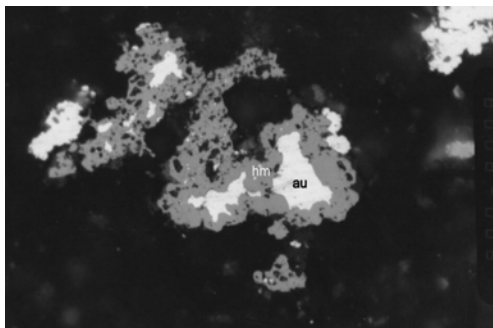


Figure 2. Native gold (au) and hematite (hm) intergrowths in the red-variety of the Kupferschiefer, Poland; size of the phot. is 1.0x1.5 mm

More than 1,200 polished samples have been studied to determine the position of the precious metals assemblage and other accompanying minerals. The following parageneses have been recognized: native gold – hematite; native gold – hematite, copper sulphides; electrum - Pd-Bi, Cu-Bi and Pb alloys; Ag-Au-Pb-Bi-Te-Se minerals – Pd-arsenides – Ag-selenides (naumanite) – clausthalite – copper sulphides. Sobolevskite (PdBi), native Pb, Pt-bearing gold and arsenides were earlier described by Kucha (1981), but Au-Ag-selenides, CuBi alloys and Pd-As-tellurium minerals are a new discovery in the Lubin-Sierszowice Kupferschiefer copper deposit. The atomic proportions of these newly discovered minerals (microprobe analyses) show the following composition: $(\text{PbAgAu})_3\text{Se}_2\text{Te}$ and $(\text{PbAgAu})_2(\text{TeSe})_1$. Also other minerals from this area contain some admixtures of tellurium. Almost all analysed minerals reveal a significant content of gold. The gold content in bornites ranges from 0.22 up to 1.27 wt%. These bornites are characterized by nonstoichiometric chemical composition. The highest gold content has been found in bornites with $\frac{1}{2}$ and $\frac{1}{4}$ of iron contents and elevated amounts of copper. Some copper sulphides e.g. chalcocite show also high concentration of gold, up to 2.78 wt% and tellurium, up to 0.13 wt% (Piestrzyński & Pieczonka 1997). Grains of hematites intergrown with high purity gold reveal also a significant gold concentration up to 2.65 wt% (Piestrzyński & Pieczonka 1997).

3.3 Definitive characteristics of the redbed gold deposit

Characteristic features of the redbed related precious metal deposit are as follows:

- basin-wide (40 sq km) distribution of the precious metals assemblage,
- dispersed character of mineralization,

- association of high purity gold with coarse-grained hematite of a hydrothermal origin,
- presence of wide spectrum of minerals e.g. native alloys, sulphides, arsenides, tellurides, selenides, and oxides,
- presence of redox barrier,
- concentrations of Au-Pt-Pd are restricted only to the secondary oxidized sections of the earlier copper deposit.

3.4 Genesis of the redbed gold deposit

The presence of a half elements from the Mendeleev list in this deposit suggests its multistage genesis. Precious metals assemblage is buffered with hematite that is a factor of the secondary oxidation of the previously existing copper deposit (Piestrzyński et al. 2002). Gold and other precious metals were deposited on the oxidized side of the redox barrier while copper on the reduced side. In this case, oxidized environment is located below the reduced zone that contains the world class copper deposit. Rotliegendes molasse was discussed by several authors as a potential source of precious metals (Pieczonka 1998; Piestrzyński & Wodzicki 2000; Piestrzyński et al. 2002).

4 DISCUSSION AND CONCLUSIONS

Some common factors can play an important role in transportation and precipitation of ore minerals in different types of precious metal deposits. A deep source of metal-bearing fluids can be the first such a factor. Precipitation of precious metal-bearing minerals can be explained on the basis of cation transportation between the environments characterized by different electric potential. It is well documented for the redbed type Au-Pt-Pd deposit in Poland (Piestrzyński et al. 2002), however its genesis is still under discussion. In such an environment a very significant redox barrier is typical. Presence of coarse-grained hematite is typical for oxidized environment (+), and copper deposit represents reducing system (-). It is therefore important that noble metal-bearing fluids, that were oxygen-saturated, can be reduced in contact with existing sulphide deposit. In the all mentioned above deposits hydrothermal fluids were responsible for the metal distribution. In Poland, Odra fault system was probably responsible for fluid transportation.

5 REFERENCES

- Berza T., Constantinescu E. & Vlad S.N., 1998: Upper Cretaceous magmatic series and associated mineralisation in the CarpathoBalkan Orogen. *Resources Geol.* 48: 291-306.

- Cabri L.J., 1981: the platinum-group minerals. In: Cabri L.J. ed., *Platinum-group elements: Mineralogy, Geology, Recovery*, Can. Inst. Min. Metall. Spec. 23: 83-150.
- Cabri L.J. & Lafamme J.H.G., 1976: The mineralogy of the platinum-group elements from some copper-nickel deposits of the Sudbury area, Ontario. *Econ. Geol.* 71: 1159-1195.
- Crocket J.H., 1993: Distribution of gold in the Earth's crust. In Foster R.P. ed., *Gold metalogeny and exploration*, Chapman & Hall: 1-30.
- Kucha H., 1981: Precious metal alloys and organic matter in the Zechstein copper deposits, Poland. *TMPM Tschermarks Min. Petr. Mitt.* 28: 1-16.
- MacCallum M.E., Loucks R.R., Carlson R.R., Cooley E.F. & Doerge T.A., 1976: Platinum metals associated with hydrothermal copper ores of the New Rambler Mine, Medicine Bow Mountains, Wyoming. *Econ. Geol.* 71: 1429-1450.
- Naldret A.J. & Cabri L.J., 1976: Ultramafic and related mafic rocks: their classification and genesis with special reference to the concentration of nickel sulphides and platinum-group elements. *Econ. Geol.* 71: 1131-1158.
- Pieczonka J., 1998: Ore mineralization in the secondary oxidized rock from the Polkowice-Sieroszowice mine, Kupferschiefer type deposit, SW Poland. PhD thesis, Univ. of Mining and Metallurgy: 158pp (in Polish)
- Pieczonka J., 2000: Secondary oxidized rocks in the copper deposit, Fore-Sudetic Monocline. *Polish Miner. Association Spec. Pap.* 16: 9-54 (in Polish).
- Piestrzyński A. & Pieczonka J., 1997: Gold and PGE on an oxide-reducing interface on Lower Zechstein sediments of the Fore-Sudetic Monocline, SW Poland. In: Papunen ed. *Mineral Deposits: Research and Exploration Where do they Meet*, Proceedings of the IVth SGA Meeting, Turku, Finland: 99-102.
- Piestrzyński A. & Wodzicki A., 2000: Origin of the gold deposit in the Polkowice-West Mine, Lubin-Sieroszowice Mining District, Poland. *Mineral. Deposita* 35/1: 37-47.
- Piestrzyński A., Schmidt S.T. & Franco H., 1994. Pd-minerals in the Sto. Tomas II, porphyry copper deposit, Tuba Benguet, Philippines. *Mineral. Polon.* 25/2: 21-31.
- Piestrzyński A., Pieczonka J. & Głuszek A., 2002: Redbed-type gold mineralisation, Kupferschiefer, south-west Poland. *Mineral. Deposita* 37: 512-528.
- Sawłowicz Z., 1994: PGE and REE in the Zechstein Cu-deposit (Kupferschiefer from the Lubin-Głogów area, Poland) In: IAGOD, IXth Symposium, Beijing, 2: 884-885.
- Schiffries C.M. & Skinner B.J., 1987: The Bushveld hydrothermal system: field and petrologic evidence *Am. J. Sci.* 187: 566-595.
- Stumpfl E.F., 1974: The genesis of platinum deposits: further thoughts. *Mineral. Sci. Eng.* 6: 120-141.
- Tarkian M. & Koopmann G., 1995: Platinum-group minerals in the Santo Tomas II (Philex) porphyry copper-gold deposit, Luzon Island, Philippines. *Mineral. Deposita*, 30: 39-47.
- Tarkian M., Hünken U., Tomakchieva M. & Bogdanov K., 2003. Precious-metal distribution and fluid-inclusion petrography of the Elatsite porphyry copper deposit, Bulgaria. *Mineral. Deposita*, 38/3: 261-281.
- Tarkian M. & Stribny B., 1999: Platinum-group elements in porphyry copper deposits: a reconnaissance study. *Mineral. Petrol.* 65: 161-183.
- Vermaak C.F. & Hendriks L.P., 1976: A review of the mineralogy of the Merensky Reef with special reference to new data on the precious metal mineralogy. *Econ. Geol.*, 71: 1222-1261.
- Wodzicki A. & Piestrzyński A 1994: An ore genetic model for the Lubin-Sieroszowice mining district, Poland. *Mineral.*

Parageneses Generated by the Oxidation During the Metamorphism of the Itabira Iron Formation in the Quadrilátero Ferrífero, Minas Gerais, Brazil

F.R.M.Pires

Department of Geology, Geosciences Institute, Federal University of Rio de Janeiro, Rio de Janeiro, Brazil

B.R.Frost

Department of Geology and Geophysics, University of Wyoming, Laramie, Wyoming, U.S.A.

ABSTRACT: The Early Proterozoic Itabira iron formation consists of three types of itabirite in the Quadrilátero Ferrífero (QF): Siliceous, Dolomitic and Amphibolitic. The Itabira was metamorphosed under high oxygen fugacity resulting in hematite along with amphiboles according to the increasing metamorphic facies, from west to east: Grunerite molecule in the amphibole decreases from $X_{Fe}=0.8$ in the western QF to 0.4 in the central part, in the actinolite from 0.6 in central to 0.1 at East and in the tremolite from 0.4 to 0.05 in the eastern QF, along with anthophyllite. Magnetite is the precursor Fe-mineral formed, being converted to hematite and to hematite+Fe/Mg-Ca amphiboles. Two oxygen producing reactions (1/2) contributed to hematite formation, consuming magnetite and oxygen (3): $7\text{magnetite}+8\text{Quartz}+\text{H}_2\text{O}=\text{hematite}+\text{grunerite}+\text{O}_2$ (1); $6\text{magnetite}+16\text{Quartz}+6\text{H}_2\text{O}=2\text{grunerite}+25\text{O}_2$ (2); $4\text{magnetite}+\text{O}_2=6\text{hematite}$ (3); $7\text{magnetite} +8\text{Quartz} + \text{H}_2\text{O} =7\text{hematite}+\text{grunerite}$ (4), and an oxygen-conserving reaction. Grunerite is stable under low, and cummingtonite under higher metamorphic conditions. Magnetite and grunerite may coexist under limited situation, because any increase in oxygen fugacity, hematite will form: $\text{grunerite}+\text{magnetite}+\text{O}_2 = \text{hematite} + \text{quartz}$ (5). Under free-magnetite condition, grunerite is oxidized in favor of hematite: $4\text{grunerite}+7\text{O}_2= 14\text{hematite}+32\text{Quartz}+4\text{H}_2\text{O}$ (6). Mg-riebeckite and biotite may be affected by similar condition.

1 INTRODUCTION

The important iron ore deposits of QF confined in the Itabira iron formation are responsible for the 40 million tons/year high grade hematitic ore. The itabirite pertains to the middle unit of the Itabira Group, Minas Supergroup overlain by dolomites and Fe-quartzites, silver phyllites with reduction spots, carbonaceous phyllites and greywackes of the Gandarela Formation and Piracicaba Group. Underneath Itabira lieserците phyllites, quartz-schist, quartzites and metaconglomerates of the Caraça Group. The itabirite consists of hematite-magnetite-quartz±ferroan dolomite, ankerite, calcite, chlorite, talc, biotite, muscovite, stilpnomelane, microcline, albite, Mg-riebeckite, aegirine, almandine, tourmaline, F-apatite. The Dolomitic itabirite contains the carbonate minerals, talc, amphiboles, chlorite, and the Na-rich phases. The Siliceous type consists of muscovite, microcline, tourmaline and scant garnet, and in the Amphibolitic, amphiboles, chlorite and talc predominate. The hematite deposits are constituted by a metamorphic derived micaceous /schistose hematite and hydrothermally derived massive/compact hematite.

The QF has been mapped in detail by the USGS-DNPM team, mainly referred in Dorr (1969), and

metamorphism studied by Herz (1978). The Minas rock sequence is strongly folded, sheared, thrust and faulted with a northwestward vergence (Harder & Chamberlin, 1915; Pires 1995). The main purpose of this work is to discuss briefly the effects of oxidation upon metamorphism of the Itabira iron formation.

2 METAMORPHISM

Mineralogical and textural changes in itabirite during metamorphism, similarly what was studied in Michigan (James 1955), have been monitored in the quartz grain-size (Dorr 1965) and compared with metamorphic zones proposed (Herz 1978; Pires 1995). In the western QF grain sizes ranges between 0.01 and 0.086 mm (average 0.035mm), in Congonhas area the range is 0.01 to 0.1mm, and in Dom Bosco, the range is 0.05-0.4mm (average 0.13). In east-QF (Itabira and Monlevade Districts) the range is 0.04 to 0.4, according to Dorr. Chlorite (West), biotite (central) and staurolite (East) zones in pelitic rocks was defined by Herz (1978) later modified and correlated with the itabirite into chlorite-sericite zone (grunerite), kyanite-chloritoid zone (cummingtonite) with stilpnomelane and biotite

subzones, and garnet-staurolite zone corresponding to the actinolite and tremolite-anthophyllite zone in the itabirite (Figure 1). As far as hematite texture and grain-size are concerned metamorphism can be defined, as submicaceous (<0.1mm) in the West, to micaceous (0.1-0.3mm) in the central part, to schistose hematite (>0.3mm, reaching 1mm) at the Eastern-QF. Muscovite micro-porphyroblasts occur mainly in the West-QF, and aegirine porphyroblasts in East-QF. Like many iron formations, the fluid in the Itabira iron formation was internally buffered during metamorphism, with the resulting CO₂ increase in respect to H₂O. Unlike most iron formations, however the Itabira shows no reduction during metamorphism. Rather, oxygen fugacity of Itabira lay on the hematite-magnetite buffer throughout metamorphism, with the result that the silicates and carbonates became enriched in Mg relative to Fe²⁺, with increasing grade. This compositional variation lead to a change in T-X_{CO2} topology, as at low grade in Fe-rich systems, the major reaction $Qz+Ank=Cumm+calcite+CO_2$, but with increasing grade the topology inverted to that for Mg-rich systems, where $Qz+Dol = Act/Trem + calcite+CO_2$, in dolomitic itabirites. In CO₂-poor, H₂O-rich systems, a set of six reactions, two oxygen-producing, one oxygen-conserving and three oxygen-consuming reactions may be studied. The relations between metamorphism and deformation might be understood through a textural study. Synkinematic/synmetamorphic hematite was formed by the massive replacement of magnetite and quartz from the iron formation, agreeing with previous ideas (Dorr 1965). The micaceous hematite is developed along with the other metamorphic silicate minerals in the axial plane foliation formed during the generation of large-scale recumbent and thrust folds. This was followed by an intense shearing which deformed the previous structures forming coaxial/coplanar cylindrical folds and the shear zones, accompanied by a strong devolatilization. Chevron, kinking and the development of décollement zone with imbricate thrust faults along the shear zones. The porphyroblast formation was provided by the devolatilization, resulted from the deformation and metamorphism. Sheaf-like amphibole, aegirine, garnet and chlorite grew in the itabirite and of muscovite micro-porphyroblasts and kyanite in the pelitic and clastic units (Figure 2).

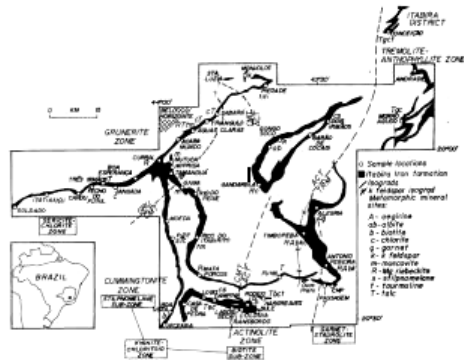


Figure 1: Metamorphic zones of Quadrilátero Ferrífero, Minas Gerais, Brazil.

Deformation pattern	Texture	Metamorphism
<p>Recumbent, large, thrust, isoclinal, similar</p> <p>Hm+Silic</p> <p>boudin</p> <p>S₁</p>	<p>Hm+Amph</p> <p>Hm+Silic</p> <p>Qz</p> <p>S₁</p>	<p>Synkinematic. Magnetite porphyroclast deformation. Generation of amphiboles, micas, talc, hematite in CPO along the main S₁-foliation. (Axial plane). L₁-mineral lineation</p>
<p>Refolding, small to large, upright fold cylindrical, concentric</p> <p>Shearing, kinking chevron</p> <p>S₁</p> <p>S₂</p>	<p>polygonal arches</p> <p>S₁</p> <p>S₂</p> <p>Sigmoids</p> <p>amphibole porphyroblast</p> <p>Sheaf like Amph</p>	<p>Coaxial. Rotation of S₁-foliation along shear zones. Crenulation Re-orientation of previous minerals into GSP0.</p> <p>Porphyroblast growth: Aegirine, garnet sheaf-like Amphibole, talc, chlorite, microline, tourmaline, albite muscovite</p>
<p>Brecciation Duplex Thrust</p> <p>S₁</p> <p>S₂</p>	<p>massive Hm itabirite micaceous Hm</p>	<p>Breccia with Hematite cement Quartz veining Compact hematite</p>

Figure 2: Textural evolution with deformation and metamorphism in the Itabira iron formation.

The last event may correspond to the retrogressive effects earlier described (Herz 1978). Crosscutting tear faults complete the structural pattern. Besides the metamorphic minerals earlier described, Mg-riebeckite, aegirine and albite in the itabirite also deserve to be mentioned. Mg-riebeckite was formerly described in dolomitic itabirite from Passagem gold mine (Leinz 1936), and later, as syndeformational mineral, in similar rock from Serra

do Cural (Pires 1995) and Gandarela Syncline. Aegirine, as porphyroblasts, was only reported from the Timbopeba mine. We believe that the source of Na as well as of K, to produce the K-micas and microcline, corresponded to the brines existing during the deposition of the iron formation, similar proposal to Brockman iron formation (Trendall & Blockley 1970).

3 MINERAL EQUILIBRIA

One of the most distinctive features of the Itabira iron formation is that it follows a very different metamorphic path from other iron formations (Yoder 1957; French 1973; Floran & Papike 1978). Most iron formations contains hematite at low grades, but lose it with increasing metamorphic grade, undergoing reduction (Frost 1979; 1988). That results, under higher metamorphic grade, the oxygen fugacity resides near FMQ buffer. A set of six mineral reactions in the system Fe-Si-O-H, involving four phases (magnetite, hematite, quartz and the Fe-rich, end-member, grunerite, can be arranged in a T-log₁₀fO₂ diagram, with three invariant points (Fig. 3). The resulting diagram was apparently developed along the HM and FMQ buffers, and the participation of Mg in the system will favor either cummingtonite, talc, chlorite or actinolite/tremolite, in the case of the presence of Ca, increasing hematite. The limited mobility of oxygen during regional metamorphism was illustrated by the association magnetite-espicularite (Kranck 1961), and also by the general idea that the in respect to oxygen the iron formations are internally constrained. In Ca-Fe-Si/skarns with both magnetite and hematite, although oxygen fugacity may be buffered by local mineral assemblages during retrograde alteration of early skarn minerals, it is unbuffered (externally controlled) during their original deposition (Burt 1971). It was studied that grunerite-forming reactions involve the breakdown of greenalite, minnesotaite and siderite (Gole 1980) and that despite greenalite coexists with hematite, minnesotaite and grunerite do not (Miyano 1978). Greenalite and minnesotaite are unstable phases for the metamorphic conditions in QF, so they were ignored in the reactions.

In addition, the origin of the magnetite in iron formations has been a matter of discussion. Gundersen & Schwartz (1962), LaBerge (1964), French (1973) and Floran & Papike (1978) support a metamorphic formation, while Klein (1983), suggests that it is the result of diagenetic recrystallization. Haase (1982) supposed that magnetite in Michigan, played a minor role in the grunerite formation, although it could be formed by a siderite-consuming reaction, and Han (1978) concludes that it is secondary, most likely formed

during regional metamorphism. In the QF, magnetite is the precursor phase, being largely oxidized to hematite, and took place in the reactions leading grunerite formation. Textural studies have demonstrated the presence of partly transformed, minute magnetite grains within the assemblage fibrous grunerite-hematite laths. Another reaction proposed $7\text{Magn}+24\text{Q}+3\text{H}_2\text{O} = 3\text{Gru}+ 7/2 \text{O}_2$, could be plotted in the diagram but it is very similar to the reaction (3), varying slightly the slope of the curve. However, it is useful to show how increasing SiO₂ activity threefold it will result in less oxygen produced.

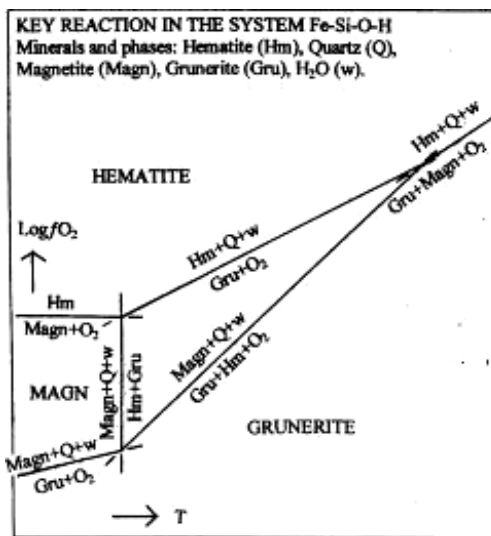


Figure 3: Log fO₂-T Diagram in the system Fe-Si-O-H, with the plot of the key reactions.

The Log fO₂-T diagrams applied to the study of metamorphic systems, particularly the Precambrian iron formation, have proved to be very useful in the understanding of the evolution of the mineral parageneses. Whenever this phase equilibria study is regarded in respect to textural features, the interpretation can be improved.

4 CONCLUSION

Hematite in the Itabira iron formation is directly derived from the oxidation of magnetite during the regional metamorphism, which produced micaceous to schistose hematite together with various silicate minerals, according to the metamorphic grade. Chlorite, muscovite and more gruneritic, fibrous Fe-Mg amphibole form in the lower grade zone, at the Western QF. Actinolitic and Fe-Mg amphibole, with

higher cummingtonite molecule content occur in the central part of QF, under higher grade conditions than the western zone and in the Eastern zone predominate tremolitic amphiboles, garnet and at the very end, anthophyllite. Biotite and microcline appear concordantly with the main foliation as well as porphyroblasts. Aegirine porphyroblasts only occur at the higher grade zone and Mg riebeckite as larger prisms. Chlorite and talc are ubiquitous, however it can be noticed the increase in the Mg-contents in both minerals. The disappearance of muscovite in this zone is characteristic. Absence of minnesotaite and greenalite in the iron formation suggests minimum temperatures of about 300°C and the absence of hypersthene, fayalite and diopside places the upper thermal limit at about 600°C. Apparently the oxygen fugacity was internally constrained, being the oxygen furnished by oxygen-producing reactions (2/3). After deformation ceased, devolatilization took place with a retrogressive event resulting in the crystallization of aegirine, chlorite, muscovite and biotite porphyroblasts and of compact and hard hematite. Whether H₂O and oxygen contents were inherited from the protolith, according to Rumble (1978) its preservation upon metamorphism is a function of the buffering capacity of the mineral assemblage and the rate of fluid migration.

It can be concluded that during the progressive metamorphism of the Itabira iron formation, the original bulk composition has controlled the composition of the fluid phase rather than the opposite. The distribution of the isograds apparently obeys the thermal gradient which defined the nature of the mineral assemblages. Also the thermal surfaces which cross cut the QF are roughly parallel to the regional isograds within the basement eastward.

5 REFERENCES

- Burt, D. (1971) Some Phase Equilibria in the System Ca-Fe-Si-C-O. Wash. Year Book, 70, 178-184.
- Dorr, J.v.N. (1965) Nature and origin of the high-grade hematite ores of Minas Gerais. *Econ. Geol.*, 60, 1-46
- Dorr, J.v.N., (1969) Physiographic, Stratigraphic and Structural Development of the Quadrilátero Ferrífero, Minas Gerais, Brazil. US Geol. Survey, Prof. Paper, 641-A, 110.
- Floran, R.J. & Papike, J.J. (1978) Petrology of the Low-grade rocks of the Gunflint iron-formation, Ontario-Minnesota. *Geol. Soc. America*, 86, 1169-1190.
- French, B.M. (1973) Mineral assemblages in diagenetic and low-grade metamorphic iron-formation. *Econ. Geol.*, 68, 1063-1074.
- Frost, B.R. (1979) Metamorphism of iron-formation: Parageneses in the System Fe-Si-C-O-H. *Econ. Geol.*, 74, 775-785.
- Frost, B.R., (1988) A review of graphite-sulfide-oxide-silicate equilibria in metamorphic rocks. *Rend. Della Soc., I. di Miner. e Petrologia*, 43, 25-40.
- Gole, M.J. (1980) Formation of grunerite in banded iron-formation (BIF), Yilgarn Block, Western Australia. *Geol. Soc. America*, abs, 12, 227.
- Gundersen, J.N. & Schwartz, G.M., 1962. The geology of the metamorphosed Biwabik iron formation, eastern Mesabi, Minnesota. *Min. Geol. Surv., Bull.* 43, 139 p.
- Haase, C.S. (1982) Metamorphic Petrology of the Negaunee iron formation, Marquette District, Northern Michigan: Mineralogy, Metamorphic reactions and phase equilibria. *Econ. Geol.*, 77, 60-81
- Han, T-M. (1978) Microstructures of magnetite as guide to its origin in some Precambrian iron formation. *Fortsch. Min.*, 56, 105-142.
- Harder, E.C. & Chamberlin, R.T. (1915), The geology of central Minas Gerais, Brazil. *Jour. Geol.* 23, 341-378.
- Herz, N., (1978) Metamorphic Rocks of the Quadrilátero Ferrífero, Minas Gerais, Brazil. US Geol. Survey, Prof. Paper 641-C, 81.
- James, H.L., (1955) Zones of regional metamorphism in the Precambrian of northern Michigan. *Geol. Soc. America*, 66, 1455-1488.
- Klein, C. (1983) Diagenesis and Metamorphism of Precambrian banded iron-formations. In Trendall & Morris, Iron-formation Facts and Problems, Elsevier 11, 417-469.
- Kranck, S.H. (1961) A study of phase equilibria in a metamorphic iron formation. *Jour. Petrol.*, 2, 137-184.
- LaBerge, G.L., (1964) Development of magnetite in iron-formations of the Lake Superior region. *Econ. Geol.*, 59, 1313-1342.
- Leinz, V., (1936) Ocorrência de Riebeckita num itabirito dolomítico, em Marianna, Minas Gerais. *Min. Metalurgia*, 9, 89-90.
- Miyano, T. (1978) Phase relations in the system Fe-Mg-Si-O-H and environments during low-grade metamorphism of some Precambrian iron-formations. *Jour. Geol. Soc. Japan*, 84, 679-690.
- Pires, F.R.M., (1979) Structural Geology and Stratigraphy at the junction of the Curral Anticline and the Moeda Syncline, Quadrilátero Ferrífero, Minas Gerais, Brazil. Unpubl. PhD thesis, Michigan Technological University, 220p.
- Pires, F.R.M., (1995) Textural and mineralogical variations during metamorphism of the Itabira Proterozoic iron formation in the Quadrilátero Ferrífero, Minas Gerais, Brazil. *Acad. Bras. Cienc. Anais* 67, 77-105.
- Rumble, D., (1978) Mineralogy, Petrology and oxygen isotopic geochemistry of the Clough Formation, Black Mountain, western New Hampshire, U.S.A. *J. Petrol.*, 19, 317-340.
- Trendall, A.F. & Blockley, J.G., (1970) The iron formation of the Hamersley Group, Western Australia. *West Austral. Geol. Surv. Bull.* 119, 366.
- Yoder, H.S., (1957) Isograd problems in metamorphosed iron-rich sediments. *Carnegie Inst. Washington, Year Book*, 56, 232-237.

Mineralogical Balance of Gold of the Bor Metallogenic Zone, Serbia

S. Radosavljevic, J. Stojanovic, & V. Kasic

Institute for Technology of Nuclear and Other Mineral Raw Materials, Applied Mineralogy Unit, P.O. Box 390, 86 Franchet d'Esperey Street, 11000 Belgrade, Serbia, Serbia and Montenegro

ABSTRACT: The Bor metallogenic zone is situated in Eastern Serbia can be considered by origin as a part of Timok-Eruptive Complex (TMC). This zone is related to the most important deposits of copper, in the Republic of Serbia. In these deposits paragenesis of sulphide copper, iron and arsenic ores as well as a number of various metals has been detected. Among this paragenesis, gold and its collectors are significant from geological and economic aspect. Our experience, related to the investigation of paragenetic and mineralogical balances of gold, show various and complex appearances of gold in these zones. The previous investigations were performed as mineralogical analyses of ores from "Veliki Krivelj", "Cerova", and the "Gallery of Bor" active mines. Gold from copper ore from mentioned ore deposits have been discussed considering the nature of gold appearance, the way of gold formation in a mineral paragenesis, and the mineralogical balance of gold.

1 INTRODUCTION

The Bor metallogenic zone, is situated in Eastern Serbia, can be considered by origin as a part of Timok-Eruptive Complex (TMC). This is one of the most significant regional metallogenetic units, where the present output of copper derives from, the ore-bearing zone, the length of which is about 80km, and the width up to 20km (Jankovic 1990).

With respect to morpho-structural types and mineral paragenesis, the following principal groups of copper deposits are recognized in the Bor metallogenetic zone: 1. Volcanic massive sulphide deposits (type: Gallery of Bor and Coka Marin); 2. Porphyry copper deposits (type: Veliki Krivelj, Cerova, Majdanpek, and etc.); 3. Conglomerate-type ore consisting of clasts of massive sulphide (type: Gallery of Bor). Deposition of porphyry copper deposits, the size of which has an economy, along the same structure below the massive sulphide bodies, represents a unique feature of some porphyry copper systems in the Bor metallogenetic zone.

Precious metals have important place in the mineral paragenesis copper deposits of East Serbia. Our experiences based on previous research on the ore from that region, show complex appearance of gold minerals as native gold and electrum as well as

exsolution in copper minerals and partially in pyrite (Radosavljevic et al. 1998b).

2 MINERALOGY

2.1 Methods

Determination methods of the nature, way of gold appearance and its distributions in investigated ore sample were:

- Mineralogical investigation, quantitative and qualitative microscopic analyze (for automatic image analysis OZARIA 2.5 was used (Tomanec et al., 1997);
- Separation of main minerals under a stereo microscope (monomineral concentrates);
- Determination of gold content;
- The distribution of gold in the ore.

2.2 Mineralogical composition of the ores

According to the quantitative mineralogical analysis in the copper ore specimen, the following minerals were summary given in Table 1.

Table 1. The quantitative mineral composition of investigated copper deposits (in wt-%)

Minerals	Cerova	The Gallery of Bor	V. Krivelj
Pyrite	2.93	17.15	3.69
Chalcopyrite	0.23	0.07	0.68
Chalcocite	0.67	0.23	<0.01
Covellite	0.03	0.49	0.03
Enargite	n.d.	0.17	n.d.
Sulvanite	n.d.	0.02	n.d.
Tetrahedrite	n.d.	<0.01	n.d.
Bornite	<0.01	<0.01	<0.01
Molybdenite	n.d.	0.02	<0.01
Sphalerite	0.03	n.d.	n.d.
Galena	0.10	n.d.	n.d.
Native gold	<0.01	<0.01	<0.01
Electrum	<0.01	<0.01	<0.01
Magnetite	0.98	0.12	0.58
Hematite	0.53	<0.01	<0.01
Rutile	0.09	<0.01	<0.01
Limonite	0.41	0.35	<0.01
Cuprite	<0.01	<0.01	<0.01
Native copper	<0.01	n.d.	n.d.
Malachite	0.03	n.d.	n.d.
Gangue minerals	93.98	81.24	94.95
Total	100.01	99.98	99.99

Note: n.d. – not detected

In the Cerova copper deposit, the major copper minerals are chalcopyrite and chalcocite, while covellite and bornite are present in trace amounts. The oxide copper minerals are identified as cuprite, malachite and native copper.

In the Gallery of Bor copper deposit, the major copper minerals are covellite, chalcocite and enargite, while chalcopyrite, sulvanite, and bornite are present in trace amounts. The oxide copper mineral is identified as cuprite.

In the Veliki Krivelj copper deposit, the major copper mineral is chalcopyrite, while covellite, chalcocite, and bornite are present in trace amounts. The oxide copper mineral is identified as cuprite.

The size distribution and association of the gold minerals were studied by optical microscopy. The gold minerals were determined to be native gold and electrum. Other gold minerals were not determined. The gold minerals were extremely rare, and commonly appeared in the form of dispersion inclusions (“droplets”; 1-5µm) in the copper and iron sulphides, or the quartz and silicates. Studied gold in chalcopyrite are mainly present as a “visible” mineral, but also there are partly bonded “invisible” minerals (Radosavljevic & Zaric 1995).

Gangue minerals are mostly quartz, silicates and less carbonates. The iron oxide mineral magnetite is also founded.

3 CHEMICAL ANALYSES

3.1 Methods

Weight of the monominerals specimen for gold assay was ~5g. Specimens were provided with applying fire assay technique and were treated with HCl and HNO₃, and after that, extraction from solution was done with methyl isobutyl ketone. Gold was determined by atomic absorption spectroscopy method, using a Perkin-Elmer, M-703 instrument (Radosavljevic et al. 1998a).

3.2 Results of chemical analyses

According to the chemical analyses in main copper and iron monominerals concentrates, the following content of gold were summary given in Table 2.

Table 2. The content of gold in the monomineral concentrates (in ppm)

Minerals	Cerova	The Gallery of Bor	V. Krivelj
Pyrite	0.20	0.40	0.05
Chalcopyrite	2.00	n.a	3.10
Chalcocite	2.65	6.55	n.a.
Covellite	n.a.	8.75	n.a
Enargite	n.a.	9.00	n.a

Note: n.a. – not analyzed for

Chalcopyrite, chalcocite, covellite, enargite, and pyrite are determined as the most important carrier of gold.

4 GOLD MINERALOGICAL BALANCE

4.1 Gold distribution in Cerova mine

Chalcopyrite, chalcocite and pyrite are the main in this ore, with combined content about 3.8-wt%. Table 2 gives the average content of gold in chalcopyrite, chalcocite and pyrite. Those three minerals are main gold bearing minerals.

On the total amount of gold, 76% is unaccounted, 20% is associated with copper mineral (chalcopyrite and chalcocite) and about 4% are associated with pyrite (see Fig. 1). These gold minerals are explicitly visible under the microscope and larger dimension size (up to 15µm). The pyrite from Cerova mine has shown a low content of gold (Table 2).

Gold content distribution is presented in the Fig.1.

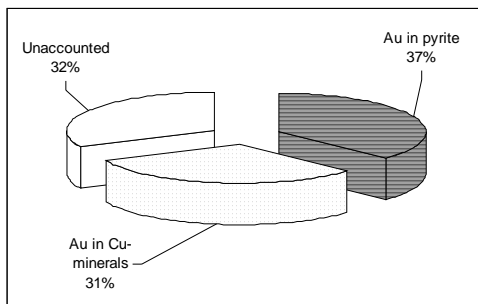


Figure 1. Gold distribution in "Cerova" copper ore

4.2 Gold distribution in Gallery of Bor mine

Covellite, chalcocite, enargite and pyrite are the main in this ore, with combined content about 18.1-wt%. Table 2 gives the average content of gold in covellite, chalcocite, enargite and pyrite. These four minerals are main gold bearing minerals.

On the total amount of gold, 32% is unaccounted, 31% is associated with copper mineral (covellite, chalcocite and enargite) and about 37% are associated with pyrite (Fig. 2). These gold minerals are explicitly visible under the microscope and larger dimension size (up to 10 μ m). The pyrite from the Gallery of Bor mine has shown a mostly content of gold (Table 2).

Gold content distribution is presented in the Fig.2.

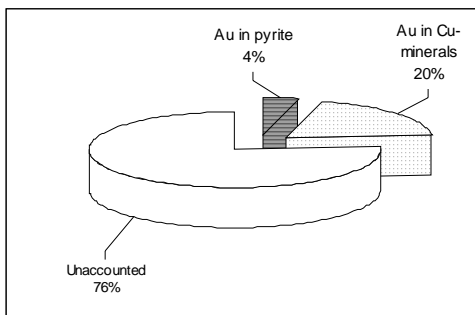


Figure 2. Gold distribution in "The Gallery of Bor" copper ore

4.3 Gold distribution in Veliki Krivelj mine

Chalcopyrite and pyrite are the main in this ore, with combined content about 4.4-wt%. Table 2 gives the average content of gold in chalcopyrite and pyrite. These two minerals are main gold bearing minerals.

On the total amount of gold, 81% is unaccounted, 12% is associated with copper mineral (chalcopyrite) and about 7% are associated with pyrite (Fig.3). These gold minerals are hardly visible under

the microscope. Probably, gold minerals could be in colloidal or diffusive submicron particles associated with gangue minerals (?) The pyrite from Veliki Krivelj deposit has shown a least content of gold (Table 2).

Gold content distribution is presented in the Fig.3.

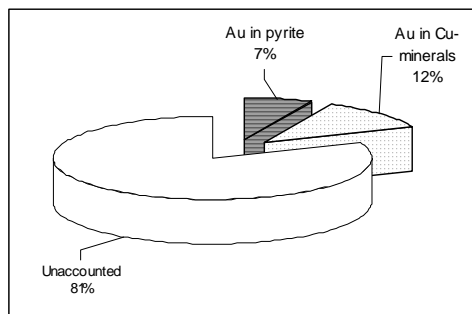


Figure 3. Gold distribution in "Veliki Krivelj" copper ore

5 CONCLUSION

The gold minerals are determined as native gold and electrum. Other gold minerals are not determined. Chalcopyrite, chalcocite, covellite, enargite, and pyrite are determined as the most important gold bearing minerals.

The main copper minerals in the Cerova deposit are chalcopyrite and chalcocite. Pyrite content is low. Gold appears in chalcopyrite and chalcocite, less in pyrite and predominantly as native gold and electrum in larger particles (up to 15 μ m.). Visible gold is mostly associated with gangue minerals. From total available amount of gold, 20% is associated with Cu-minerals, 4% is with pyrite, and the rest 76% is unaccounted.

The main copper minerals in the Gallery of Bor deposit are covellite, chalcocite, and enargite. Pyrite content is high. Gold appears in covellite, chalcocite, enargite and pyrite and predominantly as native gold and electrum in larger particles (up to 10 μ m.). From total available amount of gold, 31% is associated with Cu-minerals, 37% is with pyrite, and the rest 32% is unaccounted.

The main copper mineral in the Veliki Krivelj deposit is chalcopyrite. Pyrite content is low. Gold appears in chalcopyrite, less in pyrite and predominantly as native gold and electrum in small particles (less than 2 μ m.). Visible gold is mostly associated with gangue minerals. From total available amount of gold, 12% is associated with chalcopyrite, 7% is with pyrite, and the rest 81% is unaccounted.

This variable gold content distribution is limited with instantaneous amount and mutual relation of these minerals. Recovery of gold in flotation plants of Veliki Krivelj and Bor is the biggest from the ores of Cerova, and the lowest from the ores of Veliki Krivelj mine.

The principal utilization of gold is from copper ores of Cerova mine because of favorable relation of gold-collecting minerals and as fact that the amount of pyrite is low, and it has low content of gold. Gold minerals are clearly visible and have bigger dimensions.

The copper ore of the gallery of Bor has lower utilization because of larger number of gold-collecting minerals and as fact that the significant amount of gold is connected with pyrite.

The lowest utilization is from copper ores of Veliki Krivelj. Gold minerals are in colloidal or diffusive submicron particles associated with gangue minerals. Finally, the sequence of utilization of gold from copper ores on the basis of these examinations is next: Cerova > Bor > Veliki Krivelj.

6 REFERENCES

- Jankovic S., 1990. The Ore Deposits of Serbia. Belgrade, 1-760 (In Serbian, abstr. English).
- Radosavljevic, S. & Zaric, P. 1995. Minerogenetic characteristics of the gold in the ore of Veliki Krivelj copper mine. Bulletin of Geoinstitute, vol. 31, Belgrade, 239-244 (In Serbian, abstr. English).
- Radosavljevic, S., Canic, N., Bartulovic, Z., Stojanovic, M., & Spaskovski, B. 1998a. Mineralogical Balance and Reproducibility of Gold Recovery from Copper Deposit Veliki Krivelj – Yugoslavia. Title of publication: "Innovations in Mineral and Coal Processing". Edited by Suna Atak, Guven Onal & Mehmet Sabri Celik. A. A. Balkema/ Rotterdam/ Brookfield/, 555-559.
- Radosavljevic, S., Nikolic, M., Marinko, M., & Spaskovski, B. 1998b. Comparison Analysis Recovery of Gold in Flotation Plants of Veliki Krivelj and Bor (Yugoslavia). Proc. of 4th International Conference of Mineral Processing, Part I, Ostrava Poruba, Czech Republic, 211-217.
- Tomanec, R., Vucinic, D., Radosavljevic, S., & Jovanic, P. 1997. The characterization of ores and minerals products with the help of image analysis. Proc. 7th Balkan Confer. On Mineral Processing, Vatra Dornej, Romania, 382-387.

Dolomitic Itabirites and Generations of Carbonates in the Cauê Formation, Quadrilátero Ferrífero

C.A.Rosière & N.Brunnacci-Ferreira-Santos

CPMTC, Geosciences Institute, Federal University of Minas Gerais, Belo Horizonte, Brazil

ABSTRACT: Extremely large high-grade iron deposits like Águas Claras, Córrego de Feijão e Mutuca in the Quadrilátero Ferrífero District, Brazil, comprise friable and hard bodies associated with dolomitic itabirites. Dolomitic itabirites are irregularly distributed in the lower proterozoic Cauê Formation, and are understood as a product of the dolomitization and metamorphism of sedimentary banded iron formations. Mineralogical petrographic and microstructural analysis in carbonate and quartz of the dolomitic itabirites from the Águas Claras Deposit, western Serra do Curral show the existence of four sparitic and micro-sparitic dolomite phases with different compositions and Fe content, that may sequentially replace each other, and two distinct quartz generations. Magnesite may be present too. Dolomitization has produced the protore for friable orebodies and is probably of hydrothermal origin. It seems also to be related with the formation of the hard massive Fe-bodies. Dolomitic itabirite is commonly encountered in the eastern and western domains of the Serra do Curral structure and in the eastern limb of the Moeda Syncline where the metasediments of the Minas Supergroup are in tectonic contact with the underlying schists of the Rio das Velhas Supergroup and with granite gneisses.

1 GEOLOGICAL SETTING – THE QUADRILÁTERO FERRÍFERO

The Quadrilátero Ferrífero is located at the southern border of the São Francisco Craton (Almeida 1977), a geotectonic unit of Brasiliano age (0.8 – 0.6 Ga). In this area synclines with Paleoproterozoic metasedimentary rocks of the Minas Supergroup present a roughly rectangular arrangement and are separated by antiformal structures dominated by Archean greenstones of the Rio das Velhas Supergroup and domes of Archean and Proterozoic crystalline rocks (Machado et al. 1992; Noce 1995). The Minas Supergroup comprises, from bottom to top, the Caraça, Itabira, Piracicaba and Sabará Groups (Dorr 1969). The thickest sequence of iron formations together with enclosing high-grade iron orebodies belong to the Itabira Group, that comprise a sequence of chemical sedimentary rocks deposited in plataformal environment with subordinate metapelite units. Carbonate rocks of the upper Itabira Group, which contain algal remnants, have been dated by Babinski et al. (1995) at 2419 +/- 19 Ma (Pb-Pb isochron data). The Sabará Group comprises a 3.0 to 3.5 km-thick sequence of metavolcanoclastic rocks, turbidites and

conglomerates separated by an unconformity from the underlying Piracicaba Group.

The regional structure is the result of the superposition of two main deformation events (Chemale Jr. et al. 1994). The first produced the nucleation of regional synclines in the supracrustal sequence, uplifting of the gneissic domes during the Transamazonian Orogenesis (2.1 – 2.0 Ga), and the regional metamorphism. The second was related to a west – verging thrust belt of Brasiliano/ Pan-African age (0.8 – 0.6Ga). The latter event, which was more dramatic in the eastern half of the Quadrilátero Ferrífero, deformed the earlier structures and was responsible for the deformation gradient present in the area. Two main structural domains (Rosière et al. 2001) can be delimited regionally: the Eastern High-Strain Domain includes regional thrust systems and shear zones, whereas the Western Low-Strain Domain displays well preserved megasyndines that are discontinuously cut by discrete shear zones and faults. The iron formation of the Itabira Group delineates the main structures of the entire Quadrilátero Ferrífero as a regional marker, and high-grade iron deposits occur along the limbs of the megasyndines as well as in shear zones in the Eastern High-Strain Domain.

2 ITABIRITES AND HIGH-GRADE ORE TYPES

2.1 Itabirites

The Itabira Group is composed of two formations (Dorr 1969).

- i. The Cauê Formation comprises a thick sequence (ca. 250-300 m) of itabirites intercalated with hematitic phyllites and dolomitic phyllites
- ii. The Gandarela Formation, which conformably overlies the Cauê Formation, comprise mainly calcitic and dolomitic marbles with subordinate phyllites.

Itabirites are metamorphic, oxidized and heterogeneously deformed banded iron formations (Dorr 1969). There are several distinct mineralogical and textural types due to variation in the original composition of the sediments, intensity of deformation, and degree of metamorphism and hydrothermal alteration. Three main compositional types can be distinguished: quartz itabirite, dolomitic itabirite and amphibolitic itabirite. Manganese-rich itabirite and hematite-rich meta-pelitic rocks are also encountered. Quartz itabirite is the most oxidized variety and the more common and wide-spread type as well. It is composed of fine granular quartz alternating with iron oxide bands (hematite/martite with kenomagnetite relics). Dolomitic itabirite is a dolomitized iron formation consisting of red carbonate and black iron oxide bands. Amphibolitic itabirite present several types of amphiboles, depending on the metamorphic grade, together with quartz and eventually dolomite, alternating with iron oxide bands where martite also dominates.

2.2 High-grade iron ores

Two distinct types of high-grade iron ore bodies (>65 wt % Fe) occur in the Quadrilátero Ferrífero

- i. Hard ores both as massive and schistose bodies composed of hematite, martite, specularite and iron-deficient magnetite (kenomagnetite). The shape of the massive orebodies is totally or partially controlled by the bedding of the BIF protore, and the granoblastic fabric commonly mimics the itabirite structure. Irregular pockets of high-grade iron ore with a brecciated fabric may also occur but are not as common. Schistose orebodies composed mainly of oriented specularite plates occupy shear zones that crosscut the BIF.
- ii. Soft, friable ores, distributed as “alteration halos” around the hard orebodies. Soft high-grade orebodies may be powdery, structureless, or else present a brecciated structure or relics of the original banding. Huge cavities of several meters diameter may also be present. Soft high-grade ores do not considerably differ in mineral composition from the hard ores except in the

case of some discontinuous pockets of powdery *blue dust* composed of random textured platy hematite that occur in the middle of granoblastic ores. Goethite occurs only in the surface, with its concentration decreasing quickly with depth. Relics of gangue minerals such as quartz or dolomite, quartz, chlorite, talc and apatite may be detected.

3 DOLOMITIC ITABIRITES AND DOLOMITE GENERATIONS

Dolomitic itabirite occur mainly in the western Low-Strain Domain along the central part and western branch of the Serra do Curral Ridge and in the northern half of the western Limb of the Moeda syncline both as outcrops and diamond drill cores around mines such as Fazendão, Jangada, Aguas Claras, Mutuca and Capão Xavier (Fig.1). Contact between dolomitic rocks and normal, quartz itabirite is gradational both laterally and vertically.

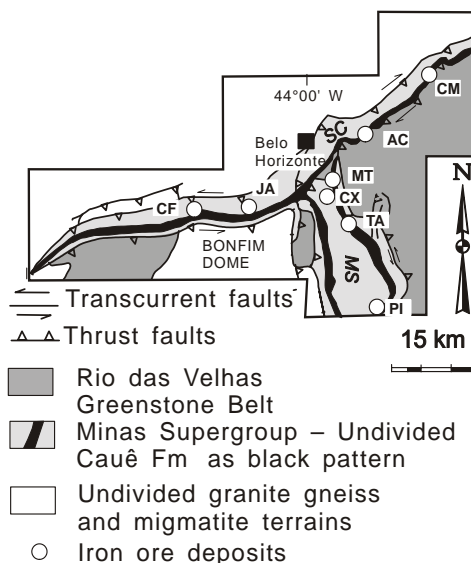


Figure 1: Geologic location map of the confluence between the Serra do Curral (SC) and Moeda Syncline (MS) with distribution area of dolomitic itabirite (Cauê Formation). Iron deposits: PI – Pico; TA – Tamanduá, MT – Mutuca; CX – Capão Xavier, AC – Águas Claras; JA – Jangada, CF – Córrego do Feijão, CM – Córrego do Meio.

This variety of itabirite present both meso- and micro- banding with alternating carbonate/quartz (reddish-white) and iron oxides (dark gray-black) bands (see Spier et al. 2003 for a detailed description). Several dolomite and quartz veins cut

across the banding (Fig.2). This structure may be entirely transposed and obliterated in shear zones with the development of schistosity and a secondary (tectonic) banding that may easily confused with the primary (sedimentary/diagenetic) structure.

Dolomitic itabirite can be hematite-rich (up to 42.5% Fe – Spier et al. 2003) and may locally develop into hard massive ore. It also gradates to the top of the sequence (Gandarela Formation) into iron-poorer banded or massive gray to pink dolomites although the contact between the lithologies is commonly sharp. Dolomitic phyllite may also occur interlayered and with gradational contact.

For the present studies, samples were selected of dolomitic itabirite from the open pit and the diamond drill hole PZ5501 from the Aguas Claras Deposit (Figure 2). This deposit is the most important occurrence of dolomitic itabirite and, at the same time, the largest single high-grade orebody of the Quadrilátero Ferrífero. It is located in the eastern branch of the Serra do Curral Range (Chemale Jr et al. 1994) near the confluence with the Moeda Syncline (see Spier et al. 2003 and references therein, for further details). The orebody is composed mainly of soft, friable ore, presenting a banded structure defined by alternating porous and compact mm to cm-thick layers.



Figure 2: Quartz dolomite itabirite. C1B Fe-dolomite (dark-grey) substitutes quartz (white) in fold hinges

3.1 Dolomite Generations

Detailed petrographic and mineralogical analysis of the carbonates from itabirite show distinct generations of dolomites: dolomite C1 is microsparitic with average grain size of 15mm and occurs in the mesobands of the itabirite. Dolomite C1A is colorless but C1B is red to pink due to its higher Fe and Mn content. C1B may substitute fine-grained quartz, especially in the fold hinges (Figure 2). Generations C2 and C3 occur in veins as coarser sparry dolomite. C2 carbonates are Fe-rich and

occur in stretched veins with *boudin* structure. C3 carbonates are colorless, Fe-poor, precipitated in veins and strain shadows from C2 *boudins*. Late calcite and quartz veins cross-cut the fabric.

4 GENETIC CONSEQUENCES AND DISCUSSION

A hypogene hydrothermal model (Oliver & Dickens 1999, Barley et al. 1999, Hagemann et al. 1999, Taylor et al. 2001, Rosière & Rios 2004) is now widely accepted to explain the origin of hard high-grade iron orebodies, probably involving both meteoric and deep-seated fluids. Rosière & Rios (2004) suggest that meteoric fluids moved downwards from the surface along normal faults and fractures during progressive uplift and extension of the crust during the collapse stage of the Transamazonian event (Alkmim & Marshak 1998). These fluids pervasively oxidized the original BIF in the entire QF, producing high-grade bodies in sites of more intensive water percolation such as along major faults and second-order folds, due to its higher permeability.

Soft high-grade ore seem to have undergone related but distinct processes with superposed supergene and hypogene mineralization events. The intimate association between large soft high-grade ore and dolomitic itabirite and the presence of large caves occasionally encountered during the mine operations presenting typical collapse structures speak for the importance of supergene processes as already pointed out by Viel et al (1999) and Spier et al. (2003).

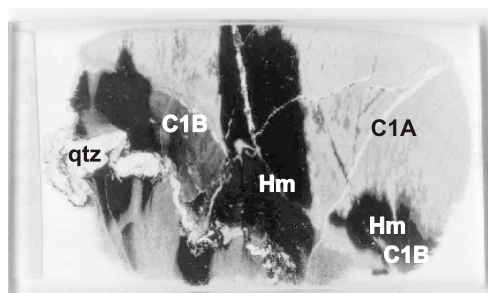


Figure 3: Thin section of partially oxidized dolomitic itabirite. C1A Microsparitic light-colored dolomite, C1B – Microsparitic Fe-dolomite. Hm – Hematite. Qtz – Quartz vein

Dolomitic itabirite probably forms from folding-related substitution of quartz to ferroan dolomite (C1B dolomites). An intense magnesium remobilization is also attested by the presence of large magnesite body partially controlled by the

hinge zone of a regional fold in the Acaba-Mundo Quarry, just a couple of kilometers distant from the Aguas Claras Mine. Further remobilization of carbonates producing coarse sparry Fe-rich dolomites (C2 dolomites) and minor calcite veins completed the process. Fe-dolomite was oxidized by hydrothermal fluids in order to form hematite (as it is possible to observe in Figure 3) in a much more efficient way than would be expected for a presumed metassomatic substitution of quartz. High-grade orebodies developed by complete substitution of dolomite, enveloped by an Fe-rich dolomitic protore.

Soft ore is therefore, the weathering product of an incomplete mineralized dolomitic itabirite. Remaining carbonates and minor quartz from the hypogene phase were leached resulting in gigantic deposits like Aguas Claras by residual enrichment. Soft high-grade bodies may also occur related to quartz-itabirite such as in the Cauê Deposit, but they are smaller, extend to much shallower levels, and are considerably different, presenting relics of interstitial quartz and gradational transition to the protore, especially close to the land surface, forming high-grade soft, friable, quartz-itabirites.

5 ACKNOWLEDGEMENTS

The authors thank the MBR in the name of O. Tessari and particularly C.A. Spier for making available the samples and for the fruitful discussions, sharing valuable information. N.B-F-S thanks the FAPEMIG and UFMG for the BIC-scholarship (PROBIC-Program) and C.A.R thanks the CNPq for the all-round financial support.

6 REFERENCES

- Alkmim, F. F., and Marshak, S. (1998) Transamazonian Orogeny in the Southern São Francisco Craton Region, Minas Gerais, Brazil: evidence for Paleoproterozoic collision and collapse in the Quadrilátero Ferrífero: *Precambrian Research*, v. 90, p. 29 - 58.
- Almeida, F. F. M. (1977) O Craton de São Francisco: *Revista Brasileira de Geociências*, v.7 (4), p. 349 - 364.
- Babinski, M., Chemale, F., Jr., and Van Schmus, W. R. (1995) The Pb/Pb age of Minas Supergroup carbonate rocks, Quadrilátero Ferrífero, Brazil, and its implications to the correlation with BIFs from South Africa and Australia: *Precambrian Research*, v.72, p. 235 - 245.
- Barley, M.E., Pickard, A.L., Hagemann, S.G., Folkert, S.L., (1999) Hydrothermal origin for the Two Billion Year Old Mount Tom Price Giant Ore Deposit, Hamersley Province, Western Australia, *Mineralium Deposita*, v. 34, p.784-789.
- Chemale, F. Jr., Rosière, C. A. & Endo, I. (1994) The tectonic evolution of the Quadrilátero Ferrífero, Minas Gerais, Brazil: *Precambrian Research*, 65, p. 25 - 54
- Dorr, J.V.N.II (1969) Physiographic, stratigraphic and structural development of the Quadrilátero Ferrífero, Minas Gerais: U. S. Geological Survey Professional Paper 641-A, 110p.
- Hagemann, S.G., Barley, M.E., Folkert, S.L., Yardley, B.W., Banks, D.A. (1999) A hydrothermal origin for the giant Tom Price iron ore deposit. In: Hughes FE (ed) *Mineral Deposits, Process to Processing*. Balkema, Rotterdam, p.41-44.
- Machado, N., Noce, C. M., Ladeira, E. A., & Belo de Oliveira, O. A (1992) U-Pb Geochronology of Archean magmatism and Proterozoic metamorphism in the Quadrilátero Ferrífero, southern São Francisco craton, Brazil: *Geological Society of America Bulletin* 104, p. 1221-1227
- Noce, C. M. (1995) *Geocronologia dos eventos magmáticos, sedimentares e metamórficos na região do Quadrilátero Ferrífero, Minas Gerais*: Unpublished Ph. D. Thesis, Universidade de São Paulo, 128 p.
- Oliver, N.H.S. and Dickens, G. (1999) Hematite ores of Australia formed by syntectonic heated meteoric fluids, in *Mineral Deposits: Processes to Processing* (Ed: Stanley), v. 2, p. 889-892.
- Pires, F. R. M. (1995) Textural and mineralogical variations during metamorphism of the Proterozoic Itabira Iron Formation in the Quadrilátero Ferrífero, Minas Gerais, Brazil: *Anais Academia Brasileira de Ciências*, v. 67, p. 77-105
- Rosière, C. A., Siemes, H., Quade, H., Brokmeier, H.-G., & Jansen, E. M. (2001) Microstructures, textures and deformation mechanisms in hematite: *Journal of Structural Geology*, v. 23, p. 1429 - 1440
- Rosière, C.C. and Rios, F.J. (2004) The origin of hematite in high grade iron ores based on infrared microscopy and fluid inclusion studies: the example of the Conceição mine, Quadrilátero Ferrífero, Brazil, *Economic Geology*, 99, 3 in press.
- Spier, C. A., Oliveira, S.M.B. & Rosière, C. A. (2003) Geology and geochemistry of the Aguas Claras and Pico Iron Mines, Quadrilátero Ferrífero, Minas Gerais, Brazil: *Mineralium Deposita*, v. 38, p. 751 - 774
- Taylor, D., Dalstra, H.J., Harding, A.E., Broadbent, G.C., Barley, M.E. (2001) Genesis of High-Grade Hematite Orebodies of the Hamersley Province, Western Australia. *Economic Geology* v. 96, p.837-873.
- Viel, R. S., Moreira, P.C.H. & Alkmim, F.F. M. (1987) *Faciologia da Formação Cauê e Gênese do Minério Friável da Mina de Águas Claras, Serra do Curral, Minas Gerais, Simpósio sobre Sistemas Depositionais no Pré-Cambriano Brasileiro, SBG, Ouro Preto. Proceedings....*, p. 137 - 153

Nugget Effect in Gold Grade Determination – An Historical Case

L.M.Sant'Agostino

Department of Sedimentary and Environmental Geology, Geosciences Institute, University of Sao Paulo, Brazil

M.M.M.L.Tassinari & G.Ratti

Department of Mining Engineering and Petroleum, Polytechnic School, University of Sao Paulo, Brazil

ABSTRACT: Appraising the nugget effect interference in gold grade determination some tests were performed to define ore sample ideal weight to be chemically analyzed. The gold mineralization is associated to a silicified shear zone developed in tonalitic gneiss, where a system of quartz veins was formed, leading to different types of ores with grades varying from 1 to 50 g/t Au. The native gold is visible by naked eye reaching milimetric grain size and is frequently associated with sulphides (pirrotite and arsenopirite). Some channel samples were collected in a research gallery, which were crushed/homogenized generating weights of around 350 kg with particles less than 3.36 mm in the mine site and sent to the laboratory for analysis. Several tests of sample preparation with different procedures of grain size reduction conjugated with weight reduction were performed generating pulverized aliquots (under 0.074 mm) of 50 g for analysis by direct dissolution and atomic absorption dosage. Three preparation procedure routes applied in six to seven aliquots totalized 950 g of analyzed weight of each sample. Two routes followed only one step of weight/grain size reduction to obtain the aliquots from the material send to the laboratory. The last route comprised four steps of weight/grain size reduction. For all the ore types a significant variability of results were obtained showing a huge nugget effect in the analysis. Independently of gold grade level, the nugget effect was exceptionally. The solution was deal with expected variability and uncertainty of grades generated as statistical parameters of this study.

1 INTRODUCTION

This study comprises tests performed in the preliminary research involving reserve evaluation, and also technological studies, of an ore presenting naked eye native gold (milimetric sized) and high grade. It was a typical case in which nugget effect was expected, and the tests intended to measure it's magnitude as well as an understanding how to deal with it.

The study was developed with ore coming from a subterraneous mine, built in fresh rock, and the samples were collected in a research gallery by channel scrapping in the roof, hanging walls and footwalls composing volumetric samples. Five samples corresponding to different ore types were considered in this study.

The volumetric samples, pre-prepared in the mine site, were submitted to different routines or procedures in laboratory.

Basically three different routines of sample preparation for the same procedure of chemical analysis were applied in the volumetric samples. The main idea was evaluated the grade variability that

can be introduced only as consequence of the way of reducing samples to analysis.

2 MINERALIZATION CHARACTERISTICS

The ore body corresponds to a silicified shear zone (de Ferran 1988) inside barren tonalitic gneiss, in which a main quartz vein is recognized, which ramifies to smaller ones locally forming two or three individualized veins; the hostess silicified zone is also mineralized, both in surrounding boundaries and between the vein ramifications.

The veins system is tabular, slopes 60 NE, being N45W oriented. It have 600m in strike length and has been traced for at least 150 m down dip; the veins present variable thickness with a maximum of 3 meters (mean 2.5 m).

For this study five different ore types were sampled: one of the ramification veins (Vein1), the main vein (Vein2), the mineralized walls between veins (ISR), the both side mineralized host silicified rock (SR1 and SR2) and the contact between the silicified zone and the tonalite rock (SRT). They

have defined spatial position and can be distinguished by their grade, mineralogical and gold grain size characteristics.

Around 85% of the total gold contained in these lithologies is in the native form and the rest is contained in sulphides (pyrite and arsenopyrite) and the same figure is observed for the mineralized host rock. Only the Intermediary material the gold mineralogical form distribution is a little different: 80% as native gold and 20% inside sulphides.

The native gold constituted granular irregular nuggets, sometimes slightly lamellar. It was estimated (Tassinari 1996) that around 70% of the gold content is granular, it occurs as millimetric grains (<2 mm) and also as micrometric inclusions in silicates or even in the sulphides

3 OBJECTIVE

Due to the abundant presence of native gold of millimetric grain size, nugget effect was commonly verified in this ore analysis. This effect has a significant role in the ore evaluation causing an uncertainty in the higher grades obtained.

The aim of this work was appraise the nugget effect interference in gold grade determination, which is essentially related with the low level of grades and gold grain size. The specific weight differences between gold particles and the silicate minerals constituents of the ore also influence the nugget effect.

Considering the sample weight limitation for chemical analysis, some tests were performed to define ore sample ideal preparation/weight to be analyzed as well as to measure the variability of the results.

4 PRACTICAL PROCEDURE

The channel samples collected in research gallery representative of each ore type were initially prepared at the mine site. The bulk samples constituted by several tons of weight were individually crushed below 3.36 mm, homogenized and splitted generating masses of around 350 kg that were sent to the laboratory for analysis.

4.1 Laboratory procedures

Three routes of sample preparation were performed in the laboratory with different procedures of grain size reduction conjugated with weight cut backing till obtain pulverized aliquots (under 0.074 mm) of 50 g for analysis by direct dissolution and atomic absorption dosage (Fig. 1).

Two routes followed only one step of grain size plus weight reduction to obtain the aliquots from the

material send to the laboratory. The last route comprised four steps of weight/grain size reduction.

In the first route, one aliquot of 200g was obtained by splitting the crushed samples, comminuted below 0.210 mm and then splitted in four aliquots of around 50 g then pulverized to minus 0.074 mm to be analyzed.

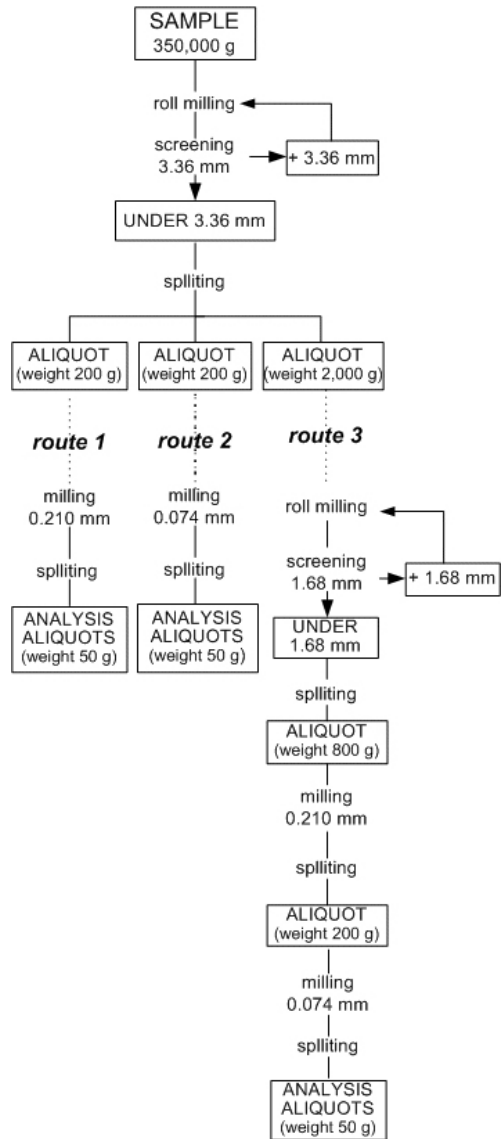


Figure 1 – Laboratory samples preparation.

The second route was quite similar to the first, but the final aliquots for analysis were maintained in the -0.210 mm, without any pulverization.

The last route meant an initial aliquot of 2.000 g, milled below 1.68 mm and reduced to 800 g; then again a particle size reduction below 0.210 mm and weight decreasing for an aliquot of 200 g; finally the pulverization to - 0.074 mm and end splitting in four aliquots of 50 g for chemical analysis.

A number of eighteen to nineteen aliquots of 50 g were analyzed, totalizing a minimum weight of 900 g for each sample.

4.2 Results

A stunning dispersion of grades was observed in the analyzed aliquots for all preparation routes and all samples (Tab.1); the results should be evaluated considering the type of ore.

The preparation route 1, compared with the others, showed for the vein samples the major grades and also the major variability of values. For the silicified zone materials evidenced a less expressive variability and the lower grades.

The preparation route 2 gave low values to the vein samples grades and similar to the silicified zone samples, in all cases showed a great variability.

Finally, the preparation route 3 maintained the great variability of values; for the vein ore presented intermediate grades face the others preparations, and for the silicified zones provided higher grades unless for the SRT.

The real grades values remain unknown; the best result should be the mean of all the dosages that is of high representation because it have a base of higher sample weight analyzed, more then 900 g. The nugget effect was critical in the studied case leading to a great variability of results in the several dosages performed, what bring a low confidence in the grades obtained with small weight samples (50 g). The only ways to deal with this effect is analyze bulk samples weighting tons or consider uncertainties and probabilities associated with small samples analysis.

Evaluating the statistics of the analyzed aliquots, apart of the preparation procedure, some interesting aspects could be verified that are in some way related to the ore characteristics. Also the statistics of hypothetical 100g aliquots, generated by mathematical combination of the same 50 g analyzed aliquots, was evaluated.

The ore types can be divided in two large domains, the vein mineralization and the silicified zone mineralization (Fig.2).

For the vein aliquots analyzed, considering both the Vein1 and Vein2 samples, it was verified that 75% of them have:

- grades between 7 and 40 ppm of Au for sample Vein1, so the data from the preparation route 1 tend to give an upper estimative; considering 100g aliquot the range enlarge to 50 ppm;
- grades between 4 and 60 ppm of Au for sample Vein2, again the preparation route 1 tends improperly and also the route 2 that showed tendency to under estimate the ore grade; considering 100 g aliquot the range stay the same.

Table 1 – Analyzed aliquots gold grade in ppm.

Route	Analysis	Vein 1	Vein2	SR1	ISR	SR2	SRT
1	1	119	77.3	0.89	5.19	3.75	1.66
	2	16.4	184	2.10	4.99	3.09	1.69
	3	35.5	60.4	1.10	5.27	2.42	2.53
	4	125	4.80	1.89	3.67	1.84	2.44
	5	21.2	59.0	1.94	5.2	1.73	4.24
	6	60.6	41.4	1.64	4.71	2.00	3.07
	mean	63.0	71.2	1.59	4.84	2.47	2.61
	desvpad	48.3	60.5	0.49	0.61	0.80	0.96
2	1	10.1	24.4	3.33	6.67	4.52	1.55
	2	31.7	27.4	1.27	8.12	2.44	2.55
	3	7.67	6.51	0.80	5.23	2.93	4.03
	4	9.42	7.28	1.40	5.2	2.58	5.96
	5	60.5	6.39	0.99	5.35	3.33	1.72
	6	25.9	6.73	1.06	5.26	2.95	3.90
	mean	24.2	13.1	1.48	5.97	3.13	3.29
	desvpad	20.3	10.0	0.93	1.20	0.75	1.68
3	1	17.2	96.8	0.92	6.27	1.74	1.92
	2	34.0	38.6	18.5	8.28	2.04	1.49
	3	18.6	53.7	1.52	4.22	32.8	1.43
	4	29.3	63.6	0.97	3.95	3.04	1.63
	5	67.0	45.9	0.98	7.08	1.70	1.93
	6	23.2	33.4	0.93	7.57	4.94	3.85
	7	22.8	26.3	na	na	2.24	na
	mean	30.3	51.2	3.97	6.23	6.93	2.04
	desvpad	17.2	23.7	7.12	1.79	11.46	0.91
Total	mean	38.7	45.5	2.35	5.68	4.32	2.64
	desvpad	34.0	42.6	4.08	1.36	6.96	1.27
	minimum	7.67	4.80	0.80	3.67	1.70	1.43
	maximum	125	184	18.5	8.28	32.6	5.96

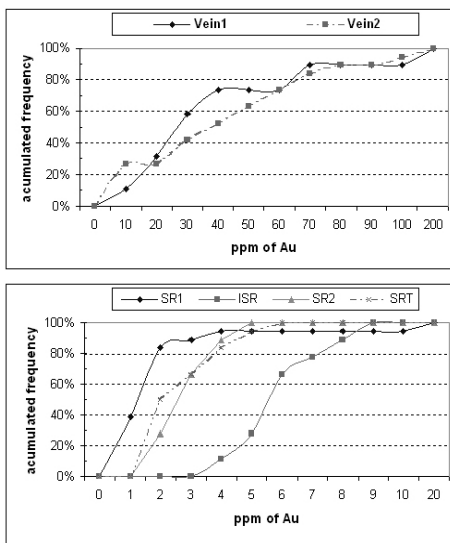


Figure 2: Analyzed aliquots grades distribution for each sample

For the samples related with the silicified zones some general aspects could be observed; 90% of the aliquots of each sample analyzed showed:

- SR1 grades ranging from 0.8 till 3 ppm of Au, pointing preparation routes 1 and 2 as more reliable;
- ISR grades between 3 and 8 ppm of Au, making acceptable the results of all the preparation route;
- SR2 and SRT grades ranging from 1.4 to 4 ppm, what indicates tendency to upper estimation in route 3 for ore type SR2.

The mathematical simulated 100 g aliquot analysis showed almost the same results.

5 CONCLUSIONS

The results obtained with the three different preparation procedures showed an extreme variability related with the gold grain size. The nugget effect could be confirmed for all ore types and was not related with the gold grade level.

So, apart of any natural variability expected in gold grade along the ore body, there is one inconsistency introduced only by sample preparation to chemical analysis, which is independent of the analytical method applied. Even analysis performed with sample weight with 50 g or the double could not afford significantly reduce the nugget effect.

For the low grades ore types, in the studied case the silicified zone samples, a sample preparation procedure comprising several steps of weight/grain size reduction, could give results in a thin range of

values. But for the ore types with high grades, in the case the vein samples, the nugget effect could not be reduced or controlled by any careful appropriated sample preparation procedure.

The solution applied was a routinely analysis of 50 g aliquots supporting the reserve evaluation and also the mining operation, in which were applied the parameters of variability and uncertainty here measured. The data obtained by this way were periodically checked applying physical separation of the gold (gravimetric methods) in volumetric samples.

The mine operated during the previous time life according to the reserve calculated based on the parameters here exposed with time and ore mean grade disparities less then 0,5% relatives, validating the criteria adopted.

6 REFERENCES

- De Ferran, A. 1988. Depósito de ouro de Salamangone e Mutum, Calçoene, Amapá. In: BRASIL. Ministério das Minas e Energia. National Department of Mineral Production. Principais depósitos minerais do Brasil. Brasília, DNPM, v.3, p.581-87.
- De Ferran, A.& Utter, T. 1987. Novo Astro: Brazil's future hard rock gold mine. Mining Magazine, v.156, n.2, p.150-2, February.
- Tassinari, M.M.M.L. 1996. Caracterização tecnológica de minérios auríferos. Um estudo de caso: O minério primário da jazida de Salamangone, AP. PHd Thesis presented to the Department of Mining Engineering and Petroleum, Polytechnic School, University of Sao Paulo, Brazil. 140 p.
- Tassinari, M.M.M.L., Kahn, H., Sant'Agostino, L.M.& Ratti, G. 1998. Characterization of primary gold from Salamangone, Ap, Brazil. 17th General Meeting of the International Mineralogical Association, Toronto, Canadá, Abstracts p. A6.

Chromites of the Polar Urals, Russia

G.N.Savelieva

Geological Institute, Russian Academy of Sciences, Moscow, Russia

ABSTRACT: Paleozoic ophiolites of the Polar Urals host numerous chromite ore bodies that display wide mineralogical variation. Distinct chromite types occupy different positions relative to the structure of the mantle sequences. The formation of the dunite and chromite bodies is related to several magmatic and mantle metasomatic events. High-Al, high Mg chromite (type 1) is related to the first event, likely formed during partial melting of peridotite, and is associated with minor fluid activity. Increasing magmatic and fluid activity resulted in crystallization of high-Cr, low-Mg chromite (type 2), within large dunite bodies, close to the Moho boundary. A further event resulted in the reaction of percolated melt with host peridotite. This reaction resulted in the formation of dunite, hosting moderately Cr, high-Mg chromite (type 3), and, with increasing volatile content and plastic, semi-brittle deformation, final crystallization of high-Cr, high-Mg metallurgic chromite (type 4).

1 GEOLOGICAL AND PETROLOGICAL BACKGROUND

1.1 Geology

The complete ophiolite sequences crop out in the Polar Urals. The massifs Voykar, Rayiz and Syumkeu form a huge allochthonous bodies of ultramafic and mafic rocks stretching from latitude $N 68^{\circ} 00'$ to $N 54^{\circ} 40'$ (up to 500 km long and 20-50 km wide). Ophiolites and volcano-sedimentary complexes of a Lower Paleozoic ocean-arc basin are thrust onto the eastern margin of the European plate (Saveliev & Samygin 1979; Savelieva & Nesbitt 1996). Ophiolite sequences include: (i) residual mantle ultramafics – harzburgite, locally lherzolite and dunite; (ii) plutonic mafic-ultramafic rocks – dunite, wherlite, pyroxenite, layered gabbro and gabbro-norite, (iii) isotropic gabbro, hornblend gabbro and sheeted diabase dikes; (iiii) fragments of pillow lavas unit.

According to paleoreconstructions, to petrological and geochemical criteria, such as the relative REE, HFSE and LILE abundances in plutonic and dike rocks of the Voykar ophiolite, this characterize the geodynamic environment of slow spreading above the ancient subduction zone, where an uprise of mantle diapir was accompanied by intermittent

intrusion of basaltic magma in Early-Middle Paleozoic time (Saveliev et al. 1999; Savelieva et al. 2002). The Rb/Sr isochron age of an intrusive tonalite, crosscutting the ophiolite gabbro and diabase dikes, is determined to be 395 ± 5 Ma (Buyakaite et al. 1983).

1.2 Petrology

Depleted residual peridotites constitute the bulk of the massifs. High depletion of ultramafics is reflected by low Ca, Al content in peridotites: olivine + enstatite + chromspinel \pm diopside (rare diopside is represented, in general, as neoblasts); abundance of dunite bodies is about of 20% of the residual mantle sequence. Low content of alumina oxide of porphyroclastic and protogranular enstatite ($Mg\# = 90-91$) correlative with high chromium number of accessory spinel ($Cr\# = 38-55$). Petrofabrics of ultramafics show a very strong lattice preferred orientation – olivine slip systems are: $[100](010)$ and $[100]\{0k1\}$. High-temperature ductile flow structures in harzburgites are marked by well expressed metamorphic banding and lineation. Flow folds are detectable and persistent throughout residual sequence, including the most depleted dunite zone.

The development of large scale high-T flow folds were accompanied in time and space with a creation of subvertical network of dunite, pyroxenite and local gabbro dykes. Some dunite bodies occur along the axial part of flow fold and they are surrounded by dunite veins (Savelieva et al. 2002).

Active interaction of hot residual harzburgites with percolating melts is clearly displayed in local occurrences of harzburgites impregnated with diopside, or, rarely, with plagioclase and in an abundance of websterite and gabbro dikes and veins cutting harzburgite banding.

2 STRUCTURAL SETTING OF CHROMITITES AND MINERAL COMPOSITION

Chromite ore bodies widespread in the ophiolite massifs and display a large mineralogical variations (Saveliev 1977; Saveliev & Savelieva 1991). Distinct chromite types occupy different positions relative to the structure of the mantle sequences (Fig.1).

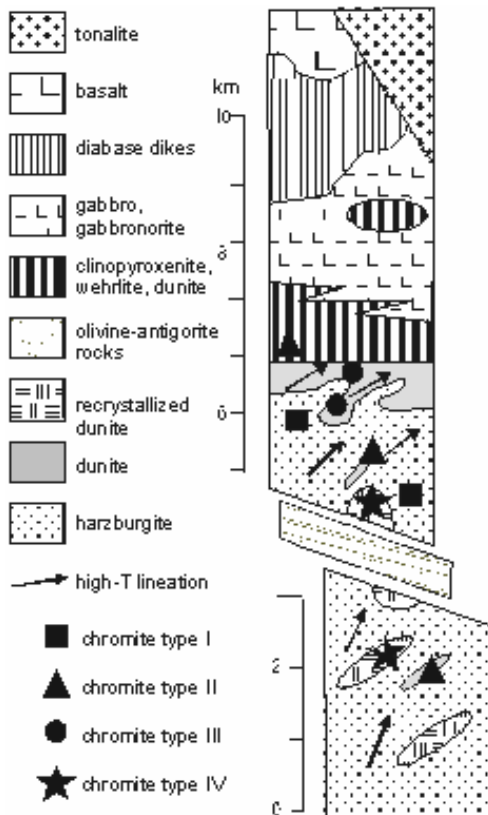


Figure 1: The position of the chromite ore bodies within schematic section of the Polar Uralian ophiolite.

2.1 Type 1

Massive and nodular chromites that form lenses and veins, occur below the petrological Moho boundary, within harzburgite. Chromite ore bodies are concordant, in general, to harzburgite banding or, to axial plane of flow folds and flexures; the plunge of bodies follows to harzburgite lineation (type 1a). Small chromite bodies of dense and disseminated ore occur in dunite veins and irregular bodies, that cut harzburgite and form the network of vein and dikes around of large dunite lenses (type 1b). The typical composition of ore is: Cr-spinel coarse grained 70-90% + Ol serpentinized 10-20% ± Di up to 10%. Mineralogical characteristics include: Cr-spinel (Cr# = 43-55, Mg# = 63-68, TiO₂ = 0.36-0.50%), olivine (Mg# = 90-95), ± high-Mg diopside ± amphibole (pargasitic) and also Ni, Fe-sulfides, and uvarovite.

2.2 Type 2

Disseminated chromites form lenticular, banded bodies within dunite in close spacial association with banded wehrlite-dunite-clinopyroxenite unite. These are characterized by a big size along the strike of chromite bands – up to 1.5 km and thickness not more, than several metres. The ratio of Cr-spinel/silicates (mostly, serpentinized olivine) is changed from 80/20 to 10/90. The orientation of chromite bodies (strike and dipping) is concordant to this of the banding of wehrlite and clinopyroxenite. Here Cr-spinel is quite variable: Cr# = 65-84, Mg# = 28-50, TiO₂ = 0.14-0.29%; and occurs with olivine (Mg# = 90-92) ± Ni, Fe-sulfides.

2.3 Type 3

Dense, middle- and fine-grained chromites, that form veins and tubes, associated with large dunite bodies that occur in the central part of mantle sequence. As a rule, chromites are situated at the periphery of dunite bodies, concordant to its boundary and discordant to harzburgite banding. The mineral composition of ore is: Cr-spinel middle-, coarse-grained 70-85%, serpentinized olivine 15-30%, ± diopside ± amphibole rare are also present Cr-spinel characteristics are: Cr# = 50-56, Mg# = 65-75, TiO₂ = 0.24-0.30%; olivine (Mg# = 90-95).

2.4 Type 4

Massive, dense fine-grained chromites, that form a series of tubular, lenses-like bodies and veins within recrystallized dunite (lower, central part of mantle sequence). A very diverse, irregular shape of chromite bodies is complicated by multistage ductile, semi-brittle and brittle deformations. The ratio of Cr-spinel/silicate is not less here, than 70/30.

Cr-spinel here has the highest Cr and Mg contents: Cr# = 72-83, Mg# = 55-70, TiO₂ = 0.20-0.51%, along with olivine (Mg# = 90-97) ± diopside ± amphibole ± Cr-chlorite. PGE-mineralization (Os-Ir alloys, laurite, irarsite, erlichmanite) is common for this type of chromite.

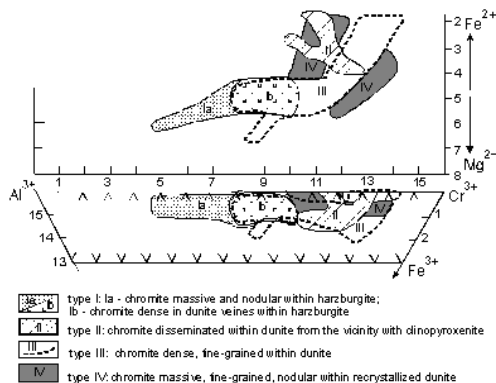


Figure 2: The compositions of chromspinellides of chromite ores within mantle residual ultramafics of the Polar Uralian ophiolites.

3 CONCLUSION

Polar Uralian ophiolite display complicated structural and magmatic evolution. Residual peridotites are highly depleted, similar to mantle ultramafic from marginal oceanic settings. The most striking features of residual ultramafics are as follows: (i) widespread veins of dunite, pyroxenite, gabbro and impregnation zones which originated by mantle residues/melt interaction at the later stages of subsolidus solid-state flow deformation; (ii) high-T metamorphism in presence of fluids expressed by recrystallization of harzburgite, dunite and chromite. Both events influenced formation of chromites (types 3, 4)

The diversity of compositions and structural settings of Polar Uralian chromites compares well with those of chromite occurrences of New Caledonia, the Troodos massif, Zambales and Newfoundland ophiolites (Cassard et al. 1981; Leblanc & Violette 1983; Hock & Friedrich 1985; Roberts et al. 1988; Roeder & Reynolds 1991; Melcher et al. 1999). The distribution of Cr- and Al-rich chromites in connection with their composition and the structure of host ultramafics have been discussed by Leblanc & Violette (1983) which related the origin of chromites to different time and places during the upwelling of mantle peridotites.

At the Polar Urals the formation of the dunite and chromite bodies also is related to several magmatic and mantle metasomatic events. The first event (high

Al, high Mg chromite (type 1), likely formed during partial melting of peridotite, and is associated with minor fluid activity. Increasing magmatic and fluid activity resulted in crystallization of high-Cr, low-Mg chromite (type 2), within large dunite bodies, close to the Moho boundary. A further event, resulted in the reaction of percolated melt with host peridotite, presumably, took place under suprasubduction environment. This reaction resulted in the formation of dunite, hosting moderately Cr, high-Mg chromite (type 3), and, with increasing volatile content and plastic, semi-brittle deformation, final crystallization of high-Cr, high-Mg metallurgic chromite (type 4).

4 REFERENCES

- Buyakaite, M.I., Vinogradov, V.I., Kuleshov, V.V., Pokrovskii, V.G., Saveliev, A.A., Savelieva, G.N., 1983. *Isotope geochemistry in ophiolite of Polar Urals*, Transactions, 376, Moscow: Nauka, 179.
- Cassard, D., Nicolas, A., Rabinovitch, M., Moutte, J., Leblanc, M., & Prinzhofer, A. 1981. Structural classification of chromite pods in southern New Caledonia. *Economic Geology*, v. 76: 805-831.
- Hock, M. & Friedrich G. 1985. Structural features of ophiolitic chromites in the Zambales Range, Luzon, Philippines. *Mineral Deposita*, 20: 290-301.
- Leblanc M. & Violette J.-F., 1983. Distribution of Alumina-Rich and Chromium-Rich Chromite Pods in Ophiolite Peridotites. *Economic Geology*, v.83: 293-301.
- Melcher, F., Grum, W., Thalhammer, T.V. & Thalhammer, O.A.R. 1999. The giant chromite deposits at Kempisai, Urals: constrains from trace elements (PGE, REE) and isotope data. *Mineralium Deposita*, 34: 250-272.
- Saveliev A.A. 1977. Chromites of the Voykar-Syn'ya massif. In: *Genesis of ultramafics and related ore deposits*. Sverdlovsk: AN USSR, USC: 63-76.
- Roberts, S., Rassios, A., Wright, L., Vacondios, I., Vragatis, G., Gtivas, E., Nesbitt, R.W., Neary, C.R., Moat, T. & Konstantopoulou, L. 1988. Structural Control on the Location and Form of the Vourinos Chromite Deposits. In: *Mineral Deposits within the European Community*, Eds. J. Boissonnas P. Omenetto, P.249-266.
- Saveliev A.A. & Samygin, S.G. 1979. Ophiolite allochthons of the Polar Urals. In: *Tectonic development of the Earth crust and faults*. Moscow: Nauka: 9-30.
- Savelieva, G.N. & Saveliev A.A. 1991. Chromite in the ophiolite sequence. *Geotectonika*, n.2: 47-58.
- Savelieva, G.N. & Nesbitt, R.W. 1996 A synthesis of the stratigraphic and tectonic setting of the Uralian ophiolites. *Jour. of Geol. Soc., London*, V.153: 525-537.
- Saveliev, A.A., Sharaskin A.Ya., D'Orazio, M. 1999. Plutonic to volcanic rocks of the Voykar ophiolite massif (Polar Urals): structural and geochemical constrains of their origin. *Ophioliti*, 24 (1): 21-30.
- Savelieva, G.N., Sharaskin A.Ya., Saveliev, A.A., Spadea, P., Pertsev, A.N., Babarina, I.I., 2002. Ophiolite and Zoned Mafic-Ultramafic Massifs of the Urals: A Comparative Analysis and Some Tectonic Implications. In: *Mountain Bulding in the Uralides: Pangea to the Present*. Geophys. Monograph, 132: 135-153.

Glide Systems of Hematite Single Crystals in Deformation Experiments

H.Siemes & B.Klingenberg

Institut für Mineralogie und Lagerstättenlehre, RWTH Aachen; D-52056 Aachen, Germany

E.Rybacki & M.Naumann

Geoforschungszentrum Potsdam, Telegrafenberg, D-14473 Potsdam, Germany

W.Schäfer & E.Jansen

Mineralogisches Institut, Universität Bonn, Forschungszentrum Jülich, D-52425 Jülich, Germany

K.Kunze

Geologisches Institut der ETH, CH-8092 Zürich, Switzerland

ABSTRACT: Experimental deformation of hematite single crystals at temperatures up to 700°C at strain rates of 10^{-5} s^{-1} and 300 MPa confining pressure extends the knowledge about the critical resolved shear stresses of twin and slip modes. Optical observations, neutron diffraction goniometry, SEM orientation contrast imaging and electron backscatter diffraction are applied in order to identify the glide modes. Additional experiments are under way to verify some questionable results.

1 INTRODUCTION

Hematite Fe_2O_3 is a trigonal mineral with corundum structure, a melting temperature of 1840 K and a hexagonal cell of $a_0 = 0.504 \text{ nm}$, $c_0 = 1.377 \text{ nm}$ to which refer the symbols for planes and directions.

Deformation experiments on hematite single crystals were performed by means of a fluid high pressure-high temperature (HTP) equipment in the temperature range 25°C to 400°C, at 400 MPa confining pressure, and a strain rate of 10^{-5} s^{-1} by Hennig-Michaeli & Siemes (1982). The critical resolved shear stresses (crss) were determined for r-twinning, c-twinning and {a}<m>-slip.

New results from compression experiments on polycrystalline hematite ores by means of an HTP Paterson gas apparatus (Paterson 1990) were described recently (Siemes et al. 2003). The analysis of the acquired preferred orientation measured by means of neutron diffraction indicated that at temperatures of 600°C and above (c)<a>-slip increasingly becomes an additional important glide system. In order to confirm the glide systems at 600°C a new series of experiments on hematite single crystals were performed under the same conditions as before. Their analysis is reported here.

2 STARTING MATERIALS AND DEFORMATION EXPERIMENTS

Natural hematite crystals collected at different locations in Minas Gerais, Brazil were used as starting material. Prismatic specimens $7 \times 7 \times 14 \text{ mm}^3$ were prepared with different orientations to the compression axis perpendicular to $c(001)$, $r\{012\}$, $f\{101\}$, $a\{110\}$, and $m\{100\}$. The specimens were strained up to 4 % in compression by means of an HTP Paterson gas apparatus. Calculation of the orientation-(Schmid-) factors for the different orientations suggest that c-specimens are most suitable for r-twinning (Tab.1) and a- and m-specimens are most suitable for {a}<m>-slip (Tab.2). The other specimens have medium to high Schmid-Factors for {a}<m>-slip, (c)<a>-slip and c-twinning.

Table 1.
Hematite twin modes

	r-twins			c-twins		
	1:	2:	3:	4:	5:	6:
$K_1 =$	(-1 0 2)	(1 -1 2)	(0 1 2)	(0 0 1)	(0 0 1)	(0 0 1)
$N_1 =$	[1 0 1]	[-1 1 1]	[0 -1 1]	[1 0 0]	[-1 1 0]	[0 -1 0]

Schmid-Factors m and strain by twinning ϵ [in %] in uniaxial compression for various crystal orientations relative to principal stress direction σ_1

r-twins	c-twins					
$\sigma_1 \perp$ to	m_1	m_2	m_3	ϵ_1	ϵ_2	ϵ_3
c (001)	0.45	0.45	0.45	9.1	9.1	9.1
r (012)	0.00	-0.05	-0.05	-2.1	-1.0	-1.0
f (101)	-0.49	0.00	0.25	-10.5	-0.7	-0.7
a (110)	-0.34	-0.34	0.00	-7.8	-7.8	0.0
m(100)	-0.45	-0.11	-0.11	-10.3	-2.7	-2.7

c-twins	r-twins					
$\sigma_1 \perp$ to	m_4	m_5	m_6	ϵ_4	ϵ_5	ϵ_6
c (001)	0.00	0.00	0.00	-18.4	-18.4	-18.4
r (012)	-0.45	0.23	0.23	-30.0	9.0	9.0
f (101)	0.29	-0.14	-0.14	18.1	-10.4	-10.4
a (110)	0.00	0.00	0.00	0.0	0.0	0.0
m(100)	0.00	0.00	0.00	0.0	0.0	0.0

Table 2
Hematite slip modes

(c)<a>-slip	{a}<m>-slip
7:c(0 0 1) a[2 -1 0] / [-2 1 0]	10:a(2 -1 0) m[0 -1 0] / [0 1 0]
8:c(0 0 1) a[-1 2 0] / [1 -2 0]	11:a(-1 2 0) m[1 0 0] / [-1 0 0]
9:c(0 0 1) a[-1 -1 0] / [1 1 0]	12:a(1 -1 0) m[-1 1 0] / [1 -1 0]

Schmid-Factors m in uniaxial compression for various crystal orientations relative to principal stress direction σ_1

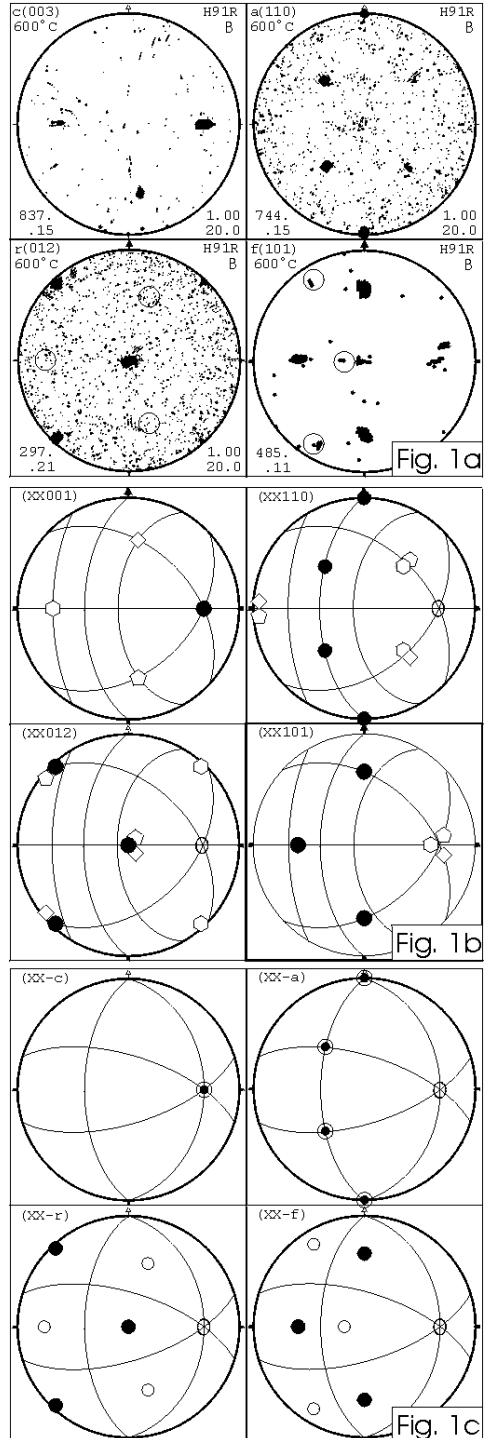
$\sigma_1 \perp$ to	m_7	m_8	m_9	m_{10}	m_{11}	m_{12}
c (001)	0.00	0.00	0.00	0.00	0.00	0.00
r (012)	0.39	0.00	0.39	0.31	0.00	0.31
f (101)	0.25	0.00	0.25	0.39	0.00	0.39
a (110)	0.00	0.00	0.00	0.00	0.43	0.43
m(100)	0.00	0.00	0.00	0.43	0.00	0.43

3 DETERMINATION OF GLIDE SYSTEMS

3.1 Neutron diffraction

Microscopic observations and neutron diffraction measurements (Jansen et al. 2000) on deformed specimens verified the development of c- and r-twinning. Figure 1 shows as an example the neutron diffraction pole figures of a specimen compressed perpendicular to r(012), therefore the (012)-pole figure shows a maximum in the center, a maximum on periphery of the (110)-pole figure indicates one of the prism planes. The second prism plane is oriented perpendicular to [0-11].

Figure 1. Interpretation of neutron pole figures of specimen H91R deformed ~4% in compression perpendicular to r(012) at 600 °C and 300 MPa confining pressure, compression direction in the center of the pole figures. a) pole figures of the c(003)-, a(110)-, r(012)-, and f(101)- reflection, circles indicate c-twin positions, b) parent crystal (●), ideal positions of the three r-twins (hexagon, pentagon, and square), c) parent crystal (●) and ideal position of the c-twin (○).



3.2 Electron back scattering diffraction

Both r- and c-twinning systems and $\{a\}\langle m \rangle$ -slip were confirmed (Fig.2a) by orientation mapping based on EBSD-measurements (Kunze et al. 1993). Besides the already known glide systems there are a few indications of the existence of $(c)\langle a \rangle$ -slip as originally indicated by the above mentioned measurements on polycrystalline hematite.

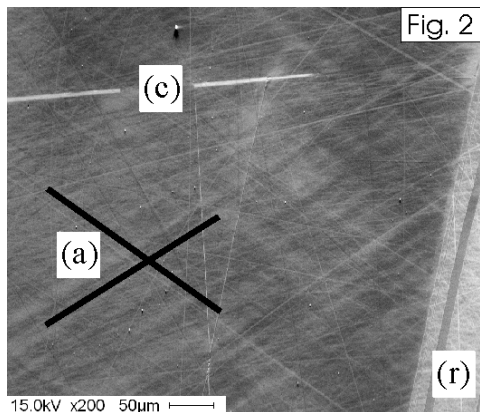


Figure 2. SEM orientation contrast micrograph (using fore-scatter electron detector) of specimen H91R deformed ~4% at 600 °C and 300 MPa confining pressure in compression perpendicular to $r(012)$, compression direction top to bottom of the micrographs: c-twin, r-twins, and small local orientation gradients aligned parallel to the trace of the slip plane for $\{a\}\langle m \rangle$ -slip systems in a plane perpendicular to $[0-11]$.

3.3 Critical resolved shear stresses (crss)

Mechanical data (Fig. 3) indicated that the crss of r-twinning decreases from 140 MPa at 25°C to ~5 MPa at 700°C and for $\{a\}\langle m \rangle$ -slip from >560 Pa to ~70 MPa. The crss for c-twinning and $(c)\langle a \rangle$ -slip seem to be below 80 MPa at 600°C. Some data in Figure 3 are still questionable.

4 FINAL REMARKS

To evaluate more precise values of the critical resolved shear stresses for c-twinning and $(c)\langle a \rangle$ -glide additional experiments are under way. The knowledge of the glide systems of hematite is important for the interpretation of the texture of metamorphic hematite ores, see e.g. Rosière et al. (2001).

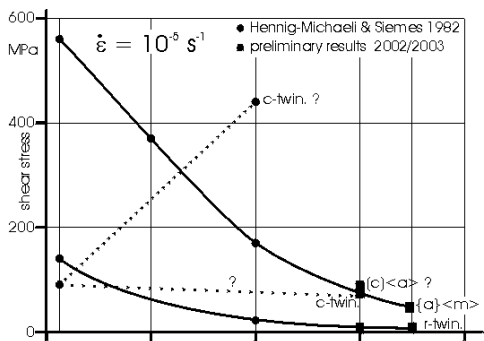


Figure 3. Critical resolved shear stresses (crss) of the glide systems of hematite.

5 ACKNOWLEDGMENTS

The support by the DFG is gratefully acknowledged. BK received a stipend from the ETH student exchange office and thanks for hospitality during a three month stay at the ETH Zürich in summer 2003. The staff of the Mineralogical Institute of the RWTH Aachen particularly M. Brand, T. Derichs, G. Paprotny and M. Wiechert contributed with a variety of preparations and measurements.

6 REFERENCES

- Hennig-Michaelli, Ch. & Siemes, H. 1982. Experimental deformation of hematite crystals between 25°C and 400°C at 400 MPa confining pressure. In: Schreyer, W. (Ed.) High Pressure Research in Geoscience, Schweizerbart'sche Verlagsbuchhandlung, Stuttgart, 133-150.
- Jansen, E., Schäfer, W. & Kirfel, A. 2000. The Jülich neutron diffractometer and data processing in rock texture investigations. *J. Struct. Geol.*, 22, 1559-1564.
- Kunze, K., Wright, S.I., Adams B.L. & Dingley D.J. 1993. Advances in automatic EBSD single orientation measurements. *Textures and Microstructures* 20, 41-54.
- Paterson M.S. 1990. Rock deformation experimentation. In: Duba, A.G., Durham, W.B., Handin, J.W. & Wang H.F. (Eds.), *The Brittle-Ductile Transition in Rocks*. The Heard Volume, American Geophysical Union Geophysical Monograph 56, 187-194.
- Rosière, C.A., Siemes, H., Quade, H., Brokmeier, H.-G. & Jansen, E.M. 2001. Microstructures, textures and deformation mechanism in hematite. *J. Struct. Geol.*, 23, 1429-1440.
- Siemes, H., Klingenberg, B., Rybacki, E., Naumann, M., Schäfer, W., Jansen, E. & Rosière, C.A. 2003. Texture, microstructure, and strength of hematite ores experimentally deformed in the temperature range 600-1100°C and at strain rates between 10^{-4} and 10^{-6} s $^{-1}$. *J. Struct. Geol.*, 25 1371-1391.

Sulfides of the Cu-S-system in the Endogenic and Exogenetic Ores

I.F.Gablina

Institute of the Lithosphere of Marginal Seas Russian Academy of Sciences, Moscow, Russia

ABSTRACT: The identification of copper sulfides from sulfide ores of different genesis was carried out. The basic objects of the investigation were represented by primary and hypogene-altered ores from cupriferous sandstones and shales (Mansfeld, Lubin-Sieroszowice, Dzhezkazgan, Udokan, Graviika, Sukharikha deposits, Western Fore-Ural region, and other trough), hypogene magmatic ores from the Talnakh deposit, the hypogene zone ores from Kounrad porphyry copper deposit, and recent oceanic ores of the Logachev and Rainbow Hydrothermal field (Mid-Atlantic Ridge). The minerals were identified by the X-ray powder diffraction (Debye, Gandolfi) method, which was combined with mineragraphic studies and MPA. Ten compounds of the Cu-S system reported in nature are ascertained: chalcocite monoclinic (Cu_2S), chalcocite tetragonal (Cu_2S), djurleite ($\text{Cu}_{1.93-1.96}\text{S}$), roxbyite ($\text{Cu}_{1.72-1.82}\text{S}$), digenite ($\text{Cu}_{1.75-1.78}\text{S}$), anilite ($\text{Cu}_{1.75}\text{S}$), geerite ($\text{Cu}_{1.5-1.6}\text{S}$), spionkopite ($\text{Cu}_{1.4}\text{S}$), yarrowite ($\text{Cu}_{1.1}\text{S}$), covellite (CuS). Non-stoichiometric minerals in which the Cu/S ratio varies from 2 to 1 are preponderant among them. Only two minerals, digenite and covellite, are encountered both exogenous and endogenous ores. The natural distribution of other minerals is restricted by the conditions of ore formation. On the whole, the confinement of stoichiometric Cu-sulfides to endogenic ores and non-stoichiometric Cu-sulfides to exogenetic ores is revealed.

1 INTRODUCTION

By now, ten natural compounds of the Cu-S system: chalcocite (Cu_2S), tetragonal form Cu_2S - $\text{Cu}_{1.96}\text{S}$ djurleite ($\text{Cu}_{1.96}\text{S}$), roxbyite ($\text{Cu}_{1.72-1.82}\text{S}$), digenite ($\text{Cu}_{1.75-1.78}\text{S}$), anilite ($\text{Cu}_{1.75}\text{S}$), geerite ($\text{Cu}_{1.5-1.6}\text{S}$), spionkopite ($\text{Cu}_{1.4}\text{S}$), yarrowite ($\text{Cu}_{1.1}\text{S}$), covellite (CuS) and two synthetic phases unstable at room temperature (hexagonal chalcocite and cubic digenite) are reported (Djurle 1958; Roseboom 1966; Morimoto et al. 1969; Goble 1980; Goble & Robinson 1980; Skinner et al. 1976; Potter 1977; Mumme et al. 1988; and others). The non-stoichiometric minerals are preponderant among them. A great diversity of non-stoichiometric minerals in the Cu-S system is related to the fact that even negligible deviation of Cu sulfide composition from stoichiometry is accompanied by structural reorganization of their crystal lattice, i.e., by formation of a new mineral.

Deviation from stoichiometry is caused by the partial penetration of bivalent (oxidized) Cu minerals into the crystal lattice (Belov 1953; Eliseev et al. 1964; Goble 1985), which is usually related to the presence of oxygen in the mineral-forming system. Goble (1985) demonstrated that the bivalent Cu content in sulfides increases with the decreasing

of the Cu/S ratio. Based on composition and physical properties of minerals, two series are discriminated: chalcocite-digenite (Cu_2S - $\text{Cu}_{1.75}\text{S}$) and geerite-covellite ($\text{Cu}_{1.6}\text{S}$ - CuS).

The attention of mineralogists has been long attracted by the possibility of using the Cu-S system minerals as indicators of the ore-forming environment. The purpose of this work is to study the occurrence of Cu-S system minerals in natural ores and reveal their indicative possibilities.

2 MATERIALS AND METHODS

The identification of copper sulfides from sulfide ores of different genesis was carried out. Data published on their synthesis, stability, and natural distribution were examined. The basic objects for the investigation were represented by primary and hypogene-altered ores from cupriferous sandstones and shales (Mansfeld, Lubin-Sieroszowice, Dzhezkazgan, Udokan, Graviika, and Sukharikha deposits, Western Fore-Ural region, and other trough), hypogene magmatic ores from the Talnakh deposit, the hypogene zone ores from Kounrad porphyry copper deposit, and recent oceanic ores of the Logachev-1, Logachev-2 and Rainbow hydrothermal field (Mid-Atlantic Ridge).

Table 1. Distribution of the Cu-S system minerals in natural ores.

Genetic types of ore: Deposits	Temperature ore formation °C	Cu-S system minerals							
		Chalcocite-digenite series (Cu ₂ S- Cu _{1.75} S)				Geerite-covellite series (Cu _{1.6} S- CuS)			
		Cc,T t Cu ₂ S	Dj Cu _{1.96} S	Dig Cu _{1.78} S- Cu _{1.8} S	Rxb,An Cu _{1.75} S- Cu _{1.8} S	Gr Cu _{1.5} S- Cu _{1.6} S	Spk Cu _{1.4} S	Yr Cu _{1.1} S	Cov CuS
Exogenic ores									
Hypergenesis zones of ancient sulfide deposits of different genesis: Udokan, Sukharikha, Dzhezkazgan, Kounrad	<0-50		+	+	+	+	+	+	+
Hypergenesis zones of present-day oceanic sulfide ores: Logachev, Rainbow (Mid-Atlantic Ridge)	4		+		+	+	+	+	+
Cupriferous sandstones and shales: Western Ural Region	75		+	+					
Endogenic ores									
Metamorphosed cupriferous sandstones and shales. Greenschist zone: Udokan	400-450		+	+					
Magmatogene: Talnakh	600		+						
Hydrothermal: Bristol* Bjutte**			+						+
Recent hydrothermal sulfide ores: Salton Sea*** Logachev, Rainbow (Mid-Atlantic Ridge)	230-400		+	+					+

*Potter & Evans 1976; ** Ramdor 1960; ***Skinner et al. 1976. Other - author's data
Cc - chalcocite, Tt - tetragonal form Cu₂S, Dj - djurleite, Dig - digenite, Rxb - roxbyite, An - anilite, Gr - geerite, Yr - yarrowite, Spk - spionkopite, Cov - covellite

The minerals were identified by the X-ray powder diffraction (Debye, Gandolfi) method, which was combined with mineragraphic studies and MPA.

3 RESULTS OF RESEARCHES

Results of the investigation are presented in Table 1. The ore types are divided into exogenous ores, formed under near-surface conditions at temperatures of no more than 75°C, and endogenous ores, formed in deeper zones of the Earth's crust at temperatures above 100°C. Ten compounds of the Cu-S system reported in nature are ascertained: chalcocite monoclinic, chalcocite tetragonal, djurleite, roxbyite, digenite, anilite, geerite, spionkopite, yarrowite, covellite. Non-stoichiometric

minerals in which the Cu/S ratio varies from 2 to 1 are predominated among them. Only two minerals, digenite and covellite, are encountered both exogenous and endogenous ores. This is explained by the wide temperature ranges of their stability. The natural distribution of other minerals is restricted by the conditions of ore formation: chalcocite often to be mixed with the tetragonal form are present in primary ores of magmatic deposits, in hydrothermal and metamorphosed ores and in the present-day oceanic sulfide ores of active tubes; djurleite is typical for non metamorphosed ores in cupriferous sandstones and shales and for recent oceanic formations; anilite and djurleite, often to be fine two phase mixtures, are widespread in recent oceanic ores and in the hypergene zones of sulfide deposits; non-stoichiometric Cu-poor sulfides are

characteristic of continental and oceanic hypergene-altered ores only. On the whole, the confinement of stoichiometric Cu-sulfides to endogenic ores and non-stoichiometric Cu-sulfides to exogenetic ores is revealed.

4 DISCUSSION

Their different temperature and chemical resistance can explain such distribution specialization of copper sulfides in nature. As it was previously demonstrated (Gablina 1992), the tetragonal Cu_2S is an indicator of relatively high-temperature ore-forming conditions. Probably, it presumably appears as a metastable transitional phase from cubic digenite to hexagonal chalcocite (near 435°C) or hexagonal chalcocite to monoclinic chalcocite (near 103°C). The wide temperature ranges of their stability explain presence of digenite and covellite in ores of different genesis.

The predominance of non-stoichiometric copper sulfides is distinguished from chalcocite, covellite, as well as digenite with low temperature stability (< 93°C for djurleite, 70°C for roxbyite, and 30°C for anilite). The available experimental data on phase stability in the Cu-S system (Rickard 1973; Whiteside & Goble 1986; and others) show that sulfides with lower copper content become more stable under both the pH of an environment decrease and Eh height. These data elucidate the predominant confinement of non-stoichiometric copper sulfides to exogenous ores, as well as presence of stoichiometric chalcocite primarily in endogenous ores. It is likely that the chalcocite formation is hampered under exogenetic conditions, because the ore-forming system contains oxygen, which leads to the oxidation of Cu^{1+} and the formation of nonstoichiometric minerals with a similar composition (djurleite, digenite and anilite). The Cu-poor sulfides of the geerite-covellite series in hypergene-altered sulfide ores are products of the leaching of Cu from the Cu-rich sulfides.

5 REFERENCES

Belov N.V. 1953. Some feature of sulfides crystallochemistry. / *Voprosy petrologii i mineralogii*. Vol. 2. Pp.7-13.

Djurle C. 1958. An x-rays study of the systems Cu-S. / *Acta Chem. Scan.* Vol. 12. No 7. 1415-1426.

Eliseev E.N. Rudenko L.E., Sisnev, L.A. et al. 1964. Polimorphism of copper sulfides in Cu_2S - $\text{Cu}_{1.86}\text{S}$ system. *Min. Sbornik L'vov. Gos. Univ.* No 18. Pp. 3385-400.

Gablina I.F.1992. Tetragonal copper sulfide (I) in the natural ores. / *Doklady Russia AS.* Vol. 323. No 6. 1170-1173.

Goble R.Y. 1980. Copper sulphides from Alberta: yarrowite Cu_9S_8 and spionkopite $\text{Cu}_{39}\text{S}_{28}$ / *Canad. Mineral.* Vol. 18. Pp. 511-518.

Goble R.Y. 1985. The relationship between crystal structure, bonding and cell dimension in the copper sulfides. *Canad. Mineral.* Vol. 23. Pp. 61-78.

Goble R.Y. & Robinson G. 1980 Geerite, $\text{Cu}_{1.6}\text{S}$, a new copper sulphide. Dekalb Township, New York. / *Canad. Mineral.* Vol. 18. 519-523.

Morimoto, N., Koto, K. & Shimasaki Y. 1969. Anilite, Cu_7S_4 , a new mineral. / *Am. Mineral.* Vol. 54. Pp. 1256-1268.

Mumme W.G., Sparrow G.J. & Walker G.S. 1988. Roxbyit, a new copper sulphide mineral from the Olympic Dam deposit, Roxby Downs, South Australia. / *Miner. Magaz.* Vol. 52. Pt. 3. P. 323-330.

Potter R.W. 1977. An electrochemical investigation on the system copper - sulfur. / *Econ. Geol.* Vol. 72. P. 1524-1542.

Potter R.W. & Evans H.T. jr. 1976. Definitive X-ray powder data for covellite, anilite, djurleite and chalcocite. / *J.Res. US Surv.* No 4. Pp. 205-212.

Ramdor P. 1960. Die Erzminerale und Ihre Verwachsungen. Berlin: Acad. Verl.

Rickard, D.J. 1973. Copper-sulfide formation chemistry at low temperatures. / *Tschermaks Mineral. Petrogr. Mag.* Vol. 19. No 1. Pp.60-75.

Roseboom E.M. 1966. An investigation of the system Cu-S and same natural copper sulphides between 25°C and 700°C. / *Econ. Geol.* Vol. 61. No 4 Pp. 641-671.

Skinner B.Y., White D.E., Rose H.J. & Mays R.E. 1967. Sulfides associated with the Solton Sea geothermal brine. / *Econ. Geol.* Vol. 62. P. 316-330.

Whiteside L.S. & Goble R.Y. 1986. Structural and compositional changes in copper sulfides during leaching and dissolution / *Canad. Mineral.* Vol. 24. No 2. Pp. 247-258.

Process Mineralogy

Correlating QemSCAN Mineralogy with Metallurgy in Feasibility Studies

C.Hamilton, C.Martin, N.McKay, S.Williams
SGS Lakefield Research Limited, Ontario, Canada

ABSTRACT: The value of QemSCAN is increasingly being recognized in feasibility and pre-feasibility studies which rely on a significantly improved understanding of ore variability for bankability of new projects. In such studies, QemSCAN data can provide a fundamentally sound link between resource evaluation and metallurgical mapping programs. In this paper, QemSCAN data from two very different ore types, a VMS Cu-Zn-Pb deposit and a Cu-Porphyry, are used to identify and quantify key ore characteristics affecting metallurgical response. The first quantitative descriptor is the phase specific surface area, or PSSA, a parameter, which was successfully applied to the San Nicolás geometallurgical mapping project (Winckers, 2002). In addition to the PSSA, the extensive database afforded by QemSCAN permits analysis of correlations between metallurgy and other measurable attributes. Specifically, the chalcopyrite-pyrite association data for the San Nicholas VMS deposit are also shown to correlate directly with metallurgical performance in certain ore types. In a second case study, data for a copper porphyry reveal the influence of disseminated, fine-grained chalcopyrite on metallurgical performance. The value of a cross-disciplinary approach in establishing correlations is also emphasized.

1 INTRODUCTION

1.1 Role of QemSCAN in Feasibility Studies

QemSCAN is used to assist mineral processing plant optimization programs and, increasingly, as part of the preparation of bankable feasibility studies for new projects. At this critical phase of a project, the objective is to establish sufficient information and confidence regarding technical risk.

Most large bankable feasibility studies currently incorporate both resource- and metallurgical information to describe the variability of the orebody in terms of geology, mineralogy, grade, grinding and metallurgical response. This approach or “geometallurgical mapping” as it is referred to (Williams & Richardson 2004) is relatively new and its’ use is an important tool in risk-reduction associated with new mine developments (or expansions), because the orebody is more fully understood. Specifically, ore variability is better characterized and the impact of ore variability can be quantified with regard to metal recovery and future project revenues.

1.2 Geometallurgical Mapping

A key premise of geometallurgical mapping is that the mineralogy of the sample and the spatial distribution of the minerals, ultimately controls the grade, recovery and hardness, thus the metallurgical performance and economic value of the project. It follows that any geometallurgical program should include a systematic mineralogical assessment.

The feasibility phase of a program is usually associated with drilling which provides samples for a geometallurgical mapping program. The number of samples sent for chemical analysis will be thousands to tens-of-thousands. The amount of samples for chemical analysis is based on the need to establish a threshold bankable resource size.

Associated metallurgical testing may consist of 100-300 standard tests and include, for example, laboratory based flotation tests and cyanidation bottle rolls. The number of samples submitted to this type of program is typically an order of magnitude less than the chemical analyses.

Mineralogical studies, particularly those employing techniques such as QemSCAN, fall in sample number between the two extremes above. Up to 1000 samples may be submitted for a QemSCAN geometallurgical mapping program. The relative unit cost of such analyses is cheaper than laboratory

based metallurgical testing, but more expensive than chemical analyses. However, an extensive mineralogical database is created and allows for prediction of metallurgical performance for the orebody. This is achieved by investigating empirical relationships between metallurgical performance and mineralogical parameter(s). Case studies that demonstrate this correlation method are presented in this paper.

2 QEMSCAN METHODOLOGY

2.1 Sampling and Measurement

The use of QemSCAN has been well established in the mineral industry and details of the methods and analytical conditions can be found in the literature (Gottlieb et al. 2000; Lotter et al. 2002).

In contrast to plant audit, size-by-size and liberation-based measurement methods (Lotter et al. 2002), feasibility projects require more rapid analyses, making the single-product ore-characterization methodology described by Sutherland et al (1989) a particularly attractive option. In the method, an ore is coarsely crushed to a particle size permitting the measurement of textural and modal attributes of unbroken ore particles. In developing an appropriate sampling protocol, issues of fundamental sampling, assay reconciliation and measurement parameters are addressed (Gottlieb et al. 2000; Lotter et al. 2002; Winckers 2002).

Depending on statistical and grade constraints, replicate polished sections are measured in the Bulk Mineralogical Analysis (BMA) mode using QemSCAN. The BMA mode is identical to the linear intercept analysis method (King & Stirling 1991) except that at a pre-defined point spacing and for each measurement point along an intercept, energy-dispersive x-ray (EDS) spectra and back-scattered electron image (BEI) information are gathered simultaneously. This allows direct measurement of mineralogical variability down to even subtle levels.

Typical measurement parameters for 95% confidence levels on both mineral composition and textural data for the San Nicolas VMS (Volcanogenic Massive Sulphide) deposit in Mexico (Winckers 2002) are presented in Table 1. Sampling and measurement protocols may vary as a function of particle size, textural complexity and grade.

The influence of measurement statistics on sensitivity of quantification is a critical issue and is addressed in this paper. In tandem with assay reconciliation and other quality controls, iterative methods of measurement and sample selection can assist in the development of appropriate sampling protocols.

Table 1. Typical QemSCAN Measurement parameters (after Winckers 2000).

Measurement Parameters	Sample Category		
	< 0.5 %	0.5-2.5 %	> 2.5 %
Cu grade	< 0.5 %	0.5-2.5 %	> 2.5 %
Measurement points	> 250,000	150-200,000	100,000
Number of intercepts	> 7,500	> 3,000	> 1,500

Table 2. Typical QemSCAN calculated elemental composition versus assayed values for preliminary scoping. Demonstrable assay reconciliation proves both precision and accuracy of QemSCAN measurements.

Elemental Composition	Sample Number			
	1	2	3	4
Fe -Calculated	5.8	6.8	6.7	2.7
Fe-Assay	6.5	7.0	7.1	3.7
S-Calculated	3.7	5.0	2.9	0.8
S-Assay	4.2	5.8	2.7	0.6
Cu - Calculated	0.2	0.4	0.3	0.3
Cu- Assay	0.2	0.3	0.3	0.3

2.2 Establishing Correlations with Metallurgy

In a metallurgical mapping project, the link between mineralogical attributes describing ore variability and metallurgical performance/concentration efficiency is sought. Once these correlations have been identified and quantified for a representative suite of samples, it should then be possible to apply the same mineralogical analyses to a larger set of samples from the mining blocks or specified domains and project the metallurgical performance with a measurable degree of confidence.

Demonstrating the link between measured attributes and performance, however, requires diligence, expertise and perseverance. In addition to issues of appropriate sampling and statistical considerations, the various techniques must satisfactorily determine both direct and indirect mineralogical influences on metallurgical performance (Canepa & Bernuy 1981). In practice, gross ore differences may be demonstrated by simple methods (e.g. mineral proportions alone) whereas more subtle differences may require the application of more sophisticated methods or multivariate analysis on a substantial database.

Since the QemSCAN linear intercept method yields many measurements with measurable precision and accuracy, merging high quality data between mineralogy and metallurgy satisfies quality requirements for statistical databasing. The need for multivariate techniques is obvious when considering the interdependence of geological and mineralogical features on metallurgical behaviour. For example, while modal mineralogy may be used to infer relative hardness and hence grindability, textural features such as recrystallization and brecciation can alter breakage characteristics (Crookes & Ryan 1998; Malvik 1982; Middlemiss & King 1993).

3 CASE STUDIES

3.1 San Nicolas VMS (Winckers 2000)

In the San Nicolas deposit, a relationship previously defined for several Australian VMS ores (Sutherland et al. 1987) was confirmed (Fig. 1). In this plot, the PSSA parameter is used, representing a grain size measurement expressed as Phase Specific Surface Area. Plotted against the PSSA is the concentration efficiency (CEI), which is a measure of overall flotation performance efficiency normalized with respect to grade. PSSA increases with decreasing grain size and is a useful index because, relative to a direct grain size measurement, the surface area increases as a square so that differences are more easily discernable relative to a direct measurement (Sutherland et al. 1987). Furthermore, since the measurements are performed on unbroken ore and assay reconciliation demonstrates that random orientation is achieved, this surface area ratio is stereologically unbiased (Gottlieb et al. 2001).

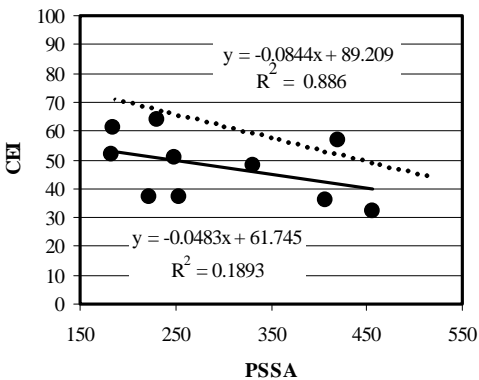


Figure 1. Correlation between CEI for San Nicolas locked cycle tests and PSSA measured on coarsely crushed ore samples by QemSCAN. The dotted line represents the correlation (upper regression equation) for samples with grades in excess of 1.5% Cu (symbols not shown). Solid symbols refer to samples grading less than 1.5% Cu. (Modified from Figures 4, 6 in Winckers 2000).

For reference ores with Cu grades between 1.5 and 4% Cu, the predominant influence on Cu concentration efficiency is the chalcopyrite grain size, as demonstrated by the dotted regression line in Figure 1. For lower grade ores, however, the correlation is poor, raising the question of the source of this variance. To investigate an alternative controlling influence, petrographic differences between the low-grade samples and higher-grade samples were sought. A key difference determined qualitatively was the presence of a network of pyrite-chalcopyrite textures.

The QemSCAN BMA routinely measures mineral association data. Based on the proportion of chalcopyrite associated with pyrite per unit of pyrite, a textural ranking scheme was developed to represent and measure the likely influence of association data on metallurgy. The association index represents the product of the percentage of chalcopyrite associated with pyrite and the modal proportion of pyrite. A significantly better correlation with CEI was established for all 0.5 to 1.5% Cu grade samples, providing a substantially improved basis for correlation among pyritic, low-Cu grade samples (Fig. 2).

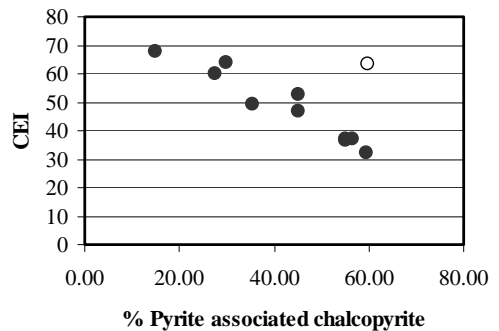


Figure 2. CEI versus pyrite-associated chalcopyrite data for the low-Cu grade data set in Figure 1. With the exception of one sample (open symbol), a significant correlation is evident.

3.2 Cu-Au Porphyry Case Study

QemSCAN analysis in this pre-feasibility study was performed on more than thirty drill core composites, as well as several master-composites representing discrete mine-blocks. The data were benchmarked against 50 laboratory flotation tests to document ore characteristics and variability.

In this study, there was no direct correlation between chalcopyrite PSSA and metallurgical performance, which led to more detailed data analysis from the outset. Probable mineralogical controls appeared to be significantly more complex, with indications that both mode of occurrence of chalcopyrite and relative sulphide proportions influence recovery behaviour (Figs. 3, 4). In Figure 3, a correlation between the relative ratio of chalcopyrite-to-pyrite and ultimate recovery is shown. Figure 4 shows comparative results for a preliminary, scoping study and a more detailed study. The second study was conducted in order to investigate the possible influence of measurement statistics on variability, especially given the low Cu grades (< 0.5% Cu).

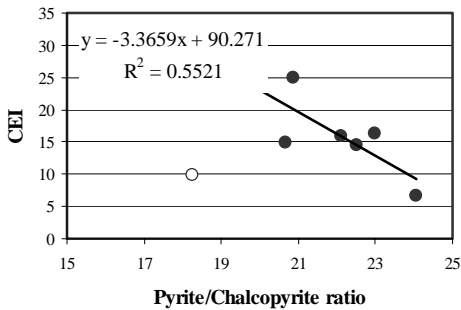


Figure 3. CEI versus pyrite-chalcopyrite ratio for a suite of Cu-porphphy block-composite samples. The outlier (open symbol) can not be explained by experimental variability.

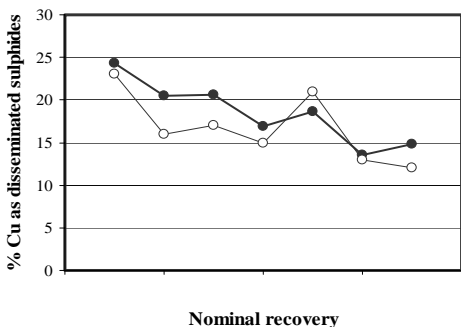


Figure 4. Disseminated chalcopyrite content versus recovery for high measurement statistics data (solid symbols) relative to the scoping phase (open symbols).

The results depicted in figure 4 show a significantly improved correlation using the high-measurement statistics data set, and provided confidence that disseminated chalcopyrite could be satisfactorily measured. This feature is consistent with drill core data. Recovery data are not reported to protect confidentiality.

4 CONCLUSIONS

Applied to two very different deposits, namely a massive sulphide and a copper porphyry, the value of an ore characterization method on carefully selected samples by QemSCAN has been demonstrated, and has been established as playing an integral role in pre-feasibility and feasibility projects.

In the San Nicolas case study, the PSSA parameter was confirmed as representing a first order influence of grain size on concentration

efficiency, while QemSCAN data also allowed the quantitative definition of a chalcopyrite-pyrite association index for low Cu grade, pyritic ores. For a copper porphyry study, the proportion of disseminated Cu mineralization was shown to correlate with decreased recovery. The ability to independently measure both attributes confirmed geologically discernable features, which unequivocally provided an important link between geological and metallurgical characteristics.

These studies underscore the value of judicious combination of optical and QemSCAN methods in establishing a rational basis for identifying key ore characteristics, as well as the value of an interdisciplinary team effort. Experience has shown that diligent application and analysis can also assist in the evaluation of apparent data outliers.

5 REFERENCES

- Canepa, C. & Bernuy, O. 1981. Mineral Beneficiation and Ore Microscopy: Some Relevant Methodological Aspects. In: Process Mineralogy: Proceedings of the 110th AIME Annual Meeting, Chicago, Illinois, February, 1981 (ed. Hausen, D. M. & Park, W. C.). 191-200.
- Crookes, R. A. & Ryan, A. J. 1998. Evaluation of the Ernest Henry Cu-Au Deposit Mineral Deposit. In: Proceeding of Australasian Institute of Mining Metallurgy Annual Conference Mount Isa, Queensland. AusIMM 98 - The Mining Cycle. 177-184.
- Gottlieb, P.; Wilkie, G.; Sutherland, Ho-Tun E.; Suthers, S.; Perera, K.; Jenkins B.; Spencer, S.; Butcher, A.; Rayner, J. 2000. Using Quantitative Electron microscopy for Process Mineralogy. JOM vol. 52, n.4. p. 24-25.
- King, R. P.; & Stirling, P. A. 1991. Linear intercept analysis of mineralogical texture. Proc. Int. Conf. Appl. Mineralogy. Pretoria, September, 1991.
- Lotter, N. O.; Whitaker, P. J.; Kormos, L.; Stickling, J. S. & Wilkie, G. J. 2002 The development of process mineralogy at Falconbridge Limited and application to the Raglan Mill. CIM Bulletin, vol. 95 n.1066, p. 85-92.
- Malvik, T. 1981. An Empirical model to establish the Liberation Properties of Minerals. In: 14th International Mineral Processing Congress, Toronto, Canada. Session VIII. p. 2.1-2.15.
- Middlemiss, S. & King, R. P. 1996. Microscale fracture measurements with application to comminution. Int. J. Miner. Process. 44-45 (1996) p. 43-58.
- Sutherland, D. N, Wilkie, G. & Johnson, C. R. 1989. Simple Prediction of the Processing Characteristics of Ores Using QEM*SEM. In: Mineralogy-Petrology Symposium Proceedings, Sydney NSW, February 1989 p. 81-84.
- Williams, S. R & Richardson, J. M. 2004. Geometallurgical Mapping: A new approach that reduces technical risk. In: Proc. 36th CMP Meeting, January, 2004. p. 241-268.
- Winckers, A. H. 2002. Metallurgical Mapping of the San Nicolas deposit. In: Proc. 34th CMP Meeting, January, 2002. p. 35-55.

Study of Electrodialysis Applied to Verde-Lodo Bentonite Clay Dispersions From Paraíba, Brazil

L.V.Amorim, H.L.Lira, H.C.Ferreira

Department of Materials Engineering, Federal University of Campina Grande, Paraíba, Brazil

F.L.H.Silva & K.B.França

Department of Chemical Engineering, Federal University of Campina Grande, Paraíba, Brazil

C.M.Gomes

Graduate Program of Materials Science Engineering, Federal University of Santa Catarina, Santa Catarina, Brazil

ABSTRACT: The aim of this work is to study the electrodialysis process applied to bentonite clay dispersions from Boa Vista City, Paraíba State, Brazil, to evaluate the influence of cations Ca^{2+} and Mg^{2+} in the rheological properties. A sample of polycationic bentonite clay namely *Verde-lodo* from Boa Vista City was studied. The electrodialysis process was done in a laboratory reactor, with two compartments (feed and cathodic compartments) separated by a cationic polymer membrane from BDH Laboratory Supplies, UK. To evaluate the influence of applied voltage and time in the rheological properties the tests was setting up according to type 2^2 factorial design, with three experiments in the central point. Quantitative analysis of exchange cations Na^+ , K^+ , Ca^{2+} and Mg^{2+} before and after electrodialysis process was done. Apparent and plastic viscosities were measure by using a viscometer Fann 35A and water loss with a filter press Fann. The results show that the electrodialysis process can remove Ca^{2+} and Mg^{2+} with approximately 23% and 22%, respectively, from the clay dispersions. Also it was show that the amount of Ca^{2+} and Mg^{2+} do not change the rheological behavior of the clay dispersions.

1 INTRODUCTION

Electrodialysis is an electrical potential driven process to remove ions from an electrolyte solution or to concentrate this solution (Krol 1969).

The electrodialysis process is traditionally use to desalting brackish water (Strathamann 1992) and in some country such as United States of América, France and Japan is the principal process to produce potable water. Nowadays, the development of new ion exchange membranes with improved selectivity, small electric resistance and better thermal, chemical and mechanical properties can be used to pharmaceutical, food and chemistry industries (Azevedo 2002).

In a laboratory scale, the electrodialysis has been studied to remove divalence cations from bentonite clay dispersions from Paraíba, Brazil, to be used as drilling oil well fluids (Gomes et al. 2002, Amorim et al. 2002a, Amorim et al. 2003a, b). Researches made by Souza Santos in the 60's (1968), showed that the rheological behavior of bentonite clay from Paraíba was not satisfactory due to the presence of Ca^{2+} and Mg^{2+} in the medium. These cations have the capacity to flocculate and cause a not swelling of the clay in an aqueous medium.

The aim of this work is to study the electrodialysis process applied to bentonite clay

dispersions from Boa Vista City, Paraíba State, Brazil, to evaluate the influence of cations Ca^{2+} and Mg^{2+} in the rheological properties.

2 METHODOLOGY

2.1 Materials

A sample of polycationic bentonite clay namely *Verde-lodo* from Boa Vista City, Paraíba State, Brazil was studied. This sample is mineralogically composed by montmorillonite, kaolinite, illite and quartz (Amorim et al. 2002b).

2.2 Electrodialysis process

It was used a laboratory cell, composed by two compartments (feed and cathodic compartments) separated to each other by a cationic polymer membrane from BDH Laboratory Supplies, United Kingdom. Detail of the reactor is described elsewhere (Amorim et al. 2003a). The clay dispersion with 4.86% w/w was placed in the feed compartment and a nitric acid solution (pH=3.0) was placed in the cathodic compartment. During the electrodialysis process, the clay dispersion was stirred at 840 rpm, with a mechanical stirrer, Fisaton model and glass tool. It was done a running with and

without stirred of the acid solution. After this process, the dispersions were treated with sodium carbonate at concentration of 150 meq $\text{Na}_2\text{CO}_3/100\text{g}$ of dry clay. It was used applied voltage of 7, 10 and 13V and time of 40, 80 and 120min according to the factorial design presented in the 2.4 item. After, the dispersions were submitted to a 5 days of cure and measured the apparent viscosity (AV), plastic viscosity (PV), in a Fann 35A viscometer, and water loss (WL), in a Fann filter press, according standard N-2605 (Petrobras 1998).

2.3 Exchange cations

It was measured the amount of exchange cations Na^+ , K^+ , Ca^{2+} and Mg^{2+} in the clay dispersion before and after the electrodialysis process, according to the chemical method described by Souza Santos (1989).

2.4 Factorial design

A type 2^2 factorial design with 3 experiments in the central point was done to evaluate the influence of the applied voltage and time over the rheological behavior of the clay dispersions. Table 1 presents the values of the voltage and time with the factors levels used in the electrodialysis process and the factorial design matrix.

3 RESULTS

It was not observed significant change in the values of AV, PV and WL for *Verde-lodo* clay dispersions after electrodialysis process and treatment with Na_2CO_3 . This behavior was observed to the electrodialysis process with and without stir of the acid solution (Tabs. 2, 3). Also it was not observed significant change in pH.

Through statistical analysis (Tab. 4), the results showed that only AV is statistically affected by the star variable (time and applied voltage). The great values were obtained to low voltage (7V) and small time (40min). These results are significant to a level of 95% of confidence.

The codified mathematical models (Tab. 5) showed that only AV, when the test were done with the acid solution under stir, is statistically affected for both star variable (applied voltage and time) and the great values are obtained to low voltages (7V) and short times (40 min).

Table 1: Start variables, codificated levels and the planning factorial matrix.

Start variables	Codificated levels		
	Level -1	Central point 0	Level +1
Voltage (V)	7	10	13
Time (min)	40	80	120

Factorial design matrix		
Experiments	Voltage [V]	Time [min]
1	-1	-1
2	+1	-1
3	-1	+1
4	+1	+1
5, 6 e 7	0	0

Nevertheless, from this study it can be observed the following tendency when the electrodialysis process was done without stir of the acid solution: (i) to obtain great values of AV it is necessary to use low voltage, under 10V and short time, below 60min and (ii) to obtain small values of WL is necessary to use high voltage, grater than 12V and long time, above 100min, or low voltage, under 8V and short time, below 50min. To the test made with acid solution under stir, it can observed the following tendency: (i) to obtain great values of AV it is necessary to use high voltage, above 12V and short time, below 60 min; (ii) to obtain great values of PV it be used any voltage and short time, below 60min and (iii) to obtain small values of WL it is necessary to use high voltage, above 12V and short time, below 60min. These tendencies are valid and put in evidence the need to extent the operational conditions of the electrodialysis process to be applied to the bentonite clay dispersions.

Table 2: Rheological properties of dispersions prepared with *Verde-lodo* clay submitted to electrodialysis process with acid solution without stirring and treated with 150 meq of Na_2CO_3 . * The values are the average of 3 measurements in the central point.

Test conditions	Acid solution without stirring			pH
	Rheological properties			
	AV (cP)	PV (cP)	WL (mL)	
7V - 40min	7.3	2.5	26.5	10.1
13V - 40min	7.0	2.5	24.0	10.1
7V - 120min	7.0	2.5	24.5	10.1
13V - 120min	6.5	2.5	27.0	10.0
10V - 80min*	6.0	2.5	25.5	10.0
Without electrodialysis process	6.5	2.5	25.5	10.0

Table 3: Rheological properties of dispersions prepared with *Verde-lodo* clay submitted to electro dialysis process with acid solution with stirring and treated with 150 meq of Na₂CO₃. * The values are the average of 3 measurements in the central point.

Test conditions	Acid solution with stirring			
	Rheological properties			pH
	AV (cP)	PV (cP)	WL (mL)	
7V - 40min	6.3	3.0	26.5	10.3
13V - 40min	7.3	3.0	24.5	10.2
7V - 120min	6.5	2.5	25.5	10.2
13V - 120min	5.8	2.0	26.0	10.1
10V - 80min*	6.8	3.0	23.0	10.2
Without electro dialysis process	6.5	2.5	25.5	10.0

The complexity of the system is due to the chemical composition of the clays and the electrical charges on the surface of the particle that can get involved in the process.

The results presented in Table 6 confirm that ions such as Na⁺, K⁺, Ca²⁺ and Mg²⁺ were eliminated from the *Verde-lodo* clay dispersions when submitted to electro dialysis process. Furthermore, it can be observed that the monovalent ions transport is greater than divalent ions. This behavior is in agreement with the results obtained by Kabay et al. (2002) and Kabay et al. (2003) about the elimination of Na⁺, K⁺, Ca²⁺ and Mg²⁺ from NaCl, KCl, CaCl₂ and MgCl₂ solutions through electro dialysis.

The condition that gives the great rate of removing cations Ca²⁺ and Mg²⁺ was 10V and 80 min, with amount of 23 % and 22 %, respectively.

Table 4: Statistical analyse of rheological properties of dispersions prepared with *Verde-lodo* clay after electro dialysis and treated with 150 meq de Na₂CO₃.

Correlation coefficient		% of explained variation*			
Acid solution without stirring					
AV (cP)	PV (cP)	WL (mL)	AV (cP)	PV (cP)	WL (mL)
0.42	ND	0.76	17.5	ND	57.9
Acid solution with stirring					
0.93	0.86	0.34	86.5	74.0	11.6

$$* R^2 = \frac{SQ_R}{SQ_T} \times 100$$

ND- not determined due to the invariance of the results. SQ_R- square regression sum, SQ_T - square total sum.

Table 5: Coded mathematical models for rheological properties of *Verde-lodo* clay dispersions after electro dialysis process and treatment with 150 meq of Na₂CO₃. V is the voltage and t is the time period. *Statistically significant to 95% of confidence level.

Acid solution without stirring	
VA	= 6.54* - 0.20V - 0.20t - 0.05Vt
VF	= 25.57* + 0.25t + 1.25Vt
Acid solution with stirring	
VA	= 6.61* + 0.07V - 0.32t - 0.42*Vt
VP	= 2.78* - 0.12V - 0.37t - 0.12Vt
VF	= 24.28* - 0.37V + 0.12t - 0.62Vt

By comparing the rheological properties (Tab. 2) with the concentration of the eliminated cations from *Verde-lodo* clay dispersions (Tab. 6), it can be observed that there is no direct correlation among these variables. On the other hand, the concentration of eliminated ions was not sufficient to modify the rheological properties of the dispersions.

According to Souza Santos (1989), there are four hypotheses to explain the rheological behavior not satisfactory to the Brazilian bentonite clays after treatment with Na⁺. First, because the nature and the proportion of the cations present in the clays that blockade the change by sodium: potassium due to the formation of illite and hydroxonium due to the attack to the octahedral sheet releasing Al³⁺ and Fe³⁺. However, this hypothesis was not acceptable because only one clay (Jundiá, SP) show high potassium content and the content of hydroxonium was high to a clay (Ponte Alta, MG) with high apparent viscosity and to a clays (Brigadão, MG and Franca, SP) with low apparent viscosity.

The second hypothesis is related to different kinetic of each clay when submitted to change the exchange cations by sodium. This hypothesis was not acceptable because the test made with radioactive sodium shows that the different clays change all the cations with 120 min and 3 days is time enough to change all exchange cations.

Table 6: Content of exchange cations from clay *Verde-lodo* before and after electro dialysis process. ND - not determined * The values are the average of 3 measurements in the central point.

Test conditions	Na ⁺	K ⁺	Ca ²⁺	Mg ²⁺
Before electro dialysis	17.2	2.5	22.3	29.5
7V-40min	11.4	2.6	20.6	26.0
13V-40min	9.6	3.2	20.3	27.3
7V-120min	9.4	ND	19.5	26.1
13V-120min	5.2	3.2	19.9	26.5
10V-80min*	6.8	2.1	17.2	23.0

In the third hypothesis, the high content of Mg and Fe, in the octahedral layer inhibits the clay swelling in water and gives low values of viscosity. This hypothesis was acceptable but the study not shows correlation between apparent viscosity and Foster swelling. Finally, in the fourth hypothesis, the divalent exchange cations Ca^{2+} and Mg^{2+} are responsible for the low values of apparent and plastic viscosity. However, in this study it was observed that the partial elimination of the cations Ca^{2+} and Mg^{2+} do not change significantly the rheological properties of the *Verde-lodo* clay dispersions.

4 CONCLUSIONS

After the analysis of the results, it can be concluded that: i) the electro dialysis process remove partially the cations Na^+ , K^+ , Ca^{2+} and Mg^{2+} from the *Verde-lodo* clay dispersions, Boa Vista, PB; ii) the elimination of 23% and 22% of Ca^{2+} e Mg^{2+} , respectively, from *Verde-lodo* clay dispersions do not change the rheological properties; iii) the start variables (applied voltage and time) do not presented effect statistically significant on the rheological properties of the dispersions, however a punctual analysis showed that the best results was obtained with 13V and 40min; iv) there is a need to improve the operational conditions and to select better membranes to the system. Nevertheless, this application seems to have potential to remove the unwanted cations from the clay dispersions.

5 ACKNOWLEDGEMENTS

This work is supported by Agência Nacional do Petróleo - ANP, FINEP, MCT and CNPq/CTPETRO.

6 REFERENCES

- Amorim, L.V., Gomes, C.M., França, K.B., Lira, H.L., Ferreira, H.C. 2002a. *Use of Electrodialysis Process to Bentonitic Clays Dispersions*. In: MRS Fall Meeting, Boston. Materials Research Society Symposium Proceeding. v. 752, 1010-1016.
- Amorim, L.V., Gomes, C.M., Kiyohara, P.K., Lira, H.L., Ferreira, H.C. 2002b. *Microstructural Characterization of Bentonite Clays From Paraíba, Brazil*. In: Micromat, Curitiba.
- Amorim, L.V., Gomes, C.M., Silva, F.L.H., França, K.B., Lira, H.L., Ferreira, H.C. 2003a. *Aplicação da Eletrodialise em Dispersões de Argilas Bentoníticas de Boa Vista, Paraíba, Brasil: Parte I - Avaliação do Reator Eletrodialítico*. In: 4º Congresso Ibero-americano em Ciência e Tecnologia de Membranas – CITEM, Florianópolis, 493-497.
- Amorim, L.V., Gomes, C.M., Silva, F.L.H., França, K.B., Lira, H.L., Ferreira, H.C. 2003b. *Aplicação da Eletrodialise em*

- Dispersões de Argilas Bentoníticas de Boa Vista, Paraíba, Brasil - Parte II - Estudo Reológico*. In: 4º Congresso Ibero-americano em Ciência e Tecnologia de Membranas - CITEM, Florianópolis, 498-503.
- Azevedo, M.G. 2002. *Membranas de Troca Iônica a Base de Polímeros Termorresistentes para Eletrodialise e Célula à Combustível*, Exame de Qualificação, COPPE/UF RJ.
- Gomes, C.M., Ferreira, H.S., Amorim, L.V., Silva, F.L.H., França, K.B., Lira, H.L., Ferreira, H.C. 2002. *Estudo da Eletrodialise de Dispersões de Argilas Bentoníticas: Resultados Preliminares*, Anais do XV CBECIMAT, Natal. No prelo.
- Kabay, N., Demircioglu, M., Ersöz, E. Kurucaovali, I. 2002. Removal of Calcium and Magnesium Hardness by Electrodialysis, *Desalination* 149: 343-349.
- Kabay, N., Arda, M., Kurucaovali, I., Ersöz, E., Kahveci, H., Can, M., Dal, S., Kopuzlu, S., Haner, M., Demircioglu, M., Yuksel, M. 2003. Effect of Feed Characteristics on The Separation Performances of Monovalent and Divalent Salts by Electrodialysis, *Desalination* 158: 95-100.
- Krol, J.J. 1969. *Monopolar and Bipolar Ion Exchange Membranes - Mass Transport Limitations*. Ph.D. Thesis, Universiteit of Twente.
- Petrobras, 1998. *Ensaio de Viscosificante para Fluido de Perfuração Base de Água na Exploração e Produção de Petróleo*, Método, N-2605.
- Souza Santos, P. 1968. *Estudo Tecnológico de Argilas Montmoriloníticas do Distrito de Boa Vista, Município de Campina Grande, Paraíba, Tese para Concurso à Cátedra de Química Industrial*, DEQ, EPUSP, São Paulo.
- Souza Santos, P. (2 ed.) 1989. *Ciência e Tecnologia de Argilas*, vol. 1, São Paulo.
- Strathmann, H. 1992. *Electrodialysis and Related Processes*, In Proceedings of the CEE - Workshop on Membrane Separation Processes, Rio de Janeiro, RJ.

“Gravitational” and “Flotational” Gold in Ores of Madneuli Copper Deposit (Georgia)

R.A.Amosov & A.S.Pariy
Mining division, INTERTECH Corp., Moscow, Russia

B.Z.Menabdishvili & Z.B.Dalakishvili
Madneuli mine, Kazreti, Georgia

ABSTRACT: The Madneuli deposit has been exploited for 30 years. Ores contain 0.92% copper and 1.06ppm gold. Until recently it was considered that gold is associated with sulphides in a finely disseminated or chemically bonded state. 40-45% of the gold is recovered in flotation, accounting for 60% of the market value of the flotation concentrate. As a result of centrifugal concentration tests carried out on various plant products with SEM analysis on concentrates, it has been established that a significant proportion of gold is presented in native form. Closed circuit flotation/gravity tests with sequential grinding between stages have indicated that the inclusion of gravity can increase recovery by 8-15%, gravity and flotation gold ratio being ~1:3.

1 INTRODUCTION

The Madneuli copper-pyrite deposit located 60 km SE of Tbilisi, has been exploited for about 30 years. The open pit comprises 6 varieties of ore of differing ratios of chalkopyrite and secondary sulfides (chalcocite, covellite). The petrographic composition of wall-rocks also differs. In the same open pit bodies of quartzites are also mined. The gold grade of the copper-pyrite ores varies from 0,6-1,5 ppm and quartzites from 2,5-3 ppm. The addition of quartzites to copper ore results in the increase of gold grade in the concentrate, but negatively influences milling characteristics and the resulting copper grade in the flotation concentrate.

Copper ores and quartzites are processed in a common flotation circuit. The plant comprises three sections with productivities of 100, 100, and 50 tph respectively. The process includes 3 stages of crushing (300, 75, 25 mm) and 2 stages of grinding to result in a nominal 55% -74 microns. The second grind stage occurs in closed circuit with a hydrocyclone, and the cyclone overflow goes to flotation. Recovery from the flotation concentrate is 83% copper, and about 40% gold. The gold accounts for 60% of the value of the flotation concentrate.

Until recently, it was accepted that the gold was either finely disseminated within the sulphides or in solid solution with them; elemental gold grains had not been observed. Subsequent plant work and a better understanding of the ore characteristics have indicated the possible presence of elemental gravity recoverable gold. In particular, the recovery of gold and copper do not appear to be connected. Furthermore, the gold grade cyclone underflow is more than twice that of the overflow and the variability of the gold grade in ores is essentially higher than that of the copper grade and of the sum of sulfides. All of the above give support to the presence of free liberated gold. It allows us to assume that the gravity-flotation circuit of gold and copper extraction, used for example in five China plants (Лодейшиков 1999; Zhang Shizhan, Du Benchen, 1992), can be successfully applied for ores from the Madneuli deposit. The work of the authors has been undertaken with the objective of increasing gold recovery.

2 MINERALOGY

In copper ores the sulfide content averages 10 %.

Copper minerals include chalkopyrite, bornite, covellite, jalpaite, chalcocite, native copper, malachite, and cuprite. According to phase analysis carried out on ores, 30 % of the copper is present as secondary sulfides and 20 % as oxides.

The native gold recovered from gravity processing of initial ore and from test products was examined by means of a scanning electronic microscope, JSM 5300. The chemical composition of gold and other minerals was determined by EDA on a Link ISIS analyzer. The form of the native gold particles is distorted, due to the matrix between grains of other minerals. Native gold intergrowths were observed not only with sulfides, but quartz and feldspar too. The size of the native gold particles varied from 0.02 to 0.4 mm, the most common size being 0.05-0.15 mm.

Due to their high malleability and density gold particles have a disproportionately high residence time in grinding circuits (Fig. 1,2). Due to work-hardening gold eventually becomes brittle and consequently fragments to a fine state, thus rendering recovery by gravity and flotation less efficient. Therefore, in order to increase gold recovery it is required to minimize its residence time in the grinding circuit.

3 GRAVITY TESTING

The samples tested were:

- sands taken from the mill during the replacement of mill liners;
- six varieties of copper ores;
- secondary quartzites from four sites, with different gold grades;
- daily average sample of hydrocyclone underflow;
- daily average samples of a hydrocyclone overflow;
- daily average samples of the current flotation tailings;
- old tailings from the copper plant.

Gravity testing of copper ores and quartzites was carried out in a Knelson KC-MD3 concentrator, in 3 stages. After crushing to -1.6mm the ore slurry was passed through the concentrator. The tailings from the first stage were then ground in a ball mill to -0.5 mm before being recycled through the concentrator and the tailings from this stage were ground once more to -0.074 mm for the same procedure. Tailings samples were taken every minute and the resulting three concentrates and tails were analysed for gold by fire assay (Амосов, Парий, 2001).

The highest gold grade (28 ppm) and the largest gold particle (0.4 mm) were observed from the mill lining sands sample, thus confirming the presence of gravity recoverability and the presence of elemental

gold! The current flotation tailings and the hydrocyclone overflow samples were processed without prior regrind.

Recoveries achieved via centrifugal gravity concentration were 12-36 % from the initial ores, 68-70 % from the hydrocyclone underflow, 17-22% from the hydrocyclone overflow and 12-16 % from the flotation tailings. This poor tailings recovery is thought to be due to fine dissemination of the gold within the sulphides coupled with an insufficiently fine grind to achieve liberation. When the initial sample weight was increased to 100kg it was possible to produce a gravity concentrate grading 1500 ppm gold, which further confirms the presence of free gold.

4 GRAVITY-FLOTATION TESTING

It is clearly apparent that the extraction of gold from hydrocyclone overflow and from the current flotation tailings are very similar. It is therefore reasonable to assume that gravity in the circuit would increase gold recovery without adversely affecting flotation recovery. To check this assumption, gravity – flotation tests were conducted against control flotation-only tests on the same samples. It was confirmed that the addition of gravity resulted in an increase of global recovery of 8-14.5 %. Extraction of gold does not appear to depend on gold content of the feed, but rather to gold in the -0.074mm size class (Table 1).

Table 1. Gold recovery on gravity-flotation and flotation

1	2 (ppm)	3 (%)	4 (%)	5 (%)
I	1,95	59,1	45,3	59,8
II	1,03	59,1	43,6	57,9
III	2,04	42,3	33,9	41,9

Explanation: I-III various blends of copper ore and quartzites; columns: 2 - the gold grade in feed; 3 – distribution in the - 0.074 mm class; 4 - gold recovery by flotation; 5 - gold recovery via gravity-flotation.

It is reasonable to assume that an increase of a share of class -0.74 mm in the hydrocyclone overflow up to 70-75 % will result in the increase of both gold and copper. The assumption that part of the gold remains unreleased because of insufficient grind is borne out by the observation that in all gravity tests the gold grade in the concentrates from the 3rd enrichment stage is higher than at 1st and 2nd stages (Table 2).

Table 2. The gold grade in a gravitational concentrate (ppm) of different stages of processing

Ore mix	Stage of processing		
	1	2	3
I	6,8	9,1	12,4
II	5,8	9,2	9,7
III	5,6	7,2	9,5

In the opinion of the authors, in order to quantify the potential economic benefits that may accrue from the introduction of gravity within the circuit, it will be necessary to undertake additional tests. The purposes of these tests are:

1) Mineralogical identification of refractory gold (Lorenzen, Van Deventer, 1992);

2) Optimization of grains size in hydrocyclone overflow for the achievement of maximum copper and gold recovery;

3) Accumulation of a gravity concentrate to allow the investigation of process options for the recovery of the contained gold, for example, the "Consep-Acacia Reactor" system.

The authors express their profound gratitude to Kevin Peacocke for his critique of this manuscript.

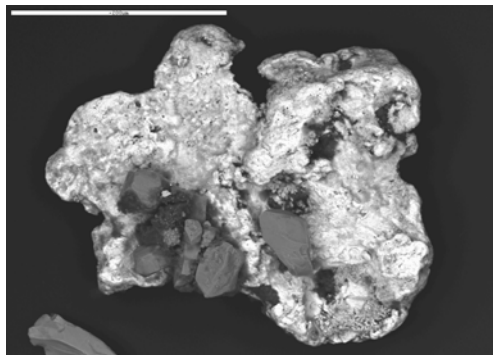


Figure 1. Native gold (white) from underflow of a hydrocyclone. Gray inclusions are pyrite. SEM, back scattered electrons.

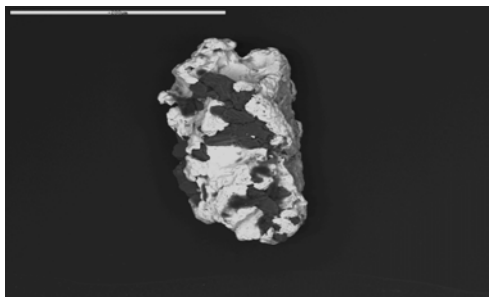


Figure 2. Native gold (white) from underflow of a hydrocyclone. Black inclusions are quartz and feldspar.

5 REFERENCES

- Амосов Р.А., Парий А.С. Методика гравитационного тестирования золотосодержащего минерального сырья // Горный журнал. 2003. №12. С.23-29.
- В.В. Технология извлечения золота и серебра из упорных руд / Т. 1, 2. Иркутск. 1999.
- Lorenzen L., Van Deventer J.S.J. The mineralogical identification of refractory gold ores by means of the selective decomposition of minerals // Extract. Met. Gold and Base Metals. Melbourne. 1992. P. 171-176.
- Zhang Shizhan, Du Benchen. A study of gold technological mineralogy evaluation of ore dressing technology in Muru , Shand ung province // Proc. 1 st Int. Conf. Mod. Process. Miner. and Miner. Process. Beijing, 1992.-P.108-112.

On-Line Measurement of Mineralogy for Ore Sorting and Characterisation

D.W.Bennett, N.G.Cutmore, D.L.Death, J.E.Eberhardt, D.G.Miljak, C.A.Rogers
CSIRO Minerals, Lucas Heights Science and Technology Centre, Lucas Heights, NSW, Australia

ABSTRACT: The mineralogy of process feed stock is often a key parameter in mineral processing. There are currently few methods in use for direct on-line surface mineralogical analysis, and none known for direct, large-volume bulk mineralogical estimation. Real-time mineralogical determination at a speed sufficient for ore sorting and on-line analysis could enable optimisation in ore blending and stockpiling leading to improved input grade control and improved extraction efficiency. This paper describes the development of mid-infrared laser reflectance techniques for rapid on-line characterisation of surface mineralogy, and radio frequency methods for on-line mineralogical analysis of bulk ores. Visible and near infrared reflectance measurements are routinely used to identify minerals. CSIRO is developing solid-state lasers to extend the wavelength range over which photometric reflectance techniques can be used. Radio frequency methods that excite mineral specific characteristic resonances are also under development for bulk mineralogical analysis. Mineral specific radio frequency resonances, that exist due to various nuclear magnetic interactions, promise potential for quantitative estimation of bulk ore stream mineralogy.

1 INTRODUCTION

1.1 Ore Sorting and Characterisation

The sorting of ore was an obvious optimisation strategy long before Georgius Agricola produced his review of mining and metals production *De Re Metallica* in 1556 (Agricola tr. by Herbert Clark Hoover and Lou Henry Hoover 1950). Ore sorting was first instituted by hand according to humanly perceived differences in the ore. Hand sorting is still used today in some mining operations and in food and waste sorting. However, today's minerals applications demand automation to cope with high tonnages in an economic fashion.

Ore sorting technology has great potential to improve the competitive position of the minerals industry by enabling the exploitation of lower grade ore reserves. Ore sorting involves the removal of gangue and below grade ore prior to comminution and downstream processing. Selective mining and ore sorting may increase mineral plant production with lower operating costs and less waste due to reduced handling and increased recovery from more-uniform higher-quality head grade.

The common requirements of all ore sorting technologies are speed and accuracy. The greatest technological challenge is the development of sensor

systems that can function reliably and quickly enough to sort between 500 and 1000 particles per second. These constraints require the integration of state of the art developments in detectors and digital signal processing with existing mechanical handling technology for the transport and selection of the sorted ore particles.

The very broad suite of sensing technologies available which may be applied for ore sorting are not currently represented in commercially available sorting equipment. Present day sorters (excluding the diamond industry) are largely based on photometric or natural radiation sensing techniques and, outside a few applications, there is often no off-the-shelf solution available. CSIRO work on ore sorting minerals on a particle-by-particle basis is concentrated on the development and refinement of new methods and sensors for discriminating mineral ores prior to mechanical sorting.

A similar set of requirements also applies to on-line characterisation of ores in process streams for the purpose of process control. However, for on-line mineralogical characterisation of an ore stream, the time constraints imposed by particle-by-particle sorting may be relaxed. Integration times of several minutes or even longer may be adequate for process control.

CSIRO is working toward sensor technology for the ore sorting and characterisation of base metals and other minerals using a range of methods including photometric and laser, X-ray, microwave and radio frequency techniques. This paper focuses on two particular techniques involving the analysis of surface mineralogy using laser reflectance and bulk mineralogy using radio frequency techniques.

2 REFLECTANCE TECHNIQUES

The surface reflectance of a mineral is the most basic indicator for ore sorting and many commercial ore sorters use colour difference as the basis for sorting. Although modifying factors, such as dust coatings and moisture, may complicate photometric techniques, discrimination of ores has been demonstrated in a number of applications. Colour difference measurements at visible wavelengths (400-700nm) typically use narrow spectral bands to maximise contrast between ore and gangue. This can be done either by band-pass filtering a passive broadband source (e.g. a lamp or the sun) or by a spectrally bright source (e.g. laser).

The visible reflectance spectra of minerals are generally broad with little structural detail, often with low contrast between ore and gangue leading to reduced selectivity. To cope with poor contrast two or more spectral bands are often used to discriminate on the basis of the relative slope of the reflectance spectrum. The infrared reflectance spectra of minerals show a range of absorption dips and reflection peaks due to fundamental vibrational bands whose position and strength depend on the mineralogy. Weaker features due to overtone and/or combination bands are often also present.

2.1 Sorting of talc

Talc is an example of a mineral where the visible reflectance spectra of various grades of talc and the gangue are quite broad, Figure 1. In addition there is also considerable talc reflectance spectral variation depending on the source of the talc. This makes it difficult to develop a generally applicable sorting technique using colour.

Measurement of a second visible band improves ore discrimination. Even so this can be insufficient when talc ores from different mines are present in the stream to be sorted. Sometimes further marginal improvement is achieved by selecting the second wavelength band in the near infrared (0.7-1.0 μ m).

While the visible reflectance of talc and its associated gangues are similar, their infrared spectra are generally quite different. OH absorption bands around 1390nm are a common feature of talc spectra which show enough variation to discriminate source location, Figure 2. The OH bands are not common to

carbonates and quartz but may appear in clays so the combination of both visible and infrared wavelength bands is more optimal for sorting talc and gangue.

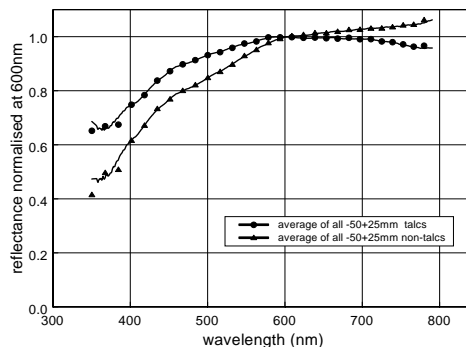


Figure 1: Visible reflectance spectra of talc.

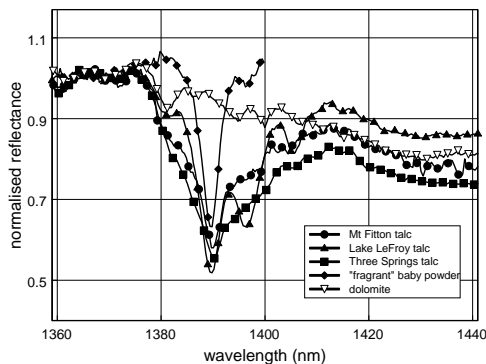


Figure 2: Infrared reflectance spectra of talc.

2.2 Sorting of phosphate

There are applications in phosphate mining where sorting can be used to enhance grade and extend the mine resource.

Sorting of phosphate from gangue can be very difficult when using colour as the discriminator of grade. It is well known (Eberhardt & Pryor 1982) that silica and apatite have reststrahlen reflection peaks around 8.6 μ m and 9.6 μ m respectively. Work at CSIRO has shown that apatite and phosphorite also have useful reflectance in the 9-11 μ m wavelength range which is accessible to CO₂ lasers.

Reflectance measurements at a handful of selected CO₂ laser wavelengths from a phosphorite sample indicated that the phosphorite was semi-transparent at the selected wavelengths. The spectra of semi-transparent materials are unlike those of opaque materials (Kortüm 1981). Their diffuse reflectance spectra are dominated by light that

penetrates into the surface through many tiny crystals before reflection at the various crystal interfaces. Such spectra are called "remission spectra". A special feature is that "remitted" light can exhibit narrow dips where the material has weak absorptions, e.g. finely powdered carbonates, sulphates and apatite (Eberhardt et al. 1985). If the illumination is polarised these dips can be enhanced by viewing the remission through a crossed polariser. Polarised laser light that undergoes reflections at many crystal boundaries is usually remitted with a different polarisation. This offers phosphate-specific identification since the remission dips are at specific wavelengths. Unfortunately, water present on the surface can modify the spectra to that of coarse-grained material as water absorbs CO₂ laser wavelengths and has a higher refractive index which reduces reflectance at grain boundaries.

A set of samples representing nine phosphate ore and gangue groups were measured to demonstrate the possibility of ore sorting based on this weak absorption. Reflectance data at up to eight discrete CO₂ laser wavelengths was recorded by scanning the laser beam across the surface of each sample as it translated across the scan line. Samples were rotated to expose four different face views. The data was subsequently normalised to the reflectance of a sand-blasted aluminium reference standard.

A sorting criterion based on reflectance at four discrete laser lines was developed to discriminate between various grades of ore and gangue. This allowed discrimination between some high grade and low grade samples, but did not adequately discriminate between phosphate and gangue.

To improve the selection of the phosphate ore samples the apparatus was modified so that the cross-polarized component of the reflectance was measured. A subset of samples representing five ore and gangue groups were measured as received and then subsequently re-measured after spraying with water and drying for several days. Spraying washed a fine powder coating from many of the samples.

The unwashed polarized results improved the discrimination of phosphate ore, however some of the unwashed gangue samples could not be discriminated from the phosphate ores. Washing and drying provided by far the best separation of phosphate ore and gangue materials. We interpret this as each sample being coated with finely divided phosphate powder during collection and delivery. If sorting were conducted using this approach, the calculated grade, expressed as the ratio of %P₂O₅ to %SiO₂, improved from 0.12 to 0.24 for the sample suite measured.

2.3 Tunable mid-infrared sensors

The measurements described above were performed using discrete fixed wavelength lasers. The inherent spectral brightness of a laser makes it a preferred choice for photometric sorting. However, the usefulness of a particular laser for a given mineral is often a matter of luck. The spectral coverage offered by commercial lasers is small compared to the range of interest. To access useful spectral features in the infrared CSIRO has built, and is testing, a versatile light source called an Optical Parametric Oscillator, which is wavelength-tunable from 1.4 to 3.5µm.

3 RADIO FREQUENCY TECHNIQUES

In contrast to the rapid techniques required for particle by particle ore sorting, on-line mineralogical estimation on ore streams may also be employed with a less stringent requirement for rapidity. For example, in some applications it may be acceptable for integrated estimates of mineralogy to be returned over periods of several minutes, in order to control downstream mineral processes such as blending and extraction. While on-line systems exist in the minerals industry for both composition (e.g., X-ray fluorescence, nuclear techniques) and mineralogy (X-ray diffraction), there are no commercial analysers used in the minerals industry for bulk (large volume and/or large particle size) mineralogical estimation that do not require significant sampling procedures.

Radio frequency techniques may potentially be suited to direct bulk mineralogical analysis on conveyor streams, flotation cells or for bore-core analysis. Some magnetic resonance phenomena have mineralogically specific resonance frequencies, such as Nuclear Quadrupole Resonance (NQR) and Antiferromagnetic Nuclear Magnetic Resonance (AFNMR) (Abragam 1961). NQR resonances occur due to the interaction of the electric quadrupole moment of the nucleus and the electric field gradient at the nucleus, the latter being strongly dependent on bonding and crystal structure. AFNMR arises due to internal hyperfine magnetic fields related to crystal structure. In both these particular cases, application of a DC magnetic field is not required to define the resonances. This is an important advantage, since the significant hardware associated with magnetic field generation and control is avoided. Most resonances of interest occur below 100MHz, where radio waves have reasonable penetration depth (typically many centimetres) into most ore streams.

CSIRO has developed a bench NQR/AFNMR system for lab-scale bulk mineralogical investigation. The resonances are observed using radio frequency pulse schemes typically used in magnetic resonance. For example, for the short

resonance relaxation times found for many ores, the Hahn echo sequence may be utilized (Das & Hahn 1958). The amplitude and shape of the echo signal may give quantitative information on the target species. The signals are generated by application of radio frequency pulses to coils or other structures that generate a radio frequency magnetic field. These structures need only surround or be in close proximity to the stream being analysed, and therefore the technique potentially offers non-intrusive analysis without need for sampling of the ore stream.

Some copper ores are amenable to radio frequency detection (Abdullin et al. 1987). Chalcopyrite, a commercially important copper ore, has a room-temperature antiferromagnetic resonance (^{63}Cu) at 18.46MHz. In laboratory bench-scale measurements on 60cm³ volumes, the resonance has been observed in a number of different samples (large crystals or powders derived from flotation). Dilution experiments in alumina powder demonstrate that resolution of concentrations below 1% is achievable within integration times useful for on-line process control. Figure 3 shows the Hahn echo signal at 6.65% dilution, obtained in 51.2 seconds.

Optimisation of the bench scale apparatus for improved resolution, with a view for larger volume analysis on actual ore streams, is continuing.

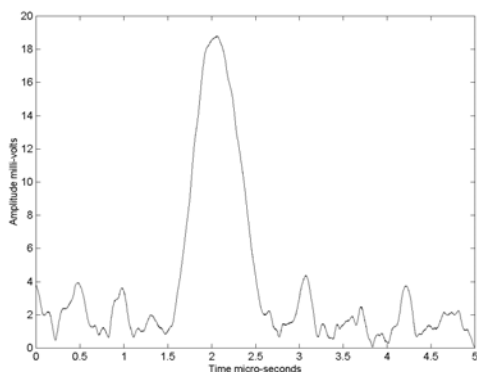


Figure 3: Hahn echo signal of 6.65% chalcopyrite diluted in alumina achieved from 512 scans in 51.2 seconds.

4 CONCLUSIONS

Efficient sorting and separation of ore and gangue depends critically on the level of discrimination offered by the sensor. For photometric sensors, the

combination of at least two wavelength bands is often required to provide adequate discrimination particularly if there is a degree of similarity between the ore and the gangue or if there is a range of acceptable ore components. Access to infrared reflectance bands can increase selectivity and enhance the sorting of complex ores. In particular, weak absorption features in remission spectra are a valuable tool for discrimination of ore and gangue. Reflectance spectra from minerals are a surface characteristic and can be subject to interference from surface dust layers and moisture.

Radio frequency detection of bulk mineralogy offers several potential advantages, such as true bulk material analysis on large volume samples, relatively simple hardware for signal generation and detection, and the avoidance of mechanical sampling and sample presentation. However, optimisation of the techniques must continue in order to improve resolution.

5 ACKNOWLEDGEMENTS

D. Bennett and D. Miljak acknowledge useful discussion with Dr David Cousens, CSIRO Exploration and Mining, and Dr Joe Khachan, University of Sydney.

6 REFERENCES

- Abdullin, R.S. Kal'chev, V.P. Pen'kov, I.N. 1987. Investigation of Copper Minerals by NQR: Crystallochemistry, Electronic Structure, Lattice Dynamics. *Phys Chem Minerals*14:258-263.
- Abragam, A. 1961. *The Principles of Nuclear Magnetism*. London: Oxford University Press.
- Agricola, G., (tr. by Herbert Clark Hoover and Lou Henry Hoover) 1950 *De Re Metallica*. New York: Dover Publications, Inc., (reprint of the 1912 edition.)
- Das, T.P. Hahn, E.L. 1958 *Nuclear Quadrupole Resonance Spectroscopy*, Supplement 1 of *Solid State Physics Advances in Research and Applications*. New York: Academic Press Inc.
- Eberhardt, J.E. Haub, J.G. & Pryor, A.W. 1985. Reflectivity of natural and powdered minerals at CO₂ laser wavelengths. *Appl. Opt.* 24: 388-395.
- Eberhardt, J.E. & Pryor, A.W. 1982. Sorting phosphate ore by infrared reflectivity. Private communication.
- Kortüm, G. 1981. *Reflectance Spectroscopy*. New York: Springer-Verlag.

Principal Component Analysis Applied to Surface Chemistry in Process Mineralogy

M.Biesinger, D.Miller, J.Francis

Surface Science Western, University of Western Ontario, London, Canada

B.Hart

Department of Earth Sciences, University of Western Ontario, London, Canada

R.StC.Smart

Ian Wark Research Institute, University of South Australia, Mawson Lakes, South Australia

ABSTRACT: Diagnosis of the surface chemical factors playing a part in flotation separation of a valuable sulfide phase requires measurement of the hydrophobic and hydrophilic species that are statistically different between the concentrate and tail streams. Time of flight secondary ion mass spectrometry (ToF-SIMS) can be used to identify sufficient particles of a specific mineral phase for reliable statistics determining a mean value for each species with 95% confidence intervals. A mass spectrum from each particle, at 1-2 monolayer sensitivity, is recorded and stored. This analysis is reported for a chalcopyrite/pyrite/sphalerite mineral mixture conditioned at pH9 for 20min to study transfer of Cu from chalcopyrite via solution to the other two mineral surfaces since this mechanism can be responsible for their inadvertent flotation in copper recovery. Particle selection by Fe/Zn indicated no statistical difference in the copper intensities on pyrite and sphalerite after this conditioning. PCA identifies combinations of factors strongly correlated (positively or negatively) in images or spectra from mass spectra recorded at each of 256x256 pixels in a selected area of particles. PCA is a better method of selecting minerals due to multi-variable recognition. It has clearly separated a statistical difference in copper intensities between the sphalerite and pyrite phases. The method has been extended to samples from an operating plant again with excellent phase recognition and diagnostic surface chemistry.

1 INTRODUCTION

In the selective separation of mineral phases by flotation, surface chemistry is the principal determinant of the average contact angle for a specific mineral phase in a flotation pulp. The average contact angle is, in turn, the principal determinant of the bubble-particle attachment efficiency (E_a) in the overall collection efficiency (E_c) from which the flotation rate constant can be determined (Ralston 1994). The recovery and selectivity in sulfide flotation is ultimately dependent on the relative rate constants of the different mineral phases. But the average contact angle is not only mineral-specific, based on a statistical average of the mineral particles in that phase, but also the contact angle for each particle is an average of hydrophobic and hydrophilic areas across the particle surface. Determination of this hydrophobic/hydrophilic balance by particle therefore requires selection of the particular mineral phase and statistical analysis of the particles with an estimation of the spread of values. In a flotation pulp containing many different mineral phases, different particle sizes of individual phases, adsorbed and precipitated species (often colloidal), and oxidised products, this is not a simple task.

The hydrophobic/hydrophilic balance by particle and its statistical average by mineral phase requires identification of the major species contributing to each category in surface layers. In addition to adsorbed collector molecules and their oxidised products (e.g. dimers), hydrophobicity can be imparted to sulfide mineral surfaces by oxidation to produce polysulfide Sn_2 - species resulting from loss of metal ions (usually Fe^{2+}) from surface layers. In acid solution, hydrophobic elemental sulfur can also be formed usually imaged in patches on the sulfide mineral surface (Smart et al. 2003). Almost all other species found on sulfide mineral surfaces, such as oxide/oxyhydroxide/hydroxides, oxy-sulfur (e.g. sulfate), carbonate, hydrous silica and fine gangue particles, are essentially hydrophilic but may be in the form of localised particles, colloids and precipitates or continuous, reacted or precipitated surface layers (Smart et al. 2003).

The action of collector molecules in inducing hydrophobicity can be assisted by activating species such as copper and lead ions that complex the collector on the surface. Previous research has shown that this activation can be inadvertently produced by dissolution and transfer via solution of these ions to mineral phases not intended to float (Smart 1991; Lascelles & Finch 2002; Finkelstein

1997). The mechanisms of activation of sphalerite (Gerson et al. 1999) and pyrite (Weisener & Gerson 2000) by copper have been elucidated. In this paper, we examine statistical evidence for this mechanism on both mixed mineral and real plant samples. The challenge in the work is to find more reliable methods of mineral phase recognition in these complex surface chemistries. This work is supported by a Canadian NSERC Discovery Grant.

2 TOF-SIMS SURFACE ANALYSIS

The time of flight secondary ion mass spectrometry technique, used in static mode, involves a very low flux of heavy ions impacting surface layers with mass spectrometric analysis of the secondary ions emitted from the surface. In the time of routine measurement, only 1-2 surface atoms in 1000 are impacted. The secondary elemental and molecular fragment ions come from the first two molecular layers of the surface and provide a very detailed set of positive and negative mass fragments from simple ions, e.g. Na^+ , OH^- through to molecular ions of specific reagents, e.g. isobutyl xanthate ($\text{CH}_3)_2\text{CHOCS}_2^-$. Identification of molecular mass peaks for collectors, activators, depressants, precipitates and adsorbed species is possible with comparative surface concentrations by particle and by phase between feed, concentrate and tail streams. A lateral distribution imaging of species by particle is combined with a statistical comparison of differences between streams by mineral phase (Piantadosi et al. 2000).

3 MIXED MINERAL SYSTEM

ToF-SIMS statistical analysis is reported for a chalcopyrite/pyrite/sphalerite mineral mixture conditioned at pH9 for 20min in order to study transfer of Cu from chalcopyrite via solution to the other two mineral surfaces since this mechanism can be responsible for their inadvertent flotation in copper recovery. In particular, preferential adsorption of copper ions between pyrite (Py) and sphalerite (Sp) was examined.

Initially, phase recognition of Py and Sp was based on +ion images for high Fe and Zn and the mass spectra from these regions (normally 30 regions selected for each phase) statistically averaged after normalisation for total ion yield (principally topographic correction) and area of each region. The difficulty of phase recognition can be appreciated from Figure 1a where the range of particle sizes is illustrated. Results for phase differentiation and Cu transfer to each mineral are shown in Figure 2. The presence of Fe (bulk and surface) in Sp and adsorbed Zn on Py complicate

this phase differentiation. In this analysis, there is no statistical difference between the copper adsorbed on Py and Sp, contrary to most studies which suggest preference for adsorption on Sp but without direct evidence (Smart 1991; Lascelles & Finch 2002; Finkelstein 1997).

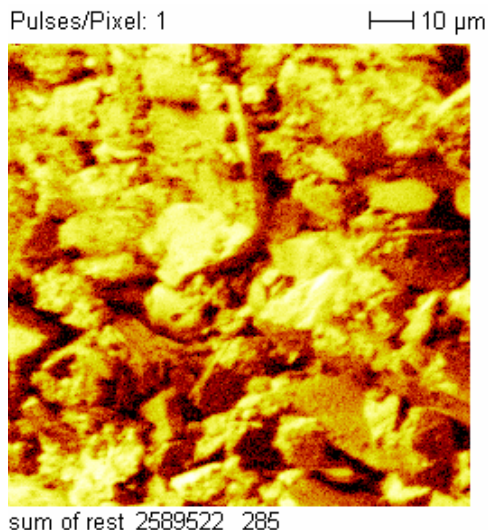


Figure 1a. ToF-SIMS image of particles in Py/Sp/Chpy mixture.

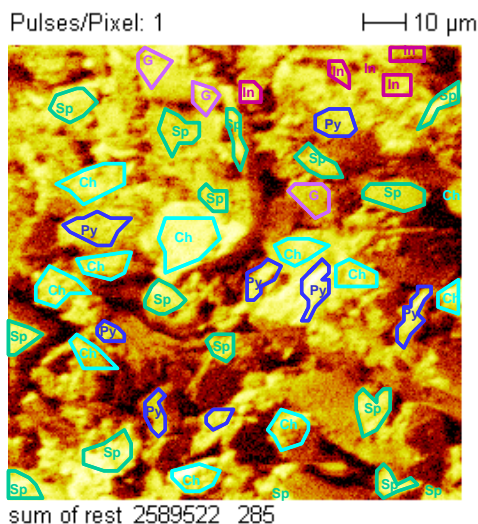


Figure 1b. PCA identification of mineral phases labelled: Py blue; Sp darker green.; Chpy lighter green; gangue purple.

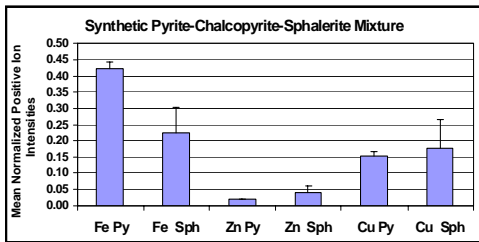


Figure 2. Statistical phase identification from images and Cu distribution between Py and Sp. Bars are 95% confidence intervals.

In an alternative statistical analysis, principal component analysis (PCA) was used to enhance phase recognition and definition of regions for mass spectral analysis. This is the first application of PCA to flotation surface chemistry. PCA identifies combinations of factors strongly correlated (positively or negatively) in images or spectra from sets of data (Biesinger et al. 2002). It can also be useful to remove systematic variance from the data – such as matrix and topographic effects. In images, PCA selects these correlations from the mass spectra recorded at each of 256x256 pixels in a selected area of particles. PCA has proved to be a much better method of selecting particles by mineral phase with clearer definition of particle boundaries due to multi-variable recognition. This selection is illustrated in Figure 1b where it is possible to recognize both Py and Sp from a specific principal component PC2, which this method selects, in which they are anti-correlated. (PC1 was largely correlated to topography). Figure 3 illustrates this PC2 in which areas with high Fe and high Zn are clearly selected from each other. The contrast difference in the image can then be used to select regions for analysis for each phase separately with higher confidence. Figure 4 gives the statistical analysis from these regions for both phase selection and Cu distribution between phases.

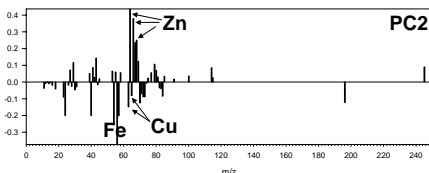


Figure 3. Principal component 2 selected from the area image in Fig. 1a differentiating Sp regions (high Zn) from Py regions (high Fe) as in Fig. 1b. Note the correlation of Cu with Fe due to the Chpy phase. Selection of the highest Fe regions in the image, however, gives good identification of Py over Chpy.

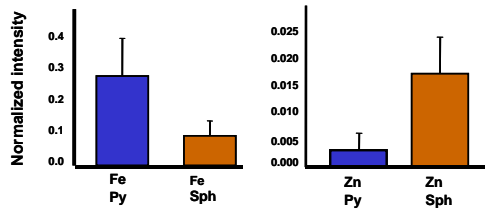


Figure 4a. PCA phase identification. Note lower contributions from Zn on Py compared with Zn on Sp (c.f. Fig. 2).

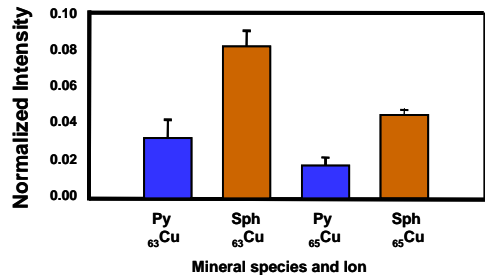


Figure 4b. Statistical analysis of Cu distribution between Py and Sp using the phase regions identified by PCA.

The selection of the Sp phase is enhanced by the higher Zn signal relative to Py. The continued presence of Fe signals from the Sp regions is consistent with a high-Fe sphalerite phase.

Importantly, using PCA phase identification, we now see a clear statistical separation of Cu distribution in favour of Sp. The close agreement between the two copper isotope provides confidence in the validity of the separation. This is also consistent with unwanted flotation of this phase in chalcopyrite circuits (Finkelstein 1997). The transfer of copper ions from chalcopyrite dissolution to both pyrite (Smart 1991) and sphalerite surfaces (Smart 1991; Lascelles & Finch 2002; Finkelstein 1997) is confirmed by the surface analysis. The new result is direct statistically-based evidence of preferential adsorption on Sp over Py in the same conditions and pulp solution.

4 PLANT SAMPLES

The Inco Nickel-Copper Matte flotation process (Sproule et al. 1945) separates chalcocite (Cc) from heazlewoodite (Hz) using a diphenylguanidine (DPG) collector and frother. The separation becomes less selective as the minerals move through the circuit possibly due to inadvertent activation of Hz by Cu ions and/or depression of Cc by adsorbed Ni ions. We have used the same PCA methods to study concentrate and tails samples from the operating plant. The principal components gave

excellent recognition of the two mineral phases with reliable statistics on the regions selected.

Figure 5 illustrates some of the results from this study, with kind permission of Inco P/L, showing direct evidence of Cu transfer from Cc to Hz on particles inadvertently collected into the concentrate.

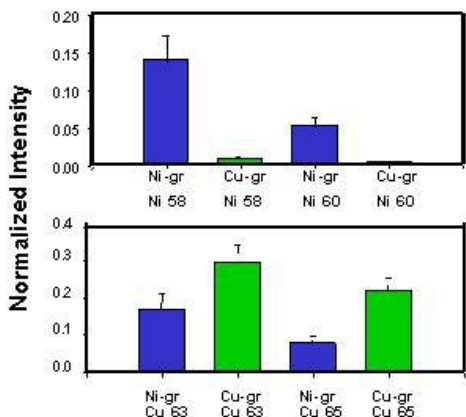


Figure 5. Matte concentrate sample. PCA phase recognition with statistical analysis of phase regions for Ni and Cu transfer. Note the relatively high surface concentrations of Cu on Hz (Ni-gr) in concentrate.

This is matched by mass signals for the Cu-DPG complex also showing relatively high surface concentrations on Hz in the concentrate compared with the tail (Figure 6).

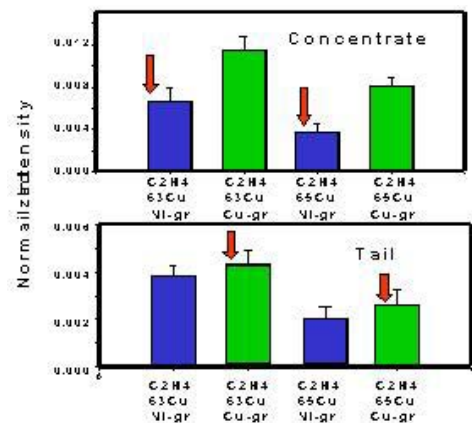


Figure 6. Comparison of Cu-DPG mass signals.

5 CONCLUSIONS

Diagnosis of the surface chemical factors playing a part in flotation separation of a valuable sulfide phase requires measurement of activating species that are statistically different between mineral phases. Time of flight secondary ion mass spectrometry (ToF-SIMS), has been used to identify sufficient particles of a specific mineral phase for reliable statistics determining a mean value for each species with 95% confidence intervals. For a chalcopyrite/pyrite/sphalerite mineral mixture conditioned at pH9 for 20min, transfer of Cu from chalcopyrite occurred via solution to the other two mineral surfaces. Analysis based on Fe and Zn images indicated no statistical difference in the copper intensities on pyrite and sphalerite after this conditioning. PCA is a better method of selecting mineral phases due to multi-variable recognition. It has clearly separated a statistical difference in copper intensities between the sphalerite and pyrite phases. The method has been extended to samples from an operating plant again with excellent phase recognition and diagnostic surface chemistry.

6 REFERENCES

- Biesinger M.C., Paepgeay P-Y., McIntyre N.S., Harbottle R.R. and Petersen N.O., (2002), *Analytical Chemistry*, 74, 5711-5716.
- Gerson A.R., Lange A.G., Prince K.P. and Smart R.St.C., (1999), *The Mechanism of Copper Activation of Sphalerite Applied Surface Sci.*, 137, 207-223.
- Finkelstein N.P., (1997), *The Activation of Sulfide Minerals for Flotation: a Review*, *Int. J. Minerals Processing*, 52, 81-120.
- Lascelles D. and Finch J.A., (2002), *Quantifying Accidental Activation I. Cu ion production*, *Minerals Engineering*, 15, 567-571.
- Piantadosi C., Jasieniak M., Skinner W. M. and Smart R.St.C., (2000), *Statistical Comparison of Surface Species in Flotation Concentrates and Tails from ToF-SIMS Evidence*, *Minerals Engineering*, 13, 1377-1394.
- Ralston J., (1994), *Bubble-Particle Capture*, in *Flotation II* (Eds. S Castro and J.Alvarez) Publ.Andros Ltd. (Chile), Vol.2, 1464 .
- Sproule K., Harcourt G.A. and Rose E.H., (1945), *Froth Flotation of Nickel-Copper Matte*, U.S. Patent No. 2,432,465.
- Smart R.St.C., (1991), *Surface Layers in Base Metal Sulphide Flotation..*, *Minerals Engineering*, 4, 891-909 .
- Smart R.St.C., Amarantidis J, Skinner W.M., Prestidge C.A., LaVanier L. and Grano S.G., (2003), *Surface Analytical Studies of Oxidation and Collector Adsorption in Sulfide Mineral Flotation in "Solid-Liquid Interfaces"* (Eds K. Wandelt and S. Thurgate), *Topics in Applied Physics*, Springer-Verlag, Berlin, 85, 3-60.
- Weisener C. and Gerson A.R., (2000), *Cu(II) Adsorption Mechanism on Pyrite: an XAFS and XPS Study*, *Surface and Interface Analysis*, 30, 454-458.

Technological Characterization of Carbonatic Raw Material Manufacture from Cajati (SP)

A.G.Brandão & L.M.Sant'Agostino

Department of Sedimentary and Environment Geology, Geosciences Institute, University of São Paulo, Brazil

T.B.Bonás

Bunge Fertilizantes S.A.

ABSTRACT: The phosphoric acid, produced from apatite concentrate obtained in the carbonatitic alkaline complex of Cajati (SP) mining activity, is applied as carbonatic raw material for manufacturing, of a calcium-phosphate mineral supplement for animal feed. The biological value of a mineral source is function of the interesting element concentration and toxics or contaminants elements grades, Mg and Fe are in this last category acting as noxious elements and Ba and Sr are cumulative in the nutritional chain. This work aim a specific litological unity that composed the ore deposit, which is an essentially carbonatitic litology with low proportions of accessory minerals. Their 3D settings show cream, orange and red litotypes confined in the neighboring of a main fault that crosses the entire mine, what is indicative that the reddish color can be result of fluids percolated through the fault opening. The technological characterization studies performed intended to obtain information to be applied in the processing of purifying the carbonatitic raw material or even in the manufacturing a new commercial product, a differentiated cream calcium-phosphate mineral supplement. It was verified that because of calcite mineralogical characteristics any process of concentration would not cause expressive reduction of Mg. In case of Fe_2O_3 , the concentration can achieve a significant reduction.

1 INTRODUCTION

Cajati mine, located in southeast Brazil, has been an important national phosphatic rock producer that exploits a low graded carbonatite ore, owned by the Bunge Fertilizantes S/A Company. The carbonatite belongs to the Jacupiranga Ultramafic Alkaline Complex, a classical geological occurrence, which was first described by Melcher (1954) as an ellipsoidal body NNW oriented, 10.5 km long and 6.7 km wide, intruded in Precambrian rocks, granodiorites at north and mica schists at south. The carbonatitic bodies occupy an area of 1 km long by 0.4 km wide, in the south portion, intruded in jacupiranguite rocks. According to Gaspar (1989), the carbonatitic orebody was formed as a sequence of at least five magmatic intrusion phases into the jacupiranguite host rocks, resulting in an internal organization as illustrated in Figure 1.

The apatite mineralization is associated with the carbonatites bodies. Mining activities began in the earlier 1940s when the carbonatites was a 250 m high hill, capped by a residual ore that could reach grades of 12% P_2O_5 . Since 1970, when the residual ore was exhausted, the fresh rock has been mined. It shows grades around 5% and the currently cut off grade is 3% P_2O_5 .

The phos-calcium (calcium-phosphate mineral supplement) has been manufacturing since the 1980's ending, moved by the high purity of the carbonatitic material obtained as tailing from apatite mineral processing.

This work aims a specific lithological unity, named COX (oxidized carbonatite), which composed the ore deposit. Currently this unity is used to produce cement, but has excellent chemical composition for phos-calcium manufacturing apart of its pale reddish color that is not adjusted for a usual white product.

The technological characterization studies performed in the carbonatic raw material aimed information to be applied in the processing of purifying it or even in the manufacturing a new commercial product, a differentiated cream phos-calcium.

1.1 Bicalcic phosphate - phos-calcium

Phos-calcium is a Bunge's trademark, corresponding to a bicalcic phosphate fluor removed that is applied as mineral supplement for animal feeding to balance Ca and P grades. This product is offered in microgranulated and dust form, has white to light gray color, pH between 5 and 6.5, high biological

availability, good palatability and stability in mineral mixture, animal supplement and ration.

It is obtained by reaction between carbonatite waste (CaO > 49% and MgO < 3.8%) and phosphoric acid.

The biological value of a mineral source is a function of the interesting element concentration and toxic or contaminants elements grades. Mg and Fe are in this last category acting as noxious elements; Ba and Sr are cumulative in the nutritional chain.

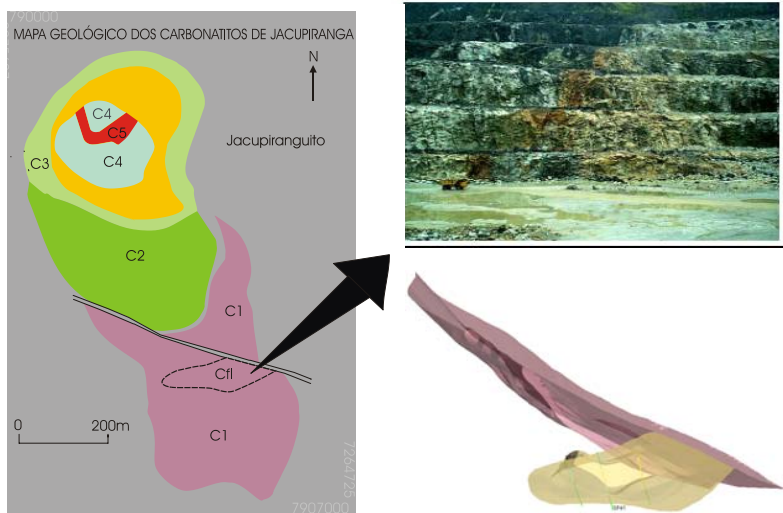


Figure 1. Carbonatite geologic map from Cajati mine (modified from Gaspar 1989). At right some details of the COX unity.

2 GEOLOGICAL SETTINGS

The unity COX outcrops in the cote -70 m in the south portion of the actual pit and has an elliptical NE/SW oriented design in plant, at NE is limited by a main faulting zone. It is a submillimetric until 5 mm grain size rock, essentially of carbonatitic composition with low proportions of accessory minerals. It is constituted by carbonates (90 %), calcite and dolomite, apatite (5 %), subidiomorphic magnetite (5 %) and idiomorphic phlogopite as trace. The absence of olivine is a distinctive characteristic of this unit.

According to physical (color, texture, grain size) and mineralogical macroscopical characteristics it was subdivided in distinct lithotypes: white, white to gray, gray, cream, orange and red.

These lithotypes show a spatial zoning mainly defined by the main faulting that crosses the orebody and truncate the unity in the north, as suggested by field correlations. The cream, the orange and the red lithotypes are confined in the neighboring of the fault what is indicative that the reddish color can be result of fluids percolated through the fault opening.

The volumetric proportions of the litotypes had been determined according to percentage of their

occurrences in vertical sections and later adjusted for the whole unity. There is a high predominance of white and white to gray lithotype (82 %) and less expressive and narrow occurrences of cream, orange and red lithotypes (18 %).

3 METHODOLOGY

Six drilling samples of the referred lithological unity were selected, which were prepared in the laboratory and after submitted to mineral separations as well as chemical, grain size and mineralogical analysis. The samples must have lengths upper to 10 m, according to mining scale, and mineralogical and physical features representation of the lithotypes recognized in the COX unity.

The sample preparation in laboratory follows the mine routine procedures, which comprises operations of dry crushing and wet milling (using jarr ball) followed by wet low intensity magnetic separation, sliming (0.037 mm), grain size classification and chemical analyses by X ray fluorescence (Alves 1999).

Additionally, some mineral separations were done, through density properties (heavy liquid tetrabromoetane with specific density 2,96 g/cm³)

and magnetic susceptibility (Frantz Isodynamic), aiming concentrate the carbonates. To investigate the carbonates characteristics techniques of microscopy, associated with chemical microanalyses were applied. An specific grain size fraction ($- 0,297 + 149$ mm) was used for these operations.

4 RESULTS

The studied samples presented similar mineralogical composition, despite of the variation on the amounts of apatite (Table 1). The analyses had also shown a weak correlation between Fe_2O_3 and reddish color; low MgO grades what is a good condition aiming phos-calcium manufacturing.

Table 1. Characteristics of three more representative samples.

SAMPLE	MINERAL COMPOSITION (% IN WEIGHT)					
	Apatite	sulfides	silicates	Fe oxides	calcite	dolomite
SP3601	8	0,4	0	6	80	5
	red orange calcitic carbonatite					
SP3602	13	0,8	1	5	77	4
	cream calcitic carbonatite					
SP3702	11	0,5	1	4	78	5
	white and white to gray calcite carbonatite					

Obs.: silicates = phlogopite + olivine; Fe oxides = magnetite + goethite + limonite; sulfides = pyrite + pyrrhotite + Cu sulfides

By dense liquid separation it was obtained light products corresponding to 88 % in weight of the analysed grain size fraction. This is composed by liberated particles of carbonates and phlogopite (95%) and non liberated particles of carbonate associated with apatite, magnetite and sulfides. The heavy products, corresponding to 12% in weight of the analysed fraction, were composed by sulfides, apatite, olivine and magnetite.

In the carbonates concentrated light product, by electromagnetic separation it was achieved a magnetic product (FLM) corresponding to 1,8 % in weight of the analyzed grain size fraction, constituted by non liberated particles of carbonates, and a non magnetic product (FLNM) corresponding to 86,2 % in weight, composed by liberated particles of carbonates.

4.1 Scanning electron microscopy (SEM)

The scanning electron microscopy, coupled with chemical analyses (SEM-EDS), indicated that in the FLNM products the non liberated particles of calcite frequently presents MgO (0.2% to 1.41%). Dolomite occurs only associated to non liberated particles of calcite. The Fe grades are associated to iron oxihydroxides that occur as fine veins and micrometrics crusts in the calcite particles and in small proportions in the structure of the calcite. Calcite crystals can present BaO grades until 0.5%.

The FLM products are composed by liberated particles of dolomite that frequently present FeO grades (1.26% a 6.3%) and rare MnO grades.

Beyond the cited mineralogical association between calcite, dolomite and iron oxihydroxides, micrometrics inclusions of barite, pyrite, apatite, phlogopite and strontium carbonate were observed in calcite particles.

The SEM-EDS studies indicated that the reddish color observed in the samples is mainly related to micrometrics iron oxihydroxides impregnations and less frequently to iron dolomite.

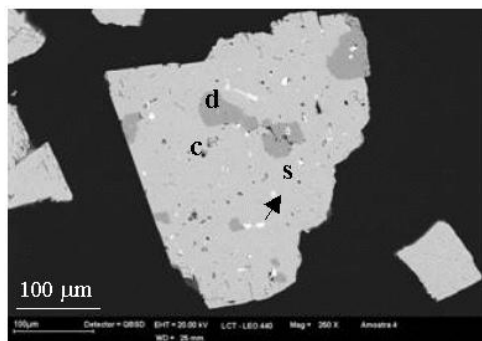


Figure 2. Non liberated calcite (c) with exsolutions of dolomite (d) and Sr carbonate (s).

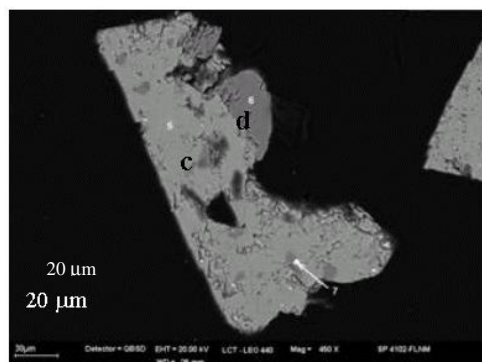


Figure 3. Mixing particle of calcite (c) and dolomite (d) with inclusions of dolomite in calcite.

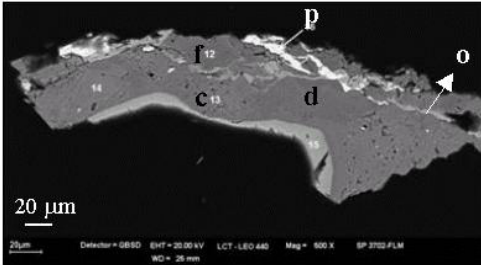


Figure 4. Particle of phlogopite (f), dolomite (d), calcite (c) with fine vein of pyrite (p) and iron oxides (o).

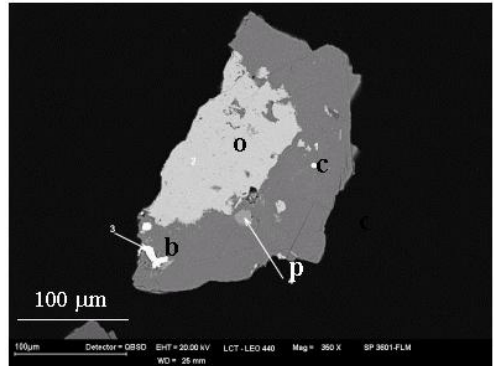


Figure 7. Mixing particle of calcite (c) and iron oxides (o) with inclusion of barite (b) and apatite (a).

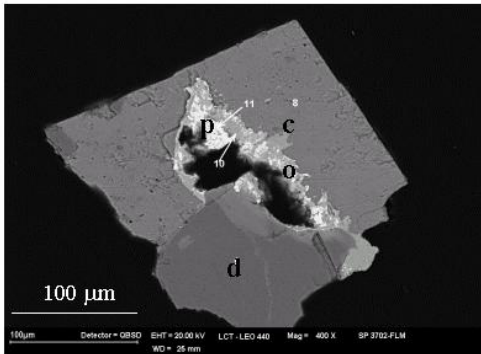


Figure 5. Particle of calcite (c) e dolomite (d) recovered by iron oxides (o) and pyrite (p).

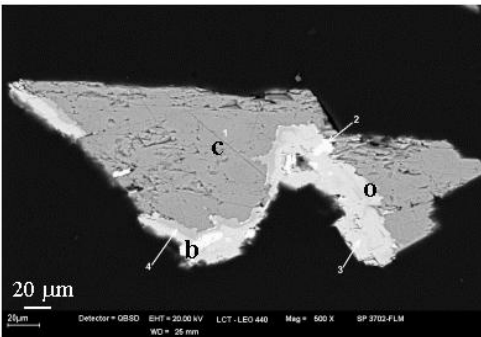


Figure 6. Calcite (c) recovered by iron oxides (o) associated to barite (b).

5 CONCLUSIONS

The attained results showed that carbonates concentrate present grades of 2% of MgO. Calcite carries between 68 to 72% of the total Mg contained in the ore. Remains of Mg are associated with dolomite, both in liberated particles and non liberated inside calcite, and silicates. Scarcely barite inclusions in carbonates particles are responsible by the low Ba grades.

Magnetite carries between 63 to 84% of the total Fe_2O_3 of the ore, and remaining amount of iron is associated with calcite: the calcite concentrates have grades of 0.15 to 0.5% Fe_2O_3 .

Therefore any process of carbonates purifying, in order to achieve a product to be applied in the classic white phos-calcium manufacturing, will not cause expressive reduction of MgO grades. But for Fe_2O_3 reduction, the processing can be interesting, because beyond that a certain cream color clearing of the product was observed.

6 REFERENCES

- Alves, P.R.P.C. 1999. Estudos de caracterização tecnológica no minério apatítico do Complexo Alcalino de Jacupiranga, SP. Monografia de trabalho de formatura, TF1999/011. Instituto de Geociências da Universidade de São Paulo, 59.
- Gaspar, J.C. 1989. Geologie el mineralogie du complexe carbonatitique de Jacupiranga, Brésil. França, Tese de Doutorado U.E.R. de Science Fundamentales et Appliquées, Université d'Orleans, 344.
- Melcher, G.C. 1954. Nota sobre os distrito Alcalino de Jacupiranga, São Paulo. Div. Geol. Min.,84.

Technological Characterization of Low Grade Phosphate from Salitre, MG-Brazil

A.B.Braz, H.Kahn, G.Ratti, M.M.M.L.Tassinari

Department of Mine and Petroleum, Polytechnic School, University of Sao Paulo, Sao Paulo, Brazil

ABSTRACT: This work presents the results of technological characterization studies made on phosphate ore samples from the northwest and southeast part of the Salitre I alkaline-carbonic Complex, municipality of Patrocínio, State of Minas Gerais. The studies, carried out on samples from bore holes, had the main purpose of evaluating the mineralogical composition and properties of the valuable and gangue minerals, such as mineral assemblages and compositions, surface coating, among other properties. The samples from drills N-112 and P-120 are the richest in terms of P_2O_5 content, 12.8% and 13.6% respectively; the lowest P content is in samples from drill P-104, with 5.3% P_2O_5 and SR composite sample (about 5.8%). Mineralogical analyses by X-ray diffraction coupled to optical microscopy and electronic scanning microscopy techniques, in association with results from chemical analyses, allowed to define that the minerals assemblage in the studied samples were quite similar: apatite, quartz, feldspars, phyllosilicates (micaceous minerals and kaolinite) and iron oxy-hydroxides; as accessory and minor minerals were found aluminum-phosphates (gorceixite and/or goyazite), titanite, perovskite, anatase, pyrochlor, manganese minerals, and rare earth phosphates. The amount of apatite coated iron oxy-hydroxides that not responds to flotation concentration is comprised between 2% and 15%; its liberation size is between 0.21 mm and 0.30 mm. The portion of apatitic P_2O_5 , for material classified above 0.037 mm, varies somewhere around 92% to 96% for all samples, while in the SR it reaches almost 100%.

1 INTRODUCTION

This work presents the results of the mineralogical and technological characterization studies carried out on samples from the phosphate deposit of the northwest and southeast areas of the Salitre I alkaline-carbonic Complex, which is located in the municipality of Patrocínio, about 245 km northwest of Belo Horizonte, in the Triângulo Mineiro area, state of Minas Gerais.

The studied ore comprises a phosphate supergenic mineralization with complex mineralogical assemblage in an area where mineralogical and technological information is scarce. The main information available in the literature comes from the studies of Barbosa et al. (1970) and Grossi Sad (1971). According to these authors, "in situ" outcrops are rare, being that substantial parts of existing descriptions were made from blocks, already in an advanced stage of alteration; an extensive overburden of lateritic ad claylike soil covers the entire complex, masking the subjacent lithologies.

The more important lithologies concern peridotites, pyroxenites and carbonatites, with

transitional types being very common among these; *peridotites*, sometimes fenitized, are rocks that present the greater area distribution.

Phosphate deposits related to alkaline-carbonic complexes have their own peculiarities, whether with respect to the phosphate minerals present, of which apatite is only one valuable, to the gangue minerals, to the mineralogical assemblages, size distribution, in addition to surface coating and apatite liberation degree, among other items. Due to the complexity of these ores, systematic mineralogical and technological characterization studies are usually needed to provide necessary information for further mineral dressing studies (Born & Kahn 1990); these studies are carried out since the mineral exploration stage up to the mine planning and industrial processing routines.

2 METHODS

The experimental procedure adopted in this study was subdivided into two stages: in the first, the samples (a total of 5) were classified and then the coarse fraction crushed in a jaw crusher. The

attained products were then homogenized and subjected to tumbling at 50% solids in mass, for a period of 10 minutes, for the purpose of disaggregating the material. The resulting material, in turn, was classified by wet-screening in sieves with 12.7 mm, 6.36 mm, 3.18 mm, 0.84 mm, 0.297 mm, 0.149 mm, 0.037 mm and 0.020 mm apertures; the fraction under 0.020 mm was further subjected to hydrocyclones classification, generating underflow and overflow products of -0.020 mm fraction size.

In the following stage, fractions with size above 0.297 mm were combined and comminuted in a roller mill, in a closed circuit with sieve screening, until obtaining all of the material going through this mesh ("*grinding product*"). This product was also subjected to size analysis distribution by wet-screening, using the same sieves (under 0.297 mm) already mentioned in the first stage, then likewise being subjected to hydrocyclones classification.

Thus, each studied sample generated two different materials, *natural fines* and a *grinding product*, that, in the sequence of the studies, were processed separately. The size fractions of natural fines and grinding product above 0.037 mm were submitted to mineral separations by heavy liquids (tetrabromoethane, $d=2.95 \text{ g/cm}^3$), followed by magnetic separation of the resulting sunk products in a Frantz separator (barrier model), employing relatively low magnetic field intensity (4.1 kGauss).

Chemical analyses by X ray fluorescence spectrometry (XRF) technique were made on all products generated in the studies; these analyses were carried out made with fused beads samples in a Philips spectrometer, Magix Pro, with systematic determinations of P_2O_5 , CaO, SiO_2 , BaO, Al_2O_3 , Fe_2O_3 , MgO and TiO_2 . Mineralogical analyses were made by combining optical microscopy by transmitted light, X-ray diffraction and scanning electron microscopy – SEM (BSE, SE and CL detectors) coupled to an energy dispersive X-ray spectrometer (EDS). The following equipment was employed in these analyses: Leica optical polarization microscope, DMRX-P model, Philips diffractometer, MPD 1880 model, with Cu K α radiation, and a LEO SEM, S440 model, with an EDS Oxford, Isis 300 model.

3 RESULTS

In this work only the results relative to the composition of the *natural fines* with the *grinding product* were considered, although, as already mentioned, these products have been characterized individually and showed some marked differences.

3.1 Chemical composition of the samples studied

Table 1 shows a comparison of the chemical compositions of the studied samples. Drill N-112 is

the one that has the highest total P_2O_5 content (15.4%), while the sample from drill P-104 has the lowest (5.3%); this sample, in turn, has the highest CaO/ P_2O_5 ratio (2.24), while drill N-112 has the lowest ratio (1.14). For all samples, the MgO content is above 4%, except for drill N-112, where it is under 1%; SiO_2 contents are similar and range between 25% and 32%. The Fe_2O_3 contents ranges between 14% and 19%, for the samples from the upper northwest area of the deposit, being a little higher for the sample composite from the more southern (GalvPat), as well as for the one from the southeast region of the alkaline complex (SR). The portion of P_2O_5 in apatite, for material classified above 0.037, varies between 92% and 96% for the samples studied, while it is almost 100% in the SR sample.

Table 1. Comparison of the chemical composition of the samples studied

Chemical composition	SAMPLE				
	SR	GalvPat	P104	N112	P120
P_2O_5	5.78	7.19	5.35	15.4	13.6
CaO	12.5	12.2	12.0	17.6	18.2
SiO_2	26.2	25.5	32.3	26.8	24.6
Fe_2O_3	24.7	23.5	19.2	14.4	18.8
Al_2O_3	5.68	5.48	6.68	7.63	4.17
MgO	5.23	4.79	5.16	0.92	4.27
CaO/ P_2O_5	2.17	1.70	2.24	1.14	1.33
Portion of phosphorus in apatite					
Fraction > 0.037mm	100%	93%	92%	94%	96%

3.2 Size distribution

The size distribution analysis of the N-112 sample indicates that about 58% in weight is above 0.037 mm and approximately 26% weight constitutes overflow. The P_2O_5 grades above 0.037 mm ranges between 7.24% and 21.3%, with an increasing tendency for fines; this fraction contains about 74% of the total P_2O_5 presented in the sample; below 0.037 mm, these grades decrease and are comprised between 6.3% and 12.5%, with a decreasing tendency for fines. The CaO/ P_2O_5 ratio above 0.037 mm varies between 1.18 and 1.26; below this fraction this ratio decreases for fines, reaching 0.69 in the overflow.

The size distribution analysis of the P-104 sample indicates that about 69% in weight is above 0.037 mm and approximately 16% weight constitutes overflow. The P_2O_5 grades above 0.010 mm range between 5.1% and 7.6%, decreasing to 3.4% in overflow; this fraction contains somewhere around 10% of the total P_2O_5 contained in the sample. The CaO/ P_2O_5 ratio above 0.010 mm are high and vary between 2.08 and 2.55, with an increasing tendency going up to 0.037 mm, reaching 1.34 in overflow.

The size distribution analysis of the P-120 sample indicates that about 60% in weight is above 0.037 mm and approximately 24% weight constitutes overflow. The P_2O_5 grades above 0.010 mm range between 7.4% and 24.6%, with an increasing tendency for fines going up to 0.074 mm; below 0.010 mm, this content decreases to 3.3%, which means about 6% of the total contained in the sample. The CaO/ P_2O_5 ratios vary between 1.27 (in overflow) and 1.40.

The size distribution analysis of the GalvPat sample indicates that 70% in weight is above 0.037 mm and approximately 20% weight constitutes overflow. The P_2O_5 grades for size fractions above 0.010 mm ranges between 6% and 9%; below 0.010 mm, this content decreases to 3.1%, which means about 8.8% of the total contained in the sample. The CaO/ P_2O_5 ratio varies between 1.37 (in overflow) and 1.82.

The size distribution analysis of the SR sample indicates that about 61% in weight is above 0.037 mm and approximately 22% in weight constitutes the overflow. The P_2O_5 grades above 0.010 mm range between 4.3% and 7.9%, with an increasing tendency for fines going up to 0.037 mm; below 0.010 mm, the P_2O_5 grade decreases to 3.2%, which means about 26% of the total P contained in the sample. The CaO/ P_2O_5 ratio are high and vary between 1.75 (overflow) up to 2.86.

3.3 Mineral Separations

The floated products form heavy liquid separations have remaining P_2O_5 grades comprised between 0.8% (SR) and 2.8% (N-112), which means between 3% (P-120) and 10% (P-104) of the total P_2O_5 content in the samples; for this product, the CaO/ P_2O_5 ratio varies between 1.02 (N-112) and 2.26 (SR); associated to this product are found the lower density gangue minerals ($d < 2.95$) such as quartz, feldspar and phyllosilicates – vermiculite, 10Å and 14Å interstratified micas (hydrobiotite) and, less frequently, kaolinite.

In the sink magnetic products, P_2O_5 grades are comprised between 2.6% (P-120), 3.3% (P-104), 3.5% (SR) and 4% (GalvPat), increasing to 6.3% in the N-112 sample, which means between 2% (P-120) and 13% (Galv-Pat) of the total P_2O_5 present in the studied samples; iron oxy-hydroxides (magnetite, hematite and goethite) are the main constituents of the sink magnetic product; ilmenite, schorlomite (Ti and Ca garnet), secondary aluminum-phosphates (gorceixite-goyazite) and manganese minerals are also present as accessory or minor minerals

In the sink nonmagnetic products, the P_2O_5 grades vary between 19.8% (P-104), 22.9% (SR) and 26.6% (GalvPat), reaching 35.1% in the other samples, which means between 75% (P-104) and 94% (P-

120) of the total P_2O_5 content in the samples; these products are essentially constituted by apatite (usually more than 80% weight), pyroxene, amphibole, titanite, perovskite, anatase and pyrochlore.

3.4 Mineralogical composition and apatite characteristics

Mineralogical compositions were established based on a combination of X-ray diffraction, optical microscopy and electronic scanning microscopy techniques and chemical analyses of attained products from the mineral separations.

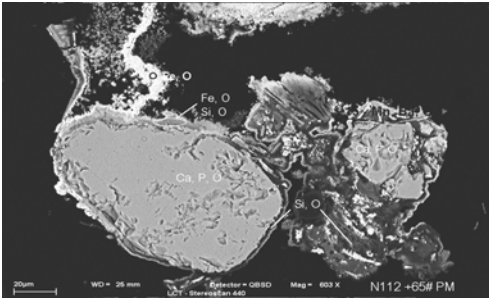
The samples studied are basically constituted by the same minerals, merely varying their relative proportion. The samples are constituted by apatite, quartz, feldspar, phyllosilicates (micaceous minerals and secondarily, kaolinite) and iron oxy-hydroxides (basically hematite and goethite). Secondary phosphates (gorceixite and/or goyazite), titanite, anatase and other (pyrochlore, manganese minerals and rare earths phosphates) were observed as accessory and minor minerals. Pyroxene + amphibole were observed mainly in the P-120, SR and GalvPat samples; both schorlomite and perovskite in P-104, SR and GalvPat samples, while ilmenite was only observed in the SR and GalvPat sample. Carbonates were not observed in any of the studied samples.

Apatite content ranges between 13%, 16% and 19% (P-104, SR and Galv-Pat respectively) to 36% and 43% (N-112 and P-120 respectively), thus drill P-120 is the richest one and drill P-104 is the poorest.

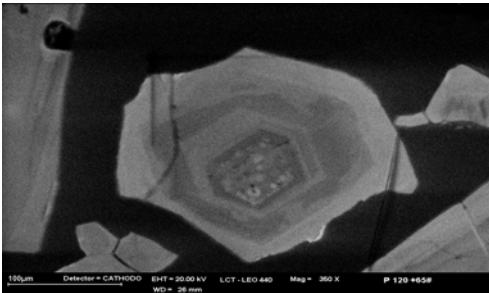
The Ca, Mg bearing minerals, major responsible for apatite selectivity losses in flotation concentration process, such as perovskite, schorlomite, titanite, and amphibole, are more abundant in the samples from drill P-104, SR and Galv-Pat (where they correspond to more than 15% in weigh); in the other samples they reach values of somewhere around 6% to 7% .

The amount of apatite impregnated or coated by iron oxy-hydroxides is comprised between 2% and 15% while its proper liberation degree is achieved for material ground bellow 0.21 or 0.30 mm, depending on the studied sample.

Backscattered electrons (BSE) and cathodoluminescence (CL) images, photos 1 and 2 respectively, shows some typical apatite superficial coating by iron oxy-hydroxides and the differences in the apatite's gray tones related variations on its chemical compositional (trace contents of rare earths elements – CL image).



Photograph 1 – Sample: N-112, grinding product; + 0.21 mm fraction. Apatite grain with surface coating by iron oxyhydroxides; SEM-BSE image.



Photograph 2 – Sample: P-120, grinding product; + 0.21 mm fraction. Typical example of apatite crystal showing its chemical zoning by SEM-CL.

4 CONCLUSIONS

The studied samples present basically the same mineralogical assemblage, merely varying in relative proportion between them. They are constituted by apatite, quartz, feldspar, phyllosilicates (micaceous minerals, and secondarily, kaolinite) and iron oxyhydroxides (hematite and goethite, in addition to magnetite). Secondary phosphates (gorceixite and/or goyazite), titanite, anatase and other (pyrochlore, manganese minerals and rare earths phosphates) are observed as accessory or minor minerals. Pyroxene and amphibole occur mainly in the P-120, SR and GalvPat samples; schorlomite and perovskite in the P-104, SR and GalvPat samples; ilmenite in the SR and GalvPat samples; carbonates were not observed in any studied sample.

The sample from drill N-112 is the one that has the highest total P_2O_5 content, while the sample from drill P-104 has the lowest; this sample, in turn, has the largest CaO/ P_2O_5 ratio, while drill N-112 has the smallest. For all samples, the MgO content is above 4%, except for drill N-112, where it is below 1%; the SiO_2 contents are similar ranging between 25% and 32%. The Fe_2O_3 contents ranges between 14% and 19%, for the samples from the northwest area of

the deposit, being a little higher for the sample composite from the more southern (GalvPat), as well as for the one from the southeast region of the alkaline complex (SR),

The portion of P_2O_5 in apatite, for material classified above 0.037, varies between 92% and 96% for the samples studied, while it is almost 100% in the SR sample.

Apatite occurs usually as limpid scarcely impregnated grains; highly impregnated apatite particles (non-flotable) corresponds to somewhere around 2% of the total presented in the N-112 and P-120 samples and 11% and 15% in the P-104 and GalvPat samples, respectively.

For the N-112 and P-104 samples, apatite is properly liberated for material ground below 0.21 mm, while for the other samples, it is achieved below 0.30 mm.

5 ACKNOWLEDGEMENTS

This research was supported by grant N. 01/1023-4 and 02/01011-1 from FAPESP – Fundação de Amparo a Pesquisa no Estado de São Paulo.

6 REFERENCES

- Barbosa, O.; Braun, O.P.G.; Dyer, R.O; Cunha, C.A.R. 1970. Geologia da Região do Triângulo Mineiro. Boletim de Fomento da Divisão da Produção Mineral, nº 136. Rio de Janeiro, p.07-141.
- Born, H.; Kahn, H. 1990. Caracterização geológica e mineralógica voltada ao aproveitamento de jazimentos fosfáticos. V Encontro Nacional de Rocha Fosfática, São Paulo. Anais, p.213-233.
- Grossi Sad, J.H. 1971. Geologia e Recursos Minerais do Complexo de Serra Negra, Minas Gerais, DNP.M.

Direct Comparison on Mechanical and Digital Size Analyses of Kemi Chromite, Finland

T.Chernet & J.Marmo

Research Laboratory, Geological Survey of Finland, Espoo, Finland

ABSTRACT: In order to compare sieve size and image size analyses of chromite particles, chromite in the concentrate should appear in size similarly to that in the ore. To meet this requirement, chromite ore samples were fragmented electro-dynamically with the advantage that this method liberates mineral grains along natural grain boundaries and existing deep fractures without unnecessary breakage of particles. The aim was to: 1) investigate the correlation between sieve and image size analysis of chromite and 2) examine the correlation of the image size analyses of unliberated chromite in the rock and sieve size analyses of liberated chromite in the crushed ore. Results show considerable correlation between mechanical and digital size analyses methods. Image size analyses of chromite in the ore are highly correlated with the sieve analyses of chromite concentrate. Moreover, the ferets average represented by number percent and the area diameter represented as weight percent are more closely correlated to the sieve analysis than to the ferets average given as weight percent and the area diameter given as number percent.

1 INTRODUCTION

1.1 Samples and scope

Chromite ore samples from the Länsiväi open pit of the Elijärvi Mine, Kemi, were taken for particle size determination of chromite. Chromite ore samples were disaggregated by electric shock device called Franka 1 at the Forschungs - Zentrum, Karlsruhe, GmbH, Germany. The objective was to recover liberated chromite grains for size analyses. Polished sections were also prepared from the ore samples for size analysis by image processing. The aim was to study the correlation between sieve and image analyses on one hand, and the correlation of the image size analyses of unliberated chromite in the rock and liberated chromite in the crushed ore on the other hand. The longer-term development objective was to have an improved predictability in mineral liberation at certain grinds.

The direct comparison of sieve and image analyses was considered to be feasible because of the simple crystal shape and grain morphology of chromite. The crystal habits of chromite include octahedral often with dodecahedral faces developed at the edges of the octahedron, which increases the sphericity of the crystal. Here, well-formed crystals are common and chromite usually occurs as massive

or granular aggregates and disseminated. Correction factors will be required for minerals of acicular, bladed, fibrous, platy, prismatic, tabular, pseudomorphic crystal shapes (Higgins 2000), if comparing sieve and image analysis is possible at all.

1.2 Application of electric pulse disaggregator

The advantage of applying electric pulse fragmentation to liberate chromite grains is that the method results in the separation of minerals along natural grain boundaries and fractures present within the solitary grains without further breakage of particles. The principle of operation is well described by (Bluhm et al. 2000) and (Sjomkin et al. 1995). The material is immersed in water-filled reactor that is subsequently subjected to high voltage pulses up to several hundreds of kilovolts. Water penetrated inside the sample along the grain boundaries and fractures has excellent breakage strength when the pulse voltage rises quickly. This resulted in the concentration of electric field within the material.

The very high pressure in the sample leads to the desired fragmentation of the material whether composite or rock into its original components or minerals.

2 SIEVE ANALYSES OF CHROMITE IN CRUSHED ORE

The treatment of the test sample gave good results, and most of the chromite grains were liberated. Major portion displayed the perfect crystal structure and deeply fractured grains broke along the fractures, thus leaving the original particle size of the chromite in the ore untouched. According to wet sieving, 99% of the crushed ore is less than 800 μm . Observation of every fraction revealed that, chromite was considerably liberated in the fractions less than 400 μm .

Liberated chromite was separated from the rest of the gangues by heavy liquid ($d=3.3$). The frequency plot of the chromite concentrate is shown in Figure 1&2. Sieve fractions between 800-400 μm contain only about 3-5% free chromite and were not treated by heavy liquid. About 85% of chromite particles, however, are less than 400 μm . In the fraction between 400 and 250 μm , almost all chromite grains are with perfect crystal shape without being broken. Fragmented particles and chips started to appear in the fractions bellow 250 μm , increasing gradually along with decreasing grain size, especially in the fraction 90-63 μm . Most of these liberated particles, however, appeared the same as in the rock.

3 IMAGE ANALYSIS OF CHROMITE IN THE CONCENTRATE AND IN THE ORE

3.1 *Image analysis and principle*

Image analysis is a technique for characterizing, classifying and comparing images by using numerical values for properties of features in images (Lastra et al. 1998). Image analysis includes image acquisition, Several images were taken from petrographic processing (e.g., enhancement, segmentation and microscope as color images). A segmentation routine was then performed on the images into separate binary images by detecting and setting the lower and upper gray levels for chromite.

3.2 *Chromite concentrate and chromite in the unbroken ore*

Based on the best liberation, polished sections were made from size fractions 160-250 μm of the chromite concentrates. Particle sizes of individual particles were analyzed from the reconstructed images. The area, maximum and minimum ferets of each particle

were measured totaling 10,000 separate features. Particle size of chromite was also analyzed directly from the ore. The analyses include all sizes in the ore. About 4500 particles are measured and frequency plots are given in Figure 1&2. Individual measurements were done for each feature in the images (object specific), which includes area, length, width and sphericity.

4 COMPARISON

According to image analyses results of the selected sieve fraction (160-250 μm), about 90.8% of the grains/particles fall between 90 and 250 μm . Although the quality of images, orientation and shape factors affect the similarity, the result generally shows a good correlation between sieve size analysis and digital size analysis. Further data manipulations, stereological conversion from comparing image-analysis measured sphere diameter with the known sieve size, and use of for e.g., method to estimate the sampling error might lead to a better correlation.

Although enough work has not yet been done on the liberated chromite particles to fully compare image analysis results of the liberated chromite and chromite from unprocessed ore, basic conclusion can be drawn. 57wt% of the heavy fraction is between 90-250 μm . Looking in to the image analysis result, 54% of chromite particles analyzed in the ore are between 90-250 μm . Thus, both methods gave quite similar result.

Furthermore, it was studied which of the feature analyses would match best with the sieve analysis. Both area diameter and feret average of chromite grains/particles in the ore are measured and plotted. Ferets, which imply maximum and minimum length of particles, are measured by the software and the average is calculated using excel. As shown in Figure 1, the sieve analysis frequency distribution of chromite concentrate almost overlaps the plot of ferets average represented by number of grains percent rather than calculated as weight percent. On the other hand, area diameter calculated as weight percent almost overlaps to that of sieve analysis rather than area diameter calculated as number percent (Fig. 2). As a result, the percent of the number of particles calculated from ferets average and the weight percent calculated from area diameter correlate more closely to that of sieve analysis represented by weight percent.

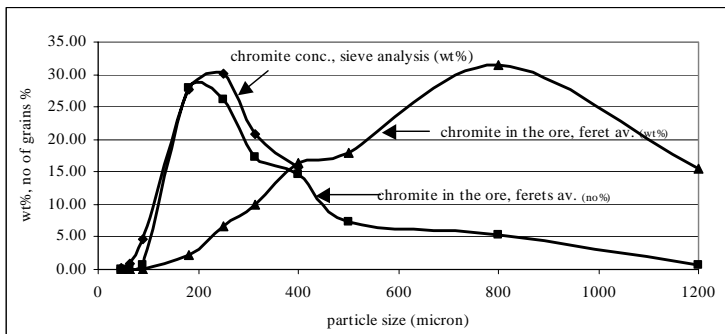


Figure 1. Comparison of image analysis results of chromite calculated from ferets average to that of chromite concentrate sieved

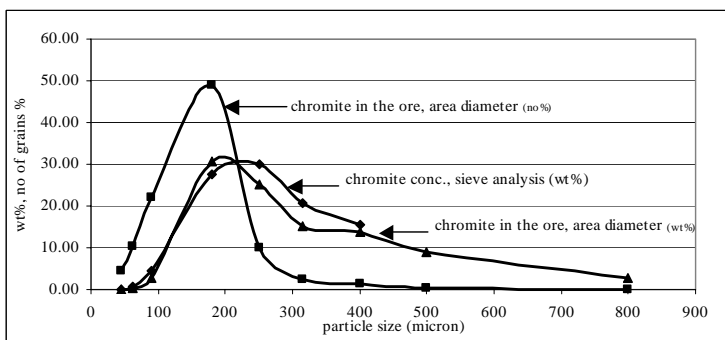


Figure 2. Comparison of image analysis results of chromite calculated from area diameter to that of chromite concentrate sieved

5 SUMMARY

Chromite grains were nearly completely liberated in grain sizes below 400µm. The electric pulse fragmentation of chromite ore turned out to be an excellent way to liberate chromite along existing boundaries to allow comparison between sieve size and image size of chromite particles. Despite the fact that only one sample was studied good correlation was found between mechanical sieve size analyses and digital size analyses. Moreover, image analyses of chromite in the ore were found to be correlated to that of sieve analysis of chromite concentrate. The ferrets average represented by number percent and area diameter represented as weight percent are more closely correlated to the sieve analysis.

6 REFERENCES

Bluhm, H., Frey, W., Giese, H., Hoppé, P., Schultheiss, C. & Strässner, R. 2000. Application of pulsed HV discharges to material fragmentation and recycling. *IEEE Transactions on Dielectrics and Electrical Insulation*, 7, 625-636.

Higgins, M.D. 2000. Measurement of crystal size distributions. *American Mineralogist* 85, 1105-1116.

Lastra R., Petruk W. & Wilson J. 1998. Image analysis techniques and applications to mineral processing. *Modern Approaches to Ore and Environmental Mineralogy*, Mineralogical Association of Canada, 27, 327-366.

Sjomkin, B., Ussov, A. & Kurets, V. 1995. The principles of electric impulse destruction of materials. *Akademi Nauk Rossija*, (in Russian).

Ore Microscopy, Origin, and Beneficiation Problems of Copper Ore from Salobo, Brazil

O.J.Choque Fernandez & M.L. da Costa

Department of Geochemistry and Petrology, Geosciences Center, University of Pará, Pará, Brazil

H.Pöllmann

Institut für Geologische Wissenschaften und Geiseltalmuseum, Martin-Luther-Universität, Halle, Germany

P.R.G.Brandão

Department of Mines and Metallurgy, University of Minas Gerais, Minas Gerais, Brazil

ABSTRACT: New mineralogical studies were carry out in ROM and comminution products of the copper ore from Salobo, Carajás, Brazil, in order to evaluate the because of the difficulties presented in its metallurgical treatment. The copper ore is constituted by bornite (4%), chalcocite (2%) and chalcopyrite (0.5%) and occur as disseminated fine grains, with fine alternated banded and/or foliated silicates, veinlets and/or long/short stringers, tiny inclusions, bornite/chalcocite and bornite/chalcopyrite mirmekitic intergrowth and bornite-chalcocite and bornite-chalcopyrite replacements in schist iron formations where the deposit is found. Although those phases are associated with several minerals in different paragenesis, the ore features have been affected drastically by metamorphism hindering the reconstruction of its pre-metamorphic evolution. Comminuted ore conserves the lepidoblastic textures of the silicates biotite, fayalite and greenalite and granoblastics of magnetite or copper sulfides grains. Crystals of copper sulfides, intergrowth with high percentage of magnetite and silicates are intensively fractured and eroded and sometimes fullfilling cracks and/or fractures of greenalite. The strong metamorphic recrystallization of the schists of ore formations, its high hardness, the extremely variable grain sizes of sulfides (5 to 300µm) and the mineralogical ore complexity, in comminution products, revealed a significant chemical variation in copper sulfides.

1 INTRODUCTION

The Salobo deposit, located in Carajás, southeastern of Pará, Brazil, is one of the largest copper reserves. Although several mineralogical studies have been developed for this ore, its origin is still controversial, with several interpretations, such as volcanogenic copper-bearing oxide and volcanogenic massive sulfide (Amaral et al. 1988; Vieira et al. 1988; Réquia et al. 1995; Souza & Vieira 1998; Lindenmayer 1990; Lindenmayer & Fyfe 1990) and iron oxide (Olympic Dam or Cu-U-Au-REE) (Huhn & Nascimento 1997; Réquia & Fontbote 2000). In comparison with other well-known deposits, it is a rare example of mineralization.

Particular characteristics such as disseminated mineralization, fine grain and its hardness impose serious difficulties to copper concentrates production (Docegeo 1988; Réquia et al. 1995; Souza & Vieira 1998; Andrade et al. 1982; CVRD/Supes/Gicor 1989; Pena et al. 1989). Due to ore complexity it is difficult the metallurgical treatment, reasons why it is constantly submitted to geological and technological reevaluations.

2 MINERALOGY

Ore microscopy, microchemical analyses using microprobe and SEM/EDS in samples of holes and ore piles (research gallery G3) of Salobo, allowed the identification of sulfide mineralization with bornite (4%), chalcocite (2%) and chalcopyrite (0.5%), and variable proportions of molybdenite, cobaltite, safflorite, niqueline, siegenite, gold, silver, graphite, ilmenite, hematite, Te-Ag, uraninite and REE minerals. These minerals occur in schist iron formations where the deposit is found: a) magnetite and massive fayalite, eventually banded and b) banded biotite and magnetite. These groups considered as gangue (magnetite 53% and silicates 40%) contain minor amounts of garnet, amphibole, quartz, plagioclase and subordinate amounts of fluorite, greenalite, minnesotaite, stülpnomelane, apatite, monazite, allanite and occasionally siderite, goethite and malachite. Sulfides are preferentially concentrated in magnetite rich iron formations.

3 TEXTURES

Copper sulfides occur as crystals less than 3.0 mm and as disseminated fine grains, with fine alternated

banded and/or foliated silicates, veinlets and/or long/short stringers, tiny inclusions, bornite/chalcocite and bornite/chalcocopyrite mirmekitic intergrowth and bornite-chalcocite and bornite-chalcocopyrite replacements.

3.1 *Crystals and disseminated fine grains*

They occur in the interstitial of the massive magnetite and sometimes close to the biotite, grunerite, almandine, fayalite and greenalite. They are not uniform and have maximum sizes of 3.0 mm.

In some cases aggregates of bornite, chalcocite and chalcocopyrite crystals assume lineal contacts with the euhedral or/and subhedral aggregates of magnetite.

Sometimes the bornite disseminates, that initially are of color orange, appear tarnishes with colors similar to the native copper the violet and blue (peacock-ore), however, without change in the composition as they indicate the XRD analyses.

3.2 *Fine alternated banded and/or foliated silicates*

Micrometric thin plates of copper sulfides occur in alternate and in parallel groups oriented along the cleavage of biotite and grunerite or in compact bands of fayalite. Those plates don't present reaction contacts and they don't substitute the silicates.

3.3 *Veinlets and stringers*

Numerous veinlets of copper sulfides associated with magnetite form irregular network without orientation filling fractures of garnet, amphibole and olivine. Sometimes the bornite form replacement textures with the chalcocopyrite. The width of those veinlets varies from fractions of micrometers up to 3mm.

3.4 *Inclusions*

Numberless and small inclusions of bornite in the form of lenses or droplets were observed in the chalcocite and chalcocopyrite. They are distributed irregularly what indicates that were not controlled by the directions crystallographic of the chalcocopyrite or chalcocite. The droplets have been form to high temperatures as exsolution products.

3.5 *Mirmekitic intergrowth and replacement*

The mirmekitic intergrowths of bornite and chalcocite (br/cc) and bornite and chalcocopyrite (br/cpy) are quite common and of irregular size.

They assume varied forms with intergrowth of thick grains with irregular textures ("thick intergrowth") or varying for lamellae intergrowths

("fine intergrowth"). Due to the absence in a crystalline form and the thick and fine appearance is difficult to explain the textural reasons of those features, although Kostov & Minceva-Stefanova (1982) suggested is an exsolution product or of simultaneous crystallization.

The mirmekitic intergrowths suggests that there was a disintegration of coarse grains of bornite, first for thick intergrowth passing later for fine intergrowth, as function of the cooling of high temperatures.

Are typical the replacements of bornite-chalcocite (br-cc) and of bornite-chalcocopyrite (br-cpy). Fine films of chalcocite are observed in margins of bornite and mainly in fractures.

4 MICROCHEMISTRY

Copper sulfides were formed by complex processes and are characterized by compositional controls, mainly for the presence of Fe in them. Solid solutions of bornite and chalcocopyrite were formed at high temperatures and gave way to those iron excesses. Atomic ratios Cu/Fe of bornite (4.3-4.9) and chalcocopyrite (average of 0.9) at high temperatures allowed the co-existence of bornite-chalcocopyrite equilibrium and therefore of bornite/chalcocopyrite. Iron contents (maximum 0.96%) in chalcocite have been incorporated at those temperatures when the structure is highly disordered.

Chalcocopyrite lamellae following the {111} orientation in bornite as well as the bornite/chalcocite and bornite/chalcocopyrite intergrowth suggest exsolution.

5 BENEFICIATION PROBLEMS

Ore grinding produced physical changes in the grain size and according to time (long or short), the mineral comminution modifies the pulp reologie.

That process originates a grain size -270 mesh (53µm), 80% wt. passing, grounding time on 4 hours (dry) and 2 hours (humid) adapted to copper concentration. Different volumetric fractions of copper sulfides in particles were obtained through both processes: larger fraction (6% volume) to grain sizes <53µm and with a prevailing fraction (7 to 15% volume) ranging from 26.9 to 7.5µm. Physical modification shows larger magnetite proportions than silicate ones with a clear incidence of magnetite density in the hydrocyclone classification.

5.1 *Metamorphism and hardness.*

Besides of finding the association of the copper sulfides with other minerals in paragenesis different, they present several features originated by the

metamorphism that affected them and that interfere in the mineral processing. In the grinding is of interest to consider the abundant crystalloblasts of magnetite and garnet of high hardness, the same consume a lot of energy during the ore comminution, since they demand larger time for the liberation of bornite, chalcocite and chalcopyrite of hardness lowers to medium. That fact also produces liberation of greenalite, minnesotaite and stilpnomelane of low hardness producing very fine grains.

5.2 Mineralogical complexity and grain size

Are predominant the copper sulfides disseminates in the ore forming mirmekitic intergrowth of br/cc and br/cpy. They rarely occur as bornite, chalcocite and chalcopyrite monominerals. The mirmekitic textures, thick and fine, occur in larger proportion in the ROM in grains $>53\mu\text{m}$ (with consequent liberation) and in smaller proportion in the grains $<53\mu\text{m}$, made a mistaking with mineral inclusions.

Many authors (Greet & Smart 1997; Chatterjee 1998) consider that the production of grains with that type of textures can be harmful when are projected circuits of metallic recovery, this because: that disseminated type produces fine to ultrafines grains forming muds with relative losses of copper sulfides and the liberation of those sulfides as fine to ultrafines increases the superficial susceptibility of the copper sulfides to the oxidation (tarnish), since small particles have larger specific areas. It is already very well-known the effect of the size of the particle in the flotation, even so the liquid effect of many physical-chemical factors related to the particle size it is very difficult of foreseeing. The fine particles of Salobo show low recovery percentages, because the same ones with areas specific great adsorb excessively reagents, besides they possess behaviors actives chemically; the liberation of the disseminated in very fine-grained as fine particles of the host rock is costly and harmful in the flotation, because particles <400 mesh ($37\mu\text{m}$) frequently are not attached by the air bubble; the mirmekitic intergrowth of br/cc and br/cpy can promote an increase of superficial oxidation in the chalcocite, harming the flotability of that intergrowth. The chalcocite as simple phase, when floated, usually produces good recovery (Tolley et al. 1996), but the flotation of this modifies in the presence of bornite or chalcopyrite, depressing it.

These occur because the present iron in those sulfides forms galvanic reactions in the surface of the chalcocite producing species of oxi-hydroxides of hydrophilic superficial iron (Fullston et al. 1999).

When comminuted the ore can be observed still the lepidoblastic textures of the silicates biotite, fayalite and greenalite and granoblastics of magnetite or bornite, chalcocite and chalcopyrite

grains. Crystals of copper sulfides liberated and mixed with high percentage of magnetite and silicates are intensively fractured and eroded and sometimes fulfilling cracks and fractures of greenalite, hindering the sulfide liberation. Copper sulfide liberations increase gradually when the grain size is finer (more than 50% in grain sizes $<29.6\mu\text{m}$). Only in fractions $<37\mu\text{m}$ (Cumulative liberation yield CLY90), the copper bearing particles begin to migrate and for higher degrees of liberation though such tendency can still be insufficient for the purposes of sulfide concentration.

5.3 Chemical variation

Mineralogically, in the comminuted products, occur the same minerals established in ROM but with chemical modifications in the copper sulfides.

Magnetite and greenalite are the main hosts for sulfides, fluorite is also less common. Proportions of S, Fe and Cu in copper sulfides are variable relative to ROM and stoichiometry, varying in function of the grain size (larger chemical variation in grain sizes of 26.9 to $7.5\mu\text{m}$ than on the 2360 to $37\mu\text{m}$ fraction). Iron can reach up to 6.0% wt. in chalcocite.

Chemical variations showed to be dependent on the grain size, with smaller oxidations in sizes $>53\mu\text{m}$ and larger oxidations in sizes $<53\mu\text{m}$, caused by a combination of superficial area and ability of chalcocite to be oxidized. Iron excess mainly as highly reactive colloidal particles could have been generated by: mill material, abrasive action of particles and probable magnetite oxidation, producing chemical variation in mill atmosphere and electrochemical corrosion processes.

The chemical variation of the copper sulfides can occur in different steps of the processing: ore in situ, in the mining operations, storage, crushing, grinding and flotation. The copper sulfides are unstable in the presence of oxygen and water, and when exposed by mining and processing tend to oxidize to complex electrochemical reactions. The fine and ultrafines grains present surfaces easily exposed to the attack of the components of the atmospheric air or of the solutions, being the copper sulfides subjects to the chemical changes owed to the superficial oxidation.

The sizes $<37\mu\text{m}$ submitted to the action of oxidizer medium easily behave as hydrophilics.

6 CONCLUSIONS

The textures and microchemical analysis in the ore copper from Salobo have received little previous study. These ore exhibit a variety of textures with phases associated with several minerals in different paragenesis, the ore features have been affected drastically by metamorphism hindering the

Reconstruction of its pre-metamorphic evolution.

Beside of the strong metamorphic recrystallization of the schists of ore formations, its high hardness, the extremely variable grain sizes of sulfides (5 to 300 μ m) and the mineralogical ore complexity (mineralogical associations, disseminations, intergrowth complexes), the microchemical investigations, in ROM and in comminution products, revealed a significant chemical variation in copper sulfides.

Iron present in sulfide mineral reticules is the main contaminant to chemical modifications (Cu/Fe ratio) influencing the quality of copper concentrate in mineral processing. It has been already established that between copper sulfides and other components of pulps during grinding and flotation (water, species collectors or modifiers) occur an interaction through electrochemical mechanisms producing oxidized species, where the chemical composition of the mineral in question is very important. The species of hydroxides of iron formed in the grinding harm the flotability and depend on the activity electrochemistry of the minerals. The presence of a reagent activator of surfaces as a collector (during the grinding) can minimize the deleterious effect of the oxidation during the mineral flotation.

7 REFERENCES

- Amaral, E.V.; Farias N.F.; Saueressig, R.; Júnior, A.V.; Andrade V.L. 1988. Jazida de Cobre Salobo 3A e 4A, Serra dos Carajás, Pará. In: DNPM (ed.) Principais depósitos minerais do Brasil, 3:43-53.
- Andrade, V.L de; Freitas, U.R. de; Viana, A. Jr. 1982. Beneficiamento do minério sulfetado de cobre do Salobo 3A da região do Carajás. CVRD revista, 3 (7):43-47.
- Chatterjee, A. 1998. Role of particle size in mineral processing at Tata Steel. International Journal of Mineral Processing, 53:1-14.
- CVRD/Supes/Gicor, 1989. Projeto cobre Salobo, minério sulfetado. Relatório final da pesquisa tecnológica (Resumo). Belo Horizonte, CVRD, Supes/Gicor. v.1. 44 p. (Relatório técnico).
- Docegeo 1988. Revisão litoestratigráfica da Província Mineral de Carajás. In: SBG (eds.) Congresso Brasileiro de Geologia 35, Proceedings Volume, Belém, SBG, 11-54.
- Freeman W.A.; Newell, R.; Quast, K.B. 2000. Effect of grinding media and NaHS on copper recovery at Northparkes mines. Minerals Engineering, 13 (13): 1395-1403.
- Fullston, D.; Fornasiero, D.; Ralston, J. 1999. Zeta potential study of the oxidation of copper sulfide minerals. Colloides and Surfaces A: Physicochemical and Engineering Aspects, 146:113-121.
- Greet C.J.; Smart R.St.C 1997. The effect of size separation by cyclizing and sedimentation/decantation on mineral surfaces. Minerals Engineering, 10 (9):995-1011.
- Huhn, S.R.B.; Nascimento, J.A.S. 1997. São os depósitos cupríferos de Carajás do tipo Cu-Au-U-ETR ?. In: Costa, M.L. & Angélica, R. (eds.). Contribuições à Geologia da Amazônia. FINEP/SBG, 143-161.
- Kostov, I.; Minceva-Stefanova, J. 1982 Sulphide Minerals. Crystal Chemistry, Parageneses and Systematics. Stuttgart, E. Schweizerbart'sche Verlagsbuchhandlung (Nägele u. Obermiller).
- Lindenmayer, Z.G. 1990. Salobo sequence, Carajás, Brazil. Geology, Geochemistry and Metamorphism. Ontario: University of Western Ontario, Department of Geology. 406p. (Doctoral Thesis).
- Lindenmayer, Z.G.; Fyfe, W. 1990. A origem da formação ferrífera do depósito de cobre do Salobo, Estado do Pará. In:SBG (eds.), Congresso Brasileiro de Geologia 36, Proceedings Volume, Natal, SBG, 109-110.
- Pena, A.T., Hilario, J.A., Pereira, C.E.; Bandeira, R.L. 1989. Projeto cobre Salobo. In: OLAMI, IBRAM (eds.) Congresso Latinoamericano de Minería, 2; Congresso Brasileiro de Mineração 3, Exposição Brasileira de Mineração, São Paulo, 287-359.
- Réquia, C.M.K.; Xavier, P.R.; Figueiredo, B. 1995. Evolução paragenética, textural e das fases fluidas no depósito polimetálico de Salobo, Província Mineral de Carajás, Pará. Boletim do Museu Paraense Emílio Goeldi. Ciências da Terra, 7: 27-39.
- Réquia, K; Fontbote, L. 2000. The Salobo iron oxide Cu (-Au) deposit, Carajás, Brazil: evidences of hydrothermal alkali metasomatism in the host amphibolites. In: International Geological Congress 31. Rio de Janeiro, Abstracts. CD-ROM.
- Souza, L.H.; Vieira, E.A.P. 1998. Jazida de cobre Salobo/ouro/prata. Relatório final de geologia, fase Salobo Metais S.A. (1997-1998), Projeto Salobo (Intern Report).
- Tolley, W.; Kotlyar, D.; Van Wagoner, R. 1996. Fundamental electrochemical studies of sulfide mineral flotation. Minerals Engineering, 9 (6):603-637.
- Vieira, E.A. P. de; Saueressig, R.; Siqueira, J.B.; Silva E.R.P. da; Regô, J.L.E. Castro, F.D.C. de 1988. Caracterização geológica da jazida polimetálica do Salobo 3A. Reavaliação. In: SBG (eds.) Congresso Brasileiro de Geologia 35, Proceedings Volume, Belém, SBG, 97-111.

Transforming Process Mineralogy Data into Improved Hydrocyclone Performance

J.M.F.Clout, A.G.Trudu, E.Donskoi, J.M.Young

CSIRO Minerals, Queensland Centre for Advanced Technologies, Kenmore, QLD, Australia

B.A.Firth

CSIRO Energy Technology, Queensland Centre for Advanced Technologies, Kenmore, QLD, Australia

ABSTRACT: Mineral tracking data derived from optical image analysis has been successfully used to develop partition curve models to describe and predict physical separation outcomes for hydrocyclone desliming of an iron ore. The mineralogical data was critical in providing specific gravity characterisation for particle populations and estimates of the iron content of the feed and products. Mineral tracking demonstrated preferential rejection of ochreous goethite and kaolinite gangue to the overflow stream and a corresponding increase in hematite and vitreous goethite in the underflow during 100 mm diameter primary hydrocyclone desliming. The experimental partition curves for the 100 mm primary hydrocyclone follow the trend of hematite having the finest separation size (~ 0.01mm) followed by vitreous goethite, with ochreous goethite and kaolinite having coarser separation sizes (~0.02 mm). The model used incorporates the impact of the density effect (via mineralogical tracking) and the potential effect of changing spigot, vortex finder or hydrocyclone diameter and was able to successfully predict the presence of coarse gangue in the overflow product.

1 INTRODUCTION

1.1 *Applied Mineralogy and Mineral Processing*

The physical and chemical nature of the ore minerals and their association with gangue minerals is the critical starting point with regard to tracking mineral through a beneficiation process and the potential pathways which can be realistically applied to a particular ore. The physical nature and mineralogy of feed and products in mineral processing applications are typically determined from either indirect or direct techniques. The most commonly used indirect techniques include calculation of mineralogy from assays, heavy liquids and assays of size fractions and diagnostic leach tests (Benson et al. 2001; Zhang & Whiten 2001). However, indirect techniques assume the minerals are stoichiometric, which may work well in restricted applications, but are often unable to detect the presence of locked inclusions or changes in texture. The complexity involved and the lack of mineralogical information often means that there is some doubt if optimum mineral processing performance has been obtained.

In contrast, direct techniques can provide more constraining data to help optimize each step in the process. More direct techniques include quantitative XRD (eg. Mandile & Johnson 1998), hand sorting

and automated image analysis using scanning electron microscopy (SEM)-based techniques, such as QemSCAN (QEM*SEM: Reid et al. 1985; Gottlieb et al. 2000) and the Mineral Liberation Analyser (MLA: Gu & Guerne 2000) or optical microscopy (Clout et al. 1997). Information that can be provided by image analysis includes modal mineralogy, texture, mineral associations, mineral grain size and size-by-size liberation or release of ore mineral/s from gangue mineral/s.

Few studies have tried to use modal mineralogy and liberation results to examine equipment separation performance but more often they have been focused towards qualitative determination of optimum grind size, particularly for flotation (Frew & Davey 1993; Griffin et al. 1993). These studies use mass balance analysis of feed and products to determine mineral grade recovery curves, which are either not predictive or at best require exhaustive iterative testing to establish optimum equipment performance.

Predictive theoretical mineral grade recovery curves have been generated from process mineralogy data by various methods. These include progressively accumulating particles from the liberated end of the particle concentration spectrum and assuming perfect separation (Batterham 1992),

mathematical treatment for breakage then subsequent liberation (Sчена & Chiaruttini 2000), use of a selectivity function for a hydrocyclone (King 1999; Srivastava et al. 2001) or separation function for breakage (Bonifazi & Massacci 1993).

1.2 The approach

Many ores can be considered as a number of simple textural types which after grinding produce characteristic combinations of either liberated or composite ore and gangue particles (Fig. 1). The ground particles can be sectioned and the proportions of minerals contained can be measured in 2D or in 3D serial sections by image analysis, although some stereological analysis is required to correct liberation volume estimates (King & Schneider 1998). Particle shape and internal porosity can also be measured. The measured individual particle information can then be used to calculate particle properties that are important for beneficiation, for example specific gravity (Fig. 2).

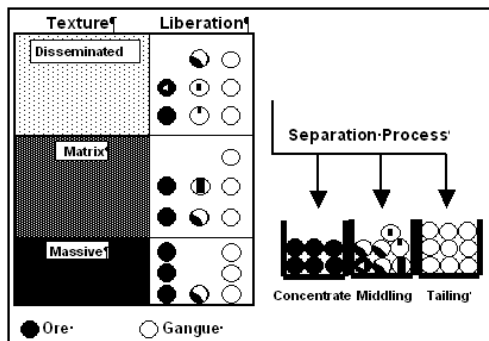


Figure 1. Ore textural types in the ore sample, corresponding mineral liberation particle types after grinding and subsequent ideal separated particle products. Modified from Clout et al. (2002).

We use this image analysis data to explore an alternative concept of mineral tracking using experimentally and theoretically derived mineral and composite particle partition curves as the basis for determining particle separation and calculation of theoretical grade-recovery curves. The concept of mineral tracking is believed to present an exciting opportunity to better understand and improve the design and operation of physical separation processes for mineral processing.

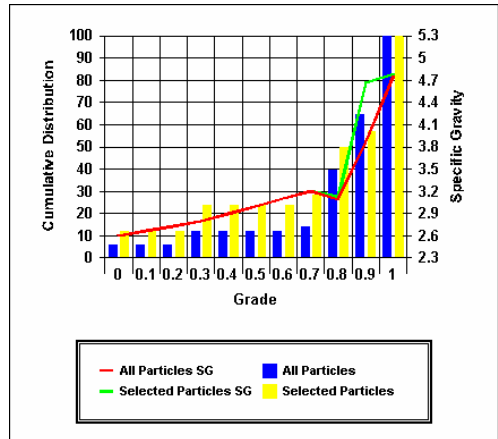


Figure 2. Example of calculated particle specific gravity distribution versus cumulative grade derived from liberation analysis. Particle 2-D section image analysis of an Australian iron ore.

Results are presented to assess the performance of a single-stage hydrocyclone separation for iron ores. Image analysis data generated for the ore feed and hydrocyclone products are used to develop actual and theoretical mineral partition curves, which in turn can be used to predict the ultimate beneficiation potential for the ore.

2 METHODS

A -0.5mm iron ore from the Pilbara region of Western Australia was deslimed using a Krebs U4 100 mm diameter hydrocyclone. Feed and underflow products were sized by wet and dry screening and cyclonizing into ten fractions to be image analyzed for mineralogy.

An aliquot of each size fraction was mounted into a 25 mm diameter round block of epoxy resin and polished on one side. Each block was image analysed under reflected plane polarized light using the Video Pro 32 MINERAL optical image analysis software (© Leading Edge Pty Ltd), described by Danti et al. (1993), to obtain mineral identification based on reflectivity, the modal abundance of each of the minerals and their liberation characteristics.

3 RESULTS

3.1 Modal Mineralogy

The ore feed is composed of largely hematite with minor ochreous (yellow) and vitreous goethite above about 20 µm. In the finer size fraction the feed is dominated by equal proportions of hematite and ochreous goethite with minor vitreous goethite. For

the hydrocyclone at optimum operating conditions (33% solids and 180 kPa), hematite and vitreous goethite are concentrated in the underflow product and there is an increase in ochreous goethite and kaolinite and a corresponding decrease in hematite and vitreous goethite in the overflow (Figs. 3, 4). The modal mineralogy results compared well when recalculated and cross checked with assay results and by reconstituting the test products and comparing with the feed (Tab. 1).

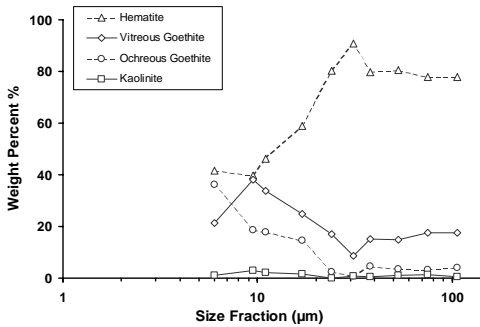


Figure 3. Change in mineralogy with size for hydrocyclone feed.

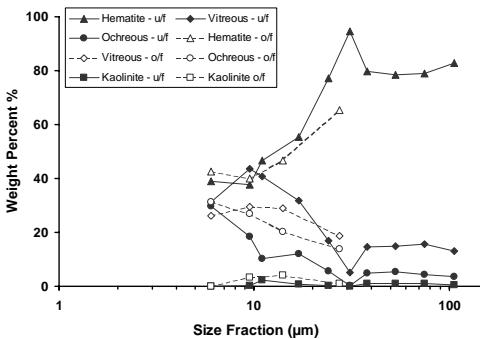


Figure 4. Hydrocyclone underflow and overflow products. Test conditions - 33% solids, 180 kPa of pressure.

Table 1. Comparison of actual head assay & reconstituted and assays calculated from mineralogy (-212 x + 2.5 µm size).

Feed Type	Fe total (%)	SiO ₂ (%)	Al ₂ O ₃ (%)	P (%)	LOI (%)	Total (%)
Actual	63.66	2.34	1.49	0.062	4.71	99.61
Reconstituted	63.57	2.28	1.56	0.064	4.80	99.60
Actual ex Mineralogy	63.22	2.39	1.57	0.069	4.81	99.24
Reconstituted ex Mineralogy	63.41	2.22	1.48	0.069	4.79	99.22

3.2 Experimental and theoretical Partition Curves

The procedure used for calculating particle density distributions from the image analysis data and ultimately the experimentally derived mineral partition curves is described in Clout et al. (2002). Figure 5 shows the actual experimental partition curves obtained for the various minerals and the overall combined size estimate. As expected, the curves follow the trend of hematite having the finest separation size (about 0.01mm) and vitreous goethite, ochreous goethite and kaolinite having coarser separation sizes. The very low levels of quartz gangue in the ore precluded any curve being developed. The vitreous goethite curve is similar to hematite, while ochreous goethite and kaolinite have the coarsest separation sizes (~0.02mm).

The partition coefficients for the very fine sizes do vary from the value for water split to the underflow stream, but the accuracy of the data in this region is considered to be low. No value was available for the porosity of the kaolinite hence no adjustment was made to the data. It also needs to be recognized that the low amounts of kaolinite present in the samples, compared to hematite, leads to potentially higher errors in determining its partition curve. The partition curve based on size is similar to that for hematite since this mineral is dominant in the sample.

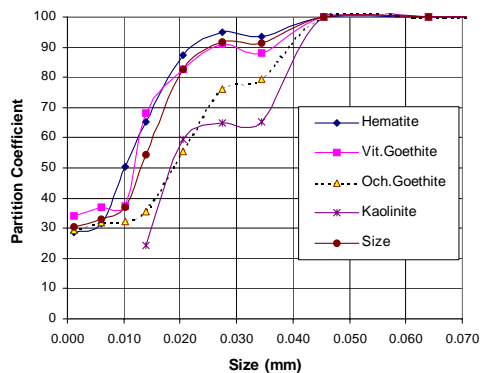


Figure 5. Experimentally determined partition coefficients for the individual minerals - 100 mm hydrocyclone optimum test.

A basic set of equations has been used to develop simple theoretical partition curve models (Firth & O'Brien 1996; O'Brien et al. 2000). A simple model of the 100mm diameter hydrocyclone for desliming of the iron ore has been developed which incorporates the impact of the density effect (via mineralogical tracking) and the potential effect of changing spigot, vortex finder or hydrocyclone diameter (Fig. 6). Whilst the model was successful

in predicting the presence of coarse gangue in an overflow product, it requires further testing and refinement, and its predictions should be used carefully.

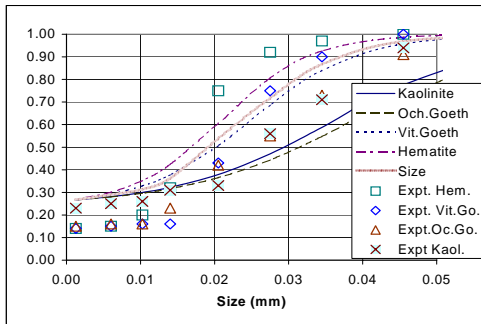


Figure 6. Comparison of experimentally derived data points (Expt.) and the partition curves generated by the general model for the 100mm hydrocyclone under optimum operating conditions.

4 CONCLUSIONS

Mineral tracking data derived from image analysis has been successfully used to develop partition curve models to describe and predict physical separation outcomes for hydrocyclone desliming of an iron ore. The mineralogical data was critical in providing specific gravity characterization for particle populations and estimates of the iron content of the feed and products. Whilst still in the early stages of development, the method is believed to provide considerable promise for prediction of mineral processing performance and design of optimum flow sheets.

5 REFERENCES

Batterham, R. J.; Grant, R. M. & Moodie, J. P. 1992. A perspective on process mineralogy and mineral processing. In: Proceedings of the First International Conference on Modern Process Mineralogy and Mineral Processing, Beijing. 3-12.

Benson, S.; Showers, G.; Loudon, P. & Rothnie, C. 2001. Quantitative and process mineralogy at Tiwest. In: International Heavy Minerals Conference, AusIMM, Fremantle. 59-68.

Bonifazi, G. & Massacci, P. 1993. Simulating separation processes by separation function. In: Proceedings of the XIX International Mineral Processing Congress, SME, Littleton, Colorado. 239-244.

Clout, J. M. F.; Firth, B. A. & O'Connor, M. T. 1997. New Advances in beneficiation of iron ore. In: Proceedings of

the National Conference on Iron Making Resources and Reserves Estimation (Eds.: V. N. Misra & J. S. Dunlop). AusIMM, Perth. 177-183.

Clout, J. M. F.; Trudu, A. G.; Campbell, J.J.; Firth, B. A.; Young, J. M.; Manuel, J. R. & Zhu, R. 2002. Improving the performance of physical separation processes using mineral tracking, TIOITT Conference. Kiruna, 2002.

Danti, K. J.; Cross, K. C. & Halsall, C. 1993. A high performance, low cost image analysis system for IBM compatible computers: practical applications in mineral processing and geology. In: Programme and Abstracts International Congress on Applied Mineralogy '93, Mineralogy. Fremantle WA. 47-49.

Firth, B. A. & O'Brien, M. 1996. Some aspects of fine particle size classification, CHEMECA '96. Sydney. 3. 41-46.

Frew, J. A. & Davey, K. J. 1993. Effect of liberation on flotation performance of a complex ore. In: Proceedings XVIII International Mineral Processing Congress, AusIMM. Melbourne. 905-911.

Griffin, L. K.; Hart, S.; Espinosa-Gomez, R. & Johnson, N. W. 1993. Chalcopyrite flotation and liberation characteristics before and after autogenous grinding at Mount Isa Mines Limited. In: Proceedings XVIII International Mineral Processing Congress, AusIMM, Melbourne. 913-922.

Gottlieb, P.; Wilkie, G.; Sutherland, D.; Ho-Tun, E.; Suthers, S.; Perera, K.; Jenkins, B.; Spencer, S.; Butcher, A. & Rayner, J. 2000. Using quantitative electron microscopy for process mineralogy applications. *Journal of Mining*. April 2000. 24-25.

Gu, Y. & Guernsey, P. 2000. Improving flotation plant performance with the JKMR/Philips Mineral Liberation Analyser. Flotation 2000. Minerals Engineering International Conference. Falmouth, Cornwall.

King, R. P.; 1999. A Users Guide to MODSIM. Department of Metallurgy, University of Utah, Salt Lake City, UT, USA.

King, R. P. & Schneider, C. 1998. Stereological correction of linear grade distributions for mineral liberation. *Powder Technol.* 98 (1): pp 21-37.

Mandile, A. J. & Johnson, N. W. 1998. Quantitative mineral analysis of ores and minerals processing products using X-ray diffraction. *The Mining Cycle*, AusIMM '98, Melbourne. 271-275.

O'Brien, M.; Firth, B. A.; Clarkson, C. & Edward, D. 2000. Operational Performance of a Large Diameter (One Metre) Classifying Cyclone. In: Proceedings of the Eighth Australian Coal Preparation Conference. 98-111.

Reid, A. F.; Gottlieb, P.; MacDonald, K. J. & Miller, R. R. 1985. QEM-SEM Image Analysis of Ore Minerals: Volume Fraction, Liberation and Observational Variances. *Applied Mineralogy* (Ed: W.C.Parks, D.H.Hausen and R.D.Hagni), TMS-AIME, Littleton, Colorado. 191-204.

Schena, G. & Chiaruttini, C. 2000. A stereologically posed mass balance for calculating the distributed efficiency of particle separation systems. *Int. J. Miner. Process.* 59:149-162.

Srivastava, M. P.; Pan, S. K.; Prasad, N. & Mishra, B. K. 2001. Characterization and processing of iron ore fines of Kiriburu deposit of India. *Int. J. Miner. Process.* 61:93-107.

Zhang, N. & Whiten, W. 2001. Determining mineral composition from assays. In: International Heavy Minerals Conference, AusIMM, Fremantle. 81-85.

Process Mineralogy Studies of a “Foscorite” Ore from Salitre Alkaline Carbonatitic Complex

H.Kahn, G.Ratti, M.M.L.Tassinari, E.S.Mano

Department of Mining and Petroleum Engineering, Polytechnic School, University of Sao Paulo, Brazil

L.A.F.Barros

Fosfertil - Fertilizantes Fosfatados S. A.

ABSTRACT: In the central area of the Salitre alkaline-carbonatitic complex there is a weathered “foscorite” deposit essentially constituted by apatite and magnetite; the accessory minerals are basically represented by quartz, ilmenite, perovskite and clay minerals. Mineralogical studies showed two distinct apatite phases; the primary one from igneous origin and the secondary phase related to the weathering process which cements the primary apatite and the other existing minerals; these apatite phases were characterized by optical microscopy, scanning electron microscopy, cathodoluminescence and microprobe analysis. In addition, process mineralogy studies were carried out focusing to evaluate an alternative of magnetic separation processes that would allow an early production stage while the detailed exploration and the feasibility studies for a large mining operation are being carried out. Five distinct comminution conditions for a volumetric outcrop sample followed by magnetic separations in RE drums and RE rolls were done; magnetic separability curves showed that for the ore ground between 2.0 - 1.2 mm was possible to achieve the higher P recoveries and separation efficiencies. In a second step the intermediate products would be reprocessed by wet magnetic separation or flotation.

1 INTRODUCTION

The Salitre alkaline carbonatitic complex is located in southeast region of Brazil. Despite the Salitre complex and their P, Ti and Nb mineralizations are known for more than 30 years, only a new foreseen of a significant growing demand of phosphate rock by the Brazilian fertilizer industry motivated new explorations activities in the recent years.

The Salitre complex is characterized by one major elliptical intrusion, with 6 by 8 km, and two others smaller ones with diameters in order of to 2 km. Less than 10 km NNW there is another larger alkaline complex, Serra Negra. The Salitre complex is constituted essentially by mica-peridotites rocks followed by pyroxenites; calcite-carbonatites occur basically as later veins or small dikes (Barbosa et al, 1970). Outcrops are very rare, since a lateritic weather mantle that can reach more than 50 m on depth covers almost the entirely complex. Mineralizations of P (apatite), Ti (anatase) and Nb (Ba-pyrochlore) are related to this lateritic material.

As a result of the recent exploration activities a “foscorite” deposit was found in the central area of the Salitre complex. Fig. 1 shows the simplified geological map and the location of the studied area.

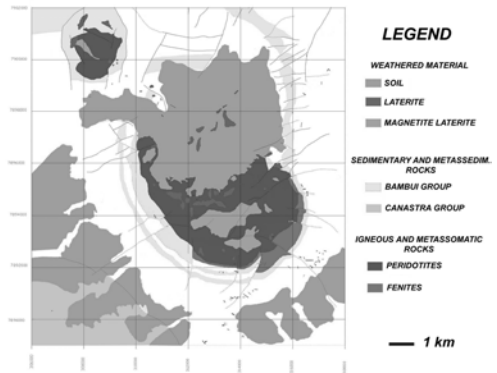


Fig. 1 Salitre simplified geological map presenting the location of the studied foscorite area (circled)

Due to the high amount of P related to the foscorite ore type and their singular mineralogy, process mineralogy studies were developed focusing to evaluate an alternative of magnetic separation processes that would allow an early production stage process while the detailed exploration and the feasibility studies for a large mining operation are being carried out.

2 METHODS

Initial studies were performed with a volumetric sample of few hundred of kilograms composed from many individual weathered cemented foscrite outcrop samples. The composed sample was then crushed to minus 3.4 mm by a hammer mill, homogenized and sampled for process mineralogy studies; additional thin-polished samples from uncrushed samples were also subject to optical and scanning electron microscopy (SEM) analyses.

The sample was split for particle size analysis by wet screening followed by chemical and mineralogical analyses as well as magnetic separation. Mineralogical analyses were performed by X-ray diffraction, optical microscopy and SEM. Cathodoluminescence microscopy (CL) coupled to optical microscope and monochromatic CL coupled to a SEM were useful techniques for discrimination between distinctly apatite phases, which were also chemically characterized by a X-ray wavelength spectrometer (WDS) coupled to the SEM.

Magnetic separability curves were carried out for five different grinding conditions (-3.4 mm, -1.7 mm, -1.2 mm, -0.84 mm and -0.60 mm) to a proper evaluation of the magnetic separation potential as an early production stage production process. Each grinding product was classified by dry size screening, with an aperture of 0.15 mm, followed by dry sequential magnetic separations on RE drums (0.15 T, 0.3 T and 0.65 T) and RE rolls (1.0 T) of the material above 0.15 mm.

Wet high intensity magnetic separation (WHIMS) was also evaluated as a further mineral processing step for the RE drums and rolls tailings coupled to the minus 0.15 mm size fraction.

3 RESULTS

3.1 Chemical composition

Chemical composition indicated that the foscrite sample is essentially constituted by P_2O_5 , 26.9%, CaO, 38.7%, and Fe_2O_3 , 25.5; other oxides represent in average 0.5-0.6% or less. Particle size analyses indicated relatively homogeneous grades among the size fractions with only a slight Fe_2O_3 enrichment for the intermediate fractions (-1.6 +0.4 mm range).

3.2 Mineralogical assemblages

The cemented foscrite outcrop sample is essentially constituted by apatite and magnetite; accessory minerals are basically represented by ilmenite, perovskite, clay minerals and goethite.

Optical, SEM and CL microscopy techniques showed two distinct apatite phases. The primary apatite, igneous in origin, usually occurs in prismatic subrounded crystals with average dimensions of 0.2

to 0.3 mm, sometimes fractured. The secondary phase, related to the weathering process, cements the primary one and the other existing minerals, occasionally presenting a zone-growing halo with optical continuity regardless to the primary apatite. The secondary apatite under optical microscopy is particularly not translucent as the primary one; the surrounding halos usually present a higher birefringence, indicating that they are probably constituted by a CO_2 enriched apatite phase, while the major cemented mass is almost "isotropic" (microcrystalline apatite).

CL images by optical microscopy showed a light blue-purple color for the primary apatite grains; deeper purple inner and lighter borders typically characterize their internal zoning. This blue-purple color is related to minor rare earth elements (REE) on apatite structure composition (Marshall, 1988). The secondary apatite presents a very weak answer to CL, sometimes in a pale yellow-green color due to the presence of minor Mn amounts.

SEM backscattered electron images with high contrast indicated that the primary one has a little higher average atomic number, as well as some internal chemical zoning. Electron microprobe analyses by WDS, Table 1, indicated that the primary apatite presents typically higher contents of P_2O_5 , REE, SrO and SiO_2 , while the secondary one shows higher contents of F, Fe_2O_3 and Al_2O_3 as well as CaO/ P_2O_5 ratio.

Table 1 – WDS microanalyses of primary and secondary apatite phases.

	Primary apatite	Std. deviation	Secondary apatite	Std. deviation
CaO	54.1	0.47	56.6	1.43
P_2O_5	41.9	0.70	38.6	1.99
F	1.48	0.21	2.23	0.48
SrO	0.93	0.21	0.26	0.06
La_2O_3	0.14	0.03	0.03	0.06
CeO_2	0.45	0.09	0.07	0.01
Nd_2O_3	0.16	0.07	0.04	0.06
SiO_2	0.12	0.11	0.01	0.05
Fe_2O_3	0.04	0.01	0.31	0.01
Al_2O_3	-	-	0.30	0.11

Magnetite grains present an average size of 0.8 to 1.5 mm, with the smaller crystals of 0.02 - 0.03 mm; they are cemented by secondary apatite and present some Mg in substitution to Fe^{2+} on their structure

3.3 Dry Magnetic separability studies

A summary of the magnetic separability studies results by RE drums and roll for five different grinding conditions (-3.4 mm, -1.7 mm, -1.2 mm, -0.84 mm and -0.60 mm) are shown on Table 2.

Table 2 - Summary of the results of magnetic separability studies by RE drums and roll for the different grinding conditions

	Grinding cond.	N.mag. conc.	Magnet. tailings	Fines -0.15mm	Total tailings
% weight	-3.4 mm	24	58	18	76
	-1.7 mm	26	53	21	74
	-1.2 mm	26	48	26	74
	-0.84 mm	22	47	31	79
	-0.60 mm	21	45	35	80
P ₂ O ₅ grade (%)	-3.4 mm	36.7	23.2	30.7	25.0
	-1.7 mm	36.9	22.9	30.6	25.1
	-1.2 mm	36.8	24.9	31.0	27.0
	-0.84 mm	36.9	25.2	30.9	27.5
	-0.60 mm	37.2	24.7	30.7	27.3
Fe ₂ O ₃ grade (%)	-3.4 mm	4.8	35.9	16.9	31.4
	-1.7 mm	4.9	36.5	16.5	30.8
	-1.2 mm	4.1	37.3	16.9	30.1
	-0.84 mm	4.4	37.5	17.4	29.4
	-0.60 mm	4.3	38.2	17.8	29.3
P ₂ O ₅ recovery (%)	-3.4 mm	32	48	20	68
	-1.7 mm	34	43	23	66
	-1.2 mm	32	40	27	68
	-0.84 mm	27	40	33	73
	-0.60 mm	26	38	36	74

Non-magnetic concentrates present P₂O₅ grades above 36% with a very slight increase for finer grinding conditions; Fe₂O₃ grades are below 5% and present opposite behavior. The higher weight and phosphate recoveries are associated to the three coarsest grinding settings, which gave very similar results, 24 to 26 % for weight recovery and 32 to 34% of P recovery. For a coarse comminution condition there are greater losses associated to the

magnetic tailings, although for a finer one there is a substantial weight increase of the -0.15 mm size fraction, despite an improvement on the magnetic separation conditions, which will mean a lower global P recovery.

Detailed magnetic separations results for a -1.7 mm grinding condition are present on Table 3 and as magnetic separability curves expressed as P₂O₅ and Fe₂O₃ grades versus weight and P₂O₅ recoveries on Fig. 2. The first magnetic product presents high magnetite content, with substantial amount as free particles; the other intermediate products are typically constituted by particles of apatite locked with fine magnetite, which must be reground for a proper liberation.

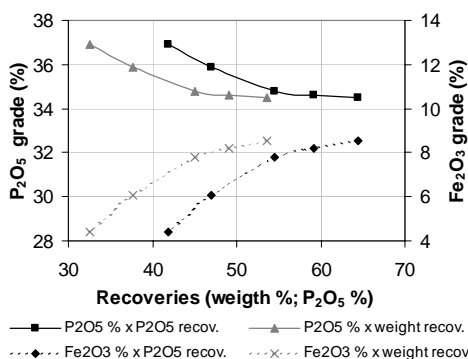


Fig. 2 - Magnetic separability curves for -1.7 mm ground material expressed as P₂O₅ and Fe₂O₃ grades versus weight and P₂O₅ recoveries

Table 3 - Magnetic separability results for the material ground to -1.7 mm

Product	Weight %	Grades (%)						CaO/ P ₂ O ₅ ratio	Assay recovery (%) Sample recovery (%)			
		P ₂ O ₅	CaO	Fe ₂ O ₃	SiO ₂	Al ₂ O ₃	MgO		P ₂ O ₅	Fe ₂ O ₃	P ₂ O ₅	Fe ₂ O ₃
REE drum mag 0.15 T	36.6	22.1	30.5	39.7	<0.10	0.30	1.25	1.38	35.6	80.0	27.7	67.2
REE drum mag 0.30 T	3.6	33.0	45.7	12.4	0.11	0.28	0.12	1.38	5.2	2.4	4.0	2.0
REE drum mag 0.65 T	3.3	32.8	45.3	12.6	0.14	0.35	0.13	1.38	4.7	2.3	3.7	1.9
REE roll mag 1	5.8	29.3	40.2	16.6	0.29	0.65	<0.10	1.37	7.5	5.3	5.9	4.5
REE roll mag 2	4.0	29.3	39.8	16.5	0.37	0.85	<0.10	1.36	5.2	3.6	4.0	3.1
REE roll non mag	25.7	36.9	51.3	4.43	0.22	0.19	<0.10	1.39	41.8	6.3	32.6	5.3
Feed -1.7 +0.15 mm	79.0	28.8	39.8	23.0	0.12	0.32	...	1.38	100.0	100.0	77.9	83.9
Fines -0.15 mm	21.1	30.6	42.2	16.5	0.29	0.51	0.32	1.38	22.1	16.1

3.4 Wet high intensity magnetic

Wet high intensity magnetic separation (WHIMS) was evaluated as a second step for processing the RE drums and rolls tailings coupled to -0.15 mm size fraction. These products were firstly ground to minus 0.3 mm, followed by a low wet magnetic separation with permanent magnet and WHIMS with

a screen matrix; the attained results are presented on Table 4. The first magnetic product is essentially constituted by magnetite; while the intermediate products are typically constituted by particles of apatite locked with fine magnetite and/or with superficial coating by iron hydroxides.

Table 4 - Wet magnetic separations for RE-Roll Tailings + Fines ground to -0.3 mm

PRODUCT	Weight %	Grades (%)					Recov. (%)	
		P ₂ O ₅	CaO	Fe ₂ O ₃	Al ₂ O ₃		P ₂ O ₅	Fe ₂ O ₃
Perman magn	17.6	5.1	7.4	80.4	0.34		3.1	64.9
Magnetic 2	9.9	22.3	30.3	34.3	1.21		7.5	15.5
Magnetic 3	4.4	21.8	27.6	32.1	1.68		3.3	10.0
Non Magnetic	42.3	37.3	49.5	4.07	0.45		53.6	7.9
Feed	74.3	26.8	35.6	27.9	0.60		67.4	94.7

3.5 Summary of magnetic separations

A summary of dry and wet magnetic separations results are presented on Table 5.

Table 5 - Summary of dry and wet magnetic separations

Product	Weight %	Grades (%)					Recov. (%)	
		P ₂ O ₅	CaO	Fe ₂ O ₃	Al ₂ O ₃		P ₂ O ₅	Fe ₂ O ₃
<i>Dry separation</i>								
REE roll conc.	25.7	36.9	51.3	4.43	0.19		32.6	5.3
Mag. tailings	53.2	24.8	32.4	31.9	0.38		45.3	78.6
-0.15 mm	21.1	30.6	42.2	16.5	0.51		22.1	16.1
<i>Wet separation</i>								
WHIMS conc.	42.3	37.3	49.5	4.07	0.45		53.6	7.9
Final tailings	32.0	12.8	17.3	59.5	0.80		13.8	86.9
<i>Total</i>								
REE roll conc.	25.7	36.9	51.3	4.43	0.19		32.6	5.3
WHIMS conc.	42.3	37.3	49.5	4.07	0.45		53.6	7.9
Total conc.	68.0	37.2	50.2	4.20	0.35		86.2	13.2

In an early project startup by a dry magnetic separation process it would be expected a non-magnetic concentrate with 37% of P₂O₅ and less than 5% of Fe₂O₃ with recoveries of 33% for P and 26% in weight. Further processing of magnetic tailing and -0.15 mm size fraction would allow to recovery up to 85% of the global P content with similar concentrate grades.

4 CONCLUSIONS

The foscrite ore type, although representing only a small portion of Salitre I phosphate resources, correspond to an expressive reserve with a high P₂O₅ grade and a singular mineralogy that would allow an early production stage while detailed exploration and the feasibility studies for a large mining operation are being carried out.

Mineralogical studies showed two distinct apatite phases. The primary or igneous apatite usually occurs in prismatic subrounded crystals with dimensions of 0.2 to 0.3 mm; the secondary phase,

related to the weathering process, cements the primary one, the magnetite and the other minor minerals. Magnetite grains present an average size of 0.8 to 1.5 mm, with the smaller crystals between 0.02 and 0.03 mm.

Mineralogical and magnetic separability studies allowed establishing the following considerations for a further mineral dressing process that would allow an early project startup:

- A first step comprising simple dry process considering comminution to minus 2.0 - 1.2 mm, classification and magnetic separations in RE drums and RE rolls. The non-magnetic concentrate would present 36% of P₂O₅ and around 5% of Fe₂O₃ with associated recoveries of 26% in mass and above 40% for the P content.
- In a second step the intermediate magnetic product should be ground to the minus 0.3 mm and together with the fine fraction size from the dry classification should be processed by a low and high intensity wet magnetic separations (drum and WHIMS). The WHIMS non-magnetic concentrate will present similar grades of the dry one with additional recoveries of other 40% of the P content. Froth flotation would be an alternative to WHIMS that must be properly evaluated.

Coupling both dry and wet magnetic separations it would be expected a final non-magnetic concentrate with grades above 36% of P₂O₅ and 5% of Fe₂O₃ with global P recoveries at about 80-85%. Since the remaining iron on the attained products are relatively high for phosphoric acid production, further chemical tests must be done for a proper evaluation of the potential products and/or process demands by the fertilizer industry, particularly considering a mix with others major phosphate rocks produced nearby.

5 ACKNOWLEDGEMENTS

This research was supported by Grant N. 01/1023-4 and 02/01011-1 from FAPESP – Fundação de Amparo a Pesquisa no Estado de São Paulo.

6 REFERENCES

- Barbosa, O. et al. 1970. Geologia da Região do Triângulo Mineiro. Boletim de Fomento da Divisão da Produção Mineral, nº 136. Rio de Janeiro, p.7-141.
- Marshall, D.J., 1988. Cathodoluminescence of Geological Materials. Unwin Hyman Ltd., 146p.
- Holland-Batt, A.B., 1985. Analysis of mineral separation systems by means of recovery functions. Trans. Inst. Min. Metall., V.94, C17-29.

Effects of Smectite and Kaolinite- rich Gangue on Sulphuric Acid Leaching of Exotic Copper Ore

U.Kelm & S.Helle

Instituto de Geología Económica Aplicada (GEA), Universidad de Concepción, Casilla 160-C, Concepción, Chile.

ABSTRACT: Smectite and kaolinite group of minerals are frequently present in the host rocks of exotic copper mineralization in the North of Chile (e.g. Mina Sur and its northward extension, Codelco Norte). In particular, when associated with low copper grades, extraction problems in heap leaching operations are frequent. To improve the understanding of gangue behavior and to contribute to mine-scale prediction procedures, synthetic compressed aggregates of chrysocolla, malachite and atacamite, inert quartz and reactive smectites and kaolinites have been short term batch leached with 15% sulphuric acid. Results are related to ore and gangue mineralogy and bottle-leach recovery from Mina Sur, Codelco Norte. Marked differences in acid resistance of the smectite phases (SWY>SAZ>NAU>Bentonite Rock) resulted in relative copper recoveries of 80 to 67% for a 0.5% total copper content of malachite and atacamite spiked aggregates. Copper is retained in the remaining exchange positions as well as adsorbed on mineral surfaces and suspended in silica gel. This copper can be easily recovered by elution with water or salt solution. Kaolinites delaminate and contribute to clogging of the leach columns. These individualized features observed for the synthetic aggregates act combined for the Mina Sur ore, where recovery rates drop to < 50% for kaolinite containing gangue. Smectite presence in gangue with no kaolinite results in recoveries of 65-80%.

1 INTRODUCTION

Heap-leach operations have gained increasing importance in the Chilean mining industry, as they offer the possibility to treat low grade exotic copper ore as well as reworking (mixed or in situ) old tailings (Domic 2001). For several deposits, this tendency requires a fresh approach to mineral characterization, taking into account the production of fines and their short-term leach behavior.

This communication contrasts the “traditional” mineral characterization by microscopy and support X-ray diffraction together with added on chemical and cation exchange capacity determinations and the leach results of Cu-mineral spiked synthetic rock aggregates of known starting composition. This juxtaposition allows to elucidate (1) the effects in terms of Cu retention, delamination, and dissolution within the smectite and kaolin phyllosilicate families and (2) recommend improved routine proceedings for the prediction of the reactivity in gangue.

2 GEOLOGY AND MINERALOGY OF MINA SUR, CODELCO NORTE

Secondary processes linked to the formation of exotic copper ore deposits have affected various Andean porphyry copper bodies, resulting in the formation of satellite deposits of e.g. chrysocolla, atacamite, malachite, brochantite, etc. depending on the pH and Eh of the mineralizing fluids as well as the alteration type of the host rock. The Mina Sur deposit is located to the South of the Chuquicamata sulphide ore body and is inserted in a SE oriented paleochannel about 8 km long. The most extensive mineralization (Late Miocene) was deposited at 2 to 6 km distance from Chuquicamata where the lens-shaped body (400-200 m wide, 60 to 40 m thick) is exploited at Mina Sur (Pincheira et al. 2003, Münchmeyer 1996). Future extraction will focus on narrow channel linking this ore body to its sulphide precursor (“Extensión Norte, Mina Sur) (Dagnino 2003 personal communication). Dominant mineralization is chrysocolla, atacamite and black copper pitch and wad. These phases form the cement of conglomerates deposited in the paleochannel as well as in fractures of the underlying Paleozoic basement. Cu saturated solutions may impregnate biotite and feldspar cleavages of grain boundaries

(Pincheira et al. 2003). Propylitic alteration prevails in the basement, whereas most of the clasts in the conglomerates and their matrix show argillic alteration, in some sectors with a marked tendency to kaolinitic advanced argillic assemblages. For propylitic alteration, chrysocolla is the main Cu phase, whereas in the argillic zones atacamite and copper wad dominate. Drill core mappings traditionally include "copper clays", as a denominator applied to faint pale blue phyllosilicates, without further definition of their mineralogy. This term may imply a submicroscopic mixture of discrete exotic Cu ore or Cu exchanged smectite phases or a mixture of both. The presence of phyllosilicates is increasingly considered one of the key factors controlling copper extraction at Mina Sur (A. Reghezza, personal communication) in particular with the change from vat to heap leaching. From a metallurgical point of view (Bartlett 1992, Domic 2001) key parameters controlling heap leach operations are: crushed rock size distribution and resulting porosity, permeability and height of the heap, acid pretreatment, acid concentration and irrigation rate, total and soluble copper content of the ore and finally, the bulk rock mineralogy and chemistry. The present study stresses the need for comprehensive mineralogical studies in order to understand copper losses once metallurgical parameters apparently have been controlled.

3 LEACHING OF SYNTHETIC ROCK AGGREGATES

Single mineral dissolution has received ample attention in weathering studies (White & Brantley 1995) as well as more recent crystallographic studies by combined TEM and atomic force microscopy (AFM) studies. Despite providing invaluable information on activation energies, preferential dissolution of individual crystal phases and leaching environments, rarely are developed below pH 2, or the individual crystals selected have much larger grain sizes than those found in ore rock. On the other hand, leaching experiments carried out on whole rock (Early et al. 1990), however well characterized, leave uncertainties as to the origin of elements found in the leachate. An additional difficulty is the impossibility to observe separately vein or fracture leaching and leaching along gangue grain boundaries or mineral cleavages.

Given the above outlined difficulties, short term batch leaching using 15% sulphuric acid of synthetic mineral aggregates was considered to be an acceptable compromise, allowing the study of the direct interaction between a finely disseminated Cu-ore phase and a highly reactive gangue. Rock aggregates were prepared by using quartz (57%, 60-

80 Tyler mesh) as permeabilizing agent, 1% Cu-mineralization (< 200 Tyler mesh, hand picked chrysocolla from a Codelco Norte specimen, Aldrich reagent malachite and a purpose synthesized atacamite - para-atacamite mixture). Short term reactive gangue (42%, <200 Tyler mesh) centered on various smectite group minerals and a high and low defect kaolinite. All materials (except one Chilean bentonite rock) were obtained from the Clay Mineral Society (CMS) source and special clay selection (Tab. 1). Details on homogenization, compaction (by XRF powder bead press) and crushing are presented in Kelm & Helle (2003). Leaching was carried out on 40 grams of crushed aggregate in columns of 4.5 cm diameter and 6.5 cm height. 50ml acid was added by slow dripping during one hour. A 20 ml aliquot of leachate was recovered after four hours (end of free dripping for all columns).

Table 1. Reactive gangue phases used in synthetic mineral aggregates. CEC-Cation Exchange Capacity; BET-Specific Surface Area.

Gangue Phase	CEC cmol/kg	BET m ² /g
Kaolinite KGa-1: 96% kaolinite, 3% anatase, 1% quartz	12.5 cmol/kg	141m ² /g
Kaolinite KGa-2: 96% kaolinite, 3% anatase, 1% other traces	0.643 cmol/kg	180m ² /g
Montmorillonite SAZ-1: 98% smectite, traces of quartz	118.1 cmol/kg	147m ² /g
Montmorillonite Swy-1: 75% smectite, 8% quartz, 17% feldspar and others	90.7 cmol/kg	117m ² /g
Nontronite Nau-1: >80% smectite, 10-15% illite and quartz	70.8 cmol/kg	97m ² /g
Bentonite rock (Chile): >90% smectite, traces Fe-oxides and vitreous matter	62.7 cmol/kg	180m ² /g

4 CHEMICAL AND MINERALOGICAL ANALYSES

Leachates were analysed by ICP-MS and ICP OES at Actlabs, Canada. Solids were characterized by XRF (Rigaku E3700), total and soluble Cu, and cation exchange capacities (CEC) were determined by AAS (Hitachi Z8100). The apparent specific surface area (BET) was determined by nitrogen adsorption at 21°C after degassing the samples for 12 hours. Changes in mineralogy were monitored by XRD (Rigaku Dmax-C) using Ni filtered Cu radiation.

For Mina Sur ore samples microscopic observation preceded X-ray diffraction. In addition the percentage of <2µm fraction present in the samples was determined by ultrasonic disaggregation, followed by centrifugation and evaporation of the separated liquid.

5 RESULTS

5.1 Observations for leaching bottle tests of samples from Mina Sur and its northward extension

Microscopic observation frequently resulted in the non-recognition or misinterpretation of the percentage of clay minerals present. This problem is partly accentuated by the loss of clay size material during the preparation of the thin section and additionally complicated by the presence of soluble atacamite and heat sensitive chrysocolla. XRD whole rock scans do not always reveal the presence of smectite phases in the $<2\mu\text{m}$ fraction. However, the estimated percentage of the $<2\mu\text{m}$ size fraction and the weighted clay mineralogy of the $<2\mu\text{m}$ fraction permit to observe the following: Cu extractions drop below 65% (based on roll bottle tests) when samples have a high smectite presence ($>70\%$) in the $<2\mu\text{m}$ fraction combined with $>10\%$ abundance of that fraction in the sample. The same drop in extraction occurs when medium amounts of smectite (30-70%) combine with minor presence of kaolinite; here the $<2\mu\text{m}$ fraction has to amount to only 5% to achieve this effect. Extreme drops ($<50\%$) in extraction are found when kaolinite become the dominating phyllosilicate, even if the $<2\mu\text{m}$ fraction only amounts to $<3\%$. Low total copper contents further accentuate the aforementioned observations. Figures 1 A and B exemplify medium and low Cu-extraction. Whole rock mineralogy is dominated by quartz, plagioclase, and the presence of mica (di- and tri-octahedral).

5.2 Observations for leaching of synthetic rock aggregates

During leaching smectite rich gangues showed an increase in volume of up to 75% and demonstrated the immediate sealing quality of the phyllosilicate group by formation of air and later acid filled cavities in the column centre. For kaolinite materials formation of acid puddles on column tops and clogging of columns was notorious until drainage channels opened. Elements present in cation exchange positions and in the octahedral layer are the principal short term cation suppliers to the leachate (Fig. 2). Figure 3 juxtaposes Cu-recovery and total cation exchange capacity of the starting mixture demonstrating preferential Cu retention in the bentonite rock, SAZ montmorillonite and NAU nontronite. Cu retention for kaolinite gangues is minimal. Greatest reduction of the basal 001 XRD reflection was observed for three high Cu retaining smectites, whereas the SWY montmorillonite appeared to be very acid stable (a similar observation was made by Madejova et al. (2003) suggesting that Cu is retained not only in exchange positions *s. str.* but also kept adsorbed and

suspended in silica gels remaining in the residue. For kaolinite the reduction of the XRD intensity of the basal reflection is directly related to the lack of lattice defects. The formation of alunogen, meta-alunogen and coquimbite (nontronite gangue) cause a temporary reduction of permeability in the residues.

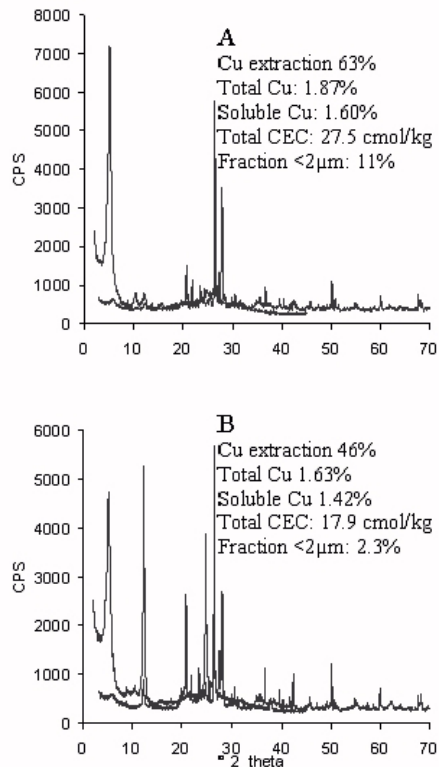


Figure 1 A and B. (next column) Bold line – XRD whole rock trace, fine line – oriented ethylene glycol solvated XRD trace, $<2\mu\text{m}$ fraction.

6 CONCLUSIONS

Variable dissolution and cation contribution to the leachate solution are observed for smectite gangues, thus making recommendable for mine operation a detailed determination of prevailing species in this group by combined XRD and CEC before the start of large scale leaching tests. Although kaolinite gangues show a copper recovery close to 100% in short term laboratory leach tests, easy delamination of this phyllosilicate causes clogging of columns and heaps by mechanical barrier formation. Depending on the X-ray equipment available and level of operator training, routine scans of $<2\mu\text{m}$ fractions are recommended to avoid overlooking minor

amounts of smectite and kaolinite in whole rock samples. Control of CEC (including Cu) in head and residues provides an easy option to monitor Cu-retention as well as predict and monitor partial cation input in the leach solutions.

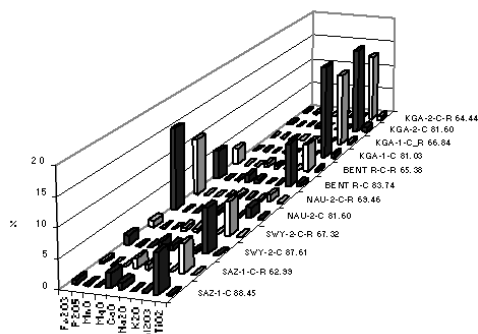


Figure 2. Major element contents of head (dark columns) and residue (R, light grey columns) samples. SiO₂ contents are stated on y-axis.

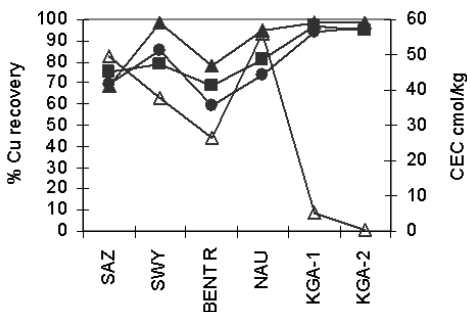


Figure 3: Percentage Cu recovery (black symbols) triangle – chrysocolla series, circle –malachite series, square atacamite series, open triangle – total CEC of head mixtures.

7 ACKNOWLEDGEMENTS

This research is supported by Fondecyt grant 1010823 (Chile). A. Reghezza and A. Dagnino (both Codelco Norte) and their respective staff are thanked for their collaboration and the opportunity to use Mina Sur information. The dedication of laboratory staff at the GEA Institute at all stages of the study is appreciated.

8 REFERENCES

Bartlett, R.W. 1992. Solution mining. Leaching and recovery of materials. Gordon and Breach Science Publishers, Philadelphia, USA.

Domic, E. M. 2001. Hidrometalurgia, fundamentos, procesos y aplicaciones. Andros Impresores Ltda., Santiago, Chile.

Early, D., Paulson, S. E., Brink, S. E. 1990. The effects of rock mineralogy, chemistry and texture on in situ leaching of oxide copper ores from the Santa Cruz deposit. SME Preprint, 90(182), 60p.

Kelm, U., Helle, S. 2003. An experimental study of malachite, atacamite and chrysocolla interaction with reactive gangue during sulphuric acid leaching. Copper 2003, Santiago, Chile, Proceedings (Hydrometallurgy), 10p.

Madejová, J., Pálková, H, Komadel, P. 2003. Acid dissolution of smectite as studied by spectroscopy in the near and middle IR regions. Euroclay 2003, Modena, Italy, Abstracts 175-176.

Münchenmeyer, 1996. Exotic deposits. Products of lateral migration of supergene solutions from porphyry copper deposits. *Soc. Econ. Geol. Special Pub.* 5: 43-58.

Pincheira, M., Dagnino, A., Kelm, U., Helle, S. 2003. Copper pitch and copper wad. Contraste entre las fases presentes en las cabezas y en los rípios en pruebas de lixiviación de materiales de Mina Sur, Chuquicamata 10° Congreso Geológico Chileno, Concepción, Chile, 10p.

Grain Size and Liberation of Chromite in Ground Chrome Ore from Kemi Mine, Finland

J.Liipo & P.Lamberg

Outokumpu Research Oy, Pori, Finland

J.Turunen & J.Pitkäljärvi

Outokumpu Chrome Oy, Kemi Mine, Kemi, Finland

ABSTRACT: The mineralogy of chromitite in Kemi Mine, northern Finland, favors the utilization of optical image analysis. Image analysis is routinely used to determine the grain size distribution of chromite from drill core samples. To broaden the use of optical image analysis to process samples, the grain size and liberation of chromites were measured from selected grinding test samples. The main object of the study was to determine the liberation degree of chromite in ground samples and also to investigate the correlation between grain size and liberation of chromite. The samples for this study were taken from Elijärvi and Pohjois-Viia ore bodies, and they are composed mainly of chromite, serpentine, talc, and carbonates. Based on the studied samples, the liberation degree of chromite can be reliably estimated based on grain size of chromite measured from the sized samples. This method offers a fast and effective tool to study the liberation of chromite in different stages of concentration process.

1 INTRODUCTION

1.1 Chrome ore

The 2.44 Ga Kemi layered intrusion's upper part consists of amphibole gabbros, central part of gabbronorites and lower part of altered ultramafic pyroxenite and peridotite layers, which are the host rocks of the chrome ore.

The thickness of the chrome ore layer varies from 5 to 110 meters, averaging about 40m. The ore contains 26% Cr₂O₃ and the Cr/Fe ratio is 1.6. The main ore mineral is chromite (Alapieti et al. 1989).

The ore is currently produced using both open pit and underground mining methods. The mine produces annually 1.2 million tonnes of chrome ore and current ore reserves are about 52 million tonnes with 91 million tonnes of additional mineral resources.

1.2 Milling

The Kemi chrome ore is concentrated into upgraded lumpy ore and metallurgical grade concentrate. During the first stage of the process the ore is crushed to a diameter of 12-100 mm. After crushing ore lumps are processed by means of heavy media separation. During this process upgraded lumpy ore,

lumpy rock and middlings are produced from the ore.

Part of the ore is concentrated into metallurgical grade concentrate by using gravity and high gradient magnetic separation methods in the concentrating plant.

Approximately 200,000 tonnes of upgraded lumpy ore and 400,000 tonnes of metallurgical grade concentrate are produced annually. The chromium content of these concentrates is on average 35% and 45%, respectively. The concentrates are shipped to the Tornio ferrochrome works by train.

1.3 Use of image analysis at the Kemi Mine

The mineralogy of chromitite in Kemi Mine, northern Finland, favors the utilization of optical image analysis, which is used at Kemi Mine for determining ore feed chromite properties like grain size and brokenness from drill cores in order to predict ore grindability and optimize the concentration process (Leinonen 1998).

Lately Chernet & Marmo (2003) compared the measurement of the grain size of Kemi chromite by image analyses and sieving.

2 SAMPLES AND APPLIED METHODS

2.1 Samples

Studied samples are the products of six different grinding tests. The ore feed for the test were taken from Elijärvi E and Pohjois-Viia ore bodies. The ground ore was sized into fractions of +4mm, 0.71/4mm, 0.18/0.71mm, 0.063/0.18mm and -0.063mm. Polished sections and XRF analyzes were done from each the sieve fractions. The mineral composition of studied samples was estimated by mass balance calculations, and the amount of chromite was measured also by image analyses.

2.2 Image analysis

The grain sizes of chromites were measured with Axioplan2 optical microscope equipped with motorized Märzhäuser stage and a ProgRes3008 color digital camera and integrated with Zeiss Vision KS400 image analysis software at Outokumpu Research.

The liberation of chromite was measured by using the back-scattered electron images (BSE) grabbed by Cambridge 360S scanning electron microscope. The BSE -images were analyzed with KS400 image analysis software. The liberation measurement procedure is similar to that described by Lastra et al. (1998).

The main object of this study was to determine the liberation of chromite and also study the correlation between the measured liberation and grain size of chromite

3 GRAIN SIZE AND LIBERATION OF CHROMITE

3.1 Mineralogy of studied samples

The studied samples are chromitites, with 46.8-56.7% chromite, 17.7-28.3% serpentine, 6.5-13.6% talc, 7.2-19.7% carbonates like dolomite and magnesite. During the grinding, the magnesite and talc enrich into finest fractions compared to the mass distribution. Chromite and serpentine follow the mass distribution.

3.2 Grain size of chromite

The grain size of chromite was measured from each sized sample by image analysis. Both the maximum and minimum diameter and area of a chromite grains were measured. Total of 64 (8×8) images were analysed from each sample. From the coarsest fractions about 4500 chromite grains and from the finest -63µm fraction about 10,000 chromite grains were measured.

The grain size of chromites is mainly below 710µm, and only in three samples a few coarser chromite grains were encountered. The average grain size of chromite in volume -% in different sieve fractions with calculated average bulk grain size is given in Table 1.

Table 1. The average grain size (µm) of chromite

Sample	1	2	3	4	5	6
+4mm	134	133	207	187	159	210
0.71/4mm	139	170	225	200	153	201
0.18/0.71mm	200	204	219	221	202	190
0.063/0.18mm	97	89	116	103	96	93
-0.063mm	22	24	28	25	25	25
Bulk.	127	138	176	166	138	159

3.3 Liberation of chromite

The liberation of chromite was measured from the BSE images from fractions finer than 4mm. Based on optical microscopy and grain size measurements, it was obvious that all the chromite grains in the coarsest fractions occur as locked particles.

In the two coarsest fractions chromite occurs mainly as locked particles with silicates. The proper liberation of chromite is reached in fraction finer than 710µm. Due to the large portion of both +4mm and 0.71/4mm fractions, the calculated bulk liberation of the studied samples remain modest. The measured liberation degree of chromite is given in Table 2.

Table 2. The liberation of chromite

Sample	1	2	3	4	5	6
+4mm	0.0	0.0	0.0	0.0	0.0	0.0
0.71/4mm	0.5	13.1	11.9	1.9	2.3	3.2
0.18/0.71mm	81.0	87.9	82.9	78.6	76.2	82.7
0.063/0.18mm	85.3	87.5	85.9	85.4	84.9	86.6
-0.063mm	90.9	86.9	91.6	95.7	92.5	93.1
Bulk	47.7	48.7	50.7	47.0	46.8	43.2

4 CORRELATION BETWEEN GRAIN SIZE AND LIBERATION

The correlation between the measured grain size and liberation was studied in order to find out whether the routine grain size measurements could be used as suitable method to predict the liberation degree of chromite from process samples at site.

When the grain size of chromite in the sized sample is finer than the used sieve it is obvious that the retained chromite must occur as locked particles. It also seems that the grain size distribution of chromite calculated as volume-% based on maximum diameter and area of a grain gives the best results.

The difference between estimated liberation value and the measured liberation is biggest in the coarsest 0.71/4mm fractions, where the difference can be up to 100%. However, the absolute values are very low, and the values are almost in the same level. In sieve fractions finer than 0.71mm the difference between the estimated liberation value and the measured one is below 15%.

Table 3. Comparison between measured and estimated liberation values

Sample	Method	+4	+0.71	+0.18	+0.063	-0.063
1	Estimated	0.0	0.0	71.8	83.3	96.5
	Measured	-	0.5	81.0	85.3	90.9
2	Estimated	0.0	14.4	75.6	80.3	96.9
	Measured	-	13.1	87.9	87.5	86.9
3	Estimated	0.0	7.8	79.8	91.2	97.5
	Measured	-	11.9	82.9	85.9	91.6
4	Estimated	0.0	2.5	80.1	89.1	97.4
	Measured	-	1.9	78.6	85.4	95.7
5	Estimated	0.0	0.0	73.8	83.5	97.8
	Measured	-	2.3	76.2	84.9	92.5
6	Estimated	0.0	0.0	71.9	84.2	97.5
	Measured	-	3.2	82.7	86.6	93.1

5 CONCLUSIONS

Based on studied samples the liberation of chromite can be reliably estimated based on its grain size distribution in sized samples. In case of Kemi chromite, the difference between the measured and estimated liberation degree is insignificant.

Since the optical image analysis is already in use in Kemi Mine (Leinonen 1998), this measurement would offer flexible and advantageous method to follow the grinding and the liberation of chromite in different parts of the concentration process.

6 REFERENCES

- Alapienti, T., Kujanpää, J. Lahtinen, J. Papunen, H. 1989. The Kemi stratoform chromitite deposit, northern Finland. *Economic Geology* 84. 1057-1077.
- Chernet, T. Marmo, J. 2003. Direct comparison on mechanical and digital size analyses of Kemi chromitite, Finland. *Minerals Engineering* 16. 1245- 1249.
- Lastra, R., Petruk, W. Wilson, J. 1998: Image analysis techniques and applications to mineral processing. In: Cabri, L. Vaughan, D (Eds.): *Modern Approaches to Ore and Environmental Mineralogy*, vol. 27. Mineralogical Association of Canada, pp.-327-366.
- Leinonen, O. 1998. Use of chromite microstructure image analysis to estimate concentration characteristics in the Kemi chrome ore. *Acta Univ. Oul.* A 305. 114 pages.

Technological Characterization of Ni-Cu-Co Ore from Fortaleza de Minas, MG, Brazil

E.S.Mano & H.Kahn

Department of Mining and Petroleum Engineering, Polytechnic School, University of Sao Paulo, Sao Paulo, Brazil

ABSTRACT: Serra da Fortaleza mine is the unique nickel sulphide mineralization in exploitation in Brazil. Its ore minerals are pentlandite, pyrrhotite, chalcopyrite and some other minor sulphide minerals related to weathering process. The gangue minerals are mainly represented by magnesium silicates, such as talc, serpentine, amphiboles, chlorite, as well as magnetite and quartz. Mineralogical studies were performed considering plant products from three distinct ore blends. The study procedure comprises mineralogical separations followed by chemical and X-ray diffraction analysis of the attained products. Optical and scanning electron microscopy (OM and SEM) analyses were also carried out in order to determine the mineralogical association of the sulphide minerals. The ore samples studied presents 1.1%-1.9% of Ni, 0.21%-0.33% of Cu, and 3.15%-6.07% de S. Pyrrhotite, the main sulphide, usually has some pentlandite associated as small exsolution lamellas. Additionally, the related final tailing samples were studied in more detail focusing the behavior of the remaining nickel in terms of its distribution among the sulphides minerals as well as liberation degree. These studies shows that pentlandite occurs mainly in the fine fractions (<0.020 mm) as liberated particles, while pyrrhotite is more common above 0.149 mm, retained with other sulphides phases or magnetite.

1 INTRODUCTION

Serra da Fortaleza or O'Toole deposit is the sole nickel sulphide mineralization in exploitation in Brazil. It is located near Fortaleza de Minas city, in Minas Gerais State, Brazil.

The nickel is presented mainly as pentlandite with 34% of Ni and secondarily as pyrrhotite which can up to 1.5% of Ni (Angeli et al. 1999); (Oliveira et al. 1998) and (Marchetto 1990). The pentlandite is associated particularly associated with pyrrhotite, chalcopyrite, and magnetite, followed by pyrite. The major gangue minerals are amphibole, talc, serpentine, chlorite, quartz and magnetite.

The mineralized zone is divided in six different sub zones, with three different lithologies. This variability can interfere on the amount of the minerals and their associations on the feed of the concentration plant with significant influences on the ore behavior – concentrate quality and/or Ni recovery.

Mineralogical studies were carried out in the final and intermediated products of the mineral processing plant considering three different ore feeds. The first one was represent by the ore of the mainly body, with 1.88% of Ni (here called D1) and

the second one by the lowest grade ore-zone with 1.14% de Ni (D3 – North orebody extension).

The third one, D2, corresponds to a mixture of the previous ones in the follow proportions: 70% of D1 and 30% D3.

Each one of these samples constituted the feed of the concentration plant in a specific period. Both feed, intermediate products and tailings were subject to mineralogical studies in a way to evaluate the behavior of the Ni sulphides and magnesium silicates in the flotation circuit. More detailed studies were done in the final tailings in order to diagnostic the Ni losses.

2 GEOLOGY

According to Cruz et al. (1986) the ore mineralization is related to the Morro do Níquel unit of the Morro do Ferro greenstone belt. Brenner et al. (1990) divided the Morro do Níquel Unit into three main sequences: upper, mineralized, and lower, as per Figure 1 schematic.

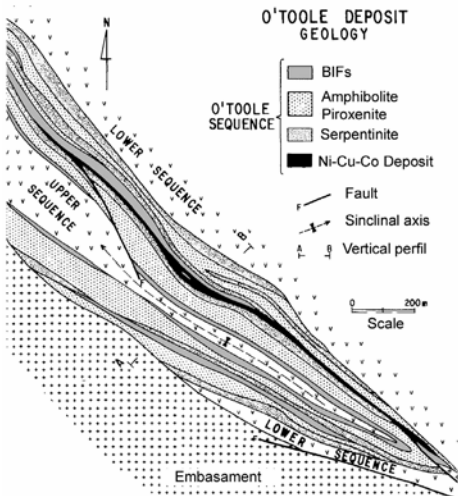


Figure 1 – Schematic cross section of Morro do Niquel unit at the O'Toole deposit (Brenner et al. 1990).

Sulphide minerals, pyrrhotite, pentlandite and chalcopyrite, represents about 25-30% of the ore composition (Brenner et al. 1990; Carvalho et al.1999). Sphalerite (ZnS), galena (PbS), cobaltite (CoAsS) with some Ni, melonite (NiTe₂), gersdorffite (NiAsS) and nicolite (NiAs) are accessories minerals (<1%).

Marchetto (1990) e Oliveira et al. (1998) by EPMA studies verify that pyrrhotite presents an average grade of 0.2-0.5% of Ni, sometimes reaching 1.5%. Pentlandite occurs as subhedral crystals, frequently associated with pyrrhotite as ex-solutions lamellas.

3 METHODOLOGY

Samples were collect by MSF in 7 distinct points of the flotation circuit as shown in Fig. 2.

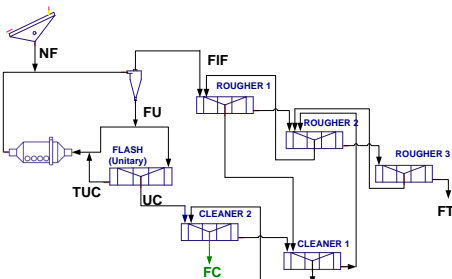
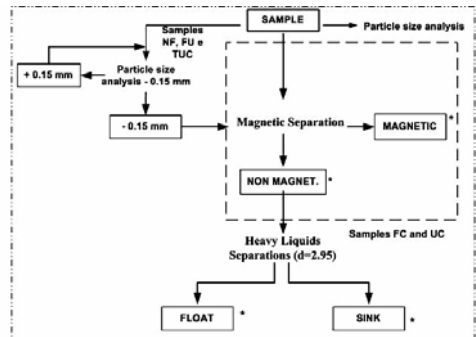


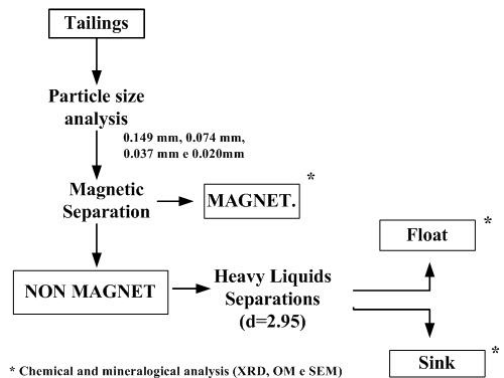
Figure 2 – Scheme of the MSF concentration plant and sampling points for thist study.

Chemical analysis and mineral separations by permanent magnet and heavy liquids (S.G 2.95 g/cm³) were carried out to help mineralogical quantification analyses and evaluation of the liberation degree of the sulphide minerals. The adopted mineral separations scheme is presented in Fig. 3. More detailed analyses were done with final tailings products according to the scheme presented in Figure 4 to assess Ni losses. All the attained products from mineral separations were submitted to chemical analysis, X-ray diffraction, and microscopy studies under optical and scanning electron microscopes.



* Chemical and mineralogical analysis (XRD, OM e SEM) Samples NF, TUC, FU, FT and FIF

Figure 3 – Schematic flow sheet of the sample processing for the mineralogical studies.



* Chemical and mineralogical analysis (XRD, OM e SEM)

Figure 4 – Schematic flow sheet of the sample processing for detailed study of tailing samples.

The mineralogical composition was defined by interaction of chemical and X-ray diffraction data. The optical and scanning electron microscopy established the mineralogical associations and assessed the liberation degree of the sulphide minerals.

4 RESULTS

Table 1 shows mineralogical compositions of the feed samples (NF).

Table 1 - Mineralogical composition of the feed samples

Minerals (%)	D1	D2	D3
Pyrrhotite	12	11	6
Pyrite	< 0.5	< 0.5	< 0.5
Chalcocopyrite	1	1	0,6
Pentlandite + Violarite	4	4	3
Magnetite + ox. Fe	4	4	3
<i>Pentlandite / violarite</i>			
• <i>Pentlandite</i>	4	3	2
• <i>Violarite</i>	0.6	0.6	0.4
Silicates	79	80	88
• Talc	8	10	10
• Serpentine	26	26	22
• Amphibole	24	20	24
• Chlorite/micaceous	7	7	9
• Quartz	9	12	17
• <i>Others silicates</i>	5	6	5

Results show that the amount of the silicates minerals on feeds D1 and D2 are almost identical. The silicates content are higher for feed D3, which presents substantial increment in quartz and lower serpentine content.

Table 2 shows compositions of final concentrates and tailings with weight and Ni recoveries. It is also important to note that the concentrate characteristics imposed by the later metallurgical process are very strict regarding the magnesium silicates (<7 % MgO), fact that limits the recovery of the sulphides minerals for low grade ores.

Table 2 - Concentrates and tailings mineralogical compositions

Minerals (%)	Concentrates			Tailings		
	D1	D2	D3	D1	D2	D3
Pyrrhotite	41	41	39	3	3	3
Pyrite	<1	1	3	<0.5	<0.5	<0.5
Chalcocopyrite	4	4	4	<0.5	<0.5	<0.5
Pentl.+Violarite	15	14	16	1	1	1
Magn + ox. Fe	4	5	3	3	6	3
Silicates	35	35	34	92	90	93
• Talc	3	4	4	6	9	9
• Serpentine	15	15	8	33	29	21
• Amphibole	9	9	13	24	27	25
• Chl./mica.	3	3	4	9	9	8
• Quartz	3	3	4	13	11	23
Weight recov. (%)	21	22	10	79	78	90
Ni recov. (%)	82	81	64	18	19	36

4.1 Occurrence form and mineral associations

Ni sulphide minerals are usually associated – pentlandita locked to Pyrrhotite or as tiny exsolution lamellas - Photo 1 (optical microscopy). Violarite presence is related to later alteration of pyrrhotite (Photo 2).

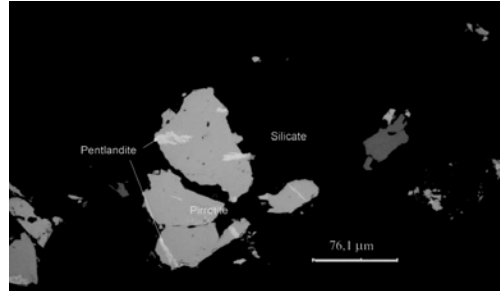


Photo 1 – Feed D1, Magnetic product. Pentlandite lamellas in pyrrhotite, that is associated with silicate.

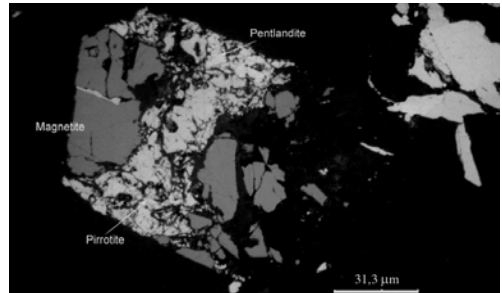


Photo 2 - NF, Magnetic product. Particle of pyrrhotite, magnetite and pentlandite with violarite related to later alteration of pyrrhotite.

4.2 Final tailing characterization

An estimate of the Ni distribution between pentlandite and pyrrhotite indicates that the major Ni losses are related to the pentlandite+violarite content in the tailing samples (Table 3).

Table 3 - Nickel distribution in the minerals of the FT.

Size (mm)	Ni as Pentland.+ Violarite (%)			Ni as Pyrrhotite (%)		
	D1	D2	D3	D1	D2	D3
+0.149	23	33	57	77	67	43
-0.149 +0.074	31	42	62	69	58	38
-0.074 +0.037	42	49	66	58	51	34
-0.037 +0.020	56	86	76	44	14	24
-0.020	94	72	94	6	28	6
<i>Total</i>	<i>66</i>	<i>70</i>	<i>73</i>	<i>34</i>	<i>30</i>	<i>27</i>

Table 4 shows results of sulphides liberation degree analysis estimated under SEM and sulphides distribution among the studied size fractions.

Table 4 – Sulphide liberation degree and sulphide distribution by particle size fraction on the final tailings.

Size (mm)	Liber. degree (%)			Sulph. distribution (%)		
	D1	D2	D3	D1	D2	D3
+0.149	10	10	10	8.80	7.10	3.70
-0.149+0.074	15	20	22	31.1	34.2	26.9
-0.074+0.037	44	35	47	32.9	29.2	31.8
-0.037+0.020	57	70	78	10.8	13.6	14.1
-0.020	96	95	95	16.5	15.9	23.5
<i>Total</i>	<i>42</i>	<i>42</i>	<i>55</i>	<i>100</i>	<i>100</i>	<i>100</i>

The observed decrease of Ni recovery in the tailings fine size fractions is essentially related to the presence of liberated sulphides, mainly pentlandite, not properly collected by the flotation process.

5 CONCLUSIONS

The studies allowed to determine the mineralogical composition of the products related to three different ore feeds at the MSF plant. Besides this, the mineralogical mass balance of the circuit had been established allowing the process engineers to know the behavior of each mineral in the plant.

D1 and D2 ore feeds present a very similar mineralogical composition, while D3 shows a significant decrease in the sulphides content and an increase in quartz and chlorite amounts.

Feed D2 corresponding to a blending of D1 and D3 (0.7:0.3) showed the higher metallurgical recoveries; this behavior can be explained by its mineralogical composition or, in other terms, by the increase the flotation selectivity with reduction of some Mg-silicates that are more critical in the flotation process.

Detailed mineralogical studies in final tailings indicated that Ni losses are mainly associated with pentlandite+violarite, which occur mainly in the fine size fractions as free particles indicating loss of flotation selectivity.

6 REFERENCES

Angeli, N., Carvalho, S.G., Ferrário, A. 1999. Ocorrência de PGE no minério sulfetado da seqüência vulcano-sedimentar de Alpinópolis do Greenstone Belt Morro do Ferro, Minas Gerais. Anais of Simpósio de Geologia do Sudeste 6, 118.

Brenner, T.L., Teixeira, N.A., Oliveira, J.A.L., Franke, N.D and Thompson, J.F.H. 1990. The O'Toole nickel deposit, Morro do Ferro Greenstone Belt, Brazil. Economic Geology, Lancaster, 85, 904-920.

Carvalho, S.G., Antonio, M.C., Brenner, T.L. 1999. A atuação

de processos tectono-metamórficos e seus efeitos modificadores na jazida de sulfeto maciço de Fortaleza de Minas: implicações na tipologia, teores e quimismo do minério. Anais of Congresso de Geoquímica dos Países de Língua Portuguesa. Porto Seguro: SBGQ, 7, 246-248.

Cruz, F.F., Brenner, T.L., Moreira, A.F.S., Cunha, C.A.B.R., Gallo, C.B.M., Franke, N.D. & Pimentel, R.C. 1986. Jazida de Ni-Cu-Co de Fortaleza de Minas, Minas Gerais. BRASIL. Ministério das Minas e Energia. Departamento Nacional de Produção Mineral. Principais depósitos minerais do Brasil. Brasília: DNPM, 2,275-306.

Marchetto, C.M.L. 1990. Platinum-group minerals in the O'Toole (Ni-Cu-Co) deposit, Brazil. Economic Geology, Lancaster, 85, 921-927.

Oliveira, S.M.B., Ibernson, R.A.L., Blot, A. & Magat P. 1998. Mineralogia, geoquímica e origem dos gossans desenvolvidos sobre o minério sulfetado de Ni-Cu do depósito de O'toole, Minas Gerais, Brasil. Revista Brasileira de Geociências, São Paulo, 28, 295-300.

Characterization and Production of Novel Ceramic Roof Tiles Obtained Using Slate Powder Waste

H.S.Mansur & A.A.P.Mansur

Department of Metallurgical & Materials Engineering, Engineering School, Federal University of Minas Gerais, Minas Gerais, Brazil

ABSTRACT: The growing world population in industrialized countries is resulting in an increasing consumption of raw materials and thus a flood of waste. The recycling of materials and waste treatment techniques have drawn the attention from all different areas including industries, technology centers and universities. In the present work we have developed a process using slate powder waste to produce ceramic pieces for roofing. The process was based on the partially substitution of the clay by fine residue of slate rocks. The thermal treatment was conducted from 50°C to 1050°C, where drying, firing and sintering of the mixtures have occurred. X-ray diffraction (XRD) techniques were used for crystallographic evaluation of the samples. Also, Scanning Electron Microscopy (SEM) analysis was carried out for microstructure characterization. The characterization included chemical composition of main elements by Electron Dispersive X-ray Spectroscopy (EDX). The results have indicated the presence of many mineral phases such as quartz, muscovite, clinocllore, hematite, albite, calcite and rutile. These results confirmed the presence of major slate minerals constituents in clays. These results, associated with the chemical analysis and SEM microstructure of ceramic pieces, gave strong evidence of the successfully substituted clay by slate powder waste. Therefore, the ceramic industry is able to reduce the environmental impact caused by slate powder, which can be used as raw material by replacing clay in roof tile production.

1 INTRODUCTION

In recent decades, the growing consumption and the consequent increasing of industrial production has led to a fast decrease of the available natural resources (raw materials or energy resources). On the other hand, a high volume of production rejects and sub-products is generated.

In order to reduce the extraction of clays natural deposits and the flood of residues, alternative ways to reuse several types of waste materials have been attempted, including the incorporation in clay-based ceramic products.

The mining of slate rocks generates 80 wt% of wastes being a quarter of them as a mud. The mud is originated from rock cutting and polishing and it is composed basically of crushed rock, water and lubricants. After a "wash stage" this residue could be used as alternative material.

In the present work the objective is to recover powder wastes from slate rock industry to produce ceramic roof tiles.

2 EXPERIMENTAL PROCEDURE

In order to assess the partially substitution of the clay by fine residue of slate rock, we first evaluated the chemical, mineralogical and morphological features of representative slate samples. The slate powder was supplied by a mining plant located in the city of Pompéu, Minas Gerais, Brazil.

Chemical analysis was performed by aqueous titration route using a powder sample. Mineralogical assays were carried out by X-ray Diffraction (XRD) using PHILIPS PW 1710 diffractometer ($\text{CuK}\alpha = 1,54 \text{ \AA}$ radiation). Mineral phases were identified by the search-match method using JCPDS database. Scanning electron photomicrographs were obtained in order to evaluate morphological aspects using a JEOL JSM 5410 microscope. Prior to SEM, the samples were coated with a thin layer of gold by sputtering to make the specimen conductive.

Ceramic pieces were manufactured by slip casting ceramic process. Mixtures of slate powder waste and kaolin were prepared in a proportion of 90 wt% slate powder and 10 wt% kaolin with 1.0 % dispersant agent (ammonium polyacrilate of Chemical Industries Arujá Ltda.) and 2.0 % binder (polyvinyl alcohol of VETEC) related to total water volume.

Kaolin was chosen because its extensive application in ceramic industry. Its proportion in ceramic products ranges from 5% to 50%, depending on the desired final properties. In this case, it was used a kaolin powder from Capim river area, Pará, Brazil.

The thermal treatment of ceramic pieces was conducted from 50°C to 1050°C where drying, firing and sintering of the mixtures have occurred.

A mineralogical analysis of the fired samples was carried out by XRD. As complementary techniques allowing the identification of structural features, fractured surfaces of ceramic samples have been studied by SEM (Scanning Electron Microscopy). The characterization procedure included evaluation of chemical composition of main elements by Electron Dispersive Spectroscopy (EDX).

3 RESULTS AND DISCUSSIONS

3.1 Slate Powder Microstructural Characterization

A typical SEM photomicrograph of slate powder particles is showed in Figure 1. These particles have presented irregular size and shape. We could see the presence of lamellar structure associated with cleavage, a feature that is characteristic of this kind of rock, indicated in the figure by an arrow (Mansur & Souza 2004).

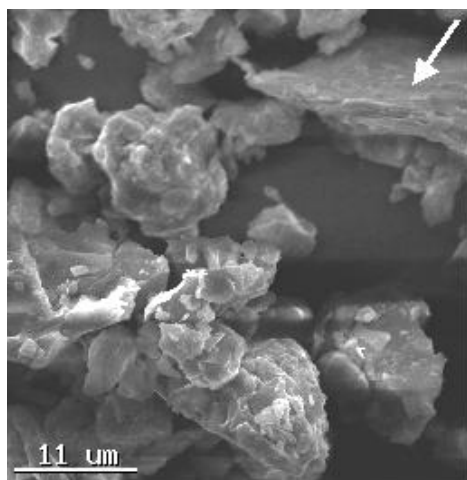


Figure 1. XRD spectrum of slate powder sample ($\times 2000$).

The chemical analysis of slate powder is presented in Table 1. The major components are silica, alumina and iron oxide.

A representative XRD spectrum for the slate sample is showed in Figure 2. The results have

revealed the presence of albite, clinocllore, calcite, hematite, muscovite and quartz as crystalline phases.

Table 1. Chemical composition of slate powder (weight %) in oxide equivalent (average of $n = 4 \pm$ standard deviation).

Oxide Equivalent (wt %)	Slate Waste Powder
SiO ₂	63.8 \pm 1.4
Al ₂ O ₃	16.5 \pm 0.5
Fe ₂ O ₃	7.5 \pm 0.5
Na ₂ O	1.3 \pm 0.0
K ₂ O	1.6 \pm 0.2
MgO	2.8 \pm 0.4
CaO	1.7 \pm 0.3
TiO ₂	0.9 \pm 0.1
PPC	3.4 \pm 1.3

Such mineralogical composition is similar to that usually found in the literature (Moore & Reynolds 1997).

Also, clays constituents found in slate powder samples, such as chlorite and mica, are those usually observed in ceramic raw materials (SACMI 1995).

The slate sample high amount of quartz would be important to guarantee a low shrinkage during firing process. Quartz also allows the outgassing of organic materials, CO₂ release during calcite decomposition and the removal of water during the drying of the ceramic piece (SACMI 1995).

Calcite will provide a neomineralization agent after its decomposition (CaO). This oxide reacts with quartz and other minerals from destroyed clays producing calcium-silicates phases after firing (Jordán et al. 2001).

The chemical analysis coupled to XRD results indicated a high amount of fluxing agents (Na₂O + K₂O + Fe₂O₃ = 10,4%) in the crystalline form of feldspar, hematite and muscovite. Although the actual eutectics in such complex systems are not well known and they depend on mica breakdown, a prediction can be derived from the consideration of less complex systems. In this case, we could expect an eutectic melting temperature from 900°C to 985°C. This temperature range is similar to the usually used in the production of roof tiles. The possibility of occurrence of sinterization in presence of liquid is interesting in this kind of product in which impermeability is an important property (Segnit & Anderson 1972).

3.2 Ceramic Pieces Microstructural Characterization

The pieces fired at 1000°C were observed at SEM coupled to EDX microprobe.

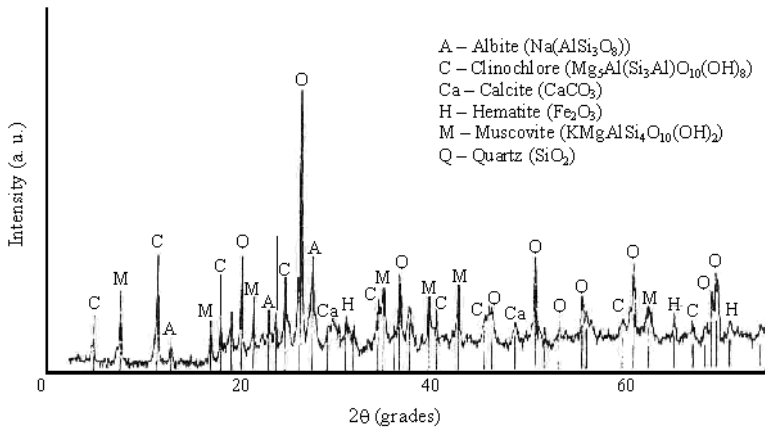


Figure 2: XRD spectrum of slate powder sample.

The EDX results have permitted us to compare the chemical composition of the mixture under evaluation with the observed in commercial products (Mansur 2002). In Figure 3, we placed the chemical data in a ternary diagram (SiO_2 - Al_2O_3 -Other oxides) and we could verify that the studied mixture was at the same composition area of other ceramic tiles.

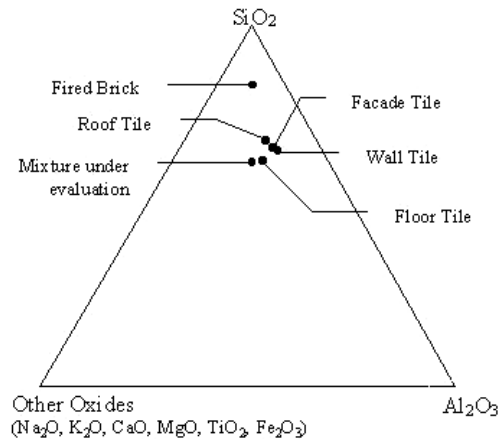


Figure 3. Ternary diagram with several compositions of ceramic products and the mixture under evaluation.

In Figure 4, we could observe the occurrence of vitrification. Quartz grains (indicated by Q) and other phases were immersed in the glassy matrix, which was identified by its smooth texture.

Figure 5 represents a typical X-ray result of specimens fired at 1000°C . The samples revealed the presence of albite, gehlenite, muscovite, mullite, quartz and a spinel phase. These phases are usually found in ceramic materials after sinterization (Mansur 2002).

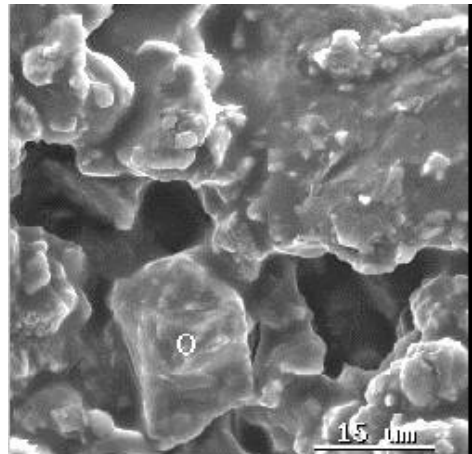


Figure 4. SEM photomicrograph of ceramic piece after firing at 1000°C ($\times 2000$).

Albite was also observed in the raw material. Most probably, firing conditions were not sufficient for the complete melting of feldspar (Abadir et al. 2002).

Formation of gehlenite was expected considering the presence of calcite as raw material. Gehlenite is formed when a CaO nuclei reacts with the Si and Al of the destroyed clay (Jordán et al. 2001).

The remaining mica pattern was probably due to the detrital muscovite flakes. These flakes were also observed by SEM images and they persist in some ceramic systems after the mica breakdown until temperatures up to 1000°C (Segnit & Anderson 1972).

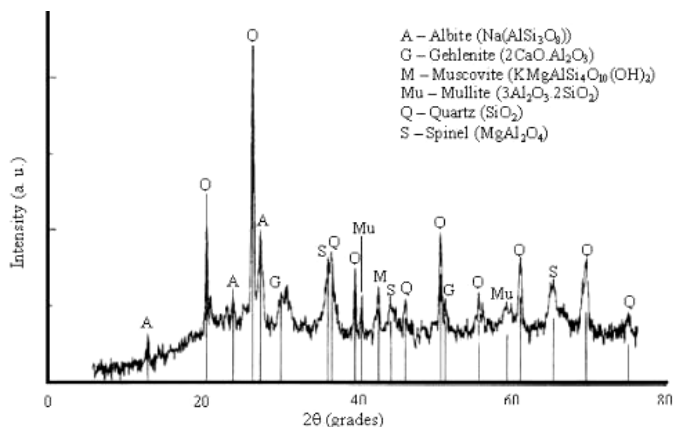


Figure 5: XRD spectrum of ceramic piece.

Neomineralization of mullite was a consequence of the amounts of quartz and alumina (binary diagram) and due to the presence of kaolin. Kaolin disappearance usually is followed by a mullite-type phase formation. Based on the sample firing temperature, this mullite should be poorly crystallized (Brindley & Nakahira 1958, Segnit & Anderson 1972). Mullite phase was also identified by SEM/EDX, as could be seen in Figure 6.

A spinel phase was also observed in the XRD spectra. The formation of spinel phase is verified in ceramic systems which are rich in chlorite and illite after their decomposition (Jordán et al. 1999).

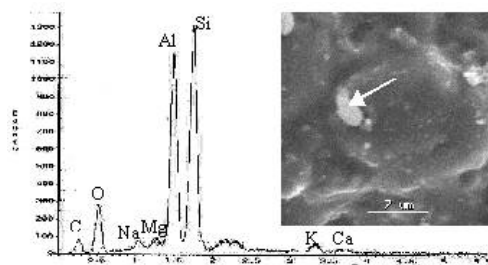


Figure 6. Scanning electron microscopy and EDX spectrum of a particle (arrow) ($\times 3500$).

4 CONCLUSIONS

The results gave strong evidence of the successfully substituted clay by slate powder waste.

Therefore, the ceramic industry is able to minimize the environmental impact caused by slate

mining plants, replacing clays by slate powder as raw materials on roof tile production.

Complementary studies are necessary in order to evaluated physical and mechanical properties.

5 REFERENCES

- Abadir, M. F. et al. 2002. Preparation of porcelain tiles from Egyptian raw materials. *Ceram. Int.*, 28: 303-310.
- Brindley, G. W. & Nakahira, M. 1958. A new concept of the transformation sequence of kaolinite to mullite. *Nature*, 181: 1333-1334.
- Jordán, M. M. et al. 1999. Firing transformations of cretaceous clays used in the manufacturing of ceramic tiles. *Appl. Clay Sci.*, 14: 225-234.
- Jordán, M. F. et al. 2001. Firing transformations of Tertiary clays used in the manufacturing of ceramic tile bodies. *Appl. Clay Sci.*, 20: 87-95.
- Mansur, A. A. P. 2002. Avaliação da Expansão por Umidade em Placas Cerâmicas de Revestimento. Minas Gerais: MSc Thesis.
- Mansur, H. S. & Souza, L. P. 2004. Production and characterization of ceramic pieces obtained by slip casting using slate powder wastes. *J. Mat. Proces. Tech.*, 145:14-20.
- Moore, M. M. & Reynolds, R.C. 1997. X-ray Diffraction and the Identification and Analysis of Clay Minerals. Oxford: Oxford University Press. (2nd).
- SACMI. 1995. Tecnologia de la fabricación de azulejos. Valencia: Asociacion Tecnicos Ceramicos.
- Segnit, E. R. & Anderson C.A. 1972. Scanning electron microscopy of fired illite. *Trans. Brit. Ceram. Soc.*, 71 (3):85-88.

6 ACKNOWLEDGEMENTS

Expressed thanks to CNPq (Brazilian Council Research) for supporting this work.

Gold Reprecipitation in the São Bento Mine Process

M.A.Márquez

Applied Mineralogy Group, Faculty of Mines, Materials Engineering School, National University of Colombia, Medellín, Colombia

J.C.Gaspar

Geosciences Institute, University of Brasilia, Brasilia, Brazil

ABSTRACT: A mineralogical characterization of samples from the alkalization stage, after the sulfide oxidation pretreatment (bacterial and pressure oxidation) from the São Bento gold mine (Brazil). It had been observed gold-rich grains occurring as aggregates, composed of gold crystals (average diameter $\sim 10\mu\text{m}$), as discontinuous layers, in a Si, Fe, Au, and As matrix. Their typical deposition textures are banded, concentric, and irregular. The sulfide oxidation can lead to the formation of thiosulfates and other sulphur compounds that can bring appropriate conditions to forming sulphur complexes, resulting in dissolution of gold during the oxidation pretreatment. The observed mineral phases, textures, and mineral chemistry indicate that the gold-rich grains are the product of precipitation in the alkalization stage of material that entered solution in the bacterial and pressure oxidation pretreatment. Mineralogical information is basic to understand the mechanisms of initial dissolution of gold and its later precipitation because this gold is not recovered in subsequent stages, causing important recovery losses.

1 INTRODUCTION

The São Bento deposit (Santa Bárbara, MG) occurs in the middle portion of the Quadrilátero Ferrífero (lato sensu), hosted by the São Bento iron formation. This is a BIF composed of fine layers of oxide, carbonate, silicate, and sulfide facies. Sulfides usually form veins of variable sizes that crosscut the BIF layering with very small angles (Ladeira 1980). The most important minerals in the deposit are: arsenopyrite, pyrrhotite, chalcopyrite, sphalerite, galena, electrum, magnetite, ilmenite, siderite, ankerite, calcite, quartz, chlorite, stilpnomelane, and muscovite (Márquez 1997). Gold crystals occur in many different forms: a) small inclusions in arsenopyrite and pyrite, sometimes associated with pyrrhotite and gangue minerals; b) large inclusions in pyrrhotite, usually in contact with arsenopyrite; c) less frequently, in mineral interfaces or fractures, associated with sulfides or not; d) rarely included in sphalerite or gangue minerals; e) rarely filling cavities in arsenopyrite associated with galena, sphalerite, chalcopyrite, and pyrrhotite (Márquez 1995). Electrum contains from 20 to 50 at % Ag. "Invisible" gold was analyzed by EPMA, SIMS, and SXRF mainly in arsenopyrite (Steele et al. 2000). It was not possible to determine whether invisible gold

occurs as structurally-bonded atoms or as extremely small inclusions.

Due to the refractory characteristic of gold, the São Bento process consists of a two step oxidation pretreatment composed of a combination of bacterial and pressure oxidation.

2 MATERIALS AND METHODS

A mineralogical characterization of the São Bento beneficiation process was performed using samples collected from the alkalization system, proceeded by a sieving step, prior cyanidation of gold. In this way, polished sections were analyzed in polarized light optical microscopy, scanning electron microscopy (SEM) and electron probe microanalyzer (EPMA).

3 RESULTS

Gold-containing grains are usually millimeter to sub-millimeter in size and vary in habit from anhedral to spherical. Their external surface textures are complex including features as flat pores, banding and films. These last are composed of quartz, iron

hydroxides, sulfides, etc., in a scorodite matrix (Figure 1).

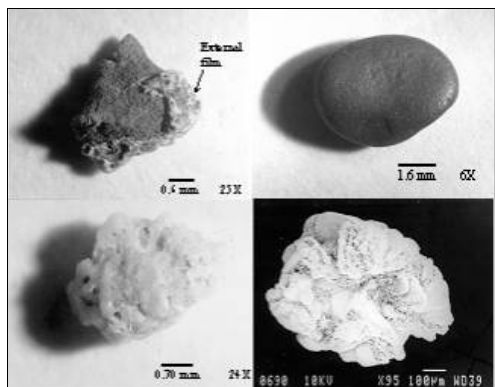


Figure 1. Upper left, scorodite grain with a thick film; upper right, rounded scorodite; lower left, porous and irregular quartz grain; lower right, gypsum grain.

The grains are aggregates composed of reddish gold crystals (average diameter $\sim 10\mu\text{m}$), forming discontinuous layers in a Si, Fe, Au, and As matrix. Scorodite is always associated with gold, either as bands, films or irregular masses (Fig. 2). Typical deposition textures are present, which may be banded, concentric, or irregular (Figs. 2- 4).

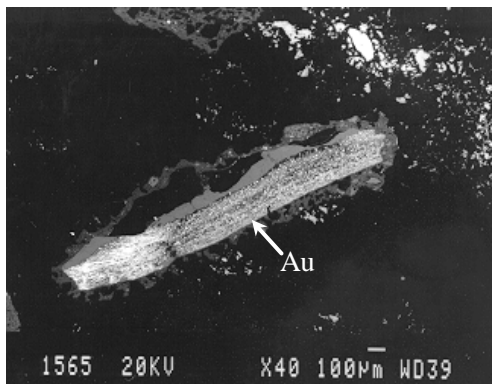


Figure 2. SEM/BSE image of a gold-rich grain showing banded texture composed of gold grains in a scorodite matrix. It is covered by an irregular film in the upper border.

Associated with the gold-rich grains are: a) prismatic gypsum crystals, sometimes showing radial porous habit, b) spherical sulphur crystals, and c) irregular porous quartz grains (Fig. 1).

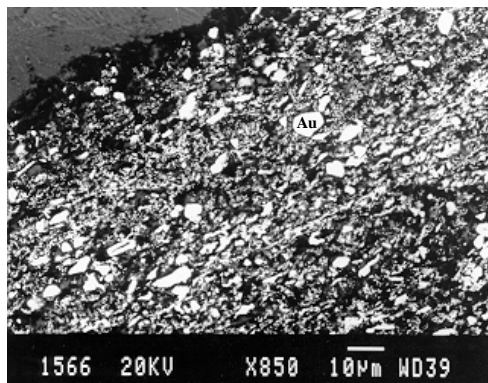


Figure 3. SEM/BSE image zoom of Figure 2, showing gold particles in a scorodite matrix.

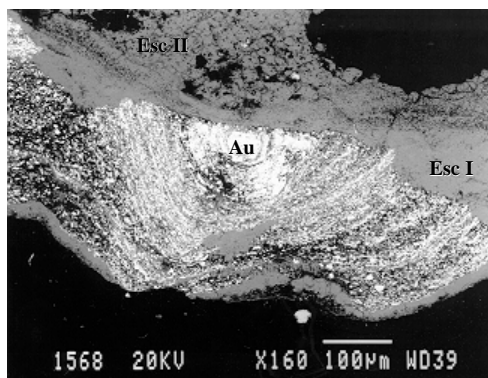


Figure 4. Concentric texture in a gold-rich grain, recovered by two stages of scorodite deposition.

4 DISCUSSION AND CONCLUSIONS

The sulfide oxidation in the São Bento ore pretreatment can lead to the formation of thiosulfates in a great range of pH conditions, which need to be controlled because they may form complexes with gold, resulting in gold dissolution during the oxidation processes (Marsden & House 1992). That is evident, according to Marsden & House (1992), in some oxidation systems under pressure where small amounts of gold are detected in effluents, without another complexant agent. Accordingly, it is necessary to control the concentration of thiosulfates in the oxidation systems to prevent a possible gold loss.

This type of gold dissolution can occur in an ample range of pH (Zipperian et al. 1988), where the dissolution rate depends on some factors as temperature, exposition time, thiosulfate concentration and dissolved oxygen (Abbruzzese et

al. 1995; Marsden & House 1992; Zipperian et al. 1988). It has been demonstrated also that the gold leaching rate is increased in the presence of copper sulphate and ammonia solutions. According to Williams (1990), Fe^{+3} can act as oxidant in the presence of thiosulfate at room temperature, explaining the transport and subsequent enrichment observed in supergenic environments.

In the São Bento mine, gold-rich grains precipitated apparently due to an increase in the proportion of bio oxidized material relative to the flotation concentrate in the input of the autoclave. This fact would result in an increased pyrite-relative proportion in the system, since most of pirrhotite is oxidized during the bacterial oxidation (Márquez 1999). Thus, an increase in the proportion of bio oxidized material would increase the relative amount of elementary sulfur, which would act as precursor to the sulphate generation in the solution, acting, at the pressure oxidation conditions (180-200°C), as a gold leaching.

The mineral phases found, textures and their mineral chemistry indicate that gold-rich grains are more likely a product of gold precipitation due to the alkalinization of the system, previously solubilized in the bacterial oxidation and the pressure oxidation systems.

Mineralogical information is basic to understand the mechanisms of initial dissolution of gold and its later precipitation because this gold is discarded in subsequent stages, causing important recovery losses.

5 REFERENCES

- Abbruzzese, C.; Fornari, P.; Massidda, F.; Vlegiò & Ubaldini, S. 1995. *Thiosulphate leaching for gold hydrometallurgy*. Hydrometallurgy, vol. 39, pp. 265-276.
- Ladeira, E.A. *Gênese do ouro na mina de Morro Velho e no distrito de Nova Lima*, Minas Gerais, Brasil. XXXI Congresso Brasileiro de Geologia, Camboriú. Bol. 2, pp. 371.
- Márquez-Godoy, M.A. 1995. *Caracterização mineralógica do minério, concentrado e rejeito da flotação da mina São Bento (MG)*. Tese de Mestrado. Instituto de Geociências, Universidade de Brasília, Brasília D.F. 237 p.
- Márquez-Godoy, M.A. 1999. *Mineralogia dos produtos de oxidação sob pressão e bacteriana do minério de ouro na mina São Bento, MG*. Tese de Doutorado. Instituto de Geociências, Universidade de Brasília, Brasília D.F. 271 p.
- Marsden, J. & House, I. 1992. *The chemistry of gold extraction*. Ellis Horwood, New York. 597 p.
- Williams, P.A. 1990. *Oxide zone geochemistry*. Ellis Horwood Series in Inorganic Chemistry (J.Burguess, ed.). Ellis Horwood, New York. 286 p.
- Zipperian, D. Raghavan, S. & Wilson, J.P. 1988. *Gold and silver extraction by ammoniacal thiosulfate leaching from a rhyolite ore*. Hydrometallurgy, vol 19, pp. 361.375.

Assessment of Uncertainties in Modal Analysis and Liberation Measurements by Synchrotron-based X-Ray Microtomography

D.Paktunc, D.Smith, R.Lastra, A.Pratt

CANMET Mining and Mineral Sciences Laboratories, 555 Booth Street, Ottawa, Ontario, K1A 0G1, Canada

ABSTRACT: Measurement of mineral modes and liberation in ground ore and rock samples are made on flat surfaces by image analysis. The amount of fully liberated particles is always overestimated with such two-dimensional measurements necessitating stereological corrections. In addition, there are uncertainties arising from the sectioning and measurement of mineral quantities. High intensity X-ray beams from a synchrotron make microtomographic imaging of solid particles possible at a resolution and sensitivity capable of resolving compositional differences between certain particles. Several sets of binary particles made of glass and epoxy, and lead borate and glass were imaged using monochromatic X-rays ranging from 15.5 to 30 keV. The samples were rotated about a vertical axis at 0.25° or 0.5° intervals to collect 720 or 360 high-resolution images. X-ray images obtained at each interval are used to reconstruct a 3-D image of the sample. Following data processing, up to 500 horizontal slices and numerous vertical slices were made from the 3-D data set. Individual slices were processed by an image analyzer to determine modal proportions and the degree of liberation. Preliminary evaluation of the data indicates the likelihood of significant measurement errors arising from random sectioning of samples. The study demonstrates that the proportion of fully liberated particles is overestimated. The variation in the measurements will be used to develop correction factors for determining the apparent mineral liberation.

1 INTRODUCTION

Routine measurements of the relative quantities of minerals and the degree of liberation of an ore mineral in ground samples have several sources of error. In essence, the errors arise from the measurement of three dimensional particle properties in 2-D on a polished section surface. Random cuts from multi-phase particles can result in single-phase particles; therefore, the amount of fully liberated particles is always over-estimated. There are numerous correction methods available; however, there does not appear to be a satisfactory methodology. Lin et al. (1999) and Latti & Adair (2001) provide a summary and a comparative review of the proposed correction techniques.

High intensity X-ray beams from a synchrotron source make microtomographic imaging of small particles in 3-D possible at a resolution and sensitivity capable of resolving compositional differences between certain particle types. With synchrotron microtomography, it is possible to produce 3-D images of the entire depth of solid objects at micrometre-scale resolution and evaluate errors arising from the two-dimensional measurements. This paper presents an evaluation of the sources and magnitudes of uncertainties arising

from the measurement of quantitative mineralogical data on two-dimensional surfaces by utilizing the synchrotron technology. In addition, this paper aims to introduce a new and potentially powerful technique in mineral processing.

2 EXPERIMENTAL

Synthetic particles that are made of binary mixtures of glass and epoxy as described by Lin & Finch (2000) were used in the experiments. Eight samples containing uniform ranges of particle compositions were analyzed. Particle compositions included the following glass proportions in volume %: 15-25, 25-35, 35-45, 45-55, 55-65, 65-75, 75-85 and 85-95. Only the results from the sample where each particle contained 15-25 % glass are presented in this paper.

In this study, the degree of liberation is simply defined as the particle composition. It is synonymous with the volumetric abundance of a mineral "locked" in a particle. As such, it is independent of the terminology used in mineral processing operations. For practical reasons, the cleaning operations refer to particle composition of 90 % as liberated, whereas it is 80 % for the rougher operations and 70 % for the scavenger operations.

To avoid confusion, these are referred to as the degree of liberation in this paper.

Experiments were performed at the GSE-CARS bending magnet beamline on sector 13 of the Advanced Photon Source (APS) at Argonne National Laboratory. The data were collected using monochromatic X-rays at 15.5 to 30 keV energy range. The radiographs were obtained by the use of a 50 mm single-crystal YAG scintillator and a high-speed 12-bit CCD camera with 1317×1035 pixels. Various objectives of up to 5x magnification were used to obtain 4 to 7 mm horizontal fields of view with resolutions ranging from approximately 7×7 μm to 13×13 μm per pixel. The camera was placed downstream of the sample at a 90° angle via a 45° mirror from the YAG scintillator (Figure 1). The samples were placed vertically and rotated counter-clockwise at 0.25° or 0.5° intervals from 0 to 180°. Exposure time at each interval was 8 to 10 seconds. Microtomography images were processed through a series of steps for the construction of volume files. The details of experimental set-up and samples are provided in Paktunc et al. (2001).

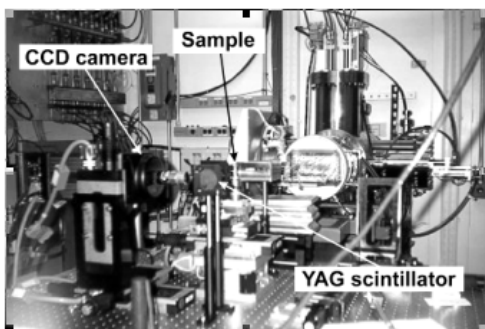


Figure 1: Photograph showing the experimental setup.

3 RESULTS

The perspective images shown in Figure 2 represent individual slices taken at 6 and 24 μm intervals. It is possible to follow the changes in the proportion of a phase within a single particle by examining the adjacent slices. For instance, particles that appear as free in an individual slice, are in fact binary particles in adjacent slices. The figure demonstrated that the proportion of fully liberated particles is always overestimated.

Such individual slices were analyzed with an image analyzer (KS400, Zeiss) to determine the modal proportion of glass and its liberation properties. Figure 3 illustrates the magnitude of deviations in average liberation and particle size

across the sample. These plots represent 335 slices and allow an assessment of the ultimate variations in the degree of liberation and particle size. On average, each slice contains 67 particles. The measured degree of liberation at the top of the sample holder is within the nominal liberation of 15-25 % of this sample. Interestingly, there is an overall trend of increasing liberation from the top to the bottom of the sample. This appears to be due to gravitational segregation of denser particles to the bottom of the sample holder. The glass has higher density (i.e. 2.47 g/cm³) than epoxy (i.e. 1.195 g/cm³); therefore, particles with higher proportions of glass (i.e. near 25 %) would be denser and settle to the bottom under the influence of gravity. The bulk particle density (ρ_{bulk}) at the top is calculated to be 1.45 g/cm³ as per the equation (1):

$$\rho_{bulk} = \sum_{i=1}^n \rho_i \times X_i \quad (1)$$

where X is the fraction of phase i and n is the number of phases. In contrast, the bulk particle density at the bottom is calculated to be 1.51 g/cm³. Accordingly, a density difference of 0.064 g/cm³ is enough to cause gravitational settling. More importantly, this plot clearly shows that significant variation in the degree of liberation could result from random sectioning. For instance, sectioning near the 900 μm distance from the top would indicate a liberation of about 35 % (Fig. 3).

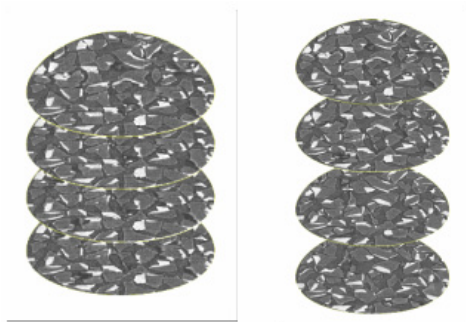


Figure 2: Slices taken at 6 μm (left) and 24 μm (right) intervals from the same volume file. White phase represents glass whereas dark grey phase is epoxy portion of the particles. Black areas between the particles represent voids filled by air.

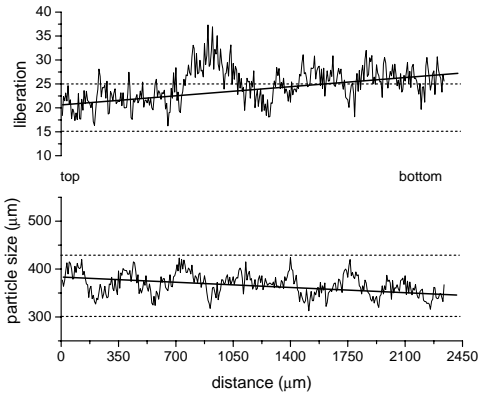


Figure 3: Variation in the degree of average liberation and particle size with distance (top to bottom) of the sample as determined by 2-D measurements on 335 slices. Dotted horizontal lines mark the nominal ranges for liberation and particle size.

Variation in the average particle size is well within the nominal particle size of 300 to 425 μm (Figure 3). Average particle size variation across the height of the sample indicates an overall trend of decreasing particle size from the top to the bottom of the sample holder. This is compatible with the observed increase in the degree of liberation. The smaller the particle size, the greater is the degree of liberation for a homogeneously distributed phase.

Variation in the liberation and particle size measurements within individual slices is shown in Figure 4. Each slice is represented by an average and error bars at 99 % confidence limits. The confidence limit (CL) is defined as:

$$CL = \pm \frac{s \times t}{\sqrt{n-1}} \quad (2)$$

where s is the standard deviation from the mean value, n is the number of particles, and t is the student-t value associated with 99 % confidence level at $n-1$ degrees of freedom. The bulk average from all 335 slices incorporating approximately 22,500 particles is represented with the diamond symbol in the centre and its error bars at 99 % confidence limit. The bulk average particle size is $366 \pm 47 \mu\text{m}$ which is within the nominal particle size range. The bulk average degree of liberation is $24.8 \pm 0.5 \%$ and coincides with the upper limit of the nominal liberation. The average liberation and its confidence limit from measurements of individual slices are 24.8 and 9.3 %, respectively. This error corresponds to 37.5 % of the measured values and is high compared to the nominal value and the measured average liberation of $24.8 \pm 0.5 \%$. This is in part due to the binary nature of the particles and

the rather narrow liberation range of the samples studied. With the consideration of the stereological bias concept of Spencer & Sutherland (2000), the high degree of measurement uncertainty reported in this study should be regarded as the maximum. According to Latti & Adair (2000), the stereological error may be insignificant for multiphase natural ore samples. Latti & Adair's (2000) cumulative liberation graphs for three silicate minerals and ilmenite appear to indicate that their 2-D measurements are representative of the true 3-D distribution of the minerals. The information provided, however, is not adequate to make an independent assessment of their findings. In addition, 50 to 80 % the mineral particles occur in the 50 % liberation class for all the minerals. This means that their findings have limited applicability for concentrate samples where the degree of liberation would be expected to be higher. The results of this study indicate that significant errors in 2-D liberation measurements are possible. Errors would be greater where the total number of ore mineral particles is low (i.e. several hundred). In summary, evaluation of routine liberation data based on single sections and samples possessing rather narrow liberation ranges should take into account of the errors presented in this study.

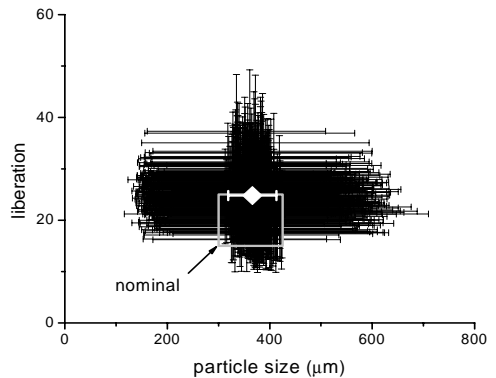


Figure 4: Variation of liberation vs. particle size in 335 individual slices. Error bars are at 99 % confidence limit. Nominal liberation and particle size is indicated by the rectangle. The mean and standard deviation of all the particles in the volume file is indicated by the white diamond symbol in the centre and error bars. The error bar of the bulk liberation is too small to be visible at this scale.

The other samples representing liberations of 25-35, 35-45, 45-55, 55-65, 65-75, 75-85 % glass are being analyzed in a similar manner. The results from these sets will provide a range of empirical errors resulting from routine liberation measurements of various compositions on 2D surfaces.

4 CONCLUSIONS

Two-dimensional measurements overestimate the proportion of fully liberated particles. The magnitude of variation resulting from measurements of liberation on 335 sections provides a statistical basis for evaluating routine liberation data. The average liberation from measurements of individual slices is 24.8 ± 9.3 %. This error which corresponds to 37.5 % of the measured values is very high in comparison to the nominal value and the measured average liberation of 24.8 ± 0.5 %. The magnitude of this error should be considered as an extreme, since it is based on binary particles with a narrow liberation range. Nevertheless, an error of this magnitude must be taken into consideration in the evaluation of routine liberation data based on single sections. Similarly, particle size measurements relying on rather limited number of particles are prone to significant errors. Analysis of individual slices from other samples will provide additional constraints, which may arise from compositional differences. The results of this study can be used to quantify possible errors in modal and liberation measurements for a range of compositions. It will be possible to derive a correction function by fitting the variability to the lowest liberation to determine a representative apparent mineral liberation. The correction functions can then be used as guides in routine liberation measurement.

5 ACKNOWLEDGEMENTS

Use of the APS was supported by the USDOE, Office of Science, Office of Basic Energy Sciences, under contract No. W-31-109-Eng-38. Technical help of Dr. Mark Rivers of the University of Chicago at APS-GSECARS is acknowledged. GSECARS is supported by the NSF – Earth Sciences, DOE - Geosciences, W.M. Keck Foundation and the USDA. Review of the paper by Glenn Poirier is acknowledged.

6 REFERENCES

- Latti, D. and Adair, B.J.I. (2001) An assessment of stereological adjustment procedures. *Minerals Engineering*, 14, 1579-1587.
- Lin, D. and Finch, J.A. (2000) A Standard Material for Stereological Correction. *Canadian Metallurgical Quarterly*, 39, 121-128.
- Lin, D., Finch, J.A. and Lastra, R. (1999) Comparison of Stereological Correction Procedures for Liberation Measurements by Use of a Standard Material. *Transactions of the Institution of Mining and Metallurgy*, (Sect. C), 108, 127-137.
- Paktunc, A.D., Rivers, M. and Lastra, R. (2001) Synchrotron-based 3-D microtomographic imaging of synthetic particles

for stereological corrections of liberation measurements and modal analysis. In: *Interactions in Mineral Processing*, COM 2001 (Eds., J.A. Finch, S.R. Rao, and L Huang) Metallurgical Society of CIM, Montreal, Canada, 459-472.

Spencer, S. and Sutherland, D. (2000) Stereological correction of mineral liberation grade distributions estimated by single sectioning of particles. *Image Analysis Stereology*, 19, 175-182.

Coal and Clay Flotation Using Dodecyltrimethylammonium Bromide (C₁₂TAB) and Sodium Dodecylsulfate (SDS)

F.G.Penha, M.P. de Oliveira, J.G. de Araújo, J.B. de Farias

Department of Analytical and Inorganic Chemistry, Chemistry and Geosciences Institute, University Federal of Pelotas, Pelotas, Brazil

N.A.Debacher

Department of Chemistry, University Federal of Santa Catarina, Florianópolis, Santa Catarina, Brazil

ABSTRACT: Brazil has its coal reserves located in the southern states. Coal and clay fines appear together in nature, within layers of coal. Flotation is the important technique used for fine coal particles processing. The surfactants are used in flotation with the purpose of changing the surface wettability properties of minerals. In this work the effects of cationic surfactant *dodecyltrimethylammonium bromide* (C₁₂TAB) and anionic surfactant *sodium dodecylsulfate* (SDS) were evaluated for the flotation of clay, coal and coal/clay mixture. Under pH = 5,00 C₁₂TAB was more efficient than SDS for clay flotation. These results indicated that the surfactant electrostatic interaction with the clay surface is dominant in the adsorption process. However, in dilute solutions both surfactants were depressants in the coal flotation, probably due to hydrophobic interaction of the surfactant with the coal surface. The flotation experiments with the coal/clay mixture in water showed that the clay was depressant in coal flotation. This outcome indicated the presence of an interaction between coal/clay which was higher in the ratio coal/clay 1,0:1,0.

1 INTRODUCTION

The exploitation of coal deposits may be used for electrical generation and steel production. In Brazil, all coal reserves are located in the southern states. The Candiota mine in the State of Rio Grande do Sul, has a reserve with resources of approximately 12.10⁹ tons, however, this exploitation is associated with environmental damage due to the high content of ash and sulfur in the presence of clay and pyrite. (Soares 1998).

Flotation is the technique of choice for fine coal cleaning. (Humeres et al. 1992). Clean coal should contain less than 2% ash and minimal sulfur. The presence of clays together with coal is partially responsible for the ash content. The effect of clay fines on coal flotation has been extensively investigated. (Xu et al. 2003).

Surfactants are reagents commonly used in flotation. These compounds can act as collectors in hydrophilic minerals or as depressant in hydrophobic minerals. (Somasundaram 1987). Adsorption of ionic surfactants on charged surfaces like clays has been studied for application in mineral flotation and to produce organic clay for environmental remediation. (Li et al. 1997).

The adsorption mechanism proposed for ionic surfactants on charged surfaces is done by electrostatic interaction with hemimicelles formation on mineral surface. The hydrophobic portion of the surfactant is oriented to aqueous solution and changes the surface from hydrophilic to hydrophobic. With high surfactant concentration bilayer is formed on mineral surface called admicelles. (Fan et al. 1997).

The objective of this work is to float coal or clay from coal/clay mixture using surfactants to obtain clean coal. With this purpose the effects of cationic surfactant *dodecyltrimethylammonium bromide* (C₁₂TAB) and anionic surfactant *sodium dodecylsulfate* (SDS) were evaluated for the flotation of clay, coal and coal/clay mixture.

2 EXPERIMENTAL

2.1 Materials

Coal and clay samples were obtained from Candiota mine – Rio Grande do Sul – Brazil. Particle size used was 62-125µm, 125-250µm and 250-500µm. The amount of kaolin in clay is more than 90%.

2.2 Procedures

The flotation experiments were realized in Hallimond Tube at 15°C. (Hunter 1993). Oxygen was utilized as carrier gas at constant flow of 3L.min⁻¹. Flotation time was 20 minutes and pH was 5,00, 4,00 and 5,00 for the coal, clay and coal/clay mixture, respectively. These pH values were those naturally obtained from coal-surfactant, clay-surfactant and coal/clay-surfactant only in the presence of water, without pH adjustment. The flotation experiments studied the effect of the clay particle size and the influence of surfactants in the coal and clay flotations. The effect of clay in the coal flotation was analyzed using a coal/clay mixture (1,0:1,0), (1,0:0,5) and (0,5:1,0) in water and also when surfactants were present.

3 RESULTS AND DISCUSSION

3.1 Effect of particle size in clay flotation with C₁₂TAB

Figure 1 shows the effect of particle size in clay flotation using C₁₂TAB as collector. Clay have a hydrophilic surface and was not recovered in water. Cationic surfactant was efficient in clay flotation due to electrostatic interaction of surfactant with negative charged clay surface. Using clay with particle size of 250-500µm flotation is more difficult than using particles of 125-250µm and 62-125µm in size.

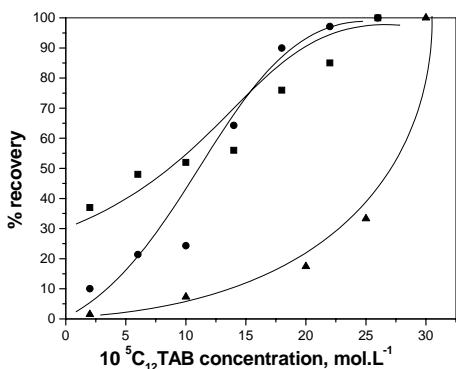


Figure1: Effect of particle size in clay flotation using C₁₂TAB: flotation time = 20 min., pH = 5,00, carrier gas = oxygen, T = 15°C, ■ d = 62-125µm, ● 125-250µm and ▲ 250-500µm.

3.2 Effect of surfactant in coal and clay flotation

Figure 2 shows the coal and clay flotation using the surfactants C₁₂TAB and SDS. Coal surface is naturally hydrophobic and 70% was recovered in water. Both surfactants in dilute solution acted as

depressants in coal flotation. The amounts of coal recovered change from 70% in water to 10% in 3.10⁻⁵ mol L⁻¹ surfactants concentration. This is due to the hydrophobic attraction of apolar portion of surfactant with the coal surface. In higher surfactant concentration, it was observed 100% of coal recovery. This can be attributed the froth formation which carry the coal particles. Under pH=5,00 C₁₂TAB was more efficient than SDS for clay flotation. Using C₁₂TAB and SDS in the concentration of 2,5. 10⁻⁴ mol L⁻¹, the results indicate that 100% of clay was recovered when C₁₂TAB was used and with SDS the clay recovery achieved 40%, only. The coal surface has a negative liquid charge under pH=5,00; therefore, electrostatic attraction in your surface with cationic surfactant is facilitated. However, the coal still has some positive sites that promote a recovery of approximate 40% using SDS.

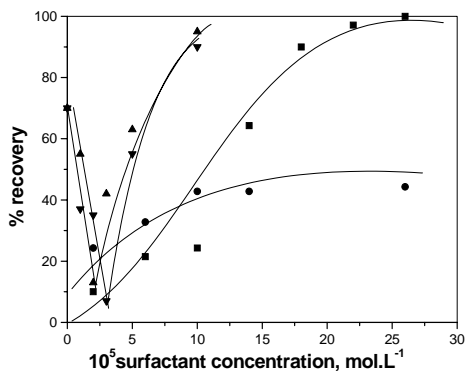


Figure 2: Effect of surfactant in coal and clay flotation: flotation time = 20 min., pH = 4,00 for coal and 5,00 for clay, carrier gas = oxygen, T = 15°C, particle size = 125-250µm; ■ clay-C₁₂TAB, ● clay-SDS, ▲ coal-C₁₂TAB and ▼ coal-SDS.

3.3 Coal/clay mixture flotation

Figure 3 shows the flotation experiments using the coal/clay mixture in water and with SDS. The presence of clay in coal flotation acted as a depressant. The coal flotation in water changed from 70% to 19% in one coal/clay mixture (1,0:1,0), to 60% in coal/clay mixture (1,0:0,5) and to 40% in coal/clay mixture (0,5:1,0). These results indicated the presence of coal/clay interaction. Clay was more efficient as depressant in coal/clay mixture (1,0:1,0) than (0,5:1,0) and (1,0:0,5). This indicated that the interaction coal/clay is higher in mixture (1,0:1,0).

When using SDS in coal/clay mixture flotation (1,0:1,0) both behaviors of the coal and the clay were observed. This result confirmed the higher interaction coal/clay in the mixture (1,0:1,0).

Probably attractive forces between charged surfaces coal and clay are responsible for this interaction, and are more efficient in coal/clay ratio (1,0:1,0). Attractive forces or repulsive forces can act and the more dominant forces will be dependent on the coal/clay ratio. In the mixture ratio (1,0:1,0) clay is more efficient as depressant in coal flotation and the attractive forces are dominant. Another important point is that in the ratio (1,0:1,0), attractive forces between coal and clay change the coal surface from hydrophobic to hydrophilic. Clay has a hydrophilic surface and it coats the coal surface. This idea agrees with what electrokinetic studies mentioned (Xu et al, 2003).

Figure 4 shows the flotation experiments using $C_{12}TAB$ with coal/clay mixture. In the mixture (1,0:1,0) both behaviors of coal and clay was observed, but in the mixture (1,0:0,5) the recovery changed from 60% in water to 70 % in the concentration $2 \cdot 10^{-5} \text{ mol L}^{-1}$ of $C_{12}TAB$. It can be concluded that there was practically no variation in the percentage recovered with concentration. The adsorption of $C_{12}TAB$ on clay is more favorable and a higher amount of mineral is recovered. The hydrophobic interaction on coal maintains the percentage of the mixture recovery around 60%. These results using $C_{12}TAB$ agree with those using SDS and show that the interaction coal/clay is higher in the mixture (1,0:1,0).

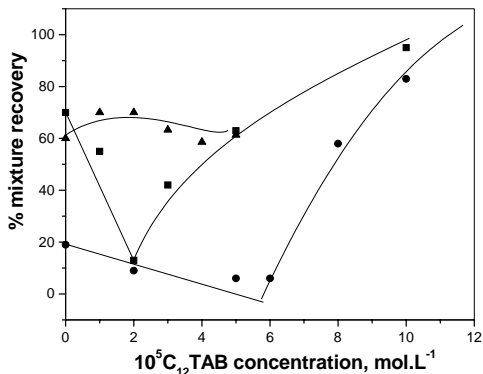


Figure 4: Coal/clay mixture flotation using $C_{12}TAB$: flotation time = 20 min., pH = 5,00, carrier gas = oxygen, T = 15°C, particle size = 125-250 μm ; ■ coal ● coal/clay 1,0:1,0, ▲ coal/clay 1,0:0,5.

4 CONCLUSIONS

Cationic surfactant was more efficient in clay flotation. Under pH=5,00 the surface clay have a negative liquid charge and electrostatic interaction is more efficient using $C_{12}TAB$ than SDS. In dilute solutions both surfactants were depressant in the coal flotation. In this case, hydrophobic interaction with coal and surfactants change coal's surface from hydrophobic to hydrophilic. The flotation experiments with the coal/clay mixture indicated the presence of a coal/clay interaction and it was dependent on the coal/clay ratio. The coal/clay interaction was higher in the coal/clay ratio 1,0:1,0. These initials tests of flotation were crucial to obtain more information about coal/clay interaction. Some further works should be done to understand the kind of coal/clay interactions in the presence/absence of surfactants to obtain clean coal by flotation. For example, the effect of pH on coal, clay and clay-coal mixture flotation; studies of adsorption mechanism of surfactants on coal, clay and clay-coal mixture; effect of other reagents used in the minerals processing industry, in coal/clay flotation, and studies of zeta potential.

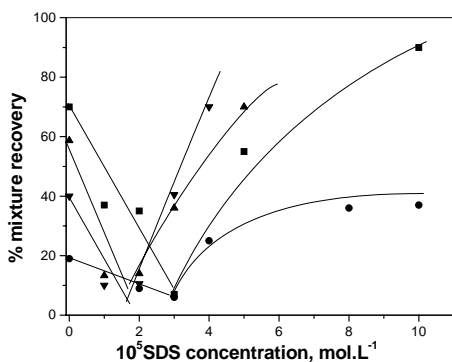


Figure 3: Coal/clay mixture flotation using SDS: flotation time = 20 min., pH = 5,00, carrier gas = oxygen, T = 15°C, particle size = 125-250 μm ; ■ coal ● coal/clay 1,0:1,0, ▲ coal/clay 1,0:0,5 and ▼ coal/clay 0,5:1,0.

5 REFERENCES

- Fan, A. et al. 1997. Adsorption of Alkyltrimethylammonium Bromides on Negatively Charged Alumina. *Langmuir*, 13, 506-510.
- Humeres, E.; et al. 1992. Mechanistic Approach to the Flotation of Pure Pyrite. *J. Braz. Chem. Soc.*, 3 (1,2), 1-7.
- Li, Z.; & Bowman, R. S. 1997. Counterion Effects on the Sorption of Cationic Surfactant and Chromate on Natural Clinoptilolite. *Environ. Sci. Technol.*, 31, 2407-2412.

Soares, E. R.; Oxidação de Pirita e Distribuição de Metais Pesados em Depósitos Carboníferos explorados em Candiota-RS, 1998. Tese de Doutorado, UFV
Somasundaram, P. & Moundgil, B. M.; Dekker 1987. Reagents in Mineral Technology, 27, New York
Xu, Z.; et al. 2003. Electrokinetic study of clay interactions with coal in flotation. Int. J. Miner. Process. 68, 183-196.

6 ACKNOWLEDGEMENTS

The authors acknowledge the financial support from FAPERGS and FAPEG.

Mixture Coal-Pyrite Flotation Using Potassium Ethylxanthate(C_2XK) and Sodium Dodecylsulfate (SDS)

F.G.Penha, M.P. de Oliveira, G.F.Fiss, L.Furlan

Department of Analytical and Inorganic Chemistry, Chemistry and Geosciences Institute, University Federal of Pelotas, Pelotas, Brazil

N.A.Debacher

Department of Chemistry, University Federal of Santa Catarina, Florianópolis, Santa Catarina, Brazil

ABSTRACT: The presence of pyrite (FeS_2) in coal produces pollution problems and has negative effects on the quality of the coal for metallurgical purposes. Flotation is the technique for fine coal particles processing, although to remove pyrite from coal by flotation is difficult because its surface acquires a degree of hydrophobicity upon superficial oxidation. Potassium ethyl xanthate (C_2XK) is the most commonly collector for pyrite flotation. The objective of this work is to float pyrite in the mixture coal-pyrite using C_2XK as collector for pyrite and sodium dodecylsulfate (SDS) as depressant for coal. In the mixture coal-pyrite (1:1) in water with particle size of 105-250 μm , 74% of coal was recovery and no pyrite was recovery. In the presence of $10 \cdot 10^{-3} mol \cdot L^{-1} C_2XK$ with particle size 105-250 μm , 60% of pyrite was recovery and 35% of coal was recovery. Using particle size of 62-125 μm and $10 \cdot 10^{-3} mol \cdot L^{-1} C_2XK$, 70% of pyrite was recovery and 38% of coal was recovery. Using SDS in concentration of $3 \cdot 10^{-5} mol \cdot L^{-1}$ in the mixture coal-pyrite in the presence of xanthate $10 \cdot 10^{-3} mol \cdot L^{-1}$, 50% of pyrite was recovery and 33% of coal was recovery. In this concentration SDS was depressant in pyrite flotation due pyrite to be more hydrophobic than coal.

1 INTRODUCTION

The pyrite is often associated with coal and has a negative environmental effect during the combustion of the coal due the production of sulfur dioxide and acid rain. The flotation process to remove pyrite from coal is difficult because the surface became hydrophobic during oxidation. (Tao et al. 1994), (Fornasiero et al. 1992).

In coal processing, pyrite can be removed using xanthate as a collector. The mechanism adsorption of xanthate on pyrite has been extensively studied. (Montalti et al. 1990; Jiang et al. 1998).

The adsorption of ethylxanthate on pyrite happens only in the presence of oxygen. The surface of pyrite changes from hydrophilic to hydrophobic after adsorption of ethyl xanthate in the concentration 0,01 $mol \cdot L^{-1}$. The contact angle determined by captive bubble method at interface solid-liquid-gas change from 0 to 35° in $pH = 8.00$ and from 0 to 90° in $pH = 5.00$. (Penha et al. 2001).

The objective of this work is to float pyrite in the mixture coal-pyrite using ethylxanthate (C_2XK) as collector to pyrite and sodium dodecylsulphate as depressant to coal.

2 EXPERIMENTAL

2.1 Materials

The samples of pyrite and coal were obtained from Candiota mine – Rio Grande do Sul – Brazil. The particle size used was 62-125 μm and 105-250 μm . Xanthate solution was prepared by dissolution of KOH in ethanol with addition of carbon disulfide.

2.2 Procedures

The flotation experiments were realized in Hallimond Tube at $20^\circ C$ after the adsorption of C_2XK on pyrite. The xanthate adsorption was accomplished in presence of oxygen, with agitation during 4 hours. Oxygen was utilized as carrier gas in flotation at constant flow of $3L \cdot min^{-1}$ in $pH = 5.00$ and the flotation time was 30 minutes.

After mixture coal-pyrite flotation was able to separate the amounts of pyrite and coal by difference of density in $CaCl_2$ saturated solution.

3 RESULTS AND DISCUSSION

The effect of ethylxanthate in pyrite and in the mixture coal-pyrite flotation in two particle sizes is

showed in Figure 1. Pyrite is hydrophilic but 17% was recovery using particle size of 105-250 μm in water at gas flow of $3\text{L}\cdot\text{min}^{-1}$. The pyrite recovery was 80% at $0,01\text{ mol L}^{-1}\text{ C}_2\text{XK}$.

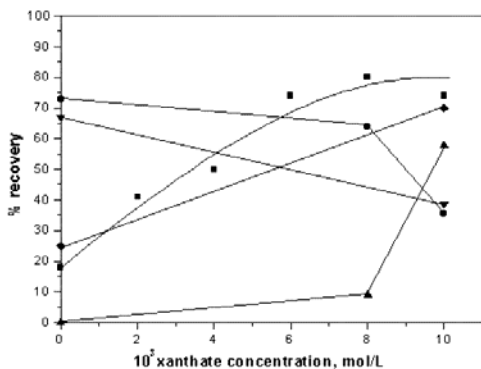


Figure 1: Pyrite flotation and mixture coal-pyrite flotation using C_2XK : flotation time = 30 min., pH = 5,00, carrier gas = oxygen, gas flow = $3\text{L}\cdot\text{min}^{-1}$: ■ pyrite pure d = 105-250 μm , ● coal in the mixture d = 105-250 μm , ▲ pyrite in the mixture d = 105-250 μm , ▼ coal in the mixture d = 62-125 μm , ◆ pyrite in the mixture d = 62-125 μm .

In the mixture coal-pyrite 1.0:1.0 in water with particle size of 105-250 μm , 74% of coal was recovery and no pyrite was recovery. The coal is hydrophobic and is naturally floated and the pyrite is hydrophilic and is not floated. Therefore coal-pyrite interaction is not observed.

Change in flotation was detected when xanthate is used as collector. The coal recovery was 35% and pyrite recovery was 60% at $0,01\text{mol L}^{-1}\text{ C}_2\text{XK}$ with particle size of 105-250 μm . Using C_2XK surface pyrite become more hydrophobic than coal.

Using particle size of 62-125 μm , the pyrite flotation was facilitated due the weigh particle and could happen an interaction coal-pyrite. In water, the pyrite recovery was around 25% and coal was 66%.

In the concentration $0,01\text{ mol L}^{-1}$ of C_2XK , the amount of pyrite recovery was 70% and coal recovery was 38%. These were the best conditions in order to separate mixture coal-pyrite using C_2XK .

Also, it was used SDS in the mixture coal-pyrite with C_2XK at $0,01\text{ mol L}^{-1}$ to decrease the amount of

coal recovery. The result obtained was 50% of pyrite recovery and 33% of coal recovery. In this concentration SDS was depressant to pyrite because its surface is more hydrophobic than coal. Therefore the SDS adsorption happens on pyrite and on coal by hydrophobic interaction.

4 CONCLUSIONS

Xanthate is a collector for pyrite flotation. In the mixture coal-pyrite, flotation in water and particle size 125-250 μm held mineral separation, coal was recovery and no pyrite was recovery. But applying particle size 62-125 μm , 25% of pyrite was recovery. Pyrite flotation is promoted with smaller sizes of particles in the mixture. In presence of xanthate the pyrite was preferentially recovery and became more hydrophobic than coal. The best conditions of separation were found using C_2XK at $0,01\text{mol L}^{-1}$ with particle size 62-125 μm . The anionic surfactant, SDS, was depressant in the pyrite adsorbed with C_2XK due the interaction hydrophobic between pyrite-surfactant. News researches are under investigation in order to find the optimum concentration and conditions foreseeing the SDS acts as depressant only in coal.

5 REFERENCES

- Fornasiero, D.; et al. 1992. An electrokinetic study of pyrite oxidation. *Colloids Surf.*, 62, 63-73.
- Jiang, C. L.; et al. 1998. The surface and solution chemistry of pyrite flotation with xanthate in the presence of iron ions. *Colloids Surf. A: Physicochem. Eng. Aspects*, 136, 51-62.
- Montalti, M.; et al. 1991. Ultraviolet-visible spectroscopic study on the kinetics of adsorption of ethylxanthate on pyrite. *J. Colloid. Int. Sci.*, 143(2), 441-450.
- Penha, F. G.; et al. 2001. Adsorção de Xantatos sobre Pirita. *Quím. Nova*, 24(5), 612-615.
- Tao, D. P.; et al. 1994. The incipient oxidation of pyrite. *Colloids Surf. A: Physicochem. Eng. Aspects*, 93, 229-239.

6 ACKNOWLEDGEMENTS

The authors acknowledge the financial support from FAPERGS and FAPEG.

Experimental Verification of the Three-phase Linear Grade Distribution Prediction Method by Direct Measurement

C.L.Schneider & R.Neumann

SCT - Division of Technological Characterization, Mineral Analysis Coordination, CETEM - Centre for Mineral Technology, Rio de Janeiro, Brazil

ABSTRACT: Linear grade distributions can be predicted using direct measurement on long strips of images generated on unbroken ore samples, under the Random Fracture assumption. The derivation of the probability equations is straightforward under the random fracture assumption. However, the direct measurement of the conditional, on chord length, linear grade distribution, is postulated and can be accomplished in at least two distinct ways, with similar results. The remaining question is whether the direct measurement procedure is sound. There is no known method to generate a sample with known conditional, on chord length, linear grade distribution, so proof can only be accomplished by comparing measured and predicted linear grade distributions. This can be done experimentally, by carrying out the procedure on a sample of unbroken ore that is later on crushed, and its particles mounted and sectioned for measurement. In this work, a sample of copper ore containing significant amounts of magnetite and silicates was used to verify the direct measurement procedure under the random fracture assumption. Results indicate that the direct measurement procedure is accurate enough for practical texture assessment and liberation prediction.

1 INTRODUCTION

The prediction of the liberation from restricted samples, as drill cores, may be a very useful tool to assess technological aspects of processing the potential ore, therefore eliminating to some extent the subjectivity of the investment decisions during the early stages of exploration. Before any laboratory-scale test results are available about the processing characteristics of the ore, only mineralogy and grade information are usually drawn from drill core and trench-type samples. At this early stage, the design of potential processing routes for the ore can be aided by simulation techniques, and the economic feasibility of the project can therefore be evaluated with some accuracy, in light of assumptions that are made about the ore characteristics. One important assumption is related to the liberation characteristics of the phases of interest.

Image analysis techniques are the only alternative for the assessment of the liberation properties of a given phase in an ore. The liberation characteristics are intimately related to the texture in which the phase is present in the mineral matrix. When liberation prediction techniques are used, only one representative sample of unbroken ore, such as a

drill core sample, many times larger than the largest liberated progeny particle of any phase, is examined by image analysis. As the texture is measured from the unbroken sample, the liberation at any progeny size from that sample can be predicted.

Two-phase liberation prediction has provided results that were sound compared to liberation measured on sized samples or compared to lab scale processing of the samples (Neumann 1999, Neumann & Schneider 2001, Schneider et al. 2001).

The prediction of three-phase liberation was first successfully carried out by Schneider et al. (2003) on coal samples. As discussed by the authors, multiphase liberation prediction by direct measurement is feasible, requiring good experimental techniques and assuming random fracture.

In this work we aim at comparing the predicted and effectively measured liberation from the same sample, in order to evaluate if prediction is accurate.

2 THEORETICAL BACKGROUND

Liberation prediction is based on linear measurements following the method due to King (1994), after a simplification made by Neumann &

Schneider (2001). The number weighted, conditional on length ℓ , linear grade distribution $p(\bar{g}_\ell | \ell)$ can be measured directly from the unbroken ore by accounting for all possible intercepts of length that can be placed on the sample of texture. This has important implications on the length of the image strip that has to be measured, as linear intercepts should exceed the largest textural expression in the ore. The smallest feature to be resolved in the image defines the necessary magnification, and the largest textural expression defines the number of images to be stitched together in a strip large enough so that the texture is fully covered.

Hence $p(\bar{g}_\ell | \ell)$ equals $f(\bar{g}_\ell | \ell)$, the conditional, on size, length-weighted linear grade distribution,

$$f(\bar{g}_\ell | D) = \int_0^{\infty} f(\bar{g}_\ell | \ell) f(\ell | D) d\ell \quad (1)$$

can be calculated for any desired particle size D , as $f(\ell | D)$ is the conditional, on size, length weighted chord-length distribution.

3 EXPERIMENTAL

A single sample of copper ore from northern Brazil, weighting about 1.1 kg, was chosen for this work. A 10 mm thick slab was randomly sawn off the sample, striking its most intensive foliation, and cut to a 50 mm diameter disc. The remaining sample was entirely hand-crushed, milled (wet rod mill, 50% solids) for 15 minutes, and immediately sieved (295, 208, 147, 104, 74, 53, 44, 38 and 20 μm), in order to avoid sulfide oxidation. The disc and the eight close-sized particulate samples were dried under vacuum, embedded in resin, and carefully polished. Images were acquired using a solid-state back-scattered electron detector on a LEO S440 SEM. Contrast and brightness were set to ensure good contrast between the gray levels of chalcopyrite, magnetite and the silicates (mainly chlorite and amphiboles).

For prediction on the unbroken ore disc, 22 images (pixel size of 1.01271 μm) were carefully stitched together for each of the six strips, called mega-images, 756 pixels high and 21,765 pixels large after cropping. Each strip encompassed, therefore, about 2 mm of sample. The image processing encompassed a delineation filter, segmentation for the three phases, elimination of artifacts, hole-filling, generation of the three-phase image and watershed for touching particles. Although simpler, as no resin shows up in the images, a routine based on fingerprinting was applied for magnetite and chalcopyrite segmentation, as fine chlorite inclusions caused

small break-offs within these minerals during polishing, which could be taken for silicates.

$f(\bar{g}_\ell | \ell)$ measurement was performed on the resulting ternary mega-images, and the measured distribution was accumulated over repeated measurement in each of the six strips. All image analyses, from stitching to measures, were conducted with MMIATM (Minerals and Metallurgical Image Analysis software, King and Schneider 1993).

Linear grade distributions were generated using a three-phase version of StereoSoftTM, applying equation (1) for particle sizes corresponding to the geometric mean particle size of the particulate samples.

The images of the eight particulate samples were also processed using MMIATM (between 45 and 70 images each), and the image processing routine was similar as the one used for the unbroken sample, including the rather complex fingerprinting. Final measurements were performed on quaternary images (resin-silicates-magnetite-chalcopyrite).

Stereological conversion for both data sets, from linear grade distribution to the presented volumetric liberation, was performed on StereoSoftTM.

4 RESULTS

Table 1 shows the measured grades of the fractions as determined by image analysis, as well as the calculated mean grade for the +20 μm sample, and the grade derived from the unbroken sample image analysis.

Table 1 – Measured grades of fractions, mean grade and grade from unbroken sample (mass %).

Sizes	Silicate	Magnetite	Chalcopyrite
295x208	32.62	64.68	2.70
208x147	37.54	59.98	2.47
147x104	28.49	69.55	1.96
104x74	22.41	75.48	2.11
74x53	23.48	74.69	1.83
53x44	24.42	73.32	2.26
44x37	28.38	69.27	2.35
37x20	27.43	69.37	3.21
295x20	27.15	70.54	2.31
From $f(\bar{g}_\ell \ell)$	23.20	73.42	3.39

The grade distributions over size fractions in Table 1 suggests that fracture is actually close to random, and so the assumption is correct. Comparison of the grades derived from the mega-images and the mean grade from the particulate image analysis should be closer, and might be due to the non analyzed -20 μm ; the balance, however,

would generate grades far too dissimilar to the other fractions, so the possibility of heterogeneous samples can not be dismissed.

The linear grade distributions, as directly measured in the particulate samples, and predicted

from $f(\bar{g}_\ell | \ell)$ using Equation (1) for the unbroken sample, are compared in Figure 1. No stereological conversion has been applied, and only the coarsest, smallest and an intermediate size fraction are presented, due to space restrictions.

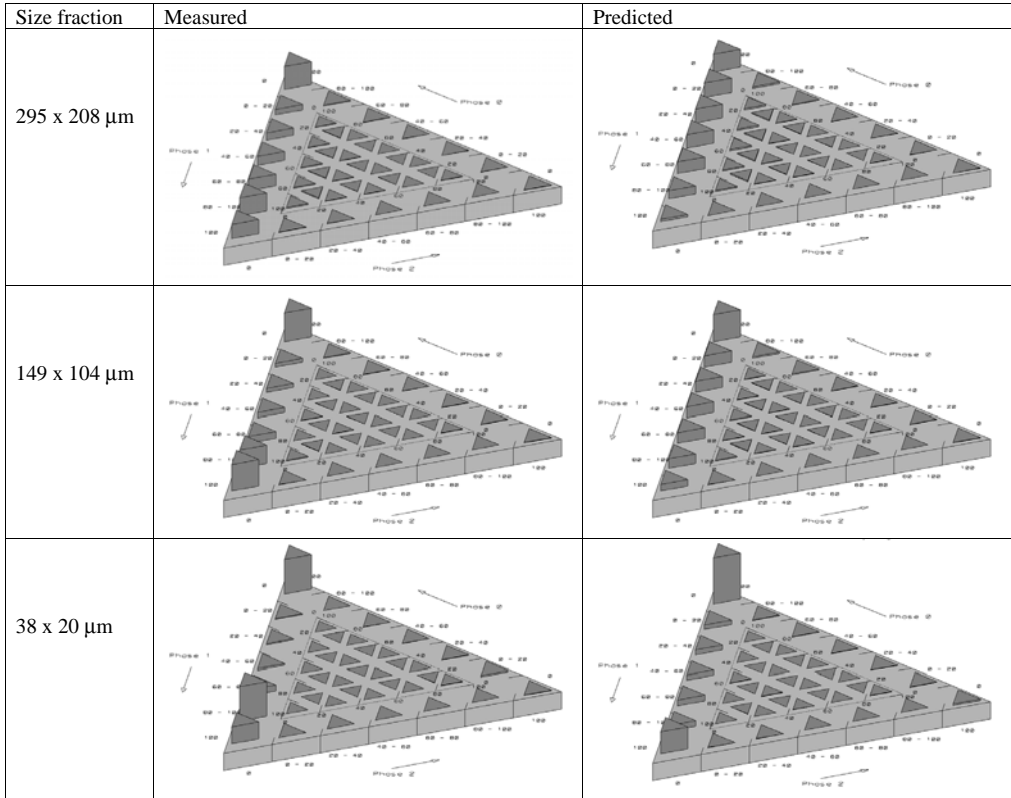


Figure 1 - Distribution of linear intercept composition, as directly measured in the particulate samples, and predicted for the unbroken sample (phase 0= silicates, 1= magnetite and 2= chalcopyrite).

Most intercepts fall on the binary magnetite-silicates axis, as expected in a low-grade ore. Intercepts are predominantly binary for the coarse fraction, but at 149x104 μm there are already several intercepts of 100% magnetite or silicates. This is also true for the silicates in the predicted spectra, although intermediary compositions are common, and 100% magnetite intercepts minor. At the 38x20 μm size class, both measured and predicted sets display mostly the high-content classes, but the measured data set indicates intercepts predominantly in the 80% magnetite, 20% silicates class. This is probably due to the higher magnifications used for

the small-sized fractions of the particle images, revealing inclusions not detected with the lower magnification used for the unbroken sample.

The texture, as a matter of fact, is well represented by the prediction, as can be observed comparing the measured and the predicted linear grade distributions in Figure 1.

Figure 2 presents the particle composition distribution, by volume, for both measured and predicted data sets, at the same size fractions as in Figure 1. Again, a fairly good correlation may be observed between the measured and the predicted liberation spectra.

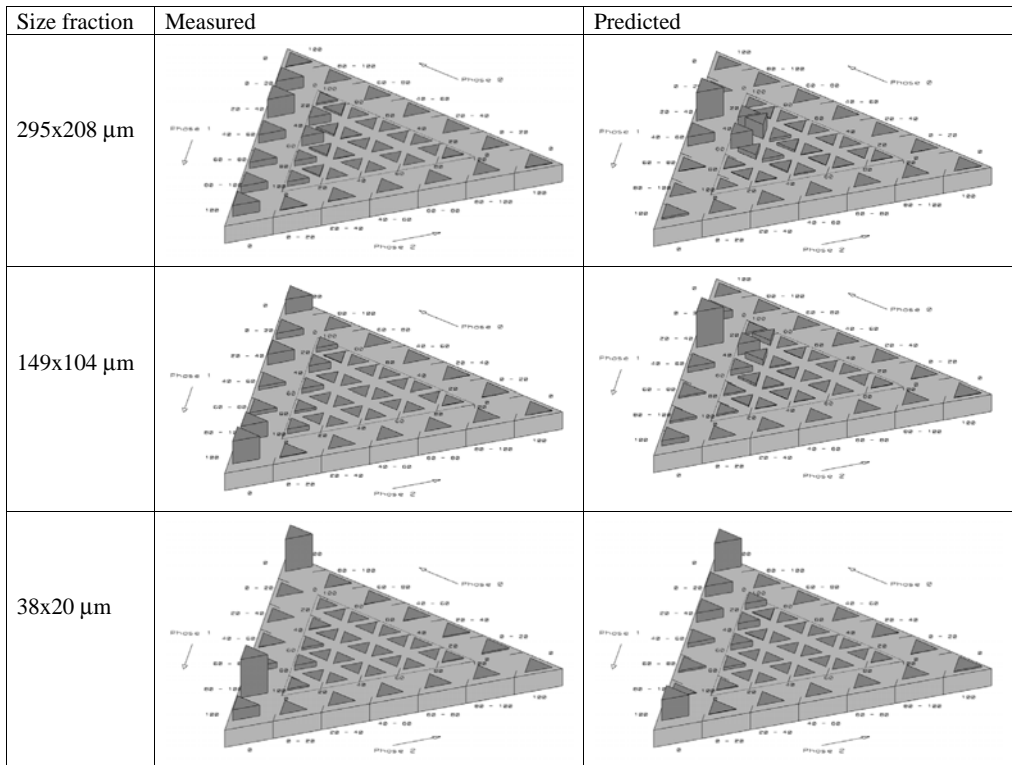


Figure 2 - Distribution of particle composition, by volume, after measured in the particulate samples and predicted for the unbroken sample data (phase 0= silicates, 1= magnetite and 2= chalcopyrite).

5 CONCLUSION

In general, the predicted liberation spectra show the same major features as seen in the measured liberation spectra. Both methods show that, for the sizes considered, the presence of 3-phase particles is reduced at about the same rate. They also show that the type of 3-phase particles present, in the larger particles, is similar. Also, both methods predict that liberation of silicates from magnetite is difficult, and that most binary particles are a combination of silicate and magnetite. The proportions of each particle type are not correctly predicted. This may be due to fractal effects and, most probably, a stereological effect from sampling only one arbitrary cross-section of the unbroken ore. Future work will be aimed at correcting this problem.

6 REFERENCES

King, R.P. 1994. Linear *Stochastic Models for Mineral Liberation*,” *Powder Technology*, 81: 217-234.

- King, R.P. and Schneider, C.L. 1993. An Effective SEM-Based Image Analysis System for Quantitative Mineralogy,” *KONA Journal* 11: 165-177.
- Neumann, R. 1999. Caracterização tecnológica dos potenciais minérios de terras-raras de Catalão I, GO. D.Sc. Thesis, University of São Paulo. São Paulo. [in portuguese, available at ftp://ftp.mines.utah.edu/pub/cmt/RNeumann_PhD/]
- Neumann, R & Schneider, C.L. 2001. Prediction of monazite liberation from the silicatic rare earth ore of Catalão I,” *Minerals Engineering*, 14(12): 1601-1607.
- Schneider, C.L., King, R.P. & Neumann, R. 2001. Assessment of liberation with optical microscopy: a fast, low cost procedure. VI Southern Hemisphere Meeting on Mineral Technology. 2001- Rio de Janeiro/Brazil. Proceedings 1: 36-39.
- Schneider, C.L., Neumann, R. & King, R.P. 2003. Prediction of Liberation from Unbroken 3-phase Texture. XXII IMPC - International Mineral Processing Congress, 2003, CapeTown, South Africa. Proceedings: 363-369.

Quantitative Measurement of Exposed Area by Image Analysis of Particle Cross-section

C.L.Schneider & R.Neumann

SCT - Division of Technological Characterization, CETEM - Centre for Mineral Technology, Rio de Janeiro, Brazil

ABSTRACT: The measurement of exposed area has sparked some interest in the literature, as it is believed exposed phase area has an important impact on particle flotation properties and metal recovery by leaching. Direct measurement has been demonstrated by computerized tomography, and the work has shown the effect of exposure on leaching rates. For scanning electron imaging, a method that is based on the measurement of the exposed perimeter has been proposed, and has produced data that seems to be factual. In this work, the concept of interphase area per unit volume, which is a quantitative measurement that has been utilized in liberation studies, is used to develop an exposed area per unit volume of phase measurement procedure. The measurement can be accomplished entirely by measuring chord length distributions on the phases and on the particles. The procedure is demonstrated on a sample of copper ore, and the calculated exposures look sound, doubling from 208 to 74 μm . Below 74 μm , exposure worsens, and it is not clear if this is due to fractal effect, polishing constrains or due to breakage along interphase boundaries generating the smaller particles. A method for calculation of exposure from cross-sections of particles has thus been developed and implemented.

1 INTRODUCTION

1.1 *The application of exposed area analysis*

At least two important problems in mineral processing may be impacted by exposed area, i.e. the area of the phase of interest that is exposed in the particle surface. These are flotation; a surface chemistry based process, and leaching. In flotation, exposed area is required, since the surfaces of the minerals are prepared, either to become hydrophobic and promote flotation, or hydrophilic, reducing flotation probability, and therefore producing an overall separation effect. When a bubble comes in contact with a particle, the particle may adhere if the conditions are adequate. Selective flotation is only possible if the mineral of interest is exposed, thus presenting a surface to interact with reagents and bubbles. Lastra (2002) has carried out comprehensive work aimed at characterizing exposure in samples from a flotation plant, measuring perimeters to obtain exposure data. In leaching, the recovery that can be obtained is established from a balance between transport phenomena and the extent of mineral exposure (Miller et al. 2003). The ultimate recovery that can be achieved by leaching for a given ore is a critical

parameter that must be known in any serious leaching study.

Flotation is a tremendously complex process, and the amount of exposed area is one of the parameters that impact directly the flotation rate constants, as well as the recovery that can be achieved for the ore. Particles with different exposed areas will be captured by rising bubbles at different rates, depending on their size and hydrophobicity, which in turn determine their specific flotation rate constant. The amount of exposed area is an important parameter that determines the particle hydrophobicity.

1.2 *Expose area, texture and particle composition*

The amount of exposure of a phase is a function of the volumetric fraction of the phase in the particle and the phase/particle texture. Figure 1 illustrates the effect of texture on phase exposure. Represented in the figure are two cross-sections of a hypothetical binary particle, with a fixed volumetric grade of phase. The texture in the left is coarse, favoring exposure of both phases while the texture in the right is dispersed, favoring exposure of the continuous phase in detriment of the dispersed phase. Both

particles are unliberated, and the sessions would be counted in the same grade class for liberation analysis. The question is whether these particles would float or leach, and what type of recovery could be achieved. Surely, the particle in the left would respond for both of these processes, but the particle in the right can only be leached or floated efficiently if the phase of interest is not the dark, dispersed phase.

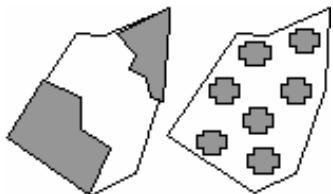


Figure 1: How texture may influence exposure.

It is of the uttermost importance to understand that although the cross-section in the right shows no exposure at all, the particle that is represented there could very well have exposed dispersed phase. This is because we only see a cross cut of the particle and exposed mineral can be located underneath that particular section, and could also have been present above it, if the section is from a polished mound. Therefore, there are stereological issues that must be taken into consideration.

Direct measurement of exposed area is possible by Cone Beam X-Ray Microtomography (Lin & Miller 2001), and this equipment and its working principles are well described in this reference. No stereological issues are directly involved in the assessment of exposure by microtomography, and the technology has been well established and is widely accepted. Here, an alternative approach is described for measurement of exposure, and that can be used by process mineralogists that have access to microscopes and image processing/analysis.

Another issue is the correlation of exposure with phase volume fraction. This is illustrated in Figure 2.

As the volume fraction of dispersed phase increases, it becomes increasingly improbable that a fracture surface (particle edge) does not hit the dispersed phase. In fact, the exposed area, for most textures, should increase linearly with the volume fraction of phase. Barbery (1991) proposes that the amount of exposed area is equal to the average volumetric grade of phase in a particle.

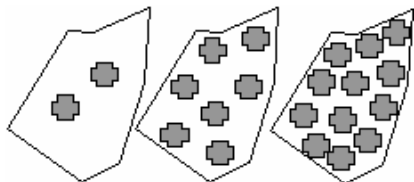


Figure 2: Phase volume fraction effect.

The implication is that for known particle composition distribution (liberation spectra) the amount of exposure can be calculated without the need for specialized measurement. Nevertheless, there might be cases for which Barbery's assumption does not hold, or is inaccurate, and it is difficult to predict if, for any given texture, exposure can be calculated based on the measured liberation spectra.

2 APPROACH

The average surface area per unit volume S_V of features on cross-sections can be measured using the stereological equation (Weibel 1980).

$$S_V = \frac{4}{\mu} \quad (1)$$

where μ is the average intercept length. Linear measurements are relatively easy to carry out provided good phase contrast is achieved on images generated on particle cross-sections, and only require frame correction for the probability that the feature intercepts the measuring frame (King & Schneider 1993). With accurate chord length distributions for each phase and for the particles, the surface area per unit volume of phase can be easily calculated using Equation 1. The volumetric fraction of each phase can also be measured easily, using the first law of stereology, and simple pixel count is sufficient.

The surface area of any phase present in the sample can be calculated using the definition of S_V ,

$$A = S_V g_v V \quad (2)$$

where g_v is the volumetric grade of phase and V is the total volume of the particles. For any type of texture, the surface area of each phase has at least two components, exposed area (A^E) and unexposed area (A^U):

$$A = A^E + A^U = S_V g_v V \quad (3)$$

If we add the exposed surface area component of all present phases, we obtain the surface area of the particles themselves, i.e.,

$$A^P = \sum_i A_i^E \quad (4)$$

where A^P is the total particle surface area and i is the phase index. For a binary system, the unexposed area of both phases must be identical, and this is a logical geometrical constraint. It follows that

$$A_1 + A_2 = A_1^E + A_1^U + A_2^E + A_2^U = A^P + 2A_1^U$$

$$\dots$$

$$A_2^U = A_1^U = \frac{A_1 + A_2 - A^P}{2} \quad (5)$$

and the exposed area of each phase can be easily calculated by

$$A_i^E = A_i - A_i^U \quad (6)$$

In terms of S_v , Equation (5) can be re-written by substituting Equation (3),

$$S_{v_2}^U g_{v_2} = S_{v_1}^U g_{v_1} = \frac{S_{v_1} g_{v_1} + S_{v_2} g_{v_2} - S_{v_p}}{2} \quad (7)$$

and

$$S_{v_i}^E = S_{v_i} - S_{v_i}^U \quad (8)$$

The fraction of phase that is exposed is simply calculated by

$$\% \text{ of phase area exposed} = 100 \frac{S_{v_i}^E}{S_{v_i}} \quad (9)$$

Also, the following constraint must be noted:

$$\sum_i g_{v_i} = 1 \quad (10)$$

The measurement procedure is illustrated in Figure 3.

Each phase is measured individually, generating information about the phase's surface area per unit volume. Then, the particles are measured. The procedure can be expanded for any number of phases, and the development follows the same rational. The measurement procedure for multiphase systems is to measure the phases individually, all possible combinations of $n-1$ phases, and the particles.

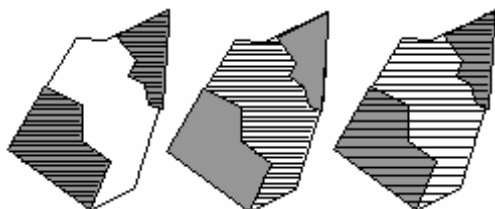


Figure 3: Measurement procedure for a binary system.

The unexposed area of a given phase is usually referred to as the interphase area per unit volume of phase. This is also an important quantity, and it is a good measure of texture. Textures with large values of interphase area per unit volume are fine, intricate textures, while textures with relatively small values of interphase area per unit volume of phase are coarse, simple textures. The procedure presented here is based on King's assessment of grain boundary fracture (King 1992).

3 EXPERIMENTAL

In order to illustrate the measurement of exposed areas, a copper ore sample from northern Brazil was prepared by hand crushing followed by milling (wet bar mill, 50% solids) for 15 minutes, and immediately sieving (295, 208, 147, 104, 74, 54, 44, 38 and 20 μm), in order to avoid sulfide oxidation. The eight closely sized samples were dried under vacuum, embedded in resin, and polished. Images were acquired using a solid-state back-scattered electron detector on a LEO S440 SEM. Contrast and brightness were set to ensure good contrast between the gray levels of chalcopyrite, and the other phases, magnetite and silicates (mainly chlorite and amphiboles).

Sets of about 60 images were generated for each sized sample. Image processing included delineation filtering, thresholding, elimination of artifacts and feature filling, assembling ternary images (epoxy, gangue and chalcopyrite) and watershed feature separation. Fingerprinting was applied for magnetite and chalcopyrite segmentation, as small polishing imperfections such as pitting and edge break-offs within these minerals could easily produce small silicate artifacts in the thresholded images.

Chord length distributions were measured, with frame correction. All image analyses, from processing to measurement, were done with MMIA™, Minerals and Metallurgical Image Analysis software (King & Schneider 1993).

The image shown on top in Figure 4 is a back-scattered electron image of 208x149 μm particles. The histogram (not shown) yields perfect phase resolution, and the peaks for the three major phases, gangue, magnetite and chalcopyrite, as well as the epoxy mounting media, can be identified with precision, although by eye the chalcopyrite is hardly distinguishable from the magnetite. The ternary image shown below results from processing and thresholding, as described. The chalcopyrite is shown as black features, all other mineralogical phases are shown as gray, and the epoxy in the background is shown in white.

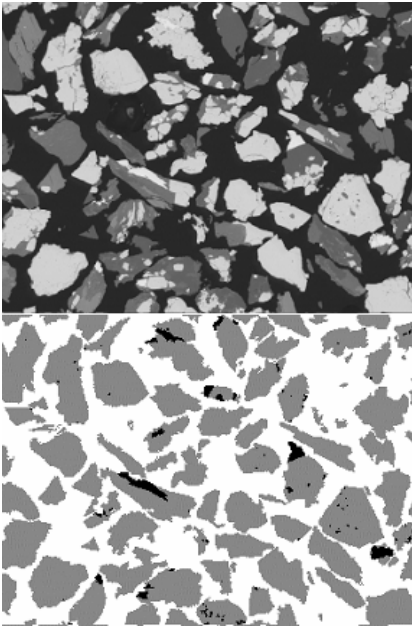


Figure 4: Top, original back-scattered electron image, and bottom, processed image.

Chord length distributions are measured in the processed image as described in Figure 3, and the average intercept lengths are calculated after proper frame correction.

4 RESULTS

The experimental results are summarized in Table 1, for each particle size analyzed.

Table 1: Average chord lengths, measured on Particles, Chalcopyrite and Gangue phases, in micrometers, and volumetric grades of Chalcopyrite.

Size, μm	% Ch	$\mu\text{m P}$	$\mu\text{m Ch}$	$\mu\text{m G}$
295x208	2.640	104.783	93.390	20.013
208x147	2.330	70.453	65.108	16.343
147x104	2.040	48.420	45.811	13.023
104x74	2.390	35.487	33.969	12.254
74x54	2.470	24.137	22.990	8.996
54x44	2.630	18.563	17.670	8.087
44x38	2.840	13.605	12.602	4.765
38x20	3.580	9.754	9.089	4.778

The calculated exposure for both gangue and chalcopyrite are shown in Table 2.

Table 2: Calculated exposures, from Equations (7), (8) and (9).

Size, μm	% Exposure Chalcopyrite	% Exposure Gangue
295x208	16.58	89.45
208x147	21.69	92.56
147x104	26.67	94.63
104x74	35.75	95.64
74x54	31.94	95.60
54x44	31.03	95.93
44x38	19.80	93.80
38x20	26.23	94.79

5 DISCUSSION AND CONCLUSIONS

The results in Table 2 show that exposure is much higher for the continuous phase, relative to the dispersed phase, chalcopyrite. In general, exposure increases as particle size decreases, and this is expected. Chalcopyrite exposure worsens below 74 μm . This may be due to fractal effects, and the phenomena will be investigated. Also, polishing quality at these sizes is never as good as for larger particle sizes. This may have contributed to the results. There is also the possibility that small particles are preferably generated along the weaker interphase boundaries in the ore (probably along chlorite's perfect basal cleavage), and in this case the behavior is real.

A method for calculation of exposure from cross-sections of particles have been developed and implemented.

6 REFERENCES

- Barbery, G. 1991. Mineral Liberation Measurement, Simulation & Practical Use in Mineral Processing. Quebec: Editions GB.
- King, R.P. 1992. Techniques for estimating the amount of grain-boundary fracture during comminution of mineralogical materials. In Comminution-Theory & Practice. S. K. Kawatra ed., SME, pp. 3-15.
- King, R.P. and Schneider, C.L. 1993. An Effective SEM-Based Image Analysis System for Quantitative Mineralogy, KONA, 11: 165.
- Lastra, R. 2002. A Comparison of Liberation Determinations by Particle Area Percentage and Exposed Particle Perimeter Percentage in a Flotation Concentrator. SME, Preprint 02-081.
- Lin, C.L. and Miller, J.D. 2001. Cone Beam X-ray Microtomography – A New Facility for 3D Analysis of Multiphase Materials. SME, Preprint 01-44.
- Miller, J.D., Lin, C.L., Garcia, C. and Arias, H. 2003. Ultimate recovery in heap leaching operations as established from mineral exposure analysis by X-ray microtomography. International Journal of Mineral Processing 72: 331-340.
- Weibel, E.R. 1980. Stereological Methods. New York: Academic Press.

Automatic Gold Process Mineralogy with the “Precious-X” Image Analysis System

P.Siegel

Mining Department, Mineral Processing Div., Engineering Faculty, Universidad de Santiago de Chile

E.Almendras

Mining Department, Minerals Identification & Characterization Div., Facultad de Ciencias Físicas y Matemáticas, Universidad de Chile, Santiago, Chile

ABSTRACT: Low metal recovery is often due to inaccurate quantitative analyses of the finer grain sizes, as well as to difficulties when gold appraisal corresponds to lower percentages of gold occurrences included within the mineral context. This is usual when mineralogical characterization of the feed, of the treated ores, products and tailings are performed using conventional methods. To overcome such problems, the authors developed the “PRECIOUS-X” automatic image analysis system (AIAS), which rapidly supplies accurate information, substituting the former irrelevant metallurgical data, thus securing the success of the process control and allowing continuous optimization of the plant’s most important metallurgical parameters. It is simple to operate, flexible and statistically reliable. Appropriate application of macros, personalize and transform valuable information supplied by this system, for routine plant practice and also for use as a powerful tool in metallurgical research. Hence, it is suitable for fast solutions in a large variety of applications of precious metals metallurgy. This friendly software, based on a windows visual C++ version, is illustrated here with three different case studies.

1 INTRODUCTION

Chile’s economically interesting gold minerals usually consist of native Au⁰ and minor quantities of electrum, amalgam and gold tellurides. Among the latter we have AuTe₂ (calaverite), mono - clinic and ortho-rhombic AuAgTe₄ (sylvanite and krennerite, respectively) and Ag₃AuTe₂ (petzite). Amalgam is seldom found as a natural deposit. The most frequent gangue mineral is quartz. Nevertheless, gold can commonly be found intimately contained in basic metallic sulfides or related minerals or in their oxidation products. A major part of gold is soluble in cyanide solutions. Control of this process implies an actual quantification of the gold ores and the associated metallic and non-metallic minerals. Traditional techniques in gold ore characterization (optical microscopy, electron micro scan) can be improved with computer aided automatic image analysis systems, increasing the reliability of the system’s information and speeding up the availability of the important metallurgical parameters, required for timely plant control and optimization.

Obviously, the same applies to most processes, such as activated carbon, flotation, amalgamation and other, where low metal recoveries are due to

insufficient or qualitatively and quantitatively inaccurate data, that is, poor characterization of the mineral’s metallurgical parameters,. For this reason automatic quantification methods to solve the real metal recovery problems have become so important. To illustrate the latter, we include three different case studies, printed in black in the proceedings. The actual original images and figures are, as shown in the session presentation, either transformed into gray levels (0 to 255), as used for their digital processing with the software, or as colored microphotographs, histograms and tables. “PRECIOUS-X”, runs on a friendly windows Visual C++ software, developed by the author’s. The basic hardware required are: a standard PC, connected to a digital camera, mounted on a mineralogical polarizing microscope and preferably high resolution color monitor. Printers plus other peripheral hardware and communication systems are optional.

Full automation of the system allows:

- creation of representative images of the gold mineral samples;
- identification of all the metallic and non-metallic phases;
- measurement of these images to quantify the desired parameters.

The work protocol is as follows:

1. The images are captured from the polarizing microscope with a digital camera, under identical conditions (light intensity, lenses, filters, etc.) in order to obtain statistically valid and reproducible results. These images are stored in the computer's secondary memory and also trespassed to the monitor to determine interference noise. The latter are eliminated to optimize image clarity, such as: focus, relief, color balance, brightness and contrast, among the main attributes.

2. The true color image is converted to a binary image and, in turn, to a gray scale image (0-256 gray levels). Both images can be shown simultaneously on the monitor.

3. The sample image is segmented according to the thresholds obtained from the respective gray levels histogram (0 to 256). A different color can be selected for each gray level range of interest and all the zones of equal gray range within the image will be shown with the same color.

4. The software performs the required statistical study of the segmented phases, allowing automatic determination of the number of particles (for each type of the selected figures of equal composition); the maximum, minimum and average sizes and areas of the particles, their contact perimeters and their modal analysis; the disseminated textures, inclusions, associations and impurities.

Next, we will further clarify the above with a few examples of the AIAS application to gold process mineralogy.

2 CASE STUDIES

The authors applied "PRECIOUS-X" to different types of occurrences, associations and intergrowths of gold bearing ores, namely to the following six samples:

Table 1. Description of the Gold Samples.

Sample	Type and description
1. M-1	Gold /Coal
2. M-2	Gold /Silicates
3. M-3	Gold /Sulfides
4. M-4	Gold /Silicates/Jarosite
5. M-5	Gold /Sphalerite /Chalcocopyrite
6. M-6	Gold /Arsenical minerals

These six samples were originally studied to prepare this manuscript and clearly show that the AIAS can be applied to large variety of cases. For seasons of space, only samples M-1, M-2 and M-3 have been included here and described as case studies.

The species identification was the first routine, as is usual in gold-minerals associations. Sulfide

minerals were found reasonably well disseminated and silicate minerals could be sufficiently well identified, with traditional microscopy and confirmed with our software. However, reliable and satisfactory quantification of gold, considering all its intergrowths and associations with other present minerals, can only be performed with a good computer program to obtain rapid and accurate results. This was done with our software.

The results are shown in Tables 1 through 3, for samples M-1, M-2 and M-3, showing modal analysis, gold size distribution and gold liberation, respectively.

Table 2. Modal analysis of samples.

	M - 1		M - 2		M-3	
	Area	weigh t %	Area	weigh t %	Area	weigh t %
Gold	16.13 2	61.64	19.514 0	52.3	2.083 8	16.8
Quartz			3.9349	1.5	0.756 8	1.0
Orthoclase					78.79 4	62.5
Plagioclase					18.36 4	19.7
Coal	83.86 7	38.6				
Chalcocopyrite			68.780 0	40.7		
Pyrite			7.7701	5.5		
Total		100.0		100.0		100.0

Table 3. Size distribution. Gold area.

Area (Pixels)	M - 1	M - 2	M-3
Total	7647	19,173	1798
Lower	5	19,173	1798
Maximum	3572	19,173	1798
Average	201	19,173	1798

Table 4. Gold liberation. Area in pixels.

Liberation	M - 1	M - 2	M-3
Totally	794	0	0
Partially	0	0	---
Not liberated	---	19.173	1798

Figures 1, 2, 3 are microphotographs of the same samples used for our case studies, that is M-1, M-2 and M-3, respectively. These were captured with the digital camera mounted on the Leitz polarizing microscope and connected to the PC and monitor.

In Figure 1 we can observe the result of a test of gold on activated carbon, in order to control the adsorption relations, such as: gold prill's sizes, the thickness of the gold deposit layers, the gold penetrations within the carbon, which allow us to optimize the related processes.

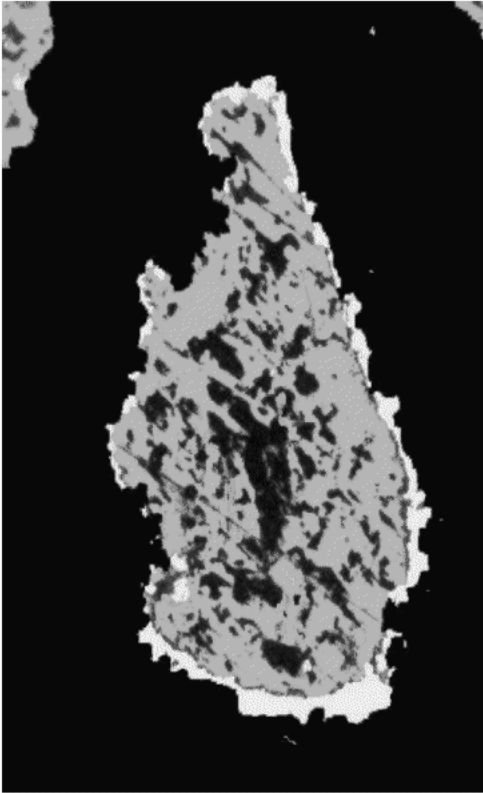


Figure 1. Microphotograph sample M-1. (Gold / Activated Carbon).

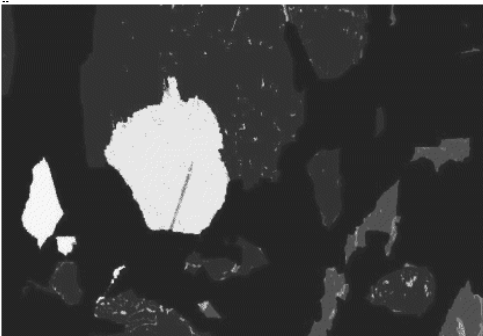


Figure 2. Microphotograph Sample M - 2. (Gold - Chalcopyrite - Quartz - Pyrite).

In Figure 3, gold is present as isolated grains in different sizes, as fine veinlets, clustered, specks aggregates frequently intergrown with silicate in intricate patterns. This interesting microphotograph shows gold as clear white particles, replacing a completely decomposed plagioclase and orthoclase.

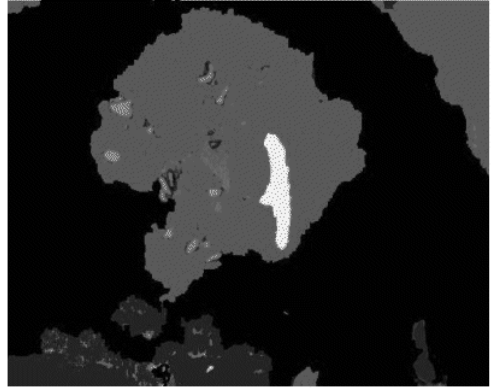


Figure 3. Microphotograph of sample M-3. (Clear-white gold replacing plagioclase/orthoclase).

ANÁLISIS CUANTITATIVO

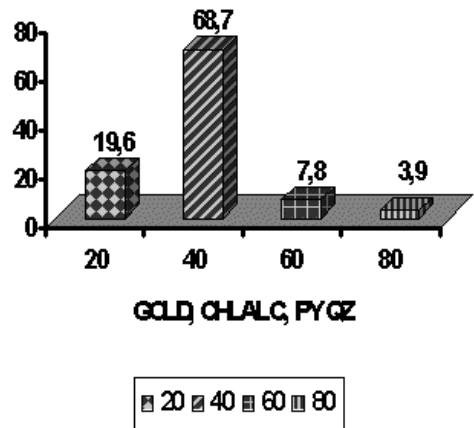


Figure 4. Quantitative analysis of sample M - 2.

Only sample M-2, showing the respective graph of the mineralogical species distribution, as resulted from the software, has been included for illustration purposes.

3 CONCLUSIONS

1. "PRECIOUS-X" is a powerful tool for evaluation of gold ore bodies, in function of the productive processes, that is, metallurgical mineralogy.
2. It is possible to determine and quantify not only macroscopic compositions of the minerals, but also the microscopic impurities therein contained.

3. From our three different case studies, it can easily be seen that with “PRECIOUS-X”, more accurate and fast assessment of the ore characteristics required can be obtained in a friendly manner, thus contributing to take better and shorter term decisions for plant operation purposes.

4. Our Automatic image analysis system, is also very useful for the evaluation ore-dressing tests and prediction of the ore’s metallurgical behavior in each stage of the productive process. It applies to intermediate optimization steps and to improve the final metal recovery. Being fast, powerful, and accurate it makes the job more productive!

4 REFERENCES

- Petruk,W. 1976. The Application of Quantitative Mineralogical Analysis of Ores to Ore Dressing. CIMM Bulletin, 146-153, Canada.
- Morrell, S. Runne, R., Finch, W. 1993. The Liberation Performance of a Grinding Circuit Treating Gold Bearing Ores. XVIII International Mineral Processing Congress. Sydney, Australia. 23-29.
- Sutherland, D. N. & Gottlieb, P. 1991. Application of Automated Quantitative Mineralogy in Mineral Processing. Minerals Engineering, vol.4: n.7-11, 753-762.
- Uytenbogaardt, W. 1971. Tables for Microscopic Identification of Ore Minerals. Elsevier Publishing Co., New York.
- Siegel,E.A.de.1999. Private communication: Pyrometallurgical Phases Characterization at Impala, South Africa.

Native Copper Analysis through Digital Microscopy

O.A.J.Soto, O.F.M.Gomes*, G.A.H.Pino & S.Paciornik

Department of Materials Science and Metallurgy, Catholic University of Rio de Janeiro, PUC-Rio, Rio de Janeiro, Brazil

** Centre for Mineral Technology, CETEM, Rio de Janeiro, Brazil*

ABSTRACT: There is no established procedure to determine native copper in a copper ore. Actually, due to its low occurrence in nature, there are not many references in the literature. This work proposes a method for copper ore analysis based on digital microscopy, image processing and chemical etching. The present case study was developed on an ore composed mainly of copper oxides, copper primary sulfides, copper secondary sulfides and native copper. Initially, several fields of a polished cross section of an ore sample were automatically imaged through a motorized optical microscope and a CCD camera connected to a computer. Then the sample suffered successive selective etchings. After each etching step, the sample was returned to the microscope and the same fields were imaged again, through the use of a computer-controlled x-y stage. Thus, three images per field were generated. Finally, the corresponding image sets (before and after each etching step) were processed and analyzed.

1 INTRODUCTION

The evaluation of head mineral for copper mining is nowadays based in just three chemical analyses: total copper, oxidized copper and copper soluble in sulfuric acid. Some companies use the sequential method for copper analysis. But none of these methods provides the amount of native copper in the sample. Moreover, copper recovery cannot be determined in these ores.

The present work proposes a method for copper ore analysis based on digital microscopy, image processing and chemical etching. Copper ore samples were imaged with a motorized optical microscope, allowing the acquisition of a large number of fields per sample. Each sample was then submitted to an etching sequence and, after each etching step, the sample was returned to the microscope and the same fields were imaged again. Thus, specific particles in each field can be located and the effect of etching can be accurately analyzed.

This correlated approach, *co-site microscopy*, improves the accuracy as compared to a traditional approach in which uncorrelated fields are analyzed before and after etching.

2 EXPERIMENTAL PROCEDURE

2.1 Material Selection

In the present work, an ore from Yauri Cusco, Peru, with $\approx 1.5\%$ of native copper was used.

The ore was classified and 4 samples (+74-100 μm , +63-74 μm , +37-63 μm , and +20-37 μm) were studied.

2.2 Sample Preparation and Etching

The samples were cold mounted by mixing the ore grains with low viscosity epoxy resin and subsequently ground, polished with 3 and 1 μm diamond paste and 0.05 μm alumina. Each sample was then glued to a glass slide in such a way that the polished surface was kept parallel to the glass plane. The glass slide was used as reference to insert the sample in the microscope sample holder. The glue used was insensitive to the chemical etchants used in the process. Thus, each sample could be observed, removed, etched and brought back to the microscope at nearly the same position, thus allowing the observation of the same fields along the etching sequence.

The first step of etching used citric acid (5% w/v) and sulfuric acid (5% v/v) for 1 hour at 25 C. Samples were then washed in deionized water and ethanol, and dried. The second step used silver sulfate (3 g/l) in sulfuric acid (5% v/v) solution in the same conditions as step 1.

The first etchant leaches all the copper oxides and part of the secondary copper sulfides. It also works as a light etchant for native copper. The second etchant leaches native copper completely and part of the sulfides.

2.3 Microscopy and Image Acquisition

A Zeiss AxioPlan 2ie mot optical microscope, with a motorized x-y stage and an AxioCam digital camera (1300 x 1030 pixels) was used in the experiments. Being fully computer-controlled, the system allows for the acquisition of any number of fields at specific x-y positions of the sample holder. Thus, within the error of the holder stepper motors, it is possible to go back to the same fields of a sample.

The system also allows for motorized control of the z-axis. Thus is possible to control the focusing for each field. An autofocus routine (Valdecasas et al. 2001, Bastos et al. 2003) was developed, allowing for automatic in focus image acquisition including compensation for sample surface inclination and local focus variation.

A set of one hundred fields was acquired from each of the samples, using a 20X objective lens, corresponding to a resolution of 0.53 $\mu\text{m}/\text{pixel}$. At this magnification each field corresponds to 685 x 543 μm^2 . Given that native copper concentration in these samples was $\approx 1.5\%$, one can expect to randomly find a few fields showing native copper particles.

The same routine was used for every sample, after each of the etching steps, leading to a total of 300 images per sample.

3 IMAGE PROCESSING AND ANALYSIS

The image processing and analysis sequence involved the steps of alignment and cropping, segmentation and measurement.

3.1 Image Alignment and Cropping

As images obtained after each etching step are to be quantitatively compared, they must be in perfect register. However, the placement of the glass slide on the microscope holder has limited repeatability and the motorized stage also presents limited

accuracy. In our experiments this led to a larger misalignment in the y-direction, of several pixels, and a smaller misalignment in the x-direction. Nevertheless, the misalignment corresponded to a few percent of the field size, allowing an automated alignment procedure.

Cross-correlation in the frequency domain (Gonzalez & Woods 1992) was used. As the misalignment was small and there are other components of the ore that are not affected by etching, the images didn't change too much due to the etching. Thus, there is always a clear correlation peak and its distance from the central pixel of the image corresponds to the displacement vector. For certain sets of images, a previous step of contrast normalization was used to improve the correlation peak definition. After alignment, all images were cropped to eliminate edge effects. The procedure runs automatically and representative results are shown in Figure 1.

3.2 Segmentation

As one of the goals of the procedure is to evaluate the leaching of native copper, this phase must be detected at each step of the etching sequence. As the microscope illumination is also computer-controlled; one can expect enough color stability to allow for stable detection thresholds.

Before the first etching, native copper and bornite (a copper/iron sulfide) appear with nearly the same color. To distinguish between them, a threshold based on the HSI color model (Gonzalez & Woods 1992) was used. In some fields the threshold had to be manually adjusted and, in some cases, it was impossible to eliminate the bornite particles without impairing the detection of copper particles.

Once the unetched copper particles were detected, they were used to mask the rest of the field in the images obtained after the etching steps.

Figure 2 shows a detail of a native copper particle before and after the two etching steps and the segmented regions detected by the procedure. It is possible to detect a small change after the first etching and the total disappearance of the particle after the second etching, leaving behind the unfocused region of the epoxy resin.

3.3 Measurement

Once the native copper particles are detected before and after each etching step, several size and shape parameters can be automatically measured.

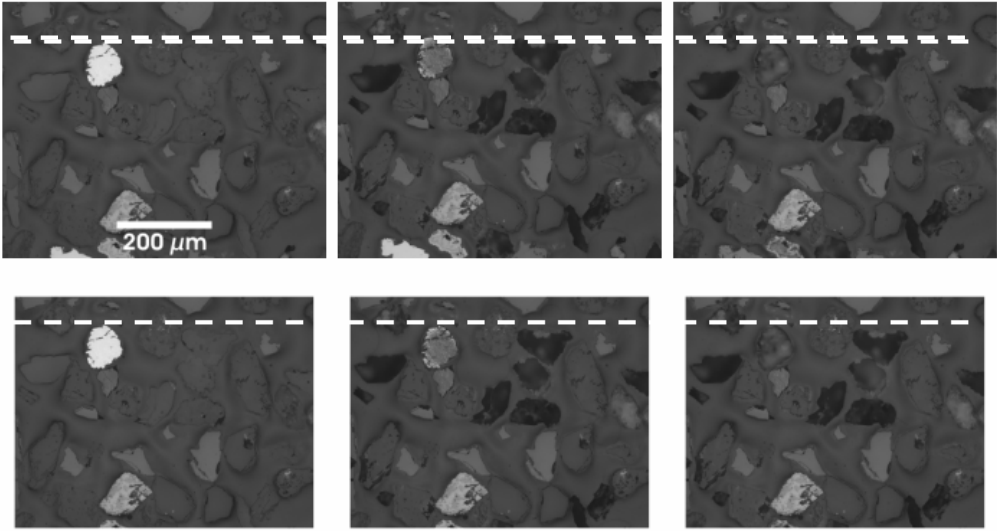


Figure 1: Image alignment through cross-correlation and cropping. The reference dashed lines highlights the vertical displacement between the images and the alignment reached after correlation.

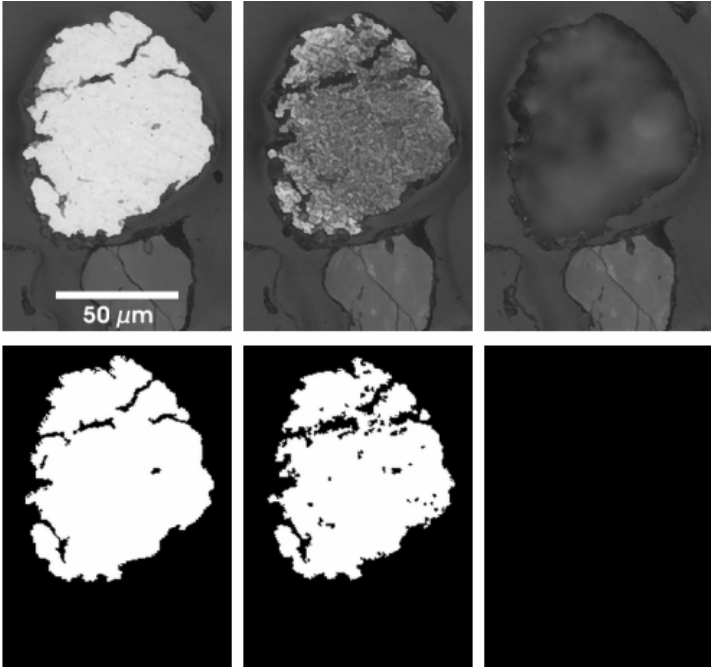


Figure 2: Detail of a native copper particle during etching and segmentation results.

4 RESULTS AND DISCUSSION

To evaluate the leaching of native copper, the area of each particle was measured before and after each etching. Table 1 shows these areas for some representative particles. A1, A2 and A3 mean area before first etching, after first etching and after second etching, respectively.

Table 1: Area measurements before and after each etching step

Particle	A1 (μm^2)	A2 (μm^2)	A2/A1 (%)	A3 (μm^2)	A3/A1 (%)
1	4683	4197	90	0	0
2	3912	3341	85	0	0
3	3781	3230	85	93	2
4	3203	2487	78	0	0
5	2490	2306	93	0	0
6	2187	2143	98	0	0
7	1315	0	0	0	0
8	1014	512	50	0	0
9	954	732	77	0	0
10	599	410	68	0	0
11	578	462	80	0	0
12	553	341	62	0	0
13	552	271	49	0	0

No correlation was found between the leaching kinetics and particle area reduction along the etching steps. We can point out some reasons for this behavior.

In line 3 of Table 1, one can see a native copper particle that apparently was not completely leached after the two etchings. Actually, as shown in Figure 3, a small silver precipitate appeared where before there was a native copper particle

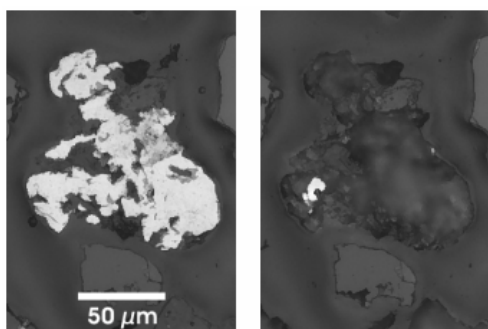


Figure 3: Native copper particle and silver precipitate after the second etching..

Referring to the particle in line 7, even though $A2=0$, indicating total leaching, this is very unlikely. Probably, the particle got detached during the etching and thus this result is not representative.

Particles 8 and 9 had similar areas, but after the first etching their area reductions were very different (Fig.4). This was a common behavior in the database of over 250 particles. It denotes the lack of correlation mentioned above. Many factors contribute to this such as porosity, polishing defects, particle shape, cross-sectional effects, among others.

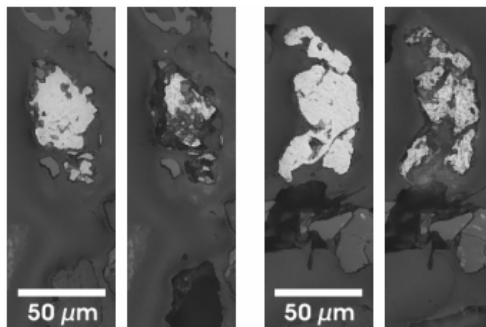


Figure 4: Particles with similar original areas and different area reduction after the first etching.

5 CONCLUSIONS

Even though no quantitative correlation between etching kinetics and area reduction was found, the approach of *co-site microscopy* opens up new possibilities of analysis.

For instance, once the particles are identified before and after each etching step, other measurements (size, shape and texture) can be automatically obtained, and may allow a better description of the process.

The technique allows the local observation of specific phenomena that would be lost in the classical multi-field statistical approach and can be applied to several other systems. Originally similar phases may change color during etching and can thus be discriminated particle by particle.

6 REFERENCES

- Bastos, A. L., Gomes, O. F. M., Maurício, M. H. P., Paciornik, S. (2003): Digital Microscopy Applied to Materials Characterization. Proceedings of XIX Congresso da Sociedade Brasileira de Microscopia e Microanálise, Caxambu, Brazil, 2003.
- Gonzalez, R. C. & Woods, R. E. (1992). *Digital Image Processing*. New York: Addison-Wesley.
- Valdecasas, A. G., Marshall, D., Becerra, J. M., Terrero, J. J. (2001): On the extended depth of focus algorithms for bright field microscopy. *Micron* 33: 559-569.

Nanometer Size Iron Oxides in Australian Iron Ores: Implications for Mineral Processing

A.G.Trudu, J.M.F.Clout, J.M.Young

CSIRO Minerals, Queensland Centre for Advanced Technologies, Kenmore, QLD, Australia

ABSTRACT: Mineralogical studies of iron ores from Australia have discovered the occurrence of iron oxide crystals, which have dimensions within the nanometer scale. Certain sections of some iron ore deposits contain iron oxides of exceedingly fine grain size, comprising a distinctly bright brick-red powder. Follow-up studies under the in-lens field emission scanning electron microscope showed that the aggregates were composed of nanometer-sized crystals of hematite plates and other unidentified iron oxide with dimensions of down to a few hundreds of nanometers, but thickness of only tens of nanometers. They formed a network within cavities hosting tiny needles and tubes, which are both smaller than the surrounding hematite microplates. The material has a very high (65-68% Fe) iron content as it is composed of practically pure iron oxides, although it has often been incorrectly identified in the field as a red clay. The very fine grain size of the iron oxides and presence within the abundant surrounding nanoplate and microplate hematite has made it difficult to isolate and identify their exact crystal structure. The ultrafine material acts as an exceptionally strong binder for iron ore agglomeration applications in mineral processing including for pelletising and in sinter granule formation. The nanometre scale iron oxides are part of the primary ore and are interpreted as the initial precipitates from the ore forming solution which replaced the carbonate and chert-rich layer of the original Banded Iron Formation host.

1 INTRODUCTION

1.1 Australian iron ore deposits

Australian iron ores can be classified into five broad genetic types and a number of subtypes, each of which have distinct ore and gangue mineralogy, ore textures and porosity (Tab.1) (Clout et al. 1997). The Banded Iron Formation (BIF)-derived Bedded Iron Deposits (BID) and the Channel Iron Deposits (CID, or pisolite ores) are the most economically important although there is also production from the much smaller metamorphosed BID and BIF-derived Detrital Iron Deposits (DID). The BIF-derived iron ore deposits of the Pilbara, Yilgarn and Gawler cratons represent a very significant iron ore resource for Australia, with current and previous production dominated by the Pilbara iron ore deposits (Tab.1). The Microplate Hematite ores and Martite-Goethite ores are the most important BIF-derived ores (Harmsworth et al. 1990).

Ore textures in the BIF-derived ores are quite complex and have formed the basis for their interpreted genesis which includes either hypogene upgrading for the Microplate Hematite ores (Dorr 1965; Li et al. 1993; Martin et al. 1998; Webb et al. 2002) or supergene upgrading followed by regional metamorphism for Microplate Hematite ores and

supergene upgrading for the Martite-Goethite ores (Morris 1985, 1986, 1987; Harmsworth et al. 1990).

There have also been a number of papers on the genesis of banded iron formation and their primary textures (Morris 1993; Barley et al. 1997). Recent work by Clout (2003) describes a new iron ore texture classification system to better understand the vertical textural zonation characteristics of Australian BIF-derived deposits in the Pilbara, Yilgarn and Gawler cratons, the interpreted role of recent supergene upgrading processes on modifying primary ore textures and their implications for downstream mineral processing.

This paper describes a new iron ore texture which contains nanometer sized iron oxides which occur in a number of Australian BIF-derived deposits, their implications for downstream mineral processing and interpreted ore genesis as the original precipitates from ore forming fluids.

Table 1. Australian iron ore deposit classifications for current and some future mines.

Classification - Deposit Type	Current and Future Mines
1 BIF (a) Magnetite and (b) Hematite	Mount Gibson, Koolanooka, Talling Peak (Yilgarn)
2 BIF-Derived (a) Bedded Iron Deposit - Martite-Goethite	Marandoo, West Angelas, Orebody 29, Mining Area C, Hope Downs (Pilbara), Koolyanobbing (Yilgarn)
- Microplaty Hematite (b) Metamorphosed Bedded Iron Deposit (c) Detrital Iron Deposit	Mount Whaleback, Mount Tom Price, Paraburdoo, Channar, Yarrie (Pilbara), Iron Duke, Iron Knight, Iron Duchess (Gawler), Cockatoo Island, Koolan Island (Pilbara) (Brockman 2 Detritals) (Pilbara)
3 Channel Iron CID	Mesa J, Yandi, Yandicoogina (Pilbara)
4 Hydrothermal/ Metasomatic (a) Hematite (b) Magnetite	Koolyanobbing –macroplaty hematite ore (Yilgarn) Savage River
5 Magmatic	-

2 METHODS

Samples were collected from a number of Australian Microplaty Hematite and Martite-Goethite iron ore deposits. Subsamples were mounted in epoxy resin, cured then ground flat to expose the surfaces of the mineral grains and polished with diamond paste. The samples were then examined using combined reflected light optical and scanning electron microscopic techniques. Natural sample powders collected directly from the mine faces were also examined using the in-lens field emission scanning electron microscope (IFESEM).

3 RESULTS

3.1 Textural characteristics

Mineralogical studies of iron ores from four Australian deposits discovered the occurrence of iron oxide crystals, which have dimensions within the nanometer scale, often amongst coarser microplates of hematite (Fig.1). Iron oxides of exceedingly fine grain size was identified during field studies: the material displayed a distinctly bright brick-red colour and was ultrafine-grained so that, when it was touched with the hands, it penetrated into the skin surface and was difficult to wash away. This material is much finer than normally found in iron ore mines across Australia. Under the reflected light optical microscope the ultrafine-grained material was identified as aggregates of submicroscopic crystals showing

either an overall brown or green-grey tinge; micron-size hematite microplates were more clearly visible under the SEM (Fig.2).

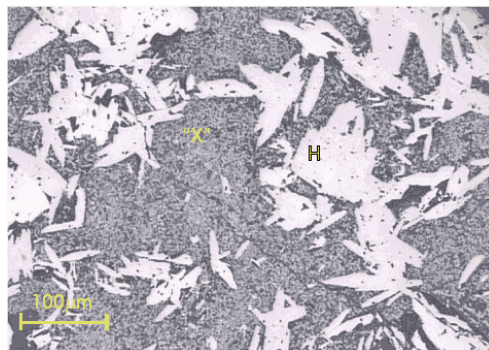


Figure 1. Photomicrograph of coarse grained microplaty hematite (H) with significant infill of soft, nanometre scale iron oxides "X". Reflected ordinary light. Sample 70-031.

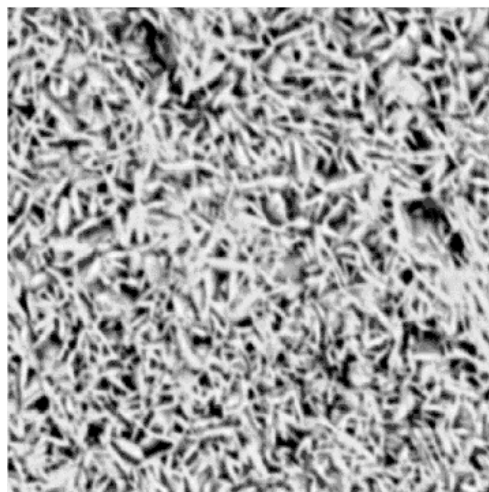


Figure 2. Distinct very fine-grained hematite microplates. Note that darker areas are pores. -2 x +1 mm size fraction. Back-scattered electron (BSE) image.

Follow-up studies under the in-lens field emission scanning electron microscope (IFESEM) showed that the aggregates were composed of nanometer-sized crystals of hematite plates with dimensions of down to a few hundreds of nanometers, but thickness of only tens of nanometers. They form a network within cavities hosting nanometre-sized needles and tubes, which are both smaller than the microplates (Figs. 3, 4, 5). The needles and tubes of iron oxides show very well defined crystal shapes.

Overall the powdery hematite ores show at least three size populations of plates (Fig. 6).

Targeting and analysis of the larger aggregates of needles (Fig. 5) by Energy Dispersive Spectrometry indicated iron and oxygen in the spectra, suggestive of either goethite or another iron oxide phase. However, bulk Rietveldt XRD analysis suggested the presence of hematite only in the samples even though at least 20% by area of the samples is composed of the needles.

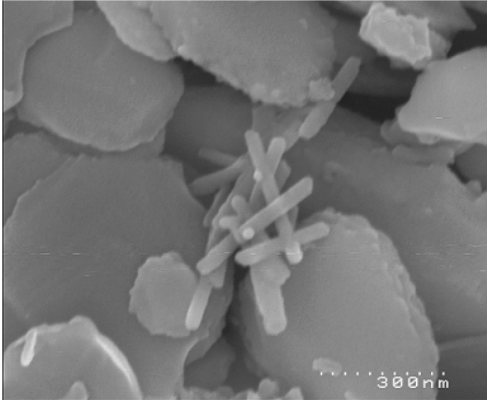


Figure 3. Distinct very fine-grained needles and larger hematite microplates of greenish-grey variant. Note that darker areas are pores. -2 x +1 mm size fraction. IFESSEM image.

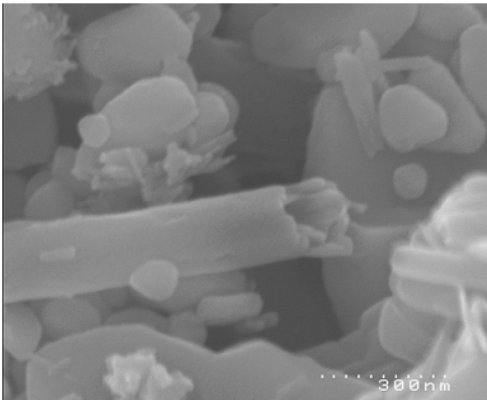


Figure 4. Nanotube and platelets of hematite. -2 x +1 mm size fraction. IFESSEM image.

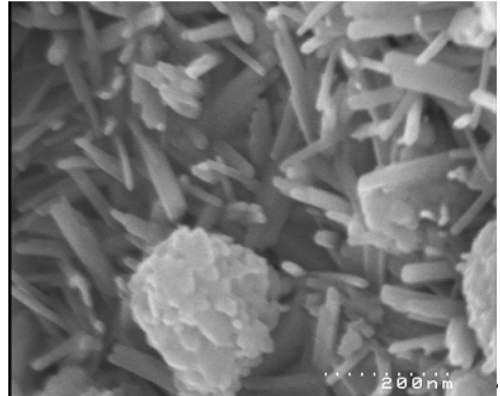


Figure 5. Nanoneedles of an unidentified phase. -2 x +1 mm size fraction. IFESSEM image.

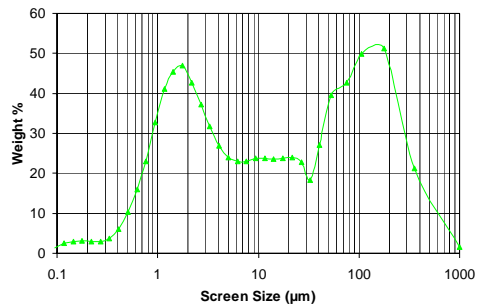


Figure 6. Size distribution of powdery microplaty hematite ore containing Nanoneedles. Analysis by laser sizer.

3.2 Implications for Mineral Processing

There are a number of mineral processing implications of our mineralogical discovery. Firstly the material has a very high (65-68% Fe) iron content as it is composed of practically pure iron oxides. This implies that it should not be removed during mineral processing of the ore, as the overall iron grade of the ore would drop. The ultrafine material acts as an exceptionally strong binder during pelletising or sintering, with higher levels resulting in very plastic green balls and granules, respectively. Whilst the desirable properties of the ultrafine iron ore can be used to benefit for pelletising and sinter granule formation, the levels must be controlled since they can lead to spalling during pellet heating. The ultrafine aggregates of iron oxides appear to allow water to penetrate, but not easily escape from it.

4 IMPLICATIONS FOR ORE GENESIS

The nanometer scale needles, tubes and hematite plates mostly occur within the less heavily mineralized primary ore and below the normal depth of weathering. There is also some which occurs in heavily dehydrated zones that form in perched water tables in the Martite-Goethite ore types (Clout 2003). There is a continuous variation in abundance of nanometer scale iron oxides relative to the enclosing coarse (>50µm) hematite plates (e.g. Fig. 3) from 80% by volume down to only a few percent. The population sizes of hematite plates varies continuously from the nanometer scale (60-600 nm), to microns (1-3µm) and hundreds of microns (100-200µm) (Fig. 6). The population of hematite plates is interpreted to represent various stages of nucleation, crystallization and progressive growth of hematite from the primary ore-forming fluid in areas that were once carbonate or silicate layers in the BIF. The nanotubes and needles are also interpreted as primary precipitates but with no other obvious coarser growth phase present.

5 CONCLUSIONS

Sampling of various Australian Microplaty and Martite-Goethite deposits has located nanometer scale plates, needles and tubes of iron oxides which form a bright red powder. The nanometre crystals are part of the primary ore and are interpreted as initial precipitates from the ore forming solution. Their high iron grade and physical binding properties makes the nanoscale crystals an excellent additive for sinter granules and pellets.

6 REFERENCES

- Barley, M. E.; Prickard, A. L. & Sylvester, P. J. 1997. Emplacement of a large igneous province as a possible cause of banded iron formation 2.45 billion years ago. *Letters to Nature*, 385:55-58.
- Clout, J. M. F., Firth, B. A. & O'Connor, M. T. 1997. New Advances in beneficiation of iron ore. Proceedings of the National Conference on Iron Making Resources and Reserves Estimation (Eds.: V. N. Misra & J. S. Dunlop). Aus IMM, Perth: p.177-183.
- Clout, J. M. F. 2003. Upgrading Processes in BIF-Derived Iron Ore Deposits: implications for ore genesis and downstream processing, IMM, Applied Earth Sciences (Trans. IMM. B), April 2003, vol. 112, B1.
- Dorr, J. van N, II, 1965. Nature and origin of high-grade hematite ores of Minas Gerais, Brazil, *Economic Geology* 60:1-46.
- Harmsworth, R. A., Kneeshaw, M., Morris, R. C., Robinson, C. J., Shrivastava, 1990. BIF-derived iron ores of the Hamersley Province, in *Geology of the Mineral Deposits of Australia and Papua New Guinea* (Ed. F E Hughes), p 617-642 (The Australasian Institute of Mining and Metallurgy: Melbourne).
- Li, X. I., Powell, C. McA. & Bowman, R. 1993. Timing and genesis of Hamersley iron-ore deposits. *Exploration Geophysics*, 24:6312-636.
- Martin, D. McB., Li, Z. X., Nemchin, A. A., Powell, C. McA. 1998. A pre-2.2 Ga age for giant hematite ores of the Hamersley Province, Australia? *Economic Geology* 93:1084-1090.
- Morris, R. C. 1985. Genesis of iron ore in banded iron-formation by supergene and supergene-metamorphic processes - conceptual model. *Handbook of Strata-Bound and Strataform Ore Deposits*, vol. 13 (Ed K H Wolf), p. 73-235 (Elsevier: Amsterdam).
- Morris, R. C. 1986. A review of geological research on the iron ores of the Hamersley Iron Province, in *Publications of the 13th CMMI Congress*, vol. 2 *Geology and Exploration* (Ed D A Berkman), pp 191-200 (13th Congress of the Council of Mining and Metallurgical Institutions: Melbourne; and the Australasian Institute of Mining and Metallurgy: Melbourne).
- Morris, R. C. 1987. Iron ores derived by the enrichment of banded iron-formation, in *The Genesis of Ores and Petroleum Associated with Sedimentary Siliceous Deposits* (Ed J R Hein), p. 231-267 (Van Nostrand Reinhold Company: New York).
- Morris, R. C. 1993. Genetic modelling for banded iron-formation of the Hamersley Group, Pilbara Craton, Western Australia. *Precambrian Research*, 60:243-286.
- Webb, A. D., Oliver, N. H. S., Dickens, G. R. 2002. Multistage evolution of high-grade hematite orebodies from the Hamersley Province, Western Australia. In: *Iron Ore 2002 Conference*, AusIMM, Perth, WA, p.91-94.
- Zhang, N. & Whiten, W. 2001. Determining mineral composition from assays, in *International Heavy Minerals Conference*, AusIMM, Fremantle: p. 81-85.

Methods of the Evaluation of Mineral Surface Wettability

V.E. Vigdergauz

Institute of Complex Exploitation of Mineral Resources, Russian Academy of Sciences, IPKON RAS, 4 Kryukovsky, 111020 Moscow, Russia

ABSTRACT: Methods of an experimental study of wetting phenomena for minerals are discussed. They are classified by the relative motion of liquid and gas phases. Measurements of air bubble detachment force, induction time, air bubble evolution pressure and mineral floatability were used to study wettability of pyrite, galena, and chalcocite. The results of the measurements of natural wettability and wettability induced by xanthates with the different length of an alkyl chain are reported. Experiments show the existence of two or more maxima of hydrophobicity on the dependences of pH or electrochemical potential. These maxima are attributed as a reflection of cationic and anionic centers on mineral surfaces with non-compensated positive and negative charges. These charges could be compensated both by regulation of pH and electrochemical potential values. Surfaces of sulfide minerals are chemically heterogeneous and wettability measurements reflect this heterogeneity. Under consideration the wetting phenomena force and energy approaches can be used. The path of the evaluation of the molecular component of the attachment energy is demonstrated. A correlation of the flotation experiments with wettability was observed.

1 INTRODUCTION

Metal sulfides are most important for industry and therefore, well-studied minerals. Electrochemical reactions on their surfaces are important for their processing by a wet mechanical dressing, flotation, and hydrometallurgy. Common practice of the operation with ores includes regulations of its redox conditions for an optimal treatment. Irreversible changes of sulfide surface composition during their polarization are well documented. In the presence of water and oxygen they are thermodynamically unstable, but their oxidation is a rather slow process. This is the reason for the existence of sulfides in ore bodies and even in flotation tails stored for many years. There has been general agreement regarding the species responsible for rendering sulfides hydrophobic and floatable. In the case of natural floatability, it is elemental sulfur and for the case of xanthate-induced flotation, it is dixanthogen and metal xanthates.

The contact angle of the bubble/mineral/solution interface has been employed for many years as a measure of wettability of minerals and, hence, of suitable conditions for mineral flotation. The available data on contact angles are rather uncertain. The main reason is hysteresis phenomena. On real

surfaces, a hysteresis of 10° or higher is quite common (Folkers et al.1992).

Alternative methods of an experimental study of wetting phenomena are classified by the relative motion of liquid and gas phases (Vigdergauz & Nedosekina 1998). Quantitative comparisons of the experimental values are possible within each group only. Results of the measurements of air bubble detachment force (DF), induction time (IT), air bubble evolution pressure (EP), and mineral floatability are discussed for sulfide minerals - pyrite and galena. The results of the measurements of natural and xanthates induced wettability are reported.

Traditional approach for an analysis of surface wetting operates with homogeneous surfaces. It predicts single maximum of hydrophobicity near potential of zero charge (pzc). Mercury was found as a suitable metal for a study of electrocapillary phenomena. Drop of mercury has isotropic and homogeneous surface. Mercury could be easily polarized and possess an electronic conductivity. Modern theories of the wetting phenomena are mainly based on the experiments with mercury. Equations of the balance of capillary and gravity forces (Frumkin-Kabanov and Wark equations) became theoretical basis for an analysis of flotation

phenomena (Klassen & Mokrousov 1959, Sutherland & Wark 1955). These equations are equations of capillary physics.

Polarization of solid electrodes changes the surface tension or surface free energy at the solid-liquid interface (γ_{sl}) that leads to the alteration of the angle of wettability. A method for the determination of a PZC for metals that is based on this phenomenon is widely known. Metal wettability has a minimum at this point. It is reasonable to assume that for the mineral-solution interface, γ_{sl} and therefore contact angle will also depend on the surface charge. So long as the charge on the mineral surface depends on the H^+ and OH^- ion concentrations, it is attractive to study pH dependences of minerals' wettability.

2 METHODOLOGY

For the evaluation of surface wettability under conditions of pH change and potentiostatic polarization the measurements of contact angle, IT, DF and EP were used. Experimental details of the measurements of an IT, DF and contact angles were described earlier (Vigdergauz & Nedosekina 1998). A torsion balance and a modified Sven-Nilsson device were used in DF and IT experiments. IT was defined as the minimum time necessary for the attachment of an air bubble to the mineral surface.

The EP experiments set-up included vacuum box with vacuum pump and manometer, potentiostat with a sweep generator, electrochemical cell with a three-electrode system and photo lens with computer for an image analysis.

Flotation experiments were carried out in an electrochemical cell based on the Hallimond tube. Electrochemical cells with a three-electrode system were used in cyclic voltammetry (CV) and potentially controlled DF, IT, EP, and flotation experiments. Potentials were measured and are reported versus a silver-silver chloride reference electrode, which had a potential of +0.22V against the standard hydrogen electrode. The potential of platinum mesh or mineral disc electrodes was controlled by a PI 50 potentiostat programmed with a sweep generator PR-8 (Izmeritel, Gomel, Byelorussia). Current passed between the working electrode and a platinum counter electrode, which was housed in the compartment, separated from the main cell by a sintered glass disc. An X-Y recorder was used for recording CV curves. To study xanthate sorption, spectral measurements were used (Chanturiya & Vigdergauz 1993).

3 RESULTS AND DISCUSSION

Measurements of stationary potentials of minerals, Figure 1, give one average PZC value for the whole particles (Vigdergauz 2003).

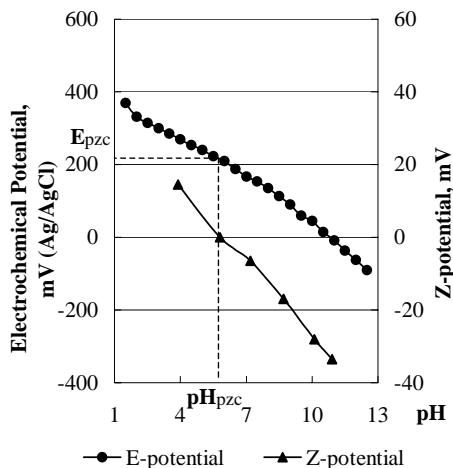


Figure 1. pH dependence of electrochemical and electrokinetic potentials of pyrite

Experimental studies of mineral surface wettability show an existence of two or more maxima of hydrophobicity on the dependences of pH or electrochemical potential, Figures 2, 3 (Vigdergauz & Nedosekina 1998, Vigdergauz & Panova 2002). The main maxima are observed for pH 6-6.5 and 9-9.5 on stationary potentials and for potentials -0.2; 0-0.2; 0.8-0.9V on pH 9.2. These maxima are attributed as a reflection of cationic and anionic centers on mineral surfaces with non-compensated positive and negative charges successively. Cathodic polarization leads to desorption of xanthate compounds from the surface of metal sulfides electrodes decreases DF and puts an end to bubble formation. Similar effects are observed under anodic polarization due the formation of hydrophilic layer of metals' oxides.

DF/potential polarization curves are similar in shape for the absence of xanthate and for the presence of all xanthates studied, Figure 2. The qualitatively similar character of the dependences of hydrophobicity functions with and without collector leads to the conclusion that xanthate ions block metal sites that give an input to the total hydrophobicity, but the basic influence is a self-induced hydrophobicity of sulfides is observed due to the influence of S-sites.

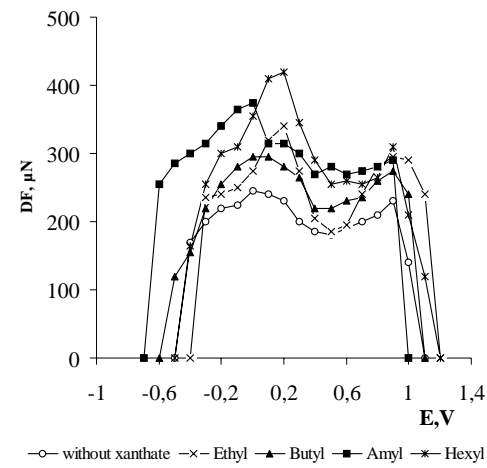


Figure 2. DF dependences on the potential of pyrite electrode

The result of increasing the carbon chain of xanthate was, as a rule, a decreasing of IT and an expansion of the area of adhesion potentials. These data are in accordance with the well known fact that in increase in the alkyl chain of xanthate collectors leads to more rapid flotation. Impulse electrochemical methods - CV and impedance measurements - reflect the presence of cationic and anionic centers on mineral surfaces. Surface of sulfide minerals is electrochemically heterogeneous and there are could be simultaneously represented cathodic and anodic areas. It was clearly shown with the help of microradiographic technique (Plaksin & Shafeev 1959). Moreover, these surfaces are chemically heterogeneous and wettability measurements could reflect this heterogeneity. On the mineral surface there are cationic and anionic sites with non-compensated positive and negative charges successively. These charges could be compensated both by regulation of pH and electrochemical potential (Vigdergauz 2001).

Flotation experiments with slurry electrodes qualitatively confirm the obtained results, Figure 4 (Chanturiya & Vigdergauz 1993). Process of bubble-mineral complex formation includes steps of microbubbles evolution on hydrophobic surfaces and subsequent coalescence of them with the bearing bubbles. The second process does not have influence on the selectivity of flotation. So, for the development of the conditions of selective flotation, the key step is an increase of the differences of wettability.

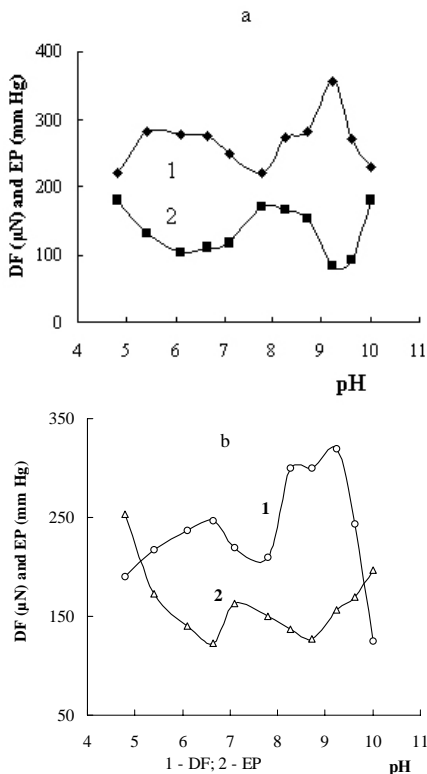


Figure 3. DF and EP dependences on the pH for galena (a) and pyrite (b)

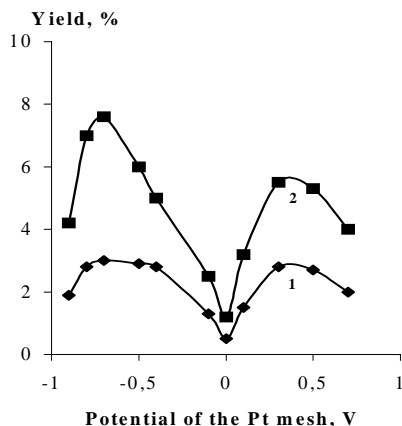


Figure 4. Self-induced pyrite floatability dependences on the potential of Pt mesh: flotation time: 1- 10 min; 2 - 20 min.

Figure 5 illustrates the influence of xanthate and oleic ions sorption at the beginning of bubbles evolution under decompression on the surfaces of pyrite and galena (Vigdergauz & Dorofeev 2003).

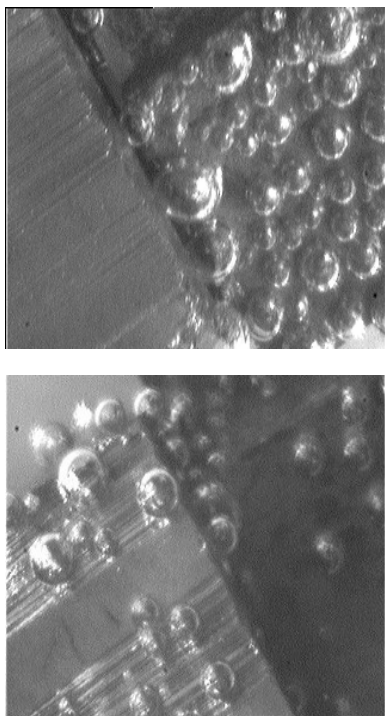


Figure 5. Pyrite (left one) and Galena (right one) in presence of xanthate (above) and xanthate and oleic-ions (below).

Under consideration the wetting phenomena force and energy approaches can be used (Bartsch 1925). Due to well-definite chemical conditions of a bubble-mineral system before and after attachment or detachment the determination of hydrophobicity through the calculation of the contact angle values considering the system's energy could become preferable. An approximate path of the evaluation of the molecular component of the attachment energy ΔG_m has been demonstrated earlier (Vigdergauz 1999). The surface free energy of the liquid-gas interface must be extracted from the detachment force value divided into the length of three-phase contact perimeter.

4 CONCLUSIONS

Measurements of mineral surface wettability reflect chemical heterogeneity of the surface. CV study of redox-transitions on sulfide's surface under cathodic

and anodic polarization leads to the conclusion that both cationic and anionic sites participate in them simultaneously. With increasing pH the hydroxides of the metals become ever more important in the surface redox reactions of sulfides. Resultant wettability is a superposition of the wettabilities of atomic or ionic sites and sorbed molecules and could be calculated through the energies of hydration of these sites.

5 ACKNOWLEDGEMENT

I thank Prof. V.A.Chanturiya for support, discussion and interest in this work.

Special thanks to the Russian Foundation of Basic Researches for research grants No. 00-05-64094 and 02-05-64225.

Grant from Mr. President of the Russian Federation (No. Nosh 472.2003.5) is gratefully acknowledged.

6 REFERENCES

- Bartsch, O., 1925. Uber Schaumssysteme. Kolloidchemie Beihefte, B20, 1-5, 42-49.
- Chanturiya, V.A., Vigdergauz, V.E., 1993. Elektrokhemija sul'fidov: Teoriya i praktika flotacii. Nauka, Moskwa, 86-125.
- Folkers, J.P., Laibinis, P.E., Whitesides, G.M., 1992. Self-assembled monolayers of alkanethiols on gold: the adsorption and wetting properties of monolayers derived from two components with alkane chains of different lengths. Journal of Adhesion Science Technology, 12, 1397-1410.
- Klassen, W.I., Mokrousov, V.A., 1959. Vvedenie v teoriju flotaczii. GNTIGD, Moskwa, 3-636.
- Plaksin, I.N., Shafeev R. Sh. 1959. To mechinizm of electrochemical heterogeneity of the surface of sulphide minerals // Dokl. Akad. Nauk SSSR V. 125, №3, P. 599-600.
- Sutherland, K.L., Wark. I.W., 1955. Principles of Flotation., AIMM, Melbourne, P. 5-230
- Vigdergauz, V.E., Nedosekina, T.V. 1998. The wettability of electrodes made of natural metal sulfides. Journal of Solid State Electrochemistry, 1, 50-57.
- Vigdergauz, V.E. 1999. Wetting hysteresis and methods of an experimental study of wetting phenomena. Proc. 8th BMPC, vol. 2, pp 819-826.
- Vigdergauz, V.E. 2001. Electrochemically modified wettability of natural metal sulfides and flotation. Proc. 9th BMPC, pp 187-191.
- Vigdergauz, V.E., Panova, M.V. 2002. Air bubbles evolution on the mineral surface under decompression: 1. Pyrite, chalcopyrite, galena. Proc.Int.Conf. Plaks. Chten., vol. 3, pp 97-98.
- Vigdergauz, V.E., Dorofeev, A.I. 2003. Prepared for publication.
- Vigdergauz, V.E. 2003. Electrochemistry of Pyrite Flotation: Second Maximum of Hydrophobicity. Proc. of 203th ECS Meeting, Paris, in press.

Definition of the Type of Refractoriness in El Zancudo Gold Mine, Antioquia, Colombia

D.M.Zapata

Geoscience Schools, National University of Colombia–Medellin. Current Address: Material Engineering School, National University of Colombia – Medellin, Colombia

A.N.Gallego

Geoscience Schools, National University of Colombia–Medellin, Colombia

M.A.Márquez

Material Engineering Schools, National University of Colombia – Medellin, Colombia

ABSTRACT: El Zancudo gold mine deposit is located in Titiribí, Antioquia in central Colombia; it has been traditionally considered as a refractory ore, however, no detailed mineralogical studies exist. The principal ore phases in the deposit are arsenopyrite and pyrite, with minor proportions of sphalerite, tetrahedrite, bournonite, galena and chalcopyrite, and pirrhotite, jamesonite, rutile, gold and silver like accessories, identified by x ray diffraction (XRD), scanning electron microscopy with energy dispersive spectroscopy (SEM/EDS) and polarized light microscopy. The principal gangue minerals are quartz, carbonates and sericite. Gold occurs mainly as small inclusions in pyrite and about 90% of gold showed sizes smaller than 70µm. In relation to the ore refractoriness these results indicate: (i) 50% of the gold is present like small inclusions (below 10µm) in sulfides and sulphosalts, and has problems with the liberation by milling, probably requiring some type of pretreatment (ii) the ore minerals will probably generate problems in the cyanidation because: (a) tetrahedrite, bournonite and jamesonite are strongly cyanicides, (b) arsenopyrite and pyrite, the most abundant ore minerals, can generate arsenites/arsenates or different kinds of sulphur compounds, consuming either cyanide or oxygen, reducing the rate of dissolution, (c) pirrhotite, present in small proportions, is one of the most reactive sulfide in cyanide solutions and it can to produce hidroxiles ions, adsorved on the gold's surfaces, (d) sericite can form waterproof coatings over gold grains, preventing the cyanide action, or causing preg-robbing.

1 INTRODUCTION

El Zancudo gold mine deposit is located in Titiribí (6° 04' 04'' N y 75° 47' 38''W), Antioquia, in the western flank of the Cordillera Central, central Colombia. This deposit corresponds to a vetiform mineralization within metamorphic rocks, correlated to the Arquía Complex (Restrepo 1986), sedimentary rocks of Amagá Formation and porphyritic rocks generally considered as associated to mineralizing events (Grosse 1926). El Zancudo gold deposit has been traditionally considered as a refractory ore, however, no detailed mineralogical studies exist, which enable to identify the causes of this refractoriness.

2 ANALYTICAL TECHNIQUES

In the development of this research, twenty eight polished thin sections were made from samples taken at different levels of the deposit.

Techniques like reflected/transmitted light microscopy, x-ray diffraction (XRD) and scanning electron microscopy with energy dispersive X-ray detector (SEM/EDS) were used, in order to

determine the components of the ore and mineral forms, sizes and associations. To quantify the different phases, modal point counting was made in each one of the polished thin sections.

3 MINERALOGY

The results of the point counting showed that the principal ore phases are arsenopyrite (53%) and pyrite (32%), with minor proportions of sphalerite (8%), tetrahedrite (3%), bournonite (1.8%), galena (1.7%) and chalcopyrite, pirrhotite, jamesonite, rutile, gold and silver as accessories. Quartz, carbonates sericite and saussurite was the principal gangue minerals identified; the presence of sericite in the deposit is remarkable.

4 GOLD MINERALOGY

Based on the distribution of the gold grains size (Fig.1) we concluded that:

- 80% of the gold grains is less than 30µm, while 96% have sizes under 70 µm.

30% of gold grains range between 5 - 10 μm in size, and 20% are under 5 μm .

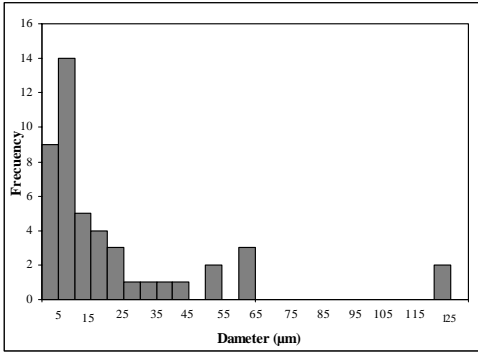


Figure 1: Size distribution of gold grains.

Gold occurs associated with other minerals, mainly as small inclusions in pyrite (Fig.2) and arsenopyrite (Fig.3) and in less proportion filling fractures in other minerals, furthermore, the gold is also found like inclusions in tetrahedrite and sphalerite.

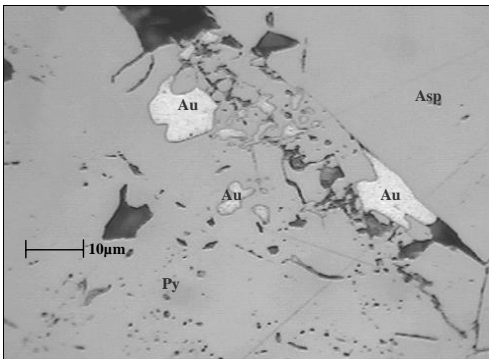


Figure 2: Gold enclosed in pyrite and intergrowth with arsenopyrite.

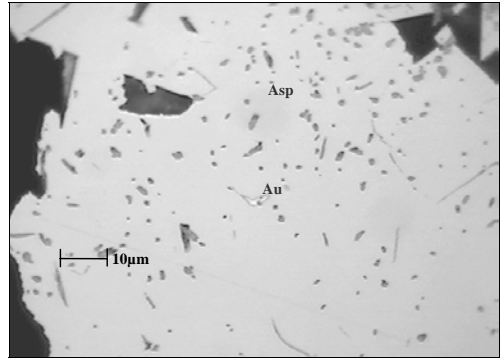


Figure 3: Gold enclosed in arsenopyrite.

In order to show the relation between gold grain size and gold association with other minerals, the next diagram was made. (Fig.4)

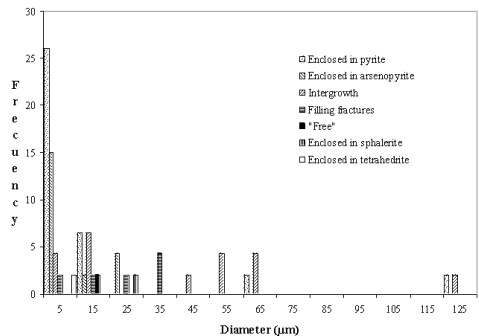


Figure 4: Relationship between size, associations and percentage of gold grains.

From this diagram it can be concluded that the gold grain's sizes smaller than 10 μm are principally included in pyrite (26%) and arsenopyrite (15%) and in lesser proportion the gold grains are intergrowth with other minerals (4.3%) and filling fractures (2%); the other side, the gold grain that are filling fractures are under 35 μm in size.

5 MINERAL CHEMISTRY

The mineral chemistry was made using EDS analysis for which the polished sections were carbon coated. Analytical conditions of 30KV to voltage, with a collection time of two minutes were used. This analysis showed that sulphides like arsenopyrite, pyrite, galena, chalcopyrite and pirrhotite present standard spectra indicating the lack of any kind of element in solid solution and

therefore that the mineral phases are relatively pure. Sphalerite, however, presents substantial amount of Fe.

According to sulphosalts analyses these phases correspond to Pb, As, Sb, Ag y Cu sulphosalts which were classified like tetrahedrite, bournonite and jamesonite. Within the analyzed sulphosalts we found that the jamesonite and some bournonite grains have a chemical composition defined by their stoichiometry. The other analyzed sulphosalts display spectra than show the presence of other elements in their composition, which are possibly in solid solution. The analyzed tetrahedrite grains show a high Ag content and present small amounts of Fe and Zn in their composition; the Zn being present in less proportion than Fe. Some grains of tetrahedrite with small amounts of As were also identified. (Fig.5). The bournonite sometimes shows small amounts of Ag.

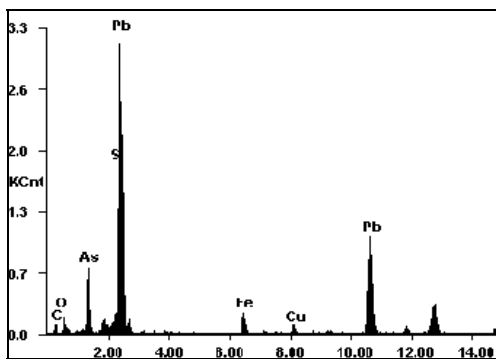


Figure 5: Typical tetrahedrite spectra.

Other mineral phases identified were defined like sulphosalts belonging to the tetrahedrite – tennantite replacement series (Ramdohr 1980) with variable amounts of As and Ag. (Fig.6).

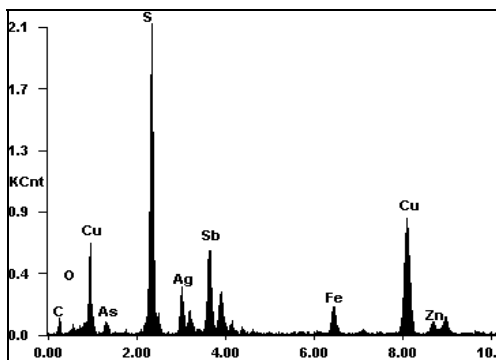


Figure 6: Typical Pb, Sb, Fe, As sulphosalts spectra.

Based on the micro-chemical analyses made by SEM/EDS in each gold grain analyzed we obtained a diagram that shows the Au/Ag ratio (Fig 7), in this diagram it can see that the Au/Ag ratio is 88/12 in average and that in general, all of the gold grains have similar ratios. From these results, the gold present in this deposit can be classified within the native gold category with small amounts of Ag (Gasparrini 1993).

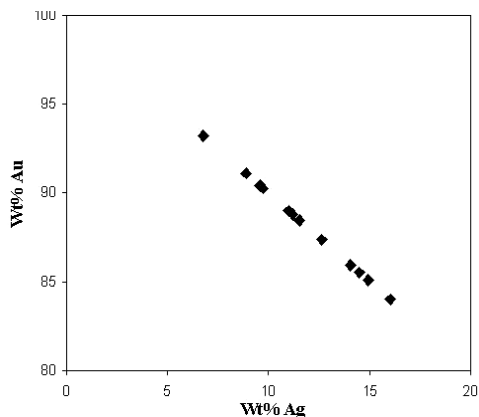


Figure 7. Au/Ag relation in the gold grains analyzed.

6 CONCLUSIONS

El Zancudo gold deposit is characterized as refractory since most of the gold grains (60%) are fine inclusions in poorly reactive cyanide sulphides like pyrite and arsenopyrite and in some sulphosalts, minerals which are difficult to break by chemical methods, suggesting the necessity to implement, during gold recuperation, some type of oxidative pretreatment like roasting, biological or pressure oxidation, to minimize the costs that would require a high mill grade and to improve the efficiency of the cyanidation process; additionally the presence of oxygen consumption minerals and/or cyanicides contribute to refractoriness. Sulphosalts like tetrahedrite, bournonite and jamesonite are strongly cyanicides; the antimony sulphosalts react with the cyanide to form complex compounds that slow down or prevent the gold dissolution due to thioantimonites and sulphur formation which can adsorb on the gold surface, inhibiting dissolution of gold (Gasparrini 1993). Arsenopyrite, the most abundant ore mineral, is a very stable mineral in cyanide solutions but can form arsenates (AsO_3^-), consuming oxygen, interfering of cyanidation process, neutralizing the solution because of ferrous sulfate formation and slowing down the dissolution velocity (Tuovinen et al. 1994). Pyrite has a high standard reduction potential, as a result it is

generally not reactive in the mildly oxidizing conditions typical of cyanide leaching (MMS 1999), in spite of that the pyrite is present in considerable amounts, it's not considered like a cyanide consumer. Pirrhotite, although present in small proportions in the deposit, is the most reactive sulphide in the cyanide solutions, consuming high amounts of both cyanide and oxygen, producing hidroxile ions that can be adsorbed on to the gold surface reducing its rate of dissolution (Marsden & House 1992).

The presence of smaller minerals like sericite and saussurite as well as the oxidation products of pyrite can produce coatings that are adsorbed on the surface of gold grains during the cyanidation process, generating a preg-robbing phenomenon and preventing high recuperations (Gasparrini 1993, Yannopoulos 1991 and Marsden & House 1992), since that the presence of sericite and saussurite in this deposit is remarkable, will be recommend that these minerals was eliminated before the ciyanidation process through a selective flotation process in order to prevent low recuperations.

7 REFERENCES

- Gasparrini, C. 1993. Gold and other precious metals : from ore to market. Hong Kong: Springer-Verlag.
- Grosee, E. 1926. Estudio geológico del Terciario Carbonífero de Antioquia en la parte occidental de la cordillera Central de Colombia entre el río Arma y Sacaoyal. Berlín: Dietrich REIMER (ERNEST VOHSEN).
- Multi Mix Systems Pty Ltd. 1992. Treatment of Ores Containing Reactive Iron Sulphides. Technical Bulletin 1. Australia.
- Marsden, J. and House, I. 1992. The chemistry of gold extraction. U.K.: Ellis Horwood, 2v.
- Ramdohr, P. 1969. The ore minerals and their intergrowths. 2 ed. Berlín: PERGAMON PRESS.
- Restrepo, J. 1986. Metamorfismo en el sector norte de la cordillera Central de Colombia. Medellín: Universidad Nacional de Colombia. Facultad de Minas.
- Tuovinen, O.; Bhatti, T.; Bigham, J.; Hallberg, K.; García, Jr. & Lindstrom, E. 1994. Oxidative dissolution of arsenopyrite by mesophilic and moderately thermophilic acidophiles. Applied Mineralogy.
- Yannopoulos, J. 1991. The extractive metallurgy of gold. Estados Unidos : Van Nostrand Reinhold.

Author Index (Volumes I & II)

Acchar, W.	293	Black, L.	245	Cid, R.	89
Addad, J.E.	579	Black, S.	395	Ciftci, E.	537, 643, 873
Afonso, M.C.	351	Blanc, P.	415	Cloete, M.	165
Alashkar, A.A.	261	Boaventura, G.R.	479	Clout, J.M.F.	993, 1047
Alba-Simionesco, C.	415	Boiocchi, M.	529	Conceição, S.I.	619, 669
Alcover-Neto, A.	103, 285, 289	Bonardi, M.	157	Correa, A.R.	403
Allard, T.	745	Bonás, T.B.	607, 861, 977	Corrêa, J.A.M.	399
Almendras, E.	1039	Boni, M.	781	Corrêa-Silva, R.H.	877
Alnæs, L.	145	Bonnes, U.	133	Correia, E.	587
Alves, A.K.	217	Böschel, D.	221	Costa, M.L.	65, 741
Alves, D.B.	819	Boschi, A.O.	337, 713	Coutinho, J.M.V.	443
Alves, P.R.	653	Bosso, S.T.	391	Couture, R.	379
Amaral Sobrinho, N.M.B.	451	Braga, G.C.B.	543	Crósta, A.P.	773
Amaral, A.M.	571	Brandão, A.G.	977	Cuchierato, G.	607
Amorim, L.V.	657, 961	Brandão, P.R.G.	233, 869, 893, 989	Cucurella, J.	881
Amosov, R.A.	965	Braz, A.B.	981	Cui, X.	697
Amouric, M.	415	Brizola, R.M.	639	Cupertino, J.A.	831
Andrade, F.R.D.	383, 759	Broekmans, M.A.T.M.	661	Cutmore, N.G.	969
Angeli, N.	849	Brum, T.M.M.	513, 559		
Angélica, R.S.	65, 273, 297	Brunet, F.	415	da Costa, M.	297
	665, 685, 741, 773	Brunnacci-Ferreira-Santos, N.	935	da Costa, M.L.	343, 373, 989
Angulo, S.C.	763	Bunds Schuh, T.	137	da Silva, F.T.	45, 53
Anjos, S.M.C.	811, 815	Butcher A.R.	37	D'Agostino, L.F.	673
Antenucci, D.	407	Bychkov, G.L.	575	D'Agostino, L.Z.	673
Aquino, J.A.	869			Dalakashvili, Z.B.	965
Arango, Y.C.	627	Cabral, A.R.	865	Daoud, W.K.	39
Arduini, M.	835	Cabrelon, M.D.	337	de Araújo, J.G.	1025
Arvidson, R.	13	Cabrol, N.	13	de Faria, D.L.A.	351
Aspandiar, M.F.	455	Caddah, L.F.G.	819	de Farias, J.B.	1025
Atanasova, M.	165	Cadille, S.	793	de Lena, J.C.	483
Atanassova, R.	387	Caffarena, V.R.	45, 49, 53	De León, A.T.	161
Atencio, D.	919	Calábria, J.	225	de Melo, H.G.	367
Auriscchio, C.	611	Caldwell, D.H.	363	de Oliveira, A.C.	479, 543
Ávila, C.A.	919	Calvin, W.	13	de Oliveira, M.P.	1025, 1029
Ávila, J.C.	521	Capitaneo, J.L.	45, 49, 53	de Pablo-Galán, L.	823
		Cardoso, D.B.	391	de Paula, S.M.	183
Bagatin, E.	443	Cardoso, M.	533	De Ros, L.F.	815, 831, 843
Banaszak, A.	923	Carneiro, B.S.	665	de Souza Filho, C.R.	309
Barbiéro, L.	411	Carvalho, C.I.P.	725	de Souza Jr., P.A.	13, 133
Barbosa, M.I.R.	657	Carvalho, F.M.S.	759	de Souza, R.S.	831
Barbosa, M.S.C.	785	Carvalho, J.O.	451	de Villiers, J.P.R.	229
Barilo, S.N.	575	Carvalho, P.R.S.	769, 777, 857	De Vito, C.	611
Barros, L.A.F.	997	Cassia de Brito Galvno, T.	479	Death, D.L.	969
Barrueto, H.R.	919	Castañeda, C.	591	Debacher, N.A.	1025, 1029
Baschini, M.T.	507	Castro, P.T.A.	745	Degen, T.	277
Basei, M.A.S.	733	Caucia, F.	529	Di Giulio, A.	835
Beljavskis, P.	111	Ceccarello, S.	395	Dias Filho, D.C.	843
Belogub, E.V.	853, 897, 915	Chambel, L.	533	Dias, G.O.	539
Benevides, T.	877	Channer, D.M. DeR.	563	Diogo Pinto, A.	533
Bennett, D.W.	969	Chapa-Cabrera, J.	85	Dixon, R.D.	901
Bendezú H., R.del P.	367	Chaves, M.	533	do Carmo, M.S.	343
Bergmann, C.P.	97, 217, 325	Chávez-García, M.L.	823	Domoney, R.M.	649
Bermanec, V.	525	Chernet, T.	985	Donchev, I.	387
Bernhard, B.	13, 133	Chodur, N.L.	513	Donskoi, E.	993
Bettencourt, J.S.	877	Choque Fernandez, O.J.	989	Drozdova, I.A.	749
Biesinger, M.	973	Christensen, P.	13	Ducart, D.F.	773
Biondi, J.C.	769, 777, 857	Chula, A.M.D.	869	Dutre, V.	407

Dziggel, A.	789	Gaspar, J.C.	1017	Holzwarth, U.	191, 195, 199
Dziubińska, B.	141, 677	Gaucher, E.	415		
		Gellert, R.	13, 133		
		Gennari, R.C.	337	Ihlen, P.M.	693
Eberhardt, J.E.	969	Gerson, A.R.	115	Ishii, K.	631
Ebina, T.	717	Gilg, H.A.	781	Ikuta, Y.	631
Edwards, H.G.M.	351	Givan, A.	583	Isaia, G.C.	639
Elsen, J.	347	Göbbels, M.	61, 179	Ishimoto, H.	435
El-Sheshtawy, A.	261	Gobbo, L.A.	249, 253, 257	Ivanova, A.S.	207
Emelchenko, G.A.	575	Goetz-Neunhoeffer, F.	179		
Enderle, R.	179	Gomes, O.F.M.	1043		
Endo, I.	889	Gomes, C.	187, 681	Jacamon, F.	693
Englert, G.	161	Gomes, C.M.	961	Jaksch, H.	525
Enzweiler, J.	391	Gomes, C.S.F.	725	Jansen, E.	947
Escudero, R.	615	Gomes, D.L.	737	Jarmolowicz-Szulc, K.	827
		Gomes, V.	681	Jdid, E.	407
		Gomes-Jr, A.A.S.	885	Joaquim, A.C.	123
Fabris, J.D.	463, 467, 471	Gonçalves, R.P.	367	John, V.M.	763
Falck, H.	547	González, I.	419	Juchem, P.L.	513, 559
Farias, K.V.	657	Gorevan, S.	13	Juliani, C.	879
Fenoll Hach-Ali, P.	495	Göske, J.	191, 195, 199, 229, 333		
Fernandes, E.F.	65	Götze, J.	203, 305, 685		
Fernandes, H.R.	33	Goulart, E.P.	713	Kachler, W.	191, 195, 199
Ferreira da Silva, E.	491	Graça, L.M.	517	Kahn, H.	123, 763, 981, 997, 1009
Ferreira, E.E.	233	Graham, R.C.	411	Kalmykov, A.E.	753
Ferreira, H.C.	657, 961	Graphchikov, A.A.	749	Kaminsky, F.V.	563
Ferreira, J.M.F.	33, 57, 619, 669	Grebenschikova, E.A.	749	Kankeleit, E.	133
Ferreira, M.Q.	619	Griffin, W.L.	563	Karfunkel, J.	525
Firth, B.A.	993	Groat, L.A.	547	Kasic, V.	931
Fischer, A.C.	513	Gross, J.M.	725	Kastner, G.F.	571
Fiss, G.F.	1029	Grossmann, J.	395	Kearsley, E.	329
Fogliata, A.S.	521	Gu, Y.	119	Kelm, U.	89, 1001
Foh, J.	133	Guastala, F.A.	337	Kerestedjian, T.	387
Fonseca, M.V.A.	285, 289	Guedes, C.C.F.	257	Kern, A.	125
Fontes, M.P.F.	107	Guedes, K.J.	539, 567	Kern, D.C.	343
França, K.B.	961	Guedes, P.J.S.	33	Khachatryan, G.K.	563
Francis, J.	973	Guerra, D.L.	65	Kihara, Y.	383
Franke, N.D.	769, 777, 857	Guimarnes, G.B.	759	Kijko, A.	901
Frank-Kamenetskaya, O.V.	359	Gurhan Yalcin, M.	643	Kisters, A.F.M.	789
Fransen, M.	277	Guttler, R.S.	551	Kitamura, S.	443
Friese, K.	483			Kleebe, H.J.	69
Fritsch, E.	595			Kleeberg, R.	129, 685
Fronzaglia, G.C.	123	Hagni, R.D.	649, 653, 873	Klingelhöfer, G.	13, 133
Frost, B.R.	927	Hall, C.	281	Klingenberg, B.	947
Furian, S.	411	Hamilton, C.	957	Kniewald, G.	525
Furlan, L.	1029	Hanna, R.A.	423	Kolayli, H.	537
Furquim, S.A.C.	411	Haralyi, N.E.	551	Komadel, P.	471
		Harben, P.W.	25	Komov, I.L.	73
		Hart, B.	973	König, U.	77, 81, 623
Gablina, I.F.	951	Hassaan, M.M.	261	Korablev, G.	439, 499
Gailhanou, H.	415	Hassaan, M.Y.	261	Köster, R.	137
Galán, E.	419	Hayashi, H.	717	Krambrock, K.	517, 539, 567
Gallego, A.N.	1055	He, C.	427	Kresten, P.	355
Gandini, A.L.	785	Heimann, R.B.	3, 203, 305	Kühn, T.	689
Garbev, K.	245	Helle, S.	1001	Kunze, Ch.	395
Garcez, L.L.	253	Henderson, I.	693	Kunze, K.	947
García, A.	627	Hengst, M.	203	Kurnevich, L.A.	575
García, N.	507	Herbert Echude, J.	313	Kusiak, M.A.	141, 677
Garda, G.M.	111	Herkenhoff, K.	13	Kuzmann, E.	543
Garg, R.	543	Heuss-Abichler, S.	431	Kwitko-Ribeiro, R.	865
Garg, V.K.	479, 543	Hjelen, J.	145	Lacerda, M.A.S.	571, 591
Gasharova, B.	245	Hofmeister, W.	555	Lagoeiro, L.	517, 885, 889

Lamberg, P.	1005	Menabdishvili, B.Z.	965	Ostrooumov, M.	595
Langhof, N.	203	Mendes, J.C.	709	Otto, A.	789
Larionov, P.M.	207	Merkle, R.K.W.	19, 805, 901	Otto, H.H.	487
Larsen, R.B.	693	Merzweiler, K.	635	Oyarzábal, J.	729, 793
Larson, R.A.	471	Meshchanova, E.V.	359	Oyarzún, J.	881
Lasnier, B.	595	Miano, S.C.	905		
Lastra, R.	1021	Miljak, D.G.	969		
Lebichot, S.	153	Miller, D.	973	Paciornik, S.	1043
Leclerq, D.	407	Miller, S.	363	Paiva, R.S.	373
Lee, K.	467	Mizusaki, A.M.	815	Paktunc, D.	379, 447, 1021
Lefrant, S.	595	Moen, K.	145	Parjy, A.S.	965
Lefter, M.G.	237, 241	Monte, M.B.M.	741	Paszkowski, M.	141, 677
Leinum, J.R.	145	Monteiro, L.V.S.	877	Patinha, C.	491
Leite, J.Y.P.	293	Morad, S.	843	Penha, F.G.	1025, 1029
Lemos, V.P.	65	Morales-Carrera, A.M.	709	Perbost, R.	415
Lengler, H.C.M.	325	Moreno, N.	237, 241	Pereira Leite, J.	313
Leonyuk, N.I.	575, 721	Moroz, I.	583	Pereira, E.	657
Li, J.	427	Moroz, T.	439	Pereira, E.A.	293
Liccardo, A.	513, 579	Morris, R.V.	13, 133	Pereira, L.	619
Liipo, J.	1005	Mortensen, J.K.	547	Pereira, M.	861
Lima, S.C.	351, 367	Motta, J.F.M.	713	Pereira, M.C.	885
Lira, H.L.	657, 961	Moura, A.	587	Pereira, R.M.	919
Lodziak, Je.	805	Moya, F.A.	737, 759	Pereira, W.C.	451, 797
López-Escobar, L.	89	Müller, I.L.	639	Persiano, A.I.C.	517
López-Galindo, A.	495, 835	Müller, T.	199	Pettinari, G.R.	507
Lorenzi, G.	407	Mussel, W.N.	463	Pieczonka, J.	923
Lu, X.	697			Piestrzyński, A.	923
Lubachesky, R.	559			Pinheiro, M.V.B.	517, 539, 567
		Nagase, T.	717	Pinho, M.S.	49
		Nakatsuka, A.	93, 631	Pino, G.A.H.	1043
Madood Hussain, T.S.	801	Nalini, H.A.	483	Pirard, E.	153
Magalhães, M.S.	893	Naumann, M.	947	Pires, F.R.M.	905, 927
Magela, G.	517	Nefyodova, I.V.	721	Pitkajarvi, J.	1005
Magnus, M.	305	Neiva, A.C.	367	Plötze, M.	685
Makovicky, E.	427	Neiva, A.M.R.	911	Pollandt, P.	221
Maltsev, V.V.	575	Nelsen, P.	407	Pöllmann, H.	77, 81, 213, 221, 297, 301, 317, 321, 329, 333, 399, 623, 635, 689, 989
Malvik, T.	145	Netto, A.M.	919		
Manjate, R.S.	33	Neubauer, J.	179		
Mano, E.S.	123, 997, 1009	Neufeld, H.	547		
Mansueto, M.S.	111	Neumann, R.	103, 285, 289, 919, 1031, 1035		
Mansur, A.A.P.	265, 1013	Neves, R.F.	273, 665, 741	Oiu, J.	697
Mansur, H.S.	265, 1013	Newman, J.A.	785	Queiroz Neto, J.P.	411
Maraschin, A.J.	815	Norman, M.	831		
Marcos, C.	269, 475, 627	Novaes, L.E.S.M.	725		
Marley, K.A.	471	Novais, R.F.	463	Radosavljevic, S.	705, 931
Marmo, J.	985	Novoselov, C.A.	853, 915	Radosavljevic-Mihajlovic, A.	705
Márquez, M.A.	1017, 1055			Raghimi, M.	455
Marshall, D.D.	547	Oba, C.A.I.	123	Rammlmair, D.	459, 805
Martelli, M.C.	273	Ogasawara, T.	49	Ratti, G.	939, 981, 997
Martin, C.	957	Okube, M.	93	Read, D.	395
Martínez, M.	269	Okudera, H.	93	Rebelo, A.M.A.	733
Mas, G.	521	Olhero, S.M.H.	57	Reimanis, I.E.	85
Masalov, V.M.	575	Oliveira, C.H.	285, 289	Reis, E.	39
Matos, M.J.	701	Oliveira, E.F.	571, 579, 591	Reis Neto, J.M.	733, 737
McGibbon, F.M.	363	Oliveira, M.C.B.	443	Remacre, A.Z.	797
McKay, N.	957	Oliveira, M.L.	57	Remus, M.V.D.	831
McSween, H.	13	Olives, J.	415	Renato Pontes, L.	313
Medeiros, S.M.	567	Olivito, J.P.R.	607	Renz, F.	13, 133
Meier, R.	277	Orlandi, P.	611	Rezende, N.G.A.M.	741
Melcher, F.	805	Ortenzi, A.	835	Ribeiro, F.R.	463, 467, 471
Melekestseva, I. Yu.	897			Rieder, R.	13
Meller, N.	281				

Riesemberg, C.E.	737	Silveira, M.	183	Viana, R.R.	601
Robles-Camacho, J.	371	Simakov, S.K.	749, 753	Vieira Coelho, A.C.	423
Rocha Filho, O.G.	865	Smart, R. StC.	973	Vieira, A.L.	423
Rocha, F.	491	Smith, D.	379, 1021	Vigdergauz, V.E.	1051
Rocha, F.J.F.T.	725	Soares, L.	673	Viladkar, S.G.	649
Rodionov, D.	13, 133	Song, R.	599	Villanova, S.N.	769, 777, 857
Rodrigues, C.R.O.	843	Sorokin, L.M.	753	Villas Boas, R.C.	451
Rodríguez, I.	269, 475, 627	Soto, O.A.J.	1043	Villegas, E.A.	403
Rogers, C.A.	969	Sousa, D.J.L.	755	Viseras, C.	495
Rogez, J.	415	Sousa, J.J.	701	Vlach, S.R.F.	849
Roggendorf, H.	221	Souza Filho, C.R.	773	Vortisch, W	169
Roldan, A.A.	713	Souza Santos, P.	423		
Romano, R.C.	885, 889	Souza, R.S.	839, 843		
Romero, A.	419	Spaeth, J.M.	567	Wagner, Ch.	635
Roquet, M.B.	729	Squyres, S.W.	13, 133	Wagner, T.	137
Rosière, C.A.	935	Stanjek, H.	107	Waichel, B.L.	559
Roth, M.	583	Stasiulevicius, R.	571, 591	Wajima, T.	435
Rubio, J.	161	Stemmermann, P.	245	Weiss, H.	395, 487
Ruckley, N.A.	363	Stirling, J.A.R.	157	Wennrich, R.	487
Rybacki, E.	947	Stöber, S.	317, 321, 635	Wiedemann, P.	685
		Stojanovic, J.	705, 931	Williams, S.	957
		Stucki, J.W.	467, 471	Winkler, N.	333
Saaro, S.	305	Stumm, A.	245	Wirth, R.	173
Sabot, B.	583	Suh, C.E.	865		
Sales, C.	293	Sunder Raju, P.V.	149, 801		
Salomão, E.P.	39	Szabó, G.A.J.	759	Xu Xin,	57
Sánchez-Hernández, R.	371				
Sanhueza, V.	89				
Sanjad, T.A.B.C.	373	Tamada, O.	435	Yagovkina, M.A.	749
Sant'Agostino, L.M.	249, 253, 257, 607, 861, 939, 977	Tassinari, M.M.M.L.	939, 981, 997	Yakovleva, V.A.	853
Santini, R.B.	383	Tavares, R.P.	893	Yalcin, G.	873
Santos, A.L.F.	479	Tavera, F.J.	615	Yalcin, M.G.	537
Santos, M.D.C.	745	Tesalina, S.G.	897	Yalcinalp, B.	537
Sasaki, O.	435	Tewelde, M.	635	Yang, Z.	599
Savelieva, G.N.	943	Titov, A.T.	207	Yasuda, M.	435
Schäfer, W.	947	Tomašić, N.	525	Yoshiasa, A.	93, 631
Schmidt, G.T.	483	Toniolo, J.C.	97, 325	Young, J.M.	993, 1047
Schneider, C.L.	103, 1031, 1035	Torres, P	33	Yvon, J.	407, 745, 755
Scholz, R.	525	Treivus, E.B.	359		
Schreck, P.	487	Trudu, A.G.	993, 1047		
Schröder, C.	13	Tuling, A.	229	Zachmann, D.W.	483
Schröder, Ch.	133	Turunen, J.	1005	Zaikovskii, V.I.	207
Schubert, M.	395, 487			Zakharchenko, O.D.	563
Schuh, A.	191, 195, 199	Ulsen, C.	763	Zambonato, E.	843
Schwertmann, U.	107			Zanardo, A.	713
Seifert, S.	305			Zanetti, A.	529
Senna, J.A.	309	Vaghetti, M.A.O.	639	Zapata, D.M.	1055
Sequeira, C.	681	Valenzuela Diaz, F.R.	423	Zauberas, R.T.	337
Serrano Pinto, L.	491	Vallés, J.M.	507	Zaykov, V.V.	897, 915
Setti, M.	495, 835	van Tonder, D.M.	165	Zeiler, G.	191, 195, 199
Shcherbakova, E.	439, 499	Vapnik, Ye.	583	Zeschky, J.	179
Sherriff, B.L.	503	Varajão, A.F.D.C.	709, 745, 755	Zhokhov, A.A.	575
Shivdasan, P.A.	649	Vasconcelos, P.	815	Zimmer, A.	97
Sidenko, N.V.	503	Vasconcelos, W.L.	225, 265		
Siegel, P.	1039	Velho, J.	619, 669		
Siemes, H.	947	Veniale, F.	495		
Silva, C.M.A.	811	Venturini, P.N.	885, 889		
Silva, D.M.	451	Verdeja, L.F.	269		
Silva, F.L.H.	961	Verryn, S.M.C.	329		
Silva, J.	187	Veschkens, M.	407		
Silveira, J.	313	Viana, J.D.	657		